

# Encyclopedia of Nanoscience and Nanotechnology

Volume 8 Number 1 2004

- |  |                            |
|--|----------------------------|
| <a href="#">▶ view</a> Near-Field Optical Properties of Nanostructures<br><i>Nicolas Richard</i>                             | <u><a href="#">1</a></u>   |
| <a href="#">▶ view</a> Noble Metal Nanoparticles<br><i>Yiwei Tan; Yongfang Li; Daoben Zhu</i>                                | <u><a href="#">9</a></u>   |
| <a href="#">▶ view</a> Noble Metal Nanocolloids<br><i>Ichiro Okura</i>   | <u><a href="#">41</a></u>  |
| <a href="#">▶ view</a> Nonlinear Optical Materials by Sol-Gel Method<br><i>Wenyan Li; Sudipta Seal</i>                       | <u><a href="#">49</a></u>  |
| <a href="#">▶ view</a> Nonlinear Optics of Fullerenes and Carbon Nanotubes<br><i>Rui-Hua Xie; Qin Rao; Lasse Jensen</i>      | <u><a href="#">67</a></u>  |
| <a href="#">▶ view</a> Nonlinear Optics of Nanoparticles and Nanocomposites<br><i>Quandou Wang; Jianfeng Xu; Rui-Hua Xie</i> | <u><a href="#">101</a></u> |
| <a href="#">▶ view</a> Nucleation Kinetics of Nanofilms<br><i>S. A. Kukushkin; A. V. Osipov</i>                              | <u><a href="#">113</a></u> |
| <a href="#">▶ view</a> Nucleoprotein Assemblies<br><i>Steven S. Smith</i>  | <u><a href="#">137</a></u> |
| <a href="#">▶ view</a> One-Dimensional Metal Oxide Nanostructures<br><i>Lionel Vayssieres; Arumugam Manthiram</i>            | <u><a href="#">147</a></u> |
| <a href="#">▶ view</a> Optical Fibers for Nanodevices<br><i>Jenny M. Tam; Sabine Szunerits; David R. Walt</i>                | <u><a href="#">167</a></u> |
| <a href="#">▶ view</a> Optical Properties of Gallium Nitride Nanostructures<br><i>Annamraju Kasi Viswanath</i>               | <u><a href="#">179</a></u> |
| <a href="#">▶ view</a> Optical Properties of Oligophenylenevinylenes<br><i>Johannes Gierschner; Dieter Oelkrug</i>           | <u><a href="#">219</a></u> |
| <a href="#">▶ view</a> Ordered Mesoporous Materials<br><i>Sebastian Polarz</i>   | <u><a href="#">239</a></u> |
| <a href="#">▶ view</a> Ordered Nanoporous Particles<br><i>Ferry Iskandar; Mikrajuddin; Kikuo Okuyama</i>                     | <u><a href="#">259</a></u> |
| <a href="#">▶ view</a> Organic Nanofilm Growth<br><i>Serkan Zorba; Yongli Gao</i>  | <u><a href="#">271</a></u> |

<a href="#">▶ view</a> Organic Polyradical Magnetic Nanoclusters <i>Andrzej Rajca</i>	<u>285</u>
<a href="#">▶ view</a> Organic Thin Film Deposition Techniques <i>M. C. Petty</i>	<u>295</u>
<a href="#">▶ view</a> Organic/Inorganic Nanocomposite Colloids <i>Elodie Bourgeat-Lami</i>	<u>305</u>
<a href="#">▶ view</a> Oxide Nanoparticles <i>K. P. Jayadevan; T. Y. Tseng</i>	<u>333</u>
<a href="#">▶ view</a> Oxide Nanowires and Nanorods <i>Guozhong Cao; Steven J. Limmer</i>	<u>377</u>
<a href="#">▶ view</a> Palladium Nanoparticles <i>Chia-Cheng Yang; Chi-Chao Wan; Chien-Liang Lee</i>	<u>397</u>
<a href="#">▶ view</a> Patterned Magnetic Nanostructures <i>Jian-Ping Wang; Tie-Jun Zhou</i>	<u>415</u>
<a href="#">▶ view</a> Pb-Based Ferroelectric Nanomaterials <i>Ki Hyun Yoon; Dong Heon Kang</i>	<u>435</u>
<a href="#">▶ view</a> Peptide Nanotubes <i>Hiroshi Matsui</i>	<u>445</u>
<a href="#">▶ view</a> Periodic Nanostructures with Interfering Femtosecond Lasers <i>Masahiro Hirano; Ken-ichi Kawamura; Hayato Kamioka; Taisuke Miura; Hideo Hosono</i>	<u>457</u>
<a href="#">▶ view</a> Pharmaceutical Nanotechnology <i>Paul A. McCarron; Maurice Hall</i>	<u>469</u>
<a href="#">▶ view</a> Phase Mixture Models for Metallic Nanomaterials <i>Yuri Estrin; Hyoung Seop Kim; Mark B. Bush</i>	<u>489</u>
<a href="#">▶ view</a> Phonon Confinement in Nanostructured Materials <i>Akhilesh K. Arora; M. Rajalakshmi; T. R. Ravindran</i>	<u>499</u>
<a href="#">▶ view</a> Phonons in GaN-AlN Nanostructures <i>J. Frandon; J. Gleize; M. A. Renucci</i>	<u>513</u>
<a href="#">▶ view</a> Photochemical Molecular Devices <i>Alberto Credi</i>	<u>527</u>
<a href="#">▶ view</a> Photochemistry in Zeolite Nanocavities <i>Masanobu Kojima</i>	<u>549</u>
<a href="#">▶ view</a> Photoconductivity of Carbon Nanotubes <i>Akihiko Fujiwara</i>	<u>569</u>

<a href="#">▶ view</a> Photodynamics of Nanoclusters	<u>575</u>
<i>M. Belkacem; M. A. Bouchene; P.-G. Reinhard; E. Suraud</i>	
<a href="#">▶ view</a> Photoexcitation Dynamics of Fullerenes	<u>593</u>
<i>Mamoru Fujitsuka; Osamu Ito</i>	
<a href="#">▶ view</a> Photonic Crystal Lasers	<u>617</u>
<i>John D. O'Brien; Wan Kuang; Po-Tsung Lee; Jiang Rong Cao; Cheolwoo Kim; Woo Jun Kim</i>	
<a href="#">▶ view</a> Phthalocyanine Nanostructures	<u>629</u>
<i>Eunyoung Kim</i>	
<a href="#">▶ view</a> Plasma Chemical Vapor Deposition of Nanocrystalline Diamond	<u>691</u>
<i>Katsuyuki Okada</i>	
<a href="#">▶ view</a> Polyacetylene Nanostructures	<u>703</u>
<i>Kevin K. L. Cheuk; Bing Shi Li; Ben Zhong Tang</i>	
<a href="#">▶ view</a> Polyaniline Fractal Nanocomposites	<u>715</u>
<i>Reghu Menon; A. K. Mukherjee</i>	
<a href="#">▶ view</a> Polymer Electrolyte Nanocomposites	<u>731</u>
<i>Mikrajuddin Abdullah; Wuled Lenggoro; Kikuo Okuyama</i>	
<a href="#">▶ view</a> Polymer Nanostructures	<u>763</u>
<i>Liming Dai</i>	
<a href="#">▶ view</a> Polymer/Clay Nanocomposites	<u>791</u>
<i>Masami Okamoto</i>	
<a href="#">▶ view</a> Polymeric Nano/Microgels	<u>845</u>
<i>Piotr Ulanski; Janusz M. Rosiak</i>	
<a href="#">▶ view</a> Polymeric Nanoparticles	<u>873</u>
<i>Bobby G. Sumpter; Donald W. Noid; Michael D. Barnes; Joshua U. Otaigbe</i>	

# Near-Field Optical Properties of Nanostructures

Nicolas Richard

*Thomson Tubes and Displays, Genlis, France*

## CONTENTS

1. Introduction
  2. Depolarization Effects in the Near-Field Optics
  3. Optical Properties of Subwavelength Objects Deposited on a Surface
  4. Analysis of the Polarization Near Subwavelength Objects
  5. Conclusion
- Glossary  
References

## 1. INTRODUCTION

During these last years, scanning near-field optical microscopy (SNOM) has become an extremely powerful technique for the analysis of surface structures with a resolution far beyond the diffraction limit [1, 2]. The role of the incident polarization associated with the incoming light is important for the understanding of optical images under the condition of total internal reflection in the near-field optics using a photon scanning tunneling microscope (so-called PSTM or STOM) [3–8] or under the illumination in normal incidence (SNOM configuration) [9]. These techniques tend to elucidate the optical properties of mesoscopic and nanoscopic particles in the near-field.

The mesoscopic regime corresponds to optical properties of the system where the size of the objects is of the order of the incident wavelength. For the visible range, it means that the object has a lateral size between 100 nm and 1000 nm. The nanoscopic regime corresponds to structures smaller than 100 nm. On the other hand, when the size of the object is much greater compared to the incident wavelength, one usually speaks of the macroscopic regime. Geometrical optics and Kirchhoff diffraction can be treated on a macroscopic scale.

Near-field optics deals with behaviors occurring with evanescent electromagnetic waves which become important

when the size of the object is of the order or lower compared to the incident wavelength. The actual theory well describes the interaction between objects and light in the microscopic or in the macroscopic regimes. A numerical approach based on Maxwell equations is needed to know the optical response of such systems in the mesoscopic range.

Many approaches were realized to model optical microscopy in the near-field optics for objects deposited on perfectly flat and rough surfaces [10–12]. Different experimental devices were used for the study of near-field optical microscopy according to the properties in transmission [13]. To understand the optical properties of mesoscopic and nanoscopic objects, many studies were performed on periodic structures in the near-field optics [14]. Main problems come from the understanding of tip detection for the electromagnetic field at a given distance from the surface and many theoretical models try to understand the basic properties of an optical microscope [15].

Optical contrasts produced by nanoscopic or mesoscopic dielectric objects according to the incident polarization associated with the incoming light for nanoscopic or mesoscopic dielectric objects are presented. First, we will describe the notion of depolarization for nanoscopic objects in the near-field optics and the impact of the object size and of the wavelength in the optical images. Second, the impact of the polarization in the near-field optics will be discussed showing optical images under several conditions of illumination and detection.

The incident polarization is chosen rectilinear under the condition of total internal reflection and in the air [16]. Circular polarization is also chosen to see the optical behaviors in normal incidence [17]. These two configurations will show effects related to the impact of the incident polarization on the optical response of the dielectric object in the near-field optics.

In both configurations (PSTM and SNOM), the probe is the main tool for the detection of the electromagnetic field or the illumination of the sample at the nanometer scale. In near-field optical microscopy, the local detection of the optical signal relies on the use of nanometer-sized probes. In the SNOM configuration, the probe acts as a local source

of evanescent optical fields whereas in the PSTM setup, the probe behaves as a local detector of light. In these devices, SNOM and PSTM tips are usually coated with a thin metal layer in order to achieve a narrow localization of the incident light on the sample (SNOM configuration) or to improve the resolution in detection for the PSTM configuration. However, Al-coated tips showed limited improvement due to the degradation of the signal-to-noise ratio related to the very low transmission through such coating in the PSTM configuration.

The scattering effects are the main problems which occur strongly in the near-field optics because these waves damage the resolution of the optical images. Scattering of the electromagnetic waves by a sphere (Mie theory) and an ellipsoid has been extensively studied in both microscopic and mesoscopic regimes [18–23]. This problem has a known solution in an analytical way. More complicated shapes involving objects with sharp edges could not be solved analytically. Far-field expressions were detailed to understand the scattering cross-section behaviors but analytical near-field expressions could not be given in the same way. Mainly, backward and forward scattering were found in the different scattering diagrams according to the size of the sphere and to the refractive index of the material.

In order to eliminate the scattering behaviors which occur in the near-field optics, polarization studies are thus necessary to understand the scattered field behaviors in the analysis of near-field optical images. This outlines effects relative to the confinement of the electric field near the objects. Main problems are involved in the diffraction pattern of the forward and backward waves scattered by the objects. The study of the different components will reject this problem and only the objects' response is taken into account.

### 1.1. Green's Dyadic Technique

The calculations are based on the Green's dyadic technique using Lippmann–Schwinger and Dyson equations for all numerical computations [24, 25]. This method is proven to be an efficient computation technique for the typical parameters of near-field optics (size of the object, height of detection, wavelength, dielectric permittivity of materials). This numerical method is reliable to solve the Maxwell equations and it is based on the knowledge of the Green's dyadic associated with a reference system which is a flat surface or vacuum in our case. The procedure considers any object deposited on the surface or placed in the air as a perturbation discretized in direct space. The electric field is determined self-consistently inside the perturbations; a renormalization associated with the depolarization effect is taken into account for the self-interaction of each discretization cell. The Huygens–Fresnel principle uses the values of the field inside the perturbations to compute the electric field or the optical magnetic field elsewhere [26].

This method for the calculation of both optical electric and magnetic fields can treat any kind of nanoscopic and mesoscopic objects in the near-field optics. The shape and the dielectric constant of the particles can be arbitrarily taken. Moreover, this numerical technique can treat anisotropic objects in near-field and in far-field optics [27]. As the discretization is performed in direct space, this

method can be thus extended to experimental samples using the topography of the surface, that is, any input geometry of the computations according to a given AFM (atomic force microscopy) data file recorded on the sample. This capability gives the opportunity to better understand the experimental images in the near-field optics.

### 1.2. Optical Initial Conditions in the Near-Field

We choose glass for the use of a dielectric material and we consider that the index of refraction of the glass, fixed to 1.5, does not depend on the incident wavelength. Other materials used for the optical properties in different wavelength ranges could be taken into account but the main physical principles are explained in the following sections. In the case of other materials, spectroscopic behaviors are important for the understanding of the near-field optical images in order to take into account resonance behaviors according to the optical response of a given structure [28–30].

Here, we will detail the case of dielectric particles deposited on a dielectric glass substrate or illuminated in the air. For the first case, the objects are bidimensional structures which are illuminated in the air. In the second case, these ones are tridimensional and illuminated under the condition of total internal reflection as in the PSTM configuration beyond the glass–air critical angle. For the circular polarization, the objects lying on a dielectric surface will be illuminated in normal incidence. We show numerical simulations which take account of the analysis for the intensity associated with the total electric field and with the optical magnetic field scattered by nanoscopic objects in transmission at constant height in the total internal reflection configuration.

In the case of a surface separating two dielectric media (glass–air interface), two modes of polarization are associated with the incoming light: TE and TM modes. The  $z$ -direction being perpendicular to the glass–air interface, as we chose the incident light to be linearly polarized, the TE mode ( $s$  polarization) corresponds to an incident electric field perpendicular to the plane of incidence ( $y$ - $z$  plane). The TM mode ( $p$  polarization) corresponds to a field parallel to the plane of incidence. In the case of bidimensional objects, the direction of the incident light is perpendicular to the infinite  $z$ -direction of the structure. In both cases, the detection is performed in the  $x$ - $y$  plane at a constant height in the case of the surface using three-dimensional structures.

## 2. DEPOLARIZATION EFFECTS IN THE NEAR-FIELD OPTICS

To understand the optical effects produced by subwavelength objects, it is important to introduce the notion of depolarization. In order to explain this behavior, one considers a bidimensional object which is illuminated along its smaller dimensions in the air; no surface is included for this model and the incident electric field is applied perpendicularly to the lateral sides of the particle. One can see that, for subwavelength objects, the negative contrast which occurs inside the object is a result of the depolarization effect which

is related to the conservation of the components normal to the object faces according to the displacement vector [31] (Fig. 1a).

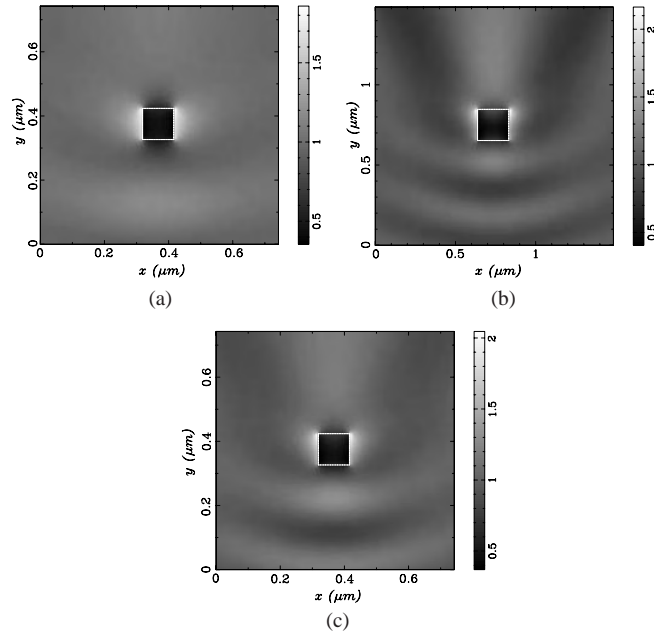
Moreover, a higher intensity can thus be found around the lateral sides of the object close to its edges (Fig. 1a). This high-intensity effect borders the structure along the direction of the applied incident electric field ( $x$ -direction).

This depolarization effect is mostly related to the size of the object which belongs to the nanometer scale (100 nm) according to the incident wavelength (633 nm). One can observe that, when the size of the object is relatively small compared to the incident wavelength, which is the present case, the field intensity distribution around the object tends to reproduce its profile. This conclusion can be extended to any nanoscopic isolated objects in the near-field optics. We took the two-dimensional case; therefore, no depolarization effect appears along the infinite  $z$ -direction. In Section 3, we will show the importance of depolarization in different directions by using a tridimensional object deposited on a dielectric glass substrate.

### 2.1. Influence of the Particle Size on the Optical Image

Let us now consider a  $200 \times 200 \text{ nm}^2$  dielectric squared structure illuminated in the same conditions as in the previous section.

By doubling the object size, one can obtain an optical image including not only depolarization effects but also scattering waves near the structure because we switch from the nanoscopic regime (previous section) to the mesoscopic



**Figure 1.** For  $\lambda = 633 \text{ nm}$ , variation of the intensity associated with the total electric field for a glass squared rod of  $100 \times 100 \text{ nm}^2$  section (a) and of  $200 \times 200 \text{ nm}^2$  section (b). For  $\lambda = 400 \text{ nm}$ , variation of the intensity associated with the total electric field for a glass squared rod of  $100 \times 100 \text{ nm}^2$  section (c). The object is illuminated along the  $y$ -direction and the incident polarization direction is along the  $x$ -axis.

range at the optical scale. One can see that a back reflected wave occurs in the optical image ( $y < 0$ ) and also a forward scattering in the direction of the incident light ( $y > 0$ ) (see Fig. 1b).

By this change, one can see the strong influence of the particle size on the resolution of the optical image. When we consider an object which has a size compared to the incident wavelength, the structure has not only depolarization properties but also scattering effects around the particle; these optical waves degrade considerably the resolution of the optical image.

### 2.2. Influence of the Incident Wavelength

The results presented in this section are a consequence of the different effects found in the previous one. To understand the impact of the wavelength in the optical image, let us consider a squared dielectric particle ( $100 \times 100 \text{ nm}^2$ ) illuminated as previously but with a different wavelength lower than 633 nm. If one turns to a wavelength dependence, the use of a particle size (100 nm) which can be compared to the wavelength of the incident light (400 nm) shows scattering effects in the optical image (see Fig. 1c).

One can see the similar behaviors shown in the previous section: backward and forward scattering can be clearly seen in the optical image as we turned to the mesoscopic regime. Consequently, these effects show the main differences between the nanoscopic regime and the mesoscopic one in the optical images when dealing with nanometric objects in the near-field and by only changing the wavelength in the visible range.

Therefore, one has to be aware that the illumination wavelength and the lateral size of the particle have a strong impact on the resolution of the optical images in the near-field optics for the visible range as one can switch from the nanoscopic regime to the mesoscopic one.

## 3. OPTICAL PROPERTIES OF SUBWAVELENGTH OBJECTS DEPOSITED ON A SURFACE

In this section, the influence of the polarization associated with the incident light on the object is shown. The index of refraction of the substrate as well as the refractive index of the object is fixed to 1.5. Depending on the size of the object and on the incident wavelength, such a protrusion can behave more or less as a obstacle to the propagation of the surface wave. For the condition of total internal reflection, the object is illuminated with an angle of incidence of  $60^\circ$  and the detection is performed in the near-field optics at constant height above the object. It is also important to see what the tridimensional case will bring to the optical image. As the object will become three-dimensional, the other direction will give more insight for the depolarization effect along this direction.

### 3.1. Optical Electric Field

For the condition of total internal reflection, the  $100 \times 100 \times 40 \text{ nm}^2$  dielectric object is illuminated with an angle of incidence of  $60^\circ$  and the detection is performed in the near-field

optics at a constant height of 10 nm above the object (see Fig. 2a and b). When the detection of the electromagnetic field is closer to the objects, one can find the same basic optical properties explained in the previous sections. Consequently, the backward and forward scattering effects cannot be seen in the optical images for both modes of polarization.

The depolarization effect occurs in the lateral sides of the particle in the TE mode as we had previously (Fig. 2a). However, this effect happens at the top of the object in the TM mode. In this mode, the incident electric field is parallel to the plane of incidence. Therefore, this field has components in both directions: parallel ( $y$ -direction) and perpendicular to the surface ( $z$ -axis). The angle of incidence ( $60^\circ$ ) is taken in such a way that the component which is perpendicular to the surface is larger compared to the parallel one. Consequently, the depolarization effect occurs in the  $z$ -direction, which produces the bright contrast in the near-field optical image (Fig. 2b).

Moreover, an inverse contrast similar to the TE polarization cannot show up in the TM mode because at short distances the vertical  $z$ -component of the electric field dominates. The matching condition of the vertical component of the displacement vector leads to a confined optical electric field close to the upper face of the pad. Therefore, in the three-dimensional case, the depolarization effect in the near-field optics could occur in the three axis according to the direction of application of the incident electric field.

A striking difference of behavior was found depending on the polarization state of the traveling wave along the

surface. In the subwavelength range, the TM polarization mode allows to reproduce the shape of the objects, whereas a TE polarized wave can be used to extract information on the contours of the objects themselves.

### 3.2. Optical Magnetic Field

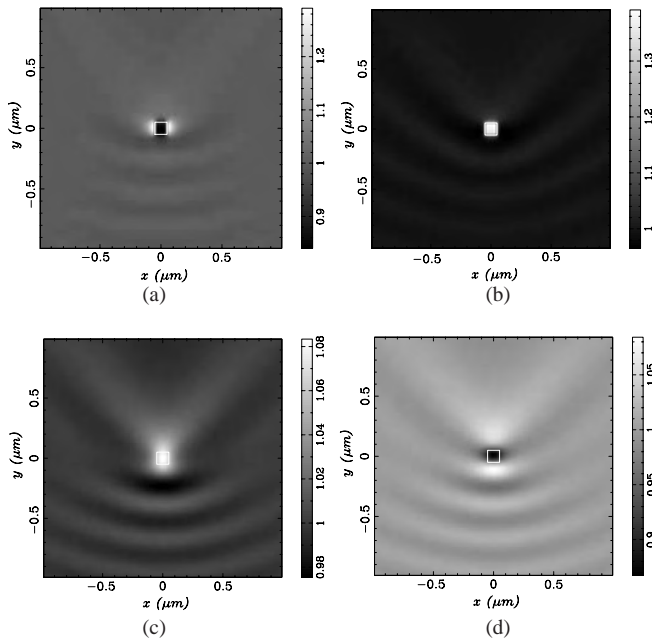
Tip detection is important according to the optical properties of the sample surfaces. In the PSTM configuration, the detection performed with dielectric tips or with dielectric tips covered by a thin noble metal film shows different optical images in the near-field. In the first case, one detects an intensity associated with the optical electric field and in the other case, one can detect a signal proportional to the optical magnetic field associated with the optical wave for wavelengths in the visible range. This behavior is mainly related to the surface plasmon effect occurring in the thin metal film which covers the dielectric tip. Therefore, this proves that the optical images depend strongly on the tip response. We will discuss later the optical image patterns obtained with the electric field associated with the optical wave and also those of the magnetic field obtained in the same conditions.

In order to achieve a better resolution in the optical images, dielectric tips coated by a thin gold film can be used. But the optical images obtained using such tips show inverted contrasts compared to the ones obtained with uncoated dielectric tips. These results indicated that the detected signal may reveal different physical behaviors according to the probe composition [32, 33].

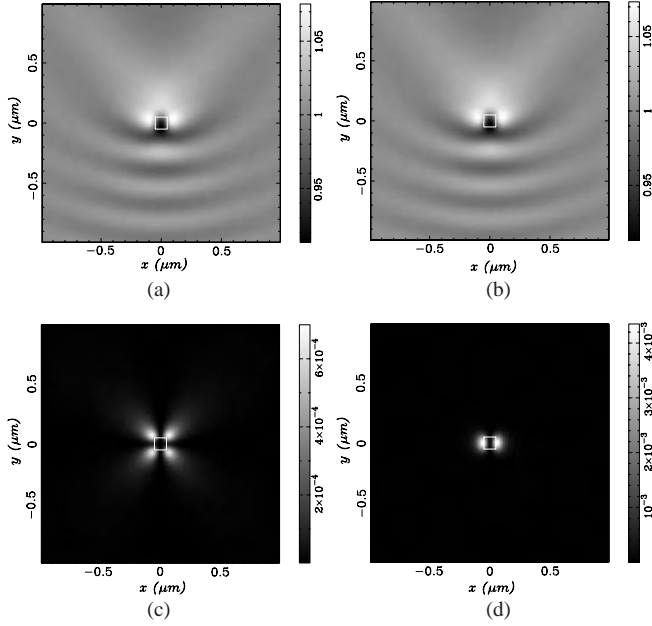
While the dielectric tip always collects a signal proportional to the square modulus of the electric near-field, using the same initial conditions, the optical images obtained with a coated gold tip display the same patterns as the theoretical maps of the square modulus of the magnetic field associated with the optical near-field. These images can be obtained under several conditions: the use of a defined gold film thickness which corresponds to a given excitation wavelength has to be achieved to obtain a signal proportional to the optical magnetic field associated with the scattered light in transmission. These conditions have to sustain a plasmon resonance mode in the thin metal film which covers the dielectric tip.

These studies show another way to detect a signal proportional to the optical magnetic field for wavelengths corresponding to the visible range. In order to show this purpose, one can compute the optical magnetic field associated with the lightwave in transmission (Fig. 2c and d). The object is illuminated as in Section 2 under the condition of total internal reflection. The height of detection is chosen to be 60 nm above the top of the dielectric object.

One can see that the depolarization effects occur at the top of the object in the TE mode while these occur on the lateral sides of the structure in the TM polarization for the optical magnetic field images (see Fig. 2c and d). These results show different behaviors compared to those found for the electric field intensities in both modes of polarization. All the optical responses are inverted for the detection of the magnetic field compared to the electric field signals: the dark contrast in the TE mode for the signal associated with the electric field gives a bright one for the optical

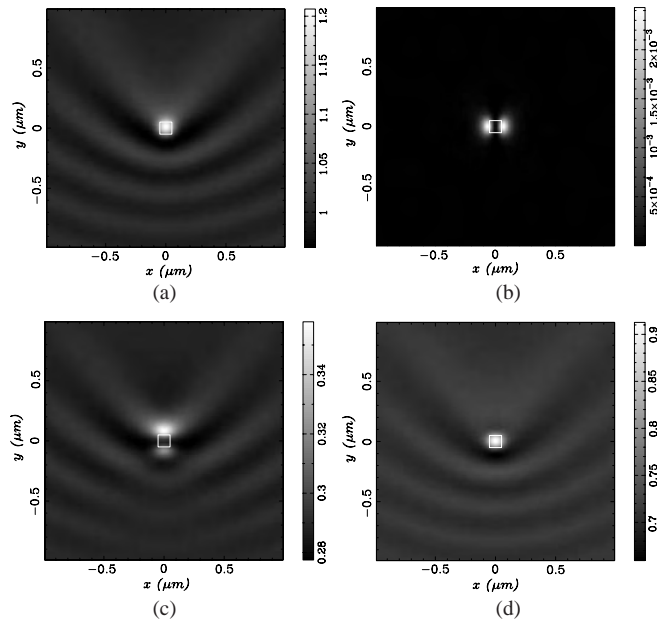


**Figure 2.** For  $\lambda = 633$  nm, variation of the intensity associated with the total electric field for the TE mode (a) and for the TM mode (b) at a constant height of 50 nm above the dielectric surface. Variation of the intensity associated with the total magnetic field for the TE mode (c) and for the TM mode (d) for a  $100 \times 100 \times 40$  nm<sup>3</sup> glass pad at a height of 100 nm above the surface. The object is illuminated by the glass substrate under the condition of total internal reflection with an angle of incidence of  $60^\circ$ .



**Figure 3.** For  $\lambda = 633$  nm, variation of the intensity associated with the total electric field (a), the  $x$ -component (b), the  $y$ -component (c), and the  $z$ -component (d) for a  $100 \times 100 \times 40$  nm<sup>3</sup> glass pad. The incident polarization direction is along the  $x$ -axis (TE or  $s$  mode). The object is illuminated under the same conditions described in Figure 2. The detection is performed at a height of 100 nm above the surface.

magnetic field (Fig. 2c and Fig. 3a). Similarly, a bright contrast for the TM mode for the intensity associated with the electric field leads to a dark one for the optical magnetic field (Fig. 2d and Fig. 4a).



**Figure 4.** For  $\lambda = 633$  nm, variation of the intensity associated with the total electric field (a), the  $x$ -component (b), the  $y$ -component (c), and the  $z$ -component (d) for a  $100 \times 100 \times 40$  nm<sup>3</sup> glass pad. The incident polarization direction is along the  $y$ - and  $z$ -axis (TM or  $p$  mode). The object is illuminated under the same conditions described in Figure 3.

## 4. ANALYSIS OF THE POLARIZATION NEAR SUBWAVELENGTH OBJECTS

As shown previously, one can detect experimentally the optical magnetic field associated with the scattered light. Using crossed polarizers, one can detect the different cartesian components associated with the electric field or with the optical magnetic field using coated gold dielectric tips at the resonance of the thin metal film or out of resonance. Choosing a proper incident polarized wave, one can detect the scattered wave obtained by eliminating the incident wave using another crossed polarizer at the fiber exit.

This could give more information on the size and shapes of the objects as the behaviors are not the same when using nanometric or mesoscopic objects compared to the incident wavelength. The cartesian components could give more insight about the shape of the object rising on the surface.

### 4.1. Detection of the Different Cartesian Components in the TE Mode

The detection is not performed close to the objects in order to show scattering effects along the dielectric surface. The aim of the following section is to show the possibility to suppress these optical waves in the near-field optics.

We illuminate a dielectric glass object at a wavelength of 633 nm through a glass substrate under the condition of total internal reflection with an angle of incidence of 60°. The lateral size of the dielectric pad is 100 nm and its height is 40 nm, placing it in the nanoscopic regime. The detection of the electromagnetic field is performed at 60 nm above the pad of dielectric permittivity of 2.25 which is equal to the one of the substrate. This detection height involves scattering behaviors around the object in the near-field optics.

The computation of the total intensity associated with electric field and to each cartesian component is realized for the TE mode (Fig. 3). The intensities are normalized according to the incident light.

It is known that in the near-field optics, a strong  $z$ -component of the electric field exists since this one does not appear in reflectivity or in transmission for thin films in the far-field. Moreover, it is also important to see its evolution with the incident polarization; this will be shown for the TM mode in the next section.

In this polarization mode, the electric field associated with the incident light is perpendicular to the plane of incidence. As shown previously, the negative contrast above the object is the depolarization effect and this can be seen in the optical images for the intensity associated with the total electric field (Fig. 3a) and also according to the  $x$ -component (Fig. 3b) which corresponds to the direction of application for the incident electric field.

In this mode, one can see first that the intensity associated to the total electric field shows a confinement of the electric field close to the lateral sides of the pad along the  $x$ -direction (Fig. 3a) which is displayed by an increase of intensity in the optical image. Nevertheless, interference phenomena due to the backward scattering effects of the incident light on the object are more accentuated in the near-field optical image (Fig. 3a) for  $y < 0$ . Moreover, the forward scattering appears on the optical image for  $y > 0$ .



Second, we can see that the  $x$ -component of the electric field, which is the incident one, is major (Fig. 3b) compared to the others ( $y$ - and  $z$ -components in Fig. 3c and d) as expected. One can see in Figure 3c that the interferences on the images due to the backscattering reflected wave on the object disappeared and only the effects due to the confinement of the field around the object show up. These ones are related to the topography of the object on the surface.

The same behavior can be seen in Figure 3d for the  $z$ -component of the electric field which shows optical effects due to the topography of the object. However, the intensities are greater for this component (Fig. 3d) compared to the other one (Fig. 3c). This shows the predominance of the  $z$ -component of the electric field compared to the one parallel to the surface ( $y$ -component) in the near-field optical images.

The image associated with the total electric field shows a negative optical response (dark contrast) above the nanoscopic object (Fig. 3a). Moreover, the  $y$ -component shows an electric field which is well confined at the corners of the dielectric pad (Fig. 3c), whereas the  $z$ -component displays the same strong effects on the lateral sides of the pad along the  $x$ -direction (Fig. 3d). By these optical patterns, one can distinguish the  $x$ -component of the electric field from the parallel  $y$ -component.

## 4.2. Detection of the Different Cartesian Components in the TM Mode

In this mode, one can see first that the optical images for the intensity associated with the total electric field and for each cartesian component are different compared to the TE mode. Consequently, the polarization plays an important role when analyzing the effects in the near-field optics.

For this mode of polarization, we can see first that the intensity associated with the total electric field shows a confinement of the electric field above the upper side of the dielectric pad along the  $z$ -direction (Fig. 4a), as shown in Section 3.1.

As in the TE mode, interference phenomena on the surface due to the backward scattering effect of the incoming light on the dielectric object show up in the optical image (Fig. 4a). Second, the  $y$ -component and more particularly, the  $z$ -component of the electric field which are associated to the incident one are major (Fig. 4c and d) compared to the other one ( $x$ -component in Fig. 4b) because they are associated with the incident electric field. The  $z$ -component is the strongest in the near-field optics, as discussed previously.

We can see in Figure 4b that the interferences on the images due to the backscattering reflected wave on the object disappeared and only the effects due to the confinement of the field around the object show up in the optical images. These are related to the topography of the object on the surface as in the TE mode.

We also show in this case that the  $z$ -component of the electric field is stronger in the near-field optical images compared to the  $y$ -component. Moreover, the  $x$ -component shows an electric field which is well confined on lateral sides of the pad (along the  $x$ -direction) whereas the  $y$ -component and the  $z$ -component display both interferences due to the incident light and a confinement of the electric

field respectively on the lateral sides along the  $y$ -direction and on the top of the pad along the  $z$ -direction (Fig. 4c and d).

It is thus possible to distinguish these three components in the near-field optics. Moreover, the forward scattering ( $y > 0$ ) shows up in the optical images (Fig. 4a, c, and d).

Thanks to this study, we show that the analysis of polarization in the near-field optics shows that one can eliminate interference behaviors on the surface. Moreover, this analysis also shows the weight of each cartesian component in the near-field optical images.

Similar effects can be found for any kind of material of real positive dielectric permittivity. The behaviors are thus accentuated as the dielectric permittivity increases raising the intensities associated with each component. Nevertheless, the intensity variations associated with the component which was not in the polarization of the incoming light (for the TE mode:  $y$ - and  $z$ -components; for the TM mode:  $x$ -component) can be detected experimentally under the condition of a good signal-to-noise ratio.

Other studies show that these intensities could get higher values using other materials. In this case, it is necessary to make spectroscopy computations by varying the incident wavelength in the visible range showing for which one the exaltation of the electric field in the near-field optics appears. This intensity enhancement is mainly due to the basic properties of matter from which the object is based [34].

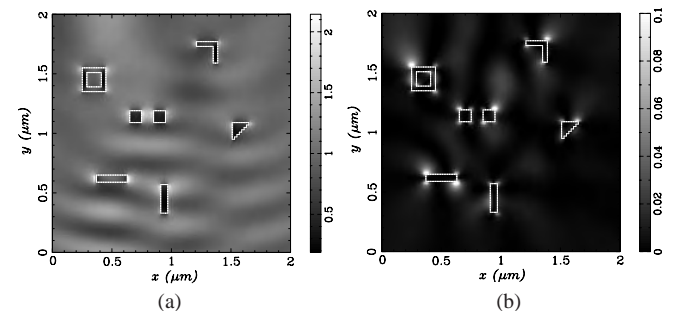
## 4.3. Dealing with Different Objects

In order to complete the previous discussion, we use several structures of different sizes and shapes. The sizes are arbitrary, taken in order to create a group which belongs to the mesoscopic regime.

Using different object sizes, one can see that scattering waves occur in the image providing difficulties to see the confinement of the electric field around each object. The case of bidimensional objects is chosen.

Using different objects sizes and shapes, it is important to see the optical signal associated with the component which is not in the incident electric field. One can see that the electric field is well confined on the edges of the different structures although surrounded by interference behaviors (see Fig. 5a).

Using different sizes of the structures in the mesoscopic regime, backward and forward scattering can be clearly seen in the optical images. One is aware that these effects



**Figure 5.** For  $\lambda = 633$  nm, variation of the intensity associated with the total electric field (a) and the  $y$ -component (b) for several dielectric bidimensional objects.

degrade strongly the resolution of the optical images in the near-field optics. The detection of the  $y$ -component shows that one can detect with a better accuracy the positions of the objects as the scattered waves are almost eliminated (see Fig. 5b).

This analysis shows a new technique to eliminate interference behaviors occurring in the near-field optics, bringing to the fore only optical effects relative to the topography of the objects on the surface.

#### 4.4. Circular Polarization

The use of circular polarized light has been developed for the case of dichroism in order to understand the optical properties of magnetic materials at the microscopic level. Circularly polarized light emitted from a scanning tunneling microscope was observed when the sample surface of a ferromagnetic material was probed with a tungsten tip in a longitudinal configuration. (The applied magnetic field is parallel to both the surface plane and the plane of light detection [35].)

The theory of radiative transfer has been used to investigate the interaction between linear or circular polarized light waves and a multiple scattering medium (spheres) according to the sizes of the objects and their relative index of refraction [36–38]. This theory shows that the circular depolarization length exhibits a strong dependence on the relative refractive index, whereas the linear one does not.

Chiral and achiral molecules show optical activity which arises from the different interaction of chiral media with left- and right-hand circularly polarized light. This optical

activity and the circular difference effects can also occur in nonlinear optics for chiral or achiral structures and magnetic materials in the second-harmonic generation signals [39, 40].

In our case, using the same computation technique, it is interesting to see the impact of circular polarization on a dielectric structure in the nanoscopic regime. We took the same dielectric object used in the previous section and illuminated under the same conditions. The detection of the electromagnetic field is performed at a height of 60 nm above the dielectric object.

In the case where the object is illuminated in normal incidence with a circular polarization ( $x$ - and  $y$ -components exist in this case), one can find that each component of the electric field gives information about the shape of the object in both directions. Therefore, an asymmetrical shape of the object can be detected with such method of illumination as the depolarization effects occur in both directions ( $x$  in Fig. 6b and  $y$  in Fig. 6c) using this particular incident polarization associated with the incident light (see Fig. 6a).

This technique could give more information about the shape of the object and also of the optical confinement of the electric field around the different structures. The main problem occurs on the detection of scattering effects along the surface and of the optical patterns produced by the mesoscopic and nanoscopic structure.

## 5. CONCLUSION

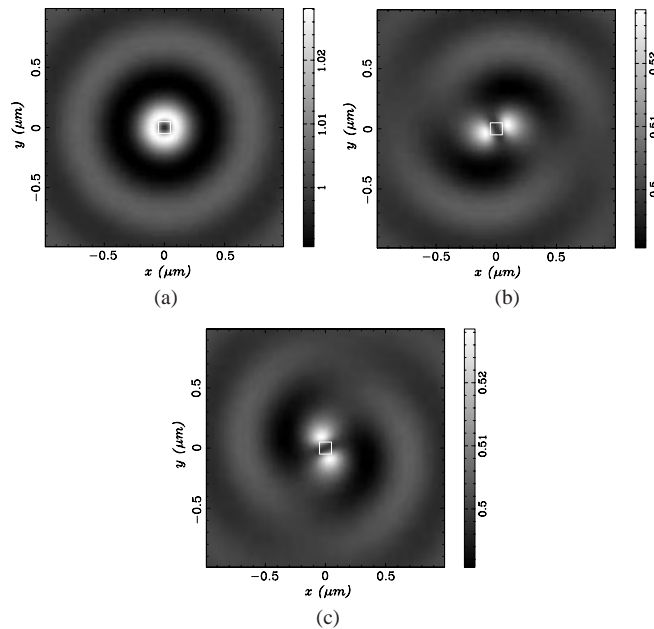
We present an accurate analysis of the optical effects produced by nanoscopic and mesoscopic structures in the near-field optics. The importance of the incident wavelength and of the particle size is one of the most important points to get a better optical resolution in the near-field optics. The depolarization effects associated with a nanoscopic object and the scattering properties of the structures were clearly shown. The analysis of polarization shows the possibility to extract optical effects relative to nanoscopic and mesoscopic objects in the near-field optics.

## GLOSSARY

**Depolarization of light** On a smaller scale, when light waves pass near a barrier, they tend to bend around that barrier and spread at oblique angles. This phenomenon is known as diffraction of light, and occurs when the light wave passes very close to the edge of an object or through a tiny opening such as a slit or aperture. The light that passes through the opening is partially redirected due to an interaction with the edges.

**Mesoscopic regime** The adjective mesoscopic is used to define the situations where the sizes of the structures are of the order of the incident wavelength. For visible light, it corresponds roughly to the length range between 0.1 and 1 micrometer. By nanoscopic, one usually means low-dimensional Structures smaller than 100 nm.

**Near-fields optics** Near-field optics studies the behavior of light fields in the vicinity of matter and deals with phenomena involving propagating and evanescent electromagnetic wave which become critically significant when the typical



**Figure 6.** For  $\lambda = 633$  nm, variation of the intensity associated with the total electric field (a), the  $x$ -component (b), and the  $y$ -component (c) for a  $100 \times 100 \times 40$  nm<sup>3</sup> glass pad. The incident polarization is circular and the object is illuminated in normal incidence by the substrate. The detection is performed at a height of 100 nm above the surface.

sizes of the object are of the order of the wavelength or smaller. Near-field optical microscopy is the straightforward application of near-field optics.

**Polarization** A light wave is an electromagnetic wave which moves through the vacuum of outer space. Light wave is produced by electric charges which vibrate in a multitude of directions. An electromagnetic wave is a transverse wave which has both an electric and a magnetic component. A light wave which is vibrating in more than one plane is referred to as unpolarized light. It is possible to transform unpolarized light into polarized light. Polarized light waves are light waves in which the vibrations occur in a single plane. The process of transforming unpolarized light into polarized light is known as polarization.

**Surface plasmon resonance** Under the condition of total internal reflection, while incident light is totally reflected the electromagnetic field component penetrates a short (tens of nanometers) distance into a medium of a lower refractive index creating an exponentially detenuating evanescent wave. If the interface between the media is coated with a thin layer of metal (gold), and light is monochromatic and p-polarized, the intensity of the reflected light is reduced at a specific incident angle producing a sharp shadow (called surface plasmon resonance) due to the resonance energy transfer between evanescent wave and surface plasmons, corresponding to a collective excitation of the electrons at the metal/lower refractive index medium interface. The resonance conditions are influenced by the material adsorbed onto the thin metal film.

**TE (s-mode) and TM (p-mode)** In the case of a surface separating two dielectric media, two modes of polarization can be associated with the incoming light: TE and TM modes. The z direction being perpendicular to the glass-air interface, as the incident light is chosen to be linearly polarized, the TE mode (s polarization) corresponds to an incident electric field perpendicular to the plane of incidence (y-z plane). The TM mode (p polarization) corresponds to a field parallel to the plane of incidence.

**Tip detection** In near-field optical microscopy, the local detection of the optical signal or the illumination of the sample relies on the use of nanometer-sized probes. In near-field optics, a tip is constituted by a pulled optical fiber which illuminates or collects the light from a sample surface. This tip can be coated with a thin metal film in order to achieve a narrow localization of the incident light on the sample or to improve the resolution in detection.

**Total internal reflection** At an interface between two transparent media of different refractive index, light coming from the side of higher refractive index is partly reflected and partly refracted. Above a certain critical angle of incidence, no light is refracted across the interface, and total internal reflection is observed.

## ACKNOWLEDGMENTS

This paper is dedicated to Jacques and Antoinette Richard and to the memory of Marie Muggéo.

## REFERENCES

1. D. W. Pohl, *Adv. Opt. Elect. Micr.* 12, 243 (1991).
2. D. W. Pohl, *Scanning Tunneling Microscopy* 2, 233 (1992).
3. R. C. Reddick, R. J. Warmack, D. W. Chilcott, S. L. Sharp, and T. L. Ferrell, *Rev. Sci. Instrum.* 61, 3669 (1990).
4. R. C. Reddick, R. J. Warmack, and T. L. Ferrell, *Phys. Rev. B* 39, 767 (1989).
5. C. Girard, A. Dereux, O. J. F. Martin, and M. Devel, *Phys. Rev. B* 52, 2889 (1995).
6. J. C. Weeber, E. Bourillot, A. Dereux, J. P. Goudonnet, Y. Chen, and C. Girard, *Phys. Rev. Lett.* 77, 5332 (1996).
7. C. Girard, A. Dereux, and C. Joachim, *Phys. Rev. E* 59, 6097 (1999).
8. J. R. Krenn, A. Dereux, J. C. Weeber, E. Bourillot, Y. Lacroute, J. P. Goudonnet, G. Schider, W. Gotchy, A. Leitner, F. R. Aussenegg, and C. Girard, *Phys. Rev. Lett.* 82, 2590 (1999).
9. E. Betzig, J. K. Trautman, J. S. Weiner, T. D. Harris, and R. Wolfe, *Appl. Opt.* 31, 4563 (1992).
10. D. Van Labeke and D. Barchiesi, *J. Opt. Soc. Am. A* 9, 732 (1993).
11. D. Barchiesi, C. Girard, D. Van Labeke, and D. Courjon, *Phys. Rev. E* 54, 4285 (1996).
12. A. A. Maradudin and D. L. Mills, *Phys. Rev. B* 11, 1392 (1975).
13. D. Courjon and C. Bainier, *Rep. Prog. Phys.* 57, 989 (1994).
14. B. Labani, C. Girard, D. Courjon, and D. Van Labeke, *J. Opt. Soc. Am. B* 7, 936 (1990).
15. C. Girard and A. Dereux, *Rep. Prog. Phys.* 59, 657 (1996).
16. M. Born and E. Wolf, "Principles of Optics." Pergamon Press, Oxford, 1959.
17. J. D. Jackson, "Classical Electrodynamics." Wiley, New York, 1983.
18. E. M. Purcell and C. R. Pennypacker, *J. Astrophys.* 186, 705 (1973).
19. B. T. Draine, *J. Astrophys.* 333, 848 (1988).
20. G. H. Goedecke and S. G. O'Brien, *Applied Optics* 27, 2431 (1988).
21. B. T. Draine and P. J. Flatau, *J. Opt. Soc. Am. A* 11, 1491 (1994).
22. J. C. Ku, *J. Opt. Soc. Am. A* 10, 336 (1993).
23. C. Bohren and D. Huffman, "Absorption and Scattering of Light by Small Particles." John Wiley, New York, 1983.
24. O. J. F. Martin, A. Dereux, and C. Girard, *J. Opt. Soc. Am. A* 11, 1073 (1994).
25. O. J. F. Martin, C. Girard, and A. Dereux, *Phys. Rev. Lett.* 74, 526 (1995).
26. C. Girard, J. C. Weeber, A. Dereux, O. J. F. Martin, and J. P. Goudonnet, *Phys. Rev. B* 55, 16487 (1997).
27. N. Richard, *Eur. Phys. J. B* 17, 11 (2000).
28. E. D. Palik, in "Handbook of Optical Constants of Solids." (E. D. Palik, Ed.) Academic Press, New York, 1991.
29. R. C. Weast, in "Handbook of Chemistry and Physics." (R. C. Weast, M. J. Astle, and W. H. Beyer, Eds.) CRC Press, Boca Raton, FL, 1985.
30. N. Richard, *J. Appl. Phys.* 88, 2318 (2000).
31. A. Yaghjian, *Proc. IEEE* 68, 248 (1980).
32. E. Devaux, A. Dereux, E. Bourillot, J. C. Weeber, Y. Lacroute, J. P. Goudonnet, and C. Girard, *Phys. Rev. B* 62, 10504 (2000).
33. U. Schröter and A. Dereux, *Phys. Rev. B* 64, 125420 (2001).
34. N. Richard, *Phys. Rev. E* 63, 026602 (2001).
35. T. Verbiest, M. Kauranen, and A. Persoons, *Phys. Rev. Lett.* 82, 3601 (1999).
36. A. D. Kim and M. Moscoso, *Phys. Rev. E* 64, 026612 (2001).
37. J. P. Macquart and D. B. Melrose, *Phys. Rev. E* 62, 4177 (2000).
38. P. Johansson, S. P. Apell, and D. R. Penn, *Phys. Rev. B* 64, 054411 (2001).
39. E. Anisimovas and P. Johansson, *Phys. Rev. B* 59, 5126 (1999).
40. S. P. Apell, D. R. Penn, and P. Johansson, *Phys. Rev. B* 61, 3534 (2000).

# Noble Metal Nanoparticles

Yiwei Tan, Yongfang Li, Daoben Zhu

*Chinese Academy of Sciences, Beijing, People's Republic of China*

## CONTENTS

1. Introduction
2. Synthesis
3. Spectroscopic Characterization
4. Properties
5. Self-Assembly
6. Applications
7. Summary
- Glossary
- References

## 1. INTRODUCTION

During the final decade of the 20th century, nanomaterials were the focus of research in the field of materials science, which is driven by the expectations concerning the application of nanomaterials as a forthcoming generation of functional materials for the new century. A large amount of knowledge about the synthesis and properties of various nanoparticles and nanocomposites was accumulated within such a short period, with numerous new insights and techniques emerging with each passing day. The physical and chemical properties of substances can be significantly altered when they are exhibited on a nanometer-length scale, and this phenomenon opens up a completely new perspective for materials design that benefits from the introduction of not only particle size, but also particle morphology as new, powerful parameters.

A brand new concept is arising in material science: to utilize nanoparticles as the building blocks to displace the conventional microdevices by nanodevices. This challenging innovation will give rise to a revolutionary development: a drastic reduction in the necessary amount of traditional materials, subsequently of the cost and pollution, and finally turning the modern manufacturing that is regarded as an industry of exhausted natural resources and environmental harm into “smart and green production.”

The substances with one dimension shrinking down to 1–100 nm can be called nanoscale substances. The nanomaterials can display various geometrical morphologies,

which include zero-dimensional nanoparticles with an aspect ratio approximately equal to 1, one-dimensional nanorods (aspect ratio  $> 1$ ), nanowires, nanofibers, nanotubes, and nanoribbons or nanobelts [1, 2], two-dimensional nanosheets [3–5] and nanoscale diskettes [6], and three-dimensional nanocages [7, 8]. Nanoparticles are the most thermodynamically stable form with respect to the other geometrically morphological nanoscale materials because they have the least surface energy. Having sizes located between those of small molecules ( $< 1$  nm) and eukaryotic cells ( $\sim 1$ – $50$   $\mu\text{m}$ ), they bridge the microscopic and macroscopic world, and provide completely novel dimensions when it comes to physical and chemical processing. Therefore, immense successes will be in gestation in this ongoing frontier research field of nanomaterials. In this chapter, the topic that will be dealt with in the following is just confined to the highlights in recent progress of noble metal nanoparticles. Additionally, copper nanoparticles are also involved since element copper belongs to Group IB.

Nanoparticles usually refer to approximately spherical particles with diameters within the range of 1–100 nm. The term nanocluster or cluster tends to be restricted for the description of nanoparticles of diameter less than 4 nm [9]. As used interchangeably in the literature, the terms nanoparticle and colloid are not clearly distinguishable. Colloidal metal nanoparticles have been known since the end of the middle ages. At that time, gold colloids were uniformly dispersed in glass to form the so-called beautiful red-colored ruby glass. In 1857, Faraday defined the “finely dispersed metal” as colloidal solutions of metal [10]. He proposed that the beautiful color of gold colloids is ascribed to metallic gold in its colloidal form. Later, at the beginning of the last century, a theory of light absorption by small metal nanoparticles was developed by Mie through solving Maxwell's equations for the absorption and scattering of electromagnetic radiation by spherical metal particles [11]. However, the research on noble metal nanoparticles is undergoing an unprecedented boom nowadays. There are a number of reasons for the resurgence of interest in nanoparticles of inorganic solids. On the one hand, new and powerful tools, both theoretical and experimental, have become available that permit a deep understanding of those fascinating materials. On the other hand, the unusual properties arise from the

material dimensions that are on the order of the electron mean-free path, which motivate their diverse application potentialities unexplored before. Perhaps most important is the finding that these materials, particularly when capped, behave almost like molecules in terms of their solubility, and the manner in which they can be crystallized in superlattices. In addition, there is the possibility of covalently modifying nanoparticle surfaces, in very much the same manner as one might take with a molecule.

It was found that some properties of metal nanoparticles may be comparable to those of semiconductor particles. There are no basic differences between metal and semiconductor nanoparticles since many effects, for example, sensitization of photoreactions of other solutes, the ability to store excess electrons and positive holes, changes in electronic properties upon surface modification, and photoelectron emission, which have been observed for semiconductor particles, can be showed in the metal nanoparticles [12]. It is known that large noble metal nanoparticles (i.e., Ag, Au, Pd, Pt, Rh, Ir, etc.) with diameters more than 10 nm have a high chemical stability due to their chemical inertness, whereas when the size of noble metal nanoparticles decreases to 2–4 nm, they are much more easily oxidized than the corresponding bulk metals in air [9]. Other transition metal nanoparticles are generally sensitive toward oxygen so that all experiments must be carried out under anaerobic conditions.

## 2. SYNTHESIS

### 2.1. Approaches to Noble Metal Nanoparticles

The accurate synthesis of colloids is never straightforward since small changes in synthesis procedures can give completely different results. Furthermore, the chemical preparation of colloids can produce nanocrystals having a crystal structure never found in bulk materials. It is thought that colloid chemistry could produce alloys of elements well known as nonalloying systems in the bulk. Noble metal nanoparticles are able to be prepared by physically or chemically forming noble metal atoms in suitable solvents, followed by an aggregation process (dispersion and condensation methods) of the noble metal atoms in the presence or absence of protective agents such as polymers, surfactants, or strong coordination ligands. The preparation of size- and shape-selected noble metal nanoparticles is always a great goal of chemists and physicists pursuing the transformation of their potential applications into reality.

Control over both the size and the shape of precious metal nanoparticles is not only of theoretical significance in the field of nanomaterials, but also an important way to modulate the catalytic and some other properties of precious metal nanoparticles. Much research work has been directed toward the preparation of shape-controlled precious metal nanoparticles. In the reported chemical preparations, there are two kinds of methods to control the morphology of precious metal nanoparticles. One is template-directed preparation, in which metal ions or complexes are reduced and the nanoparticles grow within a template, and therefore the shape of resulting products is controlled by the morphology

of the template. The other is growth-directed preparation, by which shape-selective precious metal nanoparticles are prepared using suitable precious metal precursors, protective agents, reducing agents, and reducing methods. Tables 1 and 2 show a survey of recent research activities concerning the synthesis of noble metal nanoparticles.

#### 2.1.1. Physical Methods: Condensation of Atomic Metal Vapor

The principle of physical preparative methods is the metal vapor cocondensation with organic vapors in aqueous or nonaqueous media. These methods include metal evaporation [13–18] and laser pyrolysis [19–27], of which the metal evaporation route has been known since the start of the last century and was extensively studied in the 1970s. The metal vapors are commonly generated at reduced pressure of relatively volatile metals from a resistively heated hearth or an electron-beam furnace, and subsequently condensed on the walls of the reactor together with the organic solvent vapors at low temperature. A colloidal dispersion of the metal is then obtained by warming the frozen metal/organic mixture. By this means, Klabunde and co-workers prepared various dispersions of Au and Pd nanoparticles with a wide size distribution of 5–30 nm [28–33]. The generated zerovalent nanoparticles can be stable for several months, but the size distribution is hard to control.

A recent aerosol route developed by Whetten and co-workers [34–36] gave rather uniform Ag nanoparticles with a diameter between 4 and 6 nm: elemental silver metal is evaporated at high temperatures ( $\sim 1500$  K) into a flowing, preheated atmosphere of ultrahigh-purity inert gas (Ar, He, N<sub>2</sub>, etc.). The flow stream is cooled over a short distance (and flow time) to lower temperatures, stimulating the growth of nanoparticles in the desired size range, for example, ca. 4–6 nm. Then, growth is abruptly terminated by expansion through a conical funnel accompanied by dilution in a great excess of cool inert gas. Subsequent steps may include reheating (annealing) of the separated nanocrystals and etching and passivation by molecular vapors such as long-chain alkylthiols and alkylamines introduced downstream.

Laser ablation techniques as a typical example of a dispersion method allow one to conveniently and sanitarily fabricate various noble metal nanoparticles without introducing a reductant. Here, let us give a simple description of it: a metal plate immersed in a solution containing a stabilizer was irradiated with a laser beam focused by a lens; the metal atoms were evaporated, and then condensed at the action of laser energy. Figure 1 presents a schematic diagram of laser ablation for the preparation of metal nanoparticles. The size distribution of the nanoparticles tends to be broadened because the coagulation processes of atoms are difficult to be controlled.

#### 2.1.2. Sonochemical, Photochemical, and Thermal Decomposition

High-intensity ultrasound is a powerful tool for the preparation of nanostructured materials because of ultrasonic cavitation caused by ultrasonic irradiation of a liquid. The acoustic cavitation comprises the formation, growth,

**Table 1.** Various synthetic routes for noble metal nanoparticles with the exception of chemical reduction.

Noble metal (dispersity)	Synthetic route	Ref.
Cu (5–100 nm)	laser ablation	[24]
Cu (20–100 nm)	$\gamma$ -radiolysis	[65, 247, 248]
Cu (7.5 nm)	thermal decomposition	[224]
Cu (elongated)	sonochemical synthesis	[254]
Ag (4–40 nm)	laser ablation	[25]
Ag (4–6 nm)	metal evaporation	[34–36]
Ag (13–34 nm)	sonochemical synthesis	[43]
Ag (6.5–12.5 nm)	$\gamma$ -radiolysis	[68]
Ag (2–120 nm)	$\gamma$ -radiolysis (seed mediated)	[70, 71]
Ag (5–10 nm)	UV irradiation	[78]
Ag (10–20 nm)	UV irradiation	[81]
Ag (~4 nm)	UV irradiation	[85]
Ag (nanoprism)	fluorescent light irradiation	[263]
Au (1–10 nm)	laser ablation	[26]
Au (1.7–5.5 nm)	laser ablation	[27]
Au (10–30 nm)	metal evaporation	[28]
Au (7–15 nm)	metal evaporation	[30]
Au (~2 nm)	metal evaporation	[31]
Au (2–10 nm)	metal evaporation	[32]
Au (2–9, 60 $\pm$ 30 nm)	sonochemical synthesis	[44, 268]
Au (15–22 nm)	$\gamma$ -radiolysis	[74]
Au (7.5–12.5 nm)	UV irradiation	[77]
Au (10–20 nm)	UV irradiation	[78]
Au (~6 nm)	UV irradiation	[85]
Au (0.2–5 nm)	UV irradiation	[89]
Au (triangle, hexagon)	UV irradiation	[76]
Au (platelets)	UV irradiation	[88]
Pt (1.7–3.5 nm)	sonochemical synthesis	[50]
Pt (1–10 nm)	sonochemical synthesis	[56]
Pt (1–3 nm)	$\gamma$ -radiolysis	[69, 274]
Pt (1.1 nm)	UV irradiation	[82]
Pt (0–5 nm)	UV irradiation	[83, 84]
Pt (2–4 nm)	microwave irradiation	[91]
Pt (0.6–2.2 nm)	microwave irradiation	[92]
Pt (2.5–5.0 nm)	electrochemical reduction	[214]
Pd (8 nm)	metal evaporation	[29]
Pd (6–110 nm)	sonochemical synthesis	[46]
Pd (1–6 nm)	sonochemical synthesis	[56]
Pd (0.1–12 nm)	sonochemical synthesis	[59]
Pd (2.0–40 nm)	UV irradiation	[84]
Pd (0.6–3.0 nm)	microwave irradiation	[92]
Pd (1.4–4.8 nm)	electrochemical reduction	[213, 214]
Pd (8–10 nm)	thermal decomposition of Pd complex	[235, 236]
Ru (3.5 nm)	electrochemical reduction	[214]
Rh (2.5 nm)	electrochemical reduction	[214]
Os (2.0 nm)	electrochemical reduction	[214]
Ag <sub>core</sub> Au <sub>shell</sub>	$\gamma$ -radiolysis	[72]
Au <sub>core</sub> Ag <sub>shell</sub> (60 nm)	UV irradiation	[317]
Au <sub>core</sub> Pt <sub>shell</sub>	$\gamma$ -radiolysis	[73]
Pt <sub>core</sub> Au <sub>shell</sub>	$\gamma$ -radiolysis	[73]
Ag/Pt alloy	$\gamma$ -radiolysis	[300]
Ag/Pd alloy (3–11 nm)	UV irradiation	[309]
Au/Pt alloy (1.6–13.6 nm)	$\gamma$ -radiolysis	[301]
Pt/Cu alloy (2.5 nm)	electrochemical reduction	[214]
Pt/Pd alloy (3.5 nm)	electrochemical reduction	[214]
Pt/Rh alloy (2.5 nm)	electrochemical reduction	[214]
Pt/Sn alloy (3.0 nm)	electrochemical reduction	[214]
Pd/Ni alloy (2.5–3.5 nm)	electrochemical reduction	[311]

and implosive collapse of bubbles in a liquid. When the cavitation bubbles are violently collapsing, the temperature and pressure of the bubbles reach several thousands of degrees and hundreds of atmospheres, respectively, accompanied by shock-wave generation [37, 38]. The sonochemical synthesis of novel nanostructured materials is based on such extreme conditions. The sonochemical reduction of transition salts usually proceeds in three steps: the generation of the active species, the reduction of the metal, and the growth of the colloids. These three steps occur in different compartments: (1) in the gaseous phase into the cavitation bubbles where high temperature and pressure allow water pyrolysis to form  $\bullet\text{H}$  and  $\bullet\text{OH}$ , (2) at the interface between the cavitation bubbles and the solution, and finally, (3) in the solution. Henglein first revealed that  $\bullet\text{H}$  and  $\bullet\text{OH}$  formed in the course of sonolysis of water [39], and reported the reduction of  $\text{AuCl}_4^-$  and  $\text{Ag}^+$  in an aqueous solution by ultrasonic irradiation under  $\text{Ar-H}_2$  conditions [40]. Subsequently, the synthesis of stable metal iron colloids by the sonochemical decomposition of iron-containing complexes such as  $\text{Fe}(\text{CO})_5$  was described [41, 42]. In the case of reduction of noble metal ions, the sonochemical process undergoes the sonolysis of water and organic additives, which produce  $\bullet\text{OH}$  and  $\bullet\text{H}$ , as well as the following  $\bullet\text{R}$  and  $\bullet\text{H}$ , respectively. For instance, a previous work by Nagata et al. [43] suggested that the reduction of  $\text{Ag}^+$  ions to metallic Ag under the protection of Ar atmosphere proceeded via the formation of H atoms in the sonolysis of water, and the subsequent secondary reducing radicals generated from the abstraction reaction between organic additives and OH radicals and H atoms. Due to the low vapor pressure of the metallic salts, the reduction cannot happen in the gaseous phase. The reduction occurs mainly at the bubble/solution interface and in solution. By this means, several types of metal nanoparticles have been synthesized in the presence of protective agents [44–58] or support substrates [59].

During the past few decades,  $\gamma$  radiolysis of solutions of precious metal salts has been applied to prepare nanoparticles [60–67]. The reduction of the precious metal ions occurs here by the reducing species such as organic radicals [ $(\text{CH}_3)_2\text{C}\bullet(\text{OH})$ ] which are generated in the radiolysis of the aqueous solvent (the solvated electrons or  $\bullet\text{H}$  and  $\bullet\text{OH}$  originating from water radiolysis can react with organic molecules to give new radicals to reduce metal salts). Under certain conditions, a large number of atoms are homogeneously and instantaneously produced in the course of the irradiation, thus promoting the generation of particles with a narrow size distribution. For example, by irradiating a solution of copper perchlorate ( $\text{Cu}(\text{ClO}_4)_2$ ) containing sodium formate, Cu nanoparticles are formed through the reduction of  $\text{Cu}^{2+}$  by both solvated electrons and  $\text{CO}^{2-}$  generated during radiolysis [65]. The irradiation of a solution comprising  $\text{AgClO}_4$ , sodium citrate, 2-propanol, and nitrous oxide yields rather uniform cuboctahedra and icosahedra nanoparticles [68]. Intriguingly, in an original example of radiolytic Pt colloid synthesis [69], both the nanoparticles and the protective polymer are produced simultaneously by radiolysis of a solution containing the monomer (acrylamide) and the metal salts ( $\text{H}_2\text{PtCl}_6$ ). In the presence of seeds, radiolytic reduction has also been applied to enlarge particles. Gold nanoparticles with diameters ranging from 2 to 120 nm

**Table 2.** Chemical reduction approaches to noble metal nanoparticles with different reducing and stabilizing agents.

Noble metal (dispersity nm)	Reducing agent	Stabilizer	Ref.
Cu (<5 nm)	H <sub>2</sub>	carbon nanotube (template and support)	[253]
Cu (4.8–15.0 nm)	NaBH <sub>4</sub>	PVP, PVA, dextrin, amylopectin, cellulose	[160–162]
Cu (<1.8 nm)	NaBH <sub>4</sub>	polyamidoamine	[167]
Cu (<5 nm)	NaBH <sub>4</sub>	alkylxanthate	[245]
Cu (4.5–6.0 nm)	N <sub>2</sub> H <sub>4</sub>	polyamidoamine	[166]
Cu (6.6–22.7, 15.5–30.2 nm)	N <sub>2</sub> H <sub>4</sub> · H <sub>2</sub> O	PVP	[197]
Cu (4–7, 6–9, 3–12 nm)	N <sub>2</sub> H <sub>4</sub>	AOT reverse micelles	[215, 217, 249]
Cu (3–30 nm)	N <sub>2</sub> H <sub>4</sub> · H <sub>2</sub> O	methanol	[234]
Cu (5–40 nm)	NaBH <sub>4</sub>	glycerol monooleate	[181]
Cu (5.5–12.5 nm)	NaBH <sub>4</sub>	AOT reverse micelles	[215]
Ag (5–20 nm)	methanol	poly[(vinyl alcohol)- <i>co</i> -( <i>N</i> -vinylpyrrolidone)]	[138]
Ag (3.3 nm)	KBH <sub>4</sub>	polystyrene- <i>b</i> -poly(ethylene oxide)	[85]
Ag (1.6–38.6 nm)	KBH <sub>4</sub>	cationic polyelectrolytes	[165]
Ag (<5 nm)	NaBH <sub>4</sub>	polyamidoamine	[174]
Ag	NaBH <sub>4</sub> , N <sub>2</sub> H <sub>4</sub>	polystyrene- <i>b</i> -polyvinylpyridine	[201]
Ag (4–12 nm)	NaBH <sub>4</sub>	unsaturated long-chain carboxylate	[241]
Ag (4–9 nm)	NaBH <sub>4</sub>	substituted long-chain alkanethiol	[259]
Ag (2–20 nm)	N <sub>2</sub> H <sub>4</sub>	anisic acid	[98]
Ag (hexagonal nanoplate)	N <sub>2</sub> H <sub>4</sub>	aniline	[200]
Ag (1–9.4 nm)	N <sub>2</sub> H <sub>4</sub>	AOT reverse micelles	[261, 262]
Ag (1–3 nm)	Cu nanocluster	polyamidoamine	[103]
Ag (10–60 nm)	formaldehyde	sodium dodecylbenzenesulfonic acid	[112]
Ag (25 nm)	tannins	carboxylated polystyrene latex	[112]
Ag (20–30 nm)	NaH <sub>2</sub> PO <sub>2</sub> -tannins	carboxylated polystyrene latex	[112]
Ag (nanodisk)	aging of triangular Ag nanoplate	CTAB	[115]
Ag (polygonal nanoprism)	<i>N,N</i> -dimethyl formamide	PVP	[264]
Ag (truncated triangular nanoplate)	ascorbic acid (seed-mediated growth)	CATB	[266]
Ag (3–16, 40–60 nm)	citrate	citrate	[185, 256]
Ag (2.5–25 nm)	nonionic surfactant	nonionic surfactant	[186]
Ag (1.5–5 nm)	triethylamine	dodecanethiol	[228]
Au	CO	polyvinyl sulfate	[210]
Au (2–14 nm)	ethylene glycol	PVP	[143]
Au (1–8 nm)	(CH <sub>3</sub> ) <sub>2</sub> NH · BH <sub>3</sub>	polyamidoamine	[102]
Au (3 nm)	KBH <sub>4</sub>	polystyrene- <i>b</i> -poly(methacrylic acid)	[85]
Au (5 nm)	KBH <sub>4</sub>	polystyrene- <i>b</i> -poly(ethylene oxide)	[85]
Au (1.8–3.7 nm)	NaBH <sub>4</sub>	polyamidoamine	[169, 174, 176]
Au (1.0–4.2 nm)	tetra(hydroxymethyl) phosphonium chloride	tetra(hydroxymethyl) phosphonium chloride	[230]
Au (5.1–7.4 nm)	NaBH <sub>4</sub>	polymethylphenylphosphazene	[232]
Au (1–3 nm)	NaBH <sub>4</sub>	alkanethiol	[238]
Au (5.5 nm) (refluxing with thiol)	NaBH <sub>4</sub>	alkanethiol	[227]
Au (4.5–10.5 nm)	NaBH <sub>4</sub>	tetraalkylammonium halide	[118, 384, 404]
Au (0–6 nm)	dimethylamineborane	hydrophobic polyamidoamine	[177]
Au (1–3 nm)	Cu, Ag nanocluster	polyamidoamine	[103]
Au (15–40 nm)	N <sub>2</sub> H <sub>4</sub>	CTAC, SDS, hexadecylpyridinium chloride	[198, 199]
Au (9 nm)	N <sub>2</sub> H <sub>4</sub>	polystyrene- <i>b</i> -polyvinylpyridine	[202]
Au (18, 32, 41, 56, 116 nm)	NH <sub>2</sub> OH (seed-mediated growth)	sodium citrate	[101]
Au	ascorbic acid (seed-mediated growth)	sodium citrate	[114]
Au (10–900 nm)	sodium citrate	sodium citrate	[9, 108–110, 229]
Au (26–36 nm)	formamide	PVP	[111]
Au (20, 50–200 nm)	polyaniline	<i>N</i> -methyl-2-pyrrolidone, polyaniline	[116]
Au (0–3 nm)	<i>o</i> -anisidine	<i>N</i> -methyl-2-pyrrolidone, (C <sub>7</sub> H <sub>15</sub> ) <sub>4</sub> NBr	[117]
Au (platelets)	potassium bitartrate	thiocyanuric acid	[118]
Au (~15 nm)	oligothiophene	polyelectrolytes	[131]
Pt (1–5 nm)	methanol	PVA, PVP, poly(methyl vinyl ether)	[120, 140, 144]
Pt (1.7–2.2 nm)	methanol, ethanol	polyelectrolytes	[127, 130]

continued

Table 2. Continued.

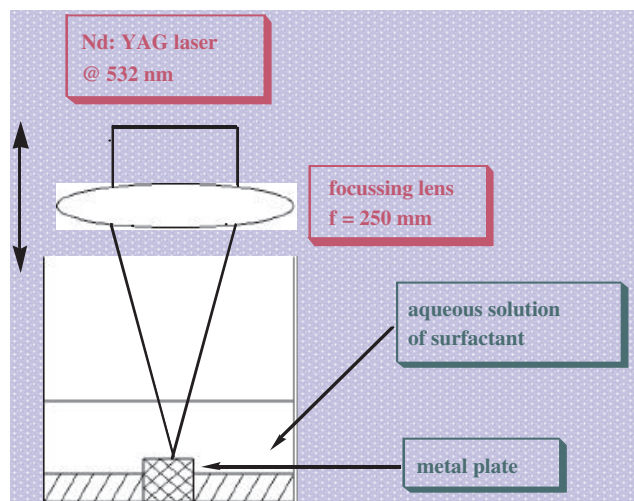
Noble metal (dispersity nm)	Reducing agent	Stabilizer	Ref.
Pt (2–4 nm)	methanol	poly[(vinyl alcohol)- <i>co</i> -( <i>N</i> -vinylpyrrolidone)]	[138]
Pt (2.2, 2.8 nm)	ethanol	polystyrene- <i>b</i> -poly(methacrylic acid)	[132]
Pt (2.6, 2.8 nm)	ethanol	polystyrene- <i>b</i> -poly(ethylene oxide)	[132]
Pt (0.25–5.5 nm)	ethanol	poly( <i>N</i> -isopropylacrylamide)	[134, 136]
Pt (0.5–4.5 nm)	ethanol	poly( <i>N</i> -vinylisobutyramide)	[135]
Pt (1.9–3.3 nm)	alcohol (MeOH, EtOH, 1-PrOH)	PVP	[368]
Pt (0.4–3.6 nm)	H <sub>2</sub>	PVP	[94, 278]
Pt (0–15.0 nm)	H <sub>2</sub>	SDS, dodecyltrimethylammonium chloride	[84]
Pt (5–10 nm)	H <sub>2</sub>	sodium citrate, NaOH	[96]
Pt (cube, tetrahedron, icosahedron, cubic octahedron, irregular prism)	H <sub>2</sub>	sodium polyacrylate	[93]
Pt (5–8 nm)	H <sub>2</sub>	sodium polyacrylate, polyphosphate	[274]
Pt (1–3, 3–5 nm)	H <sub>2</sub>	polyethyleneoxide-polyethyleneimine	[205]
Pt (3–10 nm) (cube)	H <sub>2</sub>	oxalate	[272]
Pt (cube)	H <sub>2</sub>	poly( <i>N</i> -isopropylacrylamide)	[273]
Pt (1.2, 1.5 nm)	CO	nitrocellulose, cellulose acetate	[279]
Pt (0.8–2.0 nm)	ethylene glycol	ethylene glycol	[107]
Pt (0–5.5 nm)	ethylene glycol	poly( <i>N</i> -sulfonatopropyl- <i>p</i> -benzamide)	[137]
Pt (2–12 nm)	ethylene glycol	PVP	[143]
Pt (0.25–3 nm)	formaldehyde, benzaldehyde	trioctylmethylammonium chloride, TOPO	[113]
Pt (1.3–2.2 nm)	KBH <sub>4</sub>	polyelectrolytes	[127, 130]
Pt (3.3 nm)	KBH <sub>4</sub>	polystyrene- <i>b</i> -poly(methacrylic acid)	[132]
Pt (2.2 nm)	KBH <sub>4</sub>	polystyrene- <i>b</i> -poly(ethylene oxide)	[132]
Pt (0.25–4.5 nm)	NaBH <sub>4</sub>	poly[(vinylamine)- <i>co</i> -( <i>N</i> -vinylisobutyramide)]	[133]
Pt (0.5–4.0 nm)	NaBH <sub>4</sub>	polyamidoamine	[168, 170, 174]
Pt (3–10 nm) (cubic)	NaBH <sub>4</sub> (0 °C)		[269]
Pt (2–5 nm) (highly faceted)	LiBH <sub>4</sub> , LiB(C <sub>2</sub> H <sub>5</sub> ) <sub>3</sub> H, LiAlH <sub>4</sub>	nonionic surfactants	[271]
Pt (1.3 nm)	dimethylamineborane	polyamidoamine	[175]
Pt	N <sub>2</sub> H <sub>4</sub> · H <sub>2</sub> SO <sub>4</sub>	PVA	[146]
Pt (2.5–4.0 nm)	N <sub>2</sub> H <sub>4</sub>	cetyltrimethylammonium bromide	[147, 148]
Pt (2.5–3.5 nm)	N <sub>2</sub> H <sub>4</sub>	pentaethylene glycol dodecyl ether	[147, 148]
Pt (1–5 nm)	Li (or Na,K)[B(Et) <sub>3</sub> H], H <sub>2</sub> , LiH, BEt <sub>3</sub>	tetraalkylammonium halide	[189–195]
Pt (1–3 nm)	Cu, Ag nanocluster	polyamidoamine	[103]
Pt (2.0–4.0 nm)	sodium citrate	sodium citrate	[208]
Pd (1.0, 3.4, 7.8 nm)	ethanol	polystyrene- <i>b</i> -poly(methacrylic acid)	[85, 132]
Pd (2.1, ~5, 6.8 nm)	ethanol	polystyrene- <i>b</i> -poly(ethylene oxide)	[85, 132]
Pd (1–4 nm)	alcohol (MeOH, EtOH, 1-PrOH)	PVA, PVP, poly(methyl vinyl ether)	[106, 120, 139, 144, 277]
Pd (7.5 nm)	methanol	PVP	[280]
Pd (1.5–7 nm)	ethanol	polyacids	[128]
Pd (10, 19 nm)	ethylene glycol	PVP	[143]
Pd (1–12 nm)	H <sub>2</sub>	polyethyleneoxide-polyethyleneimine	[205]
Pd (1.7–3.7 nm)	H <sub>2</sub>	PVP	[206, 277, 280]
Pd (1.0 nm)	CO	PVP	[278]
Pd (3.5 nm)	CO	nitrocellulose, cellulose acetate	[279]
Pd (5–15 nm)	N <sub>2</sub> H <sub>4</sub>	poly(acrylic acid)	[97]
Pd (5 nm)	N <sub>2</sub> H <sub>4</sub>	pentaethylene glycol dodecyl ether	[147]
Pd (2.7–10.7 nm)	N <sub>2</sub> H <sub>4</sub>	CTAB, SDS, polyoxyethylene isoctyl phenyl ether	[180, 275, 276]
Pd (3.3 nm)	N <sub>2</sub> H <sub>4</sub>	polystyrene- <i>b</i> -polyvinylpyridine	[201, 203]
Pd (6.5 nm)	N <sub>2</sub> H <sub>4</sub>	polystyrene- <i>block</i> -poly- <i>m</i> -vinyltriphenylphosphine	[207]
Pd (1.0–3.7 nm)	KBH <sub>4</sub>	polyelectrolytes	[130]
Pd (1.3–2.1 nm)	KBH <sub>4</sub>	polystyrene- <i>b</i> -poly(methacrylic acid)	[132]
Pd (1.7–3.6 nm)	KBH <sub>4</sub>	polystyrene- <i>b</i> -poly(ethylene oxide)	[132]
Pd (1–3 nm)	NaBH <sub>4</sub>	polyamidoamine	[168]
Pd (1–2.7 nm)	NaBH <sub>4</sub> , LiB(C <sub>2</sub> H <sub>5</sub> ) <sub>3</sub> H	polystyrene- <i>b</i> -polyvinylpyridine	[201, 203, 204]
Pd (2.7–9.3 nm)	NaBH <sub>4</sub>	CTAB, SDS, polyoxyethylene isoctyl phenyl ether	[275, 276]
Pd (1–2 nm)	LiB(C <sub>2</sub> H <sub>5</sub> ) <sub>3</sub> H	polystyrene- <i>block</i> -poly- <i>m</i> -vinyltriphenylphosphine	[207]
Pd (1–5 nm)	NaBH <sub>4</sub>	alkanethiolate	[231]
Pd (1–6 nm)	Li (or Na,K)[B(Et) <sub>3</sub> H], H <sub>2</sub> , LiH, BEt <sub>3</sub>	tetraalkylammonium halide	[190–195]

continued



Table 2. Continued.

Noble metal (dispersity nm)	Reducing agent	Stabilizer	Ref.
Pd (1.8–2.5 nm)	NaH <sub>2</sub> PO <sub>2</sub>	polystyrene- <i>b</i> -poly(methacrylic acid)	[132]
Pd (1.8 nm)	NaH <sub>2</sub> PO <sub>2</sub>	polystyrene- <i>b</i> -poly(ethylene oxide)	[132]
Pd (50–200)	polyaniline	polyaniline	[116]
Pd (0.8–4 nm)	sodium formate	trioctylmethylammonium chloride	[179]
Pd (2.7–20 nm)	ascorbate	CTAB, SDS, polyoxyethylene isooctyl phenyl ether	[276]
Pd (1–3 nm)	Cu, Ag nanocluster	polyamidoamine	[103]
Ir (0–3 nm)	methanol	PVA, PVP, poly(methyl vinyl ether)	[120]
Ir (3 nm)	ethylene glycol	PVP	[143]
Ir (0.6–2.7 nm)	Li (or Na,K)[B(Et) <sub>3</sub> H], H <sub>2</sub> , LiH, BEt <sub>3</sub>	tetraalkylammonium halide	[189–195]
Ir (2.5 nm)	H <sub>2</sub> (in the presence of catalyst: Al <sub>2</sub> O <sub>3</sub> /Pt(2%))	pentaethylene glycol dodecyl ether	[147]
Ir (1.4–3.0 nm)	H <sub>2</sub>	Bu <sub>4</sub> N <sup>+</sup> /P <sub>2</sub> W <sub>15</sub> Nb <sub>3</sub> O <sub>62</sub> <sup>9-</sup>	[154–157]
Ru (1.0–3.0 nm)	H <sub>2</sub>	nitrocellulose, cellulose acetate	[279]
Ru (1.1 nm)	H <sub>2</sub>	PVP, cellulose acetate	[280, 281]
Ru (2–3 nm)	H <sub>2</sub>	alkylamines, alkylthiols	[281]
Ru (12–35, 80–100 nm)	H <sub>2</sub>	methanol/THF	[282]
Ru (0.7–2.2 nm)	ethylene glycol	ethylene glycol	[107]
Ru (2 nm)	ethylene glycol	PVP	[143]
Ru (1–2 nm)	Li (or Na,K)[B(Et) <sub>3</sub> H], H <sub>2</sub> , LiH, BEt <sub>3</sub>	tetraalkylammonium halide	[189–195]
Rh (0.7–2.2 nm)	ethylene glycol	ethylene glycol	[107]
Rh (0.9–3.4 nm)	methanol	PVA, PVP, poly(methyl vinyl ether)	[119–121]
Rh (2.8 nm)	ethanol	cyclodextrine	[123]
Rh (2–3 nm)	H <sub>2</sub> , NaBH <sub>4</sub>	trisulfonate surfactant	[149, 150, 182, 183]
Rh (3 nm)	H <sub>2</sub>	pentaethylene glycol dodecyl ether	[147]
Rh (2–3 nm)	H <sub>2</sub>	trioctylmethylammonium chloride	[151–153]
Ru (2.4–6.1 nm)	H <sub>2</sub>	Bu <sub>4</sub> N <sup>+</sup> /P <sub>2</sub> W <sub>15</sub> Nb <sub>3</sub> O <sub>62</sub> <sup>9-</sup>	[158, 159]
Rh (1.3–4 nm)	Li (or Na,K)[B(Et) <sub>3</sub> H], H <sub>2</sub> , LiH, BEt <sub>3</sub>	tetraalkylammonium halide	[189–195]
Os (<1 nm)	methanol	PVA, PVP, poly(methyl vinyl ether)	[120]
Os	Li (or Na,K)[B(Et) <sub>3</sub> H], H <sub>2</sub> , LiH, BEt <sub>3</sub>	tetraalkylammonium halide	[189–195]
Cu/Pd alloy (1–4 nm)	ethylene glycol	PVP	[294–296]
Cu/Pd alloy (3.0–5.0 nm)	2-ethoxyethanol	PVP	[299]
Cu/Pt alloy (1–4.5 nm)	ethylene glycol	PVP	[294]
Cu/Au alloy (3.8 nm)	N <sub>2</sub> H <sub>4</sub>	AOT reverse micelles	[303]
Ag/Pt alloy (1.8–5.2 nm)	NaBH <sub>4</sub>	PVP	[310]
Ag/Pd alloy (4–10 nm)	ethylene glycol	PVP	[292]
Au/Pt alloy (3–4.5 nm)	N <sub>2</sub> H <sub>4</sub>	AOT reverse micelles	[304]
Au/Pd alloy (0.5–3.0 nm)	ethanol	PVP	[288]
Au/Pd cluster-in-cluster (1.0–4.5 nm)	ethanol	PVP	[312]
Pt/Pd alloy (1–4 nm)	H <sub>2</sub>	PVP	[287]
Pt/Pd alloy (0.5–3.0 nm)	ethanol	PVP	[284–286, 291]
Pt/Pd alloy (2–5 nm)	N <sub>2</sub> H <sub>4</sub>	pentaethylene glycol dodecyl ether	[302]
Pt/Ru alloy (1–4 nm)	Li (or Na,K)[B(Et) <sub>3</sub> H], H <sub>2</sub> , LiH, BEt <sub>3</sub>	tetraalkylammonium halide	[189–195]
Pt/Ru alloy (1.1–1.4 nm)	H <sub>2</sub>	PVP	[308]
Pt/Ru alloy (0.8–3.0 nm)	N(Oct) <sub>4</sub> [BEt <sub>3</sub> H]	tetraoctylammonium	[305, 306]
Pt/Rh alloy (2–7 nm)	ethanol	PVP	[289]
Pt/Fe alloy (6 nm)	1,2 hexadecanediol and thermolysis	oleic acid and oleyl amine	[320]
Pt <sub>3</sub> Co alloy (1.5–7.2 nm)	1,2 hexadecanediol and thermolysis	1-adamantanecarboxylic acid	[225, 321]
Pt <sub>3</sub> Co alloy (1.5–2.1 nm)	Co <sub>2</sub> (CO) <sub>8</sub> (transmetalation reaction)	oleic acid	[322]
PtCoFe alloy (3.5 nm)	1,2 hexadecanediol and thermolysis	oleic acid and oleyl amine	[319]
Pd/Ni alloy (1.2–2.8 nm)	ethylene glycol	PVP	[297, 298]
Pt/Sn alloy (0.4–2.8 nm)	N(Oct) <sub>4</sub> [BEt <sub>3</sub> H]	tetraoctylammonium	[307]
Pd/Rh (Ru) alloy	methanol	PVP	[291]
Ag <sub>core</sub> Pt <sub>shell</sub> (12 nm)	Co <sub>2</sub> (CO) <sub>8</sub> (transmetalation reaction)	oleic acid and tridodecylamine	[313]
Au <sub>core</sub> Ag <sub>shell</sub> (27–62 nm)	ascorbic acid	CTAB	[428]
Au <sub>core</sub> Pt <sub>shell</sub> (1–7 nm)	N <sub>2</sub> H <sub>4</sub> · H <sub>2</sub> O	AOT reverse micelles	[100]
Au <sub>core</sub> Pt(Pd) <sub>shell</sub> (~35 nm)	NH <sub>2</sub> OH · HCl	P( <i>m</i> -C <sub>6</sub> H <sub>4</sub> SO <sub>3</sub> Na) <sub>3</sub> , <i>p</i> -H <sub>2</sub> NC <sub>6</sub> H <sub>4</sub> SO <sub>3</sub> Na	[313]
Pd <sub>core</sub> Pt <sub>shell</sub> (1.5–5.5 nm)	H <sub>2</sub>	PVP	[316]
Pd <sub>core</sub> Au <sub>shell</sub> Ag <sub>shell</sub>	H <sub>2</sub>	sodium citrate	[95]
Co <sub>core</sub> Pt <sub>shell</sub> (4.0–8.0 nm)	Co nanoparticle	C <sub>12</sub> H <sub>25</sub> NC	[322]



**Figure 1.** Schematic diagram of the experimental apparatus for laser ablation. Reprinted with permission from [25], F. Mafuné et al., *J. Phys. Chem. B* 104, 9111 (2000). © 2000, American Chemical Society.

have been made by this technique [70, 71]. The amount of gold that is allowed to deposit onto the seed particles is any desired. This procedure can also be used to prepare bimetallic nanoparticles of the core-shell type. For instance,  $\text{Au}(\text{CN})_2^-$  was reduced on silver [72] and platinum [73] nanoparticles. In addition, the radiolytic preparation of transition metal nanoparticles is also possible in organized environments such as micelles or microemulsions [74].

A slow UV-reduction technique is a quite effective class of generation of nanoparticles with well-defined shapes, by which long Ag nanorods, beautiful Ag dendrites [75], and large, but thin, platelet-like Au nanoparticles with a triangular or hexagonal shape [76] are generated, respectively. Here, it should be mentioned that the concentration of noble metal ions and the amount of protective polymers is of paramount importance in the shape control. Other reports on the photolysis of metal salts include the UV-visible irradiation of Au [77–80], Ag [78–81], or Pt [82] salts in reverse microemulsions in the presence of surfactants or polymers to yield metallic nanoparticles. In the presence of micelles of a wide range of surfactants, Toshima et al. synthesized Pt [83, 84] and Pd [84] colloids by photolysis and hydrogen reduction. They found that the UV-visible irradiation technique gives smaller and better dispersed nanoparticles. Mayer and Esumi described the UV-visible photolytic synthesis of Au nanoparticles stabilized by block copolymers, polyelectrolytes [85–88], or dendrimers (polyamidoamine: PAMAM) [89]. Another aspect of utilizing the UV-visible irradiation technique is the encapsulation of Pt nanoparticles into polymerized vesicles [90]. The vesicle reticulation and the colloid formation occur simultaneously during irradiation. More recently, the microwave irradiation reduction technique has been developed to synthesize noble metal nanoparticles [91, 92]. In principle, microwave irradiation is alien to UV photolysis and  $\gamma$ -ray radiolysis. The generation of metal nanoparticles originates from the heating effect rather than the energy of the quantum of a microwave. Polar molecules can be heated quickly under the microwave irradiation, but nonpolar molecules

cannot couple with microwaves, so that the polar reaction solution can be heated to a high temperature instantaneously and homogeneously by microwaving. In comparison with conventional heating, more uniform nucleation and a shorter crystallization time will be achieved for the formation of colloids.

### 2.1.3. Chemical Reduction of Noble Metal Salts

From an efficiency point of view, the chemical reduction of a precious metal salt in an organic or aqueous medium is preferred and economical, so that it has thus motivated a vast amount of work. A series of chemical reduction approaches have been employed to prepare precious metal nanoparticles, in which the reducing agents comprise various compounds, such as  $\text{H}_2$  [93–96],  $\text{NaBH}_4$ ,  $\text{N}_2\text{H}_4$  [97–100],  $\text{NH}_2\text{OH}$  [101],  $(\text{CH}_3)_2\text{NH} \cdot \text{BH}_3$  [102], Cu or Ag (relatively active metals for metathesis reaction) [103], ethanol [104–106], ethylene glycol [107], citric acid and citrate [108–110], formamide [111], formaldehyde [112, 113], ascorbic acid [114, 115], polyaniline [116], *o*-anisidine [117], and potassium bitartrate [118]. In these preparative procedures, the formation of metal nanoparticles is strongly governed by the balance of nucleation rate and particle growth. The control of the size of nanoparticles can be realized by simply changing the ratio of the nucleation rate to the growth of particles. If the rate of particle growth is much smaller than that of nucleation, it will result in the production of a large number of small embryos, and then these embryos grow further to form tiny nanoparticles. The achievement of accurate control of the stability and reactivity of the quantum particles is also required to allow the attachment to the surface substrates or other particles without leading to coalescence, and hence losing their size-induced electronic properties.

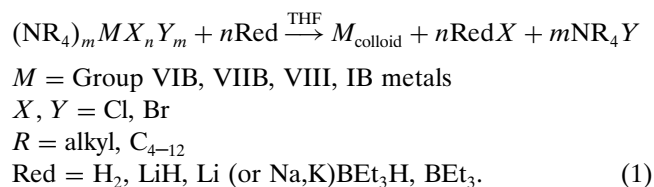
The refluxing of alcohol and some noble metal salts will lead to the formation of nanoparticles in the presence of stabilizers. In this process, the alcohol acts both as a solvent and a reducing agent. In general, the alcohols contain  $\alpha$ -hydrogen. Thus, methanol, ethanol, and isopropanol are good candidates as reducing agents, whereas *tert*-butyl alcohol is not effective. During the reduction, the alcohols are oxidized to the corresponding carbonyl compounds. The presence of water is often required to fulfill this reaction. Hirai, or more recently Delmas, have extensively used aqueous alcohols as reducing agents in the synthesis of colloids such as Rh, Pt, Pd, Os, and Ir [104, 119–125]. The effective stabilizers can be a series of polymer materials or oligomers, such as polyvinyl alcohol (PVA), poly(*N*-vinylpyrrolidinone) (PVP), polyvinyl ether (PVE), or cyclodextrine. Other types of polymers were also used for the stabilization of Au, Pd, and Pt colloids formed during the metallic salt reduction, such as various polyacids [126–129], polyelectrolytes [126, 127, 130, 131], block copolymers [85, 126, 127, 132, 133], poly(*N*-isopropylacrylamide) (PNIPAAm) [134–136], poly(*N*-sulfonatopropyl-*p*-benzamide) [137], and PVA/PVP copolymers [138]. The synthetic conditions, including the variation of stabilizer quantity [139–143], structure and quantity of alcohol [139–143], metallic precursor [142, 143], as well as the addition of a base [144] have

an impact on the particle size distribution. Several systematic studies revealed that the reduction of  $\text{H}_2\text{PdCl}_4$  [139],  $\text{H}_2\text{PtCl}_6$  [140], and  $\text{RhCl}_3$  [141] leads to smaller particles when the alcohol used had a higher boiling point. In the same way, the addition of NaOH in the course of the reduction of  $\text{H}_2\text{PtCl}_6$  or  $\text{PdCl}_2$  with methanol is accessible to a decrease in the size of the particles formed [144]. In addition, heating has an effect on particle size at times. The quick heating by microwaves of an aqueous alcoholic solution of  $\text{H}_2\text{PtCl}_6$  allows the formation of nearly monodispersed Pt nanoparticles [91].

The hydrogen reduction method is one of the most powerful tools providing access to a variety of noble metal nanoparticles. With PVA as the protecting agent, aqueous colloidal solutions of Au, Ag, Ir, Pt, Pd, Rh, and Ru were prepared by  $\text{H}_2$  reduction of the corresponding chloride salts [145]. Accordingly, hydrazine polyacrylic acid-stabilized Pt nanoparticles were fabricated [146]. A hydrogen reduction protocol was also applied to synthesize diverse precious noble metal nanoparticles in microemulsions, by which the preparation of Rh, Pt, Pd, and Ir colloids was achieved [147, 148]. In other reports, Rh nanoparticles were synthesized by hydrogen reduction of an aqueous solution of  $\text{RhCl}_3$  in the presence of a trisulfonated surfactant [149, 150]. The reduction of  $\text{RhCl}_3$  by hydrogen in water containing trioctylamine followed by extraction into  $\text{CH}_2\text{Cl}_2$  gave a stable dispersion of Rh nanoparticles [151–153]. Thus, surfactant-capped organosols were obtained by the extraction of the colloidal metal into an immiscible  $\text{CH}_2\text{Cl}_2$  phase from a preformed hydrosol. Here, the use of trioctylamine introduced both the phase transfer agent and the stabilizer as a single reagent. Finke and co-workers [154–159] studied the reduction of Ir and Rh organometallic complexes by hydrogen. Zerovalent nanoparticles stabilized by a couple ammonium ( $\text{Bu}_4\text{N}^+$ )/polyoxoanion ( $\text{P}_2\text{W}_{15}\text{Nb}_3\text{O}_{62}^{9-}$ ) generating electrostatic stabilization are formed. These nanoparticles have a great stability, and their size distributions were sufficiently narrow to be qualified as monodispersions.

The borohydrides ( $\text{NaBH}_4$  or  $\text{KBH}_4$ ) are very strong reducing agents, and can reduce most transition metal salts to elemental metal. With the borohydrides reduction method, extensive polymers (PVP, PVE, and PVA) and polysaccharides-stabilized Cu nanoparticles [160–162], PVP-stabilized Pt nanoparticles [163], and stabilizing polymers (cationic polyelectrolytes, polyacids, nonionic polymers, and block polymers)-protected Ag, Au, Pt, and Pd colloids in aqueous solution [85–88, 129, 130, 132, 164, 165] are widely investigated. Recently, borohydride reduction was used to obtain nearly monodispersed dendrimers (polyamidoamine or PAMAM)-protected Au, Ag, Pt, and Cu colloids [166–176]. The oleo-soluble dimethylamineborane has also been used to prepare Au organosol in the presence of hydrophobically modified PAMAM in toluene or chloroform [177]. Cationic, anionic, and nonionic surfactants are extensively applied to stabilize a noble metal colloidal aqueous solution prepared by borohydride reduction. By this means, the fabrication of Ru, Rh, Pd, Pt, Ag, and Au nanoparticles stabilized by quaternary ammonium, sulfates, or poly(ethylene glycol) is reported [178]. As effective stabilizers, aliquat 336 (trioctylmethylammonium chloride)

and CTAB (cetyltrimethylammonium bromide) or glycerol monooleate also show the stabilization for Pd [179, 180] or Cu [181] nanoparticles in water/oil microemulsions. In addition, aqueous solutions of colloidal Rh stabilized by a trisulfonated surfactant were obtained with the borohydride reduction method [182, 183]. The borohydride-reducing approach has been proven to be successful in the preparation of transition metal colloids in organic media. For instance, after reducing a metallic salt in aqueous phase by  $\text{NaBH}_4$  and then evaporating the water, the solid obtained can be redispersed in an organic solvent [184]. A range of approaches to the phase transfer of nanoparticles has been developed, with most studies focusing on the transfer from aqueous to organic media [185–188]. A valuable trick of the production of metal organosols involves the utilization of tetraalkylammonium hydrotriorganoborates ( $\text{NR}_4(\text{BEt}_3\text{H})$ ) in THF solution to reduce a wide range of Group VIB, VIIB, VIII, and IB metal halide salts [189–195]. The particle size locates generally between 1 and 10 nm. If appropriately substituted tetraalkylammonium salts are used, the colloidal metal nanoparticles can be solubilized in organic media. This protocol provides the possibility of large-scale production of various metal nanoclusters. However, there is a lack of exact compositional characterization of the resultant colloidal materials. Indeed, it was found that the resulting colloids contain boron from the initial  $\text{BEt}_3\text{H}^-$  reductant as a 1–2% impurity [195]. The advantage of this preparation process lies in the coupling of both the stabilizing agent (the  $\text{NR}_4^+$  group) and the reducing group in the same reagent. A high local concentration of the stabilizer is present during the reduction process, thus limiting the growth of the particles. The alternative developed by Bönemann consists of coupling the reducing agent with the transition metal salts ( $(\text{NR}_4)_m\text{MX}_n\text{Y}_m$ ). The reaction route can be denoted as



This novel compound is then reduced by hydrides (superhydride, lithium hydride) to yield colloidal metal nanoparticles, where the local concentration of the protective agent is also high, leading to the particle size being 1–10 nm. Recently, Caruso contributed a promising strategy for providing the spontaneous phase transfer of nanoparticles from organic to aqueous media. First,  $\text{HAuCl}_4$  or  $\text{Na}_2\text{PdCl}_4$  were reduced by  $\text{NaBH}_4$  in the presence of tetraoctylammonium bromide in toluene, and then the rapid and complete transfer without signs of degradation or aggregation of the nanoparticles was performed by the addition of aqueous 4-(dimethylamino)-pyridine solution [196].

Hydrazine and sodium citrate find their unique applications in the preparation of metal colloids. Hydrazine can be used in all of its forms to reduce transition metals. It allows us to reduce Cu [197] in the presence of PVA and PVP or Pd [180] in the cationic water-in-oil microemulsions of water/CTAB/*n*-butanol/isooctane at 25 °C. Hydrazine hydrochloride [145] or sulfate [146] turned

out to be efficient in the preparation of colloidal metal. The results recently reported in the literature also comprise the reduction of  $\text{HAuCl}_4$  by hydrazine in the presence of cationic or nonionic surfactants (cetyltrimethylammonium chloride (CTAC), sodium dodecyl sulfate (SDS), hexadecylpyridinium chloride, dodecylpyridinium chloride) [198, 199], the production of hexagonal Ag nanoparticles in the presence of aniline [200], the synthesis of Au, Pd, Ag, and Rh nanoparticles stabilized by block copolymers such as polystyrene-*b*-polyvinylpyridine, polystyrene-*b*-poly-*m*-vinyltriphenylphosphine, or poly(ethylene oxide)-polyethyleneimine, in which several polymer-stabilized systems show high thermal stability and can be used in drastic conditions [88, 201–207].

Sodium citrate has been known for half a century as a frequently used reducing agent in the synthesis of colloidal noble metal. Turkevich et al. [108] pointed out that the citrate is not only a reductant, but also an ionic stabilizer in the process of the nucleation and growth of Au nanoparticles reduced by sodium citrate. The preparation of Pt [208] and Ir [209] nanoparticles has also been accessible by the citrate reduction route. However, citrate anion is a noninnocent ligand, and has one significant disadvantage because of the simultaneous formation of the intermediate acetone dicarboxylic acid, which results in compositionally ill-defined colloids in opposition to focused modern nanoparticles. Carbon monoxide is also a useful reducing agent in the synthesis of metallic colloids. Kopple et al. reduced  $\text{HAuCl}_4$  in the presence of polyvinyl sulfate to obtain Au colloidal particles [210]. CO can also reduce  $\text{PtO}_2$  to form Pt nanoparticles [211].

#### 2.1.4. Electrochemical Reduction

The pioneer work in the electrochemical approach to noble metal nanoparticles was developed by Reetz and co-workers [212, 213]. This large-scale synthetic procedure can offer size-controlled nanoparticles. A sacrificial anode, which is oxidized in the presence of quaternary ammonium salt, is used as a metal source. The quaternary ammonium salt is not only an electrolyte, but also a stabilizing agent. The ions are then reduced at the cathode to yield the metallic nanoparticles. In this way, Reetz and co-workers synthesized Pd nanoparticles with various sizes dispersed in acetonitrile/THF. The formation mechanism can be divided into five steps: (1) dissolution of the anode to form metal ions (oxidation of Pd to  $\text{Pd}^{2+}$ ), (2) migration of the metal ions to the cathode, (3) reduction of the metal ions at the surface of the cathode, (4) aggregation of the particles stabilized by the ammonium ions around the metal cores, and then (5) precipitation of the Pd nanoparticles. This method allows us to produce nanoparticles of well-controlled size by varying the current intensity (higher current intensity gives smaller particles), and to obtain high yields (>95%) [212]. This synthetic procedure can be applied to easily oxidized transition metals such as Ni and Cu. The solubility of the colloids obtained can be modulated from nonpolar solvents such as pentane to polar solvents such as water by changing the polarity of the protecting agent (tetraalkylammonium halide for apolar solvents or sulfobetaine for polar solvents) [214]. For less easily oxidized metals such as Pt, Rh,

and Ru, the anode and the cathode used are made of Pt, and the metallic precursor is a transition metal salt [214]. In this new process, the anode is no longer sacrificed, and the metallic precursor is reduced by electrolysis in the presence of a quaternary ammonium salt which is both the electrolyte and the stabilizing agent.

#### 2.1.5. Size Control of Noble Metal Nanoparticles

The size of noble metal nanoparticles is greatly influenced by the kind and concentration of the reducing agent. An appropriate choice of the kind and concentration of the reducing agent is important in controlling the particle size because the reducing rate of noble metal salts to noble metal is greatly affected by those of the reducing agent. In general, an increase in the concentration of the reducing agent increases the reduction rate of noble metal ions, leading to the formation of smaller noble metal nanoparticles. In other words, the protective agents (i.e., capping agents or stabilizers), besides apparently stabilizing the noble metal nanoparticles by protecting them from aggregating, can remarkably perturb the growth of particles through the coordination of active atoms of protective agents to surface metal atoms of noble metal nanoparticles. Accordingly, the amount of protective agents added to the colloidal solutions is expected to affect the growth process for the noble metal nanoparticles. An increase in the ratio of protective agents to noble metal ions can intensively suppress the growth of noble metal particles within a shorter time, leading to smaller noble metal nanoparticles.

Alternatively, one design strategy that shows tremendous potential as a viable route by which to produce metal nanoparticles with improved size control and colloidal stability is to vary the particle growth medium. Examples of such a growth medium include a solvent, template (i.e., using micelles as the microreactor), and a specialized polymer matrix. Founded on this fact, a judicious choice of the reaction media to control the size and/or polydispersity of the particles opens new ways to such production, which is carried out using various colloidal systems such as reverse micelles [i.e., water-in-oil droplets (W/O) stabilized by a monolayer of surfactant (e.g., sodium bis(2-ethylhexyl)sulfosuccinate, usually called Na(AOT))] [99, 215–221], Langmuir–Blodgett films [222, 223], organometallic techniques [224–226], and simple single-phase or two-phase liquid–liquid systems [227–232].

One typical preparation of colloidal metals relying on reaction media is to utilize micelles or liposomes as a stabilizer containing either metal salts or a reductant, thereby acting as microreactors to control the size distribution of the noble metal particles produced. A series of morphologies that can be produced by this method have been described as “cherries” (one central metal particle), “raspberries” (multiple internal particles), “strawberries” (a layer of metal particles outside the micelle boundary), and “red currant” or “ginger root” (a dendritic type with strings of metal particles radiating away from the central micelle) [233].

The conventional strategies for the preparation of small precious metal nanoparticles in the presence of a protective agent have been greatly promoting the development

of metal colloid or nanoparticle chemistry. However stable, “unprotected” small precious metal nanoparticles in organic media with a reasonable metal concentration should be of great help for research in the active and prospective field of metal nanoparticle chemistry. “Unprotected” metal colloids do not mean that the metal nanoparticles are truly bare. In fact, they are stabilized by solvents or simple anions adsorbed on them, or by both. In the presence of protective agents, not only are the formed metal nanoparticles stabilized, but also the clustering processes are influenced by the protective agents. In the absence of protective agents, however, to effectively prepare stable “unprotected” metal nanoparticles with small size and narrow size distribution in organic media, a suitable solvent and an effective method for controlling the precious metal nanoparticle size have to be used. Up to now, some results of the preparation of nanoscopic metal colloids in organic media without traditional protective agents have been described [29, 234–238]; the products can be called “unprotected” metal colloids. The “unprotected” copper colloid in methanol was prepared by the reduction of copper (II) salts with hydrazine hydrate. The produced colloidal particles have a mean diameter of 13.3 nm [234]. The stable Pd colloids with average diameters of 6–8 nm in acetone or propanol are synthesized by using the atom clustering process [29]. These Pd colloidal particles are “living” in the sense that they can be used to produce metal film. Stable palladium colloids with average particles sizes of 8–10 nm were also prepared from thermal decomposition of palladium complexes in methyl isobutyl ketone [235, 236]. By the chemical reduction method, using polyol as the reductant as well as the protective solvent, fine powders of Cu, Ni, Co [237], and tiny noble metal nanoparticles (Pt, Rh, and Ru) with particle sizes less than 3 nm were prepared [107], respectively. In general, the species adsorbed on the “unprotected” metal nanoparticles, that is, solvent molecules and the simple anion, can easily be removed or replaced by various coordination ligands or protective agents. This characteristic makes the “unprotected” metal nanoparticles very attractive as a building block material to prepare various nanoscopic metal clusters with the same core size and demanding different modifying or protecting shells, as well as matrix materials.

## 2.2. Au Nanoparticles

Au nanoparticles are the most intensive and comprehensive research subject in metal nanoparticles. It is necessary to elucidate exclusively in detail. Gold sols are easily prepared, and are identified by the attractive color which can vary from ruby red through purple to blue. Although the history of the preparation of colloidal gold can be traced back to Faraday’s times, the past several decades have witnessed the great development of the production of gold nanoparticles. Among these, two highlighted advances are the aqueous Turkevich method [108–110] and the “phase transfer catalyst” method [238], which yield uniform and very stable Au nanoparticles in an aqueous solution and an organic solvent, respectively. By the Turkevich method, gold nanoparticles are prepared quite easily by refluxing the dilute aqueous solution of  $\text{HAuCl}_4$  with citric acid or trisodium

citrate. They are larger in size ( $\sim 12$  nm) than the typical alkanethiol-stabilized nanoparticles ( $< 4$  nm) obtained by the “phase-transfer catalyst” method, but a very narrow size distribution can be obtained with standard deviation of 10% in the presence of trisodium citrate. The nanoparticles utilize ionic interactions on the nanoparticle surface to obtain solubility. The stabilizers stem from the corresponding oxidation/decarboxylation products of citrate (such as acetone dicarboxylic and itaconic acids) and the unreacted citrate. They agglomerate irreversibly on removal of the solvent. In combination with hydroxylamine [101] or ascorbic acid [114] reduction of gold salts, a seed-mediated step growth method can produce larger nanoparticles of the desired size. The initially produced Au nanoparticles are used as seeds, and simultaneously, the metal salts are reduced on the surfaces of seed Au particles for producing large particles. Afterwards, if this route is repeated step by step, larger and larger particles will be synthesized. Au nanoparticles of 20–100 nm in diameter that have relatively narrow size distributions ( $< 20\%$  relative standard deviation) are available. In this procedure, there is, however, some drawback that seeds catalyze additional nucleation to cause the polydispersity of particle size, although not dramatically.

When long-chain thiols were used both for stabilization and for derivatization during biphasic syntheses of small gold colloids, such Au colloids behave as “molecules” solution, and have several great advantages. The resultant colloidal materials are obtained not only as stable concentrated solutions, but also as powders that can be easily redispersed after the addition of organic solvents, where they still give stable solutions, even at the highest concentration. Meanwhile, the modified nanoparticles can be stored for quite long periods in both solution and the dry state. Furthermore, the alkanethiol-stabilized nanoparticles are readily synthesized in a variety of core and shell sizes, and are able to undergo thiol substitution reactions that facilitate their self-assembly in ordered nanostructures. Despite these advantages, the solubility of such nanoparticles is limited to organic solvents. Complementarily,  $\text{Ph}_2\text{P}(m\text{-C}_6\text{H}_4\text{SO}_3\text{Na})$  and better  $\text{P}(m\text{-C}_6\text{H}_4\text{SO}_3\text{Na})_3$ -stabilized Au colloids behave as an aqueous solution of “molecules” [239, 240]. They can be isolated as solid materials, and then be redissolved in water in any concentration forming blood-red solutions.

An alternative simple procedure has also been developed to obtain thiol-derivatized particles in an organosol, where, in the presence of an agent for inducing phase transfer, metal nanoparticles of desired shape and size distribution preformed in a hydrosol are easily transferred to a nonpolar medium containing an alkanethiol [230]. These inducing phase-transfer agents include concentrated HCl, orthophosphoric acid,  $\text{NaH}_2\text{PO}_4$ , NaCl, and so forth [187, 230, 241]. To a biphasic mixture, the addition of phase-transfer agents will result in a rapid movement of metal nanoparticles from a hydrosol to a hydrocarbon layer containing thiols. By employing such a procedure, what has been achieved is not only the preparation of thiol-derivatized Au nanoparticles in organic solvents, but also the preparation of spherical, thiol-derivatized nanoparticles of silver as well as platinum in organic solvents. This is particularly advantageous since many of the water-soluble reagents may be easily washed away. Besides, this method may provide a rather

unique way of replacing polymeric or ligand shells surrounding metal nanoparticles by thiol molecules.

Intriguingly, it has been shown that the size distribution of thiolate-encapsulated Au nanocrystals can be greatly narrowed when refluxed with excess long-chain thiois ligand [227]. Further size fraction occurs by the slow lowering of the colloidal temperature, during which the excellent homogeneity in particle size of the top layer of Au nanoparticles is given. By adopting this digestive ripening process, the relative standard deviation can decrease to  $\sim 5\%$ . Other experimental evidence illustrates the evolution of both size and shape of Au nanoparticles following heating treatment [242]. After an Au nanoparticle solution is subjected to reflux at  $110^\circ\text{C}$  under reduced pressure, an increase in core size from 1.5–2.5 nm (80% populations) to 4.5–5.5 nm (>90% populations) is observed. The other striking feature is that the particle shapes evolve from irregular to a “hexagon” outline. In view of the molecular and crystal natures of such core-shell systems, the size and shape are inherently a dynamic process, and an evolution may occur as result of changes in the chemical potentials of the particles. The size and shape evolution of the encapsulated nanoparticles in the solution may involve a balance of chemical potentials via desorption and redesorption of the shell components and coalescence of the cores as the driving force for the eventual size and shape.

Besides the well-known citrate-stabilized gold nanoparticles, many studies also handle aqueous solution of gold nanoparticles. When the nanoparticles are stabilized by an alkanethiol terminating in either an ionic species or a carboxylic acid group, it can lead to water-soluble thiolate-coated gold nanoparticles. The aqueous solubility of these nanoparticles is often coupled to the pH of the solution, and the presence of functional groups that can participate in hydrogen bonding between nanoparticles will lead to particle agglomeration. Additionally, the presence of ions in the system enhances the interference during conductivity measurements and electron transport studies. Ionic effects are of particular concern in nanoelectronics applications, where they can accentuate threshold nonuniformities associated with background charges.

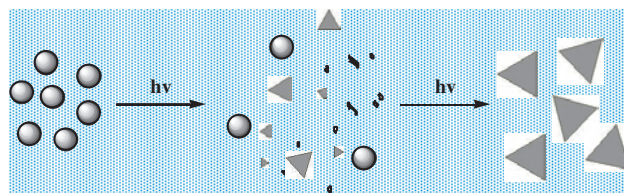
However, so far, few synthetic approaches adapted to directly preparing both water- and oil-soluble gold nanoparticles are available. The reduction of gold salts with *o*-anisidine as the reductant offers convenient access to gold nanoparticles in both aqueous and organic systems [117]. The suitable reducing environment such as in micelles and liposomes permits reduction at more moderate conditions, and results in higher colloid uniformity than usual methods. In the organic medium, polymer production (poly(*o*-anisidine) in its doping state) simultaneously occurs.

### 2.3. Cu and Ag Nanoparticles

Metallic Cu has shown the catalytic ability in the formation of aldehydes from the conversion of methanol and ethanol [243, 244]. For the nanoscale Cu entities, colloidal preparations have been the essential aspect. The preparation is generally performed under an inert atmosphere since copper nanoparticles comparatively suffer from oxidation relative to noble metal nanoparticles. A wide range of techniques, such as chemical reduction (strong reductants including hydrazine ( $\text{N}_2\text{H}_4$ ) and sodium borohydride ( $\text{NaBH}_4$ ))

can reduce copper salts to metal instantly) [197, 245],  $\gamma$ -radiolytic reduction [246–248], and the reduction of copper ions in supercritical fluids [249, 250], have been developed to synthesize spherical nanoparticles. Especially, Cu nanoparticles with rather narrow size distribution can be prepared by the clustering of acetone-solvated Cu atoms generated via metal vapor synthesis [251]. In addition, other than the Cu nanoparticles, the morphologies with the rod and fiber shapes, which were, respectively, achieved in the presence of soft template–Cu(AOT)<sub>2</sub>–isooctane–salt–water colloidal assemblies and hard template–carbon nanotubes [reduction of copper salts with  $\text{H}_2$  at high temperature ( $500^\circ\text{C}$ )], have been described [252, 253]. In the presence of soft template-surfactant (cetyltrimethylammonium *p*-toluene sulfonate), elongated copper nanoparticles of 500 nm length and 50 nm width were prepared by a pulse sonochemical method [254].

Ag nanoparticles are easily prepared by conventional chemical reduction methods. The citrate (Turkevich method) [229, 255, 256] and  $\text{NaBH}_4$  [255, 257–259] reduction method are the two standard chemical preparation routes. The synthesis of silver nanoparticles in AOT reverse micelles by mixing AOT reverse micellar solutions at the same water content containing Ag(AOT) and  $\text{N}_2\text{H}_4$  or  $\text{NaBH}_4$  offers a stable Ag colloidal solution and facile control of particle size [260]. Following the treatment by a size-selected precipitation process, nearly monodispersed Ag nanoparticles are accessible [261, 262]. Shape-controllable synthesis is always a challenging subject in nanoparticle preparation. This is, without exception, for the synthesis of silver nanoparticles. An amazing result of the shape control of Ag nanoparticles was reported by Mirkin and co-workers recently [263]. In the presence of bis(*p*-sulfonatophenyl) phenyl-phosphine dihydrate dipotassium salt (BSPP) (as a stabilizing agent), they observed that large quantities of silver nanoprisms evolve from the initial spherical nanoparticles through the fluorescent light irradiation. The production of Ag nanoprisms lies in the light-induced ripening process in which the small nanoprisms act as seeds, and then grow as the small spherical nanocrystals are digested, as shown in Figure 2. Most recently, one arresting experiment shows that triangular Ag nanoprisms are obtained by boiling  $\text{AgNO}_3$  in *N,N*-dimethyl formamide (a powerful reducing agent against  $\text{Ag}^+$  ions) in the presence of PVP [264]. The optimal experimental conditions are chosen ( $[\text{AgNO}_3] = 0.022\text{ M}$ ,  $[\text{PVP}] = 0.06\text{ mM}$ ) so that a large population of (mainly) triangular, and in general polygonal, nanoprisms are formed in solution. Another attractive experiment shows that truncated triangular Ag nanoplates can be synthesized



**Figure 2.** Fluorescent light-induced shape transformation of Ag nanospheres into triangular nanoprisms. Reprinted with permission from [263], R. Jin et al., *Science* 294, 1901 (2001). © 2001, American Association for the Advancement of Science.

in large quantities through a seed-mediated growth (by reduction of  $\text{Ag}^+$  ions with ascorbic acid on silver seeds in a basic solution) in the presence of highly concentrated micelles of CTAB [115, 265]. It is noticeable that, in these cases, the optical properties of Ag nanoprisms or triangular nanoplates varied in contrast to that of spheroidal Ag nanoparticles. An intensive in-plane dipole resonance absorption peaks at 550–675 nm, which gives a red- or blue-colored colloidal solution. Another breakthrough in the shape control of Ag nanoparticles was achieved by Xia and co-workers [266]. They fabricated monodisperse Ag nanocubes in large quantities by reducing silver nitrate with ethylene glycol in the presence of PVP. Here, the concentration of  $\text{AgNO}_3$  was high enough (0.25 M), and the molar ratio between the repeating unit of PVP and  $\text{AgNO}_3$  was kept at 1.5. Meanwhile, the presence of PVP and its molar ratio (in terms of repeating unit) relative to silver nitrate both played key roles in the determination of the geometric shape and size of the product. The generated single-crystalline Ag nanocubes were characterized by a slightly truncated shape bounded by  $\{100\}$ ,  $\{110\}$ , and  $\{111\}$  facets. Other techniques, including pulsed laser irradiation [21, 267],  $\gamma$  irradiation [68], pulsed sonoelectrochemistry [58, 268], and ultraviolet irradiation [117], have proven to be efficient methods to control the shapes of Ag nanoparticles.

## 2.4. Other Noble Metal Nanoparticles

Pt colloids are characterized by their brown color. An inimitable characteristic possessed by Pt nanoparticles is a forceful tendency for particles to form with highly faceted and irregular surfaces [93, 269–271]. Moreover, these nonspherical particles are generally single crystals. Pt colloids prepared by the reduction of Pt (II) and Pt (IV) compounds with hydrogen were described as early as 1941. This method is now experiencing a renaissance, especially in the preparation of shape-selective Pt nanoparticles. One of the elegant experiments was accomplished by changing the ratio of the concentration of the capping polymer material (sodium polyacrylate) to that of the platinum cations used in the reductive synthesis (with  $\text{H}_2$  as the reducing agent) of Pt colloidal nanoparticles in solution at room temperature, where cubic (80%), tetrahedral (60%), and truncated octahedral (TO) nanoparticles have been prepared in high percentages, thus making it possible to study the catalytic activities of nanoparticles with different shapes and crystal facets [93].

Here, the shape distribution of platinum nanoparticles at different stages of their growth is a function of time. The small nanoparticles formed during the early stages of growth or at high polymer concentration displayed distributions with a dominance of shapes having stable  $\{111\}$  faces. As the growth continues or at a low polymer-to-Pt-complex concentration ratio, the tetrahedral nanoparticles are transformed into TO, and eventually into cubic shapes. The initially rapid reduction of  $\text{Pt}^{2+}$  produces an initial growth that gives very small nanoparticles having the expected stable  $\{111\}$  faces present in tetrahedral and TO. The competition between polymer capping and  $\text{H}_2$  reduction of the  $\text{Pt}^{2+}$  complex occurring on the most catalytically active  $\{111\}$  surface determines the fate of these tetrahedral nanoparticles. If capping dominates, tetrahedral nanoparticles of small size

are formed. Otherwise, the rapid reduction of  $\text{Pt}^{2+}$  on the most active  $\{111\}$  surface leads to its disappearance and the formation of a  $\{100\}$  face due to the deposition of Pt atoms on it to give larger TO nanoparticles having both  $\{100\}$  and  $\{111\}$  faces. The TO nanoparticles continue to grow until transformed into cubic nanoparticles, which have all of their six faces of the  $\{100\}$  type. It also has been noticed that the polymer, acting both as a capping molecule and as a buffering agent, plays an important role in this competition.

Alternatively, a higher selectivity of cubic oxalate-stabilized Pt nanoparticles (>90%) are obtained through reducing  $\text{K}_2[\text{Pt}(\text{C}_2\text{O}_4)_2]$  with hydrogen [272]. Using thermosensitive poly(*N*-isopropylacryamide) as a capping polymer, it was found that the morphology of resultant Pt nanoparticles was affected by temperature, and the Pt nanoparticles prepared at temperatures above the critical solution temperature of the thermosensitive polymer had sharper size and shape distributions (68% of cubic nanoparticles) [273]. Besides organic polymers, polyphosphate [274], sodium citrate, and a mixture of sodium citrate and sodium hydroxide [96] were also adopted to stabilize Pt colloids prepared by reducing Pt (II) complexes with hydrogen. In all of these preparation examples, the resulting colloidal solutions usually contain Pt nanoparticles of different shapes, albeit one shape has a dominant distribution. However, up to now, few methods could really be applied to realize the production of nanoparticles with a single shape.

Palladium and ruthenium are the two key metals of catalytic activity. In principle, the synthetic routes are the same as for gold and platinum nanoparticles. For instance, the reduction of  $\text{H}_2\text{PdCl}_4$  and  $\text{RuCl}_3$ , respectively, with citrate leads to characteristic brown-colored colloidal solutions. Many reports regarding the preparation of Pd nanoparticles have emerged in our line of vision [230, 237, 270]. More recently, Pal and co-workers [275, 276] described the synthesis of palladium particles produced in aqueous surfactant media. Their catalytic properties toward the reduction of a number of dyes in the presence of different reducing agents, such as  $\text{NaBH}_4$ ,  $\text{N}_2\text{H}_4$ , and ascorbic acid, were investigated. The dyes used were methylene blue, phenosafranin, fluorescein, 2,7-dichlorofluorescein, eosin, and rose bengal. In fact, some zerovalent organometallic complexes can be converted into colloidal metal by reduction or ligands displacement. For example,  $\text{Pd}(\text{dba})_2$  [277] (dba = dibenzylidene acetone) and  $\text{Pd}_2(\text{dba})_3$  [278] dimer can be reduced by hydrogen at atmospheric pressure to obtain 2.5 nm Pd nanoparticles. The use of carbon monoxide also allows obtaining smaller particles of 2 nm diameter. Similarly, with this reducing agent,  $\text{Pt}(\text{dba})_2$  and  $\text{Pd}(\text{dba})_2$  can be reduced to generate nanoparticle organosols in the presence of PVP, cellulose acetate, or cellulose nitrate in THF [279, 280]. Nevertheless, the reports on the preparation of ruthenium nanoparticles are relatively scarce. Notable exceptions are outlined as follows: Ru nanoparticles of various sizes and shapes generated from the decomposition organometallic precursor of Ru ( $\text{Ru}(\text{COD})(\text{COT})$  COD = 1,5-cyclooctadiene; COT = 1,3,5-cyclooctatriene) at room temperature in the presence of polymer (PVP or cellulose acetate) or ligands (alkylthiols or alkylamines) [281]. Particularly, in the case of amine ligands, the particles display an elongated

morphology, and have a tendency to form worm- or rod-like structures at high amine concentration. Sponge-like Ru nanoparticles with a porous structure were prepared by the reaction of  $[\text{Ru}(\text{C}_8\text{H}_{10})(\text{C}_8\text{H}_{12})]$  with  $\text{H}_2$  in methanol or THF/methanol [282]. The particle size can be controlled in the range 15–100 nm by varying the MeOH/THF ratio. The particles catalyze benzene hydrogenation without modification of their size or structure. Their formation mechanism is proposed to occur in the droplets of a nanosized emulsion, which act as nanoreactors.

## 2.5. Bimetallic Nanoparticles

The interest in the synthesis of bimetallic and even trimetallic nanoparticles originates from the unique properties compared to monometallic colloids. These new properties can be ascribed to a synergy between the two metals forming particles. The synthesis of bimetallic colloids can be implemented either by simultaneous or successive reduction of two metallic precursors. Most of the synthetic procedures used to prepare monometallic particles can be suitable for the bimetallic particle synthesis.

### 2.5.1. Coreduction of Metallic Precursors

A wide range of synthetic protocols used for the monometallic particle preparation was tested to be efficient in the production of bimetallic colloids because the principles of these protocols are identical to those applied for bimetallic nanoparticles. Polymer-stabilized bimetallic nanoparticles in hydro alcoholic media can be prepared by the simultaneous reduction of two noble metal salts in refluxing alcohol. PVP-stabilized Pd/Pt bimetallic particles were produced by refluxing an aqueous/alcohol mixture containing  $\text{PdCl}_2$  and  $\text{H}_2\text{PtCl}_6$  [283–287]. Following the same procedure, colloidal Au/Pd [288], Pt/Rh [289], Pt/Ru [290], Pd/Ru [291], and Ag/Pd [292] stabilized by PVP were synthesized by coreduction in refluxing alcohol of the corresponding metal salts. Other polymer-protecting agents such as PNIPAAm [293] were also used. Easily oxidized metal colloids such as Cu or Ni are difficult to prepare in comparison with noble metal nanoparticles made of Rh, Pt, or Au. However, Cu/Pd [294–296], Cu/Pt [294], or Pd/Ni [297, 298] bimetallic nanoparticles stabilized by PVP were obtained by coreduction of the corresponding metallic hydroxides in refluxing glycol. The thermal decomposition of palladium acetate and copper acetate in a reducing alcohol solvent with a high boiling point (2-ethoxyethanol) has also been used to prepare PVP-stabilized Pd/Cu bimetallic colloids [299]. Gamma irradiation can be efficient in the production of bimetallic particles. Delcourt and co-workers demonstrated the synthesis of PVA or polyacrylic acid (PAA)-stabilized Ag/Pt [300] colloids by irradiation of a solution containing  $\text{Ag}_2\text{SO}_4$  and  $\text{K}_2\text{PtCl}_4$ . Nonionic surfactants-stabilized Au/Pt nanoparticles were fabricated with  $\gamma$  irradiation of a mixture of  $\text{NaAuCl}_4$  and  $\text{NaPtCl}_6$  [301]. The preparation of Pt/Pd, Cu/Au, and Au/Pt bimetallic nanoparticles has been conducted in water-in-oil microemulsions [302–304]. The application of tetraalkylammonium hydrotriorganoborates ( $\text{NR}_4(\text{BEt}_3\text{H})$ ) as a reducing agent was reported by Bönne-mann and co-workers for the synthesis of a series of bimetallic colloidal particles [190, 191, 305–307]. Organometallic

complexes can also be used as precursors of bimetallic colloids.  $\text{Pt}(\text{dba})_2$  and  $\text{Ru}(\text{COD})(\text{COT})$  in various proportions were reduced with hydrogen to obtain PVP-stabilized Pt/Ru nanoparticles [308]. Esumi and co-workers [309, 310] developed a procedure to synthesize Ag/Pd and Ag/Pt by photo or  $\text{NaBH}_4$  reduction of silverbis(oxalato)palladate or silverbis(oxalato)platinate complexes. The electrochemical technique developed by Reetz also allows the preparation of bimetallic nanoparticles. To do so, two different sacrificial metallic anodes and a Pt cathode were immersed in an electrolyte in the presence of a stabilizing agent (tetraalkylammonium salt) [311]. The metallic ions were generated by current, and reduced at the cathode to give tetraalkylammonium stabilized bimetallic colloids.

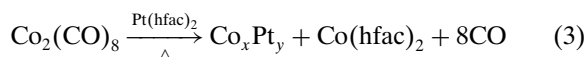
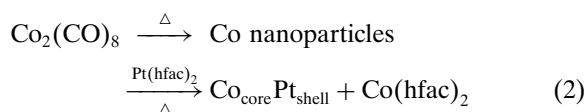
### 2.5.2. Successive Reduction of Metallic Precursors

Core/shell structured bimetallic colloids are generally synthesized by the deposition of a second metal on a preformed metallic particle through successive reduction of metallic precursors. The second metal has to be deposited on the whole surface of the performed monometallic nanoparticles. A preliminary synthesis was achieved by Toshima and co-workers [312] to generate core/shell Au/Pd nanoparticles, conducted, in fact, to randomly distributed Au/Pd bimetallic nanoparticles. On the other hand, the fabrication of Au/Pd and Au/Pt nanoparticles stabilized by such water-soluble ligands as  $\text{P}(m\text{-C}_6\text{H}_4\text{SO}_3\text{Na})_3$  or  $p\text{-H}_2\text{NC}_6\text{H}_4\text{SO}_3\text{Na}$  has been described by Schmid et al. [313, 314]. Henglein achieved the synthesis of bimetallic gold and platinum particles of the Pt/Au, Au/Pt core-shell type and bimetallic  $\text{Pd}_{\text{core}}\text{Au}_{\text{shell}}$  nanoparticles with hydrogen reduction and radiolysis techniques, respectively [73]. Likewise, he synthesized citrate-stabilized trimetallic  $\text{Pd}_{\text{core}}\text{Au}_{\text{shell}}\text{Ag}_{\text{shell}}$  particles in aqueous solution by radiolytic methods [95, 315]. Toshima designed an original synthetic route to core/shell bimetallic colloids, by which PVP-stabilized Pd/Pt bimetallic colloids with a Pd core were generated [316]. The principle of this method is that hydrogen can easily be adsorbed on a Pd surface to form a metal-H bond. This H atom is a good reducing agent, and the Pt ions added to the preformed Pd colloids are easily reduced by the adsorbed hydrogen atoms. The zerovalent Pt formed will deposit onto the Pd surface to generate a perfect core/shell structure. Additionally, Pal prepared bimetallic Au/Ag particles with a core-shell type structure by a UV-photoactivation technique [317].

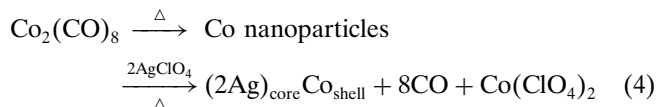
The synthesis of magnetic bimetallic and even trimetallic nanoparticles [318, 319] has been addressed in many publications. Well-known ferromagnetic alloys consist of 3d ferromagnetic metals and noble metal elements of the platinum group. The synthesis of ordinary bimetallic nanoparticles can be considered from two aspects: the coreduction of two metal salts in solution for alloy nanoparticles, and covering the “seed” with a second metal during a second reduction step for core-shell metallic nanoparticles. Nevertheless, for the preparation of magnetic alloy nanocrystals, the cases are different. The key point in the synthesis is the simultaneous reduction of noble metal salts and thermolysis of organometallic precursors. According to this principle, monodispersed FePt [320] and CoPt<sub>3</sub> [321] nanoparticles



are, respectively, prepared by the concurrent reduction of  $\text{Pt}(\text{acac})_2$  ( $\text{acac} = \text{acetylacetonate}, \text{CH}_3\text{COCHCOCH}_3$ ) with 1,2-diol and decomposition of  $\text{Fe}(\text{CO})_5$  or  $\text{Co}(\text{CO})_8$ . Similarly,  $\text{Fe}_x\text{Co}_y\text{Pt}_{100-x-y}$  alloy nanoparticles with size focusing are prepared by the simultaneous reduction of  $\text{Co}(\text{acac})_2$  and  $\text{Pt}(\text{acac})_2$  and thermal decomposition of  $\text{Fe}(\text{CO})_5$  [319]. Recently, Cheon and co-workers [322] showed the first utilization of redox transmetalation reactions for the synthesis of two different types, solid solution and core-shell, of CoPt nanoalloys under 10 nm without the need for additional reducing reagents. Stoichiometry tuned solid-solution-type CoPt nanoalloys are synthesized by the reaction between  $\text{Co}_2(\text{CO})_8$  and  $\text{Pt}(\text{hfac})_2$  ( $\text{hfac} = \text{hexafluoroacetylacetonate}$ ). Core-shell type nanoalloys in which Pt resides as a shell around a cobalt nanoparticle core are achieved by the reaction of  $\text{Pt}(\text{hfac})_2$  with cobalt nanoparticles. The obtained nanoalloys are moderately monodispersed (<10%) without any further size selection process. These two distinct reaction routes can be, respectively, elucidated as



An  $\text{Ag}_{\text{core}}\text{Co}_{\text{shell}}$  structure of bimetallic particles has been prepared using standard Schlenck techniques [323]. This method is based on the thermal decomposition of dicobalt octacarbonyl in combination with a transmetalation [322] reaction with water-free  $\text{AgClO}_4$  using oleic acid and tridodecylamine as surfactants, following the overall reaction



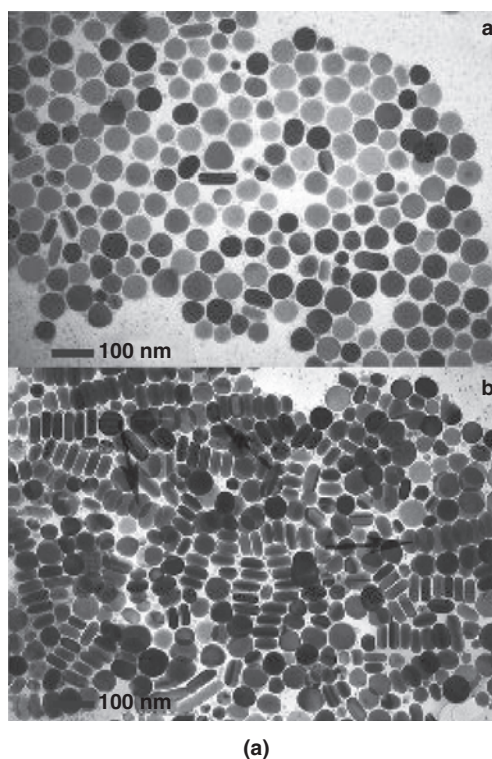
As a result, bimetallic Ag/Co nanoparticles were formed.

### 3. SPECTROSCOPIC CHARACTERIZATION

It appears that the skillful application of a wide range of different synthetic methods has catalyzed a fruitful and still growing interest in nanomaterials such as nanoparticles, nanotubes, nanorods, and nanowires. Nevertheless, one might have not imagined what the situation is in nanoscience without the coinage of various advanced physical methods to characterize these materials. We would even know little about the substance in this mesoscopic world up to now. The optimization of the analytical tools and their wide availability will contribute to a better understanding of these materials. As far as the characterization of nanoparticles is concerned, a series of spectroscopic measurement approaches have been established. Among these, transmission electron microscopy (TEM), X-ray diffraction (XRD), and dynamic light scattering (DLS) are the most efficient and extensively utilized characterization techniques.

### 3.1. TEM

Transmission electron microscopy is an indispensable tool in the identification of nanoparticle size and shape, particularly, when particle shape is more important. Although scanning tunneling microscopy (STM) and atomic force microscopy (AFM) can provide atomic-scale resolution images of large crystal surfaces, they are unable to clearly resolve the atomic lattices of nanoparticles as done by high resolution TEM (HRTEM) because of the surface coating and the wobbling of the nanocrystals under the scanning tip. Figure 3 presents a comparison of a TEM image of Ag nanodisks with their corresponding AFM image. It can be seen that, from the TEM image, the outlines of round circles can be unambiguously defined, while the AFM image shows vague outlines of Ag nanodisks. However, the advantage of using AFM as a tool for the characterization of nanoparticles is that it can provide a three-dimensional outline of an object rather than a two-dimensional projection of a three-dimensional object as given by TEM. HRTEM is very powerful in revealing the atom distributions on the nanocrystal surfaces, even if they are capped with a layer of stabilizing polymers and allow the determination of individual crystallite morphology with lattice contrast. Figure 4 shows the typical particle shapes observed by HRTEM,



**Figure 3.** Comparison of TEM images of Ag nanodisks with their AFM images. (a) TEM images of the silver nanodisks obtained after 4 h aging at 40 °C. The particles in *a* lie flat on the substrates, while those in *b* stack together. The arrows in *b* show the partially stacked particles, giving an ellipsoidal shape in projection. (b) Three-dimensional AFM images of several silver nanodisks stacked together in *a*. Horizontal and vertical line analyses of the nanodisks as shown in *b* and *c*, respectively. Reprinted with permission from [115], S. Chen et al., *J. Phys. Chem. B* 106, 10777 (2002). © 2002, American Chemical Society.

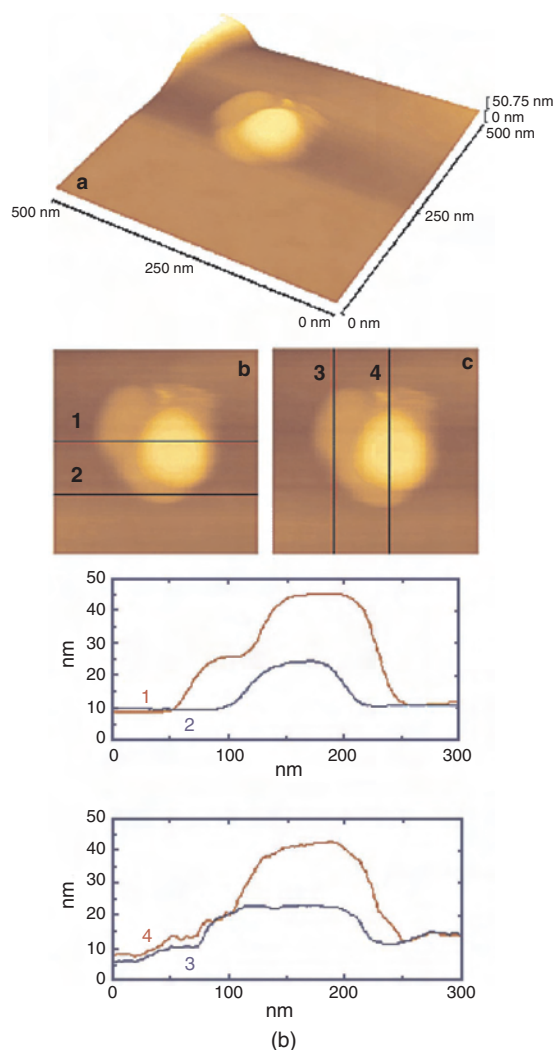


Figure 3. Continued.

in which atom rows or lattice fringes can be resolved clearly. The function of today's TEM is versatile, which offers not only the atomic-resolution lattice images, but also chemical information at a spatial resolution of 1 nm or better, and allows direct identification the chemical composition of a single nanocrystal [324–327]. With a finely focused electron probe, the structural characteristics of a single nanoparticle can be fully characterized. Moreover, TEM is unique for characterizing the *in-situ* structural evolution of nanocrystals resulting from annealing, electric field, or mechanical stress, such as imaging a single carbon nanotube when a mechanical or electrical measurement is being carried out *in-situ* [328].

A modern HRTEM is composed of an illumination system, a specimen stage, an objective lens system, the magnification system, the data recording systems, and the chemical analysis system. The electron gun is the heart of the illumination system, which typically uses an LaB<sub>6</sub> thermionic emission source or a field emission source. The LaB<sub>6</sub> gun gives a high illumination current, but the current density and the beam coherence are not as high as those of a field emission source. The field emission source is greatly

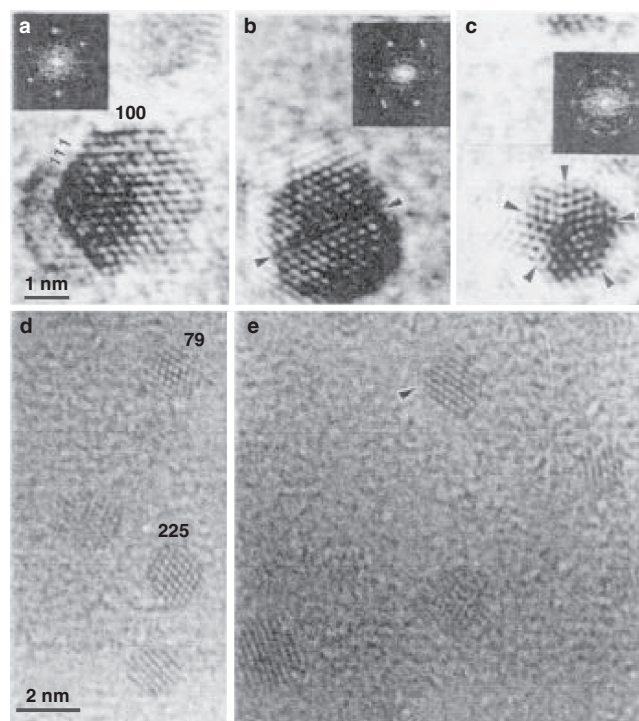


Figure 4. Typical particle shapes observed by HRTEM. (a) Truncated octahedral particle. (b) Particle with a single twin. (c) Decahedral particle. Small size (d) truncated octahedral and (e) truncated tetrahedral clusters (as one indicated by an arrow) observed by HRTEM, where 79 and 225 indicate the likely number of atoms in the corresponding nanocrystals. Reprinted with permission from [443], Z. L. Wang, *Adv. Mater.* 10, 13 (1998). © 1998, Wiley-VCH.

advantageous for performing high coherence lattice imaging, electron holography, and high spatial resolution microanalysis. The objective lens is like the human eye, and is the core device of a TEM which determines the limit of image resolution. The magnification system consists of intermediate lenses and projection lenses, and it gives a magnification up to 1.5 million. The chemical analysis system includes energy-dispersive X-ray spectroscopy (EDS) and electron energy loss spectroscopy (EELS); both can be used complementarily to quantify the chemical composition of the specimen. EDS relies on the counting of X-rays emitted from the beam-illuminated specimen region as a function of the photon energy, and it is probably the most precise microanalysis technique in TEM. EELS analyzes the intensity distribution of the transmitted electrons as a function of their energy loss. It provides not only the chemical information on the specimen, but also its electronic structure. A complementary application of the diffraction, imaging, the spectroscopy techniques available in a TEM, is likely to give a more precise and reliable determination of the crystal structure.

In theory, the image formation is a complex process. The entrance surface of a thin foil specimen is illuminated by a parallel or nearly parallel electron beam. The electron beam is diffracted by the lattices of the crystal, forming the Bragg beams which are propagating along different directions. The electron–specimen interaction results in phase and amplitude changes in the electron wave. For a thin specimen

and high-energy electrons, the transmitted wave function  $\Psi(x, y)$  at the exit face of the specimen can be assumed to be composed of a forward-scattered wave. The exit wave  $\Psi(x, y)$  contains the full structural information on the specimen. The diffracted beams are focused in the back focal plane, where an objective aperture can be applied. Electron waves leaving the specimen in the same direction (or angle  $\theta$  with the optical axis) are brought together at a point on the back focal plane, forming a diffraction pattern.

### 3.2. X-Ray Diffraction

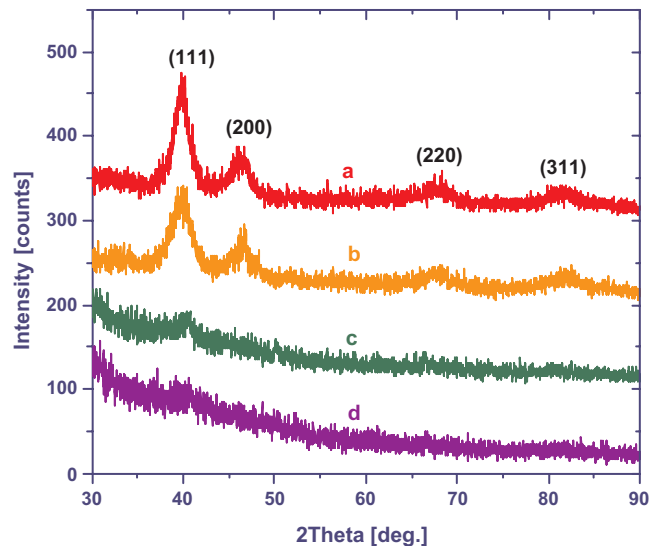
Similar to the corresponding bulk material, nanocrystal structures can be determined by X-ray diffraction. As judged from the diffraction peaks, the structure of the nanocrystallites can have characteristic features either of matching the bulk material or of a unique structure. A powder X-ray diffraction pattern of a sample of nanocrystals, unlike TEM, probes a large number of crystallites that are statistically oriented. The XRD peaks of the nanocrystallites are considerably broadened compared to those of the corresponding bulk material because of the finite size of the crystallites. The average size of the nanocrystallites can be determined from the width of the reflection according to the Debye–Scherrer equation [329]:

$$D = \frac{0.9\lambda}{\beta \cos \theta} \quad (5)$$

where  $\beta$  is the full width at half maximum (FWHM) of the peak,  $\theta$  is the angle of diffraction, and  $\lambda$  is the wavelength of the X-ray radiation. For very broad diffraction lines, a previous deconvolution of the signals in two components of strongest reflections is essential to obtain a more accurate FWHM measurement. It can be concluded that the diffraction peaks become wider gradually with a continual decrease in nanoparticle size (estimated by the Debye–Scherrer equation). Figure 5 records the wide-angle X-ray diffraction patterns of the PVP-protected Pt nanoclusters with different size. It can be found that, for the smaller noble metal nanoparticles, only a broad (111) peak is discernible. A study reported by Leff et al. shows a similar result for the long-chain alkythiol-passivated gold nanoparticles [330]. A dispersed peak is the particularity of the metal colloidal cluster for the very small size of the particles [188, 331, 332].

X-ray diffraction is powerful in refining the structure of nanoclusters, particularly those smaller than 2 nm in diameter. If the particles are oriented randomly so that the entire assembly can be treated as a “polycrystalline” specimen composed of nanocrystals with identical structure but random orientation, so that the scattering from each can be treated independently, the structure of the nanocrystals can be refined by a quantitative comparison of the theoretically calculated diffraction spectra for different nanocrystals models with the experimentally observed ones. This was recently performed by Cleveland et al. in the determination of decahedral Au nanocluster structures with 1.7–1.9 nm size [333, 334].

X-ray diffraction is also a unique tool in the study of the self-assembled nanocrystal superlattice structures.



**Figure 5.** X-ray diffraction patterns of PVP-Pt nanoparticles obtained at various initial concentration ratios of PVP/Pt. PVP (wt%)/Pt (mM)=(a) 0.5%/1.0, (b) 1.0%/1.0, (c) 2.0%/1.0, and (d) 4.0%/1.0.

The diffraction spectrum in the high-angle range is directly related to the atomic structure of the nanocrystals, while the spectrum in the small-angle region is directly associated with the ordered assembly of the nanocrystals [335, 336]. By examining the diffraction peaks that are missing from the spectrum, one may identify the crystallographic packing. This analysis is based on the assumption that each particle is identical in size, shape, and even orientation (i.e., the same X-ray scattering factor), so that the extinction rules derived from diffraction physics apply. In practice, however, a fluctuation in either the size, orientation, or shape can easily make this assumption untenable. This is the reason why a quantitative analysis of the low-angle diffraction spectrum is rather difficult. Therefore, caution must be exercised in the interpretation of the 3-D assembly using X-ray diffraction data. However, X-ray diffraction is still the most powerful technique for evaluating the average interparticle distance  $D_{\text{XRD}}$ , and is a unique technique for studying the *in-situ* pressure- and/or temperature-induced phase transformations in nanocrystals [337].

Sometimes, ordered packing is only in short range. Moreover, in the region where two layers overlap, the short-range order in each layer is overshadowed by the disordered component of the other layer. It appears that an ordered structure does not exist as the number of stacked layers is increased. This is owing to complications from the 2-D projection effect in TEM imaging. In this case, X-ray diffraction might show reasonably well-ordered structures. Although X-ray diffraction may indicate ordered packing in the assembled nanocrystals, the range of ordering is still unknown. This is similar to the X-ray diffraction spectrum of a polycrystalline specimen, in which analysis of the grain size from the diffraction spectrum is rather difficult because there are many factors, such as defects, dislocations, and structural imperfections at surfaces/interfaces, which can give rise to line broadening. In this case, TEM is effective for imaging particle packing.

### 3.3. Dynamic Light Scattering

Dynamic light scattering (DLS), also known as photon correlation spectroscopy (PCS), is an effective method to study the size of colloids (hydrodynamic radius), the kinetics of aggregation of colloids, and the structure of the aggregates formed. DLS measures the autocorrelation function  $C(t)$  of the intensity of the scattering light [338].  $C(t)$  is defined as

$$C(t) = \langle I(0)I(t) \rangle \quad (6)$$

where  $I(t)$  is the scattering intensity at time  $t$ .  $\langle \dots \rangle$  indicates averaging over the measuring time. For monodispersed particles,  $C(t)$  is an exponential decay function:

$$C(t) = B + Ae^{-t/\tau_c} \quad (7)$$

where  $B = \langle I \rangle^2$  is the background or noise level,  $A = \langle I^2 \rangle - \langle I \rangle^2$  is the signal magnitude, and  $\tau_c$  is the correlation time. Assuming spherical particles, the correlation time is related to the size of particles by

$$\tau_c = 3\pi\eta d / 2k_B T q^2 \quad (8)$$

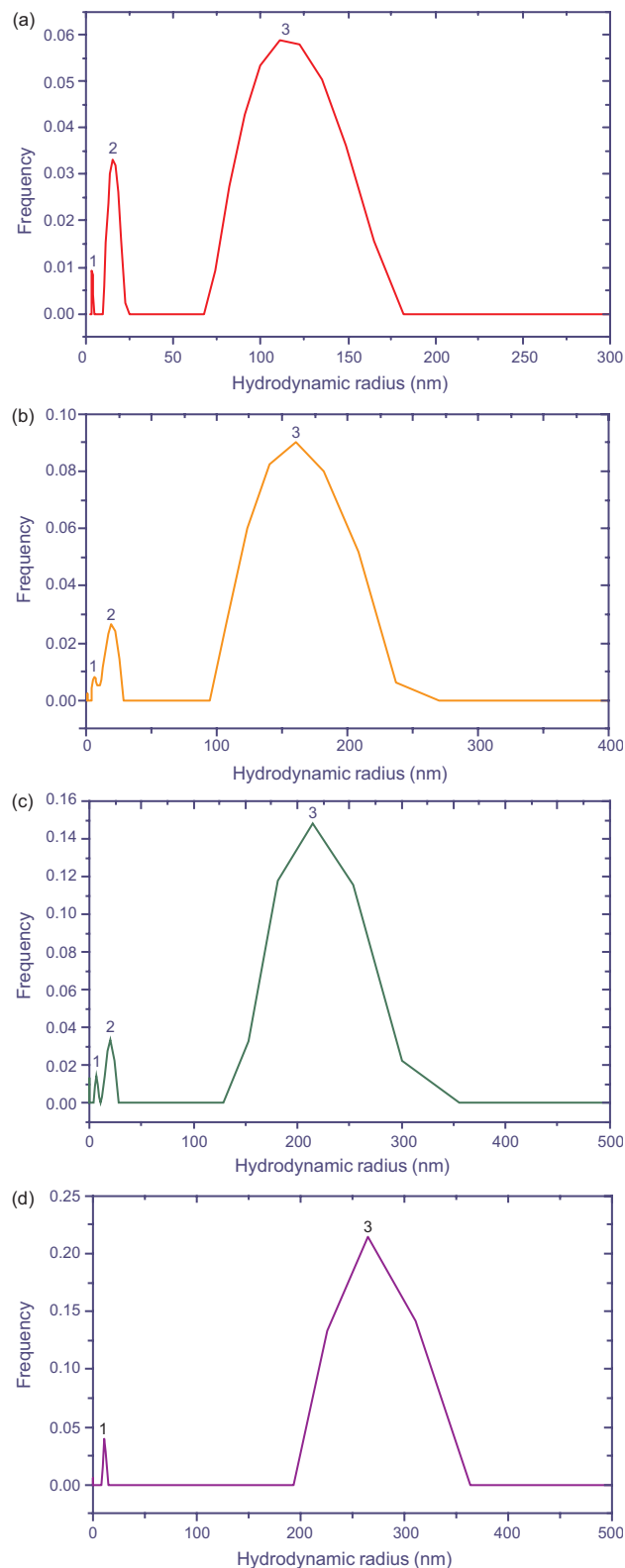
where  $\eta$  is the viscosity of the solvent,  $d$  is the average diameter of the particles,  $k_B$  is the Boltzmann constant,  $T$  is the temperature of the colloid, and  $q$  is the magnitude of the scattering wavevector. By measuring the autocorrelation function  $C(t)$  and fitting it with (7), the correlation time, and consequently, the particle size, can be found. However, the measurements of a colloidal system can sometimes be complicated by several other factors. First, the single exponential decay function for the correlation only applies to colloids with monodispersed particles. For colloids containing binary or tertiary structures with different sizes, extra exponential terms must be the following fitting function:

$$C(t) = B + A_1 e^{-t/\tau_{c1}} + A_2 e^{-t/\tau_{c2}} + A_3 e^{-t/\tau_{c3}} \quad (9)$$

where each exponential term corresponds to one component of tertiary structures. The scattering of light from colloidal particles scales as the sixth power of their size if their size is much smaller than the wavelength  $\lambda$ . Therefore, the coefficients  $A_i$  ( $i = 1, 2, 3$ ) in (9) rely heavily on the size and concentration of each component. In some cases, one or two terms in Eq. (9) might be dominant, and the contribution from others can be neglected. Secondly, strong absorption of some highly concentrated colloids induces local heating in the path of the laser beam, which in turn causes a change of the optical index of reflection of the medium and a divergence of the beam. This phenomenon, normally called thermal blooming or the thermal lensing effect [339–341], results in a faster decay of the correlation function than the exponential decay. A second cumulant term must be introduced in order to obtain the correct particle size from  $\tau_c$  [342]. The correlation function for a strongly absorbing monodispersed colloid therefore is

$$C(t) = B + Ae^{-t/\tau_c - t^2/\tau_f^2} \quad (10)$$

where the second cumulant  $\tau_f$  depends on the intensity of the incident beam and the properties of the absorbing medium. As a representative example, shown in Figure 6



**Figure 6.** Plots of the hydrodynamic radius distribution of Ag colloids protected by 2-mercaptobenzimidazole in 50% aqueous solution at 25 °C, which were obtained by DLS after the sample being left for (a) 0 h, (b) 2 h, (c) 4 h, and (d) 6 h. Reprinted with permission from [452], Y. Tan et al., *J. Phys. Chem. B* 106, 3131 (2002). © 2002, American Chemical Society.

are the hydrodynamic radii of Ag colloids measured by DLS after the sample was left for different periods. The distribution of the hydrodynamic radius of the scattering entity was calculated by the CONTIN method according to the autocorrelation function of the intensity of the scattering light.

## 4. PROPERTIES

### 4.1. Size- and Shape-Dependent Properties

The physical and chemical properties of nanoparticles have been addressed in many publications, which depend on several structural features of nanoparticles themselves, such as (1) the particle size and the size dispersity, (2) the structure of the particles, (3) the surface of the particles, (4) the shape of the particles, and (5) the organization of the particles into a nanomaterial and their dispensability. Monodispersed metal or semiconductor nanoparticles, which means uniformity in both size (the standard deviation is less than 10%) and shape, are paramount both for theoretical and practical reasons. Owing to their extremely small size, the characteristic of nanoparticles which makes them different from macroscopic solids or single atoms is mainly that the surface atoms have a very large percentage. A characteristic high surface-to-volume ratio provides sites for the efficient adsorption of reacting substrates, leading to unusual size-dependent chemical reactivity. Here, the role played by particle size is comparable, in some cases, to the particle chemical composition, thus adding another flexible parameter to the design and control of their behavior. Because of this characteristic, nanoparticles hold many novel physical and chemical properties that are size dependent, as described in many documents [11, 343–359]. Size-dependent physical properties were surveyed in a recent review article [360]. Size-dependent chemical properties of nanocrystals have been extensively discussed by Rao et al. in the other latest review [361]. These properties highlight several important aspects as follows: (1) electronic structure and properties (quantum size effects), (2) chemical reactivity, (3) self-assembly of nanocrystals, and (4) size-dependent structural and thermodynamic properties such as bond lengths, melting point, and specific heat.

Recent numerous findings added new dimensions to this subject. One representative example is that the nanoparticles with diameters usually smaller than 10 nm in size can be self-assembled. Moreover, it is in this range that many exciting and unusual physical properties are enhanced. Particularly, a decrease in the size of nanoparticles means an increase in reactivity, for example, for oxidation and a decrease of the Curie temperature of ferromagnetic materials [362]. A gigantic extensibility (elongation exceeds 50 times) without a strain-hardening effect was obtained after cold rolling of nanocrystalline copper at room temperature [363]. A size-induced transition from a positive to a negative temperature coefficient of electrical conductivity is observed by thin films of a series of (six) dodecanethiol-stabilized gold nanoparticle complexes with the Au core diameter progressively increasing from 1.7 to 7.2 nm [364]. The size of the Au core may influence both its intrinsic conductivity

and the charging energy barrier for tunneling to an adjacent monolayer-encapsulated cluster. The melting temperature of nanocrystals strongly depends on the crystal size, and is substantially lower than the bulk melting temperature. The melting points of sodium clusters consisting of 70–200 atoms are on the average 33% (120 K) lower than the sodium bulk value (371 K) [365]. A recent study shows that the electrooxidation rates of formic acid, formaldehyde, and methanol in acidic electrolyte on carbon-supported platinum nanoparticle films are changeable by varying the particle diameters [366]. The methanol electrooxidation rates on larger nanoparticles ( $d > 4$  nm) are larger than those on Pt particles with diameters below 4 nm; formic acid electrooxidation shows a reverse behavior, while formaldehyde electrooxidation displays little sensitivity to Pt nanoparticle size. Otherwise, the shift of electron energy levels as a function of particle size causes the emission of photons with unique wavelengths, potentially useful for optoelectronics.

The shape of nanoparticles is another important variant to be considered in the design of nanomaterials. The particle shape determines the crystallographic structures of the particle surface since the different geometric nanoparticles are enveloped by different oriented planes in a different number. The {111}, {100}, and possibly {110} surfaces of face-centered cubic structured metal particles are different not only in surface atom densities, but also in the electronic structure, bonding, adsorption, and possibly chemical reactivity (catalysis properties). For instance, surface energies associated with different crystallographic planes are different, and a general sequence may hold:  $\gamma_{\{111\}} < \gamma_{\{100\}} < \gamma_{\{110\}}$ . Thus, the tetrahedral Pt nanoparticles enclosed mainly by {111} facets are more stable than the {100} faces enclosed cubic Pt nanocrystals [367]. For a spherical single-crystalline particle, its surface must contain high-index crystallographic planes, which probably result in a high surface energy. Therefore, facets tend to form on the particle surface to increase the portion of the low-index planes. For particles smaller than 10 nm, they usually have a faceted shape like a truncated octahedron [139, 368]. The sublimation activation energy of Au {110} faces has been found to be significantly lower than that of {100} and {111}, giving rise to the sublimation of Au atoms from the surface at temperatures as low as 220 °C, which is much lower than the melting point of bulk gold of 1063 °C [369]. A recent molecular dynamics calculation revealed that the melting process of Au clusters is punctuated by solid-to-solid structural transformations from low-temperature optimal structures, such as a truncated octahedron and a truncated decahedron, to icosahedral structures, which are believed to be the intrinsic thermodynamic precursors to the melting transition [370]. Well-known and studiously explored is the catalytic activity of nanoparticles with different morphology. Catalytic reactions take place on the surface of metal nanoparticles. Thus, it can, of course, be concluded that the different surfaces hardly exhibit the same reactivity due to the differences among different crystallographic planes, as mentioned above. Additionally, the strongly adsorbed species act as a poison to the reaction, thereby decreasing the rate of the reaction; therefore, the low-coordination-number vertex and edge atoms on the particle surfaces, whose numbers vary with the particle shape, have high catalytic activity.

## 4.2. Aggregation Stability

A large number of studies have been directed toward understanding the mechanisms of colloids aggregation and their relationship to the structure of the aggregates formed [371]. Generally, two limiting cases have been identified [372–374]. The first, termed slow or reaction-limited aggregation, refers to the case where only a small fraction of the collisions result in the two colloidal particles involved adhering to each other [372]. It has been found that the growth kinetics of reaction-limited aggregation are described by

$$R_h(t) = R_h(t_0) \exp(ct) \quad (11)$$

where  $R_h(t_0)$  is the initial hydrodynamic radius of the aggregate, typically determined by dynamic light scattering, and  $c$  is a parameter characteristic of the experimental conditions. Related static light scattering experiments have established that the fractal dimension of such aggregates is 2.05.

The second case, termed fast or diffusion-limited aggregation, refers to the situation where each collision results in the two colloidal particles involved adhering to each other [373, 374]. It has been found that the growth kinetics of diffusion aggregation are described by

$$R_h(t) \propto t^{1/d_f} \quad (12)$$

where  $R_h(t)$  is the hydrodynamic radius of the aggregate at some time  $t$ , determined by dynamic light scattering, and  $d_f$  is the fractal dimension which has a value of 1.75. The associated physical picture can be summarized as follows. In the reaction-limited regime, the particles have a low probability of adhering upon contact, sample many possible configurations, and form aggregates which are relatively dense, possibly local ordered, and have a fractal dimension of 2.05. In the diffusion-limited regime, the particles have a high probability of adhering upon contact, sample few possible configurations, and form relatively diffuse aggregates, probably locally branch-like, and so the particles which have a fractal dimension of 1.75.

The above description of particle aggregation assumes that nanoparticle motion is diffusive, and that particle-particle aggregation is homogeneous. Furthermore, it assumes that particle aggregation is irreversible with little subsequent reorganization of the aggregate structure. In practice, there are cases in which two particles have a high probability of adhering upon contact, and in which the kinetics of aggregation growth are diffusion limited, but the strength of the interaction between aggregated particles is sufficiently small that significant restructuring leads to a larger fractal dimension [375, 376].

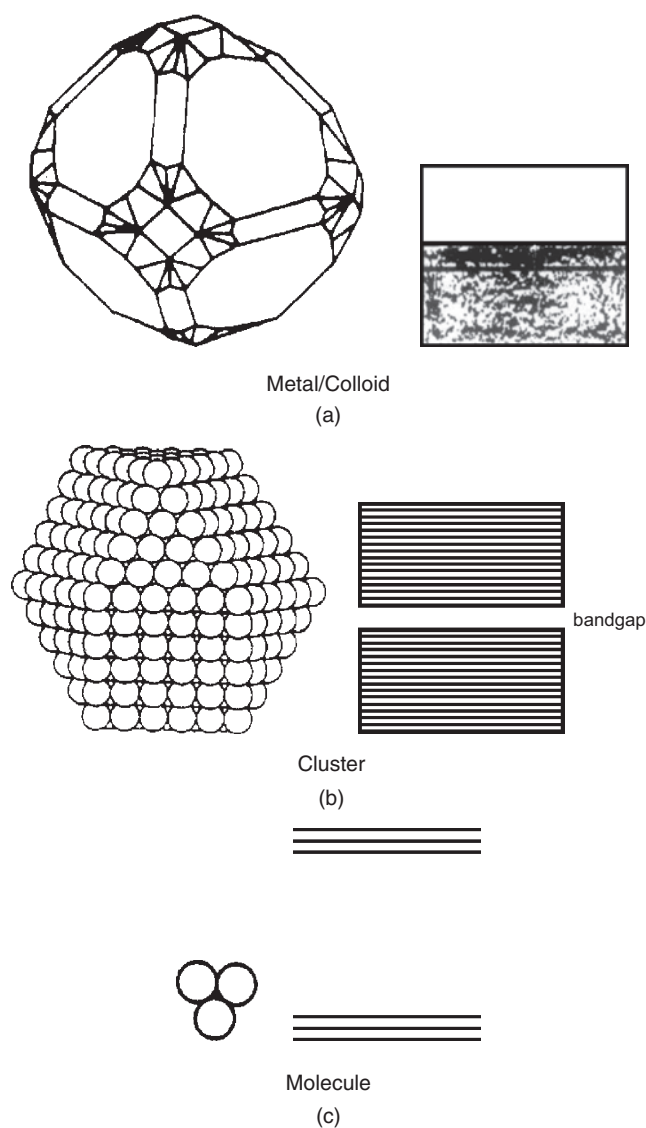
The stability against aggregation of the noble metal nanoparticles is an important prerequisite for many potential applications. The general stabilization mechanisms of colloidal materials have been explained by the Derjaguin–Landau–Verwey–Overbeek (DLVO) theory [377]. Colloid stabilization is usually discussed in terms of two general categories: (1) charge stabilization, and (2) steric stabilization. Chemical functionalization of noble metal colloids performed in an aqueous or organic medium has

often resulted in stability problems. In general, noble metal colloid aggregation is indicated by a red shift of the plasmon band. This problem is traditionally overcome by adding certain amounts of stabilizers that exhibit a high and specific affinity for the particle surface. Numerous stabilizers such as linear polymers (i.e., poly(*N*-vinyl-2-pyrrolidone [PVP]), cellulose acetate, and so on), macromolecules (highly branched dendrimer molecules [378, 379],  $\pi$ -conjugated poly(dithiafulvene) [380], and cyclodextrin [381]), ligands (alkanethiols [382–387], bi- and tri-functional thiols [118, 388, 389], acryldithiols and diisonitrile [390], dialkyl disulfides (RSSR') [391], dialkyl sulfides (RSR') [392–394], trioctylphosphine oxide (TOPO) [395, 396], and alkylamines [281, 397–400], surfactants [330, 401–403], tetraalkylammonium salts [404, 405], and heterogeneous supports [406–409] have been employed to prevent the nanoparticles from aggregation and allow one to isolate the nanoparticles. Based on these stabilizers, four types of stabilization mechanisms can be summarized: (1) the electrostatic stabilization by the surface adsorbed anions, (2) the steric stabilization by the presence of bulky groups, (3) the combination of these two kinds of stabilization with the electrosteric stabilization such as surfactants, and finally, (4) the stabilization with a ligand. The most common tools used for stabilizing nanoparticles so far have been polymers since the polymer-stabilized nanoparticles are able to be extensively used as catalysts in catalytic reactions, but they may not be useful in selected chemical or physical applications. For this reason, the use of ligands coordinated at the surface of the particles has been developed considerably in the past few years. Appropriate stabilizers play an overwhelming role in not only controlling the particle size and morphology, but also an aid to the functionalizing of the nanoparticles. For example, the incorporation of metal nanoparticles can enhance the conductivity of the  $\pi$ -conjugated polymers [410]. Nanocomposites consisting of conducting polymers and noble metal nanoparticles show the significance for catalytic applications [411].

However, stabilities at a large concentration can severely interfere with a subsequent surface functionalization due to the firm binding between stabilizer molecules and the surfaces of nanoparticles. One approach to the simultaneous solving of both the issues of colloidal stability and colloid derivatization consists of using functionalizable stabilizers such as hydrophilic polymers that are covalently grafted on the nanoparticle surfaces. For example, when biological molecules or environments are involved, the stabilizers should be compatible with biomedical requirements. As steric hindrance hampers the access to the colloid surface, the maximal amount of functional molecules that can be fixed is severely limited. Alternatively, a suitable solvent itself, such as methanol, acetone, propanol, ethylene glycol, and such, as the stabilizer has been applied to fabricate stable, “unprotected” metal nanoparticles with narrow size distribution [29, 106, 233–236]. By this means, the produced metal nanoparticles can be freely functionalized because the species adsorbed on the “unprotected” metal nanoparticles, that is, solvent molecules and the simple anions, will be easily removed or replaced by various coordination ligands or protective agents.

### 4.3. Electronic Properties

If a metal particle with bulk properties is reduced to a size of a few dozen or a few hundred atoms, the density of states in the valence band and the conduction band, respectively, decreases to such an extent that electronic properties change dramatically. In a metal, electrons are highly delocalized over a large space (i.e., least confined). This is a result of the fact that the separation between the valence and conduction bands vanishes, as shown in Figure 7(a), rendering the metal its conducting properties. As we decrease the size of the metal and confine its electronic motion, how do the electronic properties of a metal cluster have to be? The separation between the valence and the conduction bands becomes comparable to or larger than  $kT$ , and the metal becomes



**Figure 7.** Illustration of the electronic states in (a) a metal particle with bulk properties and its typical band structure, (b) a large cluster of cubic close-packed atoms with a small bandgap, and (c) a simple triatomic cluster with completely separated bonding and antibonding molecular orbitals. Reprinted with permission from [9], G. Schmid, *Chem. Rev.* 92, 1709 (1992). © 1992, American Chemical Society.

a semiconductor, as illustrated in Figure 7(b). When more confinement increases the energy separation further, for example, as demonstrated in a cluster containing three metal atoms, energetically well-defined bonding and antibonding molecular orbitals are formed [see Fig. 7(c)]. The material becomes an insulator. In the size domain at which the metal–insulator transition occurs, new properties are expected to be observed which are possessed neither by the metal nor by the molecules or atoms forming the metal. Here, the quantum size effect dominates. In other words, if the number of electronic dimensions in a bulk system is decreased from three to two, a so-called quantum well is formed. While the one dimensionality of electrons induces a quantum wire, dimension zero effects result in a quantum dot which has a dimension of a particle consisting of hundreds or thousands of atoms.

An interesting aspect of clusters (metal clusters) is the coordinatively great unsaturation of the surface atoms. They interact only with atoms inside the particle, and have free valences outside. Therefore, their electronic contribution to the behavior of the particle is different from that of the inner atoms which are fully coordinated. Surface atoms will be even more distinguishable from inner ones if they are ligated. The smaller a metal particle becomes, the larger its fraction of surface atoms is. The distinction between the total number of metal atoms forming the complete cluster and the inner atoms (i.e., exclusively with other metal atoms as neighbors) is more significant the smaller a cluster is. For example, a close-packed cluster of 13 atoms has 12 surface atoms. A two-shell cluster containing 55 atoms has a “metallic” nucleus of 13 atoms, whereas the outer shell contains 42 atoms. In general, the  $n$ th shell includes  $10n^2 + 2$  atoms. By increasing the size to a certain extent, a transition to bulk behavior will occur so that the inner metal atoms and not the total number of metal atoms should be considered.

In noble metals, the decrease in size below the electron mean-free path (the distance the electron travels between scattering collisions with the lattice centers) gives rise to intensive absorbance in the near UV–visible light. This results from the coherent oscillation of the free electrons from one surface of the particle to the other, and is called the surface plasmon absorption, which will be discussed in detail below. Noble metal nanoparticles are well known to have very efficient catalytic properties because of the large fraction of their atoms present on the surface. At this point, researchers in the high-vacuum surface science and electrochemistry fields have observed different catalytic efficiencies for the different metallic surfaces [412]. Atoms on different types of faces of a single metallic nanocrystal have different electronic structures, and thus promote different catalytic properties. The shift of the Fermi level manifests itself as a drastically increased sensitivity of the metal particles toward oxidation.

### 4.4. Optical Properties

Silver, gold, and copper colloids have been the major focus of interest because of their unique optical properties determined by the collective oscillations of electron density termed plasmons, which give rise to an intense absorption in the near UV–visible. Such strong absorption induces

the brilliant color of these metal nanoparticles in colloidal dispersion. It is produced by the strong coupling of nanoparticles to the electromagnetic radiation of incident light, leading to a collective excitation of all of the free electrons in the particles. As illustrated in Figure 8, the movement of the electrons under the influence of the electronic field vector of the incoming light leads to a dipole excitation across the particle sphere, the positive polarization charge acting as a restoring force, which makes the electrons oscillate. Thus, the electron density within a surface layer, the thickness of which is about equal to the screening length of a few angstroms, oscillates, whereas the density in the interior of the particle remains constant [“surface plasmon” (SP)]. From one up to three SP bands may be observed, corresponding to three polarizability axes of the metallic nanoparticles. A prerequisite for the formation of an intense plasmon absorption band is that  $\epsilon_2$  (the imaginary part of the dielectric constant of the metal) is not too large [11]. Silver particles have the unique property that the excitation of the collective oscillation (plasmon absorption,  $\lambda = 380$  nm) and of the interband transitions ( $\lambda = 320$  nm) occur in separate wavelength regimes. The plasmon resonances possessed by gold and copper are in the visible (Au 520 nm; Cu 570 nm), however, these resonances are superimposed by interband transitions.

In theory, the absorption spectra of metal particles smaller than the wavelength of incident light can be calculated on the basis of the Mie equation for nanoparticles whose metallic dielectric function is known and which are embedded in a medium of known dielectric constant [413–416]. The position and magnitude of the surface plasmon absorption band are intensively dependent on the size of the particles, the refractive index of the solvent, and the degree of aggregation. The surface plasmon resonance should shift slightly to high energy, and broaden

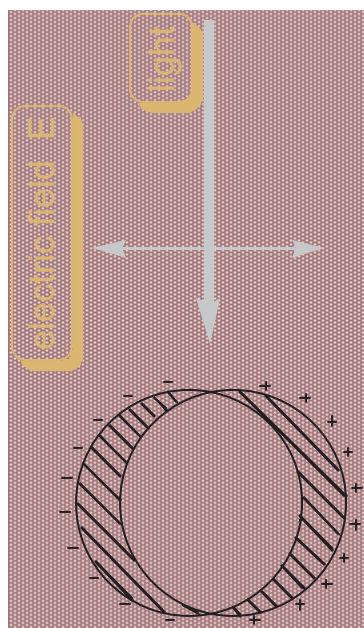
somewhat as the particle size is decreased; meanwhile, the intensity of absorption decreases remarkably until it is essentially unidentifiable for crystallites of less than 2 nm effective diameter [417, 418]. For example, a symmetric and comparatively narrow absorption peak at a shorter wavelength is usually indicative of relatively small, monodisperse, and spherical metal nanoparticles. However, it has been demonstrated both theoretically [419–422] and experimentally [423, 424] that the SP resonances of the coinage metal nanoparticles depend much more sensitively on the particle shapes than on the sizes. Typically, in the case of gold nanorods, the absorption spectra are characterized by the dominant  $SP_L$  band (at longer wavelength, ca. 620–900 nm), corresponding to longitudinal resonance and a much weaker transverse resonance than the  $SP_T$  band (at shorter wavelength, ca. 520 nm).

In general, for bimetallic Ag/Au nanoparticles, the absorption bands of alloys fall between the maxima of the respective constituent surface plasmon absorption bands, and core-shell structures manifest themselves in two distinct bands [413, 425]. Morphologies and absorption spectra of composite Ag/Au nanoparticles were, however, found to depend on the deposited metal atoms/surface ratio in a less than straightforward manner [426]. In contrast, several experimental results show that what is observed in the core-shell structured nanoparticles is only the plasmon absorption of pure metal of the core or shell constituent, probably due to particles deviating from the perfect core-shell model [427, 428]. The wavelength of the plasmon resonance of the nanoshells that are the other kind of colloidal particles, consisting of a small dielectric core covered by a thin metallic shell, can be tunable in the visible and near-infrared regions by varying the core/shell radii. This allows for the design of nanoshells with plasmon resonance across a spectral range from about 600 to 2500 nm [429]. The scattering from nanoshells adheres to the Mie scattering theory [429–431].

The efficiency for the absorption and scattering of light by metal nanoparticles can surpass that of any molecular chromophore. In addition, both absorption and scattering properties can be considerably altered by surface modification or by electronic coupling between individual nanoparticles. Together with an exceptional resistance to photodegradation, such favorable optical features are stimulating the development of new applications in analytical chemistry and in photophysics, making metal colloids attractive components for diagnostic, electronic, and photonic devices.

#### 4.5. Magnetic Properties

Nanoscale magnetic materials show novel properties that are markedly different from those of the bulk due to their very small size and fundamental change in the coordination, symmetry, and confinement [432]. For magnetic nanoparticles, the intrinsic magnetic properties are strongly influenced by the particle size; meanwhile, they exhibit specific properties such as superparamagnetism and quantum tunneling of magnetization [433, 434], which are regarded as unique features of magnetic nanoparticles. When reducing the size of



**Figure 8.** Polarization of a spherical metal nanoparticle by the electric field vector of the incoming light.



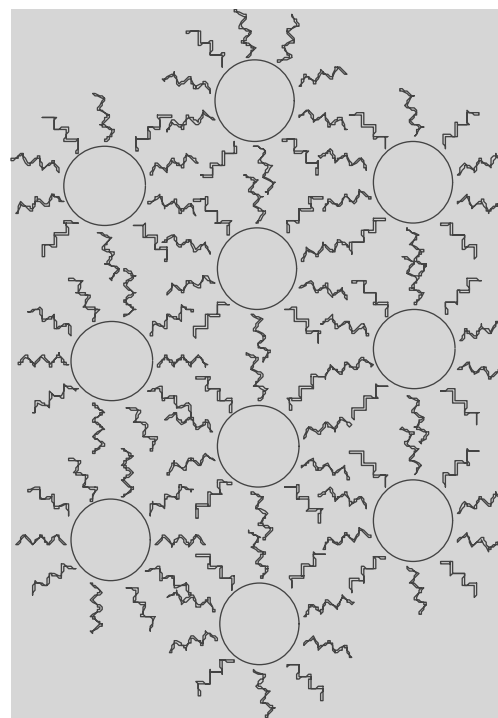
magnetic particles, a transition from poly-domain to single-domain systems occurs. If the particles of ferro- or ferri-magnetic materials are smaller than the dimensions of a single domain (which for Fe and Co is ca. 20 nm), thermal fluctuations will supersede the Weiss anisotropy above the blocking temperature. Such particles are called superparamagnetic [435]. Naturally, magnetic particles smaller than 10 nm are usually superparamagnetic, and they do not aggregate because each particle is a single magnetic domain. A permanent magnetic moment has been observed in a self-assembled array of Co particles with sizes  $<8$  nm by aligning them in a magnetic field during assembly.

The modification of the electronic band structure of nanosize magnetic particles, at the border of molecular and metallic states, induces unusual magnetic properties. As a consequence, an enhanced magnetic moment is predicted for nanoparticles of 3*d* ferromagnetic metals [436]. By applying molecular beam deflection measurements in high vacuum, such effects have been first demonstrated in the case of Fe, Co, and Ni metal nanoparticles containing fewer than 1000 atoms [437]. Bulk 4*d* metals do not display any ferromagnetic behavior; however, a spin polarization can be induced by a very small perturbation of the lattice parameter, by elaborating layered structures with a ferromagnetic material [438], and more efficiently by alloying with a 3*d* ferromagnetic metal [439, 440]. All of these fantastic phenomena motivate the preparation and characterization of magnetic nanoparticles.

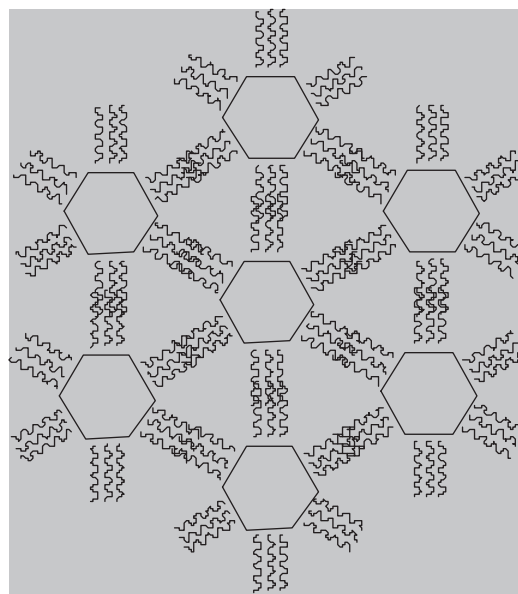
Bimetallic nanoparticles in particular have raised a wide range of scientific interests because they may exhibit unique, synergistic properties, or combinations of properties, which go beyond those of single components. The investigation in the formation of alloy nanoparticles containing ferromagnetic 3*d* and noble metal elements of the platinum group becomes rather active with respect to the magnetic behavior of large magnetic moments and high magnetocrystalline anisotropy (i.e., FePt:  $K_u \sim 6.6\text{--}10 \times 10^7$  erg/cm<sup>3</sup>) of these particles [441].

## 5. SELF-ASSEMBLY

Nonlithographic approaches based on thermodynamically driven self-organization processes are especially appealing because of their potential for low overhead in large-scale production. The spontaneous organization of monolayer-protected metal nanoparticles in periodic two-dimensional (2-D) arrays is archetypal of this approach, with many of these arrays demonstrating novel optical or electronic properties as a function of particle size or interparticle spacing. Hydrophobic compounds such as alkanethiols [34–36, 227, 238, 270] and alkylamines [224, 281, 399, 400] or cationic surfactants [404, 405] are often used to drive the nanoparticles toward self-organization at the air–aqueous interface (see Fig. 9). However, 2-D array formation by this method has mainly been successful only for small metal nanoparticles with diameters less than 10 nm, while a breakthrough, to some degree, has been achieved by the improvement of the largest unit size for a close-packed 2-D gold nanoparticle array from 18.5 to 170 nm [442]. Stabilized metal particles beyond this threshold of 10 nm become



(a)



(b)

**Figure 9.** Schematics showing self-assembled passivated nanocrystal superlattices of spherical (a) and faceted (b) particles. Apparently, long-chain thiol capping layers on the surfaces of nanoparticles are interdigitated.

increasingly prone to multilayer or three-dimensional aggregate formation, which can be attributed to the rapid increase in van der Waals attraction and the loss of surfactant chain mobility on the planar facets of the nanoparticles as a function of size.

Previously, Wang summarized that periodic arrays of nanocrystals are different from the 3-D packing of atoms

in several aspects [443]. First, to an excellent approximation, atoms or ions are spherical, while nanoparticles are faceted polyhedra; thus, the arrays of particles can be critically affected by their shape and size. Second, the atom or ion size is fixed, but the size of nanoparticles can vary slightly because their size distribution usually is within a certain range, even after size selection process. The degree of order within the close-packed domains suggests that the uniformity of arrays is determined largely by the size and shape dispersity [444] of the nanoparticles themselves. It should be noted that low size dispersity (5–10% relative standard deviation from the mean) is an important factor in the preparation of sterically stabilized colloidal crystals. Finally, atomic bonding occurs between outer shell (valence) electrons to form ionic, covalent, or metallic bonds, or mixtures of these. In most cases, the interatomic distance is fixed, while the bonding between nanoparticles is generated by a passivating surfactant whose length is variable; thus, the ratio of particle size to interparticle distance is adjustable. This is a parameter likely to determine the 3-D packing of the nanoparticles. The tunable internanocrystal spacing permits control over interparticle interactions, giving rise to novel tunable structural, optical, and transport properties.

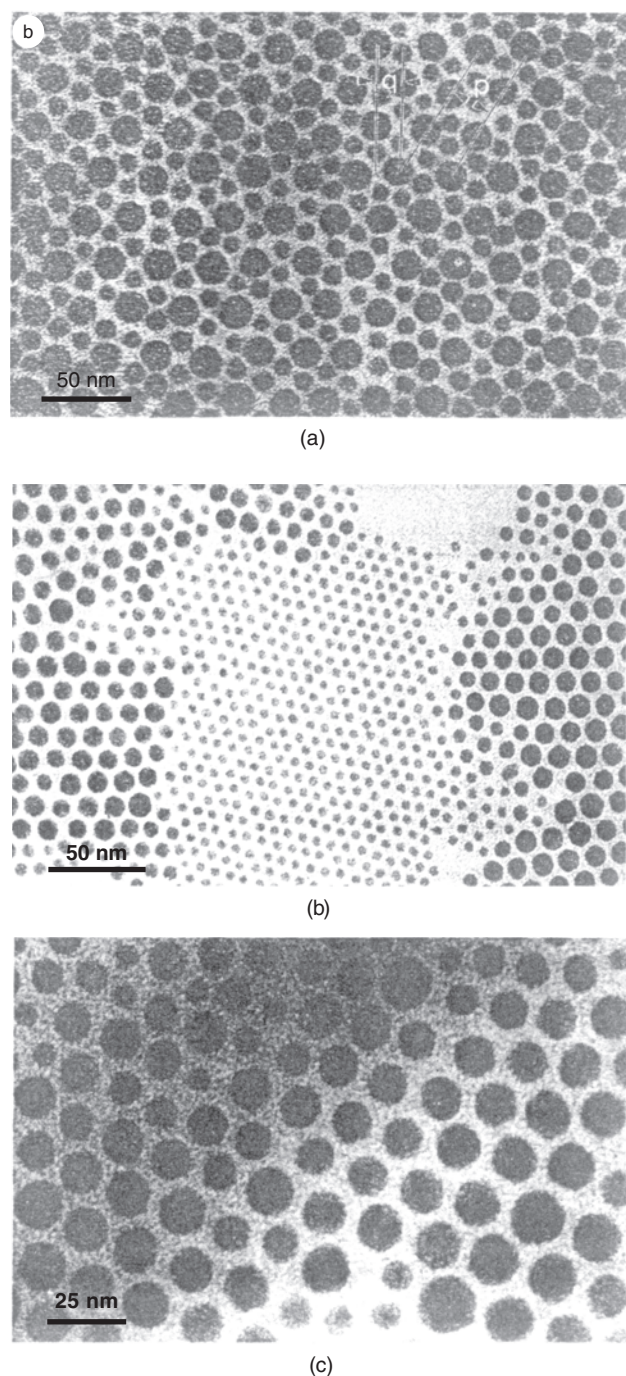
Alternatively, a molecular recognition strategy for the self-assembly of nanoparticles has been systematically developed within the past few years. One recognition principle is to make possible the synthesis of receptor molecules, incorporating appropriately designed binding sites that are capable of recognizing and selectively binding molecular substrates in solution [259, 445, 446]. For example, the diaminopyridine moiety recognizes and selectively binds the uracil moiety in chloroform through the formation of three complementary hydrogen bonds in a way similar to the interactions between base pairs in DNA. Therefore, by incorporating a diaminopyridine moiety into a fraction of alkane molecules used as capping agents at the surface of a silver nanoparticle, the resultant assembly is expected to recognize and selectively bind another nanoparticle capped using alkane molecules modified by the incorporation of the uracil moiety. Generally, it is hoped that, by programming nanocrystals, the self-assembly of complex nanostructures in solution will prove possible. The other is the recognition-directed assembly of silver nanocrystals in solution via pseudotaxane formation [446]. Specifically, a thiol modified dibenzo[24]crown-8 recognition motif was covalently linked to the surface of 7 nm diameter silver nanocrystals. Upon addition of bis-dibenzylammonium dication, an aggregation of nanocrystals was observed. The inhibition of the aggregation phenomenon by the addition of either an excess of dibeno[24]crown-8 or dibenzylammonium cation recognition motifs was further demonstrated.

To maintain a wetting layer on the surface so that nanocrystals can have a chance to self-assemble into large periodical structures, the evaporation rate of the solvent must be slowed. In analogy to molecular crystallization, it is quite reasonable to propose that better superlattices, larger and with fewer defects, are obtained when they form slowly. Once formed, these superlattices may be tough enough not to be perturbed when dewetting finally occurs. Excess low-volatile long-chain alkanethiol ligands turn out to be the ideal additive to slow the liquid droplet evaporation without

introducing other impurities. With a dependence on particle concentration, the size of the domain with a remarkable degree of ordering is routinely greater than several microns in size by maintaining a long-lasting wetting layer. A sharp transition between the ordered monolayer regime and the bare substrate regime (such as amorphous carbon film) suggests that lateral diffusion in the wetting-liquid layer is mainly driven by the interaction between particles. A slight increase in size distribution near the edge of the monolayer domain occasionally takes place, indicating the size-selective process occurring simultaneously with the assembly process. The formation of well-ordered bilayers can be achieved by increasing the nanocrystal concentration while maintaining the concentration of the solvent mixture.

The formation of regular hexagonal close-packed 2-D superlattices is frequently met in the precious metal nanoparticles with a narrow monomodal size distribution. However, what about the particles with bimodal size distributions? Two investigations give the intriguing answers [447, 448]. For alkanethiol-coated Au nanocrystals of two different well-defined size focusing, three types of ordered 2-D arrays that are primarily dependent on the local number and radius ratios of two components are observed, as shown in Figure 10 [447]: first, different-sized particles intimately mixed, forming an ordered bimodal self-organization [Fig. 10(a)], second, size-segregated regions, each containing hexagonal-close-packed monodispersed particles [Fig. 10(b)], and third, a structure in which particles of several different sizes occupy random positions in a pseudohexagonal lattice [Fig. 10c]. These different types of organization are closely related to the radius ratio of small particles to large particles. For two chemically different building blocks, such as thiol-passivated Ag and Au nanoparticles with bimodal particle sizes, they can spontaneously self-organize to true nanoscale colloidal alloy superlattices [448].

One (1-D)- and three-dimensional (3-D) arrays of nanoparticles are appealing. For the generation of low-dimension arrays, the use of templates supporting the arrangement of the particles is favorable. One-dimensional chains of Au nanoparticles linked with polypyrrole formed in porous anode oxidized alumina membranes [449]. As shown by Fitzmaurice and co-workers multiwalled carbon nanotubes can be used for supporting the 1-D arrays of Au nanoparticles up to 10  $\mu\text{m}$  [450]. In particular, long-range 1-D chains of size-controlled Au nanoparticles in planar structured substrates (nanoscale ridge- and valley-structured carbon layers) are fabricated [451], where the Au nanoparticles are predominantly immobilized in valleys and partly on ridges. The other strategy is to utilize bifunctional linkers to form 1-D arrays. A representative example is demonstrated by dithiols with which nanoparticles are bridged to fabricate 1-D arrays of Au nanoparticles [449]. Another interesting experiment shows that the self-assembly of 2-mercaptobenzimidazole (MBMZ) molecules on Ag nanoparticles results in the formation of 1-D aggregates [452]. The length of the wire-like configurations ranges from 200 to 450 nm. Here, the hydrogen bonding (i.e., N-H $\cdots$ N interactions) between MBMZ molecules on the surfaces of different Ag nanoparticles is believed to be the driving force for the formation of wire-like aggregates.



**Figure 10.** (a) Au nanocrystal superlattices comprising Au nanoparticles of two distinct sizes with  $R_B/R_A \approx 0.58$  ( $AB_2$  structure, in analogy to  $AIB_2$ ). (b) Organization of an approximately bimodal ensemble of particles for which  $R_B/R_A \approx 0.47$  ( $R_A = 9.6 \pm 1.5$  nm and  $R_B = 4.5 \pm 0.7$  nm), where phase separation of  $A + B$  mixture of Au nanoparticles in the superlattices takes place. (c) “Random alloy” of Au nanoparticles obtained for an  $R_B/R_A$  ratio greater than 0.85 ( $AB$  structure, in analogy to NaCl). Reprinted with permission from [447], C. J. Kiely et al., *Nature* 396, 444 (1998). © 1998, Macmillan Magazines Ltd.

## 6. APPLICATIONS

Nanoscale metal particles hold great promise for use as advanced materials with new electronic, magnetic, optic, and thermal properties, as well as new catalytic properties. Recent and novel applications, such as building single-electron devices [453, 454], chemical sensors [455], luminescent probes [456, 457], drug delivery [458], medical diagnostics [459], and in high-density magnetic storage devices [319], are being found. For noble metal nanoparticles, the catalytic activities that they embody are ubiquitous as a side branch of this ongoing research in the field of nanotechnology. The noble metal nanoparticles provide new opportunities for catalysis for as much as they can serve as a bridge between homogeneous and heterogeneous catalysts. For instance, the colloidal metal particles of 1–3 nm mean diameter with narrow size distributions show high activity and selectivity for the hydrogenation of olefins and dienes [104, 343–345], the hydration of acrylonitrile [346], and light-induced hydrogen generation from water [347]. Furthermore, colloidal palladium nanoparticles serve as a good catalyst for Suzuki-, Heck-, and Stille-type coupling reactions for carbon–carbon bond formation [105, 460–462]. Platinum and gold nanoparticles catalyze the oxidation of L-sorbose and carbon monoxide, respectively [463–465].

Apart from the catalytic activity of silver [466–468], for example, poly(sodium acrylate)-protected Ag nanoclusters show high activity in catalyzing the oxidation of ethylene to ethylene oxide [468], the Ag nanoparticles play an important role in photographic processes [469–471] and in the substrate for surface-enhanced Raman spectroscopy (SERS) [472, 473]. In addition, due to their large effective scattering cross section and their nonbleaching properties, Ag nanoparticles hold great promise in the field of single molecule labeling-based biological assays [474] and as output signal enhancers in near-field optical microscopy applications [475]. Noble metal particles have also found application in protein–colloid conjugates, where they are used as markers and tracers in optical and electron microscopy to help locate and quantitate antibody–antigen binding sites in cells and tissues [476, 477].

Bimetallic particles find increasing interest not only in catalysis, but also as models for the study of the formation of alloys. Catalysts made of bimetallic nanoparticles are superior compared with those made of pure metals, in terms of activity, selectivity, stability, and resistance to poisoning [478]. The magic of bimetallic nanoparticles usually originates from their structures. Many investigations have shown that the structure–function relationship involving these nanoparticles holds the key to the understanding of catalytic processes. For instance, the catalytic mechanisms of monometallic nanoparticles and bimetallic nanoparticles in petroleum refining processes and multiwalled nanotube production are understood only after the structures of these catalysts have been examined [479, 480]. With extended X-ray absorption fine-structure (EXAFS) techniques, it has been found that Cu atoms concentrate in the surface of Cu/Ru bimetallic nanoparticles [479]. Such segregation helps reduce the rate of hydrogenolysis, which requires large patches of Ru atoms to function. Pd–Pt bimetallic nanoparticles are known to be more resistive to sulfur poisoning due to the special surface arrangement [478, 481, 482].

These results clearly demonstrate that special structures of bimetallic nanoparticles can lead to novel properties and enhancement of activities such as the catalytic function. In addition, bimetallic nanoparticles are preferred heterogeneous catalysts in petroleum reforming processes [479]. Large-diameter bimetallic nanoparticles have been used to catalyze the growth of carbon filaments [483]. Nanoscopic magnetic FePt, CoPt, and  $\text{Fe}_x\text{Co}_y\text{Pt}_{100-x-y}$  alloy particles received intensive attention due to their perpendicular magnetic anisotropy [484], high chemical stability [485], and potential applications for high-density magneto-optical recording media [486–490].

## 7. SUMMARY

This frontier of nanomaterial research follows great achievements, one after another, in the laboratory, so that it becomes more and more difficult to keep up to date with all new successes, and to derive the general trends that would be the main pathways to nanotechnology. So what would be the next logical step to take to envision the prospective functional materials? The development in nanosciences will motivate the advancement in future technology. Recently, large-scale production of monodispersed thiol-derivatized Au nanoparticles in gram scale have been successfully developed by Klabunde and co-workers using the solvated metal atom dispersion method [491]. Thus, it seems that this method lays the groundwork for the scaling up of known laboratory-scale syntheses into reliable, standard manufacturing procedures for nanomaterials with uniform size and monodispersed morphologies. Nevertheless, this alone is not enough since a nanoscale substance must have superior performance. Once available at low cost, the nanoparticles should have added functionality to a great extent by means of surface modification. If all of these problems have been tackled, the probable last step left that should be considered to make technological applications possible is the alignment and addressing of nanoparticles. This is necessary in nano-devices such as nanotransistors and nanocircuits.

The immense advancement in the synthetic ability of nanoparticles is partly attributed to the diverse analytic tools and characterization methods available, which contribute to a close examination of the morphologies and a profound understanding of the structures of the nanomaterials. For example, without the high-resolution transmission electron microscope and energy dispersive X-ray spectroscopy, we would know nothing about the structures and constituents of nanomaterials.

Although nanoparticles have numerous available properties for future applications as summarized in this chapter, nothing is ever omnipotent in the world. Therefore, the role of nanoparticles as well as other nanomaterials in future nanotechnology should hardly be overstated. We are looking forward to the day when we can abandon the old-fashioned manufacturing techniques and shrink them down to an economically and actually preferable nanoscale.

## GLOSSARY

**Colloid** System in which finely divided particles, which are approximately 1–1000 nm in size, are dispersed within a

continuous medium in a manner that prevents them from being filtered easily or settled rapidly.

**Dynamic light scattering (DLS)** Also known as **photon correlation spectroscopy (PCS)**. DLS measures the autocorrelation function of the intensity of the scattering light. It is an effective method to study the size of colloids (hydrodynamic radius), the kinetics of aggregation of the colloids, and the structure of the aggregates formed.

**Energy-dispersive X-ray spectroscopy (EDS)** A precise microanalysis technique. It shows the counting of X-rays emitted from the beam-illuminated specimen region as a function of photon energy.

**Noble metal** Metal or alloy, such as gold, that is highly resistant to oxidation and corrosion.

**Plasmon absorption** Plasmons are the collective oscillations of the electron density in the metal nanoparticles of a colloid, which give rise to an intense absorption in the near UV–visible region. Plasmon absorption is produced by the strong coupling of nanoparticles to the electromagnetic radiation of incident light, leading to a collective excitation of all of the free electrons in the particles.

**Poly(N-vinyl-2-pyrrolidone) (PVP)** A widely used stabilizer in the preparation of nanoparticles.

**Stabilizer** Substance that renders or maintains a solution, mixture, suspension, or state resistant to chemical or physical change. In the field of nanoscience, a stabilizer is used to keep nanoparticles stable against aggregation.

## REFERENCES

1. Z. W. Pan, Z. R. Dai, and Z. L. Wang, *Science* 291, 1947 (2001).
2. W. Shi, H. Peng, N. Wang, C. P. Li, L. Xu, C. S. Lee, R. Kalish, and S. T. Lee, *J. Am. Chem. Soc.* 123, 11095 (2001).
3. Z. R. Dai, Z. W. Pan, and Z. L. Wang, *J. Phys. Chem. B* 106, 902 (2002).
4. S. H. Yu and M. Yoshimura, *Adv. Mater.* 14, 296 (2002).
5. T. Sasaki and M. Watanabe, *J. Phys. Chem. B* 101, 10159 (1997).
6. Z. R. Dai, Z. W. Pan, and Z. L. Wang, *J. Am. Chem. Soc.* 124, 8673 (2002).
7. R. Tenne, M. Homyonfer, and Y. Feldman, *Chem. Mater.* 10, 3225 (1998).
8. Y. Saito and T. Matsumoto, *Nature* 392, 237 (1998).
9. G. Schmid, *Chem. Rev.* 92, 1709 (1992).
10. M. Faraday, *Philos. Trans. R. Soc. London* 147, 145 (1857).
11. G. Mie, *Ann. Phys.* 25, 377 (1908).
12. A. Henglein, *J. Phys. Chem.* 97, 5457 (1993).
13. F. W. S. Benfield, M. L. H. Green, J. S. Ogden, and D. Young, *J. Chem. Soc., Chem. Commun.* 866 (1973).
14. K. J. Klabunde, P. Timms, P. S. Skell, and S. D. Ittel, *Inorg. Synth.* 19, 59 (1979).
15. M. Andrews, G. A. Ozin, and C. G. Francis, *Inorg. Synth.* 22, 116 (1981).
16. K. J. Klabunde, *Platinum Met. Rev.* 36, 80 (1992).
17. K. J. Klabunde, D. Zhang, G. N. Glavee, C. M. Sorensen, and G. C. Hadjipanayis, *Chem. Mater.* 6, 784 (1994).
18. K. J. Klabunde and G. Cárdenas-Trivino, in “Active Metals: Preparation, Characterization, Applications” (A. Fürstner, Ed.), pp. 237–278. VCH, New York, 1996.
19. G. W. Rice, in “Laser Chemistry of Organometallics” (J. Chaiken, Ed.), p. 273. American Chemical Society, Washington, DC, 1993.
20. A. Fojtik and A. Henglein, *Ber. Bunsen-Ges. Phys. Chem.* 97, 252 (1993).

21. M. Procházka, P. Mojžeš, J. Štěpánek, B. Vlčková, and P.-Y. Turpin, *Anal. Chem.* 69, 5103 (1997).
22. J. Nedderson, G. Chumanov, and T. M. Cotton, *Appl. Spectrosc.* 47, 1959 (1993).
23. M. S. Sibbald, G. Chumanov, and T. M. Cotton, *J. Phys. Chem.* 100, 4672 (1996).
24. M. S. Yeh, Y. S. Yang, Y. P. Lee, H. F. Lee, Y. H. Yeh, and C. S. Yeh, *J. Phys. Chem. B* 103, 6851 (1999).
25. F. Mafuné, J. Kohno, Y. Takeda, T. Kondow, and H. Sawabe, *J. Phys. Chem. B* 104, 9111 (2000).
26. F. Mafuné, J. Kohno, Y. Takeda, T. Kondow, and H. Sawabe, *J. Phys. Chem. B* 105, 5114 (2001).
27. F. Mafuné, J. Kohno, Y. Takeda, and T. Kondow, *J. Phys. Chem. B* 106, 7575 (2002).
28. S. T. Lin, M. T. Franklin, and K. J. Klabunde, *Langmuir* 2, 259 (1986).
29. G. Cárdenas-Trivino, K. J. Klabunde, and E. Brock Dale, *Langmuir* 3, 986 (1987).
30. K. J. Klabunde, J. Habdas, and G. Cárdenas-Trivino, *Chem. Mater.* 1, 481 (1989).
31. A. W. Olsen and Z. H. Kafafi, *J. Am. Chem. Soc.* 113, 7758 (1991).
32. E. B. Zuckerman, K. J. Klabunde, B. J. Olivier, and C. M. Sorensen, *Chem. Mater.* 1, 12 (1989).
33. K. J. Klabunde, G. Youngers, E. J. Zuckerman, B. J. Tan, S. Antrim, and P. M. Sherwood, *Eur. J. Solid State Inorg. Chem.* 29, 227 (1992).
34. S. A. Harfenist, Z. L. Wang, M. M. Alvarez, I. Vezmar, and R. L. Whetten, *J. Phys. Chem.* 100, 13904 (1996).
35. S. A. Harfenist, Z. L. Wang, R. L. Whetten, I. Vezmar, and M. M. Alvarez, *Adv. Mater.* 9, 817 (1997).
36. Z. L. Wang, S. A. Harfenist, R. L. Whetten, J. Bentley, and N. D. Evans, *J. Phys. Chem. B* 102, 3068 (1998).
37. T. J. Mason (Ed.), "Advances in Sonochemistry," Vols. 1, 2, 3. JAI Press, London, 1990, 1991, 1993.
38. Y. T. Didenko, W. B. McNamara, III, and K. S. Suslick, *J. Am. Chem. Soc.* 121, 5817 (1999).
39. A. Henglein, *Ultrason.* 25, 6 (1987).
40. M. Gutierrez, A. Henglein, and J. K. Dohrmann, *J. Phys. Chem.* 91, 6687 (1987).
41. K. S. Suslick, S.-B. Choe, A. A. Cichowlas, and M. W. Grinstaff, *Nature* 253, 414 (1991).
42. K. S. Suslick, M. Fang, and T. Hyeon, *J. Am. Chem. Soc.* 118, 11960 (1996).
43. Y. Nagata, Y. Watanabe, S. Fujita, T. Dohmaru, and S. Taniguchi, *J. Chem. Soc., Chem. Commun.* 1620 (1992).
44. S. A. Yeung, R. Hobson, S. Biggs, and F. Grieser, *J. Chem. Soc., Chem. Commun.* 378 (1993).
45. F. Grieser, R. Hobson, J. Sostaric, and P. Mulvaney, *Ultrason.* 34, 547 (1996).
46. K. Okitsu, H. Bandow, Y. Maeda, and Y. Nagata, *Chem. Mater.* 8, 315 (1996).
47. Y. Nagata, Y. Mizukoshi, K. Okitsu, and Y. Maeda, *Rad. Res.* 146, 333 (1996).
48. K. Okitsu, Y. Mizukoshi, H. Bandow, Y. Maeda, T. Yamamoto, and Y. Nagata, *Ultrason. Sonochem.* 3, 249 (1996).
49. Y. Mizukoshi, K. Okitsu, T. Yamamoto, R. Oshima, Y. Nagata, and Y. Maeda, *J. Phys. Chem. B* 101, 5470 (1997).
50. Y. Mizukoshi, R. Oshima, Y. Maeda, and Y. Nagata, *Langmuir* 15, 2733 (1999).
51. K. Okitsu, S. Nagaoka, S. Tanabe, H. Matsumoto, Y. Mizukoshi, and Y. Nagata, *Chem. Lett.* 271 (1999).
52. R. A. Caruso, M. Ashokkumar, and F. Grieser, *Colloids Surf. A* 169, 219 (2000).
53. T. Fujimoto, Y. Mizukoshi, R. Oshima, Y. Nagata, and Y. Maeda, *Trans. Mater. Res. Soc. Jpn.* 25, 95 (2000).
54. Y. Maeda, Y. Mizukoshi, E. Takagi, T. Fujimoto, R. Oshima, and Y. Nagata, *Trans. Mater. Res. Soc. Jpn.* 25, 99 (2000).
55. Y. Mizukoshi, E. Takagi, H. Okuno, R. Oshima, Y. Maeda, and Y. Nagata, *Ultrason. Sonochem.* 8, 1 (2001).
56. T. Fujimoto, S. Terauchi, H. Umehara, I. Kojima, and W. Henderson, *Chem. Mater.* 13, 1057 (2001).
57. T. Fujimoto, Y. Mizukoshi, Y. Nagata, Y. Maeda, and R. Oshima, *Scr. Mater.* 44, 2183 (2001).
58. J. Zhu, S. Liu, O. Palchik, Y. Kolytyn, and A. Gedanken, *Langmuir* 16, 6369 (2000).
59. K. Okitsu, A. Yue, S. Tanabe, and H. Matsumoto, *Chem. Mater.* 12, 3006 (2000).
60. A. Henglein and R. Tausch-Treml, *J. Colloid Interface Sci.* 80, 84 (1981).
61. M. O. Delcourt, J. Belloni, J. L. Marignier, C. Mory, and C. Colliex, *Rad. Phys. Chem.* 23, 485 (1984).
62. G. Mills and A. Henglein, *Rad. Phys. Chem.* 26, 385 (1985).
63. J. L. Marignier, J. Belloni, M. O. Delcourt, and J. P. Chevalier, *Nature* 317, 344 (1985).
64. S. Mosseri, A. Henglein, and E. Janata, *J. Phys. Chem.* 93, 6791 (1989).
65. B. G. Ershov, E. Janata, M. Michaelis, and A. Henglein, *J. Phys. Chem.* 95, 8996 (1991).
66. M. Michaelis and A. Henglein, *J. Phys. Chem.* 96, 4719 (1992).
67. B. G. Ershov, E. Janata, and A. Henglein, *Rad. Phys. Chem.* 39, 123 (1992).
68. A. Henglein and M. Giersig, *J. Phys. Chem. B* 103, 9533 (1999).
69. R. Rafaeloff, Y. Haruvy, J. Binenboym, G. Baruch, and L. A. Rajbenbach, *J. Mol. Catal.* 22, 219 (1983).
70. A. Henglein and D. Meisel, *Langmuir* 14, 7392 (1998).
71. A. Henglein, *Langmuir* 15, 6738 (1999).
72. P. Mulvaney, M. Giersig, and A. Henglein, *J. Phys. Chem.* 97, 7061 (1993).
73. A. Henglein, *J. Phys. Chem. B* 104, 2201 (2000).
74. K. Kurihara, J. Kizling, P. Stenius, and J. H. Fendler, *J. Am. Chem. Soc.* 105, 2574 (1983).
75. Y. Zhou, S. H. Yu, C. Y. Wang, X. G. Li, Y. R. Zhu, and Z. Y. Chen, *Adv. Mater.* 11, 850 (1999).
76. Y. Zhou, C. Y. Wang, Y. R. Zhu, and Z. Y. Chen, *Chem. Mater.* 11, 2310 (1999).
77. K. Torigoe and K. Esumi, *Langmuir* 8, 59 (1992).
78. Y. Yonezawa, T. Sato, M. Ohno, and H. Hada, *J. Chem. Soc., Faraday Trans.* 83, 1559 (1987).
79. P. Barnickel and A. Wokaun, *Mol. Phys.* 69, 1 (1990).
80. T. Sato, S. Kuroda, A. Takami, Y. Yonezawa, and H. Hada, *Appl. Organomet. Chem.* 5, 261 (1991).
81. Y. Yonezawa, T. Sato, S. Kuroda, and K. Kuge, *J. Chem. Soc., Faraday Trans.* 87, 1905 (1991).
82. N. Toshima, T. Takahashi, and H. Hirai, *Chem. Lett.* 35 (1986).
83. N. Toshima, T. Takahashi, and H. Hirai, *Chem. Lett.* 1245 (1985).
84. N. Toshima and T. Takahashi, *Bull. Chem. Soc. Jpn.* 65, 400 (1992).
85. A. B. R. Mayer and J. E. Mark, *Colloid Polym. Sci.* 275, 333 (1997).
86. A. B. R. Mayer and J. E. Mark, *J. Macromol. Sci., Pure Appl. Chem.* A34, 2151 (1997).
87. A. B. R. Mayer and J. E. Mark, *Eur. Polym. J.* 34, 103 (1998).
88. A. B. R. Mayer and M. Antonietti, *Colloid Polym. Sci.* 276, 769 (1998).
89. K. Esumi, A. Suzuki, N. Aihara, K. Usui, and K. Torigoe, *Langmuir* 14, 3157 (1998).
90. K. Kurihara, J. H. Fendler, I. Ravet, and J. Nagy, *J. Mol. Catal.* 34, 325 (1986).
91. W. Yu, W. Tu, and H. Liu, *Langmuir* 15, 6 (1999).
92. W. Tu and H. Liu, *Chem. Mater.* 12, 564 (2000).
93. T. S. Ahmadi, Z. L. Wang, T. C. Green, A. Henglein, and M. A. El-Sayed, *Science* 272, 1924 (1996).
94. W. Yu and H. Liu, *Chem. Mater.* 10, 1205 (1998).
95. A. Henglein, *J. Phys. Chem. B* 104, 6683 (2000).
96. A. Henglein and M. Giersig, *J. Phys. Chem. B* 104, 6767 (2000).
97. R. S. Underhill and G. Liu, *Chem. Mater.* 12, 3633 (2000).

98. D. Burshtain, L. Zeiri, and S. Efrima, *Langmuir* 15, 3050 (1999).
99. C. L. Chiang, *J. Colloid Interface Sci.* 239, 334 (2001).
100. M. L. Wu, D. H. Chen, and T. C. Huang, *Chem. Mater.* 13, 599 (2001).
101. K. R. Brown, D. G. Walter, and M. J. Natan, *Chem. Mater.* 12, 306 (2000).
102. K. Torigoe, A. Suzuki, and K. Esumi, *J. Colloid Interface Sci.* 241, 346 (2001).
103. M. Zhao and R. M. Crooks, *Chem. Mater.* 11, 3379 (1999).
104. H. Hirai, Y. Nakao, and N. Toshima, *J. Macromol. Sci., Chem.* A12, 1117 (1978).
105. O. Siiman and W. P. Hsu, *J. Chem. Soc., Faraday Trans.* 82, 851 (1986).
106. S. Pathak, M. T. Greci, R. C. Kwong, K. Mercado, G. K. S. Prakash, G. A. Olah, and M. E. Thompson, *Chem. Mater.* 12, 1985 (2000).
107. Y. Wang, J. Ren, K. Deng, L. Gui, and Y. Tang, *Chem. Mater.* 12, 1622 (2000).
108. J. Turkevich, P. C. Stevenson, and J. Hillier, *J. Discuss. Faraday Soc.* 11, 55 (1951).
109. G. Frens, *Nature* 241, 20 (1973).
110. C. H. Munro, W. E. Smith, M. Garner, J. Clarkson, and P. C. White, *Langmuir* 11, 3721 (1995).
111. M. Y. Han, C. H. Quek, W. Huang, C. H. Chew, and C. M. Gan, *Chem. Mater.* 11, 1144 (1999).
112. A. B. R. Mayer, W. Grebner, and R. Wannemacher, *J. Phys. Chem. B* 104, 7278 (2000).
113. K. Meguro, M. Torizuka, and K. Esumi, *Bull. Chem. Soc. Jpn.* 61, 341 (1988).
114. N. R. Jana, L. Gearheart, and C. J. Murphy, *Chem. Mater.* 13, 2313 (2001).
115. S. Chen, Z. Fan, and D. L. Carroll, *J. Phys. Chem. B* 106, 10777 (2002).
116. J. G. Wang, K. G. Neoh, and E. T. Kang, *J. Colloid Interface Sci.* 239, 78 (2001).
117. X. Dai, Y. Tan, and J. Xu, *Langmuir* 18, 9010 (2002).
118. Y. Tan, Y. Li, and D. Zhu, *Langmuir* 18, 3392 (2002).
119. H. Hirai, Y. Nakao, and N. Toshima, *Chem. Lett.* 545 (1978).
120. H. Hirai, Y. Nakao, and N. Toshima, *J. Macromol. Sci., Chem.* A13, 727 (1979).
121. H. Hirai, *J. Macromol. Sci., Chem.* A13, 633 (1979).
122. N. Toshima, M. Kuriyama, Y. Yamada, and H. Hirai, *Chem. Lett.* 793 (1981).
123. M. Komiyama and H. Hirai, *Bull. Chem. Soc. Jpn.* 56, 2833 (1983).
124. H. Hirai, *Makromol. Chem., Suppl.* 14, 55 (1985).
125. A. Borsla, A. M. Wilhelm, and H. Delmas, *Catal. Today* 66, 389 (2001).
126. A. B. R. Mayer and J. E. Mark, *Macromol. Rep.* A33, 451 (1996).
127. A. B. R. Mayer and J. E. Mark, *Polym. Bull.* 37, 683 (1996).
128. A. B. R. Mayer, J. E. Mark, and S. H. Hausner, *J. Appl. Polym. Sci.* 70, 1209 (1998).
129. A. B. R. Mayer, J. E. Mark, and S. H. Hausner, *Angew. Makromol. Chem.* 259, 45 (1998).
130. A. B. R. Mayer and J. E. Mark, *J. Polym. Sci. A: Polym. Chem.* 35, 3151 (1997).
131. J. H. Youk, J. Locklin, C. Xia, M. K. Park, and R. Advincula, *Langmuir* 17, 4681 (2001).
132. A. B. R. Mayer, J. E. Mark, and R. E. Morris, *Polym. J.* 30, 197 (1998).
133. C.-W. Chen, K. Arai, K. Yamamoto, T. Serizawa, and M. Akashi, *Macromol. Chem. Phys.* 201, 2811 (2000).
134. C.-W. Chen and M. Akashi, *Langmuir* 13, 6465 (1997).
135. C.-W. Chen, T. Takezako, K. Yamamoto, T. Serizawa, and M. Akashi, *Colloids Surf. A* 169, 107 (2000).
136. C.-W. Chen and M. Akashi, *J. Polym. Sci. A: Polym. Chem.* 35, 1329 (1997).
137. A. Dalmia, C. L. Lineken, and R. F. Savinell, *J. Colloid Interface Sci.* 205, 535 (1998).
138. K. Meguro, Y. Nakamura, Y. Hayashi, M. Torizuka, and K. Esumi, *Bull. Chem. Soc. Jpn.* 61, 347 (1988).
139. T. Teranishi and M. Miyake, *Chem. Mater.* 10, 594 (1998).
140. T. Teranishi, M. Hosoe, and M. Miyake, *Adv. Mater.* 9, 65 (1997).
141. G. W. Busser, J. G. Van Ommen, and J. A. Lercher, *Adv. Catal. Nanostruct. Mater.* 213 (1996).
142. F. Porta, F. Ragaini, S. Cenini, and G. Scari, *Gazz. Chim. Ital.* 122, 361 (1992).
143. F. Bonet, V. Delmas, S. Grugeon, R. Herrera Urbina, P.-Y. Silvert, and K. Tekaia-Elhsissen, *Nanostruct. Mater.* 11, 1277 (2000).
144. W. Yu, M. Liu, H. Liu, and J. Zheng, *J. Colloid Interface Sci.* 210, 218 (1999).
145. C. K. Tan, V. Newberry, T. R. Webb, and C. A. McAuliffe, *J. Chem. Soc., Dalton Trans.* 1299 (1987).
146. J. Kiwi and M. Grätzel, *J. Am. Chem. Soc.* 101, 7214 (1979).
147. M. Moutonnet, J. Kizling, P. Stenius, and G. Maire, *Colloids Surf.* 5, 209 (1982).
148. M. Moutonnet, J. Kizling, R. Touroude, G. Maire, and P. Stenius, *Appl. Catal.* 20, 163 (1986).
149. C. Larpent and H. Patin, *J. Mol. Catal.* 44, 191 (1988).
150. C. Larpent, F. Brisse-Le Menn, and H. Patin, *New J. Chem.* 15, 361 (1991).
151. P. Drogat-Landré, M. Lemaire, D. Richard, and P. Gallezot, *J. Mol. Catal.* 78, 257 (1993).
152. P. Drogat-Landré, D. Richard, M. Draye, P. Gallezot, and M. Lemaire, *J. Catal.* 147, 214 (1994).
153. K. Nasar, F. Fache, M. Lemaire, J. C. Béziat, M. Besson, and P. Gallezot, *J. Mol. Catal.* 87, 107 (1994).
154. Y. Lin and R. G. Finke, *Inorg. Chem.* 33, 4891 (1994).
155. J. D. Aiken, III, Y. Lin, and R. G. Finke, *J. Mol. Catal. A: Chem.* 114, 29 (1996).
156. M. A. Watzky and R. G. Finke, *J. Am. Chem. Soc.* 119, 10382 (1997).
157. M. A. Watzky and R. G. Finke, *Chem. Mater.* 9, 3083 (1997).
158. J. D. Aiken, III and R. G. Finke, *J. Am. Chem. Soc.* 121, 8803 (1999).
159. J. D. Aiken, III and R. G. Finke, *Chem. Mater.* 11, 1035 (1999).
160. H. Hirai, H. Wakabayashi, and M. Komiyama, *Chem. Lett.* 1047 (1983).
161. H. Hirai, H. Wakabayashi, and M. Komiyama, *Bull. Chem. Soc. Jpn.* 59, 367 (1986).
162. H. Hirai, H. Wakabayashi, and M. Komiyama, *Bull. Chem. Soc. Jpn.* 59, 545 (1986).
163. P. Van Rheenen, M. McKelvy, R. Marzke, and W. S. Glaunsinger, *Inorg. Synth.* 24, 238 (1983).
164. A. B. R. Mayer, R. W. Johnson, S. H. Hausner, and J. E. Mark, *J. Macromol. Sci., Pure Appl. Chem.* A36, 1427 (1999).
165. A. B. R. Mayer, S. H. Hausner, and J. E. Mark, *Polym. J.* 32, 15 (2000).
166. L. Balogh and D. A. Tomalia, *J. Am. Chem. Soc.* 120, 7355 (1998).
167. M. Zhao, L. Sun, and R. M. Crooks, *J. Am. Chem. Soc.* 120, 4877 (1998).
168. M. Zhao and R. M. Crooks, *Angew. Chem., Int. Ed.* 38, 364 (1999).
169. W. E. Garcia, L. A. Baker, and R. M. Crooks, *Anal. Chem.* 71, 256 (1999).
170. M. Zhao and R. M. Crooks, *Adv. Mater.* 11, 217 (1999).
171. M. Zhao, L. Sun, and R. M. Crooks, *Polym. Prepr.* 40, 400 (1999).
172. V. Chechik and R. M. Crooks, *J. Am. Chem. Soc.* 122, 1243 (2000).
173. R. M. Crooks, M. Zhao, L. Sun, V. Chechik, and L. K. Yeung, *Acc. Chem. Res.* 34, 181 (2001).
174. K. Esumi, A. Suzuki, A. Yamahira, and K. Torigoe, *Langmuir* 16, 2604 (2000).
175. K. Esumi, R. Nakamura, A. Suzuki, and K. Torigoe, *Langmuir* 16, 7842 (2000).

176. K. Esumi, A. Kameo, A. Suzuki, and K. Torigoe, *Colloids Surf. A* 189, 155 (2001).
177. K. Esumi, T. Hosoya, A. Suzuki, and K. Torigoe, *J. Colloid Interface Sci.* 229, 303 (2000).
178. Y. Nakao and K. Kaeriyama, *J. Colloid Interface Sci.* 110, 82 (1986).
179. Y. Berkovich and N. Garti, *Colloids Surf. A* 128, 91 (1997).
180. C.-C. Wang, D.-H. Chen, and T.-C. Huang, *Colloids Surf. A* 189, 145 (2001).
181. H. Itoh, M. Miura, R. Okamoto, and E. Kikuchi, *Bull. Chem. Soc. Jpn.* 64, 333 (1991).
182. C. Larpent, F. Brisse-Le Menn, and H. Patin, *J. Mol. Catal.* 65, L35 (1991).
183. C. Larpent, E. Bernard, F. Brisse-Le Menn, and H. Patin, *J. Mol. Catal. A: Chem.* 116, 277 (1997).
184. Y. Nakao and K. Kaeriyama, *Bull. Chem. Soc. Jpn.* 60, 4465 (1987).
185. H. Hirai, H. Aizawa, and H. Shiozaki, *Chem. Lett.* 1527 (1992).
186. L. M. Liz-Marzán and I. Lado-Tourino, *Langmuir* 12, 3585 (1996).
187. W. Wang, S. Efrima, and O. Regev, *Langmuir* 14, 602 (1998).
188. S. Chen, H. Yao, and K. Kimura, *Langmuir* 17, 733 (2001).
189. H. Bönnemann, W. Brijoux, R. Brinkmann, R. Fretzen, T. Jousen, R. Köppler, B. Korall, P. Neiteler, and J. Richter, *J. Mol. Catal.* 86, 129 (1994).
190. H. Bönnemann, G. Braun, W. Brijoux, R. Brinkmann, A. Schulze Tilling, K. Seevogel, and K. Siepen, *J. Organomet. Chem.* 520, 143 (1996).
191. H. Bönnemann and W. Brijoux, in "Active Metals: Preparation, Characterization, Applications" (A. Fürstner, Ed.), pp. 339–379. VCH, New York, 1996.
192. H. Bönnemann, W. Brijoux, R. Brinkmann, E. Dinjus, T. Jousen, and B. Korall, *Angew. Chem., Int. Ed. Engl.* 30, 1312 (1991).
193. H. Bönnemann, R. Brinkmann, R. Köppler, P. Neiteler, and J. Richter, *Adv. Mater.* 4, 804 (1992).
194. H. Bönnemann, W. Brijoux, R. Brinkmann, E. Dinjus, R. Fretzen, T. Jousen, and B. Korall, *J. Mol. Catal.* 74, 323 (1992).
195. H. Bönnemann, R. Brinkmann, and P. Neiteler, *Appl. Organomet. Chem.* 8, 361 (1994).
196. D. I. Gittins and F. Caruso, *Angew. Chem., Int. Ed. Engl.* 40, 3001 (2001).
197. H. H. Huang, F. Q. Yan, Y. M. Kek, C. H. Chew, G. Q. Xu, W. Ji, P. S. Oh, and S. H. Tang, *Langmuir* 13, 172 (1997).
198. H. Ishizuka, T. Tano, K. Torigoe, E. Esumi, and K. Meguro, *Colloids Surf.* 63, 337 (1992).
199. K. Esumi, N. Sato, K. Torigoe, and K. Meguro, *J. Colloid Interface Sci.* 149, 295 (1992).
200. Y. Tan, Y. Li, and D. Zhu, *J. Colloid Interface Sci.* (in press, 2003).
201. M. Antonietti, E. Wenz, L. M. Bronstein, and M. V. Seregina, *Adv. Mater.* 7, 1000 (1995).
202. J. P. Spatz, S. Mössmer, and M. Möller, *Chem. Eur. J.* 2, 1552 (1996).
203. M. V. Seregina, L. M. Bronstein, O. A. Platonova, D. M. Chernyshov, P. M. Valetsky, J. Hartmann, E. Wenz, and M. Antonietti, *Chem. Mater.* 9, 923 (1997).
204. S. Klingelhöfer, W. Heitz, A. Greiner, S. Oestreich, S. Förster, and M. Antonietti, *J. Am. Chem. Soc.* 119, 10116 (1997).
205. S. N. Sidorov, L. M. Bronstein, P. M. Valetsky, J. Hartmann, H. Cölfen, H. Schnablegger, and M. Antonietti, *J. Colloid Interface Sci.* 212, 197 (1999).
206. J. Le Bars, U. Specht, J. S. Bradley, and D. G. Blackmond, *Langmuir* 15, 7621 (1999).
207. D. M. Chernyshov, L. M. Bronstein, H. Börner, B. Berton, and M. Antonietti, *Chem. Mater.* 12, 114 (2000).
208. D. N. Furlong, A. Launikonis, W. H. F. Sasse, and J. V. Sanders, *J. Chem. Soc., Faraday Trans.* 80, 571 (1984).
209. A. Harriman, J. M. Thomas, and G. R. Millward, *New J. Chem.* 11, 757 (1987).
210. K. Kopple, D. Meyerstein, and D. Meisel, *J. Phys. Chem.* 84, 870 (1980).
211. M. R. Mucalo and R. P. Cooney, *J. Chem. Soc., Chem. Commun.* 94 (1989).
212. M. T. Reetz, W. Helbig, and S. A. Quaiser, in "Active Metals: Preparation, Characterization, Applications" (A. Fürstner, Ed.), pp. 279–297. VCH, New York, 1996.
213. M. T. Reetz and W. Helbig, *J. Am. Chem. Soc.* 116, 7401 (1994).
214. M. T. Reetz and S. A. Quaiser, *Angew. Chem., Int. Ed. Engl.* 34, 2240 (1995).
215. M. P. Pileni, *J. Phys. Chem.* 97, 6961 (1993).
216. M. P. Pileni, A. Taleb, and C. Petit, *J. Dispersion Sci. Technol.* 19, 185 (1998).
217. A. Filankembo and M. P. Pileni, *J. Phys. Chem. B* 104, 5865 (2000).
218. M. P. Pileni, *J. Phys. Chem. B* 105, 3358 (2001) and references therein.
219. M. P. Pileni, *Langmuir* 17, 7476 (2001) and references therein.
220. M. A. López-Quintela and J. Rivas, *J. Colloid Interface Sci.* 158, 446 (1993).
221. J. P. Cason, K. Khambaswadkar, and C. B. Roberts, *Ind. Eng. Chem. Res.* 39, 4749 (2000).
222. J. R. Heath, C. M. Knobler, and D. V. Leff, *J. Phys. Chem. B* 101, 189 (1997).
223. S. Chen, *Langmuir* 17, 2878 (2001).
224. J. Hambrock, R. Becker, A. Birkner, J. Weib, and R. A. Fischer, *Chem. Commun.* 68 (2002).
225. A. L. Rogach, D. V. Talapin, E. V. Shevchenko, A. Kornowski, M. Haase, and H. Weller, *Adv. Funct. Mater.* 12, 653 (2002).
226. Y. Li, J. Liu, Y. Wang, and Z. L. Wang, *Chem. Mater.* 13, 1008 (2001).
227. X. M. Lin, M. H. Jaeger, C. M. Sorensen, and K. J. Klabunde, *J. Phys. Chem. B* 105, 3353 (2001).
228. N. K. Chaki, S. G. Sudrik, H. R. Sonawane, and K. Vijayamohan, *Chem. Commun.* 76 (2002).
229. B. V. Enustun and J. Turkevich, *J. Am. Chem. Soc.* 85, 3317 (1963).
230. K. V. Sarathy, G. Raina, R. T. Yadav, G. U. Kulkarni, and C. N. R. Rao, *J. Phys. Chem. B* 101, 9876 (1997).
231. S. Chen, K. Huang, and J. A. Stearns, *Chem. Mater.* 12, 540 (2000).
232. C. H. Walker, J. V. St. John, and P. W. Neilson, *J. Am. Chem. Soc.* 123, 3846 (2001).
233. A. Mayer, *Mater. Sci. Eng. C6*, 155 (1998).
234. A. C. Curtis, D. G. Duff, P. P. Edwards, D. A. Jefferson, B. F. G. Johnson, A. I. Kirkland, and A. S. Wallace, *J. Phys. Chem.* 92, 2270 (1988).
235. K. Esumi, T. Tano, and K. Meguro, *Langmuir* 5, 268 (1989).
236. T. Tano, K. Esumi, and K. Meguro, *J. Colloid Interface Sci.* 133, 530 (1989).
237. F. Fievet, J. P. Lagier, B. Blin, B. Beaudoin, and M. Figlarz, *Solid State Ionics* 32–33, 198 (1988).
238. M. Brust, M. Walker, D. Bethell, D. J. Schiffrin, and R. Whyman, *J. Chem. Soc., Chem. Commun.* 801 (1994).
239. G. Schmid and A. Lehnert, *Angew. Chem., Int. Ed. Engl.* 28, 780 (1989).
240. G. Schmid, A. Lehnert, U. Kreibitz, Z. Adamczyk, and P. Z. Belouschek, *Naturforsch.* 45b, 989 (1990).
241. W. Wang, X. Chen, and S. Efrima, *J. Phys. Chem. B* 103, 7238 (1999).
242. C. J. Zhong, W. X. Zhang, F. L. Leibowitz, and H. H. Eichelberger, *Chem. Commun.* 1211 (1999).
243. M. Bowker and R. J. Madix, *Surf. Sci.* 95, 190 (1980).
244. M. Bowker and R. J. Madix, *Surf. Sci.* 116, 549 (1982).
245. O. Tzhayik, P. Sawant, S. Efrima, E. Kovalev, and J. T. Klug, *Langmuir* 18, 3364 (2002).
246. M. O. Delcourt and J. Belloni, *Radiochem. Radioanal. Lett.* 13, 329 (1973).
247. J. Khatouri, M. Mostafavi, J. Amblard, and J. Belloni, *Chem. Phys. Lett.* 191, 351 (1992).

248. A. Henglein, *J. Phys. Chem. B* 104, 1206 (2000).
249. J. P. Cason and C. B. Roberts, *J. Phys. Chem. B* 104, 1217 (2000).
250. K. J. Ziegler, C. Doty, K. P. Johnston, and B. A. Korgel, *J. Am. Chem. Soc.* 123, 7797 (2001).
251. G. Vitulli, M. Bernini, S. Bertozzi, E. Pitzalis, P. Salvadori, S. Coluccia, and G. Martra, *Chem. Mater.* 14, 1183 (2002).
252. M. P. Pileni, T. Gulik-Krzywicki, J. Tanori, A. Filankembo, and J. C. Dedieu, *Langmuir* 14, 7359 (1998).
253. P. Chen, X. Wu, J. Lin, and K. L. Tan, *J. Phys. Chem. B* 103, 4559 (1999).
254. R. A. Salkar, P. Jeeranandam, G. Kataby, S. T. Aruna, Y. Koltypin, O. Palchik, and A. Gedanken, *J. Phys. Chem. B* 104, 893 (2000).
255. P. C. Lee and D. Meisel, *J. Phys. Chem.* 86, 3391 (1982).
256. P. V. Kamat, M. Flumiani, and G. V. Hartland, *J. Phys. Chem. B* 102, 3123 (1998).
257. P. Matějka, B. Vlčková, J. Vohlidal, P. Pančoška, and V. Baumruk, *J. Phys. Chem.* 96, 1361 (1992).
258. B. Vlčková, P. Matějka, J. Simonová, K. Cermáková, P. Pančoška, and V. Baumruk, *J. Phys. Chem.* 97, 9719 (1993).
259. S. Fullam, S. N. Rao, and D. Fitzmaurice, *J. Phys. Chem. B* 104, 6164 (2000).
260. C. Petit, P. Lixon, and M.-P. Pileni, *J. Phys. Chem.* 97, 12974 (1993).
261. A. Taleb, C. Petit, and M. P. Pileni, *Chem. Mater.* 9, 950 (1997).
262. A. Taleb, C. Petit, and M. P. Pileni, *J. Phys. Chem. B* 102, 2214 (1998).
263. R. Jin, Y. Cao, C. A. Mirkin, K. L. Kelly, G. C. Schatz, and J. G. Zheng, *Science* 294, 1901 (2001).
264. I. Pastoriza-Santos and L. M. Liz-Marzán, *Nanolett.* 2, 903 (2002).
265. S. Chen and D. L. Carroll, *Nanolett.* 2, 1003 (2002).
266. Y. Sun and Y. Xia, *Science* 298, 2176 (2002).
267. M. Procházka, J. Štěpánek, P.-Y. Turpin, and J. Bok, *J. Phys. Chem. B* 106, 1543 (2002).
268. Y. Socol, O. Abramson, A. Gedanken, Y. Meshorer, L. Berenstein, and A. Zaban, *Langmuir* 18, 4736 (2002).
269. S.-Y. Zhao, S.-H. Chen, S.-Y. Wang, D.-G. Li, and H.-Y. Ma, *Langmuir* 18, 3315 (2002).
270. J. E. Martin, J. P. Wilcoxon, J. Odinek, and P. Provencio, *J. Phys. Chem. B* 106, 971 (2002).
271. Highly faceted Pt nanoparticles are obtained by reducing H<sub>2</sub>PtCl<sub>6</sub> using potassium bitartrate as the reducing agent in the presence of protective polymer such as PVP or PEG. Y. Tan, X. Dai, Y. Li, and D. Zhu, *J. Mater. Chem.* (submitted).
272. X. Fu, Y. Wang, N. Wu, L. Gui, and Y. Tang, *Langmuir* 18, 4619 (2002).
273. A. Miyazaki and Y. Nakano, *Langmuir* 16, 7109 (2000).
274. A. Henglein, B. G. Ershov, and M. Malow, *J. Phys. Chem.* 99, 14129 (1995).
275. N. R. Jana and T. Pal, *Langmuir* 15, 3458 (1999).
276. N. R. Jana, Z. L. Wang, and T. Pal, *Langmuir* 16, 2457 (2000).
277. J. S. Bradley, E. W. Hill, S. Behal, C. Klein, B. Chaudret, and A. Duteil, *Chem. Mater.* 4, 1234 (1992).
278. D. De Caro and J. S. Bradley, *New J. Chem.* 22, 1267 (1998).
279. A. Duteil, R. Queau, B. Chaudret, R. Mazel, C. Roucau, and J. S. Bradley, *Chem. Mater.* 5, 341 (1993).
280. J. S. Bradley, J. M. Millar, E. W. Hill, S. Behal, B. Chaudret, and A. Duteil, *Faraday Discuss.* 92, 255 (1991).
281. C. Pan, K. Pelzer, K. Philippot, B. Chaudret, F. Dassenoy, P. Lecante, and M.-J. Casanove, *J. Am. Chem. Soc.* 123, 7584 (2001).
282. O. Vidoni, K. Philippot, C. Amiens, B. Chaudret, O. Balmes, J.-O. Malm, J.-O. Bovin, F. Senocq, and M.-J. Casanove, *Angew. Chem., Int. Ed. Engl.* 38, 3736 (1999).
283. N. Toshima, K. Kushihashi, T. Yonezawa, and H. Hirai, *Chem. Lett.* 1769 (1989).
284. N. Toshima, M. Harada, T. Yonezawa, K. Kushihashi, and K. Asakura, *J. Phys. Chem.* 95, 7448 (1991).
285. M. Harada, K. Asakura, Y. Ueki, and N. Toshima, *J. Phys. Chem.* 96, 9730 (1992).
286. N. Toshima, T. Yonezawa, and K. Kushihashi, *J. Chem. Soc., Faraday Trans.* 89, 2537 (1993).
287. X. Yang, H. Liu, and H. Zhong, *J. Mol. Catal. A: Chem.* 147, 55 (1999).
288. N. Toshima, M. Harada, Y. Yamazaki, and K. Asakura, *J. Phys. Chem.* 96, 9927 (1992).
289. M. Harada, K. Asakura, and N. Toshima, *J. Phys. Chem.* 98, 2653 (1994).
290. N. Toshima and K. Hirakawa, *Appl. Surf. Sci.* 121/122, 534 (1997).
291. Z. Yu, S. Liao, Y. Xu, B. Yang, and D. Yu, *J. Mol. Catal. A: Chem.* 120, 247 (1997).
292. P. Y. Silvert, V. Vijaykrishnan, P. Vibert, R. Herrera-Urbina, and K. T. Elhissen, *Nanostruct. Mater.* 7, 611 (1996).
293. C.-W. Chen and M. Akashi, *Polym. Adv. Tech.* 10, 127 (1999).
294. N. Toshima and Y. Wang, *Langmuir* 10, 4574 (1994).
295. N. Toshima and Y. Wang, *Chem. Lett.* 1611 (1993).
296. N. Toshima and Y. Wang, *Adv. Mater.* 6, 245 (1994).
297. N. Toshima and P. Lu, *Chem. Lett.* 729 (1996).
298. P. Lu, T. Teranishi, K. Asakura, M. Miyake, and N. Toshima, *J. Phys. Chem. B* 103, 9673 (1999).
299. J. S. Bradley, E. W. Hill, C. Klein, B. Chaudret, and A. Duteil, *Chem. Mater.* 5, 254 (1993).
300. S. Remita, M. Mostafavi, and M. O. Delcourt, *Rad. Phys. Chem.* 47, 275 (1996).
301. A. Harriman, *J. Chem. Soc., Chem. Commun.* 24 (1990).
302. R. Touroude, P. Girard, G. Maire, J. Kizling, M. Boutonnet-Kizling, and P. Stenius, *Colloids Surf.* 67, 9 (1992).
303. C. Sangregorio, M. Galeotti, U. Bardi, and P. Baglioni, *Langmuir* 12, 5800 (1996).
304. M.-L. Wu, D.-H. Chen, and T.-C. Huang, *Chem. Mater.* 13, 599 (2001).
305. L. E. Aleandri, H. Bönemann, D. J. Jones, J. Richter, and J. Rozière, *J. Mater. Chem.* 5, 749 (1995).
306. T. J. Schmidt, M. Noeske, H. A. Gasteiger, R. J. Behm, P. Britz, W. Brijoux, and H. Bönemann, *Langmuir* 13, 2591 (1997).
307. H. Bönemann, P. Britz, and W. Vogel, *Langmuir* 14, 6654 (1998).
308. C. Pan, F. Dassenoy, M. J. Casanove, K. Philippot, C. Amiens, P. Lecante, A. Mosset, and B. Chaudret, *J. Phys. Chem. B* 103, 10098 (1999).
309. K. Torigoe and K. Esumi, *Langmuir* 9, 1664 (1993).
310. K. Torigoe, Y. Nakajima, and K. Esumi, *J. Phys. Chem.* 97, 8304 (1993).
311. M. T. Reetz, W. Helbig, and S. A. Quaiser, *Chem. Mater.* 7, 2227 (1995).
312. M. Harada, K. Asakura, and N. Toshima, *J. Phys. Chem.* 97, 5103 (1993).
313. G. Schmid, A. Lehnert, J. O. Malm, and J. O. Bovin, *Angew. Chem., Int. Ed. Engl.* 30, 874 (1991).
314. G. Schmid, H. West, J. O. Malm, J. O. Bovin, and C. Grenthe, *Chem. Eur. J.* 2, 1099 (1996).
315. A. Henglein, *J. Phys. Chem. B* 104, 2432 (2000).
316. Y. Wang and N. Toshima, *J. Phys. Chem. B* 101, 5301 (1997).
317. K. Mallik, M. Mandal, N. Pradhan, and T. Pal, *Nanolett.* 1, 319 (2001).
318. B. Yang, Y. Wu, B. Zong, and Z. Shen, *Nanolett.* 2, 751 (2002).
319. M. Chen and D. E. Nikles, *Nanolett.* 2, 211 (2002).
320. S. Sun, C. B. Murray, D. Weller, L. Folks, and A. Moser, *Science* 287, 1989 (2000).
321. E. V. Shevchenko, D. V. Talapin, A. L. Rogach, A. Kornowski, M. Haase, and H. Weller, *J. Am. Chem. Soc.* 124, 11480 (2002).
322. J.-I. Park and J. Cheon, *J. Am. Chem. Soc.* 123, 5743 (2001).
323. N. S. Sobal, M. Hilgendorff, H. Mhwald, M. Giersig, M. Spasova, T. Radetic, and M. Farle, *Nanolett.* 2, 621 (2002).
324. Z. L. Wang (Ed.), "Characterization of Nanophase Materials." Wiley-VCH, New York, 2000.



325. D. B. Williams and C. B. Carter, "Transmission Electron Microscopy." Plenum, New York, 1996.
326. Z. L. Wang and Z. C. Kang, "Functional and Smart Materials—Structural Evolution and Structure Analysis," Chap. 6. Plenum, New York, 1998.
327. R. F. Egerton, "Electron Energy-Loss Spectroscopy in the Electron Microscope," 2nd ed. Plenum, New York, 1996.
328. S. Frank, P. Poncharal, Z. L. Wang, and W. A. de Heer, *Science* 280, 1744 (1998).
329. B. D. Cullity, "Elements of X-ray Diffraction," 2nd ed. Addison-Wesley, Menlo Park, CA, 1978.
330. D. V. Leff, P. C. Ohara, J. R. Heath, and W. M. Gelbart, *J. Phys. Chem.* 99, 7036 (1995).
331. H. Liu, G. Mao, and S. Meng, *J. Mol. Catal.* 74, 275 (1992).
332. W. Yu, Y. Wang, H. Liu, and W. Zheng, *J. Mol. Catal. A: Chem.* 112, 105 (1996).
333. C. L. Cleveland, U. Landman, T. G. Schaaff, M. N. Shafiqullin, P. W. Stephens, and R. L. Whetten, *Phys. Rev. Lett.* 79, 1873 (1997).
334. C. L. Cleveland, U. Landman, M. N. Shafiqullin, P. W. Stephens, and R. L. Whetten, *Z. Phys. D* 40, 503 (1997).
335. R. L. Whetten, J. T. Khoury, M. M. Alvarez, S. Murthy, I. Vezmar, Z. L. Wang, C. L. Cleveland, W. D. Luedtke, and U. Landman, *Adv. Mater.* 8, 428 (1996).
336. C. B. Murray, C. R. Kagan, and M. G. Bawendi, *Science* 270, 1335 (1995).
337. A. P. Alivisatos, *J. Phys. Chem.* 100, 13226 (1996).
338. B. B. Weiner, in "Particle Size Analysis" (N. N. Stanley-Wood and R. W. Lines, Eds.), pp. 173–185. Royal Society of Chemistry, Cambridge, 1992.
339. J. P. Gorden, R. C. C. Leite, R. S. More, S. P. Porto, and J. R. Whinnery, *J. Appl. Phys. Lett.* 36, 3 (1965).
340. J. R. Whinnery, D. T. Miller, and F. Dabby, *IEEE J. Quantum Electron.* QE-3, 383 (1967).
341. W. R. Callen, B. G. Huth, and R. H. Pantell, *Appl. Phys. Lett.* 11, 103 (1967).
342. X. M. Lin, G. M. Wang, C. M. Sorensen, and K. J. Klabunde, *Appl. Opt.* 38, 1884 (1999).
343. H. Bönemann, W. Brijoux, K. Siepen, J. Hormes, R. Franke, J. Pollmann, and J. Rothe, *Appl. Organomet. Chem.* 11, 783 (1997).
344. C. W. Chen, T. Serizawa, and M. Akashi, *Chem. Mater.* 11, 1381 (1999).
345. H. R. Gao and R. J. Angelici, *J. Am. Chem. Soc.* 119, 6973 (1997).
346. H. Hirai, H. Chawanya, and N. Toshima, *React. Polym.* 3, 127 (1985).
347. N. Toshima, T. Takahashi, T. Yonezawa, and H. Hirai, *J. Macromol. Sci., Chem.* A25, 669 (1988).
348. S. Link and M. A. El-Sayed, *J. Phys. Chem. B* 103, 4212 (1999).
349. S. Link and M. A. El-Sayed, *J. Phys. Chem. B* 103, 8410 (1999).
350. J. H. Hodak, I. Martini, G. V. Hartland, S. Link, and M. A. El-Sayed, *J. Chem. Phys.* 108, 9210 (1999).
351. L. Francois, M. Mostafavi, J. Belloni, J. F. Delouis, J. Delaire, and P. Feneyrou, *J. Phys. Chem. B* 104, 6133 (2000).
352. T. P. Bigioni, R. L. Whetten, and Ö. Dag, *J. Phys. Chem. B* 104, 6983 (2000).
353. T. R. Jensen, M. D. Malinsky, C. L. Haynes, and R. P. Van Duyne, *J. Phys. Chem. B* 104, 10549 (2000).
354. X. Lin, N. J. Ramer, A. M. Rappe, K. C. Hass, W. F. Schneider, and B. L. Trout, *J. Phys. Chem. B* 105, 7739 (2001).
355. R. C. Doty, H. Yu, C. K. Shih, and B. A. Korgel, *J. Phys. Chem. B* 105, 8291 (2001).
356. S. Park, S. A. Wasileski, and M. J. Weaver, *J. Phys. Chem. B* 105, 9719 (2001).
357. K. C. Beverly, J. F. Sampaio, and J. R. Heath, *J. Phys. Chem. B* 106, 2131 (2002).
358. N. Moumen and M. P. Pileni, *Chem. Mater.* 5, 1128 (1996).
359. P. Galletto, P. F. Brevet, H. H. Girault, R. Antoine, and M. Broyer, *Chem. Commun.* 581 (1999).
360. J.-T. Lue, *J. Phys. Chem. Solid* 62, 1599 (2001).
361. C. N. R. Rao, G. U. Kulkarni, P. J. Thomas, and P. P. Edwards, *Chem. Eur. J.* 8, 29 (2002) and references therein.
362. M. J. Yacamán, J. A. Ascencio, H. B. Liu, and J. Gardea-Torresdey, *J. Vac. Sci. Technol. B* 19, 1091 (2001).
363. L. Lu, M. L. Sui, and K. Lu, *Science* 287, 1463 (2000).
364. A. W. Snow and H. Wohltjen, *Chem. Mater.* 10, 947 (1998).
365. M. Schmidt, R. Kusche, B. Von Issendorff, and H. Haberland, *Nature* 393, 238 (1998).
366. S.-H. Park, Y. Xie, and M. J. Weaver, *Langmuir* 18, 5792 (2002).
367. Z. L. Wang, J. Petroski, T. Green, and M. A. El-Sayed, *J. Phys. Chem. B* 102, 6145 (1998).
368. T. Teranishi, M. Hosoe, T. Tanaka, and M. Miyake, *J. Phys. Chem. B* 103, 3818 (1999).
369. M. Mohamed, Z. L. Wang, and M. A. El-Sayed, *J. Phys. Chem. A* 103, 10255 (1999).
370. C. L. Cleveland, W. D. Luedtke, and U. Landman, *Phys. Rev. Lett.* 81, 2036 (1998).
371. F. Family and D. Landau, (Eds.), "Kinetics of Aggregation and Gelation." North-Holland, Amsterdam, 1984.
372. D. Weitz, J. Huang, M. Lin, and J. Sung, *Phys. Rev. Lett.* 54, 1416 (1985).
373. D. Weitz and M. Olivera, *Phys. Rev. Lett.* 52, 1433 (1984).
374. D. Weitz, J. Huang, M. Lin, and J. Sung, *Phys. Rev. Lett.* 53, 1657 (1984).
375. Z. Zhou and B. Chu, *J. Colloid Interface Sci.* 143, 356 (1991).
376. Z. Zhou, P. Wu, and B. Chu, *J. Colloid Interface Sci.* 146, 541 (1991).
377. D. F. Evans and H. Wennerström, "The Colloidal Domain," 2nd ed. Wiley-VCH, New York, 1999.
378. T. Imae, K. Funayama, K. Aoi, K. Tsutsumiuchi, M. Okada, and M. Furusaka, *Langmuir* 15, 4076 (1999).
379. A. Manna, T. Imae, K. Aoi, M. Okada, and T. Yogo, *Chem. Mater.* 13, 1674 (2001).
380. Y. Zhou, H. Itoh, T. Uemura, K. Naka, and Y. Chujo, *Langmuir* 18, 277 (2002).
381. J. Liu, W. Ong, E. Román, M. J. Lynn, and A. E. Kaifer, *Langmuir* 16, 3000 (2000).
382. T. Sato, D. Brown, and B. F. G. Johnson, *Chem. Commun.* 1007 (1997).
383. X. M. Lin, G. M. Wang, C. M. Sorensen, and K. J. Klabunde, *J. Phys. Chem. B* 103, 5488 (1999).
384. X. M. Lin, C. M. Sorensen, and K. J. Klabunde, *Chem. Mater.* 11, 198 (1999).
385. P. J. Thomas, G. U. Kulkarni, and C. N. R. Rao, *J. Phys. Chem. B* 104, 8138 (2000).
386. Y.-S. Shon, S. M. Gross, B. Dawson, M. Porter, and R. W. Murray, *Langmuir* 16, 6555 (2000).
387. S. Chen and J. M. Sommers, *J. Phys. Chem. B* 105, 8816 (2001).
388. M. Brust, J. Fink, D. Bethell, D. J. Schiffrin, and C. Kiely, *J. Chem. Soc., Chem. Commun.* 1655 (1995).
389. D. E. Cliffler, F. P. Zamborini, S. M. Gross, and R. W. Murray, *Langmuir* 16, 9699 (2000).
390. R. P. Andres, J. D. Bielefeld, J. I. Henderson, D. B. Janes, V. R. Kolagunta, C. P. Kubiak, W. J. Mahoney, and R. G. Osifchin, *Science* 273, 1690 (1996).
391. L. A. Porter, D. Ji, S. L. Westcott, M. Graupe, R. S. Czeruszewicz, N. J. Halea, and T. R. Lee, *Langmuir* 14, 7378 (1998).
392. W. M. Pankau, K. Verbist, and G. Von Kiedrowski, *Chem. Commun.* 519 (2001).
393. K. Inoue, S. Shinkai, J. Huskens, and D. N. Reinhoudt, *J. Mater. Chem.* 11, 1919 (2001).
394. E. J. Shelley, D. Ryan, S. R. Johnson, M. Couillard, D. Fitzmaurice, P. D. Nellist, Y. Chen, R. E. Palmer, and J. A. Preece, *Langmuir* 18, 1791 (2002).
395. W. Shenton, D. Pum, U. B. Sleytr, and S. Mann, *Nature* 389, 585 (1997).

396. T. Cassagneau, T. E. Mallouk, and J. H. Fendler, *J. Am. Chem. Soc.* 120, 7848 (1998).
397. T. Yonezawa, T. Tominaga, and D. Richard, *J. Chem. Soc., Dalton Trans.* 783 (1996).
398. D. V. Leff, L. Brandt, and J. R. Heath, *Langmuir* 12, 4723 (1996).
399. S. Gomez, K. Philippot, V. Collière, B. Chaudret, F. Senocq, and P. Lecante, *Chem. Commun.* 1945 (2000).
400. L. O. Brown and J. E. Hutchison, *J. Phys. Chem. B* 105, 8911 (2001).
401. K. Esumi, K. Matsuhisa, and K. Torigoe, *Langmuir* 11, 3285 (1995).
402. T. Yonezawa, T. Tominaga, and N. Toshima, *Langmuir* 11, 4610 (1995).
403. N. Duxin, N. Brun, C. Colliex, and M. P. Pileni, *Langmuir* 14, 1984 (1998).
404. J. Fink, C. J. Kiely, D. Bethell, and D. J. Schiffrin, *Chem. Mater.* 10, 922 (1998).
405. M. T. Reetz, M. Winter, and B. Tesche, *Chem. Commun.* 147 (1997).
406. N. Toshima, T. Teranishi, H. Asanuma, and Y. Saito, *J. Phys. Chem.* 96, 3796 (1992).
407. T. Teranishi and N. Toshima, *J. Chem. Soc., Dalton Trans.* 2967 (1994).
408. T. Teranishi and N. Toshima, *J. Chem. Soc., Dalton Trans.* 979 (1995).
409. A. Fukuoka, H. Araki, Y. Sakamoto, N. Sugimoto, H. Tsukada, Y. Kumai, Y. Akimoto, and M. Ichikawa, *Nanolett.* 2, 793 (2002).
410. K. G. Neoh, T. T. Young, N. T. Looi, E. T. Kang, and K. L. Tan, *Chem. Mater.* 9, 2906 (1997).
411. R. Gangopadhyay and A. De, *Chem. Mater.* 12, 608 (2000).
412. M. A. El-Sayed, *Acc. Chem. Res.* 34, 257 (2001).
413. P. Mulvaney, *Langmuir* 12, 788 (1996).
414. J. A. Creighton and D. G. Eadon, *J. Chem. Soc., Faraday Trans.* 87, 3881 (1991).
415. C. F. Bohren and D. R. Huffman, "Absorption and Scattering of Light by Small Particles." Wiley, New York, 1983.
416. G. C. Papavassiliou, *Prog. Solid State Chem.* 12, 185 (1979).
417. M. M. Alvarez, J. T. Khoury, T. G. Schaaff, M. N. Shafiqullin, I. Vezmar, and R. L. Whetten, *J. Phys. Chem. B* 101, 3706 (1997).
418. S. Chen and K. Kimura, *Langmuir* 15, 1075 (1999).
419. D.-S. Wang and M. Kerker, *Phys. Rev. B* 24, 1777 (1981).
420. E. J. Zeman and G. C. Schatz, *J. Phys. Chem.* 91, 634 (1987).
421. J. A. Creighton and D. G. Eaton, *J. Chem. Soc., Faraday Trans.* 87, 3881 (1991).
422. W.-H. Yang, G. C. Schatz, and R. P. van Duyne, *J. Phys. Chem.* 99, 869 (1995).
423. I. Lisiecki, F. Billoudet, and M. P. Pileni, *J. Phys. Chem.* 100, 4160 (1996).
424. B. M. I. van der Zande, M. R. Böhmer, L. G. J. Fokkink, and C. Schönenberger, *J. Phys. Chem. B* 101, 852 (1997).
425. M. A. Hayat, "Colloidal Gold," Vol. 1, p. 23. Academic, San Diego, CA, 1989.
426. J. H. Hodak, A. Henglein, and G. V. Hartland, *J. Phys. Chem. B* 104, 9954 (2000).
427. L. Rivas, S. Sanchez-Cortes, J. V. Garcia-Ramos, and G. Morcillo, *Langmuir* 16, 9722 (2000).
428. L. Lu, H. Wang, Y. Zhou, S. Xi, H. Zhang, J. Hu, and B. Zhao, *Chem. Commun.* 144 (2002).
429. S. J. Oldenburg, J. B. Jackson, S. L. Westcott, and N. J. Halas, *Appl. Phys. Lett.* 75, 2897 (1999).
430. S. J. Oldenburg, R. D. Averitt, and S. L. Westcott, *Chem. Phys. Lett.* 288, 243 (1998).
431. J. B. Jackson and N. J. Halas, *J. Phys. Chem. B* 105, 2743 (2001).
432. D. L. Leslie-Pelecky and R. D. Rieke, *Chem. Mater.* 8, 1770 (1996).
433. Q. Chen and Z. J. Zhang, *Appl. Phys. Lett.* 73, 3156 (1998).
434. X. X. Zhang, J. Tejata, J. M. Hernandez, and R. F. Ziolo, *Nanostruct. Mater.* 9, 301 (1997).
435. I. S. Jacobs and C. P. Bean, in "Magnetism III" (G. T. Rado and H. Suhl, Eds.), pp. 71–351. Academic, New York, 1963.
436. F. Liu, M. R. Press, S. N. Khanna, and P. Jena, *Phys. Rev. B* 39, 6914 (1989).
437. I. M. L. Billas, A. Châtelain, and W. A. de Heer, *Science* 265, 1682 (1994).
438. A. Dinia, S. Zoll, M. Gester, D. Stoeffler, J. P. Jay, K. Ounadjela, H. A. M. van den Berg, and H. Rakoto, *Eur. Phys. J. B* 5, 203 (1998).
439. M. Fallot, *Ann. Phys. (Paris)* 10, 291 (1938).
440. V. W. Köster and E. Horn, *Z. Metallkd.* 43, 444 (1952).
441. D. Weller, A. Moser, L. Folks, M. E. Best, W. Le, M. F. Toney, M. Schweickert, J.-L. Thiele, and M. F. Doerner, *IEEE Trans. Magn.* 36, 10 (2000).
442. B. Kim, S. L. Tripp, and A. Wei, *J. Am. Chem. Soc.* 123, 7955 (2001).
443. Z. L. Wang, *Adv. Mater.* 10, 13 (1998).
444. Z. L. Wang, Z. R. Dai, and S. Sun, *Adv. Mater.* 12, 1944 (2000).
445. A. K. Boal, F. Ilhan, J. E. DeRouchey, T. Thurn-Albrecht, T. P. Russell, and V. M. Rotello, *Nature* 404, 746 (2000).
446. D. Ryan, S. N. Rao, H. Rensmo, D. Fitzmaurice, J. A. Preece, S. Wenger, J. F. Stoddart, and N. Zaccheroni, *J. Am. Chem. Soc.* 122, 6252 (2000).
447. C. J. Kiely, J. Fink, M. Brust, D. Bethell, and D. J. Schiffrin, *Nature* 396, 444 (1998).
448. C. J. Kiely, J. Fink, J. G. Zheng, M. Brust, D. Bethell, and D. J. Schiffrin, *Adv. Mater.* 12, 640 (2000).
449. S. M. Marinakos, L. C. Brousseau, III, A. Jones, and D. L. Feldheim, *Chem. Mater.* 10, 1214 (1998).
450. S. Fullam, D. Cottel, H. Rensmo, and D. Fitzmaurice, *Adv. Mater.* 12, 1430 (2000).
451. T. Teranishi, A. Sugawara, T. Shimizu, and M. Miyake, *J. Am. Chem. Soc.* 124, 4210 (2002).
452. Y. Tan, L. Jiang, Y. Li, and D. Zhu, *J. Phys. Chem. B* 106, 3131 (2002).
453. R. P. Andres, *Science* 272, 1323 (1996).
454. D. Davidovic and M. Tinkham, *Appl. Phys. Lett.* 73, 3959 (1998).
455. S. R. Emory, W. E. Haskins, and S.-M. Nie, *J. Am. Chem. Soc.* 120, 8009 (1998).
456. W. C. W. Chan and S. Nie, *Science* 281, 2016 (1998).
457. M. Bruchez, Jr., M. Moronne, P. Gin, S. Weiss, and A. P. Alivisatos, *Science* 281, 2013 (1998).
458. A. C. Templeton, W. P. Wuelfing, and R. W. Murray, *Acc. Chem. Res.* 33, 27 (2000).
459. J. J. Storhoff and C. A. Mirkin, *Chem. Rev.* 99, 1849 (1999).
460. Y. Li, X. M. Hong, D. M. Collard, and M. A. El-Sayed, *Org. Lett.* 2, 2385 (2000).
461. Y. Li and M. A. El-Sayed, *J. Phys. Chem. B* 105, 8938 (2001).
462. Y. Li, E. Boone, and M. A. El-Sayed, *Langmuir* 18, 4921 (2002).
463. S. N. Sidorov, I. V. Volkov, V. A. Davankov, M. P. Tsyurupa, P. M. Valetsky, L. M. Bronstein, R. Karlinsky, J. W. Zwaniger, V. G. Matveeva, E. M. Sulman, N. V. Lakina, E. A. Wilder, and R. J. Spontak, *J. Am. Chem. Soc.* 123, 10502 (2001).
464. M. N. Vargaftik, U. P. Zagorodnikov, I. P. Stolarov, A. L. Chuvilin, and K. I. Zamaraev, *J. Mol. Catal.* 53, 315 (1989).
465. M. Haruta, T. Kobayashi, H. Sano, and N. Yamada, *Chem. Lett.* 405 (1987).
466. T. Sun and K. Seff, *Chem. Rev.* 94, 857 (1994).
467. X. E. Verykios, F. P. Stein, and R. W. Coughlin, *Catal. Rev.—Sci. Eng.* 22, 197 (1980).
468. Y. Shiraishi and N. Toshima, *Colloids Surf. A* 169, 59 (2000).
469. M. Mostafavi, J. L. Marignier, J. Amblard, and J. Belloni, *J. Rad. Phys. Chem.* 34, 605 (1989).
470. M. Lewis and M. Tarlov, *J. Am. Chem. Soc.* 117, 9574 (1995).
471. R. K. Hailstone, *J. Phys. Chem.* 99, 4414 (1995).
472. B. Vlkova, X. J. Gu, D. P. Tsai, and M. Moskovits, *J. Phys. Chem.* 100, 3169 (1996).

473. P. Matejka, B. Vlkova, J. Vohlidal, P. Pancoska, and V. Baumrunk, *J. Phys. Chem.* 96, 1361 (1992).
474. S. Schultz, D. R. Smith, J. J. Mock, and D. A. Schultz, *Proc. Nat. Acad. Sci. USA* 97, 996 (2000).
475. T. J. Silva, S. Schultz, and D. Weller, *Appl. Phys. Lett.* 65, 658 (1994).
476. M. Horrisberger, in "Preparation of Biological Specimens for Scanning Electron Microscopy" (J. A. Murphy and G. M. Roomans, Eds.), p. 315. Scanning Electron Microscopy, Inc., Chicago, 1984.
477. J. DeMey, *EMSA Bull.* 14, 54 (1984).
478. J. L. Rousset, F. Aires, F. Bornette, M. Cattenot, M. Pellarin, L. Stievano, and A. J. Renouprez, *Appl. Surf. Sci.* 164, 163 (2000).
479. J. H. Sinfelt, "Bimetallic Catalysis: Discoveries, Concepts, and Applications." Wiley, New York, 1983.
480. D. S. Bethune, C. H. Kiang, M. S. Devries, G. Gorman, R. Savoy, J. Vazquez, and R. Beyers, *Nature* 363, 605 (1993).
481. L. Fiermans, R. De Gryse, G. De Doncker, P. A. Jacobs, and J. A. Martens, *J. Catal.* 193, 108 (2000).
482. H. Yasuda, N. Matsubayashi, T. Sato, and Y. Yoshimura, *Catal. Lett.* 54, 23 (1998).
483. R. T. Baker, *Carbon* 27, 315 (1989).
484. D. Weller, H. Brändle, and C. Chappert, *J. Magn. Magn. Mater.* 121, 461 (1993).
485. T. A. Tyson, S. D. Conradson, R. F. C. Farrow, and B. A. Jones, *Phys. Rev. B* 54, R3702 (1996).
486. D. Weller, H. Brändle, G. Gorman, C.-J. Lin, and H. Notarys, *Appl. Phys. Lett.* 61, 2726 (1992).
487. W. Grange, M. Maret, J.-P. Kappler, J. Vogel, A. Fontaine, F. Petroff, G. Krill, A. Rogalev, J. Coulon, M. Finazzi, and N. Brookes, *Phys. Rev. B* 58, 6298 (1998).
488. A. L. Shapiro, P. W. Rooney, M. Q. Tran, F. Hellman, K. M. Ring, K. L. Kavanagh, B. Rellinghaus, and D. Weller, *Phys. Rev. B* 60, 12826 (1999).
489. D. Weller and A. Moser, *IEEE Trans. Magn.* 35, 4423 (1999).
490. G. Chang, Y. Lee, J. Rhee, J. Lee, K. Jeong, and C. Whang, *Phys. Rev. Lett.* 87, 067208-1 (2001).
491. S. Stoeva, K. J. Klabunde, C. M. Sorensen, and I. Dragieva, *J. Am. Chem. Soc.* 124, 2305 (2002).

# Noble Metal Nanocolloids

Ichiro Okura

Tokyo Institute of Technology, Yokohama, Japan

## CONTENTS

1. Introduction
  2. Preparation and Characterization of Noble Metal Nanocolloids
  3. Catalyses with Noble Metal Nanocolloids
  4. Conclusion
- Glossary  
References

## 1. INTRODUCTION

Much attention has been paid to nanosized metal colloids, for their specific properties are different from those of bulk metal compounds. Nanosized metal colloids are usually synthesized by a *in-situ* reduction method from a suitable metal precursor, such as chemical reduction, photoreduction, electrochemical reduction, or thermal decomposition. Many small molecular ligands, surfactants, and polymers have been used to stabilize metal colloids. Some metal colloids exist stably for a long time without coagulation in a solvent. The methods for suppressing coagulation are needed to maintain the stability of metal colloids in a sol state. Additives that do not cause coagulation are steric stabilizers. Polymers such as polyvinyl alcohol and polyvinyl pyrrolidone and surfactants have frequently been used. The mechanism of the steric stabilization or suppression of the coagulation is illustrated in Figure 1, in which large adsorbed molecules that prevent coagulation can be seen. Recently many polymer-stabilized noble metal nanocolloids have been studied intensively. Stable noble metal colloids have also been obtained by a unique preparation method without a stabilizer. In this case the ionic groups on the surface of this metal colloid suppress the coagulation of metal particles by electric repulsion. The colloidal particles prepared by reduction with citrate, for example, are surrounded by an electrical double layer arising from adsorbed citrate and chloride ions and the cations that are attracted to them. This results in a Columbic repulsion decay with the interparticle distance; the net result is shown in Figure 2. Thus the metal particles are stabilized in the dispersing medium.

A counteraction can be achieved by the above two methods, electrostatic stabilization and steric stabilization. For historical details and an extensive survey of the properties of noble metal nanocolloids, the reader is referred to previous reviews [1–3].

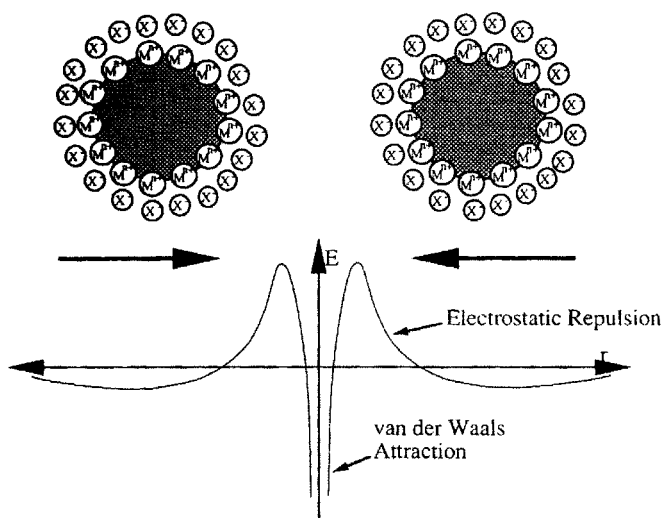
## 2. PREPARATION AND CHARACTERIZATION OF NOBLE METAL NANOCOLLOIDS

Metal colloids can be prepared in two different ways: by dispersion of larger particles or by condensation of smaller units. Sols prepared by the dispersion method are rather unstable and consist of particles with a wide size distribution. To generate uniform particles it is necessary to use chemical methods such as the reduction of metal salts in solution.

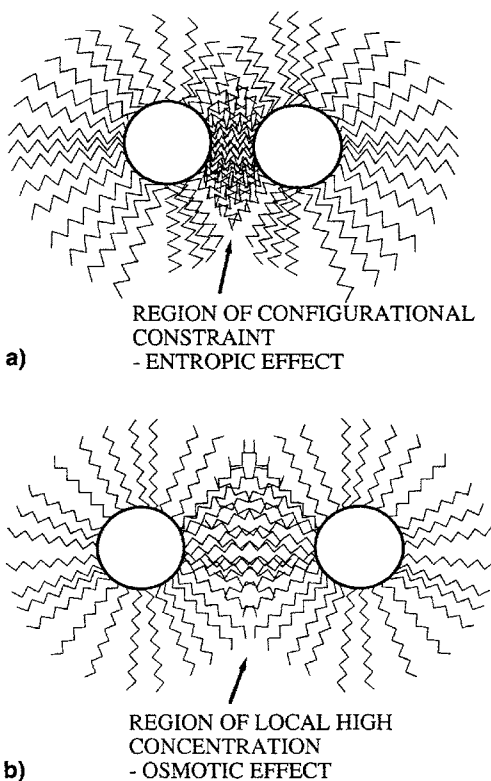
### 2.1. Platinum Nanocolloid

Application of platinum colloid in catalysis is regarded as an active research field. Many colloidal nanocatalysts have been studied intensively, and nanosized platinum metal colloids exhibit special catalytic properties different from those of conventional heterogeneous and homogeneous platinum metal catalysts. Typical platinum nanocolloids are listed in Table 1. Particle size can be kept between 1.0 to 40 nm through control of the preparation conditions. Though most platinum colloids in the table are stabilized with polymers, platinum nanoparticles without stabilizer are also prepared. The platinum colloid with electrostatic stabilization is prepared by the reduction of chloroplatinic acid with sodium citrate [20]. The platinum colloid obtained by this method is very stable and does not coagulate for several months if kept in a refrigerator. The following three points are important in the preparation of the platinum colloid:

1. The flask must be carefully washed, preferably with aqua regia.
2. Attention must be paid to the water used. Double-distilled water is recommended.
3. The flask should always be sufficiently heated, and the solution must be kept boiling.



**Figure 1.** Steric stabilization of metal colloid particles by polymers or surfactant molecules. (a) In the interparticle space the configurational freedom of the polymer chains of two approaching particles is restricted, causing a lowering of entropy. (b) The local concentration of polymer chains between the approaching particles is raised and the resulting higher local activity is osmotically counteracted by solvation. Reprinted with permission from [1], G. Schmid, "Clusters and Colloids." VCH, Weinheim, 1994, © 1994, Wiley-VCH.



**Figure 2.** Electrostatic stabilization of metal colloid particles. Attractive van der Waals forces are outweighed by repulsive electrostatic forces between adsorbed ions and associated counterions at moderate interparticle separation. Reprinted with permission from [1], G. Schmid, "Clusters and Colloids." VCH, Weinheim, 1994, © 1994, Wiley-VCH.

Unreacted chloroplatinic acid and excess sodium citrate can be removed by passing the solution through a column with the ion exchange resin Amberlite MB-1.

Figure 3 shows the relationship between the particle size of the platinum colloid prepared by the above-mentioned method and the reflux time. The diameter of the platinum particles increases gradually with time and becomes constant at 32 Å. By this method, the particle size of the platinum colloid can be controlled just through control of the reflux time. The deviations in particle sizes are very small, and the particle size is homogeneous and almost uniform. From the results it seems that the number of colloid particles does not change during the growth process of the platinum colloid and that the particle size increases because of a gradual reduction in the amount of chloroplatinic acid adsorbed on the surface of the colloid.

## 2.2. Gold Nanocolloid

Gold nanocolloid is a typical historical particle. The gold colloids, ranging from 2 to 150 nm in diameter, are available and are typical hydrophobic particles (Table 2). The properties and applications of gold nanoparticles are summarized in [3] with historical details. The major objective in using colloidal gold is the *in-situ* localization of cellular macromolecules. This information is used to elucidate biochemical properties and functions of cellular compartments and components. The silver-enhanced colloidal gold method can be used for both light and electron microscopy. Colloidal gold as a marker meets many requirements necessary for precise ultrastructural localization, distribution, and quantitation of macromolecules in living or fixed cells and tissues. During the last decade, scientific literature involving the use of colloidal gold as an immunocytochemical marker has increased, and this trend is expected to continue. The different methods for the synthesis of colloidal gold are based on controlled reduction of an aqueous solution of tetrachloroauric acid, with different reducing agents under various conditions.

## 2.3. Other Noble Metal Nanocolloids

Other noble metal nanocolloids are also prepared as platinum and gold nanocolloids with electrostatic stabilization and steric stabilization. Nanocolloids of Rh, Pd, Ru, Ir, and Ag are shown in Tables 3–7.

## 2.4. Preparation and Characterization of Noble Bimetallic Nanocolloids

Bimetallic particles have been a focus of increasing interest not only in catalysis in the fuel industry, but also as models for the study of the formation of alloys. They can be divided into two classes: alloy-like colloids consist of a homogeneous mixture of two metals with colloidal distribution and colloids with an inner nucleus of one metal, which is covered by a layer of the second metal. In the metal evaporation method, two types of preparation procedures are used [62], for example:

(1) Half SMAD: A conventional catalyst was prepared, such as Pt/Al<sub>2</sub>O<sub>3</sub>, and this catalyst was treated with solvated Re atoms (in toluene). In this way the preformed Pt particles

**Table 1.** Platinum nanocolloids.

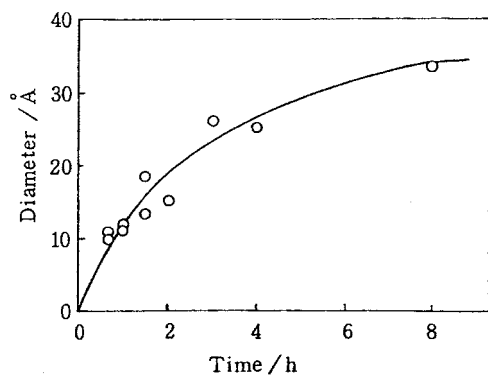
Particle size/nm	Stabilizer	Method	Ref.
2.7	PVA	Refluxing MeOH	[4]
2.7–4.1	PVP	Refluxing MeOH	[5]
1.55–1.78	PVP	Refluxing MeOH	[6]
1.1–2.7	PVP	Refluxing MeOH	[7]
1.02–2.20	PVPAA	Refluxing MeOH	[8]
	PNIPAAm	Refluxing EtOH	[9]
1.47–2.67	PNIPAAm, PVP	Refluxing EtOH	[10]
1.5	PNIPAAm	Refluxing EtOH	[11]
2.7	PVP	Refluxing EtOH	[12]
2.6	Poly(2-ethyl-2-oxazoline)	Refluxing EtOH	[12]
2.2	Poly(1-vinylpyrrolidone-co-vinylacetate)	Refluxing EtOH	[12]
~30	Poly(2-hydroxypropyl-methacrylate)	Refluxing EtOH	[12]
~40	Poly(methylvinylether-co-maleic anhydride)	Refluxing EtOH	[12]
1.5	Poly(methacrylic acid)	Refluxing EtOH	[12]
2.4	Poly(1-vinylpyrrolidone-co-acrylic acid)	Refluxing EtOH	[12]
2.3	Poly(styrene sulfonic acid)	Refluxing EtOH	[12]
2.0	Poly(2-acrylamido-2-methyl-1-propane sulfonic acid)	Refluxing EtOH	[12]
1.6	Poly(vinyl phosphonic acid)	Refluxing EtOH	[12]
~2	PS-b-PMAA	Refluxing EtOH	[13]
2.1	PS-b-PED	Refluxing EtOH	[13]
27	PVP	Refluxing EtOH	[5]
~1.5	Polystyrene	Refluxing EtOH	[14]
1.9–2.81	PNVF, PNVA, PNVIBA	Refluxing EtOH	[15]
3.9	PVP	Refluxing EtOH	[16]
2.0	PVP	Refluxing EtOH	[17]
1.12	PVPAA	Refluxing EtOH	[8]
2.09–2.53	PNVF	Refluxing EtOH	[18]
2.15–2.61	PNVA	Refluxing EtOH	[18]
2.81	PVP	Refluxing EtOH	[18]
1.9	PNVIBA	Refluxing EtOH	[18]
2.38	PNIPAAm	Refluxing EtOH	[18]
22	PVP	Refluxing PrOH	[5]
1.02–1.10	PVPAA	Refluxing PrOH	[8]
5		Citrate	[19]
2.5		Citrate	[20]
3.0		Citrate	[21]
3.0–3.5	Carbowax	Citrate	[22]
~3	Octadecanethiol	LiBH(Et) <sub>3</sub>	[23]
15	PMP, PTFE	Versatile method in supercritical CO <sub>2</sub>	[29]
3.2	PS-b-PMAA	KBH <sub>4</sub>	[13]
2.9	PS-b-PED	KBH <sub>4</sub>	[13]
7–11	Polyacrylate	H <sub>2</sub> gas	[25]
80	Cyclodextrin	H <sub>2</sub> gas	[26]
~3	1,10-Phenanthroline	UV irradiation	[27]
1.1–3.8		Microwave-dielectric heating	[28]
15	PMP, PTFE	Versatile method in supercritical CO <sub>2</sub>	[29]

Note: PVP, Polyvinyl pyrrolidone; PNIPAAm, poly(*N*-isopropylacrylamide); PVA, polyvinyl alcohol; PMP, poly(4-methyl-1-pentene); PTFE, poly(tetrafluoroethylene); PS-b-PMAA, polystyrene-*b*-poly(methacrylic acid); PS-b-PED, polystyrene-*b*-poly(ethyleneoxide); PNVF, poly(*N*-vinylformamide); PNVA, poly(*N*-vinylacetamide); PNVIBA, poly(*N*-vinylisobutylamide); PVPAA, poly(1-vinylpyrrolidone-*co*-acrylic acid).

would receive Re on their surface as a surface coating, but a homogeneous Pt-Re alloy should not form.

(2) Full SMAD: The two metals were evaporated simultaneously, and layered structures or homogeneous alloy particles could form. Some bimetallic nanocolloids are listed in Table 8. Platinum-gold alloy colloids can be prepared by a method similar to the above-described method for preparing a platinum colloid [61]. For the alloy colloid, a mixture of the gold chloride acid solution and the chloroplatinic acid solution (1 g Pt+Au/liter) at an arbitrary ratio is used.

The composition of the prepared alloy colloid corresponds to the composition of the starting material metal. Reduction with sodium citrate is completed within 4 h. This can be confirmed from a visible spectrum. Figure 4 shows a visible spectra of platinum, gold, and platinum-gold alloy colloids with various compositions. As the gold colloid has a characteristic absorption peak at 520 nm, the gold colloid does not appear to be included in the alloy colloid. The colloid thus prepared is an alloy, because the spectrum of the alloy colloid is not a summary of spectra of the pure metal



**Figure 3.** Relationship between the particle size of the platinum colloid and reflux time. Reprinted with permission from [76], Namba and Okura, *Hyomen* 21, 450 (1983). ©1983, Koshinsha Co.

**Table 2.** Gold nanocolloids.

Particle size (nm)	Color	Reducing agent	Ref.
0.82		NaBH <sub>4</sub>	[30, 31]
2.6	Yellowish	NaSCN	[32]
3	Red-orange	White phosphorus	[33]
3–17	Red	Citrate	[34]
4.2	Light brown	NaBH <sub>4</sub>	[35, 36]
5.2	Purple-brown	White phosphorus	[37]
5.7	Red	Citrate	[38]
8.5	Red	Citrate	[39]
5–12	Brown-red	White phosphorus	[40, 41]
10		EtOH	[42–44]
12		Ascorbic acid	[45–47]
12–64	Red	Citrate	[48]
Stabilizer	Method		
~3	PS-b-PMAA	KBH <sub>4</sub>	[13]
~6	PS-b-PMAA	UV irradiation	[13]
5	PS-b-PEO	KBH <sub>4</sub>	[13]
~6	PS-b-PEO	UV irradiation	[13]
2.5	DOAC, ACT	Gas flow-cold trap method	[49]

**Table 3.** Rhodium nanocolloids.

Particle size (nm)	Stabilizer	Method	Ref.
3.5	PVP	Refluxing MeOH	[51]
0.8–4	PVP	Refluxing MeOH	[52]
3–7	PVP	Refluxing MeOH	[53]
4	PVA	Refluxing MeOH	[4]
4.3	Poly(methyl vinyl- )	Refluxing MeOH	[4]
3–3.5	PVP	Refluxing MeOH	[4]
2.24–5.7	PVP	Refluxing MeOH	[54]
	PVP	Refluxing alcohol	[50]
3–20	Ion exchange resin	NaBH <sub>4</sub>	[24]
~2	Surfactant		[55]

**Table 4.** Palladium nanocolloids.

Particle size (nm)	Stabilizer	Method	Ref.
	PVP	Refluxing MeOH	[53]
5.3	PVA	Refluxing MeOH	[4]
1.9–2.7	PVP	Refluxing MeOH	[7]
3.4–7.8	PS-b-PMAA	Refluxing EtOH	[13]
5–6.8	PS-b-PEO	Refluxing EtOH	[13]
1.3–2.1	PS-b-PMAA	KBH <sub>4</sub>	[13]
3.4–5	PS-b-PEO	KBH <sub>4</sub>	[13]
3–10	Ion exchange resin	NaBH <sub>4</sub>	[24]
4.8	Tetraalkylammonium	Electrochemical	[56]

**Table 5.** Ruthenium nanocolloids.

Particle size (nm)	Stabilizer	Method	Ref.
1.3–1.8	PVP	NaBH <sub>4</sub>	[57]
1.28–1.76	PVP	NaBH <sub>4</sub>	[58]
3–20	Ion exchange resin	NaBH <sub>4</sub>	[24]

**Table 6.** Iridium nanocolloids.

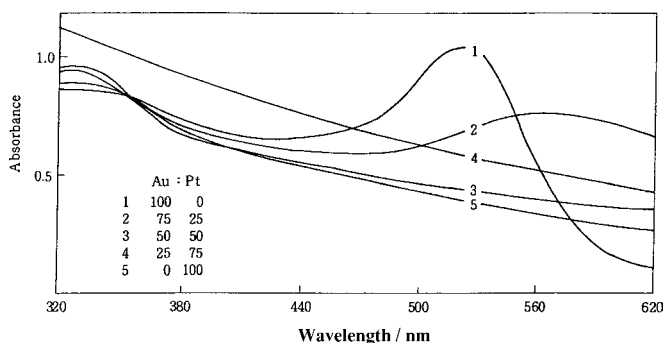
Particle size (nm)	Stabilizer	Method	Ref.
14	PVA	Refluxing MeOH	[4]
1.1–1.4	PVP	Refluxing alcohol	[59]

**Table 7.** Silver nanocolloids.

Particle size (nm)	Stabilizer	Method	Ref.
5.0, 5.5	Sodiumoleate	NaBH <sub>4</sub>	[60]
3.3	PS-b-PEO	KBH <sub>4</sub>	[13]
~4	PS-b-PEO	UV irradiation	[13]

**Table 8.** Bimetallic nanocolloids.

Metals	Particle size (nm)	Stabilizer	Method	Ref.
Pd/Pt	1.5–2.5	PVP	Refluxing EtOH	[63]
Pt/Rv	2.0	PVP	Refluxing EtOH	[66]
Ag/Pt	3.2–11.3		UV irradiation	[64]
Pt/Re			Metal evaporation	[65]



**Figure 4.** Visible spectra of platinum-gold alloy colloids with various compositions. Reprinted with permission from [76], Namba and Okura, *Hyomen* 21, 450 (1983). ©1983, Koshinsha Co.

colloids. The color of the alloy colloid is brownish black, whereas the color of the gold colloid is red. Platinum-palladium alloy colloids are prepared by a method similar to the above-described method [67]. In the case of palladium, 15 h is needed to complete the reduction with sodium citrate. The visible spectra of platinum, palladium, and these alloy colloids show alloy formation by the higher absorbance. The color of the alloy colloid is brownish black. A platinum-palladium alloy colloid with arbitrary metallic composition can be prepared.

### 3. CATALYSES WITH NOBLE METAL NANOCOLLOIDS

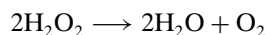
The noble metal nanocolloids and alloy nanocolloids have been used in a sol state, in which the colloid is dispersed in the solvent, and in a gel state, in which the colloid is supported on the solid surface. Some examples of catalytic reactions in the sol state and the preparation and characterization of the noble metal nanocatalyst are described. Typical catalytic reactions with noble metal nanocolloids are listed in Table 9.

#### 3.1. Hydrogenation

Hydrogenation reactions have been the most extensively studied for measuring the activity of colloids. The six platinum group metals (Ru, Os, Rh, Ir, Pd, and Pt) have been investigated as unsupported catalysts. Alcohol solutions of these metals are active catalysts with varying degrees of selectivity for the deuteration of 1,2- and 1,6-dimethylcyclohexenes. Both unsupported Pd and Pt colloids are active for selective hydrogenation of alkynes to alkenes.

#### 3.2. Hydrogen Peroxide Decomposition

Ionic platinum is not active for hydrogen peroxide decomposition. It is known that the metallic state of platinum is active for hydrogen peroxide decomposition, though the platinum ion is inert. When the platinum colloid shows a metallic character, the reaction proceeds [75]. Thus, the hydrogen peroxide decomposition reaction is a suitable model reaction. Hydrogen peroxide decomposition was carried out with platinum colloids with different particle sizes. The decomposition is easily carried out as follows by kinetic measurement:



As oxygen is generated in this reaction by the following equation, kinetic study is possible by measurement of either oxygen formation or hydrogen peroxide consumption by titration with potassium permanganate. The reaction obeys a first-order kinetics and is expressed by the following equation:

$$\ln C_0/C = kt$$

where  $C_0$  and  $C$  are the hydrogen peroxide concentrations at times 0 and  $t$ , respectively, and  $k$  is a rate constant.

Figure 5 shows the relationship between the rate constant  $k$  and the particle size of the platinum colloid. Although decomposition activity of hydrogen peroxide is not observed

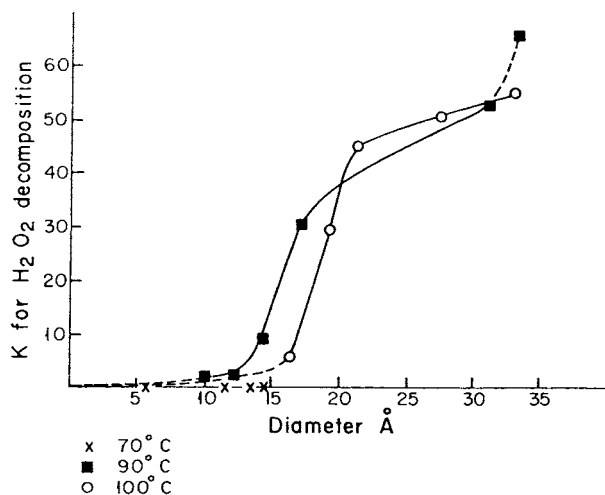
**Table 9.** Catalysis with noble metal nanocolloids.

Metals	Catalytic reactions	Ref.
Ru	Hydrogenation of	
	Cyclooctene	[57]
	<i>n</i> -Heptene	[57]
	Citronellal	[57]
	<i>o</i> -Chloronitrobenzene	[58]
	Cyclohexene	[24]
	1-Hexene	
	Benzene	[68]
	Other alkenes	[24]
	Oxidation of alkane	[69]
Rh	Hydrogenation of	
	1-Hexene	[51, 53, 24]
	Cyclohexene	[51, 52, 24]
	Styrene	[53, 24]
	Cyclooctene	[53]
	1-Octene	[70]
	Other alkenes	[53, 24, 55]
	Hydroformylation	[50]
	Methanol carbonylation	[54]
Hydrosilylation	[71]	
Pt	Hydrogenation of	
	Cinnamaldehyde	[72, 73, 74]
	Allyl alcohol	[9, 10, 11, 14]
	Cyclohexene	[12, 13, 24]
	1-Hexene	[27, 24]
	$\alpha$ -Ketoester	[16, 17]
	Styrene	[24]
	Other alkenes	[6, 7, 27, 72, 74]
	Photoinduced hydrogen evolution	[22, 27, 26]
Hydrogen peroxide decomposition	[75]	
Pd	Hydrogenation of	
	Cyclopentadiene	[53]
	Cyclohexene	[13]
	Dodecene	[7]
	Cyclooctene	[7]
	1-Hexene	[24]
Other alkenes and dienes	[24, 53]	
Ir	Hydrogenation of methyl pyruvate	[59]
Pd/Pt	Hydrogenation of cycloocta-1,3-diene	[63]
Pt/Ru	Photoinduced hydrogen evolution	[66]

*Note:* PVP, Polyvinyl pyrrolidene; PNIPAAm, poly(*N*-isopropylacrylamide); PVA, polyvinyl alcohol; PMP, poly(4methyl-1-pentene); PTFE, poly(tetrafluoroethylene); PS-*b*-PMAA, polystyrene-*b*-poly(methacrylic acid); PS-*b*-PED, polystyrene-*b*-poly(ethyleneoxide); PNVF, poly(*N*-vinylformamide); PNVA, poly(*N*-vinylacetamide); PNVIBA, poly(*N*-vinylisobutylamide); PVPAA, poly(1-vinylpyrrolidene-*co*-acrylic acid).

when a colloid with a small particle size is used, the activity increases with increasing particle size. The activity increases remarkably at a particle size of about 16 Å. A platinum colloid with a particle size of 16 Å consists of crystalline particles that each contain 108 platinum atoms, and the platinum particles may be an amorphous cluster in a platinum colloid with a particle size of less than 16 Å, which is a precursor of the crystal. The number of active sites of platinum colloids can be determined by the poisoning method in which mercuric chloride ( $\text{HgCl}_2$ ) is used as an inhibitor. The addition of  $\text{HgCl}_2$  causes a remarkable decrease in activity. If one active site is inhibited by one  $\text{HgCl}_2$  molecule, the amount of  $\text{HgCl}_2$  obtained by the extrapolation corresponds to the





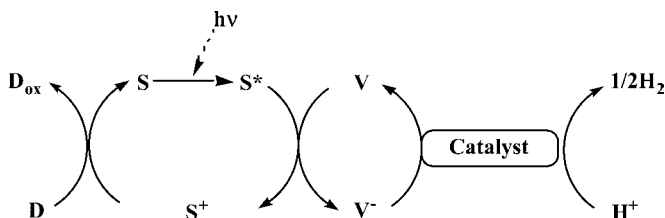
**Figure 5.** Relationship between catalytic activity for hydrogen peroxide decomposition and particle size. Reprinted with permission from [76], Namba and Okura, *Hyomen* 21, 450 (1983). © 1983, Koshinsha Co.

total active sites. For instance, in the case of platinum colloid prepared by reflex for 300 min, the number of active sites exposed on the surface is  $4.2 \times 10^{16}$ , and 37% of the platinum atoms are surface atoms. On the other hand, the activities of the hydrogen peroxide decomposition of platinum-gold and platinum-palladium alloys are strongly dependent on the alloy composition.

Gold colloid shows almost no activity. Even if up to 25% gold is added to platinum, the activity is almost the same as that of platinum alone. When 66% or more gold is added, the activity is almost lost. On the other hand, the activity decreases monotonously with the addition of palladium.

### 3.3. Photoinduced Hydrogen Evolution

Recently, hydrogen evolution by photolysis of water has been used to convert solar energy into chemical energy. The photoinduced hydrogen generation reaction and a homogeneous system can be outlined as follows:



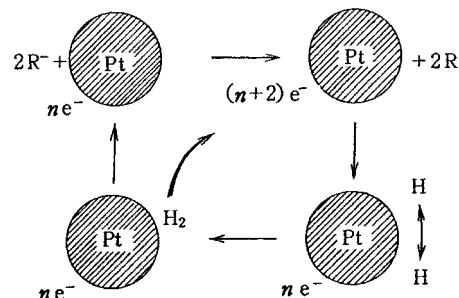
where D is an electron donor, S is a photosensitizer, and V is an electron carrier.

In this reaction, the sensitizer is first photoexcited and reduces the electron carrier, and then the sensitizer is oxidized. The oxidized photosensitizer is reduced with the electron donor and returns to its former state. On the other hand, the reduced electron carrier gives an electron to the proton of water by the catalyst, resulting in the hydrogen evolution. The catalyst for the hydrogen evolution should be

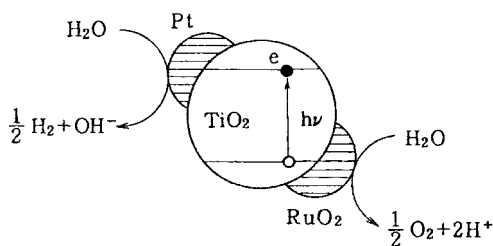
highly active and should be soluble or able to be highly dispersed in the solvent. If a dispersed solid catalyst is used, the catalyst may prevent the light from reaching the photosensitizer, and the inefficient use of irradiation light would result in a lowering of the reaction efficiency. Widely used catalysts in this reaction are platinum colloid and the enzyme hydrogenase. These are highly active for the hydrogen evolution reaction and have little effect on irradiation light. The platinum colloid receives an electron from the electron carrier, serves as an electron pool, and gives the electron to the proton. The reaction pathway is shown in Figure 6. A comparison of the hydrogen evolution efficiencies for the platinum colloid and for other platinum catalysts shows that the hydrogen evolution efficiency is much higher for platinum colloid. This is an example of photoinduced hydrogen evolution when methyl viologen (electron carrier), ethylenediamine-teraacetic acid (electron donor), and  $\text{Ru}(\text{bpy})_3^{2+}$  (photosensitizer) are used. When a semiconductor such as titania is used as the photosensitizer, water is completely decomposed. The following  $\text{RuO}_2/\text{TiO}_2/\text{Pt}$  colloid has been synthesized for efficient photolysis of water (see Fig. 7), in which the charge separation proceeds and hydrogen and oxygen are obtained. The ruthenium oxide (catalyst for oxygen evolution) and the platinum (catalyst for hydrogen evolution) are supported on a colloidal semiconductor powder.

### 3.4. Immunochromatography with Au Colloid and Pt Colloid

Immunochromatography is a method for detecting an antigen by an antigen-antibody reaction as illustrated in Figure 8. A complex (conjugate) is used in this method. The conjugate is a compound that binds with the antibody and metallic colloid, and the bare surface (the antibody not being adsorbed) is coated by bovine serum albumin. In this method, the conjugate and the antigen in the sample are reacted in advance, and a conjugate-antigen complex is formed. The conjugate-antigen complex is developed on a supported nitrocellulose film. Since the conjugate-antigen complex binds metallic colloid particles through the antigen, metallic colloid particles accumulate. When a gold colloid is used, a purple gold colloid color is observed. The detection sensitivity is  $\sim 100$  pg/ml. Sensitivity can be improved by platinum catalysis. For instance, a blue color appears when 3,3',5,5'-tetramethylbenzidine is oxidized with a platinum catalyst. The detection sensitivity in this case is 8 pg/ml.



**Figure 6.** Role of platinum colloid as an electron pool.



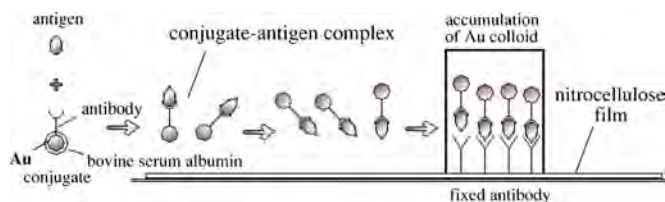
**Figure 7.** Mechanism of photodecomposition of water with  $\text{RuO}_2/\text{TiO}_2/\text{Pt}$  colloid.

### 3.5. Preparation and Characterization of Supported Platinum and Alloy Catalysts

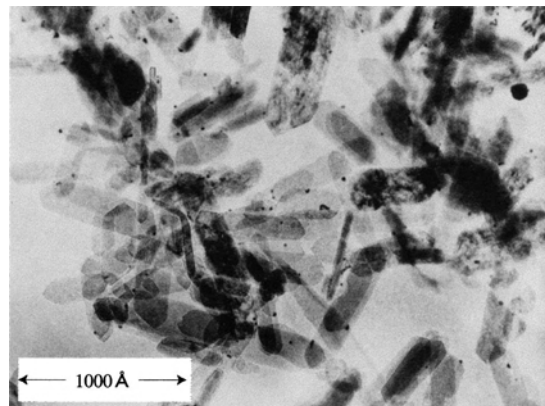
The metallic particles in a colloid are generally negatively charged. Therefore, the metallic particles are easily adsorbed to the carrier surface when the carrier contains polyvalent cations. Platinum and alloy colloids can be supported on an alumina plate as follows [20]. The hydrosol of the alumina plate is prepared as follows. Colloidal alumina is dispersed to aqueous acetic acid, and the hydrothermal reaction is allowed to proceed for 2.5 h at 200 °C. The obtained sol is deionized with the use of an ion-exchange resin (Amberlite MB-1). When the metal colloid is added to the alumina plate sol thus prepared, the metallic particles are immediately adsorbed to the alumina surface. The supported metal catalyst is obtained as a precipitate. As the adsorption of the metallic particles to the alumina surface is very fast, the metallic particles that adsorb to the surface are heterogeneous. To avoid this, the alumina plate sol is diluted 10 times and the metal colloid is dropped with vigorous stirring. The alumina plate with adsorbed metallic particles is obtained as a precipitate. This precipitate is separated by decantation and centrifugation. The precipitate is washed with clear water and dried at 105 °C.

Figure 9 shows an electron micrograph of a supported platinum catalyst prepared by the above-described method. The size of the platinum particles is the same as that of the sol, and the platinum particles are supported homogeneously on the alumina plate. The figure shows that 0.48 wt% platinum is supported on the alumina plate. The loading of the metal can easily be changed by changing the amount of metal colloid.

The platinum colloid supported on the alumina plate is active for hydrogenation of olefins and benzene and the  $\text{H}_2\text{-D}_2$  exchange reaction, as is a platinum catalyst prepared by the usual method. The thus-prepared catalyst has platinum particles of uniform sizes that are homogeneously dispersed on the surface. Such a platinum catalyst is suitable for studying the turnover numbers and selectivity change, depending on particle size. An alloy catalyst prepared by the



**Figure 8.** Mechanism of immunochromatography with gold colloid.



**Figure 9.** Electron microscopic picture of colloidal platinum on alumina. Reprinted with permission from [76], Namba and Okura, *Hyomen* 21, 450 (1983). © 1983, Koshinsha Co.

usual method may be different from an alloy catalyst prepared from a colloid. In the case of a platinum-gold alloy catalyst, it is known that only an extreme alloy (0–17% Pt, 98–100% Pt) is prepared because an immiscibility area exists in a catalyst prepared by the usual method. In a platinum-gold alloy colloid, however, the metal composition in the bulk and that of the surface are almost the same. This has been confirmed by examination of visible spectra and by hydrogen peroxide decomposition reaction. When ethylene hydrogenation was carried out with the alloy colloid, the highest activity was observed when  $\text{Pt}/\text{Au} = 2$  in the case of platinum-gold and at  $\text{Pt}/\text{Pd} = 1/2$  in the case of platinum-palladium. The high activity is caused by an increase in the turnover number, not by the exposed metal atoms or the number of active sites. Colloidal alloy catalysts are expected to have excellent activity or selectivity because various metal combinations are possible.

## 4. CONCLUSION

The nanotechnology of noble metal colloids has been making rapid progress in recent decades, and tailor-made nanocolloids of specific particle sizes have now become available. Such advances are most evident with the nanocolloids of platinum and gold as mentioned. Gold nanocolloids have been used particularly as labeling compounds of various biological materials. Catalytic reactions with platinum nanocolloids such as hydrogenation, decomposition, and hydrogen evolution have been the most extensively studied in a sol state and in a gel state. For example, platinum nanocolloids with specific sizes and Stabilizers are available for various degrees of selectivity in hydrogenation of alkenes and alkynes. Very recently, the interest in bimetallic nanocolloids has increased remarkably because of their possible use as a multifunctional catalyst, such as a fuel cell catalyst. Tailor-made multifunctional nanocolloids are strongly desired.

## GLOSSARY

**Alloy** A metal made by combining two or more metallic elements, especially to give greater strength or resistance to corrosion.

**Coagulation** A flocculate or cause of flocculate by the addition of an electrolyte to an electrostatic colloid.

**Hydrogenase** An enzyme that promotes the reduction of protonation or the oxidation of hydrogen.

**Immunochemistry** A kind of chromatography that uses the affinity of an antibody for an antigen.

**Stabilizer** Substance added to chemical compounds to prevent deterioration or the loss of desirable properties.

**Turnover number** The number of times that a catalyst or enzyme catalyzes during a given period of time.

## REFERENCES

- G. Schmid, "Clusters and Colloids." VCH, Weinheim, 1994.
- L. N. Lewis, *Chem. Rev.* 93, 2693 (1993).
- M. A. Hayat, "Colloidal Gold." Academic Press, San Diego, 1989.
- H. Hirai, Y. Nakao, and N. Toshima, *J. Macromol. Sci. A Chem.* 13, 727 (1979).
- T. Teranishi, M. Hosoe, and M. Miyake, *Adv. Mater.* 9, 65 (1997).
- X. Yang and H. Liu, *Appl. Catal., A* 164, 197 (1997).
- W. Yu, M. Liu, H. Liu, and J. Zheng, *J. Colloid Interface Sci.* 210, 218 (1999).
- W. Tu, H. Liu, and K. Y. Liew, *J. Colloid Interface Sci.* 229, 453 (2000).
- C. Chen and M. Akashi, *J. Polym. Sci. Polym. Chem.* 35, 1329 (1997).
- C. Chen and M. Akashi, *Langmuir* 13, 6465 (1997).
- C. Chen, T. Serizawa, and M. Akashi, *Chem. Mater.* 11, 1381 (1999).
- A. B. R. Mayer and J. E. Mark, *Polym. Bull.* 37, 683 (1996).
- A. B. R. Mayer and J. E. Mark, *Colloid Polym. Sci.* 275, 333 (1997).
- C.-W. Chen, M.-Q. Chen, T. Serizawa, and M. Akashi, *Chem. Commun.* 831 (1998).
- C.-W. Chen, D. Tano, and M. Akashi, *Colloid Polym. Sci.* 277, 488 (1999).
- X. Auo, H. Liu, and M. Liu, *Tetrahedron Lett.* 39, 1941 (1998).
- X. Zuo, H. Liu, D. Guo, and X. Yang, *Tetrahedron* 55, 7787 (1999).
- C.-W. Chen, D. Tano, and M. Akashi, *J. Colloid Interface Sci.* 225, 349 (2000).
- D. N. Furlong, A. Launikonis, and W. H. F. Sasse, *J. Chem. Soc. Faraday Trans. 1* 80, 571 (1984).
- K. Arai, L. L. Ban, I. Okura, S. Namba, and J. Turkevich, *J. Res. Inst. Catal. Hokkaido Univ.* 24, 54 (1976).
- L. D. Rampino and F. F. Nord, *J. Am. Chem. Soc.* 63, 2745 (1941).
- P. A. M. Brugger, P. Cuendel, and M. Gratzel, *J. Am. Chem. Soc.* 103, 2923 (1981).
- C. Yee, M. Scotti, A. Ulman, H. White, M. Rafailovich, and J. Sokolov, *Langmuir* 15, 4314 (1999).
- Y. Nakao and K. Kaeriyama, *Kobunshi Ronbunshu* 42, 223 (1985).
- T. S. Ahmadi, Z. L. Wang, T. C. Green, A. Hengleir, and M. A. El-Sayad, *Science* 272, 1924 (1996).
- V. V. Blagutina, A. I. Kokorin, and V. Ya. Shafirovich, *Kinet. Catal.* 31, 839 (1991).
- N. Toshima, K. Nakata, and H. Kitoh, *Inorg. Chem. Acta* 265, 149 (1997).
- W. Yu, W. Tu, and H. Liu, *Langmuir* 15, 6 (1999).
- J. J. Walkins and T. J. McCarthy, *Chem. Mater.* 7, 1991 (1995).
- P. A. Bartlett, B. Bauer, and S. J. Singer, *J. Am. Chem. Soc.* 100, 5085 (1978).
- J. F. Hainfeld, *Science* 236, 450 (1987).
- W. Baschong and J. Roth, *Histochem. J.* 17, 1147 (1985).
- J. Roth, *Histochem. J.* 14, 791 (1982).
- J. W. Slot and H. J. Geuze, *Eur. J. Cell Biol.* 38, 87 (1985).
- J. Tschopp, E. R. Podack, and H. J. Muller-Eberhard, *Proc. Natl. Acad. Sci. U.S.A.* 79, 7474 (1982).
- G. B. Birrell, K. K. Hedberg, and O. H. Griffith, *J. Histochem. Cytochem.* 35, 843 (1987).
- W. P. Faulk and G. M. Taylor, *Immunochemistry* 8, 1081 (1971).
- H. Mhlpfordt, *Experientia* 38, 1127 (1982).
- J. DeMey, "Immunocytochemistry, Modern Methods and Applications" (J. Polak and S. Van Noorden, Eds.), pp. 82-106. Wright-PSG, Bristol, 1986.
- W. P. Faulk and G. M. Taylor, *Immunochemistry* 8, 1081 (1971).
- P. M. P. Van Bergen en Henegouwen and J. L. M. Leunissen, *Histochemistry* 85, 81 (1986).
- C. L. Baigent and G. Muller, *Experientia* 36, 472 (1980).
- M. Rodriguez, R. J. von Wedel, R. S. Garrett, P. W. Lampert, and M. B. A. Oldstone, *Lab. Invest.* 49, 48 (1983).
- A. O. Jorgensen and K. P. Campbell, *J. Cell Biol.* 98, 1597 (1984).
- E. C. Stathis and A. Fabrikanos, *Chem. Ind. (London)* 27, 860 (1958).
- M. Horisberger, D. R. Farr, and M. Vonlanthen, *Biochim. Biophys. Acta* 542, 308 (1978).
- J. W. Slot and H. J. Geuze, *J. Cell Biol.* 90, 533 (1981).
- D. H. Handley, "Colloidal Gold, Principles, Methods, and Applications" (M. A. Hayat, Ed.), p. 13. Academic Press, San Diego, 1989.
- N. Satoh and K. Kimura, *Bull. Chem. Soc. Jpn.* 60, 1758 (1989).
- M. Han and H. Liu, *Macromol. Symp.* 105, 179 (1996).
- Y. Wang, H. Liu, and Y. Jiang, *J. Chem. Soc. Chem. Commun.* 1878 (1989).
- H. Hirai, Y. Nakao, and N. Toshima, *J. Macromol. Sci., Chem.* 12, 1117 (1978).
- H. Hirai, *J. Macromol. Sci., Chem.* 13, 633 (1979).
- Q. Wang, H. Liu, M. Han, X. Li, and D. Jiang, *J. Mol. Catal. A: Chem.* 118, 145 (1997).
- C. Larpent, F. Brisse-Le Menn, and H. Patin, *J. Mol. Catal.* 65, L35 (1991).
- M. T. Reetz and W. Helbig, *J. Am. Chem. Soc.* 116, 7401 (1994).
- W. Yu, H. Liu, M. Liu, and Q. Tao, *J. Mol. Catal. A: Chem.* 138, 273 (1999).
- M. Liu, W. Yu, and H. Liu, *J. Mol. Catal. A: Chem.* 138, 295 (1996).
- X. Zuo, H. Liu, and C. Yu, *J. Mol. Catal. A: Chem.* 147, 63 (1999).
- W. Wang, S. Efrima, and O. Regev, *Langmuir* 14, 602 (1998).
- J. Turkevich, P. C. Stevenson, and J. Hiller, *Discuss. Faraday Soc.* 11, 55 (1951).
- V. Akhmedov and K. J. Klabunde, *J. Mol. Catal.* 45, 193 (1988).
- N. Toshima, T. Yonezawa, and K. Kushihashi, *J. Chem. Soc. Faraday Trans.* 89, 2537 (1993).
- K. Torigoe and K. Esumi, *Langmuir* 9, 1664 (1993).
- K. J. Klabunde, Y. Y. X. Li, and B. J. Tan, *Chem. Mater.* 3, 30 (1991).
- N. Toshima and K. Hirakawa, *Appl. Surf. Sci.* 121/122, 534 (1997).
- J. Turkevich and G. Kim, *Science* 169, 873 (1970).
- H. Bennemann, P. Britz, and H. Ehwald, *Chem. Technik* 49, 189 (1997).
- F. Launay, A. Roucoux, and H. Patin, *Tetrahedron Lett.* 39, 1353 (1998).
- A. Borsla, A. M. Wilhelm, and H. Delmos, *Catal. Today* 66, 389 (2001).
- L. N. Lewis, R. J. Uriarte, and N. Lewis, *J. Mol. Catal.* 66, 105 (1991).
- W. Yu, H. Liu, M. Liu, and Q. Tao, *J. Mol. Catal. A: Chem.* 138, 273 (1999).
- W. Yu, H. Liu, and Q. Tao, *Chem. Commun.* 1773 (1996).
- H. Feng and H. Liu, *J. Mol. Catal. A: Chem.* 126, L5 (1997).
- J. Turkevich, R. S. Miner, Jr., I. Okura, S. Namba, and N. Zacharina, "Perspectives in Catalysis" (R. Larsson, Ed.), p. 111. CWK, Gleerup, Sweden, 1981.
- Namba and Okura, *Hyomen* 21, 450 (1983).

# Nonlinear Optical Materials by Sol–Gel Method

Wenyan Li, Sudipta Seal

University of Central Florida, Orlando, Florida, USA

## CONTENTS

1. Introduction
  2. Semiconductor–Glass Nanocomposites
  3. Metal Cluster Nanocomposites
  4. Organic–Inorganic Hybrid Composites
  5. Conclusions
- Glossary  
References

## 1. INTRODUCTION

Current developments in optical telecommunications are leading to the demand in the near future for devices capable of ultrafast signal switching and routing. These functions are presently carried out mainly by electro-optical circuits and will be performed by a photonic technique, an emerging technology in which photons, instead of electrons, are used to acquire, store, transmit, and process information [1]. All-optical integrated devices, such as optical switching devices, are to be developed to achieve fast response times. In order to realize such devices, new optical materials, exhibiting strong nonlinear properties, need be developed.

Sol–gel optics has emerged over last 20 years, along with many other applications of sol–gel technology [2, 3]. Research has been moving along several directions, ranging from semiconductors and metals to polymers, from inorganic to organic materials, and from single phase materials to composites. In this chapter, a brief survey is provided for the sol–gel synthesis of the nanocomposites with nonlinear optical properties.

### 1.1. Optical Nonlinear Effect

This section describes general concepts of nonlinear optical effects [4, 5]. When an electron is pulled from an atom, the restoring force  $F$ , to a first approximation, is proportional

to the displacement of the electron from its equilibrium position,

$$F = -kx \quad (1)$$

where  $k$  is the proportional constant, and this equation shows a linear effect.

When the force is related to the potential energy,  $V$ ,

$$F = -\nabla V \quad (2)$$

where  $\nabla$  denotes the gradient ( $\nabla = \partial/\partial x$  for the one-dimensional case), from Eqs. (1) and (2)

$$V = \frac{1}{2}kx^2 \quad (3)$$

This corresponds to a harmonic potential, and the potential energy is chosen to be zero at  $x = 0$ .

When an electric field (e.g., light) interacts with electrons in a material, the electron density can be provoked to be displaced. When the optical effect is linear, this leads to an induced dipole, or polarization, which is linearly proportional to the electric field,

$$p = \alpha E \quad (4)$$

where  $\alpha$  is the linear polarizability.

So in a linear material the charges oscillate at the same frequency as the incident light. The oscillating charges either radiate light at that frequency or the energy is transferred into nonradiative modes, such as thermal or other energy form.

In most cases, the harmonic model is a good approximation, but closer examination indicates the importance of other terms in the potential. If the restoring force can be written as

$$F = -kx - \frac{1}{2}k'x^2 \quad (5)$$

this leads to the following potential energy:

$$V = \frac{1}{2}kx^2 + \frac{1}{6}k'x^3 \quad (6)$$

As we can see, there is an additional anharmonic term, and it will give a  $V$  value which depends on the sign (or direction) of  $x$ . Similarly, the magnitude of polarization will depend on the direction of the electric field of the light. An example of such a material is one of an anisotropic charge distribution in the absence of an electric field, such as a noncentrosymmetric polar crystal. In this case, the electric field of light can displace the charge differently in different directions, resulting in nonlinear polarization. In a nonlinear optical material, or when the electric field is strong enough, the polarization can be written as a Taylor series expansion

$$p = \alpha E + \beta EE + \gamma EEE + \dots \quad (7)$$

where  $\alpha$  is the linear polarizability, while  $\beta$  and  $\gamma$  are referred to as the first and second hyperpolarizabilities, respectively. In a nonlinear optical material, the induced polarization is not a pure sine wave at the frequency of light. It can be composed of the frequency ( $\nu$ ), and its harmonics ( $2\nu, 3\nu, \dots$ ), as well as an offset, which is a dc component given by the static polarization. The hyperpolarizabilities give rise to the harmonics. The displacement of charge from its equilibrium value is a nonlinear function.

The macroscopic polarization  $P$  (i.e., the dipole moment density) can be described by

$$P = \chi^{(1)}E + \chi^{(2)}EE + \chi^{(3)}EEE + \dots \quad (8)$$

where  $\chi^{(n)}$  describes tensors of  $n$ th order, and  $\chi^{(2)}$  and  $\chi^{(3)}$  are the second- and third-order nonlinear optical susceptibilities. To have second-order nonlinear properties, there must be a preferred direction in the system, instead of an equivalent system. Most easily polar ordered dipole molecules fulfill this requirement. However, third-order nonlinear properties are nonzero for all materials, although they induced a weaker optical response.

## 1.2. Sol–Gel for Nonlinear Materials

The sol–gel method is suitable for the preparation of many nonlinear optical (NLO) materials, in the form of thin film, fibers, and even monoliths. Silica glass and other oxide glasses do not normally have high nonlinear optical parameters, but with their low optical losses and good mechanical properties, they serve as ideal matrix for nonlinear materials. Nanosized semiconductors, metal nanoclusters, and optically active organics can be introduced into the sol–gel derived transparent oxide glass and ceramic to form nanocomposites with nonlinear properties. A number of methods can be used to prepare NLO nanocomposites, which include the mixing of optically active organics into the sol–gel liquid solution, the impregnation of organics into the interconnecting pores of a stabilized oxide gel, and the direct chemical bonding of optically active organics and inorganics, metals, and semiconductors, to form NLO nanocomposites [6].

We will mainly introduce three types of NLO nanostructures made by the sol–gel process: semiconductor–glass,

metal cluster–glass, and organics–glass nanocomposites. Metal or semiconductor nanoclusters dispersed in a glass matrix have high resonant-type  $\chi^{(3)}$  [7–14]. Metal nanoclusters in glass matrix also exhibit picosecond switching and relaxation times, thermal and chemical stability, high laser damage threshold, low photon absorption, and optical tunability [15–18]. Organic polymer, such as para-nitroaniline, diethylaminonitrostyrene, *N*-(4-nitrophenyl)-(L)-prolinol, and *N*-(3-hydroxy-4-nitrophenyl)-(L)-prolinol possess high second-order optical nonlinearity, after they have been oriented by electric field poling. Conjugated polymer, like polyphenylenevinylene has emerged as a class of important third-order nonlinear optical material [1]. The composites of sol–gel processed oxide/polymer offer promising nonlinear applications.

## 2. SEMICONDUCTOR–GLASS NANOCOMPOSITES

In 1983, Jain and Lind reported that some commercially available silicate glasses containing ultrafine crystals of CdS and CdSe had high values of third-order nonlinearities and fast switching times [19]. This so-called quantum confinement effect is now well known for a variety of semiconductors and semiconductor nanocrystal-doped glasses. These materials have emerged as potential candidates for nonlinear optical devices [13, 20–27]. If the dimension of the semiconductor clusters is of the order of or smaller than the Bohr exciton radius (about 20 Å for CdS), which indicates the effective separation of hole and electron in the first excited state of the semiconductor [28], the quantization of the energy levels due to size quantization can lead to a strong improvement of the nonlinear characteristics of the material itself [29, 30].

Research has initially concentrated on commercially available SDGs (semiconductor-doped glasses), commonly used as sharp-cut optical filters [31]. Though this first approach has been important for the understanding of some basic mechanisms of the nonlinear properties enhancement, these materials were not optimized either for integrated optical applications or for optimal performance in terms of nonlinear response [32, 33].

There are two problems associated with these materials. First was the size distribution of the clusters. The size range of early samples which were obtained by usual melting processes was too broad to obtain a sharp and strong enhancement of the nonlinearity [33]. The second problem was constituted by the darkening of the glasses when exposed to light beams (*photodarkening*). This phenomenon was probably due to photochemical reactions which take place at the boundary between the semiconductor and the glass matrix, caused by impurity at those locations. Photodarkening increases optical absorption and thus can harm light propagation.

To optimize the properties of SDGs, other processes have been explored, such as radio frequency sputtering deposition [34, 35] and sol–gel deposition, which offer better prospects especially for the control of size of the nanocrystals and the impurity in the material.

The easy control of the material composition in a sol–gel system also allows an increase in the dopant concentration,

which can further improve the special characteristics of such glasses.

Various semiconductors, such as CdS, CdSe, CdTe, PbTe, and ZnTe doped glasses with nonlinear properties, have been successfully developed by the sol–gel technique [20, 22, 36–41]. A few results are summarized in Table 1.

## 2.1. CdS-Doped Films

The semiconductor particles most studied were cadmium sulfide [28, 42]. The nonlinear properties of CdS incorporated in thin film prepared by the sol–gel method and in organically modified ceramics have been studied by Reisfeld [28, 43], Mackenzie [6], Nogami et al. [21, 44, 45], and many others. Most of the earlier work was based on SiO<sub>2</sub> matrix [44, 46, 47]. More recently, Takada et al. developed Na<sub>2</sub>O–B<sub>2</sub>O<sub>3</sub>–SiO<sub>2</sub> glasses from gels and used it as the matrix material, since dense glasses could be obtained at temperature lower than 600 °C [36, 37]. CdS crystallites were prepared in glass matrix with diameters of 40 to 60 Å and concentrations up to 8 wt%. These glass nanocomposites exhibited excellent optical quality and on-resonance  $\chi^{(3)}$  values up to  $6 \times 10^{-7}$  esu [48].

Besides inorganic glass systems, organically modified silicates (Ormosils) have also been evaluated as the matrix material for semiconductor nanocrystals, as they are less brittle than pure oxide gels [49]. A simple approach was to add cadmium salt, in the form of acetate or nitrate, to a TEOS (tetraethoxysilane)–PDMS (polydimethyl siloxane) liquid solution and allow an Ormosil to form. The cadmium salt was then converted to the oxide and then to the sulfide via H<sub>2</sub>S treatment of the porous Ormosil. The resulting Ormosil was then densified to get transparent nanocomposite. The composite is then polished to achieve an excellent optical surface. Up to 20 wt% CdS nanocrystals of 30–60 Å can be dispersed in such a matrix. The off-resonance  $\chi^{(3)}$  were of the order of  $10^{-11}$  esu, and the on-resonance values around  $10^{-8}$  esu. In these Ormosil-based NLO materials, photodarkening, a deleterious process due to prolonged radiation observed in traditional matrix made by fusion and “striking” process [19], was practically unobservable.

Different techniques can be applied to the process in order to effectively control the size of the clusters, obtaining narrower size distributions of the crystallites. For instance, particle size can be controlled by applying appropriate heat-treatment schedules [41, 50]. Thermal treatments for drying and densification, at temperatures usually lower than 500 °C, do not induce unwanted effects of growth of the nanocrystals and broadening of the size distribution. In contrast, it can be used to control the particle size distribution.

Two main processes are being investigated in order to efficiently control the size of the semiconductor clusters: the first one takes the advantage of the porosity of the sol–gel matrix to put an upper limit to the growth of the crystallites (*pore doping*), while the second one uses chemical agents to control the cluster surface and to terminate it by capping groups which prevent further aggregation and growth of the nanoclusters (*surface capping*) [51].

### 2.1.1. Pore Doping

Using pore size to control the particle growth inside the pore requires a well-controlled pore size in the matrix material. Wang and Herron studied the size dependence of nonresonant third-order nonlinear susceptibility in CdS clusters and found that, in their system, the value of  $\chi^{(3)}$  reached maximum at a particle size of 60 Å [52]. It is to be noted that average size of the pores can be controlled by the pH of the starting solution [53]. They prepared porous silica glass starting from TEOS and introduced semiconductors into the pores. For the CdS system, Cd precursor can be added to the starting solution, and then the sol–gel product can be annealed in H<sub>2</sub>S atmosphere to form CdS in the porous glass. In this case, the size of CdS cluster is also influenced by the annealing time; otherwise, Cd could be introduced into the porous glass by impregnation, soaking the substrate in a cadmium nitrate solution, and then obtaining CdS by carrying out a similar annealing process. The latter technique has the advantage of possible high density of semiconductor clusters in the glass pores but also poses difficulty in achieving a uniform dispersion throughout a large substrate. The impregnation approach was also followed by Choi and Shea [54], where Na<sub>2</sub>S was used instead of H<sub>2</sub>S for the sulphidation step.

Yeatman et al. [55] investigated thoroughly the influence of the sol–gel process on the pore size distribution and obtained CdS crystals with an average size of 4 nm by annealing a silica gel in an H<sub>2</sub>S atmosphere where Cd had already been dispersed in the gel by adding cadmium acetate to the starting solution. They found that the higher the annealing temperature, the smaller the crystal obtained. Nonlinear *m*-line measurements using low and high intensities (0.76 and 8.41 μJ/pulse, respectively) were performed. The nonlinear refractive index at the wavelength of 0.532 μm was estimated to be  $n_2 = -5.5 \times 10^{-9}$  cm<sup>2</sup> kW<sup>-1</sup> [56]. However, the higher  $n_2$  obtained for thinner films (e.g.,  $3.2 \times 10^{-8}$  cm<sup>2</sup> kW<sup>-1</sup> in [57]) suggests that substantial improvements are possible. Such values of nonlinear refractive index  $n_2$  can be transformed into values of third-order nonlinear susceptibility [58], and the corresponding values of  $\chi^{(3)}$  are  $3.2 \times 10^{-10}$  and  $1.8 \times 10^{-9}$  esu, respectively.

Using a similar technique, Minti et al. [59] obtained CdS clusters with sizes mostly in the range of 2–5 nm, and they can be as high as 20 nm. Despite the rather broad size distribution, third-harmonic generation signals were observed when the sample was laser irradiated at 1.06 μm and observed at 0.355 μm: the corresponding  $\chi^{(3)}$  was evaluated to be  $10^{-12}$  esu.

### 2.1.2. Surface Capping

While the pore doping method uses pore size as a physical limit of particle growth, surface capping introduces a terminating chemical agent to control the particle size. It is a molecule which attaches to the growing cluster surface and thus controls the size to which it can grow. Research efforts have been focused on the selection of the agent and the optimization of the process developing a synthetic methodology to prepare monodisperse nanoclusters is important not only for optical devices, but also for catalysis, chemical sensing, and novel magnetic devices [60].

**Table 1.** NLO and other related properties of some sol–gel semiconductor–glass nanocomposites.

S. No.	Matrix	Particle size	Dope concentration	Optical nonlinearity	Precursors	Ref.
<b>CdS-doped Films</b>						
1	SiO <sub>2</sub>	2–5 nm	Cd/Si = 0.0077 to 0.12 (mol)		TMOS(TEOS) + H <sub>2</sub> O + EtOH + H <sub>2</sub> S + CdAc	[28]
2	SiO <sub>2</sub>	3.5–4.5 nm	CdO/SiO <sub>2</sub> = 1, 2, 5, 10 wt% before reacting with H <sub>2</sub> S	4.5 × 10 <sup>-11</sup> esu (CW laser) and 2.3 × 10 <sup>-11</sup> esu (pulse laser)		[78]
3	Na <sub>2</sub> O–B <sub>2</sub> O <sub>3</sub> –SiO <sub>2</sub>	4–6 nm	8 wt%	6 × 10 <sup>-7</sup> esu	TMOS + HCl + H <sub>2</sub> O + B(OEt) <sub>3</sub> + NaOAc + Cd(OAc) <sub>2</sub>	[6, 48]
4	ormosils	3–6 nm	20 wt%	10 <sup>-11</sup> esu (off-resonance) 10 <sup>-8</sup> esu (on-resonance)	CdAc or Cd(NO <sub>3</sub> ) <sub>2</sub> + TEOS + PDMS + H <sub>2</sub> S	[49]
5	ZrO <sub>2</sub>			4 × 10 <sup>-1</sup> esu		[79]
6	SiO <sub>2</sub> –TiO <sub>2</sub>	3.5 nm (heated at 300 °C) 5 nm (heat at 500 °C) surface capping agent: acetylacetone		n <sub>2</sub> = –2.9 × 10 <sup>-7</sup> cm <sup>2</sup> /kW, (resonant) corresponding to χ <sup>(3)</sup> 1.6 × 10 <sup>-8</sup> esu	TEOS/methyltriethoxysilane (MTES) CdAc + methnoal + acetylacetone	[80, 81]
7	SiO <sub>2</sub> –TiO <sub>2</sub>		6% (molar)	–4.67 × 10 <sup>-7</sup> esu	TEOS + Ti(OBu) <sub>4</sub> + CdAc + H <sub>2</sub> O + HCl ethanol + AcAcH + SC(NH <sub>2</sub> ) <sub>2</sub> or CH <sub>3</sub> CSNH <sub>2</sub>	[82]
8	SiO <sub>2</sub> –TiO <sub>2</sub>	2–20 nm surface capping agents: acetylacetone, 3-aminopropyltriethoxysilane, 3-aminopropyltrimethoxysilane, 3-mercaptopropyltrimethoxysilane		n <sub>2</sub> = –3 × 10 <sup>-9</sup> cm <sup>2</sup> /kW	CdAc + thioacetamide (CH <sub>3</sub> CSNH <sub>2</sub> ), TEOS + MTOS + EtOH + H <sub>2</sub> O + HCl + Ti(OBu) <sub>4</sub>	[83]
9	SiO <sub>2</sub>	4 nm		n <sub>2</sub> = –5.5 × 10 <sup>-9</sup> cm <sup>2</sup> /kW, (χ <sup>(3)</sup> 3.2 × 10 <sup>-10</sup> esu) for very thin film, n <sub>2</sub> = 3.2 × 10 <sup>-8</sup> cm <sup>2</sup> /kW, (χ <sup>(3)</sup> 1.8 × 10 <sup>-9</sup> esu)	silica gel + CdAc + H <sub>2</sub> S	[55]
10	SiO <sub>2</sub>	2–5 nm, up to 20 nm		10 <sup>-12</sup> esu	CdS prepared in glass obtained from TMOS or TEOS	[59]
11	SiO <sub>2</sub>	2.8 ± 0.9 nm surface capping agent: 3-aminopropyltriethoxysilane		10 <sup>-6</sup> esu	Silica gel + CdO + H <sub>2</sub> S	[61]
<b>CdSe-doped Films</b>						
1	SiO <sub>2</sub>	4–20 nm			TMOS + PrOH + H <sub>2</sub> O + SeO <sub>2</sub> + CdAc + glycerol + methoxyethanol	[28, 73]
2	ormosil	3–5 nm	2% (wt)		CdSe was prepared inside reverse micelles in AOT/H <sub>2</sub> O/ heptane ormosil was derived from 3-aminopropyl(trimethoxy)silane	[74, 75]
<b>CdTe-doped Films</b>						
1	ZrO <sub>2</sub>	6–20 nm		—	ZrO <sub>2</sub> sol + CdAc + TeO <sub>2</sub> + HCl + glycerol + methoxyethanol + SnCl <sub>2</sub> (or hydrazine)	[28, 77]
2	Na <sub>2</sub> O–B <sub>2</sub> O <sub>3</sub> –SiO <sub>2</sub>	2.4–8.5 nm			(a) immersing CdO doped gels in NaTe/MeOH (b) Cd(NO <sub>3</sub> ) <sub>2</sub> + H <sub>6</sub> TeO <sub>6</sub> , then reducing in H <sub>2</sub> /N <sub>2</sub>	[84]

continued

Table 1. Continued

S. No.	Matrix	Particle size	Dope concentration	Optical nonlinearity	Precursors	Ref.
PbS-doped Films						
	ZrO <sub>2</sub>	4.5 nm	5% to 30%	—	Zr(OPr) <sub>4</sub> + propanol PbAc + methoxymethanol	[28, 85]
	zirconia-ormosil	4.8 ± 0.8 nm surface capping agent: 3-mercaptopropyltrimethoxysilane		the nonlinear refractive index $n_2 = 10^{-15}$ to $10^{-16}$ m <sup>2</sup> /W	3-(trimethoxysil)propylmethacrylate + methacrylic acid + Zr(OPr) <sub>4</sub> , PbAc in methanol + thioacetamide	[86]
	SiO <sub>2</sub>	4.5–5.0 nm	5% (molar)		TEOS + MEES + H <sub>2</sub> O + HCl + EtOH PbAc + SC(NH <sub>2</sub> ) <sub>2</sub> + acetylacetone (acacH) + MeOH	[87]
	SiO <sub>2</sub> -TiO <sub>2</sub>	1.6–3.0 nm	5% (molar)		TEOS + MEES + H <sub>2</sub> O + HCl + EtOH Ti(OBu) <sub>4</sub> + acacH PbAc + SC(NH <sub>2</sub> ) <sub>2</sub> + acacH + MeOH	[87]
	SiO <sub>2</sub> -TiO <sub>2</sub>	2.3–3.5 nm surface capping agent: 3-mercaptopropyltrimethoxysilane	PbS/oxide molar ratio: 5% to 25%	$n_2 = 10^{-7}$ – $10^{-8}$ cm <sup>2</sup> /kW nanosecond excitation $n_2 = 10^{-9}$ – $10^{-10}$ cm <sup>2</sup> /kW picosecond excitations	MTES/TEOS + H <sub>2</sub> O + HCl + EtOH PbAc + CH <sub>3</sub> CSNH <sub>2</sub>	[80, 88, 89]

Takada and co-workers [61] developed CdS-doped glass samples by combining both techniques to control the cluster growth. They started producing a porous organically modified silica gel containing CdO clusters and carried out an annealing under H<sub>2</sub>S atmosphere to obtain CdS clusters. By introducing 3-aminopropyltriethoxysilane as a ligand functional to the solution, a narrow distribution of the cluster size ( $2.8 \pm 0.9$  nm) was obtained. The ligand anchors the Cd to the gel-glass matrix, avoiding precipitation during the drying step, thus improving the homogeneity of the film. A huge nonlinearity, with  $\chi^{(3)}$  of about  $10^{-6}$  esu, was observed.

Another approach is to produce colloidal particles separately using a surface capping agent to control their size and then incorporate them in the sol-gel media [54, 59, 62, 63]. For example, Gacoin et al. [60] produced semiconductor nanoclusters capped with phenylthiol and then dispersed them in a sol-gel precursor solution.

Herron and Wang [53] also obtained CdS clusters of size up to 40 Å by using thiophenolate as a capping agent. In this case, the clusters were dispersed in acetonitrile solution and showed a  $\chi^{(3)}$  of around  $10^{-14}$  esu. Since the clusters are easily soluble in a wide range of solvents, the authors suggest either to produce pure CdS films by spray pyrolysis or to incorporate them in polymeric films like polymethylmethacrylate (PMMA).

## 2.2. CdSe-Doped Films

CdSe nanoclusters are known to exhibit different colors at various particle sizes, from deep red to orange to yellow, due to the “blueshift” of the optical threshold, one of the quantum confinements.

Nanoparticles of CdSe have been prepared in colloidal solutions [64, 65] or embedded in solid and transparent

media, such as zeolites [66], glasses [67, 68], and polymers [69]. Several studies showed an attempt to passivize the surface of colloidal nanoparticles by disordered organic capping [64, 70]. However, this leaves unsaturated bonds and sensitivity to photo-oxidation [65]. Other recent reports described the development of colloidal composite nanoparticles, containing a CdSe core, surrounded with another semiconductor shell [71, 72]. These can be viewed as epitaxial heterostructures of nanoparticles, enabling crystal matching and construction of electronically passivated surfaces. The solid media diminish the particles’ surface reactivity, supply a stable chemical environment, and induce dielectric confinement [67].

CdSe nanoparticles films were prepared by chemical solution deposition and formation in a silica sol-gel matrix by Reisfeld. The silica film-dipped CdSe nanocrystals were obtained by adding the precursor solution of trimethoxyorthosilane to a solution of selenium dioxide in monomethoxyethanol and cadmium nitrate [28].

Microscopic slides dipped into the solution allowed one to obtain homogeneous films which were then thermally treated [73]. X-ray powder diffraction and transmission electron microscope measurements confirmed a cubic crystalline structure of the nanoparticles, with mean diameter varying from 4 to 20 nm. The absorption and photoluminescence spectra of the smaller crystals were strongly blueshifted due to size quantization. The results indicate that the emission band involves the recombination between trapped electrons and holes presumably located on the surface states.

Nanosized, phenyl-capped CdSe quantum dots were prepared inside reversed micelles in AOT/H<sub>2</sub>O/heptane [75, 76], and then isolated and redispersed in the amino-silicate ormosil (i.e., organically modified silicate) which was derived from 3-aminopropyl-(trimethoxy)silane by Ou and Seddon [74]. Doped ormosils were formed into films of a few micrometer thickness or small bulk samples. The ormosils



were structurally characterized by means of absorption spectroscopy in the visible and near-infrared ranges, and by  $^{29}\text{Si}$  solid state nuclear magnetic resonance spectroscopy. The siloxane matrix of the amino-silicate ormosil was found to be 84% condensed and polymeric water molecules are hydrogen bonded into the matrix, presumably at silanol and amine sites. CdSe dots of apparently good monodispersity and radius 1.5 to 2.4 nm (going from yellow to red in visual appearance) were redispersed in the amino-silicate ormosil. Attempts to prepare larger dots resulted in flocculation of the CdSe. The maximum loading of CdSe dots in the amino-silicate matrix was measured to be 2.05 wt% CdSe<sub>0.72</sub>, where the density of the amino-silicate host was around 0.5 to 0.7 of the density of a typical, melt-derived silicate glass.

### 2.3. CdTe-Doped Films

Cadmium telluride nanocrystallites were obtained by two synthetic methods in zirconia sol–gel films [77]. The nanoparticles were obtained by either chemical reduction of Te(IV) using a reducing agent (hydrazine) or tin chloride. Particle sizes ranging from 6 to 20 nm in diameter could be prepared by varying the experimental parameters. The size and crystalline structure of the particles were characterized by optical absorption, X-ray diffraction, transmission electron microscopy (TEM), and X-ray photoelectron spectroscopy. The film morphology was characterized by scanning force microscopy. The film obtained by the SnCl method is smooth and homogenous. A dense structure of CdTe nanoparticles of a few nanometers in diameter is revealed. The films prepared with hydrazine are porous as a result of evolution of the decomposition gaseous products during the reduction [77].

### 2.4. PbS-Doped Films

Lead sulfide (PbS) nanocrystals, embedded in amorphous zirconia sol–gel film with different PbS mol concentrations (5–30%), were prepared at temperatures ranging from 200 to 350 °C [28].

First, a zirconia solution is prepared. A 70% zirconium *n*-propoxide solution in 1-propanol was diluted to about 18% by *n*-propanol and stirred for 15 min. Then, glacial acetic acid was added and stirred for an additional 15 min. The solution was hydrolyzed with an acetic acid–water solution (1:1) under stirring for another 30 min, filtered, and stored in a refrigerator for 3–4 days. The solution was transparent, and its color was pale yellow. Then, to prepare the component solution, lead acetate trihydrate and ammonium thiocyanate were dissolved in 2-methoxymethanol at the boiling temperature of the solvent, 124.5 °C. An excess of sulfur, up to 50% was needed in order to bring the reaction to completion. Subsequently, the solution was stirred for 15 min, filtered, and cooled to room temperature. The solution was transparent and colorless. Finally, zirconia solution was diluted in *n*-propanol and component solution was added drop by drop. After an additional 30 min of stirring for homogenization, the final solution was transparent and pale yellow.

The films were prepared by dipping microscope glass slides or indium–tin oxide coated glass substrate into the

final solution, followed by an annealing process, which completes the chemical reaction between lead and sulfur. The mol concentrations of the PbS nanocrystals within the zirconia films were 5, 15, 20, and 30%.

The size of PbS nanocrystals was determined by TEM and by blueshift of the absorption edge. The size increased with an increase in synthesis temperature and PbS mol concentration. The PbS nanocrystals have a nearly spherical shape, have an average size of 4.5 nm, and are homogeneously dispersed in an amorphous ZrO<sub>2</sub> thin film matrix.

## 3. METAL CLUSTER NANOCOMPOSITES

Optical properties of composites consisting of nanometer-sized metal particles dispersed in solid dielectric materials, such as glass, have been of increasing interest because of their optical applications. Colloidal gold and silver has been used in stain glass techniques since the medieval age, as their absorption spectrum exhibits an extinction band in the visible region and brings beautiful colors to the glasses [90]. Photochromic glasses containing silver and copper halides were developed by Corning in the early 1960s [91]. In the last two decades, noble metal nanoparticles embedded in a dielectric medium have been reported to exhibit some attractive optical properties, such as very high third nonlinear susceptibility  $\chi^{(3)}$  of  $10^{-9}$  to  $10^{-8}$  esu [7, 92], ultrafast third nonlinear optical response [93–95], and surface plasma resonance absorption occurring in the near-ultraviolet (UV) or visible region [96, 97], which would have potential applications in nonlinear optics [92, 98, 99].

Noble metal clusters can be introduced into a glass matrix through different methods such as traditional melt quenching methods, ion implantation [100, 101], ion exchange [102, 103], and the sol–gel technique [92, 104, 105]. In recent years, sol–gel synthesis of nanocomposites containing ultra-fine particles of noble metals in oxide matrices has been rapidly developed. Sol–gel technology is becoming one of the most useful and versatile methods of oxide film fabrication, due to the following advantages: the low processing temperature, homogeneity of coatings, easy control of metal concentration and coating thickness, as well as the possibility to add reducing and oxidizing agents in small concentrations [106, 107]. For preparing coating films containing dispersed fine metal particles, the sol–gel technique has advantages over the melt-quenching method. It gives much higher metal particle contents, which is important for obtaining a nonlinear optical material with high  $\chi^{(3)}$  [93, 130].

Different metal particles were prepared in glassy matrices by the sol–gel method, such as gold [60, 108–115], silver, [104, 107, 108, 111, 112, 116–120], platinum [112, 114, 121], and copper [122, 123]. The matrices for dispersing metals include oxides, such as SiO<sub>2</sub> [124, 125], TiO<sub>2</sub> [126], ZrO<sub>2</sub> [127], AlOOH, and organic–inorganic hybrids [128]. Barium titanate thin film, with high dielectric constant and refractive indices, incorporated with noble metal nanoparticles, has also been studied as a potential nonlinear optical material [129–131].

Metal particles have been incorporated by dissolving metal salts in the precursor sols (including alkoxide, water,

and alcohol in most the cases) and reduction of the ions to metallic particles by thermal treatment in air or in a reducing atmosphere, or by irradiation with UV light or gamma rays [128]. The nonlinearities of some systems have been measured and many important results are summarized in Table 2.

### 3.1. Coating Films Containing Gold Colloids

During the last two decades, clusters of gold particles embedded in oxide glasses have been shown to exhibit very high values of  $\chi^{(3)}$  of  $10^{-9}$  to  $10^{-8}$  esu [7, 92]. The sol-gel

**Table 2.** NLO and other related properties of some sol-gel derived metal-cluster nanocomposites.

S. No.	Matrix	Particle size	Dope concentration	Optical nonlinearity	Precursors (comments*)	Ref.
<b>Au-doped Films</b>						
1	SiO <sub>2</sub>	0.7 and 3 nm	Au/Si = 0.01 (mole)	$7.7 \times 10^{-9}$ esu	NaAuCl <sub>2</sub> + TEOS + EtOH	[133]
2	SiO <sub>2</sub>	10 nm	Au/Si = 0.028 (mole)	$(0.4-2.3) \times 10^{-8}$ esu	NaAuCl <sub>2</sub> + TEOS + EtOH + H <sub>2</sub> O + HCl	[142]
3	SiO <sub>2</sub>	27-28 nm	0.5 wt%	$2.2 \times 10^{-9}$ esu	(a) HAuCl <sub>4</sub> + partially hydrolyzed tetrakis-(hydroxymethyl) phosphonium chloride + TMOS (b) silica coated Au nanoparticles + TMOS + methanol*	[143]
3	Al <sub>2</sub> O <sub>3</sub>		0.1-0.2 mol%	$(3-9) \times 10^{-8}$ esu	*particle size control by ormosil AlCl <sub>3</sub> + NH <sub>3</sub> ; + HAc (peptizing) + HAuCl <sub>4</sub> + H <sub>2</sub>	[144]
4	Al <sub>2</sub> O <sub>3</sub>		0.2-0.4 mole per alumina	$10^{-8}$ to $10^{-7}$ esu	AlCl <sub>3</sub> + NH <sub>3</sub> ; + HAc (peptizing) DR1 + cetyl-trimethylammonium bromide HAuCl <sub>4</sub> + H <sub>2</sub>	[145]
5	Al <sub>2</sub> O <sub>3</sub>	4.6-12.7 nm	0.1 mol%	$9.2 \times 10^{-6}$ to $4 \times 1.0^{-5}$ esu	*both Au and Disperse Red 1 (DR1) are doped in the film AlCl <sub>3</sub> + NH <sub>3</sub> ; + HAc (peptizing) + HAuCl <sub>4</sub> + H <sub>2</sub>	[108]
6	BaTiO <sub>3</sub>	20 nm	Au/Ba = 2:5	$10^{-9}$ to $10^{-8}$ esu	HAuCl <sub>4</sub> + Ba(CH <sub>3</sub> COO) <sub>2</sub> + Ti(OBu) <sub>4</sub> + ethanol	[131]
7	BaTiO <sub>3</sub>	20 nm		$10^{-9}$ to $10^{-8}$ esu	HAuCl <sub>4</sub> + Ba(CH <sub>3</sub> COO) <sub>2</sub> + Ti[O(CH <sub>2</sub> ) <sub>3</sub> CH <sub>3</sub> ] <sub>4</sub> + ethanol	[146]
8	BaTiO <sub>3</sub>	10-100 nm		$1.09 \times 10^{-6}$ esu	particle size grows with increasing heat-treatment temperature; narrow distribution can be reached until 16 nm	[129]
9	BaTiO <sub>3</sub>		5 vol%	$1.4 \times 10^{-6}$ esu	Ba(CH <sub>3</sub> COO) <sub>2</sub> + C <sub>2</sub> H <sub>5</sub> OH + CH <sub>3</sub> COOH + glycerol + Ti[O(CH <sub>2</sub> ) <sub>3</sub> CH <sub>3</sub> ] <sub>4</sub> + HAuCl <sub>4</sub> + ethanol	[147]
10	PGO (Pb <sub>5</sub> Ge <sub>3</sub> O <sub>11</sub> )		5 vol%	$3.5 \times 10^{-7}$ esu	Pb(CH <sub>3</sub> COO) <sub>2</sub> + 2-(2-ethoxy ethoxy) ethanol + Ge(OC <sub>4</sub> H <sub>9</sub> ) <sub>4</sub>	[147]
11	PLT (Pb <sub>1-1.5x</sub> La <sub>x</sub> TiO <sub>3</sub> )	11 nm	5 vol%	$1.0 \times 10^{-7}$ esu	HAuCl <sub>4</sub> + 2-(2-ethoxy ethoxy) ethanol La(CH <sub>3</sub> COO) <sub>3</sub> + Pb(CH <sub>3</sub> COO) <sub>2</sub> + Ti[O(CH <sub>2</sub> ) <sub>3</sub> CH <sub>3</sub> ] <sub>4</sub> + HAc + 2-ethoxy ethanol	[147]
<b>Ag-doped Films</b>						
1	Al <sub>2</sub> O <sub>3</sub>		0.3-0.5 mol%	$(1.9-5.3) \times 10^{-8}$ esu	AlCl <sub>3</sub> + NH <sub>3</sub> ; + HAc (peptizing) + AgNO <sub>3</sub> + H <sub>2</sub>	[144]
<b>Cu-doped Films</b>						
1	SiO <sub>2</sub>		Cu/Si = 0.05	$5.0 \times 10^{-8}$ esu		[12]
2	SiO <sub>2</sub>	5-15 nm		$1.25 \times 10^{-10}$ esu		[148]
3	SiO <sub>2</sub>		Cu/Si = 0.11	$n_2 = 10^{-13}$ m <sup>2</sup> /W ( $10^{-8}$ esu)	TEOS + AgNO <sub>3</sub> + Cu(NO <sub>3</sub> ) <sub>2</sub> + H <sub>2</sub> O + HNO <sub>3</sub> + solvent	[149]
<b>Ag/Cu-doped Films</b>						
1	SiO <sub>2</sub>	4-5 nm	(Ag + Cu)/Si = 0.175	$1.15 \times 10^{-9}$ esu (AgCu) $2.21 \times 10^{-9}$ esu (AgCu <sub>3</sub> ) $2.66 \times 10^{-9}$ esu (AgCu <sub>5</sub> )		[150]
2	SiO <sub>2</sub>	5 nm 50 nm	(Ag + Cu)/Si = 0.175	$n_2 = 10^{-13}$ m <sup>2</sup> /W ( $10^{-8}$ esu)	TEOS + AgNO <sub>3</sub> + Cu(NO <sub>3</sub> ) <sub>2</sub> + H <sub>2</sub> O + HNO <sub>3</sub> + solvent	[149]

method has also been used to prepare such NLO nanocomposites in thin film forms [124, 132]. Sodium tetrachloraurate ( $\text{NaAuCl}_4 \cdot 2\text{H}_2\text{O}$ ) was reacted with TEOS in EtOH solution. The dip-formed films on  $\text{SiO}_2$  substrates were heated in air up to 1000 °C. Micrographs of gold with radii of about 7 and 30 Å coexist in the glass film. The Au/Si atomic ratio was 0.01 and the  $\chi^{(3)}$  was found to be  $7.7 \times 10^{-9}$  esu [133].

Matsuoka et al. [132, 133] showed that silica coating films that contain dispersed fine gold particles, from 7 to about 40 Å in size, were prepared by the sol-gel method using  $\text{NaAuCl}_4 \cdot 2\text{H}_2\text{O}$  and TEOS as starting materials. Fine Au particles are precipitated when the film is heated at 300–400 °C in air. No special procedure for reducing  $\text{Au}^{3+}$  ions proved necessary. The glass film with an Au/Si atomic ratio of 0.01 to 0.04 was successfully prepared. The nonlinear susceptibility  $\chi^{(3)}$  of the film was  $7.7 \times 10^{-9}$  esu. Subsequent heat treatment of the films at 1000 °C changed the absorption spectra and decreased the  $\chi^{(3)}$  by a factor of two.

Kozuka and Sakka [124] obtained silica films that contained dispersed fine Au particles using  $\text{Si}(\text{OC}_2\text{H}_5)_4$  and  $\text{HAuCl}_4$  as precursors; films were formed through dip coating. The Au content was 2.8 mol%. In as-coated films, gold is present as  $\text{AuCl}_4^-$  ions. After heating at 200 °C in air, Au particles are precipitated. They are stabilized when the film is heated to 500 °C in air. It is found that some gold particles are present on the surface of the film and can be easily removed with tissue paper. The loss of gold is minimized when as-prepared coating films are exposed to monoethanolamine vapor before heating. It is assumed that the amine treatment promotes the formation of gel networks.

Partial substitution of  $\text{CH}_3\text{Si}(\text{OC}_2\text{H}_5)_3$  (MTES) for  $\text{Si}(\text{OC}_2\text{H}_5)_4$  (TEOS) in the solution for the silica film containing 4 mol% Au results in the reduction of the average size of Au particles [134]. The shape of particles is round at higher MTES contents and elongated at lower MTES contents. In addition, larger coating thickness (up to 0.5–0.7 μm in one coating step) can be obtained without cracks.

Kozuka et al. [114] employed  $\text{TiO}_2$  as matrix for dispersing fine Au particles, using  $\text{Ti}(\text{OC}_3\text{H}_7)_4$  and  $\text{HAuCl}_4$  as precursors (15 mol% Au). Films were formed by dip coating. Heating of the coating film at 500 °C in air produced spherical gold particles of 20–30 nm size. The crystalline phase of  $\text{TiO}_2$  is anatase. The optical absorption peak due to the surface plasma resonance of gold particles in the film is located at around 640 nm, compared with 540 nm for the Au/ $\text{SiO}_2$  system.

Kozuka et al. also prepared gold particles of 6–20 nm in boehmite gels of the composition  $\text{AlOOH}$  [135]. A coating sol was obtained by adding  $\text{HAuCl}_4$  to a sol prepared from  $\text{Al}(\text{OC}_4\text{H}_9)_3\text{-H}_2\text{O-HCl}$  solution until Au content reached 2.5 mol%. A gel film was deposited on a slide glass by spin coating, dried at 120 °C, and then placed over a hydrazine in ethanol solution. Very thin coating films (20–25 nm) were obtained. It is assumed that the reduction of  $\text{Au}^{3+}$  ions by hydrazine causes precipitation of gold particles at room temperature and that the texture of boehmite matrix causes the shape and alignment of elongated gold particles. The surface plasma resonance absorption is found at 660 nm for

elongated particles, compared to 600 nm for spherical gold particles of similar size.

Barium titanate was also used as matrix for dispersing nanometal particles. Barium titanate thin films have high dielectric constants and high refractive indices, which could strongly influence the local fields around the metal particles. The large third-order susceptibility  $\chi^{(3)}$  of these films has been found to be dependent on local field enhancement near the surface plasmon resonance of the metal particles by Hache et al. [92]. Recently, barium titanate thin films incorporated with noble metal nanoparticles, for example, Ag/ $\text{BaTiO}_3$  [129] and Au/ $\text{BaTiO}_3$  [130] nanocomposite films, have been investigated, but the concentration of metal particles dispersed in these films was low. In the work of Yang et al. [131], a larger volume fraction of Au nanoparticles has been successfully incorporated into  $\text{BaTiO}_3$  thin films, which exhibited high third nonlinear susceptibility and unique absorption redshift. Gold nanoparticle-dispersed  $\text{BaTiO}_3$  films were prepared by a sol-gel route combined with a dip-coating method. First,  $\text{BaTiO}_3$  precursor solution was prepared through dissolving  $\text{Ba}(\text{CHCOO})_2$  in a mixed aqueous solution of acetic acid and 2-methoxyethanol. After stirring at room temperature, acetylacetone was added to stabilize the solution. This was followed by an addition of titanium butoxide. Then,  $\text{HAuCl}_4$ -ethanol solutions were prepared by dissolving  $\text{HAuCl}_4 \cdot 4\text{H}_2\text{O}$  into ethanol. Finally, Au/ $\text{BaTiO}_3$  composite precursor solution was prepared by injecting  $\text{HAuCl}_4$ -ethanol solutions into  $\text{BaTiO}_3$  precursor solution slowly with a molar ratio of Au/Ba = 2:5. This composite solution was yellow and clear. Au-dispersed  $\text{BaTiO}_3$  thin films were coated on glass slides by dip coating. As-prepared films were dried at 60 °C and successively heated to 200–600 °C in  $\text{N}_2$  atmosphere. After heat treatment, the colors were light purplish blue.

As a result, Au nanoparticles were dispersed well in the  $\text{BaTiO}_3$  matrix with an average size of 20 nm. The absorption spectra of Au/ $\text{BaTiO}_3$  films exhibited a large redshift of the absorption edge due to the dielectric constant increase of  $\text{BaTiO}_3$  matrix with the increase of heat-treatment temperature. The nonlinear optical properties of these films were measured and the values of  $\chi^{(3)}$  were calculated to be in the range of  $10^{-8}$ – $10^{-9}$  esu.

To understand the mechanism of the stability of Au nanoparticles in glass systems, Matsuoka et al. [136] carried out a study to investigate the dependence of the maximum amount of Au microcrystals attainable in the sol-gel derived oxide films on the metal species in starting alkoxides. Au-microcrystal-doped  $\text{TiO}_2$ ,  $\text{ZrO}_2$ , and  $\text{Al}_2\text{O}_3$  films were made by a sol-gel dip-coating method using titanium isopropoxide [ $\text{Ti}(\text{OC}_3\text{H}_7)_4$ ], zirconium *n*-propoxide [ $\text{Zr}(\text{OC}_3\text{H}_7)_4$ ], and aluminum sec-butoxide [ $\text{Al}(\text{OC}_4\text{H}_9)_3$ ] with  $\text{HAuCl}_4 \cdot 4\text{H}_2\text{O}$ . At first, one of the alkoxide was diluted with anhydrous ethanol, and then the mixed solution of ethanol, water, HCl, and stabilizing agent (acetic acid) was added to form dip-coating solutions, followed by the addition of a different amount of  $\text{HAuCl}_4 \cdot 4\text{H}_2\text{O}$ . The influence of the oxide matrix composition was studied to understand how it affected maximum amount of the Au microcrystals that can be incorporated in the oxide film. Some Au microcrystals were exhausted to the surface of Au microcrystal-doped oxide

films when an excess amount of  $\text{HAuCl}_4 \cdot 4\text{H}_2\text{O}$  was dissolved in the coating solution. The maximum amount of Au that can be incorporated in the oxide film was found to increase with the increase of the pH point at zero charge (PZC) of the matrix oxide. This should be due to the fact that  $\text{AuCl}_4^-$  ions are charged negatively and also Au microcrystals tend to charge negatively, so that the oxide gel with high PZC, which has a tendency to charge positively, may fix the ions and/or microcrystals to its interior. A maximum amount of Au microcrystals as high as 12.6 vol% was attained in an  $\text{Au:Al}_2\text{O}_3$  film.

Besides inorganic oxides, inorganic-organic hybrids are also used as matrices. Compared with oxide, organic-inorganic hybrid materials (ormosils) have lower photostability and thermal resistance, but they do have several advantages over oxide matrices, such as easy formation of films, possible crack-free thick coatings, transparency, and high water durability.

Spanhel et al. [137] used coating solutions consisting of  $\text{HAuCl}_4$ ,  $\text{NH}_2[(\text{CH}_2)_2\text{NH}](\text{CH}_2)_3\text{Si}(\text{OC}_2\text{H}_5)_3$  (diamine silane), prehydrated methacryloxy-propyltrimethoxysilane, and  $\text{H}_2\text{O}$ , and the Au/Si mol ratio was 0.05. Coating films on commercial glass substrates were exposed to UV radiation. This treatment achieved both growth of the photo-induced gold metal particles and thermal curing of the film, that is, hybrid network formation, simultaneously. The resulting coating film had an absorption peak due to surface plasmon resonance at about 550 nm. Crack-free thick films up to 8  $\mu\text{m}$  thick were obtained in a one-step coating. Spanhel et al. further stated that in this procedure diamine silanes act as ligands of gold particles, thereby preventing undesirable gold particle growth and at the same time modifying the optical properties of gold particles. If  $\text{NH}_2[(\text{CH}_2)_2\text{NH}]_2(\text{CH}_2)_3\text{Si}(\text{OC}_2\text{H}_5)_3$  (triamine) was used as the gold colloid-stabilizing agent in place of diamine, photoirradiation was not required. Reduction of  $\text{Au}^{3+}$  is caused by organic materials and fine gold metal particles are spontaneously precipitated.

Tseng et al. [113] employed polydimethylsilane to prepare inorganic-organic hybrid coating films containing fine gold particles. Gold (up to 5%) and platinum (3%) cluster nanocomposites were prepared. A solution of silanol-terminated polydimethylsiloxane,  $\text{Si}(\text{OC}_2\text{H}_5)_4$ ,  $i\text{-C}_3\text{H}_7\text{OH}$ , tetrahydrofuran,  $\text{H}_2\text{O}$ , and  $\text{HCl}$  was refluxed at 80 °C for 2 h and  $\text{HAuCl}_4$  solution was added, in order to obtain a starting solution with 5 wt% gold. Gold particles were precipitated in the film heated at 100 to 300 °C or irradiated with UV, with a particle size, for example, of 2.5 nm for heating at 200 °C.

### 3.2. Coating Films Containing Silver Colloids

Silver particles have been incorporated by dissolving silver salts in the precursor sols and reduction of the silver ions to metallic particles by thermal treatment in air or in a hydrogen atmosphere, or by irradiation with UV light or gamma rays.

During the formation of Ag colloids in a thermal treatment, temperature is critical for the silver particle size and oxidation/reduction reaction of silver. It will affect the optical density and absorption wavelength of silver colloids.

While silver-containing sol-gel films and gels are heated, reversible darkening is observed in silver-containing sol-gel films and gels. Some suggest this darkening-bleaching effect occurs due to an aggregation-disaggregation of silver particles [138], while others attribute this to oxidation/reduction of silver colloids [139, 140]. The substrate being coated is also an important factor that influences the Ag colloid formation process. It seems that the silver colloids in a silica-based coating on the soda lime glass substrate have a greater tendency toward being oxidized than those on a silica substrate [139].

A simple way to form nano-silver-particle-containing silica films is through a sol-gel dip-coating method. The  $\text{SiO}_2$ -Ag sol was prepared using TEOS,  $\text{C}_2\text{H}_5\text{OH}$ ,  $\text{H}_2\text{O}$ ,  $\text{HNO}_3$ , and  $\text{AgNO}_3$  as precursors. First, solution A is prepared by mixing TEOS and ethanol in equal volume. Then, solution B is prepared by adding distilled water, different amounts of silver nitrate ( $\text{AgNO}_3$ ), and nitric acid ( $\text{HNO}_3$ ) together.  $\text{HNO}_3$  is added to adjust the pH to approximately 2. Finally, solution B was added to solution A drop by drop while stirring vigorously at room temperature. The final molar ratio is  $\text{TEOS}:\text{C}_2\text{H}_5\text{OH}:\text{H}_2\text{O}:\text{AgNO}_3 = 1:3.825:3:x$ , where  $x$  is the Ag/Si molar ratio in the glass coating. To stabilize the silver in the silica film, complete drying of the gel glass film is recommended right after the formation of the film, at about 450 °C. Without drying the film at an elevated temperature, the silver content can be lost through aggregation on the surface.

Following mixing of two solutions, the sol was left to age until the viscosity reached approximately 3 cP. It usually took two to four days for the sol to get ready, depending on the silver concentration, with sols with higher silver concentration taking less time. After the viscosity of the sol reached 3 cP, the coating was formed by dip coating at a pulling rate around 1 mm per second.

Mennig et al. [139] prepared coating films containing Ag colloids from solutions of  $\text{AgNO}_3$ ,  $N$ -(2-aminoethyl)-3-aminopropyltrimethoxysilane (DIAMO), prehydrolyzed 3-glycidoxypolytriethoxysilane, TEOS,  $\text{C}_2\text{H}_5\text{OH}$ , and  $\text{HNO}_3$ . The Ag content was 6.2 mol%. Films deposited on fused silica by dip coating and dried at 120 °C were yellow colored due to the presence of Ag colloids. Formation of Ag colloids was attributed to reduction of  $\text{Ag}^+$  ions by organic materials in the coating films. DIAMO in the coating solution acts as a stabilizing agent for Ag particles. When coating films are heated at 120–600 °C in air for decomposition of organic materials and densification of the film, some of the Ag colloids were oxidized to  $\text{Ag}_x\text{O}_y$ . Heating of this film at 500 °C reduced silver oxide particles to Ag metal colloids of 8 nm average size. When a soda-lime-silica glass substrate was used, heating of the coating films at 400–600 °C oxidized all the Ag colloids to  $\text{Ag}_x\text{O}_y$ . Heating of these films at 500 °C in 90%  $\text{N}_2$ -10%  $\text{H}_2$  atmosphere reduced  $\text{Ag}_x\text{O}_y$  to Ag colloids, producing an Ag colloid-containing film similar to that applied to the  $\text{SiO}_2$  substrate.

The effect of heating temperature on the color intensity due to silver colloids at 410 nm has been studied with silica sol-gel glass doped with 0.05 mol% silver [138]. This glass was prepared by gelling  $\text{Si}(\text{OC}_2\text{H}_5)_4$ - $\text{AgNO}_3$ - $\text{C}_2\text{H}_5\text{OH}$ - $\text{HNO}_3$  solution at 60 °C and then densifying the

film at 600 °C. When a darkened sample is heated above 400 °C, reversible bleaching took place. This darkening-bleaching was attributed to aggregation-disaggregation of fine silver particles by Ritzer et al. [138]. Another explanation for this phenomenon is that Ag particles may be oxidized to  $\text{Ag}_x\text{O}_y$  above 400 °C (but below 600 °C), and reduced to Ag particles at 600 °C.

Kozuka et al. prepared  $\text{TiO}_2$  coating films containing fine Ag particles by sol-gel processing using a  $\text{Ti}(\text{OC}_3\text{H}_7)_4$ ,  $\text{NH}(\text{CH}_2\text{CH}_2\text{OH})_2$ , *i*- $\text{C}_3\text{H}_7\text{OH}$ ,  $\text{H}_2\text{O}$ , and  $\text{AgNO}_3$  precursor solution. The Ag content was 6.2 mol%. Exposure of a gel film to formaldehyde vapor at room temperature caused reduction of  $\text{Ag}^+$  ions, forming Ag particles of 4–23 nm in size in the gel film. The gel film showed a sharp absorption peak at 441 nm due to surface plasma resonance (SPR) of Ag metal particles. Heat treatment of the gel films at 600–800 °C in air resulted in the formation of anatase or rutile polycrystalline films containing Ag particles 5–45 nm in size (5–25 nm for 600 °C and 13–45 nm for 800 °C). These films showed an absorption peak around 550 nm. The shift of the SPR absorption of Ag particles from 441 (room temperature) to 550 nm (600–800 °C) may be attributed to an increase in dielectric constant of the oxide matrix caused by its thermal densification and crystallization [120].

### 3.3. Coating Films Containing Platinum Colloids

Kozuka et al. [120] prepared  $\text{TiO}_2$  coating films containing Pt colloid particles (7 mol% Pt) on silica substrate by the sol-gel processing. Precursor solution containing  $\text{Ti}(\text{OC}_3\text{H}_7)_4$ ,  $\text{H}_2\text{O}$ ,  $\text{CH}_3\text{COOH}$ ,  $\text{C}_2\text{H}_5\text{OH}$ , and  $\text{H}_2\text{PtCl}_4 \cdot \text{H}_2\text{O}$  solutions were used to produce coating films. Platinum fine particles were precipitated by heating at 800 °C in air.

Silica based ormosil coating films containing Pt colloids were prepared by Tseng et al. [113].  $\text{Pt}^{4+}$  ion-doped gel films were prepared from coating solutions consisting of silanol terminated polydimethylsilane,  $\text{H}_2\text{O}$ ,  $\text{HCl}$ , and  $\text{H}_2\text{PtCl}_4 \cdot \text{H}_2\text{O}$ . Thermal reduction by heating at 200 °C and photoreduction by exposure to a high pressure mercury lamp are used to produce hybrid coating films containing Pt colloids of 3–5 nm in size. The color of the film was light brown.

### 3.4. Coating Films Containing Palladium Colloids

Zhao et al. [141] prepared coating solutions from titanium isopropoxide, palladium(II) chloride, deionized water, ethanol, acetic acid, and hydrochloric acid to produce  $\text{TiO}_2$  coating films containing 3 vol% Pd (7 mol%). A transparent red-brown solution resulted. Heating  $\text{TiO}_2$  coating films at 600–900 °C in air produced PdO particles in the film. Reduction of this film by heating at 500 °C in a  $\text{H}_2/\text{Ar}$  atmosphere gave films containing dispersed metal particles. The average diameter of Pd is 15–30 nm. The films containing Pd particles are brownish grey, showing optical absorption due to surface plasmon resonance. Particle size was controlled by selecting the heating time at 800 °C. It should be noted that Pd metal particles are precipitated when  $\text{TiO}_2$  coating films are heated at 1000 °C in air.

## 4. ORGANIC-INORGANIC HYBRID COMPOSITES

Many organic materials exhibit NLO properties either in the form of molecules, crystals, or polymers. NLO organic polymeric material has been an exciting area for the last two decades [151]. Following the early works [152–155] on their nonlinear properties, organic polymers have been studied extensively for nonlinear applications [156–171]. Among all nonlinear materials, organic polymeric systems provide the highest nonresonant nonlinearity [172] and therefore are very promising systems for achieving high speed. Glasses are ideal for use as a matrix for these organics, due to their highly cross-linked structures and good mechanical and chemical stability [173–193].

Through the sol-gel approach, organic/inorganic hybrid materials have rapidly become a fascinating new field of research in materials science [194–199].

The sol-gel process, based on inorganic polymerization reactions, is a synthesis method initially used for the preparation of inorganic materials, such as glasses and ceramics. Its low-temperature characteristic also provides unique opportunities to make organic/inorganic hybrid materials through the incorporation of low molecular weight and oligomeric polymeric organics with appropriate inorganics. There are several different synthetic techniques used to prepare hybrid materials [200]. The main methods for producing NLO hybrid are the following:

- (1) By simply dissolving or dispersing the active organic into inorganic sol-gel precursor solution, organics can be impregnated or entrapped as a guest within inorganic gel matrix (as a host), on gelation.
- (2) Hybrid networks can be synthesized by using low molecular weight organoalkoxysilanes as one or more of the precursors for the sol-gel reaction; as a result, organic groups are introduced into an inorganic network through the  $\equiv\text{Si}-\text{C}-$  bonds.
- (3) Hybrid material can also be formed through the co-condensation of functionalized oligomers with metal alkoxides in which chemical bonding is established between inorganic and organic phases.
- (4) A hybrid network can be formed by interpenetrating networks and simultaneous formation of inorganic and organic phases.

The properties of organic-inorganic nanocomposites depend on not only the organic and inorganic components, but also the interface between them. The precursor mixing in a homogenous solution allows organic and inorganic components to be associated at the molecular level. However, the chemical reactivities of organic and inorganic species are usually different and phase separation tends to occur. Chemical bonds have to be formed between organic and inorganic components in order to form molecular composites or organic-inorganic polymers. Hybrid materials are currently divided into two classes depending on whether the organic and inorganic phase share weak interactions such as van der Waals and hydrogen bonds (class I) or strong chemical bonds (class II). Some important optical applications of class II can be found in review articles authored by Sanchez and Lebeau [183, 201]. To accomplish superior

nonlinear optical properties in hybrid nanocomposites, it is important to have organic chromophores with high intrinsic nonlinearity, high chromophore concentration in the composites, good interfacial interaction between organic and inorganic components, and stability of the network structure. For second-order NLO composites, it is even more important to have strong bonding between the organic dye and the matrix. It is well known that second-order NLO effects cannot be observed in centrosymmetric systems, but the NLO effects can occur after poling in order to orient the organic dyes within the sol-gel matrix. However, organic dyes tend to lose their induced orientation with time due to thermal relaxation processes. Both weak and strong interactions between the NLO dyes and the matrices are used to control the relaxation behavior of the NLO chromophores. This section gives a short review of the different hybrid organic-inorganic materials with NLO properties, especially second-order nonlinearities.

As we mentioned, different synthesis routes have been developed to synthesize NLO hybrid materials; both class I (host-guest) and class II (chromophore-linked) were prepared. Chaumel et al. [202] illustrated some important hybrid network structures and the routes to achieve them (Fig. 1).

#### 4.1. Second-Order NLO Sol-Gel Hybrid Nanocomposites [201]

##### 4.1.1. Guest-Host Hybrids Containing Embedded NLO Chromophores

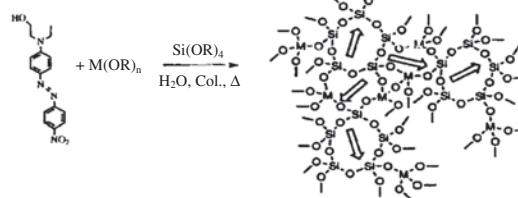
Hybrid materials with embedded NLO dyes were synthesized in the early stage of sol-gel NLO hybrid material studies, due to the simplicity of the synthesis process [2, 203]. These composites are mostly class I composites, and the interactions between organic and inorganic components are weak interactions (van der Waals, hydrogen bonds, hydrophilic-hydrophobic behavior). Figure 2 shows some usual NLO dyes that have been embedded into sol-gel matrices.

Second-harmonic generation (SHG) ( $d_{33}$  coefficient) or electro-optic coefficients ( $r_{33}$ ) have been measured in many sol-gel processed materials. Some results are shown in Table 3, along with those of other hybrid systems. Three different matrices were obtained by the sol-gel process, first, through hydrolysis of metal alkoxides  $M(OH)_n$  ( $M = Ti, Si, Zr, \dots$ ), written as  $MO_2$ ; second, through hydrolysis of trialkoxysilanes  $RSi(OR)_3$  ( $R = \text{methyl, phenyl, etc.}$ ), written as  $RSiOR_{1.5}$ ; third, through co-condensation between both precursors, which leads to  $RSiOR_{1.5}/MO_2$  matrices.

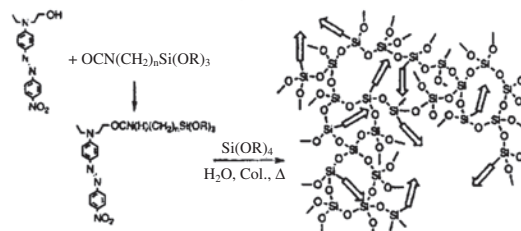
In general, organic dye molecules embedded in those hybrids are randomly oriented, and electrical-field-induced orientation (poling) is needed for second harmonic response. There are few exceptions, due to the presence of microcrystallites of chromophores [204] or possible orientation preference of NLO molecules in the glass matrix via van der Waals interactions [205].

Griesmar et al. [206] and Toussaere et al. [207] first performed the orientation of organic chromophores in hybrid sol-gel matrices by using electrical-field-induced second-harmonic and corona electrical field poling techniques. These first attempts showed the potential of using poling

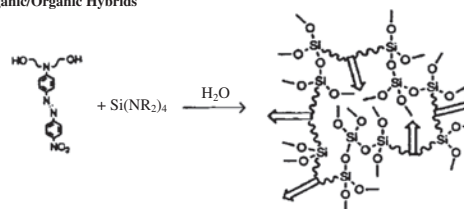
Guest-Host Organic/Inorganic Hybrids [ $M=Si, Zr, Ti, \text{etc.}$ ]



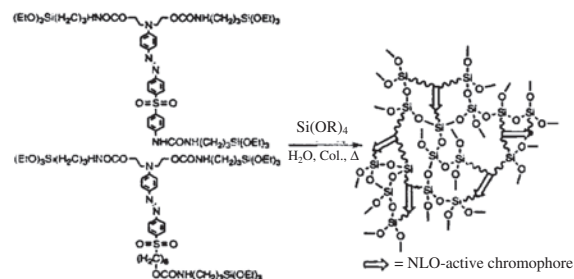
Chromophore-linked Side-chain-Tethered Hybrids



Main-Chain Inorganic/Organic Hybrids

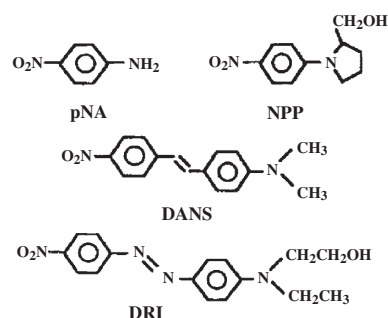


Main-Chain Inorganic/Organic Hybrids with Three points of Linkage of the Chromophore



**Figure 1.** Some important hybrid network structures and the routes to achieve them. Reprinted with permission from [202], F. Chaumel et al., *Chem. Mater.* 13, 3389 (2001). © 2001, American Chemical Society.

techniques in hybrid composites for the synthesis of second order NLO material. Unfortunately it also showed the general weakness of the guest-host system: the low efficiency and low stability of the optical nonlinearity, poor solubility



**Figure 2.** Examples of NLO dyes which are embedded in sol-gel matrices. Reprinted with permission from [239], B. Lebeau et al., *Pure Appl. Opt.* 5, 689 (1996). © 1996, IOP Publishing.

**Table 3.** NLO data for some hybrid materials with embedded NLO dyes.

NLO group	System	Matrix	$d_{33}/r_{33}$ (pm V <sup>-1</sup> )	SHG response stability		Ref.
				%	$T$ (hr)/ $T$ (°C)	
Guest–host hybrid systems						
NPP	G/H	RSiO <sub>1.5</sub> /ZrO <sub>2</sub>	0.08/—	—	—	[207]
DR1	G/H	RSiO <sub>1.5</sub> /ZrO <sub>2</sub>	0.1/—	20	4000/[25]	[213]
DR1	G/H	RSiO <sub>1.5</sub>	1.54/0.71	40	30/[100]	[212]
DR1	G/H	PMMA/SiO <sub>2</sub>	4 ( $\chi^{(2)}$ )	—	—	[214]
NPP	G/H	SiO <sub>2</sub> /TiO <sub>2</sub>	10.9/2	77	2400/[25]	[173]
DANS	G/H	TiO <sub>2</sub>	11/—	40	1200/[25]	[174]
DR1	G/H	RSiO <sub>1.5</sub>	11.4/—	—	—	[215]
DR1	G/H	SiO <sub>2</sub>	157/—	100	700/[25]	[209]
Side-chain class II hybrid systems						
DNPA	II (S-C)	R'SiO <sub>1.5</sub> /ZrO <sub>2</sub>	1.6/—	10	720/[25]	[207]
DO3	II (S-C)	R'SiO <sub>1.5</sub>	5.28/—	100	40/[100]	[215]
DNPA	II (S-C)	R'SiO <sub>1.5</sub> /SiO <sub>2</sub>	9.1/—	38	25/[60]	[182]
DO3	II (S-C)	R'SiO <sub>1.5</sub> /ZrO <sub>2</sub>	9.7/—	—	—	[216]
DNPA	II (S-C)	R'SiO <sub>1.5</sub> /SiO <sub>2</sub>	10/2	18	6000/[25]	[178]
DNPA	II (S-C)	SiO <sub>2</sub>	11.7/—	80	48/[25]	[217]
NA	II (S-C)	R'SiO <sub>1.5</sub> /SiO <sub>2</sub>	13/—	—	—	[218]
DR1	II (S-C)	R'SiO <sub>1.5</sub>	42.7/54.0	80	1/[150]	[184]
DR1	II (S-C)	R'SiO <sub>1.5</sub> /SiO <sub>2</sub>	46/—	—	—	[219]
DR1	II (S-C)	R'SiO <sub>1.5</sub> /SiO <sub>2</sub>	55/—	100	168/[25]	[180]
DR19	II (S-C)	R'SiO <sub>1.5</sub>	$37 \times 10^{-8}$ esu ( $\chi^{(2)}$ )	100	840/[80]	[220]
Main-chain class II hybrid systems						
DNPA	II (M-C)	R'SiO <sub>1.5</sub>	9–10/2–2.5	—	—	[188]
TCVA	II (M-C)	R'SiO <sub>1.5</sub>	14.3/—	35	0.5/[140]	[221]
SG-DANS	II (M-C)	R'SiO <sub>1.5</sub> /SiO <sub>2</sub>	16/—	80	3/[150]	[185]
Red17	II (M-C)	R'SiO <sub>1.5</sub> /SiO <sub>2</sub>	24/12.2	20	170/[25]	[222]
ASF	II (M-C)	R'SiO <sub>1.5</sub>	27/—	90	500/[100]	[223]
ASF	II (M-C)	R'SiO <sub>1.5</sub>	27/—	60	0.5/[200]	[223]
NA	II (M-C)	R'SiO <sub>1.5</sub>	35–37/9–10	—	—	[188]
DR19	II (M-C)	R'SiO <sub>1.5</sub> /SiO <sub>2</sub>	29/—	25	>2/[140]	[224]
DO3	II (M-C)	R'SiO <sub>1.5</sub>	38.8/—	81	144/[105]	[225]
Red 17	II (M-C)	R'SiO <sub>1.5</sub> /SiO <sub>2</sub>	78/20	50	2160/[25]	[222]
Interpenetrating network hybrid systems						
DR1	interpenetrated	polyimide/R'SiO <sub>1.5</sub>	28/—	75	168/[120]	[190]
DR1	interpenetrated	polyimide/R'SiO <sub>1.5</sub>	28/—	100	1700/[25]	[190]

Note: Chromophores: NPP: *N*-(4-nitrophenyl)-(s)-prolinol, DR1: disperse red 1, DR19: disperse red 19, DANS: 4-(dimethylamino)-4'-nitrostyrene, SG-DANS: 4-[*N,N*-bis-(2-triethoxysilanoxyethylamino)]-4'-nitrostyrene, DNPA: 2,4-dinitrophenylamine, DR1: Disperse Red 1, DO3: Disperse Orange 3, ASF: aminosulphone, NA: 4-nitroaniline, TCVA: tricyanovinylaniline, SHG response stability %: final ratio SHG response/initial SHG response,  $t$ : time after field poling cutoff in hours. Systems: S-C—side-chain, M-C—main-chain [201].

of the chromophore in the matrix, and the fast relaxation of the poling-induced order, respectively [208].

To decrease the relaxation of poling-induced order, several research groups have started to use conventional metal-oxide-based sol–gel matrices (SiO<sub>2</sub>, Al<sub>2</sub>O<sub>3</sub>, SiO<sub>2</sub>–TiO<sub>2</sub>) [173, 174, 209, 210], which exhibit high rigidity and mechanical properties. The conventional sol–gel matrix did achieve both high dye concentration and good temporal stability of the poling-induced order. The latter can be explained by the preferential interaction between the chromophore and the host matrix (hydrogen bonds and/or ionocovalent bonds) [173, 211]. However, the “conventional sol–gel matrices” also have their drawbacks. First, the type of films with good optical quality can only be obtained with thicknesses under 1  $\mu$ m. Second, there is a concern about the porous and hydrophilic nature of the matrix. Water adsorption might promote the disruption of the hydrogen-bond

network, the cleavage of the ionocovalent dye–matrix bonds, and the loss of the SHG response as a result.

To suppress those drawbacks, hybrid organic–inorganic sol–gel matrix was used to deposit dense and hydrophobic thick films (1–20  $\mu$ m) [212]. However, the problem of low chromophore concentration was not resolved in these systems.

#### 4.1.2. NLO Chromophore Grafted to Sol–Gel Matrices

The best solution so far is hybrid organic–inorganic materials with NLO dyes grafted to the inorganic network [183, 201]. It allows easy optimization of the dye concentration and better control of chemical and processing parameters. The number of covalent bonds of the organic chromophore with the inorganic matrix classifies these hybrid materials into side-chain (one covalent bond) and main-chain (two or

more bonds) hybrid materials [200]. The most common way to introduce an organic group into a silica network is to use siloxane-based trifunctional organoalkoxysilane precursors,  $R'Si(OR)_3$  (where  $R'$  is an NLO organic chromophore). Some of these precursors are presented in Figure 3.

The synthesis of a class II hybrid with second order NLO properties can be performed by hydrolysis and condensation of  $R'Si(OR)_3$  carrying the NLO dyes or through hydrolysis and co-condensation between  $R'Si(OR)_3$  and metal alkoxides [ $Si(OR)_4$ ,  $Zr(OR)_4$ , etc.].

Some important results of these class II NLO hybrids are shown in Table 3. Matrices obtained through hydrolysis of a trifunctional alcoxysilane  $R'Si(OR)_3$  ( $R'$  being the NLO group) are denoted as  $R'SiO_{1.5}$ , while those prepared via hydrolysis and co-condensation between trifunctional alcoxysilanes  $R'Si(OR)_3$  and metal alkoxides  $M(OR)_4$  ( $M = Si, Zr$ , etc.) are written as  $R'Si(OR)_3/MO_2$ .

**Class II Side-Chain Systems** It has been shown that covalent coupling of the NLO chromophore to the lattice could improve chromophore loading and consequently NLO efficiency [173, 174, 217]. Compared to class I hybrids, the side-chain hybrid efficiency is better but still needs improvement.

Two strategies are used to improve the second-order NLO response of dye-grafted hybrid coatings. First is using chromophores with a higher intrinsic NLO response, such as *N*-(4-nitrophenyl)-*L*-prolinol or disperse red one (DR1) derivatives, which exhibit higher nonlinearities than nitroaniline. Second is to control the chromophore relaxation by increasing the matrix rigidity. The most common strategies to minimize relaxation is to increase the cross-linking in the network, through adding inorganic network builders

( $MOR$ )<sub>4</sub> or polymers with well known mechanical properties such as polymethylmethacrylates or polyimide.

For the class II side-chain systems, a promising result was obtained by Riehl et al. [180] ( $d_{33} = 55 \text{ pm V}^{-1}$  at  $1.064 \mu\text{m}$ ) for an alcoxysilane-silica system functionalized with DR1. No NLO signal loss was observed at ambient temperatures 1 week after poling. The good temporal NLO response stability seems to be due to the two-step synthesis strategy. After the hydrolysis of precursors in an acidic medium, a base is added to enhance condensation reactions, therefore improving the formation of highly branched inorganic network.

**Class II Main-Chain Systems** To further increase the stability of the second-order NLO response of the hybrid composites, a main-chain system is used, with both ends of the chromophore anchored to the polymer backbone. Large second harmonic coefficient and high thermal stability can be achieved through this structure. By using a main-chain hybrid system, choosing organic dyes with a higher intrinsic NLO response (Red 17), and increasing cross-linking (adding  $SiO_2$ ), one of the best results of sol-gel NLO hybrid so far was achieved by Lebeau et al. [222].

Further increasing the number of the bonds between the organic and inorganic component will help increase the stability of the poled structure, but it also makes it difficult to reach desired order during the polling process [223]. Because class II hybrid organic-inorganic materials allow better control of film thickness, film hydrophobicity, matrix rigidity and densification, and NLO chromophore concentrations, they become very promising in the field of quadratic NLO.

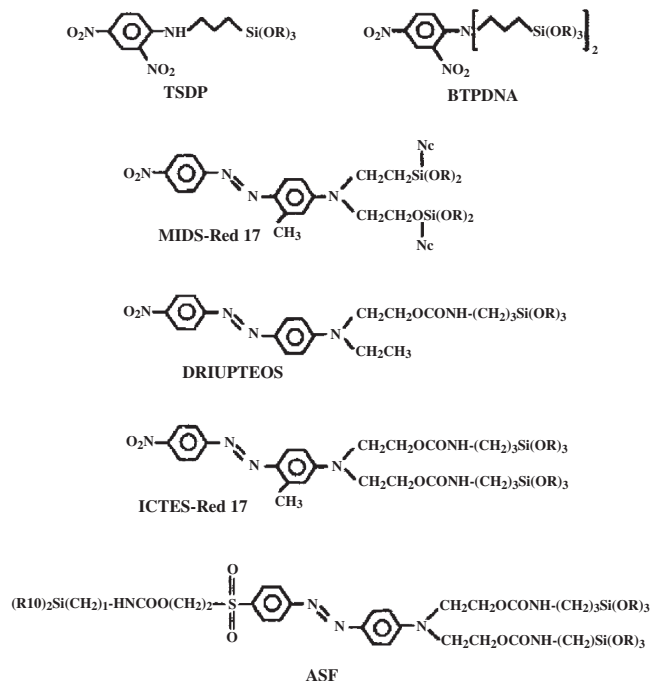
The sol-gel process is versatile, and yet it is also very complex. Many factors can be tuned in order to improve these new nanocomposites, such as the number and position of the alcoxysilyl groups, the amount and the nature of the cross-linking agent (TMOS) and catalysts, the hydrolysis ratio, the sequence of mixing, the nature of the solvent (which may influence nanophase separation), the aging time (which influence the complication of crosslinking), etc.

Poling protocol is also very important because these systems behave as thermosets or thermally hardened materials. The process must be optimized in such a way that desired noncentrosymmetric order can be introduced by electric field poling before the matrix hardening is completed.

## 4.2. Third-Order NLO Sol-Gel Hybrid Nanocomposites

Sol-gel hybrid nanocomposites for third-order NLO applications are not as well studied as second-order NLO hybrids. Prasad's group is one of the few that has been making continuing progress in developing those materials [226–229]. As we mentioned, polymer has high nonresonant third-order NLO properties. These studies are very meaningful for photonic application.

Most third-order NLO hybrid systems synthesized so far belong to guest-host hybrid materials, which are made through dissolving or dispersing the active organic into the inorganic solution. For example, poly-*p*-phenylene (PPV), a conjugated NLO polymer, was dispersed into a  $SiO_2$  gel [226]. A  $\chi^{(3)}$  value of  $3 \times 10^{-10}$  esu was obtained, using 400 femtosecond pulses from a Nd-YAG laser



**Figure 3.** NLO chromophores functionalized with trialkoxysilanes. Reprinted with permission from [239], B. Lebeau et al., *Pure Appl. Opt.* 5, 689 (1996). © 1996, IOP Publishing.



pulse compressed amplified system at 602 nm. Two PPV derivatives, poly(2-bromo-5-methoxy-1,4-phenylene vinylene) and poly(2-butoxy-5-methoxy-1,4-phenylene vinylene), and poly(2,5-disubstituted-1,4-phenylene vinylene) were also incorporated into polymer/silica composites. The third-order nonlinear susceptibilities have been investigated for the polymers themselves and their sol-gel composites. Relatively large  $\chi^{(3)}$  values ( $4 \times 10^{-10}$  to  $1 \times 10^{-9}$  esu) with a subpicosecond response were observed [227].

In order to improve the optical quality, poly(thienylene vinylene)/silica composite was prepared by sol-gel, and its optical nonlinearity was determined. The soluble methoxy pendant poly(thienylene vinylene) (PTV) precursor and the silica sol were homogeneously mixed in tetrahydrofuran and converted to the final composite material by heat treatment. The blueshift of  $\lambda_{\text{max}}$  in the UV-visible spectra was observed which provides evidence of interaction between the PTV and the silica components. The third-order optical nonlinearities,  $\chi^{(3)}$ , were measured as  $4 \times 10^{-9}$  esu and  $3 \times 10^{-9}$  esu for the pure PTV and PTV/silica [228].

Prasad et al. have also investigated the nonlinear optical performance of new UV photostable dyes, didecyl and didecyloxy substituted para-polyphenyl heptamers, in sol-gel processed composite glass, using the techniques of degenerate four-wave mixing (DFWM) and optical Kerr gate [229].

There are other organic dyes incorporated into oxide gels by similar methods [230–234]. For instance, rhodamine-6G doped  $\text{SiO}_2$ - $\text{TiO}_2$  thin films were prepared using a dip coating method. Effects of the MTMS/TEOS ratio on the cracking of the thin films during the drying stage were studied. The cracking greatly decreased on increasing the MTMS/TEOS ratio. Crack-free thin films were obtained for samples with MTMS/TEOS > 0.75. The optical absorption and fluorescence spectra of the thin films were recorded. The refractive index increases linearly with increasing  $\text{TiO}_2$  content (20, 40, 60 mol%). The third-order nonlinear susceptibility of the rhodamine-6G doped  $\text{SiO}_2$ - $\text{TiO}_2$  thin films is  $\chi^{(3)}$  approximately =  $10^{-9}$  esu, measured by the DFWM technique [235]. Other matrix systems used include  $\text{Al}_2\text{O}_3$  [236, 237] and  $\text{V}_2\text{O}_5$  [238].

While third-order nonlinear hybrids do not have the same requirements for the SHG NLO hybrids, they still share many common ones, such as high transparency, good mechanical strength, stability of the structure, and high concentration of NLO dyes. So it may be helpful to find the possibilities of synthesizing THG hybrids materials through the well defined routes for SHG hybrid materials.

## 5. CONCLUSIONS

Sol-gel is an extremely versatile technique to produce inorganic-inorganic and inorganic-organic nanocomposites. Its may open many possibilities for the development of photonic devices. Using sol-gel derived ceramics as matrix, semiconductor, metal, and polymer are incorporated into various nanocomposites to achieve high nonlinear properties. Although further studies are still needed to improve the synthesis processes of those composites, through particle size control and/or enhancing chemical bonding, the sol-gel technique has been proved to be a very promising technique for developing various NLO materials.

## GLOSSARY

**Exciton Bohr radius** The optical properties of a material are usually determined by the nature of electrons and holes existing in it. Due to Coulomb interaction, the electrons and holes existing in a material are known to form excitons. The distance between the electron and the hole within an exciton is called Bohr radius of the exciton. Typical exciton Bohr radius of semiconductors is of a few nanometers (1 nanometer =  $10^{-9}$  meter).

**Optical nonlinearity** Nonlinear effect is a general concept, and it refers to the nonlinear proportionality of the response to the input. When an electric field (e.g., light) interacts with electrons in a materials, the electron density can be provoked to be displaced. This is called polarization. In a nonlinear optical material, or when the electric field is strong enough, the polarization is a nonlinear response of the electronic field.

$$P = \chi^{(1)}E + \chi^{(2)}EE + \chi^{(3)}EEE + \dots$$

Where  $\chi^{(2)}$  and  $\chi^{(3)}$  are the second and third order nonlinear susceptibilities, respectively.

**Quantum dot** A Nanometer sized structure that is capable of trapping electrons in three dimensions. Quantum dots are made by creating an island of conductive material surrounded by insulating material. Electrons that enter the quantum dot will be confined because of the high potential required to escape.

**Sol-gel process** A process that involves the evolution of inorganic networks through the formation of a colloidal suspension (sol) and gelation of the sol to form a network in a continuous liquid phase (gel).

**Surface capping agent** A molecule which attached to the surface of a growing cluster surface to terminate its growth, thus control the particle size.

**Surface plasmon resonance** Conduction electrons (–) and ionic cores (+) in a metal form a plasma state. When external electric fields (electro-magnetic waves, electron beams etc.) are applied to a metal, electrons move so as to screen perturbed charge distribution, further move beyond the neutral states, and again return to the neutral states and so on. This collective motion of electrons is called a “plasma oscillation.” The surface plasmon resonance is a collective excitation mode of the plasma localized near the surface. Electrons confined in a nanoparticle conform the surface plasmon mode. The resonance frequency of the surface plasmon is different from an ordinary plasma frequency. The surface-plasmon mode arises from the electron confinement in the nanoparticle. Since the dielectric function tends to become continuous at the interface (surface), the oscillation mode shifts from the ordinary plasma resonance and exponentially decays along the depth from the surface.

## ACKNOWLEDGMENTS

The authors thank the Department of Mechanical, Materials, and Aerospace Engineering and the Advanced Materials Analysis and Processing Center (AMPAC) at the University of Central Florida (UCF), Orlando for continued support. Sudipta Seal is thankful to the National Science Foundation,

the Office of Naval Research through the Young Investigator Award (ONR-YIP 2002), the Florida High Tech Corridor, NASA, Florida Space Grant Consortium, Siemens Westinghouse, Energy Strategy Associates, USNR Coal Resources, psiloQuest, U.S. Filter, Pratt and Whitney, and Lucent Technologies for supporting his research activities in nanomaterials processing and applications.

## REFERENCES

- R. Burzynski and P. N. Prasad, in "Sol–Gel Optics: Processing and Applications" (L. C. Klein, Ed.), p. 417. Kluwer Academic, Boston, 1993.
- "Sol–gel Optics: Processing and Application" (L. C. Klein, Ed.). Kluwer Academic, Boston, 1994.
- "Sol–gel Optics I–VI," *Proc. SPIE*, Vols. 1328, 1758, 2288, 3136, 3943, 4804 (1990–2002); "Selected Papers on Sol–Gel for Photonics" (S. Iraj Najafi, Ed.), SPIE Optical Engineering Press, Washington, 1998.
- M. A. White, "Properties of Materials," p. 80. Oxford Univ. Press, New York, 1999.
- J. Sauer, F. Marlow, and F. Schüth, in "Handbook of Advanced Electronic and Photonic Materials and Devices" (H. S. Nalwa, Ed.), Vol. 6, p. 163. Academic Press, San Diego, 2001.
- J. D. Mackenzie, *J. Sol–Gel Sci. Technol.* 1, 7 (1993).
- D. Ricard, P. Roussignol, and C. Flytzanis, *Opt. Lett.* 10, 511 (1985).
- T. Dutton, B. Van Wonerghem, S. Saltiel, N. V. Chestony, P. M. Rentzepis, T. P. Shen, and D. Rogovin, *J. Phys. Chem.* 94, 1100 (1990).
- E. J. Heolweil and R. M. Hochstrasser, *J. Chem. Phys.* 82, 4762 (1985).
- U. Kreibig and L. Genzel, *Surf. Sci.* 156, 678 (1985).
- M. Nogami and Y. Abe, *J. Am. Ceram. Soc.* 78, 1066 (1995).
- D. Kundu, I. Honma, T. Osawa, and H. Komiyama, *J. Am. Ceram. Soc.* 77, 1110 (1994).
- M. Nogami, in "Sol–Gel Optics: Processing and Application" (L. C. Klein, Ed.), p. 329. Kluwer Academic, Boston, 1994.
- R. H. Magruder, III, Li Yang, R. F. Haglund, C. W. White, L. Yang, R. Dorsinville, and R. R. Alfano, *Appl. Phys. Lett.* 62, 1730 (1993).
- C. Flytzanis, F. Hache, M. C. Klein, D. Ricard, and P. Roussignol, in "Progress in Optics" (E. Wolf, Ed.), p. 321. North-Holland, Amsterdam, 1991.
- P. W. Smith, *Proc. SPIE* 1852, 2 (1993).
- R. H. Magruder, III, R. A. Weeks, S. H. Morgan, Z. Pan, D. O. Henderson, and R. A. Zuhr, *J. Non-cryst. Solids* 192&193, 546 (1995).
- Y. Wang and N. Herron, *J. Phys. Chem.* 95, 525 (1991).
- R. K. Jain and R. C. Lind, *J. Opt. Soc. Am.* 73, 647 (1983).
- M. Nogami, K. Nagasaka, and T. Suzuki, *J. Am. Ceram. Soc.* 75, 220 (1992).
- M. Nogami, K. Nagasaka, and M. Takata, *J. Non-cryst. Solids* 122, 101 (1990).
- M. Nogami, K. Nagasaka, and E. Kato, *J. Am. Ceram. Soc.* 73, 2097 (1990).
- N. Nogami and A. Kato, *J. Non-cryst. Solids* 163, 242 (1993).
- M. Nogami, K. Nagasaka, and K. Kotani, *J. Non-cryst. Solids* 126, 87 (1990).
- M. Nogami, S. Suzuki, and K. Nagasaka, *J. Non-cryst. Solids* 135, 182 (1991).
- M. Nogami, Y. Q. Zhu, and K. Nagasaka, *J. Non-cryst. Solids* 134, 71 (1991).
- M. Nogami, A. Kato, and Y. Tanaka, *J. Mater. Sci.* 28, 4129 (1993).
- R. Reisfeld, *J. Alloys Compounds* 341, 56 (2002).
- T. Takagahara, *Phys. Rev. B* 36, 9293 (1987).
- L. Brus, *IEEE J. Quantum Electron.* 22, 1909 (1986).
- N. F. Borrelli, D. W. Hall, H. J. Holland, and D. W. Smith, *J. Appl. Phys.* 61, 5399 (1987).
- G. C. Righini, G. P. Banfi, V. Degiorgio, F. Nicoletti, and S. Pelli, *Mater. Sci. Eng. B* 9, 397 (1991).
- R. Cingolani, C. Moro, D. Manno, M. Striccoli, C. De Blasi, G. C. Righini, and M. Ferrara, *J. Appl. Phys.* 70, 6898 (1991).
- J. Yumoto, H. Shinojima, N. Uesugi, K. Tsunetomo, H. Nasu, and Y. Osaka, *Appl. Phys. Lett.* 57, 2393 (1990).
- H. Nasu, H. Yamada, J. Matsuoka, and K. Kamiya, *J. Non-cryst. Solids* 183, 290 (1995).
- M. Yamane, T. Takada, J. D. Mackenzie, and C.-Y. Li, *Proc. SPIE* 1758, 577 (1992).
- T. Takada, T. Yano, A. Yasumori, M. Yamane, and J. D. Mackenzie, *J. Non-cryst. Solids* 147, 631 (1992).
- Y.-H. Kao, K. Hayashi, L. Yu, M. Yamane, and J. D. Mackenzie, *Proc. SPIE* 2288, 752 (1994).
- M. Nogami, I. Kojima, and K. Nagasaka, *Proc. SPIE* 1758, 557 (1992).
- G. Li, M. Nogami, and Y. Abe, *J. Am. Ceram. Soc.* 77, 2885 (1994).
- G. Li and M. Nogami, *J. Sol–Gel Sci. Technol.* 1, 79 (1993).
- M. L. Steigerwald and L. E. Brus, *Annu. Rev. Mater. Sci.* 19, 471 (1989).
- R. Reisfeld, *Structure Bonding* 85, 99 (1996).
- M. Nogami, M. Watabe, and K. Nagasaka, *Proc. SPIE* 1328, 119 (1990).
- M. Nogami, A. T. Selvanm, and H. Song, in "Handbook of Advanced Electronic and Photonic Materials and Devices" (H. S. Nalwa, Ed.), Vol. 5, p. 151.
- C. M. Bagnall and J. Zarzycki, *Proc. SPIE* 1328, 108 (1990).
- N. Tohge, M. Asuke, and T. Minami, *Proc. SPIE* 1328, 125 (1990).
- J. D. Mackenzie, *J. Ceram. Soc. Japan* 101, 1 (1993).
- C. Y. Li, J. Y. Tseng, K. Mortia, C. Lechner, Y. Hu, and J. D. Mackenzie, *Proc. SPIE* 1758, 410 (1992).
- Y. Hui, H. Dijie, J. Zhonghong, and D. Yong, *J. Sol–Gel Sci. Technol.* 3, 235 (1994).
- G. C. Righini, A. Verciant, S. Pelli, M. Guglielmi, A. Martucci, J. Fick, and G. Vitrant, *Pure Appl. Opt.* 5, 655 (1991).
- Y. Wang and N. Herron, *Int. J. Nonlinear Opt. Phys.* 1, 683 (1992).
- N. Herron and Y. Wang, *Mater. Res. Soc. Symp. Proc.* 346, 887 (1994).
- K. C. Choi and K. J. Shea, *Mater. Res. Soc. Symp. Proc.* 346, 763 (1994).
- E. M. Yeatman, M. Green, E. J. C. Dawney, M. A. Fardad, and F. Horowitz, *J. Sol–Gel Sci. Technol.* 2, 711 (1994).
- M. A. Fardad, E. M. Yeatman, E. J. C. Dawney, M. Green, J. Fick, M. Guntau, and G. Vitrant, *Proc. IEEE* 143, 298 (1996).
- E. J. C. Dawney, J. Fick, M. Green, M. Guglielmi, A. Martucci, S. Pelli, G. C. Righini, G. Vitrant, and E. M. Yeatman, "Advanced Materials in Optics, Electro-Optics and Communication Technologies," p. 15. Techna Srl, Faenza, 1995.
- P. N. Butcher and D. Cotter, "The Elements of Nonlinear Optics." Cambridge Univ. Press, Cambridge, UK, 1999.
- H. Minti, M. Eyal, and R. Reisfeld, *Chem. Phys. Lett.* 183, 277 (1991).
- T. Gacoin, F. Chaput, and J. P. Boilot, *J. Sol–Gel Sci. Technol.* 2, 679 (1994).
- T. Takada, C.-Y. Li, J. Y. Tseng, and J. D. Mackenzie, *J. Sol–Gel Sci. Technol.* 1, 123 (1994).
- L. Spahnel, *J. Non-cryst. Solids* 147–148, 657 (1992).
- Y. Gacoin, J. P. Boilot, F. Chaput, and A. Lecomte, *Mater. Res. Soc. Symp. Proc.* 272, 21 (1992).
- C. B. Murray, D. J. Norris, and M. G. Bawendi, *J. Am. Chem. Soc.* 115, 8706 (1993).
- A. Henglein, *Chem. Rev.* 89, 1861 (1989).
- Y. Wang and N. Herron, *J. Phys. Chem.* 91, 257 (1987).
- R. Reisfeld, Semiconductor Quantum Dots in Amorphous Material, in "Optical Properties of Excited States in Solids" (B. Di

- Bartolo, Ed.), NATO ASI Series B, Vol. 301, p. 601. Plenum, New York, 1992.
68. A. Ekimov, *J. Lumin.* 70, 1 (1996).
  69. Y. Wang, A. Suna, J. McHugh, E. F. Hiliniski, P. A. Lucas, and R. D. Johnson, *J. Chem. Phys.* 92, 6027 (1990).
  70. J. E. Bowen Katari, V. L. Colvin, and A. P. Alivisatos, *J. Phys. Chem.* 98, 4109 (1994).
  71. A. Eychmuller, A. Mews, and H. Weller, *J. Phys. Chem. Lett.* 208, 59 (1993).
  72. A. Mews, A. V. Kadavanich, U. Banin, and A. P. Alivisatos, *Phys. Rev. B* 53, 13242 (1996).
  73. E. Lifshitz, J. Dag, I. Litvin, G. Hodes, S. Gorer, R. Reisfeld, M. Zelner, and H. Minti, *Chem. Phys. Lett.* 288, 188 (1998).
  74. D. L. Ou and A. B. Seddon, *Proc. SPIE* 3136, 348 (1997).
  75. M. L. Steigerwald, A. P. Alivisatos, J. M. Gibson, and L. E. Brus, *J. Am. Chem. Soc.* 110, 3048 (1988).
  76. D. L. Ou and A. B. Seddon, *Phys. Chem. Glasses* 39, 154 (1998).
  77. M. Zelner, H. Minti, R. Reisfeld, H. Cohen, Y. Feldman, S. R. Cohen, and R. Tenne, *J. Sol–Gel Sci. Technol.* 20, 153 (2001).
  78. S. G. Lu, Y. J. Yu, C. L. Mak, K. H. Wong, L. Y. Zhang, and X. Yao, *Microelectron. Eng.*, 66, 171 (2003).
  79. Li Dan, Ma Guohong, Huang Weimin, and Qian Shixiong, *Acta Optica Sinica* 22, 688 (2002).
  80. G. Brusatin, M. Guglielmi, P. Innocenzi, A. Martucci, and G. Scarinci, *J. Electroceram.* 4, 151 (2000).
  81. J. Fick, A. Martucci, M. Guglielmi, and J. Schell, *Fiber Integrated Opt.* 19, 43 (2000).
  82. Zhai Jiwei, Zhang Liangying, Yao Xi, and Shi Wensheng, *J. Mater. Sci. Lett.* 18, 1107 (1999).
  83. M. Guglielmi, A. Martucci, E. Menegazzo, G. C. Righini, S. Pelli, J. Fick, and G. Vitrant, *J. Sol–Gel Sci. Technol.* 8, 1017 (1997).
  84. A. Chia, Y.-H. Kao, Y. Xu, and J. D. Mackenzie, *Proc. SPIE* 3136, 337 (1997).
  85. A. Sashchiuk, E. Lifshitz, R. Reisfeld, T. Saraidarov, and M. Zelner, *J. Sol–Gel Sci. Technol.* 24, 31 (2002).
  86. Martucci, P. Innocenzi, J. Fick, and J. D. Mackenzie, *J. Non-cryst. Solids* 244, 55 (1999).
  87. A. Martucci, M. Guglielmi, and K. Urabe, *J. Sol–Gel Sci. Technol.* 11, 105 (1998).
  88. A. Martucci, J. Fick, J. Schell, G. Battaglin, and M. Guglielmi, *J. Appl. Phys.* 86, 79 (1999).
  89. J. Fick, J. Schell, R. Levy, A. Martucci, and M. Guglielmi, *Pure Appl. Opt.* 6, 527 (1997).
  90. P. Mulvaney, *Mater. Res. Soc. Bull.* 26, 1009 (2001).
  91. W. H. Armistead and S. D. Stookey, *Science* 144, 150 (1964).
  92. F. Hache, D. Ricard, and C. Flytzanis, *J. Opt. Soc. Am. B* 3, 1647 (1986).
  93. W. Nie, *Adv. Mater.* 5, 520 (1993).
  94. K. Fukumi, A. Chayahara, K. Kadono, Y. Sakaguchi, M. Miya, K. Fujii, J. Hayakama, and M. Satou, *J. Appl. Phys.* 75, 3075 (1994).
  95. M. J. Bloemer, J. W. Haus, and P. R. Ashley, *J. Opt. Soc. Am. B* 7, 790 (1990).
  96. S. A. Kuchinskii and N. V. Nikonoro, *J. Non-cryst. Solids* 128, 109 (1991).
  97. A. Gombert, W. Graf, A. Heinzl, R. Joerger, M. Kohl, and U. Weimer, *Physica A* 207, 115 (1994).
  98. G. W. Arnold, G. De Marchi, F. Gonella, P. Mazzoldi, A. Quaranta, G. Battaglin, M. Catalano, F. Garrido, and R. F. Haglund, *Nucl. Instrum. Methods B* 116, 507 (1996).
  99. R. A. Ganeev, A. I. Rysanyansky, S. R. Kamalov, M. K. Kodirov, and T. Usmanov, *J. Phys. D* 34, 1602 (2001).
  100. A. L. Stepanov, D. E. Hole, and P. D. Townsend, *Nucl. Instrum. Methods B* 166–167, 882 (2000).
  101. G. Battaglin, *Nucl. Instrum. Methods B* 116, 102 (1996).
  102. F. Garrido, F. Caccavale, F. Gonella, and A. Quaranta, *Pure Appl. Opt.* 4, 771 (1995).
  103. E. Borsella, E. Cattaruzza, G. De Marchi, F. Gonella, G. Mattei, P. Mazzoldi, A. Quaranta, G. Battaglin, and R. Polloni, *J. Non-cryst. Solids* 245, 122 (1999).
  104. A. Samuneva, Y. Dimitriev, V. Dimitrov, E. Kashchieva, and G. Encheva, *J. Sol–Gel Sci. Technol.* 13, 969 (1998).
  105. A. Licciulli, C. Massaro, L. Tapfer, G. De, M. Catalano, G. Battaglin, P. Mazzoldi, and C. Meneghini, *J. Non-cryst. Solids* 194, 225 (1996).
  106. M. A. Garcia, S. E. Paje, J. Llopis, M. A. Villegas, and J. M. Fernandez Navarro, *J. Phys. D* 32, 975 (1999).
  107. G. Mitrikas, C. C. Trapalis, and G. Kordas, *J. Non-cryst. Solids* 286, 41 (2001).
  108. Y. Hosoya, T. Suga, T. Yanagawa, and Y. Kurokawa, *J. Appl. Phys.* 81, 1475 (1997).
  109. R. Trbojevich, N. Pellegrini, A. Frattini, O. de Sanctis, P. J. Morais, and R. M. Almeida, *J. Mater. Res.* 17, 1973 (2002).
  110. Y. Katayama, M. Sasaki, and E. Ando, *J. Non-cryst. Solids* 178, 227 (1994).
  111. P. Innocenzi, *Proc. SPIE* 2288, 87 (1994).
  112. S. Sakka, H. Kozuka, and G. Zhao, *Proc. SPIE* 2288, 108 (1994).
  113. J. Y. Tseng, C.-Y. Li, T. Takada, C. L. Lechner, and J. D. Mackenzie, *Proc. SPIE* 1758, 612 (1992).
  114. H. Kozuka, G. Zhao, and S. Sakka, *J. Sol–Gel Sci. Technol.* 2, 741 (1994).
  115. A. Kutsch, O. Lyon, M. Schmitt, M. Mennig, and H. Schmidt, *J. Non-cryst. Solids* 217, 143 (1997).
  116. A. Hinsch and A. Zastrow, *J. Non-cryst. Solids* 147&148, 579 (1992).
  117. M. Zayat, D. Einot, and R. Reisfeld, *J. Sol–Gel Sci. Technol.* 10, 67 (1997).
  118. M. Mennig, J. Spanhel, H. Schmidt, and S. Betzholz, *J. Non-cryst. Solids* 147&148, 326 (1992).
  119. S. Schneider, K. Pöppel, G. Sauer, and P. Matousek, CLRC Rutherford Appleton Laboratory Annual Report 1999/2000, RAL Report RAL-TR-2000-034, 105-106: Picosecond Dynamics of Monodisperse Nanometer-Sized Silver Colloids.
  120. H. Kozuka, G. Zhao, and S. Sakka, *Bull. Inst. Chem. Res. Kyoto Univ.* 72, 209 (1994).
  121. J. M. Tour, S. L. Pandalwar, and J. P. Cooper, *Chem. Mater.* 2, 647 (1990).
  122. S. Szu, Chung-Yi Lin, and Chung-Hung Lin, *J. Sol–Gel Sci. Technol.* 2, 881 (1994).
  123. M. Mennig, M. Schmitt, B. Kutsch, and H. Schmidt, *Proc. SPIE* 2288, 120 (1994).
  124. H. Kozuka and S. Sakka, *Chem. Mater.* 5, 222 (1993).
  125. M. Menning, M. Schmitt, U. Becher, G. Jung, and H. Schmidt, *Proc. SPIE* 2288, 130 (1994).
  126. A. Kawabata and R. Kubo, *J. Phys. Soc. Jpn.* 21, 1765 (1996).
  127. W. Huang and J. Shi, *J. Sol–Gel Sci. Technol.* 20, 145 (2001).
  128. Sakka and H. Kozuka, *J. Sol–Gel Sci. Technol.* 13, 701 (1998).
  129. S. Otsuki, K. Nishio, T. Kineri, Y. Natanade, and T. Tsuchiya, *J. Am. Ceram. Soc.* 82, 1676 (1999).
  130. R. Reisfeld, in “Optical and Electronic Phenomena in Sol–Gel Glasses and Modern Application: Structure and Bonding,” Vol. 85, p. 123. Springer, Germany, 1996.
  131. Y. Yang, J. Shi, W. Huang, S. Dai, and L. Wang, *Mater. Lett.* 56, 1048 (2002).
  132. J. Matsuoka, R. Mizutani, H. Nasu, and K. Kamiya, *J. Ceram. Soc. Japan* 100, 599 (1992).
  133. J. Matsuoka, R. Mizutani, S. Kaneko, H. Nasu, K. Kamiya, K. Kadono, T. Sakauchi, and M. Miya, *J. Ceram. Soc. Japan* 101, 53 (1993).
  134. P. Innocenzi, H. Kozuka, and S. Sakka, *J. Sol–Gel Sci. Technol.* 1, 305 (1994).
  135. H. Kozuka, M. Okuno, and T. Yoko, *J. Ceram. Soc. Japan* 103, 1305 (1995).

136. J. Matsuoka, H. Yoshida, H. Nasu, and K. Kamiya, *J. Sol-Gel Sci. Technol.* 9, 145 (1997).
137. L. Spanhel, M. Mennig, and H. Schmidt, in "Proc. XVI International Congress on Glass," 1992, Vol. 7, p. 9.
138. A. Ritzer, M. A. Villegas, and J. M. Fernandez Navarro, *J. Sol-Gel Sci. Technol.* 8, 917 (1997).
139. M. Mennig, M. Schmitt, and H. Schmidt, *J. Sol-Gel Sci. Technol.* 8, 1035 (1997).
140. M. Mennig, K. Endres, M. Schmitt, and H. Schmidt, *J. Non-cryst. Solids* 218, 373 (1997).
141. G. Zhao, H. Kozuka, and S. Sakka, *J. Sol-Gel Sci. Technol.* 4, 37 (1995).
142. M. Lee, Y. S. Choi, and T. S. Kim, *J. Non-cryst. Solids* 211, 143 (1997).
143. S. T. Selvan, T. Hayakawa, M. Nogami, Y. Kobayashi, L. M. Liz-Marzan, Y. Hamanaka, and A. Nakamura, *J. Phys. Chem. B* 106, 10157 (2002).
144. T. Ishizaka, S. Muto, and Y. Kurokawa, *Opt. Commun.* 190, 385 (2001).
145. A. Muto, T. Kubo, Y. Kurokawa, and K. Suzuki, *Thin Solid Films* 322, 233 (1998).
146. T. Kineri, E. Matano, and T. Tsuchiya, *Proc. SPIE* 2288, 145 (1994).
147. T. Tsuchiya, T. Sei, Y. Watanabe, M. Mori, and T. Kineri, *J. Sol-Gel Sci. Technol.* 8, 685 (1997).
148. M. Nogami, Y. Abe, and A. Nakamura, *J. Mater. Res.* 10, 2648 (1995).
149. G. De, L. Taper, M. Catalano, G. Battaglin, F. Caccavale, F. Gonella, P. Mazzoldi, and R. Haglund, Jr., *Appl. Phys. Lett.* 68, 3820 (1996).
150. J.-H. Gwak, L. Chae, S.-J. Kim, and M. Lee, *Nanostruct. Mater.* 8, 1149 (1997).
151. G. A. Lindsay, in "Polymers for Second-Order Nonlinear Optics" (G. A. Lindsay and K. D. Singer, Eds.), p. 1. American Chemical Society, Washington, DC, 1995.
152. L. R. Dalton, J. Thomas, and H. S. Nalwa, *Polymer* 18, 543 (1987).
153. B. P. Singh, M. Samoc, H. S. Nalwa, and P. N. Prasad, *J. Chem. Phys.* 92, 2756 (1990).
154. H. S. Nalwa, *J. Phys. D* 23, 745 (1990).
155. J. Zyss, *J. Mol. Electron.* 1, 25 (1985).
156. H. S. Nalwa, T. Watanabe, A. Kakuta, A. Mukoh, and S. Miyata, *Electron. Lett.* 28, 1409 (1992).
157. H. S. Nalwa, T. Hamada, A. Kakuta, and A. Mukoh, *Nonlinear Opt.* 6, 155 (1993).
158. H. S. Nalwa, T. Watanabe, A. Kakuta, A. Mukoh, and S. Miyata, *Polymer* 34, 657 (1993).
159. H. S. Nalwa, T. Hamada, A. Kakuta, and A. Mukoh, *Japan. J. Appl. Phys. Lett.* 32, L193 (1993).
160. H. S. Nalwa, T. Hamada, A. Kakuta, and A. Mukoh, *Synthetic Metals* 57, 3901 (1993).
161. H. S. Nalwa, T. Watanabe, A. Kakuta, A. Mukoh, and S. Miyata, *Synthetic Metals* 57, 3895 (1993).
162. H. S. Nalwa, A. Kakuta, and A. Mukoh, *J. Appl. Phys.* 73, 4743 (1993).
163. H. S. Nalwa, *Adv. Mater.* 5, 341 (1993).
164. H. S. Nalwa, T. Watanabe, A. Kakuta, A. Mukoh, and S. Miyata, *Appl. Phys. Lett.* 62, 3223 (1993).
165. H. S. Nalwa, *Thin Solid Films* 235, 175 (1993).
166. H. S. Nalwa, T. Hamada, A. Kakuta, and A. Mukoh, *Nonlinear Opt.* 7, 193 (1994).
167. H. S. Nalwa, T. Watanabe, A. Kakuta, and S. Miyata, *Nonlinear Opt.* 8, 157 (1994).
168. H. S. Nalwa, T. Watanabe, and S. Miyata, *Adv. Mater.* 7, 754 (1995).
169. T. Watanabe, X. T. Tao, J. Kim, S. Miyata, H. S. Nalwa, and S. C. Lee, *Nonlinear Opt.* 15, 327 (1996).
170. H. S. Nalwa, Y. Imanisi, and S. Ishihara, *Nonlinear Opt.* 15, 227 (1996).
171. H. S. Nalwa, *Mater. Lett.* 33, 23 (1997).
172. P. N. Prasad, *Nonlinear Opt.* 13, 91 (1995).
173. Y. Zhang, P. N. Prasad, and R. Burzynski, *Chem. Mater.* 4, 851 (1992).
174. Y. Nosaka, N. Tohriwa, T. Kobayashi, and N. Fujii, *Chem. Mater.* 5, 930 (1993).
175. R. J. Jeng, Y. M. Chen, A. K. Jain, J. Kumar, and S. K. Tripathy, *Chem. Mater.* 4, 1141 (1992).
176. S. K. Tripathy, J. Kumar, J. I. Chen, S. Martunkakul, R. J. Jeng, L. Li, and X. L. Jiang, *Mater. Res. Soc. Symp. Proc.* 346, 531 (1994).
177. G.-H. Hsiue, R.-H. Lee, and R.-J. Jeng, *Chem. Mater.* 9, 883 (1997).
178. B. Lebeau, J. Maquet, C. Sanchez, E. Toussaere, E. Hierle, and J. Zyss, *J. Mater. Chem.* 4, 1855 (1994).
179. F. Chaput, D. Riehl, Y. Levy, and J.-P. Boilot, *Chem. Mater.* 5, 589 (1993).
180. A. Riehl, F. Chaput, Y. Levy, J.-P. Boilot, F. Kajzar, and P. A. Chollet, *Chem. Phys. Lett.* 245, 36 (1995).
181. J. Kim, J. L. Plawsky, R. La peruta, and G. M. Korenowski, *Chem. Mater.* 4, 249 (1992).
182. J. Kim, J. I. Plawsky, E. Van Wagenen, and G. M. Korenowski, *Chem. Mater.* 5, 118 (1993).
183. C. Sanchez and B. Lebeau, *Pure Appl. Opt.* 5, 689 (1996).
184. D. H. Choi, J. H. Park, T. H. Rhee, N. Kim, and S.-D. Lee, *Chem. Mater.* 10, 705 (1998).
185. H. K. Kim, S.-J. Kang, S.-K. Choi, Y.-H. Min, and C.-S. Yoon, *Chem. Mater.* 11, 779 (1999).
186. B. Lebeau, S. Brasselet, J. Zyss, and C. Sanchez, *Chem. Mater.* 9, 1012 (1997).
187. Z. Yang, C. Xu, L. R. Dalton, S. Kalluri, W. H. Steier, Y. Shi, and J. H. Bechtel, *Chem. Mater.* 6, 1899 (1994).
188. H. W. Oviatt, K. J. Shea, S. Kalluri, Y. Shi, W. H. Steier, and L. R. Dalton, *Chem. Mater.* 7, 493 (1995).
189. S. J. Kang, H.-J. Lee, H. K. Kim, J. T. Park, and S.-K. Choi, *Polym. Bull.* 35, 605 (1995).
190. S. Marturunkakul, J. I. Chen, R. J. Jeng, S. Sengupta, J. Kumar, and S. K. Tripathy, *Chem. Mater.* 5, 743 (1993).
191. S. Marturunkakul, J. I. Chen, L. Li, R. J. Jeng, J. Kumar, and S. K. Tripathy, *Chem. Mater.* 5, 592 (1993).
192. B. Luther-Davies, M. Samoc, and M. Woodruff, *Chem. Mater.* 8, 2586 (1996).
193. J. Zieba, Y. Zhang, P. N. Prasad, M. K. Casstevens, and R. Ruzynski, *Proc. SPIE* 1758, 403 (1992).
194. H. Schmidt, *Mater. Res. Soc. Symp. Proc.* 73, 739 (1986).
195. H. K. Schmidt, *J. Sol-Gel Sci. Technol.* 8, 557 (1997).
196. H. Schmidt and H. Wolter, *J. Non-cryst. Solids* 121, 428 (1990).
197. B. Sanchez and F. Ribot, *New J. Chem.* 18, 1007 (1994).
198. U. Schubert, N. Huesing, and A. Lorenz, *Chem. Mater.* 7, 2010 (1995).
199. D. A. Loy and K. J. Shea, *Chem. Rev.* 96, 1431 (1996).
200. J. Wen and G. L. Wilker, *Chem. Mater.* 8, 1667 (1996).
201. B. Lebeau and C. Sanchez, *Current Opinion Solid State Mater. Sci.* 4, 11 (1999).
202. F. Chaumel, H. Jiang, and A. Kakkar, *Chem. Mater.* 13, 3389 (2001).
203. D. Avnir, D. Levy, and R. Reisfeld, *J. Phys. Chem.* 88, 5956 (1984).
204. D. R. Ulrich, *J. Non-cryst. Solids* 100, 351 (1988).
205. J. M. Boulton, J. Thompson, H. H. Fox, I. Gorodisher, G. Teowee, P. D. Calvert, and D. R. Uhlmann, *Mater. Res. Soc. Symp. Proc.* 180, 987 (1990).
206. P. Griesmar, C. Sanchez, G. Pucetti, I. Ledoux, and J. Zyss, *Mol. Eng.* 3, 205 (1991).
207. E. Toussaere, J. Zyss, P. Griesmar, and C. Sanchez, *Nonlinear Opt.* 1, 349 (1991).
208. R. J. Jeng, Y. M. Chen, A. K. Jain, J. Kumar, and S. K. Tripathy, *Chem. Mater.* 4, 972 (1992).
209. K. Izawa, N. Okamoto, and O. Sugihara, *Japan. J. Appl. Phys.* 32, 807 (1993).

210. Y. Kobayashi, S. Muto, A. Matsuzaki, and Y. Kurokawa, *Thin Solid Films* 213, 126 (1992).
211. M. Nabavi, S. Doeuff, C. Sanchez, and J. Livage, *J. Non-cryst. Solids* 121, 31 (1990).
212. R. J. Jeng, Y. M. Chen, A. K. Jain, S. K. Tripathy, and J. Kumar, *Opt. Commun.* 89, 212 (1992).
213. L. Kador, R. Fischer, D. Haarer, R. Kasermann, S. Bruck, H. Schmidt, and H. Durr, *Adv. Mater.* 5, 270 (1993).
214. L. Xu, Z. Hou, L. Liu, Z. Xu, W. Wang, F. Li, and M. Ye, *Opt. Lett.* 24, 1364 (1999).
215. R. J. Jeng, Y. M. Chen, A. K. Jain, J. Kumar, and S. K. Tripathy, *Chem. Mater.* 4, 972 (1992).
216. R. Kasermann, S. Bruck, H. Schmidt, and L. Kador, *Proc. SPIE* 2288, 321 (1994).
217. J. Kim, J. L. Plawsky, R. LaPeruta, and G. M. Korenowski, *Chem. Mater.* 4, 249 (1992).
218. C. Claude, B. Garetz, Y. Okamoto, and S. J. Tripathy, *Mater. Lett.* 14, 336 (1992).
219. P.-H. Sung, S.-L. Wu, and C.-Y. Lin, *J. Mater. Sci.* 31, 2443 (1996).
220. H. Jiang and A. K. Kakkar, *Adv. Mater.* 10, 1093 (1998).
221. J. R. Caldwell et al., *Mater. Res. Soc. Symp. Proc.* 328, 535 (1994).
222. B. Lebeau, C. Sanchez, S. Brasselet, J. Zyss, G. Froc, and M. Dumont, *New J. Chem.* 20, 13 (1996).
223. S. Kalluri, Y. Shi, W. H. Steier, Z. Yang, C. Xu, B. Wu, and L. R. Dalton, *Appl. Phys. Lett.* 65, 2651 (1994).
224. P.-H. Sung and T.-F. Hsu, *Polymer* 39, 1453 (1998).
225. R. J. Jeng, Y. M. Chen, J. I. Chen, J. Kumar, and S. K. Tripathy, *Polym. Prep.* 34, 292 (1993).
226. P. N. Prasad, *Proc. SPIE* 1328, 168 (1990).
227. K.-S. Lee, C. J. Wung, P. N. Prasad, J.-C. Kim, C. K. Park, J. Jin, and H.-K. Shim, *Mol. Cryst. Liquid Cryst.* 224, 33 (1993).
228. K.-S. Lee, H.-M. Kim, C. J. Wung, and P. N. Prasad, *Synthetic Metals* 57, 3992 (1993).
229. R. Gvishi, P. N. Prasad, B. A. Reinhardt, and J. C. R. Bhatt, *J. Sol-Gel Sci. Technol.* 9, 157 (1997).
230. P. N. Prasad, in "7th International Symp. on Electrics Proc.," 1991, p. 817.
231. P. N. Prasad, *IEEE Trans. Dielectrics Electrical Insulation* 1, 585 (1994).
232. R. Burzynski, M. K. Casstevens, Y. Zhang, J. Zieba, and P. N. Prasad, *Proc. SPIE* 1853, 158 (1993).
233. K.-S. Lee, H.-M. Kim, C. J. Wung, and P. N. Prasad, *Synthetic Metals* 57, 3992 (1993).
234. P. N. Prasad, *Int. J. Nonlinear Opt. Phys.* 3, 531 (1994).
235. Y. Zhang, Z. Cao, K. Yang, G. Long, *Proc. SPIE* 3175, 302 (1998).
236. H. Tanaka, J. Takahashi, J. Tsuchiya, Y. Kobayashi, and Y. Kurokawa, *J. Non-cryst. Solids* 109, 64 (1989).
237. H. Sasaki, Y. Kobayashi, S. Muto, and Y. Kurokawa, *J. Am. Ceram. Soc.* 75, 453 (1990).
238. Y. Zhang, Y. P. Cui, C. J. Wung, P. N. Prasad, and R. Burzynski, *Proc. SPIE* 1560, 264 (1991).
239. B. Lebeau et al., *Pure Appl. Opt.* 5, 689 (1996).

# Nonlinear Optics of Fullerenes and Carbon Nanotubes

Rui-Hua Xie, Qin Rao

Queen's University, Kingston, Ontario, Canada

Lasse Jensen

Rijksuniversiteit Groningen, Groningen, The Netherlands

## CONTENTS

1. Introduction
  2. Second-Order Optical Nonlinearities of Fullerenes
  3. Third-Order Optical Nonlinearities of Fullerenes and Carbon Nanotubes
  4. Optical Limiting of Fullerenes and Carbon Nanotubes
  5. Conclusions
- Glossary  
References

## 1. INTRODUCTION

Almost everyday we read the “nano” words (nanoscience, nanotechnology, nanoscale, nanometer, nanosecond, nanodevice, nanoelectronics, nano-optics, and so on) from television commercials, research journal papers, magazine articles, newspaper headlines, and conferences. Such excitement comes from the undisputed fact that scientists all over the world have begun to control materials at a nanometer scale resulting in a great many new techniques and skills which can be used to make new materials with unique and useful properties. Obviously, these extensive studies in nanoscience and nanotechnology have led to a range of commercial applications in electronics, photonics, spintronics, sensing, military uses, medicine, and so on. Certainly, the best and most exciting days of obtaining novel properties or other kinds of discovery in the nanoscience and nanotechnology are still ahead. In this chapter, we review the

recent development of nonlinear optical (NLO) studies on fullerenes and carbon nanotubes. Before starting our review, we briefly introduce the theory of optical nonlinearity of a material and present the brief history of the new materials, called *fullerenes* and *carbon nanotubes*.

### 1.1. Nonlinear Optical Interactions

Nonlinear optics, focusing on the studies of NLO response of a material system to an applied optical field, plays an important role in many areas of science and technology [1–15]. To introduce the concept of optical nonlinearity one can express the field-induced dipole moment per unit volume, that is, the polarization  $\mathbf{P}(t)$ , in a power series of the strength of the applied optical field  $\mathbf{E}(t)$  [9]. Assuming that this optical field vector can be represented as the discrete sum of a number of frequency components as the compact form [9]

$$\mathbf{E}(t) = \sum_n \mathbf{E}(\omega_n) e^{-i\omega_n t} \quad (1)$$

one can write the polarization  $\mathbf{P}(t)$  as a function of  $E_i(\omega_n)$  in the Gaussian system of units

$$\mathbf{P}(t) = \sum_{m=1} \sum_n \sum_{j=x,y,z} P_j^{(m)}(\omega_n) e^{-i\omega_n t} \quad (2)$$

with

$$P_j^{(1)}(\omega_n) = \sum_{i=x,y,z} \chi_{ji}^{(1)} E_i(\omega_n) \quad (3)$$

$$P_j^{(2)}(\omega_n) = \sum_{i,k=x,y,z} \sum_{(mo)} \chi_{jik}^{(2)}(\omega_n = \omega_m + \omega_o; \omega_m, \omega_o) \times E_i(\omega_m) E_k(\omega_o) \quad (4)$$

$$P_j^{(3)}(\omega_n) = \sum_{i,k,l=x,y,z} \sum_{(mop)} \chi_{jikl}^{(3)}(\omega_n = \omega_m + \omega_o + \omega_p; \omega_m, \omega_o, \omega_p) \times E_i(\omega_m) E_k(\omega_o) E_l(\omega_p) \quad (5)$$

where the indices  $ijkl$  refer to the cartesian components of the applied optical field, and the notation  $(mo)$  or  $(mop)$  indicates that the sum  $\omega_m + \omega_o$  or  $\omega_m + \omega_o + \omega_p$  is to be held fixed in performing the summation over  $m$ ,  $o$ , and  $p$ . The coefficients  $\chi^{(1)}$ ,  $\chi^{(2)}$ , and  $\chi^{(3)}$  are known as the linear optical, second-, and third-order nonlinear optical susceptibilities of the material system. Correspondingly, for atoms or molecules they are referred to as the linear polarizability  $\alpha$  ( $=\chi^{(1)}/\rho$ ), the first-order hyperpolarizability  $\beta$  ( $=\chi^{(2)}/\rho$ ), and the second-order hyperpolarizability  $\gamma$  ( $=\chi^{(3)}/\rho$ ), respectively, where  $\rho$  is the number density of molecules in a material. Assuming that the molecule-field coupling system is initially prepared in the  $g$ th state (for example, ground state), we can derive  $\alpha$ ,  $\beta$ , and  $\gamma$  by using a perturbation theory [9]. The linear optical polarizability  $\alpha(\omega_p)$  of a molecule at optical frequency  $\omega_p$  can be [33]

$$\alpha_{ij}(\omega_p) = \hbar^{-1} \sum_m \left\{ \frac{U_{gm}^i U_{mg}^j}{\omega_{mg} - \omega_p} + \frac{U_{gm}^j U_{mg}^i}{\omega_{mg}^* + \omega_p} \right\} \quad (6)$$

where  $U_{mn}$  is the transition-dipole matrix element between the  $n$ th and  $m$ th states and  $\omega_{mn}$  is the corresponding transition frequency. The first and second terms in the above equation can be interpreted as the resonant and antiresonant contributions to the linear optical polarizability.  $\beta(\omega_\sigma)$  of molecule at optical frequency  $\omega_\sigma = \omega_q + \omega_p$  is given by [33]

$$\begin{aligned} \beta_{ijk}(\omega_\sigma; \omega_q, \omega_p) &= \hbar^{-2} \Theta \sum_{mn} \left\{ \frac{U_{gn}^i U_{nm}^j U_{mg}^k}{(\omega_{ng} - \omega_p - \omega_q)(\omega_{mg} - \omega_p)} \right. \\ &\quad + \frac{U_{gn}^j U_{nm}^i U_{mg}^k}{(\omega_{ng}^* + \omega_q)(\omega_{mg} - \omega_p)} \\ &\quad \left. + \frac{U_{gn}^j U_{nm}^k U_{mg}^i}{(\omega_{ng}^* + \omega_q)(\omega_{mg}^* + \omega_p + \omega_q)} \right\} \quad (7) \end{aligned}$$

where  $\Theta$  denotes the intrinsic permutation operator. (This operator tells us to average the expression that follows it over both permutations of frequencies  $\omega_p$  and  $\omega_q$  of the

applied field. The cartesian indices  $j$  and  $k$  should be permuted simultaneously.) The second-order hyperpolarizability  $\gamma(\omega_\sigma)$  of molecule at  $\omega_\sigma = \omega_r + \omega_q + \omega_p$  can be [33]

$$\begin{aligned} \gamma_{kjih}(\omega_\sigma; \omega_r, \omega_q, \omega_p) &= \hbar^{-3} \Theta \sum_{mno} \left\{ \frac{U_{go}^k U_{on}^j U_{nm}^i U_{mg}^h}{(\omega_{ng} - \omega_r - \omega_q - \omega_p)(\omega_{ng} - \omega_p - \omega_q)(\omega_{mg} - \omega_p)} \right. \\ &\quad + \frac{U_{go}^j U_{on}^k U_{nm}^i U_{mg}^h}{(\omega_{og}^* + \omega_r)(\omega_{ng} - \omega_q - \omega_p)(\omega_{mg} - \omega_p)} \\ &\quad + \frac{U_{go}^j U_{on}^i U_{nm}^k U_{mg}^h}{(\omega_{og}^* + \omega_r)(\omega_{ng}^* + \omega_r + \omega_q)(\omega_{mg} - \omega_p)} \\ &\quad \left. + \frac{U_{go}^j U_{on}^i U_{nm}^h U_{mg}^k}{(\omega_{og}^* + \omega_r)(\omega_{ng}^* + \omega_r + \omega_q)(\omega_{mg}^* + \omega_r + \omega_q + \omega_p)} \right\} \quad (8) \end{aligned}$$

Available studies [1–4, 16] have shown that the second-order nonlinear optical interaction can occur only in non-centrosymmetric crystals which do not display inversion symmetry, while the third-order nonlinear optical interaction can occur for both centrosymmetric and noncentrosymmetric media. Assuming that the two input waves are at  $\omega_o$  and  $\omega_m$ , from Eq. (4) we have [33]

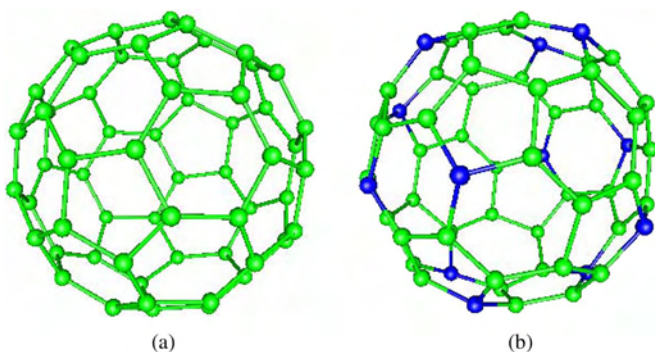
$$\begin{array}{lll} P^{(2)}(\omega_n = 2\omega) & \omega_o = \omega_m = \omega & \text{SHG} \\ P^{(2)}(\omega_n = \omega_1 + \omega_2) & \omega_o = \omega_1, \omega_m = \omega_2 & \text{SFG} \\ P^{(2)}(\omega_n = \omega_1 - \omega_2) & \omega_o = \omega_1, \omega_m = -\omega_2 & \text{DFG} \\ P^{(2)}(\omega_n = 0) & \omega_o = \omega_1, \omega_o = \omega = -\omega_m & \text{OR} \end{array} \quad (9)$$

SHG, SFG, DFG, and OR denote second-harmonic generation, sum-frequency generation, difference-frequency generation, and optical rectification, respectively. If the nonlinear crystal used in a DFG process is placed inside an optical resonator, the frequency of the output signal or idler field can build up to large values resulting in the device of optical parametric oscillator (OPO) which is used primarily at infrared wavelengths where other sources of tunable radiation are not readily available. Since the nonlinear polarization can efficiently produce an output signal only if a certain phase-matching condition is satisfied and this condition cannot be satisfied for more than one frequency component of the nonlinear polarization, no more than one of these frequency components shown in Eq. (9) will be presented with any appreciable intensity in the radiation generated by the nonlinear optical interaction. Operationally, one often chooses which frequency component will be radiated by properly selecting the polarization of the input radiation and orientation of the nonlinear crystal. Based on Eq. (5), we can get third-harmonic generation (THG) if  $\omega_m = \omega_o = \omega_p = \omega$ . Other third-order polarization can be reached by varying the three frequencies. (For more details the reader is referred to standard textbooks about nonlinear optics, e.g., [1–15].) Here we briefly describe the process of degenerate four-wave mixing (DFWM). In the DFWM experiment, a polarization is induced in the sample by the interaction between three light waves and the electrons in the nonlinear

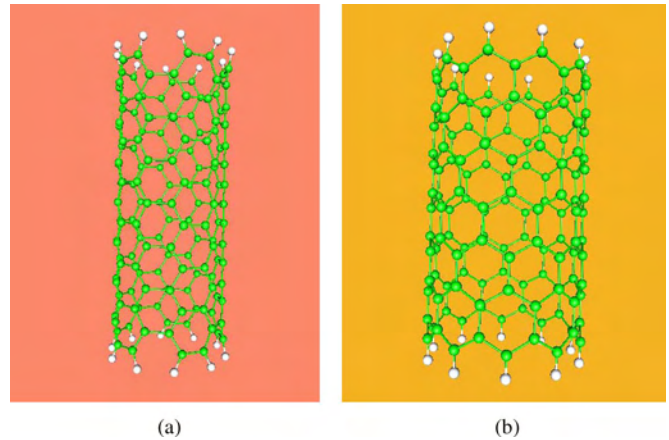
medium characterized by a third-order nonlinear optical susceptibility  $\chi^{(3)}$  through Eq. (5), but two wave beams are incident at the same region on the sample and have equal and opposite wave vectors and the same frequency  $\omega$ . The two wave beams from, for example, a He-Ne laser set up an interference grating, which interacts with the third light beam coming from the back side of a transparent sample. Then, the fourth beam, resulting from this interaction with wave vector equal and opposite to that of the third beam, is detected. So, if the frequency of the third wave is  $\omega$ , the fourth wave will be generated with the same frequency  $\omega$  but its complex amplitude everywhere will be the complex conjugate of the third wave.

## 1.2. Fullerenes and Carbon Nanotubes

Graphite is known as one stable and abundant solid form of pure carbon [17]. This form has three strong  $sp^2$  trigonal bonds with an equal distance of 0.142 nm and weak  $\pi$  bonds perpendicular to successive sheets with an inter-plane distance of 0.34 nm [18]. Diamond, known as the hardest of all natural materials, is another slightly less stable and less abundant crystallographic form of pure carbon [17]. Each carbon atom in diamond is covalently bonded to four neighbors via  $sp^3$  hybridization at the apexes of a regular tetrahedron. In 1985, Kroto et al. [19] synthesized the fascinating, truncated icosahedron molecule, named  $C_{60}$  [20] (see Fig. 1), which has 20 hexagonal and 12 pentagonal faces and 60 vertices (each vertex is at the intersection of two hexagonal and one pentagonal faces). This discovery brought us a new form of pure carbon, named fullerenes [21–26], which are made of an even number of three-coordinated  $sp^2$  carbon atoms that arrange themselves into 12 pentagonal faces and any number ( $>1$ ) of hexagonal faces. This kind of cage molecule can crystallize in a variety of three-dimensional structures [27, 28]. The macroscopic synthesis of a soot [27], which contains  $C_{60}$  and other fullerenes in large compounds, and the straightforward purification techniques of the soot, which make the pure fullerene materials available, have led to extensive studies on the structural, mechanical, electronic, magnetic, and optical properties of fullerenes [29–35]. Meanwhile, fullerenes can be doped in several different ways (e.g., endohedral, exohedral, and substitutional doping) because of their unique electronic properties [31]



**Figure 1.** Geometrical structures of fullerenes: (a)  $C_{60}$ ; (b)  $C_{48}N_{12}$ .



**Figure 2.** Geometrical structures of two kinds of carbon nanotubes: (a) armchair carbon nanotube; (b) zigzag carbon nanotube.

(see Fig. 1). These doped fullerenes can be semiconducting, metallic, or even superconducting [31].

In addition to fullerenes, it is also possible to synthesize tubular fullerenes and nested concentric fullerenes. The new field of carbon nanotube research was greatly stimulated by the discovery of the existence of carbon tubules or nanotubes [36] and the subsequent report of conditions for the synthesis of large quantities of nanotubes [31, 37–57]. Theoretically, there are three major classifications of  $C_{60}$ -based tubules or nanotubes [31, 58–62]: armchair carbon nanotubes (see Fig. 2), zigzag carbon nanotubes (see Fig. 2), and chiral carbon nanotubes, depending on whether they are related to a fivefold, a threefold, or a twofold axis relative to the  $C_{60}$  molecule. Generally speaking, a single-walled carbon nanotube (SWNT) can be made if only one graphene sheet is rolled; while a multiwalled carbon nanotube (MWNT) can be obtained if a few stacked graphitic shells are built from perfectly concentric cylinders or a single graphene sheet is rolled as a scroll. Since 1991, carbon nanotubes have been extensively studied, both theoretically and experimentally, due to their unique geometric structures and remarkable mechanical, chemical, electronic, magnetic, and transport properties. The small diameter (at scale of nanometers) and the long length (at the order of microns) lead to such large aspect ratios that the carbon nanotubes act as ideal one-dimensional systems. Their rope crystallites offer host lattice for intercalation and storage. All these characteristics make carbon nanotubes the focus of extensive studies in nanoscale science and technology with potential applications in various materials and devices. Readers can find more details about the synthesis, physical and chemical properties, and technological applications of carbon nanotubes in recent books [31, 63–70] and review articles [71–77].

## 1.3. Conventions and Outline

In nonlinear optics, there are several different systems of units [9] that are commonly used in the community. In this chapter, we use the Gaussian system of units. In the Gaussian system, both the field  $\mathbf{E}$  and polarization  $\mathbf{P}$  have the same units, statvolt/cm. Thus,  $\chi^{(1)}$  is dimensionless and the dimensions of  $\chi^{(2)}$  and  $\chi^{(3)}$  are given by



cm/statvolt ( $\equiv$  esu =  $3.3354 \times 10^{-5}$  m/V) and  $\text{cm}^2/\text{statvolt}^2$  ( $\equiv$  esu =  $1.1125 \times 10^{-9}$  m<sup>2</sup>/V<sup>2</sup>), respectively. The units of  $\chi^{(2)}$  and  $\chi^{(3)}$  are not usually stated explicitly in the Gaussian system of units, but instead quote values simply in electrostatic units (esu). For other different systems of units, the reader may refer to Appendix A of Boyd's book [9]. In addition, there are different conventions for defining hyperpolarizabilities (for example, Taylor series, perturbation series, electric field induced SHG (EFISHG), phenomenological; see [78] for details). In this chapter, we use the convention of *Taylor series*.

In this chapter, we review recent studies on the second-order optical nonlinearities (characterized by the first-order hyperpolarizability  $\beta$ ) of fullerenes and their derivatives in Section 2, and the third-order optical nonlinearities (characterized by the second-order hyperpolarizability  $\gamma$ ) of fullerenes, fullerene derivatives, and carbon nanotubes in Section 3.

Many laser sources, for example, OPO, dye lasers, and Raman lasers, are widely used in many areas of science and technology. Naturally, a potential hazard for human eyes and other optical sensors arises because of the laser power. Hence, protecting all sensors and human eyes against the hazard is a very important task which stimulates many research groups all over the world to search for good optical limiters that should have high broadband linear transmittance for low input fluences and always keep the output energy below the damage threshold of all optical sensors and human eyes. This is one NLO application. In Section 4, we review recent developments of optical limiting studies of fullerenes, fullerene derivatives, and carbon nanotubes.

In Section 5, we end this chapter by giving some remarks and outlooks for further studies about the optical nonlinearities of fullerenes and carbon nanotubes.

## 2. SECOND-ORDER OPTICAL NONLINEARITIES OF FULLERENES

Second-order NLO measurements include techniques, for example, Maker Fringe method, EFISHG, hyper-Rayleigh scattering, and the second-order NLO processes mentioned before. The detailed descriptions of Maker Fringe method and hyper-Rayleigh scattering can be found in [1–15]. The EFISHG technique involves the mixing of three optical fields and one static field of parallel polarizations and details can be found in [79].

From a symmetry consideration, both  $C_{60}$  and  $C_{70}$  possess inversion symmetry. Thus, within a dipolar approximation, no SHG activity should be detected. However, several

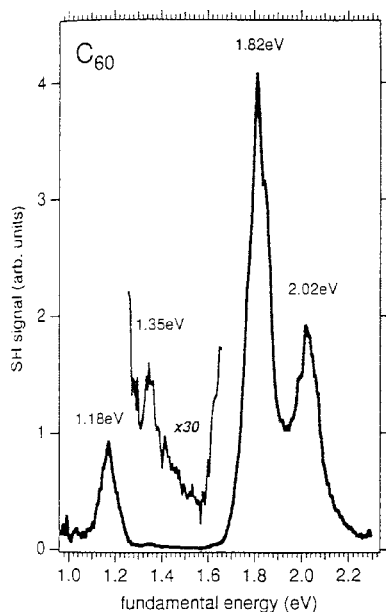
groups [80–84] have observed SHG signal from vacuum-sublimed thin films on a glass or silica substrate. Some results of fullerenes and derivatives are summarized in Tables 1 and 2 and in Figures 3 and 4.

### 2.1. $C_{60}$

Hoshi et al. [80] were the first to investigate the NLO response of  $C_{60}$  film deposited on a silica substrate by impinging an unfocused polarized Nd:YAG laser (1064 nm) on the film and measuring the dependence of the SHG intensities on the polarization of light and on the angle of incidence in the transmission geometry. A polarization analyzer and a monochromator were used to detect the transmitted SHG (532 nm). No detectable SHG was emitted from the blank substrate. For convenience, we express the polarization state of incident light by  $|I_i\rangle$  and that of the polarization analyzer by  $|O_i\rangle$  ( $i = x, y, z$ , z-axis is the direction of the incident laser beam and x-axis the rotation axis). Hoshi et al. [80] noticed that no SHG is detected under  $|I_x\rangle \otimes |O_x\rangle$  and  $|I_y\rangle \otimes |O_x\rangle$ , irrespective of the angle  $\theta$  of incidence. For  $|I_x\rangle \otimes |O_y\rangle$  or  $|I_y\rangle \otimes |O_y\rangle$ , SHG signal appears as the  $C_{60}$  film was rotated around x-axis to change the incident angle  $\theta$ . Assuming that the normal axis (i.e., z-axis here) of the  $C_{60}$  film is a  $C_\infty$  symmetry, their observed results are due to a  $C_{\infty v}$  symmetry if SHG comes from the electrical dipolar responses. If so, this implies that asymmetry exists along the z-axis direction. The presence of substrate is the only cause of the asymmetry. However, if SHG signal comes from an electrical quadrupolar response, either  $C_{\infty v}$  or  $C_{\infty h}$  symmetry is a consistent account for their observed results. Later on, Kajzar et al. [83] also observed the incidence angle dependence of SHG intensity from a sublimed  $C_{60}$  thin film: the maximum of the SHG signal is at  $\theta = 55^\circ$ . Koopmans et al. [82] performed more systematic studies on SHG from thin  $C_{60}$  films by combining frequency-, rotational-, angular-, and film-thickness-dependent measurement and gave the first SHG spectrum of pure  $C_{60}$  films or  $C_{60}$  surfaces. They found  $C_{60}$  films to show a high SHG efficiency and a strong and sharp resonance at  $2\hbar\omega = 3.60$  eV, which is close to an allowed optical transition. Meanwhile, Wang et al. [81] also found that the square root of SHG intensity of  $C_{60}$  film increases linearly with the film thickness and varies with the change of temperature (reaching a maximum at 415 K) showing a bulk second-order optical nonlinearity. All these experiments demonstrated that the SHG signal from sublimed  $C_{60}$  thin films comes from the bulk, and is not only an interface effect [85]. The large second-order NLO response

**Table 1.** Second-order optical nonlinearities of  $C_{60}$  and derivatives measured by different experimental techniques.

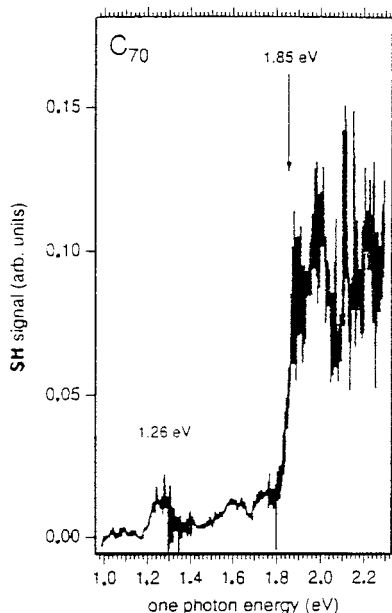
Fullerenes	$\beta$ ( $10^{-30}$ esu)	$\chi^{(2)}$ ( $10^{-9}$ esu)	Method	State of material	Ref.
$C_{60}$	1.1	1.3	ATR	film	[88]
$C_{60}/\text{DEA}$	$67 \pm 20$		EFISHG	solution	[103]
$C_{60}$ ( $C_4H_8N_2$ )	$36 \pm 12.7$	$180 \pm 80$	SHG	LB film	[115]
Carborane/ $C_{60}$ Hybrid (1a)	346		SHG	solution	[113]
Carborane/ $C_{60}$ Hybrid (1b)	483		SHG	solution	[113]
Carborane/ $C_{60}$ Hybrid (1c)	1189		SHG	solution	[113]
CFP	83	32	SHG	LB film	[121, 122]



**Figure 3.** SHG spectrum of  $C_{60}$  film. Reprinted with permission from [84], K. Kuhnke et al., *Chem. Phys. Lett.* 294, 241 (1998). © 1998, Elsevier Science.

of  $C_{60}$  films is due to small amounts of impurities (such as  $C_{60}$  isomers, other fullerenes, or oxides which have noncentral symmetry), or electric quadrupole, or magnetic dipole contributions which are allowed in centrosymmetric materials.

Kuhnke et al. [84] presented a wide SHG spectrum of  $C_{60}$  films (see Fig. 3): three pronounced resonances at 1.18 eV (1046 nm), 1.82 eV (678 nm), and 2.02 eV (611 nm), and a weak one at 1.35 eV (914 nm). The resonance peak



**Figure 4.** SHG spectrum of  $C_{70}$  film. Reprinted with permission from [84], K. Kuhnke et al., *Chem. Phys. Lett.* 294, 241 (1998). © 1998, Elsevier Science.

observed at 1.82 eV by Kuhnke et al. [84] confirms the position and width of the resonance first observed by Koopmans et al. [82]. Kuhnke et al. [84] found a significant SHG signal at 1.165 eV (1059 nm), the energy of the study at fixed wavelength by Wilk et al. [86]. Later on, Janner [87] observed the resonance at 2.02 eV in a SHG spectrum. Using the experimental technique of electro-optically modulated ATR (attenuated total reflection) spectroscopy, Wang et al. [88] have measured the second-order NLO response of Langumir–Blodgett (LB) films of  $C_{60}$  by electro-optical (Pockels) characterization for the first time. Their observed electro-optical response was the Pockels effect, and the second-order NLO susceptibility  $\chi^{(2)}$  of  $C_{60}$  film was determined to be  $1.3 \times 10^{-9}$  esu, in agreement with that of Wang et al. [81]. It should be noticed that although  $\beta$  is zero for isolated  $C_{60}$ ,  $C_{60}$  film may exhibit nonzero value if it does not display centrosymmetry. Based on the work of Rashing et al. [89], the corresponding molecular hyperpolarizability  $\beta$  of the  $C_{60}$  molecule is about  $1.1 \times 10^{-30}$  esu [88]. Such large electro-optical response of  $C_{60}$  shows that it is a promising NLO material regardless of the molecular inversion symmetry.

Theoretically, Qin et al. [90] studied the dispersion relation of the quadrupole response for single  $C_{60}$  molecule. Two resonant peaks were at 1.09 eV and 1.86 eV, respectively. The peak at 1.09 eV is only about 0.1 eV lower than the lowest peak observed by Kuhnke et al. [84], while the one at 1.86 eV is in good agreement with experiment [84]. Although their calculated peak is of asymmetric shape, no separate feature appears around the energy 2 eV. Hence, their calculation showed that the peak observed at 2.02 eV by Kuhnke et al. [84] is not caused by the electric quadrupole transition. The sharp minimum [90] between the two peaks seems to be caused by a change of amplitude sign. In the SHG spectrum of Kuhnke et al. [84], a similarly sharp minimum at 1.57 eV was observed. Hence, their theoretical calculation is in overall agreement with experiment. Finally, it should be mentioned that no SHG peak is detected at the spin-forbidden excitation of the lowest triplet exciton at 1.55 eV (0.796 nm) [91].

The  $C_{60}$  film can be crystallized in a fcc structure at room temperature [92, 93], and is therefore centrosymmetric. As mentioned above, within the electric-dipole approximation, the  $C_{60}$  film would not show SHG signal so that only the surface contribution could be detected. Nevertheless, the experiment of Wang et al. [81] showed that the surface contribution to SHG should be very small. As discussed above, the origin of the SHG signal from a  $C_{60}$  film can only be an electric quadrupole, or a magnetic-dipole contribution, or from an impurity. The recent work by Koopmans et al. [94] has convincingly shown that a fullerene's SHG at 1.8 eV comes from a magnetic-dipole interaction. However, a recent study by Munn et al. [95] showed that although the SHG signal at 1.8 eV is dominated by the magnetic-dipole response, this is not the case at other frequencies. The theoretical study of Qin et al. [90] also demonstrated that the second-order quadrupole nonlinear contribution is large enough to explain the experimental results obtained by Wang et al. [81]. Liu et al. [96] have observed a change of the SHG signal of  $C_{60}$  film with the structural phase transition of  $C_{60}$  at 245 K. Since the impurity cannot display the

properties of  $C_{60}$ , their experimental results implied that the SHG in the fcc and sc phases was not induced simply by the impurity in the  $C_{60}$  material (or say, the SHG response of impurity in  $C_{60}$  films cannot explain the change in SHG at 245 K). Thus, the SHG signal from  $C_{60}$  films cannot be attributed solely to the impurity.

## 2.2. $C_{70}$

Kuhnke et al. [84] were the first to measure the SHG response of higher fullerene  $C_{70}$  and the SHG spectrum is presented in Figure 4. They observed a weak resonance peak at 1.26 eV (979 nm) and a steep signal at 1.85 eV (667 nm) showing a broad resonance feature without resolved structure. In a Ne matrix, Sassara et al. [97] assigned the lowest singlet ( $S_1$ ) and triplet ( $T_1$ ) excitons for isolated molecules to 1.93 eV and 1.56 eV, respectively. If a shift of about 0.1 eV between matrix isolated  $C_{70}$  and the solid exists, the lowest singlet exciton may correspond very well to the onset of the SHG intensity of  $C_{70}$  film. If so, the proximity of the next higher singlet exciton ( $S_2$ ) and higher excitonic states may result in the broad resonance structure above 1.85 eV. However, the resonance peak at 1.26 eV is too low in energy to be assigned to the triplet exciton. The calculation of Shuai and Bredas [98] indicated that the SHG spectra for  $C_{70}$  come from the contribution of the electric quadrupole having a sharp peak at 1.2 eV and a broad resonance structure between 2.0 and 2.4 eV, which is in good agreement with the SHG spectrum of Kuhnke et al. [84].

$C_{70}$  has a lower symmetry than  $C_{60}$ . Thus, the low-energy part of the absorption spectrum of the  $C_{70}$  solid may be rich in dipole-allowed transitions. However, only two features were observed in the SHG spectrum of  $C_{70}$  film; that is, many dipole-allowed transitions are absent. Anyhow, this and the agreement with theoretical calculation suggest that dipole-forbidden transitions in  $C_{70}$  may be observed most easily. Indeed, Kajzar et al. [83, 99] predicted a dipole-forbidden transition at 2.49 eV.

## 2.3. Fullerene Derivatives

Charge transfer is demonstrated to be the most effective mechanism to enhance the second-order optical nonlinearity of organic molecule [100, 101]. Since fullerenes are excellent electron acceptors [102], forming charge-transfer complexes with appropriate donors would break the centrosymmetry of  $C_{60}$  or  $C_{70}$  and thus induce significant second-order optical nonlinearity.

Wang and Cheng [103] measured the second-order NLO property of  $C_{60}$  charge-transfer complexes formed with *N,N*-diethylaniline (DEA), which is an electron donor well known to form charge-transfer complexes with various aromatic acceptor molecules [104], by using EFISHG technique [105, 106]. Indeed, the formation of charge-transfer complexes with DEA breaks the centrosymmetry in  $C_{60}$  and induces its second-order optical nonlinearity [103]. The value of  $\beta_{\mu}$  in the dipolar direction for  $C_{60}$ /DEA is  $(6.7 \pm 2) \times 10^{-29}$  esu. Based on the INDO/CI-SOS (intermediate neglect of differential overlap/configuration interaction plus sum-over-state approach) method [107–109],

Feng and his co-workers [110] calculated the second-order nonlinear optical susceptibilities  $\beta_{ijk}$  and  $\beta_{\mu}$  of  $C_{60}$ /aniline (AN) (a theoretical model of the experimentally studied  $C_{60}$ /DEA [103]). The calculated value of  $\beta_{\mu}$  at 1910 nm is  $3.217 \times 10^{-29}$  esu, which is in good agreement with experiment [103]. Later on, using this theory, Liu et al. [111] found that *N*-methyl-2-(2'-thiophene)-pyrrolo[3,4] $C_{60}$  *N*-methyl-pyrrolo[3,4] $C_{60}$  and its derivatives exhibit good second-order optical nonlinearities. Both theoretically demonstrated the polarization effects, induced by the charge-transfer interaction, on the large number of hyperpolarizable  $\pi$  electrons, which have significant contribution to the higher value of  $\beta_{\mu}$  obtained by Wang and Cheng [103]. Fu et al. [112] found using INDO/CI-SOS that spiroannulated quinone-type methanofullerenes show enhanced second-order nonlinearity compared with  $C_{60}$ /AN.

Lamrani et al. [113] found experimentally that a combination of seemingly attractive carboranes and fullerene through an ethynyl  $\pi$ -system produced high  $\beta$  values. The  $\beta$  values found were  $34.6 \times 10^{-29}$ ,  $48.3 \times 10^{-29}$ , and  $118.9 \times 10^{-29}$  esu for the three carborane-fullerene hybrids investigated.

The monofunctionized derivative  $C_{60}$ -( $C_4H_8N_2$ ) has no centrosymmetry [114]. Gan et al. [115] have measured its SHG spectrum. The second-order nonlinear optical susceptibility  $\chi^{(2)}$  and molecular hyperpolarizability  $\beta$  of  $C_{60}$ -( $C_4H_8N_2$ ) are determined to be  $(1.8 \pm 0.8) \times 10^{-7}$  esu and  $(3.6 \pm 1.2) \times 10^{-29}$  esu, respectively [115].

Kajzar et al. [116] performed SHG measurements on  $C_{60}$ -based composites and multilayered charge-transfer structures with electron donors, 5,10,15,20-tetraphenyl-21*H*, 23*H*-porphine (TPP) and 5,6,11,12-tetraphenyl naphthacene (rubrene) (TPN). In thin films that contain  $C_{60}$  molecule, only the SHG signal is observed, and a significant enhancement in SHG signals is observed in the multilayered structures. The enhancement is due to a ground-state permanent electron transfer from the electron-donating molecules to  $C_{60}$  [116].

The charge separation in substituted  $C_{60}$  leading to enhancement of the second-order nonlinear optical susceptibility was also demonstrated theoretically [117, 118]. Further charge transfer can take place during the excitation process from the ground state to the excited state [118]. This kind of strong intramolecular charge transfer causes large second-order nonlinear optical susceptibility in the substituted fullerene. Among  $C_{60}$ ,  $C_{60}$ /DEA,  $C_{60}$ /AN, and  $C_{59}X$  ( $X = B, N$ ),  $C_{60}$  has the smallest  $\beta$  value and  $C_{59}X$  has the largest one [117, 118]. As discussed later, enhanced  $\beta$  value is also obtained for Si-substituted  $C_{60}$ . This means that substitute doping is a good means to achieving a large second-order nonlinear optical susceptibility of pure  $C_{60}$ .

The crown ether modified  $C_{60}$  will be typical supramolecules which combine the unique properties of  $C_{60}$  and crown ethers together. Surely, the solubility and amphiphathy of  $C_{60}$  can be improved because of the good hydrophilic properties of the crown ether moiety. This makes crowned  $C_{60}$  a kind of competitive compound to form structurally ordered fullerene thin films and may find practical applications as active surface layers in microsensors or optoelectronic devices. Several kinds of crowned fullerene

derivatives were synthesized [119], based on which Langmuir and Langmuir–Blodgett (LB) films [120] were made. Guo et al. [121, 122] investigated macroscopic SHG of a LB film of a novel crowned [60]fullero-pyrrolidine (CFP). They observed a strong SHG signal whose intensity depends linearly on the number of film layers, implying that the LB films of CFP are a promising material for SHG. The second-order molecular susceptibility  $\chi^{(2)}$  and hyperpolarizability  $\beta$  were determined to be  $3.2 \times 10^{-8}$  esu and  $8.3 \times 10^{-29}$  esu, respectively. The mechanism is still the intramolecular electron transfer.

The second-order nonlinearity of  $C_{60}$  endohedral doped with Li,  $Li@C_{60}$ , has been investigated both theoretically and experimentally by Campbell et al. [123]. They found, theoretically, that displacement of the Li off the idealized molecular center can induce a large first hyperpolarizability. An enhanced nonlinear response was also found experimentally by considering the SHG from thin films containing ~30%  $Li@C_{60}$ . From the results it was suggested that  $\chi^{(2)}$  of  $Li@C_{60}$  would be one or two orders of magnitude larger than the magnetically induced  $\chi^{(2)}$  of pristine  $C_{60}$ .

Rustagi et al. [124] studied the first- and second-order hyperpolarizability of fullerene substitutionally doped with one B or one N atom using a tight-binding method and found large enhancement of the nonlinearities in the doped fullerenes. Also, heterofullerenes substitutionally doped with silicon atoms [125] are of great interest in many aspects. One is the possibility to increase second-order optical susceptibility. Very recently, Fuks et al. [126] have shown, both theoretically and experimentally, that fullerene molecules, for example,  $C_{60}$ , can be modified by substituting fullerene with Si atoms to enhance the second-order photoinduced nonlinear optical properties. The experimental results are [126]:  $\chi_{xxx}^{(2)} = 0.21, 0.87$  pm/V for  $C_{59}Si$  and  $C_{58}Si_2$ , respectively;  $\chi_{zzz}^{(2)} = 0.66, 0.67$  pm/V for  $C_{59}Si$  and  $C_{58}Si_2$ , respectively. The substitution by two Si atoms does favor the larger second-order susceptibility in comparison with that for only one-atom substitution [126]. The indicatrice of the photoinduced second-order NLO susceptibilities for  $C_{58}Si_2$  is more isotropic than that for  $C_{59}Si$ .

Lin et al. [127] successfully incorporated  $C_{60}/C_{70}$  molecules into inorganic optical glasses with high melting temperatures. Fullerene doping leads to changes in glass properties [127]. Considering that optical glass without fullerene doping has centrosymmetry supporting no second-order optical nonlinearities, Zeng et al. [128] have recently shown that fullerene dopants can form ordered structures in the vitreous glass matrix. The fullerene doping broke the centrosymmetry of glass leading to macroscopic second-order optical nonlinearities. Nearly two orders of magnitude enhancement for the SHG was observed near the self-assembled islands [128].

It is known that high values of the first hyperpolarizability  $\beta$  tensor components for a given molecule imply optical nonlinearities as the molecule responds to applied optical fields. The so-called donor-acceptor model shows one approach to search the structure-property relationships of  $\beta$  and design our needed NLO materials. Based on this model, electronic excitation would result in charge migration from the donor to the acceptor group showing a large dipole moment along the direction bounding the two groups. Indeed, many of

donor-acceptor systems exhibit high values of  $\beta$ . This has also been demonstrated theoretically for B,N-substituted  $C_{60}$  by Jensen et al. [129] and for push-pull derivatives of  $C_{60}$  by Fanti et al. [130] where also a relation between the conjugation path length and  $\beta$  was found.

The first hyperpolarizability is made up of its dipolar and octopolar contributions. It is possible to cancel the dipolar part by symmetry and enhance the octopolar part of the  $\beta$  tensor [131, 132]. This gives us another approach designing NLO materials by exploring octopolar architectures of a number of possible molecules [132]. Such octopolar-enhanced approach has two advantages [131]: preventing the molecules from losing their optical properties in bulk by dipole cancellation on antisymmetric crystallization and raising the possibility for the system to have more than one optical axis. Barbosa and Nascimento [133] have proposed a new approach, incorporating the octopolar-enhanced approach into the donor-acceptor model, for designing molecules with large hyperpolarizabilities. In their approach, a central acceptor unit with a high value of electron affinity is used and bounded to several donor groups maximizing either the dipolar or the octopolar components of the  $\beta$  tensor.

In the late 1990s,  $C_{36}$  fullerene [134, 135] has been synthesized. This molecule with  $D_{6h}$  and  $D_{2d}$  symmetries exhibits rich structural and electronic properties [136–146]. The crystal  $D_{6h}$  structure has a very high electron affinity ( $>3$  eV) and many symmetry elements [133]. By adding two equivalent donor amino-ethylene (ME) groups to one of the three unique symmetric positions of the central acceptor group  $C_{36}$  fullerene, Barbosa and Nascimento [133] explored the second-order NLO properties of such system. The nuclear frameworks with  $C_{2h}$  point group cannot present second-order NLO properties. The framework with  $C_{2v}$  symmetry, as listed in Table 2, may exhibit high values of the  $\beta_{(z)}$  component, more than 10 times larger than those for the p-nitroaniline [147]. Because of the symmetry, most of the components of the  $\beta$  tensor vanish. Their results showed that a symmetric positioning of a great number of donor groups is more important to enhance the octopolar component of  $\beta$  than an augmentation of chain length which only influences significantly the dipolar component. According to their proposed approach, some of the designed molecules can be good candidates for building second-order NLO materials.

### 3. THIRD-ORDER OPTICAL NONLINEARITIES OF FULLERENES AND CARBON NANOTUBES

Third-order optical susceptibility  $\chi^{(3)}$  of a material can be measured by DFWM, THG, EFISHG, Z-scan, optical Kerr effect, optically heterodyned OKE (OHD-OKE), and coherent anti-Stokes Raman spectroscopy (CARS) vibrational lineshape analysis. The THG and DFWM techniques are mentioned in Section 1.1. The THG process occurs in every medium and, consequently, the harmonic intensity is a result of the superposition of harmonic fields generated in the separate media. The DFWM is a powerful tool for measuring  $\chi^{(3)}$  of a material. From the strength of the signal,

**Table 2.** The first hyperpolarizability ( $\beta$ , in  $10^{-32}$  esu) and dipole ( $\mu$ , in  $10^{-20}$  esu) for amino-ethylene (ME) substituted  $C_{36}$  fullerenes with  $C_{2v}$  symmetry.

$N$	Unique site	$\beta_{xyz}$	$\beta_{yyz}$	$\beta_{zzz}$	$\beta_{(z)}$	$\mu_{(z)}$	$\beta_{xyz}^{oct}$	$\beta_{yyz}^{oct}$	$\beta_{zzz}^{oct}$	$\beta_z^{dip}$
2	1	-1338	-686	-7468	-9492	2172	1681	3637	-1773	-5695
	2	-584	-693	21	-1256	1969				
	3	268	1756	4691	6715	-550	-3225	1234	662	4029
4	2	-28451	146	294	28011	2812	-68546	17244	17100	-16803
	3	11170	-5758	-234	5178	-3243	30403	-20381	-3341	3107

Note:  $N$  is the total ME number.  $C_{36}$  has three unique sites ( $S = 1, 2, 3$ ).  $\beta^{opt}$  and  $\beta^{dip}$  denote the octopolar and dipole parts contributed to the  $\beta$  tensor. The  $z$  axis is collinear to the  $z$  axis of the unsubstituted  $D_{6h}$   $C_{36}$  fullerene. The value  $\beta_{(z)}$  corresponds to the sum over components in the  $z$  direction.

Source: Adapted from [133].

one can determine the magnitude of  $\chi^{(3)}$ . It should be mentioned that the time-dependent behavior of the DFWM signal is related to the development and persistence of the grating and therefore provides information on the ultrafast physics of the material. The Z-scan technique [148] measures the real and imaginary parts of  $\chi^{(3)}$  simultaneously. This technique is based on the variation of transmitted radiation intensity by alteration of the geometrical parameters of the interaction region. This is achieved by gradually moving a sample along the Z-axis of propagation of a focused Gaussian beam through its focal plane and measuring the transmission of the sample for each Z position. As the sample experiences different electric field strength at different positions, the recording of the transmission as a function of the Z coordinate provides accurate information about the nonlinear effect present. In the ordinary OKE experiments the detected signal is proportional to the quadrate of  $\chi^{(3)}$ . One can only acquire the modulus of  $\chi^{(3)}$  which should be related to the excitation light because the imaginary component of  $\chi^{(3)}$  is determined by the absorption of the sample at the wavelength of the excitation light. In most cases, the real component of  $\chi^{(3)}$  is, in fact, more concerned since it is a more important parameter for the application in photonic devices. OHD-OKE determines the magnitudes and signs of  $\chi^{(3)}$  and this method greatly improves the signal-to-noise ratio of experimental data. In the CARS technique, one fits the dispersive lineshape caused by interference between the unknown nonlinearity and a Raman resonance of a standard like benzene. This CARS procedure is well accepted and has been shown to provide accurate values for  $\gamma$ . Details about CARS techniques can be found in [149].

Photonic applications, for example, data processing, eye and sensor protection, and all-optical switching, need molecules with large third-order optical nonlinearities [6–8, 10–15]. However, the  $\chi^{(3)}$  or  $\gamma$  magnitudes of most materials are usually smaller than those needed for photonic devices. Hence, searching for potential third-order NLO materials with large NLO response has been an interesting and important issue in physics, chemistry, and material science.

Quantum dots and conjugated  $\pi$ -electron organic systems (e.g., polydiacetylenes, polyacetylenes, and polythiophenes) have been shown to have large third-order optical nonlinearities [6–8, 12, 14, 150–161]. However, because of the overtones of high-energy C—H and O—H vibrations, those organic materials show strong absorption in the near-infrared region. Obviously, this would limit the application of organic materials in the infrared region, for example,

telecommunication. The advent of the technology for production of bulk quantities of fullerenes [31, 19–25] provides us another class of completely conjugated materials having quantum dot nature, a large number of delocalized  $\pi$  electrons. Since fullerenes are uniquely composed of carbon atoms, there is no C—H or O—H bond present in fullerenes. This implies that no absorption would be observed in the infrared region. On the other hand, the HOMO-LUMO energy gaps in fullerenes are narrower [162] than those in conjugated polymers. (The HOMO-LUMO energy gaps in conjugated polymers are broadened because of the conformations, polymer chain length distributions, and vibronic couplings to electronic levels.) Thus, fullerenes would exhibit narrower resonances. These novel features naturally make fullerenes appealing NLO materials for photonic applications and stimulate researchers all over the world to investigate the third-order optical nonlinearities of fullerenes. In the following, we review the experimental and theoretical studies on the third-order optical nonlinearities of  $C_{60}$ ,  $C_{70}$ , higher fullerenes, fullerene derivatives, and carbon nanotubes. The results are summarized in Tables 3–9. The NLO properties of doped carbon nanotubes are covered in our other chapter contributed to this edited book.

### 3.1. $C_{60}$

Blau et al. [163] were the first to measure the third-order optical nonlinearity of  $C_{60}$ . Although their measurement was found to have an error by more than three orders of magnitude for the final  $\gamma$  value [164, 165], their experiment did attract extensive studies of the third-order optical nonlinearities of  $C_{60}$ . As shown in Table 3 and Figure 5, which collect some of the reported optical susceptibilities  $\chi_{xxxx}^{(3)}$  and hyperpolarizability  $\gamma$  of  $C_{60}$  at a few selected wavelengths measured by DFWM, THG, and electric-field-induced second-harmonic generation (EFISHG), their error was quite indicative of the later development for obtaining the value  $\chi^{(3)}$  or  $\gamma$  of  $C_{60}$  [80, 103, 164–186]. From Table 3, we find that the third-order NLO responses are very sensitive to a great many experimental factors, for example, the incident laser power, pulse duration, the measurement techniques adopted, state of materials (sample preparation methods), and so on. Thus, it is very difficult for us to make a direct comparison of these experimental results obtained from different groups by different techniques. Surely, we see a reasonable agreement between the values measured by THG and EFISHG. From Figure 5, we

**Table 3.** Third-order optical nonlinearities of fullerenes ( $C_{60}$ ,  $C_{70}$ ,  $C_{76}$ ,  $C_{78}$ ,  $C_{84}$ ,  $C_{86}$ ,  $C_{90}$ ,  $C_{94}$ ,  $C_{96}$ ) measured by different experimental techniques.

Fullerenes	Wavelength [nm]	$\tau$	$\chi^{(3)}$ [ $10^{-14}$ esu]	$\gamma$ [ $10^{-36}$ esu]	Method	State of material	Ref.
$C_{60}$	532	70 ps	10	$(2.2 \pm 0.6) \times 10^5$	DFWM	solution	[230]
	356	50 ps	1500		THG	thin film	[172]
	405	50 ps	2100		THG	thin film	[172]
	494	50 ps	2700		THG	thin film	[172]
	497	0.5 ps	$-6.8 \pm 1.7$	$(-1.3 \pm 0.3) \times 10^4$	z-scan, DFWM	solution	[242]
	588	50 ps	2200		THG	thin film	[172]
	597	1.2 ps	38000		DFWM	thin film	[176]
	602	400 fs		$(1 \pm 0.2) \times 10^4$	DFWM	solution	[171]
		50 ps	1100		THG	thin film	[172]
	620	60 fs	22000		OKE	solution	[171]
	633	100 ps	20000		DFWM	thin film	[180]
	640	120 fs		$1.6 \times 10^5$	OKE	solution	[238]
	647	150 fs		$1.6 \times 10^5$	OKE	solution	[185]
		165 fs	$-27.5$		OHD-OKE	film	[247]
	675	1.2 ps	8200		DFWM	thin film	[176]
	686	50 ps	900		THG	thin film	[172]
	796	50 ps	450		THG	thin film	[172]
	810	120 fs		$<90$	OKE	solution	[188]
	816	13 ns	1322		THG	thin film	[83]
	825	13 ns	747		THG	thin film	[83]
	834	13 ns	1025		THG	thin film	[83]
	843	13 ns	723		THG	thin film	[83]
	850	10 ns	1500		THG	thin film	[166, 167]
	852	13 ns	1865		THG	thin film	[83]
	861	13 ns	1526		THG	thin film	[83]
	870	13 ns	1456		THG	thin film	[83]
	882	13 ns	1341		THG	thin film	[83]
	891	13 ns	1840		THG	thin film	[83]
	900	13 ns	1472		THG	thin film	[83]
	909	13 ns	2051		THG	thin film	[83]
	1022	13 ns	7148		THG	thin film	[83]
	1030	13 ns	7254		THG	thin film	[83]
	1039	13 ns	7253		THG	thin film	[83]
	1056	13 ns	7414		THG	thin film	[83]
	1064	35 ps	700		DFWM	thin film	[170]
		50 ps	$6 \times 10^6$		DFWM	solution	[163]
			330		DFWM	solid	[169]
			260	$1.6 \times 10^5$	DFWM	solution	[169]
		50 ps	1400		THG	thin film	[172]
			20000		THG	thin film	[80]
		10 ns	8200		THG	thin film	[166, 167]
		13 ns	8201		THG	thin film	[83]
		10 ns	7200	4700	THG	solution	[174]
		35 ps	700	300	DFWM	thin film	[182]
	1074	13 ns	8710		THG	thin film	[83]
	1083	13 ns	7632		THG	thin film	[83]
	1092	13 ns	7422		THG	thin film	[83]
1138	13 ns	6295		THG	thin film	[83]	
1158	13 ns	6727		THG	thin film	[83]	
1165	13 ns	7763		THG	thin film	[83]	
1177	13 ns	5122		THG	thin film	[83]	
1236	13 ns	5319		THG	thin film	[83]	
1245	13 ns	5091		THG	thin film	[83]	
1254	13 ns	5151		THG	thin film	[83]	
1263	13 ns	5385		THG	thin film	[83]	
1269	13 ns	5175		THG	thin film	[83]	
1278	13 ns	5751		THG	thin film	[83]	
1287	13 ns	5709		THG	thin film	[83]	
1291	13 ns	6000		THG	thin film	[83]	

continued

Table 3. Continued

Fullerenes	Wavelength [nm]	$\tau$	$\chi^{(3)}$ [ $10^{-14}$ esu]	$\gamma$ [ $10^{-36}$ esu]	Method	State of material	Ref.
	1296	13 ns	5736		THG	thin film	[83]
	1305	13 ns	5643		THG	thin film	[83]
	1323	13 ns	6072		THG	thin film	[83]
	1330	50 ps	3000		THG	thin film	[172]
		10 ns	6100		THG	thin film	[166, 167]
	1332	13 ns	5661		THG	thin film	[83]
	1344	13 ns	6030		THG	thin film	[83]
	1356	13 ns	6000		THG	thin film	[83]
	1368	13 ns	5817		THG	thin film	[83]
	1381	13 ns	5670		THG	thin film	[83]
	1413	13 ns	5676		THG	thin film	[83]
	1437	13 ns	5460		THG	thin film	[83]
	1456	13 ns	5610		THG	thin film	[83]
	1500	10 ns	3000	$(-1.3 \pm 0.8) \times 10^5$	THG	solution	[174]
	1815	50 ps	420		THG	thin film	[172]
	1907	13 ns	3242		THG	thin film	[83]
		13 ns	3200		THG	thin film	[168]
		13 ns	2218		THG	thin film	[240]
			2000		THG	thin film	[81]
	1910		1600	$(7.5 \pm 2) \times 10^2$	EFISHG	solution	[103]
		50 ps	900		THG	thin film	[172]
		10 ns	3200		THG	thin film	[166, 167]
		10 ns	2000		THG	thin film	[168]
	2000	10 ns	3700	$(1.6 \pm 0.8) \times 10^3$	THG	solution	[174]
	2373	50 ps	401		THG	thin film	[172]
	2380	50 ps	400		THG	thin film	[172]
$C_{70}$	532	70 ps	43	$(1.3 \pm 0.4) \times 10^6$	DFWM	solution	[230]
	597	12 ps	210000		DFWM	thin film	[176]
	633	100 ps	30000		DFWM	thin film	[180]
	647	150 fs		$4.7 \times 10^5$	OKE	solution	[185]
	675	1.2 ps	6400		DFWM	thin film	[176]
	799	13 ns	825		THG	thin film	[83]
	810	120 fs		500	OKE	solution	[243]
	816	13 ns	1132		THG	thin film	[83]
	825	13 ns	1252		THG	thin film	[83]
	834	13 ns	571		THG	thin film	[83]
	843	13 ns	636		THG	thin film	[83]
	852	13 ns	697		THG	thin film	[83]
	861	13 ns	1024		THG	thin film	[83]
	870	13 ns	568		THG	thin film	[83]
	882	13 ns	729		THG	thin film	[83]
	891	13 ns	1165		THG	thin film	[83]
	900	13 ns	1122		THG	thin film	[83]
	1013	13 ns	2974		THG	thin film	[83]
	1022	13 ns	2928		THG	thin film	[83]
	1039	13 ns	2881		THG	thin film	[83]
	1047	13 ns	2940		THG	thin film	[83]
	1056	13 ns	2558		THG	thin film	[83]
	1064	35 ps	1200		DFWM	thin film	[182]
		10 ns	560	$1.2 \times 10^6$	DFWM	solution	[175]
		10 ns	140000	$5.7 \times 10^4$	THG	solution	[174]
		13 ns	2600		THG	thin film	[99]
	1074	13 ns	2577		THG	thin film	[83]
	1129	13 ns	3584		THG	thin film	[83]
	1131	13 ns	3521		THG	thin film	[83]
	1138	13 ns	2569		THG	thin film	[83]
	1148	13 ns	3357		THG	thin film	[83]
	1158	13 ns	3861		THG	thin film	[83]
	1167	13 ns	4262		THG	thin film	[83]
	1177	13 ns	3657		THG	thin film	[83]

continued

Table 3. Continued

Fullerenes	Wavelength [nm]	$\tau$	$\chi^{(3)}$ [ $10^{-14}$ esu]	$\gamma$ [ $10^{-36}$ esu]	Method	State of material	Ref.
	1187	13 ns	3026		THG	thin film	[83]
	1216	13 ns	4740		THG	thin film	[83]
	1226	13 ns	4383		THG	thin film	[83]
	1247	13 ns	4344		THG	thin film	[83]
	1267	13 ns	1875		THG	thin film	[83]
	1278	13 ns	2895		THG	thin film	[83]
	1289	13 ns	5106		THG	thin film	[83]
	1300	13 ns	6663		THG	thin film	[83]
	1322	13 ns	6910		THG	thin film	[83]
	1333	13 ns	7056		THG	thin film	[83]
	1344	13 ns	6840		THG	thin film	[83]
	1368	13 ns	8307		THG	thin film	[83]
	1378	13 ns	6579		THG	thin film	[83]
	1390	13 ns	7649		THG	thin film	[83]
	1401	13 ns	8970		THG	thin film	[83]
	1413	13 ns	7587		THG	thin film	[83]
	1420	10 ns	9000		THG	thin film	[99]
	1425	13 ns	7157		THG	thin film	[83]
	1437	13 ns	7776		THG	thin film	[83]
	1449	13 ns	8292		THG	thin film	[83]
	1500	10 ns	5400	22000	THG	solution	[174]
	1907	13 ns	2428	$(1.1 \pm 0.1) \times 10^4$	THG	thin film	[83]
	1910		4400	$(1.3 \pm 0.3) \times 10^3$	EFISHG	solution	[103]
		10 ns	2400		THG	thin film	[99]
	2000	10 ns	9100	-3800	THG	solution	[174]
C <sub>76</sub>	532	70 ps	$28 \pm 10$	$(0.8 \pm 0.3) \times 10^6$	DFWM	solution	[230]
C <sub>78</sub>	532	70 ps	$55 \pm 10$	$(1.5 \pm 0.3) \times 10^6$	DFWM	solution	[230]
C <sub>84</sub>	532	70 ps	$39 \pm 10$	$(1.2 \pm 0.3) \times 10^6$	DFWM	solution	[230]
	647	150 fs		$5.2 \times 10^5$	OKE	solution	[185]
C <sub>86</sub>	532	70 ps	$49 \pm 15$	$(1.3 \pm 0.5) \times 10^6$	DFWM	solution	[230]
C <sub>90</sub>	532	70 ps	$72 \pm 20$	$(1.8 \pm 0.6) \times 10^6$	DFWM	solution	[229, 230]
C <sub>94</sub>	532	70 ps	$60 \pm 20$	$(1.9 \pm 0.6) \times 10^6$	DFWM	solution	[230]
C <sub>96</sub>	532	70 ps	$67 \pm 20$	$(2.1 \pm 0.6) \times 10^6$	DFWM	solution	[230]

Note:  $\lambda$  and  $\tau$  are the wavelength and pulse duration of the laser source, respectively.

Source: Some data are adapted from H. S. Nalwa [13], R. H. Xie [33], F. Kajzar et al. [83], K. C. Rustagi et al. [231], and V. P. Belousov et al. [232].

see two interesting features observed from the wavelength ( $\lambda$ )-dispersed  $\chi^{(3)}$  spectrum for C<sub>60</sub>: (i) strong resonances in  $\chi^{(3)}$  with two peaks at 1064 nm and 1210 nm; (ii) a sharp decrease of  $\chi^{(3)}$  at shorter wavelength. The three-level

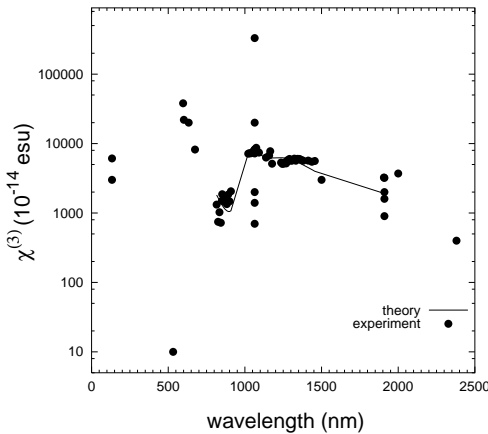


Figure 5. Wavelength dependence of the third-order nonlinear optical susceptibility  $\chi^{(3)}$  ( $-3\omega; \omega, \omega, \omega$ ) in C<sub>60</sub>. Solid line is the calculated results of Kajzar et al. [83] within three-level model, and “•” denotes the experimental values of C<sub>60</sub> films or solutions listed in Table 3.

model proposed Kajzar et al. [83] showed that the resonance observed at 1064 nm is a three-photon resonance with  $T_{1u}$  state of C<sub>60</sub>. Since several states lie in the gap between 2.3 eV (537 nm) and 2.5 eV (494 nm), a one-photon transition is forbidden. Hence, the resonance observed at 1210 nm comes from a two-photon resonance [83]. The theoretical calculations of Kajzar et al. [83], as shown in Figure 5, agree very well with most of the experimental values. In spite of the obvious discrepancy for the  $\chi^{(3)}$  or  $\gamma$  value of C<sub>60</sub> in different experimental groups, most recent experiments have demonstrated that the third-order optical nonlinearity of C<sub>60</sub> has a small value [187, 188]: the lower limit of  $\gamma$  is  $3.7 \times 10^{-35}$  esu measured by nondegenerate four-wave mixing [187], while the upper limit of  $\gamma$  is  $9.0 \times 10^{-35}$  esu determined by the femtosecond optical Kerr effect (OKE) [188]. The second hyperpolarizability  $\gamma$  of C<sub>60</sub> has been studied extensively also by theoretical methods and the results are summarized in Table 4. As seen from Table 4 also among the theoretical results there is a large spread of the result. However, if one considers the first-principles methods, such as *ab initio* Hartree Fock and density functional theory, the results are more consistent. The low value of  $\gamma$  for C<sub>60</sub> is confirmed by first-principles calculations [129, 181, 189, 190], although the experimental results tend in general to



**Table 4.** Second-order hyperpolarizabilities  $\gamma$  of  $C_{60}$  calculated by different theoretical techniques.

Technique	Wavelength [nm]	Process	$\gamma$ ( $10^{-36}$ esu)	Ref.
INDO-TDHF	$\infty$	static	29.7	[171]
INDO-TDHF	1370	OKE	30.2	[171]
INDO-TDHF	1370	EFISH	32.9	[171]
INDO-TDHF	1370	DFWM	33.1	[171]
MNDO/PM3-FF	$\infty$	static	35.9	[179]
LDA-FF	$\infty$	static	15.9	[193]
LDA-FF	$\infty$	static	42.0	[194]
VEH-SOS	$\infty$	static	204.1	[218, 219]
Tight-binding	$\infty$	static	17580	[195]
PPP-TDHF	$\infty$	static	95.6	[196]
PPP-TDHF	$\infty$	static	24.7	[197]
PPP-TDHF	1880	EFISH	29.7	[197]
PPP-TDHF	1879	THG	37.2	[198]
PPP-TDHF	1320	EFISH	37.8	[197]
PPP-TDHF	1320	THG	68.9	[198]
PPP-TDHF	1060	EFISH	51.9	[197]
PPP-TDHF	1060	THG	295.6	[198]
LDA	$\infty$	static	60.0	[199]
Coupled HF	$\infty$	static	8.4	[200]
Tight-binding	$\infty$	static	13.8	[201]
Tight-binding	$\infty$	static	3048	[124]
PPP-FF	$\infty$	static	28.6	[202]
PPP-SOS	$\infty$	static	115.8	[202]
PPP/MP2-F	$\infty$	static	35.22	[202]
Hückel	$\infty$	static	2491.2	[202]
Spherical shell	$\infty$	static	-260.0	[212]
CNDO/S-SOS	$\infty$	static	3276.6	[203]
CNDO/S-SOS	1900	THG	3564.6	[203]
CNDO/S-SOS	1830	THG	3589.2	[203]
CNDO/S-SOS	1320	THG	3928.8	[203]
CNDO/S-SOS	1064	THG	4393.2	[203]
INDO/SCI-SOS	1064	DFWM	5304	[177]
INDO/SDCI-SOS	1064	DFWM	4380	[177]
INDO/SDCI-SOS	532	DFWM	1866	[177]
INDO/SDCI-SOS	1910	EFISH	4140	[177]
LDA-RPA	$\infty$	static	29.4	[204]
CNDO/S-SOS	$\infty$	static	458	[220]
AM1/Valence-FF	$\infty$	static	24.7	[217]
AM1-FF	$\infty$	static	122.4	[205, 228]
HF-SOMO	$\infty$	static	154.6	[221]
LDA-TDDFT	$\infty$	static	44.0	[189]
LB94-TDDFT	$\infty$	static	33.0	[189]
LB94-TDDFT	830	OKE	40.1	[189]
LB94-TDDFT	1910	EFISH	36.2	[189]
HF-RPA	$\infty$	static	57.3	[186]
HF-RPA	$\infty$	static	55.0	[181]
AM1-FF	$\infty$	static	160.6	[206]
SSH-SOS	$\infty$	static	560	[213]
SSH-SOS	$\infty$	static	164	[233]
MNDO-FF	$\infty$	static	29.4	[207]
MNDO-SOS	$\infty$	static	46.1	[207]
NDDO/PM3-FF	$\infty$	static	32.4	[207]
NDDO/PM3-SOS	$\infty$	static	47.8	[207]
NDDO/AM1-FF	$\infty$	static	25.8	[207]
NDDO/AM1-SOS	$\infty$	static	44.25	[207]
HF/STO-3G-FF	$\infty$	static	8.0	[192]
HF/6-31G-FF	$\infty$	static	10.6	[192]
CNDO/S-SOS	$\infty$	static	804.6	[208]
CNDO/S-SOS	1900	THG	877.8	[208]

continued

**Table 4.** Continued

Technique	Wavelength [nm]	Process	$\gamma$ ( $10^{-36}$ esu)	Ref.
CNDO/S-SOS	1830	THG	884.4	[208]
CNDO/S-SOS	1320	THG	972.0	[208]
CNDO/S-SOS	1064	THG	1093.2	[208]
LDA-TDDFT	$\infty$	static	62.5	[190]
LDA-TDDFT	830	OKE	73.0	[190]
LDA-TDDFT	1064	DFWM	80.08	[190]
LDA-TDDFT	1910	EFISH	67.5	[190]
LDA-TDDFT	2380	THG	69.5	[190]
BLYP-TDDFT	$\infty$	static	76.6	[190]
BLYP-TDDFT	830	OKE	91.2	[190]
BLYP-TDDFT	1064	DFWM	99.2	[190]
BLYP-TDDFT	1910	EFISH	83.6	[190]
BLYP-TDDFT	2380	THG	85.6	[190]
LB94-TDDFT	$\infty$	static	47.5	[190]
LB94-TDDFT	830	OKE	55.4	[190]
LB94-TDDFT	1064	DFWM	59.9	[190]
LB94-TDDFT	1910	EFISH	51.4	[190]
LB94-TDDFT	2380	THG	52.9	[190]
INDO/SDCI-SOS	$\infty$	static	1068	[209]
INDO/SDCI-SOS	1064	DFWN	4914	[209]
INDO/SDCI-SOS	1064	EFISH	14892	[209]
INDO/SDCI-SOS	1064	THG	7068	[209]
INDO/SDCI-SOS	1910	DFWN	3666	[209]
INDO/SDCI-SOS	1910	EFISH	7914	[209]
INDO/SDCI-SOS	1910	THG	1512	[209]
LDA-TDDFT	$\infty$	static	69.48	[129]

be larger than the theoretical results. A direct comparison between experiments and theoretical predictions is difficult due to the presence of medium effects; that is, the experimental results refer to condensed phase whereas the theoretical results usually are for the gas phase. Luo et al. [191] showed that by carefully considering the intermolecular interaction and local-field corrections on the nonlinear optical properties of  $C_{60}$ , a good agreement with experiment could be obtained if care was taken to select experimental results without significant resonant contributions. Also, the vibrational contributions to the nonlinear optical properties of isolated  $C_{60}$  have been studied and shown to be significant for certain processes [192]. In Section 3.2, we shall see that a strong enhancement on third-order optical nonlinearity, for example, an increase from several tens to 100 times on the  $\gamma$  value, was even observed as  $C_{60}$  was chemically modified to form a charge-transfer complex [103, 188] or was chemically reduced to anions [210, 211].

### 3.2. $C_{70}$ and Higher Fullerenes

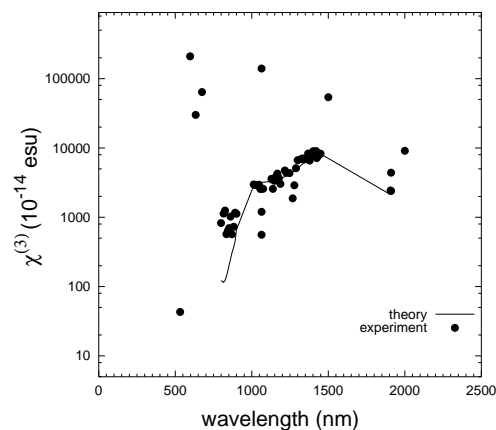
Compared with the  $C_{60}$  molecule, higher fullerenes have attracted less attention on their third-order optical nonlinearities. One reason is that large amounts of higher fullerenes are not available. That is also why the synthesis and isolation of higher fullerenes is still an active research field. Theoretical calculations [178, 179, 181, 212–228] and a few experimental results [103, 174–176, 180, 182, 185, 229, 230] have shown that higher fullerenes possess larger third-order optical nonlinearity than  $C_{60}$ .  $C_{70}$ , the most easily purified higher fullerene, was experimentally proven to have a  $\gamma$

**Table 5.** Static second-order hyperpolarizabilities  $\gamma$  of higher fullerenes calculated by different theoretical techniques.

Molecule	$\gamma$ ( $10^{-36}$ esu)	Technique	Ref.
$C_{70}$	67.8	MNDO/PM3-FF	[179]
	893.7	VEH-SOS	[218, 219]
	-390	Spherical shell	[212]
	4968	INDO/SDCI-SOS	[178]
	857	CNDO/S-SOS	[220]
	54.4	AM1/valence-FF	[217]
	170.1	AM1-FF	[205, 228]
	640	SSH-SOS	[213]
	294.5	HF-SOMO	[221]
	1050	SSH-SOS	[233]
	75.4	HF-RPA	[181]
	60.9	NDDO/PM3-FF	[207]
	461.1	NDDO/PM3-SOS	[207]
	49.8	NDDO/AM1-FF	[207]
	447.8	NDDO/AM1-SOS	[207]
	2664	INDO/SDCI-SOS	[209]
$C_{76}$	1213	CNDO/S-SOS	[220]
	368.1	HF-SOMO	[221]
$C_{78}(D_3)$	361.9	HF-SOMO	[221]
	681	SSH-SOS	[233]
	185.0	AM1-FF	[205, 228]
$C_{78}(C_{2v}(1))$	327.7	AM1/valence-FF	[236]
	369.9	HF-SOMO	[221]
	2034	SSH-SOS	[233]
$C_{78}(C_{2v}(2))$	206.4	AM1-FF	[205, 228]
	406.9	AM1/valence-FF	[236]
	440.7	HF-SOMO	[221]
$C_{78}(D_{3h}(1))$	507	SSH-SOS	[233]
	186.8	AM1-FF	[205, 228]
	336.1	AM1/valence-FF	[236]
	480	SSH-SOS	[233]
$C_{78}(D_{3h}(2))$	220.4	AM1-FF	[205, 228]
	489.7	AM1/valence-FF	[236]
	2096	SSH-SOS	[233]
$C_{84}(D_2)$	177.4	AM1-FF	[205, 228]
	316.92	AM1/valence-FF	[236]
	1812	CNDO/S-SOS	[220]
	63.5	AM1/valence-FF	[217]
$C_{84}(D_{2d})$	202.2	AM1-FF	[205, 228]
	426.9	HF-SOMO	[221]
	82.4	HF-RPA	[181]
	1800	CNDO/S-SOS	[220]
$C_{100}$	57.5	AM1/valence-FF	[217]
	198.1	AM1-FF	[205, 228]
	460.6	HF-SOMO	[221]
	879.6	HF-SOMO	[221]

Source: Some data are adapted from [33].

magnitude of 1.6 to 3 times that of  $C_{60}$  [103, 174–176, 180, 182, 185]. Tables 3 and 5 list the third-order nonlinear optical susceptibilities  $\chi^{(3)}$  of  $C_{70}$  and higher fullerenes studied by different experimental or theoretical techniques. In the following, we briefly review recent theoretical and experimental studies on the third-order optical nonlinearities of higher fullerenes. Other reviews on the nonlinear optical properties of fullerene (mainly  $C_{60}$  and  $C_{70}$  molecules) are also available in the literature; see Nalwa [13], Xie [33], Kajzar et al. [83], Rustagi et al. [231], and Belousov et al. [232].



**Figure 6.** Wavelength dependence of the third-order nonlinear optical susceptibility  $\chi^{(3)}(-3\omega; \omega, \omega, \omega)$  in  $C_{70}$ . Solid line is the calculated results of Kajzar et al. [83, 99] within three-level model, and “•” denotes the experimental values of  $C_{70}$  films or solutions listed in Table 3.

### 3.2.1. Experimental Measurements

Neher et al. [174] measured the optical susceptibilities  $\chi^{(3)}$  of  $C_{70}$  at 1064 nm, 1500 nm, and 2000 nm by THG in a toluene solution. Compared with  $C_{60}$ ,  $C_{70}$  exhibits enhanced third-order optical nonlinearity. In particular, a strong effect with  $\gamma$  exceeding  $5 \times 10^{-32}$  esu was observed in the three-photon resonant regime, and a negative real hyperpolarizability in  $C_{70}$  and a positive  $\gamma$  for  $C_{60}$  were found in the nonresonant measurements. Later on, Kajzar et al. [83, 99] reported a broad THG spectrum for  $C_{70}$ . The overall THG spectrum shows a broad resonance enhancement in  $\chi^{(3)}$  with a maximum value of  $\chi^{(3)} = (0.9 \pm 0.1) \times 10^{-10}$  esu located at 1420 nm and a dramatic decrease at short wavelengths [83, 99].

Yang et al. [175] measured for the first time the third-order NLO susceptibility of  $C_{70}$  in a toluene solution by the DWM technique using 10-ns laser pulses at 1064 nm. The third-order nonlinear optical susceptibility  $\chi^{(3)}$  is determined to be  $5.6 \times 10^{-12}$  esu for a  $C_{70}$  toluene solution at a concentration of 0.476 g/l. Later on, Flom et al. [176], Lindle et al. [182], and Rosker et al. [180] performed time-resolved DFWM measurement on the third-order optical nonlinearities of  $C_{70}$  film using a picosecond laser pulse.  $C_{70}$  was found to exhibit a two-photon resonantly enhanced third-order optical response [182]. The dynamics of  $C_{70}$  shows wavelength and fluence dependence [176]. To our interest, at high laser intensities, their experiment showed a fifth-order component to the NLO signal due to a two-photon excited-state transient grating [182].

Wang and Cheng [103] determined the optical susceptibility  $\chi^{(3)}$  of  $C_{70}$  by EFISHG measurements with 1910-nm radiation. The optical nonlinearities of  $C_{70}$  are comparable to those of linearly conjugated organics with due consideration to molecular size [103].

In Figure 6, we show the wavelength dependence of  $\chi^{(3)}$  for  $C_{70}$ . Similar to  $C_{60}$ , the  $C_{70}$  spectrum exhibits several interesting features: (i) a sharp decrease of  $\chi^{(3)}$  at shorter wavelength; (ii) strong resonance enhancement in  $\chi^{(3)}$  at 1410 nm; (iii) a shoulder around 1064 nm. Based on the three-level model proposed by Kajzar et al. [83, 99], the

observed resonance at 1410 nm is caused by a three-photon resonance with a one-photon allowed transition lying at 470 nm, while the shoulder at 1064 nm is due to a two-photon resonance.

Sun et al. [185] were the first to measure the third-order optical nonlinearity of  $C_{84}$  by using the time-resolved OKE technique with 150-fs laser pulse at 647 nm. A large instantaneous NLO response was observed for  $C_{84}$ . In comparison with  $C_{60}$  and  $C_{70}$ , the  $\gamma$  value of  $C_{84}$  is enhanced a little. Such small accretion of the optical Kerr response of  $C_{84}$  is due to the sample impurity. The experiment of Huang et al. [229] indicated that a purity of  $C_{84}$  is higher than 85%, but the impurities include  $C_{78}$ ,  $C_{82}$ ,  $C_{86}$ , and  $C_{90}$ .

Recently, Yang and his co-workers [229] have made DFWM measurements on the third-order optical nonlinearities of  $C_{90}$  (>97% purity) at 532 nm. The second-order hyperpolarizability  $\gamma$  of  $C_{90}$  is determined to be  $(1.8 \pm 0.6) \times 10^{-30}$  esu, while the  $\gamma$  value of  $C_{60}$  was  $(2.2 \pm 0.6) \times 10^{-31}$  esu. This shows the enhanced third-order optical nonlinearity of  $C_{90}$ , which is actually expected since there are more highly delocalized  $\pi$ -conjugated electrons over the spherical-like surface in  $C_{90}$  compared to  $C_{60}$ . Moreover, Yang and his co-workers [230] have systematically studied the third-order NLO response of other higher fullerenes including  $C_{76}$ ,  $C_{78}$ ,  $C_{84}$ ,  $C_{86}$ ,  $C_{94}$ , and  $C_{96}$  by using 70-ps laser pulses at 532 nm under optimized experimental conditions. The experimental  $\gamma$  or  $\chi^{(3)}$  are listed in Table 3. In general, the eightfold increase in the  $\gamma$  values from  $C_{60}$  to  $C_{96}$  is consistent with the trend predicted by theory [220–227]. But the theoretical predicted increase trend is somewhat lower than the measured one. This implies that the existence of other important factors (e.g., geometrical structure,  $\pi$ - $\pi$  overlap discussed above, resonance enhancement, etc.) contributed to the increased  $\gamma$  values for higher fullerenes.

### 3.2.2. Theoretical Calculations

Shuai and Bredas [218, 219] used the valence-effective-Hamiltonian (VEH) method to investigate the electronic structures of  $C_{60}$  and  $C_{70}$  and applied the VEH sum-over-state (SOS) approach to study the third-order NLO response of  $C_{60}$  and  $C_{70}$ . Their calculations are fully consistent with the EFISHG [103], THG [103], and DFWM [165, 170] measurements, but about three to four orders of magnitude lower than the data reported by Blau et al. [163] and Yang et al. [175]. The lowest two-photon and three-photon resonances in  $C_{70}$  were observed at almost the same frequencies for  $C_{60}$  due to the symmetry [218, 219].

Extensive theoretical studies have shown that the second-order hyperpolarizabilities  $\gamma$  of higher fullerenes scale with the mass of the all-carbon molecule [212, 216, 220–227]. The free-electron gas model proposed by Knize [212] showed that the  $\gamma$  value of higher fullerene increases as the cube of the number of carbon atoms [212]. Using the SOS-INDO/CI approach [220] or sum-over-molecular-orbitals (SOMO) approach, Fanti et al. [220, 221] found that the second-order hyperpolarizabilities of fullerenes are a nonlinear function of the number of carbon atoms. Later on, the extended Su–Schrieffer–Heeger model proposed by Xie and his co-workers [222, 223] indicated that the static  $\gamma$  values of armchair and zigzag tubular fullerenes of small size

scale with about three power of the number of carbon atoms. Using the SOS method, Harigaya [224–227] predicted that the off-resonant third-order NLO susceptibilities of higher fullerenes are nearly proportional to the fourth power of the carbon number when the on-site Coulomb repulsion is  $2t$  or  $4t$ ,  $t$  being the nearest-neighbor hopping integral. The work of both Xie et al. [222, 223] and Harigaya [224–227] has demonstrated the important roles of Coulomb interactions in higher fullerenes. Luo [216] pointed out that if  $C_{60}$  is excluded, a perfect power law dependence of the  $\gamma$  value on the number  $N$  of carbon atoms can be observed [216]:  $\gamma = 1.1 \times 10^{-4} N^{2.4}$  for the data of Fanti et al. [221], and  $\gamma = 3.2 \times 10^{-2} N^{0.75}$  for the data of Jonsson et al. [181]. Luo's work [216] reflected one important issue that  $C_{60}$  has the most exceptional electron localization among all fullerenes.

The  $C_{78}$  molecule has five topologically distinct structures: two with  $C_{2v}$  symmetry, two with  $D_{3h}$  symmetry, and one with  $D_3$  symmetry. Using the SOS method, Wan et al. [233] demonstrated numerically that molecular symmetry and the arrangement of atoms have great effect on the  $\gamma$  values of five isomers of  $C_{78}$ . From a geometric point of view, Moore et al. [217, 228] analyzed the static  $\gamma$  values of  $C_{60}$ ,  $C_{70}$ , five isomers of  $C_{78}$ , and two isomers of  $C_{84}$  in terms of the geometry symmetry (characterized by the molecular group order), aromaticity (characterized by the selection of six-member rings determined from the analysis of bond lengths), and molecular size (characterized by maximum interatomic distance and surface areas) by using the finite field method (FF), a semiempirical Hamiltonian, and molecular structures obtained from density functional theory calculations. The  $\gamma$  value is affected by a combination of the number of aromatic rings, length, and group order, in decreasing importance.

Based on the random phase approximation (RPA), Jonsson et al. [181] calculated the static  $\gamma$  values of  $C_{60}$ ,  $C_{70}$ , and  $C_{84}$ , which are determined to be 55.0, 75.4, and  $82.4 \times 10^{-36}$  esu, respectively.

An important factor governing the optical nonlinearity is the extended delocalized  $\pi$ -electron cloud along the effective conjugation length or sphere of the  $\pi$ -conjugated system. Recently, Lin et al. [235] have demonstrated the crucial role of  $\pi$ - $\pi$  overlap in determining the second-order hyperpolarizability  $\gamma$  in the  $\pi$ -conjugated framework, for example, by taking the semiempirical Austin model 1 (AM1) quantum chemical calculations on various isomers of higher fullerenes. For different isomers of the same mass of fullerene, different curvatures are exhibited and indicate that the  $\pi$ - $\pi$  overlaps are different among the isomeric fullerenes. Table 6 summarizes the orientationally averaged second-order hyperpolarizability  $\bar{\gamma}$  and the averaged pyramidalization angle  $\bar{\theta}_p$  which describes the deviation from the planar  $sp^2$  carbon and is defined as  $\theta_{\sigma\pi} - \pi/2$  ( $\theta_{\sigma\pi} = \pi/2$  for planar  $sp^2$  carbons and  $0.608\pi$  for tetrahedral  $sp^3$  centers). For isometric fullerenes of the same mass, they found an excellent correlation between  $\bar{\gamma}$  and  $\bar{\theta}_p$ :  $\bar{\gamma}$  decreases with the increase of  $\bar{\theta}_p$ . Hence, a minor change of average  $\pi$ - $\pi$  overlaps in fullerenes has a large effect on the average second-order hyperpolarizability.

Table 5 collects the static  $\gamma$  values of some fullerenes calculated by different theoretical techniques. A direct comparison between these theoretical results shows significant

**Table 6.** The averaged second-order hyperpolarizability ( $\bar{\gamma} = (\gamma_{xxxx} + \gamma_{yyyy} + \gamma_{zzzz} + 2(\gamma_{xxyy} + \gamma_{xxzz} + \gamma_{yyzz}))/5$ , in  $10^{-36}$  esu) and the averaged pyramidalization angle  $\bar{\theta}_p = \sum \theta_p/n$ , where  $n$  is the total number of carbon atoms, for the isolated-pentagon rule isomers of higher fullerenes.

Fullerene	Symmetry	$\bar{\gamma}$ ( $10^{-36}$ esu)	$\bar{\theta}_p$
$C_{76}$	$T_d$	120.5	$0.0576\pi$
	$D_2$	55.3	$0.0580\pi$
$C_{78}$	$D_{3h}(1)$	81.6	$0.0568\pi$
	$C_{2v}(1)$	67.8	$0.0570\pi$
	$C_{2v}(2)$	56.1	$0.0573\pi$
	$D_3$	54.6	$0.0574\pi$
	$D_{3h}(2)$	52.8	$0.0576\pi$
$C_{80}$	$C_s$	205.3	$0.0562\pi$
	$C_{2v}$	122.5	$0.0564\pi$
	$D_2$	58.6	$0.0567\pi$
	$D_{5d}$	56.6	$0.0569\pi$

Source: Adapted from [235].

differences. All of the SOS approaches give a second-order hyperpolarizability, which is about an order of magnitude larger than that predicted by the *ab initio* calculations. This discrepancy arises from the truncation of the expansion in excited states in the explicit summation of contributions to  $\gamma$  in SOS calculations [181]. In contrast, the  $\gamma$  values obtained in the FF methods [179, 217] are of the same order of magnitude. The described problems are absent in the analytical RPA approach [181]. On the other hand, all above theoretical studies do not consider the screening effect induced by electron-electron interaction (in time-dependent density functional theory this is to some extent taken into account). Actually, the screening effect should be considered since the polarization of the electron cloud can modify the charge density and therefore the self-consistent potential seen by each electron. Detailed analysis of the screen effect is expected.

### 3.3. Fullerene Derivatives

Fullerenes, for example,  $C_{60}$ ,  $C_{70}$ , and  $C_{82}$ , are well-known electron acceptors and thus they easily form charge-transfer complexes, or say, fullerene derivatives, with other organic groups or metal, for example, complex formed by  $C_{60}$  and polymers matrix, or trapping metal to  $C_{82}$ . Over the past 10 years, third-order optical nonlinearities of fullerene derivatives have been studied by different research groups and different experimental techniques, for example, coherent anti-Stokes Raman spectroscopy (CARS) analysis technique, optical Kerr effect (OKE), THG, DFWM, z-scan, optically heterodyned OKE (OHD-OKE). It has been demonstrated that fullerene derivatives, due to the charge transfer, do exhibit enhanced third-order optical nonlinearities at nanosecond or picosecond scales [188, 210, 211, 237–252]. The third-order optical nonlinearities of some representative fullerene derivatives are summarized in Table 7. It is seen that the chemical-modified fullerenes all exhibit enhancement on their third-order optical nonlinearities compared to small host fullerene molecules. The enhancement is greatly influenced by the measuring wavelength and pulse duration. The negative or positive  $\chi^{(3)}$  or  $\gamma$  can be understood as follows. There are two terms in the sum-over-states representation of the nonlinearity  $\gamma_{ijkl}$  [253]: the first one representing

four-wave mixing pathways which involve two-photon transitions to or between excited electronic states, and the second one describing pathways which involve transitions that return to the ground state. The final value of  $\chi^{(3)}$  or  $\gamma$  depends on the interference between the two terms. If the first term dominates,  $\chi^{(3)}$  or  $\gamma$  will be positive; they will be negative if the second term dominates.

Lascola and Wright [210, 211] determined the second-order molecular hyperpolarizability  $\gamma$  for the charged species,  $C_{60}^-$ ,  $C_{60}^{2-}$ , and  $C_{60}^{3-}$ , by using CARS vibrational line-shape analysis. Their measured  $\gamma$  values for those charged molecules are larger than that of the neutral  $C_{60}$  and are comparable to values of highly conjugated organic polymers, for example, polydiacetylene. Heflin et al. [237], Gu et al. [239], Campbell et al. [242], Mavritsky et al. [254], Qian et al. [247], and Huang et al. [245] have reported  $\chi^{(3)}$  measurement of metal-containing endohedral or exohedral fullerenes, for example,  $Er_2@C_{82}$  [237] by DFWM at 1064 nm,  $DyC_{82}$  by DFWM at 532 nm,  $LiC_{60}$  by z-scan DFWM at 497 nm,  $(Ph_3P)_2PtC_{60}$  [254] by time-resolved z-scan technique at 527.5 nm,  $C_{60}M_2$  ( $M = Pd, Pt, Sm$ ) by OHD-OKE at 647 nm, and  $CuPc-C_{60}$  by OKE at 830 nm all obtaining enhanced third-order optical nonlinearity compared to that of pristine fullerene. Recently, Wang et al. [251] have investigated the third-order optical nonlinearities of iron(III) and ruthenium(III) derivatives of organofullerene with ultrafast optical Kerr gate technique at 830 nm indicating that the electron-deficient metal ion iron(III) blocked charge transfer from the organic group to  $C_{60}$  and reduced the optical nonlinearity, while a ruthenium(III) compound, due to the chloro-bridge built by the remaining un-coordinate orbits of ruthenium ions, showed strongly enhanced optical nonlinearity. These measured results suggested that increased charge on the cage, and not asymmetric charge distribution due to metal-cage interactions, is the primary reason for increased nonlinearity, encouraging implications for the use of charge transfer and endohedral or exohedral fullerene complexes in future photonic devices.

The serial work of Gong's group [188, 243, 248, 250] showed the following order of the nonresonant  $\gamma$  value for  $C_{60}$ - or  $C_{70}$ -derived molecules:  $C_{60} < C_{60}(NH_2CN)_5 < C_{60}((NH_2)_2CNCN)_5$  and  $C_{70} < C_{70}(NH_2CN)_5 < C_{70}((NH_2)_2CNCN)_5$ . This trend indicates that the enhancement of the third-order optical nonlinearity is proportional to the increase of charge-transfer strength. This is a very important rule for us to design and synthesize new molecules for third-order optical nonlinear applications.

The fabrication of stable and efficient NLO molecules is an interesting challenge because of a large class of possible applications of these molecules. Controlled transfer multilayered structures do offer an alternative solution, well argued by the controlled fabrication and expected enhancement stability. The work of Kajzar et al. [240], Gong et al. [238], and Koudoumas et al. [249] confirmed this point by measuring the nonlinear optical properties of  $C_{60}$ -based composites and multilayered charge-transfer structures with 5,10,20-tetraphenyl-21*H*,23*H*-porphine (TPP) and 5,6,11,12-tetraphenylnaphthacene (rubrene) (TPN), poly tetrahydrofurfuryl methacrylate (PTHFMA), and

**Table 7.** The third-order optical nonlinearities of fullerene derivatives.

Material	Method	$\lambda$ [nm]	$\tau$	State of material	$\chi^{(3)}$ [ $10^{-14}$ esu]	$\gamma$ [ $10^{-36}$ esu]	Ref.
$C_{60}$	CARS			solution		$2400 \pm 1000$	[210]
$C_{60}^2$	CARS			solution		$4000 \pm 1000$	[211]
$C_{60}^3$	CARS			solution		$7600 \pm 500$	[211]
$C_{60}Pt_2$	OHD-OKE	647	165 fs	film	-49		[247]
$C_{60}Pd_2$	OHD-OKE	647	165 fs	film	-78		[247]
$C_{60}Sm_2$	OHD-OKE	647	165 fs	film	-260		[247]
$Li@C_{60}$	DFWM	497	0.5 ps	solution	$7.0 \pm 1.8$	$(-18.0 \pm 4.5) \times 10^4$	[242]
TPN: $C_{60}$ multilayer	THG	1907	13 ns	film	665		[240]
TPN: $C_{60}$ composite	THG	1907	13 ns	film	464		[240]
TPP: $C_{60}$ multilayer	THG	1907	13 ns	film	774		[240]
TPP: $C_{60}$ composite	THG	1907	13 ns	film	1157		[240]
Poly- $C_{60}$	THG	1907	13 ns	film	4777		[240]
$C_{60}:O_2$	THG	1907	13 ns	solution	4598		[240]
$C_{60}$ -poly-aminonitrile	OKE	810	120 fs	solution		3200	[188]
$C_{60}(NH_2CN)_5$	OKE	830	120 fs	solution	5.8	10000	[250]
$C_{60}[(NH)_2CNCN]_5$	OKE	830	120 fs	solution		35000	[250]
$C_{60}/Fe1$	OKE	830	120 fs	solution	3.3	7200	[251]
$C_{60}/Fe2$	OKE	830	120 fs	solution		25000	[251]
$C_{60}/Ru1$	OKE	830	120 fs	solution		240000	[251]
$C_{60}/Ru2$	OKE	830	120 fs	solution		650000	[251]
$C_{60}/Si$	OKE	820	200 fs	sol	14		[269]
$C_{60}/Si$	OKE	820	200 fs	gel	16		[269]
$C_{60}/\gamma$ -CD (1 day)	Z-scan	532	10 ns	solution		$1.3 \times 10^6$	[244]
$C_{60}/\gamma$ -CD (3 days)	Z-scan	532	10 ns	solution		$2.86 \times 10^7$	[244]
$C_{60}/\gamma$ -CD (7 days)	Z-scan	532	10 ns	solution		$5.07 \times 10^7$	[244]
$CuPc-C_{60}$	OKE	830	120 fs	solution		540000	[245]
$C_{60}$ -TTF- $\alpha$	DFWM	532	ps	solution	340		[252]
$C_{60}$ -TTF- $\beta$	DFWM	532	ps	solution	530		[252]
$C_{60}$ -( $PS$ ) <sub>6</sub> (900 Da)	OKE	800	100	solution		240000	[249]
$C_{60}$ -( $PS$ ) <sub>6</sub> (17800 Da)	OKE	800	100	solution		88000	[249]
$C_{60}$ -( $PS$ ) <sub>6</sub> (4800 Da)	OKE	800	100	solution		66000	[249]
$C_{60}$ -PTHFMA	OKE	640	fs	solution		$8.9 \times 10^5$	[238]
MTMDA- $C_{60}$	DFWM	532	15 ns	solution	53.9	248000	[241]
$C_{60}$ ( <i>biphenyl</i> ) <sub>x=3-7</sub>	Z-scan			solution	$2.3 \times 10^9$		[246]
$C_{70}$ -poly-aminonitrile	OKE	810	120 fs	solution		16000	[243]
$C_{70}(NH_2CN)_5$	OKE	810	120 fs	solution		41000	[248]
$C_{70}[(NH)_2CNCN]_5$	OKE	810	120 fs	solution		58000	[248]
$Dy@C_{82}$	DFWM	532	70 ps	solution		$(3.0 \pm 0.5) \times 10^6$	[239]
$Er_2@C_{82}$	DFWM	1064				-87000	[237]

Note: MT-MDA = mono-trimethylenediamine.  $C_{60}/Si = C_{60}[NH_2-(CH_2)_3-Si(OC_2H_5)_3]_3$ .  $C_{60}/Fe1 = C_{60}[Fe(NH_2CN)_5](NO_3)_3$ .  $C_{60}/Fe2 = C_{60}[Fe((NH)_2CNCN)_5](NO_3)_3$ .  $C_{60}/Ru1 = C_{60}[Ru_2(NH_2CN)_5]Cl_6$ .  $C_{60}/Ru2 = C_{60}[Ru_2((NH)_2CNCN)_5]Cl_6$ .  $C_{60}/\gamma$ -CD =  $C_{60}/\gamma$ -cyclodextrin.

polystyrene  $n$ -arm star polymers ( $PS$ ) <sub>$n$</sub>  ( $n = 3, 6$ ) with molecular weights of 900, 17800, and 4800 Da.

Konstantaki et al. [244] examined the third-order NLO response of the water-soluble inclusion complex  $C_{60}/\gamma$ -cyclodextrin by using z-scan technique at 532 nm. Since ageing of this complex solution results in the formation of aggregates, enhanced  $\gamma$  values were obtained (see Table 7).

Theoretical investigations of the third-order optical nonlinearities of fullerene derivatives have so far only been done for the substitute doped fullerenes [129, 124, 255–261]. Rustagi et al. [124] were the first to consider the second hyperpolarizability of  $C_{60}$  substitutionally doped with one B or one N atom. They used a tight-binding method for calculating the second hyperpolarizability and found a large enhancement in the doped fullerenes, especially for  $C_{59}N$ . Later, Dong, Jiang, Xing, and co-workers used the Su–Schrieffer–Heeger (SSH) model for calculating the second hyperpolarizability of  $C_{60-n}X_n$  ( $n = 1, 2$ ) where  $X = B$  or  $N$  [255, 256] and also found enhanced nonlinearities

compared with  $C_{60}$ , especially for the doubly substituted fullerenes. However, for the mono-substituted fullerenes they showed that by including Coulomb interactions in the SSH model they found a much smaller second hyperpolarizability [257]. Xie found, by using an SSH model with the Coulomb interactions included, enhanced third-order nonlinearity of  $C_{70}$  mono-substituted with either B or N [258]. Recently, the static second hyperpolarizability of the double substitute-doped fullerenes  $C_{58}NN$ ,  $C_{58}BB$ , and  $C_{58}BN$  has been investigated by Jensen et al. [129] using time-dependent density functional theory. They found only small changes in the second hyperpolarizability for  $C_{58}NN$  and  $C_{58}BB$ , but an enhanced second hyperpolarizability was found for the donor-accepted doped fullerene  $C_{58}BN$ . Also, using the same method, Xie et al. [259, 260] investigated the second hyperpolarizability of the heterofullerene  $C_{48}N_{12}$  and  $C_{48}B_{12}$  and found an enhanced second hyperpolarizability, especially for  $C_{48}B_{12}$  for which the average second hyperpolarizability was 180% larger than that of  $C_{60}$ . Cheng et al.

[261] studied the frequency-dependent second-order hyperpolarizability of the  $C_{59}Si$  and  $C_{58}Si_2$  heterofullerenes using the INDO/CI-SOS method. Using the results for the second-order hyperpolarizability of  $C_{59}Si$  and  $C_{58}Si_2$ , they estimated the third-order susceptibility for the DFWM optical process for Si-doped films to be about  $10^{-10}$  esu at the first excited state and  $10^{-11}$  esu at the ground state.

A main direction for searching organic materials which have enhanced third-order optical nonlinearities has focused on adding  $\pi$ -conjugated bonds, for example,  $-C=C-C=C-$ . This leads to decrease of the transparency because of narrowing of HOMO-LUMO gaps. Very recently, Fuks-Janczarek et al. [252] have reported DFWM measurements on the third-order NLO responses of a novel dyad of  $C_{60}$ -TTF with saturated ( $-C-C-C$ ) chemical bonds at 532 nm in picosecond time. The main importance of their work lies in their obtained results that the increase of the third-order optical nonlinearity is not connected with the increasing number of conjugated bonds (which increase the UV-vis transparency), but is due to the increasing number of saturated ( $-C-C-C-$ ) bonds without a decrease of the effective HOMO-LUMO gap. It should be pointed out that those  $C_{60}$ -derived compounds have large optical limiting coefficients which imply an interesting application in optical limiting systems.

Organic materials have two advantages: being optimized at the molecular engineering level for a specific application (e.g., photorefractivity [262], holographic memory [263], electro-optic modulation [264]) and combining chemical functionality with their optical properties. Apart from showing NLO properties with the inherent electron-transfer properties between donor and acceptor groups, one of these groups can have redox or proton-transfer capability [265]. This was exploited to demonstrate the reversible switching of the first-order hyperpolarizability of a donor-acceptor molecule [266]. Very recently, Asselberghs et al. [267] have investigated the proton-accepting capability of the dimethylamino electron-donor group on substituted 5,6-open azafulleroids [268], obtained through ring-opening aryl azide with  $C_{60}$  in toluene, to demonstrate reversible switching based on proton transfer. Their open azafulleroid exhibits a clear charge-transfer absorption band around 710 nm and the first-order hyperpolarizability was determined by using nanosecond hyper-Rayleigh scattering at 1064 nm in chloroform to be  $1.4 \times 10^{-28}$  esu, which is slightly resonantly enhanced because of the closeness of the charge-transfer absorption band to the second-harmonic wavelength. It should be mentioned that the side product, 6,6-closed aziridinofullerene, lacked the homoconjugation with the electron-accepting fullerene moiety and led to a lower hyperpolarizability. Their detailed studies demonstrated that the second-order NLO response was dramatically reduced upon protonation and completely restored after deprotonation. From the point of view of developing molecular photonic devices whose properties can be switched by modifying one of the component parts, the ability to switch the NLO response of a molecule "on" and "off" reversibly by a simple controllable perturbation would add significant value to the utility of NLO molecules.

Since  $C_{60}$  is not easy to mix homogeneously with organic-inorganic material, less work on the optical nonlinearity

of  $C_{60}$  doped in a solid matrix is reported. Very recently, Yu et al. [269] have used sol-gel technique and synthesized the solid compounds of  $C_{60}$  attached by three  $NH_2-(CH_2)_3-Si(OC_2H_5)_3$  groups. The nonresonant third-order optical susceptibilities measured by OKE gate technique at 820 nm are  $1.4 \times 10^{-13}$  esu and  $1.6 \times 10^{-13}$  esu for  $C_{60}[NH_2-(CH_2)_3-Si(OC_2H_5)_3]_3$  sol and gel, respectively. This off-resonant NLO response is also mainly derived from the electron-transfer process. Their results suggest a potential application of  $C_{60}$  derivatives of solid state in ultrafast optical devices.

### 3.4. Carbon Nanotubes

Compared with the extensive NLO studies of fullerenes, less work [213–215, 222, 223, 270–283] has been done on the third-order optical nonlinearities (TOON) of carbon nanotubes. Xie et al. [213–215] were the first to study theoretically the NLO properties of SWNT, predicting that SWNT has a larger TOON which would have potential applications as an ultrafast optical switch. Empirical relations for the static second-order hyperpolarizabilities  $\gamma$  of both armchair and zigzag nanotubes are established [222, 223, 270]:  $\gamma = (1 + 0.3n)^{2.98} \gamma_{C_{60}}$  for zigzag tube and  $\gamma = (1 + 0.167n)^{3.15} \gamma_{C_{60}}$  for armchair tube, where  $\gamma_{C_{60}}$  is the static  $\gamma$  value of  $C_{60}$ . The average contribution  $\Gamma$  of one carbon atom to the third-order optical nonlinearity of each chiral carbon nanotube, as listed in Table 8, is examined by Xie and Rao [271]. The chiral effect on the TOON is clearly shown. Their work demonstrated that the metallic tube favors larger  $\gamma$  values, and the smaller the diameter of a chiral carbon nanotube, the larger the average contribution  $\Gamma$ . Compared with that of a well-characterized polyenic polymer listed in Table 8, chiral carbon nanotubes can compete with the conducting polymer achieving a large  $\gamma$  value needed for photonic applications.

Liu et al. [272] and Xie et al. [273] were the first to investigate experimentally the third-order optical nonlinearities of carbon nanotubes by using the picosecond and nanosecond Nd:YAG laser and the technique of backward degenerate four-wave mixing (DFWM). Their results are listed in Table 9. They found enhancement of the TOON in the carbon nanotubes, in agreement with the theoretical predictions of Xie et al. [213–215, 222, 223, 270, 271]. The two-photon and one-photon processes, as demonstrated in the theoretical work of Xie et al., contribute to the TOON. The fast response process of the carbon nanotubes on the picosecond scale is an instantaneous electronic process due to the large polarizability arising mainly from the  $\pi \rightarrow \pi^*$  virtual transition, while the slow process on the picosecond scale is associated with an excited-state population. On the nanosecond scale, similar results are obtained.

However, Liu et al. [272] did not obtain real solution for carbon nanotubes. Thus, a large absorption was observed in the infrared region. On the other hand, their DFWM technique had limited ability to distinguish the NLO contribution from the  $\pi$ -conjugated electrons. Shi and co-workers [274, 275] have performed NLO measurements on real SWNT solutions by using the femtosecond optical Kerr technique with a Ti:sapphire laser operating at 820 nm. Their results are listed in Table 9. The magnitude of  $\Gamma$  for each carbon atom in the SWNT is about  $7.7 \times 10^{-33}$  esu, which is

**Table 8.** The static  $\gamma$  value and average contribution  $\Gamma$  of 17 chiral carbon nanotubes and 7 well-characterized polyenic polymers.

Materials	$N$	$D$ [nm]	$\theta$ [degree]	$\gamma$ [ $10^{-36}$ esu]	$\Gamma$ [ $10^{-36}$ esu]	$\zeta$
$C_{60}$	60	0.70	—	561.2	9.353	1.0
S-SWNT <sub>(6,5)</sub>	364	0.75	27.0	6355.6	17.461	1.8669
S-SWNT <sub>(9,1)</sub>	364	0.75	5.2	5199.7	14.285	1.5273
S-SWNT <sub>(8,3)</sub>	388	0.77	15.3	5401.3	13.921	1.4884
S-SWNT <sub>(9,2)</sub>	412	0.80	9.8	5719.8	13.883	1.4843
S-SWNT <sub>(7,5)</sub>	436	0.82	24.5	6017.2	13.801	1.4756
S-SWNT <sub>(8,4)</sub>	448	0.83	19.1	6176.6	13.787	1.4741
S-SWNT <sub>(10,2)</sub>	496	0.87	8.9	6704.9	13.518	1.4453
S-SWNT <sub>(7,6)</sub>	508	0.88	27.5	6850.4	13.485	1.4418
S-SWNT <sub>(9,4)</sub>	532	0.90	17.5	6915.5	12.999	1.3898
S-SWNT <sub>(10,3)</sub>	556	0.92	12.7	6881.1	12.376	1.3232
S-SWNT <sub>(8,6)</sub>	592	0.95	25.3	6815.7	11.513	1.2309
S-SWNT <sub>(9,5)</sub>	604	0.97	20.6	6764.2	11.199	1.1974
M-SWNT <sub>(7,4)</sub>	372	0.76	20.9	22999.6	61.827	6.6104
M-SWNT <sub>(10,1)</sub>	444	0.83	4.7	25039.8	56.396	6.0297
M-SWNT <sub>(9,3)</sub>	468	0.85	13.9	22187.9	47.419	5.0699
M-SWNT <sub>(8,5)</sub>	516	0.89	22.4	18159.6	35.193	3.7627
M-SWNT <sub>(10,4)</sub>	624	0.98	16.1	14883.0	23.851	2.5501
Polyenic polymer	230	—	—	3500	15	1.6038
Polyenic polymer	340	—	—	5400	16	1.7107
Polyenic polymer	450	—	—	7800	17	1.8176
Polyenic polymer	620	—	—	15500	25	2.6729
Polyenic polymer	830	—	—	26700	32	3.4214
Polyenic polymer	1460	—	—	62900	43	4.5975
Polyenic polymer	2320	—	—	85400	37	3.9559

Notes: S-SWNT<sub>( $p,q$ )</sub> and M-SWNT<sub>( $p,q$ )</sub> denote semiconducting and metallic SWNT, respectively.  $D$  and  $\theta$  are the diameter and chiral angle of carbon nanotubes.  $N$  is the total number of carbon atoms in a given material.  $\Gamma$  is the average contribution of a carbon atom to the third-order optical nonlinearity of the material.  $\zeta$  is the ratio between the  $\Gamma$  values of a material and  $C_{60}$ .

Source: Some data are adapted from [33].

about three orders larger than the value of carbon nanotube reported by Liu et al. [272]. To improve NLO performance of SWNTs, it would be of interest to test the optical nonlinearity of SWNTs of various lengths.

Very recently, using standard time-resolved pump-probe photomodulation technique with a 150-fs fiber laser at the wavelength 1550 nm, Chen et al. [276] have experimentally demonstrated that SWNTs have an exciton decay time of less than 1 ps and exhibit a high third-order optical nonlinearity. Similar experimental results from MWNTs or a SWNT/polyvinyl alcohol composite are also observed by them. Their experiment suggested that SWNT/polymide composites have the potential to become an ultrafast waveguide switch and to develop high-quality subpicosecond all-optical switches.

#### 4. OPTICAL LIMITING OF FULLERENES AND CARBON NANOTUBES

As addressed before, a currently important problem in today's science and technology is related to the task of protecting the human eye and the sensors of instruments detecting high-power light beams from radiation damage [284–287]. A solution to this problem is the use of passive optical limiters as protection devices. An ideal optical limiter exhibits linear transmission below a certain input light fluence (ILF) threshold  $W_{ILF}$ , but above the  $W_{ILF}$  value nonlinear transmission occurs and the output light fluence (OLF) will reach a saturated value  $W_{OLF}$  [284]. A good limiter should also be stable under ambient and photoradiation conditions and efficient from a few picoseconds up to

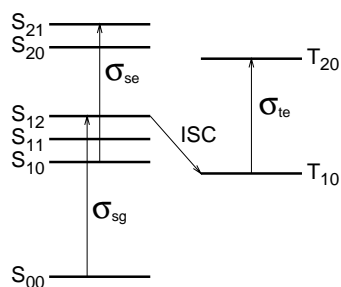
**Table 9.** Third-order optical nonlinearities of MWNTs and SWNTs.

Material	Method	$\lambda$ [nm]	$\tau$	Solvent	$\chi^{(3)}$ [ $10^{-14}$ esu]	$\Gamma$ [ $10^{-36}$ esu]	Ref.
MWNT	DFWM	1064	30 ps	PPCE	6.460	5.921	[272, 273]
	DFWM	532	30 ps	PPCE	6.303	—	[272, 273]
	DFWM	1064	8 ns	PPCE	1179	—	[272, 273]
	DFWM	1064	8 ns	PPCE	309	—	[272, 273]
SWNT	OKE	820	120 fs	DMF	40	7700	[274, 275]

Notes:  $\lambda$  and  $\tau$  are the wavelength and pulse duration of laser source.  $\Gamma$  is the averaged second-order hyperpolarizability  $\gamma$  contributed by one carbon atom in carbon nanotubes. PPCE denotes the mixing of polypyrrol and m-cresol with ethanol. DMF = dimethylformamide.

longer pulse durations from nanoseconds and milliseconds on a broad range of wavelengths (visible and near infrared). Thus, the transmitted pulse energy never exceeds the damage threshold for the optical sensor.

Optical limiting is obtained by exploiting different NLO processes [284–287]: coherent nonlinear optical absorption (reverse saturable absorption (RSA), two-, three-, or multi-photon absorption [288]), nonlinear scattering (solvent bubble formation and/or particle sublimation [289–291] or mismatched indices [292]), nonlinear refraction (electronic effects [9] or thermal lensing [293]), and so on. Among the nonlinear optical absorption, RSA is a primary mechanism for the nonlinear absorption optical limiting and is demonstrated to be one of the best processes to use for optical limiting because it reduces the total pulse energy rather than simply reducing the fluence or irradiance. It is generally accepted that RSA of a material system, for example,  $C_{60}$ , can be described by a five-level model [294–299]. As shown in Figure 7, if  $\sigma_{sg} > \sigma_{se}$ , the material is more transparent and becomes a saturable absorber. However, when the absorption cross sections of the singlet or the triplet excited states are larger than that of the ground state and the lifetime of the excited state is long enough, the total absorption of the NLO material increases and the material is then a reverse saturable absorber (i.e., a RSA process occurs). For longer laser pulses, significant intersystem crossing (ISC) to a triplet state occurs for some kinds of materials (e.g., an important feature of  $C_{60}$  is the fast and efficient ISC from the first singlet excited state to the first triplet excited state). In these cases, the excited-state absorption appears from the lowest triplet to higher excited triplet states, providing an increasing contribution to the total absorption of the system. It should be pointed out that the transition from the ground state to the first singlet electron state is forbidden because of the same parity, but becomes partially allowed due to vibronic interactions responsible for the weak absorption band in the visible region extending from 450 nm to 650 nm. In this RSA mechanism, significant parameters are the excited-state lifetimes and the ISC time, compared with the duration of the laser pulse, plus the values of the absorption cross sections.



**Figure 7.** The energy levels of singlet ( $S_j$ ) and triplet ( $T_j$ ) states of a system. The optical absorptions are related to the absorption cross sections ( $\sigma$ ) of the states. The emissions are correlated to the relaxation time ( $\tau_j$  from the  $i$ th state to the  $j$ th state).  $S_{ij}$  or  $T_{ij}$  denotes the  $j$ th vibrational state of the  $i$ th electronic state.  $S_{00}$  is the ground state.  $S_{1j}$  and  $T_{10}$  are the first singlet and triplet electronic states, respectively.  $S_{2j}$  and  $T_{20}$  are the second singlet and triplet excited electronic states.  $\sigma_{sg}$ ,  $\sigma_{se}$ , and  $\sigma_{te}$  are absorption cross sections for singlet ground and excited states and triplet excited state, respectively.

Typical reverse saturable absorbers are molecules with weak ground-state absorptions at the concerned wavelengths such as metallophthalocyanines [286, 300, 301], mixed metal complexes [302–305], and fullerenes [287]. In a more general RSA mechanism, the strongly absorbing electronic excited states can be populated by other incoherent processes, for example, internal conversion, energy transfer, and so on.

In the following, we review extensive studies of the optical limiting properties of fullerenes, fullerene-derived materials, and carbon nanotubes (see our other review chapter about the optical limiting of doped carbon nanotubes). Most of these results for fullerenes are attributed to the RSA processes, while nonlinear scattering plays an important role in the optical limiting performances of carbon nanotubes. Some important results for those materials and others are summarized in Table 10.

#### 4.1. Fullerenes

Tutt and Kost [306] were the first to observe the optical limiting performance in  $C_{60}$  solution. As listed in Table 10,  $C_{60}$  exhibits optical limiting behavior with saturation threshold lower than those reported for  $C_{70}$  and other materials currently in use. RSA is the dominant mechanism: there exist allowed broadband transitions from the first excited singlet and triplet to the higher excited states and this results in absorption in the visible and near-infrared range that is much stronger than the absorption from the ground state, leading to RSA. Because the higher ground-state absorption cross section for  $C_{70}$  leads to a smaller ratio of excited-state to ground-state cross sections, a higher threshold for optical limiting in  $C_{70}$  is observed [306, 307]. In comparison with the  $C_{60}$ -toluene system, a reduction of the saturated threshold by a factor of 3 to 5 is obtained by Belousov et al. [308] in a  $C_{60}$ - $CCl_4$  system (see Table 10). Results similar to those of the  $C_{60}$ - $CCl_4$  system are obtained in a  $C_{60}$ -decalin solution [308]. Solutions of  $C_{60}$  in methylene chloride give results similar to those of  $C_{60}$ -toluene system [306]. Sun et al. [309] have shown that the picosecond optical limiting threshold of  $C_{60}$  is higher than that of the nanosecond one. Further experiments [310] show that the optical limiting performance of  $C_{60}$  in room temperature solution toward nanosecond laser pulses at 532 nm strongly depends on the fullerene solution concentrations (see Table 10), which give significant optical limiting contribution. The optical limiting performance of the more concentrated  $C_{60}$  solution is in general stronger than that of dilute ones. For example, the  $C_{60}$  solution in toluene of  $8.2 \times 10^{-4}$  M concentration displays strong optical limiting, whereas in toluene of  $1.6 \times 10^{-4}$  M it gives a higher saturated value. In summary, RSA for excitation of  $C_{60}$  solution with picosecond duration laser pulses is due to absorption from the first singlet excited state since the population in the first triplet excited state is negligible, while for excitation with laser pulses having durations of a few nanoseconds the dominant contribution to RSA comes from absorption from the first triplet excited state. RSA is stronger for nanosecond laser pulses than for picosecond laser pulses for wavelength between 620 nm and 810 nm.

Sun et al. [311] found that the saturated threshold values of the mixture  $C_{60}/C_{70}$  solution (see Table 10) are higher



**Table 10.** Optical limiting performance of fullerenes, fullerene derivatives, single-walled carbon nanotubes (SWNT), multiwalled carbon nanotubes (MWNTs), carbon black suspension (CBS), and some other materials.

Material ( $K_m$ )	Solvent	$\tau$ [psec]	$\lambda$ [nm]	$P_t$	$W_{ILF}$ [J/cm <sup>2</sup> ]	$W_{OLF}$ [J/cm <sup>2</sup> ]	Ref.
$C_{60}$	toluene	8 ns	532	63%	0.11	0.065	[306]
	toluene	8 ns	532	70%	0.16	0.071	[306]
	toluene	8 ns	532	80%	0.51	0.24	[306]
	toluene	5 ns	532	55%	0.12	0.058	[310]
	toluene	5 ns	532	70%	0.18	0.11	[310]
	toluene	5 ns	532	70%	0.18	0.10	[352]
	toluene	40 ps	532	76%	0.32	0.12	[309]
	toluene	15 ns	532	55%	0.3	0.78	[362]
	toluene	8–10 ns	532	66%	0.6	0.1–0.12	[308]
	toluene	8 ns	532	81%	0.15	0.28	[335]
	$CCl_4$	8–10 ns	532	80%	1.0	0.46	[308]
	$CCl_4$	8–10 ns	532	65%	0.3	0.2	[308]
	$CCl_4$	8–10 ns	532	50%	0.1	0.05	[308]
	toluene	8–10 ns	308	25%	0.3	0.3	[308]
	toluene	8 ns	532	65%	0.1	0.0899	[327]
	DMF	10 ns	532	75%	0.1	0.12	[336]
$C_{60}$ (0.33)	toluene	5 ns	532	70%	0.01	0.23	[310]
$C_{60}$ (1.64)	toluene	5 ns	532	70%	0.01	0.12	[310]
$C_{60}$ (8.19)	toluene	5 ns	532	70%	0.01	0.1	[310]
$C_{60}$ (0.5)	toluene	45 ps	532	—	0.15	0.1	[324]
$C_{60}$ (2.5)	toluene	45 ps	532	—	0.05	0.05	[324]
$C_{70}$	toluene	8 ns	532	70%	0.1	0.35	[306]
	toluene	10 ns	532	70%	0.2	0.27	[307]
$C_{60}/C_{70}$ mixture	toluene	10 ns	532	14%	0.41	0.04	[311]
	toluene	10 ns	532	24%	0.45	0.07	[311]
	toluene	10 ns	532	44%	0.62	0.32	[311]
	toluene	10 ns	532	69%	1.22	0.69	[311]
	argon-degassed	10 ns	532	44%	0.11	0.12	[311]
	not argon-degassed	10 ns	532	44%	0.48	0.31	[311]
$C_{76}/C_{84}$ mixture	toluene	10 ns	1064	45%	0.7	2.0	[308]
	$C_{70}$ -II	1,2-dichlorobenzene	10 ns	532	30%	0.18	0.025
$C_{70}$ -II	1,2-dichlorobenzene	10 ns	532	50%	0.094	0.11	[307]
	1,2-dichlorobenzene	10 ns	532	70%	0.037	0.16	[307]
	1,2-dichlorobenzene	10 ns	532	70%	0.037	0.16	[307]
$CuPc-C_{60}$ (0.5)	toluene	45 ps	532	—	0.15	0.07	[324]
$CuPc-C_{60}$ (2.5)	toluene	45 ps	532	—	0.01	0.02	[324]
$DTC_{60}$	hexane	8 ns	532	65%	0.1	0.1099	[327]
$DTC_{60}$ -Ag	hexane	8 ns	532	65%	0.1	0.0716	[327]
$HDTC_{60}$	hexane	8 ns	532	70%	0.3	0.44	[331]
$HDTC_{60}$ -Ag	hexane	8 ns	532	70%	0.08	0.22	[331]
$C_{60}$ BPY	chloroform	8 ns	532	51%	0.2	0.13	[335]
$C_{60}$ TPY	chloroform	8 ns	532	51%	0.2	0.13	[335]
$C_{60}$ BPY-Au	chloroform	8 ns	532	81%	0.2	0.61	[335]
$C_{60}$ TPY-Au	chloroform	8 ns	532	81%	0.2	0.21	[335]
$C_{60}$ BPY-Au	chloroform	40 ps	532	75%	0.05	0.12	[335]
$C_{60}$ TPY-Au	chloroform	40 ps	532	75%	0.05	0.08	[335]
$C_{60}(CN)_2$	DMF	10 ns	532	55%	0.1	0.12	[336]
	DMF	40 ps	532	55%	0.07	0.05	[336]
	DMF	23 ps	532	55%	0.07	0.05	[336]
$C_{60}$ -PC	chloroform	8 ns	532	33%	0.3	0.3	[337]
PCC1	chloroform	8 ns	532	70%	0.3	0.35	[337]
PCC2	chloroform	8 ns	532	70%	0.3	0.3	[337]
PCC3	chloroform	8 ns	532	70%	0.3	0.42	[337]
PCC4	chloroform	8 ns	532	70%	0.3	0.27	[337]
PCC5	chloroform	8 ns	532	70%	0.3	0.4	[337]
PCC6	chloroform	8 ns	532	70%	0.3	0.38	[337]
TBM[60]CO (0.123)	toluene	5 ns	532	70%	0.09	0.31	[310]
TBM[60]CO (0.246)	toluene	5 ns	532	70%	0.09	0.30	[310]
TBM[60]CO (0.616)	toluene	5 ns	532	70%	0.09	0.18	[310]
TBM[60]CO (1.23)	toluene	5 ns	532	70%	0.09	0.17	[310]
TBM[60]CO (5.92)	toluene	5 ns	532	71%	0.09	0.14	[310]

continued

Table 10. Continued

Material ( $K_m$ )	Solvent	$\tau$ [psec]	$\lambda$ [nm]	$P_t$	$W_{ILF}$ [J/cm <sup>2</sup> ]	$W_{OLF}$ [J/cm <sup>2</sup> ]	Ref.
TBM[60]CO (6.16)	toluene	5 ns	532	70%	0.09	0.11	[310]
TBM[60]CO (6.4)	toluene	5 ns	532	69%	0.09	0.1	[310]
TBM[60]CO (10.4)	toluene	5 ns	532	55%	0.09	0.07	[310]
TBM[60]CO (12.3)	toluene	5 ns	532	70%	0.09	0.1	[310]
TBM[60]CO (5.92)	tol-PMMA	5 ns	532	71%	0.09	0.17	[310]
TBM[60]CO (10.4)	tol-PMMA	5 ns	532	55%	0.09	0.09	[310]
TBM[60]CO (0.123)	CHCl <sub>3</sub> -PPEI	5 ns	532	69%	0.09	0.16	[310]
SWNT suspension	water	5 ns	532	70%	0.1	0.11	[352]
	water	15 ns	532	55%	1.2	1.1	[362]
	water	15 ns	532	42%	1.1	0.76	[362]
	ethanol	15 ns	532	42%	0.4	0.45	[362]
	ethylene glycol	15 ns	532	42%	1.1	1.5	[362]
Short-SWNT suspension	water	5 ns	532	70%	0.18	0.16	[352]
Short-SWNT-PPEI-EI	chloroform	5 ns	532	70%	0.21	0.35	[352]
Short-MWNT suspension	water	5 ns	532	70%	0.16	0.14	[352]
Short-MWNT-PPEI-EI	chloroform	5 ns	532	70%	0.16	0.26	[352]
Short-MWNT-OC	chloroform	5 ns	532	70%	0.16	0.29	[352]
MWNT (large aspect ratio)	PVDF/DMF	6–8 ns	532	50%	0.2	0.35	[353]
MWNT (small aspect ratio)	PVDF/DMF	6–8 ns	532	50%	0.2	0.41	[353]
CBS	PVDF/DMF	6–8 ns	532	50%	0.2	0.33	[353]
	water	5 ns	532	70%	0.1	0.12	[352]
DT-Ag	hexane	8 ns	532	65%	0.1	0.2801	[327]
DT-Ag	hexane	8 ns	532	70%	0.3	0.33	[331]
CuPc (0.5)	toluene	45 ps	532	—	0.1	0.075	[324]
CuPc (2.5)	toluene	45 ps	532	—	0.06	0.022	[324]
HFeCo <sub>3</sub> (CO) <sub>10</sub> (P(CH <sub>3</sub> ) <sub>3</sub> ) <sub>2</sub>	methylene chloride	8 ns	532	70%	0.4	0.39	[306]
HFeCo <sub>3</sub> (CO) <sub>12</sub>	methylene chloride	8 ns	532	70%	0.4	0.55	[306]
HFeCo <sub>3</sub> (CO) <sub>10</sub> (PPh <sub>3</sub> ) <sub>2</sub>	methylene chloride	8 ns	532	70%	0.8	0.71	[306]
Indanthrone	dilute KOH	8 ns	532	70%	0.18	0.16	[306]
Chloroaluminum phthalocyanine	methanol	8 ns	532	70%	0.18	0.11	[306]
(N(C <sub>2</sub> H <sub>5</sub> ) <sub>4</sub> ) <sup>+</sup> (FeCo <sub>3</sub> (CO) <sub>12</sub> ) <sup>-</sup>	methylene chloride	8 ns	532	70%	0.38	0.55	[306]
WS <sub>4</sub> Cu <sub>4</sub> I <sub>2</sub> (py) <sub>6</sub>	DMF	40 ps	532	64%	0.15	0.059	[309]

Note:  $W_{ILF}$  denotes the ILF threshold.  $W_{OLF}$  is OLF saturation threshold.  $\tau$  and  $\lambda$  are the duration and wavelength of the laser light.  $P_t$  is the percentage of transmitting sample. The TCNEO-C<sub>60</sub>/PC ratio for PCC1, PCC2, PCC3, PCC4, PCC5 and PCC6 are 1.02, 1.06, 1.01, 1.96, 3.05, 5.03 wt%.  $K_m$  (in 10<sup>-4</sup> M) is the solution concentration. DMF = dimethylformamide. TBM(60)CO = *tert*-buty methano-C<sub>60</sub> carboxylate. C<sub>70</sub>-II = ( $\eta^2$ -C<sub>70</sub>)Mo(CO)<sub>2</sub>(*o*-phen)(DBM). PMMA = poly(methyl methacrylate). PPEI = poly(propionylethyleneimine). PPEI-EI = poly(propionylethyleneimine-co-ethyleneimine). PVDF = poly(vinylidene fluoride). OC = octadecylamine.

than that of C<sub>60</sub> solution but lower than that of C<sub>70</sub> solution, which is actually due to the lower triplet state quantum yield and stronger absorption in the visible wavelength for C<sub>70</sub> than C<sub>60</sub>. Since the triplet state of C<sub>60</sub> [312] with lifetime 330 ± 25 ns and C<sub>70</sub> [313] with lifetime 730 ± 50 ns can be quenched by <sup>3</sup>O<sub>2</sub>, the existence of <sup>3</sup>O<sub>2</sub> in the solution will influence the RSA process and the optical limiting behavior. Sun et al. [311] found that no argon-degassed solution of the mixture C<sub>60</sub>/C<sub>70</sub> has a higher ILF threshold and a higher saturated threshold than the argon-degassed solution (see Table 10).

Optical limiting performance was also observed in a mixture of higher fullerenes C<sub>76</sub> and C<sub>84</sub> at  $\lambda = 1064$  nm for  $\tau = 10$  ns [308]. Their saturated threshold value is, however, higher than that of C<sub>60</sub>-toluene in the visible region. Again, this is determined by the low quantum yield into the triplet state for the higher fullerenes.

All nonradiative relaxation processes lead to heating of the solvent. Justus et al. [293, 314] pointed out that RSA increases absorption and enhances thermal defocusing which shows additional contribution to the observed optical limiting performances in C<sub>60</sub> solution. Negative thermal lensing in C<sub>60</sub> is clearly reflected in z-scan studies of Mishra et al.

[315]. The thermal origin of negative lensing was also established on the optical limiting for different solvents [315]. C<sub>60</sub> in carbon disulfide, which has the largest thermal figure of merit, exhibits stronger optical limiting behavior [315]. A different kind of solvent dependence was also observed by Sun and Riggs [287]: the optical limiting response of C<sub>60</sub> solutions in electron-donating solvents, for example, diethylamine and dimethylamine, was much weaker than that in toluene solution. This can be understood: (i) upon photoexcitation of C<sub>60</sub>, the dominant photogenerated transient species are C<sub>60</sub> anion and diethylamine or dimethylamine cation; (ii) since absorption from the C<sub>60</sub> anion is weaker than that from the triplet C<sub>60</sub>, the optical limiting performance is degraded. It should be mentioned, however, that thermal refraction contributes to the optical limiting behavior of nanosecond laser pulses but not of picosecond laser pulses [316].

The work of Mishra et al. [317, 318] showed the significant contribution of nonlinear scattering to the observed optical limiting performance in C<sub>60</sub> solution. In their limiter geometry, the transmission could decrease at higher fluences only due to RSA or aberrations which come from the nonlinear lens. Their observed reduction in the transmission at higher

fluences was larger than that expected from a theoretical analysis including RSA and nonlinear refraction, where the difference is from the nonlinear scattering.

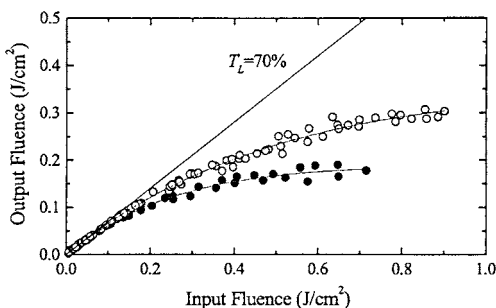
In addition, the work of Riggs and Sun [287, 310] showed us that RSA in  $C_{60}$  also has some contributions from singlet and triplet excimer-like states formed due to bimolecular processes involving  $C_{60}$  molecules in the triplet state.

## 4.2. Fullerene Derivatives

A category of metal-fullerene complexes [319–323] was synthesized in the laboratory. Their charge-transfer nature qualifies them to be promising group of excited-state absorption optical limiting materials. (Indeed, enhanced optical limiting performance of a molybdenum complex of fullerene ( $\eta^2-C_{60}$ )Mo(CO)<sub>2</sub>(o-phen)(DBM) (DBM = dibutyl maleate; o-phen = 1,10-phenanthroline) [322] was observed. Recently, Liu et al. [307] have also observed enhanced optical limiting performance of a novel molybdenum complex of fullerene ( $\eta^2-C_{70}$ )Mo(CO)<sub>2</sub>(o-phen)(DBM) relative to fullerene  $C_{70}$  with nanosecond laser pulses (see Fig. 8). This is attributed to the increment on the triplet-state absorption because of intramolecular charge transfer.

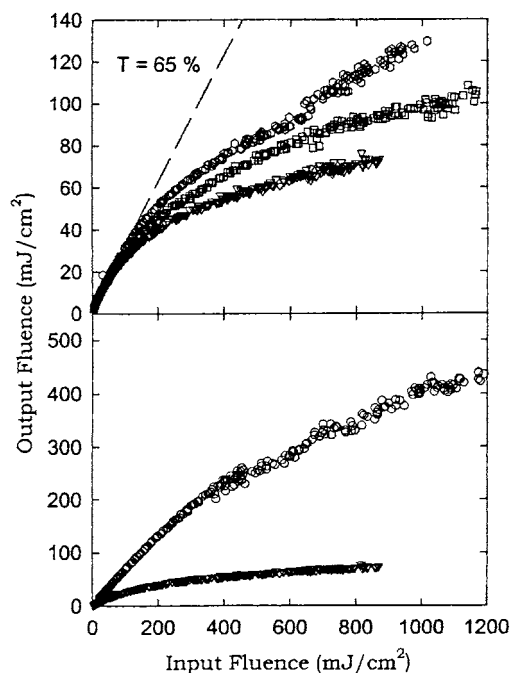
Copper (II) phthalocyanines (CuPc) and  $C_{60}$  have been used to construct practical optical limiters due to their good optical limiting properties. As far as the solubilities and aggregations of these optical limiting molecules are concerned, combining phthalocyanine and fullerene in one compound through Diels–Alder reaction has many advantages, for example, combining the optical limiting properties of both molecules, improving the solubility and stability, and avoiding the phase separation problems existing in the mixture of various materials. Recently, Zhu et al. [324] have demonstrated that in a higher-concentration solution, CuPc- $C_{60}$  shows similar optical limiting behavior to CuPc, while in a lower-concentration solution, the CuPc- $C_{60}$  shows similar optical limiting behavior to  $C_{60}$  at low input fluence (<0.2 J/cm<sup>2</sup>) and to that of CuPc at higher input fluence (>0.2 J/cm<sup>2</sup>). In this kind of combined molecule, there are two separated conjugation systems both of which independently contribute to the RSA.

The fullerene-metal nanocomposites remain as a relatively unexplored area [325, 326]. Recently, Sun et al. [327] have prepared a novel [60]fullerene-Ag nanocomposite

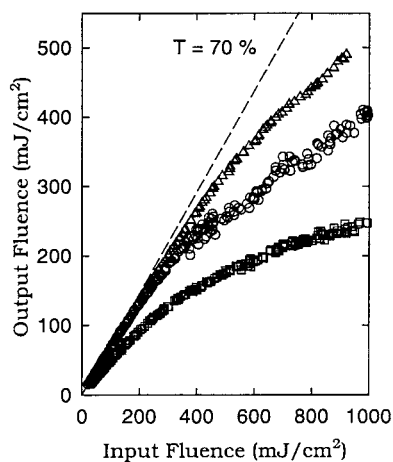


**Figure 8.** Optical limiting of  $C_{70}$  (open circles) and the molybdenum complex of ( $\eta^2-C_{70}$ )Mo(CO)<sub>2</sub>(o-phen)(DBM) (filled circles) with the same linear transmissivity at 532 nm. Reprinted with permission from [307], C. Liu et al., *Opt. Commun.* 184, 309 (2000). © 2000, Elsevier Science.

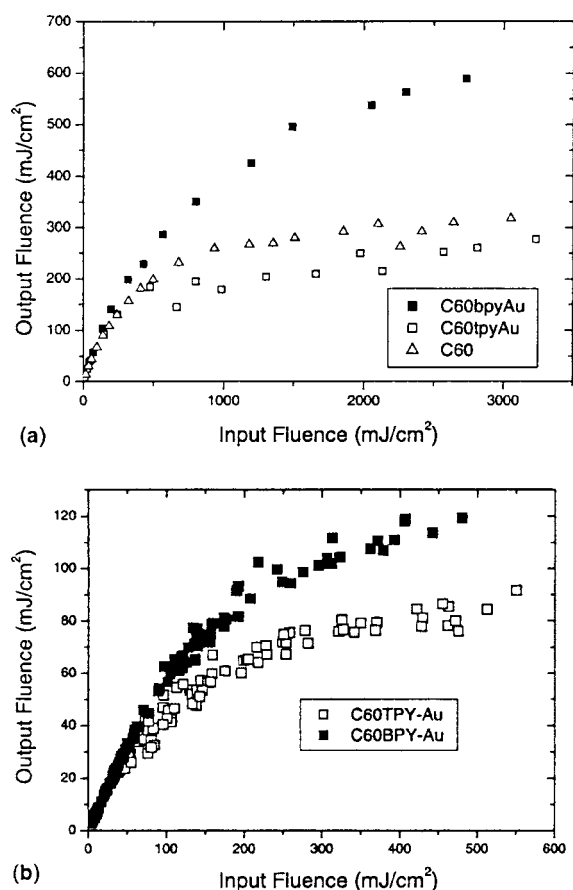
(DTC<sub>60</sub>-Ag) by the *in-situ* reduction of silver ions encapsulated in a new mono-functionalized methano-[60]fullerene derivative (DTC<sub>60</sub>) with reverse micelle-like structure. As listed in Table 10 and shown in Figure 9, their experimental measurements demonstrated that the optical limiting behavior of DTC<sub>60</sub>-Ag is better than that of both  $C_{60}$  and DTC<sub>60</sub>, even better than the results obtained with novel materials such as silver-dendrimer nanocomposite [328], the AF-380 dye [329], and single-walled carbon nanotube suspensions [330]. Similar results (see Fig. 10) [331] have been obtained for a new  $C_{60}$  hexamalonate derivative nanocomposite (HDTC<sub>60</sub>-Ag) which is a better optical power limiter compared with the parent HDTC<sub>60</sub> and DT-Ag. Recently, gold nanoparticles have attracted considerable attention due to their potential applications as promising optical devices and nanoelectronic devices because of their higher surface-to-volume ratios and small size effects [332, 333]. However, less work has been done for optical nonlinearities of these nanostructural materials, especially for those with zerovalent metal nanoparticles [334]. Very recently, Fang et al. [335] have synthesized two novel  $C_{60}$ -derived nanoparticles containing bi-pyridyl (BPY) and tri-pyridyl (TPY) groups. The optical limiting responses of  $C_{60}$ BPY,  $C_{60}$ TPY,  $C_{60}$ BPY-Au, and  $C_{60}$ TPY-Au nanoparticles in chloroform were measured by using a Nd:YAG laser at both picosecond and nanosecond scales and 532 nm. Their measured results are listed in Table 10 and shown in Figure 11. The difference between the optical limiting properties of both  $C_{60}$ BPY and  $C_{60}$ TPY is little. However, the optical limiting performance of  $C_{60}$ TPY-Au at both picosecond and nanosecond scales was much better than that of  $C_{60}$ BPY-Au. Their further



**Figure 9.** Optical limiting of hexane solution of DT-Ag (circle), DTC<sub>60</sub>-Ag (hexagon), DTC<sub>60</sub>-Ag, and toluene solution of  $C_{60}$  (square) with 8-ns, 532-nm optical laser pulses. Reprinted with permission from [327], N. Sun et al., *Chem. Phys. Lett.* 344, 277 (2001). © 2001, Elsevier Science.



**Figure 10.** Optical limiting of hexane solution of DT-Ag (circle), HDTC<sub>60</sub> (triangle), and HDTC<sub>60</sub>-Ag (square) with 8-ns, 532-nm optical laser pulses. Reprinted with permission from [331], N. Sun et al., *Chem. Phys. Lett.* 356, 175 (2002). © 2002, Elsevier Science.



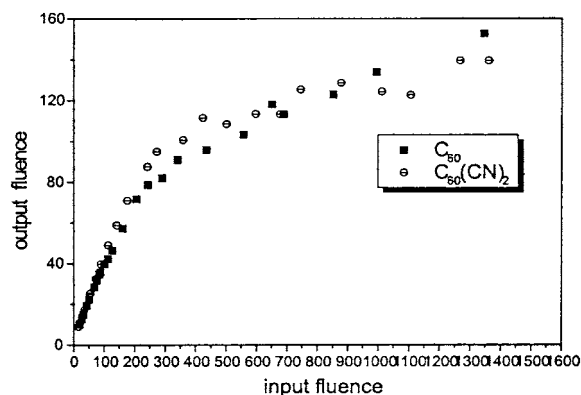
**Figure 11.** (a) Optical limiting of C<sub>60</sub> in toluene, C<sub>60</sub>TPY-Au in chloroform, C<sub>60</sub>BPY-Au in chloroform with the identical linear transmission of 81% with nanosecond optical laser pulse; (b) optical limiting of C<sub>60</sub>TPY-Au and C<sub>60</sub>BPY-Au in chloroform with the identical linear transmission of 75% with nanosecond optical laser pulse. Reprinted with permission from [335], H. Fang et al., *Chem. Phys. Lett.* 364, 290 (2002). © 2002, Elsevier Science.

Z-scan measurements indicate that nonlinear absorption (e.g., excited-state and the surface plasmon absorptions) and nonlinear scattering contribute a great deal to the optical limiting performance of C<sub>60</sub>TPY-Au, while there is no nonlinear scattering for C<sub>60</sub>BPY-Au. All these are caused by the excited-state interaction between the C<sub>60</sub> and silver or gold nanoparticles, showing the strong nonlinear refraction (or say, self-focusing effect), as well as the interband transition due to the surface plasmon resonance.

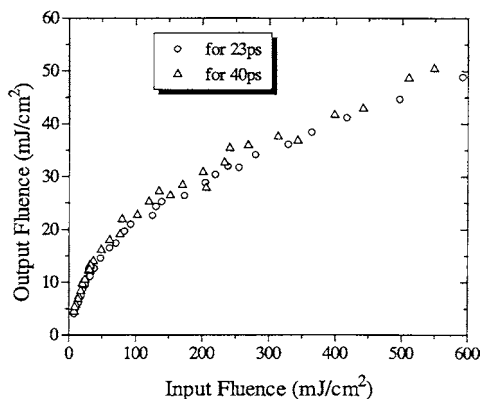
Suo et al. [336] explored the influence on the optical limiting performance of C<sub>60</sub> by attaching two strong pulling electron groups (-CN), that is, dicyanodihydrofullerene C<sub>60</sub>(CN)<sub>2</sub>. This molecule has an optical limiting performance for nanosecond laser similar to that of pristine C<sub>60</sub> (see Fig. 12). Although this molecule has an extinction coefficient of the excited triplet state larger than that of C<sub>60</sub>, its low quantum yield leads to a lower triplet-state population and thus the optical limiting behavior similar to that of C<sub>60</sub>. As mentioned before, there are generally two kinds of mechanisms for optical limiting performance because of the nonlinear absorption: dual photon absorption and RSA. Compared with the pristine C<sub>60</sub> (see Fig. 13), the picosecond optical limiting performance of C<sub>60</sub>(CN)<sub>2</sub> is power independent but assigned to the RSA of the excited singlet state [336].

The incorporation of fullerene moieties into polymer systems such as polycarbonate (PC) is a hot recent topic due to the interesting optical and electronic properties that the combined materials exhibit. The work of Li et al. [337, 338] indicated that increasing the electron-accepting ability of fullerene derivatives leads to stronger intramolecular action between TCNEO-C<sub>60</sub> moiety and PC unit and thus TCNEO-C<sub>60</sub>-PCs (e.g., PCC1, PCC3) (see Fig. 14 and Table 10 for different TCNEO-C<sub>60</sub>/PC feed ratio; TC-NEO = tetracyanomethanoxymethano) show much better optical limiting properties than C<sub>60</sub>-PCs. It should be pointed out that the optical limiting characteristics of TCNEO-C<sub>60</sub>-PC can be described by the Golovlev model [339].

Fullerene compounds are very hydrophobic. Thus, most of the related physical and chemical studies about their structure, properties, and reaction have been performed in nonpolar solvents such as toluene or benzene. However, if the fullerenes are embedded in a suitable water-soluble



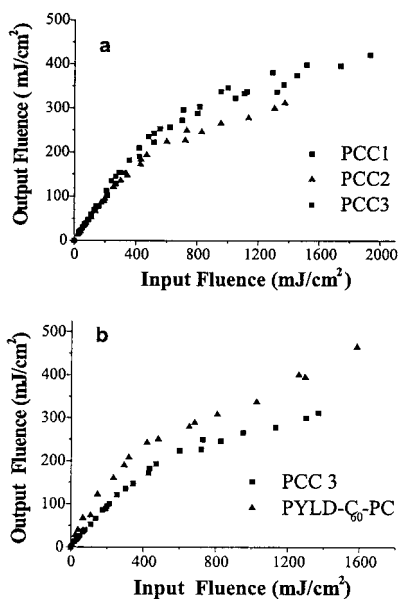
**Figure 12.** Optical limiting of C<sub>60</sub>(CN)<sub>2</sub> and C<sub>60</sub> with 10-ns optical laser. Reprinted with permission from [336], Z. Suo et al., *Chem. Phys. Lett.* 342, 497 (2001). © 2001, Elsevier Science.



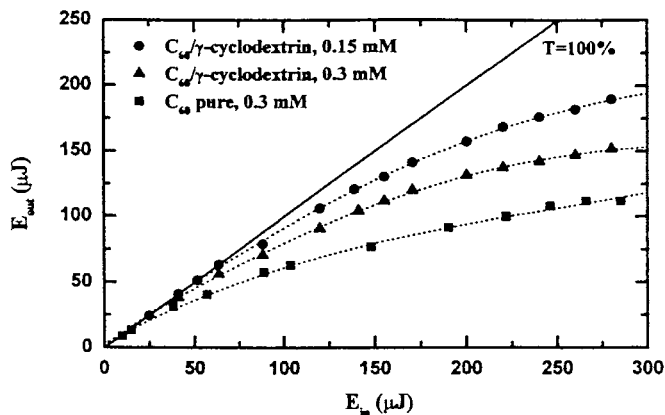
**Figure 13.** Optical limiting of  $C_{60}(CN)_2$  and  $C_{60}$  with 40-ps and 23-ps optical lasers, respectively. Reprinted with permission from [336], Z. Suo et al., *Chem. Phys. Lett.* 342, 497 (2001). © 2001, Elsevier Science.

molecule, water solubility can be achieved.  $\gamma$ -Cyclodextrin has been proved to be a rather suitable candidate for producing a water-soluble complex which has a stoichiometry of one  $C_{60}$  for two  $\gamma$ -cyclodextrins [340]. Using 532-nm, 10-ns laser pulses, Konstantaki et al. [341] observed significant optical limiting action of  $C_{60}/\gamma$ -cyclodextrin complex (see Fig. 15), the effect being slightly lower than that of the pristine  $C_{60}$ . However, ageing of the  $C_{60}/\gamma$ -cyclodextrin-water solution leads to the formation of aggregates which can enhance the optical limiting action by a factor of almost 2 [341].

It has been shown that appropriate fullerene functionalization increases the solubility in polar solvent and allows the preparation of solid materials via sol-gel method [342, 343]. Signorini et al. [343] have compared the optical limiting



**Figure 14.** Optical limiting of (a) TCNEO- $C_{60}$ -PCs and (b) MPYLD- $C_{60}$ -PC with 8-ns, 10-Hz laser pulse at 532 nm with linear transmittance 70%. Reprinted with permission from [337], Y. Li et al., *Chem. Phys. Lett.* 337, 403 (2001). © 2001, Elsevier Science.



**Figure 15.** Optical limiting of two  $C_{60}/\gamma$ -cyclodextrin water solutions (0.15 and 0.3 mM) and a pure  $C_{60}$ -toluene solution (0.3 mM) at 532 nm. The transmitted energy is normalized ( $T = 100\%$ ) with respect to the linear transmission. Reprinted with permission from [341], M. Konstantaki et al., *Chem. Phys. Lett.* 318, 488 (2000). © 2000, Elsevier Science.

behavior of a pyrrolidino-fullerene derivative (FULP) solution with a FULP doped sol-gel sample. Compared to the green spectral region (532 nm) for both  $C_{60}$  and FULP in solution, enhanced optical limiting efficiency is demonstrated in the red spectral region (690 nm), that is, it shows better optical limiting performances than pristine fullerene. The inclusion in the sol-gel matrix does not influence the optical limiting performances of the fullerene derivative. The RSA is still the predominant mechanism for the observed optical limiting behavior.

Several groups have shown that the optical limiting performance of fullerenes in solid matrix, for example, in a poly(methyl methacrylate) (PMMA) matrix, is rather different from that in solution [344–346]. The dramatic difference should be contributed to mechanisms other than the RSA since the ground-state and triplet-triplet transient absorption spectra of  $C_{60}$  in PMMA polymers film are similar to those in room-temperature toluene solution [346]. Riggs and Sun [310] have investigated systematically the optical limiting properties of *tert*-butyl methano- $C_{60}$  carboxylate (TBM[60]CO) in room-temperature toluene solutions of different concentrations, in PMMA polymers films, and in highly viscous solvent-polymer blends. Similar to  $C_{60}$ , optical limiting performance of TBM[60]CO strongly depends on the fullerene solution concentrations due to bimolecular excited-state processes of the fullerenes. Riggs and Sun [347] have studied a series of mono- and multiple functionalized fullerene derivatives [348] at different solution concentrations giving a generalized understanding of the concentration-dependent optical limiting in fullerene solutions. The medium viscosity is shown to contribute to effects on the optical limiting contribution that are also associated with excited triplet-state bimolecular processes (in particular self-quenching and triplet-triplet annihilation), resulting in weaker optical limiting performance in highly viscous solvent-polymer blends [310]. For example, for the highly viscous solution (i.e., the presence of large quantities of PMMA polymer in toluene) of TMB[60]CO at 71% linear transmittance, the fluence saturation threshold value

is about  $0.17 \text{ J/cm}^2$ , which is about 20% higher than that for TMB[60]CO in room-temperature toluene solution of the same linear transmittance [310]. For another example, at 69% linear transmittance, the fluence saturation threshold value for TBM[60]CO in a highly viscous blend of poly(propionylethyleneimine) (PPEI) polymer chloroform solution is significantly higher than in room-temperature chloroform solution [310]. Optical limiting properties of TBM[60]CO are found to be essentially film thickness independent. (Lacking meaning molecular diffusion in polymer films may explain why TBM[60]CO in both thin and thick PMMA films exhibited a poorer optical limiting behavior than that in room-temperature). Based on the modified RSA model including both unimolecular and bimolecular excited-state processes, Riggs and Sun [310] indicated that the fullerene solution concentration affects the efficiency of the bimolecular excited-state processes, whereas the medium viscosity influences the bimolecular rate constants through changes in the molecular diffusivity.

### 4.3. Carbon Nanotubes

The optical limiting properties of MWNTs [349–354] and SWNTs [352, 354–362] have been recently studied. Some of the results are listed in Table 10. Compared to  $C_{60}$  and carbon black suspension (CBS), carbon nanotubes are also good candidates for optical limiting applications.

Sun and co-workers [349, 350] were the first to measure the energy-dependent transmission of MWNTs suspended in distilled water [349] and ethanol [350], or MWNTs embedded in PMMA films [349] in the visible and infrared spectral regions (e.g., 532 nm, 700 nm, and 1064 nm) with 7-ns laser pulses. For MWNTs in ethanol, the limiting threshold  $\eta$ , defined as the value of the input fluence at which the transmittance falls to half of the linear transmittance, is about  $1.0 \text{ J/cm}^2$  at 532 nm (lower than those of  $C_{60}$  and CBS), and  $6 \text{ J/cm}^2$  at 1064 nm (lower than that of CBS). Optical limiting phenomena totally vanish for  $C_{60}$  toluene solution. For MWNTs in water,  $\eta \approx 1.0, 5.5, 13 \text{ J/cm}^2$  at 532 nm, 700 nm, 1064 nm, respectively. For MWNT in PMMA,  $\eta \approx 3.1, 4.1, 8.0 \text{ J/cm}^2$  at 532 nm, 700 nm, 1064 nm, respectively. For MWNT and carbon particles in PMMA, the  $\eta$  values at 532 nm, 700 nm, 1064 nm are almost the same as those for MWNT in PMMA. Clearly, MWNTs, unlike  $C_{60}$  which has no limiting response at 1064 nm, are a broadband limiter up to 1064 nm. Since carbon nanotubes with a lower work function, lower electron binding energy, and stronger plasma excitation have no ground-state absorption at 532 nm and 1064 nm, the broadband limiting response should result from another mechanism. Recently, the energy-dependent transmission of MWNT suspension measured with picosecond and nanosecond laser pulses has shown a strong optical limiting action on the nanosecond time scales but does not display any limiting behavior in the picosecond regime even with an input fluence as high as  $3 \text{ J/cm}^2$  [351], which is different from that of  $C_{60}$  but similar to that of CBS. Picosecond time-resolved pump-probe experiment of Sun et al. [351] indicated that it took about 0.5 ns for the nonlinear transmission to appear for both MWNT and CBS. Especially, the smaller the external diameters of MWNT, the faster and larger are the changes of the

transmission. The nonlinear scattering experiments of Sun et al. [351] with nanosecond laser pulses at 532 nm confirmed that nonlinear scattering exists in MWNT suspension since the observed limiting behavior of MWNT is similar to that in CBS. Thus, the optical limiting action in the MWNT suspension comes from a mechanism similar to that in CBS.

Vivien et al. [354–359, 361] were the first to report the NLO transmittance of SWNT in a water suspension [354–356, 359, 361] or in chloroform [354, 356–359, 361] for pulse durations ranging from 3 to 100 ns and for wavelengths from 430 nm to 1064 nm. Their results are summarized in Table 11. For SWNT in water [355, 356, 359, 361],  $\eta = 3.8 \times 10^{-6} \text{ J/cm}^2$  (a bit higher than that of CBS) for 7-ns Nd:YAG laser pulse at 532 nm, and  $2.6 \times 10^{-5} \text{ J/cm}^2$  (lower than that of CBS) for 7-ns Nd:YAG laser pulse at 1064 nm. Obviously, the detailed studies of Vivien et al. [355–361] demonstrated that SWNTs are also efficient limiters over a broad wavelength range. Also, their results clearly show the wavelength effect [359] (this effect is attributed to the larger absorption cross sections of the suspensions at shorter wavelength and to the larger scattering cross sections of the laser-induced scattering centers [356]): the shorter the wavelength, the lower the limiting threshold  $\eta$  and the better the limiting efficiency. Their experimental measurements show that the pulse-duration effects reflecting two different mechanisms, that is, vapor-bubble growth and sublimation of carbon nanotubes, contributed to the optical limiting performance: for example, only the sublimation effect at 1064 nm for 5-ns Nd:YAG laser pulse, and both mechanisms at 1000 nm for 80-ns Ti:sapphire laser pulse. The limiting performances observed with 5-ns Nd:YAG laser pulse at 532 nm are considerably better than those obtained with 2-ns Nd:YAG laser pulse at 532 nm. Such strong pulse-duration dependence of

**Table 11.** Optical limiting threshold  $\eta$  of SWNT suspended in chloroform or in water using different laser source with different wavelength  $\lambda$  and pulse duration  $\tau$ .

Solvent	Laser source	$\tau$ [ns]	$\lambda$ [nm]	$\eta$ [ $\text{J/cm}^2$ ]	
Water	Nd:YAG	7	532	$3.8 \times 10^{-6}$	
	Nd:YAG	7	1064	$2.6 \times 10^{-5}$	
	Ti:sapphire	25	700	1	
	Ti:sapphire	15	800	0.3	
	Ti:sapphire	30	900	1.1	
	OPO	3	460	0.9	
	OPO	3	580	3	
	OPO	3	680	7	
	Chloroform	Nd:YAG	5	1064	0.2
		Nd:YAG	5	532	0.2
Nd:YAG		2	532	1.1	
Ti:sapphire		100	670	0.3	
Ti:sapphire		25	700	0.18	
Ti:sapphire		12	730	1	
Ti:sapphire		15	800	0.1	
Ti:sapphire		30	900	0.3	
Ti:sapphire		80	1000	0.02	
OPO		3	460	1	
OPO	3	580	3		
OPO	3	680	6		
OPO	3	694	6		

Source: Adapted from the experimental work of Vivien et al. [354–359, 361].

the limiting performance can be explained by the fact that the maximum size of the scattering centers in the nanosecond regime is reached only after the end of the incident pulses [354]. That is also why optical limiting is not observed at all in the picosecond range, but appears in the nanosecond and longer pulses. Moreover, the solvent effects [358, 359] demonstrated that MWNTs in chloroform exhibit better limiting performance than MWNTs in water because of two main reasons [359]: (i) since the absorption cross sections of the particles are slightly larger in chloroform than in water, chloroform exhibits lower thermal conductivity and diffusivity; (ii) with longer pulses from Ti:sapphire laser, chloroform has a very low heat of vaporization, surface tension and, viscosity, which lead to faster solvent-bubble growth. Nonlinear scattering and nonlinear refraction are the dominant mechanisms [357].

Meanwhile, Mishra et al. [362] carried out a detailed study on the optical limiting behavior of SWNT suspensions in different host liquids, for example, ethanol, water, and ethylene glycol. Their results are listed in Table 10 and demonstrated that optical limiting behavior in SWNT suspension appears mainly because of absorption-induced scattering in the suspension [362]. Especially, the extent of nonlinear scattering for good limiting performance in carbon nanotubes strongly depends on the host liquid. For example, optical limiting in the ethanol suspension was the strongest among the three suspensions: water, ethylene glycol, and ethanol (see Table 10).

Riggs et al. [352] and Jin et al. [353] have investigated the size-dependent optical limiting behaviors of SWNTs and MWNTs. Their results are listed in Table 10. These experimental measurements show that carbon nanotubes of large aspect ratio (or say long nanotube) possess stronger optical limiting properties. Apparently, the carbon nanotubes exhibit significantly weaker optical limiting response in homogeneous solution than in suspensions, reflecting that the optical limiting properties of the suspended versus solubilized carbon nanotubes represent dominating contributions by a nonlinear scattering mechanism versus a nonlinear absorption mechanism [352].

Preliminary experimental results of Riggs et al. [352] pointed out that the optical limiting results of carbon nanotube suspensions of the same linear transmittance, similar to those of CBS, are independent of nanotube concentrations, whereas the solubilized carbon nanotubes, similar to fullerenes in solution discussed above, show significant solution-concentration-dependent optical limiting behaviors.

The above reviewed carbon nanotubes were suspended in liquids because of their poor solubility in most solvents. Those suspensions are unstable at high concentration. So it is necessary to get stable solutions of carbon nanotubes. Jin et al. [363] studied the optical limiting performance of several polymer-coated and polymer-grafted MWNTs (which form stable solution in DMF) using 532-nm, 7-ns Nd:YAG laser pulses. The poly(ethylene oxide)/MWNT, poly(4-vinylpyridine)/MWNT, poly(2-vinylpyridine)/MWNT, and poly(4-vinyl-phenol)/MWNT all exhibited optical limiting behaviors similar to that of MWNT suspension in DMF: the  $\eta$  values for all samples are about 1 J/cm<sup>2</sup>. Considering that there is no optical limiting effect in all polymer-DMF solutions, their observed optical limiting behaviors of

polymer/MWNT composites are obviously due to the components of MWNTs. Hence, the polymer does not change the NLO properties of MWNTs, and a large variety of polymers can be used as the matrix of carbon nanotubes for the limiting applications. Since carbon nanotubes are broadband optical limiters, the polymer/MWNT composites are also broadband limiters. The important thing is that their polymer/MWNT solutions are very stable towards air and laser radiation [363].

Doped carbon nanotubes, for example, boron- or nitrogen-doped ones, can also exhibit good optical limiting performances. More details can be found in our other chapter contributed to this encyclopedia.

## 5. CONCLUSIONS

The advantage of the type of chromophore proposed by Asselberghs et al. [267] is that the switchability can be addressed by two different ways: proton transfer and redox switchabilities. As we know, electro-optical (EO) modulation is the main application for second-order NLO materials. In EO modulators, an applied electric field changes the refractive index of the NLO material through the EO coefficient. Based on the work of Asselberghs et al. [267], embedding the chromophore with the first-order hyperpolarizability, which can be switched by proton transfer in a matrix with such a photoaddressable proton donor, can make an EO modulator which can be controlled by light, that is, “on” state without light and “off” state with light. On the other hand, the combination of a second-order NLO chromophore with a photoaddressable proton donor would constitute a composite third-order optical material since the second-order NLO polarizability of a molecule would be influenced by light. This may allow for all-optical data manipulation, and the composite materials may provide for a new driving force in the field of third-order NLO materials.

As shown before, the less is the  $\pi$ - $\pi$  overlap in the three-dimensional conjugated spheres, the isomeric fullerenes, the higher is the barrier for the  $\pi$ -conjugated electron flow and thus the lowering of the second-order hyperpolarizability. Such concepts can be extended to explain the  $\gamma$  values of one-dimensional and two-dimensional  $\pi$ -conjugated systems, for example, *trans*-1,3-butadiene, *trans*-1,3,5-hexatriene, styrene, biphenyl, and 2,2-bithiophene.

C<sub>36</sub> fullerene is much more reactive than C<sub>60</sub> and C<sub>70</sub>. It has been shown that the ground state of C<sub>36</sub> is of diradical nature and the crystal C<sub>36</sub> is formed through covalent bonds among C<sub>36</sub> units. Obviously, this is contrasted with C<sub>60</sub> and C<sub>70</sub>. On the other hand, bounding the electron donor groups to C<sub>36</sub> would remove the strong diradical character and stabilize the entire system, showing the possibility of synthesizing these molecules. Hence it is expected for the C<sub>36</sub> chemistry to be further explored, studying the possibility of using C<sub>36</sub> derivatives for building NLO materials.

The improvement of the optical limiting performance observed in the molybdenum complex of C<sub>60</sub> or C<sub>70</sub>, which is attributed to the increment on the triplet-state absorption by intramolecular charge transfer, shows that the charge-transfer nature would make metal-fullerene complexes good candidates for optical limiting applications and leads to a

new means for significantly improving the performance of fullerenes.

The solubility of  $C_{60}$  can be improved by combining it with an alkyl group of substituted CuPc through the Diels–Alder reaction. The combined molecules exhibit good optical limiting performance. Hence, based on the combination of various optical limiting molecules through covalent bonds, broadband optical limiting materials may be designed and phase separation problems, which exist in the mixture of various materials, can also be avoided.

The large optical limiting performance observed from the novel nanocomposites DTC<sub>60</sub>-Ag or HDTC<sub>60</sub>-Ag at 532 nm is due to the combination effort from the  $C_{60}$  derivative and silver nanoparticles. Thus, these kinds of novel nanocomposites would lead to novel optoelectronics as well as catalytic properties assembled by fullerene and metals. Surely, much work needs to be done to understand the interesting photo-physical phenomena observed in these systems.

The attachment of two cyano groups to  $C_{60}$  reduces its quantum yield, increases the absorption of the excited triplet state, and leads to  $C_{60}(CN)_2$  which has a similar optical limiting behavior to  $C_{60}$  for nanosecond laser at 532 nm. Since the differential absorption between the excited triplet state and the ground state in  $C_{60}(CN)_2$  is larger in the near-infrared region, we expect that this molecule may also have better optical limiting performance in the near-infrared region than at 532 nm.

## GLOSSARY

**Degenerate four-wave mixing (DFWM)** A powerful tool for measuring a third-order nonlinear optical susceptibility by using two wave beams that are incident at the same region on the sample and have equal and opposite wave vectors and the same frequency.

**Fullerene** A cage molecule made of 12 pentagonal faces and any number of hexagonal faces.

**Multiwalled carbon nanotube (MWNT)** MWNT is obtained if a few stacked graphitic shells are built from perfectly concentric cylinders or a single graphene sheet is rolled as a scroll.

**Nonlinear optics (NLO)** The study of phenomena that occur as a consequence of the modification of the optical properties of a material system by the presence of light.

**Optical Kerr effect (OKE)** A useful technique that shows the detected signal which is proportional to the quadrate of the third-order optical susceptibility.

**Optical limiter** A protection device for human eye and instrument sensors and exhibits linear transmission below a certain input light fluence threshold, but above this threshold the output light fluence reaches a saturated value.

**Second-harmonic generation (SHG)** A nonlinear optical interaction in which all of the power in the incident radiation at frequency  $w$  is converted to radiation at the second-harmonic frequency  $2w$ .

**Single-walled carbon nanotube (SWNT)** SWNT is made if only one graphene sheet is rolled.

**Third-harmonic generation (THG)** A nonlinear optical interaction in which all of the power in the incident radiation at frequency  $w$  is converted to radiation at the third-harmonic frequency  $3w$ .

**Z-scan** A technique that measures the real and imaginary parts of the third-order optical susceptibility simultaneously.

## ACKNOWLEDGMENTS

We thank Dr. H. S. Nalwa, Dr. J. F. Xu, Professor V. H. Smith, Jr., Professor J. Gao, Dr. Z. G. Li, Dr. X. H. Wang, Dr. Q. D. Wang, and Dr. J. B. Gong for valuable comments. Q. R. thanks the Queen's University for a Reinhardt Fellowship. L. J. gratefully acknowledges the Danish Research Training Council for financial support.

## REFERENCES

1. G. C. Baldwin, "An Introduction to Nonlinear Optics." Plenum Press, New York, 1969.
2. F. Zernike and J. E. Midwinter, "Applied Nonlinear Optics." Wiley, New York, 1973.
3. Y. R. Shen, "The Principles of Nonlinear Optics." Wiley, New York, 1984.
4. M. Schubert and B. Wilhelmi, "Nonlinear Optics and Quantum Electronics." Wiley, New York, 1986.
5. A. Yariv, "Quantum Electronics." John Wiley & Sons, New York, 1989.
6. J. Messier, F. Kajzar, P. N. Prasad, and D. Ulrich, "Nonlinear Optical Effects in Organic Polymers." Kluwer Academic, Dordrecht, 1991.
7. J. Messier, F. Kajzar, and P. N. Prasad, "Organic Molecules for Nonlinear Optics and Photonics." Kluwer Academic, Dordrecht, 1991.
8. P. N. Prasad and D. J. Williams, "Introduction to Nonlinear Optical Effects in Molecules and Polymers." Wiley, New York, 1991.
9. R. W. Boyd, "Nonlinear Optics." Academic Press, New York, 1992.
10. J. I. Sakai, "Phase Conjugate Optics." McGraw-Hill, Singapore, 1992.
11. H. S. Nalwa, *Adv. Mater.* 5, 341 (1993).
12. J. Zyss, "Molecular Nonlinear Optics." Academic Press, New York, 1994.
13. H. S. Nalwa, in "Handbook of Organic Conductive Molecules and Polymers" (H. S. Nalwa, Ed.), Vol. 4, Chap. 6, pp. 261–363. John Wiley & Sons, Chichester, 1997.
14. H. S. Nalwa, in "Nonlinear Optics of Organic Molecules and Polymers" (H. S. Nalwa and S. Miyata, Eds.), Chap. 11, pp. 611–797. CRC Press, Boca Raton, FL, 1997.
15. U. Woggon, "Optical Properties of Semiconductor Quantum Dots." Springer-Verlag, Berlin, 1997.
16. J. F. Nye, "The Physical Properties of Crystals." Clarendon Press, Oxford, 1985.
17. G. Benedek, P. Milani, and V. G. Ralchenko, Eds., "Nanostructured Carbon for Advanced Applications." Kluwer, Dordrecht, 2001.
18. A. A. Lucas, F. Moreau, and Ph. Lambin, *Rev. Mod. Phys.* 74, 1 (2002).
19. H. W. Kroto, J. R. Heath, S. C. O'Brien, R. E. Curl, and R. E. Smalley, *Nature (London)* 318, 162 (1985).
20. E. Osawa, *Kagaku (Kyoto)* 25, 854 (1970).
21. H. W. Kroto, J. E. Fischer, and D. E. Cox, "The Fullerenes." Pergamon, Oxford, 1993.



22. A. Hirsch, "The Chemistry of the Fullerenes." Thieme, New York, 1994.
23. R. E. Smalley, *Rev. Mod. Phys.* 69, 723 (1997).
24. R. F. Curl, *Rev. Mod. Phys.* 69, 691 (1997).
25. H. W. Kroto, *Rev. Mod. Phys.* 69, 703 (1997).
26. R. F. Curl and R. E. Smalley, *Sci. Am.* 264, 54 (1991).
27. W. Krätschmer, L. D. Lamb, K. Fostiropoulos, and D. R. Huffman, *Nature (London)* 347, 354 (1990).
28. D. R. Huffman, *Phys. Today* 44, 22 (1991).
29. P. W. Fowler and D. E. Manlopoulos, "An Atlas of Fullerenes." Clarendon Press, Oxford, 1995.
30. J. Cioslowski, "Electronic Structure Calculations on Fullerenes and Their Derivatives." Oxford University Press, New York, 1995.
31. M. S. Dresselhaus, G. Dresselhaus, and P. C. Eklund, "Science of Fullerenes and Carbon Nanotubes." Academic Press, New York, 1996.
32. W. Andreoni, Ed., "The Physics of Fullerene-Based and Fullerene-Related Materials." Kluwer, New York, 2000.
33. R. H. Xie, in "Handbook of Advanced Electronic and Photonic Materials and Devices, Vol. 9: Nonlinear Optical Materials" (H. S. Nalwa, Ed.), pp. 267–307. Academic Press, New York, 2000.
34. K. M. Kadish and R. S. Ruoff, Eds., "Fullerenes: Chemistry, Physics, and Technology." Wiley & Sons, New York, 2000.
35. E. Osawa, Ed., "Perspectives of Fullerene Nanotechnology." Kluwer, New York, 2002.
36. S. Iijima, *Nature (London)* 354, 56 (1991).
37. T. W. Ebbesen and P. M. Ajayan, *Nature (London)* 358, 220 (1992).
38. S. Iijima and T. Ichihashi, *Nature (London)* 363, 603 (1993).
39. V. P. Dravid, X. Lin, Y. Wang, X. K. Wang, A. Yee, J. B. Ketterson, and R. P. H. Chang, *Science* 259, 1601 (1993).
40. T. W. Ebbesen, H. Hiura, Y. Fujita, Y. Ochiai, S. Matsui, and K. Tanigaki, *Chem. Phys. Lett.* 209, 83 (1993).
41. T. W. Ebbesen, *Physics Today* 49, 26 (1996).
42. T. W. Ebbesen, "Carbon Nanotubes." CRC Press, Boca Raton, FL, 1997.
43. M. Endo, S. Iijima, and M. S. Dresselhaus, "Carbon Nanotubes." Pergamon, Oxford, 1996.
44. P. M. Ajayan and T. W. Ebbesen, *Rep. Prog. Phys.* 60, 1025 (1997).
45. A. Thess, R. Lee, P. Nikolav, H. Dai, P. Petit, J. Robert, C. Xu, Y. H. Lee, S. G. Kim, A. G. Rinzler, D. T. Colbert, G. E. Scuseria, D. Tomanek, J. E. Fischer, and R. E. Smalley, *Science* 373, 483 (1996).
46. C. Journet, W. K. Maser, P. Bernier, A. Loiseau, M. L. Delachapelle, S. Lefrant, P. Deniard, R. Lee, and J. E. Fischer, *Nature (London)* 388, 756 (1997).
47. Y. Zhang and S. Iijima, *Philos. Mag. Lett.* 78, 139 (1998).
48. M. Yudasaka, T. Ichihashi, T. Komatsu, and S. Iijima, *Chem. Phys. Lett.* 299, 91 (1999).
49. F. Kokai, K. Takahashi, M. Yudasaka, R. Yamada, T. Ichihashi, and S. Iijima, *J. Phys. Chem.* 103, 4346 (1999).
50. B. C. Satiskumar, A. Govindaraj, R. Sen, and C. N. R. Rao, *Chem. Phys. Lett.* 293, 47 (1998).
51. J. M. Mao, L. F. Sun, L. X. Qian, Z. W. Pan, B. H. Chang, W. Y. Zhou, G. Wang, and S. Xie, *Appl. Phys. Lett.* 72, 3297 (1998).
52. S. Bandow, S. Asaka, Y. Saito, A. M. Rao, L. Grigorian, E. Richter, and P. C. Eklund, *Phys. Rev. Lett.* 80, 3779 (1998).
53. J. Kong, A. M. Cassell, and H. Dai, *Chem. Phys. Lett.* 292, 567 (1998).
54. H. Dai, A. G. Rinzler, P. Nikolaev, A. Thess, D. T. Colbert, and R. E. Smalley, *Chem. Phys. Lett.* 260, 471 (1996).
55. M. Yudasaka, T. Komatsu, I. Ichihashi, and S. Iijima, *Chem. Phys. Lett.* 278, 102 (1998).
56. M. Yudasaka, T. Komatsu, I. Ichihashi, Y. Achiba, and S. Iijima, *J. Phys. Chem. B* 102, 4892 (1998).
57. H. M. Cheng, F. Li, G. Su, H. Y. Pan, L. L. He, X. Sun, and M. S. Dresselhaus, *Appl. Phys. Lett.* 72, 3282 (1998).
58. M. S. Dresselhaus, G. Dresselhaus, and R. Saito, *Phys. Rev. B* 45, 6234 (1992).
59. M. S. Dresselhaus, G. Dresselhaus, and R. Saito, *Carbon* 33, 883 (1995).
60. R. Saito, M. Fujita, G. Dresselhaus, and M. S. Dresselhaus, *Appl. Phys. Lett.* 60, 2204 (1992).
61. R. A. Jishi, M. S. Dresselhaus, and G. Dresselhaus, *Phys. Rev. B* 47, 16671 (1993).
62. R. A. Jishi, L. Venkataraman, M. S. Dresselhaus, and G. Dresselhaus, *Phys. Rev. B* 51, 11176 (1995).
63. T. W. Ebbesen, "Carbon Nanotubes: Preparation and Properties." CRC Press, New York, 1996.
64. R. Saito, G. Dresselhaus, and M. S. Dresselhaus, "Physical Properties of Carbon Nanotubes." Imperial College Press, London, 1998.
65. K. Tanaka, T. Yamabee, K. Fukui, T. Yamabe, and K. Fukui, "The Science and Technologies of Carbon Nanotubes." Elsevier Science, New York, 1999.
66. K. C. Venema, "Electronic Structure of Carbon Nanotubes." Delft University Press, Delft, 2000.
67. L. P. Biro, C. A. Bernardo, and G. G. Tibbetts, "Carbon Filaments and Nanotubes: Common Origins, Differing Applications." Kluwer Academic, New York, 2001.
68. M. S. Dresselhaus, G. Dresselhaus, and Ph. Avouris, Eds., "Carbon Nanotubes: Synthesis, Structures, Properties, and Applications." Springer-Verlag, New York, 2001.
69. P. J. F. Harris, "Carbon Nanotubes and Related Structures." Cambridge University Press, New York, 2001.
70. St. Reich, J. Janina, and Ch. Thomsen, "Carbon Nanotubes." Wiley & Sons, New York, 2002.
71. J. P. Lu and J. Han, *Inter. J. High Electronics and System* 9, 101 (1998).
72. L. Dai, *Polym. Adv. Technol.* 10, 357 (1999).
73. P. M. Ajayan, *Chem. Rev.* 99, 1787 (1999).
74. C. N. R. Rao, B. C. Satishkumar, A. Govindaraj, and M. Nath, *Chem. Phys. Chem.* 2, 78 (2001).
75. S. B. Sinnott and R. Andrews, *Critical Reviews in Solid State and Materials Science* 26, 145 (2001).
76. P. Avouris, *Chem. Phys.* 281, 429 (2002).
77. R. H. Baughman, A. A. Zakhidov, and W. A. de Heer, *Science* 297, 787 (2002).
78. A. Willetts, J. E. Rice, and D. M. Burland, *J. Chem. Phys.* 97, 7590 (1992).
79. G. R. Meredith, L. T. Cheng, H. Hsiung, H. A. Vanherzeele, and F. C. Zumsteg, in "Materials for Nonlinear and Electro-Optics" (M. H. Lyons, Ed.), pp. 139–150. IOP Publishing, New York, 1989.
80. H. Hoshi, N. Nakamura, Y. Maruyama, T. Nakagawa, S. Suzuki, H. Shiromaru, and Y. Achiba, *Japan. J. Appl. Phys.* 30, L1397 (1991).
81. X. K. Wang, T. G. Zhang, W. P. Lin, S. Z. Liu, G. K. Wong, M. M. Kappes, R. P. H. Chang, and J. B. Ketterson, *Appl. Phys. Lett.* 60, 810 (1992).
82. B. Koopmans, A. Anema, H. T. Jonkman, G. A. Sawatzky, and F. van der Woude, *Phys. Rev. B* 48, 2759 (1993).
83. F. Kajzar, C. Taliani, R. Zamboni, S. Rossini, and R. Danieli, *Synthetic Metals* 77, 257 (1996).
84. K. Kuhnke, M. Epple, and K. Kern, *Chem. Phys. Lett.* 294, 241 (1998).
85. Y. R. Shen, *Ann. Rev. Phys. Chem.* 40, 327 (1989).
86. D. Wilk, D. Johannsmann, C. Stanners, and Y. R. Shen, *Phys. Rev. B* 51, 10057 (1995).

87. A. M. Janner, Ph.D. Thesis, University of Groningen, Groningen, 1998.
88. G. Wang, J. Wen, Q. Houng, S. Qian, and X. Lu, *J. Phys. D: Appl. Phys.* 32, 84 (1999).
89. Th. Rashing, G. Berkovic, Y. R. Shen, S. G. Grubb, and M. W. Kim, *Chem. Phys. Lett.* 130, 1 (1986).
90. S. Qin, W. M. You, and Z. B. Su, *Phys. Rev. B* 48, 17562 (1993).
91. A. Lucas, G. Gensterblum, J. J. Pireaux, P. A. Thiry, R. Caudano, J. P. Vigneron, and W. Krätschmer, *Phys. Rev. B* 45, 13694 (1992).
92. P. A. Heiney, J. F. Fischer, A. R. McGhie, W. J. Romanow, A. M. Denenstien, J. P. McCauley, Jr., A. B. Smith III, and D. E. Cox, *Phys. Rev. Lett.* 66, 2911 (1991).
93. W. I. F. David, R. M. Ibberson, T. J. S. Dennis, J. P. Hare, and K. Prassidees, *Europhys. Lett.* 18, 219 (1992).
94. B. Koopmans, A. M. Janner, H. T. Jonkman, G. A. Sawatzky, and F. van der Woude, *Phys. Rev. Lett.* 71, 3569 (1993).
95. R. W. Munn, Z. Shuai, and J.-L. Bredas, *J. Chem. Phys.* 108, 5975 (1998).
96. Y. Liu, H. Jiang, W. Wang, Y. Li, and J. Zheng, *Phys. Rev. B* 50, 4940 (1994).
97. A. Sassara, G. Zerza, and M. Chergui, *J. Phys. Chem. A* 102, 3072 (1998).
98. Z. Shuai and J. L. Bredas, *Mol. Cryst. Liq. Cryst.* 256, 801 (1994).
99. F. Kajzar, C. Taliani, R. Danieli, S. Rossini, and R. Zamboni, *Phys. Rev. Lett.* 73, 1617 (1994).
100. B. F. Levine and C. G. Bethea, *J. Chem. Phys.* 66, 1070 (1977).
101. J. L. Qudar, *J. Chem. Phys.* 67, 446 (1977).
102. R. E. Haufler, J. Conceicao, P. F. Chibante, Y. Chai, N. E. Byrne, S. Flanagan, M. M. Haley, S. C. O'Brien, C. Pan, Z. Xiao, W. E. Billups, M. A. Ciufolini, R. H. Hauge, L. J. Wilson, R. Curl, and R. E. Smalley, *J. Phys. Chem.* 94, 8634 (1990).
103. Y. Wang and L. T. Cheng, *J. Phys. Chem.* 96, 1530 (1992).
104. A. Weller, in "Exciplex" (M. Gordon and W. R. Ware, Eds.). Academic Press, New York, 1975.
105. G. R. Meredith, L. T. Cheng, H. Hsiung, H. A. Vanherzeele, and F. C. Zumsteg, in "Materials for Nonlinear and Electro-optics" (M. H. Lyons, Ed.), pp. 139-150. IOP Publishing, New York, 1989.
106. L. T. Cheng, W. Tam, S. H. Stevenson, G. R. Meredith, G. Rikken, and S. R. Marder, *J. Phys. Chem.* 95, 10631 (1991).
107. J. Ridley and M. C. Zerner, *Theor. Chim. Acta (Berlin)* 32, 111 (1973).
108. S. D. Bella, I. L. Fragala, M. A. Ratner, and T. J. Marks, *J. Am. Chem. Soc.* 115, 682 (1993).
109. A. Ulman, C. S. Willand, W. Kohler, D. R. Robello, D. J. Williams, and L. Handley, *J. Am. Chem. Soc.* 112, 7083 (1990).
110. J. Li, J. Feng, and C. Sun, *J. Phys. Chem.* 98, 8636 (1994).
111. Y. Liu, D. Zhang, H. Hu, and C. Liu, *J. Mol. Struct. (Theochem.)* 545, 97 (2001).
112. W. Fu, J.-K. Feng, G.-B. Pan, and X. Zhang, *Theor. Chem. Acc.* 106, 241 (2001).
113. M. Lamrani, R. Hamasaki, M. Mitsuishi, T. Miyashita, and Y. Tamamoto, *Chem. Comm.* 1595 (2000).
114. K. D. Kampe, N. Egger, and M. Vogel, *Angew. Chem., Int. Ed. Engl.* 32, 1174 (1993).
115. L. B. Gan, D. J. Zhou, C. P. Luo, C. H. Huang, T. K. Li, J. Bai, X. S. Zhao, and X. H. Xia, *J. Phys. Chem.* 98, 12459 (1994).
116. F. Kajzar, Y. Okada-Shudo, C. Meritt, and Z. Kafafi, *Synthetic Metals* 94, 91 (1998).
117. N. Matsuzawa, D. A. Dixon, and T. Fukunaga, *J. Phys. Chem.* 96, 7584 (1992).
118. J. Jiang, J. Dong, Q. Xu, and D. Y. Xing, *Z. Phys. D* 37, 341 (1996).
119. P. S. Baran, R. R. Monaco, A. U. Khan, D. I. Schuster, and S. R. Wilson, *J. Am. Chem. Soc.* 119, 8363 (1997).
120. S. Wang, R. M. Leblanc, F. Arias, and L. Echegoyen, *Langmuir* 13, 1672 (1997).
121. Z. X. Guo, Y. L. Li, F. L. Bai, J. M. Yan, Z. X. Ge, D. B. Zhu, J. H. Si, P. X. Ye, L. X. Wang, and T. K. Li, *J. Phys. Chem. Solids* 61, 1089 (2000).
122. Z. X. Guo, Y. L. Li, Z. X. Ge, J. Yan, D. B. Zhu, J. H. Shi, and P. X. Ye, *Appl. Phys. B* 71, 545 (2000).
123. E. E. B. Campbell, M. Fanti, I. V. Hertel, R. Mitzner, and F. Zerbetto, *Chem. Phys. Lett.* 288, 131 (1998).
124. K. C. Rustagi, L. Ramaniah, and S. V. Nair, *Int. J. Mod. Phys. B* 6, 3941 (1992).
125. I. M. L. Billas, C. Massobrio, M. Boero, M. Parrinello, W. Branz, F. Tast, N. Malinowski, M. Heinebrodt, and T. P. Martini, *J. Chem. Phys.* 111, 15 (1999).
126. I. Fuks, I. V. Kityk, J. Kasperczyk, J. Berdowski, and I. Schirmer, *Chem. Phys. Lett.* 353, 7 (2002).
127. F. Lin, S. Mao, Z. Meng, H. Zeng, J. Qiu, Y. Yue, and T. Guo, *Appl. Phys. Lett.* 65, 2522 (1994).
128. H. Zeng, Z. Sun, Y. Segawa, F. Lin, S. Mao, Z. Xu, and S. H. Tang, *J. Phys. D: Appl. Phys.* 33, L93 (2000).
129. L. Jensen, P. Th. van Duijnen, J. G. Snijders, and D. P. Chong, *Chem. Phys. Lett.* 359, 524 (2002).
130. M. Fanti, G. Orlandi, and F. Zerbetto, *J. Phys. Chem. A* 101, 3015 (1997).
131. J. Zyss and I. Ledoux, *Chem. Rev.* 94, 77 (1994).
132. J. Zyss, S. Brasselet, V. R. Thalladi, and G. R. Desiraju, *J. Chem. Phys.* 109, 658 (1998).
133. A. G. H. Barbosa and M. A. C. Nascimento, *Chem. Phys. Lett.* 343, 15 (2001).
134. C. Piskoti, J. Yarger, and A. Zettl, *Nature (London)* 393, 771 (1998).
135. J. R. Heath, *Nature (London)* 393, 730 (1998).
136. M. Cote, J. C. Grossman, M. L. Cohen, and S. G. Louie, *Phys. Rev. Lett.* 81, 697 (1998).
137. H. Kietzmann, R. Rochow, G. Ganteför, W. Eberhardt, K. Vietze, G. Seifert, and P. W. Fowler, *Phys. Rev. Lett.* 81, 5378 (1998).
138. P. W. Fowler, D. Mitchell, and F. Zerbetto, *J. Am. Chem. Soc.* 121, 3218 (1999).
139. P. G. Collins, J. C. Grossman, M. Cote, M. Ishigami, C. Piskoti, S. G. Louie, M. L. Cohen, and A. Zettl, *Phys. Rev. Lett.* 82, 165 (1999).
140. J. C. Grossman, M. Cote, S. G. Louie, and M. L. Cohen, *Chem. Phys. Lett.* 284, 344 (1998).
141. Z. Slanina, X. Zhao, and E. Osawa, *Chem. Phys. Lett.* 290, 311 (1998).
142. E. Halac, E. Burgos, and H. Bonadeo, *Chem Phys. Lett.* 299, 64 (1999).
143. Z. Slanina, F. Uhlik, X. Zhao, and E. Osawa, *J. Chem. Phys.* 113, 4933 (2000).
144. L. Yuan, J. Yang, K. Deng, and Q. Zhu, *J. Phys. Chem. A* 104, 6666 (2000).
145. M. N. Jagadeesh and J. Chandrasekhar, *Chem. Phys. Lett.* 305, 298 (1999).
146. P. W. Fowler, T. Heine, K. M. Rogers, J. P. B. Sandall, G. Seifert, and F. Zerbetto, *Chem. Phys. Lett.* 300, 369 (1999).
147. S. P. Karna, P. N. Prasad, and M. Dupuis, *J. Chem. Phys.* 94, 1171 (1991).
148. M. Sheik-Bahae, A. A. Said, T. H. Wei, D. J. Hagan, and E. W. van Stryland, *IEEE J. Quantum Electron.* 26, 760 (1990).
149. M. O. Levenson and N. Bloembergen, *J. Chem. Phys.* 60, 1323 (1974).
150. A. F. Garito, J. R. Heflin, K. Y. Yong, and O. Zamani-Khamiri, *Proc. Soc. Photon. Opt. Instrum. Eng.* 971, 2 (1988).
151. S. R. Marder, W. E. Torruellas, M. Blanchard-Desce, V. Ricci, G. I. Stegeman, S. Gilmour, J. L. Bredas, J. Li, G. U. Bublitz, and S. G. Boxer, *Science* 276, 1233 (1997).

152. H. Thinpont, G. L. A. Rikken, E. W. Meijer, W. ten Hoeve, and H. Hynberg, *Phys. Rev. Lett.* 65, 2141 (1990).
153. F. C. Spano and Z. G. Soos, *J. Chem. Phys.* 99, 9265 (1993).
154. I. D. W. Samuel, I. Ledoux, C. Dhenaut, J. Zyss, H. H. Fox, R. R. Schrock, and R. J. Silbey, *Science* 265, 1070 (1994).
155. G. Chen, D. Lu, and W. A. Goddard III, *J. Chem. Phys.* 101, 5860 (1994).
156. D. Lu, G. Chen, and W. A. Goddard III, *J. Chem. Phys.* 101, 4920 (1994).
157. D. Lu, G. J. W. Perry, and W. A. Goddard III, *J. Am. Chem. Soc.* 116, 10679 (1994).
158. S. Mukamel, A. Tahahashi, H. X. Wang, and G. Chen, *Science* 266, 250 (1994).
159. D. Lu, B. Marten, M. Ringnalda, R. A. Friesner, and W. A. Goddard III, *Chem. Phys. Lett.* 257, 224 (1996).
160. T. Hamada, *J. Chem. Soc. Faraday Trans.* 92, 3165 (1996).
161. M. Hasan, S. J. Kim, J. L. Toto, and B. Kirtman, *J. Chem. Phys.* 105, 186 (1996).
162. E. Sohmen, J. Fink, and W. Kratschmer, *Z. Phys. B* 86, 86 (1992).
163. W. J. Blau, H. J. Byrne, D. J. Cardin, T. J. Dennis, J. P. Hare, H. W. Kroto, R. Taylor, and D. R. M. Walton, *Phys. Rev. Lett.* 67, 1423 (1991).
164. R. J. Knize and J. P. Partanen, *Phys. Rev. Lett.* 68, 2704 (1992).
165. Z. H. Kafafi, F. J. Bartoli, J. R. Lindle, and R. G. S. Pong, *Phys. Rev. Lett.* 68, 2705 (1992).
166. F. Kajzar, C. Taliani, R. Zamboni, S. Rossini, and R. Danieli, in "Fullerenes: Status and Perspectives, First Italian Workshop on Fullerenes" (C. Taliani, G. Ruani, and R. Zamboni, Eds.). World Scientific, Singapore, 1992.
167. F. Kajzar, C. Taliani, R. Zamboni, S. Rossini, and R. Danieli, *Synth. Met.* 54, 21 (1993).
168. F. Kajzar, C. Taliani, R. Zamboni, S. Rossini, and R. Zamboni, *Chem. Phys. Lett.* 217, 418 (1994).
169. Q. Gong, Y. Sun, Z. Xia, Y. H. Zou, Z. Gu, X. Zhou, and D. Qiang, *J. Appl. Phys.* 71, 3025 (1992).
170. Z. H. Kafafi, J. R. Lindle, R. G. S. Pong, F. J. Bartoli, L. J. Lingg, and J. Milliken, *Chem. Phys. Lett.* 188, 492 (1992).
171. G. B. Talapatra, N. Manickam, M. Samoc, M. E. Orczyk, S. P. Karna, and P. N. Prasad, *J. Phys. Chem.* 96, 5206 (1992).
172. J. S. Meth, H. Vanherzeele, and Y. Wang, *Chem. Phys. Lett.* 197, 26 (1992).
173. Z. Zhang, D. Wang, P. Ye, Y. Li, P. Wu, and D. Zhu, *Opt. Lett.* 17, 973 (1992).
174. D. Neher, G. I. Stegeman, F. A. Tinker, and N. Peyghambarian, *Opt. Lett.* 17, 1491 (1992).
175. S. C. Yang, Q. Gong, Z. Xia, Y. H. Zou, Y. Q. Wu, D. Qiang, Y. L. Sun, and Z. N. Gu, *Appl. Phys. B* 52, 51 (1992).
176. S. R. Flom, R. G. S. Pong, F. J. Bartoli, and Z. H. Kafafi, *Phys. Rev. B* 46, 15598 (1992).
177. J. Li, J. Feng, and J. Sun, *Chem. Phys. Lett.* 203, 560 (1993).
178. J. Li, J. Feng, and C. Sun, *Int. J. Quantum. Chem.* 52, 673 (1994).
179. N. Matsuzawa and D. A. Dixon, *J. Phys. Chem.* 96, 6241 (1992).
180. M. J. Rosker, H. O. Marcy, T. Y. Chang, J. T. Khoury, K. Hansen, and R. L. Whetten, *Chem. Phys. Lett.* 196, 427 (1992).
181. D. Jonsson, P. Norman, K. Ruud, H. Ågren, and T. Helgaker, *J. Chem. Phys.* 109, 572 (1998).
182. J. R. Lindle, R. G. S. Pong, F. J. Bartoli, and Z. H. Kafafi, *Phys. Rev. B* 48, 9447 (1993).
183. N. Tang, J. P. Partanen, R. W. Hellwarth, and R. J. Knize, *Phys. Rev. B* 48, 8404 (1993).
184. W. Ji, S. H. Tang, G. Q. Xu, H. S. O. Chan, S. H. Ng, and W. W. Ng, *J. Appl. Phys.* 74, 3669 (1993).
185. F. Sun, S. Zhang, Z. Zia, Y. H. Zou, X. Chen, D. Qiang, X. Zhou, and Y. Wu, *Phys. Rev. B* 51, 4614 (1995).
186. P. Norman, Y. Lu, D. Jonsson, and H. Ågren, *J. Chem. Phys.* 106, 8788 (1997).
187. L. Geng and J. C. Wright, *Chem. Phys. Lett.* 249, 105 (1996).
188. J. Li, S. Wang, H. Yang, Q. Gong, X. An, H. Chen, and D. Qiang, *Chem. Phys. Lett.* 288, 175 (1998).
189. S. J. A. van Gisbergen, J. G. Snijders, and E. J. Baerends, *Phys. Rev. Lett.* 78, 3097 (1997).
190. J.-I. Iwata, K. Yabana, and G. F. Bertsch, *J. Chem. Phys.* 115, 8773 (2001).
191. Y. Luo, P. Norman, P. Macak, and H. Ågren, *Phys. Rev. B* 61, 3060 (2000).
192. E. A. Perpète, B. Champagne, and B. Kirtman, *Phys. Rev. B* 61, 13137 (2000).
193. N. Matsuzawa and D. A. Dixon, *J. Phys. Chem.* 96, 6872 (1992).
194. A. A. Quang and M. R. Pederson, *Phys. Rev. B* 46, 12906 (1992).
195. K. Harigaya and S. Abe, *Jpn. J. Appl. Phys.* 31, L887 (1992).
196. A. Takahashi, H. X. Wang, and S. Mukamel, *Chem. Phys. Lett.* 216, 394 (1993).
197. M. M. Mestechkin and G. E. Whyman, *Chem. Phys. Lett.* 214, 144 (1993).
198. G. E. Whyman and M. M. Mestechkin, *Opt. Commun.* 109, 410 (1994).
199. E. Westin and A. Rosén, *Int. J. Mod. Phys. B* 6, 3893 (1992).
200. P. W. Fowler, H. M. Kelly, M. Malagoli, and R. Zanasi, *Int. J. Mod. Phys. B* 6, 3903 (1992).
201. Y. Wang, G. F. Bertsch, and D. Tomanek, *Z. Physik D* 25, 181 (1993).
202. F. Willaime and L. M. Falicov, *J. Chem. Phys.* 98, 6369 (1993).
203. T. Hara, Y. Nomura, S. Narita, and T.-I. Shibuya, *Chem. Phys. Lett.* 240, 610 (1995).
204. E. Westin and A. Rosén, *Appl. Phys. A* 60, 49 (1995).
205. B. H. Cardelino, C. E. Moore, and D. O. Frazier, *J. Phys. Chem. A* 101, 2207 (1997).
206. Y.-T. Lin and S.-L. Lee, *Int. J. Quant. Chem.* 75, 457 (1999).
207. A. Göller and U.-W. Grummt, *Int. J. Quant. Chem.* 77, 727 (2000).
208. Y. Nomura, T. Miyamoto, T. Hara, S. Narita, and T. I. Shibuya, *J. Chem. Phys.* 112, 6603 (2000).
209. W.-D. Cheng, D.-S. Wu, H. Zhang, and H.-X. Wang, *Phys. Rev. B* 66, 113401 (2002).
210. R. Lascola and J. C. Wright, *Chem. Phys. Lett.* 269, 79 (1997).
211. R. Lascola and J. C. Wright, *Chem. Phys. Lett.* 290, 117 (1998).
212. R. J. Knize, *Opt. Commun.* 106, 95 (1994).
213. R. H. Xie and J. Jiang, *Appl. Phys. Lett.* 71, 1029 (1997).
214. R. H. Xie and J. Jiang, *Chem. Phys. Lett.* 280, 66 (1997).
215. R. H. Xie, *Nuovo Cimento D* 19, 1867 (1997).
216. Y. Luo, *Chem. Phys. Lett.* 289, 350 (1998).
217. C. E. Moore, B. H. Cardelino, and X. Q. Wang, *J. Phys. Chem.* 100, 4685 (1996).
218. Z. Shuai and J. L. Bredas, *Phys. Rev. B* 46, 16135 (1992).
219. Z. Shuai and J. L. Bredas, *Phys. Rev. B* 48, 11520 (1993).
220. M. Fanti, G. Orlandi, and F. Zerbetto, *J. Am. Chem. Soc.* 117, 6101 (1995).
221. M. Fanti, P. W. Fowler, G. Orlandi, and F. Zerbetto, *J. Chem. Phys.* 107, 5072 (1997).
222. R. H. Xie and Q. Rao, *Appl. Phys. Lett.* 72, 2358 (1998).
223. R. H. Xie, *J. Chem. Phys.* 108, 3626 (1998).
224. K. Harigaya, *J. Phys.: Condens. Matter* 10, 6845 (1998).
225. K. Harigaya, *J. Lumin.* 76, 652 (1998).
226. K. Harigaya, *Synthetic Metals* 91, 379 (1997).
227. K. Harigaya, *Japan J. Appl. Phys.* 36, L485 (1997).
228. C. E. Moore, B. H. Cardelino, D. O. Frazier, J. Niles, and X. Q. Wang, *Theochem.—J. Mol. Struct.* 454, 135 (1998).
229. H. Huang, G. Gu, S. Yang, J. Fu, P. Yu, G. K. L. Wong, and Y. Du, *Chem. Phys. Lett.* 272, 427 (1997).
230. H. Huang, G. Gu, S. Yang, J. Fu, P. Yu, G. K. L. Wong, and Y. Du, *J. Phys. Chem.* 102, 61 (1998).
231. K. C. Rustagi, S. V. Nair, and L. M. Ramaniah, *Progress in Crystal Growth and Characterization of Materials* 34, 81 (1997).

232. V. P. Belousov, I. M. Belousova, V. P. Budtov, V. V. Danilov, O. B. Danilov, A. G. Kalintsev, and A. A. Mak, *J. Opt. Technol.* 64, 1081 (1997).
233. X. G. Wan, J. M. Dong, and D. Y. Xing, *J. Phys. B* 30, 1323 (1997).
234. R. H. Xie, *Z. Naturforsch. A* 54, 348 (1999).
235. Y. T. Lin, J. H. Sheu, and S. L. Lee, *Chem. Phys. Lett.* 345, 228 (2001).
236. Y.-T. Lin, R. K. Mishra, and S.-L. Lee, *Mol. Phys.* 97, 987 (1999).
237. J. R. Hefflin, D. Marciu, C. Figura, S. Wang, P. Burbank, S. Stevenson, H. C. Dorn, and J. C. Withers, *Proc. SPIE: Soc. Photo-Opt. Instrum. Eng.* 2854, 162 (1996).
238. Q. Gong, P. Yuan, Z. Xia, Y. H. Zou, J. Li, H. Yang, H. Hong, F. Yu, S. Chen, Z. Wu, X. Zhou, and F. Li, *Solid State Commun.* 103, 403 (1997).
239. G. Gu, H. Huang, S. Yang, P. Yu, J. Fu, G. K. Wong, X. Wan, J. Dong, and Y. Du, *Chem. Phys. Lett.* 289, 167 (1998).
240. F. Kajzar, Y. Okada-Shudo, C. Meritt, and Z. Kafafi, *Synth. Met.* 94, 91 (1998).
241. X. Wei, C. Hu, Z. Suo, P. Wang, W. Zhang, Z. Xu, and E. C. Alyea, *Chem. Phys. Lett.* 300, 385 (1999).
242. E. E. B. Campbell, S. Couris, M. Fanti, E. Koudoumas, N. Krawez, and F. Zerbetto, *Adv. Mater.* 11, 405 (1999).
243. T. Zhang, F. Wang, H. Yang, Q. Gong, X. An, H. Chen, and D. Qiang, *Chem. Phys. Lett.* 301, 343 (1999).
244. M. Konstantaki, E. Koudoumas, S. Couris, J. M. Janot, H. Eddaoudi, A. Deratani, P. Seta, and S. Leach, *Chem. Phys. Lett.* 318, 488 (2000).
245. W. Huang, S. Wang, R. Liang, Q. Gong, W. Qiu, Y. Liu, and D. Zhu, *Chem. Phys. Lett.* 324, 354 (2000).
246. Y. Song, L. Jiang, D. Zhu, C. Wang, K. Zhao, Z. Xia, and Y. Zou, *J. Phys. Chem. Solids* 61, 1141 (2000).
247. W. Qian, L. Lin, Z. Xia, Y. Zou, S. Qian, G. Ma, Y. Lin, R. Cai, Y. Chen, and Z. E. Huang, *Chem. Phys. Lett.* 319, 89 (2000).
248. R. Liang, S. Wang, W. Huang, Q. Gong, H. Li, H. Chen, and D. Qiang, *J. Phys. D: Appl. Phys.* 33, 2249 (2000).
249. E. Koudoumas, M. Konstantaki, A. Mavromanolakis, S. Couris, Y. Ederle, C. Mathis, P. Seta, and S. Leach, *Chem. Phys. Lett.* 335, 533 (2001).
250. S. Wang, W. Huang, R. Liang, Q. Gong, H. Li, H. Chen, and D. Qiang, *Phys. Rev. B* 63, 153408 (2001).
251. S. Wang, W. Huang, R. Liang, Q. Gong, H. Li, H. Chen, and D. Qiang, *J. Phys. Chem. B* 105, 10784 (2001).
252. I. Fuks-Janczarek, S. Dabos-Seignan, B. Sahraoui, I. V. Kityk, J. Berdowski, E. Allard, and J. Cousseau, *Opt. Commun.* 211, 303 (2002).
253. W. Zhao, H. Li, R. West, and J. C. Wright, *Chem. Phys. Lett.* 281, 105 (1997).
254. O. B. Mavritsky, A. N. Egorov, A. N. Petrovsky, K. V. Yakubovsky, W. J. Blau, D. N. Weldon, F. Z. Henary, *Proc. SPIE: Soc. Photo-Opt. Instrum. Eng.* 2854, 254 (1996).
255. J. Dong, J. Jiang, J. Yu, Z. D. Wang, and D. Y. Xing, *Phys. Rev. B* 52, 9066 (1995).
256. Q. Xu, J. Dong, J. Jiang, and D. Y. Xing, *J. Phys. B: At. Mol. Opt. Phys.* 29, 1563 (1996).
257. J. Jiang, J. Dong, and D. Y. Xing, *Solid State Commun.* 101, 537 (1997).
258. R. H. Xie, *Phys. Lett. A* 258, 51 (1999).
259. R. H. Xie, L. Jensen, G. W. Bryant, J. Zhao, and V. H. Smith, Jr., *J. Chem. Phys.*, in press.
260. R. H. Xie, G. W. Bryant, L. Jensen, J. Zhao, and V. H. Smith, Jr., unpublished.
261. W.-D. Cheng, D.-S. Wu, H. Zhang, D.-G. Chen, and H.-X. Wang, *Phys. Rev. B* 66, 85422 (2002).
262. B. Kippelen, S. R. Marder, E. Hendrickx, J. L. Maldonado, G. Guillemet, B. L. Volodin, D. D. Steele, Y. Enami, Y. J. Yao, J. F. Wang, H. Röckel, L. Erskine, and N. Peyghambarian, *Science* 279, 54 (1998).
263. S. R. Marder, B. Kippelen, A. K. Y. Jen, and N. Peyghambarian, *Nature (London)* 388, 845 (1997).
264. L. R. Dalton, W. H. Steier, B. H. Robinson, C. Zhang, A. Ren, S. Garner, A. Chen, T. Londergan, L. Irwin, B. Carlson, L. Fifield, G. Phelan, C. Kincaid, J. Amend, and A. Jen, *J. Mater. Chem.* 9, 1905 (1999).
265. M. Malaun, R. Kowallick, A. M. McDonagh, M. Marcaccio, R. L. Paul, I. Asselberghs, K. Clays, A. Persoons, B. Bildstein, C. Fiorini, J. M. Nunzi, M. D. Ward, and J. A. McCleverty, *J. Chem. Soc., Dalton Trans.* 2001, 3025 (2001).
266. M. Malaun, Z. R. Reeves, R. L. Paul, J. C. Jeffery, J. A. McCleverty, M. D. Ward, I. Asselberghs, K. Clays, and A. Persoons, *Chem. Commun.* 2001, 49 (2001).
267. I. Asselberghs, Y. Zhao, K. Clays, A. Persoons, A. Comito, and Y. Rubin, *Chem. Phys. Lett.* 364, 279 (2002).
268. J. C. Hummelen, F. Wudl, and C. Bellavia-Lund, *Top. Curr. Chem.* 199, 93 (1999).
269. B. L. Yu, H. P. Xia, C. S. Zhu, and F. X. Gan, *Appl. Phys. Lett.* 81, 2701 (2002).
270. R. H. Xie and J. Jiang, *J. Appl. Phys.* 83, 3001 (1998).
271. R. H. Xie and Q. Rao, *Chem. Phys. Lett.* 313, 211 (1999).
272. X. Liu, J. Si, B. Chang, G. Xu, Q. Yang, Z. Pan, and S. Xie, *Appl. Phys. Lett.* 74, 164 (1999).
273. S. Xie, W. Li, Z. Pan, B. Chang, and L. Sun, *J. Phys. Chem. Solids* 61, 1153 (2000).
274. Z. Shi, Y. Lian, X. Zhou, Z. Gu, Y. Zhang, S. Iijima, Q. Gong, H. Li, and S. L. Zhang, *Chem. Commun.* 461 (2000).
275. S. Wang, W. Huang, H. Yang, Q. Gong, Z. Shi, X. Zhou, D. Qiang, and Z. Gu, *Chem. Phys. Lett.* 320, 411 (2000).
276. Y. C. Chen, N. R. Raravikar, L. S. Schadler, P. M. Ajayan, Y. P. Zhao, T. M. Lu, G. C. Wang, and X. C. Zhang, *Appl. Phys. Lett.* 81, 975 (2002).
277. X. Wan, J. Dong, and D. Y. Xing, *Solid State Commun.* 107, 791 (1998).
278. V. A. Margulis and T. A. Sizikova, *Physica B* 245, 173 (1998).
279. X. Wan, J. Dong, and D. Y. Xing, *Phys. Rev. B* 58, 6756 (1998).
280. J. Jiang, J. Dong, X. Wan, and D. Y. Xing, *J. Phys. B: At. Mol. Opt. Phys.* 31, 3079 (1998).
281. J. Jiang, J. Dong, and D. Y. Xing, *Phys. Rev. B* 59, 9838 (1999).
282. V. A. Margulis, *J. Phys.: Condens. Matter* 11, 3065 (1999).
283. V. A. Margulis, E. A. Gaiduk, and E. N. Zhidkin, *Opt. Commun.* 183, 317 (2000).
284. L. Tutt and T. F. Boggess, *Prog. Quantum Electron.* 17, 299 (1993).
285. E. W. van Stryland, D. J. Hagan, T. Xia, and A. A. Said, in "Non-linear Optics of Organic Molecules and Polymers" (H. S. Nalwa and S. Miyata, Eds.), p. 841. Chemical Rubber, New York, 1997.
286. J. W. Perry, in "Nonlinear Optics of Organic Molecules and Polymers" (H. S. Nalwa and S. Miyata, Eds.), p. 813. Chemical Rubber, New York, 1997.
287. Y. P. Sun and J. E. Riggs, *Int. Rev. Phys. Chem.* 18, 43 (1999).
288. A. A. Said, M. Sheik-Bahae, D. J. Hagan, T. H. Wei, J. Wang, J. Young, and E. W. van Stryland, *J. Opt. Soc. Am. B* 9, 405 (1992).
289. K. J. McEwan, P. K. Milsom, and D. B. James, *SPIE* 3472, 42 (1998).
290. K. M. Nashold and W. D. Powell, *J. Opt. Soc. Am. B* 12, 1228 (1995).
291. K. Mansour, M. J. Soileau, and E. W. van Stryland, *J. Opt. Soc. Am. B* 9, 1100 (1992).
292. V. Joudrier, P. Bourdon, F. Hache, and C. Flytzanis, *Appl. Phys. B* 70, 105 (2000).
293. B. L. Justus, A. L. Huston, and A. J. Campillo, *Appl. Phys. Lett.* 63, 1483 (1993).
294. R. Crane, K. Lewis, E. W. van Stryland, and M. Khoshnevisa, Eds., "Materials for Optical Limiting I." Materials Research Society, Warrendale, PA, 1994.

295. P. Hood, R. Pachter, K. Lewis, J. W. Perry, D. Hagan, and R. Sutherland, Eds., "Materials for Optical Limiting II." Vol. 374. Materials Research Society, Warrendale, PA, 1997.
296. V. V. Golovlev, W. R. Garrett, and C. H. Chen, *J. Opt. Soc. Am. B* 13, 2801 (1996).
297. D. G. McLean, R. L. Sutherland, M. C. Brant, D. M. Brandelik, P. A. Fleitz, and T. Pottenger, *Opt. Lett.* 18, 858 (1993).
298. S. Guha, W. T. Roberts, and B. H. Ahn, *Appl. Phys. Lett.* 68, 3686 (1996).
299. S. R. Mishra, H. S. Rawat, and S. C. Mehendale, *Appl. Phys. Lett.* 71, 46 (1997).
300. J. S. Shirk, R. G. S. Pong, S. R. Flom, F. J. Bartoli, M. E. Boyle, and A. W. Snow, *Pure Appl. Opt.* 5, 701 (1996), and references therein.
301. J. W. Perry, K. Mansour, I. Y. S. Lee, X. L. Wu, P. V. Bedworth, C. T. Chen, D. Ng, S. Marder, and P. Miles, *Science* 273, 1533 (1996).
302. G. R. Allan, S. J. Rychnovsky, C. H. Vezke, T. F. Boggess, and L. Tutt, *J. Phys. Chem.* 98, 3570 (1994), and references therein.
303. S. Shi, W. Ji, and S. H. Tang, *J. Am. Chem. Soc.* 116, 3615 (1994).
304. T. Xia, A. Dogariu, K. Mansour, D. J. Hagan, A. A. Said, E. W. van Stryland, and S. Shi, *J. Opt. Soc. Am. B* 15, 1497 (1998).
305. M. K. M. Low, H. W. Hou, H. G. Zheng, W. T. Wong, G. X. Jin, Q. Xin, and W. Ji, *Chem. Comm.* 505 (1998).
306. L. W. Tutt and A. Kost, *Nature (London)* 356, 225 (1991).
307. C. Liu, G. Zhao, Q. Gong, K. Tang, X. Jin, P. Cui, and L. Lei, *Opt. Commun.* 184, 309 (2000).
308. V. P. Belousov, I. M. Belousova, E. A. Gavronskaya, V. A. Grigor'ev, A. G. Kalintsev, A. V. Kris'ko, D. A. Kozlovskii, N. G. Mironova, A. G. Skobelev, and M. S. Yur'ev, *J. Opt. Technol.* 68, 876 (2001).
309. Y. Song, C. Zhang, Y. Wang, G. Fang, G. Jin, C. Chang, S. Liu, X. Xin, and H. Ye, *Chem. Phys. Lett.* 326, 341 (2000).
310. J. E. Riggs and Y. P. Sun, *J. Phys. Chem. A* 103, 485 (1999).
311. Y. Sun, Q. H. Gong, S. C. Yang, Y. H. Zhou, L. Fei, Z. Zhou, and D. Qiang, *Opt. Commun.* 102, 205 (1993).
312. J. W. Arbogast, A. P. Darmanyan, C. S. Foote, Y. Rubin, F. N. Diederich, M. Alvarez, S. J. Anz, and R. L. Whetten, *J. Phys. Chem.* 95, 11 (1991).
313. J. W. Arbogast and C. S. Foote, *J. Am. Chem. Soc.* 113, 8886 (1991).
314. B. L. Justus, Z. H. Kafafi, and A. L. Huston, *Opt. Lett.* 18, 1603 (1993).
315. S. R. Mishra, H. S. Rawat, M. P. Joshi, S. C. Mehendale, and K. C. Rustagi, *Proc. SPIE* 2284, 220 (1994).
316. S. R. Mishra and S. C. Mehendale, in "Handbook of Advanced Electronic and Photonic Materials and Devices" (H. S. Nalwa, Ed.), p. 353. Academic Press, New York, 2000.
317. S. R. Mishra, H. S. Rawat, M. P. Joshi, and S. C. Mehendale, *J. Phys. B* 63, L2578 (1993).
318. S. R. Mishra, H. S. Rawat, M. P. Joshi, and S. C. Mehendale, *Appl. Phys. A* 63, 223 (1996).
319. L. Smilowitz, D. McBranch, V. Klimov, J. M. Robinson, A. Koskelo, M. Grigorova, and B. R. Mattes, *Opt. Lett.* 21, 922 (1996).
320. M. Iglesias and A. Santos, *Inorg. Chem. Acta* 248, 67 (1996).
321. K. L. Tang, S. J. Zheng, X. L. Jin, H. Zeng, Z. N. Gu, X. H. Zhou, and Y. Q. Tang, *J. Chem. Soc. Dalton Trans.* 19, 3585 (1997).
322. T. Q. Zhang, J. L. Li, P. Gao, Q. H. Gong, K. L. Tang, X. L. Jin, S. J. Zheng, and L. Li, *Opt. Commun.* 150, 201 (1998).
323. K. Dou, J. Y. Du, and E. T. Knobbe, *J. Luminescence* 83, 241 (1999).
324. P. Zhu, P. Wang, W. Qiu, Y. Liu, C. Ye, G. Fang, and Y. Song, *Appl. Phys. Lett.* 78, 1319 (2001).
325. M. Brust, C. J. Kiely, D. Bethell, and D. J. Schiffrin, *J. Am. Chem. Soc.* 120, 12367 (1998).
326. K. Fu, A. Kitaygorodsky, and Y. P. Sun, *Chem. Mater.* 12, 2073 (2000).
327. N. Sun, Y. Wang, Y. Song, Z. Guo, L. Dai, and D. Zhu, *Chem. Phys. Lett.* 344, 277 (2001).
328. R. G. Ispasiou, L. Balogh, O. P. Varnavski, D. A. Tomalia, and T. G. Goodson III, *J. Am. Chem. Soc.* 122, 11005 (2000).
329. M. P. Joshi, J. Swiatkiewicz, F. Xu, P. Prasad, B. A. Reinhardt, and R. Kannan, *Opt. Lett.* 23, 1742 (1998).
330. S. R. Mishra, H. S. Rawat, S. C. Mehendale, K. C. Rustagi, A. K. Sood, R. Bandyopadhyay, A. Govindaraj, and C. N. R. Rao, *Chem. Phys. Lett.* 317, 510 (2000).
331. N. Sun, Z. X. Guo, L. Dai, D. Zhu, Y. Wang, and Y. Song, *Chem. Phys. Lett.* 356, 175 (2002).
332. K. B. Andrew and M. R. Vincent, *J. Am. Chem. Soc.* 121, 4914 (1999).
333. G. R. Uspasiou, L. Balogh, O. P. Varnavski, A. T. Donald, and T. Goodson III, *J. Am. Chem. Soc.* 122, 11005 (2000).
334. S. Link and M. A. El-Sayed, *J. Phys. Chem. B* 103, 8410 (1999).
335. H. Fang, C. Du, S. Qu, Y. Li, Y. Song, H. Li, H. Liu, and D. Zhu, *Chem. Phys. Lett.* 364, 290 (2002).
336. Z. Suo, Y. Song, S. Yao, Y. Wang, and Z. Xu, *Chem. Phys. Lett.* 342, 497 (2001).
337. Y. Li, S. Wang, F. Li, C. Du, Z. Shi, D. Zhu, and Y. Song, *Chem. Phys. Lett.* 337, 403 (2001).
338. F. Li, Y. Li, Z. Ge, D. Zhu, Y. Song, and G. Fang, *J. Phys. Chem. Solids* 61, 1101 (2000).
339. V. V. Golovlev, W. R. Garrett, and C. H. Chen, *J. Opt. Soc. Am. B* 13, 2801 (1996).
340. K. I. Priyadarshi, H. Mohan, A. K. Tyagi, and J. P. Mittal, *J. Phys. Chem.* 98, 4756 (1994).
341. M. Konstantaki, E. Koudoumas, S. Couris, J. M. Janot, H. Eddaoudi, A. Deratani, P. Seta, and S. Leach, *Chem. Phys. Lett.* 318, 488 (2000).
342. R. Signorini, M. Meneghetti, R. Bozio, G. Brusatin, P. Innocenzi, M. Guglielmi, and F. D. Negra, *J. Sol-Gel Sci. Tech.* 22, 245 (2001).
343. R. Signorini, M. Meneghetti, R. Bozio, M. Maggini, G. Scorrano, M. Prato, G. Brusatin, P. Innocenzi, and M. Guglielmi, *Carbon* 38, 1653 (2000).
344. R. Gvishi, U. Narang, G. Ruland, D. N. Kumar, and P. N. Prasad, *Appl. Organomet. Chem.* 11, 107 (1997).
345. M. Maggini, G. Scorrano, M. Prato, G. Brusatin, P. Innocenzi, M. Guglielmi, A. Renier, R. Signorini, M. Meneghetti, and R. Bozio, *Adv. Mater.* 7, 404 (1995).
346. A. Kost, L. Tutt, M. B. Klein, T. K. Dougherty, and W. E. Elias, *Opt. Lett.* 18, 334 (1993).
347. J. E. Riggs and Y. P. Sun, *J. Chem. Phys.* 112, 4221 (2000).
348. Y. P. Sun and J. E. Riggs, in "Fullerenes, Recent Advances in the Chemistry and Physics of Fullerenes and Related Materials" (K. M. Kadish and P. V. Kamat, Eds.), p. 393. The Electrochemical Society, Pennington, 1999.
349. X. Sun, R. Q. Yu, G. Q. Xu, T. S. A. Hor, and W. Ji, *Appl. Phys. Lett.* 73, 3632 (1998).
350. P. Chen, X. Wu, X. Sun, J. Lin, W. Ji, and K. L. Tan, *Phys. Rev. Lett.* 82, 2548 (1999).
351. X. Sun, Y. Xiong, P. Chen, J. Lin, J. J. Lim, S. S. Yang, D. J. Hagan, and E. W. van Stryland, *Appl. Opt.* 39, 1998 (2000).
352. J. E. Riggs, D. B. Walker, D. L. Carroll, and Y. P. Sun, *J. Phys. Chem.* 104, 7071 (2000).
353. Z. Jin, L. Huang, S. H. Goh, G. Xu, and W. Ji, *Chem. Phys. Lett.* 352, 328 (2002).
354. L. Vivien, D. Riehl, J. F. Delouis, J. A. Delaire, F. Hache, and E. Anglaret, *J. Opt. Soc. Am. B* 19, 208 (2002).
355. L. Vivien, E. Anglaret, D. Riehl, F. Bacou, C. Journet, C. Goze, M. Andrieux, M. Brunet, F. Lafonta, P. Bernier, and F. Hache, *Chem. Phys. Lett.* 307, 317 (1999).

356. L. Vivien, D. Riehl, E. Anglaret, and F. Hache, *IEEE J. Quantum Electron.* 36, 680 (2000).
357. L. Vivien, E. Anglaret, D. Riehl, F. Hache, F. Bacou, M. Andrieux, F. Lafonta, C. Journet, C. Goze, M. Brunet, and P. Bernier, *Opt. Commun.* 174, 271 (2000).
358. L. Vivien, D. Riehl, F. Hache, and E. Anglaret, *J. Nonlinear Opt. Phys. Mater.* 9, 297 (2000).
359. L. Vivien, D. Riehl, P. Lancon, F. Hache, and E. Anglaret, *Opt. Lett.* 26, 223 (2001).
360. S. Lefrant, E. Anglaret, L. Vivien, and D. Riehl, *VIDE-Science Tech. Appl.* 56, 2888 (2001).
361. L. Vivien, P. Lancon, D. Riehl, F. Hache, and E. Anglaret, *Carbon* 40, 1789 (2002).
362. S. R. Mishra, H. S. Rawat, S. C. Mehendale, K. C. Rustagi, A. K. Sood, R. Bandyopadhyay, A. Govindaraj, and C. N. R. Rao, *Chem. Phys. Lett.* 317, 510 (2000).
363. Z. Jin, X. Sun, G. Xu, S. H. Goh, and W. Ji, *Chem. Phys. Lett.* 318, 505 (2000).



# Nonlinear Optics of Nanoparticles and Nanocomposites

Quandou Wang

*Changchun Institute of Optics, Fine Mechanics and Physics, Changchun, China*

Jianfeng Xu

*University of Arizona, Tucson, Arizona, USA*

Rui-Hua Xie

*Queen's University, Kingston, Canada*

## CONTENTS

1. Introduction
  2. Nonlinear Optics of Nanoparticles
  3. Nonlinear Optics of Nanocomposites
  4. Conclusions
- Glossary  
References

## 1. INTRODUCTION

In the past 10 years, the scientific activity of the synthesis and study of so-called “nanoparticles” [1–17], indicating particles with diameter in the range of 1 to 20 nm, has become a major interdisciplinary area [18–21] of research in the world. As the sizes of the particle become smaller, the ratio of the surface atoms to those in the interior increases, thereafter leading those kinds of particles to play an important role in the properties of novel functional material. Those significant properties, such as chemical, electronic, mechanical, and optical properties, of nanoparticles obviously distinguish them from those of the corresponding “bulk” material. In particular, one of those significant properties is the nonlinear optical (NLO) response of nanoparticles, which is enhanced remarkably with respect to the relative “bulk” materials, due not only to their atomic scale structures but also their interface and surface structures [22]. Materials with large third-order optical nonlinearity and fast response time are essential for future optical device applications [16, 17]. Thanks to such a high nonlinear optical

response of these NLO materials, they are thought to be good candidates for use in fiber-optic communication systems, such as all-optical switching [23], routing units, digital signal restoration, and multiplexing and demultiplexing, as well as optical storage media and optical limiter applications [17]. Therefore, intensive investigations on NLO of nanoparticles have recently been carried out.

In the meantime, nanocomposites [24–28] formed by metal or semiconductor nanocrystals embedded in dielectric hosts have been intensively studied as these materials might also become an attractive alternative for the development of all-optical switching devices in waveguides [29]. Strong optical nonlinearities observed due to dielectric or quantum confinement effects, such as nonlinear optical absorption and second and third optical nonlinearities, can be studied for making optical limiters, optical modulators, and laser second and third harmonic generators [16, 17].

In this chapter, we briefly highlight and review the current advances and achievements in studying the NLO properties of nanoparticles and nanocomposites in Sections 2 and 3, respectively. Remarks and outlooks are given in Section 4.

## 2. NONLINEAR OPTICS OF NANOPARTICLES

### 2.1. Theoretical Explanation

The first experimental study of nonlinear optical properties of metal nanoparticle colloids was reported by Ricard et al. [30]. Later, Hache et al. [31] gave a theoretical model calculating the electric-dipole third-order susceptibility of conduction electrons in a metal sphere. They ascribed that



the large effective third-order nonlinear susceptibility,  $\chi^{(3)}$ , of metal nanoparticle colloids is substantially enhanced by a resonance that is due to the effective medium, the surface plasma resonance: collective oscillation of the conduction electrons of the metal under the influence of an applied electromagnetic wave, as expected by direct extension of the Maxwell–Garnett theory. The enhancement of the local electric field, which occurs in the particles at frequencies close to the surface plasmon resonance, is responsible for the amplification of their NLO properties as compared with those of bulk metal. For the large third-order nonlinear susceptibility of semiconductor nanoparticles, Chemla and Miller [32] identified that the enhancement of nonlinearity is due to the combination of local field effects from dielectric confinement and saturable excitonic resonance. In addition, they predicted that these effects would be greatly enhanced since the particles are so small that they also exhibit quantum confinement. Many other authors also have predicted enhanced optical nonlinearities, resulting from quantum confinement effects, with respect to the corresponding bulk materials [33–35]. Hanamura [36] analyzed theoretically the oscillator strength and the third-order optical polarizability  $\chi^{(3)}$  due to excitons in semiconductor microcrystallites. The NLO polarizability is shown to be greatly enhanced for an assembly of such microcrystallites as the exciton is quantized due to the confinement effect and the excitons in a single microcrystallite interact strongly enough to make the excitons deviate from ideal harmonic oscillators. Cotter et al. [35] have found that three-dimensional quantum confinement can alter radically the nonlinear optical properties of semiconductors in transparency region. This discovery that introducing quantum confinement can enhance this ratio has opened new opportunities for practical exploitation of the quantum-size effect in NLO devices.

Schwarze et al. [37] have developed a new model that combines the interaction between two physical mechanisms responsible for bulk third-order optical nonlinearity. The two physical mechanisms are:

- (i) saturable absorption, due to quantum confinement in nanoparticles,
- (ii) electrostriction, causing particles to migrate in the fluid host.

Schwarze et al. [37] have shown that enhanced optical nonlinearities are predicted to result from local field coupling and those oscillations can occur under certain conditions. In such a computationally feasible theoretical model, which describes the interaction between two nonlinear optical mechanisms, particles are free to move and cluster in the presence of optical field gradients, modifying the local electric field, which in turn modifies the effective permittivity of each nanoparticle. The coupling together of these phenomena can lead to significantly enhanced  $\chi^{(3)}$  coefficients, and we have shown that oscillatory behavior can occur under certain conditions. The numerical simulations based on this model have shown the change in the bulk refractive index as a function of the particle size, concentration, and incident intensity. The model also has implications for designing some novel switching devices, which are optimal in the sense that particle sizes and concentrations can be

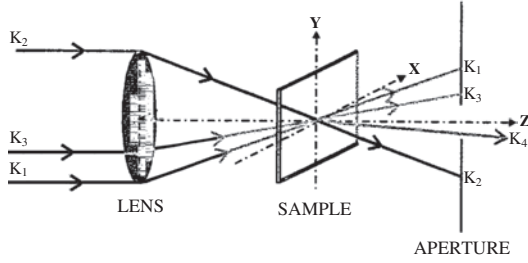
chosen to maximize the magnitude of the third-order optical susceptibility,  $\chi^{(3)}$ .

Very recently, Prot et al. [38] have initially applied a recursive transfer matrix method to calculate the electromagnetic field response for three-dimensional systems of scattering spheres to the study of nanocomposite material. Their calculations have shown that mutual interactions between nanoparticles are responsible for large local field enhancements as compared with fields inside isolated particles. According to the experimental study to measure the third-order nonlinear susceptibility of Au:SiO<sub>2</sub>, they discovered that the imaginary part of  $\chi^{(3)}$  values diverges from the theoretical predictions and does not vary linearly with the metal concentration. This discrepancy, attributed to the large enhancement of the local field, proves the qualitative agreement between the local field calculations and experimental nonlinear measurement.

## 2.2. Experimental Techniques

In the study of optical nonlinearity of nanoparticles, there are huge research works concerning the measurements of third-order nonlinear susceptibility,  $\chi^{(3)}$ . In these works, experimental technique plays a very important role in carrying out the NLO measurement of  $\chi^{(3)}$ . In our review of the NLO of nanoparticles, it is necessary to introduce several primary measurement approaches to obtain  $\chi^{(3)}$ . The most powerful or popular methods to measure the third-order nonlinear susceptibility  $\chi^{(3)}$  may be degenerate four-wave mixing experiments (DFWM) and the Z-scan technique [17]. DFWM is a nonlinear optical technique that produces a coherent signal by nonlinear interaction of light with the samples in the beam-crossing region. The coherent signal obtained with such a nonlinear technique is in the form of a laser beam that is coherent and directional. It can be spatially separated and spectrally filtered to reject the intense luminosity in many application fields. DFWM showed a great promise for sensitive measurements of transient species.

DFWM involves the interactions of three beams incident on a sample. The three beams are arranged in such a way that two of the beams (pump beams) are counterpropagating each other and the third beam acts as a probe. The fourth beam, which constitutes the conjugate beam, retraces exactly the path of the probe beam. Three input beams of nearly equal power are divided by the beamsplitters. Two of the input beams have the translation stages so that the arrival time at the sample can be varied. The beam spot size in the sample is approximately 0.5 mm in diameter. The beam geometry is shown in Figure 1. The three input beams are labeled 1, 2, and 3, and 4 is the output beam, which is generated by the input beams through  $\chi^{(3)}$ . Beam 2 is time advanced or delayed relative to beams 1 and 3 (which are coincident in time), providing the temporal response of  $\chi^{(3)}$ . The angle between beams 1 and 3 in the sample is about 1 degree. This geometry permits the generated beam, 4, to be spatially separated from the more intense incident pulses and gives a high signal-to-noise ratio. This is important for DFWM experiments because all the beams have the same frequency. The signal beam, 4, is directed to the entrance slit of a spectrometer, recorded, and then analyzed by using



**Figure 1.** The beam geometry of DFWM techniques. The three input beams are labeled 1, 2, and 3. The output beam is labeled 4.

a photomultiplier and a boxcar interfaced to a microcomputer. Three beams were polarized parallel to the  $Y$ -axis. The tensor component  $\chi_{1111}^{(3)}$  is measured, and the value of  $\chi_{1111}^{(3)}$  can be expressed as a function of beam energies by using the four-wave mixing model described in [39],

$$\chi_{1111}^{(3)} \approx \frac{cn^2}{32\pi^2} \left( \frac{\lambda_0 \omega_0^2}{2\tau l} \right) \left[ \frac{45E_4}{8E_1 E_2 E_3} \right]^{1/2} \frac{l\alpha \exp(l\alpha/2)}{1 - \exp(-l\alpha)} \quad (1)$$

where  $c$  is the speed of light in vacuum,  $n$  is the index of refraction of the sample,  $E_i$  is the pulse energy of the  $i$ th beam,  $\omega_0$  is the laser beam waist at the focus,  $\tau$  is the pulse width,  $l$  is the sample length, and  $\alpha$  is the sample absorption coefficient at the incident wavelength  $\lambda_0$ .

Z-scan [40–42] is also a simple, sensitive technique which relies on the transformation of nonlinear phase shifts into far-field amplitude deflections to obtain the complex nonlinear refractive index  $n_2 = n_2' + in_2''$ . However, the Z-scan technique has great advantages compared to the DFWM method, which consists of its ability to separate the imaginary and real parts of  $\chi^{(3)}$  and, additionally, to determine the signs of the two components. It is essentially a derivative of the ubiquitous single-beam-power-in versus power-out transmission measurement [43] but attains greater efficiency by focusing the beam and translating the sample. The technique involves the measurement of the transmittance through an aperture placed in the far field as the sample is translated through the focus of a Gaussian beam. For a sufficiently small aperture, this procedure provides a measurement of the real part of the nonlinear refractive index  $n_2'$ . If the aperture is fully opened so that the detector collects all the light, then the Z-scan provides a measurement of the imaginary part of the nonlinear refractive index  $n_2''$  or, alternatively, the nonlinear absorption coefficient  $\beta$ . If  $\beta > 0$ , then the Z-scan will result in a trough, indicative of an induced absorption. If  $\beta < 0$ , then the Z-scan will produce a peak, indicating an induced transparency. Since all the flux from the sample is collected at the detector, the transmitted power may be calculated without having to perform the free-space Fresnel propagation to the aperture. The normalized transmittance may be expressed as [44]

$$T(z) = \sum_{m=0}^{\infty} (m+1)^{-3/2} \left( \frac{-\beta I_0 L_{\text{eff}}}{1 + z^2/z_0^2} \right)^2 \quad (2)$$

where  $z$  is the longitudinal displacement of the sample from the focus,  $\beta$  is the nonlinear absorption coefficient,  $I_0$  is the

on-axis peak intensity at the focus,  $L_{\text{eff}}$  is the effective interaction length,  $z_0$  is the Rayleigh diffraction length, and the temporal profile of the pulse has been assumed to be Gaussian. Typically, if the series converge, only the first few terms are needed for numerical evaluation. Hence, the coefficient  $\beta$  may be determined from a fit of this expression to the empirical data.

Femtosecond optical kerr effect (OKE) [45–48] and transient grating scattering [49–51] techniques are also available approaches to measure nonresonant third-order optical nonlinearity of nanoparticles. Both techniques rely on an impulsive stimulated scattering [52–54]. Both the fundamental and the (anti)stokes frequency involved in this process are supplied by the ultrashort laser pulses. For 50 fs pulses the nuclear motions between 0 and 300 cm are probed.

### 2.3. Third-Order Nonlinear Optical Response

Pincon et al. [55] have studied the third-order NLO response of Au:SiO<sub>2</sub> thin films, under the influence of gold nanoparticle concentration and morphologic parameters. Based on their result, we find that, as the metal concentration reaches a few percent, the mutual electromagnetic interactions between particles greatly enlarge the nonlinear optical response of the material and cannot be neglected in the theoretical analysis. Moreover, the thermal treatment leads, for a given concentration, to a significant increase of the nonlinear response, which is ascribed to a modification of the material morphology. They finally point out that the material nonlinear properties are very sensitive to the incident wavelength through the local field enhancement phenomenon. In their study, the nonlinear optical measurements are performed by using the Z-scan technique. Values of  $\text{Im} \chi^{(3)}$  range from  $-(0.049 \pm 0.009) \times 10^{-6}$  to  $-(6.4 \pm 1.2) \times 10^{-6}$  esu as a function of the variation of metal concentrations before the thermal treatment. After anneal, it gives values from  $-(0.69 \pm 0.06) \times 10^{-6}$  to  $-(6.0 \pm 0.6) \times 10^{-6}$  esu. Smith et al. [56] also used the Z-scan technique at a wavelength (532 nm) near the transmission window of bulk gold to measure the nonlinear absorption coefficient of continuous approximately 50-Å-thick gold films, deposited onto surface-modified quartz substrates. They have fulfilled both open- and closed-aperture Z-scans to determine either the real or imaginary part of the third-order susceptibility that requires a measurement of both nonlinear absorption and nonlinear refraction. Closed-aperture Z-scans did not yield a sufficient signal for the determination of the nonlinear refraction. However, open-aperture Z-scans yielded values ranging from 51.931023 to 5.331023 cm/W in good agreement with predictions, which ascribe the nonlinear response to a Fermi smearing mechanism [31]. It should be mentioned that the sign of the optical nonlinearity is reversed from that of gold nanoparticle composites, in accordance with the predictions of mean field theories.

For the other metal nanoparticles, Takeda et al. [57] have applied a negative Cu ion-implantation technology to obtain the nanoparticle on the silica glass substrate. The DFWM method was performed to measure the  $\chi^{(3)}$  at 532 nm with a second harmonic generation (SHG) light of Nd:YAG lasers and 561 nm with a SHG-pumped dye laser. As a standard

sample, CS<sub>2</sub> was used to evaluate absolute values of  $\chi^{(3)}$ . Nonlinear optical susceptibility  $\chi^{(3)}$  of Cu implanted silica exhibits values of  $(2.0 \times 10^{-9}) \pm (2.0 \times 10^{-8})$  esu near the peak of the plasma resonance. The estimated value of  $\chi^{(3)}$  for the Cu nanoparticles is  $(9.0 \times 10^{-9}) - (8.0 \times 10^{-8})$  esu.

For semiconductor nanoparticles, the most studied is cadmium sulfide [58, 59]. The others, like InP, CdSe, CdTe, ZnS, ZnSe, Pbs, and PbSe, were reported in lots of studies. Those nanomaterials with large third-order optical nonlinearity and fast response time are essential for optical device applications in optical computing, real time holography, optical correlators, and phase conjugators [60]. Therefore, CdS and Pbs semiconductor nanoparticles as “quantum dot” materials are of interest for their large third-order NLO response and have been extensively investigated [61–64]. In works of Liu et al. [65], they use the Z-scan technique with 150-fs laser pulses at 780-nm wavelength to carry out the third-order susceptibility measurement of Pbs-coated CdS nanoparticles. The ion displacement technique was used in their work to obtain the Pbs-coated CdS nanocomposites. In such a technique, semiconductor material (Pbs) grows on a seed of CdS in microemulsion media. Their experimental result of high third-order refractive nonlinearity of confined semiconductor nanoparticles in the transparent region is in agreement with the prediction of Cotter et al. [66], who confirmed that the optical Stark effect makes a dominant contribution to the third-order refractive nonlinearity in this case when the absorptive nonlinearity can be negligible.

Other types of nanoparticles, such as magnetic nanoparticles, can be found, for example, in the review paper of Aktsipetrov [67]. In summary, three aspects of nonlinear magneto-optics of magnetic nanoparticles are considered:

- Correlation between GMR and NOMOKE has been experimentally approved [68].
- Magnetization-induced hyper-Rayleigh scattering has been observed [69].
- An internal homodyne mechanism for weakly nonlinear processes is suggested [69, 70].

Most recently, Pan et al. [71] have investigated the third-order optical nonlinearity of nanopolyacetylene using a femtosecond OKE technique at wavelengths from 790 to 860 nm. The ultrafast nonresonant effective second-order hyperpolarizability for single polyacetylene nanoparticles was estimated to be as large as  $1.0 \times 10^{-27}$  esu, which corresponds to a single carbon atom contribution equal to  $5.0 \times 10^{-33}$  esu. We ascribe such observations to the highly ordered structure of nanopolyacetylene and suppose that the delocalization of the  $\pi$  electrons along the conjugated chains is responsible for such properties.

For convenience, Table 1 summarizes some results of the third-order optical nonlinearities of nanoparticles.

### 3. NONLINEAR OPTICS OF NANOCOMPOSITES

#### 3.1. Metal Nanocomposites

We consider nanometric metal spheres dispersed in a thin dielectric film. The optical constants of the nonlinear medium are intensity dependent and can be written as

$$n' = n + \gamma I \quad (3)$$

$$\alpha' = \alpha + \beta I \quad (4)$$

where  $n$ ,  $\alpha$ , and  $I$  are linear refractive index, linear absorption coefficient, and the instantaneous light intensity, respectively. The nonlinear absorption coefficient  $\beta$  and nonlinear refraction coefficient  $\gamma$  are proportional to the imaginary or real parts of the third-order optical susceptibility  $\chi^{(3)}$  as

$$\gamma = 3\Re(\chi^{(3)})/(4\epsilon_0 cn^2) \quad (5)$$

$$\beta = 3k\Im(\chi^{(3)})/(2\epsilon_0 cn^2) \quad (6)$$

where  $k$  is the modulus of the wave vector in vacuum and  $c$  is the speed of light in vacuum. The experimentally measured optical susceptibility  $\chi^{(3)}$  of the composite material is

**Table 1.** Third-order optical nonlinearities of nanoparticles measured by different experimental techniques.

Nanoparticles	$\lambda$ (nm)	$\tau$	$\chi^{(3)}$ ( $10^{-10}$ esu)	Method	State of material	Ref.
Au:SiO <sub>2</sub> as deposited	532	7 ns	-490 to -64,000	Z-scan	film	[55]
Au:SiO <sub>2</sub> as annealed	532	7 ns	-6900 to 60,000	Z-scan	film	[55]
Au@CdS	800	100 fs	0.724±0.140	OKE	film	[108]
Cu	532		90 to 800	DFWM	film	[57]
Polyacetylene	790–860	120 fs	0.001	OKE	solution	[71]
Au:BaTiO <sub>3</sub>	800	100 fs	0.066	OKE	film	[108]
CdS:BaTiO <sub>3</sub>	800	100 fs	0.158	OKE	film	[108]
Au:TiO <sub>2</sub>	780	130 fs	2300	OKE	film	[109]
Rh:BaTiO <sub>3</sub>	308	17 ns	5710	Z-scan	film	[110]
Si-nc	813	60 fs	4 to 28	Z-scan	film	[111]
Au doped in aluminum	532		3.2 to 9.0	DFWM	film	[112]
Ad doped in aluminum	532		1.9 to 2.5	DFWM	film	[112]
ZnTe	532	5 ns	27,000	DFWM	film	[113]
PbS by PVB	595	25 ns	106,000	DFWM	film	[114]
CdS	470	400 fs	11000	DFWM	solution	[115]
Au:BaTiO <sub>3</sub>	800	120 fs	100 to 10	OKE	film	[116]

Note:  $\lambda$  and  $\tau$  are the wavelength and pulse duration of the laser source, respectively.

related to the intrinsic NLO third-order susceptibility  $\chi_m^{(3)}$  of metal crystal [72]

$$\chi^{(3)} = pf^2 |f^2| \chi_m^{(3)} \quad (7)$$

$$f = 3\epsilon_0/(\epsilon + 2\epsilon_0) \quad (8)$$

where  $p$  is the volume fraction of metal nanocrystal,  $f$  is the local field effect, and  $\epsilon_0$  and  $\epsilon$  are the dielectric constants of the matrix and metal, respectively. Near the surface plasmon resonance ( $\epsilon + 2\epsilon_0 = 0$ ),  $f$  becomes resonant and  $\chi^{(3)}$  is thus enhanced by local field effects.

Metal nanocomposites can be synthesized by several techniques, such as sol-gel [73], sputtering [74], ion implantation [75], and pulsed laser deposition [76]. These nanocomposites normally present linear optical absorption due to both surface-plasmon resonance and strong third-order nonlinear optical susceptibility. The spatial confinement of the metallic electrons by the insulating host produces an enhanced electromagnetic field due to the large dipole moment induced by an optical field. Furthermore, for very small nanocrystals, the confinement of the electronic wave functions in either the initial or final states to a volume, which is much smaller than their bulk mean free path, produces an additional contribution to the electric susceptibility.

Sella et al. [77, 78] have synthesized Au:SiO<sub>2</sub> nanocomposites by radio frequency sputtering techniques. The metal concentration varies from 8% to 35%. Several characterization techniques such as transmission electron microscopy and small angle x-ray scattering have shown that the metal particles are spherical and randomly dispersed, the mean particle size varying from 2.6 to 4.8 nm as a function of the metal concentration. The Z-scan technique [79], as described in Section 2, is a simple and useful method to measure the third-order nonlinear properties of materials. This method enables us to measure both the real and the imaginary parts of  $\chi^{(3)}$ , proportional to the nonlinear refractive index and nonlinear absorption coefficient, respectively. Sella et al. [77, 78] have measured the optical nonlinearities of these Au:SiO<sub>2</sub> films with a metal volume fraction of 20% using a Q-switched Nd:YAG laser frequency doubled at 532 nm and characterized by a pulse duration of 7 ns at a repetition rate of 10 Hz. Open aperture measurement exhibits a maximum close to the waist of light, which reveals a large negative coefficient. They derived  $\text{Im } \chi^{(3)} = -(3.0 \pm 0.5) \times 10^{-6}$  esu. The absolute value for the real part is smaller than  $3 \times 10^{-9}$  cm<sup>2</sup>/W.

Liao et al. [80] also investigated the optical nonlinearity within Au:SiO<sub>2</sub> films in the picosecond range at 532 nm by the DFWM method. They found that the third-order susceptibility increases quickly and reaches a maximum value of  $2.5 \times 10^{-6}$  esu at 40% Au. For 20% Au, their work led to  $|\chi^{(3)}| = 2.0 \times 10^{-7}$  esu, much smaller than the result of Z-scans in the nanosecond range. This is due to the fact that the third-order optical susceptibility  $\chi^{(3)}$  contains two components: a fast component and a slow one [81]. When a picosecond laser is used, the slower component would not have enough time to respond. Thus, the  $\chi^{(3)}$  signal measured by picosecond pulses could be much smaller than that measured by nanosecond pulses.

Ballesteros et al. [82] have successfully deposited Cu nanocomposite films comprising Cu nanocrystals embedded

in an amorphous Al<sub>2</sub>O<sub>3</sub> matrix by a pulsed laser deposition (PLD) technique. The mean diameter of Cu nanocrystals ranges from 3 to 6 nm. The third-order susceptibility  $\chi^{(3)}$  of the films was determined by means of a Z-scan technique using a cavity-dumped synchronously pumped, mode-locked rhodamine 6G laser tuned at 590 nm (slightly off the SPR at 578 nm) and providing 30 ps laser pulses at a repetition rate of 400 kHz. They have investigated metal size dependence of the third-order nonlinearity within Cu:Al<sub>2</sub>O<sub>3</sub> thin films. Both thermal effect and electronic components were found to contribute to the nonlinear refractive index. The thermal contribution goes up with the increase of the metal size. This is understandable because the increase of metal diameter is accompanied by an increase of absorption of the film near the SPR; thus the thermal load of the medium also increases. It was observed that the electronic contribution to nonlinear refractive index increases from  $8 \times 10^{-10}$  to  $1.4 \times 10^{-9}$  cm<sup>2</sup>/W when the nanocrystal is decreased. From the nanocrystal size dependence, the authors clearly demonstrated that the nonlinearity is caused by quantum confinement effects whose large contribution is associated to intraband electronic transitions.

The large nonlinear refractive index and  $\chi^{(3)}$  have led many authors to suggest potential applications for the metal nanocomposites in optoelectronics. However, some difficulties remain to be addressed before these types of device application will be realized. Flytzanis et al. [83] define a figure of merit for strongly absorbing nonlinear optical materials to be  $\chi^{(3)}/\alpha\tau$ , where  $\tau$  is a relaxation time. We can get metal nanocomposites with high values of  $\chi^{(3)}$ , but both  $\chi^{(3)}$  and  $\alpha$  have a peak near the same wavelength (surface plasmon resonance wavelength). The high value of  $\alpha$  and the long thermal relaxation time  $\tau$  of the insulating matrix decrease the figure of merit, particularly for laser excitation lasting longer than a few picoseconds. Recently work has been aimed at finding methods of maintaining a high  $\chi^{(3)}$  while decreasing the surface plasmon absorption. One way to accomplish this is to get a narrow size distribution of extremely small crystals.

Because there exists the difficulty of producing a suitably narrow size distribution, some researchers have aimed at forming bimetallic core-shell nanoparticles [84]. Changes in the electronic properties across the core-shell boundary add an additional degree of freedom for the reduction of  $\alpha$  and for increasing  $\chi^{(3)}$ . Recently, some researchers [85] have synthesized transparent Ag nanocomposite films by incorporating surface-modified silver nanoparticles into polystyrene through solution mixing and static casting. The Ag nanoparticles could be redispersed well in the polymer matrix. By time-resolved femtosecond OKE experiments at 830 nm, they found that the  $\chi^{(3)}$  increases with increasing the particle size.

### 3.2. Semiconductor Nanocomposites

The effects of particle size on optical properties are more pronounced in semiconductor nanoparticles. In metals, the Fermi level is in the center of the conduction band where the energy levels are closely spaced, whereas in semiconductors, the band edges control the optoelectronic behavior. As the average particle size decreased, the optical

absorption onset shifted to higher energies [86]. This is one example of quantum confinement induced shift in semiconductor nanocrystals. Semiconductor nanocrystals have been proposed as light-emitting diodes [87] and single-electron transistors [88]. They have potential applications in optical limiting, optical computing, real time holography, optical correlators, and phase conjugators because of their high optical nonlinearity. Semiconductor nanocrystals embedded in glass may be synthesized by co-sputtering and thermal annealing. Other techniques for producing nanocomposites include direct chemical reaction in aqueous or organic solution [89] or inverse microemulsion techniques [90]. Among them, more attention has been paid on the sol-gel process in recent years due to the very low temperature involved in preparing this kind of NLO material.

The third-order NLO susceptibility  $\chi^{(3)}$  can be measured by four-wave mixing or the Z-scan technique. The experiments normally were performed with a low power continuous wave, Ar ion, and high power Nd:YAG lasers operating at different laser wavelengths and pulse duration. The origin of the third-order optical nonlinearity may come from nonlinear refraction and nonlinear absorption. Normally, the optical nonlinearity is composed of an electric component (short time response) and thermal part (long time response); these can be separated by different measurements. The second-order nonlinear optical susceptibility  $\chi^{(2)}$  can be measured by second harmonic generation or Maker fringes. The optical limiting effect is easily observed in nonlinear optical materials. The need to protect optical sensors and human eyes from the damage induced by the high fluences of pulsed lasers has led to increased attention for optical limiting materials [17].

Oak et al. [91] reported earlier the intensity-dependent transmission of  $\text{CdS}_x\text{Se}_{1-x}$  and  $\text{CdSe}_x\text{Te}_{1-x}$  particle doped glasses at wavelengths of 1054 nm employing a mode-locked Nd:glass laser with a pulse width of 6 ps. They found that the transmission for the samples dropped down when the input energy increased. The linear absorption is negligible; the main mechanism of energy loss is from two-photon absorption. However, at higher intensities additional absorption induced by the laser-generated electron-hole pairs was observed.

By a modified inverse microemulsion technique, Han et al. [90] synthesized  $\text{Ag}_2\text{S}$  coated CdS nanoparticles (about 10 nm in diameter). They measured by the Z-scan technique the nonlinear absorption in the  $\text{Ag}_2\text{S}/\text{CdS}$  nanocomposites at 532 nm with both 25 ps and 7 ns pulses from two frequency-doubled Nd:YAG lasers. Enhanced nonlinear absorption in the nanocomposites was observed in comparison with the CdS nanoparticles, due to photo-excited free carriers. The relaxation times of the free carriers in the  $\text{Ag}_2\text{S}/\text{CdS}$  nanocomposites were determined to be a few nanoseconds. Furthermore, optical nonlinearities in the nanocomposites depend on the ratio of  $\text{Cd}^{2+}$  and  $\text{Ag}^+$ , which enables us to optimize and synthesize desired optical materials. Wu et al. [92] investigated the optical nonlinearity of nanosized CdO-organosol. Two samples, CdO-CTAB (cetyltrimethyl ammonium bromide) and CdO-DBS (dodecylbenzene sulfonate) organosols, were measured by using the Z-scan technique with an 85 fs pulse of a Ti:sapphire

laser operating at a wavelength of 800 nm with a repetition rate of 82 MHz. Nonlinear absorption and refraction from the samples were observed. The real and imaginary parts of  $\chi^{(3)}$  at 800 nm have been determined to be  $-1.55 \times 10^{-16} \text{ m}^2/\text{W}$  and  $0.91 \text{ cm}/\text{GW}$  for CdO-CTAB organosol, and  $-6.97 \times 10^{-16} \text{ m}^2/\text{W}$  and  $8.64 \text{ cm}/\text{GW}$  for CdO-DBS organosol. The optical Stark effect and surface trapped states are the possible origins of the observed optical nonlinearity.

Liu et al. [93] prepared PbS-polymer (C1-PEO-C11-MA-40, NMA, AN, EGDMA, etc.) nanocomposites by polymerized bicontinuous microemulsions. The size of PbS nanocrystal is about 5 nm formed in aqueous domains embedded in the NMA/AN/C1-PEO-R-MA-40 copolymer network. They measured the nonlinearity of the nanocomposites at 780 nm using 150 fs pulses delivered by a mode-locked Ti:sapphire laser, operating at a repetition rate of 76 MHz. Its third-order nonlinear refractive index ( $\gamma$ ) at 780 nm is  $-6.8 \times 10^{-12} \text{ cm}^2/\text{W}$ , three orders higher than that of commercial bulk materials. Such a large optical nonlinearity might be due to the surface-induced large separation of charges between the delocalized electrons and localized holes.

Two-photon absorption generally involves a transition from the ground state of a system to a higher lying system by simultaneous absorption of two photons and leads to a fast optical limiting phenomena in semiconductors, such as ZnO, ZnSe, InSb, etc. [94], as well as in some organic materials. Recently, Sanz and Lbanez [95] synthesized sol-gel glasses doped with nanocrystals of stilbene 3. The organic-inorganic nanocomposite materials can be highly doped with active molecules through the control of nanometer-scale crystallization. In the nanosecond regime, nonlinear absorption was observed in the spectral range from 450 to 650 nm. The nonlinear absorption occurs in a two-step process, which is characterized by two-photon absorption and excited-state absorption spectroscopies. The two-photon absorption spectrum of stilbene 3 nanocrystals shows a resonance at 620 nm with a cross-section  $\sigma_{\text{TPA}} = 3.3 \times 10^{-48} \text{ cm}^4 \text{ s}/\text{photon molecule}$ . The excited state absorption spectrum of stilbene 3 nanocrystals, which was obtained by using a pump-probe ( $\lambda = 355 \text{ nm}$ ) geometry supercontinuum laser light with a 30 ps time resolution, exhibits a broad resonance with a maximum at 670 nm and a decrease of quasilinear absorption at blue wavelengths.

It is interesting to mention that Maciel et al. [96] reported nonlinear absorption experiments which were performed with a class of ferroelectric glass-ceramic samples. The samples were prepared by heat treatment of (in molar %) 35  $\text{SiO}_2$ -31  $\text{Nb}_2\text{O}_5$ -19  $\text{Na}_2\text{O}$ -11  $\text{K}_2\text{O}$ -2  $\text{CdO}$ -2  $\text{B}_2\text{O}_3$  glass. A set of glass-ceramic samples with different volume fractions of sodium niobate ( $\text{NaNbO}_3$ ) crystallites was obtained. The samples exhibit a large transparency window from the near infrared to the visible average, and the sizes of  $\text{NaNbO}_3$  crystallites are around 10 nm. The optical transmission was measured by using a Q-switched Nd:YAG laser (532 nm, 1064 nm, 15 ns, 5 Hz). The energies of the incident and the transmitted pulses were simultaneously measured by using two large area photodetectors connected to a fast oscilloscope. The photodetector used to monitor the transmitted beam was placed in the far-field region and the light

intensity was totally collected to avoid misinterpretation of the data due to contributions of nonlinear refraction. They found that samples show a nonlinear absorption at 532 nm, and some of samples exhibit optical limiting depending on the bandgap of these samples. The nonlinear coefficients of two-photon and three-photon absorption were determined.

The approaches for increasing optical nonlinearity of nanocomposites materials are as follows:

- (i) increasing particle concentration,
- (ii) working at near-resonant wavelength,
- (iii) adding the dielectric confinement effect beside the quantum confinement effect.

For example, the  $\chi^{(3)}$  of 2% CdS doped glass was estimated to be  $1.5 \times 10^{-10}$  esu at 390 nm, while  $\chi^{(3)}$  values increase to  $6.3 \times 10^{-7}$  esu after increasing the doping concentration of CdS up to 8% by the sol-gel process [97]. Optical nonlinearity can be enhanced by the dielectric confinement effect, which is a surface polarization effect induced by trapped state and atomic vacancy defects, as discussed. This includes two cases: (a) nanoparticles with high refractive index, such as SnO<sub>2</sub>, CdS, and Pbs doped in a matrix with low refractive index, such as SiO<sub>2</sub> and PMMA; (b) nanoparticles with a high refractive index, coated with a low refractive index layer, such as stearic acid.

Very recently, Murugan and Varma [98] have fabricated glass nanocomposites in the system  $(100-x)\text{Li}_2\text{B}_4\text{O}_7-x \cdot \text{SrBi}_2\text{Ta}_2\text{O}_9$  ( $0 \leq x \leq 22.5$ ) by a melt quenching technique followed by heat treatment. They found that the optical transmission properties of these glass nanocomposites were composition dependent. The  $\chi^{(3)}$  values of the system are higher for compositions containing higher SrBi<sub>2</sub>Ta<sub>2</sub>O<sub>9</sub> (SBT) content. The heat-treated samples could have larger  $\chi^{(3)}$  values than as-quenched ones. The third-order nonlinear optical susceptibility  $\chi^{(3)}$  for glass nanocomposites  $x = 15$  is determined to be  $3.046 \times 10^{-21}$  cm<sup>3</sup>. SHG was observed in the transparent glass nanocomposites. The dependence of second harmonic intensity on the angle of incidence is weak for the compositions with  $x = 5$  and 15. However, an appreciable change in the SH intensity with the angle of incidence is observed for the composition corresponding to  $x = 20$  possibly due to larger crystallites of SBT.

### 3.3. Other Nanocomposites

Zhang et al. [99] prepared well-crystallized SBT thin films by the PLD technique. The nonlinear optical measurements were performed by using a single-beam Z-scan method. A mode-locked Nd:YAG laser (1064 nm, 38 ps, 10 Hz) was used as the light source. They performed an open aperture Z-scan measurement and no nonlinear absorption was found. However, closed-aperture Z-scan experiments revealed a signal profile with a peak followed by a valley, indicating a negative (self-defocusing) optical nonlinearity. The calculated value of the nonlinear refractive index of the sample is  $1.9 \times 10^{-6}$  esu, which compares favorably with the nonlinearities of other representative third-order NLO materials, such as V<sub>2</sub>O<sub>5</sub>, high-density Au-dispersed SiO<sub>2</sub> and TiO<sub>2</sub> composites. This shows that SBT thin films are promising materials for applications in NLO devices. In

another recent work [100], Yang et al. have reported reflection results from SBT and PbZr<sub>x</sub>Ti<sub>1-x</sub>O<sub>3</sub> (PZT,  $x = 0.30, 0.53, 0.8$ ) samples employing laser pulses of 8 ns at 1064 nm. For the SBT sample, when the input energy is low, the output energy increases linearly with incident energy. However, in excess of 270  $\mu\text{J}/\text{pulse}$ , the output energy is nearly a constant value of 185.6  $\mu\text{J}/\text{pulse}$ . Saturation occurs for higher inputs and functionally appears as typical limiting behavior. They found that the output energy of the PZT sample also shows an optical nonlinearity, and the behavior depends on the atomic ratio of Zr and Ti. As to the mechanism, the bandgap of the sample is too wide to make any nonlinear absorption. The authors suggest that the nonlinearity may result from a scattering of the incident light by the ferroelectric domains in the films.

Recently, carbon nanotubes and their nanocomposites have been investigated [15–17]. Their third-order optical nonlinearity and optical limiting properties have been reported [15–17, 101–103]. Recently, Xu et al. [104] obtained another tube-shaped material, vanadium oxide (VO<sub>x</sub>), by a sol-gel technique. These VO<sub>x</sub> nanotubes are dispersed in water or embedded in PMMA films. Their nonlinear optical transmission was measured using 8 ns pulses from a Nd:YAG laser with an  $f/40$  optical system. At 532 nm the transmittance of VO<sub>x</sub> in water drops when input fluence increases. The behavior is similar with that of carbon nanotube suspensions. However, the phenomena of VO<sub>x</sub> embedded in PMMA is much better than that of carbon nanotube-PMMA nanocomposites because the mechanism in VO<sub>x</sub> nanocomposites is two-photon absorption, different from the nonlinear scattering that occurred in carbon nanotubes.

For convenience, Table 2 summarizes some results of the third-order optical nonlinearities of nanocomposites.

### 3.4. Optical Limiting Effect

A currently important problem in science and technology is related to the task of protecting the human eye and the sensors of instruments detecting high-power light beams from radiation damage [15, 17]. A solution to this problem is the use of passive optical limiters as protection devices. An ideal optical limiter is material or device that exhibits linear transmission at low incident fluence, but output light fluence will reach a saturated value when the incident light fluence is over one threshold due to the optical nonlinearity of materials. The possibility to fabricate an applicable optical limiter based on nanocomposites materials was widely investigated. optical limiting effects can be observed in several materials and with different mechanisms [15, 17, 105], such as reverse saturable absorption (RSA), two or three absorption, nonlinear scattering, or nonlinear refraction.

Among the nonlinear optical absorptions, RSA is a primary mechanism for some organic molecules and is demonstrated to be one of the best processes to use for optical limiting because it reduces the total pulse energy rather than simply reducing the fluence or irradiance [15, 17]. RSA occurs when a larger absorption from an excited state compared to that from the ground state is observed. For example, C<sub>60</sub> and its derivatives represent such an interesting class

**Table 2.** Third-order optical nonlinearities of some nanocomposites measured by Z-scan (ZS), degenerate four-wave mixing (DFWM), nonlinear transmission (NLT), or Kerr experiment (Kerr), where  $\lambda$  and  $\tau$  are laser wavelength and pulse width, respectively.

Material and state	$\lambda$ (nm)	$\tau$	$ \chi^{(3)} $ ( $10^{-10}$ esu)	$\gamma$ ( $10^{-20}$ m <sup>2</sup> /W)	Method	Ref.
Au/SiO <sub>2</sub> film	532	7 ns	10,000		ZS	[117]
Au/SiO <sub>2</sub> film	532	70 ps	10,000		DFWM	[70]
Au/silica film	532	7 ns	30,000		ZS	[68]
Au/BaTiO <sub>3</sub> film	532	10 ns	6600		ZS	[118]
Ag/polystyrene film	830		10 <sup>11</sup>		Kerr	[75]
Ag/BaTiO <sub>3</sub> film	532	10 ns	10,000		ZS	[119]
Cu/Al <sub>2</sub> O <sub>3</sub> film	596	6 ps		2,930,000	ZS	[72]
Cu/Al <sub>2</sub> O <sub>3</sub> film	590	30 ps	1000	8,000,000	ZS	[66]
Fe/BaTiO <sub>3</sub> film	532	10 ns	7200		ZS	[120]
Si/SiO <sub>2</sub> film	813	60 fs	13		ZS	[121]
CdS/PDA film	530	5 ns		10 <sup>10</sup>	ZS	[122]
CdO/CTAB organosol	800	85 fs	1.67	-15,500	ZS	[82]
CdO/DBS organosol	800	85 fs	8.22	-69,700	ZS	[82]
PbS/polymer	780	150 fs		-68,000	ZS	[55]
PbS/CdS solution	780	150 fs		10 <sup>13</sup>	ZS	[123]
NaNbO <sub>3</sub> /glass-ceramic	532	70 ps		10	ZS	[124]
CuCl/glass	1330			3.3	ZS	[125]
Rh /BaTiO <sub>3</sub> film	532	10 ns	3590		ZS	[126]
GaSb/SiO <sub>2</sub> film	632.8			10 <sup>11</sup>	ZS	[127]
InP/SiO <sub>2</sub> film	632.8			-10 <sup>9</sup>	ZS	[128]
PbO/glass	532	5 ns		1580	ZS	[129]
Cu/silica glass	532	6 ps		10 <sup>8</sup>	ZS	[130]
Ge/silica	780	150 fs		10 <sup>8</sup>	ZS	[131]
Ge/silica	532	35 ps		10 <sup>13</sup>	ZS	[132]
PbS/microemulsion	780	150 fs		-48,000	ZS	[133]

of molecules for optical limiting in visible range [17]. C<sub>60</sub> exhibits optical limiting behavior with a saturation threshold lower than other materials. RSA is its dominant mechanism [17]: there exist allowed broadband transitions from the first excited singlet and triplet to the higher excited states and this results in absorption in the visible and near infrared range that is much stronger than the absorption from the ground state, leading to RSA. In comparison with the C<sub>60</sub>-toluene system, a reduction of the saturated threshold by a factor of 3 to 5 was obtained by Belousov et al. in a C<sub>60</sub>-CCl<sub>4</sub> system [106]. Further experiments show that the optical limiting performance of C<sub>60</sub> in room temperature solution toward nanosecond laser pulses at 532 nm strongly depends on the fullerene solution concentrations.

Optical limiting from fullerenes in solid materials, such as SiO<sub>2</sub> matrix, was reported [17]. Measurements at 532 nm on samples with two C<sub>60</sub> concentrations exhibited RSA. The sample with a larger concentration shows a lower limiting fluence. The presence of thermal effects, scattering, and other effects besides RSA makes it difficult to get their relative contributions [17]. The fullerene-metal nanocomposites remain a relatively unexplored area [17]. Recently, Sun et al. [107] prepared a novel fullerene-Ag nanocomposite (DTC<sub>60</sub>-Ag) by the *in-situ* reduction of silver ions encapsulated in a new monofunctionalized methano-[60] fullerene derivative (DTC<sub>60</sub>) with reverse micellelike structure. Their experimental measurements demonstrated that the optical limiting behavior of DTC<sub>60</sub>-Ag is better than that of both C<sub>60</sub> and DTC<sub>60</sub>.

We have observed optical limiting effects in Ag-polymer nanocomposites. Here Ag can be nanoparticles with diameter from 2 to 10 nm or nanorods with length-diameter ratios of 2:1 to 8:1. Optical limiting at different wavelength was observed by adjusting the particle size or the length-diameter ratio of the Ag rod. The limiting comes from nonlinear scattering from the Ag due to the absorption of surface-plasmon resonance. Oak et al. [91] found optical limiting within CdS<sub>x</sub>Se<sub>1-x</sub> doped glasses at 1054 nm in the range of 6 ps. They attributed the main mechanism of limiting to two-photon absorption. At higher input intensities, additional absorption due to laser-generated carriers was observed.

Recently, Sanz and Lbanez [95] synthesized sol-gel glasses doped with nanocrystals of stilbene 3. The organic-inorganic nanocomposite materials can be highly doped with active molecules through the control of nanometer scale crystallization. For sample thickness and concentration to be 1 mm and 300 g/L, in a *f*/5 optical system, laser pulse 2.6 ns, at low energy (<5  $\mu$ J), the sample is transparent and the transmitted energy increases linearly with the incident energy. At higher incident energies, the output energy is damped below 20  $\mu$ J within the visible range due to two-photon absorption and excited state absorption.

#### 4. CONCLUSIONS

We have not discussed the second-order optical nonlinearities of nanoparticles in this chapter. More details can be found in the work of Wang et al. [59].

As discussed, the novel properties of nanoparticles and nanocomposites are dominated by two major effects: surface effects and unique characteristics of electrons in confined systems. The increasing surface energy associated with the larger surface-to-volume ratio of small particles determines the physical and thermodynamic properties of the nanoparticles and nanocomposite, such as melting points. Surface effects and electron confinement combine to produce novel electronic properties that can be manifested in a wide range of effects, such as a large nonlinear optical susceptibility, etc.

For metal nanocomposites, people wish to have higher  $\chi^{(3)}$  and lower linear absorption as higher linear absorption and the corresponding long thermal relaxation time of the insulating matrix decrease the figure of merit for these materials.  $\chi^{(3)}$  varies as  $1/r^3$ . Thus, it would be the goal to produce extremely small particles with narrow size distribution and higher volume ratio of metal particles in the matrix.

For the ideal case of materials composed of linearly arranged particles, very large enhancements can be obtained provided that the particles are aligned in the polarization direction of the incident field. In this case, very high intensities are induced inside the particles at the center of the linear chain and the local field amplification is accompanied by a shift of the spectral location of the resonance.

Semiconductor nanoparticles and nanocomposites have also attracted much attention because they were shown to have large third-order optical nonlinear susceptibility. Basically, quantum size and interfacial effects are those we must consider when we want to increase the optical nonlinearity. For example, various chemical methods are developed to passivate the surface of nanoparticles. For the second case, various functional molecules are used to modify the surface of nanoparticles to form core-shell structure. Another factor to increase optical nonlinearity of nanocomposite materials is the dielectric confinement effect. This effect depends on the dielectric constant ratio, such as high refractive index nanoparticles doped in low refractive index matrix or coated with a low refractive index layer.

Finally, we would like to point out that the optical nonlinearity of nanoparticles and nanocomposites could be enhanced by the change of coupling between light and materials. We observed strong nonlinear absorption in  $\text{VO}_x$  nanotubes at 532 nm, but the nonlinear absorption vanishes when these nanotubes were unrolled into platelets. Another example is that a larger optical nonlinearity was observed in B, N doped carbon nanotubes compared to pure carbon nanotubes (see the chapter entitled "Doped Carbon Nanotubes" in this encyclopedia [15]). This means that the dimensional and electronic structures play important roles in the NLO properties of nanoparticles and nanocomposites.

## GLOSSARY

**DFWM** The nonlinear interaction of three optical waves of the same frequency to generate a fourth, re-emitted wave is known as DFWM, and the method has provided a wealth of knowledge about the behavior of excitons in III-V semiconductors.

**Gaussian beam** Lowest divergence, smallest radius laser beam possible for a given oscillator. It is created when the laser is operating in the TEM<sub>00</sub> mode.

**Hyperpolarizabilities** The coefficient of the higher than linear terms in the relation between the electric dipole moment of a molecule and the electric field which acts on the molecule.

**Kerr effect** A quadratic nonlinear electro-optic effect found in particular liquids and crystals that are capable of advancing or retarding the phase of the induced ordinary ray relative to the extraordinary ray when an electric current is applied. It varies as the square of the voltage.

**Rayleigh scattering** Scattering of radiation in the course of its passage through a medium containing particles, the sizes of which are small compared with the wavelength of the radiation. Method an OTDR uses.

**Spectrometer** A device used to measure radiant intensity or to determine the wavelengths of various radiations.

**Surface plasmon resonance (SPR) phenomenon** The collective oscillation of the conduction electrons of the metal under the influence of an applied electromagnetic (EM) wave.

**Third-order nonlinear susceptibility** Used to characterize the degree of third-order optical nonlinearity.

**Transmittance** The ratio of the radiant power transmitted by an object to the incident radiant power.

**Z-scan technique** Used to measure the sign and the magnitude of the refractive and the absorptive nonlinearities with single beam.

## ACKNOWLEDGMENTS

We thank Dr. H. S. Nalwa, Professor V. H. Smith, Jr., and Professor J. Gao for valuable comments. We thank Qin Rao for the plot of Figure 1. J. X. thanks the University of Arizona for financial support. Q. D. W. gratefully acknowledges the Changchun Institute of Optics, Fine Mechanics, and Physics for financial support.

## REFERENCES

1. A. Henglein, *Chem. Rev.* 89, 1861 (1989).
2. M. L. Stwigerwald and L. E. Brus, *Acc. Chem. Res.* 23, 183 (1990).
3. M. G. Bawendi, M. L. Stwigerwald, and L. E. Brus, *Annu. Rev. Phys. Chem.* 41, 477 (1990).
4. H. Weller, *Angew. Chem. Int. Ed. Engl.* 32, 41 (1993).
5. H. Weller, *Adv. Mater.* 5, 88 (1993).
6. A. Hagfeldt and M. Gratzel, *Chem. Rev.* 95, 49 (1995).
7. J. H. Fendler and F. C. Meldrum, *Adv. Mater.* 7, 607 (1995).
8. A. P. Alivisatos, *J. Phys. Chem.* 100, 13226 (1996).
9. R. H. Xie and J. Jiang, *Appl. Phys. Lett.* 71, 1029 (1997).
10. R. H. Xie and J. Jiang, *Chem. Phys. Lett.* 280, 66 (1997).
11. R. H. Xie and J. Jiang, *J. Appl. Phys.* 83, 3001 (1998).
12. R. H. Xie and Q. Rao, *Appl. Phys. Lett.* 72, 2358 (1998).
13. R. H. Xie and Q. Rao, *Chem. Phys. Lett.* 313, 211 (1999).
14. R. H. Xie, *Chem. Phys. Lett.* 310, 379 (1999).
15. R. H. Xie, J. Zhao, and Q. Rao, in "Encyclopedia of Nanoscience and Nanotechnology" (H. S. Nalwa, Ed.). American Scientific, Los Angeles, 2003.
16. R. H. Xie, in "Handbook of Advanced Electronic and Photonic Materials and Devices" (H. S. Nalwa, Ed.), Vol. 9, pp. 267-307. Academic Press, New York, 2000.



17. R. H. Xie, Q. Rao, and L. Jensen, in "Encyclopedia of Nanoscience and Nanotechnology" (H. S. Nalwa, Ed.). American Scientific, Los Angeles, 2003.
18. M. I. Baraton, "Synthesis, Functionalization and Surface Treatment of Nanoparticles." American Scientific, Los Angeles, 2002.
19. J. H. Fendler, "Nanoparticles and Nanostructured Films: Preparation, Characterization and Applications." Wiley, New York, 1998.
20. "Single Organic Nanoparticles (Nanoscience and Technology)" (H. Masuhara, H. Nakanishi, and K. Sasaki, Eds.). Springer-Verlag, Berlin, 2003.
21. "Metal Nanoparticles: Synthesis Characterization and Applications" (D. L. Feldheim and C. A. Foss, Eds.). Dekker, New York, 2001.
22. N. Herron and D. L. Thorn, *Adv. Mater.* 10, 1173 (1998).
23. A. J. Stentz and R. W. Boyd, in "Handbook of Photonics" (M. C. Gupta, Ed.), Ch. 5. CRC Press, Boca Raton, FL, 1997.
24. "Sol-Gel Preparation and Characterization of Metal-Silica and Metal Oxide-Silica Nanocomposites" (G. Picaluga, Ed.). Trans Tech, 2000.
25. "Polymer-Clay Nanocomposites" (T. J. Pinnavaia and G. W. Beall, Eds.). Wiley, New York, 2001.
26. R. A. Vaia and R. Krishnamoorti, "Polymer Nanocomposites: Synthesis, Characterization, and Modeling." American Chemical Society, 2001.
27. "Nanocomposite Science and Technology" (P. M. Ajayan, P. V. Braun, and L. Schadler, Eds.). Wiley, New York, 2003.
28. G. Decher and J. B. Schlenoff, "Multilayer Thin Films: Sequential Assembly of Nanocomposite Materials." VCH, Weinheim, 2003.
29. G. I. Stegeman and E. M. Wright, *Opt. Quantum Electron.* 22, 95 (1990).
30. D. Ricard, P. Roussignol, and C. Flytzanis, *Opt. Lett.* 10, 511 (1985).
31. F. Hache, D. Ricard, and C. Flytzanis, *J. Opt. Soc. Am. B* 3, 1647 (1986).
32. D. S. Chemla and D. A. B. Miller, *Opt. Lett.* 11, 522 (1986).
33. P. H. Roussignol, D. Ricard, and C. H. R. Flytzanis, *Appl. Phys. B* 51, 437 (1990).
34. E. Hanamura, *Phys. Rev. B* 37, 1273 (1988).
35. D. Cotter, M. G. Burt, and R. J. Manning, *Phys. Rev. Lett.* 68, 1200 (1992).
36. E. Hanamura, *Phys. Rev. B* 37, 1273 (1988).
37. C. R. Schwarze, D. A. Pommet, G. Flynn, and M. A. Fiddy, *Waves Random Media* 10, 43 (2000).
38. D. Prot, D. B. Stout, J. Lafait, N. Pincon, B. Palpant, and S. Debrus, *J. Opt. A* 4, S99 (2002).
39. G. M. Carter, *J. Opt. Soc. Am. B* 4, 1018 (1987).
40. M. Sheik-Bahae, A. A. Said, T. Wei, D. J. Hagan, and E. W. van Stryland, *IEEE J. Quantum Electron.* 26, 760 (1990).
41. M. C. Schanne-Klein, H. Hache, D. Ricard, and C. Flytzanis, *J. Opt. Soc. Am. B* 9, 2234 (1992).
42. D. V. Petrov, A. S. L. Gomes, and C. B. de Araujo, *Phys. Rev. B* 50, 9092 (1994).
43. J. A. Giordmaine and J. A. Howe, *Phys. Rev. Lett.* 11, 207 (1963).
44. P. D. Marker, R. W. Terhune, and C. M. Savage, *Phys. Rev. Lett.* 12, 507 (1964).
45. G. Mayer and F. Gires, *C. R. Acad. Sci. Paris* 258, 2039 (1964).
46. H. A. Duguay and J. W. Hansen, *Appl. Phys. Lett.* 15, 192 (1969).
47. E. P. Ippen and C. V. Shank, *Appl. Phys. Lett.* 26, 92 (1975).
48. S. Ruhman, L. R. Williams, A. G. Joly, and K. A. Nelson, *J. Phys. Chem.* 91, 2237 (1987).
49. J. Etchepare, G. Grillon, J. P. Chambaret, G. Harmoniaux, and A. Orszag, *Opt. Commun.* 63, 329 (1987).
50. S. Ruhman and K. A. Nelson, *J. Chem. Phys.* 94, 859 (1991).
51. Y.-X. Yan and K. A. Nelson, *J. Chem. Phys.* 87, 6240 (1987).
52. Y.-X. Yan and K. A. Nelson, *J. Chem. Phys.* 87, 6257 (1987).
53. S. Ruhman, A. G. Joly, and K. A. Nelson, *IEEE J. Quantum Electron.* QE-14, 460 (1988).
54. S. Ruhman, B. Kohler, A. G. Joly, and K. A. Nelson, *IEEE J. Quantum Electron.* QE-14, 470 (1988).
55. N. Pincon, B. Palpanta, D. Prot, E. Charron, and S. Debrus, *Eur. Phys. J. D* 19, 395 (2002).
56. D. D. Smith, Y. Yoon, R. W. Boyd, and M. George, *J. Appl. Phys.* 86, 6200 (1999).
57. Y. Takeda, V. T. Gritsyna, N. Umeda, C. G. Lee, and N. Kishimoto, *Nucl. Instrum. Methods B* 148, 1029 (1999).
58. M. L. Steigerwald and L. E. Brus, *Annu. Rev. Mater.* 19, 471 (1989).
59. X. Wang, Y. Zhang, Z. Lu, and Y. Cui, in "Encyclopedia of Nanoscience and Nanotechnology" (H. S. Nalwa, Ed.). American Scientific, Los Angeles, 2003.
60. D. F. Eaton, *Science* 253, 281 (1991).
61. A. Othmani, J. C. Plenet, E. Berstein, C. Bovier, C. Dumas, P. Riblet, P. Gilliot, R. Levy, and J. B. Grun, *J. Cryst. Growth* 144, 141 (1994).
62. H. Yao, S. Takahara, H. Mizuma, T. Kozeki, and T. Hayashi, *J. Appl. Phys. Jpn.* 35, 4633 (1996).
63. O. D. Sanctis, K. Kadono, H. Tanaka, and T. Sakaguchi, *Mater. Res. Soc. Symp. Proc.* 358, 253 (1995).
64. B. L. Yu, G. S. Yin, C. S. Zhu, and F. X. Gan, *Opt. Mater.* 11, 17 (1998).
65. B. Liu, C. H. Chew, L. M. Gan, G. Q. Xua, H. Li, Y. L. Lam, C. H. Kam, and W. X. Que, *J. Mater. Res.* 16, 1644 (2001).
66. D. Cotter, M. G. Burt, and R. J. Manning, *Phys. Rev. Lett.* 68, 1200 (1992).
67. O. A. Aktsipetrov, *Colloids Surfaces A* 202, 165 (2002).
68. T. V. Murzina, T. V. Misuryaev, A. F. Kravets, J. Gudde, D. Schuhmacher, G. Marowsky, A. A. Nikulin, and O. A. Aktsipetrov, *Surf. Sci.* 482, 1101 (2001).
69. T. V. Murzina, A. A. Nikulin, O. A. Aktsipetrov, J. W. Ostrander, A. A. Mamedov, N. A. Kotov, M. A. C. Devillers, and J. Roark, *Appl. Phys. Lett.* 79, 1309 (2001).
70. T. V. Murzina, A. A. Fedyanin, T. V. Misuryaev, G. B. Khomutov, and O. A. Aktsipetrov, *Appl. Phys. B* 68, 537 (1999).
71. X. Y. Pan, N. V. Chigarev, H. B. Jiang, W. T. Huang, Q. H. Gong, C. L. Liu, V. M. Kobryanskii, and D. Y. Paraschuk, *Chem. Phys. Lett.* 365, 117 (2002).
72. L. Yang, K. Becker, F. M. Smith, R. H. Magruder III, R. F. Haglund, Jr., R. Dorsinville, R. R. Alfano, and R. A. Zuhr, *J. Opt. Soc. Am. B* 11, 458 (1994).
73. G. De, M. Gusso, L. Tapfer, M. Catalano, F. Gonella, G. Mattei, P. Mazzoldi, and G. Battaglin, *J. Appl. Phys.* 80, 6734 (1996).
74. L. B. Liao, R. F. Xiao, H. Wang, K. S. Wong, and G. K. L. Wong, *Appl. Phys. Lett.* 72, 1817 (1998).
75. M. Falconieri, G. Salvetti, e. Cattaruzza, F. Gonella, G. Matei, P. Mazzolde, M. Piovesan, G. Battaglin, and R. Polloni, *Appl. Phys. Lett.* 73, 288 (1998).
76. J. M. Ballesteros, J. Solic, R. Serna, and C. N. Afonso, *Appl. Phys. Lett.* 74, 2791 (1999).
77. C. Sella, M. Maaza, B. Pardo, F. Dunsteter, J. C. Martin, and M. C. Sainte-Catherine, *Physica A* 241, 192 (1997).
78. S. Debrus, J. Lafait, M. May, N. Pincon, D. Prot, C. Sella, and J. Venturini, *J. Appl. Phys.* 88, 4469 (2000).
79. M. Sheik-Bahae, A. A. Said, T. Wei, D. J. Hagan, and E. W. Van Stryland, *IEEE J. Quantum Electron.* 26, 760 (1990).
80. H. B. Liao, R. F. Xiao, J. S. Fu, P. Yu, and G. K. L. Wong, *Appl. Phys. Lett.* 70, 1 (1997).
81. M. Ando, K. Kadono, M. Haruta, T. Sakaguchi, and M. Mly, *Nature (London)* 374, 625 (1995).
82. J. M. Ballesteros, R. Serna, J. Solis, C. N. Afonso, A. K. Petford-Long, D. H. Osborne, and R. F. Haglund, Jr., *Appl. Phys. Lett.* 71, 2445 (1997).
83. C. Flytzanis, F. Hache, M. C. Klein, D. Ricard, and P. Roussignol, *Progr. Opt.* 29, 321 (1991).

84. E. Cattaruzza, G. Battaglin, R. Polloni, T. Cesca, F. Gonella, and G. Mattei, *Nucl. Instrum. Methods B* 148, 1007 (1999).
85. R. Zeng, S. F. Wang, H. C. Liang, N. Z. Rong, M. Q. Zhang, H. M. Zeng, and Q. H. Gong, *Polymers Polymer Composites* 10, 291 (2002).
86. J. Xu and W. Ji, *J. Mater. Sci. Lett.* 18, 115 (1999).
87. V. L. Colvin, M. C. Schlamp, and A. P. Alivisatos, *Nature (London)* 370, 354 (1994).
88. D. L. Klein, R. Roth, A. K. L. Lim, A. P. Alivisatos, and P. L. McEuen, *Nature (London)* 389, 699 (1997).
89. F. Henneberger, S. Schmitt-Rink, and E. Gobel, "Optics of Semiconductor Nanostructures." Akademie-Verlag, Berlin, 1993.
90. M. Y. Han, W. Huang, C. H. Chew, L. M. Gan, X. J. Zhang, and W. Ji, *J. Phys. Chem. B* 102, 1884 (1998).
91. S. M. Oak, K. S. Bindra, R. CHari, and K. C. Rustagi, *J. Opt. Soc. Am. B* 10, 613 (1993).
92. X. Wu, R. Wang, B. Zou, P. Wu, L. Wang, J. Xu, and W. Huang, *Appl. Phys. Lett.* 71, 2097 (1997).
93. B. Liu, H. Li, C. H. Chew, W. Que, Y. L. Lam, C. H. Kam, L. M. Gan, and G. Q. Xu, *Mater. Lett.* 51, 461 (2001).
94. M. Sheik-Bahae, D. J. Hagan, and E. W. Van Stryland, *Phys. Rev. Lett.* 65, 96 (1990).
95. N. Sanz, A. Lbanez, Y. Morel, and P. L. Baldck, *Appl. Phys. Lett.* 78, 2569 (2001).
96. G. S. Maciel, N. Rakov, Cid B. de Araujo, A. A. Lipovskii, and D. K. Tagantsev, *Appl. Phys. Lett.* 79, 584 (2001).
97. T. Takada, T. Yano, and A. Yasumori, *J. Non-Cryst. Solids* 147, 631 (1992).
98. G. S. Murugan and K. B. R. Varma, *J. Mater. Chem.* 12, 1426 (2002).
99. W. Zhang, M. Zhang, and Z. Yin, *Appl. Phys. Lett.* 75, 902 (1999).
100. P. Yang, J. Xu, J. Ballato, R. W. Schwartz, and D. L. Carroll, *Appl. Phys. Lett.* 80, 3394 (2002).
101. R. H. Xie and Q. Rao, *Z. Naturforsch. A* 54, 645 (1999).
102. C. Stanciu, R. Ehlich, and V. Petrov, *Appl. Phys. Lett.* 81, 4064 (2002).
103. For a recent review, see C. Dekker, *Phys. Today* 52, 22 (1999).
104. J. F. Xu, R. Czerw, S. Webster, D. L. Carroll, J. Ballato, and R. Nesper, *Appl. Phys. Lett.* 81, 1711 (2002).
105. A. A. Said, M. Sheik-Bahae, D. J. Hagan, T. H. Wei, J. Wang, J. Young, and E. W. Van Stryland, *J. Opt. Soc. Am. B* 9, 405 (1992).
106. V. P. Belousov, I. M. Belousova, E. A. Gavronskaya, V. A. Grigor'ev, A. G. Kalintsev, A. V. Kris'ko, D. A. Kozlovskii, N. G. Mironova, A. G. Skobelev, and M. S. Yur'ev, *J. Opt. Technol.* 68, 876 (2001).
107. N. Sun, Y. Wang, Y. Song, Z. Guo, L. Dai, and D. Zhu, *Chem. Phys. Lett.* 344, 277 (2001).
108. Y. Yang, J. Shi, H. Chen, S. Dai, and Y. Liu, *Chem. Phys. Lett.* 370, 1 (2003).
109. G. Ma, J. He, and S.-Hai Tang, *Phys. Lett. A* 306, 348 (2003).
110. G. Yang, H.-T. Wang, G.-T. Tan, A.-Q. Jiang, Y.-L. Zhou, G.-Z. Yang, and Z.-H. Chen, *Chin. Phys. Lett.* 18, 1598 (2001).
111. G. Vijaya Prakash, M. Cazzanelli, Z. Gaburro, L. Pavesi, F. Iacona, and F. Priolo, *Mater. Res. Soc. Symp. Proc.* 722b (2002).
112. T. Ishizaka, S. Muto, and Y. Kurokawa, *Opt. Commun.* 190, 385 (2001).
113. Y. Takeda, T. Motohiro, T. Hioki, and S. Noda, *J. Vac. Sci. Technol. B* 16, 7 (1998).
114. S. W. Lu, U. Sohling, M. Mennig, and H. Schmidt, *Nanotechnology* 13, 669 (2002).
115. T. Takada, J. D. Mackenzie, M. Yamane, K. Kang, N. Peyghambarian, R. J. Reeves, E. T. Knobbe, and R. C. Powell, *J. Mater. Sci.* 31, 423 (1996).
116. Y. Yang, J. Shi, W. Huang, S. Dai, and L. Wang, *Mater. Lett.* 56, 1048 (2002).
117. N. Pincon, B. Palpant, D. Frot, E. Charron, and S. Debrus, *Eur. Phys. J. D* 19, 398 (2002).
118. W. Wang, G. Yang, Z. Chen, Y. Zhou, H. Lu, and G. Yang, *Chin. Phys.* 11, 1324 (2002).
119. G. Yang, W. Wang, Y. Zhou, H. Lu, G. Yang, and Z. Chen, *Appl. Phys. Lett.* 81, 3969 (2002).
120. W. Wang, G. Yang, Z. Chen, Y. Zhou, H. Lu, and G. Yang, *J. Appl. Phys.* 92, 7242 (2002).
121. G. V. Prakash, M. Cazzanelli, Z. Gaburro, L. Pavesi, F. Iacona, G. Franzo, and F. Priolo, *J. Appl. Phys.* 91, 4607 (2002).
122. R. E. Schwerzel, K. B. Spahr, J. P. Kurmer, Van E. Wood, and J. A. Jenkins, *J. Phys. Chem. A* 102, 5622 (1998).
123. B. Liu, C. H. Chew, L. M. Gan, G. Q. Xu, H. Li, Y. L. Lam, C. H. Kam, and W. X. Que, *J. Mater. Res.* 16, 1644 (2001).
124. G. Maciel, C. B. Acaujo, A. A. Lipovskii, and D. K. Tagantsev, *Opt. Commun.* 203, 441 (2002).
125. W. D. Xiang, *J. Inorgan. Mater.* 18, 39 (2003).
126. G. Yang, W. T. Wang, L. Yan, H. B. Lu, G. Z. Yang, and Z. H. Chen, *Opt. Commun.* 209, 445 (2002).
127. F. M. Liu, T. M. Wang, and L. D. Zhang, *Acta Physica Sinica* 51, 183 (2002).
128. M. J. Zheng, L. D. Zhang, and I. G. Zhang, *Appl. Phys. A* 73, 183 (2001).
129. T. Hashimoto, T. Yamamoto, T. Kato, H. Nasu, and K. Amiya, *J. Appl. Phys.* 90, 533 (2001).
130. G. Battaglin, P. Calvelli, E. Cattaruzza, F. Gonella, R. Polloni, G. Mattei, and P. Mazzoldi, *Appl. Phys. Lett.* 78, 3953 (2001).
131. H. Li, C. Kam, Y. Lam, Y. Jie, W. Ji, A. Wee, and C. Huan, *Appl. Phys. B* 72, 611 (2001).
132. Y. Jie, Y. Xiong, A. Wee, C. Huan, and W. Ji, *Appl. Phys. Lett.* 77, 3926 (2000).
133. H. Li, B. Liu, C. Kam, Y. Lam, W. Que, L. Gan, C. Chew, and G. Xu, *Opt. Mater.* 14, 321 (2000).



# Nucleation Kinetics of Nanofilms

S. A. Kukushkin, A. V. Osipov

*Russian Academy of Science, St. Petersburg, Russia*

## CONTENTS

1. Introduction
  2. Thermodynamics of an Adsorbed Layer
  3. Nanofilm Growth Regimes
  4. Nucleation Processes of Unstressed Nanoparticles
  5. Growth and Evolution of Isolated Nanoislands
  6. Kinetics of Nanofilm Condensation at the Initial Stage
  7. Kinetics of Nanofilm Condensation at the Late Stage
  8. Nucleation and Evolution of GaN Nanoislands
  9. Nucleation of Coherent Nanoparticles
  10. Conclusion
- Glossary  
References

## 1. INTRODUCTION

Progress in development of computer facilities, optoelectronics, and some other fields of engineering is, above all, associated with use of thin films as the ground of their elementary base. At present, a great interest is expressed in application of nanostructures and quantum dots as compared to use of continuous films [1–11]. There are reasons to suppose that application of nanostructures in optics, microelectronics, biology, or medicine can lead to a qualitative out-break in evolution of mankind.

Nanostructures can be prepared by various ways [1–5, 12, 14–18]. Here, we examine formation of nanoparticles on the surface of solid substrates. Particles whose sizes are not in excess of 100 nm are considered as nanoparticles. As for crystals of such sizes, they, in general, do not contain dislocations or some other linear defects. Films composed of such particles have a developed surface. This leads to formation of unique properties in the nanosystems, which are

not observed in ordinary materials [2–9, 12, 13]. On the surface of solid substrates, nanoparticles can be prepared by deposition from liquid or solid phases [1–5, 12, 14–19]. In addition, they can be obtained by using sol–gel technology or electrodeposition [20, 21]. Nanocrystal formation processes represent typical first-order phase transitions. While the nanocrystals formed on the surface of substrates are not elastically stressed, their nucleation can be described by means of the classical nucleation theory. In the case where nanocrystals are elastically stressed and they are formed on crystal substrates, main approaches and methods of description of their nucleation remain unchanged; however, the mechanism of formation and growth of nanoparticles is of another physical nature. Therefore, we start with analysis of nucleation of unstressed nanostructures and then, in the next section, we present new approaches to description and examination of growth of coherent nanostructures. In literature, it is common to call the new phase nuclei as islands, whereas the island ensembles are named as island films. Here and elsewhere, we follow the above notations. This helps the reader to use the results outlined in our review for description not only of nanoparticles, but also of nuclei of any sizes. During growth of films containing islands of nanosizes, experimenters and engineers are forced to control a whole number of parameters, such as material and structure of the substrate, the temperature of the substrate, composition of vapor, and intensity of its inflow. To obtain the island size and composition needed, the parameters are selected, as a rule, empirically. In this case, it is necessary to know a terminal time of the growth process, in order that the size of islands does not fall outside the nanosize limits. It is already clear today that further development will be impossible without analysis of the complicated physical chemical phenomena which take place in the nucleation process [22–46]. The study of these phenomena began in the mid-1950s. Principal attention was paid to the new phase nucleation on the solid surfaces. Initially, the main theoretical analysis of new phase nucleation was carried out in the framework of the classical nucleation theory [23–25], disregarding the variation of supersaturation during condensation and, the more so, disregarding a possible change of growth mechanisms in individual islands. Hence, the comparison of experimental results on surface new phase nucleation with the classical

nucleation theory revealed a substantial difference between them. This led the researchers to an erroneous deduction for the impossibility of using the concepts of the classical theory of phase transitions in surface processes and the necessity of rejecting them. In particular, it was assumed that such quantity as the specific interphase energy could not be used at all in the description of the early stages of thin-film nucleation. That is why, in the early 1960s, the so-called discrete models appeared that described the new phase nucleation with the help of the methods of equilibrium statistical mechanics [29]. It should be noted that these theories could not describe the nucleation of strongly metastable and unstable systems in the same measure as the rejected classical model since they ignored the most important effect, namely, the increase of long-wave density fluctuations in the spinodal region [44, 46, 47]. To establish a correspondence between the theory and experiment, it was actually quite enough to allow for the variation of the supersaturation in time and the related possibility of changing growth mechanisms of individual islands [22, 23, 37]. Furthermore, most of the models were constructed for single-component films only, while a wide variety of experiments were carried out with multicomponent systems. The needs of engineering led, in the course of time, to the necessity of obtaining composite multicomponent films with prescribed properties and composition, and the above-mentioned models could, in no way, give answers to these problems. They rather “diverted” the researchers from the straight pathway. Meanwhile, fundamental studies of the kinetics of first-order phase transitions were being conducted in the same period. It is shown that the kinetics of first-order phase transitions is a complicated multi-stage process accompanied by various nonlinear phenomena [47–65]. Such stages typically include nucleation, the separate growth of new phase nuclei, coalescence, and the late stage, that is, Ostwald ripening (OR), where the growth of the larger islands proceeds at the expense of dissolution of the smaller ones. The indicated processes have widely different time scales. The most rapid stage is the nucleation, then goes the separate growth, and so on. This time hierarchy means that the fast processes have time to “keep up” with the slow ones [63]. Solution of the equations for fast processes provides, in fact, the initial conditions for the equations of slower processes. It turned out that the solution obtained in the framework classical theory was valid at the nucleation stage only. At later stages, it is necessary to take into account the equations of conservation of matter in a system and to solve the corresponding nonlinear problems. The extension of these ideas and methods to the nucleation process of islands, as well as the development of a consistent field approach [63] providing a unified standpoint for the description of condensation under any arbitrarily high supersaturations, offered quite a new view of the problems of the formation of nanofilms. The supersaturation values were found, for which it was necessary to employ the classical nucleation theory for the description of the nucleation of islands, and also the values, for which it was necessary to use the field approach [63]. All this made it possible to apply a unified approach to the description of condensation of multicomponent nanofilms, irrespective of the type of the initial phase (vapor, gas, liquid, etc.) and condensation conditions. It was shown that the surface brings appreciable diversity

to the phase transformation, although the basic stages stay unchanged.

## 2. THERMODYNAMICS OF AN ADSORBED LAYER

An important specific feature of the new phase nucleation on the substrate surface, as compared to homogeneous nucleation in the bulk, is the presence of various defects on the substrate. Defects are typically divided into point and linear ones; the latter include steps, surface dislocations, and scratches. No rigorous theory of heterogeneous new phase nucleation on a surface has yet been developed. The existing theories of new phase nucleation on solid surfaces proceed either from the classical nucleation theory [22–24, 43] modified for the two-dimensional case and allowing for the possible role of defects in nucleation, or from the atomistic model [29]. The surfaces of solid bodies can, in the general case, be both crystalline and amorphous. The modern concepts [22, 66] distinguish between atomically “smooth” and atomically “rough” surfaces. The former usually include singular and vicinal facets, while the latter include nonsingular ones. Singular surfaces are characterized by a local minimum in the surface tension  $\sigma$  and a discontinuity in the angular derivative  $\partial\sigma/\partial\theta$  (here  $\theta$  is the angle in the polar diagram [66]). Such features of  $\sigma$  and  $\partial\sigma/\partial\theta$  behavior are typical for all directions described by rational Miller indices, the minima being sharpest and deepest in the directions normal to the close-packed planes (with minimum Miller indices). Vicinal planes have a small deviation from the alignment of close-packed facets [66]. To describe the atomic structure of vicinal facets, the TLK (terrace, ledge, kink) model [66] is most often used, which allows obtaining the binding energy of atoms that are in different positions. In terms of the TLK model, one can calculate both the number of ledges and the spacing between them and can also determine the concentration of atoms in each position, that is, in atomically smooth regions of the surface, on a step, in a ledge, etc. [66]. Thus, even ideal crystal surfaces having a slight deviation from a close-packed orientation are steplike; at  $T > 0$ , the steps are covered with ledges; the surfaces of real crystals are rough, contain surface vacancies, surface dislocations, intergrain boundaries, and other defects [8, 66–69]. They all essentially affect the parameters of the condensation and may serve as orienting centers for nucleation of nanoislands. Crystal surfaces of substrates for nanostructures could be exposed to thermal or chemical treatment [12, 14, 15, 18, 70–74]. After such a modification, crystal surfaces change their properties. The orientation and the number of free chemical bonds change in the process of the modification. Surface tension changes as well. So, the treatment of substrate surfaces allows the nucleation of nanoislands to be controlled.

The adsorption, desorption, and diffusion of atoms over the surface of a substrate have been rather well investigated [66, 75]. Adsorption is typically thought of as the first stage of film condensation [2, 4, 12, 14, 22, 23]. In condensation from a single-component vapor, monomolecular and dissociative adsorptions are most frequently distinguished [22] which, for small substrate occupation numbers, lead to a

uniform formation of adatoms over the entire nonoccupied substrate surface with a constant rate  $J$

$$J = C_g P (2\pi M k_B T_v)^{-1/2} \quad (1)$$

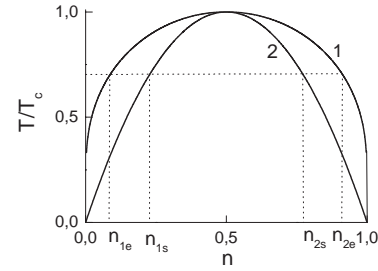
where  $P$  is the vapor pressure,  $T_v$  is the vapor temperature,  $M$  is the mass of one deposited molecule,  $k_B$  is the Boltzmann constant, and  $C_g$  is a geometric factor. The adsorbed atoms can either desorb back into vapor or jump over (diffuse) to one of the neighboring sites [29, 32, 66]. In the single-component case, the rate of desorption is described by the equation

$$\frac{dn_1}{dt} = -\frac{n_1}{\tau_r}, \quad \tau_r = \nu^{-1} \exp \frac{E_a}{k_B T} \quad (2)$$

where  $n_1$  is the surface adatom density,  $t$  is the time,  $dn_1/dt$  is the desorption rate,  $\tau_r$  is the characteristic time of monomolecular desorption (re-evaporation time),  $E_a$  is the desorption activation energy, and  $\nu$  is the frequency of tangential oscillations of an atom on the substrate surface [22, 66]. After establishing equilibrium between the surface and the surrounding initial phase, a two-dimensional “gas” of adatoms with surface density  $n_1$  is formed on the surface of the solid body [22, 24, 29]. In the case of monomolecular desorption, this proceeds approximately within a time  $\tau_r$ . A large number of papers is devoted to the study of the thermodynamic and kinetic characteristics of such an adsorbed “gas” [63, 75–77]. The most interesting and important for us are the thermodynamic stability, instability, and metastability of those systems, because it is these characteristics which are directly connected with the possibility of phase transformations in adsorbed layers. An expression for the state of an adsorbed gas on the substrate surface was derived in [63]. The equation is of the form

$$\frac{P}{k_B T_c} = \frac{T}{T_c} \ln \frac{1}{1-n} - 2n^2 \quad (3)$$

where  $n$  is the density of atoms adsorbed on the surface and  $T_c$  is the critical temperature. For  $T < T_c$ ,  $P < P_c = (\ln 2 - 1/2)k_B T_c$ , the  $P(V)$  isotherms contain a characteristic van der Waals loop testifying to a first-order phase transition of gas-liquid type. In real systems such a transition occurs only in the interval  $T_l < T < T_c$  between the triple and the critical points. The given model (the same as other models of this type) describes only the phase transition of gas-liquid type (amorphous state), that is, the amorphous film condensation and the first stage of the crystalline film condensation, which proceeds by the vapor-liquid-crystal mechanism. In spite of the simplifications made, this continual model satisfactorily describes many principal features of the behavior of the adatom system. From this equation the phase-equilibrium and spinodal curves can be obtained. The curves are plotted in Figure 1, where  $n_{1e}$  and  $n_{2e}$  are the equilibrium densities of the adsorbed gas and amorphous phase, respectively;  $n_{1s}$  and  $n_{2s}$  are the concentrations corresponding to the spinodal range. The region of metastable states,  $n_{1e} < n < n_{1s}$ , corresponds to a supersaturated vapor  $\xi = n/n_{1e} - 1$ , and the region  $n_{2s} < n < n_{2e}$  to a superheated liquid. It is precisely in the region  $n_{1e} < n < n_{1s}$  that the film condensation proceeds through nucleation, and for  $n = n_{1s}$  the critical



**Figure 1.** Phase-equilibrium curve (1) and spinodal curve (2) respectively. The values of  $n_{1e}$ ,  $n_{1s}$ ,  $n_{2s}$ , and  $n_{2e}$  are shown for  $T/T_c = 0.7$ . Reprinted with permission from [22], S. A. Kukushkin and A. V. Osipov, *Usp. Fiz. Nauk* 168, 1083 (1998). [*Phys. Usp.* 41, 983 (1998)]. © 1998, S. A. Kukushkin and A. V. Osipov.

nucleus consists of only one particle. The quantity  $\xi_{\max} = n_{1s}/n_{1e} - 1$  has the meaning of maximum possible supersaturation. For supersaturations exceeding  $\xi_{\max}$ , the adatom population becomes unstable and a spinodal decomposition begins in it [44–47, 63].

### 3. NANOFILM GROWTH REGIMES

The thin-film growth regimes are typically divided into layer-by-layer, island, and intermediate [29, 33]. Just the same regimes are realized during the growth of nanofilms. The layer-by-layer, or the Frank–van der Merwe, regime is realized in the case when the atoms of a deposited substance are bound with the substrate more strongly than with each other. Monatomic layers in this regime are occupied in turn; that is, two-dimensional nuclei (one atom thick) of a subsequent layer are formed on the upper part of the nuclei of the preceding layer after the latter is occupied. The equilibrium form of the nuclei is found by the Wulf theorem [66]. The theoretical description of the layer-by-layer growth is customarily given in the framework of the Kashchiev model [24] or its modifications [78, 79]. The island, or Volmer–Weber, regime is realized in the opposite case, that is, for the atoms of a deposited substance bound with each other more strongly than with the substrate. Island growth can only be realized under the condition [33]

$$\sigma_s < \sigma_d + \sigma_{s-d} - \text{const} \cdot k_B T \ln(\xi + 1) \quad (4)$$

where  $\sigma_s$  is the free energy of a unit substrate surface,  $\sigma_d$  is the free energy of a unit adsorbate surface, and  $\sigma_{s-d}$  is the free energy of a unit substrate-adsorbate interface. Otherwise, the layer-by-layer regime holds. In the island regime, small nuclei are formed straight on the substrate surface and then grow, transforming into large islands of the condensed phase [33]. Thereupon, these islands merge to form a continuous film after the channels between them are filled [33]. In the intermediate, or Stranski–Krastanow, regime, the first to be realized is a layer-by-layer growth and then, after one or two layers are occupied, island growth begins. There may be several reasons for the change of the growth mechanisms [33]. The principal cause is that the lattice parameter cannot remain unchanged upon occupation of an immediate

layer. Its variation entails a strong increase of the adsorbate-intermediate layer interface energy, which provides fulfillment of the island regime criterion (4). A large number of examples illustrating all three thin-film growth conditions and experimental methods of their investigation are presented in reviews [29, 33]. It was shown in [80] that under certain conditions the faceting of cap-shaped clusters at the OR stage may lead to a replacement of the island mechanism by the layer-by-layer one. In this regime, condition (4) holds at first and then the change in the condensate symmetry causes its violation. Thus, the material of the substrate and the type of its surface determine the film growth regime. At present, investigators pay particular attention to the growth of films by the Stranski–Krastanow mechanism [1–5, 12, 14]. First of all, this is associated with requirements of optoelectronics in semiconductor structures based on quantum dots. During the growth of quantum dots, an elastic energy arising along the substrate-wetting layer interface is of great importance. The elastic energy is responsible for a substantial difference in the kinetics of nanostructure nucleation. Nevertheless, the basic equations describing the nucleation processes of nanoparticles coherently conjugated with a substrate and, accordingly, the methods for their solution are, in most cases, similar to the equations describing the growth of unstrained structures, from the mathematical point of view. Therefore, we start to analyze the nucleation of nanoislands without taking into account the elastic energy, that is, the islands forming and growing by the Volmer–Weber mechanism, whereas, then, we investigate the growth of coherent nanoparticles in Section 9.

## 4. NUCLEATION PROCESSES OF UNSTRESSED NANOPARTICLES

### 4.1. The Nucleation Processes of One-Component Nanoparticles

Let us discuss the methods used to describe the nucleation processes on the surface in the cases of single- and multi-component films. The most widely employed is the so-called capillary model [24, 25, 27, 31] first formulated by Volmer and Weber, Becker and Döring, and Zel'dovich. This model postulates the following. Positive free-energy fluctuations that lead to overcoming the activation barrier are necessary for the condensation of a new phase from a supersaturated vapor in the metastable state (i.e., over the region  $n_{1e} < n_1 < n_{1s}$ ) [22, 24, 25, 27]. The presence of such a barrier is associated with the fact that the free energy of nucleation from a supersaturated vapor has a maximum at a certain critical point. Nuclei on a substrate may have various shapes [1, 2, 12, 22, 24] but theoretically they are most frequently assumed to look like a disc or a hemisphere according to the film growth mechanism [2], because many films grow by the vapor-liquid-crystal mechanism. The free energy  $F$  of the formation of disc-shaped clusters on an ideal substrate can be written in the form [23–25, 27]

$$F(i) = 2\sqrt{ai} - i \ln(\xi + 1) - \ln(n_0/n_1) \quad (5)$$

Here  $i$  is the number of particles in a nucleus,  $a = (\sigma_{st}/k_B T)^2 \pi w/h$ ,  $\sigma_{st}$  is the effective interphase energy per

unit length of the disc boundary,  $h$  is the disc height,  $w$  is the volume occupied by one particle in the nucleus,  $n_0$  is the number of adsorption sites on the substrate surface,  $n_0 \sim 1/B^2$ , where  $B$  is the substrate lattice constant, and  $F$  is expressed in  $k_B T$  units. The first term in Eq. (5) is the energy of the surface tension, the second is the chemical potential difference between the new and the old phases, and the third is a statistical correction due to the distribution of  $n_1$  atoms over  $n_0$  lattice sites [22, 24]. The maximum of the free energy (5) is positioned at the point

$$i_c = a/\ln^2(\xi + 1) \quad (6)$$

and is equal to

$$F(i_c) = a/\ln(\xi + 1) - \ln(n_0/n_1) \quad (7)$$

The nucleus has to overcome just such a potential barrier of height  $H(\xi) = F(i_c)$  owing to heterophase fluctuations in order that it might grow further regularly. According to the capillary model, an elementary act changing the nucleus size is either an attachment to it or, on the contrary, a loss of one molecule (the merging of nuclei is ignored). As regards sufficiently large nuclei containing  $i \gg 1$  particles, this change is small, and therefore the evolution of large nuclei is described by the Fokker–Planck equation [22–24]

$$\frac{\partial g}{\partial t} = -\frac{\partial I}{\partial i}, \quad I = -W(i) \left[ \frac{\partial g}{\partial i} + g \frac{dF(i)}{di} \right] \quad (8)$$

where  $g(i, t)$  is the distribution function of nuclei over the number of particles  $i$  in them,  $I$  is the nucleation rate (it vanishes for an equilibrium distribution  $g = \text{const} \cdot \exp(-F(i))$ ), and  $W(i)$  is the diffusion coefficient in the dimension space, which is equal to the number of molecules coming into the nucleus from the ensemble of adatoms per unit time. The stationary solution of this equation has the form [22–25, 27, 38, 40, 41]

$$g_s(i) = I \exp[-F(i)] \int_i^\infty W^{-1}(i') \exp F(i') di' \quad (9)$$

(the standard boundary condition  $g_s \exp F(i) \rightarrow 0$  as  $i \rightarrow \infty$  was taken into account here). The probability of fluctuations described by the second derivative of  $g$  with respect to  $i$  increases rapidly with decreasing size. Hence, the store of subcritical nuclei may be regarded as supplemented so rapidly owing to the fluctuations that their number remains in equilibrium in spite of the permanent outflow of the flux  $I$ . Consequently, the boundary condition to Eq. (8) takes the form  $g_s(i) \rightarrow n_1 \exp[-F(i)]$  as  $i \rightarrow 0$  and therefore from (9) we find

$$I = n_1 \left[ \int_0^\infty W^{-1}(i') \exp F(i') di' \right]^{-1} \quad (10)$$

The integrand in Eq. (10) has a sharp maximum at the point  $i = i_c$ , which allows us to calculate the integral using the Laplace method:

$$I = n_1 \sqrt{-F''(i_c)/2\pi W(i_c)} \exp[-F(i_c)] \quad (11)$$

The square root in Eq. (11) is sometimes called a nonequilibrium Zel'dovich factor. Let us estimate the quantity  $W(i_c)$ , which is the frequency with which adatoms are attached to a critical nucleus. To this end we shall use the lattice model. Let  $R_c$  be the radius of the critical nucleus linear boundary,  $l_0$  the length of diffusive jumps of adatoms,  $\nu$  the desorption frequency, and  $E_d$  the activation energy of surface diffusion. Then we have

$$W(i_c) = 2\pi R_c n_1 \ell_0 (\nu_d/4) \exp(-E_d/k_B T) = 2\pi R_c n_1 D_a / \ell_0 \quad (12)$$

where  $D_a = (\ell_0^2 \nu/4) \exp(-E_d/k_B T)$  is the diffusion coefficient of adatoms. From this, for disc-shaped nuclei we arrive at [23]

$$I(\xi) = C_1 n_{1e} n_0 D_a (\xi + 1) \ln^{1/2}(\xi + 1) \exp[-a/\ln(\xi + 1)] \quad (13)$$

Similarly, for nuclei in the shape of a hemisphere we have

$$I(\xi) = C_2 n_{1e} n_0 D_a (\xi + 1) \ln(\xi + 1) \exp[-b/\ln^2(\xi + 1)] \quad (14)$$

Here  $C_1 = \sqrt{2w/h\ell_0^2}$ ,  $C_2 = 2 \sin \theta [\sqrt{3/2\pi} \ell_0^3 \times (1 - \cos \theta)^2 (2 + \cos \theta)/\omega]^{-1/3} b^{-1/2}$ ,  $b = 4\pi(\sigma/k_B T)^3 \omega^3 (2 + \cos \theta)(1 - \cos \theta)^2/3$ ,  $\sigma$  is the interphase energy per unit area, and  $\theta$  is the contact angle. The time  $t_s$  of setup of a stationary nucleation rate has been repeatedly evaluated by various authors, all the values being coincident in the order of magnitude [81, 82]. The mean value is as follows

$$t_s = \frac{1}{-F''(i_c)W(i_c)} \quad (15)$$

In thin-film condensation, this time is usually very short ( $10^{-4}$ – $10^{-8}$  s) both for disc- and cap-shaped nuclei, and therefore, in practice it suffices only to calculate the stationary flow of nuclei  $I$ . The method of making allowance for nonstationary effects (necessary for the description of very fast processes) was proposed, for example, in [81–83].

## 4.2. The Nucleation Processes of Multicomponent Nanofilms

Multicomponent systems may be divided into two groups. One of them includes systems with solid solutions as islands [22, 23, 37], and the other involves systems with islands consisting of stoichiometric compounds [22, 23, 84–86]. We shall first discuss the nucleation of multicomponent stoichiometric islands and then pass over to an examination of nucleation processes in islands of solid solutions. According to [23], islands of stoichiometric compounds can be formed in the following ways:

1. The rate of the chemical reaction is much higher than the rate at which a new phase forms. In this case, molecules of the chemical compound are first formed, and then nucleation of the islands takes place.

2. The nucleation rate of the islands is much higher than the formation rate of a chemical compound on the substrate. In this case, islands of a mixture of chemical elements are formed due to heterogeneous fluctuations, and the chemical reactions then take place in the islands, producing a stoichiometric compound.
3. The rates of the chemical reaction and formation of the islands are comparable; the rate of the chemical reaction is nonlinear and the reaction product behaves as a catalyst of the reaction. In this case, self-induced oscillations in the number of the new phase nuclei and their self-organization are possible.
4. Growth of the islands proceeds as a result of the chemical reaction at their surface [23].

According to results obtained in [87, 88], the stationary flow of multicomponent stoichiometric disc-shaped islands of height  $h$  nucleating on the substrate surface is given by

$$I'_s(\xi) = \alpha'_s (\xi + 1) \ln^{1/2}(\xi + 1) \exp[-a^s/\ln(\xi + 1)] \quad (16)$$

The flow of cap-shaped nuclei can be expressed by

$$I''_s(\xi) = \alpha''_s (\xi + 1) \ln(\xi + 1) \exp[-b^s/\ln^2(\xi + 1)] \quad (17)$$

In Eqs. (16) and (17),  $\alpha'_s = A_{1s} n_0^2 D_s^0$ ;  $\alpha''_s = A_{2s} n_0^2 D_s^0$ ;  $A_{1s} = (\omega_m^s/h)^{1/2}$ ;  $A_{2s} = 2 \sin \theta [\sqrt{3/2\pi} (1 - \cos \theta)^2 (2 + \cos \theta)/\omega_m^s]^{-1/3} (b^s)^{-1/2}$ ;  $a^s = (\sigma_{st}/k_B T)^2 \pi \omega_m^s/h$ ;  $b^s = 4\pi(\sigma/k_B T)^3 (\omega_m^s)^3 (2 + \cos \theta)(1 - \cos \theta)^2/3$ ;  $\omega_m^s = \sum_{i=1}^{n^s} \nu_i \omega_i$  is the volume of a molecule of the chemical compound;  $\omega_i$  is the volume of an atom of an  $i$ th component of the chemical compound;  $\nu_i$  is a stoichiometric coefficient of an  $i$ th component;  $n_{1e}^s = n_0 \prod_{i=1}^{n^s} \rho_{i0}^{\nu_i}$  is the equilibrium density of molecules of the chemical compound on substrate

$$D_s^0 = \left[ \sum_{i=1}^{n^s} \frac{p_i^2 l_i}{D_{ai} \rho_{i0}} \right]^{-1} \quad (18)$$

is the generalized diffusion coefficient;  $\rho_{i0}$  is the equilibrium concentration;  $p_i = \nu_i / \sum_{i=1}^{n^s} \nu_i$  are the reduced stoichiometric coefficients;  $D_{ai}$  is the diffusion coefficient of an  $i$ th component;  $l_i$  the length of diffusive jumps of an  $i$ th adatom. Supersaturation  $\xi$  in the case of multicomponent systems is

$$\xi = \frac{\prod_{i=1}^{n^s} \bar{\rho}_i^{\nu_i} - K_\infty^s}{K_\infty^s} \quad (19)$$

where  $K_\infty^s = \prod_{i=1}^{n^s} \rho_{i0}^{\nu_i}$  is an equilibrium constant of the chemical reaction producing the chemical compound of composition  $s$ , and  $\bar{\rho}_i$  is the concentrations on the surface of an  $i$ th component of the multicomponent system. As it follows from Eqs. (16) and (17), the formal expression of nucleation rates in multicomponent stoichiometric systems is similar to that for single-component ones. However, kinetic coefficients in the equations depend on the kinetic coefficients for each component. In the case of nucleation of multicomponent films of solid solution, the free energy of a nucleus depends on the number of particles of each component. Its calculation is a separate, fairly complicated problem [89]. Let a nucleus be involved in the new phase nuclei representing a mixture of different components, and let the mixture be a regular solid solution. Let  $m$  be the number of



vapor components, and  $i_1, i_2, \dots, i_m$  the number of particles of each component in a nucleus. Then the free nucleation energy  $F$  expressed in the thermal units  $k_B T$  is equal to [22, 23, 89]

$$F(i_1, \dots, i_m) = \sigma(i_1, \dots, i_m)S - \sum_{j=1}^m i_j \ln \frac{n_j}{n_{je}(i_1, \dots, i_m)} - \ln \left[ n_0 / \sum_{j=1}^m n_j \right] \quad (20)$$

where  $\sigma$  is the specific interphase energy,  $S$  is the area of the nucleus phase boundary,  $n_j$  is the surface concentration of the component  $j$ ,  $n_{je}$  is the vapor concentration of the component  $j$  which is in equilibrium with the nucleus of this particular composition, and  $n_0$  is the concentration of the lattice sites on which atoms are adsorbed. The nucleus composition is determined by the set of molar concentrations  $\{\nu_k\}$  of each component, where

$$\nu_k = i_k / \sum_{j=1}^m i_j, \quad \sum_{j=1}^m \nu_j = 1 \quad (21)$$

The dependence of  $\sigma$  and  $n_{je}$  on  $\nu_k$  for a regular solid solution with a given heat of mixing of components is calculated within the thermodynamic theory of solutions [23, 89]. In particular, if a nucleus is an ideal solution, then

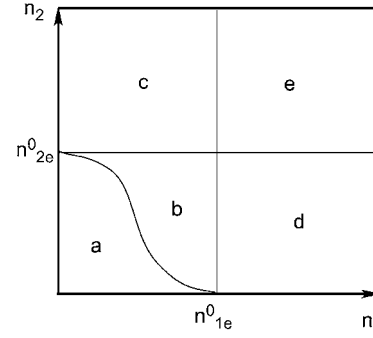
$$\sigma = \sum_{j=1}^m \sigma_j \nu_j, \quad n_{je} = n_{je}^0 \nu_j \quad (22)$$

where  $\sigma_j$  and  $n_{je}^0$  are the interphase energies and densities of a saturated vapor of pure components. Solution of the system of equations  $\partial F / \partial i_j = 0$  gives the number of particles of each component  $i_j$  in the critical nucleus, after which one can readily calculate the height of the activation barrier  $H = F(i_{1c}, \dots, i_{mc})$ . The equation  $H^{-1}(n_1, \dots, n_m) = 0$  specifies the surface that separates the regions of concentrations with and without nucleation. In the simplest case of an ideal solution with equal  $\sigma_j$ , this equation takes the form [89]

$$\sum_{j=1}^m \frac{n_j}{n_{je}^0} = 1 \quad (23)$$

Along with nuclei containing all  $m$  components, those involving a smaller number of components can be formed on the substrate, and therefore the whole range of concentration variation is divided into different phase regions with the help of  $2^m - 1$  interfaces of the type  $H^{-1}(n_j) = 0$ ,  $H^{-1}(n_j, n_k) = 0$ , etc. In particular, for  $m = 2$ , three dividing lines  $H^{-1}(n_1) = 0$  ( $n_1 = n_{1e}^0$ ),  $H^{-1}(n_2) = 0$  ( $n_2 = n_{2e}^0$ ), and  $H^{-1}(n_1, n_2) = 0$  specify five phase regions; see Figure 2.

In region **a** no new phase formation is observed; in region **b** only two-component islands nucleate, in region **c** two-component islands and those of the atoms of the second component, nucleate in region **d** two-component islands and those of the atoms of the first component nucleate, and in region **e** two-component islands and islands of the atoms of each component nucleate (the nucleation rate for islands of a mixture is as a rule much higher than the single-component nucleation rate). In the newly formed islands of



**Figure 2.** Phase diagram of a binary system. Reprinted with permission from [22], S. A. Kukushkin and A. V. Osipov, *Usp. Fiz. Nauk* 168, 1083 (1998) [*Phys. Usp.* 41, 983 (1998)]. ©1998. S. A. Kukushkin and A. V. Osipov.

a new phase, a reaction begins among the components or (if the components cannot make up a chemical compound) a eutectic decay, or the formation of a solid solution takes place. The behavior of the system is determined by the type of the corresponding state diagram for a solid mixture. In particular, for a binary system there exist five main types of state diagrams for a solid mixture [23, 89]. All possible cases of condensation are accordingly divided into 25 variants. All of them are considered in detail in [89]. Systems with three or more components are analyzed similarly but with a significantly greater number of versions. The analysis of the behavior of an ensemble of adsorbed particles shows that all the versions of multicomponent film condensation make up a set of processes, each proceeding at a certain stage [89]. We shall point out the processes that play the key role:

1. chemical reaction in an adsorbed multicomponent gas with a simultaneous nucleation of the final product of the reaction;
2. formation of nuclei representing a mixture of components;
3. chemical reaction in such nuclei;
4. growth of islands of a new phase from a supersaturated adsorbed vapor;
5. separation of a eutectic mixture;
6. evaporation of nuclei.

The methods of description of processes 1–6 are presented in [23]. In the case of nucleation of islands from solid solution, the Fokker–Planck equation becomes multidimensional, and accordingly the boundary condition at the zero point becomes more complicated. The method of its solution is based on the simultaneous diagonalization of both the equation and the boundary condition by way of a linear change of variables [57]. Then, it turns out that the nucleation rate  $I$  can be estimated as

$$I = n_0 \left( \sum_{k=1}^m d_k \right) \exp(-H_0) \quad (24)$$

where  $d_k$  are the diffusion coefficients for each of the  $m$  components in the dimension space for  $i = i_c$  [89], and  $H_0 = H + \ln(n_0 / \sum_{k=1}^m n_{1k})$  is the nucleation barrier height without the entropy correction. It has been assumed above that the nucleation takes place on an ideal substrate, namely,

in a homogeneous way. However, various substrate defects often initiate nucleation by reducing the activation barrier height  $H$ . In particular, the work of heterogeneous nucleation at the step of a substrate has recently been found by Hirth and Pound. They shown that steps may substantially increase the nucleation rate [29]. This is confirmed by numerous experimental data [24, 29, 33, 36]. The activation barrier of nucleation on a step can be so small ( $\sim k_B T$ ) that a nucleus consisting of two particles will already be supercritical, that is,  $F(2) < F(1)$  (or  $n_1 > n_{1s}$ ). In this case, as has already been mentioned, a new phase will be formed not through conventional nucleation, but through a spinodal decomposition, namely, an increase of the periodic fluctuations of substance concentration [46, 63]. At the same time, the size distribution of new phase islands on the step and their spatial distribution will already be different. Many modifications of the classical capillary model of nucleation on a substrate exist. We can point out several corrections to the height of the activation barrier, namely, the correction due to internal degrees of freedom of a cluster [22], the correction due to free-energy variation upon separation of a group of  $i$  molecules from a large ensemble [23, 24, 33], the correction due to cluster boundary smearing (see [63]), corrections due to cluster faceting [66] and non-isothermal effects [90], and so on. These corrections are, as a rule, relatively small and, moreover, have different signs. The most significant is obviously the correction due to the influence of nucleus surface curvature upon the interphase energy [63, 91]. It leads to a  $10^2 \pm 10^6$ -fold increase in the nucleation rate. We recall that the capillary model described above is only applicable for  $i_c \gg 1$ , because it is only in this case that the attachment and detachment of particles to and from critical nuclei can be described by the differential Fokker–Planck equation (8). An alternative to this model for  $i_c < 10$  is the atomistic Walton model [29] exploiting the methods of equilibrium statistical mechanics. It allows  $I$  to be expressed in terms of  $i_c$ , but does not give the dependence of  $i_c$  on  $\xi$ . Moreover, it is invalid for  $i_c = 1$  and  $i_c = 2$ , when the increase of long-wave density fluctuations is appreciable.

### 4.3. Effect of Medium Acidity on the Kinetics of Nucleation in Solutions

As it is mentioned previously, nanofilms of various materials can be prepared by deposition from ionic solutions [9, 19–21, 92–94]. In the course of film deposition, the acidity of a solution, that is, its pH, can be changed. The change in pH of the solution causes a change in equilibrium concentrations of components from which the film grows. This, in its turn, can alter supersaturation of the solution and, as a consequence, the rate of nucleation. The influence of pH on the kinetics of nucleation is examined in [95]. The investigation is performed by using as an example sedimentation of ionic compounds from liquid solutions. In [95], analytical expressions describing the nucleation rate–pH of a medium relationship are derived. The dependencies are obtained for two mechanisms of growth of nuclei. In the case where the growth of nuclei is controlled by diffusion of components

in solution, the expression for the nucleation rate is of the form

$$I_D(pH) = \frac{DN_a \rho_0 \xi(pH) \sqrt{k_B T}}{4\pi \omega \sqrt{\sigma}} \exp\left(-\frac{16\pi \sigma^3 \omega^2}{3\xi^2(pH)(k_B T)^3}\right), \quad (25)$$

where  $D$  is the diffusion coefficient of a matter dissolved in solution,  $\rho_0$  is the equilibrium concentration of a material dissolved,  $N_a$  is the density of the molecules in the solution,  $\xi(pH)$  is the dependencies of the supersaturation from the pH of solution (the specific form of this dependence can be found in [95]). In the case where the growth of nuclei is limited by the boundary kinetics, the nucleation rate depending on pH is of the form

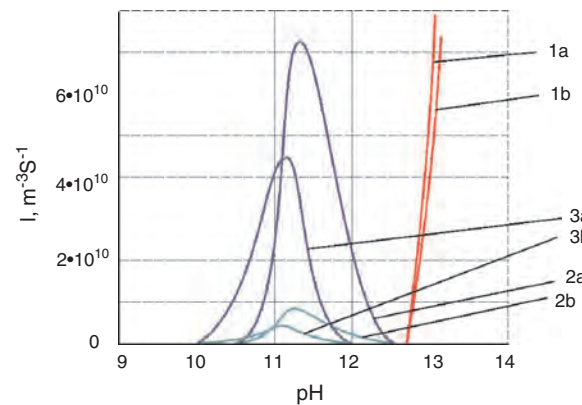
$$I_{SK}(pH) = \frac{\beta \sqrt{\sigma}}{2\pi \sqrt{k_B T}} \exp\left(-\frac{16\pi \sigma^3 \omega^2}{3\xi^2(pH)(k_B T)^3}\right) \quad (26)$$

where  $\beta$  is the specific boundary flow. Dependencies of the nucleation rate of  $\text{Pb}(\text{OH})_2$  and  $\text{CaCO}_3$  in water solutions on the pH value calculated by Eqs. (25) and (26) are given in Figure 3.

## 5. GROWTH AND EVOLUTION OF ISOLATED NANOISLANDS

### 5.1. Growth Mechanisms

After the formation of nuclei of a new phase on the substrate surface, they start growing and interacting with atoms of the old phase of which they were formed. This latter phase may be a single- or multicomponent vapor, a single- or multicomponent solution-melt, an amorphous phase, a solid solution, etc. [22, 37]. Accordingly, the island growth mechanisms are changed substantially as well. Thus, the diffusion flux of atoms of the old phase towards the surface of the nuclei is responsible for their growth from vapor medium. Both the removal of the latent heat of phase transformations



**Figure 3.** Dependencies of the nucleation rate of  $\text{Pb}(\text{OH})_2$  and  $\text{CaCO}_3$  in water solutions on the pH value; 1a— $I_D \text{Ca}(\text{OH})_2$ , 1b— $I_{SK} \text{Ca}(\text{OH})_2$ , 2a— $I_D \text{Pb}(\text{OH})_2$ , 2b— $I_{SK} \text{Pb}(\text{OH})_2$ , 3a— $I_D \text{CaCO}_3$ , 3b— $I_{SK} \text{CaCO}_3$ . Reprinted with permission from [95], S. A. Kukushkin and S. V. Nemna *Dokl. Akad. Nauk* 377, 792 (2001) [*Dokl. Phys. Chem.* 377, 117 (2001)] © 2001, S. A. Kukushkin and S. V. Nemna.

and the diffusion of atoms of the old phase are responsible for the island growth from solutions-melts and from an amorphous medium. If the film growth is due to decomposition of a supersaturated solid solution, the islands will grow via the presence of a diffusion flux of atoms of the old phase. In a case when the film growth proceeds in the course of another type of phase transformation, for instance, a film decay caused by elastic strains [14, 96] occurring at film-substrate interfaces, the islands grow owing to the diffusion atomic flux induced by elastic strains. The surface introduces an appreciable diversity into the nucleus growth mechanisms compared to the growth in the bulk of solids. According to contemporary concepts [22, 23, 37, 97], the following basic ways of atomic migration and energy, in particular, heat transfer over the surface, are distinguished as follows: three-dimensional or volume diffusion of atoms and three-dimensional heat removal; two-dimensional atomic diffusion over the substrate surface and two-dimensional heat removal; one-dimensional atomic diffusion along substrate steps, surface dislocations, and other linear defects. Islands may also grow owing to an immediate arrival of atoms from a vapor onto their surface. The ultimate goal of the study of island growth mechanisms is the determination of the islands growth rate as a function of their radius and the degree of supersaturation. With this purpose, the corresponding heat and mass transfer equations are solved [22, 23, 37]. Such problems are typically referred to as the Stefan problems [66]. They have been widely examined for three-dimensional systems [98], in particular, for crystal growth from single-component and binary melts. Similar calculations for the diffusion mechanism of island growth on surfaces have been made by Sigsbee and Chakraverty [99, 100] and others [14, 22–24]. But the authors of these papers analyzed only one of the possible mechanisms of island growth, namely, island growth due to surface diffusion of adatoms. It turned out that the island growth rate is notably governed by non-stationary effects induced by the nucleus boundary motion [23]. These effects become predominant for small values of  $R/\sqrt{D_a\tau_r}$ , where  $R$  is the island radius, and  $\sqrt{D_a\tau_r}$  is the diffusion path length of adatoms. Below, we shall only consider the quasi-stationary approximation for the island growth rate, which holds for high values of  $R/\sqrt{D_a\tau_r}$ . The structure of diffusion fields in the bulk of a vapor phase, on a substrate surface, and with linear defects was investigated in detail and the expressions for the island growth rate  $v_R$  were found in [37, 86, 101]. Islands usually grow simultaneously through several atomic diffusion mechanisms. It is, however, more convenient to consider each mechanism of island growth separately. According to [37, 86, 101], the expression for the new phase island growth rate  $v_R$  can be written in the following general form for each of the mass transfer mechanisms:

$$v_R = -M^{2-d'} w \frac{J_{DR}\Psi(\theta)}{R^{3-d'}} \quad (27)$$

Here  $w$  is the volume per atom in the islands of a new phase;  $d'$  is the dimension of the space in which the diffusion fluxes propagate:  $d' = 3$  for mass transfer in the bulk of a phase,  $d' = 2$  for mass transfer over the surface, and  $d' = 1$  for one-dimensional atomic diffusion along substrate steps or other linear defects (in this formula  $2 - d'$  is assumed

to take only nonnegative values);  $J_{DR}$  is a diffusion flux of atoms onto the island surface, which is found from the corresponding diffusion equations (for more details see [23, 37, 86, 101]), and  $\Psi(\theta)$  is the function taking into account the island geometry. For caplike islands we have  $\Psi(\theta) = 2(2 - 3\cos\theta + \cos^3\theta)^{-1}(1 - \cos\theta)$  when the diffusion of atoms proceeds in the bulk of a gas phase,  $\Psi(\theta) = 2\sin\theta/(2 - 3\cos\theta + \cos^3\theta)$  for the diffusion of atoms over the substrate surface, and  $\Psi(\theta) = [2\pi(2 - 3\cos\theta + \cos^3\theta)]^{-1}$  for the one-dimensional atomic diffusion, and, finally,  $M$  is the number showing how many linear defects are crossed by an island during its growth. To find the atomic diffusion flux of atoms  $J_{DR}$  to a nucleus, one has to solve the corresponding diffusion equations. The form of these equations, the boundary conditions on them, and the methods of their solution can be found in [23, 37, 86, 101]. The general expression for the new phase island growth rate has the form

$$v_R = \frac{K_p}{R^{p-1}} \left( \frac{R}{R_c} - 1 \right) \quad (28)$$

Here  $K_p$  is a constant involving the parameters which characterize the material of the island and the kinetic parameters of its growth (particular values of  $K_p$  in different cases can be found in [23, 37, 86, 101]), and the number  $p$  assumes the values 2, 3, 4 depending on the mass transfer mechanism. For our further purposes, it is convenient to express the number  $p$  in terms of the island dimension  $d$  and the growth index  $m$ , which takes the values 1, 3/2, 2, 3 depending on the island shape and the type of the limiting stage:  $p = d/m + 1$ . At the initial stages of phase transformation, the island radius is  $R \gg R_c$ , and therefore the unity in the right-hand side of Eq. (28) is customarily ignored as being negligibly small compared to  $R/R_c$ . Furthermore, it is convenient to write this equation not in terms of the radius growth rate but via the change of the number of atoms in the nucleus. Then, Eq. (28) will be rewritten in the form [23]

$$\frac{di}{dt} = m \frac{\xi}{t_0} i^{(m-1)/m} \quad (29)$$

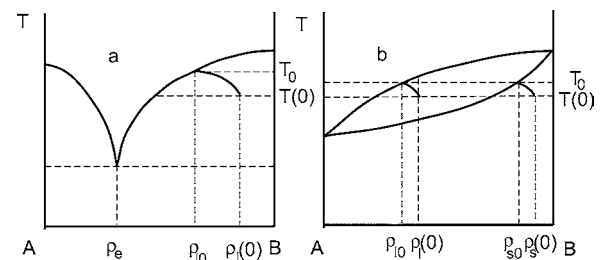
where  $\xi$  is supersaturation, and  $t_0$  is a constant having the dimension of time and called the characteristic time of island growth. It is expressed through the constant  $K_p$  and the constants relating supersaturation to the critical radius [64]. It has been shown theoretically and experimentally that the new phase island growth is determined by two principal processes, namely, a substance transfer to the island, that is, diffusion proper, and the passage of atoms through the old phase–new phase interface, that is, the boundary kinetics. Having passed through the phase interface, an atom joins the island surface. The island surface, the same as the surface of any crystal (see Section 2.1), can be atomically rough, atomically smooth, or vicinal. The ways in which the atom joins the island surface are different and depend on the type of surface [37, 66]. So, phase interfaces rough at the atomic level grow by the normal mechanism of growth. Atomically smooth surfaces grow by way of two-dimensional nucleation on their facets. Vicinal surfaces grow either through the motion of already existing steps or through the use of screw dislocations appearing on their surfaces. Island growth by the two-dimensional nucleation, as well as the evolution of

an ensemble of such islands, was described in [102]. In [37, 80], a rigorous analysis of island growth due to the motion of dislocations over their surfaces was carried out and the conditions under which this growth mechanism is realized were found. The next stage represents incorporation of adatoms into a new phase island. The growth rate (28), namely, the constant  $K_p$  and the index  $p$ , are significantly influenced by which of the processes is limiting. The particular form of the constant  $K_p$  for each type of mass transfer mechanism can be found in [23, 37, 86, 101]. In the course of formation of multicomponent nanofilms, atoms arrive at the substrate surface and they may initiate islands of various chemical compounds. Many of the islands of these compounds represent an intermediate phase in the course of growth of other phases. Islands of a chemical compound will further on be referred to as the phase  $s$ . As in single-component systems, the growth of multicomponent islands is due to the same mass transfer mechanisms [23, 37, 86, 101]. However, there is one important difference in that the chemical components of which an island of phase  $s$  is formed, may diffuse towards it in different ways. One of the components may arrive at the island surface through surface diffusion, and another through gas diffusion. In this situation one usually has to find the component responsible for the limitation and by this component determine the main flow of substance towards the island. The growth rate of a multicomponent island of an arbitrary phase  $s$  will as before be described by Eq. (27) in which, however, instead of the product of the atomic flux  $J_{DR}$  by the volume  $w$ , there stands the sum of the products of an atomic flux from each component by their volume  $w_i$ , that is,  $\sum_{i=1}^{n^s} w_i^s J_{iR}^s$ , where the subscript  $i$  stands for the corresponding sort of atoms. Since the islands have a stoichiometric composition, it follows that on their surfaces, according to [23, 37, 86, 101], the stoichiometry condition  $J_{iR}^s/\nu_i^s = J_{jR}^s/\nu_j^s$  holds. This condition allows us to express the quantity  $\sum_{i=1}^{n^s} w_i^s J_{iR}^s$  in terms of the product of the flux of one of the components  $i$  by the volume  $w_m^s$  of a molecule of the chemical compound of phase  $s$ , that is,  $J_{iR}^s w_m^s/p_i^s$ , where  $w_m^s = \sum_{i=1}^{n^s} p_i^s w_i^s$  is the volume per molecule of phase  $s$  and  $p_i^s = \nu_i^s / \sum_{i=1}^{n^s} \nu_i^s$ . Thus, to calculate the growth rate of a multicomponent island, it suffices to find the flux  $J_{iR}^s$  of only one arbitrary component. In [23, 37, 86, 101], all possible mechanisms of substance transport in multicomponent systems were investigated and analytical expressions for any type fluxes  $J_{iR}^s$  were found. Their substitution into an equation of growth rate of the type (27) leads to an equation of motion for an island of phase  $s$ , which has the form (28), where the constant  $K_p$  is replaced by a generalized constant containing kinetic and some other coefficients of each component entering the phase  $s$ . The critical radius  $R_c$  in Eq. (28) is replaced by the critical radius  $R_c^s$  for a given phase. The exact calculation of the growth rate of solid-solution islands is much more sophisticated than that for stoichiometric compounds. If the diffusion processes inside the islands are slowed down compared to the same processes outside the islands, the island composition along their radii will be inhomogeneous. Only provided the diffusion rate inside the islands appreciably exceeds the rate of variation of their radius, the island composition may be thought of as homogeneous. To determine the island growth

rate, it is necessary to know in what proportion the components are built in an island. This question can only be answered after the mixing entropy of the components is calculated [89]. The solution of this problem can be approached differently, namely, one may use the state diagram relating the composition of the old and the new phases [23, 37, 86, 101]. Solid-solution islands are formed as a rule from the vapor phase and melts. Any state diagrams of substances in which there are no chemical interactions can be represented in the form of one or other modification of the two simplest state diagrams, namely, the diagram describing melting-crystallization of substances insoluble in each other when in solid state (Fig. 4a, the diagram with a eutectic point) and the diagram describing melting-crystallization (evaporation-condensation) of substances that form a continuous solid-solution series (Fig. 4b) [66]. Islands produced from systems of the first type are single-component substances of composition A or B, respectively. At a eutectic point (see Fig. 4b), there simultaneously appear islands of both A and B compositions. In [23, 37, 103] it was shown that whenever the volume diffusion in the island matrix was fast enough, the expression for the growth rate remained the same (27), but the flux  $J_{DR}$  already consisted of the difference of atomic fluxes of components A and B. The average composition of islands changed during their growth by a definite law (see Section 7.2). The examination of island growth from single-component melts has shown that the principal mechanisms of island growth are as follows: three-dimensional heat removal into the melt, three-dimensional heat removal into the substrate, and two-dimensional heat removal from the nucleus along the substrate. The limiting stages in this process are the thermal conductivity proper and the mechanism of atomic incorporation into an island, which depends on the crystalline structure of its surface. The general expression for the island growth rate for each heat transfer mechanism takes the form

$$v_R = w \frac{J_{TR} \Psi(\theta)}{qR^{3-d}} \quad (30)$$

where  $q$  is the latent heat of phase transition per atom. Concrete expressions for the heat flows and the island growth rates can be found in [23, 37, 104]. Thus, the mechanism

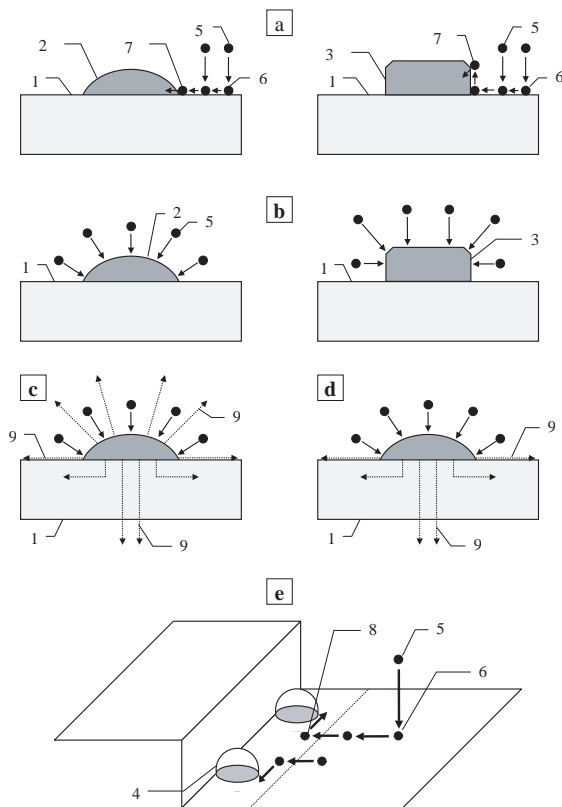


**Figure 4.** State diagrams of binary systems: (a) system with a eutectic point; (b) system with infinite component solubility in the solid phase;  $\rho_s$  and  $\rho_l$  are equilibrium concentrations in the solid and liquid phases, respectively;  $T_0$  is the equilibrium temperature,  $T(0)$  and  $\rho(0)$  are respectively the temperature and the composition at the onset of island growth. Reprinted with permission from [22], S. A. Kukushkin and A. V. Osipov, *Usp. Fiz. Nauk.* 168, 1083 (1998) [*Phys. Usp.* 41, 983 (1998)]. ©1998, S. A. Kukushkin and A. V. Osipov.

of island growth defines its rate  $v_R$  which enters the main equations of film condensation kinetics and hence ultimately determines the structure and composition of the growing nanofilm, as will be shown later.

## 5.2. Morphological Stability of Nanoislands

The main problem of the theory of morphological stability is to find out whether a given particular form of a vapor-, solution-, or melt-grown island is stable under small distortions. The analysis of stability is carried out by the following scheme: one assumes the shape of an island or a crystal to be slightly distorted, and then finds out whether this distortion increases or disappears. The necessity of examining stability stems from the fact that crystals often grow in the form of dendrites. Dendrites, or treelike crystals, consist of a central trunk and primary, secondary, etc., branches off it. They are often observed in nature and in laboratory conditions in melt



**Figure 5.** Schematic sketch of the fundamental mechanisms of island growth: (a) growth of edged and nonedged islands, when the limiting stage is the surface diffusion of adatoms; (b) the limiting process is the diffusion of atoms in the vapor phase (evaporation-condensation), (c) growth of nonedged islands, when the process is controlled by the entry of atoms from the vapor phase, but the heat removal occurs over all their surfaces; (d) the same, but with the heat removal through the substrate only; (e) growth of islands through linear diffusion along the steps of the substrate: 1—substrate, 2—non edged island, 3—edged island, to the surface of which atoms join only in specific places, 4—the island at a substrate step, 5, 6, 7, 8—the atom in the vapor phase, on the substrate surface, on an island surface, and at a substrate step, respectively, 9—heat flow angle. Reprinted with permission from [22], S. A. Kukushkin and A. V. Osipov, *Usp. Fiz. Nauk* 168, 1083 (1998) [*Phys. Usp.* 41, 983 (1998)]. © 1998, S. A. Kukushkin and A. V. Osipov.

crystallization. A quantitative analysis of the stability of the form of the growing crystal was first carried out in the classic paper by Mullins and Sekerka [105]. Numerous experiments on film growth show that the form of nuclei on the surface changes as they grow. It either becomes edged or, on the contrary, unstable or dendrite-like [66, 98]. This fact significantly influences both the nucleation and the structure of nanofilms. The growth of islands on the surface from vapor medium differs noticeably from the melt growth of three-dimensional crystals. This is first of all associated with the fact that deposited atoms are permanently supplied to the substrate surface and, having a finite lifetime (see Section 2.1), leave the surface by evaporating. This introduces essential changes and thus has a crucial effect upon the physics of the process. The morphological stability of nanoparticles growing on the surface of solid substrates is examined in [106]. The stability of shape for a flat disc-shaped island of height  $H$  and radius  $R$  is analyzed there. It is assumed that the island grows due to diffusion of adatoms. A change in the island shape is induced by two forces. On the one hand, a ledge on the island surface appears to be in the region of higher concentration gradients of adatoms and must, therefore, increase in size. On the other hand, a ledge increases the curvature and thus raises the saturated vapor density at this point, which in turn slows down the growth rate of the ledge compared to the neighboring points of the nucleus boundary.

The analysis of the corresponding diffusion equation [106] has shown that the shape of nanoislands becomes unstable in the case where island radius  $R_0$  lies within the range  $R_1(\nu) < R_0 < R_2(\nu)$ , where  $R_1(\nu) = R_c$  for  $R_c/\sqrt{D_a\tau_r} \ll 1$ ,  $R_c$  is the critical radius of a nanoparticle,  $R_2(\nu) = [(\nu^2 - 1)/2]\sqrt{D_a\tau_r}$ ,  $\nu$  are the integers corresponding to the order of modes arising in the course of an island shape change. Note that conditions needed for evolution of instability of the islands are substantially different from the conditions leading to formation of dendrites in the course of crystal growth from melts [66, 105]. A shape of the islands is more stable with respect to minor fluctuations as compared to the corresponding shape of three-dimensional crystals.

## 5.3. Structure of the Nanoparticle-Gas Interface

As it was noted before, the physical properties of nanoparticles differ significantly from the properties of volume materials. The reason for this is the influence of the surface of the particles on their properties. The problem of development of the rigorous model for the determination of the structure of interphase border nanoparticle-environment and the influence of surface active substances on the structure attracts attention of researchers (see, e.g., [24, 43, 47, 56, 57, 62, 107–109]).

The rigorous perturbation theory of the evolution of a small-sized cluster was developed in the framework of the density functional method in [110]. In this paper, for the first time, the size dependence of the surface tension for a cluster is defined and structure of the nanocluster-vapor phase interface is determined analytically. So, in the case of

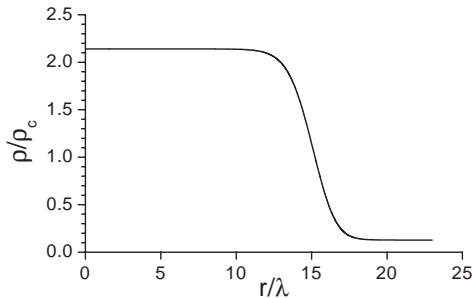
clusters, the correction to the surface tension  $\sigma(R)$  for the curvature is of the form

$$\sigma(R) = \frac{R}{R + (d-1)\delta} \quad (31)$$

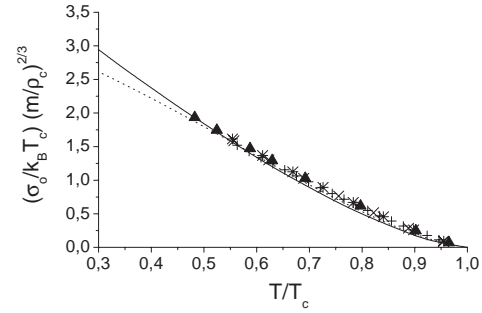
where  $R$  is the nanocluster radius,  $d$  is the space dimension ( $d = 3$  for a drop and  $d = 2$  for a disc-shaped island in the growth of nanofilms),  $\sigma_0$  is the surface tension of a solid material, which is calculated by the approach cited in [110],  $\delta$  plays the role of a correction to the surface tension for the curvature; that is,  $\delta$  the Tolman parameter,  $\delta$  is strictly estimated within the framework of the perturbation theory [110], the  $O(1/R^2)$  term denotes the corrections of higher orders within the framework of the perturbation theory. The density profile for a liquid cluster in the van der Waals three-dimensional gas at  $T = 0.7T_c$  calculated in [110] is plotted in Figure 6. The temperature dependencies of the surface tension calculated [110] for the van der Waals three-dimensional gas and the two-dimensional lattice gas are displayed in Figure 7. This figure also shows experimental values of the surface tension for four gases, namely, methane, neon, argon, and krypton [110]. As is clearly seen, the theoretical results obtained for the surface tension of the van der Waals gases are in excellent agreement with experimental data. Figure 8 depicts the temperature dependence of the Tolman parameter for the van der Waals gas. It can easily be shown that, in the temperature range  $0.5 < T/T_c < 1$ , where  $T_c$  is the critical temperature, the Tolman parameter is of the order of  $\delta \sim 0.1 \sqrt[3]{\rho_c/m} \sim 0.5 \cdot 10^{-10}$  m. This will suffice to have a pronounced effect on the nucleation [111].

#### 5.4. Surface Migration of Islands

Numerous experimental studies demonstrate that at the initial stages of crystal nanofilm condensation on foreign crystalline substrates, the nuclei of a new phase can rather rapidly transfer over the substrate surface [112–115]. This process serves as an important link in the nanofilm structure formation [113, 116]. Such migrations proceed under the action of various external forces: collisions with fast particles of the flow, the temperature gradient, the electric and

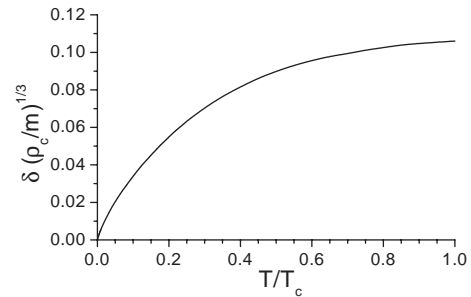


**Figure 6.** Density profile for a liquid cluster in the van der Waals gas at  $T = 0.7T_c$ . Here,  $T_c$  is the critical temperature,  $\rho$  is the density of the material at each point,  $\rho_c$  is the critical density of the material,  $r$  is the specific coordinates of a point of the medium,  $\lambda = \sqrt[3]{m/\rho_c}$ ,  $m$  is the mass of one molecule. Reprinted with permission from [110], P. V. Gordon et al., *Fiz. Tverd. Tela* 44, 2079 (2002) [*Phys. Solid State* 44, 2175 (2002)]. ©2002, P. V. Gordon, S. A. Kukushkin, and A. V. Osipov.



**Figure 7.** Temperature dependence of surface tension of the planar interface for the van der Waals gas (solid line) and the 2D lattice gas (dashed line). Points are the experimental data taken from [110]: 1  $\Delta$   $\text{CH}_4$ , 2  $+$  Ne, 3  $\times$  Ar, 4  $*$  Kr. Reprinted with permission from [110], P. V. Gordon et al., *Fiz. Tverd. Tela* 44, 2079 (2002) [*Phys. Solid State* 44, 2175 (2002)]. © 2002, P. V. Gordon, S. A. Kukushkin and A. V. Osipov.

magnetic fields, the interaction with moving steps, etc. As concerns the mechanism of island migration, only two basic models describing the island transfer have been used up to now [112]. First, particle diffusion proceeds only across the island surface, and particles attached to the boundary surface remain immobile about it. Second, an island is assumed to slide over the substrate surface. Many specific mechanisms of the morphological change of the island and of the sliding process have been proposed, but all of them yield relatively low values for the migration velocity and the diffusion coefficient compared to those actually observed in some cases [113, 114]. In the models of the first type, this is associated with the low values of the coefficients of self-diffusion of adatoms which cannot provide sufficiently fast island migration. In models of the second type, this is caused by the high values of the sliding friction forces between the island and the substrate (i.e., the high activation energy of slide) particularly during epitaxial growth. We have recently proposed [117] an essentially different model of transfer of growing islands oriented over a foreign substrate. As is well known, under certain conditions mismatch dislocations are generated on the island-substrate interface. If the Burgers vector lies in the slip plane, the motion of the island can be provided by the motion of these dislocations (solitons) [117]. Such a mechanism looks preferable to the usual



**Figure 8.** Temperature dependence of the Tolman parameter for the van der Waals three-dimensional gas. Reprinted with permission from [110], P. V. Gordon et al., *Fiz. Tverd. Tela* 44, 2079 (2002) [*Phys. Solid State* 44, 2175 (2002)]. © 2002, P. V. Gordon, S. A. Kukushkin and A. V. Osipov.

sliding because during the motion of the dislocation at every instant of time almost all the atoms of the island remain immobile with respect to the substrate, and it is only a very small group of atoms that move. The passage of a dislocation (compression or rarefaction waves) from one end of an island to the other is equivalent to island displacement by one lattice constant of the substrate [117]. If the dislocation (soliton) velocity is much smaller than the velocity of sound in the material of the film, then the energy losses during its motion are very small; that is, in such displacement of an island there is almost no friction against the substrate. The estimate of the “effective” mass of an island migrating over a substrate owing to soliton motion takes the form [117]

$$M_{\text{eff}} = 4cM \ln \frac{1}{\epsilon - \epsilon_c} \quad (32)$$

where  $M$  is the island mass,  $c$  is the ratio of forces acting on an atom from the side of other atoms of the island to those from the side of the substrate,  $\epsilon$  is the parameter of lattice mismatch between the film and substrate, and  $\epsilon_c$  is the critical lattice mismatch parameter corresponding to the onset of generating mismatch dislocations.

## 6. KINETICS OF NANOFILM CONDENSATION AT THE INITIAL STAGE

Among the whole variety of processes accompanying film growth, the principal one is, undoubtedly, the new-phase nucleation of islands, that is, the first-order phase transition. It is at this initial stage of condensation that the number of islands of a new phase determines composition and structure of nanofilms.

### 6.1. Nanofilm Condensation at Low Supersaturations

The description of the real kinetics of new phase nucleation and the occupation of a condensation surface by the nuclei is one of the most important problems of the theory of first-order surface phase transitions. A large number of papers of both classical and nonclassical direction have been devoted to this issue [17, 22–29, 31–34, 36, 38, 40, 41, 50, 64, 118, 119]. The cornerstone of any theory is a correct account of the nonlinear feedback between supersaturation and the size distribution function of new-phase islands. Indeed, growing islands absorb adatoms and thus diminish the supersaturation which is responsible for the nucleation rate and the growth rate of the islands, that is, ultimately for the distribution function [64]. One of the first models describing film condensation kinetics was posed by Zinsmeister [120]. He was the first to investigate the influence of a supersaturation decrease due to cluster growth upon the nucleation kinetics. This model has at least three shortcomings. First, the cluster growth rate is thought to be independent of cluster size. Second, the number of particles in a critical nucleus is always assumed to be equal to unity and not to increase with falling supersaturation (the decay of all the clusters is ignored). Third, the nucleation rate  $I$  is assumed to be equal

to  $\text{const} \cdot n_1^2$  over the entire nucleation stage (the possibility of a spinodal decomposition is neglected altogether). As a result, the island concentration given by the model is overestimated and increases infinitely in course of time. This model was further developed in many papers where the decay of all the clusters was also disregarded and it was assumed that  $I \sim n_1^2$  over the entire film formation stage [23, 24]. Several papers have been devoted to the calculation of the maximum surface cluster concentration  $N_{\text{max}}$  by the equation

$$I(N_{\text{max}}) = V_{\text{coal}} N_{\text{max}}^2 \quad (33)$$

where  $V_{\text{coal}}$  is the rate of pair cluster coalescence (see Section 7) calculated from various geometric considerations [121], and  $I$  depends in a certain way on  $N_{\text{max}}$  through the supersaturation  $\xi$ . Such models typically ignore the fact that the limitation on the number of clusters is not only due to coalescence, but is largely due to the deterioration of supersaturation and the associated abrupt decrease of the nucleation rate  $I$ . An important step in the development of film condensation kinetics was the model of the rate equations [122]. It is based on the division of all nuclei into subcritical and supercritical and the use of averaged condensation characteristics, such as the average number of particles in supercritical nuclei, the average rate of particle trapping by supercritical nuclei, the average radius of particles, etc. This model is frequently employed in numerical computations, which determine various characteristics of condensation. The shortcomings of the model [122] also include the absence of analytical results, the absence of data on the size distribution function of nuclei, as well as a forced assumption of an identical rate of adatom consumption by growing clusters of various sizes.

We should specially mention the nonstandard Kikuchi model which represents the nucleation and thin-film growth as an irreducible cooperative process and exploits the so-called path probability method [123]. The method of path probabilities also determines the equation of state for a system of adatoms on a lattice.

The cluster model [26] describes the nucleation, growth, and coalescence of islands of a new phase using the microscopic stochastic equations reformulated in terms of “clusters.” “Clusters” are defined as independent fluctuations of the local order parameter [26]. The division of all the variables into “relevant” and “irrelevant” (“irrelevant” properties induce random transitions in “relevant” coordinates, which are described by the Markov master equation) allows simplification of the kinetic equation. This equation is thoroughly examined in [26]. The stochastic models [124, 125] describe the film growth by various approximate stochastic equations. The characteristic feature of such models is the scaling behavior of various parameters of a growing film, for instance, its roughness.

The kinetic theory [64] yields analytical expressions for all the basic characteristics of film condensation at the initial stage using specially developed methods for an approximate account of the nonlinear feedback mentioned earlier. Finally, the continual model [63] represents thin-film condensation as the order-parameter field relaxation, the surface adatom density being the order parameter in this case. This approach is apparently the most general [63] because

it allows a description of film deposition in terms of both nucleation and spinodal decomposition, and for low supersaturations it becomes a standard kinetic model. Furthermore, there is an opinion that it is precisely this approach that will allow us to describe the appearance of the crystalline order during film growth from a vapor or melt.

## 6.2. Perturbation Theory

The variety of approaches to the description of thin-film growth is largely due to the impossibility of an exact analytical solution of the main system of equations of film formation in the opening stage, that is, the system consisting of the equation of conservation of matter on the substrate and the kinetic equation for the size distribution function of nuclei (this system is derived using the division of the whole size axis into three portions: subcritical, critical, and supercritical [64]).

Here, the set of equations is of the form [23, 64]

$$\frac{\xi_0}{\xi(t)} - 1 = \frac{(k+1)\tau_r}{n_{1c}t_0} \int_0^\infty \rho^k g(\rho, t) d\rho \quad (34)$$

$$\frac{\partial g}{\partial t} + \frac{\xi(t)}{t_0} \frac{\partial g}{\partial \rho} = 0 \quad (35)$$

$$g(0, t) = \frac{I(\xi(t))t_0}{\xi(t)}, \quad g(\rho, 0) = 0 \quad (36)$$

where Eq. (34) describes the law of conservation of matter on the substrate, Eq. (35) is the kinetic equation describing evolution of the size distribution function for nanoparticles, Eq. (36) includes the initial and boundary conditions, and  $t_0$  is the characteristic cluster growth time involved in the law of growth of stable islands (29),  $g(\rho, t)$  is the size distribution function of stable clusters  $\rho$  ( $\rho = i^{1/(k+1)}$ ),  $I(\xi)$  is the nucleation rate,  $\xi_0$  is the initial value of supersaturation,  $k = m + 1$ .

Practically all the above-mentioned models apply approximate methods for the solution of this system, which are based on some small parameter of the theory. From the physical point of view, the ‘‘principal’’ small parameter is the inverse number of particles in a critical nucleus (at the moment of maximal supersaturation). It is just this parameter that stands in the denominator of the nucleation rate exponent. Expanding all the quantities in power series of the small parameter directly, one obtains series that diverge for sufficiently long times, that is, not uniformly valid series. In order to provide convergence of the series, it is necessary to use a rigorous perturbation theory [126]. It should be noted that the presence of a small parameter does not always allow the solution to be represented in the form of a convergent series; that is, it is not always possible to provide a uniform validity of the series by way of a particular renormalization [126]. Therefore, it should be especially emphasized that the system of equations governing kinetics of the first-order phase transition in general and of thin-film condensation in particular admits an analytical solution in the form of a power series of the small parameter. The uniform convergence of this series is provided by the time renormalization procedure, that was made in [118, 119].

In the capillary nucleation model, the nucleation rate  $I(\xi)$  entering Eq. (36) has the form [see Eqs. (14), (15)]

$$I(\xi) = P(\xi)e^{-H(\xi)} \quad (37)$$

where  $H$  is the nucleation barrier height, and  $P$  is the pre-exponential factor depending on supersaturation. The most important parameter  $\Gamma$  of the phenomenological theory is connected with the function  $H$  as follows [118]:

$$\Gamma = - \xi_0 \left. \frac{dH}{d\xi} \right|_{\xi=\xi_0} \quad (38)$$

For films growing from vapor medium and high values of  $\xi_0$ , we have  $\Gamma \sim i_c \gg 1$ , where  $i_c$  is the number of particles in critical nuclei at  $\xi = \xi_0$ . Consequently, the quantity

$$\varepsilon = 1/\Gamma \quad (39)$$

is the small parameter of the given problem. As a result of the analysis performed in [118], it was proved that all the unknown functions will be expressed here in terms of the auxiliary function  $\varphi_k(x)$  specified by the equation

$$\frac{d\varphi_k}{dx} = \exp(-x^k \varphi_k), \quad \varphi_k(0) = 0 \quad (40)$$

The dependence of  $\varphi_k$  on  $x$  is plotted in Figure 9. We shall only present the net result to the first approximation in powers of  $\varepsilon$  [118]:

$$\xi(t) = \frac{\xi_0}{1 + (1/\Gamma)T^k(t)\varphi_k(T(t))} \quad (41)$$

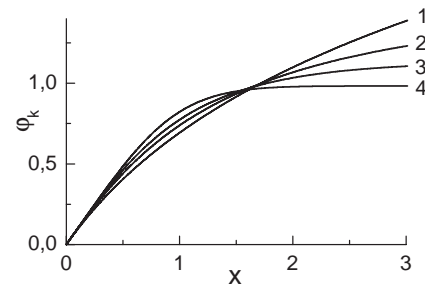
$$I(t) = I(\xi_0) \frac{\exp[-T^k(t)\varphi_k(T(t))]}{1 + (1/\Gamma)T^k(t)\varphi_k(T(t))} \quad (42)$$

$$N(t) = I(\xi_0)t_k\varphi_k(T(t)) \quad (43)$$

$$g(\rho, t) = \begin{cases} \frac{I(\xi_0)t_0}{\xi_0} \exp\left[-\left(T(t) - \frac{t_0\rho}{t_k\xi_0}\right)^k \varphi_k\left(T(t) - \frac{t_0\rho}{t_k\xi_0}\right)\right], & \rho \leq \xi_0 \frac{t_k}{t_0} T(t) \\ 0, & \rho > \xi_0 \frac{t_k}{t_0} T(t) \end{cases} \quad (44)$$

$$T = \frac{t}{t_k} - \frac{1}{\Gamma} \int_0^T x^k \varphi_k(x) dx$$

$$t_k = \frac{t_0}{\xi_0} \left[ \frac{n_{1c}\xi_0}{(k+1)\Gamma I(\xi_0)\tau} \right]^{1/(k+1)} \quad (45)$$



**Figure 9.** Dependence of the function  $\varphi_k(x)$  on  $x$ : 1 –  $k = 0$ ; 2 –  $k = 1/2$ ; 3 –  $k = 1$ ; 4 –  $k = 2$ . Reprinted with permission from [119], S. A. Kukushkin and A. V. Osipov, *Fiz. Tverd. Tela* 38, 443 (1996) [*Phys. Solid State* 38, 244 (1996)]. © 1996, S. A. Kukushkin and A. V. Osipov.



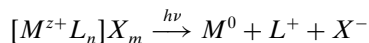
The time dependencies of the nucleation rate and the size distribution function of new-phase islands are illustrated in Figures 10 and 11.

The same method can be used to describe the growth of multicomponent films as well as inhomogeneity effects [118]. The perturbation theory technique [118] turned out to be rather effective. Application of the approach allows to describe the kinetics of phase transitions proceeding in various systems. Thus, for instance, in [127] the processes of nucleation of nanofilms from solutions or melts are described, whereas the phase transitions in ferroelectrics are investigated in [128].

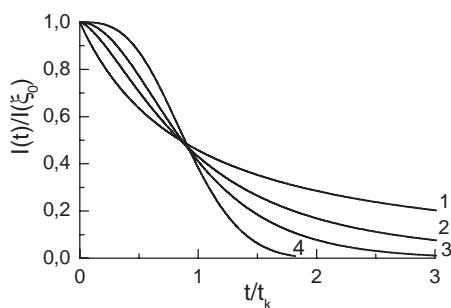
The shortcoming of the small parameter technique is the impossibility of describing a phase transition for arbitrary  $\tau_r$ ,  $\Gamma$ , and  $t_0$ , which can only be done numerically by solving the equations of condensation kinetics (35)–(37).

### 6.3. Nucleation of Islands in Solutions Under Light Exposure

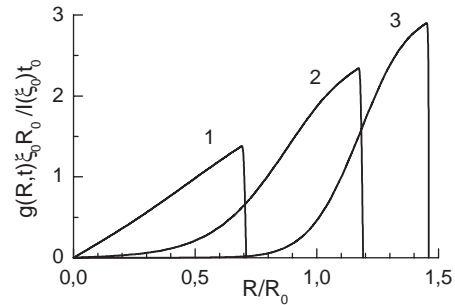
Precipitation of matter from photoactive solution is one of the methods of the island films formation. So, in [129, 130], a process of obtaining Ag, Au, Cu films on flat quartz substrates in solutions of photoactive chemical coordination compounds was experimentally investigated. The essence of this method consists in the following: supposing that one has a solution of coordination compound  $[M^{z+}L_n]X_m$ , where  $M^{z+}$  is the central metal atom ( $z+$  is the degree of oxidation),  $L$  is inner-sphere ligands and  $X$  is outer-sphere counterions. If ligand-to-metal charge transfer ( $L \rightarrow M$ ) occurs in this compound, then irradiation of the solution by light at wavelength  $\lambda = \lambda_{L \rightarrow M}$  results in the reduction of metal atom. Under irradiation of a solution the one-electron reduction of a metal atom can be produced. Thus, we are able to write the following scheme of the entire process:



One has to put the substrate to be deposited on the bottom of the vessel containing the solution. If we direct a light beam from above with its intensity decreased according to the Lambert–Buger–Behr law toward the substrate, then the beam is adsorbed on it. When a critical concentration of



**Figure 10.** Time dependence of the nucleation rate for  $\Gamma = 10$ : 1 –  $k = 0$ ; 2 –  $k = 1/2$ ; 3 –  $k = 1$ ; 4 –  $k = 2$ . Reprinted with permission from [119], S. A. Kukushkin and A. V. Osipov, *Fiz. Tverd. Tela* 38, 443 (1996) [*Phys. Solid State* 38, 244 (1996)]. © 1996, S. A. Kukushkin and A. V. Osipov.



**Figure 11.** Size distribution function of new phase islands for  $\Gamma = 10$ ,  $k = 2$ : 1 –  $t = 0.54t_k$ ; 2 –  $t = 1.7t_k$ ; 3 –  $t = 4.4t_k$ . Reprinted with permission from [119], S. A. Kukushkin and A. V. Osipov, *Fiz. Tverd. Tela* 38, 443 (1996) [*Phys. Solid State* 38, 244 (1996)]. © 1996, S. A. Kukushkin and A. V. Osipov.

metal on the substrate's surface is reached, the growth of new crystal metal phase starts.

In [129, 130] it has been noted that the essential feature of films which are obtained with the method described is the narrow size distribution of grains in the film.

The kinetics of the growth of thin metal films from solutions of photoactive chemical coordination compounds irradiated by light at certain wavelength has been theoretically investigated in [131]. In the framework of our mathematical model, the time dependencies of the basic characteristics of film growth process (size distribution function, density of nucleation, concentration of metal on surface) have been computed. Calculation of the characteristics is performed by the theory perturbation method mentioned earlier and described in [118]. These are according to experimental data. It is shown that the flux of metal (substance) from solution onto substrate's surface can be derived from stationary diffusion equation with added term taking into account the influence of photochemical substance source. It is concluded that the variation of light intensity, in wide range, saves the kinetics of the process of film deposition without drastic changes.

### 6.4. Nanofilm Condensation at High Supersaturation

If the external source of deposited particles has a large power such that a one-particle nucleus is energetically more advantageous than a two-particle nucleus, that is,  $F(2) > F(1)$ , then in the ensemble of adatoms a spinodal decomposition starts [44, 47, 63]. Any thermodynamic fluctuations increase in this case, the long-wave fluctuations increasing faster. A theory of spinodal decomposition in a system of adatoms was formulated in [63]. If the external source of deposited particles has such a power that in a metastable system it creates a supersaturation  $\xi$  close to  $\xi_{\max}$ , which corresponds to approximately  $i_c = 2 - 4$ , then the character of the nucleation process radically changes. First, the correlation radius in the system may exceed the average cluster size (for  $i_c = 1$  the correlation radius is equal to infinity). Second, the distribution of subcritical nuclei may be other than equilibrium, and, third, for small  $i_c$  the structure of critical nuclei and, therefore, the character of the interphase

energy significantly change. Hence, strongly metastable systems should be considered separately [132, 133]. It is appropriate to describe them in the framework of the continual theory [63], which represents a phase transition as a relaxation of the order-parameter field. The nucleation rate in this case depends on the supersaturation as

$$I(\xi) = I(\xi_{\max}) \exp[-\text{const}(\xi_{\max} - \xi)^2] \quad (46)$$

Thus, there exist three ways of relaxation of a supersaturated adatom population. The first is realized in weakly metastable systems where the supersaturation  $\xi$  is much lower than  $\xi_{\max} = n_{1s}/n_{1e} - 1$ . In this case the critical nucleus is so large ( $i_c \gg 1$ ) that its fluctuations lead to a change of only the coordinate of its boundary, although it has a considerable thickness. The structure of the nucleus itself will remain unchanged. In this event it is convenient to apply the capillary model, in particular, formula (14). The second way of relaxation takes place for  $\xi \leq \xi_{\max}$ . Here the critical nucleus contains only a few particles and is so small that its fluctuations affect not only the boundary, but the whole nucleus. In other words, the internal structure of the critical nucleus itself changes during fluctuations. Finally, the third way of relaxation lies through spinodal decomposition. It is realized for  $\xi \geq \xi_{\max}$ . In this event the system is unstable,  $i_c = 1$ , and thermal fluctuations generally destroy the structure of critical nuclei and lead to an increase of periodic fluctuations of substance concentration. This periodicity is a consequence of the fact that near a growing new-phase island no other islands are produced, and the whole ensemble of islands is strongly interacting [63].

## 7. KINETICS OF NANOFILM CONDENSATION AT THE LATE STAGE

The late stage of nanofilm growth is characterized by the fact that the new-phase islands generated earlier begin to interact. There exist three main types of cluster interaction. The first is cluster merging due to their migration over the surface (the migration mechanisms were briefly discussed in Section 5.4). The second is cluster merging due to their lateral growth [134]. The third is the growth of larger clusters at the expense of the evaporation of smaller ones (OR stage). The latter type of interaction is realized through the generalized diffusion or temperature field [37].

As a rule, cluster coalescence according to the first two types proceeds in a rather fast way. When merging, the islands are increased in their size. It can cause the size of islands to fall outside the limits of nanodimensions. However, investigation of the problem lies outside the scope of our chapter, and we do not discuss it here in detail. The readers interested in the phenomenon may refer to original paper [134] or reviews [22–24], where the problem is discussed more thoroughly. We only note that in preparation of nanostructures, it is necessary to avoid this process in coalescence.

The OR is a slow process. When changing such parameters as the substrate temperature, feed rate of components, and the substrate, one can effectively control the size and composition of nanoparticles. This process we shall discuss in more detail in the following subsections.

### 7.1. Ostwald Ripening Stage

The Ostwald ripening (OR) stage is the late stage of the phase transition. It begins only when the sources of evaporated adatoms are sufficiently weak and the supersaturation  $\xi$  on the substrate is small and tends to zero. No new islands are formed in this situation. The estimate of the starting point of this stage can be found in [23, 37, 84, 85, 118, 132]. The physical meaning of OR is as follows. At a late stage of evolution of an ensemble of islands, they begin to interact in a peculiar manner. This interaction is realized through a generalized self-consistent diffusion field. On a substrate, this field can be established by adatoms with a concentration  $\bar{\rho}_a$ , vapor atoms with a density  $\bar{\rho}_r$  or, if the substrate surface contains linear defects, by adatoms ( $\bar{\rho}_l$ ) adsorbed at the steps. This field depends on the size distribution function  $f(R, t)$  of islands and is in equilibrium with islands of critical size  $R_c$ . Islands of size  $R < R_c$  are dissolved in the diffusion field because near them the equilibrium concentration  $\rho_R$  of atoms exceeds the mean field concentration:  $\rho_R > \bar{\rho}_a$ ,  $\rho_R > \bar{\rho}_l$ , or  $\rho_R > \bar{\rho}_r$ . Islands of size  $R > R_c$  grow because for them  $\rho_R < \bar{\rho}_a$ ,  $\rho_R < \bar{\rho}_l$ . The critical size  $R_c$  itself goes on increasing because the islands absorb the substance from the substrate, thus lowering the supersaturation.

For this interaction and, therefore, the OR stage to take place, it is necessary that the two-dimensional island density would satisfy the inequalities [23, 37]

$$[\pi(\bar{R} + \lambda_i)^2]^{-1} < N_s < (\pi\bar{R}^2)^{-1} \quad (47)$$

where  $N_s$  is the two-dimensional island density,  $\bar{R}$  is the mean island radius,  $\lambda_i = \lambda_s$  for mass transfer over the substrate surface, and  $\lambda_i = \lambda_l$  for mass transfer along the steps,  $\lambda_s$  and  $\lambda_l$  being respectively the mean free path along the substrate surface and along the steps. Otherwise, if  $N_s \geq (\pi\bar{R}^2)^{-1}$ , the islands will “collide” and for  $N_s \leq [\pi(\bar{R} + \lambda_i)^2]^{-1}$  the adatoms on the substrate will evaporate and will not participate in the OR process provided that  $\lambda_i = \lambda_s$ . When  $\lambda_i = \lambda_l$ , the adatoms can leave the step and will not participate in ripening of the ensemble of islands located at the step.

The OR of an ensemble of islands in thin films was first investigated by Chakraverty [100, 135]. He examined the evolution of an ensemble of single-component islands with the shape of a spherical segment and located on solid substrates in the regime of complete condensation and also in the presence of atoms sputtered onto the substrate. Chakraverty [100, 135] believed that mass transfer between islands is realized only through a surface diffusion of adatoms and that the island growth rate can be controlled both by the surface diffusion (heterodiffusion) of adatoms and by the rate of consumption and emission of atoms by the islands, that is, by boundary kinetics. He assumed that the emission and absorption (building-in) of atoms are realized not by the island contour, but by its whole surface. Such an assumption corresponds to the fact that self-diffusion flows along a free island surface must exceed the heterodiffusion flows on the substrate surface. This statement should have been additionally grounded. This problem was solved more exactly by Geguzin and Kaganovskii [136]. They studied the evolution of an ensemble of islands growing by the following mechanisms: surface diffusion of atoms, gas diffusion of

atoms, evaporation-condensation of atoms, one-dimensional atomic diffusion along steps, and surface dislocations on a substrate (see Section 5.1) with allowance for a possible island growth control by boundary kinetics.

Later, the OR stage of an ensemble of single-component islands with allowance made for all possible growth mechanisms and in the presence of atoms sputtered on the substrate was investigated by various authors (see reviews [23, 37]). The authors of these papers found the laws of variation of the critical radius, height (if the islands had the shape of a flat disc), the island density in time, as well as island size distribution to a zeroth approximation. The analysis has shown that these characteristics depend substantially on the island growth mechanism and the intensity of atomic supply onto the substrate. According to [22, 23, 37], if a flux of atoms coming onto a substrate has a power-law asymptotics:  $g(t) \rightarrow ng_0 t^{n-1}$ , where  $n \geq 0$  and  $g_0$  is the constant, then there exist only two types of sources, namely, weak with  $n < d/p$  and strong with  $d/p \leq n$ .

The main idea of the OR analysis of such systems took root in the pioneering paper by Lifshitz and Slezov [137]. These authors showed that any disperse systems containing new-phase nuclei and old-phase atoms possess a whole number of common properties inherent only in disperse systems and apparent in the course of their evolutionary growth. From the thermodynamic point of view, this common property of disperse systems is their deviation from equilibrium state simultaneously in many parameters. One of the main signs showing that a disperse system resides in a nonequilibrium state is the presence of a fairly extended phase interface associated with an excess free energy. At heightened temperatures, when an appropriate diffusion mechanism becomes valid, some processes proceed in disperse systems that lead to a relaxation of the excess energy. These processes must be accompanied by a diffusive mass transfer which is responsible for the emergence of OR. This process was named after the German scientist W. Ostwald who, at the beginning of the century, examined this phenomenon experimentally during precipitation ripening. The principal system of equations describing this process has been presented in numerous works generalized in reviews and monographs [23, 37, 84, 85]. The basis for the analysis of the OR process is the Fokker–Planck equation (8) in which the term with the second derivative of the distribution function is omitted. When describing the non-isothermal ripening, we propose a more general system of equations, a particular case of which is the one given. The OR stage was also thoroughly investigated by Wagner [138], Ardell [139], Kahlweit [140], Oriani [141], Cahn [142], Voorhees and Clikman [143, 144], Enomoto, Kawasaki, Tokuyama [145, 146] and many other authors [147–152, 154–156].

The general OR theory in non-isothermal conditions was constructed in [37, 101, 153, 157]. The OR processes in multicomponent systems are richer and more diverse than similar processes in single-component systems. In multicomponent systems, substance redistribution is a consequence of not only the Gibbs–Thomson effect, but also of the chemically nonequilibrium state. Islands of a chemical substance (phase  $s$ ) may be stable from the point of view of the Gibbs–Thomson effect but unstable from the point of view of the thermodynamics of chemical reactions. At the OR stage in

multicomponent systems, when the component concentration is  $\rho_j(0) \ll 1$  (here  $\rho_j(0)$  is the concentration of the component  $j$  by the onset of OR), new islands are not formed and all the islands of the ensemble interact with each other through their generalized diffusion field. Islands of phase  $s$  with radius  $R$  smaller than the critical radius  $R_c^s$  are dissolved in the diffusion field, while islands with a radius exceeding the critical one grow. In a multiphase system, not only islands of the same phase, but also those of different phases will interact, and of all the stable phases only those for which the solution is supersaturated will be stable. For low component concentrations, when the law of mass action can be applied to the proceeding chemical reactions, this law can be written in the form

$$\sum_j \nu_j^s \mu_j^s = \ln \frac{\prod_{s^j} (\rho_j(0))^{\nu_j^s}}{K_\infty^s} \geq 0 \quad (48)$$

Here  $K_\infty^s$  is the equilibrium constant of the  $s$ th chemical reaction,  $s^j$  is the number of the phase containing the  $j$ -component, and  $\mu_j^s$  is the chemical potential of the  $j$ -component. If the islands generated in the system do not contain common components, condition (48) is necessary and sufficient since they will grow independently. Providing the islands contain common components, during their growth substance redistribution among the islands is possible and, although the solution was at first supersaturated in separate components, it may further appear to be unsaturated. In this case condition (48) is only necessary for a selection of islands capable of further competitive growth. In multicomponent systems, in the course of OR heat is liberated in chemical reactions, which affects the reaction constants. The thermal fields induced due to the heat liberation in chemical reactions affect the size distribution of islands in a nonlinear manner. The equilibrium concentration of the dissolved substance is not constant, but increases with temperature. The supersaturation will then tend to zero faster than in the isothermal case; however, the substance concentration gradient decreases in the process, which leads in turn to a decrease of the island growth rate. The amount of heat liberated in the course of phase transformation therewith decreases (if the system is conservative), which brings about stabilization of the equilibrium concentration; that is, the diffusion and thermal fields become self-consistent. Thus, the system temperature heightening may lead to a decay of some phases. A complete system of equations governing the evolution of an ensemble of multicomponent and multiphase islands at the OR stage looks like this [23, 37, 101, 153]:

$$\frac{\partial f^s(R, t)}{\partial t} + \frac{\partial}{\partial R} (f^s(R, t) v_R^s) = 0 \quad (49)$$

$$\chi^s \sum_{s^j} \int_0^\infty f^s(R, t) R^{3-d} h^{3-d} J_{DR}^s dR = n_1 |g_{D_j}| t^{n_1-1} \quad (50)$$

$$\prod_{j=1}^{n^s} (\rho_{jR}^s)^{\nu_j^s} = K_R^s(T_R) \quad (51)$$

$$\frac{J_{jR}^s}{\nu_j^s} = \frac{J_{jR}^s}{\nu_{j'}^s} \quad (52)$$

$$\sum_{s=1}^K \chi^s q^s \int_0^\infty f^s(R, t) R^{d-1} h^{3-d} J_{T,R}^s dR = n_2 |g_T| t^{n_2-1} \quad (53)$$

$$q^s \sum_{j=1}^{n^s} v_j^s J_{jR}^s = J_{TR}^s \quad (54)$$

$$K_R^s = \varphi(T_R^s) \quad (55)$$

Here  $f^s(R, t)$  is the size distribution function of islands of phase  $s$ ,  $J_{jR}^s$  is the flux of atoms of the  $j$ -component onto an island of phase  $s$ ,  $J_{TR}^s$  is the heat flux liberated during the growth of phase  $s$ ,  $\rho_j$  is the mean concentration of the  $j$ -component on the substrate (or in a vapor),  $\chi^s$  is the coefficient dependent on the island shape,  $q^s$  is the chemical reaction heat liberated during growth of islands of phase  $s$  per molecule of phase  $s$ ,  $|g_{D_j}|$  and  $|g_T|$  are the intensities of the fluxes of  $j$ -component and heat, respectively, and, finally,  $n_1$  and  $n_2$  are damping exponents. A method for the solution of this type of system was developed in [23, 37, 101, 153]. This method allows reduction of the system of equations (49)–(55) to a single-component system [23, 37, 101, 153]. Further, this set of equations can be solved by the Lifshitz and Slezov approach [137]. However, not long ago, a rigorous asymptotic theory of OR was developed in [158]. According to the rigorous results obtained in [158], the asymptotic laws of variation of the critical radius, the height and the density of islands coincide with those of [137], whereas the asymptotic size distribution function differs from the functions obtained in the zeroth approximation. In accordance with the results obtained in [158], the asymptotic solution of the set of equations (49)–(55) for sources with  $n < d/p$  are of the form

$$\bar{R}(t) = \text{const} \cdot R_c^s(t) \quad (56)$$

$$R_c(t) = \text{const} \cdot (A_{pd}^s t)^{1/p} \quad (57)$$

$$h(t) = \text{const} \cdot (A_{pd}^s t)^{1/p} \quad (58)$$

$$N(t) = \text{const} \cdot t^{n-d/p} \quad (59)$$

$$f(R, t) = \frac{N(t)}{R_c(t)} P_p \left( \frac{R}{R_c(t)} \right) \quad (60)$$

$$P_p(u) = \frac{u^p}{u^{p+1} - (p+1)u + p} \times \exp \left[ \frac{d-n(p+1)}{2} \int_u^{u^p} \frac{x^p dx}{x^{p+1} - (p+1)x + p} \right] \quad (61)$$

Here  $P_p(u)$  is the distribution function normalized to unity, so that  $\int_0^\infty P_p(u) du = 1$ , and

$$v_p(u) = \frac{p^p (p-1)^{-(p-1)} (u-1) - u^p}{p u^{p-1}} \quad (62)$$

$u = (p-1)R/pR_c$ ,  $u_p$  are constants determined from the normalization condition  $\int P_p du = 1$ ,  $N(t)$  is the density of the islands of phase  $s$ ,  $A_d^s$  is the kinetic coefficient of phase  $s$  depending on mass or heat transfer coefficients and on other constants of the deposited material. The values of these constants are given in [101, 153] for all the cases of heat and mass transfer which can be realized in the course of evolution of an ensemble of islands. As an example, we only present the value of  $A_{pd}^s$  for the case where the principal

mechanism is the surface diffusion of adatoms and the heat is transferred over the substrate surface. In this case, one can obtain

$$A_{pd}^s = \frac{27D^{os} \sigma^s n_0 K_{sb} l T_0^s (w_0^s)^2 \psi_1(\theta)}{32 [D_s^{os} n_0 (q^s)^2 \ln(H/R_1^s) + K_{sb} \lambda_{\text{eff}} k_B (T_0^s)^2]} \quad (63)$$

where

$$D^{os} = \left( \sum_{j=1}^{n^s} \frac{(p_j)^2 \ln(\lambda_j/R_1^s)}{D_{aj} \rho_{j\infty}^s} \right)^{-1}$$

is a generalized surface diffusion coefficient for  $\lambda_{sj} \gg R_1^s$ ;  $D_{aj}$  is the coefficient of Brownian motion of adatoms of the  $j$ -component,  $\psi_1(\theta) = 2(2 - 3 \cos \theta + \cos^3 \theta)^{-1}$ , with  $\theta$  as the contact angle, and the other designations were presented above.

In the case of atomic sources with  $d/p \leq n < d/(p-1)$ , both for cap-shaped and disc-shaped islands the critical radius is also specified by Eq. (57) and the distribution function can be calculated within the kinetic nucleation model [see Eq. (44)].

The solution also showed [37, 153] that at the OR stage  $N_{a,n} \sum_{s=1}^K q^s |g_D^s| = |g_T|$  and  $n_1 = n_2$ ; that is, the powers of sources (sinks) of all the phases and heat are related to one another and vary in time by one and the same law. Otherwise, the ripening process is impaired. The equations allowing the determination of regions in the concentration and temperature space which demonstrate the coexistence of phases were obtained in [37, 101, 153]. In Section 8, an example of construction of the phase diagram, that is, the coexistence of phases for the system of GaN nanoislands, is considered.

Thus, in multicomponent systems the conditions of quasi-thermodynamic equilibrium are favorable to the distribution of the substance of components in a most advantageous way over phases and to the establishment of the regions of phase coexistence, while the action of the surface tension leads to a universal size distribution of islands of the existing phases. Notice that such a distribution is only possible for low component concentrations, when the law of mass action can be applied to the chemical reactions proceeding in the system.

We shall now turn to OR of solid-solution islands. Islands of such composition are mainly produced in the growth of films from melts which have a ‘‘cigar’’ type diagram of state (Fig. 3b). The theory of OR of islands growing from binary melts of this type was developed by a number of authors (see references in [23, 37, 157]). In particular, Voorhees [143, 144], independently of the authors of works [102, 103], described the ripening of new-phase nuclei in binary melts allowing for the fact that their growth is due to both the diffusion and the removal of the latent crystallization heat into the melt. Notice that the hypothesis of a non-isothermal OR was first suggested in [37, 157], where the system of equations governing the evolution of an ensemble of islands and determining the kinetic growth diagram was derived. In these papers it was also shown that generalized diffusion-thermal fields are induced in the course of OR in binary melts. Such fields result from crystallization heat removal during the growth of islands, which causes a temperature increase in the system. This leads in turn to a change of equilibrium concentrations and the diffusion coefficients of

atoms as well as to the appearance of an involved nonlinear relation between supersaturation and supercooling on the one hand, and the size distribution and the growth rate of islands on the other. The OR theory for islands growing from a eutectic melt (Fig. 3a) was formulated in [103]. It turned out that in the course of evolution of ensembles of nuclei growing from a eutectic solution-melt, the nucleus growth at the OR stage proceeds by the thermal OR mechanism [23, 37], that is, only due to a decrease of supercooling. The solution-melt supercooling becomes equal for islands of both components, and their critical sizes and the distribution functions appear to be interrelated and similar to each other. It has been established that among some substance constants (crystallization heat, surface tension), there hold simple relations allowing us to calculate the constants of one substance through those of the other.

## 7.2. Evolution of the Composition of Nanofilms

It is a well-known fact that the properties of films are mainly determined by their composition. It is precisely the composition that determines the majority of electrophysical, optical, strength, and other properties. To gain an insight into the evolution of film composition, so as to be able to control this composition during film growth, is one of the most important problems of thin-film physics. It was shown in [157] that at the OR stage the radius of solid-solution islands and their composition are in a one-to-one correspondence. Later, a rigorous theory describing the evolution of phase composition of ensembles of such islands at the OR stage was formulated in [159]. In particular, the composition distribution function of islands  $\varphi(1/\chi_R, t)$  in the presence of substance sources with  $0 \leq n < d/p$  has the form

$$\varphi(1/\chi_R, t) = N(t)\Delta(t)P_p(U) \quad (64)$$

The average film composition changes according to the law

$$\bar{\chi}(t) = \frac{2\sigma w \rho_{L0}(1 + \gamma)}{k_B T (A_p^0 t)^{-1/p}} \quad (65)$$

Here  $\sigma$  is the specific interphase energy of the island-vapor boundary;  $\rho_{L0}$  is the equilibrium concentration of one of the components, for example, A (Fig. 3b) in the liquids line, that is, in the liquid or vapor phase;  $\gamma$  is the slope of the straight line joining the liquids and solidus lines (Fig. 3b).

## 7.3. Effect of Electromagnetic Radiation on the OR Stage

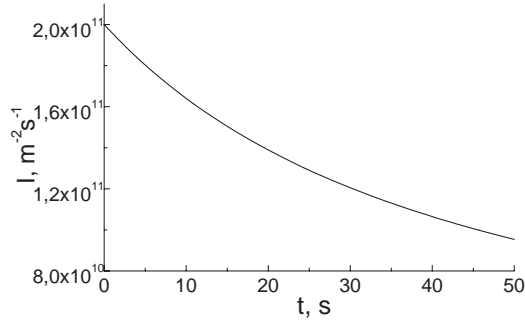
Electromagnetic radiation can markedly influence the evolution and nucleation of nanoparticles [160]. Influence of luminous radiation on the evolution of islands at the OR stage is studied in [161]. Here, we assume that a medium, where islands are present, is transparent and it does not absorb energy, whereas the islands absorb luminous radiation. In this case, the temperature of islands rises. The degree of heating of the islands is dependent on their size and thermal conductivity of the medium. As it is shown in [161], continuous influence of radiation leads to dissolution of islands.

The islands are dissolved due to increase of the equilibrium concentration in heating that causes supersaturation to fall. Under pulse action of the radiation on an island ensemble, evolution of the islands is substantially changed. It turned out that a certain critical size is established in such a system. In the case where a size of islands is less than the critical one, the islands are to dissolve, whereas in the case with a larger size they will grow. This fact makes it possible to control the size of islands efficiently, that is, to segregate the islands according to their size.

## 8. NUCLEATION AND EVOLUTION OF GaN NANOISLANDS

Processes of nucleation of GaN nanoislands prepared by the MBE and MOCVD methods are investigated in [87, 88]. The compound of GaN is a stoichiometric compound; therefore, analysis of nucleation processes is performed in parameters [87, 88] in the framework of the theory of island growth of stoichiometric compounds (see Eqs. (16)–(18)). The analysis shows that at the temperature of substrate (sapphire covered with a layer of AlN),  $T = 480$  °C, the probability of nucleation of liquid Ga islands is higher than that of nucleation of islands of GaN compound. GaN particles are formed after the nucleation of islands of liquid Ga as a result of chemical reactions between gallium and nitrogen. At  $750$  °C  $> T \geq 600$  °C, only GaN is nucleated. The physical cause for such behavior is following. Diffusion coefficients, lengths of diffusion jumps, and equilibrium concentrations of Ga and N included into the generalized coefficient of diffusion are highly dependent on the substrate temperature. At a low temperature, Ga atoms make a main contribution into diffusion mobility, therefore, the probability of nucleation of liquid GaN islands (at  $T = 480$  °C gallium is present in a liquid phase) determined by formula (14) is higher than that of nucleation for islands of GaN compound estimated by expression (17). At higher temperatures, the mobility of N atoms, equilibrium concentration of Ga, rate of chemical reaction between gallium and nitrogen are increased. It leads to the fact that the probability of nucleation for islands of GaN compound becomes higher as compared to that of Ga nucleation. Mechanisms of growth for islands of GaN within the temperature range  $T > 480$  °C and temperature conditions for a change in nanoisland growth mechanisms are described in [87, 88]. Dependencies of the nucleation rate and size distribution functions of nanoislands estimated by Eqs. (17) and (40)–(44) at the substrate temperature  $T = 650$  °C are given in Figures 12 and 13. The OR of an ensemble of GaN nanoislands is examined in [88]. It proved that at the substrate temperature  $T > 650$  °C, the process of OR of the ensemble is fairly subjected to the laws described by Eqs. (56)–(61) with subscript  $p = 3$ . Also, in [88] the kinetic phase diagram calculated by equations from [101] is plotted. The set of equations describing the phase diagram for GaN is of the form

$$\begin{aligned} Q_{0\text{Ga}} &= \rho_{0\text{Ga}} + J^{\text{Ga}} \\ &\quad + J^{\text{GaN}} \\ Q_{0\text{N}} &= \rho_{0\text{N}} + J^{\text{GaN}} \end{aligned}$$



**Figure 12.** Time dependence of the nucleation rate  $I(t)$  GaN on the substrate surface at temperature  $T = 650$  °C. Reprinted with permission from [88], S. A. Kukushkin et al., *Fiz. Tverd. Tela*, 44, 2079 (2002) [*Phys. Solid State* 44, 1399 (2002)]. © 2002, S. A. Kukushkin, V. N. Bessolov, A. V. Osipov, and A. V. Luk'yanov.

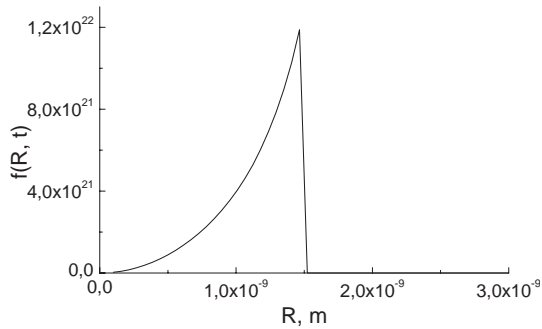
$$\left(1 - \frac{1}{Q_{0N}} J^{\text{GaN}}\right) \left(1 - \frac{1}{Q_{0\text{Ga}}} J^{\text{GaN}} - \frac{1}{Q_{0\text{Ga}}} J^{\text{Ga}}\right) = \frac{K_{\infty}^s}{Q_{0N} Q_{0\text{Ga}}} \quad (66)$$

$$\rho_{0\text{Ga}} = k^{\text{Ga}}$$

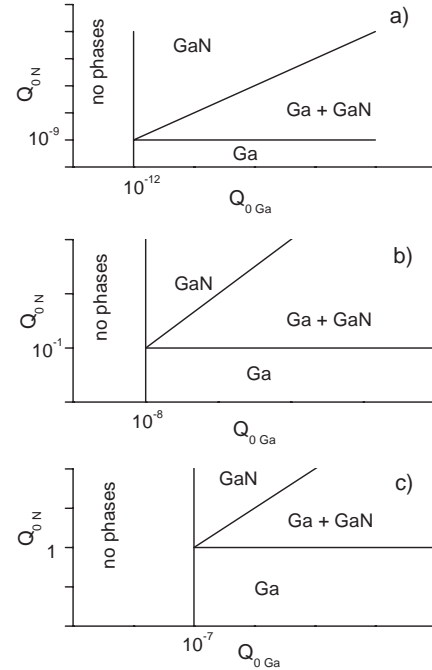
where  $Q_{0N}$  and  $Q_{0\text{Ga}}$  are relative amounts of the total initial nitrogen and gallium on the substrate and in the new-phase nuclei at the start of the ripening stage;  $J^{\text{Ga}}$ ,  $J^{\text{GaN}}$  are the total mass of the nuclei of liquid Ga and GaN at the end of the ripening stage;  $K_{\infty}^s$  is the constant of GaN dissociation on the substrate surface;  $\rho_{0\text{Ga}}$  and  $\rho_{0N}$  are the equilibrium concentrations Ga and N on a substrate;  $k^{\text{Ga}}$  is a quantity equivalent to the chemical reaction constant for single-component substances. The GaN phase diagram calculated by Eq. (66) at three different temperatures is given in Figure 14.

## 9. NUCLEATION OF COHERENT NANOPARTICLES

The elastic energy released during the formation of nanoparticles coherently connected with matrix or substrate influences significantly the nucleation process [24, 98, 162–166]. This energy can lead to either the increase



**Figure 13.** Time dependence of the size distribution function,  $f(R, t)$ , where  $R$  is the radius of islands of GaN nuclei on the substrate surface at the nucleation stage at temperature  $T = 650$  °C. Reprinted with permission from [88], S. A. Kukushkin et al., *Fiz. Tverd. Tela*, 44, 2079 (2002) [*Phys. Solid State* 44, 1399 (2002)]. © 2002, S. A. Kukushkin, V. N. Bessolov, A. V. Osipov, and A. V. Luk'yanov.



**Figure 14.** Phase diagrams of island GaN films at different temperatures: 1— $T = 480$  °C 2— $T = 850$  °C 3— $T = 1000$  °C. Reprinted with permission from [88], S. A. Kukushkin et al., *Fiz. Tverd. Tela* 44, 2079 (2002) [*Phys. Solid State* 44, 1399 (2002)]. © 2002, S. A. Kukushkin, V. N. Bessolov, A. V. Osipov, and A. V. Luk'yanov.

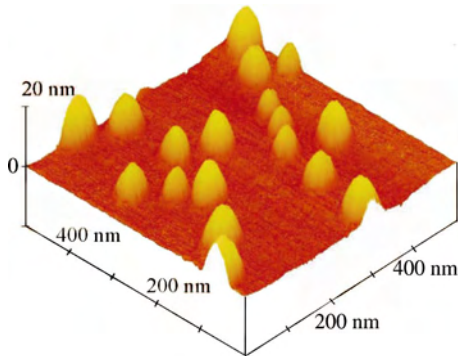
[1, 2, 4, 5, 14, 167–169] or the decrease [24, 98, 162, 163] of nucleation rate. In the process of formation of nanoparticles coherently connected with solid matrix, the formation work of nanoparticle increases by the value of an elastic energy which leads to the decrease of the nucleation rate. The elastic energy is the driving force of the nucleation process in case the nanoparticle forms on the surface of substrate from the elastically strained wetting layer. This particular process will be considered here in detail.

Let us start from the brief review of literature devoted to the analysis of growth of coherent nanoparticles. At present, the self-aligned Stranski–Krastanow growth of coherent semiconductor islands, which contain no lattice mismatch defects, is actively used for obtaining ordered structures with nanodimensional quantum dots (QDs) [1, 2]. The great interest in such structures is due to the prospects of their practical implementation in optoelectronics in relation to the localization of charge carriers in the vicinity of QDs [3]. In order to control the island shape during island growth, it is necessary to determine the driving force of nucleation. In Section 3 of this paper, we note that two principal mechanisms of nanofilm growth exist. According to the first mechanism described, the growth of nanoislands is due to a high density of adsorbed atoms on the wetting-layer surface. The islands grow in such a way by the Volmer–Weber mechanism, as a rule. In the case where there is close interaction between substrate and film materials in a film-substrate, the islands ought to grow due to the Stranski–Krastanow mechanism. In this case, the nonclassic nucleation from the atoms of the wetting layer itself proceeds under the effect of elastic energy [1, 2, 4, 5]. Thus, in the first case, the free energy

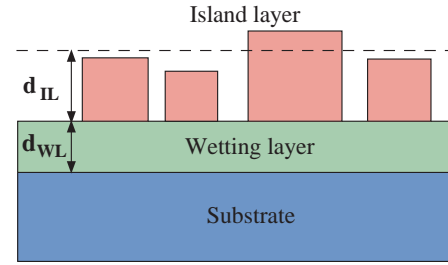
of the island decreases due to the difference in chemical potentials of the atoms in the two-dimensional adsorbate gas and in the island itself, whereas in the second case, the free energy decreases due to the difference between chemical potentials of the atoms in the wetting layer and in the island. Here, the chemical potential is determined by the difference between the elastic energy and the wetting energy. The island growth by the first mechanism occurs on a wetting layer of constant thickness. In the second case, the thickness of the wetting layer should decrease during the nucleation. The reason is that part of the atoms of the wetting layer transfer to islands in order to decrease an elastic energy [1]. A theory of growth of coherent nanoislands via the Stranski–Krastanow mechanism is outlined in [14, 96]. There, calculations and estimations are made taking the growth of Ge on (100) and (111) Si surfaces as an example. Experimental investigations to verify the extended theory are described in [96]. The Ge films were deposited by chemical vapor deposition in a vacuum chamber equipped with a spectroscopy ellipsometer and a mass-spectrometer. Digermane  $\text{Ge}_2\text{H}_6$ , which was diluted with pure He, was used as the precursor in the pressure range from 4 mbar. Depiction of coherent Ge islands on (100) surface of Si (see [96]) is given in Figure 15.

A growing-film model of the structure of Ge layers on Si surface used for ellipsometric measurements of the growth of Ge layers on (100) surface of Si (see [96]) is shown in Figure 16.

The following mechanism of the formation of coherent islands, which is based on our experimental data on the Ge on Si(100) growth, was considered in [96]. Initially, the layer-by-layer growth of the Ge film on the Si substrate occurs, since the Si surface energy is noticeably higher than the Ge surface energy, and wetting is favorable. However, Ge and Si have different lattice parameters, and the elastic energy increases with film growth (the elastic energy per atom is constant). The wetting energy per atom continuously decreases, since the Ge atoms are removed farther and farther apart from the substrate. At the instant when the elastic energy per atom is equalized to the wetting energy per atom for the upper atoms of the wetting layer, the layer itself is in equilibrium. However, the wetting layer continues to grow



**Figure 15.** SFM picture of Ge coherent islands on Si (100) at  $T = 500$  °C and the average deposition rate of 2 monolayers per minute. Reprinted with permission from [96], S. A. Kukushkin et al., *Fiz. Tekh. Poluprov.*, 36, 1177 (2002) [*Semiconductors*, 36, 1097 (2002)]. © 2002, S. A. Kukushkin, A. V. Osipov, F. Schmitt, and P. Hess.



**Figure 16.** Two-layer scheme for spectroscopic modelling of a growing film;  $d_{WL}$  and  $d_{IL}$  are thicknesses of the wetting layer (WL) and the island layer (IL), respectively. Reprinted with permission from [96], S. A. Kukushkin et al., *Fiz. Tekh. Poluprov.* 36, 1177 (2002) [*Semiconductors* 36, 1097 (2002)]. © 2002, S. A. Kukushkin, A. V. Osipov, F. Schmitt, and P. Hess.

and becomes metastable, making it possible for the elastic energy to relax. One of the possible ways of relaxation is nuclei formation on the wetting-layer surface, since the higher clusters have a higher elastic energy compared with the lower clusters. This process sets in when the nucleation barrier becomes low enough. Due to this fact, the nuclei formed grow and reduce the elastic energy of the film, and the wetting layer becomes thinner, thus supplying the growing islands with atoms. After some time, the nucleation process will be completed, since a decrease in the wetting-layer thickness will lead to heightening of the nucleation barrier. As a result of the studies, the expression of free energy is derived. The free energy of the formation of the coherent island from the wetting layer is represented by three summands

$$F = \Delta F_{\text{surf}} - (\Delta F_{\text{elas}} - \Delta F_{\text{att}}) \quad (67)$$

Here,  $\Delta F_{\text{surf}}$  is the increase in the surface energy due to the formation of an additional surface of the film material,  $\Delta F_{\text{elas}}$  is the decrease in the free energy due to the elastic energy relaxation within the island, and  $\Delta F_{\text{att}}$  is the increase in the free energy due to weakening of the attraction (wetting) of the island atoms to the substrate. It is evident that the energy parenthesized in relationship (67) is the only driving force of this nucleation process. Each of the three quantities in relationship (67) depends not only on the number of atoms in the island but also on its shape. This is the distinction of this model from the theory of nucleation of incoherent islands. To calculate the  $\Delta F_{\text{surf}}$ ,  $\Delta F_{\text{elas}}$ ,  $\Delta F_{\text{att}}$  quantities, the simplest island configuration is used. Specifically, we assume that a cuboid-shaped island with a square base  $L$  and height  $H$  lies on the wetting strained layer with a height  $h$ . For such an island configuration with two parameters  $L$  and  $H$ , all results are obtained in the analytical form. Calculations from [96] show that the coherent form of free energy (67) is as follows:

$$\frac{F(i, \beta, \xi)}{k_B T} = ai^{2/3}\beta^{1/3} + b\frac{i}{\beta} - c\xi i \quad (68)$$

Here  $k_B$  is the Boltzmann constant,  $T$  is the temperature,

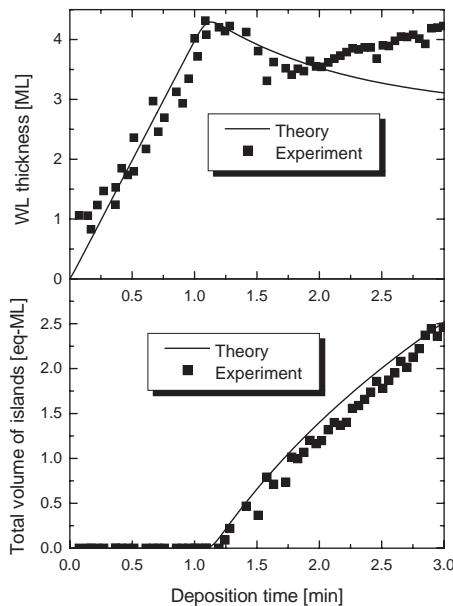
$$a = \frac{4\sigma_f(h_0 l_0^2)^{2/3}}{k_B T}, \quad b = \frac{\varkappa h_0}{6\pi l_0}, \quad c = \varkappa\gamma \quad (69)$$

$\varkappa = \lambda \varepsilon_0^2 h_0 l_0^2 / k_B T$  is the elastic-to-thermal energy ratio,  $\gamma = \ln(\Phi_\infty / \lambda \varepsilon_0^2 h_0)$  is the constant characterizing the wetting-to-elastic force ratio,  $h_0$  is the height of the monolayer film,  $l_0$  is the average interatomic distance in the same layer,  $\gamma = \ln(\Phi_\infty / \lambda \varepsilon_0^2 h_0)$  is the lattice mismatch between the film and a substrate,  $d_f$  is the lattice parameter for the film,  $d_s$  is the lattice parameter for the substrate,  $\lambda$  is the elastic modulus, and  $\Phi_\infty = \sigma_s - \sigma_f - \sigma_{s-f}$ , the surface tensions of the substrate, film, and interface between them. The expression derived for the free energy of a coherent nanoisland allows to describe the whole process of nucleation of the islands. Thus, the equations of nucleation rate, elastic energy relaxation rate time-density relations for the islands, and evolution laws of the thickness of a wetting layer in time were obtained.

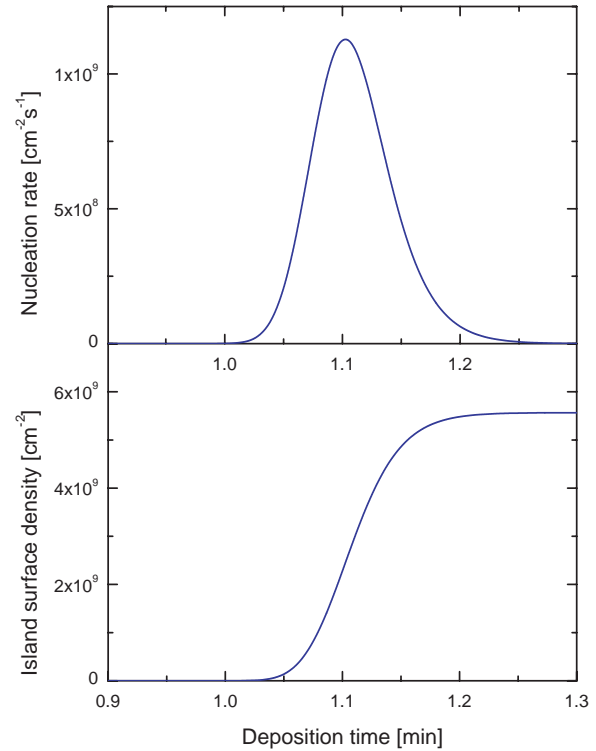
Theoretical and experimental dependencies of the wetting layer thickness and the total Ge amount in the islands measured in monolayer units in relation to the depositions time are given in Figure 17.

As for theoretical time dependencies between the nucleation rate and surface concentration of Ge islands on (100) surface of Si, they are shown in Figure 18.

A model of self-limiting growth of coherent islands is constructed in [14]. It is shown that in the case where there is a barrier for addition of atoms on the boundary of an island and the barrier is dependent on the island size, the process of secondary nucleation is probable there. Accordingly, the size distribution function of nuclei becomes binodal. This is substantially different from the size distribution function of incoherent nanoislands, which has only one maximum in all cases. Dependencies of the nucleation rate-size distribution functions of coherent Ge islands on (100) surface of Si with the barrier for addition of atoms on the island boundary can be found in [14].



**Figure 17.** Theoretical and experimental dependencies of the wetting layer thickness and the total Ge amount in the islands measured in monolayer units versus the deposition time for the Si (100). Reprinted with permission from [96], S. A. Kukushkin, et al., *Fiz. Tekh. Poluprov.* 36, 1177 (2002). [*Semiconductors*, 36, 1097 (2002)]. © 2002, S. A. Kukushkin, A. V. Osipov, F. Schmitt, and P. Hess.



**Figure 18.** Time dependencies of the main characteristics of nanoislands nucleation Ge of surface Si (100), at  $T = 550^\circ\text{C}$ . Reprinted with permission from [96], S. A. Kukushkin, et al., *Fiz. Tekh. Poluprov.* 36, 1177 (2002) [*Semiconductors*, 36, 1097 (2002)]. ©2002, S. A. Kukushkin, A. V. Osipov, F. Schmitt, and P. Hess.

## 10. CONCLUSION

We have presented all the basic modern theoretical concepts describing both the nucleation of nanoparticles and the further evolution of nanoparticles. Our presentation was based on the general theory of the first-order phase transitions. This provides a general approach allowing a unified standpoint in the investigation of processes on the substrate surface and in the surrounding volume upon nanofilms deposition from the gaseous, liquid, amorphous, and solid phases. Due to application of the generalized approach, we could investigate the influence of various factors on nucleation of nanoparticles. In this review, we considered the effects of the free energy arising between substrates and nanoparticles, composition of an environment, temperature, electromagnetic radiation, and acidity of a medium upon the processes of nanoparticle nucleation. It was shown that application of the field approach to investigation of nucleation of nanoparticles allows to calculate the structure of an interface and dependence of surface tension upon the size of a nanoparticle. It should be mentioned that experimental studies are beyond the scope of this review, because the authors do not rank themselves as skilled experimenters. At present, there is a great deal of technical literature, where experimental plants and techniques for preparation of nanostructures are described, and for details the readers can address the literature.



The authors hope that the present publication will help the reader to gain insight into these processes and to better and more quickly comprehend the range of questions described.

## GLOSSARY

**Coalescence** Interaction of nuclei of the new phase in the case of their direct contact. In the course of such a process the junction of nuclei in one particle can be realized.

**Heterogeneous fluctuations** Fluctuations of atoms or molecules in the volume of an old phase leading to the formation of the nuclei of the new phase.

**Nucleation** Formation of the nuclei of the new phase in the process of first-order phase transition.

**Nucleation rate** Number of the nuclei of the new phase formed in the unit volume (or on the unit surface) of an old phase per time unit during the process of phase transition.

**Nuclei of the critical size** Nuclei of the new phase which are in equilibrium with the initial phase under given supersaturation.

**Ostwald ripening** The late stage of first-order phase transitions on which the interaction of nuclei of the new phase with each other takes place by means of generalized diffusion, heat or another field. During such a process the bigger nuclei grow at the expense of the smaller ones.

**pH** The quantity characterizing the acidity of liquid media. *pH* is expressed by means of minus of the decimal logarithm of the concentration of hydrogen ions in a fluid (environment).

**Spinodal curve** The bounding curve of an area where phase is absolutely unstable with respect to arbitrarily small fluctuations.

**Spinodal decomposition** Non-barrier phase transition in the unstable (spinodal) region, that occurs by increasing of long-wave heterophase fluctuations.

## ACKNOWLEDGMENTS

This work was sponsored by the Russian Foundation for Basic Research (Grant 03-03-32503), the ALL-Russian Center of "Integration" Foundation (Project A0151), "Minprom-Nauka and Education of the Russian Federation" (Project 40.010.1.1.1195), and Complex Program 17 of Presidium RAS (Project 3.1.4). The authors wish to express their thanks to Mrs. E. A. Orlova and Dr. I. A. Sokolov for their help in translating the manuscript and to Mrs. T. V. Lavrova for typing it.

## REFERENCES

1. V. A. Shchukin and D. Bimberg, *Rev. Mod. Phys.* 71, 1125 (1999).
2. O. P. Pchelyakov, Yu. B. Bolkhovityanov, A. V. Dvurechenskii, A. I. Nikiforov, A. I. Yakimov, and B. Voigtlander, *Thin Solid Films* 367, 75 (2000).
3. Zh. I. Alferov, *Semiconductors* 32, 1 (1998).
4. Yu. B. Bolkhovityanov, O. P. Pchelyakov, and S. I. Chikichev, *Phys. Usp.* 171, 689 (2001).
5. P. S. Kop'ev, and D. Bimberg, *Phys. Rev. Lett.* 75, 2968 (1995).

6. M. Roco, R. Williams, P. Alivisatos, Eds., *Nanotechnology Research Directions*. Kluwer, Dordrecht, 2000.
7. G. Kiriakidis and N. Katsarakis, *Mater. Phys. Mech.* 1, 20 (2000).
8. I. A. Ovid'ko and A. G. Sheinerman, *Appl. Phys. A* 74, 273 (2002).
9. G. M. Chow, J. Ding, J. Zhang, K. Lee, and D. Surani, *Appl. Phys. Lett.* 80, 1028 (2002).
10. M. Bauer and M. Aeschlimann, *J. Electron Spectroscopy and Related Phenomena* 124, 225 (2002).
11. J. E. Wegrowe, D. Kelly, A. Franck, S. E. Gilbert, and J. Ph. Ansermet, *Phys. Rev. Lett.* 82, 3681 (1999).
12. T. I. Kamins, G. Medeiros-Ribeiro, D. A. A. Ohlberg, and R. S. Williams, *J. Appl. Phys.*, 85, 1159 (1999).
13. F. G. Shi, *J. Mater. Res.*, 9, 1307 (1994).
14. A. V. Osipov, F. Schmitt, S. A. Kukushkin, and P. Hess, *Phys. Rev. B*, 64, 205421 (2001).
15. X. Zhang, R. R. Li, P. D. Dapkus, and D. H. Rich, *Appl. Phys. Lett.*, 77, 2213 (2000).
16. R. S. Q. Fareed, J. W. Yang, J. Zhang, V. Adivarahan, V. Chaturvedi, and M. A. Khan *Appl. Phys. Lett.*, 77, 2343 (2000).
17. Z. Li, H. Chen, H. Liu, N. Yang, M. Zhang, L. Wan, O. Huang, J. Zhou, and K. Tao, *Jpn. J. Appl. Phys.*, 39, 4704 (2000)
18. F. Widmann, B. Daudin, G. Feuillet, Y. Samson, J. L. Rouviere, and N. Pelekanos, *J. Appl. Phys.*, 83, 7818 (1998).
19. Y. Gogotsi, in "Nanostructured Films and Coatings" (G. M. Chow, I. A. Ovid'ko, and T. Tsakalakos, Eds.) Vol. 78, p. 25. Kluwer Academic, Dordrecht, 1999.
20. L. K. Kurihana, in "Nanostructured Films and Coatings" (G. M. Chow, I. A. Ovid'ko and T. Tsakalakos, Eds.), Vol. 78, p. 55. Kluwer Academic, Dordrecht, 1999.
21. G. M. Chow, J. Ding, J. Zhang, K. Lee, and D. Surani, *Appl. Phys.* 83, 7818 (1998).
22. S. A. Kukushkin and A. V. Osipov, *Usp. Fiz. Nauk* 168, 1083 (1998) [*Phys. Usp.* 41, 983 (1998)].
23. S. A. Kukushkin and A. V. Osipov, *Prog. Surf. Sci.* 56, 1, 1 (1996).
24. D. Kashchiev, "Nucleation Basic Theory with Applications." Butterworth Heinemann, Oxford, 2000.
25. J. W. P. Schmelzer, *J. Colloid Interface. Sci.* 242, 354 (2001).
26. K. Binder and D. Stauffer, *Adv. Phys.* 25, 343 (1976).
27. F. M. Kuni, A. P. Grinin, and A. K. Shekin *Physica A* 252, 67 (1998).
28. D. Petersen, R. Ortner, A. Vrtala, P. E. Wagner, M. Kulmala, and A. Laaksonen, *Phys. Rev. Lett.* 87, 225703 (2001).
29. B. Lewis and J. C. Anderson, "Nucleation and Growth of Thin Films." Academic Press, New York, 1978.
30. R. Kern, G. Le Lay, and J. J. Metois, *Curr. Top. in Mat. Sci.* 3, 139 (1979).
31. J. L. Katz, J. A. Fisk, and V. M. Chakarov, *J. Chem. Phys.* 101, 2309 (1994).
32. M. Tokuyama and I. Oppenheim, *Physica A* 216, 85 (1994).
33. A. Venables, G. D. T. Spiller, and M. Hanbucken, *Rep. Prog. Phys.* 47, 399 (1984).
34. V. G. Baidakov and G. Sh. Boltashev, *Phys. Rev. E* 59, 469 (1999).
35. R. S. Berry and B. M. Smirnov, *J. Chem. Phys.* 114, 6816 (2001).
36. V. P. Koverda and V. N. Skokov, *Physica A* 262, 376 (1999).
37. S. A. Kukushkin and V. V. Slezov, "Disperse Systems on Solid Surfaces." Nauka, St. Petersburg, 1996 (in Russian).
38. V. A. Shneidman and M. C. Weinberg, *J. Chem. Phys.* 95, 9148 (1991).
39. L. Granasy, T. Borzsonyi, and T. Pusztai, *Phys. Rev. Lett.* 88, 206105 (2002).
40. Z. Kozisek and P. Demo, *J. Cryst. Growth* 147, 491 (1995).
41. H. Kumomi and F. G. Shi, *Phys. Rev. Lett.* 82, 2717 (1999).
42. V. Erukhimovitch and J. Baran, *Phys. Rev. B* 50, 5854 (1994).
43. J. W. P. Schmelzer, G. Ropke, and V. B. Priezhev. Eds., *Nucleation Theory and Applications*, JINR, Dubna, 2002.
44. J. Schmelzer, L. N. Davydov, A. S. Abyzov, and P. O. Mchedlov-Petrosyan *Physica A* 272, 459 (1999).

45. G. Fahsold and A. Pucci, *Phys. Rev. B* 61, 8475 (2000).
46. S. Maier-Paape, B. Stoth, and T. Wanner *J. Stat. Phys.* 98, 871 (2000).
47. J. S. Langer, *Ann. Phys.* 65, 53 (1971).
48. V. A. Shneidman, K. A. Jackson, and K. M. Beatty, *J. Chem. Phys.* 111, 6932 (1999).
49. H. Y. Tong, F. G. Shi, and E. J. Lavernia, *Sr. Met. et Mater.* 32, 511 (1995).
50. V. V. Slezov, J. Schmelzer, and Ya. Y. Tkatch, *J. Chem. Phys.* 105, 8340 (1996).
51. H. Reiss, *J. Stat. Phys.* 100, 73 (2000).
52. K. A. Fichtorn and M. Scheffler, *Phys. Rev. Lett.* 84, 5371 (2000).
53. L. X. Zheng, M. H. Xie, S. M. Seutter, S. H. Cheung, and S. Y. Tong, *Phys. Rev. Lett.* 85, 2352 (2000).
54. T. Ujihara and K. Osamura, *Acta Materialia* 48, 1629 (2000).
55. W. Klein, T. Lookman, A. Saxena, and D. M. Hatch, *Phys. Rev. Lett.* 88, 085701 (2002).
56. I. Gutzow and J. Schmelzer, "The Vitreous State," Springer-Verlag, Berlin, New York, 1995.
57. F. M. Kuni, A. K. Shchekin, and A. P. Grinin, *Phys. Usp.* 171, 331 (2001).
58. M. Gleiser and A. F. Heckler, *Phys. Rev. Lett.* 76, 180 (1996).
59. P. M. Lam and D. Bagayoko, *Physica A* 223, 413 (1996).
60. F. G. Shi, *Scr. Met. et Mater.* 30, 1195 (1994).
61. S. Strbac, O. M. Magnussen, and R. J. Behm, *Phys. Rev. Lett.* 83, 3246 (1999).
62. A. I. Rusanov, F. M. Kuni, and A. K. Shchekin, *Adv. Coll. Interf. Sci. A* 7, 122 (1997).
63. A. V. Osipov, *J. Phys. D.: Appl. Phys.* 28, 1670 (1995).
64. A. V. Osipov, *Thin Solid Films* 227, 111 (1993).
65. A. K. Shchekin, M. S. Kshevetskii, and V. B. Varshavskii, *Colloid J.* 64, 488 (2002).
66. A. A. Chernov, in "Modern Crystallography" (B. K. Vanshten, A. A. Chernov, and L. A. Shuvalov, Eds.), Vol. 3, p. 1. Springer, Berlin, 1980.
67. I. A. Ovid'ko, *Phys. Rev. Lett.* 88, 046103 (2002).
68. M. Yu. Gutkin and I. A. Ovid'ko, *J. Phys.: Condens. Matter* 11, 8607 (1999).
69. X. Y. Liu and P. Bennema, *Phys. Rev. B* 53, 2314 (1996).
70. H. Nienhaus, C. Schepers, S. P. Grabowski, and W. Monch, *Appl. Phys. Lett.* 77, 403 (2000).
71. Z. H. Ma, I. K. Sou, K. S. Wong, Z. Yang, and G. K. L. Wong, *J. Cryst. Growth* 201, 1218 (1999).
72. S. H. Cheung, L. X. Zheng, M. H. Xie, S. Y. Tong, and N. Ohtani, *Phys. Rev. B* 62, 033304 (2000).
73. M. Barth and P. Hess, *Appl. Phys. Lett.* 69, 1740 (1996).
74. Qi-K. Xue, Q. Z. Xue, R. Z. Bakhtizin, Y. Hasegawa, I. S. T. Tsong, T. Sakurai, and T. Ohno, *Phys. Rev. Lett.* 82, 3074 (1999).
75. H. J. Kreuzer, *Surf. Sci.* 231, 213 (1990).
76. V. P. Zhdanov and B. Kasemo, *Surf. Sci. Rep.* 20, 111 (1994).
77. M. A. Mittsev, N. D. Potekhina, and A. Y. Potekhin, *Surf. Sci.* 318, 217 (1994).
78. J. A. Nieminen and K. Kaski, *Phys. Rev. A* 40, 2096 (1989).
79. M. C. Bartelt and J. W. Evans, *J. Phys. A* 26, 2743 (1993).
80. S. A. Kukushkin and T. V. Sakalo, *Acta Met.* 41, 1237 (1993).
81. G. Shi, J. H. Seinfeld, and K. Okuyama, *Phys. Rev. A* 41, 2101 (1990).
82. V. A. Shneidman, *Phys. Rev. A* 44, 2609 (1991).
83. P. Demo and Z. Kozisek, *Philos. Mag. B* 70, 49 (1994).
84. V. V. Slezov and V. V. Sagalovich, *Sov. Phys. Usp.* 30, 23 (1987).
85. V. V. Slezov, *Phys. Rev. Rep.* 17, 1 (1995).
86. S. A. Kukushkin, *Thin Solid Films* 207, 302 (1992).
87. S. A. Kukushkin, V. N. Bessolov, A. V. Osipov, and A. V. Luk'yanov, *Phys. Solid State* 43, 2229 (2001).
88. S. A. Kukushkin, V. N. Bessolov, A. V. Osipov, and A. V. Luk'yanov, *Fiz. Tverd. Tela* 44, 2079 (2002) [*Phys. Solid State* 44, 1399 (2002)].
89. S. A. Kukushkin and A. V. Osipov, *J. Phys. Chem. Solids* 56, 831 (1995).
90. S. A. Kukushkin and A. V. Osipov, *J. Phys. Chem. Solids* 56, 211 (1995).
91. J. W. P. Schmelzer, I. Gutzow, and J. Schmelzer, *J. Coll. Interf. Sci.* 178, 657 (1996).
92. A. Pimpinelli and J. Villain, "Physics of Crystal Growth." Cambridge Univ. Press, Cambridge, 1998.
93. K. J. Parsiega and J. L. Katz, *J. Cryst. Growth* 200, 213 (1999).
94. P. Bennema and O. Sohnel, *J. Cryst. Growth* 102, 547 (1990).
95. S. A. Kukushkin and S. V. Nemna, *Doklady Akademii Nauk.* 377, 792 (2001) [*Doklady Physical Chemistry* 377, 117 (2001)].
96. S. A. Kukushkin, A. V. Osipov, F. Schmitt, and P. Hess, *Fiz. Tekh. Poluprov.* 36, 1177 (2002) [*Semiconductors* 36, 1097 (2002)].
97. Yu. S. Kaganovkii and L. N. Paritskay, *Interface Sci.* 6, 165 (1998).
98. R. W. Cahn and P. Heasen, Eds., "Physical Metallurgy". North-Holland, Amsterdam, 1983.
99. R. A. Sigsbee, *J. Appl. Phys.* 42, 3904 (1971).
100. B. K. Chakraverty, *J. Phys. Chem. Solids* 28, 2401 (1967).
101. S. A. Kukushkin, *Phys. Solid State* 35, 797 (1993).
102. P. Wynblatt and N. A. Gjostein, *Acta Met.* 24, 1165 (1976).
103. S. A. Kukushkin and D. A. Grigoriev, *Mater. Phys. Mech.* 1, 111 (2000).
104. S. A. Kukushkin, *J. Phys. Chem. Solids* 55, 779 (1994).
105. W. W. Mullins and R. F. Sekerka, *J. Appl. Phys.* 34, 323 (1963).
106. S. A. Kukushkin and A. V. Osipov, *Phys. Rev. E* 53, 4964 (1996).
107. A. Bogdan, *J. Chem. Phys.* 106, 1921 (1996).
108. A. I. Rusanov, F. M. Kuni, A. P. Grinin, and A. K. Shchekin, *Colloid J.* 64, 605 (2002).
109. A. K. Shchekin, T. M. Ykovenko, A. I. Rusanov, and F. M. Kuni, *Colloid J.* 64, 499 (2002).
110. P. V. Gordon, S. A. Kukushkin, and A. V. Osipov, *Fiz. Tverd. Tela* 44, 2079 (2002) [*Phys. Solid State* 44, 2175 (2002)].
111. E. N. Brodskaya, J. C. Enksson, A. Laaksonen, and A. A. Rusanov, *J. Colloid Interface Sci.* 180, 86 (1996).
112. R. Kern, G. Le Lay, and J. J. Metois, *Curr. Top. in Mat. Sci* 3, 139 (1979).
113. R. Kern, A. Masson, and J. J. Metois, *Surf. Sci.* 27, 483 (1971).
114. V. P. Rubets and S. A. Kukushkin, *Thin Solid Films* 221, 267 (1992).
115. S. Yu. Krylov, *Phys. Rev. Lett.* 83, 4602 (1999).
116. A. P. Belayev and B. P. Rubets, *Semiconductors* 35, 211 (2001).
117. S. A. Kukushkin and A. V. Osipov, *Surf. Sci.* 329, 135 (1995).
118. S. A. Kukushkin and A. V. Osipov, *J. Chem. Phys.* 107, 3247 (1997).
119. S. A. Kukushkin and A. V. Osipov, *Fiz. Tverd. Tela* 38, 443 (1996) [*Phys. Solid State* 38, 244 (1996)].
120. G. Zinsmeister, *Thin Solid Films* 2, 497 (1968).
121. R. M. Logan, *Thin Solid Films* 3, 59 (1969).
122. D. R. Frankl and J. A. Venables, *Adv. Phys.* 19, 409 (1970).
123. R. Kikuchi, *J. Chem. Phys.* 47, 1653 (1967).
124. R. P. U. Karunasiri, R. Bruinsma, and J. Rudnick, *Phys. Rev. Lett.* 62, 788 (1989).
125. A. J. Bernoff and S. Lichter, *Phys. Rev. B* 39, 10560 (1989).
126. A. H. Nayfeh, "Perturbation Methods." Wiley, New York, 1973.
127. S. A. Kukushkin and A. V. Osipov, *Tech. Phys.* 40, 165 (1995).
128. S. A. Kukushkin and A. V. Osipov, *Phys. Rev. B* 65, 174101 (2002).
129. A. V. Loginov, T. B. Boitsova, and V. V. Gorbunova, *Macromol. Symp.* 136, 103 (1998).
130. T. B. Boitsova, A. V. Loginov, and V. V. Gorbunova, *Appl. Chem.* 10, 1585 (1997).
131. S. A. Kukushkin and S. V. Nemenat, *Mater. Phys. Mech.* 1, 27 (2000).
132. P. Scott, *Phys. Rev. A* 42, 7447 (1990).
133. C. Unger and W. Klein, *Phys. Rev. B* 29, 2698 (1984).
134. A. V. Osipov, *Thin Solid Films* 231, 173 (1995).
135. B. K. Chakraverty, *J. Phys. Chem. Solids* 28, 2413 (1967).

136. Ya. E. Geguzin and Yu. S. Kaganovski *Sov. Phys. Usp.* 21, 611 (1978).
137. I. M. Lifshitz and V. V. Slezov, *Sov. Phys. JETP* 35, 331 (1958).
138. C. Wagner, *Z. Electrochem.* 65, 581 (1961).
139. A. J. Ardell, *Acta Met.* 20, 61 (1972).
140. M. Kahlweit, *Adv. Coll. Interf. Sci.* 5, 1 (1975).
141. R. A. Oriani, *Acta Met.* 12, 1399 (1964).
142. J. W. Cahn, *Acta Met.* 14, 83 (1966).
143. P. W. Voorhees, *Metall. Trans.* 21, 27 (1990).
144. P. W. Voorhees and M. E. Cliksmann, *J. Cryst. Growth* 72, 593 (1985).
145. Y. Enomoto, K. Kawasaki, and M. Tokuyama, *Acta Met.* 35, 915 (1987).
146. M. Tokuyama and K. Kawasaki, *Physica A* 123, 386 (1984).
147. A. Nakahara, T. Kawakatsu, and K. Kawasaki, *J. Phys. Chem. Solids* 95, 4407 (1991).
148. J. A. Margusee and J. Ross, *J. Phys. Chem. Solids* 78, 373 (1983).
149. K. Binder, *Phys. Rev. B* 15, 4425 (1977).
150. G. Venzl, *Phys. Rev. B* 31, 3431 (1985).
151. J. Schmelzer and J. Möller, *Phase Transitions* 95, 261 (1992).
152. M. P. Shepilov, *J. Non-Cryst. Solids* 146, 1 (1992).
153. S. A. Kukushkin, *Phys. Solid State* 35, 804 (1993).
154. E. A. Brener, V. I. Marchenko, H. Müller-Krumbhaar, and R. Spatschek, *Phys. Rev. Lett.* 84, 4914 (2000).
155. J. H. Yao, K. R. Elder, H. Guo, and M. Grant, *Phys. Rev. B* 45, 8173 (1992).
156. L. Alkemper, V. A. Snyder, N. Akaiwa, and P. W. Voorhees, *Phys. Rev. Lett.* 82, 2725 (1999).
157. S. A. Kukushkin and V. V. Slezov, *Phys. Solid State* 29, 2092 (1987).
158. S. A. Kukushkin and A. V. Osipov, *JETP* 113, 1201 (1998).
159. S. A. Kukushkin and A. V. Osipov, *J. Appl. Phys.* 86, 1370 (2002).
160. Yu. S. Kaganovskii and M. Rozembluh, *Appl. Phys. Lett.* 65, 3297 (1996).
161. A. G. Ambrok, E. V. Kalashnikov, and S. A. Kukushkin, *J. Appl. Phys.* 91, 4961 (2002).
162. J. K. Lee, *Mater. Transaction* 39, 114 (1998).
163. J. K. Lee, *Inorganic Materials* 395, 745 (1999).
164. J. Möller, J. Schmelzer, and I. Avramov, *Phys. Stat. Sol. (b)* 196, 49 (1996).
165. E. A. Brener, S. V. Iordanskii, and V. I. Marchenko, *Phys. Rev. Lett.* 82, 1506 (1999).
166. W. Klein, T. Lookman, A. Saxena, and D. M. Hatch, *Phys. Rev. Lett.* 88, 085701 (2002).
167. E. Korutcheva, A. M. Turiel, and I. Markov, *Phys. Rev. B* 64, 16890 (2000).
168. S. A. Chaparro, J. Drucker, Y. Zhang, D. Chandraasekhar, M. R. McCartney and D. J. Smith, *Phys. Rev. Lett.* 83, 11199 (1999).
169. P. Müller and R. Kern, *J. Cryst. Growth* 193, 257 (1998).

# Nucleoprotein Assemblies

Steven S. Smith

Kaplan Clinical Research Laboratory, City of Hope,  
Duarte, California, USA

## CONTENTS

1. Overview
  2. Supramolecular Assemblies
  3. Designs
  4. Conclusion
- Glossary  
References

## 1. OVERVIEW

Bionanotechnology is an emerging field with great promise in molecular science. The field is so new that it has yet to be formally defined. However, it can be characterized as a primitive technology that takes advantage of the properties of highly evolved natural products like nucleic acids and proteins by attempting to harness them to achieve new and useful functionalities on the nanoscale.

It is appropriate to compare bionanotechnology to the technology of the paleolithic in which natural products like wood and stone were shaped into implements and devices. Much like the paleolithic technologists who used knowledge of their surroundings to identify components and processes used in tool-making, modern bionanotechnologists use knowledge of chemistry, biochemistry, and molecular biology to identify components and processes for the construction of self-assembling materials and devices. Paleolithic technology was limited by the basic properties of natural products like wood and stone. Wood and stone could be shaped and modified, but they could not be forced into the arbitrary *de novo* designs that can be attained with our modern understanding of wood composites and ceramics. In a like fashion, bionanotechnology is limited by the basic properties of biomolecules. The field will certainly mature in the near future, but this maturation will require, among other things, advances in our understanding of the nature of nucleic acid and protein folding so that arbitrary *de novo* design of such molecules can be contemplated.

Like other forms of nanotechnology, bionanotechnology seeks to define approaches to the fabrication of useful

materials and devices. However, the construction principles utilized in the field often originate in biology and the goals are often biomimetic (e.g., the construction of biosensors [1]) or aimed at the solution of long-standing research problems (e.g., protein crystallization [2]). Nonbiological problems have also been approached in attempts at the construction of electronic circuitry using biomolecules [3] and the construction of a fuelled nanomechanical oscillator [4] and a nanomechanical switch [5]. At the heart of these approaches is the concept of self-assembly. Self-assembly of ordered elements is a defining property of living things. Moreover, the progressive increase in the complexity of the processes used by living things in self-assembly is a defining property of evolution. During the roughly 4.2 billion years of prebiotic and Darwinian evolution that have taken place on earth, an almost incomprehensible variety of molecular structures, functionalities, and associations have appeared. This evolutionary experience is stored in modern living systems. For this reason, modern living systems comprise a wealth of addressable macromolecular components. Of these, the nucleic acids and proteins are the most easily manipulated and the best understood. Thus, it is not surprising that they have been the first to be exploited to produce nucleoprotein-based addressing systems in nanobiotechnology [6–11] that attempt to exploit self-assembly and ordered proximity.

### 1.1. Creation of Biomolecular Machines by Directed Evolution

A machine is usually defined anthropomorphically as a device having a purpose [12]. A more general definition is as an assemblage of parts that transmit forces, motion, and energy one to another in a predetermined manner [13]. Such definitions are meant to encompass the spectrum of machines from the simple lever and wedge to the most complex networks of automata. In biology this definition encompasses an even broader spectrum of entities from the simplest biomolecular catalysts to the planetary biosphere. The central thesis in modern biology has been that the planetary biosphere arose spontaneously. Consequently an enormous amount of scientific research has been focused on

understanding how the earth underwent a transformation from an apparently lifeless state to the biosphere that it has now become.

A significant body of knowledge in support of this spontaneous transformation has now been accumulated in the field of prebiotic chemistry. This body of knowledge suggests pathways for the spontaneous production of each of the components of nucleic acids and proteins from conditions likely to have been present on the primitive earth [14, 15]. Most of this work has been aimed at constructing plausible routes to self-assembling chemical systems that would become subject to Darwinian natural selection. Working backward from apparent molecular fossils, the stated goal of these studies is to plausibly order the events that occurred on the prebiotic earth that gave rise to Darwinian evolution [16, 17].

The discovery of unifying principles in this area has been stimulated enormously by the discovery that nucleic acids themselves can serve as catalysts and must therefore be listed with peptides and proteins as the raw materials of simple biomachines. The current hypothesis is that the early stages of prebiotic evolution generated a series of supramolecular aggregates composed largely of RNA. These aggregates, sometimes termed metabolosomes [18], are postulated to have attained a high degree of complexity permitting them to carry out a complex series of chemical transformations. The level of complexity at which evolution by natural selection could take hold has been called the Darwinian threshold [17]. It is thought that the entity that crossed this threshold was a supramolecular aggregate that possessed the capacity for self-assembly, self-replication, and perhaps translation (i.e., the capacity to convert information stored in ribonucleic acid sequences into protein sequences [17]).

In efforts designed to recreate the basic designs for the postulated primitive nucleic acid machines, simple laboratory procedures for their construction have been developed using the principles of directed evolution *in vitro* [19–24]. Generally these techniques involve the production of a pool or library of nucleic acid sequences that are subjected to a selection process involving binding or catalysis. Those members of the library that can perform the binding or catalytic task dictated by the selection criterion are retained by the selective process. Initially, this represents only a tiny fraction of the initial library. This fraction is copied so as to increase the total number of copies of the selected species. After repeating this process many times, the resulting pool is thus reduced in complexity to a few representative molecules having the desired properties.

### 1.1.1. Aptamers

Aptamers represent perhaps the simplest class of molecular machine that has been produced by using bionanotechnology. The word aptamer is derived from the Greek word “aptus” meaning to fit, in this case, a molecule adapted to fit into another molecule. Under the first definition above [12], aptamers represent a class of molecular machine that can be considered to be devices having a specified purpose: binding to a ligand. Ligands that have been bound include organic dyes [23], proteins [25], other small molecules [26], and

other nucleic acids [27]. Aptamers have been produced from both DNA [25] and RNA [23]. Although most aptamers are essentially static machines, in the sense that a wedge is a static machine, more recently aptamers have been produced that exhibit behavior that can be regulated by a small molecule [28]. This suggests that the ligand either modifies the structure of the aptamer so that it fits into its target site properly or that the ligand forms part of a complex complementary to the targeted binding site. In short certain aptamers may be dynamic machines since they appear to move in order to bind.

### 1.1.2. Ribozymes

It is a short step from binding to catalysis because biological catalysts are selected so as to bind to and thereby stabilize transition states in a given reaction pathway. This property of catalytic biomolecules allows them to drive many organic reactions at ambient temperatures with reasonable efficiencies. RNAs with these properties are readily isolated by directed *in vitro* evolution techniques. *In vitro* selected ribozymes exhibit rate enhancements ranging from  $10^3$  to  $10^5$  over the uncatalyzed reactions. RNAs that have been isolated by these methods include those that catalyze carbon–carbon bond formation in a Diels–Alder reaction [29], phosphate bond cleavage in cleaving single-stranded DNA [22], phosphate bond formation during RNA polymerization [30], RNA ligation [31], carbon–nitrogen bond formation during self-alkylation [32], and carboxyl attack on phosphorous during amino acid activation.

### 1.1.3. Deoxyribozymes

Most secondary structure in nucleic acids involves hydrogen bonding. Since DNA lacks the 2' hydroxyl group on ribose that is present in RNA, it possesses a reduced potential for hydrogen bond formation and was initially thought to be less suitable for *in vitro* selection of aptamers and catalytic nucleic acids because it cannot adopt as many secondary structures as RNA (i.e., its conformation space [33] is restricted relative to RNA). This initial concern notwithstanding, catalytic DNAs of many types have also been selected by directed *in vitro* evolution. Porphyrin metallation [34], peroxidase activity [35], phosphoesterase activity [36], and DNA degrading activity [37] have all been documented, suggesting that the collection of accessible deoxyribozymes may be nearly as extensive as the collection of ribozymes.

### 1.1.4. Enzymes

Biologically occurring deoxyribozymes have not yet been observed. Biologically occurring ribozymes are rare, but several are known to exist. Catalytic proteins (enzymes), on the other hand, are the overwhelmingly predominant catalytic molecules in living things, with many thousands of different forms present in the average mammal, for example. Thus, by any measure, the collection of biologically occurring catalytic proteins (enzymes) is currently much larger than the collection of known catalytic nucleic acids since it encompasses the vast majority of the aggregate number of gene products contained in all species now present on earth. Even so, directed evolution techniques have been applied to the

development of new enzymes. Here, the methods are generally based on the selection of whole bacteria. In this process the bacteria develop previously unknown catalytic functions by recruiting proteins that are normally expressed in the bacteria for other purposes through a process of mutation and selection [38, 39]. For example, bacteria that are normally unable to use a certain sugar for growth are exposed to a DNA damaging agent that introduces random changes (mutations) in the genetic code of the organism. Most of these changes are deleterious and either cause the bacteria to die or grow more slowly than it would in its natural growth medium. However, if the mutated bacteria are forced to grow on the sugar that they are normally unable to use, a small fraction of them (perhaps 1 in  $10^8$ ) will be able to use the sugar in question for slow growth. Subsequent rounds of this mutagenesis and selection process yield new enzyme functionalities associated with absorbing and breaking down the sugar in question. Such *de novo* protein development completes the spectrum of currently known techniques for the *de novo* development of nanoscale components available for nanobioscience and nanobiotechnology.

Each of these *de novo* methods takes advantage of the almost incomprehensible conformation spaces available to proteins, RNAs and DNAs [33] as noted above. Given the hydrogen bonding capacities of each polymer and the number of commonly observed monomeric building blocks (4 each for nucleic acids and 20 for proteins), the number of available conformations is canonically ordered as follows: protein  $\gg$  RNA  $>$  DNA when each oligomer contains the same number of monomers. It is worth noting that even the conformations available to the most restricted system (the DNAs) is  $4^n$  (where  $n$  = sequence length in nucleotides) assuming only one conformation per sequence. It is clear that the vast collection of shapes available to oligomers of modest length ( $n > 20$ ) offers an almost inexhaustible wealth of potential devices available for nanoscale assembly.

## 1.2. Modification of Existing Biomolecular Machines

Directed evolution has provided a productive route to the *de novo* selection of new nanoscale machines; however, with proteins, it has often been simpler to modify existing molecules for purposes related to their current function. This makes recombinant DNA technology among the most powerful tools in bionanotechnology. Recombinant DNA technology is generally used to place desired proteins under the control of specific DNA sequences, called promoters, that permit the production of large quantities of the desired material. This is generally coupled with the second tool, site-directed mutagenesis, which allows the modification of the protein itself. In site-directed mutagenesis, recombinant DNA techniques from molecular biology are used to alter the genetic code so as to modify the amino acid sequence of the protein. The resulting proteins have generally been redesigned so as to suit a particular application. In general these alterations improve stability or functionality of the protein in a given application.

These techniques have been used to optimize [40, 41] the capacity of the light harvesting protein bacteriorhodopsin to

cycle between two stable photochemical states so as to permit the construction of a three-dimensional memory device. In this device the modified protein is first immobilized in a matrix. A paging laser at 570–630 nm is used to cycle the engineered bacteriorhodopsin from an all-*trans* state through a series of 13-*cis* retinal states to a light-adapted protonated all-*trans* retinal state. A full power write laser at 680 nm acting orthogonally through an active matrix liquid crystal light modulator is then used to convert volume elements of the protein-containing matrix from the light adapted all-*trans* retinal isomer to the 9-*cis* isomer to set the state of engineered protein in the matrix, thus creating a three-dimensional (3D) (volumetric) information storage pattern. The 570–630 nm paging laser is coupled with the 680 nm laser at low power to read the information by projecting the stored data onto a charge-coupled device. Bacteriorhodopsin is stable in this state and data stored in this manner are stable for decades in the absence of blue light or high temperatures. Erasure is accomplished with a 410–430 nm diode-pumped laser that converts the 9-*cis* to one of the all-*trans* states.

This working system integrates bionanotechnology (protein engineering and 3D immobilization techniques) with laser based input–output (IO) technology to achieve a storage device that is resistant to the high levels of radiation and shock required for satellite communications, while achieving a 1000-fold improvement in memory storage capacity over currently operational devices. The ultimate goal of bionanotechnology is to create devices based on biomolecules that achieve the even greater degree of complexity and miniaturization exhibited by living things.

## 2. SUPRAMOLECULAR ASSEMBLIES

A key step in the origin of life appears to have been the origin of translation [17, 18]. Translation is the process by which RNA sequence information is copied into peptide or protein sequence information. In general, this is assumed to have occurred at a time in prebiotic evolution when catalytic RNAs provided the only mechanism by which metabolic interconversion of chemical compounds could be accomplished. The appearance of translation is thought to have moved evolution to a new plane in which supramolecular aggregates (SMAs) appeared that had crossed the Darwinian threshold (i.e., the point at which the complexity of the aggregate permitted replication, self-assembly, and natural selection). This transition is thought to have been achieved by incorporating information storage and feedback to the storage mechanisms [17].

The modern ribosome is generally considered to be a molecular fossil representing a highly refined version of one of the key components of these supramolecular aggregates or SMAs. The more primitive SMAs that gave rise to them are generally thought of as metabolosomes in which nucleic acid scaffolds of RNA called organizing centers held catalytic RNAs in place by base-pairing between a short region of the nucleic acid scaffold and a short region of the catalytic RNA [18]. In this model, the alignment of sequestered catalytic RNAs was set by the sequence of the complementary RNA in the organizing center. This alignment and proximity is thought to have facilitated sequential reactions in the

metabolosome. The linear arrangement along the organizing center is thought to have been translated into the linear arrangement of amino acids, thus promoting the formation of peptides by ordering condensation reactions through appropriate juxtaposition of the amino acid adapters composed of RNAs. It is thought that these adapters ultimately evolved into modern transfer RNAs or tRNAs and that they continue to serve this purpose in modern living things. Bionanotechnological approaches to the construction of supramolecular aggregates have adapted many of these biological principles.

### 2.1. Creation of SMAs Using Base-Pairing in Complementary Nucleic Acids

Several nucleic acid scaffolds have been constructed using DNA complementarity. These scaffolds are assembled by annealing complementary DNAs followed by enzymatic ligation, or splicing, of the subsections of a larger entity. The scaffolds are defined by their connectivity. A cage having the edge connectivity of a cube [42] has been characterized, as well as a system with the connectivity of Borromean rings [43], the connectivity of a truncated octahedron [44], and the connectivity of a 2D lattice [45]. Thus, the topology available for the construction of supramolecular aggregates is quite elaborate. This topology has been used in the construction of a two-state switch that is actuated by changes in salt concentration [5] and in the construction of a DNA-fuelled oscillator [4] that is activated by the addition of oligodeoxynucleotides.

The two-state switch is based in the well-known transition of DNA from the right-handed B-form double helix seen at low salt to the left-handed Z-form double helix seen at high salt. In Z-DNA the phosphate backbone zigzags around the stacked base pairs instead of winding smoothly around them in a helical pattern as it does in B-form DNA [5]. This conformational change twists the DNA from the right- to the left-handed form, and it is favored by sequences that are rich in guanine–cytosine base pairs. Interestingly, it was found that a double-crossover molecule could be made to stabilize two duplex strands of DNA into a side by side arrangement that appears to remain in the B-form at high salt. Double-crossover is a term from genetics used to explain genetic exchanges that often occur during the DNA-strand exchanges that characterize recombination in biology. Physically a system of this type comprises four strands of DNA intertwined so that two of the strands cross over from one of the double helices to the other and back again so as to constrain them to lie side by side. This rigid system resists conformational change as salt concentration is altered. When two double-crossover systems are connected by a short double-stranded region that is rich in guanine–cytosine base pairs, the two double-crossover regions at either end of the double-stranded region can be made to lie on the same side of the double-stranded region at low salt and on opposite sides of the region after the B to Z transition induced by high salt. Resonant intramolecular energy transfer from chromophores placed at the ends of the double-crossover strands that lie near the linking region can be used to detect the change in proximity induced by the

increase in salt concentration. In effect, the system becomes a biosensor that can detect changes in salt concentration [5].

The DNA-fuelled oscillator likewise induces nanomechanical motion in a supramolecular assembly formed from DNA [4]. Here again, resonant intramolecular energy transfer is used to detect the close approach of two chromophores during the formation of a duplex waste product from the sequential addition of two complementary fuel strands. The system essentially makes use of strand displacement in DNA. Here a chromophore and a fluorescence quencher are placed at each end of a short DNA strand during synthesis. This short strand is hybridized (annealed) to two strands that are complementary to the ends of the chromophore-containing strand, extend beyond the ends by several nucleotides, but do not cover the central nucleotides of the chromophore-bearing strand. In this state the duplex DNA region is extended by the stiff stacking interactions along the Z-axes of the two duplex regions, thus maintaining the ends of the strand containing the chromophore and the fluorescence quencher at a distance adequate to prevent quenching of the fluorescent signal. Once this state is achieved, a closing fuel strand is added that is complementary to the unpaired ends of each of the previously added strands but is longer than one of them so as to leave another unpaired region. Once annealed, this strand forces the chromophore-containing strand into a hairpinlike conformation that juxtaposes the chromophore and the quencher, extinguishing the fluorescence signal by resonant intramolecular energy transfer. The system remains in this conformation until an opening fuel strand is added that is completely complementary to the closing fuel strand added previously. Annealing between the two fuel strands begins at the short unpaired region and continues by strand displacement until the opening fuel strand that maintains the chromophore containing strand in the hairpin conformation is stripped away to relax the system and permit fluorescence to reappear [4].

### 2.2. Creation of SMAs Using Complementary Protein Domains

Multisubunit proteins can exhibit a form of complementarity between subunits that results in self-assembly of defined multimolecular protein aggregates. Protein–protein interaction is not easily predicted, as can be anticipated from the increased complexity intermolecular interactions possible between the 20 common amino acids compared to that of the 5 common bases that comprise the nucleic acids. However, as the number of known 3D protein structures has increased it has become possible to catalog numerous interactions between internal protein domains that can be reproduced with synthetic peptides. For example, the SH2 and SH3 domains of the Src tyrosine kinases are known to interact with phosphotyrosine and proline rich motifs to form internal associations that influence kinase activity. SH3 and SH2 are well characterized examples of protein domains whose natural folds are spontaneously adopted by recombinant peptides containing the native peptide sequence [46, 47]. Each isolated domain retains its affinity for phosphotyrosine (SH2) or proline rich peptides (SH3)

that interact with these domains to form complex associations involving the Src kinases.

In general, domain–domain interactions also govern the spontaneous association of multisubunit proteins. Dimeric proteins often associated with DNA-binding proteins [48] represent the simplest examples of these aggregates. In addition, the multimeric assemblies that form viral capsids [49] provide examples of the complexity that is achieved in biology with simple interactions of this type. The symmetry rules that govern the self-assembly of these subunits into complex multimers are well known [49, 50].

These advances in the understanding of protein domain structure have allowed the construction of fusion proteins (i.e., chimeric proteins constructed by recombinant DNA techniques that fuse disparate functional domains in to a single unit) with predictable subunit–subunit complementarity that have been used in the formation of a closed tetrahedron protein cage and an extended protein filament [51]. The closed protein cage was designed by searching a protein database for dimeric and trimeric protein structures that begin or end in an alpha helix. Molecular modeling was then used in computer-aided design of a fusion between domains thus identified. Once models were constructed, they were examined to determine whether or not they possessed appropriate symmetry for self-assembly into a closed geometric figure. One fusion between the trimeric bromoperoxidase of *Streptomyces aureofaciens* and the dimeric M1 matrix protein of the influenza virus was shown to be capable of the formation of a tetrahedral cage by molecular modeling. Molecular cloning techniques were used to express the designed fusion protein in *E. coli*. The purified fusion protein was shown to form the expected tetrahedral cage based on sedimentation velocity, light scattering, and electron microscopy experiments. Similar methods permitted the construction of an extended filament [51].

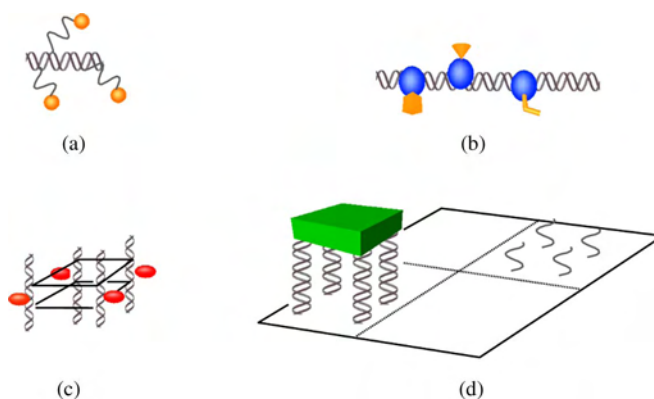
Biomolecular motors are also potential components of a variety of protein containing devices that have obvious potential in structuring or redirecting flow and mixing in nanofluidic systems. The F1-adenosine triphosphate synthase (F1-ATPase) provides a well-studied example of a molecular motor. It is also a naturally occurring supramolecular protein aggregate, comprising three alpha, three beta, and one gamma protein subunits. It is effectively a three-point stepper motor that generates ATP from ADP and inorganic phosphate by using rapid sequential conformational changes driven by a proton gradient. The conformational changes associated with the stepwise rotation of the protein rotor (i.e., the gamma subunit) between the surrounding sets of alpha and beta subunits cause the enzyme to catalyze the formation of ATP. This mechanism of action was deduced through studies of the biochemical kinetics of the system [52]. It was later supported by 3D structure determination [53] and unequivocally demonstrated by chemical means [54] and by direct real-time observation [55, 56] of the reverse reaction in which ATP is hydrolyzed. These advances in understanding of the system have permitted it to be modified using site-directed mutagenesis so that it could be mounted on an engineered substrate in order for it to be able to produce controlled rotation of synthetic arms. Rotation can be initiated by the addition of one compound (2 mM adenosine triphosphate) and halted by the addition

of another compound (sodium azide). With further protein modification, rotation could be halted by the addition of the metal ion  $Zn^{2+}$  and reinitiated by the addition of the metal ion chelator EDTA. In short, the rotation of this modified machine can now be controlled by changing its chemical environment [57–59].

### 2.3. Addressable Supramolecular Assemblies Based on Nucleic Acid Complementarity

As noted above the key feature postulated for metabolosomes is the ability of the nucleic acid scaffolds that formed the organizing centers to sequester and align nucleic acid adapters. Base-pairing between a short region of the nucleic acid scaffold and a short region of the adapter is thought to have generated the appropriate alignment of the adapters [18]. This concept has also been employed in several applications in bionanotechnology. See Figure 1.

For example gold nanoparticles can be linked to DNA by attaching alkanethiol groups to the ends of single-stranded DNA molecules [10, 11]. When the modified DNAs are



**Figure 1.** Addressable nucleoprotein assemblies. (a) Molecular addressing using nucleic acid complementarity. Here the central duplex is formed either by DNA • DNA interaction or by DNA • RNA interaction along a DNA or RNA organizing molecule. Short tethers of DNA are used to link thermostable moieties to which other molecules can be attached (e.g., gold or streptavidin molecules) indicated by the spheres [6, 11]. (b) Molecular addressing using protein–nucleic acid interaction. Here the central duplex contains 5FdC residues that form covalent complexes with DNA (cytosine-5) methyltransferase fusion proteins as they catalyze methylation of the DNA target. The fusion proteins are ordered along the DNA sequence based on the biospecificities of the cytosine methyltransferases of which more than 40 are known [8]. Each fusion protein can carry a different functionality indicated by the irregular shapes attached to each sphere. (c) Molecular addressing to a lattice. In this proposal [70] a lattice of DNA is ligated together so as to serve as a host for guest molecules (ovoid shaped objects). The purpose of this proposal is to drive crystallization so as to facilitate 3D structure determination. (d) Molecular addressing of silicon objects to a patterned DNA surface. In this proposal, DNA is patterned onto a surface (depicted here as a checkerboard). Silicon objects bearing complementary DNA strands on one of their surfaces are moved into the vicinity of their complementary strands on the surface pattern where they should attach biospecifically [9]. The attached object is linked to the DNA strands on the front left of the surface. Noncomplementary DNA states at the right rear of the surface are ignored.



exposed to a gold surface they adsorb by forming covalent bonds between the gold and sulfur atoms. Like other metal sulfur bonds the Au-S bond is very strong and can easily link a long DNA molecule tightly to the surface of the gold particle. The sequences of the attached DNA molecules can be chosen so as to be complementary to a linker strand. This permits the nanoparticles to spontaneously self-assemble into aggregates when mixed with the linker strand [10]. If they are complementary to a linear DNA strand, then they can be tethered to duplex DNA in an ordered fashion [11] around the screw axis of the B-DNA molecule ( $36^\circ/\text{base-pair}$ ). This approach can also be used to order the thermostable-protein streptavidin along the screw axis of a DNA helix [6]. Here biotinylated DNA is allowed to interact with streptavidin prior to nucleic acid hybridization. The streptavidin protein binds to the end of the DNA due to the innate capacity of streptavidin to bind extremely tightly to biotin. A DNA or an RNA organizing molecule is then used to sequester and align the tethered streptavidin molecules [6] much as originally envisioned by Gibson and Lamond [18] for the metabolosome. When DNA is used as the organizing molecule the streptavidin moieties should be arrayed in accordance with the screw axis of the B-DNA molecule ( $36^\circ/\text{base-pair}$ ). When RNA is used this orientation is expected to be in accordance with the screw axis of the RNA•DNA hybrid ( $30^\circ/\text{base-pair}$ ).

Both the gold and the streptavidin aggregates provide the opportunity for secondary assembly via the gold or streptavidin moiety. For example, the streptavidin molecule binds biotin with a stoichiometry of four biotin residues per protein moiety, leaving three unused sites on the DNA-streptavidin conjugate. These unused sites have been used to attach biotinylated antibodies to DNA-tethered streptavidin [6]. This permits the derivatization of microstructured surface arrays of DNA using the base-pairing complementarity of the array so as to convert it to a protein array of different antigen specificities [6]. Further, by adding biotin to both of the 5' ends of complementary oligodeoxynucleotides it has been possible to form ring structures or networks of DNA linked by two, three, or four biotin contacts per streptavidin residue [60].

Biotinylated proteins can be linked to streptavidin and then targeted to DNA or RNA organizing molecules. Although high-fidelity annealing is generally only achieved at temperatures above  $50^\circ\text{C}$ , annealing with bound proteins can be carried out at room temperature [61]. Alternatively, biotinylated proteins can be sequestered without regard to order along an organizing DNA or RNA molecule by incubating them at low temperature with streptavidin molecules tethered to DNA or RNA [62].

Using these methods, the effects of protein proximity have also been studied with this system. Here, the NAD(P)H/FMN oxidoreductase was placed adjacent to luciferase in order to improve the properties of light emission by the system that is normally coupled by these enzymes in their soluble form. Chemical biotinylation of proteins is not regioselective and can damage proteins. To avoid this problem, fusion proteins were prepared that contained a biotin acceptor region from the *E. coli* biotin carboxy carrier protein. This served as a biospecific attachment site for *E. coli* biotin ligase for the regiospecific attachment of biotin

to the luciferase and to the NAD(P)H/FMN oxidoreductase. Streptavidin-containing adapters were attached to the fusion proteins and annealed to a DNA-linker strand that linked the two enzymes either to the same or to different strands. The SMAs thus created were then deposited on a microplate surface again through a streptavidin-biotin linkage to the end of the carrier strand. A 2.0- to 2.5-fold rate enhancement was observed when the proteins were adjacent on a linear DNA compared to randomly placed on a surface [61].

Each of these systems results in a free (often soluble) nanoscale assembly. On a larger scale DNA sequences can be manipulated by electrophoresis in ways that immobilize them on the micro- and submicroscale [63]. Such arrays become templates for addressing silicon and gold components [9] as well as biotin linked antibodies and proteins [6, 61, 62].

## 2.4. Addressable Supramolecular Assembly Based on Protein-DNA Specificity

The feasibility of an approach to addressable self-assembly that enables the construction of ordered assemblies and devices has also been described [7, 8, 64–66]. The principal advance brought about by this work is the ability to place fusion proteins in preselected positions on a DNA scaffold under conditions that do not denature sensitive protein components. The protein-nucleic acid structures self-assemble at 5FdC [7, 8, 64] or dU substituted [66] recognition sites. Order is specified during the synthesis of the DNA by placing DNA methyltransferase recognition sites along the DNA. Two- and three-address assemblies are obtained in good yield [65], and fusion proteins have been constructed and targeted to preselected sites on linear [8] or branched targets [67].

One advantage of fusion protein-targeting over streptavidin protein-tethering is that a covalent linkage is established between the cytosine methyltransferase and the DNA that is heat stable. Thus, an array of ordered fusion proteins that might find application in a thermal cycling system could be constructed by this method without difficulty, whereas the streptavidin system would break down under repeated thermocycling not only at the level of nucleic acid but also at the streptavidin-biotin linkage. With the tethering system, one could imagine ligating the tethers in place after assembly had taken place at lower temperatures. However, steric problems would reduce yields in many cases and ligation would not solve the problems associated with the biotin-streptavidin linkage in this application.

An advantage of tethered assemblies like those ordered by streptavidin conjugation is that the length of the tether can be varied in order to accommodate proteins or other elements of unknown dimensions by trial and error. On the other hand, the use of methyltransferase fusion proteins in ordering elements on DNA or elements that contain DNA requires considerable effort in computer-aided design. This is because the structural imperatives that are imposed by such assemblies must be anticipated, insofar as is possible. As noted above for the construction of SMAs from fusion proteins [51] extensive use of the 3D structures of proteins

available in protein databases is made [7, 8, 64, 66] in developing potential fusions and SMAs based on this method. Once it is determined that the proposed design can assemble spontaneously, it is important to test these predictions in several ways. Several interesting phenomena have surfaced in producing these assemblies.

For example, as DNA is added to either side of the four base-pair binding site in a linear DNA molecule, it has been shown that the rate of the coupling reaction between methyltransferases and the targeted 5-fluorocytosine residues increases in an apparently sigmoid fashion [8]. The initial inflection point in this reaction rate occurs at about 25 to 30 bp of total length for two unrelated bacterial cytosine methyltransferases (*M•HhaI* and *M•MspI*). This was interpreted as the kinetic footprint of the enzymes (i.e., the minimum space required for unhindered approach by a methyltransferase to its targeted recognition sequence). However, the 3D structure of *M•HhaI* bound to DNA shows that it only physically covers about 13 bp of DNA [68], suggesting that it could be made to decorate DNA recognition sites that are closer than the 25 bp inferred from the kinetic experiments. This inference from the 3D structure turns out to have been correct, since three-point assembly along a linear molecule has been achieved with center to center placements as close as 17 bp [65].

### 3. DESIGNS

Although a considerable number of technical and structural feats have been achieved in bionanotechnology, an even larger number of designs for devices and assemblies based on addressable assembly have been proposed. See Table 1. Of these, many continue to be biomimetic with antecedents in prebiotic evolution. Proposals for macromolecular carcerands [69] and host-guest systems [70, 71] containing DNA form an important set of examples, since the protective nature of these assemblies touches upon one of the long-standing problems in prebiotic evolution: understanding how DNA ultimately became intertwined with the postulated RNA world. Given the rules that have emerged defining the attributes of the entity that first crossed the Darwinian threshold, it would appear that DNA was not required for the initial evolution of primitive supramolecular aggregates or metabolosomes [17, 18]. Nevertheless, the best evidence suggests that DNA was recruited early on in the evolution of these SMAs [16].

Recent discoveries on the structure of the supramolecular aggregates present in the macronucleus in protozoans and the nucleolus in primitive eukaryotes suggest that these structures may make use of the cohesive ends of DNA produced by telomerase. Telomerase is a molecular fossil with a structure resembling that of a ribosome, in that it comprises several proteins assembled on a functional RNA. In this case, however, one of the protein moieties serves to complement the RNA moiety in such a way that the supramolecular assembly becomes a primitive reverse transcriptase capable of generating short (often hexameric) DNA repeats that are capable of forming strong associations based primarily on Hoogsteen pairing between guanine residues. Many of these associations can survive even in boiling water and

**Table 1.**

Concept	Proposed	Achieved
DNA array addressing		[63]
DNA-adaptor-linked protein ordering on linear DNA		[6]
Fusion protein ordering on linear DNA		[8]
Protein assembly on branched DNA		[67]
DNA-adaptor-linked gold ordering on linear DNA		[11]
DNA directed gold particle aggregation to 2D lattice		[10]
DNA directed protein assembly on 3D lattice	[70]	
DNA directed silicon component addressing aggregation to 2D array	[9]	

thus can provide considerable integrity to a supramolecular structure. Moreover, in an RNA world, one can safely assume that competition between evolving supramolecular aggregates would involve the production of RNA degrading enzymes or ribozymes selected for their destructive power against competing metabolosomes. Thus, the evolution of a primitive ribonucleoprotein assemblage capable of generating a protective DNA cage or matrix that was impervious to RNA-degrading activities would offer an important selective advantage for such a system. In short, telomerase-like reverse transcriptases may have been both enveloped and protected by their DNA products in the distant past. This possibility is consistent with the association of the modern telomerases (as molecular fossils) with macronuclei [72, 73] and with the membraneless aggregate of nucleic acid and protein called the nucleolus [74, 75]. Of these the nucleoli of the lower eukaryotes (e.g., *D. Discodinium* and *P. polycephalum*) [76, 77] may represent living molecular fossils that evoke the freestanding supramolecular aggregate postulated as the antecedent of modern living systems [16, 17]. The DNA contained in these nucleoli is a short linear element that ends in cohesive telomeric DNA and encodes the other important molecular fossil from the RNA world: the ribosomal RNA [77, 78]. As with other nucleoli these are membraneless structures that are enclosed in an apparently freestanding fashion by the nucleus. That DNA came to be associated with the RNA world in this fashion is also consistent with the findings of Ohno who pointed out that all modern genes appear to have evolved from iterated repetitive elements of the type produced by modern telomerases [79].

These systems form biomimetic models for nanoscale cages, carcerands, and extended 3D assemblies that can be constructed with the bionanotechnological tools for supramolecular assembly and addressing described above. The utility of such assemblies lies in their potential as devices that may some day acquire the complexity attributed to nanorobots that can be directed to perform complex tasks in a nanoscale environment [80]. Targeted drug delivery, selective cell destruction, selective cell remodeling, telemetered detection of cellular abnormalities [80], and the creation of new life forms [81] are often suggested as long-range goals for these technologies.

More immediate goals for these technologies revolve around their potential for contributing to understanding

biological molecules and their interactions. A key area here has been the desire to control solid state 3D assembly of macromolecules so as to permit structure determination by X-ray diffraction. To this end, designs for extended 3D crystals based on DNA cages with oriented guests [70, 71] have also been proposed in the hope that macromolecules that interact with DNA scaffolds could be forced to adopt regular crystalline arrays that would diffract to high resolution. These nucleic acid-based proposals are supplemented by proposals for the assembly of 3D crystals based on protein cages and extended structures [51]. As with the DNA technology described above, designs for cages and shells, double-layer rings, two-dimensional layers, and helical filaments have all been proposed based on the ordered assembly of protein domain fusions [51].

Designs for nucleoprotein cages have also been proposed [69]. Here closed structures take advantage of ordered placement of methyltransferase targeted protein donors (e.g., proline rich peptides) and methyltransferase targeted protein acceptors (SH3 domains). When donors are ordered along one set of branched or linear DNA scaffolds and acceptors are ordered along another set, self-assembly can be initiated by mixing the two sets of biostructures. Using this method, it should be possible to achieve assembly of relatively large DNA cages and extended assemblies akin to those that characterize the macronucleus and the nucleolus as noted above.

Ordered assembly using biomolecules on an even larger scale has also been proposed [9]. Here, one envisions a two-step process utilizing complementary oligodeoxynucleotides. In the first step a surface is decorated with single-stranded oligodeoxynucleotides in a predetermined pattern using well known techniques [63]. In the second step, etching techniques are applied to a separate silicon-on-insulator wafer. The wafer is etched with potassium hydroxide around elements protected on their surface by a mask of Au/Cr. These islands are then released from the silicon insulator layer with hydrofluoric acid and linked to thiols at the ends of synthetic oligodeoxynucleotides through interactions with the gold surface. The silicon elements can then be moved in an electric field until they contact the complementary oligodeoxynucleotide in the previously prepared surface causing them to become fixed in a predetermined pattern [9]. In principle such a system would permit macroscale addressing for assembly of electronic devices.

Designs for ordering functional proteins so as to produce vectored chemical processes on the nanoscale have also been proposed [6–8, 82]. In this case, the implication is that ordered proximity for a set of enzymes or ribozymes performing a sequence biochemical reactions would produce advances in understanding the nature of vectored biological catalysis and its potential applications in signal amplification.

## 4. CONCLUSION

Bionanotechnology adapts not only the results (functional proteins and nucleic acids) but also the processes (e.g., directed evolution, supramolecular aggregate, and metabolosome construction) of molecular evolution. Molecular addressing systems, based on DNA complementarity and DNA–protein interaction selectivity, are now

available for the ordered assembly of a variety of functional elements from biology. Molecular motors, DNA-based switches, DNA-based oscillators, enzymes, ribozymes, deoxyribozymes, gold particles, chromophores, fluorescence quenching agents, antibodies, aptamers, and nucleic acid binding proteins can all be ordered along nucleic acid scaffolds. The potential for construction of useful devices utilizing the extraordinary wealth of functionality made possible by ordering these elements is quite broad. Given the success of this paradigm it is reasonable to assume that clues from biology will continue to be applied to the construction of useful bionanotechnological devices. It is likely that the successful construction of these devices will shed new light on both the origin and nature of living things. Moreover, one can anticipate the possibility that one of these devices might itself cross the Darwinian threshold at some time in the future.

## GLOSSARY

**Aptamer** A short nucleic acid composed of DNA or RNA that has been adapted by selection using directed evolution to fit into a molecular surface.

**Biosensor** A device designed to detect a specific biological molecule, system of biological molecules, or biologically produced signal.

**Conformation space** A three-dimensional vector space occupied by representations of the 3D shapes that can be assumed by a molecule.

**Darwinian threshold** The point at which a system can begin to evolve by self-replication variation and natural selection.

**Deoxyribonucleic acid (DNA)** A naturally occurring polymer composed of deoxy ribonucleotides. Although commonly found as a double-stranded, right-handed helix it can adopt one-, three-, and four-stranded forms having a variety of shapes.

**Directed evolution** The process by which molecules are selected from a replicable library. Multiple rounds of selection and replication generate a desired product.

**F1 ATPase** A naturally occurring multisubunit complex of proteins capable of synthesizing ATP in living systems.

**Hydrogen bond** A weak polar bond formed between two electron-rich atoms, one of which is covalently bonded to a hydrogen atom.

**Macronucleus** A large inclusion found in the cells of certain living things that contains multiple copies of genes that are in constant use by the organism.

**Membraneless structure** A substructure often present inside a living cell that is not bounded by a lipid bilayer membrane.

**Metabolosome** A nucleoprotein assembly that has been designed or selected for functionally carrying out a series of chemical reactions.

**Molecular fossil** A molecule that has been preserved by evolution over eons of geologic time stretching to or nearly to the dawn of life.

**Molecular machine** A machine comprising an assembly of a small number of molecules.

**Molecular modeling** A computer-aided design process in which computational chemistry software programs are used to create models of macromolecules based on electronic structure, and molecular mechanics calculations coupled with 3D experimental data.

**Mutation** A change in the information storage mechanism of an evolving system that alters the information it contains but may or not alter the form or function of the system.

**Nucleolus** A substructure within the cell nucleus that is composed largely of the genes responsible for the production of ribosomal RNA.

**Ribonucleic acid (RNA)** A naturally occurring polymer composed of ribonucleotides. Although commonly found in its single-stranded form, it can adopt two-, three-, and four-stranded forms having a variety of shapes.

**Selection of whole bacteria** Directed evolution in which bacteria and not macromolecules are used as the substratum for growth.

**Transition state** An intermediate and generally unstable state in a chemical reaction in which reactants are transformed into products resembling both states but identical to neither.

## REFERENCES

1. C. S. Yun, G. A. Khitrov, D. E. Vergona, N. O. Reich, and G. F. Strouse, *J. Am. Chem. Soc.* 124, 7644 (2002).
2. N. C. Seeman, *Nanotechnology* 2, 149 (1991).
3. A. Gil, P. J. de Pablo, J. Colchero, J. Gómez-Herrero, and A. M. Baró, *Nanotechnology* 13, 309 (2002).
4. B. Yurke, A. J. Turberfield, A. P. Mills, Jr., F. C. Simmel, and J. L. Neumann, *Nature* 406, 605 (2000).
5. C. Mao, W. Sun, Z. Shen, and N. C. Seeman, *Nature* 397, 144 (1999).
6. C. M. Niemeyer, T. Sano, C. L. Smith, and C. R. Cantor, *Nucleic Acids Res.* 22, 5530 (1994).
7. S. S. Smith, Biological and Biomedical Science and Technology Division, ONR 34196-3, p. 161, 1995.
8. S. S. Smith, L. Niu, D. J. Baker, J. A. Wendel, S. E. Kane, and D. S. Joy, *Proc. Natl. Acad. Sci. USA* 94, 2162 (1997).
9. R. Bashir, *Superlattices Microstruct.* 29, 1 (2001).
10. C. A. Mirkin, R. L. Letsinger, R. C. Mucic, and J. J. Storhoff, *Nature* 382, 607 (1996).
11. A. P. Alivisatos, K. P. Johnsson, X. Peng, T. E. Wilson, C. J. Loweth, M. P. Bruchez, Jr., and P. G. Schultz, *Nature* 382, 609 (1996).
12. "Encyclopedia Britannica." William Benton, Chicago, 1960.
13. "Webster's Third New International Dictionary." Merriam-Webster, Springfield, 1986.
14. D. H. Kenyon and G. Steinman, "Biochemical Predestination." McGraw-Hill, New York, 1969.
15. G. Zubay, "Origins of Life: On Earth and in the Cosmos." Academic Press, San Diego, 2000.
16. S. A. Benner, A. D. Ellington, and A. Tauer, *Proc. Natl. Acad. Sci. USA* 86, 7054 (1989).
17. C. R. Woese, *Proc. Natl. Acad. Sci. USA* 99, 8742 (2002).
18. T. J. Gibson and A. I. Lamond, *J. Mol. Evol.* 30, 7 (1990).
19. D. R. Mills, R. L. Peterson, and S. Spiegelman, *Proc. Natl. Acad. Sci. USA* 58, 217 (1967).
20. R. Levisohn and S. Spiegelman, *Proc. Natl. Acad. Sci. USA* 63, 805 (1969).
21. C. Tuerk and L. Gold, *Science* 249, 505 (1990).
22. D. L. Robertson and G. F. Joyce, *Nature* 344, 467 (1990).
23. A. D. Ellington and J. W. Szostak, *Nature* 346, 818 (1990).
24. L. Gold, *Harvey Lect.* 91, 47 (1995).
25. L. C. Bock, L. C. Griffin, J. A. Latham, E. H. Vermaas, and J. J. Toole, *Nature* 355, 564 (1992).
26. T. Kato, K. Yano, K. Ikebukuro, and I. Karube, *Nucleic Acids Res.* 28, 1963 (2000).
27. D. G. Attardi and G. P. Tocchini-Valentini, *RNA* 8, 904 (2002).
28. M. Vuyisich and P. Beal, *Chem. Biol.* 9, 907 (2002).
29. T. M. Tarasow, S. L. Tarasow, and B. E. Eaton, *Nature* 389, 54 (1997).
30. E. H. Eklund and D. P. Bartel, *Nature* 382, 373 (1996).
31. E. H. Eklund, J. W. Szostak, and D. P. Bartel, *Science* 269, 364 (1995).
32. P. A. Lohse and J. W. Szostak, *Nature* 381, 442 (1996).
33. S. S. Smith and L. Crocitto, *Molecular Carcinogenesis* 26, 1 (1999).
34. Y. Li and D. Sen, *Nat. Struct. Biol.* 3, 743 (1996).
35. P. Travascio, Y. Li, and D. Sen, *Chem. Biol.* 5, 505 (1998).
36. R. R. Breaker and G. F. Joyce, *Chem. Biol.* 2, 655 (1995).
37. N. Carmi and R. R. Breaker, *Bioorg. Med. Chem.* 9, 2589 (2001).
38. J. H. Campbell, J. A. Lengyel, and J. Langridge, *Proc. Natl. Acad. Sci. USA* 70, 1841 (1973).
39. B. G. Hall, *Genetics* 101, 335 (1982).
40. R. Birge, N. B. Gillespie, E. W. Izaguirre, A. Kusnetzow, A. F. Lawrence, D. Singh, Q. W. Song, E. Schmidt, J. Stuart, S. Seetharaman, and K. J. Wise, *J. Phys. Chem. B* 103, 10746 (1999).
41. K. Wise, N. Gillespie, J. Stuart, M. Krebs, and R. Birge, *Trends Biotechnol.* 20, 387 (2002).
42. J. H. Chen and N. C. Seeman, *Nature* 350, 631 (1991).
43. C. Mao, W. Sun, and N. C. Seeman, *Nature* 386, 137 (1997).
44. Y. Zhang and N. Seeman, *J. Am. Chem. Soc.* 116, 1661 (1994).
45. E. Winfree, F. Liu, L. A. Wenzler, and N. C. Seeman, *Nature* 394, 539 (1998).
46. V. P. Grantcharova and D. Baker, *Biochemistry* 36, 15685 (1997).
47. G. Siegal, B. Davis, S. M. Kristensen, A. Sankar, J. Linacre, R. C. Stein, G. Panayotou, M. D. Waterfield, and P. C. Driscoll, *J. Mol. Biol.* 276, 461 (1998).
48. A. C. Glasgow, M. F. Bruist, and M. I. Simon, *J. Biol. Chem.* 264, 10072 (1989).
49. D. L. D. Caspar and A. Klug, *Cold Spring Harb. Symp. Quant. Biol.* 27, 1 (1962).
50. I. Klotz, D. W. Darnall, and N. R. Langerman, in "The Proteins" (H. Neurath and R. L. Hill, Eds.), Vol. I, p. 293. Academic Press, Seattle, 1975.
51. J. E. Padilla, C. Colovos, and T. O. Yeates, *Proc. Natl. Acad. Sci. USA* 98, 2217 (2001).
52. P. D. Boyer, *Biochim. Biophys. Acta* 1140, 215 (1993).
53. J. P. Abrahams, A. G. Leslie, R. Lutter, and J. E. Walker, *Nature* 370, 621 (1994).
54. T. M. Duncan, V. V. Bulygin, Y. Zhou, M. L. Hutcheon, and R. L. Cross, *Proc. Natl. Acad. Sci. USA* 92, 10964 (1995).
55. D. Sabbert, S. Engelbrecht, and W. Junge, *Nature* 381, 623 (1996).
56. H. Noji, R. Yasuda, M. Yoshida, and K. Kinoshita, Jr., *Nature* 386, 299 (1997).
57. R. K. Soong, H. P. Neves, and J. J. Schmidt, *Biomed. Micro.* 3, 71 (2001).
58. R. K. Soong, G. D. Bachand, H. P. Neves, A. G. Olkhovets, H. G. Craighead, and C. D. Montemagno, *Science* 290, 1555 (2000).
59. C. D. Montemagno, *Nanotechnology* 10 (1999).
60. C. M. Niemeyer, M. Adler, S. Gao, and L. Chi, *Angew. Chem. Int. Ed. Engl.* 39, 3055 (2000).
61. C. M. Niemeyer, J. Koehler, and C. Wuerdemann, *ChemBiochem.* 3, 242 (2002).
62. C. M. Niemeyer, L. Boldt, B. Ceyhan, and D. Blohm, *Anal. Biochem.* 268, 54 (1999).
63. M. J. Heller, *Annu. Rev. Biomed. Eng.* 4, 129 (2002).
64. S. S. Smith, L. Niu, D. J. Baker, J. A. Wendel, S. E. Kane, and D. S. Joy, *Miami Biotechnol. Short Rep.* 8, 13 (1997).
65. S. S. Smith, *Nano Letters* 1, 51 (2001).
66. J. A. Wendel and S. S. Smith, *Nanotechnology* 9, 297 (1998).

67. A. Laayoun and S. S. Smith, *Nucleic Acids Res.* 23, 1584 (1995).
68. S. Klimasauskas, S. Kumar, R. J. Roberts, and X. Cheng, *Cell* 76, 357 (1994).
69. S. S. Smith, *Nanotechnology* 13, 413 (2002).
70. N. C. Seeman, *DNA Cell Biol.* 10, 475 (1991).
71. N. C. Seeman, *Annu. Rev. Biophys. Biomol. Struct.* 27, 225 (1998).
72. T. M. Bryan, J. M. Sperger, K. B. Chapman, and T. R. Cech, *Proc. Natl. Acad. Sci. USA* 95, 8479 (1998).
73. K. G. Murti and D. M. Prescott, *Chromosome Res.* 10, 165 (2002).
74. K. T. Etheridge, S. S. Banik, B. N. Armbruster, Y. Zhu, R. M. Terns, M. P. Terns, and C. M. Counter, *J. Biol. Chem.* 277, 24764 (2002).
75. J. S. Andersen, C. E. Lyon, A. H. Fox, A. K. Leung, Y. W. Lam, H. Steen, M. Mann, and A. I. Lamond, *Curr. Biol.* 12, 1 (2002).
76. A. F. Cockburn, W. C. Taylor, and R. A. Firtel, *Chromosoma* 70, 19 (1978).
77. V. M. Vogt and R. Braun, *J. Mol. Biol.* 106, 567 (1976).
78. S. Johansen, T. Johansen, and F. Haugli, *Curr. Genet.* 22, 305 (1992).
79. S. Ohno, *Semin. Cell Dev. Biol.* 10, 517 (1999).
80. R. J. Feitas, "Nanomedicine: Basic Capabilities." Landes Bioscience, Georgetown, 1999.
81. S. J. Sowerby, N. G. Holm, and G. B. Petersen, *Biosystems* 61, 69 (2001).
82. C. M. Niemeyer, B. Ceyhan, S. Gao, L. Chi, S. Peschel, and U. Simon, *Colloid Polym. Sci.* 279, 68 (2001).

# One-Dimensional Metal Oxide Nanostructures

Lionel Vayssieres, Arumugam Manthiram

University of Texas at Austin, Austin, Texas, USA

## CONTENTS

1. Introduction
  2. Synthesis Techniques
  3. 1D Metal Oxide Nanostructures
  4. Conclusions
- Glossary  
References

## 1. INTRODUCTION

Within the last decade, nanoscience and nanotechnology [1–7] have reached the status of leading sciences with fundamental and applied research in all basic physical, life, and earth sciences as well as engineering and materials science [8–17]. An important feature of nanoscience is that it bridges the crucial dimensional gap between the atomic and molecular scale of fundamental sciences and the microstructural scale of engineering and manufacturing [18]. Accordingly, a vast amount of true multidisciplinary fundamental knowledge is to be explored and linked [19, 20]. It shall lead to a tremendous amount of in-depth understanding as well as to the fabrication of novel high technological devices in many fields of applications from electronics to medicine [21–24]. Therefore, it should improve tremendously the level of technological advance to a much greater rate than human history has ever experienced. As a result, the technological, educational, and societal implications [25] of nanoscience and nanotechnology are of immense importance, which are attested to by the tremendous interests, the major economic efforts, and the national initiatives of many countries around the world.

At the end of the 20th century, most efforts were dedicated to develop synthesis and characterization techniques to produce and probe smaller and smaller nanoparticles. Such studies were rewarded by the generation of a new class of materials called quantum dots [26] that are characterized by zero dimensionality (0D). Such materials have revealed fascinating size-induced physical and chemical properties

due to quantum confinements and very high surface-to-volume ratio [27–33].

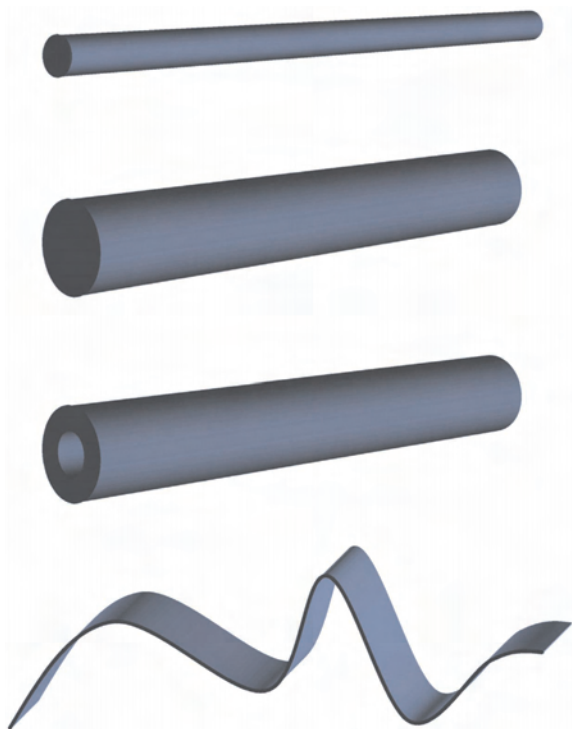
One-dimensional (1D) nanostructures, a new class of low dimensional nanomaterials, have emerged recently. These maintain one of their dimensions in the nanometer range, but with a much larger length scale, ranging from hundreds of nanometers to hundreds of microns and up to millimeters in certain cases [34–37]. Such dimensionality can give aspect ratios (length over diameter) of several thousands: for example, 10,000 for a 1D object of 10 nm in diameter and 0.1 mm in length. With no specific nomenclature, the shortest 1D nanomaterials are often called *nanorods* and the longest are called *nanowires* regardless of their diameter. Also, many straightforward names have been used to describe their morphology and appearance based on their microscale analogs. One may find them in the literature as *quantum wires*, *nanofibers*, *nanopillars*, *nanocables*, and *nanolines*. They are also referred to as *nanowhiskers* by analogy to their micrometer counterpart [38–57]. However, these names are essentially similar and all of them refer to 1D anisotropic nanoscale objects of circular cross-section. For the sake of clarity, *nanorod* will be used in this chapter for 1D anisotropic objects with length below 1 mm and *nanowire* will be used for length exceeding such dimension. Their diameter ranges from several nanometers to several hundreds of nanometers.

Such 1D objects can also be produced with a hollow interior and are referred to as *nanotubes* regardless of their length, inner, or outer diameters. Such porous anisotropic nanostructures show very large specific surface areas.

Very recently, a new class of 1D building blocks has been reported. Such novel objects are called *nanobelts* and *nanoribbons*. Compared with nanowires and nanotubes, they have extended length (up to millimeter scale) and exhibit a rectangular cross-section.

A schematic representation of 1D nanostructures is displayed in Figure 1.

The basic goals have been to develop synthetic techniques to produce a large quantity of 1D building blocks in a controllable and fashionable way. The crucial challenge remaining for scientists and engineers is to develop



**Figure 1.** Schematic representation of 1D nanostructures. From top to bottom: nanowire, nanorod, nanotube, and nanobelt/nanoribbon.

the ability and competence to hierarchically order, connect, and integrate nanowires, nanotubes, and nanobelts in functional networks, thin film coatings, and three-dimensional (3D) arrays to generate and manufacture practical nanodevices. These future devices based on such building blocks should revolutionize materials science and engineering given that they possess the unique properties of nanoscale as well as the ability to connect the nanoworld to the microworld. Along with metal oxides, several classes of materials have already been produced as 1D nanostructures [58] such as metals (Ag, Al, Au, Bi, Co, Cu, Fe, Na, Ni, Pb, Pd, W, Zn, and Zr), semimetals (B,  $\text{MgB}_2$ ,  $\text{C}_{60}$ ,  $\text{C}_{70}$ , Ge, Se, Si, and Te), chalcogenides ( $\text{Ag}_2\text{Se}$ ,  $\text{CdSe}$ ,  $\text{CuInSe}$ ,  $\text{NiSe}_2$ ,  $\text{MoSe}$ ,  $\text{PbSe}$ ,  $\text{Sb}_2\text{Se}_3$ ,  $\text{Ag}_2\text{Te}$ ,  $\text{Bi}_2\text{Te}_3$ ,  $\text{CoTe}_2$ ,  $\text{FeTe}_2$ ,  $\text{ZnTe}$ ,  $\text{Bi}_2\text{S}_3$ ,  $\text{CdS}$ ,  $\text{CuInS}$ ,  $\text{AgInS}_2$ ,  $\text{Cu}_2\text{S}$ ,  $\text{PbS}$ ,  $\text{PbSnS}_3$ ,  $\text{Cu}_3\text{SnS}_4$ ,  $\text{WS}_2$ , and  $\text{ZnS}$ ), nitrides ( $\text{AlN}$ ,  $\text{BN}$ ,  $\text{GaN}$ ,  $\text{InN}$ ,  $\text{Si}_3\text{N}_4$ , and  $\text{Ge}_3\text{N}_4$ ), carbides ( $\text{AlC}$ ,  $\text{BC}$ ,  $\text{Fe}_3\text{C}$ ,  $\text{NbC}$ ,  $\text{SiC}$ , and  $\text{TiC}$ ), phosphides ( $\text{GaAsP}$ ,  $\text{InAsP}$ ,  $\text{GaP}$ ,  $\text{InP}$ , and  $\text{Sn}_4\text{P}_3$ ), and arsenides ( $\text{GaAs}$ , and  $\text{InAs}$ ).

This chapter will focus exclusively on metal oxide compounds, which are the most common, most diverse, and richest class of materials in terms of electronic structure and physical, chemical, and structural properties. Such properties include, for instance, optical, optoelectronic, magnetic, electrical, thermal, photoelectrochemical, photovoltaic, mechanical, and catalytic ones. As a result, numerous applications of metal oxides such as ceramics, (chemical, gas, and bio-)sensors, actuators, lasers, waveguides, infrared and solar absorbers, pigments, photodetectors, optical switches, photochromics, refractories, electrochromics, (electro- and photo-)catalysts, and support for catalysts, insulators, semiconductors, superconductors, supercapacitors, transistors,

varistors, resonators, dielectrics, piezoelectrics, pyroelectrics, ferroelectrics, magnets, transducers, thermistors, thermoelectrics, protective and anticorrosion coatings, fuel cells, alkaline and lithium batteries, and solar cells have been developed.

The diversity of such applications originates from the more complex crystal and electronic structures of metal oxides compared with these of other classes of materials. The main reasons are related to their variety of oxidation states, coordination number, symmetry, ligand-field stabilization, density, stoichiometry, and acid-base properties, which yield fascinating compounds exhibiting insulating, semiconducting, conducting, or magnetic behaviors with transitions among those states.

The combinations of such a variety of distinctive properties and applications with the unique effects of low dimensionality at nanoscale make the development of 1D metal oxide nanostructures an important challenge from both fundamental and industrial standpoints. The synthesis techniques leading to the formation of rational 3D assemblies of 1D metal oxide nanostructures as well as their achievements will be presented in this chapter.

## 2. SYNTHESIS TECHNIQUES

The general deposition of metal oxides onto substrates and the fabrication of coatings such as dense thin films or nano-to microparticulate thin films have been mastered for several decades and a plethora of physical and chemical processing techniques is available. Techniques such as molecular beam epitaxy (MBE) [59–125], oxygen–plasma assisted MBE [126], ion beam-assisted deposition (IBAD) [127], electron beam evaporation [128], laser-assisted catalytic growth [129], laser photolysis [130], pulsed laser deposition (PLD) [131–191], thermal evaporation [192], metal organic vapor phase epitaxy (MOVPE) [193], vapor–liquid–solid (VLS) catalytic growth [191–197], spray pyrolysis [198, 199], chemical vapor deposition (CVD) [200, 201], radiofrequency magnetron sputtering [202–204], liquid phase deposition (LPD) [205, 206], spin coating [207], dip coating [208], electrodeposition [209, 210], electrostatic self-assembly [211], and Langmuir–Blodgett (LB) [212–222] techniques are the most utilized by scientists and engineers.

Although many thin film processing techniques are available, there are very few methods that can generate ordered and oriented anisotropic 1D metal oxide nanostructures onto various substrates in a controllable way. Such techniques can be divided in two major categories: the gas phase and the (wet) chemical methods.

### 2.1. Gas Phase Methods

#### 2.1.1. Chemical Vapor Deposition

The process of CVD involves a gas-phase chemical reaction that generates a thin solid film onto a substrate [200, 201, 223–226]. Vapors of the precursors are transported via a carrier gas onto a heated substrate (500–1000 °C) where they condense and form a thin film. Such substrates can be single crystalline and induce the oriented growth of the thin

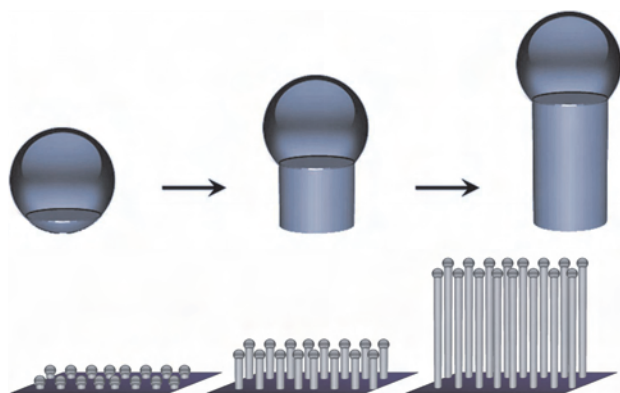
film onto the substrate by epitaxy, which is called epitaxial CVD. When such precursors are alkoxides or metallo-organics (MO), the technique is referred to as MOCVD.

### 2.1.2. Thermal Oxidation Methods

Thermal oxidation is a simple gas-phase method to produce metal oxides onto substrates [227–229]. The synthesis involves the high temperature annealing of a metal sheet in the presence of oxygen at ambient or higher pressures. It has used successfully to generate oriented crystalline metal oxide nanowires from various metal substrates despite its apparent simplicity. The formation of anisotropic features is attributed to the relaxation of thermal expansion mismatch stresses between substrates and thin films [230]. Indeed, the oxidation of various metals produces metal oxides with anisotropic crystal structure and such anisotropy promotes oxygen diffusion along specific crystallographic planes. A large volume change is induced, which leads to large compressive stresses that are relaxed by the formation of anisotropic features (i.e., hillocks).

### 2.1.3. Vapor–Liquid–Solid Processes

The VLS technique [35, 129] was developed several decades ago for the growth of single crystalline whiskers [194–196], which are the microscale equivalent of nanowires and nanorods. The mechanism involved three steps: alloying, nucleation, and axial growth (Fig. 2). The anisotropic crystal growth is promoted by the presence of a liquid alloy/solid interface. By supplying vapors of the metal at high temperature and in presence of oxygen, the alloy reaches supersaturation and consequently nucleation of the metal oxide occurs followed by the anisotropic growth of the nanowire. If such a process is carried out in presence of a substrate, large arrays of highly oriented nanowires are obtained onto the substrates. To achieve better control of the alignment and orientation of the nanowires, epitaxial VLS (VLSE) can be utilized to produce the epitaxial growth of 3D arrays of well-aligned nanowires onto selected substrates [196].



**Figure 2.** Schematic representation of the major steps (alloying, nucleation, and growth) involved in the vapor–liquid–solid (VLS) catalytic growth of 1D nanowires (top) and 3D nanowire arrays (bottom).

## 2.2. Wet Chemical Methods

Solution chemistry-based and wet chemical techniques represent the most economical and simplest techniques to produce 3D arrays on a large scale. They will contribute significantly to the manufacturing of raw nanostructures and play a large part in the fabrication of practical nanodevices. Such methods are template-based synthesis, electrodeposition techniques, and aqueous chemical growth.

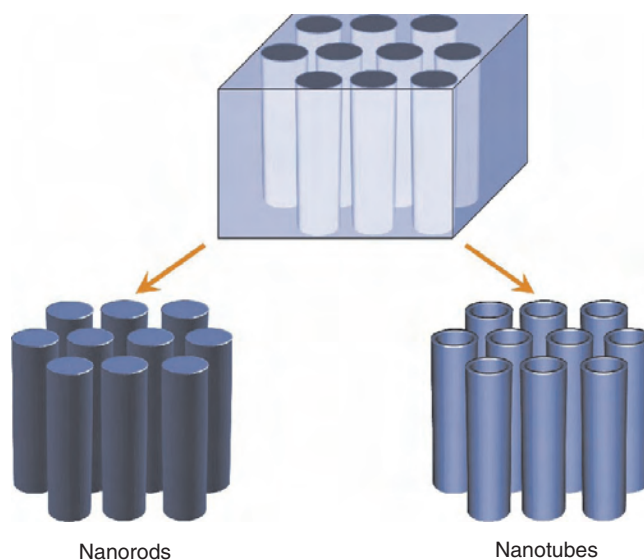
### 2.2.1. Membrane and Template Syntheses

The most common process to produce oriented anisotropic metal oxide materials (i.e., nanorod and nanotube) is the so-called *template-based synthesis* [231–233].

This method consists of growing materials within the cylindrical pore (template) of a membrane. Subsequently, the membrane is removed either by thermal decomposition or by chemical dissolution in concentrated basic solutions, yielding ordered arrays of 1D nanomaterials (Fig. 3). There are two types of available membranes: polymeric *track-etch* and *porous aluminum oxide membranes*. In addition, any porous nanostructure can also be used as a template.

**Track-Etch Membrane** The track-etch membranes are formed by bombardment of  $\alpha$  particles on nonporous targets such as polycarbonate, polyester, mica, or silica glass [234]. The result is a membrane with randomly distributed *tracks* that are subsequently chemically *etched* to form a random array of uniform pores. The size of the pores is within the range of 10 nm to 1  $\mu\text{m}$  with a typical maximum pore density of  $10^9 \text{ cm}^{-2}$ . The available thickness range is 6–20  $\mu\text{m}$ . Such membranes are commercially available from Cyclopore, Millipore, Nucleopore, Osmonics, and Poretics as filtration membranes.

**Anodic Aluminum Oxide Membrane** Porous alumina membranes are obtained by anodic oxidation (anodization) of aluminum sheets in acidic medium such as sulfuric, oxalic,



**Figure 3.** Schematic representation of the major steps involved in the fabrication of 3D arrays consisting of 1D nanostructures by the template-based synthesis method.

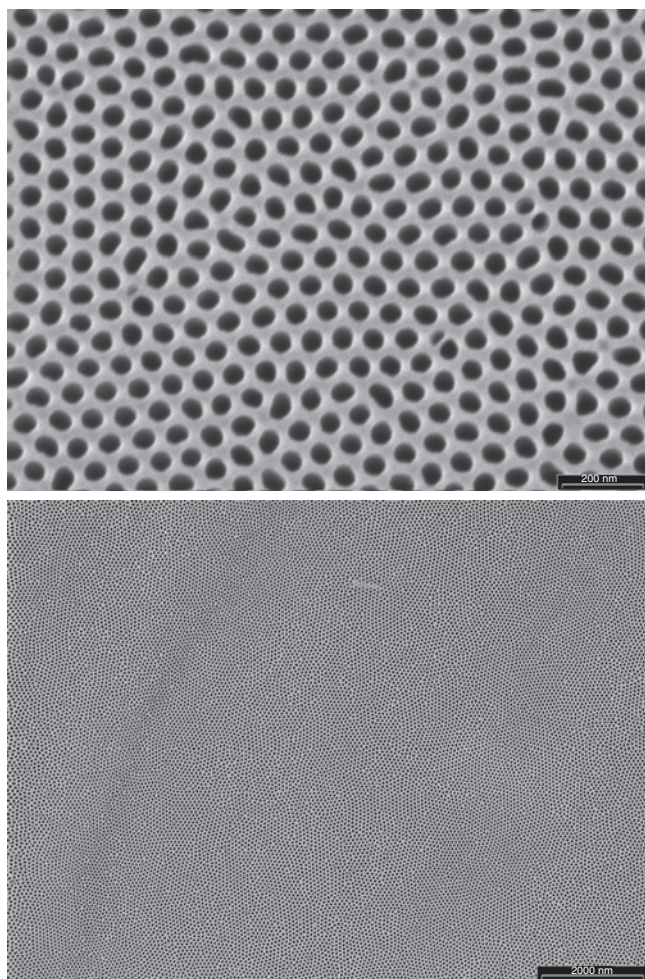


or phosphoric acid. The membranes consist of cylindrical pores of uniform diameter organized as hexagonal array with a porosity of 25–65% (Fig. 4). The dimension of the cylindrical pores is tunable from 4 to several hundred nanometers with a typical pore density of  $10^9$  to  $10^{11}$   $\text{cm}^{-2}$ . The available thickness range is 10 to 100  $\mu\text{m}$ . Such membranes are easily fabricated and commercially available from Whatman Anapore and Anotech.

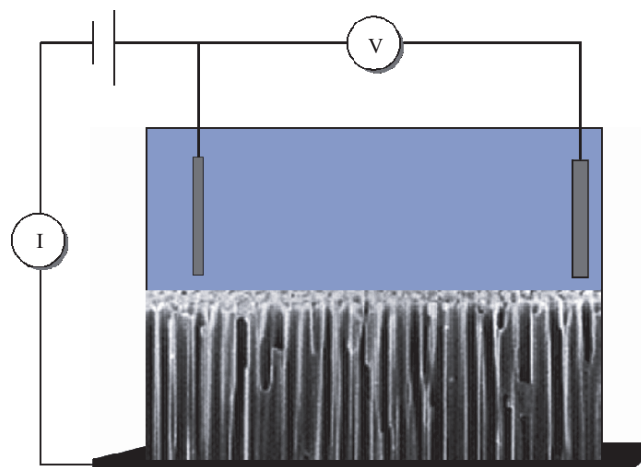
**Other Templates** Theoretically, any nanostructure could act as a template for the growth of another nanostructure. Therefore, several types of nanostructured materials have been utilized for such purposes. The most frequently used alternative nanostructure template is the carbon nanotube [235].

The synthesis paths to elaborate materials within the templates can be summarized into two categories: electrochemical deposition and chemical deposition. The former [236] involves coating one side of the membrane with a conductive material and subsequently applying a potential between the membrane and a solution consisting of metal salts or complexes (Fig. 5).

Chemical depositions involve the use of a membrane as a chemical reactor in which the reaction is performed.



**Figure 4.** Scanning electron microscopy (SEM) photographs of a typical alumina membrane obtained by anodization of aluminum sheets.



**Figure 5.** Schematic representation of the experimental set-up involved in the fabrication of 3D arrays consisting of 1D nanostructures by template-assisted electrodeposition.

In most cases, the sol–gel synthesis method is carried out within the pores of the membranes. A subsequent dissolution of the membrane is performed to release the structure. Heat treatments usually follow to assure the formation of stoichiometric oxides.

### 2.2.2. Electrodeposition

Electrodeposition [237–266] is another simple and efficient synthesis method to produce metal oxide thin films with a certain degree of orientation. There are two different generic processes of electrodeposition yielding the formation of thin films on an electrode (cathode): the electrophoretic and electrolytic depositions.

**Electrophoretic Deposition** Electrophoretic deposition is a process in which charged nanoparticles (in kinetically stable dispersions) migrate and accumulate onto the surface of an electrode under the influence of an applied electric field in a liquid medium at room temperature. No redox reaction happens at the electrode surface, and the oxide nanoparticles are deposited onto the surface at a rate of 1 to 1000  $\mu\text{m}/\text{min}$ . The deposition rate depends on the applied electric field, suspension concentration, and electrophoretic mobility of the nanoparticles. The liquid media are usually organic solvents with low conductivity rather than water because the latter could easily evolve oxygen and hydrogen gases under the influence of an applied potential. Film thicknesses of 1 to  $10^3$   $\mu\text{m}$  are commonly achieved and depend directly on the voltage, current density, and deposition time. The uniformity of the films depends on the size of the particle and the electric field.

**Electrolytic Deposition** Electrolytic deposition is a process that produces metal oxide or hydroxide thin films from the hydrolysis–condensation of metal ions or complexes in solution by a redox reaction at the electrode that is the electrogeneration of a base from water. Nanoparticles of oxides nucleate at the interface at a rate of  $10^{-3}$  to 1  $\mu\text{m}/\text{min}$ . Such a process is governed by Faraday’s law, which means that the amount of material deposited is monitored by the deposition time and current density. The liquid medium is usually

a mixing of water and organic solvent with high conductivity. Film thicknesses of  $10^{-3}$  to  $10\ \mu\text{m}$  are commonly achieved. The uniformity of the films is excellent due to the use of molecular scale species.

**Epitaxial Electrodeposition** A more advanced electrodeposition technique is the *epitaxial electrodeposition* [267–276] in which thin films are deposited in epitaxy onto a substrate; that is, the crystal structure and crystallographic lattice parameters of the substrate induce a crystal orientation of the thin film. This method has the ability to produce metal oxide nanoparticulate thin films with fairly large area, and many devices have been developed by such techniques.

### 2.2.3. Aqueous Chemical Growth

This novel technique has emerged recently as a simple and powerful tool to fabricate, at low cost and mild temperatures, large areas of metal oxide nano- to microparticulate thin films [277]. 3D arrays consisting of oriented anisotropic nanoparticles are easily generated with enhanced control over orientations and dimensions. The synthesis involves the controlled heteronucleation of metal oxides onto substrates from the hydrolysis–condensation of metal salts in aqueous solutions. The most pertinent parameter to control the nucleation and growth and therefore the overall design and architecture of a thin film is the interfacial free energy of the system [278].

**Theoretical Concepts** The main idea here is to play on the thermodynamics and kinetics of nucleation, growth, and aging of the systems by controlling experimentally their interfacial tension [279]. The ability to segregate the nucleation and the growth stage enables control of the monodispersity of the system. Indeed, performing the aqueous precipitation far from the typical point of zero charge (PZC) of the metal oxide allows enhanced control of the nucleation, growth, and aging processes. According to the well-known acid–base surface properties of metal oxides, decreasing (or increasing) the pH of precipitation from the PZC will increase the surface charge density by adsorption of protons (or hydroxyl ions) and consequently reduce the interfacial tension of the system. In addition, a high ionic strength will also increase the surface charge density by screening the electrostatic repulsion at the interface, allowing more surface sites to develop a charge. The surface charge may therefore reach its maximum, which is directly related to the composition and structure of surface oxygen. This will contribute to a further lowering of the interfacial tension of the system. From then on, thermodynamic colloidal stability may thus be reached, resulting in a considerable lowering of the secondary aging processes and henceforth maintaining constant the size and shape of the nanoparticles as well as avoiding crystal phase (and morphological) transformations. By careful consideration of the parameters involved in the nucleation and growth processes, the free enthalpy of nucleation shows a maximum as a function of the particle size, which depends on the interfacial tension at the cubic power. Therefore, reducing the interfacial tension leads to an important lowering of the nucleation energy barrier, leading to the reduction of the particle size and its distribution [280].

The experimental verification on the aqueous precipitation of spinel iron oxide (i.e., magnetite  $\text{Fe}_3\text{O}_4$ ) at room temperature [281] has clearly illustrated that the thermodynamic stability of metal oxide nanoparticles does exist. It also demonstrated that the average particle size may experimentally be monitored and empirically predicted over an order of magnitude in the nanometer range with narrow size distribution. The excellent agreement between theory and experiments has yielded strong evidence for efficient growth control of metal oxide nanoparticles under low interfacial tension conditions; it has also produced great expectations for future development of nanomaterials devices and the optimization of their physical properties. Moreover, when the thermodynamic stabilization is achieved, not only is the size tailored but also the shape as well as the crystallographic structure may be controlled. For instance, at low interfacial tension, the particle shape does not need to be spherical; indeed, very often nanoparticles are spherical to minimize the surface energy because the sphere represents the smallest surface for a given volume. However, if the synthesis or dispersion condition is suitable (i.e., yielding to the thermodynamic stabilization of the system), the shape of the crystallites will be driven by the symmetry of the crystal structure and an anisotropy may therefore be developed. Manipulating and controlling the interfacial tension enables one to grow nanoparticles with various sizes and shapes. Applying the appropriate solution chemistry (precipitation and dispersion media) to transition metal ions along with the natural crystal symmetry and anisotropy or forcing the material to grow along a certain crystal direction by controlling chemically the thermodynamics and kinetics of nucleation, growth, and aging phenomena, one can reach the ability to develop novel crystal morphologies. In addition to particle size and shape control, precipitating nanoparticles at “zero” interfacial tension allows stabilization of metastable crystal phases.

Crystal phase transition in solution usually operates through a dissolution–re-crystallisation process to minimize the surface energy of the system. Indeed, when a solid offers several allotropic phases, it is generally the one with the highest solubility and consequently the lowest stability (i.e., the crystallographic metastable phase that precipitates first). This is understood by considering the nucleation kinetics of the solid. At a given supersaturation ratio, the germ size is as small and the nucleation speed as fast as the interfacial tension of the system is low. Thus, because the solubility is inversely proportional to the interfacial tension, the precipitation of the most soluble phases and consequently the thermodynamically less stable phases is therefore kinetically promoted. Indeed, due to its solubility and metastability, this particular phase is more sensitive to secondary growth and aging that lead to crystallographically more stable phases essentially by heteronucleation. This is typically the case for aluminum hydroxide (boehmite to bayerite or gibbsite), titanium dioxide (anatase to rutile), and ferric oxyhydroxides (goethite, akaganeite, and lepidocrocite to hematite). Usually, the growth and aging processes are delicate to control and the phase transformation appears within a few hours to a few days in solution, resulting in an undesired mixing of various allotropic phases. However, by careful consideration of the precipitation conditions, such a phenomenon might

be avoided when systems are precipitated at low interfacial tension [278].

In summary, by adjusting the experimental conditions to obtain the thermodynamic stability conditions, the particle size, shape, and crystal structure may be tuned and optimized and shape anisotropy may be generated and/or maintained.

**Thin-Film Processing** By applying the above-mentioned thermodynamic concepts to the thin film processing technology, an inexpensive and effective aqueous growth technique at mild temperatures has been developed to produce functionalized coating of metal oxide materials onto various substrates [282]. Such a technique allows generation of advanced nano/microparticulate thin films without any template, membrane, surfactant, or specific requirements in substrate activation, thermal stability, or crystallinity. Given that the crystallites grow from the substrate, a large choice of thin film/substrate combinations is offered, which provides consequently better flexibility and a higher degree of materials engineering and design. To understand the possibility of growing nano- and microparticulate thin films from aqueous solution as well as the ability to grow and align anisotropic nanoparticles into large arrays on a substrate, one has to take into account the differences between homogeneous and heterogeneous nucleation phenomena. In most cases, homogeneous nucleation of solid phases from solution requires a higher activation energy barrier and therefore heteronucleation will be promoted and energetically more favorable. Indeed, the interfacial energy between two solids is usually smaller than the interfacial energy between a solid and a solution, and therefore nucleation may take place at a lower saturation ratio onto a substrate than in solution. Nuclei will appear onto the substrate and various morphologies and orientations can be reached depending on the chemical composition of the medium.

For instance, if the nucleation rate is controlled and the number of nuclei is limited by the precipitation conditions, the growth will take place according to the crystal symmetry and relative face velocities along the favorable direction of crystallization. A condensed phase of anisotropic single-crystalline nanorods parallel to each other and perpendicular to the substrate will be generated. However, if the number of nuclei is further limited and if the crystal symmetry allows it, the system will promote twinning. The preferential growth of the rods along the favorable axis from the same nuclei will induce a star-shape (or flower-shape) morphology. Finally, if the rate is enhanced by the precipitation conditions, the fast appearance of a large number of nuclei will result in 2D growth, promoting therefore, the formation of the anisotropic nanoparticles with a parallel orientation with respect to the substrate.

The ability to design materials with different orientations stimulates the study of the influence of such parameters on the physical properties of materials and gives further opportunities for materials design.

The aqueous chemical growth method consists of heating an aqueous solution of metal salts (or complexes) in the presence of a substrate at moderated temperatures (below 100 °C) in a closed vessel. Therefore, such technique does not require high-pressure containers and is also

entirely recyclable, safe, and environment friendly because only water is used as solvent. Such a process avoids the safety hazards of organic solvents and their eventual evaporation and potential toxicity. In addition, because no organic solvents or surfactants are present, the purity of the materials is substantially improved. The residual salts are easily washed out by water due to their high solubility. In most cases, no additional heat or chemical treatments are necessary, which represents a significant improvement compared with surfactant-, template-, or membrane-based synthesis methods.

Full coverage of the substrate is obtained within a few hours provided that the heat capacity of water and surface coverage control are achieved by monitoring the synthesis time in the early stages of the thin film growth. Partial coverage is obtained within the first hours, which may be necessary for certain applications to adjust and tune the overall physical properties of devices (e.g., optical properties of multi-bandgap thin films). Such a technique is a multi-deposition technique and the growth of layer-by-layer of thin films is readily obtainable. The development of multilayer thin films of various morphologies and/or of various chemical compositions, that is, composite, multi-bandgap, and doped thin films, is reached. The complete thin film architecture may thus be modeled, designed, and monitored to match the application requirements. In most cases, it should improve the physical and chemical properties of the devices. It also gives the capacity to create novel and/or improved thin film integrated devices. Growing thin layers directly from the substrate does substantially improve the adherence and the mechanical stability of the thin film compared with the standard solution and colloidal deposition techniques such as spin and dip coating, chemical bathing, screen printing, or doctor blading. Moreover, given that such materials do precipitate in homogeneous solution from molecular scale compounds (i.e., condensed metal complex), they will grow on virtually any substrate. It goes without saying that the overall mechanical stability of the thin films does vary from substrate to substrate, but in most cases, strong adhesion is observed. Scale-up is potentially easily feasible, and this concept and synthesis method are theoretically applicable to all water-soluble metal ions likely to precipitate in solution. Large-scale manufacturing at low cost is therefore achievable with such a technique. In addition to all these industrial related advantages, such a technique is also potentially very interesting due to the compatibility of water and aqueous solution to biological compounds. For instance, 3D arrays of composite bionanomaterials have been obtained using the aqueous chemical growth. Such concepts and thin film processing technique have been applied successfully to basic oxides and oxyhydroxides of transition metals [283–289] (Figs. 6, 7, and 8).

### 3. 1D METAL OXIDE NANOSTRUCTURES

One-dimensional metal oxide nanostructures such as nanorods, nanowires, and nanotubes are defined by their aspect ratio, which is essentially the ratio of the (outer) diameter to their length (Fig. 9).

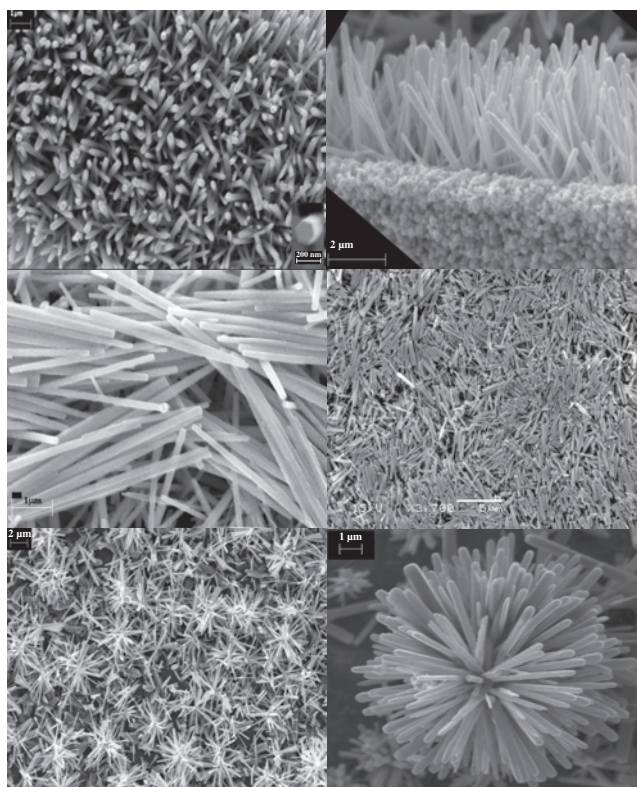
**Nanorods and Nanowires** A literature survey of the synthesis and investigations of nanorods and nanowires of metal oxides, hydroxides, and oxyhydroxides is given below (sorted by alphabetic order of chemical formula):

- Aluminum  
 $\alpha$ -Al<sub>2</sub>O<sub>3</sub> [290–292],  $\gamma$ -AlOOH, and  $\gamma$ -Al<sub>2</sub>O<sub>3</sub> [293]
- Boron  
Al<sub>18</sub>B<sub>9</sub>O<sub>33</sub> and MgB<sub>4</sub>O<sub>7</sub> [294]
- Cadmium  
CdO [295–297]
- Cobalt  
CoO [298] and Co<sub>3</sub>O<sub>4</sub> [299]
- Chromium  
 $\alpha$ -Cr<sub>2</sub>O<sub>3</sub> [300] and BaCrO<sub>4</sub> [301]
- Copper  
CuO [302–305], Cu(OH)<sub>2</sub> [306], Cu<sub>2</sub>O [303, 307, 308], GdBa<sub>2</sub>Cu<sub>3</sub>O<sub>6.5</sub> [309], and YBaCu<sub>3</sub>O<sub>7</sub> [310]
- Europium  
Eu<sub>2</sub>O<sub>3</sub> [311]
- Iron  
 $\alpha$ -FeOOH [312, 313],  $\beta$ -FeOOH [285],  $\alpha$ -Fe<sub>2</sub>O<sub>3</sub> [314, 315], and Fe<sub>3</sub>O<sub>4</sub> [316]
- Gallium  
 $\beta$ -Ga<sub>2</sub>O<sub>3</sub> [317–329]
- Germanium  
GeO<sub>2</sub> [330–332]
- Indium  
In<sub>2</sub>O<sub>3</sub> [296, 333–341] and SnIn<sub>2</sub>O<sub>3</sub> [342]
- Iridium  
IrO<sub>2</sub> [343]
- Lanthanum  
La(OH)<sub>3</sub> [344]
- Magnesium  
MgO [345–351] and Mg(OH)<sub>2</sub> [349, 352]
- Manganese  
 $\gamma$ -MnOOH [353],  $\alpha$ - and  $\beta$ -MnO<sub>2</sub> [354],  $\delta$ -MnO<sub>2</sub> [355], LaBaMnO<sub>3</sub> [356], LaCaMnO<sub>3</sub> [357], LaSrMnO<sub>3</sub> [358], and Mn<sub>3</sub>O<sub>4</sub> [359]
- Molybdenum  
MoO<sub>2</sub> [343] and  $\alpha$ -MoO<sub>3</sub> [343, 360–362]
- Nickel  
NiO [363, 364] and  $\alpha$ -Ni(OH)<sub>2</sub> [365]
- Lead  
PbO<sub>2</sub> [296, 338, 339]
- Ruthenium  
RuO<sub>2</sub> [343, 366]
- Antimony  
Sb<sub>2</sub>O<sub>3</sub> [367], Sb<sub>2</sub>O<sub>4</sub> [368], and Sb<sub>2</sub>O<sub>5</sub> [343, 367]
- Silicon  
SiO<sub>2</sub> [300, 369–372]
- Tin  
SnO<sub>2</sub> [296, 373–377]
- Tantalum  
NaTaO<sub>3</sub> [378]
- Titanium  
TiO<sub>2</sub> [379–383] and BaTiO<sub>3</sub> [384]
- Vanadium  
VO<sub>2</sub> [385], LiV<sub>2</sub>O<sub>4</sub> [386], and V<sub>2</sub>O<sub>5</sub> [343, 387–389]
- Tungsten  
WO<sub>x</sub> [390], WO<sub>2</sub> [391], WO<sub>3</sub> [343, 391–393], BaWO<sub>4</sub> [394], and CdWO<sub>4</sub> [395, 396]

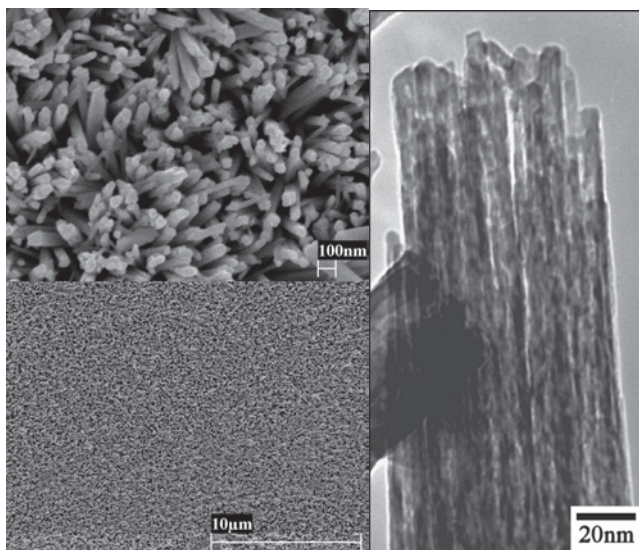
- Zinc  
ZnO [193, 296, 397–415]
- Zirconium  
ZrO<sub>2</sub> [416, 417].

**Nanotubes** Hitherto, one may find in the literature the synthesis and experimental investigations of the following metal oxide nanotubes:  $\alpha$ -Al<sub>2</sub>O<sub>3</sub> [418], CeO<sub>2</sub> [419], Co<sub>3</sub>O<sub>4</sub> [420, 421], Dy(OH)<sub>3</sub> and Dy<sub>2</sub>O<sub>3</sub> [422], Er<sub>2</sub>O<sub>3</sub> [423], Ho<sub>2</sub>O<sub>3</sub> [422], Lu<sub>2</sub>O<sub>3</sub> [423], MgO [424], MoO<sub>3</sub> [343], RuO<sub>2</sub> [343], SiO<sub>2</sub> [336–338, 418, 425], SnO<sub>2</sub> [426], TiO<sub>2</sub> [382, 427–433], H<sub>2</sub>Ti<sub>3</sub>O<sub>7</sub> [434], Tm<sub>2</sub>O<sub>3</sub> [423], VO<sub>x</sub> [435–445], V<sub>2</sub>O<sub>5</sub> [418], Na<sub>2</sub>V<sub>3</sub>O<sub>7</sub> [446], WO<sub>3</sub> [300], Y<sub>2</sub>O<sub>3</sub> [447], Yb<sub>2</sub>O<sub>3</sub> [423], ZnO [448, 449], and ZrO<sub>2</sub> [450].

**Nanobelts and Nanoribbons** The latest class of 1D nanostructures has emerged recently, which consists of ultra-long (up to millimeter) belt-like (or ribbons) nanostructured building blocks and are called nanobelts and nanoribbons. The specificity of such novel 1D nanostructures is that the cross-section is rectangular in contrast to cylindrical for nanowires and nanotubes. So far, nanobelts and nanoribbons of  $\alpha$ -Al<sub>2</sub>O<sub>3</sub> [291], Cu(OH)<sub>2</sub> [451], CdO [296, 410],  $\beta$ -Ga<sub>2</sub>O<sub>3</sub> [296, 327, 410, 452–455], In<sub>2</sub>O<sub>3</sub> [296, 410], NiO [456], Mg<sub>2</sub>Mn<sub>5</sub>O<sub>12</sub> [457], MgO [348, 350, 458–461],  $\alpha$ -MoO<sub>3</sub> [361, 462, 463], SnO [464], SnO<sub>2</sub> [296, 410, 465–472],  $\beta$ -PbO<sub>2</sub> [410, 473], TiO<sub>2</sub> [474], K<sub>2</sub>Ti<sub>8</sub>O<sub>17</sub> [475], WO<sub>3</sub> [392], CdWO<sub>4</sub> [396], and ZnO [296, 404, 406, 410, 470, 471, 476–478] have been successfully synthesized and promising physical properties are currently being investigated.

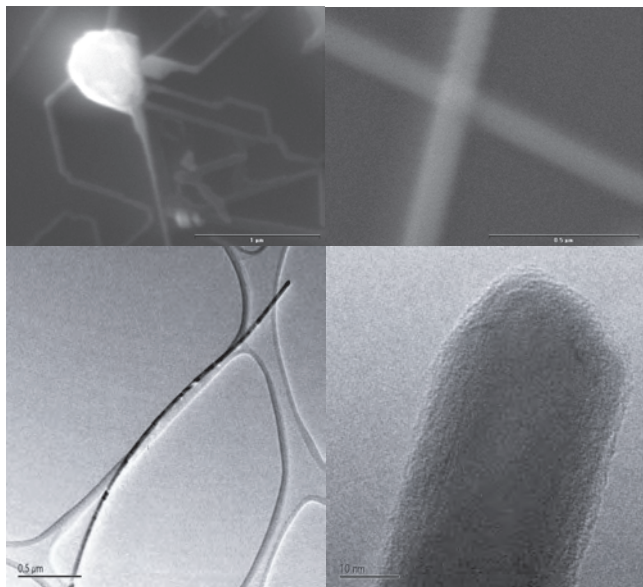


**Figure 6.** Scanning electron microscopy (SEM) photographs of various 3D arrays of ZnO grown by the aqueous chemical growth method.

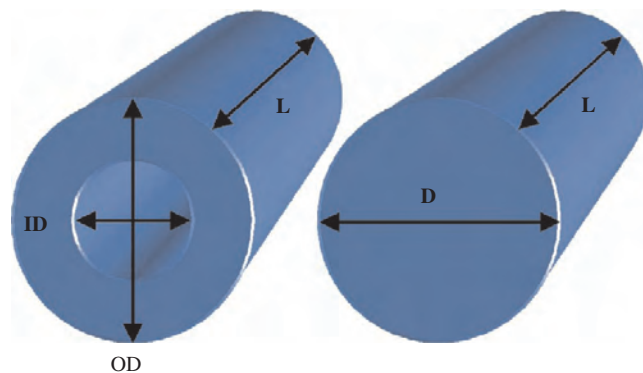


**Figure 7.** Scanning electron microscopy (SEM) photographs of 3D arrays consisting of 1D nanorods  $\alpha\text{-Fe}_2\text{O}_3$  grown by the aqueous chemical growth method. Reprinted with permission from [283], L. Vayssieres, *J. Phys. Chem. B* 107, 2623 (2003). © 2003, American Chemical Society.

A more important challenge in nanowire technology is to develop economical synthesis methods to produce ordered, oriented, and aligned 1D nanostructures onto various substrates. The following section consists of a literature survey of the major achievements of two- and three-dimensional ordering of 1D nanostructures. 2D arrays are developed to probe and optimize collective physical properties, mostly optical (nematic–smectic phases) and magnetic. The goal of generating 3D arrays is to develop practical devices such as chemical, gas, and bio sensors as well as optoelectronic devices such as lasers, photodetectors, optical switches, photovoltaics, and photocatalytic cells.



**Figure 8.** Electron micrographs of 1D nanowires; SEM images of ZnO (top) and TEM images of  $\gamma\text{-MnOOH}$  (bottom) synthesized by the aqueous chemical growth method.



**Figure 9.** Schematic representation of the dimensional characteristics of 1D nanostructures; length ( $L$ ), diameter ( $D$ ), inner diameter ( $ID$ ), and outer diameter ( $OD$ ).

### 3.1. 2D Arrays

Anisotropic nanoparticles and their collective optical and magnetic properties are of fundamental and industrial importance. However, besides a few examples based on spherical metal oxide nanoparticles of CoO [479, 480],  $\gamma\text{-Fe}_2\text{O}_3$  [481],  $\text{CoFe}_2\text{O}_4$  [482],  $\text{Fe}_3\text{O}_4$  [481, 482],  $\text{SiO}_2$  [483, 484], and  $\text{TiO}_2$  [485, 486], reports of two-dimensional ordered arrays in general and of metal oxide 1D nanostructures in particular are very seldom in the literature. The lack of such nanostructure assemblies is most probably due to the limitations in available synthesis techniques. Indeed, basically a couple of generic methods to produce ordered 2D arrays exist: self-assembly by solvent evaporation on substrate [487, 488] and the LB technique. The LB technique is usually utilized to fabricate ultrathin and layer-by-layer thin films and several metal oxide thin films have been produced by such a technique [212–222, 489]. However, only a few ordered 2D arrays of anisotropic nanoparticles of metal oxides have been reported. They involve  $\text{BaCrO}_4$  [490, 491],  $\beta\text{-FeOOH}$  [492],  $\text{TiO}_2$  [485], and  $\text{BaWO}_4$  [493].

### 3.2. 3D Arrays

Besides the low-cost synthesis of well-defined 1D nanostructures, the most crucial challenge is to develop the ability to order and orientate them in functional network and oriented 3D periodic arrays. Although a plethora of synthesis techniques is available to produce metal oxide 1D nanostructures, only a few among them can generate anisotropic and oriented 1D nanomaterials assembled as 3D arrays.

Table 1 summarizes the dimensions, synthesis methods, and type of oriented arrays of 1D nanostructures (nanorods, nanowires, and nanotubes) that have been produced so far. Many 3D arrays of 1D oxides have already been produced with various dimensions, ranging from a few nanometers to several hundreds of nanometers in diameter with length ranging from a few hundred nanometers to several tens of microns. Ordered 3D arrays of porous 1D nanostructures have also been produced with various metal oxides, ranging from basic unary oxides to more complex oxides.  $\text{TiO}_2$  and ZnO are, by far, the most representative 1D nanomaterials produced to date due to their established importance as

**Table 1.** Literature survey of oriented 3D arrays consisting of 1D metal oxide nanostructures (sorted alphabetically by chemical formula and by ascending diameter).

Material	Morphology	Dimension (D * L)	Synthetic Method	Ref.
<i>Monoxide</i>				
CdO	Nanowire	60 nm * few $\mu\text{m}$	Alumina membrane	[494]
CuO		30–100 nm * 15 $\mu\text{m}$	Thermal oxidation	[495]
Cu <sub>2</sub> O		25–45 nm * 3–5 $\mu\text{m}$ 80–100 nm * 10 $\mu\text{m}$	Electrodeposition	[496]
ZnO	Nanorod	15–40 nm * 1 $\mu\text{m}$	Molecular beam epitaxy	[497]
		20 nm * 400 nm	Pulsed laser deposition	[498]
		25 nm * 800 nm	Metallorganic vapor-phase epitaxy	[499]
		45 nm * 200 nm 70 nm * 600 nm	Chemical vapor deposition	[500, 501]
	Nanowire	85–95 nm * 500 nm	Epitaxial electrodeposition	[502]
		55 nm * 2.6 $\mu\text{m}$ 190 nm * 15 $\mu\text{m}$	Metal vapor deposition	[503]
		90 nm * 1 $\mu\text{m}$	Electrodeposition in alumina membrane	[504]
		150–250 nm * 2 $\mu\text{m}$	Electrodeposition	[505]
		100–200 nm several $\mu\text{m}$ in length	Aqueous chemical growth	[405]
		10–200 nm * 2–20 $\mu\text{m}$ 20–120 nm * 5–20 $\mu\text{m}$	Vapor–liquid–solid growth	[506, 507]
		15–90 nm * few $\mu\text{m}$	Alumina membrane	[508]
	200 nm * 50 $\mu\text{m}$	[509]		
	150 nm inner diameter 200 nm outer diameter 60 $\mu\text{m}$ in length	[510]		
Microtube	1 $\mu\text{m}$ inner diameter 2 $\mu\text{m}$ outer diameter 10 $\mu\text{m}$ in length	Aqueous chemical growth	[511]	
<i>Dioxide</i>				
CeO <sub>2</sub>	Nanowire	100 nm * 1 $\mu\text{m}$	Chemical vapor deposition	[512]
LiCoO <sub>2</sub>		100 nm several $\mu\text{m}$ in length	Alumina membrane	[513]
LiNi <sub>0.5</sub> Co <sub>0.5</sub> O <sub>2</sub>				[514]
LiNiO <sub>2</sub>		100 nm * 50 $\mu\text{m}$		[515]
$\alpha$ -MnO <sub>2</sub>		200 nm * 50 $\mu\text{m}$		[516]
LiMnO <sub>2</sub>		100 nm * 50 $\mu\text{m}$		[517]
LiCo <sub>0.5</sub> Mn <sub>0.5</sub> O <sub>2</sub>	Nanorod	100 nm * 500 nm		[518]
PdO <sub>2</sub>	Nanocone	40 nm * 500 nm	Thermal oxidation	[519]
		200 nm * 1.2 $\mu\text{m}$		[520]
SiO <sub>2</sub>	Nanowire	50 nm mm in length	Sol–gel electrophoresis in polycarbonate membrane	[521]
		125–200 nm * 10 $\mu\text{m}$		[522]
	Nanoflower	20–120 * 10–250 $\mu\text{m}$		Catalytic gas–solid reaction
SnO <sub>2</sub>	Nanotube	16–24 nm inner diameter 30 nm outer diameter 6 $\mu\text{m}$ in length	Alumina membrane	[523]
		70 nm several $\mu\text{m}$ in length		[524]

continued

Table 1. Continued.

Material	Morphology	Dimension (D * L)	Synthetic Method	Ref.
<i>Dioxide</i>				
TiO <sub>2</sub>	Nanowire	10–40 nm * 2–10 μm	Electrodeposition in alumina membrane	[525]
		15 nm * 6 μm	Alumina membrane	[526]
	Nanorod	40–50 nm * 140 nm	Photoelectrochemical etching	[527]
	Nanowire	125–200 nm * 10 μm	Sol-gel electrophoresis in polycarbonate membrane	[521]
		200 nm * 2 μm 500 nm * 8 μm	Magnetron sputtering	[528]
		15 nm * 30 μm		[516]
	Nanotube	2.5–5 nm inner diameter 20–40 nm outer diameter 0.3–0.9 μm in length	Alumina membrane	[529]
		200 nm outer diameter 50 μm in length		[516]
		25–60 nm inner diameter 250 nm in length	Anodic oxidation	[530]
		50–70 nm inner diameter 120 nm outer diameter several μm in length	Electrodeposition in polymer-coated alumina membrane	[531]
		170–180 nm inner diameter 200–233 nm outer diameter 3 μm in length		[532]
ZrO <sub>2</sub>		170 nm inner diameter 190 nm outer diameter 50 μm in length	Alumina membrane	[533]
		170 nm inner diameter 280 nm outer diameter several μm in length		[534]
<i>Trioxide</i>				
MoO <sub>3</sub>	Nanotube	20–150 nm inner diameter 50–300 nm outer diameter 5–8 μm in length	Chemical vapor deposition	[535]
WO <sub>3</sub>	Nanowire	200 nm * 50 μm	Alumina membrane	[536]
<i>Sesquioxide</i>				
Al <sub>2</sub> O <sub>3</sub>	Nanorod	5 nm * 860 nm 20–80 nm * 30–200 nm	Anodization	[537]
	Nanotube	10–20 nm inner diameter 40 nm outer diameter 450 nm in length		[538]
		12 nm inner diameter 35 nm outer diameter 650 nm in length		[539]
α-Fe <sub>2</sub> O <sub>3</sub>	Nanorod	5 * 500 nm Bundles of 50 nm	Aqueous chemical growth	[540]
In <sub>2</sub> O <sub>3</sub>	Nanowire	60 nm several μm in length	Electrodeposition in alumina membrane	[541, 542]
	Nanotube	100 nm inner diameter 200 nm outer diameter 50 μm in length	Alumina membrane	[543]
β-Ga <sub>2</sub> O <sub>3</sub>	Nanowire	20–100 nm * 10–100 μm	Microwave plasma	[544]
		60–150 nm several μm in length	Chemical vapor deposition	[545]
	Nanotube	100 nm inner diameter 200 nm outer diameter 50 μm in length	Alumina membrane	[543]

continued

Table 1. Continued.

Material	Morphology	Dimension (D * L)	Synthetic Method	Ref.
<i>Perovskite oxide</i>				
BaTiO <sub>3</sub>	Nanowire	125–200 nm * 10 μm	Sol-gel electrophoresis in polycarbonate membrane	[521]
	Nanotube	200 nm outer diameter 60 μm in length	Alumina membrane	[546]
PbTiO <sub>3</sub>				
PbZr <sub>0.52</sub> Ti <sub>0.48</sub> O <sub>3</sub>	Nanowire	125–200 nm * 10 μm	Sol-gel electrophoresis in polycarbonate membrane	[521]
<i>Spinel oxide</i>				
LiMn <sub>2</sub> O <sub>4</sub>	Nanotube	100 nm inner diameter 200 nm outer diameter several μm in length	Alumina membrane	[547]
				Co <sub>3</sub> O <sub>4</sub>
<i>Pentoxide</i>				
V <sub>2</sub> O <sub>5</sub>	Nanowire	300–600 nm several μm in length	Electrodeposition in polycarbonate membrane	[516]
<i>Miscellaneous</i>				
β-FeOOH	Nanorod	5 nm * 500 nm Bundles of 50 nm	Aqueous chemical growth	[540]
γ-MnOOH	Nanowire	100 nm several μm in length		[353]
La <sub>0.7</sub> Sr <sub>0.3</sub> MnO <sub>3</sub>	Nanorod	100 nm * 500 nm–1.5 μm	Pulsed laser deposition	[548]
La <sub>0.8</sub> Sr <sub>0.2</sub> MnO <sub>3</sub>		25 nm * 70 nm		[549]
Sr <sub>2</sub> Nb <sub>2</sub> O <sub>7</sub>	Nanowire	125–200 nm * 10 μm	Sol-gel electrophoresis in polycarbonate membrane	[521]
VO <sub>x</sub>	Nanotube	5–50 nm inner diameter 15–150 outer diameter 1–15 μm in length	Ligand-assisted template	[550]
		15–45 nm inner diameter 50–100 outer diameter 0.8–3 μm in length		[551]
		20–35 nm inner diameter 70–140 outer diameter 2–12 μm in length		
WO <sub>x</sub>	Nanorod	10–30 nm * 300 nm	Electrochemical etching	[552]
		10–30 nm * 500 nm–1.6 μm	Thermal oxidation	

basic materials for catalysis and large bandgap semiconducting properties.

Many applications of 1D metal oxides are currently under investigation. Because of the very recent development of ordered 3D arrays of oriented 1D nanostructures, only a very few applications have been demonstrated. Most of the research and development have focused on developing new synthesis techniques to order and align 1D nanostructures. However, applications in the field of optoelectronic and photoelectrochemistry have been reported and are briefly presented below.

Room temperature lasing properties have been demonstrated based on highly ordered ZnO nanowires grown by epitaxial VLS (see 2.1.2) on sapphire substrate. Such arrays

consist of perpendicularly oriented nanowires of ZnO of 100 nm in diameter and a few microns in length. Such hexagonal nanowires are well crystalline and faceted and behave as a natural (Fabry–Perot) resonating optical cavity. When pumped by a laser, inversion of electronic population and ultraviolet (UV) lasing action are observed at room temperature and at a much lower threshold compared with conventional lasers [553–557].

Another successful application of oriented nanowire arrays is found in the fields of photoelectrochemistry and energy conversion. For instance, the design of photovoltaic or photocatalytic cells that can, respectively, generate a current or induce a chemical reaction under UV/visible illumination has been achieved. Such photoelectric effects are well



known, and many attempts to produce economical solar cells or to photo-oxidize water with sunlight have been made. Well-aligned single-crystalline nanorods with a typical diameter of 5 nm, self-assembled as bundles of about 50 nm in diameter, grown in fairly perpendicular fashion onto the substrate and arranged in very large uniform arrays have been tested for such purposes. The length of the nanorods, which essentially represents the thickness of the thin film, may be experimentally tailored to any required dimension of up to about 1  $\mu\text{m}$  by varying the time or temperature of aging in solution. For instance, nanorods of 100 nm in length have been produced after 1 h at 100 °C. The aspect ratio is 1 to 20 for the nanorod bundles and 1 to 200 for the individual nanorods. Such quantum-size 1D rods arranged in oriented 3D bundles feature an oriented, direct, grain boundary-free electron pathway. In addition, as the diameter of a single nanorod matches the minority carrier diffusion length, fast electron-hole recombination is prevented, allowing fast generation, transfer, and collection of photogenerated electrons. Accordingly, a high photoefficiency was achieved; more than 50% of the incident photon was converted to electrons at a wavelength of 350 nm [558]. Such materials have also been tested as photocatalytic cells [559] for the photo-oxidation of water [560].

Besides optoelectronics and photoelectrochemistry, sensor technologies [561–574] will also benefit from such ordered arrays of 1D metal oxide nanostructures. Metal oxides are already well established as basic materials for chemical, gas, and bio-sensors and promising improvements in terms of detection threshold limit and sensitivity, selectivity, response time, and temperature of operation could be demonstrated with the use of such nanostructures.

In addition to applications, fundamental knowledge regarding the effects of anisotropy, ordering, and orientation on the physical properties and electronic structure of 1D metal oxides can be developed. A recent study was performed on II–VI semiconductor 3D arrays consisting of oriented ZnO rods. In addition to the strong anisotropic effects that are not observed in the isotropic (spherical) samples, researchers were able to probe and demonstrate the symmetry contribution of oxygen orbitals to the conduction band of ZnO by means of polarization dependent soft X-ray spectroscopy and first principle calculations [575]. Such fundamental knowledge is of great importance for understanding and consequently optimizing the existing optoelectronic devices.

The production of novel 1D nanostructures and their controlled assemblies in 2D and 3D arrays are evolving at such a rapid rate that many physical properties and forthcoming applications as well as fundamental understanding are foreseen with confidence.

#### 4. CONCLUSIONS

As for many new fields and emerging technologies, most of the efforts have been focused on the exploration and development of synthesis techniques and manufacturing processes to produce a variety of 1D metal oxide nanomaterials in a simple and economical, yet reliable approach. Mass production of nanorods, nanowires, nanotubes, and the latest nanobelts and nanoribbons is soon to be accomplished

owing to the intensive efforts and dedication of scientists and engineers. However, much remains to be explored fundamentally to understand the unique effects of low dimensionality on the electronic structure and structural, physical, and chemical properties of such advanced materials. Such fundamental knowledge will in turn help the optimization of current devices and most certainly the creation of new ones based on one-dimensional nanostructures and their ordered two- and three dimensional assemblies. Many fields of applications in basic physical, life, and earth sciences are directly targeted and the outcome should truly impact our society and its level of technological advance.

#### GLOSSARY

**Allotropic phases** Solids of same elemental composition but with different atomic arrangements (i.e. crystal structure).

**Anisotropic nanoparticles** Nanoparticles with a shape defined by distinct longitudinal and lateral dimensions and thus an aspect ratio different from unity.

**Array** Arrangement of objects (e.g. nanoparticles) in orderly fashion.

**Interfacial tension** Variation of the surface free energy by unit surface area. The interfacial tension  $g$  is given in  $\text{mJ}/\text{m}^2$  or  $\text{mNm}^{-1}$ .

**Nucleation** Formation within an unstable, supersaturated solution of the first object (nucleus) capable of spontaneous growth into larger crystals of a more stable solid phase.

**Particulate thin film** Polycrystalline thin film consisting of fine particles deposited or grown onto a substrate.

**Point of zero charge (PZC)** pH at which the electrostatic surface charge density (per unit area) equals to zero.

**Template** A form (mask, pattern, mold) used as a guide to generate a product of similar morphology.

#### REFERENCES

1. E. K. Drexler, "Engines of Creation: The Coming Era of Nanotechnology." Doubleday, New York, 1987.
2. E. K. Drexler, "Nanosystems: Molecular Machinery, Manufacturing, and Computation." Wiley, New York, 1992.
3. M. Wilson, "Nanotechnology: Basic Science and Emerging Technologies" (M. Simmons, G. Smith, and K. Kannangara, Eds.). CRC Press, Boca Raton, FL, 2002.
4. E. Regis and M. Chimsy, "Nano: The Emerging Science of Nanotechnology," Vol. 1. Little, Brown, Boston, 1996.
5. B. C. Crandall and J. Lewis, Eds., "Nanotechnology: Research and Perspectives." MIT Press, Cambridge, MA, 1992.
6. M. Krummenacker and J. Lewis, Eds., "Prospects in Nanotechnology: Toward Molecular Manufacturing." Wiley, New York, 1994.
7. G. Timp, Ed., "Nanotechnology." AIP Press, New York, 1999.
8. K. J. Klabunde, Ed., "Nanoscale Materials in Chemistry." Wiley-Interscience, New York, 2001.
9. A. J. Bard, "Integrated Chemical Systems: A Chemical Approach to Nanotechnology." Wiley, New York, 1994.
10. S. Kawata, "Nano-Optics" (M. Irie and M. Ohtsu, Eds.). Springer-Verlag, New York, 2002.
11. M. Grundmann, Ed., "Nano-Optoelectronics: Concepts, Physics, and Devices." Springer-Verlag, New York, 2002.

12. H. S. Nalwa, "Handbook of Nanostructured Materials and Nanotechnology." Academic Press, San Diego, 1999.
13. S. Mitura, "Nanomaterials." Elsevier Science, New York, 2000.
14. H. S. Nalwa, "Nanostructured Materials and Nanotechnology." Academic Press, San Diego, 2001.
15. A. S. Edelstein and R. C. Cammarata, Eds., "Nanomaterials: Synthesis, Properties, and Applications." Institute of Physics, Bristol, PA, 1998.
16. H. Hofmann, Z. Rahman, and U. Schubert, Eds., "Nanostructured Materials." Wien: Springer-Verlag, Wien, 2002.
17. C. C. Koch, Ed., "Nanostructured Materials: Processing, Properties and Potential Applications." Noyes Publications/William Andrew, Norwich, NY, 2002.
18. B. Bhushan, Ed., "Fundamentals of Tribology and Bridging the Gap between the Macro and Micro/Nanoscales." Kluwer Academic, 2001.
19. N. J. DiNardo, Ed., "Nanoscale Characterization of Surfaces and Interface." VCH, Weinheim, 1994.
20. Z. L. Wang, Ed., "Characterization of Nanophase Materials." Wiley, New York, 2000.
21. M. A. Reed and T. Lee, Eds., "Molecular Nanoelectronics." American Science Publishers, Stevenson Ranch, CA, 2003.
22. R. A. Freitas, Jr., "Nanomedicine." Landes Bioscience, 1999.
23. D. Robinson, in "Nanotechnology in Medicine and the Biosciences" (R. Coombs, Ed.). Gordon & Breach, 1996.
24. H. C. Hoch, L. W. Jelinski, and H. G. Craighead, Eds., "Nanofabrication and Biosystems: Integrating Materials Science, Engineering, and Biology." Cambridge University Press, Cambridge, UK, 1996.
25. M. C. Roco and W. S. Bainbridge, Eds., "Societal Implications of Nanoscience and Nanotechnology." Kluwer Academic, 2002.
26. S. Bandyopadhyay and H. S. Nalwa, Eds., "Quantum Dots and Nanowires." American Science Publishers, Stevenson Ranch, CA, 2003.
27. K. K. Likharev, *IBM J. Res. Develop.* 32, 144 (1988).
28. M. G. Bawendi, M. L. Steigerwald, and L. E. Brus, *Annu. Rev. Phys. Chem.* 41, 477 (1990).
29. D. L. Klein, R. Roth, A. K. L. Lim, A. P. Alivisatos, and P. L. McEuen, *Nature (London)* 389, 699 (1997).
30. G. Markovich, C. P. Collier, S. E. Henrichs, F. Remacle, R. D. Levine, and J. R. Heath, *Acc. Chem. Res.* 32, 415 (1999).
31. C. B. Murray, C. R. Kagan, and M. G. Bawendi, *Annu. Rev. Mater. Sci.* 30, 545 (2000).
32. V. I. Klimov, A. A. Mikhailovsky, S. Xu, A. Malko, J. A. Hollingsworth, C. A. Leatherdale, H. J. Eisler, and M. G. Bawendi, *Science (Washington, DC)* 314, 290 (2000).
33. T. Rueckes, K. Kim, E. Joselevich, G. Y. Tseng, C.-L. Cheung, and C. M. Lieber, *Science (Washington, DC)* 94, 289 (2000).
34. J. Hu, T. W. Odom, and C. M. Lieber, *Acc. Chem. Res.* 32, 435 (1999).
35. P. Yang, Y. Wu, and R. Fan, *Int. J. Nanosci.* 1, 1 (2002).
36. Y. Zhang and J. Zhu, *Micron* 33, 523 (2002).
37. S. G. Louie, *Opt. Appl. Phys.* 80, 113 (2001).
38. J. Q. Hu, Q. Li, N. B. Wong, C. S. Lee, and S. T. Lee, *Chem. Mater.* 14, 1216 (2002).
39. Z. Wei, H. Qi, P. Ma, and J. Bao, *Inorg. Chem. Commun.* 5, 147 (2002).
40. R. Funahashi, I. Matsubara, and M. Shikano, *Chem. Mater.* 13, 4473 (2001).
41. M. Satoh, N. Tanaka, Y. Ueda, S. Ohshio, and H. Saitoh, *Jpn. J. Appl. Phys.* 38, L586 (1999).
42. S. I. Castaneda, F. Rueda, R. Diaz, J. M. Ripalda, and I. Montero, *J. Appl. Phys.* 83, 1995 (1998).
43. S. Hashimoto and A. Yamaguchi, *J. Am. Ceram. Soc.* 79, 491 (1996).
44. L. C. Pathak, S. K. Mishra, D. Bhattacharya, and K. L. Chopra, *Mater. Res. Bull.* 31, 1 (1996).
45. T. Yamazaki, K. Ryochi, S. Wada, T. Noma, and T. Suzuki, *J. Mater. Sci. Lett.* 14, 1479 (1995).
46. N.-W. Chen, D. W. Readey, and J. J. Moore, *Ceram. Trans.* 46, 73 (1994).
47. T. Yoshida, H. Naito, M. Okuda, S. Ehara, T. Takagi, O. Kusumoto, H. Kado, K. Yokoyama, and T. Tohda, *Appl. Phys. Lett.* 64, 3243 (1994).
48. H. Kado, S. Yamamoto, K. Yokoyama, T. Tohda, and Y. Umetani, *J. Appl. Phys.* 74, 4354 (1993).
49. H. Kado, K. Yokoyama, and T. Tohda, *Ultramicroscopy* 42, 1659 (1992).
50. R. J. O. Jarvinen, E. E. Podkletnov, T. A. Mantyla, J. T. Laurila, and T. K. Lepisto, *Appl. Phys. Lett.* 59, 3027 (1991).
51. M. Egashira, Y. Yoshida, and S. Kawasumi, *Sens. Actuators* 9, 147 (1986).
52. M. Nagano, *J. Cryst. Growth* 66, 377 (1984).
53. S. Hayashi and H. Saito, *J. Cryst. Growth* 24, 345 (1974).
54. A. H. Heuer and P. Burnett, *J. Am. Chem. Soc.* 50, 327 (1967).
55. F. Takei, *Jpn. J. Appl. Phys.* 4, 152 (1965).
56. T. Homma and S. Issiki, *Acta Metall.* 12, 1092 (1964).
57. W. R. Lasko and W. K. Tice, *Anal. Chem.* 34, 1795 (1962).
58. P. Yang, Y. Wu, and R. Fan, *Int. J. Nanosci.* 1, 1 (2002).
59. H. Kato, M. Sano, K. Miyamoto, and T. Yao, *J. Cryst. Growth* 237-239, 538 (2002).
60. N. J. C. Ingle, R. H. Hammond, and M. R. Beasley, *J. Appl. Phys.* 91, 6371 (2002).
61. Y. Adachi, I. Sakaguchi, H. Haneda, and K. Takahashi, *Thin Solid Films* 406, 224 (2002).
62. R. Koltun, M. Herrmann, G. Guntherodt, and V. A. M. Brabers, *Appl. Phys. A: Mater. Sci. Process.* 73, 49 (2001).
63. J. P. Liu, P. Zaumseil, E. Bugiel, and H. Osten, *J. Appl. Phys. Lett.* 79, 671 (2001).
64. B. J. Gibbons, M. E. Hawley, S. Trolier-McKinstry, and D. G. Schlom, *J. Vac. Sci. Technol., A* 19, 584 (2001).
65. S.-H. Lim, D. Shindo, H.-B. Kang, and K. Nakamura, *J. Cryst. Growth* 225, 208 (2001).
66. S.-H. Lim, D. Shindo, H.-B. Kang, and K. Nakamura, *J. Cryst. Growth* 225, 202 (2001).
67. G. W. Pickrell, K. L. Chang, H. C. Lin, K. C. Hsieh, and K. Y. Cheng, *J. Vac. Sci. Technol., B* 19, 1536 (2001).
68. K. Sakurai, M. Kanehiro, K. Nakahara, T. Tanabe, S. Fujita, and S. Fujita, *J. Cryst. Growth* 214-215, 92 (2000).
69. K. Nakamura, T. Shoji, and H.-B. Kang, *Jpn. J. Appl. Phys.* 39, L534 (2000).
70. G. W. Brown, M. E. Hawley, C. D. Theis, J. Yeh, and D. G. Schlom, *Thin Solid Films* 357, 13 (1999).
71. S. Gota, E. Guiot, M. Henriot, and M. Gautier-Soyer, *Phys. Rev. B* 60, 14387 (1999).
72. D. J. Rogers, P. Bove, F. H. Teherani, *Supercond. Sci. Technol.* 12, R75 (1999).
73. K. L. Chang, L. J. Chou, K. C. Hsieh, D. E. Wohlert, G. W. Pickrell, and K. Y. Cheng, *J. Cryst. Growth* 201-202, 633 (1999).
74. K. Sakurai, D. Iwata, S. Fujita, and S. Fujita, *Jpn. J. Appl. Phys.* 38, 2606 (1999).
75. S. I. Yi, Y. Liang, S. Thevuthasan, and S. A. Chambers, *Surf. Sci.* 443, 212 (1999).
76. F. C. Voegt, T. Fujii, P. J. M. Smulders, L. Niesen, M. A. James, and T. Hibma, *Phys. Rev. B.* 60, 11193 (1999).
77. H. Ota, S. Migita, Y. Kasai, H. Matsuhata, and S. Sakai, *Physica C* 311, 42 (1999).
78. S. Thevuthasan, Y. J. Kim, S. I. Yi, S. A. Chambers, J. Morais, R. Denecke, C. S. Fadley, P. Liu, T. Kendelewicz, and G. E. Brown, Jr., *Surf. Sci.* 425, 276 (1999).
79. H. J. Ko, Y. F. Chen, J. M. Ko, T. Hanada, Z. Zhu, T. Fukuda, and T. Yao, *J. Cryst. Growth* 207, 87 (1999).

80. K. P. Muthe, J. C. Vyas, S. N. Narang, D. K. Aswal, S. K. Gupta, D. Bhattacharya, R. Pinto, G. P. Kothiyal, and S. C. Sabharwal, *Thin Solid Films* 324, 37 (1998).
81. N. Taga, M. Maekawa, Y. Shigesato, I. Yasui, M. Kakei, and T. E. Haynes, *Jpn. J. Appl. Phys.* 37, 6524 (1998).
82. H.-B. Kang, K. Nakamura, S.-H. Lim, and D. Shindo, *Jpn. J. Appl. Phys.* 37, 781 (1998).
83. J. T. Torvik, J. I. Pankove, E. Iliopoulos, H. M. Ng, and T. D. Moustakas, *Appl. Phys. Lett.* 72, 244 (1998).
84. J. M. Gaines, P. J. H. Bloemen, J. T. Kohlhepp, C. W. T. Bulle-Lieuwma, R. M. Wolf, A. Reinders, R. M. Jungblut, P. A. A. van der Heijden, J. T. W. M. van Eemeren, J. de Stegge, and W. J. M. de Jonge, *Surf. Sci.* 373, 85 (1997).
85. F. C. Voogt, T. Hibma, P. Smulders, and L. Niesen, *J. Cryst. Growth* 174, 440 (1997).
86. F. Hamdani, A. E. Botchkarev, H. Tang, W. Kim, and H. Morkoc, *Appl. Phys. Lett.* 71, 3111 (1997).
87. K. Kawaguchi, G. Pindoria, R. Kita, M. Nishiyama, and T. Morishita, *J. Cryst. Growth* 172, 156 (1997).
88. Y. J. Kim, Y. Gao, and S. A. Chambers, *Surf. Sci.* 371, 358 (1997).
89. S. A. Chambers, Y. Gao, S. Thevuthasan, S. Wen, K. L. Merkle, N. Shivaparan, and R. Smith, *J. Mater. Res. Soc. Symp. Proc.* 436, 475 (1997).
90. J. F. Anderson, M. Kuhn, U. Diebold, K. Shaw, P. Stroyanov, and D. Lind, *Mater. Res. Soc. Symp. Proc.* 474, 265 (1997).
91. A. Brazdeikis, U. O. Karlsson, and A. S. Flodstroem, *Thin Solid Films* 281–282, 57 (1996).
92. C. D. Theis and D. G. Schlom, *J. Vac. Sci. Technol., A* 14, 2677 (1996).
93. Y. Gao and S. A. Chambers, *J. Mater. Res.* 11, 1025 (1996).
94. C. P. Flynn and M. H. Yang, *Mater. Res. Soc. Symp. Proc.* 401, 3 (1996).
95. Y. Gao and S. A. Chambers, *Mater. Lett.* 26, 217 (1996).
96. S. Ikegawa and Y. Motoi, *Appl. Phys. Lett.* 68, 2430 (1996).
97. R. Jansen, H. van Kempen, and R. M. Wolf, *J. Vac. Sci. Technol., B* 14, 1173 (1996).
98. T. Ishibashi, H. Soutome, Y. Okada, and M. Kawabe, *J. Cryst. Growth* 150, 1094 (1995).
99. H.-S. Wang, W. Dietsche, and X. Z. Pan, *Phys. Rev. B: Condens. Matter* 96, 305 (1995).
100. Y. Jaccard, A. Cretton, E. J. Williams, J.-P. Locquet, E. Machler, C. Gerber, T. Schneider, O. Fischer, and P. Martinoli, *Proc. SPIE* 2158, 200 (1994).
101. R. Kita, *Int. J. Mod. Phys., B* 8, 183 (1994).
102. E. S. Hellman and E. H. Jr. Hartford, *Mater. Res. Soc. Symp. Proc.* 341, 127 (1994).
103. J. Anderson, J. Conner, and R. Raj, *Ferroelectrics* 157, 353 (1994).
104. K. Kawaguchi, R. Kita, M. Nishiyama, and T. Morishita, *J. Cryst. Growth* 143, 221 (1994).
105. S. A. Chambers, T. T. Tran, and T. A. Hileman, *J. Mater. Res.* 9, 2944 (1994).
106. T. Ishibashi, T. Fujita, K. H. Song, Y. Okada, and M. Kawabe, *Jpn. J. Appl. Phys.* 32, L257 (1993).
107. A. Catana and J. P. Locquet, *J. Mater. Res.* 8, 1373 (1993).
108. H. Nonaka, T. Shimizu, and K. Arai, *Physica C* 217, 280 (1993).
109. T. Miura and Y. Ishizuka, *Thin Solid Films* 228, 189 (1993).
110. H. S. Wang, W. Dietsche, A. Fischer, and K. Ploog, *J. Cryst. Growth* 127, 655 (1993).
111. M. Kawai and T. Hanada, *RIKEN Rev.* 2, 31 (1993).
112. Y. Watanabe, F. Maeda, M. Oshima, and O. Michikami, *J. Cryst. Growth* 127, 672 (1993).
113. W. Schindler, P. van Hasselt, P. Tontsch, J. Markl, J. Burger, P. Bauer, and G. Saemann-Ischenko, *J. Cryst. Growth* 127, 1088 (1993).
114. H. S. Wang, W. Dietsche, A. Fischer, and K. Ploog, *Solid State Commun.* 84, 695 (1992).
115. T. Matsumoto, T. Kawai, and S. Kawai, *Mater. Res. Soc. Symp. Proc.* 237, 535 (1992).
116. K. Yamano, K. Shimaoka, K. Takahashi, T. Usuki, Y. Yoshisato, and S. Nakano, *Jpn. J. Appl. Phys.* 31, 1765 (1992).
117. T. Siegrist, D. A. Mixon, E. Coleman, and T. H. Tiefel, *Appl. Phys. Lett.* 60, 2489 (1992).
118. F. J. Walker and R. A. McKee, *J. Cryst. Growth* 116, 235 (1992).
119. J. G. Hu, D. J. Miller, D. B. Buchholz, S. J. Duray, D. Schulz, T. J. Marks, and R. P. H. Chang, *Mater. Res. Soc. Symp. Proc.* 275, 885 (1992).
120. K. Norimoto, R. Sekine, M. Mori, T. Hahada, M. Kudo, and M. Kawai, *Appl. Phys. Lett.* 61, 1971 (1992).
121. H. S. Wang, D. Eissler, Y. Kershaw, W. Dietsche, A. Fischer, K. Ploog, and D. Brunner, *Appl. Phys. Lett.* 60, 778 (1992).
122. V. Agrawal, N. Chandrasekhar, Y. J. Zhang, V. S. Achutharaman, M. L. Mecartney, and A. M. Goldman, *J. Vac. Sci. Technol., A* 10, 1531 (1992).
123. S. Sakai, Y. Kasai, and P. Bodin, *Jpn. J. Appl. Phys.* 31, L399 (1992).
124. K. Suzuki, T. Karaki, K. Iwashima, M. Shibata, H. Okada, H. Onnagawa, and K. Miyashita, *Jpn. J. Appl. Phys.* 31, L1339 (1992).
125. T. Fujii, F. M. F. de Groot, G. A. Sawatzky, F. C. Voogt, T. Hibma, and K. Okada, *Phys. Rev. B* 59, 3195 (1999).
126. Y. Gao, *Rec. Res. Devel. in Cryst. Growth Res.* 1, 13 (1999).
127. F. Yubero, M. Ocana, A. Caballero, and A. R. Gonzalez-Elipe, *Acta Mater.* 48, 4555 (2000).
128. T. Tsuchiya, A. Watanabe, H. Niino, A. Yabe, I. Yamaguchi, T. Manabe, T. Kumagai, and S. Mizuta, *Appl. Surf. Sci.* 186, 173 (2002).
129. A. M. Morales and C. M. Lieber, *Science (Washington, DC)* 279, 208 (1998).
130. S. Choopun, R. D. Vispute, W. Yang, R. P. Sharma, T. Venkatesan, and H. Shen, *Appl. Phys. Lett.* 80, 1529 (2002).
131. B. S. Qadri and H. J. Kim, *J. Appl. Phys.* 92, 227 (2002).
132. A. Essahlaoui, A. Boudrioua, J. C. Loulergue, R. Chety, E. Millon, and E. J. Perriere, *Opt. Mater.* 19, 389 (2002).
133. C. Mitra, P. Raychaudhuri, J. John, S. K. Dhar, A. K. Nigam, and R. J. Pinto, *Appl. Phys.* 89, 524 (2001).
134. R. Chety, E. Millon, A. Boudrioua, J. C. Loulergue, A. Dahoun, and H. J. Perriere, *J. Mater. Chem.* 11, 657 (2001).
135. H. Huhtinen, J. Jarvinen, R. Laiho, P. Paturi, and J. Raittila, *J. Appl. Phys.* 90, 1521 (2001).
136. M. A. El Khakani, R. Dolbec, A. M. Serventi, M. C. Horriilo, M. Trudeau, R. G. Saint-Jacques, D. G. Rickerby, and I. Sayago, *Sens. Actuators, B* B77, 383 (2001).
137. Y.-Z. Yoo, T. Fukumura, Z. Jin, K. Hasegawa, M. Kawasaki, P. Ahmet, T. Chikyow, and H. Koinuma, *J. Appl. Phys.* 90, 4246 (2001).
138. H. Yoshioka, F. O. Adurodija, H. Izumi, T. Ishihara, and M. Motoyama, *Electrochem. Solid-State Lett.* 3, 540 (2000).
139. M. Noda, Y. Adachi, H. Sugiyama, T. Nakaiso, and M. Okuyama, *Appl. Phys. A* 71, 113 (2000).
140. X. Fang, M. Tachiki, and T. Kobayashi, *Thin Solid Films* 368, 227 (2000).
141. R. Lyonnet, A. Khodan, A. Barthelemy, J.-P. Contour, O. Durand, J. L. Maurice, D. Michel, and J. De Teresa, *J. Electroceram.* 4, 369 (2000).
142. A. N. Khodan, J.-P. Contour, D. Michel, O. Durand, R. Lyonnet, and M. Mihet, *J. Cryst. Growth* 209, 828 (2000).
143. S. S. Kim, B. I. Kim, Y. B. Park, and J. H. Je, *Appl. Phys. A* 69, S625 (1999).
144. T. Aoki, A. Suzuki, T. Matsushita, H. Kaimi, and M. Okuda, *Jpn. J. Appl. Phys.* 38, 4802 (1999).
145. R. J. Gaboriaud and F. Pailloux, *Appl. Surf. Sci.* 138–139, 549 (1999).
146. E. Vasco, L. Vazquez, and C. Zaldo, *Appl. Phys. A* 69, S827 (1999).

147. W. Zhang, X. Wang, M. Elliott, W. Herrenden-Harkerand, and I. W. Boyd, *Appl. Surf. Sci.* 138–139, 569 (1999).
148. E. A. F. Span, F. J. G. Roesthuis, D. H. A. Blank, and H. Rogalla, *Appl. Phys.* 69, S783 (1999).
149. J. E. Mathis, A. Goyal, D. F. Lee, F. A. List, M. Paranthaman, D. K. Christen, E. D. Specht, D. M. Kroeger, and P. M. Martin, *Jpn. J. Appl. Phys.* 37, L1379 (1998).
150. A. Ohtomo, M. Kawasaki, T. Koida, H. Koinuma, Y. Sakurai, Y. Yoshida, M. Sumiya, S. Fuke, T. Yasuda, and Y. Segawa, *Mater. Sci. Forum* 264–268, 1463 (1998).
151. T. Yotsuya, T. Kusaka, Y. Kakehi, and S. Ogawa, *Mater. Chem. Phys.* 54, 169 (1998).
152. A. Di Trollo, U. Gambardella, A. Morone, S. Orlando, and G. P. Parisi, *Appl. Surf. Sci.* 127–129, 959 (1998).
153. Z. Fu, M. Zhou, Q. Qin, S. Zhang, and F. Lu, *Jpn. J. Appl. Phys.* 36, 6714 (1997).
154. W. S. Hu, Z. G. Liu, X. L. Guo, J. Sun, S. B. Xiong, and D. Feng, *Ferroelectrics* 195, 179 (1997).
155. M. Zhou, Z. Fu, H. Yang, Z. Zhang, and Q. Qin, *Appl. Surf. Sci.* 108, 399 (1997).
156. A. Tsukamoto, K. Nakanishi, K. Yamamoto, and H. Yamauchi, *Thin Solid Films* 274, 138 (1996).
157. K. A. Striebel, C. Z. Deng, S. J. Wen, and E. J. Cairns, *J. Electrochem. Soc.* 143, 1821 (1996).
158. R. I. Tomov, P. A. Atanasov, and V. S. Serbesov, *Proc. SPIE* 2777, 174 (1996).
159. S. L. King, J. G. E. Gardeniers, and I. W. Boyd, *Appl. Surf. Sci.* 96–98, 811 (1996).
160. B. Dam, J. H. Rector, J. Johansson, S. Kars, and R. Griessen, *Appl. Surf. Sci.* 96–98, 679 (1996).
161. P. Tiwari, X. D. Wu, S. R. Foltyn, I. H. Campbell, Q. X. Jia, R. E. Muenchausen, D. E. Peterson, and T. E. Mitchell, *J. Electron. Mater.* 25, 51 (1996).
162. T. Nagaishi and H. Itozaki, *J. Vac. Sci. Technol., A* 14, 1995 (1996).
163. Q. X. Jia, S. G. Song, S. R. Foltyn, and X. D. Wu, *J. Mater. Res.* 10, 2401 (1995).
164. H. S. Choi, J. S. Ahn, W. Jo, and T. W. Noh, *J. Korean Phys. Soc.* 28, 636 (1995).
165. K. A. Striebel, C. Z. Deng, and E. Cairns, *J. Mater. Res. Soc. Symp. Proc.* 393, 85 (1995).
166. D. L. Perry, A. C. Thompson, R. E. Russo, and X. L. Mao, *Mater. Res. Soc. Symp. Proc.* 375, 307 (1995).
167. H. Jiang, A. J. Drehman, R. J. Andrews, J. A. Horrigan, and C. Vittoria, *Appl. Phys. Lett.* 65, 3132 (1994).
168. M. Fukutomi, S. Aoki, K. Komori, R. Chatterjee, and H. Maeda, *Physica C* 219, 333 (1994).
169. B. Shen, R. Izquierdo, and M. Meunier, *Proc. SPIE* 2045, 91 (1994).
170. K. Terryll, C. Bjoermander, A. M. Grishin, J. H. Xu, L. N. Wang, M. Muhammed, and K. V. Rao, *Physica C* 235–240, 683 (1994).
171. F. Mattheis and H.-U. Krebs, *J. Alloys Compd.* 195, 275 (1993).
172. M. D. Strikovsky, E. B. Klyuenkov, S. V. Gaponov, J. Schubert, and C. A. Copetti, *Appl. Phys. Lett.* 63, 1146 (1993).
173. J. T. Cheung, P. E. D. Morgan, and R. Neugaonkar, *Integrated Ferroelectrics* 3, 147 (1993).
174. M. Schilling, F. Goerke, and U. Merkt, *Thin Solid Films* 235, 202 (1993).
175. G. A. Giardini, I. Pettiti, A. Morone, V. Marotta, M. Snels, G. P. Parisi, and G. Bentivenga, *Appl. Surf. Sci.* 69, 365 (1993).
176. D. Chambonnet, C. Fages, C. Belouet, H. Moriceau, M. Schwerdtfeger, J. C. Villegier, and D. Keller, *J. Alloys Compd.* 195, 243 (1993).
177. T. Fujii, A. Fujishima, T. Hirano, and T. Kobayashi, *Appl. Phys. Lett.* 62, 3204 (1993).
178. A. Kumar, J. Narayan, and B. Patnaik, *Physica C* 209, 421 (1993).
179. S. F. Xu, Y. J. Tian, H. B. Lu, Y. L. Zhou, Z. H. Chen, D. F. Cui, L. Li, and G. Z. Yang, *Mod. Phys. Lett. B* 7, 1741 (1993).
180. A. Gupta, B. W. Hussey, and M. W. Chern, *Physica C* 200, 263 (1992).
181. J. Lee, E. Narumi, C. Li, S. Patel, and D. T. Shaw, *Physica C* 200, 235 (1992).
182. H. S. Kwok, *Thin Solid Films* 218, 277 (1992).
183. P. Schwab, X. Z. Wang, and D. Baeuerle, *Appl. Phys. Lett.* 60, 2023 (1992).
184. G. Brorsson, P. A. Nilsson, E. Olsson, S. Z. Wang, T. Claeson, and M. Lofgren, *Appl. Phys. Lett.* 61, 486 (1992).
185. N. Sugii, K. Kubo, M. Ichikawa, K. Yamamoto, H. Yamauchi, and S. Tanaka, *Jpn. J. Appl. Phys.* 31, L1024 (1993).
186. E. V. Pechen, S. I. Krasnosvobodtsev, G. Kessler, A. Richter, A. M. Panzner, O. Grossmann, and A. Teresiak, *Phys. Status Solidi A* 131, 179 (1992).
187. X. L. Mao, P. Berdahl, R. E. Russo, H. B. Liu, and J. C. Ho, *Physica C* 183, 167 (1991).
188. E. Narumi, L. Song, C. Li, Y. H. Kao, S. Patel, D. T. Shaw, S. Shue, and K. Fujino, *Jpn. J. Appl. Phys.* 30, L585 (1991).
189. S. Y. Lee, Q. X. Jia, W. A. Anderson, and D. T. Shaw, *J. Appl. Phys.* 70, 7170 (1991).
190. J. S. Horwitz, D. B. Chrisey, M. S. Osofsky, K. S. Grabowski, and T. A. Vanderah, *J. Appl. Phys.* 70, 1045 (1991).
191. B. M. Moon, C. E. Platt, R. A. Schweinfurth, and D. Van Harlingen, *J. Appl. Phys. Lett.* 59, 1905 (1991).
192. P. Cacciafesta, K. R. Hallam, C. A. Oyedepo, A. D. L. Humphris, M. J. Miles, and K. D. Jandt, *Chem. Mater.* 14, 777 (2002).
193. K. Ogata, K. Maejima, S. Z. Fujita, and S. G. Fujita, *J. Cryst. Growth* 248, 25 (2003).
194. R. S. Wagner and W. C. Ellis, *Appl. Phys. Lett.* 4, 89 (1964).
195. R. S. Wagner in “Whisker Technology” (A. P. Levitt, Ed.), pp. 47–119. Wiley, New York, 1970.
196. R. S. Wagner, W. C. Ellis, K. A. Jackson, and S. M. J. Arnold, *Appl. Phys.* 35, 2993 (1964).
197. Y. Wu, H. Yan, M. M. Huang, B. Messer, J. H. Song, and P. Yang, *Chem. Eur. J.* 8, 1261 (2002).
198. S. U. M. Khan and J. Akikusa, *J. Phys. Chem. B* 103, 7184 (1999).
199. I. Yamaguchi, T. Terayama, S. Ohnishi, T. Manabe, T. Shimizu, T. Kumagai, and S. Mizuta, *Thin Solid Films* 391, 157 (2001).
200. M. L. Hitchman and K. F. Jensen, “Chemical Vapor Deposition.” Academic Press, San Diego, CA, 1993.
201. J.-H. Park and T. S. Sudarshan, “Chemical Vapor Deposition.” ASM International, Materials Park, OH, 2001.
202. O. Auciello, A. I. Kingon, A. R. Krauss, and D. Lichtenwalner, *NATO ASI Ser. E* 234, 151 (1993).
203. I. Safi, *Surf. Coat. Technol.* 135, 48 (2000).
204. K. Zhang, F. Zhu, C. H. A. Huan, and A. T. S. Wee, *Thin Solid Films* 376, 255 (2000).
205. S. Deki, H. Y. Y. Ko, T. Fujita, K. Akamatsu, M. Mizuhata, and A. Kajinami, *Eur. Phys. J. D* 16, 325 (2001).
206. S. Deki and Y. Aoi, *J. Mater. Res.* 13, 883 (1998).
207. C. Santato, M. Odziemkowski, M. Ulmann, and J. Augustynski, *J. Am. Chem. Soc.* 123, 10639 (2001).
208. W. Lu, D. Yang, Y. Sun, Y. Guo, S. Xie, and H. Li, *Appl. Surf. Sci.* 147, 39 (1999).
209. S. L. Limmer, S. Seraji, M. J. Forbes, Y. Wu, T. P. Chou, C. Nguyen, and G. Cao, *Adv. Mater.* 13, 1269 (2001).
210. I. Zhitomirsky and L. Gal-Or, in “Intermetallic and Ceramic Coatings” (N. B. Dahotre and T. S. Sudarshan, Eds.), pp. 83–145. Marcel Dekker, New York, 1999.
211. A. Rosidian, Y. Liu, and R. O. Claus, *Proc. SPIE* 3675, 113 (1999).
212. K. B. Blodgett, *J. Am. Chem. Soc.* 56, 495 (1934).
213. K. B. Blodgett, *J. Am. Chem. Soc.* 57, 1007 (1935).
214. D. V. Paranjape, S. Murali, and P. Ganguly, *Appl. Phys. Lett.* 63, 18 (1993).
215. D. M. Taylor and J. N. Lambi, *Thin Solid Films* 243, 384 (1994).
216. D. Brandl, Ch. Schoppmann, Ch. Tomaschko, J. Markl, and H. Voit, *Thin Solid Films* 249, 113 (1994).

217. D. J. Amm, D. J. Johnson, N. Matsuura, T. Laursen, and G. Palmer, *Thin Solid Films* 242, 74 (1994).
218. T. Faldum, W. Meisel, and P. Gütllich, *Surf. Interface. Anal.* 24, 68 (1996).
219. T. Faldum, W. Meisel, and P. Gütllich, *Hyperfine Interact.* 92, 1263 (1994).
220. D. T. Amm, D. J. Johnson, T. Laursen, and S. K. Gupta *Appl. Phys. Lett.* 61, 522 (1992).
221. M. Schurr, J. Hassmann, R. Kügler, Ch. Tomaschko, and H. Voit, *Thin Solid Films* 307, 260 (1997).
222. N. Matsuura, D. J. Johnson, and D. T. Amm, *Thin Solid Films* 295, 260 (1997).
223. H. A. Bullen and S. J. Garrett, *Chem. Mater.* 14, 243 (2002).
224. M. L. Hitchman, and S. E. Alexandrov, *Electrochem. Soc. Interface* 10, 40 (2001).
225. S. Jain, T. T. Kodas, and M. Hampden-Smith, *Chem. Vap. Deposition* 4, 51 (1998).
226. M. Yoshimaru, S. Koizumi, and K. Shimokawa. *J. Vac. Sci. Technol., A* 15, 2908 (1997).
227. B. H. Lee, L. Kang, R. Nieh, W. J. Qi, and J. C. Lee, *Appl. Phys. Lett.* 76, 1926 (2000).
228. X. T. Zhang, Y. C. Liu, L. G. Zhang, J. Y. Zhang, Y. M. Lu, D. Z. Shen, W. Xu, G. Z. Zhong, X. W. Fan, and X. G. Kong, *J. Appl. Phys.* 92, 3293 (2002).
229. Y. Li and T. Ishigaki, *Chem. Phys. Lett.* 367, 561 (2003).
230. F. M. d'Heurle, *Int. Mater. Rev.* 34, 53 (1989).
231. R. W. Baker, "Membrane Technology and Applications." McGraw-Hill, New York, 2000.
232. C. R. Martin, *Acc. Chem. Res.* 28, 61 (1995); *Science* 266, 1961 (1994).
233. A. Huczko, *Appl. Phys. A* 70, 365 (2000).
234. R. L. Fleischer, P. B. Price, and R. M. Walker, "Nuclear Tracks in Solids." University of California Press, Berkeley, CA, 1975.
235. C. N. R. Rao and A. Govindaraj, *Proc. Indian Acad. Sci. Chem. Sci.* 113, 375 (2001).
236. A. Despic and V. P. Parkhutik, in "Modern Aspects of Electrochemistry" (J. O. Bockris, R. E. White, and B. E. Conway, Eds.). Plenum Press, New York, 1989.
237. S. J. Gani, *Ind. Ceram.* 14, 163 (1994).
238. O. Van der Biest and L. J. Vandeperre, *Annu. Rev. Mater. Sci.* 29, 327 (1999).
239. G. H. A. Therese and R. V. Kamat, *Chem. Mater.* 12, 1195 (2000).
240. I. Zhitomirsky, *Am. Ceram. Soc. Bull.* 79, 57 (2000).
241. I. Zhitomirsky, *J. Eur. Ceram. Soc.* 18, 849 (1998).
242. M. Shirkhazadeh, *J. Mater. Sci.* 9, 67 (1998).
243. E. M. Wong and P. C. Searson, *Chem. Mater.* 11, 1959 (1999).
244. M. Izaki and T. Omi, *J. Electrochem. Soc.* 144, 1949 (1997).
245. S. Peulon and D. Lincot, *Adv Mater.* 8, 166 (1996).
246. S. Peulon and D. Lincot, *J. Electrochem. Soc.* 145, 864 (1998).
247. M. Izaki and T. Omi, *Appl. Phys. Lett.* 68, 2439 (1996).
248. M. Izaki and T. Omi, *J. Electrochem. Soc.* 143, L53 (1996).
249. I. Zhitomirsky, *Nanostruct. Mater.* 8, 521 (1997).
250. I. Zhitomirsky and L. Gal-Or, *J. Eur. Ceram. Soc.* 16, 819 (1996).
251. Y. Ishikawa and Y. Matsumoto, *Electrochim. Acta* 46, 2819 (2001).
252. J. Tamaki, G. K. L. Goh, and F. F. Lange, *J. Mater. Res.* 15, 2583 (2000).
253. I. Zhitomirsky and L. Gal-Or, *Mater. Lett.* 31, 155 (1997).
254. I. Zhitomirsky, *J. Eur. Ceram. Soc.* 19, 2581 (1999).
255. R. Chaim, I. Silberman, and L. Gal-Or, *J. Electrochem. Soc.* 138, 1942 (1991).
256. I. Zhitomirsky and L. Gal-Or, *J. Mater. Sci.* 33, 699 (1998).
257. A. R. Boccaccini, U. Schindler, and H.-G. Kruger, *Mater. Lett.* 51, 225 (2001).
258. L. Gal-Or, S. Liubovich, and S. Haber, *J. Electrochem. Soc.* 139, 1078 (1992).
259. P. E. de Jongh, D. Vanmaekelbergh, and J. J. Kelly, *Chem. Mater.* 11, 3512 (1999).
260. B. O'Regan, V. Sklover, and M. Graetzel, *J. Electrochem. Soc.* 148, C498 (2001).
261. J. A. Switzer, M. J. Shane, and R. J. Phillips, *Science (Washington, DC)* 247, 444 (1990).
262. Y.-C. Wang, I.-C. Leu, and M.-H. Hon, *Electrochem. Solid-State Lett.* 5, C53 (2002).
263. A. Dierstein, H. Natter, F. Meyer, H.-O. Stephan, C. Kropf, and R. Hempelmann, *Scripta Mater.* 44, 2209 (2001).
264. I. Zhitomirsky and A. Petric, *Ceram. Int.* 27, 149 (2001).
265. S. Kenane and L. Piroux, *J. Mater. Res.* 17, 401 (2002).
266. P. M. Vereecken, I. Shac, and P. C. Searson, *J. Electrochem. Soc.* 147, 2572 (2000).
267. A. A. Vertegel, E. W. Bohannon, M. G. Shumsky, and J.-A. Switzer, *J. Electrochem. Soc.* 148, C253 (2001).
268. J. K. Barton, A. A. Vertegel, E. W. Bohannon, and J.-A. Switzer, *Chem. Mater.* 13, 952 (2001).
269. R. Liu, A. A. Vertegel, E. W. Bohannon, T. A. Sorenson, and J.-A. Switzer, *Chem. Mater.* 13, 508 (2001).
270. E. W. Bohannon, M. G. Shumsky, and J.-A. Switzer, *Chem. Mater.* 11, 2289 (1999).
271. J.-A. Switzer, M. G. Shumsky, and E. W. Bohannon, *Science (Washington, DC)* 284, 293 (1999).
272. J.-A. Switzer, E. W. Bohannon, T. D. Golden, C.-H. Hung, L.-Y. Huang, and M. Shumsky, *Mater. Res. Soc. Symp. Proc.* 451, 283 (1997).
273. Th. Pauporte and D. Lincot, *Appl. Phys. Lett.* 75, 3817 (1999).
274. A. A. Vertegel, M. G. Shumsky, and J.-A. Switzer, *Electrochim. Acta* 38, 3233 (2000).
275. A. A. Vertegel, M. G. Shumsky, and J.-A. Switzer, *Chem. Mater.* 12, 596 (2000).
276. M. P. Nikiforov, A. A. Vertegel, M. G. Shumsky, and J.-A. Switzer, *Adv. Mater.* 12, 1351 (2000).
277. L. Vayssieres, *Int. J. Mater. Prod. Technol.* 18, 1–25 (2003).
278. L. Vayssieres, PhD Thesis, Université Pierre et Marie Curie, Paris, (1995).
279. L. Vayssieres, A. Hagfeldt, and S.-E. Lindquist, *Pure Appl. Chem.* 72, 47 (2000).
280. L. Vayssieres, "Proceedings of the 3rd IUPAC International Conference and UNESCO Virtual Teaching Encyclopedia on Macromolecules and Materials Science on CDROM," 2000, pp. 1–100.
281. L. Vayssieres, C. Chaneac, E. Tronc, and J. P. Jolivet, *J. Colloid Interface Sci.* 205, 205 (1998).
282. L. Vayssieres, *Int. J. Nanotechnol.* 1, 1 (2003).
283. L. Vayssieres, *J. Phys. Chem. B* 107, 2623 (2003).
284. L. Vayssieres, L. Rabenberg, and A. Manthiram, *NanoLett.* 2, 1393 (2002).
285. L. Vayssieres, N. Beerermann, S.-E. Lindquist, and A. Hagfeldt, *Chem. Mater.* 13, 233 (2001).
286. L. Vayssieres, J.-H. Guo, and J. Nordgren, *J. Nanosci. Nanotechnol.* 1, 385 (2001).
287. L. Vayssieres, K. Keis, S.-E. Lindquist, and A. Hagfeldt, *J. Phys. Chem. B* 105, 3350 (2001).
288. L. Vayssieres, K. Keis, A. Hagfeldt, and S.-E. Lindquist, *Chem. Mater.* 13, 4395 (2001).
289. L. Vayssieres, in "Surface Engineering: Science and Technology II" (A. Kumar, Y.-W. Chung, J. J. Moore, G. L. Doll, K. Yatsui, and D. S. Misra, Eds.), pp. 51–59. The Minerals, Metals and Materials Society, Warrendale, PA, 2002.
290. Z. L. Xiao, C. Y. Han, U. Welp, H. H. Wang, W. K. Kwok, G. A. Willing, J. M. Miller, R. E. Cook, D. J. Miller, and G. W. Crabtree, *NanoLett.* 2, 1293 (2002).
291. X. S. Peng, L. D. Zhang, G. W. Meng, X. F. Wang, Y. W. Wang, C. Z. Wang, and G. S. Wu, *J. Phys. Chem. B* 106, 11163 (2002).
292. J. Zhou, S. Z. Deng, J. Chen, J. C. She, and N. S. Xu, *Chem. Phys. Lett.* 365, 505 (2002).
293. R. W. Hicks and T. J. Pinnavaia, *Chem. Mater.* 15, 78 (2003).
294. R. Ma, Y. Bando, and T. Sato, *Appl. Phys. Lett.* 81, 3467 (2002).

295. Y. Liu, C. Yin, W. Wang, Y. Zhan, and G. Wang, *J. Mater. Sci. Lett.* 21, 137 (2002).
296. Z. W. Pan, Z. R. Dai, and Z. L. Wang, *Science (Washington, DC)* 291, 1947 (2001).
297. X. S. Peng, X. F. Wang, Y. W. Wang, C. Z. Wang, G. W. Meng, and L. D. Zhang, *J. Phys. D: Appl. Phys.* 35, L101 (2002).
298. C. Xu, Y. Liu, G. Xu, and G. Wang, *Chem. Phys. Lett.* 366, 567 (2002).
299. H.-Q. Wu, M.-W. Shao, X.-W. Wei, J.-S. Gu, and M.-Z. Qu, *Chin. J. Chem.* 20, 610 (2002).
300. Y. J. Chen, J. B. Li, Y. S. Han, Q. M. Wei, and J. H. Dai, *Appl. Phys. A* 74, 433 (2002).
301. M. Li, H. Schnablegger, and S. Mann, *Nature (London)* 402, 393 (1999).
302. W. Wang, Y. Zhan, X. Wang, Y. Liu, C. Zheng, and G. Wang, *Mater. Res. Bull.* 37, 1093 (2002).
303. S. Wang, Q. Huang, X. Wen, X. Li, and S. Yang, *Phys. Chem. Chem. Phys.* 4, 3425 (2002).
304. C. Xu, Y. Liu, G. Xu, and G. Wang, *Mater. Res. Bull.* 2049, 1 (2002).
305. W. Wang, Z. Liu, Y. Liu, C. Xu, C. Zheng, and G. Wang, *Appl. Phys. A* 76, 417 (2003).
306. W. Wang, C. Lan, Y. Li, K. Hong, and G. Wang, *Chem. Phys. Lett.* 366, 220 (2002).
307. W. Wang, G. Wang, X. Wang, Y. Zhan, Y. Liu, and C. Zheng, *Adv. Mater.* 14, 67 (2002).
308. S. Kenane and L. Piraux, *J. Mater. Res.* 17, 401 (2002).
309. R. S. Decca, H. D. Drew, B. Maiorov, J. Guimpel, and E. Osquiguil, *Appl. Phys. Lett.* 73, 120 (1998).
310. Y. F. Zhang, Y. H. Tang, X. F. Duan, Y. Zhang, C. S. Lee, N. Wang, I. Bello, and S. T. Lee, *Chem. Phys. Lett.* 323, 180 (2000).
311. V. G. Pol, O. Palchik, A. Gedanken, and I. Felner, *J. Phys. Chem. B* 106, 9743 (2002).
312. R. J. Atkinson, A. M. Posner, and J. P. Quirk, *J. Phys. Chem.* 71, 550 (1967).
313. Y. Ni, X. Ge, H. Liu, Z. Zhang, Q. Ye, and F. Wang, *Mater. Lett.* 49, 185 (2001).
314. Y. Fu, J. Chen, and H. Zhang, *Chem. Phys. Lett.* 350, 491 (2001).
315. K. Matsui, T. Kyotani, and A. Tomita, *Mol. Cryst. Liq. Cryst. Sci. Technol., Sect. A* 387, 1 (2002).
316. R. V. Kumar, Y. Kolytyn, X. N. Xu, Y. Yeshurun, A. Gedanken, and I. Felner, *J. Appl. Phys.* 89, 6324 (2001).
317. K.-W. Chang, S.-C. Liu, L. Y. Chen, C.-N. F. Hong, and J.-J. Wu, *Mater. Res. Soc. Symp. Proc.* 703, 129 (2002).
318. C. H. Liang, G. W. Meng, G. Z. Wang, Y. W. Wang, L. D. Zhang, and S. Y. Zhang, *Appl. Phys. Lett.* 78, 3202 (2001).
319. G.-S. Park, W.-B. Choi, J.-M. Kim, Y. C. Choi, Y. H. Lee, and C.-B. Lim, *J. Cryst. Growth* 220, 494 (2000).
320. X. C. Wu, W. H. Song, W. D. Huang, M. H. Pu, B. Zhao, Y. P. Sun, and J. J. Du, *Chem. Phys. Lett.* 328, 5 (2000).
321. Y. C. Choi, W. S. Kim, Y. S. Park, S. M. Lee, D. J. Bae, Y. H. Lee, G.-S. Park, W. B. Choi, N. S. Lee, and G. M. Kim, *Adv. Mater.* 12, 746 (2000).
322. J. Y. Li, Z. Y. Qiao, X. L. Chen, L. Chen, Y. G. Cao, M. He, H. Li, Z. M. Cao, and Z. Zhang, *J. Alloys Compd.* 306, 300 (2000).
323. H. Z. Zhang, Y. C. Kong, Y. Z. Wang, X. Du, Z. G. Bai, J. J. Wang, D. P. Yu, Y. Ding, Q. L. Hang, and S. Q. Feng, *Solid State Commun.* 109, 677 (1999).
324. W. Q. Han, P. Kohler-Redlich, F. Ernst, and M. Rhle, *Solid State Commun.* 115, 527 (2000).
325. G.-S. Park, W.-B. Choi, J.-M. Kim, Y. C. Choi, Y. H. Lee, and C.-B. Lim, *J. Cryst. Growth* 220, 494 (2000).
326. C. C. Tang, S. S. Fan, M. L. de la Chapelle, and P. Li, *Chem. Phys. Lett.* 333, 12 (2001).
327. D. P. Yu, J.-L. Bubendorff, J. F. Zhou, Y. Leprince-Wang, and M. Troyon, *Solid State Commun.* 124, 417 (2002).
328. R. Ma and Y. Bando, *Chem. Phys. Lett.* 367, 219 (2003).
329. B. C. Kim, K. T. Sun, K. S. Park, K. J. Im, T. Noh, M. Y. Sung, S. Kim, S. Nahm, Y. N. Choi, and S. S. Park, *Appl. Phys. Lett.* 80, 479 (2002).
330. Z. G. Bai, D. P. Yu, H. Z. Zhang, Y. Ding, Y. P. Wang, X. Z. Gai, Q. L. Hang, G. C. Xiong, and S. Q. Feng, *Chem. Phys. Lett.* 303, 311 (1999).
331. Y. Zhang, J. Zhu, Q. Zhang, Y. Yan, N. Wang, and X. Zhang, *Chem. Phys. Lett.* 317, 504 (2000).
332. Y. H. Tang, Y. F. Zhang, N. Wang, I. Bello, C. S. Lee, and S. T. Lee, *Appl. Phys. Lett.* 74, 3824 (1999).
333. X. S. Peng, G. W. Meng, J. Zhang, X. F. Wang, Y. W. Wang, C. Z. Wang, and L. D. Zhang, *J. Mater. Chem.* 12, 1602 (2002).
334. X. S. Peng, Y. W. Wang, J. Zhang, X. F. Wang, L. X. Zhao, G. W. Meng, and L. D. Zhang, *Appl. Phys. A* 74, 437 (2002).
335. C. Liang, G. Meng, Y. Lei, F. Philipp, and L. Zhang, *Adv. Mater.* 13, 1330 (2001).
336. P. Yang and C. M. Lieber, *J. Mater. Res.* 12, 2981 (1997).
337. P. Yang and C. M. Lieber, *Science (Washington, DC)* 273, 1836 (1996).
338. Z. L. Wang, R. P. Gao, Z. W. Pan, and Z. R. Dai, *Adv. Eng. Mater.* 3, 657 (2001).
339. Z. R. Dai, Z. W. Pan, and Z. L. Wang, *Solid State Commun.* 118, 351 (2001).
340. D. Zhang, C. Li, S. Han, L. Song, T. Xiaolei, T. Tang, W. Jin, and C. Zhou, *Appl. Phys. Lett.* 82, 112 (2003).
341. C. Li, D. Zhang, S. Han, X. Liu, T. Tang, and C. Zhou, *Adv. Mater.* 15, 143 (2003).
342. H. Yumoto, T. Sako, Y. Gotoh, K. Nishiyama, and T. Kaneko, *J. Cryst. Growth* 203, 136 (1999).
343. B. C. Satishkumar, A. Govindaraj, M. Nath, and C. N. R. Rao, *J. Mater. Chem.* 10, 2115 (2000).
344. Y. Deng, J. Wu, J. Liu, G.-D. Wei, and C.-W. Nan, *J. Phys. Chem. Solids* 64, 607 (2003).
345. Y. Yin, G. Zhang, and Y. Xia, *Adv. Funct. Mater.* 12, 293 (2002).
346. Z. Cui, G. W. Meng, W. D. Huang, G. Z. Wang, and L. D. Zhang, *Mater. Res. Bull.* 35, 1653 (2000).
347. P. Yang and C. M. Lieber, *Science (Washington, DC)* 273, 1836 (1996).
348. Y. Chen, J. Li, Y. Han, X. Yang, and J. Dai, *J. Cryst. Growth* 245, 163 (2002).
349. L. Yan, J. Zhuang, X. Sun, Z. Deng, and Y. Li, *Mater. Chem. Phys.* 76, 119 (2002).
350. K. L. Klug and V. P. Dravid, *Appl. Phys. Lett.* 81, 1687 (2002).
351. W. D. Huang, W. H. Song, Z. Cui, B. Zhao, M. H. Pu, X. C. Wu, T. Hu, Y. P. Sun, and J. J. Du, *Supercond. Sci. Technol.* 13, 1499 (2000).
352. Y. Li, M. Sui, Y. Ding, G. Zhang, J. Zhuang, and C. Wang, *Adv. Mater.* 12, 818 (2000).
353. L. Vayssieres and A. Manthiram, in "Three-Dimensional Nano-engineered Assemblies" (K. Ikuta, L. Merhari, T. Orlando, and D. P. Taylor, Eds.), Materials Research Society Symposium Proceedings, 739 Warrendale, PA, 2003.
354. X. Wang and Y. Li, *J. Am. Chem. Soc.* 124, 2880 (2002).
355. X. Wang and Y. Li, *Chem. Eur. J.* 9, 300 (2003).
356. D. Zhu, H. Zhu, and Y. Zhang, *Appl. Phys. Lett.* 80, 1634 (2002).
357. X. Ma, H. Zhang, J. Xu, J. Niu, Q. Yang, J. Sha, and D. Yang, *Chem. Phys. Lett.* 363, 579 (2002).
358. D. Zhu, H. Zhu, and Y. Zhang, *J. Cryst. Growth* 249, 172 (2003).
359. W. Wang, C. Xu, G. Wang, Y. Liu, and C. Zheng, *Adv. Mater.* 14, 837 (2002).
360. M. Niederberger, F. Krumeich, H.-J. Muhr, M. Miller, and R. Nesper, *J. Mater. Chem.* 11, 1941 (2001).
361. X. W. Lou and H. C. Zeng, *Chem. Mater.* 14, 4781 (2002).
362. G. R. Patzke, F. Krumeich, and R. Nesper, *Angew. Chem., Int. Ed., Engl.* 41, 2446 (2002).
363. W. Wang, Y. Liu, C. Xu, C. Zheng, and G. Wang, *Chem. Phys. Lett.* 362, 119 (2002).

364. K. Matsui, T. Kyotani, and A. Tomita, *Adv. Mater.* 14, 1216 (2002).
365. P. Jeevanandam, Yu. Koltypin, and A. Gedanken, *NanoLett.* 1, 263 (2001).
366. J. V. Ryan, A. D. Berry, M. L. Anderson, J. W. Long, R. M. Stroud, V. M. Cepak, V. M. Browning, D. R. Rolison, and C. I. Merzbacher, *Nature (London)* 406, 169 (2000).
367. L. Guo, Z. Wu, T. Liu, W. Wang, and H. Zhu, *Chem. Phys. Lett.* 318, 49 (2000).
368. Z. Zhang, *J. Mater. Res.* 17, 1698 (2002).
369. Y. W. Wang, C. H. Liang, G. W. Meng, X. S. Peng, and L. D. Zhang, *J. Mater. Chem.* 12, 651 (2002).
370. B. Zheng, Y. Wu, P. Yang, and J. Liu, *Adv. Mater.* 14, 122 (2002).
371. W.-J. Kim and S.-M. Yang, *Adv. Mater.* 13, 1191 (2001).
372. D. A. Dikin, X. Chen, W. Ding, G. Wagner, and R. S. Ruoff, *J. Appl. Phys.* 93, 226 (2003).
373. Y. Liu, C. Zheng, W. Wang, Y. Zhan, and G. Wang, *J. Crystal Growth* 233, 8 (2001).
374. J. K. Jian, X. L. Chen, T. Xu, Y. P. Xu, L. Dai, and M. He, *Appl. Phys. A* 75, 695-697 (2002).
375. C. Xu, X. Zhao, S. Liu, and G. Wang, *Solid State Commun.* 125, 301 (2003).
376. Y. Liu, Y. Dong, and G. Wang, *Appl. Phys. Lett.* 82, 260 (2003).
377. Y. Chen, X. Cui, K. Zhang, D. Pan, S. Zhang, B. Wang, and J. G. Hou, *Chem. Phys. Lett.* 369, 16 (2003).
378. J. A. Nelson and M. J. Wagner, *J. Am. Chem. Soc.* 125, 332 (2003).
379. X. Y. Zhang, B. D. Yao, L. X. Zhao, C. H. Liang, L. D. Zhang, and Y. Q. Mao, *J. Electrochem. Soc.* 148, 398 (2001).
380. Y. Lei, L. D. Zhang, and J. C. Fan, *Chem. Phys. Lett.* 338, 231 (2001).
381. D. K. Yi, S. J. Yoo, and D.-Y. Kim, *NanoLett.* 2, 1101 (2002).
382. M. Zhang, Y. Bando, and K. Wada, *J. Mater. Sci. Lett.* 20, 167 (2001).
383. S. U. M. Khan and T. Sultana, *Sol. Energy Mater. Sol. Cells* 76, 211 (2003).
384. W. S. Yun, J. J. Urban, Q. Gu, and H. Park, *NanoLett.* 2, 447 (2002).
385. R. Lopez, T. E. Haynes, L. A. Boatner, L. C. Feldman, and R. F. Haglund, Jr., *Opt. Lett.* 27, 1327 (2002).
386. H. T. Zhang, Z. Gui, R. Fan, and X. H. Chen, *Inorg. Chem. Commun.* 5, 399 (2002).
387. J. Muster, G. T. Kim, V. Krstic, J. G. Park, Y. W. Park, S. Roth, and M. Burghard, *Adv. Mater.* 12, 420 (2000).
388. J. Livage, *Chem. Mater.* 3, 578 (1991).
389. G. N. Kryukova, G. A. Zenkovets, N. Pfänder, D.-S. Su, and R. Schlögl, *Mater. Sci. Eng.* 343, 8 (2003).
390. W. G. Gu, B. Zheng, W. Q. Han, S. Roth, and J. Liu, *NanoLett.* 2, 849 (2002).
391. Yu. Koltypin, S. I. Nikitenko, and A. Gedanken, *J. Mater. Chem.* 12, 1107 (2002).
392. Y. B. Li, Y. Bando, D. Golberg, and K. Kurashima, *Chem. Phys. Lett.* 367, 214 (2003).
393. X.-L. Li, J.-F. Liu, and Y.-D. Li, *Inorg. Chem.* 42, 921 (2003).
394. S. Kwan, F. Kim, J. Akana, and P. Yang, *Chem. Commun.* 447 (2001).
395. H.-W. Liao, Y.-F. Wang, X.-M. Liu, Y.-D. Li, and Y.-T. Qian, *Chem. Mater.* 12, 2819 (2000).
396. S.-H. Yu, M. Antonietti, H. Cölfen, and M. Giersig, *Angew. Chem., Int. Ed. Engl.* 41, 2356 (2002).
397. J. Zhang, L. Sun, H. Pan, C. Liao, and C. Yan, *New J. Chem.* 26, 33 (2002).
398. Y. C. Kong, D. P. Yu, B. Zhang, W. Fang, and S. Q. Feng, *Appl. Phys. Lett.* 78, 407 (2001).
399. J. Y. Li, X. L. Chen, H. Li, M. He, and Z. Y. Qiao, *J. Cryst. Growth* 233, 5 (2001).
400. C. Pacholski, A. Kornowski, and H. Weller, *Angew. Chem.* 114, 1234 (2002).
401. C. Pacholski, A. Kornowski, and H. Weller, *Angew. Chem., Int. Ed. Engl.* 41, 1188 (2002).
402. Y. W. Wang, L. D. Zhang, G. Z. Wang, X. S. Peng, Z. Q. Chu, and C. H. Liang, *J. Cryst. Growth* 234, 171 (2002).
403. Y. C. Kong, D. P. Yu, B. Zhang, W. Fang, and S. Q. Feng, *Appl. Phys. Lett.* 78, 407 (2001).
404. P. Gao and Z. L. Wang, *J. Phys. Chem. B* 106, 12653 (2002).
405. L. Vayssieres, *Adv. Mater.* 15, 464 (2003).
406. B. D. Yao, Y. F. Chan, and N. Wang, *Appl. Phys. Lett.* 81, 757 (2002).
407. K. Park, J.-S. Lee, M.-Y. Sung, and S. Kim, *Jpn. J. Appl. Phys.* 41, 7317 (2002).
408. J.-S. Lee, M.-I. Kang, S. Kim, M.-S. Lee, and Y.-K. Lee, *J. Cryst. Growth* 249, 201 (2003).
409. S. Y. Li, C. Y. Lee, and T. Y. Tseng, *J. Cryst. Growth* 247, 357 (2003).
410. Z. L. Wang, Z. W. Pan, and Z. R. Dai, *Microsc. Microanal.* 8, 467 (2002).
411. L. Guo, Y. L. Ji, H. Xu, P. Simon, and Z. Wu, *J. Am. Chem. Soc.* 124, 14864 (2002).
412. Z. R. Tina, J. A. Voigt, J. Liu, B. McKenzie, and M. McDermot, *J. Am. Chem. Soc.* 124, 12954 (2002).
413. X. M. Sun, X. Chen, Z. X. Deng, and Y. D. Li, *Mater. Chem. Phys.* 78, 99 (2003).
414. J. Y. Lao, J. Y. Huang, D. Z. Wang, and Z. F. Ren, *NanoLett.* 3, 235 (2003).
415. H. Kim and W. Sigmund, *Appl. Phys. Lett.* 81, 2085 (2002).
416. Y. Liu, C. Zheng, W. Wang, Y. Zhan, and G. Wang, *J. Am. Ceram. Soc.* 85, 3120 (2002).
417. Z. Q. Shen, L. L. He, E. D. Wu, Y. Y. Fan, J. F. He, H. M. Cheng, D. X. Li, and H. Q. Ye, *J. Mater. Res.* 17, 2761 (2002).
418. C. Satishkumar, A. Govindaraj, E. M. Vogl, L. Basumallick, and C. N. R. Rao, *J. Mater. Res.* 12, 604 (1997).
419. M. Adachi, Y. Murata, I. Okada, and S. Yoshikawa, *Trans. Mater. Res. Soc. Jpn.* 27, 505 (2002).
420. X. Shi, S. Han, R. J. Sanedrin, F. Zhou, and M. Selke, *Chem. Mater.* 14, 1897 (2002).
421. X. Shi, S. Han, R. J. Sanedrin, C. Galvez, D. G. Ho, B. Hernandez, F. Zhou, and M. Selke, *NanoLett.* 2, 289 (2002).
422. A.-W. Xu, Y.-P. Fang, L.-P. You, and H.-Q. Liu, *J. Am. Chem. Soc.* 125, 1494 (2003).
423. M. Yada, M. Mihara, S. Mouri, M. Kuroki, and T. Kijima, *Adv. Mater.* 14, 309 (2002).
424. P. Wilson, *J. Phys. Chem. B* 101, 4917 (1997).
425. W. Shenton, T. Douglas, M. Young, G. Stubbs, and S. Mann, *Adv. Mater.* 11, 253 (1999).
426. Z. R. Dai, J. L. Gole, J. D. Stout, and Z. L. Wang, *J. Phys. Chem. B* 106, 1274 (2002).
427. G. H. Du, Q. Chen, R. C. Che, Z. Y. Yuan, and L.-M. Peng, *Appl. Phys. Lett.* 79, 3702 (2001).
428. T. Kasuga, M. Hiramatsu, A. Hoson, T. Sekino, and K. Niihara, *Langmuir* 14, 3160 (1998).
429. C.-H. Lin, S.-H. Chien, J.-H. Chao, C.-Y. Sheu, Y.-C. Cheng, Y.-J. Huang, and C.-H. Tsai, *Catal. Lett.* 80, 153 (2002).
430. Q. Zhang, L. Gao, J. Sun, and S. Zheng, *Chem. Lett.* 2, 226 (2002).
431. T. Kasuga, M. Hiramatsu, A. Hoson, T. Sekino, and K. Niihara, *Adv. Mater.* 11, 1307 (1999).
432. S. Uchida, R. Chiba, M. Tomiha, N. Masaki, and M. Shirai, *Electrochemistry* 70, 418 (2002).
433. B. D. Yao, Y. F. Chan, X. Y. Zhang, W. F. Zhang, Z. Y. Yang, and N. Wang, *Appl. Phys. Lett.* 82, 281 (2003).
434. Q. Chen, W. Zhou, G. H. Du, and L.-M. Peng, *Adv. Mater.* 14, 1408 (2002).
435. J.-F. Xu, R. Czerw, S. Webster, D. L. Carroll, J. Ballato, and R. Nesper, *Appl. Phys. Lett.* 81, 1711 (2002).
436. X. Chen, X. Sun, and Y. Li, *Inorg. Chem.* 41, 4524 (2002).

437. F. Bieri, F. Krumeich, H.-J. Muhr, and R. Nesper, *Helv. Chim. Acta* 84, 3015 (2001).
438. A. Doble, K. Ngala, S. Yang, P. Y. Zavalij, and M. S. Whittingham, *Chem. Mater.* 13, 4382 (2001).
439. F. Krumeich, H.-J. Muhr, M. Niederberger, F. Bieri, and R. Nesper, *Z. Anorg. Allg. Chem.* 626, 2208 (2000).
440. J. M. Reinoso, H.-J. Muhr, F. Krumeich, F. Bieri, and R. Nesper, *Helv. Chim. Acta* 83, 1724 (2000).
441. F. Krumeich, H.-J. Muhr, M. Niederberger, F. Bieri, M. Reinoso, and R. Nesper, *Mater. Res. Soc. Symp.* 581, 393 (2000).
442. H.-J. Muhr, F. Krumeich, U. P. Schonholzer, F. Bieri, M. Niederberger, L. J. Gauckler, and R. Nesper, *Adv. Mater.* 12, 231 (2000).
443. F. Krumeich, H.-J. Muhr, M. Niederberger, F. Bieri, B. Schnyder, and R. Nesper, *J. Am. Chem. Soc.* 121, 8324 (1999).
444. M. E. Spahr, P. Bitterli, R. Nesper, M. Muller, F. Krumeich, and F. H. U. Nissen, *Angew. Chem., Int. Ed. Engl.* 37, 1263 (1998).
445. K. S. Pillai, F. Krumeich, H.-J. Muhr, M. Niederberger, and R. Nesper, *Solid State Ionics* 141–142, 185 (2001).
446. P. Millet, J. Y. Henry, F. Mila, and J. Galy, *J. Solid State Chem.* 147, 676 (1999).
447. C. Wu, W. Qin, G. Qin, D. Zhao, J. Zhang, S. Huang, S. Lü, H. Liu, and H. Lin, *Appl. Phys. Lett.* 82, 520 (2003).
448. J.-J. Wu, S.-C. Liu, C.-T. Wu, K.-H. Chen, and L.-C. Chen, *Appl. Phys. Lett.* 81, 1312 (2002).
449. J. Q. Hu, Q. Li, X. M. Meng, C. S. Lee, and S. T. Lee, *Chem. Mater.* 15, 305 (2003).
450. C. N. R. Rao, B. C. Satishkumar, and A. Govindaraj, *Chem. Commun.* 1581 (1997).
451. X. Wen, W. Zhang, S. Yang, Z. R. Dai, and Z. L. Wang, *NanoLett.* 2, 1397 (2002).
452. L. Dai, X. L. Chen, X. N. Zhang, A. Z. Jin, T. Zhou, B. Q. Hu, and Z. Zhang, *J. Appl. Phys.* 92, 1062 (2002).
453. J. Zhang and L. Zhang, *Solid State Commun.* 122, 493 (2002).
454. G. Gundiah, A. Govindaraj, and C. N. R. Rao, *Chem. Phys. Lett.* 351, 189 (2002).
455. Z. R. Dai, Z. W. Pan, and Z. L. Wang, *J. Phys. Chem. B* 106, 902 (2002).
456. K. Matsui, B. K. Pradhan, T. Kyotani, and A. Tomita, *J. Phys. Chem. B* 105, 5682 (2001).
457. J. Liu, J. Cai, Y.-C. Son, Q. Gao, S. L. Suib, and M. Aindow, *J. Phys. Chem. B* 106, 9761 (2001).
458. J. Zhang, L. Zhang, Z. Peng, and X. Wang, *Appl. Phys. A* 73, 773 (2001).
459. J. Zhang and L. Zhang, *Chem. Phys. Lett.* 363, 293 (2002).
460. Y. Li, Y. Bando, and T. Sato, *Chem. Phys. Lett.* 359, 141 (2002).
461. K. L. Klug and V. P. Dravid, *Appl. Phys. Lett.* 81, 1687 (2002).
462. Y. B. Li, Y. Bando, D. Golberg, and K. Kurashima, *Appl. Phys. Lett.* 81, 5048 (2002).
463. X.-L. Li, J.-F. Liu, and Y.-D. Li, *Appl. Phys. Lett.* 81, 4832 (2002).
464. Z. L. Wang and Z. Pan, *Adv. Mater.* 14, 1029 (2002).
465. E. Comini, G. Faglia, G. Sberveglieri, Z. Pan, and Z. L. Wang, *Appl. Phys. Lett.* 81, 1869 (2002).
466. E. R. Leite, J. W. Gomes, M. M. Oliveira, E. J. H. Lee, E. Longo, J. A. Varela, C. A. Paskocimas, T. M. Boschi, F. Lanciotti, P. S. Pizani, and P. C. Soares, *J. Nanosci. Nanotechnol.* 2, 125 (2002).
467. J. Q. Hu, X. L. Ma, N. G. Shang, Z. Y. Xie, N. B. Wong, C. S. Lee, and S. T. Lee, *J. Phys. Chem. B* 106, 3823 (2002).
468. Z. R. Dai, J. Gole, J. D. Stout, and Z. L. Wang, *J. Phys. Chem. B* 106, 1274 (2002).
469. Z. R. Dai, Z. W. Pan, and Z. L. Wang, *Solid State Commun.* 118, 351 (2001).
470. K. McGuire, Z. W. Pan, Z. L. Wang, D. Milkie, J. Menendez, and A. M. Rao, *J. Nanosci. Nanotechnol.* 2, 499 (2002).
471. M. S. Arnold, P. Avouris, Z. W. Pan, and Z. L. Wang, *J. Phys. Chem. B* 107, 659 (2003).
472. X. Kong, D. Yu, and Y. Li, *Chem. Lett.* 32, 100 (2003).
473. Z. W. Pan, Z. R. Dai, and Z. L. Wang, *Appl. Phys. Lett.* 80, 309 (2002).
474. Z.-Y. Yuan, J.-F. Colomer, and B.-L. Su, *Chem. Phys. Lett.* 363, 362 (2002).
475. X. Sun, X. Chen, and Y. Li, *Inorg. Chem.* 41, 4996 (2002).
476. Y. B. Li, Y. Bando, T. Sato, and K. Kurashima, *Appl. Phys. Lett.* 81, 144 (2002).
477. J. Zhang, W. Yu, and L. Zhang, *Phys. Lett. A* 299, 276 (2002).
478. Y. Berta, C. Ma, and Z. L. Wang, *Micron* 33, 687 (2002).
479. J. S. Yin and Z. L. Wang, *Phys. Rev. Lett.* 79, 2570 (1997).
480. J. S. Yin and Z. L. Wang, *J. Phys. Chem. B* 101, 8979 (1997).
481. S. A. Iakovenko, A. S. Trifonov, M. Giersig, A. Mamedov, D. K. Nagesha, V. V. Hanin, E. C. Soladto, and N. A. Kotov, *Adv. Mater.* 11, 388 (1999).
482. T. Friend, G. Shemer, and G. Markovich, *Adv. Mater.* 13, 1158 (2001).
483. C. Wang, Y. Zhang, L. Dong, L. Fu, Y. Bai, T. Li, J. Xu, and Y. Wei, *Chem. Mater.* 12, 3662 (2000).
484. S. Matsushita, T. Miwa, D. A. Tryk, and A. Fujishima, *Langmuir* 14, 6441 (1998).
485. A. Chemseddine and T. Moritz, *Eur. J. Inorg. Chem.* 235 (1999).
486. Cao, H. Wan, L. Huo, and S. Xi, *J. Colloid Interface Sci.* 244, 97 (2001).
487. K. P. Velikov, F. Durst, and O. D. Velev, *Langmuir* 14, 1148 (1998).
488. N. D. Denkov, O. D. Velev, P. A. Kralchevsky, I. B. Ivanov, H. Yoshimura, and K. Nagayama, *Langmuir* 8, 3183 (1992).
489. S. I. Matsushita, T. Miwa, and A. Fujishima, *Langmuir* 17, 988 (2001).
490. M. Li, H. Schnablegger, and S. Mann, *Nature (London)* 402, 393 (1999).
491. F. Kim, S. Kwan, J. Akana, and P. Yang, *J. Am. Chem. Soc.* 123, 4360 (2001).
492. H. Maeda and Y. Maeda, *Langmuir* 12, 1446 (1996).
493. P. Yang and F. Kim, *Chem. Phys. Chem.* 3, 503 (2002).
494. Y. W. Wang, C. H. Liang, G. Z. Wang, T. Gao, S. X. Wang, J. C. Fan, and L. D. Zhang, *J. Mater. Sci. Lett.* 20, 1687 (2001).
495. X. Jiang, T. Herricks, and Y. Xia, *NanoLett.* 2, 1333 (2002).
496. L. Huang, H. Wang, Z. Wang, A. Mitra, D. Zhao, and Y. Yan, *Chem. Mater.* 14, 876 (2002).
497. Y. W. Heo, V. Varadarajan, M. Kaufman, K. Kim, D. P. Norton, F. Ren, and P. H. Fleming, *Appl. Phys. Lett.* 81, 3046 (2002).
498. S. V. Prasad, S. D. Walckb, and J. S. Zabinski, *Thin Solid Film* 360, 107 (2000).
499. W. I. Park, D. H. Kim, S.-W. Jung, and G.-C. Yi, *Appl. Phys. Lett.* 80, 4232 (2002).
500. S.-C. Liu and J.-J. Wu, *J. Mater. Chem.* 12, 3125 (2002).
501. J.-J. Wu and S.-C. Liu, *Adv. Mater.* 14, 215 (2002).
502. R. Liu, A. A. Vertegel, E. W. Bohannon, T. A. Sorenson, and J. A. Switzer, *Chem. Mater.* 13, 508 (2001).
503. S. C. Lyu, Y. Zhang, H. Ruh, H. J. Lee, H.-W. Shim, E.-K. Suh, and C. J. Lee, *Chem. Phys. Lett.* 363, 134 (2002).
504. M. J. Zheng, L. D. Zhang, G. H. Li, and W. Z. Shen, *Chem. Phys. Lett.* 363, 123 (2002).
505. L. Dloczik, R. Engelhardt, K. Ernst, S. Fiechter, I. Sieber, and R. Konenkamp, *Appl. Phys. Lett.* 78, 3687 (2001).
506. Y. Wu, H. Yan, and P. Yang, *Top. Catal.* 19, 197 (2002).
507. P. Yang, H. Yan, S. Mao, R. Russo, J. Johnson, R. Saykally, N. Morris, J. Pham, R. He, and H.-J. Choi, *Adv. Funct. Mater.* 12, 323 (2002).
508. Y. Li, G. W. Meng, L. D. Zhang, and F. Phillipp, *Appl. Phys. Lett.* 76, 2011 (2000).
509. B. B. Lakshmi, P. K. Dorhout, and C. R. Martin, *Chem. Mater.* 9, 857 (1997).
510. Z. Wang and H. L. Li, *Appl. Phys. A* 74, 201 (2002).
511. L. Vayssieres, K. Keis, A. Hagfeldt, and S.-E. Lindquist, *Chem. Mater.* 13, 4395 (2001).



512. R. L. Nigro, G. Malandrino, and I. L. Fragala, *Chem. Mater.* 13, 4402 (2001).
513. Y. Zhou, C. Shen, and H. Li, *Solid State Ionics* 146, 81 (2002).
514. Y. Zhou and H. Li, *J. Mater. Sci.*, 37, 5261 (2002).
515. Y. Zhou, J. Huang, C. Shen, and H. Li, *Mater. Sci. Eng.* A335, 260 (2002).
516. B. B. Lakshmi, C. J. Patrissi, and C. R. Martin, *Chem. Mater.* 9, 2544 (1997).
517. Y.-K. Zhou, J. Huang, and H.-L. Li, *Appl. Phys. A* 76, 53 (2003).
518. Y. Zhou and H. Li, *J. Solid State Chem.* 165, 247 (2002).
519. S. Aggarwal, A. P. Monga, S. R. Perusse, R. Ramesh, V. Ballarotto, E. D. Williams, B. R. Chalamala, Y. Wei, and R. H. Reuss, *Science (Washington, DC)* 287, 2235 (2000).
520. J. Q. Hu, Y. Jiang, X. M. Meng, C. S. Lee, and S. T. Lee, *Chem. Phys. Lett.* 367, 339 (2003).
521. S. L. Limmer, S. Seraji, Y. Wu, T. P. Chou, C. Nguyen, and G. Cao, *Adv. Funct. Mater.* 12, 59 (2002).
522. Y.-Q. Zhu, W.-K. Hsu, M. Terrones, N. Grobert, W.-B. Hu, J. P. Hare, H. W. Kroto, and D. R. M. Walton, *Chem. Mater.* 11, 2709 (1999).
523. M. Zhang, Y. Bando, K. Wada, and K. Kurashima, *J. Mater. Sci. Lett.* 18, 1911 (1999).
524. M. Zheng, G. Li, X. Zhang, S. Huang, Y. Lei, and L. Zhang, *Chem. Mater.* 13, 3859 (2001).
525. Z. Miao, D. Xu, J. Quyang, G. Guo, X. Zhao, and Y. Tang, *NanoLett.* 2, 717 (2002).
526. X. Y. Zhang, L. D. Zhang, W. Chen, G. W. Meng, M. J. Zheng, and L. X. Zhao, *Chem. Mater.* 13, 2511 (2001).
527. H. Masuda, K. Kanezawa, M. Nakao, A. Yokoo, T. Tamamura, T. Sugiura, H. Minoura, and K. Nishio, *Adv. Mater.* 15, 159 (2003).
528. J. Rodriguez, M. Gomez, J. Lu, E. Olsson, and C.-G. Granqvist, *Adv. Mater.* 12, 341 (2000).
529. S. M. Liu, L. M. Liu, W. D. Zhang, and H. C. Zeng, *Chem. Mater.* 14, 1391 (2002).
530. D. Gong, C. A. Grimes, O. K. Varghese, W. Hu, R. S. Singh, Z. Chen, and E. C. Dickey, *J. Mater. Res.* 16, 3331 (2001).
531. P. Hoyer, *Langmuir* 12, 1411 (1996).
532. S. Z. Chu, K. Wada, S. Inoue, and S.-I. Todoroki, *Chem. Mater.* 14, 266 (2002).
533. J. Bao, C. Tie, Z. Xu, and Q. Ma, *Adv. Mater.* 14, 44 (2002).
534. J. Bao, D. Xu, Q. Zhou, and Z. Xu, *Chem. Mater.* 14, 4709 (2002).
535. Y. Li and L. Bando, *Chem. Phys. Lett.* 364, 484 (2002).
536. C. R. Martin, *Chem. Mater.* 9, 862 (1997).
537. Z. Huan, H. Huang, and S. Fan, *Adv. Mater.* 14, 303 (2002).
538. J. Zou, L. Pu, X. Bao, and D. Feng, *Appl. Phys. Lett.* 80, 1079 (2002).
539. L. Pu, X. Bao, J. Zou, and D. Feng, *Angew. Chem., Int. Ed. Engl.* 40, 1490 (2001).
540. L. Vayssieres, N. Beermann, S.-E. Lindquist, and A. Hagfeldt, *Chem. Mater.* 13, 233 (2001).
541. M. Zheng, L. Zhang, X. Zhang, J. Zhang, and G. Li, *Chem. Phys. Lett.* 334, 298 (2001).
542. M. J. Zheng, L. D. Zhang, G. H. Li, X. Y. Zhang, and X. F. Wang, *Appl. Phys. Lett.* 79, 839 (2001).
543. B. Cheng and E. T. Samulski, *J. Mater. Chem.* 11, 2901 (2001).
544. S. Sharma and M. K. Sunkara, *J. Am. Chem. Soc.* 124, 12288 (2002).
545. K.-W. Chang, S.-C. Liu, L.-Y. Chen, F. C.-N. Hong, and J.-J. Wu, *Mater. Res. Soc. Symp. Proc.* 703, 129 (2002).
546. B. A. Hernandez, K.-S. Chang, E. R. Fisher, and P. K. Dorhout, *Chem. Mater.* 14, 480 (2002).
547. M. Nishizawa, K. Mukai, S. Kuwabata, C. R. Martin, and H. Yoneyama, *J. Electrochem. Soc.* 144, 1923 (1997).
548. I. Satoh and T. Kobayashi, *J. Appl. Phys.* 91, 6529 (2002).
549. J. C. Juang, E. I. Meletis, and K. I. Gnanasekar, *Appl. Phys. Lett.* 80, 4831 (2002).
550. H.-J. Muhr, F. Krumeich, U. P. Schonholzer, F. Bieri, M. Niederberger, L. J. Gauckler, and R. Nesper, *Adv. Mater.* 12, 231 (2000).
551. M. Niederberger, H.-J. Muhr, F. Krumeich, F. Bieri, D. Gunther, and R. Nesper, *Chem. Mater.* 12, 1995 (2000).
552. G. Gou, B. Zheng, W. Q. Han, S. Roth, and J. Liu, *NanoLett.* 2, 849 (2002).
553. M. H. Huang, S. Mao, H. Feick, H. Yan, Y. Wu, H. Kind, E. Weber, R. Russo, and P. Yang, *Science (Washington, DC)* 292, 1897 (2001).
554. J. C. Johnson, H. Yan, R. D. Schaller, L. H. Haber, R. J. Saykally, and P. Yang, *J. Phys. Chem. B* 105, 11387 (2001).
555. S. S. Mao, R. E. Russo, and P. Yang, *Proc. SPIE* 4608, 225 (2002).
556. S. S. Mao, *Int. J. Nanotechnol.* 1, 42 (2003).
557. J. C. Johnson, H. Yan, R. D. Schaller, P. B. Petersen, P. Yang, and R. J. Saykally, *NanoLett.* 2, 279 (2002).
558. N. Beermann, L. Vayssieres, S.-E. Lindquist, and A. Hagfeldt, *J. Electrochem. Soc.* 147, 2456 (2000).
559. T. Lindgren, H. Wang, N. Beermann, L. Vayssieres, A. Hagfeldt, and S.-E. Lindquist, *Sol. Energy Mater. Sol. Cells* 71, 231–243 (2002).
560. T. Lindgren, L. Vayssieres, H. Wang, and S.-E. Lindquist, in “Chemical Physics of Nanostructured Semiconductors” (A. I. Kokorin and D. W. Bahnemann, Eds.), pp. 93–126. VSP-International Science Publishers, 2003.
561. D. D. Lee and W. T. Chung, *Sens. Actuators* 20, 301 (1989).
562. G. Sberveglieri, S. Groppelli, and G. Coccori, *Sens. Actuators* 15, 235 (1988).
563. S. W. Lee, R. P. Tsai, and H. Chen, *Sens. Actuators, B* 67, 122 (2000).
564. S.-S. Park and J. D. Mackenzie, *Thin Solid Films* 274, 154 (1996).
565. R. K. Sharma and M. C. Bhatnagar, *Sens. Actuators, B* 56, 215 (1999).
566. D. Davazoglu and K. Georgouleas, *J. Electrochem. Soc.* 145, 1346 (1998).
567. V. Guidi, D. Boscarino, L. Casarotto, E. Comini, M. Ferroni, G. Martinelli, and G. Sberveglieri, *Sens. Actuators, B* 77, 55 (2001).
568. T. Miyata and T. Minami, *Thin Solid Films* 355–356, 35 (1999).
569. V. V. Kissine, S. A. Voroshilov, and V. V. Sysoev, *Thin Solid Films* 348, 304 (1999).
570. S. Xue, W. O. Benoman, and R. A. Lessard, *Thin Solid Films* 250, 194 (1994).
571. G. Sberveglieri, G. Groppelli, and R. Nelli, *Sens. Actuators* 4, 457 (1991).
572. G. Faglia, P. Nelli, and G. Sberveglieri, *Sens. Actuators* 18–19, 497 (1994).
573. F. Cosandey, G. Skandan, and A. Singhal, *JOM* 52 (2000).
574. S. R. Morrison, *Sens. Actuators* 2, 32 (1982).
575. J.-H. Guo, L. Vayssieres, C. Persson, R. Ahuja, B. Johansson, and J. Nordgren, *J. Phys.: Condens. Matter* 14, 6969 (2002).

# Optical Fibers for Nanodevices

Jenny M. Tam, Sabine Szunerits,<sup>1</sup> David R. Walt

Tufts University, Medford, Massachusetts, USA

## CONTENTS

1. Introduction
  2. Optical Fibers
  3. Optical Fiber Modifications for Nanoscale Applications
  4. Fiber Optic-Based Nanodevices
  5. Conclusions
- Glossary  
References

## 1. INTRODUCTION

Optical fibers offer a unique platform for the fabrication of a variety of nanostructures and nanodevices. Nanotechnology applications incorporating optical fibers have grown during the past twenty years, and modified optical fibers have been increasingly used in the fabrication of nanodevices. For example, optical fibers have been used in microscopy tools, such as near-field scanning optical microscopy (NSOM), to examine the optical properties of nanostructures. Analyzing the optical properties of nanometer-sized structures has become difficult as measurements and resolution have become diffraction limited [1–3], but NSOM has overcome this hurdle. NSOM uses an optical fiber tapered to a nanometer-sized aperture to bypass the diffraction limit of light. Illuminating a NSOM fiber probe and placing it close to the sample surface can make it possible to examine optical characteristics at the nanometer scale. In addition, NSOM has spawned a variety of devices to tackle some of the limitations with current lithographic technologies for data storage.

Optical fibers have also been used as transducers in sensing devices capable of monitoring and detecting a variety of chemical and biological analytes in different environments (e.g., blood, water, food, waste water) [4, 5]. Intracellular

<sup>1</sup>Permanent address: CEA Grenoble, UMR SPrAM 5819, 17, avenue des Martyrs, 38054 Grenoble Cedex, France.

processes inside living cells are more complicated to measure, but optical fibers have been tapered to a nanometer-sized apex and inserted into living cells without damaging them in order to measure cellular responses. As a result, these sensors have been able to further elucidate complex intracellular processes.

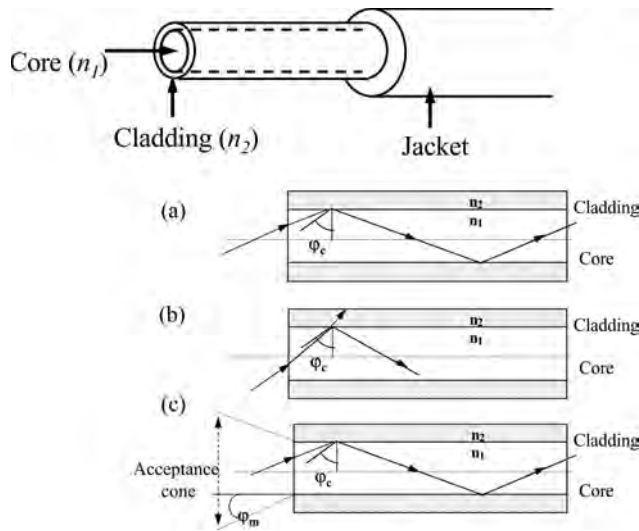
The nanometer physical aspects of tapered fibers and bundles of tapered fibers have also been used as templates to fabricate a variety of nanostructures. With the direction of light at nanometer-sized tip apices, photopolymerization can be controlled to form nanometer-sized polymer spots [6]. The nanotips have also been immersed in a heated polymer film, indenting the surface and forming nanometer-sized wells. Fiber optic bundles have also been modified to form arrays of nanowells [7] that have been used as templates for nanofabrication. With the immersion of the nanowell array in a polymer solution, arrays of nanocones were produced.

Fundamental characteristics of fibers and fiber bundles will be examined, as well as how they can be modified for nanodevices. Applications incorporating modified fibers, such as nanotips and nanowells, will be described, as well as new approaches to utilize these devices to overcome limitations that face current technologies.

## 2. OPTICAL FIBERS

### 2.1. Fundamental Characteristics of Optical Fibers

Optical fibers act as wave guides, efficiently transmitting light from one end of the fiber to the other. Optical fibers can be made out of glass or plastic, resulting in a strong, flexible, and durable component for a variety of applications. An optical fiber is composed of a core, with a refractive index  $n_1$ , surrounded by a cladding with a *lower* refractive index  $n_2$  (Fig. 1). The refractive index mismatch results in total internal reflection at the core-clad interface, effectively acting like a mirror and confining the transmission of light to the fiber core with minimal attenuation. Several principles govern the light transmission through an optical fiber and are significant in their function in nanodevices.



**Figure 1.** Schematic diagram of an optical fiber with the core and clad structure. Propagation of light through an optical fiber occurs through total internal reflection. Total internal reflection occurs at the interface between the core ( $n_1$ ) and the clad ( $n_2$ ), where  $n_1 > n_2$ . (a) Total internal reflection occurs when the light angle is greater than the critical angle  $\phi_c$ . (b) Light is partially reflected and partially refracted if the light angle is less than the critical angle  $\phi_c$ . (c) Total internal reflection will occur only if the entering light angle is within the acceptance cone  $\phi_m$  of the fiber.

### 2.1.1. The Critical Angle

The guiding principle for light in an optical wave guide is total internal reflection (Fig. 1). According to Snell's law of refraction

$$n_1 \times \sin \Theta_1 = n_2 \times \sin \Theta_2 \quad (1)$$

For a step-index fiber, where  $n_1 > n_2$ , total internal reflection occurs when the incident angle  $\Theta_1$  meets the criterion  $90^\circ > \Theta_1 > \Theta_c$ , where  $\Theta_c$  is given by

$$\Theta_c = \sin^{-1}(n_2/n_1) \quad (2)$$

The critical angle  $\Theta_c$  depends on the indices of refraction between the core and the cladding. Provided that total internal reflection occurs at the core-clad interface, a ray of light propagates down the core as shown in Figure 1.

### 2.1.2. Acceptance Cone

High transmission efficiencies in optical fibers are achieved if the angle of the light entering the fiber is within the acceptance cone as shown in Figure 1c. The acceptance cone depends on the refractive indices of the core, clad, and the surrounding medium ( $n_o$ )

$$\sin \Theta_a = \frac{\sqrt{n_1^2 - n_2^2}}{n_o}$$

### 2.1.3. Numerical Aperture

The efficiency of the light collection of the fiber depends on the width of the acceptance cone and can be described in terms of its numerical aperture (NA)

$$NA = n_o \sin \Theta_a$$

A wide acceptance cone can gather light more efficiently, symbolized by a high NA.

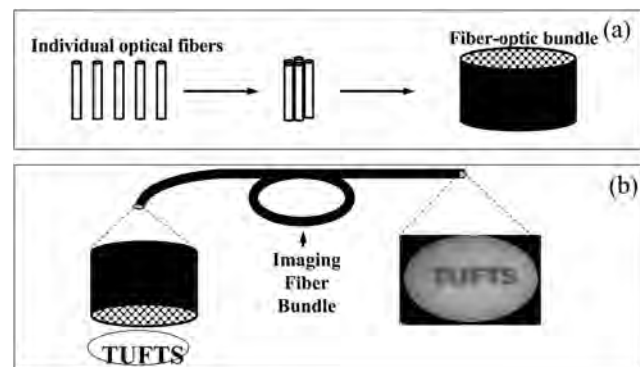
## 2.2. Types of Optical Fibers

Optical fibers are made from a variety of materials, but the most common material is silica. Pure silica has a refractive index of approximately 1.45, and doping it with various impurities will alter this value. For example, impurities that raise the refractive index include titania ( $\text{TiO}_2$ ), alumina ( $\text{Al}_2\text{O}_3$ ), and germania ( $\text{GeO}_2$ ), whereas boria ( $\text{B}_2\text{O}_3$ ) and fluorine ( $\text{F}_2$ ) will lower it [8]. Fibers with silica cores surrounded by plastic cladding are also available, as are all-plastic fibers.

## 2.3. Optical Fiber Configurations

Optical fibers are produced in many different configurations, sizes, and formats. One type of optical fiber consists of a single core surrounded by a clad material. Fiber optics is mainly used in telecommunications applications, but it has also been incorporated into new applications such as microscopy and sensing. Recently, optical fibers have also been integrated into devices to analyze and create nanostructures. For some fiber-optic nanodevices, optical fibers with diameters ranging from 50 to 500  $\mu\text{m}$  are tapered to a nanometer-sized tip for use in nanotechnology applications such as NSOM.

Fiber optic technology can go one step further—instead of using only one strand of fiber, thousands to tens of thousands of optical fibers can be bundled together and used for imaging applications. Single optical fibers cannot transmit images because the light signal mixes as it is carried from one end of the fiber to the other. Fiber optic bundles, on the other hand, are composed of thousands of individual fibers melted and drawn together coherently (Fig. 2), such that an



**Figure 2.** (a) Fiber-optic bundles are composed of thousands to tens of thousands of individual fibers that are coherently fused together. (b) Fiber bundles can be used for imaging purposes. Reprinted with permission from [7], P. Pantano and D. R. Walt, *Chem. Mater.* 8, 2832 (1996). © 1996, American Chemical Society.

image is carried and maintained throughout the length of the bundle. The spatial resolution of the bundle depends on the diameter of each fiber in the bundle. Fiber bundles have been used in devices such as medical endoscopes to transmit images from inaccessible parts of the body to a detector. Optical fiber bundles have also been incorporated into optical sensors and nanodevices [4, 5]. Similar to single core fibers, the surface of the fiber bundles can be mechanically or chemically modified to produce arrays of nanostructures such as nanotips and nanowells.

### 3. OPTICAL FIBER MODIFICATIONS FOR NANOSCALE APPLICATIONS

#### 3.1. Optical Fibers as Probes in Near-Field Scanning Optical Microscopy

Conventional, far-field optical techniques have limited spatial resolution [9–11]. The typical rules of interference and diffraction are defined by the Abbe diffraction limit, in which the optical resolution is approximately  $\lambda/2(\text{NA})$ , where  $\lambda$  is the wavelength and NA is the numerical aperture [9]. The rapid development of nanotechnology demands better spatial resolution and has led to the development of alternative microscopy techniques such as near-field optics (NFO) and NSOM. NSOM offers enhanced spatial resolution, bypassing the Abbe diffraction limit by using a small, subwavelength-sized light source that effectively focuses photons through an aperture that may be as small as  $\lambda/50$  [9].

NSOM is a scanning technique that developed from principles derived from two other related scanning techniques, scanning tunneling microscopy (STM) and atomic force microscopy (AFM) [12–14]. In 1982, G. Binnig and H. Rohrer at the IBM Research Center in Zürich showed that topographic pictures of surfaces on an atomic scale could be obtained by a method they called STM or scanning tunneling microscopy [12]. STM consists of two electrodes, the tip and the sample, and measures the tunneling current between the tip and surface. STM obtains information about both the topographical and electronic surface structure. STM led to the development of other types of microscopy, particularly AFM.

An atomic force microscope creates a topographical image of a surface through physical interactions between a nanometer-sized probe and the sample surface [13, 14]. The probe consists of a sharp tip attached to a cantilever, and an image is created based on the deflection of the tip as it rasters over the sample surface. As a result, each point in the image directly corresponds to the surface structure.

Unlike STM or AFM, NFO images sample through the interaction of light with the surface through simple refraction/reflection contrast or absorption and fluorescence. Introduced by U. Düring in 1986 [15], NSOM illuminates a specimen through a subwavelength-sized aperture, typically a tapered fiber probe, while keeping the specimen close to the probe, typically 100 Å to tens of nanometers from the fiber. NSOM picks up information contained in the optical field just above the surface of the illuminated sample called the near-field region, where the sample and the probe light closely interact [3]. Radiation emitted from the

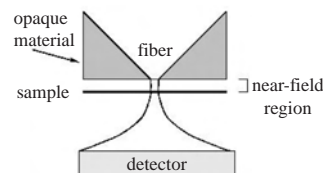


Figure 3. Schematic of near-field optics.

nanometer-sized probe is highly collimated in the near-field regime, decaying exponentially as photons move away from the surface, as shown in Figure 3. In NSOM, the spatial resolution of a sample is no longer limited by the diffraction limit of light—it is independent of the wavelength of light used and depends only on the size of the aperture. As a result, the quality of NSOM measurements is fully dependent on optical tip parameters, and the resolution is directly related to the size of the probe aperture, which is typically 50–200 nm [16]. Betzig and Chichester have reported the development of one such probe that has an optimum spatial resolution of 12 nm [17]. A NSOM can also supply additional physical information about a sample such as spectroscopic properties, optical thickness, topography, lateral structure, transparency, as well as its chemical behavior. NSOM has been mainly used for analytical applications, but several new NSOM-based applications have been proposed recently for nanotechnology; these are described in Section 4.

The formation of nanometer-sized fiber probes for microscopy applications, such as NSOM, progressed rapidly during the 1980s and 1990s. In these applications, the formation and characterization of the tips are crucial to instrument performance and image interpretation [18]. Several methods have been used to scale micrometer-size optical fibers for nanotechnology applications.

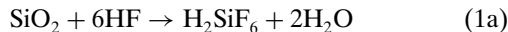
##### 3.1.1. Mechanical Pulling

One of the preferred methods for fabricating nanometer-sized probes is the mechanical pulling of heated fibers, with either a micropipette puller or a CO<sub>2</sub> laser [19–23]. In a micropipette puller, a small area of the fiber is situated in the center of a heating coil and then the tip of the fiber is pulled until it separates, leaving a long tip [23]. An apparatus used by Tan and co-workers [6] consists of a modified micropipette puller and a 25-W CO<sub>2</sub> infrared laser. The CO<sub>2</sub> laser replaces the heating coil. The laser beam is reflected off a mirror and directed to heat the optical fiber. Similar to the micropipette puller, the fiber is heated and then pulled until the fiber separates into two fibers, each with a long tip. To create nanometer-sized apertures, metal is coated along the length of the tapered fiber. To avoid metallizing and blocking the tip, the tip surface must be positioned essentially orthogonal to the pulled fiber wall [24]. The deposition angle also has to be carefully adapted to the tip geometry.

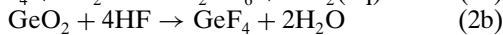
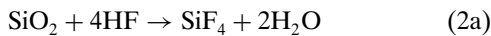
Mechanical pulling is fast compared with chemical etching (*vide infra*) and is quite controllable, since there is precise control over the heating and pulling parameters. Although transmission is low through pulled fibers, they have well-defined apertures, with diameters as small as 50 nm.

### 3.1.2. Chemical Etching

Chemical etching produces shorter tapers with larger cone angles, resulting in higher transmission efficiency (shown in Fig. 4) [18, 25–42]. Furthermore, chemical etching offers a simple and inexpensive fabrication method, especially compared with mechanical pulling. Depending on the composition of the glass, different acidic solutions are used. Silica fibers are chemically etched in a one-step procedure with a solution of hydrofluoric acid (HF) and ammonium fluoride ( $\text{NH}_4\text{F}$ ) buffer. The etch rate depends on the dopant concentration in the fiber and the concentration of the acid solution. Single core optical fibers and fiber bundles can be etched to form either nanotips or nanowells. For example, in the fiber bundles used by Pantano and Walt [7, 43], the pure  $\text{SiO}_2$  of the fiber cladding etches at a different rate than the  $\text{GeO}_2$ -doped  $\text{SiO}_2$  of the core, and depending on the dopant concentration of the core and cladding, either nanotips or nanowells can be formed. Figures 5 and 6 show images of the nanotips and nanowells that can be fabricated. The chemical reaction of  $\text{SiO}_2$  and  $\text{GeO}_2$  with HF acid can be summarized by reactions (1)–(3) [44].



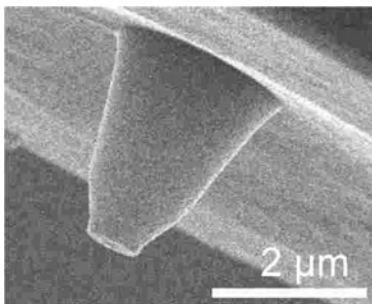
The fluorosilicic acid ( $\text{H}_2\text{SiF}_6$ ) and the hexafluorogermanic acid ( $\text{H}_2\text{GeF}_6$ ) are produced directly as outlined by reactions (1a) and (1b) but also can arise from



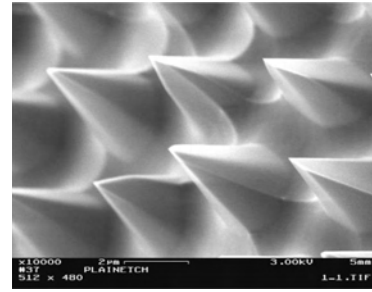
If an ammonium fluoride-buffered etching solution is used, there is a further possible dissolution step that arises from the involvement of ammonia ionized from the solution (reaction (3)).



The difference in solubility of the resultant  $(\text{NH}_4)_2\text{SiF}_6$  and  $(\text{NH}_4)_2\text{GeF}_6$  leads to different etching rates between the core and cladding. Therefore, the tip cone angle is a



**Figure 4.** Etched fiber optic for use as a NSOM probe. Reprinted with permission from JASCO Inc.



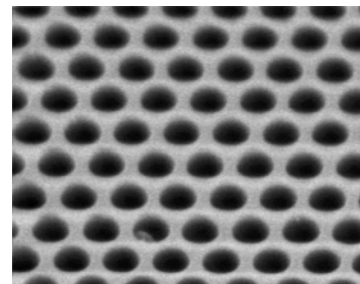
**Figure 5.** Scanning electron micrograph of an array of nanotips formed by chemical etching of a fiber-optic bundle.

function of the concentration of etchant solution and the  $\text{GeO}_2$  dopant level of the fiber core. Temperature can also influence the tip cone angle [18].

Etching parameters such as solvent type, acid concentration, etching time, and temperature are crucial for optical and geometrical characteristics (e.g., cone angle, aperture diameter, well size); Table 1 lists some of the conditions used in the literature. Recently, it was shown that a multiple-step etching process followed by application of an organic protecting layer improved optical characteristics of the fibers [37]. Stöckle developed a specific chemical etching method called tube etching. It involves etching fiber tips surrounded with an organic cladding where the acid first etches away the tip of the fiber without destroying the cladding [45]. The polymer cladding is thus acting as a wall, creating microcurrents in the acid, which, coupled with capillary action, cause the fiber to be etched into the shape of a cone with a large, smooth taper.

### 3.1.3. Fracturing

Fischer and co-workers [46, 47] fabricated tetrahedral tips for NSOM, using modified ultramicrotome glass blades. A rectangular slab of glass was cleaved twice at an angle. A tetrahedral tip consists of a pyramidal glass fragment, which is then coated with a gold film. The tetrahedral tip is mounted on the oblique end face of a glass support by an index matching glue. A beam of light incident at an angle of  $45^\circ$  can irradiate the tip.



**Figure 6.** Scanning electron micrograph of a nanowell array formed by chemical etching of a fiber-optic bundle. The doping concentration in the core and clad material determines whether nanotips or nanowells will be formed.

**Table 1.** Etching conditions and the optical fiber apertures obtained.

	Mode	Fiber	Time temp.	Solution	Characteristics	Comments	Ref.
1	SM	Silica glass fiber FS-SN-3224, 3 M C 4 $\mu\text{m}$ / G 125 $\mu\text{m}$	21 °C 140 min	HF (40%)	CA 50°–80°	Bevelling	[93, 94]
2	SM	Silica glass fiber Newport F-SF		HF (48%), NH <sub>4</sub> F (40%) water ratio = 1:x:1 x = 1.5, 7	CA 8°–90°	Organic solvent as protection	[37]
3	SM	Silica glass fiber FS-SN-3224, 3 M C 3 $\mu\text{m}$	10–50 °C, 90 min	HF (21, 28, 34, 40%)	CA 18°–35°	<i>p</i> -Xylene as protection	[45]
		Silica glass fiber 40-692.11, Cablotioc, C 3 $\mu\text{m}$					
		Silica glass fiber 91-9116.136, Alcatel C 3 $\mu\text{m}$					
	MM	HCG-M0100T-14, Laser Components C 100 $\mu\text{m}$					
	MM	HCG-M0200T-14, Laser Components C 200 $\mu\text{m}$ core					
4	SM	Bent SNOM tip	132 min	HF (48%), acetic acid ratio = 7:1	CA 40° 50-nm tip radii	Two-stage hexadecane	[39]
5	SM	GeO <sub>2</sub> -doped core	—	—	CA 150° 25 nm	Three-stage etching	[28]
7	IF	Sumitomo Electric Industries, IGN-035/06	RT 16 h	HF (50%), NH <sub>4</sub> F (40%) water ratio = 1:5:1	Tip diameter 300 nm		[43]
8	MM	Silica glass fiber Corning 6 62-125-900 ST	24–50 °C 1–20 h	HF (50%), NH <sub>4</sub> F (40%) water ratio = 1:x:1 x = 2, 4, 6	CA 36°–140°		[18, 95]
9	IF	Sumitomo Electric Industries, IGN-035/06	RT 7.5 h	HF (49%), NH <sub>4</sub> F (40%) water glacial acetic acid ratio = 1:6:1:1	CA 25° Radius of tip 15–50 nm		[88]
10	SM	GeO <sub>2</sub> -doped silica fibers (3.6–23 mol%)	22 °C 180 min	HF (50%), NH <sub>4</sub> F (40%) water ratio = 1:x:1 x = 4, 5, 6, 7	CA 20° Tip diameter 10 nm		[36]

Note: SM, single mode; MM, multiple mode; IF, imaging fiber; C, cone; G, cladding; CA, cone angle.

## 4. FIBER OPTIC-BASED NANODEVICES

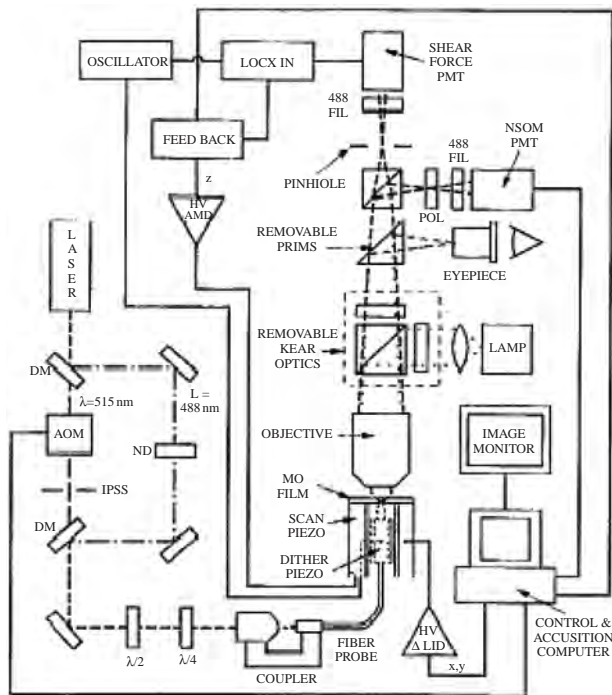
### 4.1. NSOM-Based Applications in Nanotechnology

#### 4.1.1. NSOM-Based Optical Storage

In addition to its use in analytical applications as well as in the detection of nanostructures ([48–50] and references therein), NSOM is also used for data storage applications. Data are written and read off of optical storage devices by using a focused laser beam on a storage medium [51]. The data density on optical storage disks is determined by the size of the focused laser spot, which is determined by the diffraction limit of light, approximately  $\lambda/2(\text{NA})$ . The diffraction limit can be overcome, however, by NFO

techniques, as discussed previously. Smaller spot sizes can increase the areal density over what is currently available on storage devices.

Near-field techniques were used to write and read data [52–60] domains as small as 60 nm in thin-film magneto-optic materials [61]. As shown in Figure 7, a dichroic mirror splits a beam from an Ar laser into two distinct wavelengths. One beam is used for reading, and another is used for writing. The beam used for reading is attenuated with a neutral-density filter, while the writing beam is controlled with an acousto-optic modulator. The beams are then recombined and coupled into an optical fiber NSOM probe. Half-wave ( $\lambda/2$ ) and quarter-wave ( $\lambda/4$ ) plates, positioned before the fiber coupler, adjust the polarization of the laser light to an almost purely linear state. The Faraday effect rotates



**Figure 7.** Schematic of system used for near-field magneto-optic imaging and recording. Reprinted with permission from [61], E. Betzig et al. *Appl. Phys. Lett.* 61, 142 (1992). © 1992, American Institute of Physics.

the polarization of the light slightly as it passes through the magneto-optical film. The direction of the rotation is determined by the orientation of the magnetization immediately under the probe. A conventional optical microscope then collects the light, and the image is viewed with a polarizer/photomultiplier tube combination.

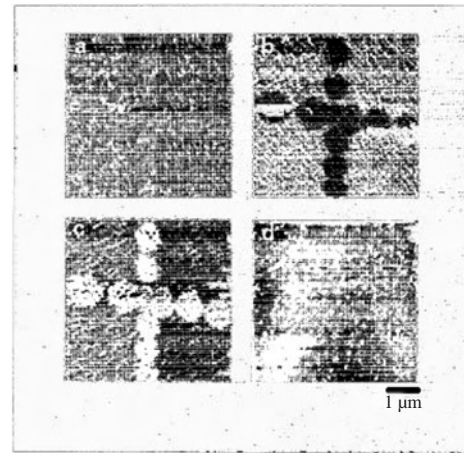
The acousto-optical modulated laser beam writes data on the magneto-optical storage medium by heating the data region under the probe near the Curie temperature [61], magnetizing the domain in a direction opposite that of the surrounding medium. After writing, the data are then read with the lower power read beam. An example of written data is shown in Figure 8.

The data domains are approximately 100 nm in diameter with a 200-nm center-to-center spacing. The polarization of the aperture is rotated by approximately  $+1^\circ$  and  $-1^\circ$  (Fig. 9a and b, respectively). The pattern on the storage medium is imaged as it appears, composed of alternating contrast regions. Although high laser power may be required, the entire reading and writing process is straightforward.

#### 4.1.2. NSOM Optical Lithography

The smallest structures that can be achieved with conventional optical lithography are determined by the Abbe diffraction limit. Although shorter wavelengths (UV, X-rays) and particle beams have brought the feature sizes down to a few nanometers, the setups are costly. NFO lithography was investigated as a method to bypass the limitations faced in conventional optical lithography [62–64].

A near-field lithographic probe was fabricated by drawing an optical fiber while it was heated with a  $\text{CO}_2$  laser. The tapered ends were subsequently coated with an approximately



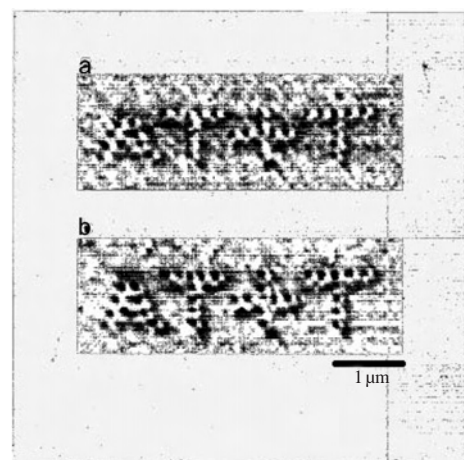
**Figure 8.** (a–c) Near-field magneto-optic images of conventionally written domains at three different polarization states. (d) Topographical image of the same region obtained with shear force microscopy. Reprinted with permission from [61], E. Betzig et al., *Appl. Phys. Lett.* 61, 142 (1992). © 1992, American Institute of Physics.

100-nm layer of aluminum. Typical aperture sizes of about 50 nm were achieved.

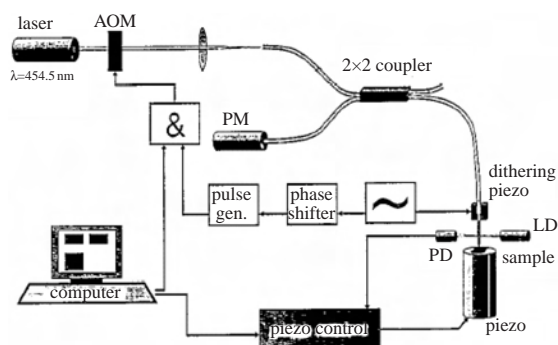
As shown in Figure 10, a photoresist sample was mounted on a piezoelectric motor and was placed in proximity to the near-field probe, approximately 10 nm away. An Ar laser was coupled into the optical fiber that was connected to a fiber coupler. An acousto-optical modulator was placed in the laser beam to control the exposure of the laser light to the photoresist. Lines about 80 nm wide and 10 nm deep were written on the surface upon exposure to laser light emitted from the probe. The surface structures were analyzed with an AFM, as shown in Figure 11.

#### 4.1.3. Near-Field Optical Array

Single probes in conventional NSOMs are limited in that they can only examine one particular region at a time [6, 65]. Pantano and Walt [7, 43] fabricated a NFO array



**Figure 9.** Written domains with  $\sim 100$ -nm diameters formed and imaged with near-field techniques. Two different polarization states are shown in (a) and (b). Reprinted with permission from [61], E. Betzig et al. *Appl. Phys. Lett.* 61, 142 (1992). © 1992, American Institute of Physics.

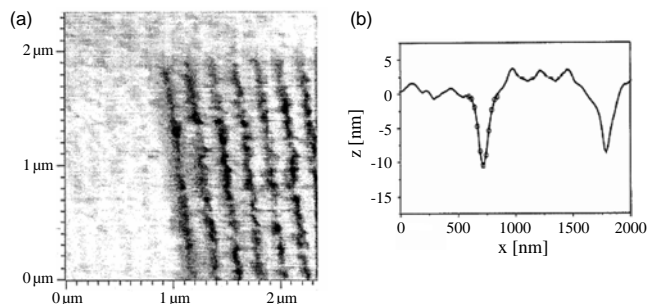


**Figure 10.** Schematic view of experimental setup used for NSOM lithography. Reprinted with permission from [96], G. Krausch et al., *Thin Solid Films* 264, 264 (1995). © 1995, Elsevier Science.

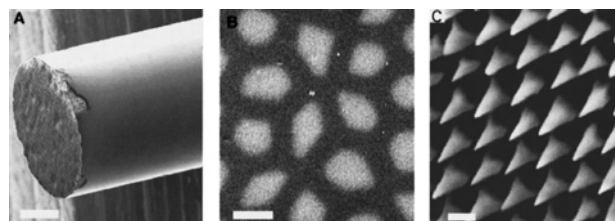
that can overcome this limitation. A 300- $\mu\text{m}$ -diameter imaging fiber bundle, comprising approximately 6000 coherently fused optical fibers, was chemically etched in a buffered HF solution for 16 h, yielding an array of near-field tips (shown in Fig. 12).

To prevent light leakage from the sidewalls of each tip in the array, a gold layer coated the entire array. The entire array was crudely ground on a spinning mirror to create nanoapertures on each tip. Metal-coated tips with apertures as small as 300 nm were fabricated, and the height differences between near-neighbor tips were as small as approximately 20 nm, as shown in Figure 13. The optical properties of the array were also investigated by directing light through the proximal end of the fiber and imaging a small portion of the distal face through a microscope objective.

The major advantage of a near-field array is that it can scan a larger area of a sample. For example, in an equivalent period of time, an array of several thousand 100-nm-diameter near-field tips on the distal face of a 300- $\mu\text{m}$ -diameter fiber bundle could scan over an area approximately three orders of magnitude larger than that of a single 100-nm-sized tip. In addition, commercial imaging fibers are available with up to 100,000 individually clad optical fibers such that very large regions can be imaged with subwavelength resolution.



**Figure 11.** AFM images of lines created by near-field scanning lithography. (a) Top view of a set of parallel lines created by a single path exposure through the tapered tip of an optical fiber. (b) A cross-sectional view of two written lines. The open circles represent a least-squares fit of a Gaussian profile to the data. Reprinted with permission from [96], G. Krausch et al., *Thin Solid Films* 264, 264 (1995). © 1995, Elsevier Science.



**Figure 12.** (A) A low-magnification scanning electron micrograph of a chemically etched fiber bundle. The white bar denotes a 50- $\mu\text{m}$  distance. (B) A high-magnification image of the fiber surface before it was chemically etched. The white bar denotes a 2.5- $\mu\text{m}$  distance. (C) A high-magnification image of the fiber bundle after it was chemically etched, forming an array of nanotips. The white bar denotes a 2.0- $\mu\text{m}$  distance. Reprinted with permission from [43], P. Pantano and D. R. Walt, *Rev. Sci. Instrum.* 68, 1357 (1997). © 1997, American Institute of Physics.

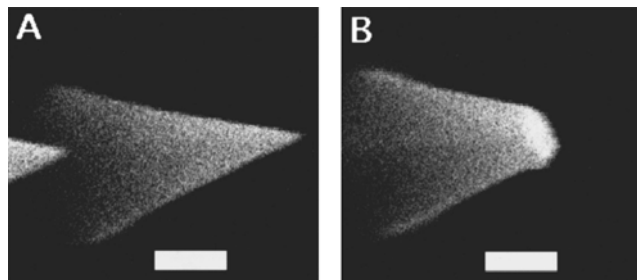
## 4.2. Nanosensors

The resolution obtained in near-field microscopy has become useful for single molecule detection [66–69]. Nano-probes have detected single dye and dye-labeled DNA molecules [48, 70]. The probes had a 100-nm resolution and were able to image labeled DNA molecules. Nanofibers can probe for specific chemicals in highly localized areas, capable of monitoring concentration gradients and spatial homogeneities in cellular environments. Kopelman et al. [6, 71] reported the first nanobiosensor to monitor the environment inside rat embryos. Measurements of  $\text{Na}^+$  and  $\text{Ca}^{2+}$  were also analyzed [72]. These conventional sensors are based on the measurement of fluorescence intensity or on the measurement of luminescence decay time [73].

### 4.2.1. Nano-Bio-Optrodes

The recent drive in nanotechnology research has led to the development of the nano-bio-optrode, a device that is able to monitor biomolecular concentrations inside a single living cell, elucidating more about the complex intracellular processes that occur [6, 10, 74].

Nano-bio-optrodes are composed of optical fibers a few nanometers in diameter. The optical fiber initially has a diameter of a few micrometers before a modified micropipette puller heats and pulls it to form the bio-optrode.



**Figure 13.** High-magnification scanning electron micrographs of a gold-coated, chemically etched fiber before (A) and after (B) it was ground on a spinning mirror. The white bars denote a 0.5- $\mu\text{m}$  distance. Reprinted with permission from [43], P. Pantano and D. R. Walt, *Rev. Sci. Instrum.* 68, 1357 (1997). © 1997, American Institute of Physics.



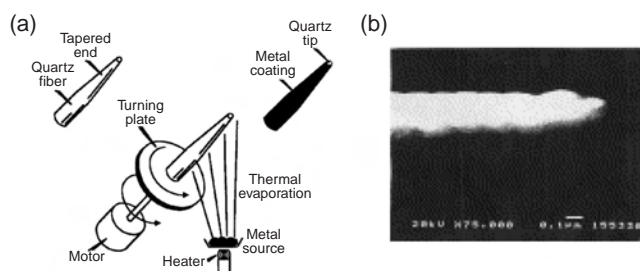
The distal tip of the tapered fiber typically has a diameter between 20 and 80 nm. Kopelman and co-workers [65] used this technique to fabricate nano-fiber-optic chemical sensors to monitor the pH inside living cells. A pH-sensitive dye was immobilized on the surface of the fiber tip in a polymer hydrogel to measure the pH changes.

An enzyme-based nano-bio-optrode was also used to measure nitric oxide content [75]. Fluorescently labeled cytochrome *c'* was immobilized on the tip of the fiber. In the presence of NO, cytochrome *c'* undergoes a conformational change. Nitric oxide concentration changes were correlated to changes in the energy transfer between cytochrome *c'* and the fluorescent dye.

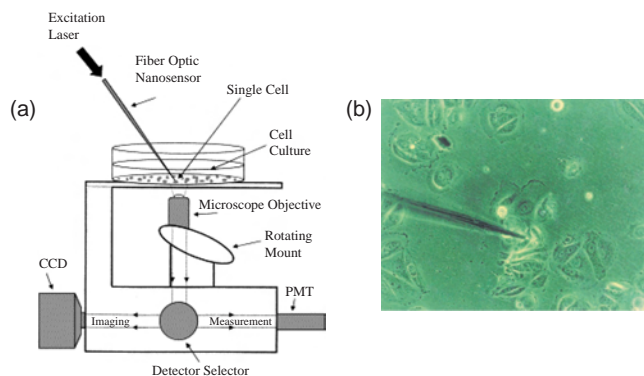
Vo-Dinh and co-workers fabricated an antibody-based nano-bio-optrode to detect benzo[a]pyrenetetrol (BPT) [76–78]. The outer walls of the tapered end of a 200-nm to 300-nm fiber were coated with a thin silver, gold, or aluminum layer with the use of a vacuum evaporator as shown in Figure 14. A turning plate/motor device held and rotated the fiber in the deposition chamber. The fiber was held at an angle relative to the metal vapor, and as it rotated, the metal evenly coated the sides of the fiber while leaving the tip uncoated. The metal coating prevents light from leaking from the fiber walls and maximizes the light intensity at the fiber tip. The uncoated tip surface was then silanized to covalently attach anti-BPT antibodies.

Figure 15 shows how the nano-bio-optrode measured BPT concentrations inside a single living cell. The tapered end of the fiber was inserted at an angle inside a living cell and incubated for 5 min to allow the antibodies to bind the antigen (BPT). Laser light was transmitted through the fiber and excited the fluorescent BPT. Bound BPT molecules changed the fluorescence signal. The fiber was then removed from the cell, and the fluorescence signal obtained from the bound BPT was collected through a microscope objective and measured and analyzed with a photomultiplier tube.

Nano-bio-optrodes are advantageous over larger bio-optrodes in that they have higher sensitivities and faster response times. Nano-bio-optrodes could detect BPT concentrations as low as 300 zeptomoles.



**Figure 14.** Fabricating nano-bio-optrodes. (a) An optical fiber heated and then tapered to submicron dimensions. Metal is then thermally evaporated on the fiber sidewalls to prevent light leakage. The fiber is mounted on a rotating plate, evaporating an even coating while creating an aperture. Antibodies can be immobilized on the bare distal tip. Reprinted with permission from [77], T. Vo-Dinh et al., *Nat. Biotechnol.* 18, 264 (2000), © 2000, Nature Publishing Group; and [78], T. Vo-Dinh et al., *Sens. Actuators, B* 74, 2 (2001), © 2001, Elsevier Science.



**Figure 15.** (a) The optical measurement system to monitor living cells. (b) A nano-bio-optrode inside a living cell. Reprinted with permission from [77], T. Vo-Dinh et al., *Nat. Biotechnol.* 18, 264 (2000), © 2000, Nature Publishing Group; and [78], T. Vo-Dinh et al., *Sens. Actuators, B* 74, 2 (2001), © 2001, Elsevier Science.

#### 4.2.2. Fiber Bundle-Based Nanotip pH Sensor

The desire to miniaturize analytical detectors such that data throughput can be increased while small volume samples are used has fueled the rapid development of nanobioanalytical techniques. Another desire in new imaging methodologies involves remote analysis of samples, without having to bring the sample to the microscope stage. A nanotip array, fabricated by chemically etching an imaging fiber bundle, was used to measure oxidative stress in biological cells [22].

Oxidative stress results in an overload of reactive oxygen species, such as hydrogen peroxide, and causes a pH change in cells. Oxidative stress is thought to be an important causative agent in a variety of pathologies such as aging, cardiovascular disease, some carcinogenesis, and possibly in AIDS. Conventional amperometric measurement techniques analyze oxidative stress by inserting the tip of a 5- $\mu\text{m}$  carbon-fiber microelectrode into a biological cell. Analysis indicated that the hydrogen peroxide was generated as a direct result of the microelectrode insertion [79–82]. A nanotip array would improve conventional oxidative stress monitoring techniques because the nanometer dimensions of the tip would be less intrusive to the cell. A nanotip array should also increase measurement throughput by providing sampling through many probes instead of using only one, and the nanotip array's sensing layer can be readily modified to allow investigation of a variety of biologically relevant analytes.

A nanotip array was fabricated by chemically etching a fiber bundle with HF, as discussed in Section 4.1.3, and a chemical sensing layer was deposited across the array such that the nanotip architecture was retained. In addition to its remote sensing abilities and measurement throughput improvements, the small nanotip diameters (ca. 200 nm) of the nanotip array should more closely mimic the size scale of biological entities such as bacteria and viruses in comparison with a conventional 5- $\mu\text{m}$  microelectrode tip.

### 4.3. Fiber Bundle-Based Photoimprint Lithography

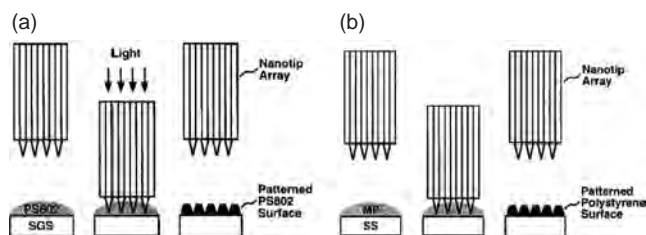
Well-established methods such as electron beam, X-ray, and UV lithographic methods have been used to create nanostructures [83–86] (Sun, 2002 #152, 87). Dam and Pantano [88] created a nanotip array by chemically etching fiber-optic imaging bundles as described in the previous sections. An array of tips was produced as a lithographic template for surface patterning applications. As shown in Figure 16, two methods were used to pattern a polymer surface: photoimprint lithography and imprint lithography.

Both techniques produced arrays of picoliter-volume wells suitable for microanalytical applications. In photoimprint lithography, a patterned surface was created when the nanotip array was brought into contact with a photopolymerizable monomer film, and photoinitiation was directed through the array. With this method, an array of 1- $\mu\text{m}$  wells was produced with a 4- $\mu\text{m}$  center-to-center spacing. In imprint lithography, bringing the nanotip array into contact with a heated polystyrene-covered surface created a patterned surface. With this technique, an array of 0.8- $\mu\text{m}$ -radii wells was produced with 3- $\mu\text{m}$  cone depths and 25° cone angles, as shown in Figure 17.

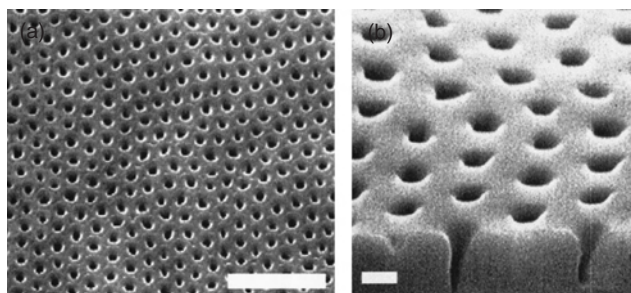
### 4.4. Ordered Nanowell Arrays

Lithographic procedures such as microcontact printing [89], high-throughput imprint lithographic methods [90, 91], and nanochannel array glass materials [92] have been used to form ordered, periodic structures on a variety of materials. Arrays of nanowells were fabricated from fiber-optic bundles as another form of templating. Pantano and Walt [7, 43] produced arrays of nanowells with approximately 300-nm diameters, using an embossing template to create patterned polymeric films.

Fiber-optic imaging bundles were polished with a series of lapping films. The fiber bundle was then pulled with a standard micropipette puller and potted in epoxy such that the length of the imaging fiber's distal tip protruded from the polishing apparatus. Adjusting the length of the fiber



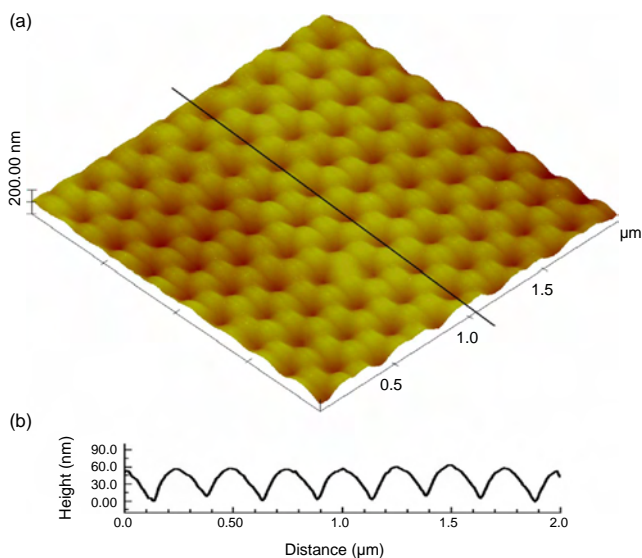
**Figure 16.** (a) Photoimprint lithography through a nanotip array. A PS802 polymer film is placed on a silicon glass surface. The nanotip array is then brought into contact with the film and glass surface, and light is directed through the fiber bundle, exposing the surface to light. The tip array is then removed, leaving a polymerized, patterned surface. (b) Imprint lithography with a nanotip array. An aluminum surface is coated with melted polystyrene. The nanotip array is then brought into contact with the warm polymer film. The array is then removed, leaving a patterned polystyrene surface. Reprinted with permission from [88], T. H. Dam and P. Pantano, *Rev. Sci. Instrum.* 70, 3982 (1999). © 1999, American Institute of Physics.



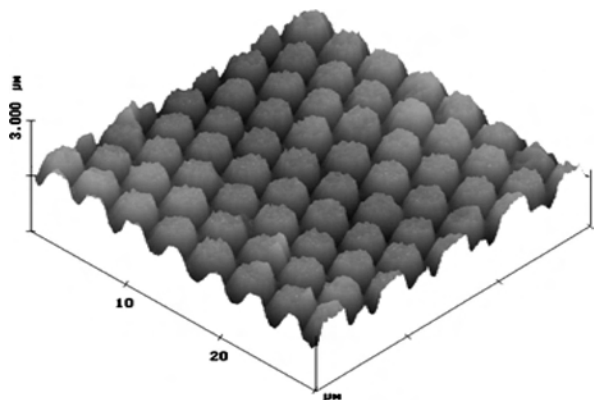
**Figure 17.** (a) Scanning electron micrograph of a patterned PS802 polymer surface using photoimprint lithography through a nanotip array. The white scale bar denotes a 5- $\mu\text{m}$  distance. (b) A patterned polystyrene surface using imprint lithography through a nanotip array. The white scale bar denotes a 2- $\mu\text{m}$  distance. Reprinted with permission from [88], T. H. Dam and P. Pantano, *Rev. Sci. Instrum.* 70, 3982 (1999). © 1999, American Institute of Physics.

yielded the final, desired diameter of the tapered fiber. The fiber bundle was then chemically etched in a buffered HF solution, yielding an array of nanowells. Scanning electron microscopy and AFM were used to characterize the surface of the modified fiber bundle, as shown in Figure 18. Nanowells with diameters as small as 480 nm with 4.5- $\mu\text{m}$  center-to-center spacings and 300-nm well depths (corresponding to  $\sim 2$  fL volumes) could be obtained. Such small wells could be used, in principle, as nanoreaction vials for molecule trapping.

The resulting nanowell arrays were used to emboss polymeric films with nanometer-sized structures. The nanowell array was dipped into a siloxane copolymer solution and allowed to cure. The polymer cured upon solvent evaporation, and the dip process was repeated five times. The polymer film was then peeled off of the fiber, resulting in a



**Figure 18.** Atomic force micrograph of a modified fiber bundle. The fiber was first mechanically pulled and then was chemically etched to form an array of nanowells. Reprinted with permission from [7], P. Pantano and D. R. Walt, *Chem. Mater.* 8, 2832 (1996). © 1996, American Chemical Society.



**Figure 19.** A patterned polymer surface fabricated from an array of nanowells. A polymer layer was deposited on the surface of the nanowell array and removed to form an array of nanocones. Reprinted with permission from [7], P. Pantano and D. R. Walt, *Chem. Mater.* 8, 2832 (1996). © 1996, American Chemical Society.

hexagonally packed array with 600-nm tall cones, as shown in Figure 19.

## 5. CONCLUSIONS

A variety of techniques have been used to fabricate nanometer-sized optical fiber tips and arrays of nanotips and nanowells from optical fiber bundles. The nanoprobe and arrays of nanoprobe have been successfully applied in NSOM, near-field data storage, and near-field lithography. These systems overcome the diffraction limit, enabling one to study materials science and biomedical phenomena on the nanometer scale. Near-field methods have also been applied to data storage with the potential to create data densities higher than those currently available. NFO lithography can provide a potentially low-cost alternative to conventional lithographic techniques while improving the spatial resolution on substrates. With nanoprobe and arrays of nanoprobe, nanosensors for nitric oxide monitoring and oxidative stress monitoring can be created with higher temporal resolution, greater data throughput, and increased sensitivity. The large variety of nanoprobe will lead to new techniques and applications where progress has been limited by present technologies. In addition, arrays of nanowells have been fabricated for use as nanometer-sized templates for polymer films. As nanotechnology research advances, optical fibers will be further integrated with nanodevices, producing tools that will improve and enhance conventional tools used in scientific research and development.

## GLOSSARY

**Chemical etching** Process of etching by a chemical reaction between a chemically reactive etching species and the material.

**Near-field scanning optical microscopy (NSOM)** [Also referred to as scanning near-field microscopy (SNOM)]. A scanning probe microscopy technique that analyzes the optical properties of a surface (e.g., fluorescence transmission, reflectance). The specimen is placed less than a wavelength

away from the probe, and light is transmitted through a subwavelength-sized aperture as the surface is scanned.

**Optical fiber** Glass or plastic rod consisting of a core surrounded by a cladding material with a higher refractive index that results in total internal reflection light and confines light to the core. As a result, light is efficiently transmitted with minimal attenuation.

## REFERENCES

1. D. W. Pohl, "Advances in Optical and Electron Microscopy." Academic Press, New York, 1991.
2. D. W. Pohl and D. Courjon, "Near Field Optics," NATO ASI Series E. Kluwer, Dordrecht, the Netherlands, 1993.
3. D. Courjon and D. Bainier, *Rep. Prog. Phys.* 57, 1029 (1994).
4. O. S. Wolfbeis, *Anal. Chem.* 72, 81 (2000).
5. O. S. Wolfbeis, *Anal. Chem.* 74, 2663 (2002).
6. W. Tan, Z.-Y. Shi, and R. Kopelman, *Anal. Chem.* 64, 2985 (1992).
7. P. Pantano and D. R. Walt, *Chem. Mater.* 8, 2832 (1996).
8. J. Wilson and J. Hawkes, "Optoelectronics, An Introduction." Prentice Hall, London, 1998.
9. E. Abbe, *Arch. Mikrosk. Anat.* 9, 413 (1873).
10. A. Lewis, M. Issacson, A. Muray, and A. Harootunian, *Ultramicroscopy* 13, 227 (1984).
11. K. Lieberman, S. Harush, A. Lewis, and R. Kopelman, *Science* 247, 59 (1990).
12. G. Binning, H. Rohrer, C. Gerber, and W. Weibel, *Phys. Rev. Lett.* 49, 57 (1982).
13. G. Binning, C. F. Quate, and C. Gerber, *Phys. Rev. Lett.* 56, 930 (1986).
14. M. Y. Reetz, W. Helbig, S. A. I. Quaiser, U. Stimming, N. Breuer, and R. Vogel, *Science* 267, 367 (1990).
15. U. Durig, D. W. Pohl, and F. Rohner, *J. Appl. Phys.* 59, 3318 (1986).
16. S. Seebacher, W. Osten, V. P. Veiko, and N. B. Voznessenski, *Opt. Lasers Eng.* 36, 451 (2001).
17. E. Betzig and R. Chichester, *Science* 262, 1422 (1993).
18. B. A. F. Pygranier and P. Dawson, *Ultramicroscopy* 85, 235 (2000).
19. E. Betzig, J. K. Trautman, T. D. Harris, J. S. Weiner, and R. L. Kostelak, *Science* 251, 1468 (1991).
20. W. P. Ambrose, P. M. Goodwin, J. C. Martin, and R. A. Keller, *Science* 265, 364 (1994).
21. N. Essaidi, Y. Chen, V. Kottler, E. Cambriel, C. Mayeux, N. Ronarch, and C. Vieu, *Appl. Opt.* 37, 609 (1998).
22. Y.-H. Liu, T. H. Dam, and P. Pantano, *Anal. Chim. Acta* 419, 215 (2000).
23. G. A. Valaskovic, M. Holton, and G. H. Morrison, *Appl. Opt.* 34, 1215 (1995).
24. W. Tan and R. Kopelman (1996).
25. S. Mononobe, M. Naya, T. Saiki, and M. Ohtsu, *Appl. Opt.* 36, 1496 (1997).
26. S. Mononobe and M. Ohtsu, *J. Lightwave Technol.* 14, 2231 (1996).
27. S. Mononobe and M. Ohtsu, *J. Lightwave Technol.* 15, 1051 (1997).
28. T. Yatsui, M. Kourogi, and M. Ohtsu, *Appl. Phys. Lett.* 73, 2090 (1998).
29. P. Hofmann and R. Slathe, *Ultramicroscopy* 61, 165 (1995).
30. R. U. Maheswari, S. Mononobe, and M. Ohtsu, *J. Lightwave Technol.* 13, 2308 (1995).
31. M. Ohtsu, *J. Lightwave Technol.* 13, 1200 (1995).
32. T. Saiki, S. Mononobe, M. Ohtsu, N. Saito, and J. Kusano, *Appl. Phys. Lett.* 68, 2612 (1996).
33. H.-D. Lee, H.-J. Lee, C.-K. Kim, and C.-H. Han, *Appl. Phys. Lett.* 66, 3272 (1995).
34. S. Ottow, V. Lehmann, and H. Foll, *J. Electrochem. Soc.* 143, 385 (1996).
35. T. Pangaribuan, S. Jiang, and M. Ohtsu, *Electron. Lett.* 29, 1978 (1993).

36. T. Pangaribuan, K. Yamada, S. Jiang, H. Ohsawa, and M. Ohtsu, *Jpn. J. Appl. Phys.* 31, L1302 (1992).
37. Y.-H. Chuang, K.-G. Sun, C.-J. Wang, J. Y. Huang, and C.-L. Pan, *Rev. Sci. Instrum.* 69, 437 (1998).
38. M. Datta, *J. Electrochem. Soc.* 142, 3801 (1995).
39. J. F. Wolf, P. E. Hillner, R. Bilewicz, P. Kolsch, and J. P. Rabe, *Rev. Sci. Instrum.* 70, 2751 (1999).
40. A. Sayah, C. Philipona, P. Lambelet, M. Pfeffer, and F. Marquis-Weible, *Ultramicroscopy* 71, 59 (1998).
41. K. Kobayashi, Y. Nishida, and K. Fujiura, Japanese Patent 09328335, 1997.
42. E. Oesterschulze, O. Rudow, C. Mihalcea, W. Scholz, and S. Werner, *Ultramicroscopy* 71, 85 (1998).
43. P. Pantano and D. R. Walt, *Rev. Sci. Instrum.* 68, 1357 (1997).
44. E. G. Rochow, "Comprehensive Inorganic Chemistry." Pergamon Press, Oxford, 1973.
45. R. Stöckle, C. Fokas, V. Deckert, R. Zenobi, B. Sick, B. Hecht, and U. P. Wild, *Appl. Phys. Lett.* 75, 160 (1999).
46. U. C. Fischer, J. Koglin, and H. Fuchs, *J. Microsc.* 176 (Part 3), 231 (1994).
47. J. Ferber, U. C. Fischer, N. Hagedorn, and H. Fuchs, *Appl. Phys. A* 69, 581 (1999).
48. R. Zenobi and V. Deckert, *Angew. Chem. Int. Ed.* 39, 1746 (2000).
49. K. Nakajima, R. Micheletto, K. Mitsui, T. Isoshima, M. Hara, T. Wada, H. Sasabe, and W. Knoll, *Appl. Surf. Sci.* 144–145, 520 (1999).
50. J. M. Freyland, R. Eckert, and H. Heinzlmann, *Microelectron. Eng.* 53, 653 (2000).
51. S. M. Meteov and V. P. Veiko, "Laser Assisted Micro-technology." Springer-Verlag, New York, 1998.
52. M. B. Lee, M. Kourogi, T. Yatsui, K. Tsutsui, N. Atoda, and M. Ohtsu, *Appl. Opt.* 38, 3566 (1999).
53. K. Goto, *J. Appl. Phys.* 37, 2274 (1998).
54. S. Jinang, J. Ichihashi, H. Monobe, M. Fujihira, and M. Ohtsu, *Opt. Commun.* 106, 173 (1994).
55. H. Ueki, Y. Kawata, and S. Kawata, *Appl. Opt.* 35, 2457 (1996).
56. E. B. Cooper, S. R. Manalis, H. Fang, H. Dai, K. Matsumoto, S. C. Minne, T. Hunt, and C. F. Quate, *Appl. Phys. Lett.* 75, 3566 (1999).
57. P. N. Minh, T. Ono, S. Tanaka, K. Goton, and M. Esashi, *Sens. Actuators, A* 95, 168 (2002).
58. C. E. Talley, G. A. Cooksey, and R. C. Dunn, *Appl. Phys. Lett.* 69, 3809 (1996).
59. I. I. Smolyaninov, D. L. Mazzoni, and C. C. Davis, *Appl. Phys. Lett.* 67, 3859 (1995).
60. G. Eggers, A. Rosenberger, N. Held, A. Münnemann, G. Güntherodt, and P. Fumagalli, *Ultramicroscopy* 71, 249 (1998).
61. E. Betzig, J. K. Trautman, R. Wolfe, E. M. Gyorgy, P. L. Finn, M. H. Kryder, and C.-H. Chang, *Appl. Phys. Lett.* 61, 142 (1992).
62. E. S. Snow and P. M. Cambell, *Science* 1639 (1995).
63. M. F. Crommie, C. P. Lutz, and D. M. Eigler, *Science* 262 (1993).
64. V. Foglietti, E. Cianci, and G. Giannini, *Microelectron. Eng.* 57–58, 807 (2001).
65. W. Tan, Z.-Y. Shi, S. Smith, and R. Kopelman, *Mol. Cryst. Liq. Cryst. Sci. Technol., Sect. A* 252, 535 (1994).
66. K. Albert, N. S. Lewis, C. L. Schauer, G. A. Sotzing, S. E. Stitzel, T. P. Vaid, and D. R. Walt, *Chem. Rev.* 100, 2595 (2000).
67. W. R. Seitz, *CRC Crit. Rev. Anal. Chem.* 19, 135 (1988).
68. D. Uttamchandani and S. McCulloch, *Adv. Drug Delivery Rev.* 21, 239 (1996).
69. S. Nie and D. T. Chiu, *Science* 266, 1018 (1994).
70. D. e. a. Zeisel, *Chem. Phys. Lett.* 283, 381 (1998).
71. W. Tan, Z.-Y. Shi, S. Smith, D. Birnbaum, and R. Kopelman, *Science* 258, 778 (1992).
72. B. M. Cullum and T. Vo-Dinh, *Thin Solid Films* 19, 388 (2000).
73. I. Koronczai, J. Reichert, H.-J. Ache, C. Krause, T. Werner, and O. S. Wolfbeis, *Sens. Actuators, B* 74, 47 (2001).
74. D. W. Lubbers, *Sens. Actuators, B* 51, 5 (1998).
75. S. L. Barker, R. Kopelman, T. E. Meyer, and M. A. Cusanovich, *Anal. Chem.* 70, 971 (1998).
76. T. Vo-Dinh, J. P. Alarie, and B. M. Cullum, *Fresenius J. Anal. Chem.* 366, 540-551 (2000).
77. T. Vo-Dinh, J. P. Alarie, B. M. Cullum, and G. D. Griffin, *Nat. Biotechnol.* 18, 764 (2000).
78. T. Vo-Dinh, B. M. Cullum, and D. L. Stokes, *Sens. Actuators, B* 74, 2 (2001).
79. S. Arbault, P. Pantano, J. A. Jankowski, M. Vuillaume, and C. Amatore, *Anal. Chem.* 67, 3382 (1995).
80. C. Amatore, S. Arbault, D. Bruce, P. De Oliveira, M. Erard, and M. Vuillaume, *Port. Electrochim. Acta* 19, 145 (2001).
81. C. Amatore, S. Arbault, D. Bruce, P. De Oliveira, M. Erard, and M. Vuillaume, *Chem.—Eur. J.* 7, 4171 (2001).
82. M. T. Kawagoe, J. A. Jankowski, and R. M. Wightman, *Anal. Chem.* 63, 1589 (1991).
83. Y. Nakayama, S. Okazaki, N. Saitou, and H. Wakabayashi, *J. Vac. Sci. Technol., B* 8, 1836 (1990).
84. H. I. Smith, M. L. Schattenburg, S. D. Hector, J. Ferrera, E. E. Moon, I. Y. Yang, and M. Burkhardt, *Microelectron. J.* 32, 143 (1996).
85. L. L. Sohn and R. L. Willett, *Appl. Phys. Lett.* 67, 1552 (1995).
86. Y. Wada, *Microelectron. J.* 29, 601 (1998).
87. S. Sun and G. J. Leggett, *NanoLetters* 2, 1223 (2002).
88. T. H. Dam and P. Pantano, *Rev. Sci. Instrum.* 70, 3982 (1999).
89. Y. Xia, E. Kim, and G. M. Whitesides, *J. Electrochem. Soc.* 143, 1070 (1996).
90. S. Y. Chou, P. R. Krauss, and P. J. Renstrom, *Science* 272, 85 (1996).
91. Y. X. X.-M. Zhao and G. M. Whitesides, *J. Mater. Chem.* 7, 1069 (1997).
92. D. H. Pearson and R. J. Tonucci, *Science* 270, 68 (1995).
93. P. Lambelet, A. Sayah, M. Pfeffer, C. Philipona, and F. Marquis-Weible, *Appl. Opt.* 37, 7289 (1998).
94. T. Held, S. Emonin, O. Martin, and O. Hollricher, *Rev. Sci. Instrum.* 71, 3118 (2000).
95. B. A. F. Puygranier, S. Montgomery, J. Ashe, R. J. Turner, and P. Dawson, *Ultramicroscopy* 86, 233 (2001).
96. G. Krausch, S. Wegscheider, A. Kirsch, and J. Mlynek, *Thin Solid Films* 264, 264 (1995).



# Optical Properties of Gallium Nitride Nanostructures

Annamraju Kasi Viswanath

Ministry of Information Technology, Pune, India

## CONTENTS

1. Introduction
  2. Gallium Nitride (GaN) Nanostructures
  3. Photoluminescence Spectroscopy of InGaN
  4. Time-Domain Photoluminescence of InGaN
  5. Laser Action in InGaN
  6. Light-Emitting Diodes and Semiconductor Lasers Based on InGaN
  7. Mechanism of Laser Action in InGaN
  8. Conclusions
- Glossary  
References

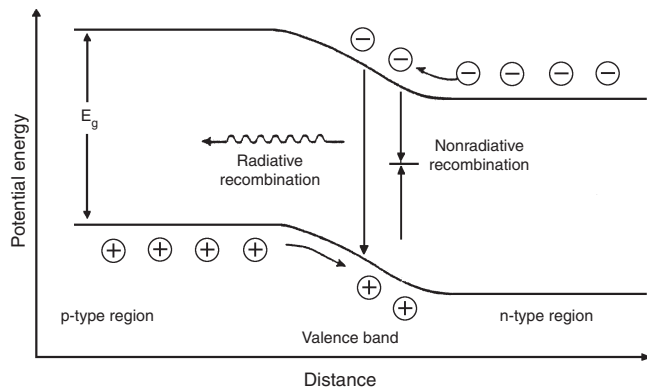
## 1. INTRODUCTION

In the last decade, there have been dedicated efforts to develop the materials and solid-state devices based on III-V nitrides and other wide bandgap semiconductors [1–22]. The III-V nitrides belong to the general class of wide bandgap semiconductors. These semiconductors are particularly suitable to develop light-emitting diodes (LED), semiconductor lasers, ultraviolet (UV) detectors, field-effect transistors, etc. Short wavelength LEDs have very important applications in high-density optical storage, full-color display technology, color photocopy, digital video-disk, lighting, underwater communications. Nitride-based LEDs already are being used in traffic lights, automobile lights, home lighting, and entertainment. InN, GaN and AlN belong to the III-V nitride family. They have bandgaps in the range 1.9 to 6.2 eV, and hence, it is possible to make ternary and quaternary alloys of these materials to obtain bandgaps in the red to UV energies. One can use the well-known semiconductor fabrication techniques such as molecular beam epitaxy (MBE) and metal organic chemical vapor deposition (MOCVD) to achieve various nanostructures of quantum wells and superlattices.

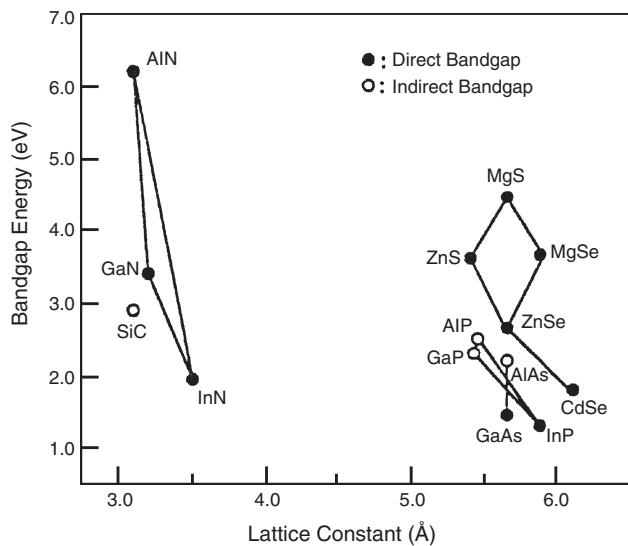
Figure 1 shows the schematic diagram of a LED [14]. It has a p-n junction of a semiconductor with a bandgap  $E_g$ .

When current is passed through the junction, electrons in the conduction band flow across the junction from the n-type semiconductor, while the holes in the valence band flow from the p-type semiconductor. A large number of electrons and holes recombine at the junction, giving rise to radiation that has the energy equivalent to the bandgap. In direct bandgap semiconductors, the luminescence radiation obeys the relation  $h\nu = E_g$ , where  $\nu$  is the frequency of emitted radiation,  $h$  is the Planck's constant, and  $E_g$  is the bandgap of the semiconductor. The plot of bandgaps as a function of the lattice constant for some semiconductors is shown in Figure 2 [1]. The first LED was made in the red region of the visible spectrum by using a GaAsP direct bandgap semiconductor [16]. The emission wavelength of this red LED was 610 nm. Figure 3 shows the evolution of LED technology, the performance of LEDs has improved over the years [19]. As can be seen in the figure, several materials were used to achieve various colors. These semiconductors include GaAsP, GaP:Zn, O, AlGaAs/GaAs, AlGaInP/GaAs, etc. Figure 3 also shows the wavelengths that can be obtained from InGaN-based LEDs. These are in the blue and green region of the electromagnetic spectrum, which were very much wanted for a long time for a number of applications. Nakamura, at Nichia in Japan, made it possible to achieve this important breakthrough in solid-state display technology. Nakamura's team made several LEDs and semiconductor lasers in the pulsed and continuous wave (cw) mode. It also was shown that the InGaN-based LEDs have better luminous intensities than the SiC-based LEDs, which were the only commercially available blue-light-emitting devices before the GaN-based devices came onto the market. It also was shown that III-V nitride devices were useful for high-temperature and high-power electronics.

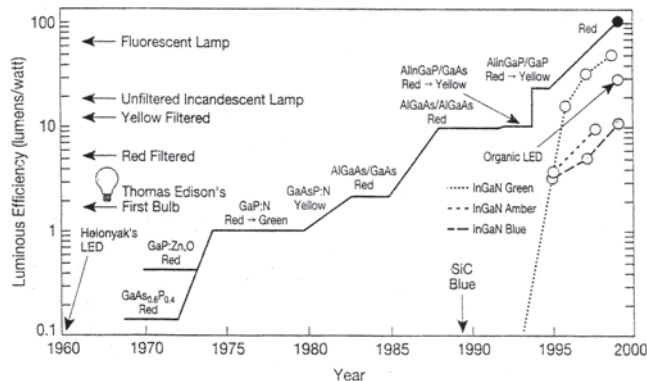
To develop blue- and green-light-emitting devices II-VI based semiconductor materials were investigated for a long time. An excellent review on optical properties of these materials was given by Morkoc et al. [2]. ZnSe is nearly lattice matched to GaAs, and, hence, integration of II-VI based technology with the well-established GaAs technology could be anticipated. Also, high-quality GaAs substrate



**Figure 1.** Schematic of a LED. Electrons injected across a p-n junction combine with holes to produce photons in radiative recombination. However, in nonradiative recombination photons are not produced. The wavelength of the emitted radiation depends on the bandgap of the semiconductor material.



**Figure 2.** Energy gaps of different compound semiconductors as a function of lattice constant. Reprinted with permission from [1], S. Nakamura and G. Fasol, "The Blue Laser Diode," 1997. © 2001, Springer-Verlag, Berlin.



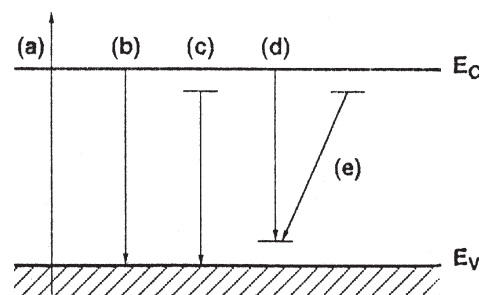
**Figure 3.** Evolution of LED technology, showing approximately a tenfold improvement per decade in performance. Reprinted with permission from [19], M. G. Craford, *MRS Bull.* 25, 27 (2000). © 2000, Materials Research Society.

can be easily obtained. It also is possible to make several quantum structures because ternary and quaternary compounds of II-VI materials can be made that will have different bandgap energies. In the ternary system of ZnCdSe, the wavelength could be tuned in the blue to green region by changing composition. The quaternary ZnMgSse was used to make the cladding layers. However, the LEDs and lasers with these materials have a short lifetime because of crystal defects. Therefore, commercialization of these devices could not be made.

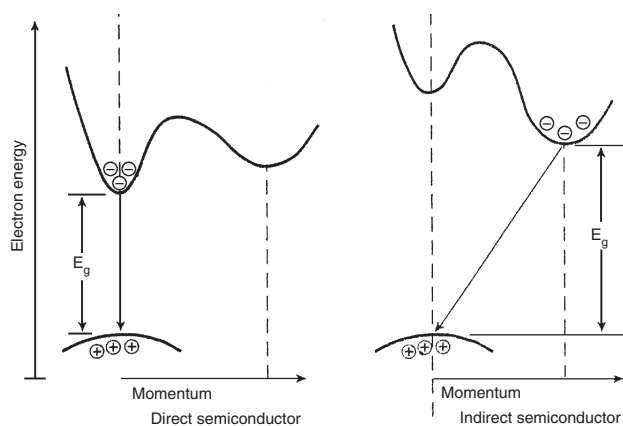
Figure 4 shows the schematic energy level diagram describing the optical processes in semiconductors. The recombination phenomena gives valuable information about excitons, donors, acceptors, phonon interactions, etc. Figure 5 shows the band diagrams of direct and indirect semiconductors. In a direct bandgap semiconductor, the electrons and holes combine directly without any need of momentum conservation, whereas, in the indirect bandgap semiconductors, phonon participation is required for momentum conservation.

In this review, we discuss the optical properties of nanostructured GaN and related materials and their applications in fabricating LEDs and semiconductor lasers. A large number of papers have been published on the growth and photoluminescence properties of GaN. A variety of commonly available substrates have been used to grow epitaxial GaN. A detailed discussion on this topic is out of the scope of the present review. The review chapters written by the author cover these topics [10]. The present chapter emphasizes the optical properties of nanostructures such as nanowires, nanodots, nanobelts, nanoparticles, nanorods, nanocrystals, etc. The properties of epitaxial thin films are given for comparison purposes. We also discuss in great detail the quantum well structures of InGaN that form the heart of LEDs and semiconductor lasers.

We will give a very brief introduction to quantum confinement in semiconductors. There are several special editions that deal with the development of the exciting field of semiconductor nanostructures [23–27]. The article by Weisbuch [28] gives a very comprehensive description of various quantum-confined semiconductor structures and their optical and electronic properties. Basically, the thin film quantum structures initially were developed at IBM and AT and T Bell laboratories. This was possible by the novel MBE technique by which atomic layers can be grown one on top of



**Figure 4.** Most common optical processes in semiconductors. (a) is absorption of photons that generates electron and hole pairs in the conduction and valence bands, followed by various recombinations, (b) is band-to-band recombination, (c) is donor to valence band, (d) is conduction band to acceptor, (e) is donor-acceptor pair recombination.



**Figure 5.** Band diagrams of direct and indirect band gap semiconductors. In a direct band gap semiconductor electron and hole combine directly producing a photon, whereas in an indirect semiconductor conservation of momentum is required for recombination to occur.

the other. Esaki and Chang [29] were the first to observe the perpendicular differential conductance due to resonant electron tunneling across potential barriers. Soon after that Dingle et al. [30] showed in their optical experimental results, the quantization of energy levels. This has proved beyond a doubt that very thin semiconductor layers of small nanometer dimensions can be grown that behave like quantum mechanical objects. Quantum phenomena come into play when the actual size of the material is of the order of DeBroglie wavelengths. The simplest confined structure is a quantum well, which is a very thin semiconductor with a thickness of a few nanometers or less that is placed between two barrier layers having higher bandgap energies. These also are called quasi two-dimensional (2D) systems. The free motion of the carriers occurs in only two directions perpendicular to the growth direction, while the motion in the third direction,  $z$ , is restricted. Several solid-state devices were achieved by using the quantum phenomena in semiconductors. These include the quantum well lasers [31, 32], high-electron mobility transistors, modulation-doped transistors [33–35], etc. Modulation-doped quantum wells also give us the opportunity to study very interesting physical phenomena such as Landau quantization, Fermi edge singularity, many body effects, etc. [36–41]. The nonlinear optical properties of the quantum wells were found to be useful in fabricating optical switches based on optical bistability [42].

Semiconductor structures with higher degrees of confinement of carriers have been achieved. A quantum wire is a one-dimensional electron system in which quantum confinement occurs in two dimensions and a quantum box or a quantum dot is a zero-dimensional system, and the confinement of electron motion occurs in all three directions. The method of tailoring the materials to custom design the structure and desired properties also is called bandgap engineering. Sakaki [43] has predicted that in a single-channel quantum wire, the electron scattering is minimal and the electron mobility will be extremely high. Arakawa et al. [44] have theoretically studied the use of quantum wires in semiconductor lasers. Quantum wires are expected to be suitable for high-gain and low-threshold current lasers

and for high-electron mobility transistors because the density of states is very high. Free-standing quantum whiskers of GaAs were grown for the first time by MOCVD at Hitachi Central Research Laboratory, and very intriguing aspects of surface and interface recombination were studied by the author and his collaborators [45–48]. Lieber and coworkers have written very interesting articles on the physics and chemistry of wirelike structures [49–61]. Confined movement of electrons in the crystal gives very unique properties. The study of dimensionality and its effects on the material properties is not at all new and has been known in the chemistry for several decades [62, 63]. For example, in bulk single crystals that contain square planar complexes of Ni, Pd, and Pt, which show the quasi one-dimensional behavior, the electron motion is confined in the  $z$  direction. The author and his collaborators at the University of Maine, have published a series of papers on the electronic structure, extended Huckel molecular orbital calculations, optical properties, and time-resolved phenomena in single crystal Ni, Pd, and Pt compounds that contain square planar configurations [64–71]. Very interesting observations that can be directly related to quasi one-dimensional behavior of electrons, such as energy transfer along the one-dimensional chains, energy migration and trapping, optical anisotropy, bandgap formation due to the orbital overlap along the one-dimensional chains, etc., were observed. These crystals may be called natural quantum wires. These are “natural” in the sense that no special efforts have to be made to fabricate them and the crystal structure offers the possibility of restricted motion of the electrons. These crystals also serve as the model systems to understand the more complicated bandgap engineered, semiconductor, low-dimensional nanostructures.

It is possible to further reduce the dimension of the semiconductor in such a way that the motions of the electrons are confined in all the three directions to obtain a quantum dot, which also is known as a quantum box, a nanocrystal, or a nanoparticle [72]. In this situation, the translational symmetry is completely removed, and the traditional band structure of the solid splits into a bunch of discrete energy levels. This kind of energy-level scheme has several implications in the design of a number of semiconductor devices. When the size of the nanocrystal becomes much smaller than the bulk Bohr radius, the confinement affects not only the center-of-mass motion but also the relative motion of an electron and a hole. So the excited electron–hole pair does not behave like a true exciton in the bulk. The quantum confinement effects of a system containing the nanocrystals has been observed as the blue shift in the absorption spectrum, which increases with the decrease of the crystal size [72]. In the strong confinement case, where the electrons and holes are completely confined in all the three directions, the electronic states can be described by molecular orbitals rather than the Bloch functions in momentum space. The author and his collaborators at the Korea Research Institute of Standards and Science have investigated the special properties of self-assembled quantum dots such as bandgap renormalization and screening of carriers by femtosecond laser spectroscopy [73].

There are two main approaches to making the nanostructures. First is the top-to-bottom approach. This generally is used by physicists and semiconductor technologists



and involves very complicated procedures such as MBE, metal organic chemical vapor deposition, masking, etching, lithography, etc. Second is the bottom-to-top approach, which is a very inexpensive and easy method used by chemists. In this method, nanostructures are made by wet chemical methods, LB film formation, etc.

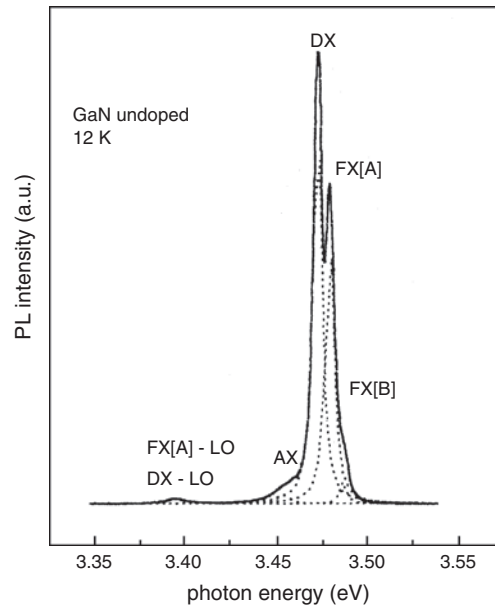
## 2. GALLIUM NITRIDE (GaN) NANOSTRUCTURES

Among the III–V nitrides, most work has been done on GaN because its bandgap is very suitable for developing UV lasers. Several papers have been published on the growth and photoluminescence properties of GaN. A variety of commonly available substrates have been used to grow epitaxial GaN. Sapphire has excellent properties required for a substrate to grow epitaxial layers. Most of the work on GaN has been done by using sapphire as a substrate. It is very stable, even at high temperatures, and has good chemical stability. Dingle et al. [74], Monemar [75] and Pankove et al. [76] have done the early pioneering work on the optical properties of GaN. The development of GaN devices was hampered by the lack of good-quality single crystals. The major problems were the lack of suitable lattice-matching substrates, very-high background n-type carrier concentration, and the difficulty in achieving p-type material. Two Japanese research teams, led by Nakamura and by Amano and Akasaki, who have used GaN [78] and AlN [90] buffer layers on the top of the substrates just before growing the epitaxial layers, have solved these problems [77–104].

### 2.1. Optical Properties of Thin Films of GaN

The early work on GaN was on absorption and reflection. Generally, the donor- and acceptor-bound exciton emissions were observed only in the photoluminescence spectra. Free-exciton transitions were found very rarely in the luminescence. The observation of free-exciton transitions is an indication of the good quality of the sample. Also, it is better to understand valence-band physics based on the luminescence properties rather than on absorption or reflection, because optoelectronic devices like LEDs and semiconductor lasers are based on emission phenomena. Hence, it is absolutely necessary to carefully investigate the effects of crystal fields, spin-orbit coupling, strain-induced deformation potentials, etc., on degenerate valence bands and how these are manifested in photoluminescence spectra.

Photoluminescence studies of high quality GaN epilayers grown by rotating disk MOCVD were reported by Viswanath et al. [105]. They have deduced several important parameters, such as exciton energies, delocalization energies of donor- and acceptor-bound excitons, Varshni's coefficients, exciton–phonon interaction parameters, etc. Figure 6 shows the photoluminescence spectrum of a GaN epitaxial layer grown on (0001) sapphire substrate at 12 K. The dotted lines show the individual peaks obtained by a curve-fitting procedure that uses a Lorentzian line-shape function. Assignment of various transitions was made by considering the electronic and band structures of GaN. The lattice mismatch between GaN and sapphire substrate generates strain



**Figure 6.** Photoluminescence spectrum of a GaN epitaxial layer grown on a (0001) sapphire substrate at 12 K. FX(A): free-exciton A; FX(B): free-exciton B; DX: donor-bound exciton; AX: acceptor-bound exciton; FX(A)-LO: phonon-assisted free exciton transitions; DX-LO: phonon-assisted donor-bound exciton transition. The dotted lines show Lorentzian fitting to various peaks. A He–Cd laser is used for excitation. Reprinted with permission from [105], A. K. Viswanath et al., *J. Appl. Phys.* 84, 3848 (1998). © 1998, American Institute of Physics.

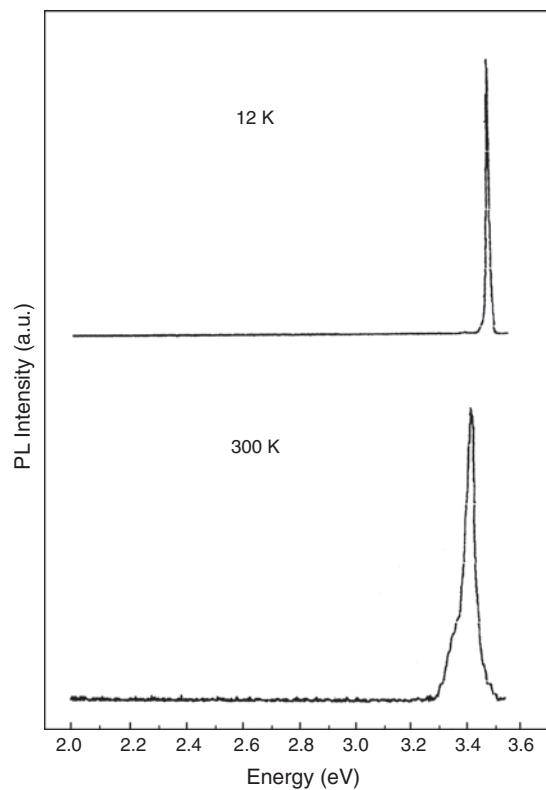
in the epilayers. When the strained layer epitaxy occurs along (0001), the corresponding strain keeps the wurtzite symmetry but alters the valence and conduction-band energies via strain-induced modifications of the chemical bonds. GaN conduction band ( $\Gamma_5^c$ ) is mainly constructed from s states of gallium, whereas the valence band is mainly from the p states of nitrogen. When there is no perturbation, the valence band is a threefold degenerate. But the crystal fields of the hexagonal symmetry of the wurtzite crystal lift the threefold degeneracy partially into a doubly degenerate  $\Gamma_5$  state and a lower-lying  $\Gamma_1$  state. The degeneracy is further removed through the spin–orbit interaction, and, in this case, the top of the valence band consists of  $\Gamma_5^v$ ,  $\Gamma_7^v$ , and  $\Gamma_7^v$ , where  $\Gamma_5^v$  is the highest level. These three levels also are called A, B, and C valence bands, respectively.

Viswanath et al. [105] have assigned the peak at 3.479 eV to free exciton A or FX(A), the 3.486 eV peak to free exciton B or FX(B), the peak at 3.472 eV to donor-bound exciton DX, and the peak at 3.454 eV to acceptor-bound exciton AX. Temperature-dependent photoluminescence studies were made to confirm these assignments.

Dingle et al. [74] reported the free exciton transitions for A, B, and C at 3.474, 3.481, and 3.501 eV, respectively, based on their polarized reflection experiments at 2 K. From the photoluminescence excitation spectroscopy studies, Monemar [75] has observed these exciton transitions at 3.4751, 3.481, and 3.493 eV, respectively. It is important to note that the exciton energy values reported by Dingle et al. [74] and Monemar [75] represent strain-free values because they have used very thick GaN samples. In the case of thin epilayers, there is a large mismatch between the lattice constants

of the sapphire substrate and the GaN crystal. Also, there is a large difference in the thermal expansion coefficients, which gives rise to misfit strain, which, in turn, generates many crystal defects and dislocations. This strain has a significant effect on the optical and electrical properties and also on the bandgap. In the case of sapphire substrate, the compressive biaxial stress in the epitaxial layers increases the energy values of the excitonic transitions and also the separations between them. The strain decreases with an increase in the layer thickness. The relationship between the strain and epilayer thickness has been investigated by Akasaki and coworkers [100]. They have studied the donor-bound exciton transition in the Photoluminescence (PL) spectra. Deviation of free-exciton values in thin ( $<4 \mu\text{m}$ ) epilayers from the values reported for thick samples was explained by the strain effects. The quality of the sample is estimated from the magnitude of the deviation.

Viswanath et al. [105] have also studied the free-exciton transitions at 12 K and room temperature over a wide energy range. The PL spectra are shown in Figure 7. At both the temperatures, the normally observed yellow band at 2.2 eV and the donor-acceptor pair recombination at 3.27 eV could not be observed. From this result, it was inferred that the quality of the sample was very good. The separation between the energy positions of FX(A) and FX(B) transitions,  $\Delta_{AB}$ , was found to be 7 meV. Viswanath et al. [105] have

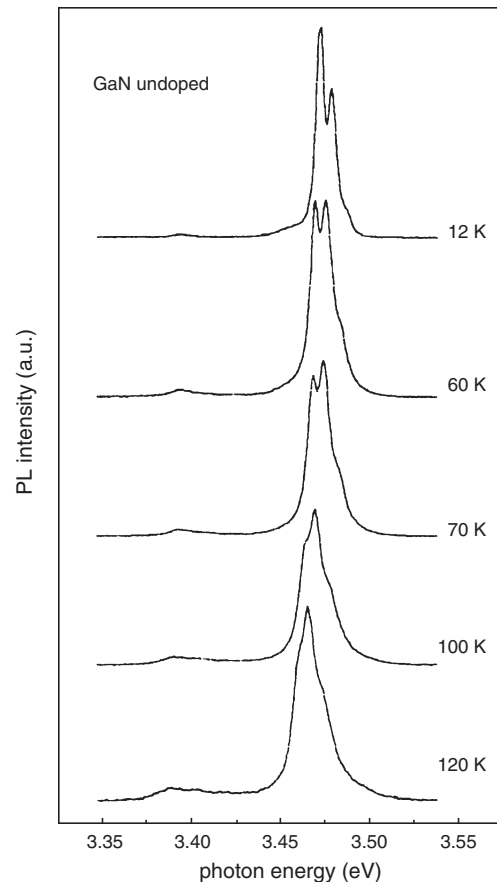


**Figure 7.** Photoluminescence spectrum of GaN showing the free-exciton transition at 12 K and room temperature. Note that there are no traces of yellow luminescence peaks and donor-acceptor transition due to background impurities or defects at both temperatures. Reprinted with permission from [105], A. K. Viswanath et al., *J. Appl. Phys.* 84, 3848 (1998). © 1998, American Institute of Physics.

concluded that the strain in their samples due to lattice mismatch is small since the  $\Delta E_{AB}$ , value of 7 meV they observed is close to that of the unstrained value of 6 meV.

The DX peak was found to be at 3.472 eV, which is shown in Figure 6 [105]. The exciton binding energy to the donor or the localization energy of the donor is 7 meV. The donor binding energy can be evaluated by considering the Haynes rule [109] for semiconductors, which states that the localization energy is  $\alpha E_D$ , where  $E_D$  is the binding energy of the donor and  $\alpha$  is a constant of proportionality generally taken as 0.2. Viswanath et al. [105] obtained the binding energy of donor as 35 meV. These shallow donors may be nitrogen vacancies or Ga interstitials. The peak at 3.454 eV was interpreted as due to AX. The binding energy between the acceptor and exciton is 25 meV. Considering the Haynes rule [109], a value of 250 meV for acceptor binding energy was estimated. In the case of acceptors, the constant of proportionality is 0.1.

Figure 8 shows the temperature dependence of the PL spectrum. As the temperature increases, FX(A) intensity increases at the expense of the DX peak. The donor-bound exciton dissociates into a free exciton and a neutral donor. The intensity ratio of the free exciton A peak to the donor-bound exciton peak, i.e.,  $I_{FX(A)}/I_{DX}$  is shown as a function



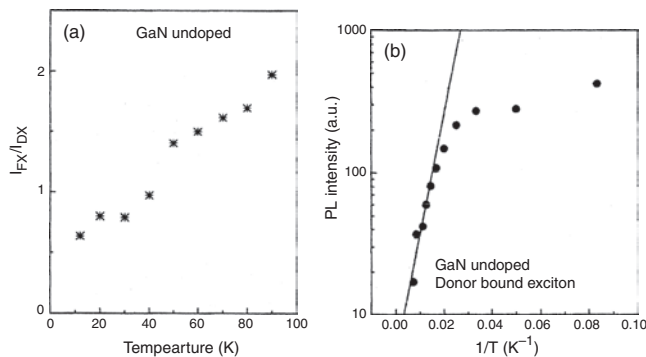
**Figure 8.** Photoluminescence spectra at selected temperatures for GaN epitaxial layers on sapphire. The changes in the relative intensities of free-exciton A and the donor-bound exciton can be noticed. Reprinted with permission from [105], A. K. Viswanath et al., *J. Appl. Phys.* 84, 3848 (1998). © 1998, American Institute of Physics.

of temperature in Figure 9a, and we can see that the ratio increases. From this the authors have concluded that the donor-bound exciton dissociates into a free exciton and a neutral donor,  $DX \rightarrow FX + D$ . The PL intensities of a donor-bound exciton are plotted as a function of  $1/T$ , as shown in Figure 9b. The thermal activation energy of donor was estimated as 6 meV. The PL peak positions were plotted as shown in Figure 10. The experimental points were fitted to the Varshni's equation for variation of the bandgap with temperature

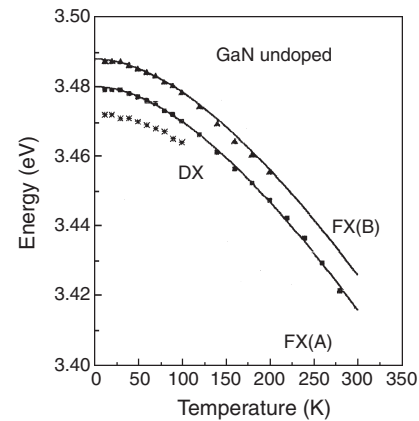
$$E(T) = E(0) - [\alpha T^2 / (\beta + T)] \quad (1)$$

In this equation,  $E(T)$  is the transition energy at any temperature  $T$ ,  $E(0)$  is the corresponding energy at 0 K, and  $\alpha$  and  $\beta$  are Varshni's thermal coefficients. The solid lines were obtained by least-square fitting. For FX(A), the best-fit values are  $E(0) = 3.480$  eV,  $\alpha = 5.0 \times 10^{-4}$  eV/K, and  $\beta = 400$  K; and, for FX(B),  $E(0) = 3.488$  eV,  $\alpha = 5.2 \times 10^{-4}$  eV/K, and  $\beta = 450$  K. In the case of GaAs, the  $\beta$  value is the same as the Debye temperature of the lattice. However, in the case of GaN, the exact relationship between  $\beta$  and the Debye temperature is not known yet. Figures 11a and b show the plots of PL peak energies as a function of  $T^2/(\beta + T)$  for free excitons A and B, respectively. The authors have obtained a straight line in each case from which it was concluded that the excitons exist up to room temperature in GaN.

Based on the observation of excitons up to room temperature, it was proposed [105] that GaN can be used in fabricating nonlinear optical devices working at room temperature. These devices have applications in the area of nonlinear optical signal processing, digital optical switching, optical computing, and optical communication. The longitudinal optical (LO) phonon-assisted transitions of the donor-bound exciton, free exciton A, and free exciton B were observed at 3.383, 3.392, and 3.398 eV, respectively, as shown in Figure 12. The separations of these peaks from their zero-phonon peaks are 89, 87, and 87 meV, respectively. These energy separations are in the range of LO phonon



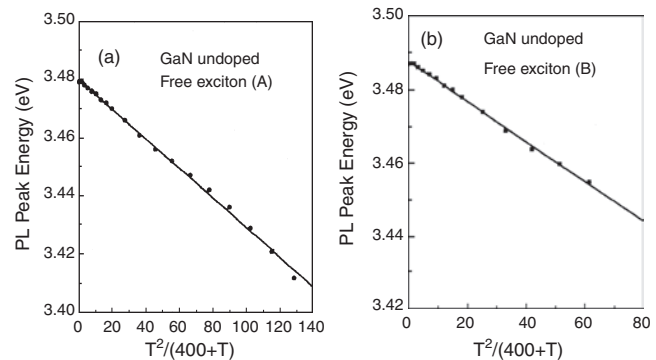
**Figure 9.** Intensity ratio of the free exciton A peak to the donor-bound exciton peak  $I_{FX}/I_{DX}$  as a function of temperature. (b) PL intensities of the donor-bound exciton as a function of  $1/T$ . The thermal activation energy of the donor-bound exciton is obtained as 6 meV from the slope of the straight line. Reprinted with permission from [105], A. K. Viswanath et al., *J. Appl. Phys.* 84, 3848 (1998). © 1998, American Institute of Physics.



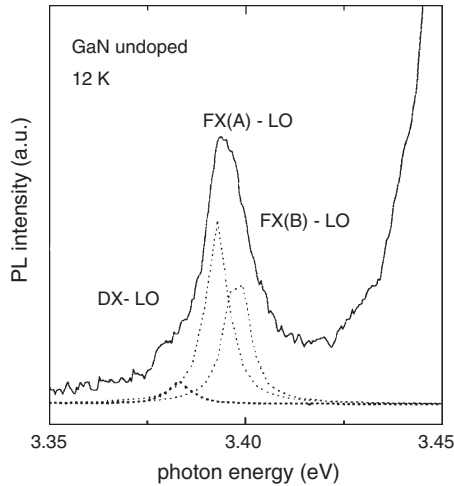
**Figure 10.** Temperature variation of the various transitions in the PL spectra of GaN/sapphire. The experimental points are represented by solid squares for free-exciton A, FX(A); solid triangles for free-exciton B, FX(B); and stars for the donor-bound exciton, DX. The solid lines are the theoretical fit curves following Varshni's equation for variation of the bandgap as a function of temperature. Reprinted with permission from [105], A. K. Viswanath et al., *J. Appl. Phys.* 84, 3848 (1998). © 1998, American Institute of Physics.

energy of GaN, which is 90 meV. The energy separation between FX(A)-LO and FX(B)-LO is 7 meV, while the separation between DX-LO and FX(A)-LO also is 7 meV. These energy separations agree with the corresponding energy differences of the zero-phonon transitions observed in the 12 K spectrum. The phonon replicas reveal that phonon-assisted exciton formation is very efficient in GaN. In polar semiconductors, Frohlich polar intraband scattering [110], which is the interaction between free excitons and LO phonons, is strong. Frohlich interactions were observed in other wide bandgap semiconductors [111–115].

Figure 13 shows the PL intensities of the free exciton A as a function of  $1/T$ . The activation energy of the free exciton was estimated as 26 meV [105]. Viswanath et al. [105] have estimated the bandgaps of GaN as 3.505 and 3.437 eV at 12 K and room temperature, respectively.



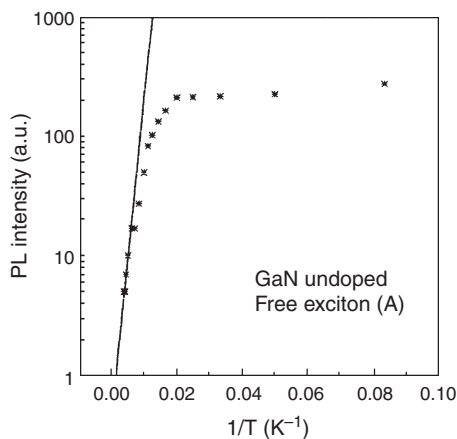
**Figure 11.** (a) Plot of PL peak energy of free-exciton A as a function of  $T^2/(\beta + T)$ , where  $\beta = 400$  K; (b) Plot of PL peak energy of free-exciton B as a function of  $T^2/(\beta + T)$ , where  $\beta = 450$  K. Reprinted with permission from [105], A. K. Viswanath et al., *J. Appl. Phys.* 84, 3848 (1998). © 1998, American Institute of Physics.



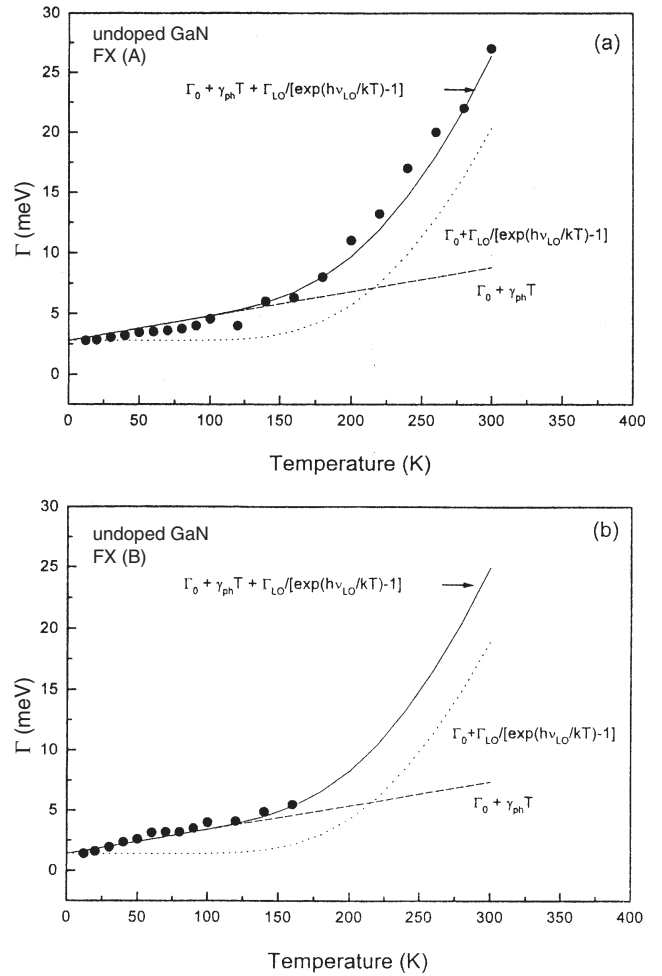
**Figure 12.** Photoluminescence spectrum for GaN/sapphire at 12 K showing the phonon-assisted exciton transitions. The dotted lines show the fit to multiple peaks assuming a Lorentzian line-shape function. Reprinted with permission from [105], A. K. Viswanath et al., *J. Appl. Phys.* 84, 3848 (1998). © 1998, American Institute of Physics.

### 2.1.1. Exciton Phonon Interactions in GaN

The lasing mechanism in GaN-based devices—excitonic versus band-to-band recombination—has not been understood so far. Viswanath et al. [106] have done the detailed analysis of exciton linewidths in the PL of GaN. Figures 14a and b show the temperature dependence of the linewidths of the free exciton A and B, respectively. Solid circles are experimental linewidths. The observed linewidths were fitted to a theoretical model. The basic formalism for phonon-assisted optical absorption and exciton lifetimes was developed by Toyozawa [116] and by Segall and Mahan [117]. Segall [118] applied it to describe absorption and emission in a number of materials. The temperature dependence of the width of the lowest 1S exciton in semiconductors initially was reported by Segall [119], and the most comprehensive



**Figure 13.** Photoluminescence intensities of the free-exciton A transition (shown as stars) as a function of  $1/T$ . The activation energy of free-exciton A is estimated as 26 meV from the slope of the straight line. Reprinted with permission from [105], A. K. Viswanath et al., *J. Appl. Phys.* 84, 3848 (1998). © 1998, American Institute of Physics.



**Figure 14.** Temperature dependence of the linewidths of (a) free exciton A and (b) free exciton B in GaN. Solid circles are the experimental points. Solid curve is the fitting of the experimental linewidths considering acoustic-phonon scattering and LO-phonon scattering. Dashed lines show the contribution from the acoustic-phonon scattering alone, and dotted lines show the contributions from the LO phonons only. In both the cases, inhomogeneous broadening was added. Adapted with permission from [106], A. K. Viswanath et al., *Phys. Rev. B* 58, 16333 (1998). © 1998, American Physical Society.

treatment was later given by Rudin et al. [120]. According to them, the exciton linewidth  $\Gamma(T)$  at any temperature  $T$  can be written as

$$\Gamma(T) = \Gamma_0 + \gamma_{ph}T + \Gamma_{LO}N_{LO}(T) \quad (2)$$

In polar semiconductors, linewidth is dominated by LO-phonon broadening.  $\Gamma_0$  is inhomogeneous broadening in the above equation. At very low temperatures, phonons are not active, and the contribution to the linewidth is mainly from inhomogeneous broadening. The second and third terms on the right-hand side of Eq. (2) are the homogeneous linewidths and are due to acoustic-phonon and LO-phonon scattering, respectively. The contribution due to acoustic phonons increases linearly with temperature  $T$  and is represented as  $\gamma_{ph}T$ , where  $\gamma_{ph}$  is the exciton-acoustic-phonon coupling strength. The last term in Eq. (2) arises from interactions with LO phonons and is proportional to the Bose

function  $N_{LO}(T)$  for LO-phonon occupation, which is equal to  $1/[\exp(h\nu_{LO}/kT) - 1]$ , where  $h\nu_{LO}$  is the LO-phonon energy in GaN, and  $\Gamma_{LO}$  represents the strength of exciton-LO phonon coupling.

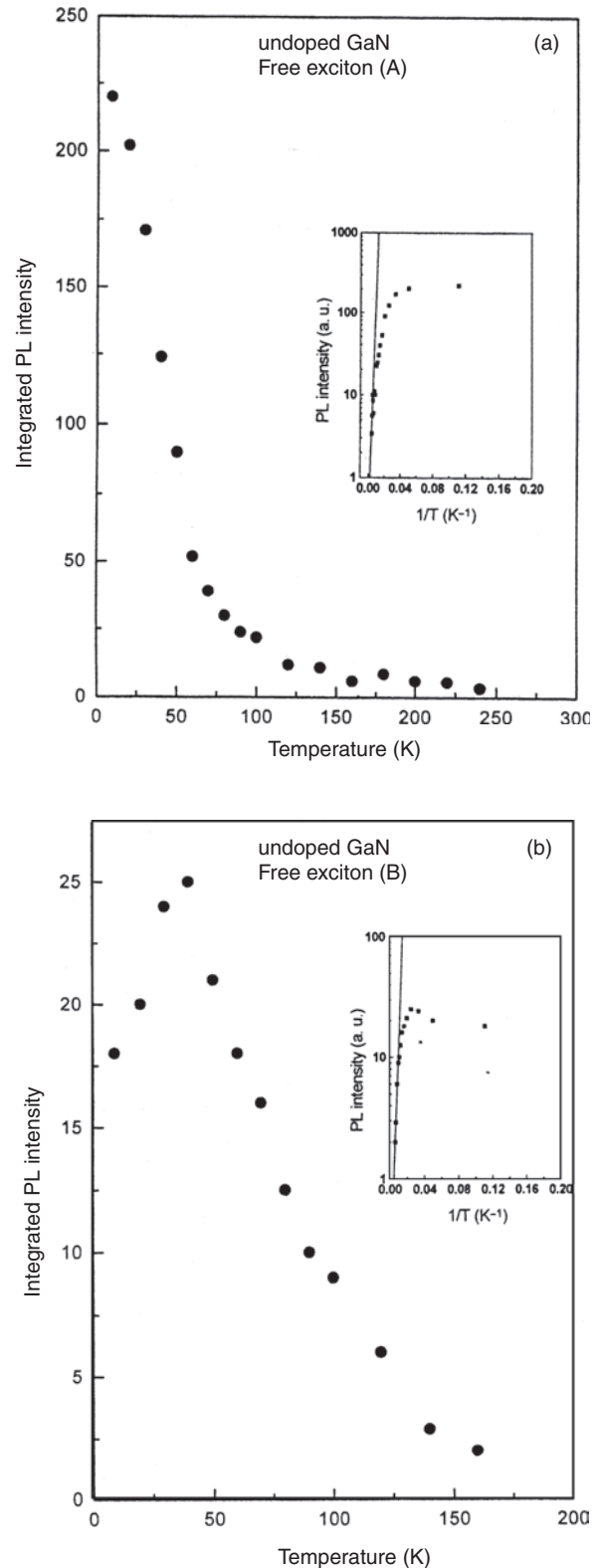
The solid lines in Figure 14 are the least-squares fitting considering acoustic-phonon scattering and LO-phonon scattering, in addition to inhomogeneous broadening. The LO-phonon energy was taken as 91.5 meV. The fitting parameters are  $\Gamma_0 = 2.8$  meV,  $\gamma_{ph} = 21 \mu\text{eV/k}$ , and  $\Gamma_{LO} = 525$  meV for FX(A), and  $\Gamma_0 = 1.4$  meV,  $\gamma_{ph} = 22 \mu\text{eV/k}$ , and  $\Gamma_{LO} = 495$  meV for FX(B).

In Figure 14, the dashed lines show the contribution from acoustic-phonon scattering and the dotted lines show the contribution from LO phonons to the linewidth. In all the cases, the inhomogeneous broadening also is added. The acoustic phonons contribute up to 120 K very significantly, but the contribution from LO phonons is negligible up to this temperature. From 120 K, the LO phonon contribution is very significant, and the linewidth increases sharply, because of the exponential factor. At 200 K, there is a crossover, and LO phonons dominate over the acoustic phonons.

The value of exciton-LO-phonon coupling parameter,  $\Gamma_{LO}$ , reported by Viswanath et al. [106] is very high. It indicates very strong interaction between excitons and LO-phonons. GaN is a polar material and has a very high Frohlich constant, which is responsible for the large  $\Gamma_{LO}$  value. The exciton-phonon interactions can be seen in the optical spectra in two ways. First is the line broadening of absorption or emission spectra. Second is the occurrence of phonon-assisted transitions in the absorption and emission spectra [105] as discussed in the previous sections.

It is necessary to have excitons that can exist up to room temperature, in order to realize room-temperature photonic devices. The existence of room-temperature excitons depends upon the delicate balance between two competing factors. The first is the exciton-LO-phonon interaction parameter, and the second is the exciton binding energy. A very large value of  $\Gamma_{LO}$  will make the exciton line broaden, so much so that at high temperatures the line will vanish completely. But the larger binding energy of the exciton can resist the phonon interaction, and it is possible to observe room-temperature excitons. This is what actually happens in the case of GaN, which has a larger binding energy of 26 meV. Viswanath et al. [106] have suggested that to realize stable room-temperature devices, it is better to work with quantum-confined systems of GaN, which have higher binding energy and lower LO-phonon coupling as a direct consequence of quantum phenomena. Added to this, quantum wells have a much narrower emission due to smaller inhomogeneous broadening.

In the same publication Viswanath et al. [106] have reported the temperature dependence of the PL intensities of both free exciton A and B. These are shown in Figure 15. While the intensity of free exciton A decreases steadily with an increase in temperature, the intensity of free exciton B initially increases up to 40 K and then decreases. The initial increase in intensity was explained by the authors as due to the higher energy position of free exciton B compared with free exciton A.



**Figure 15.** Temperature dependence of integrated PL intensity of (a) FX(A) and (b) FX(B). The insets show the activation energy plots. Adapted with permission from [106], A. K. Viswanath et al., *Phys. Rev. B* 58, 16333 (1998). © 1998, American Physical Society.

### 2.1.2. Acceptors in GaN

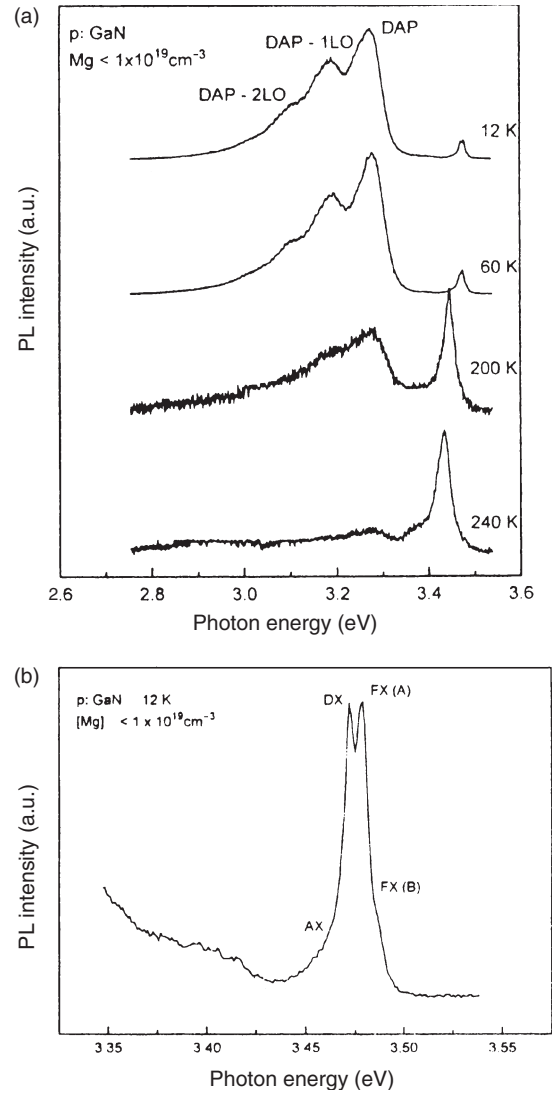
The first LEDs made of GaN were based on the metal-insulator-semiconductor structure. These devices required very high operating voltages, and, hence, they were not useful in practical devices. Several acceptor impurities were tried to make p-GaN with Zn, Cd, Be, Mg, Hg, and Li. It was observed that all these impurities effectively compensate the electrons in GaN, leading to highly resistive material. Amano et al. [95] achieved p-GaN by low-energy electron-beam irradiation (LEEBI) of Mg doped GaN. They also demonstrated the p-n junction LED by using LEEBI treated Mg-doped GaN as the p-type material. Nakamura et al. [80] have successfully obtained p-type GaN by thermal annealing. Mg was recognized as the most suitable acceptor impurity.

Photoluminescence of Mg/GaN grown by MOCVD was reported by Viswanath et al. [121]. Energy levels of these acceptors were investigated by systematic photoluminescence measurements in the temperature range of 12–300 K. Mg concentration was varied from less than  $1 \times 10^{19}$  to higher than  $5 \times 10^{19} \text{ cm}^{-3}$ . Figures 16, 17, 18, and 19 show the PL spectra for different Mg concentrations and for different annealing conditions. In the 12 K spectrum shown in Figure 16a, a strong line at 3.276 eV and satellites on the low-energy side at 3.184 and 3.092 eV were observed. The main line at 3.276 eV was attributed to zero-phonon donor-acceptor pair transition. The separation between two consecutive lines is about 92 meV. In the Raman spectra of undoped and Mg-doped GaN, the authors also observed the transitions due to the LO phonons with an energy of 91 meV. By this argument, the first satellite at 3.184 eV was assigned as the first phonon replica and the line at 3.092 eV as the second phonon replica of the donor-acceptor pair transition. The donors may be nitrogen vacancies. They have estimated the binding energy of the acceptor as 209 meV. Figure 13b shows the PL spectrum in the excitonic region at 12 K for the as-grown Mg-doped GaN with [Mg] less than  $1 \times 10^{19} \text{ cm}^{-3}$ . The FX(A) is the free exciton A, FX(B) is the free exciton B, DX is the donor-bound exciton, and AX is the acceptor-bound exciton transition. The spectrum for the doped samples shown in Figure 16b has exactly the same features as those found in undoped GaN [105]. Figure 17 shows PL spectra at certain selected temperatures for the annealed samples of Mg-doped GaN with [Mg] less than  $1 \times 10^{19} \text{ cm}^{-3}$ . The DA pair transitions were observed at low temperatures, which almost vanish at 120 K, and a new broad peak was seen at around 2.94 eV, which was attributed to conduction-band electron transition to a Mg acceptor.

### 2.1.3. Donors in GaN

The native defects were supposed to give high carrier concentrations in undoped GaN [10]. Nitrogen vacancy and oxygen impurities were considered as background donors.

Photoluminescence studies of shallow donors in GaN were done by Viswanath et al. [108]. Ionized donor-bound excitons have been observed, in addition to donor-bound excitons, as shown in Figure 20. The donor-binding energy was deduced as 35 meV. Figure 21 shows the temperature dependence of the full width at half maximum (FWHM) of the neutral donor-bound exciton PL peak reported by

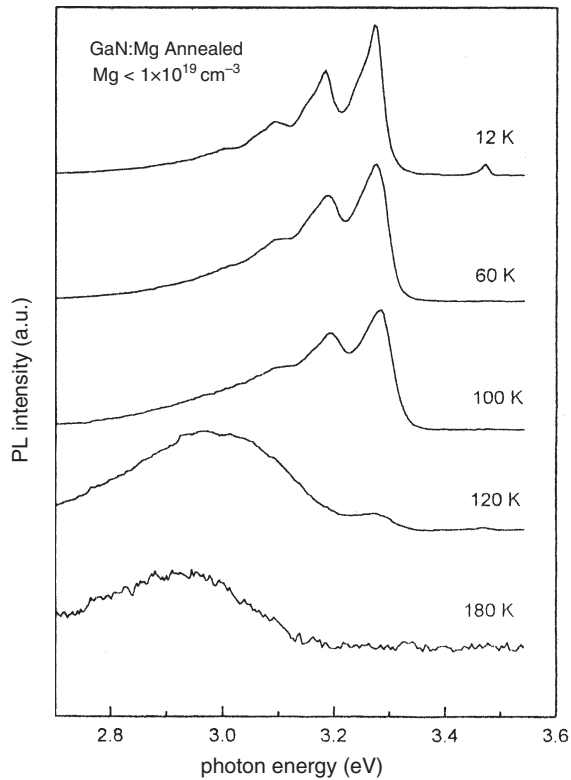


**Figure 16.** (a) Photoluminescence spectra at selected temperatures for magnesium-doped GaN, Magnesium concentration is less than  $1 \times 10^{19} \text{ cm}^{-3}$ . DAP is the zero phonon donor-acceptor pair transition. DAP-1LO and DAP-2LO are the first and second phonon replicas. (b) Excitonic region PL spectrum at 12 K. Reprinted with permission from [121], A. K. Viswanath et al., *J. Appl. Phys.* 83, 2272 (1998). © 1998, American Institute of Physics.

Viswanath et al. [108]. The solid squares are the experimental points, and the straight line is the linear fit of the experimental points. The experimental linewidths may be described by

$$\Gamma(T)(\text{FWHM}) = \Gamma_0 + \gamma_{\text{ph}}T \quad (3)$$

Here  $\Gamma(T)$  is the linewidth at temperature  $T$ ;  $\Gamma_0$  is the low-temperature limit of the linewidth and contains the contributions due to collision with other excitons, scattering by the crystal imperfections, or radiative recombination; and  $\gamma_{\text{ph}}$  is a measure of the exciton-acoustic-phonon coupling strength. From the linear increase of the linewidth with temperature, it was concluded by the authors that only acoustic phonons



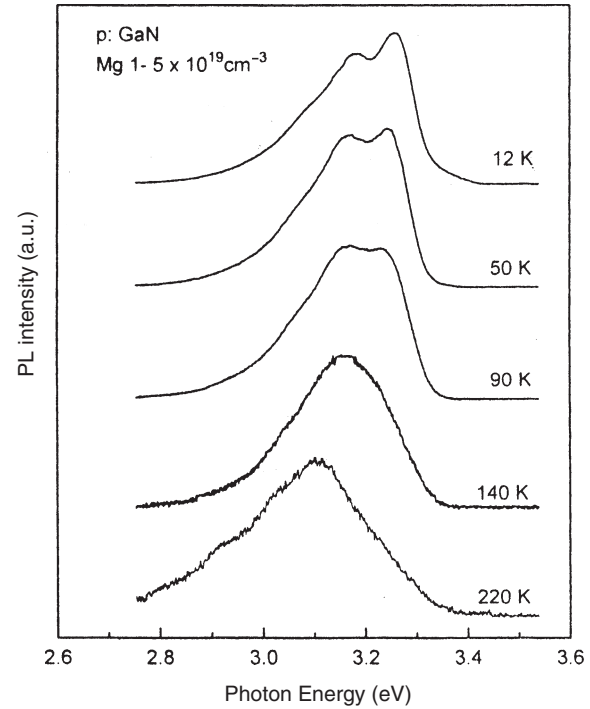
**Figure 17.** Photoluminescence spectra at selected temperatures for the annealed samples of Mg-doped GaN. Magnesium concentration is less than  $1 \times 10^{19} \text{ cm}^{-3}$ . The broad peak at 2.94 eV, which appears at higher temperatures is due to conduction band to acceptor transition. Reprinted with permission from [121], A. K. Viswanath et al., *J. Appl. Phys.* 83, 2272 (1998). © 1998, American Institute of Physics.

contribute to the homogeneous broadening. From the analysis of the linewidths, the following values were evaluated:  $\Gamma_0 = 1.55 \text{ meV}$  and  $\gamma_{\text{ph}} = 0.14 \text{ meV/K}$ .

Figure 22 illustrates the plot of the integrated emission intensity of the neutral donor-bound exciton as a function of  $1/T$ . The activation energy was reported as 9 meV. Figure 23 is a plot of the ratio of total intensity of free excitons to the total intensity of bound excitons, which includes both neutral and ionized donors, as a function of temperature. From the figure, it is clear that the bound excitons dissociate thermally, releasing free excitons and neutral donors as well as ionized donors. At 100 K, donor-bound excitons completely dissociate, forming free excitons and neutral donors. This temperature corresponds to the dissociation energy of the donor-bound exciton.

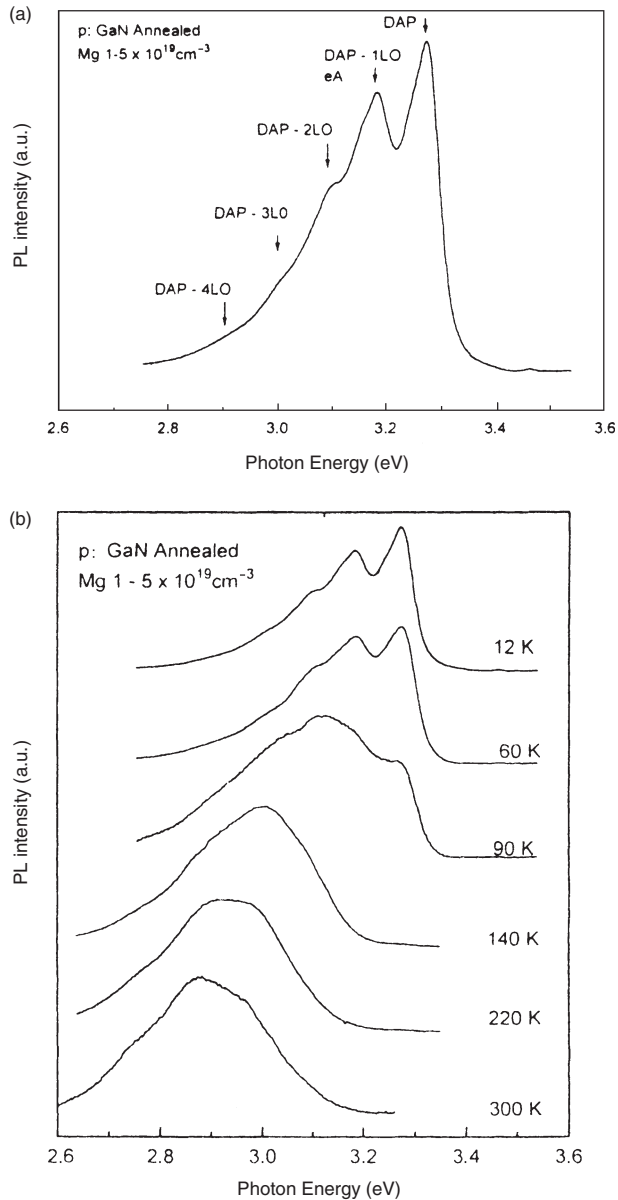
## 2.2. GaN Nanowires

Chen and Yeh [122] have reported the large scale production of GaN nanowires by a very simple method. They have reacted gallium and ammonia by using polycrystalline indium powder as a catalyst. The fiber-like semiconductors of GaAs, InP, etc. were grown by several groups by the vapor-liquid-solid crystal growth mechanism. The important ingredient in this method is the catalyst between the vapor and the solid at high temperatures that are normally required for the chemical vapor deposition technique.



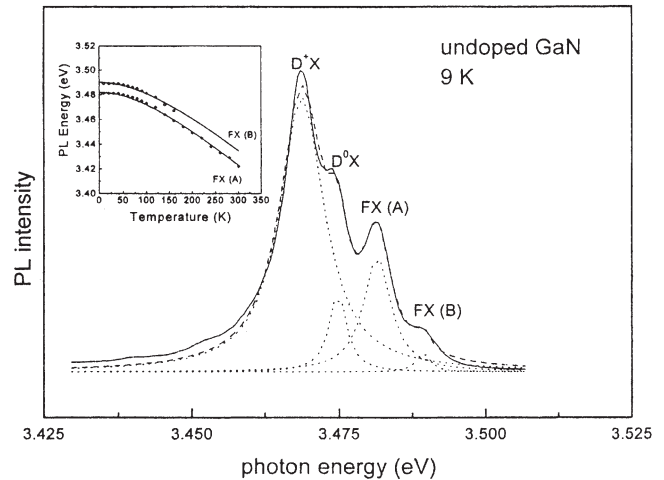
**Figure 18.** Temperature dependence of the PL spectra for as grown Mg:GaN. Magnesium concentration is in the range of  $1\text{--}5 \times 10^{19} \text{ cm}^{-3}$ . Reprinted with permission from [121], A. K. Viswanath et al., *J. Appl. Phys.* 83, 2272 (1998). © 1998, American Institute of Physics.

Generally, gold metal has been used as the catalyst for the wire-like structures of both III-V and II-VI semiconductors. Chen and Yeh have realized that elemental indium was better than gold as a catalyst. It was thought that very small In-GaN miscible droplets were formed during the heating process of the reaction, which act as nucleation sites in the VLS growth of GaN nanowires. However, the authors could not give any evidence for their mechanism. The diameters of the wires were estimated to be about 20 to 50 nm from the scanning electron microscopy results. Nanowires were found to be uniformly distributed over 95% of the substrate area, and the rest was filled with nanoparticles of GaN. Chen et al. [123] have examined the effect of various catalysts and reaction parameters on the size of the nanowires and their properties. In these trials, they have modified their experimental setup and tried to separate the residual gallium and bulk gallium nitride from resulting GaN nanowires after the catalysis reaction was complete. When the reaction was going on, several combinations of metals were tried to act as catalysts. To increase the yield and control the diameter of the nanowire, the parameters, which were varied, include the temperature of reaction, time, and heating rates. Figure 24 shows the scanning electron microscopy (SEM) images of GaN nanowires grown on a silicon substrate. It was noticed that when cobalt phthalocyanine or nickel phthalocyanine was used as a catalyst, the diameter of the nanowire was reduced to as low as 6 nm. Based on the experimentation with several metals and their compounds, it was concluded that the usage of metal complexes gives nanowires with very small diameter. Varying the reaction time has helped the authors to understand the growth mechanism.



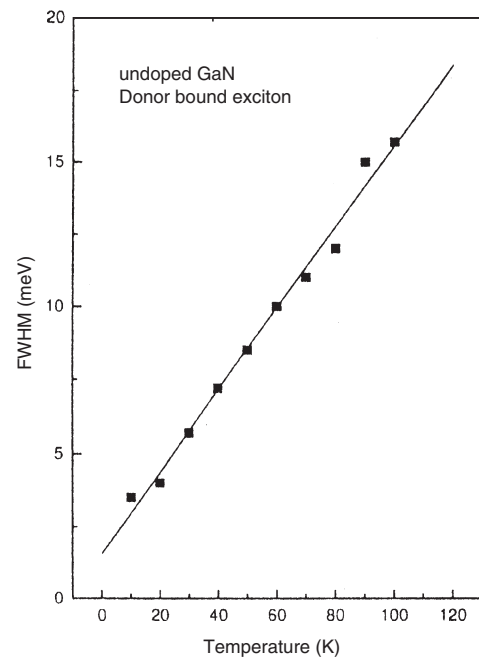
**Figure 19.** Photoluminescence spectrum at 12 K for the annealed GaN doped with magnesium. Magnesium concentration is in the range of  $1\text{--}5 \times 10^{19} \text{ cm}^{-3}$ . The zero-phonon and various phonon-assisted donor-acceptor pair transitions can be seen. The eA is the conduction band to Mg acceptor transition, which overlaps with the first phonon replica of DA transition. (b) Temperature variation of the photoluminescence of GaN:Mg epilayers, which are annealed. (Mg):  $1\text{--}5 \times 10^{19} \text{ cm}^{-3}$ . Reprinted with permission from [121], A. K. Viswanath et al., *J. Appl. Phys.* 83, 2272 (1998). © 1998, American Institute of Physics.

It was concluded from these experiments that the total reaction time controls the diameter and the length of the wire. Figure 25 shows the SEM image of the sample that was heated for three hours. A large number of rodlike structures with diameters of several hundred nanometer were found. When the heating time was increased, the short, rodlike structures increased in length along the axial direction to form wirelike structures with the simultaneous reduction in their diameter. Based on these results, the authors have given the possible pathways of the vapor-liquid-solid (VLS)



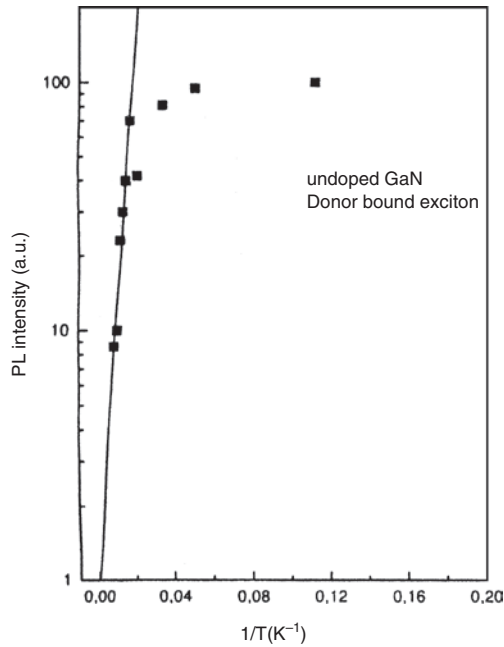
**Figure 20.** Luminescence spectrum of GaN epilayer at 9 K. Dotted lines show the deconvolution into Lorentzian fitting of various transitions. Dashed line is the Lorentzian fitting of the experimental spectrum. The inset shows the temperature dependence of the transition energies of free excitons A and B. D<sup>+</sup>X is due to ionized donor-bound exciton transition. Reprinted with permission from [106], A. K. Viswanath et al., *Phys. Rev. B* 58, 16333 (1998). © 1998, American Physical Society.

growth of GaN nanowires as shown in Figure 26. The photoluminescence and Raman spectra of the GaN nanowires also were reported. In a later publication, the same group has reported the temperature dependence of the photoluminescence [124]. A very simple chemical route to prepare GaN nanowires and nanotubes, without using any catalyst or



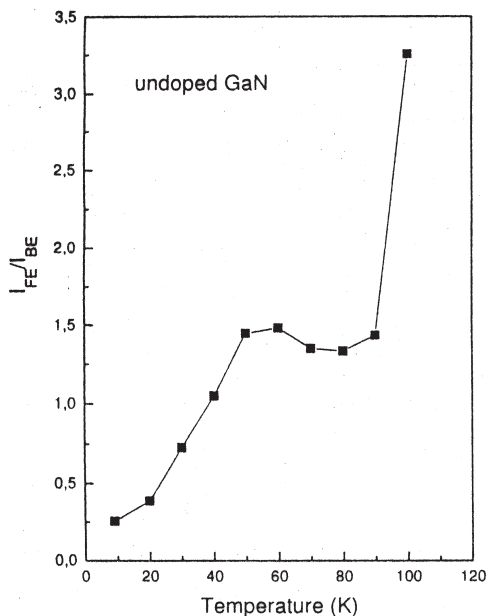
**Figure 21.** Variation of FWHM as a function of temperature for the neutral donor-bound exciton PL peak. The squares are experimental linewidths. The straight line is a linear fit of the experimental linewidths considering the acoustic phonon scattering. Reprinted with permission from [108], A. K. Viswanath et al., *Appl. Phys. A* 67, 551 (1998). © 1998, Springer Verlag.



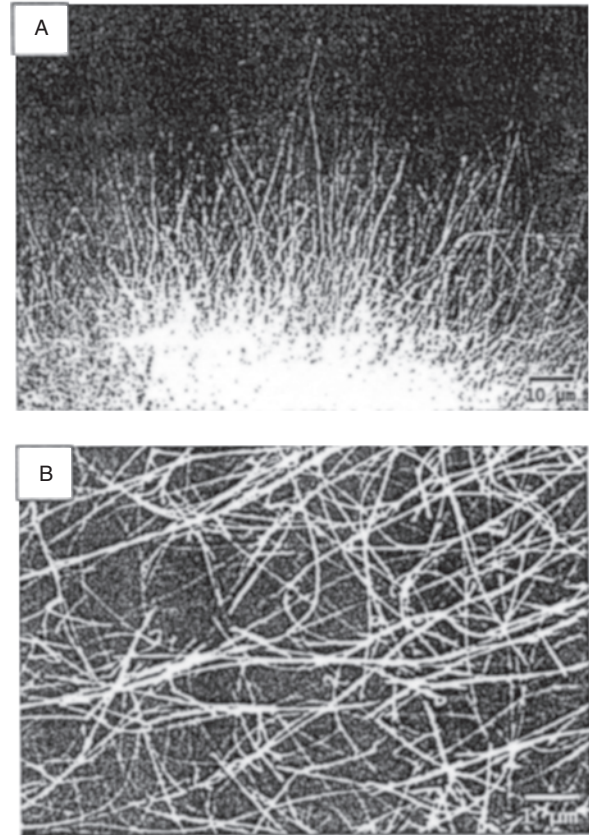


**Figure 22.** Activation energy plot of the PL intensities of the neutral donor-bound excitons vs.  $1/T$ . The slope of the straight line gives the thermal activation energy of neutral donor bound excitons as 9 meV. Reprinted with permission from [108], A. K. Viswanath et al., *Appl. Phys. A* 67, 551 (1998). © 1998, Springer Verlag.

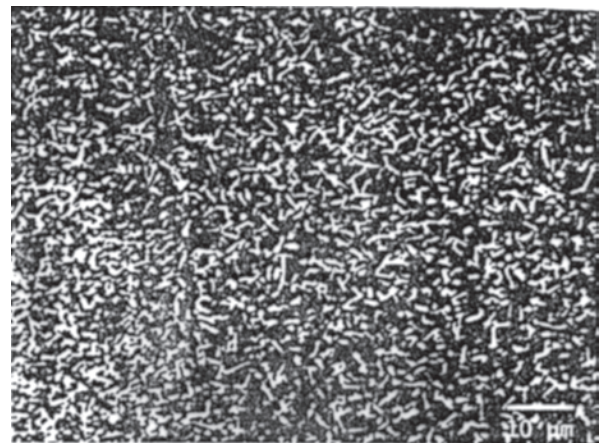
a template was described by He et al. [125]. A direct reaction between Ga metal with flowing ammonia at a temperature of around 900 °C in a horizontal furnace was conducted. The diameters of the GaN nanowires thus obtained were in the range of 26 to 100 nm. The controlling parameters of the reaction were determined to be the temperature of reaction



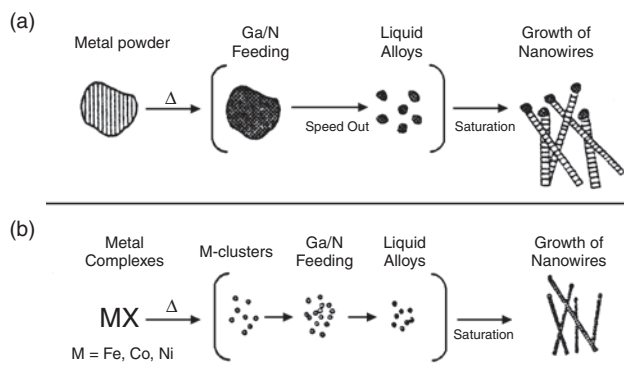
**Figure 23.** The ratio of total intensity of free excitons (A and B) to total intensity of bound excitons (neutral and ionized donor),  $I_{FE}/I_{BE}$  as a function of temperature. Reprinted with permission from [108], A. K. Viswanath et al., *Appl. Phys. A* 67, 551 (1998). © 1998, Springer Verlag.



**Figure 24.** Typical SEM images of GaN nanowires grown on a silicon substrate (a) Cross-sectional image showing a large number of nanowires grown on the substrate. (b) Top-view image of nanowires. The lengths of nanowires are up to several micrometers, and their diameters are around 20–50 nm. The nanowires show a smooth surface and no ramification over their length. Reprinted with permission from [123], C. C. Chen et al., *J. Am. Chem. Soc.* 123, 2791 (2001). © 2001, American Chemical Society.

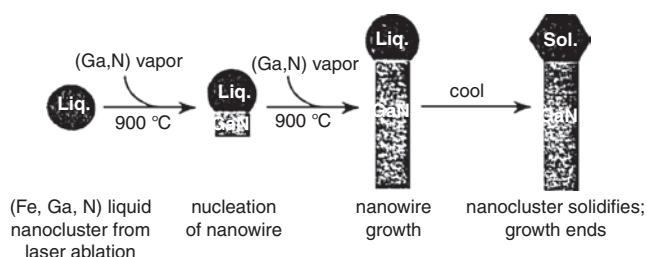


**Figure 25.** SEM image of the sample heated for 3 h. A large number of short rodlike structures with diameter of several hundred nanometers are found. Reprinted with permission from [123], C. C. Chen et al., *J. Am. Chem. Soc.* 123, 2791 (2001). © 2001, American Chemical Society.



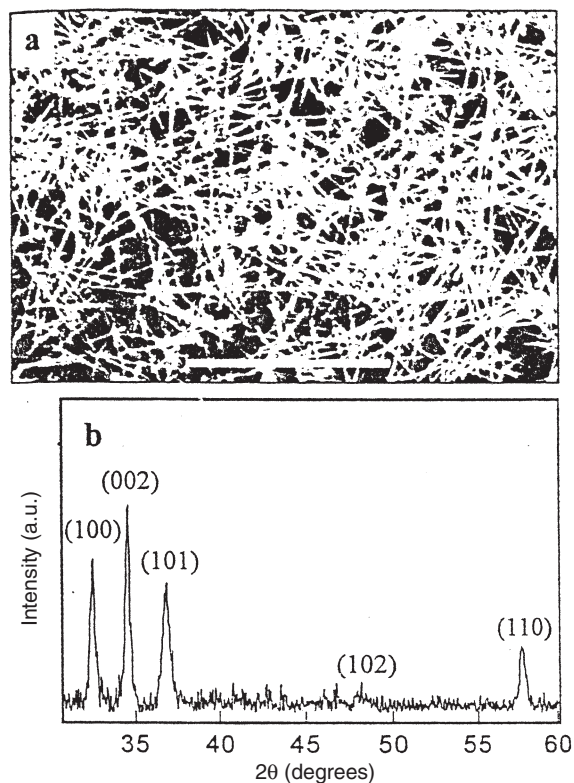
**Figure 26.** Schematic illustration of two possible pathways of the VLS growth of GaN nanowires (a) At the beginning, the catalysts of metal powder gradually form catalyst–gallium–nitrogen alloys after gallium vapor transport to the catalysts on the substrate. Each alloy turns into a miscible liquid droplet and then spreads out, becoming many smaller droplets. Hence, after the concentration of gallium nitride reaches saturation in the droplet, the droplet can act as a nucleation site, and a GaN nanowire begins to grow in one direction. (b) At the initial heating stage, metal complexes are decomposed rapidly in the gas phase or on the substrate and sequentially generate many small metal clusters. These clusters form small Ga–N–catalyst liquid droplets and serve as nucleation sites after gallium and ammonia vapors are fed in. In comparison to pathway (a), the nanowires with smaller diameters could be obtained when the reaction goes through pathway (b). Reprinted with permission from [123], C. C. Chen et al., *J. Am. Chem. Soc.* 123, 2791 (2001). © 2001, American Chemical Society.

and the flow rate of ammonia. Nanoparticles of transition metal oxides such as NiO as catalysts were used by Chen et al. [126] to grow GaN nanowires of diameters of 10 to 40 nm. These nanowires, which were made without any template, were found to be straight and smooth compared to the twisted ones obtained by other workers from the confined reactions. In another approach, Ga and SiO<sub>2</sub> were reacted with ammonia in the presence of Fe<sub>2</sub>O<sub>3</sub> catalyst to get GaN nanowires of diameters in the range of 10 to 50 nm [127]. The authors also have proposed a growth mechanism of the wires. Peng et al. [128] have used a hot filament in the chemical vapor deposition chamber and obtained GaN nanowires of the diameters of 5 to 22 nm and lengths of a few micrometers. Structural studies have shown them to be of a wurtzite structure. In this method, a mixture of Ga<sub>2</sub>O<sub>3</sub> and C was placed above the hot filament and ammonia gas was passed at a pressure of 200 Torr. The temperature of the substrate was at 900 °C. A two-step reaction path was proposed for the growth of the nanowires. Duan and Lieber [129] have demonstrated a very novel method of laser-assisted catalytic growth to grow GaN nanowires. A laser is used to vaporize a solid target containing the desired material and a catalyst. Nanowires were supposed to grow by following the vapor–liquid–solid growth mechanism. The authors have stressed the importance of a rational approach in choosing the catalyst. The catalyst should form a miscible liquid phase with GaN but should not form a more stable solid phase under the nanowire growth conditions. According to this principle, Fe was chosen as the catalyst and quasi one-dimensional structures with diameters of 10 nm and lengths exceeding 1 mm were obtained. Figure 27 shows the growth



**Figure 27.** Schematic of the mechanism of formation of GaN nanoclusters from laser ablation. Reprinted with permission from [129], X. Duan and C. M. Lieber, *J. Am. Chem. Soc.* 122, 188 (2000). © 2000, American Chemical Society.

mechanism, and the SEM picture of these wires is shown in Figure 28. In a later study, Lieber and his group at Harvard have demonstrated the fabrication of several logic gates in which the basic building blocks were made by the bottom-up approach [130]. Kim et al. [131] have made use of the thermal chemical vapor deposition method to grow GaN nanowires with a wurtzite crystal structure. In this method, a Ni catalyst was used in a direct reaction between Ga metal and GaN powder in the presence of flowing ammonia at 1000 °C. InN nanowires were grown by a Taiwanese team on p-type silicon substrate that was patterned with gold [132a].



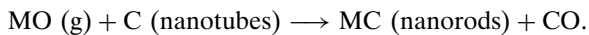
**Figure 28.** (a) FE–SEM image of bulk GaN nanowires synthesized by LCG. The scale bar corresponds to one micron. (b) PXRD pattern recorded on bulk GaN nanowires. The numbers above the peaks correspond to the (hkl) values of the wurtzite structure. Reprinted with permission from [129], X. Duan and C. M. Lieber, *J. Am. Chem. Soc.* 122, 188 (2000). © 2000, American Chemical Society.

Nanoscale structures also were made by using self-ordered nanochannel material that acts as a template. This is prepared by the anodization of Al in a suitable acid [132b–132d]. The anodic alumina membrane (AAM) contains a hexagonal-ordered porous structure with nanochannel diameters that lie in the range of 10 to 200 nm, and the channel density is in the range of  $10^{10}$  to  $10^{12}/\text{cm}^2$ . The main advantage of these templates is that the aspect ratio of their channels, which is defined as the ratio of depth to width, is very high and that cannot be achieved by the conventional lithographic techniques. Several groups have made use of such templates and different nanowires were grown [132c–g]. Cheng et al. [132h] have grown GaN wires in the alumina template. Here, GaN was created by a reaction between  $\text{Ga}_2\text{O}_3$  and ammonia gas. Zhang et al. [132i] have made highly ordered GaN wires in AAM templates. These workers have used indium nanoparticles as catalyst into the nanochannels of AAM through electrochemical deposition, instead of sputtering a layer of indium onto the side of AAM. The evidence for the catalytic activity of indium was found from the EDX analysis, which has shown that the nanoparticle on the tip contains In, Ga, and N. However, nanowire was found to consist of only Ga and N. The authors also have discussed the VLS mechanism for the formation of the nanowires that is similar to the proposals by Leiber. However, no quantum confinement effects were observed in the photoluminescence spectrum.

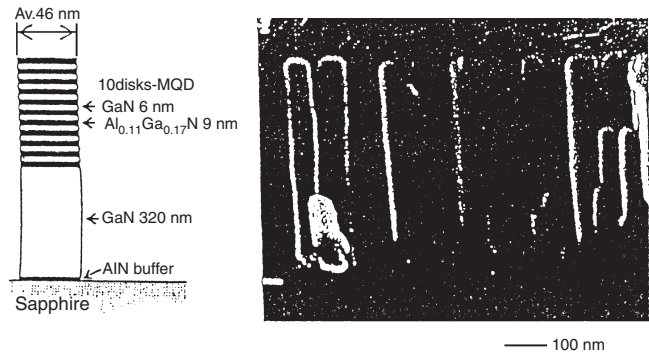
Yoshizawa et al. [132j] have grown nanocolumns of GaN on c-face sapphire by molecular-beam epitaxy. The SEM pictures of these nanostructures are shown in Figure 29. By controlling the Ga-cell temperature, the diameter of nanocolumn could be reduced to about 40 nm. These workers also have achieved GaN/AlGaIn multiple quantum disks. Here nanostructures were grown by the self-organization process. Figure 30 shows the schematic of the multiple quantum structure and the SEM picture of the quantum disks. Quantum size effects were observed in the PL spectra.

### 2.3. Nanorods

Leiber's group at Harvard was the first to report a novel approach to synthesize nanoscale structures based on carbon nanotubes [133, 134]. In this method, the nanotubes were converted into carbide (MC) nanorods by reaction with a volatile oxide species. The reaction can be expressed as

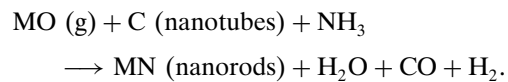


**Figure 29.** (a) SEM photograph of GaN nanocolumn, in which AlN buffer was grown. Growth time of buffer is for 40 sec. (b) SEM photograph of GaN in which AlN buffer was grown. Growth time of buffer is for 10 sec. Reprinted with permission from [132j], M. Yoshizawa et al., *J. Cryst. Growth* 189–190, 138 (1998). © 1998, Elsevier Science.

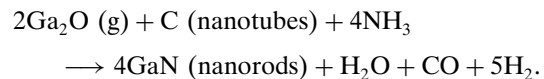


**Figure 30.** (a) Schematic of GaN/AlGaIn 10 disks MQD (b) Cross-sectional SEM photograph of MQD structure. Reprinted with permission from [132j], M. Yoshizawa et al., *J. Cryst. Growth* 189–190, 138 (1998). © 1998, Elsevier Science.

Where MO is a volatile metal or nonmetal oxide with a reasonably high vapor pressure at the reaction temperature. Han et al. [135] have adopted the similar procedure to prepare GaN nanorods. They have carried out the following reaction



Here  $\text{Ga}_2\text{O}$  was taken for MO, which was prepared by the reaction of Ga and  $\text{Ga}_2\text{O}_3$ . Carbon nanotubes were made by metal catalyzed decomposition of ethylene and hydrogen in a chemical vapor deposition chamber. By this procedure, the research team could achieve the multishell carbon nanotubes with approximate diameters of 15 nm. The actual reaction in which GaN nanorods were prepared can be represented as



The  $\text{Ga}_2\text{O}$  gas that was generated from the reaction of Ga and  $\text{Ga}_2\text{O}_3$  powder reacts with ammonia gas to form the GaN. Transmission electron microscopy (TEM) results have shown that GaN rods of diameters in the range of 4 to 50 nm were formed. The GaN nanorods were solid, while the carbon nanotubes have a hollow-core structure. A strong broad band with a peak at 384 nm was observed in the photoluminescence spectrum at room temperature, in addition to the yellow band due to impurities. By using the methods similar to those described above, Han et al. [136–138] have made silicon nitride and boron nitride nanorods, boron nitride nanotubes with or without filling. Later, Han et al. [139] have prepared GaN–carbon composite nanotubes and GaN nanorods by arc discharge in nitrogen atmosphere. Ebbesen's special edition [140] on carbon nanotubes gives a complete discussion on the synthesis in the arc discharge of a variety of carbon nanostructures by using the high temperature of the plasma. Carbon whiskers [141], fullerenes [142], nanotubes [143], and carbon nanotubes filled with metals and nonmetals and their carbides and oxides [140, 144–150] were synthesized by arc discharge methods. Han

et al. [139] obtained the nanorods of GaN by dc arc discharge between a graphite anode filled with a mixture of GaN, graphite, and nickel powders, and a graphite cathode in a nitrogen atmosphere. The cathode was a graphite rod with a diameter of 12 mm. The nitrogen pressure was maintained at 400 to 500 Torr. The experiment could be completed in about 10 minutes. The authors also concluded that the nitrogen atmosphere played a very important role in synthesis of GaN nanorod fillings and also isolated GaN nanorods. For example, the experiments done in the helium atmosphere could not produce the nanostructures of GaN. Another observation by these workers was that Ni catalyst has yielded very high quantities of GaN nanomaterials. High-resolution transmission spectroscopy imaging has shown that the carbon tubes were filled with GaN nanorods and the isolated GaN rods with diameters of the order of 7 to 45 nm. The authors also have given a five-step process as the mechanism of growth of the nanostructures: (1) boiling GaN, Ni, and graphite powder in the anode; (2) plasma formation at the anode, (3) transport of Ga, N, Ni, and C ions toward the cathode, and formation of N radicals from the nitrogen atmosphere that goes along with the plasma processes; (4) crystalline growth of GaN nanorods that occurs as a result of reaction between Ga ions and surrounding N ions at the cathode; (5) agglomeration of carbon around the GaN rods that is catalyzed by Ni.

Tiginyanu et al. [151] have achieved columnar GaN nanostructures by electrochemical etching of GaN layers. In the micro-Raman spectroscopy of these samples, frequencies of Frohlich modes that lie between the LO and transverse optic phonon frequencies could be observed. It was argued that the nanotexturing will change the density of phonon states, induces surface-related vibrations, and spatially confines the bulk phonon modes. Kang's group in South Korea has demonstrated the growth of high-quality, well-aligned GaN nanorods by hydride vapor phase epitaxy [152]. The samples were grown on a sapphire substrate. The substrate temperature was kept at 480 °C in a horizontal reactor. The main advantage in this method is that the nanorods are straight and parallel to each other, unlike the ones made by other methods that have very irregular shapes, and, hence, they are very suitable for the device fabrication purpose. Quantum confinement effects also were observed in the luminescence spectra. Zettl's group at Berkeley has used a pyrolysis approach to synthesize GaN nanorods [153]. In this method, both the Ga and the catalyst come from organic sources. A two-stage furnace system fitted with temperature controllers was used for the pyrolysis. Gallium dimethylamide and ferrocene powders were mixed in a quartz tube, and the ammonia gas was passed through the tube throughout the reaction. The analysis of TEM revealed that the GaN nanorod is a single crystalline with a hexagonal structure, and the interface between the nanorod and the tip is polycrystalline. The energy dispersive spectra shows that the tip contains Ga, N, Fe, and O, whereas the nanorod contains only Ga and N in approximately a 1:1 ratio. Ferrocene was known to be a very good catalyst for the growth of nanotubes. The authors have found very firm evidence for the catalytic activity of ferrocene by doing the pyrolysis experiments with and without ferrocene. Nanotubes and nanorods could not be formed in the absence of ferrocene. The growth

process was thought to be by the vapor–liquid–solid mechanism. At high temperatures used in the pyrolysis experiment, ferrocene, gallium dimethylamide, and ammonia will decompose. The iron particles are surrounded by N, Ga, C, and other radicals, which leads to the increase in the size of the F clusters on the surface of the quartz tube. Later, Ga and N, in vapor phase, dissolve in the iron oxide clusters to form liquid catalyst centers. A supersaturated solution is created when Ga and N dissolve continuously. GaN nanorod growth takes place by precipitation from the supersaturated liquid of the catalyst centers. After cooling down the system, solid GaN nanorods are formed. In a recent report, Han and Zettl [160] have described the growth of GaN nanorods coated with insulating boron nitride.

## 2.4. Nanobelts and Nanoribbons

Nanobelts and nanoribbons of semiconducting oxides were first reported by Pan et al. [161]. These authors have described a chemical route synthesis of very novel nanostructures of oxides of zinc, tin, indium, cadmium, and gallium, which have a rectangular cross section, with widths in the range of 30 to 300 nm. Nanoribbons and nanoribbon rings of GaN were made by Chen's group by the reaction of Ga and ammonia in which silver particles were used as catalyst and with the sublimation of ball-milled GaN powders in the presence of ammonia flow [162, 163]. Bae et al. [164] have reported a synthesis of GaN nanobelts by the thermal CVD method. They have reacted a mixture of Ga and GaN with ammonia in the presence of boron oxide at 1100 °C.

## 2.5. Nanopillars

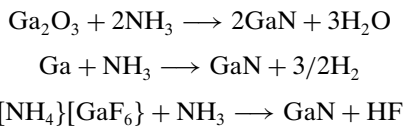
Pearson et al. [165] have discussed the application of reactive ion etching in the growth of nitrides. GaN pillar arrays were made by Grandjean and his coworkers in France [166–168]. First, 300-nm-thick GaN layers were grown along the [0001] direction on top of a 400-nm-thick AlN layer deposited on a sapphire substrate by molecular-beam epitaxy. Patterning was done by electron-beam lithography on poly-methylmethacrylate resist and then metallic mask was deposited by sputtering. Reactive ion etching was performed by using silicon tetrachloride at a pressure of 2 mT. The research team has done very detailed characterization of the pillars thus obtained. Seven pillars of different sizes, ranging from 5 μm, to 100 nm, spaced by 50 μm, were grown. Two unetched zones were used to compare the properties of the etched material with the grown material. Very large surface roughness was observed in the atomic force microscopy (AFM) pictures, which was attributed to the fact that the as-grown layer itself was very rough. In addition to this, ion etching leads to the surface roughness. The authors have measured the Raman and photoluminescence spectra of the GaN pillars.

## 2.6. Nanoparticles and Nanocrystals

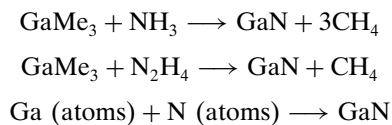
Williams's group in Australia has reported a very novel method of preparation of GaN nanocrystalline powders by ball milling [169]. They have used high-purity elemental gallium ingot and high-purity ammonia gas as starting materials. Ga was milled in a specially designed laboratory ball

mill with perfect control of ball movement. In their design of the equipment, they also could control the temperature of heating. Ga metal was kept as a liquid by keeping the temperature at 100 °C. The TEM analysis has shown that the powder consists of small crystals of diameters ranging between 10 and 30 nm. There also are larger crystals with diameters of about 70 nm. It also was found that the nanocrystalline phase changes to polycrystalline GaN on thermal treatment.

Gladfelter's group has achieved the GaN nanocrystals by a molecular route [170]. The molecular precursor used for this purpose is cyclotrigallazane  $[H_2GaNH_2]_3$ , its molecular structure is shown in Figure 31. It should be noted that this compound does not have any carbon or organic substituents, which makes it a best candidate to prepare carbon-free GaN. Bulk GaN with a hexagonal structure has been chemically prepared by the following chemical reactions [171–173]:

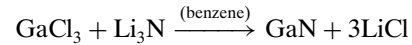


GaN thin films also were made by different research groups according to the following chemical reactions [174–176]:



Nanocrystalline GaN was obtained by the pyrolysis of powdered samples of cyclotrigallazane under different conditions. From the TEM studies, the size of the nanocrystals was estimated to be 6 nm. In the initial products, both cubic and hexagonal phases of GaN were identified. If this mixture of nanocrystals is heated to 900 °C the nanocrystals convert to a pure hexagonal phase. The removal of hydrogen by a series of bimolecular reactions, followed by Ga–N bond formation, was thought to be the mechanism of formation of GaN from the original precursor molecule. The authors have argued that the cyclotrigallazane molecule has the correct formula, connectivity, and conformation so that solid-state polymerization takes place, which gives rise to a GaN crystalline state. Janik and Wells [177] have discovered a new polymeric precursor, gallium imide, with the formula  $[Ga(NH)_{3/2}]_n$ , which upon pyrolysis yielded nanocrystalline GaN. The authors have argued that the main advantage of

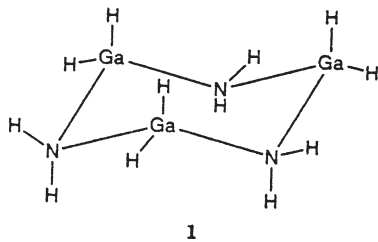
this precursor is that it does not contain any organic groups, and, hence, it is expected that relatively pure GaN without carbon content can be obtained. Also, it is easy to eliminate ammonia at low temperatures, through stepwise deamination. The preparation of the precursor also was described in the publication. Xie et al. [178] have discussed the preparation of nanocrystalline GaN by liquid–solid reaction,



This reaction was called the benzene thermal process, which is similar to the hydrothermal process. Here benzene is used instead of water.

A Chinese group has used the dc arc plasma method to prepare nanocrystals of GaN [179]. Bulk gallium was placed in a water-cooled copper crucible, which acts as an anode. A mixture of nitrogen and ammonia gases were sent into the chamber. The flow rates of the gases can be controlled, and, hence, the proportion of the two gases can be adjusted easily. The nitride reaction takes place when an arc plasma was generated with the mixture of nitrogen and ammonia as the discharge gas. The morphology of the nanocrystals was found to be hexagonal, with a particle size of about 20 to 200 nm. The authors have noted that it is very difficult to prepare GaN by using only nitrogen gas, because it is very stable up to very high temperatures. For this reason, ammonia is preferred as the nitrogen source. However, if only ammonia is used, the generated plasma will be very unstable and so a mixture of nitrogen and ammonia has to be used. The larger nanoparticles were found to be due to the wurtzite phase GaN monocrystals from the diffraction patterns. A few nanoparticles grew into larger particles of several hundred nanometers as a result of collision and secondary nucleation. To study the thermal stability of the synthesized nanopowders, the research group has done annealing experiments. It was found that  $Ga_2O_3$  oxide was formed when the GaN powder was heated in the temperature range of 200 to 900 °C. Benaissa et al. [180] have fabricated the composites of PMMA doped with GaN nanoparticles. First, the chemical reaction of  $LiN(CH_3)_2$  with  $GaCl_3$  in hexane was conducted at room temperature to obtain the precursor  $Ga_2[NMe_2]_6$ , which was decomposed under flowing ammonia gas for 4 h at 600 °C. The nano GaN thus obtained was reacted with methylmethacrylate and thermally polymerized at 72 °C for 50 minutes. It was observed that the GaN was highly dispersed in the polymer matrix, and the size of the GaN nanocrystals is around 5 nm.

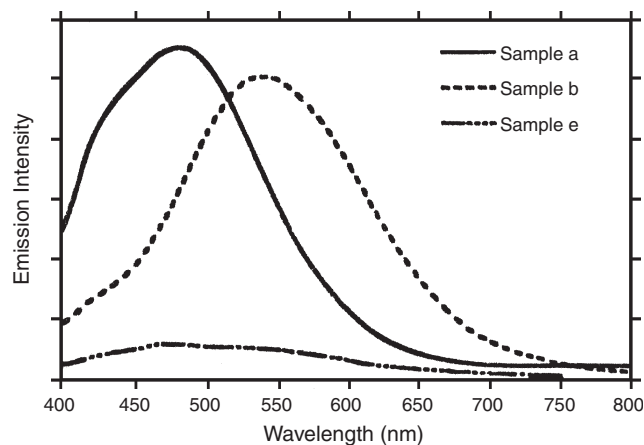
Coffer et al. [181] have done a very detailed investigation on the effect of the precursor route on the photoluminescence of bulk and nanocrystalline GaN. They have experimented with two precursors namely gallium imide and cyclotrigallazane. This research team also has discovered a new chemical reaction to prepare cyclotrigallazane [182]. Nanocrystals of GaN with a diameter of about 12 nm were obtained after the pyrolysis of a gallium imide precursor at or above 500 °C in a vacuum or in the ammonia atmosphere. These samples have shown very low quantum efficiency and strong defect emission. The weak luminescence was thought to be due to the nonradiative centers at interfaces or in the interior of the sample. Very



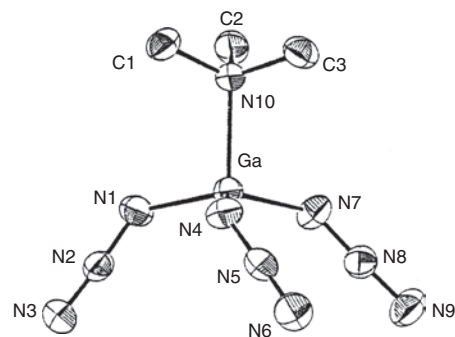
**Figure 31.** Molecular structure of cyclotrigallazane. Reprinted with permission from [170], J. Hwang et al., *Chem. Mater.* 7, 517 (1995). © 1995, American Chemical Society.

strong luminescence was observed if the pyrolysis temperature was lowered or the reaction medium was changed. In the samples, which were obtained after the pyrolysis of a gallium imide precursor in ammonia atmosphere at a lower temperature of 300 °C, an intense defect luminescence with peak maximum at 560 nm was observed. From the temperature-dependent luminescence measurements, it was concluded that multiphonon-related nonradiative transitions take place, which have an identical character of the donor-acceptor transitions observed in nanocrystals of CdS [183]. Very strong luminescence in the blue with a peak at 460 nm was observed if the pyrolysis of the gallium imide was done in the refluxing  $N,N,N',N'$ -tetramethyl-1,6-hexane diamine. The variation in the luminescence for various conditions of preparation of GaN nanoparticles is shown in Figure 32. Experiments also were done to remove the surface defects on GaN nanoparticles by treating the samples with HF and  $HNO_3$ . Yamane et al. [184] have prepared GaN nanocrystals by using Na flux. Pyrolysis of  $Ga_2[N(CH_3)_2]_6$  [185] and  $[Ga(N_3)_3]_n$  [186] also yielded nanocrystalline GaN. Microwave-assisted nitridation of  $Ga_2O_3$  [187] and also in combination with carbothermal reduction [188] were used successfully to prepare nanocrystals of GaN.

Fischer and his collaborators in Germany have used a very novel method of detonation chemistry to synthesize nanocrystals of GaN [189–191]. The main idea in using detonation for synthesis is that it acts like an arc discharge since very high temperatures and pressures are used for a very short time duration. The detonation chemistry of gallium azides was made use of to prepare nanosize GaN. It was proposed that the optimal mixing of Ga and N can be controlled at the molecular level. The molecular structure of gallium azide is shown in Figure 33. At very high temperatures, the nitrogen from the azide groups can be removed, and GaN can be formed. The sensitivity of the highly explosive triazidogallium unit  $[Ga(N_3)_3]$  can be tuned by using the trialkylamine adducts  $(R_3N)[Ga(N_3)_3]$  where  $R_3N = Me_3N, Et_3N, Me_2C_8H_{17}N$  instead of the parent triazido compound.

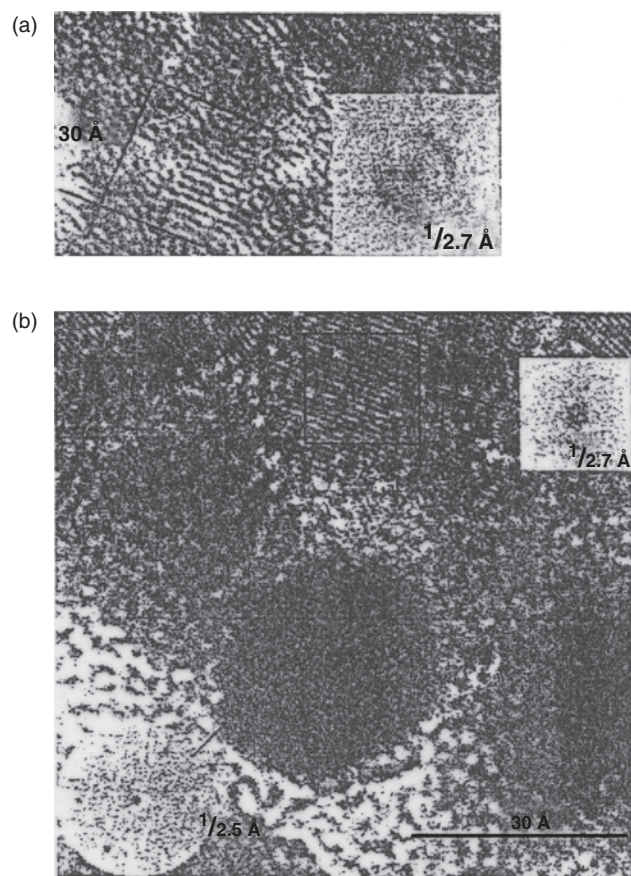


**Figure 32.** Room-temperature PL spectra for GaN samples prepared by pyrolysis of gallium imide: spectrum a (solid line), reflux in  $N,N,N',N'$ -tetramethyl-1,6-hexane diamine, bp 210 °C, 48 h; spectrum b (dashed line), 300 °C,  $NH_3$ , 4h; spectrum e (dot-dashed line), 600 °C, vacuum, 3h. Reprinted with permission from [181], J. L. Coffey et al., *Chem. Mater.* 9, 2671 (1997). © 1997, American Chemical Society.

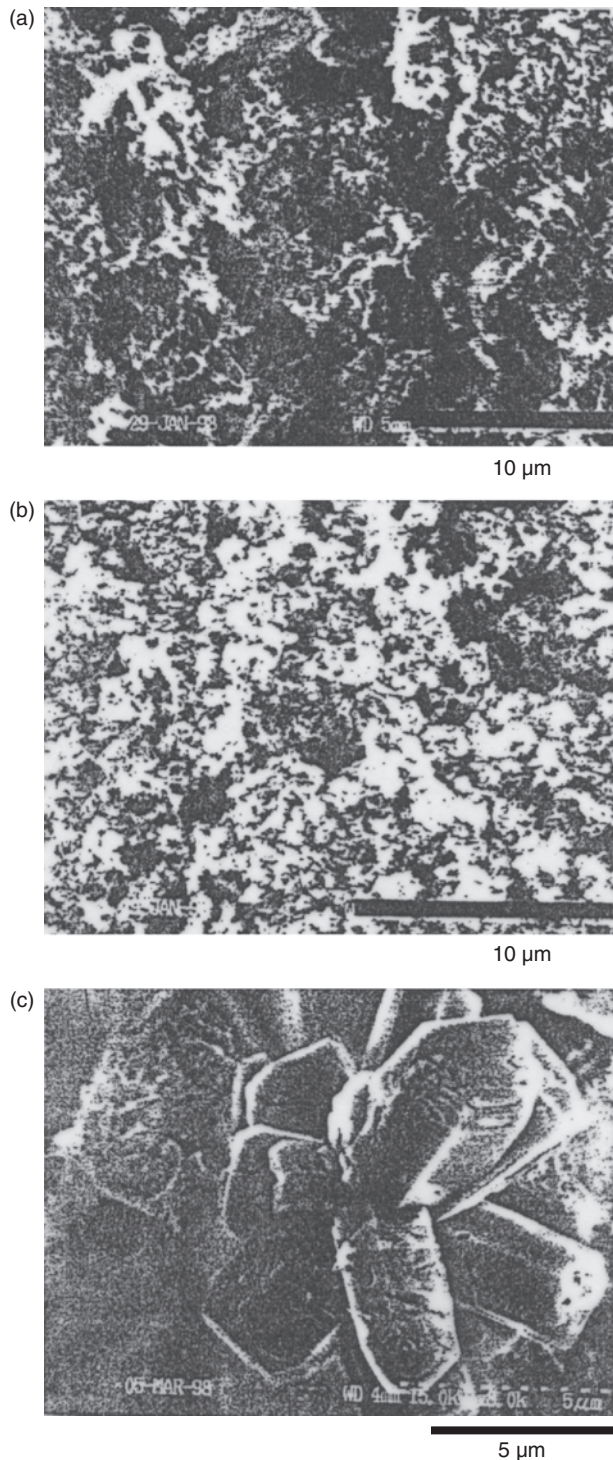


**Figure 33.** Molecular structure of  $(Me_3N)Ga(N_3)_3$  in the solid state as a representative example of the homologous series of  $(R_3N)Ga(N_3)_3$ . Reprinted with permission from [191], A. C. Frank et al., *Adv. Mater.* 10, 961 (1998). © 1998, John Wiley and Sons.

Figure 34 shows the high-resolution TEM micrographs and electron diffraction patterns of two representative samples. Figure 35 shows the SEM pictures of GaN nanoparticles of different sizes. The particle size could be controlled by the total amount of the precursor, the protecting amine ligand, the condensation time at 150 °C, and the starting pressure. Photoluminescence spectra of these nanoparticles were



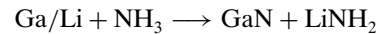
**Figure 34.** High-resolution TEM micrographs and electron diffraction patterns of two representative samples (a and b). The 7-nm nanocrystals of samples a and b exhibit a characteristic plate-like shape. Reprinted with permission from [191], A. C. Frank et al., *Adv. Mater.* 10, 961 (1998). © 1998, John Wiley and Sons.



**Figure 35.** Scanning electron micrographs of a typical sample of nano-crystalline GaN as-prepared (a) and after purification in nitrogen (600 °C; 10 h) (b). The porosity of the material is enhanced after removing the hydrocarbon matrix. (c) for GaN needles or nanorods. Reprinted with permission from [191], A. C. Frank et al., *Adv. Mater.* 10, 961 (1998). © 1998, Wiley-VCH.

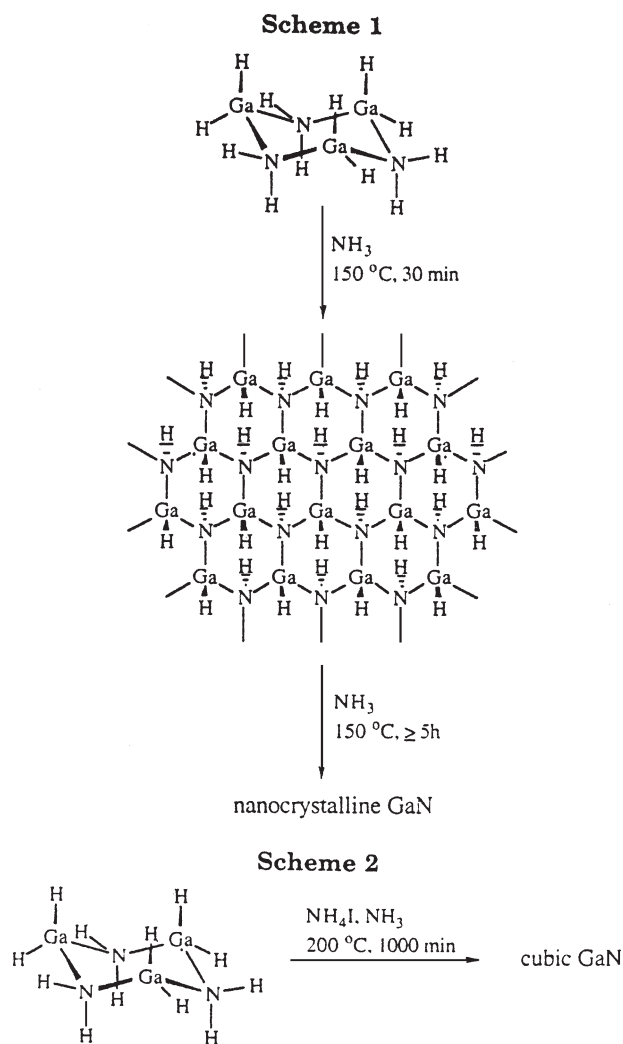
taken, and the authors have observed blue luminescence and yellow luminescence due to defects. Gladfelter et al. [192] have described a solution-based route to nanosized GaN. They have isolated a polymeric intermediate in the conversion of cyclotrigallazane to GaN in supercritical ammonia. Initially, cyclotrigallazane  $[\text{H}_2\text{GaNH}_2]_3$  was prepared, and then it was dissolved in liquid ammonia. This solution, upon heating, was converted to a product that was identified as polymeric hydridogallium imide  $[\text{HGaNH}]_n$ . Thermolysis of this compound for four hours at 600 °C under a flow of nitrogen produced nanocrystalline GaN.

Barry et al. [193a] have chemically prepared GaN particles with sizes in the micron large by using lithium as a nitrogen fixant. Such a procedure was used several decades ago by Grimmiess et al. [193b] to prepare bulk GaN crystal. They have used Li/Ga alloy and flowing ammonia. The alloy composition consists of an equal proportion of Li and Ga, and the temperatures used were in the range of 400 to 500 °C. Grimmiess et al. could obtain millimeter size GaN crystals with this method. The main intention of Barry et al. [193a] was to prepare very pure GaN microcrystalline powders, which should be white in color, by reacting a mixture of Li and Ga in the presence of ammonia. The reaction, which was originally proposed by Grimmiess, can be represented as

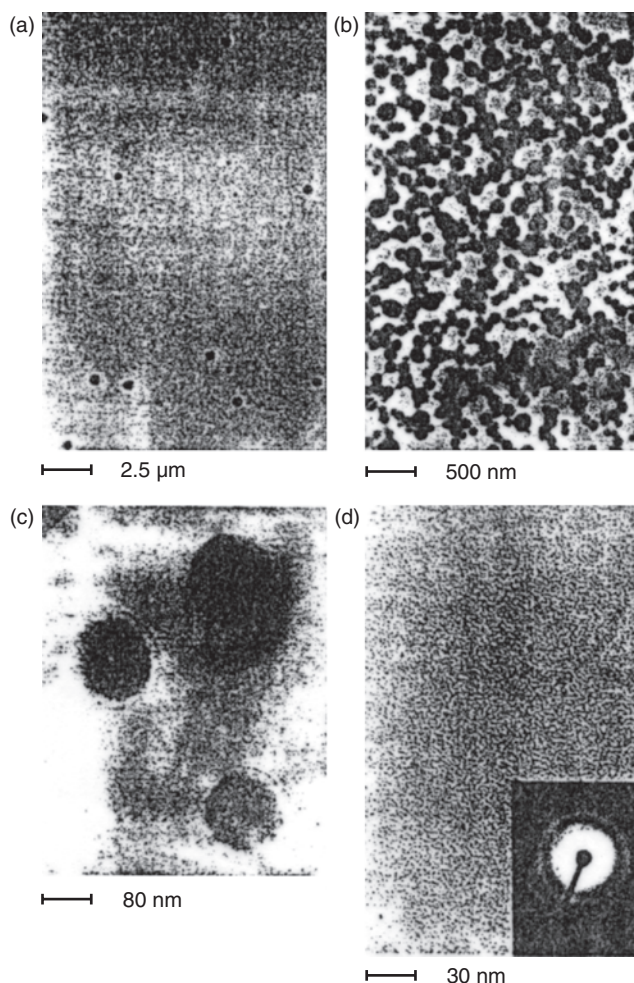


The mixture of GaN and lithium nitride was found to be white in color. This mixture was washed in water and aquaregia, and pure GaN without lithium metal contamination could be obtained easily. The earliest method by Grimmiess has produced GaN with a substantial amount of lithium as an impurity. Barry et al. [193a] also have developed a second method to produce GaN in which an alloy of Li and Ga were used instead of a physical mixture of Li and Ga. However, this method did not give pure GaN. Micic et al. [194] have obtained colloidal GaN nanoparticles. They have used the chemical procedures developed by Wells and coworkers to synthesize nanosize GaN by pyrolysis of  $[\text{Ga}(\text{NH})_{3/2}]$  [177, 181]. The  $[\text{Ga}(\text{NH})_{3/2}]$  was slowly heated in trioctylamine at 360 °C for over 24 h. The GaN nanoparticles were dispersed in a nonpolar solvent to get the colloidal solutions. The synthesis was conducted in an air-free and a water-free atmosphere. The authors also have found that using the mixture of trioctylamine and hexadecylamine has decreased the carbon adsorption on the quantum dot particles. The diameters of the nanoparticles were in the range of 2 to 4 nm. Photoluminescence of the colloidal GaN particles was recorded. Evidence for quantum confinement effects was obtained from the peak position of the luminescence peak. Coffey et al. [195] have done micro-Raman studies of nanocrystalline GaN and found that the spectra were dependent on the pyrolysis temperature used for the synthesis. For example, in the samples obtained with low pyrolysis temperature, many extra peaks were observed, which were very similar to those observed in the GaN samples ion implanted with  $\text{Ar}^+$ ,  $\text{P}^+$ ,  $\text{C}^+$ , and  $\text{Ca}^+$ . The Raman modes at 360, 420, and 670  $\text{cm}^{-1}$  were thought to be due to the lattice damage by ion bombardment. It also was shown that these defect-related peaks can be removed by subsequent heating of GaN at 900 °C or higher temperatures.

These studies have proved the necessity of using relatively high temperatures in the preparation of GaN. Purdy [196] and Jegier et al. [197] have discussed the control of the coherent length of GaN powders derived from cyclotrigallazane  $[\text{H}_2\text{GaNH}_2]_3$ . They also have shown the conditions for achieving a zinc blend structure of GaN. The summary of their findings is given in Figure 36. Fischer's research team has followed the research work of Micic et al. [194] on colloidal GaN nanoparticles and has investigated the thermolysis of the molecular gallium azides [198]. The TEM images of GaN colloidal particles obtained from various precursors are shown in Figure 37. The particles sizes were estimated from the dynamic light-scattering experiments. The light scattering depends on the hydrodynamic radius of the particle. In the photoluminescence spectra of these samples, very broad peaks were observed. Diffraction patterns of these samples are not good, indicating that the sample quality is very poor. The researchers were of the opinion that the low temperatures at which the synthesis was made was the reason for the poor quality of the samples. Balkas and Davis [199] have studied the thermodynamics of several chemical reactions to



**Figure 36.** Schematic of formation of nanocrystalline GaN from cyclotrigallazane. Reprinted with permission from [197], J. A. Jegier et al., *Chem. Mater.* 12, 1003 (2000). © 2000, American Chemical Society.

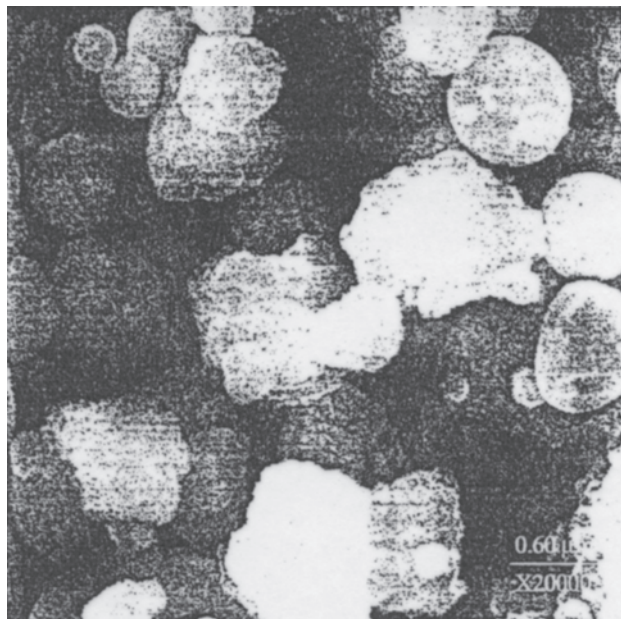


**Figure 37.** TEM images of GaN nanoparticles (a) prepared from  $[\text{Me}_2\text{N}(\text{CH}_2)_3]_3\text{-Ga}(\text{N}_3)_2$  in triglyme, (b) prepared with  $\text{Et}_3\text{N Ga}(\text{N}_3)_3$  in solution, (c) obtained from the pyrolysis of  $\text{Et}_3\text{N Ga}(\text{N}_3)_3$ , and (d) obtained from precursor  $[\text{Et}_2\text{N Ga}(\text{N}_3)_3]_3$  with electron diffraction pattern in the inset. Reprinted with permission from [198], A. Manz et al., *Adv. Mater.* 12, 569 (2000). © 2000, John Wiley and Sons.

prepare GaN and concluded that nanosized particles can be made by using Ga metal,  $\text{Ga}_2\text{O}_3$ , and ammonia gas.

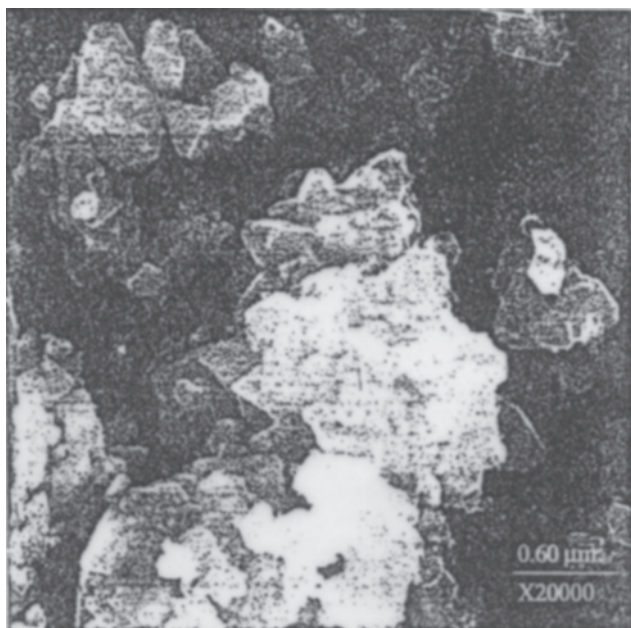
Wood et al. [200] have described the aerosol-assisted vapor phase synthesis (AAVS) [201, 202] of GaN particles with different sizes. These researchers have taken up this work encouraged by their earlier achievement of the submicron-sized h-BN [203] and AlN [204] by simply using inexpensive precursors such as aqueous solutions of boric acid and aluminum nitrate. To prepare GaN by the AAVS method, Ga metal or gallium oxides cannot be used. One has to use the soluble gallium salts, and the authors have used aqueous gallium nitrate and ammonia gas in a two-step AAVS nitridation chemistry. Figure 38 shows the SEM picture of the partially nitrided powder  $\text{GaN}_x\text{O}_y$ . As can be seen, the particles have a spherical structure with a cauliflower-like texture. The complete nitridation is achieved by heating the sample of  $\text{GaN}_x\text{O}_y$  in ammonia atmosphere for about 5 h at a temperature of 1050 °C. The product was found to be a yellow powder, which was identified as pure h-GaN. The SEM picture of



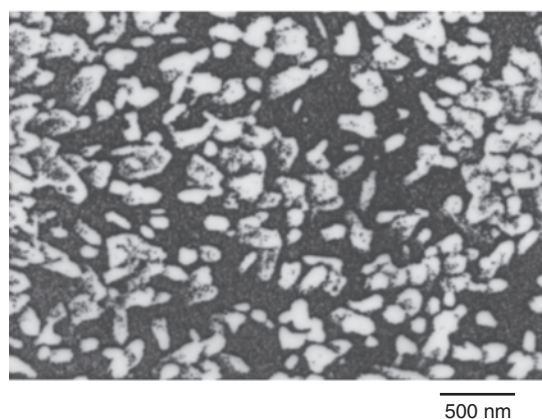
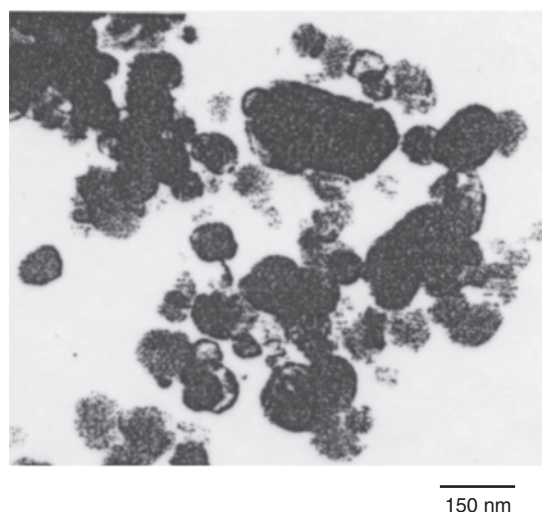
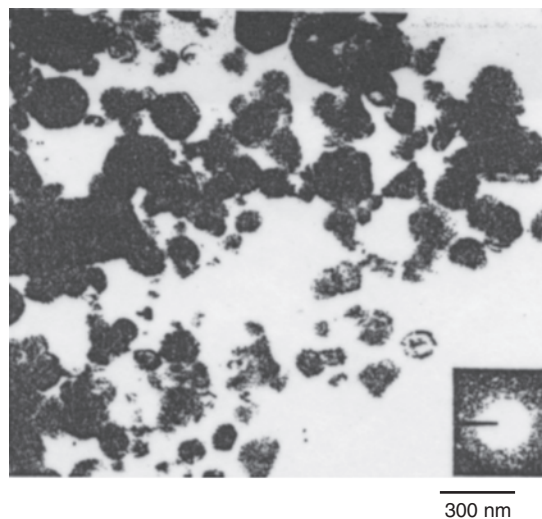


**Figure 38.** SEM of  $\text{GaN}_x\text{O}_y$  aerosol particles. Reprinted with permission from [200], G. L. Wood et al., *Chem. Mater.* 13, 12 (2001). © 2001, American Chemical Society.

these samples, displayed in Figure 39, shows that the particles are agglomerated. The sample contains many unagglomerated particles, also with sizes in the range of 20 to 50 nm. The agglomerated particles contain a range of crystals in the sizes 20 to 200 nm. Grocholl et al. [205] have synthesized a number of nanostructures of GaN, including nanoparticles and nanorods by solvothermal decomposition of azides. The decomposition of azides was done in superheated toluene or tetrahydrofuran. Figure 40 shows the



**Figure 39.** SEM of GaN aerosol particles. Reprinted with permission from [200], G. L. Wood et al., *Chem. Mater.* 13, 12 (2001). © 2001, American Chemical Society.



**Figure 40.** Transmission and scanning electron microscopic images for GaN nanoparticles synthesized from toluene, then annealed at 1000 °C (top) or annealed at 1000 °C, then washed with water (middle), or washed with glycerol/ethanol, then annealed at 1000 °C (bottom). An electron diffraction pattern is shown in the inset on the top. Reprinted with permission from [205], L. Grocholl et al., *Chem. Mater.* 13, 4290 (2001). © 2001, American Chemical Society.

TEM and SEM images of GaN nanoparticles obtained from toluene and subjected to different annealing conditions. Li et al. [206] have investigated the resonant Raman scattering of GaN nanocrystals prepared by the arc plasma method. An enhancement in the intensities of the signals was observed when the exciting laser light coincided with the energy of the yellow band in GaN.

## 2.7. Nanoislands and Quantum Dots

Copel et al. [207] were the first to discuss the effect of surfactants on the crystal growth by MBE or any other epitaxial techniques. The technique developed by them is being widely used now in semiconductor technology to grow self-assembled quantum dots and nanoislands. They have pointed out that lattice strain and surface free energy are the ultimate determining factors to decide whether a film grows by layer-by-layer growth (Frank–Van der Merwe), islanding (Volmer–Weber), or layer-by-layer growth followed by islanding (Stranski–Krastanov [SK]).

Whether the epitaxial layer can wet the substrate or not is determined by the following inequality

$$\sigma_s > \sigma_f + \sigma_i$$

Here,  $\sigma_s$  is the free energy of the substrate surface,  $\sigma_i$  is the interface free energy, and  $\sigma_f$  is the surface free energy of the heteroepitaxial layer. When the above inequality is satisfied, Frank–Van der Merwe growth takes place, and, if the inequality has the opposite sign, then the Volmer–Weber growth will occur and there will not be any wetting of the substrate. The SK growth takes place when there is a wetting of the substrate but the overlayer strain is unfavorable or when there is interface mixing or surface reconstruction. Therefore, if element A can be grown on element B in Frank–Van der Merwe or SK mode, then B will grow on A in Volmer–Weber mode. In a situation like this, there will be problems in growing multiple layered structures such as multiple quantum wells or superlattices. For example, Ge grows on Si in SK mode, whereas Si grows on Ge in Volmer–Weber mode. In the attempts to grow Si/Ge/Si quantum well structures, the Si cap layer was found to contain islands. To solve this problem, Copel et al. [207] have passivated the Si surface by one monolayer (ML) of As prior to the growth. The unsatisfied dangling bonds on the Si surface are passivated by the one extra valence electron of As. By using the As-passivated surface as a stage for MBE growth, it was possible to change the growth mode of an epitaxial layer to induce wetting of the substrate. It should be noted that As itself will not be incorporated into the lattice since it segregates to the surface during growth. Therefore, the most important requirements for the surfactant are the following: (1) it should reduce the surface free energies of both the substrate and the overlayer and (2) it should be very mobile and segregate to the surface.

Self-assembled quantum dots of InGaAs, InAs, AlInAs, and various phosphides have been grown by a number of groups by the SK method [208–213]. Dmitriev et al. [214] were the first to make GaN quantum dots on SiC substrates by MOCVD. Aoyagi's group at RIKEN, Japan, have achieved the self-assembled GaN quantum dots on AlGaN

surface by using tetraethyl silane as a surfactant [215]. One of the aims in growing the GaN quantum dots is to develop ultraviolet (UV) LEDs and semiconductor lasers. At present, the threshold currents required for the nitride-based lasers are in the range of 9 kA/cm<sup>2</sup>. Comparatively, these are much higher than those in other III–V lasers. The present nitride-based lasers use only the quantum well structures. On the other hand, if one uses the quantum wire or quantum dots as the active region, then the threshold currents are expected to be smaller, since the exciton-binding energy is very high in the case of quantum dots. Also, because of many-body effects, one may have lasing in the quantum dot systems due to biexcitons and other novel mechanisms. Aoyagi's group have grown multilayer structures with GaN quantum dots on Si faces of SiC substrate by MOCVD. They have used AlGaIn as the cladding layer and also as the capping layer. A thin layer of AlN also was used as the buffer layer. After growing the atomically smooth AlGaIn cladding layer, which was identified by AFM images, tetraethylsilane, with the hydrogen carrier gas, was sent into the reactor, followed by a short supply of trimethylgallium and ammonia gases. This has resulted in the growth of GaN quantum dots with an average width of 40 nm and a height of 6 nm. It should be noted that the surfactant was introduced to enhance the growth of GaN islands, and this is quite contrary to the use of surfactant in the growth of Si/Ge multiple quantum wells (MQW), in which case, the As surfactant was used to suppress the island formation. The exact role of the surfactant in the growth of GaN quantum dots is not known. The size of the quantum dots was controlled by the doping rate of TESI, the Al content in AlGaIn, and the growth temperature. The photoluminescence spectrum revealed a strong peak at 3.55 eV with a FWHM of 60 meV. In a later publication, Aoyagi's group has reported the optically pumped lasing in a laser structure of GaN quantum dots [216]. The procedure to grow the dots is the same as discussed before. The structure consists of an Al<sub>0.23</sub>Ga<sub>0.77</sub>N cladding layer (100 nm thick), an Al<sub>0.09</sub>Ga<sub>0.91</sub>N barrier layer (100 nm thick), GaN quantum dots, an Al<sub>0.12</sub>Ga<sub>0.88</sub>N barrier layer (300 nm thick), and an Al<sub>0.20</sub>Ga<sub>0.80</sub>N cladding layer (600 nm thick). The optical pumping experiments were done with a nitrogen laser with an emission wavelength of 337.1 nm and a pulse width of 7 ns. Stimulated emission was observed at high-excitation densities. It also was noted that the laser emission has shown a red shift of about 50 meV, with peak at 3.49 eV. The threshold pump power density was estimated to be 0.75 MW/cm<sup>2</sup>, which was thought to be somewhat high. The reasons for this are the following: the confinement of the carriers in GaN quantum dots is very poor, the absorption of the pump power in the AlGaIn barrier lasers is rather small, and the Al mole fractions in each AlGaIn layer also were too small to achieve high carrier and optical confinements.

Daudin et al. [217] have grown the GaN quantum dots in the SK mode by MBE by using lattice mismatched heterostructures. The occurrence of the SK mode was found to be dependent on the growth temperature. They have found that at low temperature, the growth was purely 2D. When three-dimensional (3D) islands were formed, further deposition of GaN resulted in the coalescence, followed by a plastic relaxation through misfit dislocation formation.

*In-situ* reflection high-energy electron diffraction (RHEED) was used to study the characteristics of the grown layers and surfaces. The results observed from the RHEED experiments were confirmed by the AFM images and high-resolution electron microscopy of the superlattices. AlN and GaN with wurtzite structures were grown on a sapphire substrate. Substrate temperature was varied, and three types of behavior were observed, corresponding to high  $T_s$  ( $>700$  °C), low  $T_s$  ( $<620$  °C), and intermediate  $T_s$ . In the intermediate  $T_s$  temperature range, a relaxation to island formation is followed by a decrease of the relaxation value corresponding to island coalescence. At high  $T_s$ , the relaxation rapidly reaches a plateau corresponding to 3D growth mode, and, at low  $T_s$ , the relaxation is small, correlated to 2D growth. After island coalescence, a gradual relaxation was observed for long deposition times. It should be noted that in this work, GaN quantum dots were achieved without using any surfactant and the 3D growth of islands occurs because of strain relaxation in the lattice mismatched heterostructures.

In a later publication, Daudin and coworkers have demonstrated the growth of a quantum dot superlattice [218]. They also have studied the various experimental conditions for the control of the size and the density of dots. The effect of substrate temperature was initially examined. The AFM pictures of GaN quantum dots grown at three different substrate temperatures, viz. 725 °C, 705 °C, and 685 °C were taken. It was shown that, as the substrate temperature increases, the dot density decreases. At 685 °C, many dots have coalesced, whereas they were isolated at 725 °C. The dependence of dot density on temperature was thought to be due to Ga surface diffusion. The ripening effects were investigated by studying the morphology of GaN quantum dots as a function of time under vacuum and under nitrogen plasma flux. GaN dots were grown at 700 °C by depositing 3 ML on an AlN surface. The dots were left either under vacuum at 700 °C before cooling under vacuum, or they were exposed to nitrogen plasma after growth and during cooling. The AFM pictures of GaN dots when the surface was exposed under vacuum and under nitrogen flux were taken. A ripening effect was noted when the dots were grown under vacuum. The dots were bigger in size and less dense compared to the other case of growth under nitrogen. Periodic, stacked layers of GaN quantum dots separated by AlN spacer also were fabricated. When the thickness of AlN was small, in the range of 8 nm, vertical correlation between the GaN dots also was observed in high-resolution electron microscopy pictures. The AFM studies were made to confirm the vertical correlation of the dots. Morphology of dots in a sample consisting of 20 layers of GaN quantum dots separated by 5-nm-thick AlN layers was investigated. The dot density was smaller compared to the case of no correlation. The authors have reported the photoluminescence and cathodoluminescence of these samples. Samuelson's group in Sweden has investigated the SEM and cathodoluminescence of GaN quantum dots and has shown the correlation between the actual position of the dots and the luminescence from these dots [219]. These samples were grown by Aoyagi's group in Japan. Very low intermixing between GaN and AlN layers was observed in the high-resolution TEM images

of MBE-grown samples containing self-assembled quantum dots of GaN [220].

Damilano et al. [221] have observed very intense room-temperature photoluminescence, from blue to orange, from the GaN quantum dots of various sizes. Also, white-light emission was observed by properly mixing quantum dots of various sizes. GaN and AlN layers were grown by MBE on a Si(111) surface. Ammonia was used as the nitrogen source. The native oxide on the silicon surface was removed by rapid thermal annealing at 900 °C. The quantum dots were obtained by strain induced 2D to 3D transition. The room temperature PL spectra of GaN/AlN quantum dots on Si were studied. The authors also have observed the PL of GaN dots from stacked planes, giving rise to white-light emission. Kuball et al. [222] have reported the resonant Raman scattering of GaN quantum dots grown by MOCVD. The dots were grown on AlGaIn by using tetraethylsilane as the surfactant. The Raman spectra were recorded for dots of different sizes by changing the excitation laser energy. It was noted that very little Si enters the GaN lattice, though it was used as the surfactant. Most of the Si was thought to remain on the AlGaIn surface, where it was deposited before the growth of GaN. The authors have investigated the Raman spectra of sample A, which consists of GaN quantum dots on  $\text{Al}_{0.15}\text{Ga}_{0.85}\text{N}$ , and of sample B, which consists of GaN layer on  $\text{Al}_{0.15}\text{Ga}_{0.85}\text{N}$ , for various excitations of the laser. In resonant Raman scattering, the exciting laser light or the scattered light coincides in energy with an electronic transition of the material. In such a situation, the Raman spectra are dominated by the Frohlich scattering arising due to the longitudinal polar optical phonons. Therefore, it is possible to distinguish the lines arising from GaN and AlGaIn. The fundamental transitions of GaN and  $\text{Al}_{0.15}\text{Ga}_{0.85}\text{N}$  are at 3.42 and 3.66 eV, respectively. Both the spectra show Raman peaks at 736 and at 1474  $\text{cm}^{-1}$ . The authors have assigned these transitions to first- and second-order Raman scattering from the  $A_1$  LO phonons of GaN. These were supposed to be enhanced under UV excitation. The authors gave a detailed discussion on the effects of quantum confinement and the effects of Si, which was used as an antisurfactant. These workers have taken the Raman spectra of sample A, containing GaN quantum dots, and also sample B, containing the GaN layer, under 5.08 eV excitation. For this case, a shift of 9  $\text{cm}^{-1}$  was observed for the GaN  $A_1$  (LO) frequency of sample A toward lower wave numbers. Based on these results, the  $A_1$  (LO) peak was assigned to the GaN quantum dots.

Daudin's group in France has done a very exhaustive investigation on the effects of surfactant on the growth of GaN quantum dots grown by MBE [223]. Ga was found to form a bilayer on the GaN surface during the growth in Ga-rich conditions. The study conducted dealt with the growth kinetics and relaxation mechanisms in the presence of a Ga film. The GaN dots were fabricated under various experimental conditions such as the V/III ratio, the substrate temperature, etc. The results were analyzed by using a set of important analytical techniques such as RHEED, AFM, TEM etc. When the Ga effusion cell temperature is  $T_{\text{Ga}} = 1040$  °C GaN, growth is nearly stoichiometric and the SK growth mode takes place with the formation of GaN islands. If the Ga flux was increased above  $T_{\text{Ga}} = 1040$  °C, the growth

conditions become Ga-rich and a Ga bilayer was formed because of excess Ga. In these conditions, no 2D to 3D transition occurs. However, when the Ga flux was in the intermediate range, a transition from 2D to 3D was observed. The GaN layer undergoes a lot of strain, leading to the formation of GaN pyramids, followed by the coalescence of grown islands and the formation of a smooth surface. As discussed before under Ga-rich conditions, there was no growth of GaN islands. However, it was observed that the 2D to 3D transition takes place under the N flux. It was noted in the AFM images that there is no difference between the quantum dots grown under N flux and those formed during the SK growth mode. When the substrate temperature was low,  $T_s = 660$  °C formation of GaN platelets was observed. These dots were obtained with growth interruption under N after Ga-rich GaN growth on AlN. In these conditions, SK growth cannot occur since the 2D wetting layer was absent. The platelets were found to be flat islands with heights of around 4 ML (1 nm) and diameters of around 15 nm. In their very interesting paper, Daudin and coworkers also have made detailed discussion on the mechanisms related to the effect of surfactants on the SK growth mode. The inhibition of 2D to 3D transition was thought to be due to the surface stress caused by Ga adsorbate. It also was argued that under Ga-rich conditions, the adsorbed Ga layer is almost instantly formed without allowing the formation of GaN layers, and, hence, islanding of GaN never takes place.

Andreev and O'Reilly [224] have done the theoretical calculations on the radiative lifetimes in GaN/AlN self-assembled quantum dots. Gleize et al. [225] have measured the resonant Raman scattering of GaN dots in the MBE grown samples. They have changed the laser energies in the range 2.33 and 3.81 eV, which enabled them to select the quantum dots with specific size and energy. Resonance enhancement in the signals was observed. The Raman frequencies were related to the lattice mismatch strain between GaN and AlN. Multilayered superlattices of GaN quantum dots grown by MBE were characterized by Chamard et al. [226] by the technique of grazing incidence X-ray scattering. This method was shown to be complimentary to AFM and TEM.

Wolk et al. [227] at Berkeley, California, have demonstrated the growth of GaN nanocrystals by sequential ion implantation of Ga and N ions into a sapphire substrate. The TEM studies allowed the authors to identify the phase of GaN as wurtzite and the size of the quantum dots was found to be in the range of 1 to 5 nm. Photoluminescence experiments also were done on these samples. Band-edge luminescence and yellow peaks due to defects were recorded in the PL spectra. The main advantages of the ion implantation technique are the following. Firstly, it is possible to introduce a well-defined concentration of nanocrystals at a precalculated depth below the surface. Secondly, it is most suitable for integration into the standard semiconductor processing. Nanocrystals of GaN have been achieved by N implantation into GaAs [228]. Sequential ion implantation of Ga and As into sapphire and SiO<sub>2</sub> has been done to fabricate GaAs. [229]. The crystalline phase was found to be dependent on the dose of the N ions. In a later publication by Borcella et al. [230] ion implantation of Ga and N ions in a number of dielectrics such as crystalline quartz

or amorphous silica was reported to achieve GaN quantum dots. These authors have examined the influence of implantation conditions, the annealing procedures, and the role of substrate on the formation and morphology of GaN dots. Quantum confinement effects also were observed in the luminescence spectra. Morkoc's group has observed a drastic reduction in the dislocation density of GaN layers that were grown by using GaN buffer layers containing quantum dots [231].

Atomic layer epitaxy (ALE) was used for the first time by Daudin's group in France to grow GaN quantum dots on (0001) AlN [232]. This epitaxy also is called the migration enhanced epitaxy. Here, the growth proceeds by alternately exposing the surface to cation and anion fluxes. Another advantage of this method is that the layer thickness is independent of flux values and deposition time but depends on the number of growth cycles. When more than one ALE cycle was performed, GaN island formation was observed. The research group has done the optical characterization experiments on various samples. For the sample containing five quantum wells grown by one ALE cycle, an emission peak at a photon energy of 5.1 eV was recorded in the cathodoluminescence. In the samples with GaN quantum dots, the main emission peak was observed at 3.8 eV, which was found to be in agreement with the expected energy position of dots of the size 1.6 to 1.8 nm. In the sample made from four ALE cycles, another luminescence band was observed at around 3.2 eV, which was interpreted as the second mode of the island height distributions. This work has demonstrated the feasibility of using ALE to grow stable Ga film on the AlN surface, which was independent of the precise Ga flux between 0.2 and 0.8 ML/s at a substrate temperature of 740 °C.

Arakawa's group in Japan has grown the self-assembled GaN quantum dots on AlN by low-pressure MOCVD [233]. Trimethyl gallium and trimethylaluminum were used as the group III sources. an AlN layer of 110 nm thickness was grown on (0001) SiC at 1180 °C. After the growth of an AlN layer, the growth temperature was reduced to 960 to 990 °C to grow GaN quantum dots. The growth of GaN quantum dots was done at a very low V/III ratio. The research group has observed that the growth temperature and the V/III ratio are the most important factors to form quantum dots of GaN. These parameters will decide the migration and evaporation of Ga atoms on the GaN surface. The AFM pictures of GaN quantum dots, illustrating the dependence of dot density on the GaN coverage, which was changed systematically between 3.4 and 9.2 ML, were reported. It can be easily seen from the AFM images that the dots are formed only when the critical thickness of the GaN layer is around 4ML. After depositing over the critical thickness of GaN, quantum dots are immediately formed on the 2D GaN layer. It should be noted that such a sudden transition from 2D to 3D growth also was observed before in the literature in the case of InAs quantum dots grown by Petroff's group at the University of California, Santa Barbara California [234]. It can be observed in Figure 62 that no quantum dots were formed when the coverage was 3.4 ML, and the density of dots increases as the GaN coverage is higher. It also was observed that the density of dots saturated above the GaN coverage of 8 ML, which happens because of the increase in the size

of the dots. The AFM pictures of GaN quantum dots grown at different temperatures, e.g., 960, 975, and 990 °C were reported. The dots grown at 960 °C have smaller diameters and higher densities than those grown at 975 °C. Suppression of migration of Ga atoms as the growth temperature decreases is thought to be the reason for this observation. Tsong's group has grown the self-assembled GaN quantum dots by vapor-liquid-solid mechanism [235]. Daudin's group has demonstrated that Ga-covered GaN layers thicker than about 2.5 ML are stable against annealing under Ga flux but they transform into islands when the Ga layer is evaporated under vacuum at substrate temperature of 750 °C [236]. The AFM pictures of GaN quantum dots and the GaN 2D layer grown under different conditions were reported. Northrup et al. [237] have discussed, theoretically, the microscopic origin of the increased nucleation under different conditions of growth. They have performed the *ab initio* calculations on GaN surface structures. The interested readers should see references [238] and [239] for general reviews on quantum dots in semiconductors.

## 2.8. Quantum Wells

Morkoc's group has studied the optical properties of a Si-doped GaN/AlGaIn quantum well [240]. The calculated confinement energies could be matched to the observed band-to-band transition, assuming a band offset of 67:33 and effective masses of 0.3 and 0.19 for the heavy hole and conduction electron, respectively. Time-resolved PL of GaN/AlGaIn MQW indicated strong quantum confinement effects [241]. The researchers have compared these results with those of GaN epilayers and GaAs/GaAlAs MQW. The exciton-LO phonon interactions in AlGaIn barriers were noted to be enhanced. Localized excitons at low temperatures and free excitons at higher temperatures were identified. An increase in the lifetime of an exciton up to 60 K was observed, which gave an indication of radiative recombination. In the photoluminescence spectrum of MBE grown MQW, A, B, and C excitons and their phonon replicas were observed [242]. From the intensity dependence of the luminescence, the assignments of the transitions were confirmed. The  $n = 1$  band persists up to room temperature, whereas the extrinsic emission bands are ionized above 120 K. The thermal shift of the  $n = 1$  band follows the thermal shift of the bulk GaN energy gap. Morkoc and coworkers have fabricated a 50 Å/50 Å GaN/Al<sub>x</sub>Ga<sub>1-x</sub>N ( $x = 0.07$ ) MQW by the MBE technique [243]. Dry etching was used to pattern an array of microdisks of approximately 9 μm diameter and 50 μm spacing. Picosecond time-resolved spectroscopy was used to study the emission dynamics. A strong enhancement of the intrinsic exciton transition quantum efficiency was observed in the microdisk compared to MQW.

Radiative and nonradiative recombination dynamics were studied in GaN/AlGaIn double heterostructures by using time-domain spectroscopy in picosecond scale [244]. The diffusion constant for the minority carriers in the AlGaIn barrier layers was estimated. In another time-resolved study, the effects of well thickness and Si-doping on the optical properties of MQWs of GaN/AlGaIn were identified [245]. Quantum confinement was observed in quantum wells of well thickness less than 40 Å. The exciton lifetimes in

MQWs with well thickness less than 40 Å increase linearly with temperature up to 60 K. It also was observed that the Si doping improves the quality of the crystals. Fabrication of GaN/AlGaIn quantum wells by MBE was discussed by a French group [246]. The quantum well width could be controlled up to ML scale. The quantum well transition energy increases as the thickness decreases. Each quantum well exhibits a clearly resolved emission peak. This is due to relatively narrow PL linewidths, ranging between 20 and 30 meV. However, the luminescence from AlGaIn barriers is not detected. This was thought to be due to strong capture of the excitons by the quantum wells. When the thickness of the well is decreased, the intensity of the quantum well emission vanishes. This was explained as due to thermal escape of carriers from the quantum well to the barrier due to insufficient confinement. In the time-resolved PL experiments of GaN/AlGaIn MQW, a very high excitation was used [247]. This excitation condition will simulate the pumping powers required for lasing. It was found that under these conditions, the carrier distributions are characterized by plasma temperatures. Leroux et al. [248] have grown high-quality MQWs of GaN/AlGaIn by MBE. They have examined the quantum confined Stark effect by temperature-dependent luminescence and reflectivity.

Picosecond time-resolved studies by Hangleiter's group enabled them to understand the piezoelectric fields in GaN/AlGaIn quantum wells [249]. A reduction in oscillator strength was observed, which was attributed to piezoelectric fields. An increase in luminescence decay time, with increasing well width, was observed, along with a red shift of the emission peaks. Lefebvre et al. [250] have published a series of interesting papers on the recombination dynamics of free and localized excitons in MQWs of GaN/AlGaIn. The decay times of excitons in both the wells and barriers was found to be ~330 ps at 8 K. Spectral distribution of lifetimes was attributed to the localization of carriers by potential fluctuations that arise due to alloy disorder and well width and depth variations. The radiative lifetime of free excitons in the low-temperature limit was estimated as 2.4 ps, which is much smaller than that for GaAs/GaAlAs MQW. Grandjean et al. [251] have measured the PL of GaN quantum wells for different Al contents. Strong internal electric fields were found that have a linear relationship with Al content.

## 3. PHOTOLUMINESCENCE SPECTROSCOPY OF InGaIn

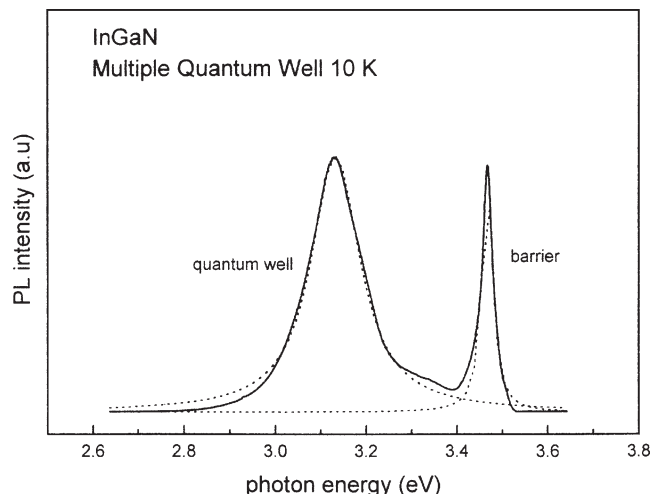
The ternary compound InGaIn is an active layer for both blue and green emission. The bandgap of this material can be changed from 1.95 to 3.4 eV by varying the concentration of In. In this section, we discuss the cw photoluminescence of InGaIn epitaxial layers and quantum wells. Many papers were published on this topic [252–280]. Katsui et al. [252] at NTT were the first to propose the quaternary InGaAlIn system in which a lattice-matched double heterostructure is possible for high-performance light-emitting devices. Nakamura and Mukai [255] have reported the PL of high-quality InGaIn epilayers in which sharp band-edge emissions between 400 and 445 nm were observed, and the deep level emissions were barely observed at room temperature.

Multiple quantum wells of  $\text{In}_{0.08}\text{Ga}_{0.92}\text{N}/\text{GaN}$  were grown by Amano and Akasaki [257]. In these samples, strong cathodoluminescence was measured compared to bulk material of InGaN. Chichibu et al. [258] have studied the emission mechanisms of InGaN SQW (SQW) and MQW structures. The electroluminescence (EL) from InGaN QWs was assigned to the recombination of excitons localized at certain potential minima in the QW plane. The blue shift of the EL caused by an increase of the driving current was explained by the combined effects of the quantum confinement Stark effect, screening of the piezoelectric field, and band filling of the localized states by excitons. Narukawa et al. [259] have proposed that the main radiative recombination was due to excitons localized at deep traps, which originate from the In-rich region in the wells, acting as quantum dots.

The compositional dependence of PL peak energy in InGaN-strained quantum wells was reported by a Japanese team [260]. When excitation intensity was increased, the PL peak energy was shown to be blue shifted. The well-width dependence of PL peak energies were calculated and found to agree with experiment. It was proposed that the quantum confined Stark effect occurs due to piezoelectric fields. Chichibu et al. [261] have attributed the emission from  $\text{In}_x\text{Ga}_{1-x}\text{N}$  to the recombination of excitons localized at the potential minima originating from large compositional fluctuations. Ploog's group has grown cubic  $\text{In}_{0.17}\text{Ga}_{0.83}\text{N}$  by MBE, which has given blue luminescence [262]. Chichibu et al. [263] have investigated the exciton localization by spatially resolved CL mapping. The InN-rich quantum disks originating from compositional undulation in InGaN SQWs were identified. Shan et al. [264] have studied low-temperature photoluminescence in InGaN alloys as a function of pressure. The pressure coefficients for the direct  $\Gamma$  bandgaps of  $\text{In}_{0.08}\text{Ga}_{0.92}\text{N}$  and  $\text{In}_{0.14}\text{Ga}_{0.86}\text{N}$  have been estimated from the pressure dependencies of the radiative decay of the charge carriers localized in the tail states of the alloy fluctuations. Chichibu et al. [265] have reported the bandgap separation in  $\text{In}_x\text{Ga}_{1-x}\text{N}$  layers ( $0.05 \leq x \leq 0.2$ ).

Self-assembled InGaN quantum dots were grown, and their PL was measured by Hirayama et al. [266]. Vertiko et al. [267] have demonstrated the applicability of near-field optical microscopy to study the influence of defects on the photoluminescence of InGaN. It was found that the pinholes do not have any effect on the radiative recombination in the epitaxial layers. McCluskey et al. [268, 269] have evaluated the bowing parameter as 3.5 eV for  $\text{In}_x\text{Ga}_{1-x}\text{N}$  ( $x \leq 0.12$ ). Mitchel and Saxler [270] have proposed a hopping conduction model in InGaN/GaN multiple quantum wells.

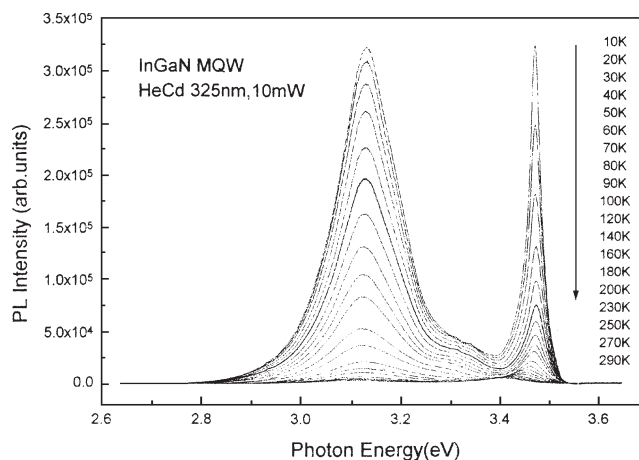
PL studies of  $\text{In}_{0.13}\text{Ga}_{0.87}\text{N}/\text{GaN}$  multiple quantum wells were made by Viswanath et al. [271]. The thickness of the quantum wells in these structures is 10 Å, and barriers have width of 50 Å. The MOCVD method was used to grow these samples, which were grown on (0001) sapphire substrate. Figure 41 shows cw photoluminescence spectrum of the InGaN MQW, recorded at 10 K. The dotted lines show the individual peaks obtained by the curve-fitting procedure by using Lorentzian line-shape function. The broad peak 3.134 eV is interpreted as due to the InGaN quantum well, and the narrow peak at 3.471 eV is due to the GaN barrier. The large blue shift was interpreted as due to strong



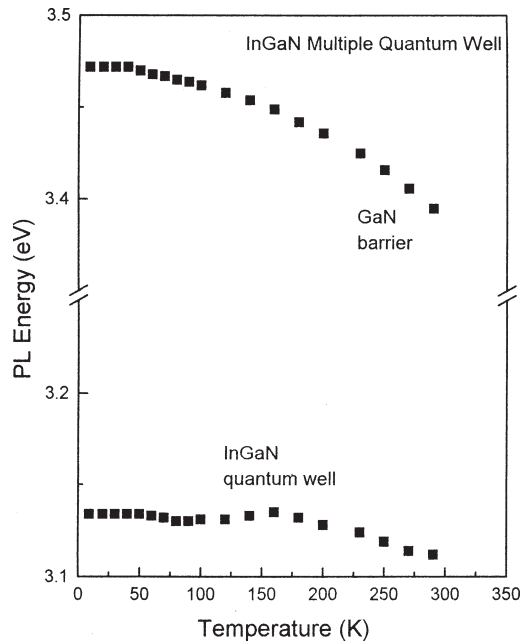
**Figure 41.** Photoluminescence spectrum at 10 K for InGaN/GaN MQW. It may be noted that the emission from GaN barrier is observed very clearly. Reprinted with permission from [271], A. K. Viswanath et al. (unpublished results).

quantum confinement effects in ultrathin quantum wells. At 10 K, the linewidth of the InGaN quantum well was estimated as 129 meV and was interpreted as due to inhomogeneous broadening. The origin of a solid-phase miscibility gap in nitrides was discussed by Ho and Stringfellow [272]. Localized excitons were considered to explain the luminescence. The observed PL linewidths were thought to be due to the effects of strong quantum confinement.

A display of photoluminescence spectra at different temperatures is shown in Figure 42. The PL peak positions were determined from the curve-fitting procedure. Figure 43 shows the temperature variation of PL peak energies of InGaN quantum wells and GaN barriers. From the temperature variation of the peak energies, it was inferred that the species involved in the luminescence of the InGaN quantum wells were localized excitons, which also were confirmed



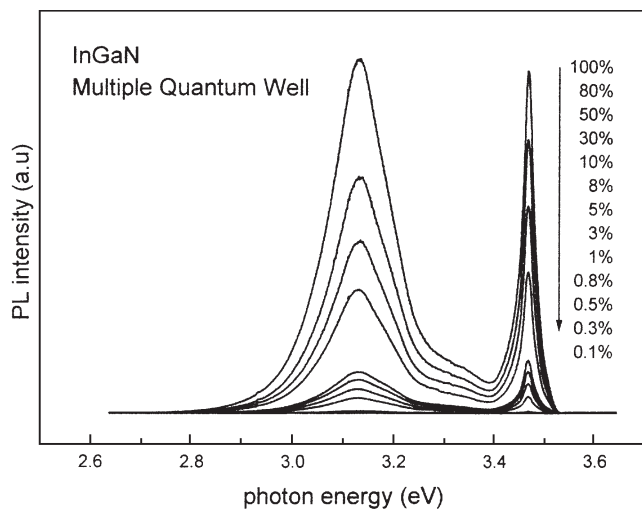
**Figure 42.** Photoluminescence spectra of InGaN/GaN MQW at some selected temperatures. A He-Cd laser is used for excitation. Reprinted with permission from [271], A. K. Viswanath et al. (unpublished results).



**Figure 43.** Temperature variation of PL peak energies of InGaN quantum well and GaN barrier. Reprinted with permission from [271], A. K. Viswanath et al. (unpublished results).

by various techniques. The activation energy of 69 meV also gave an indication of the localized nature of the excitons. Band-filling effects were noted in the power dependence studies of photoluminescence, as shown in Figure 44. Chichibu et al. [274–276] recently have reported on the localization of excitons in a number of InGaN quantum wells emitting in various wavelengths.

Li et al. [277] have observed a blue shift in the InGaN/ GaN single quantum well bandgap energy, after

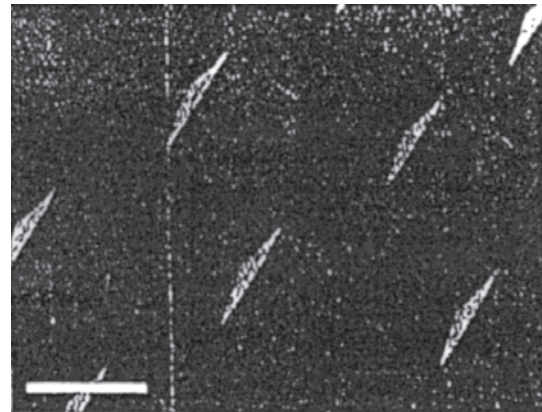


**Figure 44.** Excitation power dependence of the PL spectra of InGaN/ GaN MQW. It may be noted that the emission energy of GaN barrier does not show any power dependence, while the InGaN quantum well emission shows a slight blue shift due to band filling. Reprinted with permission from [271], A. K. Viswanath et al. (unpublished results).

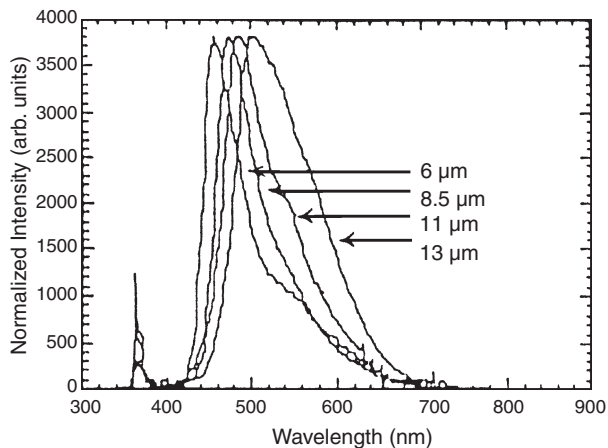
rapid thermal annealing in nitrogen atmosphere. This was explained as due to the flattening of the potential fluctuation as a result of spatial redistribution of atomic In and Ga in the InGaN quantum well. Luminescence from the phase-separated InGaN grown by MOCVD was reported by Li et al. [278]. The dominant peaks were observed around 2.9 and 2.8 eV. The low-energy peak at 2.8 eV was thought to be due to the phase-separated regions, which are rich in In content. They also have recorded very strong luminescence of the low-energy peak at room temperature. This was interpreted as due to quantum confinement enhancement in the form of nanostructures of quantum dots. Zhang et al. [279] have used a novel technique to improve the luminescence efficiency from the MQWs of InGaN/GaN. They have used a multilayer buffer on Si substrate. Hao et al. [280a] have reported the observation of electron-hole plasma emission from InGaN/GaN quantum wells. They have conducted the photoluminescence experiments at room temperature by using a He–Cd laser. Only exciton-related transitions were observed at low excitation powers. When the excitation power was increased, a peak has been observed on the low energy side of the exciton transition, which was interpreted as due to the electron plasma recombination. The assignment was also confirmed by the fact that the integrated PL intensity has shown a 1.9 power dependence.

Mishra's group at the University of California, Santa Barbara, California, have demonstrated that selective epitaxy of InGaN can be done by MOCVD [280b]. They have used templates consisting of arrays of circular etched holes in SiO<sub>2</sub> mask layer, with pregrown GaN hexagonal pyramid structures. Figure 45 shows the SEM picture of GaN/InGaN pyramids. In the PL experiments, it was observed that the PL peak wavelength increased with an increase in mask opening spacing for a constant mask opening diameter (Fig. 46).

The same group also has achieved the InGaN nanoscale islands by MOCVD [280c]. A growth mode transition from step-flow into 3D spiral growth mode by predeposition of Si prior to InGaN was found to enhance the PL efficiency and the radiative recombination lifetimes. Figure 47 show the AFM images of GaN grown under different conditions.

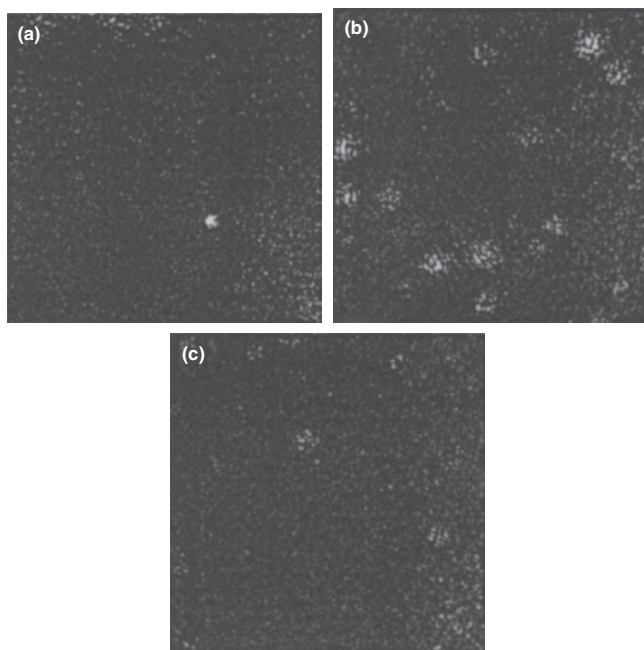


**Figure 45.** Scanning electron microscope image of GaN/InGaN pyramids (bar = 5  $\mu\text{m}$ ). Reprinted with permission from [280b], D. Kapolnek et al., *J. Cryst. Growth* 189–190, 83 (1998). © 1998, Elsevier Science.

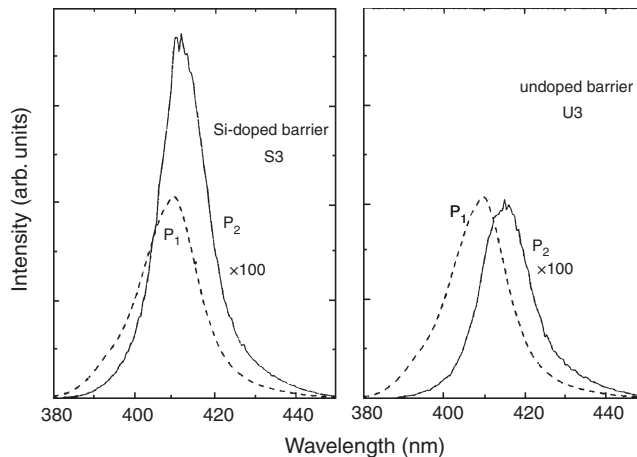


**Figure 46.** Photoluminescence spectra obtained from GaN/InGaN pyramid arrays with original mask opening diameter of 5 μm, and various spacings between openings. Reprinted with permission from [280b], D. Kapolnek et al., *J. Cryst. Growth* 189–190, 83 (1998). © 1998, Elsevier Science.

Oh et al. [280d] have investigated the effect of Si doping in the barriers of InGaN MQWs by PL spectroscopy. They have observed that the PL intensity was enhanced with Si doping under low-excitation conditions as shown in Figure 48. It also was shown that the blue shift with an increase in excitation intensity is larger for larger well width, and the blue shift for Si-doping is larger for lower-excitation density (Fig. 49). The increase in PL intensity with Si-doping was less pronounced at higher excitation densities, as shown in Figure 50.



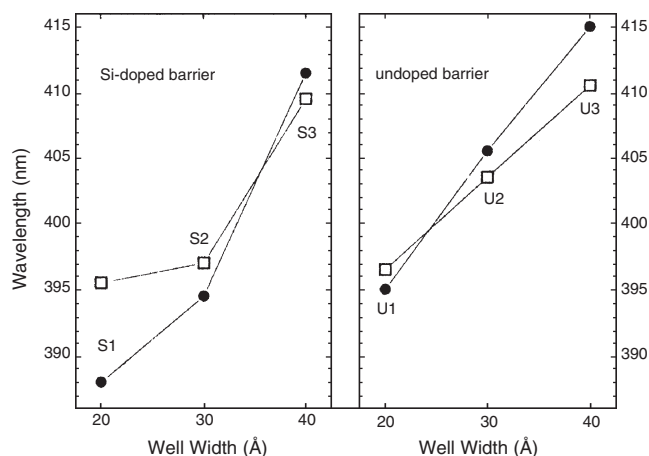
**Figure 47.** 2 × 2 μm<sup>2</sup> AFM images of (a) GaN (1060 °C); (b) GaN/Si/InGaN (790 °C); (c) GaN/InGaN (790 °C). Reprinted with permission from [280c], S. Keller et al., *J. Cryst. Growth* 189–190, 29 (1998). © 1998, Elsevier Science.



**Figure 48.** Photoluminescence spectra of Si-doped and undoped InGaN MQWs, taken with excitation densities of  $P_1 = 100 \text{ kW/cm}^2$  (dashed curves) and  $P_2 = 1 \text{ kW/cm}^2$  (solid curves) at room temperature. The spectra taken with  $P_2$  are multiplied by 100. Reprinted with permission from [280d], E. Oh et al., *Phys. Status Solidi B* 216, 487 (1999). © 1999, John Wiley and Sons.

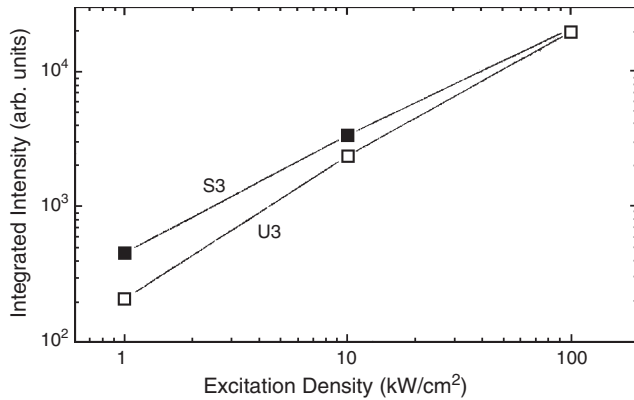
#### 4. TIME-DOMAIN PHOTOLUMINESCENCE OF InGaN

A number of research papers were published on the time-domain spectroscopy of InGaN [271, 273, 281–297]. The present author and his collaborators have done complete analysis of time-resolved photoluminescence of InGaN MQWs [271]. In the picosecond time-resolved spectroscopy experiments, a coherent synchronously pumped dye laser was used. This laser was pumped by a mode-locked Ar-ion laser, which has about 2 ps pulse width at 3.8 MHz repetition rate. The dye laser beam frequency was doubled by using a β-barium borate nonlinear optical crystal. The UV light thus generated was used to excite the sample. The PL



**Figure 49.** Photoluminescence peak wavelengths as a function of well widths in InGaN quantum wells for excitation densities of  $P_1 = 100 \text{ kW/cm}^2$  (open squares) and  $P_2 = 1 \text{ kW/cm}^2$  (solid circles). The blue shift, with increasing excitation density, is larger for larger well width, and the blue shift for Si-doping is larger for lower excitation density. Reprinted with permission from [280d], E. Oh et al., *Phys. Status Solidi B* 216, 487 (1999). © 1999, John Wiley and Sons.

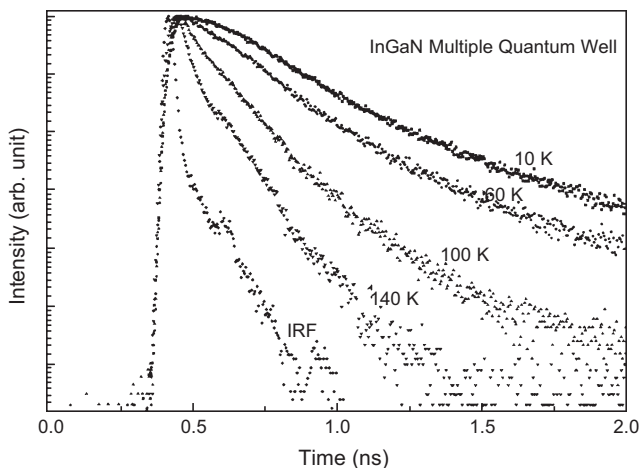




**Figure 50.** Comparison of excitation density dependence of PL intensity at 300 K with (solid squares) and without (open squares) Si-doping in InGaN barriers. The intensity is significantly enhanced with Si-doping at lower excitation densities, whereas, the enhancement is less pronounced at higher densities. Reprinted from [280d], E. Oh et al., *Phys. Status Solidi B* 216, 487 (1999). © 1999, John Wiley and Sons.

signal was dispersed by a McPherson monochromator and detected by a Hamamatsu photomultiplier tube. The time dependence of the decay was measured by a time-correlated single photon counting. The setup has a time resolution of 10 psec after deconvolution.

A display of spectra for different temperatures obtained in the time-resolved experiments is shown in Figure 51. At 10 K, the decay time was deduced as 720 psec. For reference, the lifetime of GaN epilayers also was measured, and it was found to be 100 psec at 10 K. The lifetimes of GaN and related materials are expected to be very short. This is because of the strong exciton-acoustic phonon interactions due to which fast energy relaxation of free excitons to the bottom of the exciton band takes place. But the lifetime observed in the InGaN MQW is about seven times that of the lifetime of free excitons in undoped GaN. This clearly shows that the excitons in InGaN are not in the free state. The slow down in the exciton relaxation in InGaN must be due to the trapping of excitons in potential fluctuations



**Figure 51.** Time-resolved photoluminescence decay curves of InGaN quantum well emission from InGaN/GaN MQW, at different temperatures. Reprinted with permission from [271], A. K. Viswanath et al. (unpublished results).

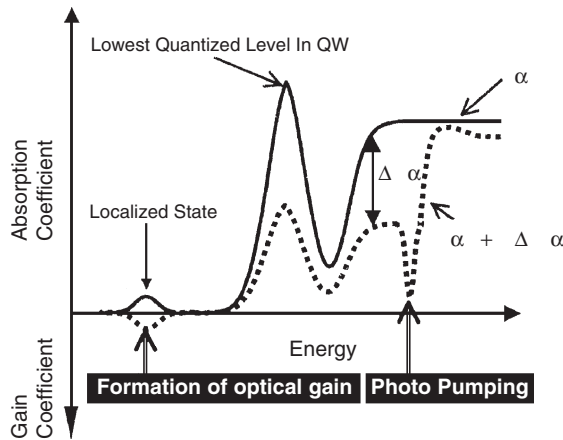
in the lattice. The lifetime was found to decrease with an increase in temperature. This shows that the nonradiative processes come into play as the temperature is increased. This should be considered very important, since the actual photonic devices like LEDs and semiconductor lasers are operated at high temperatures such as room temperature. The nonradiative relaxation has deleterious effects on the performance and efficiency of the semiconductor lasers. Time-resolved spectroscopy of  $\text{In}_{0.20}\text{Ga}_{0.80}\text{N}$  (2.5 nm)/ $\text{In}_{0.05}\text{Ga}_{0.95}\text{N}$  (6.0 nm) MQW has revealed two peaks at 2.920 eV and 3.155 eV [273]. The main peak at 2.920 eV was attributed to localized excitons and the weak peak at 3.155 eV to free excitons. Satake et al. [287] have studied the exciton localization in  $\text{In}_x\text{Ga}_{1-x}\text{N}$  epitaxial layers. In the 2 K photoluminescence spectrum, they observed a Stokes shift from the absorption shoulder and broadening at the lower photon energy side. In ternary alloys, the spatial fluctuations due to composition fluctuations can localize excitons. The mobility edge was determined by site-selective experiments in which the excitation photon energy is changed and PL spectra are recorded for different excitation energies.

Picosecond studies of MQWs of  $\text{In}_{0.20}\text{Ga}_{0.80}\text{N}$  (3 nm)/ $\text{In}_{0.05}\text{Ga}_{0.95}\text{N}$  (6 nm) and  $\text{In}_{0.10}\text{Ga}_{0.90}\text{N}$  (3 nm)/ $\text{In}_{0.02}\text{Ga}_{0.98}\text{N}$  (6 nm) have identified localized and delocalized excitons [292]. The decay times for different emission energies were studied. Decay times of localized excitons were found to be very long in the range of several nanoseconds. Photoluminescence and time-resolved spectroscopy of self-assembled InGaN quantum dots has been reported [293]. Lefebvre et al. [294] have studied the well-width dependence of luminescence and the PL lifetimes of InGaN quantum wells. In these samples, the In composition was kept constant. In the cw PL spectra, the FWHM was found to be constant for different well widths. The PL energies cover the entire visible range. In the PL time-resolved experiments, the decay times were found to increase with a decrease of peak energy. Lefebvre et al. [295] also have investigated the effects of the AlGaIn barrier and of dimensionality on InGaN systems. Their studies have confirmed the carrier localization on potential fluctuations. Kuroda et al. [296] have performed the picosecond time-resolved experiments on  $\text{In}_{0.12}\text{Ga}_{0.88}\text{N}/\text{In}_{0.03}\text{Ga}_{0.97}\text{N}$  MQWs. They investigated the excitation power dependence on the lifetimes and PL energy. The carrier recombination rate and the PL energy decreased nonlinearly with the decrease of carrier density. Ozgur et al. [297] have observed ultrafast carrier capture in InGaN MQWs by the four wave mixing experiments.

Kawakami et al. [297b] have described various time-resolved experiments carried out by them to understand the optical phenomena in GaN-based semiconductors. The experiments include time-resolved photoluminescence, time-resolved EL, transient grating, scanning near-field optical microscopy, pump-probe spectroscopy, etc. They also have given a model for the carrier dynamics in a localized system, which is shown in Figure 52.

## 5. LASER ACTION IN InGaN

Many laboratories in the world have studied the laser action in InGaN [287, 298–306]. Hangleiter and coworkers have measured the optical gain in InGaN/GaN heterostructures



**Figure 52.** Schematic of carrier dynamics in a localized system.  $\alpha$  and  $\alpha + \Delta\alpha$  denote absorption coefficient under low photoexcitation and under photo-pumping, respectively. Reprinted with permission from [297b], Y. Kawakami et al., *Phys. Status Solidi A* 183, 41 (2001). © 2001, John Wiley and Sons.

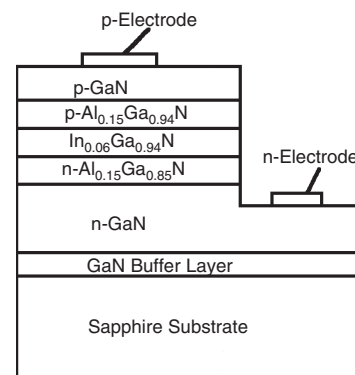
under optical pumping [289]. The measurements were made at room temperature. The stripe excitation method has been used to measure the gain in the system. Stimulated emission (SE) experiments on an epitaxial layer of InGaN were reported for different excitation powers [287]. When the laser power was greater than  $10 \mu\text{J}/\text{cm}^2$ , stimulated emission was observed. Above threshold, a superlinearly grown sharp emission band was recorded. The laser emission was just below the mobility edge. The SE has shown a red shift with the increase of excitation energy density. A multimode lasing spectrum was observed [300] in optically pumped lasing experiments on InGaN/GaN. A multimode lasing spectrum was observed for the input power density of  $11 \text{ MW}/\text{cm}^2$ . Stimulated emission in a number of samples of InGaN/GaN MQWs, with different well widths and barrier heights, revealed the dependence of the emission peak position on quantum-well thickness [301]. As the thickness of the quantum well decreased, the stimulated emission shifted to higher energies. The effective conduction and valence-band discontinuities also were estimated. In the samples used by Bidnyk et al. [304] for the optical pumping experiments, the GaN barriers were intentionally doped with Si. The concentration of Si was varied from  $1 \times 10^{17}$  to  $3 \times 10^{19} \text{ cm}^{-3}$ . The threshold at room temperature was found to be 12 times as low as that of a high-quantity GaN epitaxial layer. Spectral narrowing was observed at higher excitation densities. The authors have interpreted the low SE threshold as due to large localization of excitons in quantum wells of InGaN. This research group has shown the applicability of InGaN MQWs for high-temperature laser operation by observing laser action up to 550 K. The threshold necessary at high temperatures is also high because nonradiative processes are very dominant at these temperatures. Laser action in the MOCVD-grown InGaN/GaN MQWs that have high In content also was studied by one research team [306]. The experiments were done at room temperature and 25 K. Annealing experiments have revealed that the potential fluctuations can be reduced.

## 6. LIGHT-EMITTING DIODES AND SEMICONDUCTOR LASERS BASED ON InGaN

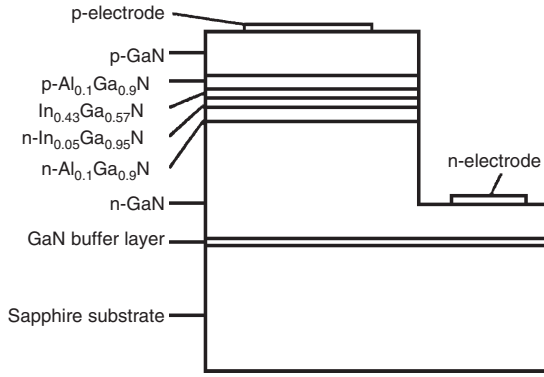
There are several excellent reviews on LEDs and lasers based on InGaN [1, 307–311]. Many research groups in universities and industry have fabricated the light-emitting devices of InGaN [312–356]. Nakamura et al. [313] have fabricated blue LEDs from a p-GaN/n-InGaN/n-GaN double heterostructure. The output power of this laser was twice that of the II–VI-based blue LEDs, at the same forward current. When a Zn-doped InGaN active layer was used, a candela class high-brightness blue LED could be achieved [315].

In a later work, Nakamura et al. [1] could increase the output power and lower the forward voltage. In the previous studies, electron-beam irradiation was performed instead of thermal annealing for as-grown InGaN/GaN epilayers to obtain a high-quality p-type GaN layer. In this case, the output power was not high since the entire p layer was not uniformly converted into a highly p-type GaN layer by electron irradiation. Thermal annealing could easily change the entire high-resistivity p-type GaN layer into a low-resistivity p-type GaN layer. The structure of the InGaN/AlGaIn double heterostructure LED is shown in Figure 53.

Blue-green LEDs were fabricated [314] with InGaN/AlGaIn double heterostructure in which the In mole fraction was increased to 0.23. Also, the active layer of InGaN was co-doped with both Zn and Si. Donor–acceptor pair recombination was the recombination channel. The peak wavelength in the EL was 500 nm. High-brightness InGaN blue, green, and yellow LEDs with quantum well structure based III–V nitrides were grown on sapphire substrates [316]. The In mole fraction was varied from 0.2 to 0.7 to change the peak wavelength of the InGaN SQW LEDs from blue to yellow. Super bright green InGaN single quantum well structure, p-AlGaIn/InGaN/n-GaN, with a luminous intensity of 12 cd were fabricated [317] in which the  $\text{In}_{0.45}\text{Ga}_{0.55}\text{N}$  active layer was undoped (Fig. 54). The luminous intensity of this LED was about 100 times higher than of conventional GaP LEDs. Amano and Akasaki's group have fabricated a double heterostructure of p-GaN/ $\text{In}_{0.2}\text{Ga}_{0.8}\text{N}$ /n-GaN by MBE,



**Figure 53.** The structure of the InGaN/AlGaIn double-heterostructure LEDs. Reprinted with permission from [1], S. Nakamura and G. Fasol, “The Blue Laser Diode.” © 1997, Springer-Verlag.

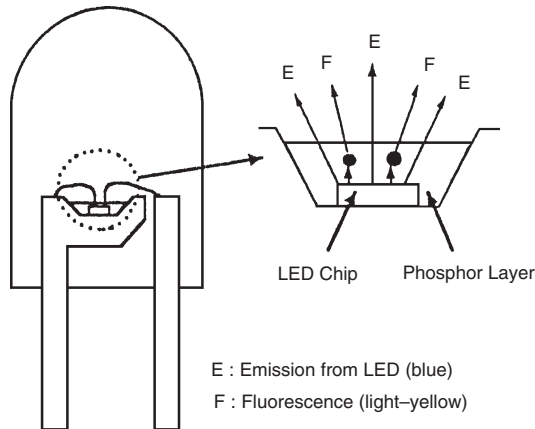


**Figure 54.** The structure of a green SQW LED. Reprinted from [1], S. Nakamura and G. Fasol, "The Blue Laser Diode." © 1997, Springer-Verlag.

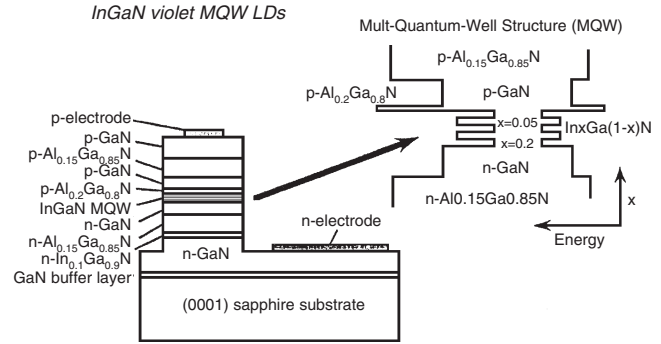
which has given violet emission upon current injection at room temperature [318].

Nakamura et al. [1, 317] have made breakthroughs in making white LEDs. There are several applications for white LEDs. They can be used in full-color liquid-crystal displays, fluorescent lamps, etc. White LEDs could be fabricated by exciting phosphors by using blue LEDs with high excitation energy. The structure of white LEDs is shown in Figure 55. The structure of this LED is almost the same as the blue LED chip except that a phosphor layer is used on top of the blue LED. When current is supplied to the single quantum well LED, blue light is emitted from the quantum well of InGaN. The phosphor is excited by this light and emits yellow luminescence. The mixture of blue light from InGaN and yellow light from phosphor gives white light.

Nakamura et al. [319] have fabricated InGaN MQW semiconductor lasers by MOCVD on (0001) sapphire substrate. Etching of III-V nitride films was done to get the mirror facets for the laser cavity. The active layer was a MQW consisting of 25 Å thick In<sub>0.2</sub>Ga<sub>0.8</sub>N well layers and 50 Å thick In<sub>0.05</sub>Ga<sub>0.95</sub>N barrier layers, with 26 periods. The n- and p-type Al<sub>0.15</sub>Ga<sub>0.85</sub>N layers were cladding layers (Fig. 56). Under current injection, pulsed lasing was obtained at room temperature at a wavelength of 417 nm.

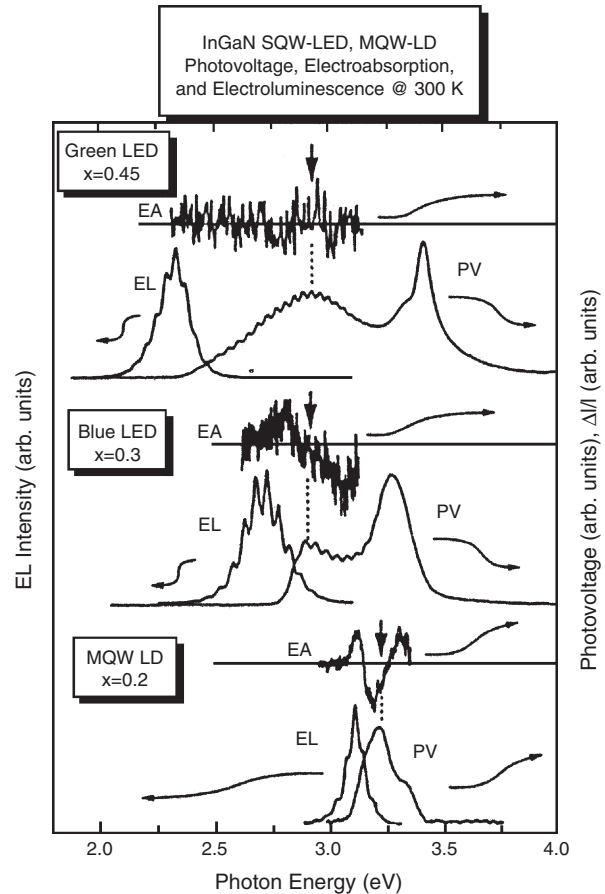


**Figure 55.** Structure of white LED. Reprinted with permission from [1], S. Nakamura and G. Fasol, "The Blue Laser Diode." © 1997, Springer-Verlag.



**Figure 56.** The structure of the InGaN MQW semiconductor laser. Reprinted with permission from [1], S. Nakamura and G. Fasol, "The Blue Laser Diode." © 1997, Springer-Verlag.

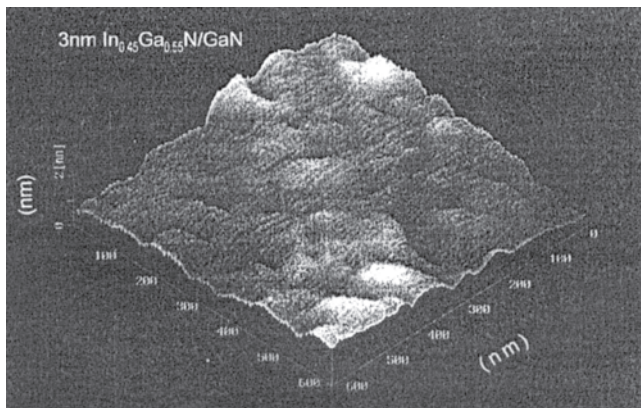
Figure 57 shows the room temperature EL, PV, and EA spectra of green, blue SQW LED, and MQW laser diode structures. The EL spectrum of the MQW laser diode was measured below the threshold density. The lasing emission



**Figure 57.** EL, PV, and EA (EA) spectra for InGaN green (510 nm) and blue (450 nm) SQW LED structures and a MQW laser structure, whose lasing wavelength is 406 nm. The EL spectrum of the MQW structure was measured below the threshold current. The In compositions in the InGaN quantum well for green, blue, and MQW LED are 0.45, 0.3, and 0.2, respectively. The structure in the EA spectra corresponds to the free exciton resonances. Reprinted with permission from [1], S. Nakamura and G. Fasol, "The Blue Laser Diode." © 1997, Springer-Verlag.

of this MQW LD appeared at 3.052 eV (406 nm). From these results, Nakamura's group has concluded that the EL emissions are from localized excitons in the quantum wells. In the MQW laser device, even the inhomogeneous column-like structures have shown lasing. From this observation, Nakamura et al. have concluded that the oscillator strength and gain at local potential minima are very large. The emissions were interpreted as due to inhomogeneity of InGaN layers, which are equivalent to quantum-dot-like states in InGaN quantum well layers. Figure 58 shows the surface morphology of InGaN well layers observed in AFM. The roughness of InGaN well layers was about 10 to 30 Å, with periods of about 1000 Å horizontally in the plane parallel to the junction. These islands-like structures were not found for layers thicker than 40 Å. It was thought that the In-rich regions in InGaN well layers can form potential minima to confine the carriers.

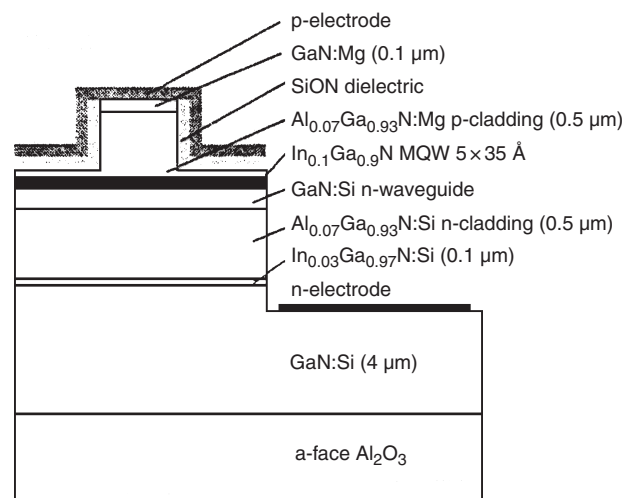
Nakamura et al. [325] has demonstrated the cw operation of a InGaN MQW semiconductor laser at room temperature, which has shown a single peak when the forward current was increased above the threshold current. Continuous-wave operation of InGaN MQW laser structure with a lifetime of 27 h [86] was demonstrated. The best method to reduce the number of threading dislocations is by using epitaxially overgrown GaN on sapphire [329, 330]. The GaN layer above the SiO<sub>2</sub> mask area surrounding the window, was found to have almost no dislocations. A high density of threading dislocations was observed in the window regions. InGaN MQW semiconductor lasers were fabricated on such GaN substrates. In these structures, Al<sub>0.14</sub>Ga<sub>0.86</sub>N–GaN modulation doped-strained-layer superlattice cladding layers were used. With these structures, operating lifetime of 10,000 hours was demonstrated in the cw mode at room temperature. Amber-[331] and violet-[332] color-emitting InGaN semiconductor lasers on a GaN substrate were reported by Nakamura's group. The semiconductor lasers with cleaved mirror facets have given much higher output powers [334, 336]. Kneissl et al. [338] have fabricated the mirrors by chemical-assisted ion-beam etching for their InGaN/GaN semiconductor lasers. From these lasers, emission was observed in the wavelength range of 419 to 423 nm in the pulsed current-injection conditions. Hofstetter et al. [339] have reported



**Figure 58.** AFM image of the 30 Å thick In<sub>0.45</sub>Ga<sub>0.55</sub>N layer on n-GaN/sapphire. Reprinted with permission from [1], S. Nakamura and G. Fasol, "The Blue Laser Diode." © 1997, Springer-Verlag.

the threshold current density of 16 kA/cm<sup>2</sup> in an electrically injected InGaN/GaN distributed feedback laser. The emission of this laser was at 403 nm and was found to be in a single longitudinal mode. Kneissl et al. [340] have characterized the mirrors made by chemical etching with the help of AFM and SEM. Bour et al. [341] have studied the dependence of threshold current density on the stripe width in the gain-guided InGaN MQW lasers. The lasing wavelength was 400 nm. The threshold current density was found to increase very rapidly as the stripe width was narrowed. The same group has later accomplished the room temperature cw operation of InGaN MQW semiconductor laser [342].

Low-threshold current operation is a desirable requisite for the utilization of semiconductor lasers for color printing and optical memory systems. To realize the low-threshold operation, it is essential that the injected carriers are confined. Generally, the injected electrons leak away from the quantum well region into the p-cladding layer, where they recombine with the holes. These electrons, which leak into the neighboring cladding layers, do not populate the quantum well active region, and, hence, they do not contribute to the stimulated emission. This results in the increase in the threshold current and a decrease in the internal quantum efficiency. To prevent the leakage effects, Nakamura et al. [1] have used a thin, high bandgap, p-type AlGaIn layer that is placed immediately after the quantum well layer. Bour et al. [343] have designed and studied the characteristics of InGaN MQW lasers with an asymmetric waveguide. The device structure is shown in Figure 59. The active region consists of five 35 Å In<sub>0.1</sub>Ga<sub>0.9</sub>N QWs separated by 60 Å In<sub>0.02</sub>Ga<sub>0.98</sub>N:Si barriers. The cladding layers are 0.5-μm-thick Al<sub>0.07</sub>Ga<sub>0.93</sub>N. A room-temperature cw operation was achieved with this structure. Kneissl et al. [344] have examined the effects of compositional fluctuations on the optical gain characteristics in InGaN semiconductor lasers. Bour et al. [345] have demonstrated a cw operation of InGaN lasers with threshold current densities as low as 7 kA/cm<sup>2</sup> and an emission wavelength at 400 nm. Improvements in the



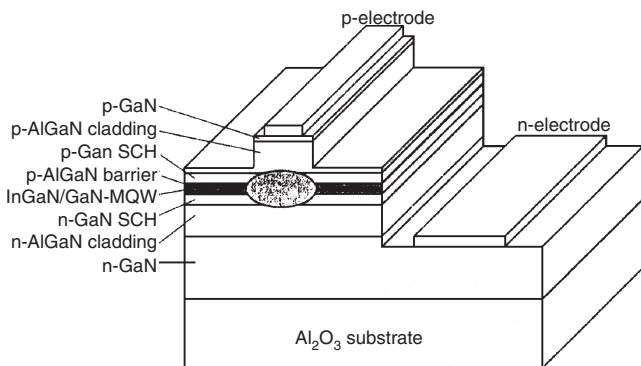
**Figure 59.** Ridge waveguide device structure incorporating asymmetric transverse waveguide. Reprinted with permission from [343], D. P. Bour et al., *IEEE J. Quantum Elect.* 36, 184 (2000). © 2000, Institute of Electrical and Electronics Engineers.

beam quality were observed when thick, superlattice, n-type cladding layer was used (Fig. 60). From theoretical considerations, it also was shown that thinning the sapphire substrate will give a better room-temperature cw operation of the laser. The cw operation was observed up to a temperature of 60 °C as shown in Figure 61. Bour et al. [348] have shown that polycrystalline LEDs of InGaN could be fabricated on quartz substrate. The active layer is an  $\text{In}_{0.2}\text{Ga}_{0.8}\text{N}$  SQW with an emission wavelength of 430 nm. These polycrystalline LEDs were thought to be useful for large-area displays. Huh et al. [353] have described the fabrication and characterization of InGaN/GaN MQW LED by using a Pt thin film as a current spreading layer. The emission wavelength was at 453 nm and had a FWHM of 23 nm.

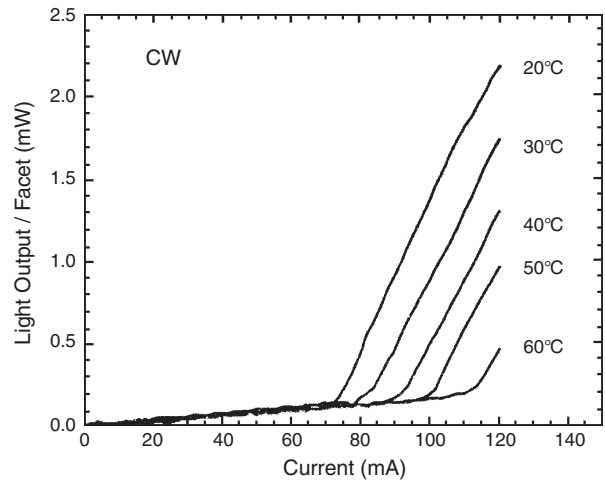
## 7. MECHANISM OF LASER ACTION IN InGaN

Lasing mechanisms in the InGaN epitaxial layer and quantum wells were discussed by several authors based on the optical experiments. However, it is still a controversial topic. Chichibu et al. [258] were the first who identified localized excitons in SQWs and MQWs of InGaN and proposed that they are responsible for the lasing in these materials. Later, Narukawa et al. [259] have demonstrated photo-pumped lasing from the localized exciton states. Kuball et al. [283] suggested that the microscopic crystalline order influences the laser action. Satake et al. [287] have reported stimulated emission characteristics in InGaN epilayers. They were of the opinion that localized states can be easily filled by optical pumping, since the density of localized states in the band tail is lower than that of the extended states. If the optical gain from the filled localized states exceeds the losses due to light propagation, stimulated emission sets in. Similar phenomena have been very thoroughly investigated by Ding et al. [357] in the case of II–VI semiconducting quantum wells.

From the optical gain spectroscopy measurements, Frankowsky et al. [298] concluded that optical gain in GaN/GaN heterostructures is due to direct band-to-band transitions in an electron-hole plasma. The electron-hole plasma state under high optical excitation was also observed by Jiang et al. [302]. Song et al. [303] have performed



**Figure 60.** Typical nitride laser heterostructure on a sapphire substrate. Reprinted with permission from [345], D. P. Bour et al., *Phys. Status Solidi A* 180, 139 (2000). © 2000, John Wiley and Sons.



**Figure 61.** cw light-current characteristics of  $2 \times 500 \mu\text{m}^2$  nitride diode with HR-coated mirrors. Reprinted with permission from [345], D. P. Bour et al., *Phys. Status Solidi A* 180, 139 (2000). © 2000, John Wiley and Sons.

the gain spectroscopy studies on InGaN/GaN quantum well lasers and concluded that the filling of localized band-edge states is a prerequisite for achieving lasing.

Viswanath et al. [106] have discussed the importance of the exciton binding energy in realizing the room-temperature semiconductor lasers based on GaN. Mohs et al. [358] have investigated the optical gain in Nichia company's InGaN blue LED. Experiments were conducted at room temperature by using the variable stripe-length method and nanosecond Nd:YAG laser. Plasma recombination from a quantum-confined level was thought to be the gain mechanism. Mohs et al. [359] have performed absorption and gain spectroscopy experiments and arrived at a conclusion that the conventional electron-hole plasma recombination model is valid to explain lasing in  $\text{In}_{0.18}\text{Ga}_{0.82}\text{N}/\text{In}_{0.06}\text{Ga}_{0.94}\text{N}$  MQWs.

Mukai et al. [360] have studied the current and temperature dependence of EL in InGaN SQW lasers with different In compositions. For the lasers that emit shorter wavelengths (less than 375 nm), the emission was attributed to band-to-band recombination, while for the InGaN lasers with higher In composition, which emit in the longer wavelength region, lasing was due to the localized excitons.

## 8. CONCLUSIONS

Optical properties of GaN nanostructures and devices have been reviewed in this article. The discussion includes photoluminescence and time-resolved spectroscopy of these materials. Most of the work on material growth and device development has been done by using the MOCVD technique. However, other techniques, such as MBE, also were tried. To date, the MOCVD method has provided better materials and optoelectronic devices compared to MBE. Similarly, sapphire has been the most used substrate.

Now GaN and other III–V nitrides are realized as potential candidates in photonics. Light-emitting diodes and semiconductor lasers, which emit in a variety of wave lengths from blue to yellow, are now commercially available. They

are being used in full-color displays and traffic lights. By combining the three primary colors, white light LEDs also were developed. The LEDs emitting various colors also are substitutes for traditional fluorescent lamps and can be used in homes and shops. The market for this is very huge. Blue LEDs also find applications in laser printers and underwater optical communications. In conclusion, the future of nitrides looks extremely bright.

## GLOSSARY

**Laser** Light amplification by stimulated emission of radiation.

**Light-emitting diode** This is the p-n junction of a semiconductor and emits light when current is passed through it.

**Luminescence** This is the phenomena of emission of radiation when the material is excited by suitable energy. If the excitation is caused by photons it is called photoluminescence and if the excitation is caused by electrons it is called as cathodoluminescence.

**Quantum dot** This is a zero-dimensional system in which the confinement of electron occurs in all the three directions.

**Quantum well** This is a very thin semiconductor with thickness of few nanometers or less and is placed between two barrier layers which have higher bandgap energies. In this case the free carrier motion occurs in two directions. Here quantum confinement occurs in one direction.

**Quantum wire** This is a one-dimensional electron system in which the quantum confinement occurs in two directions.

**Semiconductor laser** This is a solid state laser in which the active medium is a semiconductor.

## ACKNOWLEDGMENTS

I would like to thank the brain pool program of South Korea for providing me the opportunity of working in South Korea for three years. The original work of the author discussed in this article was done at National Creative Research Initiative Center for Ultrafast Optics Control at Korea Research Institute of Standards and Science (KRISS) Taejon. I would like to thank Dr. Dongho Kim for providing me the finest laser laboratory to investigate the optical phenomena. I would like to thank a number of collaborators, Dr. Joo In Lee, Dr. Sunkyu Yu, Dr. Eunjoon shin, Dr. S. C. Jeoung, of KRISS. I am very grateful to many scientists who have provided me a number of samples of GaN and InGaN. Thanks are due to Dr. Chang Hee Hong, who was the group leader of the GaN project at L. G. Electronics, presently, at Department of physics and National Semiconductor Research Centre, Jeoungbuk National University, Korea, for giving me the first batch of samples that I have worked with. I also would like to thank Dr. Yoonho Choi, present group leader of GaN project, and Dr. Baeyoung Kim of LG Electronics. I thank C. R. Lee and J. Y. Leem of KRISS, and S. T. Kim and A. G. Lee of Chungbuk National University, Korea, for their cooperation. I also thank my wife Mrs. Annapurna Viswanath and my son Mr. A. Srinivas for their support and understanding during the time of investigation and also during the writing of this chapter.

## REFERENCES

1. S. Nakamura and G. Fasol, "The Blue Laser Diode" Springer, Berlin, 1997. S. Nakamura, *Solid State Commun.* 102, 237 (1997).
2. S. Strite, M. E. Lin, and H. Morkoc, *Thin Solid Films* 231, 197 (1993). H. Morkoc, S. Strite, G. S. Gao, M. E. Lin, B. Sverdlov, and M. Burns, *J. Appl. Phys.* 73, 1363 (1994). S. N. Mohammad, A. A. Salvador, and H. Morkoc, *P. IEEE*, 83, 1306 (1995). H. Morkoc, in "Semiconductor Heteroepitaxy" (B. Gil and R. L. Aulombard, Eds.), pp. 238–249. World Scientific, Singapore, 1995. S. Strite and H. Morkoc, *J. Vac. Sci. Technol., B* 10, 1237 (1992). H. Morkoc, "Wide Bandgap Nitrides and Devices." Springer Verlag, Berlin, 1998. S. N. Mohammad and H. Morkoc, *Prog. Quant. Electron.* 20, 361 (1996).
3. T. D. Moustakas, J. I. Pankove, and Y. Hamakawa (Eds.), "Wide Bandgap Semiconductors," Vol. 242. MRS, Pittsburgh, 1992.
4. M. Razeghi and A. Rogalski, *J. Appl. Phys.* 79, 7433 (1996).
5. R. F. Davis, *P. IEEE*, 79, 702 (1991).
6. J. H. Edgar (Ed.), "Group III Nitrides." INSPEC, London, 1994.
7. "Proceedings of International Symposium on Blue Lasers and Light Emitting Diodes," Chiba University, Japan, 1996.
8. S. J. Pearton, J. C. Zolper, R. J. Shul, and F. Ren, *J. Appl. Phys.* 86, 1 (1999).
9. S. C. Jain, M. Willander, J. Narayan, and R. van Overstraeten, *J. Appl. Phys.* 87, 965 (2000).
10. A. K. Viswanath, in "Handbook of Advanced Electronic and Photonic Materials and Devices" (H. S. Nalwa, Ed.), Academic Press, San Diego, 2001; A. K. Viswanath, in "Semiconductors and Semimetals" (H. S. Nalwa, R. Willardson, and E. Weber, Eds.), Vol. 73, Academic Press, San Diego, 2001.
11. B. Gil (Ed.), "Group III Nitride Semiconductor Compounds." Clarendon Press, Oxford, 1998.
12. J. W. Orton and C. T. Foxon, *Rep. Prog. Phys.* 61, 1 (1998).
13. "Proceedings of International Conference on Nitride Semiconductors," Tokushima, Japan, 1997.
14. F. A. Ponce and D. P. Bour, *Nature* 386, 351 (1997).
15. D. P. Bour, in "Quantum Well Lasers" (P. S. Zory, Ed.), Academic Press, San Diego, 1993.
16. H. Holonyak Jr. and S. E. Bevacqua, *Appl. Phys. Lett.* 1, 82 (1962).
17. M. G. Craford and F. M. Steranka, in "Encyclopedia of Applied Physics" Vol. 8, p. 485 VCH, New York, 1994.
18. M. G. Craford, *IEEE Circuits Device.* 8, 25 (1992).
19. M. G. Craford, *Mater. Res. Bull.* 25, 27 (2000).
20. M. G. Craford, in "Semiconductors and Semimetals" (M. G. Craford and B. Stringfellow, Eds.), Vol. 48. Academic Press, San Diego, 1997.
21. M. A. Khan, J. N. Kuznia, A. R. Bhattarai, and D. T. Olson, *Appl. Phys. Lett.* 62, 1786 (1993). M. A. Khan, A. Bhattarai, J. N. Kuznia, and D. T. Olson, *Appl. Phys. Lett.* 63, 1214 (1993).
22. G. Popovici, H. Morkoc, and S. N. Mohammad, in Ref. 10.
23. B. Kramer (Ed.), "Quantum Coherence in Mesoscopic Systems." Plenum, New York, 1991.
24. D. K. Ferry (Ed.), "Granular Nanoelectronics." Plenum Press, New York, 1991.
25. H. Haug and L. Banyai (Eds.), "Optical Switching in Low Dimensional Systems." Plenum Press, New York, 1989.
26. R. Dingle (Ed.), "Applications of Multi Quantum Wells, Selective Doping and Superlattices." Academic Press, New York, 1987.
27. F. Henneberger, S. Schmitt Rink, and E. Gobel (Eds.), "Optics of Semiconductor Nanostructures." Akademie Verlag, 1993.
28. C. Weisbuch, in [26].
29. L. Esaki and L. L. Chang, *Phys. Rev. Lett.* 33, 495 (1974).
30. R. Dingle, W. Wiegman, and C. H. Henry, *Phys. Rev. Lett.* 33, 827 (1974).
31. W. T. Tsang, in [26].
32. R. D. Burnham, W. Streifer, and T. L. Paoli, *J. Cryst. Growth* 68, 370 (1984).

33. H. Morkoc, in [26].
34. N. Linh, in [26].
35. M. Abe, T. Mimura, K. Nishiushi, A. Shibatomi, M. Kobayashi, and T. Misugi, in [26].
36. R. Stepniewski, M. Potemski, H. Buhmann, D. Toet, J. C. Mann, G. Martinez, W. Knap, A. Raymond, and B. Etienne, *Phys. Rev. B* 50, 11895 (1994).
37. M. S. Skolnick, J. M. Rorison, K. J. Nash, D. J. Mowbray, P. R. Tapster, S. J. Bass, and A. K. Pitt, *Phys. Rev. Lett.* 58, 2130 (1987).
38. M. S. Skolnick, K. J. Nash, S. J. Bass, P. E. Simmonds, and M. J. Kane, *Solid State Commun.* 67, 637 (1988).
39. Q. X. Zhao, P. O. Holtz, B. Monemar, T. Lundstrom, J. Wallin, and G. Landgren, *Phys. Rev. B* 48, 11890 (1993).
40. W. Chen, M. Fritze, W. Walecki, A. V. Nurmikko, D. Ackley, J. M. Hong, and L. L. Chang, *Phys. Rev. B* 45, 8464 (1992).
41. J. I. Lee, A. K. Viswanath, S. Yu, E. J. Shin, K. S. Lee, H. G. Lee, and G. Ihm, *Solid State Commun.* 110, 633 (1999).
42. D. S. Chemla, D. A. B. Miller, and P. W. Smith, in [26].
43. H. Sakaki, *Jpn. J. Appl. Phys.* 19, L735 (1980).
44. Y. Arakawa, K. Vahala, and A. Yariv, *Appl. Phys. Lett.* 45, 950 (1984).
45. A. Kasi Viswanath, K. Hiruma, K. Ogawa, and T. Katsuyama, *Applied Physics Communications*. 13, 55 (1994).
46. A. Kasi Viswanath, K. Hiruma, K. Ogawa, and T. Katsuyama, "Proceedings of the International Conference on Solid State Devices and Materials," Tsukuba, Japan, 1992.
47. A. Kasi Viswanath, K. Hiruma, M. Yazawa, K. Ogawa, and T. Katsuyama, *Microw. and Opt. Techn. Lett.* 7, 94 (1994).
48. A. Kasi Viswanath, K. Hiruma, K. Ogawa, and T. Katsuyama, *Superlattices and Microstruct.* 14, 105 (1993).
49. C. M. Lieber, *Solid State Commun.* 107, 607 (1998).
50. C. M. Lieber and X. L. Wu, *Acc. Chem. Res.* 24, 223 (1991).
51. H. Dai and C. M. Lieber, *Annu. Rev. Phys. Chem.* 44, 237 (1993).
52. C. M. Lieber, J. Liu, and P. E. Sheehan, *Angew. Chem., Int. Ed. Engl.* 35, 686 (1996).
53. C. M. Lieber, A. M. Morales, P. E. Sheehan, E. W. Wong, and P. Yang, Proceedings of the Robert A. Welch Foundation 40th "Conference on Chemical Research: Chemistry on the Nanometer Scale, Welch Foundation," Houston, 1997.
54. P. Yang and C. M. Lieber, *Science* 273, 1836 (1996).
55. S. S. Wong, J. D. Harper, P. T. Lansbury, and C. M. Lieber, *J. Am. Chem. Soc.* 120, 603 (1998).
56. S. S. Wong, E. Joselevich, A. T. Woolley, C. Cheung, and C. M. Lieber, *Nature* 394, 52 (1998).
57. H. Dai, E. W. Wong, Y. Z. Lu, S. Fan, and C. M. Lieber, *Nature* 375, 769 (1995).
58. M. Morales and C. M. Lieber, *Science* 279, 208 (1998).
59. P. Kim, T. W. Odom, J. L. Huang, and C. M. Lieber, *Phys. Rev. Lett.* 82, 1225 (1999).
60. J. Zhang, J. Liu, J. L. Huang, and C. M. Lieber, *Science* 274, 757 (1996).
61. H. Jiangtao, T. W. Odom, and C. M. Lieber, *Acc. Chem. Res.* 32, 435 (1999).
62. J. Voit, *Rep. Prog. Phys.* 57, 977 (1994).
63. J. T. Devreese, R. P. Evrard, V. E. van Doren (Eds.), "Highly Conducting One-Dimensional Solids." Plenum, New York, 1979.
64. A. Kasi Viswanath, Jeanette Vetuskey, Rosemary Leighton, Mary Beth Krogh Jespersion, and Howard H. Patterson, *Mol. Phys.* 48, 567 (1983).
65. A. Kasi Viswanath, M. B. Krogh Jespersion, J. Vetuskey, C. Baker, W. Ellenson, and Howard H. Patterson, *Mol. Phys.* 42, 1431 (1981).
66. A. Kasi Viswanath, W. L. Smith, and Howard H. Patterson, *Chem. Phys. Lett.* 87, 612 (1982).
67. Marilyn Martin, M. B. Krogh Jespersion, M. Hsu, J. Tewkesbury, Michel Laurent, A. Kasi Viswanath, and H. H. Patterson, *Inorg. Chem.* 22, 647 (1983).
68. A. Kasi Viswanath and Howard H. Patterson, *Chem. Phys. Lett.* 82, 25 (1981).
69. W. D. Ellenson, A. Kasi Viswanath, and Howard H. Patterson, *Inorg. Chem.* 20, 780 (1981).
70. A. Kasi Viswanath, J. Vetuskey, M. B. Krogh Jespersion, W. Ellenson, and Howard H. Patterson, *Inorg. Chem.* 20, 3493 (1981).
71. Howard H. Patterson, J. Tewkesbury, M. Martin, M. B. Krogh Jespersion, J. Lomenzo, H. Hooper, and A. Kasi Viswanath, *Inorg. Chem.* 20, 2297 (1981).
72. K. Misawa, S. Nomura, and T. Kobayashi, in [27].
73. J. I. Lee, H. G. Lee, E. J. Shin, S. Yu, A. Kasi Viswanath, D. Kim, and G. Ihm, *Mater. Sci. Eng. B* 51, 122 (1998).
74. R. Dingle, D. D. Sell, S. E. Stokowski, and M. Ilegems, *Phys. Rev. B* 4, 1211 (1971).
75. B. Monomar, *Phys. Rev. B* 10, 676 (1974).
76. J. I. Pankove, J. E. Berkeyheiser, H. P. Maruska, and J. Wittke, *Solid State Commun.* 8, 1051 (1970).
77. S. Nakamura, M. Senoh, and T. Mukai, *Jpn. J. Appl. Phys.* 32, L8 (1998).
78. S. Nakamura, T. Mukai, and M. Senoh, *Appl. Phys. Lett.* 64, 1686 (1994).
79. S. Nakamura and T. Mukai, *Jpn. J. Appl. Phys.* 31, L1457 (1992).
80. S. Nakamura, T. Mukai, M. Senoh, and N. Isawa, *Jpn. J. Appl. Phys.* 31, L139 (1992).
81. S. Nakamura, M. Senoh, S. I. Nagahama, N. Isawa, T. Yamada, T. Matsushita, H. Kiyoku, and Y. Sugimoto, *Jpn. J. Appl. Phys.* 35, L74 (1996).
82. S. Chichibu, T. Azuhata, T. Sota, and S. Nakamura, *J. Appl. Phys.* 79, 2784 (1996).
83. Y. Kawakami, Z. G. Peng, Y. Narukawa, S. Fujita, S. Fujita, and S. Nakamura, *Appl. Phys. Lett.* 69, 1414 (1996).
84. S. Chichibu, A. Shikanai, T. Azuhata, T. Sota, A. Kuramata, K. Horino, and S. Namamura, *Appl. Phys. Lett.* 68, 3766 (1996).
85. A. Shikanai, T. Azuhata, T. Sota, S. Chichibu, A. Kuramata, K. Horino, and S. Nakamura, *J. Appl. Phys.* 81, 417 (1997).
86. S. Nakamura, S. Masayuki, S. Nagahama, N. Iwasa, T. Yamada, T. Matsushita, Y. Sugimoto, and K. Hiroyuki, *Appl. Phys. Lett.* 70, 1417 (1997).
87. A. Alemu, B. Gil, M. Julier, and S. Nakamura, *Phys. Rev. B* 57, 3761 (1998).
88. M. Julier, J. Campo, B. Gil, J. P. Lascaray, and S. Nakamura, *Phys. Rev. B* 57, R6791 (1998).
89. S. Chichibu, H. Okumura, S. Nakamura, G. Feuillet, T. Azuhata, T. Sota, and S. Yoshida, *Jpn. J. Appl. Phys.* 36, 1976 (1997).
90. S. Chichibu, T. Mizutani, T. Shoida, H. Nakanishi, T. Deguchi, T. Azuhata, T. Sota, and S. Nakamura, *Appl. Phys. Lett.* 70, 3440 (1997).
91. S. Nakamura, *Jpn. J. Appl. Phys.* 30, 1620 (1991).
92. H. Amano, K. Hiramatsu, and I. Akasaki, *Jpn. J. Appl. Phys.* 27, L1384 (1988).
93. K. Naniwae, S. Itoh, H. Amano, K. Itoh, K. Hiramatsu, and I. Akasaki, *J. Cryst. Growth* 99, 381 (1990).
94. K. Hiramatsu, T. Detchprohm, and I. Akasaki, *Jpn. J. Appl. Phys.* 32, 1528 (1993).
95. H. Amano, M. Kito, K. Hiramatsu, and I. Akasaki, *Jpn. J. Appl. Phys.* 28, L2112 (1989).
96. D. Volm, K. Oettinger, T. Streibl, D. Kovalev, M. Ben-chorin, J. Diener, B. K. Meyer, J. Mejewski, L. Eckey, A. Hoffmann, H. Amano, I. Akasaki, K. Hiramatsu, and T. Detchprohm, *Phys. Rev. B* 53, 16 543 (1996).
97. C. Wetzel, D. Volm, B. K. Meyer, K. Pressel, S. Nilsson, E. N. Mokhov, and P. G. Baranov, *Appl. Phys. Lett.* 65, 1033 (1994).
98. D. Kovalev, B. Averboukh, D. Volm, B. K. Meyer, H. Amano, and I. Akasaki, *Phys. Rev. B* 54, 2518 (1996).
99. B. K. Meyer, D. Volm, A. Graber, H. C. Alt, T. Detchprohm, A. Amano, and I. Akasaki, *Solid State Commun.* 95, 597 (1995).

100. T. Detchprohm, K. Hiramatsu, K. Itoh, and I. Akasaki, *Jpn. J. Appl. Phys.* 31, L1454 (1992).
101. D. Volm, T. Streibl, B. K. Meyer, T. Detchprohm, H. Amano, and I. Akasaki, *Solid State Commun.* 96, 53 (1995).
102. M. Drechsler, D. M. Hofmann, B. K. Meyer, T. Detchprohm, H. Amano, and I. Akasaki, *Jpn. J. Appl. Phys.* 34, L1178 (1995).
103. I. A. Buyanova, Mt. Wagner, W. M. Chen, B. Monemar, J. L. Lindstrom, H. Amano, and I. Akasaki, *Appl. Phys. Lett.* 73, 2968 (1998).
104. S. Hearne, E. Chason, J. Han, J. A. Floro, J. Figiel, J. Hunter, H. Amano, and I. S. T. Tson, *Appl. Phys. Lett.* 74, 356 (1999).
105. A. Kasi Viswanath, J. I. Lee, S. Yu, D. Kim, Y. Choi, and C. H. Hong, *J. Appl. Phys.* 84, 3848 (1998).
106. A. Kasi Viswanath, J. I. Lee, D. Kim, C. R. Lee, and J. Y. Leem, *Phys. Rev. B* 58, 16 333 (1998).
107. A. Kasi Viswanath, J. I. Lee, C. R. Lee, J. Y. Leem, and D. Kim, *Solid State Commun.* 108, 483 (1998).
108. A. Kasi Viswanath, J. I. Lee, C. R. Lee, J. Y. Leem, and D. Kim, *Appl. Phys. A* 67, 551 (1998).
109. J. R. Haynes, *Phys. Rev. Lett.* 4, 351 (1960).
110. H. Frohlich, *Adv. Phys.* 3, 325 (1954).
111. J. Conradi and R. R. Haering, *Phys. Rev. Lett.* 20, 1344 (1968).
112. E. Gross, S. Permogrov, V. Travnikov, and A. Selkin, *J. Phys. Chem. Solids* 31, 2595 (1970).
113. S. Permogrov, in "Modern Problems in Condensed Matter Sciences," (E. I. Rashba and M. D. Sturge, Eds.), Vol. 2. North Holland, Amsterdam, 1982.
114. Y. S. Park and J. R. Schneider, *Phys. Rev. Lett.* 21, 798 (1968).
115. A. A. Klochikhin, S. A. Permogrov, and A. N. Reznitsky, *Sov. Phys. JETP* 44, 1176 (1976).
116. Y. Toyozawa, *Prog. Theor. Phys.* 20, 53 (1958). Y. Toyozawa, *J. Phys. Chem. Solids* 25, 59 (1964).
117. B. Segall and G. D. Mahan, *Phys. Rev.* 171, 935 (1968).
118. B. Segall, *Phys. Rev.* 150, 734 (1966); 163, 769 (1967). G. E. Hite, D. T. F. Marple, M. Aven, and B. Segall, 156, 850 (1967).
119. B. Segall, in "Proceedings of the IX Conference on the Physics of Semiconductors" (S. M. Ryvkin, Ed.), p. 425. Moscow, 1968.
120. S. Rudin, T. L. Reinecke, and B. Segall, *Phys. Rev. B* 42, 11218 (1990).
121. A. Kasi Viswanath, E. J. Shin, J. I. Lee, S. Yu, D. Kim, B. Kim, Y. Choi, and C. H. Hong, *J. Appl. Phys.* 83, 2272 (1998).
122. C. Chen and C. Yeh, *Adv. Mater.* 12, 738 (2000).
123. C. Chen, C. Yeh, C. Chen, M. Yu, H. Liu, J. Wu, K. Chen, L. Chen, J. Peng, and Y. Chen, *J. Am. Chem. Soc.* 123, 2791 (2001).
124. M. Lee, H. Z. Twu, C. Chen, and C. Chen, *Appl. Phys. Lett.* 79, 3693 (2001).
125. M. He, I. Minus, P. Zhou, S. Mohammed, J. Halpern, R. Jacobs, W. L. Sarney, L. S. Riba, and R. D. Vispute, *Appl. Phys. Lett.* 77, 3731 (2000).
126. X. Chen, J. Li, Y. Cao, Y. Lan, H. Li, M. He, C. Wang, Z. Zhang, and Z. Qiao, *Adv. Mater.* 12, 1432 (2000).
127. C. C. Tang, S. S. Fan, H. Y. Dang, P. Li, and Y. M. Liu, *Appl. Phys. Lett.* 77, 1961 (2000).
128. H. Y. Peng, X. T. Zhou, N. Wang, Y. F. Zheng, L. S. Liao, W. S. Shi, C. S. Lee, and S. T. Lee, *Chem. Phys. Lett.* 327, 263 (2000).
129. X. Duan and C. M. Lieber, *J. Am. Chem. Soc.* 122, 188 (2000).
130. Y. Huang, X. Duan, Y. Cui, L. J. Lauhon, K. Kim, and C. M. Lieber, *Science* 294, 1313 (2001).
131. J. R. Kim, H. M. So, J. W. Park, J. J. Kim, J. Kim, C. J. Lee, and S. C. Lyu, *Appl. Phys. Lett.* 80, 3548 (2002).
132. (a) C. H. Liang, L. C. Chen, J. S. Hwang, K. H. Chen, Y. T. Hung, and Y. F. Chen, *Appl. Phys. Lett.* 81, 22 (2002). (b) H. Masuda and K. Fukuda, *Science* 268, 1466 (1995). (c) M. Saito, K. Kirihara, T. Taniguchi, and M. Miyagi, *Appl. Phys. Lett.* 55, 607 (1994). (d) D. Routkevich, T. Bigioni, and M. Moskovits, *J. Phys. Chem.* 100, 14037 (1996). (e) D. Routkevich, A. A. Tager, J. Haruyama, D. Almawlawi, M. Koskovits, and J. M. Xu, *IEEE Trans. Electron Devices* 42, 1646 (1996). (f) D. Al-Mawlawi, C. Z. Liu, and M. Moskovits, *J. Mater. Res.* 9, 1014 (1998). (g) S. A. Sapp, B. B. Lakshmi, and C. R. Martin, *Adv. Mater.* 11, 402 (1999). (h) G. S. Cheng, L. D. Zhang, and Y. Zhu, *Appl. Phys. Lett.* 75, 2455 (1999). (i) J. Zhang, L. D. Zhang, X. F. Wang, C. H. Liang, X. S. Peng, and Y. W. Wang, *J. Chem. Phys.* 115, 5714 (2001). (j) M. Yoshijawa, A. Kikuchi, N. Fujita, K. Kushi, H. Sasamoto, and K. Kishino, *J. Cryst. Growth* 189–190, 138 (1998).
133. H. Dai, W. W. Wong, Y. Z. Lu, S. Fan, and C. Lieber, *Nature* 375, 769 (1995).
134. W. Wong, B. W. Maynor, L. D. Burns, and C. M. Lieber, *Chem. Mater.* 8, 2041 (1996).
135. W. Han, S. Fan, Q. Li, and Y. Hu, *Science* 277, 1287 (1997).
136. W. Han, S. Fan, Q. Li, B. Gu, X. Zhang, and D. Yu, *Appl. Phys. Lett.* 71, 2271 (1997).
137. W. Han, Y. Bando, K. Kurashima, and T. Sato, *Appl. Phys. Lett.* 73, 3085 (1998).
138. W. Han, Ph. Redlich, F. Ernst, and M. Ruhle, *Appl. Phys. Lett.* 75, 1875 (1999).
139. W. Han, P. Redlich, F. Ernst, and M. Ruhle, *Appl. Phys. Lett.* 76, 652 (2000).
140. T. W. Ebbesen (Ed.) "Carbon Nanotubes: Preparation and Properties." CRC, Boca Raton, 1997.
141. R. Bacon, *J. Appl. Phys.* 283, 31 (1960).
142. W. Kratschmer, L. D. Lamb, K. Fostiropoulos, and D. R. Huffman, *Nature* 347, 354 (1990).
143. S. Iijima, *Nature* 354, 56 (1991).
144. J. Sloan, J. Cook, M. L. H. Green, J. L. Hutchison, and R. Tenne, *J. Mater. Chem.* 7, 1089 (1997).
145. S. C. Tsang, Y. K. Chen, P. J. F. Harris, and M. L. H. Green, *Nature* 372, 159 (1994).
146. C. Guerret-Piecourt, Y. Le Bouar, A. LLoiseau, and H. Pascard, *Nature* 372, 761 (1994).
147. P. M. Ajayan, O. Stephan, P. Redlich, and C. Colliex, *Nature* 375, 564 (1995).
148. D. Ugarte, A. Chatelain, and W. A. de Heer, *Science* 274, 1897 (1996).
149. M. Terrones, N. Grobert, N. W. K. Hsu, Y. Q. Zhu, W. B. Hu, H. Terrones, J. P. Hare, H. W. Kroto, and D. R. M. Walton, *MRS Bull.* 24, 43 (1999).
150. N. Demoncy, O. Stephan, N. Brun, C. Colliex, A. Loiseau, and H. Pascard, *Eur. Phys. J. B* 4, 147 (1998).
151. I. M. Tiginyanu, A. Sarua, G. Irmer, J. Monecke, S. M. Hubbard, D. Pavlidis, and V. Valiaev, *Phys. Rev. B* 64, 233317 (2001).
152. H. M. Kim, D. S. Kim, T. W. Kang, Y. H. Cho, and K. S. Chung, *Appl. Phys. Lett.* 81, 2193 (2002).
153. W. Han and A. Zettl, *Appl. Phys. Lett.* 80, 303 (2002).
154. M. Terrones, N. Grobert, J. Livares, J. P. Zhang, H. Terrones, K. Kordatos, H. K. Hsu, J. P. Hare, P. D. Townsend, K. Prassides, A. K. Cheetham, H. W. Kroto, and D. R. M. Walton, *Nature* 388, 52 (1997).
155. C. N. Rao, R. Sen, B. C. Satishkumar, and J. Govindaraj, *J. Chem. Soc., Chem. Commun.* 15, 1525 (1998).
156. W. Han, P. Kohler-Redlich, F. Ernst, M. Rhle, N. Grobert, W. K. Hsu, B. H. Chang, Y. Q. Zhu, H. W. Kroto, D. R. M. Walton, M. Terrones, and H. Terrones, *Appl. Phys. Lett.* 77, 1807 (2000).
157. W. Han, J. Cumings, and A. Zettl, *Appl. Phys. Lett.* 78, 2769 (2001).
158. R. S. Wagner and W. C. Ellis, *T. Metall. Soc. AIME* 233, 1054 (1965).
159. J. V. Milewski, F. D. Gac, J. J. Petrovic, and S. R. Skaggs, *J. Mater. Sci.* 20, 1160 (1985).
160. W. Han and A. Zettl, *Appl. Phys. Lett.* 81, 5051 (2002).
161. Z. W. Pan, Z. R. Dai, and Z. L. Wang, *Science* 291 1947 (2001).
162. Z. Y. Li, X. L. Chen, H. J. Li, Q. Y. Tu, Z. Yang, X. P. Yu, and B. Q. Hu, *Appl. Phys. A* 72, 629 (2001).



163. J. Li, Z. Qiao, X. Chen, Y. Cao, and M. He, *J. Phys. Condens. Matter* 13, L285 (2001).
164. S. Y. Bae, H. W. Seo, J. Park, H. Yang, J. C. Park, and S. Y. Lee, *Appl. Phys. Lett.* 81, 126 (2002).
165. S. J. Pearton, J. C. Zolper, R. J. Shul, and F. Ren, *J. Appl. Phys.* 86, 1 (1999).
166. D. Peyrade, Y. Chen, L. Manin-Ferlazzo, A. Lebib, N. Grandjean, D. Coquillat, R. Legros, and J. Lascaray, *Microelectron. Eng.* 57–58, 843 (2001).
167. F. Demangeot, J. Gleize, J. Frandon, M. A. Renucci, M. Kuball, D. Peyrade, L. Manin-Ferlazzo, Y. Chen, and N. Grandjean, *J. Appl. Phys.* 91, 6520 (2002).
168. F. Demangeot, J. Gleize, J. Frandon, M. A. Renucci, M. Kuball, D. Peyrade, L. Manin-Ferlazzo, Y. Chen, and N. Grandjean, *J. Appl. Phys.* 91, 2866 (2002).
169. P. Millet, A. Calka, J. S. Williams, and G. J. H. Vantenaar, *Appl. Phys. Lett.* 63, 2505 (1993).
170. J. Hwang, J. P. Campbell, J. Kozubowski, S. A. Hanson, J. F. Evans, and W. L. Gladfelter, *Chem. Mater.* 7, 517 (1995).
171. R. C. Schoonmaker and C. E. Burton, *Inorg. Synth.* 7, 16 (1963).
172. W. C. Johnson, J. B. Parsons, and M. C. Crew, *J. Phys. Chem.* 36, 2651 (1932).
173. R. Juza and H. Hahn, *Anorg. Allg. Chem.* 244, 111 (1940).
174. M. Mizuta, S. Fujieda, Y. Matsumoto, and T. Kawamura, *Jpn. J. Appl. Phys.* 25, L945 (1986).
175. M. J. Paisley, Z. Sitar, J. B. Posthill, and R. F. Davis, *J. Vac. Sci. Technol. A* 7, 701 (1989).
176. R. Powell, C. A. Tomasch, Y. W. Kim, J. A. Thornton, and J. E. Greene, "Fall Meeting, Materials Research Society," Pittsburgh, 1989.
177. J. F. Janik and R. L. Wells, *Chem. Mater.* 8, 2708 (1996).
178. Y. Xie, Y. Qian, W. Wang, S. Zhang, and Y. Zhang, *Science* 272, 1926 (1996).
179. H. D. Li, H. B. Yang, S. Yu, G. T. Zou, Y. D. Li, S. Y. Liu, and S. R. Yang, *Appl. Phys. Lett.* 69, 1285 (1996).
180. M. Benaissa, M. Jose-Yacamán, J. M. Hernandez, Bokhimi, K. E. Gonslaves, and G. Carlson, *Phys. Rev. B* 54, 17763 (1996).
181. J. L. Coffey, M. A. Johnson, L. Zhang, R. L. Wells, and J. F. Janik, *Chem. Mater.* 9, 2671 (1997).
182. J. Janik and R. L. Wells, *Inorg. Chem.* 36, 4135 (1997).
183. Y. Wang and N. Herron, *J. Phys. Chem.* 92, 4988 (1988).
184. H. Yamane, M. Shimada, S. J. Clarke, and F. J. DiSalvo, *Chem. Mater.* 9, 413 (1997).
185. K. E. Gonsalves, G. Carlson, S. P. Rangarajan, M. Benaissa, and K. J. Jose-Yacamán, *J. Mater. Chem.* 6, 1451 (1996).
186. R. A. Fischer, A. Miehr, E. Herdtweck, M. R. Mattner, O. Ambacher, T. Metzger, E. Born, S. Weinkauff, C. R. Pulham, and S. Parsons, *Chem. —Eur. J.* 2, 1353 (1996).
187. J. D. Houmes and H. C. zur Loye, *Chem. Mater.* 8, 2551 (1996).
188. B. Vaidyanathan and K. J. Rao, *Chem. Mater.* 9, 1196 (1997).
189. A. Miehr, M. R. Mattner, and R. A. Fischer, *Organometallics* 15, 2053 (1996).
190. A. C. Frank, F. Stowasser, H. Sussek, H. Pritzkow, C. R. Miskys, O. Ambacher, M. Giersig, and R. A. Fischer, *J. Am. Chem. Soc.* 120, 3512 (1998).
191. A. C. Frank and R. A. Fischer, *Adv. Mater.* 10, 961 (1998).
192. J. A. Jegier, S. McKernan, and W. Gladfelter, *Chem. Mater.* 10, 2041 (1998).
193. (a) S. T. Barry, S. A. Ruoff, and A. L. Ruoff, *Chem. Mater.* 10, 2571 (1998). (b) H. G. Grimmiess, R. Groth, and J. Z. Maak, *Naturforsch.* 15a, 799 (1960).
194. O. I. Micic, S. P. Ahrenkiel, D. Bertram, and A. Nozik, *Appl. Phys. Lett.* 75, 478 (1999).
195. J. L. Coffey, T. Waldek Zerda, R. Appel, R. L. Wells, and J. F. Janik, *Chem. Mater.* 11, 20 (1999).
196. A. Purdy, *Chem. Mater.* 11, 1648 (1999).
197. J. A. Jegier, S. McKernan, A. Purdy, and W. L. Gladfelter, *Chem. Mater.* 12, 1003 (2000).
198. A. Manz, A. Birkner, M. Kolbe, and R. A. Fischer, *Adv. Mater.* 12, 569 (2000).
199. C. M. Balkas and R. F. Davis, *J. Am. Ceram. Soc.* 79, 2309 (1996).
200. G. Wood, E. A. Pruss, and R. T. Paine, *Chem. Mater.* 13, 12 (2001).
201. T. T. Kodas and M. J. Hampden-Smith, "Aerosol Processing of Materials," Wiley, New York, 1999.
202. M. K. Akhtar and S. E. Pratsinis, in "Carbide, Nitride and Boride Materials Synthesis and Processing (A. W. Weimer, Ed.), Chapman and Hall, London, 1997.
203. E. A. Pruss, G. L. Wood, W. J. Kroenke, and R. T. Paine, *Chem. Mater.* 12, 19 (2000).
204. E. A. Pruss, T. Tinsley, W. J. Kroenke, and R. Paine (unpublished results).
205. L. Grocholl, J. Wang, and E. G. Gillan, *Chem. Mater.* 13, 4290 (2001).
206. H. D. Li, S. L. Zhang, H. B. Yang, G. T. Zou, Y. Y. Yang, K. T. Yue, X. H. Wu, and Y. Yan, *J. Appl. Phys.* 91, 4562 (2002).
207. M. Copel, M. C. Reuter, E. Kaxiras, and R. M. Tromp, *Phys. Rev. Lett.* 63, 632 (1989).
208. D. Leonard, M. Krishnamurthy, C. M. Reaves, S. P. Denbaars, and P. M. Petroff, *Appl. Phys. Lett.* 63, 3203 (1993).
209. R. Notzel, J. Temmyo, and T. Tamamura, *Nature* 369, 131 (1994).
210. J. Oshinowo, M. Nishioka, S. Ishida, and Y. Arakawa, *Appl. Phys. Lett.* 65, 1421 (1994).
211. N. Carlsson, W. Seifert, A. Petersson, P. Castrillo, M. E. Pistol, and L. Samuelson, *Appl. Phys. Lett.* 65, 3093 (1994).
212. M. Sapanen, H. Lipsanen, and J. Ahopelto, *Appl. Phys. Lett.* 67, 3768 (1995).
213. A. Ponchet, A. L. Corre, H. L'Harodon, B. Lambert, and S. Salaun, *Appl. Phys. Lett.* 67, 1850 (1995).
214. V. Dmitriev, K. Irvine, A. Zubrilov, D. Tsvetkov, V. Nikolaev, M. Jakobson, D. Nelson, and A. Sitnikova, in "Gallium Nitride and Related Materials" (R. D. Dupuis, J. A. Edmond, F. A. Ponce, and S. Nakamura, Eds.), Materials Research Society, Pittsburgh, 1996.
215. S. Tanaka, S. Iwai, and Y. Aoyagi, *Appl. Phys. Lett.* 69, 4096 (1996).
216. S. Tanaka, H. Hirayama, Y. Aoyagi, Y. Narukawa, Y. Kawakami, S. Fujita, and S. Fujita, *Appl. Phys. Lett.* 71, 1299 (1997).
217. B. Daudin, F. Widmann, G. Feuillet, Y. Samson, M. Arlery, and J. L. Rouviere, *Phys. Rev. B* 56, R 7069 (1997).
218. F. Widmann, B. Daudin, G. Feuillet, Y. Samson, J. L. Rouviere, and N. Pelekanos, *J. Appl. Phys.* 83, 7618 (1998).
219. A. Petersson, A. Gustafsson, L. Samuelson, S. Tanaka, and Y. Aoyagi, *Appl. Phys. Lett.* 74, 3513 (1999).
220. M. Arlery, J. L. Rouviere, F. Widmann, B. Daudin, G. Feuillet, and H. Mariette, *Appl. Phys. Lett.* 74, 3287 (1999).
221. B. Damilano, N. Grandjean, F. Semond, J. Massier, and M. Leroux, *Appl. Phys. Lett.* 75, 962 (1999).
222. M. Kuball, J. Gleize, S. Tanaka, and Y. Aoyagi, *Appl. Phys. Lett.* 78, 987 (2001).
223. G. Mula, C. Adelman, S. Moehl, J. Oullier, and B. Daudin, *Phys. Rev. B* 64, 195406 (2001).
224. A. D. Andreev and E. P. O'Reilly, *Appl. Phys. Lett.* 79, 521 (2001).
225. J. Gleize, F. Demangeot, J. Frandon, M. A. Renucci, M. Kuball, B. Damilano, N. Grandjean, and J. Massies, *Appl. Phys. Lett.* 79, 686 (2001).
226. V. Chamrad, T. H. Metzger, E. Bellet-Amalric, B. Daudin, C. Adelman, H. Mariette, and G. Mula, *Appl. Phys. Lett.* 79, 1971 (2001).
227. J. A. Wolk, K. M. Yu, E. D. Bourret-Courchesne, and E. Johnson, *Appl. Phys. Lett.* 70, 2268 (1997).
228. X. W. Lin, M. Behar, R. Maltez, W. Swider, Z. Liliental-Weber, and J. Washburn, *Appl. Phys. Lett.* 67, 2699 (1995).
229. C. W. White, J. D. Buda, J. G. Zhu, S. P. Withrow, and M. J. Aziz, *Appl. Phys. Lett.* 68, 2389 (1996).

230. E. Borsella, M. A. Garcia, G. Mattei, C. Maurizio, P. Mazzoldi, E. Cattaruzza, F. Gonella, G. Battaglin, A. Quaranta, and F. D'Acapito, *J. Appl. Phys.* 90, 4467 (2001).
231. D. Huang, M. A. Reshchikov, F. Yun, T. King, A. A. Baski, and H. Morkoc, *Appl. Phys. Lett.* 80, 216 (2002).
232. C. Adelman, J. Brault, J. L. Rouviere, H. Mariette, G. Mula, and B. Daudin, *J. Appl. Phys.* 91, 5498 (2002).
233. M. Miyamura, K. Tachibana, and Y. Arakawa, *Appl. Phys. Lett.* 80, 3937 (2002).
234. D. Leonard, K. Pond, and P. M. Petroff, *Phys. Rev. B* 50, 11687 (1994).
235. C. W. Hu, A. Bell, F. A. Ponce, D. J. Smith, and I. S. T. Tsong, *Appl. Phys. Lett.* 81, 3236 (2002).
236. C. Adelman, N. Gogneau, E. Sarigiannidou, J. L. Rouviere, and B. Daudin, *Appl. Phys. Lett.* 81, 3064 (2002).
237. J. E. Northrup, J. Neugebauer, R. M. Feenstra, and A. R. Smith, *Phys. Rev. B* 61, 9932 (2000).
238. W. Seifert, N. Carlsson, M. Miller, M. E. Pistol, L. Samuelson, and L. R. Wallenberg, *Prog. Cryst. Growth Ch.* 33, 423 (1996).
239. D. Brimberg, M. Grundmann, and N. N. Ledentsov, "Quantum Dot Heterostructures." Wiley, Chichester, UK, 1999.
240. A. Salvador, G. Liu, W. Kim, O. Aktas, A. Botchkarev, and H. Morkoc, *Appl. Phys. Lett.* 67, 3322 (1995).
241. M. Smith, J. Y. Lin, H. X. Jiang, A. Salvador, A. Botchkarev, W. Kim, and H. Morkoc, *Appl. Phys. Lett.* 69, 2453 (1996).
242. R. Cingolani, G. Coli, R. Rinaldi, L. Calcagnile, H. Tang, A. Botchkarev, W. Kim, A. Salvador, and H. Morkoc, *Phys. Rev. B* 56, 1491 (1997).
243. R. A. Mair, K. C. Zeng, J. Y. Lin, H. X. Jiang, B. Zhang, L. Dai, H. Tang, A. Botchkarev, W. Kim, and H. Morkoc, *Appl. Phys. Lett.* 71, 2898 (1997).
244. W. Shan, S. Xu, B. D. Little, X. C. Xie, J. J. Song, G. E. Bulman, H. S. Kong, M. T. Leonard, and S. Krishnankutty, *J. Appl. Phys.* 82, 3158 (1997).
245. K. C. Zeng, J. Y. Lin, H. X. Jiang, A. Salvador, G. Popovici, H. Tang, W. Kim, and H. Morkoc, *Appl. Phys. Lett.* 71, 1368 (1997).
246. N. Grandjean and J. Massies, *Appl. Phys. Lett.* 73, 1260 (1998).
247. K. C. Zeng, R. Mair, J. Y. Lin, H. X. Jiang, W. W. Chow, A. Botchkarev, and H. Morkoc, *Appl. Phys. Lett.* 73, 2476 (1998).
248. M. Leroux, N. Grandjean, M. Laugt, J. Massies, B. Gil, P. Lefebvre, and P. Bigenwald, *Phys. Rev. B* 58, R 13371 (1998).
249. J. S. Im, H. Kollmer, J. Off, A. Sohmer, F. Scholz, and A. Hangleiter, *Phys. Rev. B* 57, R 9435 (1998).
250. P. Lefebvre, J. Allegre, B. Gil, A. Kavokine, H. Mathieu, W. Kim, A. Salvador, A. Botchkarev, and H. Morkoc, *Phys. Rev. B* 57, R 9447 (1998). B. Gil, P. Lefebvre, A. Allegre, H. Mathieu, N. Grandjean, M. Leroux, J. Massies, P. Bigenwald, and P. Christol, *Phys. Rev. B* 59, 10246 (1999). P. Lefebvre, J. Allegre, and H. Mathieu, *Mat. Sci. Eng. B* 59, 307 (1999). P. Lefebvre, J. Allegre, B. Gil, H. Mathieu, N. Grandjean, M. Leroux, J. Massies, and P. Bigenwald, *Phys. Rev. B* 59, 15363 (1999). P. Lefebvre, M. Gallart, T. Taliercio, B. Gil, J. Allegre, H. Mathieu, N. Grandjean, M. Leroux, J. Massier, and P. Bigenwald, *Phys. Status Solidi B* 216, 361 (1999). T. Taliercio, P. Lefebvre, M. Gallart, and A. Morel, *J. Phys. Condens. Matter* 13, 7027 (2001).
251. N. Grandjean, J. Massies, and M. Leroux, *Appl. Phys. Lett.* 74, 2361 (1999).
252. T. Matsuoka, H. Tanaka, T. Sasaki, and A. Katsui, *Inst. Phys. Conf. Ser.* 106, 141 (1989).
253. T. Nagamoto, T. Kuboyama, H. Minamino, and O. Omoto, *Jpn. J. Appl. Phys.* 28, L1334 (1989).
254. N. Yoshimoto, T. Matsuoka, T. Sasaki, and A. Katsui, *Appl. Phys. Lett.* 59, 2251 (1991).
255. S. Nakamura and T. Mukai, *Jpn. J. Appl. Phys.* 31, L1457 (1992).
256. S. Nakamura, *J. Microelec.* 25, 651 (1994).
257. M. Koike, S. Yamasaki, S. Nagai, N. Koide, S. Asami, H. Amano, and I. Akasaki, *Appl. Phys. Lett.* 68, 1403 (1996).
258. S. Chichibu, T. Azuhata, T. Sota, and S. Nakamura, *Appl. Phys. Lett.* 69, 4188 (1996).
259. Y. Narukawa, Y. Kawakami, M. Funato, S. Fujita, S. Fujita, and S. Nakamura, *Appl. Phys. Lett.* 70, 981 (1997).
260. T. Takeuchi, H. Takeuchi, S. Sota, H. Sakai, H. Amano, and I. Akasaki, *Jpn. J. Appl. Phys.* 36, L177 (1997). T. Takeuchi, S. Sota, M. Katsuragawa, M. Komori, H. Takeuchi, H. Amano, and I. Akasaki, *Jpn. J. Appl. Phys.* 36, L382 (1997).
261. S. Chichibu, T. Azuhata, T. Sota, and S. Nakamura, *Appl. Phys. Lett.* 70, 2822 (1997).
262. J. R. Mullhauser, B. Jenichen, M. Wassermeier, O. Brandt, and K. H. Ploog, *Appl. Phys. Lett.* 71, 909 (1997).
263. S. Chichibu, K. Wada, and S. Nakamura, *Appl. Phys. Lett.* 71, 2346 (1997).
264. W. Shan, J. J. Song, Z. C. Feng, M. Schurman, and R. A. Stall, *Appl. Phys. Lett.* 71, 2433 (1997). W. Shan, P. Perlin, J. W. Ager III, W. Walukiewicz, E. E. Haller, M. D. McCuskey, N. M. Johnson, and D. P. Bour, *Appl. Phys. Lett.* 73, 1613 (1998). W. Shan, J. W. Ager III, W. Walukiewicz, E. E. Haller, M. D. McCuskey, N. M. Johnson, and D. P. Bour, *Phys. Rev. B* 58, R10191 (1998).
265. S. Chichibu, M. Arita, H. Nakanishi, J. Nishio, L. Sugiura, Y. Kokubun, and K. Itaya, *J. Appl. Phys.* 83, 2860 (1998).
266. H. Hirayama, S. Tanaka, P. Ramvall, and Y. Aoyagi, *Appl. Phys. Lett.* 72, 1736 (1998).
267. A. Vertikov, M. Kuball, A. V. Nurmikko, Y. Chen, and S. Y. Wang, *Appl. Phys. Lett.* 72, 2645 (1998).
268. M. D. McCluskey, C. G. Van de Walle, C. P. Master, L. T. Romano, and N. M. Johnson, *Appl. Phys. Lett.* 72, 2725 (1998).
269. L. T. Romano, B. S. Krusor, M. D. McCluskey, D. P. Bour, and K. Nauka, *Appl. Phys. Lett.* 73, 1757 (1998).
270. I. Lo, K. Y. Hsieh, S. L. Hwang, L. W. Tu, W. C. Mitchel, and A. W. Saxler, *Appl. Phys. Lett.* 74, 2167 (1999).
271. A. Kasi Viswanath, J. I. Lee, D. Kim, and H. G. Lee (unpublished).
272. I. Ho and G. B. Stringfellow, *Appl. Phys. Lett.* 69, 2701 (1996).
273. Y. Narukawa, Y. Kawakami, S. Fujita, S. Fujita, and S. Nakamura, *Phys. Rev. B* 55, R 1938 (1997).
274. S. F. Chichibu, K. Wada, J. Mullhauser, O. Brandt, K. H. Ploog, T. Mizutani, A. Setoguchi, R. Nakai, M. Sugiyama, H. Nakanishi, K. Korii, T. Deguchi, T. Sota, and S. Nakamura, *Appl. Phys. Lett.* 76, 1671 (2000).
275. S. F. Chichibu, T. Azuhata, T. Sota, T. Mukai, and S. Nakamura, *J. Appl. Phys.* 88, 5153 (2000).
276. S. F. Chichibu, T. Azuhata, T. Sota, and T. Mukai, *Appl. Phys. Lett.* 79, 341 (2001).
277. G. Li, S. J. Chua, J. H. Teng, W. Wang, Z. C. Feng, Y. H. Huang, and T. Osipowicz, *J. Vac. Sci. Technol. B* 17, 1507 (1999).
278. P. Li, S. J. Chua, G. Li, W. Wang, X. C. Wang, and Y. P. Guo, *Phys. Status Solidi B* 216, 145 (1999).
279. X. Chang, S. J. Chua, W. Liu, and P. Li, *Phys. Status Solidi B* 216, 307 (1999).
280. (a) M. Hao, S. J. Chua, X. H. Zhang, W. Wang, E. K. Sia, L. S. Wang, A. Ramam, P. Li, and W. Liu, *Phys. Rev. B* 63, 121308 (2001). (b) D. Kopolnek, S. Keller, R. D. Underwood, P. Kozodoy, S. P. Den Baars, and U. K. Mishra, *J. Cryst. Growth* 189–190, 83 (1998). (c) S. Keller, B. P. Keller, M. S. Minsky, J. E. Bowers, U. K. Mishra, S. P. Den Baars, and W. Seifert, *J. Cryst. Growth* 189–190, 29 (1998). (d) E. Oh, C. S. Sone, H. Park, O. H. Nam, and Y. Park, *Phys. Status Solidi B* 216, 487 (1999).
281. E. S. Jeon, V. Kozlov, Y. K. Song, A. Vertikov, M. Kuball, A. V. Nurmikko, H. Liu, C. Chen, R. S. Kern, C. P. Kuo, and M. G. Craford, *Appl. Phys. Lett.* 69, 4194 (1996).
282. C. K. Sun, T. L. Chiu, S. Keller, G. Wang, M. S. Minsky, S. P. DenBaars, and J. E. Bowers, *Appl. Phys. Lett.* 71, 425 (1997).
283. M. Kuball, E. S. Jeon, Y. K. Song, A. V. Nurmikko, P. Kozodoy, A. Abare, S. Keller, L. A. Coldren, S. P. DenBaars, and D. A. Steigerwald, *Appl. Phys. Lett.* 70, 2580 (1997).

284. W. Li, P. Bergman, B. Monemar, H. Amano, and I. Akasaki, *J. Appl. Phys.* 81, 1005 (1997).
285. K. C. Zeng, M. Smith, J. Y. Lin, H. X. Jiang, J. C. Robert, E. L. Piner, F. G. McIntosh, S. M. Bedair, and J. Zavada, *J. Vac. Sci. Technol. B* 15, 1139 (1997).
286. Y. H. Cho, G. H. Gainer, A. J. Fischer, J. J. Song, S. Keller, U. K. Mishra, and S. P. DenBaars, *Appl. Phys. Lett.* 73, 1370 (1998).
287. A. Satake, Y. Masumoto, T. Miyajima, T. Asatsuma, F. Nakamura, and M. Ikeda, *Phys. Rev. B* 57, R2041 (1998).
288. Y. H. Cho, J. J. Song, S. Keller, M. S. Minsky, E. Hu, U. K. Mishra, and S. P. DenBaars, *Appl. Phys. Lett.* 73, 1128 (1998).
289. T. J. Schmidt, Y. H. Cho, G. H. Gainer, J. J. Song, S. Keller, U. K. Mishra, and S. P. DenBaars, *Appl. Phys. Lett.* 73, 1892 (1998).
290. Y. Narukawa, S. Saijou, Y. Kawakami, S. Fujita, T. Mukai, and S. Nakamura, *Appl. Phys. Lett.* 74, 558 (1999).
291. S. F. Chichibu, H. Marchand, M. S. Minsky, S. Keller, P. T. Fini, J. P. Ibbetson, S. B. Fleischer, J. S. Speck, J. E. Bowers, E. Hu, U. K. Mishra, S. P. DenBaars, T. Deguchi, T. Sota, and S. Nakamura, *Appl. Phys. Lett.* 74, 1460 (1999).
292. Y. Narukawa, Y. Kawakami, S. Fujita, and S. Nakamura, *Phys. Rev. B* 59, 10283 (1999).
293. T. Taliercio, P. Lefebvre, A. Morel, M. Gallart, J. Allegre, B. Gil, H. Mathieu, N. Grandjean, and J. Massies, *Mater. Sci. Eng., B* 82, 151 (2001).
294. P. Lefebvre, A. Morel, M. Gallart, T. Taliercio, J. Allegre, B. Gil, H. Mathieu, B. Damilano, N. Grandjean, and J. Massies, *Appl. Phys. Lett.* 78, 1252 (2001).
295. P. Lefebvre, T. Taliercio, A. Morel, M. Gallart, B. Gil, H. Mathieu, B. Damilano, N. Grandjean, and J. Massies, *Appl. Phys. Lett.* 78, 1538 (2001).
296. T. Kuroda, A. Tackeuchi, and T. Sota, *Appl. Phys. Lett.* 76, 3753 (2000).
297. U. Ozgur, M. J. Bergmann, H. C. Casey Jr., H. O. Everitt, A. C. Abare, S. Keller, and S. P. DenBaars, *Appl. Phys. Lett.* 77, 109 (2000).
298. G. Frankowsky, F. Steuber, V. Harle, F. Scholz, and A. Hangleiter, *Appl. Phys. Lett.* 68, 3746 (1996).
299. C. T. Sun, J. W. Yang, Q. Chen, B. W. Lim, M. Z. Anwar, M. A. Khan, H. Temkin, D. Weismann, and I. Brenner, *Appl. Phys. Lett.* 69, 668 (1996).
300. I. K. Shmagin, J. F. Muth, R. M. Kolbas, S. Krishnankutty, S. Keller, U. K. Mishra, and S. P. DenBaars, *J. Appl. Phys.* 81, 2021 (1997).
301. C. J. Sun, M. Z. Anwar, Q. Chen, J. W. Yang, M. A. Khan, M. S. Shur, A. D. Bykhovski, Z. Liliental-Weber, C. Kisielowski, M. Smith, J. Y. Lin, and H. X. Jiang, *Appl. Phys. Lett.* 70, 2978 (1997).
302. H. X. Jiang, J. Y. Lin, M. A. Khan, Q. Chen, and J. W. Yang, *Appl. Phys. Lett.* 70, 984 (1997).
303. Y. K. Song, M. Kuball, A. V. Nurmikko, G. E. Bulman, K. Dover-spice, S. T. Sheppard, T. W. Weeks, M. Leonard, H. S. Kong, H. Dieringer, and J. Edmond, *Appl. Phys. Lett.* 72, 1418 (1998).
304. S. Bidnyk, T. J. Schmidt, Y. H. Cho, G. H. Gainer, J. J. Song, S. Keller, U. K. Mishra, and S. P. DenBaars, *Appl. Phys. Lett.* 72, 1623 (1998).
305. T. J. Schmit, Y. H. Cho, G. H. Gainer, J. J. Song, S. Keller, U. K. Mishra, and S. P. DenBaars, *Appl. Phys. Lett.* 73, 560 (1998). T. J. Schmidt, S. Bidnyk, Y. H. Cho, A. J. Fischer, J. J. Song, S. Keller, U. K. Mishra, and S. P. DenBaars, *Appl. Phys. Lett.* 73, 3689 (1998).
306. C. C. Chen, H. W. Chuang, G. C. Chi, C. C. Chu, and J. I. Chyi, *Appl. Phys. Lett.* 77, 3758 (2000).
307. S. Nakamura, *J. Vac. Sci. Technol., A* 13, 705 (1995).
308. S. Nakamura, *IEEE J. Sel. Top. Quant.* 4, 483 (1998).
309. I. Akasaki and H. Amano, *Jpn. J. Appl. Phys.* 36, 5393 (1997).
310. D. P. Bour, M. Kneissl, L. T. Romano, M. D. McCluskey, C. G. van de Walle, B. S. Krusor, R. M. Donaldson, J. Walker, C. J. Dunnrowicz, and N. M. Johnson, *IEEE J. Sel. Top. Quant.* 4, 498 (1998).
311. A. C. Abare, M. P. Mack, M. Hansen, R. K. Sink, P. Kozodoy, S. Keller, J. S. Speck, J. E. Bowers, U. K. Mishra, L. A. Coldren, and S. P. DenBaars, *IEEE J. Sel. Top. Quant.* 4, 505 (1998).
312. S. Nakamura, M. Senoh, and T. Mukai, *Appl. Phys. Lett.* 62, 2390 (1993).
313. S. Nakamura, M. Senoh, and T. Mukai, *Jpn. J. Appl. Phys.* 32, L8 (1993).
314. S. Nakamura, T. Mukai, and M. Senoh, *J. Appl. Phys.* 76, 8189 (1994).
315. S. Nakamura, T. Mukai, and M. Senoh, *Appl. Phys. Lett.* 64, 1687 (1994).
316. S. Nakamura, M. Senoh, N. Iwasa, and S. Nagahama, *Jpn. J. Appl. Phys.* 34, L797 (1995).
317. S. Nakamura, M. Senoh, N. Iwasa, S. Nagahama, T. Yamada, and T. Makai, *Jpn. J. Appl. Phys.* 34, L1332 (1995).
318. H. Sakai, T. Koide, H. Suzuki, M. Yamaguchi, S. Yamasaki, M. Koike, H. Amano, and I. Akasaki, *Jpn. J. Appl. Phys.* 34, L1429 (1995).
319. S. Nakamura, M. Senoh, S. Nagahama, N. Iwasa, T. Yamada, T. Matsushita, H. Kiyoku, and Y. Sugimoto, *Jpn. J. Appl. Phys.* 35, L74 (1996).
320. S. Nakamura, M. Senoh, S. Nagahama, N. Iwasa, T. Yamada, T. Matsushita, H. Kiyoku, and Y. Sugimoto, *Jpn. J. Appl. Phys.* 35, L217 (1996).
321. S. Nakamura, M. Senoh, S. Nagahama, N. Iwasa, T. Yamada, T. Matsushita, H. Kiyoku, and Y. Sugimoto, *Appl. Phys. Lett.* 68, 2105 (1996).
322. S. Nakamura, M. Senoh, S. Nagahama, H. Iwasa, T. Yamada, T. Matsushita, H. Kiyoku, and Y. Sugimoto, *Appl. Phys. Lett.* 68, 3269 (1996).
323. S. Nakamura, M. Senoh, S. Nagahama, N. Iwasa, T. Yamada, T. Matsushita, Y. Sugimoto, and H. Kiyoku, *Appl. Phys. Lett.* 69, 1477 (1996).
324. J. W. Yang, Q. Chen, C. J. Sun, B. Lim, M. Z. Anwar, M. Asif Khan, and H. Temkin, *Appl. Phys. Lett.* 69, 369 (1996).
325. S. Nakamura, M. Senoh, S. Nagahama, N. Iwasa, T. Yamada, T. Matsushita, Y. Sugimoto, and H. Kiyoku, *Appl. Phys. Lett.* 69, 3034 (1996).
326. S. Nakamura, M. Senoh, S. Nagahama, N. Iwasa, T. Yamada, T. Matsushita, Y. Sugimoto, and H. Kiyoku, *Appl. Phys. Lett.* 70, 616 (1997).
327. S. Nakamura, M. Senoh, S. Nagahama, N. Iwasa, T. Yamada, T. Matsushita, Y. Sugimoto, and H. Kiyoku, *Appl. Phys. Lett.* 70, 868 (1997).
328. S. Nakamura, M. Senoh, S. Nagahama, N. Iwasa, T. Yamada, T. Matsushita, Y. Sugimoto, and H. Kiyoku, *Appl. Phys. Lett.* 70, 2753 (1997).
329. S. Nakamura, M. Senoh, S. Nagahama, N. Iwasa, T. Yamada, T. Matsushita, H. Kiyoku, Y. Sugimoto, T. Kozaki, H. Umemoto, M. Sano, and K. Chocho, *Jpn. J. Appl. Phys.* 37, L309 (1998).
330. S. Nakamura, M. Senoh, S. Nagahama, N. Iwasa, T. Yamada, T. Matsushita, H. Kiyoku, Y. Sugimoto, T. Kozaki, H. Umemoto, M. Sano, and K. Chocho, *Appl. Phys. Lett.* 72, 211 (1998).
331. T. Mukai, H. Narimatsu, and S. Nakamura, *Jpn. J. Appl. Phys.* 37, L479 (1998).
332. S. Nakamura, M. Senoh, S. Nagahama, N. Iwasa, T. Yamada, T. Matsushita, H. Kiyoku, Y. Sugimoto, T. Kozaki, H. Umemoto, M. Sano, and K. Chocho, *Jpn. J. Appl. Phys.* 37, L627 (1998).
333. T. Mukai, K. Takekawa, and S. Nakamura, *Jpn. J. Appl. Phys.* 37, L839 (1998).
334. S. Nakamura, M. Senoh, S. Nagahama, N. Iwasa, T. Yamada, T. Matsushita, H. Kiyoku, Y. Sugimoto, T. Kozaki, H. Umemoto, M. Sano, and K. Chocho, *Jpn. J. Appl. Phys.* 37, L1020 (1998).

335. S. Nakamura, M. Senoh, S. Nagahama, N. Iwasa, T. Yamada, T. Matsushita, H. Kiyoku, Y. Sugimoto, T. Kozaki, H. Umemoto, M. Sano, and K. Chocho, *Appl. Phys. Lett.* 73, 832 (1998).
336. S. Nakamura, M. Senoh, S. Nagahama, T. Matshshita, H. Kiyokyu, Y. Sugimoto, T. Kozaki, A. Umemoto, M. Sano, and T. Mukai, *Jpn. J. Appl. Phys.* 38, L226 (1999).
337. L. T. Romano, B. S. Krusor, M. D. McCluskey, D. P. Bour, and K. Nauka, *Appl. Phys. Lett.* 73, 1757 (1998).
338. M. Kneissl, D. P. Bour, N. M. Johnson, L. T. Romano, B. S. Krusor, R. Donaldson, J. Walker, and C. Dunnrowicz, *Appl. Phys. Lett.* 72, 1539 (1998).
339. D. Hofstetter, R. L. Thornton, L. T. Romano, D. P. Bour, M. Kneissl, and R. M. Donaldson, *Appl. Phys. Lett.* 73, 2158 (1998).
340. M. Kneissl, D. Hofstetter, D. P. Bour, R. Donaldson, J. Walker, and N. M. Johnson, *J. Cryst. Growth* 189–190, 846 (1998).
341. D. P. Bour, M. Kneissl, L. T. Romano, R. M. Donaldson, C. J. Dunnrowicz, N. M. Johnson, and G. A. Evans, *Appl. Phys. Lett.* 74, 404 (1999).
342. M. Kneissl, D. P. Bour, C. G. van de Walle, L. T. Romano, J. E. Northrup, R. M. Wood, M. Teepe, and N. M. Johnson, *Appl. Phys. Lett.* 75, 581 (1999).
343. D. P. Bour, M. Kneissl, C. G. van De Walle, G. A. Evans, L. T. Romano, J. Northrup, M. Teepe, R. Wood, T. Schmidt, S. Schofferger, and N. M. Johnson, *IEEE J. Quantum Elect.* 36, 184 (2000).
344. M. Kneissl, C. G. van de Walle, D. P. Bour, L. T. Romano, L. L. Goddard, C. P. Master, J. E. Northrup, and N. M. Johnson, *J. Lumin.* 87–89, 135 (2000).
345. D. P. Bour, M. Kneissl, C. G. van de Walle, J. Northrup, L. T. Romano, M. Teepe, R. Wood, T. Schmidt, and N. M. Johnson, *Phys. Status Solidi A* 180, 139 (2000).
346. M. Kneissl, D. P. Bour, and N. M. Johnson, *SPIE Proc.* 3947, 174 (2000).
347. D. Hofstetter, J. Faist, and D. P. Bour, *Appl. Phys. Lett.* 76, 1495 (2000).
348. D. P. Bour, N. M. Nickel, C. G. van de Walle, M. S. Kneissl, B. S. Krusor, P. Mei, and N. M. Johnson, *Appl. Phys. Lett.* 76, 2182 (2000).
349. L. L. Goddard, M. Kneissl, D. P. Bour, and N. M. Johnson, *J. Appl. Phys.* 88, 3820 (2000).
350. W. S. Wong, T. Sands, N. W. Cheung, M. Kneissl, D. P. Bour, P. Mei, L. T. Romano, and N. M. Johnson, *Appl. Phys. Lett.* 77, 2822 (2000).
351. M. Kneissl, D. P. Bour, L. Romano, C. G. van de Walle, J. E. Northrup, W. S. Wong, D. W. Treat, M. Teepe, T. Schmidt, and N. M. Johnson, *Appl. Phys. Lett.* 77, 1931 (2000).
352. W. S. Wong, M. Kneissl, P. Mei, D. W. Treat, M. Teepe, and N. M. Johnson, *Appl. Phys. Lett.* 78, 1198 (2001).
353. A. Huh, H. S. Kim, S. W. Kim, J. M. Lee, D. J. Kim, I. H. Lee, and S. J. Park, *J. Appl. Phys.* 87, 4464 (2000).
354. H. Kim, J. M. Lee, S. W. Kim, D. J. Kim, S. J. Park, and H. Hwang, *Appl. Phys. Lett.* 77, 1903 (2000).
355. A. Huh, S. W. Kim, H. S. Kim, H. M. Kim, H. Hwang, and S. J. Park, *Appl. Phys. Lett.* 78, 1766 (2001).
356. T. Hino, T. Asano, T. Tojyo, S. Kijima, S. Tomiya, T. Miyajima, S. Uchida, and M. Ikeda, to be published in *Phys. Stat. Sol.*
357. J. Ding, H. Jeon, T. Ishihara, M. Hagerott, A. V. Nurmikko, H. Luo, N. Samarth, and J. Furdyna, *Phys. Rev. Lett.* 69, 1707 (1992).
358. G. Mohs, T. Aoki, M. Nagai, R. Shimano, M. K. Gonokami, and S. Nakamura, *Solid State Commun.* 104, 643 (1997).
359. G. Mohs, T. Aoki, R. Shimano, M. K. Gonokami, and S. Nakamura, *Solid State Commun.* 108, 105 (1998).
360. T. Mukai, M. Yamada, and S. Nakamura, *Jpn. J. Appl. Phys.* 37, L1358 (1998).



# Optical Properties of Oligophenylenevinylenes

Johannes Gierschner, Dieter Oelkrug

University of Tübingen, Tübingen, Germany

## CONTENTS

1. Introduction
  2. Materials
  3. Optical and Photophysical Properties in Solution
  4. Model Compounds for OPV–OPV Interaction Studies
  5. Optical and Photophysical Properties in the Solid State
- Glossary  
References

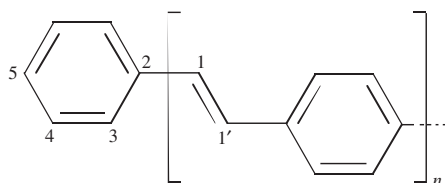
## 1. INTRODUCTION

In the last 20 years, polyene-like organic molecules have attracted much attention as active components in organic light-emitting diodes (OLEDs), microlasing cavities, ultrafast photoswitches and detectors, as well as organic field effect transistors (FETs) [1]. Among the varieties of materials, polyphenylenevinylene (PPV)-based materials are widely investigated due to their use in OLEDs [2]. In order to improve the optical and photophysical properties, that is, tunable emission wavelengths and high fluorescence quantum yields, the interplay of *intramolecular* effects (the effective conjugation length and band shifts by chemical substitution) and *intermolecular* interactions (mutual geometrical orientations, electronic and vibrational coupling between the chromophores) has to be understood. Oligophenylenevinylenes (OPVs, see Fig. 1) make possible the systematic study of these parameters, since the oligomers provide well-defined conjugation lengths, variable substitution patterns, and a variety of intermolecular orientations in the condensed phases.

OPVs have been studied since the 1960s as scintillators [3], laser dyes [4], and optical whiteners [5]. The photochemistry of stilbenoid compounds, especially the *trans*–*cis*

photo-isomerization of stilbene, has been extensively analyzed [6] and is still under investigation [7–12]. Since the early 1990s, with the synthesis of homologous series of soluble *t*-butyl-substituted OPVs by Schenk and co-workers [13], the oligomers have become a widely used model system for PPV. Since then, a great variety of substitution patterns has been established, allowing the tuning of the emission wavelength over the visible range [14, 15]. Quantum chemical investigations and theoretical modeling of the OPVs permit the precise prediction of the electronic transition energies and spectra of the oligomers in solution and extrapolation to the ideally conjugated polymer. Experimental and theoretical studies of intermolecular orientations in different model systems enlightened the correlation of structural and optical properties in the condensed phases and opened the opportunity to achieve full control of the photophysics of these systems. In the recent years, films, single crystals, dendrimer systems, and host–guest compounds of the OPVs have attracted growing attention for potential applications in optoelectronic devices due to their electroluminescent [16–23], lasing [24, 25], (photo) conductive [26–31], or photovoltaic properties [32, 33]. Substituted OPVs with large two-photon absorption cross sections are attractive materials for fluorescence microscopy, optical limiting, and optical data storage [34].

The article focuses on the photophysics of individual and condensed *para*-oligophenylenevinylenes and their correlation to *intra*- and *intermolecular* structural effects. In Section 2, an overview of the materials is given, including the variety of substitution patterns and the geometrical structures of the molecules. Section 3 discusses the features of the molecules in solution (absorption and fluorescence spectra, electronic transition energies, fluorescence quantum yields, and decay times) and the influence of mesomeric and inductive substituent effects, solvent shifts, and thermal effects. In Section 4, model compounds for the investigation of intermolecular interactions and their impact on the optical properties are discussed. In Section 5, the photophysics of condensed phases such as films, nanoparticles, and single crystals of OPVs are addressed.



**Figure 1.** Structure and notation of the atoms for oligophenylenevinylenes (*n*PVs).

## 2. MATERIALS

### 2.1. Substitution Patterns

The homologous series of unsubstituted oligophenylenevinylenes, *n*PV, where *n* denotes the number of phenylenevinylene units (see Fig. 1 and Table 1), has been synthesized up to *n* = 7 [5, 27, 35, 36]. In order to enlarge the solubility of the oligomers, alkyl or alkoxy groups were introduced. The series of *t*-butyl-substituted oligomers (*Bn*PV, see Table 2) with *n* = 1–6 was synthesized by Schenk et al. [13], and series of alkoxy-substituted OPVs were synthesized by Stalmach et al. (*n*POPVs with *n* = 1–11, see Table 3) [37] and Peeters et al. (*n*BOPVs, with *n* = 1–6, see Table 4) [38]. Recently, the syntheses of further homologous series with alkyl [39–42] and alkoxy [16, 40–43] substituents was reported. Finally, homologous series of donor–acceptor (DA)-substituted OPVs were synthesized, with D,A substituents either in the terminal 5,5' positions (see Fig. 1, D,

dialkylamino, and A, cyano, carbonyl, nitro groups) [44] or in the vinylene units (1,1' positions with D, dibutylamino, A, cyano) [45].

The substitution pattern was widely varied, especially on *para*-distyrylbenzene (2PV), including ring substitutions (Tables 5, 6) with alkyl [13, 26, 36, 39, 46–49], alkoxy [16, 26, 36–38, 43, 49–53], cyano [36, 49, 54–57], amino [34, 49, 58], nitro [26, 49], fluoro [59–61], bromo [49], carbonyl [62], carboxyl [49], sulfonyl [53], and silyl groups [63, 64] or push–pull systems [44, 53], as well as substitutions in the vinylene unit (Tables 7, 8) with sulfonyl [50, 65, 66] or cyano groups [48, 50, 66–71]. A systematic variation of cyanosubstitution was also performed on 4PV (Table 9) [72–75]. Thus, different substitution patterns with mesomeric ( $\pm$ M) and/or inductive ( $\pm$ I) groups, but also with varying sterical requirements, are now available. Recently, general procedures of OPV syntheses were reviewed [14].

### 2.2. Molecular Structure

According to X-ray studies on *trans*-stilbene (1PV) [76–79], 2PV [80], and 4PV [17], the unsubstituted OPVs are only slightly twisted, with torsional angles around the C<sub>1</sub>–C<sub>2</sub> single bonds (Fig. 1) of  $\phi \approx 5^\circ$ . A perfect planar structure (C<sub>2h</sub> symmetry) of 1PV is found in the gas phase at low temperatures according to jet-cooled spectra [81–84]. The C<sub>2h</sub> symmetry is also predicted by density functional (B3LYP) [8, 85–88] and semiempirical PM3 [89–92] quantum chemical

**Table 1.** Experimental and calculated adiabatic and vertical electronic transition energies (10<sup>3</sup> cm<sup>-1</sup>) of unsubstituted oligophenylenevinylenes *n*PV *in vacuo*.

			1PV	2PV	3PV	4PV	Ref.	
Adiabatic transition energies $\nu_{00}$	Experiment <sup>a</sup>	<i>In vacuo</i>	31.5	27.7	26.0	25.1	[91]	
		<i>Ab initio</i>	31.7	28.1	26.3	— <sup>b</sup>	[91]	
	Calculation	Semiempirical	33.8	29.9	28.7	27.4 <sup>c</sup>	[246]	
			30.0	26.4	24.4	23.3 <sup>d</sup>	[97]	
Vertical transition energies $\nu_{\text{vert}}$	Experiment <sup>c</sup>	<i>In vacuo</i>	33.8	29.8	28.0	27.0	[91]	
		<i>Ab initio</i>	33.9	29.7	28.2	— <sup>f</sup>	[91]	
	Calculation	TDFT	41.8	36.6	34.3	33.0 <sup>g</sup>	[246]	
		Semiempirical		32.5	26.1	22.9	21.1 <sup>h</sup>	[245]
				32.9	29.1	26.9	25.7 <sup>i</sup>	[97]
			33.8	29.3	27.3	26.2 <sup>j</sup>	[91]	
			33.1	28.7	26.9	25.9 <sup>k</sup>	[243]	
		31.9	28.0	26.2	25.2 <sup>l</sup>	[107]		
Fluorescence	$\Phi_{\text{F}}$		0.036 <sup>m</sup>	0.90	0.85	—	[148]	
	$\tau_{\text{F}}$ / ns		0.09 <sup>m</sup>	1.20	1.10	—	[148]	

Note: Fluorescence quantum yields ( $\Phi_{\text{F}}$ ) and decay times ( $\tau_{\text{F}}$ ) in solution are shown.

<sup>a</sup> Obtained from experiments in solution by extrapolation to a refractive index *n* = 1.

<sup>b</sup> RCIS/6–311G\*.

<sup>c</sup> RCIS/3–21G.

<sup>d</sup> AM1 CAS.

<sup>e</sup> Obtained from the experimental adiabatic transition energies by addition of the equilibration energy  $\Delta\nu_{\text{exp}}$ .

<sup>f</sup> From  $\nu_{00}$  (RCIS/6–311G\*) by addition of the explicitly calculated [91] equilibration energy  $\Delta\nu_{\text{calc}}$ .

<sup>g</sup> RCIS/3–21G (direct calculation).

<sup>h</sup> Time-dependent density functional B3LYP/6–31G\*.

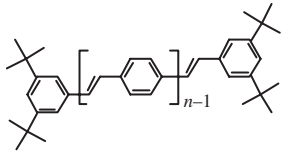
<sup>i</sup> AM1.

<sup>j</sup> ZINDO/S-CI, involving (2*n* + 1) occupied and unoccupied molecular levels.

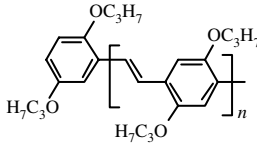
<sup>k</sup> ZINDO/S-CI (full configuration interaction).

<sup>l</sup> PPP.

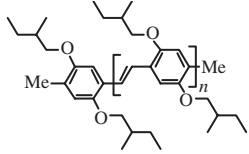
<sup>m</sup> [278].

**Table 2.** Absorption maxima ( $\lambda_{\max}$ ), oscillator strengths ( $f$ ), fluorescence subbands ( $\lambda_1, \lambda_2$ ), fluorescence quantum yields ( $\Phi_F$ ), fluorescence decay times ( $\tau_F$ ), and radiative rate constant ( $k_F$ ) of *t*-butyl-substituted oligophenylenevinylene B*n*PVs in solution (dichloromethane) at  $T = 293$  K. [175].


	Absorption		Fluorescence			
	$\lambda_{\max}/\text{nm}$	$f$	$\lambda_1, \lambda_2/\text{nm}$	$\Phi_F$	$\tau_F/\text{ns}$	$k_F/10^9 \text{ s}^{-1}$
B1PV	316	0.53	344, 361	0.10	—	—
B2PV	360	0.89	397, 419	0.86	1.10	0.78
B3PV	387	1.21	428, 456	0.82	1.06	0.77
B4PV	403	1.60	448, 478	0.75	0.97	0.77
B5PV	410	1.80	459, 490	0.71	0.73	0.97
B6PV	417	1.88	464, 495	0.71	0.65	1.09

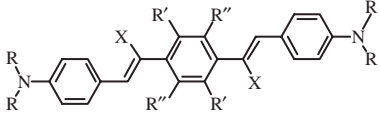
**Table 3.** Absorption maxima ( $\lambda_{\max}$ ), extinction coefficient ( $\epsilon$ ), fluorescence maxima ( $\lambda_1, \lambda_2$ ), fluorescence quantum yields ( $\Phi_F$ ), fluorescence decay times ( $\tau_F$ ), and radiative rate constant ( $k_F$ ) of propyloxy-substituted oligophenylenevinylene *n*POPVs in solution at  $T = 293$  K.


	Absorption <sup>a</sup>		Fluorescence <sup>b</sup>			
	$\lambda_{\max}/\text{nm}$ [37]	$\epsilon_{\max}/10^3 \text{ l mol}^{-1} \text{ cm}^{-1}$ [37]	$\lambda_1, \lambda_2/\text{nm}$ [283]	$\Phi_F$ [283]	$\tau_F/\text{ns}$ [283]	$k_F/10^9 \text{ s}^{-1}$ [283]
1POPV	354	17	(408), 425	0.45	1.89	0.23
2POPV	401	41	460, 486	0.82	1.60	0.51
3POPV	431	59	500, 529	0.94	1.72	0.55
4POPV	450	85	522, 555	0.70	1.10	0.64
6POPV	466	117	543, 580	0.43	0.62	0.70
8POPV	475	146	549, 586	0.48	0.62	0.77
11POPV	481	196	551, 590	0.48	0.64	0.75

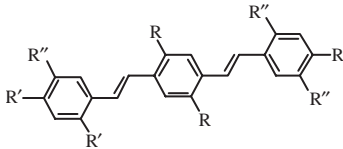
<sup>a</sup> In chloroform.<sup>b</sup> In dichloromethane.**Table 4.** Absorption maxima ( $\lambda_{\max}$ ), extinction coefficient ( $\epsilon$ ), fluorescence maxima ( $\lambda_1, \lambda_2$ ), fluorescence quantum yields ( $\Phi_F$ ), fluorescence decay times ( $\tau_F$ ), and radiative rate constant ( $k_F$ ) of methylbutoxy-substituted oligophenylenevinylene *n*BOPVs in chloroform at  $T = 293$  K [173].


	Absorption		Fluorescence			
	$\lambda_{\max}/\text{nm}$	$\epsilon_{\max}/10^3 \text{ l mol}^{-1} \text{ cm}^{-1}$	$\lambda_{\max}/\text{nm}$	$\Phi_F$	$\tau_F/\text{ns}$	$k_F/10^9 \text{ s}^{-1}$
1BOPV	357	21	409	—	—	—
2BOPV	407	44	466	0.62	1.70	0.37
3BOPV	437	68	502	0.76	1.32	0.58
4BOPV	454	88	523	0.49	0.73	0.67
5BOPV	464	107	534	0.41	0.52	0.80
6BOPV	475	142	541	0.25	0.45	0.55



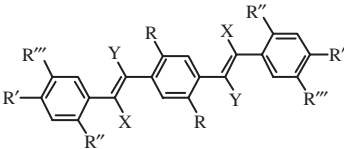
**Table 5.** Absorption maxima ( $\lambda_{\max}$ ), extinction coefficient ( $\epsilon$ ), fluorescence maxima ( $\lambda_{\max}$ ), fluorescence quantum yields ( $\Phi_F$ ), fluorescence decay times ( $\tau_F$ ), two-photon excitation maximum ( $\lambda_{\max}^{\text{tpa}}$ ), and two-photon absorption cross section ( $\delta$ ) of substituted distyrylbenzenes in toluene at  $T = 293$  K.


R	R'	R''	X	One-photon absorption		Fluorescence			Two-photon absorption		Ref.
				$\lambda_{\max}/\text{nm}$	$\epsilon_{\max}/10^3 \text{ l mol}^{-1} \text{ cm}^{-1}$	$\lambda_{\max}/\text{nm}$	$\Phi_F$	$\tau_F/\text{ns}$	$\lambda_{\max}^{\text{tpa}}/\text{nm}$	$\delta/10^{-50} \text{ cm}^4/\text{s/photon}$	
<i>n</i> -Butyl	H	H	H	410	74	455	0.88	1.35 <sup>a</sup>	730	955	[270, 268]
<i>n</i> -Butyl	F	F	H	430	77	456	0.58	0.79	760	1400	[271]
<i>n</i> -Butyl	OMe	H	H	428	67	480	0.88	1.38 <sup>a</sup>	730	900	[268, 34]
<i>n</i> -Butyl	SO <sub>2</sub> C <sub>3</sub> H <sub>7</sub>	H	H	439	43	528	0.31	1.01	816	4100	[271]
<i>n</i> -Butyl	CN	H	H	490	66	536	0.69	1.30	830	1750	[270]
Phenyl	CN	H	H	475	66	528	0.87	1.46	830	1640	[270]
<i>n</i> -Butyl	H	H	CN	438	54	504	0.003	<0.015	790	890	[270]

<sup>a</sup> In acetonitrile.**Table 6.** Absorption maxima ( $\lambda_{\max}$ ), fluorescence maxima ( $\lambda_{\max}$ ), fluorescence quantum yields ( $\Phi_F$ ), and fluorescence decay times ( $\tau_F$ ) of distyrylbenzene (2PV) derivatives with substituents in the phenylene moieties.


R	R'	R''	Absorption		Fluorescence			Solvent	Ref.
			$\lambda_{\max}/\text{nm}$	$\lambda_{\max}/\text{nm}^a$	$\Phi_F$	$\tau_F/\text{ns}$			
H	H	H	355	388, 410	0.90	1.29	Dioxane	[48]	
OC <sub>8</sub> H <sub>17</sub>	H	H	387	440	0.83	1.74	Dioxane	[48]	
OC <sub>8</sub> H <sub>17</sub>	Ph	H	405	460	0.90	1.35	Dioxane	[48]	
OC <sub>8</sub> H <sub>17</sub>	OPh	H	392	444	0.91	1.49	Dioxane	[48]	
OC <sub>8</sub> H <sub>17</sub>	COPh	H	415	487	0.70	1.52	Dioxane	[48]	
OCH <sub>3</sub>	NPh <sub>2</sub>	H	425	480	0.75	1.26	Dioxane	[48]	
OCH <sub>3</sub>	H	OCH <sub>3</sub>	393	446, 470	0.92	1.55	C <sub>6</sub> H <sub>12</sub>	[69]	

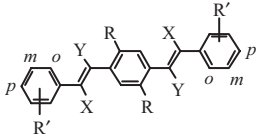
Note: Data in solution are shown.

<sup>a</sup>For structured spectra the spectral positions of the two high energetic subbands are given.**Table 7.** Absorption maxima ( $\lambda_{\max}$ ), fluorescence maxima ( $\lambda_{\max}$ ), fluorescence quantum yields ( $\Phi_F$ ), and fluorescence decay times ( $\tau_F$ ) of distyrylbenzene (2PV) derivatives with substituents in the vinylene moieties.


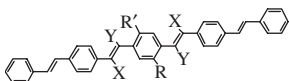
Type	R	R'	R''	R'''	X	Y	Absorption		Fluorescence			Solvent	Ref.
							$\lambda_{\max}/\text{nm}$	$\lambda_{\max}/\text{nm}^a$	$\Phi_F$	$\tau_F/\text{ns}$			
A	OC <sub>3</sub> H <sub>7</sub>	H	H	H	CN	H	425	489	—	—	CHCl <sub>3</sub>	[50]	
	OC <sub>8</sub> H <sub>17</sub>	H	H	H	CN	H	422	512	0.36	2.90	Dioxane	[48, 284]	
	OC <sub>8</sub> H <sub>17</sub>	OPh	H	H	CN	H	428	511	0.49	2.23	Dioxane	[48, 284]	
B	OCH <sub>3</sub>	H	OCH <sub>3</sub>	H	CN	H	408	478	0.06	0.3 (25%) 1.0 (75%)	C <sub>6</sub> H <sub>12</sub>	[69]	
	OCH <sub>3</sub>	H	OCH <sub>3</sub>	H	H	CN	410	445, 475	0.10	0.2 (12%) 0.9 (88%)	CH <sub>2</sub> Cl <sub>2</sub>	[69]	
C	C <sub>6</sub> H <sub>13</sub>	H	H	H	CN	H	375	435, 458	0.002	<0.01	CH <sub>2</sub> Cl <sub>2</sub>	[146]	
	C <sub>6</sub> H <sub>13</sub>	H	H	H	H	CN	304	410	~0.5–0.8	1.5	EPA, 77 K	[146]	
	C <sub>6</sub> H <sub>13</sub>	H	C <sub>6</sub> H <sub>13</sub>	C <sub>6</sub> H <sub>13</sub>	CN	H	325	441	0.001	—	CH <sub>2</sub> Cl <sub>2</sub>	[237]	
									0.003	—	CH <sub>2</sub> Cl <sub>2</sub>	[146]	

Note: Data in solution are shown.

<sup>a</sup>For structured spectra the spectral positions of the two high energetic subbands are given.

**Table 8.** Fluorescence properties of (substituted) distyrylbenzenes (2PV) in solution, thin films, and nanoparticles (NP): fluorescence maxima ( $\lambda_{\max}$ ; u.s., unstructured), quantum yields ( $\Phi_F$ ), decay times ( $\tau_F$ , n.e., nonexponential), natural lifetimes ( $\tau_F^0$ ), and fluorescence anisotropy ( $r_F$ ).


R	R'	X	Y	State	$\lambda_{\max}/\text{nm}$	$\Phi_F$	$\tau_F/\text{ns}$	$\tau_F^0/\text{ns}$	$r_F$	Remarks	Ref.
H	H	H	H	Solution	388, 409	0.92	1.2	1.3			[54]
				Film/NP 293 K	(415), 441	0.05–0.1	2.5 (n.e.)	~30	0.25	H aggregates	[54]
				15 K	(421), 448	0.3–0.5	9–12 (n.e.)				
Hex	H	H	H	Solution	403, 424	0.82	1.1	1.3			[54]
				Film	417, 440	0.18	0.4	2.2	0.30	J aggregates	[54]
HexO	H	H	H	Solution	446, 467	0.66	1.6	2.4			[237]
				Film	583 u.s.	~0.15	21 (n.e.)	~140	0.00	Excimer emission	[54, 57]
HexO	H	H	CN	Solution	497 u.s.	—	0.9	—			[237]
				Film	478 u.s.	—	2.2 (n.e.)	—	—		[237]
HexO	H	CN	H	Solution	520 u.s.	0.32	2.1	6.6			[237]
				Film	622 u.s.	~0.3	30 (n.e.)	~100	—	Excimer emission	[237]
HexO	<i>o</i> -CN	H	H	Solution	487 u.s.	0.65	2.0	3.1			[57]
				Film	580 u.s.	0.03–0.06	9.5	~200	0.01	Excimer emission	[54, 57]
HexO	<i>m</i> -CN	H	H	Solution	460 u.s.	0.72	1.9	2.6			[57]
				Film	576 u.s.	0.04–0.08	2.3	~40	0.25	Excimer emission	[54, 57]
HexO	<i>p</i> -CN	H	H	Solution	500 u.s.	0.81	1.8	2.2			[57]
				Film	482, 514	0.7–0.8	0.5–1.0	~1	0.20	J aggregates	[54]
H	<i>p</i> -CN	H	H	Solution	409, 433	0.80	1.2	1.5			[55]
				NP (methanol/H <sub>2</sub> O)	(430), 460	0.2	1.3	6.5	0.30	H aggregates	[319]
				Film, fast deposited	436, 463	~0.2	~0.3 (n.e.)	~1.5	0.30	J aggregates	[55]
				Film, annealed	560 u.s.	0.4–0.5	12 (n.e.)	~30	—	Excimer emission	[55]
				NP (dioxane/H <sub>2</sub> O)	560 u.s.	0.4	20 (n.e.)	~50	0.23	Excimer emission	[319]

**Table 9.** Fluorescence properties of (substituted) distyryl(distyrylbenzene)s (4PV) in solution, thin films, nanoparticles (NP), and single crystals: fluorescence maxima ( $\lambda_{\max}$ ; u.s., unstructured), quantum yields ( $\Phi_F$ ), and decay times ( $\tau_F$ , mono- or biexponential fits).


Name	R	R'	X	Y	State	$\lambda_{\max}/\text{nm}$	$\Phi_F$	$\tau_F/\text{ns}$	Remarks	Ref.
4PV	H	H	H	H	Solution	440, 471	—	—		[91]
					NP	(483), 515	~0.1	—	H aggregates	[174]
MEH-4PV	EtHexO <sup>a</sup>	MetO	H	H	Solution	480, 510	—	0.65		[152, 154, 155]
					Film	(500), 530	0.15	1.2		[153, 320]
Oct-4PV	Oct	H	H	H	Solution	455, 485	0.85–0.9	—		[305]
					Film	505, 533	—	—		[303]
OctO-4PV	OctO	H	H	H	Solution	483, 515	0.7–0.9	~1.0		[25, 305]
					Film, as deposited	529	0.5	1.1	J aggregates	[24, 306]
					Film, annealed	539	0.7	1.7		[24, 306]
					Single crystal	539, (563)	0.5	1.0	Cofacial <i>x</i> , <i>z</i> -shifted	[306]
OctO-4PV-CN <sub>o</sub>	OctO	H	CN	H	Solution	537, (570)	0.7–0.9	1.4		[25, 110, 275]
					Film, as deposited	595, (620)	0.4	1.4, 7.0		[306, 110]
					Film, annealed	615 u.s.	0.6	3.4, 8.0	Excimer emission	[306]
					Single crystal	630 u.s.	0.5	8.0	Cofacial <i>z</i> -shifted	[110, 306]
OctO-4PV-CN <sub>i</sub>	OctO	H	H	CN	Solution	510 u.s.	0.04	0.08		[25]
					Single crystal	560, 593	0.4	2.2	Cofacial <i>x</i> , <i>z</i> -shifted	[306]

<sup>a</sup> EtHexO is 2-ethyl-hexyloxy.

calculations on 1PV. *Ab initio* Hartree–Fock (HF) [86, 87, 92–95] and semiempirical AM1 [89, 90, 92, 93, 96, 97] calculations yield a slightly nonplanar structure ( $C_2$  symmetry) of 1PV; however, the ring-torsional potential is very flat for  $\phi < 30^\circ$ . The bond lengths and angles of the *n*PVs, as determined by X-ray measurements [17, 76–80], are quite well reproduced by theory, resulting in pronounced bond alterations in the vinylene units [8–10, 87–94, 98–103]. In the gas phase at higher temperatures, the *average* geometrical structure, according to electron diffraction [104] and photoelectron studies [105, 106] of 1PV, is nonplanar, due to the low torsional barrier for rotations around the ethenyl–phenyl ( $C_1$ – $C_2$ ) single bonds [8, 85, 89–93, 95–97, 107].

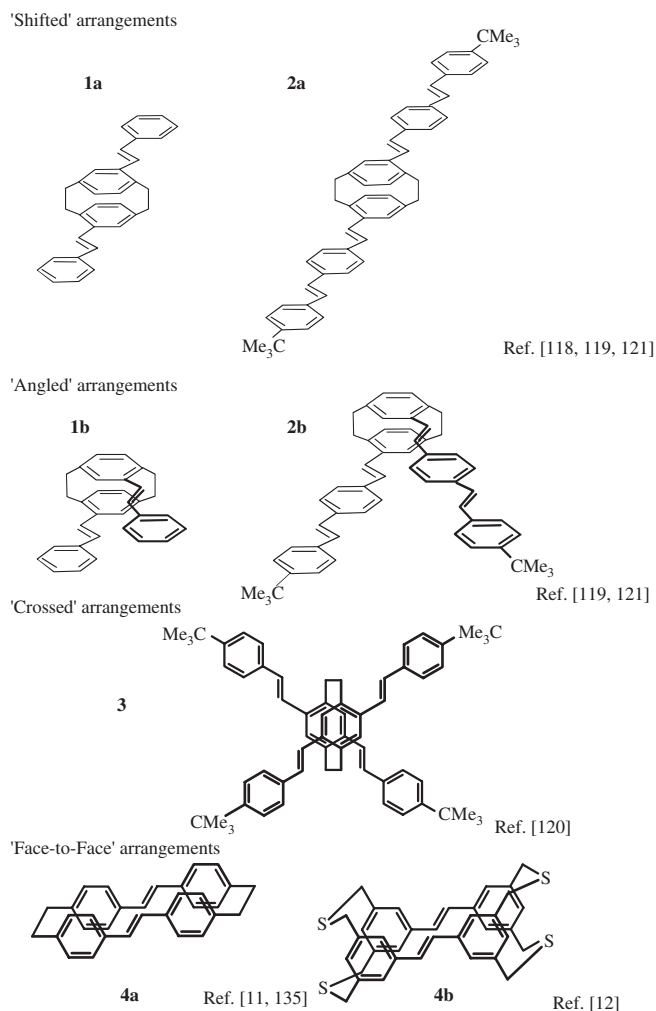
Deviations from planarity in the solid state are observed in several substituted OPVs. According to quantum chemical calculations [69, 92, 93], the deviations from planarity depend sensitively on the kind and positions of substituents [93]. However, the torsional angles in most of the reported X-ray structures [17, 47, 60, 73, 74, 80, 108–114] do not exceed  $11^\circ$ – $18^\circ$ . Larger deviations from planarity are found for 2PV derivatives with cyanosubstituents in the vinylene moiety and additional alkyl substituents at the central phenyl ring (see Tables 7–9) [68].

### 2.3. Bridged Oligophenylenevinylenes

Oligophenylenevinylenes with defined mutual geometric alignment are represented by (i) hydrogen-bonded OPV pairs, introduced by Meijer and co-workers [115–117], and by (ii) covalently linked oligomers, which were synthesized by Schenk et al. [13], Anger et al. [11], Rau and Waldner [12], Bazan [118–129], and Song et al. [130–133]. The covalently linked OPVs cover dimeric stilbenoid cyclophanes with partial  $\pi$ – $\pi$  overlap and different intermolecular orientations [13, 118–125, 134] (Fig. 2), stilbenophanes with perfect face-to-face alignment [11, 12, 135] (Fig. 2), tetrameric systems with tetrahedral OPV orientation [126–128, 136] (Fig. 3), and dendrimers [128, 136–141]. Dimeric OPVs were also prepared by Lewis and Letsinger using 1:1 mixtures of complementary oligonucleotides containing stilbene units [142–145].

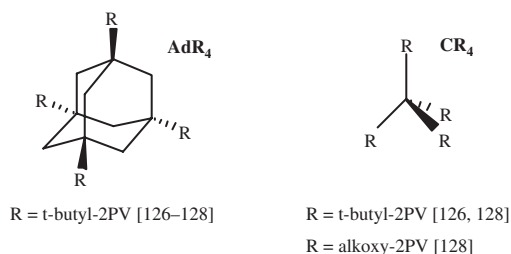
### 2.4. Condensed Phases

Films of OPVs were prepared by vapor deposition from high vacuum [20, 28, 74, 146–155], by spin or drop coating from solution [21, 23, 156–158], and by the Langmuir–Blodgett technique [131, 159–170]. Nanoparticles were obtained by fast precipitation from solutions of the oligomers by addition of a poor solvent (i.e., water) and measured in suspension [38, 54, 116, 146, 148, 170–178]. The size of the nanoparticles (20–500 nm) can be controlled by the preparation conditions (concentration, solvent, temperature, mixing ratio). Nanoparticles were also prepared by cooling saturated solutions of the OPVs [62, 179–182]. General procedures for nanoparticle preparation were reviewed recently [183, 184]. Single crystals were grown from solution [60, 61, 68, 75–78, 108–112, 163, 185], melt [186], and gas phase [31, 79, 187, 188].



**Figure 2.** Structures of stilbenoid cyclophanes.

Host–guest compounds (HGCs), where the OPVs are incorporated in an inert host material such as  $\gamma$ -cyclodextrin [189] or channel-forming perhydrotriphenylene (PHTP) [55, 190, 191], were prepared by cocrystallization from solution. The cavities of the cyclodextrin HGCs permit the inclusion of cofacially oriented stilbene pairs. PHTP HGCs open the opportunity to investigate specific “head-to-tail” interactions of the oligomers.

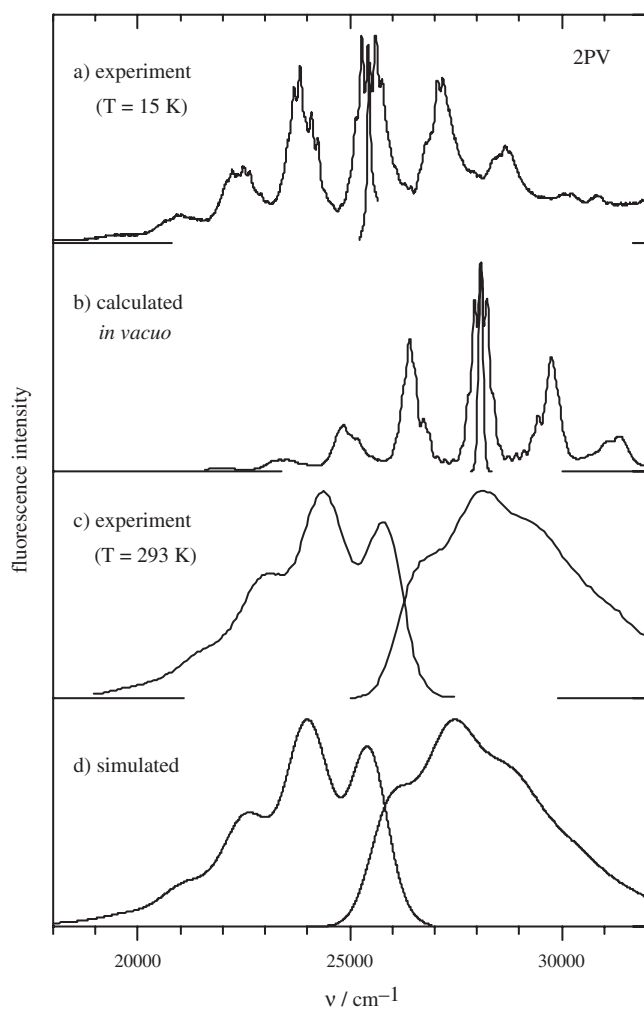


**Figure 3.** Structures of tetrahedral oligophenylenevinylenes.

### 3. OPTICAL AND PHOTOPHYSICAL PROPERTIES IN SOLUTION

#### 3.1. Absorption and Fluorescence Spectra

At low temperatures ( $T < 20$  K), the  $S_0 \rightarrow S_1$  absorption and  $S_1 \rightarrow S_0$  fluorescence spectra of 1PV [192] and the longer oligomers [91] show very small 0–0 bandgaps and the spectra are almost mirror symmetrical (Fig. 4). Thus, the frequencies and nuclear displacements of the totally symmetrical  $a_g$  vibrational modes which couple to the electronic transition must be very similar in  $S_0$  and  $S_1$ , in agreement with *ab initio* quantum chemical calculations [91]. Detailed vibrational analyses of the electronic spectra were carried out on (substituted) *trans*-stilbenes under collision-free conditions [81–84, 193–196]. The fine structures of the experimental spectra are dominated by the progressions and combinations of a few prominent modes, which also becomes evident for the longer oligomers in solid solution



**Figure 4.** Fluorescence emission (left) and excitation (right) spectra of distyrylbenzene (2PV). (a) Experimental spectra in tetradecane at  $T = 15$  K. (b) Calculated low temperature spectra (HF/RCIS 6–311G\*) [91]. (c) Experimental spectra in dioxane at  $T = 293$  K. (d) Simulated spectra, obtained by convolution of the experimental low temperature spectra with a Gaussian and an exponential distribution [91].

[91, 118, 179, 197, 198]. Theoretical calculations, obtained by a Franck–Condon approach [85, 91, 99, 100, 199, 200] from *ab initio* quantum chemical calculations, demonstrate that the nuclear displacements of the prominent modes essentially coincide with the geometrical changes upon the electronic transition. Among these modes, the low-frequency longitudinal in-plane deformation mode ( $\nu = 204$   $\text{cm}^{-1}$  for 1PV [193]) strongly decreases with  $n$ , resulting in  $\nu \rightarrow 0$  for  $n \rightarrow \infty$  [91], whereas the vinylene  $C_1-C'_1$  stretching mode around  $1650$   $\text{cm}^{-1}$  [201–208] decreases only very little with  $n$  [96, 209–211]. The optical spectra of the  $n$ PVs were calculated at different levels of theory for 1PV [85, 99, 100, 212] and the longer oligomers [91, 200, 213], and good agreement with the experiment was obtained at the *ab initio* HF/restricted configuration interaction singles (RCIS) 6–311G\* level, including the progressions and combinations of the complete sets of  $a_g$  modes (Fig. 4).

With increasing temperature, the mirror symmetry of absorption and fluorescence is lost and a 0–0 bandgap opens, which extends to  $200$   $\text{cm}^{-1}$  at  $77$  K [173, 175, 214] and to  $1000$   $\text{cm}^{-1}$  at room temperature (Fig. 4). The room temperature fluorescence spectra still exhibit distinct vibronic structure, whereas the absorption spectra are only slightly structured and asymmetrically shifted to the blue [91, 96, 146, 210, 214–219] (see Fig. 4). The differences in the spectral characteristics of fluorescence and absorption are due to the different torsional barriers of the ground and excited state structures. Compared to the  $S_0$  state, the  $C_1-C_2$  bond is rigidified in the  $S_1$  state [8, 9, 89–91, 95, 100–103, 220], leading to a steeper potential of the torsional modes [8, 90, 91, 97, 212]. The torsional barrier can be investigated in the gas phase, where the low-frequency torsional mode of 1PV was determined to  $\nu = 8$   $\text{cm}^{-1}$  in the  $S_0$  state and  $\nu = 48$   $\text{cm}^{-1}$  in the  $S_1$  state [81]. Therefore, the room temperature absorption spectra arise from superimposed transitions of different nonplanar conformers of the molecules [91, 96, 146, 215, 216, 221], and the total band shapes are well described by a combination of a Gaussian-shaped and an exponential convolution of the low temperature spectra (Fig. 4). The Gaussian part accounts for inhomogeneities of the environment, and the exponential part accounts for the increase in the torsional potential in  $S_1$  against  $S_0$  [212]. Since the potential in  $S_1$  is high against the thermal energy, the room temperature fluorescence spectra can be exclusively fitted by the Gaussian contribution to line broadening. In rigid environments, where the potential in  $S_0$  is also high against the thermal energy, the absorption spectrum can also be reasonably fitted by a Gaussian convolution [178, 222].

#### 3.2. Electronic Transition Energies

The energetic positions of the absorption spectra of the OPVs are strongly affected by the conjugation length and to a smaller extent also by the solvent and the temperature (Fig. 4) [36, 223] due to changes in the polarizability of the environment [224–226]. In nonpolar solvents, the polarizability shift becomes a linear function of the Onsager relation [224], which allows the extrapolation to the spectral positions *in vacuo* with a refractive index of  $n_{\text{solv}} = 1$  [91]. The solvent red shift amounts to  $\Delta\nu_R = 2500$   $\text{cm}^{-1}$  compared to the values *in vacuo* (Fig. 4); thus solvent effects

should be considered if experimental transition energies are compared to calculated ones. Specific solvent interactions in polar solvents are observed for OPVs with electron withdrawing substituents like cyano, nitro, triflyl ( $\text{SO}_2\text{CF}_3$ ), or fluoro groups [59, 75] and for donor–acceptor-substituted OPVs [225–227], resulting in unstructured, red-shifted fluorescence spectra and large Stokes shifts between the absorption and fluorescence maxima due to the contribution of charge separation not only in the  $S_1$ , but also in the  $S_0$  state [228].

Vertical transition energies  $\nu_{\text{vert}}$  for the  $S_0 \rightarrow S_1$  transition were calculated at different levels of theory for 1PV [85, 88, 89, 99, 100, 229–233], substituted OPVs [8, 16, 55, 60, 67, 92, 119, 232–239], and the homologues series of the  $n$ PVs [91, 97, 101, 103, 107, 218, 234, 240–251]. The latter reproduce the experimental result of an inverse chain length dependence  $1/N$  (with  $N = 3n + 2$ ) of  $\nu_{\text{vert}}$  [91, 96, 173, 216, 237, 247, 248]. However, the results obtained by semiempirical methods depend sensitively on the number of electron configurations considered in the calculations [89]. Time-dependent density functional (TDFT) methods tend to underestimate the vertical transition energies (Table 1) and to overestimate the slope of the  $1/N$  dependence [245]. Reliable results were obtained by the *ab initio* RCIS/6–311G\* method, where the vertical transition energies were calculated from adiabatic transition energies  $\nu_{00}$  by addition of the equilibration energy [91] (see Table 1). In contrast, the direct calculation of the vertical transition energies by *ab initio* methods [246] yields unreasonably high values for  $\nu_{\text{vert}}$  (see Table 1). For longer oligomers ( $n > 4$ ), a deviation from the linear  $1/N$  dependence is observed both experimentally [27, 37, 173, 175] and theoretically [234, 246, 247], which results in a faster convergence for  $n \rightarrow \infty$ . The experimental transition energies can be reasonably fitted by empirical functions [44, 246], within the extended Hückel Molecular Orbital [252] and free electron gas model [253] including bond alternation, Simpson's exciton model [254], or the classical oscillator approach by Kuhn [255]. The extrapolation to idealized PPV yields  $\nu_{00} \approx 20,300 \text{ cm}^{-1}$  in solution ( $23,400 \text{ cm}^{-1}$  *in vacuo*). The equilibration energy for PPV was calculated to  $\nu_{\text{vert}} - \nu_{00} \approx 1750 \text{ cm}^{-1}$  [91].

The introduction of substituents in the *terminal* phenyl rings with +M effect (e.g., alkoxy [16, 215, 223, 256] or amino [34, 49, 58] groups), –M effect (e.g., carbonyl [62] or cyano [36, 49, 54–57] groups), or +I effect (e.g., alkyl groups [39, 96, 107, 175, 216, 218, 223, 257, 258]) shifts the  $S_0 \rightarrow S_1$  transitions slightly to lower energies. The additional introduction of alkoxy substituents [18, 38, 43, 48, 51, 69, 173, 234, 237] in the *central* phenyl rings ( $n$ POPVs, Table 3,  $n$ BOPVs, Table 4) leads to a splitting of the low energetic absorption band with a systematic bathochromic shift of the  $S_0 \rightarrow S_1$  transition compared to that of the  $n$ PVs. According to quantum chemical calculations, this effect is ascribed to the interaction between carbon and oxygen  $\pi$  orbitals, destabilizing the highest occupied molecular orbital (HOMO) more strongly than the lowest unoccupied molecular orbital (LUMO) [238, 259]. In addition, a blue-shifted “RO band” appears, due to strong configuration interactions between the HOMO and phenyl orbital branches [234]. Extrapolation of the  $n$ BOPV spectral positions to  $n \rightarrow \infty$  yields

$\nu_{00} \approx 17,600 \text{ cm}^{-1}$  for the idealized polymer (experimentally:  $\nu_{00}(\text{BOPPV}) = 18,100 \text{ cm}^{-1}$  [260]). The fluorescence and absorption spectra of OPVs with cyanosubstituents in the vinylene unit are strongly red-shifted against the unsubstituted ones (Tables 7–9), in agreement with quantum chemical calculations [238, 259, 261]. Terminal donor–acceptor substitution of 1PV, for example, 4-(dialkylamino)-4'-nitrostilbene [122, 225–227], causes a large bathochromic shift in the transition energies due to the intramolecular charge transfer (CT) character of the transition. These results are also well reproduced by quantum chemical calculations [239, 247]. With increasing chain length  $n$ , the extent of the CT character decreases [44, 239, 247]. Thus, for some donor–acceptor-substituted homologous series, the decrease in the CT character overcompensates the bathochromic shift induced by the increase in  $n$ , thus causing a hypsochromic shift with  $n$  [44].

According to polarized absorption [262] and fluorescence studies [148, 263, 264] in stretched polyethylene films and to the rotational resolved fluorescence excitation spectrum of 1PV under collision-free conditions [84], the  $S_0 \rightarrow S_1$  transition moment  $\mu$  of the  $n$ PVs is oriented approximately parallel to the long geometrical axes of the molecules (defined as the distance between the terminal carbon atoms  $d_{\omega, \omega'}$ ). The experimental results are supported by quantum chemical calculations, [9, 218, 229, 265, 266], yielding for 2PV an angle of approximately  $8^\circ$  between  $d_{\omega, \omega'}$  and  $\mu$  [266]. The oscillator strengths increase roughly linearly with the chain length (Tables 2–4). The energetic positions, orientations, and oscillator strengths of the higher  $S_0 \rightarrow S_n$  transitions of the OPVs were assigned by polarized absorption spectroscopy on 1PV [262, 263] and fluorescence excitation measurements (1PV [265, 267],  $Bn$ PVs [218]) and correlated with quantum chemical calculations [9, 218, 229, 265, 272].

Two-photon absorption studies allowed the assignment of the weak  $S_0 \rightarrow S_2$  transition in 1PV [267] and substituted OPVs [270, 268] (Table 5) located about  $4000 \text{ cm}^{-1}$  above the  $S_0 \rightarrow S_1$  transition, in qualitative agreement with quantum chemical calculations [270, 97, 232, 269]. Substituted  $n$ PV derivatives with donor–donor, donor–acceptor–donor, and acceptor–donor–acceptor structural motifs exhibit large two-photon absorption cross sections,  $\delta$  [34, 268, 270, 271], in combination with high fluorescence quantum yields (Table 5). According to quantum chemical calculations, the magnitude of  $\delta$  can be correlated with the degree of intramolecular charge transfer from the terminal donor groups to the  $\pi$  bridge [34, 268] and the calculated  $\delta$  values are in reasonable agreement with the experimental ones [34, 286, 271].

Triplet  $T_1 \rightarrow T_n$  transitions of  $n$ PVs ( $n = 1$  [273],  $n = 2$  [221]) alkoxy OPVs [173, 274] and differently substituted 4PVs [275] were determined by photoinduced absorption spectroscopy and by pulse radiolysis, respectively. The transition energies decrease with increasing chain length [173, 257], in agreement with quantum chemical calculations [101, 103], whereby the decrease is somewhat stronger than the one in the  $S_0 \rightarrow S_1$  transition [173]. The equilibration energies of the triplet transition decrease rapidly with chain length  $n$  [173] in agreement with theoretical results [101]. The triplet lifetimes at  $T = 100 \text{ K}$  are in the range of 3–8 ms [173].

### 3.3. Fluorescence Quantum Yields and Decay Times

The fluorescence quantum yields  $\Phi_F$  of the parent *n*PVs and their derivatives with substituents at the phenylene moieties are fairly high (Tables 2–6) [16, 36, 48, 54, 59, 60, 66, 69, 146, 175, 237, 276, 277]. An exception is 1PV (*trans*-stilbene) due to the crossing of the  $S_1$  potential surface with the  $S_2$  state in the twisted geometry, leading to efficient nonradiative decay and *trans*–*cis* photoisomerization [6, 278]. Consequently,  $\Phi_F$ (1PV) strongly increases in highly viscous [279] or rigid environments [190], at low temperatures [279–281], and in stiffed *trans*-stilbenes [7, 279, 282], where the flexibility of 1PV is strongly reduced. The radiative rate constants  $k_r$  for the  $S_1$  deactivation of the OPVs in solution (Tables 2–4) increase with increasing conjugation length  $n$ , saturating at  $k_r^\infty = (1 \pm 0.3)10^9 \text{ s}^{-1}$  [146, 173]. The increase in the nonradiative rate constant with  $n$  is even stronger, due to the increase in torsional phonon state density with decreasing  $S_1 \rightarrow S_0$  transition energy, leading to an overall decrease in  $\Phi_F$  with  $n$  (Tables 2–4) [16, 173, 175, 283].

Compared to the alkyl- and alkoxy-substituted OPVs, the fluorescence quantum yields are significantly lowered for OPVs with cyanosubstituents in the vinylene unit. The reduction is a sensitive function of the additional substitution patterns (Table 7). Medium quantum yields ( $\Phi_F = 0.3$ – $0.5$ ) are observed if the central phenyl ring of 2PV is additionally substituted with alkoxy groups (molecules of Type A, see Table 7) [48, 50, 284]. Further alkoxy substitution at the terminal phenyl rings reduces  $\Phi_F$  to 5–10% (Type B) [69, 146]. Finally, the oligomers become practically nonfluorescent if the central phenyl ring is substituted with alkyl groups (Type C) [146, 237]. Fluorescence quenching of these compounds is mainly a sterical effect. While molecules of Type A are almost planar [74], the structures of Type C molecules are far from planarity in the  $S_0$  state [68], thus enhancing torsional induced nonradiative deactivation [146]. Rigid environments enforce planarization of the C-type molecules in the  $S_1$  state; thus  $\Phi_F$  increases by 2 orders of magnitude in EPA glass at 77 K [146] (see Table 7).

## 4. MODEL COMPOUNDS FOR OPV–OPV INTERACTION STUDIES

Intermolecular interactions between OPV chromophores and their impact on optical and photophysical properties can be studied on model compounds, which are formed of a small number of oligomers with defined intermolecular geometrical alignment. Simple tetrameric structures were obtained with 2PV derivatives, where the oligomers are covalently linked via a central  $sp^3$  carbon atom or via adamantane (Fig. 3) [126–128]. One-dimensional head-to-tail alignments could be realized in channel-forming host–guest compounds [55, 190, 191, 285]. Since in these structures the OPV–OPV distances are large, the interactions between the oligomers are only of weak dipolar character. An increase in interactions is expected for arrangements with  $\pi$ – $\pi$  overlap, represented by stilbenoid cyclophane compounds [11–13, 118–124, 134] and 1:1 mixtures of complementary oligonucleotides containing stilbene units [142–144].

### 4.1. Arrangements with Weak Dipolar Coupling

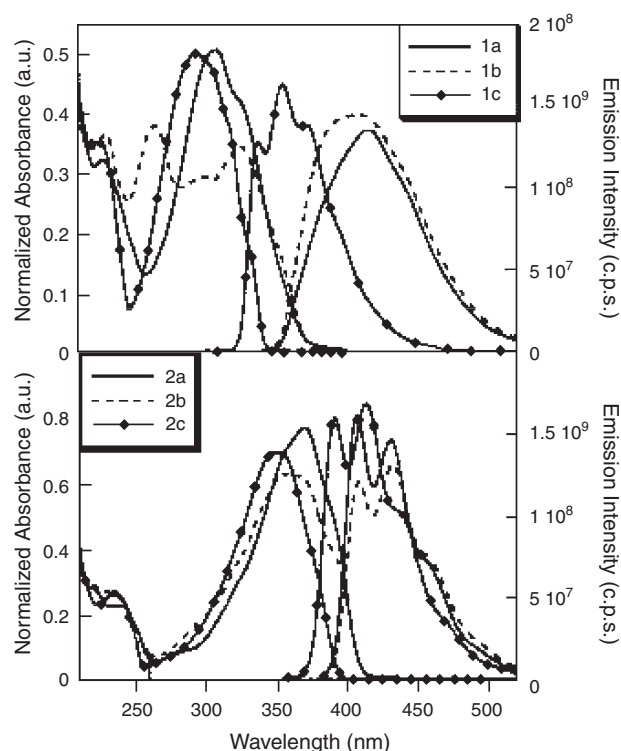
In order to investigate specific head-to-tail interactions, HGCs were prepared, where OPVs and their *p,p'*-substituted derivatives are incorporated in the channels of the pseudo-hexagonal host lattice of PHTP [55, 190, 191]. The intrachannel distances of the oligomers are given by the long axis dimensions and the van der Waals distances. The interchannel distances are in the order of  $r_{a,b} \approx 1.5 \text{ nm}$  [190, 286], so that side-by-side interactions between the oligomers are suppressed. The fine structures and spectral positions of the fluorescence spectra are very similar to those observed in solution [55, 190, 191], thus indicating only small dipolar OPV–OPV interactions. The observed red shift of the spectra  $\Delta\nu_R \approx 700 \text{ cm}^{-1}$  against solution is partly due to the high polarizability of the host lattice, and only a portion of  $\Delta\nu_R \approx 300 \text{ cm}^{-1}$  can be attributed to OPV–OPV interactions [55, 191]. The intermolecular excitation transfer of energy (ET) in the HGCs was investigated by time-resolved fluorescence on doped systems [191]. The results were interpreted according to the Förster-type ET mechanism, considering homo- and heterotransfer as well as *intra*- and *interchannel* transfer steps [191, 287].

The spectral features of the OPV tetramers in Figure 3 are also comparable with those of solutions of the monomers [126–128]. The spectra remain structured and are red-shifted by  $\Delta\nu_R \approx 350 \text{ cm}^{-1}$  against the monomers. This also indicates that in these compounds the interactions between the OPV units are only of weak dipolar character. However, very fast ET is observed. The monoexponential fluorescence anisotropy decay of **AdR<sub>4</sub>** can be reasonably fitted assuming a Förster-type energy transfer, again indicating a weak coupling of the OPV units [128]. For **CR<sub>4</sub>** a biexponential decay was observed, which may suggest the presence of short-range exchange (Dexter)-type interaction [128].

### 4.2. Arrangements with $\pi$ – $\pi$ Overlap

Stronger interactions are expected in OPV pairs with partial  $\pi$ – $\pi$  electron overlap of the OPV units, as in cyclophanes [118–125]. For the “shifted” and “angled” arrangements of the 2PV cyclophanes (structures **2a**, **2b** in Fig. 2), a red shift of  $\Delta\nu_R = 1100 \text{ cm}^{-1}$  against the spectra of the parent monomer unit (**2c** in Fig. 5) is observed [119, 121]. The intermolecular coupling is still of dipolar character, since the vibronic features of the room temperature spectra as well as the fluorescence quantum yields and decay times [119] are very similar to those of the monomer. A monomer-like emitting state was also predicted by theoretical calculations on the basis of the collective electronic oscillator (CEO) method [119]. However, differences between **2a** and the monomer become apparent at low temperatures. In contrast to the monomer, well-resolved phonon lines could not be observed in the fluorescence spectrum of **2a**, probably due to an increase in the Franck–Condon activity in low-frequency chain deformation modes [118].

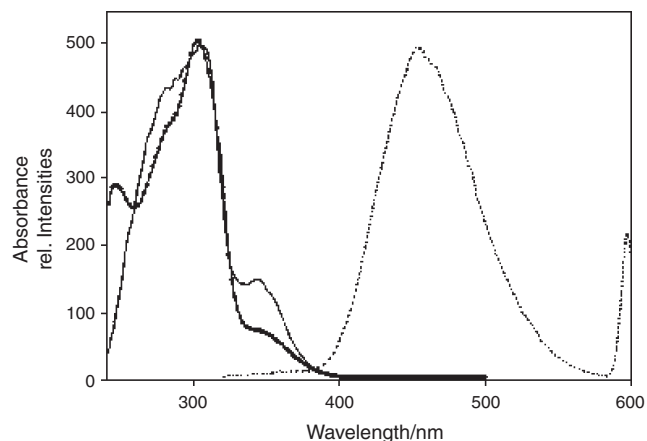
Significant changes in the optical properties are observed if the relative extent of  $\pi$ – $\pi$  overlap between the oligomers is enhanced. Thus, the shifted and angled arrangements of 1PV cyclophanes [119, 134] (structures **1a**, **1b** in Fig. 2)



**Figure 5.** Absorption and fluorescence spectra of stilbenoid cyclophanes. (Top) Spectra of compounds **1a**, **1b** (see Fig. 2) and of the parent monomer unit (**1c**). (Bottom) Spectra of compounds **2a**, **2b** (see Fig. 2) and of the parent monomer unit (**2c**). Reprinted with permission from [121], W. J. Oldham Jr. et al., *J. Am. Chem. Soc.* 120, 419 (1998). © 1998, American Chemical Society.

both show structureless, strongly red-shifted emission bands (Fig. 5) with low radiative rate constants [119], reminiscent of excimer emission. According to CEO calculations the emission of the 1PV cyclophanes occurs from a low-lying state with a significant contribution of the through-space delocalized paracyclophane core [119]. The main absorption band of **1b** shows a splitting of about  $9700\text{ cm}^{-1}$ , in good agreement with CEO calculations, due to the “Davydov-like” splitting of the  $S_0 \rightarrow S_1$  transitions of the monomer units in the angled arrangement [119]. An equivalent explanation accounts for the properties of the “crossed” 2PV cyclophane [120, 134] (structure **3** in Fig. 2), where the  $\pi$ - $\pi$  overlap of the monomer units is increased against **2a** and **2b**, respectively.

Perfect face-to-face alignment in 1PV cyclophane dimers was realized in the dimers **4a** and **4b** of Figure 2. In contrast to the stilbenophane **4a**, which can form *ZZ*, *ZE*, and *EE* isomer pairs [11] due to the flexibility of the ethyl linkers, **4b** is unable to undergo *E-Z* isomerization [12]. The main absorption band of **4b** shows two components, an intense one at  $\lambda_1 \approx 300\text{ nm}$ , slightly blue-shifted against the monomer peak at  $\lambda = 308\text{ nm}$ , and a red-shifted weak one at  $\lambda_2 \approx 350\text{ nm}$  (Fig. 6). Due to the strong  $\pi$ - $\pi$  overlap of the stilbene units, the fluorescence mimics excimer emission with an even stronger red-shifted emission spectrum than **1a** and **1b** and a fluorescence lifetime of  $\tau_F = 11\text{ ns}$  [12]. Similar



**Figure 6.** Absorption (dots), fluorescence excitation (solid line), and emission (dashed line) spectra of stilbenophane **4b**. Reprinted with permission from [12], H. Rau and I. Waldner, *Phys. Chem. Chem. Phys.* 4, 1776 (2002). © 2002, Royal Society of Chemistry.

features are also observed for 1:1 mixtures of complementary oligonucleotides containing stilbene units [142–144] and ternary complexes of 1PV/ $\gamma$ -cyclodextrin/cyclohexane [189].

The electronic properties of cofacial *n*PV dimers were theoretically treated by Cornil [242, 288–290] and by Tretiak and Mukamel [291] and Tretiak et al. [292] as a function of the interchain distance. For large interchain separations ( $d \gtrsim 5\text{ \AA}$ ), a symmetrical splitting of the first single chain transition into a dipole allowed higher energetic components and a forbidden lower one was calculated (H-type interaction), in agreement with Kasha’s molecular exciton model [293, 294]. The excitation energy is still localized on a single chain. Below a critical distance of  $d \approx 5\text{ \AA}$  the splitting becomes unsymmetrical due to second-order perturbations, inducing an additional stabilization of the both states [242]. The lower state is delocalized over both chromophores, whereas the upper state has small interchromophore coherence [292]. The splitting tends to decrease nonlinearly with the chain length of the oligomers [242, 288, 295–297], in contrast to the predictions of the molecular exciton model, which states that there is an increase with chain length [293]. The splitting for a cofacial 1PV dimer [242] at a distance of  $d = 3.5\text{ \AA}$ , which roughly corresponds to the average interchromophore distance in **4b** [298], is  $\Delta\nu = 5800\text{ cm}^{-1}$  at the INDO/S-CI level, in reasonable agreement with experiments (see Fig. 6). Analogous to considerations on 2,2’-paracyclophane [299], the symmetrically forbidden lower excited electronic  $B_g$  state in **4b** may borrow intensity from the higher  $B_u$  state via an  $a_u$  vibrational mode. The weakly allowed  $B_g$  state is responsible for the low radiative rate constant of **4b**. The large red shift of the fluorescence spectra of **1a** and **1b** and particularly **4b** is mainly due to strong intermolecular vibronic coupling between the chromophore units: Quantum chemical calculations of 2,2’-paracyclophane [300] and **4b** [298] predict a strong decrease in the interring distance after  $S_0 \rightarrow S_1$  excitation, which results in extremely high Franck–Condon activity of interring breathing modes [298].

## 5. OPTICAL AND PHOTOPHYSICAL PROPERTIES IN THE SOLID STATE

The optical and photophysical properties of OPVs in the solid state are extensively studied on vapor-deposited (VD) films. Many experimental data are available on the absorption and fluorescence spectra [20–22, 28, 51, 54, 55, 67, 110, 146–149, 153, 158, 237, 258, 301–304], fluorescence quantum yields [22, 54, 55, 237], and fluorescence decay kinetics [22, 54, 55, 110, 158, 237, 258]. However, in only a few cases were the geometrical arrangements of the oligomers in the films determined by atomic force microscopy [149] or by polarized absorption studies [148, 159, 169, 301]; thus structure–property correlations are often missing. On the other hand, the structures of several single crystals have been determined by X-ray measurements [17, 25, 47, 60, 61, 68, 73–80, 108–114, 163, 185, 305, 306], and in some samples the fluorescence properties were also investigated [80, 110, 163, 185–188, 306]. VD films, formed from the same molecules as the corresponding single crystals, are expected to form similar structures, but substrate-induced orientation effects and the formation of meta-stable phases cannot be excluded.

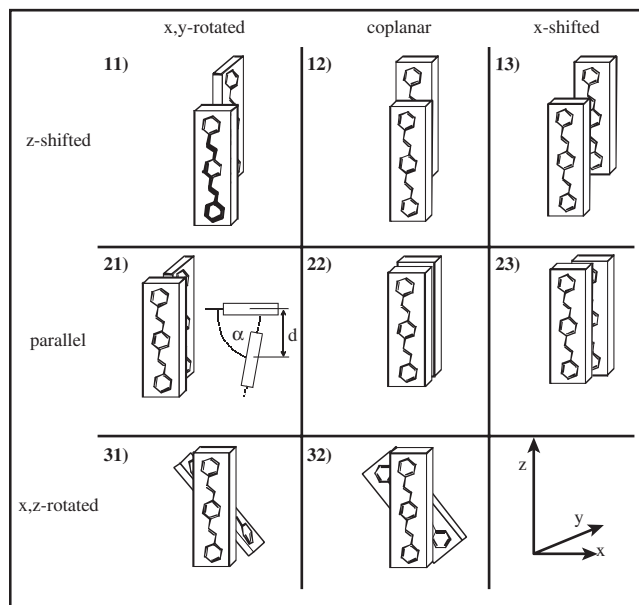
The model compounds of Section 4 demonstrated how the optical and photophysical properties of the individual molecules are changed by specific intermolecular electronic interactions and vibrational coupling. Similar interactions are expected in the solid state structures, but the extension to three dimensions will induce an increase in the total intermolecular coupling strength. Moreover, the photophysical properties in the solid state are influenced by additional effects, such as exciton diffusion, structural defects, and chemical impurities. However, most of the spectral characteristics in OPV condensed phases can be explained by (short-range) molecular ordering. A schematic matrix representation of nearest neighbor arrangements is given in Figure 7.

### 5.1. Unsubstituted Oligomers

#### 5.1.1. Structure

In 4PV single crystals the molecules are oriented with their long axes parallel to each other, where the short axes of adjacent molecules are arranged in a T-shaped manner (Fig. 7.21) with a short-axis inclination angle of  $\alpha \approx 71^\circ$  [17]. The T-shaped short-axis arrangement of adjacent molecules is also found for 2PV [80]. The corresponding “herringbone” arrangement is also predicted for 7PV by force field calculations [307]. A different packing was observed for 1PV single crystals [76–79]. The unit cell contains two molecules that are oriented with their long axes almost perpendicular to each other. Nearest neighbor molecules are cofacially arranged with a slight shift in the  $x,z$  plane (Fig. 7.23).

On the other hand, T-shaped arrangements are also assumed for small aggregates of phospholipids with 1PV substituents [130–133]. The “unit” aggregate consists of a chiral tetramer “pinwheel,” as determined by induced circular dichroism spectra [131, 133]. Analogous structures are assumed in self-organized nanoparticles [146, 148, 174–179] or VD films [20, 21, 28, 51, 146–148, 301] of unsubstituted  $n$ PVs ( $n = 2-4$ ) as well as in Langmuir–Blodgett (LB) films



**Figure 7.** Schematic matrix representation of simple unit cells of oligophenylenevinylenes in the solid state.

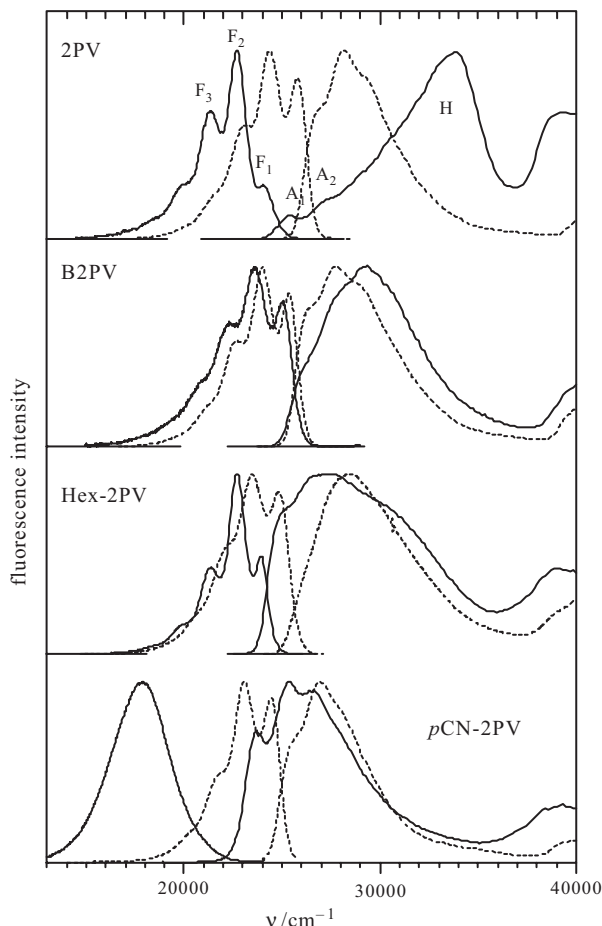
of terminal-substituted  $n$ PVs ( $n = 1$  [131, 159–164], 2 [165–169]), since the spectral and photophysical features are very similar for all of these systems. Especially, both LB [159, 169] and VD films [148, 301] exhibit strong optical linear dichroism, indicating a preferential parallel alignment of the transition dipole moments.

#### 5.1.2. Absorption Spectra

The absorption characteristics can be well studied in systems with low optical density, such as VD films (film thickness  $< 50$  nm), small nanoparticles ( $\varnothing < 100$  nm), or LB films. In thick films [21, 28, 51, 301, 308] or micro [51, 174, 309] or single crystals [80] the increase in the optical density masks most of the spectral characteristics by saturation effects.

The absorption spectra of thin VD films and nanoparticles of unsubstituted  $n$ PVs consist of some weak bands ( $A_1$ ,  $A_2$ ) followed by the main maximum (H band, e.g., for 2PV [175] see Fig. 8), which is blue-shifted by  $\Delta\nu \approx 6000$   $\text{cm}^{-1}$  against the monomer spectrum. The blue shift is a consequence of exciton coupling of the transition dipole moments (H-type aggregation). According to the theoretical treatment by Spano [266, 310–314], the weak low energy peaks ( $A_1$ ,  $A_2$ ) of the spectrum are ascribed to vibrationally dressed excitons in pinwheels [266, 312] which may be present in the inhomogeneous distribution of different aggregate sizes [266]. The “noninteracting domains model” [313], which accounts for the distribution of molecular transition frequencies caused by disorder, reproduces the fine structure of the spectrum. The deviation from perfect parallel alignment of the transition dipoles was determined from the decrease in the time-resolved fluorescence anisotropy from the initial value  $r_{F,0} = 0.4$  to the steady-state value of  $r_F = 0.2-0.3$  [146, 148, 175–178], which yields a mean deviation angle of  $\theta \approx 30^\circ$  between the emitting species and the originally excited absorber. The forbidden lower exciton state (J band) is seen as a very weak shoulder at the low energy side of the spectrum [146, 313],





**Figure 8.** Fluorescence emission (left) and excitation (right) spectra of (substituted) distyrylbenzene (2PV) nanoparticles (solid lines) and spectra in solution (dashed lines).

where the energetic position in 2PV nanoparticles coincides well with the electronic origin ( $\nu_{00} = 23,900 \text{ cm}^{-1}$ ) observed in single crystals of 2PV [188]. The  $\nu_{00}$  position is red shifted against solution by  $\Delta\nu_R = 1800 \text{ cm}^{-1}$  and against vacuum by  $\Delta\nu_R = 3800 \text{ cm}^{-1}$  due to the high optical polarizability of the solid samples in the direction of the long molecular axes. The anisotropic polarizability of 2PV nanoparticles was demonstrated by polarized light scattering measurements [176] and the spectral positions of the sensitized fluorescence of dopants [178].

### 5.1.3. Fluorescence Properties

The room temperature steady-state fluorescence spectra of the unsubstituted *n*PVs are very similar for VD films, LB films, and nanoparticles, whereas in thick films and microcrystals the high energy side of the emission spectra is suppressed by reabsorption [80, 146, 187]. The spectra reveal some vibronic structure (progression  $F_i$ , see Fig. 8) where the energy spacing of the subbands resembles the one in solution. Cooling of the films and nanoparticles does not significantly enhance the vibrational resolution of the spectra, which is due to the spatial inhomogeneity of these systems. Rich vibronic fine structure of the spectra was observed in

2PV single crystals [188] at low temperatures, clearly demonstrating that the vibronic progressions and intercombinations are very similar to those observed in the spectra of the isolated molecules. Thus the contribution of intermolecular vibrational modes is small. However, the electronic origins as well as the  $F_1$  features (Fig. 8) are only of very weak intensity, in significant contrast to the solution spectra. According to the theoretical investigations by Spano [310–314] and Meskers et al. [158], this effect is ascribed to electronic interactions in the medium coupling regime. In the nanoparticles, the  $F_1$  band shows varying intensities [174], which are caused by distributions of zero-order excited state energies [158] and/or distributions of interchain interactions [158, 310–314] due to (point) defects [312, 313]. The fluorescence lifetimes (2PV:  $\tau_F \approx 2.5 \text{ ns}$ , Table 8) are considerably longer than those in solution (2PV:  $\tau_F = 1.2 \text{ ns}$ ), whereas the fluorescence quantum yields are reduced from  $\Phi_F = 0.9$  in solution to  $\Phi_F = 0.05$ – $0.1$  in the films and nanoparticles. Thus the radiative rate constant  $k_F$  decreases against solution by 1 order of magnitude. At  $T = 20 \text{ K}$ ,  $\Phi_F$  increases by a factor of 4–5 [54, 309], similar to PPV [258, 309], reaching the room temperature value of the 2PV single crystal ( $\Phi_F = 0.65$  [80]). The increase in  $\Phi_F$  is accompanied by an increase in  $\tau_F$  of the same order [54, 146, 177]; thus in a first approximation  $k_F$  is independent of temperature.

Energy migration of the  $S_1$  excitation energy in *n*PV films is due to a diffusion-enhanced Förster transfer process, as revealed from the bimolecular rate constant of  $S_1$ – $S_1$  annihilation [308]. The exciton diffusion (diffusion constant  $D \approx 8 \cdot 10^{-4} \text{ cm}^2 \text{ s}^{-1}$ ) [308] allows the deactivation via intrinsic or extrinsic traps. For 6BOPV (Table 4), which also forms H aggregates [38, 158, 173], a distribution of disorder-induced trap sites was deduced from time-resolved and site-selective fluorescence spectra [158]. With increasing excitation wavelength, the fluorescence decay becomes exponential on the time scale of the first nanoseconds [158]. However, on longer time scales, up to the ms regime [315], the fluorescence decay traces of the *n*PVs are strongly nonexponential [146, 148, 177]. This may be due to the recombination of bounded polaron pairs, whose generation was observed in a photoinduced absorption (PIA) study [308]. In this study evidence for fission of vibrationally hot  $S_1$  states into triplet pairs was also found, a process which additionally reduces  $\Phi_F$ . PIA studies on alkoxy-substituted 4PV films (MeH4PV, see Table 9) [152–157, 316, 317] show that at low excitation densities, singlet excitons are formed as the only photoexcitations. At higher excitation densities, the singlet excitons are subject to bimolecular annihilation. In contrast to unsubstituted OPV, no evidence of exciton diffusion is found [153]. An additional contribution to the PIA at high excitation densities is ascribed to biexciton states that are stable in solution but dissociate into charged pairs in thin films [154]. The dissociation of singlet excitons into charged states is found to be a common process in conjugated polymers [157].

### 5.1.4. Doping with Acceptor Molecules for Electronic Excitation Transfer

Doping of the *n*PVs with suitable acceptor molecules, such as longer OPVs [146, 177], oligothiophenes [178], or acenes [186], leads to efficient energy transfer to these extrinsic

traps, resulting in sensitized fluorescence of the dopants. At doping ratios of  $x_{\text{dop}} > 5 \cdot 10^{-4}$  the emission is almost completely dominated by the acceptor emission [146, 177, 178]. The appropriate choice of the acceptors allows tuning of the emission wavelength over the visible range. The acceptor molecules possess the same preferential orientation as the surrounding *n*PV molecules, as revealed from the constant fluorescence anisotropy over the whole emission range [177, 178]. The deactivation kinetics depend strongly on the choice of the dopant. OPVs as acceptors enhance the overall fluorescence quantum yield of doped 2PV nanoparticles up to  $\Phi_{\text{F,tot}} = 0.6$  [146, 177]. Doping with oligothiophenes does not change  $\Phi_{\text{F,tot}}$ , which is probably a consequence of the competition between energy transfer and photoinduced electron transfer [178] from the HOMO of quinquethiophene to the HOMO of 2PV, which is approximately 1 eV lower in energy [150, 318]. The strong decrease in donor emission is not accompanied by a comparable decrease in fluorescence decay, thus indicating spatial inhomogeneities in these systems [146, 178].

## 5.2. Substituted Oligomers

### 5.2.1. *t*-Butyl-Substituted OPVs

Space-consuming substituents like tertiary butyl groups (*Bn*PVs, see Table 2) hinder the coplanar or side-by-side alignments of adjacent molecules (Fig. 7.21, 7.22), since now these structures are energetically less favored than, for example, pairs with *x,z*-rotated axes (Fig. 7.31, 7.32). The lack of short-range parallel intermolecular orientation was demonstrated by the very fast complete fluorescence depolarization, occurring in the first ps after excitation [148, 176, 177]. Due to the different orientations of neighboring transition dipoles, the absorption spectra are very similar to those in solution [148, 176, 177] (see Fig. 8) and no indication of a blue-shifted H band can be observed. Also the energy spacings and relative intensities of the  $F_i$  bands in the fluorescence spectra are almost identical to the ones in solution. The small red shift of  $\Delta\nu_{\text{R}} \approx 400 \text{ cm}^{-1}$  against solution is due to the high, approximately isotropic polarizability of the condensed material. The polarizability in the nonabsorbing region of B2PV nanoparticles was determined as isotropic by polarized light scattering measurements [176, 178]. The calculated isotropic value of the refractive index is in good agreement with the averaged value obtained from the polarizabilities of the constituting atoms and the one derived from the spectral positions of the sensitized fluorescence spectra of dopants [178]. The fluorescence quantum yields are low at room temperature (e.g., B2PV:  $\Phi_{\text{F}} = 0.12$ ) [148], increasing by a factor of three at  $T = 20 \text{ K}$  [258].

### 5.2.2. OPVs with Alkyl or Alkoxy Side Chains

Alkyl or alkoxy side chains (e.g., *n*POPVs, *n*BOPVs, Tables 3, 4) destabilize T-shaped arrangements (Fig. 7.21) and favor partial  $\pi$ - $\pi$  overlap. Thus in general cofacial arrangements, displaced in the *x,z* plane (Fig. 7.12, 7.13, 7.23), are observed. The 4PV oligomer with octyloxy side chains in the central phenyl ring (OctO-4PV, see Table 9) [24, 25, 74, 114, 305, 306] may serve as an example: The unit cell of the single crystal contains eight molecules, where

the conjugated backbones lie parallel to each other. Neighboring molecules are oriented in a cofacial arrangement, shifted in the *x,z* plane [305]. The highly anisotropic character of the cofacial arrangement becomes evident from the high degree of fluorescence polarization [114]. The crystal shift of the fluorescence spectrum against solution yields  $\Delta\nu_{\text{R}} \approx 900 \text{ cm}^{-1}$  (Table 9). This value is significantly higher than that in isotropic solids (e.g., *Bn*PVs) but much smaller than that in the herringbone-arranged unsubstituted 4PV sample ( $\Delta\nu_{\text{R}} \approx 1800 \text{ cm}^{-1}$ , see Table 9). The smaller shift is due to the displacement of the OctO-4PV molecules in the *x,z* plane, but also to the decrease in the packing density by 11% compared to 4PV [17, 306]. The displacement gives rise to J aggregation with a well-structured, red-shifted absorption spectrum and high fluorescence quantum yields and decay rates [24, 306] (see Table 9). Similar considerations also apply for Oct-4PV [303] (Table 9) and Hex-2PV [54] (Fig. 8, Table 8), which all display well-structured fluorescence spectra similar to the ones in solution. No evidence for contributions of intermolecular vibrational modes to the fluorescence spectra is found for these systems.

On the other hand, microcrystals of hexyloxy-substituted 2PV (HexO-2PV, Table 8) show excimer-like emission [54], thus indicating a strong  $\pi$ - $\pi$  overlap of the emitting adjacent molecules. The fluorescence is completely depolarized, which may be due to a random distribution of small  $\pi$ -stacked aggregates or to self-trapping of the excitation energy in excimer-like states [54].

### 5.2.3. Cyanosubstituted OPVs

The tendency to arrange in a  $\pi$ -stacked structure increases by introduction of cyanosubstituents. However, the crystal structure of cyanoderivatives depends sensitively on the substitution position. Thus cyanosubstitution at the *inner* position of the central vinyl moieties of octyloxy-4PV (OctO-4PV-CN<sub>*i*</sub>, see Table 9) results in a cofacial *x,z*-shifted arrangement of neighboring molecules (Fig. 7.13) [73], where the displacement between the molecules is too large to allow intermolecular vibrational coupling. Concomitantly the fluorescence spectrum is structured and no excimer emission is observed [306].

On the other hand, cyanosubstitution at the *outer* positions of the central vinyl linkages (OctO-4PV-CN<sub>*o*</sub>, see Table 9) results in a *z* shift of neighboring molecules (Fig. 7.12) by one phenylene unit [306]. The  $\pi$ - $\pi$  overlap is now large and gives rise to high Franck-Condon activity of intermolecular vibrational modes, leading to excimer emission with a long fluorescence decay time of 8 ns, with a considerably high quantum yield of  $\Phi_{\text{F}} = 0.5$  [306]. Excimer-like emission spectra are also observed for most of the cyanosubstituted 2PVs with additional hexyloxy substituents in the central phenyl ring (Table 8) [54, 57, 237]. However, it should be emphasized that the preparation conditions play a crucial role in the resulting arrangement of the molecules and hence, in the optical and photophysical properties. An illustrative example is *p,p'*-dicyanosubstituted 2PV (*p*CN-2PV). Depending on the preparation conditions (Table 8), H aggregates [319], J aggregates with well-structured emission spectra, or arrangements with excimer-like emission spectra (Fig. 8) [55] are observed (Table 8). In all these arrangements the molecules show a preferential parallel orientation

of the long molecular axes, as revealed from the high values of the fluorescence anisotropy,  $r_F$  (see Table 8). The differences in the absorption and fluorescence spectra of the systems indicate that small changes in the geometrical alignment may induce strong changes in the optical and photophysical properties of the materials.

Extended  $\pi$ - $\pi$  stacks of adjacent molecules were observed for single crystals of various fluorosubstituted distyrylbenzenes [60] and binary cocrystals, containing pairs of unsubstituted and fluorinated *n*PVs, respectively [61, 109]. Nanoparticles and VD films of these materials exhibit H-type absorption spectra and excimer-like emission [321]. Excimer emission is also observed for single crystals of 3,5-dichloro-*trans*-stilbene (Fig. 1), which also crystallizes in a cofacial arrangement [185].

## NOTE

Since the submission of the review chapter a number of new papers in the field of oligophenylenevinylenes have been published [322–363], which could not be included in the text, but should be brought to the attention of the reader. Further studies on the *trans*-*cis* photoisomerization of *trans*-stilbene (1PV) were published by several authors [322–324]. Room temperature Raman studies on 1PV suggest a distorted structure in solution [325]. In a theoretical paper, Møller-Plesset (MP2, MP3) calculations suggest a strictly planar geometry of 1PV in its absolute energy minimum [326]. Several papers described the preparation and spectroscopic characterization of new phenyl [327], alkyl [328], alkoxy [329–331], alkoxysilyl [332], amino [333, 334], bromo [335], and push-pull [336, 337] substituted OPVs. The effects of conformational [338, 339] and environmental disorder [338] on the optical properties were investigated both experimentally [338] and theoretically [338, 339]. A new method for the correlation of molecular shape and polarized luminescence, examined on OPVs, was introduced in Ref. [340]. The electronic transition energies of (substituted) OPVs were investigated at different quantum-chemical levels of theory [341–345], which *inter alia* allow the extrapolation for several ideally conjugated substituted PPV chains [341]. Two-photon properties of substituted OPVs were determined both experimentally [346] and theoretically [347, 348]. Molecular interactions in model compounds and their impact on the optical and photophysical properties were studied in OPV dimers with biphenyl linkage center [349], complementary oligonucleotides containing 1PV units [350], tetrahedral OPV structures [351], polystyrene bearing stilbenoid side chains [352], and supramolecular OPV ensembles [353]. Reference [354] shows that excimer formation of substituted OPVs might be used as strain sensors in polymer blends. Photo- [355–358] and electroluminescence [359–362] of films formed by substituted OPVs were investigated by a number of groups, addressing the influence of substituents [362], crystal structure [355] and morphology of the sample [356, 360]. OPVs have also been used as active material for energy transfer in gelation-assisted light harvesting [363] and for photoinduced electron transfer in TiO<sub>2</sub> hybrid materials [364]. Silver nanoparticles with OPV coating may act as ultrabright two-photon fluorescent nanobeacons [365].

## GLOSSARY

**Bridged oligomers** Model systems of a defined number of chromophores whose conformational degrees of freedom are reduced by hydrogen or covalent bonds between the chromophores. These systems can be used to understand intermolecular interactions of adjacent molecules in the solid state and to build up supramolecular architectures, for example, dendrimers and helical self-organized structures.

**Nanochannel-forming host-guest compounds** Host-guest compounds (HGCs), in which chromophores are incorporated into the channels of inorganic (e.g., zeolites, nanoporous silica) or organic host materials (e.g., perhydrotriphenylene). HGCs provide ideal systems for studying weak dipolar interactions of chromophores and open up the opportunity to overcome the drawbacks of conventional condensed phase device structures for organic optoelectronic applications: Improved chemical stability by exclusion of oxygen, high fluorescence quantum yields by avoiding intermolecular aggregation, intrinsic polarization, high NLO efficiencies, and spatially directed energy transfer.

**Nanoparticles** Nanoparticles of organic chromophores are obtained by precipitation from solutions by addition of a poor solvent. Nanoparticles allow the investigation of substrate-free self-organized systems, easy color tuning by chemical doping with appropriate acceptor molecules, and preparation of optoelectronic devices.

**Oligomer approach** Oligomeric  $\pi$ -conjugated organic molecules provide well-defined conjugation lengths compared to polymers, variable substitution patterns, and defined intermolecular orientations in the condensed phase. Hence oligomers with variable conjugation lengths and substituents make possible the systematic study of the interplay of *intramolecular* (optical) properties and *intermolecular* interactions as well as the understanding of the properties of the polymers. These well-defined systems permit theoretical modeling of solid state properties for molecular engineering of optoelectronic devices.

## REFERENCES

1. M. G. Harrison and R. H. Friend, in "Electronic Materials: The Oligomer Approach" (K. Müllen and G. Wegner, Eds.), p. 515. Wiley-VCH, Weinheim 1998.
2. R. H. Friend, R. W. Gymer, A. B. Holmes, J. H. Burroughes, R. N. Marks, C. Taliani, D. D. C. Bradley, D. A. dos Santos, J. L. Brédas, M. Löglund, and W. R. Salaneck, *Nature (London)* 397, 121 (1999).
3. L. Pichat, P. Peistel, and J. Clement, *J. Chem. Phys.* 50, 26 (1953).
4. (a) V. P. Kotsubanov, L. Ya. Malkes, Yu. V. Naboikin, L. A. Ogurtsova, A. P. Podgorny, F. S. Potrovskaia, and L. V. Shubina, *Zh. Prik. Spektrosc.* 10, 152 (1969); (b) H. Furumato and H. Ceccon, *J. Appl. Phys.* 40, 4204 (1969); (c) J. T. Warden and L. Gough, *Appl. Phys. Lett.* 19, 345 (1971); (d) H. Tell, U. Brinkmann, and P. Raue, *Opt. Commun.* 24, 248 (1978).
5. A. E. Siegrist, P. Liechti, H. R. Meyer, and K. Weber, *Helv. Chim. Acta* 52, 2521 (1969).
6. (a) D. H. Waldeck, *Chem. Rev.* 91, 415 (1991) and references cited therein; (b) T. Arai and K. Tokumaru, *Chem. Rev.* 93, 23 (1993) and references cited therein.
7. G. Hohlneicher, R. Wrzal, D. Lenoir, and R. Frank, *J. Phys. Chem. A* 103, 8696 (1999).

8. W. G. Han, T. Lovell, T. Liu, and L. Noodleman, *Chem. Phys. Chem.* 2002, 167 (2002).
9. V. Molina, M. Merchán, and B. O. Roos, *J. Phys. Chem. A* 101, 3478 (1997).
10. J. Quenneville and T. J. Martínez, *J. Phys. Chem. A* 107, 829 (2003).
11. I. Anger, K. Sandros, M. Sundahl, and O. Wennerström, *J. Phys. Chem.* 97, 1920 (1993).
12. H. Rau and I. Waldner, *Phys. Chem. Chem. Phys.* 4, 1776 (2002).
13. R. Schenk, H. Gregorius, K. Meerholz, J. Heinze, and K. Müllen, *J. Am. Chem. Soc.* 113, 2634 (1991).
14. Y. Geerts, G. Klärner, and K. Müllen, in "Electronic Materials: The Oligomer Approach" (K. Müllen and G. Wegner, Eds.), p. 1. Wiley-VCH, Weinheim (1998).
15. R. E. Martin and F. Diederich, *Angew. Chem. Int. Ed.* 38, 1350 (1999).
16. M. S. Wong, Z. H. Li, M. F. Shek, K. H. Chow, Y. Tao, and M. D'Iorio, *J. Mater. Chem.* 10, 1805 (2000).
17. P. F. van Hutten, J. Wildeman, A. Meetsma, and G. Hadziioannou, *J. Am. Chem. Soc.* 121, 5910 (1999).
18. V. Gebhardt, A. Bacher, M. Thelakkat, U. Stalmach, H. Meier, H.-W. Schmidt, and D. Haarer, *Synth. Met.* 90, 123 (1997).
19. U. Stalmach, H. Detert, H. Meier, V. Gebhardt, D. Haarer, A. Bacher, and H.-W. Schmidt, *Opt. Mater.* 9, 77 (1998).
20. F. Meghdadi, G. Leising, W. Fischer, and F. Stelzer, *Synth. Met.* 76, 113 (1996).
21. H. S. Woo, J. G. Lee, H. K. Min, E. J. Oh, S. J. Park, K. W. Lee, J. H. Lee, S. H. Cho, T. W. Kim, and C. H. Park, *Synth. Met.* 71, 2173 (1995).
22. T. Goodson III, W. Li, A. Gharavi, and L. Yu, *Adv. Mater.* 9, 639 (1997).
23. V. Gebhardt, A. Bacher, M. Thelakkat, U. Stalmach, H. Meier, H.-W. Schmidt, and D. Haarer, *Adv. Mater.* 11, 119 (1999).
24. H.-J. Brouwer, V. V. Krasnikov, T.-A. Pham, R. E. Gill, and G. Hadziioannou, *Appl. Phys. Lett.* 73, 708 (1998).
25. P. F. van Hutten, V. V. Krasnikov, and G. Hadziioannou, *Acc. Chem. Res.* 32, 257 (1999).
26. Z. Yang, H. J. Geise, M. Mehbod, G. Debrue, J. W. Visser, E. J. Sonneveld, L. Van't Dack, and R. Gijbels, *Synth. Met.* 39, 137 (1990).
27. G. Drefahl, R. Kühmstedt, H. Oswald, and H.-H. Hörhold, *Makromol. Chem.* 131, 89 (1970).
28. H.-J. Egelhaaf, M. Brun, S. Reich, and D. Oelkrug, *J. Mol. Struct.* 267, 297 (1992).
29. L. Lüer, H.-J. Egelhaaf, and D. Oelkrug, *Synth. Met.* 119, 621 (2001).
30. L. Lüer, H.-J. Egelhaaf, and D. Oelkrug, *Opt. Mater.* 9, 454 (1998).
31. J. H. Schön, C. Kloc, J. Wildeman, and G. Hadziioannou, *Adv. Mater.* 13, 1273 (2001).
32. B. de Boer, U. Stalmach, C. Melzer, and G. Hadziioannou, *Synth. Met.* 121, 1541 (2001).
33. B. de Boer, U. Stalmach, H. Nijland, and G. Hadziioannou, *Adv. Mater.* 12, 1581 (2000).
34. M. Albota, D. Beljonne, J. L. Brédas, J. E. Ehrlich, J.-Y. Fu, A. A. Heikal, S. E. Hess, T. Kogej, M. D. Levin, S. R. Marder, D. McCord-Maughon, J. W. Perry, H. Röckel, M. Rumi, G. Subramaniam, W. W. Webb, X.-L. Wu, and C. Xu, *Science* 281, 1653 (1998).
35. (a) S. Misumi, M. Kuwana, K. Murashima, and M. Nakagawa, *Bull. Chim. Soc. Jpn.* 34, 1833 (1961); (b) S. Misumi, M. Kuwana, and M. Nakagawa, *Bull. Chim. Soc. Jpn.* 35, 135 (1962).
36. R. Erckel and H. Fröhbeis, *Z. Naturforsch.* 37b, 1472 (1982).
37. U. Stalmach, H. Kolshorn, I. Brehm, and H. Meier, *Liebigs Ann.* 1996, 1449 (1996).
38. E. Peeters, R. A. J. Janssen, S. C. J. Meskers, and E. W. Meijer, *Polym. Prepr. (Am. Chem. Soc. Div. Polym. Chem.)* 40, 519 (1999).
39. R. Reetz, O. Narwark, O. Herzog, S. Brocke, and E. Thorn-Csányi, *Synth. Met.* 119, 539 (2001).
40. O. Narwark, O. Herzog, and E. Thorn-Csányi, *Synth. Met.* 121, 1375 (2001).
41. O. Herzog, O. Narwark, and E. Thorn-Csányi, *Synth. Met.* 119, 141 (2001).
42. E. Thorn-Csányi and P. Kraxner, *Macromol. Chem. Phys.* 198, 3827 (1997).
43. A. P. H. J. Schenning, A. El-ghayoury, E. Peeters, and E. W. Meijer, *Synth. Met.* 121, 1253 (2001).
44. H. Meier, J. Gerold, H. Kolshorn, W. Baumann, and M. Bletz, *Angew. Chem. Int. Ed.* 41, 292 (2002).
45. G. Klärner, C. Former, X. Yan, R. Richert, and K. Müllen, *Adv. Mater.* 11, 932 (1996).
46. I. Anger, M. Sundahl, O. Wennerström, K. Sandros, T. Arai, and K. Tokumaru, *J. Phys. Chem.* 96, 7027 (1992).
47. H. Irngartinger, J. Lichtenthaler, and R. Herpich, *Struct. Chem.* 5, 283 (1994).
48. E. Birckner, U.-W. Grummt, H. Rost, A. Hartmann, S. Pfeiffer, H. Tillmann, and H.-H. Hörhold, *J. Fluoresc.* 8, 73 (1998).
49. S. Nakatsuji, K. Matsuda, Y. Uesugi, K. Nakashima, S. Akiyama, G. Katzer, and W. Fabian, *J. Chem. Soc. Perkin Trans. 2*, 6, 861 (1991).
50. U. Stalmach and H. Detert, *J. Prakt. Chem.* 342, 10 (2000).
51. N. N. Barashkov, D. J. Guerrero, H. J. Olivos, and J. P. Ferraris, *Synth. Met.* 75, 153 (1995).
52. F. Babudri, G. M. Farinola, L. C. Lopez, M. G. Martinelli, and F. Naso, *J. Org. Chem.* 66, 3878 (2001).
53. M. S. Wong, M. Samoc, A. Samoc, B. Luther-Davies, and M. G. Humphrey, *J. Mater. Chem.* 8, 2005 (1998).
54. K.-H. Schweikhart, M. Hohloch, E. Steinhuber, M. Hanack, L. Lüer, J. Gierschner, H.-J. Egelhaaf, and D. Oelkrug, *Synth. Met.* 121, 1641 (2001).
55. J. Gierschner, H.-J. Egelhaaf, H.-G. Mack, D. Oelkrug, R. Martinez-Alvarez, and M. Hanack, *Synth. Met.* 137, 1449 (2003).
56. M. S. Liu, X. Jiang, S. Liu, P. Herguth, and A. K.-Y. Jen, *Macromolecules* 35, 3532 (2002).
57. K.-H. Schweikart, M. Hanack, L. Lüer, and D. Oelkrug, *Eur. J. Org. Chem.* 2001, 293 (2001).
58. H. Detert and E. Sugiono, *Synth. Met.* 127, 233 (2002).
59. B. Strehmel, A. M. Sarker, J. H. Malpert, V. Strehmel, H. Seifert, and D. C. Neckers, *J. Am. Chem. Soc.* 121, 1226 (1999).
60. M. L. Renak, G. P. Bartholomew, S. Wang, P. J. Ricotto, R. J. Lachicotte, and G. C. Bazan, *J. Am. Chem. Soc.* 121, 7787 (1999).
61. G. W. Coates, A. R. Dunn, L. M. Henling, J. W. Ziller, E. B. Lobkovsky, and R. H. Grubbs, *J. Am. Chem. Soc.* 120, 3641 (1998).
62. K. Sandros and M. Sundahl, *J. Phys. Chem.* 98, 5705 (1994).
63. E. Sugiono, T. Metzroth, and H. Detert, *Adv. Synth. Catal.* 343, 351 (2001).
64. H. Detert and E. Sugiono, *Synth. Met.* 127, 237 (2002).
65. A. C. Freydank, M. G. Humphrey, R. W. Friedrich, and B. Luther-Davies, *Tetrahedron* 58, 1425 (2002).
66. S. E. Döttinger, M. Hohloch, J. L. Segura, E. Steinhuber, M. Hanack, A. Tompert, and D. Oelkrug, *Adv. Mater.* 9, 233 (1997).
67. P. Martinez-Ruiz, B. Behnisch, K.-H. Schweikhart, M. Hanack, L. Lüer, and D. Oelkrug, *Chem. Eur. J.* 2000, 1294 (2000).
68. M. Hohloch, C. Maichle-Mössmer, and M. Hanack, *Chem. Mater.* 10, 1327 (1998).
69. M. M. de Souza, G. Rumbles, I. R. Gould, H. Amer, I. D. W. Samuel, S. C. Moratti, and A. B. Holmes, *Synth. Met.* 111–112, 539 (2000).
70. M. Leuze, M. Hohloch, and M. Hanack, *Chem. Mater.* 14, 3339 (2002).
71. M. M. de Souza, G. Rumbles, D. L. Russel, I. D. W. Samuel, S. C. Moratti, A. B. Holmes, and P. L. Burn, *Synth. Met.* 119, 635 (2001).
72. H. Detert and E. Sugiono, *J. Phys. Org. Chem.* 13, 587 (2000).
73. R. E. Gill, P. F. van Hutten, A. Meetsma, and G. Hadziioannou, *Chem. Mater.* 8, 1341 (1996).

74. R. E. Gill, A. Hilberer, P. F. van Hutten, G. Berentschott, M. P. L. Werts, A. Meetsma, J.-C. Wittmann, and G. Hadziioannou, *Synth. Met.* 84, 637 (1996).
75. H. Detert, D. Schollmeyer, and E. Sugiono, *Eur. J. Org. Chem.* 2001, 2927 (2001).
76. J. Bernstein, *Acta Crystallogr. B* 31, 1268 (1975).
77. C. J. Finder, M. G. Newton, and N. L. Allinger, *Acta Crystallogr. B* 30, 411 (1974).
78. A. Hoeckstra, P. Meertens, and A. Voss, *Acta Crystallogr. B* 31, 2813 (1975).
79. J. A. Bouwstra, A. Schouten, and J. Kroon, *Acta Crystallogr. C* 40, 428 (1984).
80. C. C. Wu, M. C. DeLong, Z. V. Vardeny, and J. P. Ferraris, *Synth. Met.* 137, 939 (2003).
81. T. Suzuki, N. Mikami, and M. Ito, *J. Phys. Chem.* 90, 6431 (1986).
82. (a) L. H. Spangler, R. van Zee, S. C. Blankespoor, and T. S. Zwier, *J. Phys. Chem.* 91, 6077 (1987); (b) L. H. Spangler, R. van Zee, and T. S. Zwier, *J. Phys. Chem.* 91, 2782 (1987).
83. W.-Y. Chiang and J. Laane, *J. Chem. Phys.* 100, 8755 (1994).
84. B. B. Champagne, J. F. Pfanstiel, D. F. Plusquellic, D. W. Pratt, W. M. van Herpen, and W. L. Meerts, *J. Phys. Chem.* 96, 6 (1990).
85. S. P. Kwasniewski, M. S. Deleuze, and J. P. Francois, *Int. J. Quantum Chem.* 85, 557 (2001).
86. L. Claes, S. Kwasniewski, M. S. Deleuze, and J. P. François, *J. Mol. Struct. (Theochem)* 549, 63 (2001).
87. C. H. Choi and M. Kertesz, *J. Phys. Chem. A* 101, 3823 (1997).
88. S. P. Kwasniewski, M. S. Deleuze, and J. P. Francois, *Int. J. Quantum Chem.* 80, 672 (2000).
89. Z. G. Soos, S. Ramasesha, D. S. Galvão, and S. Etemad, *Phys. Rev. B* 47, 1742 (1993).
90. D. S. Galvão, Z. G. Soos, S. Ramasesha, and S. Etemad, *J. Chem. Phys.* 98, 3016 (1993).
91. J. Gierschner, H.-G. Mack, L. Lüer, and D. Oelkrug, *J. Chem. Phys.* 116, 8596 (2002).
92. C.-J. Kim, *Bull. Korean. Chem. Soc.* 23, 330 (2002).
93. O. Lhost and J. L. Brédas, *J. Chem. Phys.* 96, 5279 (1992).
94. G. Baranović, Z. Meić, and A. H. Maulitz, *Spectrochim. Acta A* 54, 1017 (1998).
95. G. C. Claudio and E. R. Bittner, *Chem. Phys.* 276, 81 (2002).
96. a) B. Tian, G. Zerbi, R. Schenk, and K. Müllen, *J. Chem. Phys.* 95, 3191 (1991); (b) B. Tian, G. Zerbi, and K. Müllen, *J. Chem. Phys.* 95, 3198 (1991).
97. S. Karabunarliev, M. Baumgarten, and K. Müllen, *J. Phys. Chem. A* 104, 8236 (2000).
98. J. F. Arenas, I. L. Tocón, J. C. Otero, and J. I. Marcos, *J. Phys. Chem.* 99, 11392 (1995).
99. L. Gagliardi, G. Orlandi, V. Molina, P.-A. Malmqvist, and B. Roos, *J. Phys. Chem. A* 106, 7355 (2002).
100. F. Negri, G. Orlandi, and F. Zerbetto, *J. Phys. Chem.* 93, 5124 (1989).
101. D. Beljonne, Z. Shuai, R. H. Friend, and J. L. Brédas, *J. Chem. Phys.* 102, 2042 (1995).
102. H. Watanabe, Y. Okamoto, K. Furuya, A. Sakamoto, and M. Tasumi, *J. Phys. Chem. A* 106, 3318 (2002).
103. D. Beljonne, J. Cornil, J. L. Brédas, and R. H. Friend, *Synth. Met.* 76, 61 (1996).
104. M. Trættemberg, E. B. Frantsen, F. C. Mijehoff, and A. Hoeckstra, *J. Mol. Struct.* 26, 57 (1975).
105. T. Kobayashi, H. Suzuki, and K. Ogawa, *Bull. Chem. Soc. Jpn.* 55, 1734 (1982).
106. P. Rademacher, A. L. Marzinzik, K. Kowski, and M. E. Weiß, *Eur. J. Org. Chem.* 2001, 121 (2001).
107. S. Karabunarliev, M. Baumgarten, N. Tyutyulkov, and K. Müllen, *J. Phys. Chem.* 98, 11892 (1994).
108. U. Stalmach, D. Schollmeyer, and H. Meier, *Chem. Mater.* 11, 2103 (1999).
109. G. P. Bartholomew, X. Bu, and G. C. Bazan, *Chem. Mater.* 12, 2311 (2000).
110. P. F. van Hutten, H.-J. Brouwer, V. V. Krasnikov, L. Ouali, U. Stalmach, and G. Hadziioannou, *Synth. Met.* 102, 1443 (1999).
111. M. Verbruggen, Yang Zhou, A. T. H. Lenstra, and H. J. Geise, *Acta Crystallogr. C* 44, 2120 (1988).
112. K. Ogawa, H. Suzuki, T. Sakurai, K. Kobayashi, A. Kira, and A. Toriumi, *Acta Crystallogr. C* 44, 505 (1988).
113. M. Hakansson, S. Jagner, M. Sundahl, and O. Wennerström, *Acta Chem. Scand.* 46, 1160 (1992).
114. H. J. Brouwer, V. V. Krasnikov, T. A. Pham, R. E. Gill, P. F. van Hutten, and G. Hadziioannou, *Chem. Phys.* 227, 65 (1998).
115. A. El-ghayoury, E. Peeters, A. P. H. J. Schenning, and E. W. Meijer, *Chem. Commun.* 2000, 1969 (2000).
116. A. P. H. J. Schenning, P. Jonkheijm, E. Peeters, and E. W. Meijer, *J. Am. Chem. Soc.* 123, 409 (2001).
117. A. El-ghayoury, A. P. H. J. Schenning, P. A. van Hal, K. J. van Duren, R. A. Janssen, and E. W. Meijer, *Angew. Chem. Int. Ed.* 40, 3660 (2001).
118. N. Verdal, J. T. Godbout, T. L. Perkins, G. P. Bartholomew, G. C. Bazan, and A. Myers Kelley, *Chem. Phys. Lett.* 320, 95 (2000).
119. G. C. Bazan, W. J. Oldham Jr., R. J. Lachicotte, S. Tretiak, V. Chernyak, and S. Mukamel, *J. Am. Chem. Soc.* 120, 9188 (1998).
120. S. Wang, G. C. Bazan, S. Tretiak, and S. Mukamel, *J. Am. Chem. Soc.* 122, 1289 (2000).
121. W. J. Oldham Jr., Y.-J. Mio, R. J. Lachicotte, and G. C. Bazan, *J. Am. Chem. Soc.* 120, 419 (1998).
122. A. M. Moran, G. P. Bartholomew, G. C. Bazan, and A. Myers Kelley, *J. Phys. Chem. A* 106, 4928 (2002).
123. J. Zyss, I. Ledoux, S. Volkov, V. Chernyak, S. Mukamel, G. P. Bartholomew, and G. C. Bazan, *J. Am. Chem. Soc.* 122, 11956 (2000).
124. G. P. Bartholomew, I. Ledoux, S. Mukamel, G. C. Bazan, and J. Zyss, *J. Am. Chem. Soc.* 124, 13480 (2002).
125. J. W. Hong, B. S. Gaylord, and G. C. Bazan, *J. Am. Chem. Soc.* 124, 11868 (2002).
126. S. Wang, W. J. Oldham, Jr., R. A. Hudack, Jr., and G. C. Bazan, *J. Am. Chem. Soc.* 122, 5695 (2000).
127. M. R. Robinson, S. Wang, G. C. Bazan, and Y. Cao, *Adv. Mater.* 12, 1701 (2000).
128. O. P. Varnavski, J. C. Ostrowski, L. Sukhomlinova, R. J. Twieg, G. C. Bazan, and T. Goodson III, *J. Am. Chem. Soc.* 124, 1736 (2002).
129. M. A. Summers, M. R. Robinson, G. C. Bazan, and S. K. Buratto, *Chem. Phys. Lett.* 364, 542 (2002).
130. X. Song, C. Geiger, U. Leinhos, J. Perlstein, and D. G. Whitten, *J. Am. Chem. Soc.* 116, 10340 (1994).
131. X. Song, C. Geiger, M. Farahat, J. Perlstein, and D. G. Whitten, *J. Am. Chem. Soc.* 119, 12481 (1997).
132. X. Song, C. Geiger, I. Furman, and D. G. Whitten, *J. Am. Chem. Soc.* 116, 4103 (1994).
133. D. G. Whitten, L. Chen, C. Geiger, J. Perlstein, and X. Song, *J. Phys. Chem. B* 102, 10098 (1998).
134. B. König, B. Knieriem, and A. de Meijere, *Chem. Ber.* 126, 1643 (1997).
135. Y. Ito, S. Miyata, M. Nakatsuka, T. Saegusa, M. Takamoto, and Y. Wada, *J. Chem. Soc., Chem. Commun.* 375 (1982).
136. O. Varnavski, I. D. W. Samuel, L.-O. Pålson, R. Beavington, P. L. Burn, and T. Goodson III, *J. Chem. Phys.* 116, 8893 (2002).
137. C. C. Kwok and M. S. Wong, *Macromolecules* 34, 6821 (2001).
138. S. C. J. Meskers, M. Bender, J. Hübner, Y. V. Romanovskii, M. Oestreich, A. P. H. J. Schenning, E. W. Meijer, and H. Bässler, *J. Phys. Chem. A* 105, 10220 (2001).
139. D. M. Guldi, A. Swartz, C. Luo, R. Gómez, J. L. Segura, and N. Martin, *J. Am. Chem. Soc.* 124, 10875 (2002).
140. J. M. Lupton, I. D. W. Samuel, and P. L. Burn, *Phys. Rev. B* 66, 155206 (2002).

141. L.-O. Pålson, R. Beavington, M. J. Frampton, J. M. Lupton, S. W. Magennis, J. P. J. Markham, J. N. G. Pillow, P. L. Burn, and I. D. W. Samuel, *Macromolecules* 35, 7891 (2002).
142. R. L. Letsinger and T. Wu, *J. Am. Chem. Soc.* 116, 811 (1994).
143. F. D. Lewis, T. Wu, E. L. Burch, D. M. Bassani, Y.-S. Yang, S. Schneider, W. Jäger, and R. L. Letsinger, *J. Am. Chem. Soc.* 117, 8785 (1995).
144. R. L. Letsinger and T. Wu, *J. Am. Chem. Soc.* 117, 7323 (1995).
145. F. D. Lewis, Y.-S. Yang, and C. L. Stern, *J. Am. Chem. Soc.* 118, 2772 (1996).
146. D. Oelkrug, A. Tompert, J. Gierschner, H.-J. Egelhaaf, M. Hanack, M. Hohloch, and E. Steinhuber, *J. Phys. Chem. B* 102, 1902 (1998).
147. D. Oelkrug, J. Haiber, R. Lege, H. Stauch, and H.-J. Egelhaaf, *Thin Solid Films* 284–285, 581 (1996).
148. H.-J. Egelhaaf, J. Gierschner, and D. Oelkrug, *Synth. Met.* 83, 221 (1996).
149. J. P. Ni, Y. Ueda, T. Hanada, N. Takada, Y. Ichino, Y. Yoshida, N. Tanigaki, K. Yase, D. K. Wang, and F. S. Wang, *J. Appl. Phys.* 86, 6150 (1999).
150. A. Schmidt, M. L. Anderson, D. Dunphy, T. Wehrmeister, K. Müllen, and N. R. Armstrong, *Adv. Mater.* 7, 722 (1995).
151. S. C. Veenstra, U. Stalmach, V. V. Krasnikov, G. Hadziioannou, H. T. Jonkman, A. Heeres, and G. A. Sawatzky, *Appl. Phys. Lett.* 76, 2253 (2000).
152. V. Klimov, D. McBranch, N. Barashkov, and J. Ferraris, *SPIE* 3145, 58 (1997).
153. E. S. Maniloff, V. I. Klimov, and D. W. McBranch, *Phys. Rev. B* 56, 1876 (1997).
154. V. I. Klimov, D. W. McBranch, N. Barashkov, and J. Ferraris, *Phys. Rev. B* 58, 7654 (1998).
155. V. I. Klimov, D. W. McBranch, N. N. Barashkov, and J. P. Ferraris, *Chem. Phys. Lett.* 277, 109 (1997).
156. D. W. McBranch, B. Kraabel, S. Xu, R. S. Kohlman, V. I. Klimov, D. D. C. Bradley, B. R. Hsieh, and M. Rubner, *Synth. Met.* 101, 291 (1999).
157. B. Kraabel, V. I. Klimov, R. Kohlman, S. Xu, H.-L. Wang, and D. W. McBranch, *Phys. Rev. B* 61, 8501 (2000).
158. S. C. J. Meskers, R. A. J. Janssen, J. E. M. Haverkort, and J. H. Wolter, *Chem. Phys.* 260, 415 (2000).
159. W. F. Mooney III, P. E. Brown, J. C. Russell, S. B. Costa, L. G. Pedersen, and D. G. Whitten, *J. Am. Chem. Soc.* 106, 5659 (1984).
160. W. F. Mooney and D. G. Whitten, *J. Am. Chem. Soc.* 108, 5712 (1986).
161. S. P. Spooner and D. G. Whitten, *J. Am. Chem. Soc.* 116, 1240 (1994).
162. J. Heesemann, *J. Am. Chem. Soc.* 102, 2167 (1980).
163. S. Vaday, H. C. Geiger, B. Cleary, J. Perlstein, and D. G. Whitten, *J. Phys. Chem. B* 101, 321 (1997).
164. D. G. Whitten, *Acc. Chem. Res.* 26, 502 (1993).
165. M. Era, J. Koganemaru, T. Tsutsui, A. Watakabe, and T. Kunitake, *Synth. Met.* 91, 83 (1997).
166. A. Watakabe and T. Kunitake, *J. Colloid Interface Sci.* 145, 90 (1991).
167. A. Watakabe and T. Kunitake, *Chem. Lett.* 1991, 905 (1991).
168. A. Watakabe and T. Kunitake, *Thin Solid Films* 186, L21 (1990).
169. A. Watakabe, H. Okoda, and T. Kunitake, *Langmuir* 10, 2722 (1994).
170. P. Jonkheijm, M. Fransen, A. P. H. J. Schenning, and E. W. Meijer, *J. Chem. Soc., Perkin Trans. 2* 2001, 1280 (2001).
171. C. J. Collison, V. Treemanekarn, W. J. Oldham, Jr., J. H. Hsu, and L. J. Rothberg, *Synth. Met.* 119, 515 (2001).
172. B.-K. An, S.-K. Kwon, S.-D. Jung, and S. Y. Park, *J. Am. Chem. Soc.* 124, 14410 (2002).
173. E. Peeters, A. M. Ramos, S. C. J. Meskers, and R. A. J. Janssen, *J. Chem. Phys.* 112, 9445 (2000).
174. J. Gierschner, Dissertation, Tübingen, 2000.
175. D. Oelkrug, H.-J. Egelhaaf, J. Gierschner, and A. Tompert, *Synth. Met.* 76, 249 (1996).
176. J. Gierschner, H.-J. Egelhaaf, and D. Oelkrug, *Synth. Met.* 84, 529 (1997).
177. J. Gierschner, H.-J. Egelhaaf, D. Oelkrug, and K. Müllen, *J. Fluoresc.* 8, 37 (1998).
178. H.-J. Egelhaaf, J. Gierschner, and D. Oelkrug, *Synth. Met.* 127, 221 (2002).
179. I. A. Vasileva, M. D. Galanin, A. N. Nikitina, and Z. A. Chizhikova, *Opt. Spektrosk.* 60, 976 (1986).
180. B. Brocklehurst, D. C. Bull, M. Evans, P. M. Scott, and G. Stanney, *J. Am. Chem. Soc.* 97, 2977 (1975).
181. K. Henderson, A. B. Dalton, G. Chambers, A. Drury, S. Maier, A. G. Ryder, W. Blau, and H. J. Byrne, *Synth. Met.* 119, 555 (2001).
182. J. Catalán, L. Zimányi, and J. Saltiel, *J. Am. Chem. Soc.* 122, 2377 (2000).
183. D. Horn and J. Rieger, *Angew. Chem. Int. Ed.* 40, 4330 (2001).
184. H. Kasai, H. S. Nalwa, S. Okada, H. Oikawa, and H. Nakanish, in “Handbook of Nanostructured Materials and Nanotechnology” (H. S. Nalwa, Ed.), Vol. 5, Chap. 8, pp. 4330–4361. Academic Press, New York, 2000.
185. M. D. Cohen, B. S. Green, Z. Ludmer, and G. M. J. Schmidt, *Chem. Phys. Lett.* 7, 486 (1979).
186. R. M. Hochstrasser, *J. Mol. Spectrosc.* 8, 485 (1962).
187. A. F. Prikhot’ko and I. Fugol’, *Opt. Spektrosk.* 7, 19 (1959).
188. C. C. Wu, O. J. Korovyanko, M. C. DeLong, Z. V. Vardeny, and J. P. Ferraris, *Synth. Met.* 139, 735 (2003).
189. R. A. Agbaria, E. Roberts, and I. M. Warner, *J. Phys. Chem.* 99, 10056 (1995).
190. J. Gierschner, L. Lüer, D. Oelkrug, E. Musluoğlu, B. Behnisch, and M. Hanack, *Adv. Mater.* 12, 757 (2000).
191. J. Gierschner, L. Lüer, D. Oelkrug, E. Musluoğlu, B. Behnisch, and M. Hanack, *Synth. Met.* 121, 1695 (2001).
192. R. H. Dyck and D. S. McClure, *J. Chem. Phys.* 36, 2326 (1962).
193. J. A. Syage, P. M. Felker, and A. H. Zewail, *J. Chem. Phys.* 81, 4685 (1984).
194. Z. Arp, W.-Y. Chiang, A. Sakamoto, and M. Tasumi, *J. Phys. Chem. A* 106, 3479 (2002).
195. R. A. Rijkenberg, D. Beelaar, W. J. Buma, and J. W. Hofstraat, *J. Phys. Chem. A* 106, 2446 (2002).
196. T. Urano, H. Hamaguchi, M. Tasumi, K. Yamanouchi, S. Tsuchiya, and T. L. Gustafson, *J. Chem. Phys.* 91, 3884 (1989).
197. (a) R. Mahrt, J. Yang, A. Greiner, and H. Bässler, *Makromol. Chem.* 11, 415 (1990); (b) S. Heun, R. F. Mahrt, A. Greiner, U. Lemmer, H. Bässler, D. A. Halliday, D. D. C. Bradley, P. L. Burns, and A. B. Holmes, *J. Phys. Condens. Matter* 5, 247 (1993).
198. T. Pauck, H. Bässler, J. Grimme, U. Scherf, and K. Müllen, *Chem. Phys.* 210, 219 (1996).
199. F. Negri and M. Z. Zgierski, *J. Chem. Phys.* 100, 2571 (1994).
200. S. Karabunarliev and E. R. Bittner, *J. Chem. Phys.* 118, 4291 (2003).
201. G. Baranović, Z. Meić, H. Güsten, J. Mink, and G. Keresztury, *J. Phys. Chem.* 94, 2833 (1990).
202. Z. Meić and H. Güsten, *Spectrochim. Acta* 34A, 101 (1978).
203. A. Bree and R. Zwarich, *Spectrochim. Acta* 38A, 719 (1982).
204. X. Ci and A. B. Myers, *Chem. Phys. Lett.* 158, 263 (1989).
205. S. L. Schultz, J. Qian, and J. M. Jean, *J. Phys. Chem. A* 101, 1000 (1997).
206. K. Palmö, *Spectrochim. Acta* 44A, 341 (1988).
207. T. Nakabayashi, H. Okomoto, and M. Tasumi, *J. Phys. Chem. A* 102, 9686 (1998).
208. T. Nakabayashi, H. Okomoto, and M. Tasumi, *J. Phys. Chem. A* 101, 7189 (1997).
209. I. Orion, J. P. Buisson, and S. Lefrant, *Phys. Rev. B* 57, 7050 (1998).
210. T. P. Nguyen, V. H. Tran, P. Destruel, and D. Oelkrug, *Synth. Met.* 101, 633 (1999).

211. V. Hernandez, C. Castiglioni, M. Del Zoppo, and G. Zerbi, *Phys. Rev. B* 50, 9815 (1994).
212. A. B. Myers, M. O. Trulson, and R. A. Mathies, *J. Chem. Phys.* 83, 5000 (1985).
213. S. Karabunarliev, M. Baumgarten, E. R. Bittner, and K. Müllen, *J. Chem. Phys.* 113, 11372 (2000).
214. E. Mulazzi, A. Ripamonti, J. Wery, B. Dulieu, and S. Lefrant, *Phys. Rev. B* 60, 16519 (1999).
215. Y. Ichino, J. P. Ni, Y. Ueda, and D. K. Wang, *Synth. Met.* 116, 223 (2001).
216. J. Cornil, D. Beljonne, C. M. Heller, I. Campbell, B. K. Laurich, D. L. Smith, D. D. C. Bradley, K. Müllen, and J. L. Brédas, *Chem. Phys. Lett.* 278, 139 (1997).
217. J. Cornil, D. Beljonne, Z. Shuai, T. W. Hagler, I. Campbell, D. D. C. Bradley, J. L. Brédas, C. W. Spangler, and K. Müllen, *Chem. Phys. Lett.* 247, 425 (1995).
218. H.-J. Egelhaaf, L. Lüer, A. Tompert, P. Bäuerle, K. Müllen, and D. Oelkrug, *Synth. Met.* 115, 63 (2000).
219. J. Dale, *Acta Chem. Scand.* 11, 971 (1957).
220. A. Warshel, *J. Chem. Phys.* 62, 214 (1975).
221. D. Oelkrug, S. Reich, F. Wilkinson, and P. A. Leicester, *J. Phys. Chem.* 95, 269 (1991).
222. J. Gierschner, H.-G. Mack, H.-J. Egelhaaf, S. Schweizer, B. Doser, and D. Oelkrug, *Synth. Met.* 138, 311 (2003).
223. T. E. Bush and G. W. Scott, *J. Phys. Chem.* 85, 146 (1981).
224. L. Onsager, *J. Am. Chem. Soc.* 58, 1486 (1936).
225. E. Lippert, *Z. Elektrochem.* 61, 962 (1957).
226. W. Liptay, *Z. Naturforsch.* 20a, 1441 (1965).
227. H. Gruen and H. Görner, *J. Phys. Chem.* 93, 7144 (1989).
228. B. Boldrini, E. Cavalli, A. Painelli, and F. Terenziani, *J. Phys. Chem. A* 106, 6286 (2002).
229. C. W. M. Castleton and W. Barford, *J. Chem. Phys.* 117, 3570 (2002).
230. W. G. Han, T. Lovell, T. Liu, and L. Noodleman, *Chem. Phys. Chem.* 2002, 167 (2002).
231. J. Fabian, L. A. Diaz, G. Seifert, and T. Niehaus, *J. Mol. Struct. (Theochem.)* 594, 41 (2002).
232. G. P. Das, A. T. Yeates, and D. S. Dudis, *Chem. Phys. Lett.* 361, 71 (2002).
233. E. Zojer, D. Beljonne, T. Kogej, H. Vogel, S. R. Marder, J. W. Perry, and J. L. Brédas, *J. Chem. Phys.* 116, 3646 (2002).
234. D. Oelkrug, J. Gierschner, H.-J. Egelhaaf, L. Lüer, A. Tompert, K. Müllen, U. Stalmach, and H. Meier, *Synth. Met.* 121, 1693 (2001).
235. X. Zhou, A.-M. Ren, J.-K. Feng, and X.-J. Liu, *Chem. Phys. Lett.* 362, 541 (2002).
236. F. Guo, *Chem. Phys. Lett.* 355, 89 (2002).
237. D. Oelkrug, A. Tompert, H.-J. Egelhaaf, M. Hanack, E. Steinhuber, H. Meier, and U. Stalmach, *Synth. Met.* 83, 231 (1996).
238. J. Cornil, D. A. dos Santos, D. Beljonne, and J. L. Brédas, *Synth. Met.* 99, 5604 (1995).
239. Y. Shuto, *Int. J. Quantum Chem.* 58, 407 (1996).
240. J. Obrzut and F. E. Karasz, *J. Chem. Phys.* 87, 2349 (1987).
241. J. Obrzut and F. E. Karasz, *J. Chem. Phys.* 87, 6178 (1987).
242. J. Cornil, D. A. dos Santos, X. Crispin, R. Silbey, and J. L. Brédas, *J. Am. Chem. Soc.* 120, 1289 (1998).
243. J. Cornil, D. Beljonne, and J. L. Brédas, *J. Chem. Phys.* 103, 834 (1995).
244. M. Chandross, S. Mazumdar, M. Liess, P. A. Lane, Z. V. Vardeny, M. Hamaguchi, and K. Yoshino, *Phys. Rev. B* 55, 1486 (1997).
245. A. Pogantsch, G. Heimel, and E. Zojer, *J. Chem. Phys.* 117, 5921 (2002).
246. J. B. Lagowski, *J. Mol. Struct. (Theochem.)* 589–590, 125 (2002).
247. W. B. Davis, M. R. Wasielewski, and M. A. Ratner, *Int. J. Quantum Chem.* 72, 463 (1999).
248. J. Yu, W. S. Fann, F. J. Kao, D. Y. Yang, and S. H. Lin, *Synth. Met.* 66, 143 (1994).
249. W. Barford and R. J. Bursill, *Synth. Met.* 89, 155 (1997).
250. T. Wagenstreiter and S. Mukamel, *J. Chem. Phys.* 104, 7086 (1996).
251. J. L. Brédas, J. Cornil, D. Beljonne, D. A. dos Santos, and Z. Shuai, *Acc. Chem. Res.* 32, 267 (1999).
252. (a) B. E. Kohler, *J. Chem. Phys.* 93, 5838 (1990); (b) J. E. Lennard-Jones, *Proc. R. Soc. London, Ser. A* 158, 280 (1937).
253. (a) H. Kuhn, *Fortschr. Chem. Org. Naturst.* 16, 169 (1958); (b) H. Kuhn, *Fortschr. Chem. Org. Naturst.* 17, 404 (1959).
254. W. T. Simpson, *J. Am. Chem. Soc.* 77, 6164 (1955).
255. W. Kuhn, *Helv. Chim. Acta* 31, 1780 (1948).
256. H.-K. Ryu, W. Y. Kim, K. S. Nahm, Y. B. Hahn, Y.-S. Lee, and C. Lee, *Synth. Met.* 128, 21 (2002).
257. H. S. Woo, O. Lhost, S. C. Graham, D. D. C. Bradley, R. H. Friend, C. Quattrocchi, J. L. Brédas, R. Schenk, and K. Müllen, *Synth. Met.* 59, 13 (1993).
258. C. M. Heller, I. H. Campbell, B. K. Laurich, D. L. Smith, D. D. C. Bradley, P. L. Burn, J. P. Ferraris, and K. Müllen, *Phys. Rev. B* 54, 5516 (1996).
259. J. Cornil, D. Beljonne, D. A. dos Santos, and J. L. Brédas, *Synth. Met.* 76, 101 (1996).
260. L. Chiavarona, M. Di Terlizzi, G. Scamarcio, F. Babudri, G. M. Farinola, and F. Naso, *Appl. Phys. Lett.* 75, 2053 (1999).
261. D. A. dos Santos, D. Beljonne, J. Cornil, and J. L. Brédas, *Chem. Phys.* 227, 1 (1998).
262. P. Usnanski, M. Kryszewski, and E. W. Thulstrup, *Spectrochim. Acta* 46A, 23 (1990).
263. A. Yogeve and L. Margulies, *Isr. J. Chem.* 16, 258 (1977).
264. (a) T. Damerou and M. Hennecke, *J. Chem. Phys.* 103, 6232 (1995); (b) M. Hennecke, T. Damerou, and K. Müllen, *Macromolecules* 26, 3411 (1993).
265. M. S. Gudipati, M. Maus, J. Daverkausen, and G. Hohlneicher, *Chem. Phys.* 192, 37 (1995).
266. F. C. Spano and S. Siddiqui, *Chem. Phys. Lett.* 314, 481 (1999).
267. G. Hohlneicher and B. Dick, *J. Photochem.* 27, 215 (1984).
268. M. Rumi, J. E. Ehrlich, A. A. Heikal, J. W. Perry, S. Barlow, Z. Hu, D. McCord-Moughon, T. C. Parker, H. Röckel, S. Thayumanavan, S. R. Marder, D. Beljonne, and J.-L. Brédas, *J. Am. Chem. Soc.* 112, 9500 (2000).
269. D. Beljonne, Z. Shuai, J. Cornil, D. A. dos Santos, and J. L. Brédas, *J. Chem. Phys.* 111, 2829 (1999).
270. S. J. K. Pond, M. Rumi, M. D. Levin, T. C. Parker, D. Beljonne, M. W. Day, J.-L. Brédas, S. R. Marder, and J. W. Perry, *J. Phys. Chem. A* 106, 11470 (2002).
271. B. Strehmel, A. M. Sarker, and H. Detert, *Chem. Phys. Chem.* 4, 249 (2003).
272. S. Mukamel, S. Tretiak, T. Wagersreiter, and V. Chernyak, *Science* 277, 781 (1997).
273. F. S. Dainton, C. T. Peng, and G. A. Salmon, *J. Phys. Chem.* 72, 3801 (1968).
274. L. P. Candéias, J. Wildeman, G. Hadziioannou, and J. M. Warman, *J. Phys. Chem. B* 104, 8366 (2000).
275. L. P. Candéias, G. H. Gelinck, J. J. Piet, J. Piris, B. Wegewijs, E. Peeters, J. Wildeman, G. Hadziioannou, and K. Müllen, *Synth. Met.* 119, 339 (2001).
276. D. Oelkrug, K. Rempfer, E. Prass, and H. Meier, *Z. Naturforsch.* 43a, 583 (1988).
277. M. M. de Souza, G. Rumbles, I. D. W. Samuel, S. C. Moratti, and A. B. Holmes, *Synth. Met.* 101, 631 (1999).
278. U. Mazzucato, *Pure Appl. Chem.* 54, 1705 (1982).
279. J. Saltiel and J. T. D'Agostino, *J. Am. Chem. Soc.* 94, 6445 (1972).
280. S. Sharafy and K. A. Muszkat, *J. Am. Chem. Soc.* 93, 4119 (1971).
281. (a) J. L. Charlton and J. Saltiel, *J. Phys. Chem.* 81, 1940 (1977); (b) J. Saltiel, A. S. Waller, D. F. Sears Jr., and C. Z. Garrett, *J. Phys. Chem.* 97, 2516 (1993); (c) J. Saltiel, A. S. Waller, D. F. Sears, Jr.,

- E. A. Hoburg, D. M. Zeglinski, and D. H. Waldeck, *J. Phys. Chem.* 98, 10689 (1994).
282. J. Saltiel, O. C. Zafiriou, E. D. Megarity, and A. A. Lamola, *J. Am. Chem. Soc.* 90, 4759 (1968).
283. D. Oelkrug, A. Tompert, H. Maier, and U. Stalmach, unpublished results.
284. H. Tillmann and H.-H. Hörhold, *Synth. Met.* 101, 138 (1999).
285. (a) A. Colombo and G. Allegra, *Macromolecules* 5, 579 (1971); (b) O. König, H.-B. Bürgi, T. Armbruster, J. Hulliger, and T. Weber, *J. Am. Chem. Soc.* 119, 10632 (1997); (c) G. Bongiovanni, C. Botta, J. L. Brédas, J. Cornil, D. R. Ferro, A. Mura, A. Piaggi, and R. Tubino, *Chem. Phys. Lett.* 278, 146 (1997).
286. M. Farina, G. de Silvestro, and P. Sozzani, in "Comprehensive Supramolecular Chemistry" (D. D. McNicol, F. Toda, and R. Bishop, Eds.), Vol. 6. Elsevier, Oxford, 1996.
287. N. Gfeller and G. Calzaferri, *J. Phys. Chem. B* 101, 1396 (1997).
288. D. Beljonne, J. Cornil, R. Silbey, P. Millié, and J. L. Brédas, *J. Chem. Phys.* 112, 4749 (2000).
289. J. Cornil, D. Beljonne, D. A. dos Santos, J. Ph. Calbert, and J. L. Brédas, *Thin Solid Films* 363, 72 (2000).
290. J. Cornil, D. Beljonne, J.-P. Calbert, and J. L. Brédas, *Adv. Mater.* 13, 1053 (2001).
291. S. Tretiak and S. Mukamel, *Chem. Rev.* 102, 3171 (2002).
292. S. Tretiak, A. Saxena, R. L. Martin, and A. R. Bishop, *J. Phys. Chem. B* 104, 7029 (2000).
293. (a) M. Kasha, *Rev. Mod. Phys.* 31, 162 (1959); (b) R. M. Hochstrasser and M. Kasha, *Photochem. Photobiol.* 3, 317 (1964); (c) E. G. McRae and M. Kasha, *J. Chem. Phys.* 28, 721 (1958); (d) M. Kasha, H. R. Rawls, and M. A. El-Bayoumi, *Pure Appl. Chem.* 11, 371 (1965).
294. (a) V. Czikkely, H. D. Försterling, and H. Kuhn, *Chem. Phys. Lett.* 6, 11 (1970); (b) V. Czikkely, H. D. Försterling, and H. Kuhn, *Chem. Phys. Lett.* 6, 207 (1970); (c) H. Nolte and V. Buss, *Chem. Phys. Lett.* 19, 395 (1973); (d) H. Nakahara, K. Fukuda, D. Möbius, and H. Kuhn, *J. Phys. Chem.* 90, 6144 (1986); (e) C. E. Evans and P. W. Bohn, *J. Phys. Chem.* 97, 12302 (1993).
295. M. J. McIntire, E. S. Manas, and F. C. Spano, *J. Chem. Phys.* 107, 8152 (1997).
296. E. S. Manas and F. C. Spano, *J. Chem. Phys.* 109, 8087 (1999).
297. Z. G. Soos, G. W. Hayden, P. C. M. McWilliams, and S. Etemad, *J. Chem. Phys.* 93, 7439 (1990).
298. J. Gierschner, H.-G. Mack, D. Oelkrug, I. Waldner, and H. Rau, *J. Phys. Chem. A*, in press.
299. S. Canuto and M. C. Zerner, *J. Am. Chem. Soc.* 112, 2114 (1990).
300. S. Canuto and M. C. Zerner, *Chem. Phys. Lett.* 157, 353 (1989).
301. D. Oelkrug, H.-J. Egelhaaf, B. Lehr, J. Gierschner, L. Lüer, P. Matousek, and M. Towrie, *Tech. Rep.—Counc. Cent. Lab. Res. Counc.* 1999, 1 (1999).
302. T. Damerau and M. Hennecke, *J. Polym. Sci.* 33, 2219 (1995).
303. R. E. Gill, G. Hadziioannou, P. Lang, F. Garnier, and J. C. Wittmann, *Adv. Mater.* 9, 331 (1997).
304. A. Menon, H. Dong, Z. I. Niazimbetova, L. J. Rothberg, and M. E. Galvin, *Chem. Mater.* 14, 3668 (2002).
305. R. E. Gill, A. Meetsma, and G. Hadziioannou, *Adv. Mater.* 8, 212 (1996).
306. P. F. van Hutten, V. V. Krasnikov, H.-J. Brouwer, and G. Hadziioannou, *Chem. Phys.* 241, 139 (1999).
307. L. Claes, J.-P. François, and M. S. Deleuze, *Chem. Phys. Lett.* 339, 216 (2001).
308. G. Cerullo, G. Lanzani, S. De Silvestri, H.-J. Egelhaaf, L. Lüer, and D. Oelkrug, *Phys. Rev. B* 62, 2429 (2000).
309. N. F. Colaneri, D. D. C. Bradley, R. H. Friend, P. L. Burn, A. B. Holmes, and C. W. Spangler, *Phys. Rev. B* 42, 11670 (1990).
310. F. C. Spano, *Chem. Phys. Lett.* 331, 7 (2000).
311. F. C. Spano, *Synth. Met.* 116, 339 (2001).
312. (a) F. C. Spano, *J. Chem. Phys.* 114, 5376 (2001); (b) F. C. Spano, *J. Chem. Phys.* 117, 9961 (2002).
313. F. C. Spano, *J. Chem. Phys.* 116, 5877 (2002).
314. F. C. Spano, *J. Chem. Phys.* 118, 981 (2003).
315. L. Lüer, H.-J. Egelhaaf, and D. Oelkrug, in preparation.
316. S. Brazovskii, A. Kirova, A. R. Bishop, V. Klimov, D. McBranch, N. N. Barashkov, and J. P. Ferraris, *Opt. Mater.* 9, 472 (1998).
317. N. Kirova, S. Brazovskii, A. R. Bishop, D. McBranch, and V. Klimov, *Synth. Met.* 101, 188 (1999).
318. D. Jones, M. Guerra, L. Favaretto, A. Modelli, M. Fabrizio, and G. Distefano, *J. Phys. Chem.* 94, 5761 (1990).
319. J. Gierschner, H.-J. Egelhaaf, D. Oelkrug, R. Martinez Alvarez, M. Hanack, D. Nädle, and J. Strähle, in preparation.
320. M. D. Joswick, I. H. Campbell, N. N. Barashkov, and J. P. Ferraris, *J. Appl. Phys.* 80, 2883 (1996).
321. J. Gierschner, H.-J. Egelhaaf, D. Oelkrug, H. Benmansour, and G. Bazan, in preparation.
322. K. Iwata, R. Ozawa, and H. Hamaguchi, *J. Phys. Chem. A* 106, 3614 (2002).
323. (a) Y. Dou and R. E. Allen, *Chem. Phys. Lett.* 378, 323 (2003), (b) Y. Dou and R. E. Allen, *J. Chem. Phys.* 119, 10658 (2003).
324. J.-H. Perng, *J. Fluorescence* 12, 311 (2002).
325. K. Furuya, K. Kawato, H. Yokoyama, A. Sakamoto, and M. Tasumi, *J. Phys. Chem. A* 107, 8251 (2003).
326. S. P. Kwasniewski, L. Claes, J.-P. Francois, and M. S. Deleuze, *J. Chem. Phys.* 118, 7823 (2003).
327. Q.-L. Fan, S. Lu, Y.-H. Lai, X.-Y. Hou, and W. Huang, *Macromolecules*, 36, 6976 (2003).
328. O. Narwark, A. Gerhard, S. C. J. Meskers, S. Brocke, E. Thorn-Csányi, and H. Bässler, *Chem. Phys.* 294, 17 (2003).
329. O. Narwark, S. C. J. Meskers, R. Peetz, E. Thorn-Csányi, and H. Bässler, *Chem. Phys.* 294, 1 (2003).
330. Z. I. Niazimbetova, A. Menon, M. E. Galvin, and D. H. Evans, *J. Electroanal. Chem.* 529, 43 (2002).
331. Y. Chen and S.-P. Lai, *J. Polym. Sci. A* 39, 2571 (2001).
332. H. Detert and E. Sugiono, *Synth. Met.* 138, 181 (2003).
333. H. Detert and O. Sadovski, *Synth. Met.* 138, 185 (2003).
334. C.-L. Li, S.-J. Shieh, S.-C. Lin, and R.-S. Liu, *Org. Letters* 5, 1131 (2003).
335. A. M. Sarker, Y. Kaneko, P. M. Lahti, and F. E. Karasz, *J. Phys. Chem. A* 107, 6533 (2003).
336. M. S. Wong, Z. H. Li, Y. Tao, and M. D'Iorio, *Chem. Mater.* 15, 1198 (2003).
337. H. Meier, J. Gerold, and D. Jacob, *Tetrahedron Letters* 44, 1915 (2003).
338. S. Wachsmann-Hogiu, L. A. Peteanu, L. A. Liu, D. J. Yaron, and J. Wildeman, *J. Phys. Chem. B* 107, 5133 (2003).
339. S. P. Kwasniewski, J. P. Francois, and M. S. Deleuze, *J. Phys. Chem. A* 107, 5168 (2003).
340. M. A. Summers, P. R. Kemper, J. E. Bushnell, M. R. Robinson, G. C. Bazan, M. T. Bowers, and S. K. Buratto, *J. Am. Chem. Soc.* 125, 5199 (2003).
341. J.-S. K. Yu, W.-C. Chen, and C.-H. Yu, *J. Phys. Chem. A* 107, 4268 (2003).
342. F. C. Grozema, R. Telesca, J. G. Snijders, and L. D. A. Siebbeles, *J. Chem. Phys.* 118, 9441 (2003).
343. P. C. Chen and Y. C. Chieh, *J. Mol. Struct. (Theochem.)* 624, 191 (2003).
344. B.-C. Wang, J.-C. Chang, J.-H. Pan, C. Xue, and F.-T. Luo, *J. Mol. Struct. (Theochem.)* 636, 81 (2003).
345. J. B. Lagowski, *J. Mol. Struct. (Theochem.)* 634, 243 (2003).
346. B. J. Zhang and S.-J. Jeon, *Chem. Phys. Lett.* 377, 210 (2003).
347. F. Guo and Z. Y. Shih, *Chem. Phys. Lett.* 370, 572 (2003).
348. W. Bartkowiak, R. Zalesny, and J. Leszczynski, *Chem. Phys.* 287, 103 (2003).
349. F. He, G. Cheng, H. Zhang, Y. Zheng, Z. Xie, B. Yang, Y. Ma, S. Liu, and J. Shen, *Chem. Commun.*, 2206 (2003).



350. M. Egli, V. Tereshko, G. N. Mushudov, R. Sanishvili, X. Liu, and F. D. Lewis, *J. Am. Chem. Soc.* 125, 10842 (2003).
351. Y. Wang, M. I. Ranasinghe, and T. Goodson, III, *J. Am. Chem. Soc.* 125, 9562 (2003).
352. W. Dermaut, C. Wuyts, G. Aerts, E. Goovaerts, and H. J. Geise, *Synth. Met.* 135–136, 249 (2003).
353. (a) L. M. Herz, C. Daniel, C. Silva, F. J. M. Hoeben, A. P. H. J. Schenning, E. W. Meijer, R. H. Friend, and R. T. Phillips, *Synth. Met.* 139, 839 (2003); (b) L. M. Herz, C. Daniel, C. Silva, F. J. M. Hoeben, A. P. H. J. Schenning, E. W. Meijer, R. H. Friend, and R. T. Phillips, *Phys. Rev. B* 64, 045203 (2003).
354. (a) B. R. Crenshaw and C. Weder, *Chem. Mater.* (2003) in press; (b) C. Löwe and C. Weder, *Adv. Mater.* 14, 1625 (2003).
355. R. Capelli, M. A. Loi, C. Taliani, H. B. Hansen, M. Murgia, G. Ruani, M. Muccini, P. W. Lovenich, and W. J. Feast, *Synth. Met.* 139, 909 (2003).
356. M. A. Summers, M. R. Robinson, G. C. Bazan, and S. K. Buratto, *Synth. Met.* 137, 957 (2003).
357. J. De Ceuster, E. Goovaerts, A. Bouwen, and V. Dyakonov, *Phys. Rev. B* 68, 125202 (2003).
358. J. E. Wong, M. S. Weaver, T. Richardson, D. D. C. Bradley, and D. W. Bruce, *Mater. Sci. Engineer. C* 22, 393 (2002).
359. J. E. Wong, S. Schrader, H. Detert, S. Katholy, and L. Brehmer, *Mater. Sci. Engineer. C* 22, 413 (2002).
360. C. Melzer, V. V. Krasnikov, and G. Hadziioannou, *J. Polym. Sci. B* 41, 2665 (2003).
361. A. Yoshiki, N. Matsuoka, M. Kondo, and H. Yanagi, *Thin Solid Films* 438–439, 308 (2003).
362. M. Hanack, B. Behnisch, H. Häckl, P. Martinez-Ruiz, and K.-H. Schweikart, *Thin Solid Films* 417, 26 (2002).
363. A. Ajayaghosh, S. J. George, and Y. K. Praveen, *Angew. Chem. Int. Ed.* 42, 332 (2003).
364. P. A. van Hal, M. M. Wienk, J. M. Kroon, and R. A. J. Janssen, *J. Mater. Chem.* 13, 1054 (2003).
365. F. Stellacci, C. A. Bauer, T. Meyer-Friedrichsen, W. Wenseleers, S. R. Marder, and J. W. Perry, *J. Am. Chem. Soc.* 125, 328 (2003).

# Ordered Mesoporous Materials

Sebastian Polarz

*Ruhr-University Bochum, Bochum, Germany*

## CONTENTS

1. Introduction
  2. Preparation of Ordered Mesoporous Materials
  3. Analysis of Ordered Mesoporous Materials
  4. Examples for Ordered Mesoporous Materials
  5. Conclusions
- Glossary  
References

## 1. INTRODUCTION

Ordered mesoporous materials are a subgroup of, or even prototypes, for so-called nanoporous materials. It is, therefore, necessary to give some comments on (nano)porous materials in general.

The most general definition of a porous material is a continuous and solid network material filled through and through with voids. The voids are of the order of  $\approx 1\text{--}100$  nm in the case of nanoporous materials. A material is obviously porous when the voids are filled with gas. However, the voids might be filled with a liquid or even a solid. Then, some authors prefer to label materials nanostructured instead of using the expression nanoporous. However, for this review, this not very exact distinction will not be made. Once a pore can possibly be emptied without destroying the material, the material is regarded as a porous material no matter what is momentarily in the pores.

The general definition given above already indicates that porous materials are actually a classical type of dispersion known for a long time in classical colloid science [1]. This is a solid foam. The voids show a translational repetition in three-dimensional space, while no regularity is necessary for a material to be termed porous. Correlating to this, the most common way is to consider a porous material showing gas-solid interfaces as the most dominant characteristic. This indicates that the creation of interfaces due to nucleation phenomena (in this case, nucleation of wholes), decreasing interface energy, and stabilization of interfaces is of elemental importance during the formation process of nanoporous materials [1]. Often, these factors are omitted because the final products are stable. Indeed, they are just metastable.

This metastability is gained by the rigid character of the void surrounding network that is covalently crosslinked in most cases. However, it should be noticed that most of the nanoporous materials reported in the literature or those that are of technical high relevance are not stable by thermodynamic means. As soon as activation-energy boundaries are overcome, materials start to break down. One example should elucidate this. Porous silica, for instance, is just metastable. As soon as temperature is raised and the melting point is reached, primary particles in the network begin to fuse and it comes to phase separation into a nonporous silica phase (and bulk air). Finally, at very high temperatures, the thermodynamic stable phase of  $\text{SiO}_2$ , quartz emerges. Control over interface energy and metastabilization of nanodimensional wholes becomes of special importance when the task is to produce nanoporous materials.

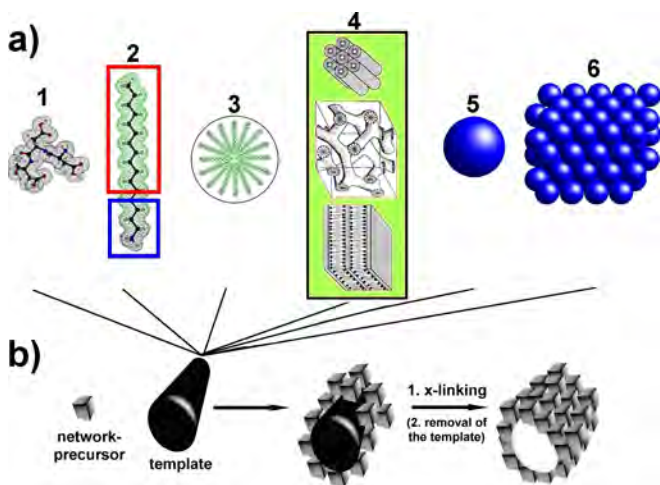
Ordered mesoporous materials exhibit some special features. These materials are characterized by pores of the order of 2 nm to 50 nm, the pores have a regular shape and a mutual correlation to each other, and the polydispersity of the pore radius is small ( $\approx 10\text{--}20\%$ ), sometimes less.

## 2. PREPARATION OF ORDERED MESOPOROUS MATERIALS

### 2.1. The Templating Concept

The most successful way to produce all sorts of nanoporous materials and ordered mesoporous materials, in particular, is the templating method as schematically shown in Figure 1.

An organic (or sometimes inorganic) compound acts as the placeholder, what later becomes the void space in the nanoporous material. The templating concept mainly allows the control of the criterium of pore size but also pore shape, obviously. At first, a suitable template structure has to be provided (see Fig. 1a). By suitable is meant that this template structure has to be compatible all the time with solvents involved in the process and the final network materials throughout the whole process. In other words, the free interface energy between the template structure and the network material has to be smaller than  $kT$ , despite the huge created interface area. Otherwise, the material can rearrange or demix to more stable, unporous phases.



**Figure 1.** Schematic representation of the approach to obtain nanoporous materials by templating strategies. (a) shows a range of applicable templates beginning with single molecules (1) or amphiphiles (2), followed by assemblies of amphiphiles as micelles (3) or lyotropic phases (4), followed by polymeric spheres (5) or assemblies of spheres (6). These units are surrounded or bonded to the network precursor systems in the actual templating step (b). The created pore resembles the size, shape, and even functional characteristics of the template in an ideal case. Finally, the template is removed. Therefore, it is possible to tune the properties, and most importantly, the size and interconnectivity of the pore and pore system in the order (1)–(6).

The template structure can have sizes on many different length scales. The smallest pores are achieved for molecules as templates (Fig. 1a-1). The created pores have similar shape and size than the used molecules. The pores can be spatially uncorrelated to each other. In this case, one speaks about molecular imprinting [2–4]. Molecular imprinting is even successful for organic materials as network material and is, therefore, very often used for imprinting biomolecules to a matrix for biochemical applications [2, 4–8]. Highly ordered materials with pores that have a mutual correlation to each other are found for zeolitic materials. The template units for zeolites are also single molecules (primary amines and ammonium cations) and therefore, pore size normally does not exceed 2 nm. Zeolites are microporous solids.

Larger pores can be achieved by assemblies of molecules to form templates. Here, assemblies of amphiphiles (Fig. 1a-3) are ideal due to their self-organizing properties and their capability to lower interface energy. An amphiphilic molecule (Fig. 1a-2) has typically one hydrophilic and one hydrophobic part which tend to lead to microphase separation [1]. The resulting template structures are micelles or ultimately lyotropic phases with different possible symmetries (lamellar, hexagonal, or gyroid as depicted in Fig. 1a-3). Materials with pores of the order of 2–50 nm react with sometimes surprisingly high order. The structure of the liquid crystal, the pore size, and shape are imprinted into the solid materials. Therefore, the current review article focuses on these template structures derived from the amphiphilic organization of matter (underlined in green in Fig. 1).

Alternatively, hydrophilic polymers can be adopted as templates which is not pursued further in this article [9–14]. Even larger pores are obtained when polymer spheres or colloidal crystals of these spheres are used as templates [15].

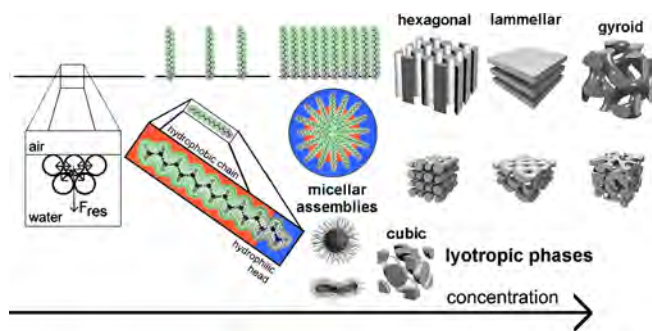
In conclusion, suitable central structures as well as network builders with the property of being able to surround and cast these structures on a scale smaller than the template, have to be available. This is of importance because if the network building blocks are (i) too large in size (then they create cavities by themselves just by packing effects and are not able to cast a template structure smaller than the cavities), and (ii) if there is a “wrong” interaction (zero interaction or repulsion) between the network building units and the template, no casting is possible. Instead, these two mistakes are often found in the literature when some authors claim that their materials are ordered mesoporous materials, just because they used a surfactant in the recipe. Instead, phase separation (isotropic distributions of the two phases but not mesoscopic ordering) could occur. Therefore, a certain degree of attraction is elemental.

### 2.1.1. Creation of Templates Through Amphiphilic Self-Assembly Processes

It is evident in the previous section that the formation of the template via amphiphiles is of extraordinary relevance. Therefore, this section briefly explains the formation of these templates.

Special structures in water (or other selective solvents) may emerge when molecules contain two parts in its architecture that are chemically very different. In most cases, one part is hydrophilic (ionic, hydroxy-, or polar groups) while the other part is hydrophobic (aliphatic, aromatic, or fluorinated groups). Molecules with these characteristics are called amphiphiles. Surfactants (special cases of amphiphiles) are characterized by a relatively short hydrophilic and hydrophobic block. The most striking feature of amphiphiles is their behavior at interfaces (see Fig. 2).

Due to the interface force pointing into the bulk phase (see Fig. 2), creation of additional interface requires energy. This force is given by the surface tension (force per length), which is defined via the free interface energy  $dG_i$  as  $dG_i = \gamma dA$ .



**Figure 2.** Schematic representation of the processes leading to self-assembly of amphiphilic molecules (the headgroup is printed in blue) in water. In the upper part of the figure, the behavior at interfaces is shown and how micelles and lyotropic phases are formed. The different symmetries of lyotropic liquid crystals are graphically demonstrated.

Due to their amphiphilic character, surfactant molecules are enriched on the air-water interface. This creates a new interface (the air-hydrophobic tail interface) and, consequently, the interface is energetically stabilized and surface tension decreases. When the concentration of the amphiphile is increased, the interface gets more and more enriched at the air-water interface until a monolayer of densely packed molecules is reached. Because all of the interface is now occupied, every additional amphiphile molecule has to be now located in continuous liquid phase. This state is not very favorable for the hydrophobic parts; thus, the aggregation to micellar structures is observed, where the hydrophobic chains are shielded from the water by the hydrophilic head groups. The structure of micelles is determined mainly by pure geometric factors of the amphiphile described by the so-called packing parameter  $N_s$  (with  $v$  = volume;  $l$  = length;  $a$  = area).

$$N_s = \frac{v_{tail}}{l_{tail}a_{head}} \quad (1)$$

For  $N_s$  up to 0.33 (wedge-shaped surfactants) spherical micelles, for  $0.33 > N_s > 0.5$  cylindrical micelles, and for  $0.5 > N_s > 1$ , planar bilayers are the most favorable structures.

When the surfactant or amphiphile concentration is increased more and more, more and more micelles are also formed. A dense and ordered packing of micelles (cubic symmetry or others) is the consequence. At some point, the micelles come into contact with each other and fuse together. The formation of continuous structures, so-called lyotropic phases (liquid crystals), can be explained by this fusion [16]. First, hexagonal structures evolve which can be transformed at higher surfactant concentration to lamellar assemblies. It is possible to find bicontinuous gyroid structures in the region between the hexagonal and lamellar phases. For special amphiphile compositions, more exotic lyotropic structures can be obtained (see Fig. 2). Because the liquid crystals do not allow the penetration of the hydrophilic sol-gel precursors (for instance, silicic acid) into the continuous core of the amphiphile assembly, formation of  $\text{SiO}_2$  in the hydrophobic domains is excluded and only allowed in the hydrophilic domains. This creates the pores.

## 2.2. Categorization of Ordered Mesoporous Materials

Directly from the range of possible amphiphilically organized templates, one can conclude certain criteria for ordered mesoporous materials. First of all, the template determines the size of the pore. If larger templates are used, larger pores result. Although the mesopore size is defined by the International Union of Pure and Applied Chemistry (IUPAC) for 2–50 nm, the majority of ordered mesoporous materials are found in the size range 3–10 nm. Secondly, the template determines the shape of the pores and the mutual correlation of the pores to each other. Mainly independent from the template, as long as suitable interaction modes are present (as described before), is the composition of the void-surrounding network material.

### 2.2.1. Categorization by Dimensionality

As already expected from the possible template structures and the templating concept, different pore dimensionalities are possible. “Zero-dimensional” pores are obtained when spherical templates, for instance, micelles, are used (see Fig. 3a).

One-dimensional pores are realized for cylindrical pores as shown in Figure 3b. Three-dimensional pore systems are obtained when three dimensionally intertwined templates are applied as shown in Figure 3c.

### 2.2.2. Categorization by Network Material

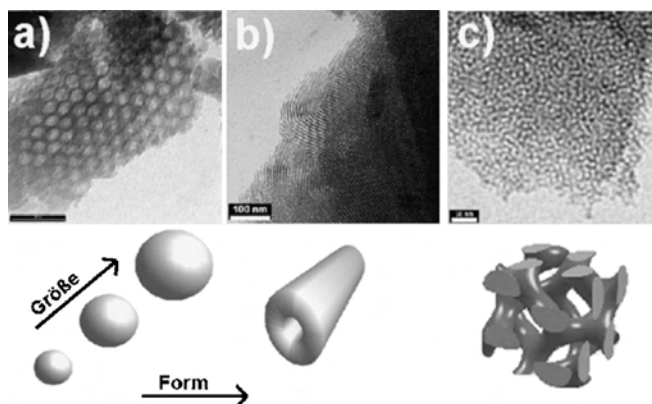
One of the highest goals in the field of nanoporous materials is to achieve any possible chemical composition in the network materials “hosting” the pores. It makes sense to divide the materials into two categories:

1. inorganic materials
2. organic materials.

Among the inorganic materials, which is the larger group, we will find:

- 1a. Inorganic oxide-type materials. This is the field of the most commonly known ordered mesoporous: silica-, porous titania-, porous zirconia materials.
- 1b. A category of its own is given for nanoporous carbon materials. Contributed to this category are the highly important active carbons but also some examples for ordered mesoporous carbon materials.
- 1c. Other binary compounds such as sulfides, nitrides, etc. In this category fall also the famous  $\text{AlPO}_4$  materials.
- 1d. There are already some examples in addition to carbon where just one element, for instance, a metal, could be prepared in a nanoporous state. The most prominent member of this class of materials is likely to be nanoporous silicon with its luminescent properties [17, 18].

There are far fewer examples for nanoporous organic materials as polymers, for instance [8]. Some of the known



**Figure 3.** TEM images demonstrating the possible shapes of pores: (a) spherical pores, (b) cylindrical but curved pores, and (c) highly curved, bicontinuous pores.

examples for ordered mesoporous polymers will be discussed in Section 4.3 and it will be explained what the limits are for the preparations of these materials.

### 3. ANALYSIS OF ORDERED MESOPOROUS MATERIALS

#### 3.1. Gas Adsorption Methods

Gas sorption represents a widely used technique to characterize micro- and mesoporous materials and also provides porosity parameters such as pore size distributions, surface areas, and pore volumes. In the following, a brief description of classical methods to analyze sorption data is followed by an overview on recent advances in the interpretation of sorption experiments.

In a typical sorption experiment, the uptake of gases such as nitrogen, krypton, and CO<sub>2</sub> is measured as a function of relative pressures  $p/p_0 < 1$  at constant temperature.  $p$  and  $p_0$  are the equilibrium vapor pressures of the liquid in the pores and that of the bulk liquid, respectively. The interaction between the pore walls and the adsorbate is based on physisorption (van der Waals interaction) and leads to the formation of adsorbate layers at low  $p/p_0$ . Simplistically, the macroscopic laws of classical thermodynamics predict that the confinement of pores with radii on the nanometer scale leads to the condensation of gas inside the pores at a smaller pressure than  $p_0$ . In a typical sorption experiment, the adsorbed volume is plotted versus  $p/p_0$ , and this “sorption isotherm” is the superposition of different uptake mechanisms. At low  $p/p_0$ , adsorption in micropores takes place, which is supposed to be a process of volume filling rather than capillary condensation [19, 20]. The isotherms of microporous materials are characterized by a steep increase in the isotherm at low  $p/p_0$ , ending up in a plateau at larger  $p/p_0$ . In a mesoporous substrate, with increasing values of  $p/p_0$ , a liquid-like adsorbate film of statistical thickness  $t(p/p_0)$  is formed on the pore walls. At a certain pressure, capillary condensation takes place filling the mesopores with liquid, which is apparent in isotherms as a pronounced increase of the adsorbed amount. The total pore volume (“porosity”) is given by the overall uptake of adsorbate. Zsigmondy proposed the first explanation of the capillary condensation in a single, infinite cylindrical mesopore based on the macroscopic Kelvin equation:

$$\ln\left(\frac{p}{p_0}\right) = \frac{2\sigma V_L}{RT r_m}$$

where  $V_L$  and  $\sigma$  are the molal liquid volume and the liquid-gas surface tension at temperature  $T$ , respectively, and  $r_m$  is the mean radius of curvature of the liquid-gas interface (cylindrical for the condensation, spherical for desorption [21]). Based on the classical treatment of Cohan and the Kelvin equation [22], the condensation of a liquid in a nanoporous material at a certain  $p/p_0$  can be related to the corresponding mesopore size, thus also providing a pore size distribution (PSD). Since the condensation starts at a relative pressure  $p/p_0$ , where the walls are covered by a film of thickness  $t(p/p_0)$ , in the so-called modified Kelvin equation,  $2/r_m$  is replaced by  $f/(r - t(p/p_0))$ , where  $r$  is the

“true” mesopore radius and  $f$  the meniscus shape factor, which is 1 or 2 for the filling or emptying of the mesopore, respectively. This procedure represents the basis for the well-known “Barrett–Joyner–Halenda (BJH)” method, currently the most frequently used procedure to determine PSDs [23]. The dependence  $t(p/p_0)$  can be described by the approach of Frenkel–Halsey–Hill describing the sorption on nonporous silica [24]. In addition, the pore geometry significantly affects thermodynamic properties of confined fluids and their adsorption behavior [25, 26]. The confinement is stronger in spherical pores compared to cylindrical pores of the same diameter leading to a shift of the capillary condensation to lower  $p/p_0$ ; therefore the aforementioned procedures are restricted to cylindrical pores [27]. The progress in synthesizing ordered mesoporous materials (see Section 4) with well-defined pore morphologies in terms of uniform mesopore sizes and pore shapes allowed the testing, optimization, and further development of these classical approaches [28–30].

Furthermore, widely used methods to determine structural parameters are comparative plots such as the  $t$ -plot and  $\alpha$ -plot methods [19, 31, 32]. Typically, the amount adsorbed on the porous solid under study is plotted as a function of the amount adsorbed on an ideally nonporous reference solid with similar surface characteristics, providing parameters such as the overall pore volume, specific surface area, and micropore volumes. This procedure has been used to determine microporosity in ordered mesoporous silicas [33–35]. It has turned out that the macroscopic, thermodynamics of the classical methods already described do not provide reliable descriptions of materials with mesopore sizes below about 4 nm for oxidic materials [36]. One of the main shortcomings of these approaches lies with the nonconsideration of fluid-wall interactions. Recent progress in understanding capillary condensation deals with molecular level models. The methods of the grand canonical Monte Carlo (GCMC) simulations [37], molecular dynamics [38], and density functional theory (DFT) [39, 40] allow direct modeling of capillary condensation/desorption phase transitions, and are capable of generating hysteresis loops of simple fluids sorbed in model pores. Neimark and Ravikovitch have shown that the nonlocal density functional theory (NLDFT) with properly chosen parameters of fluid-fluid and fluid-solid intermolecular interactions quantitatively predicts desorption branches of hysteretic isotherms of nitrogen and argon on reference mobil composition of matter (MCM)-41 samples with pore channels narrower than 5 nm [41–44]. This method was tested against Monte Carlo simulations and was shown to provide reliable pore sizes and wall thicknesses in MCM-41-type materials [34, 37, 44–46].

In spite of the recent progress in the theoretical understanding of sorption phenomena, certain issues of sorption are still unclear:

1. The nature of the hysteresis in ordered mesoporous materials is still subject to intensive theoretical and experimental research and not yet fully understood [14, 34, 47–49]. Recent NLDFT studies were able to shed some more light on the hysteresis phenomenon. It was concluded that in the range of pore sizes  $> 5$  nm, the experimental desorption branch corresponds to the

equilibrium evaporation, while the capillary condensation branch corresponds to the spontaneous (spinodal) condensation [34, 45].

2. The dependence  $t(p/p_0)$  is still a matter of discussion due to the lack of independent techniques in determining film thicknesses, and usually reference data from nonporous materials are used [50]. An exact knowledge of  $t(p/p_0)$  is needed for the determination of mesopore sizes by the classical methods, as well as for the testing of DFT models. Smarsly et al. have determined  $t(p/p_0)$  by a combination of nitrogen sorption and small-angle neutron scattering [49].

### 3.2. Mercury Porosimetry

In mercury porosimetry (MP), gas is evacuated from the sample, which is then immersed into mercury, and an external pressure is applied to gradually force the nonwetting mercury into the sample. By monitoring the incremental volume of mercury intruded for each applied pressure, the pore size distribution of the sample can be estimated in terms of the volume of the pores intruded for a given diameter  $D$ . The evaluation of pore sizes from MP is based on the Washburn equation, quantifying the pressure  $p$  required to force a nonwetting fluid into a circular cross-section capillary of diameter  $D$  [51, 52]. Mercury porosimetry allows the determination of PSD between 3 nm and 200 nm and is, therefore, inappropriate for microporous materials, but more suitable for pore sizes above ca. 30 nm compared to nitrogen sorption. In addition, the total pore volume  $V_{\text{tot}}$  is accessible from the total intruded volume of mercury at the highest pressure determined, and the total pore surface  $S$  is calculated from

$$S = \frac{1}{\gamma |\cos \theta|} \int_0^{V_{\text{tot}}} p dV$$

Mercury porosimetry has inherent shortcuts in determining mesopore sizes, especially below 20 nm. During the measurement, high pressures to force mercury into small pores may compress the sample [53]. Damage or compression of highly porous silica has been reported previously [53, 54]. In addition, mercury porosimetry overestimates the volume of the smallest pores in case of ink-bottle shaped pores by the small openings [55].

### 3.3. Electron Microscopy

Electron microscopy (transmission electron microscopy (TEM) for micro- and mesoporous samples, and scanning electron microscopy (SEM) for macroporous samples) are an unrenouncable tool for the investigation of porous materials. The biggest advantage of these techniques is that they deliver an optical image of the samples. However, giving an overview above these techniques is definitely behind the scope of this review. Sakamoto et al. presented a method to obtain three-dimensional imaging of pores in a mesoporous system [56]. These authors use electron diffraction in a high-resolution electron microscope preserving phase information of the scattered electrons. The obtained two-dimensional scattering patterns equipped with this phase information allows the calculation of the three-dimensional spatial structure of the material by Fourier transformation.

### 3.4. Diffraction Techniques

Experiments using elastic X-ray and neutron scattering have turned out to be an invaluable tool for the characterization of various types of porous materials, providing quantitative parameters such as the pore size, surface area, and pore volume. In addition, diffraction techniques allow the determination of the shape and, in particular, the spatial distribution of the pores, both for highly ordered arrays such as in MCM-41 and a more disordered arrangement of pores, for instance, in activated carbons. In the early 1900's, Max von Laue, W. L. Bragg, and W. H. Bragg, and others laid the groundwork for X-ray crystallography, which has become a powerful method of visualizing complex inorganic and organic crystalline materials [57–59]. In spite of the variety of different diffraction techniques that are available nowadays, they all are based on the same physical phenomenon, namely, the scattering of X-rays and neutrons by the atoms through their electrons or nuclei, respectively. In the Fraunhofer approximation, the interaction of X-rays with the electrons leads to the superposition of the coherent scattering of the basic scattering centers (atoms, molecules, or pores), without changing the energy of the incoming X-rays (“elastic scattering”). The resulting coherent scattering pattern is directly related to the mutual position, size, and scattering power of these scattering units. For almost all types of ordered mesoporous materials, no single crystal diffraction data are obtainable. Therefore, these materials are studied in diffraction experiments as a polycrystalline powder. In this case, the powder diffraction raw data are obtained as one-dimensional plots of the coherent scattering intensity versus the scattering angle  $2\theta$ . Only in the case of thin porous films with an oriented alignment of the pores relative to the substrate, two-dimensional diffraction patterns can be obtained [60–63]. The main problem in analyzing scattering patterns of any kind of polycrystalline, nanoporous materials lies with the extraction of a maximum of structural information. Depending on the length scale of the pore size, two methods can be distinguished regarding both the experimental realization and the theoretical treatment. Basically, the characteristic length scale  $d$ , describing the pore system and the corresponding diffraction angle  $2\theta$ , are related by the Bragg equation

$$s = \frac{1}{d} = \frac{2 \sin \theta}{\lambda}$$

where  $\lambda$  is the wavelength and  $s$  the corresponding scattering vector.

Several excellent textbooks are available on the general principles of diffraction theory and experiments [64–66]. Mesoporous materials with pores sizes above 1 nm are studied by so-called “small-angle scattering” (SAS), either using X-rays (SAXS) or neutrons (SANS). The evaluation of SAS data of porous materials is usually based on the approximation that the material can be regarded as a so-called “two-phase system”: in case of X-ray scattering, basic theoretical considerations show that the SAS of such materials arises from the scattering at the void-solid interface and is related to the scattering contrast  $(\delta_1 - \delta_2)^2$ , where  $\delta_1$  is the average electron density of the voids ( $\delta_1 = 0$ ) and  $\delta_2$  represents the *average* electron density of the solid. The SAS

of a sufficiently ordered nanoporous material with pores of a distinct shape is also given by Eq. (1), where the lattice factor  $Z$  has the same meaning as in wide-angle scattering, while the form factor  $F$  here corresponds to the shape of the mesopore/solid rather than the electron density of single atoms [67–69]. Polycrystalline-ordered mesoporous materials with a distinct pore shape and a well-defined two- or three-dimensional alignment, give rise to SAS patterns with a characteristic sequence of reflections (“peaks”). Therefore, the SAS patterns of the limited number of possible regular mesopore structures and space groups can serve as “fingerprints,” allowing an almost unambiguous assignment of a certain mesopore lattice structure, if a sufficient number of reflection peaks is obtained. In combination with TEM, SAXS experiments turned out to be a powerful technique to determine the alignment and structure in a variety of ordered mesoporous materials and other structures [70]. As the main information, SAXS provides the crystallographic space group of the mesopore arrangement and the corresponding lattice parameter. While the three-dimensional alignment of the mesoporous can be obtained from the bare SAS peak positions, the determination of mesopore sizes from single-peak analyses involves substantial uncertainties, because both the peak profiles and intensities can be substantially superimposed by various factors such as smearing, incoherent background scattering, in the arrangement of the mesopores and background fluctuations, and the presence of additional intrawall micropores. In particular, no satisfactory approach has been developed so far to quantitatively simulate the influence of two- and three-dimensional disorder on SAS. Even highly ordered mesopore systems such as MCM-41 show a certain two-dimensional displacement of the cylindrical mesopores on the hexagonal lattice, which together with the polydispersity of the pores may result in a nonnegligible overlap of the peaks, thus severely aggravating a meaningful pore size analysis [71–73].

A different approach for the evaluation of SAS data, without assuming a specific model, was recently pursued by using the concept of the so-called “chord-length distribution” (CLD)  $g(r)$ .  $g(r)$  is a statistical function describing the probability of finding a chord of length  $r$ , which is a connector of two points on the solid-void interface [74, 75]. The only preassumption of this concept is the formal description of the pore system as a two-phase system, but no assumptions about the pore shape and distribution are needed. Therefore, the CLD approach is most appropriate for disordered pore systems [14, 49].

### 3.5. Positron Annihilation

In the past 20 years, positron annihilation lifetime spectroscopy (PALS) has been developed as a powerful tool for the detection and quantification of defects on the atomic scale in various types of solids. Positron annihilation lifetime spectroscopy is sensitive to different kinds of defects such as dislocations and vacancies in metals or crystals, grain boundaries, as well as voids and pores. Similar to scattering techniques, PALS is a noninvasive technique and thereby allows the detection of inaccessible pores. In the area of micro- and mesoporous materials, Positron annihilation lifetime spectroscopy is predominantly applied to porous polymers and thin porous films. Positron annihilation lifetime

spectroscopy is based on the decay of positrons into two gamma photons (“annihilation”) and has been described in various publications [76–80]. Using  $^{22}\text{Na}$  as the radioactive source, the formation of positrons ( $\beta^+$ ) by radioactive decay is accompanied by the simultaneous emergence of a  $\gamma$ -quantum of 1.273 MeV, which defines the starting signal of the positron lifetime measurement. Entering the sample, the positrons lose their high energy by inelastic collisions with electrons. These “thermalized” positrons have energies on the order of few meV, form positroniums (Ps, the electron-positron-bound state) and diffuse through the solid until annihilation after their specific lifetime in the solid, which is measured as the time difference between the creation of the 1.273 MeV  $\gamma$ -quantum and the annihilation radiation (two 511 keV gamma rays). The natural lifetime of Ps of 142 ns is reduced by annihilation with electrons during collisions. The lifetimes, inverse of the annihilation rates, become longer when a positron or positronium is localized at spaces with lower electron density such as voids. Thus, positrons can be used as a probe to investigate average sizes of the free volume, size distribution, and the free volume concentration by measuring their lifetimes [81]. The raw data of PALS are plots of the annihilation radiation signal as a function of time. In case of not too high defect concentrations porosities, there will be at least two or three lifetime components  $\tau_i$  in the spectra, which are usually analyzed as a sum of exponentials after background subtraction.

### 3.6. Homogeneity of Materials

The pore-size regime for nanoporous materials ranges from the 1 nm-region to 1000 nm = 1 m $\mu$ . According to IUPAC, three distinctions can be made [82, 83]:

- Microporous materials 0–2 nm pores
- Mesoporous materials 2–50 nm pores
- Macroporous materials >50 nm pores.

Especially in the field of mesoporous materials, the mistake is often made to mix up the terms mesoporous and ordered materials. When a sorption isotherm indicates that a material is mesoporous, it does not mean that it is ordered as well, nor does a single reflex in X-ray diffraction (XRD). Ordered mesoporous materials are judged to be much more interesting due to the control over pore sizes and pore shapes. Their disordered counterparts exhibit high polydispersity in pore sizes and the shapes of the pores are irregular (a good example of such a material can be found in [84]). Ordered porous materials seem to be much more homogeneous. But one has to be careful with this statement because it is often led by aesthetic arguments caused by the beauty of images. In many cases, a material possesses more than one porosity. These can be:

- For microporous materials: an additional meso- or macroporosity caused by random grain packing;
- For mesoporous materials: an additional macroporosity caused by random grain packing, or an additional microporosity in the continuous network;
- For macroporous materials: an additional meso- and microporosity.

These factors should be taken into consideration when materials are classified concerning their homogeneity. A material possessing just one type of pore even when they are disordered might be more homogenous than one having just a fraction of nicely ordered pores.

#### 4. EXAMPLES FOR ORDERED MESOPOROUS MATERIALS

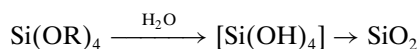
As previously described, mesoporous materials have pore sizes in the range between 2 nm and 50 nm. If a high porosity (larger than 50%) for materials can be achieved, porosity on the meso scale is always equivalent to high surface area. For instance, a material that has 80% of spherical 5 nm, voids can theoretically contribute 480 m<sup>2</sup>/g mesopore surface area. However, there is one very important differentiation that has to be made, namely, if the pore system is ordered or not. The typical features of an ordered pore system is that the pores are monodisperse in size, have a specific shape and a mutual three-dimensional correlation between each other. When on the other hand, a template above its percolation threshold has been applied, disordered pore systems result. Both of these classes of materials (ordered or disordered) are highly important for practical applications as in sensing [85, 86], catalysis [87–89], dielectric coatings [90–92], and of course, typical molecular sieve applications [93–96]. The following section will focus on materials with ordered pore systems because it is believed that the properties of these materials can be designed to a very high degree.

##### 4.1. Ordered Mesoporous Silica Materials

So far, the highest degree of perfection in materials design has been achieved for ordered mesoporous silica materials. As will be described in more detail later, ordered mesoporous silica materials can be obtained in a variety of pore sizes (2–80 nm), a variety of pore shapes (from spheres to lamellae), and a variety of surface properties. This makes ordered mesoporous silica materials a very active field of research. In 1992, Beck, Kresge et al. published their work about the first-ordered mesoporous silica material—the so-called mobile composition of matter (MCM)-41 [70, 97].

Before major achievements and the state-of-the-art in this field are presented, one might ask the more general question, “Why, especially for silica, these big improvements could be made?” There are three main reasons to mention:

1. Silica can be produced by sol–gel methods. The precursors used are not very reactive, despite other precursors for oxidic materials as titania, tin oxide, etc. This makes the silica sol–gel process very easy to control. Alkoxysilane compounds are used in most cases. The general process which is going on is given by the reaction scheme



Furthermore, there has been a great deal of investigation about the silica sol–gel process and nearly every detail is known. The description of the silica sol–gel

process is behind the scope of this article but very good presentations can be found in the books by Iler, Brinker, and Scherer [98–100].

2. The free energy of silica is very close to its most stable form crystalline quartz [101]. Furthermore, are the Si–O bonds so strong that the silica sol–gel process has highly irreversible character! Silica forms in its amorphous form and this amorphous silica is stable over a very high temperature range and period of time. This means that the shape of silica can be formed at room temperature and then be retained practically infinitely. Once more, this distinguishes silica from other oxidic materials where crystallization frequently leads to a restructuring in the network and therefore can destroy the mesostructure.
3. Finally, the interactions between surfactants and amphiphiles as surfactants or block copolymers can be tuned because silica units are available in anionic, neutral, or cationic form with dependence on the pH. Further, the charge density on these silica precursors matches the charge density of the surfactant head groups quite well. Silica precursors and amphiphiles are compatible.

##### 4.1.1. The M41S Family

A description of morphologies of porous silica materials derived by supramolecular organic assemblies as structure-directing agents should begin with the pioneering work of Beck, Kresge et al. in 1992 [70, 97]. They termed their silica materials M41S family.

The “family” has three members, the most famous one MCM-41 with a hexagonal pore structure, MCM-48 with a bicontinuous, gyroid structure, and MCM-50, which is lamellar. The preparation of MCM-41 itself has already been reported in 1971 but obviously Chiola et al. did not realize their important discovery [102].

Supposedly, Beck, Kresge et al. wanted to synthesize something similar to a zeolite structure under the influence of the quite large surfactant hexadecyltrimethylammonium chloride/bromide (CTAB). They worked in a diluted solution of CTAB. The concentration of the surfactant was far away from the corresponding hexagonal lyotropic phase.

Most research interest in the field of ordered mesoporous silica materials focused on the preparation, investigation of formation, modification, and application of MCM-41. It was seen rapidly after the first publication in 1992 that the addition of alumina is negligible and pure SiO<sub>2</sub> MCM-41 can be obtained. Many silica sources such as tetraalkoxysilanes, sodium silicate, fumed silica, or Ludox worked out fine. In the original publication, only a fraction of the obtained silica materials was MCM-41. The yield and ordering was improved by various methods like the addition of acids [103–105], changing the pH-conditions [104, 106], the addition of fluoride anions [107, 108], modifications in the hydrothermal treatment [109–111], or changes in the electrolyte concentration [112]. The addition of cosolvents, on the other hand, decreased the order [113, 114]. Several scientists could influence the MCM-41 particle morphology as well [115–118]. An amazing example is given by Huo et al. in 1997 with their production of 1–3 mm-sized silica MCM-41



spheres [119]. Even the preparation of MCM-41 at room temperature is common in the meantime [106]. Already Beck, Kresge et al. studied the influence of surfactant chain length variations [97]. As expected, the pore diameter was adjusted from 1.5 nm (zeolite like) to 4 nm (MCM-41) in the row  $C_6^- \rightarrow C_{16}^-$  surfactants. Well-ordered materials are obtained only for surfactant chains  $C_{14}^-$ - $C_{16}^-$ , although Sayari and Wang reported the preparation of high-quality MCM-41 also for  $C_{12}^-$  surfactants [120]. It was already pointed out by Beck, Kresge et al. in their original contribution that a change in the surfactant to a silica-source ratio leads to other structures than MCM-41 [70, 97]. The correct structure of MCM-48 was a point of discussion for quite a long time. First approximations assumed a cubic structure but in the meantime it is accepted to assign the minimal gyroid surface [113, 121]. The reason for the initial disorientation is nicely demonstrated by Anderson in his article "Simplified Description of MCM-48" [114] where he shows all different perspective modes of the complicated MCM-48 structure. An accurate synthesis procedure for MCM-48 was reported in 1993 [122]. When the surfactant-to-silica ratio exceeds the value 1, the main product of the M41S preparation is MCM-48 [123]. A systematic study of systems involving the corresponding surfactants was performed by Huo et al. in 1996 [124]. They also described the phase transitions between MCM-41 to MCM-48. It is seen that a key factor is the presence of ethanol which is suspected of suppressing the growth of one-dimensional cylinders (MCM-41) [121]. To provide easy and reproducible methods for the preparation of MCM-48 silica is still of interest as some recent reports indicate [121, 125, 126]. An interesting improvement was made by Schumacher et al. in 1999. They were able to prepare MCM-48 in the form of monodisperse spheres of approximately 500 nm size [127]. The last member of the M41S family is MCM-50. MCM-50 has a lamellar structure but it cannot be transferred to the porous state via surfactant removal by calcination. The pores collapse and the porosity is lost. Two models for the structure are discussed at the moment (i) ordinary silica sheets with intercalated surfactant or (ii) a special type of stacking of the surfactant rods to layers.

A common feature in the M41S family is that the cationic surfactant ( $S^+$ ) is combined with the anionic silica species ( $I^-$ ).

#### 4.1.2. Other Examples for the $S^+I^-$ Approach

McGrath et al. reported about the preparation of a new silica having a sponge-like  $L_3$ -phase [128, 129]. McGrath et al. claim that using a  $L_3$ -phase of cetylpyridinium chloride in 1:1 replication process, the corresponding silica is formed. The template phase consists of a surfactant bilayer system that is bent so strongly that a bicontinuous phase is created that divides the solvent (water) volume. Although the results are somewhat questionable, their characterization is not absolutely convincing; the preparation of a silica of this type is a real progress. The reasons are the following: According to McGrath et al., it is possible to adjust the pore size to any value between from 1 to 100 nm [128] simply by adding more water to the reaction system. Due to the fact that the pores

are filled with water and not with surfactant, as in other cases, the removal of the pore size directing agent is just drying. Furthermore, McGrath et al. claim that by removing the surfactant by calcination, an additional porosity appears.

Also, Huo et al. could show that completely new and unexpected morphologies could be reached via the  $S^+I^-$  route. Also, here the morphologies had no counterpart in the pure surfactant/water mixtures. Huo et al. presented a systematic study using the  $S^+I^-$  approach and a hole variety of cationic surfactants in 1996 [124]. They call their silica materials Santa Barbara (SBA) plus an additional number. SBA-1 was prepared in acidic media. The structure can be understood by assuming a densely packed cubic arrangement of spherical micelles (space group  $Pm\bar{3}n$ ). Maybe even more interesting is the structure of SBA-2. Gemini surfactants  $C_nH_{2n+1}N^+(CH_3)_2(CH_2)_sN^+CH_3)_2C_mH_{2m+1}$  were used in the synthesis. As can be seen from the formula, the two cationic head groups are separated by an adjustable hydrocarbon spacer. The surfactant packing parameter  $N_s$  can, therefore, be adjusted to several different values. In this case, a dense packing of globular micelles in a hexagonal fashion leads to a bicontinuous, three-dimensional  $P6_3/mmc$  structure [125]. The silica can be understood best as an analogue of zeolite cages just on a different pore size level and noncrystalline. The  $P6_3/mmc$  symmetry has no counterpart for pure surfactant-micelle/aqueous systems. A two-dimensional silica with a centered rectangular symmetry (SBA-8), which has been achieved by using related bolaform surfactants  $(CH_3)_3N^+(CH_2)_n-O-Ph-Ph-O-(CH_2)_nN^+(CH_3)_3$ , also has no counterpart [130]. It only exists as the silica-surfactant hybrid. Its structure is related to MCM-41 (hexagonal) by elongation of the crystallographic b-axis (space group  $cmm$ ).

However, the  $S^+I^-$  pathway is not the only possibility in obtaining ordered mesoporous materials via the synergistic coassembly mechanism. Every combination that results in an attraction between surfactant and silica source can be chosen in principle. There are also  $S^-X^+I^-$  (counter-ion mediated) and  $S^+X^-I^+$  (reverse charge matching) approaches [131–133]. But much more important and widely used is the neutral  $S^0X^0$  approach, using nonionic template systems.

#### 4.1.3. Neutral Interactions $S^0I^0$

The first ones to utilize neutral template assemblies were Pinnavaia and, independently, Goeltner. The  $S^0I^0$  approach is governed by hydrogen bonding between the template and the inorganic matrix [132]. Pinnavaia and Tanev tried to avoid the problems that appear concerning the recovery of the template, and to grant access to the porosity avoiding calcination. For ionic interactions between the silica walls and the template, a liquid-liquid removal is very difficult (time-consuming ion-exchange processes) or sometimes impossible. Tanev and Pinnavaia solved the problem by using primary amines  $C_{8-18}NH_2$  as the template with EtOH as co-solvent [134]. They found larger wall thicknesses and smaller domain sizes in their hexagonally ordered materials in comparison to MCM-41 [135, 136]. An additional textural porosity is created by this decrease in domain size. A similar approach with polyethylene oxide (PEO)-based surfactants ( $C_{11-15}$ -PEO) led them to the preparation of silica materials with 2–6 nm pores [137]. The pore structure was not

so well ordered in this case. They found a bicontinuous “worm-type” morphology. Bagshaw et al. described already in this work the use of nonionic block copolymers Pluronic (PEO-PPO-PEO) as templates [137]. Later, they figured out that one further difference between the  $S^0I^0$  and the ionic strategies is that the best-ordered materials are obtained at ambient temperature, while well-ordered MCM-41 required hydrothermal conditions [135]. Kim et al. also thought about the costs involved in the preparation of ordered mesoporous silica materials due to the use of silica tetra-alkoxysilanes. They extended the nonionic  $S^0I^0$  approach to water soluble silicates as precursors [138].

Independently, Goeltner and Attard used poly(ethylene glycol) alkyl ethers like  $C_{12/16}(EO)_8$  for the production of hexagonally ordered silica materials [139]. Their invention was to work with high-concentrated surfactant/water phases, namely, at concentrations where the lyotropic phase already exists. This allowed a 1:1 cast of the lyotropic template phase into the silica and was the beginning of the so called “nano-casting” [140, 141]. Then Goeltner et al. switched over to amphiphilic block copolymer systems to obtain larger pore materials [142, 143]. With poly(styrene) poly(ethyleneoxide), block copolymers worm-type pore systems with diameters from 4.5–10 nm were obtained. In the meantime, the structure of those silica is known in great detail. Large spherical mesopores are interconnected by smaller “bottleneck” channels. As all silicas that are derived by the use of amphiphilic block copolymers feature an additional microporosity created by the PEO chains. Even larger and beautiful morphologies were obtained with poly(butadiene)-poly(ethylene oxide) (PB-PEO) block copolymers [144, 145]. For these templates, the nanocasting (1:1 copy) could be nicely demonstrated and a phase transition between hexagonal cylinders and the lamellar phase was depicted. First, a lyotropic phase was prepared. Because the hydrophobic block of the copolymer contained polymerizable groups, treatment with  $\gamma$ -radiation led to crosslinking. The lyotropic phase was fixed this way and, therefore, accessible for TEM investigations. A comparison of this pure organic phase with the resulting silica revealed a match of 100% which means that the exact imprint could be shown. Also, ionic block copolymer systems have been used like poly(ethylene)-poly(styrenesulfonate) (anionic) or poly(butadiene)-poly(vinylpyridinium) (cationic). They produced casts of differently sized micelles and could even observe a micelle-lamella phase transition via the nanocasting [146].

At the same time (1998), Zhao et al. used a similar approach which led to various ordered mesoporous materials as  $C_{16}(EO)_{10}$  (SBA-11; cubic  $Pm\bar{3}n$ ),  $C_{18}(EO)_{10}$  (SBA-12; hexagonal  $P6_3/mmc$ ), and Pluronic [147] PEO-PPO-PEO (SBA-15; hexagonal and SBA-16; cubic  $Im\bar{3}m$ ) [148]. Much of the later work of Melosh et al. was devoted to SBA-15, which is in the meantime well known and used by many other groups as the prototype of a block copolymer-derived, ordered mesoporous silica material. In 1999, they presented the preparation of a SBA-15 monolith that was dry indeed but still template-containing (no accessible pores) [149]. For the first time, Kim et al. tried to give a mechanistic interpretation of the nanocasting process using amphiphilic block copolymers. They gave an explanation for

the microporous character of the mesoporous silicas and performed  $^{29}\text{Si}$  nuclear magnetic resonance (NMR) studies to explain the state of the PEO chains in the silica walls. The order of the silica phase can be increased by the addition of a small amount of fluoride ions  $\text{F}^-$  [150].

A new way to create interesting silica structures as vesicles and others was recently discovered by Jung et al. They use organogel systems as templates. With crown-appended cholesterol derivatives, large multilayer vesicles were obtained [151]. Chiral amide gelators connected to a cyclohexane ring directed the silica growth to helical fibers [152], modified cholesterol organogelators too [153], and sugar-derived gelators to a lotus shape [154]. Even organic crystals of dl-tartaric acid were used as a template by Mann et al. for the creation of hollow fibers with rectangular shape [155].

#### 4.1.4. Mechanistic Considerations

Figure 4 shows the formation mechanism of ordered mesoporous silica materials. There are two different pathways: The synergistic coassembly mechanism (a), and the nanocasting or true-liquid crystal mechanism (b). The surfactant (hexadecyltrimethylammonium bromide, CTAB, for instance) concentration that was used for the preparation



**Figure 4.** Schematic representation of the mechanisms involved in formation of hexagonally ordered porous materials within the scope of templating strategies. One pathway is characterized by an interaction of amphiphile and network precursor leading to the nanostructured composite phase (synergistic coassembly). In the other case, a template structure is formed at first, and imprinted precisely into a solid mold.

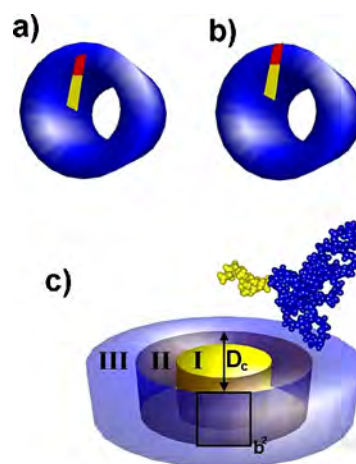
of MCM-41 was way behind the critical micelle concentration [1] and extremely far away from the lyotropic phase regime. It was, therefore, quite surprising in the beginning that MCM-41, with its hexagonal pore system mimicking a hexagonal liquid crystal, had formed. In the meantime, it is accepted that the first step in the formation of MCM-41 is an interaction between the cationic surfactant head group and an anionic silica species (shown as black cubes in Fig. 4). This special interaction between silica species and surfactant is generally denoted as  $S^+I^-$ . If one considers the packing parameter (see Eq. 1) [1], one realizes that bonding of the silica species to the surfactant will modify the head-group region. In principle, this creates a new, silica-organic hybrid surfactant with a different packing parameter and, therefore, also a different phase behavior. The morphology of the MCM-41 pores caused the assumption that a hexagonal arrangement of surfactant cylinders (a lyotropic phase) acted as the template for the formation of the final material. The silica could be formed by a direct solidification of this phase. But it was instantaneously clear that this could not be the truth because MCM-41 can be produced in concentration regimes below the critical micelle concentration (cmc) up to true liquid crystalline phases [156]. Consequently, Beck et al. proposed two general mechanistic ways [97]. One pathway involves the silica condensation in the hydrophilic domains of a preorganized liquid crystal and the other alternative suggests a cooperative interaction between the cationic surfactant and the anionic silica species. These two models were named *liquid crystal templating (LCT)* mechanism. More than one model was published to explain the final emergence of MCM-41 within the LCT. Chen et al. argued via  $^{14}\text{NMR}$  spectroscopy that at first, two to three layers of silica preliminary stages are deposited on isolated cylindrical surfactant micelles [157]. Via crosslinking of the isolated silica-surfactant composites, ordering and the final MCM-41 occurs. This model was supported by electron paramagnetic resonance (EPR) measurements [158]. On the other hand, Steel et al. founded on the same technique a formation of silica layers with intercalated surfactant rods [159]. By aging, the layers are bent and finally result in MCM-41 (puckering layer model). This model was further supported by TEM [159] and  $^{29}\text{Si-NMR}$  [160]. Monnier et al. introduced a related model, but they also considered charge density matching between the surfactant and silica [122]. The oligomeric silicate polyanions act as multidendate ligands which are connected to the surfactant. This leads to a lamellar silica-surfactant phase. The silica precursors now polycondensate primarily in these interface regions which reduces the negative charge. To obey the rules of charge density matching (the cationic charge of the surfactant head groups have to be compensated), the silica sheets have to bend. This phase transformation leads to MCM-41. Therefore, the formation of MCM-41 is a cooperative process. Although this process leads to the highly defined porous material MCM-41, a pre-determination of the pore morphology is not possible via this route.

It would be possible if a pre-existing template is casted into the silica by a 1:1 copy process. When the materials derived by block copolymer nanocasting are analyzed not only are the expected mesopores found but also a significant ratio of smaller pores. The micropores can contribute

as much as 80% to the total surface area in some cases [14]. In the meantime, it is accepted that the microporosity is caused by the PEO chain imbedded in the network matrix during nanocasting [14, 149, 161–163]. The hydrophilic PEO domains of the template are dispersed in the water/silicic acid mixture during the casting process and remain there when the network solidifies. When the materials are calcined, these imbedded, single polymer chains lead to micropores.

Further investigations of this fact showed that the micropores, which are responsible for approximately 70–80% of the total inner surface area, are caused by PEO chains dispersed in the silica wall [14]. A “one-phase” situation within the template, where the hydrophobic and hydrophilic blocks fully contribute to the mesopore volume, is excluded (see Fig. 5a).

A situation depicted in Figure 5b, where the two blocks of the amphiphile are strongly microphase separated (the PEO is now fully dispersed in the hydrophilic silica/water phase), was also excluded in a recent work by Smarsly et al. [163]. In this work it was found that the size of the mesopores  $D_c$  for materials prepared with Brij (alkyl- poly(ethylene oxide) surfactants) depends on the length of the hydrophobic as well as on the length of the hydrophilic block. Smarsly et al. assumed that only a fraction of the PEO chains are dispersed in the silica wall while a significant amount is located in the mesopore volume next to the hydrophobic core of the alkyl chains (see Fig. 5c). One empirical and a physically reasonable relationship was derived which allowed to predict the pore size dependant on the length of the blocks in the amphiphiles. They could also show that every pore size between two boarders given by the “parent” template systems can be reached simply mixing different ratios of two amphiphilic block copolymers of different length together in the templating mixture. Obviously, the nanocasting allows the gathering of inside views into self-assembly processes of soft matter by investigating the pore structure of the corresponding ordered porous material. Besides the production of the porous materials, the analysis of the pore



**Figure 5.** Schematic representation of the three different phase models related to the nanocasting mechanism. (a) one-phase model, (b) two-phase model, and (c) three-phase model. The organization of the template units (amphiphiles) is indicated as well.

structure itself led to the proposed “three-phase model.” Because only weak interactions between the template and the network phase are given within the nanocasting concept, nearly all structures occurring in the aqueous phase can be analyzed using this procedure. Polarz et al. demonstrated this by elucidating the proposed but unknown structures for cyclodextrins in water [164]. Cyclodextrins, cyclic oligo-saccharides, self-assemble to “worm-type” aggregates which can be depicted by transferring these structures into the solid silica replica.

When trimethylbenzene (TMB) is added to the lyotropic phase to increase the pore size by swelling, mesocellular foams are obtained at a certain ratio as Lettow et al. and Kim et al. pointed out independently [165, 166]. The ideal hexagonal structure of SBA-15 is maintained only for relatively low concentrations of TMB. When the oil to polymer ratio is 0.2–0.3, the silica walls begin to buckle forming nodes accompanied by an increase in the pore size. If the amount of oil is increased further, the nodes undergo a transition to spherical pores ( $d \approx 20$  nm)—the so-called mesocellular foam. The explanation for this phase transition lies in the reaction of the lyotropic phase due to a change in the surfactant parameter by adding a hydrophobic solvent [167–169]. The TMB is located in the hydrophilic poly(propylene oxide) (PPO) regions of the amphiphilic assemblies, which changes the packing parameter of the surfactant and finally leads to the transition of micelles to microemulsions [165]. That emulsions could indeed act as templates was shown in 1997 by Imhof and Pine [170].

While the synergistic coassembly (MCM route) naturally leads to powder-like materials, or in best cases, larger particles [127], the nanocasting allows the production of monoliths or thin films. For the first time, this allows one to divide a macroscopic volume into well-defined, nanometer-sized compartments. A crucial problem in maintaining the macroscopic and microscopical integrity of the materials is the removal of the template and drying of the samples. Calcination fails for the production of crack-free monolithic samples. Fortunately, the templates can be removed by liquid-liquid extraction. However, capillary stress due to evaporation [171] can very easily lead to cracks. Capillary pressures generated by a phase transition of the pore fluid to the gas state can be avoided by supercritical drying [172]. Cracks can be further avoided by adding silica fibers to the sol which is used for the nanocasting process.

#### 4.1.5. Adjustment of and Understanding of Pore Sizes

One blemish of the chemistry involved in the preparation of mesoporous materials is that most of the obtained silica structures were not discovered by planning but more by trying. Some work has been devoted to gain more knowledge regarding the silica morphologies (pore shape and size). Especially in the field of influencing the pore size, success was reached. Roughly, this was already shown in the previous section. Here, these different strategies should be summarized in a more general way.

Navrotsky et al. were able to show that there is, in principle, no limitation for accessible pore sizes in amorphous silica materials [101]. They demonstrated that the amorphous

silica in materials like MCM-41 is insignificantly less stable than the most stable form of  $\text{SiO}_2$ , crystalline quartz. This means that only suitable experimental pathways have to be found to reach a certain pore size. Then the materials are absolutely stable.

To determine the pore size, three independent methods exist:

- variation of the amphiphile size (especially the hydrophobic part);
- swelling of the lyotropic phase by addition of selective solvents;
- change in reaction parameters like temperature or electrolyte concentration [173].

All these methods include the problem that their application changes the packing parameter of the amphiphile and can, therefore, change the desired lyotropic phase (phase transitions). For a modification of the hydrophobic block length, this is obvious as  $N_s$  directly depends on this parameter. Swelling of the lyotropic phase changes the volume of the hydrophobic chain which also appears in equation [165, 167–169]. One way to change pore sizes is to vary the temperature during preparation of the material [174, 175]. The higher the temperature, the larger the pores get and also the electrolyte concentration is an important factor [173]. A change in the electrolyte concentration (which also means the addition of electrolytes) changes the physical character of the aqueous phase, and due to interactions of the ions, with the ionic head of the surfactant the head group area.

The dependence of the pore size on the length of the hydrophobic chain was already demonstrated by the first works of Beck, Vartuli et al. [70, 97, 176]. An investigation in our group on Brij surfactants  $C_x(\text{EO})_y$  showed that this dependency is true as well for nonionic approaches, but that in this case the length of the hydrophilic chain influences the pore size as well [163]. Expanding pore sizes by addition of selective solvents can also be used for  $\text{S}^+\text{I}^-$  [177, 178] and  $\text{S}^0\text{I}^0$  [165]. Preparation conditions or post-treatment [179, 180] are also important for both systems. So far, the most comprehensive study on the nanocasting process and the creation of micropores was published by Smarsly et al. [163]. A quantitative relation between the size of the mesopore  $D_c$  and the composition of the used block copolymer (length of hydrophobic and hydrophilic block) was derived. This dependence  $D_c \propto N_{\text{hydrophobic}}^{0.4} N_{\text{hydrophilic}}^{0.25}$  is described in more detail in [163]. It was shown in this article [163] that quantitatively the size of a pore depends in principle just on the average number of monomer units in the amphiphile. This average number can be simply varied if one uses mixtures of amphiphiles (for instance, a small and a large surfactant) in different amounts. Besides the prediction of pore sizes from the molecular composition of pore sizes, it now becomes possible to achieve a fine tuning of pore sizes by using mixtures of amphiphiles as templates. With the most commonly available amphiphiles (even pluronics), it is now possible to achieve every pore size between 1.5 to 10 nm.

#### 4.1.6. Chemistry with Ordered Mesoporous Silica Materials

Certain fractions of other elements than silicon can be imbedded into materials mostly of the MCM-41 type. These materials can be obtained when a source for this metal is added directly to the precursor sols. The most prominent example, which was already prepared in the original work by Kresge, Beck et al. [70, 97], is Al-MCM-41, a MCM-41 where some Si atoms are substituted by Al. Through the incorporation of aluminum, the material obtains Lewis acidity. Therefore, Al-MCM-41 has been used for the catalytic cracking of various organic compounds [181–183]. The performance of the competing zeolites is often better [182], although sometimes higher product selectivities with mesoporous materials were observed. Other catalytic materials with acidic functions are Ni-MCM-41 and Mo-MCM-41 [184]. These materials have some importance for the removal of sulfur from raw oil hydrodesulfuration (HDS) process [185–187]. The latter cases (hydrocracking and HDS) are examples for the reasons why some major oil companies are even today quite interested in ordered mesoporous materials [188–191]. The acidic forms of MCM-41 have also been used for some classical organic synthesis catalyst such as Friedel–Crafts reactions and others [192–197]. The big advantage of ordered mesoporous materials in comparison to zeolites is that MCM can also be used for large and bulky molecules even when the reactivity is not so high. Basic forms of MCM-41 have also been prepared but here silica-organic hybrid materials are much more important and will be discussed later. Just Cs-MCM-41 has some importance as a catalyst for Knoevenagel reactions [198–200]. Another modified MCM-41, Ti-MCM-41, has been used for a variety of redox catalysis [201]. Other examples for MCM-41 redox catalysts are Ti-, Fe-, Cr-, V-, B-, Al-, and Mn-MCM-41 materials [202], but also Sn- [203–205], Zr- [206], or Ru-MCM-41 [207] have been invented.

A different way to enrich silica MCM-41 with catalytic properties is to deposit metal or oxidic nanoparticles inside the mesoporous framework. It was shown recently that the size of the resulting nanoparticles can be fine tuned by the size of the pore restriction and that the wall properties are of major significance [208].

It is possible to create noble metals particles which resemble exactly the size of the hosting mesopore after reduction of suitable precursors. If the same process is applied to a material that is able to interact with these precursors (in the case shown, a silanol-rich silica monolith interacts with  $[\text{PdCl}_4]^{2-}$  ions), the created metal particles are bound to the pore surface and Ostwald-ripening is suppressed. Just subnanometer large particles are created [208]—not visible in TEM images. One is, therefore, able to create ordered silica materials carrying a great variety of nanoparticles, semiconductor nanoparticles, or even oxide nanoparticles [209–219]. Therefore, much of the work has been devoted to prepare semiconductor nanoparticles this route. Examples are gallium nitride [217], cadmium selenide [212], cadmium sulfide [220], silicon [221, 222], titanium dioxide [223], germanium [224], galliumarsenide [225], zinc sulfide [226], and indium phosphide [227]. Since then, preparation of colloidal particles inside mesoporous hosts has become a versatile

tool to produce different kinds of nanostructures [228]. One ideal example can be found in the work of Huang et al. where silver nanowires were produced inside MCM-41 [210]. Similarly, metal nanowires have also been produced with Pd [229, 230], and Pt [213].

The last work already indicated that it is possible to transform the whole pore system of a material into a new material which would not be accessible otherwise. The ordered mesopores act as a template again for new materials which is released by removal of  $\text{SiO}_2$  via HF etching. For instance, when an ordered mesoporous material is filled with a suitable precursors for carbon, depending on the pore morphology particle-like carbon [231], or nanoporous carbons (for instance, with the *Ia3d* structure of MCM-48) have been prepared [47, 232–234]. Similar results can be obtained by preparing a replica of the pore structure with platinum. These results are extraordinary because the new material now resembles the structure of the organic liquid crystal, which was originally used as a template for the production of the ordered mesoporous silica materials. Having an “artificial carbon liquid crystal” in hand could be very beneficial because carbon is stable to very high temperatures. The mesostructured carbon might, therefore, be taken as a new template for many materials that are not accessible with organic templates.

It should be mentioned that many of the host-guest compounds with ordered mesoporous materials are not of the inorganic-inorganic type. In many cases, organic compounds as dyes or polymers have been immobilized in the porous framework preferentially of MCM-41 [235]. Polymers like polymethyl-methacrylate were directly created inside the pores and it was shown that the spatial confinement had some impact on the physical properties of the polymers [236]. Kageyama et al. reported about a titanocene containing MCM-41 material, which was used as a solid-state catalyst for the preparation of a unique, high molecular weight poly(ethylene) [237]. Very important in this respect are also ordered mesoporous silica materials containing conductive polymers as found, for instance, in the work of Gangopadhyay and De [238] and Wu and Bein for poly(aniline). The created organic-inorganic hybrid materials have often unique properties. One example for such unique features are new ordered mesoporous laser materials. Generally, an active laser dye is brought into a porous environment and its laser activity is studied. It was envisioned by Marlow et al. that a whole laser could be produced by using the self-assembly laws [240]. They could prepare a silica-surfactant laser dye (Rhodamine 6G) hybrid material which had a fibrous morphology. The laser dye is located in the hydrophobic domains of the lyotropic template phase. The fiber was pumped perpendicular to the fiber direction and above a certain threshold laser activity was detected. Wirnsberger and Stucky et al. extended their works [241, 242] and recently they prepared impressive waveguides by a combination of self-assembly and soft lithography techniques [243]. Mesoporous silica (template removed) was deposited on silicon and as the third layer, there were the waveguides containing the dye-doped-ordered mesoporous silica [242]. The cylindrical channels were aligned throughout the whole waveguides and even the dye seemed to be oriented in the template phase.

In all of the preceding cases was the organic part of the material just immobilized inside the pore system of the ordered mesoporous silica material. An alternative is to covalently link organic groups to the silica network and change the material properties this way. After calcination, ordered mesoporous silica still possesses a certain amount of active silanol groups Si-OH [244]. These groups can be reacted with a variety of organically modified sol-gel (ORMOSIL) precursors which have the general formula  $R-Si(OR')_3$ . The attachment of a terminal organic group in a post-modification procedure leads to new, mesostructured silica-organic hybrids. However, the organic groups loom into the pore volume and not every pore surface Si-group gets modified this way. These are two clear disadvantages of the post-functionalization method. In most cases, amino functions have been introduced this way to ordered mesoporous silica materials [245–248]. But also materials containing ephidrine for asymmetric catalysis [249, 250] or organometallic complexes were invented [87]. As was pointed out, it would be quite desirable if the pore wall itself is modified, instead having the organic groups located in the pore volume. Therefore, materials scientists tried with some success to add the ORMOSIL precursors directly to the synthesis mixture. This approach has two problems. The Si—O—R bond is not stable enough under most commonly needed synthesis conditions (high or low pH) and the organic group can negatively influence the interface energy, which is important when the amphiphile microphase separates and, thus, structures the material. Burkett et al. could show that this pathway is successful for octyl- and phenyl-groups [251], later also thiols, amines, epoxides, imidazoles, and other alkyl-groups [252], when the ORMOSIL precursors with Si-C motives are used. The template can now just be removed by liquid-liquid extraction due to the presence of the organic groups. Therefore, and due to the effect of the organic ligand on the condensation rates, one obtains not fully condensed, quite weak, or collapsed materials. Still, the amount of organic groups that can be incorporated in the materials remains with 25% quite low. If higher amounts of ORMOSIL precursor are taken, the structuring of the material via self-assembly is not successful.

A big improvement was made by MacLachlan, Asefa et al., when they used bridging ligands (Si-R-Si) to modify the pore wall [253, 254]. These groups are truly incorporated in the material; they even seem to cover the pore walls. Now it was possible to use 100% of the organically modified sol-gel precursor for the synthesis, the materials are stable, and the pore walls are 100% covered with different organic groups as ethylene or benzene [253–258].

#### 4.1.7. Conclusions

It has been shown in this section that ordered mesoporous materials have become “designer” materials. They can be prepared with a great variety of or properties as pore size, pore shape, organic groups on pore walls, organic groups in pore volume, and any desired macroscopic shape of the materials. Next, it is considered if the structure principles that work for silica can be extended to other inorganic network materials (Section 3.2.3).

## 4.2. Other Inorganic-Ordered Mesoporous Materials

It was already suspected in 1993, briefly after the invention of MCM-41, that one would be able to create mesoporous materials of different compositions than silica by surfactant templating routes, because similar interactions between the network precursor and the amphiphile might be created [131]. However, creating other network sources than silica always involves two general problems. The precursors for these networks are much more reactive which makes the whole process less controllable. Secondly, most other networks tend to exist in the crystallized rather than amorphous form. The crystallization can result in major restructuring processes in the material and, therefore, might destroy the mesostructure. Most frameworks begin to crystallize at higher temperatures, when the surfactant is removed by calcination. This makes it often difficult to remove the template.

The first nonsiliceous example for a comparable material followed in 1994 about tungsten oxide, molybdenum oxide, antimony oxide, or vanadium oxide related materials, but it was not possible at that time to remove the organic template because lamellar structures were obtained [259–263]. Ying and Antonelli [264] were the first ones to obtain transition metal oxides with similar structures than MCM-41. For instance, a mesoporous titania material  $TiO_2$  was obtained when the reactivity of the precursors was decreased by the addition of a complexing ligand as acac. Later, nicely structured niobium oxide and tantalum oxide materials were obtained by tuning the interaction of the amphiphile with the precursors (ligand-assisted route) for the inorganic framework [265–267].

### 4.2.1. Transition Metal Oxides

Due to their high relevance in many areas of catalysis and their variable redox and magnetic properties, much work was devoted to the creation of stable-ordered mesoporous, transition metal oxides. In the meantime, many compositions with Ti, Zr [268–273], V [270, 274], Nb [265, 267, 270, 275, 276], Ta [266, 270, 277], Mo [278, 279], W [278, 280, 281], Mn [282, 283], and Y [284, 285], as the central element have been introduced. In comparison, most of the work has focused on ordered mesoporous titania because of its potential use in solar cells [286, 287] and electrochromic devices [288]. Ordered mesoporous titania is a quite representative example for transition, metal-based materials. The reactivity of titania precursors goes in the order  $TiCl_4 > Ti(iOPr)_4 > Ti(OBu)_4 > Ti(OEt)_4$  [289, 290]. These precursors all react rapidly with moisture and form  $TiO_2$ . In order to control the growth of a titania network around a template phase, the reactivity has to be decreased. The most frequently used approach is to take  $TiCl_4$  as a titania source and react it with anhydrous ethanolic solutions of the template (surfactant or block copolymer) [270, 291]. The reaction between  $TiCl_4$  and EtOH releases high amounts of HCl. High concentrations of HCl stabilize titania nanoclusters and, therefore, prevent uncontrolled condensation. Additionally, one deals with an anhydrous solvent. The water needed for the self-organization of the amphiphile and for the condensation of the titania is provided exclusively by the atmospherical

humidity. The humidity is the crucial point in these preparations and it should be around 50%. It is also interesting to note that the water seems unable to diffuse from the top of a deposited film into the material, presumably due to densely packed surfactant hydrophobic chains on this surface. Diffusion of water and ordering of the material begins at cracks and propagates from there. As prepared, the materials have amorphous framework which is often undesired for many applications. Crystallization of titania occurs at temperatures above 400 °C, which might also disrupt the mesostructure and leads just to 3 nm large crystallites. As a possible solution, titania nanocrystals were proposed as the starting material for ordered mesoporous titania as well [292].

#### 4.2.2. Metal Sulfides

Tohver, Osenar, Braun et al. used a true liquid crystal approach to prepare various mesostructured metal sulfide materials [293–295]. A lyotropic block copolymer phase is swollen by an inorganic salt solution as  $\text{Cd}^{2+}$  salts and then treatment with  $\text{H}_2\text{S}$  vapor follows. A nanocrystalline, ordered, mesoporous  $\text{CdS}$  material is the result. Soon, a  $\text{ZnS}$  material followed [296]. Similar to the work, where titania nanoclusters have been used for the preparation of mesostructured titania [297], several groups prepared ordered mesostructured germanium sulfide materials with  $\text{Ge}_4\text{S}_{10}$  clusters in the initial state [86, 298–300].

#### 4.2.3. $\text{AlPO}_4$

Due to the similarity between silica molecular sieves (zeolites) and aluminium phosphates (ALPOs), there have been many attempts to synthesize MCM-41 analogous ALPO materials. In most of these cases, nonstable materials are obtained or the pore systems are quite different from MCM-41 [301, 302]. Kimura et al. reported a nicely ordered hexagonal ALPO material in 1999 [303] and Holland et al. reported on an interesting approach using an  $\text{Al}_{13}$  Keggin species as the source for aluminum [304].

#### 4.2.4. Silicon Nitride

Similar to ALPOs, one could suspect that it will be possible to produce ordered, mesostructured silicon nitride because the  $\text{NH}$  unit as in imides or amines is isoelectronic to oxygen, which would allow a similar sol–gel chemistry as for silica. There have been attempts to synthesize these compounds with silicon amines, ammonia, and nonaqueous solvents and surfactant [305].

#### 4.2.5. $\text{Al}_2\text{O}_3$

Ordered mesoporous alumina would also be a very interesting material due to its high relevance in catalysis. The classic way of preparing mesoporous alumina is by electrolytic etching (anodized alumina) and the obtained results are impressive for the production of thin films [306]. This technique is restricted to surfaces. Therefore, preparing ordered mesoporous alumina via templating routes should be very promising. It was found that it was very difficult for alumina to achieve highly ordered materials and to achieve control over pore size although some examples exist [270, 307]. It seems that the  $\text{S}^0\text{X}^0$  pathway is appropriate for alumina.

#### 4.2.6. Metals

Attard and Goltner succeeded in the preparation of hexagonally ordered metal sponges via templating techniques [308]. This technique is very similar to the described approaches although the network is now formed by reduction of noble metal precursors.

### 4.3. Ordered Mesoporous Organic Materials

The templating concept introduced in Section 2 can be extended towards pure organic or polymeric compositions of materials. Similarly, an organic monomer is polymerized around a prefabricated template structure. The chemical and physical parameters of the obtained polymer differ very much from the monomer species if one compares it to the sol–gel process of inorganic oxides. Often, restructuring processes occur during polymerization which can lead to partial or complete phase separation. Therefore one has to distinguish:

- Transcriptive synthesis: The pore structure is a 1:1 imprint of the template structure.
- Reconstructive synthesis: The polymerization takes place under the spatial confinement imposed by the template and morphological rearrangements lead to the final material.
- Synergistic synthesis: The monomer itself self-organizes.

Similar to all the approached previously discussed, the interactions between the template phase and the network builder (or in other words, charge density matching considerations) are of crucial importance. Additionally, entropic forces, such as restriction of polymer segment mobility due to spatial restrictions, can become important. These factors determine whether a synthesis is transcriptive or reconstructive. One problem that also remains is that the porous materials are just metastable. In the case of polymeric materials, this fact becomes much more important than for most inorganic networks. Due to the swelling of polymers and their high flexibility, polymer systems might be unable to retain the porous structure in the long run.

One important field is the transcriptive translation of molecules into pores designed on a molecular level which is also known as molecular imprinting [309]. The synthesis pathway is similar to a key lock or antibody/antigene mechanism. The template molecules (often amino acids [310, 311], sugars [312], peptides [313], or steroids [314, 315]) exhibit a certain pattern of distinct, spatially distributed functional groups. Suitable functional groups in the monomer systems interact with these patterns and this leads to an imprint of the shape and functional structure. Finally, the template molecules are removed by extraction or chemical cleavage. Typical monomers that have been used are methacrylic acid and ethylene glycol dimethacrylate. More detailed reviews about molecular imprinting to obtain porous polymers can be found in the recent literature [316–319].

The second type for a clear transcriptive synthesis of porous, organic polymer materials are found when colloidal crystals (opals) are used as templates [320, 321]. Large mesopore materials or macroporous structures are obtained. Possible polymer compositions involve polyurethane [322, 323],

poly(acrylate-methacrylates) [324], poly(divinylbenzene)-copoly(ethyleneglycoldimethacrylate) [325], polystyrene and poly(methyl methacrylate) [326], and polypyrrole [327].

Already, when micelles are used as templates, a clear transcription to pores is questionable. Styrene/divinylbenzene polymers with spherical pores of 10–20 nm were obtained by templating with water swollen AOT (sodium bis(2ethylhexyl) sulfosuccinate) micelles [328, 329]. The pore size appears to be too large to be caused even by swollen AOT micelles. In a similar work, water swollen AOT micelles were used for the preparation of ethylene trimethacrylate polymers in supercritical CO<sub>2</sub> with 20 nm pores [330–332]. When supercritical CO<sub>2</sub> was omitted, pores of 100 nm were obtained indicating the reconstructive character of the synthesis.

The micelles in the previous cases were already swollen with a polar solvent as water, while the continuous phase contained the hydrophobic monomer. The next logical step is to use microemulsions as templates for the production of porous polymers. Microemulsions are thermodynamically stable systems with droplet sizes in the range of 10–100 nm [1]. Of particular interest for this application are bicontinuous microemulsions.

It was seen in all reported cases that the pore morphology was no longer directly related to the structure of the microemulsion. Very often just latex particles were obtained [333, 334]. However, when hydrophilic (as acrylic acid) and hydrophobic (as methylmethacrylate) are copolymerized in the presence of a microemulsion, true porous materials have been obtained [335]. The final product was, as mentioned, very different as expected from the morphology of the microemulsion. Therefore, one has to conclude a reconstructive synthesis pathway. The transformation from a microemulsion to the final porous system for such a system was studied and not less than four phase transitions have been observed during the polymerization reaction [336].

The next level of complexity is reached when lyotropic phases are used as templates for porous polymers. First attempts to imprint a lyotropic structure into a polymer failed due to demixing [337, 338]. However, it was possible to get nicely ordered, reconstructed morphologies this way [338, 339].

It can be concluded that a variety of nanoporous polymer materials can be obtained. But due to thermodynamic factors during the polymerization, demixing processes lead to the formation of different materials than was planned. Also, nonequilibrium conditions might play an important role. Although the prepared structures are very interesting and might have applications, it seems hard to synthesize designed nanoporous polymers. Furthermore, it seems that there are currently restrictions to just a few polymer systems.

## 5. CONCLUSIONS

It was shown in this review that the field of mesoporous materials is very interdisciplinary. It ranges from a variety of network compositions (inorganic, organic, and metallo-organic), different pore shapes (disordered, spherical, cylindrical, lamellar), different pores sizes (from 2 nm to several tenths of nanometers), and last but not least, different pore-surface properties.

This high level of knowledge for these types of materials creates several new challenges which would fill pages if one considers all the different classes of materials in the mesoporous materials family. However, some relevant future directions should be mentioned.

During the next few years, scientists are going to achieve compositions as much as possible for this class of materials. It is also somewhat surprising that so far, no significant application has been established for ordered mesoporous materials. It can be envisioned that the more it is possible to create materials with designer properties as electronic, magnetic, or mechanical properties, applications will be found. One interesting application could be photocatalysis. It is still unanswered if the narrow pore size distribution and the regularity in shapes of the pore channels has some special effects on processes in pores. Therefore, these effects will have to be studied on a more fundamental basis.

All porous materials presented so far have some kind of static character. This means that once the materials have been prepared, they don't change their properties any longer. Smart porous materials, that is, materials changing their properties in dependence on outer stimuli (for instance, pH or electric fields), are a very interesting goal. As a first problem one might address changing pore sizes due to a chemical stimulus. However, it cannot be overlooked that mesoporous materials are just metastable once the template is removed. This metastability has to be retained whatever smart or intelligent materials are to be created. Therefore, it seems that neither pure inorganic nor pure organic materials are able to fulfill this task. Inorganic-organic composites might be able to have these desired properties once the complexity of the materials has been increased.

Much progress can also be expected from the field of colloidal crystals (which also can create mesoporous materials) and photonic materials. Ideally, several disciplines—chemistry physics, and engineering—will fuse to predict and realize materials and device properties. The future will tell if the next computer generation will run with light.

## GLOSSARY

**Amphiphile** Molecules containing hydrophilic and hydrophobic parts.

**Cetyltrimethylammoniumbromide (CTAB)** A cationic surfactant.

**MCM-41** The first ordered mesoporous material with hexagonally aligned cylindrical pores.

**Mesoporous materials** Materials with pores between 2–50 nm.

**Micropores** Pores below 2 nm in size.

**Self-assembly** Process due to weak intermolecular forces which leads to higher organized structures.

**Template** A central structure which acts as some kind of a place-holder.

## REFERENCES

1. D. F. Evans and H. Wennerström, "The Colloidal Domain." Wiley-VCH, 1999.
2. K. Mosbach, *Trends Biochem. Sci.* 19, 9 (1994).



3. K. Mosbach and O. Ramstrom, *Bio-Technology* 14, 163 (1996).
4. T. Takeuchi, D. Fukuma, and J. Matsui, *Analytical Chemistry* 71, 285 (1999).
5. S. A. Piletsky, K. Piletskaya, E. V. Piletskaya, K. Yano, A. Kugimiya, A. V. Elgersma, R. Levi, U. Kahlow, T. Takeuchi, I. Karube, T. I. Panasyuk, and A. V. Elskaya, *Anal. Lett.* 29, 157 (1996).
6. S. Dai, Y. S. Shin, C. E. Barnes, and L. M. Toth, *Chem. Mat.* 9, 2521 (1997).
7. J. Matsui, T. Kato, T. Takeuchi, M. Suzuki, K. Yokoyama, E. Tamiya, and I. Karube, *Analytical Chemistry* 65, 2223 (1993).
8. H. P. Hentze and M. Antonietti, *Curr. Opin. Solid State Mat. Sci.* 5, 343 (2001).
9. E. J. A. Pope, M. Assami, and J. D. MacKenzie, *J. Mater. Res.* 4, 1018 (1989).
10. C. J. T. Landry and B. K. Coltrain, *Polym. Prep. (Am. Chem. Soc., Div. Polym. Chem.)* 32, 514 (1991).
11. T. Hino, K. Mochida, and S. Okumara, *Kobunshi Ronbunshu* 40, 225 (1983).
12. P. B. Messerschmidt and S. I. Stupp, *Polym. Prep. (Am. Chem. Soc., Div. Polym. Chem.)* 32, 536 (1991).
13. T. Saegusa, *J. Macromol. Sci. Chem. A* 28, 817 (1991).
14. C. G. Göltner, B. Smarsly, B. Berton, and M. Antonietti, *Chem. Mater.* 13, 1617 (2001).
15. A. Stein, *Microporous Mesoporous Mat.* 44, 227 (2001).
16. K. Fontell, C. Fox, and E. Hansson, *Mol. Cryst. Liq. Cryst.* 1, 9 (1985).
17. N. Koshida and B. Gelloz, *Curr. Op. Colloid Interf. Sci.* 4, 309 (1999).
18. K. L. Kavanagh and M. J. Sailor, *Science* 255, 66 (1992).
19. S. J. Gregg and K. S. W. Sing, "Adsorption, Surface Area and Porosity." Academic Press, London, 1982.
20. K. W. Sing, *Adv. Colloid Interf. Sci.* 76-77, 3 (1998).
21. R. Zsigmondy, *Z. Anorg. Allgem. Chem.* 71, 356 (1911).
22. L. H. Cohan, *J. Am. Chem. Soc.* 60, 433 (1938).
23. E. P. Barret, L. G. Joyner, and P. H. Halenda, *J. Am. Chem. Soc.* 73, 373 (1951).
24. A. V. Neimark and P. I. Ravikovitch, *Microporous Mesoporous Mat.* 44, 697 (2001).
25. P. B. Balbuena and K. E. Gubbins, *Characterization of Porous Solids III* 87, 41 (1994).
26. R. Evans, U. M. B. Marconi, and P. Tarazona, *J. Chem. Soc. Faraday Transactions II* 82, 1763 (1986).
27. J. C. Broekhof and J. H. Deboer, *J. Cata.* 10, 153 (1968).
28. M. Kruk, M. Jaroniec, and A. Sayari, *Microporous Mesoporous Mat.* 27, 217 (1999).
29. M. Kruk, M. Jaroniec, and A. Sayari, *J. Phys. Chem. B* 101, 583 (1997).
30. M. Kruk, M. Jaroniec, and A. Sayari, *Langmuir* 13, 6267 (1997).
31. M. Jaroniec and K. K. Langmuir 13, 6589 (1997).
32. M. Kruk, M. Jaroniec, R. Ryoo, and J. M. Kim, *Microporous Mater.* 12, 93 (1997).
33. B. L. Newalkar and S. Komarneni, *Chem. Mat.* 13, 4573 (2001).
34. P. I. Ravikovitch and A. V. Neimark, *J. Phys. Chem. B* 105, 6817 (2001).
35. M. Jaroniec, M. Kruk, C. H. Ko, and R. Ryoo, *Chem. Mater.* 12, 1961 (2000).
36. K. E. Gubbins, in "Physical Adsorption: Experiment, Theory and Physical Applications" (J. Fraissard, Ed.). Kluwer, Dordrecht, 1991.
37. M. W. Maddox, J. P. Olivier, and K. E. Gubbins, *Langmuir* 13, 1737 (1997).
38. P. Tarazona, U. M. B. Marconi, and R. Evans, *Mol. Phys.* 60, 573 (1987).
39. A. Dekeizer, T. Michalski, and G. H. Findenegg, *Pure Appl. Chem.* 63, 1495 (1991).
40. P. Tarazona, *Phys. Rev. A* 31, 2672 (1985).
41. P. I. Ravikovitch, S. C. Odomhnaill, A. V. Neimark, F. Schuth, and K. K. Unger, *Langmuir* 11, 4765 (1995).
42. P. I. Ravikovitch, D. Wei, W. T. Chueh, G. L. Haller, and A. V. Neimark, *J. Phys. Chem.* 101, 3671 (1997).
43. P. I. Ravikovitch, G. L. Haller, and A. V. Neimark, *Adv. Colloid Interf. Sci.* 76-77, 203 (1998).
44. A. V. Neimark, P. I. Ravikovitch, M. Grun, F. Schuth, and K. K. Unger, *J. Colloid Interface Sci.* 207, 159 (1998).
45. A. V. Neimark and P. I. Ravikovitch, *Stud. Surf. Sci. Catal.* 128, 51 (2000).
46. P. I. Ravikovitch and A. V. Neimark, *Langmuir* 18, 1550 (2002).
47. M. Kruk, M. Jaroniec, Y. Sakamoto, O. Terasaki, R. Ryoo, and C. H. Ko, *J. Phys. Chem. B* 104, 292 (2000).
48. M. Thommes, R. Kohn, and M. Froba, *J. Phys. Chem. B* 104, 7932 (2000).
49. B. Smarsly, C. Goltner, M. Antonietti, W. Ruland, and E. Hoinkis, *J. Phys. Chem. B* 105, 831 (2001).
50. M. Jaroniec and M. Kruk, *Langmuir* 15, 5410 (1999).
51. E. W. Washburn, *Proc. Nat. Acad. Sci.* 7, 115 (1921).
52. J. van Brakel, *Powder Technol.* 29, 1 (1981).
53. G. P. Johnston, D. M. Smith, I. Melendez, and A. J. Hurd, *Powder Technol.* 61, 289 (1990).
54. S. M. Brown and E. W. Lard, *Powder Technol.* 9, 187 (1974).
55. T. Allen, in "Particle Size Measurements," p. 251. Chapman and Hall, New York, 1997.
56. Y. Sakamoto, M. Kaneda, O. Terasaki, D. Y. Zhao, J. M. Kim, G. D. Stucky, H. J. Shin, and R. Ryoo, *Nature* 408, 449 (2000).
57. W. H. Bragg and W. L. Bragg, *Proc. R. Soc. Lond.* 88, 428 (1913).
58. P. P. Ewald, *Zeit. f. Krist.* 56, 129 (1921).
59. M. von Laue, *Physikal. Zeitschr.* 14, 1075 (1913).
60. S. Inagaki, S. Guan, T. Ohsuna, and O. Terasaki, *Nature* 416, 304 (2002).
61. C. J. Brinker, Y. F. Lu, A. Sellinger, and H. Y. Fan, *Adv. Mater.* 11, 579 (1999).
62. H. Y. Fan, S. Reed, T. Baer, R. Schunk, G. P. Lopez, and C. J. Brinker, *Microporous Mesoporous Mat.* 44, 625 (2001).
63. D. Grosso, G. Soler-Illia, F. Babonneau, C. Sanchez, P. A. Albouy, A. Brunet-Bruneau, and A. R. Balkenende, *Adv. Mater.* 13, 1085 (2001).
64. B. D. Cullity and S. R. Stock, "Elements of X-Ray Diffraction." Prentice-Hall, Upper Saddle River, NJ, 2001.
65. C. Hammond, "The Basics of Crystallography and Diffraction." Oxford University Press, Oxford, 1997.
66. A. Guinier, "X-Ray Crystallographic Technology." Hilger and Watts, London, 1952.
67. A. Guinier and G. Fournet, "Small-Angle Scattering of X-Rays." John Wiley, New York, 1955.
68. O. Glatter and O. Krattky, "Small Angle X-Ray Scattering," Academic Press, London, 1982.
69. L. A. Feigin and D. I. Svergun, "Structure Analysis by Small Angle X-ray and Neutron Scattering" (G. W. Taylor, Ed.). Plenum, 1987.
70. C. T. Kresge, M. Leonowicz, W. J. Roth, J. C. Vartuli, and J. S. Beck, *Nature* 359, 710 (1992).
71. M. Imperor-Clerc, P. Davidson, and A. Davidson, *J. Am. Chem. Soc.* 122, 11925 (2000).
72. J. Sauer, F. Marlow, and F. Schüth, *Phys. Chem. Chem. Phys.* 3, 5579 (2001).
73. S. Schacht and F. Schüth, *Microp. Mesop. Mater.* 22, 485 (1998).
74. D. Tchoubar-Vallat and J. Méring, *J. C. R. Acad. Sci. Paris* 261, 3096 (1965).
75. P. J. Mering and D. Tchoubar, *J. Appl. Crystallogr.* 1, 153 (1968).
76. O. E. Mogensen, in "Positron Annihilation in Chemistry" (V. I. Goldanskii, F. P. Schaffer, and J. P. Toennis, Eds.). Springer, Berlin, 1995.
77. D. M. Schrader and Y. C. Jean, "Positron and Positronium Chemistry." Elsevier, Amsterdam, 1988.

78. V. P. Shantarovich, I. B. Kevdina, Y. P. Yampolskii, and A. Y. Alentiev, *Macromolecules* 33, 7453 (2000).
79. T. E. M. Staab, R. Krause-Rehberg, and B. Kieback, *J. Mater. Sci.* 34, 3833 (1999).
80. G. Dlubek, C. Hubner, and S. Eichler, *Phys. Status Solidi A-Appl. Res.* 172, 303 (1999).
81. D. W. Gidley, W. E. Frieze, T. L. Dull, A. F. Yee, E. T. Ryan, and H. M. Ho, *Physical Review B* 60, R5157 (1999).
82. J. Rouquerol, D. Avnir, C. W. Fairbridge, D. H. Everett, J. H. Haynes, N. Pernicone, J. D. Ramsay, K. S. W. Sing, and K. K. Unger, *Pure Appl. Chem.* 66, 1739 (1994).
83. K. S. W. Sing, D. H. Everett, R. A. W. Haul, L. Moscou, R. A. Pierotti, J. Rouqu  rol, and T. Siemieniewska, *Pure Appl. Chem.* 57, 603 (1985).
84. T. J. Barton, L. M. Bull, W. G. Klemperer, D. A. Loy, B. McEnaney, M. Misono, P. A. Monson, G. Pez, G. W. Scherer, J. C. Vartuli, and O. M. Yaghi, *Chem. Mater.* 11, 2633 (1999).
85. P. Zhang, J. H. Guo, Y. Wang, and W. Q. Pang, *Mater. Lett.* 53, 400 (2002).
86. M. J. MacLachlan, N. Coombs, and G. A. Ozin, *Nature* 397, 681 (1999).
87. T. Maschmeyer, F. Rey, G. Sankar, and J. M. Thomas, *Nature* 378, 159 (1995).
88. J. H. Clark, P. M. Price, K. Martin, D. J. Macquarrie, and T. W. Bastock, *J. Chem. Res.-S*, 430 (1997).
89. H. H. Kung, *Abstr. Pap. Am. Chem. Soc.* 222, 16 (2001).
90. G. Wirnsberger, P. D. Yang, B. J. Scott, B. F. Chmelka, and G. D. Stucky, *Spectroc. Acta Pt. A-Molec. Biomolec. Spectr.* 57, 2049 (2001).
91. C. M. Yang, A. T. Cho, F. M. Pan, T. G. Tsai, and K. J. Chao, *Adv. Mater.* 13, 1099 (2001).
92. H. Y. Fan, H. R. Bentley, K. R. Kathan, P. Clem, Y. F. Lu, and C. J. Brinker, *J. Non-Cryst. Sol.* 285, 79 (2001).
93. B. L. Newalkar, N. V. Choudary, P. Kumar, S. Komarneni, and T. S. G. Bhat, *Chem. Mat.* 14, 304 (2002).
94. R. I. Nooney, E. Maginn, and D. Moore, *Abstr. Pap. Am. Chem. Soc.* 219, 288 (2000).
95. S. V. Mattigod, X. D. Feng, G. E. Fryxell, J. Liu, and M. L. Gong, *Sep. Sci. Technol.* 34, 2329 (1999).
96. J. Liu, X. Feng, G. E. Fryxell, X. Chen, M. Gong, L. Wang, and K. M. Kemner, *Abstr. Pap. Am. Chem. Soc.* 214, 344 (1997).
97. J. S. Beck, J. C. Vartuli, W. J. Roth, M. E. Leonowicz, C. T. Kresge, K. D. Schmitt, C. T. Chu, D. H. Olson, E. W. Sheppard, S. B. McCullen, J. B. Higgins, and J. L. Schlenker, *J. Am. Chem. Soc.* 114, 10834 (1992).
98. R. K. Iler, "The Chemistry of Silica." New York, 1955.
99. R. K. Iler, "The Chemistry of Silica." New York, 1968.
100. C. J. Brinker and G. W. Scherer, "Sol-Gel Science: The Physics and Chemistry of Sol-Gel Processing." Academic Press, London, 1990.
101. A. Navrotsky, I. Petrovic, Y. Hu, C. Chen, and M. E. Davies, *J. Non-Cryst. Sol.* 192-193, 474 (1995).
102. V. Chiola, J. E. Ritsko, and C. D. Vanderpool, US Patent 3556725 (1971).
103. R. Ryoo and J. M. Kim, *J. Chem. Soc. Chem. Comm.* 7, 711 (1995).
104. K. J. Edler and J. W. White, *Chem. Mater.* 9, 1226 (1997).
105. H. P. Lin, S. Cheng, and C. Y. Mou, *Microp. Mater.* 10, 111 (1997).
106. A. C. Voegtlin, F. Ruch, J. L. Guth, J. Patarin, and L. Huve, *Microp. Mater.* 10, 137 (1997).
107. F. H. P. Silva and H. O. Pastore, *J. Chem. Soc. Chem. Comm.* 7, 833 (1996).
108. A. C. Voegtlin, F. Ruch, J. L. Guth, J. Patarin, and L. Huve, *Microp. Mater.* 9, 95 (1997).
109. D. Kushalani, A. Kuperman, G. A. Ozin, K. Tanaka, J. Garces, M. M. Olken, and N. Coombs, *Adv. Mater.* 7, 842 (1995).
110. M. Kruk, M. Jaroniec, and A. Sayari, *Microp. Mesop. Mater.* 27, 217 (1999).
111. L. Chen, T. Horiuchi, T. Mori, and M. Maeda, *J. Phys. Chem. B* 103, 1216 (1999).
112. G. Oye, J. S  blom, and M. St  cker, *Microp. Mesop. Mater.* 27, 171 (1999).
113. V. Alfredsson and M. W. Anderson, *Chem. Mater.* 8, 1141 (1996).
114. M. W. Anderson, *Zeolites* 19, 220 (1997).
115. G. Schulz-Ekloff, J. Rathousk  y, and A. Zukal, *Microp. Mesop. Mater.* 27, 273 (1999).
116. M. Gr  n, I. Lauer, and K. K. Unger, *Adv. Mater.* 9, 254 (1997).
117. M. Gr  n, K. K. Unger, A. Matsumoto, and K. Tsutsumi, *Microp. Mesop. Mater.* 27, 207 (1999).
118. H. P. Ling, S. Cheng, and C. Y. Mou, *Chem. Mater.* 10, 581 (1998).
119. Q. Huo, J. Feng, F. Sch  th, and G. D. Stucky, *Chem. Mater.* 9, 14 (1997).
120. A. Sayari and Y. Yong, *J. Phys. Chem. B* 104, 4835 (2000).
121. A. Sayari, *J. Am. Chem. Soc.* 122, 6504 (2000).
122. A. Monnier, F. Sch  th, Q. Huo, D. Kumar, D. Margolese, R. S. Maxwell, G. D. Stucky, M. Krishnamurty, P. Petroff, A. Firouzi, M. Janicke, and B. F. Chmelka, *Science* 261, 1299 (1993).
123. P. Behrens, A. Glaue, C. Haggem  ller, and G. Schechner, *Solid State Ionics* 101-103, 255 (1997).
124. Q. Huo, D. I. Margolese, and G. D. Stucky, *Chem. Mater.* 8, 1147 (1996).
125. Q. Huo, R. Leon, P. M. Petroff, and G. D. Stucky, *Science* 268, 1324 (1995).
126. R. Ryoo, S. H. Joo, and J. M. Kim, *J. Phys. Chem. B* 103, 7435 (1999).
127. K. Schumacher, M. Gr  n, and K. K. Unger, *Microp. Mesop. Mater.* 27, 201 (1999).
128. K. M. McGrath, D. M. Dabbs, N. Yao, K. J. Edler, I. A. Aksay, and S. M. Gruner, *Langmuir* 16, 398 (2000).
129. K. M. McGrath, D. M. Dabbs, N. Yao, I. A. Aksay, and S. M. Gruner, *Science* 277, 552 (1997).
130. D. Zhao, Q. Huo, J. Feng, J. Kim, Y. Han, and G. D. Stucky, *Chem. Mater.* 11, 2668 (1999).
131. Q. Huo, D. I. Margolese, U. Ciesla, D. G. Demuth, P. Feng, T. E. Gier, P. Sieger, A. Firouzi, B. F. Chmelka, F. Sch  th, and G. D. Stucky, *Chem. Mater.* 6, 1176 (1994).
132. J. Y. Ying, C. P. Mehnert, and M. S. Wong, *Angew. Chem.* 38, 58 (1999).
133. U. Ciesla and F. Sch  th, *Microp. Mesop. Mater.* 27, 131 (1999).
134. P. T. Tanev and T. J. Pinnavaia, *Science* 267, 865 (1995).
135. P. T. Tanev and T. J. Pinnavaia, *Chem. Mater.* 8, 2068 (1996).
136. N. Ulagappan, N. Battaram, B. V. N. Raju, and C. N. R. Rao, *J. Chem. Soc. Chem. Comm.* 2243 (1996).
137. S. A. Bagshaw, E. Prouzet, and T. J. Pinnavaia, *Science* 269, 1242 (1995).
138. S. Kim, T. R. Pauly, and T. J. Pinnavaia, *Chem. Comm.* 835 (2000).
139. G. S. Attard, J. G. Glyde, and C. G. Goltner, *Nature* 378, 366 (1995).
140. C. Goltner, H. C  lfen, and M. Antonietti, *Ch. i. u. Zeit* 33, 200 (1999).
141. C. G. Goltner and M. Antonietti, *Adv. Mater.* 9, 431 (1997).
142. M. C. Wei  nberger, C. G. Goltner, and M. Antonietti, *Ber. Bunsenges. Phys. Chem.* 101, 1679 (1997).
143. C. G. Goltner, S. Henke, M. C. Wei  nberger, and M. Antonietti, *Angew. Chem.* 110, 633 (1998).
144. C. G. Goltner, B. Berton, E. Kr  mer, and M. Antonietti, *Adv. Mater.* 11, 395 (1999).
145. H. P. Hentze, E. Kr  mer, B. Berton, S. F  rster, and M. Antonietti, *Macromolecules* 32, 5803 (1999).
146. E. Kr  mer, S. F  rster, C. Goeltner, and M. Antonietti, *Langmuir* 14, 2027 (1998).
147. P. Alexandridis, *Curr. Op. Coll. Interf. Sci.* 2, 478 (1997).
148. D. Zhao, Q. Huo, J. Feng, B. F. Chmelka, and G. D. Stucky, *J. Am. Chem. Soc.* 120, 6024 (1998).

149. N. A. Melosh, P. Lipic, F. S. Bates, F. Wudl, G. D. Stucky, G. H. Fredrickson, and B. F. Chmelka, *Macromolecules* 32, 4332 (1999).
150. J. M. Kim, Y.-J. Han, B. F. Chmelka, and G. D. Stucky, *Chem. Comm.* 2437 (2000).
151. J. H. Jung, Y. Ono, K. Sakurai, and S. Shinkai, *J. Am. Chem. Soc.* 122, 8648 (2000).
152. J. H. Jung, Y. Ono, and S. Shinkai, *Chem. Eur. J.* 24, 4552 (2000).
153. J. H. Jung, Y. Ono, and S. Shinkai, *Angew. Chem.* 112, 1931 (2000).
154. J. H. Jung, M. Amai, and S. Shinkai, *Chem. Comm.* 2343 (2000).
155. F. Miyaji, S. A. Davies, J. P. H. Charamant, and S. Mann, *Chem. Mater.* 11, 3021 (1999).
156. C.-F. Cheng, Z. Luan, and J. Klinowski, *Langmuir* 11, 2815 (1995).
157. C.-Y. Chen, S. L. Burkett, H.-X. Li, and M. E. Davies, *Microp. Mater.* 2, 27 (1993).
158. J. Zhang, Z. Luz, and D. Goldfarb, *J. Phys. Chem.* 101, 7087 (1997).
159. A. Steel, S. W. Carr, and M. W. Anderson, *J. Chem. Soc. Chem. Comm.* 1571 (1994).
160. A. Steel, S. W. Carr, and M. W. Anderson, *Chem. Mater.* 7, 1829 (1995).
161. P. F. W. Simon, R. Ulrich, H. W. Spiess, and U. Wiesner, *Chem. Mat.* 13, 3464 (2001).
162. S. M. De Paul, J. W. Zwanziger, R. Ulrich, U. Wiesner, and H. W. Spiess, *J. Am. Chem. Soc.* 121, 5727 (1999).
163. B. Smarsly, S. Polarz, and M. Antonietti, *J. Phys. Chem. B* 105, 10473 (2001).
164. S. Polarz, B. Smarsly, L. Bronstein, and M. Antonietti, *Angew. Chem.-Int. Edit.* 40, 4417 (2001).
165. J. S. Lettow, Y. J. Han, P. Schmidt-Winkel, P. Yang, D. Zhao, G. D. Stucky, and J. Y. Ying, *Langmuir* 16, 8291 (2000).
166. S. Kim, T. R. Pauly, and T. J. Pinnavaia, *Chem. Comm.* 1661 (2000).
167. J. N. Israelachvili, D. J. Mitchell, and B. W. Ninham, *J. Chem. Soc. Faraday Trans.* 72, 1525 (1976).
168. J. Israelachvili, "Intermolecular and Surface Forces." Academic Press, London, 1991.
169. D. J. Mitchell and B. W. Ninham, *J. Chem. Soc. Faraday Trans.* 77, 601 (1981).
170. A. Imhof and D. J. Pine, *Nature* 389, 948 (1997).
171. N. Hüsing and U. Schubert, *Angew. Chem.* 110, 22 (1998).
172. N. Hüsing, F. Schwertfeger, W. Tappert, and U. Schubert, *J. Non-Cryst. Sol.* 186, 37 (1995).
173. A. Corma, Q. Kan, M. T. Navarro, J. Pérez-Pariente, and F. Rey, *Chem. Mater.* 9, 2123 (1997).
174. E. Prouzet and T. J. Pinnavaia, *Angew. Chem.* 109, 533 (1997).
175. D. Zhao, J. Feng, Q. Huo, N. Melosh, G. H. Fredrickson, B. F. Chmelka, and G. D. Stucky, *Science* 279, 548 (1998).
176. J. S. Beck and J. C. Vartuli, *Curr. Op. Sol. State. Mat. Sci.* 1, 76 (1996).
177. A. Sayari, Y. Yang, M. Kruk, and M. Jaroniec, *J. Phys. Chem. B* 103, 3651 (1999).
178. A. Sayari, *Angew. Chem.* 112, 3042 (2000).
179. A. Sayari, M. Kruk, M. Jaroniec, and I. L. Moudrakovski, *Adv. Mater.* 10, 1376 (1998).
180. M. Kruk, M. Jaroniec, and A. Sayari, *J. Phys. Chem. B* 103, 4590 (1999).
181. B. A. Aufdembrink, A. W. Chester, J. A. Herbst, and C. T. Kresge, US Patent 5258 (1993).
182. A. Corma, M. S. Grande, V. Gonzalez Alfaro, and A. V. Orchilles, *J. Cata.* 159, 375 (1996).
183. J. Aguado, D. P. Serrano, M. D. Romero, and J. M. Escola, *Chem. Commun.* 725 (1996).
184. C. T. Kresge, M. E. Leonowicz, W. J. Roth, J. C. Vartuli, K. M. Keville, S. S. Shih, T. F. Degnan, F. G. Dwyer, and M. E. Landis, US Patent 5344553 (1993).
185. A. Corma, A. Martinez, V. Martinezsoria, and J. B. Monton, *J. Catal.* 153, 25 (1995).
186. K. M. Reddy, B. L. Wei, and C. S. Song, *Catal. Today* 43, 261 (1998).
187. C. S. Song, K. M. Reddy, and H. Leta, *Abstr. Pap. Am. Chem. Soc.* 216, 010 (1998).
188. M. R. Apelian, T. F. Degnan, D. O. Marler, and D. Mazzone, US Patent 5227353 (1993).
189. T. F. Degnan, K. M. Keville, M. E. Landis, D. O. Marler, and D. N. Mazzone, US Patent 5183557 (1993).
190. T. F. Degnan, K. M. Keville, M. E. Landis, D. O. Marler, and D. N. Mazzone, US Patent 5290744 (1994).
191. K. M. Reddy and C. S. Song, *Catal. Today* 31, 137 (1996).
192. E. A. Gunnewegh, S. S. Gopie, and H. vanBekum, *J. Mol. Catal. A-Chem.* 106, 151 (1996).
193. K. R. Kloetstra, J. C. Jensen, and H. Vanbekum, *Abstr. Pap. Am. Chem. Soc.* 211, 68 (1996).
194. E. Armengol, A. Corma, H. Garcia, and J. Primo, *Appl. Catal. A-Gen.* 126, 391 (1995).
195. H. Vanbekum, A. J. Hoefnagel, M. A. Vankoten, E. A. Gunnewegh, A. H. G. Vogt, and H. W. Kouwenhoven, *Zeolites and Microporous Crystals* 83, 379 (1994).
196. E. Armengol, A. Corma, L. Fernandez, H. Garcia, and J. Primo, *Appl. Catal. A-Gen.* 158, 323 (1997).
197. E. Armengol, A. Corma, H. Garcia, and J. Primo, *Appl. Catal. A-Gen.* 149, 411 (1997).
198. K. R. Kloetstra and H. van Bekkum, *Progress in Zeolite and Microporous Materials, Pts A-C* 105, 431 (1997).
199. K. R. Kloetstra and H. van bekkum, *J. Chem. Soc.-Chem. Commun.* 1005 (1995).
200. K. R. Kloetstra, J. vandenbroek, and H. van Bekkum, *Catal. Lett.* 47, 235 (1997).
201. A. Corma, M. T. Navarro, J. Perezpariente, and F. Sanchez, *Zeolites and Related Microporous Materials: State of the Art 1994* 84, 69 (1994).
202. F. Rey, G. Sankar, T. Maschmeyer, J. M. Thomas, R. G. Bell, and G. N. Greaves, *Top. Catal.* 3, 121 (1996).
203. K. G. Severin, T. M. Abdel-Fattah, and T. J. Pinnavaia, *Chem. Commun.* 1471 (1998).
204. T. M. Abdel-Fattah and T. J. Pinnavaia, *Chem. Commun.* 665, (1996).
205. T. K. Das, K. Chaudhari, A. J. Chandwadkar, and S. Sivasanker, *J. Chem. Soc.-Chem. Commun.* 2495 (1995).
206. S. Gontier and A. Tuel, *Progress in Zeolite and Microporous Materials, Pts A-C* 105, 1085 (1997).
207. M. Florea, M. Sevinci, V. I. Parvulescu, G. Lemay, and S. Kaliaguine, *Microporous Mesoporous Mat.* 44, 483 (2001).
208. L. M. Bronstein, S. Polarz, B. Smarsly, and M. Antonietti, *Adv. Mater.* 13, 1333 (2001).
209. J. H. Fendler, "Nanoparticles and Nanostructured Films." Wiley-VCH, 1998.
210. M. H. Huang, A. Choudrey, and P. Yang, *Chem. Comm.* 1063 (2000).
211. K. Moller and T. Bein, *Stud. Surf. Sci. Cat.* 117, 53 (1998).
212. H. Parala, H. Winkler, M. Kolbe, A. Wohlfart, R. A. Fischer, R. Schmechel, and H. van Seggern, *Adv. Mater.* 12, 1050 (2000).
213. J. Han, J. M. Kim, and G. D. Stucky, *Chem. Mater.* 12, 2068 (2000).
214. K. Moller and T. Bein, *Chem. Mater.* 10, 2950 (1998).
215. I. V. Kozhevnikov, K. R. Kloetstra, A. Sinnema, H. W. Zandbergen, and H. van Bekkum, *J. Mol. Catal. A-Chem.* 114, 287 (1996).
216. I. V. Kozhevnikov, A. Sinnema, R. J. J. Jansen, K. Pamin, and H. van Bekkum, *Catal. Lett.* 30, 241 (1995).
217. H. Winkler, A. Birkner, V. Hagen, I. Wolf, R. Schmechel, H. van Seggern, and R. A. Fischer, *Adv. Mater.* 11, 1444 (1999).
218. T. Abe, Y. Tachibana, T. Uematsu, and M. Iwamoto, *J. Chem. Soc., Chem. Comm.* 1617 (1995).
219. K. Miyazawa and S. Inagaki, *Chem. Comm.* 2121 (2000).
220. T. Hirai, H. Okubo, and I. Komasa, *J. Phys. Chem. B* 103, 4228 (1999).

221. O. Dag, G. A. Ozin, H. Yang, C. Reber, and G. Bussiere, *Adv. Mater.* 11, 474 (1999).
222. E. Chomski, O. Dag, A. Kuperman, N. Coombs, and G. A. Ozin, *Chem. Vapor Depos.* 2, 8 (1996).
223. B. J. Aronson, C. F. Blanford, and A. Stein, *Chem. Mat.* 9, 2842 (1997).
224. R. Leon, D. Margolese, G. Stucky, and P. M. Petroff, *Physical Review B* 52, R2285 (1995).
225. V. I. Srdanov, I. Alxneit, G. D. Stucky, C. M. Reaves, and S. P. Den Baars, *J. Phys. Chem. B* 102, 3341 (1998).
226. W.-H. Zhang, J.-L. Shi, H.-R. Chen, Z.-L. Hua, and D.-S. Yan, *Chem. Mater.* 13, 648 (2001).
227. J. R. Agger, M. W. Anderson, M. E. Pemble, O. Terasaki, and Y. Nozue, *J. Phys. Chem. B* 102, 3345 (1998).
228. G. A. Ozin, E. Chomski, D. Khushalani, and M. J. MacLachlan, *Curr. Op. Coll. Interf. Sci.* 3, 181 (1998).
229. H. Kang, Y. Jun, J. Park, K. Lee, and J. Cheon, *Chem. Mater.* 12, 3530 (2000).
230. K. B. Lee, S. M. Lee, and J. Cheon, *Adv. Mater.* 13, 517 (2001).
231. Y. Mastai, S. Polarz, and M. Antonietti, *Adv. Funct. Mater.* 12, 197 (2002).
232. R. Ryoo, S. H. Joo, and S. Jun, *J. Phys. Chem. B* 103, 7743 (1999).
233. S. Jun, S. H. Joo, R. Ryoo, M. Kruk, M. Jaroniec, Z. Liu, T. Ohsuna, and O. Terasaki, *J. Am. Chem. Soc.* 122, 10712 (2000).
234. J. Lee, S. Yoon, T. Hyeon, S. M. Oh, and K. B. Kim, *Chem. Commun.* 2177 (1999).
235. P. L. Llewellyn, U. Ciesla, H. Decher, R. Stadler, F. Schuth, and K. K. Unger, *Zeolites and Related Microporous Materials: State of the Art 1994* 84, 2013 (1994).
236. K. Moller, T. Bein, and R. X. Fischer, *Chem. Mater.* 10, 1841 (1998).
237. K. Kageyama, J. Tamazawa, and T. Aida, *Science* 285, 2113 (1999).
238. R. Gangopadhyay and A. De, *Chem. Mat.* 12, 608 (2000).
239. C. G. Wu and T. Bein, *Science* 264, 1757 (1994).
240. F. Marlow, M. D. Mc Gehee, D. Y. Zhao, B. F. Chmelka, and G. D. Stucky, *Adv. Mater.* 11, 632 (1999).
241. G. Wirnsberger and G. D. Stucky, *Chem. Mat.* 12, 2525 (2000).
242. P. D. Yang, G. Wirnsberger, H. C. Huang, S. R. Cordero, M. D. Mc Gehee, B. Scott, T. Deng, G. M. Whitesides, B. F. Chmelka, S. K. Buratto, and G. D. Stucky, *Science* 287, 465 (2000).
243. G. Wirnsberger, P. D. Yang, H. C. Huang, B. Scott, T. Deng, G. M. Whitesides, B. F. Chmelka, and G. D. Stucky, *J. Phys. Chem. B* 105, 6307 (2001).
244. X. S. Zhao, G. Q. Lu, A. K. Whittaker, G. J. Millar, and H. Y. Zhu, *J. Phys. Chem. B* 101, 6525 (1997).
245. J. H. Clark, J. C. Ross, D. J. Macquarrie, S. J. Barlow, and T. W. Bastock, *Chem. Commun.* 1203 (1997).
246. M. A. Marshall and H. A. Mottola, *Analytical Chemistry* 55, 2089 (1983).
247. P. M. Price, J. H. Clark, and D. J. Macquarrie, *J. Chem. Soc.-Dalton Trans.* 101 (2000).
248. A. J. Butterworth, J. H. Clark, P. H. Walton, and S. J. Barlow, *Chem. Commun.* 1859 (1996).
249. D. Brunel, N. Bellocq, P. Sutra, A. Cauvel, M. Lasperas, P. Moreau, F. Di Renzo, A. Galarneau, and F. Fajula, *Coordination Chemistry Reviews* 180, 1085 (1998).
250. M. Lasperas, N. Bellocq, D. Brunel, and P. Moreau, *Tetrahedron: Asymmetry* 9, 3053 (1998).
251. S. L. Burkett, S. D. Sims, and S. Mann, *Chem. Commun.* 1367 (1996).
252. C. E. Fowler, S. L. Burkett, and S. Mann, *Chem. Commun.* 1769 (1997).
253. M. J. MacLachlan, T. Asefa, and G. A. Ozin, *Chem. Eur. J.* 6, 2507 (2000).
254. T. Asefa, M. J. MacLachlan, H. Grondy, N. Coombs, and G. A. Ozin, *Angew. Chem.* 112, 1878 (2000).
255. T. Asefa, M. J. MacLachlan, N. Coombs, and G. A. Ozin, *Nature* 402, 867 (1999).
256. S. Inagaki, S. Guan, Y. Fukushima, T. Ohsuna, and O. Terasaki, *J. Am. Chem. Soc.* 121, 9611 (1999).
257. C. Yoshina-Ishii, T. Asefa, N. Coombs, M. J. MacLachlan, and G. A. Ozin, *Chem. Commun.* 2539 (1999).
258. T. Asefa, C. Yoshina-Ishii, M. J. MacLachlan, and G. A. Ozin, *J. Mater. Chem.* 10, 1751 (2000).
259. U. Ciesla, D. Demuth, R. Leon, P. Petroff, G. D. Stucky, K. Unger, and F. Schuth, *J. Chem. Soc. Chem. Comm.* 1387 (1994).
260. G. G. Janauer, A. Doble, J. Guo, P. Zavalij, and M. S. Whittingham, *Chem. Mater.* 8, 2096 (1996).
261. T. Abe, A. Taguchi, and M. Iwamoto, *Chem. Mater.* 7, 1429 (1995).
262. T. Doi and T. Miyake, *Chem. Commun.* 1635 (1996).
263. G. G. Janauer, A. D. Doble, P. Y. Zavalij, and M. S. Whittingham, *Chem. Mater.* 9, 647 (1997).
264. D. M. Antonelli and J. Y. Ying, *Angew. Chem. Int. Ed. Engl.* 34, 2014 (1996).
265. D. M. Antonelli, A. Nakihara, and J. Y. Ying, *Inorg. Chem.* 35, 3126 (1996).
266. D. M. Antonelli and J. Y. Ying, *Chem. Mater.* 8, 874 (1996).
267. D. M. Antonelli and J. Y. Ying, *Angew. Chem.* 108, 461 (1996).
268. D. Khushalani, G. A. Ozin, and A. Kuperman, *J. Mater. Chem.* 9, 1491 (1999).
269. U. Ciesla, M. Fröba, G. D. Stucky, and F. Schuth, *Chem. Mater.* 11, 227 (1999).
270. P. D. Yang, D. Y. Zhao, D. I. Margolese, B. F. Chmelka, and G. D. Stucky, *Chem. Mat.* 11, 2813 (1999).
271. M. S. Wong, H. C. Huang, and J. Y. Ying, *Chem. Mat.* 14, 1961 (2002).
272. F. Schuth, U. Ciesla, S. Schacht, M. Thieme, Q. Huo, and G. Stucky, *Mater. Res. Bull.* 34, 483 (1999).
273. M. S. Wong and J. Y. Ying, *Chem. Mat.* 10, 2067 (1998).
274. P. Liu, I. L. Moudrakovski, J. Liu, and A. Sayari, *Chem. Mat.* 9, 2513 (1997).
275. M. Vetraino, M. L. Trudeau, and D. M. Antonelli, *Adv. Mater.* 12, 337 (2000).
276. S. Cabrera, J. El Haskouri, C. Guillem, J. Latorre, A. Beltran-Porter, D. Beltran-Porter, M. D. Marcos, and P. Amoros, *Solid State Sci.* 2, 405 (2000).
277. J. N. Kondo, Y. Takahara, B. Lee, D. L. Lu, and K. Domen, *Top. Catal.* 19, 171 (2002).
278. Q. S. Hue, D. I. Margolese, U. Ciesla, P. Y. Feng, T. E. Gier, P. Sieger, R. Leon, P. M. Petroff, F. Schuth, and G. D. Stucky, *Nature* 368, 317 (1994).
279. T. B. Liu, Q. Wan, Y. Xie, C. Burger, L. Z. Liu, and B. Chu, *J. Am. Chem. Soc.* 123, 10966 (2001).
280. A. Stein, M. Fendorf, T. P. Jarvie, K. T. Mueller, A. J. Benesi, and T. E. Mallouk, *Chem. Mat.* 7, 304 (1995).
281. U. Ciesla, D. Demuth, R. Leon, P. Petroff, G. Stucky, K. Unger, and F. Schuth, *J. Chem. Soc.-Chem. Commun.* 1387 (1994).
282. Z. Tian, W. Tong, N. Duan, V. V. Krishnan, and S. L. Suib, *Science* 276, 926 (1997).
283. J. Luo and S. L. Suib, *Chem. Commun.* 1031 (1997).
284. M. Yada, H. Kitamura, A. Ichinose, M. Machida, and T. Kijima, *Angew. Chem.* 111, 3716 (1999).
285. M. Yada, H. Kitamura, M. Machida, and T. Kijima, *Inorganic Chemistry* 37, 6470 (1998).
286. M. Gratzel, *Curr. Opin. Colloid Interface Sci.* 4, 314 (1999).
287. G. Rothenberger, P. Comte, and M. Gratzel, *Sol. Energy Mater. Sol. Cells* 58, 321 (1999).
288. P. Bonhote, E. Gogniat, F. Campus, L. Walder, and M. Gratzel, *Displays* 20, 137 (1999).

289. D. C. M. Dutoit, M. Schneider, and A. Baiker, *J. Cata.* 153, 165 (1995).
290. E. Haroponiatowski, R. Rodrigueztalavera, M. Delacruzheredia, O. Canocorona, and R. Arroyomurillo, *J. Mater. Res.* 9, 2102 (1994).
291. L. Kavan, J. Rathousky, M. Gratzel, V. Shklover, and A. Zukal, *Microporous Mesoporous Mat.* 44, 653 (2001).
292. Y. K. Hwang, K. C. Lee, and Y. U. Kwon, *Chem. Commun.* 1738 (2001).
293. V. Tohver, P. V. Braun, M. U. Pralle, and S. I. Stupp, *Chem. Mat.* 9, 1495 (1997).
294. P. Osenar, P. V. Braun, and S. I. Stupp, *Adv. Mater.* 8, 1022 (1996).
295. P. V. Braun, P. Osenar, and S. I. Stupp, *Nature* 380, 325 (1996).
296. J. Q. Li, H. Kessler, M. Soulard, L. Khouchaf, and M. H. Tuilier, *Adv. Mater.* 10, 946 (1998).
297. G. Soler-Illia, A. Louis, and C. Sanchez, *Chem. Mat.* 14, 750 (2002).
298. K. K. Rangan, P. N. Trikalitis, and M. G. Kanatzidis, *J. Am. Chem. Soc.* 122, 10230 (2000).
299. M. Wachhold, K. K. Rangan, M. Lei, M. F. Thorpe, S. J. L. Billinge, V. Petkov, J. Heising, and M. G. Kanatzidis, *J. Solid State Chem.* 152, 21 (2000).
300. K. K. Rangan, S. J. L. Billinge, V. Petkov, J. Heising, and M. G. Kanatzidis, *Chem. Mat.* 11, 2629 (1999).
301. D. Zhao, Z. Luan, and L. Kevan, *Chem. Comm.* 1009 (1997).
302. B. Chakraborty, A. C. Pulikottil, S. Das, and B. Viswanathan, *Chem. Commun.* 911 (1997).
303. T. Kimura, Y. Sugahara, and K. Kuroda, *Chemistry Letters*, 983 (1997).
304. B. T. Holland, P. K. Isbester, C. F. Blanford, E. J. Munson, and A. Stein, *J. Am. Chem. Soc.* 119, 6796 (1997).
305. D. Farrusseng, K. Schlichte, B. Spliethoff, A. Wingen, S. Kaskel, J. S. Bradley, and F. Schuth, *Angew. Chem.-Int. Edit.* 40, 4204 (2001).
306. J. W. Diggle, T. C. Downie, and C. W. Goulding, *Chem Rev.* 69, 365 (1969).
307. S. A. Bagshaw and T. J. Pinnavaia, *Angew. Chem. Int. Ed. Engl.* 35, 1102 (1996).
308. G. S. Attard, C. G. Göltner, S. M. Covker, S. Henke, and R. H. Templer, *Angew. Chem.* 109, 1372 (1997).
309. G. Wulff, *Angew. Chem.-Int. Edit. Engl.* 34, 1812 (1995).
310. J. M. Lin, T. Nakagama, K. Uchiyama, and T. Hobo, *Chromatographia* 43, 585 (1996).
311. J. M. Lin, K. Uchiyama, and T. Hobo, *Chromatographia* 47, 625 (1998).
312. A. G. Mayes, L. I. Andersson, and K. Mosbach, *Anal. Biochem.* 222, 483 (1994).
313. J. U. Klein, M. J. Whitcombe, F. Mulholland, and E. N. Vulson, *Angew. Chem.-Int. Edit.* 38, 2057 (1999).
314. A. E. Rachkov, S. H. Cheong, A. V. Ef'skaya, K. Yano, and I. Karube, *Polym. Adv. Technol.* 9, 511 (1998).
315. S. H. Cheong, A. E. Rachkov, J. K. Park, K. Yano, and I. Karube, *J. Polym. Sci. Pol. Chem.* 36, 1725 (1998).
316. B. Sellergren, *Trac-Trends Anal. Chem.* 16, 310 (1997).
317. O. Ramstrom and R. J. Ansell, *Chirality* 10, 195 (1998).
318. S. A. Piletsky, T. L. Panasyuk, E. V. Piletskaya, I. A. Nicholls, and M. Ulbricht, *J. Membr. Sci.* 157, 263 (1999).
319. H. Asanuma, T. Hishiya, and M. Komiyama, *Adv. Mater.* 12, 1019 (2000).
320. Y. Xia, B. Gates, Y. Yin, and Y. Lu, *Adv. Mater.* 12, 693 (2000).
321. O. D. Velev and A. M. Lenhoff, *Curr. Opin. Colloid Interface Sci.* 5, 56 (2000).
322. S. H. Park and Y. N. Xia, *Adv. Mater.* 10, 1045 (1998).
323. S. H. Park and Y. N. Xia, *Chem. Mat.* 10, 1745 (1998).
324. B. Gates, Y. D. Yin, and Y. N. Xia, *Chem. Mat.* 11, 2827 (1999).
325. S. A. Johnson, P. J. Ollivier, and T. E. Mallouk, *Science* 283, 963 (1999).
326. P. Jiang, K. S. Hwang, D. M. Middleman, J. F. Bertone, and V. L. Colvin, *J. Am. Chem. Soc.* 121, 11630 (1999).
327. T. Sumida, Y. Wada, T. Kitamura, and S. Yanagida, *Chem. Commun.* 1613 (2000).
328. X. X. Zhu, K. Banana, and R. Yen, *Macromolecules* 30, 3031 (1997).
329. X. X. Zhu, K. Banana, H. Y. Liu, M. Krause, and M. Yang, *Macromolecules* 32, 277 (1999).
330. A. I. Cooper, W. P. Hems, and A. B. Holmes, *Macromol. Rapid Commun.* 19, 353 (1998).
331. A. I. Cooper and A. B. Holmes, *Adv. Mater.* 11, 1270 (1999).
332. A. I. Cooper, W. P. Hems, and A. B. Holmes, *Macromolecules* 32, 2156 (1999).
333. C. Holtzschere, J. C. Wittmann, D. Guillon, and F. Candau, *Polymer* 31, 1978 (1990).
334. M. T. Carver, E. Hirsch, J. C. Wittmann, R. M. Fitch, and F. Candau, *J. Phys. Chem.* 93, 4867 (1989).
335. W. R. P. Raj, M. Sasthav, and H. M. Cheung, *J. Appl. Polym. Sci.* 47, 499 (1993).
336. M. Antonietti and H. P. Hentze, *Colloid and Polymer Science* 274, 696 (1996).
337. M. Antonietti, R. A. Caruso, C. G. Goltner, and M. C. Weissenberger, *Macromolecules* 32, 1383 (1999).
338. M. Antonietti, C. Goltner, and H. P. Hentze, *Langmuir* 14, 2670 (1998).
339. H. P. Hentze, C. G. Goltner, and M. Antonietti, *Ber. Bunsen-Ges. Phys. Chem. Chem. Phys.* 101, 1699 (1997).

# Ordered Nanoporous Particles

Ferry Iskandar

*Japan Chemical Innovation Institute, Hiroshima, Japan*

Mikrajuddin, Kikuo Okuyama

*Hiroshima University, Hiroshima, Japan*

## CONTENTS

1. Introduction
  2. Synthesis
  3. Characterization
  4. Properties
  5. Summary
- Glossary  
References

## 1. INTRODUCTION

Porous materials are of scientific and technological interest because of their potential for applications in separation processes, catalysts, chromatography, the controlled release of drugs, low dielectric constant fillers, pigments, microelectronics, electro-optics, and other emerging nanotechnologies [1–4].

Based on the IUPAC (International Union of Pure and Applied Chemistry) definition, the pores of materials are classified according to size: pore sizes in the range of 2 nm and below are defined as micropores, those in the range of 2 nm to 50 nm, as mesopores, and those above 50 nm, as macropores [5]. A direct relationship exists between the distribution of sizes, shapes, and volumes of the void spaces in porous materials and their ability to perform the desired function in a particular application. Hence, a need exists to create uniformity within a pore size, shape, and volume, since such properties can lead to superior applications. For example, a material with uniform micropores could be used to separate molecules on the basis of their size by selectively adsorbing a small molecule from a mixture containing molecules that are too large to enter its pores [1]. In another example, the controllability of pore size as well as the morphology of a material are important in the development of

size-selective filters and selective optical cavities. The wavelength of the optical mode in a cavity is dependent on cavity size and the bandgap of optical crystals depends on the crystal periodicity, typically denoted as a photonic crystal [6].

In 1988, the first report of a crystalline microporous material, aluminophosphate ( $\text{AlPO}_4$ ; VPI-5), with uniform pores of 1.2 nm was reported [7]. Following the discovery of VPI-5, numerous extra-large pore materials were synthesized. In 1992, Mobil researchers disclosed the first family of highly ordered mesoporous molecular sieves M41S (pore size in the range 2–10 nm) where surfactants were used as the template or pore forming agents during a hydrothermal sol-gel synthesis [8, 9]. The use of appropriate starting materials and synthesis conditions permitted the preparation of different mesoporous silica oxides with ordered structures in hexagonal form (denoted as MCM-41), cubic form (denoted as MCM-48), and lamellar form (denoted as MCM-50). Several reviews dealing with microporous and mesoporous materials have appeared [1, 2]. In 1997, the first ordered macroporous materials produced via a template were reported [10]. A variety of macroporous ceramics, metals, semiconductors, and polymers with well-defined pore sizes in the submicrometer range have been successfully synthesized using self-assembled templates of a colloid as well as self-assembled templates of emulsion [10, 11]. Several reviews on the subject of macroporous materials have appeared in the literature [3, 4]. The above methods for preparing ordered porous materials have, thus far, resulted in irregular shapes and/or thin-film shapes. However, for practical applications, ordered porous materials must have the shape of a usable object. It would be desirable, for example, to produce ordered porous materials having a particular form.

Reviews of previous methods used in the preparation of well-ordered porous particles are described here with the following main subjects: (1) synthesis, (2) characterization, and (3) properties.

## 2. SYNTHESIS

The preparation of ordered nanoporous particles was carried out in several ways as shown in Table 1. Surfactants, which function as templates for forming ordered porous materials, were typically used, particularly for the preparation of ordered microporous and mesoporous particles. A colloidal templating procedure was also used for the preparation of ordered macroporous particles. For the materials, silica was typically used in this process.

### 2.1. Emulsion Templating

Schacht et al. [12] reported on the preparation of the mesostructured and macroscopically structured ordered porous particles by interfacial reactions conducted in oil/water emulsions. The use of emulsion biphasic chemistry offers the possibility of simultaneously controlling shape on the micrometer to centimeter scale and the ordered mesostructure at the molecular scale. The cetyltrimethylammonium bromide (CTAB), or other related surfactants as the pore structure directing agent, was used as surfactant. The surfactant was dissolved in water and an aqueous solution of HCl was then added to the solution. To this solution a mixture of the auxiliary (typically mesitylene) and tetraethoxysilane (TEOS) was added slowly with stirring at room temperature, resulting in the formation of an emulsion. The morphology of the final product can be controlled by the simple tuning of the stirring speed in the synthesis mixture. A flat mesoporous silica film, mesoporous silica fibers, and hollow porous silica particles form can be produced by appropriate control of the stirring speed.

Huo et al. [13] extended this general emulsion-based approach to the preparation of mesoporous particles with a diameter of 0.1–2.0 mm. A similar synthesis method was employed, using CTAB as a surfactant. NaOH, as an optional source of basic catalyst, was added to the CTAB solution. To this solution, tetrabutyl orthosilicate (TBOS) was added with stirring. The resulting product, a collection of hard spheres, was filtered, and air-dried at room temperature. They reported that the size of the silica spheres can be controlled by varying the reaction conditions and the volume.

### 2.2. Biomimetic Templating

Tanev and Pinnavaia [14] condensed silica in the interlayer regions of multilamellar vesicles, a biomimetic templating approach, to form roughly spherical particles. The procedure is based on the hydrolysis and cross-linking of a neutral silicon alkoxide precursor in the interlayered regions of multilamellar vesicles formed from a neutral diamine bola-amphiphile. Unlike surfactant templating approaches, this method produces porous lamellar silicas with vesicular particle morphology. In a typical preparation, TEOS as the silica source was added to a 1,12-diaminododecane (DDAD) template in ethanol and deionized water. The reaction mixture was vigorously stirred at ambient temperature to give the templated lamellar product with a vesicular morphology. The crystalline product was recovered by filtration, washed with deionized water, and air-dried. The template was removed either by calcination in air or by solvent extraction. Complete cross-linking of the structure of the ethanol-extracted product was accomplished by subsequent calcination in air.

The use of 1-alkylamine as a templating agent in the synthesis of mesoporous silica particles has also been reported by Kosuge and Singh [15]. In a typical preparation, TEOS was mixed with dilute aqueous HCl and stirred at a constant speed. To this solution, 1-alkylamine (designated by using carbon numbers such as C<sub>6</sub>, C<sub>8</sub>, C<sub>10</sub>, or C<sub>12</sub>) was added and the solution was then stirred. The resulting mesoporous silica particles were collected by centrifugation, dried, and calcined. Appropriate control of the synthesis conditions led to the production of various morphologies of mesoporous silica particles.

### 2.3. Liquid-Phase Surfactant Templates

#### 2.3.1. Preparation under Acidic Conditions

Ozin and co-workers [16] reported on the preparation of mesoporous silicates particles using an extremely dilute aqueous acidic solution using cetyltrimethylammonium chloride (CTACl) as cationic surfactant template and TEOS as silica precursor. The prepared particles show the co-presence of various morphologies, for example, toroidal, disklike, spiral, and spheroidal shapes.

**Table 1.** Synthesis method for the fabrication of ordered nanoporous particles.

Synthesis method	Template	Materials	Porous structure	Ref.
Oil–water interface emulsion templating	Surfactants	Silica	Mesoporous	[12, 13]
Biomimetic templating	Diamines	Silica	Micro- and mesoporous	[14]
Liquid-phase surfactant templating under acidic and basic condition	Surfactants	Silica	Mesoporous	[16–18]
Liquid-phase surfactant templating with modification of Stöber method	Surfactants	Silica, composite	Mesoporous	[19, 20, 22–25]
Aerosol spray surfactant templating	Surfactants	Silica	Mesoporous	[26, 27]
Aerosol spray colloidal templating	Latex	Silica	Macroporous	[30, 31]
Aerosol spray surfactant and colloidal templating	Surfactant and latex	Silica	Meso- and macroporous	[32]
Micromolding in inverted polymer opals	Surfactant and latex	Silica	Mesoporous	[32]
Air–oil interface colloidal templating	Latex	Silica, titania	Macroporous	[34]
Double templating	Polystyrene latex, silica spheres	Silica, titania	Macroporous	[35]

This synthesis method was extended by Qi et al. [17] to the synthesis of micrometer-sized mesoporous silica spheres by mixed cationic-nonionic surfactant templating. The mixed surfactants used were cetyltrimethylammonium bromide (CTAB) and decaethylene glycol monohexadecyl ether ( $C_{16}EO_{10}$ ). In a typical synthesis, CTAB and  $C_{16}EO_{10}$  were dissolved in HCl aqueous solution. To this solution, TEOS was added at room temperature with stirring. After the complete addition of TEOS, the mixture was allowed to age either without stirring or with additional stirring. The white precipitate was then recovered by filtration, washed with water, and dried. Finally, the product was calcined in air to remove the surfactants.

### 2.3.2. Preparation under Basic Conditions

Chai et al. [18] reported on the preparation of mesoporous particles using a dilute aqueous basic medium. Silica particles with several morphologies were prepared. In this study, CTAB was used as a cationic surfactant, while TEOS served as the silica source. Aqueous sodium hydroxide or ammonia was used as the catalyst. The synthetic conditions, both stirring speed and surfactant concentration, were varied so as to control the morphologies and size of the prepared particles. Typically, a solution of CTAB, TEOS, NaOH, and water, in a known ratio, was mixed at different stirring speeds. The resulting product was filtered, washed, dried, and then subjected to calcination.

### 2.3.3. Modification of Stöber Method

Unger and co-workers [19, 20] first reported the synthesis of spherical silica particles featuring a hexagonal (MCM-41) mesoporous structure, using a modification of the Stöber synthesis [21] by adding surfactants to the reaction mixture during particle formation. The synthesis was carried out in an alcohol-water-ammonia system. Porosity was created by adding two different types of pore structure directing agents to the starting solution: one was an n-alkyltrialkoxysilane which was covalently bonded to the silica framework, while the other was an n-alkylamine which acted as a nonionic template. Water hydrolyzes the tetraethoxysilane (TEOS) to silicic acid which further condenses to oligomers, and these primary particles agglomerate to the final silica spheres in sizes up to 1.5  $\mu\text{m}$ . Ethanol acts as a cosolvent to produce a homogeneous solution, and ammonia acts as a morphological catalyst. The particle size can be adjusted by the ratio of water, alcohol, ammonia, and silane. After removal of the solvent, the product was calcined to remove the porogen and to form porous silica particles.

In another paper [22], they extended this method to the preparation of submicrometer-sized solid core/mesoporous shell (SCMS) silica particles. The particles were nearly perfectly spherical in shape, with the pores being randomly distributed over the silica shell, whereas the core was composed of dense silica. The formation of the pore structure of the shell was studied as a function of the amount of n-octadecyltrimethoxysilane ( $C_{18}\text{-TMS}$ ) as the porogen in the starting solution during the growth process.

Yoon et al. [23] extended this approach to the production of mesoporous carbon hollow spheres. In this synthesis, silica (or aluminosilicate) spheres with SCMS structures

were used as template materials and an *in-situ* polymerized phenol-resin or poly(divinylbenzene) as carbon source. Aluminum was incorporated into the silicate framework via an impregnation method to generate strongly acidic catalytic sites for the polymerization of phenol and formaldehyde. Phenol and formaldehyde were incorporated into the mesopores of SCMS aluminosilicate, and further carbonized to obtain carbon/aluminosilicate nanocomposite. The dissolution of the aluminosilicate template using either NaOH or HF solutions generated HCMS carbon capsules.

Schumacher et al. [24] reported a similar synthesis route for the formation of submicrometer- to micrometer-sized particles with a three-dimensional cubic structured (MCM-48) pore system. n-Hexadecyltrimethylammonium bromide was used as template. Aluminum-, chromium-, gallium-, niobium-, and vanadium-MCM-48 were also synthesized using this general procedure by using different metallic precursors (e.g.,  $\text{Al}_2(\text{SO}_4)_3 \cdot 18 \text{H}_2\text{O}$  and  $\text{V}_2\text{O}_5$ ).

### 2.3.4. Mesoporous Nanocomposite Particles

The preparation of monodisperse spherical mesoporous silica/gold nanocomposites consisting of mesoporous silica and a single gold particle approximately 60 nm in diameter using a liquid-phase self-assembly process was reported by Nooney et al. [25]. To prepare gold vitreophilic, a bifunctional ligand, mercaptopropyl trimethoxysilane (MPTS) was bound to the surface of the gold. Following this, an organic mesopores template and tetraethylorthosilicate (TEOS) were added using a Stöber method. The template used in this work was a quaternary ammonium salt, cetyltrimethylammonium bromide (CTAB). In an aqueous solution this surfactant forms an ordered hexagonal micellar array, which serves as a template for the polymerization of silicate, and the length of the carbon chain controls the radius of the mesopores. After 2 h of growth at room temperature, the sample was filtered and washed.

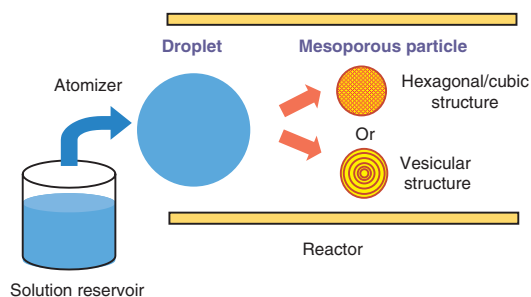
## 2.4. Aerosol Spray Method

### 2.4.1. Surfactant Templating

Bruinsma et al. [26] first used an aerosol spray method (spray drying) to prepare mesoporous powders by the rapid evaporation of hydrolyzed silicon alkoxide-surfactant in an acidic alcohol/water mixture. During solvent drying, the silica and surfactant, cetyltrimethylammonium chloride, self-assemble to form a hexagonally ordered mesophase structure and all of the nonvolatile components (silica, polymer, and surfactant) are incorporated into the mesophase. Spray-dried particles, consisting of hollow particles with mesoporous shells, were produced.

Lu and co-workers [27, 28] extended this method to the preparation of spherical well-ordered mesoporous particles via the self-assembly of surfactant templates. The synthesis process starts by using a homogeneous solution of soluble silica plus a surfactant prepared in an ethanol/water solvent. The solution was generated in the form of an aerosol dispersion within a tubular reactor (Fig. 1). In a continuous process, the aerosol particles are dried, heated, and collected on a filter. Preferential alcohol evaporation during drying enriches the particles in the surfactant, water, and silica,



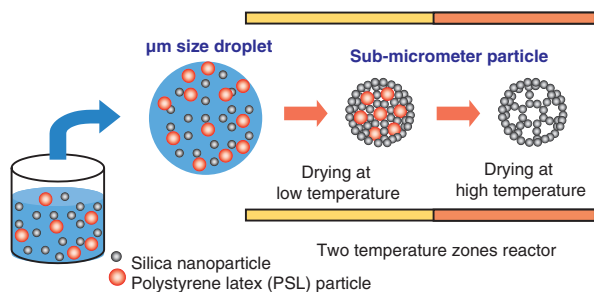


**Figure 1.** Schematic for the preparation of ordered mesoporous particles via a surfactant template using aerosol spray method.

inducing micelle formation and the successive co-assembly of silica–surfactant micellar species into liquid-crystalline mesophases. Typically, particles produced by this method are solid, with highly ordered hexagonal, cubic, or vesicular mesostructures. Rao et al. [29] extended this method to the preparation of mesoporous particles with diameters in the range of 5 to 10  $\mu\text{m}$ .

### 2.4.2. Colloidal Templating

The production of spherical-shaped porous particles with a nanoscale ordering porosity by means of an aerosol spray method via a colloidal crystal template has been reported by Iskandar et al. [30, 31]. The synthesis via colloid crystallization permits pore sizes to be controlled in the range of nanometers to micrometers. Figure 2 depicts the schematic for the preparation of such ordered porous particles. Colloidal silica nanoparticles were mixed with polystyrene (PS) latex, in a certain fraction in water, which was then atomized to generate droplets. The size of the silica particles varied from 5 nm to 25 nm and the PS latex from 42 nm to 178 nm. The reactor consisted of two heating zones: the first was used to evaporate the solvent in the droplet and the second was used to evaporate the PS latex particles, resulting in the formation of porous silica particles. This method is rapid and relatively simple. A large amount of porous particles can be produced in just several seconds. The production rate can be easily controlled by the appropriate control of the rate of flow of the nitrogen carrier gas. This method is an *in-situ* process. No post treatment is required to produce porous particles. Particle size can be controlled by altering the droplet size as well as the concentration of primary particles in the precursor, which represents additional advantages of this method.



**Figure 2.** Schematic for the preparation of ordered macroporous particles via a colloidal template using aerosol spray method.

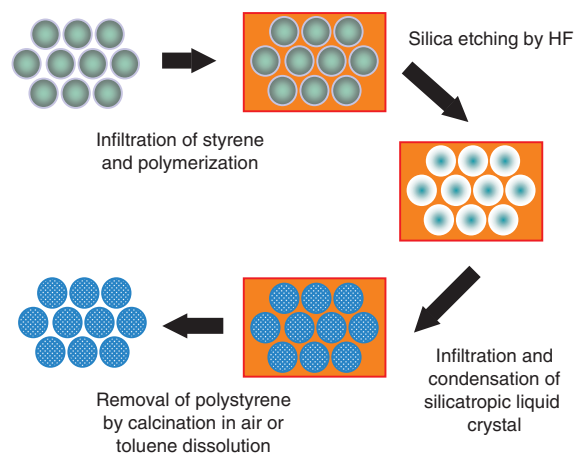
### 2.4.3. Combining of Surfactant and Colloidal Templating

The synthesis of hierarchical porous silica nanoparticles with well-defined pore sizes (or cells) templated by combining colloidal particles with surfactants, or microemulsions, through an aerosol process has been reported by Fan et al. [32]. Adjustable meso- or macroporosity nanoporous silica particles could be produced using a soft microemulsion and solid polystyrene beads as templates.

The synthesis process starts by using a homogeneous solution of polystyrene spheres/silica, polystyrene spheres/surfactant/silica, or microemulsions/silica. The method for preparing the porous silica particles was similar to that used for the preparation described in Figures 1 and 2. After removal of surfactants and polymer spheres, the resulting materials exhibited a controlled meso- and macroporosity.

### 2.5. Micromolding in Inverted Polymer Opals

The synthesis of silica spheres composed of the hexagonal symmetry form of mesoporous silica using micromolding in inverted polymer opals (MIPO) was reported by Yang et al. [33]. MIPO begins with the synthesis of a polystyrene micro-mold having the structure of an inverted opal (Fig. 3). This is achieved by the radical polymerization of styrene monomer within the void spaces of a silica opal that had been grown and sintered followed by removal of the silica opal by fluoride-based etching. The polystyrene micrometer-scale structure is well ordered and within each spherical void regular arrangements of smaller holes that originate from the necking points between silica spheres in the sintered fcc opal template can be observed. The polystyrene inverted opal is subsequently infiltrated with a silicatropic liquid crystal composed of a nonionic surfactant  $\text{C}_{12}\text{H}_{25}(\text{OCH}_2\text{CH}_2)_{10}\text{OH}$ , water, hydrochloric acid, and TEOS, which slowly undergoes hydrolytic polycondensation to a monolithic periodic mesoporous silica. Removal of the polystyrene mold either by solvent extraction or by calcination in air leaves behind



**Figure 3.** Schematic for the preparation of ordered mesoporous particles via a surfactant template using micromolding in inverted polymer opals. Reprinted with permission from [33], S. M. Yang et al., *Adv. Mater.* 12, 1940 (2000). © 2000, Wiley-VCH.

a well-ordered opal replica in which the individual particles are composed of periodic mesoporous silica.

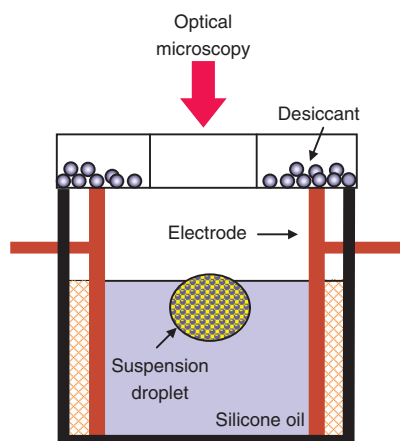
## 2.6. Air–Oil Interface Colloidal Templating

Ordered macroporous particles of silica and titania fabricated by colloidal templating in aqueous droplets straddling an air–oil interface have been investigated by Yi et al. [34]. The procedures involve the initial preparation of spherical colloidal crystalline particles of polystyrene latex spheres followed by infusion with metal precursor solutions that form silica or titania in the interstices (Fig. 4). Finally, calcination is employed to decompose the polystyrene latex spheres, leaving macropores at their sites. The shape of the template can be controlled by the presence of added surfactant or by the action of an applied electric field. Specifically, spherical, concaved disklike, and ellipsoidal colloidal crystals were successfully prepared and used as templates in the fabrication of ordered macroporous particles.

An electric field can be applied to the droplet-template colloidal crystallization cell with electrodes that are connected to an alternating current (ac) electric power supply. The suspension droplet of the monodisperse PS latex spheres straddles the air–oil interface, but most of the suspension droplet is immersed in the oil phase. If necessary, an ac electric field can be applied to deform the suspension droplets. During the evaporation of the drop-phase liquid (i.e., water in the present case), the PS latex spheres in the suspension droplets begin to order into a macrocrystalline structure. In the presence of an applied electric field, the suspension droplets are deformed into spheroids. A viscous silicone oil or a partially fluorine-substituted silicone oil was used as the continuous oil phase.

The suspension droplets underwent shrinkage during incubation. Finally, the oil that had infiltrated into the macrocrystalline structure was extracted with hexane and drying gave supraparticle assemblies having various shapes.

The prepared macrocrystalline particles were soaked in a solution of a metal alkoxide precursor, which penetrated the interstices between the PS latex spheres by capillary force.

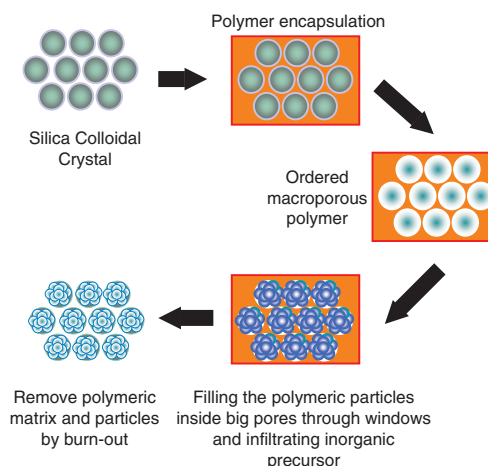


**Figure 4.** Schematic of the colloidal crystallization cell with a suspension droplet as a template. Reprinted with permission from [34], G.-R. Yi et al., *Chem. Mater.* 13, 2613 (2001). © 2001, American Chemical Society.

The macrocrystalline spheres into which the precursor had fully infiltrated were removed and then exposed to air. The metal oxide precursor was then hydrolyzed by moisture in the air. It is especially noteworthy that before the hydrolysis reaction proceeded, the residual alkoxide precursor remaining on the surface of spherical colloidal assemblies must be removed. Otherwise, a thick skin is formed on the ordered macroporous sphere. Skin formation can be avoided by removing the precursor solution on the surface of colloidal assemblies in a moisture-free space or by treatment with n-propanol. Finally, the polystyrene latex spheres constituting the organic-inorganic composite microstructured particles were removed by calcination, leaving ordered spherical air voids at their sites in a matrix of titanium oxide or silicon oxide.

## 2.7. Double Templating

Yi et al. [35] reported on a fabrication method for preparing an array of uniform micron-sized ceramic spheres with ordered macropores by double templating. The synthetic method for preparing the macroporous particles is a two-step template-assisted fabrication process, as illustrated in Figure 5. Micrometer-sized silica particles are initially assembled into a close-packed colloidal crystalline array and are then encapsulated by polymerizing a polymer in the interstices. The silica spheres are then removed by selective chemical etching, leaving behind micrometer-sized air cavities. The polymer latex particles are then injected into the spherical air cavities inside the polymer matrix. The polymeric particles assemble within the voids to form an ordered close-packed structure. Finally, an inorganic precursor is infiltrated into the interstices between the latex particles and gelled to capture the ordered structure. A key feature of the polymer template is that the macropores are interconnected with windows sufficiently large for small polystyrene latex with size of about 500 nm to pass through.



**Figure 5.** Schematic for the preparation of ordered mesoporous particles via a colloidal template by double templating method. Reprinted with permission from [35], G.-R. Yi et al., *J. Am. Chem. Soc.* 124, 13354 (2002). © 2002, American Chemical Society.

### 3. CHARACTERIZATION

Characterization of the morphology and porous structure of prepared particles usually involves the use of scanning electron microscopy (SEM), transmission electron microscopy (TEM), X-ray diffraction (XRD), and adsorption analysis. In this section, the characterization of the prepared particles will be described from the following points of view: (1) microscopy observation, (2) X-ray diffraction, and (3) adsorption analysis. Table 2 shows some data relative to the characterization of ordered nanoporous particles.

#### 3.1. Microscopy Observation

Using SEM and TEM observation techniques, the morphology, size distribution, and porous structure of the prepared particles can be observed. In the following subsections, the microscopy characterization of the prepared particles will be summarized according to the synthesis method used.

##### 3.1.1. Emulsion Templating

In the preparation of ordered porous particles via oil–water interface emulsion templates, Schacht et al. [12] reported that the final product morphology can be controlled by the stirring speed used in the synthesis (see Section 2.1). Stirring is one mechanism for controlling emulsion properties through modification of long-range hydrodynamic forces and is crucial in the formation of the secondary morphology. Under low stirring speed, a fiber type morphology was observed. By increasing the stirring speed, more spherical particles were formed and the fiber morphology disappeared. The spherical particle size decreased with increasing stirring speed. However, the size distribution was broad and some of the particles were agglomerated. By carefully controlling the synthesis conditions, a relatively narrow

size distribution of spherical particles was obtained. From other SEM images, these particles were shown to be hollow and most were crushed after the organic phase had been removed. Silica particles in the form of fibers have a size of 50–1000  $\mu\text{m}$  in length, and in the hollow spherical form have a diameter of 10 to 500  $\mu\text{m}$ .

Using a similar method, Huo et al. [13] reported that by combining different surfactants and basic catalysts, the prepared particles have a solid and spherical morphology, where the stirring speed influences the condition of the particles. A low stirring speed resulted in the formation of soft gel particles, a medium stirring speed give millimeter-sized particles, and high stirring speeds resulted in smaller particle sizes. The size of the silica particles was uniform and could be controlled in the range of 0.1 to 2  $\mu\text{m}$ . TEM images suggest that the particles exhibit a small pore size in the nanometer range (1–5 nm) and a preferentially ordered hexagonal form (MCM-41), while other areas show pores that appear to have a narrow size distribution but with a random orientation.

##### 3.1.2. Biomimetic Templating

In the preparation of ordered porous particles via diamine templating, elliptical well-ordered multilamellar regions near the vesicles of 300 to 800 nm were observed, as evidenced by TEM and SEM observations [14]. The multilamellar regions near the vesicle surface are populated by a dense inorganic phase. This structural feature is indicative of biomimetic nucleation and the growth of lamellar silica material, as the self-assembly process occurs in the interlayered regions of the multilamellar bola-amphiphile vesicles. Tanev and Pinnavaia postulated that the formation of vesicular materials occurs in a manner reminiscent of natural biomineralization processes.

**Table 2.** Characterization data of ordered nanoporous particles.

Preparation method	Morphology	Ordered type	Size [ $\mu\text{m}$ ]	Pore size [nm]	Specific surface area [ $\text{m}^2/\text{g}$ ]	Specific pore volume [ $\text{cm}^3/\text{g}$ ]	Ref.
Oil–water interface emulsion templating	Fibers, spherical solid and hollow	Hexagonal	1–2000	1.4–10	~1100	0.24 ~ 0.61	[12, 13]
Biomimetic templating	Spherical hollow	Vesicle	0.3–0.8	0.6, 1.2	~984	0.47 ~ 0.56	[14]
Liquid–phase surfactant templating under acidic/basic condition	Toroidal, disklike, spiral, spherical	Hexagonal	2–20	2.5 ~ 5	~1042	0.70	[16–18]
Liquid–phase surfactant templating with modification of Stöber method	Spherical	Hexagonal, cubic	0.4–2.3	2.10–11.2	~1600	0.49 ~ 1.2	[19, 20, 22–25]
Aerosol spray surfactant templating	Spherical	Hexagonal, cubic, vesicular	0.05–0.5	1.8–9.2	~1770	—	[26, 27]
Aerosol spray colloidal templating	Spherical, doughnut-like	Hexagonal	0.3	42–178	—	—	[30, 31]
Aerosol spray surfactant and colloidal templating	Spherical	Hexagonal	0.1	4.0–100	~480	0.53–0.88	[32]
Micromolding in inverted polymer opals	Spherical	Hexagonal	0.28 ~ 0.36	4.1	~560	—	[32]
Air–oil interface colloidal templating	Spherical, concave disklike, ellipsoidal	Hexagonal	2000	190–275	—	—	[34]
Double templating	Spherical	Hexagonal	60	500	—	—	[35]

In the preparation of ordered porous particles via diamine templating, various types of spherical morphologies of spirals, hollow and solid mesoporous silica with submicrometer-sized diameters were obtained [15]. By changing the mixing order of the reactants used in the synthesis, mesoporous solid particles of several tens of micrometers in size were obtained. The morphologies of the particles produced and their porous properties are strongly influenced by the alkyl chain length of the 1-alkylamine template and the concentration and volume of the acidic aqueous solution used in the synthesis mixture. A longer alkyl chain ( $C_{10}$ ,  $C_{12}$ ) leads to production of a flaky, ultrathin lamina morphology, while a short alkyl chain ( $C_6$ ,  $C_8$ ) produces a spherical morphology,  $C_6$  templating produces hard mesoporous silica spheres, and  $C_8$  templating, spiral or hollow spheres. With a very long alkyl chain (above  $C_{12}$ ) or a short alkyl chain (below  $C_6$ ), the amorphous qualities significantly increase, indicating instability or incomplete solubility of the 1-alkylamine.

### 3.1.3. Liquid-Phase Surfactant Templating under Acidic and Basic Conditions

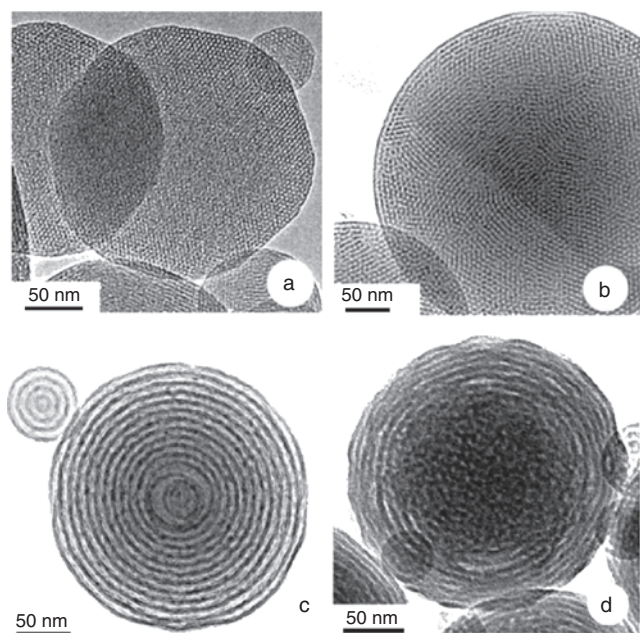
Mesoporous particles prepared by this method have spherical and curved morphologies including toroidal, disklike, spiral, and spheroidal shapes [16–18]. In the case of the use of a cationic surfactant under acidic conditions, SEM images reveal that the morphologies are extraordinary in terms of their diverse and remarkable shapes and impressive range of curvature [16]. However, for the use of cationic-nonionic surfactants, SEM images reveal the production of entirely spherical particles, although some agglomeration is evident. The size of these silica spheres ranges from 2 to 6  $\mu\text{m}$ . In the case where a cationic-nonionic surfactant is used, the exterior surface of the particles is very smooth, in contrast to the faceted and corrugated surfaces exhibited by the mesoporous silica bodies synthesized by cationic surfactant templating. TEM images of the basic morphologies clearly show the presence of hexagonally close-packed channels with a center-to-center spacing of  $\sim 5$  nm.

### 3.1.4. Liquid-Phase Surfactant Templating: Modification of Stöber Method

The morphologies of particles prepared by the Stöber method using the CTAB surfactant as a template were almost spherical with a size range from 400 to 1100 nm. In the case where *n*-alkylamines were employed as templates, spherical particles in a wide range of sizes, from 0.5 to 2.3  $\mu\text{m}$ , were obtained. The particles are nearly completely dispersed although some agglomeration was visible.

### 3.1.5. Aerosol Spray Surfactant Templating

In the preparation of particles by aerosol spray surfactant templating, particles with ordered mesoporous structures and a spherical morphology were obtained. Different surfactant templates, that is, CTAB, Brij-58, Brij-56, or P123, exhibited different structural mesopores of the prepared particles. The use of the CTAB surfactant gave particles that exhibit a highly ordered hexagonal mesophase (Fig. 6a). Many of the particles adopted a polyhedral shape that is hexagonal in cross section. The use of nonionic surfactants (Brij-56/58) commonly resulted in vesicular mesostructures,



**Figure 6.** Representative TEM micrographs of mesostructured silica particles. (a) Faceted, calcined particles with hexagonal mesophases. The sol was prepared using 5 wt% CTAB as the surfactant template. (b) Calcined particles showing a cubic mesostructure. The sol was prepared using 4.2 wt% Brij-58. (c) Calcined particles showing a vesicular mesophase. The sol was prepared using 5% P123. (d) Uncalcined silica particles showing the “growth” of ordered vesicular domains from the liquid–vapor interface. The sol was prepared using 2.5% Brij-56. Reprinted with permission from [27], Y. Lu et al., *Nature* 398, 223 (1999). © 1999, Macmillan Magazines Ltd.

but cubic and hexagonal mesostructures could also be produced (Fig. 6b and d). The use of the P123 surfactant as the triblock copolymer template typically resulted in a vesicular mesophase (Fig. 6c).

Evaporation during aerosol processing creates a radial gradient in surfactant concentration within each droplet that steepens with time and maintains a maximum concentration at the droplet surface. Starting with an initially homogeneous solution, the surfactant critical micelle concentration is exceeded first at the surface of the droplet, and, as evaporation proceeds, is progressively exceeded throughout the droplet. This surfactant enrichment induces a silica–surfactant self-assembly into the micelles and further organization into liquid-crystalline mesophases. The radial concentration gradient and the presence of a liquid–vapor interface causes the rapid inward growth of ordered silica–surfactant liquid-crystalline domains (Fig. 6d) rather than in the outward direction from a seed.

Unlike films—which have flat liquid–vapor interfaces and show a progressive change in mesostructure (disordered  $\rightarrow$  hexagonal  $\rightarrow$  cubic  $\rightarrow$  lamellar) with increasing surfactant concentration, particles prepared with comparable CTAB concentrations show only disordered or hexagonal mesophases. The reason for this is because the liquid–vapor interface serves as a nucleating surface for liquid-crystal growth; the high curvature imposed by this interface alters the generally observed relationship between the surfactant packing parameter and the resulting mesostructure.

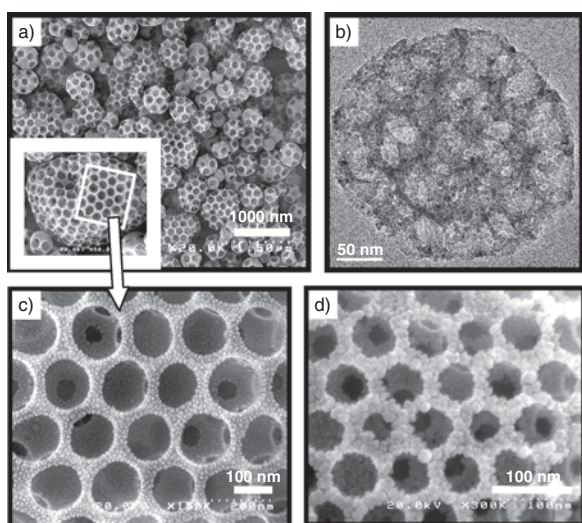
Although the use of CTAB typically leads to the formation of lamellar mesophases in bulk and thin-film samples, it appears that this molecule cannot pack into a cone that is truncated by surfaces of high and opposite curvature, as is required to direct the vesicular mesostructure. Only surfactants containing ethylene oxide (EO) blocks consistently gave vesicular mesophases.

### 3.1.6. Aerosol Spray Colloidal Templating

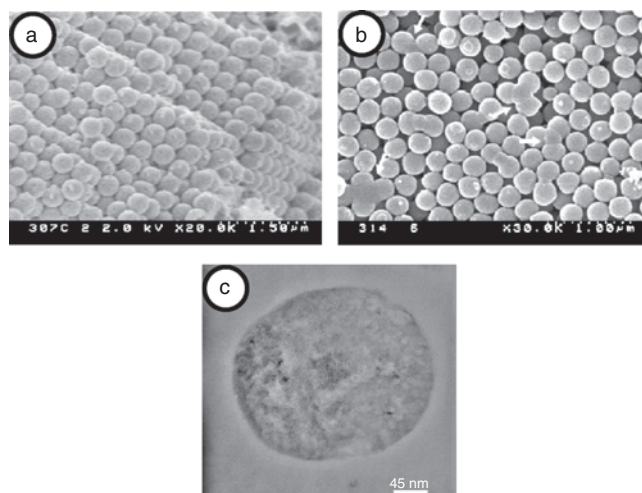
In the preparation of particles by aerosol spray colloidal templating, ordered macroporous particles were obtained. The resulting powders are almost spherical (Fig. 7a). Ordered pores with a close-packed hexagonal arrangement are clearly observed on their surfaces, indicating that a self-organization of the PSL particles occurred spontaneously during the evaporation process. The area of organization (arrangement) increased with an increase in powder particle size, which was obtained using a larger-sized droplet. TEM images reveal that the pore arrangement persists throughout the entire volume of the particles (Fig. 7b). The pore sizes are similar to the PS latex particle sizes. This suggests that the pore size can be easily controlled by appropriately altering the size of the PS latex particles (Fig. 7c and d). There is an optimum fraction of PS latex and primary silica particles to result in the formation of spherical particles with an organized pore arrangement.

### 3.1.7. Micromolding in Inverted Polymer Opals

SEM images of prepared porous particles using this method showed that the morphology of particles was spherical (Fig. 8). The diameter of the product of mesoporous silica



**Figure 7.** (a) Typical SEM image of ordered macroporous silica particles synthesized by templating spherical colloidal 178-nm PS particles using a spray drying method. (b) Typical TEM image of ordered macroporous silica particles. (c) SEM image at high magnification shows the hexagonal packing of macroporous particles. (d) SEM image of ordered macroporous silica particles synthesized by templating 79-nm PS particles. Reprinted with permission from [31], F. Iskandar et al., *Nano Lett.* 2, 389 (2002). © 2002, American Chemical Society.



**Figure 8.** Microscope images of mesoporous silica particles prepared by micromolding in inverted polymer opals. (a) SEM image of calcined mesoporous spheres, (b) a triplet coalescence defect, and (c) TEM image of a microtomed thin section. Reprinted with permission from [33], S. M. Yang et al., *Adv. Mater.* 12, 1940 (2000). © 2000, Wiley-VCH.

depends on the colloidal template (silica microspheres) size used. In the case where a silica microspheres size of 460 nm is used, the diameter of the air microspheres in the inverted mold is ca. 460 nm. The mesoporous silica opal showed that the size of the as-synthesized mesoporous silica microspheres is ca. 420 nm and this observed shrinkage is due to the condensation of silicate to silica (Fig. 8a). The mesoporous silica particles further shrink to ca. 390 nm after calcination because of further condensation polymerization of Si-OH groups on the surface of the mesoscale channels (Fig. 8c). In the case where a silica opal consisting of smaller ca. 360 nm microspheres is used, the diameter of the as-synthesized mesoporous silica microspheres is ca. 280 nm. The monodisperse mesoporous silica microspheres are packed in a regular fcc array. In addition, intriguing coalescence defect structures are observed, as depicted in Figure 8b. These structures are most pronounced when templating the mesoporous silica opal with smaller microspheres. TEM images of a thin microtomed section show hexagonally ordered mesoscale pores with a diameter ca. 5 nm.

### 3.1.8. Air–Oil Interface Colloidal Templating

The shape of the prepared colloidal crystals was either spherical or nonspherical (oblate or prolate spheroids) and could be successfully controlled by applying an ac electric field or by adding a surfactant. Specifically, spherical, concaved disklike, and ellipsoidal colloidal crystal were successfully prepared and used as a template in the fabrication of ordered macroporous particles. The SEM images of the prepared macroporous particles showed that the pores were interconnected and ordered into a hexagonal arrangement. The sizes of the pores ranged from 190 to 275 nm, depending on the colloidal template size. All samples underwent shrinkage during calcination. Nevertheless, the spherical shapes of the colloidal crystals remained, as shown from a low-magnification image of an optical

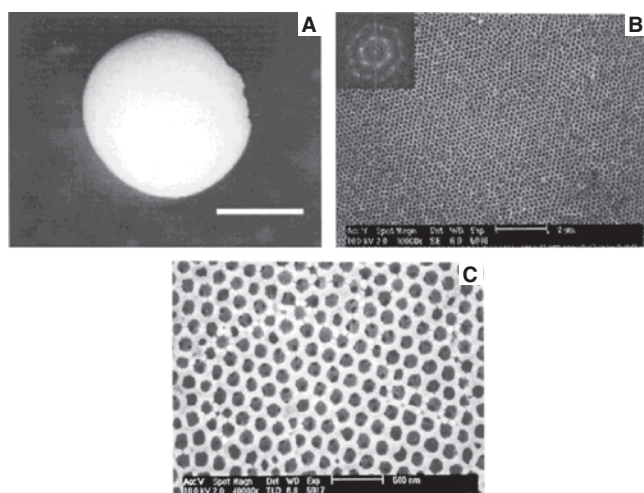
microscope (Fig. 9a). The SEM images reproduced in Figure 9b showed that calcined samples of titanium oxides were highly ordered in three dimensions over the entire range, resembling a cubic close packing of cages. However, the cubic close packing structure can clearly be seen from the two-dimensional Fourier transforms (FFTs) of the corresponding SEM images (see the insets in Fig. 9b). The resulting spot pattern indicates that the image plane is close to the (111) plane of an fcc lattice. The void spaces were interconnected in three dimensions through windows, the diameters of which typically exceeded 40 nm, and the wall thickness was about 40 nm (Fig. 9c).

### 3.1.9. Double Templating

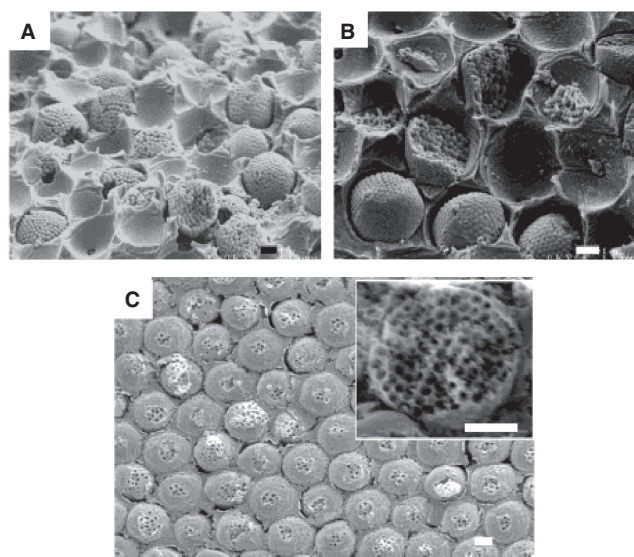
SEM images of mesoporous silica particles prepared by the double templating method are shown in Figure 10. Figure 10a shows several millimeter-sized polymer skeletons filled with small latex particles. After the large pores were filled with the polymer particles and the remaining water was removed by drying, the metal alkoxide precursor of silica or titania was infiltrated into the interstices formed between the latex particles (Fig. 10b), after the organic polymer matrix and latex particles were removed. Figure 10c shows that photonic balls with ordered spherical macropores were successfully produced. The size distribution of the photonic balls was determined by the size of the silica particles that were used in the original templating process. The inset of Figure 10c shows that the internal structure of each photonic ball is highly ordered.

### 3.2. X-Ray Diffraction

X-ray diffraction techniques are frequently used to characterize the porous structure of ordered nanoporous particles. XRD patterns of hexagonal ordered mesoporous materials



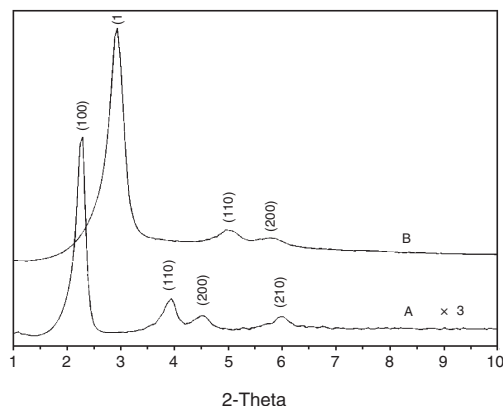
**Figure 9.** (A) Optical microscope images of an ordered macroporous titania sphere synthesized by templating the spherical colloidal assembly formed from the 230-nm PS spheres. (B) Typical SEM image of an ordered macroporous titania sphere. The inset shows the fast Fourier transform of the SEM image. (C) SEM image at large magnification showing the interconnected cavity pores. Reprinted with permission from [34], G.-R. Yi et al., *Chem. Mater.* 13, 2613 (2001). © 2001, American Chemical Society.



**Figure 10.** SEM images show (A) shaped colloidal crystals in a polyurethane skeleton, (B) composite of shaped colloidal crystals and an infiltrated titanium alkoxide precursor solution, and (C) ordered macroporous titanium spheres by removal of the organic polymer phase of the previous composite. (Scale bars are 1  $\mu\text{m}$ ). Reprinted with permission from [35], G.-R. Yi et al., *J. Am. Chem. Soc.* 124, 13354 (2002). © 2002, American Chemical Society.

usually exhibit three or five reflections, or Bragg peaks, between  $2\theta = 2^\circ$  and  $6^\circ$ . Figure 11 shows XRD patterns of dried and calcined fibers prepared by an aerosol spray surfactant templating method [26]. The reflections are due to the ordered hexagonal array of pores and can be indexed assuming a hexagonal unit cell as (100), (110), (200), and (210) after calcination.

The XRD pattern of lamellar mesoporous materials typically shows one intense peak between  $2\theta = 2^\circ$  and  $6^\circ$ , along with a broad weak shoulder [14]. However, samples with only one distinct reflection have also been reported to contain substantial amounts of hexagonal structure [16]. The XRD patterns of cubic structure mesoporous materials typically exhibit three or five Bragg peaks, between  $2\theta = 2^\circ$  and



**Figure 11.** XRD patterns of mesoporous silica fibers: (A) air-dried fibers; (B) calcined fibers. Reprinted with permission from [26], P. J. Bruinsma et al., *Chem. Mater.* 9, 2507 (1997). © 1997, American Chemical Society.

$6^\circ$ . The reflections can be indexed assuming a cubic unit cell as (211), (220), (421), (332), and (431) [24].

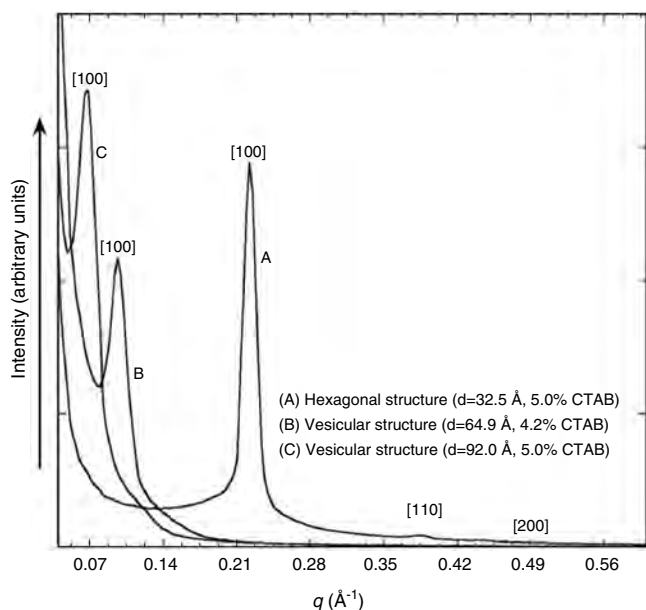
Since the materials are not crystalline at the atomic level, no reflections at higher angles are observed. Moreover, these reflections would only be very weak in any case, owing to the strong decrease of the structure factor at high angles. It is not possible to quantify the purity of the materials by means of XRD. Samples with only one distinct reflection have also been found to contain substantial amounts of hexagonal materials. Using XRD patterns, the pore center-to-center diameter, or d-spacing, can be calculated.

A small-angle X-ray scattering (SAXS) was also used to characterize the porous structure of the particles [27]. Figure 12 shows small-angle X-ray scattering (SAXS) patterns for silica particles prepared by aerosol spray surfactant templating method and different surfactants. The main peak is indexed as the [100] reflection of the hexagonal (A, prepared using CTAB surfactant) and vesicular mesophases (B and C).

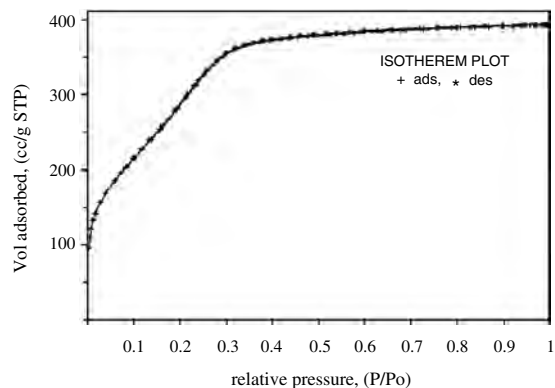
### 3.3. Adsorption Analysis

Adsorption analysis has been widely used to determine surface area and to characterize the pore-size distribution of ordered nanoporous particles.  $N_2$ ,  $O_2$ , and Ar gases are typically used to characterize the porosity of mesoporous materials [36–38]. Figure 13 shows the adsorption-desorption isotherm of  $N_2$  for ordered nanoporous particles [13].

To determine the pore-size distribution, several methods based on geometrical considerations [39], thermodynamics [40], or a statistical thermodynamic approach have been used [41]. In addition, freezing point depression can be used, as well as nuclear magnetic resonance (NMR) [42]. A method for analyzing in the mesopores range is the Barret–Joyner–Halenda (BJH) method [43, 44] which is



**Figure 12.** Small-angle X-ray scattering (SAXS) patterns of silica particles with (A) hexagonal or (B and C) vesicular mesophase. Reprinted with permission from [27], Y. Lu et al., *Nature* 398, 223 (1999). © 1999, Macmillan Magazines Ltd.



**Figure 13.** Adsorption-desorption isotherm of nitrogen at 77 K for ordered mesoporous particles. Reprinted with permission from [13], Q. S. Huo et al., *Chem. Mater.* 9, 14 (1997). © 1997, American Chemical Society.

based on the Kelvin equation. Figure 14 shows a sample of a BJH pore-size distribution plot from the adsorption branch of the sample shown in Figure 13 [13].

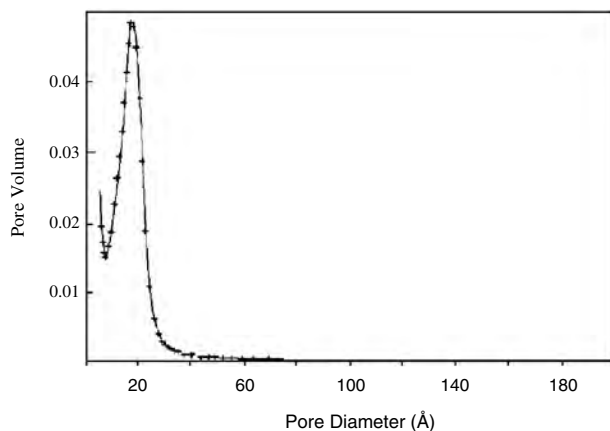
## 4. PROPERTIES

### 4.1. Pore Size and Surface Area

Ordered nanoporous materials are used technically as adsorbents, catalysts and catalysts supports, and separation materials due to their high surface area and well-ordered pore size. The extremely high surface areas are conducive to high catalytic activity. From Table 2, it was found that mesoporous particles prepared using an aerosol spray surfactant template had the highest surface area,  $1770 \text{ m}^2/\text{g}$  [26]. Well-ordered mesoporous materials also offer interesting potential for use in separation and adsorption [45].

### 4.2. Thermal Properties

Thermal stability by annealing nanoporous silica particles has been investigated [24, 31]. By annealing particles below  $750^\circ\text{C}$ , the porous structure of silica particles (mesoporous



**Figure 14.** BJH pore-size distribution plot from adsorption branch. Reprinted with permission from [13], Q. S. Huo et al., *Chem. Mater.* 9, 14 (1997). © 1997, American Chemical Society.

[24] and macroporous [31]) remains stable. At higher temperatures in the vicinity of 1000 °C, the XRD patterns of materials show that several peaks disappear. From SEM images, by annealing at 1200 °C, some silica nanoparticles collapse from the pore wall and give rise to smaller pore sizes inside the particles. The morphology of the powder becomes smoother and smaller, due to the sintering of silica, which occurs at this temperature. When the annealing temperature reaches 1500 °C, the pores collapse and, finally, solid spherical silica particles are obtained. The difference in powder particle volume before and after annealing determines the porosity of the powder [31].

### 4.3. Optical Properties

Chang and Okuyama [46] reported on the optical properties of ordered macroporous particles prepared by an aerosol spray colloidal surfactant method. Light scattering by solid and macroporous silica particles was investigated using a laser particle counter (LPC) coupled with a pulse height analyzer. The measured partial scattering cross section of solid and macroporous silica particles with same diameter showed significant differences. The effective relative indices of solid and macroporous silica particles were computed by the best fitting of the scattering intensity measurements. The result showed that the macroporous silica particles have a low effective refractive index, 1.147 (for solid silica particles, the effective refractive index was 1.46). By changing the porosity of the porous particles, the refractive index could be easily controlled.

## 5. SUMMARY

Ordered nanoporous particles have been synthesized by several methods, in the liquid process as well as in the aerosol phase using a surfactant and/or colloidal templates. The morphology of prepared particles, the pore size, and the porous structure are typically influenced by the template types, the synthesis method, and the synthesis procedures. The use of a surfactant template led to the formation of micro- and/or mesoscaled structured porous particles. The use of a colloidal template gave particles with macroscale ordered pores. A high surface area and well-ordered nanoporous particles would be potentially useful as catalyst, adsorbent, separation materials, and low refractive index materials. Research in the preparation of particles that contain ordered nanopores (microporous, mesoporous, and macroporous) with a controlled morphology is in its infancy. It remains to be seen if these systems can be developed for other applications such as low dielectric constant, microelectronics, and electro-optics.

## GLOSSARY

**Aerosol** A substance composed of solid or liquid particles that are small but larger than most molecules in gas phase.

**Aerosol spray method** A method for material processing by spraying the droplets containing precursor in gas phase.

**Biomimetic** Biomimetic refers to human-made processes, substances, devices, or systems that imitate nature.

**Colloid** A substance composed of particles that are small but larger than most molecules. The particles in a colloid do not actually dissolve but remain suspended in a suitable liquid or solid. Among the colloids are polymers, such as rubber, plastics, and synthetic fibers.

**Emulsion** A stable dispersion of one liquid in a second immiscible liquid, such as milk (oil dispersed in water).

**Macroporous materials** Materials which have pore size above 50 nm.

**Mobil oil composite of matter (MCM)** Silicate-surfactant composite structures that possess mesoscopic order which have attracted large interest since the pioneering work of the Mobil Oil group published in 1992.

**Mesoporous materials** Materials which have pore size between 2 and 50 nm.

**Microporous materials** Materials which have pore size below 2 nm.

**Scanning electron microscopy (SEM)** The use of a stream of electrons controlled by electric or magnetic fields to obtain the profile materials surface. The examined object is scanned with a focused beam of accelerated electrons in a vacuum cannon. Under the influence of the bombardment the object emits various sorts of radiations that can be captured by fluorescence screen or film.

**Transmission electron microscopy (TEM)** A fine electron beam passes through the specimen, which must therefore be sliced extremely thinly. The transmission electron may be thrown on a fluorescent screen or may be photographed to produce specimen image.

## REFERENCES

1. M. E. Davis, *Nature* 417, 813 (2002).
2. F. Schüth and W. Schmidt, *Adv. Mater.* 14, 629 (2002).
3. O. D. Velev and A. M. Lenhoff, *Curr. Opin. Colloid Interface Sci.* 5, 56 (2000).
4. A. Stein, *Microporous and Mesoporous Mater.* 44–45, 227 (2000).
5. K. S. W. Sing, D. H. Everett, R. H. W. Haul, L. Moscou, R. A. Pierotti, J. Rouquerol, and T. Siemieniowska, *Pure Appl. Chem.* 57, 603 (1985).
6. E. Yablonovitch, *J. Opt. Soc. Am. B.* 10, 283 (1993).
7. M. E. Davis, C. Saldarriaga, C. Montes, J. Garces, and C. A. Crowder, *Nature* 331, 698 (1988).
8. C. T. Kresge, M. E. Leonowicz, W. J. Roth, J. C. Vartuli, and J. S. Beck, *Nature* 359, 710 (1992).
9. J. S. Beck, J. C. Vartuli, W. J. Roth, M. E. Leonowicz, C. T. Kresge, K. D. Schmitt, C. T.-W. Chu, D. H. Olson, E. W. Sheppard, S. B. McCullen, J. B. Higgins, and J. L. Schlenker, *J. Am. Chem. Soc.* 114, 10834 (1992).
10. O. D. Velev, T. A. Jede, R. F. Lobo, and A. M. Lenhoff, *Nature* 389, 447 (1997).
11. A. Imhof and D. J. Pine, *Nature* 389, 948 (1997).
12. S. Schacht, Q. Huo, I. G. Voigt-Martin, G. D. Stucky, and F. Schüth, *Science* 273, 768 (1996).
13. Q. S. Huo, J. L. Feng, F. Schüth, and G. D. Stucky, *Chem. Mater.* 9, 14 (1997).
14. P. Tanev and T. Pinnavaia, *Science* 271, 1267 (1996).
15. K. Kosuge and P. S. Singh, *Microporous and Mesoporous Mater.* 44–45, 139 (2001).
16. H. Yang, N. Coombs, and G. A. Ozin, *Nature* 386, 692 (1997).
17. L. Qi, J. Ma, H. Cheng, and Z. Zhao, *Chem. Mater.* 10, 1623 (1998).



18. Q. Chai, Z.-S. Luo, W.-Q. Pang, Y.-W. Fan, X.-H. Chen, and F.-Z. Cui, *Chem. Mater.* 13, 258 (2001).
19. M. Grun, I. Laueur, and K. K. Unger, *Adv. Mater.* 9, 254 (1997).
20. G. Buchel, M. Grun, K. K. Unger, A. Matsumoto, and K. Tsutsumi, *Supramolecular Sci.* 5, 253 (1998).
21. W. Stöber, A. Fink, and E. Bohn, *J. Colloid Interface Sci.* 26, 62 (1968).
22. G. Buchel, K. K. Unger, A. Matsumoto, and K. Tsutsumi, *Adv. Mater.* 10, 1036 (1998).
23. S. B. Yoon, K. Sohn, J. Y. Kim, C. H. Shin, J. S. Yu, and T. Hyeon, *Adv. Mater.* 14, 19 (2002).
24. K. Schumacher, M. Grün, and K. K. Unger, *Microporous Mesoporous Mater.* 27, 201 (1999).
25. R. I. Nooney, T. Dhanasekaran, Y. Chen, R. Josephs, and A. E. Ostafin, *Adv. Mater.* 14, 529 (2002).
26. P. J. Bruinsma, A. Y. Kim, J. Liu, and S. Baskaran, *Chem. Mater.* 9, 2507 (1997).
27. Y. Lu, H. Fan, A. Stump, T. L. Ward, T. Rieker, and C. J. Brinker, *Nature* 398, 223 (1999).
28. C. J. Brinker, Y. Lu, A. Selinger, and H. Fan, *Adv. Mater.* 11, 579 (1999).
29. G. V. Rao, G. P. Lopez, J. Bravo, H. Pham, A. K. Datye, H. Xu, and T. L. Ward, *Adv. Mater.* 14, 1301 (2002).
30. F. Iskandar, Mikrajuddin, and K. Okuyama, *Nano Lett.* 1, 231 (2001).
31. F. Iskandar, Mikrajuddin, and K. Okuyama, *Nano Lett.* 2, 389 (2002).
32. H. Fan, F. van Swol, Y. Lu, and C. J. Brinker, *J. Non-Crystal. Solids* 285, 71 (2001).
33. S. M. Yang, N. Coombs, and G. A. Ozin, *Adv. Mater.* 12, 1940 (2000).
34. G.-R. Yi, J. H. Moon, and S.-M. Yang, *Chem. Mater.* 13, 2613 (2001).
35. G.-R. Yi, J. H. Moon, V. N. Manoharan, D. J. Pine, and S.-M. Yang, *J. Am. Chem. Soc.* 124, 13354 (2002).
36. P. J. Branton, P. G. Hall, and K. S. W. Sing, *J. Chem. Soc., Chem. Commun.* 1527 (1993).
37. P. J. Branton, P. G. Hall, K. S. W. Sing, H. Reichert, F. Schüth, and K. K. Unger, *J. Chem. Soc. Faraday Trans.* 90, 2956 (1994).
38. O. Franke, G. Schulz-Ekloff, J. Rathousky, J. Starck, and A. Zukal, *J. Chem. Soc., Chem. Commun.* 724 (1993).
39. M. Kruk, M. Jaroniec, and A. Sayari, *J. Phys. Chem.* 101, 583 (1997).
40. S. J. Gregg and K. S. W. Sing, "Adsorption, Surface Area and Porosity," 2nd ed. Academic Press, London, 1995.
41. P. I. Ravikovitch, S. C. O'Domhnaill, A. V. Neimark, F. Schüth, and K. K. Unger, *Langmuir* 11, 4765 (1995).
42. D. Akporiaye, E. W. Hansen, R. Schmidt, and M. Stöcker, *J. Phys. Chem.* 98, 1926 (1994).
43. E. P. Barrett, L. G. Joyner, and P. P. Halenda, *J. Am. Chem. Soc.* 73, 373 (1951).
44. M. Kruk, M. Jaroniec, and A. Sayari, *Langmuir* 13, 6267 (1997).
45. J. Y. Ying, C. P. Menhert, and M. S. Wong, *Angew. Chem. Int. Ed.* 38, 57 (1999).
46. H. Chang and K. Okuyama, *J. Aerosol Sci.*, 33, 1701 (2002).

# Organic Nanofilm Growth

Serkan Zorba, Yongli Gao

*University of Rochester, Rochester, New York, USA*

## CONTENTS

1. Introduction
  2. Growth Modes
  3. Modeling the Nanofilm Growth
  4. Organic Nanofilm Growth and Interplay Between Morphology and Charge Transport
  5. Characterization and Application of Organic Nanofilms
  6. Summary
- Glossary  
References

## 1. INTRODUCTION

The last couple of decades have seen the emergence of organic or “plastic” electronics, a term that would probably have sounded peculiar to scientists half a century ago, to take its deserved place among today’s scientific and technological endeavors. It all started with the discovery of the conducting polymers by Shirakawa et al. and Adam in the mid 1970’s [1, 2]. Organic electronics has been a hot and prolific field of science and technology since then. With important discoveries made recently, scientists became even more excited and encouraged about the feasibility of plastic circuitry. Among these recent discoveries are relatively high electron and hole mobilities, and high on/off current ratios observed in single crystals of simple conjugated molecules such as pentacene, perylene, and sexithiophene, etc., when used in thin-film transistor (TFT) applications [3–8]. These achieved results rival those of conventional hydrogenated amorphous silicon. This is by no means suggesting that organic electronics will supersede the inorganic electronics in its high performance and high device density. Rather, the former presents a host of new possibilities like flat panel displays, smart cards, and identification tags with numerous advantages, such as ease of fabrication, reduced cost and power, mechanical flexibility, and other desirable features [3–10].

It has been shown by many research groups in the field that there is a strong relationship between the microstructure and the charge-carrier mobility in organic nanofilms [11–16]. In this article, we will review the recent progress made in organic semiconductor nanofilms as they are used in thin-film field-effect transistors (OTETs) and organic light-emitting diodes (OLEDs). We will outline the basic modes of organic thin-film growth with selected examples and discuss the effect of morphology on charge transport. It seems that molecular ordering is of crucial importance. Charge carriers can hop easily from one molecule to another if there is ordering between them. However, lack of molecular ordering and presence of grain boundaries can be the greatest bottlenecks to charge transport in polycrystalline organic semiconductor nanofilms [11–18]. We will also deal with organic thin-film growth from kinetic roughening considerations, and examine pentacene and perylene more extensively as two model organic semiconductor materials, as they are among the most favorable material due to their relatively high electron and hole mobilities [6, 19, 20].

A direct and easy way of measuring conductance and morphology, and charge injection barrier in organic nanofilms is an effective and desirable way of learning about transport characteristics and potential hurdles to charge transport in these films. To this end, new, reliable, and very powerful scanning probe microscopy (SPM)-based techniques of measurements, such as conducting probe atomic force microscopy (CP-AFM) [7, 8, 12, 16–18, 21–25], and height versus potential ( $z$ - $V$ ) scanning tunneling microscopy (STM) measurements [26–28] on organic semiconductor nanofilm interfaces, are described. These versatile tools let us investigate the structure, structure-transport relationship, charge-carrier transport characteristics, and potential hurdles to charge transport in organic semiconductor nanofilms and interfaces with nanometer-scale spatial resolution.

This review consists of two main parts: structure and morphology aspects, and their effects on the application aspects of organic semiconductor nanofilms. In the first part (Sections 1–4), we will briefly summarize the fundamental principles of organic thin-film growth, and give some background as to the growth dynamics of thin films. We will finish the first section by reviewing the recent works done on some of the selected organic semiconducting materials from

a growth and morphology perspective. In the second part (Section 5), some of the recent results on the applications of organic semiconductor nanofilms will be reviewed, elaborating more on the organic thin-film transistor (OTFT) and OLED applications. The subject of organic semiconductor thin films is such a broad topic that reviewing all the work done in this area so far would require extensive discussion and space. We will, therefore, focus more on the morphology and morphology-transport correlation, and leave the rest to be outside the scope of this article.

## 2. GROWTH MODES

Organic molecules (Chart 1 displays typical chemical structures of some of the promising organic materials), when deposited onto an inorganic substrate, can result in three different growth modes (see Fig. 1), depending on the relative strengths of the adsorbate-adsorbate and adsorbate-substrate interactions [20, 29, 30]. First, if the substrate is chemically inert, the adsorbate-substrate interaction will be very small having almost no influence on the growth of the organic film. This will enable the organic molecules to move freely on the surface and form large, separated islands of crystals after adsorption. This type of growth is known as Volmer–Weber or three-dimensional island growth. Second, if the substrate has highly reactive bonds, the adsorbate-substrate interaction will be very large, and as soon as the organic molecules hit the surface they will be bound strongly to the substrate. This will prevent a self-ordering mechanism of the organic molecules, which is of crucial importance for ordered growth; hence, result in disorder. This mode of growth is known as Frank–van der Merwe or layer-by-layer growth. The third type of growth is a moderate combination of the first two scenarios. That is, the adsorbate-substrate interaction is neither too strong, nor too weak. It is such that the substrate has strong enough influence on the deposited particles to impose its crystallinity to the grown organic film, and the deposited particles have enough mobility to self-order themselves. This type of growth goes by the name of Stranski–Krastanov mode or layer island growth.

Producing very thin defect-free organic nanofilms with high structural order and well-controlled interfaces is a prerequisite for improving charge-carrier speed in electronic device applications. One way to accomplish that is to use organic molecular beam epitaxy (OMBE). Due to the fact that the lattice spacing of organic materials are much larger than that of inorganic ones, it is a difficult task to obtain true epitaxial organic layers. However, well-defined crystal orientations of organic nanofilms are obtained in spite of the absence of lattice matching. This phenomenon is known as quasi-epitaxy. Over the last few years, researchers have tried a number of substrates that might be suitable for epitaxial growth. Noble metals such as gold and silver, therefore, provide the necessary conditions for making highly ordered monolayers with large and defect-free domains. Fenter et al. and Umbach et al. succeeded in fabricating quasi-epitaxial layers of perylene-tetracarboxylic dianhydride (PTCDA), one of the most favorable and intensely studied molecules used in getting highly ordered organic films, on gold [31] and silver [32] substrates, respectively. In their study of the fundamentals of quasi-epitaxy

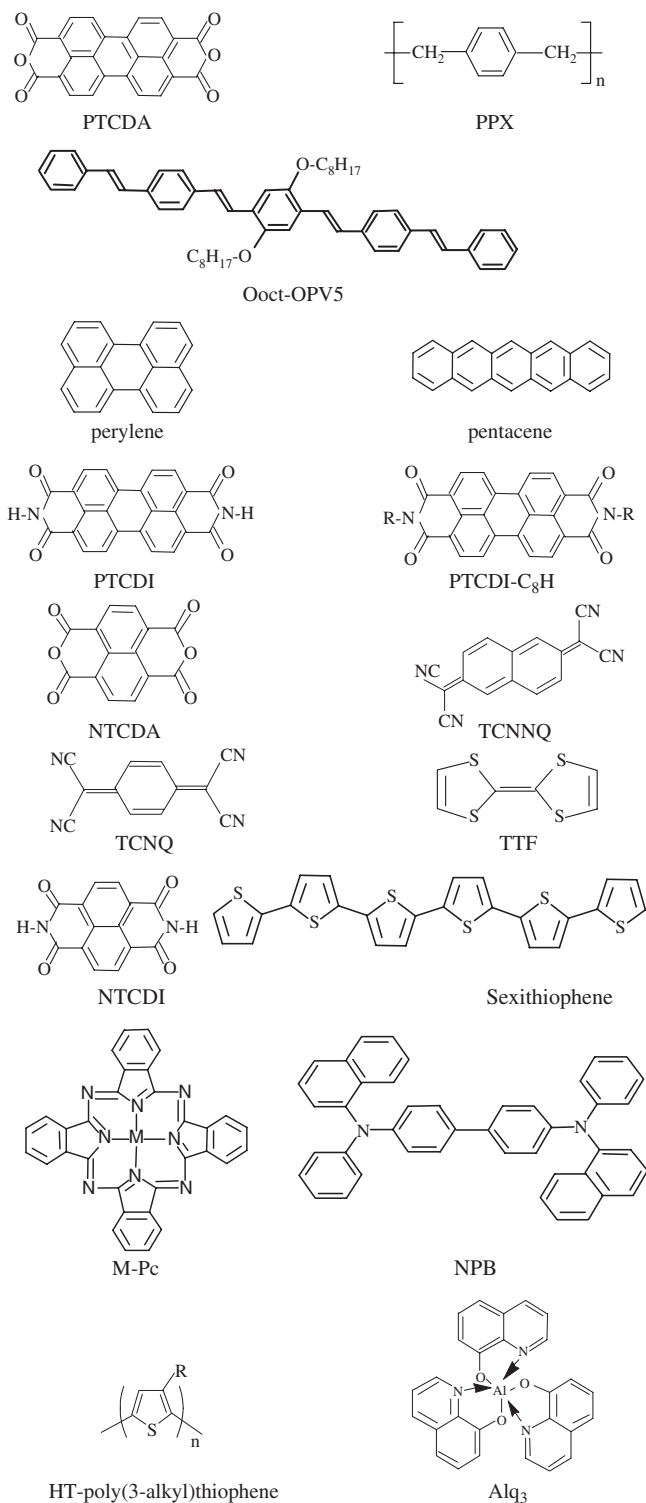
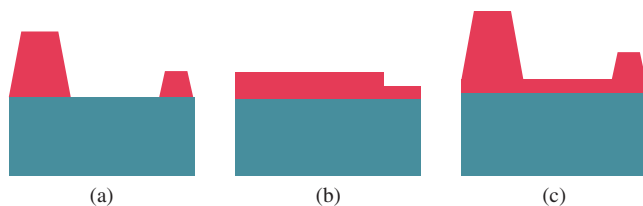


Chart 1. Chemical structures of some of the molecular semiconductors.

of PTCDA Kendrick and Kahn observed that this planar molecule reveals all of three possible growth modes mentioned at the outset of this section when deposited on Se-passivated GaAs (100) ( $2 \times 1$ ), graphite, and InAs (001) ( $4 \times 2$ ) substrates, respectively [29]. We will discuss more about PTCDA and other perylene derivatives later in this article.



**Figure 1.** Three different modes of nanofilm growth: (a) Volmer–Weber or three-dimensional island, the adsorbate-adsorbate interaction dominates and thus deposition results in multilayer islands. (b) Frank–van der Merwe or layer-by-layer, the adsorbate-substrate interaction dominates the adsorbate-adsorbate interaction and thus a new layer can begin to grow only after the previous one is completed. (c) Stranski–Krastanov or layer + island, after the formation of a couple complete layers, the adsorbate-substrate interaction becomes weaker and the adsorbate-adsorbate interaction dominates, forming islands on top of the complete layers.

### 3. MODELING THE NANOFILM GROWTH

Devices based on organic nanofilms, such as light-emitting diodes, field-effect transistors, and solar cells have been demonstrated in recent years [19, 33–39]. In spite of the fact that the performance of these devices has been shown to largely depend on the morphology of the organic thin films [11, 28, 30, 40], only recently has there been a growing interest in studying the growth properties of these films [41–44]. The roughness studies on polymer and small organic molecule films have shed some light on the way the organic interfaces nucleate and evolve to form the desired thin films. In what follows is a brief discussion on the theory of kinetic roughening. We will then review some of the recently published articles dealing with the growth dynamics of organic thin films.

In order to study the growth kinetics of a surface, one can use the  $q$ th-order height-height correlation function, which we can be defined as [45]:

$$C_q(r, t) = \left( \frac{1}{N} \sum_{i=1}^N |h(r_i, t) - h(r_i + r, t)|^q \right)^{1/q}$$

where  $N$  is the number of sites with single-valued heights  $h(r_i, t)$ . By definition, the  $q = 2$  case refers to the height-height correlation function, which is the rms fluctuation in the height difference between two surface points separated by a lateral distance  $r$ . It scales as follows according to the scaling hypothesis [46–48]:

$$C_2(r, t) \sim t^\beta g(r/\xi(t))$$

where  $r$  is the lateral separation,  $t$  is time,  $\beta$  is a scaling exponent, and  $g$  is a scaling function which depends on  $r$  and  $\xi$ , where  $\xi$  is the correlation length. The correlation length is the critical distance over which two heights are correlated.  $C_2(r, t)$  takes the following asymptotic behavior:

$$C_2(r, t) \sim t^\beta$$

Namely, for distances much larger than the correlation length,  $C_2(r, t)$  increases as a power of time.  $\beta$  in the above equation is called the growth exponent. It characterizes the time-dependant dynamics of the growth. For distances much

less than the correlation length  $\xi$ ,  $C_2(r, t)$  is independent of time for surfaces that obey the normal scaling law. It reads as

$$C_2(r, t) \sim \rho r^H$$

where  $\rho$  is the local slope of the interface, and  $H$  is a second scaling exponent called the Hurst exponent. The Hurst exponent  $H$  characterizes the roughness of the saturated interface. As for the local slope  $\rho$ , it is literally the approximate average slope of the local structure. Its value is related to the intersection of  $C_2(r, t)$  with the vertical axis. For normal scaling, it does not depend on time [49, 50]. If  $\rho$  does depend on time, the scaling becomes anomalous. As one can see, to be able to characterize a growing interface, one needs the height-height correlation function  $C_2(r, t)$ , and more specifically, the critical exponent  $H$  and  $\beta$ .

Zhao et al. have shown in their study of roughness evolution of a simple polymer growth system,  $-(C_8H_{10})-$ , called p-xylylene, that monomer bulk diffusion is the dominant growth mechanism in the formation of linear poly(p-xylylene) (PPX) (with the tradename Parylene<sup>®</sup>) via vapor deposition polymerization (VDP) [41]. Parylene<sup>®</sup> is a conformal protective polymer-coating material with high thermal stability and excellent electric and dielectric properties which is used for coating electronic components and insulating applications. In a VDP process, the monomer from the gas phase condenses on the substrate and reacts to form high molecular weight polymers. The monomer can take part in two chemical reactions: initiation and propagation. In initiation reactions, new polymer molecules are spawned, and in propagation reactions, existing polymer molecules are made longer by the addition of new monomers. When a monomer condenses on a substrate from the gas phase, the reaction can only occur at the ends of a polymer chain. This is contrary to what happens in the physical vapor deposition (PVD), where deposited atoms can attach to the nearest neighbors of nucleated sites making the film dense and compact. In PVD, the growth is affected by the surface dynamics, such as surface and edge diffusion, step barrier effects, etc. In VDP, on the other hand, surface diffusion, intermolecular interaction, and chain relaxation can occur during growth. The latter two processes are very different from the atomistic processes of PVD, and this gives rise to a distinct dynamic behavior for the VDP film morphology. In the case of Parylene<sup>®</sup>, this is realized as monomer bulk diffusion with the growth exponent  $\beta = 0.25$ , roughness exponent  $\alpha = 0.72$ , and dynamic exponent  $1/z = 0.31$ , where  $z = \alpha/\beta$ . This type of scaling behavior belongs to a novel universality class.

Other types of mechanisms might also be present in organic thin-film growth. Tsamouras et al., for example, have observed that the Kardar–Parisi–Zhang (KPZ) type of growth, in which desorption or vacancy formation are the dominant relaxation mechanisms, is the best model to describe roughening in the growth of Oligomer van der Waals thin films [44]. They based their conclusion on the fact that the height distribution was not Gaussian, and the Hurst exponent,  $H$ , was 0.45, the growth exponent,  $\beta$ , was 0.28. These observations agree with what the KPZ model predicts.

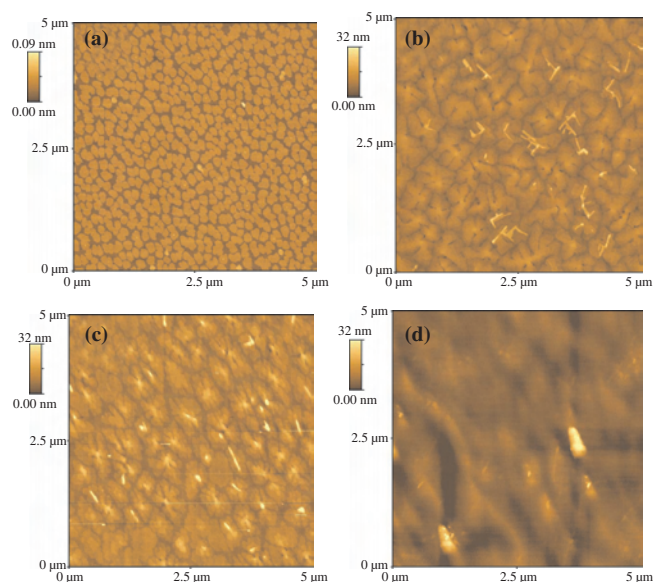
We have studied the growth dynamics of perylene on glass and Au substrates grown side-by-side by vapor deposition

using AFM. Higher order height-height correlation functions have been calculated for the perylene thin films on glass and Au substrates [51]. The results show a complex, multifractal behavior on both substrates evidenced by order dependence of the Hurst exponent [45, 52], and point to a critical thickness value for both substrates that might have important implications regarding the film substrate interactions. We will discuss this issue later on in this article.

It is desirable to have high enough mobility in organic semiconductors for any kind of realistic device applications. The best mobilities can be obtained with single-crystal organic thin films in comparison to polycrystalline ones. The reason being the least amount of grain boundaries and discontinuities, the higher the structural order found in single-crystal films. However, it is not easy to obtain single-crystal semiconducting films as most semiconductor depositions result in polycrystalline structures. The grain size and continuity of polycrystalline thin films depend strongly on the substrate temperature, deposition rate, and substrate material itself. The underlying physical principles governing organic thin-film growth and crystallization are not as well understood as those of metal and inorganic semiconductor thin films, and very little has been done to relate the experimental findings to growth theories. By studying the growth dynamics of organic materials, we are exploring more about the structure of these materials, which has a substantial effect on their transport properties.

#### 4. ORGANIC NANOFILM GROWTH AND INTERPLAY BETWEEN MORPHOLOGY AND CHARGE TRANSPORT

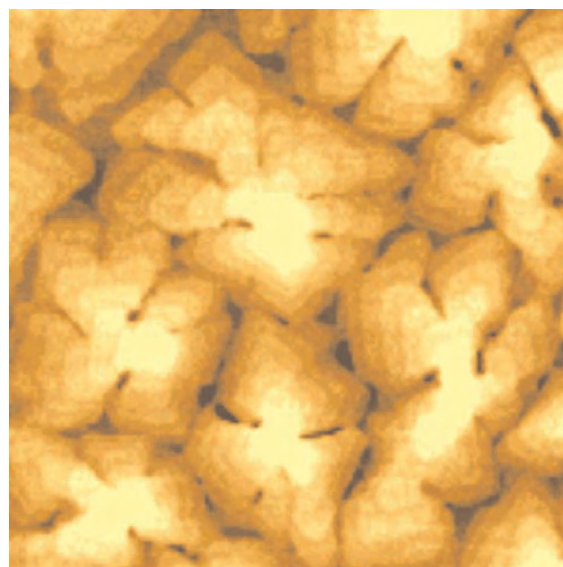
Among the organic semiconductor materials that are being used extensively by researchers worldwide in molecular device applications, pentacene has been one of the most promising material due to its relatively high hole mobility [3–6]. In fact, field effect mobility as large as  $2.2 \text{ cm}^2/\text{Vs}$  has been observed in OTFTs that use pentacene as the active layer [6]. Pentacene is an aromatic hydrocarbon molecule consisting of five linearly fused benzene rings. It is a p-type semiconductor. When deposited onto a  $\text{SiO}_2$  substrate, as would be the case in a field-effect transistor application, pentacene initially grows in almost a layer-by-layer fashion (Frank–van der Merwe mode) over the substrate. After a while islands start forming, making it layer + island type of growth (Stranski–Krastanov). Figure 2 shows the tapping mode images of pentacene films on  $\text{SiO}_2$  substrate [43]. In Figure 2(a), we can first see monolayer steps of pentacene developing and forming the dendritic grains of about  $1 \mu\text{m}$  in size (Figs. 2(b), 2(c), and 2(d)). From X-ray diffraction experiments, it has been shown that this kind of dendritic growth of pentacene on  $\text{SiO}_2$  has well-ordered crystalline structure [11]. The step size of the monolayer steps have been obtained from the line analysis to be about  $15 \text{ \AA}$ , which is the length of one pentacene molecule. The mobility measurements have shown that pentacene films on  $\text{SiO}_2$  with such dendritic grains have higher mobility than the ones with granular structure obtained by flash evaporation on the same kind of substrate. In fact, high mobility can only be obtained if



**Figure 2.** Tapping mode AFM images of different coverages of pentacene on  $\text{SiO}_2$  substrate. (a)  $7 \text{ \AA}$ , (b)  $20 \text{ \AA}$ , (c)  $50 \text{ \AA}$ , (d)  $150 \text{ \AA}$ . Image sizes are  $5 \times 5 \mu\text{m}$ .

the pentacene film is highly ordered, making it easier for the charge carriers to hop from one molecule to another.

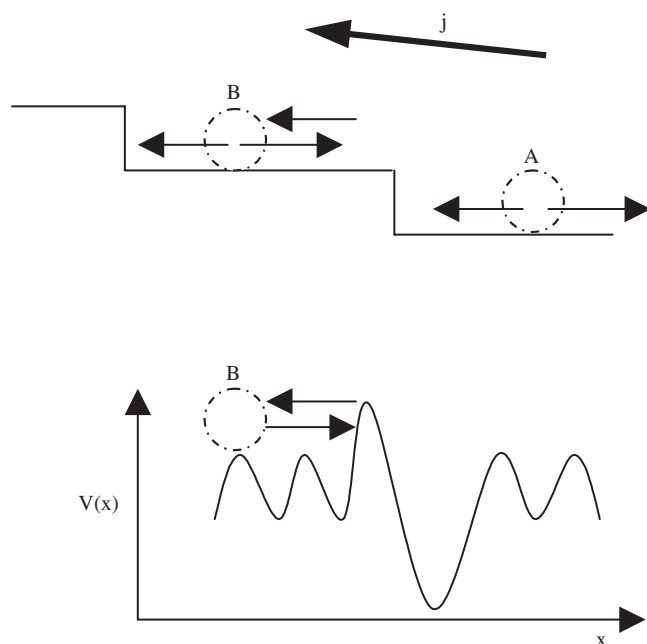
The ordered growth of pentacene thin films is a very peculiar one that involves many contrasting growth mechanisms. As can be seen in Figure 3, pentacene grains form mounded structures with diffusion limited aggregation (DLA)-type dendritic crystal growth. The mounded growth with well-established facets, such as we see in Figure 3, is predicted to be a result of step barrier effect [48]. This type of faceting may indicate the existence of a potential barrier, which is



**Figure 3.** A close-up image of  $50 \text{ \AA}$  pentacene on  $\text{SiO}_2$ . One can see many growth mechanisms involved in the ordered pentacene nanofilm growth. Mounded growth, DLA-type growth, and dendritic growth are all copresent as is seen in the image.

also called a Schwoebel barrier, at the step edge of well-defined pentacene terraces. It can be shown that there exists a potential barrier at the edge of a step that generates a bias in the diffusion process. If a molecule diffuses towards an ascending step, it sticks to the molecules of the step. If it diffuses towards the edge of a descending step, it will most likely be reflected back from the step without jumping down the step due to the existing edge barrier. This asymmetry in the diffusion process will force molecules to move uphill on a stepped surface, producing an average upward current (see Fig. 4). If there is sufficient nucleation of islands on terraces, mounds will develop and with time they will get bigger and bigger, finally to coalesce and form one single big mound on the order of the size of the substrate [53]. Diffusion limited aggregation, which is another mode of growth observed in ordered pentacene, forms via diffusion of molecules through pure random walk and their sticking to a cluster to create irregularly branched and chaotic patterns. The striking thing is that, in addition to the mounded and DLA-type growth, there is also dendritic crystal formation, as was mentioned earlier. Dendritic crystals have regularly branched structure, such as observed in snowflakes [54]. One can see that DLA and dendritic growth are two competing mechanisms. This competition can result in one of the following three scenarios:

- (i) DLA-like crystal growth occurs when random perturbation, such as roughness, is very strong or substrate lattice anisotropy is very weak;
- (ii) dendritic crystal growth occurs when crystal anisotropy is very strong;



**Figure 4.** Molecule B may go to the left or right (top drawing). If it goes to the left, it will stick to the edge, as the energy is minimal at that spot. Going to the right to jump down the edge, however, there is no atom to the right of the edge to help molecule B to diffuse in that direction. This asymmetry in the lattice potential (bottom drawing) creates a higher probability of moving to the left than to the right. This bias in diffusion will generate an average uphill particle current.

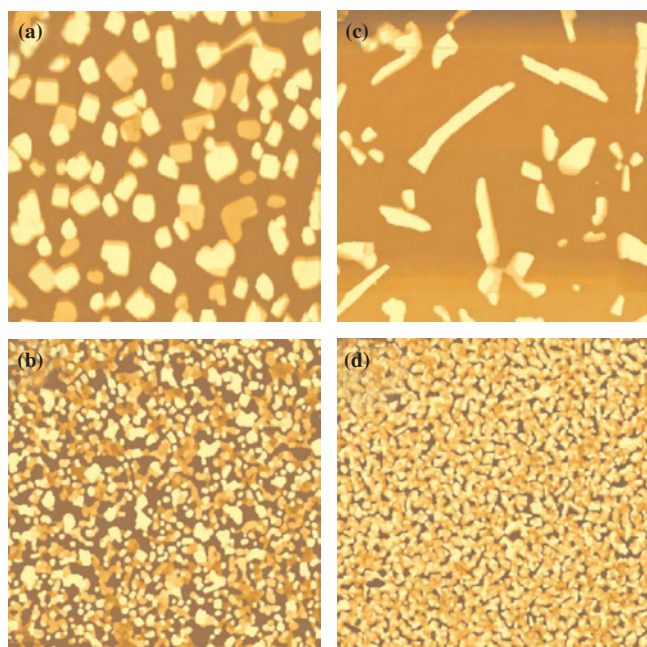
- (iii) a peaceful existence of both growth types when random perturbation and crystal anisotropy both contribute to the growth.

In the context of a  $\text{SiO}_2$  substrate that is used in Figures 3 and 4, the adsorbate-substrate interaction must be such that pentacene molecules once deposited onto the  $\text{SiO}_2$  have enough mobility to diffuse randomly on the surface to attach to the already formed clusters (DLA). Yet the substrate anisotropy must be strong enough to introduce dendritic crystal growth alongside DLA. As previously, this kind of interplay between the adsorbate-substrate and adsorbate-adsorbate interactions is found in the layer + island (Stranski-Krastanov) growth mode. Pentacene achieves high mobility only if it has formed the ordered thin-film structure that we have just discussed. In addition, the larger the size of those grains, the higher mobility one would get [42]. It is intriguing that there are so many mechanisms involved for the pentacene thin films to be ordered and to have a relatively high mobility.

Perylene is another favorite organic semiconductor molecule that has attracted a great deal of interest especially among the organic solar cell, and more recently, the organic thin-film transistor communities [19, 28]. It has been observed to not only have relatively high hole mobility, but also high electron mobility [28, 55, 56], which might enable it to be used in  $n$ -channel, as well as  $p$ -channel, device applications. This is very significant because most organic semiconductors are  $p$ -type, and hence only show  $p$ -channel conductivity. However, a broad variety of circuit designs call for the development of both types of materials.

We have, extensively investigated in our laboratory the growth morphology of perylene on glass and Au substrates as a function of the deposition rate. The shape and size of perylene single crystals varied from glass substrate to Au substrate (see Fig. 5). However, the single crystal size, in both substrates, increased as the deposition rate decreased. Perylene, for slower deposition rates, forms large-scale mounds that are almost of a regular size on the glass substrate but irregular on the Au substrate. This might indicate that the adsorbate-adsorbate interaction is stronger when perylene is deposited on Au rather than glass. This naturally results in the formation of large islands of single crystals. This growth scheme falls under the three-dimensional island (Volmer-Weber) growth scenario. Perylene on glass also forms islands, but the individual islands are well spread over the substrate, hinting at the fact that the adsorbate-substrate interaction is not negligible. For faster deposition rates, small perylene grains are formed and uniformly spread over both substrates.

We applied the kinetic roughening theory for the initial coverages of perylene crystals on these surfaces. The initial crystal sizes on both substrates were observed to be much smaller than the length scales we investigated. This allowed us to use the theory of kinetic roughening to investigate the evolution of the nucleation process of perylene thin-film interfaces [51]. The height-height correlation function and the Hurst exponent saturate once the nominal perylene film thickness reaches the critical value of 40 Å on glass, and 100 Å on Au substrates. Once these critical thickness values are reached, overhang structures develop and dynamic scaling analysis becomes inappropriate. This shows that there is



**Figure 5.** Tapping mode AFM images of 200 Å of perylene on glass ((a) and (b)) and Au ((c) and (d)) substrates. The deposition rate for the top images was about 0.1 Å/s, and for the bottom images about 10 Å/s. The image sizes are  $10 \times 10 \mu\text{m}$ .

a critical thickness for each substrate until which the organic semiconductor perylene develops nucleation sites during its initial growth. The critical thickness might be where the interaction between the incoming flux and the substrate weakens dramatically, even though the surface might not be altogether covered.

Wang et al. recently found that the interaction between aromatic molecules and substrate increases with the increase of aromatic rings in their investigation of pyrene and perylene on Cu(111) [57]. Derivatives of perylene, such as PTCDA—a symmetric planar stacking molecule have—also been investigated as potential players in molecular device technologies [28–32, 58, 59]. Our group at the University of Rochester has also studied the quasi-epitaxial growth of PTCDA on highly oriented pyrolytic graphite (HOPG) using STM in air. Perylene-tetracarboxylic acid-dianhydride formed highly ordered large domains on HOPG (see Fig. 6). The growth mode that it follows is layer-by-layer growth. It is remarkable that STM can obtain molecular resolution images, as seen in Figure 6, in air, a difficult environment to work with. In spite of the highly ordered structure of quasi-epitaxial PTCDA films, devices based on these films gave poor transport characteristics. The maximum mobilities reported were about  $0.03 \text{ cm}^2/\text{Vs}$  [60]. The poor mobility of PTCDA is explained partly by the morphology. The PTCDA molecules lie flat on the dielectric. Molecular planes are parallel to the transport direction in a TFT. Electrons move along this direction where  $\pi$  orbital overlap is minimal. Hole transport dominates in the direction normal to the molecular planes, where the  $\pi$  orbital overlap is maximal. However, this does not do any good as holes move in a direction perpendicular to that of transport in a TFT [59]. Another



**Figure 6.** Grayscale STM image of an ordered nanofilm of PTCDA molecules on HOPG surface. The film thickness is 30 Å and the size of the image is  $500 \times 500 \text{ Å}$ . The image was taken in the constant current mode in air with a tip current of 300 pA and a voltage of 150 mV. PTCDA grows in a layer-by-layer fashion on HOPG.

setback for PTCDA, like much of the other n-type organic semiconductors, is that it is not stable in wet air. This is attributed to the fact that oxygen acts as trap centers for the electrons in such organic materials [9, 60].

More recently, Malenfant et al. reported mobilities up to  $0.6 \text{ cm}^2/\text{Vs}$  and current on/off ratios larger than  $10^5$  obtained with another perylene derivative, perylene tetracarboxylic diimide (PTCDI- $\text{C}_8\text{H}$ ), used as the active material in a TFT device [61]. They explain the observed good characteristics by highly ordered extended structures, which were formed by interdigitation of alkyl substituents.

Naphthalene tetracarboxylic dianhydride (NTCDA) is another symmetric and planar organic molecule. Like PTCDA, NTCDA also forms quasi-epitaxial layers on substrates such as HOPG [28]. Laquindanum and Katz et al. have studied naphthalene-based materials, such as NTCDA and naphthalene diimides [62, 63]. They measured higher mobilities when the substrate during deposition was held at elevated temperatures. More continuous films were obtained at higher temperatures. Their devices were unstable in air. Better air stability was achieved with tetracyanonaphthoquinodimethane (TCNNO), another naphthalene-based substance. Furthermore, TCNNO gave higher mobilities than its relative molecule tetracyanoquinodimethane (TCNQ) [64]. A short note on TCNQ: it is a strong electron acceptor, which is why it easily forms ionic salts with good electron donors such as tetrathiofulvalene (TTF). The donor-acceptor compounds such as TTF-TCNQ are also called charge-transfer compounds because their conductivity depends on the transfer of charge from the donor molecule to the acceptor molecule. Katz et al. also observed that changing the substitution in naphthalene diimides varied the transport characteristics drastically [63]. Fluorinated naphthalene diimides (NTCDI- $\text{C}_3\text{F}$ , NTCDI- $\text{BnCF}_3$ ) showed high

mobilities in air. On the other hand, alkyl functionalized diimides (NTCDI-C<sub>8</sub>H, NTCDI-C<sub>12</sub>H, NTCDI-C<sub>18</sub>H) revealed high mobilities under vacuum only.

C<sub>60</sub> has also been explored as a potential player in organic electronic business. It has been used as the active material in OTFT applications. In fact, it is one of the few n-type materials that show very high mobilities [65]. In addition, contrary to other materials that require highly ordered morphology with peculiar shapes (e.g., pentacene), isotropic films of C<sub>60</sub> provide good device characteristics. This might be due to its approximately spherical shape, as compared with the elongated and/or planar shape that other organic semiconductors have. However, there is an air-stability issue with C<sub>60</sub> as well, that one has to deal with [9, 60].

Since the introduction of molecular crystals as TFT semiconductor active materials [36, 37], oligothiophenes have been investigated widely due to their favorable characteristics [7, 9, 10, 13–15]. They have been found forming highly ordered self-assembled thin films on Si/SiO<sub>2</sub> and S-treated Au substrates. As will be discussed later in the next section, Seshadri and Frisbie were able to obtain large enough sexithiophene (6T), an oligothiophene molecule, single crystals to achieve relatively high hole mobilities [8]. In their work on the mobility dependence of polycrystalline oligothiophene thin films, Horowitz and Hajlaoui found that the mobility increases roughly linearly with grain size [14]. They further observed that temperature dependence of mobility in these thin films changes drastically from small grains to larger grains. For small grains, they found that mobility is thermally activated, whereas for larger grains, mobility becomes practically temperature-independent. Recently, Hajlaoui et al. reported that heating the substrate during octithiophene (8T) film deposition enhances the molecular order and leads to large crystallites, which in turn, gives rise to high-charge carrier mobilities [15]. The carrier mobility was observed to rapidly increase once the substrate temperature exceeded 120 °C, reaching a value as high as 0.33 cm<sup>2</sup>/Vs.

Metallophthalocyanines (M-Pcs) have found applications in areas such as solar cells, optical limiters, photoconductors, OLEDs, and OTFTs [60–70]. Copper phthalocyanine (CuPc) has been an especially important molecule for improving OLED device stability when deposited between the anode and hole transport layer. Forsythe et al. showed that growth morphology of the hole transport layer,  $\alpha$ -naphthylphenyl biphenyl diamine (NPB), is changed significantly by the interposing CuPc layer [69]. Without that interlayer, NPB grows on the anode in isolated islands (three-dimensional island mode). With the CuPc interlayer, NPB grows in layer-by-layer fashion (at least for relatively thinner coverages), making the interface much more smoother and thus resulting in improved adhesion as compared to NPB deposited directly on the anode substrate.

Bao et al. have explored a number of M-Pcs exhaustively for OTFT applications [66–68]. They reported that highly ordered M-Pcs can be obtained by heating the substrate during deposition. This way, they were able to get relatively high mobility and on/off ratios. However, they also observed that after some critical temperature value, the mobility starts decreasing even though the crystal size keeps getting larger. This is most likely due to the increasing gaps formed

between very large, non-space-filling crystals when the temperature is too high. Furthermore, their results show that there is a great difference in mobility with different metal coordinations even when the films are deposited under the same conditions. They obtained the optimal results with a perfluorinated phthalocyanine with M = Cu (F<sub>16</sub> CuPc) and T = 125 °C. Electron-withdrawing groups are known to lower the highest occupied molecular orbital (HOMO) and the lowest occupied molecular orbital (LUMO) energy levels. The LUMO level of F<sub>16</sub> MPC has been shown to drop by 1.6 eV. This opens up new possibilities of converting p-type materials to n-type materials by simply lowering the LUMO levels via substitution with strong electron-withdrawing groups. With such an option, fabrication of high-performance all-plastic complimentary circuits and ring oscillators become possible. In addition, these materials might be of great interest as n-channel semiconductors in photovoltaic devices and electron-transporting materials in OLED applications. Bao et al. also showed that these devices are very stable in air, and do not show any degradation for half a year.

In an effort to study the growth structure of thick evaporated CuPc layers on Si (111) surface by STM, Hiesgen et al. found that the CuPc molecules arrange themselves in a slipped stacking order rather than in the expected zig-zag orientation normally encountered in CuPc crystals [70]. This leads to polycrystalline film formation after initial coverages. The growth mode in this case resembles the layer + island mode (Stranski–Krastranov).

Last in this section, we would like to mention about solution-processable, organic semiconductor materials. The use of such materials has the potential to eliminate the costly lithography and reduce the need to use expensive and cumbersome high-temperature, vacuum deposition techniques. Poly (3-hexylthiophene) (P3HT) is among the widely used, soluble organic semiconductor materials. The solubility of this polymer increases with the addition of long insulating alkyl side-chains without any harm to the electrical properties of the polymer [71, 72]. Since its first use in an OTFT, the mobility of polythiophene materials has been improved dramatically from  $\sim 10^{-5}$  through  $\sim 0.1$  [71, 73]. Bao et al. reported that the solvent used effects the film quality and field-effect mobility strongly [74]. Solution-processed films of regioregular P3HT self-orient into well-ordered lamellar structures. Siringhaus et al. showed that depending on the processing conditions the lamellae can adopt two different orientations—parallel and normal to the substrate [75]. The difference in mobility between these two orientations is more than two orders of magnitude. In the case where the lamellae are parallel to the substrate ( $\pi$ - $\pi^*$  stacking direction perpendicular to the substrate), the mobility is minimal. On the other hand, for the case where the lamellae are normal to the substrate ( $\pi$ - $\pi^*$  stacking direction parallel to the substrate), the mobility is maximal. This is very telling as far as the role that the structure plays in charge transport in such organic materials. Furthermore, this work indicates that a  $\pi$ - $\pi^*$  stacking direction is very critical in determining the final mobility of organic semiconductor materials. Some of the other organic semiconductor materials that have enough solubility to allow them to be used by solution-processing techniques are oligothiophenes.



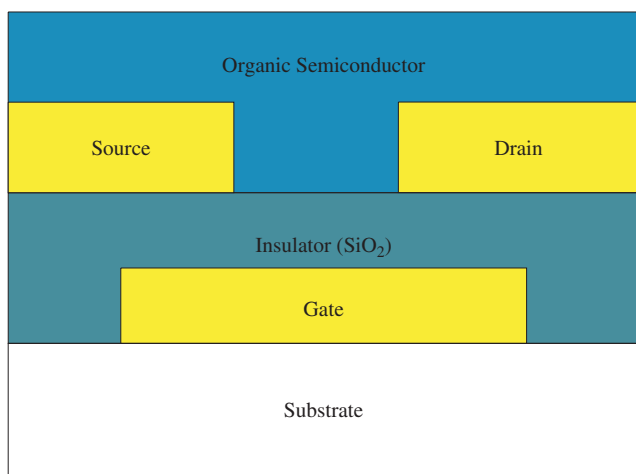
However, semiconductor materials with very poor solubility, such as pentacene, can also be processed via their soluble nonsemiconducting precursor molecules. Upon deposition of the precursor molecule, the sample is heated to convert back to the insoluble semiconducting molecule [76, 77].

In fact, there are plenty of organic semiconductor materials that need to be explored and exploited by the scientists, thanks to the infinite variety of organic materials. Understanding the growth mechanisms of these molecules is imperative in improving the charge-transport properties of such materials.

## 5. CHARACTERIZATION AND APPLICATION OF ORGANIC NANOFILMS

Organic semiconductor nanofilms find a broad range of applications among which are organic thin-film transistors, organic light-emitting diodes, solar cells, photo detectors, lasers, sensors, rectifiers, electro-optic switches, waveguides, and optical couplers, to name a few [9, 28]. Instead of treating all of these devices here, we will just focus on the thin-film transistor and light-emitting diode applications. In particular, we will review some of the new SPM-related techniques that have been developed to learn more about these devices and their characteristics.

Organic TFTs are perhaps one of the most exciting applications of plastic electronics. It is especially suitable for “all plastic” applications where every device element is designed to be organic [36, 37, 78–80]. Figure 7 shows a schematic diagram of a typical field effect transistor (FET). The transistor is said to be in “on” state when substantial current flows from source to drain at a given source-drain voltage, while it is in “off” state when little or no current flows between source and drain at that voltage. The switching between these two states is done by the application and removal of



**Figure 7.** Schematic diagram of a typical “bottom contact” FET, where the source and drain electrodes are fashioned directly on the gate dielectric and underneath the organic semiconductor material. There is also “top contact” geometry, where the source and drain electrodes are fashioned on top of the organic material. For more information about the variability of OTFT structures, please see [9].

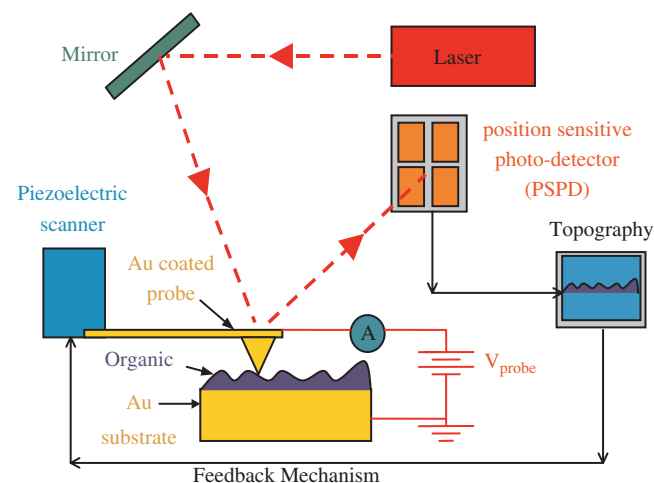
an electric field, respectively. In a typical FET characteristic measurements, the mobility can be determined using the following formula of a standard FET equation in the saturation regime [81]

$$I_{DS} = WC_i\mu/2L(V_G - V_T)^2$$

where  $I_{DS}$  is the drain saturation current,  $W$  is the channel width,  $L$  is the channel length, and  $C_i$  is the capacitance per unit area of the insulating dielectric layer. If the square root of  $I_{DS}$  is drawn versus  $V_G$ , the mobility can easily be derived from the slope of that plot.

Before we move further on to reviewing the recent findings on OTFTs, let us briefly describe a very powerful and versatile instrument that is being used in investigating these and other types of devices. Conducting probe-AFM (hereafter referred to as CP-AFM) has been proven to be an indispensable tool in studying and correlating morphological, electronic, and mechanical properties of organic molecules with high spatial resolution [7, 8, 12, 16–18, 20–24, 43]. Conducting probe-AFM is a scanning probe method that incorporates the standard AFM technique with point contact electrical measurements using a metal-coated tip that serves both as a movable electrode and force sensor (see Fig. 8). It is an ideal tool to quantify the effects of microstructure, such as grain boundaries and contacts on the performance of organic semiconductor devices.

Frisbie et al. have used the CP-AFM technique extensively to study the electrical transport properties, nanostructure-transport correlation, and possible bottlenecks to electrical transport in organic thin-film transistors based on 6T [7, 8, 12, 16–18, 22]. Field-effect conductance measurements made on a 6T-based transistor have shown no discernible dependence of the carrier mobility on thickness, even down to monolayer thickness. This suggests that much of the current is carried by the first monolayer next to the dielectric layer. This can be expected, as the field-induced carriers will be electrostatically confined to the organic-oxide interface. Hole mobility as large as  $0.5 \text{ cm}^2/\text{Vs}$  has been observed for



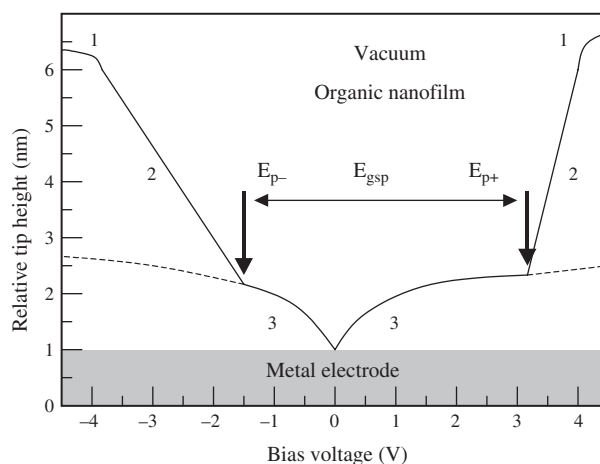
**Figure 8.** Schematic diagram of CP-AFM. CP-AFM incorporates the standard AFM technique with point-contact electrical measurements using a metal-coated tip that serves both as a movable electrode and force sensor.

6T-based OTFTs. Electrical measurements done on polycrystalline 6T-based OTFTs show that grain boundaries (such as seen in Figure 4 for ordered pentacene) can be the primary hurdles to charge transport in such materials. As high as  $10^{10} \Omega$  resistance has been observed for a  $1\text{-}\mu\text{m}$  boundary length. However, the grain boundary resistance is found to be gate voltage dependant. The device's turn-on voltage depends on the potential barrier that exists on the grain boundary. It cannot be turned on until this barrier is reduced to allow charge-carrier flow. Another important stumbling block to charge transport in organic molecular devices are the contacts. The potential profile across the channel of an operating 6T-based FET reveals that, for any given source-drain bias, most of the potential drops at the source and drain contacts. This means that the FET is contact limited. Moreover, the potential drop depends on the applied drain and gate voltages. In order to lessen the effects of contacts, researchers are resorting to various techniques, such as employment of self-assembled monolayers (SAMs), [82–85]. Choosing the right SAM would enable chemical bonding at the contacts, which would in turn minimize the contact resistance giving rise to higher mobility. It is quite clear that in order for OTFTs to be satisfactorily used in plastic electronic applications, these obstacles to transport need to be overcome.

Pentacene has also been widely used in OTFTs since they were first demonstrated [3, 4, 6, 10]. Gundlach et al. reported a mobility of  $2.2 \text{ cm}^2/\text{Vs}$ , and on/off current ratio of  $10^8$  for thermally evaporated pentacene-based OTFTs [6]. These values compare favorably with the conventional amorphous silicon-based TFT technology. In an effort to take the performance of small-molecular organic semiconductor-based OTFTs to even higher values, Gundlach et al. treated the dielectric substrate with octadecyltrichlorosilane (OTS) before deposition of the organic. This OTS pretreatment really did increase the device performance [86]. The pre-deposited OTS layer seems to increase the molecular order, which is beneficial for the transfer of charge carriers between molecules.

Another exciting application of plastic electronics is OLEDs, which was demonstrated during late 1980's by Kodak scientists [33] to be realistic candidates for display applications. Since then, the giants of the display industry have been eagerly investing a wealth of resources in this exciting field to acquire their shares of this growing market. Naturally, there are obstacles in this endeavor as well, such as device stability and efficiency, which need to be improved for high-end applications. These problems can be solved by developing new organic materials [87]. For this, one needs to have the necessary techniques to investigate possible candidates. One of the most challenging tasks in trying to find and investigate such materials is to understand and characterize the energy-level alignments of organic/metal, organic/organic interfaces that are involved in such devices. Substantial efforts worldwide have been made on the characterization of the alignment of the occupied and unoccupied states of those interfaces using different techniques [25–27, 88–97]. Scanning tunnel microscopy has long secured its position as a critical instrument to be used in the characterization of surfaces and interfaces [98–100]. Razafitrimo et al. [101] and Rasmusson et al. [102] have

employed STM and AFM to study the morphology of polymer films. Their study reveals nanometer-scale structures in polymeric LEDs caused by the substrate, polymer film, and top electrode. These nanostructures may significantly alter the local electric field and therefore profoundly affect the performance and lifetime of polymeric LEDs. Lidzey et al. used STM to induce electroluminescence on polymer films [103]. This might be very crucial for the realization of electrically pumped laser diodes. Electroluminescence can be generated by tunneling injection from an STM tip [104]. Electrons can tunnel from the tip directly into unoccupied states of polymer, and upon combination with holes injected from the anode, excitons are formed that can decay radiatively with the emission of light. Other SPM-related spectroscopy methods have also been used to study the organic and polymer semiconductors. Conventional scanning tunneling spectroscopy (STS) technique has helped researchers in getting the density of states (DOS) of materials [105, 106]. In STS, the feedback is turned off for the tip to scan at constant height. The bias voltage is then ramped, and the current is collected. One gets the DOS from the normalized conductance calculations. This way, energy as a function of the DOS is obtained. Scanning tunneling microscopy  $z$ - $V$  spectroscopy, which is a relatively new technique [25–27, 107], on the other hand, probes the DOS via the voltage-dependant tip displacement at a constant tunneling current. It has the capability of providing direct access to molecular level alignments of the occupied and unoccupied states. This means that it is even possible to probe charge-carrier injection into optically forbidden electronic states. Figure 9 shows a schematic  $z$ - $V$  spectrum of a thin film. Such a plot consists of three consecutive phases, indicated in Figure 9 as 1, 2, and 3. Under normal conditions, the tunneling resistance is much higher than the resistance of the organic layers. Charge-carrier injection takes place through the vacuum barrier into



**Figure 9.** Schematic drawing of an STM  $z$ - $V$  curve (solid line). The dashed curve represents typical STM tip displacement measured for a clean metal substrate.  $E_{p-}$  and  $E_{p+}$  are the corresponding charge injection thresholds for electrons and holes, respectively, into polaronic states.  $E_{gsp}$  is the single-particle energy gap. Note that the slopes in region 2 are drawn depending on the polarity of the bias voltage. The above scheme represents a hole-conducting material, as the slope of  $z$ - $V$  curve in the positive bias region is drawn to be higher than that in the negative bias region.

the organic material. This means that the applied bias voltage drops completely at the tunneling barrier. In phase 1, where each  $z$ - $V$  run begins, the tip is biased at a potential difference high enough to ensure that the tip is above the surface of the organic film to avoid modifying or damaging the organic thin-film structure before the actual acquisition of data. As the magnitude of the bias voltage is decreased under constant current conditions, the tip moves toward the organic thin film until a characteristic threshold bias voltage is reached, at which point the tip makes an abrupt penetration into the film [107, 108]. This threshold voltage is approximately the LUMO level of the organic thin film. At this point, the Fermi level of the tip will be very close to the edge of the forbidden energy gap of the organic material. The tip will move down in a step-like fashion, by only one or two molecular spacings initially until full penetration (phase 2). The rate of penetration,  $dz/dV$ , is a measure of the mobilities of the electron and hole polarons. In fact, the average slope of  $z$ - $V$  curves in phase 2 is directly proportional to the conductivity of the organic material which is being investigated. However, one should be prudent to note that the slope of the  $z$ - $V$  curves can be influenced by different factors such as the potential drop within the organic material and the shape of the injection barrier and the sharpness of the tip. In addition, the charge-carrier mobility is a field-dependant quantity. As a result, the slope of a  $z$ - $V$  curve could only be a qualitative measure of the local electron and hole polaron mobilities.

Another point to note is that the high electrical field across the organic layer causes band bending and the formation of a Schottky-like diode. The gradient of the electrical field strongly depends on the curvature of the injecting electrodes. Thus, the highest electrical field drop occurs at the STM tip apex. It will be the predominant site for charge-carrier injection into the organic thin film under ideal conditions. Finally, when the tunneling voltage is reduced to the value at which the Fermi level of the tip enters the forbidden energy gap at the interface with the metal electrode, the charge carriers are injected into the organic material (phase 3). The point at which this transition occurs determines the position of the lowest electron polaron state ( $E_{p-}$ ) for negative bias voltages, or the highest polaron state ( $E_{p+}$ ) for positive bias voltages.

Using STM  $z$ - $V$  spectroscopy technique, Alvarado et al. were able to directly measure the electron and hole injection barriers [26],  $E_{p-}$  and  $E_{p+}$ , respectively, of some of the organic semiconductor materials, such as tris-(8-hydroxyquinoline) aluminum ( $Alq_3$ ), phthalocyanine (CuPc), and (NPB), which are of potential use for OLED applications. From these measurements, together with the optical bandgap, they were able to calculate the single-particle energy gaps,  $E_{gsp}$ , and the exciton binding energies,  $E_b$ , of these materials. Furthermore, they were able to learn qualitatively about the local mobility of electrons and holes from the slopes of  $z$ - $V$  curves.

We note that STM-based methods have been used extensively to study the organic semiconductor materials that are potential candidates to be used in OLEDs.

## 6. SUMMARY

In this article, we have described the principal growth modes of organic nanofilms on inorganic substrates with examples. We have shown that worldwide efforts are being made in trying to understand the growth dynamics of organic nanofilms. The application of scaling theories in understanding the mechanisms involved in the evolution of organic interfaces is especially noteworthy, considering the fact that the major efforts in applying such theories have been thus far focused on the study of the growth of inorganic thin films. We have seen that, generally, more than one growth mechanism is involved in organic nanofilm growth, which makes the topic at hand a challenging subject. However, encouraging and exciting results that are being obtained in improving the morphological, and hence, transport properties of organic nanofilms, are the impetus that derives this newly flourishing field.

Important and recent SPM-based characterization techniques, such as CP-AFM and  $z$ - $V$  spectroscopy, have been discussed. These tools will contribute immensely to the investigation of organic materials by providing information about the structure, structure-transport, and electronic properties of these materials.

Many obstacles are on the road to fully utilizing the organic semiconductor nanofilms fully in organic device applications. Among these obstacles are charge-carrier speed—depending on how fast the device will operate—and the long-term device stability. Basic research of such issues will have potential benefits. In addition, organic electronics is an area closely intertwined with nanotechnology and molecular electronics, all of which might be the driving force for the next industrial revolution.

## GLOSSARY

**Atomic force microscope (AFM)** A very high resolution microscope with a small stylus attached to a cantilever which in turn is attached to a piezoelectric scanner. As the cantilever is approached to the surface of a sample via the computer controlled piezoelectric scanner, it is bent due to the interatomic forces between the probe and the sample. The extent of the bending of the cantilever is detected via a laser that is being reflected off of the back of the cantilever, and is proportional to interatomic forces present. Appropriate mapping of these forces would give properties of the sample such as morphology, stiffness, viscoelasticity, etc., at very high resolution. Since AFM's operation principle involves interatomic forces, there is no restriction on the conductivity of the sample under investigation. It could be a conductor, semiconductor, or insulator.

**Conducting-probe atomic force microscope (CP-AFM)** If the probe used in AFM is a conducting one, then AFM can be used to perform electrical measurements. This system is known as conducting-probe AFM. It is also called conducting AFM.

**Diffusion-limited aggregation (DLA)** A famous cluster growth model. A seed particle is fixed in the center of the lattice, and another particle is released at some distant point traveling on the lattice in a random fashion. The meandering particle may either stick to the seed, or escape

to infinity. As more particles are released, the sticking probability will increase and an aggregate will start forming. The aggregate will have random branching due to the random nature of the process. This branching will prevent the newcoming particles to diffuse into the inner regions of the aggregate ending up with a wispy fractal structure.

**Highly ordered pyrolytic graphite (HOPG)** It is manufactured at around 3273 K. HOPG consists of highly oriented atomic layers of carbon. It is very smooth, easy to cleave, and non-polar. When used as substrate, it will provide favorable background with only carbon in the elemental signature. All of this makes HOPG a good candidate as a research material.

**Kardar-Parisi-Zhang (KPZ)** An nonlinear differential equation to describe a particular self-affine growth in which the growth direction is along the local surface normal.

**Organic light emitting diode (OLED)** A structure in which a hole transport layer and an electron transport layer are sandwiched between anode and cathode electrodes. Upon application of voltage across the terminals, the organic layer emits light. OLED, in comparison with its inorganic counterparts such as LED and liquid crystal display, has higher brightness, longer lifetimes, lower power consumption. Due to its organic nature, it is more robust, and can be made flexible as well.

**Organic molecular beam epitaxy (OMBE)** Deposition of highly ordered organic films by sublimating organic material from an oven. Contrary to the conventional inorganic MBE, organic MBE does not result in lattice-matched growth. Because organic lattice spacings are much larger than those of inorganic substrates. However, it is still possible to obtain well-ordered organic nanofilms by choosing the right substrate. This is known as quasi-epitaxial growth. The interaction between the substrate and the growing organic film must provide necessary mobility to the growing film and also have enough strength that the crystallinity of the substrate will be dictated into the growing film.

**Organic thin film transistor (OTFT)** A transistor whose active material is an organic semiconductor film the thickness of which is no more than about 5000 Å. It is crucial in implementing "all plastic electronics."

**Physical vapor deposition (PVD)** The particles are deposited by heating and evaporating the source material. The deposited particles can attach to the nearest neighbors of nucleated sites making the film dense and compact. In PVD, the growth is affected by the surface dynamics, such as surface and edge diffusion, step barrier effects, etc.

**Scanning tunneling microscope (STM)** A sharp metal tip is brought in close proximity of the conducting or semiconducting surface. When the tip is close enough to the surface but not yet touching, due to the quantum mechanical phenomenon of tunneling, there will be current flowing between the tip and the sample upon application of a small electrical potential. The magnitude of the current that will flow is exponentially dependent upon the distance between the tip and the sample surface. A very small change in the distance will produce significant change in the current. This in turn provides STM with remarkable sensitivity to the morphology of the sample. However, since the interaction parameter is

current, only conducting and semiconducting materials can be studied with STM.

**Vapor deposition polymerization (VDP)** In a VDP process, the monomer from the gas phase condenses on the substrate and reacts to form high molecular weight polymer. Surface diffusion, intermolecular interaction, and chain relaxation can occur during growth.

## ACKNOWLEDGMENT

This work was supported by NSF DMR-9982988 and AFOSR Grant 96NL245.

## REFERENCES

1. H. Shirakawa, E. J. Louis, A. G. MacDiarmid, C. K. Chiang, and A. J. Heeger, *J. C. S. Chem. Commun.* 578 (1977).
2. D. Adam, *Nature* 407, 662 (2000).
3. Y. Lin, D. J. Gundlach, S. F. Nelson, and T. N. Jackson, *IEEE Electron. Trans. Electron. Device* 44, 1325 (1997).
4. H. Klauk, D. J. Gundlach, J. A. Nichols, and T. N. Jackson, *IEEE Trans. Electron. Device* 46, 1258 (1999).
5. J. G. Laquindanum, H. E. Katz, A. J. Lovinger, and A. Dodabalapur, *Chem. Mater.* 8, 2542 (1996).
6. D. J. Gundlach, C. C. Kuo, S. F. Nelson, and T. N. Jackson, *57th Device Research Conference Digest*, 164 (1999).
7. M. J. Loiacono, E. L. Granstrom, and C. D. Frisbie, *J. Phys. Chem.* 102, 1679 (1998).
8. K. Seshadri and C. D. Frisbie, *Appl. Phys. Lett.* 78, 993 (2001).
9. H. E. Katz, *J. Mater. Chem.* 7, 369 (1997), and references therein.
10. H. E. Katz and Z. Bao, *J. Phys. Chem. B* 104, 671 (2000).
11. D. J. Gundlach, Y. Y. Lin, T. N. Jackson, S. F. Nelson, and D. G. Schlom, *IEEE Electron. Device Lett.* 18, 87 (1997).
12. T. W. Kelley, E. L. Granstrom, and C. D. Frisbie, *Adv. Mater.* 11, 261 (1999).
13. G. Horowitz, B. Bachet, A. Yassar, P. Lang, F. Demanze, J.-L. Fave, and F. Garnier, *Chem. Mater.* 7, 1337 (1995).
14. G. Horowitz and M. Hajlaoui, *Adv. Mater.* 12, 1046 (2000).
15. M. Hajlaoui, F. Garnier, L. Hassine, F. Kouki, and H. Bouchriha, *Synth. Met.* 129, 215 (2002).
16. T. W. Kelley and C. D. Frisbie, *J. Phys. Chem. B* 105, 4538 (2001).
17. A. B. Chwang and C. D. Frisbie, *J. Appl. Phys.* 90, 1342 (2001).
18. T. W. Kelley and C. D. Frisbie, *J. Vac. Sci. Technol. B* 18, 632 (2000).
19. L.-S. Mende, A. Fechtenkötter, K. Mullen, E. Moons, R. H. Friend, and J. D. MacKenzie, *Science* 293, 1119 (2001).
20. S. R. Forrest, *Chem. Rev.* 97, 1793 (1997).
21. H. Dai, E. W. Wong, and C. M. Lieber, *Science* 272, 523 (1996).
22. D. Klein and P. McEuen, *Appl. Phys. Lett.* 66, 2478 (1995).
23. E. L. Granstrom and C. D. Frisbie, *J. Phys. Chem.* 103, 8842 (1999).
24. D. J. Wold and C. D. Frisbie, *J. Am. Chem. Soc.* 122, 2970 (2000).
25. D. J. Wold and C. D. Frisbie, *J. Am. Chem. Soc.* 123, 5549 (2001).
26. S. F. Alvarado, P. F. Seidler, D. G. Lidzey, and D. D. C. Bradley, *Phys. Rev. Lett.* 81, 1082 (1998).
27. S. F. Alvarado, L. Rossi, P. Müller, and P. F. Seidler, *IBM J. Res. Develop.* 45, 89 (2001).
28. P. Müller, S. F. Alvarado, L. Rossi, and W. Rieß, *Mater. Phys. Mech.* 4, 76 (2001).
29. C. Kendrick and A. Kahn, *Appl. Surf. Sci.* 123/124, 405 (1998).
30. M. Sokolowski and E. Umbach, *Vacuum Solutions* July/August, 15 (1999).
31. P. Fenter, P. E. Burrows, P. Eisenberger, and S. R. Forrest, *J. Cryst. Growth* 152, 65 (1995).
32. E. Umbach, M. Sokolowski, and R. Fink, *Appl. Phys. A* 63, 565 (1996).

33. C. W. Tang and S. A. Van Slyke, *Appl. Phys. Lett.* 51, 913 (1987).
34. J. H. Burroughes, D. D. C. Bradley, A. R. Brown, R. N. Marks, K. Mackay, R. H. Friend, P. L. Burns, and A. B. Holmes, *Nature* 347, 539 (1990).
35. A. Tsumura, H. Koezuka, and T. Ando, *Appl. Phys. Lett.* 49, 1210 (1986).
36. F. Garnier, G. Horowitz, X. Peng, and D. Fichou, *Adv. Mater.* 2, 592 (1990).
37. F. Garnier, R. Hajlaoui, A. Yassar, and P. Srivastava, *Science* 265, 1684 (1994).
38. D. Wöhrle and D. Meissner, *Adv. Mater.* 3, 129 (1991).
39. J. J. M. Halls, K. Pichler, R. H. Friend, S. C. Moratti, and A. B. Holmes, *Appl. Phys. Lett.* 68, 3120 (1996).
40. Z. Q. Gao, W. Y. Lai, T. C. Wong, C. S. Lee, I. Bello, and S. T. Lee, *Appl. Phys. Lett.* 74, 3269 (1999).
41. Y.-P. Zhao, J. B. Fortin, G. Bonvallet, G.-C. Wang, and T.-M. Lu, *Phys. Rev. Lett.* 85, 3229 (2000).
42. F.-J. Meyer zu Heringdorf, M. C. Reuter, and R. M. Tromp, *Nature* 412, 517 (2001).
43. S. Zorba, Q. T. Le, N. J. Watkins, L. Yan, and Y. Gao, *J. Nanosci. Nanotechnol.* 1, 317, (2001).
44. D. Tsamouras, G. Palasantzas, and J. Th. M. De Hosson, *Appl. Phys. Lett.* 79, 1801 (2001).
45. A.-L. Barabási and T. Vicsek, *Phys. Rev. A* 44, 2730 (1991).
46. F. Family and T. Vicsek, *J. Phys. A* 18, L75 (1985).
47. P. Meakin, "Fractals, Scaling and Growth Far from Equilibrium." Cambridge University Press, Cambridge, UK, 1998.
48. A.-L. Barabási and H. E. Stanley, "Fractal Concepts in Surface Growth." Cambridge University Press, Cambridge, UK, 1995.
49. T.-M. Lu, H.-N. Yang, and G.-C. Wang, *Mat. Res. Soc. Symp. Proc.* 367, 283 (1995).
50. Y. Zhao, G.-C. Wang, and T.-M. Lu, "Characterization of Amorphous and Crystalline Rough Surface: Principles and Applications." Academic Press, New York, 2001.
51. S. Zorba, L. Yan, N. J. Watkins, and Y. Gao, *Appl. Phys. Lett.* 81, 5195 (2002).
52. A.-L. Barabási, R. Bourbonnais, M. Jensen, J. Kertesz, T. Vicsek, and Y.-C. Zhang, *Phys. Rev. A* 45, R6951 (1992).
53. M. D. Johnson, C. Orme, A. W. Hunt, D. Graff, J. Sudijono, L. M. Sander, and B. G. Orr, *Phys. Rev. Lett.* 72, 116 (1994).
54. H. Honjo, S. Ohta, and M. Matsushita, *J. Phys. Soc. Jpn.* 55, 2487 (1986).
55. E. A. Silinsh and V. Capek, "Organic Molecular Crystals." AIP Press, New York, 1994.
56. J. L. Brédas, J. P. Calbert, D. A. da Silva Filho, and J. Cornil, *PNAS* 99, 5804 (2002).
57. D. Wang, L.-J. Wan, Q.-M. Xu, C. Wang, and C.-L. Bai, *Surf. Sci.* 478, L320 (2001).
58. C. W. Tang, *Appl. Phys. Lett.* 48, 183 (1986).
59. J. R. Ostrick, A. Dodabalapur, L. Torsi, A. J. Lovinger, E. W. Kwock, T. M. Miller, M. Galvin, M. Berggren, and H. E. Katz, *J. Appl. Phys.* 81, 6804 (1997).
60. C. D. Dimitrakopoulos and P. R. L. Malenfant, *Adv. Mater.* 14, 99 (2002).
61. P. R. L. Malenfant, C. D. Dimitrakopoulos, J. D. Gelorme, L. L. Kosbar, T. O. Graham, A. Curioni, and W. Andreoni, *Appl. Phys. Lett.* 80, 2517 (2002).
62. J. G. Laquindanum, H. E. Katz, A. Dodabalapur, and A. J. Lovinger, *J. Am. Chem. Soc.* 118, 11331 (1996).
63. H. E. Katz, J. Johnson, A. J. Lovinger, and W. Li, *J. Am. Chem. Soc.* 122, 7787 (2000).
64. A. R. Brown, D. M. de Leeuw, E. J. Lous, and E. E. Havinga, *Synth. Met.* 66, 257 (1994).
65. R. C. Haddon, A. S. Perel, R. C. Morris, T. T. M. Palstra, A. F. Hebard, and R. M. Fleming, *Appl. Phys. Lett.* 67, 121 (1995).
66. Z. Bao, A. J. Lovinger, and A. Dodabalapur, *Adv. Mater.* 9, 42 (1997), and references 4–6 therein.
67. Z. Bao, A. J. Lovinger, and J. Brown, *J. Am. Chem. Soc.* 120, 207 (1998).
68. Z. Bao, A. J. Lovinger, and A. Dodabalapur, *Appl. Phys. Lett.* 69, 3066 (1996).
69. E. W. Forsythe, M. A. Abkowitz, Y. Gao, and C. W. Tang, *J. Vac. Sci. Technol. A* 18, 1869 July/August (2000).
70. R. Hiesgen, M. Rübisch, H. Böttcher, and D. Meissner, *Sol. Energ. Mat. C* 61, 73 (2000).
71. A. Assadi, C. Svensson, M. Willander, and O. Inganäs, *Appl. Phys. Lett.* 53, 195 (1988).
72. A. Tsumura, H. Fuchigami, and H. Koezuka, *Synth. Met.* 41, 1181 (1991).
73. H. Sirringhaus, N. Tessler, and R. H. Friend, *Science* 280, 1741 (1998).
74. Z. Bao, A. Dodabalapur, and A. J. Lovinger, *Appl. Phys. Lett.* 69, 4108 (1996).
75. H. Sirringhaus, P. J. Brown, R. H. Friend, M. M. Nielsen, K. Bechgaard, B. M. W. Langeveld-Voss, A. J. H. Spiering, R. A. J. Janssen, E. W. Meijer, P. Herwig, and D. M. de Leeuw, *Nature* 401, 685 (1999).
76. A. R. Brown, A. Pomp, D. M. de Leeuw, D. B. M. Klaassen, E. E. Havinga, P. Herwig, and K. Mullen, *J. Appl. Phys.* 79, 2136 (1996).
77. P. T. Herwig and K. Müllen, *Adv. Mater.* 11, 480, (1999).
78. C. J. Drury, C. M. J. Mutsaers, C. M. Hart, M. Matters, and D. M. de Leeuw, *Appl. Phys. Lett.* 73, 108 (1998).
79. G. H. Gelinck, T. C. T. Geuns, and D. M. de Leeuw, *Appl. Phys. Lett.* 77, 1487 (2000).
80. B. Crone, A. Dodabalapur, Y.-Y. Lin, R. W. Filas, Z. Bao, A. La Duca, R. Sarpeshkar, H. E. Katz, and W. Li, *Nature* 403, 521 (2000).
81. S. M. Sze, "Physics of Semiconductor Devices," 2nd Ed. Wiley, New York, 1981.
82. K. W. Hipps, *Science* 294, 536 (2001).
83. X. D. Cui, A. Primak, X. Zarate, J. Tomfohr, O. F. Sankey, A. L. Moore, T. A. Moore, D. Gust, G. Harris, and S. M. Lindsay, *Science* 294, 571 (2001), and references therein.
84. I. Amlani, A. M. Rawlett, L. A. Nagahara, and R. K. Tsui, *Appl. Phys. Lett.* 80, 2761 (2002), and references therein.
85. J. Wang, D. J. Gundlach, C. C. Kuo, and T. N. Jackson, *41st Electronic Materials Conference Digest*, 16 (1999).
86. D. J. Gundlach, H. Klauk, C. D. Sheraw, C. C. Kuo, J. R. Huang, and T. N. Jackson, *1999 International Electron Devices Meeting Technical Digest*, 111 (1999).
87. J. Kido, *Physics World*, March, 27 (1999).
88. T. P. Nguyen, V. Massardier, V. H. Tran, and A. Guyot, *Synth. Met.* 55, 235 (1993).
89. V. Choong, Y. Park, Y. Gao, T. Wehrmeister, K. Mullen, B. R. Hsieh, and C. W. Tang, *Appl. Phys. Lett.* 69, 1492 (1996).
90. V. Choong, Y. Park, B. R. Hsieh, C. W. Tang, T. Wehrmeister, K. Mullen, and Y. Gao, *J. Vac. Sci. Technol. A* 15, 1745 (1997).
91. K. Seki, E. Ito, and H. Ishii, *Synth. Met.* 91, 137 (1997).
92. A. Rajagopal and A. Kahn, *Adv. Mater.* 10, 140 (1998).
93. M. Probst and R. Haight, *Appl. Phys. Lett.* 70, 1420 (1997).
94. S. T. Lee, X. Y. Hou, M. G. Mason, and C. W. Tang, *Appl. Phys. Lett.* 72, 1593 (1998).
95. N. Johansson, F. Cacialli, K. Z. Xing, G. Beamson, D. T. Clark, R. H. Friend, and W. R. Salaneck, *Synth. Met.* 92, 207 (1998).
96. L. Yan, N. J. Watkins, S. Zorba, and Y. Gao, *Appl. Phys. Lett.* 79, 4148 (2001).
97. N. J. Watkins, L. Yan, and Y. Gao, *Appl. Phys. Lett.* 80, 4384 (2002).
98. G. Binnig, H. Rohrer, Ch. Gerber, and E. Weibel, *Phys. Rev. Lett.* 49, 57 (1982).
99. G. Binnig, H. Rohrer, Ch. Gerber, and E. Weibel, *Phys. Rev. Lett.* 50, 120 (1983).
100. M. Kasaya, H. Tabata, and T. Kawai, *Surf. Sci.* 400, 367 (1998), and references therein.

101. H. Razafitrimo, Y. Gao, and B. R. Hsieh, *Synth. Met.* 79, 103 (1996).
102. J. R. Rasmusson, P. Broms, J. Birgeron, R. Erlandsson, and W. R. Salaneck, *Synth. Met.* 79, 75 (1996).
103. D. G. Lidzey, D. D. C. Bradley, S. F. Alvarado, and P. F. Seidler, *Nature* 386, 135 (1997).
104. J. K. Gimzewski, B. Reihl, J. H. Coombs, and R. R. Schlitter, *Z. Phys. B* 72, 497 (1988).
105. R. M. Feenstra, *Phys. Rev. B* 50, 4561 (1994).
106. R. Wiesendanger, "Scanning Probe Microscopy and Spectroscopy, Methods and Applications." Cambridge University Press, Cambridge, UK, 1994.
107. S. F. Alvarado, L. Libioulle, and P. F. Seidler, *Synth. Met.* 91, 69 (1997).
108. S. F. Alvarado, L. Rossi, P. Muller, and W. Rieß, *Synth. Met.* 122, 73 (2001).



# Organic Polyradical Magnetic Nanoclusters

Andrzej Rajca

University of Nebraska, Lincoln, Nebraska, USA

## CONTENTS

1. Introduction
  2. Prerequisites for “Single-Molecule Magnet” Behavior
  3. Molecular Organic Radical-Metal Nanoclusters
  4. Nanometer-Sized Organic Polyradicals
  5. Summary
- Glossary  
References

## 1. INTRODUCTION

In 1980, Lis reported  $\text{Mn}_{12}$  synthesis, structure, and magnetic susceptibility measurements for nanometer-sized  $[\text{Mn}_{12}\text{O}_{12}(\text{CH}_3\text{COO})_{16}(\text{H}_2\text{O})_4]$  molecules [1]. Subsequent magnetic studies determined the  $S = 10$  ground state ( $S =$  total spin quantum number), primarily arising from uncompensated magnetic moment from antiferromagnetic interactions between eight  $S = 2$   $\text{Mn}^{\text{III}}$  and four  $S = 3/2$   $\text{Mn}^{\text{IV}}$  ions. (All spins of one valence point up and the remainder point down.) In 1993, a significant magnetic anisotropy barrier ( $\Delta E_A$ ) for reversal of magnetization ( $\Delta E_A/k = 60$  K,  $k =$  Boltzman constant), which manifested itself as magnetic hysteric cycle at temperatures below 4 K, was found [2]. Because this hysteric behavior is analogous to that for nanometer-sized magnetic particles or bulk magnets, except it is of purely molecular origin, the designation “single-molecule magnet” (SMM) was coined. Numerous organometallic molecules, based on Mn, Fe, Ni, Mo, W, etc., with large magnetic moments ( $S$  up to  $5\ 1/2$ ) were prepared but none of them had  $\Delta E_A/k$  exceeding room temperature (or even 60 K for Lis’  $\text{Mn}_{12}$  cluster); also, selected nanoclusters showed non-negligible intermolecular interactions, which interfere with the SMM behavior [3, 4]. Thus,

significant obstacles remain in the development of molecule-based magnetic memories, based upon classical reversal of magnetization.

More recently, quantum effects in reversal of magnetization (tunneling of magnetization) were discovered for Lis’  $\text{Mn}_{12}$  and other related clusters; that is, steplike hysteric cycles were found at temperatures below 4 K [5]. This quantum behavior, which is associated with greatly accelerated reversal of magnetization at certain applied magnetic fields, has attracted wide interest for both fundamental reasons and potential technological applications of SMMs in so-called quantum computing [6, 7].

The advances in transition metal ion based magnetic nanoclusters open an interesting question as to whether alternative sources of electron spin, such as organic radicals, could be used for SMMs. In this chapter, we will briefly summarize the selected aspects of magnetism of SMMs and then review two classes of organic radical-based nanometer-sized molecules: organometallic metal-radical nanoclusters and organic polyradicals.

## 2. PREREQUISITES FOR “SINGLE-MOLECULE MAGNET” BEHAVIOR

The magnetic anisotropy barrier ( $E_A$ ) for inversion of magnetization (between up- and down-spin states) in a molecular cluster may be related to  $S^2|D|$ , where  $S$  is the total spin quantum number for the molecule and  $D$  is the axial zero-field splitting parameter for the molecule [8]. When  $E_A/k$  significantly exceeds the temperature ( $T$ ) at which the experiment is carried out, the inversion of magnetization becomes slow on the experimental time scale; for example, for a relatively slow experiment, such as hysteric cycle,  $E_A/kT \approx 10$  is usually needed. Therefore, attaining relatively large values for  $E_A$  through optimization of  $S$  and  $D$  will be the primary goal. Furthermore, the energies associated with intermolecular interactions ( $E_{\text{inter}}$ ) should be significantly



lower than thermal energies (i.e.,  $E_{\text{inter}} \ll kT$ ), to prevent bulk magnetic ordering interfering with the SMM behavior.

## 2.1. Total Spin Quantum Number $S$

Three generic coupling schemes for individual spins, associated with organic radicals and/or metal ions, and leading to large values of  $S$  are illustrated in Figure 1A. In the ferromagnetic scheme, all nearest neighbor pairs of individual spins are ferromagnetically coupled. Another coupling scheme relies on antiferromagnetic coupling of the nearest neighbor spins connected in such a way that the spins are not compensated, giving an overall value of  $S > 1/2$ . The third coupling scheme may be referred to as ferromagnetic (i.e., it relies on antiferromagnetic coupling of unequal spins). For all coupling schemes, the exchange coupling (ferromagnetic or antiferromagnetic) has to be sufficiently strong so the energy difference(s) between the high-spin ground state with the large value of  $S$  and the low-spin lowest energy excited states significantly exceeds the thermal energy ( $kT$ ) at the temperature of the experiment.

Conceptually pairwise ferromagnetic and antiferromagnetic couplings may be visualized as transmitted through ferromagnetic coupling units (FCUs) and antiferromagnetic coupling units, respectively (Fig. 1B) [9, 10]. These coupling units may correspond to organic radical-metal linkage or, in polyradicals, the  $\pi$ -system bridging two nearest neighbor radical sites. For an  $S = 1$  ground state diradical, such as a Schlenk hydrocarbon, a 1,3-phenylene FCU links two arylmethyl spin sites (Fig. 1B) [11]. A ferromagnetic coupling scheme may be implemented via connection in an alternating mode of the FCUs and the spin sites to provide polyradicals with  $S = n/2$ , where  $n$  is the number of spin sites [9, 10].

Ferromagnetic coupling is attained when the orbitals containing unpaired electron spins are orthogonal and coinciding in space [12, 13]. This situation is found in an  $S = 1$  ground state diradical (Fig. 1B) with unpaired electron spins located in nearly degenerate, coinciding in space, and orthogonal molecular orbitals, which are characteristic of 1,3-phenylene moiety (an FCU). Other examples of strong and moderate ferromagnetic couplings are  $\text{Cu}^{\text{II}}$  (and  $\text{Ni}^{\text{II}}$ ) complexes with *o*-semiquinone and  $\text{Cu}^{\text{I}}$  complexes with nitroxide in the axial position, respectively [14]. A ferromagnetic coupling scheme may be implemented via connection

in an alternating mode of the FCUs and the spin sites to provide polyradicals with  $S = n/2$ , where  $n$  is the number of spin sites [9, 10].

Antiferromagnetic coupling is associated with an effective overlap of nonorthogonal orbitals; thus, it may be viewed as a weak chemical bonding. This situation may be found in an  $S = 0$  ground state diradical with 3,3'-biphenylene bridging two arylmethyl sites (Fig. 1B) [15]. Other examples of strong antiferromagnetic couplings are  $\text{Mn}^{\text{II}}$  complexes with nitroxides [14, 16, 17].

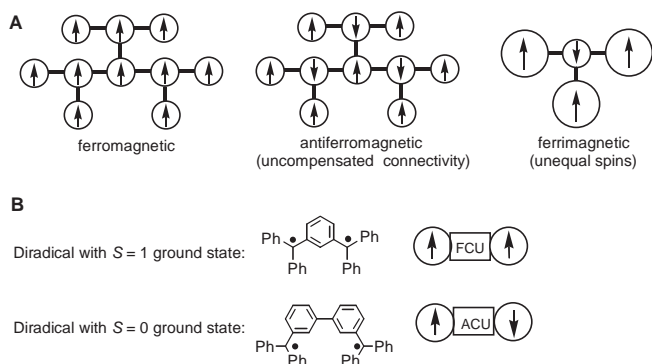
## 2.2. Zero-Field Splitting Parameter $D$

For a molecule with the ground state with  $S \geq 1$ , a splitting of its Zeeman energy levels in a zero applied magnetic field leads to anisotropy of magnetic properties, including a barrier for inversion of magnetization. Only states without first-order angular momentum will be considered;  $D$  is the axial zero-field splitting (ZFS) parameter, which is related to the principal value of the corresponding tensor  $\mathbf{D}$ . There are two primary mechanisms for ZFS. The first mechanism involves coupling of the ground state with the excited states through spin-orbit coupling. The second mechanism involves magnetic dipole-dipole interactions. Of the two mechanisms, the spin-orbit coupling is capable of attaining much greater values of  $D$  than the magnetic dipole-dipole interactions. This is the situation found in selected transition metal ions, such as  $\text{Mn}^{\text{III}}$ ,  $\text{Ni}^{\text{II}}$ ,  $\text{Cr}^{\text{III}}$ , etc., in their numerous complexes [18, 19]. Jahn-Teller distortions may lead to large values of the parameter  $D$  for single ion. In derivatives of  $\text{Mn}_{12}$ , where single ion  $D$  is main contributor to the large value of  $D$  for the cluster, the relative phases of Jahn-Teller distortions for  $\text{Mn}^{\text{III}}$  have a large effect on the value of  $D$  of the cluster [20]. For a cluster, in which the exchange coupling is the dominant interaction between the ions, overall values of  $D$  for each state with a value of  $S$  can be derived from tensors  $\mathbf{D}$  for single ions [14].

Because spin-orbit coupling is a relativistic effect, it is very small in the elements of organic molecules such as C, N, and O [18]. There are several methods for estimating values of  $D$  from classical magnetic dipole-dipole interactions [14]. Perhaps the most straightforward method involves indirect estimate of  $D$  through the shape anisotropy; this estimate is especially applicable to molecules or clusters with large numbers of approximately uniformly distributed and ferromagnetically coupled electron spins [21]. Such estimates may be applied to organic polyradicals [22].

## 3. MOLECULAR ORGANIC RADICAL-METAL NANOCLUSTERS

A plethora of organic radical-metal one-dimensional chains and extended networks, in which organic radicals act as bridging groups between the metal ions, leading to relatively large  $E_A$  and/or magnetic ordering are known. Organic radicals involved in such one-dimensional chains and networks are nitronyl nitroxides, [23, 24] di- and trinitroxides, [25] nitroxides with nitrogen base, [26] and pyridine-based photochemically generated carbenes [27–29].



**Figure 1.** (A) Coupling schemes leading to large net values of  $S$ . (B) Pairwise ferromagnetic and antiferromagnetic couplings in diradicals with  $S = 1$  and  $S = 0$  ground states, respectively.

Analogous molecular organic radical-metal nanoclusters, in which organic radicals act as bridging groups between the metal ions, are relatively scarce.

One of the pioneering examples of organic radical-metal nanoclusters is a macrocyclic  $[\text{Mn}(\text{hfac})_2\text{NITPh}]_6$  cluster with  $S = 12$  ground state (hfac, hexafluoroacetyl acetate; NITPh, 2-phenyl-4,4,5,5-tetramethyl-4,5-dihydro-1H-imidazolyl-1-oxy-3-oxide) [30]. In  $[\text{Mn}(\text{hfac})_2\text{NITPh}]_6$ , the manganese(II) ions with  $S = 5/2$  are antiferromagnetically coupled to  $S = 1/2$  organic radicals (nitronyl nitroxides), resulting in an overall spin value of  $6(5/2 - 1/2) = 12$ . Both the oblate shape of the cluster and the small spin-orbit couplings associated with high-spin  $\text{Mn}^{\text{II}}$  (half-filled  $d$ -shell) and nitronyl nitroxide may contribute to its overall low magnetic anisotropy.

More recently, a  $S = 7$  nanocluster,  $[\text{Fe}_2(\text{CN})_{12}\text{Ni}_3(\text{IM-2Py})_6] \cdot 4\text{H}_2\text{O}$ , in which two  $\text{Fe}^{\text{III}}$  and three  $\text{Ni}^{\text{II}}$  ions are bridged with cyanides and six organic radicals (IM-2py, 2-pyridyl substituted imino nitroxide), was reported [31]. The  $S = 7$  value is accounted for by a weak ferromagnetic coupling between three high-spin  $S = 2$   $[\text{Ni}(\text{IM-2-Py})_2]$  and two low-spin  $S = 1/2$   $[\text{Fe}(\text{CN})_6]$  fragments. Below 1.2 K, magnetic hysteresis is observed, though magnetic relaxation studies reveal nonexponential time dependence and temperature dependence down to 0.05 K, precluding SMM behavior. Most likely, intercluster interactions are responsible for magnetic ordering.

$[\text{Mn}_{12}]$  anion modified with organic radical cation, that is, salt of  $[\text{Mn}_{12}\text{O}_{12}(\text{PhCOO})_{16}(\text{H}_2\text{O})_4]^-$  anion (Ph = phenyl) and  $S = 1/2$  cation (*m-N*-methylpyridinium nitronyl nitroxide), was found to undergo relatively fast inversion of magnetization; at 1.7 K, hysteresis was almost negligible compared to  $[\text{Mn}_{12}]$  anions with diamagnetic cations or the unmodified  $[\text{Mn}_{12}]$  [32]. Recent studies of analogous salts of  $[\text{Mn}_{12}]$  anion with  $S = 1/2$  ferrocenium cation and related diamagnetic cations led to the conclusion that the counterion may have a direct influence on the  $E_A$  by affecting alignment of Jahn-Teller elongation axes of the eight  $\text{Mn}^{\text{III}}$  ions [33].

Synthesis of organic radical-metal ion clusters, and metal ion clusters in general, relies largely on finding the right mixture of the reagents that would produce a crystalline material suitable for X-ray crystallography. The development of self-assembly approaches to organic ligand-metal ion clusters provides hope for future rational syntheses of metal ion clusters of increasing size with predetermined magnetic properties [34].

## 4. NANOMETER-SIZED ORGANIC POLYRADICALS

Organic polyradicals (i.e., molecular organic radical-based nanoclusters) possess covalently linked organic radicals. Unlike metal-based nanoclusters, they are amenable to the rational stepwise syntheses, employing powerful methodologies of organic chemistry. Furthermore, powerful chromatographic techniques are available for fast purification of organic molecules; that is, those products and intermediates at each synthetic step, which are stable at ambient conditions, can be isolated and purified even from complex reaction mixtures. Such a rational synthetic approach

is especially important if clusters with specific values of  $S$  or particular shapes are sought. The major drawbacks of organic polyradicals include moderate, at best, stability of organic radicals. Also, single crystals for X-ray crystallography are relatively difficult to grow for large organic molecules (as opposed to metal-based clusters); the structural characterization of organic polyradicals is largely based upon spectroscopic (or scattering) techniques as applied to polyradicals and their synthetic intermediates.

From the viewpoint of magnetism, nanometer-sized organic polyradicals can be classified as possessing either weak or strong exchange coupling. The thermal energy at a readily accessible temperature of 2 K is designated as a relative measure of strength for exchange coupling. Thus, weak exchange coupling will imply that the  $S = 1/2$  radicals are effectively noninteracting above a temperature of 2 K. The more interesting situation for the potential SMM behavior is the case of strong exchange coupling, implemented with one of the coupling schemes in Figure 1, leading to large values of  $S$ .

### 4.1. Nanometer-Sized Organic Polyradicals with Strong Exchange Coupling

Polyradicals with strong exchange coupling are primarily based upon a  $\pi$ -conjugated system mediating exchange coupling between the radicals. The majority of nanometer-sized  $\pi$ -conjugated polyradicals rely on the ferromagnetic coupling scheme, though the ferrimagnetic coupling scheme using unequal spins recently became important (Fig. 1) [35]. 1,3-Phenylene is by far the most dominant FCU. The most developed types of nanometer-sized organic polyradicals with strong exchange coupling are polyarylmethyls, polyphenylcarbenes, and polyphenoxyls.

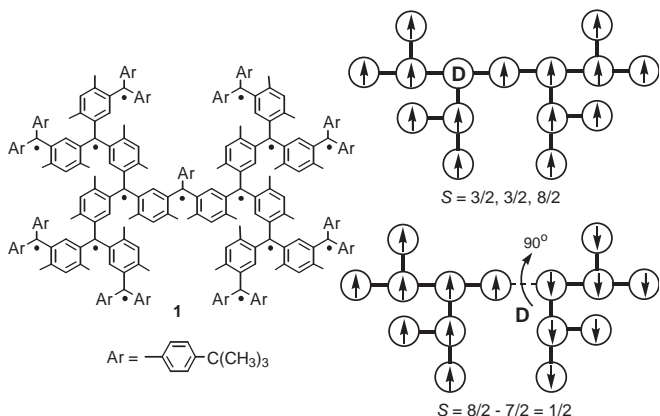
#### 4.1.1. Polyarylmethyls

Polyarylmethyls have long history dating to Gomberg's triphenylmethyl [36] and Schlenk and Brauns' hydrocarbon [11] reported in 1900 and 1915, respectively. In the 1990s, the first attempts at synthesis of nanometer-sized polyarylmethyls were made, using branched or dendritic connectivities of 1,3-phenylene FCUs and arylmethyls. However, values of  $S$  for such dendrimers with up to up to 31 arylmethyls did not exceed  $S = 5$  [22, 37–39]. With increasing number of radicals per molecule, the generation of unpaired electrons at the radical sites must approach perfection. Otherwise, even relatively small numbers of failures in generation of unpaired electrons (i.e., chemical defects) may disrupt  $\pi$ -conjugation, and consequently exchange coupling. The chemical defects may arise from incomplete oxidation of polycarbanion, protonation, or hydrogen transfer leading to  $\text{Ar}_3\text{CH}$  moieties, or reaction of radicals with excess of iodine giving  $\text{Ar}_3\text{CI}$  moieties [40, 41]. As illustrated for pentadecaradical **1** in Figure 2, a chemical defect at one of the inner radical sites will cut the  $\pi$ -conjugated system into noninteracting segments, with low values of  $S$ , for example, a mixture of  $S = 3/2, 3/2, 8/2$  vs  $S = 15/2$  for a "perfect" **3** with all 15 radicals intact and ferromagnetically coupled [22]. Another type of defect involves severe out-of-twisting of the  $\pi$ -conjugated system, which may lead to antiferromagnetic

coupling through the twisted linkage; such a defect in the inner part of **1** could severely reduce the overall value of  $S$  in the twisted conformation (Fig. 2) [35, 42, 43].

Another approach relied on dendrimers with macrocyclic cores, such as 24-radical **2** (Fig. 3) [44–47]. The macrocyclic core provides the second exchange pathway, preserving exchange coupling in the presence of one chemical defect located at one of the four inner radical sites. Overall, 24-radical **2** possess only four radical sites (those adjacent to biphenyl moieties), where a defect would interrupt exchange coupling. The ferromagnetic coupling scheme is implemented in 24-radical **2** using two types of FCU: 1,3-phenylene and 3,4'-biphenylene. Model studies showed that the pairwise ferromagnetic couplings mediated by 1,3-phenylenes (within the dendritic branches and the macrocyclic core) are significantly stronger than those mediated by four 3,4'-biphenylenes (between the branches and the core) [45, 48]. Therefore, 24-radical **2** may be viewed as a cluster of five component spins,  $5/2, 5/2, 5/2, 5/2, 4/2$ , associated with the branches and the core. Magnetic studies corroborate this pentamer model, though the average value of  $S = 10$  is below the expected  $S = 12$  for a 24-radical with 24 ferromagnetically coupled unpaired electron spins. A small density of chemical defects may account for this discrepancy in the values of  $S$  [47]. Alternatively, the presence of conformations, in which one or two dendritic branches are significantly out-of-plane twisted at the biphenylene moieties, may decrease the overall value  $S$  too because of antiferromagnetic coupling between the twisted branch and the core.

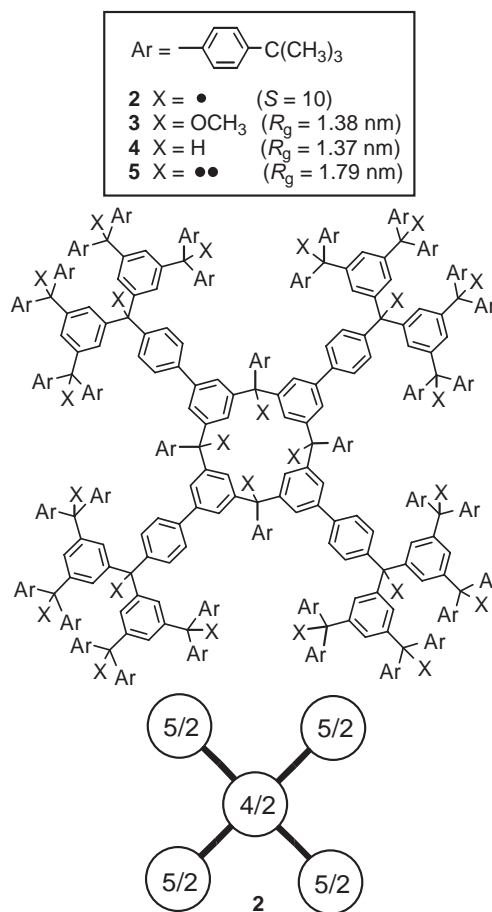
Synthetic precursor to 24-radical **2** (i.e., polyether **3**) was employed to obtain the size and shape estimate (**2** is obtained from **3** by replacing 24 triarylmethyl ether,  $\text{Ar}_3\text{C}-\text{OCH}_3$ , groups with 24 triarylmethyl radicals,  $\text{Ar}_3\text{C}^\bullet$ , through a two-step sequence of chemical transformations) [47]. The fast atom bombardment mass spectrum shows the expected molecular fragment ion corresponding to the loss of one  $\text{OCH}_3$  group; the isotopic multiplet fits well with the expected  $\text{C}_{503}\text{H}_{589}\text{O}_{23}$  formula for the  $[\text{M}-\text{OCH}_3]^+$  ion [47]. Small angle neutron scattering (SANS) for **3** in tetrahydrofuran- $d_8$  (THF- $d_8$ ) gives a radius of gyration  $R_g = 1.38$  nm (Table 1). Preliminary numerical fitting of the SANS data using simulated annealing programs suggests an



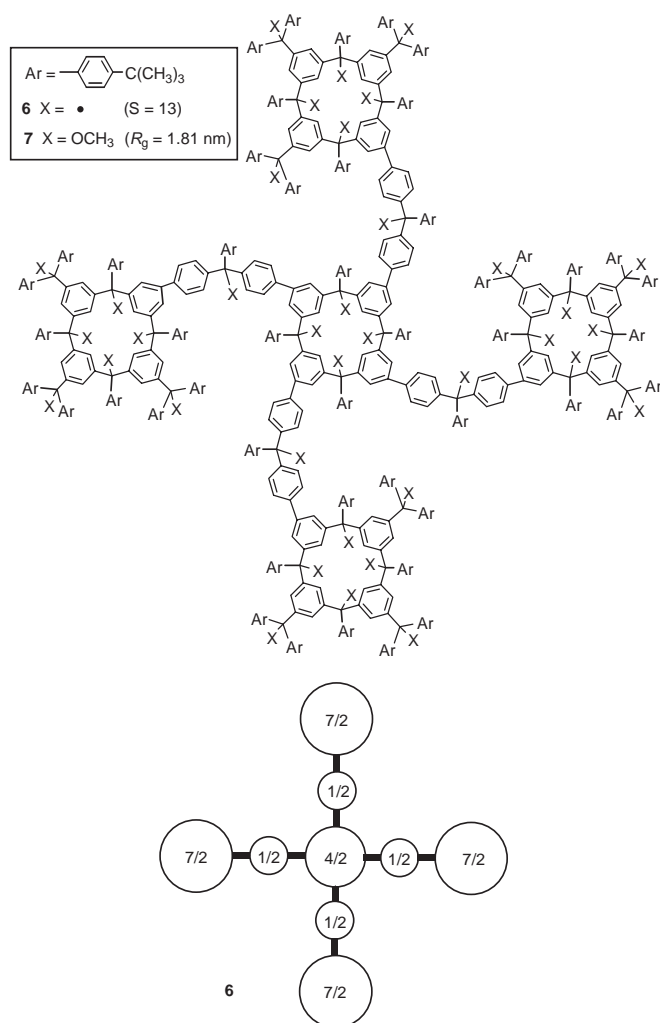
**Figure 2.** Polyarylmethyl dendritic pentadecaradical **1** and possible defects (D): missing unpaired electron (top) and large out-of-plane twisting (bottom).

approximately dumbbell-like shape. Similar values of  $R_g$  and analogous shapes are found for hydrocarbon **4**, though carbopolyanion **5** has relatively large  $R_g$ , presumably due to increased solvation. Assuming similar shapes for 24-radical **2** and its derivatives **3–5**, and approximating them with a prolate spheroid with half-axes of 2 and 1 nm, shape anisotropy based  $E_A/k \approx 0.06$  K is estimated for  $S = 12$  (Fig. 3).

Further evolution of dendritic architecture is illustrated by 36-radical **6**, which possesses macrocyclic branches and a macrocyclic core; that is, five calix[4]arene macrocycles are linked with four bis(biphenylene)methyls (Fig. 4) [35, 49]. The macrocycles provide additional exchange pathways; 36-radical **6** has only four radical sites (those bridging biphenylene moieties), where a defect would interrupt exchange coupling. The exchange coupling within the  $\pi$ -system of **6** may be described in terms of strong 1,3-phenylene FCUs and weak 3,4'-biphenylene FCUs, which connect radical sites within macrocycles and outside macrocycles, respectively. Therefore, **6** may be viewed as a cluster of nine component spins, associated with the macrocyclic branches ( $4 \times 7/2$ ), the linkers ( $4 \times 1/2$ ), and the macrocyclic core ( $4/2$ ) (Fig. 4). The component spins are exchange coupled through the weak 3,4'-biphenylene FCUs. Notably, the nearest neighbor component spins have significantly unequal values (i.e., component spins  $1/2$  are located between the



**Figure 3.** Polyarylmethyl dendritic-macrocyclic 24-radical **2** and its diamagnetic derivatives.

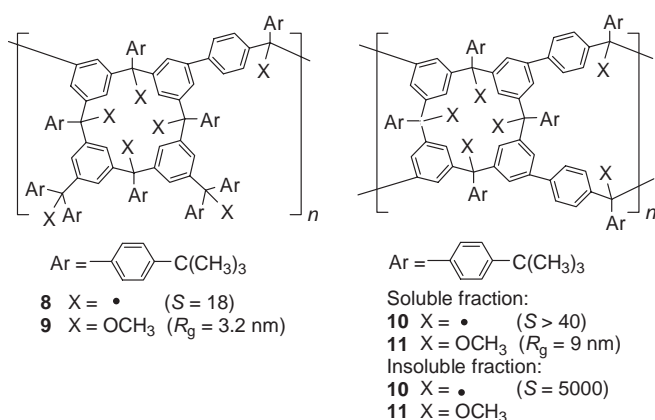


**Figure 4.** Polyarylmethyl macrocyclic–macrocyclic 36–radical **6** and its diamagnetic derivative.

larger spins of  $7/2$  and  $4/2$ ). Consequently, large out-of-plane distortion at the biphenylene moieties, leading to antiferromagnetic coupling between component spins, could be expected to lower the overall value of  $S$  only moderately. Magnetic studies show an average  $S \approx 13$  for **6**, below the expected  $S = 18$  for a 36–radical with 36 ferromagnetically coupled unpaired electron spins [49].

SANS for a polyether **7** (synthetic precursor to 36–radical **6**) in THF- $d_8$  gives a radius of gyration  $R_g = 1.81$  nm (Table 1). Assuming that the shape for 36–radical **6** is a prolate spheroid with  $a/b = 2$ , analogous to that in 24–radical **2**, shape anisotropy based  $E_A/k \approx 0.09$  K is estimated for  $S = 18$  (Fig. 4).

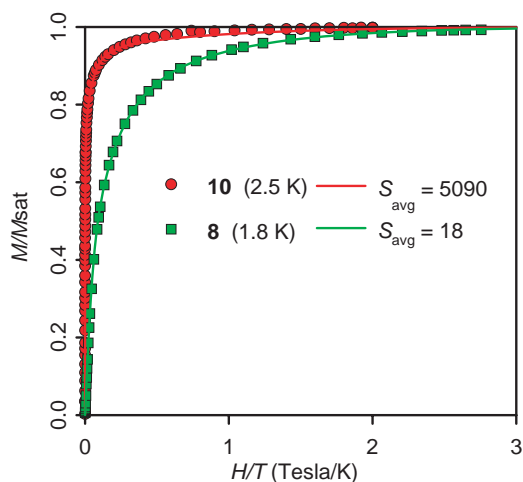
The alternating connectivity of unequal spins was applied to polyarylmethyl polymers **8** and **10** by linking calix[4]arene with bis(biphenyl)methyls (Fig. 5). Polymer **8** had an average value of  $S \approx 18$  (Fig. 6). SANS and multiangle light scattering (MALS) studies showed that the corresponding polyether **9** had  $R_g = 3.2$  nm and  $M_w \approx 30$  kDa. Polymer **10** possessed even higher values of  $S$  that depended on the polymerization conditions leading to the corresponding polyether **11** (Fig. 5). The benzene soluble fractions of



**Figure 5.** Polyarylmethyl polymers **8** and **10** and their diamagnetic derivatives.

polyethers **11** with  $M_w = 300$ – $500$  kDa gave polymers **10** with average values of  $S > 40$  [50]. SANS studies gave  $R_g \approx 9$  nm for benzene-soluble polyethers **11**. The benzene insoluble fractions of polyethers **11**, which were polymerized for a long time beyond the gel point, gave polymers **10** with average values of  $S \approx 5000$  (Fig. 6). Polymers **10** with  $S \approx 5000$  showed the onset of magnetic ordering near the temperature of 10 K. The blocking behavior for the inversion of magnetization is analogous to that in insulating spin glasses and blocked superparamagnets but closer to spin glasses [51].

In conclusion for polyarylmethyls, polyradical **10** showed magnetic ordering and slow inversion of magnetization below a temperature of about 10 K. Whether this magnetic behavior is associated with single macromolecules is difficult to establish because of the insoluble network nature of **10**. For the soluble polyradicals **2**, **6**, and **8**, possessing  $S = 10$ – $18$ , magnetic studies in the milliKelvin range would be needed to search for SMM behavior (slow inversion of magnetization) due to the shape anisotropy. The requirements for sample handling with present state-of-the-art microSQUID techniques would make such studies



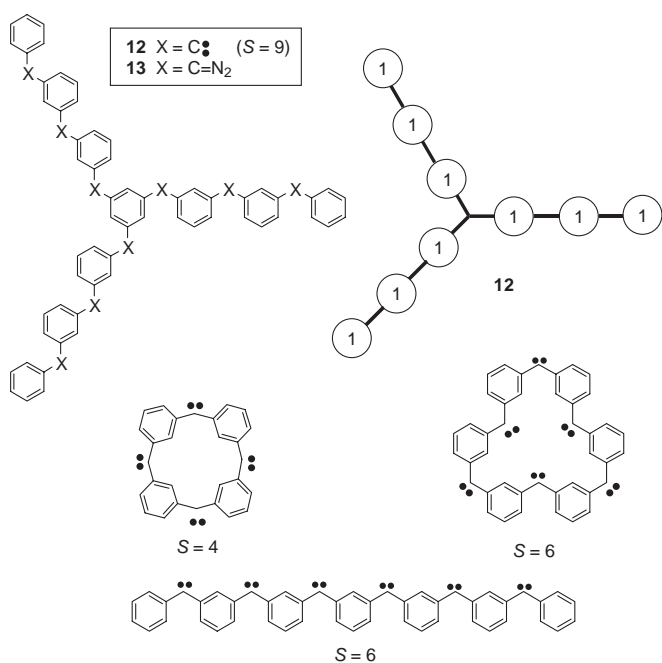
**Figure 6.** Plot of reduced magnetization ( $M/M_{\text{sat}}$ ) vs the ratio of applied magnetic field and temperature ( $H/T$ ) for polymers **8** and **10** with an average  $S \approx 18$  and  $S \approx 5000$ , respectively.

difficult because such polyarylmethyls decompose above 170 K and are sensitive to oxygen. Polyradicals with stability at ambient conditions, in which triarylmethyl radicals are replaced with more stable radicals such as nitroxides, would be desirable for such studies.

#### 4.1.2. Polyphenylcarbenes and Other Organic Polyradicals with Significant Values of $S$

In addition to polyarylmethyls, very few organic polyradicals are known, in which significant values of  $S$  have been achieved. Those include polyphenylcarbenes, trimethylenemethanes, aminium-based polyradicals, and polyphenoxyis. Among those, polyphenoxyis stand out because of their size characterization by microscopy and relative thermal stability.

Iwamura and co-workers prepared numerous polyphenylcarbenes with large values of  $S$ ; the leading example is the  $S = 9$  nonacarbene **12**, which was prepared from the corresponding nona-diazo precursor **13** (Fig. 7) [52–56]. The solid state photolysis of the diazo precursors, such as **13**, is reported to proceed essentially quantitatively for molecules with up to nine diazo groups, providing polyphenylcarbenes with significant values of  $S$ , as shown in Figure 7. Attempts to prepare polyphenylcarbenes with more than nine carbene centers were not successful [56]. For **12** and the related polyphenylcarbenes, the ferromagnetic coupling scheme, using 1,3-phenylene and 1,3,5-phenylene as FCUs, is implemented in the star-branched structure of nine  $S = 1$  carbenes. Although the initial report on **12** suggested the possibility of slow inversion of magnetization below 5 K for **12** in 2-methyltetrahydrofuran (2-MeTHF), [53] it is most likely that slow interconversion between conformations with



**Figure 7.** Selected phenylcarbenes with large values of  $S$ , including  $S = 9$  nonacarbene **12** and the corresponding coupling scheme.

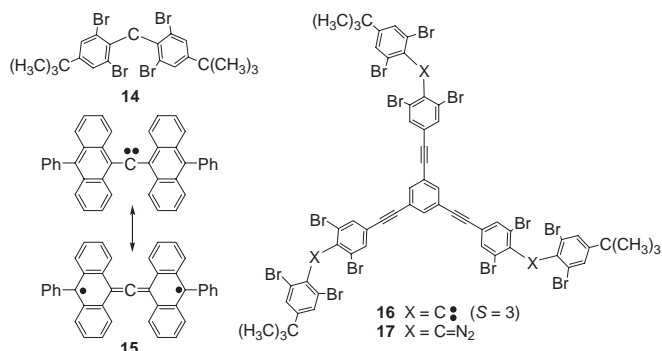
different values of  $S$  is involved, as observed in organic diradicals in 2-MeTHF matrices [57, 58].

Polyphenylcarbenes, such as **12**, are extremely reactive and typically have to be generated in frozen matrices below 77 K. Recently, more stable  $S = 1$  carbenes were prepared; for example, **14** and **15** have a half-life of 16 s and 19 min in degassed benzene at room temperature, respectively (Fig. 8) [59, 60]. For **15**, this fair persistence may be derived from its triphenylmethyl-like structure. These values of half-life are several orders of magnitude longer than the half-life of  $2 \mu\text{s}$  for the parent diphenylcarbene under the same conditions. Polycarbenes derived from those relatively stable carbenes are still rare. The leading example is the  $S = 3$  tricarbene **16**, which is generated from the corresponding tris(diazo) derivative **17** and characterized by two-dimensional electron paramagnetic resonance (EPR) spectroscopy (Fig. 8) [61].

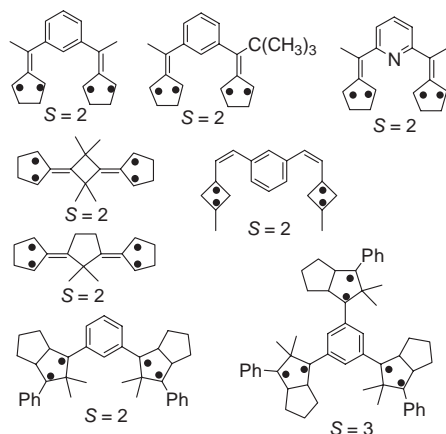
Dougherty and co-workers developed a so-called “bisTMM” (TMM = trimethylenemethane) approach to design and prepare numerous  $S = 2$  tetradicals [62–65]. Their ferromagnetic coupling scheme employs 1,3-phenylene, cyclobutane, or cyclopentane as FCU (Fig. 9). More recently, this approach is extended to an  $S = 3$  hexaradical, with 1,3,5-phenylene and cyclopentane as FCUs (Fig. 9). [66–68] In each case, the polyradical is prepared by ultraviolet photolysis of the corresponding bis- or tris-azoalkanes at cryogenic temperatures; typically, efficient and complete conversions are difficult to attain, resulting in mixtures of polyradicals from the successive loss of dinitrogen. The resultant mixtures of polyradicals are quite unstable requiring handling in frozen matrix at temperatures of 77 K or below. Magnetic characterization of these tetra- and hexaradicals is limited to EPR spectroscopy.

Bushby and co-workers prepared aminium based polyradicals; the leading example is polyradical **18** with an average value of  $S \approx 4$  at temperatures below 10 K (Fig. 10) [69]. The ferromagnetic coupling scheme in **18** relies on the FCU composed of 1,3-phenylene and two 1,4-phenylene spacers; this rather long coupling pathway results in a relatively weak ferromagnetic coupling. Polyradical **18** was generated from the corresponding polyamine **19** with  $M_w > 10$  kDa; no size measurements are reported [69].

Polymeric aminium-based polyradicals may be viewed as examples of the “polaronic” approach to organic polymers with large values of  $S$ , in which the source of electron spin is



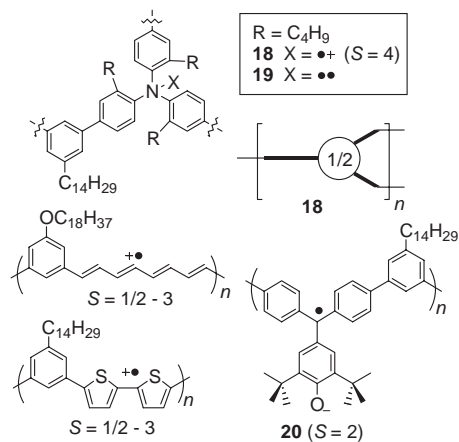
**Figure 8.** Selected persistent carbenes and tricarbene **16**. (Ph corresponds to a phenyl group.)



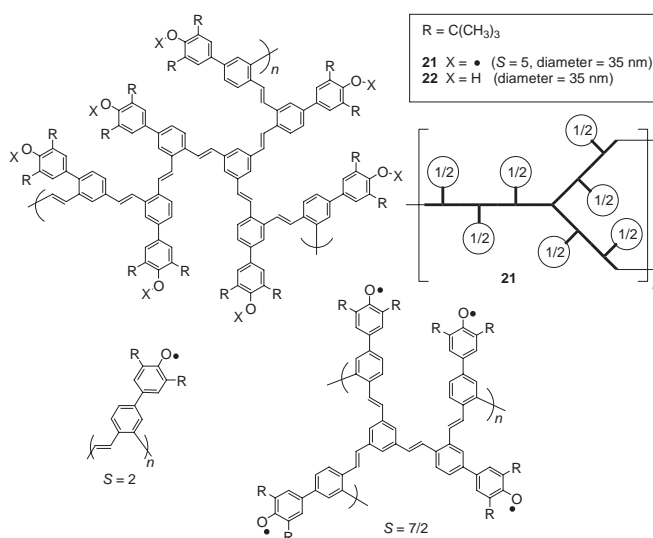
**Figure 9.** Selected bis(TMM)  $S = 2$  tetradicals and  $S = 3$  hexaradical. (Ph corresponds to a phenyl group.)

relatively localized aminium radical cations [70]. Dougherty and co-workers examined various polymers and oligomers, in which short fragments of the  $\pi$ -system are linked together with 1,3-phenylene couplers. The studied  $\pi$ -systems include radical cations of polyacetylene, radical cations of aromatic heterocycles, and radical anions of fuchson (Fig. 10). The variable values of  $S$  up to 3 were reported for such polymers [71, 72]. However, only electrochemically generated fuchson-based radical anions (polymer **20** with  $S \approx 2$ ) have significant concentration of electron spin (0.5 radical per repeat unit) [72]. Radical ion based polymers are generally stable at room temperature. Their main drawbacks are complicated ion multiplet equilibria and tendency for formation of diamagnetic aggregates [73–75].

Nishide and co-workers prepared many examples of polyphenoxyls with significant values of  $S$  (up to 5) (Fig. 11) [76–80]. The leading example is polyphenoxyl **21**, which possesses an average value of  $S \approx 5$  at low temperatures below 10 K (Fig. 11) [80]. The ferromagnetic coupling scheme in **21** is implemented using phenoxyl pendants attached to the poly(1,2-phenylenevinylene) FCU. Polyphenoxyl **21** was obtained from the corresponding polyphenol **22** ( $M_w \approx 32$  kDa,  $M_w/M_n \approx 1.2$ ). Dichloromethane solutions of **21**



**Figure 10.** Aminium-based polyradical **18** and other radical ion based polymers with significant values of  $S$ .



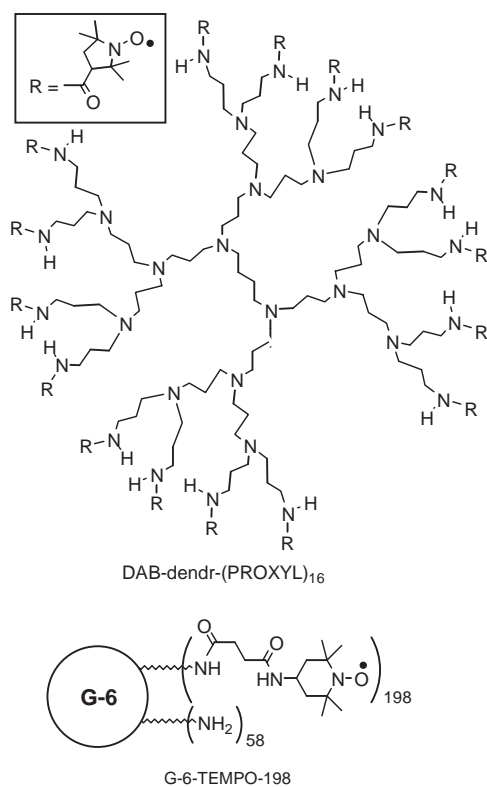
**Figure 11.** Polyphenoxyl **21**, coupling scheme for polyphenoxyl **21**, and other selected polyphenoxyls with significant values of  $S$ .

and **22** are transferred to a highly oriented pyrolytic graphite surface and examined with atomic force microscopy (AFM), followed by magnetic force microscopy (MFM). Notably, both AFM and MFM studies are carried out at ambient temperature (i.e., polyphenoxyl **21** has a value of  $S = 1/2$ , corresponding to an ensemble of a large number of independent  $S = 1/2$  electron spins, at these conditions). AFM images for **21** and **22** are similar (i.e., the horizontal distance of 35 nm and the vertical distance of 0.6 nm are determined). The follow-up MFM images, using a tip coated with ferromagnetic CoCr film (magnetic moment of  $10^{-13}$  emu), are observed only for paramagnetic **21**, with the 35-nm size analogous to the AFM images. The MFM contrast weakens and ultimately disappears following slow decomposition of paramagnetic polyphenoxyl **21** to the undetermined (perhaps diamagnetic) products after one day; however, the 35-nm sized image of the decomposition products remains visible in AFM even after one week [80]. The detection limits for MFM for small paramagnetic moments and the effects involved in magnetization of the tip in the opposite direction as found for this  $S = 1/2$  paramagnet will need more detailed analysis. If confirmed, these preliminary MFM results may open the way for organic polyradical-based magnetic dots.

## 4.2. Nanometer-Sized Organic Polyradicals with Weak Exchange Coupling

In organic polyradicals with weak exchange coupling, the energy level splitting due to the exchange coupling is smaller than the thermal energy ( $RT$ ) at the readily accessible temperatures down to 2 K. Such polyradicals possess a value of  $S = 1/2$  above temperature of 2 K. The barrier for inversion of magnetization for  $S = 1/2$  paramagnets will be very low if not absent [8].

The magnetic susceptibility for a paramagnetic polyradical with a large number ( $n$ ) of  $S = 1/2$  electron spins scales with  $n$  as approximately  $n^2$  and  $n$  for the strong and the weak



**Figure 12.** Third generation of nitroxide-functionalized poly(propylene imine) dendrimer DAB-dendr-(PROXYL)<sub>16</sub> and sixth generation PAMAM dendrimer functionalized with 198 nitroxides (G-6-TEMPO-198).

ferromagnetic couplings, respectively. Therefore, even in the absence of large values of  $S$ , the magnetic susceptibility for an  $S = 1/2$  polyradical with  $n$  weakly coupled (effectively independent)  $S = 1/2$  electron spins will still be greater by a factor of  $n$  than that for a single  $S = 1/2$  monoradical. This is the situation for polyphenoxyl **16**, which is weakly coupled at ambient temperature but still reported as detectable at ambient temperature by the current MFM technology [80].

The review of nanometer-sized weakly coupled polyradicals will be limited to well-defined dendrimers. Janssen and co-workers reported five generations of nitroxide-functionalized dendrimers, with up to 64 nitroxide radicals [81]. Poly(propylene imine) dendrimers were functionalized with 3-carboxy-2,2,5,5-tetramethyl-1-pyrrolidinyloxy radical (PROXYL) end groups [DAB-dendr-(PROXYL) <sub>$n$</sub> ] (Fig. 9). Because DAB-dendr-(PROXYL) <sub>$n$</sub>  dendrimers are prepared via divergent synthetic routes, substantial contamination with nonseparable dendrimers with a smaller than nominal number of PROXYL end groups, especially for higher generations, is expected. Already for intermediate generations with  $n = 8$  and  $n = 16$  PROXYLs, the matrix-assisted laser desorption ionization time-of-flight (MALDI-TOF) mass spectra showed the impurity mass peaks corresponding to dendrimers with  $n = 7$  and  $n = 15$  PROXYLs. The EPR spectra in solution were consistent with the presence of a weak but detectable exchange coupling, as shown by the hyperfine splitting patterns for the lowest generations [81].

Few examples of poly(amidoamine) (PAMAM) dendrimers, functionalized with spin carrying end groups (radicals or radical ions), have been reported [82–84]. Because PAMAM dendrimers are prepared according to divergent synthetic routes, significant contamination with incompletely end-functionalized dendrimers is expected. In particular, the commercially available sixth generation PAMAM (G-6 PAMAM<sup>TM</sup>) dendrimers possess oblate spheroidal shape with nominally 256 amine end groups on the surface of the macromolecule.

Miller and co-workers reported a conducting film formed from a PAMAM dendrimer that had been functionalized with naphthalene diimide radical anions [82]. The defects in these modified dendrimers prepared according to divergent synthetic routes were not estimated. The radical anions of this type are known to form conducting  $\pi$ -stacks, rendering the dendrimer effectively diamagnetic. In high humidity, the third generation dendrimer had conductivities in the 0.12–11 S cm<sup>-1</sup> range depending on the content of radical anions vs nonreduced diimide moieties [82].

PAMAM dendrimers with relatively low densities of nitroxide radical end groups for their studies in vesicles are known. For example, the sixth generation dendrimer (G-6 PAMAM<sup>TM</sup>, diameter of 7 nm from dynamic light scattering) was functionalized 2,2,6,6-tetramethylpiperidine-*N*-oxyl (TEMPO) with only 3% conversion of the amino end groups [83].

Much higher densities of radicals are reported in a polynitroxyl G-6 PAMAM<sup>TM</sup> with 198 (G-6-TEMPO-198) or with 80 (G-6-TEMPO-80) TEMPO end groups for possible applications in EPR imaging [84]. MALDI-TOF mass spectra showed the expected mass averages for G-6-TEMPO-198 and G-6-TEMPO-80, with a difference of about 1 kDa between the number and weight averages for both dendrimers. One of the possible drawbacks for their application as intravenous contrast agents may be their affinity for aggregation in aqueous solution because of the relatively lipophilic surface for the nitroxyl labeled dendrimers. MALS analyses identify particles with an average molecular weights of 549 kDa (degree of aggregation  $\approx 5.4$ , radius of gyration  $\approx 19$  nm) and 113 kDa (degree of aggregation  $\approx 1.6$ , radius of gyration  $< 10$  nm) for G-6-TEMPO-198 and G-6-TEMPO-80, respectively [84].

Octaferrocenyl dendrimer (with ethylene silane backbone) was reported to undergo 8-electron oxidation to the corresponding dendrimer with eight ferrocenium radical cations. However, neither the exchange coupling between the radical cations nor the size of this relatively low molecular mass dendrimer were characterized [85].

## 5. SUMMARY

The development of rational synthetic methods for organic radical-metal ion nanoclusters may provide a new library of organometallic SMMs with predetermined magnetic properties. Through incorporation of di- and polyradicals into such nanoclusters, SMMs responsive to the external stimuli may be designed (e.g., photomagnetic SMMs).

The rational synthetic methods for the unstable organic polyradicals should be extended to the ambient stable organic polyradicals with large values of  $S$  and elongated

shapes. This will greatly facilitate the search for organic SMMs. Intriguing questions will be whether the magnetic anisotropy barrier arising from purely classical magnetic dipole–dipole interactions could be achieved and whether quantum tunneling of magnetization could be observed in such magnetic nanoclusters.

## GLOSSARY

**Exchange coupling or exchange interaction** The interaction between electron spins that originates from a quantum exchange term of the Coulomb interaction between electrons. Although electrostatic in its origin, the exchange coupling is one of the key aspects of magnetism.

**Magnetic nanocluster** Nanometer-sized cluster of magnetic metals, metal ions, or other magnetic subunits.

**Organic polyradical** Organic molecule that possesses more than several unpaired electrons.

**Single-molecule magnet (SMM)** Individual molecule that functions as a nanoscale magnet, effectively a single domain magnetic particle that shows magnetic hysteresis below its blocking temperature.

## ACKNOWLEDGMENTS

Support from the National Science Foundation for this research is gratefully acknowledged. The author thank Dr. Suchada Rajca, Dr. Paul Butler, and Dr. Sungmin Choi for assistance with unpublished SANS data collection and numerical fittings.

## REFERENCES

1. T. Lis, *Acta Crystallogr. B* 36, 2042 (1980).
2. R. Sessoli, D. Gatteschi, A. Caneschi, and M. A. Novak, *Nature* 365, 141 (1993).
3. J. Larionova, M. Gross, M. Pilkington, H. Andres, H. Stoeckli-Evans, H. U. Gudel, and S. Decurtins, *Angew. Chem. Int. Ed.* 39, 1605 (2000).
4. H. Andres, R. Basler, A. J. Blake, C. Cadiou, G. Chaboussant, C. M. Grant, H.-U. Gudel, M. Murrie, S. Parsons, C. Paulsen, F. Semadini, V. Villar, W. Wernsdorfer, and R. E. P. Winpenny, *Chem. Eur. J.* 8, 4867 (2002).
5. J. R. Friedman, M. P. Sarachik, J. Tejada, and R. Ziolo, *Phys. Rev. Lett.* 76, 3830.
6. M. N. Leuenberger and D. Loss, *Nature* 410, 789 (2001).
7. W. Wernsdorfer, N. Allaga-Alcalde, D. N. Hendrickson, and G. Christou, *Nature* 416, 406 (2002).
8. W. Wernsdorfer, *Adv. Chem. Phys.* 118, 99 (2001).
9. A. Rajca, *Chem. Rev.* 94, 871 (1994).
10. P. M. Lahti, Ed., "Magnetic Properties of Organic Materials." Dekker, New York, 1999.
11. W. Schlenk and M. Brauns, *Chem. Ber.* 48, 661 (1915).
12. W. T. Borden and E. R. Davidson, *J. Am. Chem. Soc.* 99, 4587 (1977).
13. A. A. Ovchinnikov, *Theor. Chim. Acta* 47, 297 (1978).
14. A. Bencini and D. Gatteschi, "Electron Paramagnetic Resonance of Exchange Coupled Systems." Springer-Verlag, Berlin, 1990.
15. W. Schlenk and M. Brauns, *Chem. Ber.* 48, 716 (1915).
16. A. Rajca, S. Rajca, J. Wongsriratanakul, and C. R. Ross II, *Polyhedron* 20, 1669 (2001).
17. G. Görlitz, T. Hayamizu, T. Itoh, K. Matsuda, and H. Iwamura, *Inorg. Chem.* 37, 2083 (1998).
18. K. Yosida, "Theory of Magnetism," Springer-Verlag, Berlin, 1996.
19. O. Kahn, "Molecular Magnetism," Ch. 2 and 3. VCH, New York, 1993.
20. C. Boskovic, M. Pink, J. C. Huffman, D. N. Hendrickson, and G. Christou, *J. Am. Chem. Soc.* 123, 9914 (2001).
21. A. Aharoni, "Introduction to the Theory of Ferromagnetism," 2nd ed. Oxford Univ. Press, Oxford, 2000.
22. A. Rajca and S. Utamapanya, *J. Am. Chem. Soc.* 115, 10688 (1993).
23. A. Caneschi, D. Gatteschi, and P. Rey, *Progr. Inorg. Chem.* 39, 331 (1991).
24. A. Caneschi, D. Gatteschi, N. Lalioti, R. Sessoli, L. Sorace, V. Tangoulis, and A. Vindigni, *Chem. Eur. J.* 8, 286 (2002).
25. H. Iwamura, K. Inoue, and N. Koga, *New J. Chem.* 201 (1998).
26. A. B. Burdukov, V. I. Ovcharenko, V. N. Ikorski, N. V. Perukhina, N. V. Podberezskaya, I. A. Grigor'ev, S. V. Larionov, and L. B. Volodarsky, *Inorg. Chem.* 30, 972 (1991).
27. N. Koga, Y. Ishimaru, and H. Iwamura, *Angew. Chem. Int. Ed.* 35, 755 (1996).
28. Y. Sano, M. Tanaka, N. Koga, K. Matsuda, H. Iwamura, P. Rabu, and M. Drillon, *J. Am. Chem. Soc.* 119, 8246 (1997).
29. S. Karasawa, H. Kumada, N. Koga, and H. Iwamura, *J. Am. Chem. Soc.* 123, 9685 (2001).
30. A. Caneschi, D. Gatteschi, J. Laugier, P. Rey, R. Sessoli, and C. Zanchini, *J. Am. Chem. Soc.* 110, 2795 (1988).
31. K. E. Vostrikova, D. Luneau, W. Wernsdorfer, P. Rey, and M. Verdager, *J. Am. Chem. Soc.* 122, 718 (2000).
32. K. Takeda and K. Awaga, *Phys. Rev. B* 56, 14560 (1997).
33. T. Kuroda-Sowa, M. Lam, A. L. Rheingold, C. Frommen, W. M. Reiff, M. Nakano, J. Yoo, A. L. Maniero, L. C. Brunel, G. Christou, and D. N. Hendrickson, *Inorg. Chem.* 40, 6469 (2001).
34. T. Kusukawa and M. Fujita, *J. Am. Chem. Soc.* 124, 13576 (2002).
35. A. Rajca, *Chem. Eur. J.* 8, 4834 (2002).
36. M. Gomberg, *J. Am. Chem. Soc.* 22, 757 (1900).
37. A. Rajca, *J. Am. Chem. Soc.* 112, 5890 (1990).
38. A. Rajca, S. Utamapanya, and S. Thayumanavan, *J. Am. Chem. Soc.* 114, 1884 (1992).
39. A. Rajca and S. Utamapanya, *J. Am. Chem. Soc.* 115, 2396 (1993).
40. S. Utamapanya and A. Rajca, *J. Am. Chem. Soc.* 113, 9242 (1991).
41. S. Rajca and A. Rajca, *J. Am. Chem. Soc.* 117, 9172 (1995).
42. M. Dvornitzky, R. Chiarelli, and A. Rassat, *Angew. Chem. Int. Ed. Engl.* 31, 180 (1992).
43. A. Rajca and S. Rajca, *J. Chem. Soc. Perkin Trans. 2* 1077 (1998).
44. A. Rajca, S. Rajca, and K. Padmakumar, *Angew. Chem. Int. Ed. Engl.* 33, 2091 (1994).
45. A. Rajca, S. Rajca, and S. R. Desai, *J. Am. Chem. Soc.* 117, 806 (1995).
46. A. Rajca, J. Wongsriratanakul, and S. Rajca, *J. Am. Chem. Soc.* 119, 11674 (1997).
47. A. Rajca, J. Wongsriratanakul, S. Rajca, and R. Cerny, *Angew. Chem. Int. Ed.* 37, 1229 (1998).
48. A. Rajca and S. Rajca, *J. Am. Chem. Soc.* 118, 8121 (1996).
49. J. Wongsriratanakul, A. Rajca, and S. Rajca, in "Book of Abstracts," 219th ACS National Meeting, San Francisco, CA, 26–30, March, 2000.
50. A. Rajca, S. Rajca, and J. Wongsriratanakul, *J. Am. Chem. Soc.* 121, 6308 (1999).
51. A. Rajca, J. Wongsriratanakul, and S. Rajca, *Science* 294, 1503 (2001).
52. H. Iwamura and N. Koga, *Acc. Chem. Res.* 26, 346 (1993).
53. N. Nakamura, K. Inoue, and H. Iwamura, *Angew. Chem. Int. Ed.* 32, 872 (1993).
54. K. Matsuda, N. Nakamura, K. Inoue, N. Koga, and H. Iwamura, *Chem. Eur. J.* 2, 259 (1996).
55. K. Matsuda, N. Nakamura, K. Takahashi, K. Inoue, N. Koga, and H. Iwamura, *J. Am. Chem. Soc.* 117, 5550 (1995).



56. K. Matsuda, N. Nakamura, K. Inoue, N. Koga, and H. Iwamura, *Bull. Chem. Soc. Jpn.* 69, 1483 (1996).
57. A. Rajca, K. Lu, S. Rajca, and C. R. Ross, II, *Chem. Commun.* 1249 (1999).
58. D. A. Schultz, A. K. Boal, and G. T. Farmer, *J. Am. Chem. Soc.* 119, 3846 (1997).
59. H. Tomioka, M. Hattori, K. Hirai, and S. Murata, *J. Am. Chem. Soc.* 118, 8723 (1996).
60. H. Tomioka, E. Iwamoto, H. Itakura, and K. Hirai, *Nature* 412, 626 (2001).
61. K. Itoh, and M. Kinoshita, Eds. "Molecular Magnetism," p. 260. Gordon and Breach (Kodansha), Tokyo, 2000.
62. S. J. Jacobs, D. A. Schultz, R. Jain, J. Novak, and D. A. Dougherty, *J. Am. Chem. Soc.* 115, 1744 (1993).
63. S. K. Silverman and D. A. Dougherty, *J. Phys. Chem.* 97, 13273 (1993).
64. S. J. Jacobs and D. A. Dougherty, *Angew. Chem. Int. Ed.* 33, 1104 (1994).
65. A. P. West, Jr., S. K. Silverman, and D. A. Dougherty, *J. Am. Chem. Soc.* 118, 1452 (1996).
66. W. Adam and W. Maas, *J. Am. Chem. Soc.* 122, 6735 (2000).
67. W. Adam and W. Maas, *J. Org. Chem.* 65, 7650 (2000).
68. W. Adam, W. Maas, and W. M. Nau, *J. Org. Chem.* 65, 8790 (2000).
69. R. J. Bushby, D. R. McGill, K. M. Ng, and N. Taylor, *J. Chem. Soc. Perkin Trans. II* 7, 1405 (1997).
70. H. Fukutome, I. Takahashi, and M. Ozaki, *Chem. Phys. Lett.* 133, 34 (1987).
71. M. M. Murray, P. Kaszynski, D. A. Kaisaki, W. Chang, and D. A. Dougherty, *J. Am. Chem. Soc.* 116, 8152 (1994).
72. K. K. Anderson and D. A. Dougherty, *Adv. Mater.* 10, 688 (1998).
73. A. Rajca, S. Rajca, and S. R. Desai, *Chem. Commun.* 1957 (1995).
74. L. L. Miller and K. R. Mann, *Acc. Chem. Res.* 29, 417 (1996).
75. J. A. E. H. van Haare, M. van Boxel, and R. A. J. Janssen, *Chem. Mater.* 10, 1166 (1998).
76. H. Nishide, T. Kaneko, T. Nii, K. Katoh, E. Tsuchida, and P. M. Lahti, *J. Am. Chem. Soc.* 118, 9695 (1996).
77. H. Nishide, M. Miyasaka, R. Doi, and T. Araki, *Macromolecules* 35, 690 (2002).
78. H. Nishide, R. Doi, K. Oyaizu, and E. Tsuchida, *J. Org. Chem.* 66, 1680 (2001).
79. H. Nishide, M. Miyasaka, and E. Tsuchida, *Angew. Chem. Int. Ed.* 37, 2400 (1998).
80. H. Nishide, T. Ozawa, M. Miyasaka, and E. Tsuchida, *J. Am. Chem. Soc.* 123, 5942 (2001).
81. A. W. Bosman, R. A. J. Janssen, and E. W. Meijer, *Macromolecules* 30, 3606 (1997).
82. R. G. Duan, L. L. Miller, and D. A. Tomalia, *J. Am. Chem. Soc.* 117, 10783 (1995).
83. M. F. Ottaviani, P. Matteini, M. Brustolon, N. J. Turro, S. Jockusch, and D. A. Tomalia, *J. Phys. Chem. B* 102, 6029 (1998).
84. A. T. Yordanov, K. Yamada, M. C. Krishna, J. B. Mitchell, E. Woller, M. Cloninger, and M. W. Brechbiel, *Angew. Chem. Int. Ed.* 40, 2690 (2001).
85. B. Alonso, M. Moran, C. M. Casado, F. Lobete, J. Losada, and I. Cuadrado, *Chem. Mater.* 7, 1440 (1995).

# Organic Thin Film Deposition Techniques

M. C. Petty

University of Durham, Durham, United Kingdom

## CONTENTS

1. Introduction
  2. Langmuir–Blodgett Film Deposition
  3. Self-Assembly
  4. Layer-by-Layer Electrostatic Deposition
  5. Spin-Coating
  6. Physical Vapor Deposition
  7. Nanopatterning
- Glossary  
References

## 1. INTRODUCTION

The success of many nanotechnology ideas will depend on the ability to process and pattern ultrathin films (1–100 nm in thickness). Techniques such as spin-coating, thermal evaporation, and chemical vapor deposition are routinely used for the fabrication of electronic and optoelectronic components where the nanoscale is not yet critical [1–7]. Organic compounds are becoming increasingly useful to the electronics industry, although, for fast and efficient signal processing, it is unlikely that these materials will outperform inorganic semiconductors such as silicon and gallium arsenide in the foreseeable future. However, in niche areas, organic compounds can have significant advantages over their inorganic counterparts. Perhaps the best known example is the liquid crystal display. Organic and biological compounds are also being exploited in chemical sensors, light-emitting displays, photocopiers, and infrared detectors [8]. The field of plastic electronics is developing rapidly for the fabrication of low-cost electronic components for use where high-speed operation is not essential, for example, in smart cards.

In their bulk form, many organic materials are difficult to handle and single crystals can be extremely fragile. The ability to form high-quality thin layers of these materials can therefore present particular difficulties. Here, an overview of the methods that can be used is presented. Emphasis will be given to those techniques that can be used to build up thin films of organic molecules at the molecular level (i.e., film

thicknesses of a few nanometers). Such molecular engineering approaches offer much scope for the development of *molecular and nanoscale electronics* [8].

## 2. LANGMUIR–BLODGETT FILM DEPOSITION

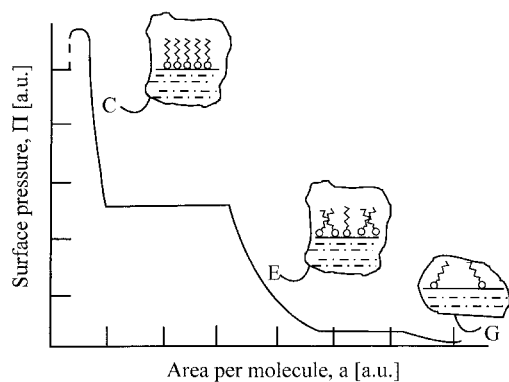
A method that allows the manipulation of materials on the nanometer scale is the Langmuir–Blodgett (LB) technique [9–12]. Langmuir–Blodgett films are prepared by first depositing a small quantity of an amphiphilic compound (i.e., one incorporating both polar and nonpolar groups—the classical materials being long-chain fatty acids), dissolved in a volatile solvent, onto the surface of purified water, the subphase. When the solvent has evaporated, the organic molecules may be compressed to form a floating two-dimensional solid. Monolayer films can exhibit a multiplicity of phases during this compression; these are similar to the mesophases shown by liquid crystals.

The surface pressure  $\Pi$  of the floating organic film is defined as the reduction of the subphase surface tension by the film, that is,

$$\Pi = \gamma_0 - \gamma \quad (1)$$

where  $\gamma_0$  is the surface tension of the pure subphase and  $\gamma$  is the surface tension of the film-covered surface. In the case of a water subphase (almost all the work on LB films has involved a water subphase), values of  $\Pi$  of the order of  $\text{mN m}^{-1}$  are generally encountered; the maximum value of  $\Pi$  is  $72.8 \text{ mN m}^{-1}$  at  $20^\circ\text{C}$ , the surface tension of pure water.

Figure 1 shows a surface pressure versus area isotherm (i.e., measurement at constant temperature) for a hypothetical long-chain organic material. This generic diagram is not meant to represent that observed for a particular substance, but shows most of the features observed for long-chain compounds. In the “gaseous” state (G in Fig. 1) the molecules are far enough apart on the water surface that they exert little force on one another. As the surface area of the monolayer is reduced, the hydrocarbon chains will begin to interact. The “liquid” state that is formed is generally called the expanded monolayer phase (E). The hydrocarbon chains

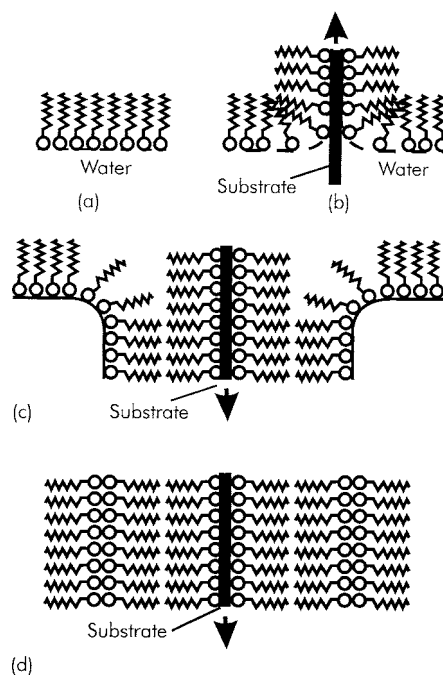


**Figure 1.** Surface pressure versus area isotherm for a long-chain fatty acid material.

of the molecules in such a film are in a random, rather than a regular orientation, with their polar groups in contact with the subphase. As the molecular area is progressively reduced, condensed (C) phases may appear; there may be more than one of these. In the condensed monolayer states, the molecules are closely packed and are oriented with the hydrocarbon chains pointing away from the water surface. The limiting area per molecule in such a state will be similar to the cross-sectional area of the hydrocarbon chain, that is, approximately  $0.19 \text{ nm}^2 \text{ molecule}^{-1}$ .

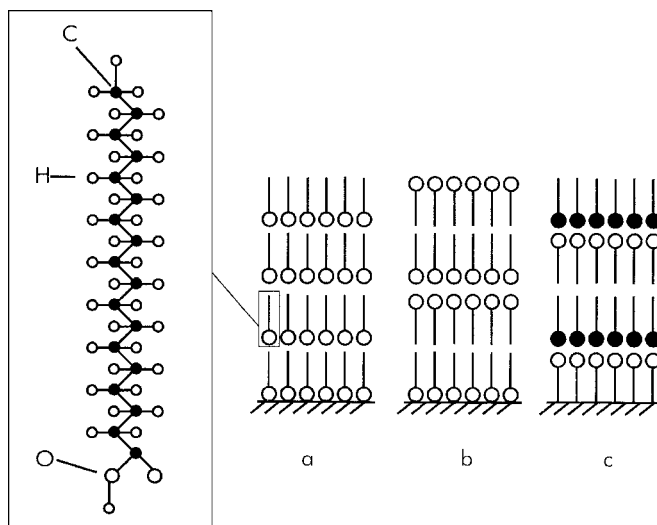
If the surface pressure of the monolayer is held constant in one or more of the condensed phases, then the film may be transferred from the water surface onto a suitable solid substrate simply by raising and lowering the latter through the monolayer–air interface. Monolayer transfer speeds are usually of the order of a few millimeters per second. Several deposition modes are possible depending on the interactions between the polar and nonpolar parts of the molecules, and the nature of the bond between the first layer and the substrate surface. Figure 2 shows the most common form of LB film deposition. The substrate is hydrophilic and the first monolayer is transferred, like a carpet, as the substrate is raised through the water (Fig. 2b). Subsequently, a monolayer is deposited on each traversal of the monolayer–air interface (Fig. 2c). As shown, these stack in a head-to-head and tail-to-tail pattern; this deposition mode is called Y-type (Fig. 2d). Although this is the most frequently encountered situation, instances in which the floating monolayer is only transferred to the substrate as it is being inserted into the subphase, or only as it is being removed, are often observed. These deposition modes are called X-type (monolayer transfer on the downstroke only) and Z-type (transfer on the upstroke only); the molecular arrangements in Z-type and Y-type films are contrasted in Figure 3. Mixed deposition modes are sometimes observed and, for some materials, the deposition type can change as the LB film is built up. Film transfer is characterized by the measurement of a deposition, or transfer, ratio,  $\tau$ . This is the decrease in the area occupied by the monolayer (held at constant pressure) on the water surface divided by the coated area of the solid substrate, that is,

$$\tau = \frac{A_L}{A_S} \quad (2)$$



**Figure 2.** Langmuir–Blodgett film deposition: (a) condensed monolayer on water surface; (b) transfer of monolayer on upstroke of solid substrate; (c) subsequent transfer on downstroke; (d) Y-type multilayer film.

where  $A_L$  is the decrease in the area occupied by the monolayer on the water surface and  $A_S$  is the coated area of the solid substrate. Transfer ratios significantly outside the range 0.95 to 1.05 suggest poor homogeneity. Fatty acid and fatty acid salt (obtained by the addition of metallic cations, such as  $\text{Cd}^{2+}$ , to the aqueous subphase) monolayers normally deposit as Y-type films. However, X-type deposition is possible with suitable changes in the dipping conditions; X-type deposition is favored by high pH values.



**Figure 3.** Molecular arrangements for LB molecular assemblies: (a) Z-type deposition; (b) Y-type deposition; (c) alternate-layer deposition.

It is possible to construct LB films using more than one type of molecular film. In the simplest case, condensed floating monolayers of two different amphiphilic materials are confined (using mechanical barriers) to different regions of the water surface. By lowering the solid substrate through the first layer of, say, material A, and raising it up through the other, material B, alternate layers of structure ABABAB... may be built up, Figure 3c. This permits the fabrication of organic superlattices with precisely defined symmetry properties. Such molecular assemblies can exhibit pyroelectric (electric charge generation on heating), piezoelectric (charge generation on the application of a mechanical stress), and second-order nonlinear optical phenomena (frequency doubling) [9, 10, 13].

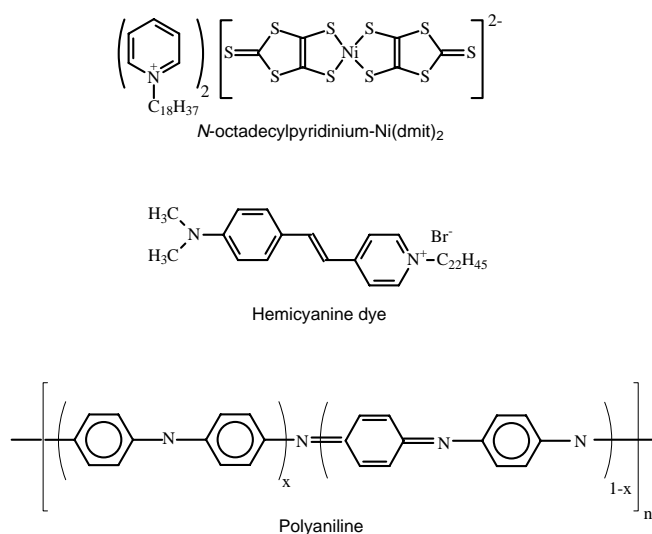
The final molecular arrangement in an LB layer may not be always as depicted in the “molecular stick” diagrams. For fatty acids, early experiments using X-ray diffraction revealed that the spacings between the hydrophilic head groups was nearly the same, and equal to twice the length of the hydrocarbon chain, whether they were deposited as X-type or Y-type films. This suggests that the molecules in some LB films rearrange, during or shortly after deposition [9].

Although fatty acids and their salts are the “classical” materials for LB film formation, much activity has focused on the incorporation of electroactive groups into such long-chain compounds. Some examples are depicted in Figure 4. Charge-transfer materials, such as the *N*-octadecylpyridinium-Ni(dmit)<sub>2</sub> complex, are important organic conductors. These are formed from a variety of molecules, primarily aromatics that can behave as electron donors (D) and electron acceptors (A) [8]. Complete transfer of an electron from a donor to an acceptor molecule results in a system that is electrically insulating (e.g., the transfer of a valence electron in a Cl atom to a Na atom to form the compound NaCl). However, if the ratio of the number of donor molecules to the number of acceptor molecules differs from 1:1 (e.g., the stoichiometry is 1:2 or

2:3), or if there is incomplete transfer of an electron from a donor to an acceptor (say, six electrons in every ten donor atoms are transferred), then partially filled electron bands can be formed and electrical conduction is possible.

Well-known donor and acceptor molecules are tetrathiafulvalene (TTF) and tetracyanoquinodimethane (TCNQ), respectively. A 1:1 TCNQ:TTF salt exhibits a high room-temperature conductivity ( $5 \times 10^4 \text{ S m}^{-1}$ ) and metallic behavior is observed as the temperature is reduced to 54 K (i.e., the conductivity increases with decreasing temperature). The molecules in such compounds are arranged in segregated stacks, in which donors and acceptors form separate donor stacks (DDDDDD...) and acceptor stacks (AAAAA...). The possibility of imitating this structural arrangement in multilayer LB films has resulted in the synthesis of many amphiphilic derivatives of TTF and TCNQ and related compounds [14]. The organometallic Ni(dmit)<sub>2</sub> compound shown in Figure 4 is an electron acceptor. The long-chain pyridinium counterion allows this compound to form an insoluble layer at the air–water interface and to be built up as a multilayer structure using the LB technique [15]. Following iodine doping, a relatively high in-plane conductivity ( $10^2$ – $10^3 \text{ S m}^{-1}$ ) is observed. Such thin films show electrical behavior associated with inorganic semiconductors and can be used as the basis of a field effect transistor (FET) device [16]. Although the carrier mobility (carrier velocity per unit applied electric field) is much lower in these devices than in single crystalline silicon or gallium arsenide, the values are comparable to those found in amorphous silicon and auger well for the development of devices that can be processed using low-cost methods. Metallic behavior (i.e., conductivity decreasing with increasing temperature) has also been reported in LB films based on the electronic molecule bis(ethylenedioxy)tetrathiafulvalene (BEDO-TTF) [17, 18]. The results of low-temperature conductance and magnetoconductance experiments have been interpreted in terms of a weakly localized two-dimensional electronic system formed in the conducting donor layers. Other relevant electroactive materials that can be manipulated by the LB technique have been based on fullerene derivatives [19] and on carbon nanotubes [20, 21]. In the latter case, the nanotubes were either mixed with surfactant molecules or grafted with poly(ethylene oxide) to form condensed floating films.

An intriguing possibility is that of observing molecular rectification using monolayer or multilayer films. This follows from the prediction of Aviram and Ratner [22] that an asymmetric organic molecule containing a donor and acceptor group separated by a short  $\sigma$ -bonded bridge (allowing quantum mechanical tunnelling) should exhibit diode type characteristics. There have been many attempts to obtain this effect in LB systems [9]. Asymmetric current versus voltage behavior has certainly been recorded for many metal–LB film–metal structures, although the results have often been open to several interpretations because of the asymmetry of the metallic electrodes and the presence of oxide layers. However, data obtained using gold for both electrodes suggests that molecular rectification can be observed using appropriate LB films of charge-transfer complexes [23, 24].



**Figure 4.** Examples of amphiphilic organic compounds suitable for LB film deposition.

As noted above, an area of interest is the fabrication of asymmetric nanostructures that exhibit second-order nonlinear optical effects. The hemicyanine dye shown in Figure 4 is an example of a compound that has been extensively investigated in this respect. The molecule possesses both donor and acceptor groups separated by a conjugated  $\pi$ -electron system; the long hydrocarbon chain facilitates molecular alignment on a water surface. By alternating the hemicyanine dye with a “spacer” molecule (e.g., a simple fatty acid) or with a compound with a complementary donor–acceptor configuration (i.e., a similar compound, but with the donor moiety positioned adjacent to the hydrocarbon chain), an LB film may be assembled that exhibits significant second harmonic generation [25]. Some LB film materials may be built up to over a hundred layers in thickness, where they might be suitable for use in electro-optic devices [9, 26].

A further field of endeavor is that of chemical sensors [27–29]. Gas detectors with high sensitivity, reversibility, and appropriate selectivity continue to be sought for process control and environmental monitoring. For most gas sensors, advantages accrue by using the sensing element in thin film form (not least, the high surface-to-volume ratio). A simple sensor exploits the variation of electrical resistance of a thin layer of gas-sensitive material, for example, a phthalocyanine or conductive polymer. The conductivity of such organic semiconductors changes in the presence of oxidizing or reducing agents. The effect is analogous to the doping of an inorganic semiconductor, such as silicon, with acceptor or donor impurities. A problem associated with these chemiresistor devices is that the resistance of the organic layer is usually very high. Consequently, the output currents are low (typically picoamperes), requiring elaborate detection electronics and careful shielding and guarding of components. This difficulty may be overcome by incorporating the organic sensing layer into a diode or field effect transistor [29].

An optical transduction method that is often used with ultrathin films, such as LB films, is that of surface plasmon resonance [30, 31]. Surface plasma waves are collective oscillations of the free electrons at the boundary of a metal and a dielectric. These can be excited by means of evanescent electromagnetic waves. This excitation is associated with a minimum in the intensity of the radiation reflected from the thin film system, called surface plasmon resonance (SPR). The sensitivity of SPR is noteworthy, and changes in refractive index of  $10^{-5}$  may be monitored; thus the technique compares favorably with ellipsometry. The method has been used with LB films to provide both gas detectors [29] and sensors for metal ions in solution [32].

One criticism that is often levelled at the LB approach is that the amphiphilic compounds necessary for film formation are not particularly stable. Long-chain fatty acid type materials possess relatively low melting points and have poor mechanical properties. Furthermore, the incorporation of a long hydrocarbon chain can “dilute” the electroactive part of the molecule. Certain LB film materials, however, such as phthalocyanines, other dyes, and polymers (see next paragraph), can be deposited without the need for long aliphatic chains [33, 34], although the molecules of such compounds may not possess a high degree of order when deposited as LB multilayers.

Improvements in film stability can be achieved by using polymeric materials. There are broadly two different methods available to produce polymeric multilayer structures [9]. First, a monomeric amphiphile, which can be deposited using the LB approach, can be used. The molecules in the LB film can then be cross-linked, for example by exposure to ultra-violet radiation. An alternative is to build up LB films from a polymeric monolayer, that is, a preformed polymer. In some cases, it is not necessary to use a “traditional” LB material, for example, a long chain with hydrophilic and hydrophobic terminal groups. Rod-type preformed polymers, based on porphyrins or phthalocyanines, can undergo self-organization on the water surface. During the LB transfer, the long axes of the rods are preferentially aligned parallel to the dipping direction so that oriented multilayers with nematic-like order are formed [9]. Figure 4 shows an example of the conductive polymer polyaniline that can be deposited in this way [35], although, as noted in the previous paragraph, the molecular order in such films is not always high [36]. Polyaniline possesses three reversible oxidation states, each with a distinct backbone structure composed of different proportions of quinoid and phenylene rings; the compound in Figure 4 represents a generic formula for this polymer. To form a multilayer film, polyaniline, in its emeraldine base form ( $x = 0.5$  in Fig. 4), is mixed first with a small quantity of acetic acid; this improves spreading on the subphase surface. The mixture is then dissolved in 1-methyl-2-pyrrolidinone. Following spreading on a water surface and compression, electrically conductive Z-type LB films can then be deposited, up to 50 layers in thickness, on a solid substrate.

The LB technique may also be combined with solid-state chemistry methods to produce novel molecular architectures. For example, a network of conductive polypyrrole (molecular “wires”) may be obtained in a fatty acid matrix [37, 38]. First, monolayers of the iron salt of a long-chain fatty acid (e.g., ferric palmitate) are assembled on an appropriate substrate. The multilayer film is then exposed to saturated HCl vapor at room temperature for several minutes. During this process, a chemical reaction transforms the fatty acid salt into layers of ferric chloride separated by layers of fatty acid. In the third and final step, the film is exposed to pyrrole vapor and a reaction occurs between the pyrrole and the ferric chloride, producing polypyrrole distributed within the multilayer assembly.

Highly ordered layers of nondispersive colloids may also be formed with the Langmuir–Blodgett technique [39]. The interest in such structures lies in the fact that it is possible to induce the particles to coalesce into a structure analogous to a close-packed crystal. It is possible to obtain repeat distances large enough so that radiation in the optical region can be diffracted, just as X-rays are diffracted in an ordinary crystal. Such photonic crystals may have many practical uses in optoelectronics.

Many biological molecules form condensed monolayers on a water surface [9, 10]. Phospholipids, chlorophyll a, the green pigment in higher plants, vitamins A, E, and K, and cholesterol are all examples. Biochemists and biophysicists have also been long aware that monomolecular films bear a close resemblance to naturally occurring biological membranes and many revealing experiments may be undertaken

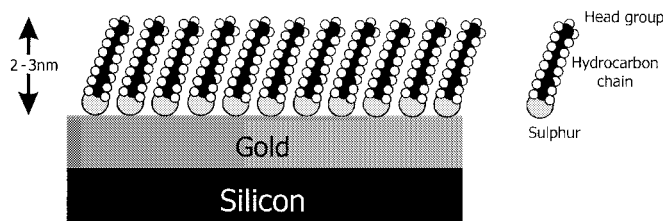
with floating and transferred layers of biological compounds. The structurally similar proteins streptavidin and avidin have been the model system for protein binding studies. Each tightly binds biotin at four symmetrically located sites. Streptavidin in an aqueous subphase will bind to a biotin lipid at the air/water interface [40]. The resulting complex forms two-dimensional crystalline domains.

The vertical dipping LB process is not the only way to transfer a floating molecular film to a solid substrate or to build up multilayer films. Other methods are based on touching one edge of a hydrophilic substrate with the monolayer-covered subphase or lowering the substrate horizontally so that it contacts the ends of the floating molecules [9]. This is useful for the transfer of highly rigid monolayers to solid supports.

### 3. SELF-ASSEMBLY

In principle, self-assembly is a much simpler process than that of LB deposition [12]. Monomolecular layers are formed by the immersion of an appropriate substrate into a solution of the organic material, Figure 5. The best known examples of self-assembled systems are organosilicon on hydroxylated surfaces ( $\text{SiO}_2$ ,  $\text{Al}_2\text{O}_3$ , glass, etc.) and alkanethiols on gold, silver, and copper. However, other combinations include dialkyl sulphides on gold; dialkyl disulphides on gold; alcohols and amines on platinum; and carboxylic acids on aluminum oxide and silver. The self-assembly process is driven by the interactions between the head group of the self-assembling molecule and the substrate, resulting in a strong chemical bond between the head group and a specific surface site, for example, a covalent Si—O bond for alkyltrichlorosilanes on hydroxylated surfaces. Molecules possessing one or more electroactive groups may be deposited by self-assembly. For example, the incorporation of an amphiphilic TTF unit into a metal-binding macrocyclic structure allows the resulting self-assembled monolayer to act as a sensor for metal ions [41]. The presence of the metal cation imposes an inductive effect on the polarizable TTF system, resulting in an anodic shift of the first oxidation potential as indicated by cyclic voltammetry experiments. Thus, self-assembled monolayers represent an attractive method for device fabrication, having the advantages of straightforward preparation and generally being very robust (stable to solvents, acids, and bases).

The self-assembly process is usually restricted to the deposition of a single molecular layer on a solid substrate. However, chemical means can be exploited to build up multilayer organic films. A method pioneered by Sagiv is based



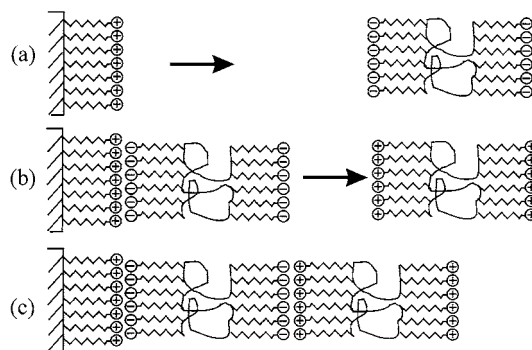
**Figure 5.** Self-assembled monolayer film of an alkane-thiol on an Au-coated substrate.

on the successive absorption and interaction of appropriate molecules [42, 43]. The headgroups react with the substrate to give a permanent chemical attachment and each successive layer is chemically attached to the one before in a very similar way to that used in systems for supported synthesis of proteins.

Functionalized metallic nanoclusters represent a hybrid material that can combine the advantages of organic specificity with the robustness and processability of inorganic materials. Such nanoparticles can be chemically modified with a variety of terminal groups, including OH,  $\text{CH}_3$ ,  $\text{NH}_2$ , and COOH [44] and combined with the self-assembly technique to provide selective coatings, for example, for chemical sensing.

### 4. LAYER-BY-LAYER ELECTROSTATIC DEPOSITION

In another method, shown in Figure 6, the ionic attraction between opposite charges is the driving force for the multilayer buildup [45, 46]. In contrast to the Sagiv technique, which requires a reaction yield of 100% to maintain surface functional density in each layer, no covalent bonds need to be formed. A solid substrate with a positively charged planar surface is immersed in the solution containing the anionic polyelectrolyte and a monolayer of the polyanion is adsorbed (Fig. 6a). Since the adsorption is carried out at relatively high concentrations of the polyelectrolyte, most ionic groups remain exposed to the interface with the solution and the surface charge is reversed. After rinsing in pure water, the substrate is immersed in the solution containing the cationic polyelectrolyte. Again, a monolayer is adsorbed but now the original surface charge is restored (Fig. 6b), resulting in the formation of multilayer assemblies of both polymers (Fig. 6c). This method has been used to build up layers of partially doped polyaniline and a polyanion, sulphonated polystyrene [47]. Biocompatible surfaces consisting of alternate layers of charged polysaccharides and oppositely charged synthetic polymers can also be deposited in this way [48].



**Figure 6.** Buildup of multilayer assemblies by consecutive adsorption of anionic and cationic polyelectrolytes: (a) substrate with a positively charged surface is immersed in an anionic polyelectrolyte; (b) following monolayer adsorption and washing, the substrate is immersed in a cationic polyelectrolyte; (c) resulting multilayer assembly.

Bilayer films of poly(ethyleneimine) (positively charged) and poly(ethylene-co-maleic acid) have been used for chemical sensing [49]. The technique of surface plasmon resonance was used to monitor, *in-situ*, the deposition of these films. Subsequent exposure to aqueous solutions of metal acetate (metal = copper, nickel) resulted in a shift in position of the SPR curve. Phase-separated polyelectrolyte multilayer films that undergo a reversible pH-induced swelling transition have also been exploited for erasable nanoporous antireflection coatings, opening up applications for bioreponsive materials and membrane applications [50].

A related, but alternative, approach uses layer-by-layer adsorption driven by hydrogen-bonding interactions [51]. This has been accomplished with polyvinylpyrrolidone, polyvinyl alcohol, polyacrylamide, and polyethylene oxide. In the case of polyaniline, comparisons with films assembled via the electrostatic mechanism, using sulphonated polystyrene, indicate that the nonionic polymers adsorb onto polyaniline with a greater density of loops and tails and form highly interpenetrated bilayers with high polyaniline content.

## 5. SPIN-COATING

Spin-coating is a method that is extensively used by the microelectronics industry for depositing layers of photoresist, generally polyimides, onto silicon wafers [7, 52–54]. A quantity of a polymer solution is first placed on the semiconductor wafer, which is then rotated at a fixed speed of several thousand rpm (or the solution can be applied while the wafer is slowly rotating). The resist solution flows radially outwards, reducing the fluid layer thickness. Evaporation of the solvent results in a uniform thin film. The initial stage involves delivering a quantity of solution to the surface of the substrate. The substrate surface may be pretreated with an adhesion promoter, such as hexamethyldisilazane (HMDS), to improve wetting. This is often used when coating silicon wafers. The HMDS consists of six methyl groups and a Si<sub>2</sub>NH group. This reacts with the thin layer of oxide on the silicon surface to form a new surface layer of hydrophobic methyl groups, allowing the organic solution to make intimate contact with the substrate.

The initial volume of the fluid dispensed onto the rotating disk and the rate of fluid delivery have a negligible effect on the final film thickness. In contrast, the resist viscosity (dependent on the concentration of the starting solution) and final film speed are both important process parameters. An increase in angular velocity decreases the film thickness; an inverse power-law relationship generally holds for the thickness dependence on the final spin speed. For a given speed, the film thickness decreases rapidly at first, but then slows considerably at longer times. A simple theory predicts the following relationship between the thickness of the spun film,  $d$ , the viscosity coefficient of the solution,  $\eta$ , its density,  $\rho$ , the angular velocity of the spinning,  $\omega$ , and the spinning time,  $t$  [7]

$$d = \left( \frac{\eta}{4\pi\rho\omega^2} \right)^{1/2} t^{-1/2} \quad (3)$$

More sophisticated models have been developed to allow for changes in the resist resulting from solvent evaporation and

the non-Newtonian character of the rheological behavior of the photoresist [52–54].

Organic compounds that have been deposited successfully by spin-coating include electrically insulating polymers such as polyvinylidene fluoride, conductive polymers, and dyes developed for electroluminescent (EL) displays [55–62]. A selection of such compounds is shown in Figure 7. A key polymeric material for use in EL displays is poly(p-phenylene vinylene) or PPV [59, 60]. This is a conjugated polymer that has the advantage of being readily processable to form thin films over large areas, which are stable over a wide temperature range and relatively cheap to manufacture. Changing the chemical structure of the polymer can alter the emission color and the electrical transport properties. Figure 7 shows the structure of one PPV derivative that has been extensively used—poly(2-methoxy-5-(2'-ethylhexyloxy)-1,4-phenylene vinylene), MEH-PPV. Spin-coating can be used to prepare high-quality films of MEH-PPV of a few hundred nanometers in thickness [61, 62]. This polymer can also be processed into much thinner films using the LB technique [63].

Amorphous elastomeric polymers represent an important category of materials for the electronics industry that can be processed by spin-coating. Materials such as silicones

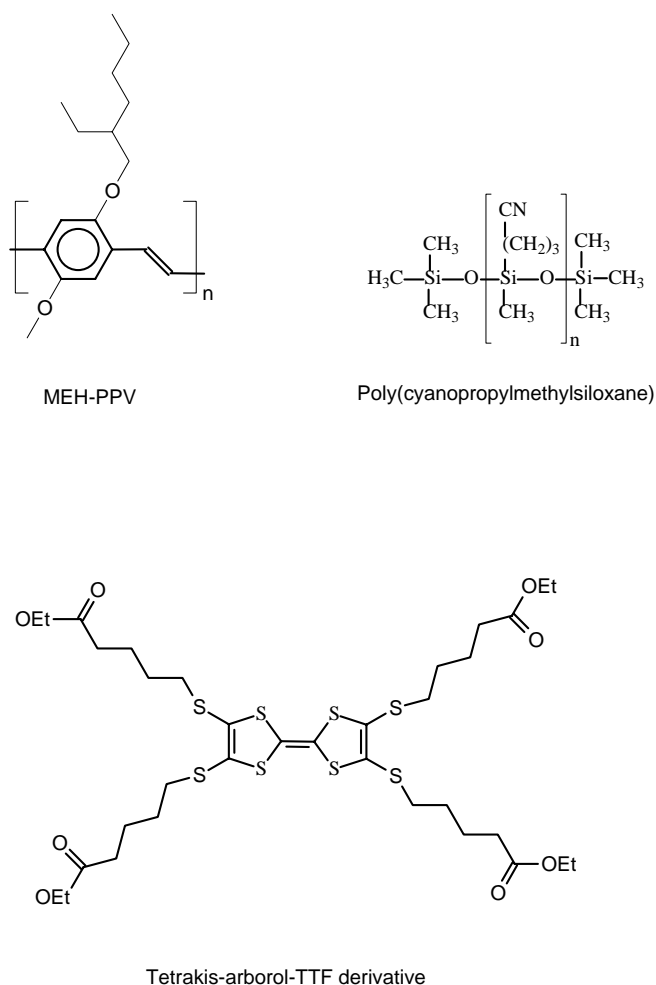


Figure 7. Examples of compounds suitable for spin-coating.

are used extensively as sealants and encapsulants [64], but are also finding use as nonconductive sensor coatings [29]. In the elastomeric phase (i.e., above the glass transition temperature), constant thermal motion of the polymer chains allows rapid vapor diffusion. Adsorption and desorption of a vapor leaves the material in the same state. The softness of elastomeric materials has an additional advantage for piezoelectric sensors such as surface acoustic wave devices that are sensitive to changes in material stiffness. An example of such materials is the family of polysiloxanes, which are characterized by a repeat unit (-RR'-Si-O-) where R and R' are generic functional groups. By modifying the side chains, nonpolar, polar, and polarizable polymers can be obtained. One such example, poly(cyanopropylmethylsiloxane), is shown in Figure 7. Chemical vapor sensors based on a number of different transduction methods have been demonstrated with this polymer [65–67].

Figure 7 also shows the structure of a tetrakis-arboral-TTF derivative that can be processed by spin-coating to form potentially conductive nanowires [68]. The TTF inner core of these molecules self-assembles into supermolecular aggregates possessing a redox-active interior and a hydrophilic exterior sheath [69].

## 6. PHYSICAL VAPOR DEPOSITION

Solid materials vaporize when heated to sufficiently high temperatures; this process may proceed through the liquid phase. A thin film is obtained by the condensation of the vapor onto a colder substrate [4]. This thermal evaporation method is applied to deposit films of inorganic materials, such as metals and their alloys. However, the technique is being used increasingly for the formation of layers of low molecular weight organic compounds.

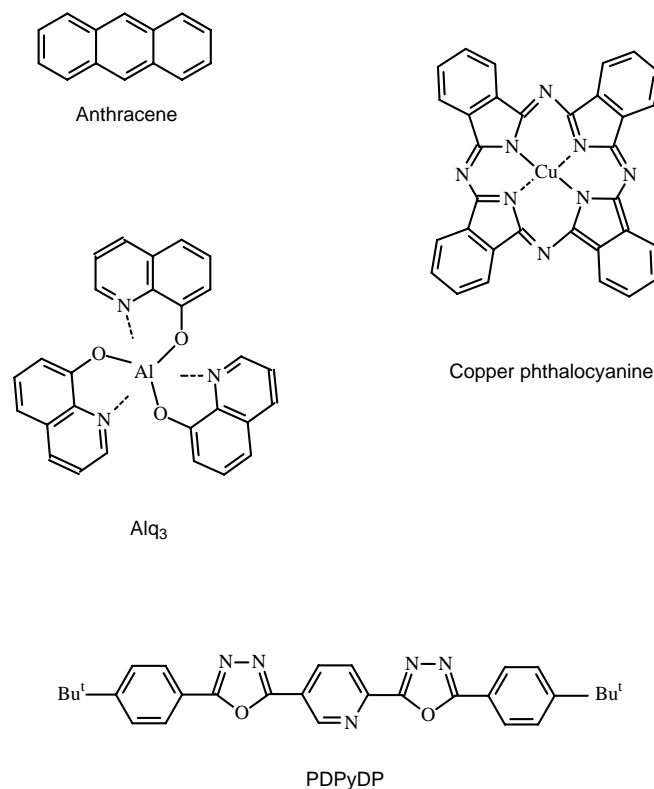
Because of collisions with ambient gas atoms, a fraction of the vapor atoms will be scattered. For a straight-line path between the evaporating material (source) and the substrate, it is necessary to use low pressures ( $<10^{-4}$  mbar), where the mean free path of the gas atoms is much greater than the source–substrate distance. This allows the use of a shadow mask immediately in front of the substrate to define patterns. The low pressure also prevents contamination of the source material (e.g., by oxidation). A typical evaporation system, which can be made out of glass or metal, is evacuated to a pressure of  $10^{-4}$ – $10^{-6}$  mbar, normally with two types of vacuum pump operating in series (a rotary and diffusion pump).

Although commonly thought of as a single process, the deposition of thin films by thermal evaporation consists of several distinguishable steps: (i) transformation of the condensed phase, solid or liquid, into the gaseous state; (ii) vapor molecules traversing the space between the source and the substrate; and (iii) condensation of the vapor upon arrival on the substrate.

The first step requires the conversion of thermal to mechanical energy, which is achieved by a variety of physical methods. Resistive heating has been used to deposit fluorescent dyes, charge-transfer salts, and large macromolecules,

such as the phthalocyanines [70–74]; many of these compounds are finding use as the light-emitting layer or charge-transport layer in organic light-emitting devices [59, 60]. The molecular structures of some of these compounds are shown in Figure 8. Typical evaporation rates are  $1$ – $10$  nm  $\text{min}^{-1}$ . Other techniques include arc evaporation; RF heating; or heating by electron bombardment. Deposition of polymer films by laser ablation is an area that offers some promise [75]. Laser pulsed methods have been used successfully for polyethylene, polycarbonate, polyimide, and polymethylmethacrylate; typical film growth rates are  $0.02$ – $0.1$  nm per laser pulse. As an alternative to traditional thermal evaporation or spin-coating, this method has also been used to deposit organic materials for organic electroluminescence [76]. An organic pellet target was ablated with two wavelengths,  $532$  nm and  $355$  nm, of a Q-switched Nd/YAG laser at a base pressure of  $2 \times 10^{-5}$  torr. Films deposited in this way were more amorphous than films fabricated by excimer lasers.

Materials that dissociate in the vapor phase may provide solid films with a stoichiometry that differs from that of the source. Therefore, special techniques have been devised. One approach is to use the method of “flash” evaporation. Rapid evaporation is achieved by continuously dropping fine particles of the materials onto a hot surface. Although fractionation occurs during the evaporation of each particle (the more volatile component evaporating first), at any time there will be several particles at different stages of fractionation. Consequently, the vapor phase will possess a similar



**Figure 8.** Examples of organic compounds suitable for thermal evaporation.



composition to that of the source material. A further technique is to evaporate from two or more sources, and control the vapor flux from each to obtain a vapor with the required composition. This has been used effectively to deposit thin films of doped organic charge-transfer salts [77]: one source is the charge-transfer salt, for example, tetrathiafulvalene, while the other is the dopant, for example, iodine. Laser co-ablation techniques can be used to deposit films of metal-polymer composite films [75].

The microstructure of an evaporated thin film depends on the evaporation rate, substrate temperature, and chemical and physical nature of the substrate surface. The size of the grains in a polycrystalline film will generally be larger for high source and substrate temperatures. However, if the kinetic energy of the incoming molecules is too high, the surface mobility of the adsorbed species is reduced because the vapor molecules will penetrate the condensed film. The effect of substrate temperature on grain size is greater for relatively thicker films. For a given material-substrate combination and under a fixed set of deposition conditions, the grain size increases as the film thickness increases. However, beyond a certain thickness, the grain size remains constant, suggesting that coherent growth with the underlying grains does not go on forever.

The physical nature of evaporated films can be changed by post-deposition heat treatment (annealing). This is usually associated with a change in the crystallinity of the film. For example, following thermal evaporation, the dc in-plane conductivity of thin films of the electron donor bis(ethylenedithio) tetrathiafulvalene (BEDT-TTF) can be increased by many orders of magnitude by doping with iodine and then annealing at 60 °C [78].

Molecular beam epitaxy (MBE) is, in principle, very similar to the method of vacuum evaporation described in the previous section [8]. However, an ultrahigh vacuum ( $<10^{-9}$  mbar) is required to eliminate the scattering by residual gas molecules. The technique consists of directing controlled "beams" of the required molecules towards a heated substrate. Multiple sources, Knudsen cells, can be shuttered and used to create a superlattice structure on the substrate and control the molecular composition, orientation, and packing in two dimensions. Each Knudsen cell encloses an evaporating surface that is large compared to the orifice. The diameter of the orifice must be about one-tenth or less of the mean free path of the gas molecules, and the wall around the orifice must be vanishingly thin so that gas molecules leaving the enclosure are not scattered, adsorbed, and desorbed by the orifice wall. MBE has been used to produce ordered films of phthalocyanines and other molecular crystals on inorganic single-crystal substrates [8, 79, 80].

Sputtering is based on the momentum transfer exchange of accelerated ions incident on a target of source material [4]. The principle advantage of sputtering is that almost any material can be deposited. Since no heating is required, materials that are difficult to evaporate by thermal means are readily sputtered. The method has found application for the formation of thin films of certain organic polymers, for example, polytetrafluoroethylene, PTFE. However, a relatively large amount of the material is needed. This is not always practical for many novel organic compounds that may only be available in small quantities.

## 7. NANOPATTERNING

Planar microelectronic components are patterned using photolithography. A surface is covered first with a light-sensitive photoresist and then exposed to ultraviolet light through a mask. Either the exposed photoresist (positive resist) or the unexposed regions (negative resist) can be washed away subsequently to leave positive or negative image of the mask on the surface.

Conventional photolithography has feature sizes greater than about 100 nm. However, structures of less than 10 nm may be fabricated using techniques of shadowing and edge-step deposition [7]. Substrate steps with a square profile are first formed by ion-beam etching. Ion-etching the film-coated substrate at an angle then produces wires of triangular cross section, so that the wire is formed in the shadow of the step. Metal wires as narrow as 30 nm and as long as 0.5 mm have been fabricated in this way. Chemical approaches to the deposition of ultrathin organic films offer some control over the composition and structure of a surface [81]. Here, a substrate is patterned with gold and aluminum strips by conventional photolithography. The aluminum spontaneously oxidizes in air and presents aluminum oxide at the solid-vapor interface; in contrast, the gold remains "clean." Two adsorbates are then chosen (in this case an alkane thiol and a carboxylic acid) so that they adsorb strongly and selectively on the gold and alumina.

Brittain et al. describe a series of "soft" lithographic methods that may be suited to the patterning of organic layers [82]. A pattern-transfer element is formed by pouring a liquid polymer, such as poly(dimethylsiloxane), onto a "master" made from silicon. The polymer is allowed to cure to form an elastomer, which can then be removed from the master. This replica can be used subsequently as a stamp to transfer chemical ink, such as a solution of an alkanethiol, to a surface. Features with dimensions of 40–100 nm can be produced with the technique of near-field, phase-shift photolithography [82].

Scanning microscopy methods offer a powerful means of manipulating molecules and are able to reposition molecules, such as the fullerene C<sub>60</sub>, on surfaces or to break up an individual molecule [83]. A further approach that has recently been developed is called dip-pen nanolithography (DPN) [84, 85]. This technique is able to deliver organic molecules in a positive printing mode. An atomic force microscope (AFM) tip is used to "write" alkanethiols on a gold thin film in a manner analogous to that of a fountain pen. Molecules flow from the AFM tip to a solid substrate ("paper"), making DPN a potentially useful tool for assembling nanoscale devices. A range of different materials can be used with the DPN process, including proteins [86] and magnetic nanoparticles [87]. The method has also been used to write organic patterns with sub-100-nm dimensions directly onto silicon and gallium arsenide surfaces [88].

The need to combine large area coatings with device patterning has resulted in the development of ink-jet printing [89, 90]. Although ink-jet printhead droplet ejection can be achieved with thermal (bubble-jet) and piezoelectric modes of operation, the majority of published literature on ink-jet printing as a tool for manufacturing organic devices has been the result of using piezoelectric actuated printers. Piezoelectric printhead technology is favored primarily because it

applies no thermal load to the organic “inks” and is compatible with the printing of digital images. The combination of solution-processable emissive polymers with ink-jet printing offers some promise in the development of low-cost, high-resolution displays [91]. The technique has also been applied to the manufacture of all-polymer transistor circuits [92].

## GLOSSARY

**Dip-pen nanolithography** An atomic force microscope is used to transfer a chemical ink to a surface in a manner analogous to that of a fountain pen.

**Ink-jet printing** Ink droplet ejection from a reservoir to a surface using either thermal (bubble-jet) or piezoelectric means.

**Langmuir–Blodgett (LB) film deposition** Transfer of a condensed monomolecular film from a liquid subphase (usually water) surface to a solid substrate by raising and lowering the latter through the monolayer/air interface.

**Layer-by-layer electrostatic deposition** Formation of multilayers of organic compounds on a solid substrate by sequential immersion of the latter in solutions of positively and negatively charged polyelectrolytes.

**Molecular beam epitaxy (MBE)** A variation on physical vapor deposition. The technique consists of directing controlled “beams” of the required molecules towards a heated substrate. The deposition takes place in ultrahigh vacuum.

**Molecular electronics** Exploitation of organic compounds in electronic or optoelectronic devices.

**Photolithography** The method used to pattern microelectronic devices. A surface is covered first with a light-sensitive photoresist and then exposed to UV light through a mask. Either the exposed photoresist (positive resist) or the unexposed regions (negative resist) can be washed away subsequently to leave a positive or negative image of the mask on the surface.

**Physical vapor deposition** Thin film formation by vaporization under reduced vacuum followed by condensation of the vapor onto a solid surface.

**Self-assembly** Spontaneous formation of a monolayer on a surface by the immersion of an appropriate solid substrate (e.g., Au) into a solution of an organic compound (e.g., alkanethiol).

**Soft lithography** The pattern-transfer element is formed by pouring a liquid polymer onto a master made from silicon. This replica can be used as a stamp to transfer chemical ink, such as a solution of alkanethiol, to a surface.

**Spin-coating** Thin film formation by deposition of a solution onto a solid, which is then rotated at a speed of several thousand revolutions per minute.

**Sputtering** Thin film deposition technique based on the momentum transfer between accelerated ions and a target of source material. The process is undertaken at reduced pressure.

**Surface plasmon/surface plasma wave** Collective oscillations of the free electrons at the boundary between a metal (e.g., Ag, Au) and a dielectric (e.g., air, water).

## REFERENCES

1. K. D. Leaver and B. N. Chapman, “Thin Films.” Wykeham Publishers, London, 1971.
2. O. S. Heavens, “Thin Film Physics.” Methuen, London, 1970.
3. K. L. Chopra, “Thin Film Phenomena.” McGraw-Hill, New York, 1969.
4. L. I. Maissel and R. Glang, Eds., “Handbook of Thin Film Technology.” McGraw-Hill, New York, 1970.
5. T. J. Coutts, Ed., “Active and Passive Thin Film Devices.” Academic Press, London, 1978.
6. M. Ohring, “The Materials Science of Thin Films.” Academic Press, San Diego, 1992.
7. I. Brodie and J. J. Muray, “The Physics of Micro/Nano-Fabrication.” Plenum, New York, 1992.
8. M. C. Petty, M. R. Bryce, and D. Bloor, Eds., “An Introduction to Molecular Electronics.” Edward Arnold, London, 1995.
9. M. C. Petty, “An Introduction to Langmuir–Blodgett Films.” Cambridge Univ. Press, Cambridge, 1996.
10. G. G. Roberts, Ed., “Langmuir–Blodgett Films.” Plenum, New York, 1990.
11. R. H. Tredgold, “Order in Thin Organic Films.” Cambridge Univ. Press, Cambridge, 1994.
12. A. Ulman, “An Introduction to Organic Thin Films.” Academic Press, San Diego, 1991.
13. T. H. Richardson, Ed., “Functional Organic and Polymeric Materials.” Wiley, Chichester, 2000.
14. M. R. Bryce and M. C. Petty, *Nature* 374, 771 (1994).
15. C. Pearson, A. S. Dhindsa, L. M. Goldenberg, R. A. Sing, R. Dieing, A. J. Moore, M. R. Bryce, and M. C. Petty, *J. Mater. Chem.* 5, 1601 (1995).
16. C. Pearson, A. J. Moore, M. C. Petty, and M. R. Bryce, *Thin Solid Films* 244, 932 (1994).
17. Y. Ishizaki, M. Izumi, H. Ohnuki, K. Kalita-Lipinska, T. Imakubo, and K. Kobayashi, *Phys. Rev. B* 63, 134201 (2001).
18. Y. Ishizaki, M. Suzuki, H. Ohnuki, T. Imakubo, and M. Izumi, *Mol. Cryst. Liq. Cryst.* 376, 263 (2002).
19. M. Carano, P. Ceroni, F. Paolucci, S. Roffia, T. Da Ros, M. Prato, M. I. Sluch, C. Pearson, M. C. Petty, and M. R. Bryce, *J. Mater. Chem.* 10, 269 (2000).
20. V. Krstic, J. Muster, G. S. Duesberg, G. Philipp, M. Burghard, and S. Roth, *Synth. Met.* 110, 245 (2000).
21. M. Sano, A. Kamino, J. Okamura, and S. Shinkai, *Langmuir* 17, 5125 (2001).
22. A. Aviram and M. A. Ratner, *Chem. Phys. Lett.* 29, 277 (1974).
23. G. J. Ashwell and D. S. Gandolfo, *J. Mat. Chem.* 12, 411 (2002).
24. N. Okazaki, J. R. Sambles, M. J. Jory, and G. J. Ashwell, *Appl. Phys. Lett.* 81, 2300 (2002).
25. H. Ancelin, G. Briody, J. Yarwood, J. P. Lloyd, M. C. Petty, M. M. Ahmad, and W. J. Feast, *Langmuir* 6, 172 (1990).
26. G. J. Ashwell and A. J. Whittam, *Mol. Cryst. Liq. Cryst.* 337, 1 (1999).
27. J. W. Gardner, “Microsensors.” Wiley, Chichester, 1994.
28. P. T. Moseley and A. J. Crocker, “Sensor Materials.” IOP Publishing, Bristol, 1996.
29. M. C. Petty and R. Casalini, *Eng. Sci. Ed. J.* 10, 99 (2001).
30. J. Homola, S. S. Yee, and G. Gauglitz, *Sensors and Actuators B* 54, 3 (1999).
31. J. M. Brockman, B. P. Nelson, and R. M. Corn, *Ann. Rev. Phys. Chem.* 51, 41 (2000).
32. I. K. Lednev and M. C. Petty, *Adv. Mater.* 8, 615 (1996).
33. S. Baker, M. C. Petty, G. G. Roberts, and M. V. Twigg, *Thin Solid Films* 99, 53 (1983).
34. G. J. Ashwell and M. A. Amiri, *J. Mater. Chem.* 12, 2181 (2002).
35. N. E. Agbor, M. C. Petty, A. P. Monkman, and M. Harris, *Synth. Met.* 55–57, 3789 (1993).
36. V. I. Troitsky, T. S. Berzina, and M. P. Fontana, *Synth. Met.* 129, 39 (2002).

37. R. B. Rosner and M. F. Rubner, *Chem. Mater.* 6, 581 (1994).
38. R. Casalini, L. M. Goldenberg, C. Pearson, B. K. Tanner, and M. C. Petty, *J. Phys. D* 31, 1 (1998).
39. M. Bardosova and R. H. Tredgold, *J. Mater. Chem.* 12, 2835 (2002).
40. M. Hoffman, W. Müller, H. Ringsdorf, A. M. Rourke, E. Rump, and P. A. Suci, *Thin Solid Films* 210/211, 780 (1992).
41. A. J. Moore, L. M. Goldenberg, M. R. Bryce, M. C. Petty, A. P. Monkman, C. Marengo, J. Yarwood, M. J. Joyce, and S. N. Port, *Adv. Mater.* 10, 395 (1998).
42. L. Netzer and J. Sagiv, *J. Amer. Chem. Soc.* 105, 674 (1983).
43. L. Netzer, R. Iscovici, and J. Sagiv, *Thin Solid Films* 99, 235 (1983).
44. H. L. Zhang, S. D. Evans, J. R. Henderson, R. E. Miles, and T. H. Shen, *Nanotechnology* 13, 439 (2002).
45. G. Decher, J. D. Hong, and J. Schmitt, *Thin Solid Films* 210/211, 831 (1992).
46. G. Decher, Y. Lvov, and J. Schmitt, *Thin Solid Films* 244, 772 (1994).
47. J. H. Cheung, W. B. Stockton, and M. F. Rubner, *Macromolecules* 30, 2712 (1997).
48. Y. Lvov, M. Onda, K. Ariga, and T. Kunitake, *J. Biomater. Sci. Polymer Edn.* 9, 345 (1998).
49. C. Pearson, J. Nagel, and M. C. Petty, *J. Phys. D: Appl. Phys.* 34, 285 (2001).
50. J. A. Hiller, J. D. Mendelsohn, and M. F. Rubner, *Nature Materials* 1, 59 (2002).
51. W. B. Stockton and M. F. Rubner, *Macromolecules* 30, 2717 (1997).
52. W. W. Flack, D. S. Soong, A. T. Bell, and D. W. Hess, *J. Appl. Phys.* 56, 1199 (1984).
53. D. E. Bornside, C. W. Macosko, and L. E. Scriven, *J. Imaging Technology* 13, 122 (1987).
54. D. E. Bornside, C. W. Macosko, and L. E. Scriven, *J. Appl. Phys.* 66, 5185 (1989).
55. D. Chinn and J. Janata, *Thin Solid Films* 252, 145 (1994).
56. M. Scully, M. C. Petty, and A. P. Monkman, *Synthetic Metals* 55–57, 183 (1993).
57. S. M. Critchley, M. R. Willis, M. J. Cook, J. McMurdo, and Y. Maruyama, *J. Mater. Chem.* 2, 157 (1992).
58. M. Petty, J. Tsibouklis, M. C. Petty, and W. J. Feast, *Ferroelectrics* 150, 267 (1993).
59. S. Miyata and H. S. Nalwa, Eds., "Organic Electroluminescent Materials and Devices." Gordon and Breach, Amsterdam, 1997.
60. R. Farchioni and G. Grosso, Eds., "Organic Electronic Materials," Vol. 41. Springer, Berlin, 2001.
61. I. D. Parker, *J. Appl. Phys.* 75, 1656 (1994).
62. T. Q. Nguyen, R. C. Kwong, M. E. Thompson, and B. J. Schwartz, *Appl. Phys. Lett.* 76, 2454 (2000).
63. M. I. Sluch, C. Pearson, M. C. Petty, M. Halim, and I. D. W. Samuel, *Synth. Met.* 94, 285 (1988).
64. J. H. Davis, in "Plastics for Electronics." (M. T. Goosey, Ed.), p. 67. Elsevier, New York, 1985.
65. M. Haug, K. D. Schierbaum, H. E. Endres, S. Drost, and W. Göpel, *Sensors and Actuators A* 32, 326 (1992).
66. M. Haug, K. D. Schierbaum, G. Gauglich, and W. Göpel, *Sensors and Actuators B* 11, 383 (1993).
67. K. D. Schierbaum, *Sensors and Actuators B* 18–19, 71 (1994).
68. T. Le Gall, M. R. Bryce, A. J. Moore, C. Pearson, and M. C. Petty, *Synth. Met.* 121, 1409 (2001).
69. M. R. Bryce, *J. Mater. Chem.* 10, 589 (2000).
70. K. O. Lee and T. T. Gan, *Chem. Phys. Lett.* 51, 120 (1977).
71. Y. Saitoh, M. Matsuoka, Y. Nakao, and T. Kitao, *Chem. Lett.* 285 (1991).
72. M. Kilitziraki, C. Pearson, A. S. Dhindsa, M. R. Bryce, and M. C. Petty, *Thin Solid Films* 284–285, 516 (1996).
73. A. W. Snow and W. R. Barger, in "Phthalocyanines: Properties and Applications" (C. C. Leznoff and A. B. P. Lever, Eds.). VCH Publishers, New York, 1989.
74. C. Wang, G. Y. Jung, Y. Hua, C. Pearson, M. R. Bryce, M. C. Petty, A. S. Batsanov, A. E. Goeta, and J. A. K. Howard, *Chem. Mater.* 13, 1167 (2001).
75. D. B. Chrisey and G. K. Hubler, Eds., "Pulsed Laser Deposition of Thin Films." Wiley Interscience, New York, 1994.
76. C. Hong, H. B. Chae, K. H. Lee, S. K. Ahn, C. K. Kim, T. W. Kim, N. I. Cho, and S. O. Kim, *Thin Solid Films* 409, 37 (2002).
77. J. J. Breen, J. S. Tolman, and G. W. Flynn, *Appl. Phys. Lett.* 62, 1074 (1993).
78. M. Kilitziraki, A. J. Moore, M. C. Petty, and M. R. Bryce, *Thin Solid Films* 335, 209 (1998).
79. M. Nakamura, T. Matsunobe, and H. Tokumoto, *J. Appl. Phys.* 89, 7860 (2001).
80. N. Nicoara, I. Cerrillo, D. Xueming, J. M. García, C. Gómez-Navarro, J. Méndez, and A. M. Baró, *Nanotechnology* 13, 352 (2002).
81. G. M. Whitesides and P. E. Laibinis, *Langmuir* 6, 87 (1990).
82. S. Brittain, K. Paul, X.-M. Zhao, and G. Whitesides, *Physics World*, 11, 31 (1998).
83. J. Gimzewski, *Physics World* 11, 25 (1998).
84. R. D. Piner, J. Zhu, F. Xu, S. Hong, and C. A. Mirkin, *Science* 283, 661 (1999).
85. P. V. Schwartz, *Langmuir* 18, 4041 (2002).
86. K. B. Lee, S. J. Park, C. A. Mirkin, J. C. Smith, and M. Mrksich, *Science* 295, 1702 (2002).
87. X. G. Liu, L. Fu, S. H. Hong, V. P. Dravid, and C. A. Mirkin, *Adv. Mater.* 14, 231 (2002).
88. A. Ivanisevic and C. A. Mirkin, *J. Amer. Chem. Soc.* 123, 7887 (2001).
89. S. P. Speakman, G. G. Rozenberg, K. J. Clay, W. I. Milne, A. Ille, I. A. Gardner, E. Bresler, and J. H. G. Steinke, *Organic Electronics* 2, 65 (2001).
90. G. Perçin and B. T. Khuri-Yakub, *Rev. Sci. Instr.* 73, 2193 (2002).
91. I. D. Rees, K. L. Robinson, A. B. Holmes, C. R. Towns, and R. O'Dell, *MRS Bull.* 27, 451 (2002).
92. H. Sirringhaus, T. Kawase, and R. H. Friend, *MRS Bull.* 26, 539 (2001).

# Organic/Inorganic Nanocomposite Colloids

Elodie Bourgeat-Lami

*Laboratoire de Chimie et Procédés de Polymérisation, CNRS–CPE, Villeurbanne, France*

## CONTENTS

1. Introduction
  2. Nanocomposite Colloids  
via Self-Assembly Techniques
  3. Nanocomposite Colloids  
via Polymerization Techniques
  4. Hybrid Colloids
  5. Conclusion
- Glossary  
References

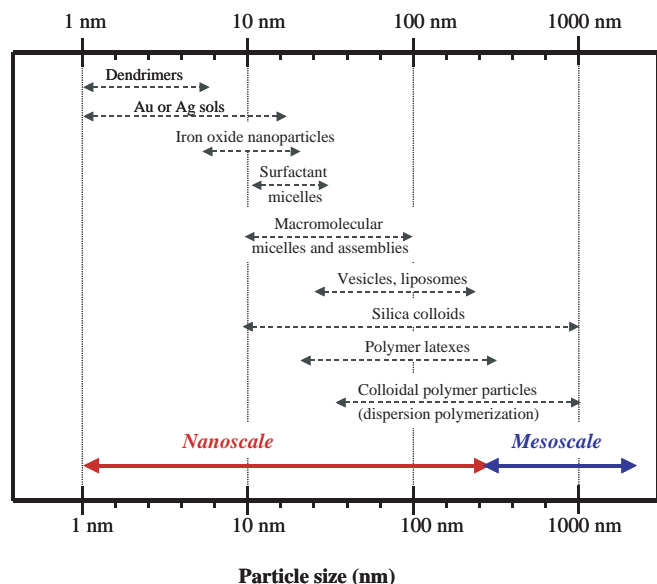
## 1. INTRODUCTION

At the dawn of the 21st century, members of the U.S. Interagency Working Group on Nanoscience, Engineering and Technology (IWGN) wrote in a report to the National Science and Technology Council: “The emerging fields of nanoscience and nanoengineering are leading to unprecedented understanding and control over the fundamental building blocks of all physical things. This is likely to change the way almost everything—from vaccines to computers to automobile tires to objects not yet imagined—is designed and made” [1–3]. This futurist vision of nanomaterials construction from the bottom up (atom by atom) rather than the top down (via nanophysics ultraminiaturization fabrication methods) is shared by many scientists all over the world who aim to create new materials with the control of matter on the nanometer length scale [4]. As a matter of fact, it is now well established that the way molecules of various shapes and surface features organize into patterns on nanoscales determines important material properties including electronic, optical, and magnetic properties and mechanical strength [5]. So, by manipulating atoms and molecules, chemists are learning how to synthesize perfect nanosize objects with new sets of properties [6–8].

One important class of nanomaterials is organic/inorganic (O/I) hybrids and nanocomposites. These materials are nanostructured materials that combine the characteristics of organic and inorganic constituents at the nanoscale.

Nanocomposite materials can be elaborated as fibers, gels, thin films, or particles. By tailoring the structure of these materials at the nanometer length scale, it should be possible in principle to significantly change their properties at a larger scale. Applications are various and concern optics, electronics, catalysis, coatings, and biotechnologies [9–11]. Nanocomposite materials have gained intense interest in recent literature and a variety of significantly different preparation methods have been described and recently reviewed [12–17]. Among the various synthetic techniques, the so-called sol–gel methodology has been extensively investigated as a well-established wet chemical route for creating glassy and hybrid materials [18–23]. But despite the recent interest in nanotechnologies, it is to be underlined that nanoscaled materials are old products that have been produced for several years. Colloidal science [24–26], for instance, affords an extremely broad variety of such nanomaterials ranging from surfactant and macromolecular aggregates to polymer latexes [27–28] including metal colloids (Au, Ag) [29–33], semiconductor nanocrystallites [34–37], and metal oxide nanoparticles [38–43]. Colloidal particles constitute one of the major components of many industrial products such as food, ink, paint, adhesives, papers, and cosmetics. Some typical examples of colloidal particles with their respective range of particle sizes are reported in Figure 1. Since colloidal materials are an important class of products with applications in material science, chemistry, and biology, they have been the subject of extensive research for a long time, the most studied and best established examples being silica colloids and polymer latexes. However, it is only very recently that the combination of organic and inorganic components into colloidal nanocomposites has been considered with interest [44–48]. The earliest developments in this field were principally motivated by the coating industry and concerned the elaboration of polymer encapsulated pigments [49]. Surface modification of pigments is of major technological importance for ink and paint applications. Now, an extremely broad range of seemingly different materials is concerned with those developments.

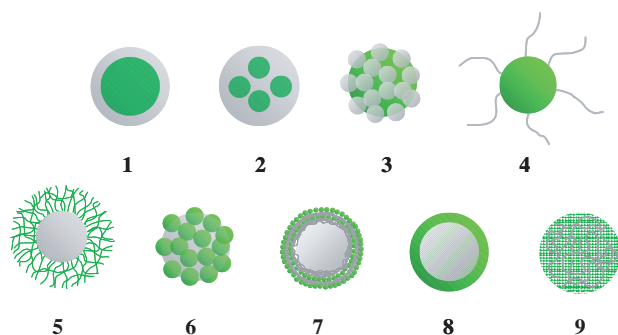
We aim in this chapter to give an overview of the techniques recently developed for the elaboration of O/I



**Figure 1.** Particle size range of different types of colloidal systems.

nanocomposite colloids with diameters in the range of 10 up to several hundred nanometers. These systems are characterized by the fact that each particle of the colloidal suspension is a composite particle. Either *ex-situ* or *in-situ* techniques can be used for the elaboration of nanocomposite colloids. Figure 2 shows idealized spherical morphologies of the different types of organic/inorganic colloidal particles that can be produced through assembly, precipitation, organic polymerization, and/or inorganic polycondensation processes. Although in practice nanocomposite colloids can exhibit a variety of shapes and geometries, we have exclusively represented spherical and isotropic morphologies.

This chapter is divided into three parts. In the first part, physicochemical processes based on supramolecular assembly of preformed nanoparticles and/or macromolecules, including heterocoagulation and the sequential deposition of preformed colloids and polyelectrolytes onto latex seeds, are described. Such strategies enable us to associate a variety of polymeric and colloidal materials in one step or using multisequential procedures. In the second part, nanocomposite



**Figure 2.** Idealized morphologies of different types of O/I nanocomposite particles. Core-shell (1, 8), occluded (2), raspberry-like (3, 6), hairy (4), shell-cross-linked (5), multilayered (7), and hybrid interpenetrated organic/inorganic networks (9).

particles are produced *in-situ* giving rise to nanostructured colloids with various morphologies (core-shell, multicore, raspberry-like, hairy, and shell-cross-linked). In this synthetic strategy, preformed colloidal nanoparticles are used as seeds for polymer growth or inorganic condensation on their surface either in solution or in multiphase systems. Unusual colloidal materials, for instance vesicles or block copolymers, can also be used as host or templates as will be briefly discussed in a short section. The third part deals with the elaboration of hybrid colloids from the simultaneous reaction of organic and inorganic molecular precursors. The emphasis is put here on the unusual properties of the so-produced particles. Finally, the potential applications of nanocomposite colloids and nanocapsules will be briefly presented and illustrated by typical examples.

## 2. NANOCOMPOSITE COLLOIDS VIA SELF-ASSEMBLY TECHNIQUES

The development of self-assembly methodologies in the creation of new materials has veritably expanded the range of supramolecular structures that can be built up in the field of nanotechnology [50, 51]. Not only can organic molecules and block copolymers be assembled onto inorganic substrates but the assembly process can also take place between two types of colloidal particles or between colloids and macromolecules. The interaction of surfactants with pigments and inorganic particles, for instance, is a well established process and this will not be discussed here [52]. Similarly, a large range of polymeric materials such as dendrimers and block copolymers have demonstrated huge potentialities as unique nanoscale reactors, templates, or building blocks for higher order nanoscale construction. The elaboration of nanostructured colloidal materials (nanoparticles, nanocrystals, and clusters) by organic templating and the construction of higher hierarchical assemblies (for instance colloidal crystals) will not be covered in this chapter. These aspects have been discussed and reviewed in more detail elsewhere [53–58]. We are mainly interested, here, in the creation of complex nanoparticle structures through the assembly of binary colloidal materials. The assembly process is driven by weak interactions (e.g., steric, electrostatic, hydrophobic, and hydrogen bonding) or chemical and biomolecular recognition. This section describes the main synthetic strategies and briefly reports on the recent advances in this area.

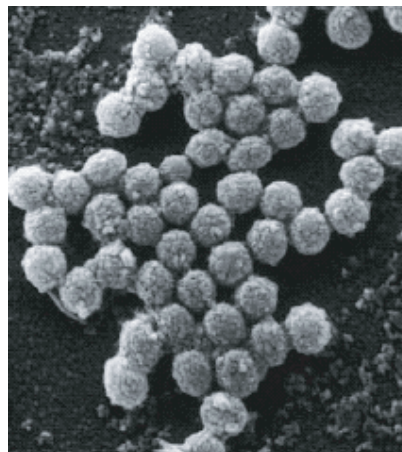
### 2.1. Electrostatically Driven Self-Assembly

#### 2.1.1. Heterocoagulation

Aggregation between particles of different characteristics (sizes, charges, and chemical composition) is generally known as heterocoagulation. This kind of process is common in nature and frequently encountered in many industrial and biological processes. Due to its major technological implications, the fundamental aspects associated with the stability behavior of mixed colloidal dispersions, including the mechanisms and kinetics of the heterocoagulation process, have been extensively studied both experimentally and theoretically for a long time [59–61]. Systematic studies have been performed using different types of inorganic and polymer

colloids such as metal oxides and polymer latexes. By changing the pH, both the sign and the surface potential of the colloids can be finely tuned, making it possible to evaluate the effects of these determinant parameters on the interactions of unlike particles. In addition to these theoretical considerations, attractive interactions between positively charged particles and negatively charged colloids also provide a possible mechanism for the encapsulation of inorganic particles giving a core mineral surrounded by small heterocoagulated polymer particles. The interaction of preformed amphoteric latex particles with titanium dioxide pigments, for instance, has been studied by Kato et al. [62]. The latex particles were synthesized in the presence of a zwitterionic emulsifier, *N,N'*-dimethyl *n*-lauryl betaine at pH 7.0 and showed an isoelectric point in the range of pH 7–8. Strong interactions were observed between pH 3 and 8, where the latexes were positively charged while titanium dioxide particles were negatively charged. As evidenced by turbidity measurements, the mixed heterocoagulated suspensions were destabilized upon addition of an increased number of latex particles due to the neutralization of the surface charge of the pigment, but restabilization occurred with further addition of the latexes. Similarly, the adsorption of cationic polystyrene latexes onto spherical rutile titanium dioxide particles has been investigated by Marston and co-authors [63]. It was shown that the ionic strength of the suspension medium had a great influence on the adsorption behavior. More latex particles were heterocoagulated on the TiO<sub>2</sub> surface when the electrolyte concentration was increased due to the diminution of the electrostatic repulsion between neighboring adsorbed particles. Using the heterocoagulation technique, a large variety of O/I nanocomposite colloids can be successfully produced. Among them, magnetic colloids are important class of materials with potential applications in biotechnology and medicine including bioseparation, diagnostics, magnetic resonance imaging, therapy, and drug targeting. The elaboration of magnetic colloidal supports and their utilization in the biomedical field have been extensively described and reviewed in recent years, and only few typical examples will be reported here [64, 65]. Monodisperse hydrophilic magnetic polymer latexes have been synthesized for example using a two-step procedure. In the first step, magnetic iron oxide particles have been separately obtained by procedures known for a long time [66], and adsorbed onto various cationic latexes [e.g., polystyrene, core-shell poly(styrene-*N*-isopropylacrylamide)(NIPAM), and poly(NIPAM)] via electrostatic interactions [67]. Figure 3 shows the raspberrylike morphology of the so-produced nanocomposite colloids. In the second step, the iron oxide-coated polymer latexes were encapsulated by poly(NIPAM) after separation of the excess free iron oxide particles in a magnetic field [68].

Trilayer composite microspheres containing small Fe<sub>2</sub>O<sub>3</sub> or NiO–ZnO–Fe<sub>2</sub>O<sub>3</sub> oxide particles in middle layer have been elaborated by a similar procedure [69, 70]. In the first step, the magnetic ultrafine powder was heterocoagulated on the surface of the core latex particles by adjusting the pH of the mixed dispersion to 2, 5. Then, sodium methyl acrylate [69] or sodium oleate [70] was added in order to improve the hydrophobicity of the heterocoagulates and to ensure the formation of a third polymer layer at the surface of the composite seed latexes. Under these conditions,

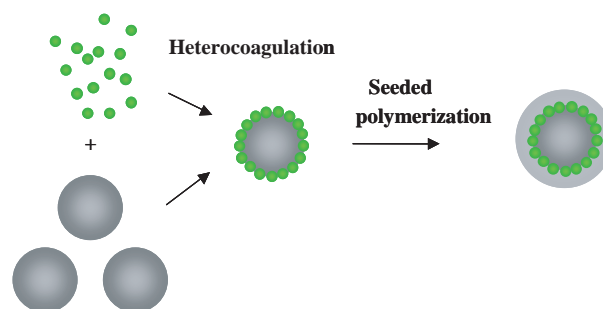


**Figure 3.** Scanning electron micrograph of polystyrene latex particles coated with iron oxide colloids. Reprinted with permission from [67], F. Sauzedde et al., *Colloid Polym. Sci.* 277, 846 (1999). © 1999, Springer-Verlag.

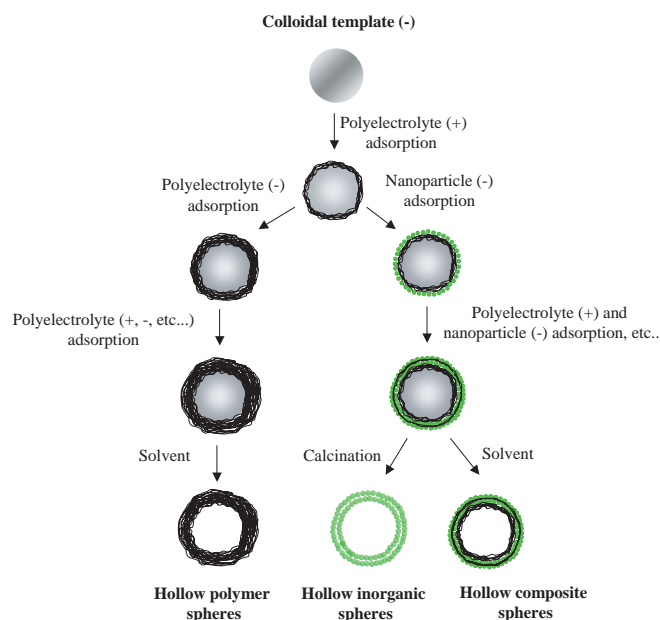
a polymer shell was obtained giving composites with a trilayer morphology (Fig. 4). In a related work by Lee and Senna, composite magnetic particles of the core-shell type were prepared by emulsion polymerization of styrene in the presence of polystyrene (PS) seed microspheres and ultrafine magnetite colloids coated with sodium oleate [71]. Small composite particles were produced in the continuous phase through emulsion polymerization. These nanoparticles were shown to adhere to the seed surface giving rise to the formation of large PS microspheres covered with a uniform layer of smaller nanocomposite particles.

### 2.1.2. Layer-by-Layer Assembly

A versatile technique that combines colloidal assembly and polymer adsorption strategies, first developed by Caruso and Möhwald's research group, has been extensively described in the last five years [72]. The general concept involves forming a sequential alternate layer-by-layer (LbL) deposition of polyelectrolytes [73–75] or polyelectrolytes and nanoparticles [76–79] through electrostatic self-assembly onto sacrificial polymeric colloidal templates. Removal of the organic core and the bridging polymer by chemical (dissolution, etching) or thermal treatments generates hollow polymeric or nanocomposite structures (Fig. 5) [80–85].

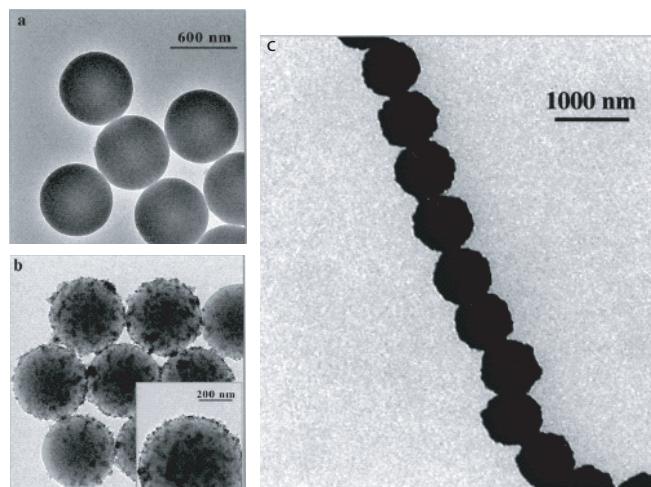


**Figure 4.** Schematic picture showing the process of encapsulation of Fe<sub>2</sub>O<sub>3</sub> particles with a trilayer structure. Reprinted with permission from [69], H. Du. et al., *Polym. Int.* 43, 274 (1997). © 1997, Wiley-VCH.



**Figure 5.** Schematic representation of the different steps involved in the LbL self-assembly technique and the synthesis of hollow nanoparticles. Reprinted with permission from [80], *Chem. Eur. J.* 6, 413 (2000). © 2000, Wiley-VCH.

Due to their low density, large surface area, stability, and surface permeability, the resulting nanocapsules are of major technological and scientific interest. Hollow particles offer a lot of promising applications in various domains of advanced materials, especially in architectural coatings, optics, electronics, and biotechnologies. Hollow latex particles, for instance, are used as synthetic pigments in paper coating [86] and paint materials [87, 88]. By scattering light, the voids contribute to increase hiding and opacity, whereas microspheres with large voids (typically 10–100  $\mu\text{m}$  in size) are inefficient in such processes. Nanometer-sized capsules are also very promising materials for encapsulation and controlled release of various substances—dyes, drugs, cosmetics, and inks—and are particularly suited for biological applications such as drug targeting, artificial cells, and diagnostics. By using the LbL technique, determinant parameters such as size, composition, geometry, wall thickness, and uniformity can be precisely controlled. A huge variety of such hollow spheres has been successfully produced over a wide range of micrometer and submicrometer inner diameters, and the thickness and permeability of the walls have been varied by proven formulation variations. The organic templates involved in these coating procedures were either melamine–formaldehyde resins [73–75] or PS latex particles [76–85]. Poly(allylamine hydrochloride) (PAH), poly(sodium 4-styrene sulfonate), and poly(diallyl dimethylammonium chloride) (PDADMAC) were used as the polyelectrolytes. Among the coating materials, silica [76, 77], titanium dioxide [84], clays [84], zeolites [78, 83], and iron oxide [79, 85] have been successively reported. As mentioned in the previous section, magnetic colloids are of particular interest in diagnostics and bioseparations where the particles can be selectively oriented and directed by application of an external magnetic field. Figure 6 shows the type of anisotropic



**Figure 6.** (a), (b) TEM micrographs of PS particles and PS particles coated with three layers of polyelectrolyte (PSA and PAH), respectively, and (c) TEM image of the nanocomposite particles aligned in a magnetic field. Reprinted with permission from [79], F. Caruso et al., *Adv. Mater.* 11, 950 (1999). © 1999, Wiley-VCH.

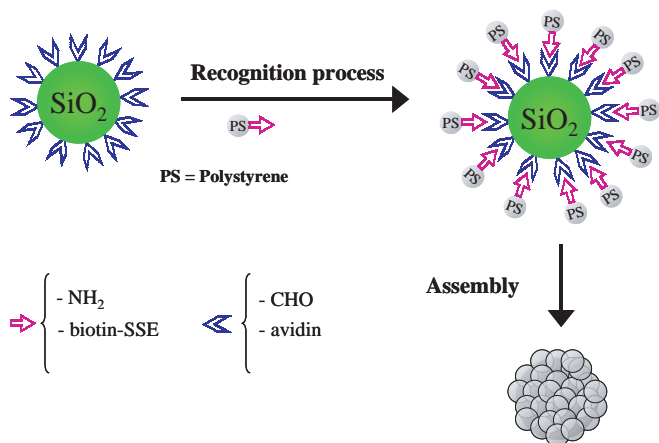
orientation that can be obtained from latex particles coated with alternate layers of PDADMAC and iron oxide nanoparticles. In alternative procedures, inorganic precursors can be used instead of preformed nanoparticles [89, 90]. For example, water soluble titanium (IV) bis(ammonium lactato) dihydroxide was employed to uniformly coat PS templates with a thin titania layer. A regular and smooth coating was obtained by this approach. LbL nanoengineered capsules are versatile materials. They can be used for instance as microreactors for chemical reactions to be conducted inside the hollow spheres. Preformed hollow capsules are particularly well suited for such applications since they provide effective size limitations because of the compartmentalization of the precipitation chemistry [91]. Different species can be incorporated into the nanocapsules making them attractive for a wide range of applications from biotechnology to catalysis. For example, hollow polyelectrolyte shells have been used as microenvironments for the precipitation of inorganic salt and crystal deposition in the inner part of the capsules [92]. Nanoscale objects with controlled sizes and shapes have been successfully obtained by this technique. In a typical example, the spheres are first suspended in a solvent for the organic solid to be precipitated. The solubilized reactive compound then permeates the sphere wall and enters the nanocapsules. A nonmiscible solvent is subsequently slowly introduced into the suspension to initiate precipitation of the principal compound contained inside the hollow spheres by osmotically shifting the original solvent. Precipitation can be alternatively induced by change in pH or by addition of a trigger. The key limitation of the LbL technique, however, is the difficulty one may encounter to produce stable nonaggregated hollow spheres in large quantities without damaging the shell properties. For scaling-up procedures, the technology must be carefully optimized to reduce time scale experiments and limitate the amount of free polyelectrolyte that must be removed from the suspension. A complete description of these systems encompasses the goal of this chapter. More detailed information on the LbL concept

including the limitations and potential applications of the technique can be found elsewhere [93].

## 2.2. Nanosphere–Microsphere Assembly

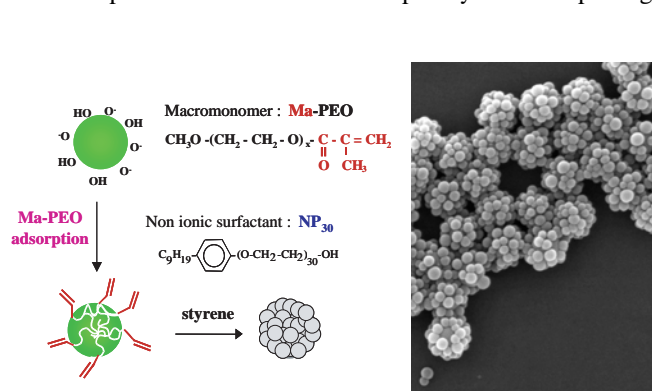
Mixtures of organic and inorganic colloids of different sizes and number ratios can also arrange into supramolecular colloidal architectures by means of chemical or biological interactions. Fleming and co-workers have demonstrated for instance that polymer colloids, functionalized with amine groups, can be assembled onto glutaraldehyde-activated silica microspheres [94]. The assembled composite particles were subsequently heated above the glass transition temperature of the polymer nanospheres to produce uniform core–shell composite microparticles. Alternatively, the introduction of suitable biological functions on both parts, for instance avidin and biotin groups, allowed the two sets of particles to be assembled via a specific biomolecular recognition mechanism (Fig. 7). Assembly procedures of this type, based on both biological and nonbiological molecular recognition, have been largely reported in recent literature for binary dispersions of polymer colloids [95] and inorganic particles [96, 97], respectively. However, there are only few examples of supramolecular recognition-directed assembly of organic and inorganic nanoparticles.

Controlling the assembly of unlike colloidal particles in a binary suspension requires control over the surface properties of each of the two colloidal materials as illustrated in the example in Figure 7. However, systems can also be specifically designed to undergo self-colloidal organization by using a bifunctional mediating molecule bearing reactive groups on both ends capable of bonding particles together, as recently reported in our group for binary mixtures of silica and polymer colloids [98]. Biologically programmed assembly of nanoparticles was first described by Mirkin et al. [99] and Alivisatos et al. [100, 101]. They showed that complementary DNA antigens could be used to self-assemble nanoparticles. The concept was recently applied to gold colloids by Mann and co-workers who used antigen/antibody recognition assembly to induce the reversible aggregation of the inorganic nanoparticles and



**Figure 7.** Schematic representation of the colloidal assembly of dissimilar particles in a binary suspension via chemical and biospecific interactions. Adapted with permission from [94], M. S. Fleming et al., *Chem. Mater.* 13, 2210 (2001). © 2001, American Chemical Society.

produce a conjugated hybrid material with long-range interconnectivity [102]. Recent examples also include the elaboration of colloid/colloid [103], dendrimer/colloid [55], and polymer/colloid [104] composite superstructures. According to this general principle, we recently demonstrated that addition of a small amount (only  $0.1 \text{ g} \cdot \text{L}^{-1}$ ) of a monomethylether monomethylmethacrylate poly(ethylene oxide) macromonomer allowed us to direct the self-assembly of nanometric polystyrene latex particles on the surface of submicronic silica particles through an *in-situ* nucleation and growth process (Fig. 8) [98]. The two sets of particles were assembled in a raspberry-like morphology via the formation of hydrogen bonds at the interface of the inorganic and organic colloids. The size and shape of the assembly can be easily controlled by varying the sizes and stoichiometries of the colloidal components. In a related work, hydrophilic poly(vinyl pyrrolidone) (PVP)-based macromonomers having styrene end groups were shown to be efficient compatibilizers during the coating reaction of large colloidal silica particles by dispersion polymerization of styrene into a mixture of ethanol and tetrahydrofuran (THF) [105]. The encapsulation was shown to take place via the copolymerization of styrene with the terminal group of the macromonomer adsorbed on the inorganic surface. A large variety of amphiphilic block copolymers and nonionic water soluble polymers like polystyrene-*b*-poly(ethylene oxide) (PS-*b*-PEO) and hydroxypropyl cellulose (HPC), respectively, can be used for this purpose. For example, it was found that HPC strongly adsorbed on silica and that the saturated amount of adsorption was dependent on temperature. The adsorption value (around  $1.5 \text{ mg/m}^2$ ) at temperatures higher than the lower critical solution temperature (LCST) of the polymer was 1.5 times larger than the value obtained at room temperature. Furusawa et al. [106] described that the dense layer of HPC adsorbed at the LCST allowed synthesis of composite polystyrene latexes containing silica beads in their core through hydrophobic-mediated interactions. When the emulsion polymerization reaction was performed in presence of an anionic emulsifier at concentrations higher than the critical micellar concentration, nanocomposite colloids with a raspberry-like morphology



**Figure 8.** (a) Schematic representation of the macromonomer mediated assembly process of polymer latexes onto colloidal silica nanoparticles. (b) Scanning electron microscope image of the assembled nanocomposite particles with a raspberry-like morphology. Reprinted with permission from [98], S. Reculosa et al., *Chem. Mater.* 14, 2354 (2002). © 2002, American Chemical Society.



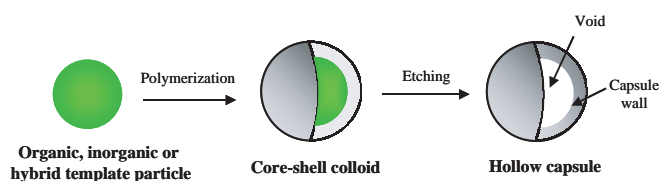
were produced by the spontaneous and controlled heterogeneous coagulation of the polymer particles formed in the continuous phase onto the hydrophobized silica surface. A similar behavior was observed by Long et al. during the seeded emulsion polymerization of methyl methacrylate in the presence of silica particles and hydropropyl methyl cellulose [107]. Such cooperative effects have been reported as well when using “adhesive” monomers, that is, monomers with strong interaction with the inorganic surface [108, 109]. 4-Vinylpyridine, aniline, and pyrrole are typical examples of such mediating monomers. The possibility to produce O/I nanocomposite colloids through acid/base chemistry will be discussed in the following section. Although the idea of colloidal nanocomposites construction via a building block approach is still in its infancy, it can be anticipated that the concept of bottom-up recognition-mediated multiscale ordering of dissimilar organic and inorganic nanoparticles will find extensive and innovative developments in the near future.

### 3. NANOCOMPOSITE COLLOIDS VIA POLYMERIZATION TECHNIQUES

The possibility to synthesize O/I nanocomposite colloids by direct polymerization techniques (i.e., solution, emulsion, miniemulsion, dispersion, and precipitation reactions) has gained much interest in recent years due to the large range of applications of those colloidal nanomaterials. Nanocomposite colloids are of major technological importance in the coating industry as well as in electronics, catalysis, optics, and medicine. Composite colloids are elaborated for a variety of reasons. The incorporation of, for instance, magnetic, optical, or catalytic functions enables us to produce multifunctional colloids, the properties of which can be finely tuned by controlling the proportions and spatial organizations of the inorganic and organic constituents. In addition, coating of minerals with a polymer layer can be of particular interest in order to protect the nanoparticles from chemical (oxidative, thermal, photochemical) and physical degradations and to improve their dispersion state. The coated surfaces have significantly different properties leading to increased durability or stability and better end-use performance. Nanocoating technologies have been extensively developed in recent years and reviewed [110–112]. In addition to the aforementioned interest, nanoengineering of particle surfaces also offers the possibility to control the shape of the resulting material by using templates of well defined sizes and characteristics. Since the coating can be done in a variety of ways, the nanocomposite particles can display a large range of morphologies as illustrated in Figure 2. Once the template is removed from the composite particles, replicas are formed that present interesting structural properties (Fig. 9).

#### 3.1. Synthetic Strategies

In order to circumvent the inherent incompatibility of polymers and minerals, synthetic strategies need to be developed in order to establish a physicochemical or chemical link at the interface of the organic and inorganic constituents. The



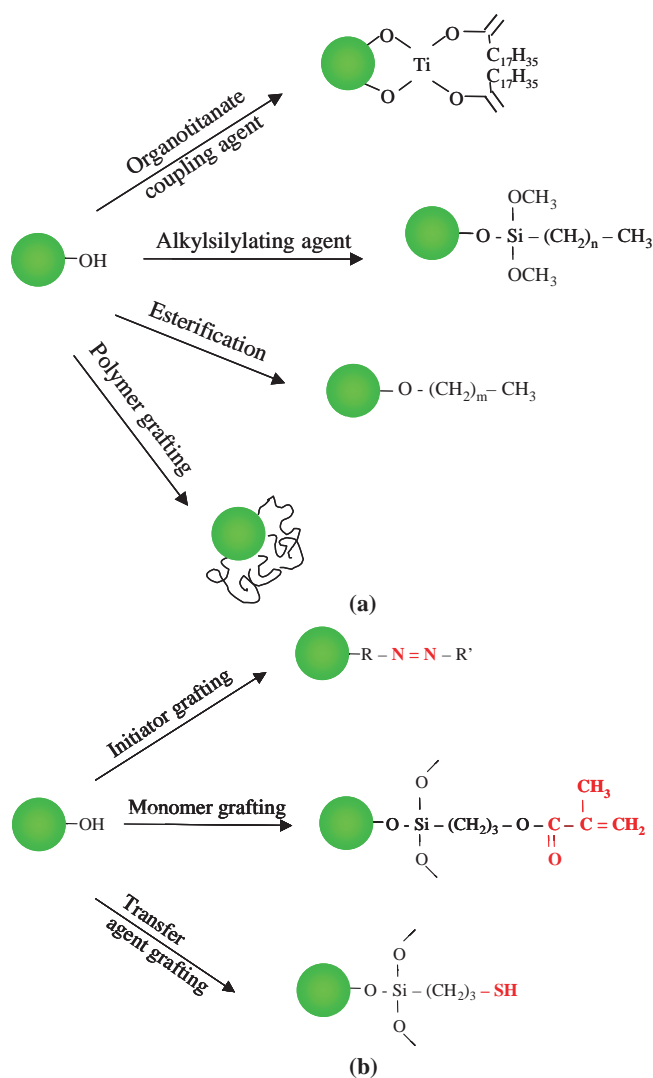
**Figure 9.** Synthetic scheme for synthesis of hollow particles by colloidal templating.

affinity of polymers for inorganic substrates, in terms of wetting or adhesion, can be substantially increased for instance by the prior adsorption by hydrogen bonding or electrostatic interactions of suitable organic substances over the inorganic particle surface. If covalent bonding is required, organic or inorganic reactive groups need to be grafted onto the surface of the nanoparticles. The general synthetic approach to O/I colloids thus involves two successive steps: (1) synthesis of the core material with the desired surface group and chemical reactivity and (2) coating of the templating core with an organic, inorganic, or hybrid shell. Figure 10 illustrates the kind of surface modification that can be done with the purpose of compatibilizing the core and shell components. Among the different strategies, organic functionalization of metal oxide nanoparticles has been much described in recent years and a full description of these systems will not be attempted here [113–115]. Initiating, propagating, or terminating groups can be attached to the seed surface in order to promote in a subsequent step anchoring of the growing polymer chains [17, 44–48]. Electrostatic interactions also provide a driving force for noncovalent association of organic and inorganic constituents into colloidal nanocomposites as briefly discussed in the previous section. Finally, it can also be envisaged to perform polymerization reactions at the interface of inorganic colloids with water provided that some amphiphilic molecules have been previously adsorbed on the nanoparticle surface. Inversely, inorganic polycondensates and metallic nanoparticles can be grown on the surface of polymer latexes if care is taken to use inorganic precursor molecules (e.g., metal salts or organometallic compounds) with sufficient affinity for the organic templates. Only a few directions are given here. A more complete description of these strategies will be reported in the following section.

#### 3.2. Organic Polymerization

##### 3.2.1. Polymerization in Multiphase Systems

**Polymer-Encapsulated Pigments** Pigments are important class of solid materials that enter into the composition of a variety of industrial products such as inks, paints, papers, and cosmetics. They are used for instance as additives in the coloration of thermoplastic materials or in the pigmentation of resins and synthetic fibers. One major drawback of pigmented formulations, however, is that high energy and cost-productive milling operations are necessary in order to disperse the pigment into particles of pigmentary dimensions throughout the plastic mass. Pigment agglomeration is also of major inconvenience during film formation in water-based paint formulations. Pigment flocculation creates zones locally enriched in pigment particles with undesirable



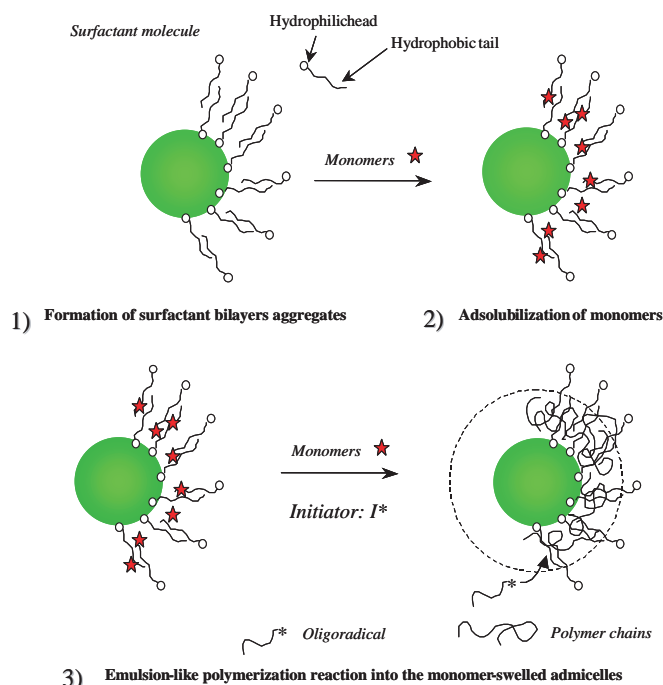
**Figure 10.** Different reaction schemes for (a) the graft polymerization of vinyl monomers from functionalized oxide surfaces via initiation, propagation, or termination, and (b) the hydrophobization of mineral surfaces for compatibilization with hydrophobic polymers.

effects on the hiding power of the latex paints. To improve and stabilize a paint dispersion, it is common to use polymeric dispersants [116]. However, this is generally not sufficient and a lot of pigments need a surface treatment to maximize their efficiency. Among the various surface modification techniques (use of derivatives, coating with inorganic materials), *in-situ* polymerization offers interesting perspectives. The coating of pigments with a thin polymer layer enables one to control interparticle spacing and reach better paint performances (hiding power, tinting strength, gloss, scrub resistance, stability, ...). Since the paint properties are highly dependent on pigment dispersibility, various encapsulation techniques have been described so far in order to achieve an optimal disposition of the pigment particles within the polymeric film [117]. This section describes the main synthetic strategies and briefly reports on the recent advances in this area.

Owing to the major technological importance of pigments in industry, it is not very surprising to see that

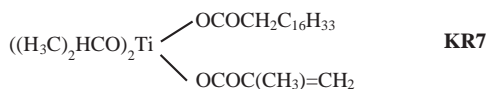
most published works in this field are in the patent literature [49, 118–125]. Among the various solid particles to be coated, titanium dioxide pigments ( $\text{TiO}_2$ ) have gained more and more interest since they constitute one of the major ingredients of water-borne coatings. Similarly, there have been a number of attempts to produce polymer encapsulated inorganic solids, but emulsion polymerization is by far the approach most frequently used [126]. In a typical procedure, the pigment particles are dispersed into water with the help of surfactant. High shear mixing is carried out to help dissociate the pigment agglomerates. Alternatively, fine pigment dispersions can also be produced by applying ultrasound as reported by Templeton-Knight [127–129]. A monomer or a mixture of monomers is then introduced into the suspension medium, and a water-soluble free radical initiator is subsequently added to start polymerization. The nature of the surfactant obviously plays an important role in the coating mechanism. It has been shown for instance that the presence of an amphiphatic polymer in combination with a companion surfactant allows one to produce more uniform coverages and reach better coating efficiencies [124, 130]. Solc [120, 123] and Hasegawa et al. [131, 132] claimed the use of water-soluble anionic surfactants, while Martin [121, 125] recommended the use of nonionic oxyethylene amphiphiles. In reality, the role of the surfactant is somewhat complex. It is generally admitted that the process begins with the adsorption of the surfactant molecules on the particle surface. Interaction takes place through the hydrophilic head group of the surfactant, the hydrophobic part being consequently directed toward the aqueous phase. A second layer of emulsifier molecules is then adsorbed on the first layer to provide an energetically stable arrangement. The net result is the formation of a surfactant bilayer that can solubilize monomer molecules in the hydrophobic interlayer and promote polymerization at the interface of the pigment particles with water (Fig. 11).

This process, also known as admicellization/adpolymerization, is of course highly dependent on the geometry of the bilayer structure and on the surfactant packing density, which in turn are functions of the nature and concentration of the soap. Too low emulsifier concentrations may lead to incomplete pigment coverage while a too large a concentration may result in the formation of free polymer particles that do not participate in the coating. Better results are usually obtained when the monomers are introduced under starved feed conditions. Various attempts have been made in the literature in order to achieve higher coating efficiencies. For example, Caris and co-workers used diisopropyl methacryl isostearoyl titanate molecules (Structure 1) to covalently attach polymer chains on the surface of  $\text{TiO}_2$  pigments [133, 134]. Modification of the titanium dioxide pigments was carried out by suspending  $\text{TiO}_2$  into an organic solution of the coupling agent and shaking for several hours. The authors recommended the use of aprotic solvents like diethylether or dichloromethane to avoid the rapid solvolysis of the titanates. When  $\text{TiO}_2$  was modified in isopropanol, low levels of grafting were obtained in contrast to diethylether. The high sensitivity of the titanate bonding toward hydrolysis could be reduced by incorporating a small amount of another titanate coupling



**Figure 11.** Schematic illustration of pigment encapsulation through an emulsionlike polymerization reaction. The process involves (1) formation of surfactant bilayers, (2) solubilization of monomer, and (3) free radical polymerization.

agent bearing long hydrophobic chains which provided effective protection of the methacrylic acid ester groups against hydrolysis by steric hindrance. In a subsequent work, they determined the polymer content of the encapsulated pigments and found that the highest amount of surface polymer was obtained when the initiator was chemically bound or strongly attracted to the particle surface [135]. Similar results were obtained by Haga et al. who used a diazoic amidinium initiator to promote anchoring of the polymer chains onto  $\text{TiO}_2$  pigments [136]. It is worthwhile to mention also the work of Janssen et al. [137], who used redox initiators to improve the efficiency of the encapsulation reaction of surface modified titanium dioxide pigments by PMMA and polystyrene. Although a real benefit was achieved with the nature of the initiator, in particular in the case of MMA, there was still competition between the formation of surface polymer and free latex particles in these systems. Another critical aspect of encapsulation reactions is the stability of the encapsulated powders. The occurrence of severe coagulation during the encapsulation process has been evidenced by several authors. The temporary decrease in the polymerization rate observed by Caris et al. during PMMA encapsulation of titanium dioxide pigments has been attributed to pigment agglomeration in the course of the coating reaction [138]. Hasegawa et al. [139] also described that  $\text{CaCO}_3$  powders have a strong tendency to aggregate in a certain



**Structure 1.** Diisopropyl methacryl isostearyl titanate.

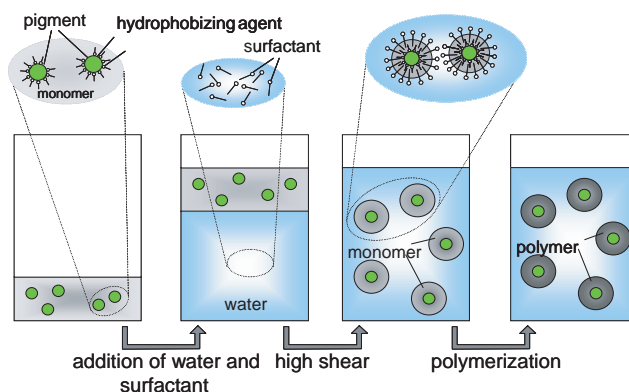
range of SDS surfactant concentrations. The decrease in polymerization rates with increasing SDS concentration was found to follow the sedimentation curves of the inorganic pigment which supported the fact that aggregated rather than individual pigments had been encapsulated. Such instability appeared to be even more pronounced in the case of titanium dioxide pigments for which it was described that coagulation can take place under certain experimental conditions. In order to prevent the formation of agglomerates or coagulum during encapsulation reactions, the evolution of the surfactant concentration has been controlled by Janssen and co-authors using on-line conductivity measurements [140, 141]. It was found that the critical micellar concentration (CMC) of the soap determined in the presence of monomer and initiator, the so-called apparent CMC ( $\text{CMC}_{\text{app}}$ ), was significantly lower than the CMC measured in pure water. On the other hand,  $\text{CMC}_{\text{app}}$  increased with increasing amount of pigment since more and more surfactant molecules were adsorbed on the mineral surface. By measuring the conductivity signal of the suspension, it was thus possible to follow the surfactant concentration evolution during the encapsulation reaction. Of course, an increase in the total surface area, due to polymer particle growth or renucleation, leads to a decrease in the conductivity because surfactant is adsorbed from the continuous phase ( $\text{CMC}_{\text{app}}$  is increased). On the contrary, when coagulation takes place, surfactant is released from the agglomerated particles due to a decrease in the surface area and thus the conductivity is increased. The occurrence of severe coagulation during batch encapsulation reactions was then clearly manifested on the conductivity curves by one maximum in the conductivity signal. In order to prevent coagulation, extra surfactant must be introduced in the course of the coating reaction. On-line conductivity measurements were shown to provide an effective way to optimize the surfactant addition profile in order to obtain the best efficiency with maximum stability.

As mentioned previously, polymer-encapsulated pigments are of major implication in the coating industry and, consequently, a variety of monomers have been used to produce the shell, including vinyl acetate as well as combinations of vinyl acetate, isobutyl acrylate, styrene, *n*-butyl acrylate, methyl methacrylate, acrylonitrile, and isobutyl vinyl ether. In principle, a huge number of inorganic solids including metal powders, such as iron, steel, titanium, cobalt, nickel, gold, platinum, or copper, metal oxides ( $\text{CuO}$ ,  $\text{ZnO}$ ,  $\text{Al}_2\text{O}_3$ ,  $\text{CeO}_2$ , ...), and various fillers, such as talc, mica, barytes, calcium carbonate, china clay, and dolomite, can be covered with polymers according to the general synthetic procedure described previously. However, in practice, the synthesis needs to be adapted to every individual situation. Metallic surfaces do not display for instance the same reactivity as metal oxides or carbonates and sulfates, and specific strategies need to be developed. Similarly, it is clear that the surface properties of metal oxides may suffer significant changes from one oxide to another depending on the pH of the suspension, the ionic strength, as well as the acidic or basic character of the surface. Batzilla and Tulke described for instance the encapsulation reaction of commercial aluminum pigments through an emulsionlike polymerization process [142]. They reported the use

of phosphorous-containing protecting agents to provide a good dispersion of the Al pigment and control its reactivity. They also recommended using monomers with strong adhesion with the metal surface (e.g., carboxylic acid derivatives). In a related work, silver nanoparticles have been recovered with a thin polymer layer via emulsion polymerization of styrene and MMA monomers in presence of oleic acid [143]. The fatty acid derivative was shown to be essential to achieve pigment encapsulation. Yu et al. recently reported the preparation of  $\text{CaCO}_3$ /polystyrene composite particles using a polymerizable silane derivative previously attached on the mineral surface [144]. The pretreated  $\text{CaCO}_3$  particles were shown to act as comonomers during the emulsion polymerization process as will be fully discussed in the case of silica.

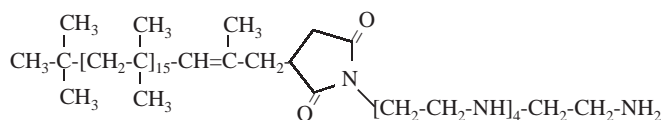
Apart from the aforementioned technologies, miniemulsion polymerization also provides a versatile route to polymer encapsulation of pigments and nanoparticles. Contrary to emulsion polymerization which involves the formation of large monomer droplets dispersed in the aqueous phase, in a miniemulsion process, the monomer phase is stabilized in the form of small droplets with diameters in the range of typically 30–500 nm. Miniemulsions are typically obtained by shearing a system containing water, an oil phase, a surfactant, and an hydrophobe. The role of the hydrophobe is to suppress the Ostwald ripening process responsible for droplet coalescence. The hydrophobe must be able therefore to regulate the osmotic pressure inside the monomer droplets in order to ensure both size and composition stability of the oil phase. Many different molecules (hexadecane, hexadecanol, silanes, cyclosiloxanes, ...) or macromolecules (high molecular weight polystyrenes, polyesters, silicone oils, ...) can be used for this purpose. Because of their small size and large surface area, the monomer droplets can efficiently compete for radical capture and hence become the major locus of particle nucleation. Consequently, polymerization can take place into the monomer droplets which play the role of nanoreactors. This concept of nanoreactor is particularly attractive for the design of a variety of nanoparticulate materials as well as for encapsulation purposes. The potential of miniemulsion in the preparation of new nanoparticles including polycondensates, metals, ceramics, hybrid polymers, and nanocomposites has been recently reviewed [145,146].

Based on the miniemulsion principle, a variety of inorganic particles have been successfully encapsulated including titanium dioxide pigments [147–149], carbon black [150, 151], calcium carbonate [150], magnetic nanoparticles [152], and organic pigments [153]. The principle of pigment encapsulation through miniemulsion polymerization is schematically illustrated in Figure 12. The general process involves forming a stable dispersion of the pigment particles in the monomer and polymerizing the nanoparticle-loaded miniemulsion. In an alternative procedure, a cominiemulsification technique was developed that allowed the monomer droplets to split and heterocoagulate onto the surface of carbon black particles previously dispersed in water [151]. Monomer deposition on the pigment surface was promoted by a fusion/fission process induced by ultrasound.



**Figure 12.** Principle of pigment encapsulation through miniemulsion polymerization. Reprinted with permission from [145], K. Landfester, *Macromol. Rapid Commun.* 22, 896 (2001). © 2001, Wiley-VCH.

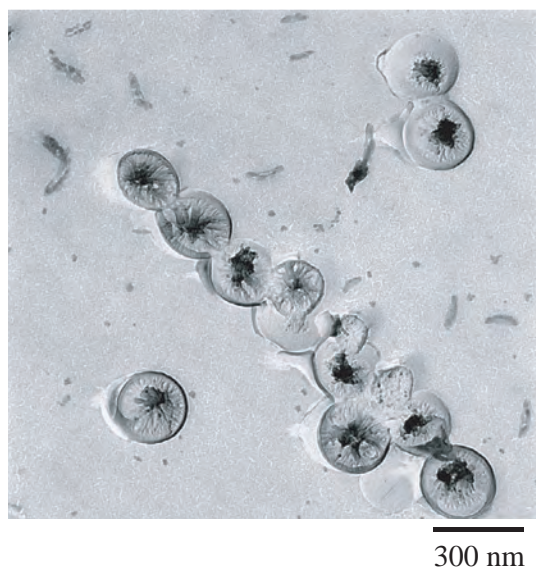
Because miniemulsion droplets have small sizes, the pigment particles must be highly dispersed in the monomer to accommodate them inside the droplets. To reach this goal, Erdem and co-workers described the use of a polybutene succinimide pentamine dispersing agent (OLOA 370, Structure 2) that proved to be an efficient stabilizer in case of titanium dioxide pigments and styrene monomer [147]. Stearic acid derivatives were shown to play the same role during the encapsulation reaction of  $\text{CaCO}_3$  powders by polystyrene [150]. Figure 13 shows a transmission electron microscopy (TEM) image of core-shell  $\text{CaCO}_3$ /polystyrene particles obtained by this technique.



**Structure 2.** Chemical structure of OLOA 370 (polybutene-succinimide pentamine).

The problem of nanoparticle dispersion is much less critical for organic pigments since they can be readily dispersed in the monomer phase. We recently described the encapsulation reaction of an organic phthalocyanine blue pigment (Structure 3) via miniemulsion polymerization. We showed that the organic pigment played the role of hydrophobe and was able to stabilize the miniemulsion. Better long-term stability was observed, however, when the pigment was used in combination with a costabilizer such as hexadecane or a low molecular weight polystyrene [153]. Pigmented latex particles as well as pure polystyrene latexes were produced in this work suggesting that both monomer droplet nucleation and conventional homogeneous nucleation mechanisms were taking place under our experimental conditions. Similar results have been reported by Chern and Liou during the miniemulsion polymerization of styrene in the presence of a blue dye molecule, sparingly soluble in water [154].

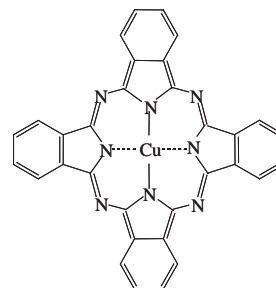
**Magnetic Colloids** Another important class of nanocomposite particles is the magnetic colloid. As mentioned previously, magnetic latexes are of major interest in the biological and medical fields [155–157]. It has been shown for instance that thermosensitive magnetic latexes with covalently immobilized antigens (so-called magnetic



**Figure 13.** TEM image of calcium carbonate nanoparticles encapsulated in polystyrene by miniemulsion polymerization. Reprinted with permission from [150], N. Bechthold et al., *Macromol. Symp.* 151, 549 (2000). © 2000, Wiley-VCH.

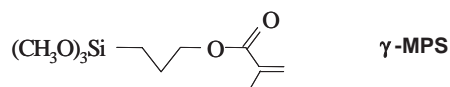
immunomicrospheres) are particularly suitable for antibody purification applications [158]. The immunomicrospheres were prepared by covalent immobilization of bovine serum albumin onto magnetic poly(styrene/NIPAM/methacrylic acid) latex particles using the carbodiimide method. The thermosensitive encapsulated magnetic particles could be easily flocculated or redispersed by controlling the temperature or the ionic strength and could be quickly separated upon application of a magnetic field. Encapsulated magnetic microspheres tagged with fluorescent dyes also proved to have interesting applications in labeling and separation of cells [159, 160]. They have been used in the magnetic separation of red blood and lymphoid cells and in the detection of the labeled cells by fluorescent microscopy. As patented by Richard and Vaslin [161], magnetic particles can be widely used for therapeutic or analytical purposes and provide useful applications in, for instance, radioimmunological assays, enzyme immobilization, drug targeting, and so on. Magnetically responsive particles are usually prepared by conventional emulsion polymerization methods (similar to those described previously) using colloidal iron oxides (so-called ferrofluids) as magnetic seeds. As before, oleic acid derivatives with strong interactions with the magnetic particles have been preconized in order to stabilize the nanoparticles against aggregation and enhance the affinity of the growing polymer chains for the inorganic surface [155]. Highly charged, monodisperse superparamagnetic latex particles, prepared according to this procedure, have been assembled into colloidal crystals and were found particularly suitable for the creation of unique magnetically induced photonic bandgap materials [162–164]. Alternatively, polymerizable olefin-terminated surfactants have been reported in order to increase the long-term stability of the coating. The fatty acid surfactant was shown to form bilayers on the iron oxide surface and to actively participate to the polymerization reaction [165]. Other techniques include polymerizations in

reverse emulsion [166, 167] and microemulsion [168], emulsification processes [169, 170], and the controlled assembly of preformed polymer latexes and magnetic nanoparticles through electrostatic attraction as described in the previous section. Only a few typical examples of magnetic colloids are described here. Extensive details on synthesis and applications of magnetically responsive nanospheres and nanocomposites can be found elsewhere [64, 65].



**Structure 3.** Chemical structure of the phthalocyanine blue pigment.

**Silica-Based Colloidal Nanocomposites** Colloidal silica is widely used as a reinforcing agent in the coating and rubber industries, as the thickener or thixotropic agent of liquid resins, and as fillers for plastics. The incorporation of silica particles into nanocomposite colloids offers a lot of promising perspectives. It is expected that the mechanical strength, stiffness, impact resistance, and optical properties of the resulting composite materials could be significantly improved if the inorganic particles were finely dispersed into the polymeric matrix. Various methods have been thus developed in the last 20 years to improve silica dispersibility by coating the inorganic fine particles with a polymer layer [171–193]. The first studies have been reported by Hergeth who described the elaboration of composite particles made of quartz powders and polyvinyl acetate through seeded emulsion polymerization [171–174]. He showed that the number of seed particles must exceed a minimal value to prevent formation of new particles and thus promote seed particle growth. The polymerization was proved to take place in the vicinity of the surface and the so-produced “interfacial” polymer was shown to display physical properties different than those of the bulk polymer. In the 1990s, Espiard and co-workers described the use of a polymerizable silane coupling agent (3-trimethoxysilyl propyl methacrylate: Structure 4) to covalently attach the polymer shell on the seed surface [175–180]. The silane molecule allowed the grafting of a significant amount of polymer since the early stages of polymerization. The grafted polymer chains formed tight loops on the silica surface into which the free polymer chains were entangled. The films prepared by coalescence of the latexes were fully transparent up to high silica contents and showed remarkable mechanical properties similar to those of vulcanized elastomers reinforced with solid particles [181–183].



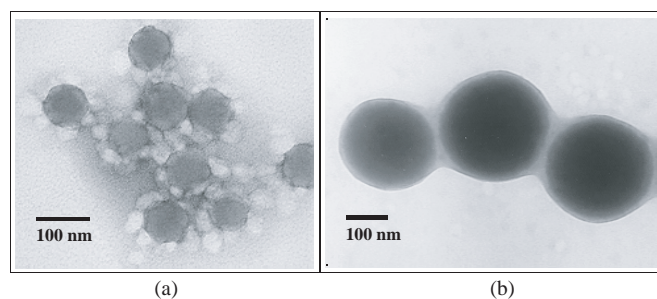
**Structure 4.** Methacryloxy propyl trimethoxy silane ( $\gamma$ -MPS) coupling agent.



[197, 198]. The presence of the 4-VP comonomer ensured strong interaction of the vinyl polymers with the acidic silica surface resulting in the formation of nanocomposite colloids with a “currant-bun” morphology characterized by silica beads assembled into colloidal aggregates cemented together by the polymer synthesized during the emulsion polymerization reaction. The small silica particles emerging from the composite surface were shown to participate to the colloidal stability of the particles. Similar conclusions have been addressed by Tiarks et al. concerning the miniemulsion polymerization of styrene using silica nanoparticles as spickering stabilizer [109]. Based on this same general idea, colloidal dispersions of nanocomposite particles made of silica cores and polymeric overlayers have been successfully prepared using appropriate cationic radical initiators and cationic vinyl monomers as described in a recent Japanese patent [199]. Recently, our group also demonstrated the successful formation of nanosize silica/PMMA composite colloids using a cationic initiator, 2, 2'-azobis (isobutyramidine) dihydrochloride (AIBA), and a nonionic polyoxyethylene surfactant (NP<sub>30</sub>) [200–203]. Composite particles made of silica beads surrounded by small heterocoagulated PMMA latexes or a thin polymer layer were produced depending on the size of the silica beads (Fig. 15). The role of the suspension pH and the influence of the monomer, silica, and initiator concentrations on the assembly process have been investigated in depth and analyzed in a quantitative way. Electrostatic attraction between the polymer end groups and the negatively charged silica surface proved to be the driving force of polymer assembly at high pH whereas polymerization in the adsorbed surfactant bilayers appeared to be the predominant mechanism at lower pH. Finally, it is worth noting also the recent work by Percy and Armes on the surfactant-free synthesis of colloidal silica/PMMA nanocomposites in the absence of auxiliary comonomers using a commercial dispersion of silica beads into isopropyl alcohol [204]. The assembly process was suspected to be driven in this case by simple hydrophobic interactions.

### Conducting Metal Oxide/Polymer Nanocomposites

Electrically conducting organic polymers have drawn the attention of scientists for several decades due to their unique physical and chemical properties (redox, acid–base, ion-exchange, ...). Conducting polymers have been found to

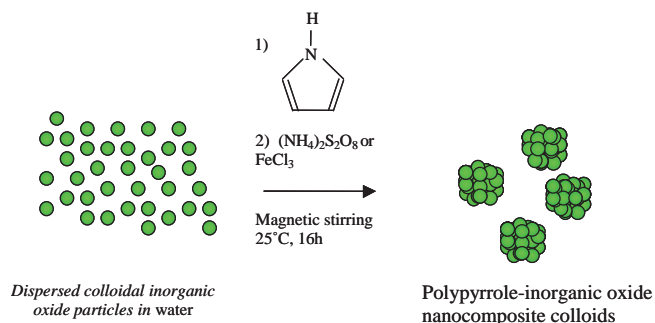


**Figure 15.** TEM micrographs of the silica/PMMA nanocomposite particles obtained through emulsion polymerization in alkaline solutions using AIBA as a cationic initiator. (a)  $D_p$  SiO<sub>2</sub> = 68 nm and (b)  $D_p$  SiO<sub>2</sub> = 230 nm. Reprinted with permission from [202], J. L. Luna-Xavier et al., *J. Colloid Interf. Sci.* 250, 82 (2001). © 2001, Elsevier Science.

be particularly suitable for numerous applications as optical and electrical sensors, molecular electronic devices, and anticorrosion, and antistatic coatings [205–207]. Polypyrrole (Ppy) and polyaniline (PAN) are two important examples of conducting materials with high electrical conductivity and significantly good stability in air and water. These highly conjugated conducting materials, however, have some inherent limitations such as poor mechanical strength and poor processability. Bulk Ppy and PAN are infusible, intractable, and insoluble in common solvents which drastically reduces their potential uses as thin films or coatings. Various attempts have been made to improve the processability of these otherwise intractable conducting powders. Sterically stabilized dispersions of conducting polymers have been elaborated for instance using various types of polymeric dispersants [208–211]. The particles usually exhibit good long-term conductivity and conductive films can be easily fabricated from the colloidal dispersions. Another alternative solution consists of the elaboration of conducting nanocomposites that combine the advantages of conducting polymers and those of inorganic particles. There have been numerous publications describing the preparation of conducting O/I nanocomposite colloids in recent literature [212–240].

Matijevic et al. [212–215] described for instance the formation of PAN and Ppy coatings over a series of metal oxide particles ( $\alpha$ -Fe<sub>2</sub>O<sub>3</sub>, CeO<sub>2</sub>, CuO, TiO<sub>2</sub>, SiO<sub>2</sub>). The conducting polymers were produced by chemical oxidation of the monomers in a mixture of ethanol and water in the presence of poly(vinyl alcohol) in order to produce stable colloidal suspensions. The coating reaction was catalyzed by air in the case of  $\alpha$ -Fe<sub>2</sub>O<sub>3</sub> and SiO<sub>2</sub> and the metal oxide surface was found to be inactive in the oxidation mechanism. On the contrary, the hydroxylated surfaces of CuO or CeO<sub>2</sub> could initiate the polymerization of the adsorbed monomer through a reductive-dissolution process, in which the monomer was oxidized while the metal oxide was reduced into metal ions. In the case of copper oxide, the released Cu<sup>+</sup> ions were reoxidized by air to Cu<sup>2+</sup> cations which in turn were able to extend further the molecular chain and increase the thickness of the shell or give new independent polyaniline or polypyrrole (latex) particles in addition to the coated CuO particles. A regular core-shell morphology or more irregular coatings with free polymer particles coagulated on the core surface were obtained depending on the experimental conditions.

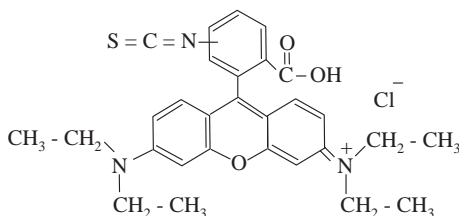
Armes and co-workers [216–223] and Perruchot et al. [224] also described the synthesis of composite materials made of various ultrafine inorganic oxide particles (silicium, tin, titanium, yttria, ...) and polypyrrole or polyaniline. The polymerization reactions were performed in water without any stabilizer and using FeCl<sub>3</sub> or (NH<sub>4</sub>)<sub>2</sub>S<sub>2</sub>O<sub>8</sub> as chemical oxidants. Macroscopic precipitation of the conducting polymer was prevented by the presence of the inorganic sol resulting in the formation of stable colloidal dispersions of organic–inorganic particles, the metal oxide playing the role of a *particulate* colloidal dispersant (Fig. 16). The resulting nanocomposites were made of microaggregates of the original oxide nanoparticles “glued” together by the polypyrrole or the polyaniline components as demonstrated by small-angle X-ray scattering [225]. Chemical analysis of the surface composition of polymer/silica nanocomposites by X-ray



**Figure 16.** Schematic representation of the formation of polypyrrole-inorganic oxide nanocomposite colloids by dispersion polymerization of pyrrole in aqueous medium. Reprinted with permission from [219], S. Maeda and S. P. Armes, *Chem. Mater.* 7, 171 (1995). © 1995, American Chemical Society.

photoelectron spectroscopy [226] proved that they had silica rich surfaces suggesting that the conducting polymer was somewhat depleted from the surface of the nanocomposite particles. The raspberry colloids were shown to display large surface area making them suitable for catalysis or chromatographic applications [227]. A similar approach has been developed in the case of zirconium dioxide [228], and similar results were obtained. The resulting polypyrrole/ZrO<sub>2</sub> nanocomposites showed a significant increase in conductivity in comparison to bare polypyrrole. Other typical examples include the elaboration of conducting polyaniline-coated barium sulfate nanoparticles in inverse microemulsion [229], the elaboration and physical characterization of polyaniline and polypyrrole-montmorillonite nanocomposites [230–233], the uptake of palladium [234] or gold [235] from aqueous solutions of conducting particles, and the synthesis of polypyrrole-ferric oxide conducting nanocomposites [236].

The elaboration of conducting nanocomposites is not restricted to silica and metal oxide colloids. In an original approach, Selvan and Nogami described for instance the synthesis of gold/polypyrrole core/shell nanoparticles via a simultaneous cooperative precipitation/polymerization mechanism [237]. Gold particles have also been reported to be useful templates for the growth polymerization of conductive polypyrrole and poly(*N*-methyl pyrrole) on their surface [238–240]. The polymer-gold composite particles were converted in a subsequent step into hollow polymeric nanocapsules by chemical etching of the colloidal gold template. Not only were the gold particles useful templates but they also made it possible to entrap guest molecules in the capsule core: rhodamine B isothiocyanate (Structure 6). The



**Structure 6.** Rhodamine B isothiocyanate.

loaded dye remained encapsulated in the hollow spheres after gold etching. This synthetic method obviously offers an interesting approach to guest encapsulation and could potentially be extended to the entrapment of enzymes and proteins.

### 3.2.2. Polymerization Initiated by Inorganic Particles

Apart from the formation of dense coatings, core-shell O/I particles can also be elaborated by templating inorganic colloids with polymer brushes using living polymerization techniques. The grafting reaction can be done in various ways through anionic [241–243], cationic [244, 245], or free radical processes [246, 247]. A variety of colloidal materials including silica and gold nanoparticles are concerned by these approaches. Since the growth reaction of polymers from inorganic surfaces is a very broad field of research [17, 248–253] a full description of these systems will not be attempted here. Only recent and typical examples will be reported in this section.

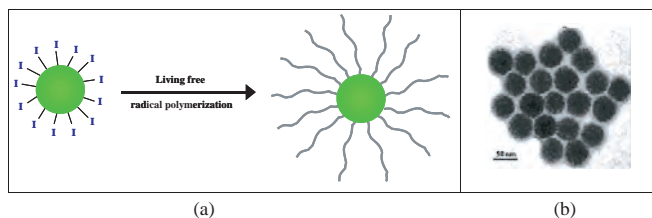
Hybrid nanoparticles with a block copolymer shell structure have been synthesized for instance by ring opening polymerization of norbornenyl groups immobilized onto gold colloids [254]. Ring opening polymerization of  $\epsilon$ -caprolactone has also been recently conducted from the surface of silica gel and cadmium sulfide nanoparticles [255, 256]. Amine or alcohol groups have been attached to the inorganic surface using silane coupling agents in order to provide a covalent anchoring of the macromolecules into hydrolytically stable polymer brushes. Tsubokawa et al. described the grafting of various polymers from the surface of silica nanoparticles [257–261]. Cationic polymerization of styrene was initiated by surface-grafted acylium perchlorate groups whereas peroxyester and diazo functions were involved in free radical polymerizations of styrene and methyl methacrylate monomers, respectively. In azo-initiated reactions, ungrafted polymer chains were also produced since the initiator was attached to the surface by only one end. In order to achieve better control of the grafting density, Prucker and Ruhe described the designed synthesis of an asymmetric diazo silane coupling agent [262–264]. The azo compound contained a cleavable ester group in order to facilitate degrafting of the polymer chains for analytical purposes and was monofunctional to control self-assembly of the chlorosilane azo initiator on the silica surface. Polymerization was performed in toluene at 60 °C and afforded grafted and free polymer chains. The graft density was found to be dependent on the silane concentration and polymerization time. Despite the confinement of the growing active centers on the silica surface, high molecular weight polymers were formed without the occurrence of excessive branching or cross-linking reactions. In recent years, several groups have reported the synthesis of polymer-grafted nanoparticles with controlled molecular weights and molecular weight distributions, using the atom transfer radical polymerization (ATRP) technique [265–270]. The general synthetic strategy involves the covalent attachment of various halide-functionalized ATRP macroinitiators on the inorganic surface (Table 1) and the subsequent controlled/living growth reaction of the polymer



**Table 1.** Chemical structures of the macroinitiators involved in the CRP from nanoparticulate inorganic surfaces.

Initiators	Abbreviation	Ref.
	BPDS	[265–268]
	BIDS	[265–268, 272]
	BIDS	[277–278]
	CDES	[271]
	/	[269]
	/	[274]
	/	[279]

chains from the anchored initiator molecules (Fig. 17). One key advantage of controlled radical polymerization (CRP) in comparison to conventional free radical processes is the possibility to synthesize well-defined polymers which can



**Figure 17.** (a) Reaction scheme for the synthesis of polymer-grafted inorganic particles via controlled radical polymerization using chemically anchored CRP macroinitiators. (b) TEM illustration of the CdS@SiO<sub>2</sub>/PMMA hybrid nanoparticles produced by atom transfer radical polymerization initiated from the CdS@SiO<sub>2</sub> nanoparticle surface. Reprinted with permission from [278], S. C. Farmer and T. E. Patten, *Chem. Mater.* 13, 3920 (2001). © 2001, American Chemical Society.

be grown with the desired thickness and composition. The technique allowed the formation of densely grafted and hairy outer polymer layers on nanoparticulate silica surfaces. Owing to the narrow molecular weight polydispersity of the polymer chains, the grafted particles organized into two-dimensional (2D) arrays with controlled interparticle distances a function of the degree of advancement of the reaction. Hollow polymeric microspheres have been produced by this technique by templating silica microspheres with poly(benzyl methacrylate) and subsequently removing the core by chemical etching [271]. The ATRP technique has also been recently reported to work effectively in aqueous media using hydrophilic water-soluble acrylic monomers [272]. Not only silica but also aluminum oxide particles [273], magnetic colloids [274], gold [275, 276], and photoluminescent cadmium sulfide nanoparticles [277, 278] have been used as macroinitiators. When cast from solution, the resulting nanocomposite film materials exhibited hexagonal ordering of the photoconductive cores (Fig. 17b) and were

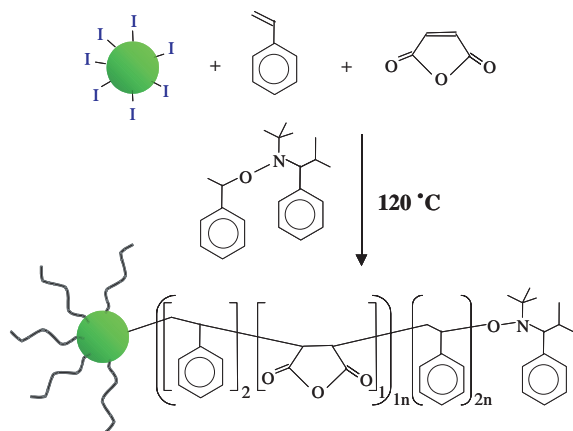
shown to retain the photoluminescent properties of the precursor CdS nanoparticles, but no mention was made of the colloidal stability of these systems.

It has been shown recently that the so-called stable free radical polymerization can also be used to initiate the polymerization of vinyl monomers from inorganic surfaces [279]. Following this route, shell-cross-linked polymeric capsules have been elaborated in a multistep procedure by templating colloidal silica with polymeric compounds and cross-linking the polymer shell. Micrometric silica beads were first modified by grafting on their surface a chlorosilane alkoxyamine initiator (see Table 1). Copolymers were then grown from the surface-attached initiator using an appropriate amount of sacrificial "free" alkoxyamine. The copolymer chains were designed to carry maleic anhydride functional groups for further cross-linking reactions (Fig. 18). A diamine cross-linker was added in a third step to effect interchain coupling via the formation of a bisimide. The inorganic silica template was finally removed in a last step by chemical etching. In an alternative strategy, styrene monomer was copolymerized with 4-vinylbenzocyclobutene, and the resulting nanocomposite core/shell particles were heated at 200 °C for thermal cross-linking.

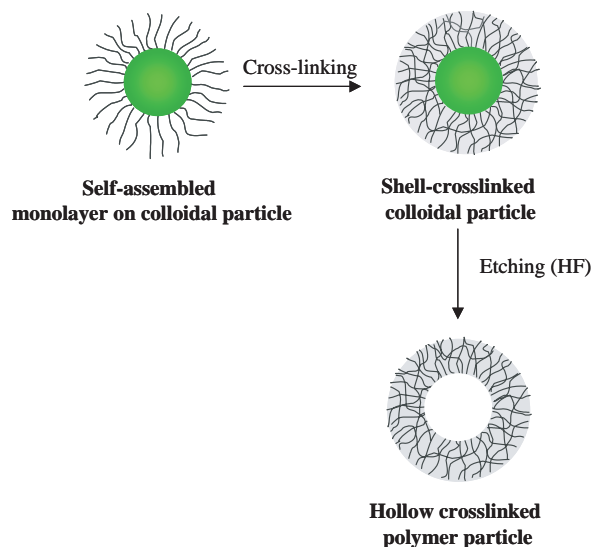
### 3.2.3. Cross-Linking of Self-Assembled Monolayers

As mentioned previously (Section 2), self-assembly also provides an original and efficient way to modify inorganic particle surfaces [280]. The formation and structure of self-assembled monolayers (SAMs) and their use in surface engineering have been much described and reviewed in recent years [281]. Alkane-thiol derivatives for instance are known to self-assemble onto gold colloid surfaces in a monolayer fashion via a surface complexation reaction [282]. If convenient reactive groups are incorporated into the SAM, further chemical reactions can be envisaged in order to elaborate core-shell particles and hollow capsules after degradation of the internal core (Fig. 19).

Shell-cross-linked polymeric nanocapsules have been synthesized for instance by metathesis polymerization of

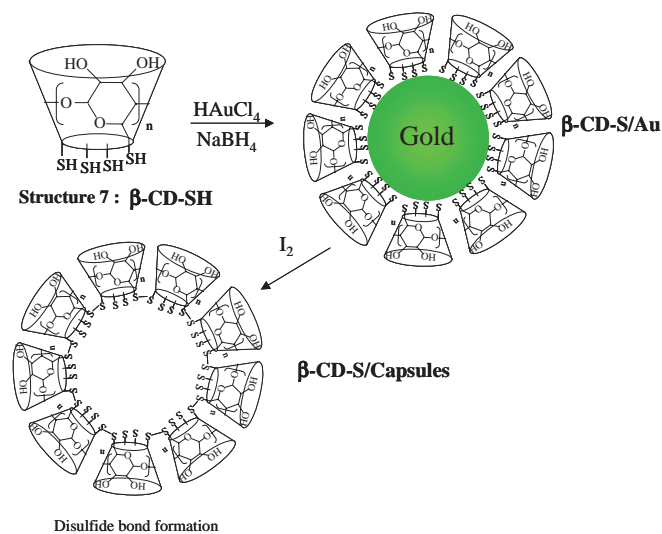


**Figure 18.** Synthetic scheme for the preparation of maleic anhydride-functionalized silica beads. Reprinted with permission from [279], S. Blomberg et al., *J. Polym. Sci. A* 40, 1309 (2002). © 2002, Wiley-VCH.



**Figure 19.** Principle of formation of shell-cross-linked nanocomposite particles from self-assembled monolayers on colloidal surfaces and the resulting polymeric capsules after core removal by chemical etching.

alkene-functionalized alkylthiolate monolayers attached on gold surfaces [283]. The thiolated ligands were designed to maximize polymer cross-linking and contained three alkene groups. In a related work, Sun and co-workers reported the preparation of monolayer-thick polymeric spheres by assembling thiolated- $\beta$ -cyclodextrins ( $\beta$ -CD-SH) (Structure 7) around gold nanoparticles (Fig. 20) [284]. The core dissolved upon addition of iodine to the suspension while simultaneously disulfide bonds were formed on the surface to produce structurally rigid cross-linked nanocapsules.



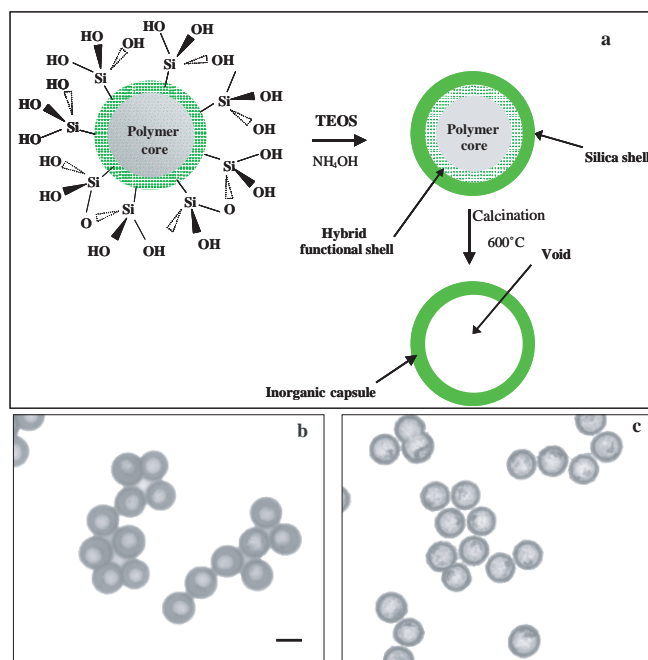
**Figure 20.** Preparation of polycyclodextrin hollow spheres by templating  $\beta$ -CD-SH monolayers around gold nanoparticles. Disulfide bridges were formed upon reaction with iodine while simultaneously the core dissolved into metallic complexes to give shell-cross-linked hollow spheres. Reprinted with permission from [284], L. Sun et al., *Chem. Commun.* 359 (2001). © 2001, Royal Society of Chemistry.

### 3.3. Polymer Latexes as Colloidal Templates

Coating of polymer colloids with materials of different chemical compositions gives access to nanocomposite particles with tailored structures and morphologies. Contrary to inorganic templates that require relatively harsh conditions to decompose, organic colloids can be easily removed either chemically or thermally from the nanocomposite particles without damaging the shell materials. A large variety of such structures involving polymer latexes as sacrificial templates can be found in recent literature.

#### 3.3.1. Sol-Gel Nanocoating

The coating of organic templates by metal oxides can be easily conducted in solution by the sol-gel technique. The sol-gel process involves the reaction of metal salts or organometallic precursor molecules to produce a three-dimensional inorganic polymer network. The coating of polystyrene latex particles with amorphous titanium dioxide has been achieved for instance by the hydrolysis of titanium tetrabutoxide [285, 286] and titanium tetraethoxide [287] in ethanolic suspensions. Due to the fast reactivity of the titanium alkoxide precursor in the sol-gel process, mixed suspensions with secondary titania particles were mostly produced. Optimal conditions were found to avoid the formation of separate particles and afford a regular coating. In order to overcome these difficulties, another approach, which consists of using cationic polystyrene particles as the seed, has been developed [288]. The positive charges on the surface ensured quick deposition of the titania precursors on the seed particles in the early stages of the sol-gel reaction. Very thin (in the range typically a few nanometers up to 50 nm) and smooth coatings were thus produced in a one-step method. Crystalline hollow spheres were further obtained by calcination of the  $\text{TiO}_2$ -coated particles at elevated temperatures. Increasing the temperature up to 600 °C yielded hollow crystalline anatase titania particles whereas the rutile form of  $\text{TiO}_2$  was obtained by calcining at 900–1000 °C. As an alternative solution, the latex core was dissolved by suspending the coated particles in toluene, a good solvent for the polymer. Using a similar technique, Margel and co-workers described the coating of large polymer beads with silica and magnetic iron oxide [289]. The coating was performed by seeded polymerization of tetraethoxysilane and iron salts on micrometer-sized polystyrene seed particles. The polymer surface contained adsorbed PVP which obviously played an active role in the coating procedure. Freestanding inorganic nanoparticles were also produced in this process but they could be easily separated from the coated polymer beads by repeated centrifugations. Core removal was performed thermally and the hollow capsules were visualized by TEM from cross-sections of the particles. With the aim to improve chemical interaction between the core and shell materials, we have recently developed a coating strategy based on a two-step procedure (Fig. 21). Polymer latex particles carrying silanol groups on their surface were first synthesized in emulsion polymerization using  $\gamma$ -MPS as a functional comonomer [290, 291]. The SiOH-functionalized latexes have been extensively characterized using AUGER, solid state nuclear magnetic resonance, and infrared spectroscopies [291]. The surface charge



**Figure 21.** (a) Synthetic scheme for the formation of silica/coated polymer latexes and the resulting hollow silica nanoparticles using SiOH-functionalized latex particles as colloidal templates. TEM image of (a) the core-shell colloid and (c) the hollow silica spheres. Scale bar: 100 nm. Reprinted with permission from [290], I. Tissot et al., *Macromolecules* 34, 5737 (2001). © 2001, American Chemical Society.

density was determined by chemical titration and was found to vary between 1.15 and 3.7  $\mu\text{C}/\text{cm}^2$  depending on the MPS content in the monomer mixture. Then, a silica shell was produced onto the functionalized PS seed particles by addition of tetraethoxysilane and ammonia to the colloidal suspension either in water [290] or in a mixture of ethanol and water [291]. No separate silica particles were formed in this work, indicating the strong affinity of the sol-gel precursor for the polymer colloid. Burning of the latex core resulted in the formation of hollow nanometer sized silica capsules. The nature of the core, the particle size, and the shell thickness can be finely tuned by conventional polymer colloid chemistry. Core-shell latexes with a soft polybutylacrylate core and a rigid silica shell have also been successfully produced by this technique.

Not only can inorganic precursors be used for coating, but preformed particles can also be homogeneously deposited onto colloidal templates to generate core-shell structures. For instance, colloidal clay nanosheets have been adsorbed onto cationic polystyrene latexes as a thin and crystalline layer [292]. Tetramethoxysilane was used as inorganic precursor to consolidate the coating and increase shell stability. The polymer template was removed in the next step to generate hollow silicate capsules. Hollow titania shells have been produced in a similar way by alternate deposition of polyethylenimine and titania nanosheets on polymer latexes and removal of the organic template by heat or ultraviolet (UV) treatment of the core-shell nanocomposite particles [293]. Valtchev also recently reported the coating of micrometer-sized polystyrene beads by zeolite

A nanocrystals using a cationic polymeric agent as binder between the core and shell materials [294].

In addition to polymer latexes, inorganic colloids can also be advantageously used as templates to generate inorganic capsules. A range of hollow spheres have been prepared in this manner using silica materials as sacrificial templates. For example, monodisperse core-shell colloidal spheres of silica ( $\text{SiO}_2$ ) and zinc sulfide (ZnS) have been elaborated by templating silica colloids [295]. Coating of  $\text{SiO}_2$  with ZnS was performed in water/ethanol solutions by direct precipitation of ZnS onto the silica seed using thermally activated thioacetamide as a source of sulfide ions and acidic zinc nitrate aqueous solutions. Hollow ZnS spheres were obtained in a subsequent step by dissolving the  $\text{SiO}_2$  core in hydrofluoric acid. Surprisingly, the ZnS shell only dissolved slowly under these conditions and the particles retained their original shape. The reverse structure composed of ZnS core coated with silica was elaborated in a similar way by templating zinc sulfide colloids with tetraethoxysilane using a seeded growth technique adapted from the Stöber method. A mineral nitric acid, much less aggressive than HF, was used in this case to selectively dissolve the ZnS core from the structured particles. The resulting hollow spheres (either the silica shells or the high dielectric ZnS capsules) were shown to display interesting optical properties with potential applications as colloidal crystals in photonic devices. Another extensively described templating material is gold colloid [296, 297]. The coating of gold nanoparticles with silica has been reported by Mulvaney and co-workers. The coating serves first to stabilize particles against coagulation and also promotes ordering of the nanoparticles into two-dimensional arrays. Their method involves three successive steps. The gold surface was first rendered vitreophilic by addition of 3-aminopropyl trimethoxysilane which strongly adsorbed on the metal. The anchored silanol groups were then involved in the formation of a thin silica layer by direct precipitation of a native sodium silicate solution. In the final step, extensive growth was performed in ethanol/water mixtures to afford silica-coated gold nanoparticles with shell thickness up to 80 nm. Again, the coated nanosized silica/gold colloids were shown to display very interesting optical properties [298]. Hollow silica capsules were obtained from the coated colloids by exposing the particles to cyanide ions. The oxidized gold cores completely dissolved and diffused out of the silica shell. Several studies on silica particles grown using TEOS clearly attest to the presence of micropores ranging in size from 2 to 50 nm. The resulting microporous and hollow shell particles are potential carriers for slow release and drug delivery.

### 3.3.2. Metal Deposition

The immobilization of fine metal colloids onto nanoparticle surfaces has received a lot of attention in recent years because of the potential use of metal-decorated particles in optics, electronics, and heterogeneous catalysis [299, 300]. A variety of methods have been successfully reported for the coating of colloidal templates with metallic nanoparticles. Two approaches can be distinguished. In the first method, the nanoparticles are precipitated *in-situ* onto the colloidal templates by the reaction of the metal salt precursors previously adsorbed on their surface through ion exchange or

complexation chemistry [301–310], whereas in the second method, preformed metal colloids are adsorbed onto colloidal templates of opposite charges through electrostatic interaction as extensively reported in the previous section. In both methods, the colloidal templates must contain surface groups with strong affinity for the metal precursors and/or the nanoparticles. Functional groups such as carboxylic acid (-COOH), hydroxy (-OH), thiol (-SH), and amine (-NH<sub>2</sub>) derivatives can be easily introduced into polymer latexes by copolymerizing their corresponding monomers. The surface-complexed metal salts are then directly transformed into metal colloids by the addition of reducing agents. Following this route, palladium [301–303, 306, 310], rhodium [301–303, 309], nickel [305], cobalt [305], silver [304], and gold [310] nanoparticles have been successively anchored onto the surface of a series of functional polymer microspheres. The resulting composite colloids were shown to display high catalytic activity in, for instance, the hydrogenation of alkenes. In alternative procedures, the coating can also be produced by the controlled hydrolysis of the metal salts into metal oxide followed by reduction of the oxide into the corresponding metal [311–316]. Submicrometer-sized composite spheres of yttrium and zirconium compounds and hollow metallic spheres have been prepared this way by coating cationic polystyrene latex particles with basic yttrium carbonate [311–312] and basic zirconium sulfate [313], respectively, followed by calcination of the so-coated latexes at elevated temperatures. Uniform coatings of copper [314] and iron oxide [315, 316] compounds have been formed in a similar procedure by aging at high temperature aqueous solutions of the metal salt in presence of urea, PVP, and anionic polystyrene latexes. The coating was shown to proceed by *in-situ* heterocoagulation of the precipitating metal colloids on the organic seed surface. Voids were produced in a subsequent step by complete thermal oxidative decomposition of the polymer core.

Not only metal but also semiconductor nanoparticles can be used for coating. Polymer micro- and nanoparticles have been successively reported as host matrices for CdS nanocrystal formation [317, 318]. Monodisperse poly(methyl methacrylate-co-methacrylic acid) (PMMA-PMAA) latex particles were prepared by emulsion polymerization and ion exchanged with a  $\text{Cd}(\text{ClO}_4)_2$  solution. The  $\text{Cd}^{2+}$  ions thus introduced into the electrical double layer were further reduced into CdS nanoclusters by addition of a  $\text{Na}_2\text{S}$  solution. The CdS loaded nanocomposite particles were subsequently recovered by a film forming polymer shell by reacting methyl methacrylate and butyl acrylate monomers. The resulting colloidal nanocomposites were finally assembled in 3D periodic arrays consisting of rigid PMMA-PMAA/CdS core particles regularly distributed within the soft polymer matrix. Periodic structures of polyacrylic/silver colloids have been elaborated in a similar way using  $\text{Ag}^+$  ions as precursors. The method obviously opens a new avenue for producing optically responsive materials with a controlled periodicity. Nanocomposite materials with several other functions can be elaborated by this technique using different types of nanoparticles and organic polymers.

### 3.4. Vesicle and Block Copolymer Templating

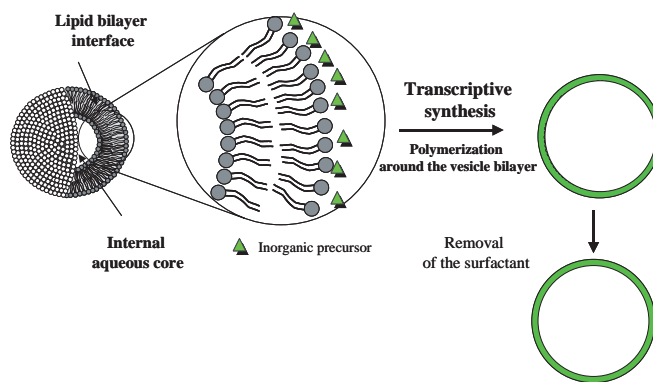
O/I nanocomposite colloids can also be elaborated from the assembly of preformed polymers into spherical aggregates and their subsequent use as host materials or templates for the growth reaction of metal oxides and metal colloids. The ability of amphiphilic diblock copolymers, dissolved in a selective solvent, to self-assemble into colloidal size aggregates has been studied for several decades and their use as nanoreactors has been much described. Core-shell architecture of micelles prepared from amphiphilic polymers permits the dissolution of large amounts of poorly water soluble drugs, for instance, and affords protection against a potentially damaging environment. On the other hand, phospholipid molecules and synthetic amphiphiles with two long aliphatic chains attached to an ionic head group are insoluble in water and are known to form highly ordered layers. The bilayer structures separate an aqueous interior from an aqueous exterior and are versatile carriers in the area of drug delivery. The elaboration of vesicular, micellar, and related aggregate structures as host materials for inorganic polymerization is briefly reviewed in this section. A complete description of these systems can be found elsewhere [319, 320].

#### 3.4.1. Vesicle Templating

Surfactant vesicles are an important class of bilayer aggregates extensively used as model membranes for artificial cells. They are nonequilibrium structures mostly kinetically stabilized. Vesicles are usually produced by shear-assisted means including sonication and extrusion. However, owing to the noncovalent interactions responsible for their formation, these nanoobjects have only a limited stability and inherently return to their native lamellar phase state. A variety of techniques have been employed in order to increase vesicle stability. One method involves using reactive polymerizable surfactants and polymerizing the vesicle. Another technique takes advantage of the bilayer morphology of the surfactant aggregates to solubilize organic substances such as monomers. Subsequent polymerization of the vesicles gives hollow spheres whose shape is the replica of the original bilayer structure (so-called morphosynthesis). The shell is cross-linked so as to afford rigid and stable capsules after extraction of the templating surfactant matrix. In addition to morphosynthesis, vesicles can also be used as templating materials for transcription into inorganic capsules as described by Hubert and colleagues [321]. The transcriptive synthesis approach (see Fig. 22) is identical to the colloidal templating strategy described in the previous section. Cationic dioctadecyldimethylammonium vesicles were shown to provide effective receptors for silica growth due to electrostatic interaction of the alkoxy silane precursors with the surfactant molecules. The so-produced "petrified" vesicles were stable to dehydration and could be visualized by conventional TEM without additional staining agents.

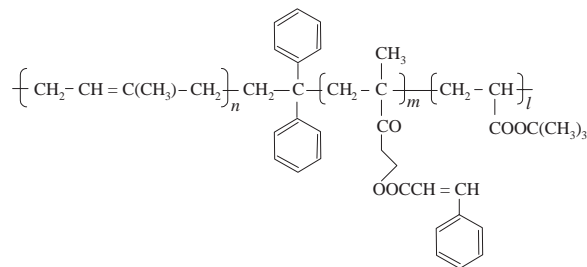
#### 3.4.2. Block Copolymer Templating

Block copolymers can adopt a variety of supramolecular structures in selective solvents. Gohy and co-workers described for instance the synthesis of pH-sensitive core-shell-corona (CSC) polystyrene-*b*-poly(2-vinyl pyridine)-*b*-poly(ethylene oxide) triblock copolymer micelles [322]. The



**Figure 22.** Schematic representation of the vesicle-templating strategy (transcriptive synthesis) for the elaboration of hollow inorganic spheres.

micelles were loaded with  $\text{HAuCl}_4$  gold salt, which was transformed in the next step into metal colloids by  $\text{NaBH}_4$  reduction. Due to preferred interaction between the protonated P2VP block of the terpolymer and the metal ions, precipitation of gold nanoparticles took place on the P2VP outerlayer of the triblock micelle. Similarly, CSC polyisoprene-*b*-poly(2-cinnamoyl ethyl methacrylate)-*b*-poly(*tert*-butyl acrylate) micelles (PI-*b*-PCEMA-*b*-PtBA; Structure 8) have been produced by Stewart and Liu [323]. The micelles were solidified by UV cross-linking of the PCEMA shell while the PI block was degraded by ozonolysis to generate nanospheres with a central cavity. The so-obtained nanocapsules were loaded with rhodamine B (Structure 6), a model molecule which size is similar to that of drug compounds. In a related work, iron oxide magnetic nanoparticles have been precipitated inside the core of the PI-*b*-PCEMA-*b*-PtBA triblock micelles [324]. For that purpose, the triblock nanospheres were first rendered water dispersible by hydroxylation of the polyisoprene block. The PtBA block was then converted into polyacrylic acid (PAA) by hydrolysis. The resulting polymeric triblock nanospheres were loaded with  $\text{Fe}^{2+}$  metal ions by exchange of the PAA protons and the iron oxide nanoparticles were finally precipitated by addition of  $\text{NaOH}$ . Based on the same general concept, the synthesis of a variety of triblock and diblock copolymer micelles has been reported in the literature [325–327]. Hollow particles have been produced for instance from shell-cross-linked (SCL) micelles after degradation of the internal part of the micellar aggregates. These SCL micelles can serve further as nanoreactors to precipitate organic and/or inorganic particles using strategies

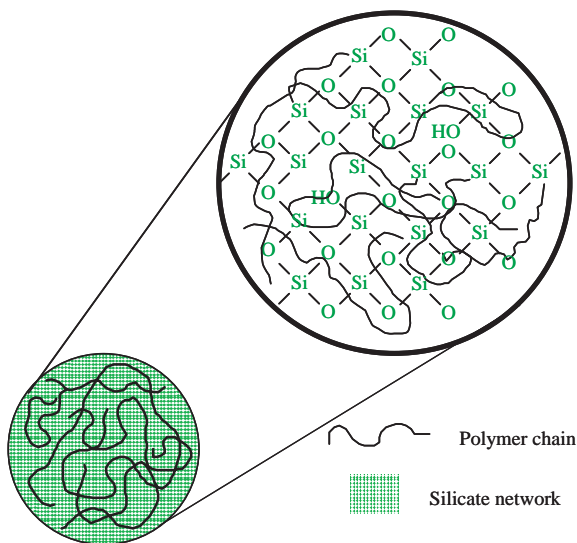


**Structure 8.** Polyisoprene-*b*-poly(2-cinnamoyl ethyl methacrylate)-*b*-poly(*tert*-butyl acrylate) (PI-*b*-PCEMA-*b*-PtBA).

similar to those reported previously for CSC micelles. pH-responsive SCL micelles have been used for instance as reservoirs for the preparation of gold colloids [328]. Organic polymerization reactions can also be conducted in the confined space of nanocapsules. As a typical example, an aqueous solution of hydrophilic monomers containing acrylamide has been entrapped inside the water pool of hollow spheres. Subsequent polymerization produced cross-linked poly(acrylamide) gels filling the whole volume of the capsule. The imprinted latexes were found to adopt the dimensions and spherical shape of the mold [329].

#### 4. HYBRID COLLOIDS

Composite materials where the organic and inorganic components are intimately intertwined within one another on the molecular level are an important class of materials whose properties are controlled by the functionality and connectivity of the molecular precursors. There have been a huge number of works in recent years describing the elaboration of hybrid structures of this type by, for instance, *in-situ* polymerization of inorganic precursors within a polymer matrix or by embedding of organic polymers into inorganic glasses [16–22]. Such materials are usually produced by the sol–gel technique and processed as thin films, powders, gels, or monoliths [330]. But, surprisingly, there are only few examples of nanoparticle synthesis by reacting simultaneously organic and inorganic precursor molecules into a kind of organic/inorganic interpenetrated network. An example of morphology that can be produced by this strategy is reported in Figure 23 which represents a colloidal particle composed of an organic–inorganic network condensed into a gellike structure. It is expected that the properties of those hybrid colloids will be significantly different than



**Gel-type colloidal particle with interpenetrated organo-mineral network**

**Figure 23.** Schematic representation of nanocomposite colloids with organic/inorganic interpenetrated network.

a simple combination of the properties of the two components. We describe in this section typical examples of this general approach.

#### 4.1. Poly(organosiloxane/vinylic) Copolymer Hybrids

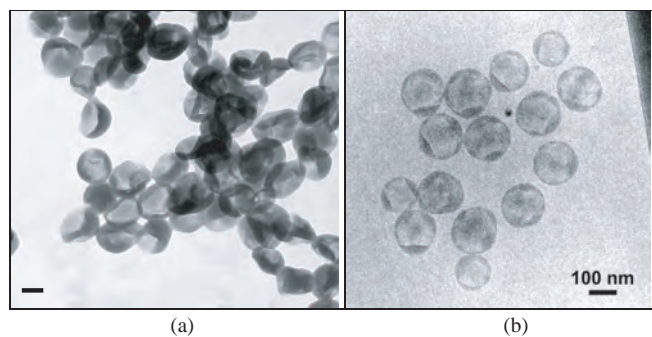
The combination of various polymers and copolymers with inorganic structures, like silica and silsesquioxanes, to yield inorganic particles doped with organic polymers or vitreophilic polymer colloids can be readily conducted in multiphase media. As a matter of fact, silica networks and structured silicate for instance are easily obtained by hydrolysis and condensation of tetrafunctional  $[\text{Si}(\text{OR})_4]$  or trifunctional  $[\text{R}'_n\text{Si}(\text{OR})_{4-n}]$  alkoxy silanes in various dispersion systems. In addition, the polymerization reaction of a variety of acrylic monomers and comonomers can be carried out in these systems as well. So, provided that the rates of both reactions are not too much different and that a coupling agent is used to link the inorganic network and the organic polymer, hybrid colloids with interpenetrated organic–inorganic networks could be formed. Microemulsion for instance is a convenient system for both metal oxide and polymer latex synthesis. On one hand, alcohols are usually used as short chains cosurfactants in conjunction with sodium dodecyl sulfate to stabilize the microemulsion. On the other hand, the sol–gel reaction can take place in alcohol–water mixtures. Consequently, the sol–gel reaction of TEOS and the polymerization of acrylic monomers can be performed simultaneously in microemulsion systems in which the continuous phase is a mixture of alcohol (typically methanol) and water and the organic phase is composed of TEOS and the acrylic monomer. In a typical recipe, the inorganic precursor, the organic monomer, and the coupling agent are added simultaneously, and interpenetrated networks can be obtained by adjusting the kinetics of the organic and inorganic reactions. Organoalkoxysilane molecules with a terminal double bond reactive in free radical polymerization processes are particularly well suited in order to attach the polymer chains to the inorganic network as described in the previous section. Methacryloxypropyl trimethoxysilane ( $\gamma$ -MPS) is the most commonly used functional monomer for such applications.

Following this route, Donescu et al. have synthesized hybrid materials by the simultaneous reaction of TEOS and methyl methacrylate in the presence of alcohol [331]. A cross-linker was introduced to promote the formation of the polymer network and  $\gamma$ -MPS was used to avoid phase separation. Although it is not clear whether colloidal particles have been successfully obtained in this work, the formation of simultaneous interpenetrated polymer–inorganic networks was indirectly evidenced by the increase in glass transition temperature and the improved thermal resistance of the organic network in the presence of the inorganic phase. In a related study from the same group, vinyl acetate was used as the organic monomer and it was argued that monostructured materials or dispersed particles were obtained depending on the ratio of the organic over the aqueous phase and the nature of the comonomer (e.g., butyl acrylate versus di-2-ethyl hexyl maleate) [332]. It has also been reported in a recent work from Uricanu

and Panayiotou that silica–polystyrene nanocomposites can be obtained in one reaction step through miniemulsion polymerization [333]. However, the silica nanoparticles were shown to form agglomerates in the final composite latexes, and phase separation occurred during polymerization.

We have recently demonstrated in our group that the MPS molecule can also be reacted with acrylic and styrene monomers to produce functional hybrid copolymer latexes with interpenetrated organic/inorganic networks via emulsion polymerization [290, 291, 334]. The polymer latex particles were synthesized in batches or semibatches. In the semibatch reactions, the silane molecule was introduced as a shot after consumption of part of the acrylic and styrene monomers. Core–shell colloids with a polymer core and a hybrid shell were thus produced by this technique. The core-to-shell ratio could be easily adjusted by addition of the silane molecule at different seed conversions. The silane concentration was varied from 5 to 40 wt% with respect to the monomer without significant influence on particle size and particle stability except when nonionic surfactants were used as stabilizers. Not only did the presence of the silanol group enable the successful overgrowth of a silica layer on the polymer particle surface, but the hybrid structure of the shell also proved to have unusual solubility behavior [335]. Hybrid polymeric capsules were produced from the core–shell nanocomposite colloids by suspending the hybrid latexes into a good solvent of the core, THF. The latex core was shown to diffuse through the hybrid shell and instantaneously dissolve into THF giving rise to hybrid and soft nanocapsules. Figure 24 shows the morphology of the hybrid capsules after observation with a conventional transmission electron microscope and by cryogenic transmission electron microscopy, respectively. While the dried capsules collapsed on the grid support due to the very low shell thickness and presumably also because of the low  $T_g$  of the hybrid copolymer membrane, cryo-TEM observation enabled visualization of the spherical shape of the capsules by preserving their morphology into a thin film of freeze-dried water. The hybrid shell structure thus played the role of a dialysis membrane that enabled water exchange in and out of the capsules.

Film forming copolymer latexes were also produced by this technique by reacting MPS, styrene, and butyl acrylate monomers. The composite films were fully transparent up to 15% MPS content suggesting an homogeneous distribution



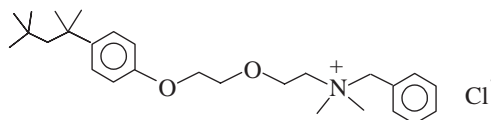
**Figure 24.** (a) Conventional TEM picture and (b) cryo-TEM micrograph of poly(styrene-co-MPS) hybrid capsules. Scale bar: 100 nm.

of the silane units within the organic/inorganic network and the absence of macroscopic phase separation. The resulting materials were characterized by dynamic mechanical spectroscopy and were shown to display significantly improved mechanical properties in comparison to their polymeric counterparts.

Not only can tetrafunctional and trifunctional alkoxy silanes be reacted with vinylic monomers, but polysiloxanes with difunctional repeating units can also be incorporated into polymer latexes via the emulsion copolymerization reaction of silicon monomers, namely octomethyltetracyclosiloxane and methacryloxypropyl trimethoxysilane, and a series of acrylic compounds (e.g., MMA, butyl acrylate, acrylic acid, and *N*-hydroxyl methyl acrylamide) [336–341]. In order to obtain stable latexes, the copolymerization reaction must be carried out under specific experimental conditions. It was shown for instance that stable monodispersed particles were formed only when the monomers were pre-emulsified in water and added dropwise at 85 °C into an aqueous solution of the initiator. The silane coupling agent was used to control particle morphology and provide a successful incorporation of the silicone polymers into the acrylic latexes. The films produced from the hybrid latexes were shown to display improved water resistance and a higher gloss.

## 4.2. Polyorganosiloxane Colloids

Organoalkoxysilanes of the type described previously  $[R_nSi(OR')_{4-n}]$  can also be processed separately as fine particles by emulsion polymerization as extensively reported by Schmidt and co-workers in recent literature [342–348]. The colloids were elaborated by the sol–gel process in aqueous solution through hydrolysis and condensation of various organoalkoxysilane precursors in the presence of benzethonium chloride surfactant (Structure 9) and a base catalyst. Spherical elastomeric micronetworks (so-called organosilicon microgels) of narrow size distribution were produced by this technique. Typical examples of alkoxy silane derivatives which have been used in these syntheses are listed in Table 2. From the mechanistic point of view, the inorganic polymerization reaction can be regarded more as a polycondensation in microemulsion than a conventional emulsion polymerization process. Particle sizes were principally governed by the ratio of surfactant to monomer concentration, and in a limited range, the final microgel diameters could be well described by the theory of  $\mu$ -emulsion although the suspensions were not fully transparent. The main interest of the technique is the possibility to synthesize highly functionalized nanoparticles with nearly uniform diameters typically in the range 10–40 nm. The cross-linking density of the microgel particles could be finely



**Structure 9.** Benzethonium chloride surfactant.

tuned by using a mixture of trifunctional (T) trialkoxysilane and difunctional (D) dialkoxysilane molecules. Particle sizes were shown to increase with increasing content of D units suggesting intraparticle gelation. Other critical parameters influencing colloidal stability were the dispersion concentration, the amount of catalyst, the temperature, and the monomer addition rate. The particles could be additionally rendered chemically inert toward further interparticle condensation reactions and hydrophobic by end capping of the  $-\text{SiOH}$  groups into  $-\text{SiOSi}(\text{CH}_3)_3$  or  $-\text{SiOSi}(\text{CH}_3)_2\text{H}$  moieties. The curing process was performed by addition of trimethyl methoxysilane or dihydridotetramethyldisiloxane, respectively. The resulting colloids could be easily solubilized or redispersed into organic solvents making it possible to grow polystyrene chains from their surface by the hydrosilylation reaction of vinyl-terminated polystyrene macromonomers with the SiH functional groups [345]. Those model systems have been shown to be particularly suitable for the elaboration of thermodynamically stable homogeneous mixtures of the hybrid colloids with linear polymeric chains.

In addition to copolycondensates, well defined core/shell structures can also be prepared by the subsequent addition of different types of monomers on particle seeds [346, 347]. The cores were made for instance of linear chains of polydimethylsiloxane while the shell was cross-linked by reacting different trialkoxysilane precursors. One important feature of these core-shell colloids is that specific reactivities can be imparted to the cores by the reaction of convenient functional monomers. These topologically entrapped functional molecules are confined reactive sites that can undergo further chemical reactions. According to this principle, organic dye molecules have been selectively attached to microgel particles by the reaction of the dye labels with chlorobenzyl functional groups previously incorporated in the internal part of the colloid [348, 349]. In a similar procedure, functionalized  $\mu$ -network gel particles were used as nanoreactors to entrap metal clusters [350, 351]. The microstructure of

the host microgel particles was designed so as to contain reducing SiH moieties in their core. Metal ions were subsequently loaded into the microgel particles by diffusion of the metal salt solution  $[\text{H}(\text{AuCl}_4)]$  through the shell. Metal salt reduction was taking place *in-situ* by means of the confined SiH reactive sites. The aqueous dispersion of the metal cluster entrapped colloids was finally transferred to organic solvents by reaction of SiOH with monoalkoxy silanes as reported previously.

An original approach that combines templating techniques and organoalkoxysilane chemistry has been reported by Büchel and co-workers [352]. The authors described the synthesis of silica core/mesoporous shell (SCMS) colloids by reacting a mixture of triethoxysilane and *n*-octadecyl trimethoxysilane (C18-TMS; see Table 2) on the surface of nanometer-sized silica particles produced by the Stöber process. Calcination of the C18-TMS porogen molecules resulted in the formation of inorganic spheres whose surface porosity can be finely tuned by the concentration of the organoalkoxysilane precursor incorporated into the shell. Following this line, Yoon et al. reported the fabrication of carbon capsules by templating the mesopores of the SCMS colloid with a phenolic resin followed by carbonization [353]. Hollow spheres were produced in the last step by dissolution of the silica core. More recently, the technique was extended to the synthesis of complex shell-in-shell nanocomposite particles and gold loaded nanocapsules using silica-coated gold colloid as the seed instead of pure silica spheres [354]. Hall and co-workers also recently described the use of silica-coated gold particles as templates for the subsequent overgrowth of a polyorganosiloxane shell on their surface [355]. The process involves the hydrolysis and condensation reaction of a mixture of functional alkoxysilanes on the surface of gold colloids previously rendered vitreophilic according to the procedure of Liz-Marzan and co-workers [296]. Gold/polysiloxane core/shell nanoparticles with various functionalities (allyl, phenyl mercapto, amino,

**Table 2.** Examples of organoalkoxysilanes involved in the preparation of organosilicon microgel colloids.

Organoalkoxysilanes	Chemical structure	Abbreviation
Tetraethoxysilane	$(\text{CH}_3\text{CH}_2\text{O})_4\text{Si}$	TEOS
Methacryloxypropyl trimethoxysilane	$(\text{CH}_3\text{O})_3\text{Si}(\text{CH}_2)_3\text{OCOC}(\text{CH}_3)=\text{CH}_2$	$\gamma$ -MPS
Triethoxysilane	$(\text{CH}_3\text{CH}_2\text{O})_3\text{SiH}$	TMS
Vinyl trimethoxysilane	$(\text{CH}_3\text{O})_3\text{SiCH}=\text{CH}_2$	VMS
Allyl trimethoxysilane	$(\text{CH}_3\text{O})_3\text{SiCH}_2\text{CH}=\text{CH}_2$	AMS
Mercaptopropyl trimethoxysilane	$(\text{CH}_3\text{O})_3\text{Si}(\text{CH}_2)_3\text{SH}$	MPTMS
Mercaptopropyl triethoxysilane	$(\text{CH}_3\text{CH}_2\text{O})_3\text{Si}(\text{CH}_2)_3\text{SH}$	MPTES
Methyl trimethoxysilane	$(\text{CH}_3\text{O})_3\text{SiCH}_3$	MMS
Dimethyl dimethoxysilane	$(\text{CH}_3\text{O})_2\text{Si}(\text{CH}_3)_2$	DMMS
Trimethyl methoxysilane	$(\text{CH}_3\text{O})\text{Si}(\text{CH}_3)_3$	TMMS
Dihydridotetramethyl disiloxane	$\text{HSi}(\text{CH}_3)_2\text{OSi}(\text{CH}_3)_2\text{H}$	DTDS
Hexamethyldisilazane	$(\text{CH}_3)_3\text{SiNHSi}(\text{CH}_3)_3$	HMDS
Cyanatopropyl triethoxysilane	$(\text{CH}_3\text{CH}_2\text{O})_3\text{Si}(\text{CH}_2)_3\text{CN}$	CPTMS
Chlorobenzyl trimethoxysilane	$(\text{CH}_3\text{O})_3\text{SiPh}(\text{CH}_2)\text{Cl}$	CMS
Phenyl trimethoxysilane	$(\text{CH}_3\text{O})_3\text{SiPh}$	PMS
Glycidoxypropyl triethoxysilane	$(\text{CH}_3\text{CH}_2\text{O})_3\text{Si}(\text{CH}_2)_3\text{OCH}_2\text{CHOCH}$	GLYMO
Aminopropyl trimethoxysilane	$(\text{CH}_3\text{O})_3\text{Si}(\text{CH}_2)_3\text{NH}_2$	APTMS
<i>n</i> -Octadecyl trimethoxysilane	$(\text{CH}_3\text{O})_3\text{Si}(\text{CH}_2)_{17}\text{CH}_3$	C18-TMS



cyano, . . .) and controlled shell thicknesses have been successfully prepared by this technique.

## 5. CONCLUSION

Although organic/inorganic colloids represent a relatively new category of nanocomposite materials, they have demonstrated a lot of potential in a variety of domains from the coating industry to the biomedical field. O/I colloids have indeed attracted increasing attention in the last 10 years because they offer the unique possibility to combine the properties of organic and inorganic components within a nanoparticle space. Catalytic, electronic, and optical features of inorganic colloids can thus be combined with the mechanical characteristics of polymers such as film formation, structural flexibility, and easy processing. In addition to combining distinct properties, new and unexpected synergistic phenomena may also arise from the nanometer-scale dimensions of the composite material. Because small particles offer the promise of large interfacial areas and size confinement effects, new physical, chemical, or biological properties can be expected by size scaling. Many new properties may also result from the possibility of ordering the inorganic components into the polymer matrix. As such, it can be anticipated that nanocomposite colloids will provide numerous exciting and new opportunities in the near future.

O/I colloids can be elaborated in a variety of ways through seeded-growth reactions, structure-directing templates, and self-assembly strategies using chemical or physicochemical routes, and a variety of nanocomposite particles of different compositions and structural characteristics can be produced by these techniques. Among the various synthetic schemes, emulsion polymerization offers great potential that has been largely exploited in the paint industry. The unique flexibility of emulsion processing makes it possible to produce coated particles with controlled size, composition, and shell thickness in large volumes. Nanoengineering of particle surfaces (coating and encapsulation) enables the elaboration of a new class of composite products of higher quality and better end-use properties.

The synthesis of O/I colloids in multiphase systems, including miniemulsion and dispersion polymerizations, can be successfully achieved provided that the inorganic surface has been previously modified and rendered compatible with the organic polymer. A number of compatibilizing synthetic approaches have been described in this chapter. These include polymer grafting from inorganic surfaces via the covalent attachment of initiator or monomer molecules, *in-situ* polymer precipitation through electrostatic attraction, or polymerization in adsorbed surfactant bilayers. The nature of the link at the interface between the organic and inorganic components (i.e., ionic, ionocovalent, van der Waals, hydrogen bonding, . . .) and the functional group concentration are of paramount importance in controlling particle morphology. The variety of different types of connections which have been investigated have indeed demonstrated the possibility to achieve different degrees of control over the assembly process. Thin polymer layers or nanoparticles can be deposited on the seed surface depending on the affinity between the organic and inorganic entities. Each partner obviously plays an active role in this process by directing

their dual association by means of complementary functionalities. Preformed organic and inorganic particles can also be connected this way into "supracolloidal" architectures.

Templating of polymer latexes with minerals also provides a versatile way for the elaboration of nanocomposite colloids and capsules using either organic or hybrid particles as sacrificial templates. The general LbL nanocoating strategy gives access to tailor-made, reproducible, and optimized systems for biotechnological applications. Among the advantages is the possibility to manipulate the size and permeability of the capsules. One major limitation, however, is the time consuming elaboration process of the shell membrane. To this respect, direct inorganic polymerization techniques offer alternative strategies to grow smooth and controlled mineral oxide layers on organic templates. We also described in this work the use of block copolymer and surfactant assemblies into vesicles and related aggregate structures to produce nanocomposite colloids and small permeable capsules. These hollow spheres can be additionally loaded with metal ions and provide confined spaces for further chemical reactions. The copolymers can also be designed to carry recognition groups and affinity ligands to be directed toward specific target sites. Supramolecular assemblies and their use as structure directing agents is a very broad field of research, and only a limited number of examples have been presented here.

Hybrid colloids with interpenetrated organomineral networks also constitute a real challenge. Not only can the mechanical and physical properties of these materials be significantly enhanced, but new, unexpected properties can also arise from the intimate association of the organic and inorganic components. The preliminary investigations in this field are promising but further knowledge is needed to develop this new area of research.

Obviously, the synthesis of organic-inorganic colloids has opened interesting perspectives in the field of colloidal science. It can be expected that these early achievements will see further expansion and find extensive development in the near future. For example, the elaboration of multi-scale nanocomposite particles with complex morphologies and containing colloids of different nature could provide a new class of materials and expand the range of properties that can be achieved in the field of nanotechnologies. To this end, a variety of inorganic compounds having different sizes and shapes could be used as precursors from layered silicate, nanofibers, and colloidal metals to ordered mesoporous silica and other related materials. These multicomposite colloids additionally could be assembled into higher hierarchical superstructures to fabricate novel types of sensor devices with optical or electro-optical properties.

## GLOSSARY

**Colloidal nanocomposites** Particles which are inhomogeneous in composition and contain at least two incompatible domains.

**Colloids** Organic and/or inorganic particles stabilized in a suspension medium and which have at least in one direction a dimension in the colloidal range (i.e., comprised roughly between 1 nm and 1  $\mu\text{m}$ ).

**Core-shell particles** Nanostructured colloids comprised of at least two phases, one of which is in the center (core) and the other which forms a concentric outer layer (shell).

**Heterocoagulation** The interaction of unlike colloidal particles (e.g., for instance organic and inorganic colloids) with different sign of charge by means of electrostatic attraction.

**Latex** A colloidal dispersion of polymer particles in a liquid phase (water, alcohols, or organic solvents). Surfactants or polymeric dispersants are typically used to stabilize the suspension.

**Living free radical polymerization (LFRP)** Controlled/living free radical polymerization techniques that allow the formation of organic polymers with controlled molecular weights and narrow molecular weight distributions.

**Miniemulsion** Oil in water (O/W) or water in oil emulsions in which the diameter of the disperse phase is typically in the range from around 50 to 500 nm. The emulsion droplets are stabilized against diffusion degradation (Ostwald ripening) by a molecule contained in the disperse phase. This compound is typically a water-insoluble substance in case of the O/W miniemulsions.

**Nanocapsules/Hollow particles** Core-shell particles of colloidal dimension wherein the core is a liquid (nanocapsule) or a gas (hollow particles).

**Nanostructured colloids** Multicomponent particles which have been designed in an attempt to obtain specific structures.

**Polymerizations in multiphase systems** Organic and/or inorganic polymerizations (including free radical processes, organic and inorganic polycondensations) resulting in the formation of organic and/or inorganic polymer particles suspended in a liquid phase.

**Self-assembly** The assembly of molecules and/or polymeric substances into micelles, vesicles, and related aggregates. Polymers and/or modifying agents, for instance polyelectrolytes and silane or organothiols, can also be assembled onto colloidal templates giving rise to molecules and/or macromolecules surrounding (covering) the core material. Colloids can also be assembled into aggregates of controlled shapes and size (e.g., with for instance raspberry-like morphologies) the process of which is most often known as heterocoagulation.

**Silane coupling agents** Organosilane molecules (halides or alkoxydes) of the type  $R_{4-n}SiX_n$  ( $n = 1 - 3$ , X = halide or OR) carrying an organic functionality R useful for the derivatization of inorganic materials. R is typically a thiol, an amine, an epoxy, or a methacryloyl group.

**Sol-gel nanocoating** Formation of inorganic coatings on templates (for instance polymer particles or any other substrate) by the polycondensation/precipitation reaction of metal alkoxides and/or metal salts through the sol-gel route.

## REFERENCES

- I. Amato, Nanotechnology—Shaping the World Atom by Atom, NSTC report, 1999. Available on the Web at <http://itri.loyola.edu/nano/IWGN.Public.Brochure/>.
- Nanostructure Science and Technology, A Worldwide Study, Report on Nanostructure Science and Technology: R&D Status and Trends in Nanoparticles, Nanostructured Materials, and Nanodevices (R. W. Siegel, E. Hu, and M. C. Rocco, Eds.), WTEC, Loyola College, MD, Hyper Librarian, 1999.
- Nanotechnology Research Directions: IWGN Workshop Report, Vision for Nanotechnology Research and Development in the Next Decade (M. C. Roco, S. Williams, and P. Alivisatos, Eds.), WTEC, Loyola College, MD, Hyper Librarian, 1999. Available on the Web at <http://wtec.org/loyola/nanobase/>.
- G. A. Ozin, *Adv. Mater.* 4, 612 (1992).
- "Handbook of Nanostructured Materials and Nanotechnology" Vols. 1–5. (H.-S. Nalwa, Ed.), Academic Press, New York, 1999.
- R. Rajagopalan, "Book Review: Nanoparticles in Solids and Solution" (J. H. Fendler and I. Dekany, Eds.), 1996.
- C. Roco, *J. Nanoparticles Res.* 1, 1 (1999).
- J. H. Fendler, *Chem. Rev.* 87, 877 (1987).
- M. Alexandre and P. Dubois, *Mater. Sci. Eng. Rep.* 28, 1 (2000).
- K. Rajeshwar, N. R. de Tacconi, and C. R. Chenthamarakshan, *Chem. Mater.* 13, 2765 (2001).
- L. L. Beecroft and C. Ober, *Chem. Mater.* 9, 1302 (1997).
- "Hybrid Organic-Inorganic Composites" (J. E. Mark, C. Y.-C. Lee, and P. A. Bianconi, Eds.), ACS Symposium Series 585. *Am. Chem. Soc.*, Washington DC, 1995.
- A. Loy, *Mater. Bull.* 26, 364 (2001).
- D. Pomogailo, *Russian Chem. Rev.* 69, 53 (2000).
- H. Rostein, R. Tannenbaum, Polymer metal nanocluster composites, in "Synthesis, Functionalization and Surface Treatment of Nanoparticles" (M.-I. Baraton, Ed.), pp. 103–126. American Scientific Publishers, Los Angeles, 2003.
- U. Schubert, *Chem. Mater.* 13, 3487 (2001).
- G. Kickelbick and U. Schubert, *Monatsh. Chem.* 132, 13 (2001).
- C. Guizard and P. Lacan, *New J. Chem.* 18, 1097 (1994).
- P. Judeinstein and C. Sanchez, *J. Mater. Chem.* 6, 511 (1996).
- Z. Ahmad and J. E. Mark, *Chem. Mater.* 13, 3320 (2001).
- C. Sanchez, G. J. de A. A. Soler-Illia, F. Ribot, T. Lalot, C. R. Mayer, and V. Cabuil, *Chem. Mater.* 13, 3061 (2001).
- G. Schottner, *Chem. Mater.* 13, 3422 (2001).
- K. C. Kwiatkowski and C. M. Lukehart, in "Handbook of Nanostructured Materials and Nanotechnology," Concise Edition (H. S. Nalwa, Ed.), Ch. 2, p. 57. Academic Press, San Diego, 2002.
- D. H. Everett, "Basic Principles of Colloid Science," Royal Society of Chemistry, London, 1988.
- W. B. Russel, D. A. Saville and W. R. Schowalter, "Colloidal Dispersions." Cambridge Univ. Press, Cambridge, UK, 1989.
- R. J. Hunter, "Introduction to Modern Colloid Science." Oxford Univ. Press, Oxford, 1993.
- "Emulsion Polymerization" (I. Piirma, Ed.). Academic Press, New York, 1982.
- "Science and Technology of Polymer Colloids" (G. W. Poehlein, R. H. Ottewill, and J. W. Goodwin, Eds.), Vol. II, Nijhoff, Boston, 1983.
- A. Henglein, *Chem. Rev.* 89, 1861 (1989).
- G. Schmid, *Chem. Rev.* 92, 1709 (1992).
- D. V. Goia and E. Matijevic, *New J. Chem.* 1203 (1998).
- K. E. Gonsalvez, S. P. Rangarajan, and J. Wang, in "Handbook of Nanostructured Materials and Nanotechnology," Concise Edition (H. S. Nalwa, Ed.), Ch. 1, p. 1. Academic Press, London, 2002.
- D. L. Feldheim and C. A. Foss, "Metal Nanoparticles, Synthesis, Characterization and Applications." Dekker, New York, 2002.
- M. L. Steigerwald and L. E. Brus, *Acc. Chem. Res.* 23, 183 (1990).
- T. Trindade, P. O'Brien, and N. L. Pickett, *Chem. Mater.* 13, 3843 (2001).
- P. V. Kamat, K. Murakoshi, Y. Wada, and S. Yanagida, in "Handbook of Nanostructured Materials and Nanotechnology," Concise Edition (H. S. Nalwa, Ed.), Ch. 4, p. 129. Academic Press, San Diego, 2002.
- O. I. Micic and A. J. Nozik, in "Handbook of Nanostructured Materials and Nanotechnology," Concise Edition (H. S. Nalwa, Ed.), Ch. 5, p. 183. Academic Press, London, 2002.

38. P. McFadyen and E. Matijevic, *J. Colloid Interf. Sci.* 44, 95 (1973).
39. "Sol-Gel Science" (C. J. Brinker and G. W. Scherer, Eds.). Academic Press, San Diego, 1990.
40. "The Chemistry of Silica" (R. K. Iler, Ed.). Wiley, New York, 1979.
41. E. Matijevic, in "Controlled Particle, Droplet and Bubble Formation" (D. J. Wedlock, Ed.), p. 39. Butterworth-Heinemann, Oxford, 1994.
42. E. Matijevic, *Current Opinion Colloid Interface Sci.* 1, 176 (1996).
43. Nanoparticles, Part I, Special issue of *New J. Chem.* edited by J. S. Bradley and B. Chaudret, 22 (1998).
44. C. H. M. Hofman-Caris, *New J. Chem.* 18, 1087 (1994).
45. J. A. Fendler and F. C. Meldrum, *Adv. Mater.* 7, 607 (1995).
46. A. M. van Herk and A. L. German, in "Microspheres, Microcapsules and Liposomes" (R. Arshady, Ed.), Vol. 1, Ch. 17, p. 457. Citus Book, London, 1999.
47. E. Bourgeat-Lami, in "Dendrimers, Assemblies and Nanocomposites" (R. Arshady and A. Guyot, Eds.), MML Series 5, Ch. 5, p. 149. Citus Books, London, 2002.
48. E. Bourgeat-Lami, *J. Nanosci. Nanotechnol.* 2, 1 (2002) and references therein.
49. P. Newman, U.S. Patent 3, 133, 893, 1964.
50. J. H. Fendler, *Chem. Mater.* 13, 3196 (2001).
51. M. G. Warner and J. E. Hutchison, in "Synthesis, Functionalization and Surface Treatment of Nanoparticles" (M.-I. Baraton, Ed.), pp. 67-89. American Scientific, Los Angeles, 2002.
52. See, for instance, K. Esumi, *J. Colloid Interf. Sci.* 241, 1 (2001).
53. J. M. Lehn, *J. Nanopart. Res.* 1, 7 (1999).
54. M. Zhao, L. Sun, and R. M. Crooks, *J. Am. Chem. Soc.* 120, 4877 (1998).
55. V. Chechik and R. M. Crooks, *Langmuir* 15, 6364 (1999).
56. K. Torigoe, A. Suzuki, and K. Esumi, *J. Colloid Interf. Sci.* 241, 346 (2001).
57. I. Gitsov and K. R. Lambrych, in "Dendrimers, Assemblies and Nanocomposites" (R. Arshady and A. Guyot, Eds.), Ch. 2, p. 31. MML Series 5, Citus Books, London, 2002.
58. Y. Xia, B. Gates, Y. Yin, and Y. Lu, *Adv. Mater.* 12, 693 (2000).
59. E. Bleier and E. Matijevic, *J. Colloid Interf. Sci.* 55, 510 (1976).
60. H. Sasaki, E. Matijevic, and E. Barouch, *J. Colloid Interf. Sci.* 76, 319 (1980).
61. K. Csoban and E. Pefferkorn, *J. Colloid Interf. Sci.* 205, 516 (1998).
62. K. Kato, M. Kobayashi, K. Esumi, and K. Meguro, *Colloids Surfaces* 23, 159 (1987).
63. N. J. Marston, B. Vincent, and N. G. Wright, *Progr. Colloid Polym. Sci.* 109, 278 (1998).
64. For a review, see for instance R. Arshady, D. Poulinquen, A. Halbreich, J. Roger, J.-N. Pons, J.-C. Bacri, M. de F. Da Silva, and U. Häfeli, in "Dendrimers, Assemblies, Nanocomposites" (R. Arshady and A. Guyot, Eds.), MML Series 5, Ch. 6, p. 283. Citus Book, London, 2002.
65. F. Sauzedde and A. Elaïssari, in "Colloid Polymers: Preparation and Biomedical Applications" (A. Elaïssari, Ed.). Dekker, New York, in press, and references therein.
66. J. Lefort, *C. R. Acad. Sci. Paris* 34, 488 (1852).
67. F. Sauzedde, A. Elaïssari, and C. Pichot, *Colloid Polym. Sci.* 277, 846 (1999).
68. F. Sauzedde, A. Elaïssari, and C. Pichot, *Colloid Polym. Sci.* 277, 1041 (1999).
69. H. Du, P. Zhang, S. Liu, D. Wang, T. Li, and X. Tang, *Polym. Int.* 43, 274 (1997).
70. K. Furusawa, K. Nagashima, and C. Anzai, *Colloid Polym. Sci.* 272, 1104 (1994).
71. J. Lee and M. Senna, *Colloid Polym. Sci.* 273, 76 (1995).
72. F. Caruso, R. Caruso, G. B. Sukhorukov, E. Donath, and H. Möhwald, PCT-European Patent 99/01854, 1999.
73. E. Donath, G. B. Sukhorukov, F. Caruso, S. A. Davis, and H. Möhwald, *Angew. Chem. Int. Ed.* 37, 2201 (1998).
74. G. B. Sukhorukov, E. Donath, S. Davis, H. Lichtenfeld, F. Caruso, V. I. Popov, and H. Möhwald, *Polym. Adv. Technol.* 9, 759 (1998).
75. C. Gao, S. Leporatti, S. Moya, E. Donath, and H. Möhwald, *Langmuir* 17, 3491 (2001).
76. F. Caruso, H. Lichtenfeld, M. Giersig, and H. Möhwald, *J. Am. Chem. Soc.* 120, 8523 (1998).
77. F. Caruso and H. Mohwald, *Langmuir* 15, 8276 (1999).
78. K. H. Rhodes, S. A. Davis, F. Caruso, B. Zhang, and S. Mann, *Chem. Mater.* 12, 2832 (2000).
79. F. Caruso, A. S. Sussha, M. Giersig, and H. Mohwald, *Adv. Mater.* 11, 950 (1999).
80. F. Caruso, *Chem. Eur. J.* 6, 413 (2000) and references therein.
81. F. Caruso, R. A. Caruso, and H. Möhwald, *Science* 282, 1111 (1998).
82. F. Caruso, R. A. Caruso, and H. Mohwald, *Chem. Mater.* 11, 3309 (1999).
83. X. D. Wang, W. L. Yang, Y. Tand, Y. J. Wang, S. K. Fu, and Z. Gao, *Chem. Commun.* 2161 (2000).
84. R. A. Caruso, A. Sussha, and F. Caruso, *Chem. Mater.* 13, 400 (2001).
85. F. Caruso, M. Spasova, A. Sussha, M. Giersig, and R. A. Caruso, *Chem. Mater.* 13, 109 (2001).
86. C. P. Hemenway, J. J. Latimer, and J. E. Young, *Tappi J.* 68, 102 (1985).
87. R. W. Hislop and P. L. McGinley, *J. Coatings Tech.* 50, 69 (1978).
88. D. M. Fasano, *J. Coatings Tech.* 59, 109 (1987).
89. F. Caruso, X. Shi, R. A. Caruso, and A. Sussha, *Adv. Mater.* 13, 740 (2001).
90. D. Wang and F. Caruso, *Chem. Mater.* 14, 1909 (2002).
91. G. Sukhorukov, L. Dähne, J. Hartmann, E. Donath, and H. Möhwald, *Adv. Mater.* 12, 112 (2000).
92. G. B. Sukhorukov, A. S. Sussha, S. Davis, S. Leporatti, E. Donath, J. Hartmann, and H. Möhwald, *J. Colloid Interf. Sci.* 247, 251 (2002).
93. For a review, see for instance G. B. Sukhorukov, in "Dendrimers, Assemblies, Nanocomposites" (R. Arshady and A. Guyot, Eds.), MML Series 5, Ch. 4, p. 111. Citus Book, London, 2002.
94. M. S. Fleming, T. K. Mandal, and D. R. Walt, *Chem. Mater.* 13, 2210 (2001).
95. A. L. Hiddessen, S. D. Rodgers, D. A. Weitz, and D. A. Hammer, *Langmuir* 16, 9744 (2000).
96. T. H. Galow, A. K. Boal, and V. M. Rotello, *Adv. Mater.* 12, 576 (2000).
97. S. Fullam, H. Rensmo, S. Nagaraja Rao, and D. Fitzmaurice, *Chem. Mater.* 14, 3643 (2002).
98. S. Reculosa, C. Poncet-LeGrand, S. Ravaine, C. Mingotaud, E. Duguet, and E. Bourgeat-Lami, *Chem. Mater.* 14, 2354 (2002).
99. C. A. Mirkin, R. L. Letsinger, R. C. Mucic, and J. J. Storhoff, *Nature* 382, 607 (1996).
100. P. Alivisatos, K. P. Johnsson, X. Peng, T. E. Wilson, C. J. Loweth, M. Bruchez, and P. G. Schultz, *Nature* 382, 609 (1996).
101. C. J. Loweth, W. B. Caldwell, X. G. Peng, A. P. Alivisatos, and P. G. Schultz, *Angew. Chem. Int. Ed.* 38, 1808 (1999).
102. S. Mann, W. Shenton, M. Li, S. Connolly, and D. Fitzmaurice, *Adv. Mater.* 12, 147 (2000).
103. P. Jiang, J. Cizeron, J. F. Bertone, and V. L. Colvin, *J. Am. Chem. Soc.* 121, 7957 (1999).
104. B. L. Frankamp, O. Uzun, F. Ilhan, A. K. Boal, and V. M. Rotello, *J. Am. Chem. Soc.* 124, 892 (2002).
105. K. Yoshinaga, T. Yokoyama, and T. Kito, *Polym. Adv. Technol.* 4, 38 (1993).
106. K. Furusawa, Y. Kimura, and T. Tagawa, *J. Colloid Interf. Sci.* 109, 69 (1986).
107. F. Long, W. Wang, Y. Xiu, and T. Cao, *Gaofenzi Cailiao Kexue Yu Gongcheny* 7, 13 (1991).
108. C. Barthet, A. J. Hickey, D. B. Cairns, and S. P. Armes, *Adv. Mater.* 11, 408 (1999).

109. F. Tiarks, K. Lanfester, and M. Antonietti, *Langmuir* 17, 5775 (2001).
110. R. Davies, G. A. Schurr, P. Meenan, R. D. Nelson, H. E. Bergna, C. A. S. Brevett, and R. H. Goldbaum, *Adv. Mater.* 10, 1264 (1998) and references therein.
111. R. A. Caruso and M. Antonietti, *Chem. Mater.* 13, 3272 (2001).
112. F. Caruso, *Adv. Mater.* 13, 11 (2001) and references therein.
113. G. Kickelbick and U. Schubert, in "Synthesis, Functionalization and Surface Treatment of Nanoparticles" (M.-I. Baraton, Ed.), Ch. 6, pp. 91–102. American Scientific Publishers, Los Angeles, 2002.
114. P. Van Der Voort and E. F. Vansant, *J. Liq. Chromatogr. Relat. Technol.* 19, 2723 (1996).
115. W. Yoshida, R. P. Castro, J.-D. Jou, and Y. Cohen, *Langmuir* 17, 5882 (2001).
116. P. Bugnon, *Progr. Org. Coat.* 29, 39 (1996).
117. W.-H. Hou, T. B. Lloyd, and F. M. Fowkes, in "Polymer Latexes: Preparation, Characterization and Applications" (E. S. Daniels, T. Sudol, and M. El-Aasser, Eds.), ACS Symposium Series 492, Ch. 25, p. 405. *Am. Chem. Soc.*, Washington DC, 1992.
118. P. R. Sperry, R. J. Wiersema, and K. Nyi, U.S. Patent 4, 102, 843, 1978.
119. J. D. Schofield, U.S. Patent 4, 349, 389, 1982.
120. J. Solc, U.S. Patent 4, 421, 660, 1983.
121. R. W. Martin, Eur. Patent 0104498, 1984.
122. R. W. Martin, U.S. Patent 4, 608, 401, 1986.
123. J. Solc, U.S. Patent 4, 680, 200, 1987.
124. K. L. Hoy, C. W. Glancy, and J. M. O. Lewis, Eur. Patent 0392065, 1990.
125. R. W. Martin, U.S. Patent 4, 771, 086, 1992.
126. E. A. W. G. Janssen, A. M. van Herk, and A. L. German, *ACS Div. Polym. Chem. Polym. Prep.* 34, 532 (1993).
127. R. L. Templeton-Knight, *J. OCCA* 73, 459 (1990).
128. R. L. Templeton-Knight, *Chem. Ind.* 512 (1990).
129. J. P. Lorimer, T. J. Mason, D. Kershaw, I. Livsey, and R. L. Templeton-Knight, *Colloid Polym. Sci.* 269, 392 (1991).
130. K. L. Hoy and O. W. Smith, *ACS Polym. Preprint* 65, 78 (1991).
131. M. Hasegawa, K. Arai, and S. Saito, *J. Polym. Sci. A* 25, 3117 (1987).
132. M. Hasegawa, K. Arai, and S. Saito, *J. Appl. Polym. Sci.* 33, 411 (1987).
133. C. H. M. Caris, L. P. M. van Elven, A. M. van Herk, and A. German, in "19th FATIPEC Conference Book," Vol. 3, p. 341, 1988.
134. C. H. M. Caris, L. P. M. van Elven, A. M. van Herk, and A. German, *British Polym. J.* 21, 133 (1989).
135. C. H. M. Caris, A. M. van Herk, A. L. German, in "20th FATIPEC Conference Proceedings," p. 325, 1990.
136. Y. Haga, T. Watanabe, and R. Yosomiya, *Die Angew. Makromol. Chem.* 189, 23 (1991).
137. R. Q. F. Janssen, A. M. van Herk, A. L. German, in "22nd FATIPEC Conference Proceedings," Vol. 1, p. 104, 1994.
138. C. H. M. Caris, R. P. M. Kuijpers, A. M. van Herk, and A. L. German, *Makromol. Chem. Macromol. Symp.* 35/36, 535 (1990).
139. M. Hasegawa, K. Arai, and S. Saito, *J. Chem. Eng. Japan* 21, 30 (1988).
140. R. Q. F. Janssen, Polymer Encapsulation of Titanium Dioxide, Ph.D. Thesis, Eindhoven University of Technology, The Netherlands, 1995.
141. R. Q. F. Janssen, A. M. van Herk, and A. L. German, *J. Oil Colour Chem. Ass.* 11, 455 (1993).
142. Th. Batzilla and A. Tulke, *J. Coat. Technol.* 70, 77 (1998).
143. L. Quaroni and G. Chumanov, *J. Am. Chem. Soc.* 121, 10642 (1999).
144. J. Yu, J. Yu, Z.-X. Guo, and Y.-F. Gao, *Macromol. Rapid Commun.* 22, 1261 (2001).
145. K. Landfester, *Macromol. Rapid Commun.* 22, 896 (2001).
146. K. Landfester, *Adv. Mater.* 13, 765 (2001).
147. B. Erdem, D. Sudol, V. L. Dimonie, and M. El-Aasser, *J. Polym. Sci. A* 38, 4419 (2000).
148. B. Erdem, D. Sudol, V. L. Dimonie, and M. El-Aasser, *J. Polym. Sci. A* 38, 4431 (2000).
149. B. Erdem, D. Sudol, V. L. Dimonie, and M. El-Aasser, *J. Polym. Sci. A* 38, 4441 (2000).
150. N. Bechthold, F. Tiarks, M. Willert, K. Landfester, and M. Antonietti, *Macromol. Symp.* 151, 549 (2000).
151. F. Tiarks, K. Landfester, and M. Antonietti, *Macromol. Chem. Phys.* 202, 51 (2001).
152. D. Hoffmann, K. Landfester, and M. Antonietti, *Magneto-hydrodynamics* 37, 217 (2001).
153. S. Lelu, C. Novat, C. Graillat, A. Guyot, and E. Bourgeat-Lami, *Polymer Int.* 52, 542 (2003).
154. C. S. Chern and Y. C. Liou, *Polymer* 9, 3767 (1998).
155. N. Yanase, H. Noguchi, H. Asakura, and T. Suzuta, *J. Appl. Polym. Sci.* 50, 765 (1993).
156. H. Noguchi, N. Yanase, Y. Uchida, and T. Suzuta, *J. Appl. Polym. Sci.* 48, 1539 (1993).
157. X. Li and Z. Sun, *J. Appl. Polym. Sci.* 58, 1991 (1995).
158. A. Kondo, H. Kamura, and K. Higashitani, *Appl. Microbiol. Biotechnol.* 41, 99 (1994).
159. R. S. Molday, S. P. S. Yen, and A. Rembaum, *Nature* 268, 437 (1977).
160. A. Rembaum, S. P. S. Yen, and W. Volksen, *Chemtech.* 8, 182 (1978).
161. J. Richard and S. Vaslin, French Patent 2, 735, 778, 1995.
162. X. Xu, G. Friedman, K. D. Humfeld, S. A. Majetich, and S. A. Asher, *Adv. Mater.* 13, 1681 (2001).
163. X. Xu, G. Friedman, K. D. Humfeld, S. A. Majetich, and S. A. Asher, *Chem. Mater.* 14, 1249 (2002).
164. O. Kwon and J. Solc, *J. Magn. Magn. Mater.* 54, 1699 (1986).
165. L. Shen, A. Stachowiak, T. Alan Hatton, and P. E. Laibinis, *Langmuir* 16, 9907 (2000).
166. T. C. C. Huang, The Model Microencapsulation of Iron Oxides in Latex Particles by Preparation and Characterization of Magnetic Latex Particles, Ph.D. Thesis, Lehigh University, 1986.
167. K. Wormuth, *J. Colloid Interf. Sci.* 241, 366 (2001).
168. P. A. Dresco, V. S. Zaitsev, R. Gambino, and B. Chu, *Langmuir* 15, 1945 (1999).
169. S. A. Gomez-Lopera, R. P. Plaza, and A. V. Delgado, *J. Colloid Interf. Sci.* 240, 40 (2001).
170. C. Menager and V. Cabuil, *Colloid Polym. Sci.* 272, 1295 (1994).
171. W. D. Hergeth, M. Peller, and P. Hauptmann, *Acta Polym.* 37, 468 (1986).
172. W. D. Hergeth, P. Starre, K. Schmutzler, and S. Wartewig, *Polymer* 29, 1323 (1988).
173. W. D. Hergeth, U. J. Steinau, H. J. Bittrich, G. Simon, and K. Schmutzler, *Polymer* 30, 254 (1989).
174. W. D. Hergeth, U. J. Steinau, H. J. Bittrich, K. Schmutzler, and S. Wartewig, *Progr. Colloid Polym. Sci.* 85, 82 (1991).
175. P. Espiard, J.E. Mark, and A. Guyot, *Polym. Bull.* 24, 173 (1990).
176. P. Espiard, A. Revillon, A. Guyot, and J. E. Mark, in "Polymer Latexes: Preparation, Characterization and Applications" (E. S. Daniels, T. Sudol, and M. El-Aasser, Eds.), ACS Symposium Series 492, Ch. 24, pp. 387–403. *Am. Chem. Soc.*, Washington DC, 1992.
177. P. Espiard, A. Guyot, and J. E. Mark, *J. Inorganic Organometallic Polym.* 5, 391 (1995).
178. E. Bourgeat-Lami, P. Espiard, and A. Guyot, *Polymer* 36, 4385 (1995).
179. P. Espiard and A. Guyot, *Polymer* 36, 4391 (1995).
180. E. Bourgeat-Lami, P. Espiard, A. Guyot, S. Briat, C. Gauthier, G. Vigier, and J. Perez, in "Hybrid Organic-Inorganic Composites" (J. E. Mark, C. Y.-C. Lee, and P. A. Bianconi, Eds.), American Chemical Society Symposium Series 585, Ch. 10, pp. 112–24. *Am. Chem. Soc.*, Washington DC, 1995.

181. J. C. Daniel, P. Espiard, and A. Guyot, Eur. Patent 505230, Rhône-Poulenc, 1992.
182. P. Espiard, A. Guyot, J. Perez, G. Vigier, and L. David, *Polymer* 36, 4397 (1995).
183. E. Bourgeat-Lami, P. Espiard, A. Guyot, C. Gauthier, L. David, and G. Vigier, *Die Angew. Makromol. Chem.* 242, 105 (1996).
184. K. Shiratsuchi and H. Hokazono, U.S. Patent 5, 856, 379, 1999.
185. E. Bourgeat-Lami and J. Lang, *J. Colloid Interf. Sci.* 197, 293 (1998).
186. E. Bourgeat-Lami and J. Lang, *J. Colloid Interf. Sci.* 210, 281 (1999).
187. F. Corcos, E. Bourgeat-Lami, C. Novat, and J. Lang, *Colloid Polym. Sci.* 277, 1142 (1999).
188. E. Bourgeat-Lami and J. Lang, *Macromol. Symp.* 151, 377 (2000).
189. I. Sondi, T. H. Fedynshyn, R. Sinta, and E. Matijevic, *Langmuir* 16, 9031 (2000).
190. K. Yoshinaga, R. Horie, F. Saigoh, T. Kito, N. Enomoto, H. Nishida, and M. Komatsu, *Polym. Adv. Technol.* 3, 91 (1992).
191. K. Yoshinaga, K. Sueishi, and H. Karakawa, *Polym. Adv. Technol.* 7, 53 (1995).
192. K. Yoshinaga, M. Iwasaki, M. Teramoto, and H. Karakawa, *Polym. Polym. Composites* 4, 163 (1996).
193. K. Yoshinaga, K. Kondo, and A. Kondo, *Colloid Polym. Sci.* 275, 220 (1997).
194. K. Nagai, Y. Ohishi, K. Ishiyama, and N. Kuramoto, *J. Appl. Polym. Sci.* 38, 2183 (1989).
195. K. Nagai, *Macromol. Symp.* 84, 29 (1994).
196. K. Yoshinaga, F. Nakashima, and T. Nishi, *Colloid Polym. Sci.* 277, 136 (1999).
197. M. J. Percy, C. Barthet, J. C. Lobb, M. A. Khan, S. F. Lascelles, M. Vamvakaki, and S. P. Armes, *Langmuir* 16, 6913 (2000).
198. J. I. Amalvy, M. J. Percy, and S. P. Armes, *Langmuir* 17, 4770 (2001).
199. T. Sakurai, H. Murata, T. Mizutani, Y. Kimura, and M. Miyamoto, Japanese Patent 11-209622, 1999.
200. E. Bourgeat-Lami, J.-L. Luna-Xavier, and A. Guyot, *Mater. Res. Symp. Symp. Proc.* 628, CC3.5 (2000).
201. J. L. Luna-Xavier, E. Bourgeat-Lami, and A. Guyot, *Colloid Polym. Sci.* 279, 947 (2001).
202. J. L. Luna-Xavier, A. Guyot, and E. Bourgeat-Lami, *J. Colloid Interf. Sci.* 250, 82 (2001).
203. J. L. Luna-Xavier, A. Guyot, and E. Bourgeat-Lami, submitted for publication.
204. M. J. Percy and S. P. Armes, *Langmuir* 18, 4562 (2002).
205. J. Stejskal, in "Dendrimers, Assemblies, Nanocomposites" (R. Arshady and A. Guyot, Eds.), MML Series 5, p. 195. Citus Book, London, 2002.
206. J. Stejskal, in "Dendrimers, Assemblies, Nanocomposites" (R. Arshady and A. Guyot, Eds.), MML Series 5, p. 245. Citus Book, London, 2002 and references therein.
207. S. P. Armes, *Current Opinion Colloid Interf. Sci.* 1, 214 (1996).
208. D. H. Napper, "Polymer Stabilization of Colloidal Dispersions." Academic Press, London, 1983.
209. T. K. Mandal and B. M. Mandal, *Polymer* 36, 1911 (1995).
210. S. P. Armes and M. Aldissi, *Polymer* 31, 569 (1990).
211. P. M. Beadle, L. Rowan, J. Mykytiuk, N. C. Billingham, and S. P. Armes, *Polymer* 34, 1561 (1993).
212. R. E. Partch, S. G. Gangolli, D. Owen, C. Ljungqvist, and E. Matijevic, in "Polymer Latexes: Preparation, Characterization and Applications" (E. S. Daniels, T. Sudol, and M. El-Aasser, Eds.), ACS Symposium Series 492, Ch. 23, p. 369. *Am. Chem. Soc.*, Washington DC, 1992.
213. R. E. Partch, S. G. Gangolli, E. Matijevic, W. Cai, and S. Arajs, *J. Colloid Interf. Sci.* 144, 27 (1991).
214. C. H. Huang, R. E. Partch, and E. Matijevic, *J. Colloid Interf. Sci.* 170, 275 (1995).
215. C. H. Huang and E. Matijevic, *J. Mater. Res.* 10, 1327 (1995).
216. S. P. Armes, S. Gottesfeld, J. G. Beery, F. Garzon, and S. F. Agnew, *Polymer* 32, 2325 (1991).
217. S. Maeda and S. P. Armes, *J. Colloid Interf. Sci.* 159, 257 (1993).
218. S. Maeda and S. P. Armes, *J. Mater. Chem.* 4, 935 (1994).
219. S. Maeda and S. P. Armes, *Chem. Mater.* 7, 171 (1995).
220. S. Maeda and S. P. Armes, *Synth. Metals* 69, 499 (1995).
221. R. Flitton, J. Johal, S. Maeda, and S. P. Armes, *J. Colloid Interf. Sci.* 173, 135 (1995).
222. J. Stejskal, P. Kratochvil, S. P. Armes, S. F. Lascelles, A. Riede, M. Helmstedt, J. Prokes, and I. Krivka, *Macromolecules* 29, 6814 (1996).
223. S. F. Lascelles, G. P. McCarthy, M. D. Butterworth, and S. P. Armes, *Colloid Polym. Sci.* 276, 893 (1998).
224. C. Perruchot, M. M. Chehimi, D. Mordenti, M. Briand, and M. Delamar, *J. Mater. Chem.* 8, 2185 (1998).
225. N. J. Terrill, T. Crowley, M. Gill, and S. P. Armes, *Langmuir* 9, 2093 (1993).
226. S. Maeda, M. Gill, and S. P. Armes, *Langmuir* 11, 1899 (1995).
227. S. Maeda and S. P. Armes, *Synth. Metals* 73, 151 (1995).
228. A. Bhattacharya, K. M. Ganguly, A. De, and S. Sarkar, *Mater. Res. Bull.* 31, 527 (1996).
229. L. M. Gan, L. H. Zhang, H. S. O. Chan, and C. H. Chew, *Mater. Chem. Phys.* 40, 94 (1995).
230. S. H. Hong, B. H. Kim, J. Joo, J. W. Kim, and H. J. Choi, *Current Appl. Phys.* 1, 447 (2001).
231. B. H. Kim, J. H. Jung, J. W. Kim, H. J. Choi, and J. Joo, *Synth. Metals* 117, 115 (2001).
232. B. H. Kim, J.-H. Jung, S.-H. Hong, J. Joo, A. J. Epstein, K. Mizoguchi, J. W. Kim, and H. J. Choi, *Macromolecules* 35, 1419 (2002).
233. J. Lu and X. Zhao, *J. Mater. Chem.* 12, 2603 (2002).
234. S. W. Huang, K. G. Neoh, E. T. Kang, H. S. Han, and K. L. Tan, *J. Mater. Chem.* 8, 1743 (1998).
235. K. G. Neoh, K. K. Tan, P. L. Goh, S. W. Huang, E. T. Kang, and K. L. Tan, *Polymer* 40, 887 (1999).
236. R. Gangopadhyay and A. De, *Eur. Polym. J.* 35, 1985 (1999).
237. S. T. Selvan and M. Nogami, *J. Mater. Sci. Lett.* 17, 1385 (1998).
238. S. M. Marikanos, L. C. Brousseau III, A. Jones, and D. L. Feldheim, *Chem. Mater.* 10, 1214 (1998).
239. S. M. Marikanos, J. P. Novak, L. C. Brousseau III, A. B. House, E. M. Edeki, J. C. Feldhaus, and D. L. Feldheim, *J. Am. Chem. Soc.* 121, 8518 (1999).
240. S. M. Marikanos, D. A. Shultz, and D. L. Feldheim, *Adv. Mater.* 11, 34 (1999).
241. Q. Zhou, X. Fan, C. Xia, J. Mays, and R. Advincula, *Chem. Mater.* 13, 3057 (2001).
242. X. Fan, Q. Zhou, C. Xia, W. Cristofoli, J. Mays, and R. Advincula, *Langmuir* 18, 4511 (2002).
243. Q. Zhou, S. Wang, X. Fan, R. Advincula, and J. Mays, *Langmuir* 18, 3324 (2002).
244. N. Tsubokawa, H. Ishida, and K. Hashimoto, *Polym. Bull.* 31, 457 (1993).
245. N. Tsubokawa, T. Kimoto, and T. Endo, *Polym. Bull.* 33, 187 (1994).
246. N. Fery, R. Hoene, and K. Hamann, *Angew. Chem. Int. Ed. Engl.* 11, 337 (1972).
247. M. Jiang, S. Wang, and X. Jin, *J. Mater. Sci. Lett.* 9, 1239 (1990).
248. See for instance R. Kroker, M. Schneider, and K. Hamann, *Progr. Org. Coat.* 1, 23 (1972).
249. R. Laible and K. Hamann, *Adv. Colloid Interf. Sci.* 13, 65 (1980).
250. N. Tsubokawa, *Progr. Polym. Sci.* 17, 417 (1992).
251. D. L. Huber, G. Carlson, and K. Gonsalves, in "Interfacial Aspects of Multicomponent Polymer Materials" (Lohse et al., Eds.), p. 107. Plenum Press, New York, 1997.
252. K. Yoshinaga, *Surfactant Sci. Ser.* 92, 626 (2000).
253. Y. Cohen, W. Yoshida, V. Nguyen, N. Bei, and J.-D. Jou, *Surfactant Sci. Ser.* 103, 321 (2001), and references therein.

254. K. J. Warson, J. Zhu, S. T. Nguyen, and C. A. Mirkin, *J. Am. Chem. Soc.* 121, 462 (1999).
255. G. Carrot, D. Rutot-Houzé, A. Pottier, P. Degée, J. Hilborn, and P. Dubois, *Macromolecules* 35, 8400 (2002).
256. M. Joubert, C. Delaite, E. Bourgeat-Lami, and Ph. Dumas, *Macromol.* submitted.
257. N. Tsubokawa, K. Maruyama, Y. Sone, and M. Shimomura, *Polym. J.* 21, 475 (1989).
258. N. Tsubokawa, A. Kogure, K. Maruyama, Y. Sone, and M. Shimomura, *Polym. J.* 22, 827 (1990).
259. N. Tsubokawa and H. Ishida, *Polym. J.* 24, 809 (1992).
260. N. Tsubokawa and H. Ishida, *J. Polym. Sci. A* 30, 2241 (1992).
261. N. Tsubokawa, Y. Shirai, H. Tsuchida, and S. Handa, *J. Polym. Sci. Polym. Chem.* 32, 2327 (1994).
262. O. Prucker and J. Rühle, *Polymer* 37, 1087 (1996).
263. O. Prucker and J. Rühle, *Macromolecules* 31, 602 (1998).
264. O. Prucker and J. Rühle, *Macromolecules* 31, 592 (1998).
265. T. von Werne and T. E. Patten, *J. Am. Chem. Soc.* 121, 7409 (1999).
266. T. von Werne and T. E. Patten, *PMSE Preprints* 80, 465 (1999).
267. T. von Werne, I. M. Suehiro, S. Farmer, and T. E. Patten, *PMSE Preprints* 82, 294 (2000).
268. T. von Werne and T. E. Patten, *J. Am. Chem. Soc.* 123, 7497 (2001).
269. H. Böttcher, M. L. Hallensleben, S. Nuß, and H. Wurm, *Polym. Bull.* 44, 223 (2000).
270. J. Bai, J.-B. Pang, K.-Y. Qiu, and Y. Wei, *Chinese J. Polym. Sci.* 20, 261 (2002).
271. T. K. Mandal, M. S. Fleming, and D. R. Walt, *Chem. Mater.* 12, 3481 (2000).
272. C. Perruchot, M. A. Khan, A. Kamitsi, S. P. Armes, T. von Werne, and T. E. Patten, *Langmuir* 17, 4479 (2001).
273. B. Gu and A. Sen, *Macromolecules* 35, 8913 (2002).
274. C. R. Vestal and Z. J. Zhang, *J. Am. Chem. Soc.* 124, 14312 (2002).
275. S. Nub, H. Böttcher, H. Wurm, and M. L. Hallensleben, *Angew. Chem. Int. Ed.* 40, 4016 (2001).
276. K. Ohno, K. M. Koh, Y. Tsujii, and T. Fukuda, *Macromolecules* 35, 8989 (2002).
277. S. C. Farmer and T. E. Patten, *PMSE Preprints* 82, 237 (2000).
278. S. C. Farmer and T. E. Patten, *Chem. Mater.* 13, 3920 (2001).
279. S. Blomberg, S. Ostberg, E. Harth, A. W. Bosman, B. van Horn, and C. J. Hawker, *J. Polym. Sci. A* 40, 1309 (2002).
280. D. E. Bergbreiter, *Angew. Chem. Int. Ed.* 38, 2870 (1999).
281. A. Ulman, *Chem. Rev.* 96, 1533 (1996).
282. A. C. Templeton, W. P. Wuelfing, and R. W. Murray, *Acc. Chem. Res.* 33, 27 (2000).
283. M. Wu, S. A. O'Neill, L. C. Brousseau, W. P. McConnell, D. A. Shultz, R. J. Linderman, and D. L. Feldheim, *Chem. Commun.* 775 (2000).
284. L. Sun, R. M. Crooks, and V. Chechik, *Chem. Commun.* 359 (2001).
285. H. Shiho and N. Kawahashi, *Colloid Polym. Sci.* 278, 270 (2000).
286. H. Shiho, Y. Manabe, and N. Kawahashi, *J. Mater. Chem.* 10, 333 (2000).
287. S. Eiden and G. Maret, *J. Colloid Interf. Sci.* 250, 281 (2002).
288. A. Imhof, *Langmuir* 17, 3579 (2001).
289. H. Bamnolker, B. Nitzan, S. Gura, and S. Margel, *J. Mater. Sci. Lett.* 16, 1412 (1997).
290. I. Tissot, C. Novat, F. Lefebvre, and E. Bourgeat-Lami, *Macromolecules* 34, 5737 (2001).
291. I. Tissot, J. P. Reymond, F. Lefebvre, and E. Bourgeat-Lami, *Chem. Mater.* 14, 1325 (2002).
292. B. zu Putlitz, K. Landfester, H. Fischer, and M. Antonietti, *Adv. Mater.* 13, 500 (2001).
293. L. Wang, T. Sasaki, Y. Ebina, K. Kurashima, and M. Watanabe, *Chem. Mater.* 14, 4827 (2002).
294. V. Valtchev, *Chem. Mater.* 14, 956 (2002).
295. K. P. Velikov and A. van Blaaderen, *Langmuir* 17, 4779 (2001).
296. L. M. Liz-Marzan, M. Giersig, and P. Mulvaney, *Langmuir* 12, 4329 (1996).
297. M. Giersig, T. Ung, L. M. Liz-Marzan, and P. Mulvaney, *Adv. Mater.* 9, 570 (1997).
298. P. Mulvaney, L. M. Liz-Marzan, M. Giersig, and T. Ung, *J. Mater. Chem.* 10, 1259 (2000).
299. S. J. Oldenburg, R. D. Averitt, S. L. Westcott, and N. J. Halas, *Chem. Phys. Lett.* 288, 243 (1998).
300. S. L. Westcott, S. J. Oldenburg, T. R. Lee, and N. J. Halas, *Langmuir* 14, 5396 (1998).
301. H. Tamai, S. Sakurai, Y. Hirota, F. Nishiyama, and H. Yasuda, *J. Appl. Polym. Sci.* 56, 441 (1995).
302. H. Tamai, S. Hamamoto, F. Nishiyama, and H. Yasuda, *J. Colloid Interf. Sci.* 171, 250 (1995).
303. H. Tamai, T. Sumi, F. Nishiyama, and H. Yasuda, *J. Appl. Polym. Sci.* 60, 1727 (1996).
304. C.-W. Chen, M.-Q. Chen, T. Serizawa, and M. Akashi, *Adv. Mater.* 10, 1122 (1998).
305. P. H. Wang and C.-Y. Pan, *Colloid Polym. Sci.* 278, 581 (2000).
306. P. H. Wang and C.-Y. Pan, *J. Appl. Polym. Sci.* 75, 1693 (2000).
307. P. H. Wang and C.-Y. Pan, *Colloid Polym. Sci.* 279, 171 (2001).
308. C. H. Reynolds, N. Annan, K. Beshah, J. H. Huber, S. H. Shaber, R. E. Lenkinski, and J. A. Wortman, *J. Am. Chem. Soc.* 122, 8940 (2000).
309. S. Mecking and R. Thomann, *Adv. Mater.* 12, 953 (2000).
310. A. Dokoutchaev, J. Thomas James, S. C. Koene, S. Pathak, G. K. Surya Prakash, and M. E. Thompson, *Chem. Mater.* 11, 2389 (1999).
311. N. Kawahashi and E. Matijevec, *J. Colloid Interf. Sci.* 138, 534 (1990).
312. N. Kawahashi and E. Matijevec, *J. Colloid Interf. Sci.* 143, 103 (1991).
313. N. Kawahashi, C. Persson, and E. Matijevec, *J. Mater. Chem.* 1, 577 (1991).
314. N. Kawahashi and H. Shiho, *J. Mater. Chem.* 10, 2294 (2000).
315. H. Shiho and N. Kawahashi, *J. Colloid Interf. Sci.* 226, 91 (2000).
316. H. Shiho, Y. Manabe, and N. Kawahashi, *J. Mater. Chem.* 10, 333 (2000).
317. H. Yao, Y. Takada, and N. Kitamura, *Langmuir* 14, 595 (1998).
318. J. Zhang, N. Coombs, and E. Kumacheva, *J. Am. Chem. Soc.* 124, 14512 (2002).
319. "Vesicles" (M. Rosoff, Ed.). Dekker, New York, 1996.
320. R. Zana, in "Surfactants in Solution" (K. J. Mitall and P. Botherel, Eds.), pp. 115. Plenum, New York, 1986, and references therein.
321. D. H. W. Hubert, M. Jung, P. M. Frederik, P. H. H. Bomans, J. Meuldijk, and A. L. German, *Adv. Mater.* 12, 1286 (2000).
322. J. F. Gohy, N. Willet, S. Varshney, J. X. Zhang, and R. Jérôme, *Angew. Chem. Int. Ed.* 40, 3214, 2001.
323. S. Stewart and G. Liu, *Chem. Mater.* 11, 1048 (1999).
324. R. S. Underhill and G. Liu, *Chem. Mater.* 12, 2082 (2000).
325. M. Antonietti, S. Förster, and S. Oestreich, *Macromol. Symp.* 121, 75 (1997).
326. S. Förster and M. Antonietti, *Adv. Mater.* 10, 195 (1998).
327. C. Goltner, *Surfactant Sci. Ser.* 100, 797 (2001).
328. S. Liu, J. V. M. Weaver, M. Save, and S. P. Armes, *Langmuir* 18, 8350 (2002).
329. A. L. Klibanov, N. N. Ivanov, H. Ringsdorf, and B. Schlarb, *Makromol Chem. Rapid Commun.* 8, 457 (1987).
330. F. Chaumel, H. Jiang, and A. Kakkar, *Chem. Mater.* 13, 3389 (2001).
331. D. Donescu, M. Teodorescu, S. Serban, L. Fusulan, and C. Petcu, *Eur. Polym. J.* 35, 1679 (1999).
332. D. Donescu and S. Serban, *Synt. Polym. J.* 3, 32 (1996).

333. V. Uricanu and C. Panayiotou, in "International Symposium on Polymers in Dispersed Media," Abstract Book, p. 274, 1999.
334. E. Bourgeat-Lami, I. Tissot, and F. Lefebvre, *Macromolecules* 35, 6185 (2002).
335. E. Bourgeat-Lami, J. L. Putaux, and F. Lefebvre, submitted for publication.
336. C. Kan, Q. Yuan, M. Wang, and X. Kong, *Polym. Adv. Technol.* 7, 95 (1996).
337. C. Y. Kan, X. L. Zhu, Q. Yuan, and X. Z. Kong, *Polym. Adv. Technol.* 8, 631 (1997).
338. S. Huang, Z. Xu, H. Peng, and S. Cheng, *J. Appl. Polym. Sci.* 71, 2209 (1999).
339. J. R. Caille, D. Teyssié, L. Bouteiller, R. Bischoff, and S. Boileau, *Macromol. Symp.* 153, 161 (2000).
340. Y. Wu, H. Duan, Y. Yu, and C. Zhang, *J. Appl. Polym. Sci.* 79, 333 (2001).
341. C. Y. Kan, D. S. Liu, X. Z. Kong, and X. L. Zhu, *J. Appl. Polym. Sci.* 82, 3194 (2001).
342. F. Baumann, M. Schmidt, B. Deubzer, M. Geck, and J. Dauth, *Macromolecules* 27, 6102 (1994).
343. F. Baumann, B. Deubzer, M. Geck, J. Dauth, and M. Schmidt, *Macromolecules* 30, 7568 (1997).
344. N. Jungmann, M. Schmidt, and M. Maskos, *Macromolecules* 34, 8347 (2001).
345. G. Lindenblatt, W. Schärfl, T. Pakula, and M. Schmidt, *Macromolecules* 33, 9340 (2000).
346. F. Baumann, B. Deubzer, M. Geck, J. Dauth, S. Sheiko, and M. Schmidt, *Adv. Mater.* 9, 955 (1997).
347. N. Jungmann, M. Schmidt, M. Maskos, J. Weis, and J. Ebenhoch, *Macromolecules* 35, 6851 (2002).
348. C. Graf, W. Schärfl, K. Fischer, N. Hugenberg, and M. Schmidt, *Langmuir* 15, 6170 (1999).
349. C. Graf, W. Schärfl, M. Maskos, and M. Schmidt, *J. Chem. Phys.* 112, 3031 (2000).
350. C. Roos, M. Schmidt, J. Ebenhoch, F. Baumann, B. Deubzer, and J. Weis, *Adv. Mater.* 11, 761 (1999).
351. W. Schärfl and C. Roos, *Phys. Rev. E* 60, 2020 (1999).
352. G. Büchel, K. K. Unger, A. Matsumoto, and K. Tsutsumi, *Adv. Mater.* 10, 1036 (1998).
353. S. B. Yoon, K. Sohn, J. Y. Kim, C.-H. Shin, J.-S. Yu, and T. Hyeon, *Adv. Mater.* 14, 19 (2002).
354. M. Kim, K. Sohn, H. Bin Na, and T. Hyeon, *Nano Lett.* 2, 1383 (2002).
355. S. R. Hall, S. A. Davis, and S. Mann, *Langmuir* 16, 1454 (2000).

# Oxide Nanoparticles

K. P. Jayadevan, T. Y. Tseng

*National Chiao-Tung University, Hsinchu, Taiwan*

## CONTENTS

1. Introduction
  2. Synthesis
  3. Spectroscopic Characterization
  4. Properties
  5. Applications
  6. Summary
- Glossary  
References

## 1. INTRODUCTION

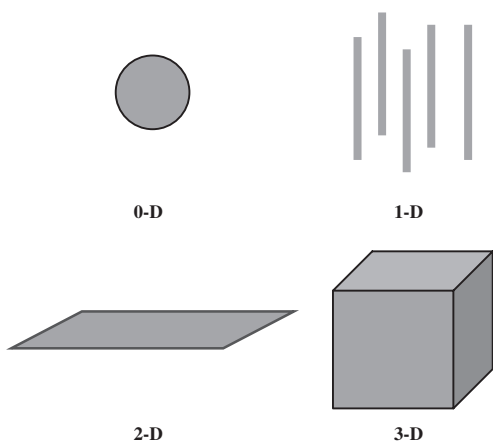
Nanotechnology has emerged as one of the most exciting fields in science and engineering in recent years. Major academic institutions as well as industries around the world have opened exclusive centers to focus on nanoscale research as a part of miniaturization in devices. The trend in miniaturization had been foreseen forty years ago by Feynmann in the most often quoted text of his lecture, "There's plenty of room at the bottom" [1], in which he intuitively suggested the idea of storing bits of information in atomic dimensions. The predictions of Feynmann were partly realized when information storage at such a minute scale was made possible in two dimensions using a scanning tunneling microscope (STM) [2]. In particular, the field of electronics has focused on the fabrication of scaled-down data storage devices to meet the predictions of Moore's law [3]. The rapid advancements in feature size reduction in electronic circuits can be attributed partly to the successful implementation of a wide variety of nanostructured materials in various devices. Now at the dawn of the new century, nanotechnology has become the most fascinating area of research, as it encompasses almost all fields of science and engineering. For instance, in biomedical applications, it has been found that nanotechnology has a major role to play in medical diagnostics and drug delivery as demonstrated by the investigations into nanocrystal fluorophores for imaging, nanoscale biodevices as sensors, and nanobubbles for drug delivery [4–7]. A novel concept termed "nanoclinic"

in medical diagnostics refers to exploitation of the unique properties of oxide nanoparticles for biomedical applications. A typical example of a "nanoclinic" is the iron oxide ( $\text{Fe}_2\text{O}_3$ ) nanoparticles encapsulated by silica shell, which can be used in contrast magnetic resonance imaging in medical diagnosis [8]. There are also examples of biomolecules being used for the derivatization of nanoparticle surfaces to form novel nanostructures [9]. Moreover, the presence of a large number of cavities and bonded networks that result from intra- and intermolecular interactions in biomolecules make them attractive templates for developing technologically useful nanomaterials [10].

### 1.1. Size and Dimensionality

Nanomaterials have unique features that are suitable to a variety of industrial applications. To examine these features, let us consider the definition of the term "nanomaterial." A material can be termed as a nanomaterial if one of its linear dimensions is less than 100 nm. In other words, at least in one dimension, the size of a nanomaterial is in between the sizes of atoms and bulk materials, which results in size- and dimension-dependent unique material properties. By taking into consideration the metastable nature of the nanomaterial, defining the size limits for the formation of a stable nanocrystal would be difficult. However, it is possible to define the tentative size limits for nanomaterials with the lowest limit corresponding to the clusters of molecules having sizes on the order of 1 nm or even less. The highest size limit would correspond to a few crystallites (grains), forming a nanoparticle of dimension close to 100 nm. As the grain size approaches the particle size, we have single-crystal nanoparticles. However, depending on the dimension in which the size-effect on the resultant property becomes apparent, the nanomaterials can be classified as zero-dimensional (spherical nanoparticles of ~5 nm diameter), one-dimensional (quantum wires), two-dimensional (thin films), or three-dimensional (nanostructured material built of nanoparticles as building blocks) [11]. The schematic diagram in Figure 1 illustrates the typical dimensional characteristics of nanomaterials. In this chapter, we intend to focus on the recent developments in synthesis, spectroscopic





**Figure 1.** Schematic illustration of dimensionality in nanostructured materials: zero-dimensional nanoparticles (0-D), one-dimensional nanowires (1-D), two-dimensional nanostructured thin films (2-D), and three-dimensional nanostructure (3-D).

characterization, properties, and industrial applications of oxide nanoparticles and nanostructures.

## 1.2. Selection of Synthesis Route

The drive for finding novel routes for the synthesis of nanomaterials has gained considerable momentum in recent years, owing to the ever-increasing demand for smaller particle sizes. In particular, controlling the microstructure at the atomic level has been of great multidisciplinary interest to fields such as physics, chemistry, materials science, and biology.

Nanomaterials and related devices can be classified into three major categories, and suitable preparative routes are identified depending on the desired resultant structure as proposed by Gleiter [12]. i) The first category of nanomaterials consists of isolated, substrate-supported, or embedded nanoparticles, which can be synthesized by physical vapor deposition (PVD); chemical vapor deposition (CVD); inert gas condensation; aerosol processing; precipitation from supersaturated vapors, liquids, or solids; or relatively novel routes such as ultrasonication. Nanostructured metal oxide catalysts [13] and electronic devices incorporating quantum dots [14] are examples wherein this class of nanoparticles have been employed. ii) The second category refers to materials having a thin nanometer-sized surface layer, which can be processed by techniques such as PVD, CVD, ion implantation, or laser ablation. The major advantage associated with these techniques is that the processing parameters can be suitably tuned to obtain a nanometer-sized surface layer. A recent study demonstrates the formation of a self-organized and ordered oxide nanostructure on the surface of nonstoichiometric metal oxides under ultra-high vacuum deposition conditions [15]. The self-organization and chemical self-assembly are also emerging as very important techniques for the deposition of materials layer-by-layer with controlled particle size and composition [16–18]. A single protective layer grown on the surface of bulk materials also provides enhanced stability, such as lower susceptibility to corrosion [19, 20].

iii) Three-dimensional (3-D) materials having nanometer-sized grains belong to the third category. The crucial aspect related to the processing of these materials is control of the chemical composition and the grain size. For example, the metastable 3-D nanostructures such as glass, gels, supersaturated solid solutions, or implanted materials can be prepared by quenching the high-temperature phases at equilibrium to the room temperature. The quenching helps to freeze the disordered structure with the composition varying on an atomic scale. Nanostructured-glass ceramics, which belong to the category of metastable three-dimensional nanostructures, have been studied with immense interest in recent years because of the potential engineering applications [21]. Another type of material that belongs to this group is a three-dimensionally ordered solid having building blocks as nanocrystals [22]. The microstructures of such solids comprise crystals with varying orientations separated by interfaces, which may be coherent, semicoherent, or incoherent. The ideal preparative route for such structures would involve the optimization of the processing conditions to ensure the formation of a microstructure with controlled grain growth so that the unique properties of the nanobuilding blocks are preserved.

## 1.3. Microstructure

As the particle size is scaled down to a few nanometers, the constituting atoms exhibit highly defective coordination environments. Most of the atoms have unsatisfied valences and reside at the surface. In short, microstructural features such as small grain size, large number of interfaces and grain boundary junctions, pores, and various lattice defects that result from the chosen routes for their synthesis contribute significantly to the unique physical and chemical properties of nanomaterials [23–25].

### 1.3.1. Grains

Grains are crystallized domains that combine to form a larger polycrystalline particle. Except for a single-crystal nanoparticle, in which the grain size and the particle size are identical, the nanoparticles have randomly oriented grains. The atomic planes within a grain can be directly imaged using high-resolution transmission electron microscopy (HRTEM) [26–30]. For example, it has been demonstrated that HRTEM characterization provides a clear insight into the grain structure for a cluster-deposited nanophase material [28]. The size distribution of the clusters formed in the gas-condensation method is very narrow ( $\pm 25\%$  Full-width at half maximum (FWHM)) as evidenced by a dark-field TEM study for cluster-consolidated nanophase  $\text{TiO}_2$ . However, methods such as mechanical activation and crystallization result in a broader grain size distribution [27].

The higher density of the consolidated nanophase material as compared to the theoretical density (74%) of powder compact may be attributed to the filling up of the pores by the enhanced diffusion, which arises out of an extrusion-like deformation in the consolidated nanophase. This process has been experimentally verified by the STM and the atomic force microscopy (AFM) studies on metal nanoparticles [31]. The grains of the consolidated nanophase

materials do not exhibit any preferred orientations in contrast to the micrograined samples. The random orientations of the grains in nanophase suppress the dislocation motion in these materials.

### 1.3.2. Interfaces

In order to account for the unique properties of nanomaterials, it is imperative to understand the interface characteristics, perhaps on an atomic scale. In nanomaterials, the randomly oriented crystals have incoherent interfaces where the atoms are far from being in a perfect order, as in a lattice. The misfit among the crystals also results in the modification of the grain boundary atomic structure by reducing the atomic density and altering the coordination numbers of the atoms. The characterization of the Fe-containing nanomaterials by Mossbauer spectroscopy revealed the grain boundary structures of these materials with defective coordination environments compared to a perfect lattice [32]. The defective coordination environments also make the atoms at the interface more reactive. In other words, the relatively positive enthalpies and Gibbs energies associated with the formation of nanocrystalline ceramic oxides can be attributed to the reactive surfaces or interfaces present in the samples [33, 34]. The quantitative determination of the thermodynamic parameters may help to correlate the size of the nanoparticles to the degree of metastability and the crystal structure. For instance, in the case of oxide ceramics, which are known to crystallize in systems different from that of the bulk (e.g., cubic  $\text{BaTiO}_3$  [35], tetragonal  $\text{ZrO}_2$  [36], monoclinic  $\text{Y}_2\text{O}_3$  [37], and  $\gamma\text{-Al}_2\text{O}_3$  [38, 39]), a quantitative estimation of the thermodynamic parameters for the nanocrystalline state would provide much needed insight into the resultant microstructure, as well as the hierarchy of transition states [34]. The parameter, strain, may also govern the stability of the finely divided particles, as it has been found that the presence of large number of interfaces in a nanomaterial leads to the generation of intrinsic strain in nanosized particles [40]. Apart from the intrinsic strain, the method of preparation may induce an extrinsic strain in these materials. The line broadening obtained by X-ray diffraction helps to estimate the strain present in the sample [41].

### 1.3.3. Defects

Siegel et al. [26], Eastman et al. [42], and Balachandran et al. [43] have demonstrated the cluster deposition method for the synthesis of metal oxide nanoparticles. One of the major issues during such processing is to minimize the formation of defects, which can be done by annealing the sample at a suitable temperature in a chosen atmosphere. It has been found that annealing at a fixed partial pressure of oxygen would compensate the oxygen vacancies in metal oxide nanophase samples. The increase in oxygen permeability through the nanophase material can be attributed to the highly defective surfaces of the metal oxide nanoparticles, which eventually provides easy pathways for the oxygen diffusion. For instance, the nonstoichiometry in the as-prepared nanophase  $\text{TiO}_2$  ( $\text{TiO}_{1.89}$ ) samples caused the broadening and the shifting of Raman bands, but could be oxidized to stoichiometric  $\text{TiO}_2$  without a change in nanometer grain size ( $\sim 12$  nm) when annealed in oxygen

atmosphere [44–46]. It has been experimentally verified that the defects such as dislocations are rare in nanoparticles [28, 47, 48]. The reason for the lack of dislocations in nanophase materials can be attributed to the image forces in the finite atomic ensembles that pull the dislocations out of the grains. The absence of dislocations also affects the mechanical properties of nanoparticles [49].

### 1.3.4. Pores

Porous solids have been recognized as an important class of materials that can find applications in various fields [50–52]. Therefore, the determination of porosity in a consolidated solid product has become very relevant in recent times. Upon consolidation, the nanoparticles form a porous structure, which can be characterized by positron annihilation spectroscopy (PAS) [26, 53, 54], Archimedes densitometry [55], porosimetry [56–58], and small angle neutron scattering (SANS) [59]. The percentage of porosity varies from  $\sim 5\%$  to  $\sim 25\%$  in nanophase materials. The value is higher for the consolidated oxide nanoparticles compared to the metal nanoparticles. The pore sizes obtained from the various measurement techniques mentioned above have dimensions comparable to the grains of the ceramic. Pores are usually associated at the triple junction grain boundaries with interconnected structures and intersections at the surface. The consolidation of nanoparticles at elevated temperature would uniformly remove the porosity without significant increase in the grain growth. The porosity also enhances the diffusion in nanophase ceramics. However, the diffusion rate would tend to be lower for the high-temperature-sintered fully dense ceramic. For example, the diffusion of Hf in sintered nanophase  $\text{TiO}_2$  has been suppressed after the densification [60]. In the case of fully dense nanomaterial, the diffusion of the impurity atoms is mostly through the grain boundaries. Doping of oxide nanomaterials with various types of dopants enables tuning of the properties to fit in a variety of applications. This has been a major area of research in recent years.

## 1.4. Size Effects on the Properties of Oxide Nanoparticles

In this section, we summarize the important consequences of size reduction on various properties of oxide nanoparticles. Over the years, numerous studies have been carried out to understand the interesting properties exhibited by nanomaterials [61, 62]. Careful examinations of the microstructure and the atomic structure of nanomaterials supported by strong theoretical understanding of the phenomenon under investigation are required in order to arrive at a satisfactory explanation for the observed characteristics. For example, in the case of electrically conducting nanoceramics, microstructure effects such as highly defective grain boundaries have been found to have a great influence on the resultant characteristics. At reduced grain sizes, the interfacial contribution dominates the total conductivity. Theoretically, the enhancement in electrical conductivity is predicted for nanosized conducting ceramics as a result of space charge contribution from the interfaces [63]. The experimentally obtained value of the enhanced conductivity of the nanocomposite  $\text{AgI}:\text{Al}_2\text{O}_3$  [64] could be

explained based on the interfacial and the space charge effects. Increase in conductivity has also been observed in nanocrystalline  $\text{CeO}_2$  [65] and  $\text{Y}_2\text{O}_3$ -stabilized  $\text{ZrO}_2$  [66].

Size effects play a crucial role in influencing the domain-dependent magnetic and dielectric characteristics. As the particle size of the oxide is progressively reduced to nano-dimensions, the size ultimately becomes identical to that of a single domain in which the magnetic or dipole moments are aligned. At this critical size, the magnetization or the polarization is no longer nonlinear in the presence of an applied field with the disappearance of hysteresis loops. For example, the critical size for  $\gamma\text{-Fe}_2\text{O}_3$  and ferroelectric  $\text{PbTiO}_3$ , which exhibit distinctly different behaviors compared to larger particles, is about 8 nm [67, 68]. However, the critical size may vary depending on the processing history of the sample, which will be discussed in detail while considering size-dependent properties in a subsequent section in this chapter.

Another interesting effect is size quantization in semiconducting nanoparticles [69]. As the sizes of the semiconductor particles are reduced to dimensions (<5 nm) comparable to an exciton diameter, the energy gap between the valence and the conduction band increases. Consequently, the optical absorption shows a blue shift. For example, semiconducting  $\text{ZnO}$  nanoparticles exhibit a blue shift in the optical spectra due to quantum size effect [70].

Reduction in particle size also enhances self-diffusion, solute diffusion, and solute solubility in nanomaterials. Enhanced diffusivity and solubility can be attributed to defective atomic coordination at the grain boundaries in the nanocrystals [23]. The higher fraction of the grain boundaries in nanocrystals also results in higher values of specific heat compared to conventional polycrystals [71]. Consolidated  $\text{TiO}_2$  nanoparticles have improved mechanical properties such as hardness comparable to the coarse-grained  $\text{TiO}_2$  [72]. The improved ductility of a brittle ceramic oxide when prepared in nanocrystalline form is worth noting. The enhanced interdiffusion among the grains in nanocrystals helps the grain boundaries slide by one another, thereby improving the ductility [73].

### 1.5. The Need for High Surface Area Nanomaterials

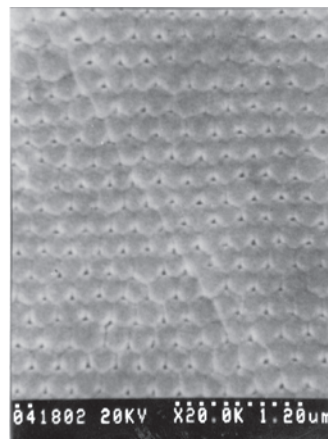
High surface area (300–2,000  $\text{m}^2/\text{g}$ ) is an important feature of nanosized and nanoporous materials, which can be exploited in many potential industrial applications, such as separation science and catalytic processing, because of the enhanced chemical reactivity [74, 75]. The major drive is to develop inexpensive materials that exhibit superior properties. High surface area nanomaterials have already been used in applications that require rapid and responsive sampling, selective separations, high throughput catalytic processing, enhanced chemical activity, or 3-D packaging of supported or entrained nanoscopic structured species [76–78]. The detection sensitivities of the high surface areas lie in the range of parts per billion on a short time scale. This enables rapid sampling and chemical processing of large volumes of reactants. By controlling the pore sizes or surface structures at the nanostructure level (<1 Å), several orders

of enhancement in separation or catalytic process selectivities can be realized. Magnetic high surface area materials for oxygen separation and optically transparent high surface area monoliths (films, spheres, fibers) for chemical sensor applications [79–82] are some of the industries where high surface area materials such as nanostructures and nanoporous materials have potential applications. Figure 2 illustrates the pore formation in silica glass ( $\text{SiO}_2$ ) [83]. The dimensions of the pores are on the order of a few nanometers. High surface area nanostructures should be characterized to determine certain figure-of-merit variables that are relevant in a variety of applications. Some of the important variables are the void space in the case of porous structures for molecular recognition, transition state lifetimes, sorption and the desorption rates in the case of catalytic processes, surface activity, chemical and the mechanical stability, defect, and interface properties in the case of synthesis and tuning of the properties of composites.

High surface area materials are also useful in the preparation of metastable phases by creating the necessary interfaces for the stability of processed composites, as well as promoting the thermal transport in low-density packaging. The major challenge is to fabricate the appropriate form of the nanostructure, for example, in thin film forms, fibers, or microspheres for the desired applications. After the selection of the appropriate structure, the nano-building units have to be carefully assembled to obtain multidimensional control of their properties. This, undoubtedly, is one of the most exciting areas in materials technology [84, 85].

### 1.6. Relevance of Nanoparticles in Device Fabrication

Nanoparticles form the basic building unit for 3-D nanostructures, which can be considered as primary components in nanostructure-based devices. For the successful fabrication of nanostructure-based devices, the synthesized nanostructures have to be suitably incorporated to device structures. The ultimate objective of the modern day industry is to fabricate cost-effective, nanostructure-based, miniaturized devices with superior characteristics. For



**Figure 2.** Nanopore formation in  $\text{SiO}_2$ -glass sintered at 1000 °C for 10 min [83].

instance, nanostructure-based memory devices have high information storage and computational capacity. These characteristics result from the packing density and the short information transit time from site to site. For optical applications, a wide range of nanostructure-based optical sources that include high performance lasers to general illumination can be fabricated. These industrial requirements can be accomplished by selecting an appropriate fabrication method of functional nanostructures with controlled size, shape, and composition. However, assembling nanoparticles to form a nanostructure is a complex process. Numerous research groups are working out different synthetic strategies to find economically affordable ways for fabricating the nanostructures and simultaneously preserving the superior characteristics of the basic building units (the nanoparticles) in various devices. For example, self-organization and chemical self-assembly are promising techniques that provide inexpensive routes for the fabrication of nanostructures [16–18]. In the immediate future, one can expect the miniaturization revolution in device fabrication to reach its peak in various industries. However, a recent study predicts that there is an optimum limit for miniaturization, beyond which the second law of thermodynamics no longer holds [86]. The study is significant as it implies a possible device breakdown at molecular or atomic scale because of energy accumulation.

Oxide nanoparticles are of particular interest in the fabrication of electronic devices based on the ultra-large scale integration (ULSI). Integrated circuits become more and more complex with increasing layers of metallization and interlayer dielectrics. This has led to the search for a method to planarize the wafers between the deposition and the processing steps. The method adopted is chemical mechanical polishing (CMP), which involves pressing the Si wafers against a polishing pad in the presence of colloidal slurries of metal oxides such as  $\text{SiO}_2$ ,  $\text{Al}_2\text{O}_3$ ,  $\text{CeO}_2$ , or  $\text{ZrO}_2$ . The size, shape, surface chemistry, and stability of the oxide particles govern the efficiency of the process. The CMP process has turned out to be an important step in the semiconductor industry [87].

## 2. SYNTHESIS

Prior to the synthesis of a nanophase material, the size and the dimensional features of the material to be prepared have to be defined. Accordingly, a suitable preparative method can be adopted. This is very crucial because the particle size, dimensionality, and composition govern the resultant properties of the nanostructured materials that are assembled from nanoparticles as building units in order to achieve certain desired properties. For instance, the fascinating electronic, electrical, optical, catalytic, thermal, and mechanical properties of the nanoparticles and the nanostructured materials have triggered enormous multipronged research activities in recent years in this area.

Several methods have been developed over the years for the synthesis of nanomaterials. The various routes include synthesis using liquid, solid, or gas phase precursors, which come under physical or chemical processing. The major issues for the synthesis of nanoparticles are i) the control of the particle size and composition, and ii) the control of the

interfaces and the distributions of the nanobuilding blocks within the fully formed nanostructured materials.

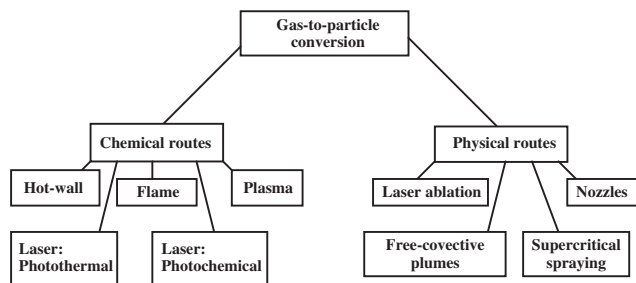
The oxide nanomaterials are of interest in a variety of structural and functional applications. The advantages of equiaxed, dispersive, submicron ceramic oxide particles with a narrow size distribution have been discussed much before the onset of the present nano era in materials research [88]. Typical nanoparticles are agglomerates of several primary particles. The agglomerates are termed as secondary particle. The secondary particle size is obtained by scanning electron microscopy (SEM), whereas the X-ray line broadening helps to estimate the primary particle size or crystallite size. Minimizing the agglomeration and deriving the properties exclusive to the primary particles are the important objectives in the synthesis of oxide nanoparticles. In the subsequent sections, important methods for the preparation of oxide nanoparticles are described.

### 2.1. Gas Phase Condensation Methods

The production of nanoparticles by condensation of gaseous precursor molecules generally comes under the category of aerosol processes [89, 90]. For the synthesis of nanoparticles or ultra-fine particulates (particle size  $<100$  nm), the gas phase condensation is a suitable method. The initial step in this process is the formation of gaseous precursor molecules by a suitable physical or chemical method in aerosol reactors [91–95]. The precursor molecules then react in the vapor phase to form tiny nuclei of the desired phase (gas-to-particle conversion). The size of a typical nucleus thus formed has dimensions comparable to that of a molecule of a refractory oxide. Subsequently, the primary particles undergo collision and coalescence to form aggregates, which in turn form agglomerates held together by the weak van der Waals forces [96, 97]. The method is suitable for the production of nanoparticles in laboratories as well as in industries. The mechanism involved in the gas phase condensation process allows one to link the properties of gaseous precursor to the nanoparticles formed. The important parameters involved in the processing are time, temperature, and the amount of particles produced per unit volume. The decisive characteristics of the prepared nanoparticles include the size distribution of the primary particles, the grain boundaries, the pore sizes, the defect concentrations, and crystallinity. Apart from these characteristics, the fractal dimension of the aggregates and the particle bond energies are also of interest for investigation. The various methods used for the gas phase condensation of oxide nanoparticles are summarized as a block diagram in Figure 3 [98]. We discuss two important preparative routes—flame processing and laser ablation and related techniques such as sputtering for oxide nanoparticles. The microwave plasma-assisted chemical reactions in the gas phase for the preparation of oxide nanoparticles will be described in a subsequent section on microwave plasma processing.

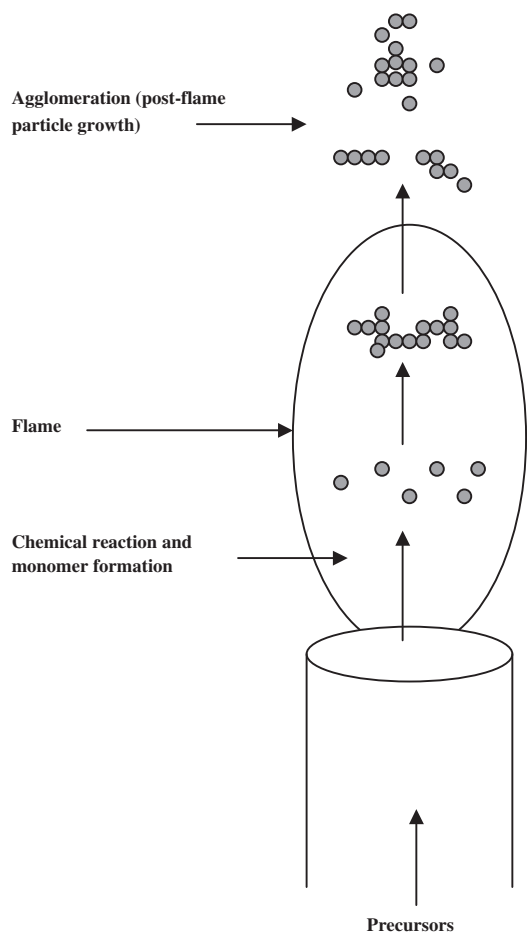
#### 2.1.1. Flame Processing

Oxide nanoparticles are produced commercially on a large scale in a flame reactor [94, 95]. The precursor in vapor phase is fed into a reactor in the presence of oxygen and ignited. The burning step may also take place in



**Figure 3.** Methods used for gas phase condensation of nanoparticles. Reprinted with permission from [98], T. T. Kodas and M. J. H. Smith, "Aerosol processing of materials," Wiley-VCH, New York, 1999. © 1999, Wiley.

other gaseous atmospheres such as inert gas, hydrogen, or methane. The schematic diagram for the particle formation in a flame reactor is shown in Figure 4 [98], which illustrates the eventual formation of nanoparticles through collision, coalescence, and agglomeration in an aerosol reactor. Temperatures as high as 1200–2500 K can be achieved in a typical flame reactor. The method is commercially used for the production of industrially useful silica ( $\text{SiO}_2$ ) from silicon



**Figure 4.** Schematic representation of particle formation in a flame reactor. Reprinted with permission from [98], T. T. Kodas and M. J. H. Smith, "Aerosol processing of materials," Wiley-VCH, New York, 1999. © 1999, Wiley.

tetrachloride vapor. It is also important to correlate the particle size of the material produced to the processing conditions and the material properties in order to standardize the production method for the nanoparticles. The particle size and the surface area of the oxide can be tuned by adjusting the process temperature. The lower the process temperature, the smaller the particle size and larger the surface area. The sizes of the oxide nanoparticles that are produced using the aerosol technique fall in the range of 7 to 27 nm. Other examples of oxides prepared using aerosol process are  $\text{Al}_2\text{O}_3$  and  $\text{TiO}_2$  from  $\text{AlCl}_3$  and  $\text{TiCl}_4$ , respectively.

Large-scale production of nanoparticles in industrial aerosol generators is governed by particle collision and coalescence. Industrial flame reactors are operated at high particle concentrations, which result in high rates of particle collisions. The particle size of the product is determined by the rates of the particle collision and the subsequent coalescence. The collision/coalescence mechanism for the particle formation is based on a series of steps assumed to proceed as follows [96, 97]: i) transformation of gaseous precursors to condensable molecules, ii) formation of a cloud of stable nuclei from condensable molecules, iii) coalescence of the stable nuclei to form larger particles, iv) formation of the agglomerates of the phase, and v) coalescence within the agglomerate.

The above five steps may proceed either step by step or simultaneously at a faster rate. The monomer molecules produced from the precursor coalesce to form a primary particle. The size of the primary particle, which is formed as a result of the coalescence of the monomer molecules, depends on the temperature/time history of the process. For example, at a high temperature, the enhanced coalescence leads to the formation of the particle agglomerates with reduced specific surface area, whereas at a low temperature, with the slower coalescence rate fractal-like agglomerates are produced with a high specific surface area. The size of the primary particle also depends on the diffusion characteristics of the material; the higher the diffusion coefficient, the larger the primary particle size. Also, the solid-state diffusion being a thermally activated process, high temperature heat treatment enhances the formation of larger particles with minimum surface area.

In the processing of ceramic powder compacts, one should have a clear understanding of the bond energies and the agglomerate rigidity of the particles. After deriving sufficient experimental evidence for agglomeration, the processing conditions can be optimized for obtaining desired particle characteristics. The processing can also be tuned as a function of temperature, from which the activation energy for the process can be estimated.

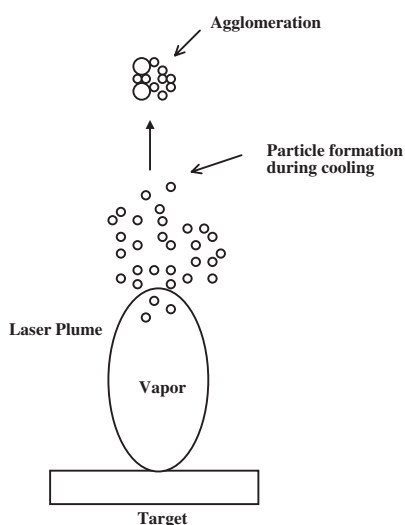
### 2.1.2. Laser Ablation and Related Methods

Recently, researchers have developed a laser vaporization technique to synthesize nanoparticles of controlled particle sizes and compositions [70, 99–102]. The technique involves the vaporization of a target using pulsed laser, which is then followed by controlled condensation in a diffusion cloud chamber under well defined conditions of temperature and pressure. A wide variety of metal oxides, carbides, and nitrides can be synthesized in nanoscale dimensions using

this technique. The process of laser ablation is schematically illustrated in Figure 5 [98].

An ArF excimer laser ( $\lambda = 193$  nm) can be used for the ablation of the target. The sintered pellet that can be used as a target is mounted on a rotating target holder in the ablation chamber and is rotated during the laser irradiation. The sputtering technique can also be used to prepare nanoparticles from a preformed solid target. Nanoparticles are collected on a selected substrate such as carbon-coated mica, quartz glass, and silicon wafers at room temperature. The substrate is placed at an off-axial position in order to suppress the deposition of the droplet-like large particles and collect the monodispersed nanoparticles. The background gas pressure can be varied from 0.133 Pa to 13.3 kPa of Ar gas.

By varying the ablation pressure, the morphology of the nanoparticles can be controlled. Sasaki et al. [103], Li et al. [104], Koshizaki et al. [105], and Zbroniec et al. [106] have investigated in detail the dependence of the particle morphology on the ablation pressure. They observed that the deposited products have morphologies that are typically dependent on the different pressure regions of Ar at 200 mJ/pulse. At a pressure of 26.7 Pa and below, a continuous film formation was observed on the substrate, whereas the nanoparticles of sizes in the range 2–9 nm formed under higher values of gas pressures in the range 66.7 Pa to 133 Pa. Upon increasing the gas pressure to about 1.07 kPa and above, the sizes of the primary particles did not change. However, the higher values of gas pressure affected the sizes of the aggregates. The formation of the aggregates indicated that the nanoparticles when formed in the gas phase undergo collisions with gaseous molecules dissipating their kinetic energy. A similar dependence of nanoparticle morphology has been reported for cobalt oxide nanoparticles [104]. Interesting observations were also made on the evolution of various cobalt oxide phases as a function of gas pressure using X-ray diffraction.



**Figure 5.** Schematic diagram to illustrate particle formation during laser ablation. Reprinted with permission from [98], T. T. Kodas and M. J. H. Smith, "Aerosol processing of materials," Wiley-VCH, New York, 1999. © 1999, Wiley.

The mechanism leading to the formation of thin films, nanoparticles, and aggregates can be sequenced against increasing gas pressure [104–106]. At low pressure, the ablated molecules have larger available volume for expansion. Molecules have higher kinetic energy with fewer collisions in the gas phase. But as the ambient gas pressure increases, the number of collisions between the metal and the oxygen species in the gas phase increases, leading to the formation of primary nanoparticles. With further increase in the ambient pressure, the primary particles lose their kinetic energy due to frequent collisions, resulting in the quenching of the nanophase. The small nanoparticles stick together by weak van der Waals forces to form nanoparticle agglomerates. The recent advancements in the laser ablation process indicate that nanoparticles with desired microstructure and properties can be synthesized by suitably optimizing the experimental conditions.

## 2.2. Microwave Plasma Processing

Microwave plasma processing has emerged as a major processing route for oxide ceramics [107–109]. The method is attractive because the kinetic and thermodynamic barriers that are usually encountered in conventional solid-state synthesis can be overcome with a short processing time. The faster reaction rate may be attributed to the reverse heating profile during the exposure of reactants to microwaves as compared to conventional furnace heating. Moreover, the basic reaction mechanism involving various species in the microwave plasma can be exploited for the synthesis of nanophase oxide powders [108, 110–114]. The compound forms when energy transfer occurs between the electrons and the other species in the plasma. Stable plasma can be achieved in a microwave cavity by reducing the pressure, thereby controlling the collision frequency to less than the source frequency (2.45 GHz and 0.915 GHz) [115]. The parameters that decide the energy transfer between the electrons and the neutral or ionized species in the plasma are the frequency of the source and the number of collisions made. A recent thermodynamic study on the oxidation of silver in oxygen-microwave plasma indicates that the gaseous species in the plasma have very high chemical potentials, which are equivalent to normally unattainable high pressures of neutral diatomic oxygen ( $\sim 10^{10}$  MPa) [116]. This extraordinarily high thermodynamic driving force in the microwave plasma can be exploited for the synthesis of a wide variety of nanoscale metastable materials.

The precursor used for the preparation of nanophase oxide powders can be a homogeneous solution or a gaseous precursor. The precursor solution is introduced into the microwave cavity through a nozzle [117]. Both aqueous and nonaqueous solutions are used for the synthesis of oxide powders. The aqueous precursor solution is usually a nitrate solution containing the metal ions of the desired phase [112]. Water, being highly polar, absorbs the microwaves quickly and evaporates from the precursor solution. The residual material, upon further exposure to the plasma, reacts with the oxygen species in the plasma. This results in the formation of fine metal oxide particles. The technique has been used for the preparation of some model binary oxides

such as zirconia ( $\text{ZrO}_2$ ), alumina ( $\text{Al}_2\text{O}_3$ ), or solid solution between them. It is interesting to note that the nanocrystallites of metastable cubic zirconia ( $\text{ZrO}_2$ ) complex solid solution with 3%  $\text{Y}_2\text{O}_3$  and 20%  $\text{Al}_2\text{O}_3$  could be processed at a much lower temperature in a short amount of time compared to the conventional high-temperature solid-state synthesis [108]. Nonaqueous solutions such as metal halides can also be used as precursors for the processing of nanopowders. For example, for the synthesis of  $\text{ZrO}_2$  powders, the nonaqueous solution can be  $\text{ZrCl}_4$  in  $\text{CH}_3\text{CN}$  [108]. The various steps involved in the processing of oxide nanoparticles from a nonaqueous halide solution are vaporization of the solvent in the plasma, evaporation of the metal halide, oxidation of the metal halide, and formation of the oxide powder particles by agglomeration. The particle sizes of the oxides formed depend on the final temperature of the oxidation, which implies that at a higher oxidation temperature, larger zirconia particles are produced.

In order to reduce the processing complexities of using a precursor solution for the synthesis of oxide nanoparticles, high vapor pressure metal halide can be directly exposed to microwave plasma in an oxidizing atmosphere. This ensures better homogeneity, as the reactant species are all in the gas phase. The ionized gaseous species in the plasma reacts with the metal halide vapors and promotes oxidation, resulting in the formation of fine metal oxide particles. Synthesis of single crystalline cubic  $\text{ZrO}_2$  nanoparticles of sizes  $\sim 4$  nm with a narrow size distribution have been realized by this method [108].

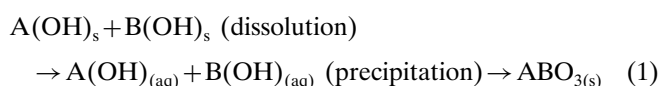
### 2.3. Hydrothermal Synthesis

Hydrothermal synthesis involves the exploitation of the properties of water under high pressure and temperature for the preparation of fine powders of advanced ceramic oxides [118]. The typical values of the reaction temperatures are between the boiling point of water and the critical temperature of  $374^\circ\text{C}$  and pressures up to 15 MPa. However, continued revision of the process has led to high temperature hydrothermal processes at greater pressures [118]. The advantage of the hydrothermal method over other solution routes is that the final product readily forms at a low temperature without calcination. Fine crystallites of the desired phase with excellent composition, morphology control, powder reactivity, and purity can be obtained using the hydrothermal method [119].

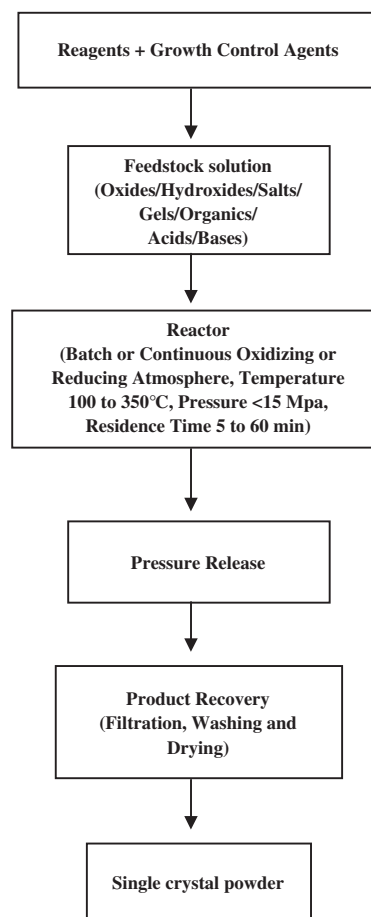
The precursor sol is prepared from oxides, hydroxides, nitrates, or halides of the corresponding metallic elements. The prepared sol is subjected to hydrothermal synthesis, which is carried out in a high-pressure apparatus or hydrothermal bomb (autoclave) [120]. The basis of the technique is the enhanced solubility of the precursor in water under hydrothermal conditions, which ensures the formation of the product with very good composition control and uniformity. Under hydrothermal conditions, water may be termed as a superior solvent with the ability to dissolve even nonpolar entities. This anomalous solvation characteristic under hydrothermal conditions effectively brings down the activation energy for the formation of the final phase, which otherwise forms only when heated at high temperature as

in the case of a conventional solid-state reaction or calcination of the coprecipitated powders. The hydrothermal technique has been demonstrated as a very effective route for the preparation of nanoscale ceramic oxides [121–123] and many novel materials such as porous and open-framework solids [124].

The hydrothermal process is advantageous for the preparation of electronic ceramic powders and their solid solutions, with a potential for commercial scale-up because of the relatively low temperature associated with the crystallization of the final phase when compared to conventional solid-state synthesis or coprecipitation route [125, 126]. A typical flow chart for the hydrothermal process is presented in Figure 6 [119]. For an  $\text{ABO}_3$  perovskite oxide, the general hydrothermal reaction that involves dissolution and precipitation can be written as



The perovskite  $\text{BaTiO}_3$  with several dopants has been prepared by the hydrothermal technique [127]. Fine powders of the hydrothermally prepared dielectric ceramics exhibit improved dielectric characteristics. For instance, a thin layer



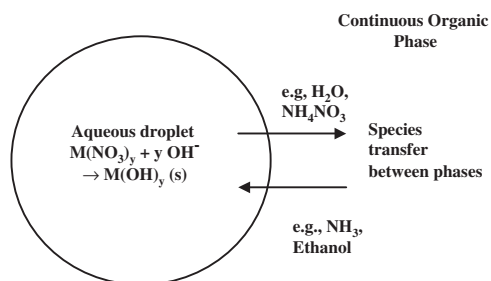
**Figure 6.** Flow chart for the synthesis of oxide nanoparticles using hydrothermal process. Reprinted with permission from [119], W. J. Dawson, *Am. Ceram. Soc. Bull.* 67, 1673 (1988).

of fine-grained ceramic can enhance the capacitance stored per unit volume in a multilayered capacitor, which is relevant from the point of view of miniaturization.

Hydrothermal synthesis also promotes the crystallization of high temperature metastable phases at much lower temperatures. For example, zirconia has several polymorphs—cubic, tetragonal, or monoclinic—and can crystallize in any of these systems, depending on the process variables such as the reaction time and the temperature, the presence of impurities, and the concentration of the precursor solution. By the conventional solid-state technique, the synthesis of metastable phases requires higher energy input, with the resultant products being far from pure. Apart from being a single process for the synthesis of fine powders, various other techniques can be combined with the hydrothermal technique to form a kind of hybrid technique for the synthesis of nanoparticles. Examples of such techniques are hydrothermal-sonochemical [128] and hydrothermal-microwave processing [129].

## 2.4. Electric Dispersion Reaction

The electric dispersion reaction is a precipitation reaction that is carried out in the presence of a pulsed electric field to synthesize ultrafine precursor powders of advanced ceramic materials. The technique involves subjecting the reactor liquid (metal-alkoxide solution) to a dc electric field (3 to 10 kV/cm at pulsing frequencies in the range 1 to 3 kHz). Under the applied electric field, the sol is shattered to micron-sized droplets, termed as microreactors, that contain hydrous precursor precipitate. The formed precursor powders can be thermally processed to obtain oxide nanoparticles. Harris and coworkers have developed this technique for the synthesis of various ultrafine ceramic powders from the corresponding metal alkoxide solution [130–133]. A typical microreactor droplet for the formation of nanosized oxide particles is schematically represented in Figure 7. Metal alkoxide and metal salt solutions have been used for the synthesis of ceramic precursor powders (including  $\text{SiO}_2$ ,  $\text{Al}_2\text{O}_3$ ,  $\text{ZrO}_2$ , and 1:2:3 yttrium-barium-copper oxide) with chemical homogeneity at submicrometer level [130]. The method also allows control and modification of the particle morphology. Moreover, the method has been shown to be a viable means for the production of microspheres and porous spherical shells. A scanning electron micrograph of hydrous 1:2:3 Y-Ba-Cu oxide particles synthesized by an electric dispersion reaction from the corresponding metal



**Figure 7.** Typical microreactor droplet for the formation of nanosized oxide particles during an electric dispersion reaction [130].

nitrate revealed that the particle sizes were in the micrometer range ( $\sim 5 \mu\text{m}$ ), which on further thermal processing form submicrometer powders [130].

## 2.5. Combustion Synthesis

Another interesting method for the preparation of oxide nanoparticles is the combustion technique, which involves the exploitation of an excess heat-generating or exothermic reaction to overcome the activation energy barrier for the formation of products [134–138]. The precursor is a redox mixture that contains an organic compound (fuel) as the reducing agent and a metal salt as the oxidizing agent. When heated to the ignition point of the fuel, the mixture instantaneously burns to form the product. Large volumes of gas produced during the process also help the precursor particles to disintegrate to smaller particles. The major advantage of the method is that it is fast, requiring the least external energy input. Moreover, the synthesis gives high output with the possibility of producing a wide variety of ceramic oxides. The carbonaceous residue left over as a result of the combustion can be detrimental to the powder characteristics. Therefore, the fuel or organic compound should have a relatively low carbon content, but at the same time should ignite easily. For the preparation of yttria ( $\text{Y}_2\text{O}_3$ )-stabilized zirconia ( $\text{ZrO}_2$ ) powders, for example, the precursor solution was first prepared by dissolving the metal nitrate in distilled water followed by the addition of the fuel (oxalic dihydrazide) [135]. The solution was then spray-dried prior to combustion. By controlled heating of a small amount of the dried precursor, combustion was initiated. Less vigorous reactions that do not form flames during combustion can be initiated by directly placing the precursor solutions inside a preheated furnace or a microwave oven [138].

The rate of the reaction depends on the amount of the fuel in the initial mixture. Upon increasing the fuel concentration, the reaction propagates to completion in a self-sustained manner producing large volumes of gases as by-products. However, an optimum fuel concentration has to be selected for obtaining high surface area nanoparticles with the sizes in the range of 10–20 nm. By suitably tuning the various parameters in the combustion synthesis, the crystallization of high temperature metastable phases such as the cubic/tetragonal phase in  $\text{Y}_2\text{O}_3$ -stabilized  $\text{ZrO}_2$  can be achieved at a lower temperature from precursor solutions with moderately high fuel content [136].

Because of the vigorous reaction during a combustion process, particles formed in the gas phase undergo collision and form agglomerates. The agglomerate formation during the combustion synthesis has to be controlled by suitably tuning the properties of the precursor. The method is economically affordable and has the potential for commercial production of oxide nanoparticles.

## 2.6. Sol–Gel (Colloidal) Processing

Sol–gel processing is a popular processing route for the synthesis of a wide variety of materials in desired shapes (particles, fibers, or films). The formation of a sol by dissolving the metal alkoxide, metal-organic, or metal-inorganic salt precursors in a suitable solvent is the primary step in a sol–gel



process. Upon drying the sol, a polymeric network is formed in which the solvent molecules are trapped inside a solid (gel) [139, 140]. Subsequent drying of the gel followed by calcination and sintering leads to the final ceramic product. As the reacting species are homogenized at the atomic level in a sol-gel process, the diffusion distances are considerably reduced compared to a conventional solid-state reaction; thereby the product forms at much lower temperatures.

Depending on the nature of the precursor, which can be an aqueous solution of an inorganic salt or metal-organic compound, the species involved in the intermediate steps of the sol-gel process differ. The nature and composition of the intermediate species formed also depend on the oxidation state, the pH, or the concentration of the solution. These factors are crucial in the formation of a colloid and its stability. Metal alkoxides are noted for the very high reactivity toward hydrolysis and are therefore being used as a common starting material for the sol-gel synthesis [141]. Electronegativity, valence states, and the coordination number of the metal affect the rate of hydrolysis and hence the nature of the colloidal solution. The resultant properties of the synthesized powder depend on the colloidal aggregate formed as a result of the hydrolysis step. This has been demonstrated in the case of many ceramics, as the chemical tuning of the precursor sol and the nature of the colloid formed have affected the final product [142, 143].

The preparation of powders with the desired microstructure from colloids depends on the tuning of the interparticle forces in the colloid, which differ depending on the nature of the suspension—well-dispersed, weakly flocculated, or strongly flocculated. The total interparticle potential energy can be expressed as

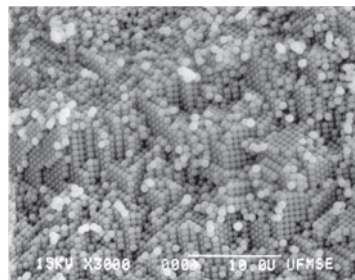
$$V_{\text{total}} = V_{\text{vdW}} + V_{\text{elect}} + V_{\text{steric}} + V_{\text{structural}} \quad (2)$$

where  $V_{\text{vdW}}$  is the attractive potential energy due to long range van der Waals interaction between particles,  $V_{\text{elect}}$  is the electrostatic repulsive potential energy between like-charged particles,  $V_{\text{steric}}$  is the potential energy arising out of the steric interactions among bulky groups present on the particle surface, and  $V_{\text{structural}}$  is the potential energy due to various nonadsorbed species in solution [144]. Tseng and coworkers have demonstrated the use of sol-gel (colloidal) method for the synthesis of advanced ceramic oxides such as silica ( $\text{SiO}_2$ ) [16, 83, 145–147], stabilized zirconia ( $\text{ZrO}_2$ ) [148–150], ferrites [22, 151, 152], and superconducting oxides [153–156]. The grain sizes in the nanometer range were obtained when samples were sintered from nanoparticles with a uniform green microstructure prepared through colloidal processing. Recently, our group has demonstrated that the grain sizes of high permittivity thin films can be suitably tuned by varying the sol-gel precursor concentration as well as the subsequent annealing temperatures of the films [157]. Some of our major results that are relevant to oxide nanoparticle synthesis are summarized in the subsequent paragraphs.

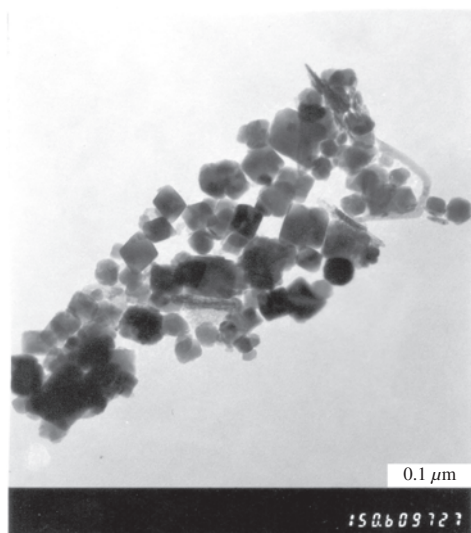
Silica ( $\text{SiO}_2$ ) is a potential material in optical, electrical, and thermal applications. To understand the densification and sintering characteristics of silica powders, monodisperse, spherical hydrous silica ( $\text{SiO}_2$ ) was synthesized through a colloidal sol-gel process and the resultant powder

was characterized in detail [16, 83, 146, 147]. The preparative step involved the addition of tetraethylorthosilicate ( $\text{Si}(\text{OC}_2\text{H}_5)_4$ , TEOS) to a reagent-grade ethanol and concentrated  $\text{NH}_4\text{OH}$  solution with constant stirring at room temperature. The TEOS undergoes hydrolysis/condensation reactions, forming polysilicic acid, which is then followed by the precipitation of silica particles. The reactant concentration controlled the average diameter of the particles that are formed during the synthesis. The precipitate was washed with distilled water, dried, and subsequently calcined in loose stack in the temperature range of 200 °C to 1050 °C. The diameters of the spherical particles ranged from 200 to 600 nm. However, by tuning the reactant concentration and the thermal processing conditions, the particles can be crystallized within the nanograin size range. The sample calcined at 200 °C was suspended in distilled water using ultrasonication and pH adjustments. The powder was then allowed to settle down in plastic tube under gravity to form a green compact. The SEM characterization of the green compact formed by the particle sedimentation showed the two-dimensional, hexagonal close-packed array of particles with an ordered array extending to a few micrometers. Figure 8 illustrates the hexagonal pore formation in  $\text{SiO}_2$  [83]. The hcp layers are stacked one over the other to form a self-organized three-dimensional ordered structure. The striking feature of these investigations was the tuning of the diameter of the nano-sized pores in the compact, which was prepared by dispersion and flocculation techniques. The green compact of the dispersed particles had smaller pores compared to that of flocculated particles. The pore size distributions were narrower and bimodal in nature because of the presence of three-particle and four-particle pore channels. The study showed that by appropriate tuning of the sol preparation, colloid formation, and dispersion conditions, three-dimensional ordered  $\text{SiO}_2$  powder compact can be formed.

Low magnetic loss is the characteristic of soft ferrites with highly dense fine-grained microstructure of nanoparticles. In order to obtain the desired microstructure for low loss soft ferrites, a colloidal precipitation technique was selected [22, 151, 152]. The TEM image of the highly sinter-active Ni-Zn ferrite ( $\text{Ni}_{0.5}\text{Zn}_{0.5}\text{Fe}_2\text{O}_4$ ) powders prepared by the colloidal precipitation technique is presented in Figure 9 [152]. The particle size of the prepared powder was 26.7 nm with specific surface area of 116  $\text{m}^2/\text{g}$  obtained from BET measurements. The samples when sintered at temperatures in the range of 1000 °C–1200 °C showed that the dense



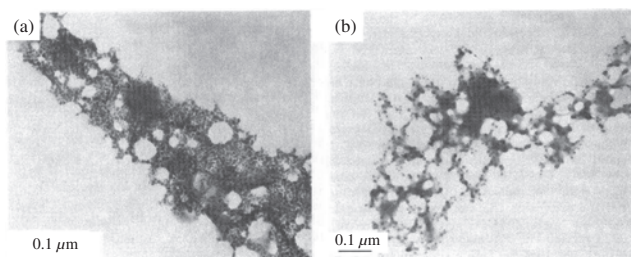
**Figure 8.** SEM picture illustrating the formation of hexagonal and cubic ordered array in  $\text{SiO}_2$  [83].



**Figure 9.** TEM picture of  $\text{Ni}_{0.5}\text{Zn}_{0.5}\text{Fe}_2\text{O}_4$  powders prepared by colloidal precipitation [22].

microstructure with some intergranular porosity and had a very low magnetic loss [22]. The sintered samples were magnetically characterized to obtain the grain-size dependence of magnetic permeability [22]. At temperatures below  $1100\text{ }^\circ\text{C}$ , the magnetic permeability was found to be proportional to  $(\text{grain size})^{1/2}$ , which was in accordance with the model proposed by Igarashi and Okazaki [158]. However, at high temperature, the permeability data did not agree with the model, perhaps due to the loss of zinc from the sample, which could have affected the  $\text{Fe}^{2+}/\text{Fe}^{3+}$  ratio. Moreover, the high-temperature sintered sample exhibited higher magnetic loss, possibly because of the formation of larger pores.

Using ethylene di-amine tetra-acetic acid as a chelating agent in a sol-gel process, the 2223 superconducting ceramic powder belonging to the Bi-Pb-Sr-Ca-Cu-O system was prepared and characterized by Chen et al. [156]. The TEM micrographs obtained from the ultrastructures of Bi-Pb-Sr-Ca-Cu-O EDTA colloid after aging treatments at  $40\text{ }^\circ\text{C}$  and  $90\text{ }^\circ\text{C}$  are shown in the Figure 10. It can be inferred from the pictures that each EDTA cluster exhibited a fractal structure at two different temperatures. The absence of an additional aggregation of clusters could be due to the evaporation of the solvent when the colloid was placed on a highly hydrophilic grid and exposed to the electron beam. The average size of the primary colloidal particle was about



**Figure 10.** TEM micrographs for the ultrastructures of Bi-Pb-Sr-Ca-Cu-O EDTA colloid after aging treatments at  $40\text{ }^\circ\text{C}$  and  $90\text{ }^\circ\text{C}$  [156].

$10\text{ nm}$ , implying that the particles had a large specific surface area along with very high chemical reactivity during subsequent heat treatment. Moreover, the ultrastructures shown in Figure 10 exhibited different fractal dimensions. The fractal structure of colloidal EDTA formed at  $90\text{ }^\circ\text{C}$  is more open than that formed at  $40\text{ }^\circ\text{C}$ . The temperature dependence of the fractal formation could be explained by two distinct mechanisms of cluster aggregation, namely reaction-limited aggregation (RLA) and diffusion-limited aggregation (DLA). The RLA mechanism was probably responsible for the formation of dense aggregates formed at  $40\text{ }^\circ\text{C}$ , whereas DLA caused the formation of less dense aggregates at  $90\text{ }^\circ\text{C}$ .

## 2.7. Sonochemical Processing

Application of ultrasound in chemical synthesis has initiated a new fascinating field in processing technology [159]. As the name of the route suggests, the sound waves act as the energy source, when the respective sol of the material to be prepared is exposed to high-intensity ultra sound ( $50\text{ to }500\text{ W/cm}^2$ ). The underlying mechanism of sonochemical processing route consists of the formation, growth, and collapse of the bubbles of the sol upon exposure to acoustic waves to form the product phase. The collapse of the bubbles leads to very high temperature ( $\sim 5273\text{ K}$ ), high pressure ( $\sim 1.01325 \times 10^8\text{ Pa}$ ), high heating and cooling rate ( $10^{10}\text{ K/s}$ ), and short-lived transient species [160]. The extreme conditions during acoustic cavitation enable the reactants to cross the activation energy barrier in a very short amount of time to form the product phase. The rapid heating and cooling rate during acoustic cavitation leads to the formation of amorphous nanoparticles [161]. Apart from the liquid sol, a dispersion of the ceramic (liquid-solid systems) can be subjected to ultrasonic irradiation. The sonicated dispersions are characterized by enhanced mass transport due to turbulent mixing and acoustic streaming, surface damage at liquid-solid interfaces by shock waves and microjets, generation of high-velocity interparticle collisions in slurries, and increase in surface area of the particles [162–165]. Interparticle collision during the ultrasonic agitation leads to changes in particle morphology, composition, and reactivity.

The magnetite  $\text{Fe}_3\text{O}_4$  is useful as a magnetic ferrofluid in applications such as data storage. In order to prepare fine-grained magnetite particles, an efficient alternative to high-energy milling is the use of sonochemical preparation from volatile organometallic precursors. Suslick and coworkers were able to prepare a stable ferromagnetic colloid from an organometallic precursor [163]. The  $\text{Fe}_3\text{O}_4$  particles had a narrow particle size distribution and exhibited superparamagnetic properties. By varying the concentration of the sol used, the particle size of the oxide powder can be tuned. Nanosized powders are obtained when dilute sol is subjected to sonochemical processing. Moreover, the type of the surfactant used in the sol preparation also influences the morphology of the oxide nanoparticles [166, 167]. Sonochemical processing has been found to be very useful for the preparation of mesoporous materials [168]. The ultrasonic method is superior to other techniques for the preparation of porous solids having fine, dense spherical pores. Recently,

nested fullerene-like oxides, which can be used as a host material for organic molecules, have been synthesized using this technique [169]. The ability of porous solids to act as host material for organic molecules may be exploited for the removal of toxic organic substances from the environment so that major ecological disasters can be prevented. However, tuning of pore sizes in porous solids and their large-scale commercial production at affordable cost are desirable in order to achieve this objective.

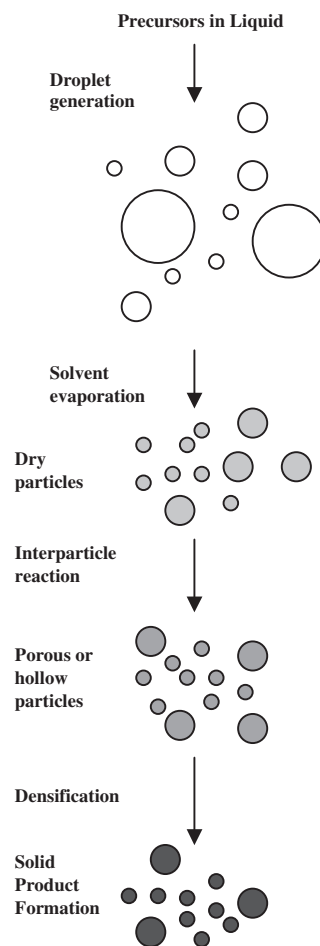
## 2.8. Spray Pyrolysis

As an alternate method to sophisticated processing routes with the potential for commercial scale-up, spray pyrolysis has been widely used for the synthesis of ultrafine particles [170–174] and thin films [175]. The method can be briefly described as follows: The precursor solution (sol), which contains the metal ions dissolved in the desired stoichiometry, is sprayed through a nozzle and suspended in gaseous atmosphere (aerosol generator). The suspended droplets are thermally processed to the product phase by allowing the sol droplets to drift through the heated zone of a furnace. Spray pyrolysis has many variations based on the differences in thermal processing step. Some of them are aerosol decomposition, evaporative decomposition, spray roasting, and spray calcination [98]. The schematic diagram in Figure 11 illustrates the sequence of transformation of the sol droplets to final particulate material in spray pyrolysis.

Compared to the gas phase condensation techniques, spray pyrolysis is more advantageous because of its simplicity and the ability to produce complex multicomponent oxides in particulate as well as thin film forms from comparatively cheaper nonvolatile starting materials. In comparison with the sol–gel method and related precipitation techniques, the powders produced by spray pyrolysis are less agglomerated with improved crystallinity. Submicrometer-sized composite particles with excellent compositional homogeneity can be prepared by this method. For instance,  $\text{Ag-YBa}_2\text{Cu}_3\text{O}_7$  composite powders synthesized by spray pyrolysis maintained identical Ag to ceramic ratio in each particle [176]. However, it is difficult to control the particle morphology of powders prepared through spray pyrolysis. Moreover, the production costs can be high when large volumes of gases have to be handled during the spray pyrolysis.

## 2.9. Mechanochemical Synthesis

The drive for low cost commercial production of nanophase materials has led to the development of a mechanical milling process, which involves continuous milling of the reactive powders over a period of time. The apparatus used for milling should have the following features: generating high energy through high impact velocity and frequency during the milling process to enhance the reaction rate and the productivity, and easy scale-up of the mill capacity. In order to improve the design of conventional mills (planetary, vibratory, or attrition mills), Basset et al. [177] incorporated a modified design for the milling apparatus. The goal of design was to rectify the drawbacks of conventional mills by enhancing the generated energy as well as the capacity for production in large quantities.



**Figure 11.** The sequence of formation of solid particles from sol droplets in spray pyrolysis. Reprinted with permission from [98], T. T. Kodas and M. J. H. Smith, “Aerosol processing of materials,” Wiley-VCH, New York, 1999. © 1999, Wiley.

The reactive components, after prolonged milling, undergo reduction in size and increase in surface area, which leads to enhanced diffusion of the reactants. Hence, the product phase crystallizes at much lower temperatures compared to conventional solid state synthesis. Moreover, the incorporation of high energy and generation of defects in the crystalline lattice during the intense grinding contribute to higher diffusion rates. The process has been employed for the synthesis of a wide variety of oxide nanoparticles [178–182].

The nanocrystalline ferroelectric  $\text{Bi}_2\text{VO}_{5.5}$  (BiV) has been synthesized by a mechanochemical processing of stoichiometric amounts of  $\text{Bi}_2\text{O}_3$  and  $\text{V}_2\text{O}_5$  powders [178]. The evolution of the product phase has been systematically characterized by X-ray diffraction (XRD) and differential thermal analysis (DTA) of the samples milled for different durations. Based on the detailed characterizations, it was concluded that the nanocrystalline (BiV) phase nucleated through a ferroelastic intermediate phase  $\text{BiVO}_4$  and the reaction reached completion in 54 h to yield 30 nm BiV crystallites.

Though the process can be used for the preparation of large amounts of nanophase materials at low cost, there are certain disadvantages associated with the process. As the process involves physically dividing the solid reactant particles through high energy collisions, the resultant product obtained through this method may have inherent strain present in the lattice. Also, there are chances of contamination after prolonged milling. Although the time required for the completion of the reaction depends on the kinetics of specific systems, relatively longer duration is required for the completion of the reaction in mechanochemical processing.

## 2.10. Microemulsion Synthesis

During the past few years, there has been tremendous motivation among scientists to find novel preparative routes that can precisely control the particle size of the final solid product. Among the various techniques, the microemulsion-mediated synthesis has been particularly of interest to size-selective preparation and self-assembly of nanoparticles because of the excellent control on the particle size that can be achieved through appropriate surface modification of the micelle [183]. Microemulsion can be defined as an isotropic, thermodynamically stable system constituting the micrometer-sized droplets (micelle) dispersed in an immiscible solvent and an amphiphilic surfactant species on the surface of the micelle [184, 185]. The crucial aspect of the microemulsion route is the control of the nanoparticle size through suitable selection and addition of a surfactant prior to the hydrolysis of the metal alkoxide sol (reverse micelle or water-in-oil emulsion). The addition of the surfactant molecules creates aqueous domains (nanoreactors) in the range of 0.5–10 nm. By properly tuning the water/surfactant ratio, which is critical in deciding the final particle size, the diameter of the aqueous droplets can be tuned. The difference between the conventional sol-gel method and emulsion-mediated synthesis is that the rate of hydrolysis is controlled by the diffusion of the precursors from the oil phase to the aqueous droplets. The method has been recognized as the most appropriate for the synthesis of ultra-fine magnetic nanoparticles for potential applications in magnetic recording media, biomedical, and related fields [186–188]. The ability to control the particle size when prepared through an emulsion route has also prompted the synthesis of nanosized ferroelectric materials with a motivation to implement them in various electronic devices [189–191]. The microemulsion-derived size-selective oxide nanoparticles are also potential materials for catalytic applications as demonstrated in recent years [192–194].

When the metal ions have different reactivities, the conventional preparative routes do not yield a homogeneous product. In such cases, the microemulsion route may be preferred for the oxide nanoparticle synthesis. For instance, as a potential catalyst for the hydrocarbon decomposition, Zarur et al. [192] have synthesized nanoparticles of barium hexa-aluminate ( $\text{BaO} \cdot 6\text{Al}_2\text{O}_3$ , BHA) with good homogeneity, which cannot be achieved through conventional synthesis, because of the different reactivities of barium and aluminium, using a reverse microemulsion route. The prepared nanoparticles showed excellent catalytic activity for

methane combustion, high surface area, high thermal stability and ultrahigh dispersion of cerium oxide on their surfaces. The morphology, structure, and surface area of the synthesized BHA nanoparticles have been carefully tailored by the water to oil ratio, aging time, powder recovery, and drying time. For water content in the range 5–20 wt%, discrete spherical BHA particles of 3–10 nm were reported. These nanoparticles were subsequently subjected to thermal processing at relatively low temperatures (1050 °C) to obtain fully crystallized BHA phase with high surface area. Even though the microemulsion method is effective in the size-selective preparation of nanoparticles, the as-prepared powder may have organic impurities. Table 1 summarizes the advantages and disadvantages of different synthesis routes for oxide nanoparticles discussed in this section.

## 3. SPECTROSCOPIC CHARACTERIZATION

The exciting developments in nanoparticle research must be effectively supported by a variety of structural characterization tools, as the characterization of nanoparticles provides invaluable information on the various microstructural, crystallographic, molecular, and atomic features, which can shed light on unique properties exhibited by these fascinating materials. In the previous sections, we have illustrated the use of electron microscopy in obtaining the microstructural features of some of the oxides (Figs. 2, 8, 9, and 10). In this section, we briefly summarize the use of various spectroscopic characterization tools in nanoparticle research in light of some recent studies on a variety of oxide nanoparticles.

### 3.1. X-Ray Diffraction

As a primary characterization tool for obtaining the critical features such as crystal structure, crystallite size, and strain, X-ray diffraction (XRD) patterns have been widely used in nanoparticle research [104, 194–197]. Except for single crystalline nanoparticles, the randomly oriented crystals in nanoparticles cause broadening of the diffraction peaks. This has been attributed to the absence of total constructive and destructive interferences of X-rays in a finite-sized lattice [195]. The effect becomes more pronounced when the crystallite sizes are on the order of a few nanometers. Moreover, inhomogeneous lattice strains and structural faults also lead to broadening of peaks in diffraction patterns. Detailed analytical procedures for XRD patterns for polycrystalline and amorphous materials have been discussed by Klug and Alexander [198]. The simplest and most widely used method for estimating the crystallite size is from the full width at half maximum (FWHM) of a diffraction peak using the Scherrer equation, which can be expressed as,

$$D = \frac{K\lambda}{\beta \cos \theta} \quad (3)$$

where  $D$  is the crystallite size,  $\lambda$  is the wavelength of the X-ray used,  $\beta$  is the FWHM,  $\theta$  is the diffraction angle, and  $K$  is a constant close to unity. The major assumptions are that the sample is free of residual strain and has a narrow grain

**Table 1.** Major advantages and disadvantages of different synthesis routes for oxide nanoparticles.

Process	Advantages	Disadvantages
Gas phase deposition methods	Particle formation can be controlled by tuning the gas pressure in the reactor, narrow particle size distribution, high purity	Sophisticated instrumentation and costly reactants, unsuitable for large scale production, difficulty in producing multicomponent oxides, agglomerate formation at high particle concentration
Microwave plasma processing	Short processing time, preparation of metastable materials, use of solid or liquid reactants, small particle size of the product with narrow size distribution	High reaction rate with inside-out heating profiles, difficult to measure exact process temperature, microwave susceptible starting materials needed
Hydrothermal synthesis	Less agglomerated fine powders with narrow size distribution, good control on chemical composition, microstructure, crystallinity, no separate calcination step, synthesis of metastable materials	Hydrothermal slurries are potentially corrosive, careful release of the pressure from the hydrothermal bomb, prior knowledge on solubility of starting materials required
Electric dispersion reaction	Liquid-liquid reaction system requires less energy compared to liquid-gas systems, soft agglomerates, use of surfactant (water-in-oil) to control green body density	Complex reaction setup, difficult for commercial scale up
Combustion synthesis	Exothermic reaction gives product almost instantaneously, preparation of multicomponent oxide, high surface area materials, low cost for commercial scale-up	Contamination due to carbonaceous residue, particle agglomeration, no control on particle morphology, reliable data on fuel characteristics needed, violent reaction—requires special protection
Sol-gel (colloidal) processing	Fine sinter-active powders, crystallization at low temperature, simple apparatus, preparation of wide variety of oxides, metastable materials in desired shapes, particle size controllable by changing reactant concentration	Costly starting materials such as metal alkoxides, particle agglomeration, contamination due to undecomposed group in the low-temperature crystallized samples
Sonochemical processing	Processibility of a wide variety of materials including metastable materials, fine powders with high surface area and green density, amorphous nanoparticles, and nanoporous materials for catalytic applications	The enormous energy concentration during the collapse of the bubble may leave residual strain in the powders, interparticle collision may lead to change in morphology or composition
Spray pyrolysis	Preparation of multicomponent oxides, volatile precursors are not required, more crystalline and less agglomeration compared to liquid-phase precipitation, ability to produce composite particles	Relatively low production rate and high processing costs when large volumes of reactants have to be handled
Mechanochemical processing	Low cost starting materials, ability to produce large amounts of nanoparticles at low production cost, crystallization at low temperature	Long processing time, chance of contamination due to prolonged milling, no control on particle morphology, formation of agglomerates, residual strain in the crystallized phase
Micro-emulsion synthesis	Size-selective oxide nanoparticles with very narrow size distribution, less agglomeration compared to sol-gel	Undecomposed organic contaminants in low-temperature crystallized samples, complex route compared to sol-gel

size distribution. However, the analysis becomes more complex when contribution due to strain is taken into consideration. The Warren–Averbach method involves separating the crystallite size and strain effects on line broadening using Fourier analysis [199]. Another analytically simpler technique for the estimation of strain is the Williamson–Hall procedure, which involves plotting the breadth of reciprocal lattice points ( $1/D = \beta \cos \theta / K\lambda$ ) as a function of their distance from the origin ( $d_{hkl} = 2 \sin \theta / \lambda$ ) [200]. The method, which is more popular among metallurgists for the diffraction profile analysis of nanocrystalline metals [201], has been used recently to characterize the strain in a variety of oxide samples [34, 202, 203]. A horizontal Williamson–Hall plot would signal the absence of strain in the prepared ceramic powders as reported in the case of nanocrystalline  $\text{MgAl}_2\text{O}_4$

[34]. By recording the XRD patterns as a function of pressure and temperature, several important characteristics such as grain boundary and thermal and elastic properties of the nanocrystals can be estimated [195]. Highly intense XRD peaks at low angle indicate the formation of an ordered superstructure of nanoparticles [204].

### 3.2. Energy Dispersive X-Ray (EDX) Spectroscopy

The main use of energy dispersive spectrometers is to accurately determine the composition of the sample under investigation. While electron microscopic images provide real-time pictures of the size and morphology of the nanoparticles, the supplementary EDX analysis provides exact

composition of the sample. Upon exposing the samples to high energy electron beams, the various atoms present in the sample emit characteristic X-rays, which can be observed as several distinct peaks on an energy scale. The intensities of the peaks can be compared with the peaks of a standard sample to obtain the relative amounts of each atomic species; thereby accurate composition of the sample can be determined. The EDX composition analysis has been proven to be very critical, especially when the composition plays a crucial role in the resultant properties as in the case of high- $T_c$  cuprates [205–207].

The use of EDX has been demonstrated in oxide nanoparticle research, particularly in the determination of the composition of substituted or nanoparticle composite materials as reported for Zn-substituted  $\text{Fe}_3\text{O}_4$  magnetic colloids [208],  $\text{Eu}_2\text{O}_3$ -coated spherical  $\text{ZrO}_2$  or stabilized  $\text{ZrO}_2$  [209], and polymer  $\gamma\text{-Fe}_2\text{O}_3$  nanocomposites [210]. The EDX analysis provides information on the concentration of Eu on the surface of the spherical  $\text{ZrO}_2$  nanoparticles, which supplements the TEM evidence for the presence of  $\text{Eu}_2\text{O}_3$  coating on spherical  $\text{ZrO}_2$  nanoparticles [209]. Similarly, the EDX analysis of polystyrene  $\gamma\text{-Fe}_2\text{O}_3$  nanoparticle composite has signature peaks of Fe, confirming the presence and concentration of iron in the nanocomposite samples. The EDX analysis has been used for obtaining the composition of  $\text{TiO}_2$  nanotubes as reported in a recent study by Du et al. [211]. The results of their EDX analysis of several  $\text{TiO}_2$  nanotubes showed that the ratios of intensities of Ti peaks and O peaks are not identical in all nanotubes, which indicates that the composition of the nanotubes can be represented as  $\text{TiO}_x$ .

### 3.3. Extended X-Ray Absorption Fine Structure Spectroscopy

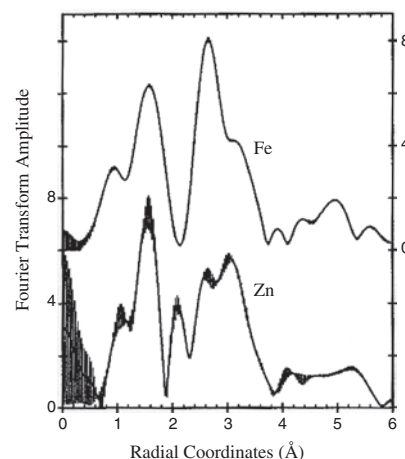
Probing the local order in disordered systems such as glass and nanostructures has been of great interest to scientists. Extended X-ray absorption fine structure spectroscopy (EXAFS), which involves obtaining the characteristic X-ray absorption spectrum for individual elements present in the sample, provides a partial radial distribution function (RDF) for each element as compared to a single averaged RDF from conventional diffraction techniques [212]. The technique has been extensively used in obtaining the local order in glass systems and amorphous alloys [213–216].

Advancements in the preparative strategies of oxide nanoparticles have led to further reduction in derived particle sizes, which implies that the increasingly disordered surfaces, interfaces, or atomic sites contribute significantly to the resultant properties of nanoparticles. This has prompted scientists to look for more effective techniques such as EXAFS to probe the local order in nanoparticles. For instance, the technique has been proven to be very effective in probing the local structure in nanoferrites [217, 218], luminescent phosphors [219, 220], and surface-modified nanostructured catalysts [221]. Spinel ferrites exhibit structural disorder at the cationic sites. As an accurate method for the determination of the cationic disorder parameter  $x$  in spinel, the EXAFS technique can be used [222]. Recently, Oliver et al. [218] carried out EXAFS study on nanocrystalline  $\text{ZnFe}_2\text{O}_4$  in order to obtain the cationic disorder ( $x$ ) in their spinel sample  $(\text{Zn}_{1-x}^{2+}\text{Fe}_x^{3+})_t[\text{Zn}_x^{2+}\text{Fe}_{2-x}^{3+}]_o\text{O}_4$  where “t” and

“o” refer to tetrahedral and octahedral sites, respectively. The typical Fourier-transformed EXAFS spectrum of nanocrystalline  $\text{ZnFe}_2\text{O}_4$  is presented in Figure 12 [218]. The intense peaks at  $r$ -space values 2.6 Å and 3.1 Å have been attributed to the octahedral and the tetrahedral occupancies of cations, respectively. By comparing the intensities of the peaks for Zn and Fe cations in the respective spectra, it is possible to qualitatively infer the extent of cation mixing at the two sites. The disorder parameter can be quantitatively determined by least squares fitting of the Fe and Zn EXAFS spectra to the idealized scattering results for a spinel lattice [223]. From the EXAFS-derived disorder parameter, Oliver et al. [218] obtained the quantitative distribution of the Zn and Fe cations in tetrahedral and octahedral sites for their nanocrystalline ferrite spinel sample, which can be expressed as  $(\text{Zn}_{0.55}\text{Fe}_{0.18})_t[\text{Zn}_{0.45}\text{Fe}_{1.82}]_o\text{O}_4$ . The degree of disorder at the grain boundaries of nanocrystalline samples can be derived from the EXAFS study of doped nanocrystalline sample with an impurity that is not soluble in the lattice and segregate at the grain boundaries. The local order around the impurity element would provide an estimate on the grain boundary order in a nanocrystalline sample under investigation [224].

### 3.4. X-Ray Photoelectron Spectroscopy

Reactive solid surfaces have generated lot of interest among researchers because of their potential in catalyzing chemical reactions and influencing various transport properties. In particular, determining the structure and composition of the surfaces is of utmost importance for understanding the basic mechanisms in catalytic reactions, as well as for fabricating novel nanostructured catalysts [225, 226]. One of the important characterization tools in surface chemical analysis is X-ray photoelectron spectroscopy (XPS), which has the ability to probe the surface to a few atomic layers deep (2–20 atomic layers, 0.5–5 nm) and obtain a semiquantitative elemental analysis of the surface without standards [227]. The valence states of the elements that constitute the surfaces can also be deduced from the XPS characterization.



**Figure 12.** Fourier transform EXAFS spectra of Fe (top) and Zn (bottom) atoms for the nanocrystalline spinel  $\text{ZnFe}_2\text{O}_4$  plotted against radial coordinates with a  $k^3$  weighting [218].

The technique involves measurement of the binding energy of the ejected electrons from the atomic core shells of the material when bombarded with monochromatic soft X-rays. XPS has been extensively used for thin film characterization in order to monitor the surface layer growth as well as to obtain the valence states of various elements at the surface [116, 228–230].

As a part of innovative design of nanoparticles, oxide nanoparticles with surfaces different in chemical composition from the grain interior have attracted attention. For example,  $\text{CrO}_2$  nanoparticles with  $\text{Cr}_2\text{O}_3$  surface layers have been characterized for exploring magneto-transport properties through intergranular tunnel junctions [196]. XPS study of the  $\text{CrO}_2$  nanoparticles indicates that the Cr is in a trivalent state on the 1–3 nm thick surface layer, which confirms the presence of the  $\text{Cr}_2\text{O}_3$  on the surface of  $\text{CrO}_2$ . Similar studies have been reported for the XPS characterization of oxide nanoparticle surfaces such as CuO surface layers on  $\text{Cu}_2\text{O}$  nanoparticles [231] and  $\text{Co}_3\text{O}_4$  layers on CoO [232]. XPS spectroscopy is an inevitable technique for the study of metal nanoclusters with oxide coated surface layers. For instance, systems like Sn/ $\text{SnO}_2$  are important candidates for the study of confinement effects on core level XPS spectra of clusters and quantum dots, the development of metal supported catalysts, and the understanding of various electronic transport properties [233]. Another related effect of photoelectron emission is the Auger electron emission or secondary electron emission, which is essentially a relaxation process of the ionized atom [234]. The technique is noted for high lateral resolution and relatively high sensitivity along with the ability to probe the surface to  $\sim 10$  nm depth [227]. Oxide layer formation on the surfaces can be characterized using Auger spectroscopy [116, 235].

### 3.5. Secondary Ion Mass Spectroscopy

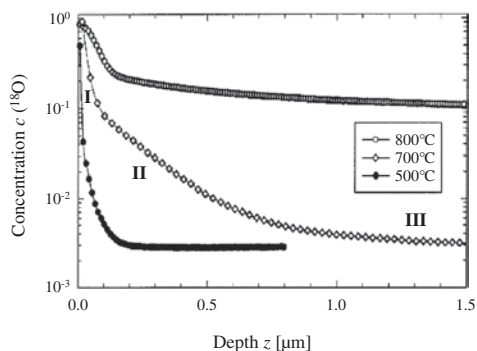
Another important surface analytical technique is secondary ion mass spectroscopy (SIMS), which has been extensively used for the characterization of thin film heterostructures [236–240]. The sample under investigation is exposed to a primary ion beam, which then sputters atoms and molecules from the surface to the interior of the sample. The masses of the sputtered species are then analyzed using a time-of-flight analyzer and recorded as mass spectrum. The SIMS depth profile, which provides elemental concentrations in the sample as a function of depth, is the most commonly sought after information, especially in thin film heterostructure characterization.

SIMS profiling has great potential in characterizing the concentration profiles of self-organized or consolidated nanostructures. In particular, being a highly sensitive technique with sensitivity levels on the order of parts-per-billion (ppb), SIMS is the most appropriate technique to study diffusion reactions. As an example, it is worth noting the studies on oxygen diffusion through nanocrystalline zirconia [241]. The study involved monitoring the diffusion of the isotopic oxygen ( $^{18}\text{O}$ ) tracer in densified monoclinic  $\text{ZrO}_2$  samples with grain sizes in the range of 80–300 nm. The densified  $\text{ZrO}_2$  nanocrystals have large number of interfaces, which provide easy pathways for oxygen diffusion compared to microcrystalline ceramic samples. SIMS depth

profiles corresponding to the  $^{18}\text{O}$  diffusion through nanocrystalline  $\text{ZrO}_2$  are presented in Figure 13 for densified samples diffusion-annealed at three different temperatures for 1 h: 500 °C, 700 °C, and 800 °C [241]. The variation of the tracer concentration profile with annealing temperature is obvious from the figure. For samples annealed at 500 °C, the  $^{18}\text{O}$  concentration decreases dramatically to  $\sim 5\%$  of its initial value at a depth of about 100 nm. This can be attributed to the small bulk diffusion distances at relatively low temperature. For samples annealed at 700 °C, the tracer concentration registers a slower rate of decrease, due to the enhanced diffusion through well-formed interfaces of the densified nanocrystalline  $\text{ZrO}_2$  samples. The  $^{18}\text{O}$ -depth profile for sample annealed at 800 °C shows that the isotopic tracer penetrates to greater depths on the order of several micrometers. As a sensitive technique for the detection of impurities and related diffusion, SIMS has been used for the characterization of photonic materials such as porous silicon (Si) [242] or doped ZnO [243], in which the presence of trace impurities affects the resultant optical characteristics. A recent study probes the potential application of SIMS in the characterization of inorganic materials by recording the mass spectra of oxide species in the binary Cu-O and the ternary Fe-Cr-O systems [244].

### 3.6. Optical Absorption-Emission Spectroscopy

Spectacular changes in optical characteristics of nanocrystalline oxides when compared to those of bulk counterparts have triggered tremendous interest among scientists in order to understand the basic mechanisms responsible for the fascinating optical absorption-emission, which also would help to examine their potential use in a variety of optical applications [245–251]. Optical absorption and emission arise as a result of electronic transitions in solids upon exposure to excitation energies in the range  $\sim 10^2$  to  $10^3$   $\text{kJmol}^{-1}$  that cover the near infrared through visible to ultraviolet. There are various types of optical transitions in solids. One type of transition is the promotion of an electron from a localized orbital to a higher energy localized orbital of the same atom ( $d$ - $d$ ,  $f$ - $f$  transitions) or from a localized orbital



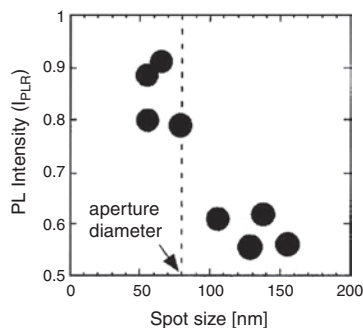
**Figure 13.** SIMS profile for  $^{18}\text{O}$  diffusion through sintered nanocrystalline  $\text{ZrO}_2$  for diffusion anneals for durations of 1 h at three different temperatures as quoted in the diagram [241].

in one atom to a higher energy localized orbital on an adjacent atom (charge-transfer spectra). Another type of transition can be the promotion of electrons from a localized orbital in one atom to the delocalized energy band (conduction band) of the solid as seen in the case of photoconductive materials. The transition that helps to quantify the band gap in solids is the transfer of electrons from the valence band to the conduction band. The transition energies associated with these processes differ, thereby requiring different excitation frequencies for obtaining their absorption and emission spectra [212].

Understanding the quantum confinement effect on optical absorption and emission characteristics has been the major objective of optical characterization of oxide nanocrystals. For example, the photoluminescence spectra of  $\text{In}_2\text{O}_3$  nanocrystals dispersed in mesoporous silica indicate a blue shift for smaller crystallites, which also implies an expansion in the energy gap between the valence and conduction band upon size reduction [245]. Particularly interesting is the investigation of size effects on the photoluminescence imaging of ZnO nanocrystals [249]. The intensities of the high energy components of the PL spectrum increased with decreasing spot sizes or crystallite sizes (Fig. 14), implying a size quantization effect in ZnO nanocrystals. Recently, optical characterization of nanocrystalline rare earth doped oxides, which are termed as phosphor materials, has become a major area of research because of their potential applications in the development of display devices [252–255]. From the optical absorption-emission spectra of nanophosphor materials, the various optical transition mechanisms such as charge-transfer or host-matrix absorption can be identified [255].

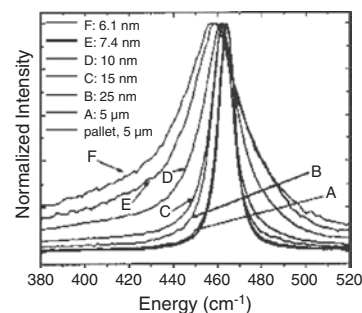
### 3.7. Raman Spectroscopy

The Raman spectroscopic technique has been extensively used for structure, composition, and phase characterization of materials. For example, the information derived from the Raman spectra of superconducting cuprates [256] and colossal magnetoresistive manganates [257] helps to explain the fascinating electronic transport properties in these materials. The Raman spectra provide various characteristic vibrational frequencies, such as those associated with lattice defects or surfaces, and derive crucial data on the electronic band structures in solids.



**Figure 14.** Relative PL intensities ( $I_{\text{PLR}} (=I_{\text{PL}} \text{ at } 370 \pm 2.5 \text{ nm}) / (I_{\text{PL}} \text{ at } 380 \pm 2.5 \text{ nm})$ ) of PL-imaging of ZnO nanocrystallites as a function of spot sizes (representing the corresponding crystallite sizes) [249].

In nanoparticle research, monitoring the characteristic vibrational frequencies of atoms would be of great interest in understanding the bonding and coordination environments of the increased fraction of atoms residing at the surface. Raman spectroscopy, which measures the inelastic light scattering due to the excitation of various vibrational modes in materials [227], can be used for obtaining the characteristic frequencies associated with surface states in nanoparticles. In one of the earlier investigations into vibrational modes in nanophase oxides, the Raman spectra of oxygen-deficient  $\text{TiO}_2$  nanoparticles showed characteristic broadening and shifting of peaks due to the oxygen vacancies present in the rutile or anatase  $\text{TiO}_2$  lattice [45]. Raman analysis of  $\text{SnO}_2$  nanoparticles of sizes in the range of 3–90 nm indicates the appearance of two additional peaks in the Raman spectrum for the particle sizes below 10 nm. These additional peaks are ascribed to the surface phonon modes of  $\text{SnO}_2$  [258]. The evidence for optical phonon confinement appear in Raman spectra as asymmetric broadening of Raman bands as obtained for ZnO nanoparticles of sizes 4.5 nm and 8.5 nm [259]. The experimental results are fitted into a theoretical optical phonon confinement model, which takes into account various asymmetric phonon modes in nanosized ZnO wurtzite structure. Asymmetric broadening of the Raman peak, which is in comparison with symmetric Raman peak at a wavenumber  $464 \text{ cm}^{-1}$  for an ideal  $\text{CeO}_2$  crystal, has been observed in a systematic Raman characterization of single crystal nanocrystalline  $\text{CeO}_2$  of sizes in the range of 6 to 25 nm. The peak also shifts to lower energy values for smaller crystals. The peaks corresponding to micrometer-sized single crystal  $\text{CeO}_2$  appear to be symmetric, sharp, and intense (Fig. 15) [260]. The characteristic changes in Raman peak for smaller crystallites can be attributed to the expansion of the nanocrystalline  $\text{CeO}_2$  lattice due to increased point defects. A similar systematic Raman characterization for nanocrystalline  $\text{CeO}_2$  thin films has shown a similar trend with varying grain sizes of  $\text{CeO}_2$  from nanometers (4–150 nm) to micrometer-sized single crystals [261]. The quantitative analysis on the effects of phonon confinement, strain, size dispersion, and defects on the Raman spectral lines have been discussed recently by Spanier et al. [262] for oxygen-deficient ceria ( $\text{CeO}_{2-x}$ ).



**Figure 15.** Raman spectroscopic characterization of  $464 \text{ cm}^{-1}$  Raman peaks for nano- and micrometer-sized  $\text{CeO}_2$  particles [260]. Peaks shift to lower energy with asymmetric broadening as particle size decreases.



### 3.8. Infrared (IR) Spectroscopy

The characteristic vibrations of atoms in solids have frequencies in the range  $10^{12}$  to  $10^{13}$  Hz, which implies that an infrared (IR) excitation source can resonate these vibrations, thereby exciting them to higher energy levels [212]. A plot of  $I/I_0$  versus frequency, which is represented as wavenumber ( $\text{cm}^{-1}$ ), is the typical IR spectrum. The IR absorption bands characterize qualitatively and quantitatively the chemical species, stress, and structural inhomogeneity in solids and thin film materials [227]. The use of IR spectroscopy for the characterization of phase transformation in gel-derived stabilized zirconia powders has been demonstrated by Tseng et al. [148]. In particular, the IR technique can be the most appropriate method to characterize various functional groups present on surface-modified oxide nanoparticles as shown in the case of amorphous  $\text{Fe}_2\text{O}_3$  nanoparticles [263]. When it is required to obtain the surface characteristics of a few monolayers or even a single atomic layer of the nanosized particles, the Fourier transform infrared (FTIR) technique has been found to be highly suitable [264]. For example, the FTIR spectra for the molybdenum oxide ( $\text{Mo}_2\text{O}_5 \cdot x\text{H}_2\text{O}$ )-silica ( $\text{SiO}_2$ ) nanocomposite [265],  $\text{Eu}_2\text{O}_3$ -coated  $\text{ZrO}_2$  nanoparticles [209], or hydrothermally derived  $\text{CeO}_2$  nanoparticles [266] exhibit characteristic absorption bands of chemical species present at the surface. Another very important application of FTIR is to delineate the mechanism of adsorption and formation of various species on the catalytic metal oxide surfaces such as the carbonate decomposition on metal oxide to form metal carbonyl bonds [267].

### 3.9. Mössbauer Spectroscopy

Mössbauer spectroscopic analysis involves exciting various nuclear transitions that are induced in the Fe or Sn nuclei of the sample when bombarded by  $\gamma$ -rays, which are emitted by corresponding radioactive nuclei ( $^{57}\text{Fe}^*$  or  $^{119}\text{Sn}^*$ ) from a  $\gamma$ -ray source. The energy of the incident monochromatic  $\gamma$ -rays is varied by movement of the source either toward or away (Doppler shift) from the Mössbauer-active sample [212]. A typical Mössbauer spectrum is a plot of  $\gamma$ -ray absorption against Doppler velocity. When the  $\gamma$ -ray emitting nuclei and absorbing nuclei are identical, the absorption peak appears as a sharp dip at 0 Doppler velocity. However, the chemical environments such as valence state, outer electronic configuration, and coordination number of the nuclei in Mössbauer-active samples are not the same as those in the  $\gamma$ -ray source. These effects are reflected in the spectra as characteristic chemical shifts,  $\delta$ , of the absorption peaks of the spectrum. Moreover, the hyperfine splitting in the Mössbauer absorption spectra indicate the possible effects of quadrupole splitting or magnetic exchange interaction in the sample.

The Mössbauer spectrum has been extensively used for the characterization of Fe-containing oxides [268]. In particular, the technique provides crucial information about the local order and associated magnetic properties in nanocrystalline ferrites [269–275]. For instance, the Mössbauer spectroscopic characterization of  $\text{Mn}_{0.5}\text{Zn}_{0.5}\text{Fe}_2\text{O}_4$  (MnZn-ferrite) reveals the effect of temperature on the hyperfine

field effect in Mössbauer spectra. The calculated values of the isomer shifts at two temperatures 295 K and 78 K correspond to the trivalent Fe in the nanocrystalline MnZn-ferrite samples [272]. The Mössbauer spectra recorded at two different temperatures (300 K and 4.2 K) for the polymer- $\text{CoFe}_2\text{O}_4$  nanocomposite exhibit distinct features due to quadrupole splitting and magnetic hyperfine splitting. At 300 K, the quadrupole splitting dominates the magnetic splitting, which indicates the superparamagnetic nature of the sample, whereas at 4.2 K, only the magnetic splitting is present, implying the ferrimagnetic nature of the sample [273]. The presence of both types of splitting has been attributed to the typical particle size distribution of the ferrite ( $4.8 \pm 1.4$  nm) in the composite. It is also possible to estimate the ratio of distribution of Fe on A and B sites in spinel ferrites as obtained by Moumen and Pileni [274] for nanosized  $\text{CoFe}_2\text{O}_4$  and Morales et al. [275] for  $\gamma$ - $\text{Fe}_2\text{O}_3$  nanoparticles.

## 4. PROPERTIES

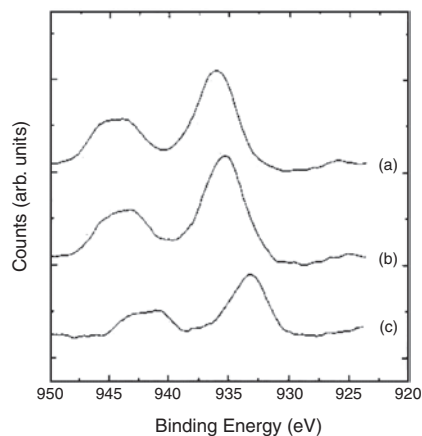
### 4.1. Electronic Structure

Electronic transition in solids is a major physical phenomenon that accounts for varied and interesting properties of solids such as electronic conduction and optical absorption. The overlapping energy levels in the valence and conduction bands of a bulk solid separate as the size of the solid is reduced. The major effects of size reduction include the discretization of the electron energy levels, concentration of the oscillator strength, formation of the highly polarizable excited states, and increased electron-electron correlation [276]. In particular, the size effects on the electronic energy levels in semiconductors are of interest because of their potential applications in the fabrication of a wide range of electronic and optoelectronic devices. For solids of dimensions on the order of a few nanometers, the increased separation between the valence and the conduction band results in bandgap expansion [277]. The consequences of bandgap expansion are reflected in the resultant electronic structure and the binding energy values of the core electrons [278–281]. The optical properties of the material also undergo remarkable changes upon reduction in size, as evidenced by the peaks shifting to higher energy levels in the photoluminescence spectra [282–285]. Other noteworthy effects of size quantization are the suppression of the dielectric constant and the blue shift in the photo absorption, as the particle dimension approaches the limit of an exciton diameter (electron-hole separation) [286–288].

Among the various models proposed, the quantum confinement theory satisfactorily explains the effects of size quantization [289–291]. According to this theory, which has been developed based on the concept of “particle in a box,” the electrons in the conduction band and the holes in the valence band are confined spatially by the potential barrier of the surface. As the particle size approaches the limit of the exciton diameter, the charge carriers gain more energy, and the width of the confined band gap increases or expands. The confinement of electrons and holes leads to the shifting of the lowest energy optical transition to higher energy values. While a large amount of literature is available on

the synthesis, characterization, and related quantum size effects in II-VI sulfide and selenide semiconductors [292], relatively fewer studies have focused on the size quantization in oxide nanoparticles. Semiconducting oxide nanoparticles such as CuO, NiO, CoO, and ZnO have been characterized to understand the effect of size quantization on the electronic energy levels [279, 293–295].

Being a narrow band covalent semiconductor of band gap between 1.21 and 1.5 eV [296, 297], cupric oxide (CuO) has strong electron correlation and hence complicated optical properties [279]. XPS has been used by Borgohain et al. [279] to study the electronic structure of electrochemically prepared CuO nanoparticles (4 nm, 6 nm and 25 nm). When the particle size decreases, the transitions of electrons in various energy levels are affected. This is reflected in the recorded XPS spectrum for different particle sizes of CuO. The  $2p$  core level XPS spectra obtained by Borgohain et al. [279] for CuO nanoparticles are shown in Figure 16. The broad peaks indicate the presence of a large number of atoms residing at the surface of the nanoparticle. The broadening of the peaks can also be attributed to the adsorbed oxygen and the surface passivated groups on the defective nanoparticle surface. Similar studies on CoO and NiO nanoparticles have proved that oxygen and the water vapor adsorption on the defective surface indeed contribute to the peak broadening [232, 293]. As shown in Figure 16, the Cu  $2p_{3/2}$  peaks shift toward higher energy as the particle size decreases. For all the three different sizes of CuO nanoparticles, the recorded XPS spectra have satellite peaks, which confirmed the absence of Cu<sub>2</sub>O [279]. The ratio of the satellite peak (Cu  $2p_{1/2}$ ) intensity to the major peak (Cu  $2p_{3/2}$ ) intensity ( $I_s/I_m$ ) increases systematically with decreasing particle size. The energy separation between the two maxima registers a slight decrease for smaller CuO particles. On comparing these observations with the XPS study on divalent copper halides, CuX<sub>2</sub> (X=Br, Cl, or F) [298], where increase in ionicity of the ligand from Br to Cl to F led to similar results, it was concluded that the Cu-O bonds have higher ionicity in smaller CuO particles. The contributing factors that cause an increase in the ionicity of Cu-O bonds were presumed to be the defective coordination of the atoms



**Figure 16.** Cu  $2p_{3/2}$  core level XPS spectra for CuO nanoparticles: (a) 4.0 nm, (b) 6.0 nm, (c) 25 nm [279].

near the surface and the formation of discrete energy levels in the CuO nanoparticles [279].

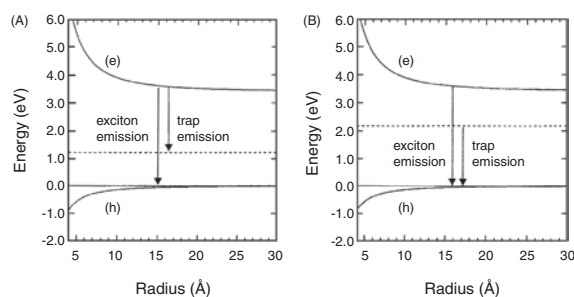
In the present era of advanced technology, low-voltage, high-efficiency phosphors are potential materials for the development of vacuum fluorescent displays (VFD) and field-emission displays (FED) [299]. As an efficient low-voltage blue-green emitting phosphor, the semiconductor ZnO has been identified as an important material for the fabrication of display devices [295, 300]. Recently, van Dijken et al. [300] have studied the particle size effects on the energy band structure and the related emission process in ZnO nanoparticles. The authors suggested two possible mechanisms for visible emission as either the recombination of a delocalized electron with deeply trapped hole or delocalized hole with deeply trapped electron, and experimentally verified the transition. The two possible mechanisms for the visible emission were explained using a schematic energy level diagram as shown in Figure 17. The dashed lines in the Figure 17A and 17B depict the energy levels associated with the deeply trapped hole and electron, respectively. The size dependence of the band gap  $E^*$  can be represented by the following equation:

$$E^* = E_g + \frac{h^2}{8\mu R^2} - \frac{1.8e^2}{4\pi\epsilon_0\epsilon_\infty R} \quad (4)$$

where  $E_g$  is the band gap of the macrocrystalline material,  $h$  is the Planck's constant,  $\mu$  ( $1/\mu = 1/m_e^* + 1/m_h^*$ ) is the effective mass of the exciton,  $\epsilon_\infty$  is the high frequency dielectric constant, and  $R$  is the radius of the particle [301]. The variations of the conduction band ( $1/m_e^*R^2$ ) and valence band ( $1/m_h^*R^2$ ) as a function of particle size ( $R$ ) are schematically represented in Figure 17 as curves (e) and (h). The  $R^{-2}$  variation corresponds to the confinement potential, whereas  $R^{-1}$  variation is the Coulomb potential in Equation (4). Effective mass approximation has been used by van Dijken et al. [300] for their ZnO nanocrystalline samples to sketch the energy level diagram, as the samples were made up of 50 to 5000 molecular units of ZnO (0.7 nm–3.5 nm). By taking into consideration the effective mass approximation, the absolute values for the shift of the band edges can be written as

$$(e) = E_g + \frac{h^2}{8m_e^*R^2} - \frac{0.9e^2}{4\pi\epsilon_0\epsilon_\infty R} \quad (5)$$

$$(h) = \frac{h^2}{8m_h^*R^2} - \frac{0.9e^2}{4\pi\epsilon_0\epsilon_\infty R} \quad (6)$$



**Figure 17.** Schematic energy level diagram as a function of particle size for ZnO nanoparticles illustrating the two possible mechanisms for trap emission [300].

where all symbols have the same meaning as in Equation (4). The variation of the conduction band edge as a function of the particle size is determined by the effective mass of the electron ( $m_e^*$ ). The value is  $0.28m_e$  for ZnO. Similarly, the valence band edge variation is decided by the effective mass of the hole ( $m_h^*$ ,  $0.50 m_e$  for ZnO) [302]. The difference in these values is shown in the respective band edge variations for the ZnO sample. However, the energy levels of the trapped charge carriers are size-independent as shown by the dashed lines in Figure 17A and 17B. The shift in the visible emission is governed by the variation of the conduction band against particle size as shown in Figure 17A for the emission process involving the recombination of delocalized electrons and deeply trapped holes. Similarly, for the delocalized holes and deeply trapped electrons, the variation of the valence band with particle size decides the energy associated with the recombination leading to the visible emission.

By plotting the maximum values of the exciton emission energy and the trap emission energy obtained for each particle size of ZnO, van Dijken et al. [300] found that the relationship is linear with a slope of  $\mu/m_e^* = 0.6$ , which represents the situation in Figure 17A and agrees with the calculated value of 0.64. The important conclusion from the plot was that the visible emission in ZnO nanocrystals involves the transition of an electron from the conduction band to the trap level approximately 2 eV below the conduction band edge. In other words, the recombination of electrons with deeply trapped holes (in the case of nanocrystalline ZnO, positively charged oxygen vacancies  $V_O^+$ ) was responsible for the visible emission in ZnO nanocrystals [303].

## 4.2. Optical Properties

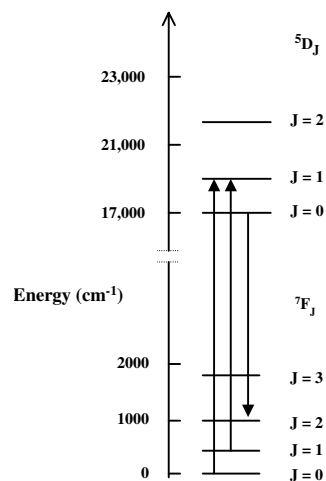
We have discussed the effect of particle size reduction on the electronic band structure and the resultant optical absorption and emission for nanosized ZnO [300] in the previous section. In this section, we briefly review the studies on optical properties of oxide nanoparticles including the rare-earth-doped luminescent phosphors. As a material of immense interest to the microelectronics industry, it is worth noting the optical characterization of thermally oxidized Si nanoparticles [304]. Light emission from thermally oxidized Si nanoparticles exhibited a shift toward higher energy for smaller particles due to the quantum size effect. Molecular dynamic simulations of optical properties of Si clusters constituting varying number of atoms ( $Si_{20}$ ,  $Si_{60}$ , and  $Si_{70}$ ) indicate that the optical response has a strong dependence on the configuration of the atoms in various clusters [305]. Such studies indeed contribute to the basic understanding of the complex correlation among atomic configuration, size quantization, and optical properties of nanoparticles. The more recent optical absorption studies on  $SnO_{2-x}$  [251],  $Cu_2O$  [306], and ZnO [307] nanoparticles, which have dimensions comparable to the exciton diameter, provide further experimental evidence for the size quantization effect as shown by the blue shifts in the corresponding absorption spectra.

The phenomenon of luminescence in ultrafine powders (phosphors) has been attracting great attention in recent years. The absorbed energy (UV photons in photoluminescence) is emitted as light in phosphor materials that

are in focus for the development of various optical devices [308, 309]. The two types of processes in luminescent phosphors are fluorescence and phosphorescence, which are distinguished by the time delay between the absorption of the energy and its emission (decay time  $\leq 10^{-8}$  s for fluorescence, longer decay time for phosphorescence) [212]. A typical doped photoluminescent material has a host lattice having small amounts of activator ions as guest species. It is the optical absorption-emission characteristics of these activator ions and their interaction with the host lattice that decide the resultant luminescent properties. Of particular interest is the study of nanocrystalline rare-earth-doped phosphor materials, which include a lanthanide ion doped in an insulating nanocrystalline ceramic oxide [252, 253, 255, 310, 311]. The interest in this particular class of materials is to understand the changes in the energy levels of the guest species when confined in a nanometer-sized host, as well as to explore their potential use in a wide variety of applications [312, 313]. The spatial confinement would also result in interesting optical properties that are different from the corresponding bulk counterparts.

A trivalent lanthanide ion has the characteristic electronic configuration in which the overlying  $5s$  and  $5p$  electronic shells effectively shield the inner  $4f$  levels from interacting with the neighboring atoms, thereby preserving the hydrogenic character [314]. Hence, the transitions within the  $4f$  levels are sharp regardless of the host material. However, the number of lines appearing in the optical spectra of the lanthanide ions depends on the characteristic chemical environment in the host lattice, as the  $4f$  shells are split by the crystal field effect of the host lattice, thereby generating various possibilities for electronic transition. The observed spectral characteristics of lanthanide-doped luminescent phosphors would, therefore, provide much needed insight into complex ion-lattice interactions, which will be helpful for the design of novel phosphor materials.

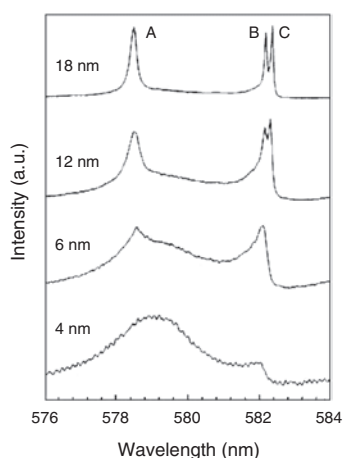
A schematic representation of the partial energy level diagram for  $Eu^{3+}$  ion in solids is depicted in Figure 18 [312].



**Figure 18.** Schematic partial energy level diagram of  $Eu^{3+}$  ions in solids. The two upward arrows correspond to absorptions, and the downward arrow corresponds to the strong red emission  ${}^5D_0 \rightarrow {}^7F_2$ . Reprinted with permission from [312], B. M. Tissue, *Chem. Mater.* 10, 2837 (1998). © 1998, American Chemical Society.

Each energy level can be further split into  $2J + 1$  levels. The two upward arrows in Figure 18 correspond to absorption transitions, whereas the downward arrow represents the strong red luminescence for the transition  ${}^5D_0 \rightarrow {}^7F_2$ . For nanoparticles, the luminescence spectrum is expected to show a shift toward higher energy. No significant shifts in spectral lines were observed at a measuring temperature of 93 K, which may be attributed to the thermal broadening effect for high surface area  $\text{Eu}_2\text{O}_3$  powders having particle diameters  $\leq 100$  nm [315]. However, the excitation spectra corresponding to the transition  ${}^7F_0 \rightarrow {}^5D_0$  when recorded at a much lower temperature of 12 K for  $\text{Eu}_2\text{O}_3$  nanoparticles in the size range 4 to 18 nm exhibited sharp peaks for 18 nm and broadened peaks for 4 nm sample. The broadening of the spectral lines for smaller particles can be attributed to the high degree of disorder in the corresponding samples (Fig. 19) [312, 316].

Apart from quantum confinement, which influences the electronic transitions and luminescence in nanocrystals [317], the increased fraction of interfaces would also contribute to the observed optical properties and sometimes dominate size quantization [318, 319]. The luminescence characteristics of nanocrystalline  $\text{Eu}^{3+}:\text{Y}_2\text{O}_3$  phosphors have been extensively studied [252, 253, 255, 310, 312], as the relatively high quantum efficiency (close to unity) of their red emission makes them a future material in a variety of photonic applications [320]. In addition to the red emission, there could also be a charge transfer (CT) band in the optical spectra, which arises due to the transfer of electrons from the  $2p$  orbital of  $\text{O}^{2-}$  to  $4f$  orbital of  $\text{Eu}^{3+}$  [321]. In order to understand the surface effects on the CT spectra of nanocrystalline  $\text{Eu}^{3+}:\text{Y}_2\text{O}_3$  phosphors, Song et al. [310] excited the phosphors using UV-light and studied the characteristics of the resultant emission spectra. It has been reported that the changes in the CT band spectra could have been caused by the increased fraction of surface atoms ( $\sim 80\%$  for 5 nm crystal) in  $\text{Eu}^{3+}:\text{Y}_2\text{O}_3$  phosphors as the local environments of  $\text{Eu}^{3+}$  ions at or near the surface of the nanoparticles get rearranged upon UV irradiation. Apart from the red

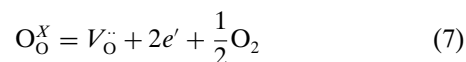


**Figure 19.**  ${}^7F_0 \rightarrow {}^5D_0$  excitation spectra of nanocrystalline  $\text{Eu}_2\text{O}_3$  at  $\sim 12$  K for different particle sizes. Reprinted with permission from [312], B. M. Tissue, *Chem. Mater.* 10, 2837 (1998). © 1998, American Chemical Society.

emission and the CT band, a weak size-dependent excitonic band corresponding to  $\text{Y}^{3+}-\text{O}^{2-}$  host matrix absorption has been reported in this system on UV excitation [255]. The observed excitonic absorption and optical storage luminescence of nanocrystalline  $\text{Eu}^{3+}:\text{Y}_2\text{O}_3$  phosphors (10–20 nm) have been attributed to the possible existence of various defects, as well as chemisorbed species on the surface of the nanocrystals. Recently, the studies on the visible up-conversion emissions in  $\text{Lu}_{1.98}\text{Er}_{0.02}\text{O}_3$  (50 nm) and  $\text{Y}_{1.98}\text{Er}_{0.02}\text{O}_3$  (20 nm) nanoparticles indicate comparable features in the emission processes, except for the strong blue up-conversion emission recorded for Er-doped lutetia ( $\text{Lu}_{1.98}\text{Er}_{0.02}\text{O}_3$ ) [311]. This may be due to reduced surface area and less porosity of lutetia samples compared to the yttria counterpart. Another important area in photonics is the development of optical band gap materials, which will be reviewed briefly later in this chapter as potential materials for future photonic applications.

### 4.3. Electrical Conductivity

Electrical conductivity in ceramics has been a topic of immense interest for researchers due to the potential applications in the development of various electrochemical devices [321–323]. The electrical conductivity ( $\sigma$ ) of a material can be considered as the sum of the contributions from electronic conductivity ( $\sigma_e$ ) and ionic conductivity ( $\sigma_i$ ); the former type is caused by the transport of electrons or holes, whereas the latter type can be attributed to the ion transport through the vacant or interstitial lattice sites [324]. A recent review presents a detailed picture on the dependence of ionic and electronic conductivities as a function of concentration and spacing of interfaces in nanosized mixed oxide ion conductors [325]. For an oxygen-deficient metal oxide ( $\text{MO}_{1-\delta}$ ), the defect equation corresponding to the formation of charged oxygen vacancies is represented by



The condition for electroneutrality corresponds to

$$2[V_\text{O}^{\cdot\cdot}] = n + [A'_M] \quad (8)$$

where the  $A'_M$  is the acceptor-type lower valent dopant impurity that substitutes a cationic site in the lattice. According to the defect formation equation, the electronic conductivity of an oxygen-deficient metal oxide ( $\text{MO}_{1-\delta}$ ) is dependent on the partial pressure of oxygen  $P_{\text{O}_2}$ , which can be written as

$$\sigma_e = ne\mu_e = \frac{A_0}{T} \exp\left(-\frac{E_a}{kT}\right) P_{\text{O}_2}^{-x} \quad (9)$$

where the Arrhenius expression for electronic conductivity has  $n$  as the charge carrier concentration,  $e$  the charge of an electron,  $\mu_e$  the electron mobility,  $A_0 (=ne\mu_0)$  the pre-exponential factor,  $E_a$  the activation energy for conduction, and  $x$  the exponent that represents the variation of conductivity with partial pressure of oxygen. The expression for the ionic conductivity in  $\text{MO}_{1-\delta}$  lattice can be written as

$$\sigma_i = 2e[V_\text{O}^{\cdot\cdot}]\mu_{V_\text{O}^{\cdot\cdot}} \quad (10)$$

The total conductivity ( $\sigma$ ), which can be represented by the following equation as a sum of the Equations (9) and (10), is a function of the partial pressure  $P_{O_2}$  as well as temperature  $T$ :

$$\sigma = \frac{A_0}{T} \exp\left(-\frac{E_a}{kT}\right) P_{O_2}^{-x} + 2e[V_{O^{\cdot\cdot}}]\mu_{V_{O^{\cdot\cdot}}} \quad (11)$$

From the variation of the conductivity ( $\log \sigma$ ) with partial pressure of oxygen ( $\log P_{O_2}$ ), it is possible to distinguish between the two distinct regions of the conductivity—extrinsic and intrinsic—as indicated by the slopes ( $x$ ). For the extrinsic region, where the ionic defects predominate, the electroneutrality condition gets modified to  $2[V_{O^{\cdot\cdot}}] = [A'_M]$ . Consequently, the partial pressure dependence has a value of 1/4 (slope  $x$ ). In the intrinsic region, the electroneutrality condition is  $2[V_{O^{\cdot\cdot}}] = n$ , as the electronic charge carrier concentration ( $n$ ) predominates  $[A'_M]$ . The value of  $x$  for the intrinsic region corresponds to 1/6. The activation energy associated with the conductivity can be estimated from a plot of  $\ln \sigma T$  vs  $1/T$ . The activation energies for extrinsic and intrinsic conductivity can be related to the enthalpy of defect formation ( $\Delta H$ ) by the expressions

$$\text{Extrinsic conduction: } E_a = \frac{\Delta H}{2} + E_h \quad (12)$$

and

$$\text{Intrinsic conduction: } E_a = \frac{\Delta H}{3} + E_h \quad (13)$$

where  $E_h$  is the hopping energy [326].

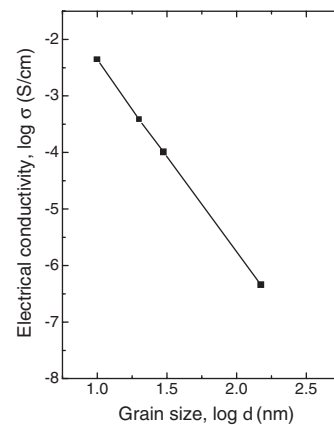
Recently, the defect model for oxygen-deficient oxides has been employed to explain the observed conductivity behavior of nanocrystalline  $CeO_{2-\delta}$  [327]. The study focused on the conductivity measurements of a series of thin film samples having grain sizes in the nanometer range (20 to 150 nm). It has been inferred from the conductivity measurements on  $CeO_{2-\delta}$  samples that the films with the largest grains (150 nm) exhibited predominantly extrinsic behavior at very low partial pressures  $<10^{-10}$ , such that conductivity increases with decreasing partial pressure showing a 1/4 power dependence. The conductivity ( $\sigma$ ) was independent of  $P_{O_2}$  at partial pressures in the range  $\sim 10^{-8}$ – $10^0$  at the lowest measurement temperature of 600 °C. The pressure-independent conductivity behavior for larger grains of n-type nonstoichiometric oxide such as ceria may be due to the presence of the acceptor-type impurities that can pin the oxygen vacancy concentration [328]. For the samples with 65 nm grain size, the 1/6 power dependence became apparent at higher measurement temperature, or in other words the onset of intrinsic conductivity was evident at 900 °C, with the conductivity no longer independent of  $P_{O_2}$ . Further reduction in grain size led to predominantly intrinsic conduction in the sample at relatively lower temperatures and higher partial pressures with the 20 nm sample exhibiting only intrinsic conduction in the higher partial pressure range ( $10^{-5}$ – $10^0$ ). In the case of finer nanoparticles, the energy required for the oxygen defect formation would be considerably less when compared to fully grown larger grains because of the larger number of interfaces as well as lack of pinning along grain boundaries; therefore the conductivity

registers an increase with decreasing particle size (Fig. 20). The conductivity measurements by impedance spectroscopy have been found to be useful to separate the contributions from the bulk and the interface as well as to propose a possible mechanism for conductivity in finer nanoparticles. For instance, the impedance measurements on finer oxide nanocrystals ( $\leq 20$  nm) such as  $CeO_{2-x}$  [327, 328],  $ZrO_2$  [329, 330], and  $ZnO$  [331] provided evidence for the reduction in grain boundary impedance with decreasing particle size, which may be attributed to reduced pinning as well as increase in vacancy concentration at the interfaces for finer nanoparticles having larger interfacial area [328–331].

#### 4.4. Ferroelectric and Dielectric Characteristics

In recent years, studies on ferroelectric and related ceramics have been major fields of research because of the potential applications of thin films of these materials in the fabrication of memory devices [332]. The particle size effects on ferroelectricity are analogous to magnetic characteristics. Corresponding to the magnetization in the presence of a magnetic field, ferroelectricity involves alignment of dipole moments (polarization) in the presence of an electric field. Comparison also arises from the assumption that both phenomena are governed by the mechanism of formation of domains and domain wall motion [333]. However, for particle sizes much less than the critical domain size, there is scarcity of experimental data that can provide evidence for a superparaelectric state analogous to superparamagnetic state, which will be discussed in a subsequent section on magnetic nanoparticles. The particle size effect on the ferroelectric phase transition in these materials has been well documented in the literature [334–342].

As a classical example of a displacive ferroelectric with excellent dielectric, pyroelectric, and piezoelectric properties,  $PbTiO_3$  has been characterized for the size effects on its phase transition [336–341]. The size effects have been found to be predominant below 100 nm in these ferroelectric oxides. The phase transition studies on nanocrystalline  $PbTiO_3$  with crystallite sizes in the range of 20–80 nm showed that the nanocrystals exhibited a reduction



**Figure 20.** Electrical conductivity ( $\sigma$ ) as a function of the grain size ( $d$ ) for nanocrystalline  $CeO_2$  thin films at 1000 K. Data from Ref. [327].

in tetragonal distortion according to an exponential function  $\sim 1-e^{-d}$ , ultimately transforming to a cubic phase for smaller particles (critical size  $\sim 7$  nm at room temperature) [339]. The transition was in accordance with the internal stress model predicted by Buessem et al. [343]. The model assumes that when particles of dimensions close to single domains are cooled to  $T_c$ , each grain experiences a complex system of internal stresses that are developed depending on the orientation of the surrounding grains. In order to relieve these stresses, the crystal transforms from a spontaneously polarized distorted tetragonal phase (ferroelectric) to a less-polarized cubic phase (paraelectric). The consequences of this transformation being the gradual reduction in permittivity, a shift in  $T_c$  values to lower temperatures ( $\sim 20$  °C lower) and a diffused phase transition, which almost disappears eventually for particle sizes in the range 26 nm (Fig. 21) [339]. The dielectric constant in the vicinity of the ferroelectric phase transition  $T_c$  can be expressed by a semiempirical relation [344, 345]

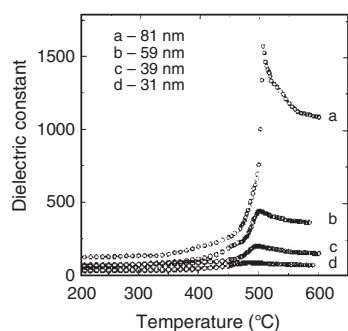
$$\frac{1}{\varepsilon} - \frac{1}{\varepsilon_{\max}} = \frac{1}{A}(T - T_c)^\gamma \quad (14)$$

where  $\varepsilon$  is the dielectric constant,  $\varepsilon_{\max}$  is the maximum dielectric constant value at the transition temperature  $T_c$ ,  $A$  is a constant, and  $\gamma$  is the order of phase transition within the range  $1 < \gamma < 2$ . When  $\gamma$  equals 1, the phase transition is Curie–Weiss type, and when  $\gamma$  approaches 2, the phase transition can be regarded as diffused type. The  $\gamma$  value is  $\sim 1$  for 80 nm  $\text{PbTiO}_3$  crystals and increases to 1.5 for 30 nm crystals [339].

The critical dimension for the phase transformation of  $\text{PbTiO}_3$  nanocrystals from ferroelectric to paraelectric phase at room temperature can be estimated by extrapolating the experimentally determined  $c/a$  ratio and crystallite size  $d$  from the X-ray diffraction data of the nanocrystalline samples. The least-squares fitted expression for the  $c/a$  ratio versus average crystallite size  $d$  can be written as

$$y = y_\infty - C \exp[C(d_{\text{crit}} - x)] \quad (15)$$

where  $x \equiv d_{\text{XRD}}$ ,  $y \equiv c/a$ ,  $y_\infty = 1.065$ , and  $C \equiv y_\infty - 1$ . The critical crystallite size corresponds to the  $c/a$  ratio being unity. The estimated value of the critical crystal dimension was around 7 nm for nanocrystalline  $\text{PbTiO}_3$  [339]. The phase transformation in  $\text{PbTiO}_3$  is probably similar to the



**Figure 21.** Dielectric constant as a function of temperature for different average grain sizes of the nanocrystalline  $\text{PbTiO}_3$  [339].

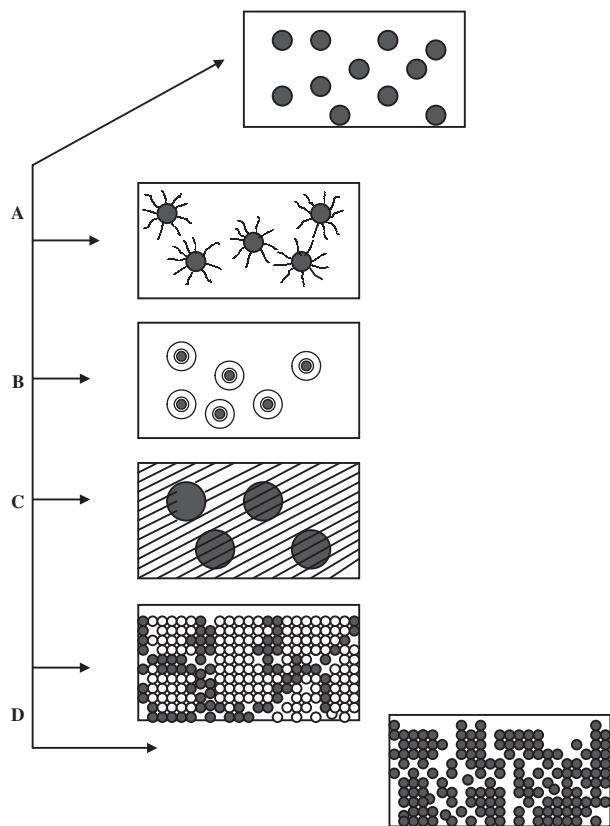
crystallization of a more symmetric phase for nanocrystals in a certain model of binary oxide systems such as  $\text{Al}_2\text{O}_3$  and  $\text{Fe}_2\text{O}_3$  [346]. The driving force for such crystallization may be attributed to the tendency to minimize the surface Gibbs energy associated with high surface area. The molecular dynamic simulation of relative enthalpies of alumina polymorphs predicted the possibility of a more symmetric  $\gamma$ -alumina phase being stabilized compared to the  $\alpha$ -phase [347].

The characteristics of the ferroelectric phase transition, such as lowering of the dielectric constant peak, the diffused maximum, and the shift in  $T_c$  values have been observed to register a reverse trend when the nanocrystalline ferroelectric materials have charged ion-vacancy dipoles. These dipoles contribute to the space charge effect along grain boundaries; thereby the total polarization in the material is increased. Moreover, the defect formation is energetically more favorable in finer particles due to the large surface-to-volume ratio in the material. For instance, a reverse trend in  $\varepsilon$ - $T$  curves has been reported for ferroelectric phase transitions in nanocrystalline  $\text{Bi}_4\text{Ti}_3\text{O}_{12}$  [348] and  $\text{Bi}_2\text{VO}_{5.5}$  [349]. The crystal structure of  $\text{Bi}_4\text{Ti}_3\text{O}_{12}$  comprises layers of ionic conducting  $[\text{Bi}_2\text{O}_2]^{2+}$  layers stacked between insulating perovskite-like  $(\text{Bi}_2\text{Ti}_3\text{O}_{10})^{2-}$  layers [350]. Jiang et al. [348] explained the  $\varepsilon$ - $T$  curves for  $\text{Bi}_4\text{Ti}_3\text{O}_{12}$  samples of crystallite sizes in the nanometer range (19 to 56 nm) by taking into consideration the formation of defect dipoles, which orient in the applied electric field and contribute to the total polarization. The contribution to the dielectric constant from the defect dipoles decreased when the crystallite size was increased as a result of annealing out of the defects. The observed enhancement in the dielectric constant for  $\text{Bi}_2\text{VO}_{5.5}$  ceramics on crystallite size reduction has been attributed to the increase in oxygen vacancy concentration [349].

#### 4.5. Magnetic Properties

In the present era of advanced technology, magnetic materials have a significant role in the development of various devices. Ferromagnets have been identified as potential materials for the development of information storage devices [351], magnetic refrigeration [352], and ferrofluids [353, 354]. The enormous potential of magnetic fluids has been currently expanded to biological processes. For instance, the magnetic fluid based on maghemite ( $\gamma\text{-Fe}_2\text{O}_3$ ) has been proved to be a biocompatible material for the purpose of transporting antibodies through human tissue [355].

The observed magnetic properties of oxide nanoparticles depend on the particle size or large surface area-to-volume ratio. The correlation between the nanostructure and the magnetic properties has been investigated for the model oxide  $\gamma\text{-Fe}_2\text{O}_3$  nanoparticles [275, 356–359]. In analyzing these results, one can conclude that the chosen preparative route also governs the nanostructure and the resultant magnetic properties. Pelecky and Rieke [360] have classified different types of magnetic nanostructures according to a schematic diagram shown in Figure 22. The illustration provides insight into the possible interparticle interactions and the extent to which it affects the magnetic properties.



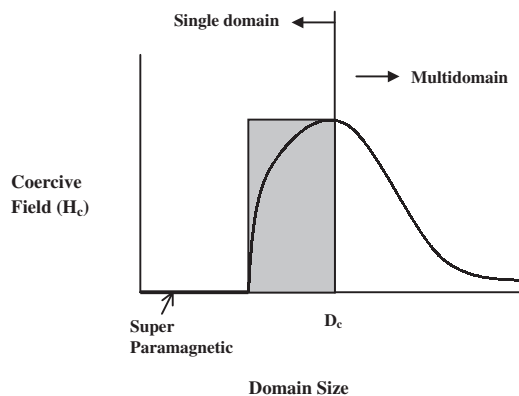
**Figure 22.** Schematic representation of the different types of magnetic nanostructures [360]. Type A—noninteracting nanoparticles, Type B—nanoparticles with core-shell morphology, Type C—nanocomposite, and Type D—nanocrystals (ordered regions represented by hollow spheres or black spheres) dispersed in a disordered solid matrix (black colored circles). Reprinted with permission from [360], D. L. L. Pelecky and R. D. Rieke, *Chem. Mater.* 8, 1770 (1996). © 1996, American Chemical Society.

The classification ranges from type A material of noninteracting particles to type D with dominant interparticle interactions. An example of type A material is a ferrofluid in which the particle surfaces have been modified by surfactant molecules, thereby minimizing the interaction through steric hindrance between the particles [361–363]. Type D material comprises a three-dimensional solid built of nanoparticles dispersed in a disordered solid matrix, wherein the interparticle or intergranular interactions predominantly contribute to the total magnetization. When the atoms that constitute the nanoparticles and the corresponding solid matrix are the same, we may describe the Type D system as fully grown grains separated by disordered interfaces as shown schematically in the second possibility for Type D [22]. The intermediate nanostructure of type B depicts the ultrafine particles with core shell morphology (e.g., a shell of oxide layer formed over a magnetic core, Co/CoO [364]), and type C refers to nanocomposite materials (e.g.,  $\gamma$ -Fe<sub>2</sub>O<sub>3</sub> nanoparticles dispersed in SiO<sub>2</sub> matrix in which the magnetic interactions are determined by volume fraction of the magnetic nanoparticles [358, 365]).

The magnetic characterization of a material includes tracing of a hysteresis loop ( $M$ – $H$  curve, where  $M$  is the

magnetization and  $H$  is the applied field) to obtain typical values of saturation magnetization ( $M_s$ ), remanent magnetization ( $M_r$ ), and coercive field ( $H_c$ ). Ideally, the hysteresis loop for a material should have a near square shape with high value of remanent magnetization ( $M_r$ ), and moderate coercivity [360]. Magnetization in a material has been found to be dependent on various types of anisotropies arising out of the crystal system, particle morphology, stress, external field, and exchange interaction [366]. A large magnetic particle can be considered as made up of several magnetic domains or multidomains. Within each domain, spins have the same orientation and are associated with a critical dimension and energy depending on the material. The applied magnetic field provides the necessary activation energy for the spins in multidomains to align and reach a state of saturation magnetization. When the field is applied in the opposite direction, domain wall motion reverses the magnetization. However, as the particle size decreases and reaches a value close to the critical single domain dimension,  $D_c$ , the multidomain formation becomes energetically unfavorable. The underlying domain wall mechanism involving the reversal of the magnetic moments in bulk particles no longer holds true for single domain particles. The reversal of the magnetic moments in the single domain particles takes place through a coherent rotation of spins, which require higher coercive fields. For particles smaller than the critical domain dimension, the spins are increasingly affected by thermal fluctuations, coercivity decreases, and the system becomes superparamagnetic [360]. Magnetic behavior as a function of particle size is schematically represented in Figure 23. The shaded region refers to the decrease in coercivity as the particle sizes decrease below  $D_c$ . The surface modified noninteracting nanoparticles with sizes less than  $D_c$  have superparamagnetic properties [273, 274, 361, 363].

From the magnetization measurements, it is possible to draw an important conclusion regarding the distribution of particle size, provided that the form of the distribution is known [367]. The magnetization in a system of noninteracting magnetic particles as in the case of a surface modified



**Figure 23.** Schematic variation of the coercivity ( $H_c$ ) as a function of the domain size in ultrafine magnetic nanoparticle systems. Reprinted with permission from [360], D. L. L. Pelecky and R. D. Rieke, *Chem. Mater.* 8, 1770 (1996). © 1996, American Chemical Society.

ferrofluid can be represented by Langevin function

$$L\left(\frac{\mu H}{k_B T}\right) = \coth\left(\frac{\mu H}{k_B T}\right) - \frac{k_B T}{\mu H} \quad (16)$$

where  $\mu = M_s V$  is the magnetic moment of a single particle and  $H$  is the external field. In a real system, the field dependence of the magnetization is the integral of the Langevin function over the size distribution. A lognormal distribution, which was suggested by O'Grady and Bradbury [368], has been proved to be adequate to describe the magnetization in a noninteracting nanoparticle assembly [274]. The width and mean particle size can also be estimated from the distribution. The expressions for calculating the particle diameter ( $D_{\text{mag}}$ ) and standard deviation ( $\sigma$ ) can be written as

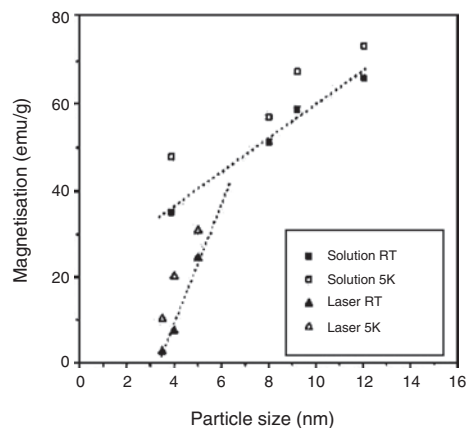
$$D_{\text{mag}} = \left[ \frac{18kT}{\pi m_s} \sqrt{\frac{\chi_i}{3M_s H_0}} \right]^{1/3}; \quad \sigma = 1/3 \left[ \ln\left(\frac{3\chi_i}{M_s H_0}\right) \right]^{1/2} \quad (17)$$

where  $M_s$  and  $m_s$  are the saturation magnetization of the nanoparticles and the bulk phase, respectively.  $\chi_i$  is the initial susceptibility calculated at low fields, in the region where the variation of  $M$  against  $H$  is linear. The factor  $1/H_0$  is obtained by extrapolating  $M$  to 0 at high fields, in the region where the relationship between  $M$  and  $1/H$  is a straight line [275]. Exact superposition of  $M-H$  curves at different temperatures implies a very narrow particle size distribution in the sample [360].

Moumen and Pileni [274] estimated the average particle size of the cobalt ferrite ( $\text{CoFe}_2\text{O}_4$ ) superparamagnetic sample (2–5 nm) using the Langevin function assuming a lognormal size distribution based on the magnetization measurements for dry nanoparticles and particles dispersed in a fluid. The calculated average particle size for dry powder was greater than the value obtained by TEM or XRD. The differences in the particle diameters obtained for the dry powder and the ferrofluid implied that the magnetization curves of the two samples were different. In the dry powder, the interparticle interactions are no longer weak compared to ferrofluid where the weight fraction of the particles in the fluid is very low. Moreover, the bulky surfactants on the particles provided steric hindrances; therefore the interactions between the particles were minimized. The interparticle interactions in dry powder would have perturbed the Langevin function and caused an increase in apparent magnetic diameter of the particle. The authors also reported the magnetic property measurements on samples heated at 200 °C, 400 °C, and 600 °C for 30 min. The thermally processed samples had larger particle size. The adsorbed surfactant molecules decomposed with increasing annealing temperature, resulting in higher values of reduced remanence ( $M_r/M_s$ ) and the coercivity ( $H_c$ ) for  $\text{CoFe}_2\text{O}_4$  nanoparticles. Moreover, the samples annealed at higher temperatures showed improvement in coercivity due to better crystallinity and the release of surfactant to the particle interface.

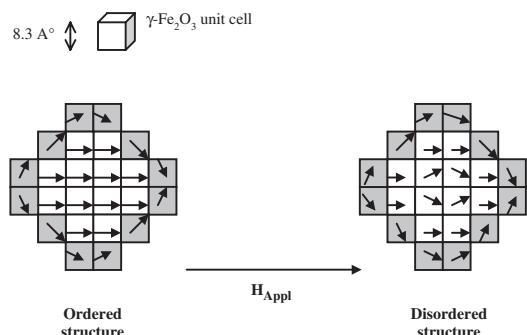
The intrinsic cationic vacancy disorder in  $\gamma\text{-Fe}_2\text{O}_3$  has been found to influence the orientation of magnetic moments through a phenomenon termed as canting effect [369] that affects the resultant magnetic properties. The

effect is more pronounced for particle diameters less than 20 nm [370]. Below 20 nm, the surface contribution to the total magnetization also becomes significant. Morales et al. [275] studied the size effect and structural ordering on the magnetic properties of  $\gamma\text{-Fe}_2\text{O}_3$  nanoparticles less than 20 nm prepared through a coprecipitation technique and laser ablation. The saturation magnetization ( $M_s$ ) for  $\gamma\text{-Fe}_2\text{O}_3$  nanoparticles decreased with decreasing particle size as shown in Figure 24 as two distinct regimes—one for particle sizes greater than 5 nm and the steeper region for particle sizes less than 5 nm. The observed reduction in the saturation magnetization has been explained based on the spin canting effect and the vacancy disorder. The change in the slope of the  $M_s$  versus particle size plot signaled a possible order-disorder transformation of cationic sites in  $\gamma\text{-Fe}_2\text{O}_3$  nanoparticles of sizes below 5 nm. Compared to the earlier reports on the particle size limit for the cationic order-disorder transformation in  $\gamma\text{-Fe}_2\text{O}_3$  [370], the study by Morales et al. [275] set a lower size limit for order-disorder transformation. As the size limit also depends on the method of preparation, samples prepared through different routes would have different degree of order-disorder in the lattice. This would apparently explain the reason for difference in magnetization ( $M_s$ ) values for similar sized particles that are prepared by different synthesis routes. The high value of coercivity ( $H_c$ ) measured for  $\gamma\text{-Fe}_2\text{O}_3$  nanoparticles particles less than 5 nm at low temperature (5 K) was attributed to the pinning of core magnetic moments through direct exchange interaction with frozen spin-glass surface layer. The order-disorder transformation for  $\gamma\text{-Fe}_2\text{O}_3$  nanoparticles of average diameter 5 nm when placed in a magnetic field can be explained using a schematic diagram (Fig. 25) [275]. The spinel-like  $\gamma\text{-Fe}_2\text{O}_3$  lattice has cationic vacancies that may be ordered in a tetragonal superstructure, partially ordered in a cubic superstructure, or completely disordered resulting in vacancy aggregation. The completely disordered state gives rise to spin canting effect in  $\gamma\text{-Fe}_2\text{O}_3$  nanoparticles as schematically shown in Figure 25. The shaded outer layer represents the



**Figure 24.** Plot of saturation magnetization ( $M_s$ ) versus particle size for  $\gamma\text{-Fe}_2\text{O}_3$  nanoparticles for samples prepared through different synthesis routes [275]. For experimental details, see Ref. [275]. Reprinted with permission from [275], M. P. Morales et al., *Chem. Mater.* 11, 3058 (1999). © 1999, American Chemical Society.





**Figure 25.** Schematic illustration of the order-disorder transformation in the spinel-like lattice of  $\gamma\text{-Fe}_2\text{O}_3$  nanoparticles of diameter 5 nm. Each square in the diagram is a projection of the  $\gamma\text{-Fe}_2\text{O}_3$  unit cell. The shaded squares represent the unit cells close to the surface. Magnetic orientation associated with each unit cell is inscribed in the projection [275]. Reprinted with permission from [275], M. P. Morales et al., *Chem. Mater.* 11, 3058 (1999). © 1999, American Chemical Society.

surface layer. The studies on magnetic oxide nanoparticles indicate that magnetic properties are strongly dependent on parameters such as the preparative conditions, particle size, surface area, and degree of vacancy disorder.

#### 4.6. Catalytic Properties

The research on catalysis and related materials has become very relevant at present as an effective means of disposing the increasing amounts of pollutants from industry and automobiles. Catalytic converters are already being used in automobiles to reduce the levels of carbon monoxide emission. Of the two types of catalytic processes, heterogeneous and homogeneous, heterogeneous catalysis has been widely used in industries. The heterogeneous catalysis can be further divided into two categories—structure-insensitive and structure-sensitive catalysis [371]. As the term indicates, in structure-insensitive catalysis, the process does not depend on the individual microstructure such as the crystallite size and the crystal structure of the catalytic material, but only on the composition, the number of active catalytic sites available, and the electronic structure of the active species involved in the process. The structure-sensitive catalytic process is affected by the microstructure of the catalytic material such as its crystallite size, crystal structure, and interatomic spacing [372].

Utilizing high surface area nanoparticles having a large number of active sites is one way to boost the reaction rate in the two types of heterogeneous processes mentioned above. The role of nanoparticles is more pronounced in the structure-sensitive catalytic process where small crystallite size affects the overall rate of the reaction. Various methods for the preparation of oxide-supported-nanostructured metal catalysts have been established. The process involves dispersing metal clusters on oxide by ion-exchange or impregnation [373–378]. Relatively recently, the processing and catalytic applications of nanostructured nonmetallic systems have been developed [379]. In order to produce high surface area oxide nanoparticles for catalytic applications,

suitable synthesis techniques can be chosen. Table 2 summarizes different oxide materials used for catalytic applications, their preparative routes, and catalytic activities.

Nanocrystalline catalysts have high surface-to-volume ratio and exhibit size quantization effect for very small grain sizes (<5 nm). Because of these unique features, catalytic activities of nanocrystals are different from the bulk. The large fraction of unsatisfied valences at the surfaces, interfaces, and grain boundaries of nanocrystals provide active catalytic centers, thereby influencing the rate of formation and the nature of the intermediate species. The study of the catalytic activity of nanocrystals would be complete only if extensive surface characterization is carried out to understand the reaction mechanism leading to the formation of final product. For instance, by coupling scanning tunneling electron microscopy (STEM) and energy dispersive X-ray analysis (EDX), precise compositional mapping of the surface for doped polycrystalline  $\text{TiO}_2$  has been reported [386]. Another efficient procedure for composition analysis would be to combine STEM and electron energy loss spectroscopy (EELS), which could provide insight into the atomic and the electronic structure of the surfaces. The morphological examination of the surface is carried out by the atomic force microscopy (AFM) [371]. Besides providing the surface morphology of the nanocrystalline compact, the formation of pores can also be clearly observed from the AFM picture.

Enhanced catalytic activity has been demonstrated recently in catalytic combustion of methane using barium hexa aluminate ( $\text{BaO} \cdot 6\text{Al}_2\text{O}_3$ , BHA) nanoparticles [192]. The difference in catalytic activities of sol-gel-derived conventional BHA, reverse microemulsion-derived BHA nanoparticles, and reverse-microemulsion-derived  $\text{CeO}_2$ -BHA nanocomposite is depicted as curves c, b, and a, respectively, in Figure 26. The reactant stream consisted of 1 vol%  $\text{CH}_4$  in air at a space velocity of  $60,000 \text{ h}^{-1}$ . Combustion (light-off) was initiated at temperature as low as  $590 \text{ }^\circ\text{C}$  for nanocrystalline BHA (curve b) compared to  $710 \text{ }^\circ\text{C}$  (curve c) required for conventional BHA. For the  $\text{CeO}_2$ -BHA nanocomposite particles, the combustion was initiated at a very low temperature of  $400 \text{ }^\circ\text{C}$  (curve a).

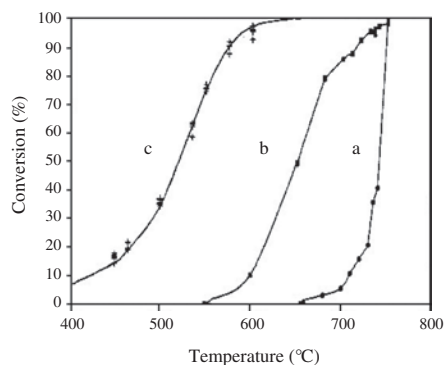
Another interesting development in catalysis is the exploitation of the typical surface chemical properties of the metal oxide nanoparticles to reduce the polluting effects of toxic gases. Besides being ionic with good thermal stability, the edges and corners of fine-grained metal oxides may exhibit acid/base properties [387, 388], which enable the oxides to react chemically with a wide range of toxic materials, thereby reducing the pollution. A well-known example of a Lewis type acid-base reaction is the adsorption of CO onto the surface of a metal-oxide catalyst by metal-carbonyl bonding. The bonding results from the donation of a pair of electrons from carbon to the empty orbitals of metals. This particular type of binding has been found to be prevalent at low temperature in the oxidation of CO by  $\text{SO}_2$  in the presence of nanocrystalline  $\text{CeO}_2$  [389].

Nanocrystalline metal oxides with intrinsic oxygen deficiency are potential materials in catalysis [389]. Examples of these types of oxides are substoichiometric titanium oxide ( $\text{TiO}_{2-x}$ ) [390], tungsten oxide ( $\text{WO}_{3-x}$ ) [391], and cerium oxide ( $\text{CeO}_{2-x}$ ) [382, 385, 389]. Particularly,  $\text{CeO}_{2-x}$  is of interest because of its ability to oxidize CO and  $\text{CH}_4$

**Table 2.** Different types of nanostructured oxide catalysts, their preparative routes, and catalytic activities.

Oxide catalyst	Preparative route	Catalytic activity	Ref.
Zirconia ( $ZrO_2$ )-Silica ( $SiO_2$ ) composite aerogel	Sol-gel	Isomerization of 1-butene	[380]
Titanium dioxide, $TiO_2$	Sol-gel	Photocatalysis	[381]
Cerium oxide, $CeO_{2-x}$	Gas phase deposition	Selective reduction of $SO_2$ by CO at a low temperature of 460 °C	[382, 385, 389]
Vanadium phosphorous oxide ( $\gamma$ - $VOPO_4$ )	Flame processing	Selective oxidation of $C_4$ carbons to maleic anhydride	[383]
$\alpha$ -alumina ( $Al_2O_3$ )	High energy milling of $\gamma$ - $Al_2O_3$	Inert catalyst support for partial oxidation and high temperature combustion applications	[384]
Mesoporous transition metal oxides ( $TiO_2$ , $ZrO_2$ , $V_2O_5$ , $Nb_2O_5$ , $MoO_3$ , Ni/Co oxides)	Modified sol-gel route	Photocatalytic decomposition of organic compounds ( $TiO_2$ ), solid acid isomerization, and alkylation (sulfated $ZrO_2$ ), partial oxidation ( $V_2O_5$ , $MoO_3$ ), and hydro-desulfurization (Ni/Co oxide)	[371]
Barium hexa aluminate ( $BaO \cdot 6Al_2O_3$ , BHA)	Microemulsion route	Catalytic oxidation of methane	[192]
Nanocrystalline CaO, ZnO, $Al_2O_3$ , MgO	Sol-gel or aerogel synthesis	Enhanced catalytic activity towards $H_2S$	[392, 393]

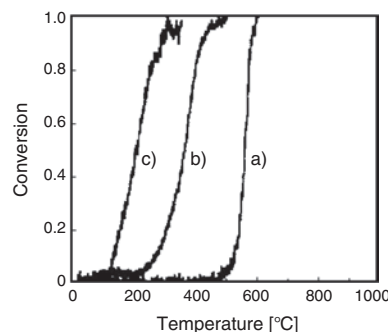
[389]. Studies on the ceria-based catalysts by Tschöpe et al. [389], involved a detailed characterization and comparison of microcrystalline and nanocrystalline ceria, nonstoichiometric ceria, and ceria-supported metal catalysts. The nanoparticles of ceria prepared by inert gas condensation were nonstoichiometric. The nonstoichiometric ceria,  $CeO_{2-x}$ , catalyzes the oxidation of CO in the presence of  $O_2$  at a lower temperature (200 °C; curve c in Fig. 27) compared to the oxidation of CO by  $SO_2$  in the presence of stoichiometric nanocrystalline  $CeO_2$  (560 °C curve a in Fig. 27). For comparison, the simple oxidation CO by  $O_2$  is presented as curve b in Figure 27 (360 °C). The intermediate species involved in the oxidation of CO in the presence of stoichiometric nanocrystalline  $CeO_2$  has been characterized using Fourier transform infra-red spectroscopy (FTIR) at various stages [389]. The study showed that the mechanism involved the chemical adsorption of CO to the metal followed by the formation of bidentate carbonate with low-coordinated terminating oxygen. The metal-carbonyl bonds were stable



**Figure 26.** Comparison of catalytic activities of sol-gel-derived conventional BHA (curve c), reverse microemulsion-derived BHA (curve b) nanoparticles, and reverse-microemulsion-derived  $CeO_2$ -BHA nanocomposite (curve a) [192]. Reprinted with permission from [192], A. J. Zarur and J. Y. Ying, *Nature* 403, 65 (2000). © 2000, Macmillan Magazines Ltd.

only at low temperature, whereas the carbonates were stable up to 500 °C. On the other hand, the electrons associated with charged oxygen vacancies in the nonstoichiometric ceria lattice,  $CeO_{2-x}$ , might have enhanced the chemisorption of oxygen, thereby promoting the oxidation of CO at a much lower temperature [389].

Klabunde et al. [75], Carnes and Klabunde [392], Richards et al. [393], and Khaleel et al. [394] have reported excellent catalytic properties for the high surface area nanocrystalline oxides such as CaO, ZnO,  $Al_2O_3$ , and MgO. These oxides are also associated with high surface chemical reactivity. A recent study from the same group sequenced a series of nanocrystalline oxides based on their reactivity towards  $H_2S$  [299]. They found that at selected elevated temperatures, the order of the reactivity of the oxides towards  $H_2S$  was  $CaO > ZnO > Al_2O_3 > MgO$ . At lower temperatures, the reactivity sequence was  $ZnO > CaO > Al_2O_3 \approx MgO$ . As the reaction enthalpy is the most important factor that decides the course of the reaction with  $H_2S$ , an optimum temperature should be selected to achieve a favorable reaction rate. The  $Al_2O_3$  and MgO have thermodynamically less favorable enthalpies of reaction with  $H_2S$  in this series.



**Figure 27.** Comparison of catalytic oxidation of CO a) by  $SO_2$  in the presence of nanocrystalline stoichiometric ceria, b) by  $O_2$ , c) by  $O_2$  in presence of nonstoichiometric ceria [389].

Therefore, heating to a moderately elevated temperature would have increased the reaction rate for  $\text{Al}_2\text{O}_3$  and  $\text{MgO}$ , whereas the reaction rate reached optimum value at lower temperature for  $\text{CaO}$  and  $\text{ZnO}$ . The reaction temperature should be selected in such way as to compensate for the unfavorable enthalpy as well as to avoid sintering, which will lower the surface area for the consolidated sample at elevated temperature [392].

#### 4.7. Thermal Conductivity

Another topic of great industrial interest is the thermal transport properties exhibited by oxide nanoparticles. As a part of miniaturization in devices, particularly in the microelectronics industry, a comprehensive knowledge of thermal transport at reduced dimension is essential to minimize possible device failures due to localized heating. Heat transfer through solids depends on the microstructure such as particle size, porosity, and type of material. For instance, heat-transfer fluids that consist of metal-oxide or metal nanoparticles dispersed in water or ethylene glycol have improved thermal conductivity [395, 396], whereas nanocrystalline zirconia coatings with grain sizes on the order of 40 nm or less have reduced thermal conductivity [397]. According to the kinetic theory of heat transfer, the thermal conductivity,  $k$ , of a material is directly proportional to the heat capacity  $C_p$ , the sound velocity  $v$ , and the phonon mean free path  $l$  [398]. The heat capacity measurements indicate that there is only a slight increase (up to 15%) in the  $C_p$  of the nanocrystalline materials compared to their coarse-grained counterparts [399, 400]. However, further studies on the heat capacities of different types of nanocrystalline solids are required in order to derive a final conclusive picture of their grain size dependence. Heat conduction is indirectly related to sound velocity ( $v$ ) through the Young's modulus, which has insignificant dependence on grain size, but depends on the processing-induced porosity [401]. The thermal conductivity ( $k$ ) value, however, may have a stronger dependence on the phonon mean free path ( $l$ ). For instance, in defect-free crystals such as diamond, the  $l$  value is significantly reduced by about three orders of magnitude from a few mm for single crystals to a few  $\mu\text{m}$  for polycrystals having micrometer-sized grains [402]. In defective crystals such as yttria-stabilized zirconia (YSZ), the reduction in mean free path is less pronounced compared to the defect-free crystals because of the relatively small separation between the oxygen vacancies in single crystals and polycrystals [403]. Small mean free path implies a lower thermal conductivity, which can be exploited for thermal barrier applications [404, 405]. In other words, the interfaces in oxide nanoparticles scatter phonons and resist heat flow, which ultimately results in a temperature discontinuity between the grains in the presence of a temperature gradient (Kapitza resistance) [406, 407]. There have been efforts to understand the thermal transport across interfaces in polycrystalline and nanocrystalline materials [408–411]. Assuming that the grain boundaries are associated with identical thermal resistance, Yang et al. [411] formulated expressions for determining the Kapitza resistance in nanocrystalline YSZ sample. The heat

flux ( $q$ ) through a polycrystalline sample in a temperature gradient ( $dT/dx$ ) can be represented by

$$q = -k \left( \frac{dT}{dx} \right) \quad (18)$$

where  $k$  refers to thermal conductivity. For grains of width  $d$ ,  $dT/dx$  is equivalent to  $T^*/d$  where  $T^*$  is the temperature across a single grain consisting two distinct temperature regions, namely,  $T_0$  as the grain interior temperature and  $T_{\text{gb}}$  as the average temperature discontinuity at each grain boundary. The temperature  $T^*$  across a single grain can be written as

$$T^* = T_0 + T_{\text{gb}} \quad (19)$$

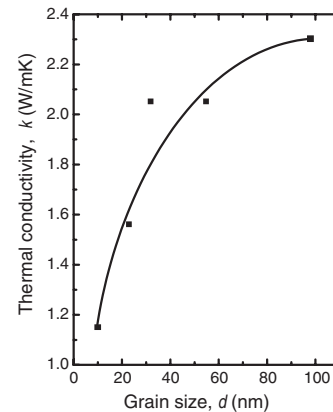
By considering the above assumptions, the expression for effective thermal conductivity ( $k$ ) of a polycrystalline material becomes

$$k = \frac{-qd}{T_0 + T_{\text{gb}}} \quad (20)$$

where  $T_0 = \frac{-qd}{k_0}$  and  $T_{\text{gb}} = -qR_k$  where  $k_0$  is the bulk or single crystal thermal conductivity and  $R_k$  is the Kapitza resistance. Substituting the various parameters in Equation (20), the equation for the thermal conductivity can be expressed as

$$k = \frac{k_0}{1 + \frac{k_0 R_k}{d}} \quad (21)$$

The Kapitza resistance ( $R_k$ ) of the 10 nm-sized YSZ has been found to be relatively low ( $R_k = 4.5 \times 10^{-10} \text{ m}^2 \cdot \text{K/W}$ ) when compared to identical grain-sized  $\text{Si}_{0.8}\text{Ge}_{0.2}$  samples ( $R_k = 1 \times 10^{-8} \text{ m}^2 \cdot \text{K/W}$ ) [411]. The grain-size dependence of thermal conductivity for nanocrystalline YSZ samples indicates that thermal conductivity gradually increases with increasing grain size (Fig. 28). The rate of increase is rapid for crystallites below 40 nm. For grain sizes above 40 nm, the thermal conductivity registers a lesser rate of increase. The rapid rise in conductivity for small nanocrystals (<40 nm)



**Figure 28.** Thermal conductivity of nanocrystalline yttria-stabilized zirconia (YSZ) as a function of grain size at 480 K. Data taken from [411].

may be attributed to the high rate of reduction in the number of grain boundary interfaces when subjected to thermal processing. The important challenge is to understand the various factors that control the thermal conductivity in oxide nanoparticles and optimize them in order to implement in device fabrication.

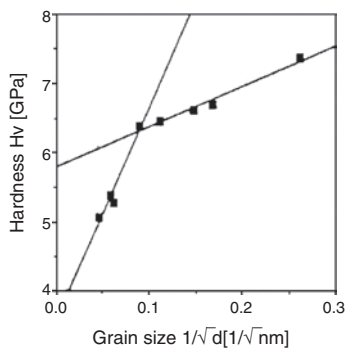
#### 4.8. Mechanical Properties

Unique and fascinating mechanical properties of nanocrystalline materials, especially gas-phase deposited nanoparticles, have motivated detailed theoretical and experimental studies on characteristics such as elastic moduli, high hardness and strength, and increased ductility reaching the superplastic behavior for the nanosized grains, when compared to their coarse-grained counterparts [412].

The verification of the empirical Hall–Petch equation [413, 414] helps to draw important conclusions on the mechanical properties of nanocrystalline materials. The expression that relates the yield stress ( $\sigma_y$ ) to the average grain size ( $d$ ) and can be written as

$$\sigma_y = \sigma_0 + \frac{k}{\sqrt{d}} \quad (22)$$

where  $\sigma_0$  is a friction stress and  $k$  is a constant. As the grain size decreases to nanometer dimensions, the yield strength increases. For example, the yield strength increases by a factor of about 30, as the grain size decreases by about two orders of magnitude from 10  $\mu\text{m}$ . However, this is an ideal prediction and in reality the relation is yet to be completely satisfied for a wide range of nanocrystalline metals studied. A similar inverse relation holds true for grain size dependence of hardness [415]. In the case of nanocrystalline ceramics, mechanical characterization has been reported on model oxide systems such as  $\text{TiO}_2$  [72]. The Hall–Petch plot that relates the hardness ( $H_v$ ) and the grain size ( $d$ ) for the nanocrystalline  $\text{TiO}_2$  is presented as Figure 29. Although the reduction in slope of the curves was observed for the grain sizes smaller than 200 nm, the increase in the hardness of the  $\text{TiO}_2$  samples with decreasing grain size was not in accordance with Hall–Petch relation. The break in the slope of the curve at smaller grain sizes (Fig. 29) indicates a reduction in the rate of increase in hardness values with decreasing grain sizes for the low temperature crystallized  $\text{TiO}_2$  samples. This abrupt rate change in the measured



**Figure 29.** Hall–Petch plot relating hardness ( $H_v$ ) and grain size ( $d$ ) for nanocrystalline  $\text{TiO}_2$  [415].

hardness values can be attributed to decreased diffusion through the grain boundaries for samples crystallized at low temperature ( $T \leq 400^\circ\text{C}$ ). The observations were consistent with the studies on the nanostructured alloy TiAl [416–418]. Comparable hardness values have been reported for dense  $\text{TiO}_2$  nanocrystals by Karch and Birringer [419]. The dense nanosized  $\text{TiO}_2$  also had high values of fracture toughness ( $\sim 14 \text{ MPa m}^{-1/2}$ ). The verification of the Hall–Petch relation provided insight into improving the strength and hardness of nanomaterials.

Another important mechanical property is superplasticity, which refers to the ability of materials to undergo extensive tensile deformation without necking or fracture. Though the superplastic deformation is a well-established industrial process in metals [420], in the case of brittle materials, the phenomenon needs to be explored further for large-scale industrial use. Among the oxide ceramics, polycrystalline tetragonal zirconia has been characterized for superplasticity [421]. The decisive factors for a material to exhibit superplasticity are small grain sizes ( $< 5 \mu\text{m}$ ), equiaxed grains, high energy grain boundaries, and crystallization from a heterogeneous phase [422]. These features are invariably present in nanocrystalline materials and hence in principle should exhibit superplasticity. For instance, enhanced diffusion along the grain boundaries of a nanomaterial implies the high energy associated with it as compared to coarse-grained samples [423]. This can also lead to rapid grain growth in nanomaterials at moderately elevated temperatures. However, in nanocomposite materials, the additional phase present in the sample hinders the grain growth, thereby preserving the essential small grain size feature for superplasticity [424].

The condition for superplasticity can be derived from the general expression for diffusional creep mechanism, which can be represented as

$$\dot{\varepsilon} = \frac{AD_bGb}{kT} \left(\frac{b}{d}\right)^p \left(\frac{\sigma}{G}\right)^n \quad (23)$$

where  $A$  is a constant,  $G$  the shear modulus,  $b$  the Burger's vector,  $n$  the stress exponent,  $p$  the grain size exponent,  $\dot{\varepsilon}$  the diffusional creep rate, and  $\sigma$  is the stress [422, 425, 426]. The condition for superplasticity is that the strain rate sensitivity  $m$  must be greater than 1/3, which can be expressed by the following equation:

$$m = \partial \ln \sigma / \partial \ln \dot{\varepsilon} > 1/3 \quad (24)$$

For materials with grain sizes less than 10  $\mu\text{m}$ , the stress exponent  $n \geq 2$  ( $m \leq 0.5$ ) and the grain size exponent  $p \approx 2$  [422, 425].

Superplasticity was observed in nearly nanometer-sized ( $\sim 300 \text{ nm}$ ) yttria-stabilized tetragonal zirconia crystals (Y-TZP), as the crystals elongated to about 100% under applied load [421, 427]. Another well-studied example is the mechanical characterization of composite crystals of 20 wt%  $\text{Al}_2\text{O}_3$  and Y-TZP. The value of the grain size exponent  $p$  was in the range 1.5–1.8 and the stress exponent  $\sim 2$  for the alumina-doped Y-TZP composite [428, 429]. The basic microstructure for superplasticity was maintained in these composite crystals by hindering the grain growth. These studies have derived the grain size and the stress exponents

using a diffusion model [Eq. (23)] for nearly nanocrystalline stabilized zirconia, and hence can be considered as fundamental experimental data to understand the superplastic behavior in fine-grained oxide ceramics.

In one of the earlier studies on model oxides such as titania ( $\text{TiO}_2$ ), a low temperature deformation bending was observed at 180 °C for nanocrystals with grain sizes less than 20 nm [430]. The  $\text{TiO}_2$  nanocrystals were also found to exhibit a brittle-to-ductile transition at room temperature. The strain rate sensitivities [ $m$  in Eq. (24)] of nanocrystalline ZnO and  $\text{TiO}_2$ , obtained by Mayo et al. [431], were found to decrease from 0.04 to 0.015 during sintering. The higher values of  $m$  in nanocrystalline oxides may imply the onset of superplasticity in these materials. But the values are much less than the ideal value of  $m$  for superplasticity, that is, 1/3. Recently, mechanical characterization has been reported for a variety of technologically important ceramics [432–441]. The studies ranged from simple oxide such as stabilized  $\text{ZrO}_2$  [433] to complex garnets [436], 1-2-3  $\text{YBa}_2\text{Cu}_3\text{O}_{7-x}$  superconductor [437], and composites [441]. However, the grain sizes of the oxide ceramics in these studies were on the order of 0.5  $\mu\text{m}$  or above. A recent study discusses the superplasticity behavior for the  $\text{ZrO}_2$ -reinforced

$\text{Al}_2\text{O}_3$  nanocomposite with finer grains of the constituent phases ( $\sim 100\text{--}400$  nm) [442]. From the technology point of view, it is important to obtain sufficient data on plasticity and ductility of nanocrystalline ceramic oxides for various industrial uses. Superplasticity finds use in net shape forming processes, extrusion or rolling, whereas ductile nature of a ceramic can be exploited to develop various composite materials [23]. Table 3 summarizes preparative routes, particle sizes, size-dependent properties, and potential areas of application of important oxide nanoparticles, which we have identified as representative classes of oxides having unique properties with tremendous application potential in various fields.

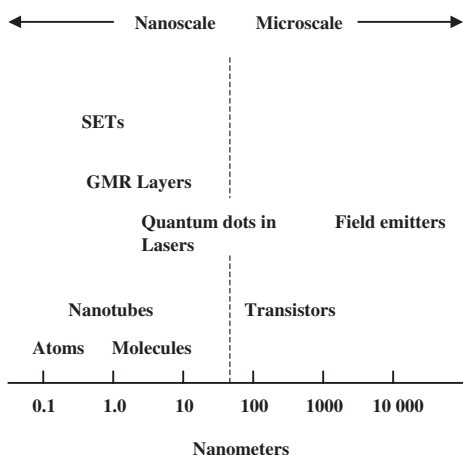
## 5. APPLICATIONS

### 5.1. Electronics

The present revolutionary changes in dimensions of functional nanoscale and microscale devices are summarized in a schematic diagram in Figure 30 [443]. The dimensions of nanoscale devices range between 0.1 nm to 50 nm. However, 0.1 nm represents only the possible lowest size limit and

**Table 3.** Summary of some model oxide nanoparticles noted for their unique size-dependent properties.

Oxide	Preparative route	Particle/Crystallite size (nm)	Size-dependent properties	Potential areas of application	Ref.
CuO	Electrochemical route	4, 6, 25	Electronic band structure	Catalysis	[279]
ZnO	Sol-gel	$3.5 \pm 1.5$	Optical absorption-emission	Optical display devices	[300]
$\text{SiO}_2$	Thermal oxidation of Si nanoparticles prepared through microwave plasma-gas phase synthesis	$\sim 8$ nm core with 1–1.5 nm oxide layer	Optical absorption-emission	Microelectronic and optoelectronic devices	[304]
$\text{Eu}_2\text{O}_3$	Laser ablation	4, 6, 12, 18	Optical absorption-emission	Optical display devices	[312]
$\text{Eu:Y}_2\text{O}_3$	Sol-gel	Range: 10–20	Optical absorption-emission	Optical display devices	[255]
$\text{CeO}_{2-\delta}$	Sol-gel	10, 20, 30, 150	Electrical conductivity	Gas sensors, fuel cells, and ionic membranes	[327]
$\text{PbTiO}_3$	Coprecipitation	31, 39, 59, 81	Dielectric constant and phase transition	Nonvolatile memory devices	[339]
$\gamma\text{-Fe}_2\text{O}_3$	Coprecipitation and laser pyrolysis	Range: 3–14	Magnetization, superparamagnetism at a critical size of $\sim 5$ nm	Information storage devices, medical imaging	[275]
$\text{CoFe}_2\text{O}_4$	Microemulsion	Range: 2–5	Comparison of magnetic susceptibility of as prepared ferrofluids and samples annealed at different temperatures	Magnetic memory, ferrofluids, medical diagnosis, bioprocessing	[274]
$\text{Ni}_{0.48}\text{Zn}_{0.48}\text{Fe}_{2.04}\text{O}_4$	Colloidal precipitation	Range: 10–30	Magnetic permeability	Low loss soft ferrites in memory devices	[22]
$\text{BaO} \cdot 6\text{Al}_2\text{O}_3$	Microemulsion	30	Enhanced catalytic activity	Catalytic combustion of hydrocarbons	[192]
$\text{CeO}_{2-x}$	Inert gas condensation	—	Catalytic conversion of CO to $\text{CO}_2$ at lower temperatures	Catalytic converters	[389]
$(\text{Y}_2\text{O}_3)/\text{ZrO}_2$	Metal-organic chemical vapor deposition	Range: 10–100	Thermal conductivity	Thermal barrier coating	[411]
$\text{TiO}_2$	—	Range: $\sim 14\text{--}400$	Hall-Petch behavior	Net shape forming processes, extrusion, rolling, fabrication of ductile composites	[415]



**Figure 30.** Schematic classification of functional devices on a nanometer scale [443].

requires addressing of several issues related to the device fabrication based on particles of such small dimensions. For example, complexities associated with the electrical measurements on quantum dots have been a major area of research [444]. Among various nanodevices, nanoparticle-based single electron tunneling (SET) devices are of interest to electronics. The SET devices have been developed based on the concept of controlling the charge transfer through the Coulomb gap by applying a suitable potential across a nanoparticle, which when connected in circuit can be described as an island surrounded by high potential walls [445]. The island can be considered as electrically neutral initially with a specified number of electrons present as in any other material. In order to add an electron to the island, the electrostatic repulsive forces between the electrons present in the island and incoming electrons have to be overcome with sufficient electric field potential. The electric field  $E$  is inversely proportional to the island size, implying that charging of nanoscale islands takes place under strong electric field. The charging phenomenon is more adequately explained based on the charging energy  $E_c$ , which is given by the expression

$$E_c = e^2/2C \quad (25)$$

where  $e$  is the electronic charge and  $C$  is the capacitance of the island [446]. As the island sizes approach De Broglie wavelength, discretization or size quantization of the energy levels set in [447, 448]. The electron addition energy ( $E_a$ ) under such conditions can be expressed as a sum of charging energy [ $E_c$ ; Eq. (25)] and quantum kinetic energy ( $E_k$ ) of the added electron. The expression can be written as

$$E_a = E_c + E_k \quad (26)$$

where  $E_k = 1/g(\epsilon_F)V$  in which  $g(\epsilon_F)$  is the density of states and  $V$  is the volume of the island. For devices having nanoscale islands of dimensions  $\sim 100$  nm, the electron addition energy is dominated by the term  $E_c$  and is about 1 meV for temperature corresponding to 10 K. Thermal fluctuations suppress the single electron charging phenomenon when  $E_a < 10k_B T$ . However, for islands of sizes on the order of  $\sim 10$  nm,  $E_a$  is about 100 meV and single electron charging

may occur at much higher temperatures close to room temperature [445]. In most of the digital single electron devices, the  $E_a$  limit has to be even higher (a few electron volts) in order to overcome the thermal fluctuations and facilitate single electron conduction. In other words, the island size must be scaled down to  $\sim 1$  nm so that the two energy terms,  $E_k$  and  $E_c$ , in Eq. (26) are comparable. The successful fabrication of devices based on islands of such small dimensions (quantum dots) is of utmost importance for the purpose of operating the device at temperatures close to room temperature. However, the device fabrication processes are highly complicated and require advanced preparative routes, especially to incorporate nanoparticles in large-scale integrated circuits.

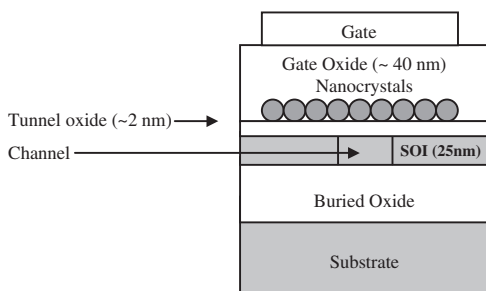
Single electron conductivity through nanoparticles results in a characteristic I–V curve, which shows step-like behavior (Coulomb staircase) [444, 449]. This step-like behavior can be attributed to the increase in the potential energy for each electron transfer, which arises out of the electrostatic repulsion between the incoming electron and the additional electron(s) already present in the nanoparticle. Another feature of the mono-electron conductivity in nanoparticle systems is the negative differential resistance (NDR), which is related to the quantized energy levels due to the zero-dimensional sizes of the particles [450]. As an important development in the exploration of the single electron conductivity phenomenon, the use of a scanning tunneling microscope (STM) for measurements on nanoparticles was experimentally demonstrated [451]. Some of the important results on single electronic conductivity through the nanoparticles are the studies on Coulomb gap in single junctions [452], Coulomb gaps and Coulomb staircases in a single metal granule [453], the correlation of nonlinear current characteristics to the particle sizes [454], and the peculiar effects of energy level quantization [455, 456]. These contributions have initiated urgent research activities for further exploitation of their use in electronic device fabrication.

The use of single charge trapping in the design of digital memory was demonstrated as early as in 1986 by Averim and Likharev [457]. The sustained efforts in subsequent years have resulted in the fabrication of a number of devices based on the principle of single electron tunneling. Some examples are sensitive high-frequency electromagnetic wave detectors and digital electronic devices [458], high sensitivity electrometers [459], and quantum dot transistors [460]. Presently, there is increasing interest in the fabrication of nanoelectronic devices aided by the simulation studies called quantum computing, which has been developed based on the laws of quantum mechanics [461]. Apart from the objective of miniaturization in electronic devices, exploitation of single electron tunneling may greatly simplify electronic circuits, as well as improve device performance. In particular, oxide nanoparticles, which are characterized by a relatively high chemical and thermal stability, can be incorporated in the fabrication of various electronic devices. Presently, fine oxide nanoparticle slurries are being used in the microelectronic industry for the chemical mechanical planarization (CMP) process [87, 462, 463]. The process enables multi-level metallization (MLM) on planar wafers. However, the sizes of the particles used for CMP are very critical and

have to be in the nanometer range, as larger particles damage the wafer surface, and the effects would be detrimental to further fabrication process [87]. The potential use of oxide nanoparticles in the development of information storage devices will be discussed in the next section. Currently, researchers are also trying to implement high dielectric constant polymer-ceramic nanocomposite materials in decoupling capacitor applications [464], which will have a promising impact on microelectronic device packaging. Further development in integrated circuit (IC)-related devices is the exploitation of ultra-low  $k$  nanoporous  $\text{SiO}_2$  dielectric for interconnect dielectrics [465].

## 5.2. Information Storage Devices

The storage of voluminous information or data in a small chip is a major requirement in academia as well as in industry. This ever-increasing demand for high information storage capacity has led to the development of innovative fabrication of memory devices. In particular, nanocrystal-based memory devices have attracted great attention in recent years [466–476]. A typical nanocrystal-based flash memory device has metal-oxide semiconductor field effect transistor (MOSFET) configuration in which the conventional gate dielectric is replaced by a gate stack consisting of a thin tunneling oxide layer, a layer of semiconductor nanocrystals (crystallite size  $<10$  nm) embedded in  $\text{SiO}_2$ , and a thicker oxide layer (Fig. 31). The storage process can be initiated by applying a positive potential to the gate. Consequently, the conduction band of the thin tunneling oxide layer is lowered. This results in the tunneling of electrons from the substrates to the nanocrystals. The Coulomb blockade effect controls the flow of electrons to the nanocrystals, thereby making single-electron charging a self-limited process. The electrons get trapped inside the nanocrystals, as the overlying thick oxide layer acts as a barrier and inhibits further tunneling. The charging potential for nanocrystals increases in steps (Coulomb staircase), which in this case is called the MOSFET threshold potential. The step-like increase in the threshold potential enables the storage of the multibit information in the device [475]. The information stored in the device can be read by measuring the saturation current corresponding to a gate potential significantly less than that required for programming. The application of a reverse potential leads to erasing of the memory as the



**Figure 31.** Schematic diagram of a nanocrystal gate stack used in a memory device. Reprinted with permission from [473], A. Dutta et al., *Jpn. J. Appl. Phys.* 39, L855 (2000). © 2000, Japan Society of Applied Physics.

reverse electron flow takes place from the nanocrystals to the channel.

The thickness of the tunneling oxide layer in a nanocrystal memory device is on the order of 2 nm, which is less than the oxide layer thickness ( $>7$  nm) in conventional electrically erasable programmable read-only memory (EEPROM). EEPROM requires programming voltages larger than 10 V, whereas nanocrystal memory works at a much lower operating voltages (3 V). Therefore, the endurance to write-erase cycles and power consumption are superior in nanocrystal memories compared to EEPROM [470]. But the retention time of the nanocrystal memories is poor compared to commercially available EEPROM ( $\sim 10$  years). Barring the poor retention time, the nanocrystal memory can be considered for applications in quasi-nonvolatile memory where write-erase cycles and low power consumption are considered important [475]. King et al. [470] fabricated a quasi-nonvolatile memory cell incorporating nanocrystalline Si-rich oxide as the charge storage layer, which was deposited using a low-pressure chemical vapor deposition process (LPCVD). The refresh time and the endurance of the device were found to be improved when compared to the devices incorporating Si or Ge nanocrystals as charge storage layers [468]. The device performance was assessed by recording the write/erase time at different operating voltages (4 to 6 V). The device registered fast write/erase time approaching that of dynamic random access memory (DRAM) at a relatively low operating voltage.

On the other hand, we have witnessed outstanding growth in the fabrication of high-density information storage devices based on magnetic materials. Remarkable storage capacity has been achieved in such devices [477–480]. As the bit density increases, the issues related to the integration of the device also become complex. Among the various challenges, obtaining an acceptable signal-to-noise ratio in high-density recording media needs considerable attention. One way to achieve low noise in magnetic recording devices is to incorporate completely decoupled single domain particles or particles having dimensions comparable to that of a single magnetic domain in high-density recording bits. The spin reversal in these small particles takes place at much higher coercive fields ( $H_c$ ,  $\sim 2000$ – $3000$  Oe) through coherent rotation of magnetization [481]. The magnetic recording medium is a continuous multigrain film with no specific patterning. The decisive parameter in the fabrication of magnetic recording device is the width-to-length ratio of the rectangular shaped bit. As the bit size is scaled down, the grain size becomes comparable to the bit length. This essentially leads to an increase in noise level, which can be imaged directly using magnetic force microscopy (MFM). The MFM image reveals the irregular transition between bits as the total bit length gets reduced to about 200 nm (longitudinal recording media) [481]. The solution for smoothing the bit edges, thereby reducing the noise level, is the incorporation of magnetic nanoparticles in the recording devices. Surface-modified single domain superparamagnetic oxide nanoparticles [273, 274, 361, 363] are potential candidates for this purpose. However, the issues related to the stability of superparamagnetic nanoparticles have to be addressed in order to implement them successfully in the fabrication of magnetic recording devices [481].

### 5.3. Photonics

In recent years, nanoparticles of sizes in the range 1–10 nm are being studied as potential optoelectronic materials. Their unique features, which can be attributed to electron-hole pair (exciton) quantum confinement, lead to bright luminescence or appearance of forbidden transitions [482]. The prospective areas of application of these materials include the development of solid-state lasers for color displays [483], high-density optical data reading and storage [484, 485], and infrared laser viewers and indicators [486, 487]. Among oxides, rare-earth ion-doped oxide nanocrystals have been an important class of materials because of their interesting luminescence properties, which can be exploited in various multicolor phosphor applications [488, 489]. The luminescence properties are dependent on the electronic structure and the concentration of the dopant ion when confined in a host matrix. The emission characteristics become enhanced when the matrix crystallites are on the order of a few nanometers, so that the rare earth ions are quantum confined in crystals of sizes comparable to the exciton diameter (<10 nm). Under these confined states, the luminescence efficiency is enhanced due to the hybridization of various electronic states of the rare earth ion in a nanoparticle environment [490].

Fluorescence intermittency has been observed in II-VI CdSe semiconductor quantum dots on a variable time scale [491]. Recently, Barnes et al. [488] have demonstrated spectacular “on-off” blinking characteristics on a variable time scale in  $\text{Eu}^{3+}$  ion doped  $\text{Y}_2\text{O}_3$  nanocrystals (5–15 nm) on continuous illumination of the sample with an Ar ion laser. From the varying intensities of the diffraction limited spots as a function of time, the “on-off” profiles in the luminescence of the doped nanocrystals were sketched. The duty factor (“on” time as a percentage of total measurement time) was found to vary significantly from particle to particle. The intensity-versus-time spectra indicated an inverse relation between the two variables, that is, some nanoparticles exhibited a very short “on” time with high intensity, whereas for some other lower intensity has been recorded for longer “on” time. The possible reasons for the intermittent fluorescence were attributed to local symmetry fluctuations and resultant excited state partitioning. It is interesting to correlate the effect of local symmetry variations on the observed intermittent fluorescence. Upon schematically plotting the electric dipole transition moment against the local symmetry coordinate, one can derive various logic states that can be randomly accessed by the dopant ion in the crystal. Depending on the number of ions in a single particle, there would also be multiple bright states due to transitions between intermediate states [488]. The laser source provided the required amounts of thermal energy for dipole transitions among various intermediate states within the oxide nanocrystal. The distinct “on-off” states in fluorescent emission of the doped oxide nanocrystals can be suitably tuned for the development of relatively faster and efficient data storage devices. However, for the larger particles, the fluorescence was no longer discrete due to the overlap of emissions from various energy levels.

Silicon (Si)-based nanostructures have been the focus of research in photonics due to their potential use in the fabrication of various optical and optoelectronic devices [492].

The quantum confinement mechanism responsible for the photoluminescence in Si nanocrystals has been well documented in the literature [100, 493]. Being the luminescent centers in porous Si, studies on the photoluminescence of small clusters of Si has been of great interest [494]. Photoluminescence of small clusters of  $\text{SiO}_x$  (1 to 10 nm) prepared by laser vaporization of c-Si target has been investigated *in-situ* during processing and compared with *ex-situ* scanning electron microscopy (SEM) analysis by Geohagan et al. [495]. The study reveals the advantage of probing the luminescence of individual nanoparticles prior to their deposition onto a substrate to form a thin film. By carefully controlling the oxidation, the interfacial oxide thickness and hence the resultant properties of individual nanoparticles can be varied.

Nanostructures with three-dimensional periodicity comparable to the wavelength of visible light have great significance, as they play a major role in the development of a variety of modern day optoelectronic devices. With such materials, it is possible to have microscopic light manipulation by tuning the photonic bandgap [496, 497]. The optical band gap arises in this special class of three-dimensional photonic crystals due to periodic variations in the dielectric constant, which essentially prohibits electromagnetic wave propagation throughout a specified frequency band. Self-assembly has been developed in recent years as a cost effective and efficient method for the preparation of such three-dimensionally ordered structures. Processing of a typical self-assembled three-dimensionally ordered structure of colloidal spherical silica have been discussed and illustrated under Section 2.6 Sol-Gel (Colloidal) Processing (Fig. 8) [83]. The method can easily replace conventional lithographic techniques because of less complexity associated with the process. The three-dimensional self-assembled colloidal spherical silica ( $\text{SiO}_2$ ) particles have characteristic photoluminescence and are called as opals [498]. However, the theoretical calculations showed that the opals have a pseudo-optical band gap [499]. This has further triggered the quest for finding novel materials with complete optical band gap. The result was the discovery of “inverse opals,” which have a characteristic microstructure of air spheres separated by dielectric medium [500–502]. Blanco et al. [502] used inverse silica ( $\text{SiO}_2$ ) opal as a template and replaced the  $\text{SiO}_2$  spheres with Si using a CVD process to prepare a complete three-dimensional optical band gap material. The SEM pictures of the sample clearly showed the microstructure comprising air spheres surrounded by Si. The photoluminescence study of the three-dimensional inverse opal crystals indicated that the center and the width of the optical band gap were sensitive to the degree of Si filling. The study also illustrated an effective method of tuning the optical band gap of an inverse opal photonic crystal by appropriate filling.

### 5.4. Sensors

Detecting the presence of various types of gases so as to prevent health hazards to people in industry as well as to reduce pollution in the environment is a major modern day requirement. As traditional methods such as gas chromatography and chemical routes are tedious and time consuming, the motivation is to find an alternative technique involving



miniaturized, highly sensitive solid state “electronic noses” or sensors [503]. Semiconducting metal oxide materials have been especially attractive for this purpose because of their easy availability, relatively low cost, and simplicity. An example of such a sensor is the semiconductor oxide-based multi-sensor array fabricated for environmental monitoring, which is carried out by measuring the change in oxide ion conductivity due to space charge effect arising out of gas adsorption or defect formation on the surface [504]. As the critical parameters that improve the sensitivity and selectivity of the sensing devices are the contributions from surfaces and interfaces to the total conductivity, a comprehensive knowledge of atomic level diffusion along surfaces and interfaces is highly desirable. Because of the higher values of surface to bulk ratio, the gas sensors based on nanomaterials exhibit improved performance. Some of the semiconducting oxide materials that have been used for environmental and air quality monitoring are listed in Table 4.

Critical parameters such as sensitivity and selectivity can be improved by suitably doping or tuning the materials’ microstructures. The gas sensitivity implies quantifying the gas concentration at the ppm level in a gaseous mixture, whereas the gas selectivity is the detection of specific gases from the mixture. The gas sensitivities of nanocrystalline semiconductor oxides have been found to increase with decreasing particle size. Improved sensitivities have been reported for oxide particle sizes in the range of 5–50 nm [514, 517–519]. For instance, the sensitivity of the H<sub>2</sub> gas sensor based on SnO<sub>2</sub> has been found to improve dramatically (~an order of magnitude increase) for particle sizes smaller than 10 nm (Fig. 32) [503]. However, the critical particle size for dramatic improvement in sensitivity depends on the sample history, such as the electronic structure, the dopant concentration, and the preparative method used.

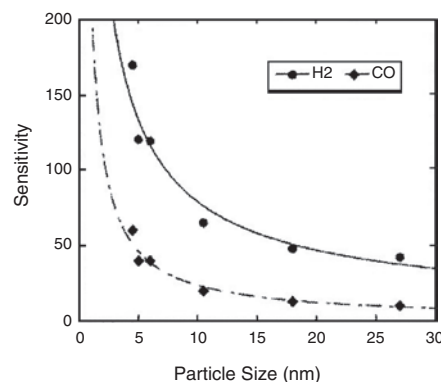
The particle size effect on the observed improvement in sensitivity can be explained by relating the depth of the space charge formation (surface depleted layer) to the particle size. The depth of the space charge formation can be represented by Debye length, which can be related to other experimental parameters such as temperature and carrier concentration by the expression

$$L_D = (\epsilon_0 K T / n_0 e^2)^{1/2} \quad (27)$$

where  $L_D$  is the Debye length,  $\epsilon_0$  is the static dielectric constant,  $n_0$  is the total carrier concentration,  $e$  is the carrier charge,  $K$  is the Boltzmann constant, and  $T$  is the absolute temperature. When  $L_D$  is less than or close to particle

**Table 4.** Nanocrystalline oxide gas sensors [503].

Oxide type	Sensitive to	Ref.
SnO <sub>2</sub>	H <sub>2</sub> , CO, NO <sub>2</sub> , H <sub>2</sub> S, CH <sub>4</sub>	[504–506]
TiO <sub>2</sub>	H <sub>2</sub> , C <sub>2</sub> H <sub>5</sub> OH, O <sub>2</sub>	[507, 508]
Fe <sub>2</sub> O <sub>3</sub>	CO	[509]
Cr <sub>1.8</sub> Ti <sub>0.2</sub> O <sub>3</sub>	NH <sub>3</sub>	[510, 511]
WO <sub>3</sub>	NO <sub>2</sub> , NH <sub>3</sub>	[512, 513]
In <sub>2</sub> O <sub>3</sub>	O <sub>3</sub> , NO <sub>2</sub>	[514, 515]
LaFeO <sub>3</sub>	NO <sub>2</sub> , NO <sub>x</sub>	[516]



**Figure 32.** The particle size effect on the sensing characteristics of SnO<sub>2</sub>-based gas sensors. Reprinted with permission from [503], F. Cosandey et al., JOM-e 52, October (2000). © 2000, The Minerals, Metals, & Materials Society.

radius, the oxide nanoparticles have maximum sensitivity. Under these conditions, the sensitivity ( $S$ ), which can be expressed as a ratio of change in the conductivity to the total conductivity, can be related to the Debye length ( $L_D$ ) by a proportionality constant ( $\Delta n/n_0$ ) where  $\Delta n$  is the charge carrier concentration. The equation for sensitivity ( $S$ ) corresponds to

$$S = \Delta\sigma/\sigma_0 = (\Delta n/n_0)L_D \quad (28)$$

The above expression helps to optimize various parameters that improve the sensitivity of sensors based on semiconducting oxide nanoparticles [503]. Another parameter, selectivity, of the gas sensor shows marked improvement with enhanced gas adsorption on nanoparticles with larger surface to volume ratio or chemically modified particles [506, 520]. A recent study illustrates the successful synthesis of various nanostructured semiconducting oxides (ZnO, SnO<sub>2</sub>, In<sub>2</sub>O<sub>3</sub>, CdO, and Ga<sub>2</sub>O<sub>3</sub>) in a belt-like morphology [521]. The unique features of these oxide nanobelts, such as well-defined geometry and perfect crystallinity, could be exploited for the development of novel gas sensors.

## 5.5. Catalysts and Fuel Cells

We have discussed some of the frontier areas where oxide nanoparticles have been identified as potential materials for future developments. Now we will briefly scan other possible areas wherein these versatile materials can be used. Table 5 presents a summary of emerging applications of oxide nanoparticles in different fields. The second and third columns list the energy, catalysis, structural, and biological applications of nanoparticles [522, 523].

Oxide nanoparticles having very high surface area are attractive in catalytic applications. Recent advances in sol-gel and aerogel preparative routes have enabled the preparation of high surface area powders, which when consolidated form a porous structure [524]. The consolidated porous nanostructures have enormous potential in catalytic applications. Moreover, the surface chemical properties of consolidated nanocrystalline powders can be exploited to adsorb toxic chemicals [388]. Recently, inorganic mesoporous oxides with well-controlled pore sizes in the range

**Table 5.** Summary of emerging areas of application of oxide nanoparticles [522, 523].

Electronic, magnetic, and optoelectronic applications	Energy, catalytic, and structural applications	Biological applications
Information storage devices	Fuel cells	Drug delivery
Single electron tunneling (SET) devices	Ceramic membranes	Biomagnetic separations
Chemical mechanical polishing (CMP) supports	Automotive catalysts	Biodetection and labeling
Multilayer ceramic capacitors (MLC)	Photocatalysts	Antimicrobial detoxification of microorganisms
Electroconductive coatings	Propellants	Magnetic resonance imaging (MRI) contrast agents
Magnetic fluid seals	Scratch-resistant coatings	Orthopedics
Quantum optical devices	Structural ceramics	
	Thermal spray coatings	

1 to 10 nm have been developed [525]. The applications of these oxides include catalysis, filtration, and separation. The role of nanostructured metal oxides in catalyzing various chemical reactions has already been summarized in Table 2. Many of these reactions have the potential for commercial production or have already been employed in various industrial processes.

Apart from potential use in catalytic applications, mesoporous transition metal oxides are also suitable for use in electrochemical applications as anode materials [526], as they improve cell performance by increasing storage capacities, lifetimes, and charge/discharge rates. The use of nanoporous or mesoporous materials in the development of fuel cells results in superior characteristics such as high storage capacity, higher rates of charge and discharge, and good control over absorption and charge transfer process. For example, materials with high storage capacity for H<sub>2</sub> (or CH<sub>4</sub>) in small volume are of particular interest to the fuel cell industry for developing cost effective, efficient, environmentally friendly fuel cell-powered vehicles or fuel cell power generation units [527–529]. The porous nanostructured materials can also be used in the effective removal of H<sub>2</sub>S, H<sub>2</sub>O, CO, and/or CO<sub>2</sub> from natural gas wells; therefore the oil transfer process from the well to the end-user takes place efficiently.

## 5.6. Structural and Biological Applications

Rapid advancements in nanoscience have led to the discovery of various forms of nanostructured materials having unique features, which could probably revolutionize diverse fields ranging from electronics to biology. A recent overview examines the future potential applications of a variety of exciting nanomaterials including nanotubes, nanobundles, nanoparticles, and supramolecular nanostructures [530]. Oxide nanoparticles embedded in a polymer matrix form a nanocomposite structure, which is of interest in a variety of industrial applications such as microelectronic packaging [464]. Composite materials can also be very effective candidates in lightweight replacement for conventional metals in automobiles in order to improve fuel efficiency and stability against corrosive environments. However, successful dispersion of nanoparticles in polymer matrix and moulding them to desired shapes require advanced processing routes. The range of application of nanocomposites is not only restricted to automobiles but also to manufacturing various components for the building and construction industry, and various home appliances [523].

The beginning of the new century has witnessed groundbreaking preparations by nations to counter unconventional warfare against humanity. One of the major threats is the biological weapon, which becomes operative when small amounts of deadly disease-causing microorganisms are easily spread among living beings. It is interesting to note that the ultrafine powders can play a rescuer's role in such situations. For example, airborne heat-resistant anthrax bacteria are killed at room temperature by the airborne formulation of MgO nanoparticles and other reactive components. The entire colony forming units (CFU) of the deadly bacteria are detoxified within 5–20 minutes when bombarded with the nanoparticle formulations. Similarly, several nanoparticle formulations are found to be effective in the treatment against *E. coli* bacteria [523, 531].

Another prospective field for the application of nanoparticles is the pharmaceutical industry, where nanoparticles act as vehicles for drug delivery. The hydrophobicity of pharmaceutical drugs often prevents their assimilation in the body. Suitable nanoparticle formulations allow the drugs to be assimilated in the body by acting as an effective medium for the transportation [523]. Mesoporous silica (SiO<sub>2</sub>) coatings are being investigated as potential materials for medical applications [532].

## 6. SUMMARY

In this chapter, we have reviewed various processing routes, characterization, properties, and potential areas of applications of oxide nanoparticles. Significant progress has been made in the development of processing routes for oxide nanoparticles. These routes range from the simplest possible solution techniques to sophisticated laser ablation processes. Over the years, each processing route has been modified to prepare oxide nanoparticles with desired properties. In particular, plasma-assisted processing, sonication, hydrothermal, and sol–gel (colloidal) processing have been regularly used for the synthesis of a wide variety of oxide nanoparticles. Being one of the earliest well-established methods, sol–gel (colloidal) processing has been proven to be very effective for the synthesis of oxide nanoparticles and their self-assembly, which is currently being pursued as one of the frontier areas in the processing of nanostructured materials. Another major achievement in processing is the successful synthesis of surface-modified single-domain superparamagnetic nanoparticles.

As nanoparticle dimensions are progressively scaled down, highly accurate spectroscopic measurements are often required for obtaining crucial information about the structure of oxide nanoparticles. Frequently used spectroscopic characterization techniques have been reviewed based on the developments in oxide nanoparticle characterization. X-ray diffraction (XRD) continues to be the most common technique for the determination of grain size, strain, and phase characterization of oxide nanoparticles. However, for very small particles of dimensions less than 5 nm, probing the local structure using extended X-ray absorption fine structure (EXAFS) spectroscopy is preferred. While techniques such as X-ray photoelectron spectroscopy (XPS) and secondary ion mass spectra (SIMS) probe the surface structure and composition, the optical absorption-emission spectra reflect the band gap expansion due to quantum confinement in oxide nanoparticles. As for the characterization of the vibrational frequencies of various atoms in oxide nanoparticles, Raman and IR spectroscopies have been used. More specialized technique such as Mössbauer spectroscopy correlates the local order and magnetic properties of nanoferrites.

The unique properties of nanoparticles have always been subjects of interest since their discovery. We have reviewed the varied and interesting properties of oxide nanoparticles (electronic, optical, electrical, ferroelectric and dielectric, magnetic, catalytic, thermal, and mechanical) based on selected recent studies from the literature. The objectives of these studies were to understand the changes in properties as a function of particle size. An important conclusion from the extensive review of the properties of the oxide nanoparticles is that there exists a critical size regime below which the properties are truly unique. The review indicates that the critical size regimes for various characteristics need further investigation. Hence, the major future challenge would be to obtain concrete experimental evidence to prove theoretical predictions in those critical size regimes and delineate the transition in properties, which would help to unravel the intricate processing-nanostructure-property relationship in oxide nanoparticles. Research in this direction will also be helpful in selecting the critical size and dimension for the purpose of implementing oxide nanoparticles in various devices.

Potential areas of application of oxide nanoparticles have been identified with a major focus in areas such as electronics, information storage devices, photonics, and sensors. The applications in other areas such as catalysis and biology have significant relevance at present. We have briefly scanned the catalytic, structural, and biological applications of oxide nanoparticles. As nanoparticle research spreads its wings at a rapid pace, a complete review on this subject is an arduous task. However, we have made a modest attempt to analyze significant developments in the oxide nanoparticle research and their possible applications in various industries.

## GLOSSARY

**Agglomeration** The term refers to the formation of agglomerates (secondary particles) when primary particles are held together by weak surface forces (soft agglomerates) such as van der Waals forces or capillary forces or by strong

chemical bonds (hard agglomerates) during the synthesis of ceramic powders.

**Domains** Under favorable energetics, certain regions termed domains are formed in materials within which a given property is identical with respect to magnitude and direction. For example, the formation of domains, wherein each domain has identical electric or magnetic dipole moments aligned in a particular direction, in ferroelectric or ferromagnetic samples.

**Grains** Individual crystals, which combine to form a polycrystalline structure. The sizes of the grains in a material can be estimated from the broadening of the peaks in X-ray diffraction (XRD) patterns.

**Microstructure** A term used to describe details such as the grain size, structure of interfaces, various defects, and pores present in a synthesized material.

**Nanomaterials** A broad class of materials that includes nanometer-sized crystallites, nanometer-sized powders, macroscopic objects, and films composed of nanometer-sized particles or any phases combined with a spatial distribution that involves nanometer length scale of less than 100 nm in at least one dimension.

**Nanoparticles** The term refers to particles of sizes in the range of 1–100 nm. Depending on the preparative conditions, nanoparticles may have polycrystalline or single crystalline structure. Nanoparticles of sizes less than 5 nm are termed as quantum dots.

**Nanoscale devices** Nanostructure-based devices that exhibit unique characteristics such as multistate switching phenomena, resonant tunneling, quantum interference, and single electron effects due to quantum size effect.

**Nanostructure** Typical structure of a material with nanometer-sized microstructure.

**Quantum size effect** The size effects on the properties of nanoparticles, as the charge carriers in nanoparticles are quantum confined for particle sizes comparable to the wavelengths of the de Broglie electrons or phonons, or the mean-free-paths or diameters of the excitons.

**Self-assembly** Spontaneous stepwise assembly of molecules or nanoparticles onto a substrate.

## ACKNOWLEDGMENT

The authors thank Mr. M. C. Li for assistance with the preparation of the manuscript.

## REFERENCES

1. R. P. Feynmann, *Eng. Sci.* 23, 22 (1960).
2. D. M. Eigler and E. K. Schweizer, *Nature* 344, 524 (1990).
3. G. E. Moore, Proc. IEEE IEDM, IEEE cat. No. 75CH1023-1 ED 11 (1975).
4. J. Kreuter, *J. Anat.* 189, 503 (1996).
5. J. Kreuter, *Pharm. Biotechnol.* 6, 463 (1995).
6. B. R. Rosen and T. J. Brady, *J. Comput. Assist. Tomog.* 17, S36 (1993).
7. A. G. Tibbe, B. G. de Groot, J. Greve, P. A. Liberti, G. J. Dolan, and L. W. Terstappen, *Nat. Biotechnol.* 17, 1210 (1999).
8. L. Levy, Y. Sahoo, K.-S. Kim, E. J. Bergey, and P. N. Prasad, *Chem. Mater.* 14, 3715 (2002).

9. C. A. Mirkin, R. L. Letsinger, R. C. Mucic, and J. J. Storhoff, *Nature* 382, 607 (1996).
10. F. C. Meldrum, B. R. Heywood, and S. Mann, *Science* 257, 522 (1992).
11. R. W. Siegel, *Mater. Sci. Eng., A* 168, 189 (1993).
12. H. Gleiter, *Nanostruct. Mater.* 6, 3 (1995).
13. Y. Li, Q. Fu, and M. Stephanopoulos, *Appl. Catal. B: Environmental* 27, 179 (2000).
14. Y. Shi, K. Saito, H. Ishikuro, and T. Hiramoto, *J. Appl. Phys.* 84, 2358 (1998).
15. T. Kubo and H. Nozoye, *Nano Lett.* 2, 1173 (2002).
16. M. D. Sacks and T. Y. Tseng, *J. Am. Ceram. Soc.* 67, 526 (1984).
17. J. A. Switzer, C. J. Hung, L. Y. Huang, E. R. Switzer, D. R. Kammiller, T. D. Golden, and E. W. Bohannon, *J. Am. Chem. Soc.* 120, 3530 (1998).
18. J. H. Fendler, *Chem. Mater.* 13, 3196 (2001).
19. R. Boukherroub, D. D. M. Wayner, G. I. Sproule, D. J. Lockwood, and L. T. Canham, *Nano Lett.* 1, 713 (2001).
20. A. Vertes, Gy. Vanko, Z. Nemeth, Z. Klencsar, E. Kuzmann, Z. Homonnay, F. H. Karman, E. Szocs, and E. Kalman, *Langmuir* 18, 1206 (2002).
21. G. H. Beall and L. R. Pinckney, *J. Am. Ceram. Soc.* 82, 5 (1999).
22. T. Y. Tseng and J. C. Lin, *IEEE Trans. Magn.* 25, 4405 (1989).
23. H. Gleiter, *Prog. Mater. Sci.* 33, 223 (1989).
24. R. W. Siegel, in "Encyclopaedia of Applied Physics," edited by G. L. Trigg, VCH, Weinheim, 1994, Vol. 11.
25. R. W. Siegel, in "Nanomaterials: Synthesis, Properties and Applications," edited by A. S. Edelstein and R. C. Cammarata, IOP Publishing, Philadelphia, 1998, p. 201.
26. R. W. Siegel, S. Ramasamy, H. Hahn, Z. Li, T. Lu, and R. Gronsky, *J. Mater. Res.* 3, 1367 (1988).
27. R. W. Siegel, *Annu. Rev. Mater. Sci.* 21, 149 (1991).
28. G. J. Thomas, R. W. Siegel, and J. A. Eastman, *Scr. Metall. Mater.* 24, 201 (1990).
29. W. Wunderlich, Y. Ishida, and R. Maurer, *Scr. Metall. Mater.* 24, 403 (1990).
30. S. K. Ganapathi and D. A. Rigney, *Scr. Metall. Mater.* 24, 1675 (1990).
31. K. Sattler, G. Raina, M. Ge, N. Venkateswaran, J. Xhie, Y. X. Liao, and R. W. Siegel, *J. Appl. Phys.* 76, 546 (1994).
32. S. Ramasamy, J. Jiang, H. Gleiter, R. Birringer, and U. Gonser, *Solid State Commun.* 74, 851 (1990).
33. J. M. McHale, A. Auroux, A. J. Perrotta, and A. Navrotsky, *Science* 277, 788 (1997).
34. K. T. Jacob, K. P. Jayadevan, R. M. Mallya, and Y. Waseda, *Adv. Mater.* 12, 440 (2000).
35. S. S. Flaschen, *J. Am. Chem. Soc.* 77, 6194 (1955).
36. R. C. Garvie, *J. Phys. Chem.* 82, 218 (1978).
37. G. Skandan, C. M. Foster, H. Frase, M. N. Ali, J. C. Parker, and H. Hahn, *Nanostruct. Mater.* 1, 313 (1992).
38. G. P. Johnston, R. Muenchausen, D. M. Smith, W. Fahrenholtz, and S. Foltyn, *J. Am. Ceram. Soc.* 75, 3293 (1992).
39. P. M. Kumar, P. Borse, V. K. Rohatgi, S. V. Bhoraskar, P. Singh, and M. Sastry, *Mater. Chem. Phys.* 36, 354 (1994).
40. D. Wolf and J. F. Lutsko, *Phys. Rev. Lett.* 60, 1170 (1988).
41. B. D. Cullity, "Elements of X-ray Diffraction," Addison-Wesley, New York, 1978.
42. J. A. Eastman, Y. X. Liao, A. Narayanaswamy, and R. W. Siegel, *Mater. Res. Symp. Proc.* 155, 255 (1989).
43. U. Balachandran, R. W. Siegel, and T. Askew, *Nanostruct. Mater.* 5, 505 (1995).
44. C. A. Melendres, A. Narayanaswamy, V. A. Maroni, and R. W. Siegel, *J. Mater. Res.* 4, 1246 (1989).
45. J. C. Parker and R. W. Siegel, *J. Mater. Res.* 5, 1246 (1990).
46. J. C. Parker and R. W. Siegel, *Appl. Phys. Lett.* 57, 943 (1990).
47. P. Gao and H. Gleiter, *Acta Metall.* 35, 1571 (1990).
48. W. W. Milligan, S. A. Hackney, M. Ke, and E. C. Aifantis, *Nanostruct. Mater.* 2, 267 (1993).
49. R. W. Siegel and G. E. Fougere, *Mater. Res. Symp. Proc.* 362, 219 (1995).
50. L. W. Miller, M. I. Tejedor, B. P. Nelson, and M. A. Anderson, *J. Phys. Chem. B* 103, 8490 (1999).
51. P. Yang, D. Zhao, D. I. Margolese, B. F. Chmelka, and G. D. Stucky, *Chem. Mater.* 11, 2813 (1999).
52. D. N. Srivastava, N. Perkas, A. Gedanken, and I. Felner, *J. Phys. Chem. B* 106, 1878 (2002).
53. H. E. Schaefer, R. Wurschum, M. Scheytt, R. Birringer, and H. Gleiter, *Mater. Sci. Forum* 15–18, 955 (1987).
54. H. E. Schaefer, R. Wurschum, R. Birringer, and H. Gleiter, *Phys. Rev. B* 38, 9545 (1988).
55. G. W. Nieman, J. R. Weertman, and R. W. Siegel, *J. Mater. Res.* 6, 1012 (1991).
56. M. D. Sacks, T. Y. Tseng, and S. Y. Lee, *Am. Ceram. Soc. Bull.* 63, 301 (1984).
57. H. Hahn, J. Logas, and R. S. Averback, *J. Mater. Res.* 5, 609 (1990).
58. W. Wagner, R. S. Averback, H. Hahn, W. Petry, and A. Wiedenmann, *J. Mater. Res.* 6, 2193 (1991).
59. P. G. Sanders, J. R. Weertman, J. G. Barker, and R. W. Siegel, *Scr. Metall. Mater.* 29, 91 (1993).
60. R. S. Averback, H. Hahn, H. J. Hofler, J. L. Logas, and T. C. Chen, *Mater. Res. Soc. Symp. Proc.* 153, 3 (1989).
61. H. Gleiter, *Acta Mater.* 48, 1 (2000).
62. N. Setter and R. Waser, *Acta Mater.* 48, 151 (2000).
63. J. Maier, *Solid State Ionics* 23, 59 (1987).
64. J. Maier, *J. Eur. Ceram. Soc.* 19, 675 (1999).
65. Y. M. Chiang, E. B. Levik, I. Kosacki, H. L. Tuller, and J. Y. Ying, *J. Electro. Ceram.* 1, 7 (1997).
66. P. Mondal, A. Klein, W. Jaegermann, and H. Hahn, *Solid State Ionics* 118, 331 (1999).
67. C. Pascal, J. L. Pascal, F. Favier, and M. L. E. Moubtassim, *Chem. Mater.* 11, 141 (1999).
68. K. Ishikawa and K. Nagareda, *J. Korean Phys. Soc.* 32, 56 (1998).
69. L. E. Brus, *J. Chem. Phys.* 80, 4403 (1984).
70. S. Li, S. J. Silvers, and M. S. El-Shall, *Mater. Res. Symp. Proc.* 452, 389 (1997).
71. J. Rupp and R. Birringer, *Phys. Rev. B* 36, 7888 (1987).
72. R. W. Siegel, H. Hahn, S. Ramasamy, L. Zongquan, L. Ting, and R. Gronsky, *J. Phys. C* 49, 681 (1988).
73. J. Karch, R. Birringer, and H. Gleiter, *Nature* 330, 556 (1987).
74. S. Decker and K. J. Klabunde, *J. Am. Chem. Soc.* 118, 12465 (1996).
75. K. J. Klabunde, J. V. Stark, O. Koper, C. Mohs, O. G. Park, S. Decker, Y. Jiang, and I. Lagadic, *J. Phys. Chem.* 100, 12142 (1996).
76. G. L. Hornyak, C. J. Patrissi, and C. R. Martin, *J. Phys. Chem. B* 101, 1548 (1997).
77. R. Leon, D. Margolese, P. Petroff, and G. D. Stucky, *Phys. Rev. B* 52, R2285 (1995).
78. N. P. Blake, V. I. Srdanov, G. D. Stucky, and H. Metiu, *J. Chem. Phys.* 104, 8721 (1996).
79. S. Schacht, Q. Huo, I. G. Voigt-Martin, G. D. Stucky, and F. Schüth, *Science* 273, 768 (1996).
80. Q. Huo, J. Feng, F. Schüth, and G. D. Stucky, *Chem. Mater.* 9, 14 (1997).
81. T. A. Dickinson, J. White, J. S. Kauer, and D. R. Walt, *Nature* 382, 697 (1996).
82. R. A. Dunbar, J. D. Jordan, and F. V. Bright, *Anal. Chem.* 68, 604 (1996).
83. T. Y. Tseng, Unpublished research.
84. M. Sarikaya and I. A. Aksay (Eds.), "Design and processing of materials by biomicking," Am. Inst. Physics, New York, 1994.
85. A. M. Belcher, X. H. Wu, R. J. Christensen, P. K. Hansma, G. D. Stucky, and D. E. Morse, *Nature* 381, 56 (1996).

86. G. M. Wang, E. M. Sevick, E. Mittag, D. J. Searles, and D. J. Evans, *Phys. Rev. Lett.* 89, 50601 (2002).
87. G. B. Basim, J. J. Adler, U. Mahajan, R. K. Singh, and B. M. Moudgil, *J. Electrochem. Soc.* 147, 3523 (2000).
88. H. K. Bowen, *Mater. Sci. Eng.* 44, 1 (1980).
89. S. K. Friedlander, "Smoke, dust and haze: Fundamentals of aerosol behavior," Wiley Interscience, New York 1977.
90. R. W. Siegel, in "Physics of new materials," edited by F. E. Fujita, Springer-Verlag, Berlin, Germany, 1994.
91. C. G. Grandqvist and R. A. Buhrman, *J. Appl. Phys.* 47, 2200 (1976).
92. A. Gurav, T. Kodas, T. Pluym, and Y. Xiong, *Aerosol Sci. Technol.* 19, 411 (1993).
93. S. R. Nagel, J. B. MacChesney, and K. L. Walder, in "Optical fiber communications," edited by L. Tingye, Academic Press, NY, Vol. 1, 1985.
94. S. E. Pratsinis and S. V. R. Mastrangelo, *Chem. Eng. Prog.* 85, 62 (1989).
95. S. E. Pratsinis and T. T. Kodas, in "Aerosol measurement," edited by K. Willeke and P. A. Baron, Van Nostrand Reinhold, New York, 1993.
96. G. D. Ulrich, *Chem. Eng. News* 62, 22 (1984).
97. M. K. Wu, R. S. Windeler, C. K. R. Steiner, T. Bors, and S. K. Friedlander, *Aerosol Sci. Technol.* 19, 527 (1993).
98. T. T. Kodas and M. J. H. Smith, "Aerosol processing of materials," Wiley-VCH, New York, 1999.
99. W. J. Stark and S. E. Pratsinis, *Powder Technol.* 126, 103 (2002).
100. S. Li, S. J. Silvers, and M. S. El-Shall, *J. Phys. Chem.* 101, 1794 (1997).
101. M. S. El-Shall and S. Li, *SPIE* 3123, 98 (1997).
102. T. Sasaki, X. Zeng, and N. Koshizaki, *Mater. Res. Soc. Symp. Proc.* 526, 67 (1998).
103. T. Sasaki and N. Koshizaki, *Rev. Laser Eng.* 28, 348 (2000).
104. Q. Li, T. Sasaki, and N. Koshizaki, *Appl. Phys. A* 69, 115 (1999).
105. N. Koshizaki, A. Narazaki, and T. Sasaki, *Scr. Mater.* 44, 1925 (2001).
106. L. Zbroniec, T. Sasaki, and N. Koshizaki, *Scr. Mater.* 44, 1869 (2001).
107. W. H. Sutton, *Am. Ceram. Soc. Bull.* 68, 376 (1989).
108. D. Vollath and K. E. Sickafus, *J. Mater. Res.* 8, 2978 (1993).
109. Z. Xie, J. Yang, X. Huang, and Y. Huang, *J. Eur. Ceram. Soc.* 19, 381 (1999).
110. A. K. Singh, P. Mehta, and A. I. Kingon, *Ceram. Trans.* 21, 421 (1991).
111. D. Vollath and K. E. Sickafus, *Nanostruct. Mater.* 1, 427 (1992).
112. D. Vollath, K. E. Sickafus, and R. Varma, *Mater. Res. Soc. Symp. Proc.* 269, 379 (1992).
113. P. Rigneau, K. Bellon, I. Zahreddine, and D. Stuerger, *Eur. Phys. J., A* 7, 41 (1999).
114. S. S. Manoharan, Swati, S. J. Prasanna, M. L. Rao, and R. K. Sahu, *J. Am. Ceram. Soc.* 85, 2469 (2002).
115. A. D. MacDonald, "Microwave breakdown in gases," John Wiley & Sons, New York, 1966.
116. K. P. Jayadevan, N. V. Kumar, R. M. Mallya, and K. T. Jacob, *J. Mater. Sci.* 35, 2429 (2000).
117. D. Vollath, *J. Mater. Sci.* 25, 2227 (1990).
118. S. Somiya and R. Roy, *Bull. Mater. Sci.* 23, 453 (2000).
119. W. J. Dawson, *Am. Ceram. Soc. Bull.* 67, 1673 (1988).
120. G. W. Morey, *J. Am. Ceram. Soc.* 36, 279 (1953).
121. M. Hirano and E. Kato, *J. Am. Ceram. Soc.* 82, 786 (1999).
122. C. C. Wang and J. Y. Ying, *Chem. Mater.* 11, 3113 (1999).
123. M. Hirano, M. Imai, and M. Inagaki, *J. Am. Ceram. Soc.* 83, 977 (2000).
124. S. Feng and R. Xu, *Acc. Chem. Res.* 34, 239 (2001).
125. C. R. Peterson and E. B. Slamovich, *J. Am. Ceram. Soc.* 82, 1702 (1999).
126. R. K. Roeder and E. B. Slamovich, *J. Am. Ceram. Soc.* 82, 1665 (1999).
127. D. Hennings, *Int. J. High Technol. Ceram.* 3, 91 (1987).
128. A. M. Milia, "Sonochemistry and cavitation," Gordon and Breach Publishers, Luxembourg, 1995.
129. S. Komarneni, R. Pidugu, Q. H. Li, and R. Roy, *J. Mater. Res.* 10, 1687 (1995).
130. M. T. Harris, T. C. Scott, and C. H. Byers, *Mater. Sci. Eng. A* 168, 125 (1993).
131. M. T. Harris, W. G. Sisson, T. C. Scott, O. A. Basaran, C. H. Byers, W. Renand, and T. Meek, *Mater. Res. Soc. Symp. Proc.* 271, 945 (1992).
132. M. T. Harris, T. C. Scott, O. A. Basaran, and C. H. Byers, *AIChE Symp. Series, Superconducting Engineering* 88, 44 (1992).
133. M. T. Harris, T. C. Scott, O. A. Basaran, and C. H. Byers, *Mater. Res. Soc. Symp. Proc.* 180, 153 (1990).
134. P. Ravindranathan and K. C. Patil, *Am. Ceram. Soc. Bull.* 66, 688 (1987).
135. K. Kouratakis, M. Robbins, P. K. Gallagher, and T. Tiefel, *J. Mater. Res.* 4, 1289 (1989).
136. K. R. Venkatachari, D. Huang, S. P. Ostrander, W. A. Schulze, and G. C. Stangle, *J. Mater. Res.* 10, 748 (1995).
137. K. C. Patil, S. T. Aruna, and S. Ekambaram, *Current Opinion in Solid State & Materials Science* 2, 158 (1997).
138. T. Mimani and K. C. Patil, *Mater. Phys. Mech.* 4, 134 (2001).
139. J. Livage, M. Henry, and S. Sanchez, *Prog. Solid State Chem.* 18, 259 (1988).
140. C. J. Brinker and G. W. Scherer, "Sol-gel science," Academic Press, San Diego, 1990.
141. D. C. Bradely, R. C. Mehrotra, and D. P. Gaur, "Metal alkoxides," Academic Press, London, 1978.
142. I. A. Aksay, in "Forming of ceramics," edited by J. A. Mangels and G. L. Messing, American Ceramic Society, Columbus, OH, 1984.
143. C. J. Brinker and G. W. Scherer, *J. Non-Cryst. Solids* 70, 301 (1985).
144. J. A. Lewis, *J. Am. Ceram. Soc.* 83, 2341 (2000).
145. M. D. Sacks and T. Y. Tseng, *J. Am. Ceram. Soc.* 67, 532 (1984).
146. T. Y. Tseng and J. J. Yu, *J. Mater. Sci.* 21, 3615 (1986).
147. T. Y. Tseng and J. C. Lee, *Am. Ceram. Soc. Bull.* 52, 443 (1987).
148. T. Y. Tseng, C. C. Lin, and J. T. Liaw, *J. Mater. Sci.* 22, 965 (1987).
149. T. Y. Tseng, J. M. Huang, J. G. Lin, and Y. L. Lin, *J. Mater. Sci.* 24, 2735 (1989).
150. Y. S. Fran, T. Y. Tseng, Y. L. Lin, and C. P. Chang, *J. Mater. Sci.* 26, 1834 (1991).
151. T. Y. Tseng and C. C. Fu, *J. Mater. Sci. Lett.* 6, 351 (1987).
152. T. Y. Tseng and J. C. Lin, *J. Mater. Sci. Lett.* 8, 261 (1989).
153. F. H. Chen, H. S. Koo, T. Y. Tseng, R. S. Liu, and P. T. Wu, *Mater. Lett.* 8, 228 (1989).
154. T. S. Heh, J. R. Chen, and T. Y. Tseng, *Jpn. J. Appl. Phys.* 29, 650 (1990).
155. F. H. Chen, H. S. Koo, and T. Y. Tseng, *J. Mater. Sci.* 25, 3338 (1990).
156. F. H. Chen, H. S. Koo, and T. Y. Tseng, *J. Am. Ceram. Soc.* 75, 96 (1992).
157. M. Nayak and T. Y. Tseng, *Thin Solid Films* 408, 194 (2002).
158. H. Igarashi and K. Okazaki, *J. Am. Ceram. Soc.* 60, 51 (1977).
159. K. S. Suslick and G. J. Price, *Annu. Rev. Mater. Sci.* 29, 295 (1999).
160. K. S. Suslick, S. B. Choe, A. A. Cichowlas, and M. W. Grinstaff, *Nature* 353, 414 (1991).
161. T. G. Leighton, "The acoustic bubble," Academic, London, 1994.
162. S. J. Doktycz and K. S. Suslick, *Science* 247, 1067 (1990).
163. K. S. Suslick, M. Fang, and T. Hyeon, *J. Am. Chem. Soc.* 118, 11960 (1996).
164. N. De la Rosa-Fox, L. Esquivias, A. F. Craievich, and J. Zarzycki, *J. Non-Cryst. Solids* 121, 211 (1990).
165. R. Litran, E. Blanco, M. Ramirezdelsolar, and L. Esquivias, *J. Sol-Gel Sci. Technol.* 8, 985 (1997).

166. K. V. P. M. Shafi, I. Felner, and A. Gedanken, *J. Phys. Chem. B* 103, 3358 (1999).
167. S. Avivi, Y. Mastai, G. Hodes, and A. Gedanken, *J. Am. Chem. Soc.* 121, 4196 (1999).
168. X. Tang, S. Liu, Y. Wang, W. Huang, Y. Koltypin, and A. Gedanken, *Chem. Commun.* 21, 19 (2000).
169. S. Avivi, Y. Mastai, and A. Gedanken, *J. Am. Chem. Soc.* 122, 4331 (2000).
170. J. M. Nedeljkovic, Z. V. Saponjic, Z. Rakocevic, V. Jokanovic, and D. P. Uskokovic, *Nanostruct. Mater.* 9, 125 (1997).
171. A. S. Gandhi, V. Jayaram, and A. H. Chokshi, *J. Am. Ceram. Soc.* 82, 2613 (1999).
172. D. Majumdar, H. D. Glicksman, and T. T. Kodas, *Powder Technol.* 110, 76 (2001).
173. R. Baranwal, M. P. Villar, R. Garcia, and R. M. Laine, *J. Am. Ceram. Soc.* 84, 951 (2001).
174. H. Xu, L. Gao, H. Gu, J. Guo, and D. Yan, *J. Am. Ceram. Soc.* 85, 139 (2002).
175. P. S. Patil, *Mater. Chem. Phys.* 59, 185 (1999).
176. T. L. Ward, T. T. Kodas, A. H. Carim, D. M. Kroeger, and H. J. Hsu, *J. Mater. Res.* 7, 827 (1992).
177. D. Basset, P. Matteazzi, and F. Miani, *Mater. Sci. Eng. A* 168, 149 (1993).
178. K. Shantha, G. N. Subbanna, and K. B. R. Varma, *J. Solid State Chem.* 142, 41 (1999).
179. J. Z. Jiang, F. W. Polsen, and S. Morup, *J. Mater. Res.* 14, 1343 (1999).
180. M. Simoneau, G. L'Esperance, M. L. Trudeau, and R. Schulz, *J. Mater. Res.* 9, 535 (1994).
181. J. Xue, D. Wan, S. E. Lee, and J. Wang, *J. Am. Ceram. Soc.* 82, 1687 (1999).
182. L. B. Kong, J. Ma, H. Huang, and R. F. Zhang, *Mater. Res. Bull.* 37, 1087 (2002).
183. M. P. Pileni, *J. Phys. Chem. B* 105, 3358 (2001).
184. V. Degiorgio and M. Corti (Eds.), "Physics of amphiphilic micelles, vesicles and microemulsions," North-Holland, Amsterdam, 1985.
185. S. H. Chen and R. Rajagopal (Eds.), "Micelles, Solutions and Microemulsions: Structure, Dynamics and Statistical Thermodynamics," Springer, New York, 1990.
186. J. A. L. Pérez, M. A. L. Quintela, J. Mira, J. Rivas, and S. W. Charles, *J. Phys. Chem. B* 101, 8045 (1997).
187. J. Fang, J. Wang, L. M. Gan, S. C. Ng, J. Ding, and X. Liu, *J. Am. Ceram. Soc.* 83, 1049 (2000).
188. S. Santra, R. Tapec, N. Theodoropoulou, J. Dobson, A. Hebard, and W. Tan, *Langmuir* 17, 2900 (2000).
189. D. E. Collins and E. B. Slamovich, *Chem. Mater.* 11, 2319 (1999).
190. C. H. Lu and S. K. Saha, *J. Am. Ceram. Soc.* 83, 1320 (2000).
191. J. J. Urban, W. S. Yun, Q. Gu, and H. Park, *J. Am. Chem. Soc.* 124, 1186 (2002).
192. A. J. Zarur and J. Y. Ying, *Nature* 403, 65 (2000).
193. A. J. Zarur, H. H. Hwu, and J. Y. Ying, *Langmuir* 16, 3042 (2000).
194. H. Althues and S. Kaskel, *Langmuir* 18, 7428 (2002).
195. C. A. Huber, in "Hand book of nanophase materials," edited by A. N. Goldstein, Marcel Dekker Inc., New York, 1997, p. 317.
196. J. Dai, J. Tang, H. Xu, L. Spinu, W. Wang, K. Wang, A. Kumbhar, M. Li, and U. Diebold, *Appl. Phys. Lett.* 77, 2840 (2000).
197. T. Nutz and M. Haase, *J. Phys. Chem. B* 104, 8430 (2000).
198. H. P. Klug and L. E. Alexander, "X-ray diffraction procedures for polycrystalline and amorphous materials," Wiley, New York, 1974.
199. B. E. Warren, "X-ray diffraction," Addison-Wesley, Reading, MA, 1969.
200. G. K. Williamson and W. H. Hall, *Acta Metall.* 1, 22 (1953).
201. T. Ungar, J. Gubicza, P. Hanak, and I. Alexandrov, *Mater. Sci. Eng. A* 319–321, 274 (2001).
202. K. Santra, P. Chatterjee, and S. P. Sengupta, *Sol. Energy Mater. Sol. Cells* 57, 345 (1999).
203. S. A. M. Lima, F. A. Sigoli, M. Jafelicci, and M. R. Davolos, *Int. J. Inorg. Mater.* 3, 749 (2001).
204. C. B. Murray, C. R. Kagan, and M. G. Bawendi, *Science* 270, 1335 (1995).
205. R. Ramesh, G. Thomas, S. M. Green, M. L. Rudee, and H. L. Luo, *Appl. Phys. Lett.* 53, 520 (1988).
206. J. M. Liang, L. Chang, S. F. Tang, Y. C. Chen, P. T. Wu, and L. J. Chen, *Appl. Phys. Lett.* 53, 913 (1988).
207. A. Cohen, P. Allenspacher, M. M. Brieger, I. Jeuck, and H. Opower, *Appl. Phys. Lett.* 59, 2186 (1991).
208. C. H. Lin, P. C. Kuo, J. L. Pan, and D. R. Huang, *J. Appl. Phys.* 79, 6035 (1996).
209. A. Gedanken, R. Reisfeld, E. Sominski, O. Palchik, Y. Koltypin, G. Panczer, M. Gaft, and H. Minti, *J. Phys. Chem. B* 104, 7057 (2000).
210. X. Xu, G. Friedman, K. D. Humfeld, S. A. Majetich, and S. A. Asher, *Chem. Mater.* 14, 1249 (2002).
211. G. H. Du, Q. Chen, R. C. Che, Z. Y. Yuan, and L. M. Peng, *Appl. Phys. Lett.* 79, 3702 (2001).
212. A. R. West, "Solid state chemistry and its applications," John Wiley & Sons, Singapore, 1989.
213. D. A. McKeown, I. S. Muller, K. S. Matlack, and I. L. Pegg, *J. Non-Cryst. Solids* 298, 160 (2002).
214. J. Choi, S. J. Gurman, and E. A. Davis, *J. Non-Cryst. Solids* 297, 156 (2002).
215. S. H. Messaddeq, V. R. Mastelaro, A. Y. Ramos, M. S. Li, D. Lezal, S. J. L. Ribeiro, and Y. Messaddeq, *J. Non-Cryst. Solids* 304, 160 (2002).
216. A. Mizuno, T. Itami, A. S. Miguel, G. Ferlat, J. F. Jal, and M. Borowski, *J. Non-Cryst. Solids* 312–314, 74 (2002).
217. E. E. Carpenter, C. J. O'Connor, and V. G. Harris, *J. Appl. Phys.* 85, 5175 (1999).
218. S. A. Oliver, V. G. Harris, H. H. Hamdeh, and J. C. Ho, *Appl. Phys. Lett.* 76, 2761 (2000).
219. Y. L. Soo, S. W. Huang, Y. H. Kao, V. Chhabra, B. Kulkarni, J. V. D. Veliadis, and R. N. Bhargava, *Appl. Phys. Lett.* 75, 2464 (1999).
220. Z. Qi, C. Shi, W. Zhang, W. Zhang, and T. Hu, *Appl. Phys. Lett.* 81, 2857 (2002).
221. S. Decker, I. Lagadic, K. J. Klabunde, J. Moscovici, and A. Michalowicz, *Chem. Mater.* 10, 674 (1998).
222. V. G. Harris, N. C. Koon, C. M. Williams, Q. Zhang, M. Abe, J. P. Kirkland, and D. A. McKeown, *IEEE Trans. Magn.* 31, 3473 (1995).
223. V. G. Harris, N. C. Koon, C. M. Williams, Q. Zhang, M. Abe, and J. P. Kirkland, *Appl. Phys. Lett.* 68, 2082 (1996).
224. J. Weismuller, in "Nanomaterials: Synthesis, properties and applications," edited by A. S. Edelstein and R. C. Cammarata, IOP Publishing, Philadelphia, 1998, p. 219.
225. G. A. Somorjai, *J. Mol. Catal. A* 107, 39 (1996).
226. G. Rupprechter, A. S. Eppler, A. Avoyan, and G. A. Somorjai, *Suod. Surf. Sci. Catal.* 130A, 215–220 (2000).
227. R. E. Loehman and L. E. Fitzpatrick, "Characterization of ceramics," Butterworth-Heinemann, Boston, 1993.
228. Q. Guo and R. W. Joyner, *Appl. Surf. Sci.* 144, 375 (1999).
229. C. C. S. Bob, S. O. Saied, and J. L. Sullivan, *Appl. Surf. Sci.* 183, 126 (2001).
230. H. Piao, M. S. Fuller, D. Miller, and N. S. McIntyre, *Appl. Surf. Sci.* 187, 266 (2002).
231. B. Balamurugan, B. R. Mehta, and S. M. Shivaprasad, *Appl. Phys. Lett.* 79, 3176 (2001).
232. L. Soriano, M. Abbate, A. Fernandez, A. R. G. Elipse, F. Sirotti, G. Rossi, and J. M. Sanz, *J. Phys. Chem. B* 103, 6676 (1999).
233. D. Schmeißer, O. Böhme, A. Yfantis, T. Heller, D. R. Batchelor, I. Lundstrom, and A. L. Spetz, *Phys. Rev. Lett.* 83, 380 (1999).

234. D. L. Perry, in "Applications of Analytical Techniques to the Characterization of Materials," edited by D. L. Perry, Plenum Press, New York, 1991, p. 1.
235. W. H. Thompson, Z. Yamani, L. AbuHassan, O. Gurdal, and M. Nayfeh, *Appl. Phys. Lett.* 73, 841 (1998).
236. M. S. Tsai, S. C. Sun, and T. Y. Tseng, *J. Am. Ceram. Soc.* 82, 351 (1999).
237. E. Chatzitheodoridis, G. Kiraikidis, and I. Lyon, in "Handbook of thin film materials," edited by H. S. Nalwa, Academic Press, San Diego, 2002, Vol. 2, p. 638.
238. Y. F. Chong, K. L. Pey, A. T. S. Wee, M. O. Thompson, C. H. Tung, and A. See, *Appl. Phys. Lett.* 81, 3786 (2002).
239. L. F. Schloss, P. C. McIntyre, B. C. Hendrix, S. M. Bilodeau, J. F. Roeder, and S. R. Gilbert, *Appl. Phys. Lett.* 81, 3218 (2002).
240. S. H. Jang, T. Kang, H. J. Kim, and K. Y. Kim, *Appl. Phys. Lett.* 81, 105 (2002).
241. U. Brossmann, R. Wurschum, U. Sodervall, and H. E. Schaefer, *J. Appl. Phys.* 85, 7646 (1999).
242. T. V. Torchynska, N. E. Korsunskaya, B. R. Dzhumaev, and L. Yu. Khomenkova, *J. Phys. Chem. Solids* 61, 937 (2000).
243. N. Ohashi, T. Ishigaki, N. Okada, T. Sekiguchi, I. Sakaguchi, and H. Haneda, *Appl. Phys. Lett.* 80, 2869 (2002).
244. F. Aubriet, C. Poelunis, N. Chaoui, B. Maunit, E. Millon, J. F. Muller, and P. Bertrand, *Appl. Surf. Sci.* 186, 315 (2002).
245. H. Zhou, W. Cai, and L. Zhang, *Appl. Phys. Lett.* 75, 495 (1999).
246. T. A. Konovalova, L. D. Kispert, and V. V. Konovalov, *J. Phys. Chem. B* 103, 4672 (1999).
247. U. Felde, M. Haase, and H. Weller, *J. Phys. Chem. B* 104, 9388 (2000).
248. D. Cummins, G. Boschloo, M. Ryan, D. Corr, S. N. Rao, and D. Fitzmaurice, *J. Phys. Chem. B* 104, 11449 (2000).
249. A. Gedanken, R. Reisfeld, L. Sominski, Z. Zhong, Yu. Kolytynin, G. Panczer, M. Gaft, and H. Minti, *Appl. Phys. Lett.* 77, 945 (2000).
250. T. Yatsui, T. Kawazoe, T. Shimizu, Y. Yamamoto, M. Ueda, M. Kourogi, M. Ohtsu, and G. H. Lee, *Appl. Phys. Lett.* 80, 1444 (2002).
251. S. Tsunekawa, J. Kang, K. Asami, and A. Kasuya, *J. Appl. Phys.* 91, 10098 (2002).
252. D. K. Williams, B. Bihari, B. M. Tissue, and J. M. McHale, *J. Phys. Chem. B* 102, 916 (1998).
253. K. Hong, R. S. Meltzer, B. Bihari, D. K. Williams, and B. M. Tissue, *J. Lumin.* 76-77, 234 (1998).
254. A. Eychmuller, *J. Phys. Chem. B* 104, 6514 (2000).
255. J. Dhanaraj, R. Jagannathan, T. R. N. Kutty, and C. H. Lu, *J. Phys. Chem. B* 105, 11098 (2001).
256. E. Faulques and R. E. Russo, in "Applications of analytical techniques to the characterization of materials," edited by D. L. Perry, Plenum Press, New York, 1991, p. 59.
257. C. Roy and R. C. Budhani, *J. Appl. Phys.* 85, 3124 (1999).
258. J. Zuo, C. Xu, X. Liu, C. Wang, C. Wang, Y. Hu, and Y. Qian, *J. Appl. Phys.* 75, 1835 (1994).
259. M. Rajalakshmi, A. K. Arora, B. S. Bendre, and S. Mahamuni, *J. Appl. Phys.* 87, 2445 (2000).
260. F. Zhang, S. W. Chan, J. E. Spanier, E. Apak, Q. Jin, R. D. Robinson, and I. P. Herman, *Appl. Phys. Lett.* 80, 127 (2002).
261. I. Kosacki, T. Suzuki, H. U. Anderson, and P. Colomban, *Solid State Ionics* 149, 99 (2002).
262. J. E. Spanier, R. D. Robinson, F. Zhang, S. W. Chan, and I. P. Herman, *Phys. Rev. B* 64, 245407 (2001).
263. K. V. P. M. Shafi, A. Ulman, X. Yan, N. L. Yang, C. Estournès, H. White, and M. Rafailovich, *Langmuir* 17, 5093 (2001).
264. M. I. Baraton, in "Handbook of nanostructured materials," edited by H. S. Nalwa, Academic Press, San Diego, 2000, Vol. 2, p. 89.
265. N. Aruldas and A. Gedanken, *Chem. Mater.* 9, 3144 (1997).
266. T. Masui, H. Hirai, N. Imanaka, G. Adachi, T. Sakata, and H. Mori, *J. Mater. Sci. Lett.* 21, 489 (2002).
267. F. Boccuzzi, A. Chiorino, and M. Manzoli, *Surf. Sci.* 502-503, 513 (2002).
268. F. J. Berry, in "Applications of analytical techniques to the characterization of materials," edited by D. L. Perry, Plenum Press, New York, 1991, p. 41.
269. E. Wu, S. J. Campbell, and W. A. Kaczmarek, *J. Magn. Magn. Mater.* 177-181, 355 (1998).
270. A. S. Albuquerque, J. D. Ardisson, and W. A. A. Macedo, *J. Magn. Magn. Mater.* 192, 277 (1999).
271. S. R. Mekala and J. Ding, *J. Alloys Compd.* 296, 152 (2000).
272. D. J. Fatemi, V. G. Harris, M. X. Chen, S. K. Malik, W. B. Yelon, G. J. Long, and A. Mohan, *J. Appl. Phys.* 85, 5172 (1999).
273. S. R. Ahmed, S. B. Ogale, G. C. Papaefthymiou, R. Ramesh, and P. Kofinas, *Appl. Phys. Lett.* 80, 1616 (2002).
274. N. Moumen and M. P. Pileni, *Chem. Mater.* 8, 1128 (1996).
275. M. P. Morales, S. V. Verdager, M. I. Montero, C. J. Serna, A. Roig, L. Casas, B. Martýnez, and F. Sandiumenge, *Chem. Mater.* 11, 3058 (1999).
276. A. D. Yoffe, *Adv. Phys.* 42, 173 (1993).
277. C. Q. Sun, B. K. Tay, S. Li, X. W. Sun, S. P. Lau, and T. P. Chen, *Mater. Phys. Mech.* 4, 129 (2001).
278. L. T. Canham, *Appl. Phys. Lett.* 57, 1046 (1990).
279. K. Borgohain, J. B. Singh, M. V. R. Rao, T. Shripathi, and S. Mahamuni, *Phys. Rev. B* 61, 11093 (2000).
280. D. Schmeißer, O. Bohme, A. Yfantis, T. Heller, D. R. Batchelor, I. Lundstrom, and A. L. Spetz, *Phys. Rev. Lett.* 83, 380 (1999).
281. M. Zaccagna, C. Astaldi, M. Sastry, C. Comicioli, R. Rosei, C. Quaresima, C. Ottaviani, C. Crotti, A. Antonini, M. Matteucci, and P. Perfetti, *Surf. Sci.* 347, 53 (1996).
282. G. G. Qin and Y. Q. Jia, *Solid State Commun.* 86, 559 (1993).
283. T. S. Iwayama, D. E. Hole, and I. W. Boyd, *J. Phys.: Condens. Matter* 11, 6595 (1999).
284. A. P. Alivisatos, *Science* 271, 933 (1996).
285. R. T. Collins, P. M. Fauchet, and M. A. Tischler, *Phys. Today* 1, 24 (1997).
286. S. Lizzit, A. Baraldi, A. Groso, K. Reuter, M. V. G. Pirovano, C. Stampfl, M. Scheffler, M. Stichler, K. Keller, W. Wurth, and D. Menzel, *Phys. Rev. B* 63, 205419 (2001).
287. L. W. Wang and A. Zunger, *Phys. Rev. B* 53, 9579 (1996).
288. R. Tsu, D. Babic, and L. Loriai, Jr., *J. Appl. Phys.* 82, 1327 (1997).
289. L. E. Brus, *J. Lumin.* 31, 381 (1984).
290. G. Hackenbroich, W. D. Heiss, and H. A. Weidenmüller, *Phys. Rev. Lett.* 79, 127 (1997).
291. C. Q. Sun, X. W. Sun, B. K. Tay, S. P. Lau, H. Huang, and S. Li, *J. Phys. D* 34, 2359 (2001).
292. C. B. Murray, C. R. Kagan, and M. G. Bawendi, *Annu. Rev. Mater. Sci.* 30, 545 (2000).
293. L. Soriano, M. Abbate, A. Fernandez, A. R. G. Elipe, F. Sirotti, G. Rossi, and J. M. Sanz, *Chem. Phys. Lett.* 266, 184 (1997).
294. S. Mahamuni, K. Borgohain, B. S. Bendre, V. J. Leppert, and S. H. Risbud, *J. Appl. Phys.* 85, 2861 (1999).
295. Mikrajuddin, F. Iskandar, K. Okuyama, and F. G. Shi, *J. Appl. Phys.* 89, 6431 (2001).
296. F. Marabelli, G. B. Parravicini, and F. S-Drioli, *Phys. Rev. B* 52, 1433 (1995).
297. T. Ito, H. Yamaguchi, T. Masumi, and S. Adachi, *J. Phys. Soc. Jpn.* 67, 3304 (1998).
298. G. van der Laan, C. Westra, C. Haas, and G. A. Sawatzky, *Phys. Rev. B* 23, 4369 (1981).
299. S. Shionoya and W. M. Yen (Eds.), "Phosphor handbook," CRC, Boca Raton, FL, 1998.
300. A. van Dijken, E. A. Meulenkaamp, D. Vanmaekelbergh, and A. Meijerink, *J. Lumin.* 90, 123 (2000).
301. L. E. Brus, *J. Phys. Chem.* 90, 2555 (1986).
302. L. Landolt-Bornstein, in "Numerical data and functional relationships in science and technology, Semiconductors," edited by O. Madelung, Springer, Berlin, 1988, Vol. III-17.

303. A. van Dijken, E. A. Meulenkaamp, D. Vanmaekelbergh, and A. Meijerink, *J. Phys. Chem. B* 104, 1715 (2000).
304. D. Zhang, R. M. Kolbas, P. D. Milewski, D. J. Lichtenwalner, A. I. Kingon, and J. M. Zavada, *Appl. Phys. Lett.* 65, 2684 (1994).
305. C. Noguez and S. E. Ulloa, *Phys. Rev. B* 56, 9719 (1997).
306. K. Borgohain, N. Murase, and S. Mahamuni, *J. Appl. Phys.* 92, 1292 (2002).
307. L. Madler, W. J. Stark, and S. E. Pratsinis, *J. Appl. Phys.* 92, 6537 (2002).
308. T. Hase, T. Kano, E. Nakazawa, and H. Yamamoto, *Adv. Electron. Phys.* 79, 271 (1990).
309. T. Justel, H. Bechtel, H. Nikol, C. R. Ronda, and D. U. Weichert, *Proc. VII Int. Symp. Luminescent Mater. Electrochem. Soc. Proc.* 98-24, 103 (1998).
310. H. Song, B. Chen, H. Peng, and J. Zhang, *Appl. Phys. Lett.* 81, 1776 (2002).
311. J. A. Capobianco, F. Vetrone, J. C. Boyer, A. Speghini, and M. Bettinelli, *Opt. Mater.* 19, 259 (2002).
312. B. M. Tissue, *Chem. Mater.* 10, 2837 (1998).
313. C. Fouassier, *Curr. Opin. Solid State Mater. Sci.* 2, 231 (1997).
314. G. H. Dieke, "Spectra and energy levels of rare earth ions in crystals," Interscience, New York, 1968.
315. K. C. Sheng and G. M. Korenowski, *J. Phys. Chem.* 92, 50 (1988).
316. H. Eilers and B. M. Tissue, *Chem. Phys. Lett.* 251, 74 (1996).
317. R. N. Bhargava, D. Gallagher, X. Hong, and A. Nurmikko, *Phys. Rev. Lett.* 72, 416 (1994).
318. A. Trave, F. Buda, and A. Fasolino, *Phys. Rev. Lett.* 77, 5405 (1996).
319. J. R. Agger, M. W. Anderson, M. E. Pemble, O. Terasaki, and Y. Nozue, *J. Phys. Chem. B* 102, 3345 (1998).
320. C. R. Ronda, *J. Lumin.* 72, 49 (1997).
321. I. Kosacki and H. U. Anderson, *Sens. Actuators, B* 48, 263 (1998).
322. H. Aono, M. Sato, E. Traversa, M. Sakamoto, and Y. Sadaoka, *J. Am. Ceram. Soc.* 84, 341 (2001).
323. P. Vernoux, E. Djurado, and M. Guillodo, *J. Am. Ceram. Soc.* 84, 2289 (2001).
324. W. D. Kingery, H. Bowen, and D. R. Uhlmann, "Introduction to ceramics," John Wiley & Sons, New York, 1975.
325. J. Maier, *Solid State Ionics* 148, 367 (2002).
326. H. L. Tuller, *Solid State Ionics* 52, 135 (1992).
327. T. Suzuki, I. Kosacki, H. U. Anderson, and P. Colombon, *J. Am. Ceram. Soc.* 84, 2007 (2001).
328. Y. M. Chiang, E. B. Lavik, I. Kosacki, H. L. Tuller, and J. Y. Ying, *Appl. Phys. Lett.* 69, 185 (1996).
329. M. Aoki, Y. M. Chiang, I. Kosacki, J. R. Lee, H. L. Tuller, and Y. Liu, *J. Am. Ceram. Soc.* 79, 1169 (1996).
330. C. W. Nan, A. Tschöpe, S. Holten, H. Kliem, and R. Birringer, *J. Appl. Phys.* 85, 7735 (1999).
331. C. D. Terwilliger and Y. M. Chiang, *Acta Metall. Mater.* 43, 319 (1995).
332. K. P. Jayadevan and T. Y. Tseng, *J. Mater. Sci.: Materials in Electronics* 13, 439 (2002).
333. T. M. Shaw, S. T. McKinstry, and P. C. McIntyre, *Annu. Rev. Mater. Sci.* 30, 263 (2000).
334. T. Kanata, Y. Yoshikawa, and K. Kubota, *Solid State Commun.* 62, 765 (1987).
335. K. Uchino, E. Sadanaga, and T. Hirose, *J. Am. Ceram. Soc.* 72, 1555 (1989).
336. O. Yamaguchi, A. Narai, T. Komatsu, and K. Shimizu, *J. Am. Ceram. Soc.* 69, C-256 (1986).
337. K. Ishikawa, K. Yoshikawa, and N. Okada, *Phys. Rev. B* 37, 5852 (1988).
338. W. L. Zhong, B. Jiang, P. L. Zhang, J. M. Ha, H. M. Cheng, Z. H. Yang, and L. X. Li, *J. Phys.: Condens. Matter* 5, 2619 (1993).
339. S. Chattopadhyay, P. Ayyub, V. R. Palkar, and M. Multani, *Phys. Rev. B* 52, 13177 (1995).
340. Y. Park, K. M. Knowles, and K. Cho, *J. Appl. Phys.* 83, 5702 (1998).
341. B. Jiang, J. L. Peng, L. A. Bursill, and W. L. Zhong, *J. Appl. Phys.* 87, 3462 (2000).
342. A. Q. Jiang, Z. X. Hu, and L. D. Zhang, *Appl. Phys. Lett.* 74, 114 (1999).
343. W. R. Buessem, L. E. Cross, and A. K. Goswami, *J. Am. Ceram. Soc.* 49, 33 (1966).
344. P. Ayyub, V. R. Palkar, S. Chattopadhyay, and M. S. Multani, *Phys. Rev. B* 51, 6135 (1995).
345. K. Uchino and S. Nomura, *Ferroelectrics Lett. Sect.* 44, 55 (1982).
346. R. Clarke and J. C. Burfoot, *Ferroelectrics* 8, 505 (1974).
347. A. Navrotsky, B. A. Wechsler, K. Geisinger, and F. Seifert, *J. Am. Ceram. Soc.* 69, 418 (1986).
348. A. Q. Jiang, G. H. Li, and L. D. Zhang, *J. Appl. Phys.* 83, 4878 (1998).
349. K. Shantha and K. B. R. Varma, *J. Am. Ceram. Soc.* 83, 1122 (2000).
350. H. S. Shulman, M. Testorf, D. Damjanovic, and N. Setter, *J. Am. Ceram. Soc.* 79, 3124 (1996).
351. L. Gunther, *Phys. World* 3, 28 (1990).
352. R. D. Shull, *IEEE Trans. Magn.* 29, 2614 (1993).
353. R. F. Ziolo, E. P. Giannelis, B. Weinstein, M. P. O'Horo, B. N. Ganguly, V. Mehrotra, M. W. Russell, and D. R. Huffman, *Science* 257, 219 (1992).
354. K. Raj, B. Moskowitz, and R. Casciari, *J. Magn. Magn. Mater.* 149, 174 (1995).
355. U. Hafeli, W. Schut, J. Teller, and M. Zborowski (Eds.), in "Scientific and clinical applications of magnetic carriers," Plenum Press, New York, 1997.
356. D. Vollath, D. V. Szabo, R. D. Taylor, and J. O. Willis, *J. Mater. Res.* 12, 2175 (1997).
357. B. Martinez, A. Roig, X. Obrador, E. Molins, A. Rouanet, and C. Monty, *J. Appl. Phys.* 79, 2580 (1996).
358. L. Zhang, G. C. Papaefthymiou, and J. Y. Ying, *J. Appl. Phys.* 81, 6892 (1997).
359. C. Pascal, J. L. Pascal, F. Favier, M. L. E. Moubtassim, and C. Payen, *Chem. Mater.* 11, 141 (1999).
360. D. L. L. Pelecky and R. D. Rieke, *Chem. Mater.* 8, 1770 (1996).
361. N. Mouten and M. P. Pileni, *J. Phys. Chem.* 100, 1867 (1996).
362. M. H. Sousa, F. A. Tourinho, J. Depuyrot, G. J. da Silva, and M. C. F. L. Lara, *J. Phys. Chem. B* 105, 1168 (2001).
363. P. J. Thomas, P. Saravanan, G. U. Kulkarni, and C. N. R. Rao, *Pramana* 58, 371 (2002).
364. M. Verelst, T. O. Ely, C. Amiens, E. Snoeck, P. Lecante, A. Mosset, M. Respaud, J. M. Broto, and B. Chaudret, *Chem. Mater.* 11, 2702 (1999).
365. C. Cannas, D. Gatteschi, A. Musinu, G. Piccaluga, and C. Sangregorio, *J. Phys. Chem. B* 102, 7721 (1998).
366. B. D. Cullity, "Introduction to magnetic materials," Addison-Wesley Publishing Company, Reading, MA, 1972.
367. R. W. Chantrell, J. Popplewell, and S. W. Charles, *IEEE Trans. Magn.* 5, 975 (1978).
368. K. O'Grady and A. Bradbury, *J. Magn. Magn. Mater.* 39, 91 (1994).
369. M. P. Morales, C. J. Serna, F. Bødker, and S. Mørup, *J. Phys.: Condens. Matter* 9, 5461 (1997).
370. B. Martinez, X. Obradors, L. Balcells, A. Rouanet, and C. Monty, *Phys. Rev. Lett.* 80, 181 (1998).
371. F. Zaera, A. Gellman, and G. A. Somorjai, *Acc. Chem. Res.* 19, 24 (1986).
372. J. Y. Ying and T. Sun, *J. Electroceram.* 1, 219 (1997).
373. J. R. Anderson, "Structure of metallic catalysts," Academic Press, New York, 1975.
374. W. M. H. Sachtler, *Acc. Chem. Res.* 26, 283 (1993).
375. F. G. Ciapetta and D. N. Wallace, *Catal. Rev.* 5, 67 (1971).
376. J. H. Sinfelt, "Bimetallic catalysts: Discoveries, concepts and applications," Wiley, New York, 1983.



377. T. R. Huges, W. C. Buss, P. W. Tamm, and R. L. Jacobson, "Proceedings of the 7th International Zeolite Conference," edited by Y. Murakami, A. Lijima, and J. W. Ward, Elsevier, Japan, 1986.
378. D. V. Law, P. W. Tamm, and C. M. Detz, *Energy Prog.* 7, 215 (1987).
379. M. L. Trudeau and J. Y. Ying, *Nanostruct. Mater.* 7, 245 (1996).
380. J. B. Miller, S. E. Rankin, and E. I. Ko, *J. Catal.* 148, 673 (1994).
381. C. C. Wang, Z. Zhang, and J. Y. Ying, *Nanostruct. Mater.* 9, 583 (1997).
382. A. Tshope, W. Liu, M. F. Stephanopoulos, and J. Y. Ying, *J. Catal.* 157, 42 (1995).
383. P. F. Miquel and J. L. Katz, *J. Mater. Res.* 9, 746 (1994).
384. M. L. Panchula and J. Y. Ying, *Nanostruct. Mater.* 9, 161 (1997).
385. J. Y. Ying and A. Tshope, *Chem. Eng. J.* 64, 225 (1996).
386. J. A. S. Ikeda, Y. M. Chiang, A. J. G. Reed, and J. B. V. Sande, *J. Am. Ceram. Soc.* 76, 2447 (1993).
387. E. Knozinger, K. H. Jakob, S. Singh, and P. Hoffman, *Surf. Sci.* 290, 288 (1993).
388. O. Koper, I. Lagadic, A. Volodin, and K. J. Klabunde, *Chem. Mater.* 9, 2468 (1997).
389. A. Tshope, D. Schaadt, R. Birringer, and J. Y. Ying, *Nanostruct. Mater.* 9, 423 (1997).
390. D. D. Beck and R. W. Siegel, *J. Mater. Res.* 7, 2840 (1992).
391. H. M. Lin, C. Y. Tung, C. M. Hsu, and P. Y. Lee, *J. Mater. Res.* 10, 1115 (1995).
392. C. L. Carnes and K. J. Klabunde, *Chem. Mater.* 14, 1806 (2002).
393. R. Richards, W. Li, S. Decker, C. Davidson, O. Koper, V. Zaikovski, A. Volodin, T. Rieker, and K. J. Klabunde, *J. Am. Chem. Soc.* 122, 4921 (2000).
394. A. Khaleel, P. N. Kapoor, and K. J. Klabunde, *Nanostruct. Mater.* 11, 459 (1999).
395. S. Lee, S. U. S. Choi, S. Li, and J. A. Eastman, *ASME J. Heat Transfer* 121, 280 (1999).
396. J. A. Eastman, S. U. S. Choi, S. Li, W. Yu, and L. J. Thompson, *Appl. Phys. Lett.* 78, 718 (2001).
397. G. Soye, J. A. Eastman, L. J. Thompson, R. J. DiMelfi, G.-R. Bai, and P. M. Baldo, *Appl. Phys. Lett.* 77, 1155 (2000).
398. A. Majumdar, in "Microscale energy transport," edited by C. L. Tien, A. Majumdar, and F. M. Gerner, Taylor and Francis, Washington, DC, 1998.
399. K. Lu, R. Lück, and B. Predel, *Z. Metallkd.* 84, 740 (1993).
400. C. Moelle, M. Werner, F. Szücs, D. Wittorf, M. Sellschopp, J. von Borany, F. J. Fecht, and C. Johnston, *Diamond Relat. Mater.* 7, 499 (1998).
401. P. G. Sanders, J. A. Eastman, and J. R. Weertman, *Acta Mater.* 45, 4019 (1997).
402. V. B. Efimov and L. P. M. Deglin, *Physica B* 263–264, 745 (1999).
403. D. G. Cahill, S. K. Watson, and R. O. Pohl, *Phys. Rev. B* 46, 6131 (1992).
404. P. G. Klemens and M. Gell, *Mater. Sci. Eng. A* 245, 143 (1998).
405. J. R. Nicholls, K. J. Lawson, A. Johnstone, and D. S. Rickerby, *Surf. Coat. Technol.* 151–152, 383 (2002).
406. P. L. Kapitza, *J. Phys. (Moscow)* 4, 181 (1941).
407. E. T. Swartz and R. O. Pohl, *Rev. Mod. Phys.* 61, 605 (1989).
408. C. W. Nan and R. Birringer, *Phys. Rev. B* 57, 8264 (1997).
409. A. Maiti, G. D. Mahan, and S. T. Pantelides, *Solid State Commun.* 102, 517 (1997).
410. S. Fayette, D. S. Smith, A. Smith, and C. Martin, *J. Eur. Ceram. Soc.* 20, 297 (2000).
411. H. S. Yang, G. R. Bai, L. J. Thompson, and J. A. Eastman, *Acta Mater.* 50, 2309 (2002).
412. C. Koch, in "WTEC panel report on nanostructure science and technology," edited by R. W. Siegel, E. Hu, and M. C. Roco, Kluwer Academic Publishers, Dordrecht, Netherlands, 1999, p. 93.
413. E. O. Hall, *Proc. Phys. Soc., London B* 64, 747 (1951).
414. N. J. Petch, *J. Iron Steel Inst.* 17, 25 (1953).
415. J. R. Weertman and R. S. Averback, in "Nanomaterials: Synthesis, properties and applications," edited by A. S. Edelstein and R. C. Cammarata, IOP Publishing, Philadelphia, 1998, p. 323.
416. H. J. Hofler and R. S. Averback, *Scr. Metall. Mater.* 24, 2401 (1990).
417. H. Chang, C. J. Alstetter, and R. S. Averback, *J. Mater. Res.* 7, 2962 (1992).
418. M. Guermazi, H. J. Hofler, R. Hahn, and R. S. Averback, *J. Am. Ceram. Soc.* 74, 2672 (1991).
419. J. Karch and R. Birringer, *Ceram. Int.* 16, 291 (1990).
420. C. H. Hamilton and N. E. Paton, "Superplasticity and superplastic forming," Metallurgical Society, Warrendale, PA, 1988.
421. F. Wakei, S. Sakaguchi, and Y. Matsuno, *Adv. Ceram. Mater.* 1, 259 (1986).
422. O. D. Sherby and J. Wadsworth, *Prog. Mater. Sci.* 33, 169 (1989).
423. H. J. Hofler, R. S. Averback, H. Hahn, and H. Gleiter, *J. Appl. Phys.* 74, 3832 (1993).
424. U. Herr, J. Jing, U. Gonser, and H. Gleiter, *Solid State Commun.* 76, 197 (1990).
425. T. G. Langdon, *Mater. Sci. Eng. A* 166, 67 (1993).
426. O. A. Kaibyshev, "Superplasticity of alloys, intermetallics and ceramics," Springer, Berlin, 1992.
427. T. G. Nieh and J. Wadsworth, *Acta Metall. Mater.* 38, 1121 (1990).
428. F. Wakei and H. Kato, *Adv. Ceram. Mater.* 3, 71 (1988).
429. T. G. Nieh, C. M. Mc Nally, and J. Wadsworth, *Scr. Metall.* 23, 457 (1989).
430. J. Karch, R. Birringer, and H. Gleiter, *Nature* 330, 556 (1987).
431. M. J. Mayo, R. W. Siegel, Y. X. Liao, and W. D. Nix, *J. Mater. Res.* 7, 973 (1992).
432. T. Shiono, H. Ishitomi, Y. Okamoto, and T. Nishida, *J. Am. Ceram. Soc.* 83, 645 (2000).
433. B. Sudhir and A. H. Chokshi, *J. Am. Ceram. Soc.* 84, 2625 (2001).
434. T. Nagano, H. Gu, K. Kaneko, G. D. Zhan, and M. Mitomo, *J. Am. Ceram. Soc.* 83, 2497 (2000).
435. T. Nagano, H. Gu, K. Kaneko, G. D. Zhan, and M. Mitomo, *J. Am. Ceram. Soc.* 84, 2045 (2001).
436. M. J. Melendo, H. Haneda, and H. Nozawa, *J. Am. Ceram. Soc.* 84, 2356 (2001).
437. J. Yun, Y. T. Chou, and M. P. Harmer, *J. Am. Ceram. Soc.* 85, 1190 (2002).
438. J. Mimurada, M. Nakano, K. Sasaki, Y. Ikuhara, and T. Sakuma, *J. Am. Ceram. Soc.* 84, 1817 (2001).
439. D. C. Dunand and J. L. Grabowski, *J. Am. Ceram. Soc.* 83, 2521 (2000).
440. K. Sasaki, M. Nakano, J. Mimurada, Y. Ikuhara, and T. Sakuma, *J. Am. Ceram. Soc.* 84, 2981 (2001).
441. R. J. Xie, M. Mitomo, G. D. Zhan, and H. Emoto, *J. Am. Ceram. Soc.* 83, 2529 (2000).
442. J. M. C. Moreno, M. Schehl, and M. Popa, *Acta Mater.* 50, 3973 (2002).
443. H. Goronkin, P. von Allmen, R. K. Tsui, and T. X. Zhu, in "WTEC panel report on nanostructure science and technology," edited by R. W. Siegel, E. Hu, and M. C. Roco, Kluwer Academic Publishers, Dordrecht, Netherlands, 1999, p. 67.
444. S. Carrara, in "Nanoparticles and nanostructured films," edited by J. H. Fendler, Wiley-VCH, New York, 1998, p. 349.
445. K. K. Likharev, *Proc. IEEE* 87, 606 (1999).
446. P. J. M. van Bentum, R. J. M. Smokers, and H. van Kempen, *Phys. Rev. Lett.* 60, 2543 (1988).
447. M. A. Kastner, *Physics Today* 46, 24 (1993).
448. U. Meirav and E. B. Foxman, *Semicond. Sci. Technol.* 10, 255 (1995).
449. K. Mullen, E. B. Jacob, R. C. Jaklevic, and Z. Shuss, *Phys. Rev. B* 37, 98 (1988).
450. M. A. Reed, J. N. Randall, R. J. Aggarwal, R. J. Matyi, T. M. Moore, and A. E. Wetsel, *Phys. Rev. Lett.* 60, 535 (1988).
451. S. Weiner, H. F. Hess, R. B. Robinson, T. R. Hayes, D. L. Sivco, A. Y. Cho, and M. Ranade, *Appl. Phys. Lett.* 58, 2402 (1991).

452. P. J. M. van Bentum, H. van Kempen, L. E. C. van de Leemput, and P. A. A. Teunissen, *Phys. Rev. Lett.* 60, 369 (1988).
453. P. J. M. van Bentum, R. T. M. Smokers, and H. van Kempen, *Phys. Rev. Lett.* 60, 2543 (1988).
454. R. Wilkins, E. B. Jacob, and R. C. Jaklevic, *Phys. Rev. Lett.* 63, 801 (1989).
455. M. F. Crommie, C. P. Lutz, and D. M. Eigler, *Science* 262, 218 (1993).
456. J. G. A. Dubois, J. W. Gerritsen, S. E. Shafranjk, E. J. G. Boon, G. Schmid, and H. van Kempen, *Europhys. Lett.* 33, 279 (1996).
457. D. V. Averim and K. K. Likharev, *J. Low Temp. Phys.* 62, 345 (1986).
458. H. Grabert and M. H. Devoret (Eds.), "Single charge tunneling—coulomb blockade phenomena in nanostructures," NATO ASI B, New York, 1992, Vol. 294.
459. R. J. Haug and K. von Klitzing, *FED Journal* 6, 4 (1995).
460. E. Leobandung, L. Guo, and S. Y. Chou, *Appl. Phys. Lett.* 67, 2338 (1995).
461. K. K. Likharev and A. N. Korotkov, *Science* 273, 763 (1996).
462. D. Gräf, A. Schnegg, R. Schmolke, M. Suhren, H. A. Gerber, and P. Wagner, in "Chemical mechanical planarization in IC device manufacturing," edited by I. Ali and S. Raghavan, The Electrochemical Society Proceedings Series, Pennington, NJ, 1996, Vol. 96-22.
463. R. Schmolke, R. Deters, P. Thieme, R. Pech, H. Schwenk, and G. Diakourakis, *J. Electrochem. Soc.* 149, G 257 (2002).
464. J. M. Hobbs, H. Windlass, V. Sundaram, S. Chun, G. E. White, M. Swaminathan, and R. R. Tummala, IEEE Electronic Components and Technology Conference, 2001, p. 339.
465. C. Jin, J. D. Luttmer, D. M. Smith, and T. A. Ramos, *MRS Bull.* October (1997).
466. S. Tiwari, F. Rana, H. Hanafi, A. Hartstein, E. F. Crabble, and K. Chan, *Appl. Phys. Lett.* 68, 1377 (1996).
467. S. Tiwari, F. Rana, K. Chan, L. Shi, and H. Hanafi, *Appl. Phys. Lett.* 69, 1232 (1996).
468. H. I. Hanafi, S. Tiwari, and I. Khan, *IEEE Trans. Electron Devices* 43, 1553 (1996).
469. I. Kim, S. Han, H. Han, J. Lee, and H. Shin, *IEEE Electron Device Lett.* 20, 630 (1999).
470. Y. C. King, T. J. King, and C. Hu, *IEEE Electron Device Lett.* 20, 409 (1999).
471. E. Nagata, N. Takahashi, Y. Yasuda, T. Inukai, H. Ishikuro, and T. Hiramoto, *Jpn. J. Appl. Phys.* 38, 7230 (1999).
472. I. Kim, S. Han, K. Han, J. Lee, and H. Shin, *Jpn. J. Appl. Phys.* 40, 447 (2001).
473. A. Dutta, Y. Hayafune, and S. Oda, *Jpn. J. Appl. Phys.* 39, L855 (2000).
474. T. Gebel, J. von Borany, H. J. Thees, M. Wittmaack, K. H. Stegmann, and W. Skorupa, *Microelectron. Eng.* 59, 247 (2001).
475. G. Iannaccone and P. Coli, *Appl. Phys. Lett.* 78, 2046 (2001).
476. E. Kapetanakis, P. Normand, D. Tsoukalas, and K. Beltsios, *Microelectron. Eng.* 61–62, 505 (2002).
477. C. Tsang, T. Lin, S. MacDonald, M. Pinarbasi, N. Robertson, H. Santini, M. Doerner, T. Reith, L. Vo, T. Diola, and P. Arnett, *IEEE Trans. Magn.* 33, 2866 (1997).
478. H. Kanai, J. Kane, K. Yamada, K. Aoshima, M. Kanamine, J. Toda, and Y. Mizoshita, *IEEE Trans. Magn.* 33, 2872 (1997).
479. H. L. Hu, K. Ju, C. C. Han, D. Chhabra, Y. Guo, C. Horng, J. W. Chang, T. Torng, G. Yeh, B. B. Lal, S. Malhotra, Z. Jiang, M. Yang, M. Sullivan, and J. Chao, *IEEE Trans. Magn.* 35, 683 (1999).
480. C. Tsang, M. Pinarbasi, H. Santini, E. Marinero, P. Arnett, R. Olson, R. Hsiao, M. Williams, R. Payne, J. Moore, B. Gurney, T. Lin, and R. Fontana, *IEEE Trans. Magn.* 35, 689 (1999).
481. R. L. White, *J. Magn. Mater.* 209, 1 (2000).
482. W. L. Wilson, P. F. Szajowski, and L. E. Brus, *Science* 262, 1242 (1993).
483. R. A. McFarlane, *J. Opt. Soc. Am. B* 11, 871 (1994).
484. R. Brede, T. Danger, E. Heumann, G. Huber, and B. Chai, *Appl. Phys. Lett.* 63, 729 (1993).
485. D. Lande, S. S. Orlov, A. Akella, L. Hesselink, and R. R. Neurgaonkar, *Opt. Lett.* 22, 1722 (1997).
486. S. F. Collins, G. W. Baxter, S. A. Wade, T. Sun, K. T. V. Grattan, Z. Y. Zhang, and A. W. Palmer, *J. Appl. Phys.* 84, 4649 (1998).
487. G. S. Maciel, A. Biswas, R. Kapoor, and P. N. Prasad, *Appl. Phys. Lett.* 76, 1978 (2000).
488. M. D. Barnes, A. Mehta, T. Thundat, R. N. Bhargava, V. Chhabra, and B. Kulkarni, *J. Phys. Chem. B* 104, 6099 (2000).
489. A. Patra, C. S. Friend, R. Kapoor, and P. N. Prasad, *J. Phys. Chem. B* 106, 1909 (2002).
490. R. N. Bhargava, V. Chhabra, B. Kulkarni, and J. V. Veliadis, *Phys. Status Solidi B* 210, 621 (1998).
491. M. Nirmal, B. O. Dabbousi, M. G. Bawendi, J. J. Macklin, J. K. Trautman, T. D. Harris, and L. E. Brus, *Nature* 383, 802 (1996).
492. S. M. Prokes, in "Nanomaterials: Synthesis, properties and applications," edited by A. S. Edelstein and R. C. Cammarata, IOP Publishing, Philadelphia, 1998, p. 439.
493. N. Hill and K. Whaley, *Phys. Rev. Lett.* 75, 1130 (1995).
494. S. Schuppler, S. L. Friedman, M. A. Marcus, D. L. Adler, Y. H. Xie, F. M. Ross, Y. J. Chabal, T. D. Harris, L. E. Brus, W. L. Brown, E. E. Chaban, P. F. Szajowski, S. B. Christman, and P. H. Citrin, *Phys. Rev. B* 52, 4910 (1995).
495. D. B. Geohegan, A. A. Puzos, G. Duscher, and S. J. Pennycook, *Appl. Phys. Lett.* 73, 438 (1998).
496. S. John, *Phys. Rev. Lett.* 58, 2486 (1987).
497. E. Yablonovitch, *Phys. Rev. Lett.* 58, 2059 (1987).
498. G. Kumaraswamy, A. M. Dibaj, and F. Caruso, *Langmuir* 18, 4150 (2002).
499. K. M. Ho, C. T. Chan, and C. M. Soukoulis, *Phys. Rev. Lett.* 65, 3152 (1990).
500. J. E. G. J. Wijnhoven and W. L. Vos, *Science* 281, 802 (1998).
501. B. T. Holland, C. F. Blanford, and A. Stein, *Science* 281, 538 (1998).
502. A. Blanco, E. Chomski, S. Gratchak, M. Ibisate, S. John, S. W. Leonard, C. Lopez, F. Meseguer, H. Miguez, J. P. Mondia, G. A. Ozin, O. Toader, and H. M. van Driel, *Nature* 405, 437 (2000).
503. F. Cosandey, G. Skandan, and A. Singhal, JOM-e 52, Internet edition of the Publication of The Minerals, Metals and Materials Society, October (2000).
504. G. Martinelli, M. C. Carotta, E. Traversa, and G. Ghiotti, *MRS Bull.* 24, 30 (1999).
505. A. M. Azad, S. A. Akbar, S. G. Mhaisalkar, L. D. Birkefeld, and K. S. Goto, *J. Electrochem. Soc.* 139, 3690 (1992).
506. W. Gopel, *Sens. Actuators, B* 18–19, 1 (1994).
507. G. Sberveglieri, *Sens. Actuators, B* 23, 103 (1995).
508. L. D. Birkefeld, A. M. Azad, and S. A. Akbar, *J. Am. Ceram. Soc.* 75, 2964 (1992).
509. H. Tang, K. Prasad, R. Sanjines, and F. Levy, *Sens. Actuators, B* 26–27, 71 (1995).
510. T. Kobayashi, M. Haruta, S. Tsubota, and H. Sano, *Sens. Actuators, B* 1, 222 (1990).
511. P. Moseley and D. E. Williams, *Sens. Actuators, B* 1, 113 (1990).
512. V. Jayaraman, K. I. Gnanasekar, E. Prabhu, T. Gnanasekaran, and G. Periaswami, *Sens. Actuators, B* 55, 175 (1999).
513. D. Manno, A. Serra, M. D. Giulio, G. Micocci, and A. Tepore, *Thin Solid Films* 324, 51 (1998).
514. Y. Shimizu and M. Egashira, *MRS Bull.* 24, 18 (1999).
515. A. Gurlo, N. Barsan, M. Ivanovskaya, U. Weimar, and W. Gopel, *Sens. Actuators, B* 47, 92 (1998).
516. G. Martinelli, M. C. Carotta, M. Ferroni, Y. Sadaoka, and E. Traversa, *Sens. Actuators, B* 55, 99 (1999).
517. N. Yamazoe, *Sens. Actuators, B* 5, 7 (1991).
518. C. Xu, J. Tamaki, N. Miura, and N. Yamazoe, *Sens. Actuators, B* 3, 147 (1991).

519. S. G. Ansari, P. Boroojerdian, S. R. Sainkar, R. N. Karekar, R. C. Aiyer, and S. K. Kulkarni, *Thin Solid Films* 295, 271 (1997).
520. V. Demarne and R. Sanjines, in "Gas sensors—principles, operation and developments," edited by G. Sberveglieri, Dordrecht, Kluwer Academic, Netherlands, 1992.
521. Z. W. Pan, Z. R. Dai, and Z. L. Wang, *Science* 291, 1947 (2001).
522. M. Rittner, [www.ceramicbulletin.org](http://www.ceramicbulletin.org), Vol. 81, March (2002).
523. "Nanotechnology research directions: IWGN Workshop report," edited by M. C. Roco, Kluwer Academic Publishers, Netherlands, 2000, p. 95, 139, 153, 173.
524. C. G. Guizard, A. C. Julbe, and A. Ayrat, *J. Mater. Chem.* 9, 55 (1999).
525. P. D. Yang, T. Deng, D. Y. Zhao, P. Y. Feng, D. Pine, B. F. Chemelka, G. M. Whitesides, and G. D. Stucky, *Science* 282, 2244 (1998).
526. D. R. Rollison and B. Dunn, *J. Mater. Chem.* 11, 963 (2001).
527. K. Kendall and M. Palin, *J. Power Sources* 71, 268 (1998).
528. N. M. Sammes and R. Boersma, *J. Power Sources* 86, 98 (2000).
529. G. Cacciola, V. Antonucci, and S. Freni, *J. Power Sources* 100, 67 (2001).
530. C. N. R. Rao and A. K. Cheetham, *J. Mater. Chem.* 11, 2887 (2001).
531. P. K. Stoimenov, R. L. Klinger, G. L. Marchin, and K. J. Klabunde, *Langmuir* 18, 6679 (2002).
532. J. M. G. Vega, M. Iyoshi, K. Y. Kim, A. Hozumi, H. Sugimura, and O. Takai, *Thin Solid Films* 398–399, 615 (2001).

# Oxide Nanowires and Nanorods

Guozhong Cao, Steven J. Limmer

University of Washington, Seattle, Washington, USA

## CONTENTS

1. Introduction
2. Spontaneous Growth
3. Template-Based Synthesis
4. Lithography
5. Summary
- Glossary
- References

## 1. INTRODUCTION

Oxides possess many important physical properties conducive to a wide range of applications. Examples include electronic or ionic conductors, semiconductors, dielectrics, ferroelectrics, piezoelectrics, pyroelectrics, electro-optics, ferrites, and high  $T_c$  superconductors. In addition, they offer excellent thermal and chemical stabilities. The physical properties of these materials are sensitively dependent on the chemical stoichiometry, crystallinity, and microstructure and thus can be tailored by doping or alloying, or control of crystal structure and microstructures. There is, therefore, no doubt that nanostructured oxides would play a very important role in nanotechnology. Nanostructured materials can be generally grouped into (1) zero-dimensional structures (i.e., quantum dots and core-shell nanostructures), (2) one-dimensional structures (i.e., nanorods and nanowires), (3) two-dimensional structures (thin films), and (4) three-dimensional structures (bulk materials with nanoscale building blocks).

In this chapter, we discuss the synthesis and fabrication of one-dimensional structures. Although the focus is on the oxide nanorods and nanowires, significant attention has been paid to the review of fundamental concepts, which determine the synthesis and fabrication of one-dimensional nanostructures. For the completeness of the discussion, a large number of nonoxide nanorods and nanowires have been discussed in detail to illustrate the practical approaches, when no suitable examples of oxide nanorods are available. It should be noted that it is not our intention to exhaust all the work on the synthesis and fabrication of oxide nanorods and nanowires published in the open

literature, and therefore, many excellent works have not been included in this chapter. The aim of the chapter is to provide the reader a systematic and fundamental understanding of various methods applied in the fabrication of one-dimensional nanostructures of all types of materials, albeit with more emphasis on oxides.

One-dimensional nanostructures have been called a variety of names including whiskers, fibers or fibrils, nanowires, and nanorods. In many cases, nanotubules and nanocables are also considered one-dimensional structures. Although whiskers and nanorods are in general considered to be shorter than fibers and nanowires, the definition is often a little arbitrary. In addition, one-dimensional structures with diameters ranging from several nanometers to several hundred micrometers were referred to as whiskers and fibers in early literature, whereas nanowires and nanorods with diameters not exceeding a few hundred nanometers are used predominantly in recent literature. One will find, from reading this chapter, the fact that many fundamental understandings and techniques of growth of one-dimensional nanostructures are based on the early work on the growth of whiskers and fibers, albeit with less emphasis on nanometer scale. In this chapter, various terms of one-dimensional structures will be used interchangeably, though nanowires in general have a higher aspect ratio than that of nanorods.

Many techniques have been developed in the synthesis and formation of one-dimensional nanostructured materials, though some techniques have been explored extensively, while other techniques attracted far less attention. These techniques can be generally grouped into three categories:

1. Spontaneous growth
  - a. evaporation (or dissolution)–condensation
  - b. vapor (or solution)–liquid–solid (VLS or SLS) growth
  - c. stress–induced recrystallization
2. Template-based synthesis
  - a. electroplating and electrophoretic deposition
  - b. colloid dispersion, melt, or solution filling
  - c. conversion with chemical reaction
3. Lithography

Spontaneous growth and template-based synthesis are considered bottom-up approaches, whereas lithography is a top-down technique. Spontaneous growth commonly results in the formation of single crystal nanowires or nanorods along a preferential crystal growth direction depending on the crystal structures and surface properties of the nanowire materials. Template-based synthesis mostly produces polycrystalline or even amorphous products. All the above techniques for the preparation of one-dimensional nanostructured materials will be discussed in this chapter, following the above order just for the sake of clarity. Further, lithography will be discussed briefly only, considering the maturity of the technique.

## 2. SPONTANEOUS GROWTH

Spontaneous growth is a process driven by the reduction of Gibbs free energy or chemical potential. The reduction of Gibbs free energy is commonly realized by phase transformation or chemical reaction or the release of stress. For the formation of nanowires or nanorods, anisotropic growth is required (i.e., the crystal grows along a certain orientation faster than other directions). Uniformly sized nanowires (i.e., the same diameter along the longitudinal direction of a given nanowire) can be obtained when crystal growth proceeds along one direction, whereas there is no growth along other directions. In spontaneous growth, for given material and growth conditions, defects and impurities on the growth surfaces can play a significant role in determining the morphology of the final products.

### 2.1. Evaporation (Dissolution)–Condensation

The evaporation–condensation process is also referred to as a vapor–solid (VS) process; however, the discussion in this section will not only be limited to the simple evaporation–condensation process. Chemical reactions among various precursors may be involved to produce desired materials. Of course, the growth of nanorods from solution is also included. The driving force for the synthesis of nanorods and nanowires by spontaneous growth is a decrease in Gibbs free energy, which arises from either recrystallization or a decrease in supersaturation. Nanowires and nanorods grown by evaporation–condensation methods are commonly single crystals with fewer imperfections. The formation of nanowires, nanorods, or nanotubules through evaporation (or dissolution)–condensation is due to the anisotropic growth. Several mechanisms are known to result in anisotropic growth, for example:

1. Different facets in a crystal with different growth rates. For example, in silicon with a diamond structure, the growth rate of {111} facets is smaller than that of {110}.
2. Presence of imperfections in specific crystal directions such as screw dislocation.
3. Preferential accumulation of or poisoning by impurities on specific facets.

Before discussing the growth of various nanowires by the evaporation–condensation method in detail, let us first review the fundamentals of crystal growth. Crystal growth

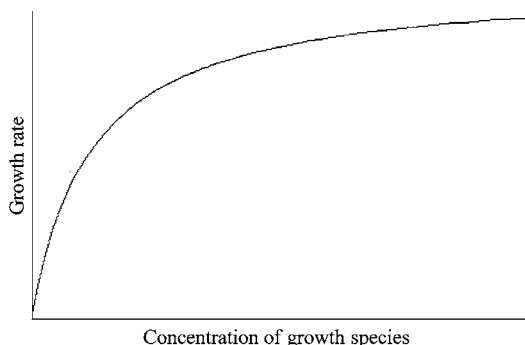
can generally be considered as a heterogeneous reaction, and a typical crystal growth proceeds following the sequences:

1. Diffusion of growth species from the bulk (such as vapor or liquid phase) to the growing surface, in general, is considered to proceed rapidly enough, and thus is not a rate-limiting process.
2. The adsorption and desorption of growth species onto and from the growing surface can be rate limiting, if the supersaturation or concentration of growth species is low.
3. During surface diffusion, an adsorbed species may either be incorporated into a growth site, which contributes to crystal growth, or escape from the surface.
4. Surface growth can occur by irreversibly incorporating the adsorbed growth species into the crystal structure. When a sufficient supersaturation or a high concentration of growth species is present, this step will be the rate-limiting process and determines the growth rate.
5. If by-product chemicals were generated on the surface during the growth, by-products would desorb from the growth surface, so that growth species can adsorb onto the surface and the growth process can continue.
6. By-product chemicals diffuse away from the surface so as to vacate the growth sites for continuing growth.

For most crystal growth, the rate-limiting step is either adsorption–desorption of growth species on the growth surface (step 2) or surface growth (step 4). When step 2 is rate limiting, the growth rate is determined by condensation rate  $J$  (atoms/cm<sup>2</sup>sec), which is dependent on the number of growth species adsorbed onto the growth surface, which is directly proportional to the vapor pressure or concentration,  $P$ , of the growth species in the vapor as given by

$$J = \alpha \sigma P_0 (2\pi mkT)^{-1/2} \quad (1)$$

where  $\alpha$  is the accommodation coefficient,  $\sigma = (P - P_0)/P_0$  is the supersaturation of the growth species in the vapor in which  $P_0$  is the equilibrium vapor pressure of the crystal at temperature  $T$ ,  $m$  is the atomic weight of the growth species, and  $k$  is the Boltzmann constant. Here,  $\alpha$  is the fraction of impinging growth species that becomes accommodated on the growing surface and is a surface specific property. A surface with a high accommodation coefficient will have a high growth rate as compared with low  $\alpha$  surfaces. A significant difference in accommodation coefficients in different facets would result in anisotropic growth. When the concentration of the growth species is very low, the adsorption is more likely a rate-limiting step. For a given system, the growth rate increases linearly with the increase in the concentration of growth species. Further increase in the concentration of growth species would result in a change from an adsorption limited to surface growth limited process. When the surface growth becomes a limiting step, the growth rate becomes independent of the concentration of growth species as schematically shown in Figure 1. A high concentration or vapor pressure of growth species in the vapor phase would increase the probability of defect formation, such as impurity inclusion and stacking faults. Further, a high concentration may result in a secondary nucleation on the growth surface



**Figure 1.** A schematic of crystal growth when the surface growth is rate limiting. At higher concentrations of growth species, the reaction rate is independent of the concentration.

or even homogeneous nucleation, which would effectively terminate the epitaxial or single crystal growth.

An impinging growth species onto the growth surface can be described in terms of the residence time and/or diffusion distance before escaping back to the vapor phase. The residence time,  $\tau_s$ , for a growth species on the surface is described by

$$\tau_s = \frac{1}{\nu} \exp\left(\frac{E_{\text{des}}}{kT}\right) \quad (2)$$

where  $\nu$  is the vibrational frequency of the adatom (i.e., adsorbed growth species) on the surface (typically  $10^{12} \text{ sec}^{-1}$ ), and  $E_{\text{des}}$  is the desorption energy required for the growth species escaping back to the vapor. While residing on the growth surface, a growth species will diffuse along the surface with the surface diffusion coefficient,  $D_s$ , given by

$$D_s = \frac{1}{2} a_0 \nu \exp\left(\frac{-E_s}{kT}\right) \quad (3)$$

where  $E_s$  is the activation energy for surface diffusion and  $a_0$  is the size of the growth species. So the mean diffusion distance,  $X$ , for a growth species from the site of incidence is

$$X = \sqrt{2} D_s \tau_s = a_0 \exp\left(\frac{E_{\text{des}} - E_s}{kT}\right) \quad (4)$$

It is clear that in a crystal surface, if the mean diffusion distance is far longer than the distance between two growth sites such as kinks or ledges, all adsorbed growth species will be incorporated into the crystal structure and the accommodation coefficient would be unity. If the mean diffusion distance is far shorter than the distance between growth sites, all adatoms will escape back to the vapor and the accommodation coefficient will be zero. The accommodation coefficient is dependent on desorption energy, activation energy of surface diffusion, and the density of growth sites.

When step 2 proceeds, sufficiently rapid surface growth (i.e., step 4) becomes a rate-limiting process. Different facets in a given crystal have different atomic densities and atoms on different facets have a different number of unsatisfied bonds (also referred to as broken or dangling bonds), leading to different surface energy. Such a difference in surface

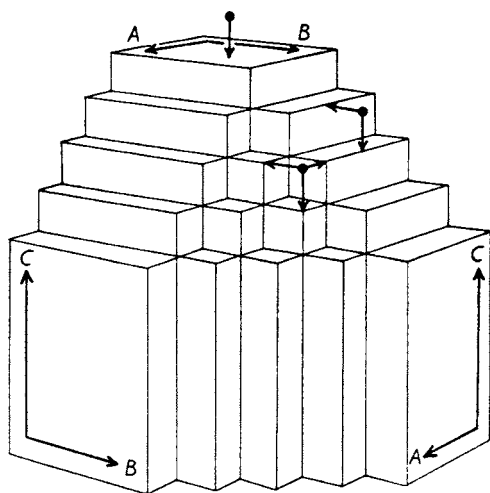
energy or number of broken chemical bonds leads to different growth mechanisms and varied growth rates. According to periodic bond chain (PBC) theory developed by Hartman and Perdok [1], all crystal facets can be categorized into three groups based on the number broken periodic bond chains on a given facet: flat surface, stepped surface, and kinked surface. The number of broken periodic bond chains can be understood as the number of broken bonds per atom on a given facet in a simplified manner. Let us first review the growth mechanisms on a flat surface.

For a flat surface, the classic step growth theory was developed by Kossel, Stranski, and Volmer, which is also called the KSV theory [2]. They recognized that the crystal surface, on the atomic scale, is not smooth, flat, or continuous, and such discontinuities are responsible for the crystal growth. To illustrate the step growth mechanism, we consider a  $\{100\}$  surface of a simple cubic crystal as an example and each atom as a cube with a coordination number of six (six chemical bonds). When an atom adsorbs onto the surface, it diffuses randomly on the surface. When it diffuses to an energetically favorable site, it will be irreversibly incorporated into the crystal structure, resulting in the growth of the surface. However, it may escape from the surface back to the vapor. On a flat surface, an adsorbed atom may find different sites with different energy levels. An atom adsorbed on a terrace would form one chemical bond between the atom and the surface; such an atom is called an adatom, which is in a thermodynamically unfavorable state. If an adatom diffuses to a ledge site, it would form two chemical bonds and become stable. If an atom were incorporated to a ledge-kink site, three chemical bonds would be formed. An atom incorporated into a kink site would form four chemical bonds. Ledge, ledge-kink, and kink sites are all considered as growth sites; incorporation of atoms into these sites is irreversible and results in growth of the surface. The growth of a flat surface is due to the advancement of the steps (or ledges). For a given crystal facet and a given growth condition, the growth rate will be dependent on the step density. A misorientation would result in an increased density of steps and consequently lead to a high growth rate. An increased step density would favor the irreversible incorporation of adatoms by reducing the surface diffusion distance between the impinging site and the growth site, before adatoms escape back to the vapor phase.

The obvious limitation of this growth mechanism is the regeneration of growth sites, when all available steps are consumed. Burton, Cabrera, and Frank [3] proposed that screw dislocations serve as a continuous source to generate growth sites so that the stepped growth would continue. The crystal growth proceeds in a spiral growth, and this crystal growth mechanism is now known as BCF theory. The presence of screw dislocation will not only ensure the continuing advancement of the growth surface but also enhance the growth rate. The growth rate of a given crystal facet under a given experimental condition would increase with an increased density of screw dislocations parallel to the growth direction. It is also known that different facets can have a significantly different ability to accommodate dislocations. The presence of dislocations on certain facets can result in anisotropic growth, leading to the formation of nanowires or nanorods.

The PBC theory offers a different perspective in understanding the different growth rates and behavior in different facets. Let us take a simple cubic crystal as an example to illustrate the PBC theory as shown in Figure 2. According to the PBC theory,  $\{100\}$  faces are flat surfaces (denoted as F-faces) with one PBC running through one such surface,  $\{110\}$  are stepped surfaces (S-faces) that have two PBCs, and  $\{111\}$  are kinked surfaces (K-faces) that have three PBCs. For  $\{110\}$  surfaces, each surface site is a step or ledge site, and thus any impinging atom would be incorporated wherever it adsorbs. For  $\{111\}$  facets, each surface site is a kink site and would irreversibly incorporate any incoming atom adsorbed onto the surface. For both  $\{110\}$  and  $\{111\}$  surfaces, the above growth is referred to as a random addition mechanism and no adsorbed atoms would escape back to the vapor phase. It is obvious that both  $\{110\}$  and  $\{111\}$  faces have a faster growth rate than that of the  $\{100\}$  surface in a simple cubic crystal. In general terms, S-faces and K-faces have a higher growth rate than F-faces. For both S- and K-faces, the growth process is always adsorption limited, since the accommodation coefficients on these two type surfaces are unity, that all impinging atoms are captured and incorporated into the growth surface. For F-faces, the accommodation coefficient varies between zero (no growth at all) and unity (adsorption limited), depending on the availability of kink and ledge sites.

The above theories enable us to understand better why some facets in a given crystal grow much faster than other facets. However, facets with fast growth rates tend disappear (i.e., surfaces with high surface energy will disappear). In a crystal at thermodynamic equilibrium, only those surfaces with the lowest total surface energy will survive. Therefore, the formation of high aspect ratio nanorods or nanowires entirely based on different growth rates of various facets is limited to materials with special crystal structures. In general, other mechanisms are required for the continued growth along the axis of nanorods or nanowires, such as defect-induced growth and impurity-inhibited growth.



**Figure 2.** The types of crystal faces in PBC theory. Reprinted with permission from [1], P. Hartman and W. G. Perdok, *Acta Cryst.* 8, 49 (1955). © 1955, International Union of Crystallography.

It should be noted that for an anisotropic growth, a low supersaturation is required. Ideally, the concentration is higher than the equilibrium concentration (saturation) of the growth surface, but equal or lower than that of other nongrowth surfaces. A low supersaturation is required for anisotropic growth, whereas a medium supersaturation supports bulk crystal growth, and a high supersaturation results in secondary or homogeneous nucleation leading to the formation of polycrystalline or powder samples.

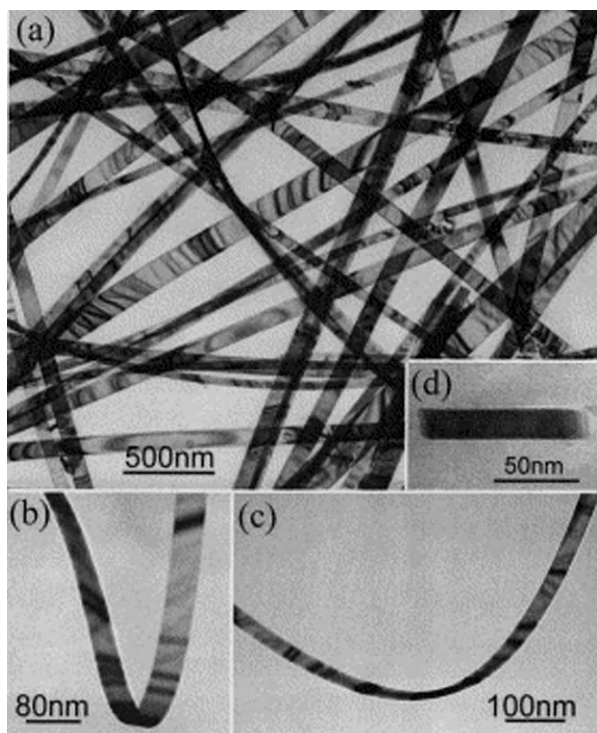
Sears [4] was the first one to explain the growth of mercury whiskers (or nanowires, with a diameter of  $\sim 200$  nm and a length of 1–2 mm) by axial screw-dislocation induced anisotropic growth in 1955. The mercury whiskers or nanowires were grown by a simple evaporation–condensation method, with a condensation temperature of  $-50$  °C under vacuum, and the estimated axial growth rate was of approximately  $1.5$   $\mu\text{m}/\text{sec}$  under a supersaturation of 100, which is defined as a ratio of pressure over equilibrium pressure. However, it was found that the whiskers or nanowires remained at constant radius throughout the axial growth and thus implied that there was no or negligible lateral growth. In a subsequent article, Sears [5] also demonstrated that fine whiskers of other materials including zinc, cadmium, silver, and cadmium sulfide could be grown by the evaporation–condensation method. The experimental conditions varied with the material in question. The growth temperature varied from  $250$  °C for cadmium to  $850$  °C for silver whiskers, with a supersaturation ranging from  $\sim 2$  for cadmium sulfide to  $\sim 20$  for cadmium.

Subsequently, a lot of research has been devoted to confirm the presence of axial screw dislocation for the growth of nanowires; however, in most cases, various techniques including electron microscopy and etching all failed to reveal the presence of axial screw dislocation [6]. Microtwins and stacking faults are observed in many nanowires or nanorods grown by the evaporation–condensation method and are suggested to be responsible for the anisotropic growth [7]. However, many other researchers revealed no axial defects at all in the grown nanorods and nanowires. Such an anisotropic growth is also not possible to explain by means of anisotropic crystal structures. Obviously, more work is needed to understand the growth of nanowires and nanorods by the evaporation–condensation method.

Another related issue is the fact that the observed growth rate of the nanowires exceeds the condensation rate calculated using the equation for a flat surface [Eq. (1)], assuming the accommodation coefficient is unity. That means the growth rate of nanowires is faster than all the growth species arriving at the growth surface. To explain such a significantly enhanced growth rate of a whisker or nanowire, a dislocation–diffusion theory was proposed [8]. In this model, the fast growth rate was explained as follows: the depositing materials at the tip originated from two sources: direct condensation of growth species from the vapor and the migration of adsorbed growth species on side surfaces to the growth tip. However, an adatom migrating over an edge from side surfaces to the growth surface on the tip is unlikely, since the edge serves as an energy barrier for such a migration [9–11].

Pan et al. [12, 13] reported the growth of single crystal nanobelts of various semiconducting oxides simply by

evaporating the desired commercially available metal oxides at high temperatures under a vacuum of 300 Torr and condensing on an alumina substrate, placed inside the same alumina tube furnace, at relatively lower temperatures. The oxides include zinc oxide (ZnO) of wurtzite hexagonal crystal structure, tin oxide ( $\text{SnO}_2$ ) of rutile structure, indium oxide ( $\text{In}_2\text{O}_3$ ) with C-rare-earth crystal structure, and cadmium oxide (CdO) with NaCl cubic structure. Figure 3 shows the scanning electron microscope (SEM) and transmission electron microscope (TEM) pictures of  $\text{SnO}_2$  nanobelts. We will just focus on the growth of ZnO nanobelts to illustrate their findings, since similar phenomena were found in all four oxides. The typical thickness and width-to-thickness ratios of the ZnO nanobelts are in the range of 10 to 30 nm and  $\sim 5$  to 10, respectively. Two growth directions were observed: [0001] and [0110]. No screw dislocation was found throughout the entire length of the nanobelt, except a single stacking fault parallel to the growth axis in the nanobelts grown along [0110] direction. The surfaces of the nanobelts are clean, atomically sharp, and free of any sheathed amorphous phase. Their further TEM analysis also revealed the absence of amorphous globules on the tip of nanobelts. The above observations imply that the growth of nanobelts is not due to the VLS mechanism, which will be discussed later in this chapter. The growth of nanobelts cannot be attributed to either screw dislocation induced anisotropic growth, nor impurity inhibited growth. Furthermore, since four oxides in question all have different crystal structures, it is not likely that the growth of nanobelts is directly related to their crystal structures. It seems worthwhile to note that the shape of nanowires and

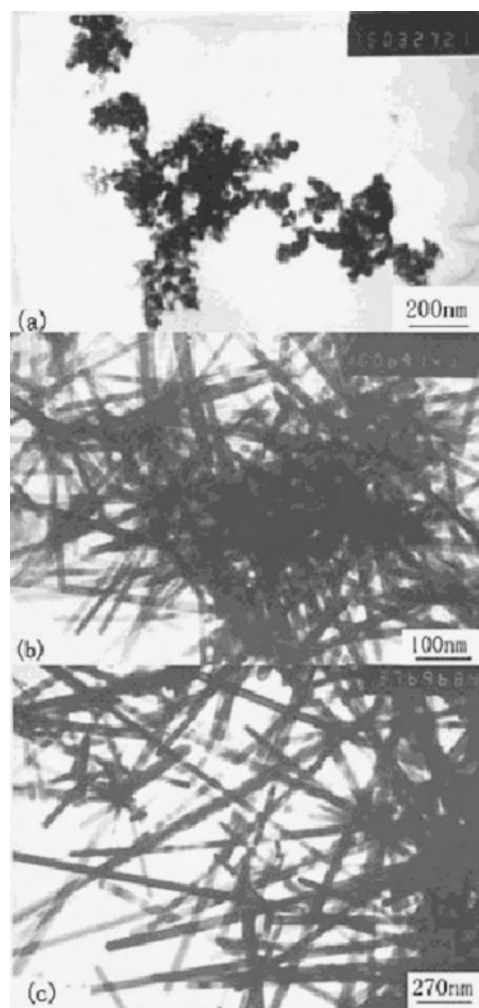


**Figure 3.**  $\text{SnO}_2$  nanobelts grown by evaporation of powders. Reprinted with permission from [13], Z. R. Dai et al., *Solid State Commun.* 118, 351 (2001). © 2001, Elsevier Science.

nanobelts may also depend on growth temperature. Early work showed that single crystal mercury grown at different temperatures would have either a platelet shape or a whisker form [4, 14]. CdS ribbons were also grown by the evaporation–condensation method [5].

Liu et al. [15] synthesized  $\text{SnO}_2$  nanorods by converting nanoparticles at elevated temperatures. The nanoparticles were chemically synthesized from  $\text{SnCl}_4$  by inverse microemulsion using nonionic surfactant, have an average size of 10 nm, and are highly agglomerated.  $\text{SnO}_2$  nanoparticles are likely amorphous. When heated to temperatures ranging from 780 to 820 °C in air, single crystal  $\text{SnO}_2$  nanorods with rutile structure were formed. These nanorods are straight and have uniform diameters ranging from 20 to 90 nm and lengths from 5 to 10  $\mu\text{m}$ , depending on annealing temperature and time. Figure 4 shows  $\text{SnO}_2$  nanowires grown by this method.

Silicon nanowires could be synthesized by thermal evaporation of silicon monoxide under a reducing environment [16]. SiO powder was simply heated to a temperature of 1300 °C, and the vapor of silicon monoxide was carried by a mixture of argon and 5% hydrogen. The (100) silicon



**Figure 4.**  $\text{SnO}_2$  nanorods grown by heating of powders nanoparticles. Reprinted with permission from [15], Y. Liu et al., *Adv. Mater.* 13, 1883 (2001). © 2001, Wiley-VCH.



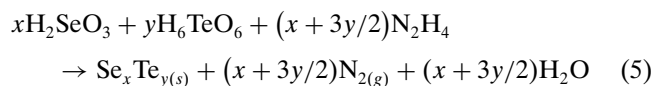
substrate was maintained at 930 °C for the growth. It was found that the as-grown nanowires of 30 nm in diameter consist of a silicon core of 20 nm in diameter and a shell of silicon dioxide of 5 nm in thickness. The silicon core is believed to form through the reduction of silicon monoxide by hydrogen. The silicon dioxide shell may serve as a stopper for the side growth, resulting in a uniform diameter throughout a nanowire.

Although it is known that the impurities have differential adsorption on various crystal facets in a given a crystal and the adsorption of impurity would retard the growth process, no nanorods have been grown by vapor condensation methods based on impurity poisoning by design. However, impurity poisoning has often been cited as one of the reasons for anisotropic growth during the synthesis of nanowires and nanorods.

The dissolution–condensation process differs from evaporation–condensation in growth media. In the dissolution–condensation process, the growth species first dissolve into a solvent or a solution and then diffuse through the solvent or solution and deposit onto the surface resulting in the growth of nanorods or nanowires.

Gates et al. [17] prepared uniform single crystal nanowires of selenium by dissolution–condensation methods. In the first step, spherical colloidal particles of amorphous selenium with sizes of ~300 nm in aqueous solution were prepared through the reduction of selenious acid with excess hydrazine at 100 °C. When the solution was cooled to room temperature, some nanocrystalline selenium with trigonal structure precipitated. In the second step, when the solution aged at room temperature in dark, amorphous selenium colloid particles dissolved into the solution, whereas the selenium crystallites grew. In this solid–solution–solid transformation, the morphology of the crystalline selenium products was determined by the anisotropic growth, which is attributed to the one-dimensional characteristics of the infinite, helical chains of selenium in the trigonal structure. Trigonal Se crystals were found to grow predominantly along the [001] direction [18]. Se nanowires grown by this method were found free of defects, such as kinks and dislocations.

The chemical solution method was also explored for the synthesis of nanorods of crystalline  $\text{Se}_x\text{Te}_y$  compound [19]. In an aqueous medium (refluxed at ~100 °C), a mixture of selenious acid and orthotelluric acid was reduced by excess hydrazine [20]

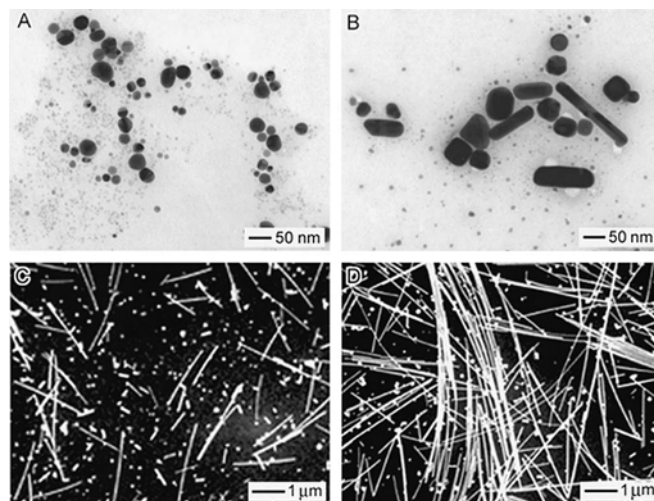


Tellurium could easily precipitate out as crystalline hexagonal nanoplatelets under the experimental conditions through a homogeneous nucleation process [21]. It is postulated that the selenium and tellurium atoms subsequently produced by the above reduction reaction would grow into nanorods on the nanoplatelet tellurium seeds with a growth direction along [001]. The as-synthesized nanorods typically have a mean length of <500 nm and a mean diameter of ~60 nm, with a stoichiometric chemical composition of  $\text{SeTe}$ , and a trigonal crystal structure, similar to that of Se and Te. Hydrazine can also promote the growth of nanorods directly from metal powders in solution; for example, single crystal

ZnTe nanorods with diameters of 30–100 nm and lengths of 500–1200 nm were synthesized using Zn and Te metal powders as reactants and hydrazine hydrate as solvent by a solvothermal process [22]. It was postulated that hydrazine could promote anisotropic growth in addition to its role as a reduction agent.

Wang et al. have grown single crystal  $\text{Mn}_3\text{O}_4$  nanowires of 40–80 nm diameter and lengths up to 150  $\mu\text{m}$  in a molten NaCl flux [23].  $\text{MnCl}_2$  and  $\text{Na}_2\text{CO}_3$  were mixed with NaCl and nonylphenyl ether (NP-9) and heated to 850 °C. After cooling, the NaCl was removed by washing in distilled water. NP-9 was used to prevent the formation of small particles at the expense of nanowires. The nanowires are believed to grow through Ostwald ripening, with NP-9 acting to reduce the eutectic temperature of the system, as well as stabilizing the smaller precursor particles. This technique has been applied to a wide variety of single crystal oxide nanorods.

Nanowires can grow on alien crystal nanoparticles, which serve as seeds for heteroepitaxial growth, by solution processing. Sun et al. [24] synthesized crystalline silver nanowires of 30–40 nm in diameter and ~50  $\mu\text{m}$  in length using platinum nanoparticles as growth seeds. The growth species of Ag is generated by the reduction of  $\text{AgNO}_3$  with ethylene glycol, whereas the anisotropic growth was achieved by introducing surfactants such as polyvinyl pyrrolidone in the solution. Polymer surfactants adsorbed on some growth surfaces, kinetically blocking (or poisoning) the growth, resulting in the formation of uniform crystalline silver nanowires. TEM analyses further revealed that the growth directions of face-centered-cubic silver nanowires were [211] and [011]. Figure 5 shows the silver nanowires grown in solution using Pt nanoparticles as growth seeds. Dissolution–condensation can also grow nanowires on a substrate. Govender et al. formed ZnO nanorods on glass substrates from a solution of zinc acetate or zinc formate and hexamethylenetetramine at room temperature [25]. These faceted nanorods were preferentially oriented in the [0001] direction (that is, along the *c*-axis), with diameters of about 266 nm and a length of ~3  $\mu\text{m}$ .



**Figure 5.** Silver nanowires grown from solution. Reprinted with permission from [24], Y. Sun et al., *Nano Lett.* 2, 165 (2002). © 2002, American Chemical Society.

Hydrothermal growth is another method being explored in the formation of nanorods from inorganic salts.  $\text{CdWO}_4$ , with a monoclinic crystal structure, nanorods were synthesized directly by the reaction of cadmium chloride ( $\text{CdCl}_2$ ) and sodium tungstate ( $\text{NaWO}_4$ ) at  $130^\circ\text{C}$  under pressure at a pH ranging from 3 to 11 for 5 hours. Such grown cadmium tungstate nanorods have diameters of 20–40 nm and lengths ranging from 80 to 280 nm [26]. The growth of nanorods is attributed to anisotropic growth, though no specific growth direction was identified. Nanotubes of  $\text{H}_2\text{Ti}_3\text{O}_7$  have been hydrothermally synthesized from  $\text{TiO}_2$  powder dissolved in a  $\text{NaOH}$  aqueous solution at  $130^\circ\text{C}$  by Chen et al. [27]. The synthesized products were hollow tubes about 9 nm in diameter, with lengths from 100 to several hundred nanometers.

Nanowires or nanorods by the evaporation (dissolution)–condensation deposition most likely have faceted morphology and are generally short in length with relatively small aspect ratios, particularly when grown in liquid medium. However, anisotropic growth induced by axial imperfections, such as screw dislocation, microtwins, and stacking faults, or by impurity poisoning, can result in the growth of nanowires with very large aspect ratios.

## 2.2. Vapor (or Solution)–Liquid–Solid Growth

In VLS growth, a second phase material, commonly referred to as either impurity or catalyst, is purposely introduced to direct and confine the crystal growth on a specific orientation and within a confined area. Catalyst forms a liquid droplet by itself or by alloying with growth material during the growth, which acts as a trap of growth species. Enriched growth species in the catalyst droplets subsequently precipitates at the growth surface resulting in the one-directional growth. Wagner et al. [28, 29] first proposed the VLS theory over 40 years ago to explain the experimental results and observations in the growth of silicon nanowires or whiskers that could not be explained by the evaporation–condensation theory. These phenomena include:

1. There are no screw dislocations or other imperfections along the growth direction.
2. The growth direction  $\langle 111 \rangle$  is the slowest as compared with other low index directions such as  $\langle 110 \rangle$  in silicon.
3. Impurities are always required.
4. A liquidlike globule is always found in the tip of nanowires.

Wagner summarized the experimental details, results, and the VLS theory in a truly elegant way in a classical paper [30], and Givargizov [6] further elaborated the experimental observations, models, and theories developed regarding the VLS process. The readers who want to learn more about this subject are strongly recommended to read those literatures. Although extensive research in this field has been carried out in recent years, fundamentals of the VLS method have not been changed significantly. Wagner summarized the requirements for the VLS growth 30 years ago [30], which are still valid in today's understanding.

1. The catalyst or impurity must form a liquid solution with the crystalline material to be grown at the deposition temperature.

2. The distribution coefficient of the catalyst or impurity must be less than unity at the deposition temperature.
3. The equilibrium vapor pressure of the catalyst or impurity over the liquid droplet must be very small. Although the evaporation of the catalyst does not change the composition of the saturated liquid droplet, it does reduce the total volume of the liquid droplet. Unless more catalyst is supplied, the volume of the liquid droplet reduces. Consequently, the diameter of the nanowire will reduce and the growth will eventually stop, when all the catalyst is evaporated.
4. The catalyst or impurity must be inert chemically. It must not react with the chemical species such as by-products presented in the growth chamber.
5. The interfacial energy plays a very important role. The wetting characteristics influence the diameter of the grown nanowire. For a given volume of liquid droplet, a small wetting angle results in a large growth area, leading to a large diameter of nanowires.
6. For a compound nanowire growth, one of the constituent can serve as the catalyst.
7. For controlled unidirectional growth, the solid–liquid interface must be well defined crystallographically. One of the simplest methods is to choose a single crystal substrate with desired crystal orientation.

In VLS growth, the growth species is evaporated first and then diffuses and dissolves into a liquid droplet. The surface of the liquid has a large accommodation coefficient and is therefore a preferred site for deposition. Saturated growth species in the liquid droplet will diffuse to and precipitate at the interface between the substrate and the liquid. The precipitation will follow first nucleation and then crystal growth. Continued precipitation or growth will separate the substrate and the liquid droplet, resulting in the growth of nanowires.

Let us take the growth of silicon nanowires with gold as a catalyst as an example to illustrate the experimental process of the VLS growth. A thin layer of gold is sputtered on a silicon substrate and annealed at an elevated temperature (above the eutectic point of  $\sim 360^\circ\text{C}$  of the silicon–gold system), which is typically the same as the growth temperature. During the annealing, silicon and gold react and form a liquid mixture, which forms a droplet on the silicon substrate surface. During the growth, an equilibrium composition is reached at the growth temperature as determined by the binary phase diagram. When silicon species is evaporated from the source and preferentially condensed at the surface of the liquid droplet, the liquid droplet will become supersaturated with silicon. Subsequently, the supersaturated silicon will diffuse from the liquid–vapor interface and precipitate at the solid–liquid interface resulting in the growth of silicon. The growth will proceed unidirectionally perpendicular to the solid–liquid interface. Once the growth species is adsorbed onto the liquid surface, it will dissolve into the liquid. The material transport in the liquid is diffusion-controlled and occurs under essentially isothermal conditions. At the interface between the liquid droplet and growth surface, the crystal growth proceeds essentially the same as that in the Czochraski crystal growth.

The catalyst can be introduced *in-situ* as well. In this case, the growth precursor is mixed with the catalyst and evaporated simultaneously at a higher temperature. Both the growth precursor or species and the catalyst condense at the substrate surface when supersaturation is reached at a temperature lower than the evaporation temperature. The mixture of the growth species and catalyst reacts either in the vapor phase or on the substrate surface to form a liquid droplet. The subsequent nanowire growth would proceed as discussed before.

Crystalline defects, such as screw dislocations, are not essential for VLS growth. However, defects present at the interface may promote the growth and lower the required supersaturation. From the above discussion, it is clear that the growth of nanowires by the VLS method is not restricted by the type of substrate material and the type of catalysts. The nanowires can be single crystal, polycrystalline, or amorphous depending on the substrates and growth conditions.

The preferential adsorption of growth species onto the liquid droplet surface can be understood. For a perfect or an imperfect crystal surface, an impinging growth species diffuses along the surface. During the diffusion, the growth species may be irreversibly incorporated into the growth site (ledge, ledge-kink, or kink). If the growth species did not find a preferential site in a given period of time (the residence time), the growth species will escape back to the vapor phase. A liquid surface is distinctly different from a perfect or imperfect crystal surface and can be considered as a "rough" surface. Rough surface is composed of only ledge, ledge-kink, or kink sites. That is, every site over the entire surface is to trap the impinging growth species. The accommodation coefficient is unit. Consequently, the growth rate of the nanowires or nanorods by the VLS method is much higher than that without liquid catalyst. Wagner and Ellis [31] reported that the growth rate of silicon nanowires using a liquid Pt-Si alloy is about 60 times higher than directly on the silicon substrate at 900 °C. It is likely that in addition to acting as a sink for the growth species in the vapor phase, the catalyst or impurity forming the liquid with the growth material can act as a catalyst for the heterogeneous reaction or deposition.

Bootsma and Gassen compared the axial ( $V_{||}$ ) and lateral ( $V_{\perp}$ ) growth rates for Si and Ge nanowires as well as the substrate (i.e., film) growth rate of these materials, with  $\text{SiH}_4$  and  $\text{GeH}_4$  as precursors and numerous metals (Au, Ag, Cu, Ni, Pd) as catalysts [32]. They found that the lateral and the substrate growth rates are essentially the same, whereas the axial rates by the VLS process for both Si and Ge nanowires are approximately two orders of magnitude higher than the VS growth rates under the same conditions.

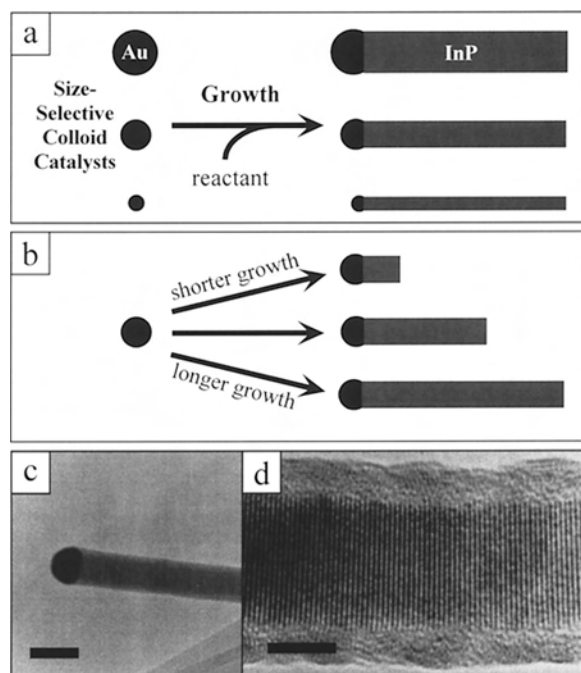
The enhanced growth rate can also be partly due to the fact that the condensation surface area for the growth species in the VLS growth is larger than the surface area of the crystal growth. While the growth surface is the interface between the liquid droplet and the solid surface, the condensation surface is the interface between the liquid droplet and vapor phase. Depending on the contact angle, the liquid surface area can be several times the growth surface.

Growth of elementary Si and Ge nanowires has been well established [33–35]. Although gold was initially used for the

growth of silicon nanowires with the VLS method, other catalysts have been found to be effective in the formation of nanowires of various materials. For example, Si nanowires can be synthesized using Fe as a catalyst [36, 37] at a relatively high growth temperature of 1200 °C. A mixture of silicon powder with 5 wt% Fe was ablated by either laser or simple heating to 1200 °C, which was also the growth temperature. The nanowires have nominal diameters of ~15 nm and a length varying from a few tens to several hundreds micrometers. An amorphous layer of silicon oxide of ~2 nm in thickness overcoated the outside of silicon nanowires. The amorphous oxide layer was likely formed during the growth at high temperature, when a small amount of oxygen leaked into the deposition chamber.

The size of nanowires grown by VLS method is solely determined by the size of the liquid catalyst droplets. To grow thinner nanowires, one can simply reduce the size of the liquid droplets. A typical method used to form small liquid catalyst droplets is to coat a thin layer of catalyst on the growth substrate and to anneal at elevated temperatures [38]. During annealing, catalyst reacts with the substrate to form a eutectic liquid and further ball up to reduce the overall surface energy. Au as a catalyst and silicon as a substrate is a typical example. The size of the liquid catalyst droplets can be controlled by the thickness of the catalyst film on the substrate. In general, a thinner film forms smaller droplets, giving smaller diameters of nanowires subsequently grown. For example, 10 nm Au film yields single crystal germanium nanowires of 150 nm in diameter, while 5 nm Au film results in the growth of 80 nm sized germanium nanowires [39]. However, further reduction in the catalyst film thickness did not result in a decreased diameter of germanium nanowires [39]. No further reduction in diameter of nanowires indicated that there is a minimum size of liquid droplets achievable by applying thin films.

Further reduction of diameters of nanowires could be achieved by dispersing monosized catalyst colloids on the substrate surface, instead of a thin film of catalyst [40, 41]. GaP nanowires were grown by a laser catalytic growth synthetic method [35] using gold colloids [41]. Gold colloids or nanoclusters were supported on a silica substrate and the reactants Ga and P were generated from a solid target of GaP by laser ablation. Single crystal GaP nanowires show a growth direction of [111] and have a stoichiometric composition of 1:0.94 confirmed by energy dispersive X-ray analysis (EDAX). The diameters of GaP nanowires were determined by the size of the catalyst gold nanoclusters. GaP nanowires grown from 8.4, 18.5, and 28.2 nm diameter gold colloids were found to be 11.4, 20, and 30.2 nm, respectively. A similar technique was applied to the growth of InP nanowires [40]. The growth substrate temperature was controlled to be approximately 500–600 °C, and a constant flow of Ar at 100 standard cubic centimeters per minute under a pressure of 200 Torr was maintained during the growth. The laser for ablation used was an ArF excimer laser with a wavelength of 193 nm. InP nanowires were found to be single crystal and grew along the [111] direction. Figure 6 shows the general concepts of control of the diameters and length of nanowires grown by catalyst colloids [40]. Detailed analysis further revealed an amorphous oxide layer of 2–4 nm in thickness presented on all nanowires. The existence of an



**Figure 6.** Length and diameter control in nanowires grown from colloidal catalysts. Reprinted with permission from [40], M. S. Gudiksen et al., *J. Phys. Chem. B* 105, 4062 (2001). © 2001, American Chemical Society.

amorphous oxide layer was explained by the overgrowth of an amorphous InP on the side faces and subsequent oxidation after the samples were exposed to air. The overgrowth on side faces is not catalyst activated and implies supersaturated vapor concentrations of growth constituents in the system.

The equilibrium vapor pressure or solubility is dependent on the surface energy and a radius (or curvature of a surface) at a given condition defined by the Kelvin equation

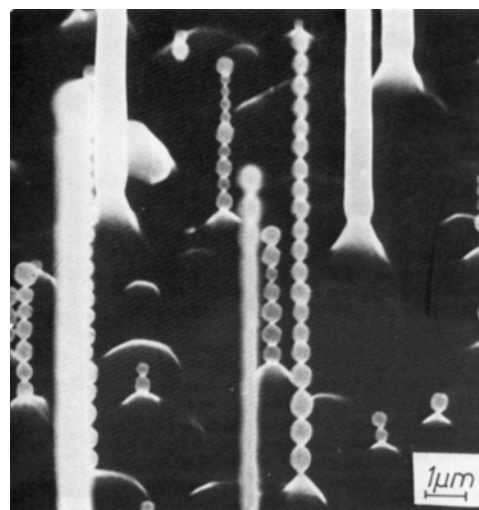
$$\ln\left(\frac{P}{P_0}\right) = -\frac{2\gamma\Omega}{kTr} \quad (6)$$

where  $P$  is the vapor pressure of a curved surface,  $P_0$  is the vapor pressure of a flat surface,  $\gamma$  is the surface energy,  $\Omega$  is the atomic volume,  $r$  is the surface radius, and  $k$  is the Boltzmann constant. For the growth of nanowires, if facets are developed during the growth, longitudinal and lateral growth rates of nanowires or nanorods will be solely determined by the growth behavior of individual facets. However, if nanowires were cylindrical in shape, the lateral growth rate would be significantly smaller than the longitudinal one, assuming all surfaces have the same surface energy. Convex surfaces (the side surface) with very small radius (<100 nm) would have a significantly higher vapor pressure as compared with that of a flat growing surface. A supersaturated vapor pressure or concentration of the growth species for the growing surface may be well below the equilibrium vapor pressure of the convex surface of thin nanowires. For the growth of uniform high quality crystalline nanowires or nanorods, in general supersaturation should be kept relatively low, so that there would be no growth on the side surface. A high supersaturation would result in growth of other

facets, just as in the vapor–solid growth discussed before. Further high supersaturation would lead to secondary nucleation on the growth surface or homogeneous nucleation, resulting in termination of epitaxial growth.

Since the diameters of nanowires grown by the VLS method are solely controlled by the size of the liquid catalyst droplets, thinner wires can be grown by using smaller liquid droplets. However, this approach has its limit. From Eq. (6), we already know that the equilibrium vapor pressure of a solid surface is dependent on the surface curvature. The same dependence is found for a solubility of a solute in a solvent. As the size of the droplets is reduced, the solubility would increase. For the growth of very thin nanowires, a very small droplet is required. However, a convex surface with a very small radius would have a very high solubility. As a result, a high supersaturation in the vapor phase has to be generated. A high supersaturation in the vapor phase may promote the lateral growth on the side surface of nanowires with the vapor–solid mechanism. Therefore, a conical structure may be developed instead of uniformly sized nanowires. Further, a high supersaturation may initiate homogeneous nucleation in the gas phase or secondary nucleation at the surface of nanowires.

Another characteristic in the VLS method should be noted. According to the Kelvin equation, an equilibrium solubility and supersaturation of growth species in larger liquid catalyst droplets can be obtained more easily than in smaller droplets. The growth of nanowires will proceed only when the concentration of growth species is above the equilibrium solubility. When the concentration or supersaturation in the vapor phase is appropriately controlled, vapor pressure could be kept below the equilibrium solubility in small liquid droplets, and the growth of nanowires of thinnest nanowires would terminate. When the growth proceeds at high temperatures and the grown nanowires are very thin, radial size instability is often observed as shown in Figure 7. Such instability is explained by the oscillation of the size of the liquid droplet on the growth tip and the concentration of



**Figure 7.** Radial size instability in nanowires grown by VLS. Reprinted with permission from [6], E. I. Givargizov, “Highly Anisotropic Crystals.” Reidel, Dordrecht, 1986. © 1986, Kluwer Academic Publishers.

the growth species in the liquid droplet [6]. Alternately, this instability may be thought of as similar to the necking of thin streams of liquids [42]. The instability is only observed in very thin wires, where the surface energy is quite high, and at high temperatures where roughening may occur. Such instability could be another barrier for the synthesis of very thin nanowires, which may require high deposition temperatures.

The diameter of nanowires grown by the VLS method is determined by the minimum size of the liquid catalyst droplet under the equilibrium conditions [30]. Methods to achieve small sizes of liquid catalyst droplets are straightforward. For example, laser ablation can be used to deposit catalytic material on a heated substrate to form nanometer diameter clusters with controlled pressure and temperature [43]. In a similar manner, many other evaporation techniques could be used to deposit nanometer catalyst clusters on substrates for the growth of nanowires. Controlling the catalyst placement on the substrate can be used to achieve other novel morphologies. For example, patterned arrays of ZnO nanorods on a surface have been grown, simply by patterning the Au catalyst film prior to VLS growth [44].

Nanowires or nanorods grown by the VLS method in general have a cylindrical morphology (i.e., without facets on the side surface and having a uniform diameter). The physical conditions of both Czochraski and VLS methods are very similar; growth proceeds very close to the melting points or liquid–solid equilibrium temperature. Surfaces may undergo a transition from faceted (smooth) to “rough” surface, known as the roughening transition [45]. Below the roughening temperature, a surface is faceted, and above this temperature, thermal motion of the surface atoms overcomes the interfacial energy and causes a faceted crystal to roughen. From melt, only a restricted group of materials including silicon and bismuth can grow faceted single crystals [46]. However, facets may develop if there is VS deposition on the side surface. Although the VS deposition rate is much smaller than the VLS growth rate for a given temperature, it is still effective in controlling the morphology. Since the difference in the two deposition rates decreases with increasing temperature, the VS deposit will greatly influence the morphology in the high temperature range. It is noted that the diameter of the nanowire may change if the growth conditions vary or the catalyst evaporates or is incorporated into the nanowires.

Numerous precursors have been used for the VLS growth as evaporation–condensation methods. Gaseous precursors such as  $\text{SiCl}_4$  for silicon nanowires [38] are convenient sources. Evaporation of solids by heating to elevated temperatures is another common practice [47]. Laser ablation of solid targets is yet another method used in generating vapor precursors [35, 48]. To promote the evaporation of solid precursors, formation of intermediate compounds may be an appropriate approach. For example, Wu et al. [39] used a mixture of Ge and  $\text{GeI}_4$  as precursors for the growth of Ge nanowires. The precursors evaporated through the formation of volatile compound via the following chemical reaction



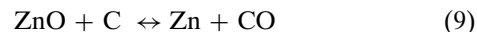
The  $\text{GeI}_2$  vapor was transported to the growth chamber, condensed into the liquid catalyst (here is Au/Si) droplets, and disproportionated according to



Other precursors have also been explored in the VLS growth of nanowires including ammonia and gallium acetylacetonate for GaN nanorods [49], closo-1,2-dicarbododecaborane ( $\text{C}_2\text{B}_{10}\text{H}_{12}$ ) for  $\text{B}_4\text{C}$  nanorods [50], and methyltrichlorosilane for SiC [51].

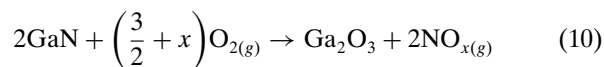
Other materials can be used as catalysts as well. For example, silicon nanowires were grown using iron as a catalyst [35]. Any material or mixture can be used as catalyst as long as they meet the requirements described by Wagner [30]. For example, a mixture of Au and Si was used for the growth of germanium nanowires [39].

ZnO nanowires have been grown using the VLS method [52] on Au-coated (thickness ranging from 2 to 50 nm) silicon substrates by heating a 1:1 mixture of ZnO and graphite powder to 900–925 °C under a constant flow of argon for 5–30 min. The grown ZnO nanowires vary with the thickness of the initial Au coatings. For a 50 nm Au coating, the diameters of the nanowires normally range from 80 to 120 nm and their lengths are 10–20  $\mu\text{m}$ . Thinner nanowires of 40–70 nm with lengths of 5–10  $\mu\text{m}$  were grown on 3 nm Au-coated substrates. The grown ZnO nanowires are single crystal with a preferential growth direction of  $\langle 001 \rangle$ . The growth process of ZnO is believed to be different from that of elementary nanowires. The process involves the reduction of ZnO by graphite to form Zn and CO vapor at high temperatures (above 900 °C). The Zn vapor is transported to and reacted with the Au catalyst, which would have already reacted with silicon to form a eutectic Au–Si liquid on silicon substrates, located downstream at a lower temperature to form Zn–Au–Si alloy droplets. As the droplets become supersaturated with Zn, crystalline ZnO nanowires are formed, possibly through the reaction between Zn and CO at a lower temperature. The above process could be easily understood by the fact that the reaction



is reversible at temperatures around 900 °C [53, 54]. Although the presence of a small amount of CO is not expected to change the phase diagram significantly, no ZnO nanowires were grown on substrates in the absence of graphite.

Single crystal monoclinic gallium oxide ( $\beta\text{-Ga}_2\text{O}_3$ ) nanowires were synthesized with a conventional dc arc-discharge method [55]. GaN powder mixed with 5 wt% of transition metal powders (Ni/Co = 1:1 and Ni/Co/Y = 4.5:4.5:1) was pressed into a small hole of the graphite anode. A total pressure of 500 Torr of argon and oxygen gases in a ratio of 4:1 was maintained during the growth. The typical diameter of the nanowires is about 33 nm with a growth direction of  $[001]$ , and no amorphous layer was founded on the surface. A possible chemical reaction for the formation of  $\text{Ga}_2\text{O}_3$  is proposed to be



Single crystal GeO<sub>2</sub> nanowires were grown by evaporation of a mixture of Ge powder and 8 wt% Fe at 820 °C under a flow (130 sccm) of argon gas under a pressure of 200 Torr [56]. The nanowires have diameters ranging from 15 to 80 nm. Although Fe was added as a catalyst to direct the growth of nanowires, no globules were found in the tips of grown nanowires. The authors argued that the GeO<sub>2</sub> nanowires were grown by mechanisms other than the VLS method. It is also noticed that during the experiment, no oxygen was intentionally introduced into the system. Oxygen may leak into the reaction chamber and react with germanium to form germanium oxide.

Yu et al. [57] reported the synthesis of amorphous silica nanowires by the VLS method. A mixture of silicon with 20 wt% silica and 8 wt% Fe was ablated using an excimer laser of 246 nm wavelength under flowing argon at 100 Torr. Fe was used as a catalyst and the growth temperature was 1200 °C. The nanowires have a chemical composition of Si:O = 1:2 and a uniform size distribution with a diameter of 15 nm and a length up to hundreds micrometers.

In general, a high temperature and a vacuum are required in the growth of nanowires by the VLS method. An alternative method called the solution–liquid–solid (SLS) growth method was developed by Buhro's research group [58, 59] and first applied for the synthesis of InP, InAs, and GaAs nanowires with solution-phase reactions at relatively lower temperatures ( $\leq 203$  °C). The SLS method is very similar to VLS theory [58]. Nanowires were found to be polycrystalline or near single crystal with diameters of 10–150 nm and lengths up to several micrometers. Let us take the growth of InP nanowires as an example to illustrate the SLS growth process. Precursors used were typical organometallic compounds: In(*t*-Bu)<sub>3</sub> and PH<sub>3</sub>, which were dissolved into hydrocarbon solvent with protic catalyst such as MeOH, PhSH, Et<sub>2</sub>NH<sub>2</sub>, or PhCO<sub>2</sub>H. In the solution, precursors reacted to form In and P species for the growth of InP nanowires with the following organometallic reaction, which is commonly used in chemical vapor deposition [60]



Indium metal functions as the liquid phase or catalyst for the growth of InP nanowires. Indium melts at 157 °C and forms liquid drops. It is postulated that both P and In dissolve into the In droplets and precipitate to form nanowires of InP. The growth direction of InP nanowires was found to be predominated by  $\langle 111 \rangle$ , similar to that with the VLS method.

### 2.3. Stress-Induced Recrystallization

It is worth noting that nanowires can be synthesized by stress-induced recrystallization, though it has attracted little attention in the nanotechnology community. Application of pressure on solids at elevated temperatures is known to result in the growth of whiskers or nanowires with diameters as small as 50 nm [61]. It was demonstrated that the growth rate of tin whiskers increased proportionally with the applied pressure [61] and could be four orders of magnitude when a pressure of 7500 psi was applied [62]. The growth of such nanowires or whiskers is based on a dislocation at

the base of the whisker [63, 64] and the growth proceeds from the base and not from the tip [65]. The formation of metallic nanorods is likely due to the confined growth at the surface between the metallic film and the grown nanowires, whereas no growth is possible in other directions (side faces of nanowires). It should be noted that this technique is not widely explored in the recent studies on the growth of nanorods and nanowires (see Table 1).

## 3. TEMPLATE-BASED SYNTHESIS

Template-based synthesis of nanostructured materials is a very general method and can be used in fabrication of nanorods, nanowires, and nanotubules of polymers, metals, semiconductors, and oxides. Various templates with nano-size channels have been explored for the template growth of nanorods and nanotubules. The most commonly used and commercially available templates are anodized alumina membrane [66] and radiation track-etched polymer membranes [67]. Other membranes have also been used as templates such as nanochannel array glass [68], radiation track-etched mica [69], mesoporous materials [70], porous silicon by electrochemical etching of silicon wafer [71], zeolites [72], and carbon nanotubes [73, 74]. Alumina membranes with uniform and parallel porous structure are made by anodic oxidation of aluminum sheets in solutions of sulfuric, oxalic, or phosphoric acids [66, 75]. The pores are arranged in a regular hexagonal array, and densities as high as 10<sup>11</sup> pores/cm<sup>2</sup> can be achieved [76]. Pore size ranging from 10 nm to 100 μm can be achieved [76, 77]. The polycarbonate membranes are made by bombarding a nonporous polycarbonate sheet, with typical thickness ranging from 6 to 20 μm, with nuclear fission fragments to create damage tracks, and then chemically etching these tracks into pores [67]. In radiation track-etched membranes, pores have a uniform size as small as 10 nm, though randomly distributed. Pore densities can be as high as 10<sup>9</sup> pores/cm<sup>2</sup>.

In addition to the desired pore or channel size, morphology, size distribution, and density of pores, template materials must meet certain requirements. First, the template materials must be compatible with the processing conditions. For example, an electrical insulator is required for a template to be used in electrochemical deposition. Except for the template directed synthesis, template materials should be chemically and thermally inert during the synthesis and following processing steps. Second, depositing materials or solution must wet the internal pore walls. Third, for the synthesis of nanorods or nanowires, the deposition should start from the bottom or one end of the template channels and proceed from one side to another. However, for the growth of nanotubules, the deposition should start from the pore wall and proceed inwardly. Inward growth may result in pore blockage, so that should be avoided in the growth of "solid" nanorods or nanowires. Kinetically, enough surface relaxation permits maximal packing density, so a diffusion-limited process is preferred. Other considerations include the easiness of release of nanowires or nanorods from the templates and of handling during the experiments.

**Table 1.** A summary of the oxide nanorods mentioned in this chapter.

Material	Form	Method	Diameter (or width for beltlike structures)	Length	Ref.
ZnO, SnO <sub>2</sub> , In <sub>2</sub> O <sub>3</sub> , CdO, Ga <sub>2</sub> O <sub>3</sub>	Nanobelts	Evaporation–condensation	30–300 nm	Up to a few mm	[12, 13]
SnO <sub>2</sub>	Nanorods	Evaporation–condensation	70–90 nm	5–10 μm	[15]
Mn <sub>3</sub> O <sub>4</sub>	Nanowires	Dissolution–condensation (molten salt flux)	40–80 nm	Up to 150 μm	[23]
ZnO	Nanorods	Dissolution–condensation	~200–300 nm	~3 μm	[25]
CdWO <sub>4</sub>	Nanorods	Dissolution–condensation (hydrothermal)	20–40 nm	80–280 nm	[26]
H <sub>2</sub> Ti <sub>3</sub> O <sub>7</sub>	Nanotubes	Dissolution–condensation (hydrothermal)	9 nm	100 to several hundred nanometers	[27]
ZnO	Nanowires	VLS	20–150 nm	2–10 μm	[51, 54]
β-Ga <sub>2</sub> O <sub>3</sub>	Nanowires	VLS	33 nm	Up to 100 μm	[55]
GeO <sub>2</sub>	Nanowires	VLS or VS	15–80 nm	Up to a few tens of μm	[56]
Amorphous SiO <sub>2</sub>	Nanowires	VLS	~15 nm	Up to hundreds of μm	[57]
TiO <sub>2</sub> , amorphous SiO <sub>2</sub> , BaTiO <sub>3</sub> , Pb(Ti,Zr)O <sub>3</sub> , Sr <sub>2</sub> Nb <sub>2</sub> O <sub>7</sub>	Nanorods	Template electrophoretic deposition	40–200 nm	Up to 10 μm	[102, 103]
ZnO	Nanowires and nanotubes	Template electrophoretic deposition	~200 nm	~25–55 μm	[104]
TiO <sub>2</sub>	Nanowires	Template electrophoretic deposition (electrochemically induced sol–gel)	10–40 nm	2–10 μm	[105]
TiO <sub>2</sub> , MnO <sub>2</sub> , V <sub>2</sub> O <sub>5</sub> , Co <sub>3</sub> O <sub>4</sub> , ZnO, WO <sub>3</sub> , SiO <sub>2</sub>	Nanotubes and nanorods	Template filling with colloidal dispersion	22–600 nm	Tens of μm	[107, 109]
Bi <sub>2</sub> O <sub>3</sub>	Nanowires	Oxidation of metal nanowires (melt filling)	~10–100 nm	Up to tens of μm	[112]
ZnO	Nanowires	Oxidation of metal nanowires (electrodeposited)	15–90 nm	Up to 50 μm	[129]

### 3.1. Electrochemical Deposition

Electrochemical deposition can be understood as a special electrolysis resulting in the deposition of solid material on an electrode. This process involves (1) oriented diffusion of charged growth species (typically positively charged cations) through a solution when an external electric field is applied, and (2) reduction of the charged growth species at the growth or deposition surface, which also serves as an electrode. In general, electrochemical deposition is only applicable to electrically conductive materials such as metals, alloys, semiconductors, and electrical conductive polymers, since after the initial deposition, the electrode is separated from the depositing solution by the deposit and the electrical current must go through the deposit to allow the deposition process to continue. Electrochemical deposition is widely used in making metallic coatings; the process is also known as electroplating [78]. When deposition is confined inside the pores of template membranes, nanocomposites are produced. If the template membrane is removed, nanorods or nanowires are prepared.

Electrochemical deposition has been explored in the fabrication of nanowires of metals, semiconductors, and conductive polymers and the growth of nanowires of conductive materials is a self-propagating process [79]. Once a little fluctuation yields the formation of small rods, the growth of rods or wires will continue, since the electric field and the density

of current lines between the tips of nanowires and the opposing electrode are greater, due to a shorter distance, than that between two electrodes. The growth species will more likely deposit onto the tip of nanowires, resulting in continued growth. However, this method is hardly used in practice for the synthesis of nanowires, since it is very difficult, if not impossible, to control the growth. Possin [69] prepared various metallic nanowires by electrochemical deposition inside pores of radiation track-etched mica. Williams and Giordano [80] grew silver nanowires with diameters below 10 nm. The potentiostatic electrochemical template synthesis yielded different metal nanowires, including Ni, Co, Cu, and Au with nominal pore diameters between 10 and 200 nm, and the nanowires were found to be true replicas of the pores [81]. Whitney et al. [82] fabricated the arrays of nickel and cobalt nanowires by electrochemical deposition of the metals into track-etched templates. Single crystal antimony nanowires have been grown by Zhang et al. in anodic alumina membranes using a pulsed electrodeposition [83]. Semiconductor nanorods by electrodeposition include CdSe and CdTe synthesized by Klein et al. in anodic alumina templates [84], and Schönenberger et al. [85] have made conducting polypyrrole electrochemically in porous polycarbonate.

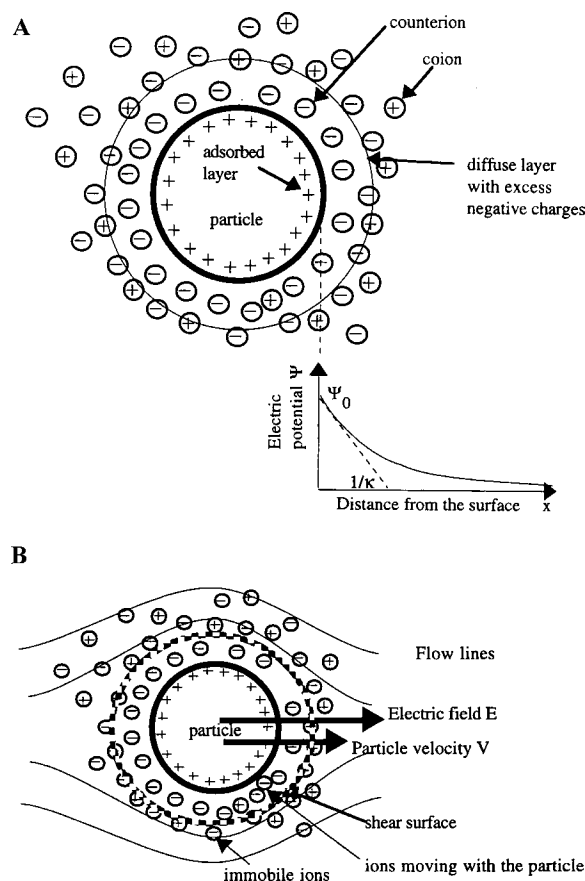
Hollow metal tubules can also be prepared using electrochemical deposition [86, 87]. For growth of metal tubules, the pore walls of the template need to be chemically derivatized

first so that the metal will preferentially deposit onto the pore walls instead of the bottom electrode. Such surface chemistry of the pore walls is achieved by anchoring silane molecules. For example, the pore surface of an anodic alumina template was covered with cyanosilanes; subsequent electrochemical deposition resulted in the growth of gold tubules [88].

An electroless electrolysis process has also been applied in the fabrication of nanowires or nanorods [86, 89–91]. Electroless deposition is actually a chemical deposition and involves the use of a chemical agent to plate a material from the surrounding phase onto a template surface [92]. The significant difference between electrochemical deposition and electroless deposition is that in the former, the deposition begins at the bottom electrode and the deposited materials must be electrically conductive, whereas the latter method does not require the deposited materials to be electrically conductive and the deposition starts from the pore wall and proceeds inwardly. Therefore, in general, electrochemical deposition results in the formation of “solid” nanorods or nanowires of conductive materials, whereas the electroless deposition often grows hollow fibrils or nanotubules. For electrochemical deposition, the length of nanowires or nanorods can be controlled by the deposition time, whereas the length of the nanotubules is solely dependent on the length of the deposition channels or pores, which often equal to the thickness of membranes. Variation of deposition time would result in a different wall thickness of nanotubules. An increase in deposition time leads to a thick wall and a prolonged deposition may form solid nanorods. However, a prolonged deposition time does not guarantee the formation of solid nanorods. For example, the polyaniline tubules never closed up, even with prolonged polymerization time [93].

### 3.2. Electrophoretic Deposition

The electrophoretic deposition technique has been widely explored, particularly in film deposition of ceramic and organoceramic materials on cathode from colloidal dispersions [94]. Electrophoretic deposition differs from electrochemical deposition in several aspects. First, the deposit by the electrophoretic deposition method need not be electrically conductive. Therefore, this method is particularly useful for oxide systems. Second, nanosized particles in colloidal dispersions are typically stabilized by electrostatic or electrosteric mechanisms. When dispersed in a polar solvent or an electrolyte solution, the surface of nanoparticles develops an electrical charge via one or more of the following mechanisms: (1) preferential dissolution or (2) deposition of charges or charged species, (3) preferential reduction or (4) oxidation, and (5) adsorption of charged species such as polymers. Charged surfaces will electrostatically attract oppositely charged species (typically called counterions) in the solvent or solution. A combination of electrostatic forces, Brownian motion and osmotic forces would result in the formation of a so-called double layer structure, as schematically illustrated in Figure 8A. The figure depicts a positively charged particle surface, the concentration profiles of negative ions (counterions), and positive ions (surface-charge-determining ions), and the electric potential profile. The concentration of counterions gradually decreases with



**Figure 8.** (A) A schematic of the electrical double layer surrounding a particle in a colloidal suspension. (B) Diagram of the features of electrophoretic motion. Reprinted with permission from [98], A. C. Pierre, “Introduction to Sol–Gel Processing.” Kluwer Academic, Boston, 1998. © 1998, Kluwer Academic Publishers.

distance from the particle surface, whereas that of charge-determining ions increases. As a result, the electric potential decreases with distance. Near to the particle surface, the electric potential decreases linearly, in the region known as the Stern layer. Outside of the Stern layer, the decrease follows an exponential relationship, and the region between Stern layer and the point where the electric potential equals zero is called the diffusion layer. Together, the Stern layer and diffusion layer are called the double layer structure in the classic theory of electrostatic stabilization.

Upon application of an external electric field to a colloidal system or a sol, the constituent charged particles are set in motion in response to the electric field, as schematically illustrated in Figure 8B. This type of motion is referred to as electrophoresis. When a charged particle is in motion, some of the solvent or solution surrounding the particle will move with it, since part of the solvent or solution is tightly bound to the particle. The plane that separates the tightly bound liquid layer from the rest of the liquid is called the slip plane. The electric potential at the slip plane is known as the zeta potential. The zeta potential is an important parameter in determining the stability of a colloidal dispersion or a sol; a zeta potential larger than about 25 mV is typically required to stabilize a system [95]. The zeta potential is determined



by a number of factors, such as the particle surface charge density, the concentration of counterions in the solution, solvent polarity, and temperature. The zeta potential around a spherical particle can be described as [96]

$$\zeta = \frac{Q}{4\pi\epsilon_r a(1 + \kappa a)} \quad (12)$$

with

$$\kappa = \left( \frac{e^2 \sum n_i z_i^2}{\epsilon_r \epsilon_0 kT} \right)^{1/2}$$

where  $Q$  is the charge on the particle,  $a$  is the radius of the particle out to the shear plane,  $\epsilon_r$  is the relative dielectric constant of the medium, and  $n_i$  and  $z_i$  are the bulk concentration and valence of the  $i$ th ion in the system, respectively. It is worthwhile to note that a positively charged surface results in a positive zeta potential in a dilute system. A high concentration of counterions, however, can result in a zeta potential of the opposite sign.

The mobility of a nanoparticle in a colloidal dispersion or a sol is dependent on the dielectric constant of the liquid medium, the zeta potential of the nanoparticle, and the viscosity of the fluid. Several forms for this relationship have been proposed, such as the Hückel equation [96]

$$\mu = \frac{2\epsilon_r \epsilon_0 \zeta}{3\pi\eta} \quad (13)$$

Double layer stabilization and electrophoresis are extensively studied subjects. Readers may find additional detailed information in books on sol-gel processing [97–99] and colloidal dispersions [96, 100].

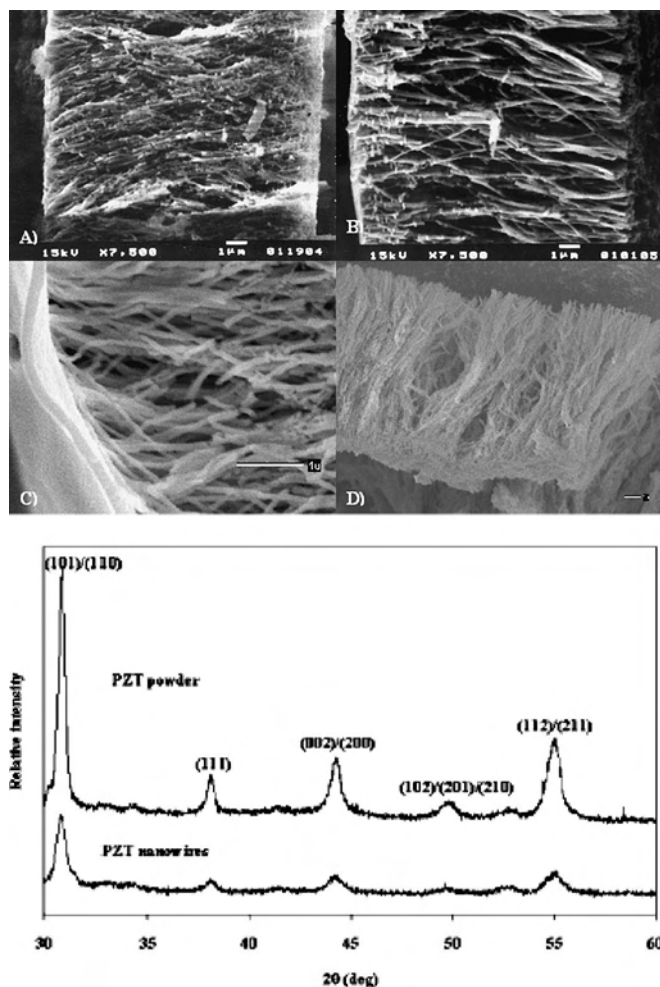
Electrophoretic deposition simply uses such an oriented motion of charged particles to grow films or monoliths by enriching the solid particles from a colloidal dispersion or a sol onto the surface of an electrode. If particles are positively charged (more precisely speaking, having a positive zeta potential), then the deposition of solid particles will occur at the cathode. Otherwise, deposition will be at the anode. At the electrodes, surface electrochemical reactions proceed to generate or receive electrons. The electrostatic double layers collapse upon deposition on the growth surface, and the particles coagulate. There is not much information on the deposition behavior of particles at the growth surface. Some surface diffusion and relaxation is expected. Relatively strong attractive forces, including the formation of chemical bonds between two particles, develop once the particles coagulate. The films or monoliths grown by electrophoretic deposition from colloidal dispersions or sols are essentially a compaction of nanosized particles. Such films or monoliths are porous (i.e., there are voids inside). Typical packing densities, defined as the fraction of solid (also called green density), are less than 74%, which is the highest packing density for uniformly sized spherical particles [101]. The green density of films or monoliths by electrophoretic deposition is strongly dependent on the concentration of particles in sols or colloidal dispersions, zeta potential, externally applied electric field, and reaction kinetics between particle surfaces. Slow reaction and slow arrival of nanoparticles onto the surface would allow sufficient particle relaxation

on the deposition surface, so that a high packing density is expected.

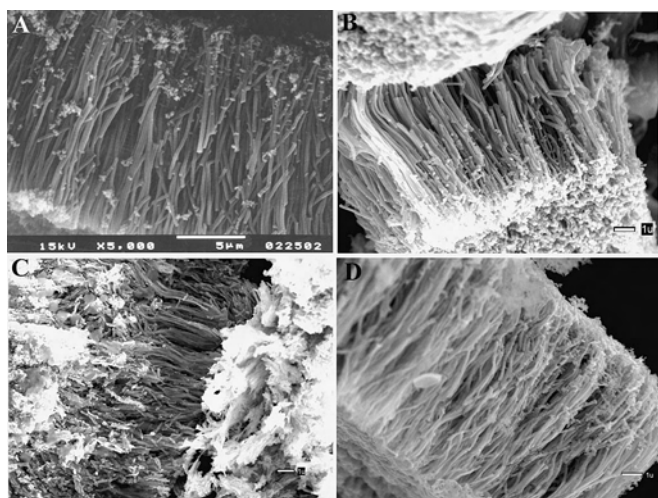
Many theories have been proposed to explain the processes at the deposition surface during electrophoretic deposition. The electrochemical process at the deposition surface or electrodes is complex and varies from system to system. However, in general, a current exists during electrophoretic deposition, indicating reduction and oxidation reactions occur at electrodes and/or deposition surface. In many cases, films or monoliths grown by electrophoretic deposition are electric insulators. However, the films or monoliths are porous and the surface of the pores would be electrically charged just like the nanoparticle surfaces, since surface charge is dependent on the solid material and the solution. Furthermore, the pores are filled with solvent or solution that contains counterions and charge-determining ions. The electrical conduction between the growth surface and the bottom electrode could proceed via either surface conduction or solution conduction.

Limmer et al. [102, 103] combined sol-gel preparation and electrophoretic deposition in the growth of nanorods of various oxides, including complex oxides such as lead zirconate titanate and barium titanate. In their approach, conventional sol-gel processing was applied for the synthesis of various sols. By appropriate control of the sol preparation, nanometer particles with desired stoichiometric composition were formed, electrostatically stabilized by adjusting to an appropriate pH and uniformly dispersed in the solvent. When an external electric field is applied, these electrostatically stabilized nanoparticles will respond and move toward and deposit on either a cathode or an anode, depending on the surface charge (more precisely speaking, the zeta potential) of the nanoparticles. Using radiation-tracked etched polycarbonate membranes with an electric field of  $\sim 1.5$  V/cm, they have grown nanowires with diameters ranging from 40 to 200 nm and a length of 10  $\mu$ m corresponding to the thickness of the membrane. The materials include anatase  $\text{TiO}_2$ , amorphous  $\text{SiO}_2$ , perovskite structured  $\text{BaTiO}_3$  and  $\text{Pb}(\text{Ti},\text{Zr})\text{O}_3$ , and layered structured perovskite  $\text{Sr}_2\text{Nb}_2\text{O}_7$ . Nanorods grown by sol electrophoretic deposition are polycrystalline or amorphous. One of the advantages of this technique is the ability of synthesis of complex oxides and organic-inorganic hybrids with desired stoichiometric composition; Figure 9 shows the nanorods and X-ray diffraction spectra of  $\text{Pb}(\text{Zr},\text{Ti})\text{O}_3$  nanorods. Another advantage is the applicability for a variety of materials; Figure 10 shows the nanorods of  $\text{SiO}_2$ ,  $\text{TiO}_2$ ,  $\text{Sr}_2\text{Nb}_2\text{O}_7$ , and  $\text{BaTiO}_3$ .

Wang et al. used electrophoretic deposition to form nanorods of ZnO from colloidal sols [104]. ZnO colloidal sol was prepared by hydrolyzing an alcoholic solution of zinc acetate with NaOH, with a small amount of zinc nitrate added to act as a binder. This solution was then deposited into the pores of anodic alumina membranes at voltages in the range of 10–400 V. It was found that lower voltages led to dense, solid nanorods, while higher voltages caused the formation of hollow tubules. The suggested mechanism is that the higher voltages cause dielectric breakdown of the anodic alumina, causing it to become charged similarly to the cathode. Electrostatic attraction between the ZnO nanoparticles and the pore walls then leads to tubule formation.



**Figure 9.** Electron micrographs and X-ray diffraction data for Pb (Zr, Ti) $O_3$  (PZT) nanorods grown by sol-gel electrophoresis. Reprinted with permission from [102], S. J. Limmer et al., *Adv. Mater.* 13, 1269 (2001). © 2001, Wiley-VCH.

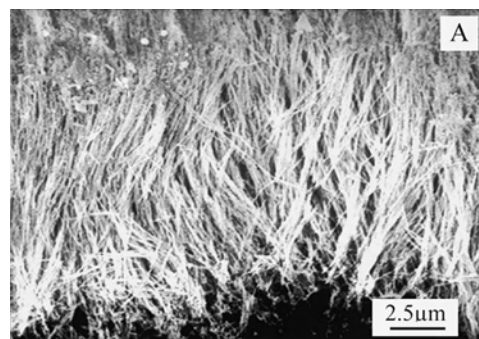


**Figure 10.** Other nanorods grown by sol-gel electrophoresis: (A)  $SiO_2$ , (B)  $TiO_2$ , (C)  $Sr_2Nb_2O_7$ , and (D)  $BaTiO_3$ . Adapted with permission from [103], S. J. Limmer et al., *Adv. Funct. Mater.* 12, 59 (2002). © 2002, Wiley-VCH.

Miao et al. [105] prepared single crystalline  $TiO_2$  nanowires by template-based electrochemically induced sol-gel deposition. Titania electrolyte solution was prepared using a method developed by Natarajan and Nogami [106], in which Ti powder was dissolved into a  $H_2O_2$  and  $NH_4OH$  aqueous solution, forming  $TiO^{2+}$  ionic clusters. When an external electric field was applied,  $TiO^{2+}$  ionic clusters diffused to cathode and underwent hydrolysis and condensation reactions, resulting in deposition of nanorods of amorphous  $TiO_2$  gel. After heat treatment at  $240\text{ }^\circ\text{C}$  for 24 hr in air, nanowires of single crystal  $TiO_2$  with anatase structure and with diameters of 10, 20, and 40 nm and lengths ranging from 2 to  $10\text{ }\mu\text{m}$  were synthesized. However, no axis crystal orientation was identified. The formation of single crystal  $TiO_2$  nanorods here is different from that reported by Martin's group [107]. Here the formation of single crystal  $TiO_2$  is via crystallization of amorphous phase at an elevated temperature, whereas nanoscale crystalline  $TiO_2$  particles are believed to assemble epitaxially to form single crystal nanorods. Epitaxial agglomeration of two nanoscale crystalline particles has been reported [108], though no large single crystals have been produced by assembly of nanocrystalline particles. Figure 11 shows such single crystal nanorods grown by electrophoretic deposition.

### 3.3. Template Filling

Direct template filling is the most straightforward and versatile method in preparation of nanorods and nanotubules. Most commonly, a liquid precursor or precursor mixture is used to fill the pores. There are several concerns in the template filling. First, the wettability of the pore wall should be good enough to permit the penetration and complete filling of the liquid precursor or precursor mixture. For filling at low temperatures, the surface of pore walls can be easily modified to be either hydrophilic or hydrophobic by introducing a monolayer of organic molecules. Second, the template materials should be chemically inert. Third, control of shrinkage during solidification is required. If adhesion between the pore walls and the filling material is weak or solidification starts at the center, or from one end of the pore, or uniformly, solid nanorods are most likely to form.



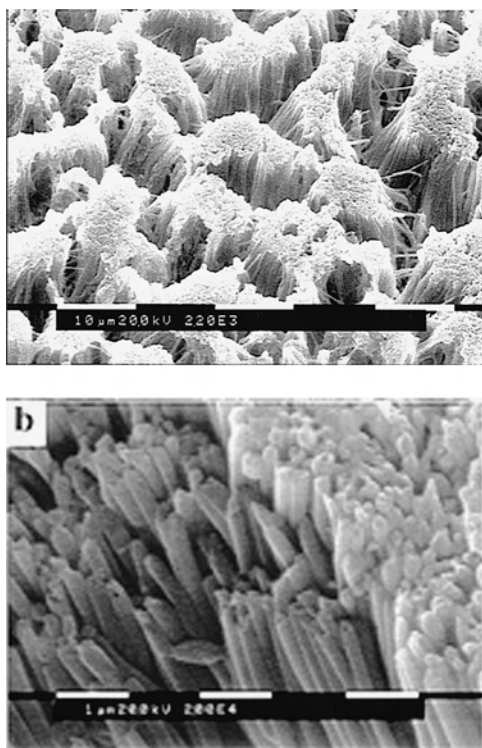
**Figure 11.** Single crystal  $TiO_2$  nanorods growth by electrochemically induced sol-gel processing. Reprinted with permission from [105], Z. Miao et al., *Nano Lett.* 2, 717 (2002). © 2002, American Chemical Society.

However, if the adhesion is very strong, or the solidification starts at the interfaces and proceeds inwardly, it is most likely to form hollow nanotubules.

### 3.3.1. Colloidal Dispersion Filling

Martin and co-workers [107,109] have studied the formation of various oxide nanorods and nanotubules by simply filling the templates with colloidal dispersions. Colloidal dispersions were prepared using appropriate sol-gel processing. The filling of the template was to place a template in a stable sol for a various period of time. The capillary force is believed to drive the sol into the pores, when the surface chemistry of the template pores was appropriately modified to have a good wettability for the sol. After the pores were filled with sol, the template was withdrawn from the sol and dried prior to firing at elevated temperatures. The firing at elevated temperatures served two purposes: removal of template so that freestanding nanorods can be obtained and densification of the sol-gel-derived green nanorods. Figure 12 shows some typical examples of oxide nanorods made by filling the templates.

In previous work, we discussed sol-gel processing and knew that the typical sol consists of a large volume fraction of solvent up to 90% or higher [97]. Although the capillary force may ensure the complete filling of colloidal dispersion inside pores of the template, the amount of the solid filled inside the pores can be very small. Upon drying and subsequent firing processes, a significant amount of shrinkage would be expected. However, the results showed that

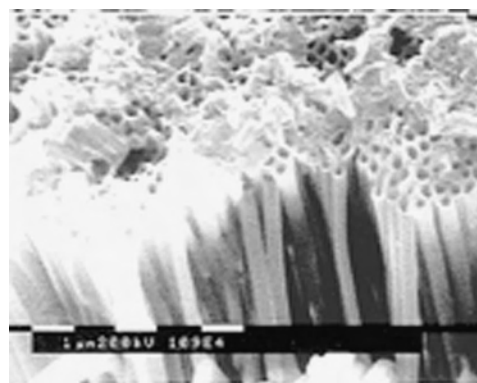


**Figure 12.** Oxide nanorods ( $\text{TiO}_2$  top and  $\text{ZnO}$  bottom) grown by template filling with sol-gel. Adapted with permission from [107], B. B. Lakshmi et al., *Chem. Mater.* 9, 857 (1997). © 1997, American Chemical Society.

most nanorods shrank only a little as compared with the size of the template pores. For example, Lakshmi et al. found that  $\text{TiO}_2$  nanorods synthesized in this manner had the same diameter as the template pores, even after heating to  $400^\circ\text{C}$  [107]. The results indicated that there are some unknown mechanisms which enrich the concentration of solid inside pores. One possible mechanism could be the diffusion of solvent through the membrane, leading to the enrichment of solid along the internal surface of template pores, a process used in ceramic slip casting [110]. The observation of formation of nanotubules (as shown in Fig. 13) by such a sol filling process may imply such a process is indeed present. However, considering the fact that the templates typically were emerged into sol for just a few minutes, the diffusion through membrane and enrichment of solid inside the pores must be a rather rapid process. It is also possible that electrostatic attraction between the positive particles and negative pore walls is responsible for this enrichment. This is a very versatile method and can be applied for any material, which can be made by sol-gel processing. However, the drawback is that it is difficult to ensure the complete filling of the template pores. It is also noticed that the nanorods made by template filling are commonly polycrystalline or amorphous. An exception was found: when the diameter of nanorods is smaller than 20 nm, single crystal  $\text{TiO}_2$  nanorods were made [107].

### 3.3.2. Melt and Solution Filling

Metallic nanowires can also be synthesized by filling a template with molten metals [111]. One example is the preparation of bismuth nanowires by pressure injection of molten bismuth into the nanochannels of an anodic alumina template [112]. The anodic alumina template was degassed and immersed in the liquid bismuth at  $325^\circ\text{C}$  ( $T_m = 271.5^\circ\text{C}$  for Bi), and then high pressure Ar gas of  $\sim 4500$  psi was applied to inject liquid Bi into the nanochannels of the template for 5 hours. Bi nanowires with diameters of 13–110 nm and large aspect ratios of several hundred have been obtained. Individual nanowires are believed to be single crystal. When exposed to air, bismuth nanowires are readily oxidized. An amorphous oxide layer of  $\sim 4$  nm in thickness was observed after 48 hours. After 4 weeks, bismuth nanowires of 65 nm in



**Figure 13.** Hollow nanotubes formed by incomplete filling of the template. Reprinted with permission from [107], B. B. Lakshmi et al., *Chem. Mater.* 9, 857 (1997). © 1997, American Chemical Society.

diameter were found to be completely oxidized. Nanowires of other metals, In, Sn, and Al, and semiconductors, Se, Te, GaSb, and Bi<sub>2</sub>Te<sub>3</sub>, were prepared by injection of melt liquid into anodic alumina templates [111].

Polymeric fibrils have been made by filling a monomer solution, which contains the desired monomer and a polymerization reagent, into the template pores and then polymerizing the monomer solution [113–116]. The polymer preferentially nucleates and grows on the pore walls, resulting in tubules at short deposition times, as discussed previously in the growth of conductive polymer nanowires or nanotubules by electrochemical deposition and fibers at long times. Cai et al. [117] synthesized polymeric fibrils using this technique.

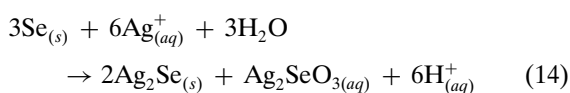
Similarly, metal and semiconductor nanowires have been synthesized through solution techniques. For example, Han et al. [118] have synthesized Au, Ag, and Pt nanowires in mesoporous silica templates. The mesoporous templates were filled with aqueous solutions of the appropriate metal salts (such as HAuCl<sub>4</sub>), and after drying and treatment with CH<sub>2</sub>Cl<sub>2</sub> the samples were reduced under H<sub>2</sub> flow to convert the salts to pure metal. Chen et al. filled the pores of a mesoporous silica template with an aqueous solution of Cd and Mn salts, dried the sample, and reacted it with H<sub>2</sub>S gas to convert to (Cd,Mn)S [119]. Ni(OH)<sub>2</sub> nanorods have been grown in carbon-coated anodic alumina membranes by Matsui et al. [120], by filling the template with ethanolic Ni(NO<sub>3</sub>)<sub>2</sub> solutions, drying, and hydrothermally treating the sample in NaOH solution at 150 °C.

### 3.3.3. Chemical Vapor Deposition

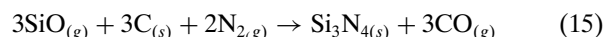
Some researchers have used chemical vapor deposition as a means to form nanowires. Ge nanowires were grown by Leon et al. by diffusing Ge<sub>2</sub>H<sub>6</sub> gas into mesoporous silica and heating [121]. They believed that the precursor reacted with residual surface hydroxyl groups in the template, forming Ge and H<sub>2</sub>. Lee et al. have used a platinum organometallic compound to fill the pores of mesoporous silica templates, followed by pyrolysis under H<sub>2</sub>/N<sub>2</sub> flow to yield Pt nanowires [122].

### 3.3.4. Converting through Chemical Reactions

Nanorods or nanowires can also be synthesized using consumable templates [123]. Nanowires of compounds can be synthesized or prepared using a template-directed reaction. First nanowires or nanorods of a constituent element are prepared and then reacted with chemicals containing the desired element to form final products. Gates et al. [124] converted single crystalline trigonal selenium nanowires into single crystalline nanowires of Ag<sub>2</sub>Se by reacting with aqueous AgNO<sub>3</sub> solutions at room temperature. The trigonal selenium nanowires were prepared first also using a solution synthesis method [17]. Selenium nanowires were either dispersed in water or supported on TEM grids during reaction with aqueous AgNO<sub>3</sub>. The following chemical reaction was suggested:



Nanorods can also be synthesized by reacting volatile metal halide or oxide species with formerly obtained carbon nanotubes to form solid carbide nanorods with diameters between 2 and 30 nm and lengths up to 20 μm [125, 126]. Carbon nanotubes were used as removable templates in the synthesis of silicon and boron nitride nanorods [127]. Silicon nitride nanorods of 4–40 nm in diameter were also prepared by reacting carbon nanotubes with a mixture of silicon monoxide vapor and flowing nitrogen at 1500 °C [128]:



Silicon monoxide is generated by heating a solid mixture of silicon and silica in an alumina crucible at 1500 °C. The total transformation of carbon nanotubes into silicon nitride nanorods was observed.

ZnO nanowires were prepared by oxidizing metallic zinc nanowires [129]. In the first step, polycrystalline zinc nanowires without preferential crystal orientation were prepared by electrodeposition using anodic alumina membrane as a template, and in the second step, grown zinc nanowires were oxidized at 300 °C for up to 35 hr in air, yielding polycrystalline ZnO nanowires with diameters ranging from 15 to 90 nm and lengths of ~50 μm. Although ZnO nanowires are embedded in the anodic alumina membranes, freestanding nanowires may be obtained by selectively dissolving alumina templates.

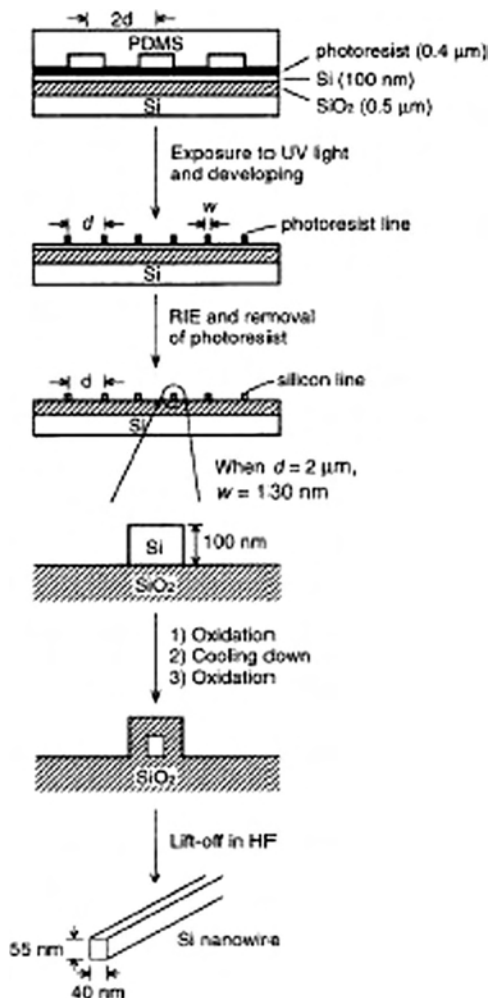
Hollow nanotubules of MoS<sub>2</sub> of ~30 μm long and 50 nm in external diameter with wall thickness of 10 nm were prepared by filling a solution mixture of molecular precursors, (NH<sub>4</sub>)<sub>2</sub>MoS<sub>4</sub> and (NH<sub>4</sub>)<sub>2</sub>Mo<sub>3</sub>S<sub>13</sub>, into the pores of alumina membrane templates. Then template filled with the molecular precursors was heated to an elevated temperature and the molecular precursors thermally decomposed into MoS<sub>2</sub> [130].

Certain polymers and proteins were also reported to have been used to direct the growth of nanowires of metals or semiconductors. For example, Braun et al. [131] reported a two-step procedure to use DNA as a template for the vectorial growth of silver nanorods of 12 μm in length and 100 nm in diameter. CdS nanowires were prepared by polymer-controlled growth [132]. For the synthesis of CdS nanowires, cadmium ions were well distributed in a polyacrylamide matrix. The Cd<sup>2+</sup> containing polymer was treated with thiourea (NH<sub>2</sub>CSNH<sub>2</sub>) solvothermally in ethylenediamine at 170 °C, resulting in degradation of polyacrylamide. Single crystal CdS nanowires of 40 nm in diameter and up to 100 μm in length with a preferential orientation of [001] were then simply filtered from the solvent.

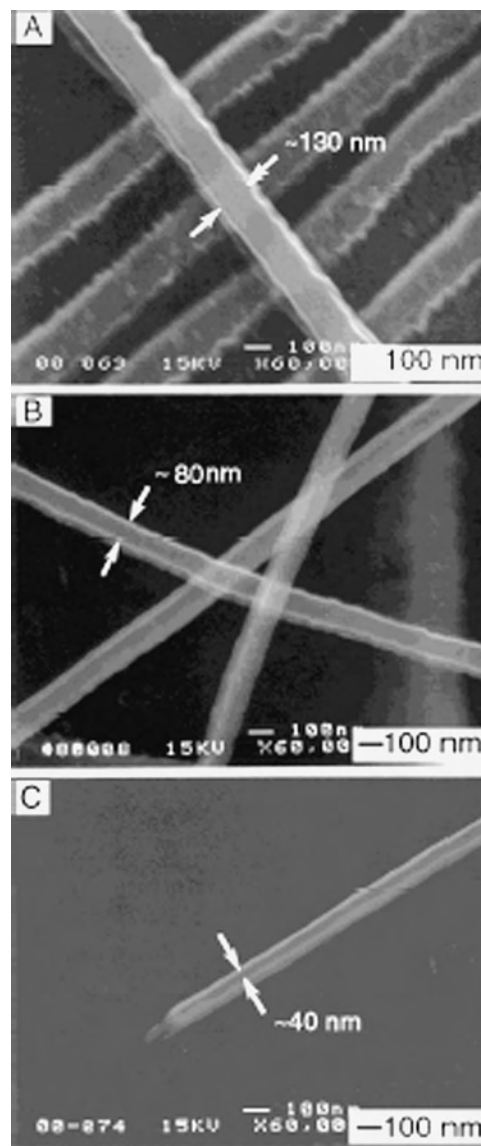
## 4. LITHOGRAPHY

Lithography represents another route to the synthesis of nanowires. Various techniques have been explored in the fabrication of nanowires, such as electron beam lithography [133, 134], ion beam lithography, scanning tunnelling microscope lithography, X-ray lithography, proximal-probe lithography, and near-field photolithography [135]. Nanowires with diameters less than 10 nm and an aspect ratio of 100 can be readily prepared. Here we just take the fabrication of single crystal silicon nanowires

reported by Yin et al. [136] as an example to illustrate the general approach and the products obtained. Figure 14 outlines the schematic procedures used for the preparation of single crystal silicon nanowires. The nanoscale features were defined in a thin film of photoresist by exposing it to an ultraviolet light source through a phase shift mask made of a transparent elastomer, such as poly(dimethylsiloxane) (PDMS). The light passing through this phase mask was modulated in the near field such that an array of nulls in the intensity was formed at the edges of the relief structures patterned on the PDMS mask. Therefore, nanoscale features were generated in a thin film of photoresist and the patterns were transferred into the underlying substrate using a reactive ion etching or wet etching process. Silicon nanostructures were separated from the underlying substrate by slight overetching. Figure 15 shows SEM images of silicon nanostructures fabricated using such near-field optical lithography, followed by pattern transfer into silicon with reactive ion etching, oxidation of silicon at 850 °C in air for ~1 hr, and finally lift-off in HF solution.



**Figure 14.** An outline of the procedure used for the near-field lithographic preparation of single crystal silicon nanowires. Reprinted with permission from [136], Y. Yin et al., *Adv. Mater.* 12, 1426 (2000). © 2000, Wiley-VCH.



**Figure 15.** SEM images of silicon nanostructures fabricated using near-field optical lithography. Reprinted with permission from [136], Y. Yin et al., *Adv. Mater.* 12, 1426 (2000). © 2000, Wiley-VCH.

## 5. SUMMARY

This chapter summarizes the fundamentals and general approaches for the preparation of one-dimensional nanostructures, with emphasis on the synthesis and fabrication of oxide nanorods and nanowires. For a given fundamental concept, many different approaches can be taken and indeed have been developed. However, not all the synthesis methods have been included in this chapter. The coverage is limited so that the important fundamentals and concepts are included. It is certain that many new synthesis techniques will be developed soon.

## GLOSSARY

**Electrophoretic deposition** The motion of charged particles in a sol or suspension under an applied electric field.

**Electrostatic stabilization** The surface of particles in a suspension becomes charged and counterions in the solvent will distribute in such a way that an electrical double layer at the vicinity of each particle will be formed. This layer is due to a combination of electrostatic force, entropic force, and Brownian motion. Such an electrical double layer will keep the nanoclusters from agglomerating, and thus a stable suspension is obtained.

**Sol-gel processing** A solution chemical route for forming oxide materials. Metal-organic (or inorganic) precursors undergo hydrolysis and condensation reactions, forming a stable suspension of nanoparticles (sol) or a continuous oxide network (gel).

**Template growth** The use of a physical template (such as a porous filtration membrane) to direct the formation of nanorods.

**VLS growth** Growth in which a catalyst is purposely introduced to direct and confine the crystal growth on a specific orientation and within a confined area. The catalyst forms a liquid droplet by itself or by alloying with growth material, trapping growth species. An enriched growth species in the catalyst droplets subsequently precipitates at the growth surface resulting in the one-directional growth.

## REFERENCES

- P. Hartman and W. G. Perdok, *Acta Cryst.* 8, 49 (1955).
- A. W. Vere, "Crystal Growth: Principles and Progress." Plenum, New York, 1987.
- W. Burton, N. Cabrera, and F. C. Frank, *Philos. Trans. Roy. Soc. London* 243, 299 (1951).
- G. W. Sears, *Acta Metal.* 3, 361 (1955).
- G. W. Sears, *Acta Metal.* 3, 367 (1955).
- E. I. Givargizov, "Highly Anisotropic Crystals." Reidel, Dordrecht, 1986.
- G. Bögles, H. Meeke, P. Bennema, and D. Bollen, *J. Phys. Chem. B* 103, 7577 (1999).
- W. Dittmar and K. Neumann, in "Growth and Perfection of Crystals" (R. H. Doremus, R. W. Roberts, and D. Turnbull, Eds.), p. 121. Wiley, New York, 1958.
- R. L. Schwoebel and E. J. Shipsey, *J. Appl. Phys.* 37, 3682 (1966).
- R. L. Schwoebel, *J. Appl. Phys.* 40, 614 (1969).
- Z. Y. Zhang and M. G. Lagally, *Science* 276, 377 (1997).
- Z. W. Pan, Z. R. Dai, and Z. L. Wang, *Science* 291, 1947 (2001).
- Z. R. Dai, Z. W. Pan, and Z. L. Wang, *Solid State Commun.* 118, 351 (2001).
- M. Volmer and I. Estermann, *Z. Phys.* 7, 13 (1921).
- Y. Liu, C. Zheng, W. Wang, C. Yin, and G. Wang, *Adv. Mater.* 13, 1883 (2001).
- W. Shi, H. Peng, Y. Zheng, N. Wang, N. Shang, Z. Pan, C. Lee, and S. Lee, *Adv. Mater.* 12, 1343 (2000).
- B. Gates, Y. Yin, and Y. Xia, *J. Am. Chem. Soc.* 122, 12582 (2000).
- B. Wunderlich and H.-C. Shu, *J. Cryst. Growth* 48, 227 (1980).
- B. Mayers, B. Gates, Y. Yin, and Y. Xia, *Adv. Mater.* 13, 1380 (2001).
- A. A. Kudryavtsev, "The Chemistry and Technology of Selenium and Tellurium." Collet's, London, 1974.
- B. Gates, Y. Yin, and Y. Xia, *J. Am. Chem. Soc.* 122, 582 (1999).
- Y. Li, Y. Ding, and Z. Wang, *Adv. Mater.* 11, 847 (1999).
- W. Wang, C. Xu, G. Wang, Y. Liu, and C. Zheng, *Adv. Mater.* 14, 837 (2002).
- Y. Sun, B. Gates, B. Mayers, and Y. Xia, *Nano Letters* 2, 165 (2002).
- K. Govender, D. S. Boyle, P. O'Brien, D. Brinks, D. West, and D. Coleman, *Adv. Mater.* 14, 1221 (2002).
- H. W. Liao, Y. F. Wang, X. M. Liu, Y. D. Li, and Y. T. Qian, *Chem. Mater.* 12, 2819 (2000).
- Q. Chen, W. Zhou, G. Du, and L.-M. Peng, *Adv. Mater.* 14, 1208 (2002).
- R. S. Wagner and W. C. Ellis, *Appl. Phys. Lett.* 4, 89 (1964).
- R. S. Wagner, W. C. Ellis, K. A. Jackson, and S. M. Arnold, *J. Appl. Phys.* 35, 2993 (1964).
- R. S. Wagner, VLS mechanism of crystal growth, in "Whisker Technology" (A. P. Levitt, Ed.). Wiley, New York, 1970.
- R. S. Wagner and W. C. Ellis, *Trans. Metal. Soc. AIME* 233, 1053 (1965).
- G. A. Bootsma and H. J. Gassen, *J. Cryst. Growth* 10, 223 (1971).
- C. M. Lieber, *Solid State Commun.* 107, 106 (1998).
- J. Hu, T. W. Odom, and C. M. Lieber, *Acc. Chem. Res.* 32, 435 (1999).
- A. M. Morales and C. M. Lieber, *Science* 279, 208 (1998).
- D. P. Yu, Z. G. Bai, Y. Ding, Q. L. Hang, H. Z. Zhang, J. J. Wang, Y. H. Zou, W. Qian, G. C. Xiong, H. T. Zhou, and S. Q. Feng, *Appl. Phys. Lett.* 72, 3458 (1998).
- D. P. Yu, C. S. Lee, I. Bello, X. S. Sun, Y. TH Tang, G. W. Zhou, Z. G. Bai, and S. Q. Feng, *Solid State Commun.* 105, 403 (1998).
- E. I. Givargizov, *J. Vac. Sci. Technol. B* 11, 449 (1993).
- Y. Wu and P. Yang, *Chem. Mater.* 12, 605 (2000).
- M. S. Gudiksen, J. Wang, and C. M. Lieber, *J. Phys. Chem. B* 105, 4062 (2001).
- M. S. Gudiksen and C. M. Lieber, *J. Am. Chem. Soc.* 122, 8801 (2000).
- A. W. Adamson and A. P. Gast, "Physical Chemistry of Surfaces," 6th ed. Wiley, New York, 1997.
- T. Dietz, M. Duncan, M. Liverman, and R. E. Smalley, *J. Chem. Phys.* 73, 4816 (1980).
- M. H. Huang, S. Mao, H. Feick, H. Yan, Y. Wu, H. Kind, E. Weber, R. Russo, and P. Yang, *Science* 292, 1897 (2001).
- H. N. V. Temperley, *Proc. Cambridge Philos. Soc.* 48, 683 (1952).
- K. A. Jackson, "Growth and Perfection of Crystals." Wiley, New York, 1958.
- Y. Wang, G. Meng, L. Zhang, C. Liang, and J. Zhang, *Chem. Mater.* 14, 1773 (2002).
- Y. Q. Chen, K. Zhang, B. Miao, B. Wang, and J. G. Hou, *Chem. Phys. Lett.* 358, 396 (2002).
- K.-W. Chang and J.-J. Wu, *J. Phys. Chem. B* 106, 7796 (2002).
- D. Zhang, D. N. McIlroy, Y. Geng, and M. G. Norton, *J. Mater. Sci. Lett.* 18, 349 (1999).
- I.-C. Leu, Y.-M. Lu, and M.-H. Hon, *Mater. Chem. Phys.* 56, 256 (1998).
- M. H. Huang, Y. Wu, H. Feick, N. Tran, E. Weber, and P. Yang, *Adv. Mater.* 13, 113 (2001).
- D. R. Gaskell, "Introduction to the Thermodynamics of Materials." Taylor and Francis, Washington, DC, 1995.
- D. R. Askeland, "The Science and Engineering of Materials." PWS, Boston, 1989.
- Y. C. Choi, W. S. Kim, Y. S. Park, S. M. Lee, D. J. Bae, Y. H. Lee, G.-S. Park, W. B. Choi, N. S. Lee, and J. M. Kim, *Adv. Mater.* 12, 746 (2000).
- Z. G. Bai, D. P. Yu, H. Z. Zhang, Y. Ding, Y. P. Wang, X. Z. Gai, Q. L. Hang, G. C. Xiong, and S. Q. Feng, *Chem. Phys. Lett.* 303, 311 (1999).
- D. P. Yu, Q. L. Hang, Y. Ding, H. Z. Zhang, Z. G. Bai, J. J. Wang, Y. H. Zou, W. Qian, G. C. Xiong, and S. Q. Feng, *Appl. Phys. Lett.* 73, 3076 (1998).
- T. J. Trentler, K. M. Hickman, S. C. Goel, A. M. Viano, P. C. Gobbons, and W. E. Buhro, *Science* 270, 1791 (1995).
- W. E. Buhro, *Polyhedron* 13, 1131 (1994).
- M. J. Ludowise, *J. Appl. Phys.* 58, R31 (1985).
- J. Franks, *Acta Metal.* 6, 103 (1958).
- R. M. Fisher, L. S. Darken, and K. G. Carroll, *Acta Metal.* 2, 368 (1954).

63. F. C. Frank, *Philos. Mag.* 44, 854 (1953).
64. J. D. Eshelby, *Phys. Rev.* 91, 775 (1953).
65. S. E. Koonce and S. M. Arnold, *J. Appl. Phys.* 24, 365 (1953).
66. R. C. Furneaux, W. R. Rigby, and A. P. Davidson, *Nature* 337, 147 (1989).
67. R. L. Fleisher, P. B. Price, and R. M. Walker, "Nuclear Tracks in Solids." Univ. of California Press, Berkeley, 1975.
68. R. J. Tonucci, B. L. Justus, A. J. Campillo, and C. E. Ford, *Science* 258, 783 (1992).
69. G. E. Possin, *Rev. Sci. Instrum.* 41, 772 (1970).
70. C. Wu and T. Bein, *Science* 264, 1757 (1994).
71. S. Fan, M. G. Chapline, N. R. Franklin, T. W. Tomblor, A. M. Cassell, and H. Dai, *Science* 283, 512 (1999).
72. P. Enzel, J. J. Zoller, and T. Bein, *Chem. Commun.* 633 (1992).
73. C. Guerret-Piecourt, Y. Le Bouar, A. Loiseau, and H. Pascard, *Nature* 372, 761 (1994).
74. P. M. Ajayan, O. Stephan, P. Redlich, and C. Colliex, *Nature* 375, 564 (1995).
75. A. Despic and V. P. Parkhuitik, "Modern Aspects of Electrochemistry," Vol. 20. Plenum, New York, 1989.
76. D. AlMawawi, N. Coombs, and M. Moskovits, *J. Appl. Phys.* 70, 4421 (1991).
77. C. A. Foss, M. J. Tierney, and C. R. Martin, *J. Phys. Chem.* 96, 9001 (1992).
78. J. B. Mohler and H. J. Sedusky, "Electroplating for the Metallurgist, Engineer and Chemist." Chemical Publishing Co., New York, 1951.
79. F. R. N. Nabarro and P. J. Jackson, in "Growth and Perfection of Crystals" (R. H. Doremus, B. W. Roberts, and D. Turnbull, Eds.), pp. 13–101. Wiley, New York, 1958.
80. W. D. Williams and N. Giordano, *Rev. Sci. Instrum.* 55, 410 (1984).
81. B. Z. Tang and H. Xu, *Macromolecules* 32, 2569 (1999).
82. T. M. Whitney, J. S. Jiang, P. C. Searson, and C. L. Chien, *Science* 261, 1316 (1993).
83. Y. Zhang, G. Li, Y. Wu, B. Zhang, W. Song, and L. Zhang, *Adv. Mater.* 14, 1227 (2002).
84. J. D. Klein, R. D. Herrick, II, D. Palmer, M. J. Sailor, C. J. Brumlik, and C. R. Martin, *Chem. Mater.* 5, 902 (1993).
85. C. Schönenberger, B. M. I. van der Zande, L. G. J. Fokink, M. Henny, C. Schmid, M. Krüger, A. Bachtold, R. Huber, H. Birk, and U. Staufer, *J. Phys. Chem. B* 101, 5497 (1997).
86. C. J. Brumlik, V. P. Menon, and C. R. Martin, *J. Mater. Res.* 268, 1174 (1994).
87. C. J. Brumlik and C. R. Martin, *J. Am. Chem. Soc.* 113, 3174 (1991).
88. C. J. Miller, C. A. Widrig, D. H. Charych, and M. Majda, *J. Phys. Chem.* 92, 1928 (1988).
89. C.-G. Wu and T. Bein, *Science* 264, 1757 (1994).
90. P. M. Ajayan, O. Stephan, and Ph. Redlich, *Nature* 375, 564 (1995).
91. W. Han, S. Fan, Q. Li, and Y. Hu, *Science* 277, 1287 (1997).
92. "Electroless Plating: Fundamentals and Applications" (G. O. Mallory and J. B. Hajdu, Eds.). American Electroplaters and Surface Finishers Society, Orlando, FL, 1990.
93. C. R. Martin, *Chem. Mater.* 8, 1739 (1996).
94. I. Zhitomirsky, *Adv. Colloid Interf. Sci.* 97, 297 (2002).
95. J. S. Reed, "Introduction to the Principles of Ceramic Processing." Wiley, New York, 1988.
96. R. J. Hunter, "Zeta Potential in Colloid Science: Principles and Applications." Academic Press, London, 1981.
97. C. J. Brinker and G. W. Scherer, "Sol-Gel Science: The Physics and Chemistry of Sol-Gel Processing." Academic Press, San Diego, CA, 1990.
98. A. C. Pierre, "Introduction to Sol-Gel Processing." Kluwer Academic, Boston, 1998.
99. J. D. Wright and N. A. J. M. Sommerdijk, "Sol-Gel Materials: Chemistry and Applications." Gordon and Breach, Amsterdam, 2001.
100. D. H. Everett, "Basic Principles of Colloid Science." Royal Society of Chemistry, London, 1988.
101. W. D. Callister, "Materials Science and Engineering: An Introduction." Wiley, New York, 1997.
102. S. J. Limmer, S. Seraji, M. J. Forbess, Y. Wu, T. P. Chou, C. Nguyen, and G. Z. Cao, *Adv. Mater.* 13, 1269 (2001).
103. S. J. Limmer, S. Seraji, M. J. Forbess, Y. Wu, T. P. Chou, C. Nguyen, and G. Z. Cao, *Adv. Funct. Mater.* 12, 59 (2002).
104. Y. C. Wang, I. C. Leu, and M. N. Hon, *J. Mater. Chem.* 12, 2439 (2002).
105. Z. Miao, D. Xu, J. Ouyang, G. Guo, Z. Zhao, and Y. Tang, *Nano Lett.* 2, 717 (2002).
106. C. Natarajan and G. Nogami, *J. Electrochem. Soc.* 143, 1547 (1996).
107. B. B. Lakshmi, P. K. Dorhout, and C. R. Martin, *Chem. Mater.* 9, 857 (1997).
108. R. L. Penn and J. F. Banfield, *Geochim. Cosmochim. Acta* 63, 1549 (1999).
109. B. B. Lakshmi, C. J. Patrissi, and C. R. Martin, *Chem. Mater.* 9, 2544 (1997).
110. J. S. Reed, "Introduction to Principles of Ceramic Processing." Wiley, New York, 1988.
111. C. A. Huber, T. E. Huber, M. Sadoqi, J. A. Lubin, S. Manalis, and C. B. Prater, *Science* 263, 800 (1994).
112. Z. Zhang, D. Gekhtman, M. S. Dresselhaus, and J. Y. Ying, *Chem. Mater.* 11, 1659 (1999).
113. W. Liang and C. R. Martin, *J. Am. Chem. Soc.* 112, 9666 (1990).
114. S. M. Marinakos, L. C. Brousseau, III, A. Jones, and D. L. Feldheim, *Chem. Mater.* 10, 1214 (1998).
115. P. Enzel, J. J. Zoller, and T. Bein, *Chem. Commun.* 633 (1992).
116. H. D. Sun, Z. K. Tang, J. Chen, and G. Li, *Solid State Commun.* 109, 365 (1999).
117. Z. Cai, J. Lei, W. Liang, V. Menon, and C. R. Martin, *Chem. Mater.* 3, 960 (1991).
118. Y.-J. Han, J. M. Kim, and G. D. Stucky, *Chem. Mater.* 12, 2068 (2000).
119. L. Chen, P. J. Klar, W. Heimbrodt, F. Brieler, and M. Fröba, *Appl. Phys. Lett.* 76, 3531 (2000).
120. K. Matsui, T. Kyotani, and A. Tomita, *Adv. Mater.* 14, 1216 (2002).
121. R. Leon, D. Margolese, G. Stucky, and P. M. Petroff, *Phys. Rev. B* 52, R2285 (1995).
122. K.-B. Lee, S.-M. Lee, and J. Cheon, *Adv. Mater.* 13, 517 (2001).
123. C.-G. Wu and T. Bein, *Science* 264, 1757 (1994).
124. B. Gates, Y. Wu, Y. Yin, P. Yang, and Y. Xia, *J. Am. Chem. Soc.* 123, 11500 (2001).
125. H. Dai, E. W. Wong, Y. Z. Lu, S. Fan, and C. M. Lieber, *Nature* 375, 769 (1995).
126. E. W. Wong, B. W. Maynor, L. D. Burns, and C. M. Lieber, *Chem. Mater.* 8, 2041 (1996).
127. W. Han, S. Fan, Q. Li, B. Gu, X. Zhang, and D. Yu, *Appl. Phys. Lett.* 71, 2271 (1997).
128. A. Huczko, *Appl. Phys. A* 70, 365 (2000).
129. Y. Li, G. S. Cheng, and L. D. Zhang, *J. Mater. Res.* 15, 2305 (2000).
130. C. M. Zelenski and P. K. Dorhout, *J. Am. Chem. Soc.* 120, 734 (1998).
131. E. Braun, Y. Eichen, U. Sivan, and G. Ben-Yoseph, *Nature* 391, 775 (1998).
132. J. Zhan, X. Yang, D. Wang, S. Li, Y. Xie, Y. Xia, and Y. Qian, *Adv. Mater.* 12, 1348 (2000).
133. K. Kurihara, K. Iwadate, H. Namatsu, M. Nagase, and K. Murase, *J. Vac. Sci. Technol. B* 13, 2170 (1995).
134. H. I. Liu, D. K. Biegelsen, F. A. Ponce, N. M. Johnson, and R. F. Pease, *Appl. Phys. Lett.* 64, 1383 (1994).
135. Y. Xia, J. A. Rogers, K. E. Paul, and G. M. Whitesides, *Chem. Rev.* 99, 1823 (1999).
136. Y. Yin, B. Gates, and Y. Xia, *Adv. Mater.* 12, 1426 (2000).

# Palladium Nanoparticles

Chia-Cheng Yang, Chi-Chao Wan

*National Tsing-Hua University, Hsin-Chu, Taiwan, R.O.C.*

Chien-Liang Lee

*Industrial Technology Research Institute, Hsin-Chu, Taiwan, R.O.C.*

## CONTENTS

1. Introduction
  2. Synthesis of Palladium and Its Alloy Nanoparticles
  3. Spectroscopic Characterizations
  4. Catalytic Properties
- Glossary  
References

## 1. INTRODUCTION

Mono- and bimetallic nanoparticles are of great interest due to their prominent chemical and physical properties. These nanoparticles, which are usually defined as isolable particles between 1 and 50 nm in size, could be newly categorized as mesoscopic materials [1]. This new category of materials, different from bulk material or atoms, can be defined as an “atom assembly” or “molecule” rather than the classical term “colloid.” If the nanoparticles are well controlled in structure, the term “cluster” is often used [2]. In this chapter, we focus on the nanocluster of palladium and its alloy, which shows outstanding performance in a catalyst [3]. Various potential applications are also being explored owing to its extremely high surface area and different electronic structure.

Palladium and its bimetallic nanoparticles can be prepared from reduction of the corresponding metal salt encapsulated in various stabilizers, such as reversed micelle [4–7], dendrimer [8–9], and biomolecules [10–11]. In the early stage of nucleation, the metal salt is reduced to a zero-valent metallic state. Then, the metal atoms further collide with other atoms or clusters to form irreversible nuclei in the solution [1]. These stable nuclei provide (usually well below 1 nm, depending on the metal–metal bonds and the redox potential) seeds for the subsequent growth of particles. To prevent further agglomeration, the addition of protective

agents is essential to control the particle in nanosize. These protective agents can be grouped as electrostatic and steric effects on the basis of different modes of stabilization [12]. Electrostatic stabilization is based on the coulombic repulsion force between individual nanoparticles, where ligands (e.g., sodium citrate) are adsorbed on the surface of clusters, while steric stabilization is accomplished by the coordination of organic molecules, including polymers, surfactants, thiol derivatives, and long-chain alcohols, on the particle surfaces.

Now, those electronic, surface-to-volume, and optical properties are all size dependent for metal colloidal particles. The technology for the mass production of nanoparticles with enough uniformity becomes important and essential. With proper choices of precursor concentration, reductants, and stabilizers, highly monodispersed nanoparticles can be achieved, and much effort is being directed to this area.

## 2. SYNTHESIS OF PALLADIUM AND ITS ALLOY NANOPARTICLES

Colloidal Pd nanoparticles are, in general, prepared by the reduction of metal salt in a chemical, sonochemical, or electrochemical system. The system can be confined space or free space surrounded by appropriate templates, including surfactants, soluble polymers, and mesoporous materials.

### 2.1. Confined-Space Reduction Method

#### 2.1.1. Reverse Micelle

Reverse micelle is an isotropic and thermodynamically stable system consisting of water nanodroplets surrounded by proper organic surfactants. These well-established nanostructures make microemulsion an ideal vehicle to synthesize metal nanoparticles by exchanging materials within hydrophilic nanodroplets. Furthermore, manipulation of the particle sizes can be achieved by simply altering the micellar radius. This is of great importance to control the particle dimension since nanomaterials reveal a “size-dependent” property.



In a reverse micelle system, exchanging reactants occur within water droplets by collisions to form dimers, and subsequently to form two separate nanodroplets again. The material exchange process is governed by: (1) the dimers formed by contacting micelles, and (2) the exchange process between two water pool droplets [13]. The first factor is related to the attractive interaction and collision of two micelles. The latter is due to the interface rigidity arising from the dynamic property of the interface. Controlling these parameters could affect the reaction rate, and thus change the particle size [4].

Palladium nanoclusters have been prepared in a water/sodium bis(2-ethylhexyl) sulfosuccinate (AOT)/*n*-heptane microemulsion system [7]. In addition, a systematic study of the synthesis of Pd nanoparticles, including the kinetics of particle formation, was reported by Chen et al. [6]. The palladium particle size is mainly affected by the molar ratio of water to AOT ( $\omega_0$ ) and the concentration of palladium salt. Other factors, such as the AOT concentration, temperature, and pH of the aqueous phase, are less influential under the experimental conditions. During the particle formation, nucleation occurs without the formation of particles in the fast few minutes. In the following tens of minutes, the particles form, and gradually reach their final sizes. In addition to a systematic kinetic study, Chen et al. compare the diameter differences between reverse micelle and the formed metallic nanoparticles. The hydrodynamic diameters of reverse micelles, which are characterized by dynamic light scattering, are smaller than those of palladium nanoparticles. This phenomenon suggests that micelles might be enlarged by the growth of particles, although the reverse micelles limit the growth of particles.

In addition to palladium ultrafine particles, other Pd-based bimetallic nanoparticles prepared in a water/oil (w/o) microemulsion system have also been studied [5, 14]. In a Pd/Pt bimetallic system, the nanoclusters reveal a homogeneous alloy structure, and the composition is roughly identical to that of the feeding solution, while the Pd/Au alloy appears Pd-rich in the outer part of the nanoparticles. Thus, the reverse micelle technique, which provides versatile choices of materials, is shown to be a powerful method to prepare colloidal metal particles.

### 2.1.2. Dendrimer

Dendrimers are monodisperse, well-structured, and hyperbranched polymers with a high concentration of functional groups. They are extensively used as templates for the synthesis of palladium nanoparticles [8–9]. The advantages of dendrimers can be described as follows. (1) The monodisperse nanoparticles can be accomplished due to the highly uniform and well-defined porosity of the dendrimer template. (2) The hyperbranched dendrimers prevent particles from agglomeration stemming from the steric effect. (3) The surfaces of nanoparticles are only partially encapsulated by dendrimers, and therefore leave a substantial portion of the surface atoms for the following catalytic reactions, whereas some stabilizers will strongly absorb on the surface, and thus block the active sites for subsequent catalytic reactions. (4) By adjusting generations of dendrimers, different solvents, and functional groups, a dendrimer could act

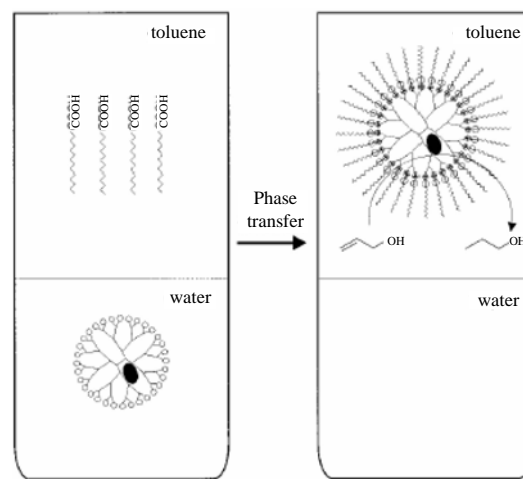
as a “nanofilter” to control the access of small molecules (substrates) to the catalytic nanoparticles. (5) The terminal groups on the dendrimers can be linked to other functional groups, and therefore change the solubility of the nanocomposite between the hydrophilic and hydrophobic phases [15].

Two dendrimers, poly(amidoamine) (PAMAM) and poly(propylene imine) (PPI), were widely used to synthesize colloidal palladium particles [7–8, 15]. The dendrimers retain a guest molecule by covalent bonding, complex, electrostatic, or van der Waals force, and so on. Besides the formation of uniform palladium nanoparticles, the dendrimer-encapsulated Pd particles undergo phase transfer by adjusting the pH value, as illustrated in Figure 1 [8]. This reversible approach, which is driven on the basis of acid base and ion pairing, can shuttle the guests encapsulated in dendrimers between the hydrophobic and hydrophilic phases. This is of great importance, especially in homogeneous and colloidal catalytic reactions, because the catalyst is difficult to separate from the organic reaction mixture. So the recycling of a colloidal catalyst, an important “green chemistry” approach, can be accomplished by extracting the catalyst from the organic reaction mixture to the water phase through adjustment of the pH values.

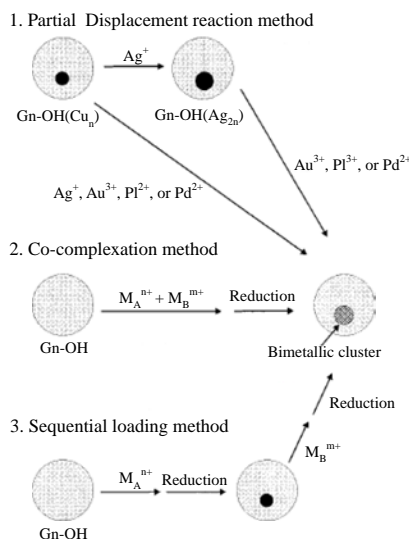
In addition to Pd nanoparticles, bimetallic ultrafine particles can also be prepared in a dendrimer. Bimetallic nanomaterial can be prepared by the partial displacement reaction, cocomplexation, and sequential loading methods, as shown in Figure 2. Based on these procedures, a trimetallic or core/shell nanostructure might also be achieved with the aid of the encapsulation of dendrimers [15].

### 2.1.3. Hard Template

Many mesoporous materials, such as polycarbonate, aluminum oxide, carbon tube, and silica, can be used as hard templates for the synthesis of nanomaterials in different shapes, including nanowire, nanoball, and dendritic nanostructures [16–19]. Metal salts or organometallic precursors are reduced to their corresponding zero-valent state



**Figure 1.** Schematic illustration of spontaneous assembly of fatty acid onto the surface of amine-terminated PAMAM resulting in the extraction of dendrimer-encapsulated Pd nanoparticles from aqueous to non-polar phases. Reprinted with permission from [15], R. M. Crooks et al., *Acc. Chem. Res.* 34, 181 (2001). © 2001, American Chemical Society.

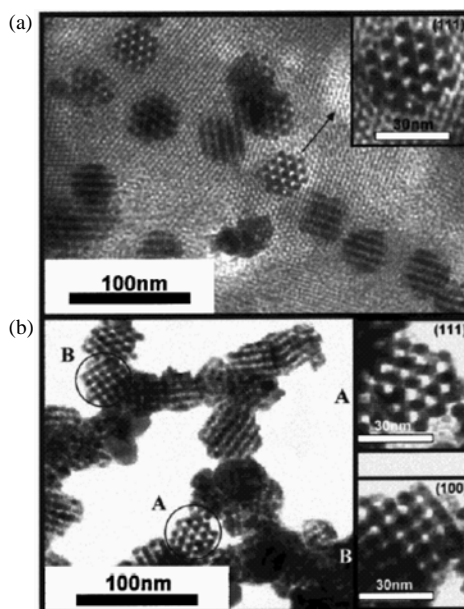


**Figure 2.** Three possible routes for the synthesis of bimetallic nanoparticles encapsulated in dendrimer. Reprinted with permission from [15], R. M. Crooks et al., *Acc. Chem. Res.* 34, 181 (2001). © 2001, American Chemical Society.

in the well-defined mesoporous templates. The skeleton of nanomaterials is therefore identical to the nanosized porous architecture. Among these hard templates, mesoporous silica is the most frequently used for preparing Pd nanomaterial. In order to fabricate a mesoscopically well-defined silica template, surfactants and silicate species are used for the self-assembly process under hydrothermal treatment. On the basis of the nanostructure, the M41S mesoporous silica can be categorized into hexagonal (MCM-41), cubic (MCM-48), and unstable lamellar (MCM-50). Furthermore, the architecture of mesoporous silica can be manipulated by adjusting the temperature and the addition of alcohol [20–21]. Therefore, the resulting structure of the nanomaterial can be significantly varied in shape by changing the template structure.

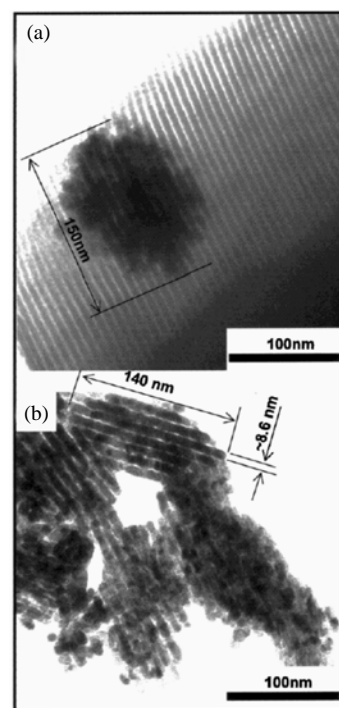
Porous palladium nanoballs and nanowires, as illustrated in Figures 3 and 4, can be prepared with the aid of mesoporous silica [16–17]. In this work, palladium nanostructures were produced in a silica matrix via chemical vapor infiltration (CVI), by which the organometallic precursor is decomposed under a mild thermal condition without deterioration of the silica template. Characterization by X-ray diffraction (XRD) reveals that the crystal structure is identical to that of bulk palladium. Moreover, the melting point of Pd nanowires is observed around 300 °C, which is significantly lower than that of the bulk material (1552 °C). This phenomenon is due to the high surface-to-volume ratio of the nanomaterials.

In addition to mesoporous silica, carbon material can serve as a template for the production of nanomaterials. Figure 5 shows the growth of hexagonal quasi-2-D palladium nanoparticles with the assistance of a carbon template [22]. The graphite sheet is used for the monolayer intercalation of the palladium precursor. The palladium ion is reduced to a hexagonal quasi-2-D structure, followed by H<sub>2</sub> reduction at a high temperature. Furthermore, the formation of the hexagonal crystal structure of Pd atoms results

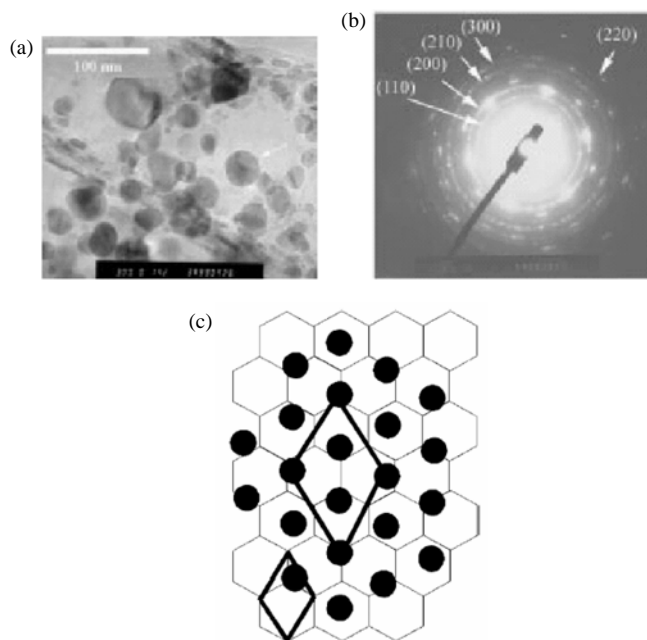


**Figure 3.** TEM images of (a) Pd@MCM-48 and (b) porous Pd superlattice nanoballs. Reprinted with permission from [17], H. Kang et al., *Chem. Mater.* 12, 3530 (2000). © 2000, American Chemical Society.

from their interaction and induction with a hexagonal host lattice. The carbon sheet template controls the formation of the nanostructure in not only the lateral direction, but also in a vertical orientation, resulting in hexagonal quasi-2-D palladium nanoparticles.



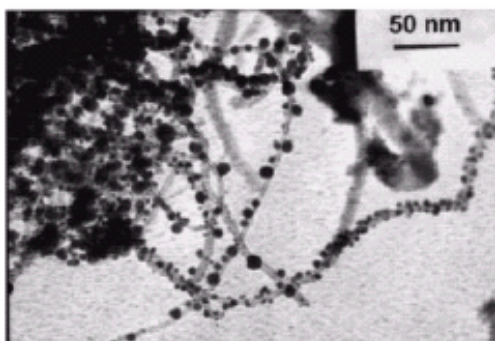
**Figure 4.** TEM images of (a) Pd@SBA-15 and (b) Pd nanowires. Reprinted with permission from [17], H. Kang et al., *Chem. Mater.* 12, 3530 (2000). © 2000, American Chemical Society.



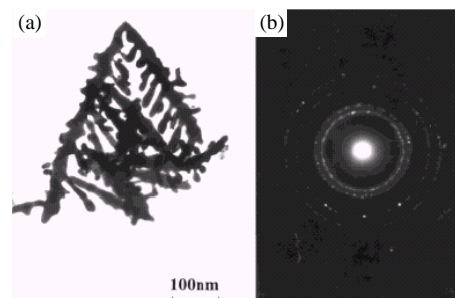
**Figure 5.** (a) TEM photograph of the Pd particle. (b) SAED pattern of a polycrystalline particle. (c) Graphene lattice (thin lines) with hexagonal Pd lattice; the unit cell of graphite and of a hexagonal Pd particle is indicated by thick bars. Reprinted with permission from [22], J. Walter, *Adv. Mater.* 12, 31 (2000). © 2000, Wiley-VCH Verlag GmbH.

Besides lamellar graphite, carbon nanotubes can also be applied for nanoparticle fabrication. Carbon nanotubes, which are different in structure from graphite and diamond, are rolled up cylindrically with a diameter in the nanoscale. The structure and morphology of the carbon nanotube justify its use as a template for synthesizing nanoparticles. Figure 6 shows the transmission electron microscopy (TEM) images of Pd nanoparticles grown on carbon nanotubes [23]. Most palladium nanoparticles developed on the outer surface of the carbon nanotubes and XRD characterization reveal well-crystallized Pd with lattice contraction.

Recently, another novel method for the preparation of palladium dendritic nanostructures was proposed, as shown in Figure 7 [18]. Raney nickel, which is derived from a Ni–Al alloy, is composed of a porous pattern, which is suit-



**Figure 6.** TEM images of Pd samples prepared by solid-state reaction between  $\text{HPdCl}_3$  and carbon nanotubes at 873 K under a flow of  $\text{H}_2$ . Reprinted with permission from [23], B. Xue et al., *J. Mater. Chem.* 11, 2378 (2001). © 2001, Royal Society of Chemistry.



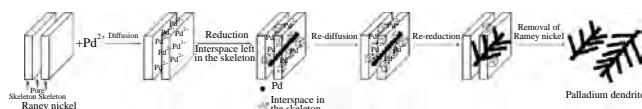
**Figure 7.** (a) TEM images of palladium dendrites. (b) The corresponding SAED pattern using Raney nickel as a template with the assistance of ultrasonic waves. Reprinted with permission from [18], J. Xiao et al., *Adv. Mater.* 13, 1887 (2001). © 2001, Wiley-VCH Verlag GmbH.

able to be a host material. In addition to the well-established nanostructure, Raney nickel can be easily removed with dilute HCl without damage to the dendritic Pd structure. Figure 8 illustrates a typical process for the fabrication of palladium dendrites. First,  $\text{Pd}^{2+}$  diffuses into the pores of Raney nickel with the aid of ultrasonic waves. Then, an interspace in the skeleton of the template is formed, and  $\text{Pd}^{2+}$  is reduced by Raney nickel. This process continues until the complete reduction of  $\text{Pd}^{2+}$ . In this case, Raney nickel works not only as a template, but also as a reductant, while other templates, such as mesoporous silica and a carbon nanotube, only play the role of a template. Moreover, a presumable mechanism of a diffusion-limited aggregation (DLA) model is also proposed to account for the dendritic growth.

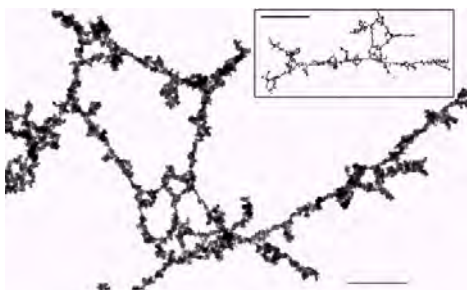
## 2.2. Free-Space Reduction Method

### 2.2.1. Quasione-Dimensional DNA Template

In a biological system, a metal cluster can be used as an additional tool for the investigation of micromanipulation. Among these biological molecules, deoxyribonucleic acid (DNA) is particularly important since it is 2 nm in diameter and several micrometers in length with well-ordered sequent bases. The quasione-dimensional Pd nanostructure can be accomplished by metallization of DNA, as shown in Figure 9 [10]. The surface of the DNA was first activated with a Pd ion, and then immersed in a reduction solution consisting of sodium citrate, lactic acid, and dimethyl amine borane (DMAB). The separated metal clusters, which were formed in the beginning, gradually aggregated into a quasi-1-D metallic structure with a 3–5 nm diameter. In addition to formation of metallic DNA in solution, they could be immobilized with alignment on the substrate by controlling the evaporation of the solution. Accordingly, metallic DNA can be fixed between electrical contacts for further investigation.



**Figure 8.** Schematic illustration of the growth process of palladium dendrites. Reprinted with permission from [18], J. Xiao et al., *Adv. Mater.* 13, 1887 (2001). © 2001, Wiley-VCH Verlag GmbH.



**Figure 9.** Detail of a metallized DNA strand illustrating the small-scale networks of the nanowires (scale bar: 200 nm). Inset: the complete DNA strand (scale bar: 1  $\mu\text{m}$ ). Reprinted with permission from [10], J. Richter et al., *Adv. Mater.* 12, 507 (2000). © 2000, Wiley-VCH Verlag GmbH.

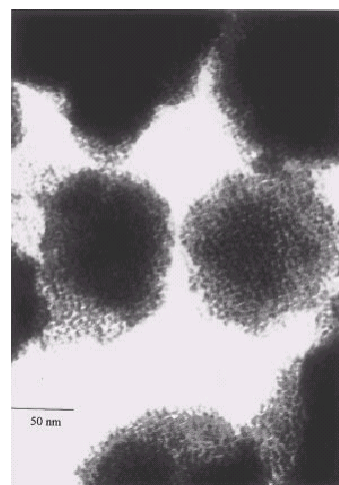
### 2.2.2. Sonochemical Reduction

Sonochemistry relates to chemical reaction under the influence of acoustic cavitations, which generate extremely high temperature (thousands of degrees), pressure (megapascal), as well as a high cooling rate ( $\approx 10^{10}$  K/s). It can be applied for manufacturing Pd nanoparticles [24–25]. The radicals arising from pyrolysis of the solvent and/or stabilizer can reduce  $\text{Pd}^{2+}$  to  $\text{Pd}^0$ , resulting in the formation of metallic particles. To prevent agglomeration, the addition of a biotemplate or solid template is essential [24–27]. In the sonochemical process, there are two different regions where the reaction might occur, that is, (1) the gas phase within the cavity, where extremely high temperature and pressure are generated, and (2) the liquid layer surrounding the collapsing cavity, where the chemical environment is still capable of conducting the sonochemical reaction even though the temperature is lower than that of the gas phase. In general, the liquid phase plays the major part in the sonochemical decomposition of the precursor since the low vapor pressure of the precursor in the gas phase eliminates the possibility of reaction within this zone.

A novel palladium nanostructure, an amorphous and carbon-activated porous nanoparticle, has been prepared with the assistance of ultrasound irradiation [26]. The organometallic precursor, tris- $\mu$ -[dibenzylideneacetone]dipalladium [ $\text{Pd}_2(\text{DBA})_3$ ], is decomposed, and therefore reduced to nanosize palladium particles with DBA ligands absorbing on the metal surface. These carbon-rich ligands may further crack into atomic carbon atoms or other volatile fragments due to the vigorous chemical environment, which cannot be obtained by conventional synthetic techniques. The carbon species so obtained form a protecting shell, and prevent Pd particles from coalescence, as demonstrated in Figure 10. Furthermore, the result of differential scanning calorimetry reveals that carbon-activated Pd particles have a broad peak with a long tail, while typical amorphous metal particles exhibit a sharp exothermic characterization. This interesting phenomenon might result from the presence of atomic carbons, which inhibit the crystallization process and influence the surface free energy of Pd particles.

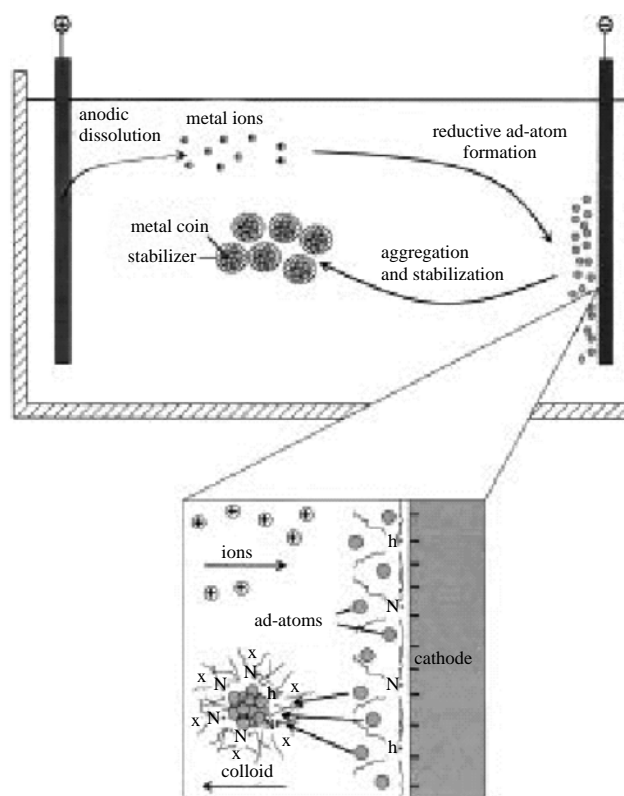
### 2.2.3. Electrochemical Preparation

An electrochemical technique is commonly employed to reduce the metal ion to a metallic state on an electrode. Naturally, it has also been used widely for the size-selective



**Figure 10.** Transmission electron micrographs of initial carbon-activated Pd; scale bar: 50 nm. Reprinted with permission from [26], N. A. Dhas et al., *J. Phys. Chem. B* 101, 6834 (1997). © 1997, American Chemical Society.

preparation of Pd and its alloy nanomaterial [28–31]. A sacrificial anode usually serves as the metal source, while the surfactants (e.g.,  $\text{R}_4\text{N}^+\text{X}^-$ ) act as an electrolyte and stabilizer in organic solvent, as illustrated in Figure 11. The metal ions arising from the oxidation of the anode migrate to the cathode, and are reduced to ad atoms. These metal clusters



**Figure 11.** Schematic representation of electrochemical formation of  $\text{R}_4\text{N}^+\text{X}^-$ -stabilized transition metal colloids. Reprinted with permission from [29], M. T. Reetz et al., *Chem. Eur. J.* 7, 1084 (2001). © 2001, Wiley-VCH Verlag GmbH.

are then trapped by stabilizers, and form colloidal nanoparticles rather than metallic powders.

A systematic investigation of the electrochemical parameters on particle size has been carried out by Reetz and co-workers [29]. The first factor is the solvent effect. With increasing polarity of the medium (e.g., the addition of acetonitrile), the particle size also increases due to the reduced electrostatic interaction between the colloids in a polar solution. The second parameter is the charge flow. The particle sizes increase with increasing charge flow, and the effect is especially pronounced in the early stage of electrolysis. This phenomenon suggests that the diameter of the particle is largely influenced by the growth mechanism. The third effect is the current density. A fast nucleation rate, which results from the high current density, accounts for the formation of smaller particle sizes. The fourth is the temperature effect. The particle size increases with elevating temperature. This consequence arises from the higher diffusion, migration, and dissociation rate of the palladate intermediate, as well as the decreasing viscosity of the medium.

A combination of scanning tunneling microscopy (STM) and transmission electron microscopy is used to examine the actual structure of surfactant-protected nanomaterials [11]. The TEM study reveals the diameter of the metal core, while the STM can probe the outer dimensions of the nanostructure. The difference between these two diameters is directly related to the thickness of the stabilizer. On the basis of these studies, a model of a monolayer-coated palladium nanoparticle is proposed.

In addition to colloidal palladium, the electrochemical system has been extended to prepare a bimetallic colloid [30–31]. Reetz has shown that the colloidal alloy structure can be synthesized simultaneously by using two sacrificial anodes. Alternatively, one can start with the first colloidal metal, and subsequently reduce the second metal onto the formed particles electrochemically. Thus, electrochemical preparation provides various choices in materials, and the control of sizes could be easily accomplished by adjustment of the experimental conditions.

#### **2.2.4. Metal Salt Reduction via Wet Chemical Method**

The basic principle for the wet chemical preparation of colloidal nanoparticles is the reduction of the metal precursor with reductants under the protection of stabilizers. The choices of stabilizers can be versatile, including ligands [32–36] and soluble polymers [37–39]. These stabilizers, which play an important role in synthesis, can affect the particle size and the stability of the colloid. Owing to its reasonable cost and convenience, this approach has become one of the most common and powerful methods for the preparation of colloidal particles.

**Protection by Ligands** A palladium colloid can be protected by nitrogen-containing ligands such as phenanthroline, sodium sulfanilate [32], and water-soluble isocyanide [33]. A systematic study concerning the control of particles size has been reported by Quiros et al. [35]. In general, a long chain of ligands, increasing the amount of the stabilizer, and lengthening the reaction time all favor the diminution of colloidal particles. It seems that the formation of

self-assembly by a long-chained stabilizer occurs faster than that of the shorter one, due to the increase in hydrophobic interaction. This trend is also consistent with isocyanide-protected Pd nanoparticles [33].

These common synthetic methods, unfortunately, usually limit the diameter of palladium particles (<45 nm). In order to synthesize larger Pd particles (25–100 nm), a seeding growth method, protected by citric acid, has been proposed [36]. 12 nm diameter Au nanoparticles, used as “heterogeneous seeds” for the subsequent procedure, were prepared by the reduction of citric acid. The larger Pd particles were formed, following the reduction of Pd<sup>2+</sup> onto the surface of preformed Au particles. The mean size of the particles increases from 25 to 100 nm by decreasing the gold seed concentration. Furthermore, the approach could be scaled up to produce larger and monodispersed palladium nanoparticles.

**Stabilized by Polymer** A solvent soluble polymer, poly(N-vinyl-2-pyrrolidone) (PVP), is widely chosen as a protective agent for the preparation of Pd ultrafine particles. PVP prevents the preformed particles from coalescence by the steric effect stemming from tail or loop segments of the polymer dispersing in the solvent. The higher the molecular weight of PVP is, the larger is the particle size [37]. This phenomenon is attributed to the larger fraction of high molecular weight adsorbing on the particle surface compared to that of low molecular weight. In addition, the thickness of the adsorbed layer on palladium increases by increasing the molecular weight on the basis of sedimentation with an ultracentrifugation study.

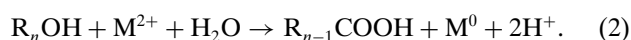
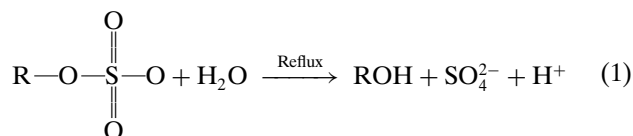
Besides the effect of PVP, there are other factors affecting the particle size [38]. The pH value, reaction temperature, and the types of reductants all play important roles in controlling the nucleation and crystal growth rate, and therefore affect the diameter of the size. A series of alcohols, including methanol, ethanol, propan-1-ol, propan-2-ol, butan-1-ol, and ethylene glycol, served as reducing agents. In general, the particle size is inversely proportional to the reducing power provided by the alcohol. In addition, a higher pH value and lower reaction temperature both result in the formation of smaller particle.

Different particle sizes of palladium nanoclusters can be accomplished by a stepwise procedure without changing other experimental conditions [39]. The preformed Pd nanoparticles are used as “homogeneous seeds” for the subsequent growth of palladium. Furthermore, the XRD patterns reveal that different sizes of Pd nanoparticles have a face-center cubic (fcc) structure in spite of the dilation of the lattice constant with decreasing particle sizes.

#### **2.2.5. Metal Salt Reduction via Reactive Micelle as Template**

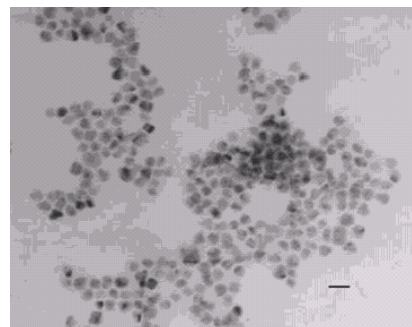
When metal nanoparticles are prepared by chemical methods, the metal ions are often reduced by a reducing agent that is externally added. A protective agent is also added to stabilize the nanoparticles produced. Typical reducing agents are N<sub>2</sub>H<sub>4</sub> [40], NaBH<sub>4</sub> [41], H<sub>2</sub> [42], and alcohol [38–39]. The choice of reductant and its concentration can drastically affect the nucleation rate and particle size: this highlights the complexity and delicacy of this reaction.

Recently, a method to chemically prepare noble metal nanoparticles without externally added reductant was developed [43]. The reductant is *in-situ* generated through the gradual decomposition of the surfactant contained in the solution as a protective agent. The surfactant chosen is an alcohol-type surfactant, sodium alkyl sulfate, which simultaneously acts as both the reductant and protective agent. In this method, sodium alkyl sulfate can gradually release the nonpolar alcohol of a long carbon chain in the system during refluxing [Eq. (1)]. Then, metal ions that had diffused into the core of the micelle are reduced by the alcohol [Eq. (2)].



The typical transmission electron microscopy (TEM) images of Pd nanoparticles reduced by sodium dodecyl sulfate (SDS) are shown in Figure 12. One remarkable finding is that the size of the nanoparticles can be controlled by varying the length of the carbon chain of the sodium alkyl sulfate (Table 1). Obviously, the time needed for the solution to turn dark brown, which signals the completion of the reaction, is a function of the length of the carbon chain. The reaction time increases with an increasing carbon chain length. The reducing power follows the trend  $\text{C}_8 \geq \text{C}_{10} > \text{C}_{12} > \text{C}_{14}$ , and the diameter of the particles decreases as the carbon chain lengthens. This trend is closely related to the nucleation and growth rate of the nanoparticles. As the rate increases, the nanoparticles grow in size accordingly. The alcohol reduces the metal ions to metal particles in the core of the micelles. The steric effect between the carbon chains of a micelle and the alcohol becomes more critical when the chain length of the hydrophobic group is sufficiently long, for example,  $\text{SC}_{14}\text{S}$  and  $\text{SC}_{12}\text{S}$  (SDS), and results in a slowing down of the growth rate of the Pd nanoparticles. In contrast, the effect is less pronounced in the case of  $\text{SC}_8\text{S}$  and  $\text{SC}_{10}\text{S}$  systems.

Auvray et al. [45] reported that a transformation of the liquid crystal phase of the surfactant could occur under an elevated temperature and a high surfactant concentration. Consequently, the following intermediate phases have been



**Figure 12.** TEM images of Pd nanoparticles formed via reduction by sodium octyl sulfate ( $\text{SC}_8\text{S}$ ) (mean diameter of the particles: 9.41 nm). Scale bar = 20 nm. Reprinted with permission from [43], C. L. Lee et al., *Adv. Funct. Mater.* 11, 344 (2001). © 2001, Wiley-VCH Verlag GmbH.

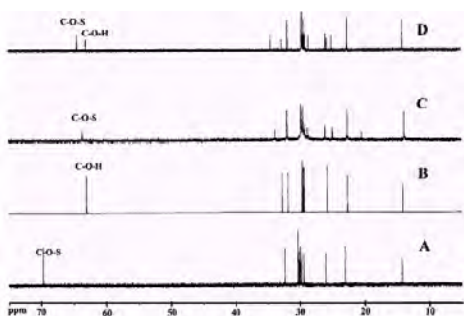
identified: disordered micellar phase  $\text{I}\alpha \rightarrow$  two-dimensional hexagonal  $\text{H}\alpha \rightarrow$  bicontinuous cubic phase  $\text{Q}\alpha \rightarrow$  lamellar phase  $\text{L}\alpha$ . The synthesis of various mesoporous silica-based nanostructures can be achieved by controlling the pH, the amount of alcohol, and the concentration of the surfactant. The micellar phases of the surfactant could be altered due to various experimental conditions. Consequently, different nanostructures could be obtained by adding inorganic silica compounds to link onto those soft cages, for example, MCM-41 (2-D hexagonal phase,  $\text{P6m}$ ), MCM-48 (cubic phase,  $1a3d$ ), or MCM-50 (lamellar phase) [45]. Moreover, Hendriks and Pansu [47] also found that, in  $\text{H}_2\text{O}$ , the liquid crystal phase of the  $\text{SC}_{10}\text{S}$  surfactant could transform into a ternary structure that contained 2-octanol. In this case, 1-dodecanol was detected by  $^{13}\text{C}$  NMR (see Fig. 13), which demonstrates how the alkyl sulfate surfactant could exhibit reducing power. Similarly, the Pd nanoparticle/ $\text{SC}_{10}\text{S}$  system can produce 1-octanol, which then reduces the Pd ions to Pd, and affects the transformation of the liquid-crystal phase of the surfactant. This mild reaction of the alkyl sulfate compounds to generate an alcohol provides a self-regulated, stable supply of reductant to the metal ion, thereby eliminating the need for any other reducing agent.

Another remarkable finding regarding hydrophilic and hydrophobic colloids can be obtained by simple adjustment of the reaction time [48]. This dual hydrophilic–hydrophobic property involves the production of hydrophobic lipid acid

**Table 1.** Average particle size, reaction time, and reaction conditions for the various Pd/ $\text{S}_n\text{S}$  nanoparticles.

Surfactant	Average diameter of the particles (nm)	Reaction time: time taken for the solution to turn dark brown (h)	Conditions	
			Concentration of surfactant (M)	Reflux temperature ( $^{\circ}\text{C}$ )
Sodium <i>n</i> -octyl sulphate ( $\text{SC}_8\text{S}$ )	$9.41 \pm 1.44$	0.5	0.1	70
Sodium decyl sulfate ( $\text{SC}_{10}\text{S}$ )	$2.12 \pm 0.4$	0.5	0.1	70
Sodium dodecyl sulfate (SDS)	$7.81 \pm 1.8$			
Sodium dedecyl sulfate (SDS)	$3.36 \pm 0.71$	4	0.1	110
Sodium <i>n</i> -terdecyl sulphate ( $\text{SC}_{14}\text{S}$ )	$3.25 \pm 0.6$	5	0.1	110

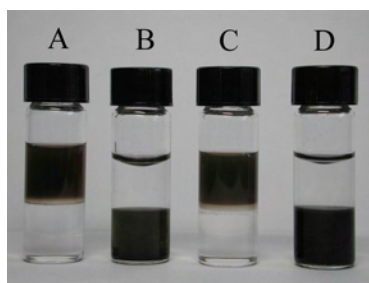
Source: Reprinted with permission from [43], C. L. Lee et al., *Adv. Funct. Mater.* 11, 344 (2000). © 2000, Wiley-VCH Verlag GmbH.



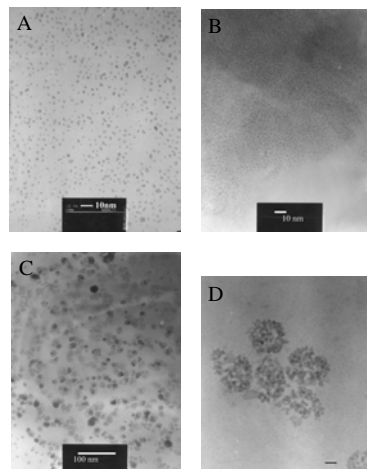
**Figure 13.**  $^{13}\text{C}$  NMR spectra of: (A) SDS (not heat treated) in  $\text{D}_2\text{O}$ . (B) The oily phase that forms on top of an aqueous SDS solution after heating in  $\text{CDCl}_3$ . (c) Pd nanoparticles/SDS in  $\text{D}_2\text{O}$ . (D) Pd nanoparticles/SDS in  $\text{CDCl}_3$ . Reprinted with permission from [43], C. L. Lee et al., *Adv. Funct. Mater.* 11, 344 (2001). © 2001, Wiley-VCH Verlag GmbH.

from the oxidation of the self-generated alcohol from the long carbon chain within the lyophobic micellar core throughout the reaction. The surface modification can render the particle from hydrophilic to hydrophobic by lengthening the synthesis time.

Figure 14 shows pictures of hydrophilic ( $\text{hy-Pd}_{nm}$ ) and hydrophobic Pd nanoclusters ( $\text{hp-Pd}_{nm}$ ) templated within two micelle systems, sodium *n*-dodecyl sulfate (SDS) and sodium *n*-tetradecyl sulfate ( $\text{SC}_{14}\text{S}$ ). Figure 14(A) and (B) are, respectively, hydrophilic and hydrophobic Pd nanoparticles, which are prepared from the aqueous solution of SDS micelles, and then well dispersed in  $\text{H}_2\text{O}$  and  $\text{CHCl}_3$ , whereas Figure 14(C) and (D) are  $\text{hy-Pd}_{nm}$  and  $\text{hp-Pd}_{nm}$ , prepared from the aqueous solution of  $\text{SC}_{14}\text{S}$  micelles, and then dispersed in  $\text{H}_2\text{O}$  and  $\text{CHCl}_3$ , respectively. It is interesting to find that, no matter within which micellar system,  $\text{hy-Pd}_{nm}$  is stably dispersed in  $\text{H}_2\text{O}$  indefinitely, and  $\text{hp-Pd}_{nm}$  is also well dispersed in  $\text{CHCl}_3$  for at least several months. In addition to Pd nanoparticles, this novel method can be extended to prepare other materials, including Pt, Ru, Ag [46] as well as an Ag/Pd colloid [49]. Figure 15 illustrates the typical images of these nanoparticles. A further study of the synthesis and characterization of an Ag/Pd bimetallic colloid will be done in due course.



**Figure 14.** Photoimage of  $\text{hy-Pd}_{nm}$  and  $\text{hp-Pd}_{nm}$  within  $\text{SC}_{12}\text{S}$  and  $\text{SC}_{14}\text{S}$ . (A) Pd nanoparticles/ $\text{SC}_{12}\text{S}$  suspended in the upper aqueous solution. (B) Pd nanoparticles/ $\text{SC}_{12}\text{S}$  suspended in the lower  $\text{CHCl}_3$  solution. (C) Pd nanoparticles/ $\text{SC}_{14}\text{S}$  suspended in the upper aqueous solution. (D) Pd nanoparticles/ $\text{SC}_{14}\text{S}$  suspended in the lower  $\text{CHCl}_3$  solution.



**Figure 15.** TEM images and mean diameters of (A) Pt nanoparticles/SDS ( $d = 2.04 \pm 0.42$  nm), (B) Ru nanoparticles/SDS ( $d = 2.04 \pm 0.34$  nm), (C) Ag nanoparticles/SDS ( $d = 11.12 \pm 3.40$  nm), (D) Ag/Pd (1/1) bimetallic nanoparticles/SDS ( $d = 3.98 \pm 0.75$  nm).

### 3. SPECTROSCOPIC CHARACTERIZATIONS

#### 3.1. TEM Observation

##### 3.1.1. Transmission Electron Microscopy

Transmission electron microscopy can be best applied to characterize the shape and sizes of nanoparticles; although there are still other methods, such as dynamic light scattering (DSL) and small-angle X-ray scattering (SAXS) [50], which can be used to measure the particle size, TEM exclusively provides the real images and shapes of nanostructures.

Owing to the improvement of the high-voltage electron beam, the high-resolution TEM (HRTEM) is designed to produce the images of nanoparticles at an angstrom level. Thus, some defects, like distortion and dislocation, and the interatomic length of the nanomaterial, can be observed from HRTEM images [39]. The sample preparation of a colloidal solution for TEM is rather simple, involving the evaporation of the colloidal solution on carbon-coated metal grids. However, there may be some additives, including stabilizers and unreacted reactants, which can dissolve the colloid as well. These organic compounds, which may react under the influence of a high-voltage electron beam, will affect the resolution of TEM images. In order to obtain clear images, dilution or filtration may be necessary in some cases [2]. Besides, some studies [51] also reveal the possibility of coalescence during TEM observation.

An electron energy loss spectrometer (EELS) and an energy dispersive spectrometer (EDX), which are usually coupled with TEM, can provide an elemental analysis of the nanoparticles being examined. In addition, selected area diffraction patterns also characterize the crystal structure for single-crystalline or randomly oriented polycrystalline nanomaterial.

### 3.2. Ultraviolet–Visible Absorption Spectrum

Metal colloids usually exhibit absorption bands in the ultraviolet–visible (UV–vis) range due to excitation of the plasma resonance or interband transition. Therefore, the UV–vis spectrum is a convenient method of characterization for colloidal nanoparticles as long as they are synthesized. Some colloidal materials, which are different from bulk materials, show distinct absorption peaks in the visible region, and thus can be used for colorants. Bulk silver is gray, for example, while silver sol shows yellow in color. Copper, silver, and gold are the typical materials that show prominent absorption peaks, and thus are frequently used in colored glasses or decorative glazes. On the other hand, other colloidal metals, such as palladium and platinum, exhibit only broad absorption throughout the region of the UV–vis spectrum, and these colloids are brown or gray in appearance.

Creighton and Eadon [52] systematically computed 52 metallic elements in 10 nm diameters of spherical particles on the basis of the Mie theory. For the majority of the colloidal metallic elements, there is only a continuous absorption in the visible range. In addition, the size dependence is more pronounced with decreasing diameter due to the approximation between the particle diameter and the mean-free path of the conduction electrons.

Although many studies associated with the optical property of nanoparticles have been reported, there are still some discrepancies in metal sols owing to their complicated double-layer, metal–water interface. Mulvaney [53] found that the surface plasmon absorption was directly related to the electrochemical processes involved, which include polarization, chemisorption, metal ad atom deposition, and alloying. When the electrical charge is accumulated on the particle surface, a blue-shifted absorption peak is usually observed. Furthermore, dramatic optical shifts are correlated to the electrodeposition of metal atoms onto the preformed metal clusters to form bilayer colloids. In a core–shell bimetallic mesostructure, underpotential deposition (UPD) can be amenable to the blue-shifted spectrum.

In addition to optical properties, the colloidal particles of certain metals are extensively studied for surface-enhanced Raman scattering (SERS). There are two mechanisms to account for this effect [52]. First, the metal surface can enhance the nearby electromagnetic field when the incident radiation lies within the absorption band of the nanoparticles. Second, the scattering close to the metal–adsorbate charge-transfer transitions can improve the tensor of Raman scattering. The wavelength of colloidal metals corresponding to the most efficient excitation wavelengths for SERS has also been verified experimentally.

### 3.3. Fourier Transform Infrared Absorption Spectrometry

Infrared spectroscopy has been widely used to investigate the surface structure by adsorption of a small molecule on the metal surface. Carbon monoxide, which is frequently used for a surface probe molecule, has distinguishable IR characteristic absorption due to its strong adsorption ability to a metal's surface. In addition, the wavenumber of CO

changes drastically with different surface structures, and thus is suitable to characterize the surface sites.

Bradley and co-workers studied a series of Pd and its alloy nanoparticles using CO as the surface probe molecule [54–56]. A size-dependence effect was observed in the Pd colloidal solution [54]. The smallest particles show the highest ratio of terminal to bridged CO, while the smallest particles possess only bridged CO. Terminal CO is more stable on the low coordination number atoms at edges and vertices. On the contrary, the bridged CO is preferred on atoms with a higher coordination number at the face terrace. With decreasing particle size, the relative portion of low coordination atoms increases, and therefore increases the ratio of the terminal to bridged CO peaks.

IR spectroscopy of CO adsorption can also provide information on the surface structure of bimetallic nanoparticles. One can evaluate the surface structure by a comparison of the CO adsorption at various compositions of bimetallic clusters. After subtraction of the adsorptions due to the colloid solution prior to CO addition, a clean spectrum of adsorbed CO is obtained to interpret the surface structure. The segregation of palladium on the surface of Pd/Cu clusters was investigated with an IR spectrum [55]. The formation of a palladium-rich surface was observed, and may result from the dissolution of surface copper atoms into the interior palladium. It is clear that, even under a mild deposition condition, copper atoms could readily diffuse into the palladium in order to form a maximal CuPd bond, which would decrease the energy of alloy formation.

### 3.4. X-Ray Methods

#### 3.4.1. X-Ray Diffraction

X-ray diffraction is a powerful method to determine the palladium crystalline structure. From the characteristic peaks of diffraction patterns, we can characterize palladium nanoparticles with an fcc crystal structure, which is the same as bulk material. In addition, the primary particle size can be calculated from the calculation of the half width of the corresponding peaks, as illustrated in Eq. (3):

$$d = \frac{\alpha\lambda}{\beta \cos \theta} \quad (3)$$

where  $d$  is the particle's diameter,  $\alpha$  is a geometric factor,  $\lambda$  is the X-ray wavelength, and  $\beta$  is the half width of the corresponding diffraction peak at angle  $2\theta$ . According to Eq. (3), a broader peak yields a smaller primary particle diameter. Therefore, nanoparticles usually show broader peaks than bulk material.

XRD can also be used to characterize the lattice constant from the diffraction patterns. When the substance is down to nanoscale, the interatomic length of nanoparticles may change with the particle size. Most materials, such as copper and platinum [57], show lattice contraction properties due to surface stress. In general, the interatomic length will decrease with decreasing particle size. However, most studies [51, 58–61] clearly illustrate that palladium nanoparticles possess lattice expansion rather than lattice contraction. This unique property can be explained by structure



change [51, 58], pseudomorphism [59], and the diffusion of impurities [60–61].

When the palladium nanoclusters are deposited on the solid supports, the lattice dilation phenomenon might be explained in terms of two reasons: structure change and pseudomorphism. Giorgio et al. [51] reported that, when the nanoparticles were deposited on an MgO substrate, an isotropic lattice expansion increased from 2 to 8%, while the particle sizes decreased from 6 to 2 nm. The truncated octahedral could be observed at the top and at the interface with the aid of HRTEM, and the structure change could account for the lattice dilation. Another mechanism, pseudomorphism [59], has frequently been mentioned to explain this special property. Pseudomorphism, which causes lattice strain due to the mismatch between palladium nanoclusters and the substrate, is the possible cause for the lattice expansion of palladium nanoparticles. However, for amorphous substrates such as carbon or SiO<sub>2</sub>, pseudomorphism does not exist since the substrate is not single crystal.

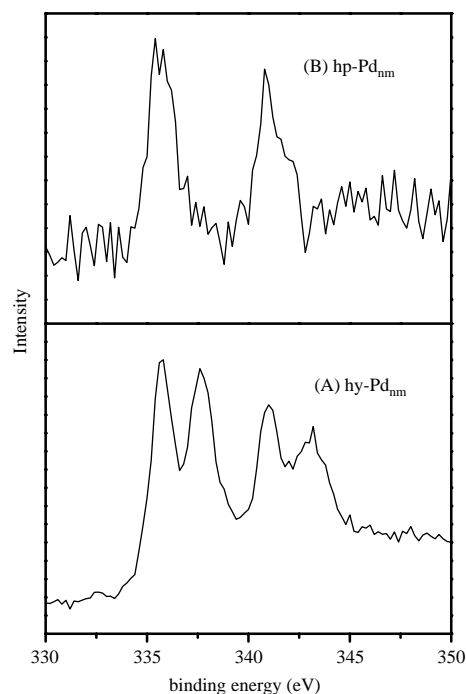
It has also been found that the lattice dilation was correlated with the diffusion of hydrogen. Bulk palladium, which interacts with hydrogen easily, forms metal hydride and exhibits lattice dilation up to about 3%. Kuhrt and Anton [60] demonstrated the hydrogen diffusion into palladium nanoclusters by secondary-ion mass spectroscopy (SIMS) and X-ray photoelectron spectroscopy (XPS). The incorporation of hydrogen in the palladium lattice at an interstitial position leads to an isotropic expansion of the lattice parameter. The origin of hydrogen could result from dissociation of the hydrogen-containing molecules such as H<sub>2</sub>, H<sub>2</sub>O, or C<sub>x</sub>H<sub>y</sub>. In addition to Pd nanoparticles, Pd–Au alloy clusters also possess a nonlinear dependence of lattice expansion due to the different hydrogen diffusion coefficients in various alloy compositions.

Although the expansion of the lattice parameter is usually explained by hydrogen diffusion, an expansion as large as 6% for Pd [59] cannot be similarly explained since the maximum of the dilation for Pd–H formation is only 3.6%. Therefore, Jacobs and Schryvers [61] discussed the palladium lattice parameter dilation in terms of oxygen diffusion. They suggested that the distorted fcc structure, which was observed by TEM, represented Pd–O alloys. The dissolution of oxygen in the Pd nanoparticles might be responsible for the expansion of the interatomic length.

Most studies so far have focused on the expansion of the lattice constant for palladium clusters, and there are still a few works observing the lattice contraction phenomenon [62–63], which is the same as other materials. The presence of methyl and vinyl groups, followed by the activated diffusion of carbon atoms through the metal lattice, can lead to the formation of a Pd–C phase and the subsequent expansion of the lattice parameter.

### 3.4.2. X-Ray Photoelectron Spectroscopy

In contrast to other electron spectroscopies, X-ray photoelectron spectroscopy provides information regarding not only the atomic composition, but also the structure and oxidation state of the samples. Before XPS measurement, the colloidal particles must be precipitated by ultrahigh-speed centrifuge, and dried in the vacuum. Figure 16 [48] shows a



**Figure 16.** XPS spectra of the hy-Pd<sub>nm</sub> and hp-Pd<sub>nm</sub>.

typical XPS spectrum of hy-Pd<sub>nm</sub> and hp-Pd<sub>nm</sub> powders protected by sodium dodecyl sulfate. The detailed preparation method was discussed in Section 2.5.5. For the hy-Pd<sub>nm</sub>, the resulting spectrum of the Pd element (Fig. 16) clearly reveals four bands, 335.6, 337.6, 341, and 343.2 eV, respectively. Two bands at 335.6 and 341 eV correspond to the 3d<sub>5/2</sub> and 3d<sub>3/2</sub> of zero-valence palladium, while the other two peaks represent the precursors (palladium acetate). It clearly indicates that Pd nanoparticles and precursors (Pd(OAc)<sub>2</sub>) coexist in the core of the hydrophilic micelle mesostructure. In contrast to the XPS result of the hy-Pd<sub>nm</sub>, the XPS spectrum of the hp-Pd<sub>nm</sub> (Fig. 16) only shows Pd<sup>0</sup> (335.6 and 340.8 eV). It seems that, during the transformation from hy-Pd<sub>nm</sub> to hp-Pd<sub>nm</sub>, the particle growth reaches an end, so there is no longer a detectable palladium ion inside the hp-Pd<sub>nm</sub> structure.

XPS can also be used to investigate the surface composition of palladium and its alloy nanoparticles. If the nanoclusters are synthesized by a chemical method, the surface of nanoparticles is coated with a thick layer of organic protecting agents, which influence the detection of XPS. To overcome this problem, a coordination capture method is usually employed to remove the protective agents [2]. The surface composition of nanoclusters can then be quantitatively determined.

Wu et al. [5] also used the thiophenol-capped Pd–Au bimetallic nanoparticles to investigate the composition on the outer surface of the particles. The Pd atoms were found to concentrate in the outer part of nanoclusters, which suggests an incomplete Au-core/Pd-shell mesostructure. Although XPS provides an indispensable method to investigate the surface composition of nanoparticles, a problem may arise because the structure might change

during the coordination capture process, resulting in experimental deviation.

Further, for the determination of the surface composition of nanoparticles, the concept of coordination capture can also be employed to immobilize two-dimensional nano-clusters onto a solid substrate [64–66]. The achievement of well-ordered metal clusters on the substrate makes the fabrication of a nanodevice possible.

## 4. CATALYTIC PROPERTIES

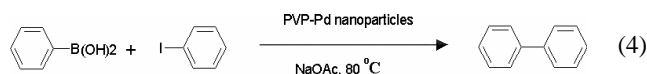
The high material cost of palladium naturally restricts the application of palladium nanoparticles. Catalysis is the most important application for palladium or its alloy clusters, and has been extensively investigated. Transition metal nanoparticles are known to be effective catalysts owing to their large surface area arising from the drastic reduction of size [12]. For the past decades, palladium nanoparticles have played an important role in organic catalysis. In general, the catalysis of organic reactions can be grouped as structure-sensitive, such as Suzuki coupling reactions [67] and Heck coupling reactions [68], or structure-insensitive, including hydrogenation reactions [69]. Pd nanoparticles show outstanding performance in reactivity and selectivity for catalyzing these organic reactions.

Besides catalyzing these organic reactions, pure palladium clusters can work as activators for electroless copper deposition [70]. Electroless deposition is an important technology to prepare circuits for industries, including printed-circuit boards (PCBs) and semiconductors. It was found that copper could be successfully deposited and filled in 0.25  $\mu\text{m}$  vias and trenches on a TaN/SiO<sub>2</sub>/Si wafer surface [70]. The effects of particle size and carbon-chain length of surfactants (sodium alkyl sulfate) on the deposition kinetics were studied by electrochemical quartz crystal microgravimetry (EQCM).

### 4.1. Catalysis for Organic Coupling Reaction

#### 4.1.1. Suzuki Coupling Reaction

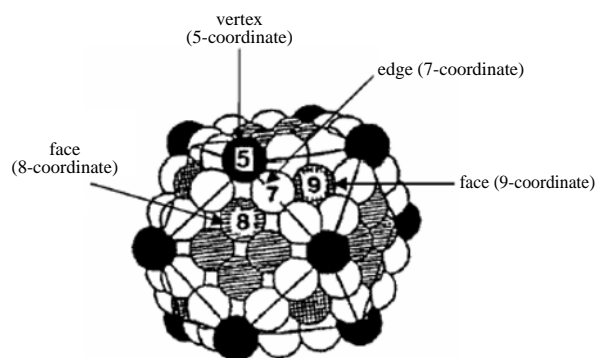
The coupling reactions of aryl halides with arylboronic acids, namely Suzuki coupling reactions [Eq. (4)], provide a versatile route for synthesizing biaryls, which are important precursors for pharmaceutical, nucleoside analogs, polymers, and liquid crystals [67].



Traditionally, these reactions are catalyzed by the phosphine-ligand palladium complex. In general, homogeneous catalysis is preferred because it is often highly selective toward the formation of a desired product. These homogeneous catalysts, however, involved problems such as separation from the reaction mixture and recovery of the catalyst. Recently, colloidal palladium has shown high reactivity, and the separation of the Pd catalyst can be easily carried out by using water as the reaction medium [71]. Accordingly, colloidal palladium has become a promising candidate as a commercial catalyst for the Suzuki coupling reaction for environmental and economical reasons.

The effects of size on the catalytic activity in Suzuki reactions have been systematically studied by El-Sayed's group [67]. They used a stepwise procedure to synthesize PVP-protected palladium nanoparticles with different particle sizes of 3.0, 3.9, 5.2, and 6.6 nm, respectively. The Suzuki reaction between phenylboronic acid and iodobenzene has been studied to probe the reactivity of Pd clusters. The activity of Pd nanoparticles is expressed in terms of the initial turnover frequency (TOF; moles of the product per mole of total surface Pd atoms per minute). They found the reactivity of the reaction in the order of Pd (3.9 nm) > Pd (3.0 nm)  $\approx$  Pd (5.2 nm) > Pd (6.6 nm). The TOF changes significantly with different particles sizes, indicating that the activity is not the same for all surface atoms, since if all of the surface atoms were equally active, there would be no particle size dependence of TOF. In addition, the structure of the cuboctahedron model, as shown in Figure 17, suggests the different types of surface atoms and coordination numbers. The relative proportion of edge and vertex sites increases as the particle decreases. Accordingly, the general trend that the reactivity increases as the particle size decreases suggests that the Suzuki reaction is "structure-sensitive," that is, the low-coordination number of vertex and edge atoms on the particle surface is active for this coupling reaction. However, the lower catalytic activity for the smallest Pd (3.0 nm) nanoparticles might be due to stronger adsorption of the reaction intermediates on the surface, which retard the reaction rate and act as poison to the reaction by Piccolo and Henry [73]. They also found that the intrinsic activity depends not only on particle size, but also on particle shape.

The effect of the stabilizer on the activity and stability of a palladium colloid has also been studied El-Sayed and his co-workers [71]. A series of different stabilizers, hydroxyl-terminated poly(amido-amine) (PAMAM) dendrimers ( $G_n\text{-OH}$ , where  $G_n$  represents the  $n$ th generation), block copolymer polystyrene-*b*-poly (sodium acrylate), and poly (N-vinyl-2-pyrrolidone) (PVP), were used to investigate the activity and stability in Suzuki coupling reactions between phenylboronic acid and iodobenzene in an aqueous medium. The Suzuki reaction being refluxed at about 100  $^\circ\text{C}$  for 24 h is a good "acid test" for examining the stability of the colloid. It is found that the Pd clusters protected by PVP,

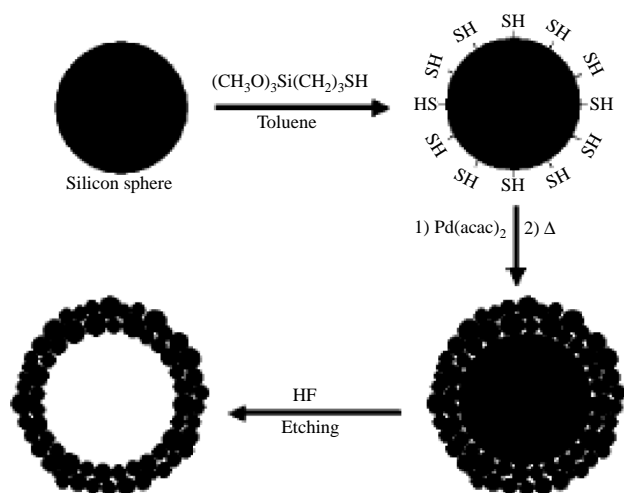


**Figure 17.** Structure of a three-shell cuboctahedron showing the different types of surface atoms and their coordination numbers. Reprinted with permission from [67], Y. Li et al., *Langmuir* 18, 4921 (2002). © 2002, American Chemical Society.

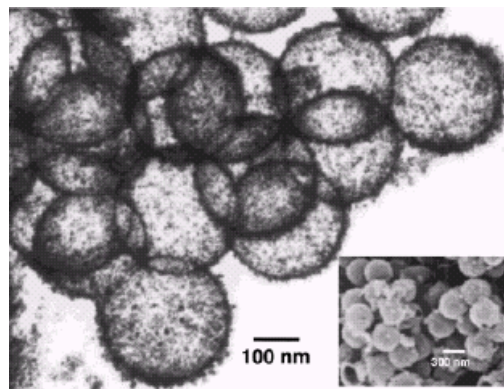
a block copolymer, and the G3 dendrimer are effective catalysts for the Suzuki reaction, while the palladium colloid encapsulated by the G4 dendrimer shows good stability, but results in the loss of activity. We may expect, that the activity and stability are found to be anticorrelated, that is, the most stable is the least catalytically active [71].

Recently, the fabrication of hollow palladium spheres and its application to Suzuki coupling reaction have been reported [74]. First, uniform silica spheres were synthesized, and the surfaces of silica spheres were modified with a thiol group. Then palladium acetylacetonate ( $\text{Pd}(\text{acac})_2$ ) was introduced, and  $\text{Pd}^{2+}$  ions were adsorbed onto the thiol-functionalized surfaces of these silica spheres. The  $\text{Pd}^{2+}$  solution was heated at  $250\text{ }^\circ\text{C}$  for 3 h to form  $\text{Pd}^0$  metal-coated silica spheres, as illustrated in Figure 18. The reductant probably came from the CO generated *in-situ* from the thermal decomposition of acetylacetonate. Finally, 10 M HF was used to remove the silica template, and the hollow Pd spheres were then produced. Their TEM images, shown in Figure 19, illustrate that nearly monodispersed 300 nm hollow spheres with a uniform shell of 15 nm were obtained. The BET surface area of the palladium hollow spheres was measured to be  $64\text{ m}^2\cdot\text{g}^{-1}$ , which is much larger than the surface of dense spheres. Iodothiophene and phenylboronic acid were used as test substrates for the Suzuki reaction. The palladium hollow spheres are shown to be extremely active for this reaction, and by simply filtrating the reaction mixture, this catalyst can be easily retrieved without losing its activity, even after seven recycles.

Besides Pd monometallic catalyst, mixed nanocluster colloids, including other metals like copper and platinum, were used for Suzuki coupling reaction [75]. An experimental design method was applied to investigate the monometallic and the combined catalysts, including palladium, ruthenium, platinum, and copper. A wide range of aromatic compounds were used for test substrates in Suzuki reactions. The designed mixed nanocluster can effectively catalyze these organic reactions, and provides an inexpensive and economic alternative to replacing the noble metal catalyst.



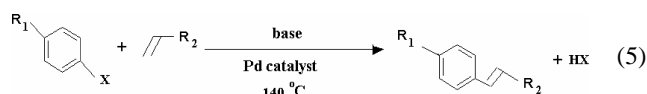
**Figure 18.** Experimental procedure for production of hollow palladium spheres. Reprinted with permission from [74], S. W. Kim et al., *J. Am. Chem. Soc.* 124, 7642 (2002). © 2002, American Chemical Society.



**Figure 19.** Transmission electron micrograph and scanning electron micrograph (inset) of hollow palladium spheres. Reprinted with permission from [74], S. W. Kim et al., *J. Am. Chem. Soc.* 124, 7642 (2002). © 2002, American Chemical Society.

#### 4.1.2. Heck Coupling Reaction

The Heck reaction, including coupling reactions between aryl halides and olefins [Eq. (5)], provides an important synthetic method for the production of intermediates of pharmaceuticals and fine chemicals. In general, coupling reactions, which occur on the surface defects rather than terrace sites in a heterogeneous catalyst, can be regarded as “structure-sensitive,” which is significantly influenced by the particle size of the catalyst [76]. A conventional heterogeneous catalyst differing only in particle size, however, is technically very difficult to prepare, since different supports or preparation conditions produce catalysts intrinsically different from one another. Recently, colloidal methods [77], which can synthesize nanoparticles with constant properties except varying in particle sizes, provide a possible way to investigate the structure-sensitive reactions.



A series of well-defined PVP-stabilized palladium nanoparticles reduced by  $\text{H}_2$  has been used for the Heck coupling reaction [68]. This systematic study confirms that these defect sites are responsible for the C–C bond coupling reaction other than terrace sites in Heck reaction. Furthermore, the activity of colloidal palladium is comparable to that of the most efficient homogeneous Pd catalyst in a similar reaction.

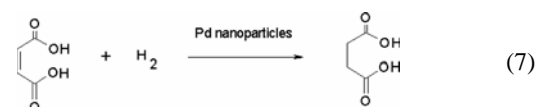
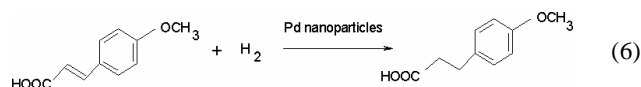
Although Pd nanoparticles show high activity toward the organic coupling reaction, the stability of colloid, which is especially important for pharmaceutical applications, has much room for improvement. A well-stabilized palladium colloid can be accomplished by being prepared in block copolymer micelles of polystyrene-*b*-poly-4-vinylpyridine [78]. The activity of the block-copolymer-stabilized Pd colloid ranks about equal to that of conventional palladium complexes, but the former has higher stability. In addition, adjustment of the outer block to the environment allows the Heck reaction to proceed in many “simple” solvents, such as toluene, instead of amidic solvent.

In recent years, some homogeneous catalyst systems, such as  $\text{Pd}(\text{OAc})_2$  in the presence of  $n\text{Bu}_4\text{N}^+\text{Cl}^-$  or  $\text{Pd}(\text{OAc})_2$  in an aqueous medium, have been extensively used in the Heck reaction and Suzuki reaction. Although the phosphane was regarded as an activity agent before, the role of phosphane-free catalysts in a coupling reaction is uncertain. A mechanistic study, supported by TEM analysis, indicates the involvement of Pd nanoparticles as intermediate in the reaction [79]. The palladium salt undergoes thermolytic decomposition or  $\text{RCO}_2^-$ -induced electron transfer to form a Pd colloid simultaneously in the Heck reaction. The resulting Pd colloid acts as a catalyst for the C–C bond-forming process. Thus, the phosphane-free palladium complex, which is traditionally regarded as a homogeneous catalyst in the Heck reaction, actually belongs to the area of a heterogeneous colloidal heterogeneous catalyst system.

## 4.2. Catalysis for Hydrogenation of Olefins

Polymer-stabilized Pd, Pt, Rh, and Ir nanoparticles have been used as catalysts for the hydrogenation of many unsaturated olefins [2]. In particular, palladium colloid was used as an effective catalyst for the partial hydrogenation of dienes to alkenes due to their high activity and selectivity.

A palladium cluster utilizing water-in-supercritical  $\text{CO}_2$  has been tried as a catalyst for hydrogenation [80]. The palladium salt dissolved in the water core was reduced by the hydrogen gas. Hydrogen gas is a suitable reductant in supercritical  $\text{CO}_2$  due to its miscibility and simplicity. Furthermore, the hydrogen gas can also serve as a starting material for the subsequent hydrogenation process. Besides the simplicity of the process, the water-in- $\text{CO}_2$  microemulsion system can dissolve hydrophobic organic compounds in the supercritical fluid and hydrophilic organic compounds in the water core. This unique property allows the hydrogenation of hydrophobic organic compounds, such as 4-methoxy-cinnamic acid to 4-methoxyhydrocinnamic acid [Eq. (6)], or the hydrogenation of water-soluble compounds in  $\text{CO}_2$  [Eq. (7)]. Moreover, Pd nanoparticles in water-in- $\text{CO}_2$  microemulsion can also catalyze other hydrogenation reactions, including the conversion of the nitro group ( $\text{NO}_2$ ) to amine ( $\text{NH}_2$ ).

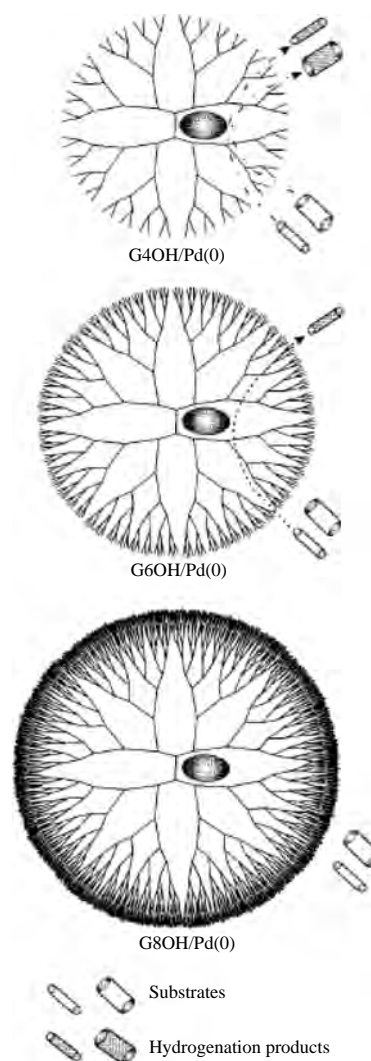


Another novel method for catalyzing the hydrogenation of olefins is to utilize dendrimers as stabilizers. Dendrimers have been proven to be effective for the separation of chemical species due to their crowding structures. Traditionally, dendrimers can be used as stationary phases in various liquid separation techniques. These separation processes involve physical interactions between small molecules and dendrimers, such as size, shape, and electronic interaction, including surface charge and polarity. With the progress

of nanotechnology, dendrimers have been used for capping metal nanoparticles [8, 9].

Crooks and co-workers systematically studied the hydrogenation of olefins by dendrimer-encapsulated palladium nanoparticles, and they showed that the selectivity can be adjusted by the surrounding dendrimer [81–82]. Nearly monodisperse ( $1.7 \pm 0.2$  nm) Pd nanoparticles were prepared within the interior of three different generations of hydroxyl-terminated poly(amidoamine) (PAMAM) dendrimers. Importantly, the Pd encapsulated in PAMAM dendrimers can act as an adjustable-mesh “nanofilter” by changing the generation of dendrimers; that is, a higher generation of dendrimer-encapsulated catalysts or larger substrates resulted in a lower hydrogenation reaction rate, as shown in Figure 20. In addition, the dendrimer-encapsulated Pd composite shows higher activity and good stability for months, even after several cycles of hydrogenation reactions.

Dendrimer-encapsulated Pd nanoparticles can also be synthesized as a fluorous phase-soluble catalyst [9]. This



**Figure 20.** Palladium nanoparticles encapsulated in different dendrimer generations, which can act as an adjustable-mesh “nanofilter.” Reprinted with permission from [81], Y. Nui et al., *J. Am. Chem. Soc.* 123, 6840 (2001). © 2001, American Chemical Society.

catalyst is selectively soluble in the fluorous phase, while the reactants are preferentially soluble in the organic solvent. Stirring or sonicating the mixture leads to the formation of fine emulsion and partial homogenization, and the catalytic reaction proceeds at the interface between the two liquids, as shown in Figure 21. When the reaction is over, the liquid phases are separated, the product is isolated from the organic phase, and the catalyst-containing phase layer is recycled. Such easy separation and recycling are preferred owing to the economic and environmental concerns.

In addition to dendrimer-protected colloids, qualitative work concerning polyacid-stabilized palladium nanoclusters has been conducted to investigate the hydrogenation of cyclohexene [83]. This type of polymer can significantly influence the particle sizes, which affect the catalytic property, and the stability as well. The introduction of functional groups of the polymer, such as hydrogen transfer units, can create a certain surrounding environment, which subsequently allows or hinders the pathway of the reactions. Moreover, additional ions could be used to tune the catalytic reaction rate due to interaction with the surrounding polymer matrix.

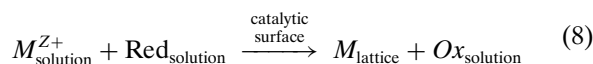
### 4.3. Activation for Electroless Metal Deposition

#### 4.3.1. Introduction to Electroless Metal Deposition

Electroless deposition has been widely used for the metallization of a nonconductive substrate. The best known application is the plating-through-hole (PTH) for a printed-circuit board and copper interconnection of ultralarge-scale integration in a semiconductor [84]. So the most common metal to be plated is copper, although nickel and cobalt are both electrolessly plated to prepare a device with special mechanical or magnetic properties [85].

Electroless metal deposition in theory should cover all chemical processes for metal deposition, except conventional electrodeposition. In practice, it only refers to the process of autocatalytic electroless deposition which involves metal reduction on a catalytic surface. Two electrochemical reactions, the reduction of metal ions and the oxidation of a

reducing agent, occur at the same place at the electrode-electrolyte interface. The overall reaction is shown as follows:

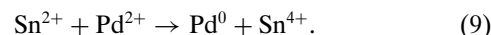


where  $M^{Z+}$  is a metal salt,  $\text{Red}_{\text{solution}}$  is a reducing agent in the electrolyte,  $M_{\text{lattice}}$  is solid-state metal, and  $\text{Ox}$  is the oxidized product of the reducing agent. The catalytic surface can be the substrate itself or a surface coated with catalytic colloids. A reducing agent, Red, binds to the catalytic colloids on the surface, and is oxidized, providing electrons to reduce metal ions so that metal is deposited on the substrate. As the reduction continues, the hydrogen generated due to the reduction provides new catalytic sites promoting the deposition. Hence, the process is called autocatalytic electroless deposition.

A similar process is called direct metallization. The process also needs to activate the surface with a catalyst, yet the catalyzed surface needs no electroless deposition to make it conductive, and can accept metal deposition directly [87]. The catalyst used is also similar to that for electroless deposition.

#### 4.3.2. Conventional Pd/Sn Colloidal Activator

The Pd/Sn colloid is the most common catalyst for electroless metal deposition. In related industries, the catalyst is specially called an activator, and the process to render the surface catalytic is called activation. In a common commercial process [88],  $\text{PdCl}_2$  and  $\text{SnCl}_2$  were mixed and heated up to 80 °C for 8 h. The  $\text{Pd}^{2+}$  was then reduced by  $\text{Sn}^{2+}$  to form Pd/Sn colloids with stannic ions adsorbed as a stabilizer [Eq. (9)]:



However, this colloidal solution has limited stability due to the oxidation of the stannic ion by the air, and usually can last for at most only a few months; obviously, this is a costly drawback to users. Recently, a novel method for the synthesis of noble metal nanoparticles was developed [43], and the Pd colloid so produced was studied as a possible new activator for electroless copper deposition.

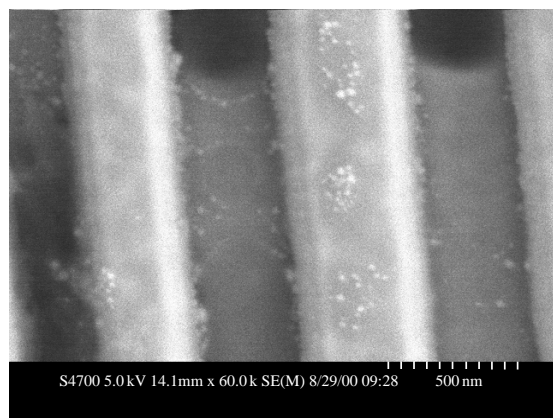
#### 4.3.3. Evaluation of Pd Colloidal Activator

Nanotechnology has gained increasing importance in many fields; however, there are a few studies concerning the possibility of using Pd nanoparticles as a catalyst for activating electroless copper deposition.

Recently, the kinetics of electroless copper deposition catalyzed by palladium nanoclusters and the effect of the surrounding functional group were investigated [53]. Pd nanoparticles were synthesized via reactive micelles with sulfate-type surfactants with different chain lengths (the detailed experimental procedure was previously discussed in Section 2.2.5). In order to test the catalytic activity of Pd nanoparticles for electroless copper deposition, a 0.25  $\mu\text{m}$  TaN/SiO<sub>2</sub>/Si wafer pattern was activated by Pd nanoparticles/SC<sub>12</sub>S (sodium dodecyl sulfate) (Fig. 22). Then copper was deposited and filled in the microtrench by immersing the pattern in an electroless copper bath.



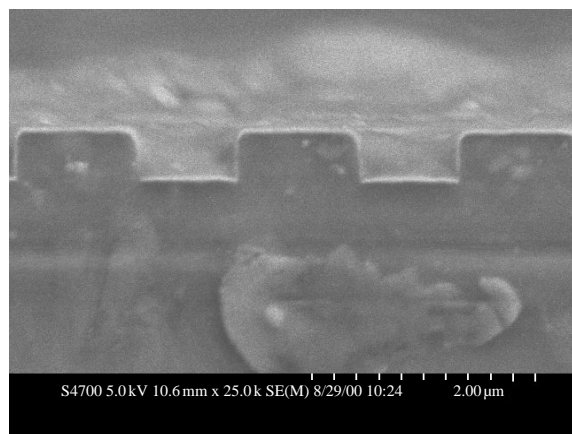
**Figure 21.** Illustration of the approach used to carry out fluorous biphasic catalysis using dendrimer-encapsulated metal nanoparticles modified on their exterior with perfluoroether “ponytails.” Here, the catalyst is a G4-NH<sub>2</sub> PAMAM dendrimer electrostatically functionalized with a perfluoroether fatty acid. Reprinted with permission from [15], R. M. Crooks et al., *Acc. Chem. Res.* 34, 181 (2001). © 2001, American Chemical Society.



**Figure 22.** FE-SEM image of 0.25  $\mu\text{m}$  TaN substrate of ULSI after activation with Pd nanoparticles/ $\text{SC}_{12}\text{S}$  (top view; the white spots represent the Pd nanoparticles). Reprinted with permission from [70], C. L. Lee et al., *J. Electrochem. Soc.* (Mar. 2003). © 2003, Electrochemical Society.

Figure 23 shows that electroless copper can be deposited with this kind of Pd nanoparticle as the activator. A quantitative evaluation of the process was carried out with the aid of quartz crystal microgravimetry (QCM).

The results are summarized in Table 2. A comparison of the rate of the electroless copper deposition between systems with Pd nanoparticles/sodium alkyl sulfate and systems with a conventional Pd/Sn activator indicates that the newly developed Pd/alkyl nanoclusters can be effectively used as an activator for electroless copper deposition. In fact, Pd nanoparticles protected with  $\text{SC}_8\text{S}$  micelles are more catalytically active than the Pd/Sn colloids. Another surprising finding is that, not only the diameter of Pd nanoparticles, but also the carbon chain length of the surfactant influences the electroless rate. Based purely on the surface-volume area and available site of the catalyst, the rate of electroless deposition should theoretically increase with decreasing diameter of the catalytic particle without a protection agent. However, in our case, the Pd nanoparticle/ $\text{SC}_8\text{S}$



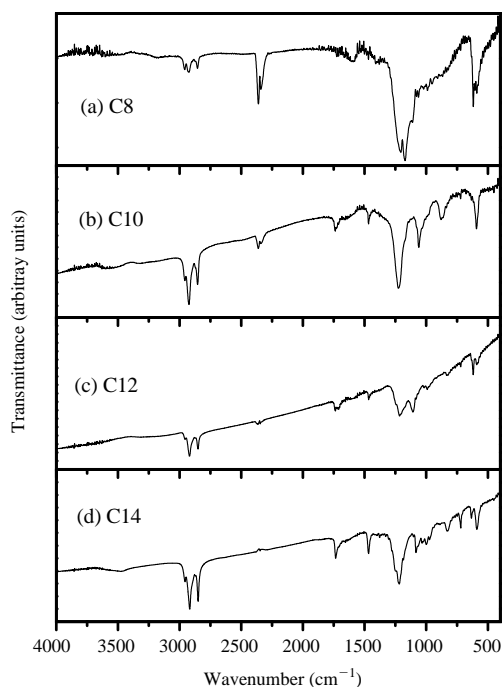
**Figure 23.** FE-SEM image of electroless copper deposition on 0.25  $\mu\text{m}$  TaN/ $\text{SiO}_2$ /Si pattern wafer after activation with Pd nanoparticles/ $\text{SC}_{12}\text{S}$  (cross section). Reprinted with permission from [70], C. L. Lee et al., *J. Electrochem. Soc.* (Mar. 2003) © 2003, Electrochemical Society.

**Table 2.** Summary of kinetics of electroless copper deposition and the induction time which is measured by QCM.

Pd nanoparticle	Induction period (s)	Starting potential (mV)	$\Delta F$ (Hz)	Rate of electroless copper ( $\text{ng}/\text{cm}^2\cdot\text{s}$ )
$\text{C}_8$	0	-1200	-751,987	70.69
$\text{C}_{10}$	62	-911	-307,625	28.92
$\text{C}_{12}$	0	-1116	-489,586	46.03
$\text{C}_{14}$	350	-800	-106,552	9.87
Pd/Sn	140	-985	-555,402	52.36

Source: Reprinted with permission from [70], C. L. Lee et al., *J. Electrochem. Soc.* (Mar. 2003). © 2003, Electrochemical Society.

system, which has a larger particle diameter than the Pd nanoparticles/ $\text{SC}_{10}\text{S}$  system, turns out to be more active. Similarly, the Pd nanoparticle/ $\text{SC}_{12}\text{S}$  is also more active than the Pd nanoparticle/ $\text{SC}_{14}\text{S}$  since  $\text{SC}_{12}\text{S}$  has a shorter carbon chain than  $\text{SC}_{14}\text{S}$ . Other evidence can be found from the FTIR spectra ( $2800\text{--}3000\text{ cm}^{-1}$ ), as shown in Figure 24. This means that the alkyl groups of sodium alkyl sulfate strongly adsorb on the surface of Pd nanoparticles, which may result in a barrier for adsorption of formaldehyde during the incubation period. However, a faster deposition rate could also be attributed to smaller particles when comparing  $\text{C}_{12}$  with  $\text{C}_{10}$  system, even if lengthening the carbon chain has an influence. Overall, the activity of these four types of Pd nanoparticles is in the following order:  $\text{C}_8 > \text{C}_{12} > \text{C}_{10} > \text{C}_{14}$ , which shows that both the carbon chain length of the protection agent and the



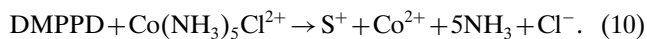
**Figure 24.** The FT-IR spectra of Pd nanoparticles attached with sodium alkyl sulfate with various carbon chains: (a)  $\text{C}_8$ , (b)  $\text{C}_{10}$ , (c)  $\text{C}_{12}$ , (d)  $\text{C}_{14}$ . Reprinted with permission from [70], C. L. Lee et al., *J. Electrochem. Soc.* (Mar. 2003). © 2003, Electrochemical Society.

size of Pd nanoparticles are essential factors in controlling the catalytic activity.

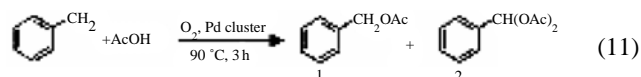
Thus, electroless copper can be successfully deposited and filled in microtrenches of a 0.25  $\mu\text{m}$  TaN/SiO<sub>2</sub>/Si pattern wafer by using a newly developed Pd nanoparticle protected by sodium alkyl sulfate. In addition to Pd monometallic nanoparticles, Ag/Pd bimetallic nanoparticles can also be synthesized via reactive micelles. The bimetallic colloids are of great interest due to their tailed structures, resulting in the improvement of the catalytic properties [49]. Accordingly, the Ag/Pd bimetallic colloid is a promising candidate as a catalyst since it is significantly less expensive than Pd nanoparticles based on the material cost.

#### 4.4. Other Catalytic Aspects

In recent years, a nanosized particle has been utilized for the synthesis of various transition metals in a hydrazine-reduced water/sodium bis(2-ethylhexyl) sulfosuccinate (AOT)/*n*-heptane microemulsion system [90]. However, only a few reports correlate the kinetic and mechanical study in a catalytic reaction. Spiro and co-workers [91–92] presented a qualitatively kinetic study on the reaction between *p*-Me<sub>2</sub>NC<sub>6</sub>H<sub>4</sub>NH<sub>2</sub> (DMPPD) and Co(NH<sub>3</sub>)<sub>5</sub>Cl<sup>2+</sup> catalyzed by reversed-micelle Pd nanoparticles [Eq. (10)]. The activation energy and rotating Pd electrode were also used to investigate the catalytic mechanism. However, one should bear in mind that the hydrodynamics are quite different between the actual surface of the nanoparticles and that of the rotating disk electrode.



Acetoxylation is a powerful method to functionalize various kinds of C–H bonds in hydrocarbons [Eq. (11)]. Recently, acetoxylation of toluene in the presence of oxygen was systematically studied by Kaneda and co-workers [93].



They used a novel method to prepare different palladium particle sizes containing Pd<sup>0</sup>, Pd<sup>2+</sup>, and Pd<sup>+</sup> species on the particle surface by simply adjusting the concentration of palladium nitrate. On the basis of this mechanism, they found that mixed-valence states, which is similar to supported metal particles, lead to a powerful colloidal catalyst, and this finding gives us a clue in understanding the roles of heterogeneous catalysts on the solid supports.

#### 4.5. Hydrogen Storage

Metals in the form of hydride can exhibit useful properties, such as hydrogen storage [94] and conductivity [95]. Owing to the promotion of clean energy, bulk palladium has been extensively studied in the field of hydrogen storage due to its extremely high hydrogen storage ability at room temperature [96]. A cuboctahedral Pd<sub>13</sub>/H model has been proposed to interpret the mechanism of phase transition.

With the advance of nanotechnology, the palladium cluster has been studied for its properties as a metal hydride [94]. Ligand-stabilized Pd nanoparticles of different sizes, Pd<sup>2</sup>, Pd<sup>5</sup>, as well as Pd<sup>7</sup>, were synthesized to investigate the size effect on the capacity and kinetics. These clusters show prominent improvement in the discharge kinetics compared to the bulk. Pd nanoparticles with a diameter of 1.2 nm show a reversible hydrogen uptake, which is not observed in bulk material. Furthermore, X-ray diffraction data reveal that the crystalline structure of the nanoparticles is not influenced by adsorption/ desorption cycles.

### GLOSSARY

**Colloid** Colloid is a substance typically larger than 10 nm in diameter, with broader dispersion ( $\gg 15\%$  size dispersion), and poorly defined in composition. It is a classical and traditional term to describe these tiny substances suspended in the solutions.

**Micelle** When the concentration of surfactants is above critical concentration, surfactants will aggregate with their hydrophobic or hydrophilic groups to form micelles. The shapes of micelles could be spherical, rod-like, or lamellar. Micelles are extremely tiny, usually below 10 nm, and transparent to light. They can be used as soft templates to control the size and shape of nanoparticles.

**Nanocluster** Nanoclusters are substances about 1–10 nm in diameter, near monodisperse ( $\leq 15\%$  size dispersion), and well defined in composition.

**Nanotechnology** Nanotechnology concerns methods to produce useful materials, devices, and systems through the control of matter on the nanometer scale (1–100 nm), and the study of novel properties and phenomena developed at this scale.

**Template** Templates are host materials where the nanoparticles can nucleate and grow. The geometry and dimensions of the templates can manipulate the shape and size of the nanoparticles.

### REFERENCES

1. H. Bönemann and R. M. Richards, *Eur. J. Inorg. Chem.* 2455 (2001).
2. N. Toshima and T. Yonezawa, *New J. Chem.* 1179 (1998).
3. G. Schmid, M. Harm, J. O. Bovin, J. V. Ruitenbeck, H. W. Zandbergen, and W. T. Ruitenbeck, *J. Am. Chem. Soc.* 115, 2046 (1993).
4. M. P. Pileni, *Langmuir* 13, 3266 (1997).
5. M. L. Wu, D. H. Chen, and T. C. Huang, *Langmuir* 17, 3877 (2001).
6. D. H. Chen, C. C. Wang, and T. C. Huang, *J. Colloid Interface Sci.* 210, 123 (1999).
7. V. Arcoletto, G. Cavallaro, G. L. Manna, and V. T. Liveri, *Thermochimica Acta.* 254, 111 (1995).
8. V. Chechik, M. Zhao, and R. M. Crooks, *J. Am. Chem. Soc.* 121, 4910 (1999).
9. V. Chechik, M. Zhao, and R. M. Crooks, *J. Am. Chem. Soc.* 122, 1243 (2000).
10. J. Richter, R. Seidel, R. Kirsch, M. Mertig, W. Pompe, J. Plaschke, and H. K. Schackert, *Adv. Mater.* 12, 507 (2000).
11. M. T. Reetz, W. Helbig, S. A. Quaiser, U. S. Timming, N. Breuer, and R. Vogel, *Science* 267, 367 (1995).
12. “Clusters and Colloids: From Theory to Applications” (G. Schmid, Ed.), p. 469. VCH, Weinheim, New York, 1994.
13. T. K. Jain, G. Cassin, J. P. Badiali, and M. P. Pileni, *Langmuir* 12, 2408 (1996).

14. M. L. Wu, D. H. Chen, and T. C. Huang, *J. Colloid Interface Sci.* 243, 102 (2001).
15. R. M. Crooks, M. Zhao, L. Sun, V. Chechik, and L. K. Yeung, *Acc. Chem. Res.* 34, 181 (2001).
16. K. B. Lee, S. M. Lee, and J. Cheon, *Adv. Mater.* 13, 517 (2001).
17. H. Kang, Y. W. Jun, J. I. Park, K. B. Lee, and J. Cheon, *Chem. Mater.* 12, 3530 (2000).
18. J. Xiao, Y. Xie, R. Tang, M. Chen, and X. Tain, *Adv. Mater.* 13, 1887 (2001).
19. K. N. Mbindyo, T. E. Mallouk, J. B. Mattzela, I. Kratochvilova, B. Razavi, T. N. Jackson, and T. S. Mayer, *J. Am. Chem. Soc.* 124, 4020 (2002).
20. L. Z. Wang, J. L. Shi, J. Yu, W. H. Zhang, and D. S. Yan, *Mater. Lett.* 45, 273 (2000).
21. H. P. Lin, Y. R. Cheng, S. B. Liu, and C. Y. Mou, *J. Mater. Chem.* 9, 1197 (1999).
22. J. Walter, *Adv. Mater.* 12, 31 (2000).
23. B. Xue, P. Chen, Q. Hong, J. Lin, and K. L. Tan, *J. Mater. Chem.* 11, 2378 (2001).
24. N. A. Dhas and A. Gedanken, *J. Mater. Chem.* 8, 445 (1998).
25. K. Okitsu, H. Bandow, and Y. Maeda, *Chem. Mater.* 8, 315 (1996).
26. N. A. Dhas, H. Cohen, and A. Gedanken, *J. Phys. Chem. B* 101, 6834 (1997).
27. W. Chen, W. Cai, Y. Lei, and L. Zhang, *Mater. Lett.* 50, 53 (2001).
28. M. T. Reetz and W. Helbig, *J. Am. Chem. Soc.* 116, 7401 (1994).
29. M. T. Reetz, M. Winter, R. Breinbauer, T. A. Thomas, and W. Vogel, *Chem. Eur. J.* 7, 1084 (2001).
30. M. T. Reetz, W. Helbig, and S. A. Quaiser, *Chem. Mater.* 7, 2227 (1995).
31. T. Teranishi and M. Miyake, *Chem. Mater.* 11, 3414 (1999).
32. G. Schmid and L. F. Chi, *Adv. Mater.* 10, 515 (1998).
33. T. Yonezawa, K. Imamura, and N. Kimizuka, *Langmuir* 17, 4701 (2001).
34. D. E. Cliffl, F. P. Zamborini, S. M. Gross, and R. W. Murray, *Langmuir* 16, 9699 (2000).
35. I. Quiros, M. Yamada, K. Kubo, J. Mizutani, M. Kurihara, and H. Nishihara, *Langmuir* 18, 1413 (2002).
36. L. Lu, H. Wang, S. Xi, and H. Zhang, *J. Mater. Chem.* 12, 156 (2002).
37. H. Hirai, N. Yakura, Y. Seta, and S. Hodoshima, *React. Funct. Polym.* 37, 121 (1998).
38. H. P. Choo, K. Y. Liew, and H. Liu, *J. Mater. Chem.* 12, 934 (2002).
39. T. Teranishi and M. Miyake, *Chem. Mater.* 10, 594 (1998).
40. A. Taleb, C. Petit, and M. P. Pileni, *Chem. Mater.* 9, 950 (1997).
41. A. Badia, W. Gao, S. Singh, L. Demers, L. Cuccia, and L. Reven, *Langmuir* 12, 1262 (1996).
42. K. Naka, M. Yaguchi, and Y. Chujo, *Chem. Mater.* 11, 849 (1999).
43. C. L. Lee, C. C. Wan, and Y. Y. Wang, *Adv. Funct. Mater.* 11, 344 (2000).
44. A. Miyazaki, I. Balint, K. I. Aika, and Y. Nakano, *J. Catal.* 204, 364 (2001).
45. X. Auvray, C. Petipas, A. Lattes, and I. RicoLattes, *Colloid Surf. A* 123, 247 (1997).
46. Q. S. Huo, D. I. Margolese, and G. D. Stucky, *Chem. Mater.* 8, 1147 (1996).
47. Y. Hendrikx and B. Pansu, *J. Phys. II* 6, 33 (1996).
48. C. L. Lee, C. C. Wan, and Y. Y. Wang (to be published).
49. C. C. Yang, C. C. Wan, and Y. Y. Wang (unpublished).
50. I. W. Lenggoro, B. Xia, and K. Okuyama, *Langmuir* 18, 4584 (2002).
51. S. Giorgio, C. R. Henry, C. Chapon, and J. M. Penisson, *J. Cryst. Growth* 100, 254 (1990).
52. J. A. Creighton and D. G. Eadon, *J. Chem. Soc. Faraday Trans.* 87, 3881 (1991).
53. P. Mulvaney, *Langmuir* 12, 788 (1996).
54. J. S. Bradley, E. W. Hill, S. Behal, and C. Klein, *Chem. Mater.* 4, 1234 (1992).
55. J. S. Bradley, G. H. Via, L. Bonneviot, and E. W. Hill, *Chem. Mater.* 8, 1895 (1996).
56. D. D. Caro and J. S. Bradley, *Langmuir* 13, 3067 (1997).
57. H. J. Wasserman and J. S. Vermaak, *Surface Sci.* 32, 168 (1972).
58. C. R. Berry, *Phys. Rev.* 88, 596 (1952).
59. C. Goyhenex, C. R. Henry, and J. Urban, *J. Philos. Mag. A* 69, 1073 (1994).
60. C. Kuhrt and R. Anton, *Thin Solid Films* 198, 301 (1991).
61. J. W. Jacobs and D. Schryvers, *J. Catal.* 103, 436 (1987).
62. R. Lamber, S. Wetjen, and N. I. Jaeger, *Phys. Rev. B* 51, 10986 (1995).
63. S. B. Ziemecki, G. A. Jones, D. G. Swartzfager, and R. L. Harlow, *J. Am. Chem. Soc.* 107, 4547 (1985).
64. T. Yonezawa, S. Y. Onoue, and T. Kunitake, *Adv. Mater.* 10, 414 (1998).
65. K. C. Grabar, K. R. Brown, C. D. Keating, S. J. Stranick, S. L. Tang, and M. J. Natan, *Anal. Chem.* 69, 471 (1997).
66. K. C. Grabar, K. J. Allison, B. E. Baker, R. M. Bright, K. R. Brown, R. G. Freeman, A. P. Fox, C. D. Keating, M. D. Musick, and M. J. Natan, *Langmuir* 12, 2353 (1996).
67. Y. Li, E. Boone, and M. A. El-Sayed, *Langmuir* 18, 4921 (2002).
68. J. L. Bars, U. Specht, J. S. Bradley, and D. G. Blackmond, *Langmuir* 15, 7621 (1999).
69. J. G. Ciebien, R. E. Cohen, and A. Duran, *Supramol. Sci.* 5, 31 (1998).
70. C. L. Lee, C. C. Wan, and Y. Y. Wang, *J. Electrochem. Soc.* (Mar. 2003).
71. Y. Li and A. El-Sayed, *J. Phys. Chem. B* 105, 8938 (2001).
72. T. Teranishi and M. Miyake, *Chem. Mater.* 10, 594 (1998).
73. L. Piccolo and C. R. Henry, *J. Mol. Catal. A: Chem.* 167, 181 (2001).
74. S. W. Kim, M. Kim, W. Y. Lee, and T. Hyeon, *J. Am. Chem. Soc.* 124, 7642 (2002).
75. M. B. Thathagar, J. Beckers, and G. Rothenberg, *J. Am. Chem. Soc.* 124, 11858 (2002).
76. R. L. Augustine and S. T. O'Leary, *J. Mol. Catal. A: Chem.* 95, 277 (1995).
77. J. S. Bradley, E. W. Hill, S. Behal, C. Klein, B. Chaudret, and A. Duteil, *Chem. Mater.* 4, 1234 (1992).
78. S. Klingelhöfer, W. Heitz, A. Greiner, S. Oestreich, S. Förlster, and M. Antoneitti, *J. Am. Chem. Soc.* 119, 10116 (1997).
79. M. T. Reetz and E. Westermann, *Angew. Chem. Int. Ed.* 39, 165 (2000).
80. H. Ohde, C. M. Wai, H. Kim, J. Kim, and M. Ohde, *J. Am. Chem. Soc.* 124, 4540 (2002).
81. Y. Nui, L. K. Yeung, and R. M. Crooks, *J. Am. Chem. Soc.* 123, 6840 (2001).
82. M. Zhao and R. M. Crooks, *Angew. Chem. Int. Ed.* 38, 364 (1999).
83. A. B. R. Mayer, J. E. Mark, and S. H. Hausner, *J. Appl. Polym. Sci.* 70, 1209 (1998).
84. S. D. Yosi, V. Dubin, and M. Angyal, *Thin Solid Films* 262, 93 (1995).
85. T. Osaka and H. Nagasak, *J. Electrochem. Soc.* 128, 1686 (1980).
86. M. Paunovic and M. Schlesinger, "Fundamentals of Electrochemical Deposition." Wiley, New York, 1998.
87. C. H. Yang, Y. Y. Wang, and C. C. Wan, *J. Electrochem. Soc.* 146, 4473 (1999).
88. C. R. Shipley, U.S. Patent 3,011,920, 1961.
89. A. J. Bard and L. R. Faulkner, "Electrochemical Methods." Wiley, New York, 2001.
90. M. L. Wu, D. H. Chen, and T. C. Huang, *Langmuir* 17, 3877 (2001).
91. M. Spiro and D. M. de Jesus, *Langmuir* 16, 2464 (2000).
92. D. M. de Jesus and M. Spiro, *Langmuir* 16, 4896 (2000).
93. K. Ebitani, K. M. Choi, T. Mizugaki, and K. Kaneda, *Langmuir* 18, 1849 (2002).
94. C. Nützenadel, A. Züttel, D. Chartouni, G. Schmid, and L. Schlappbach, *Eur. Phys. J. D* 8, 245 (2000).
95. J. N. Huiberts, R. Griessen, J. H. Rector, R. J. Wijnaarden, J. P. Dekker, D. G. deGroot, and N. J. Koeman, *Nature* 380, 231 (1996).
96. N. W. tari, S. Ohnishi, and Yishii, *J. Phys.: Cond. Matter* 12, 6799 (2000).





# Patterned Magnetic Nanostructures

Jian-Ping Wang

*University of Minnesota, Minneapolis, Minnesota, USA*

Tie-Jun Zhou

*Data Storage Institute, National University of Singapore, Singapore*

## CONTENTS

1. Introduction
  2. Magnetic Nanopatterning—Fabrication of Patterned Magnetic Nanostructures
  3. Applications of Patterned Magnetic Nanostructures
  4. Conclusion
- Glossary  
References

## 1. INTRODUCTION

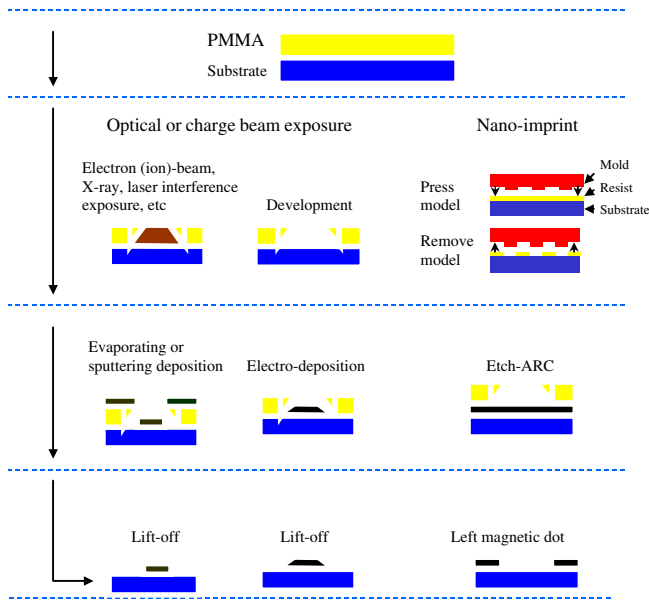
Patterned magnetic nanostructures and related magnetic quantum effects have been studied extensively, not only from a basic view point of understanding spin-electron quantum phenomena but also for various applications of ultra-high density magnetic recording [1–18] and new magnetic devices such as read heads, memory cells, magnetic sensors, magnetic logic elements, magnetic cellular automata, and so forth [19–32]. However, fabrication of patterned magnetic nanostructures is still a major challenge. To date, a lot of top-down methods have been used for producing patterned magnetic nanostructures with magnetic elements down to the nanometer scale [33–60]. Of all the top-down approaches, some of them can produce patterned magnetic nanostructures by one step, while others do this by a multistep process of resist coating, energy-beam exposure, etching, magnetic material deposition and liftoff, and so on. Some bottom-up methods of producing patterned magnetic nanostructures, including template growth [61–65] and mononanoparticle self-assembly [66–80], also have been developed. In this review, we will briefly describe traditional multistep lithography methods, and the single-step methods will be introduced in detail. Finally, the potential applications of patterned magnetic nanostructures for ultra-high density magnetic recording, new magnetic devices, and strong permanent magnets are briefly addressed.

## 2. MAGNETIC NANOPATTERNING— FABRICATION OF PATTERNED MAGNETIC NANOSTRUCTURES

Magnetic nanopatterning with the feature size down to deep submicron is beyond the reach of conventional optical lithography. Instead, a few multistep nanolithography techniques, which are combined with magnetic materials deposition and pattern transfer processes, have been used to pattern magnetic nanostructures. These methods include electron-beam lithography, X-ray lithography, nanoimprint lithography, and laser interference lithography, etc. Several single-step magnetic nanopatterning approaches also have been newly developed to simplify the patterning process and also for time and cost saving. Besides these lithography methods, bottom-up self-assembly methods also have been demonstrated by which magnetic particles are synthesized chemically or by ion-beam bombardment and are assembled as close-packed structures on a surface. Since magnetic nanopatterning technology and its application are not mature, a lot of efforts are still put on how to make patterned magnetic nanostructures efficiently with the smallest features and long-range order.

### 2.1. Multistep Magnetic Nanopatterning Approaches

A typical multistep magnetic nanopatterning process consists of four successive steps: (i) coating a substrate with an irradiation-sensitive polymer layer (resist); (ii) generating a desired pattern by exposing the resist layer to a charge beam (electron or ion) and optical light (laser or X-ray), followed by developing the resist image with a proper chemical solution, or by nanoimprint; (iii) depositing a magnetic layer into the template by evaporating, sputtering, or electrodepositing; and (iv) using the liftoff process to remove the resist from the substrate or by reactive ion etching to leave the magnetic dot on the substrate. The whole process is schematically illustrated in Figure 1.



**Figure 1.** Schematic fabrication step for making patterned magnetic nanostructures. The first step is the resist coating on substrate. The second step is the pattern generation by optical or charge beam exposure or by nanoimprint. The third step is the evaporating or sputtering a magnetic layer on the template. Alternatively, the magnetic layer also can be electrodeposited into template. The last step is liftoff process to remove the resist from the substrate or by etching to leave the magnetic dot on the substrate.

During the process, the pattern generation can be fulfilled by a few methods, including ion- or electron-beam lithography [19–22], X-ray or optical lithography [23–24], nanoimprint lithography [25–26], proximal probe lithography assisted by scanning probe microscopes, such as the scanning tunnel microscope and the atomic force microscope (AFM), or by the scanning near-field optical microscope [81–90]. Magnetic nanopatterning then can be accomplished by additive or subtractive processes [19–26]. In an additive process, magnetic material is deposited after patterning, for instance, by sputtering or evaporating a magnetic film over the pattern or by electrodeposition through holes in a lithographically prepared template, followed by the liftoff process to remove the resist on the substrate (Fig. 1). In a subtractive process, a magnetic layer is deposited firstly and then is etched. Based on the mask generated by the lithography process, various desired patterns can be formed after etching.

Electron-beam or ion-beam lithography has been the most widely used nanopatterning method for fabricating small magnetic structures with dimensions of 10 nm and above. Because the electron-beam writing process is a serial method, it is unsuitable for making large-area samples but has been used to pattern relatively small (submillimeter) areas with fine enough features. Triangle, rectangle, pentagon, ellipsoidal, and circular dot arrays, wires, rings, and other shapes of nanomagnetic elements have been made by evaporation or sputtering and liftoff [91, 92]. Ion-beam or electron-beam lithography is very convenient for making patterns of arbitrary geometry, but its throughput is very low so far, and, also, because of the stitching errors between the

different written fields, the long-range coherence of the pattern can be distorted when one wants to make a large-area pattern. However, recently developed projection electron-beam or ion-beam lithography may solve the low-throughput and long-range miscoherence problem.

X-ray lithography, laser interference lithography, and nanoimprint lithography are the other techniques that can pattern large-area samples. In X-ray lithography, a thin-membrane mask is placed in close proximity to a resist-coated substrate and is illuminated with soft X-rays of 0.5–4 nm wavelength. A typical mask consists of 2-micron-thick membrane of silicon carbide and absorber features of heavy metals such as Au, W, or Ta. In nanoimprint lithography, a rigid mold is used to physically deform a heated resist layer coated on a substrate. The mold can be made of metal or thermal silicon dioxide produced on a silicon substrate. The imprint can be carried out by applying a typical pressure of about 50 bar in the temperature of 100–200 °C depending on the resist used. This process has developed rapidly in the past few years. Features as small as 10-nm dots on a 40-nm period have been made by using evaporation and liftoff. The mold can be reused many times without damage. In both X-ray lithography and nanoimprint lithography, a mask or master mold must first be produced by using traditional lithography methods, but the large number of replications made from each mask or mold would justify this time-consuming step.

Interference lithography is a maskless method. In interference lithography, a resist layer is exposed by an interference pattern generated by two obliquely incident laser beams. After the development of the resist, lines are formed. The period of the pattern is given by  $\lambda/2 \sin \theta$ , where  $\theta$  is the half angle of intersection of the two laser beams, and  $\lambda$  is the laser wavelength exposure. Dot or hole array can simply be fabricated by a second exposure after rotating the substrate in the plane over  $\pm 90$  degrees. The minimum period of the pattern is just over  $\lambda/2$ , typically 180–200 nm, by using an Ar-ion laser. Interference lithography has been used to make a variety of dot or ellipse arrays from evaporated Ni, Co, or Co/Pt multilayers, pillar arrays from electroplated Ni or Co, and dots or ellipses etched from single-layer or multilayer sputtered films.

A probe tip direct writing also can fulfill magnetic nanopatterning. For example, material can be evaporated from a fine tip under pulsed voltage to form sub-100-nm-diameter pillars. Cobalt and iron particles of heights up to 200 nm and diameters of 10 nm and greater were made by the decomposition of cobalt and iron pentacarbonyl under a probe tip in a chemical vapor deposition process. Although these methods are relatively slow, they allow tall structures to be made in precise locations on a substrate.

## 2.2. Single-Step Magnetic Nanopatterning Approaches

Besides the multistep nanopatterning methods, a few single-step magnetic nanopatterning approaches, which include electron-beam radiation induced nanoscale magnetic phase change [93–97] and direct interferometric laser annealing [98–104], anisotropy patterning [105–115], magnetization patterning [116–117], laser-assisted direct imprint

[118, 119], ion-beam-induced chemical vapor deposition (IBICVD) [120–125], and ion projection direct patterning [126] also have been newly developed to simplify the patterning process.

### 2.2.1. Electron-Beam-Radiation-Induced Nanoscale Magnetic Phase Change

Zhou et al. [93–97] proposed and demonstrated a novel method of direct magnetically nanopatterning a non- or weak-magnetic thin film by electron-beam radiation-induced nanoscale magnetic phase change. This is a simple single-step magnetic nanopatterning method. Firstly, a non- or weak-magnetic film (amorphous CoC or CoZr alloy films), which can be converted into a magnetic state upon annealing, is deposited. Then, the film is subjected to a focused electron-beam radiation to locally heat the irradiated region. The temperature of the irradiated region will rise. Under the proper condition, the region will undergo magnetic phase change to a magnetic state, as the whole film does after annealing. All kinds of nanostructured patterns can be produced easily by this method. So far, nanoscale dot and line array have been fabricated by using this method. Examples of the magnetic dot array and line array are shown in Figure 2.

With this method, the magnetic dots or lines are produced through a magnetic phase change. This phase change from nonmagnetic status to magnetic status is a kinetic process, which occurs under certain conditions and also takes time. This is the reason why the shorter dwell time per dot (0.95 and 1.9 sec) could not induce a magnetic phase change in the irradiated area.

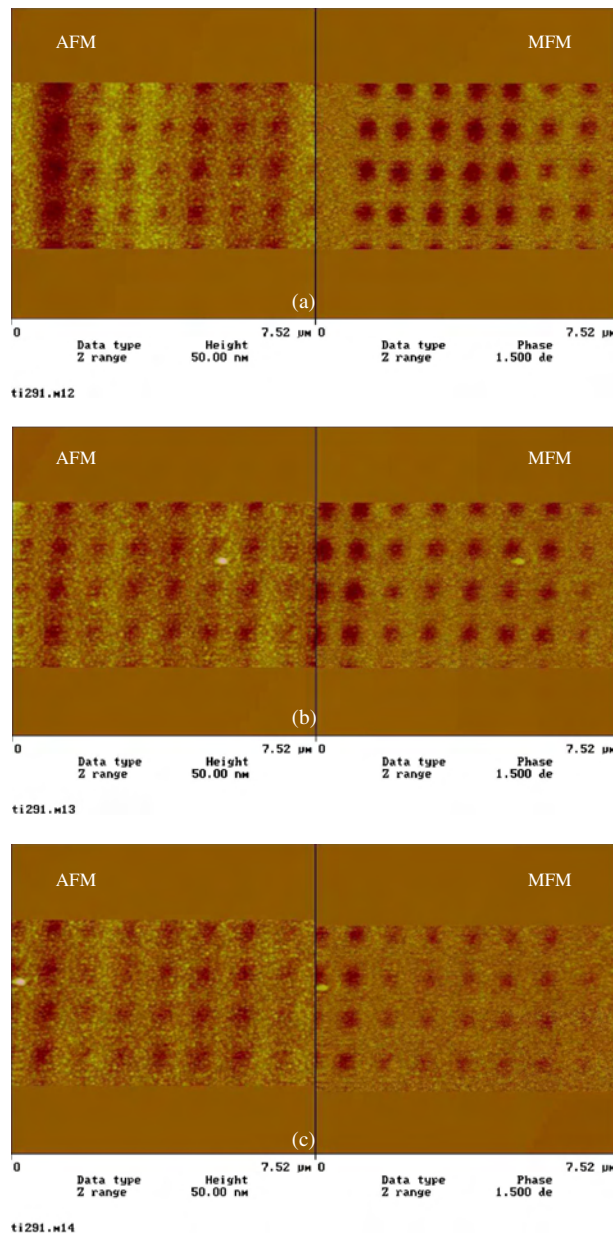
When the as-deposited nonmagnetic films were subjected to electron-beam radiation, primary electrons penetrate the films and undergo scattering, and produce secondary electrons. As the primary electrons slow down continuously, some of their energy transfers into the film. The transferred energy is absorbed partly by the film. Once the film absorbs some energy, thermal diffusion occurs within the film. Because of the thermal diffusion, the phase change occurs not only in the irradiated area. One can expect that the phase change takes place within the scale of thermal diffusion length  $L_{ex}$ , which is described by:

$$L_{ex} \propto \sqrt{kt},$$

where  $t$  is the beam dwell time per dot and  $k$  is the thermal conductivity of the film [127–128]. This means that the thermal diffusion length rather than the electron beam size determines the magnetic dot size produced by such method. This is the reason why we observed that the magnetic dot diameter increases linearly with the square root of dwell time per dot (Fig. 3). By fitting the experimental data, the slope of magnetic dot size divided by the square root of dwell time can be obtained, and the thermal conductivity of the film can be calculated out.

Presently, the magnetic properties of such fabricated patterns are somewhat poor. The  $H_c$  is only about 75 Oe, indicating that the dots are magnetically soft. When using a magnetized MFM (MFM) tip to measure the MFM images, the field produced by the MFM tip can magnetize regions

that have undergone a phase change, since they are magnetically soft, whereas the MFM tip did not interact with regions that did not undergo a phase change. These give rise to the MFM contrast, consisting of dark regions (due to



**Figure 2.** Examples of the magnetic dot (a–c) and line (d–e) array and line arrays. (a) AFM and MFM images of the fabricated dot array with dwell time of 15.2 and 7.6 sec per dot for the first five and last two columns, respectively; (b) AFM and MFM images of the fabricated dot array with dwell time of 15.2, 7.6, and 3.8 sec per dot for the first two, second five, and last one columns, respectively; (c) AFM and MFM images of the fabricated dot array with dwell time of 7.6, 3.8, and 1.9 sec per dot for the first two, second five, and last one columns, respectively; (d) AFM and MFM images of the fabricated line array with dwell time of 1.9 and 0.95 sec per pixel for the first three and last seven columns, respectively; and (e) AFM and MFM images of the fabricated line array with dwell time of 4 and 2 sec per pixel for the first six and last five columns, respectively.

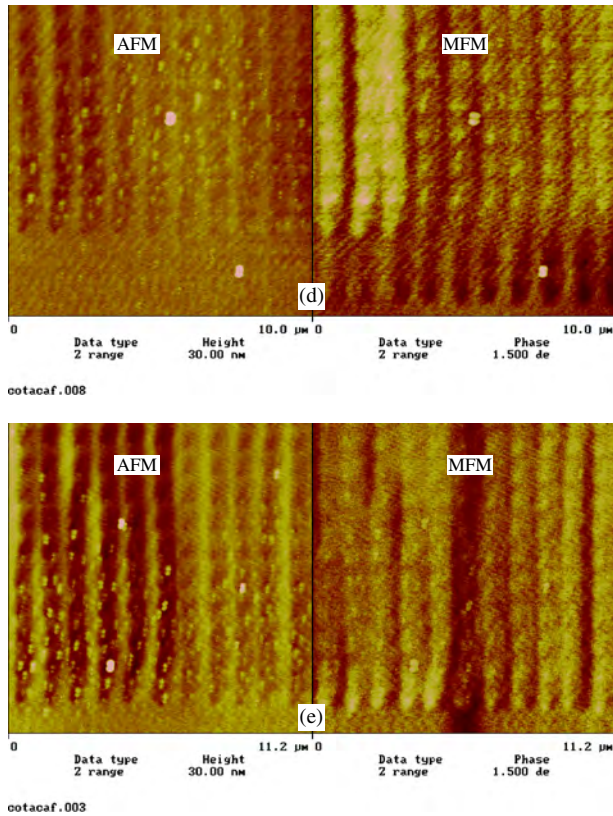


Figure 2. Continued.

the attractive magnetic force) embedded in a bright matrix (nonmagnetic).

The present single-step nanolithography eliminates the cumbersome traditional processes and is potentially a new and flexible alternative for fabricating patterned magnetic nanostructures for ultrahigh density magnetic recording and various magnetic devices.

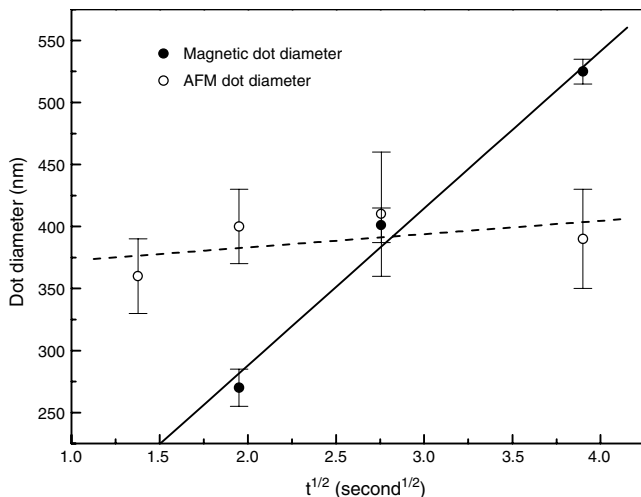


Figure 3. Time dependence of AFM (open circle) and magnetic (solid circle) dot size. Reprinted with permission from [94], T. J. Zhou et al., *IEEE Trans. Magn.* 38, 1970 (2002). © 2002, IEEE.

### 2.2.2. Direct Interferometric Laser Annealing

Zheng et al. reported an approach to magnetic nanopatterning by direct laser interference annealing, which can produce 2-dimensional (2D) hexagonal dot arrays with a dot size around 250 nm [98–102]. This also is a single-step magnetic nanopatterning method. Firstly, nonmagnetic CoC films with a thickness of 40 nm were deposited onto a water-cooled glass substrate. Then the sputtered films were exposed to a 10-ns-pulsed excimer laser having a wavelength of 308 nm and a flux of 0.17 J/cm<sup>2</sup>. The laser beam was split into two beams of an approximately equal intensity, and then were recombined, generating an interference pattern and a periodic modulation of the light intensity. The interference of the four beams leads to the formation of 2D arrays of modified regions, having a minimum lattice periodicity equal to half of the radiation wavelength. The size and shape of the regions depend on the incident angles of the beam, on the pulse duration, and on the flux. Examples of the magnetic dot array are shown in Figure 4.

With this method, the magnetic nanopatterning is attributed to the phase separation or precipitation of Co under local heating at the laser intensity maxima (also magnetic phase change) [129–131]. The as-deposited Co–C film actually contains some Co-rich nanoclusters that are superparamagnetic at room temperature. After laser local annealing, local atomic rearrangements will occur, and more strongly interacting magnetic Co or Co-rich clusters are formed or Co clusters grow bigger, to become a magnetic state in room temperature and yield the observed magnetic phase at room temperature. This method holds the promise to make a big-area pattern quickly and economically but has the drawback of low resolution and low flexibility, and also is limited only to patterns with a linear alignment.

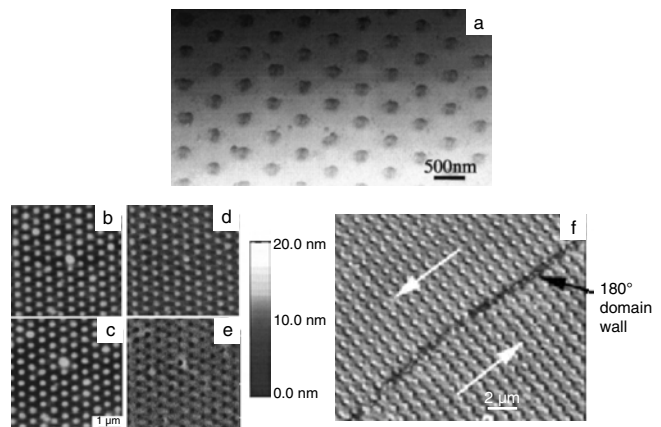


Figure 4. Examples of the magnetic dot array. (a) TEM image of periodic arrays of patterned Co–C films, (b) and (c) AFM and (d) and (e) MFM images of a periodic array of patterned Co–C films after exposing the film to interference laser and a perpendicular field of 1700 Oe was applied parallel (d) and antiparallel (e) to the film-plane normal during scan. (f) MFM image of the patterned Co–C film under higher laser power. Reprinted with permission from [99 and 100], M. Zheng et al., *IEEE Trans. Magn.* 37, 2070 (2001) and M. Zheng et al., *Appl. Phys. Lett.* 79, 2606 (2001). © 2001, IEEE and AIP respectively.

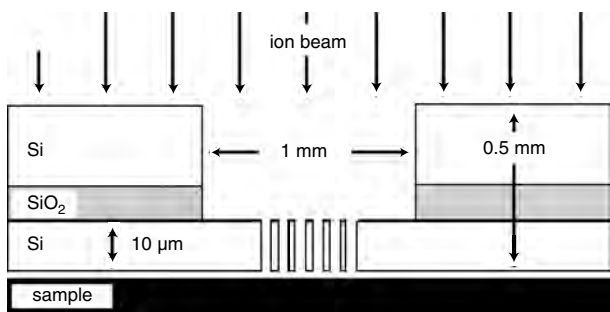
### 2.2.3. Anisotropy Engineering

Ion-beam irradiation has been shown to be an effective way to alter the magnetic properties of thin multilayer films by roughening the interface or by mixing. Chappert et al. [105, 107–115] reported an alternative of planar patterning a magnetic media by ion-beam-radiation-induced change of magnetic anisotropy of (Co/Pt) multilayer film, and this was further developed by Terris et al. [106] by using a stencil masks. Figure 5 illustrates the schematic of an ion-beam patterning on a Co/Pt multiplayer film through a silicon stencil mask.

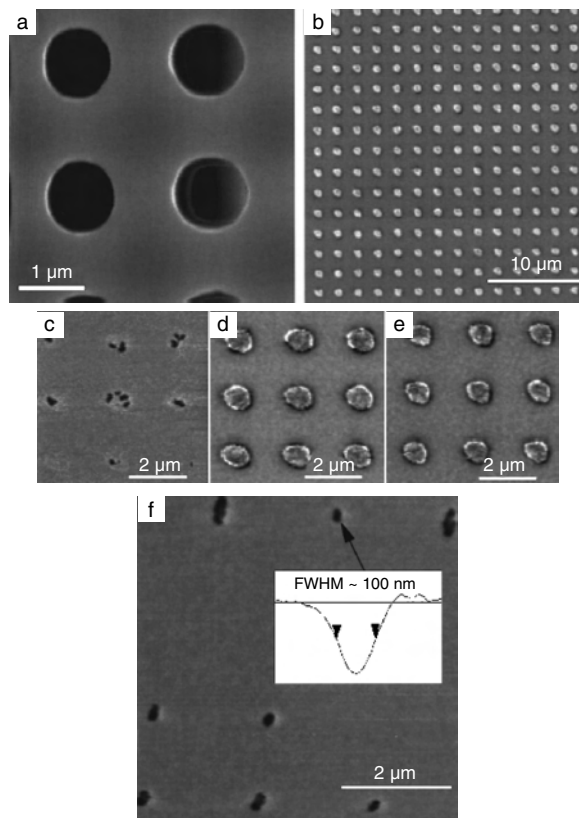
To pattern the film, a mask is placed on it and then the mask-covered films are bombarded with an ion beam. Because of the mask-effect, only those portions through which the ions pass will undergo anisotropy change (from out-of-plane to in-plane) by ion-beam induced mixing of interfaces, but this does not affect the parts of the film that are hidden from the radiation by the mask shadow. Thus an array of magnetic elements with a much smaller coercive force and in-plane anisotropy in a magnetic matrix with perpendicular anisotropy is produced. The size of each soft magnetic element is dependent on the resolution of the mask. Examples of the magnetic dot array are shown in Figure 6.

With this method, the magnetic media is patterned into areas with vastly different magnetic characteristics by ion-beam mixing, but the required dose is quite high, and the mask lifetime also is a concern. Additionally, since the coercive field of irradiated area is very low and are inappropriate for magnetic recording purposes. The magnetic contrast between irradiated and nonirradiated areas needs to be maximized, while the topographic variations caused by the ions need to be minimized by the judicious choice of substrate, ions species, and ion energy. However, this technique holds promise for ultra-high-density magnetic recording applications if magnetic properties of the irradiated areas can be improved.

Anisotropy also can be engineered to be out-of-plane and in-plane alternatively by using selective epitaxial growth. Li et al. [132, 133] reported an approach to anisotropy patterning by using selective epitaxial growth. In this method, a modulated single/polycrystalline substrate surface to modify locally the magnetic anisotropy in subsequently deposited magnetic films, which induces the desired artificial magnetic



**Figure 5.** Schematic of ion-beam patterning a Co/Pt multiplayer through a silicon stencil mask. Reprinted with permission from [106], B. D. Terris et al., *Appl. Phys. Lett.* 75, 403 (1999). © 1999, American Institute of Physics.

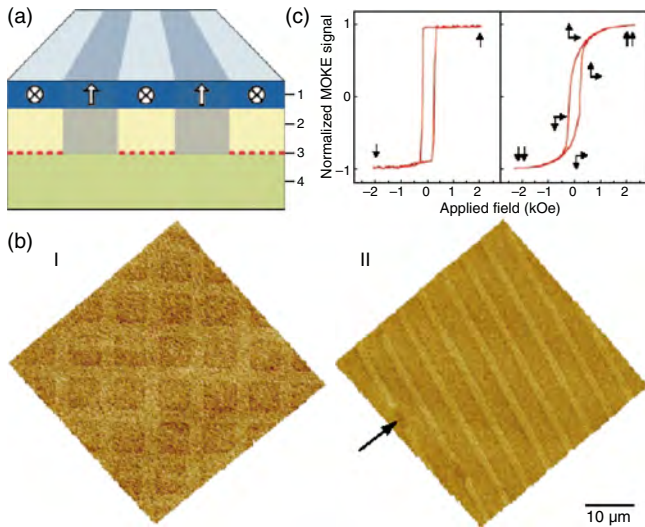


**Figure 6.** Examples of the magnetic dot array produced by ion-beam mixing. (a) is SEM image of an area of a mask with 1- $\mu\text{m}$ -dia. holes at 2-mm pitch. (b) is MFM image showing the magnetic contrast that arises from the ion-beam patterning. (c), (d), and (e) are MFM images of Co/Pt multilayers (14 periods of 4 Å Co and 10 Å Pt deposited on fused silica) of irradiated with  $10^{15}$ ,  $5 \times 10^{15}$ , and  $10^{16}$  ions/cm<sup>2</sup> of 700 keV N<sup>+</sup> ions, respectively, and the circular regions were formed by irradiating the sample through a silicon stencil mask with 1-mm-dia. holes on a 2-mm pitch. Reprinted with permission from [106], B. D. Terris et al., *Appl. Phys. Lett.* 75, 403 (1999). © 1999, American Institute of Physics.

structure. Selective epitaxial growth introduces an alternation between single-crystal and polycrystalline structures in the film, according to the substrate patterning (Fig. 7a). Ni/Cu(001) films with appropriate thickness show perpendicular magnetization, which is due to the magneto-elastic interaction induced by the Ni/Cu(001) interface [134]. In contrast, the magnetization of polycrystalline nickel lies in the film plane because of the dominant demagnetizing field. This magnetic anisotropy patterning opens up new avenues for controlling the spin structure of magnetic materials within the nanometer scale. The simulation results show that the patterned bit resolution can be smaller than 30 nm. Such modulated structures can be used as patterned magnetic media either perpendicularly or longitudinally. Figure 7 shows the pattern produced by using this method.

### 2.2.4. Magnetization Patterning

Terris et al. reported that magnetic nanopatterning also could be fulfilled by magnetization patterning in one step [116–117]. It is found that magnetic properties of CoCrPt

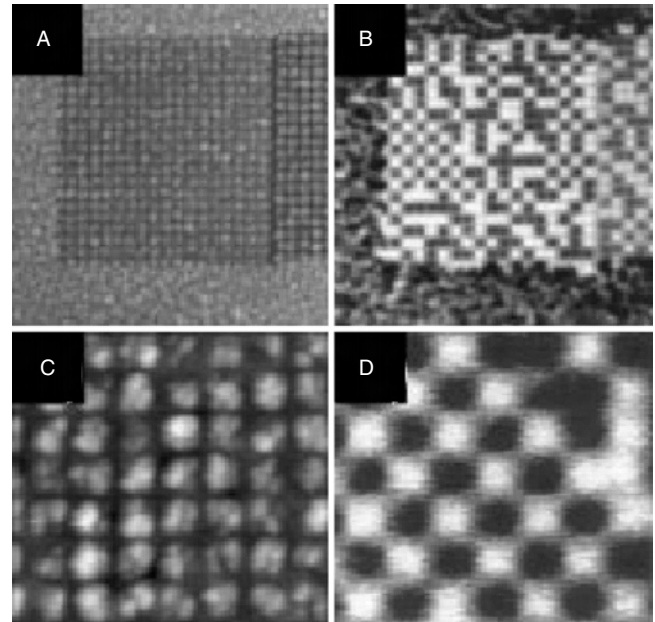


**Figure 7.** Selective epitaxy in spin engineering and magnetic characterization. (a) Selective epitaxial growth of Cu/Ni/Cu/Co structure. Layer 1, magnetic layer of nickel; symbols: crosses, magnetization in the plane of the film; arrows: magnetization perpendicular to the film. Layer 2, Cu/Co underlayer. Ultrathin NiO was used as the embedded template (layer 3) on a GaAs(001) substrate (layer 4). The wire arrays are  $2\ \mu\text{m}$  wide and separated by  $4\ \mu\text{m}$ ; the square dots are  $7 \times 7\ \mu\text{m}^2$  and are separated by  $3\ \mu\text{m}$ . (b) MFM images of the dot (I) and wire (II) samples in zero field after perpendicular field saturation. Arrow indicates a switch of the perpendicular Ni induced by the external stray field of the MFM tip. (c) Polar magneto-optic Kerr-effect hysteresis loops for the unpatterned reference sample (left panel) and the wire sample (right panel). Solid and dotted arrows indicate the magnetization orientation in the epitaxial and polycrystalline regions, respectively, of the Ni film. Reprinted with permission from [132], S. P. Li et al., *Nature* 415, 601 (2002). © 2002, Macmillan Magazines Ltd.

films with perpendicular anisotropy can be changed by ion-beam irradiation. Figure 8 shows the hysteresis loops of CoCrPt measured by Kerr rotation as a function of an irradiated  $\text{Ga}^+$  dose. It is clear that the coercivity drops with the dose, as does the remanent magnetization. Under the proper dose, the coercivity and remanence will vanish. With this method, a focused ion beam (FIB) is used to machine a grid pattern into thin-film CoCrPt media to leave isolated magnetic islands. The cuts were made by moving the beam in 5 nm steps to cover the desired grid. To ensure a regular period, the patterns were cut by repeated sweeps, rather than by making a single pass. Examples of such a produced dot array are shown in Figure 8.

Writing and reading on such produced media also were done with much better recording performance compared with unpatterned media [135–137].

The chemically ordered  $\text{CrPt}_3$  with  $\text{L1}_2$  ( $\text{Cu}_3\text{Au}$ ) phase (the Cr atoms site at the corners and Pt atoms at the faces of a unit cell) also can be magnetically patterned by using magnetization patterning [138–142]. Neutron diffraction studies of magnetic measurements have shown that chemically ordered  $\text{CrPt}_3$  is ferrimagnetic, with localized moments of 2.33 and  $-0.27\ \text{m}$  for Cr and Pt, respectively. The chemically disordered  $\text{CrPt}_3$ , which is nonmagnetic, is structurally face-centered cubic (fcc) and the sites are randomly substituted. Hellwig et al. found that ion irradiation can locally

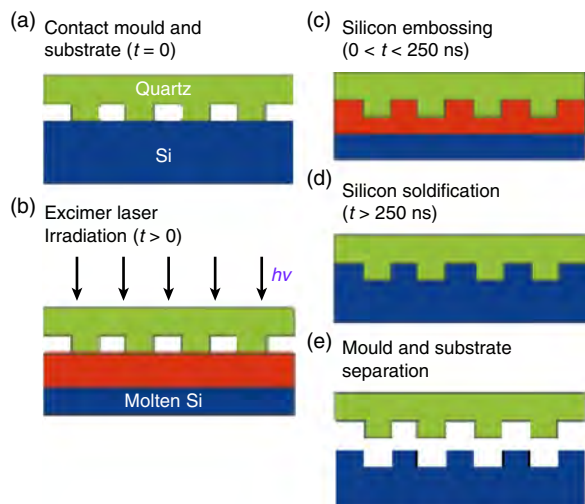


**Figure 8.** AFM and MFM images of a  $2\ \mu\text{m} \times 2\ \mu\text{m}$  patterned region are shown in (a) and (b), respectively, along with higher magnification images of small regions in (c) and (d), respectively. The pattern period is  $\sim 100\ \text{nm}$ . This pattern was made with a 60 sec exposure to a 1 pA 30 keV beam. Reprinted with permission from [116], C. T. Rettner et al. *IEEE Trans. Magn.* 37, 1649 (2001). © 2001, IEEE.

transform chemically ordered  $\text{CrPt}_3$  into the chemically disordered fcc phase. This suppresses the ferrimagnetism and thus provides a mechanism for patterning magnetic and non-magnetic regions within a magnetic film.

### 2.2.5. Laser-Assisted Direct Imprint

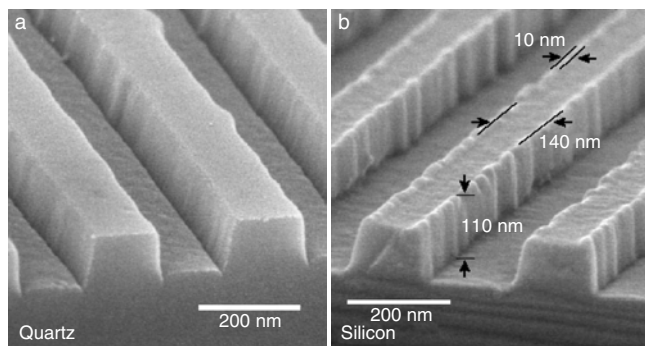
Chou et al. [118] reported one ultrafast approach to nanopatterning by direct imprint of nanostructures. With this method, a single XeCl excimer laser pulse (308 nm wavelength and 20 ns pulse duration) passes through a quartz mold (which does not absorb the laser energy because it has a bandgap larger than the photon energy) and melts a thin surface layer of the silicon substrate within picoseconds [118, 119]. The molten silicon layer (which can be about 300 nm deep and remain molten for hundreds of nanoseconds) is then embossed by the quartz mold. After the liquid silicon solidifies, the mold is separated from the imprinted silicon for the next imprint. Figure 9 shows the process schematically. Chou et al. created features of 140-nm dimension (the limit of their mask). But detail at the level of 10 nm on these features also was replicated, indicating the extraordinary resolution of the process. This technique also can be used for patterning polycrystalline films of silicon, one of the most critical steps in patterning silicon chips. Because there is no need for expensive focusing optics, the printing equipment is much simpler than a stepper. And the absence of a resist eliminates the cost. The nanostructures fabricated by using this method, as an example, are shown in Figure 10. After direct imprinting, magnetic films can be deposited into the template to form patterned magnetic nanostructures.



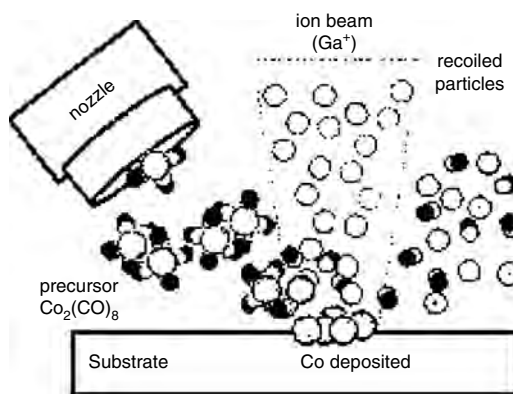
**Figure 9.** Schematic of the process. (a) A quartz mold is brought into contact with the silicon substrate. A force presses the mold against the substrate. (b) A single XeCl (308 nm wavelength) excimer laser pulse (20 nm pulse width) melts a thin surface layer of Si. (c) The molten silicon is embossed, while the silicon is in the liquid phase. (d) The silicon rapidly solidifies. (e) The mold and silicon substrate are separated, leaving a negative profile of the mold patterned in the silicon. Reprinted with permission from [118], S. Y. Chou et al. *Nature*, 417, 802 (2002). © 2002, Macmillan Magazines Ltd.

### 2.2.6. Ion-Beam-Induced Chemical Vapor Deposition

Fabrication of magnetic dot arrays by IBICVD was proposed and demonstrated by Lapicki et al. [120, 121, 123]. The principle of the method is illustrated in Figure 11 [120]. It is dependent on the energy and momentum exchange between incident ions and molecules of a precursor suitable for the metal of interest (Fe, Co, Ni, etc.). Collisionally induced decomposition of the precursor occurs near the substrate surface, and it is followed by dynamic deposition of the metal into top layers of the substrate. Dot arrays of alloys and compounds, such as FeNi, FeCo, FePt, CoPt, SmCo<sub>5</sub>, which have potential applications in data storage and information processing, can be produced by introducing two or



**Figure 10.** SEM image of the cross section of samples patterned by using LADI. (a) A quartz mold. (b) Imprinted patterns in silicon. The imprinted silicon grating is 140 nm wide, 110 nm deep, and has a 300-nm period, an inverse of the mold. Reprinted with permission from [118], S. Y. Chou et al. *Nature*, 417, 802 (2002). © 2002, Macmillan Magazines Ltd.



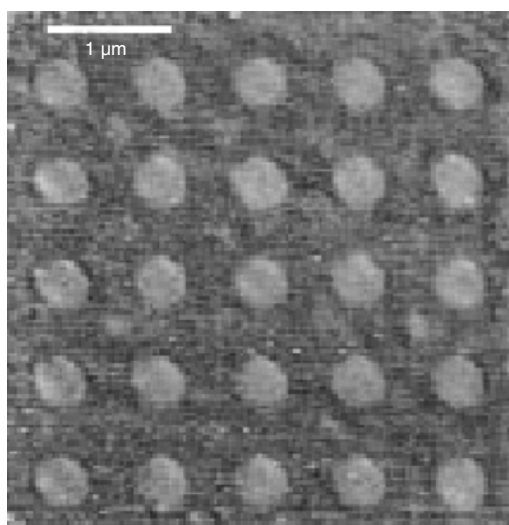
**Figure 11.** Scheme of IBICVD experiments. Reprinted with permission from [120], A. Lapicki et al., *IEEE Trans. Magn.* 38, 2589 (2002). © 2002, IEEE.

more precursors. Figure 12 shows the cobalt dot arrays fabricated by IBICVD on a glassy carbon substrate, and this is an *in-situ* imaging by secondary electron microscopy of the FIB system.

Such fabricated dots are rather flat and are partially embedded in the substrate layer, and post annealing usually is needed to obtain better magnetic properties. Although this method is best suitable for the laboratory scale, it has its analog among projection schemes, which can produce a large enough area for practical usage.

### 2.2.7. Ion Projection Direct Patterning of Magnetic Nanostructures

Ion-beam irradiation has been demonstrated to be an effective way to modify the magnetic properties of Co–Pt multilayers with strong perpendicular magnetic anisotropy, and patterning of magnetic nanostructures can be fulfilled by local ion-beam exposure-induced mixing. However, focused



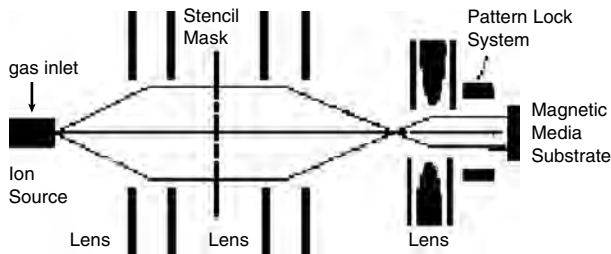
**Figure 12.** Cobalt dots fabricated by IBICVD on glassy carbon. *In-situ* imaging by secondary electron microscopy of the FIB system. Reprinted with permission from [120], A. Lapicki et al., *IEEE Trans. Magn.* 38, 2589 (2002). © 2002, IEEE.



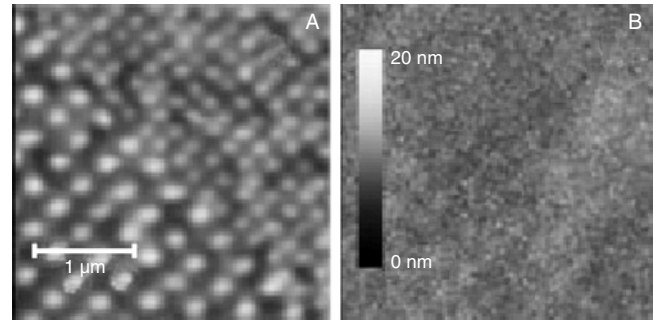
ion-beam direct writing is too slow to be of practical usage. Ion-projection direct structuring (IPDS), as sketched in Figure 13, was proposed and demonstrated by Dietzel et al. [126]. This method facilitates a large-area patterning process, which potentially is of commercial use for manufacturing future magnetic storage media. The structures required for reading and writing on spinning disks in hard-disk drives (HDD), including bit cells in a circular arrangement and servo (head positioning) structures, can be integrated in a single stencil mask. By IPDS, the stencil mask patterns can be transferred into the magnetic medium at a given demagnification factor, which relaxes the resolution requirements for the stencil mask process.

By IPDS, at  $8.7\times$  demagnification, the smallest mask openings currently available in the mask test structures could be successfully transferred into a magnetic pattern, as shown in Figure 14. The nominal feature size can be deduced from the dimensions of square mask openings and the projector demagnification factor as  $57\text{ nm} \times 57\text{ nm}$ . Figure 14(a) confirms dot diameters of less than  $100\text{ nm}$ . Potential reasons for the observed widening and rounding in the MFM images are the following: blur in the ion optics, magnetic-coupling phenomena, and, to some degree, MFM resolution. A second type of deviation from the geometrically projected array of mask openings is that some of the islands, especially in the denser pattern, are slightly shifted from their regular position. This can be attributed to local charging effects in the masks as presently used for the experiments. The unmodified surface roughness observed after exposure by means of AFM (Fig. 14b) confirms that IPDS is compliant with requirements regarding the surface quality of magnetic storage media.

Ion projection facilitates a direct structuring, which is an attractive potential manufacturing process for patterned storage media. In contrast to conventional resist processes or direct-contact printing techniques, this is a noncontact process, and the surface quality of the as-grown storage media is preserved. Nevertheless, further work, including improvements in mask technology, material development, and adaptation of the ion projector to the some specific requirements,



**Figure 13.** Sketch of the IPDS technique. Ions are generated in a gas ion source and a broad ion-beam illuminates the stencil mask. A demagnified image of the stencil mask is projected onto the ion-sensitive magnetic medium. The ion energy at the stencil mask is lower than the ion energy at the magnetic medium and the medium surface is at significant distance from the stencil mask. A pattern lock system can compensate for a drift of the image parameters such as linear drift, rotational drift, and magnification shift. Reprinted with permission from [126], A. Dietzel et al., *IEEE Trans. Magn.* 38, 1952 (2002). © 2002, IEEE.



**Figure 14.** (a) MFM analysis of a Co-Pt ML sample exposed through a stencil mask with  $3\times 10^6\text{ Xe/cm}$ . The upper right part corresponds to a Cartesian configuration of  $0.5\text{-}\mu\text{m}$ -wide square mask openings. The image was taken after fully magnetizing the sample with an external field of  $1.4\times 10^6\text{ A/m}$  and subsequently counter-magnetizing the irradiated islands by applying a field of  $0.4\times 10^6\text{ A/m}$  in opposite direction. (b) AFM analysis of the same area. From this scan, a surface roughness (rms value) of  $1.1\text{ nm}$  is determined. Reprinted with permission from [126], A. Dietzel et al., *IEEE Trans. Magn.* 38, 1952 (2002). © 2002, IEEE.

have to be carried out to demonstrate the application of IPDS for patterned magnetic media with areal densities well beyond  $15\text{ Gbit/cm}^2$  ( $100\text{ Gbit/in}^2$ ).

### 2.3. Template Growth Approach

There are two main methods that have been developed for making arrays of magnetic particles with using self-organized templates. One is the use of anodized alumina films with ordered and variable-sized holes as templates for electrodeposition [61–65]. The anodized alumina films or foils have an oxide layer that contains a close-packed arrangement of fine holes, with the hole spacing and size controlled by anodization conditions such as voltage, current density, or pH value, and a subsequent pore-widening process. The magnetic materials, such as cobalt, nickel, iron, alloys, can be deposited electrically into the holes to form patterned magnetic nanostructures. This method is well suited to the fabrication of arrays of longer nanowires with lengths of microns or more.

The other is self-assembled block copolymers with various geometries as a template to grow patterned magnetic nanostructures [143–158]. A block copolymer consists of chains of two chemically distinct, immiscible monomers, A and B, joined together to form a polymer  $\text{An-Bm}$ . Self-organized copolymers are spun onto a substrate to form copolymer films followed by selectively removing one domain to form a template. The template can be used to grow patterned magnetic nanostructures as anodized aluminum films do.

The drawback of these template methods is that the structures typically are lacking long-range order, even though the short-range order is good. By combination with traditional lithography, the long-range order could be improved. Alternatively, by growth in a field, to align the self-assembled structure over large distances, the long-range ordering also can be improved. These combined processes are still in the early stages of exploration.

## 2.4. Self-Assembly Approach

There are various approaches to self-assemble magnetic nanostructures. The first, which is widely used, is the wet self-assembly (chemical route) [66–80]. The other, which is far from mature, is the dry self-assembly by ion-beam bombardment [159, 160], cluster deposition [161–169], and thermal deposition [170–174].

### 2.4.1. Wet Self-Assembly

For wet self-assembly (chemical route), monodispersed magnetic nanoparticles are needed. The monodispersed nanoparticles can be synthesized by a few chemical ways, such as sol-gel or coprecipitation, and then are assembled on a surface to form a regular array without the need for lithography. This has the potential for making very-fine-scale structures over large areas in a rapid process and thus has attracted considerable attention. Structures with a period of less than 10 nm and a particle size around 3 nm can be made, and so tiny a feature is beyond that of traditional lithography techniques. An example of such a produced FePt dot array is shown in Figure 15.

The challenge for this method is that it is not easy to control the size distribution of the particles to obtain uniform properties. The second problem is that the long-range ordering is poor, although the short-range ordering is quite good. For this method, the ordering is very good at keeping within several microns, and in combination with lithography, this could be a way to overcome the short-range ordering.

Many other methods to grow nanoparticles besides chemical synthesis, have been developed including vapor phase growth by sputtering, laser ablation, arc discharge, and so forth. These methods typically produce a distribution of sizes from which highly monodisperse samples can be made by size-selective precipitation.

### 2.4.2. Dry Self-Assembly

Chen et al. [159] demonstrated that patterned magnetic nanostructures can be fabricated by depositing perpendicular magnetic films on self-assembled surfaces by ion-beam

bombardment. By this method, the magnetic nanopatterning is realized by two steps. Firstly, by ion-beam bombardment, a self-assembled surface is formed, and then by depositing magnetic films on the patterned surface to form patterned magnetic nanostructures.

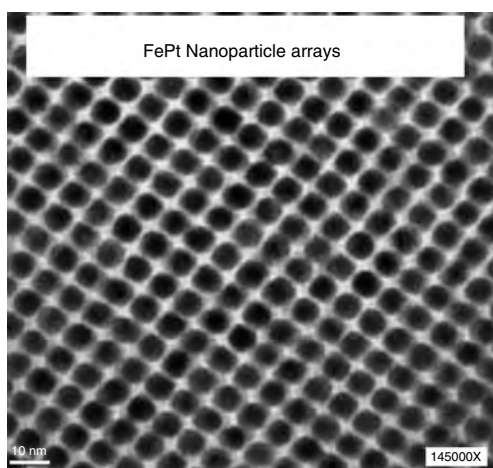
Chen et al. used a commercial broad ion-beam source with good uniformity (beam-current density better than  $\pm 5\%$  within the bombarded area) to bombard epitaxial GaSb(100) substrate surfaces. Ion-beam bombardment was carried out with  $\text{Ar}^+$  (420 eV) ions under normal incidence at a beam current density of  $\sim 0.4 \text{ mA/cm}^2$  (i.e., a flux of  $\sim 2.5 \times 10^{15}$  ions/cm<sup>2</sup> s) and a dosage of  $\sim 6 \times 10^{18}$  ions/cm<sup>2</sup>. Then perpendicular magnetic Co/Pd multilayer films with a  $\sim 2.5$  nm NiP seedlayer are deposited on the bombarded substrate surfaces to form patterned magnetic nanostructures. The mechanism of forming a patterned surface is due to the interplay between roughening due to the sputtering and smoothing because of a surface diffusion-viscous flow. Examples of such a patterned surface and magnetic nanopatterning are shown in Figure 16.

Further processing steps, such as etching or polishing, are needed to isolate the magnetic elements from each other to make ultrahigh-density magnetic storage media.

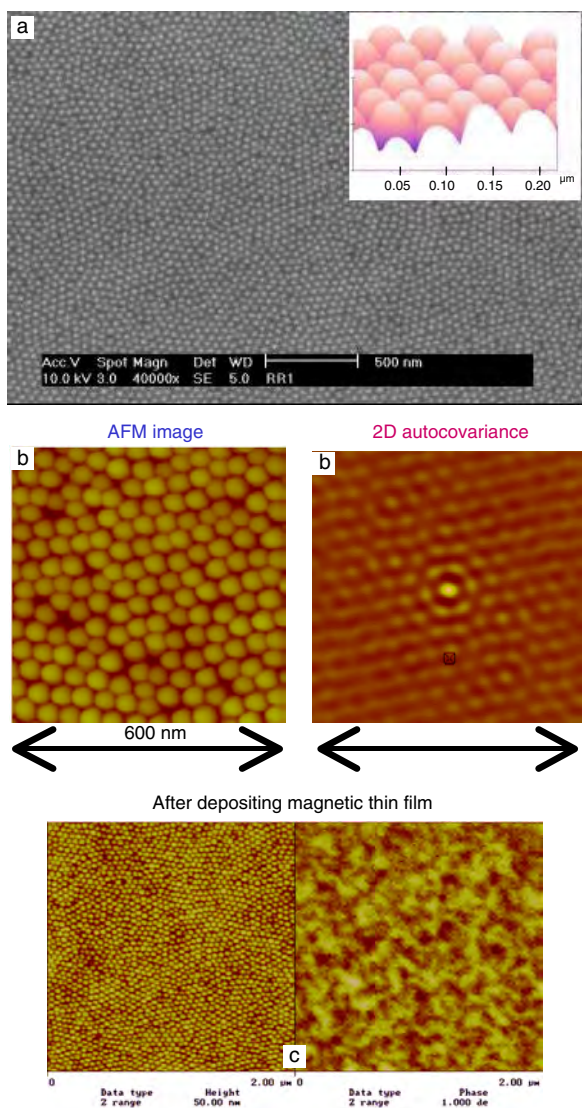
Two-dimensional superlattice of molecularly linked metal clusters is another approach to magnetic nanopatterning via dry self-assembly [161]. Andres et al. reported on a process that uses molecular self-assembly to fabricate a 2D superlattice of uniform metal nanocrystals linked by organic interconnects [161–169, 175, 176].

There are four steps involved in the synthesis of a linked cluster network (LCN): (i) synthesis of ultrafine metal crystals with uniform diameters in the nanometer range, (ii) adsorption of a self-assembled monolayer of organic surfactant on the surface of these particles to produce stable macromolecular entities that can be manipulated, (iii) formation of a close-packed monolayer film of these coated particles on a solid substrate, and (iv) displacement of the organic surfactant with a molecular interconnect that covalently bonds adjacent particles to each other without destroying the order in the monolayer film. This method is quite general with respect to the choice of metal, surfactant, and interconnect. If conductive and nonmagnetic metals (Au, Cu, etc.) are selected, the fabricated LCN can be used for nanoscale electronic devices, such as single-electron transistor. If magnetic metals or alloys are chosen, the produced LCN can be used for magnetic data storage and information processing. For the magnetic nanopatterning, the fourth step may not be needed as it is not necessary to bond the adjacent particles to each other covalently.

Figure 17 shows a schematic of the gas-phase cluster source that was used by Andres et al. in their study (Au was used in the study as an example). Au clusters with a controlled mean diameter in the range from 1 to 20 nm and a size distribution characterized by a full-width at half-maximum of 0.5 nm at the low end of this range and 5 nm at the high end have been synthesized in this source at total production rates of 100 mg per h. In order to assure that all of the clusters are single crystals, a dilute aerosol stream of clusters suspended in inert gas is passed through a meter-long tube in which the clusters are first heated to be crystallized and then cooled to room temperature. Then the

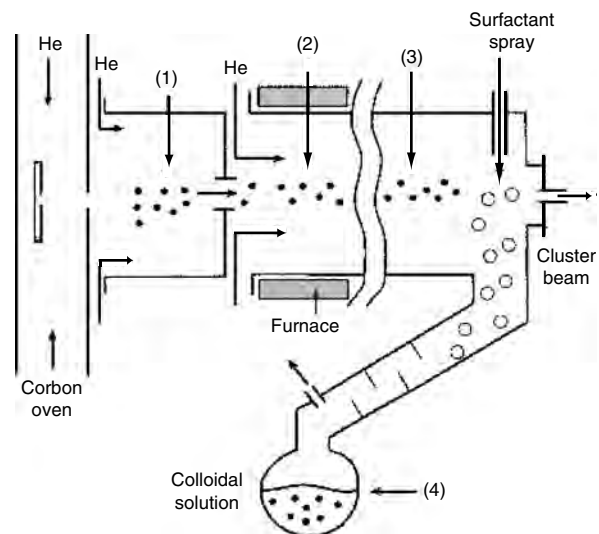


**Figure 15.** FePt dot array produced by wet self-assembly. Reprinted with permission from [67], S. H. Sun et al., *Science* 287, 1989 (2000). © 2002, American Association for the Advancement of Science.



**Figure 16.** Examples of ion beam bombarded surface. (a) SEM micrograph (inset: 3D AFM topography) for self-assembled nanostructures on bombarded GaSb(100) surfaces. (b) AFM image (left) and corresponding 2D autocovariance analysis (right) for bombarded substrate surfaces. (c) AFM (left) and MFM (right) images of a perpendicular magnetic Co/Pd multilayer film on self-assembled GaSb(100) surface by ion bombardment. Reprinted with permission from [159], Y. J. Chen et al., *J. Appl. Phys.* 91, 7323 (2002). © 2002, American Institute of Physics.

aerosol-containing Au clusters were passed through a spray chamber in which the clusters are captured by contact with a fine spray of organic solvent and surfactant. The spray droplets subsequently are removed from the gas stream and collected in a liquid receiver. The key for successful operation of this collection technique is a surfactant that rapidly adsorbs onto the surface of the clusters and prevents aggregation. With the proper surfactant, it is possible to capture nanometer-diameter metal clusters in various organic solvents without altering the cluster-size distribution [176]. Figure 18 is a schematic representation of the self-assembly process involved in the formation of these close-packed arrays, and Figure 19 is a TEM micrograph of such an unlinked array. The mean diameter of the clusters in

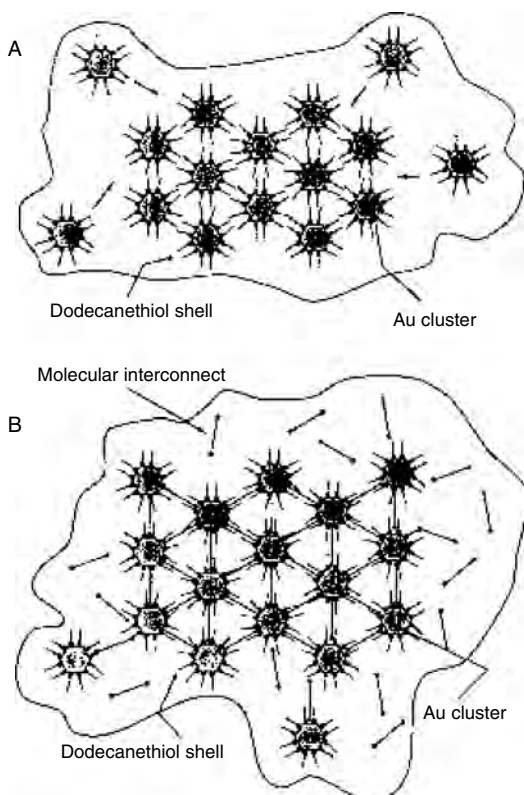


**Figure 17.** Schematic of process for synthesizing a stable colloidal suspension of crystalline gold clusters. Gold atoms evaporated from a carbon crucible in a resistively heated carbon tube are entrained in He and induced to condense into nanoclusters by mixing the hot flow with a room temperature stream of He. Controlling conditions in the oven and the flow downstream from the oven (see 1) controls the mean cluster size. The clusters are melted (see 2) and recrystallized (see 3) while still in the gas phase. They are scrubbed from the gas phase by contact with a mist of organic solvent containing 1-dodecanethiol and collected as a stable colloidal suspension (see 4). Before each run, a sample of the cluster aerosol is expanded as a cluster beam into a vacuum chamber and deposited on a TEM substrate for subsequent analysis. Reprinted with permission from [161], R. P. Andres et al., *Science* 272, 1323 (1996). © 1996, American Association for the Advancement of Science.

Figure 19 is 3.7 nm, and the average center-to-center distance between adjacent clusters is 5.0 nm.

By using Co, Fe, Ni, CoPt, FePt, and so forth, as precursors, magnetic nanostructures can be easily fabricated by this approach. The drawback of this method is that the long-range ordering is poor.

Self-assembly of nanoscale magnetic dots with narrow size distributions on an insulating substrate also is a way of magnetic nanopatterning via dry self-assembly. It has been realized that the strain energy associated with the lattice mismatch between the dot and the substrate materials can be exploited to induce a self-assembled formation of quantum dots with narrow size distributions [177–182]. Gai et al. introduced a growth method of magnetic dot array by strain-mediated dry self-assembly [170, 174]. They found that the iron dots could be self-assembled on insulating NaCl substrate by thermal deposition. It is shown that, by properly choosing the growth conditions, nanometer-scale magnetic iron dots with remarkably narrow size distributions can be achieved in the absence of a wetting layer. Furthermore, by changing the dosage of iron, both the vertical and lateral sizes of the dots can be tuned without introducing apparent size broadening, even though the clustering is already in the strong coarsening regime, signified by the decrease in dot density as a function of the iron dosage. The self-assembly is mediated by the strain between the iron dots and substrate. Figure 20 give an example of the fabricated iron dot array.



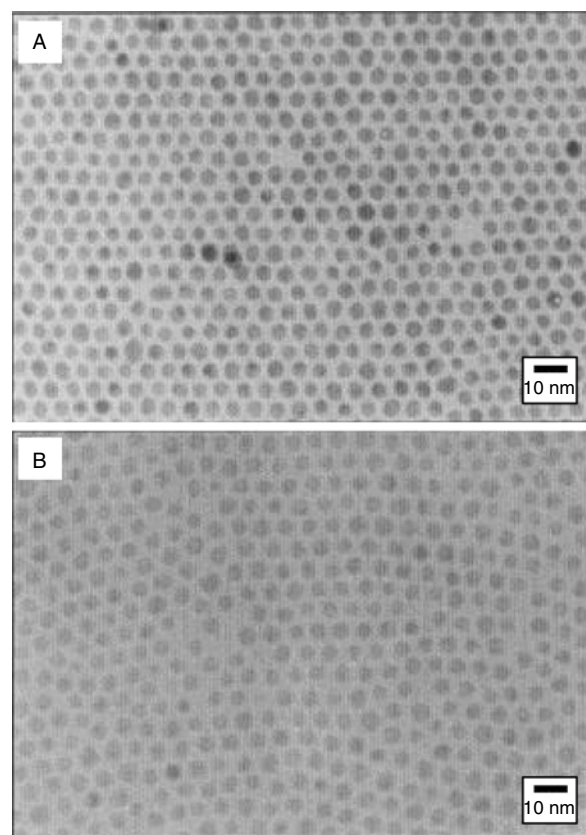
**Figure 18.** Self-assembly of a LCN. (A) A drop of organic solvent containing dodecanethiol-encapsulated gold clusters is cast on a smooth substrate. On evaporation of the solvent the long-range dispersion forces between clusters cause them to coalesce into a close-packed monolayer. A TEM micrograph of such an unlinked array is shown in Figure 19A. (B) The substrate with its unlinked cluster array is immersed in an acetonitrile solution containing aryl dithiol or diisocyanide molecules. The molecular interconnects displace the dodecanethiol molecules from the clusters and form rigid molecular linkages between adjacent clusters. A TEM micrograph of such a linked network is shown in Figure 19B. Reprinted with permission from [161], R. P. Andres et al., *Science* 272, 1323 (1996). © 1996, American Association for the Advancement of Science.

### 3. APPLICATIONS OF PATTERNED MAGNETIC NANOSTRUCTURES

The applications of patterned magnetic nanostructures are quite broad (biology, drug delivery, spintronics, data storage, information processing, magnetic sensors, etc.) and this review cannot cover all these aspects. Instead, this review will briefly describe their important applications for ultrahigh-density magnetic recording as a medium, with information processing, with magnetic sensors, and with strong permanent magnets.

#### 3.1. Ultrahigh-Density Magnetic Recording Medium

The increase in areal density of magnetic storage devices of >100% annually has been accomplished over the past few years by reducing the physical dimensions while maintaining the principle of storing information on a continuous, granular magnetic medium with in-plane magnetization. However, increases of areal density of hard-disk drives will be limited

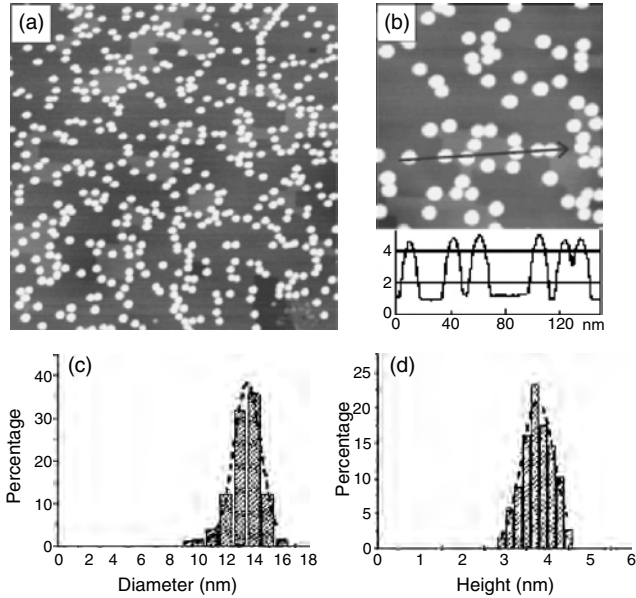


**Figure 19.** Bright-field TEM micrographs of monolayer films of 3.7-nm gold clusters supported on a thin flake of  $\text{MoS}_2$ . (A) Unlinked array encapsulated by dodecanethiol. (B) Cluster network linked by 20 ADT. Reprinted with permission from [161], R. P. Andres et al., *Science* 272, 1323 (1996). © 1996, American Association for the Advancement of Science.

by thermal instability of the thin-film medium because of the superparamagnetism effect. Perpendicular recording was suggested to push the recording density higher, but it still is ultimately limited by the same effect. Patterned media, in which data are stored in an array of single-domain magnetic particles, have been proposed as an approach to overcome the limitation of superparamagnetism and to enable recording densities of over 1 Tbit/in<sup>2</sup> to be achievable.

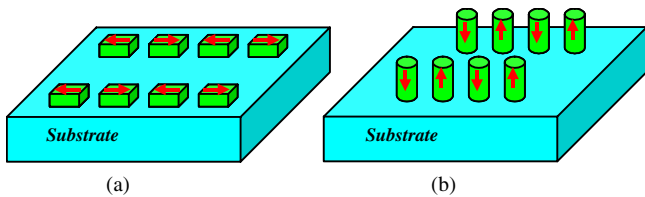
A patterned recording medium, shown schematically in Figure 21, consists of an array of magnetic nanoelements, each of which has uniaxial magnetic anisotropy. The easy axis can be oriented parallel or perpendicular to the substrate. Each element stores one bit, depending on its magnetization direction; for instance, magnetization up could represent 1, and down could represent 0. Each element is a single crystalline particle or consists of some grains that are strongly coupled so that the entire element behaves as a single magnetic domain. The medium is incorporated into a system capable of reading and writing data, for example, a spinning-disk system with an ultra-narrow recording head or a system with an array of scanning probes that address the elements.

For a patterned media recording system, it must offer significantly higher data densities than can be achieved in a conventional hard drive. There is confidence that hard drives

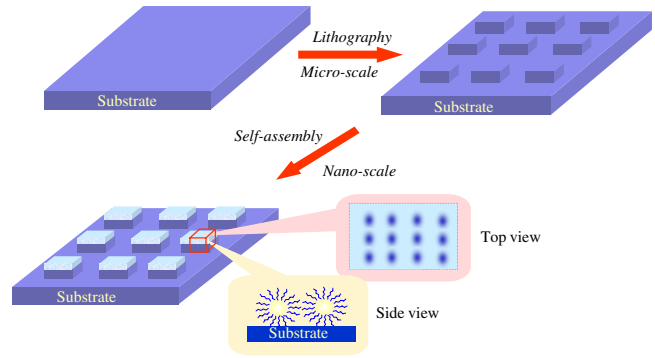


**Figure 20.** Nanometer-scale iron dots grown on NaCl(001) with a nominal Fe dose of 1.7 ML. (a) A typical NC-AFM image. Scan area 500 nm × 500 nm. (b) Close-up and line profile (150 nm long) of the dots. Scan area 200 nm × 200 nm. The unit in the line profile is nm. (c) (d) Diameter and height distributions of the dots shown in (a) and the corresponding Gaussian fits. The center and dispersion for the diameter distribution are 13.5 and 1.1 nm, respectively; and for the height distribution they are 3.76 and 0.36 nm, respectively. Reprinted with permission from [170], Z. Gal et al., *Phys. Rev. Lett.* 89, 235502 (2002). © 2002, American Physical Society.

that use longitudinal media will be able to reach 300 Gbit/in<sup>2</sup> or higher, so, patterned media designs must be capable of reaching densities of 500 Gbit/in<sup>2</sup> and beyond. This implies a periodicity of less than 40 nm, for instance, 20-nm elements with 15-nm separation. A 35-nm period corresponds to a density of 522 Gbit/in<sup>2</sup>. However, fabrication of sub-20-nm features over large areas is somewhat beyond the traditional lithography techniques. The combination of lithography with self-assembly is a possible way to fabricate such required tiny features over large area. This combination is schematically shown in Figure 22. Firstly, using the lithography method, micron-sized features over a large area are fabricated and then self-assemble the nanoparticles onto the micron-sized features to solve the problem of long-range ordering. Nowadays, monodisperse particles with a size of 3 nm can be synthesized. The ultimate patterned medium may consist of an array of magnetic particles with a size down to a few nanometers, self-assembled on a substrate with the aid of lithography to produce an array with long-range ordering.

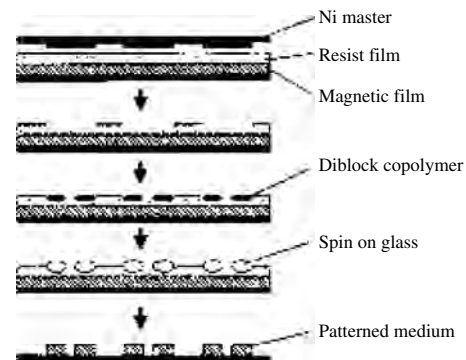


**Figure 21.** Schematic of longitudinal (a) and perpendicular patterned media (b).

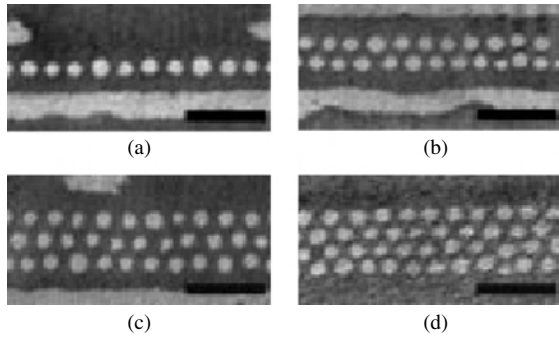


**Figure 22.** Schematic of combination of traditional lithography with nanoparticle self-assembly.

Recently, circumferential magnetic patterned media were prepared on a 2.5-inch-diameter glass plate and on a 3-inch-diameter silicon plate by combination of traditional lithography with self-assembly [183]. Figure 23 shows a schematic explanation of the preparation method by Naito et al. A Ni master disk with spiral patterns with 60-, 100-, 150-, 200-, and 250-nm-width lands and a 400-nm-width groove (110-nm depth) was purchased from the Nikon Corporation. The master disk was pressed onto a resist-covered magnetic film of either a CoPt or CoCrPt at room temperature and a pressure of 1000 bar. The magnetic film was prepared by sputtering CoPt or CoCrPt onto the disk substrate with a 40-nm Ti underlayer. A diblock copolymer solution [polymethylmethacrylate (PMMA) (Mw41500)–polystyrene (Mw172 000)] was cast into the obtained grooves, and then annealed to prepare self-assembling dot structures aligned along the grooves. The PMMA dots were selectively removed by the oxygen plasma treatment [184]. The resulting holes were filled by spin-on-glass (SOG). The underlying magnetic films were patterned by ion milling by using the SOG dots as a mask. As an example, Figure 24 shows the dot structures of the diblock copolymer in the grooves with different widths. One to four dot lines could be obtained by changing the groove width [185]. Another example, Figure 25(a) shows the SEM image of the patterned magnetic dots with about a 40 nm diameter. The image of the whole patterned media disk prepared on a



**Figure 23.** Scheme of the preparation method of patterned medium. Reprinted with permission from [183], K. Naito et al., *IEEE Trans. Magn.* 38, 1949 (2002). © 2002, IEEE.



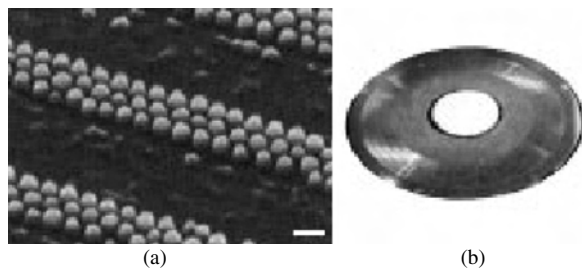
**Figure 24.** Phase-separation dot patterns of the diblock copolymers in grooves with different widths: (a) 60, (b) 150, (c) 200, and (d) 250 nm. The scale bar indicates 300 nm. Reprinted with permission from [183], K. Naito et al., *IEEE Trans. Magn.* 38, 1949 (2002). © 2002, IEEE.

2.5-inch-diameter HDD glass plate is shown in Figure 25b. This is the first report on disk-level magnetic nanopatterning for patterned magnetic recording.

### 3.2. Magnetic Sensors

Cowburn et al. [27] has proposed a new approach to high-sensitivity magnetic field sensing, based on an array of dots that are superparamagnetic. A particle that shows superparamagnetic behavior is because its anisotropy energy  $K_u V$  becomes smaller than or comparable to the thermal fluctuation energy  $k_B T$ . The M~H loops of superparamagnetic particles lose all hysteresis and have a shape that is determined by the Langevin function. The lack of hysteresis makes superparamagnetic particles interesting candidates for field sensors.

For magnetically hard materials, as their  $K_u$  is high, the superparamagnetic behavior normally is observed in particles with size of ~10 nm, in which case, the thermal fluctuation field,  $k_B T/m$  ( $m$  is the moment carried by the particle), is large due to the small value of  $m$ . Consequently, the sensitivity of such sensors would be very low because the saturation field of the particles is typically thousands of Oe. Cowburn et al. found that the offset in the linear dependence of configurational anisotropy on size results in thin planar permalloy nanomagnets losing all anisotropy at relatively large sizes, typically 100 nm. This means that magnetically soft permalloy magnets become superparamagnetic



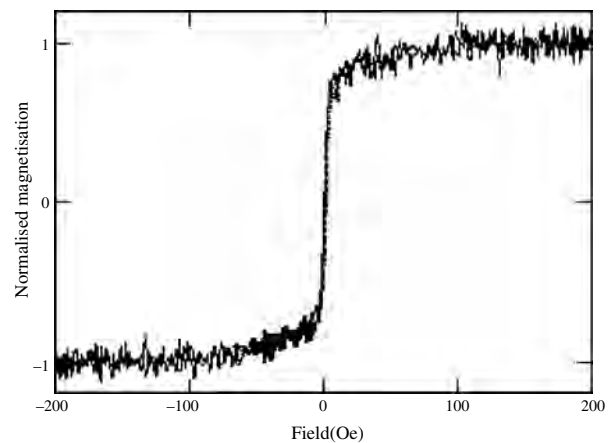
**Figure 25.** (a) SEM image of the patterned magnetic medium (Co Cr Pt) with a 40 nm diameter. The scale bar indicates 100 nm. (b) Whole image of the patterned media disk prepared on a 2.5-inch HDD glass plate. Reprinted with permission from [183], K. Naito et al., *IEEE Trans. Magn.* 38, 1949 (2002). © 2002, IEEE.

at a large size with large moment on the particles. Consequently, the fluctuation field (and hence saturation field) is very low. The magnetic response is, therefore, guaranteed to be a hysteresis-free response while retaining high sensitivity. Figure 26 shows a hysteresis loop of such dot array. One observes a completely hysteresis-free response combined with very high sensitivity.

### 3.3. Information Processing—Magnetic Logical Elements

Devices for information processing have been dominated by electronics. However, the emerging of spintronic technologies, which are based on electron spin, as well as charge, may offer new types of devices that outstrip the performance of traditional electronic devices. Spintronic devices use magnetic moment to carry information. To date, two classes of spintronic device have been proposed: semiconductor and metallic. Semiconductor devices will use spin-population imbalances between electrons or nuclei. Metallic devices, including magnetic read heads in hard drive and MRAM (MRAM), represent the information by magnetization direction in a ferromagnetic metal. However, the extent to which information can be manipulated in the magnetic form has, to date, been very limited; MRAM cells, for instance, can only store information. The scope of spintronics could be greatly expanded if, in addition to data storage, magnetic data bits could interact to perform some computation between being written and detected. In the future, one can dream of programmable magnetic logic elements configured to form magnetic central processor units, the brain of the computer. So far, a few magnetic logic elements, such as magnetic quantum molecular automata [30] and magnetic NOT (NOT) gate and shift register [28, 29] have been proposed and demonstrated.

Cowburn et al. proposed magnetic quantum molecular automata. In their proposal, the networks of interacting sub-micrometer magnetic dots are used to perform logic operations and propagate information at room temperature. The



**Figure 26.** A hysteresis loops measured from 3-nm-thick square nanostructures of lateral size 150 nm. The magnetization of the entire structure can be reversed with ~20Oe of applied field and has zero hysteresis. Reprinted with permission from [27], R. P. Cowburn, *J. Magn. Magn. Mater.* 242–245, 505 (2002). © 2002, JMMM.

logic states are signaled by the magnetization direction of the single-domain magnetic dots; the dots couple to their nearest neighbors through magnetostatic interactions. Magnetic solitons carry information through the networks, and an applied oscillating magnetic field feeds energy into the system and serves as a clock. Figure 27 shows the networks of quantum molecular automata.

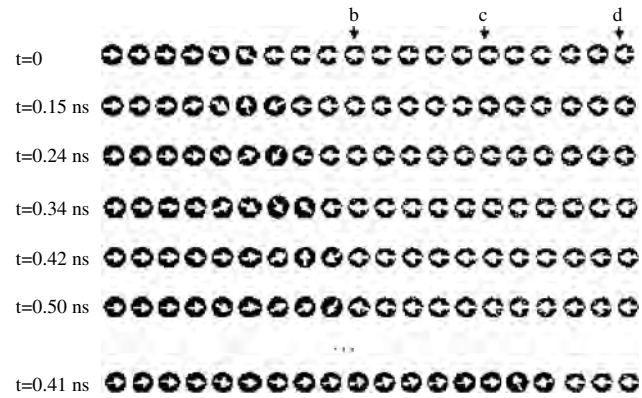
Figure 28 shows the calculated evolution of a soliton propagating along a chain of coupled nanomagnets under the action of a 30 Oe field applied from left to right ( $x$  direction). The propagation speed of the soliton is dependent on the applied field. These networks offer a several-thousands-fold increase in integration density and a hundredfold reduction in power dissipation over current microelectronic technology.

Cowburn et al. also proposed magnetic NOT gate and shift register. They use a trick of geometry to manipulate magnetization as conventional devices manipulate an electric charge. The NOT gate consists of a simple track of naturally magnetic nickel-iron wire, shaped like an upside-down Y (shown in Fig. 29). The magnetism of the alloy naturally runs parallel to the track, but it can be made to flip direction within a short length of the wire. In that case, the two opposing magnetizations meet at a region called a “domain wall.” There they either both point toward the domain wall (head to head) or both point away from it (toe to toe). Those two magnetic configurations can be used to encode 0 and 1 values for bits of information. Up to 11 of these junctions are then directly linked together to create a magnetic shift register as shown in Figure 30.

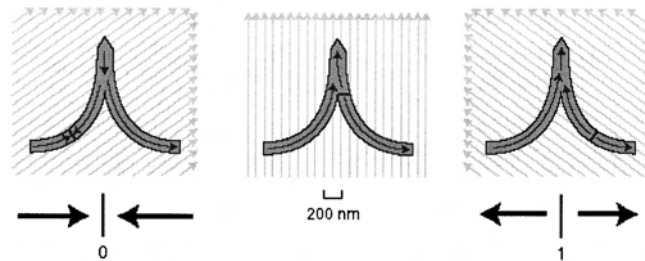
This tiny device that answers “no” when it is told “yes” and vice versa could mark the first step toward microchips that calculate magnetically.

### 3.4. Strong Permanent Magnets

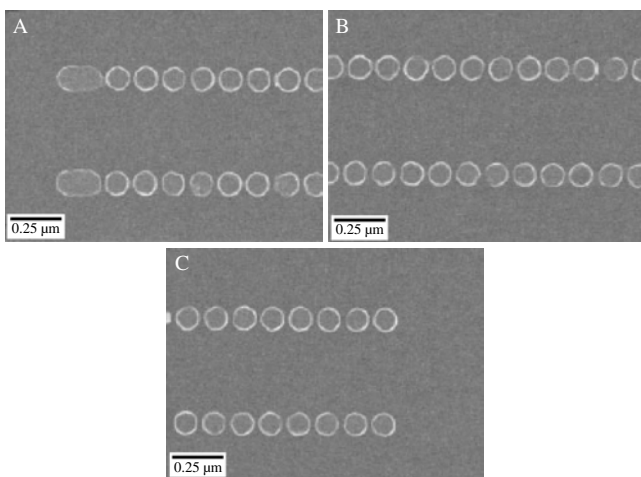
Exchange-spring magnets are nanocomposites that consist of magnetically hard and soft phases that interact through magnetic exchange coupling [186–191]. Such systems are



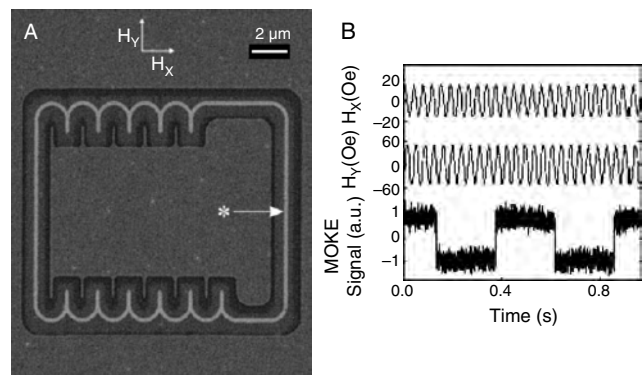
**Figure 28.** The calculated evolution of a soliton propagating along a chain of coupled nanomagnets under the action of a 30 Oe field applied from left to right ( $x$  direction). Reprinted with permission from [27], R. P. Cowburn, *J. Magn. Magn. Mater.* 242–245, 505 (2002). © 2002, JMMM.



**Figure 29.** Magnetic NOT gate. In this NOT gate, a rotating magnetic field (gray arrows) changes the value of a bit by moving and then flipping the boundary of magnetized wire. Reprinted with permission from [28], D. A. Allwood et al., *Science* 296, 2003 (2002). © 2002, American Association for the Advancement of Science.

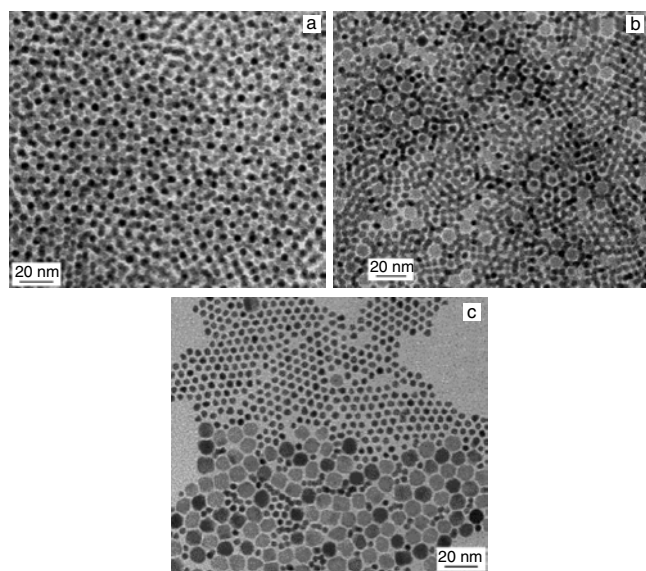


**Figure 27.** Scanning electron micrographs of the left (A), center (B), and right (C) regions of two of the room temperature MQCA networks. Reprinted with permission from [30], R. P. Cowburn and M. E. Welland, *Science* 287, 1466 (2000). © 2000, American Association for the Advancement of Science.

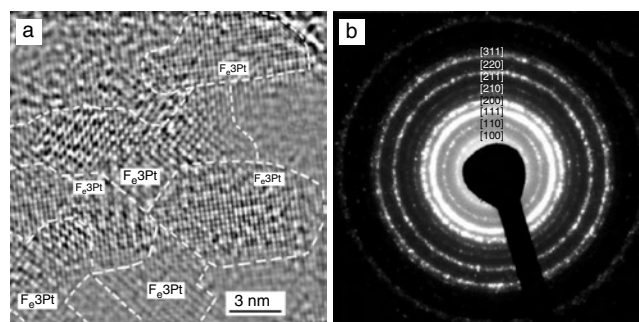


**Figure 30.** (A) FIB image of a magnetic ring, including 11 NOT junctions, with the asterisk indicating the position of subsequent MOKE analysis. The directions of elliptical magnetic field components,  $H_x$  and  $H_y$ , are also indicated. (B) MOKE analysis of an identical structure within a clockwise-rotating magnetic field ( $H_x = 15$  Oe and  $H_y = 50$  Oe). Reprinted with permission from [28], D. A. Allwood et al., *Science* 296, 2003 (2002). © 2002, American Association for the Advancement of Science.

promising for advanced permanent magnetic applications, as they have a large energy product—the combination of large coercivity field of permanent magnet and high magnetization of soft magnet—compared to traditional, single-phase materials [192–194]. Conventional techniques, including sputtering [195–197], mechanical milling [198–200], and melt-spinning [201–203], have been used to produce exchange-coupled magnets. However, it is still a big challenge to structurally control the hard and soft phases at the nanometer scale to fulfill exchange coupling efficiently. The recent and timely introduction of a fabrication method of exchange-coupled nanocomposites by using nanoparticle self-assembly by Zeng et al. [204] has opened a new window to structurally control the hard and soft phases at the nanometer scale. In their approach, both FePt and  $\text{Fe}_3\text{O}_4$  particles are incorporated as nanometer-scale building blocks into binary assemblies. Subsequent annealing converts the assembly into FePt– $\text{Fe}_3\text{Pt}$  nanocomposites, where FePt is a magnetically hard phase and  $\text{Fe}_3\text{Pt}$ , a soft phase. An optimum exchange coupling and, therefore, an optimum energy product, can be obtained by independently tuning the size and composition of the individual building blocks. They have produced exchange-coupled isotropic FePt– $\text{Fe}_3\text{Pt}$  nanocomposites with an energy product of 20.1 MGOe, which exceeds the theoretical limit of 13 MGOe for nonexchange-coupled isotropic FePt by over 50 per cent. Figure 31 exemplifies the TEM images of  $\text{Fe}_3\text{O}_4$ : $\text{Fe}_{58}\text{Pt}_{42}$  binary assemblies with different sizes and a fixed mass ratio of 1:10. Figure 32 shows a typical high-resolution TEM image of a sintered sample obtained from a 4 nm:4 nm assembly.



**Figure 31.** TEM images showing binary nanoparticle assemblies. (a)  $\text{Fe}_3\text{O}_4$  (4 nm): $\text{Fe}_{58}\text{Pt}_{42}$  (4 nm) assembly; (b)  $\text{Fe}_3\text{O}_4$  (8 nm): $\text{Fe}_{58}\text{Pt}_{42}$  (4 nm) assembly; and (c)  $\text{Fe}_3\text{O}_4$  (12 nm): $\text{Fe}_{58}\text{Pt}_{42}$  (4 nm) assembly. The assembly contained  $\text{Fe}_3\text{O}_4$  and FePt binary nanoparticles with a mass ratio of  $\text{Fe}_3\text{O}_4$ :FePt = 1/10 and was formed by solvent vaporation of the mixed nanoparticle dispersions on amorphous carbon-coated TEM grids. All images were acquired using a Philips CM12 microscope at 120 kV. Reprinted with permission from [204], H. Zeng et al., *Nature* 420, 395 (2002). © 2002, Macmillan Magazines Ltd.



**Figure 32.** Structural analyses of the FePt– $\text{Fe}_3\text{Pt}$  nanocomposite obtained from the annealed  $\text{Fe}_3\text{O}_4$  (4 nm): $\text{Fe}_{58}\text{Pt}_{42}$  (4 nm) assembly. (a) A typical HRTEM image for a sintered FePt– $\text{Fe}_3\text{Pt}$  particle. The FePt and  $\text{Fe}_3\text{Pt}$  phases are in coexistence as different domains within the particle, with each domain having a dimension of about 5 nm, showing a modulated FePt– $\text{Fe}_3\text{Pt}$  spatial distribution. Here, the FePt (ordered f.c.t structure) and  $\text{Fe}_3\text{Pt}$  (ordered fcc structure) phases were identified by their different [001] projected potential, owing to their different composition modulation periodicities. The image was acquired by using a Jeol 4000EX HRTEM at 400 kV. To prepare the TEM samples, the composite was deposited on a solid NaCl substrate. The substrate was then removed in water, and the composite was thinned by using ion milling for TEM observation. (b) A typical SAD pattern of the FePt– $\text{Fe}_3\text{Pt}$  nanocomposite. The f.c.t.-structured FePt was indexed in the ring pattern. The diffraction rings of the fcc-structured  $\text{Fe}_3\text{Pt}$  cannot be resolved from those of the FePt phase. The ring pattern of the diffraction demonstrates that the nanocrystallites in the nanocomposite are three-dimensionally randomly oriented. Reprinted with permission from [204], H. Zeng et al., *Nature* 420, 395 (2002). © 2002, Macmillan Magazines Ltd.

Although progress has been made by using a self-assembled composite of nanoparticles, there are still many practical challenges to be faced if energy products approaching the magic number of 144 MGOe are to be achieved. For instance, ways of compressing the two-phase material into a high-density compact must be explored, as well as improved alignment of the axes of the hard grains to exploit the full magnetic potential of the nanocomposite system.

## 4. CONCLUSION

We have attempted to review some of the current topics for magnetic nanopatterning methods and their applications. The starting point was the magnetic nanopatterning technology, including the most expensive and traditional approaches and some newly developed nontraditional methods. It is appears that all lithography methods presented are useful in enabling certain applications. As the feature size scales down further to sub 10 nm, which is aiming for, but not only limited to, advanced information technologies such as molecular electronics (moletronic), data storage (nanoBIT), and quantum information processing, it is necessary to develop new nanofabrication technologies with the help of molecular self-assembling and self-organization to produce tiny enough feature size with long-range ordering and large area.

Data storage, magnetic memory and sensors, magnetic information processing, and even biological microsystems are the well-identified application areas of patterned magnetic nanostructures. Due to the too many aspects of magnetic nanopatterning and too rapid development of their



applications today, it was not possible to cover the topic in an exhaustive manner, and a selection of the most important issues was thus chosen by the authors. However, we hope that the stimulating conjunctures in this chapter will encourage new exploration of this exciting area.

## GLOSSARY

**Anisotropy patterning** A method to pattern magnetic film by engineering the anisotropy of the magnetic film to be out-of-plane and in-plane alternatively via ion beam radiation or selective epitaxial growth.

**Anodized alumina template** A film or foil having alumina layer which contains a close packed arrangement of fine holes, with the hole spacing and size controlled by anodization conditions such as voltage, current density, or pH value.

**Block copolymers** A polymer mixture consisting of chains of two chemically distinct, immiscible monomers A and B.

**Electron beam lithography** A lithography approach with which an electron beam is used to write pattern into resist layer.

**Exchange-spring magnet** Magnetic nanocomposites consisting of magnetically hard and soft phases that interact through magnetic exchange coup.

**Ferromagnetism** A term used to characterize strongly magnetic behavior with spontaneous magnetization.

**Laser-assisted direct imprint (LADI)** An ultrafast approach to nanopatterning by direct imprint of nanostructures on laser-melted surface.

**Laser interference lithography** A lithography approach using laser interference to write pattern into resist layer.

**Lithography** The art or process of putting writings or designs on stone with a greasy material and producing printed impressions therefrom; also, any process based on the same principle, as one using zinc, aluminium, or some other substance instead of tone.

**Longitudinal medium** A recording medium with which the magnetization of the recorded bit lies in the plane of the disk.

**Magnetic NOT gate** A magnetic logical element consisting of a simple track of naturally magnetic nickel-iron wire, shaped like an upside-down Y, which answers “no” when it’s told “yes” and vice versa.

**Magnetic quantum molecular automata (MQCA)** A magnetic logical element using the networks of interacting sub-micrometer magnetic dots to perform logic operations and propagate information.

**Magnetic random access memory (MRAM)** Information is carried by magnetic moment.

**Magnetization patterning** A method to pattern magnetic film by selectively altering the magnetization of magnetic films via laser and ion beam radiation.

**Paramagnetism** A term describing a feeble magnetism, which exhibits positive susceptibility of the order of  $10^{-5}$  to  $10^{-2}$ .

**Patterned magnetic nanostructure** A 1- or 2-dimensional magnetic nanoelement array or 3 dimensional superlattice.

**Patterned medium** A recording medium consisting of an array of magnetic nanoelements with uniaxial magnetic anisotropy.

**Perpendicular medium** A recording medium with which the magnetization of the recorded bit is perpendicular to the plane of the disk.

**Resist** A polymer or polymer mixture used as a thin coating over some base and subsequently exposed in an image-wise fashion for micron or nano patterning.

**Superparamagnetism** A magnetic particle or particle assembly which exhibits paramagnetic behavior due to its anisotropy energy  $K_u V$  becoming smaller than or comparable to the thermal fluctuation energy  $k_B T$ .

**Thermal diffusion length** A length, described by  $L_{ex} \propto \sqrt{kt}$ , referring to the thermal conducting distance in a material with thermal conductivity  $k$  within time  $t$ .

## REFERENCES

1. S. Y. Chou, M. S. Wei, P. R. Krauss, and P. B. Fischer, *J. Appl. Phys.* 76, 6637 (1994).
2. M. H. Kryder, W. Messner, and L. R. Carley, *J. Appl. Phys.* 79, 4485 (1996).
3. S. Y. Chou, *P. IEEE* 85, 652 (1997).
4. L. Kong, L. Zhuang, and S. Y. Chou, *IEEE Trans. Magn.* 33, 3019 (1997).
5. C. A. Ross, *Ann. Rev. Mater. Res.* 31, 203 (2001).
6. M. Chou, P. R. Wei, P. B. Krauss, and J. Fisher, *J. Vac. Sci. Technol., B* 12, 3695 (1994).
7. R. L. White, R. M. H. New, and R. F. W. Pease, *IEEE Trans. Magn.* 33, 990 (1997).
8. S. Y. Chou, R. C. Shi, and L. S. Kong, *J. Appl. Phys.* 81, 4673 (1997).
9. R. L. White, *J. Magn. Magn. Mater.* 242, 21 (2002).
10. S. Ganesan, C. M. Park, K. Hattori, H. C. Park, R. L. White, H. Koo, and R. D. Gomez, *IEEE Trans. Magn.* 36, 2987 (2000).
11. M. E. Walsh, Y. W. Hao, C. A. Ross, and H. I. Smith, *J. Vac. Sci. Technol., B* 18, 3539 (2000).
12. J. U. Thiele, D. J. Pocker, and R. L. White, *J. Appl. Phys.* 87, 2989 (2000).
13. H. Takano, Y. Nishida, A. Kuroda, H. Sawaguchi, Y. Hosoe, T. Kawabe, H. Aoi, H. Muraoka, Y. Nakamura, and K. Ouchi, *J. Magn. Magn. Mater.* 235, 241 (2001).
14. S. Iwasaki, *J. Magn. Magn. Mater.* 235, 227 (2001).
15. R. M. H. New, R. F. W. Pease, and R. L. White, *J. Magn. Magn. Mater.* 155, 140 (1996).
16. M. Todorovic, S. Schultz, J. Wong, and A. Scherrer, *Appl. Phys. Lett.* 74, 2516 (1999).
17. G. F. Hughes, *IEEE Trans. Magn.* 36, 521 (2000).
18. J. Zhu, X. Lin, L. Guan, and W. Messner, *IEEE Trans. Magn.* 36, 23 (2000).
19. J. L. Simonds, *Phys. Today* 48, 26 (1995).
20. G. A. Prinz, *Science* 282, 1660 (1998).
21. G. A. Prinz, *J. Magn. Magn. Mater.* 200, 57 (1999).
22. M. M. Miller, G. A. Prinz, S. F. Cheng, and S. Bounnak, *Appl. Phys. Lett.* 81, 2211 (2002).
23. S. A. Wolf, D. D. Awschalom, R. A. Buhrman, J. M. Daughton, S. von Molnar, M. L. Roukes, A. Y. Chtchelkanova, and D. M. Treger, *Science* 294, 1488 (2001).
24. J. G. Zhu, Y. F. Zheng, and G. A. Prinz, *J. Appl. Phys.* 87, 6668 (2000).
25. S. A. Wolf and D. Treger, *IEEE Trans. Magn.* 36, 2748 (2000).
26. G. A. Prinz, *Science* 283, 330 (1999).
27. R. P. Cowburn, *J. Magn. Magn. Mater.* 242–245, 505 (2002).

28. D. A. Allwood, G. Xiong, M. D. Cooke, C. C. Faulkner, D. Atkinson, N. Vernier, and R. P. Cowburn, *Science* 296, 2003 (2002).
29. A. Cho, *Science* 296, 1948 (2002).
30. R. P. Cowburn and M. E. Welland, *Science* 287, 1466 (2000).
31. D. J. Monsma, J. C. Lodder, Th. J. A. Popma, and B. Dieny, *Phys. Rev. Lett.* 74, 5260 (1995).
32. D. J. Monsma, R. Vlutters, and J. C. Lodder, *Science* 281, 407 (1998).
33. R. M. H. New, R. F. W. Pease, and R. L. White, *J. Vac. Sci. Technol., B* 13, 1089 (1995).
34. S. Y. Chou, P. R. Krauss, and P. B. Fischer, *Science* 272, 85 (1996).
35. H. C. Pferffer, *J. Vac. Sci. Technol.* 15, 887 (1978).
36. F. J. Hohn, *J. Vac. Sci. Technol., B* 7, 1405 (1989).
37. R. Ferre, K. Ounadjela, J. M. George, L. Pirauz, and S. Dubois, *Phys. Rev. B* 56, 14066 (1997).
38. M. Thielen, S. Kirsch, H. Weinforth, A. Carl, and E. F. Wassermann, *IEEE Trans. Magn.* 34, 1009 (1998).
39. R. P. Cowburn, *J. Phys. D: Appl. Phys.* 33, R1 (2000).
40. M. Walsh, Y. Hao, C. A. Ross, and H. I. Smith, *J. Vac. Sci. Technol., B* 18, 3539 (2000).
41. C. A. Ross, M. Farhoud, H. I. Smith, M. Hwang, M. Redjidal, and F. Humphrey, *J. Appl. Phys.* 89, 1310 (2001).
42. S. Evoy, D. W. Carr, L. Sekaric, Y. Suzuki, J. M. Parpia, and H. C. Craighead, *J. Appl. Phys.* 87, 404 (2000).
43. R. M. H. New, R. F. W. Pease, and R. L. White, *J. Vac. Sci. Technol., B* 12, 3196 (1994).
44. M. A. M. Haast, J. R. Schuirhuis, L. Abelman, J. C. Lodder, and Th. J. Popma, *IEEE Trans. Magn.* 34, 1006 (1998).
45. J. F. Smyth, S. Schultz, D. Kern, H. Schmid, and D. Yee, *J. Appl. Phys.* 63, 4237 (1988).
46. R. M. H. New, R. F. W. Pease, R. L. White, R. M. Osgood, and K. Babcock, *J. Appl. Phys.* 79, 5851 (1996).
47. R. P. Cowburn, D. K. Koltsov, A. O. Adeye, M. E. Welland, and D. M. Tricker, *Phys. Rev. Lett.* 85, 1042 (1999).
48. K. J. Kirk, J. N. Chapman, and C. D. W. Wilkinson, *J. Appl. Phys.* 85, 5237 (1999).
49. M. Lederman, G. A. Gibson, and S. Schultz, *J. Appl. Phys.* 73, 6961 (1993).
50. R. O'Barr, S. Y. Yamamoto, S. Schultz, W. Xu, and A. Scherer, *J. Appl. Phys.* 81, 4730 (1997).
51. J. Wong, A. Scherer, M. Todorovic, and S. Schultz, *J. Appl. Phys.* 85, 5489 (1999).
52. H. I. Smith, *J. Vac. Sci. Technol., B* 13, 2323 (1995).
53. B. Cui, W. Wu, L. Kong, X. Sun, and S. Y. Chou, *J. Appl. Phys.* 85, 5534 (1999).
54. G. Meier, M. Kleiber, D. Grundler, D. Heitmann, and R. Wiesendanger, *Appl. Phys. Lett.* 72, 2168 (1998).
55. A. Fernandez, M. R. Gibbons, M. A. Wall, and C. J. Cerjan, *J. Magn. Magn. Mater.* 190, 71 (1998).
56. T. A. Savas, M. Farhoud, H. I. Smith, M. Hwang, and C. A. Ross, *J. Appl. Phys.* 85, 6160 (1999).
57. R. O'Barr, R. M. Lederman, S. Schultz, W. Xu, A. Scherer, and R. J. Tonucci, *J. Appl. Phys.* 79, 5303 (1996).
58. Y. Chen and A. Pepin, *Electrophoresis* 22, 187 (2001).
59. W. Ehrfeld and A. Schmidt, *J. Vac. Sci. Technol., B* 16, 3526 (1998).
60. J. P. Silverman, *J. Vac. Sci. Technol., B* 16, 3137 (1998).
61. F. Keller, M. S. Hunter, and D. L. Robinson, *J. Electrochem. Soc.* 100, 411 (1953).
62. H. Masuda and K. Fukada, *Science* 268, 1466 (1995).
63. F. Müller, A. Birner, J. Schilling, A. P. Li, K. Nielsch, U. Gösele, and V. Lehmann, *Microsyst. Technol.* 8, 7 (2002).
64. A. P. Li, F. Müller, A. Birner, K. Nielsch, and U. Gösele, *Advanced Materials* 11, 483 (1999).
65. G. Sauer, G. Brehm, S. Schneider, K. Nielsch, R. B. Wehrspohn, J. Choi, H. Hofmeister, and U. Gösele, *J. Appl. Phys.* 91, 3243 (2002).
66. M. C. Roco, *Computational Nanoscience and Nanotechnology* 2002,
67. S. H. Sun, C. B. Murray, D. Weller, L. Folks, and A. Moser, *Science* 287, 1989 (2000).
68. C. L. Chien, *J. Appl. Phys.* 69, 5267 (1991).
69. J. Hong, E. Kay, and S. X. Wang, *IEEE Trans. Magn.* 32, 4475 (1996).
70. J. Y. Li, C. L. Platt, M. L. Rudee, A. E. Berkowitz, and T. L. Cheeks, *J. Appl. Phys.* 79, 5072 (1996).
71. D. S. Gangopadhyay, G. C. Hadjipanayis, C. M. Sorensen, and K. Klabunde, *IEEE Trans. Magn.* 29, 2602 (1993).
72. S. H. Sun and C. B. Murray, *J. Appl. Phys.* 85, 4325 (1999).
73. R. H. Ottewill, *J. Appl. Crystallogr.* 24, 436 (1991).
74. T. G. Schaaff, M. N. Shafiqullin, J. T. Khoury, I. Vezmar, and R. L. Whetten, *J. Phys. Chem. B* 101, 7885 (1997).
75. C. J. Kiely, J. Fink, M. Brust, D. Bethell, and D. J. Schiffrin, *Nature* 396, 444 (1998).
76. A. Taleb, C. Petit, and M. P. Pileni, *J. Phys. Chem. B* 102, 2214 (1998).
77. C. Petit, A. Taleb, and M. P. Pileni, *J. Phys. Chem. B* 103, 1805 (1999).
78. J. S. Yin and Z. L. Wang, *Phys. Rev. Lett.* 79, 2570 (1997).
79. M. Li, H. Schnablegger, and S. Mann, *Nature* 402, 393 (1999).
80. A. C. Levi and M. Kotrla, *J. Phys: Condens. Matter* 9, 299 (1997).
81. H. J. Manin, P. H. Guthner, and D. Rugar, *Phys. Rev. Lett.* 65, 2418 (1990).
82. K. Bessho, Y. Iwasaki, and S. Hashimoto, *IEEE Trans. Magn.* 32, 4443 (1996).
83. S. Kondo, S. Heike, M. Lutwyche, and Y. Wada, *J. Appl. Phys.* 78, 155 (1995).
84. A. D. Kent, S. Molnar, S. Gider, and D. D. Awschalom, *J. Appl. Phys.* 76, 6656 (1994).
85. U. Staufer, R. Wiesendanger, L. Eng, L. Rosenthaler, H. R. Hidber, H. J. Guntherodt, and N. Garcia, *Appl. Phys. Lett.* 51, 244 (1987).
86. S. Tomino, H. Saito, and S. Ishio, *J. Magn. Magn. Mater.* 212, 69–74 (2000).
87. S. Hosaka, S. Hosoki, T. Hasegawa, H. Koyanagi, T. Shintani, and M. Miyamoto, *J. Vac. Sci. Technol., B* 13, 2813 (1995).
88. K. Bessho, Y. Iwasaki, and S. Hashimoto, *IEEE Trans. Magn.* 32, 4443 (1996).
89. S. Wirth, M. Field, D. D. Awschalom, and S. von Molnar, *Phys. Rev. B* 57, R14028 (1998).
90. S. Wirth, S. von Molnar, M. Field, and D. D. Awschalom, *J. Appl. Phys.* 85, 5249 (1999).
91. R. P. Cowburn, A. O. Adeyeye, and M. E. Welland, *Phys. Rev. Lett.* 81, 5414 (1998).
92. R. P. Cowburn and M. E. Welland, *Appl. Phys. Lett.* 72, 2041 (1998).
93. T. J. Zhou, Y. Zhao, J. P. Wang, J. T. L. Thong, and T. C. Chong, *J. Appl. Phys.* 91, 8019 (2002).
94. T. J. Zhou, Y. Zhao, J. P. Wang, J. T. L. Thong, and T. C. Chong, *IEEE Trans. Magn.* 38, 1970 (2002).
95. Y. Zhao, T. J. Zhou, J. P. Wang, and T. C. Chong, "INTERMAG 2002," GS-04.
96. Y. Zhao, T. J. Zhou, J. P. Wang, J. T. L. Thong, and T. C. Chong, *J. Appl. Phys.* (in press).
97. Y. Zhao, T. J. Zhou, J. P. Wang, J. T. L. Thong, and T. C. Chong, "INTERMAG 2003," Boston, FQ-10.
98. M. Yu, Y. Liu, and D. J. Sellmyer, *J. Appl. Phys.* 85, 4319 (1999).
99. M. Zheng, M. Yu, Y. Liu, R. Skomski, S. H. Liou, D. J. Sellmyer, V. N. Petryakov, Yu. K. Verevkin, N. I. Polushkin, and N. N. Salashchenko, *IEEE Trans. Magn.* 37, 2070 (2001).
100. M. Zheng, M. Yu, Y. Liu, R. Skomski, S. H. Liou, D. J. Sellmyer, V. N. Petryakov, Yu. K. Verevkin, N. I. Polushkin, and N. N. Salashchenko, *Appl. Phys. Lett.* 79, 2606 (2001).

101. A. E. Tselev, N. I. Polushkin, Y. K. Verevkin, A. A. Gorbunov, V. N. Petryakov, and W. Pompe, *Appl. Phys. A* 69 [Suppl.], S819 (1999).
102. N. I. Polushkin, S. A. Gusev, and M. N. Drozdov, *J. Appl. Phys.* 81, 5478 (1997).
103. N. I. Polushkin and N. N. Salashchenko, *J. Magn. Magn. Mater.* 124, 347 (1993).
104. Yu. Blyakhman, N. I. Polushkin, A. D. Akhsakhalyan, S. A. Gusev, N. N. Salashchenko, and V. G. Semenov, *Phys. Rev. B* 52, 10 303 (1995).
105. C. Chappert, H. Bernas, J. Ferre, V. Kottler, J. P. Jamet, Y. Chen, E. Cambril, T. Devolder, F. Rousseaux, V. Mathet, and H. Launois, *Science* 280, 1919 (1998).
106. B. D. Terris, L. Folks, D. Weller, J. E. E. Baglin, A. J. Kellock, H. Rothuizen, and P. Vettiger, *Appl. Phys. Lett.* 75, 403 (1999).
107. T. Devolder, C. Chappert, Y. Chen, E. Cambril, H. Bernas, J. P. Jamet, and J. Ferré, *Appl. Phys. Lett.* 74, 3383 (1999).
108. T. Devolder, C. Chappert, and H. Bernas, *J. Magn. Magn. Mater.* 249, 452 (2002).
109. T. Devolder, C. Chappert, V. Mathet, H. Bernas, Y. Chen, J.-P. Jamet, and J. Ferre, *J. Appl. Phys.* 87, 8671 (2000).
110. V. Kottler, C. Chappert, N. Essaidi, and Y. Chen, *IEEE Trans. Magn.* 34, 2012 (1998).
111. H. Bernas, T. Devolder, C. Chappert, J. Ferre'e, V. Kottler, Y. Chen, C. Vieu, J. P. Jamet, V. Mathet, E. Cambril, O. Kaitanov, S. Lemerle, F. Rousseaux, and H. Launois, *Nucl. Instrum. Methods Phys. Res., Sect. B* 148, 872 (1999).
112. T. Aign, P. Meyer, S. Lemerle, J. P. Jamet, J. Ferre', V. Mathet, C. Chappert, J. Gierak, C. Vieu, F. Rousseaux, H. Launois, and H. Bernas, *Phys. Rev. Lett.* 81, 5656 (1998).
113. J. Ferre', C. Chappert, H. Bernas, J. P. Jamet, P. Meyer, O. Kaitasov, S. Lemerle, V. Mathet, F. Rousseaux, and H. Launois, *J. Magn. Magn. Mater.* 198, 191 (1998).
114. T. Devolder, J. Ferre, C. Chappert, H. Bernas, J. P. Jamet, and V. Mathet, *Phys. Rev. B* 64, 064415 (2001).
115. C. Vieu, J. Gierak, H. Launois, T. Aign, P. Meyer, J. P. Jamet, J. Ferré, C. Chappert, V. Mathet, and H. Bernas, *Microelectron. Eng.* 53, 191 (2000).
116. C. T. Rettner, M. E. Best, and B. D. Terris, *IEEE Trans. Magn.* 37, 1649 (2001).
117. T. Devolder, *Phys. Rev. B* 62, 5794 (2000).
118. S. Y. Chou, C. Keimel, and J. Gu, *Nature* 417, 835 (2002).
119. R. F. Pease, *Nature* 417, 802 (2002).
120. A. Lapicki, K. Kang, and T. Suzuki, *IEEE Trans. Magn.* 38, 2589 (2002).
121. A. Lapicki, E. Ahmad, and T. Suzuki, *J. Magn. Magn. Mater.* 240, 47 (2002).
122. J. Melngailis and P. G. Blauner, *Proc. Material Research Soc. Symp.* 147, 111 (1989).
123. A. Lapicki, E. Ahmad, and T. Suzuki, "Proceedings of the 25th Conference Magnetism in Japan," Akita, Japan, p. 249.
124. P. G. Blauner, J. S. Ro, Y. Butt, and J. Melngailis, *J. Vac. Sci. Technol., B* 7, 609 (1989).
125. P. G. Blauner, Y. Butt, J. S. Ro, and J. Melngailis, *J. Vac. Sci. Technol., B* 7, 1816 (1989).
126. A. Dietzel, R. Berger, H. Grimm, W. H. Bruenger, C. Dzionk, F. Letzkus, R. Springer, H. Loeschner, E. Platzgummer, G. Stengl, Z. Z. Bandic', and B. D. Terris, *IEEE Trans. Magn.* 38, 1952 (2002).
127. M. Berger and S. Seltzer, *Natl. Acad. Sci.-Natl. Res. Council. Publ.* 1133, 205 (1964).
128. A. Neukermans and W. Saperstein, *J. Vac. Sci. Technol.* 16, 1847 (1980).
129. T. J. Konno and R. Sinclair, *Acta Metall. Mater.* 42, 1231 (1994).
130. H. L. Bai, E. Y. Jiang, C. D. Wang, and R. Y. Tian, *J. Phys.: Condens. Matter* 8, 8763 (1996).
131. T. Hayashi, S. Hirono, M. Tomita, and S. Umemura, *Nature* 38, 772 (1996).
132. S. P. Li, W. S. Lew, J. A. C. Bland, L. Lopez-Diaz, M. Natali, C. A. F. Vaz, and Y. Chen, *Nature* 415, 601 (2002).
133. S. P. Li, W. S. Lew, J. A. C. Bland, L. Lopez-Diaz, M. Natali, C. A. F. Vaz, and Y. Chen, *Phys. Rev. Lett.* 88, 087202 (2002).
134. G. Bochi, C. A. Ballentine, H. E. Ingelfield, C. V. Thompson, and R. O'Handley, *Phys. Rev. B* 53, 1729 (1996).
135. M. Albrecht, C. T. Rettner, A. Moser, M. E. Best, and B. D. Terris, *Appl. Phys. Lett.* 81, 2875 (2002).
136. C. T. Rettner, S. Anders, T. Thomson, M. Albrecht, Y. Ikeda, M. E. Best, and B. D. Terris, *IEEE Trans. Magn.* 38, 1725 (2002).
137. M. Albrecht, S. Anders, T. Thomson, C. T. Rettner, M. E. Best, A. Moser, and B. D. Terris, *J. Appl. Phys.* 91, 6845 (2002).
138. S. J. Pickart and R. Nathans, *J. Appl. Phys.* 34, 1203 (1963).
139. T. D. Leonhardt, Y. Chen, M. Rao, D. E. Laughlin, D. N. Lambeth, and M. H. Kryder, *J. Appl. Phys.* 85, 4307 (1999).
140. M. Maret, M. Albrecht, J. Koehler, R. Poinot, C. Ulhaq-Bouillet, J. M. Tonnerre, J. F. Berar, and E. Bucher, *J. Magn. Magn. Mater.* 218, 151 (2000).
141. P. M. Oppeneer, V. N. Antonov, T. Kraft, H. Eschrig, A. N. Yaresko, and A. Ya Perlov, *J. Phys.: Condens. Matter* 8, 5769 (1996).
142. Olav Hellwig, Dieter Weller, A. J. Kellock, J. E. E. Baglin, and Eric E. Fullerton, *Appl. Phys. Lett.* 79, 1151 (2001).
143. N. S. Cameron, M. K. Corbierre, and A. Eisenberg, *Can. J. Chem.* 77, 1311 (1999).
144. M. W. Matsen and F. S. Bates, *Macromolecules* 29, 7641 (1996).
145. A. K. Khandpur, S. Förster, F. S. Bates, I. W. Hamley, A. J. Ryan, W. Bras, K. Almdhal, and K. Mortensen, *Macromolecules* 28, 8796 (1995).
146. M. J. Fasolka and A. M. Mayes, *Ann. Rev. Mater. Res.* 31, 323 (2001).
147. P. Minsky, C. K. Harrison, P. M. Chaikin, R. A. Register, and N. Yao, *Appl. Phys. Lett.* 68, 2586 (1996).
148. M. Park, C. Harriuson, P. M. Chaikin, R. A. Register, and D. H. Adamson, *Science* 276, 1401 (1996).
149. G. Liu, J. F. Ding, T. Hashimoto, K. Kimishima, F. M. Winnik, and S. Nigam, *Chem. Mater.* 11, 2233 (1999).
150. E. Huang, L. Rockford, T. P. Russell, and C. J. Hawker, *Nature* 395, 757 (1998).
151. K. Amundson, E. Helfand, D. D. Davis, X. Quan, S. S. Patel, and S. D. Smith, *Macromolecules* 24, 6546 (1991).
152. K. Amundson, E. Helfand, X. Quan, S. D. Hudson, and S. D. Smith, *Macromolecules* 27, 6559 (1994).
153. S. Zhu, R. J. Gambino, M. H. Rafailovich, J. Sokolov, S. A. Schwarz, and R. D. Gomez, *IEEE Trans. Magn.* 33, 3022 (1997).
154. K. Nielsch, F. Muller, A.-P. Li, and U. Gosele, *Adv. Mater.* 12, 582 (2000).
155. H. Hieda, N. Gemma, and K. Naito, *Jpn. J. Appl. Phys.* 40, L1071 (2001).
156. R. A. Segalman, H. Yokoyama, and E. J. Kramer, *Adv. Mater.* 3, 1152 (2001).
157. K. Asakawa and T. Hiraoka, "Proceedings of the Annual APS Meeting," Vol. I33-2, 2000.
158. M. J. Fasolka, D. J. Harris, A. M. Mayes, M. Yoon, and S. G. J. Mochrie, *Phys. Rev. Lett.* 79, 3018 (1997).
159. Y. J. Chen, J. P. Wang, E. W. Soo, L. Wu, and T. C. Chong, *J. Appl. Phys.* 91, 7323 (2002).
160. S. Facsko, T. Dekorsy, C. Koerdt, C. Trappe, H. Kurz, A. Vogt, and H. L. Hartnagel, *Science* 285, 1551 (1999).
161. R. P. Andres, J. D. Bielefeld, J. I. Henderson, D. B. Janes, V. R. Kolagunta, C. P. Kubiak, W. J. Mahoney, and R. G. Osifchin, *Science* 272, 1323 (1996).
162. G. Schön and U. Simon, *Colloid Polym. Sci.* 273, 101 (1995).
163. G. Schön and U. Simon, *Colloid Polym. Sci.* 273, 202 (1995).
164. S. Rubin, G. Bar, T. N. Yaylor, R. W. Cutts, and T. A. Zawodzinski, *J. Vac. Sci. Technol., A* 14, 1870 (1996).

165. M. Brust, M. Walker, D. Bethell, D. J. Schiffrin, R. Whyman, *J. Chem. Soc., Chem. Commun.* 1994, 801 (1994).
166. D. V. Leff, P. C. Ohara, J. R. Heath, W. M. Gelbart, *J. Phys. Chem.* 99, 7036 (1995).
167. R. L. Whetten, *Adv. Mater.* 8, 428 (1996).
168. R. S. Bowles, J. J. Kolstad, J. M. Calo, and R. P. Andres, *Surf. Sci.* 106, 117 (1981).
169. G. E. Poirier and E. D. Pylant, *Science* 272, 1145 (1996).
170. Z. Gai, B. Wu, J. P. Pierce, G. A. Farnan, D. Shu, M. Wang, Z. Zhang, and J. Shen, *Phys. Rev. Lett.* 89, 235502 (2002).
171. L. Huang, S. J. Chey, and J. H. Weaver, *Phys. Rev. Lett.* 80, 4095 (1998).
172. S. J. Chey, L. Huang, and J. H. Weaver, *Surf. Sci.* 419, L100 (1998).
173. G. Brown, H. K. Lee, T. C. Schulthess, B. Ujfalussy, G. M. Stocks, W. H. Butler, D. P. Landau, J. P. Pierce, J. Shen, and J. Kirschner, *J. Appl. Phys.* 91, 7056 (2002).
174. Z. Y. Zhang and J. F. Wendelken, U.S. Patent 6,313,479, 2001.
175. A. N. Patil, D. Y. Paithankar, N. Otsuka, and R. P. Andres, *Z. Phys. D: at., mol. clusters* 26, 135 (1993).
176. L. C. Chao and R. P. Andres, *J. Colloid Interface Sci.* 165, 290 (1994).
177. V. A. Shchukin and D. Bimberg, *Rev. Mod. Phys.* 71, 1125 (1999).
178. J. Tersoff, C. Teichert, and M. G. Lagally, *Phys. Rev. Lett.* 76, 1675 (1996).
179. I. Daruka and A. L. Barabasi, *Phys. Rev. Lett.* 79, 3708 (1997).
180. L. Huang, S. J. Chey, and J. H. Weaver, *Phys. Rev. Lett.* 80, 4095 (1998).
181. M. Bäumer and H. J. Freund, *Prog. Surf. Sci.* 61, 127 (1999).
182. A. Sugawara and M. R. Scheinfein, *Phys. Rev. B* 56, R8499 (1997).
183. K. Naito, H. Hieda, M. Sakurai, Y. Kamata, and K. Asakawa, *IEEE Trans. Magn.* 38, 1949 (2002).
184. K. Asakawa and T. Hiraoka, "Proceedings of the Annual APS Meeting," Vol. I33-2, 2000.
185. M. J. Fasaloka, D. J. Harris, A. M. Mayes, M. Yoon, and S. G. J. Mochrie, *Phys. Rev. Lett.* 79, 3018 (1997).
186. E. F. Kneller and R. Hawig, *IEEE Trans. Magn.* 27, 3588 (1991).
187. R. Skomski and J. M. D. Coey, *Phys. Rev. B* 48, 15812 (1993).
188. T. Schrefl, H. Kronmuller, and J. Fidler, *J. Magn. Mag. Mater.* 127, L273 (1993).
189. J. M. D. Coey, *J. Magn. Magn. Mater.* 248, 441 (2002).
190. J. M. D. Coey, *J. Magn. Magn. Mater.* 226, 2107 (2001).
- 191.
192. J. M. D. Coey, *J. Alloys Comp.* 326, 238 (2001).
193. R. Skomski and J. M. D. Coey, "Permanent Magnetism," Institute of Physics, Bristol, 1999.
194. E. F. Kneller and R. Hawig, *IEEE Trans. Mag.* 27, 3588 (1991).
195. E. E. Fullerton, J. S. Jiang, C. H. Sowers, J. E. Pearson, and S. D. Bader, *Appl. Phys. Lett.* 72, 380 (1997).
196. J. P. Liu, C. P. Luo, Y. Liu, and D. J. Sellmyer, *Appl. Phys. Lett.* 72, 483 (1998).
197. J. P. Liu, Y. Liu, R. Skomski, and D. J. Sellmyer, *J. Appl. Phys.* 85, 4812 (1999).
198. W. Gong, G. C. Hadjipanayis, and R. F. Krause, *J. Appl. Phys.* 75, 6649 (1994).
199. J. Zhang, S. Y. Zhang, H. W. Zhang, B. G. Shen, and B. H. Li, *J. Appl. Phys.* 89, 2857 (2001).
200. D. J. Sellmyer and R. Skomski, *Scripta Mater.* 47, 531 (2002).
201. R. Coehoorn, D. B. De Mooij, and C. De Waard, *J. Magn. Mag. Mater.* 80, 01 (1989).
202. D. H. Ping, K. Hono, and S. Hirosawa, *J. Appl. Phys.* 83, 7769 (1998).
203. T. Kobayashi, M. Yamasaki, and M. Hamano, *J. Appl. Phys.* 87, 6579 (2000).
204. H. Zeng, J. Li, J. P. Liu, Z. L. Wang, and S. Sun, *Nature* 420, 395 (2002).
205. D. J. Sellmyer, *Nature* 420, 374 (2002).



# Pb-Based Ferroelectric Nanomaterials

Ki Hyun Yoon

*Yonsei University, Seoul, Korea*

Dong Heon Kang

*University of Suwon, Suwon, Korea*

## CONTENTS

1. Introduction
  2. Synthesis of Lead-Based Ferroelectric Thin Films
  3. Physical Properties of PMN and PZT Thin Films
  4. Electrical Fatigue of PZSTN Thin Films
  5. Conclusions
- Glossary  
References

## 1. INTRODUCTION

There has been significant interest in the ferroelectric and antiferroelectric perovskite thin films such as  $\text{Pb}(\text{Mg}_{1/3}\text{Nb}_{2/3})\text{O}_3$  (PMN),  $\text{Pb}(\text{Zr,Ti})\text{O}_3$  (PZT),  $(\text{Ba,Sr})\text{TiO}_3$  (BST), and  $\text{Pb}(\text{Zr,Sn,Ti,Nb})\text{O}_3$  (PZSTN) because of their potential advantages for electro-optic and microelectronic applications including capacitors, pyroelectric detectors, ultra-high-density data storage systems, nonvolatile semiconductor memories, piezoelectric sensors and devices [1–9]. Recently, with miniaturization and integration of electronic circuits, the electronic devices with high performance in their small size up to nano scale are increasingly required. Current microelectromechanical systems (MEMS) technology, which is typically constructed on the micrometer scale, is being pushed into the nanometer range as well, leading to the nanoelectrochemical system (NEMS) [10–13]. It is well known that such a regime will be attainable by not only nanomachining technique such as lithography and printing but also proper thin-film techniques with homogeneous and fine grains under 100 nm in size. However, in the early stage, the interest in this nanotechnology has been mainly focused on the ceramic powders, which increased enormously with the availability and the possibility of consolidation into dense nanostructured ceramics. The most

important factors limiting this goal are powder agglomeration, contamination during processing, and the residual pores on various length scales in the bodies [14–16]. Nowadays, the nanocrystalline structure has been obtained more frequently and actually through the thin-film process rather than through the powder process. For such submicron-scale applications very fine-grained thin films with highly uniform and highly textured microstructures are preferable. Thus intensive and extensive studies have been attempted to prepare the applicable thin films with nanocrystalline structures by using various fabrication methods, such as wet-chemical processes, physical and chemical vapor depositions [17–31]. In the case of solution-based (wet)-chemical method, it has been known to offer numerous advantages, including excellent compositional control, uniform homogeneity, ease of fabrication over large area, and especially low cost. And so several wet-chemical methods utilizing metallorganic compounds and sol-gel processing have been extensively employed to prepare thin films of the lead-based ferroelectric materials [32, 33]. The methoxyethanol route in which 2-methoxyethanol was conventionally used as a solvent has been applied to the alkoxide-based sol-gel process for the film preparation because 2-methoxyethanol can act as a bridging ligand and has a sufficient solubility for alkoxides and salts [34, 35]. However, lead-based thin films deposited on the Pt or oxide electrode by conventional methoxyethanol sol-gel process suffer from the presence of irregular microstructures which are detrimental to submicron device performance. Modified processes using different solvents and/or chelating agents are often applied to overcome some problems of solution and film such as the instability against moisture and difficulty of multicomponent synthesis [36–38].

In this study we introduced the solution-derived lead-based perovskite thin films with different chemical compositions and electric phases such as ferroelectric  $\text{Pb}(\text{Mg}_{1/3}\text{Nb}_{2/3})\text{O}_3$  (PMN), ferroelectric  $\text{PbTiO}_3$  (PT), antiferroelectric  $\text{PbZrO}_3$  (PZ), ferroelectric/antiferroelectric  $\text{Pb}(\text{Zr}_{1-x}\text{Ti}_x)\text{O}_3$  (PZT), and ferroelectric/antiferroelectric

$\text{Pb}_{0.99}[(\text{Zr}_{0.6}\text{Sn}_{0.4})_{1-x}\text{Ti}_x]_{0.98}\text{Nb}_{0.02}\text{O}_3$  (PZSTN) by using the modified and conventional methoxyethanol routes [39–41]. Their microstructures could be controlled in the respect of solution chemistry, phase transformation kinetics, and composition control, respectively. The solution processing, film heat-treatment condition, film composition, and deposition sequence are widely discussed in terms of the nanocrystallization of the thin film. Considering the fact that in case of chemical solution-derived thin films, most of fabrication processes were limited to the hydrothermal and spray pyrolysis methods [19–27], this study seems to be meaningful. Furthermore, the recent approaches have been to acquire a long-term reliability of the ferroelectric thin films including resistance to electric fatigue, imprint, and leakage. It has been suggested that the fatigue in the antiferroelectric ceramics and thin films is much less severe than that in the ferroelectric counterparts [42, 43]. Also, the modification of nanocrystalline size is thought to be related closely with electrical fatigue. So the novel method has been introduced to modify nanocrystalline microstructure and to study its effect on electrical fatigue in PZT and PZSTN with the Pt electrode system. Therefore, the main topics of this chapter are to explain and analyze the effects of the modified solution chemistry, crystallization, and compositional variation on the nano-scale microstructure and related characteristics of the ferroelectric and antiferroelectric lead-based thin films.

## 2. SYNTHESIS OF LEAD-BASED FERROELECTRIC THIN FILMS

### 2.1. Solution Preparation

The Pb-based complex perovskite films were prepared by a conventional methoxyethanol chemical solution deposition [44] and a modified version of the route described by Yi et al. [35] and Park et al. [39, 45]. The starting materials were lead acetate ( $\text{Pb}(\text{CH}_3\text{COO})_2 \cdot 3\text{H}_2\text{O}$ ), zirconium *n*-propoxide ( $\text{Zr}(\text{O}-n\text{C}_3\text{H}_7)_4$ ), magnesium ethoxide ( $\text{Mg}(\text{OC}_2\text{H}_5)_2$ ), tin acetate ( $\text{Sn}(\text{CH}_3\text{COO})_4$ ), titanium isopropoxide ( $\text{Ti}(\text{O}-i\text{C}_3\text{H}_7)_4$ ), and niobium ethoxide ( $\text{Nb}(\text{OC}_2\text{H}_5)_2$ ). Propylenglycol, deionized water, and 2-methoxyethanol ( $\text{CH}_3\text{OC}_2\text{H}_4\text{OH}$ ) were used as a solvent. For the PMN and PZT precursors prepared by modified process, triethanolamine (TEA) and acetylacetonate (AcAc) were used as a complexing agent to control hydrolysis reaction with metal alkoxides, respectively. In the case of PMN solution, the A-site and B-site precursors of  $\text{ABO}_3$  perovskite structure were prepared separately. The appropriate amounts of the B-site precursors, such as magnesium ethoxide and niobium ethoxide, were mixed in 2-methoxyethanol and heated to  $\sim 110^\circ\text{C}$  for 24 h in a dry atmosphere. The solutions were then cooled to room temperature and then TEA ( $R = 1$ ; where  $R = \text{mole of TEA}/\text{mole of metal alkoxides}$ ) was added to create the B-site complex compound. In a separate vessel, to make the A-site precursor, lead acetate trihydrate was mixed with propyleneglycol and water in a 1:12:44 molar ratio. The solution was then heated to  $\sim 70^\circ\text{C}$  for dissolution of lead acetate trihydrate. This method was used to prepare all of Pb precursors. Finally, the A-site and

B-site precursors were mixed and allowed to react at room temperature for 3 h to form the PMN solution.

For the preparation of PT and PZ solutions, titanium isopropoxide and AcAc ( $R = 1$ ; where  $R = \text{mole of AcAc}/\text{mole of metal alkoxides}$ ) were added in 2-methoxyethanol. The refluxing and distillation of this mixture resulted in gold-colored solutions with a concentration of about 0.5 M. After refluxing for 3 h in air, the solution was cooled to room temperature. Finally, the PT chemical solution was prepared by mixing of the Pb and Ti solutions and diluting with 2-methoxyethanol. Similarly, PZ solution was prepared by the same solution processing method mentioned above.  $\text{Pb}(\text{Zr}_{0.5}\text{Ti}_{0.5})\text{O}_3$  (PZT) solution was obtained by mixing and reacting equal amounts of PT and PZ precursors. For  $(x)\text{PMN}-(1-x)\text{PZT}$  and  $(x)\text{PMN}-(1-x)\text{PT}$  solutions, the corresponding amounts of PZT, PT, and PMN precursors were mixed and allowed to react for 3 h to obtain a desired composition.

In the conventional process, all starting sources of lead for A-site cation and others such as Zr, Nb, Sn, Ti for B-site cation were refluxed and distilled in 2-methoxyethanol as described elsewhere [42, 43]. Then each solution was admixed to the corresponding  $\text{Pb}_{0.99}[(\text{Zr}_{0.6}\text{Sn}_{0.4})_{1-x}\text{Ti}_x]_{0.98}\text{Nb}_{0.02}\text{O}_3$  (PZSTN), PZ, and PZT compositions. Various PZSTN compositions with different electric phases were obtained by changing  $x$ ; as  $x = 0.03$  for antiferroelectrics (40/3/2) and  $x = 0.15$  for ferroelectrics (40/15/2). All mixed-precursor solutions prepared by the modified and conventional processes were partially hydrolyzed to give a 0.3 M stable sol by diluting them with 2-methoxyethanol. After refluxing at room temperature for 24 h in air, they were aged for 24 h for the film coating process.

### 2.2. Thin-Film Fabrication

Film deposition was carried out on the Pt (111)-coated {100} silicon substrates ( $\text{Si}/10,000\text{\AA}-\text{SiO}_2/200\text{\AA}-\text{Ti}/1500\text{\AA}-\text{Pt}$ ) by spin-coating at 2800 rpm for 30 s. Following pyrolysis at  $350\text{--}380^\circ\text{C}$  for 3 min, additional layers were spin-coated to build up the desired thickness. The films were crystallized by the rapid insertion heating process at  $700\text{--}750^\circ\text{C}$  for 10 min. The final film thicknesses were about 330–350 nm. In order to investigate the effect of heat-treatment procedure on microstructure and related characteristics, three different conditions (F I, F II, F III) for the ferroelectric PMN-PT thin-film series and two different conditions (AF I, AF II) for the antiferroelectric/ferroelectric PZSTN thin-film series were selected, respectively. For the F I process, the film was singly crystallized at  $730^\circ\text{C}$  for 5 min after deposition of multilayer amorphous film. For the F II, the film was crystallized at  $730^\circ\text{C}$  for 5 min after heating the first layer at the same condition, while layer-by-layer heating at  $730^\circ\text{C}$  for 5 min was done in sequence for the F III process [39].

The antiferroelectric/ferroelectric PZSTN thin films were formed by crystallizing at  $700^\circ\text{C}$  for 10 min after heating each layer at  $350^\circ\text{C}$  (AF I) and after crystallizing each layer at  $700^\circ\text{C}$  for 5 min without pyrolysis at  $350^\circ\text{C}$  (AF II), respectively. In case of the thin films having the buffered structure, a total of seven layers was deposited with varying stacking sequences such as AFE layer/FE layer/AFE layer

(AFE buffered FE), and FE layer/AFE layer/FE layer (FE buffered AFE), where PZT(50/50) and PZNST (40/15/2) thin films, and PZ and PZNST (40/3/2) thin films were applied as ferroelectric and antiferroelectric layers, respectively. The total thickness of the annealed films was about 330 nm.

## 2.3. Measurements and Characterization

### 2.3.1. Spectroscopic Characterization

The structure and crystallinity of the films were characterized by an X-ray diffraction (XRD; Rigaku Co., Japan) using  $\text{CuK}\alpha$  radiation. Typically step scans from  $20^\circ$  to  $60^\circ$ , at  $0.04$  increments and  $4$  s count time, were used. A differential thermal analysis (DTA) and thermogravimetry (TG) were performed on dried gel powders which were prepared by heating to  $150^\circ\text{C}$  for  $24$  h. DTA diagrams were obtained at a heating rate of  $10^\circ\text{C}/\text{min}$  and an airflow rate of  $40\text{ cm}^3/\text{min}$ . Also organic residue of the film after coating each layer was analyzed by using FT-IR (1600, Perkin Elmer, USA), where the film was deposited on  $\text{MgO}(100)$  single crystal. The film morphology was observed by a scanning electron microscope (SEM; S4200, Hitachi, Japan).

### 2.3.2. Electrical Measurements

Electrical measurements were made through the film thickness using Pt top electrode  $0.5$  mm in diameter prepared by sputtering through a shadow mask. Electrical contact was made to the bottom electrode with a probe wire, whereas the top contact was made with a microprobe tip. Low field dielectric properties were determined by an impedance/gain phase analyzer (4194A, Hewlett-Packard, USA) with an oscillation of  $10$  mV and frequencies of  $0.1$  kHz to  $100$  kHz. The hysteresis loop of polarization (P) versus electric field (E) and the fatigue characteristics of each film were obtained with a modified computer-controlled Sawyer–Tower circuit using an RT66A ferroelectric tester (Radiant Tech., USA) in conjunction with an external function generator (19, Wavetek, USA) and digitizing oscilloscope (VC6025, Hitachi, Japan).

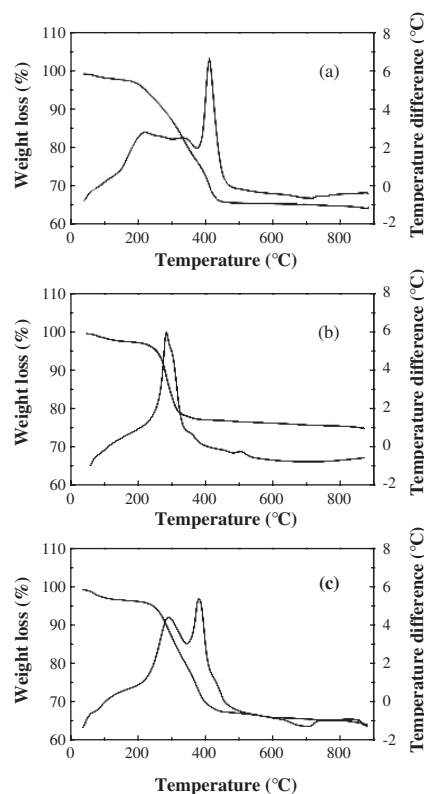
## 3. PHYSICAL PROPERTIES OF PMN AND PZT THIN FILMS

### 3.1. Solution Chemistry

Since Budd et al. [34] first demonstrated the methoxyethanol route, the modification of this route has been done in many ways. Especially to control the hydrolysis and condensation reaction of parent alkoxides during solution preparation, a number of related sol–gel methods using several alkoxides stabilized by chelating agents, or using other alcohol solvent, have been proposed. Alkoxides of some metals, such as Zr, Ti, and Nb, react with  $\beta$ -dikonates, diethanolamine, or triethanolamine to form chelate complexes [35, 39, 46]. These chelated complexes are less sensitive to moisture and result in stability to hydrolysis and precipitation during the solution preparation. Generally, thin films prepared by using solution stabilized by chelating agent show relatively high crystallization temperature and small grain size but little porous

microstructure because they contain more carboxyl ligand and require high thermodynamic driving force to decompose the organic compound. A good understanding of organic decomposition behavior of solution precursor and/or gel in chemical solution processing is essential to obtain more dense microstructure in chemical solution-derived thin films.

DTA/TG diagrams of PMN, PZT, and 0.5PMN-0.5PZT are represented in Figure 1a, b, and c. The main exothermic peaks at  $300$ – $400^\circ\text{C}$  are due to the combustion of the carboxylate compounds bound to the alkoxy groups in the precursors. This is also confirmed by a distinct weight loss in the TG data of Figure 1 [47]. It is noted that the temperature at which organic pyrolysis occurred is slightly different for the different compositions. In case of PMN gel powder, a large exothermic peak due to organic combustion appears at around  $400^\circ\text{C}$ , while for the PZT and 0.5PMN-0.5PZT gel powders, it appeared at about  $288^\circ\text{C}$  and  $360^\circ\text{C}$ , respectively. The difference of organic pyrolysis temperature is mainly attributed to different chelating agents used in the preparation of each chemical solution as explained in the previous experimental section. This suggests that the pyrolysis behavior is related to the character of carboxylate groups in the PMN and PZT solution because different complexing agent was used to stabilize each solution. Tahan et al. [48] reported that DTA diagrams of dried gels were dependent on the mixed ratio of acetic acid to ethyleneglycol in  $(\text{Ba}, \text{Sr})\text{TiO}_3$  solution processing. Thus, this difference is



**Figure 1.** (a) DTA/TG curves of PMN solution-derived gel powder, (b) PZT solution-derived gel powder, and (c) 0.5PMN-0.5PZT solution-derived gel powder. Reprinted with permission from [47], J. H. Park et al., *Ferroelectrics* 260, 75 (2001). © 2001, Gordon and Breach.



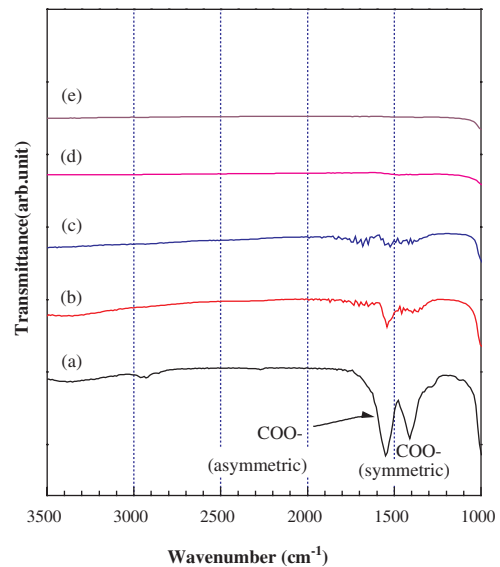
also explained by comparison of physical properties of the constituents used in this study. Table 1 represents the physical constants of typical solvent and various chelating agents [49]. As shown in Table 1, TEA has higher molecular weight and boiling point than those of acetylacetone or acetic acid. This reason is why organic pyrolysis temperature of the PMN solution is higher than that of the PZT solution. Two exothermic peaks of the Figure 1c solution also indicate the behavior of different chelating agents in 0.5PMN-0.5PZT solution, where peak temperatures were slightly different. In case of the modified chemical solution process, it may be more worthwhile to consider appropriate heat-treatment condition to eliminate organic content in the amorphous films and minimize the film cracking during the crystallization. Organic pyrolysis behavior was also investigated by FT-IR spectroscopy analysis. The typical FT-IR transmittance spectra shown in Figure 2 ascertain that in case of 0.5PMN-0.5PZT thin films, most organic groups were burned out in the temperature ranges of 350–380 °C. Therefore, an intermediate pyrolysis at 380 °C was performed in case of PMN-containing thin films, while PZSTN thin films prepared by the conventional process based on 2-methoxyethanol were pyrolyzed at 350 °C as explained in the experimental section. Figure 3 shows XRD patterns of the PMN, PZT, and 0.5PMN-0.5PZT thin films crystallized at optimum temperature that was experimentally determined in the range of 700–750 °C. It can be found that all the films prepared by chemical solution have a single-phase perovskite structure within X-ray detection limit. In analyzing the lattice spacing of the materials, the thin-film spacings were slightly larger than in the bulk material. It may be due to the mechanical stress present in thin films caused by lattice or thermal expansion mismatch between the film and substrate, resulting in differences in lattice constant of bulk and corresponding thin-film materials. SEM photographs of the thin films corresponding to above compositions are shown in Figure 4. The PMN and PZT films showed uniform grain structures with an average grain size of about 400 nm and 150 nm, respectively. The 0.5PMN-0.5PZT films also showed uniform and dense microstructure with an average grain size

**Table 1.** Physical properties of typical solvents and chelating agents.

Chemical name Formula	$M_w$	$b_p$	$\rho$	$n_D$
2-methoxyethanol $C_3H_8O_2$	76.10	124.43	0.9663	1.4028
Propylenglycol $C_3H_8O_2$	76.10	188.2	1.036	1.4324
Acetic acid $C_2H_4O_2$	60.05	118	1.053	1.049
Acetylacetone $C_5H_8O_2$	100.12	140.05	0.976	1.4512
Water $H_2O$	18.01	100.00	1.000	1.333
Triethanolamine $C_6H_{15}NO_3$	149.19	335.4	1.1242	1.4852

Note:  $M_w$ : molecular weight (g),  $b_p$ : boiling point (°C) at 1 atm.,  $\rho$ : density ( $g/cm^3$ ) at 20° C,  $n_D$ : refractive index at R.T.

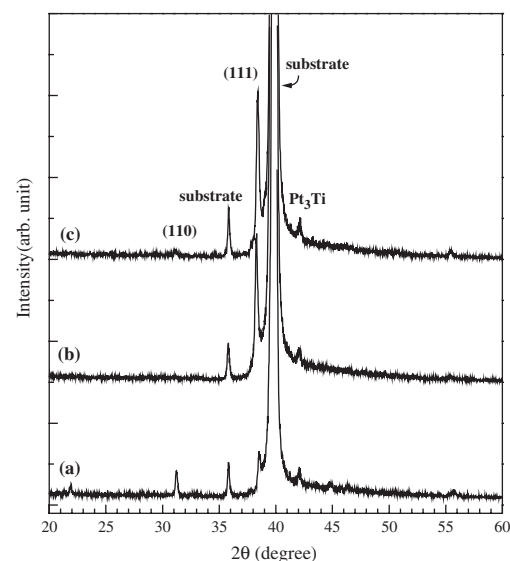
Source: Reprinted with permission from [49], C. R. Hammond, in "CRC Handbook of Chemistry and Physics" (D. R. Lide, Ed.). CRC Press, Boca Raton, FL, 1995. © 1995, Chemical Rubber Company Press.



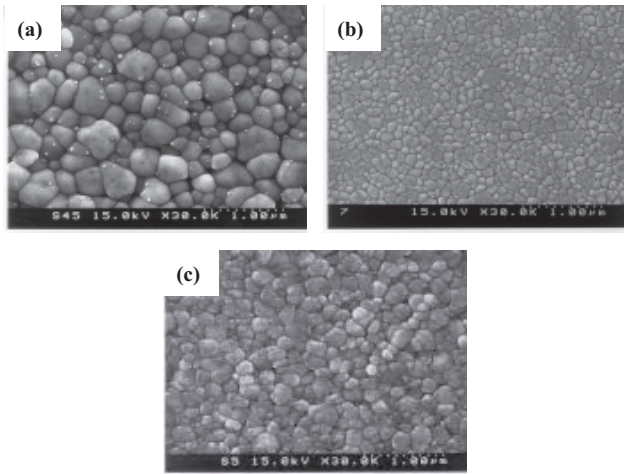
**Figure 2.** FT-IR transmittance spectra collected from thin layers by heating at different temperatures, (a) as deposited, (b) 200 °C for 3 min, (c) 300 °C for 3 min, (d) 350 °C for 3 min, and (e) 380 °C for 3 min.

around 200 nm. For the precursor modified with complexing agent or specific catalyst, it requires relatively higher temperature to decompose the organic compound and resulted in smaller grain size distribution or higher crystallization temperature. Similarly, Francis and Payne [50] reported that more uniform and small-grain-sized PMNT thin films were developed by adding benzoic acid as a catalyst.

Figure 5 shows the frequency dependency of the dielectric constant and loss for various films by chemical solution. The room-temperature dielectric constants, measured at 1 kHz, of the PMN, PZT, 0.5PMN-0.5PZT, 0.9PMN-0.1PZT, and 0.9PMN-0.1PT films, are summarized in Table 2

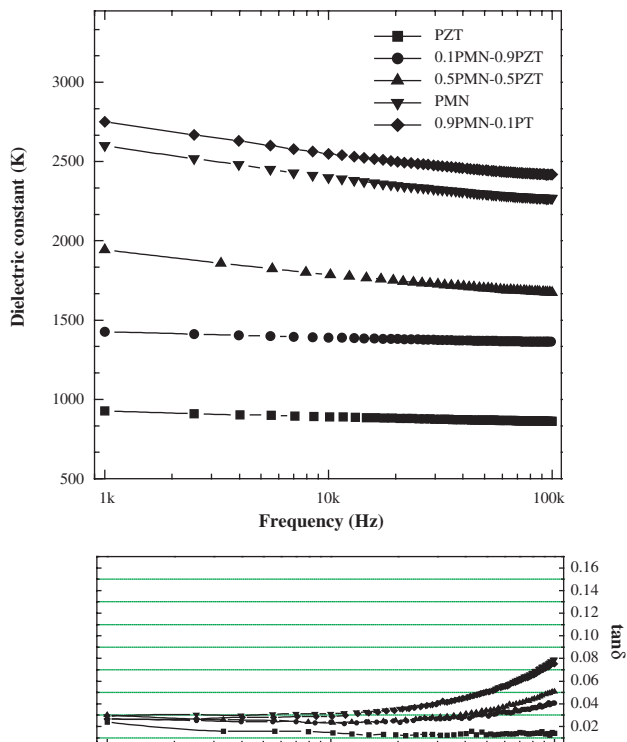


**Figure 3.** XRD patterns of solution-derived ferroelectric thin films. (a) PMN, (b) PZT, and (c) 0.5PMN-0.5PZT thin film. Reprinted with permission from [47], J. H. Park et al., *Ferroelectrics* 260, 75 (2001). © 2001, Gordon and Breach.



**Figure 4.** SEM photographs of chemical solution-derived ferroelectric thin films. (a) PMN, (b) PZT, and (c) 0.5PMN-0.5PZT thin film. Reprinted with permission from [47], J. H. Park et al., *Ferroelectrics* 260, 75 (2001). © 2001, Gordon and Breach.

[47, 51, 52]. The dielectric properties of the Pb-based thin films were comparable or superior to those of the films with same composition prepared by conventional sol-gel process as reported previously [50, 53, 54]. This confirms that the chemical solution method modified by the chelating agent used in this study can be applied to prepare a reliable ferroelectric thin film with a variety of lead-based compositions.



**Figure 5.** Frequency dependencies of dielectric constant and  $\tan \delta$  for the various ferroelectric thin films by chemical solution deposition.

**Table 2.** Summary of the dielectric and hysteresis properties of solution-derived Pb-based ferroelectric thin films by chemical solution deposition.

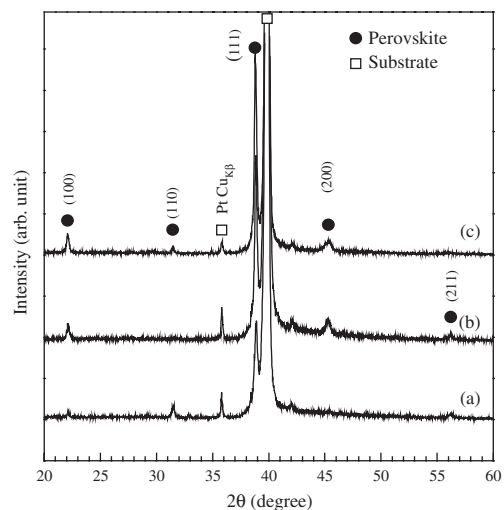
Thin films	$\epsilon_{r,1\text{kHz}}$	$\delta$ (%) <sup>a</sup>	$\tan \delta$	$P_r$ ( $\mu\text{C}/\text{cm}^2$ )	$E_c$ (kV/cm)
PMN	2600	13.1	0.03	1.3	4.5
0.5PMN-0.5PZT	1994	13.5	0.03	14.3	34.8
0.1PMN-0.9PZT	1420	7.1	0.03	18	40
PZT	926	6.8	0.027	11.3	48.5
0.9PMN-0.1PT	2750	12.7	0.031	5.8	11

<sup>a</sup>Degree of dispersion for the dielectric constant with frequency ( $\delta$ ) was calculated from the equation  $(\epsilon_{r,1\text{kHz}} - \epsilon_{r,100\text{kHz}})/\epsilon_{r,1\text{kHz}} \times 100$  (%).

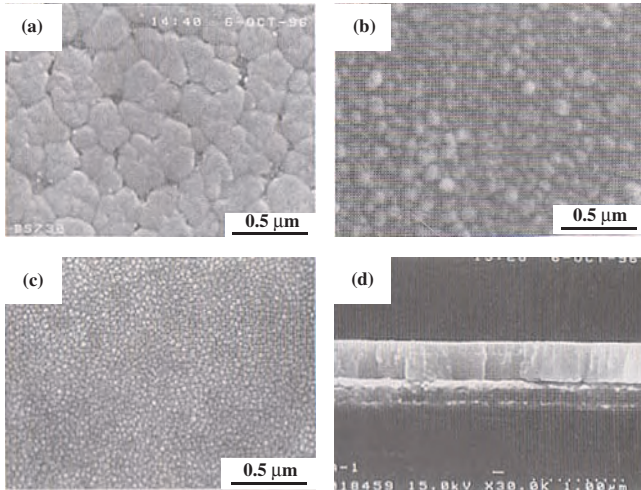
Source: Reprinted with permission from [47], J. H. Park et al., *Ferroelectrics* 260, 75 (2001). © 2001, Gordon and Breach.

### 3.2. Nucleation and Grain Growth

Figure 6 shows typical XRD patterns for 0.5PMN-0.5PT(50PMNT) thin films prepared according to the multilayer film formation and heating process as explained in experimental part. These diffraction patterns showed that they were developed highly (100)-oriented ones (F I film) (Fig. 3a) while the highly (111)-oriented films were obtained for F I and F II films (Fig. 3b and c). In regard to both (111)- and (100)-oriented thin films, Liu and Phule [55] reported that the (111) nuclei grew and a strong (111) texture developed in sol-gel-derived PZT film, when the film that had a perovskite seed layer formed *in-situ* was subjected to a higher-temperature heat treatment. Tani et al. [56] suggested that (100) PLZT texture was developed, when the film was deposited onto platinumized Si substrate which was free of any intermetallic phase between Pt and Ti. Further, they also concluded that this (100) texture represented minimum surface energy. Figure 7 shows the SEM photographs of the 50PMNT films with different multilayer film formation conditions. The thin film deposited by F I process consisted of small and large grains with grain size distribution of



**Figure 6.** XRD patterns of solution-derived 0.5PMN-0.5PT thin films deposited on Pt-passivated Si by (a) F I, (b) F II, and (c) F III processes. Reprinted with permission from [41], J. H. Park et al., *J. Am. Ceram. Soc.* 82, 2116 (1999). © 1999, American Ceramic Society.



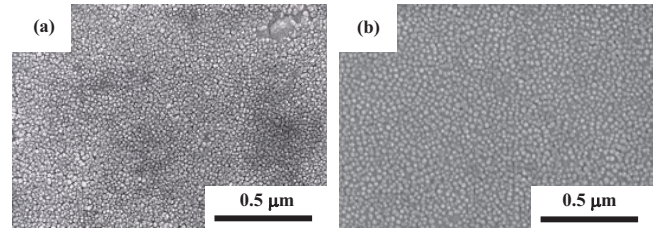
**Figure 7.** SEM photographs of the 0.5PMN-0.5PT thin films by (a) F I, (b) F II, (c) F III processes, and (d) cross-sectional view of (b). Reprinted with permission from [41], J. H. Park et al., *J. Am. Ceram. Soc.* 82, 2116 (1999). © 1999, American Ceramic Society.

about 50 to 200 nm. On the other hand, the grain size of the film by F II process became smaller. For the film by the F III process shown in Figure 4c, its grain size reduced effectively up to average grain size under 20 nm. It means that introduction of a perovskite seed layer before a crystallization of amorphous thin film could facilitate the microstructural change of the films into more small and uniform grain size distribution. It is possibly ascribed to the presence of more nucleation sites between Pt substrate and the film or in the film, resulting in smaller grain size distribution [40, 57, 58]. The dielectric and ferroelectric properties of the films with different multilayer film formation conditions are summarized in Table 3. The dielectric constant of the F I film was slightly larger compared to that of F II or F III films heat-treated at 730 °C. These results imply that the degree of orientation and microstructure with different grain sizes have effects on the weak-field dielectric properties. A similar correlation between the orientation and grain size distribution has been also noticed by Aoki et al. [59] on sol-gel-derived PZT films, even when no pure perovskite phase was observed. Figure 8 indicates that the microstructure of PZT thin film effectively changed through the addition of relaxor compound and an increase of zirconium to titanium ratio, confirming that nanocrystallization of thin film can be controlled by compositional modification as well as crystallization condition.

**Table 3.** Comparison of dielectric properties of the 0.5PMN-0.5PT thin films deposited with various annealing conditions.

Annealing condition	Dielectric constant (at 1 kHz)	$\tan \delta$ (at 1 kHz)	Preferential orientation
F I	1690	0.02	$\langle 100 \rangle$
F II	1378	0.03	$\langle 111 \rangle$
F III	1413	0.03	$\langle 111 \rangle$

Source: Reprinted with permission from [41], J. H. Park et al., *J. Am. Ceram. Soc.* 82, 2116 (1999). © 1999, American Ceramic Society.



**Figure 8.** SEM photographs of the (a) 10 mol% PMN modified PZT(50/50) and (b) Zr/Ti modified PZT (80/20).

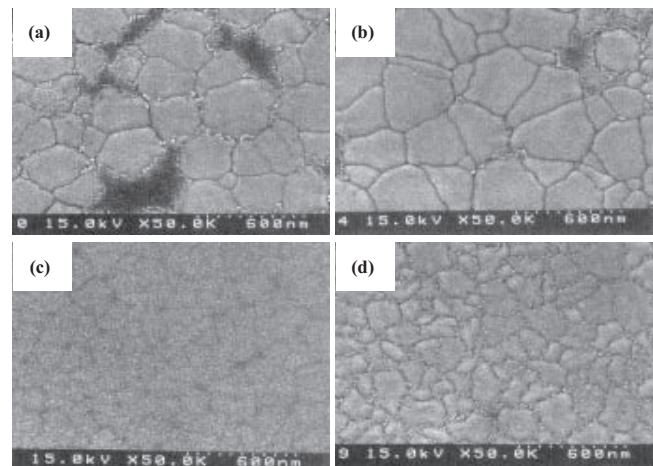
## 4. ELECTRICAL FATIGUE OF PZSTN THIN FILMS

### 4.1. Grain Size Effect

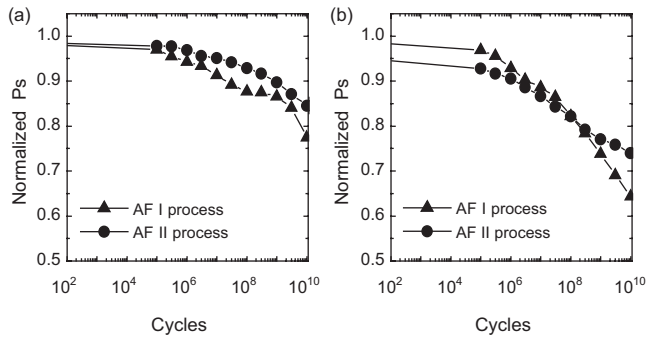
PZSTN compositions are also known to be attractive material for actuator and transducer applications due to relatively easier introduction of antiferroelectric and ferroelectric phase, leading to large displacement [60–63].

The antiferroelectric (40/3/2) and ferroelectric (40/15/2) PZSTN thin films were prepared by different heat treatments (AF I, AF II, AF III) and their SEM photographs are shown in Figure 9. The films prepared by the AF I process consisted of the large grains for both films (Fig. 9a, b), while, in the films prepared by the AF II, the nanocrystalline microstructure of very fine grains under 100 nm was obtained, where the 40/15/2 film showed a little larger grains than 40/15/2 possibly due to the higher content of ferroelectric (PZT) phase.

The antiferroelectric film (40/3/2) has small values of switchable polarization compared to those of the ferroelectric film (40/15/2). The saturated polarization ( $P_s$ ), corresponding to the difference between switched polarization ( $P^*$ ) and the half value of switchable polarization ( $(P^*_r - P^*_r)/2$ ), has been introduced [32, 40]. The change of normalized  $P_s$  in the PZSTN thin films is shown in Figure 10. The degradation of polarization in the ferroelectric composition (40/15/2) was steeper than that in the



**Figure 9.** SEM photographs of the PZSTN thin films with antiferroelectric (40/3/2) composition (a) by the AF I and (c) by the AF II process; and ferroelectric (40/15/2) composition (b) by the AF I process and (d) by the AF II process.

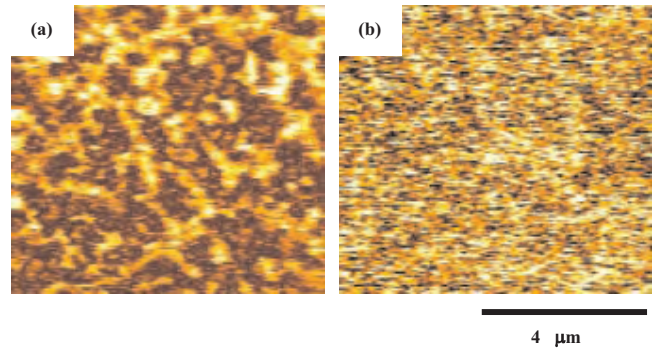


**Figure 10.** Comparison of the fatigue curves between the films prepared by the AF I process and the AF II process for (a) antiferroelectric (40/3/2) and (b) antiferroelectric (40/15/2) compositions.

antiferroelectric composition (40/3/2). It was considered that the antiferroelectrics contained mainly  $180^\circ$  domains which had smaller internal stress during switching cycles compared to  $90^\circ$  domains as reported elsewhere [64].

The following things seem to be more interesting. The PZSTN thin films prepared by the AF I process (the large and irregular grain size) showed more degradation of polarization than the films prepared by the AF II process showing nanocrystalline structure with regular grain size for both compositions. The steeper degradation of polarization in the films prepared by the AF I process could be mainly attributed to the larger grains and irregular microstructure. The different distributions of the applied electric field and internal stress between the large perovskite grains and the grain boundaries (or the different phases between grains) during repetitive switching should generate the electrical and mechanical defects especially at the interfaces of the two different phases. The uniformly distributed nanocrystalline structure could release the stress coming from the above reason more than the microstructure consisting of the large grains. Similar phenomena will be found in the results shown in the next section.

The phase images of electrostatic charge were taken using a commercial scanning force microscope. Initially, a dc voltage of  $-10$  V was applied while a conductive tip scanned over the desired area. Subsequently, the phase images were obtained under applying an ac voltage of  $1$  V and a frequency of  $17$  kHz. Details of instrumentation and mechanisms for the imaging have already been published [65]. Figure 11 shows phase images of electrostatic charge of the 40/3/2 and 40/15/2 compositions. After being scanned with a conductive tip held under an applied dc voltage of  $-10$  V, the thin film having 40/3/2 composition showed a quite different phase image compared with the film having 40/15/2 composition. In the 40/3/2 film [Fig. 11a], the bright regions of the phase image result from the polarization directions toward the bottom electrode while the dark regions result from the polarization directions toward the top electrode. The bright and dark regions seemed to consist of several nanocrystalline grains. This behavior implies that the very small nano-sized domains have their antiferroelectric properties. It was confirmed that the antiferroelectric 40/3/2 composition was switched by  $180^\circ$ . On the other hand, the phase image of the 40/15/2 film [Fig. 11b] showed no contrast in the whole area. This configuration also means that the full



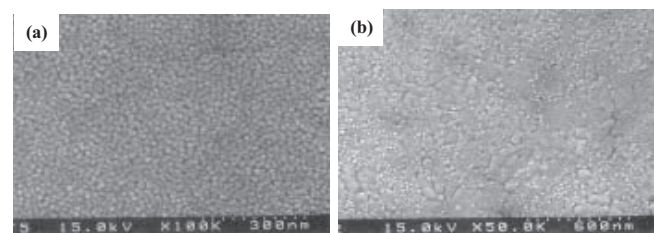
**Figure 11.** Phase images of electrostatic charge of the PZSTN thin films with (a) antiferroelectric (40/3/2) and (b) ferroelectric (40/15/2) compositions after applying  $-10$  V. Reprinted with permission from [68], J. H. Jang et al., *Appl. Phys. Lett.* 73, 1823 (1998). © 1998, American Institute of Physics.

nano domains of the 40/15/2 have switched to the unipolar direction and switched by  $90^\circ$ .

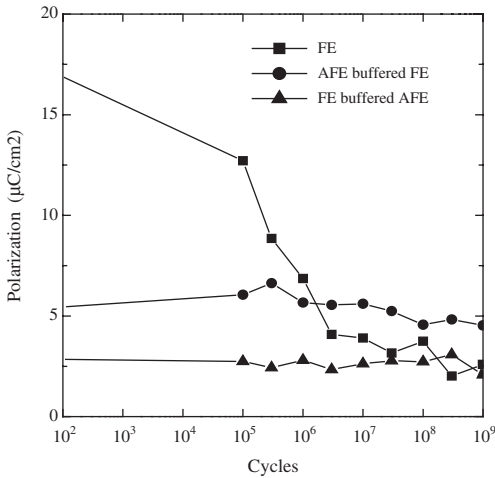
## 4.2. Buffer-Layer Effect

In addition to the effect of the overall grain size of the PZSTN thin films on the electrical properties, we have modified the grain size of very thin buffer layers existing on the interface between the electrode and the main body. The buffer layers have the PZT and PZSTN system but utilized different compositions to the main dielectric films. The PZ buffer layer on PZT body has grain size less than  $20$  nm as shown in Figure 12a. The PZT buffer layer on PZ body has two different grain sizes of about  $20$  nm, same as PZ buffer, and  $60$ – $70$  nm as shown in Figure 12b.

The change of  $P^*r$ - $P^{\wedge}r$  as a function of switching cycles of PZT, PZ buffered PZT, and PZT buffered PZ is shown in Figure 13 [64].  $P^*r$  is the switched remanent polarization between two opposite polarity pulses, and  $P^{\wedge}r$  is the non-switched remanent polarization between two same polarity pulses. The difference between  $P^*r$  and  $P^{\wedge}r$  denotes the switchable remanent polarization, an important variable for nonvolatile memory application. The PZT films showed a significant drop in polarization after  $10^5$  cycles. The PZ buffered PZT did not show any drop of polarization up to  $10^9$  cycles with sufficient remanent polarization of about  $5 \mu\text{C}/\text{cm}^2$ . The virgin state of the PZ buffered PZT has smaller remanent polarization than that of the PZT. However, the relative values were reversed after  $2 \times 10^6$  cycles. This implies that the nanocrystalline antiferroelectric

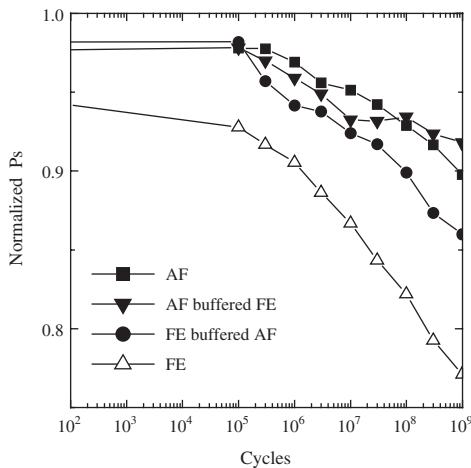


**Figure 12.** SEM photographs of (a) AFE-PZ buffer on FE-PZT and (b) FE-PZT buffer on AFE-PZ thin films.



**Figure 13.** Switchable polarization ( $P^*r-P^r$ ) based on ferroelectric PZT(FE) and antiferroelectric PZ(AFE) thin films. Reprinted with permission from [64], J. H. Jang and K. H. Yoon, *Appl. Phys. Lett.* 75, 130 (1999). © 1999, American Institute of Physics.

layer should act as a barrier to degradation of polarization. Reduced stress related to  $180^\circ$  domains during switching would suppress the formation of electrical and mechanical defects, which cause the generation of the oxygen vacancies [42, 43]. The near zero fatigue in the PZ buffered PZT compared with that of the PZT films was attributed to the relatively low stress and the resulting low number of oxygen vacancies induced at the ferroelectric or antiferroelectric phase, the nanocrystalline microstructure played an important role to reduce the internal stress. It was confirmed by the fact that PZT buffered PZ also showed very good fatigue endurance as shown in Figure 13, although it had an insufficient remanent polarization value for FRAM application. The saturated polarization ( $P_s$ ) of AF, AF buffered FE, FE buffered AF, and FE is shown in Figure 14 [67]. All films except FE showed near zero fatigue after  $10^9$  cycles.



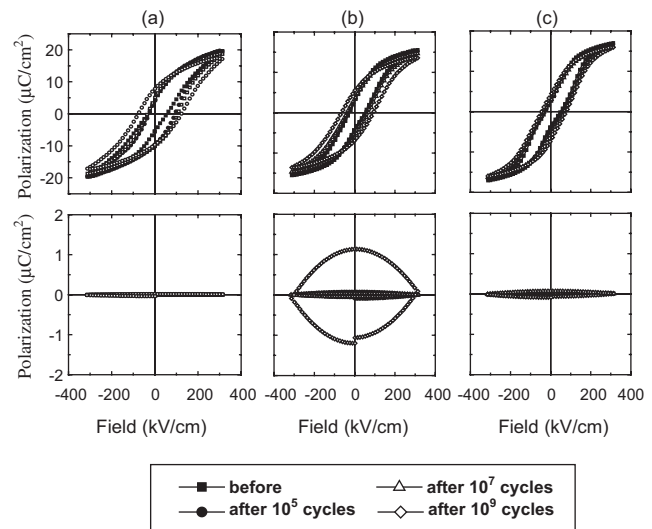
**Figure 14.** Switchable polarization based on ferroelectric PZSTN(FE) and antiferroelectric PZSTN(AFE) thin films. Reprinted with permission from [67], J. H. Jang and K. H. Yoon, *Thin Solid Films* 401, 67 (2001). © 2001, Elsevier Science.

The FE and AF buffered FE showed sufficient remanent polarization, while FE buffered AF and AF showed insufficient remanent polarization. The AF buffered FE showed excellent fatigue properties maintaining more than 90% of initial polarization values after  $10^9$  cycles. FE showed the stiffest degradation of polarization. FE buffered AF showed better fatigue endurance than FE. The near zero fatigue in the AF buffered FE was attributed to the fact that the nanocrystalline microstructure having antiferroelectric phase should act as a barrier to degradation of polarization. The relatively lower stress and the resulting smaller number of oxygen vacancies should be induced at the nanocrystalline buffer-Pt electrode interface than at the large grains-Pt electrode interface.

Figure 15 shows the hysteresis loops and the leakage current component of the PZ buffered PZT film with different switching cycles [64, 67]. The hysteresis loops and leakage current component of the corresponding hysteresis loop were measured using the same sample, using “Analysis” software in RT66A ferroelectric tester. During the voltage step, the change in charge ( $dQ$ ) due to the leakage current can be estimated from the measured resistance by the following equation:

$$dQ = (V \times A \times \Delta T) / R \tag{1}$$

where  $V$  is the voltage applied across the film,  $A$  is the capacitor area,  $\Delta T$  is the time increment, and  $R$  is the resistance for polarity of the applied voltage. In the hysteresis loop after  $10^5$  cycles, the remanent polarization increased compared with the initial state, and such behavior agreed with the  $P^*r-P^r$  data in Figure 13. The increase of remanent polarization near  $10^5$  cycles should be related to the release of the suppressed polarization originating from the difference in lattice parameters between PZT and PZ. The



**Figure 15.** The change of P-E hysteresis loops and leakage current component of (a) the PZ buffered PZT thin film, (b) the FE, and (c) the AF buffered FE during fatigue. Reprinted with permission from [64], J. H. Jang and K. H. Yoon, *Appl. Phys. Lett.* 75, 130 (1999). © 1999, American Institute of Physics; and from [67], J. H. Jang and K. H. Yoon, *Thin Solid Films* 401, 67 (2001). © 2001, Elsevier Science.

release of polarization occurred asymmetrically. This behavior was attributed to the different natures of crystallization between the two PZ layers, because one PZ layer was crystallized on the Pt bottom electrode and the other PZ layer was crystallized on PZT layers during the deposition process of the films. As well as near  $10^5$  cycles, the leakage current component of the corresponding hysteresis loop (Fig. 15a) increased negligibly after  $10^9$  cycles. This result supports the release of the suppressed polarization. The resistivity measurement also indicated that the resistivity of the PZ1/PZT5/PZ1 film did not change after  $10^9$  cycles. In the hysteresis loop of FE (Fig. 15b), the increase of remanent polarization in hysteresis loop of FE was found after  $10^7$  cycles. The increase in FE should come from the leakage current component of the corresponding hysteresis loop increased after  $10^7$  cycles. The reason for leakage in fatigued FE could be explained by the large displacement of the grains under the applied field and the large stress during the  $90^\circ$  domain switching. The AF buffered FE showed nearly no increase of remanent polarization and leakage current component after  $10^9$  cycles as shown in Figure 15c. There should be a small amount of defect dipoles due to nanocrystalline antiferroelectric buffer. The negligible leakage current component could be explained by the reason that the antiferroelectric buffer has very small grain size and internal stress during  $180^\circ$  switching acts as a barrier to fatigue between the electrode and the ferroelectric layers. Therefore, the antiferroelectric buffer could be resistant to mechanical stress and resulting microcracking or production of electrical defects. The AF buffered FE showed somewhat different fatigue properties from the PZ buffered PZT. In the PZ buffered PZT, there was the release of the suppressed polarization originating from the mismatches in lattice parameters and microstructures between PZT and PZ, while there was no significant change in AF buffered FE during  $10^9$  cycles of  $\pm 10$  V due to the similar lattice parameters and microstructures [64].

## 5. CONCLUSIONS

We have outlined the chemical synthesis of Pb-based nanocrystalline perovskite thin films and their effects on the electrical properties such as dielectric constant, hysteresis loop, and especially fatigue character. For Pb-based perovskites, the modification of metal alkoxide by a chemical solution processing gave rise to the formation of a stable complex against hydrolysis, and eventually enhanced reliability and uniformity of the films. Surface microstructural characteristics resulting from the crystallization of as-prepared thin films were found to depend strongly on the various multilayer film formations as well as solution chemistry. Moreover, with proper control of multilayer thin-film formation procedure, it may be possible to control its related dielectric properties as well as preferred orientation of the ferroelectric thin films.

For antiferroelectric and ferroelectric PZSTN thin films, nanocrystalline microstructure was obtained with various heat treatments and compositional change, and the modified multilayer processes improved the electric fatigue

endurance. From the scanning force microscopy, it was confirmed that the very small nano domains have their ferroelectric and antiferroelectric properties.

The nanocrystalline antiferroelectric buffer has improved the electric fatigue endurance of the PZT-based ferroelectric thin films prominently. The  $P^*r-P^*r$  of the PZ buffered PZT films and AF buffered FE (PZSTN) showed near zero degradation of polarization after  $10^9$  cycles on the Pt electrode. The nanocrystalline antiferroelectric PZ and AF buffers acted as barriers to fatigue due to their  $180^\circ$  domain switching and stress release in the nanocrystalline microstructure. It is expected to be applied to other popular thin-film processes for nonvolatile memory applications and other fields, such as the actuator which needs long-term reliability.

## GLOSSARY

**Antiferroelectric (AFE)** There is no net polarization of a cell in the absence of an electric field, but the cell is polarized when a field is applied. An antiferroelectric material will be strongly repelled by an electric field. The dipole moments in an antiferroelectric are arranged with an equal number pointing in each direction.

**Electric fatigue** The loss in switchable polarization at a fixed drive voltage as a function of the continuous switching of a ferroelectric capacitor.

**Ferroelectric (FE)** A kind of electric phase in crystal where the centers of the positive and negative charges do not coincide even without the application of external electric field. In this case, spontaneous polarization exists in the crystal. And the polarization of the dielectric can be reversed by an electric field.

**Microelectromechanical system (MEMS)** Devices that have a characteristic length of less than 1 mm but more than  $1 \mu\text{m}$ , that combine electrical and mechanical components that are fabricated using integrated circuit batch-processing technologies.

**Nano electromechanical system (NEMS)** The NEMS devices that have the dimension of nanometer range.

**Sol-gel process** Colloidal route used to synthesize chemicals with an intermediate stage including a sol/or a gel state. (Sol-gel is restricted to the gels synthesized from alkoxides).

## REFERENCES

1. J. F. Scott and C. A. Paz de Araujo, *Science* 246, 1400 (1989).
2. D. Dimos, S. J. Lockwood, and R. W. Schwartz, *IEEE Trans. Comp. Pack. Man. Tech.* A18, 174 (1995).
3. V. Bobnar, Z. Kutnjak, A. Levstik, J. Holc, M. Kosec, T. Hauke, R. Steinhausen, and H. Beige, *J. Appl. Phys.* 85, 622 (1999).
4. T. Tani, J. Li, D. Viehland, and D. A. Payne, *J. Appl. Phys.* 75, 3017 (1994).
5. H. D. Chen, K. R. Udayakumar, C. J. Gaskey, and L. E. Cross, *Appl. Phys. Lett.* 67, 3411 (1995).
6. V. Nagarajan, S. P. Alpay, C. S. Ganpule, B. K. Nagaraj, S. Aggarwal, E. D. Williams, A. L. Roytburd, and R. Ramesh, *Appl. Phys. Lett.* 77, 438 (2000).
7. T. Haccart, E. Cattin, D. Remiens, S. Hiboux, and P. Muralt, *Appl. Phys. Lett.* 76, 3292 (2000).

8. A. M. Flynn, L. S. Tavrow, S. F. Bart, R. A. Brooks, D. J. Ehrlich, K. R. Udayakumar, and L. E. Cross, *J. Microelectromechan. Syst.* 1, 44 (1992).
9. K. R. Udayakumar, J. Chen, A. M. Flynn, S. F. Bart, L. S. Tavrow, D. J. Ehrlich, L. E. Cross, and R. A. Brooks, *Ferroelectrics* 160, 347 (1994).
10. G. H. Berrstein, H. V. Goodson, and G. L. Snider, in "The MEMS Handbook" (M. Gad-el-Hak, Ed.). CRC Press, Boca Raton, FL, 2002.
11. R. P. Feynman, *J. Microelectromechan. Syst.* 1, 60 (1992).
12. F. Cerrina, *Proc. IEEE* 84, 644 (1997).
13. S. Matsui, *Proc. IEEE* 84, 629 (1997).
14. M. J. Mayo, D. C. Hague, and D. J. Chen, *Mater. Sci. Eng.* A166, 145 (1993).
15. K. P. Kumar, K. Kelzer, A. J. Burggraaf, T. Okuba, H. Nagamoto, and S. Morooka, *Nature* 358, 48 (1992).
16. W. H. Rhodes, *J. Am. Ceram. Soc.* 64, 19 (1981).
17. K. I. Choy, in "Handbook of Nanostructured Materials and Nanotechnology" (H. S. Nalwa, Ed.), Vol. 1, p. 533. Academic Press, San Diego, 2000.
18. Q. Yitai, in "Handbook of Nanostructured Materials and Nanotechnology" (H. S. Nalwa, Ed.), Vol. 1, p. 459. Academic Press, San Diego, 2000.
19. Q. W. Chen, Y. T. Qian, Z. Y. Chen, W. B. Wu, Z. W. Chen, G. E. Zhou, and Y. H. Zhang, *Appl. Phys. Lett.* 66, 1 (1995).
20. Q. W. Chen, Y. T. Qian, Z. Y. Chen, G. E. Zhou, and Y. H. Zhang, *Mater. Lett.* 22, 93 (1995).
21. Q. W. Chen and Y. T. Qian, *Thin Solid Films* 264, 25 (1995).
22. Q. W. Chen, Y. T. Qian, Z. Y. Chen, Y. Xie, G. E. Zhou, and Y. H. Zhang, *Mater. Lett.* 24, 85 (1995).
23. Q. W. Chen, Y. T. Qian, Z. Y. Chen, L. Shi, X. G. Li, G. E. Zhou, and Y. H. Zhang, *Thin Solid Films* 272, 1 (1996).
24. Y. Xie, W. Z. Wang, Y. T. Qian, L. Yang, and Z. Chen, *J. Crystal Growth* 167, 656 (1996).
25. W. J. Desisto, Y. T. Qian, C. Hanni Gan, J. O. Edward, R. Kershaw, K. Dwight, and A. World, *Mater. Res. Bull.* 25, 183 (1990).
26. Q. W. Chen, X. G. Li, Y. T. Qian, J. S. Zhu, G. E. Zhou, W. P. Zhang, and Y. H. Zhang, *Appl. Phys. Lett.* 68, 1 (1995).
27. Y. T. Qian, Y. Xie, Z. Chen, J. Lu, and J. Zhu, *J. Chem. Phys.* 8, 549 (1995).
28. W. S. Hu, Z. G. Liu, Z. C. Wu, and D. Feng, *Mater. Lett.* 28, 369 (1996).
29. T. C. Chou, D. Adamson, J. Mardinly, and T. G. Nieh, *Thin Solid Films* 205, 131 (1991).
30. X. Mei, M. Tao, H. Tan, Y. Han, and W. Tao, *Mater. Res. Soc. Symp. Proc.* 286, 179 (1993).
31. T. Sugino, K. Tanioka, S. Kawasaki, and J. Shirafuji, *Diamond Related Mater.* 7, 632 (1998).
32. T. Atsuki, N. Soyama, G. Sasaki, T. Yonezawa, K. Ogi, K. Sameshima, K. Hoshiba, Y. Nakao, and A. Kamisawa, *Jpn. J. Appl. Phys.* 33, 5196 (1994).
33. M. N. Kamalasanan, N. D. Kumar, and S. Chandra, *J. Appl. Phys.* 76, 4603 (1994).
34. K. D. Budd, S. K. Dey, and D. A. Payne, *Brit. Ceram. Soc. Proc.* 36, 107 (1985).
35. G. Yi, Z. Wu, and M. Sayer, *J. Appl. Phys.* 64, 2717 (1988).
36. Y. L. Tu and S. J. Milne, *J. Mater. Res.* 10, 3222 (1995).
37. Y. Takahashi, Y. Matsuoka, K. Yamaguchi, M. Matski, and K. Kobayashi, *J. Mater. Sci.* 25, 3960 (1990).
38. K. H. Yoon, J. H. Park, and D. H. Kang, *J. Am. Ceram. Soc.* 78, 2267 (1995).
39. J. H. Park, K. H. Yoon, and D. H. Kang, *J. Am. Ceram. Soc.* 82, 2683 (1999).
40. K. H. Yoon, J. H. Park, and J. H. Jang, *J. Mater. Res.* 14, 2933 (1999).
41. J. H. Park, K. H. Yoon, and D. H. Kang, *J. Am. Ceram. Soc.* 82, 2116 (1999).
42. J. H. Jang and K. H. Yoon, *Ferroelectrics* 225, 193 (1999).
43. Q. Y. Jiang, E. C. Subbarao, and L. E. Cross, *J. Appl. Phys.* 75, 7433 (1995).
44. S. S. Sengupta, D. Roberts, J.-F. Li, M. C. Kim, and D. A. Payne, *J. Appl. Phys.* 78, 1171 (1995).
45. J. H. Park, K. H. Yoon, and D. H. Kang, *Thin Solid Films* 396, 84 (2001).
46. Y. Takahashi and Y. Wada, *J. Electrochem. Soc.* 137, 267 (1990).
47. J. H. Park, K. H. Yoon, and D. H. Kang, *Ferroelectrics* 260, 75 (2001).
48. D. M. Tahan, A. Safari, and L. C. Klein, *J. Am. Ceram. Soc.* 79, 1593 (1996).
49. C. R. Hammond, in "CRC Handbook of Chemistry and Physics" (D. R. Lide, Ed.). CRC Press, Boca Raton, FL, 1995.
50. L. F. Francis and D. A. Payne, *J. Am. Ceram. Soc.* 74, 3000 (1991).
51. J. H. Park, K. H. Yoon, D. H. Kang, and E. S. Kim, *Ferroelectrics* 258, 303 (2001).
52. J. H. Park, K. H. Yoon, D. H. Kang, and J. H. Park, *Mater. Chem. Phys.* 79, 151 (2003).
53. K. Okuwada, M. Imai, and K. Kakuno, *Jpn. J. Appl. Phys.* 28, L1271 (1989).
54. K. R. Udayakumar, J. Chen, P. J. Schuele, L. E. Cross, V. Kumar, and S. B. Krupanidhi, *Appl. Phys. Lett.* 60, 1187 (1992).
55. Y. Liu and P. P. Phule, *J. Am. Ceram. Soc.* 79, 495 (1996).
56. T. Tani, Z. Xu, and D. A. Payne, *Ferroelectric Thin Films III* 310, 269 (1993).
57. K. C. Chen and J. D. Mackenzie, *Mater. Res. Soc. Symp. Proc.* 180, 663 (1990).
58. C. H. Peng and S. B. Desu, *Mater. Res. Soc. Symp. Proc.* 243, 335 (1992).
59. K. Aoki, Y. Fukuda, K. Numata, and A. Nishimura, *Jpn. J. Appl. Phys.* 32, 5155 (1994).
60. K. Uchino, *Jpn. J. Appl. Phys.* 24, 460 (1985).
61. C. Zhiming, L. Jingyu, and W. Yongling, *Ferroelectrics* 101, 225 (1990).
62. P. Yang and D. A. Payne, *J. Appl. Phys.* 71, 1361 (1992).
63. D. Viehland, D. Forst, Z. Xu, and J.-F. Li, *J. Am. Ceram. Soc.* 78, 2101 (1995).
64. J. H. Jang and K. H. Yoon, *Appl. Phys. Lett.* 75, 130 (1999).
65. J. Lee, S. Esayan, A. Safari, and R. Ramesh, *Appl. Phys. Lett.* 65, 254 (1994).
66. J. H. Jang, K. H. Yoon, and K. Y. Oh, *Mater. Res. Bull.* 35, 393 (2000).
67. J. H. Jang and K. H. Yoon, *Thin Solid Films* 401, 67 (2001).
68. J. H. Jang, K. H. Yoon, and H. J. Shin, *Appl. Phys. Lett.* 73, 1823 (1998).

# Peptide Nanotubes

Hiroshi Matsui

*The City University of New York, New York, USA*

## CONTENTS

1. Introduction
  2. Development of Peptide Nanotubes
  3. Characterization of Peptide Nanotubes
  4. Peptide Nanotube Applications
  5. Summary
- Glossary  
References

## 1. INTRODUCTION

Recently, there has been enormous interest in nanomaterials such as nanotubes and nanowires which show superior electronic, magnetic, and mechanical properties that may not be obtained in the bulk states [1–5]. Therefore, it is natural for material scientists to use such excellent nanometer-sized materials as building blocks to build various miniaturized devices. One of the interesting applications is to build these nanotube-based devices in solution [6–11]. If nanotubes are soluble in aqueous solution (i.e., nanotubes are not aggregated in solution), they will be very practical in use for biological and medical applications. The water-soluble nanotubes are also advantageous to organize nanotubes in solution by using self-assembly and supramolecular processes.

Among various nanotubes, peptide molecule-assembled nanotubes satisfy those features. Peptide nanotubes are water-soluble and functional groups of peptides such as amide and carboxylic acid can highly enhance their self-assemblies via hydrogen bonding in solution. Peptide nanotubes usually possess high affinity to biological molecules via hydrogen bonding with their amide and carboxylic acid groups and this feature enables peptide nanotubes to decorate with various molecules or to sense biological molecules. This versatile functionalization capability makes peptide nanotubes flexible templates to create various exotic nanotubes. Addition of functionality to peptide nanotubes can also be achieved by incorporating the functional groups into peptide monomers [12] via organic synthesis. Once this modified peptide monomer is assembled

into nanotubes, the functional groups are also incorporated in the nanotubes. However, one needs to be careful because addition of functional groups to peptide monomers may affect their assembled nanotube structures. In other words, the certain additions may totally prevent nanotube formation because molecular self-assembly is very sensitive to the chemical structures of monomers [13]. Therefore, optimization of growth conditions for peptide nanotubes may be necessary when peptide monomers are modified to add new functionalities.

Another advantage of peptide nanotubes is that the nanotube structure and size can be controlled by external environments such as surfactant, solvent, temperature, and pH. One of the important factors to determine assembled nanotube structures is the degree of protonation in amide and carboxylic acid groups under these environmental changes. The protonation states of those groups have a significant effect on intermolecular hydrogen bonding and hydrophobicity of peptide monomers, which are driving forces of the peptide nanotube formation. Therefore, the strengths of hydrogen bonding and hydrophobicity of peptide monomers, controlled by the environments, determine the assembled nanotube structure. This feature allows us to synthesize peptide nanotubes in certain dimensions with high reproducibility by controlling experimental conditions. Once peptide monomers are assembled into peptide nanotubes, they are quite stable and can be used as building blocks for device fabrication in relatively harsh environments. Peptide assemblies may seem unstable; however, the peptide monomers are assembled into crystalline nanotubes via three-dimensional hydrogen bonds, which makes peptide nanotubes fairly rigid (See Fig. 4 later in this chapter). For example, the melting point for one of the peptide nanotubes is 235 °C which is high enough for various device fabrication conditions [14]. In neutral solution, peptide nanotubes are stable for more than a year, although the solution must be microorganism free because it can consume peptide nanotubes.

The third advantage of peptide nanotubes is that the nanotube structure can be well defined in the molecular level [15]. Since the locations and the orientations of specific functional groups of peptide monomers in the peptide nanotubes are understood, modification of peptide



monomers can design chemical properties of inner and outer walls of peptide nanotubes respectively. Of course, peptide monomers have to be functionalized through appropriate chemical structures to be assembled as the nanotube form. For example, cyclic D,L,-peptide nanotubes were designed to have hydrophobic outer walls and hydrophilic inner walls, which were suitable to fabricate artificial ion channels [16].

For some peptide nanotubes, the nanotube structures and the sizes are not consistent with the ones expected from the peptide monomer structures. It seems that the assembled structure of peptide nanotubes should be predictable from the monomer structure since charge distribution and strength of intermolecular hydrogen bonding of peptide monomers at various pHs are well understood. However, the peptide monomer could undergo conformation changes via pH change and the structure of peptide nanotubes is very sensitive to the peptide monomer conformation. As a result, it is not always straightforward to predict the structure and the size of peptide nanotube from the chemical structure of the peptide monomer.

It should be noted that the use of peptide nanotubes is not limited to biological applications. Biological recognitions of peptide nanotubes can be used to guide the nanotubes to desired locations in solution for nonbiological devices such as electronics and sensors. In this concept, device designs can be developed by biological interactions between the nanotubes and biological surfaces instead of patterning the designs with photolithography. This method may simplify nanometer-scale device fabrication procedures and reduce fabrication costs because synthesis of most of peptides described here is fairly inexpensive.

This chapter consists of three major sections; “Development of Peptide Nanotubes,” “Characterization of Peptide Nanotubes,” and “Peptide Nanotube Applications.” Since this field is extremely young, there are more reports about peptide nanotube synthesis than their applications. However, recently several promising reports about their applications began to appear and they are summarized in Section 4.

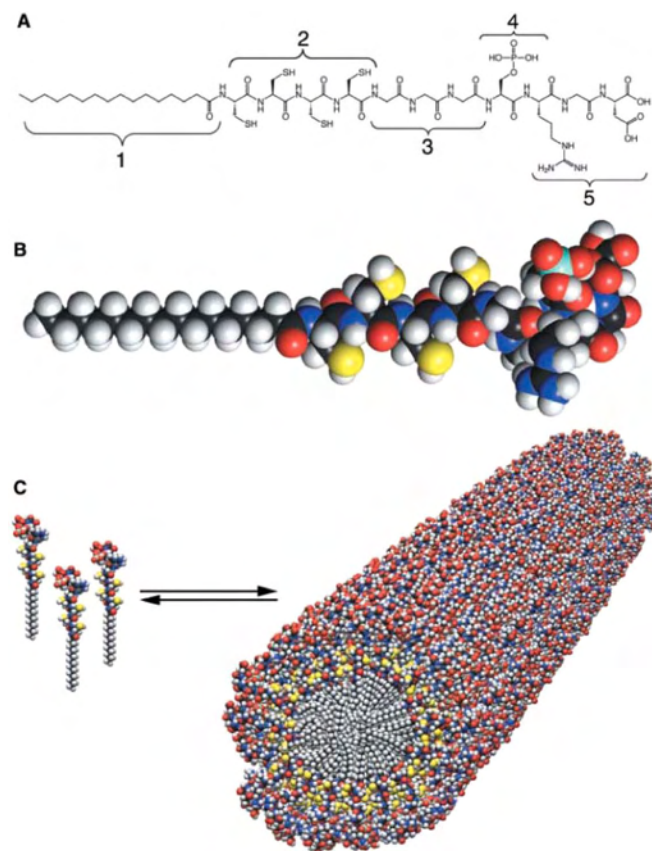
## 2. DEVELOPMENT OF PEPTIDE NANOTUBES

### 2.1. From Linear Peptides to Nanotubes

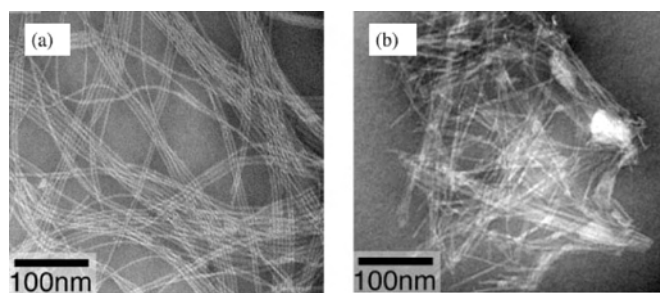
Self-assemblies of linear amphiphiles (i.e., molecules with charged head groups and nonpolar tail groups) have been studied to mimic biological membrane structures for decades. Those simple linear amphiphiles were self-assembled by hydrophilic/hydrophobic interactions between the amphiphiles and surfactants. Phase diagrams of those assemblies have been well established as functions of temperature and pressure [17]. Then it was natural to evolve from the simple amphiphile self-assembly to peptide-derivatized amphiphile assembly to introduce a new parameter to control self-assemblies, hydrogen bonding [18–20]. Self-assembled peptide amphiphile structures are sensitive to pH that changes the strength of intermolecular hydrogen bonding between amide and carboxylic acid groups. When the peptide nanotubes are self-assembled in aqueous solution, the hydrophobicity of peptide monomers also becomes

an important factor to determine the dimension of peptide nanotubes [21].

Figure 1 is an example illustrating how linear peptide monomers self-assemble into nanotubes [22]. The peptide amphiphile monomers in Figure 1a are assembled to orient the hydrophobic alkyl chain to the core and the amide group to the outer surface. While this assembled structure seems to have the same structure as micelles, protonation states of amides still play an important role to organize this structure, which is supported by the observation that the appearance of nanotube depended on pH of solution [23]. Since the nanotube structure from this type of linear peptide monomer is well defined (i.e., tail group inside and polar head group outside), functionalization of peptide nanotubes can be obtained by introducing the functional groups into the peptide monomer via chemical synthesis. If some functional groups are incorporated into the head groups, those groups appear on the outer surfaces of nanotubes, which determines the surface properties of nanotubes. For example, a certain peptide sequence for cell adhesion was incorporated into the head group of peptide to anchor cells onto the peptide nanotubes [22]. Figure 2 shows that nanotube structures are sensitive to chemical structures of peptide



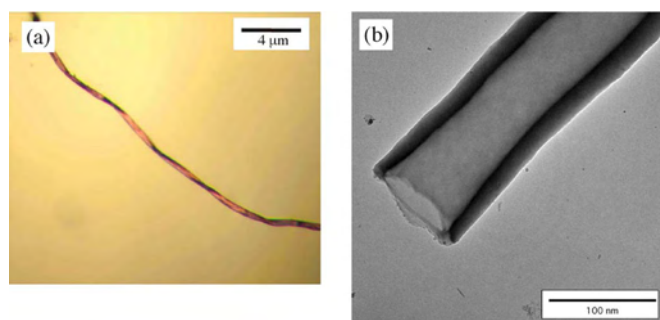
**Figure 1.** (A) Chemical structure of the peptide amphiphiles, highlighting five key structural features by 1 through 5. (B) Molecular model of the peptide amphiphiles. C: black, H: white, O: red, N: blue, P: cyan, S: yellow. (C) Schematic showing the self-assembly of the peptide amphiphile molecules into nanotubes. Reprinted with permission from [22], J. D. Hartgerink et al., *Science* 294, 1684 (2001). © 2001, American Association for the Advancement of Science.



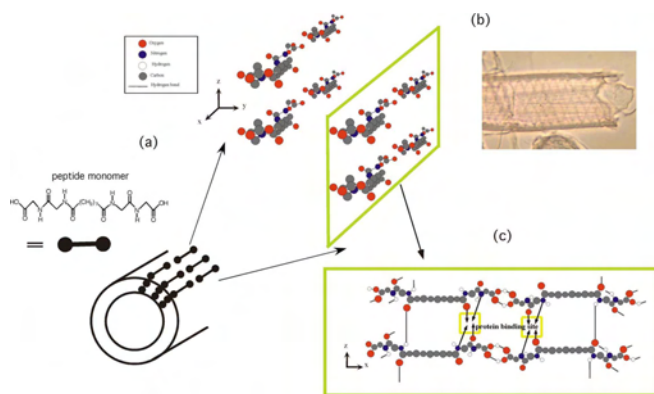
**Figure 2.** TEM images of peptide nanotubes from peptide amphiphiles with (a) 10 carbons in the hydrophobic chain and (b) 16 carbons in the hydrophobic chain. Reprinted with permission from [23], J. D. Hartgerink et al., *Proc. Natl. Acad. Sci. USA* 99, 5133 (2002). © 2002, National Academy of Science.

monomers. The transmission electron microscope (TEM) image in Figure 2a shows that the peptide nanotubes, formed from peptide amphiphiles with 10 hydrocarbons in the hydrophobic chain, aligned in parallel, while the peptide nanotubes from peptide amphiphiles with 16 hydrocarbons in the hydrophobic chain were grown shorter and aggregated in random orientation as seen in Figure 2b [23]. The comparison of those TEM images indicates that the chemical structure of peptide monomers is very sensitive to the nanotube structure.

There is another type of linear peptide monomer with two amide head groups connected by a hydrocarbon tail group (called bolaamphiphile), which showed pH dependence in the assembled structures. This peptide bolaamphiphile monomer assembled into the helical form at pH 8 (Fig. 3a) and the nanotube form at pH 5 (Fig. 3b) [24]. This peptide monomer is assembled into the nanotube and the helical form via three-dimensional hydrogen between amide and carboxylic acid groups (Fig. 4a, c). X-ray diffraction and Raman microscopy indicate that lower pH induces stronger protonation to amide and carboxylic acid groups that results in stronger intermolecular hydrogen bonds [24–26]. This change increases the tilting angle of the peptide monomer alignment and more surface curvature of the



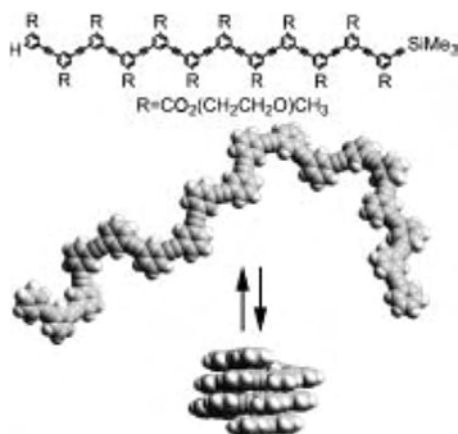
**Figure 3.** Visible microscopic images of self-assembled structures from the peptide bolaamphiphiles. (a) In a pH = 8 solution, the peptide bolaamphiphile assembled into helical ribbons. The width of the helices is about 2 μm and the length varies from 10 to 40 μm. The helical structures appeared after one week. (b) In a pH = 5 solution, the peptide bolaamphiphile monomers assembled into nanotube structures. The diameter of the nanotube is 10–1000 nm. The peptide nanotubes appeared after two weeks [24].



**Figure 4.** (a) Chemical structure of peptide bolaamphiphile monomer. (b) Chemical structure of peptide nanotube from the peptide monomer. The nanotube surface has free amide groups (shown by arrows and yellow squares) to immobilize biological molecules and ions to functionalize the peptide nanotubes [28–30, 62].

peptide assembly results in the nanotube formation as if a sheet of paper is rolled up to a cigar [24]. The observation of stripes in zigzags on the nanotubes in Figure 4b supports this nanotube-assembly mechanism. The monomer conformation of the peptide bolaamphiphile also shows a significant effect on the self-assembled form. The helix-to-nanotube transformation was observed in the peptide bolaamphiphile with the seven-hydrocarbon chain (Fig. 4a). However, the same peptide monomer with a six-hydrocarbon chain only forms nanotubes in pH 5 and the helical form did not appear at higher pH in solution. Spectroscopic studies indicate that the peptide nanotubes from the six-hydrocarbon chain peptide monomer are assembled via stronger hydrogen bonding than the peptide monomer with the seven-hydrocarbon chain [27]. It seems that the stronger intermolecular hydrogen bonding between peptide monomers with the six-hydrocarbon chain prevents the structural transformation between the helix and the nanotube. For this type of peptide nanotube, functionalization can be obtained by anchoring molecules onto the nanotube surfaces. While the peptide nanotube is assembled via intermolecular hydrogen bonds between amide groups and carboxylic acid groups, an interesting characteristic of the peptide nanotubes is that their free amide groups can capture and incorporate biological molecules such as DNAs, proteins, and porphyrins via hydrogen bonding (Fig. 4c) [28, 29]. This free amide group also captures metal ions such as Pt, Pd, Cu, Co, and Ni to form square planar complexes and the further electroless plating results in stable metallic coatings [30]. Therefore, instead of chemically modifying peptide monomer structure, this type of peptide nanotube can be used as an efficient template to produce various exotic nanotubes.

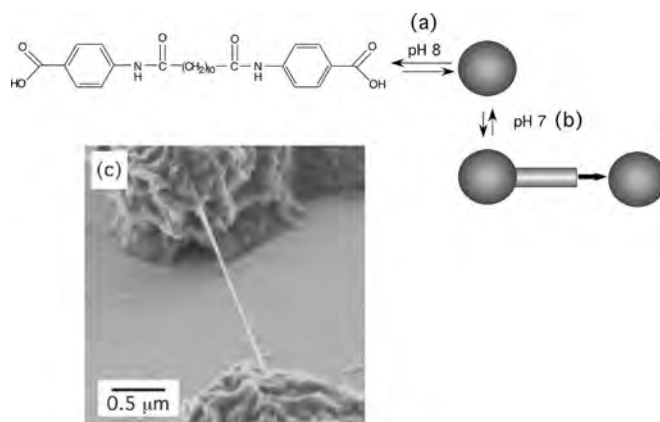
Another scheme to produce peptide nanotubes is to fold linear peptide monomers to the helical structure (i.e., a shape like a rattled snake). Oligophenylacetylenes were folded into helical forms as shown in Figure 5 [31]. This structural transformation is induced by solvophobic interaction between backbone phenyl rings. The peptide nanotube from the oligophenylacetylenes preserves a hollow coil structure because the turning angle of the helical conformation is wide enough to prevent a close-packed



**Figure 5.** Oligophenylacetylene folding equilibrium between the open state and the helical folded structure [31]. Reprinted with permission from [39], D. T. Bong et al., *Angew Chem. Int. Ed. Engl.* 40, 988 (2001). © 2001, Wiley-VCH.

core. The folded peptide monomers produce nanotubes of 4 Å in diameter. The ease to add additional derivatives into oligophenylacetylenes is advantageous for this type of folding peptide nanotubes [32]; however, the dimensions of the nanotubes in both diameter and length may be limited by the size of the monomer unless these nanotubes are integrated by noncovalent interactions to form longer tubes [33].

Peptide nanotubes have been produced from various linear peptide monomers [34]. Whereas the peptide nanotube dimension via changes of peptide chain length, functional groups in the chain, and pH of solution has been studied systematically [14, 35, 36], the complexity is that those factors cannot be treated separately. For example, the pH change will alter charge distributions and intermolecular hydrogen bonds between peptide monomers. However, it will also change the peptide monomer conformation via intramolecular charge interactions and/or intramolecular hydrogen bonds [23]. Since self-assembled nanotube dimension is also very sensitive to the peptide monomer conformation, sometimes it is difficult to predict the formation of peptide nanotubes from peptide monomer conformations. However, it is advantageous that the formation of peptide nanotubes via molecular self-assembly is very reproducible and the size of peptide nanotubes is quite monodisperse under the proper nanotube growth conditions. This feature is strength for the use of self-assembly in the nanotube formation [37]. In fact, the sensitivity of the assembled structure changes with experimental conditions may turn to an advantage when the exotic combined structures are aimed to be fabricated by controlling the growth conditions. For example, the monomer in Figure 6, which self-assembled into a microsphere at pH 8 and a nanotube at pH 7, can be formed as the combined structure between the microsphere and the nanotube (i.e., dumbbell) by switching pHs between the spherical growth and the tubular growth conditions [38]. The monomers in Figure 6 were first assembled into microspheres in a pH 8 solution. Once the microspheres were grown in diameter of 1 μm, the self-assembly condition was switched to the nanotube formation by tuning pH to 7. After 12 hours, the nanotubes (50 nm in

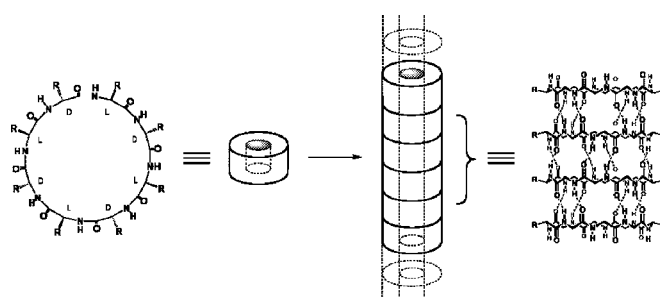


**Figure 6.** Strategy to produce nanotube-bridge geometry by controlling the molecular self-assembly mechanisms between microspheres and nanotubes. (a) First, the monomers are self-assembled in a pH 8 solution. (b) Then the nanotubes are assembled on the microspheres by changing pH to 7. The nanotubes grow to connect with other microspheres. (c) TEM image of the nanotube bridge between the microspheres [38].

diameter) were observed between the microspheres. Therefore, the adjustment of experimental conditions during self-assembling peptide monomers alters the growth processes in the intermediate time and it will produce exotic nanotube-based structures such as bridges, dumbbells, and multibranches.

## 2.2. From Cyclic Peptides to Nanotubes

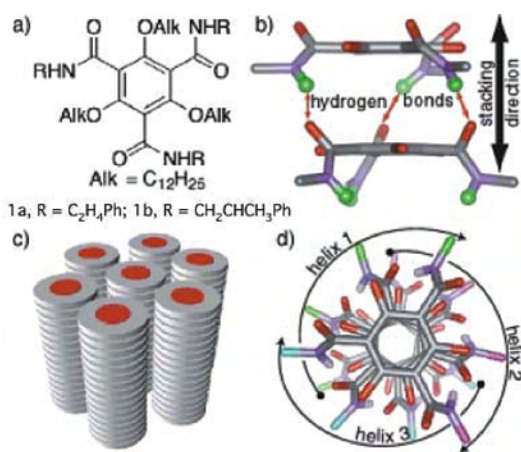
Peptide nanotubes can also be self-assembled by stacking cyclic peptide monomers [39–41]. A typical assembling mechanism of a cyclic D,L-peptide monomer is shown in Figure 7 [42]. Those peptide rings were stacked through the backbone–backbone hydrogen bonding between neighboring amide groups. The sequence of octapeptide *cyclo*[-(L-Gln-D-Ala-L-Glu-L-Ala)<sub>2</sub>-] was used to prevent subunit association through Columbic repulsion in basic aqueous solution. A cyclic D,L-octapeptide containing bis-aspartic acid was also self-assembled into nanotubes via pH control of solution [43]. One of the simplest cyclic monomers, benzene, can also be stacked to grow as nanotubes if benzene is derivatized with right functional groups at the right positions. When benzene rings were derivatized with secondary



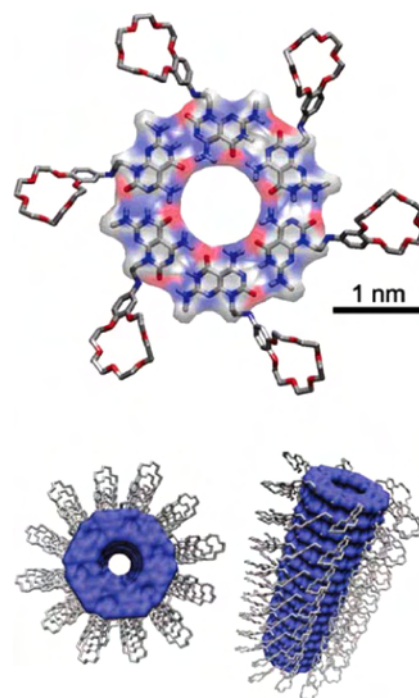
**Figure 7.** Schematic diagram of peptide nanotube assembly from cyclic D,L-α-peptides. Reprinted with permission from [39], D. T. Bong et al., *Angew Chem. Int. Ed. Engl.* 40, 988 (2001). © 2001, Wiley-VCH.

amides at the 1,3,5-positions, those monomers stack with amide–amide intermolecular hydrogen bonding and  $\pi$  overlap (Fig. 8) [44]. At higher concentration of the peptide monomer, these stacks self-organized into spherical arrays [45]. This two-dimensional hexagonal array (Fig. 8c) can be directed with external electric fields because the stacked column has a macroscopic dipole moment parallel to the stacking direction. The stacked column can be self-organized into hexagonally arranged fibers or liquid crystalline phases by controlling chirality of the peptide monomer via chemical synthesis. Those types of cyclic peptide nanotubes may have limitations in the nanotube dimensional control over wide ranges. For example, the cyclic D,L-peptide monomer was sequenced between 9 and 13 Å in diameter and nanotubes needed to be bundled as arrays to obtain larger nanotube diameters [39].

To produce a larger diameter of peptide nanotubes from cyclic peptide monomers, the ring diameter of the cyclic peptide monomers needs to be larger. Whereas peptide sequencing may have limitations in the ring size of peptide monomers, combination of peptide molecules into an integrated cyclic structure via hydrogen bonding is possible. These integrated rings can be stacked in the length direction to form nanotubes. For example, a heteroaromatic bicyclic base G $\wedge$ C, possessing the Watson–Crick donor–donor–acceptor of guanine and acceptor–acceptor–donor of cytosine, was self-assembled into nanotubes (Fig. 9a) [46]. This monomer formed a six-membered supermacrocycle held by 18 hydrogen bonds. Then this substantially more hydrophobic supermacrocycle self-assembled as a stack to produce nanotubes. The diameter of the nanotubes is 4 nm and the hydrodynamic radius is between 10 and 100 nm, depending on the monomer concentration. The inner space of the nanotube is determined by the distance separating the hydrogen bonding arrays within G $\wedge$ C. The peripheral diameter and its chemistry depend on the choice of functional groups conjugated to this motif. Crown ether (Fig. 9a) was conjugated with the motif because of its broad



**Figure 8.** (a) Chemical structure of the monomer. (b) The intermolecular hydrogen bond conformation between monomers in the stacking direction. (c) The hexagonal arrays. (d) Model of a tetramer showing three helices of hydrogen bonds surrounding the exterior of the column. Reprinted with permission from [45], M. L. Bushey et al., *Angew Chem. Int. Ed. Engl.* 41, 2828 (2002). © 2002, Wiley–VCH.



**Figure 9.** Hierarchical self-assembly of heteroaromatic bicyclic base G $\wedge$ C into a six-membered supermacrocycle and resulting nanotube. Each crown ether site within the assembled structure provides 328 Å<sup>3</sup> of open space for binding of a molecular guest. Reprinted with permission from [49], H. Fenniri et al., *J. Am. Chem. Soc.* 124, 11064 (2002). © 2002, American Chemical Society.

solvent compatibility, synthetic accessibility, and functionality as versatile receptors [47]. The crown ether plays an important role in controlling chiroptical properties by using chiral-promoting molecules, which induce a rapid transition from racemic to chiral nanotubes via electrostatic interactions between the crown ether moiety and the promoter [48]. The promoter molecules could even induce self-assembly of the monomer in the low concentration that the nanotubes were not assembled spontaneously [49]. The degree of chiral induction was sensitive to the chemical structure of the promoter. Similar cyclic peptide nanotube assemblies from noncyclic peptide monomers were reported with series of small dipeptides, L-Leu-L-Leu, L-Leu-L-Phe, L-Phe-L-Leu, and L-Phe-L-Phe [50].

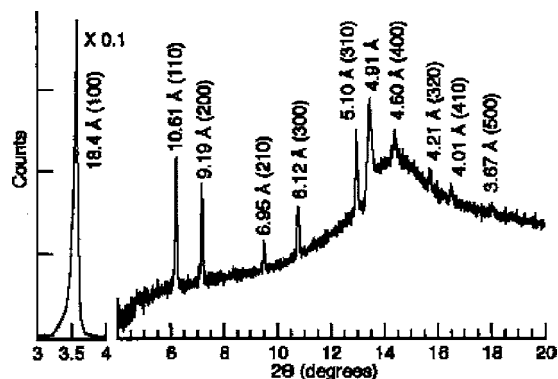
One of characteristic features of the cyclic peptide nanotubes is the precise diameter control of the nanotubes, determined by the chain length, the size of side chains, and the bond angles of the peptide monomer. Proper side chain functionalization also enables those peptide nanotubes to possess distinct surface properties on the inner surfaces and the outer surfaces respectively. As pointed out in Section 1, hydrogen bond-driven self-assemblies are very naive against the environment. However, the peptide nanotubes from cyclic peptide monomers may be less sensitive to the external conditions such as pH and solvent because hydrogen bonds in only one direction need to stack the peptide monomers to produce the nanotubes. Therefore, the optimization of experimental conditions to grow nanotubes from the cyclic peptide monomers may be much more straightforward than the one from linear peptide monomers.

The cyclic peptide nanotubes from linear peptide monomers may require more delicate experimental optimization than sequenced cyclic peptide monomers because this system must first form peptide rings from hydrogen-bonding linear peptide monomers and then stack them into tubular structures.

### 3. CHARACTERIZATION OF PEPTIDE NANOTUBES

Since chemical structures of peptide monomers are well defined, it is relatively straightforward to probe peptide nanotube structures if we have additional spectroscopic information. Conventional X-ray diffraction is a powerful spectroscopy to identify the nanotube structures [41, 50]. However, peptide nanotubes are necessary to grow as a perfectly aligned single crystal in the scale of  $\text{mm}^3$  to resolve fine structures of peptide nanotubes in the X-ray diffraction. Recently, synchrotron X-ray diffraction has been applied to peptide nanotubes. For example, the synchrotron X-ray diffractogram of **1a** in Figure 8a resolved a single sharp peak at low angle that indicates their columnar assemblies and the hexagonal lattice structure was indexed by the diffraction peaks up to fifth order (Fig. 10) [44]. The fluidic packing of the side chain was also probed by the diffuse reflection at  $4.5 \text{ \AA}$  [51]. The lateral core-to-core separation was  $21 \text{ \AA}$ , which is consistent with the column separation with extended side chains,  $27 \text{ \AA}$  [44].

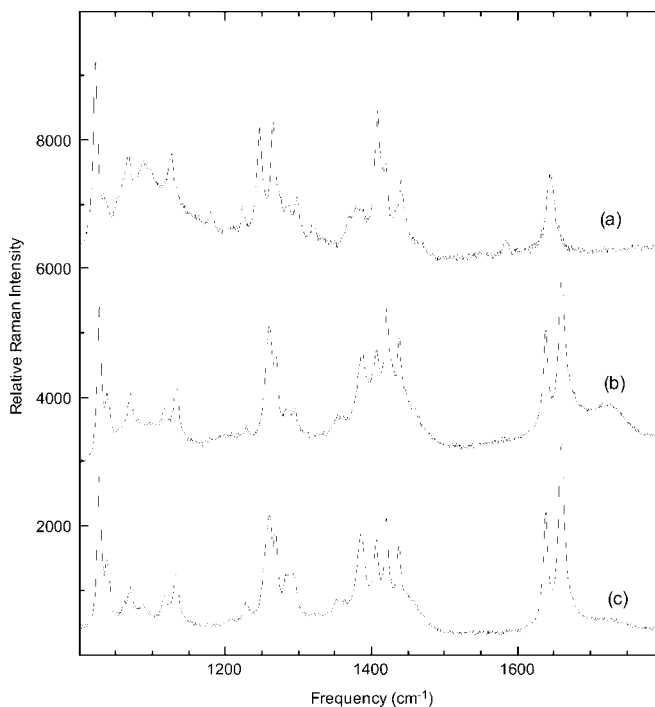
Another technique to resolve peptide nanotube structures is vibrational spectroscopy. The most common vibrational spectroscopies to study chemical structures of peptide nanotubes are Fourier transform infrared spectroscopy and Raman spectroscopy [14, 16, 24, 35, 36, 52]. An advantage for these spectroscopies is that no sample preparation is required. Recently, Raman microscopy has been applied to study single carbon nanotubes [53] and peptide nanotubes [24, 54]. For peptide nanotubes, vibrational frequencies of amide groups are very important to monitor because the frequency shifts reflect the strength of hydrogen bonding with the amides. This information helps one to build the structural model: how the hydrogen bonding assembles peptide



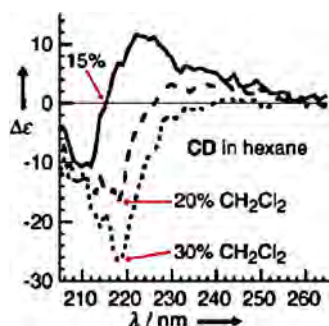
**Figure 10.** Synchrotron X-ray diffraction of the nanotubes from **1a** in Figure 8a. Reprinted with permission from [44], M. L. Bushey et al., *J. Am. Chem. Soc.* 123, 8157 (2001). © 2001, American Chemical Society.

monomers into peptide nanotubes. For example, the structure of the peptide nanotube from the monomer (Fig. 4a) was investigated with a Raman microscope. When the structural transformation between the helical form (Fig. 3a) and the nanotube (Fig. 3b) was monitored, the helical phase (Fig. 11a) has a peak for the C=O stretch at  $1644 \text{ cm}^{-1}$  while the nanotube (Fig. 11b) and the crystalline form (Fig. 11c) have two C=O peaks at  $1637$  and  $1660 \text{ cm}^{-1}$ . The C=O stretch with the highest frequency is assigned as the free C=O of the amide group. The C=O frequencies at  $1637$  and  $1644 \text{ cm}^{-1}$  are redshifted from the free C=O stretch since these C=O stretches bind the amide NH group via intermolecular hydrogen bonds (Fig. 4c). These assignments suggest that the C=O group in the nanotube and the crystal phase binds to NH stronger than the C=O group in the helical form due to a redshift of the vibrational frequency. This is consistent with the structural transformation model for the peptide bolaamphiphile that shortening amide–amide and acid–acid hydrogen bonds induces further tilt of the peptide monomer arrangement and makes the assembly surface more convex. This greater molecular tilting leads the assembled structure to the nanotubes by scrolling the sheetlike helical form into the tubular form (Fig. 4b). Nuclear magnetic resonance spectroscopy is an alternative way to study hydrogen bonding schemes of peptides in nanotubes [55].

Helicity of the peptide nanotube structure can be analyzed by CD spectroscopy [31, 45, 46]. The monomer concentration dependence of the structural change for the nanotubes stacked from monomer **1b** in Figure 8a was probed by CD spectroscopy, as shown in Figure 12 [45]. When the solution of **1b** in hexane was diluted with ca. 15%  $\text{CH}_2\text{Cl}_2$ , the helical order of nanotubes was observed



**Figure 11.** Raman spectra of (a) helical form, (b) nanotube, (c) crystal from the peptide monomer in Figure 4a [24].



**Figure 12.** CD spectra of the nanotubes from **1b** in Figure 8a in hexane. Reprinted with permission from [45], M. L. Bushey et al., *Angew Chem. Int. Ed. Engl.* 41, 2828 (2002). © 2002, Wiley-VCH.

via an exciton coupling between degenerate chromophores. As the concentration of  $\text{CH}_2\text{Cl}_2$  increased, the helical complex dissociated and the transition dipoles were not observed to couple. The series of CD spectra show that the monomers self-assembles through hydrogen bonds with their side chains close enough to interact with each other only when the solvent is hydrocarbonlike [45].

## 4. PEPTIDE NANOTUBE APPLICATIONS

### 4.1. Tissue Engineering

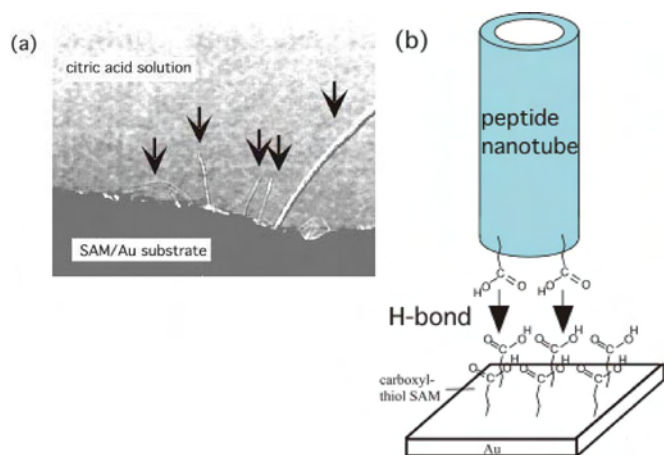
In nature, self-assembled fibrils and their biomineralization routinely produce various composite materials. Bone tissue is one of those examples. The collagen fibrils are formed by self-assembled collagen triple helices and the hydroxyapatite crystals grow in these fibrils with the hierarchical organization of their *c* axes along the long axes of the fibrils [56]. The peptide nanotube was applied as an artificial fibril to serve as crystal nucleation and growth of the inorganic hydroxyapatite crystals [22]. This peptide nanotube was self-assembled from the peptide amphiphile monomer shown in Figure 1a. This synthetic peptide monomer incorporates four important functions. The tail group (region 1 in Fig. 1a) and amide group (region 3 in Figure 1a) stabilize the nanotube structure via hydrophobic interactions and hydrogen bonds. The amide group also plays an important role in promoting the hydroxyapatite crystal growth because their negative charges established the local ion supersaturation [57]. The sulfide group (region 2 in Fig. 1a) provides extra stability to the nanotubes via disulfide bonds with adjacent peptide monomers. The phosphorylated group (region 4 in Fig. 1a) was introduced to nucleate calcium phosphate minerals. As this peptide monomer forms the peptide nanotube, the phosphoserine residue locates at the outer wall of the nanotube. This peptide nanotube with a highly phosphorylated nanotube surface resembles the collagen fibrils. To proceed with the biomineralization efficiently, the fibrils should promote the adhesion growth of cells on their surfaces. The peptide sequence Arg–Gly–Asp (RGD), contained in collagen-associated fibronectin, is important for integrin-mediated cell adhesion [22] and this peptide sequence was also incorporated in the peptide monomer shown as region 5 in Figure 1a. When the assembled peptide nanotubes are treated with  $\text{CaCl}_2$  and  $\text{Na}_2\text{HPO}_4$  solution,

the crystalline minerals were observed on the nanotubes after 20 minutes [22]. The hydroxyapatite crystallographic *c* axis was aligned with the peptide nanotube long axis, which mimics the natural bone growth with collagen fibrils. The ability of the peptide nanotube to orient crystalline nuclei and subsequent crystal growth in the specific direction can be applied to other mineralized tissue repairs.

### 4.2. Electronics

While various nanocomponents have been applied as building blocks to construct nanodevices [9–14], more reproducible methods to assemble them onto precise positions are desirable. The improved fabrication method will be extremely significant to interconnect electronic components with nanotubes. The configurations of nanotubes on those components depend on the type of devices to develop. For example, when two nanowires are crossed perpendicularly at the centers of the nanowires, this configuration acts as an electric switch [58]. More complex nanowire configurations of logic gates such as OR, AND, and NOR have been fabricated [2, 59]. One of the simpler ways to align nanotubes for complex device configurations is to use freestanding nanotubes in solution. This strategy will allow nanotubes to freely move and attach at the target locations in solution via noncovalent interactions, charge interactions, or molecular recognitions. However, it remains highly challenging to fabricate freestanding nanotubes in solution. Biologically compatible peptide nanotubes are soluble in aqueous solution and therefore their aggregations are not a concern. Therefore, the use of peptide nanotubes as building blocks for electronics and sensor devices may be appropriate in the solution-based fabrications. Our strategy has been to use those functionalized peptide nanotubes, which can recognize and selectively bind a well-defined region on patterned substrates, as building blocks to assemble three-dimensional nanoscale architectures at uniquely defined positions [8, 38, 60] and then decorate the nanotubes with various materials such as metals [30, 61], quantum dots [62], and metalloporphyrins [29] for electronics and sensor applications. Complex device configurations may be achieved by using peptide nanotubes incorporating multiple recognition functions such as antibodies and antigens in solution [28]. When a large number of the monodisperse peptide nanotubes are required for practical applications, the peptide nanotubes can be grown in microporous membranes [63]. In this case, the peptide nanotube diameter is controlled by a porous size of polycarbonate membranes. After the nanotubes are grown inside the membrane pores, the membranes are dissolved by  $\text{CH}_2\text{Cl}_2$  to extract the size-controlled nanotubes. When the peptide nanotubes are necessary to have higher mechanical strength for harsher environmental applications, the peptide nanotubes can be bundled via the ligand-ion bridge formations [54].

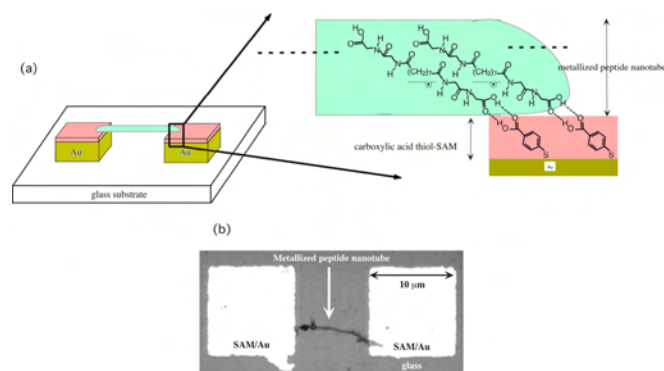
Patterning of peptide nanotubes in the desired device configurations is achieved before the functionalization of peptide nanotubes. We have demonstrated that the peptide nanotubes can be assembled as an array on Au surfaces via a 4-mercaptobenzoic acid self-assembled monolayer (SAM) [60]. The nanotube array was grown when peptide monomers were assembled to nanotubes with the SAM/Au substrates, as shown in Figure 13a. The SAM, with thiol



**Figure 13.** (a) Visible micrograph of the nanotubes grown on the 4-mercaptobenzoic acid monolayer/Au substrate in a citric acid/sodium citrate solution (black arrows shows the positions of nanotubes). (b) Proposed mechanism of the nanotube attachment on a mercaptobenzoic acid SAM/Au substrate [60].

groups at one end and carboxylic acid groups at the other end, serves as a junction between Au and the nanotubes because the thiol groups are attached firmly onto the Au surface while the carboxylic acid groups bind the carboxylic acid groups of the nanotubes via hydrogen bonds (Fig. 13b).

To demonstrate the surface-specific immobilization of nanotubes for the nanotube-cross-linking configuration, we connected carboxylic acid groups of SAM/Au surfaces with carboxylic acid groups of the peptide nanotubes via hydrogen bonds (Fig. 14) [60]. All peptide nanotubes were placed on the SAMs parallel to the substrates when we processed the tube immobilization in two steps; first the peptide nanotubes were grown in suspension and then placed in solution containing the 4-mercaptobenzoic acid SAM/Au substrates. The carboxylic acid groups of peptide nanotubes recognized the carboxylic acid groups on the SAM via the

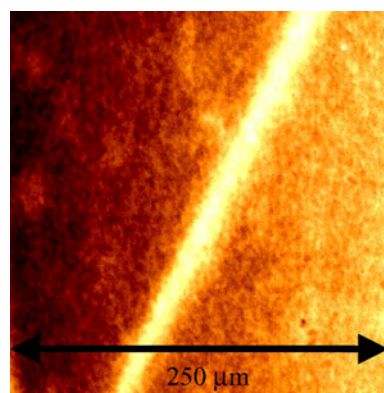


**Figure 14.** Visible micrograph of the peptide nanotubes immobilized onto two separated 4-mercaptobenzoic acid SAM/Au substrates. Two bright squares of the Au layers ( $10\ \mu\text{m} \times 10\ \mu\text{m} \times 0.2\ \mu\text{m}$ ), patterned on a glass substrate by photolithography, were deposited by the 4-mercaptobenzoic acid SAM. The peptide nanotubes, assembled in suspension, were placed on the carboxylic acid SAM/Au substrate and then complete the immobilization in a pH 6 citric acid/sodium citrate solution [60].

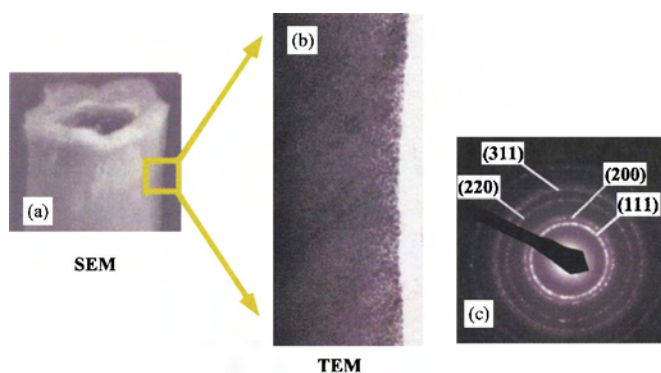
acid–acid hydrogen bonds to interconnect two substrates. After the site-specific immobilization of peptide nanotubes on the SAM surfaces, the nanotubes were coated with Ag by an electroless coating process (Fig. 14a). The surface of the nanotube was quite rough due to the nonuniform Ag coating on the nanotube and the concentrations of Ag ions and reducing agents need to be optimized to obtain smooth metallic coatings on the peptide nanotubes.

Whereas the peptide nanotubes have been patterned into simple device configurations in solution, those nanotubes must be conductive for use in electronics and sensors. Using the characteristic of the peptide nanotubes that their free amide groups can intercalate metal ions (Fig. 4c) [30], side-walls of the peptide nanotubes can be coated with metals via electroless plating to form metallic nanowires [24, 30]. The difficulty in organic nanotube metallization is the creation of organic–inorganic junctions on the nanotube surfaces. But the peptide nanotubes can overcome this difficulty through the intercalating of free amide sites. For example, Figure 15 shows an X-ray photoelectron spectroscopy (XPS) microscopic image of the Ni  $2p$  peak on the single peptide nanotube [64]. In Figure 15, brighter colors correspond to higher concentration of Ni. This image indicates that a uniform Ni coating is possible on the peptide nanotubes via a simple electroless coating. Au nanocrystals can also be coated on the peptide nanotube surfaces and they behave as metallic or semiconductor depending on the size and the density of Au nanocrystals [65]. The strategy is to use carboxylic acid-thiol capped Au nanocrystals that can be intercalated by the free amide group on the peptide nanotubes [62]. Figure 16 shows the Au nanocrystal-capped nanotube developed by coating carboxylic acid-thiol capped Au nanocrystals on the peptide nanotube templates. The magnified TEM image in Figure 16c shows multilayer coatings of Au nanocrystals as dots on the peptide nanotubes seen as a dark continuous background. The coated Au nanocrystals have preferred crystal orientations as (111), (200), (220), and (311). Hydrogen bonding between the amide groups of the peptide nanotube and the carboxylic acid groups of the Au nanocrystals was used as a driving force for this fabrication process.

While the peptide nanotubes can be conductive by coating metals on the nanotubes, recent computational studies



**Figure 15.** XPS microscopic image of Ni on the peptide nanotubes via electroless coating. The intensity of the Ni  $2p$  peak on the substrate was mapped [64].

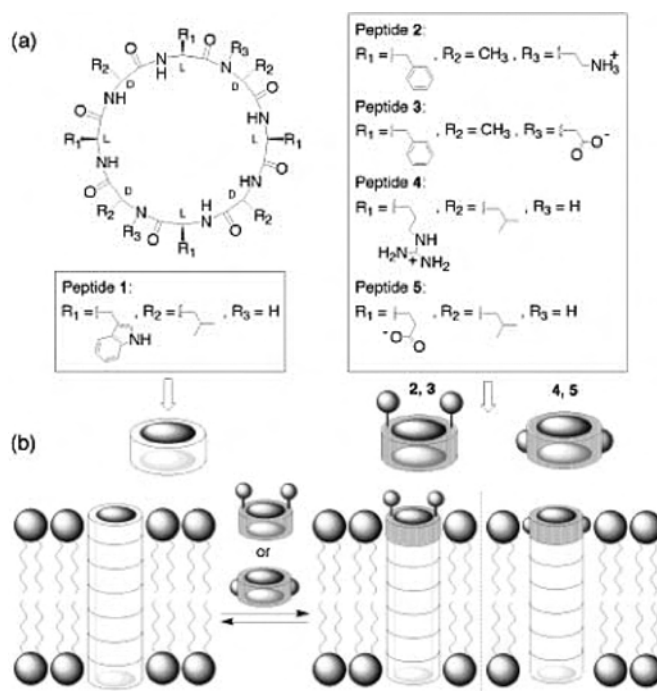


**Figure 16.** (a) Scanning electron microscope image of the peptide nanotube coated with the carboxylic acid-terminated thiol-capped Au nanocrystals. (b) TEM image of the peptide nanotube coated with the carboxylic acid-terminated thiol-capped Au nanocrystals in the higher magnification around the surface of nanotube. (c) Electron diffraction pattern of the peptide nanotube coated with the carboxylic acid-terminated thiol-capped Au nanocrystals [62].

showed that some of peptide nanotubes may be conductive without any metallic coatings. For example, cyclic *D,L*-octapeptide nanotubes may be conductive due to delocalizations of electrons and holes through the hydrogen bonds between the peptide rings [66]. Because theory suggests that strengths of the intermolecular hydrogen bonds via the nanotube axis affect the electronic band-edge states sensitively [67], proper structures of peptide nanotubes may possess adequate electronic transport properties to build electronics. For example, the highest occupied molecular orbital/lowest unoccupied molecular orbital gap of the cyclic *D,L*-octapeptide nanotube was computed approximately as 5 eV [68].

### 4.3. Ion Channels and Biosensors

When functionalized peptide nanotubes were incorporated into membranes, Sanchez-Quesada and co-workers demonstrated that this system mimics transmembrane channels [69]. Transmembrane channels involved in electrical signaling in cells display ion selectivity and rectification, gated by their potentials [70]. While monomeric peptide nanotubes incorporated in membranes were used for size selective transmembrane transport of small molecules [52], membranes with heteromeric peptide nanotube channels showed altered conductance and rectification properties. In this demonstration, peptide nanotubes from the cyclic *D,L*- $\alpha$ -peptide monomers (Fig. 7) were used as templates to incorporate into membranes. The template nanotubes were capped with two different subunits and these heteromeric peptide nanotubes were assembled in membranes with locating designed functional groups of the nanotubes at the channel ends (Fig. 17). The ion conductivity and conductance of the nanotube channels were modulated via local electrostatic perturbation from the cap subunits bearing ionizable functionalities. When *L*- $\alpha$ -phosphatidyl-choline (*L*- $\alpha$ -lecithin) planar bilayers were applied as membranes and transferred into symmetric KCl solution, the conductance of the peptide nanotubes decreased after capping the nanotubes with a positively charged functional group (cap peptides 2 and



**Figure 17.** Chemical structures of the cyclic *D,L*- $\alpha$ -peptides and schematic representation of the mode of interaction of the tube cap informing heteromeric transmembrane channels. The cyclic peptide monomer self-assembles in lipid membranes to form the core transmembrane channel structure, while the peptides 2–5 serve as the cap subunits creating the heteromeric channel assemblies with altered ion conductance properties. Reprinted with permission from [69], J. Sanchez-Quesada et al., *J. Am. Chem. Soc.* 124, 10004 (2002). © 2002, American Chemical Society.

4 in Fig. 17), while the conductance increased after the nanotubes were capped with a negatively charged functional group (cap peptides 3 and 5 in Fig. 17).

If biological recognition functions are incorporated into the capping groups of peptide nanotubes, the membrane–nanotube complex will be applied to biosensors [39]. In this configuration, coupling of target antigen with antibody on the peptide nanotubes modulates the conductance, and the conductivity change will be analyzed to identify the target antigen. Thus, the introduction of the molecular recognition function to the membrane–nanotube complex will dramatically improve the signal-to-noise ratio and sensitivity [71, 72].

### 4.4. Antibacterial Agents

The technique to incorporate peptide nanotubes into membranes as described in the previous section can also be applied to kill bacteria. When cyclic *D,L*- $\alpha$ -peptides were functionalized to selectively target bacterial membranes, they were self-assembled in the bacterial membranes and exert antibacterial activity by increasing the membrane permeability [73]. From the library of antibacterial peptides, a series of six- and eight-residue amphiphilic cyclic *D,L*- $\alpha$ -peptides were designed to bear at least one basic residue to enhance their target specificity toward negatively charged



bacterial membranes [74, 75]. In order to determine the efficacy of the peptide nanotubes with respect to *in vivo* protection of mice from bacterial infection, groups of mice were infected with lethal doses of methicillin-resistant *S. aureus* (MRSA) and then each group was treated intraperitoneally with a given bolus dose of the peptide nanotubes at 45–60 min after initial infection [73]. In this study, the amino acid sequences of cyclic peptides to target MRSA were **KKKWLWLW**, **RRKWLWLW**, and **KKLWLW**, where bold letters indicate D-amino-acid residues. After seven days, single appropriate doses of the peptide nanotubes were sufficient to completely protect various groups of mice from MRSA infections. This result will be very useful in developing new therapeutic treatments of existing and emerging infectious diseases by designing peptides rationally via combinatorial peptide libraries.

## 5. SUMMARY

The field of device fabrication based on peptide nanotubes is still very young. At this stage, material development and fundamental mechanistic study of self-assemblies in peptide nanotubes have been very active and there is some progress in organizing peptide nanotubes in device configurations. These two areas are necessary to be coupled to develop real-world devices from peptide nanotubes, which have just started appearing in literature very recently. The biocompatibility of peptide nanotubes makes them valuable to build biotechnology-related devices such as biosensors and biomolecular filters, and their potential to position them into device configurations via biological recognitions may help build improved electronics. Physical properties of peptide nanotubes may not be suitable for certain applications; however, functionalization of peptide nanotubes will give them flexibility in physical properties to overcome it. As explained, functionalization can be achieved via peptide monomer modification or coating on the peptide nanotubes with functional groups.

## GLOSSARY

**Amphiphile** A molecule with a functional group as a head and alkyl chain as a tail.

**Bolaamphiphile** A molecule with two functional groups as heads connected by an alkyl chain.

**Functional group** Systematic chemical structures with specific chemical/physical properties.

**Functionalization** Addition of specific chemical/physical properties onto self-assembled structures.

**Intermolecular hydrogen bond** Hydrogen bonding among multiple molecules.

**Intramolecular hydrogen bond** Hydrogen bonding within single molecule.

**Peptide nanotube** A nanometer-sized tubular structure self-assembled from monomers containing amino acids or amino acid-like molecules linked with peptide bonds.

**Self-assembly** Spontaneous organization of molecules into stable, larger-scaled structures.

## ACKNOWLEDGMENTS

I thank my co-workers for the past four years for their hard work in the development of peptide nanotubes and their applications: B. Gologan, S. Pan, G. E. Douberly, S. Jonas, E. Goun, P. Porrata, R. MacCuspie, Dr. Catherine Thaler, and Dr. B. P. Tonner. I also acknowledge the financial support from the National Science Foundation CAREER Award (EIA-0133493), the National Science Foundation NER program (ECS-0103430), the U.S. Department of Energy (DE-FG-02-01ER45935), and Florida Hospital, Gala Endowed Program for Oncologic Research.

## REFERENCES

1. Y. Cui, Q. Q. Wei, H. K. Park, and C. M. Lieber, *Science* 293, 1289 (2001).
2. Y. Huang, X. Duan, Y. Cui, L. J. Lauhon, K. H. Kim, and C. M. Lieber, *Science* 294, 1313 (2001).
3. M. R. Diehl, S. N. Yaliraki, R. A. Beckman, M. Barahona, and J. R. Heath, *Angew. Chem. Int. Ed. Engl.* 41, 353 (2001).
4. P. G. Collins, M. S. Arnold, and P. Avouris, *Science* 292, 706 (2001).
5. A. Bachtold, P. Hadley, T. Nakanishi, and C. Dekker, *Science* 294, 1317 (2001).
6. E. Braun, Y. Eichen, U. Sivan, and G. Ben-Yoseph, *Nature* 391, 775 (1998).
7. O. Harnack, W. E. Ford, A. Yasuda, and J. M. Wessels, *Nano Lett.* 2, 919 (2002).
8. H. Matsui, P. Porrata, and G. E. J. Douberly, *Nano Lett.* 1, 461 (2001).
9. J. K. N. Mbindyo, B. D. Reiss, E. R. Martin, C. D. Keating, M. J. Natan, and T. E. Mallouk, *Adv. Mater.* 13, 249 (2001).
10. E. Dujardin and S. Mann, *Adv. Mater.* 14, 775 (2002).
11. E. Dujardin, L.-B. Hsin, C. R. C. Wang, and S. Mann, *Chem. Commun.* 1264 (2001).
12. In this chapter, the word “monomer” was used for a peptide molecule from which peptide nanotubes are self-assembled.
13. G. M. Whitesides, E. E. Simanek, J. P. Mathias, C. T. Seto, D. N. Chin, M. Mammen, and D. M. Gordon, *Acc. Chem. Res.* 28, 37 (1995).
14. M. Kogiso, S. Ohnishi, K. Yase, M. Masuda, and T. Shimizu, *Langmuir* 14, 4978 (1998).
15. S. Zhang, D. M. Marini, W. Hwang, and S. Santoso, *Curr. Opin. Chem. Biol.* 6, 865 (2002).
16. J. D. Hartgerink, J. R. Granja, R. A. Milligan, and M. R. Ghadiri, *J. Am. Chem. Soc.* 118, 43 (1996).
17. J.-H. Fuhrhop and J. Koning, “Membranes and Molecular Assemblies: The Synkinetic Approach.” Royal Society of Chemistry, Cambridge UK, 1994.
18. N. Nakashima, S. Asakuma, and T. Kunitake, *J. Am. Chem. Soc.* 107, 509 (1985).
19. J.-H. Fuhrhop and W. Helfrich, *Chem. Rev.* 93, 1565 (1993).
20. T. Shimizu and M. Hato, *Biochim. Biophys. Acta* 1147, 50 (1993).
21. P. L. Privalov and S. J. Gills, *Pure Appl. Chem.* 61, 1097 (1989).
22. J. D. Hartgerink, E. Beniash, and S. I. Stupp, *Science* 294, 1684 (2001).
23. J. D. Hartgerink, E. Beniash, and S. I. Stupp, *Proc. Natl. Acad. Sci. USA* 99, 5133 (2002).
24. H. Matsui and B. Gologan, *J. Phys. Chem. B.* 104, 3383 (2000).
25. T. Shimizu, M. Kogiso, and M. Masuda, *J. Am. Chem. Soc.* 119, 6209 (1997).
26. M. Kogiso, M. Masuda, and T. Shimizu, *Supramol. Chem.* 9, 183 (1998).
27. B. Gologan and H. Matsui, unpublished results.
28. G. J. Douberly, S. Pan, D. Walters, and H. Matsui, *J. Phys. Chem. B.* 105, 7612 (2001).

29. H. Matsui and R. MacCuspie, *Nano Lett.* 1, 671 (2001).
30. H. Matsui, S. Pan, B. Gologan, and S. Jonas, *J. Phys. Chem. B.* 104, 9576 (2000).
31. R. B. Prince, J. S. Barnes, and J. S. Moore, *J. Am. Chem. Soc.* 122, 2758 (2000).
32. J. C. Nelson, J. K. Young, and J. S. Moore, *J. Org. Chem.* 61, 8160 (1996).
33. J. S. Moore, *Acc. Chem. Res.* 30, 402 (1997).
34. S. Vauthey, S. Santoso, H. Gong, N. Watson, and S. Zhang, *Proc. Natl. Acad. Sci. USA* 99, 5335 (2002).
35. M. Kogiso, Y. Okada, T. Hanada, K. Yase, and T. Shimizu, *Biochim. Biophys. Acta* 1475, 346 (2000).
36. T. Shimizu, R. Iwaura, M. Masuda, T. Hanada, and K. Yase, *J. Am. Chem. Soc.* 123, 5947 (2001).
37. G. M. Whitesides, *Sci. Am.* 273, 146 (1995).
38. H. Matsui and C. Holtman, *Nano Lett.* 2, 887 (2002).
39. D. T. Bong, T. D. Clark, J. R. Granja, and M. R. Ghadiri, *Angew. Chem. Int. Ed. Engl.* 40, 988 (2001).
40. D. Seebach, J. L. Matthews, A. Meden, T. Wessels, C. Naerlocher, and L. B. McCusker, *Helv. Chim. Acta* 80, 173 (1997).
41. D. Ranganathan, C. Lakshmi, and I. L. Karle, *J. Am. Chem. Soc.* 121, 6103 (1999).
42. M. R. Ghadiri, J. R. Granja, R. A. Milligan, D. E. McRee, and N. Khazanovich, *Nature* 366, 324 (1993).
43. M. E. Polaskova, N. J. Ede, and J. N. Lambert, *Aust. J. Chem.* 51, 535 (1998).
44. M. L. Bushey, A. Hwang, P. W. Stephens, and C. Nuckolls, *J. Am. Chem. Soc.* 123, 8157 (2001).
45. M. L. Bushey, A. Hwang, P. W. Stephens, and C. Nuckolls, *Angew. Chem. Int. Ed. Engl.* 41, 2828 (2002).
46. H. Fenniri, B.-L. Deng, A. E. Ribbe, K. Hallenga, J. Jacob, and P. Thiyagarajan, *Proc. Natl. Acad. Sci. USA* 99, 6487 (2002).
47. B. Dietrich, P. Viout, and J.-M. Lehn, "Macrocyclic Chemistry: Aspects of Organic and Inorganic Supramolecular Chemistry." VCH, Weinheim, 1993.
48. H. Fenniri, P. Mathivanan, K. L. Vidale, D. M. Sherman, K. Hallenga, K. V. Wood, and J. G. Stowell, *J. Am. Chem. Soc.* 123, 3854 (2001).
49. H. Fenniri, B.-L. Deng, and A. E. Ribbe, *J. Am. Chem. Soc.* 124, 11064 (2002).
50. C. H. Gorbits, *Chem. Eur. J.* 7, 5153 (2001).
51. A. M. Levelut, *J. Chim. Phys. Phys.-Chim. Biol.* 80, 149 (1983).
52. J. Sanchez-Quesada, H. S. Kim, and M. R. Ghadiri, *Angew. Chem. Int. Ed. Engl.* 40, 2503 (2001).
53. X. L. Zhao, Y. Ando, L. C. Qin, H. Kataura, Y. Maniwa, and R. Saito, *Appl. Phys. Lett.* 81 (2002).
54. H. Matsui and G. E. J. Douberly, *Langmuir* 17, 7918 (2001).
55. T. D. Clark, K. Kobayashi, and M. R. Ghadiri, *Chem. Eur. J.* 5, 782 (1999).
56. W. Traub and H. D. Weiner, *Proc. Natl. Acad. Sci. USA* 86, 9822 (1989).
57. H. D. Weiner and L. Addadi, *J. Mater. Chem.* 7, 689 (1997).
58. T. Rueckes, K. Kim, E. Joselevich, G. Y. Tseng, C.-L. Cheung, and C. M. Lieber, *Science* 289, 94 (2000).
59. A. Javey, Q. Wang, A. Ural, Y. M. Li, and H. J. Dai, *Nano Lett.* 2, 929 (2002).
60. H. Matsui, B. Gologan, S. Pan, and G. J. Douberly, *Eur. Phys. J. D.* 16, 403 (2001).
61. R. Djalali, Y.-F. Chen, and H. Matsui, *J. Am. Chem. Soc.* 124, 13660 (2002).
62. H. Matsui, S. Pan, and G. E. J. Douberly, *J. Phys. Chem. B.* 105, 1683 (2001).
63. P. Porrata, E. Goun, and H. Matsui, *Chem. Mater.* 14, 4378 (2002).
64. H. Matsui, P. Porrata, E. Goun, M. Kilmov, and B. P. Tonner, unpublished results.
65. J. L. Sample, K. C. Beverly, P. R. Chaudhari, F. Remacle, J. R. Heath, and R. D. Levine, *Adv. Mater.* 14, 124 (2002).
66. K. Fukusaki, K. Takeda, and K. Shiraishi, *J. Phys. Soc. Jpn.* 66, 3387 (1997).
67. H. Okamoto, M. Kasahara, K. Takeda, and K. Shiraishi, *Pept. Sci.* 36, 67 (1999).
68. J. P. Lewis, N. H. Pawley, and O. F. Snakey, *J. Phys. Chem. B.* 101, 10576 (1997).
69. J. Sanchez-Quesada, M. P. Isler, and M. R. Ghadiri, *J. Am. Chem. Soc.* 124, 10004 (2002).
70. B. Hille, "Ionic Channels of Excitable Membrane." Sinauer, Sunderland, MA, 1992.
71. O. Braha, B. Walker, S. Cheley, J. J. Kasianowicz, L. Song, J. E. Gouaux, and H. Bayley, *Chem. Biol.* 4, 497 (1997).
72. L.-Q. Gu, O. Braha, S. Conlan, S. Cheley, and H. Bayley, *Nature* 398, 686 (1999).
73. S. Fernandez-Lopez, H. S. Kim, E. C. Choi, M. Delgado, J. R. Granja, A. Khasanov, K. Kraehenbuehl, G. Long, D. A. Weinberger, K. Wilcoxon, and M. R. Ghadiri, *Nature*, 412, 452 (2001).
74. D. M. Pitterle, J. L. Johnson, and K. V. Rajagopalan, *J. Biol. Chem.* 268, 13506 (1993).
75. J. E. Walker, M. Saraste, M. J. Runswick, and N. J. Gay, *EMBO J.* 1, 945 (1982).



# Periodic Nanostructures with Interfering Femtosecond Lasers

Masahiro Hirano, Ken-ichi Kawamura, Hayato Kamioka,  
Taisuke Miura

*Japan Science and Technology Agency, Kawasaki, Japan*

Hideo Hosono

*Tokyo Institute of Technology, Nagatsuda, Japan*

## CONTENTS

1. Introduction
  2. Progress in Encoding Technology
  3. Features of Encoding
  4. Encoding Mechanism
  5. Encoding System
  6. Encoded Hologram
- Glossary  
References

## 1. INTRODUCTION

Introduction of femtosecond (fs) laser pulse, which is characterized as an ultrashort time domain with good coherence over the whole pulse duration, significantly influences trends in various laser application fields. Specifically, when the fs pulse is applied to material processing, it provides additional advantages to conventional laser processing, including the capability of processing in transparent materials, nanosized patterning, and clean processing nearly free from thermal effects. Those features originate from the inherent nature of the pulse. First, fs laser pulses have extremely short time durations, leading to very high peak powers due mostly to the temporal compression of the laser energy. Such high peak powers can process almost all kinds of materials, typically by laser ablation [1–3]. When the energy is a little smaller than the ablation threshold, it can still induce structural changes, which are inevitably accompanied by refractive index modulation [4–8]. As the laser energy can be absorbed efficiently through a multiphoton

process in such a high-power pulse, materials to be processed are not necessarily opaque against the laser wavelength. In other words, the fs laser processing is particularly suited to transparent materials, which are difficult to process by conventional lasers such as CO<sub>2</sub> and YAG:Nd<sup>3+</sup> lasers. Second, with the aid of nonlinear effects such as multiphoton absorption and selffocusing, we can concentrate the laser energy onto a very small spot. In addition, materials suffered ablation or structural changes only in a limited area where the accumulated energy exceeded a certain threshold value. Nanoscale structures may be formed in this way. Finally, the pulse terminates before the completion of energy transfer from photoexcited electrons or electron-hole plasma to the lattice, which minimizes thermal effects during the machining process and makes the process clean [1, 2, 6–9], specifically when only a single pulse is involved. By using these features, a large number of excellent works have been performed recently in fabricating various kinds of fine-scale structures on the surface and inside of transparent dielectrics, semiconductors, polymers, and metals.

Further, if we combine another distinct feature of the fs pulse, which is good coherence [10], with the above mentioned features, we can encode holograms, having a very fine internal structure in various materials, by splitting a single pulse into multiple beams and allowing interference. In this chapter, we will focus on an emerging technology of the formation of periodic microstructures with interfering fs laser pulses.

## 2. PROGRESS IN ENCODING TECHNOLOGY

Phillips et al. [11] at Rice University, performed an initial work, where they used a fs KrF excimer laser to record holographic gratings in polyimide with the intention to realize

fine patterning resulting from the thermal diffusion-free process. Also, an observation of a periodical fringe in diamond has been reported, which was accidentally encoded, presumably due to interference of the incident fs laser beam with a reflected beam [12]. In spite of these reports, material processing with the interfering fs pulses had not attracted much attention before Hosono's group succeeded in encoding holographic gratings in versatile materials, including transparent dielectrics, semiconductors, polymers, and metals with an interfering Ti:Sapphire laser pulse [13–18]. Since then, several groups have reported the formation of the periodic structures in polymers and glasses with the interfering fs pulse. Misawa's group, at Tokushima University, recorded three-dimensional structures in photoresist material with the interference of five beams split from a single fs pulse with the intention to form a photonic crystal [19]. Hirao's group at Kyoto University [20], and Ito's group at Osaka University [21], have succeeded in encoding embedded gratings in polymers and glass materials. The number of research groups involved in this technique is increasing, with an expectation that the interfering fs pulses will open a new frontier in laser processing.

### 3. FEATURES OF ENCODING

Features of the encoding technique that uses interference fs laser pulses are summarized. As is fs laser processing, almost all kinds of materials can be processed with the interfering fs pulses, and the structures are formed in a designated position in materials. Especially, embedded structures can be formed in transparent materials. The process can be completed in a single shot, thus, throughput of the process is potentially very high. Overall size of gratings is as small as  $\sim 100 \mu\text{m}$ , where the fringe spacing is in the range of  $0.1\text{--}5 \mu\text{m}$ , depending on the colliding angle of the beams and laser wavelength. As the spacing is proportional to the laser wavelength for a fixed crossing angle of the beams, use of fs pulse with a shorter wavelength is effective in narrowing the fringe spacing. On the other hand, as is common to the fs laser processing, minimum structure sizes for line width or dot diameter in the periodic structures can be reduced to the nanometer scale, which seems to be almost insensitive to the irradiated laser wavelength [22]. An additional novel feature of the technique is that two- and three-dimensional periodic structures can be fabricated by a double exposure and multiple-beam interfering methods.

### 4. ENCODING MECHANISM

As fs laser pulses exhibit good coherency over the entire pulse duration, interference takes place when multiple fs pulse beams split from a single pulse and overlap with each other both spatially and temporally. The interference pattern resulting from this overlapping can immediately lead to the modulation of the electron-hole plasma density in the irradiated materials through multiphoton absorption or avalanche ionization processes, where the plasma is excited more densely in an enhanced region of the interference than in a depressed region. The density modulation of the plasma causes the refractive index modulation. That is, a transient

grating is immediately formed in the material just after the irradiation of the interfering fs pulse. The transient grating, which likely lasts for several picoseconds (ps), may induce reconstructed beams that could interfere with the incident beams to form additional gratings. The plasma energy in the material is likely relaxed to the lattice within  $\sim 1$  ps to accumulate locally in the lattice.

With the relaxation proceeding, the transient grating is converted into a permanent grating when the local energy in the lattice exceeds a threshold for laser ablation or structural changes of the material. That is, the permanent gratings can be formed when the laser energy in the enhanced region of the interference is over a threshold value.

## 5. ENCODING SYSTEM

### 5.1. General Feature

A hologram encoding system by fs laser pulses does not differ significantly from conventional laser hologram exposure systems. A major difference between the two systems is that an fs laser pulse is used instead of a continuous wave light, typically from a gas laser having a long coherent length. A fs KrF excimer laser (248 nm,  $\sim 400$  fs) [11], Ti:sapphire laser (800 nm,  $\sim 100$  fs) [13–18, 20–25], second harmonics of Ti:sapphire (380 nm,  $\sim 80$  fs) [19], and third harmonics of Ti:sapphire (290 nm,  $\sim 100$  fs) [26,27] have been used so far as a fs pulse source. Because of a very short coherent length of the fs pulse, which is restricted by the spatial extent of the pulse, an optical delay line and a mechanism for detecting the time coincidence of the two beams, with a spatial accuracy of  $\sim \mu\text{m}$ , is, in general, required to ensure a spatial and temporal overlap. It also is desirable for the time-coincidence measurement to be independent of the angle between interference beams. By varying this angle, we can control over-fringe intervals in gratings and over shapes of unit elements in two-dimensional periodic structures. The sum of the frequency generation of the pulses due to optical nonlinear crystals (colliding angle dependent) [20] or third harmonic generation in air (colliding angle independent) [23] is effectively used for most of the systems, but alternative time-coincidence detecting system, without using the up-frequency conversion process, is necessary when a shorter wavelength fs pulse is used. A distributed feedback dye laser technique was used for the fs KrF laser [11], and for the pump and probe techniques, based on the optical Kerr effect and transient absorption, have been developed for the THG of the Ti:sapphire laser [26, 27]. On the other hand, use of a diffractive beam splitter in a multiple beam interfering system allows for the temporal coincidence without installing any adjusting mechanism [19].

When comparing the encoding systems developed so far, optical configurations are basically the same, and differences exist in the types of fs lasers and the detecting mechanisms for the temporal coincidence of the split beams, which are shown in Table 1.

### 5.2. Experimental Setup

Figure 1 shows, as a representative example, a schematic diagram of an experimental setup for grating encoding that uses near infrared (IR) fs laser pulses developed by

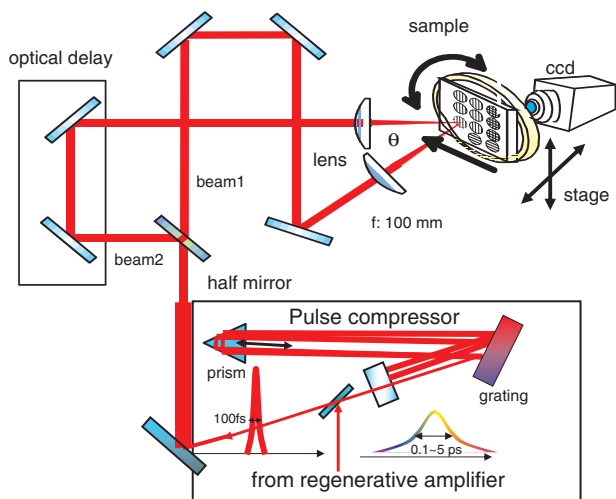
**Table 1.** Type of lasers and detection mechanisms for temporal coincidence used in encoding systems developed so far, together with encoded structures and materials in each encoding system.

	Type of laser	Detection for temporal coincidence	Encoded structure	Materials	Ref.
I	KrF excimer 274 nm ~400 fs	Distributed feedback dye laser	Surface grating	Polyimide	[11]
II-1	Ti: sapphire 800 nm ~100 fs	THG in air	Surface grating Embedded grating Two-dimensional periodic structure	SiO <sub>2</sub> glass, SiO <sub>2</sub> thin film LiNbO <sub>3</sub> , ZnO, ZrO <sub>2</sub> , MgO, TiO <sub>2</sub> , diamond, carbon, SiC, ZnSe, Si, WC, Pt, Au	[13, 14, 15, 16, 17, 18, 22, 23]
II-2	Ti: sapphire 800 nm 100 fs~5 ps (chirped)	THG in air before chirping	Embedded grating Embedded two-dimensional periodic structure	SiO <sub>2</sub> glass	[24, 25]
III	Ti: sapphire 380 nm (SHG) ~80 fs	none	Multidimensional periodic structures	Negative photoresist (SU-8)	[19]
IV	Ti: sapphire 290 nm (SHG) ~100 fs	Transient optical absorption and optical Kerr gate	Surface grating	SiO <sub>2</sub> glass ZnO	[26, 27]
V	Ti: sapphire 800 nm ~150 fs	SFC in nonlinear optical crystal	Embedded grating	Azodye-doped PMMA	[20]
VI	Ti: sapphire 800 nm ~130 fs	Transilluminated optical microscope	Embedded grating	Soda-lime glass	[21]

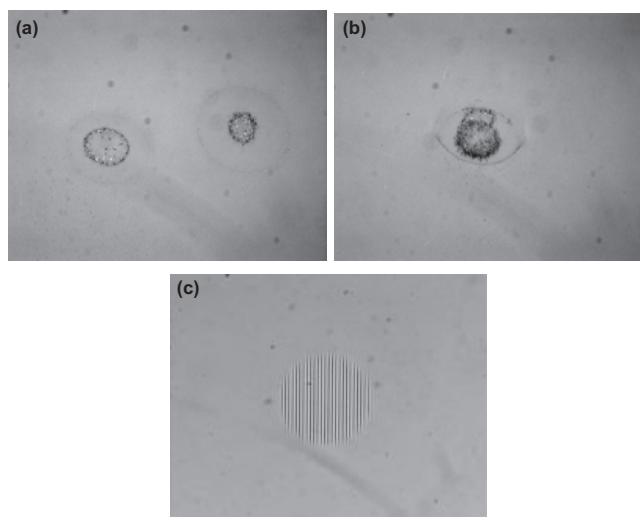
Kawamura et al. [13]. A Ti:sapphire laser system, consisting of a Ti:sapphire oscillator, a stretcher, a regenerative amplifier pumped by the second harmonic of an Nd:YAG laser, and a compressor, is used as a light source. It generated 800-nm light pulses with a repetition rate of 10 Hz, a pulse duration of ~100 fs (an effective coherence length of ~30 μm), and a maximum energy of 3 mJ/pulse. A fs laser pulse from the laser system was divided into two beams by a half-silvered mirror. The separated beams propagated along different optical paths, with one having a variable path length (optical delay line). The two beams were focused onto a single spot of 50–100 μm in diameter by lenses with a focal length of 5–10 cm. The angle of intersection ( $\theta$ ) between these two beams was varied from 10° to 160°. The spatial

length of each optical path was equalized with a precise movement of mirrors in the optical delay line, while monitoring the time coincidence signal. Third harmonic generation (THG) from air was used for the signal [23], as will be described.

Once the time coincidence of the two beams was realized, samples were placed at the beam-focus position. Encoding of the gratings was confirmed *in-situ* by detecting diffracted light from an incident He–Ne laser. Figure 2



**Figure 1.** Experimental setup for hologram encoding system using IR fs laser pulses. Reprinted with permission from [24], M. Hirano et al., *Proc. SPIE* 506, 89 (2003). © 2003, SPIE.



**Figure 2.** Images showing that spatial and temporal coincidence of two fs laser beams are required for encoding gratings. (a) No gratings are recorded when two fs beams are not in spatial coincidence. (b) No gratings are recorded when two fs beams are in coincidence spatially, but not temporally. (c) Gratings are encoded when two fs beams are in coincidence both spatially and temporally. Reprinted with permission from [18], M. Hirano et al., *Appl. Surf. Sci.* 197–198, 688 (2002). © 2002, Elsevier Science.

shows that both spatial and temporal coincidences were simultaneously required for encoding gratings.

As will be described, chirping of the fs pulse, which results in the stretching of the pulse width from  $\sim 100$  fs to  $\sim 10$  ps, keeping the total pulse energy unchanged, is very effective in encoding embedded gratings due mostly to the reduction of the surface damage [24, 25]. In using the stretched pulse for the encoding, the fs pulse is chirped by controlling the degree of the compression in the compressor, while keeping other optical configurations unchanged.

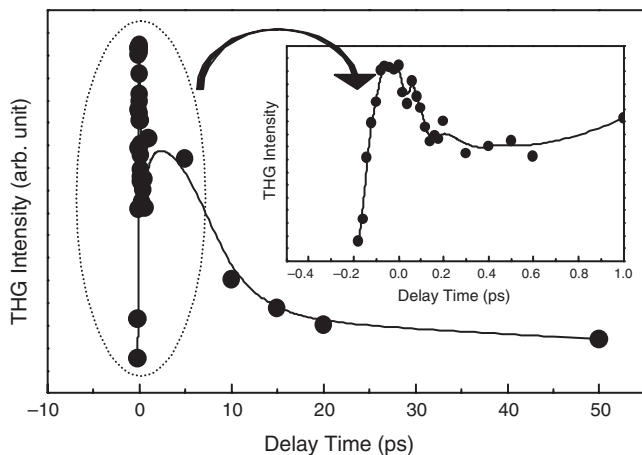
### 5.3. Detecting Mechanism

Representative examples of the detecting mechanism for the temporal coincidence of the beams are introduced in this session.

#### 5.3.1. Third Harmonic Generation in Air

It has been reported that THG is induced when an intense fs laser pulse is focused in various gases such as air [28] or argon [29]; the mechanism has been discussed theoretically [30]. This phenomenon has been applied to monitoring the time coincidence of the two fs pulses [23].

When pulse energy of the first fs laser beam exceeds 1.5 mJ/pulse, a blue spot is observed at the beam center of the far field pattern, which is confirmed as the third harmonic of the laser fundamental (800 nm) at 266 nm. The THG was not observed when the pulse was focused in a vacuum, indicating that air was responsible for the THG. Then, a second focused beam, having an energy of 50  $\mu$ J/pulse, which was too small to induce the THG light by itself, was directed at the focal point so as to overlap spatially with the first beam. The far field pattern of the second beam on the luminescence screen yielded only weak white continuum light without the blue spot, likely due to the self-phase modulation in air when the relative time delay of the two pulses was large. While tuning the optical path length, the blue THG spot suddenly appeared at the center of the white continuum spot. Figure 3 shows the THG intensity in the



**Figure 3.** Third harmonic generation light intensity as a function of delay time between two fs laser pulses. Inset: expanded curve around zero delay time. Reprinted with permission from [18], M. Hirano et al. *Appl. Surf. Sci.* 197–198, 688 (2002). © 2002, Elsevier Science.

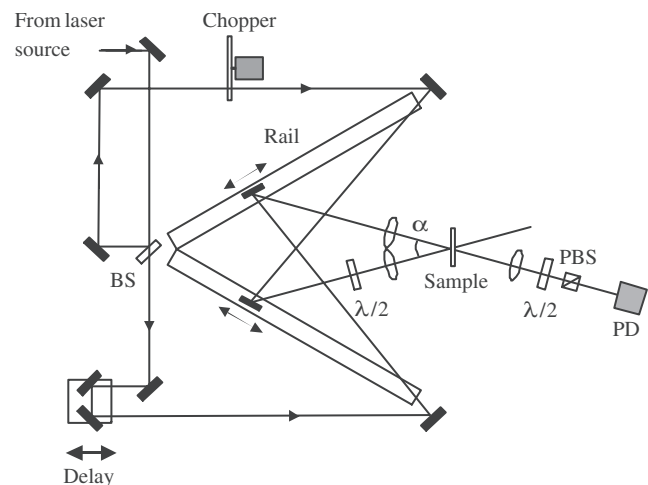
second beam as a function of the delay time calculated from the change in the optical path length.

The intensity increases abruptly as the delay time approaches zero from below. The rise time for the THG enhancement estimated from the inset figure was  $\sim 200$  fs, which is in reasonable agreement with a pulse width of  $\sim 100$  fs. With a further increase in the delay time, the intensity, at first, decreases sharply. The decrease then becomes gradual and is still observed at delay times above 50 ps. Despite the gradual decay on the long delay time side, the peak in Figure 3 is sharp enough to determine the exact time coincidence of the two fs pulses. The trend in Figure 3 was independent of the angle of intersection of the two beams, as expected from the inherent nature of THG in the gas phase. The use of THG in air makes it possible to arrange the time coincidence of two fs pulses over a wide range of angles of intersection.

#### 5.3.2. Pump and Probe Technique

The techniques using up-frequency conversion processes are not applicable for monitoring the time coincidence of ultraviolet fs pulses, because the resultant sum frequency light in the process has a too short wavelength to propagate in nonlinear crystals or even in air. To overcome this problem, alternative methods using a distributed feedback dye laser technique and two kinds of pump-probe techniques based on optical Kerr and transient absorption effects have been developed.

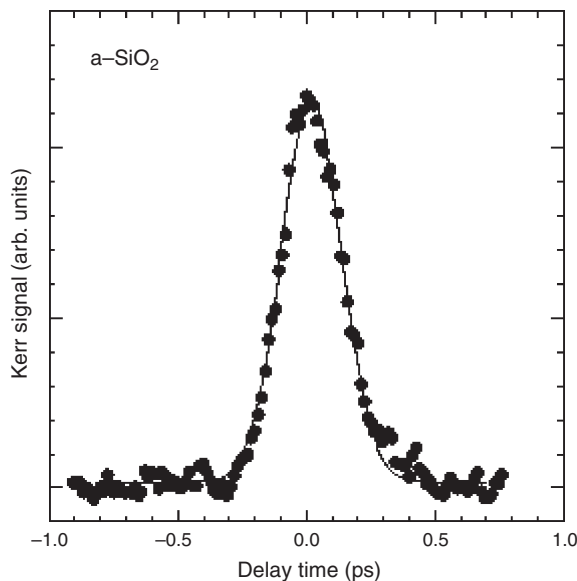
In the pump and probe techniques, the two beams to be interfered are used, respectively, as pump and probe pulses under the low intensity condition below the threshold for the ablation [26, 27]. In the optical Kerr gating method, the pump pulse is polarized perpendicular to the probe pulse by using a  $\lambda/2$  plate, which is inserted in the pump beam path before a quartz plate (Fig. 4). On the other hand, the probe pulse goes into another  $\lambda/2$  plate after passing through the quartz plate and then into polarized beam splitter (PBS) placed at the front of a photodiode detector (PD) equipped with a phase-sensitive detection system.



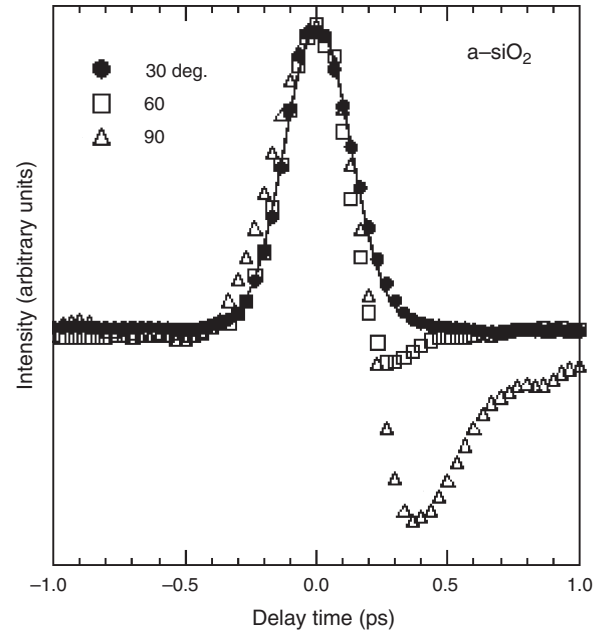
**Figure 4.** Experimental setup for hologram encoding system by using interfering UV fs pulse beams. Reprinted with permission from [26], H. Kamioka et al., *Proc. SPIE* 4760, 994 (2002). © 2002, SPIE.

Silica has third-order susceptibility, with a very fast time response, and thus the pump pulse induces a birefringence through the electronic Kerr effect, also known as the non-linear refractive index change. When the  $\lambda/2$  plates are rotated by 45 degree with each other, the probe pulse can go through PBS only when the silica plate is irradiated simultaneously with the pump pulse (Fig. 5). That is, this geometry yields an autocorrelation measurement of the pulse. Although the observed pulse width stretches from that of the fundamental wavelength (870 nm) and the exact reason for that has not been clarified, the time zero is determined at the center position of the band.

In the transient absorption method, the probe pulse is directly collected at the PD without both the  $\lambda/2$  plates and the PBS device. The absorbance change of the probe pulse perturbed by the pump-pulse irradiation is detected by the same procedure as the Kerr measurement. Because the laser energy (4.3 eV) is below the bandgap energy of silica, the absorption occurs through two photon processes. The electron hole plasma is momentarily created and decays to a self-trapped exciton or transient defect centers with a fast relaxation time. Figure 6 shows the experimental result of the transient absorption measurement. The pulse width (FWHM) is obtained as 300 fs, which is a little larger compared to that obtained by the optical Kerr measurement. However, it is accurate enough to determine the time zero between the two pulses from the absorption band profile. Spectra for different colliding angles of two pulses also were demonstrated in Figure 6, indicating that the peak width has hardly changed with the angle, although dip structures become prominent in a longer delay time region with increasing the angle. These results indicate that the transient absorption measurement is a useful method to obtain the time zero, not restricted by the colliding angle between two pulses.



**Figure 5.** Optical Kerr gate signal in silica plate as a function of delay time between pump and probe pulses. The crossing angle between the two beams is 30°. Reprinted with permission from [26], H. Kamioka et al., *Proc. SPIE* 4760, 994 (2002). © 2002, SPIE.



**Figure 6.** Optical transient transmission intensity as a function of delay time between pump and probe beams for several crossing angles. Solid line shows Gaussian fitting curve. Reprinted with permission from [26], H. Kamioka et al., *Proc. SPIE* 4760, 994 (2002). © 2002, SPIE.

### 5.3.3. Distributed Feedback Dye Laser Technique

When the beams overlap with each other spatially and temporally in a dye cell placed at the focal point of colliding fs KrF laser beams, a grating is induced in the cell, which in turn acts as a Bragg mirror, thereby forming a distributed feedback dye laser [11]. In this way, monitoring the output of the dye cell while tuning an optical delay line makes it possible to achieve the temporal coincidence of the two KrF laser beams.

## 6. ENCODED HOLOGRAM

Several types of holographic structures have been encoded by the above mentioned exposure techniques in various materials, including dielectrics (SiO<sub>2</sub> glass, SiO<sub>2</sub> thin films, LiNbO<sub>3</sub>, ZnO, ZrO<sub>2</sub>, MgO, TiO<sub>2</sub>, diamond, carbon), semiconductors (SiC, ZnSe, Si), metals (WC, Pt, Au, Al) and polymers (polyimide, PMMA, negative photoresist SU-8). Table 1 also summarizes types of periodic structures and encoded materials. Representative examples among them are shown in detail in this section.

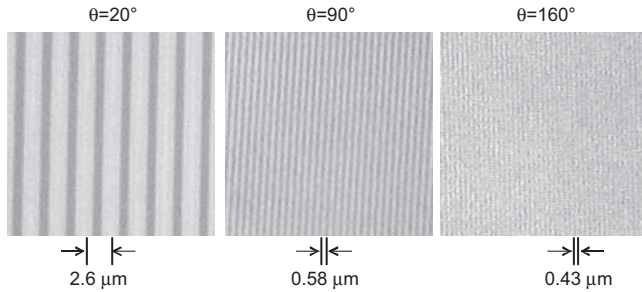
### 6.1. Surface Relief Hologram

#### 6.1.1. Silica Glass by IR fs Laser

When the intersecting beams were focused onto the surface, surface-reliefs type gratings were encoded because of material ablation.

Figure 7 shows surface-relief gratings encoded in silica glass for several  $\theta$  values, with a total fluence of 0.3 mJ/pulse. Each grating forms a circle with a diameter of  $\sim 100 \mu\text{m}$  and





**Figure 7.** Optical microscope images of gratings recorded in silica glasses for various beam intersecting angles ( $\theta$ ). Fringe interval  $d$  varies with  $\theta$  according to the equation  $d = \lambda/[2 \sin(\theta/2)]$ . Reprinted with permission from [18], M. Hirano et al., *Appl. Surf. Sci.* 197–198, 688 (2002). © 2002, Elsevier Science.

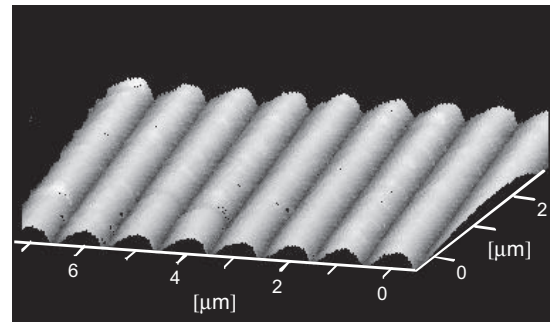
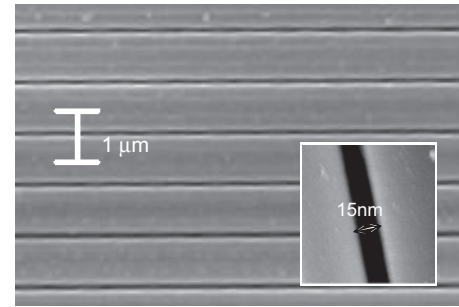
is composed of parallel fringes with a constant spacing equal to  $\lambda/[2 \sin(\theta/2)]$ , where  $\lambda$  is the laser wavelength (800 nm). This observation constitutes clear evidence that the gratings were encoded as the result of interference between the two fs pulses of the fundamental wavelength (800 nm). The formation of a periodic valley structure at the surface is revealed by (AFM) images. The deposition of debris or molten materials onto the surface indicates that the grating structure results from laser ablation at this fluence level.

Infrared spectra suggested O–Si–O bond angles in the laser-irradiated area suffered photo-induced changes, leading to the densification of the silica glass. Such structural changes have been observed in silica glasses during high-energy ion implantation or neutron bombardment; densification typically saturates at  $\sim 3\%$  [31]. As this compaction is accompanied by a refraction index increase of  $\sim 0.7\%$ , a refraction index modulation type grating can be simultaneously formed beneath the surface relief type grating.

High-resolution images of the grating acquired with a field emission scanning electron microscope (SEM) (Fig. 8) show periodic valleys in the internal structure of the grating. These valleys are very narrow, down to 15 nm. The compaction of silica glass in very localized areas due to intense laser irradiation generates tensile forces directed parallel to the surface, which likely play an important role in the formation of such narrow valleys.

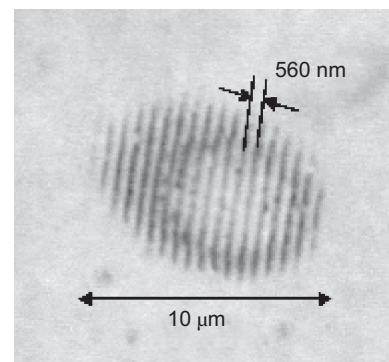
### 6.1.2. Silica Glass by Ultraviolet fs Laser

When the interference UV fs pulse (290 nm), with a total energy of  $20 \mu\text{J}$ , was irradiated at bulk silica glass, the micrograting structure was encoded at the surface through an ablation, as shown in Figure 9. A colliding angle was set to be  $30^\circ$ . The fringe spacing is in good agreement with the calculated value of 560 nm for  $\lambda = 290 \text{ nm}$ . The net fluence of the two laser pulses at the sample surface was  $0.25 \text{ J/cm}^2$ , which is similar to that of the 800 nm fs laser that encoded the surface grating on silicon surface. The slight dependence of the threshold power on the laser wavelength implies that the multiphoton absorption is not a major process, but the avalanche ionization is responsible for the excitation of electron-hole pairs in silica glass. The

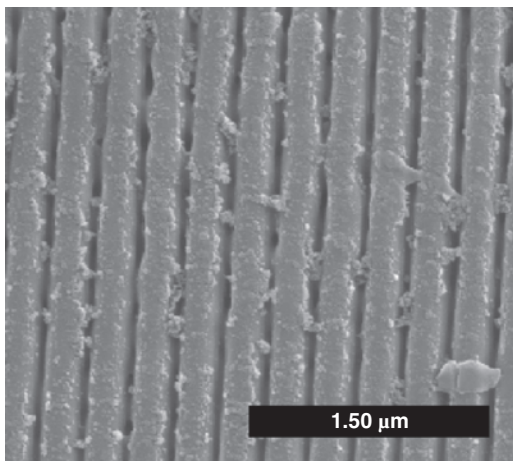


**Figure 8.** SEM image (upper) and AFM profile (lower) of a grating encoded in silica glass. Reprinted with permission from [18], M. Hirano et al., *Appl. Surf. Sci.* 197–198, 688 (2002). © 2002, Elsevier Science.

smaller spacing between grooves is expected when increasing the colliding angle of the two pulses. The SEM picture of the grating is shown in Figure 10 for the colliding angle of  $60^\circ$ . The spacing agrees with the predicted value of 290 nm, which will be further narrowed down to  $\sim 150 \text{ nm}$  with increasing of the angle.



**Figure 9.** Optical microscope image of a grating on silica surface encoded by UV fs pulse (290 nm). The colliding angle is  $30^\circ$ . Reprinted with permission from [26], H. Kamioka et al., *Proc. SPIE* 4760, 994 (2002). © 2002, SPIE.



**Figure 10.** SEM image of a grating on silica surface encoded by UV fs pulse (290 nm). The colliding angle is  $60^\circ$ . Reprinted with permission from [26], H. Kamioka et al., *Proc. SPIE* 4760, 994 (2002). © 2002, SPIE.

### 6.1.3. Polyimide by fs KrF Laser

Surface-relief-type gratings with a spacing of 167 nm were produced at polyimide surface by a single shot of a 400 fs KrF excimer laser with an average energy of  $83 \text{ mJ/cm}^2$ . The colliding angle was 45 degree.

### 6.1.4. Silica Thin Film

Surface-relief-type gratings with a valley depth as shallow as 3.5 nm were recorded in thin-film silica on a silicon wafer by reducing the total fluence to 0.015 mJ. The surface profile of the fabricated grating was smooth and neither small deposits nor macroscopic laser damage or cracking was observed at this fluence, suggesting that the formed grating resulted from the densification of the films, not from laser ablation. The valley depth of the grating (3.5 nm) relative to the film thickness (114 nm) supported this suggestion, as it coincides with the saturation level ( $\sim 3\%$ ) of radiation-induced densification in amorphous  $\text{SiO}_2$ . A difference in the properties of undensified and densified amorphous  $\text{SiO}_2$  is manifested in the etching rates during stress-enhanced corrosion [32]. An AFM image and a cross section of grating structures formed by etching with 1% HF solution (Fig. 11) show that etching increases the depth of the valley by a factor of 5–6 relative to that before etching. In other words, chemical etching converted the refractive index modulation-type grating into a surface-relief-type grating.

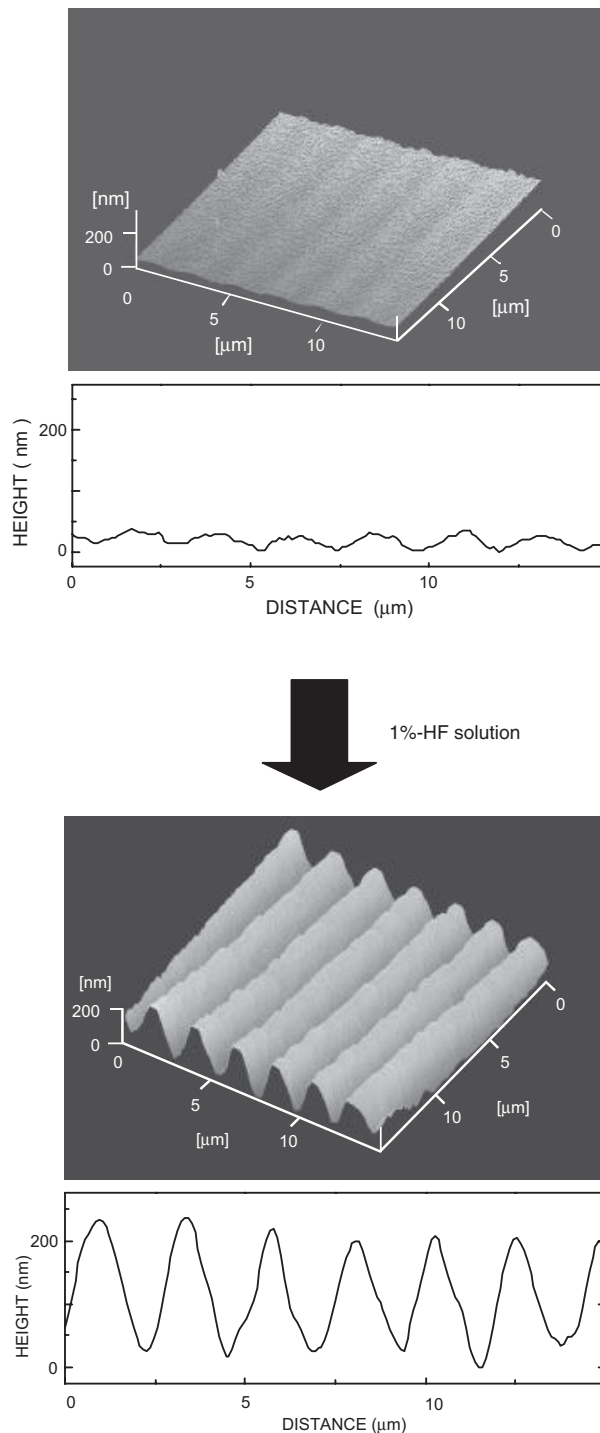
## 6.2. Embedded Hologram

### 6.2.1. Full Compressed Pulse

When the focal point of the interfering fs laser pulses is positioned inside the target materials, an embedded grating is recorded through a refractive index modulation, either due to structural alternations such as densification in silica glass, crystallographic phase changes from crystalline to amorphous states, or the formation of micropores due to the evaporation of a small amount of the materials.

Such an embedded grating was recorded inside a diamond crystal [14]. Confocal microscopic images reveal the grating

lies  $0.45\text{--}1.05 \mu\text{m}$  beneath the surface. Raman spectra for the grating encoded area suggest that the refractive index modulation was caused by a structural change from diamond to diamond-like carbon or amorphous carbon [33]. Similar embedded gratings in a multicomponent glass plate [21] and



**Figure 11.** AFM images of surface-relief-type gratings encoded in silica thin films before and after etching by 1% HF solution. The valley depth was deepened due to preferential etching in the densified areas. Reprinted with permission from [18], M. Hirano et al., *Appl. Surf. Sci.* 197–198, 688 (2002). © 2002, Elsevier Science.

polymer [20] have been reported by using fully compressed fs laser pulse.

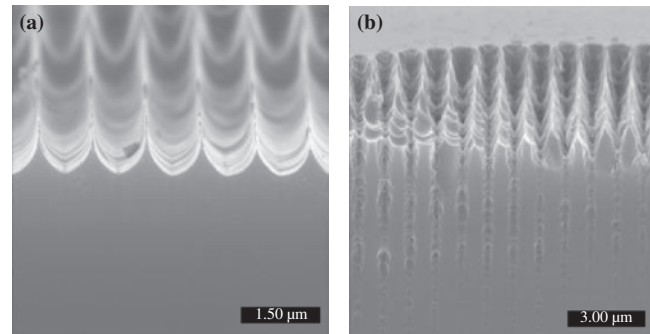
### 6.2.2. Chirped Pulse

In spite of the successes in encoding the embedded gratings by fully compressed fs pulse ( $\sim 100$  fs), it is still difficult to encode embedded gratings deep inside versatile materials. The major reason for such a shallow processing depth is likely attributed to the fact that absorption coefficient is larger at the surface than the inside of materials, thereby, most of the pulse energy being lost around surface and the penetrating pulse is not intense enough for the encoding. The deterioration of the coherency of the pulse due to the interaction between the intense pulse and materials during the propagation may be an additional cause for the difficulty in encoding the gating inside of materials.

One possible approach to overcome the difficulty is to use focal lenses with a large numerical aperture, which makes it possible to reduce the laser-power density at the surface much lower than that at the focal area inside the material, thereby keeping accumulated energy at the surface below the threshold, while enhancing the energy at the focal point above the threshold. This approach is successfully used to encode embedded gratings for specific materials such as diamond [14], multicomponent glass [21], and polymers [20], as mentioned before. But, this approach alone unlikely provides enough controllability and flexibility to the encoding process of the embedded gratings.

An essential solution to overcome the difficulty is to reduce the peak energy of the pulse keeping the total energy of the pulse unchanged by expanding the pulse width. A chirped pulse, which is a partially compressed fs pulse, may meet the requirements. Before encoding embedded gratings with the chirped pulses, surface-relief-type gratings were encoded to confirm their effectiveness [24, 25]. The diameters of the surface-relief-type gratings at the surface slightly decrease with an increase in the pulse width from 100 to 5000 fs, each pulse having a constant total energy. As the energy density at the periphery of the recorded area corresponds to the threshold for the encoding, this observation implies that the threshold is more dominantly governed by the total energy than by the peak energy of the pulse in this pulse width range.

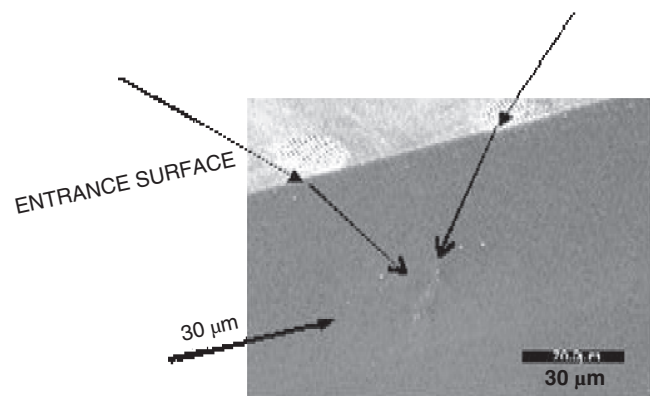
Figure 12 shows (FE)-SEM images of a cross section of the surface-relief-type gratings recorded by 100 fs and 400 fs pulses with the total energy of  $50 \mu\text{J}/\text{pulse}$ . The 100 fs pulse encodes the grating with very shallow grooves of  $\sim 1 \mu\text{m}$  located at the surface. On the other hand, the groove depth becomes deeper for the 400 fs pulse irradiation, indicating the pulse energy penetrates deeper with an increase in the pulse width or a decrease in the peak power. The shallow processing depth by 100 fs pulse may be explained as follows. When the 100 fs pulse with an energy of  $\sim 5 \text{ TW}/\text{cm}^3$  is irradiated at the silica glass, it generates the electron-hole pairs with a density of  $\sim 10^{21}/\text{cm}^3$  around the surface within the pulse duration via multiphoton absorption and avalanche ionization processes as predicated by Stuart et al. [34]. The resultant dense plasma strongly absorbs IR light through one photon process, thereby dramatically enhancing the plasma density and thus preventing the penetration of the pulse into



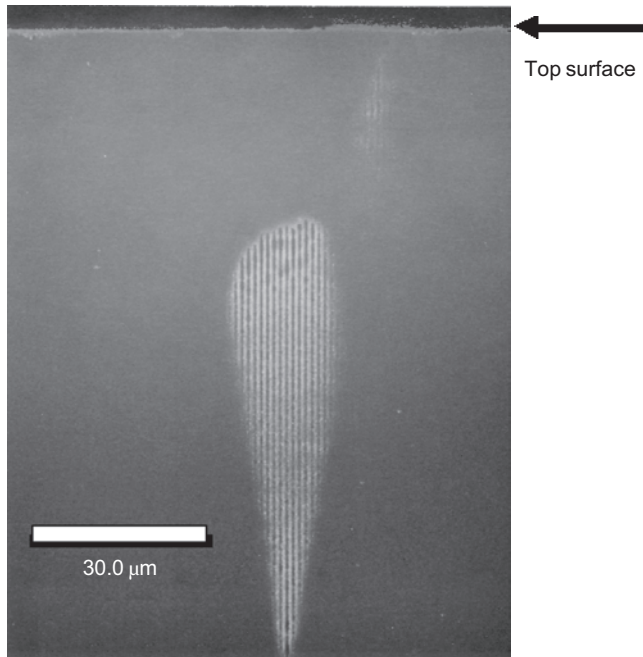
**Figure 12.** FE-SEM images of cross section of the surface-relief-type gratings recorded by 100 fs (a) and 400 fs (a) pulses in silica glass. Reprinted with permission from [24], M. Hirano et al., *Proc. SPIE* 506, 89 (2003). © 2003, SPIE.

the silica more than  $\sim 1 \mu\text{m}$ . On the other hand, the front part of the stretched pulse may penetrate into materials before the electron-hole pair density at the surface becomes greater than  $\sim 10^{21}/\text{cm}^3$ . These observations encourage the use of a stretched pulse for the formation of embedded gratings.

Then, the cross area of the two stretched pulse beams was shifted to the inside of the material to encode the embedded grating, as demonstrated in Figure 13, where the beam colliding angle of  $45^\circ$ , cross area of  $30 \mu\text{m}$  below the surface, laser pulse width of 500 fs, and total pulse energy of  $50 \mu\text{J}/\text{pulse}$  were used. No gratings are observed in the crossing area in the as-cut sample, but faint gratings are seen in the beam entrance areas on the surface. After the chemical etching, an embedded grating appears at the crossing area due to the stress-enhanced etching, as described previously. An expanded SEM image for the cross area shown in Figure 14, clearly demonstrates that the grating is encoded inside the silica glass at a depth of  $\sim 30 \mu\text{m}$ . Periodic line grooves with a constant spacing ( $d$ ) of  $\sim 1 \mu\text{m}$  is visible in the grating. The spacing agrees with that given by the equation of  $d = \lambda/[2 \sin(\theta/2)]$ , where  $\lambda$  is the wavelength of the laser (800 nm), and  $\theta$  is the colliding angle between two incident pulses ( $45^\circ$ ). Those gratings are observed directly without the chemical etching by a confocal microscope as shown in Figure 15b. The faint gratings in the beam entrance



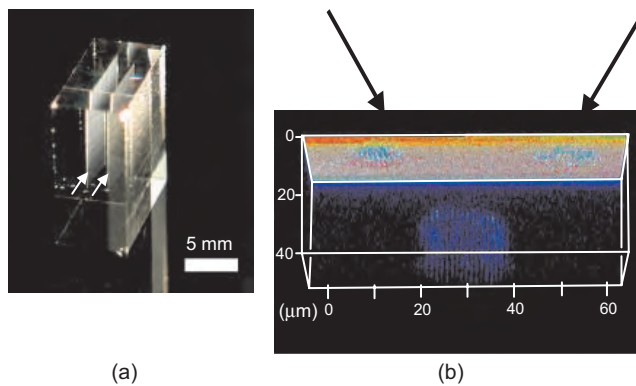
**Figure 13.** FE-SEM image of the propagation of the two stretched pulses. Reprinted with permission from [24], M. Hirano et al., *Proc. SPIE* 506, 89 (2003). © 2003, SPIE.



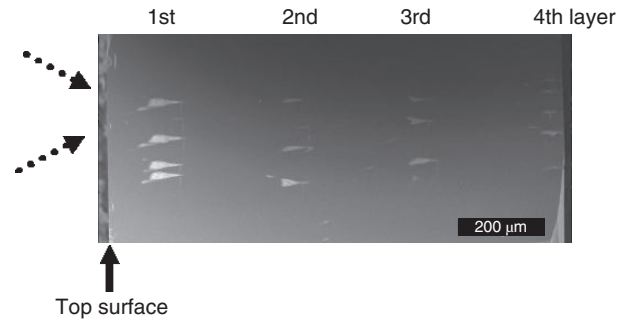
**Figure 14.** Expanded FE-SEM image of the crossed area of the two stretched pulse beams. Reprinted with permission from [25], K. Kawamura et al., *Appl. Phys. Lett.* 81, 1137 (2002). © 2002, American Institute of Physics.

areas on the surface, whose line spacing is  $\sim 1 \mu\text{m}$ , equaling to that of the embedded grating, are most likely created as results of the interference between an incident beam and a conjugated beam reconstructed from the transient grating, formed by the periodic density distribution of the laser-induced excited state or by electron-hole plasma.

Figure 16 shows a cross-sectional FE-SEM image of multiple gratings vertically located inside the silica glass. Each grating was recorded by a single shot. These gratings, which were encoded in four layers separated by  $300 \mu\text{m}$ , show long tails downward to the beam propagation direction. When an array of gratings is encoded in each layer, it can be visualized by illuminating white light, as shown in Figure 15a.



**Figure 15.** Embedded gratings in silica glass. (a) Array of embedded gratings in two layers are visualized by illuminating white light. (b) Confocal microscope image of embedded grating. Two surface gratings at the beam entrances also are observed. Reprinted with permission from [25], K. Kawamura et al., *Appl. Phys. Lett.* 81, 1137 (2002). © 2002, American Institute of Physics.



**Figure 16.** Cross-sectional SEM images for multiple gratings located vertically inside silica glass. Reprinted with permission from [25], K. Kawamura et al., *Appl. Phys. Lett.* 81, 1137 (2002). © 2002, American Institute of Physics.

No noticeable difference is observed between the gratings encoded by down- and up-chirped pulses, suggesting the nonlinear optical interaction, which may degrade the coherence of the pulse, does not play a significant role, at least in the stretched pulse.

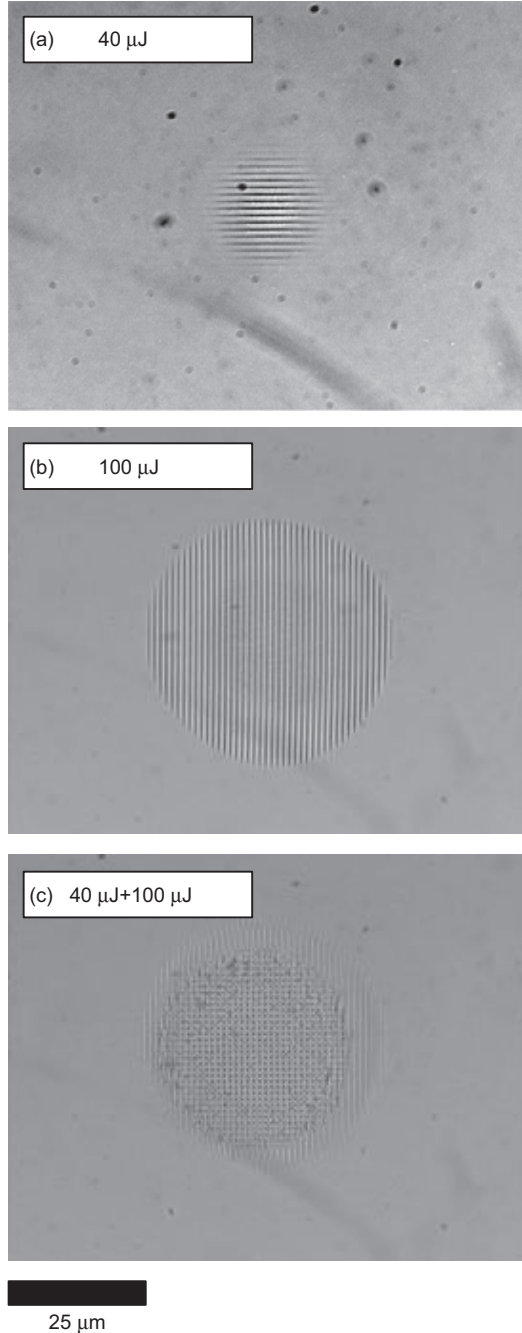
These results clearly indicate that use of chirped pulses instead of a fully compressed fs pulse, which results in stretching of the pulse width from  $\sim 100$  to  $\sim 5000$  fs, provides controllability and flexibility to the encoding system, particularly giving rise to the capability in encoding embedded gratings in versatile materials. The optimized pulse width, which may be of material dependent, is  $\sim 500$  fs for silica glass.

### 6.3. Multidimensional Periodic Structure

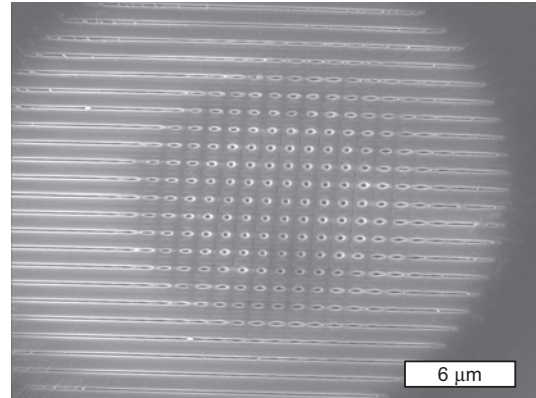
#### 6.3.1. Double Exposure Technique

Two-dimensional periodic structures can be formed by a double-exposure technique [22]. A series of optical microscope images of the gratings in Figure 17 demonstrate the double-exposure procedure. Photos (a) and (b) in this figure show gratings with diameters of  $\sim 15 \mu\text{m}$  and  $\sim 50 \mu\text{m}$  encoded by laser pulse energies of  $40 \mu\text{J}$  and  $100 \mu\text{J}$ , respectively. After the first grating was encoding, the samples were rotated by  $90^\circ$  and a second grating was recorded superposed on the first grating. The resultant structure is not always a simple superposition of two kinds of gratings, but a complicated structure results from interactions between the two encoding processes. Figure 18 is an SEM image of a crossed grating encoded when energy in the second pulse ( $80 \text{ mJ}$ ) was larger than in the first one ( $40 \text{ mJ}$ ) with a  $45^\circ$  angle between the beams for both exposures. The periodic vertical lines represent fringes of the grating encoded by the first exposure, since the periodicity of  $1.0 \mu\text{m}$  equals  $\lambda/[2 \sin(\theta/2)]$ . It is noted that an array of round dots with a diameter of  $\sim 140 \text{ nm}$  is observed in the center part of the crossed grating. The dots become ellipsoidal as one moves toward the edge of the grating and connect with each other to form periodic horizontal lines. Since the first grating was not encoded in the outer area and the spacing is consistent with the second exposure, the horizontal lines here are fringes of the second grating. The formation of the dot array in the central part results from the interaction between the first grating and the incident beams in the second exposure.

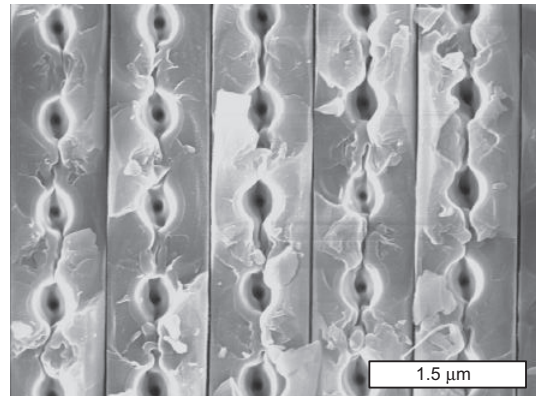
When the first pulse energy ( $80 \mu\text{J}/\text{pulse}$ ) is larger than that of the second pulse ( $40 \mu\text{J}/\text{pulse}$ ), a resultant structure is composed of periodic narrow valleys recorded by the first exposure and a two-dimensional dot array with exfoliations and cracks around the dot (Fig. 19). Diameters of the dots are  $\sim 100 \text{ nm}$  and each dot seems to have a smaller dot



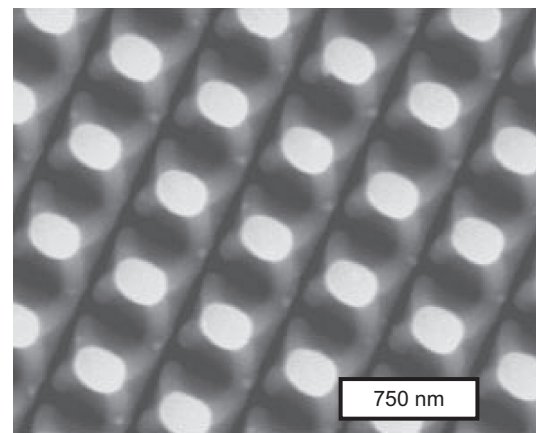
**Figure 17.** Procedure for double exposure. (a) Optical microscopic image of a grating encoded at a total laser fluence of  $40 \mu\text{J}/\text{pulse}$  (first grating). (b) Optical microscopic image of a grating encoded at a total laser fluence of  $80 \mu\text{J}/\text{pulse}$  after the sample was rotated by  $90^\circ$  (second grating). (c) Optical microscopic image of a crossed grating, encoded by superposing the second grating onto the first grating. Reprinted with permission from [18], M. Hirano et al., *Appl. Surf. Sci.* 197–198, 688 (2002). © 2002, Elsevier Science.



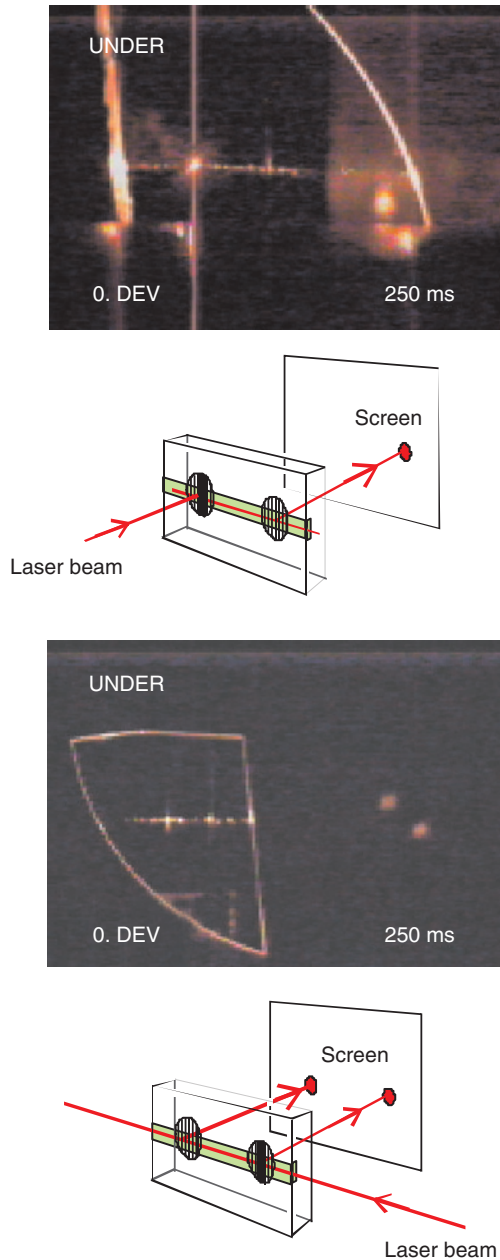
**Figure 18.** Scanning electron microscope image of a crossed grating encoded at a total fluence of  $40 \mu\text{J}/\text{pulse}$  for the first exposure and  $80 \mu\text{J}/\text{pulse}$  for the second exposure. The beams intersected at an angle of  $45^\circ$  for both exposures. Reprinted with permission from [18], M. Hirano et al., *Appl. Surf. Sci.* 197–198, 688 (2002). © 2002, Elsevier Science.



**Figure 19.** Scanning electron microscope image of a crossed grating encoded at a total fluence of  $80 \mu\text{J}/\text{pulse}$  for the first exposure and  $40 \mu\text{J}/\text{pulse}$  for the second exposure. The beams intersected at an angle of  $45^\circ$  for both exposures. Reprinted with permission from [18], M. Hirano et al., *Appl. Surf. Sci.* 197–198, 688 (2002). © 2002, Elsevier Science.



**Figure 20.** Scanning electron microscope image of a crossed grating encoded at a total fluence of  $100 \mu\text{J}/\text{pulse}$  and the beams intersected at right angle for each exposure. Reprinted with permission from [18], M. Hirano et al., *Appl. Surf. Sci.* 197–198, 688 (2002). © 2002, Elsevier Science.



**Figure 21.** Photographs of two gratings encoded on an optical waveguide fabricated in  $\text{LiNbO}_3$ . Light coupling and decoupling functions of the gratings are demonstrated. Reprinted with permission from [18], M. Hirano et al., *Appl. Surf. Sci.* 197–198, 688 (2002). © 2002, Elsevier Science.

inside, whose diameter becomes smaller with a decrease in the pulse energy. The dot array results from the interaction between the periodic valleys and the incident beams in the second exposure, most likely due to the interference among two incident beams and reconstructed beams from the first grating. If this were the case, encoded structures would be equivalent with those by the interference among four beams divided from a pulse. By increasing  $\theta$  from  $45^\circ$  to  $90^\circ$ , an array of trapezoid structures could be produced; this array looks like a simple superposition of two orthogonal gratings (Fig. 20).

These results indicate that the double-exposure technique of using fs laser pulses offers a new tool for the formation of two-dimensional nanostructures in various kinds of materials.

### 6.3.2. Multibeam Interference Technique

Results of the double-exposure process suggest that multi-beam interference provides a novel technique in encoding multidimensional periodic structures. Especially, when we use the interference among five beams, we can fabricate three-dimensional periodic structures in transparent materials. Such three-dimensional structures have been encoded in polymers by using a Q-switched YAG: $\text{Nd}^{3+}$  laser [35]. Three-dimensional periodic structures were encoded in negative photoresist SU-8 with interfering five beams split from a SHG of Ti:sapphire laser pulse [19], where the pulse was split into five beams by a diffractive beam splitter, making it possible to achieve the temporal coincidence without the detecting mechanism.

### 6.4. Application to Optical Device

Because sizes of the recorded gratings ( $\sim 50 \mu\text{m}$ ) are slightly smaller than that of optical devices, gratings could be used as building blocks of the optical devices. For example, two gratings capable of coupling and decoupling of light to waveguide were encoded on a waveguide fabricated on a  $\text{LiNbO}_3$  substrate. Figure 21 demonstrates that He–Ne laser light is coupled and decoupled to the waveguide through these gratings.

## GLOSSARY

**Chirped femto second laser pulse** Not fully compressed pulse with a pulse width of  $100\sim 3,000$  fs from regenerated amplified fs pulse laser system.

**Double exposure technique** An interference fs pulse are irradiated exactly on as encoded grating which was rotated by  $90^\circ$  degree.

**Embedded grating** Refractive index type grating encoded inside transparent materials.

**Interference fs laser pulse** When two fs laser pulses split from a single pulse collided with spatial and temporal coincidences, interference of fs laser pulse occurs due to good coherency of the pulse.

**Multi-dimensional periodic structure** Two or three dimensional periodic structures are encoded by the interference among four of five fs laser pulses. Two dimensional structures are also fabricated by a double exposure technique.

**Structural alternation** Structural changes induced by the irradiation of fs laser pulse including densification of silica glass, crystallographic phase change from crystal to amorphous states in diamond, which accompany with the refractive index modulation.

**Surface grating** Surface relief type grating encoded by material ablation.

## REFERENCES

1. E. E. B. Campbell, D. Ashkenasi, and A. Rosenfeld, *Mater. Sci. Forum* 301, 123 (1999).
2. J. Kruger and W. Kautek, *Appl. Surf. Sci.* 96–98, 430–438 (1996).
3. J. Ihlemann, B. Wolff, and P. Simon, *Appl. Phys. A* 54, 363 (1992).
4. J. H. Strickler and W. W. Webb, *Opt. Lett.* 16, 1780 (1991).
5. E. N. Glezer and E. Mazur, *Appl. Phys. Lett.* 71, 882 (1997).
6. K. H. Davis, K. Miura, N. Sugimoto, and K. Hirao, *Opt. Lett.* 21, 1729 (1996).
7. D. von der Linde, K. Sokolowski-Tinten, and J. Bialkowski, *Appl. Surf. Sci.* 109/11, 1–10 (1997).
8. K. Hirao, T. Mitsu, J. Si, and J. Qui, “Active Glass for Photonic Devices.” Springer Series in Photonics. P47, 2002.
9. B. C. Stuart, M. D. Feit, A. M. Rubenchik, B. W. Shore, and M. D. Perry, *Phys. Rev. Lett.* 74, 2248 (1995).
10. E. P. Ippen and C. V. Shank, in “Ultrashort Light Pulses” (S. L. Shapiro, Ed.), Chap. 3. Springer Verlag, New York, 1997.
11. H. M. Phillips and R. L. Sauerbrey, *Opt. Eng.* 32, 2424 (1993).
12. A. M. Ozkan, A. P. Malshe, T. A. Railkar, W. D. Brown, M. D. Shirk, and P. A. Molian, *Appl. Phys. Lett.* 75, 3716 (1999).
13. K. Kawamura, N. Sarukura, M. Hirano, and H. Hosono, *Appl. Phys. B* 71, 119 (2000).
14. K. Kawamura, N. Sarukura, M. Hirano, and H. Hosono, *Jpn. J. Appl. Phys.* 39, L767 (2000).
15. K. Kawamura, N. Sarukura, M. Hirano, and H. Hosono, *Appl. Phys. Lett.* 78, 1038 (2001).
16. H. Hosono, K. Kawamura, S. Matsui, and M. Hirano, *Nucl. Instrum. Methods Phys. Res., Sect. B* 191, 89 (2002).
17. K. Kawamura, N. Motomitsu, M. Hirano, and H. Hosono, *J. J. Appl. Phys.* 41, 4400 (2002).
18. M. Hirano, K. Kawamura, and H. Hosono, *Appl. Surf. Sci.* 197–198, 688 (2002).
19. T. Kondo, S. Matsuo, S. Juodkazis, and H. Misawa, *Appl. Phys. Lett.* 79, 725 (2001).
20. J. Si, J. Qiu, J. Zhai, Y. Shan, and K. Hirao, *Appl. Phys. Lett.* 80, 359 (2002).
21. Y. Li, W. Watanabe, K. Yamada, T. Shinagawa, K. Itoh, J. Nishii, and Y. Jiang, *Appl. Phys. Lett.* 80, 1508 (2002).
22. K. Kawamura, N. Sarukura, M. Hirano, and H. Hosono, *Appl. Phys. Lett.* 79, 1228 (2001).
23. K. Kawamura, N. Ito, N. Sarukura, M. Hirano, and H. Hosono, *Rev. Sci. Instrum.* 73, 1711 (2002).
24. M. Hirano, K. Kawamura, and H. Hosono, *Proc. SPIE (International Symposium on Photonic Glasses '02)* 506, 89 (2003).
25. K. Kawamura, M. Hirano, T. Kamiya, and H. Hosono, *Appl. Phys. Lett.* 81, 1137 (2002).
26. H. Kamioka, K. Kawamura, T. Miura, M. Hirano, and H. Hosono, *Proc. SPIE* 4760, 994 (2002).
27. H. Kamioka, K. Kawamura, T. Miura, M. Hirano, and H. Hosono, *J. Nanosci. Nanotech.* 2, 321 (2002).
28. S. Backus, J. Peatross, Z. Zeek, A. Rundquist, G. Taft, M. M. Murnane, and H. C. Kapteyn, *Opt. Lett.* 21, 665 (1996).
29. C. W. Siders, N. C. Turner III, M. C. Downer, A. Babine, A. Stepanov, and A. M. Sergeev, *J. Opt. Soc. Am. B* 12, 330 (1996).
30. G. Marcus, A. Zigler, and Z. Henis, *J. Opt. Soc. Am. B* 16, 792 (1999).
31. S. K. Sharma, D. W. Matson, J. A. Philpotts, and T. L. Roush, *J. Non-Cryst. Solids* 68, 99 (1984).
32. F. N. Schwettman, D. J. Dexter, and D. F. Cole, *J. Electrochem. Soc.* 120, 1566 (1973).
33. J. Roberson, *Adv. Phys.* 35, 317 (1986).
34. B. C. Stuart, M. D. Feit, S. Herman, A. M. Rubenchik, B. W. Shore, and M. D. Perry, *J. Opt. Soc. Am. B* 13, 459 (1996).
35. M. Campbell, D. N. Sharp, M. Harrison, R. G. Denning, and A. J. Turberfield, *Nature* 404, 53 (2000).

# Pharmaceutical Nanotechnology

Paul A. McCarron, Maurice Hall

*The Queen's University of Belfast, Belfast, Ireland*

## CONTENTS

1. Introduction
  2. Definition of Nanoparticles
  3. Preparation
  4. Characterization
  5. Drug Loading
  6. Incorporation of Water-Soluble Drugs
  7. Incorporation of 5-Fluorouracil into Nanoparticles
  8. Drug Release
  9. Conclusions
- Glossary  
References

## 1. INTRODUCTION

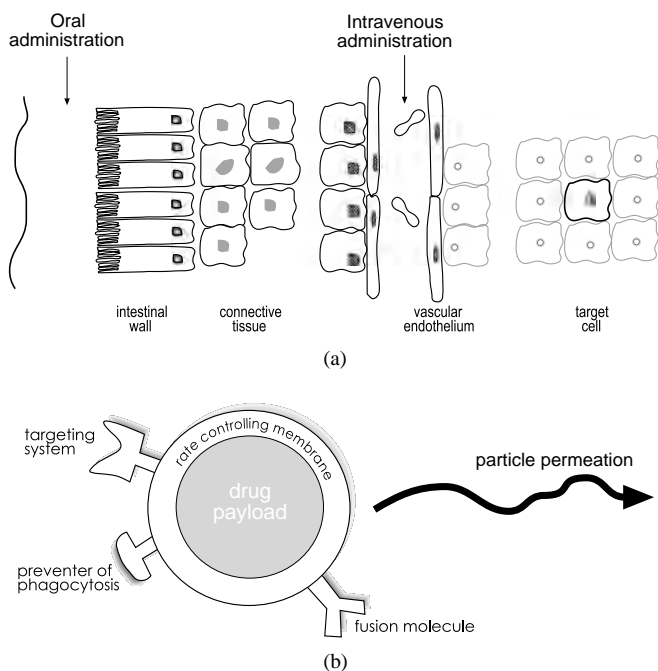
The dream of delivering a pharmaceutically active molecule to a specific site in the body has been a long-held aspiration with beginnings that may be traced back to Paul Ehrlich, who in the early 20th century coined the phrase “magic bullet” to describe such an entity [1]. Today, extensive pharmaceutical research has led to the development of drug delivery systems and strategies, which go some way to fulfilling this idea, but few which could be described as “magic bullets.” Side-effects and toxicities still afflict these approaches and, hence, Ehrlich’s visionary thinking has not yet been fully realized. This is especially relevant in tumor chemotherapy, where selective delivery to neoplastic cells in comparison to surrounding normal cells is an important principle [2]. As can be seen in Figure 1a, the challenge faced in site-specific delivery of drugs is immense due to the numerous obstacles barricading the drug along its desired route. Cellular structures and indeed the very components of the cell itself will either prevent or act in some selective manner to hinder to the migration of drug from its point of administration to the intended destination site.

On moving forward into the 21st century, it is apparent that modern medicine still faces many challenges. Nanotechnology is indeed one area that may offer scientific advances in the coming years, which could lead to significant progress in the improvement of therapeutic outcomes. In particular, the development of nanoparticulate drug delivery systems may enhance the probability of getting a drug to its target site [3]. Instead of relying on the physicochemical properties of the drug to dictate its biodistribution, the drug is incorporated as a payload into a particle resulting in a different transit mechanism for the drug after administration [4]. This can be enhanced further by virtue of the flexible nature of the nanoparticle scaffold, on to which subsections may be chemically bolted, producing a tailor-made and multifaceted device. This can be represented in Figure 1b, which gives the blueprint of an idealized nanoparticulate delivery system that must make its way to the target cell.

The particle in Figure 1b has several properties which are incorporated onto the particle, mostly by covalent bonding to surface groups. A targeting system, such as a monoclonal antibody, will recognize binding sites that are unique to the target cell and allow the particle to dock onto the exposed surface [5]. This has been the focus of much current research into developing strategies for targeting nanoparticles to the site of drug action [6–8]. A fusion protein will instigate the process of merging with the target cell, thereby bringing the particle into the cytoplasm [9]. As polymeric nanoparticles are recognized as foreign by the body’s immune system, they are removed quite effectively by phagocytosis on exposure to the endorecticular system [10]. This will prevent the particle from reaching the target site and must be prevented. Steps toward this goal have already been taken with the production of so-called “stealth” nanoparticles. These are nanoparticles which incorporate a biomimetic polymer, usually polyethylene glycol, into their structure to avoid elicitation of an immune response [11–13]. Presently, such an idealized nanoparticle with these three important properties has yet to be realized, but attempts have been made to attach some of the subsystems described.

The construction of an idealized particle must start with the formation of a solid polymeric sphere with a diameter





**Figure 1.** (a) A simplified overview depicting the barriers to drug localization at a target cell after oral administration into the gut or intravenous administration to the systemic circulation. For example, the path from a capillary to a target cell may involve crossing the vascular endothelium and various connective tissue structures. (b) An idealized draft of a multifaceted nanoparticulate system containing a drug payload that must also permeate in some way to the target cell. Pendant molecules, such as a targeting ligand, add to the functionality of the device.

of approximately 200 nm. This is followed closely by loading the drug into the naked particle. This is dependent on the physicochemical properties of the drug molecule, which may often present problems in terms of efficient loading, especially if the drug has appreciable water solubility. This scenario may not be uncommon given that the majority of candidate molecules for inclusion in nanoparticulate systems will possess some degree of aqueous solubility. This chapter discusses the construction of nanoparticles and describes their characterization. In particular, the process of incorporating a water-soluble payload is discussed and the problems associated with this are used to illustrate the complexities encountered during the proposed construction of a device, as typified in Figure 1b.

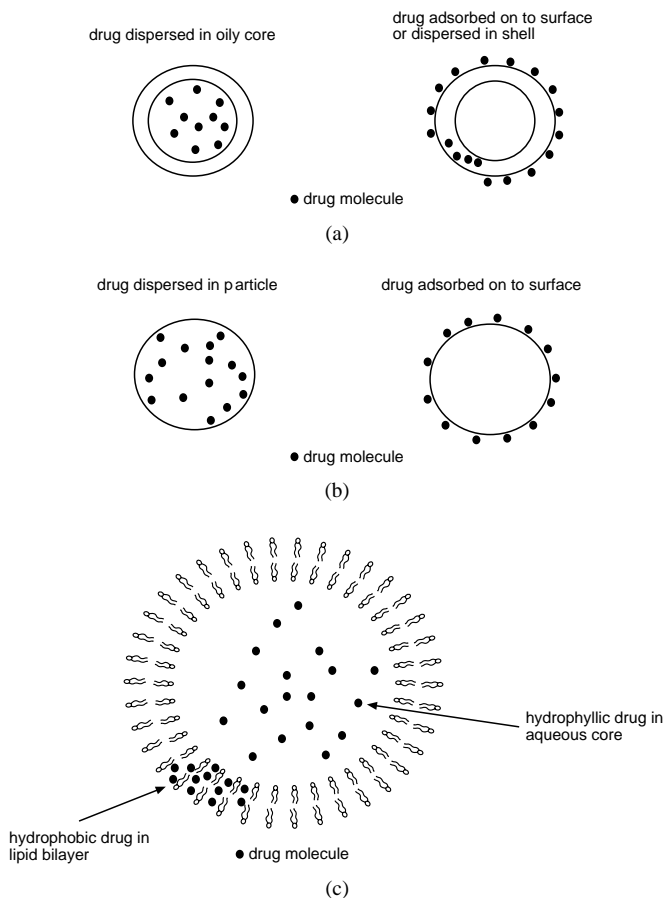
## 2. DEFINITION OF NANOPARTICLES

Nanoparticles have been studied extensively as carriers for drugs employed in a wide variety of routes of administration, including parenteral [14], ocular [15], and peroral [16] pathways. The term nanoparticle is a collective name for any colloidal carrier of submicrometer dimension and includes nanospheres, nanocapsules, and liposomes. They can all be defined as solid carriers, approximately spherical and ranging in size from 10 to 1000 nm. They are generally polymeric in nature (synthetic or natural) and can be biodegradable

or nonbiodegradable in character. Biodegradable polymers used include poly(alkylcyanoacrylates) [17, 18], poly(lactide-co-glycolide) [19, 20], chitosan [21, 22], and gelatin [23], while nonbiodegradable polymers include poly(styrene) [24], poly(acrylamide) [25], and poly(methylmethacrylate) [26]. Nanospheres represent the simplest carrier and are solid, monolithic systems in which the drug is dissolved or entrapped throughout the particle matrix. Alternatively, it may be adsorbed onto the surface. No continuous membrane surrounds the particle, as illustrated in Figure 2a.

Nanocapsules are reservoir type systems comprising an oily liquid core surrounded by a polymeric shell [27]. The drug is usually dissolved in this liquid core but may be more closely associated with the shell polymer and the exposed surface, as illustrated in Figure 2b.

Liposomes are closely related to nanocapsules in structural layout but consist of an aqueous core surrounded by a bilayer membrane composed of lipid molecules, such as phospholipids [28], as illustrated in Figure 2c. The drug can be located in the aqueous core or in the bilayer membrane.



**Figure 2.** (a) The morphology of nanospheres, where drug can be either dispersed throughout the polymeric matrix of the particle or adsorbed onto the surface. (b) The morphology of nanocapsules, where drug is dispersed mostly in a liquid core. Drug can also be associated with the polymeric shell, either by dispersal through the polymer or adsorption to it. (c) The morphology of a small single lamellar liposome of submicrometer dimensions showing the possible location of a drug payload.

From a historical prospective, liposomes have been the most extensively studied nanoparticulate carrier [29–32]. However, their full development leading to extensive clinical use has been restricted by pharmaceutical problems entailing drug leakage, stability, and problems with scale-up procedures. These all arise due to their liquid and semisolid nature leading to a lack of rigidity and subsequent fragility. However, the important early work by Couvreur and co-workers [33] introduced nanoparticles prepared from biodegradable poly(alkylcyanoacrylates). This has prompted much research into nanoparticles made from polymeric materials and, furthermore, into finding polymers that are pharmaceutically acceptable, biodegradable, and nontoxic [34]. A wide variety of preparation methods for nanoparticles have now evolved, which encapsulate many different types of drug compounds [35, 36].

### 3. PREPARATION

Both nanospheres and nanocapsules are prepared from either a polymerization reaction of dispersed monomers or from a solvent dispersion procedure using preformed polymers. In many instances, the latter procedure using preformed polymer is desirable, as potential reactions between drug and monomer are avoided and the potential toxicity of residual monomers, surfactant, and initiator is reduced [37]. The final properties of nanoparticles, such as their size, morphology, drug loading, release characteristics, and biodistribution, are all influenced by the method of preparation [38].

#### 3.1. Nanoparticles Prepared from Polymerization Reactions

Most examples of polymerization used to create nanoparticles occur by a free radical mechanism involving distinct initiation, propagation, and termination processes [39]. Polymerization occurs within a continuous liquid medium, which also comprises the monomer, initiator, and a surfactant. Four different polymerization techniques are described to polymerize vinyl type monomers, namely:

- emulsion polymerization, resulting in 0.05–0.2  $\mu\text{m}$  particles
- dispersion polymerization, resulting in 0.3–10  $\mu\text{m}$  particles
- precipitation polymerization, resulting in nonspherical 0.1–10  $\mu\text{m}$  particles
- suspension polymerization, resulting in 20–2000  $\mu\text{m}$  particles

##### 3.1.1. Emulsion Polymerization in a Continuous Aqueous Phase

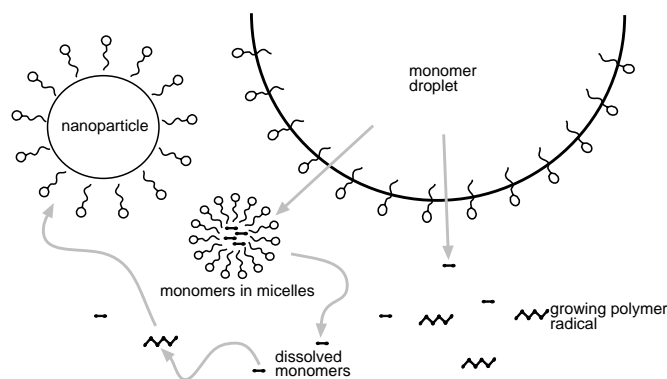
Continuous aqueous phase emulsion polymerization is one of the most widely used procedures to make nanoparticles for drug delivery purposes, especially those prepared from the alkylcyanoacrylate monomers. An oil-in-water emulsion system is employed where the monomer is emulsified in a continuous aqueous phase containing soluble initiator and surfactant [39, 40]. Under these conditions, the monomer is partly solubilized in micelles (5–10 nm), emulsified as large

monomer droplets (1–10  $\mu\text{m}$ ), and partly dissolved in the continuous aqueous phase. The polymerization takes place in the outer continuous phase and not in the micelle interior [41]. Initiation of polymerization occurs in the aqueous phase when a monomer molecule collides with an initiator molecule, which may be an ion or a free radical [42]. Alternatively, the monomer can be struck by a high-energy photon, such as gamma radiation and ultraviolet or intense visible light. Propagation occurs when nascent monomeric radicals interact with other monomer molecules forming primary particles [39]. The polymerization is maintained by the continuous supply of monomer from the monomer reservoirs, such as droplets and micelles, and is illustrated in Figure 3.

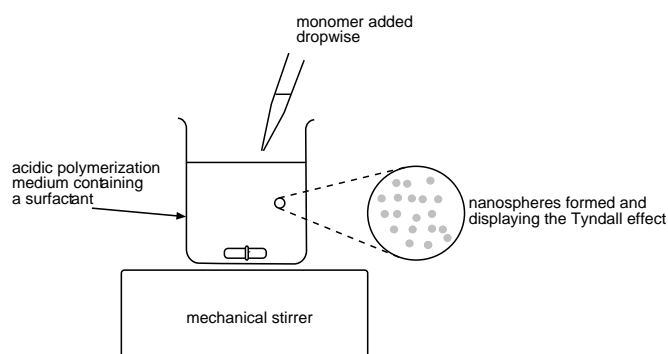
The surfactant is an important component of this process and acts to stabilize the growing polymeric particles by surface adsorption. Phase separation and the formation of solid particles occur before or after termination of the polymerization process [42]. Polymerization can occur in some systems without the presence of surfactants [40]. Various particulate systems have been prepared by this method, including poly(styrene) [43], poly(vinylpyridine) [44, 45], poly(acrolein) [46, 47], and poly(glutaraldehyde) [48–50].

Considerable work has been done using poly(alkylcyanoacrylate) (PACA) nanospheres due to their biodegradability, bioelimination, ease of preparation, low toxicity, and stability [18, 51, 52]. Although initially used as hemostatic aids in surgery [53, 54], their preparation was first recorded by Couvreur et al. [33]. Monomer was emulsified in a stirred, acidic, aqueous medium containing a nonionic surfactant, as illustrated in Figure 4. The suspension obtained displays a blue coloration due to the scattering of light by the particles known as the Tyndall effect. Glucose, Tween, Dextran 70, and Pluronic F68 have been used to stabilize and protect the particles from agglomeration [52]. Various monomers are available, such as methyl, ethyl, butyl, and isohexyl monomers, to prepare PACA nanoparticles, which differ in the length of their alkyl side chains.

The polymerization is an anionic mechanism initiated by hydroxide ions or any bases present [42]. The reaction scheme can be seen in Figure 5. The polymerization rate is regulated by hydroxyl ion concentration and hence is carried out at pH values below 3.5. Above this pH, the reaction rate is too rapid to allow discrete particle formation [55, 56].



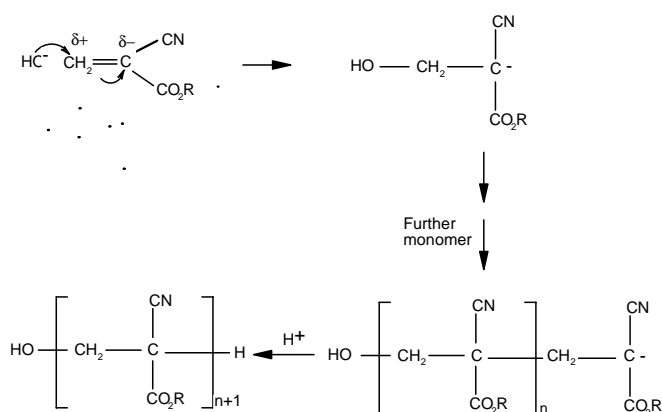
**Figure 3.** Presentation of the emulsion-polymerization mechanism in an aqueous phase.



**Figure 4.** Preparation conditions used in the preparation of poly(alkylcyanoacrylate) nanoparticles.

The main advantage of this polymerization is that it can be carried out at room temperature without an energy input. PACA nanoparticles have been prepared reproducibly at a semi-industrial level and can be made aseptically [57].

Spherical particles of around 200 nm in diameter are prepared by this technique as demonstrated by scanning electron microscopy [58, 59]. Particles as small as 10 nm were obtained by altering the concentration of surfactant and by increasing amounts of sulphur dioxide [60, 61]. Freeze fracture studies confirmed that PACA nanospheres have a dense solid spherical core with no distinguishable surrounding membrane [27]. The contents of the polymerization medium, such as pH, concentration, type of surfactant, and monomer type have been shown to influence the particle size [55, 62–64]. A large variety of drugs, such as cytostatics and antibiotics, have been encapsulated in PACA nanospheres successfully, in part due to their porosity and high specific surface area [35, 65–68]. Drugs are incorporated into these nanospheres during polymerization or adsorbed onto the surface of preformed particles [52]. The loading of lipophilic drugs is limited by their solubility in the aqueous acidic continuous phase. Acid labile drugs can be incorporated using poly(dialkylmethylenemalonate) esters as they polymerize at neutral pH [69, 70]. This is due to the presence of the less electrophilic alkoxy carbonyl group compared to the cyano



**Figure 5.** Anionic polymerization mechanism for alkylcyanoacrylate monomers ( $R = n$ -butyl).

group of the alkylcyanoacrylates. Their use, however, has been limited due to slow biodegradability [71].

### 3.1.2. Emulsion Polymerization in a Continuous Organic Phase

This procedure involves emulsifying a water-soluble monomer in a continuous organic phase containing a soluble initiator and surfactant. This constitutes a water-in-oil emulsion, as the different phases are reversed from the more common continuous aqueous phase based methods. The first process reported for nanoparticle formation by Birrenbach and Speiser is an example of this procedure [72]. Poly(acrylic) nanoparticles were prepared by dissolving acrylamide and  $N,N'$ -methylene bisacrylamide in an outer hexane phase containing anionic surfactants. The polymerization was initiated by gamma, ultraviolet, or visible radiation. Biologically active, antigenic materials were encapsulated and showed intact biological activity and high antibody production after encapsulation [72]. Spherical particles of 80 nm were produced based on electron microscopic studies. Kreuter [59] reported that transmission electron microscopy (TEM) revealed these particles to have a solid dense interior, forming matrix type nanopellets. Ekman and Sjöholm [73] investigated the polymerization of these monomers by radical initiation in a toluene/chloroform mixture, but higher particle sizes were obtained.

The main disadvantage in using poly(acrylamide) systems is that they are not biodegradable and the monomers are toxic. Extensive purification is also required to remove the organic solvents, anionic surfactants, and residual monomers. Edman et al. [74] produced biodegradable poly(acryldextran) particles by incorporating dextran into the poly(acrylamide) chain. These particulate systems were metabolized and eliminated faster, both *in vivo* and *in vitro*, than poly(acrylamide) particles.

### 3.1.3. Dispersion Polymerization

In dispersion polymerization, the monomer and initiator are dissolved in the continuous phase, which acts as a nonsolvent for the developing polymer. The continuous phase can be organic, aqueous, or a mixture of miscible phases. Two methods of initiation have been employed, including gamma radiation [75] and chemical initiation by potassium peroxydisulphate [76]. As the polymer is formed, it precipitates as nanoparticles. These particles are not polymeric precipitates as in precipitation polymerization. Rather, they are swollen by a mixture of the monomer and the continuous phase [39].

Kreuter and Speiser [77] developed a dispersion polymerization producing adjuvant nanospheres of poly(methylmethacrylate) (PMMA). The monomer is dissolved in phosphate buffered saline and initiated by gamma radiation in the presence and absence of influenza virions. These systems showed enhanced adjuvant effect over aluminum hydroxide and prolonged antibody response. PMMA particles could be distinguished by TEM studies and the particle size was reported elsewhere to be 130 nm by photon correlation spectroscopy [75]. The particle size could be reduced, producing monodisperse particles by inclusion of protective colloids, such as proteins or casein [40]. Poly(methylmethacrylate) nanoparticles are also prepared

by chemical means using potassium peroxodisulphate as initiator combined with heating at 65 or 85 °C [76]. Increasing monomer concentration and temperature resulted in an increase in particle size.

Copolymerization of PMMA has been carried out for the purpose of producing more hydrophilic particles [45, 78, 79]. Methylmethacrylate has been copolymerized with methacrylic acid, ethylene glycol dimethacrylate, hydroxypropyl dimethacrylate, or 2-hydroxyethylmethacrylate, by emulsion polymerization. Particle sizes from 30 to 340 nm in diameter can be produced by chemical initiation and 0.3–3.0  $\mu\text{m}$  particles produced using gamma radiation [45, 80]. Antibodies, amino acids, and fluorescent molecules can be covalently bound to the active surface groups on these particles by cyanogen bromide, carbodiimide, and glutaraldehyde methods [78, 80]. The polymerization of PMMA and its copolymers avoids the use of organic solvents and anionic surfactants. However, PMMA is not biodegradable and, thus, persists in the body [18, 81]. The hydrolysis of these polymers requires an acid environment not generally found in body fluids.

### 3.2. Nanospheres Prepared from Preformed Polymers

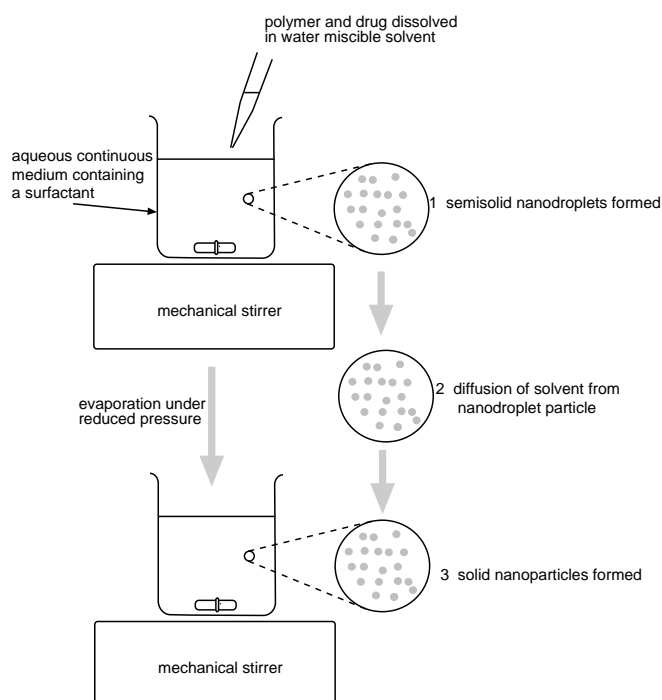
Synthetic and natural polymers have been investigated which are biodegradable and biocompatible. The nanospheres are formed by precipitation of synthetic polymers or by denaturation/solidification of polymers of natural origin. Four techniques have been reported for preparing nanoparticles from synthetic preformed polymers. These include:

- emulsion–evaporation,
- salting out technique,
- emulsion–diffusion,
- coacervation/phase separation technique.

#### 3.2.1. Emulsion–Evaporation

This method was first reported by Vanderhoff [82] for the preparation of artificial latexes. The polymer and drug are dissolved or dispersed in a volatile water-immiscible organic solvent, such as dichloromethane, chloroform, or ethyl acetate. This is emulsified in an aqueous continuous phase containing a surfactant, such as poly(vinylalcohol), to form nanodroplets. The organic solvent diffuses out of the nanodroplets into the aqueous phase and evaporates at the air/water interface, as illustrated in Figure 6. The solvent is removed under reduced pressure. The nanodroplets solidify and can be separated, washed, and dried to form a free-flowing powder.

Poly(D,L-lactic acid) (PLA) nanospheres containing testosterone, with a particle size of 450 nm, were first produced by Vanderhoff et al. [83]. Microfluidization produced spherical particles of less than 200 nm with a narrow size distribution [84]. Krause et al. [85] produced PLA nanoparticles of 500 nm using sonication. The polymer and drug, triamcinolone acetonide, were dissolved in chloroform and emulsified, with sonication, for 45 minutes at 15 °C in a gelatin solution. The solvent was evaporated by heating to 40 °C for 45 minutes under continuous stirring. TEM



**Figure 6.** Preparation scheme for the emulsion–evaporation method.

showed these particles to have a highly porous interior structure. Scholes et al. [86] and Julienne et al. [87] optimized the particle size of poly(lactide-co-glycolide) (PLGA) nanospheres by altering preparation conditions in the emulsion–evaporation method. These conditions included the phase volume ratio of the emulsion formed, concentration and molecular weight of the polymer and surfactant, as well as homogenization time and pressure. Tice and Gilley [88] reported that size of the particles formed depended on the initial size of the emulsion droplets.

It is desirable to use good film forming polymers for the emulsion–evaporation process [88]. For example, Eudragit® RL, Eudragit® RS, ethyl cellulose, PMMA, and cellulose acetate butyrate polymers formed nanoparticles by this method [89]. Biodegradable poly( $\beta$ -hydroxybutyrate) has been used to prepare nanospheres by this process [90, 91]. Particle sizes from 170 to 220 nm were obtained using high pressure emulsification with Brij® surfactants [90].

The successful entrapment of drugs by this preparation procedure involves minimizing the loss of drug to the aqueous continuous phase. Various strategies employed include the use of drugs with low water solubility in the continuous aqueous phase, a high concentration of polymer in the organic phase, and a fast precipitation rate of the polymer in the continuous phase [92, 93]. By pH adjustment of the continuous aqueous phase, the loss of ionizable drugs, such as quinidine, can be reduced [94]. The emulsion–evaporation method is most suited to the encapsulation of lipophilic drugs, such as hydrocortisone, progesterone, diazepam, and indomethacin [84, 94].

Adding water miscible solvents to the organic phase enhanced the encapsulation of water-soluble drugs due to rapid polymer precipitation in the aqueous phase [93, 95]. Bodmeier and McGinity [93] investigated using co-solvents

such as acetone, ethyl acetate, methanol, and dimethylsulphoxide (DMSO) with PLA to increase quinidine loadings. Niwa et al. [95] produced nanospheres of PLA and PLGA enhancing peptide encapsulation by incorporating acetone with DCM. Organic phases have been employed to improve the encapsulation of water-soluble drugs by the emulsion–evaporation method. Tsai et al. [96] first reported using light mineral oil as the continuous phase with Span 65 as the surfactant, but microspheres were produced. This was also reported by other authors [38, 97, 98].

### 3.2.2. Salting Out Technique

The salting out technique was first proposed by Bind-schaedler et al. [99]. This preparation method involves adding a water-soluble polymer, such as poly(vinylalcohol) (PVA), to a concentrated solution of an electrolyte or non-electrolyte forming a viscous gel. This is emulsified in a water-miscible solvent, such as acetone containing the polymer and drug. The saturated aqueous phase prevented acetone from mixing with the water by a salting out process. On further addition of the gel to the organic phase, an oil-in-water emulsion is formed. Sufficient water is then added to allow complete diffusion of the acetone into the aqueous continuous phase, thereby forming nanospheres [100, 101]. Typically, magnesium chloride and magnesium stearate are used as salting out agents. This method avoids the use of surfactants and chlorinated solvents, which offers distinct advantages over the emulsion–evaporation method. However, the hydrocolloidal PVA is employed as a viscosity increasing agent and stabilizing agent. The PVA, electrolyte, and acetone were removed from the nanospheres by cross flow filtration, as described by Allémann et al. [101].

The preparation conditions of the salting out technique could be altered to produce nanospheres of monomodal distributions with particle sizes in the range 170 to 900 nm using Eudragit® S as polymer [102]. The conditions investigated include homogenization, stirring rate, internal/external phase ratio, viscosity of the external phase, concentration of polymer in the organic phase, type of salting out agent, and concentration and type of stabilizing agent in the aqueous phase. The size of the droplets in the emulsion determined the size of the final particles [102]. Leroux et al. [103] prepared PLA particles of 70 nm using benzyl alcohol and high PVA concentrations.

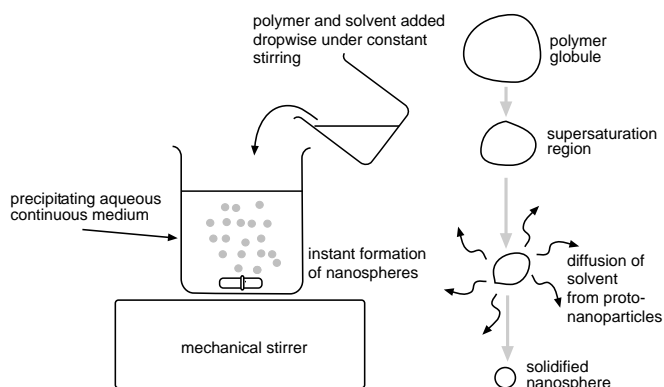
Different polymers have been used to produce nanoparticles by the salting out process, such as Eudragit® S, Eudragit® E, poly(DL-lactic acid), polycaprolactone, ethyl cellulose, cellulose acetate and cellulose acetate butyrate [99, 100, 102, 103]. Other salting out agents, such as sucrose, and solvents, such as THF, ethyl acetate, and isopropyl alcohol, also produced nanoparticles [102]. The salting out technique was found to entrap lipophilic drugs successfully, such as savoxepine and chlorambucil, due to the continuous aqueous phase used [35, 103, 104]. Leroux et al. [103] commented on the pharmaceutical acceptability of the salting out process as the use of acetone and large amounts of salt may pose problems concerning salt recycling and compatibility with some drug substances. These authors used benzyl alcohol as the organic solvent and low amounts of salt and gelatin as the stabilizing hydrocolloid to improve the pharmaceutical acceptability.

### 3.2.3. Emulsion–Diffusion

This procedure is also referred to as the precipitation method and was first reported by Fessi et al. [105]. In this type of preparation, as shown in Figure 7, the polymer is dissolved in a water-miscible solvent and then poured under stirring into a nonsolvent, which is usually water. This leads to the polymer precipitating as nanospheres. Prior emulsification and inclusion of surfactants are not necessary.

The proposed mechanism for formation of nanospheres by this technique is by a diffusion and stranding mechanism, as illustrated in Figure 10 (Section 4.2) [106]. Polymer globules are formed as the polymer solution is added to the aqueous phase. As the solvent diffuses into the water from the polymer globule, the polymer precipitates out of solution and is stranded in the water in the form of fine emulsion droplets or “protonanoparticles.” Complete diffusion of solvent from these protonanoparticles will provoke polymer solidification in the form of nanospheres of about 200 nm in diameter. Turbidity measurements are consistent with this mechanism [106]. In summary, the diffusion of the solvent causes regions of supersaturation from which nanoparticles are formed, due to phase transformation in these regions. The size of the resulting particles is dependent on this process.

This precipitation procedure has been successfully applied to a wide variety of polymers such as poly(lactide), poly(lactide-co-glycolide), poly( $\epsilon$ -caprolactone), ethylcellulose, poly(alkylcyanoacrylate), and poly(styrene) [107]. More recent biodegradable polyesters, called poly( $\beta$ -malic acid-co-benzyl malate) copolymers, have formed nanospheres of 200 nm in diameter by the precipitation method [108, 109]. Solvent/nonsolvent mixtures that have been used include ethanol/water, acetone/water, and propylene carbonate/water [110]. Murakawi et al. [19] employed solvent mixtures, such as ethanol/acetone and methanol/acetone, providing high yields of PLGA nanometer sized particles with less aggregation. This preparation method is best suited to the encapsulation of lipophilic drugs as an aqueous continuous phase is used [111]. The lipophilic drugs are usually dissolved in with the polymer-rich phase. High encapsulation was reported for peptides, such as TRH and elcatonin, with this method [112].



**Figure 7.** Preparation procedure for precipitating technique. Shown also is the schematic illustration of the diffusion stranding mechanism for nanosphere formation that occurs during the precipitation method.

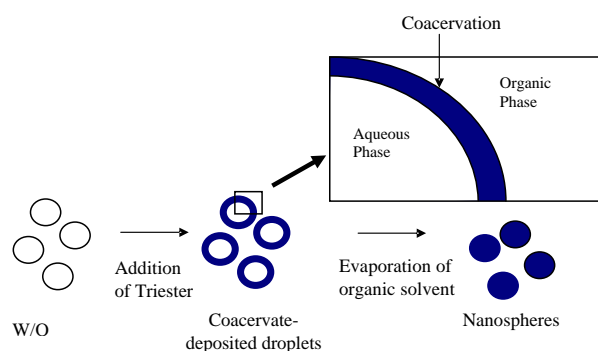
A major advantage of this procedure is that a surfactant is not required. This avoids its removal by purification procedures. However, poly(vinyl alcohol) has been used as a stabilizer in some instances and was found to adsorb strongly, resisting washing procedures [19, 106]. Without surfactant, nanoparticle formation and stability are dependent on the initial polymer concentration, the volume ratio of the solvent to nonsolvent, and the dielectric constant of the final mixture [111]. Ternary phase diagrams have been constructed to find the optimal region of nanoparticle formation [110, 111]. Another advantage of this procedure from an industrial point of view is that high-pressure homogenizers and ultrasonication are not required as spontaneous emulsification occurs [106].

### 3.2.4. Coacervation

Coacervation is a phase separation technique. It was first introduced by Bungenberg de Jong and Kruyt [113] who described a process in which aqueous colloidal solutions are separated into two liquid phases, a colloid-rich phase or coacervate and a colloid-poor phase. Many synthetic polymers are water-insoluble and consequently, nonaqueous coacervation systems have been employed. Coacervation usually consists of binary and ternary systems [114, 115]. Binary systems consist of one polymer dissolved in a solvent and ternary systems of either a single polymer in a binary solvent mixture or two polymers in a single solvent. For binary systems, phase separation can occur by changing the temperature or pH or by the addition of electrolytes, such as sodium sulphate, to gelatin [116]. For ternary systems, phase separation can be induced by adding a nonsolvent for a single polymer system or by adding a polymer incompatible with the second polymer for a two polymer system [117]. Solidification of the particles produced by coacervation can be effected by temperature, chemical cross-linking, adjustment of pH, or rinsing with a nonsolvent for the polymer.

The coacervation process is controlled by the interactions between polymer/solvent/nonsolvent. The formation of stable coacervates is influenced by the polymer type, molecular weight, and hydrophobicity and by the amount and viscosity of the added coacervating agent [118, 119]. By careful adjustment of these parameters, optimum coacervation conditions can be achieved by the use of phase diagrams. The classical coacervation method for nonaqueous systems has been modified to produce nanoparticles by using an emulsion-phase separation method in an oil system [120]. An aqueous solution of the drug, a peptide in this instance, was emulsified in a DCM–acetone mixture containing the dissolved PLGA using homogenization [112, 120]. Triester oil (caprylate and caprate triglyceride) was added gradually, inducing phase separation of the PLGA at the interface between the aqueous and oily phase. The aqueous droplets are covered with the coacervate droplets of PLGA and the evaporation of the organic solvent reduces the solubility of the PLGA and deposits it around the aqueous droplets containing the drug. This mechanism is illustrated in Figure 8.

Nanoparticles encapsulating 5-fluorouracil were prepared by coacervation using cellulose derivatives [121]. An ethanolic solution of ethyl cellulose was desolvated by stirring in distilled water producing particles with an average diameter of 472 nm, as determined using scanning electron



**Figure 8.** Preparation mechanisms of PLGA nanospheres by the emulsion-phase separation method in an oil system.

microscopy (SEM). Nanospheres of methyl cellulose were prepared by desolvating an aqueous solution of the polymer with sodium sulphate solution [121]. An average particle size of 540 nm was obtained.

The main drawback to coacervation is the toxicological implication of residual solvents, coacervating agents, and hardening agents left in the particles. More biocompatible coacervating and hardening agents are being investigated along with approaches to minimize solvent residues [114]. The triester oil used in the coacervation of PLGA by Niwa et al. [120] is nontoxic and biocompatible and an alternative to silicone oil usually used in the coacervation of PLGA. Biocompatible hardening agents suggested include fatty acid esters, such as isopropyl myristate for PLGA [114]. For low molecular weight polymers, drying near the glass transition temperature of the polymer was found to be effective in lowering DCM content [114].

### 3.3. Nanoparticle Production Using Supercritical Fluids

Supercritical fluids are defined as those substances whose temperature and pressure have been raised above the point where the densities of the liquid and gaseous states are the same. When substances exist in a supercritical state, they can be used as solvents or antisolvents and, hence, used in the production of particulates in a similar manner to other solvent systems. The use supercritical fluids has increased significantly over the last few years, with many drugs either being encapsulated within, or being formed into, nanoparticles using this technique [122–125]. However, there are a number of advantages to using supercritical fluids over conventional solvent systems. Production is usually a one-step process, with little polydispersity in particle size and, perhaps, most importantly, much less organic solvent is used, with carbon dioxide being the most frequently used supercritical fluid. This is obviously of significance environmentally, especially if production is on the commercial scale.

A number of techniques are based on supercritical fluid technology. Three are of particular pharmaceutical interest, namely the supercritical antisolvent (SAS) system, the rapid expansion of supercritical solution (RESS) method, and the gas antisolvent (GAS) technique [126].

The SAS method involves the introduction of the supercritical fluid into a solution of solute in an organic solvent.

At high pressures, the fluid acts as an antisolvent, becoming soluble enough in the organic solvent to precipitate out the solute. At the final operating pressure, the supercritical fluid flows through the precipitation vessel stripping away any residual organic solvent. Finally, the vessel is depressurized and the solid product is collected. The GAS technique is a modified version of this method, with the organic solution being rapidly introduced into the supercritical fluid through a fine nozzle [127, 128]. The solution is quickly extracted into the fluid, resulting in instantaneous precipitation of the solute as fine particles.

In the RESS method, the solute of interest is solubilized in a supercritical fluid, which is then rapidly expanded through a nozzle. As the fluid expands, it loses its solvent capabilities and the solute precipitates out. While this technique has the advantage of not using any organic solvent, it is restricted by the generally poor solubility of most polymers in supercritical fluids. Indeed, polymers generally have to be below 10,000 MW in order to be eligible for this method of particle production [126].

## 4. CHARACTERIZATION

The physicochemical characterization of a colloidal carrier is necessary because important characteristics, such as particle size, hydrophobicity, and surface charge, determine the biodistribution after administration [129–132]. Preparation conditions, such as the pH of the polymerization medium, monomer concentration, and surfactant concentration, can influence the physicochemical characteristics of the particles [60, 62, 64]. It is, therefore, essential to perform a comprehensive physicochemical characterization of nanoparticles, which has been reviewed by Magenheimer and Benita [133].

### 4.1. Particle Size

Clearly, the definitive characteristic of any nanoparticulate drug delivery system will be its submicrometer diameter. Sizing such particles in the suboptical region can be difficult as the measuring technique itself may alter size and properties by either hydrating or aggregating the particles. This will have a profound influence on the size of the particle [59]. Haskell [134] has discussed the various optical techniques available to measure the size of nanoparticles.

Photon correlation spectroscopy (PCS) has been used extensively for the sizing of submicrometer particles and is now the accepted technique in most sizing determinations. PCS is based on the Brownian motion that colloidal particles undergo, where they are in constant, random motion due to the bombardment of solvent (or gas) molecules surrounding them. The time dependence of the fluctuations in intensity of scattered light from particles undergoing Brownian motion is a function of the size of the particles. Smaller particles move more rapidly than larger ones and the amount of movement is defined by the diffusion coefficient or translational diffusion coefficient, which can be related to size by the Stokes–Einstein equation, as described by

$$d(H) = \frac{kT}{3\pi\eta D} \quad (1)$$

where  $D$  is the diffusion coefficient,  $k$  is the Boltzmann's constant,  $T$  is the absolute temperature,  $\eta$  is the viscosity, and  $d(H)$  is the hydrodynamic diameter. The hydrodynamic diameter, or Stokes diameter, measures how a particle moves within a fluid. To obtain mass or volume diameters, the full Mie theory should be used, which requires knowledge of the refractive indices of the particulate material and sizing medium. The upper limit of size for PCS is determined by the density of the particle and, most importantly, its onset of sedimentation, rather than limitations on the technique itself.

PCS is a rapid, nondestructive technique which enables the measurement of many types of spherically shaped entities, including discrete living cells, without causing alteration or damage [133]. However, the use of PCS is not possible when the size distribution of the sample is broad, the sample material is nonspherical, and multimodal distributions are present. PCS is also susceptible to errors from the presence of larger particles, such as dust, microbial contamination, crystallization of ingredients, or secondary particle agglomerates. Larger particles scatter more light than smaller particles, as shown by the Rayleigh ratio, and thus will swamp the scattered light from smaller particles. Samples for PCS measurements must be clean and filtered to ensure removal of contaminating dust particles. Another disadvantage of this method is that the particle size is influenced by the surrounding medium, such as adsorbed surfactants or hydration layers.

PCS has been applied in nanoparticulate characterization to investigate the effect of altering preparation parameters on the particle size of various nanoparticulate carriers, such as poly(alkylcyanoacrylates) [55, 60, 61, 135]. The effect of the incorporation of drugs on nanoparticle size has also been investigated [136, 137]. PCS has been used to examine the degradation of PACA nanoparticles [138]. This technique has been useful in determining the influence on size of using different surfactants in the preparation process and also the thickness of the surfactant coating layer on the surface of the nanoparticle [139, 140].

Electron microscopy techniques, such as SEM and TEM, have been used to measure the particle size of nanoparticles. TEM has the additional advantage in that interior particle morphology can be determined by freeze fracturing [133]. TEM has been used to size poly(acrylic) acid and cellulose nanoparticles and it was shown that the sizes obtained were comparable to PCS [59, 121]. TEM has been used to optimize the preparation conditions of poly(methylmethacrylate) nanoparticles to obtain small particle sizes [141]. SEM requires the particles to be coated with gold to make them conductive. This coating varies in thickness from 30 to 60 nm and has to be subtracted in order to determine the size of the uncoated particles. On comparison to other sizing techniques, the particle sizes of poly(acrylic) acid nanoparticles by SEM were in good agreement [59]. Although electron microscopy allows the measurement of individual particles, this may be unrepresentative of the whole sample. The low vacuum used, gold coating, and any surfactants present may alter the particle size [59].

## 4.2. Surface Charge

Particles in a suspending medium carry a thin layer of ions and solvent around them, which will cause the particle to drift when placed in an electric field. The surface separating the stationary medium from the moving particle and its bound ions and solvent is called the surface of hydrodynamic shear [142]. The potential at this surface is called the zeta potential, as illustrated in Figure 9. This surface potential can originate from the dissociation of surface polymeric groups or preferential adsorption of ions or other ionic molecules from the aqueous suspending medium. The zeta potential of the particle is dependent on electrolyte concentration and pH of the suspending particle medium [142, 143].

The zeta potential can be measured by electrophoresis, which determines the velocity of particles in an electric field of known strength [144]. This particle velocity,  $v$ , can then be related to the electrical field strength,  $E$ , as the electrophoretic mobility,  $\mu$ . This is shown by

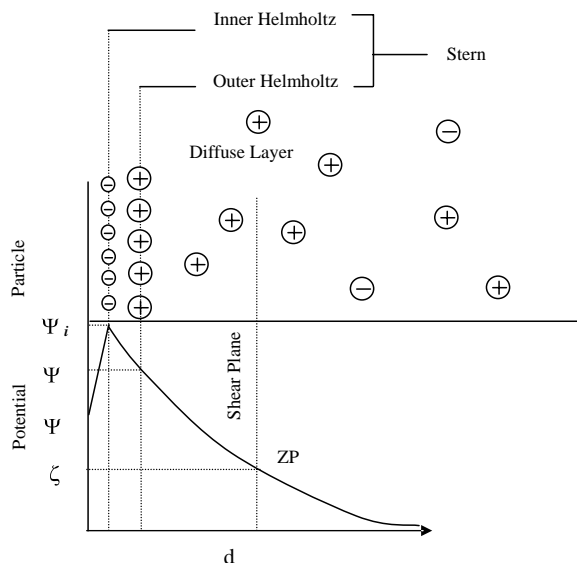
$$\mu = \frac{v}{E} \quad (2)$$

The electrophoretic mobility,  $\mu$ , can be converted to a zeta potential by using the Smoluchowski equation,

$$Z_p = \frac{\mu 4\pi\eta}{\varepsilon} \quad (3)$$

where  $Z_p$  is the zeta potential (mV),  $\mu$  is the electrophoretic mobility [(cm/s)/(Volt/cm)],  $\eta$  is the dynamic viscosity of the dispersion medium (poise), and  $\varepsilon$  is the dielectric constant.

Electrophoretic mobility measurements can be performed by laser Doppler anemometry (LDA). LDA is fast and capable of high resolution of particle velocities [144]. It measures particle velocity, which is measured in the stationary



**Figure 9.** Formation of Stern plane and diffuse layer on particle surface ( $\Psi_0$  = surface or Nernst potential,  $\Psi_i$  = potential of inner Helmholtz plane,  $\Psi_s$  = Stern potential,  $\zeta$  = thickness of Stern plane, ZP = zeta potential at surface of shear,  $d$  = distance from particle surface).

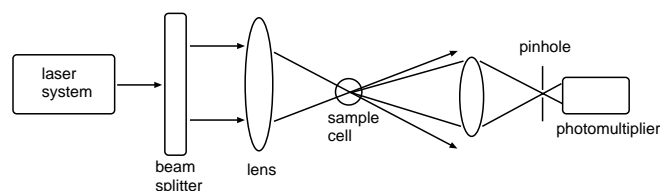
layer, where the particles are moving solely with a velocity due to their charge [142]. This stationary layer is defined by the crossing of two laser beams, as illustrated in Figure 10. Interference fringes are produced by the crossing of the two beams. Particles inside the scattering volume interact with these fringes to produce scattered light, which is detected by the photomultiplier tube. The frequency of the scattered light by the particles differs from the frequency of the incident laser beam. This shift in frequency is caused by the Doppler effect and is a function of the particle velocity [142].

Zeta potential measurements have been used to determine the stability of particle suspensions. Particles with large negative or positive zeta potentials (+30 and -30 mV) will form stable colloidal suspensions as they tend to repel each other and reduce aggregation [143, 145]. Zeta potential measurements have been used to estimate particle opsonization, a process whereby specific proteins in blood plasma adsorb to the particle surface. It is relevant to this discussion as such proteins make the particle more susceptible to phagocytosis and subsequent unwanted removal by the body. High negative zeta potential values in the presence of serum are indicative of particles that have become highly opsonized [10] and may indicate a poor formulation. Zeta potential measurements have also been applied to investigate drug/polymer association. Alonso et al. [67] found the negative charge of poly(alkylcyanoacrylate) nanoparticles was neutralized by the adsorption of the polar drug, amikacin sulphate, indicating an electrostatic association.

An alternative technique to LDA for zeta potential measurement using Bragg cells is amplitude weighted phase structuration (AWPS). It is a laser light scattering technique allowing the simultaneous determination of particle size and zeta potential [142]. The major difference between AWPS and LDA is in the theoretical treatment and signal processing. A major advantage of this technique over LDA is the ability to measure at low field strengths, which can be important for sensitive biological samples [144].

## 4.3. Surface Hydrophobicity

Surface hydrophobicity can be evaluated using several techniques. One method involves determining the contact angle of a polymer film that is representative of the surface of the particle. This is performed by removing all the water from nanoparticulate suspension, dissolving in a suitable solvent, and casting as a film on a microscope slide [59]. The contact angles can then be determined by a goniometer. The contact angles increase with increasing hydrophobicity.



**Figure 10.** Optical setup for LDA, consisting of a laser beam being split and focused by a lens through a suspension of particles in a sample cell. Scattered light is focused through a pinhole and detected by a photomultiplier tube.



This method has been used to determine the hydrophobicity of poly(methylmethacrylate) nanoparticles and acrylic acid copolymer nanoparticles [146–148].

An alternative procedure is the adsorption of the hydrophobic dye Rose Bengal [144]. This particular dye shows different degrees of affinity for the particle surface depending on the surface hydrophobicity. After incubating the particles in Rose Bengal, the dye undergoes partitioning between the surface of the particles and the dispersion medium and is determined by spectroscopic measurements at 542.7 nm [142]. This enables the partition quotient of Rose Bengal for the particles to be calculated and plotted against the surface area of the particles. The slope of this plot is a measure of hydrophobicity, with a steep gradient indicating high hydrophobicity. This approach was used by Lukowski et al. [147] to investigate the decrease in hydrophobicity on increasing the acrylic acid content of acrylic acid copolymer nanoparticles.

Hydrophobic interaction chromatography (HIC) is a column chromatography technique which can determine particle hydrophobicity by interaction with a hydrophobic gel matrix [142, 149, 150]. Hydrophilic particles pass through the column without interaction, whereas particles with increased hydrophobicity show a retarded elution and are retained by the column. Hydrophobicity measurements are used to determine the hydrophobicity of nanoparticulate carriers and correlate this to their *in vivo* biodistribution [10, 149].

The components of the HIC apparatus are essentially similar to those found on basic high performance liquid chromatographic systems and consist of a column, pump, and ultraviolet spectrophotometer. Particles are detected by a reduction in optical density at 400 nm. A miniaturized version of HIC with a 1 ml bed volume has been developed to establish a rapid and less costly screening method [151]. Alkyl agarose gels are used as the column packing and their hydrophobicity increases with alkyl-chain length. Phosphate buffered saline is usually used as the elution medium. The chromatograms obtained are analyzed with regard to the elution volume and the area under the elution peak, which enables quantitation.

HIC enables the particles to be determined in their original suspending medium preserving their true surface properties. Contact angle and Rose Bengal partitioning require removal of the particles from their dispersion medium, which could result in a modification of the surface properties. These two methods only determine an average value for hydrophobicity and are unable to detect subpopulations differing in surface hydrophobicity. The detection of subpopulations is possible with HIC, which also allows the polydispersity in surface properties to be determined.

#### 4.4. Molecular Weight Characterization

The determination of the molecular weight of nanoparticles is performed by gel permeation chromatography (GPC). The experimental setup consists of a high performance liquid chromatography system with a size exclusion column and a refractive index detector. The nanoparticles are usually freeze-dried and dissolved in tetrahydrofuran for analysis on the system. Poly(styrene) or poly(methylmethacrylate) standards are used to calibrate the column, to enable the determination of number average molecular weight ( $M_n$ ), as in

Eq. (4), and the weight average molecular weight ( $M_w$ ), as in Eq. (5),

$$\bar{M}_n = \frac{\sum Q_i}{\sum (Q_i/M_i)} \quad (4)$$

$$\bar{M}_w = \frac{\sum (Q_i \cdot M_i)}{\sum Q_i} \quad (5)$$

where  $Q_i$  represents the amount of polymer having a molecular weight  $M_i$ . The polymer molecular weight distribution can be estimated by calculating  $\bar{M}_w/\bar{M}_n$ .

Molecular weight determinations have been used to elucidate the polymerization mechanism of polymers [152, 153]. Poly(butylcyanoacrylate) (PBCA) polymers were reported to be made up of numerous oligomeric subunits rather than one or a few polymer chains due to rapid termination at the low pH values required for preparation [153]. The pH and monomer and surfactant concentrations were found to influence the resulting molecular weight of the PBCA nanoparticles produced [153, 154]. Interaction between the drug and polymer could be detected by molecular weight measurements [60, 137, 155]. The biodegradation of nanoparticles can be monitored by molecular weight measurements and the mechanism of degradation can also be elucidated [156–158].

It is not possible to determine the molecular weight of highly cross-linked polymers and natural polymers by GPC as they do not dissolve in tetrahydrofuran. Accurate results for molecular weight can only be obtained if the polymer standards used have similar properties to the polymer employed to prepare the nanoparticles. In most cases, this similarity is absent.

#### 4.5. Microscopic Characterization

The two main techniques used to characterize nanoparticles by microscopy are scanning electron microscopy and transmission electron microscopy. SEM has been used to determine particle size, morphology, surface roughness, and porosity of nanoparticles made from various materials [27, 33, 159, 160]. SEM can also provide information on the behavior of adsorbed drugs [161]. Aprahamian et al. [162] characterized lipiodol nanocapsules by the X-ray emission of iodine using SEM fitted with an energy-dispersive X-ray spectrometer. The preparation of samples for SEM involves drying a portion of the particle suspension at room temperature and then coating it with a thin metallic film, such as gold, which is usually 30–60 nm in thickness [59]. A 10 nm layer was obtained by spraying the nanoparticle suspension onto an aluminum foil with the aid of an atomizer [85]. Samples for SEM analysis must be capable of withstanding a vacuum environment. This technique is limited for sizing due to the interference from surfactants in the nanoparticles, but their presence is necessary to prevent the particles from agglomerating [59].

TEM has been used to determine the shape and particle size of nanoparticles [27, 33]. Samples are prepared by placing a drop of preparation on copper grids, followed by negative staining with an aqueous solution of sodium phosphotungstate, phosphotungstic acid, or uranyl acetate [27, 163, 164]. Freeze fracturing with TEM has been

used to investigate the internal structure of nanoparticles and applied to samples which are not suitable for staining or which melt or sinter when irradiated by the electron beam. Nanospheres were shown to have a dense, solid internal matrix and nanocapsules a hollow internal structure [27]. The interior morphology and surface roughness have been characterized for various nanoparticulate carriers [33, 59, 165]. TEM has been used to establish the wall thickness of nanocapsules, which was found to be 3 nm for PBCA nanocapsules [135]. TEM is not useful for routine measurements as the sample preparation is time-consuming and laborious.

Other more advanced microscopic techniques have been developed, including near-field scanning optical microscopy [166] and scanning probe microscopy techniques, such as atomic force microscopy and scanning tunnelling microscopy [166, 167].

## 5. DRUG LOADING

Drugs may be incorporated into nanoparticles by addition to the polymerization medium or by adsorption to preformed particles [168]. Depending on the drug, polymer, and preparation method used, the drug can exist as:

- a solid solution of the drug in the particle,
- a solid dispersion of the drug in the polymer,
- surface adsorption of the drug,
- chemical binding of the drug to the polymer [169].

Determination of drug content in nanoparticles is mainly concerned with the effective separation of the free drug from the bound drug. Various techniques have been employed including:

- ultracentrifugation,
- ultrafiltration,
- gel filtration,
- dialysis.

The separation must be as rapid as possible to prevent desorption of drug from the particle [170].

Ultracentrifugation is the most extensively used separation technique, where the particle suspension is spun at high speeds, usually at 100,000 g for one hour [171–173]. The supernatant is carefully removed and analyzed for the amount of free drug present. This is subtracted from the total drug added to the system, to determine the amount of drug bound to the particles. However, the pellet itself can be analyzed directly to measure the amount of drug bound to the particles [174, 175]. Usually, both the supernatant and pellet are analyzed together [176–178]. The main disadvantage of this technique is that drug desorption and caking of the pellet can occur due to the long centrifugation times and large centrifugal forces required. Undissolved free drug in the form of nanocrystals may spin down with the sedimented pellet, leading to inaccurate determination of loading [133].

Reszka et al. [168] used ultrafiltration to separate free mitoxantrone from PBCA nanoparticles. The particle suspension was passed through a cellulose nitrate membrane with a pore size of 20 nm with magnetic stirring and pressurized nitrogen. The filtrate obtained was analyzed for free drug content. Recovery of the particles is not possible with

this method and the particles themselves can clog the filter. Undissolved drug may be removed with the particulate carrier and it must be ensured that drug adsorption to the filter membrane does not occur.

Gel filtration employs a column containing a packing material, such as Sephadex® media, to separate free drug from the particles. The particles elute first in the void volume followed by the drug, which is retained on the column, thus enabling its separation. The eluted fractions are collected from the column and analyzed by ultraviolet/visible spectrophotometry. Beck et al. [170] used gel filtration with Sephadex® G50 packing to separate five model drugs from PBCA nanoparticles. This media was also used to separate free mitoxantrone and ampicillin from liposomes [168, 173]. This technique is rapid and does not alter the particle size, but desorption of the bound drug can occur. It can be scaled up and equipment costs are low [179].

Dialysis has been used by Labhasetwar and Dorle [180] to determine free drug concentration in particle suspensions. The suspension is placed in a dialysis bag and then positioned in an aqueous continuous phase until there is no change in drug concentration. The main disadvantages of dialysis are that the equilibration times are long, causing drug desorption. Large volumes of continuous phase are required and particle aggregation can occur [170, 181].

A potentially new separation method called field flow fractionation has been introduced only on a preliminary basis for the determination of adsorbed substances to particles [182]. A novel method was developed by Illum et al. [68] to determine both free and bound drug on PBCA nanoparticles without prior separation. For example, a bathochromic shift was observed in the ultraviolet/visible (UV/vis) spectrum of Rose Bengal after binding to PBCA nanoparticles. The amount of free drug was determined at 540 nm and bound drug at 548 nm. This type of analysis is very specific to the drug under investigation.

The end result of the separation techniques described is to calculate the particle drug loading. The drug loading usually expresses the bound drug as a percentage of the total drug content used in the preparation or as a percentage of the weight of the dried nanoparticles. The total drug content is usually taken as the amount of drug added to the preparation medium initially [66, 136], but errors may result if drug degradation occurs [183]. Alternatively, total drug content can be expressed by dissolving the whole nanoparticle suspension in a suitable solvent and analyzing both the free and bound drug contents [171, 184]. Total drug content used can also be calculated from the bound and free drug contents analyzed separately in the supernatant and pellet [137, 185]. The drug loading efficiency is a measure of the total amount of drug recovered on analyzing the particles compared to the total amount of drug added initially at the preparation stage.

Various analytical techniques have been employed to determine the drug content in nanoparticles after the separation procedures. High performance liquid chromatography and UV/vis spectroscopy are two of the most extensively used techniques [133]. Other techniques used include scintillation counting [186], spectrofluorodensitometry [176], microbiological assays [136], spectrofluorimetry [187], and polarization fluoroimmunoanalysis [67].

## 6. INCORPORATION OF WATER-SOLUBLE DRUGS

When introducing a water-soluble drug into a nanoparticulate system, a number of factors must be considered. Different preparation methods will give rise to particles with a wide range of surface properties, sizes, and drug incorporations. Some methods may appear to offer the solution to a particular loading problem, but the efficiency of particle formation may be preclusive to their use. In our experience, there are a number of factors that can be optimized in terms of loading and particle manufacture, but unfortunately the level of optimization may not reach that which is deemed acceptable in a therapeutic context. Many of the problems encountered by those attempting to encapsulate a water-soluble drug have been experienced in our own work studying the incorporation of 5-fluorouracil. As such, it represents a good model drug for testing the incorporation efficiency of nanoparticle production methods.

Much information exists in the literature about the various payloads introduced into nanoparticles. The choice of pharmaceutically active compound that is incorporated is dictated by many considerations but is driven primarily by the potency of the drug, its route of administration, and the need to give the compound some protection against enzymatic degradation. It must be remembered that nanoparticles have a low capacity for carrying drugs and large doses cannot be administered by this means. As can be seen from Table 1, the range of drugs that have been incorporated is wide, with many of high potency and some requiring protection from proteolytic attack. Other applications exploit the unique properties of nanoparticles in enhancing drug delivery to the eye, with many examples to be found in the literature. This list is by no means absolute, with further work produced regularly using new drug payloads for novel applications.

## 7. INCORPORATION OF 5-FLUOROURACIL INTO NANOPARTICLES

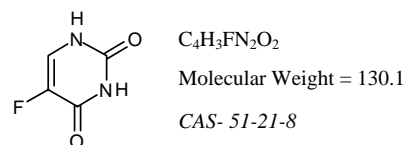
5-Fluorouracil (5FU) is 5-fluoropyrimidine-2,4(1*H*, 3*H*)-dione. Its structure is illustrated in Figure 11. The hydrogen in the naturally occurring pyrimidine, uracil, is substituted by fluorine in the 5 position. The presence of the heteroatoms in the structure imparts hydrophilicity to the compound as they are capable of hydrogen bonding.

The incorporation of 5FU into particulate carriers made from both natural and synthetic polymers has been reported extensively. The natural carriers investigated have included albumin [188], chitosan [189], casein [190], liposomes [191], and fibrinogen [192]. The drug-loaded particles are usually prepared by an emulsion-cross-linking procedure, which can be performed chemically or by heat. The loading of 5FU in albumin and chitosan particles by this procedure has been reported to be low [193, 194]. Nanospheres of chitosan loaded with 5FU derivatives were coated with anionic poly(saccharides) for targeting studies involving cell-specific recognition [189]. Methyl and ethyl cellulose nanospheres containing 5FU have been prepared by a desolvation technique with drug loading efficiencies of 45% for ethyl

**Table 1.** The diverse range of pharmaceutically active compounds that have been incorporated into nanoparticles or nanocapsules.

Active compound	Ref.
Peptides and proteins	
insulin	[207–219]
muramyl dipeptide	[220–222]
salmon calcitonin	[223–227]
chymotrypsin	[228–230]
Steroids	
triamcinolone	[231]
hydrocortisone	[232]
dexamethasone	[233, 234]
prednisolone	[235, 236]
progesterone	[237, 238]
Nonsteroidal anti-inflammatory drugs	
indomethacin	[238–240]
diclofenac	[241–248]
Polysaccharides	
Antibiotic drugs	
Antisense	
Beta receptor blocking drugs	
timolol	[249–254]
carteolol	[255–268]
Anticonvulsant drugs	
primidone	[269–278]
Cytotoxic drugs	
fluorouracil	[24, 279–284]
cisplatin	[285, 286]
doxorubicin	[287]
paclitaxel	[288]
methotrexate	[289–293]
vinblastine	[294]
Antiarrhythmic drugs	
Miscellaneous	
chlorhexidine	[295–298]
diazepam	[299–301]
cyclosporin	[302–310]
pilocarpine	[311–316]
primaquine	[317, 318]
	[319, 320]
	[321]
	[322, 323]
	[324–326]
	[327–334]
	[335–337]
	[338–340]

cellulose and 11.6% for methyl cellulose [121]. Synthetic carriers have also been used to incorporate 5FU, including PMMA [195], PLGA [196], PLA [197], PBCA [198], and poly(glutaraldehyde) (PGL) [50]. The most widely used carriers for 5FU are the PLA and PLGA polymers. An emulsion–evaporation preparation technique is frequently used to prepare the drug-loaded particles [196, 199]. Such a method loaded 5FU up to 30% w/w in PLGA particles with a diameter of 20–540  $\mu\text{m}$ , which were implicated for the treatment of cerebral tumors by implantation [200].



**Figure 11.** Chemical structure of 5FU.

Nanospheres of PLGA were prepared by emulsion–evaporation by employing homogenization and a solvent system consisting of acetone in which both the drug and polymer were dissolved [95]. The encapsulation of 5FU in these nanospheres was low compared to the more hydrophobic drug, indomethacin. It was reported that the hydrophilic 5FU leaked to the aqueous phase. PGL nanoparticles were prepared by aldol condensation loading 5FU with an efficiency of 14.32% [50].

The process of loading 5FU into a nanoparticulate system proves to be far from simple and is representative of other water-soluble drugs. The methods used to encapsulate drugs tend toward low drug loading encapsulation efficiency by the nature of the solvent systems used. Our work focused on the use of the emulsion–polymerization scheme with a continuous aqueous phase. In order to assess the most suitable parameters for particle formation, response surface methodology was used. Three variables were analyzed—surfactant concentration, pH of the polymerization medium, and monomer concentration. By varying these parameters and then analyzing the resultant particles produced, it was possible to predict the set of conditions which would lead to the formation of an optimized nanoparticulate system. Using this methodology enabled the production of particles that could be tailored to meet specific requirements, such as a certain diameter with a low polydispersity, and so on. When the optimum conditions were known, work involving the encapsulation of 5FU could proceed.

Preliminary results using the optimized system from the response surface model proved disappointing. Particle loadings were below 1% and this value was even lower when a washing step was introduced. In fact, around 90% of the drug which was “encapsulated” was removed upon the washing of the particles, indicating a large surface bound fraction, which was freely soluble in the wash. A number of strategies were used in order to raise the loading efficiency of the system. Various surfactants were tried to assess whether there was an advantage in the use of one over another with respect to drug loading. Indeed, there is evidence that the type of surfactant used can influence drug loadings of nanoparticles [62]. Sodium lauryl sulphate was found to be effective in increasing the loading of the polar drug, amikacin sulphate, in PBCA nanoparticles [67], with the percentage drug loading efficiency increasing from 4.76% to 60.47%. It was reported that this surfactant reduced the aqueous solubility of the drug, thereby improving its incorporation into nanoparticles. These authors also reported that poloxamer 188 (Pluronic F68) appeared to hinder the drug–polymer interaction for the sorption of amikacin sulphate onto freeze-dried PBCA nanoparticles. Similar results were also obtained by Harmia et al. [201]. The most appropriate surfactant depends on the drug under investigation. Surfactants can further affect the molecular weight and size of the drug-loaded particles obtained as well as the drug release [62, 202]. However, in our work, despite definite advantages being seen in the use of particular surfactants, the loading could not be increased significantly solely by their careful selection.

Alterations to the concentration of 5FU, surfactant concentration, pH, and monomer concentration were also made to effect an increase in the loading. However, in each

case the changing of the preparatory conditions made little impact upon the loading of the particles. It was found that changes could lead to various particle size differences and zeta potential changes, but any variation in loading was in the manner of 1–2%. It was clear that the absence of any dynamic for the water-soluble drug to move into the monomer-rich micelles during particle formation was fundamental to the lack of success in the incorporation of 5FU. Hence, other methods of particle formation were employed, including an oil-in-oil emulsion/solvent diffusion method. It was reasoned that if all sources of water could be eliminated from the manufacturing process, there was a much greater likelihood of achieving significant incorporation into the nanoparticles.

## 8. DRUG RELEASE

Drug release can be defined as the fraction of drug released from the nanoparticulate system as a function of time after the system has been administered [203]. The release of drug from nanoparticles depends on the location and physical state of the drug loaded into the colloidal carrier [133]. The drug can be released by:

- desorption of surface-bound drug,
- diffusion through the nanoparticulate matrix,
- diffusion through the polymer wall of nanocapsules,
- nanoparticle matrix erosion,
- a combined erosion diffusion process [169].

Measurement of true release profiles requires good sink or infinite dilution conditions so that the drug has the greatest opportunity to be released [204]. Therefore, the release must occur into a large volume of sink or continuous phase. However, as the sink volume is increased the concentration of drug being measured decreases. As a compromise, it is recommended that the drug concentration in the continuous phase be kept below 10% of saturation [203]. Good sink conditions are required to avoid errors from the reabsorption of the drug to the carrier and saturating the sink with drug, especially if it is poorly water-soluble. Two techniques have been employed to determine drug release from nanoparticulate carriers, which include membrane diffusion techniques and the sample and separate techniques. Drug release from submicrometer carriers has been reviewed by Washington [203] and Magenheimer and Benita [133].

### 8.1. Membrane Diffusion Techniques

A volume of the particle suspension is placed in a dialysis bag, which is sealed and placed into the continuous sink phase, which is usually phosphate buffered saline. The entire system is kept at 37 °C with continuous magnetic stirring of the sink [203]. The drug in the particles diffuses into the aqueous phase in the dialysis bag with a rate constant,  $k_i$ . This drug concentration in the dialysis bag diffuses through the dialysis membrane to the sink phase with rate constant  $k_m$ . The drug concentration in the sink is periodically assayed to determine the amount of drug released. The main disadvantage of this method is that the release of drug from particles in the dialysis bag is driven by the partitioning of the drug between the particle and its continuous phase in

the dialysis bag [204]. The release is determined by  $K_p$ , the partition coefficient, and is independent of  $k_p$ . This reduces the amount of drug available for release through the dialysis membrane and  $k_m$  becomes the rate-limiting step in the release. In contrast, the diffusion of free drug across the membrane is rapid, as the release is driven by the drug's concentration gradient as all the drug is available for release [204]. The rate constant,  $k_m$ , is fast in this instance. Another disadvantage is that the membrane diffusion experiment is not performed under sink conditions. This is because the particulate sample itself is never diluted in the sink, since it is separated from it by the dialysis membrane. Therefore, the membrane diffusion technique is not a measure of the true release rate and has been found limited for the prediction of release from nanoparticles *in vivo* [205]. The technique is less prone to error where dissolution or disintegration of the carrier occurs [203]. However, the technique has been extensively used to determine release from nanoparticulate carriers *in vitro* for many different carriers, including liposomes and emulsions [159, 160, 206].

## 9. CONCLUSIONS

Nanoparticles represent a unique drug delivery system due to their small size, which allows them to pass through the narrowest components of the circulatory system. They also represent a generic system that has the potential for adaptation so that they can be tailor-made to specific applications. Because of this, more sophisticated drug delivery is possible, based on active targeting methods, allowing localization to sites that can be accessed from the circulation. An attached monoclonal antibody can be used to recognize an exposed antigen and so effect attachment. Consequent drug release will be concentrated around the target cells and will increase the probability that drug will diffuse into the cell of choice and not into those that do not require drug administration.

Incorporating water-soluble drugs has proved to be problematic. However, much work is underway to develop methods to achieve loadings in the particle that can be used in clinical problems. Development of particles with targeting capabilities has been less successful and more investigations are awaited, although one potential opportunity remains to be exploited and involves the integration of technology, more commonly seen in solid state-based electronic technology, with the design of particles described herein. Whether a particle can be controlled by onboard processing capabilities remains a debatable possibility, but an exciting one with no shortage of potential clinical applications.

## GLOSSARY

**Coacervation** The separation of two liquid phases in colloidal systems.

**Liposome** A spherical capsule consisting of a liquid core surrounded by a lipid bilayer.

**Nanocapsule** A spherical particle of submicrometer diameter consisting of an outer polymeric wall which encapsulates an inner core.

**Nanoparticle** Any solid particle ranging in size from 10 to 1000 nm.

**Nanosphere** A spherical particle of submicrometer diameter consisting of a solid monolithic polymer matrix with no discernable core.

**Photon correlation spectroscopy** A technique for measuring the size of submicrometer particles by analyzing their size-dependent scattering of laser light.

**Supercritical fluid** A substance whose temperature and pressure has been raised beyond the point where its gaseous and liquid states have equal density.

**Tyndall effect** The scattering of light as it passes through colloidal suspensions.

**Ultracentrifugation** The centrifugation of samples at very high speeds.

**Zeta potential** The potential existing between the suspending medium and the effective electrical surface of a particle.

## REFERENCES

1. R. Sykes, *Int. J. Antimicrobial Agents* 14, 1 (2000).
2. P. K. Gupta, *J. Pharm. Sci.* 79, 949 (1990).
3. P. R. Lockman, R. J. Mumper, M. A. Khan, and D. D. Allen, *Drug Devel. Ind. Pharm.* 28, 1 (2002).
4. C. Damge, M. Aprahamian, G. Balboni, A. Hoeltzel, V. Andrieu, and J. P. Devissaguet, *Int. J. Pharm.* 36, 121 (1987).
5. L. Illum, P. D. E. Jones, J. Kreuter, R. W. Baldwin, and S. S. Davis, *Int. J. Pharm.* 17, 65 (1983).
6. S. S. Davis, L. Illum, S. M. Moghimi, M. C. Davies, C. J. H. Porter, I. S. Muir, A. Brindley, N. M. Christy, M. E. Norman, P. Williams, and S. E. Dunn, *J. Controlled Release* 24, 157 (1993).
7. J. Kreuter, *European J. Drug Metabolism Pharmacokinetics* 3, 253 (1994).
8. S. M. Moghimi, *Adv. Drug Delivery Rev.* 17, 1 (1995).
9. M. Silhol, M. Tyagi, M. Giacca, B. Lebleu, and E. Vives, *European J. Biochem.* 269, 494 (2002).
10. R. H. Muller, K. H. Wallis, S. D. Troster, and J. Kreuter, *J. Controlled Release* 20, 237 (1992).
11. M. T. Peracchia, E. Fattal, D. Desmaele, M. Besnard, J. P. Noel, J. M. Gomis, M. Appel, J. d'Angelo, and P. Couvreur, *J. Controlled Release* 60, 121 (1999).
12. D. Bazile, C. Prud'homme, M. T. Bassoullet, M. Marlard, G. Spenlehauer, and M. Veillard, *J. Pharm. Sci.* 84, 493 (1995).
13. Y. P. Li, Y. Y. Pei, Z. H. Zhou, X. Y. Zhang, Z. H. Gu, J. Ding, J. J. Zhou, X. J. Gao, and J. H. Zhu, *Biol. Pharm. Bull.* 24, 662 (2001).
14. T. Verrecchia, G. Spenlehauer, D. V. Bazile, A. Murry-Brelier, Y. Archimbaud, and M. Veillard, *J. Controlled Release* 36, 49 (1995).
15. C. L. Boursais, L. Acar, H. Zia, P. A. Sado, T. Needham, and R. Leverage, *Progr. Retinal Eye Res.* 17, 33 (1998).
16. J. Kreuter, *Adv. Drug Delivery Rev.* 7, 71 (1991).
17. P. Couvreur and C. Vauthier, *J. Controlled Release* 17, 187 (1991).
18. J. Kreuter, *Methods Enzymol.* 112, 129 (1985).
19. H. Murakami, M. Kobayashi, H. Takeuchi, and Y. Kawashima, *Int. J. Pharm.* 187, 143 (1999).
20. T. Govender, S. Stolnik, M. C. Garnett, L. Illum, and S. S. Davis, *J. Controlled Release* 57, 171 (1999).
21. K. A. Janes, M. P. Fresneau, A. Marazuela, A. Fabra, and M. J. Alonso, *J. Controlled Release* 73, 255 (2001).
22. P. Calvo, C. Remunan-Lopez, J. L. Vila-Jato, and M. J. Alonso, *Pharm. Res.* 14, 1431 (1997).

23. E. Leo, M. Angela Vandelli, R. Camerini, and F. Forni, *Int. J. Pharm.* 155, 75 (1997).
24. H. Fritz, M. Maier, and E. Bayer, *J. Colloid Interface Sci.* 195, 272 (1997).
25. G.-H. Hsiue, S.-h. Hsu, C.-C. Yang, S.-H. Lee, and I.-K. Yang, *Biomaterials* 23, 457 (2002).
26. F. J. Papatheofanis and R. Barmada, *J. Biomed. Mater. Res.* 25, 761 (1991).
27. J. M. Rollot, P. Couvreur, L. Roblot-Treupel, and F. Puisieux, *J. Pharm. Sci.* 75, 361 (1986).
28. R. R. C. New, "Liposomes: A Practical Approach." IRL Press, Oxford, 1990.
29. G. Gregoriadis, "Liposomes as Drug Carriers: Recent Trends and Progress." Wiley, New York, 1988.
30. G. Gregoriadis, A. T. Florence, and H. M. Patel, "Liposomes in Drug Delivery." Harwood, London, 1993.
31. Y. Barenholz and D. J. Crommelin, in "Encyclopedia of Pharmaceutical Technology" (J. C. Boylan, Ed.), pp. 1–39. Dekker, New York, 1994.
32. T. M. Allen, *Drugs* 54, 8 (1997).
33. P. Couvreur, B. Kante, M. Roland, P. Guiot, P. Bauduin, and P. Speiser, *J. Pharmacy Pharmacol.* 31, 331 (1979).
34. S. S. Davis, L. Illum, and S. Stolnik, *Current Opinion Colloid Interface Sci.* 1, 660 (1996).
35. E. Allemann, R. Gurny, and E. Doelker, *European J. Pharm. Biopharm.* 39, 173 (1993).
36. P. Couvreur, C. Dubernet, and F. Puisieux, *European J. Pharm. Biopharm.* 41, 2 (1995).
37. M. Gallardo, L. Roblot-Treupel, J. Manhuteau, I. Genin, P. Couvreur, M. Plat, and F. Puisieux, Nanocapsules et nanosphères d'alkyl-cyanoacrylate, interactions principe actif/polymère, in "1989 Proc. 5th Int. Conf. Pharm. Tech." pp. D36–D45.
38. R. Jalil and J. R. Nixon, *J. Microencapsulation* 7, 25 (1989).
39. R. Arshady, *J. Microencapsulation* 5, 101 (1988).
40. J. Kreuter, *Pharm. Acta Helvetica* 58, 196 (1983).
41. R. M. Fitch, M. M. B. Prenosil, and K. J. Sprick, *J. Polymer Sci. A* 27, 95 (1969).
42. J. Kreuter, in "Microcapsules and Nanoparticles in Medicine and Pharmacy" (M. Donbrow, Ed.), pp. 125–245. CRC Press, Boca Raton, 1992.
43. V. U. E. Berg, J. Kreuter, P. P. Speiser, and M. Soliva, *Pharm. Ind.* 48, 75 (1986).
44. A. Schwarz and A. Rembaum, in "Methods in Enzymology" (R. Green, Ed.), pp. 175–194. Academic Press, Orlando, 1985.
45. A. Rembaum, S. P. S. Yen, and R. S. Molday, *J. Macromol. Sci. A* 13, 603 (1979).
46. M. Chang, G. Richards, and A. Rembaum, in "Methods in Enzymology" (R. Green, Ed.), pp. 150–164. Academic Press, Orlando, 1985.
47. S. Margel and E. Wiesel, *J. Polymer Sci. A* 22, 145 (1984).
48. S. Margel, S. Zisblatt, and A. Rembaum, *J. Immunol. Methods* 28, 341 (1979).
49. A. D. McLeod, F. C. Lam, P. K. Gupta, and C. T. Hung, *J. Pharm. Sci.* 77, 704 (1988).
50. G. Mukherji, R. S. R. Murthy, and B. D. Miglani, *Int. J. Pharm.* 50, 15 (1989).
51. S. J. Douglas, S. S. Davis, and L. Illum, *CRC Critical Rev. Therapeutic Drug Carrier Syst.* 3, 233 (1987).
52. P. Couvreur and C. Vauthier, *J. Controlled Release* 17, 187 (1991).
53. D. K. Ousterhout, W. T. Tumbusch, P. M. Margetis, and F. Leonard, *British J. Plastic Surgery* 24, 23 (1971).
54. J. A. Collins, K. C. Pani, M. M. Seidenstein, G. Brandes, and F. Leonard, *Surgery* 65, 256 (1969).
55. S. J. Douglas, L. Illum, S. S. Davis, and J. Kreuter, *J. Colloid Interface Sci.* 101, 149 (1984).
56. P. Couvreur, *CRC Critical Rev. Therapeutic Drug Carrier Syst.* 5, 1 (1988).
57. C. Verdun, P. Couvreur, and H. Vranckx, *J. Controlled Release* 3, 205 (1986).
58. P. Maincent, J. P. Devissaguet, R. Leverage, P. A. Sado, and P. Couvreur, *Appl. Biochem. Biotechnol.* 10, 263 (1984).
59. J. Kreuter, *Int. J. Pharm.* 14, 43 (1983).
60. B. Seijo, E. Fattal, L. Roblot-Treupel, and P. Couvreur, *Int. J. Pharm.* 62, 1 (1990).
61. V. Lenaerts, P. Raymond, J. Juhasz, M. A. Simard, and C. Jolicoeur, *J. Pharm. Sci.* 78, 1051 (1989).
62. G. Puglisi, G. Giammona, M. Fresta, B. Carlisi, N. Micali, and A. Villari, *J. Microencapsulation* 10, 353 (1993).
63. T. Harmia-Pulkkinen, A. Tuomi, and E. Kristoffersson, *J. Microencapsulation* 6, 87 (1989).
64. P. A. McCarron, A. D. Woolfson, and S. M. Keating, *Int. J. Pharm.* 193, 37 (1999).
65. J. Kreuter, in "Encyclopedia of Pharmaceutical Technology" (J. C. Boylan, Ed.), pp. 1–29. Dekker, New York, 1988.
66. N. Bapat and M. Boroujerdi, *Drug Devel. Ind. Pharm.* 18, 65 (1992).
67. M. J. Alonso, C. Losa, P. Calvo, and J. L. Vilajato, *Int. J. Pharm.* 68, 69 (1991).
68. L. Illum, M. A. Khan, E. Mak, and S. S. Davis, *Int. J. Pharm.* 30, 17 (1986).
69. F. Lescure, C. Seguin, P. Breton, P. Bourrinet, D. Roy, and P. Couvreur, *Pharm. Res.* 11, 1270 (1994).
70. T. K. M. Mbela, J. H. Poupaert, P. Dumont, and A. Haemers, *Int. J. Pharm.* 92, 71 (1993).
71. J. L. De Keyser, J. H. Poupaert, and P. Dumont, *J. Pharm. Sci.* 80, 67 (1991).
72. G. Birrenbach and P. P. Speiser, *J. Pharm. Sci.* 65, 1763 (1976).
73. B. Ekman and I. Sjöholm, *J. Pharm. Sci.* 67, 693 (1978).
74. P. Edman, B. Ekman, and I. Sjöholm, *J. Pharm. Sci.* 69, 838 (1980).
75. J. Kreuter and P. P. Speiser, *J. Pharm. Sci.* 65, 1624 (1976).
76. U. Berg, "Immunstimulation durch hochdisperse polymersuspensionen." ETH, Zurich, 1979.
77. J. Kreuter and P. P. Speiser, *Infection Immunity* 13, 204 (1976).
78. R. S. Molday, W. J. Dreyer, A. Rembaum, and S. P. S. Yen, *J. Cell Biol.* 64, 75 (1975).
79. A. Rolland, D. Gibassier, P. Sado, and R. Leverage, *J. Pharm. Belgique* 41, 94 (1986).
80. A. Rembaum, S. P. S. Yen, E. Cheong, S. Wallace, R. S. Molday, and W. J. Deyer, *Macromolecules* 9, 328 (1976).
81. J. Kreuter, U. Tauber, and V. Illi, *J. Pharm. Sci.* 68, 1443 (1979).
82. J. W. Vanderhoff, M. S. El-Aasser, and J. Ugelstad, U.S. Patent 4, 177, 177, 1979.
83. R. Gurny, N. A. Peppas, D. D. Harrington, and G. S. Banker, *Drug Devel. Ind. Pharm.* 7, 1 (1981).
84. R. Bodmeier and H. G. Chen, *J. Controlled Release* 12, 223 (1990).
85. H. J. Krause, A. Schwarz, and P. Rohdewald, *Int. J. Pharm.* 27, 145 (1985).
86. P. D. Scholes, A. G. A. Coombes, L. Illum, S. S. Davis, M. Vert, and M. C. Davies, *J. Controlled Release* 25, 145 (1993).
87. M. C. Julienne, M. J. Alonso, J. L. Gomez-Amoza, and J. P. Benoit, *Drug Devel. Ind. Pharm.* 18, 1063 (1992).
88. T. R. Tice and R. M. Gilley, *J. Controlled Release* 2, 343 (1985).
89. R. Bodmeier and H. Chen, Preparation and evaluation of drug containing polymeric nanosuspensions, in "1989 Proc. 5th Int. Conf. Pharm. Tech.," pp. B265–268.
90. F. Koosha and R. H. Muller, *Arch. Pharm.* 320, 913 (1987).
91. F. Koosha, R. H. Muller, S. S. Davis, and M. C. Davies, *J. Controlled Release* 9, 149 (1989).
92. R. Bodmeier and H. Chen, *J. Controlled Release* 10, 167 (1989).
93. R. Bodmeier and J. W. McGinity, *Int. J. Pharm.* 43, 179 (1988).
94. R. Bodmeier and J. W. McGinity, *Pharm. Res.* 4, 465 (1987).
95. T. Niwa, H. Takeuchi, T. Hino, N. Kunou, and Y. Kawashima, *J. Controlled Release* 25, 89 (1993).

96. D. C. Tsai, S. A. Howard, T. F. Hogan, C. J. Malanga, S. J. Kandzari, and J. K. Ma, *J. Microencapsulation* 3, 181 (1986).
97. R. Jalil and J. R. Nixon, *J. Microencapsulation* 7, 25 (1990).
98. R. Wada, S. H. Hyon, and Y. Ikada, *J. Pharm. Sci.* 79, 919 (1990).
99. C. Bindschaedler, R. Gurny, and E. Doelker, Swiss Patent 1497/88, 1988.
100. H. Ibrahim, C. Bindschaedler, E. Doelker, P. Buri, and R. Gurny, *Int. J. Pharm.* 87, 239 (1992).
101. E. Allemann, E. Doelker, and R. Gurny, *European J. Pharm. Biopharm.* 39, 13 (1993).
102. E. Allemann, R. Gurny, and E. Doelker, *Int. J. Pharm.* 87, 247 (1992).
103. J. C. Leroux, E. Allemann, E. Doelker, and R. Gurny, *European J. Pharm. Biopharm.* 41, 14 (1995).
104. S. Massen, E. Fattal, R. H. Müller, and P. Couvreur, *S.T.P. Pharma Sci.* 3, 11 (1993).
105. H. Fessi, F. Puisieux, and J. P. Devissaguet, European Patent 274961, 1987.
106. D. Quintanar-Guerrero, E. Allemann, E. Doelker, and H. Fessi, *Colloid Polymer Sci.* 275, 640 (1997).
107. P. Couvreur, C. Dubernet, and F. Puisieux, *European J. Pharm. Biopharm.* 41, 2 (1995).
108. S. Stolnik, M. C. Davies, L. Illum, S. S. Davis, M. Boustta, and M. Vert, *J. Controlled Release* 30, 57 (1994).
109. S. Stolnik, M. C. Garnett, M. C. Davies, L. Illum, M. Boustta, M. Vert, and S. S. Davis, *Colloids Surfaces A* 97, 235 (1995).
110. S. Stainmesse, A. M. Orecchioni, and E. Nakache, Modelling of an original process to obtain biocompatible polymeric nanospheres, in "1992 6th International Conference on Pharmaceutical Technology," pp. 89–97.
111. S. Stainmesse, A. M. Orecchioni, E. Nakache, F. Puisieux, and H. Fessi, *Colloid Polymer Sci.* 273, 505 (1995).
112. Y. Kawashima, H. Yamamoto, H. Takeuchi, T. Hino, and T. Niwa, *European J. Pharm. Biopharm.* 45, 41 (1998).
113. H. G. Bungenberg de Jong and H. R. Kruyt, Chemistry co-ervation (partial miscibility in colloid systems) (preliminary communication), in "1929 Proc. Konink. Nederl. Akad. Wetensch.," pp. 849–856.
114. C. Thomasin, N. T. Ho, H. P. Merkle, and B. Gander, *J. Pharm. Sci.* 87, 259 (1998).
115. M. Donbrow, "Microcapsules and Nanoparticles in Medicine and Pharmacy." CRC Press, Boca Raton, 1992.
116. P. B. Deasy, "Microencapsulation and Related Processes." Dekker, New York, 1984.
117. L. M. Sanders, J. S. Kent, G. I. McRae, B. H. Vickery, T. R. Tice, and D. H. Lewis, *J. Pharm. Sci.* 73, 1294 (1984).
118. J. M. Ruiz, B. Tissier, and J. P. Benoit, *Int. J. Pharm.* 49, 69 (1989).
119. C. Thomasin, H. P. Merkle, and B. Gander, *J. Pharm. Sci.* 87, 269 (1998).
120. T. Niwa, H. Takeuchi, T. Hino, M. Nohara, and Y. Kawashima, *Int. J. Pharm.* 121, 45 (1995).
121. G. Mukherji, R. S. R. Murthy, and B. D. Miglani, *Int. J. Pharm.* 65, 1 (1990).
122. E. Reverchon, I. De Marco, and G. Della Porta, *Int. J. Pharm.* 243, 83 (2002).
123. P. Chattopadhyay and R. B. Gupta, *Int. J. Pharm.* 228, 19 (2001).
124. P. Chattopadhyay and R. B. Gupta, *AICHE J.* 48, 235 (2002).
125. P. Chattopadhyay and R. B. Gupta, *Ind. Eng. Chem. Res.* 40, 3530 (2001).
126. K. S. Soppimath, T. M. Aminabhavi, A. R. Kulkarni, and W. E. Rudzinski, *J. Controlled Release* 70, 1 (2001).
127. U. Foerter-Barth, U. Teipel, and H. Krause, Formation of particles by applying the gas anti-solvent (GAS) process, in "Nottingham, 1999 Supercritical fluids: Chemistry and Materials," Institut National Polytechnique de Lorraine, pp. 175–180.
128. N. Elvassore, A. Bertucco, and P. Caliceti, *J. Pharm. Sci.* 90, 1628 (2001).
129. L. Illum, S. S. Davis, C. G. Wilson, N. W. Thomas, M. Frier, and J. G. Hardy, *Int. J. Pharm.* 12, 135 (1982).
130. D. J. Wilkins and P. A. Meyers, *British J. Exp. Pathol.* 47, 568 (1966).
131. C. J. Van Oss, C. F. Gillman, and A. W. Neumann, "Phagocytic Engulfment and Cell Adhesiveness as Surface Phenomena." Dekker, New York, 1975.
132. L. Grislain, P. Couvreur, V. Lenaerts, M. Roland, D. Deprezdecampeneere, and P. Speiser, *Int. J. Pharm.* 15, 335 (1983).
133. B. Magenheimer and S. Benita, *STP Pharma Sci.* 1, 221 (1991).
134. R. J. Haskell, *J. Pharm. Sci.* 87, 125 (1998).
135. N. A. Fallouh, L. Roblottreupel, H. Fessi, J. P. Devissaguet, and F. Puisieux, *Int. J. Pharm.* 28, 125 (1986).
136. S. Henry-Michelland, M. J. Alonso, A. Andreumont, P. Maincen, J. Sauzieres, and P. Couvreur, *Int. J. Pharm.* 35, 121 (1987).
137. R. Gaspar, V. Preat, and M. Roland, *Int. J. Pharm.* 68, 111 (1991).
138. R. H. Muller, C. Lherm, J. Herbot, and P. Couvreur, *Biomaterials* 11, 590 (1990).
139. S. J. Douglas, L. Illum, and S. S. Davis, *J. Colloid Interface Sci.* 103, 155 (1985).
140. R. H. Muller and K. H. Wallis, *Int. J. Pharm.* 89, 25 (1993).
141. A. Malaiya and S. P. Vyas, *J. Microencapsulation* 5, 243 (1988).
142. R. H. Muller, "Colloidal Carriers for Controlled Drug Delivery and Targeting: Modification, Characterisation and In Vivo Distribution." CRC Press, Stuttgart, 1991.
143. A. Zimmer, J. Kreuter, and J. R. Robinson, *Proc. Int. Symp. Control. Rel. Bioact. Mater.* 18, 642 (1991).
144. R. H. Muller, S. S. Davis, L. Illum, and E. Mak, in "Targeting of Drugs with Synthetic Systems." (G. Poste, Ed.), Vol. 113. Plenum Press, New York, 1986.
145. S. E. Dunn, A. G. A. Coombes, M. C. Garnett, S. S. Davis, M. C. Davies, and L. Illum, *J. Controlled Release* 44, 65 (1997).
146. S. D. Troster and J. Kreuter, *J. Microencapsulation* 9, 19 (1992).
147. G. Lukowski, R. H. Muller, B. W. Muller, and M. Dittgen, *Int. J. Pharm.* 84, 23 (1992).
148. G. Lukowski, R. H. Muller, B. W. Muller, and M. Dittgen, *Colloid Polymer Sci.* 271, 100 (1993).
149. H. Carstensen, B. W. Muller, and R. H. Muller, *Int. J. Pharm.* 67, 29 (1991).
150. T. Blunk, E. Mak, and R. H. Muller, *Pharm. Ind.* 55, 612 (1993).
151. K. H. Wallis and R. H. Muller, *Pharm. Ind.* 55, 1124 (1993).
152. V. Bentele, U. E. Berg, and J. Kreuter, *Int. J. Pharm.* 13, 109 (1983).
153. S. J. Douglas and S. S. Davis, *British Polymer J.* 17, 339 (1985).
154. L. Vansnick, P. Couvreur, D. Christiaens-Leyh, and M. Roland, *Pharm. Res.* 36 (1984).
155. C. Damge, C. Michel, M. Aprahamian, P. Couvreur, and J. P. Devissaguet, *J. Controlled Release* 13, 233 (1990).
156. W. R. Vezin and A. T. Florence, *J. Biomed. Mater. Res.* 14, 93 (1980).
157. F. Leonard, R. K. Kulkarni, G. Brandes, J. Nelson, and J. Cameron, *J. Appl. Polymer Sci.* 10, 259 (1966).
158. V. Lenaerts, P. Couvreur, D. Christiaens-Leyh, E. Joiris, M. Roland, B. Rollman, and P. Speiser, *Biomaterials* 5, 65 (1984).
159. M. S. El-Samaligy, P. Rohdewald, and H. A. Mahmoud, *J. Pharm. Pharmacol.* 38, 216 (1986).
160. H.-J. Krause, A. Schwarz, and P. Rohdewald, *Drug Devel. Ind. Pharm.* 12, 527 (1986).
161. M. El-Samaligy and P. Rohdewald, *Pharm. Acta Helvetiae* 57, 201 (1982).
162. M. Aprahamian, C. Michel, W. Humbert, J. P. Devissaguet, and C. Damge, *Biol. Cell* 61, 69 (1987).
163. H. Fessi, F. Puisieux, J. P. Devissaguet, N. Ammouray, and S. Benita, *Int. J. Pharm.* 55, R1 (1989).
164. H. J. Krause and P. Rohdewald, *Pharm. Res.* 239 (1985).
165. B. Kante, P. Couvreur, V. Lenaerts, P. Guiot, M. Roland, P. Bauduin, and P. Speiser, *Int. J. Pharm.* 7, 45 (1980).

166. G. Binnig, C. F. Quate, and C. Gerber, *Phys. Rev. Lett.* 56, 930 (1986).
167. D. R. Denley, *Ultramicroscopy* 33, 83 (1990).
168. R. Reszka, P. Beck, I. Fichtner, M. Hentschel, J. Richter, and J. Kreuter, *J. Pharm. Exp. Therapeutics* 280, 232 (1997).
169. J. Kreuter, in "Encyclopedia of Pharmaceutical Technology" (J. C. Boylan, Ed.), pp. 165–190. Dekker, New York, 1994.
170. P. Beck, D. Csherer, and J. Kreuter, *J. Microencapsulation* 7, 491 (1990).
171. J. L. Grangier, M. Puygrenier, J. C. Gautier, and P. Couvreur, *J. Controlled Release* 15, 3 (1991).
172. F. Nemati, C. Dubernet, A. C. Deverdiere, M. F. Poupon, L. Treupelacar, F. Puisieux, and P. Couvreur, *Int. J. Pharm.* 102, 55 (1994).
173. E. Fattal, J. Rojas, L. Roblot-Treupel, A. Andremont, and P. Couvreur, *J. Microencapsulation* 8, 29 (1991).
174. G. Cavallaro, M. Fresta, G. Giammona, G. Puglisi, and A. Villari, *Int. J. Pharm.* 111, 31 (1994).
175. A. Sanchez, J. L. Vila-Jato, and M. J. Alonso, *Int. J. Pharm.* 99, 263 (1993).
176. P. Maincent, R. Le Verge, P. Sado, P. Couvreur, and J. P. Devisageut, *J. Pharm. Sci.* 75, 955 (1986).
177. M. Fresta, G. Puglisi, G. Giammona, G. Cavallaro, N. Micali, and P. M. Furneri, *J. Pharm. Sci.* 84, 895 (1995).
178. M. Radwan, I. Zaghoul, and Z. Aly, *European J. Pharm. Sci.* 8, 95 (1999).
179. P. Beck, D. Scherer, and J. Kreuter, *J. Microencapsulation* 7, 491 (1990).
180. V. D. Labhasetwar and A. K. Dorle, *J. Controlled Release* 12, 113 (1990).
181. J. J. Marty, R. C. Oppenheim, and P. Speiser, *Pharm. Acta Helveticae* 53, 17 (1978).
182. S. Levin, *Israel J. Chem.* 30, 257 (1990).
183. J. Kreuter, M. Nefzger, E. Liehl, R. Czok, and R. Voges, *J. Pharm. Sci.* 72, 1146 (1983).
184. N. Bresseur, D. Brault, and P. Couvreur, *Int. J. Pharm.* 70, 129 (1991).
185. M. A. Radwan, *Drug Devel. Ind. Pharm.* 21, 2371 (1995).
186. C. Verdun, F. Bresseur, V. Vranckx, P. Couvreur, and M. Roland, *Cancer Chemother. Pharmacol.* 26, 13 (1990).
187. P. Calvo, J. L. Vila-Jato, and M. J. Alonso, *J. Pharm. Sci.* 85, 530 (1996).
188. E. J. Truter, *Artificial Cells Blood Substitutes Immobilization Biotechnol.* 23, 579 (1995).
189. T. Ouchi, H. Kobayashi, and T. Banba, *British Polymer J.* 23, 221 (1990).
190. M. S. Latha, A. Jayakrishnan, K. Rathinam, and M. Mohanty, *J. Pharm. Pharmacol.* 46, 858 (1994).
191. B. Elorza, M. A. Elorza, G. Frutos, and J. R. Chantres, *Biochim. Biophys. Acta* 1153, 135 (1993).
192. S. Miyazaki, N. Hashiguchi, M. Sugiyama, M. Takada, and Y. Morimoto, *Chem. Pharm. Bull.* 34, 1370 (1986).
193. K. Sugibayashi, Y. Morimoto, T. Nadai, Y. Kato, A. Hasegawa, and T. Arita, *Chem. Pharm. Bull.* 27, 204 (1979).
194. J. Akbuga and N. Bergisadi, *J. Microencapsulation* 13, 161 (1996).
195. H. S. Yalabik-Kas, J. Kreuter, A. A. Hincal, and P. P. Speiser, *J. Microencapsulation* 3, 71 (1986).
196. M. Boisdron-Celle, J. M. Ruiz, and J. P. Benoit, Preparation and characterisation of 5-fluorouracil-loaded microspheres as biodegradable anti-cancer drug carriers, in "1992 6th International Conference on Pharmaceutical Technology," pp. 52–61.
197. K. Ciftci, A. A. Hincal, H. S. Kas, M. T. Ercan, and S. Ruacan, *European J. Pharm. Sci.* 1, 249 (1994).
198. J. Kreuter and H. R. Hartmann, *Oncology* 40, 363 (1983).
199. K. Ciftci, A. A. Hincal, and H. S. Kas, Microspheres of 5-fluorouracil using poly(DL-lactic acid), effect of polymer molecular weight on release characteristics, in "1992 6th International Conference on Pharmaceutical Technology," pp. 62–71.
200. M. Boisdron-Celle, P. Menei, and J. P. Benoit, *J. Pharm. Pharmacol.* 47, 108 (1995).
201. T. Harmia, P. Speiser, and J. Kreuter, *Int. J. Pharm.* 33, 45 (1986).
202. M. A. Vandelli, M. Fresta, G. Puglisi, and F. Forni, *J. Microencapsulation* 11, 531 (1994).
203. C. Washington, *Int. J. Pharm.* 58, 1 (1990).
204. C. Washington, *Int. J. Pharm.* 56, 71 (1989).
205. M. Y. Levy and S. Benita, *Int. J. Pharm.* 66, 29 (1990).
206. N. Ammoury, H. Fessi, J. P. Devissaguet, F. Puisieux, and S. Benita, *STP Pharma Sci.* 5, 647 (1989).
207. H. Yuan, F. q. Hu, and X. y. Ying, *Chinese Pharm. J.* 37, 349 (2002).
208. Z. Ma, H. H. Yeoh, and L. Y. Lim, *J. Pharm. Sci.* 91, 1396 (2002).
209. Y. Pan, H. Xu, H. Y. Zhao, G. Wei, and J. M. Zheng, *Acta Pharm. Sinica* 37, 377 (2002).
210. N. Elvassore, A. Bertucco, and P. Caliceti, *J. Pharm. Sci.* 90, 1628 (2001).
211. N. Behan and C. Birkinshaw, *Macromole. Rapid Comm.* 22, 41 (2001).
212. P. Venugopalan, A. Sapre, N. Venkatesan, and S. P. Vyas, *Pharmazie* 56, 217 (2001).
213. L. M. Ma, Q. Zhang, and Y. Z. Li, *Chinese Pharm. J.* 36, 38 (2001).
214. Q. Zhang, Z. Shen, and T. Nagai, *Int. J. Pharm.* 218, 75 (2001).
215. Z. N. Yin and B. Lu, *Chinese J. Pharm.* 31, 349 (2000).
216. S. Watnasirichaikul, N. M. Davies, T. Rades, and I. G. Tucker, *Pharm. Res.* 17, 684 (2000).
217. Z. N. Yin, B. Lu, and G. J. Wang, *West China J. Pharm. Sci.* 15, 250 (2000).
218. M. Aboubakar, P. Couvreur, H. Pinto-Alphandary, B. Gouritin, B. Lacour, R. Farinotti, F. Puisieux, and C. Vauthier, *Drug Dev. Res.* 49, 109 (2000).
219. C. X. Zheng, M. X. Duan, Z. C. Yue, H. Ma, and J. H. Guo, *Polymer Preprints* 40, 351 (1999).
220. I. Seyler, M. Appel, J. P. Devissaguet, P. Legrand, and G. Barratt, *Int. J. Immunopharmacol.* 18, 385 (1996).
221. G. M. Barratt, C. Morin, M. Appel, and I. Seyler, Intracellular delivery of a muramyl dipeptide derivative by poly(DL-lactide) nanocapsules, in "In vitro and ex vivo test systems to rationalize drug design and delivery," Paris, 1993, pp. 265–268.
222. C. Morin, G. Barratt, H. Fessi, and J. P. Devissaguet, *Int. J. Immunopharmacol.* 16, 451 (1994).
223. S. Sakuma, N. Suzuki, R. Sudo, K. I. Hiwatari, A. Kishida, and M. Akashi, *Int. J. Pharm.* 239, 185 (2002).
224. S. Sakuma, Y. Ishida, R. Sudo, N. Suzuki, H. Kikuchi, K. I. Hiwatari, A. Kishida, M. Akashi, and M. Hayashi, *Int. J. Pharm.* 159, 181 (1997).
225. S. Sakuma, N. Suzuki, H. Kikuchi, K. I. Hiwatari, K. Arikawa, A. Kishida, and M. Akashi, *Int. J. Pharm.* 149, 93 (1997).
226. S. Sakuma, N. Suzuki, H. Kikuchi, K. I. Hiwatari, K. Arikawa, A. Kishida, and M. Akashi, *Int. J. Pharm.* 158, 69 (1997).
227. H. Vranckx, M. Demoustier, and M. Deleers, *Eur. J. Pharm. Biopharm.* 42, 345 (1996).
228. N. O. Fischer, C. M. McIntosh, J. M. Simard, and V. M. Rotello, *Proc. Nat. Acad. Sci. USA* 99, 5018 (2002).
229. Y. E. Shapiro and E. G. Pykhteeva, *Appl. Biochem. Biotechnol.* 74, 67 (1998).
230. Y. E. Shapiro, E. G. Pykhteeva, and G. V. Fedorova, *Russian J. Bioorganic Chem.* 23, 156 (1997).
231. A. M. da Silveira, D. Duchene, and G. Ponchel, *STP Pharma Sci.* 10, 309 (2000).
232. J. Valero, M. A. Egea, M. Espina, F. Gamisans, and M. L. Garcia, *Drug Dev. Ind. Pharm.* 22, 167 (1996).
233. R. Cavalli, E. Peira, O. Caputo, and M. R. Gasco, *Int. J. Pharm.* 182, 59 (1999).



234. A. K. Zimmer, P. Maincent, P. Thouvenot, and J. Kreuter, *Int. J. Pharm.* 110, 211 (1994).
235. M. G. Cascone, P. M. Pot, Z. Zhu, and L. Lazzeri, *J. Mater. Sci. Mater. Med.* 13, 265 (2002).
236. C. X. Song, V. Labhasetwar, H. Murphy, X. Ou, W. R. Humphrey, R. J. Shebuski, and R. J. Levy, *J. Control. Release* 43, 197 (1997).
237. J. H. Chen, M. Shagufra, and S. S. Davis, *Acta Pharm. Sinica* 37, 473 (2002).
238. A. Zur Muehlen and W. Mehnert, *Pharmazie* 53, 552 (1998).
239. E. Lemos-Senna, D. Wouessidjewe, and D. Duchene, *Colloids Surfaces B* 10, 303 (1998).
240. J. Jansen, C. Treiner, and C. Vaution, *J. Colloid Interface Sci.* 179, 578 (1996).
241. A. Raffin Pohlmann, V. Weiss, O. Mertins, N. Pesce da Silveira, and S. Staniscuaski Guterres, *Eur. J. Pharm. Sci.* 16, 305 (2002).
242. C. W. Maboundou, G. Paintaud, Y. Ottignon, J. Magonette, Y. Bechtel, H. Fessi, F. Gouchet, P. Carayon, and P. Bechtel, *Therapie* 51, 88 (1996).
243. F. Fawaz, F. Bonini, M. Guyot, A. M. Lagueny, H. Fessi, and J. P. Devissaguet, *Int. J. Pharm.* 133, 107 (1996).
244. P. Calvo, M. J. Alonso, J. L. Vila-Jato, and J. R. Robinson, *J. Pharm. Pharmacol.* 48, 1147 (1996).
245. M. Skiba, C. Morvan, D. Duchene, F. Puisieux, and D. Wouessidjewe, *Int. J. Pharm.* 126, 275 (1995).
246. F. Fawaz, F. Bonini, M. Guyot, and A. M. Lagueny, *Pharm. Res.* 10, 750 (1993).
247. N. Ammourey, M. Dubrasquet, H. Fessi, and J. P. Devissaguet, in "Biomedical Polymers" (D. Cohn and J. Kost, Eds.), Vol. 13, Number 1/4, p. 121. Elsevier Applied Science, 1993.
248. P. Calvo, J. L. Vila-Jato, and M. J. Alonso, Corneal penetration of 14C-indomethacin-loaded nanocapsules, in "Methods to Overcome Biological Barriers in Drug Delivery," Kuopio, Finland, 1993, Kuopio University, Department of Pharmaceutical Technology, p. 93.
249. C. R. Muller, S. R. Schaffazick, A. R. Pohlmann, L. de Lucca Freitas, N. Pesce da Silveira, T. Dalla Costa, and S. S. Guterres, *Pharmazie* 56, 864 (2001).
250. S. S. Guterres, H. Fessi, G. Barratt, F. Puisieux, and J. P. Devissaguet, *J. Biomater. Sci. Polymer Ed.* 11, 1347 (2000).
251. S. S. Guterres, C. R. Muller, C. B. Michalowski, A. R. Pohlmann, and T. D. Costa, *STP Pharma Sci.* 11, 229 (2001).
252. A. R. Kulkarni, K. S. Soppimath, and T. M. Aminabhavi, *J. Microencapsul.* 17, 449 (2000).
253. O. Valls, M. L. Garcia, X. Pages, J. Valero, M. A. Egea, M. A. Salgueiro, and R. Valls, in "Trends in Colloid and Interface Science X," (C. Solans, M. R. Infante, and M. J. Garcia-Celma, Eds.), Vol. 100, pp. 107–111. (Steinkopff-Verlag, 1996).
254. S. S. Guterres, H. Fessi, G. Barratt, and J. P. Devissaguet, *Int. J. Pharm.* 113, 57 (1995).
255. X. W. Li, J. L. Liu, Y. Q. Wei, A. S. C. Chan, and K. L. D. Lee, *J. Pharm. Pharmacol.* 51, 176 (1999).
256. K. Akiyoshi, S. Kurumada, E. C. Kang, J. Sunamoto, T. Principi, and F. M. Winnik, *J. Network Polymer Japan* 20, 171 (1999).
257. C. Passirani, G. Barratt, J. P. Devissaguet, and D. Labarre, *Life Sci.* 62, 775 (1998).
258. J. Sunamoto, S. Deguchi, Y. Kato, I. Taniguchii, Y. Sasaki, K. Kuroda, and K. Akiyoshi, in "Proceedings of the American Chemical Society Division of Polymeric Materials: Science and Engineering," Vol. 79, pp. 230–231. *Amer. Chem. Soc.*, Washington, DC, 1998.
259. X. G. Gu, M. Schmitt, A. Hiasa, Y. Nagata, H. Ikeda, Y. Sasaki, K. Akiyoshi, J. Sunamoto, H. Nakamura, and K. Kuribayashi, *Cancer Res.* 58, 3385 (1998).
260. C. Passirani, G. Barratt, J. P. Devissaguet, and D. Labarre, *Pharm. Res.* 15, 1046 (1998).
261. N. C. Santos, M. J. E. Prieto, A. Morna-Gomes, D. Betbeder, and M. A. R. B. Castanho, *Biopolymers* 41, 511 (1997).
262. K. Akiyoshi, T. Nishikawa, S. I. Kobayashi, and J. Sunamoto, in "Biomedical Functions and Biotechnology of Natural and Artificial Polymers" (M. Yalpani, Ed.), Vol. 3, pp. 115–126. Atl Press, 1996.
263. I. Taniguchi, K. Akiyoshi, and J. Sunamoto, in "SPSJ 45th Symposium on Macromolecules," Vol. 45, Number 2, p. E1019. The Society of Polymer Science, 1996.
264. K. Akiyoshi, S. Deguchi, H. Tajima, and T. Nishikawa, *Proc. Japan Acad. Ser. B Phys. Biol. Sci.* 71, 15 (1995).
265. K. Akiyoshi, T. Nishikawa, S. Shichibe, and J. Sunamoto, *Chem. Lett.* 707 (1995).
266. Y. Kakizawa, K. Akiyoshi, K. Nakamura, and J. Sunamoto, in "Enzymatic Activity of Lipase Complexed with Nanoparticle of Hydrophobized Polysaccharide," Kyoto, Japan, 1998, p. III-806. Society of Polymer Science, Japan (Spsj).
267. S. Xu and M. Yonese, in "Charge Densities and Nanoparticle Formation of Complexes Composed of Acid Polysaccharides and Protein," Nagoya, Japan, 1998, p. E1076.
268. X. W. Li, J. L. Liu, Y. Q. Wei, and A. S. C. Chan, Preparation of polysaccharide nanoparticles for controlled gene release, in "British Pharmaceutical Conference," p. 176. Pharmaceutical Society of Great Britain, Cardiff, 1999.
269. N. S. Santos-Magalhaes, A. Pontes, V. M. Pereira, and M. N. Caetano, *Int. J. Pharm.* 208, 71 (2000).
270. P. Chattopadhyay and R. B. Gupta, *Ind. Eng. Chem. Res.* 40, 3530 (2001).
271. H. Lin and J. Xue-hua, *Chinese J. Antibiotics* 25, 272 (2000).
272. X. Jiang and G. Liao, *Chinese J. Antibiotics* 24, 35 (1999).
273. H. Pinto-Alphandary, A. Andreumont, and P. Couvreur, *Int. J. Antimicrob. Agents* 13, 155 (2000).
274. E. Reverchon and G. Della Porta, *Powder Technol.* 106, 23 (1999).
275. M. E. Page-Clisson, H. Pinto-Alphandary, M. Ourevitch, A. Andreumont, and P. Couvreur, *J. Control. Release* 56, 23 (1998).
276. A. E. Gulyaev, B. A. Ermekbaeva, G. Y. Kivman, T. G. Radchenko, A. Y. Sherstov, and V. G. Shirinskii, *Pharm. Chem. J.* 32, 115 (1998).
277. M. S. Espuelas, P. Legrand, J. M. Irache, C. Gamazo, A. M. Orecchioni, J. P. Devissaguet, and P. Ygartua, *Int. J. Pharm.* 158, 19 (1997).
278. G. Cavallaro, M. Fresta, G. Giammona, and G. Puglisi, *Int. J. Pharm.* 111, 31 (1994).
279. G. Lambert, J. R. Bertrand, E. Fattal, F. Subra, H. Pinto-Alphandary, C. Malvy, C. Auclair, and P. Couvreur, *Biochem. Biophys. Res. Commun.* 279, 401 (2000).
280. H. P. Zobel, M. Junghans, V. Maisenschein, D. Werner, M. Gilbert, H. Zimmermann, C. Noe, J. Kreuter, and A. Zimmer, *Eur. J. Pharm. Biopharm.* 49, 203 (2000).
281. E. Fattal, C. Vauthier, I. Aynie, Y. Nakada, G. Lambert, C. Malvy, and P. Couvreur, *J. Control. Release* 53, 137 (1998).
282. H. P. Zobel, J. Kreuter, D. Werner, C. R. Noe, G. Kuemel, and A. Zimmer, *Antisense Nucleic Acid Drug Dev.* 7, 483 (1997).
283. O. Balland, T. Saison-Behmoaras, T. Garestier, and C. Helene, in "Targeting of Drugs: 5 Strategies for Oligonucleotide and Gene Delivery in Therapy" (G. Gregoriadis and B. McCormack, Eds.), Vol. 290, pp. 131–142. Plenum Press, New York, 1996.
284. I. Aynie, C. Vauthier, E. Fattal, and M. Foulquier, Alginate nanoparticles as a novel carrier for antisense oligonucleotides, in "Future Strategies for Drug Delivery with Particulate Systems," Stuttgart, 1997, pp. 11–16.
285. E. Benoit, O. Prot, P. Maincent, and J. Bessiere, *Pharm. Res.* 11, 585 (1994).
286. O. Prot, E. Benoit, P. Maincent, and J. Bessiere, *J. Colloid Interface Sci.* 184, 251 (1996).
287. T. K. De and A. S. Hoffman, *Artificial Cells Blood Substitutes Immobilization Biotechnol.* 29, 31 (2001).
288. L. Marchal-Heussler, D. Sirbat, M. Hoffman, and P. Maincent, *Pharm. Res.* 10, 386 (1993).

289. J. M. Irache, M. Berrabah, P. Verite, and S. Menager, Phenobarbitone-loaded poly-curly epsilon-caprolactone nanocapsules; In vitro kinetics and in vivo behaviour by the oral route, in "Formulation of Poorly-Available Drugs for Oral Administration," Paris, 1996, pp. 334-337.
290. M. Berrabah, D. Andre, F. Prevot, and A. M. Orecchioni, *J. Pharm. Biomed. Anal.* 12, 373 (1994).
291. H. Goto, T. Isobe, and M. Senna, Controlled dissolution of phenytoin by complexing with silica nanoparticles modified by acrylamide, in "International Conference on Silica Science and Technology," Mulhouse, France, 1998, pp. 573-576.
292. H. Goto, T. Isobe, and M. Senna, *Mater. Res. Soc. Symp. Proc.* 501, 321 (1998).
293. M. Fresta, G. Cavallaro, G. Giammona, E. Wehrli, and G. Puglisi, *Biomaterials* 17, 751 (1996).
294. V. Ferranti, H. Marchais, C. Chabenat, A. M. Orecchioni, and O. Lafont, *Int. J. Pharm.* 193, 107 (1999).
295. P. A. McCarron, A. D. Woolfson, and S. M. Keating, *J. Pharm. Pharmacol.* 52, 1451 (2000).
296. S. Keating, P. A. McCarron, and A. D. Woolfson, *J. Pharm. Pharmacol.* 52, 4 (2000).
297. B. T. Yu, Z. R. Zhang, and R. J. Zeng, *Acta Pharm. Sinica* 35, 705 (2000).
298. H. S. Ch'ng, in "Formulation and Release Studies of 5-Fluorouracil from Chitosan-Nanoparticles," Penang, Malaysia, 1999, Malaysian Society of Pharmacology and Physiology/Singapore University Press, p. S56.
299. K. N. J. Burger, R. W. H. M. Staffhorst, H. C. de Vijlder, M. J. Velinova, P. H. Bomans, P. M. Frederik, and B. de Kruijff, *Nat. Med.* 8, 81 (2002).
300. K. Avgoustakis, A. Beletsi, Z. Panagi, P. Klepetsanis, A. G. Karydas, and D. S. Ithakissios, *J. Control. Release* 79, 123 (2002).
301. M. A. Ecea, F. Gamisans, J. Valero, and M. E. Garcia, *Farmaco* 49, 211 (1994).
302. L. Barraud, P. Merle, E. Soma, L. Lefrancois, S. Guerret, M. Chevallier, C. Dubernet, P. Couvreur, C. Trepo, and L. Vitvitski, *J. Hepatol.* 36, 82 (2002).
303. S. E. Gelperina, A. S. Khalansky, I. N. Skidan, Z. S. Smirnova, A. I. Bobruskin, S. E. Severin, B. Turowski, F. E. Zanella, and J. Kreuter, *Toxicol. Lett.* 126, 131 (2002).
304. W. Ai-dong, C. Jiang-hao, and W. Dao-cheng, *Chinese J. Antibiotics* 26, 464 (2001).
305. S. Mitra, U. Gaur, P. C. Ghosh, and A. N. Maitra, *J. Control. Release* 74, 317 (2001).
306. K. A. Janes, M. P. Fresneau, A. Marazuela, A. Fabra, and M. Alonso, *J. Control. Release* 73, 255 (2001).
307. H. S. Yoo, K. H. Lee, J. E. Oh, and T. G. Park, *J. Control. Release* 68, 419 (2000).
308. S. C. Yang, H. X. Ge, Y. Hu, X. Q. Jiang, and C. Z. Yang, *J. Appl. Polym. Sci.* 78, 517 (2000).
309. A. Fundaro, R. Cavalli, A. Bargoni, D. Vighetto, G. P. Zara, and M. R. Gasco, *Pharmacol. Res.* 42, 337 (2000).
310. H. S. Yoo and T. G. Park, *Polymer Preprints* 41, 992 (2000).
311. F. D. Kolodgie, M. John, C. Khurana, A. Farb, P. S. Wilson, E. Acampado, N. Desai, P. Soon-Shiong, and R. Virmani, *Circulation* 106, 1195 (2002).
312. C. Fonseca, S. Simoes, and R. Gaspar, *J. Control. Release* 83, 273 (2002).
313. D. B. Chen, T. Z. Yang, W. L. Lu, and Q. Zhang, *Acta Pharm. Sinica* 37, 58 (2002).
314. N. K. Ibrahim, N. Desai, S. Legha, P. Soon-Shiong, R. L. Theriault, E. Rivera, B. Esmaeli, S. E. Ring, A. Bedikian, and G. N. Hortobagyi, *Clin. Cancer Res.* 8, 1038 (2002).
315. B. Damascelli, F. Mattavelli, P. Tamplenizza, P. Bidoli, E. Leo, F. Dosio, A. M. Cerrolla, G. Di Tolla, L. F. Frigerio, and F. Garbagnati, *Cancer* 92, 2592 (2001).
316. D. B. Chen, T. Yang, W. L. Lu, and Q. Zhang, *Chem. Pharm. Bull.* 49, 1444 (2001).
317. M. G. Cascone, L. Lazzeri, C. Carmignani, and Z. Zhu, *J. Mater. Sci. Mater. Med.* 13, 523 (2002).
318. M. I. Llovet, M. A. Egea, J. Valero, and M. A. Alsina, *Drug Dev. Ind. Pharm.* 21, 1761 (1995).
319. M. Simeonova and M. Antcheva, *Acta Physiol. Pharmacol. Bulg.* 20, 31 (1994).
320. M. Simeonova, M. Ilarionova, T. Ivanova, and C. Konstantinov, *Acta Physiol. Pharmacol. Bulg.* 17, 43 (1991).
321. A. Lamprecht, Y. Bouligand, and J. P. Benoit, *J. Control. Release* 84, 59 (2002).
322. H. Lboutounne, J. F. Chaulet, C. Ploton, F. Falson, and F. Pirot, *J. Control. Release* 82, 319 (2002).
323. H. Lboutounne, F. Pirot, M. A. Belfihadj, G. Degobert, J. Y. Dusseau, and F. Falson, Antimicrobial activity and percutaneous absorption of chlorhexidine base from poly-epsilon-caprolactone nanocapsules, "Perspectives in Percutaneous penetration," p. 102. STS Publishing, La Grande Motte, France, 2000.
324. M. Sznitowska, M. Gajewska, S. Janicki, A. Radwanska, and G. Lukowski, *Eur. J. Pharm. Biopharm.* 52, 159 (2001).
325. P. Calvo, C. Remuan-Lopez, J. L. Vila-Jato, and M. J. Alonso, *Colloid Polym. Sci.* 275, 46 (1997).
326. R. Cavalli, O. Caputo, M. E. Carlotti, M. Trotta, C. Scarnecchia, and M. R. Gasco, *Int. J. Pharm.* 148, 47 (1997).
327. E. Ugazio, R. Cavalli, and M. R. Gasco, *Int. J. Pharm.* 241, 341 (2002).
328. Q. Zhang, G. Yie, Y. Li, Q. Yang, and T. Nagai, *Int. J. Pharm.* 200, 153 (2000).
329. Q. Zhang, G. Q. Ye, Y. Li, and Q. S. Yang, *Acta Phara. Sinica* 34, 308 (1999).
330. J. Molpeceres, M. Chacon, M. Guzman, L. Berges, and M. del Rosario Aberturas, *Int. J. Pharm.* 187, 101 (1999).
331. P. Calvo, A. Sanchez, J. Martinez, M. I. Lopez, M. Calonge, J. C. Pastor, and M. J. Alonso, *Pharm. Res.* 13, 311 (1996).
332. S. Bonduelle, M. Carrier, C. Pimienta, J. P. Benoit, and V. Lenaerts, *Eur. J. Pharm. Biopharm.* 42, 313 (1996).
333. E. Harris, Z. Ramtoola, and J. G. Kelly, *Pharm. Technol. Conf.* 1, 301 (1995).
334. J. Miones, E. Yebra-Pimentel, O. Conde, and E. Iribarnegaray, *Langmuir* 10, 1888 (1994).
335. S. D. Desai and J. Blanchard, *Drug Delivery* 7, 201 (2000).
336. A. Zimmer and J. Kreuter, in "Ocular Drug Delivery" (R. D. Schoenwald, Ed.), Vol. 16, Number 1, p. 61. Elsevier Science Division, New York, 1995.
337. A. Zimmer, E. Mutschler, G. Lambrecht, and D. Mayer, *Pharm. Res.* 11, 1435 (1994).
338. B. Heurtault, P. Legrand, V. Mosqueira, J. P. Devissaguet, G. Barratt, and C. Bories, *Ann. Trop. Med. Parasitol.* 95, 529 (2001).
339. J. M. Rodrigues, H. Fessi, C. Bories, F. Puisieux, and J. P. Devissaguet, *Int. J. Pharm.* 126, 253 (1995).
340. J. M. Rodrigues, S. L. Croft, H. Fessi, and C. Bories, *Trop. Med. Parasitol.* 45, 223 (1994).



# Phase Mixture Models for Metallic Nanomaterials

Yuri Estrin

*Clausthal University of Technology,  
Clausthal-Zellerfeld, Germany*

Hyoung Seop Kim

*Chungnam National University, Daejeon, Korea*

Mark B. Bush

*The University of Western Australia, Crawley, Australia*

## CONTENTS

1. Introduction
  2. Phase Mixture Model for Plasticity of Nanocrystalline Materials
  3. Phase Mixture Model for Elastic Modulus
  4. Young's Modulus of a Nanocomposite
  5. Conclusions
- Glossary  
References

## 1. INTRODUCTION

The mechanical properties of bulk materials are known to change with grain refinement. Extreme changes are expected when the average grain size is of the order of 100 nm or less. At the time when nanostructured materials (often defined as polycrystals with the average grain size of less than 100 nm) are becoming a major focus of materials research, the attention of researchers is turning more and more to their mechanical performance. Mechanical properties of nanostructured materials were recently reviewed by D. G. Morris [1]. His report provided an analysis of experimental literature and a comprehensive overview of the relevant deformation mechanisms. Still, the mechanical behavior of nanocrystalline materials remains a controversial

issue and the roles of the different deformation mechanisms, such as dislocation glide and grain boundary processes, are not fully understood. Most recent molecular dynamics simulations [2] suggest that mechanical twinning may also play an important part in the plasticity of nanocrystalline materials, thus adding to the complexity of the emerging picture of the operating deformation mechanisms.

Grain boundary sliding is often considered a deformation mechanism in nanostructured materials that permits a high level of strain before failure and may be responsible for superplastic forming (see [1] and references therein). Yamakov et al. [3] observed grain boundary sliding in their molecular dynamic simulations. As this mechanism would require grain boundary diffusion as an accommodation mechanism, it is claimed that grain boundary diffusion and grain boundary sliding “are closely connected and, perhaps, represent one and the same deformation mechanism”—a view the present authors subscribe to.

In this chapter, we give an account of the mechanical properties of ultra-fine grained materials from our current viewpoint. It is based on recent modeling that appears to provide a conclusive description of the phenomenology and mechanisms underlying the mechanical properties of nanostructured materials. Common to the proposed models is the concept of a “phase mixture” in which the grain boundaries are treated as a separate phase. The volume fraction of this “phase” may be quite appreciable in a nanostructured material. The issues covered include strength, ductility, and the elastic properties of single-phase materials as well as the elastic properties of nanocomposites.

Experimental data on the mechanical properties of nanocrystalline metallic materials are appearing in literature at an ever-increasing rate. However, the range of data is still somewhat limited, except in the case of copper, where an extensive experimental database already exists. The various published mechanical properties of nanocrystalline Cu are summarized in Table 1. The table highlights a fundamental difficulty associated with the interpretation of experimental measurements made on nanomaterials. Residual porosity is an omnipresent feature of specimens manufactured using common production techniques. Porosity influences the observed bulk mechanical properties and, in fact, may dominate the behavior. Care must therefore be taken when drawing conclusions based on the bulk behavior. However, as will be seen later, porosity may be included in the phase mixture model to permit the effects of pores to be isolated from the grain size effects.

## 2. PHASE MIXTURE MODEL FOR PLASTICITY OF NANOCRYSTALLINE MATERIALS

It is generally believed that grain refinement leads to enhancement of strength of metallic materials. Indeed, the classical Hall–Petch relation predicts an inverse square root dependence of the yield strength on the average grain size. However, it is clear that there must be a limit to an increase of strength with decreasing grain size. Grain refinement will reduce the characteristic length for vacancy diffusion. Mass transport by diffusion across the grains and along grain boundaries therefore becomes more significant and may eventually prevail over dislocation glide-controlled plastic flow. In addition, the very mechanism of dislocation glide may become inoperative when the grain size drops below a certain critical level, perhaps around 10 nm [4], when dislocation sources in the grain interior or in grain boundaries cannot be activated. The rate of plastic flow will then be controlled by vacancy diffusion through the bulk (the Nabarro–Herring mechanism) or along grain boundaries (the Coble

mechanism). In both cases, the plastic strain rate is proportional to stress and inversely proportional to the average grain size,  $d$ , raised to the power  $n$ , where  $n = 2$  for the Nabarro–Herring mechanism and  $n = 3$  for the Coble mechanism [5]. Hence, for a fixed strain rate, the stress turns out to increase with the average grain size as  $d^2$  or  $d^3$ , respectively. There is evidence in literature [6–7] that a pronounced departure from, or even inversion of the Hall–Petch behavior, is observed for nanostructured materials. Unfortunately, the picture is clouded by the inevitable presence of porosity, as fully dense specimens of very fine-grained materials are difficult to prepare. In such cases, mathematical modelling offers a unique opportunity to provide further insight into the behavior of such materials.

Ductility usually decreases with increase of strength, but expectations have been expressed in literature [8] that for the grain size in the submicrometer range, enhancement of strength without loss, or even with an increase, of ductility can be achieved. Such expectations were raised [9], particularly with regard to materials that have undergone severe plastic deformation, for example, by equal-channel angular pressing.

The challenge in modelling the effects of ultra-fine grained structures is not only to capture the relevant physical phenomena, including dislocation glide and diffusion mechanisms, but also to correctly represent their relative contributions to the mechanical behavior of the material. In modelling the behavior of actual test specimens, porosity or other embedded flaws may represent an important component of the model.

A constitutive model has been proposed that provides an adequate description of the grain size dependence of strain hardening in a broad range of grain sizes, down to the nanometer scale [10–12]. A distinctive feature of the model is that grain boundaries are treated as a distinct separate phase [4, 13], which is assumed to deform by a diffusion mechanism [12]. The grain interiors are considered to represent another phase. This phase is assumed to deform by a combination of two mechanisms: dislocation glide and diffusion transport. A transition between the regimes where the different mechanisms prevail can therefore be incorporated.

**Table 1.** The mechanical properties of nanocrystalline copper.

Property	(Grain size, property value, density)	Ref.
Young's modulus E	(10 nm, 108 GPa, 97.6%), (16 nm, 113 GPa, 98.6%), (22 nm, 116 GPa, 98.9%), (100 $\mu$ m, 131 GPa, 100%)	[21]
Ultimate tensile strength	(16 nm, 340 MPa, 98.6%), (26 nm, 425 MPa, 99%), (49 nm, 460 MPa, 99.1%), (110 nm, 415 MPa, 99.4%), (22 nm, 480 MPa, 98.8%), (20 $\mu$ m, 290 MPa, 100%)	[21]
Tensile elongation	(16 nm, 2.4%, 98.6%), (26 nm, 1.8%, 99%), (49 nm, 1.6%, 99.1%), (110 nm, >8%, 99.4%), (22 nm, 1.6%, 98.8%), (20 $\mu$ m, >8%, 100%)	[21]
	(15 nm, 1.52%), (20 nm, 0.79%), (25 nm, 6.3%), (50 nm, 2.2%), (61 nm, 2.2%)	[26]
	(209 nm, 10%), (206 nm, 17%)	[28]
	(29 nm, 0%), (32 nm, 2%), (31 nm, 7%), (41 nm, 5%), (58 nm, 5%), (175 nm, 5%)	[27]
	(26 nm, 0.7%), (39 nm, 0.3%), (49 nm, 1.2%), (110 nm, 10%), (20000 nm, 15%)	[18]
	(210 nm, 5%)	[29]
Micro-hardness	(34 nm, 797 MPa), (26 nm, 802 MPa), (25 nm, 779 MPa), (24 nm, 767 MPa), (22 nm, 752 MPa), (22 nm, 773 MPa), (18 nm, 696 MPa), (18 nm, 748 MPa), (18 nm, 769 MPa), (19 nm, 801 MPa), (21 nm, 822 MPa), (21 nm, 884 MPa), (18 nm, 889 MPa), (16 nm, 877 MPa), (16 nm, 854 MPa), (16 nm, 810 MPa), (16 nm, 812 MPa), (12 nm, 849 MPa), (11 nm, 773 MPa), (10 nm, 793 MPa), (10 nm, 828 MPa), (7 nm, 806 MPa)	[21]
	(7.8 nm, 144 MPa), (8.4 nm, 173 MPa), (14 nm, 207 MPa), (15 nm, 223 MPa)	[51]

Combined with a rule of mixtures, the constitutive equations for the mechanisms considered provide a simple description of the deformation behavior [10–12]. This model is illustrated by application to ultra-fine grained Cu—the material for which a most extensive experimental database is available.

The grain boundary phase is considered to deform by a vacancy diffusion mechanism [12]. The corresponding plastic strain rate is given by

$$\dot{\epsilon}_{GB} = A \frac{\Omega \sigma_{GB}}{kT} \frac{D_{GB}}{d^2} \quad (1)$$

Here  $\sigma_{GB}$  is the stress acting in the grain boundary (GB) phase,  $\Omega$  the atomic volume,  $T$  the absolute temperature,  $k$  the Boltzmann constant,  $D_{GB}$  the self-diffusion coefficient for grain boundary diffusion, and  $A$  is a numerical constant. This formula represents an interesting “hybrid” of the Nabarro–Herring and the Coble equations in that the grain size dependence is that of Nabarro–Herring, while the (grain boundary) diffusivity is that of the Coble mechanism. A similar relation was recently obtained through molecular dynamics simulations [3].

Plastic flow of the crystalline grain interiors is considered to be carried by two mechanisms that operate in parallel: the dislocation glide mechanism (contributing the plastic strain rate  $\dot{\epsilon}_{disl}$ ) and the diffusion-controlled mechanism. In principle, both bulk and grain boundary diffusion need to be considered. However, for most cases of interest in connection with ultra-fine grained materials, the bulk diffusion contribution can be neglected [10]. Accordingly, the plastic strain rate for the grain interior (GI) phase can be written as

$$\dot{\epsilon}_{GI} = \dot{\epsilon}_{disl}(\sigma_{GI}) + \dot{\epsilon}_{Coble} \quad (2)$$

where

$$\dot{\epsilon}_{Coble} = 14\pi \frac{\Omega \sigma_{GI}}{kT} \cdot \frac{w}{d} \cdot \frac{D_{GB}}{d^2} \quad (3)$$

Here  $\sigma_{GI}$  is the stress acting in the grain interior and  $w$  is the grain boundary width. We note that the latter contribution to the strain rate is similar to the expression for the plastic strain rate of the grain boundary phase, Eq. (1)—apart from the exponent in the grain size dependence.

The dislocation glide contribution to the plastic strain rate of the grain interior phase is described in terms of a model [14] based on the dislocation density evolution. The total dislocation density is considered to be an internal variable. The evolution of dislocation density is affected by the grain size through its influence on the dislocation mean free path. The relation between the plastic strain rate  $\dot{\epsilon}_{disl}$  and stress is given by

$$\dot{\epsilon}_{disl} = \dot{\epsilon}_o \left( \frac{\sigma_{GI}}{\sigma_o} \right)^{m_i} Z^{-m_i/2} \Theta(d - d_c) \quad (4)$$

where  $Z$  denotes the dislocation density normalized with respect to its initial value, and the parameters  $\dot{\epsilon}_o$ ,  $\sigma_o$ , and  $m_i$  can be considered constant for a given temperature. The values of these parameters for Cu are known [15]. The Heviside step-function  $\Theta(d - d_c)$  expresses the fact that for  $d$  below some critical value,  $d_c$ , the dislocation mechanism becomes

inoperative and its contribution to plastic strain rate,  $\dot{\epsilon}_{disl}$ , drops to zero. Following Wang et al. [4], the value of  $d_c$  for Cu was taken to be 8 nm.

The evolution equation for the dislocation density is

$$\frac{dZ}{dt} = \dot{\epsilon}_{disl} \left[ C + C_1 \sqrt{Z} - C_2 \left( \frac{\dot{\epsilon}_{disl}}{\dot{\epsilon}_o} \right)^{-1/n} Z \right] \quad (5)$$

Here  $t$  denotes the time,  $C$ ,  $C_1$ ,  $C_2$ , and  $\dot{\epsilon}_o$  are constants, while  $n$  is constant if the temperature is fixed. Grain size effects, which are of main concern here, enter through the term  $C$ , which is inversely proportional to  $d$  [14].

It is further assumed that the strain in both phases is the same (and equal to the macroscopic strain). Henceforth, the subscripts “GI” and “GB” in the respective strain rates will be dropped. The stress is determined using a rule of mixtures,

$$\sigma = f\sigma_{GB} + (1 - f)\sigma_{GI} \quad (6)$$

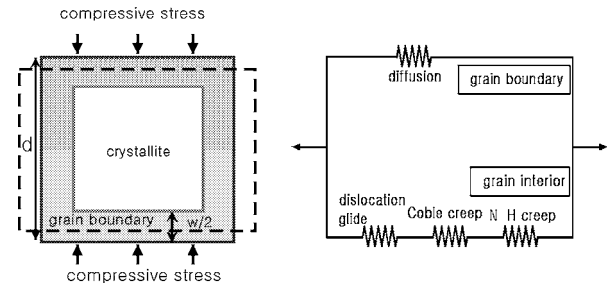
where  $f$  is the volume fraction of the grain boundary phase given by

$$1 - f = \left( 1 - \frac{w}{d} \right)^3 \quad (7)$$

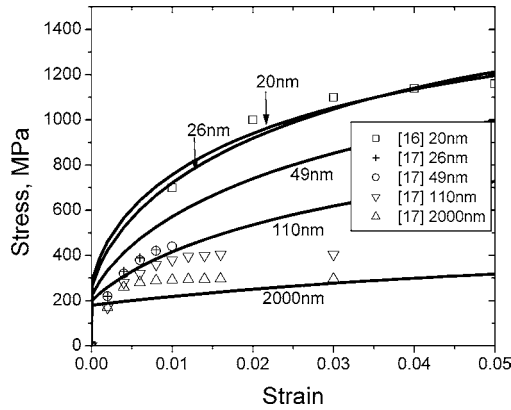
Equation (7) reflects the assumption of cube-shaped grains. A schematic illustrating the phase mixture model is shown in Figure 1.

The set of Eqs. (1–7) furnish a full constitutive description for a “single-phase” material, which, in fact, is treated at the microscopic level as consisting of two subphases. It has been applied to the case of Cu [10–12] for which the parameters pertaining to the dislocation mechanism and the grain boundary diffusion mechanism are known from previous work [5, 15–16]. As an example, the stress versus strain curves for tensile deformation with constant strain rate are presented in Figure 2. The curves show a good agreement with reported experimental data [17–18].

The dependence of the offset yield stress,  $\sigma_{0.2}$ , on the calculated grain size using this model is plotted in the “Hall–Petch” diagram of Figure 3. It is seen that a Hall–Petch-like behavior in the range of large grain sizes breaks down for  $d$  below about 50 nm, and an “inverse” Hall–Petch behavior



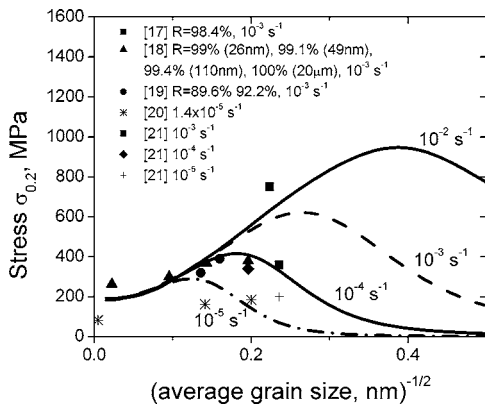
**Figure 1.** Schematic of two-phase model of grain deformation. The contribution of the Nabarro–Herring (N–H) creep mechanism in the grain interior becomes insignificant for very small grain size,  $d$ . Reprinted with permission from [10], H. S. Kim et al., *Acta Mater.* 48, 493 (2000). © 2000, Elsevier Science.



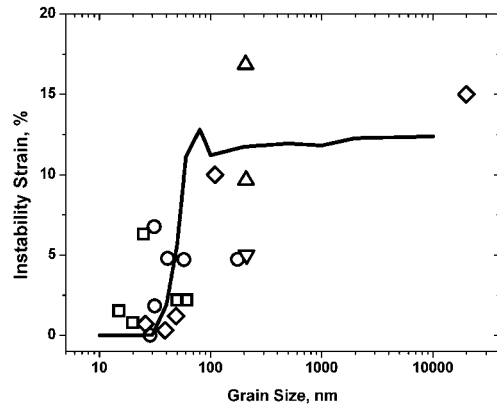
**Figure 2.** Calculated and experimental stress-strain curves for Cu at the strain rate of  $10^{-3} \text{ s}^{-1}$ . The solid lines are the model predictions, while the symbols refer to experimental data [17–18]. Reprinted with permission from [10], H. S. Kim et al., *Acta Mater.* 48, 493 (2000). © 2000, Elsevier Science.

is predicted for small values of  $d$  and  $\dot{\epsilon}$ . The numerical correspondence between the calculated curves and the experimental results is rather poor, but the main trends predicted seem to be confirmed by experiments. It should be noted, however, that the experimental data were obtained for specimens manufactured by different methods [17–21], but in all cases, residual porosity and other imperfections may be responsible for the over-prediction of strength by the model considered.

The model can also be used to study the grain size dependence of the tensile ductility. Koch and Malow [22], in their compilation of ductility data, demonstrated that ultra-fine grained single-phase materials exhibit little room-temperature ductility in tension. For elemental metals that are ductile when coarse grained, the data show a clear trend for decreasing tensile ductility with decreasing grain size (Fig. 4). A similar behavior was recently observed in Al alloys [23]. The effect of grain size on ductility was



**Figure 3.** Average grain size dependence of  $\sigma_{0.2}$  for fine grain Cu at strain rates of  $10^{-2}$ ,  $10^{-3}$ ,  $10^{-4}$ , and  $10^{-5} \text{ s}^{-1}$  calculated using the phase mixture model with a log-normal distribution of the grain volume. Also shown are the experimental data points (see Fig. 2). Reprinted with permission from [12], H. S. Kim et al., *Mater. Sci. Eng.* 316A, 195 (2001). © 2001, Elsevier Science.



**Figure 4.** Strain to necking (calculated) and experimental tensile room temperature ductility as a function of the average grain size  $d$ . Symbols:  $\square$  Ref. [26],  $\circ$  Ref. [27],  $\triangle$  Ref. [28],  $\nabla$  Ref. [18],  $\diamond$  Ref. [29]. Reprinted with permission from [24], H. S. Kim and Y. Estrin, *Appl. Phys. Lett.* 79, 4115 (2001). © 2001, American Institute of Physics.

considered [24] using Hart’s condition for the onset of necking [25]:

$$\theta \leq \sigma(1 - 1/m) \tag{8}$$

Here the strain hardening coefficient and the effective strain rate sensitivity parameter are defined as  $\theta = (\partial\sigma/\partial\epsilon)_\epsilon$  and  $1/m = (\partial \log \sigma / \partial \log \dot{\epsilon})_\epsilon$ , respectively. It can easily be seen from this criterion that for extremely fine-grained materials, when plasticity is carried chiefly by the diffusion mechanisms and  $m$  tends to unity, tensile deformation will always be stable, strain-to-necking tending to infinity, as long as strain hardening is nonzero. That is to say, the material will never fail by necking, its ductility being limited by other failure mechanisms. In a real case, however, even for a very small grain size, the fulfillment of the necking condition, indicated by the equality in Eq. (8), will depend on the interplay of  $m$ ,  $\sigma$ , and  $\theta$ . For  $d$  in the range, where diffusion mechanisms of plasticity prevail over the dislocation glide mechanism,  $1/m$  tends to unity and the strain-hardening coefficient tends to zero. Indeed, diffusion-controlled mechanisms do not exhibit any strain hardening. It is apparent that the loss of strain hardening as grain size is decreased cannot be compensated for by the stabilizing effect of the growing strain rate sensitivity, as it is not close enough to unity to outstrip the destabilizing effect.

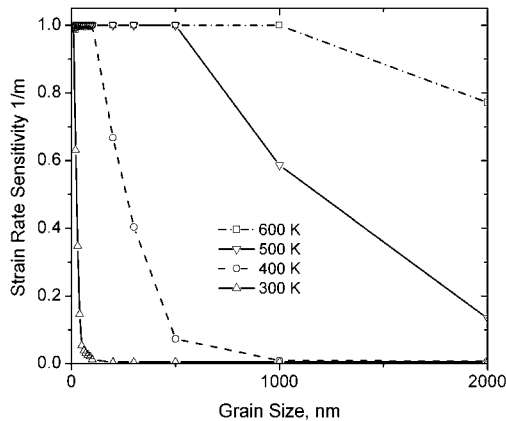
Numerical simulations of a strain rate jump test can be used to determine the dependence of the instantaneous strain rate sensitivity  $1/m$  on the grain size. These numerical experiments show that the strain dependence of the rate sensitivity parameter  $1/m$  is fairly weak. Substituting the values of  $\sigma$ ,  $\theta$ , and  $1/m$  (calculated for strain of 0.2%) into Hart’s condition, the grain size dependence of strain-to-necking was determined. This dependence is shown as a solid line in Figure 4.

The results presented in Figure 4 demonstrate that the experimentally observed reduction of tensile room temperature ductility with grain refinement is in close quantitative agreement with the model. The loss of ductility with grain refinement found for room temperature deformation of copper does not necessarily represent a generic trend with all

materials at all temperatures. In fact, a simple linear stability analysis shows that the characteristic strain required for an incipient neck to grow to a sizable defect,  $\varepsilon_{growth}$ , is of the order of  $(1 - \theta/\sigma) \cdot 1/m$ . That is, it scales with  $1/m$ . As seen in Figure 5, which shows the grain size and temperature dependence of  $1/m$  for small grain sizes (below 50 nm, for instance),  $\varepsilon_{growth}$  increases with temperature quite significantly and rapidly becomes more important than the strain to the onset of necking. In other words, a tensile specimen can sustain a significant strain as the pace of neck development is slow. The effect becomes more pronounced with decrease of the grain size. It can be stated that while nanostructured materials do not possess good room temperature ductility, their ductility at elevated temperatures is much better than for their coarse-grained counterparts. Thus, a common expectation that the temperature and strain rate range for superplastic forming may be moved to lower temperatures and higher strain rates by grain refinement down to the submicrometer range is qualitatively supported by these calculations.

### 3. PHASE MIXTURE MODEL FOR ELASTIC MODULUS

There are some conflicting results in the literature regarding the variation of elastic modulus  $E$  with grain size in nanostructured materials [20–21, 30–34]. Most of the experimental results indicate a reduction in  $E$  when the grain size is reduced to nanoscale [20–21, 30–31], although some reports suggest there is only little, if any, grain size effect [32–34]. Many authors [20–21, 31–32, 35] attribute the decrement of  $E$  to porosity and assume the intrinsic elastic modulus of the material itself is independent of the grain size. For example, Sanders et al. [21] relate the decrement of  $E$  for nanocrystalline Cu to the degree of porosity by analogy with the porosity dependence of  $E$  for coarse-grained Cu. By contrast, several investigators [30, 36] assumed an intrinsic grain size dependence of  $E$ . Weller et al. [30] attributed a reduction in the shear modulus  $G$  for nanocrystalline Pd to increased atomic interaction distance in the interface region. Similarly, Chen [36] explained a reduction



**Figure 5.** Grain size and temperature dependence of  $1/m$ . Reprinted with permission from [24], H. S. Kim and Y. Estrin, *Appl. Phys. Lett.* 79, 4115 (2001). © 2001, American Institute of Physics.

in  $E$  for nanocrystalline Fe in terms of increased spacing between atoms in the grain boundary. Since the elastic modulus is a measure of the bonding between atoms, an overall decrease in  $E$  is expected in nanostructured materials as a result of the increased volume fraction of the less stiff grain boundary phase. Porosity can be taken into account by including pores as a *third phase* with bulk modulus  $K$  and shear modulus  $G$  set to zero. The phase mixture model is combined with Budiansky's self-consistent method [37] for a random mixture of isotropic constituents. Since the bulk modulus and shear modulus of the pore are both zero, the bulk modulus  $K$  and the shear modulus  $G$  of the composite are related, in Budiansky's self-consistent approach, to the moduli  $K_i$  and  $G_i$  of the  $i$ th constituents by the following equations:

$$\frac{f_{GI}}{1 - a + a \frac{K_{GI}}{K}} + \frac{f_{GB}}{1 - a + a \frac{K_{GB}}{K}} + \frac{f_{PORE}}{1 - a} = 1 \quad (9)$$

and

$$\frac{f_{GI}}{1 - b + b \frac{G_{GI}}{G}} + \frac{f_{GB}}{1 - b + b \frac{G_{GB}}{G}} + \frac{f_{PORE}}{1 - b} = 1 \quad (10)$$

where

$$a = \frac{1}{3} \left( \frac{1 + \nu}{1 - \nu} \right) \quad (11)$$

$$b = \frac{2}{15} \left( \frac{4 - 5\nu}{1 - \nu} \right) \quad (12)$$

and  $\nu$ , Poisson's ratio of the phase mixture, is, in turn, given by

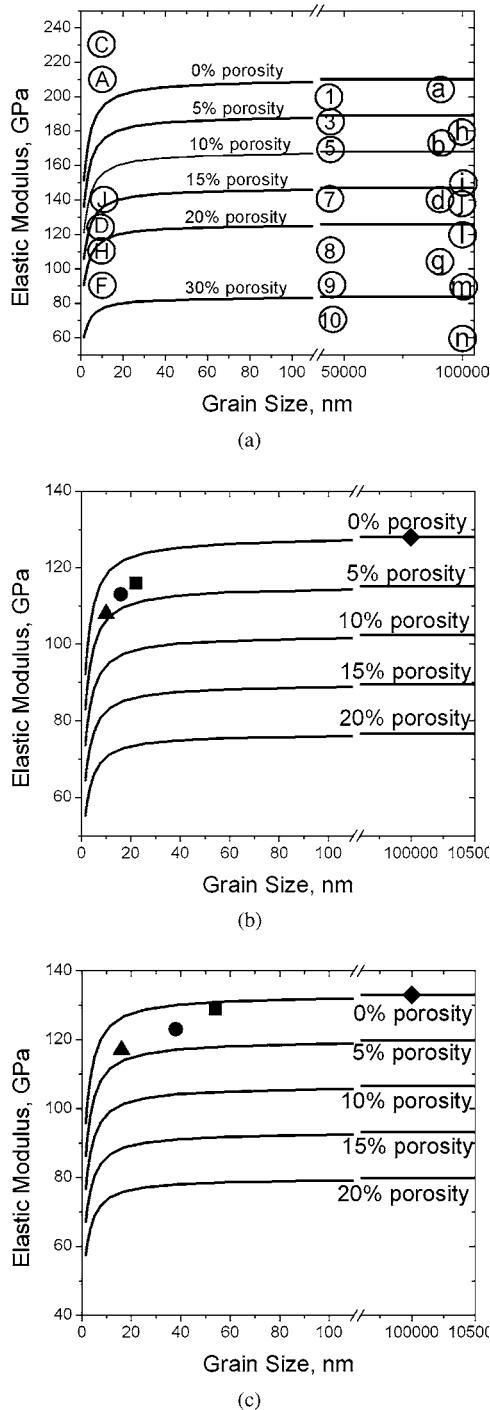
$$\nu = \frac{3K - 2G}{6K + 2G} \quad (13)$$

Here, the pore volume fraction,  $f_{PORE}$ , was introduced, in addition to the volume fractions of the GIs and the GBs. In this formulation, the volume fractions of the grain boundaries proper, the triple lines, and the quaternary nodes were lumped together in the quantity  $f_{GB}$ . An alternative approach was adopted in [38], where these regions were treated separately. The Newton–Raphson method was used to obtain the solution of the set of coupled Eqs. (9–13). The model was applied to three metallic systems (Cu, Fe, and Pd), as data for these materials in the nanocrystalline range are available in literature.

The local elastic constants for the grain boundary region were calculated by atomistic simulation to be around 70% of the values for the crystalline phase [39]. Thus, the elastic modulus of the grain boundary was taken to be 70% of that for the corresponding coarse-grained polycrystal.

Figure 6 shows the calculated elastic modulus as a function of grain size for Fe, Pd, and Cu for various levels of porosity [21, 31]. It can be seen that the elastic modulus decreases very slowly with decreasing grain size as long as  $d$  remains in the range of relatively coarse grain size ( $>20$  nm), but this decrease becomes very rapid when the grain size is below about 20 nm. It was also found that for a given level of porosity, the shape of the  $E$  versus  $d$  curve follows the grain size dependence of the volume fraction of the crystallite phase  $f_{CR}$ . The effect of porosity is clearly much





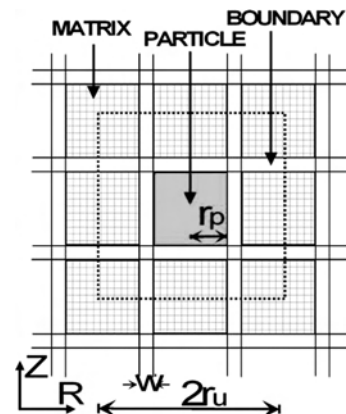
**Figure 6.** Effect of grain size and porosity on the elastic modulus  $E$  for Fe, Cu, and Pd. (a) Fe, data points from [31], experimental porosity level (%): (1) = 5.5, (3) = 10, (5) = 12.5, (7) = 18.5, (8) = 24, (9) = 28, (10) = 35.5, (a) = 4, (b) = 10, (d) = 18, (g) = 25, (h) = 5, (i) = 10, (j) = 11.5, (l) = 15, (m) = 20, (n) = 25, (A) = 0, (C) = 6, (D) = 19, (F) = 22, (H) = 25, (J) = 30; (b) Cu, data points from [21], experimental porosity level (%):  $\blacklozenge$  = 0,  $\blacksquare$  = 1.1,  $\bullet$  = 1.4,  $\blacktriangle$  = 2.4; (c) Pd, data points from [21], experimental porosity level (%):  $\blacklozenge$  = 0,  $\blacksquare$  = 1.5,  $\bullet$  = 2.1,  $\blacktriangle$  = 4.9. Reprinted with permission from [38], H. S. Kim and M. B. Bush, *Nanostructured Mater.* 11, 361 (1999). © 1999, Elsevier Science.

more significant than that of the grain size. Since nanostructured materials usually contain some porosity (whose level depends on the processing route and conditions), the effect of the grain size on the elastic modulus will, in many cases, be insignificant. The calculated values of  $E$  for the Cu and Pd specimens correlate reasonably well with the experimental data. In the case of Fe, the theoretical results show a good agreement with experimental data, both for relatively coarse grained ( $d = 100$  nm, 90 nm, and 44 nm) and ultra-fine-grained ( $d = 4 \sim 20$  nm) material.

#### 4. YOUNG'S MODULUS OF A NANOCOMPOSITE

Using the same concept of a phase mixture, Young's modulus of a nanocomposite—a particle reinforced metal matrix composite with an ultra-fine grain size—can be evaluated [40]. The composite is now treated as a mixture of a metallic matrix phase, a reinforcing ceramic particle phase, and a boundary phase. Porosity—an inevitable companion of nanostructured materials—can be treated as a separate phase, but it can also be considered to reside in the boundary phase [40]. Indeed, residual pores are usually found at the interfaces between reinforcement particles and the matrix, as well as at the boundaries between matrix grains themselves. For example, Kizuka et al. [41] reported the evidence of voids residing on grain boundaries rather than in the grain interiors: an observation valid for many compacted MMCs.

Figure 7 shows a schematic representation of the phase mixture model identifying a unit cell [40]. The material is considered to be constructed by a periodic reproduction of this unit cell in three dimensions. The unit cell consists of a reinforcing particle and the matrix material separated from each other by the boundary phase. It should be noted that the matrix is not considered to be a contiguous phase, but is rather taken to consist of compacted matrix material "particulate." The model has been applied to a composite containing ceramic inclusions with an average diameter of 200 nm, a grain size of 247 to 126 nm, and an interparticle spacing of 330 to 137 nm [40].



**Figure 7.** Phase mixture model for a particle reinforced composite with ultra-fine microstructure. Reprinted with permission from [11], H. S. Kim et al., *Mater. Sci. Eng.* 276A, 175 (2000). © 2000, Elsevier Science.

The model of Figure 7 has the provision for distinguishing between the properties of the boundaries between matrix particles and matrix/inclusion interfaces; however, the same properties were assumed for both kinds of interface. A cylindrical geometry was assumed for the ceramic particles. The overall effective relative density,  $R_{eff}$ , of the composite can be represented in terms of the volume  $V$  and density  $\rho$  of each phase as [11]:

$$R_{eff} = \frac{V_p \rho_p + V_m \rho_m + V_b \rho_b}{V_p \rho_p + V_m \rho_m + V_b \rho_m} \quad (14)$$

Here the subscripts  $m$ ,  $p$ , and  $b$  refer, respectively, to the matrix, particles, and boundaries. From Eq. (14), the density of the boundary phase  $\rho_b$  can be obtained when the volume and density of the other two phases and the overall density are known.

The unit cell dimensions used in the calculations are based on experimental data [42]. Three kinds of ball-milled, compacted, and sintered composites with reinforcement volume fractions of 0, 10, 20, and 30% (referred to as C-00, C-10, C-20, and C-30) were prepared. A fully dense bulk Al material (referred to as “Al standard”) was used as a reference material. The details (volume fraction, hardness, grain size, and density) of these materials are summarized in Table 2. Although these materials are not fine scaled enough to be referred to as genuinely nanocrystalline, the general trends observed can be translated to nanocomposites. The particle radius was taken to be 100 nm. The unit cell size (radius) was considered to be 247 nm, 215 nm, 171 nm, and 149 nm, which corresponds to the particle volume fraction of 0, 10, 20, and 30%, respectively.

The notion of a “generalized” boundary phase in the current model includes various imperfections, such as voids and cracks in the interface region. Hence, its properties need not be identical with those of the grain boundary proper. The effective width of the grain boundary was selected by taking into account the following considerations [16]. Using Auger electron spectroscopy of the surface products on atomized stainless steel powder particles, as well as on the particle boundaries that existed prior to compaction [43], the average oxide thickness was estimated to be 6 nm. This is much larger than a typical grain boundary thickness in elemental

metals usually taken to be of the order of 1 nm. The inhomogeneous surface region, as indicated by the variations of the chemical composition, reached an even larger depth of up to 10 nm. This value may be taken as representative of the effective boundary thickness scale for the case considered. Fortunately, the sensitivity of the mechanical properties of interest here to the boundary thickness is fairly weak: both the magnitude of the strength and the effective Young’s modulus of the composite vary with the boundary width only slightly, the general trends remaining unchanged. The calculations that follow were done for a constant thickness of the boundary phase (assumed to be amorphous and porous) set at 1, 6, and 10 nm.

The dependence of mechanical properties on porosity can be represented by various empirical equations [44]. Spriggs’ empirical relation [45] for Young’s modulus,  $E$ , was adopted for the grain boundary phase where porosity was assumed to be concentrated [40]:

$$E_{GB} = E_0 e^{-s(1-R)} \quad (15)$$

Here,  $E_0$  is zero-porosity Young’s modulus of the grain boundary material,  $R$  is the relative density (the ratio of the actual and the theoretical density), and  $s$  is a material constant that was found to range between 3 and 4.5 [45]. Young’s modulus and Poisson’s ratio of the particle material ( $\text{Al}_2\text{O}_3$ , in the particular case of an Al- $\text{Al}_2\text{O}_3$  composite considered) were taken to be 380 GPa and 0.22 [42], respectively. Fracture of particles and debonding between a particle and the matrix were not included.

The modulus of elasticity of the grain boundary phase in the absence of porosity cannot be calculated from the available experimental data. The boundary phase was considered to be amorphous in character. Indeed, glass-like behavior in nanocrystalline alloys has been reported in the literature [46]. This provides certain albeit indirect support for the above assumption. It is generally accepted that the modulus of elasticity of an amorphous material  $E_{am}$  amounts to 60~75% of that of the corresponding equilibrium crystalline alloy [47]. This value is further reduced by the effect of porosity, in accordance with Eq. (15). Thus, the modulus of elasticity of the Al matrix, the  $\text{Al}_2\text{O}_3$  reinforcement, and the boundary phase used in the calculations were 70, 380, and 47.3 GPa, respectively.

The classical models of Voigt and Reuss determine, respectively, the upper and the lower bounds of Young’s modulus of the composite in the form

$$\begin{aligned} E_{upper} &= \sum f_i E_i, \\ E_{lower} &= (\sum f_i / E_i)^{-1} \end{aligned} \quad (16)$$

where  $f_i$  and  $E_i$  are the volume fraction and Young’s modulus of the component  $i$ . In a nontextured polycrystalline material, the effective modulus often lies between these two bounds, as determined by Hashin and Shtrikman [48]. Results very similar to those by Hashin and Shtrikman may be obtained by making use of Hill’s approach [49], in which an effective Young’s modulus is determined simply as the average of the upper and the lower bounds:

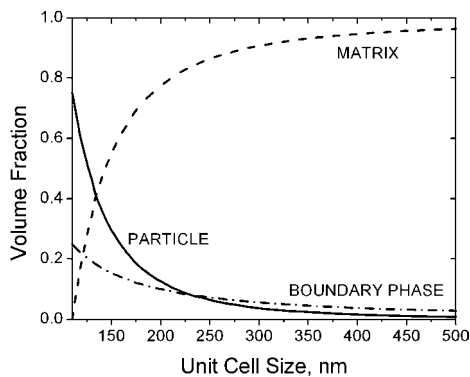
$$E_{eff} = (E_{upper} + E_{lower})/2 \quad (17)$$

**Table 2.** Microstructure and measured properties of the composite materials investigated.

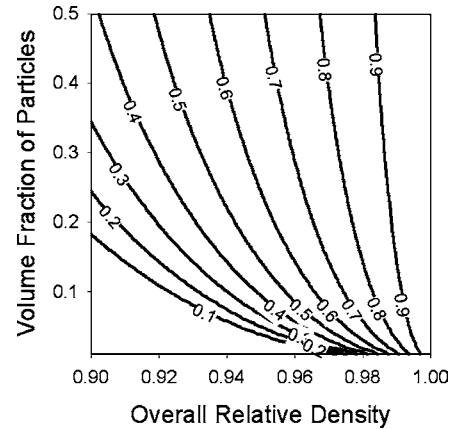
	Al Standard	C-00	C-10	C-20	C-30
Volume fraction of reinforcement, %	0	0	10	20	30
Volume fraction of boundary phase, %	0	6	9	13	15
Matrix grain size (diameter), nm	—	247	218	162	126
Unit cell size (radius), nm	—	247	215	171	149
Overall relative density, %	100	95.8	92.4	95.2	96.9
Local relative density of boundary phase, % as obtained using Eq. (2)	100	29.4	11.1	58.4	77.1

The volume fractions of the reinforcing particle, matrix, and boundary phases as a function of the unit cell size are shown in Figure 8 for the boundary width of 10 nm and the particle radius of 100 nm. As the radius of the unit cell  $r_u$  increases, the volume fraction of the matrix increases as well, while those of the particles and the boundary decrease. The trends seen in Figure 8 are consistent with the results presented in Table 2. It should also be noted that as the volume fraction of reinforcing particles increases, the grain size of the matrix decreases, and the volume fraction of the boundary phase increases.

While the density of the grain boundary phase taken in isolation is hardly accessible to experimental determination, it can be deduced from the overall density of the composite and the volume fraction of reinforcement particles. Figure 9 represents the contour plot for the relative density of the boundary phase as a function of the volume fraction of the particles and the relative density. As the overall relative density increases at a constant volume fraction of reinforcement particles, the local relative density of the boundary phase increases as well. When the volume fraction of the reinforcement particles is low, the relative density of the boundary phase is also low for a constant overall relative density. It should be noted that the effect of the overall relative density on the relative density of the boundary phase is much more significant than the effect of the volume fraction of the reinforcement particles. That is, the relative density of the boundary phase is inversely proportional to its volume fraction, since the volume occupied by pores, given by the product of the local porosity and the boundary volume, is constant. As shown in Table 2, the overall densities of the C-00, C-10, C-20, and C-30 specimens are 95.8, 92.4, 95.2, and 96.9% and the local relative densities in the boundary phase are 29.4, 11.1, 58.4, and 77.1%, respectively. The substantial variation in the derived density of the boundary phase may come as a surprise. However, it must be remembered that the model assumes that all the porosity resides in the grain boundary phase and the relative density of the grain interior is 100%. When the volume fraction of the grain boundary phase is small (For instance, <10%), the resulting calculation of relative density of the grain boundary will be very sensitive to the level of porosity. It follows



**Figure 8.** Volume fractions of the constituent phases of the composite. Reprinted with permission from [11], H. S. Kim et al., *Mater. Sci. Eng.* 276A, 175 (2000). © 2000, Elsevier Science.



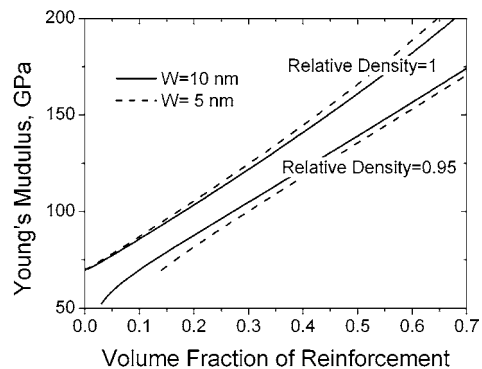
**Figure 9.** Contours of relative density of the boundary phase on a particle volume fraction versus overall relative density map. Reprinted with permission from [40], H. S. Kim et al., *Z. Metallkd.* 90, 863 (1999). © 1999, Carl Hanser Verlag.

that this calculation will also be very sensitive to the accuracy with which measurements of overall relative density are made, and caution must therefore be exercised in interpreting the results.

The effect of the volume fraction of the reinforcing particles is therefore not limited to a hardening role due to the particles themselves, but it also has an influence through the change in the volume fraction and the local density of the boundary phase. Small variations in the global density can be a result of large variations in the local density, such as in the grain boundaries.

In order to assess the relative importance of the overall relative density, the volume fraction of the reinforcement particles and the width of the boundary phase, we can view the overall (effective) Young's modulus  $E_{eff}$  in Figure 10. The calculation is based on Hill's rule of mixtures, Eq. (17).

In all cases, the effective elastic modulus increases with the volume fraction of the reinforcement particles. When

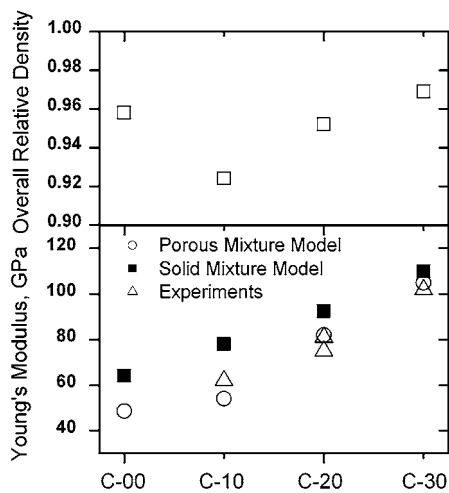


**Figure 10.** Effective Young's modulus of the composite consisting of three phases (reinforcement, matrix, and boundary) as a function of volume fraction of the reinforcement particles calculated using Hill's modification to the rule of mixtures (Eq. (5)). The cases when the width of the boundary phase is 5 and 10 nm, and the overall relative density is 1 and 0.95 are compared. Reprinted with permission from [40], H. S. Kim et al., *Z. Metallkd.* 90, 863 (1999). © 1999, Carl Hanser Verlag.

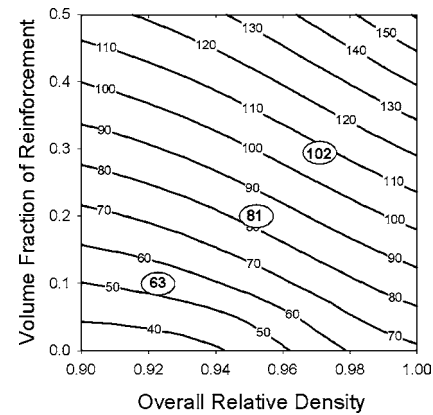
the specimen has no porosity, the material with less boundary phase ( $w = 5$  nm) shows a higher overall Young's modulus than the material with more boundary phase, thereby reflecting the lower modulus exhibited by the boundary phase. However, in the presence of porosity, a composite with a fixed overall density will possess a higher elastic modulus, if it has a larger volume fraction of boundary material. Indeed, for a fixed overall density  $R$ , the local density within the boundary phase increases with its volume fraction.

Figure 11 shows the calculated and experimental values of Young's modulus of the Al-Al<sub>2</sub>O<sub>3</sub> composites as well as the measured overall relative density. The agreement between experimental data and the results obtained using the rule of mixtures is satisfactory. As can be seen in the figure, the experimental data are better represented by the calculations that include local porosity than by the calculations for a material with zero porosity. The relatively large difference between the calculated results for a porous and a nonporous material for the C-10 specimen can be attributed to the relatively high level of porosity in the test samples.

The relation between the volume fraction of particles, the overall relative density, and the effective Young's modulus of the composite is shown in Figure 12. As expected for a fixed overall relative density, the effective Young's modulus increases nearly linearly with the volume fraction of reinforcement particles. Its dependence on the overall relative density  $R_{eff}$  for a fixed volume fraction of particles is much stronger: it follows an exponential law. The circled numbers represent the experimental values of Young's modulus. The calculated and experimental data are in good agreement. The diagrams in Figure 12 provide a useful tool for predicting the value of Young's modulus as a function of the volume fraction of reinforcement particles and the relative density that can be controlled by the degree of compaction.



**Figure 11.** The overall density and elastic modulus of the nanocomposites. The open circles correspond to the model predictions, while the triangles represent the experimental data. Filled squares correspond to calculations for a porosity free composite. Reprinted with permission from [40], H. S. Kim et al., *Z. Metallkd.* 90, 863 (1999). © 1999, Carl Hanser Verlag.



**Figure 12.** Contours of the effective Young's modulus as a function of the overall relative density and volume fraction of reinforcement. The values of the effective Young's modulus (in GPa) are shown on the respective contours. Reprinted with permission from [40], H. S. Kim et al., *Z. Metallkd.* 90, 863 (1999). © 1999, Carl Hanser Verlag.

## 5. CONCLUSIONS

In this overview, it was demonstrated that the phase mixture modelling concept, based on the notion that the grain boundaries can be treated as a separate phase, is very productive in accounting for mechanical behavior of nanostructured materials. Various aspects of this behavior, particularly plastic and elastic properties, were considered using different variants of the phase mixture modelling. Such salient features of plastic behavior as the breakdown of the Hall-Petch behavior and a drop in room temperature ductility of single-phase nanostructured metals with decreasing grain size were recovered adequately. Similarly successful is the description of the grain size dependence of the elastic modulus. The approach taken was also shown to be suitable for dealing with the elastic properties of ultra-fine grained metal-matrix composites. Plasticity of such materials (not considered here) can also be successfully modelled using similar approaches [10]. To summarize, mechanical properties of nanostructured single-phase and composite materials can be rationalized from a unifying viewpoint based on the phase mixture approach. A critical proof of the models presented will come from experiments done on porosity-free nanocrystalline materials on one side and molecular dynamic simulations [2, 3, 50] on the other. The latter are needed for checking the assumptions made in the above models regarding the role of grain boundaries as impenetrable obstacles to dislocations and their elastic and plastic properties.

## GLOSSARY

**Coble mechanism** A mechanism of plastic flow in a polycrystalline material controlled by matter transfer along grain boundaries.

**Constitutive model** A set of equations establishing relations between macroscopic mechanical quantities and describing the mechanical behavior of a material, usually in terms of the evolution of internal variables.

**Dislocation glide** A mechanism of plastic deformation of crystalline materials controlled by the movement of dislocations on crystallographic slip systems.

**Hall-Petch relation** An inverse square root dependence of strength or hardness of a polycrystalline material on the average grain size.

**Metal matrix composite (MMC)** A composite material consisting of particles or fibers of reinforcing material (usually ceramic) embedded in a metal matrix.

**Nabarro-Herring mechanism** A mechanism of plastic flow in a polycrystalline material controlled by matter transfer across crystallites by bulk diffusion.

## REFERENCES

1. D. G. Morris, "Mechanical Behaviour of Nanostructured Materials," Materials Science Foundations, Vol. 2., Trans Tech Publications Ltd., Switzerland, 1998.
2. V. Yamakov, D. Wolf, S. R. Phillpot, A. K. Mukherjee, and H. Gleiter, *Nature Materials* 1, 45 (2002).
3. V. Yamakov, D. Wolf, S. R. Phillpot, and H. Gleiter, *Acta Mater.* 50, 61 (2002).
4. N. Wang, Z. Wang, K. T. Aust, and U. Erb, *Acta Mater.* 43, 519 (1995).
5. H. J. Frost and M. F. Ashby, "Deformation Mechanism Maps, The Plasticity and Creep of Metals and Ceramics," Pergamon Press, Oxford, 1982.
6. G. E. Fougere, J. R. Weertman, and R. W. Siegel, *Scripta Metall. Mater.* 26, 1879 (1992).
7. K. Lu, W. D. Wie, and J. T. Wang, *Scripta Metall. Mater.* 24, 2319 (1990).
8. G. E. Dieter, "Mechanical Metallurgy," McGraw-Hill, London, 1988.
9. R. Z. Valiev, R. K. Islamgaliev, and I. V. Alexandrov, *Prog. Mater. Sci.* 45, 103 (2000).
10. H. S. Kim, Y. Estrin, and M. B. Bush, *Acta Mater.* 48, 493 (2000).
11. H. S. Kim, M. B. Bush, and Y. Estrin, *Mater. Sci. Eng.* 276A, 175 (2000).
12. H. S. Kim, Y. Estrin, and M. B. Bush, *Mater. Sci. Eng.* 316A, 195 (2001).
13. J. E. Carsley, J. Ning, W. M. Milligan, S. A. Hackney, and E. C. Aifantis, *Nanostruct. Mater.* 5, 441 (1995).
14. Y. Estrin, in "Unified Constitutive Laws of Plastic Deformation," (A. S. Krausz and K. Krausz, Eds.), Academic Press, New York, 1996, p. 69.
15. Y. Estrin and H. A. Mecking, *Acta Metall.* 32, 57 (1984).
16. H. Gleiter, *Prog. Mater. Sci.* 33, 224 (1989).
17. C. J. Youngdahl, P. G. Sanders, J. A. Eastman, and J. R. Weertman, *Scripta Mater.* 37, 809 (1997).
18. P. G. Sanders, J. A. Eastman, and J. R. Weertman, in "Processing and Properties of Nanocrystalline Materials," (C. Suryanarayana, J. Singh, and F. H. Froes, Eds.), TMS, 1996, p. 379.
19. R. Suryanarayana, C. A. Frey, S. M. L. Sastry, B. E. Waller, S. E. Bates, and W. E. Buhro, *J. Mater. Res.* 11, 439 (1992).
20. G. W. Nieman, J. R. Weertman, and R. W. Siegel, *J. Mater. Res.* 6, 1012 (1991).
21. P. G. Sanders, J. A. Eastman, and J. R. Weertman, *Acta Mater.* 45, 4019 (1997).
22. C. C. Koch and T. R. J. Malow, *Metastable and Nanocryst. Mater.* 2-6, 565 (1999).
23. T. Mukai, M. Kawazoe, and K. Higashi, *Nanostruct. Mater.* 10, 755 (1998).
24. H. S. Kim and Y. Estrin, *Appl. Phys. Lett.* 79, 4115 (2001).
25. E. W. Hart, *Acta Metall.* 15, 351 (1967).
26. G. W. Nieman, J. R. Weertman, and R. W. Siegel, *Nano Struct. Mater.* 1, 185 (1992).
27. B. Günther, A. Baalman, and H. Weiss, H. in "Physical Phenomena in Granular Materials" (G. D. Cody, T. H. Geballe, and P. Sheng, Eds.), Materials Research Society, Pittsburgh, 1990, p. 611.
28. V. T. Gertsman, M. Hoffmann, H. Gleiter, and R. Birringer, *Acta Metall. Mater.* 42, 3539 (1994).
29. R. Z. Valiev, E. V. Kozlov, Yu. F. Ivanov, J. Lian, A. A. Nazarov, and B. Baudelet, *Acta Mater.* 42, 2467 (1994).
30. M. Weller, J. Diehl, and H.-E. Schaefer, *Phil. Mag.* A63, 527 (1991).
31. G. E. Fougere, L. Riestler, M. Ferber, J. R. Weertman, and R. W. Siegel, *Mater. Sci. Eng.* A204, 1 (1995).
32. T. D. Shen, C. C. Koch, T. Y. Tsui, and G. M. Pharr, *J. Mater. Res.* 10, 2892 (1995).
33. L. Wong, D. Ostrander, U. Erb, G. Palumbo, and K. T. Aust, in "Proc. Symp. on Nanophase and Nanocrystalline Structures" (R. D. Shull and J. M. Sanchez, Eds.), Metallurgical Society of AIME, Warrendale, PA, 1994, p. 85.
34. M. J. Mayo, "Structure/Property Relationships for Metal/Metal Interface," Vol. 229. (A. D. Romig, D. E. Fowler, and P. D. Bristow, Eds.), MRS, Pittsburgh, 1991, p. 197.
35. V. Krstic, U. Erb, and G. Palumbo, *Scripta. Mater.* 29, 1501 (1993).
36. D. Chen, *Mater. Sci. Eng.* A190, 193 (1995).
37. B. Budiansky, *J. Composite Mater.* 4, 286 (1970).
38. H. S. Kim and M. B. Bush, *Nanostructured Mater.* 11, 361 (1999).
39. M. D. Kulge, D. Wolf, J. F. Lutsko, and S. R. Phillpot, *J. Appl. Phys.* 67, 2370 (1990).
40. H. S. Kim, Y. Estrin, and M. B. Bush, *Z. Metallkd.* 90, 863 (1999).
41. T. Kizuka, H. Ichinose, and Y. Ishida, *J. Mater. Sci.* 32, 1501 (1997).
42. H. Huang and M. B. Bush, *Mater. Sci. Eng.* A232, 63 (1997).
43. M. Norell, N. Nyborg, and M. Friesel, *Powder Metall.* 41, 31 (1998).
44. R. W. Rice, *Key Eng. Mater.* 115, 1 (1996).
45. R. M. Spriggs, *J. Am. Ceram. Soc.* 44, 628 (1961).
46. J. E. Carsley, W. W. Milligan, S. A. Hackney, and E. C. Aifantis, *Metall. Mater. Trans.* 26A, 2479 (1995).
47. D. E. Polk, B. C. Giessen, and F. G. Gardner, *Mater. Sci. Eng.* 23, 309 (1976).
48. Z. Hashin and S. Shtrikman, *J. Mech. Phys. Solids* 11, 127 (1963).
49. R. Hill, *Proc. Phys. Soc. London* A65, 349 (1952).
50. P. M. Derlet and H. Van Swygenhoven, *Scripta Mater.* 47, 719 (2002).
51. A. H. Chokshi, A. Rosen, J. Karch, and H. Gleiter, *Scripta Metall.* 23, 1678 (1989).

# Phonon Confinement in Nanostructured Materials

Akhilesh K. Arora, M. Rajalakshmi, T. R. Ravindran

*Indira Gandhi Centre for Atomic Research, Kalpakkam, India*

## CONTENTS

1. Introduction
  2. Optical Phonons
  3. Results
  4. Acoustic Phonons
  5. Summary
- Glossary  
References

## 1. INTRODUCTION

There is considerable current interest in the physics of nanostructured materials in view of their numerous technological applications [1, 2] in a variety of areas such as catalysis [3], magnetic data storage [4], ferrofluids [5], soft magnets [6], machinable ceramics and metallurgy [7], non-linear optical and optoelectronic devices [8], and sensors [9]. In addition, obtaining an understanding of the properties of nanostructured materials is of interest from a fundamental point of view. Only a proper understanding of the dependence of a given property on the grain/particle size can lead to design/tailoring of the nanostructured material for the related application. It is also important to understand when a material could be considered as nanostructured. Although one can in principle classify materials with grain size less than 1000 nm as nanostructured, several properties such as optical [10] and vibrational [11] properties do not differ much from the corresponding bulk value unless the grain/particle size is less than typically 20 nm. In view of this it is reasonable to treat a material with a grain size smaller than a certain value as nanostructured only if the property of interest differs from the bulk value at least by a few percent. It is also possible that a material with nanometer grain size may behave as nanostructured for a specific property while it could act like bulk for other properties. In addition to the grain size, the properties of the nanostructured materials may sometimes depend on the method of their synthesis. Generally nanostructured materials are synthesized in

one of the three forms: (a) as isolated or loosely connected nanoparticles in the form of powder [12], (b) as composites of nanoparticles dispersed in another host [13], or (c) as compact collection of nanograins as pellets [14] or thin films [15]. The last form is also called nanophase material. This chapter reviews the vibrational properties of the various forms of nanostructured materials.

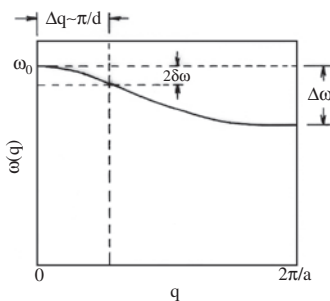
Phonons are quanta of atomic vibrations in crystalline solids. In a simple monoatomic solid with only one atom per primitive cell (for example,  $\alpha$ -iron, copper), one can have only three acoustic phonon branches corresponding to the three degrees of freedom of atomic motion. On the other hand, for monoatomic solids with two atoms per primitive cell such as diamond, magnesium, or diatomic compounds such as GaAs, one also has three optic phonon branches in addition to the three acoustic phonons [16]. In compounds with a greater number of atoms and complex crystal structures, the number of optic phonons is more than three. If the crystal unit cell contains  $N$  atoms, then  $3N$  degrees of freedom result in 3 acoustic phonons and  $3N - 3$  optical phonons. These phonons can propagate in the lattice of a single crystal as a wave and exhibit dispersion depending on their wavelength or equivalently their wavevector in the Brillouin zone [17]. Phonon propagation is interrupted when a grain boundary is encountered in a polycrystalline material. In an isolated grain the phonon can get reflected from the boundaries and remain confined within the grain. However, from the point of view of phonons, a well-crystallized polycrystalline sample with several micrometer grain size can be treated as a bulk/infinite crystal for all practical purposes. The consequences of phonon confinement are noticeable in the vibrational spectra only when the grain size is smaller than typically 20 lattice parameters.

The atomic vibrational frequencies in crystalline solids range from zero to about 100 THz. A more common unit to describe the vibrational frequencies is wavenumber ( $\text{cm}^{-1}$ ) obtained by dividing the actual frequency by the velocity of light or by inverting the wavelength. Acoustic phonons have frequencies from zero to about a few hundred

wavenumbers while the optic phonons have higher frequencies. Hence the vibrational spectra could be probed using infrared absorption/reflectivity or using Raman spectroscopy [18]. The wavevector of the IR photon for these energies is of the order of  $10^2\text{--}10^3\text{ cm}^{-1}$ . On the other hand, in a Raman scattering experiment the magnitude of scattering vector is  $2k_0 \sin(\theta/2)$ , where  $k_0$  is the wavevector of the incident light and  $\theta$  is the scattering angle. Thus the maximum value of the scattering vector could at best be  $2k_0$  (corresponding to the backscattering geometry), which has a value  $\sim 5 \times 10^4\text{ cm}^{-1}$  for visible light. Hence the wavevector probed by either of these two techniques is much smaller than the wavevector  $q$  of the full phonon dispersion curve, which extends up to the boundary of the Brillouin zone ( $\pi/a \sim 10^8\text{ cm}^{-1}$ , where  $a$  is the lattice parameter). Thus these techniques sample only the optical phonons close to the zone center ( $q \sim 0$ ). This  $q \sim 0$  selection rule is essentially a consequence of the infinite periodicity of the crystal lattice [19]. However, if the periodicity of the crystal lattice is interrupted, as in the case of nanocrystalline materials, this rule is relaxed and phonons away from the Brillouin zone center also contribute to the phonon lineshape observed in spectroscopic measurements. This can be qualitatively explained in the following manner. Consider the phonon dispersion curve of a typical diatomic solid as shown in Figure 1. For a particle/grain of size  $d$ , the phonon wavefunction must decay to a very small value close to the boundary. This restriction on the spatial extent of the wavefunction, via a relationship of the uncertainty principle type, results in an uncertainty  $\Delta q \sim \pi/d$  in the wavevector of the zone-center optical phonon and a corresponding uncertainty  $2\delta\omega$  in its frequency [20]. Now the light scattering can take place from quasi-zone-center optical phonons with wavevectors  $\Delta q$  up to  $\pi/d$ . This results in asymmetric broadening of the phonon lineshape. In addition to the changes in the optical phonon lineshape, confinement of acoustic phonons also leads to other interesting changes in the spectra. A quantitative formalism of phonon confinement will be discussed in subsequent sections.

### 1.1. Dimensionality of Confinement

It is important to distinguish between the dimensionality of the system and the dimensionality/degree of confinement. A bulk material is a 3D system and is unconfined; that is, dimensionality/degree of confinement is zero. The first



**Figure 1.** Schematic representation of the optical phonon dispersion curve and the range  $\Delta q$  of the wavevectors probed in Raman scattering from a nanoparticle of diameter  $d$ .  $2\delta\omega$  is the corresponding range of phonon frequencies that contribute to the first-order Raman scattering.

level of confinement occurs in single- and multilayer thin films grown using layered deposition on substrates. Semiconductor superlattices, single-quantum well structures, and multiple-quantum well structures [21] are well-known examples of 2D systems because the phonons and charge carriers are confined within a plane, say, the x-y plane; however, the degree of confinement is 1D because phonons and charge carriers are restricted along the z direction. Similarly, 2D confinement occurs in nanowires [22] and in carbon nanotubes [23], whereas the dimensionality of the system reduces to 1D. The highest degree of confinement (3D) occurs in quantum dots [24] and nanoparticles [25, 26] where the propagation is restricted in all three directions. Here the dimensionality of the system is zero.

## 2. OPTICAL PHONONS

As mentioned in the Introduction, only zone-center optical phonons can be observed in ideal single crystals using optical techniques such as Raman spectroscopy. However, this  $q = 0$  selection rule is relaxed due to interruption of lattice periodicity in a nanocrystalline material. In this section we present a phenomenological model of phonon confinement in an isolated nanoparticle. The case of spherical nanoparticle is considered first.

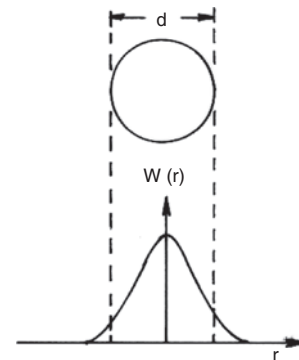
### 2.1. Phenomenological Confinement Model

A quantitative formalism for the confined-phonon lineshape [27] involves taking into account the contributions of the phonons over the complete Brillouin zone with appropriate weight factors. Consider a spherical nanoparticle of diameter  $d$  as shown in Figure 2. A plane-wave-like phonon wavefunction cannot exist within the particle because the phonon cannot propagate beyond the crystal surface. In view of this, one must multiply the phonon wavefunction with a confinement function or envelope function  $W(r)$ , which decays to a very small value close to the boundary.

The wavefunction of a confined phonon of wavevector  $q_0$  can be written as

$$\Psi(q_0, r) = W(r)u(q_0, r) \exp(-iq_0 \cdot r) \quad (1)$$

$$\Psi(q_0, r) = \Psi'(q_0, r)u(q_0, r) \quad (2)$$



**Figure 2.** The Gaussian confinement function  $W(r)$  for a spherical nanocrystal of diameter  $d$ .

where  $u(q_0, r)$  has the periodicity of the lattice. In order to calculate the effect on the Raman spectrum, we expand  $\Psi'(q_0, r)$  in Fourier series:

$$\Psi'(q_0, r) = \int C(q_0, q) \exp(iq \cdot r) d^3q \quad (3)$$

where the Fourier coefficients  $C(q_0, q)$  are given by

$$C(q_0, q) = (2\pi)^{-3} \int \Psi'(q_0, r) \exp(-iq \cdot r) d^3r \quad (4)$$

The particle (nanocrystal) phonon wavefunction is a superposition of plane waves with  $q$  vectors centered at  $q_0$ . Gaussian confinement functions have been extensively used as the confinement function [27–29]. One can write  $W(r)$  as

$$W(r) = \exp(-\alpha r^2/d^2) \quad (5)$$

where the value of  $\alpha$  decides how rapidly the wavefunction decays as one approaches the boundary. This gives  $C(q_0, q)$  as

$$C(q_0, q) = \exp\{-d^2(q - q_0)^2/4\alpha\} \quad (6)$$

Richter et al. (RWL model) [27] used the boundary condition that the phonon amplitude  $|\Psi|^2 \propto W^2(r)$  reduced to  $1/e$  at the boundary  $r = d/2$  of the particle. This corresponds to  $\alpha = 2$ . Other values of  $\alpha$  such as  $8\pi^2$  used by Campbell and Fauchet (CF model) [28] and 9.67 (bond polarizability model) [29] have also been proposed. Thus  $\Psi'$  are the eigenfunctions of the phonons with wavevectors  $q$  in an interval  $|q - q_0| < \pi/d$  centered at  $q_0$  and the weight factors  $C(q_0, q)$  also have a Gaussian distribution. As one-phonon Raman scattering probes zone-center phonons, one can set  $q_0 = 0$ . This yields

$$|C(0, q)|^2 = \exp(-q^2 d^2/2\alpha) \quad (7)$$

The first-order Raman spectrum is then given as

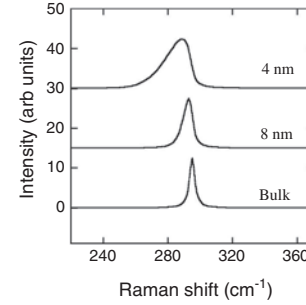
$$I(\omega) = \int \frac{|C(0, q)|^2 d^3q}{[\omega - \omega(q)]^2 + (\Gamma_0/2)^2} \quad (8)$$

where  $\omega(q)$  is the phonon dispersion curve and  $\Gamma_0$  is the natural linewidth of the zone-center optical phonon in the bulk. In order to simplify the calculations, one can assume a spherical Brillouin zone and consider the phonon dispersion curve to be isotropic. These assumptions are valid when only a small region of the Brillouin zone, centered at  $\Gamma$  point, contributes to the scattering. The optical phonon dispersion curve could then be approximated to an analytical function of the type

$$\omega(q) = \omega_0 - \Delta\omega \sin^2(qa/4) \quad (9)$$

where  $a$  is the lattice parameter,  $\omega_0$  is the zone-center optical phonon frequency, and  $\Delta\omega$  is the width of the phonon dispersion curve.

The calculated Raman lineshapes of 4- and 8-nm GaAs nanoparticles are compared in Figure 3 with that of the bulk. One can see that as the particle size reduces, the



**Figure 3.** Calculated Raman spectra of confined LO phonon in GaAs nanoparticles. The bulk spectrum is also shown for comparison. Note the asymmetric broadening of the lineshape and also the shift of the peak towards the low-frequency side.

Raman spectra develop marked asymmetry towards the low-frequency side and exhibit marginal shift in the peak position also towards the same side. As the optical phonon dispersion curves in most solids have negative dispersion, that is, phonon frequency decreases as a function of wavenumber, the increased intensity in the wing of the Raman spectra on the low-frequency side basically arises from the contribution from the phonon branch away from the zone center. The dependence of the peak shift and the line broadening on the particle size is shown in Figure 4 for the longitudinal optic phonon in GaAs. Note that both peak shift and the linewidth increase as the particle size reduces. However, the changes are marginal if the particle size is larger than 10 nm.

It is sometimes useful to combine the results of Figure 4 into a single curve of peak shift versus line broadening. This is particularly useful while analyzing data on nanocrystalline systems where information about the particle size is not available. For ion-implanted GaAs, Tiong et al. [30] argued that crystallite size reduced due to irradiation-induced damage in the lattice; however, spatial correlation (size of crystalline region) persisted over a small length. In view of this the changes in the peak shift and line broadening as a function of fluence were ascribed to the residual spatial correlation over the nanocrystalline grains in the implanted sample. Figure 5 shows peak shift as a function of line broadening for GaAs nanoparticles.

In addition to the Gaussian function, other analytic functions such as sinc and exponential have also been considered as confinement functions. In analogy with the ground-state wavefunction of an electron in a spherical potential well, a sinc ( $\sin(x)/x$ ) function was considered [28]:

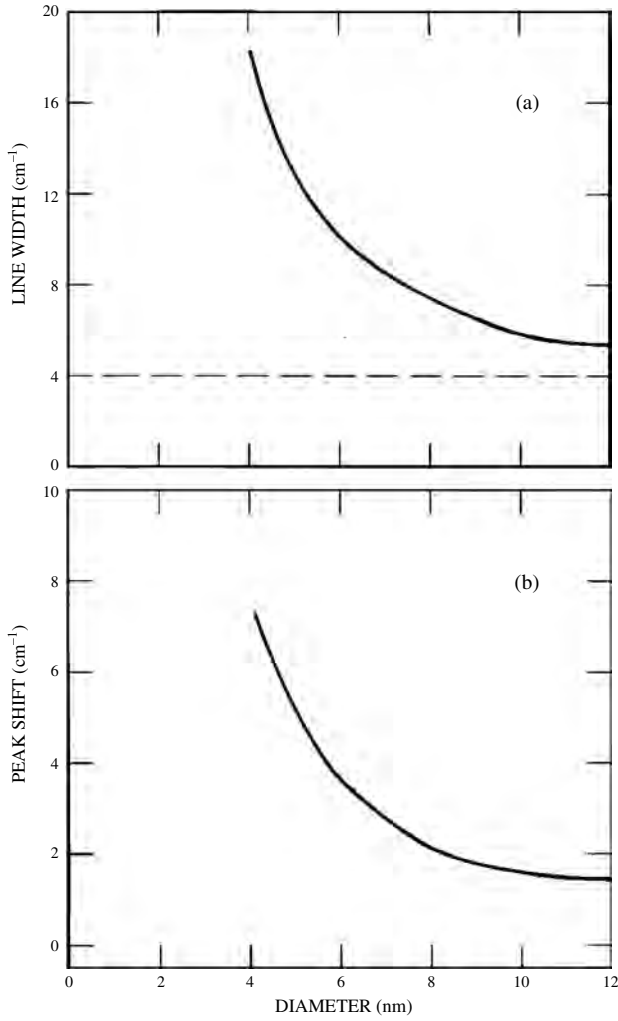
$$W_S(r) = \begin{cases} \sin(2\pi r/d)/(2\pi r/d) & \text{if } r < d/2 \\ 0 & \text{otherwise} \end{cases} \quad (10)$$

Here the wavefunction becomes zero at the boundary of the particle. The Fourier coefficient in this case becomes [29]

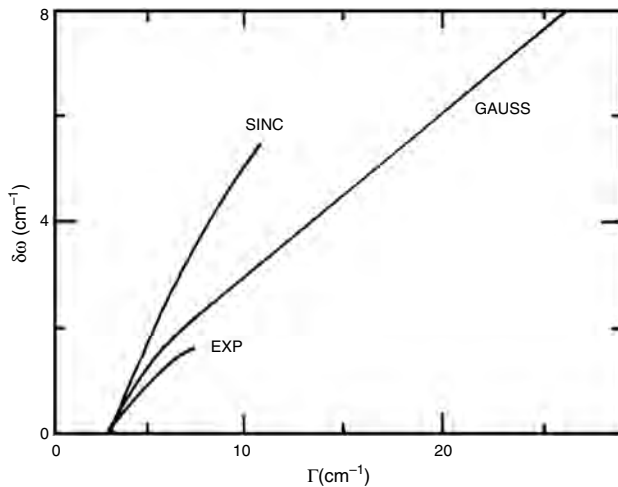
$$C_S(0, q) \cong \frac{\sin(qd/2)}{q(4\pi^2 - q^2 d^2)} \quad (11)$$

Similarly, in analogy with the propagation of a wave in a lossy medium, an exponential decay of phonon amplitude





**Figure 4.** The dependence of linewidth (a) and peak shift (b) of the longitudinal optic phonon on the particle size for GaAs nanoparticles. Dashed line is the linewidth of the bulk phonon.



**Figure 5.** The relationship between peak shift  $\delta\omega$  and line broadening  $\Gamma$  for the three different confinement functions. Adapted with permission from [28], I. H. Campbell and P. M. Fauchet, *Solid State Commun.* 58, 739 (1986). © 1986, Elsevier Science.

has also been considered [28]. The confinement function used in this case was

$$W_E(r) = \exp(-4\pi^2 r/d) \quad (12)$$

The Fourier coefficient is then given by [28]

$$C_E(0, q) \cong \frac{1}{(16\pi^4 - q^2 d^2)^2} \quad (13)$$

These confinement functions yield different dependence of peak shift on the line broadening. Figure 5 also compares the dependencies for the sinc and exponential confinement functions with that of Gaussian. Note that each confinement function has a different shape of  $\delta\omega$  versus  $\Gamma$  curve. From the analysis of their data and other reported results [27, 31], Campbell and Fauchet [28] have shown that a Gaussian confinement with  $\alpha = 8\pi^2$  fits best to the data. This corresponds to a strong/rigid confinement of phonons within the nanoparticle with zero amplitude near the boundary.

We now consider other confinement geometries. As mentioned earlier, rodlike shape corresponds to 2D confinement and platelike (thin-film) shape gives 1D confinement. A rodlike particle is characterized by two length scales, its diameter  $d_1$  being much smaller than its length  $d_2$ . Again using  $\alpha = 8\pi^2$  in Gaussian confinement, the expressions for the Fourier coefficients  $C(0, q_1, q_2)$  have been obtained [28]:

$$|C(0, q_1, q_2)|^2 \cong \exp(-q_1^2 d_1^2 / 16\pi^2) \exp(-q_2^2 d_2^2 / 16\pi^2) \times \left| 1 - \operatorname{erf}\left(\frac{iq_2 d_2}{\sqrt{32}\pi}\right) \right|^2 \quad (14)$$

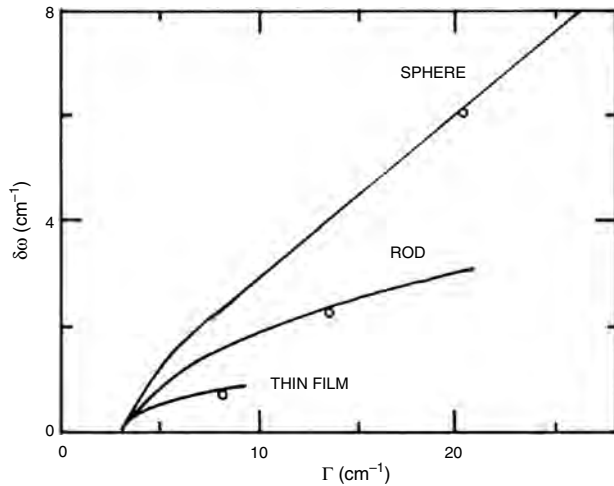
On the other hand, a thin film has only its thickness  $d$  as the confining dimension. For a thin film, the Fourier coefficient is given by [28]

$$|C(0, q)|^2 \cong \exp(-q^2 d^2 / 16\pi^2) \left| 1 - \operatorname{erf}\left(\frac{iqd}{\sqrt{32}\pi}\right) \right|^2 \quad (15)$$

The changes in the Raman lineshape, quantified in terms of line broadening and peak shift, are compared in Figure 6 for 1-, 2-, and 3D confined systems within the framework of Gaussian confinement. Note that as the dimensionality of confinement reduces, the magnitude of peak shift and line broadening reduce dramatically. The departure from bulk is maximum for a particle while it is least for a thin film of the same dimension.

## 2.2. Bond Polarizability Model

In addition to the phenomenological models of phonon confinement, there have been some attempts to theoretically obtain [29] the Raman spectrum of nanocrystals using bond polarizability model [32] within the framework of partial density approximation [33]. In this method eigenvalues and eigenvectors are obtained by diagonalizing the dynamical matrix, while the force constants are obtained by using partial density approach. The eigenvectors thus obtained are analyzed to give vibrational amplitude as a function of distance from the center of the particle. The phonon amplitude in a Si nanosphere was shown to closely



**Figure 6.** The relationship between peak shift  $\delta\omega$  and line broadening  $\Gamma$  for three different shapes of the nanoparticles. In all the three curves the open circles correspond to a size of 4 nm. Adapted with permission from [28], I. H. Campbell and P. M. Fauchet, *Solid State Commun.* 58, 739 (1986). © 1986, Elsevier Science.

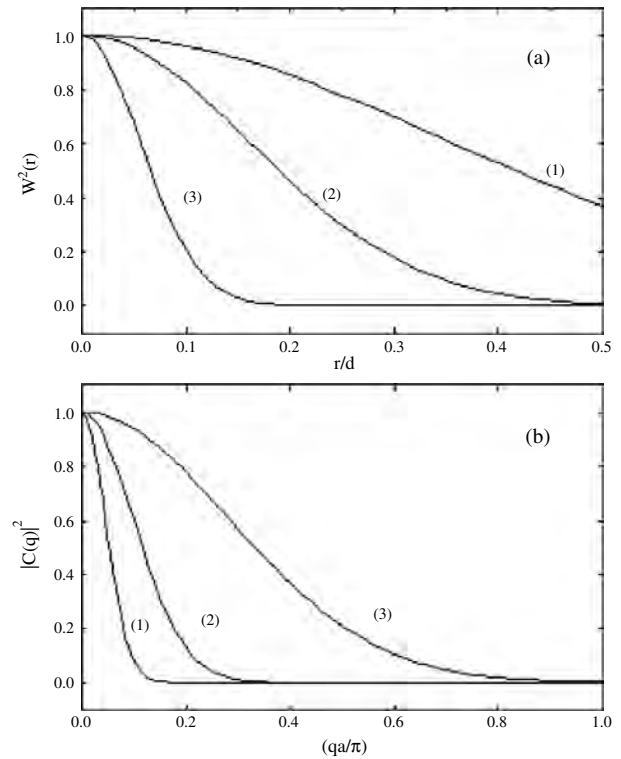
resemble a sinc function or a Gaussian with  $\alpha = 9.67$  [29]. Amplitude at the boundary was calculated to be around 3.6%. This is much smaller than  $1/e$  used by Richter et al. [27] and much larger than  $\exp(-4\pi^2)$  used by Campbell and Fauchet (CF) [28]. The Gaussian confinement functions and the corresponding Fourier coefficients corresponding to three different  $\alpha$  (2, 9.67, and  $8\pi^2$ ) are compared in Figure 7. Note that weight factor  $|C(q)|^2$  for the Raman intensity drops too rapidly for  $\alpha = 2$  and too slowly for  $\alpha = 8\pi^2$  as one moves away from the Brillouin zone center. Consequently the RWL model predicts only a marginal change in the Raman spectra while that of CF model causes maximum departure from the bulk for the same particle size. On the other hand, the calculations of Zi et al. suggest an effect intermediate between the two limiting cases. It is important to point out that a large number of results have been satisfactorily explained on the basis of Gaussian confinement model using  $\alpha = 8\pi^2$  [20, 34–38].

### 3. RESULTS

In this section we discuss various results reported on phonon confinement in 1-, 2-, and 3D confined systems.

#### 3.1. 1D Confined Systems

Superlattices consisting of alternate thin layers of a pair of semiconducting materials such as GaAs and AlAs, grown on a substrate using molecular beam epitaxy, have been extensively studied [21] in view of their applications in light-emitting diodes and diode lasers [39]. In these superlattices GaAs layer constitutes the quantum well while the AlAs layer forms the barrier layer. It is important to point out that the range of optical phonon frequencies of GaAs does not overlap with that of AlAs. Hence the phonons of GaAs layer cannot propagate into the neighboring AlAs layers and vice versa. Thus phonons in each of the GaAs and AlAs



**Figure 7.** Squares of the Gaussian confinement functions  $W(r)$  (a) and the corresponding Fourier transform  $C(q)$  (b) for different values of  $\alpha$ . Curve (1)  $\alpha = 2.0$  (RWL model), (2)  $\alpha = 9.67$  (bond-polarizability model), and (3)  $\alpha = 8\pi^2$  (CF model). The phonon amplitude  $W^2$  is plotted up to the boundary of the particle ( $r = d/2$ ) and  $C^2$  up to the Brillouin zone boundary  $q = \pi/a$ .

layers are confined within those layers. The confined optical phonons in such superlattices can be described as modes of a thin slab, arising from the standing wave pattern formed within each slab. A set of modes at discrete wavevectors  $q_j = \pi j/d_1$ , where  $d_1$  is the thickness of the GaAs layer, are allowed. The confined phonon frequencies  $\omega_j$  then correspond to the discrete  $q_j$  points on the dispersion curve of GaAs [40]. Similarly the confined optical phonons of AlAs layer of thickness  $d_2$  correspond to the  $q_j = \pi j/d_2$  discrete points on the AlAs dispersion curve. In GaAs/AlAs superlattices the confined optical phonons in the GaAs layers have been observed only under resonant conditions, that is, when the incident photon energy is close to that of an electronic excitation of the GaAs quantum well [40]. Under nonresonant conditions the intensities of these modes are weak.

In many cases one of the layers is an alloy  $\text{Al}_x\text{Ga}_{1-x}\text{As}$  [21]. This mixed crystal system exhibits a “two-mode” behavior [41]; that is, it exhibits both GaAs-like and AlAs-like modes. Hence AlAs-like phonons remain confined in the barrier layer ( $\text{Al}_x\text{Ga}_{1-x}\text{As}$ ) in a GaAs/ $\text{Al}_x\text{Ga}_{1-x}\text{As}$  superlattice. On the other hand, the GaAs-like modes of the quantum-well layer (GaAs) can propagate in the barrier layer and vice versa. In view of this one expects “zone folding” to take place with new periodicity of  $(d_1 + d_2)$  at  $q_j = \pi j/(d_1 + d_2)$ ; however, this effect has not been observed for propagating optical phonons in GaAs/ $\text{Al}_x\text{Ga}_{1-x}\text{As}$  superlattices because of the highly dispersive character of the optical

modes [42]. It may be mentioned that the acoustic phonons, whose dispersion curves overlap over a wide range of frequencies, propagate through both the layers exhibiting zone-folding effects due to new periodicity [43].

Confined optical phonons have been found also in single GaAs quantum wells under resonant conditions [44]. Resonance was achieved at a fixed photon energy by exploiting the temperature dependence of electronic excitations in the quantum well. Recently, IR absorption measurements have been used for studying confined optical phonons in  $(\text{PbTe})_m/(\text{EuTe})_n$  superlattices [45]. The confined phonons manifest themselves as minima in the transmission spectrum. In the normal incidence only transverse optic (TO) phonons are observed, while in oblique incidence both TO and longitudinal optic (LO) phonons are seen. From the frequencies of these confined phonons the dispersion curve along the  $\langle 111 \rangle$  direction could be deduced. In contrast to GaAs/ $\text{Al}_x\text{Ga}_{1-x}\text{As}$  superlattices, zone-folding effects have been observed in GaN/ $\text{Al}_x\text{Ga}_{1-x}\text{N}$  superlattices [46]. As this mixed crystal system exhibits “one-mode behaviour,” it is argued that the overlap between the density of states in the two layers is significant. In superlattices and in quantum-well structures, interface optical phonons have also been observed [47, 48]. Phenomenological models [49] predict that these modes have frequencies between TO and LO phonons of the constituent layers. If the interfaces are sharp, the interface phonons are found to be weak [46].

### 3.2. 2D Confined Systems

Recently, several tens of micrometers long nanowires of a variety of materials such as Si [22, 50], Ge [51], GaAs [52], SiC [53–55], and TiC [56] have been synthesized using laser ablation [57] and other methods. The diameter of these nanowires ranges from 5 to 50 nm. Their optical properties are strongly influenced by the confinement of electrons and holes in these 1D systems. In view of their unique properties, they find applications in several devices [56]. In analogy with electron confinement, phonon confinement has also been found to give rise to interesting changes in the vibrational spectra.

Raman spectra of the  $F_{2g}$  optical phonon in Si nanowires show broadening and peak shifts [50] similar to those predicted by Gaussian confinement model. For a 10-nm-diameter nanowire the peak is found to shift to  $505 \text{ cm}^{-1}$  from  $519 \text{ cm}^{-1}$  and also broaden to  $13 \text{ cm}^{-1}$  from  $3.5 \text{ cm}^{-1}$ . Additional peaks at  $302$  and  $964 \text{ cm}^{-1}$  have also been reported. These were assigned to overtones of the zone-boundary phonons [50]. Appearance of zone-boundary phonons in crystals with large density of defects [58] or in mixed crystals [59] has often been reported. This arises due to the relaxation of the  $q = 0$  selection rule due to the presence of disorder in the crystal. Similarly, overtones and combinations constitute the second-order spectra and these also are enhanced in the presence of disorder. On the other hand, Wang et al. [50] apply the phonon confinement model also to the overtones of zone-boundary phonon and try to interpret their shifts and broadening. In fact, the changes in the Raman spectra of overtones, etc., as a consequence of reducing the nanowire diameter should only be ascribed to higher defect density resulting in the appearance of peaks

corresponding to one- and two-phonon density of states. Quite interestingly, Wang et al. also introduce a new term “phonon confinement length” (in analogy with exciton confinement length). By this they imply a size of nanostructure below which the phonon confinement effects are noticeable in the Raman spectra. In this context it is important to point out that for a given material the confinement effects may be different for phonons of different symmetries [37], making such terms lose their physical significance. This will be discussed further in a subsequent section.

Germanium nanowires with an oxide layer coating have been synthesized using laser ablation technique [51]. As expected, larger core diameters in the range 20–51 nm do not exhibit any noticeable change in the Raman spectra. On the other hand, nanowires with 6–17 nm core show asymmetric broadening; however, no quantitative analysis has been carried out. Gallium arsenide nanowires with a  $\text{GeO}_x$  sheath have exhibited broad TO and LO phonon modes [52]; however, the broadening was found to be nearly symmetric. Surprisingly, the red shift of the LO phonon was very large,  $\sim 40 \text{ cm}^{-1}$  for nanowires with diameters in the range 10–120 nm with an average diameter of 60 nm. Such a large shift cannot be accounted for based on phonon confinement effect alone. Other factors such as defects and residual stresses have been argued to contribute to the decrease of LO phonon frequency. Silicon carbide nanowires of average diameter 80 nm with a coating of 17 nm  $\text{SiO}_x$  [53] have also shown very broad Raman spectra that resemble those arising from phonon density of states rather than from phonon confinement effects. The red shifts of 12 to  $34 \text{ cm}^{-1}$  for the TO and LO phonons were attributed to confinement effects and internal stresses [53]. CdSe nanofilaments incorporated in fibrous magnesium silicate (chrysotile asbestos) have shown polarized Raman spectrum [60].

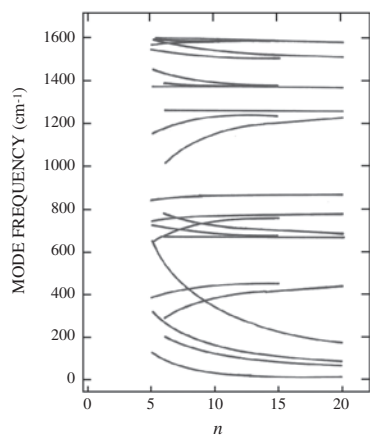
Carbon nanotubes are unique one-dimensional systems [61, 62], whose diameters are typically 1–2 nm and whose lengths are up to several tens of micrometers. Vibrational properties of these hollow tubes are quite different from those of solid nanorods discussed earlier. A single-wall carbon nanotube (SWNT) can be described as a single atomic layer of graphite rolled up into a seamless cylinder. A SWNT is specified by a pair of indices ( $m, n$ ) that represent the number of unit vectors  $n\mathbf{a}_1$  and  $m\mathbf{a}_2$  on the 2D hexagonal honeycomb lattice contained in the chiral vector. Folding of the graphite sheet is done such that the chiral vector is perpendicular to the axis of the nanotube (see, e.g., Fig. 1 of [63]). The magnitude of the chiral vector gives its circumference. The diameter of the nanotube is related to the ( $m, n$ ) indices as

$$d = 3^{1/2}(m^2 + mn + n^2)^{1/2}a_{c-c}/\pi$$

where  $a_{c-c}$  is the nearest-neighbor C-C distance (1.421 Å in graphite). The phonon dispersion relations in a carbon nanotube are obtained from those of an isolated 2D graphite layer (graphene sheet) by using the zone-folding approach [64]. Zone folding of acoustic branches leads to several low-frequency modes, whose frequencies depend strongly on the diameter of the nanotube. Notable among these are the  $E_{2g}$  mode, the  $E_{1g}$  mode, and the  $A_{1g}$  radial breathing mode. For a (10, 10) nanotube of diameter 1.36 nm, these modes

have frequencies of 17, 118, and 165  $\text{cm}^{-1}$  [63]. For tube diameters ranging between 0.6 and 1.4 nm, a power law dependence of the mode frequencies has been found [65]. The exponent for the  $E_{1g}$  and  $A_{1g}$  modes is close to  $-1$  while that for the lowest energy  $E_{2g}$  mode is close to  $-2$ . Figure 8 shows the dependence of the frequencies of several Raman active modes on the index  $n$  for  $(n, n)$  armchair nanotubes [66]. The inverse dependence of the radial breathing mode frequency on the tube diameter serves as a secondary characterization to estimate the mean diameter of SWNTs. In addition to these features, the internal modes associated with the hexagonal ring stretching vibration of the graphite sheet around 1581  $\text{cm}^{-1}$  exhibits splitting into  $A_{1g} + E_g$ . This splitting arises due to the curvature of the nanotube graphene sheet. A novel feature of the Raman spectra of SWNTs is the diameter selective scattering at different excitation energies, arising from the 2D quantum confinement of electrons. Resonance Raman spectroscopic studies in the energy range 1–4.8 eV have proved to be a powerful probe of these quasi-1D materials [67–69]. Depending on its chirality (i.e.,  $n$  and  $m$ ), an individual SWNT could be semiconducting or metallic. Any sample of SWNTs is a mixture of  $\sim 1/3$  metallic and  $\sim 2/3$  semiconducting tubes. Raman excitations at different energies could selectively probe either of these sets of tubes.

Specific-heat measurements at low temperature have shown evidence of quantized phonon spectrum of SWNT [70]. The data show the expected linear  $T$  dependence and were found to be significantly different from that of 3D graphite and 2D graphene. The analysis also yielded an energy of 4.3 meV for the lowest quantized phonon subband. The nanotubes that are produced in either an electric arc or pulsed laser vaporization are mostly in the form of bundles, where nanotubes are aligned in a close-packed triangular lattice. Intertube interactions that arise in the lattice are usually weak and are approximated by van der Waals interaction. This is similar to coupling between adjacent graphene layers in 3D crystalline graphite. This coupling causes a slight increase ( $\sim 7\%$ ) in the frequency of radial breathing



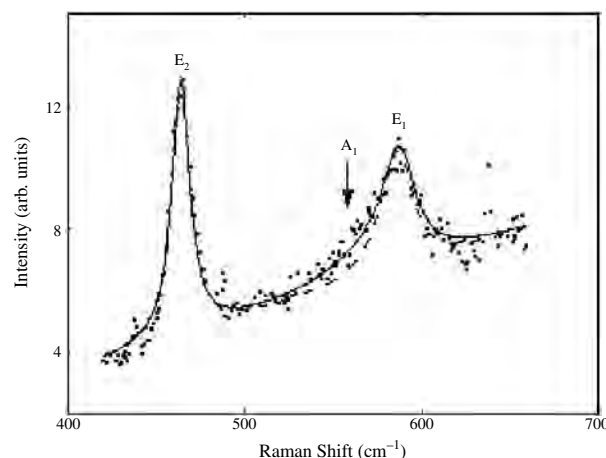
**Figure 8.** Dependence of the vibrational frequencies of  $(n, n)$  armchair single-walled carbon nanotubes on the index  $n$ . The diameter of the nanotube is  $d_n = 1.357n \text{ \AA}$ . The frequencies of the  $A_{1g}$  radial breathing mode and other low-frequency modes depend strongly on the diameter. Adapted with permission from [66], P. C. Eklund et al., *Carbon* 33, 959 (1995). © 1995, Elsevier Science.

mode, independent of the tube diameter. This arises from additional restoring force due to the nearest-neighbor tube-tube interaction [71].

### 3.3. 3D Confined Systems

Isolated or loosely connected nanoparticles as self-supporting powders and nanoparticles dispersed in other hosts have been the most extensively studied nanostructured systems. In many investigations quantitative fitting of phonon lineshape has also been carried out [20, 38, 72]. The extent of peak shift and line broadening is expected to depend on the shape of the dispersion curve. For phonon branches with less dispersion the effects are expected to be small. On the other hand, the phonons that exhibit large dispersion would get modified significantly. This was demonstrated for the first time [37] in the case of zinc oxide nanoparticles by examining the phonons of different symmetries (irreducible representations). Zinc oxide has wurtzite structure and consequently has phonons of symmetries  $A_1$ ,  $E_1$ , and  $E_2$  at 393, 591, and 465  $\text{cm}^{-1}$ , respectively. For a 4-nm particle size,  $E_1$ -LO mode exhibited a change in linewidth from 18 to 38  $\text{cm}^{-1}$  whereas  $E_2$  mode showed an increase of only 2  $\text{cm}^{-1}$ . Figure 9 shows the fitted lineshape for 4-nm particles along with the data. Because of insufficient intensity,  $A_1$  mode was not analyzed in detail. The widely different behavior of  $E_1$  and  $E_2$  phonons could be understood when the widths of the corresponding dispersion curves  $\Delta\omega$  were taken into account. Table 1 shows the peak shift and line broadening data for these modes in 4-nm particles.

There are a number of Raman spectroscopic studies on nanocrystalline powders which exhibit broadening and peak shifts similar to those expected for phonon confinement [73–75]; however, quantitative analyses have not been carried out. In the case of composites synthesized either as thin films using co-sputtering [15] or by doping melt-quenched oxide glasses [76], nanocrystalline precipitates form during annealing at elevated temperatures [77, 78]. A departure of LO phonon frequency from the expected behavior for



**Figure 9.** Raman spectrum of 4-nm ZnO nanoparticles. The continuous curve is the calculated spectrum from Gaussian confinement model. Adapted with permission from [37], M. Rajalakshmi et al., *J. Appl. Phys.* 87, 2445 (2000). © 2000, American Institute of Physics.

**Table 1.** Peak shift  $\delta\omega$  and line broadening  $\Gamma$  data for optical phonons of different symmetries for 4-nm zinc oxide nanoparticles.

Phonon	$\Delta\omega$ (cm <sup>-1</sup> )	$\Gamma_0$ (cm <sup>-1</sup> )	$\Gamma$ (cm <sup>-1</sup> )	$\delta\omega$ (cm <sup>-1</sup> )
E <sub>2</sub>	12	12	14	1
E <sub>1</sub> -LO	60	18	38	7

Note:  $\Delta\omega$  is the width of the dispersion curve and  $\Gamma_0$  is the natural linewidth of the phonon.

CdS nanoparticles smaller than 5 nm dispersed in GeO<sub>2</sub> matrix has been attributed to defects [79]. Evidence of the presence of CdO surface capping layer on pulsed laser deposited CdS nanoparticles in SiO<sub>2</sub> matrix has been found from the presence of its characteristic peak in the Raman spectrum [80]. A comparison of the Raman spectra of Si doped SiO<sub>2</sub> films with those of theoretically calculated vibrational density of states of Si<sub>33</sub> and Si<sub>45</sub> clusters suggested the presence of such clusters in SiO<sub>2</sub> [81]. Semiconductor mixed crystals such as CdS<sub>x</sub>Se<sub>1-x</sub> [82] and Cd<sub>1-x</sub>Zn<sub>x</sub>S [77] dispersed in oxide glasses as nanocrystalline precipitates have been extensively studied in view of their interesting optical properties and applications as long-pass optical filters. The system CdS<sub>x</sub>Se<sub>1-x</sub> exhibits two-mode behavior and both CdSe-like and CdS-like confined LO phonons are observed [20]. On the other hand, Cd<sub>1-x</sub>Zn<sub>x</sub>S system exhibits single-mode behavior. The shift of the LO phonon frequency during late stage of annealing of Cd<sub>1-x</sub>Zn<sub>x</sub>S nanoparticles dispersed in oxide glass host containing 20% ZnO suggested a change in the stoichiometry ( $x$ ) in the nanoparticle [77]. A few monolayers of AlSb deposited on GaAs substrate using molecular beam epitaxy are found to self-assemble in the form of platelike quantum dots during annealing at 500 °C [83]. In addition to phonon confinement effects, sometimes compressive stresses also play a role in determining Raman lineshapes [84]. Nanopores of zeolites have also been used to capture nanoparticles of Se and Te [85]. Raman spectra showed evidence of trapping of either a molecular Se<sub>8</sub> or Te<sub>8</sub> or formation of an irregular array of chains and clusters depending on the size and connectivity of pores. The lifetime of phonons in nanocrystalline Si has also been measured and found to be more than that in amorphous Si [86].

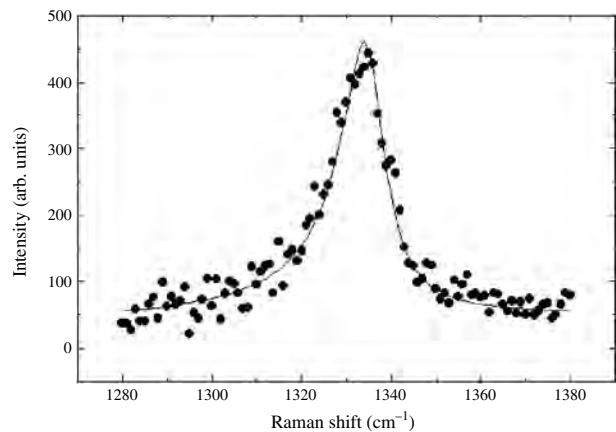
As pointed out earlier, in most of the systems the optical phonon frequency decreases as one moves away from the Brillouin zone center; that is, the optical phonon branch exhibits negative dispersion. In this context, thorium oxide is a unique system, whose optical phonon branch splits into two components; one exhibits a negative dispersion with  $\Delta\omega = -50$  cm<sup>-1</sup>, while the other undergoes a positive dispersion of  $\Delta\omega = +160$  cm<sup>-1</sup> [87]. For nanocrystalline thorium oxide both the branches are expected to contribute to the Raman lineshape. Recently, Raman spectra of nanocrystalline ThO<sub>2</sub> have been reported, which are found to be less asymmetric as compared to other crystals [88]. This is attributed to the broadening arising on the left and the right side of the peak from the contributions from branches of the dispersion curve with negative and positive dispersions, respectively.

In addition to the confined optic phonons, the presence of surface phonons in the Raman spectra of nanostructured materials has been reported in a number of systems

[72, 89–91]. Surface phonons are expected to have frequencies between TO and LO phonons [72]. As the fraction of surface atoms increases as the grain size of a nanostructured material reduces, the surface phonons are observed with noticeable intensity for small size particles. The dependence of surface phonon frequency on the dielectric constant of the surrounding medium has also been examined [90]. In the nanoparticles of mixed crystals such as CdS<sub>x</sub>Se<sub>1-x</sub>, two surface phonons, one each of CdSe-like and CdS-like, have been reported [89].

Porous-silicon (p-Si), obtained from electrochemical etching of Si [92], has been a subject of considerable interest in view of its efficient photo- and electroluminescence at ambient temperature [93]. The pore diameter and consequently the size of interconnected Si-nanostructure depends on the electrochemical conditions [94]. Raman spectrum of p-Si consists of an asymmetrically broadened F<sub>2g</sub> phonon line characteristic of nanocrystalline Si and an overlapping broad peak at 480 cm<sup>-1</sup> associated with amorphous Si [95, 96]. Fitting of the Raman spectrum to a confined phonon lineshape has frequently been carried out to estimate the average particle size [97]. Confined phonons of p-Si have been found to be responsible for the photoluminescence arising from radiative recombination of carriers across the indirect transition [98] similar to that found in crystalline Si.

As mentioned earlier, if the phonon spectrum of the particle overlaps significantly with that of the surrounding medium, phonons of the particles can propagate into the surrounding medium. In such cases a strong confinement model of the Gaussian type is not expected to be satisfactory. This was indeed found to be true [99] in the case of nanocrystalline diamond particles surrounded by amorphous-carbon region. Figure 10 shows the Raman spectrum of nanocrystalline diamond embedded in amorphous-carbon matrix. The observed linewidth was found to be much more than expected for a Gaussian confinement model. In order to understand these results, an alternate confinement model was proposed, which took into account the reflection of the phonon from the dielectric/elastic boundary of the particle. This leads to the existence of a



**Figure 10.** Raman spectrum of 26-nm diamond particles embedded in amorphous-carbon host. The continuous curve is the calculated spectrum based on the discrete model of phonon confinement. Adapted with permission from [99], A. K. Arora et al., *Diamond Relat. Mater.* 10, 1477 (2001). © 2001, Elsevier Science.

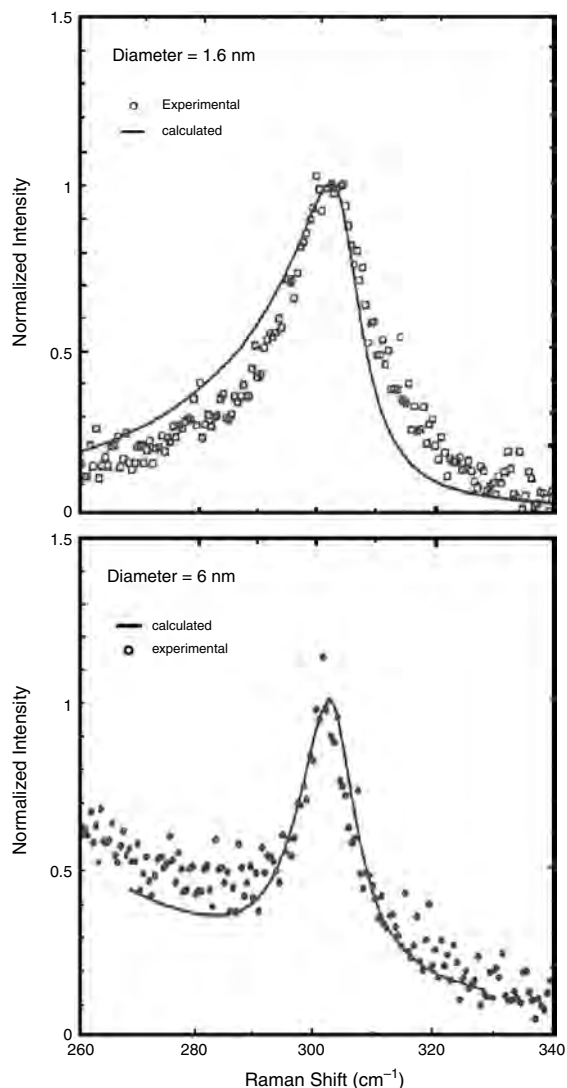
standing wave pattern in the particle with phonon wavevector sampling the Brillouin zone at discrete points  $q_n = nQ_B/N$  ( $1 \leq n \leq N$ ), where  $Na$  is the size of the particle. The intensities  $I_n$  from the discrete phonons  $\omega(q_n)$  were taken to vary according to a power law  $I_n \sim b^n$  ( $b < 1$ ). The discrete model of the phonon confinement yielded a satisfactory fit to the experimental phonon lineshape.

In order to probe the changes in the electron-phonon interaction, resonance Raman scattering from confined optical phonons has been investigated in a number of systems. Effect of valence band mixing, arising from the degeneracy at  $\Gamma$  point in the Brillouin zone of zinc-blende semiconductors, on the electron phonon coupling has been studied [100] in GaP nanoparticles. Surface phonons with angular momentum  $l = 2$  were found to participate in the resonance Raman scattering, while in another study [101] only the transitions with  $l = 0, 2$  have been argued to contribute to the resonance Raman scattering. In addition to the LO phonons, zone-boundary TO phonons and their overtones have also been observed [102] in the nanoparticles of indirect gap semiconductor AgBr under resonant conditions. Using a phenomenological model, the ratio of intensities of the overtone and the fundamental Raman spectra have been analyzed [103] and the results suggested that electron-phonon coupling decreased as the particle size reduced. Interference effects in the resonance Raman efficiency profile [104] of 1- and 2-LO confined phonons in  $\text{Cd}_{1-x}\text{Zn}_x\text{S}$  mixed crystal nanoparticles, arising from a nonresonant contribution to the polarizability, have also been reported. A detailed theory [105] of the one-phonon resonance Raman scattering from spherical nanoparticles has shown that in the dipole approximation, only  $l = 0$  phonon modes couple to the photon. On the other hand, in the electric quadrupole approximation  $l = 1$  phonon modes can be excited and their polarizability amplitude is proportional to the wavevector of the photon.

In most of the analyses of the phonon lineshapes, the bulk phonon dispersion curves have been assumed to be still applicable. However, this is not guaranteed for very small particles. Recent studies have shown that use of bulk phonon dispersion in Gaussian confinement model gives a good agreement for 6-nm CdS particle; on the other hand, for 1.6-nm particles the predicted lineshape is more asymmetric (Fig. 11) than that observed [106]. This disagreement has been attributed to the inapplicability of the bulk phonon dispersion curves. It may be pointed out that the phonon density of states (DOS) of nanocrystalline iron [107] measured using neutron scattering exhibits smearing of sharp features and broadening on both low- and high-frequency side as compared to the bulk. Molecular dynamics simulations show that the increased density of states at low energies arises from the vibrations of atoms at surface/grain boundaries [108], whereas the increase in the DOS at high frequencies has been attributed to shortening of bond length [109] and lifetime broadening [110] due to anharmonic effects.

#### 4. ACOUSTIC PHONONS

Similar to the optical phonons, the acoustic phonons also get confined within the particles. In the elastic continuum limit, the confinement of long-wavelength acoustic phonons



**Figure 11.** Raman spectra of CdS nanoparticles of diameter 1.6 and 6 nm. The disagreement of the calculated lineshape and the data for the 1.6-nm particles suggests inapplicability of bulk phonon dispersion curves. Reprinted with permission from [106], P. Nandakumar et al., *Physica E* 11, 377 (2001). © 2001, Elsevier Science.

(sound waves) leads to the emergence of discrete modes of particle which depend on the elastic properties through the longitudinal and transverse sound velocities [111]. These are spheroidal and torsional modes of the particle and their frequencies depend on the angular momentum associated with the vibration. We now briefly describe the procedure to obtain the frequencies of these modes.

##### 4.1. Vibrational Modes of a Small Particle

By considering a spherical particle to be a homogeneous elastic body, its free vibrations can be obtained by solving the equation of motion [111–113],

$$\rho \partial^2 D / \partial t^2 = (\lambda + \mu) \nabla(\nabla \cdot D) + \mu \nabla^2 D \quad (16)$$

where  $D$  is the displacement,  $\rho$  is the density, and  $\lambda$  and  $\mu$  are Lamé's constants. The solutions are obtained by introducing scalar and vector potentials and by using appropriate boundary conditions for spheroidal and torsional modes. The eigenvalue equation for the spheroidal modes is [111]

$$2[\eta^2 + (l-1)(l+2)\{\eta j_{l+1}(\eta)/j_l(\eta) - (l+1)\}] \\ \times \xi j_{l+1}(\xi)/j_l(\xi) - \frac{1}{2}\eta^4 + (l-1)(2l+1)\eta^2 \\ + \{\eta^2 - 2l(l-1)(l+2)\}\eta j_{l+1}(\eta)/j_l(\eta) = 0 \quad (17)$$

where  $l$  is the angular momentum,  $\eta = \omega R/c_t$  and  $\xi = \eta c_t/c_l$  are dimensionless variables,  $\omega$  is the spheroidal mode frequency,  $R$  is the radius of the particle, and  $c_t$  and  $c_l$  are the transverse and longitudinal sound velocities, respectively.  $j_l(\eta)$  is the spherical Bessel function of the first kind. The angular momentum quantum number  $l$  can take values  $0, 1, 2, \dots$ . The eigenvalue equation for torsional modes is [114]

$$j_{l+1}(\eta) - \frac{(l-1)}{\eta} j_l(\eta) = 0 \quad \text{for } l \geq 1 \quad (18)$$

Solving these equations for discrete values of  $l$  results in a set of eigenvalues for each  $l$ , labeled as  $\eta_{(l,n)}^S$  and  $\eta_{(l,n)}^T$  for spheroidal and torsional modes, respectively. The index  $n$  represents the branch number. It may be mentioned that  $l=0$  torsional mode has null displacement. In addition, the eigenvalues of the torsional modes do not depend on the material, whereas those of spheroidal modes are completely determined by the ratio  $c_l/c_t$ . The eigenvalues of these modes have been reported for many materials with widely different values of the velocity ratio, such as 1.54 ( $\text{MgAl}_2\text{O}_4$ ) [115], 2.00 (Se) [38], 2.28 (CdS) [116, 114], 2.32 (CdSe) [117], 2.51 (Pb) [111], and 2.77 (In) [111]. The lowest eigenvalues for  $n=0$  for both spheroidal and torsional modes correspond to the surface modes. These modes have large amplitude near the surface. The subsequent eigenvalues ( $n \geq 1$ ) correspond to the inner modes. These discrete modes for different values of  $l$  are essentially similar to the acoustic phonons at discrete  $q$ -points in the Brillouin zone given by  $\pi(l+1/2)/R$  up to a maximum value  $\pi/a$  at the zone boundary [111]. These modes modify the density of states of the bulk [118] and have been argued to be responsible for excess specific heat of small particles at low temperatures [119, 120].

The symmetries of the particle vibrations correspond to the irreducible representations of the rotation inversion group  $O(3)$  of the sphere. The spheroidal modes transform according to the irreducible representations  $D_1^g, D_2^u, D_3^g, \dots$  [121]. The subscripts represent the angular momentum, and the superscripts  $g$  and  $u$  imply symmetry and antisymmetry with respect to inversion. In addition, the components of electric dipole moment transform according to  $D_1^u$ . On the other hand, the components of the symmetric polarizability tensor for Raman scattering will transform according to the irreducible representations resulting from the symmetric product  $[D_1^u \times D_1^u]_{\text{sym}} = D_0^g + D_2^g$ . Therefore the only allowed Raman active modes are the spherical mode  $D_0^g$  and the quadrupolar mode  $D_2^g$ . The torsional modes are not Raman active [121]. This is different from the assignment by other

researchers [114, 122] based only on the parity of the wavefunctions, where all spheroidal modes with even  $l$  and all torsional modes of odd  $l$  were argued to be Raman active.

In addition to the elastic continuum model, a microscopic lattice dynamical calculation of confined acoustic phonons in nanocrystalline Si has been carried out [123]. For this the bond polarizability model within the partial density approximation has been used, similar to the confined optical phonon calculation [29]. The disagreement of the calculated confined acoustic phonon frequencies with the experimental data [124] was attributed to the fact that the calculations were carried out for free Si particles while the data was for Si nanoparticles dispersed in  $\text{SiO}_2$  matrix. On the other hand, studies of the effect of host matrix on the spheroidal mode frequencies [111, 125] suggest only marginal changes. In a recent formalism the linewidth of the confined acoustic phonon has also been taken into account by making the eigenvalue complex [126].

## 4.2. Low-Frequency Raman Scattering

The frequencies of the spheroidal and torsional modes can be calculated from the eigenvalues  $\eta_{(l,n)}^S$  and  $\eta_{(l,n)}^T$ , respectively, as

$$\omega_{(l,n)}^S = \eta_{(l,n)}^S c_t / R \quad (19a)$$

and

$$\omega_{(l,n)}^T = \eta_{(l,n)}^T c_t / R. \quad (19b)$$

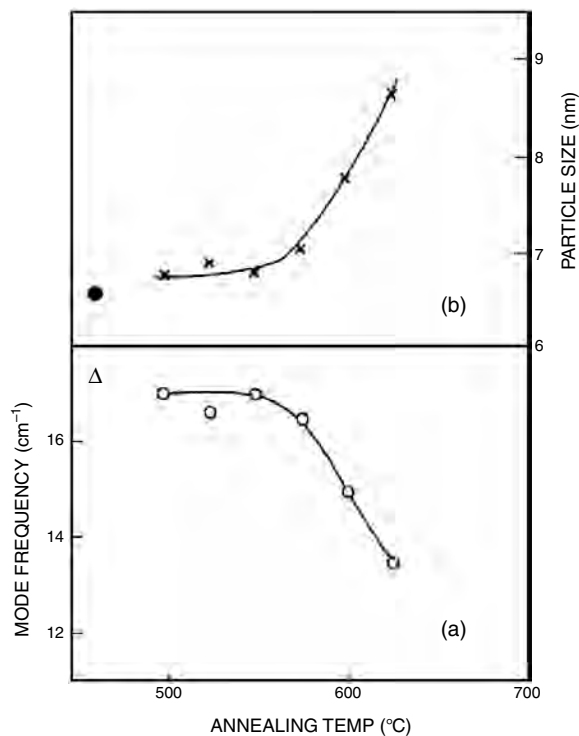
In order to express the vibrational frequencies in  $\text{cm}^{-1}$ , one can divide Eqs. (19) by the velocity of light in vacuum  $c$ . In most materials, for particles of diameter less than 10 nm, these frequencies lie in the range of 5 to 50  $\text{cm}^{-1}$ . Hence it is possible to observe the modes, allowed by the selection rules, in the low-frequency Raman scattering. It is noteworthy that Brillouin spectroscopy is extensively used for probing the acoustic phonon branch close to the zone center in crystalline solids. The Brillouin shifts of the order of 1  $\text{cm}^{-1}$  are conveniently measured by interferometric techniques using Fabry–Perot etalon. However, the range of confined acoustic phonon frequencies makes Brillouin spectroscopy unsuitable for this purpose. On the other hand, the particle modes were observed for the first time by Duval et al. [115] in the spinal ( $\text{MgAl}_2\text{O}_4$ ) particles dispersed in oxide glass in the low-frequency Raman scattering. The inverse dependence of the mode frequencies on the particle size was also established experimentally. Subsequently, confined acoustic phonons have been reported in metal [127–129] and semiconductor [124, 130, 131] nanoparticles.

Often the assignment of the peaks observed in the low-frequency Raman spectrum in terms of angular momentum quantum number  $l$  and branch number  $n$  may be tricky and nonunique. In order to obtain unambiguous assignment, it is useful to know the size of the particle from independent measurements such as high-resolution transmission electron microscopy (HRTEM) [122], X-ray diffraction (XRD) [132], or small-angle X-ray scattering (SAXS) [117] and plot the observed mode frequencies as a function of inverse diameter along with the theoretically expected linear dependencies

[72, 114]. In addition, making a polarized measurement is useful in the assignment, as the spheroidal mode appears only in the polarized geometry while the quadrupolar mode occurs in both polarized and depolarized geometry.

Silver nanoparticles dispersed in different hosts such as alkali halides [128], soda-lime glass [129],  $\text{SiO}_2$  [122, 127], and  $\text{ZrO}_2$  [132] have been studied in great detail. Fuji et al. found the frequencies of Ag particles of sizes between 2 and 5 nm close to those expected for  $l = 0$  and  $l = 2$  spheroidal modes [122]. The strong Raman signal was attributed to resonance associated with localized surface plasmons. The growth of Ag nanoparticles in  $\text{SiO}_2$  during isochronal annealing has been recently examined [127]. In view of its depolarized characteristics, the Raman peak was assigned to the  $l=2$  quadrupolar mode. The average size thus estimated was found to be consistent with that obtained from the width of the surface plasmon absorption. Quadrupolar mode has been observed also for Ag nanoparticles dispersed in soda-lime glass [129]. Silver nanoparticles synthesized in  $\text{ZrO}_2$  by annealing a polycrystalline pellet coated with Ag, at 1073 K exhibited as many as four peaks in the Raman spectra [132] which were assigned to the quadrupolar mode. These were interpreted as arising from a multimodal distribution of particle sizes ranging between 3.5 and 7 nm. However, the average particle diameters obtained from the width of the XRD peak and TEM were of the order of 23 nm. The quadrupolar mode frequency corresponding to such a large average size is much smaller and not expected to be observed in the low-frequency Raman spectrum. This makes their assignment to quadrupolar modes doubtful. The average size of gold clusters found in  $\text{SiO}_2$  due to ion beam mixing and subsequent annealing has been estimated to be around 4 nm from low-frequency Raman scattering [133].

Semiconductor nanoparticles dispersed in oxide glass [77, 116, 134],  $\text{SiO}_2$  [135], and  $\text{GeO}_2$  [114] have been extensively studied. Many of these composites are synthesized by doping the glass by the semiconductor up to about 2% in the melt and rapidly cooling to room temperature. The solid solution thus formed is supersaturated and semiconductor nanoparticles nucleate and grow upon annealing the “semiconductor doped glass” above 500 °C [136]. Synthesis of composites in the form of thin films is carried out using the technique of co-sputtering. There have been several studies on commercial long-pass optical filters such as GG495, GG475, and RG630 from SCHOTT, which contain  $\text{CdS}_x\text{Se}_{1-x}$  mixed crystals dispersed in oxide glass [137]. In the early studies the lowest energy surface mode and the lowest energy breathing mode were identified in the Raman spectra [116]. The frequencies of these modes were found to decrease during annealing, suggesting growth of particles [117]. Figure 12 shows the dependence of spheroidal mode frequency and the estimated particle size on the annealing temperature in  $\text{Cd}_{1-x}\text{Zn}_x\text{S}_{0.95}\text{Se}_{0.05}$  nanoparticles dispersed in oxide glass. During annealing the zinc concentration  $x$  in the nanoparticle was reported to increase, if the host glass contained ZnO as one of the constituents [77]. Some studies have revealed very large width of the confined acoustic phonon  $\omega_{(2,2)}$  in semiconductor doped glass GG495 [134]. This has been attributed to the existence of a log-normal particle size distribution. In addition, resonance enhancement of the quadrupolar



**Figure 12.** Dependence of confined acoustic phonon frequencies (a) and average particle size (b) of  $\text{CdS}_{1-x}\text{Se}_x$  nanoparticles dispersed in borosilicate glass (GG475) on annealing temperature. Symbols ‘●’ and ‘Δ’ represent the corresponding values for the unannealed filter. Reprinted with permission from [77], M. Rajalakshmi et al., *J. Phys.: Condens. Matter* 9, 9745 (1997). © 1997, IOP Publishing.

mode was found for excitation with green wavelength but not with blue line. For CdS nanoparticles dispersed in  $\text{GeO}_2$  glass, a linear dependence of confined phonon frequencies on inverse diameter has been reported [114]. From this analysis the mode was identified as the  $l = 0$  spheroidal mode. In addition to the confined acoustic phonons, another broad peak called “boson peak” arising from the glassy host has been observed in the low-frequency Raman spectra of semiconductor doped glasses [72]. Confined acoustic phonons have also been reported in selenium nanoparticles dispersed in a polymer host [38].

## 5. SUMMARY

In this chapter we have examined the consequences of confinement of the optical and acoustic phonons within a grain of nanostructured materials on the vibrational spectra. These are the shift and asymmetric broadening of the optical phonon lineshape and the appearance of spheroidal and quadrupolar modes of the nanoparticle in the low-frequency Raman spectra. Among the confined acoustic phonons, only the spherical mode with angular momentum  $l = 0$  and quadrupolar mode with  $l = 2$  are Raman active. The inverse dependence of the particle mode frequencies on its diameter is useful as a secondary method for the estimation of particle size. Changes in the optical phonon Raman lineshape arise from the contribution of phonon with finite wavevector whose magnitude is of the order of inverse diameter of the



grain. Noticeable differences in the spectra are found only when the particle/grain size is smaller than about 20 lattice parameters. Furthermore, the effect of confinement is least for 1D confinement and maximum for 3D confinement. For very small grain size the phenomenological models that use the bulk phonon dispersion curves as inputs fail because for these sizes, phonon density of states differs significantly from that of the bulk. Detailed theoretical studies are required to obtain a full understanding of the vibrational spectra of very small size particles.

## GLOSSARY

**Acoustic phonons** Phonons created by atoms vibrating in phase with each other.

**Anharmonic effects** Effects such as thermal expansion, arising from non-parabolic nature of interaction potential between atoms. Parabolic atomic potential leads to harmonic atomic vibrations.

**Brillouin scattering** Inelastic scattering of photons by acoustic phonons in a solid.

**Brillouin zone** Unit cell formed in the reciprocal space by reciprocal lattice vectors.

**Carbon nanotube** A graphene layer rolled up into a tube of diameter of the order of a few nanometers and length several micrometer.

**Chiral vector** A vector formed from the superposition of integral multiples of unit vectors of a 2D-hexagonal plane of graphite. This vector is perpendicular to the axis of the carbon nano-tube, and its magnitude determines the circumference of the tube.

**Dispersion curve** Plot of phonon frequency versus wavevector for a phonon of specific symmetry.

**Long-pass filter** An optical filter that allows light longer than a given wavelength to pass through.

**Nanowire** Wire/rod of a few nanometers diameter and several micrometer length.

**Optical phonon** Phonons in the high frequency region created by atoms in a crystal vibrating out-of-phase with each other.

**Phonon** Quantum of atomic vibrations in crystalline solids.

**Quantum dot** A small particle surrounded by vacuum or a material of larger band gap, capable of exhibiting effects of quantum mechanical confinement of charge carriers.

**Quantum well** A thin layer of a material of smaller band gap sandwiched between adjacent layers of another material with larger band gap, capable of exhibiting effects of quantum mechanical confinement of charge carriers.

**Raman scattering** Inelastic scattering of photons by atomic vibrations or other elementary excitations in solids/molecules.

**Resonance Raman scattering** Enhancement of efficiency of Raman scattering when the incident photon energy is close to one of the electronic transitions in a solid/molecule.

**Scattering vector** Wavevector transferred in the scattering of light by elementary excitations.

**Superlattice** A periodic arrangement formed by depositing thin alternate layers of two materials on a substrate.

**Wavevector** A vector in the direction of propagation of phonon with a magnitude that is inverse of wavelength of the phonon.

## ACKNOWLEDGMENTS

It is a pleasure to acknowledge very fruitful collaborations with Professors S. Mahamuni, D. S. Misra, B. R. Mehta, and C. Vijayan. We also thank Dr. B. Viswanathan for interest in the work, Dr. Baldev Raj for support, and Mr. S. B. Bhoje for encouragement.

## REFERENCES

1. W. M. Tolles, in "Nanotechnology" (G. M. Chow and K. E. Goncalves, Eds.), p. 1. American Chemical Society, Washington, DC, 1996.
2. B. C. Crandall, in "Nanotechnology" (B. C. Crandall, Ed.), p. 1. Massachusetts Institute of Technology, Cambridge, MA, 1996.
3. M. M. Maye, Y. Lou, and C. J. Zhong, *Langmuir* 16, 7520 (2000).
4. M. Hwang, M. C. Abraham, T. A. Savas, H. I. Smith, R. J. Ram, and C. A. Ross, *J. Appl. Phys.* 87, 5108 (2000).
5. K. Butter, P. H. N. Bomans, P. M. Frederik, G. J. Vroege, and A. P. Philipse, *Nature Mater.* 2, 88 (2003).
6. M. E. McHenry, M. A. Willard, and D. E. Laughlin, *Progr. Mater. Sci.* 44, 291 (1999).
7. T. Kusunose, Y. H. Choa, T. Sekino, and K. Niihara, *Ceramic Trans.* 94, 443 (1999).
8. R. K. Jain and R. C. Lind, *J. Opt. Soc. Am.* 73, 647 (1983).
9. A. T. Wu and M. J. Brett, *Sensors Mater.* 13, 399 (2001).
10. U. Woggon, "Optical Properties of Semiconductor Quantum Dots." Springer, Berlin, 1997.
11. P. Milani and C. E. Bottani, in "Handbook of Nanostructured Materials & Nanotechnology" (H. S. Nalwa, Ed.), Vol. 2, p. 213. Academic, New York, 2000.
12. T. R. Ravindran, A. K. Arora, B. Balamurugan, and B. R. Mehta, *NanoStruct. Mater.* 11, 603 (1999).
13. B. G. Potter, Jr., J. H. Simmons, P. Kumar, and C. J. Stanton, *J. Appl. Phys.* 75, 8039 (1994).
14. G. W. Nieman, J. R. Weertman, and R. W. Siegel, *Scr. Metall.* 23, 2013 (1989).
15. Y. Maeda, N. Tsukamoto, Y. Yazawa, Y. Kanemitsu, and Y. Matsumoto, *Appl. Phys. Lett.* 59, 3168 (1991).
16. C. Kittel, "Introduction to Solid State Physics," 4th ed. Wiley, New York, 1971.
17. H. Bilz and W. Kress, "Phonon Dispersion Relations in Insulators." Springer, Berlin, 1979.
18. G. Turrell, "Infrared and Raman Spectra of Crystals." Academic Press, London, 1972.
19. D. A. Long, "Raman Spectroscopy." McGraw Hill, New York, 1977.
20. W. S. O. Rodden, C. M. S. Torres, and C. N. Ironside, *Semicond. Sci. Technol.* 10, 807 (1995).
21. T. Ruf, "Phonon Raman Scattering in Semiconductors, Quantum Wells and Superlattices." Springer-Verlag, Berlin, 1998.
22. B. Li, D. Yu, and S. L. Zhang, *Phys. Rev. B* 59, 1645 (1999).
23. S. Iijima, *Nature* 354, 56 (1991).
24. L. Banyai and S. W. Koch, "Semiconductor Quantum Dots." World Scientific, Singapore, 1993.
25. R. L. Bley and S. M. Kauzlarich, in "Nanoparticles and Nanostructured Films" (J. H. Fender, Ed.), p. 101. Wiley-VCH, New York, 1998.
26. M. Rajalakshmi and A. K. Arora, *Solid State Commun.* 110, 75 (1999).

27. H. Richter, Z. P. Wang, and L. Ley, *Solid State Commun.* 39, 625 (1981).
28. I. H. Campbell and P. M. Fauchet, *Solid State Commun.* 58, 739 (1986).
29. J. Zi, K. Zhang, and X. Xie, *Phys. Rev. B* 55, 9263 (1997).
30. K. K. Tiong, P. M. Amirharaj, F. H. Pollak, and D. E. Aspnes, *Appl. Phys. Lett.* 44, 122 (1984).
31. Z. Iqbal and S. Veprek, *J. Phys. C: Solid State Phys.* 15, 377 (1982).
32. S. Go, H. Bilz, and M. Cardona, *Phys. Rev. Lett.* 34, 580 (1975).
33. C. Falter, *Phys. Rep.* 161, 1 (1988).
34. Z. Sui, P. P. Leong, I. P. Herman, G. S. Higashi, and H. Temkin, *Appl. Phys. Lett.* 60, 2086 (1992).
35. A. Nakajima, Y. Nora, Y. Sugita, T. Itakura, and N. Nakayama, *Jap. J. Appl. Phys.* 32, 415 (1993).
36. J. C. Tsang, M. A. Tischler, and R. T. Collins, *Appl. Phys. Lett.* 60, 2279 (1992).
37. M. Rajalakshmi, A. K. Arora, B. S. Bendre, and S. Mahamuni, *J. Appl. Phys.* 87, 2445 (2000).
38. M. Rajalakshmi and A. K. Arora, *NanoStruct. Mater.* 11, 399 (1999).
39. S. Nakamura, G. Fasol, and S. Pearton, "The Blue Laser Diode." Springer, Heidelberg, 2000.
40. A. K. Sood, J. Menendez, M. Cardona, and K. Ploog, *Phys. Rev. Lett.* 54, 2111 (1985).
41. L. Genzel, T. P. Martin, and C. H. Perry, *Phys. Stat. Sol. (b)* 62, 83 (1974).
42. S. Venugopalan, L. A. Kolodziecki, R. L. Gunshor, and A. K. Ramdas, *Appl. Phys. Lett.* 45, 974 (1984).
43. C. Colvard, T. A. Gant, M. V. Klein, R. Merlin, R. Fischer, H. Morkoc, and A. C. Gossard, *Phys. Rev. B* 31, 2080 (1985).
44. A. K. Arora, E. K. Suh, A. K. Ramdas, F. A. Chambers, and A. L. Moretti, *Phys. Rev. B* 36, 6142 (1987).
45. M. Aigle, H. Pascher, H. Kim, E. Tarhan, A. J. Mayur, M. D. Sciacca, A. K. Ramdas, G. Springholz, and G. Bauer, *Phys. Rev. B* 64, 035316 (2001).
46. C. H. Chen, Y. F. Chen, A. Shih, S. C. Lee, and H. X. Jiang, *Appl. Phys. Lett.* 78, 3035 (2001).
47. A. K. Sood, J. Menendez, M. Cardona, and K. Ploog, *Phys. Rev. Lett.* 54, 2115 (1985).
48. A. K. Arora, A. K. Ramdas, M. R. Melloch, and N. Otsuka, *Phys. Rev. B* 36, 1021 (1987).
49. R. E. Camley and D. L. Mills, *Phys. Rev. B* 29, 1695 (1984).
50. R. P. Wang, G. W. Zhou, Y. L. Liu, S. H. Pan, H. Z. Zhang, D. P. Yu, and Z. Zhang, *Phys. Rev. B* 61, 16827 (2000).
51. Y. F. Zhang, Y. H. Tang, N. Wang, C. S. Lee, I. Bello, and S. T. Lee, *Phys. Rev. B* 61, 4518 (2000).
52. W. Shi, Y. F. Zheng, N. Wang, C. S. Lee, and S. T. Lee, *Appl. Phys. Lett.* 78, 3304 (2001).
53. W. Shi, Y. Zheng, H. Peng, N. Wang, C. S. Lee, and S. T. Lee, *J. Am. Ceram. Soc.* 83, 3228 (2000).
54. S. L. Zhang, B. F. Zhu, F. Huang, Y. Yan, E. Y. Shang, S. Fan, and W. Han, *Solid State Commun.* 111, 647 (1999).
55. Y. Ward, R. J. Young, and R. A. Shatwell, *J. Mater. Sci.* 36, 55 (2001).
56. Y. Zhang, T. Ichihashi, E. Landree, F. Nihey, and S. Iijima, *Science* 285, 1719 (1999).
57. A. M. Morales and C. M. Lieber, *Science* 279, 208 (1998).
58. V. K. Malinovsky and A. P. Sokolov, *Solid State Commun.* 57, 757 (1986).
59. A. K. Arora, D. U. Bartholomew, D. L. Peterson, and A. K. Ramdas, *Phys. Rev. B* 35, 7966 (1987).
60. V. V. Poborchii, V. I. Alperovich, Y. Nozue, N. Ohnishi, A. Kasuya, and O. Terasaki, *J. Phys.: Condens. Matter* 9, 5687 (1997).
61. A. M. Rao, E. Richter, S. Bandow, B. Chase, P. C. Eklund, K. W. Williams, M. Menon, K. R. Subbaswamy, A. Thess, R. E. Smalley, G. Dresselhaus, and M. S. Dresselhaus, *Science* 275, 187 (1997).
62. M. S. Dresselhaus, G. Dresselhaus, and P. C. Eklund, "Science of Fullerenes and Carbon Nanotubes." Academic Press, New York 1996.
63. M. S. Dresselhaus and P. C. Eklund, *Adv. Phys.* 49, 705 (2000).
64. E. Richter and K. R. Subbaswamy, *Phys. Rev. Lett.* 79, 2738 (1997).
65. R. Saito, T. Takeya, T. Kimura, G. Dresselhaus, and M. S. Dresselhaus, *Phys. Rev. B* 57, 4145 (1998).
66. P. C. Eklund, J. M. Holden, and R. A. Jishi, *Carbon* 33, 959 (1995).
67. A. Thess, R. Lee, P. Nikolaev, H. Dai, P. Petit, J. Robert, C. Xu, Y. H. Lee, S. G. Kim, A. G. Rinzler, D. T. Colbert, G. E. Scuseria, D. Tomanek, J. E. Fischer, and R. E. Smalley, *Science* 273, 483 (1996).
68. S. Bandow, S. Asaka, Y. Saito, A. M. Rao, L. Grigorian, E. Richter, and P. C. Eklund, *Phys. Rev. Lett.* 80, 3779 (1998).
69. T. R. Ravindran, B. R. Jackson, and J. V. Badding, *Chem. Mater.* 13, 4187 (2001).
70. J. Hone, B. Batlogg, Z. Benes, A. T. Johnson, and J. E. Fischer, *Science* 289, 1730 (2000).
71. D. Kahn and J. P. Lu, *Phys. Rev. B* 60, 6535 (1999).
72. P. Verma, L. Gupta, S. C. Abbi, and K. P. Jain, *J. Appl. Phys.* 88, 4109 (2000).
73. J. F. Xu, W. Ji, Z. X. Shen, S. H. Tang, X. R. Ye, D. Z. Jia, and X. Q. Xin, *J. Solid State Chem.* 147, 516 (1999).
74. K. K. Nanda, S. N. Sarangi, S. N. Sahu, S. K. Deb, and S. N. Behra, *Physica B* 262, 31 (1999).
75. A. G. Rolo, M. I. Vasilevskiy, N. P. Goponik, A. L. Rogach, and M. J. M. Gomes, *Phys. Stat. Sol. (b)* 229, 433 (2002).
76. A. Tanaka, S. Onari, and T. Arai, *Phys. Rev. B* 45, 6587 (1992).
77. M. Rajalakshmi, T. Sakuntala, and A. K. Arora, *J. Phys.: Condens. Matter* 9, 9745 (1997).
78. S. Y. Ma, Z. C. Ma, W. H. Zong, H. X. Han, Z. P. Wang, G. H. Li, and G. Qin, *J. Appl. Phys.* 84, 559 (1998).
79. A. Tanaka, S. Onari, and T. Arai, *J. Phys. Soc. Jpn.* 61, 4222 (1992).
80. H. Wang, Y. Zhu, and P. P. Ong, *J. Appl. Phys.* 90, 964 (2001).
81. Y. Kanzawa, S. Hayashi, and K. Yamamoto, *J. Phys.: Condens. Matter* 8, 4823 (1996).
82. G. Mei, *J. Phys.: Condens. Matter* 4, 7521 (1992).
83. B. R. Bennet, B. V. Shanabrook, and R. Magno, *Appl. Phys. Lett.* 68, 958 (1996).
84. J. W. Ager III, D. K. Veirs, and G. M. Rosenblatt, *Phys. Rev. B* 43, 6491 (1991).
85. V. V. Poborchii, M. S. Ivanova, V. P. Pebranovskii, Y. A. Barnakov, A. Kasuya, and Y. Nishina, *Mater. Sci. Eng.* A217/218, 129 (1996).
86. M. van der Voort, G. D. J. Smit, A. V. Akimov, J. I. Dijkhuis, N. A. Feoktistov, A. A. Kaplyanskii, and A. B. Pevtsov, *Physica B* 263–264, 473 (1999).
87. M. Ishigame and M. Kojima, *J. Phys. Soc. Jpn.* 41, 202 (1976).
88. M. Rajalakshmi, A. K. Arora, S. Dash, and A. K. Tyagi, *J. Nanosci. Nanotechnol.* 3, (2003), in press.
89. A. Roy and A. K. Sood, *Phys. Rev. B* 53, 12127 (1996).
90. S. Hayashi and H. Kanamori, *Phys. Rev. B* 26, 7079 (1982).
91. A. Ingale and K. C. Rustagi, *Phys. Rev. B* 58, 7197 (1998).
92. L. T. Canham, *Appl. Phys. Lett.* 57, 1046 (1990).
93. K. Li, D. C. Diaz, Y. He, J. Campbell, and C. Tsai, *Appl. Phys. Lett.* 64, 2394 (1994).
94. I. Sagnes and A. Halimaoui, *Appl. Phys. Lett.* 62, 1155 (1993).
95. R. Tsu, H. Shen, and M. Dutta, *Appl. Phys. Lett.* 60, 112 (1992).
96. A. K. Sood, K. Jayaram, and D. V. S. Muthu, *J. Appl. Phys.* 72, 4963 (1992).
97. J. D. Moreno, F. A. Rueda, E. Montoya, M. L. Marcos, J. G. Velasco, R. G. Lemus, and J. M. M. Durat, *Appl. Phys. Lett.* 71, 2166 (1997).
98. G. W. 't Hooft, Y. A. R. R. Kessener, G. L. J. A. Rikken, and A. H. J. Venhuizen, *Appl. Phys. Lett.* 61, 2344 (1992).
99. A. K. Arora, T. R. Ravindran, G. L. N. Reddy, A. K. Sikder, and D. S. Misra, *Diamond Relat. Mater.* 10, 1477 (2001).

100. A. L. Efros, A. I. Ekimov, F. Kozlowski, V. P. Koch, H. Schmidbauer, and S. Shumilov, *Solid State Commun.* 78, 853 (1991).
101. A. V. Baranov, Y. S. Bobovich, and V. I. Petrov, *J. Raman Spectrosc.* 24, 767 (1993).
102. H. Vogelsang, H. Stolz, and W. von der Osten, *J. Lumin.* 70, 414 (1996).
103. J. J. Shiang, S. H. Risbud, and A. P. Alivisatos, *J. Chem. Phys.* 98, 8432 (1993).
104. A. K. Arora and M. Rajalakshmi, *J. Appl. Phys.* 88, 5653 (2000).
105. M. P. Chamberlain, C. T. Giner, and M. Cardona, *Phys. Rev. B* 51, 1680 (1995).
106. P. Nandakumar, C. Vijayan, M. Rajalakshmi, A. K. Arora and Y. V. G. S. Murthi, *Physica E* 11, 377 (2001).
107. B. Fultz, C. C. Ahn, E. E. Alp, W. Sturhahn, and T. S. Toellner, *Phys. Rev. Lett.* 79, 937 (1997).
108. P. M. Derlet, R. Meyer, L. J. Lewis, U. Stuhr, and H. V. Swygenhoven, *Phys. Rev. Lett.* 87, 205501 (2001).
109. A. Kara and T. S. Rahman, *Phys. Rev. Lett.* 81, 1453 (1998).
110. H. Frase, B. Fultz, and J. L. Robertson, *Phys. Rev. B* 57, 898 (1998).
111. A. Tamura, K. Higeta, and T. Ichinokawa, *J. Phys. C: Solid State Phys.* 15, 4975 (1982).
112. H. Lamb, *Proc. Math. Soc. London* 13, 189 (1882).
113. A. E. H. Love, "A Treatise on the Mathematical Theory of Elasticity." Dover, New York, 1944.
114. A. Tanaka, S. Onari, and T. Arai, *Phys. Rev. B* 47, 1237 (1993).
115. E. Duval, A. Boukenter, and B. Champagnon, *Phys. Rev. Lett.* 56, 2052 (1986).
116. B. Champagnon, B. Andrianasolo, and E. Duval, *J. Chem. Phys.* 94, 5237 (1991).
117. B. Champagnon, B. Andrianasolo, A. Ramos, M. Gandais, M. Allais, and J. P. Benoit, *J. Appl. Phys.* 73, 2775 (1993).
118. A. Tamura and T. Ichinokawa, *J. Phys. C: Solid State Phys.* 16, 4779 (1983).
119. N. Nishiguchi and T. Sakuma, *Solid State Commun.* 38, 1073 (1981).
120. V. Novotony and P. P. M. Meincke, *Phys. Rev. B* 8, 4186 (1973).
121. E. Duval, *Phys. Rev. B* 46, 5795 (1992).
122. M. Fujii, T. Nagareda, S. Hayashi, and K. Yamamoto, *Phys. Rev. B* 44, 6243 (1991).
123. J. Zi, K. Zhang, and X. Xie, *Phys. Rev. B* 58, 6712 (1998).
124. M. Fujii, Y. Kanzawa, S. Hayashi, and K. Yamamoto, *Phys. Rev. B* 54, 8373 (1996).
125. M. Montagna and R. Dusi, *Phys. Rev. B* 52, 10080 (1995).
126. P. Verma, W. Cordts, G. Irmer, and I. Monecke, *Phys. Rev. B* 60, 5778 (1999).
127. P. Gangopadhyay, R. Kesavamoorthy, K. G. M. Nair, and R. Dhandapani, *J. Appl. Phys.* 88, 4975 (2000).
128. G. Mariotto, M. Montagna, G. Vilianni, E. Duval, S. Lefrant, E. Rzepka, and C. Mai, *Europhys. Lett.* 6, 239 (1988).
129. M. Ferrari, F. Gonella, M. Montagna, and C. Tosello, *J. Appl. Phys.* 79, 2055 (1996).
130. N. N. Ovsyuk, E. B. Gorkov, V. V. Grishchenko, and A. P. Shebanin, *JETP Lett.* 47, 298 (1988).
131. A. V. Baranov, V. I. Petrova, and Ya. B. Bobovich, *Opt. Spectrosc.* 72, 314 (1992).
132. R. Govindaraj, R. Kesavamoorthy, R. Mythili, and B. Viswanathan, *J. Appl. Phys.* 90, 958 (2001).
133. S. Dhara, R. Kesavamoorthy, P. Magudapathy, M. Premila, B. K. Panigrahi, K. G. M. Nair, C. T. Wu, K. H. Chen, and L. C. Chen, *Chem. Phys. Lett.* 370, 254 (2003).
134. A. Roy and A. K. Sood, *Solid State Commun.* 97, 97 (1996).
135. A. Nakamura, H. Yamada, and T. Tokizaki, *Phys. Rev. B* 40, 8585 (1989).
136. N. F. Borrelli, D. W. Hall, H. J. Holland, and D. W. Smith, *J. Appl. Phys.* 61, 5399 (1987).
137. M. Rajalakshmi, Ph.D. Thesis, University of Madras, 2001.

# Phonons in GaN-AlN Nanostructures

J. Frandon, J. Gleize, M. A. Renucci

*Université Paul Sabatier, Toulouse, France*

## CONTENTS

1. Introduction
  2. Raman Scattering in Hexagonal Crystals and Nanostructures
  3. Phonons in Quantum Wells and Superlattices
  4. Phonons in Quantum Dots Structures
  5. Summary
- Glossary  
References

## 1. INTRODUCTION

The scope of this chapter is the review of recent experimental studies of phonons in nanostructures made of nitride semiconductors with an hexagonal structure. First let us recall some basic definitions. A quantum well (QW) is described as a thin layer exhibiting semiconducting properties, located between a couple of layers made of another semiconductor and playing the role of barriers. Indeed, the electronic bandgap energy in the latter is higher than its counterpart in the former, thus favoring carrier confinement and electrical transport inside the well. Single or multiple QW structures can be fabricated as well as superlattices (SL) which are periodic arrays of QWs. A quantum dot (QD) is an island made of a given semiconductor embedded in another semiconductor acting as barrier. It is usually characterized by a pyramidal shape and a small height (typically 5 nm). The samples are periodic stackings of planes containing the QDs, which can be self-assembled by the effect of vertical correlation.

The purpose of the extensive work recently devoted to GaN-AlN or GaN-AlGaIn nanostructures is the development of new devices, particularly laser diodes emitting in the ultraviolet range. Their light emission is expected to be much stronger than from heterostructures made of GaN and AlN (or AlGaIn) thick layers grown in the nineties, due to the low-dimensional geometry of nanostructures. In addition, the crystallographic structure of nitride semiconductors is responsible for their piezoelectric properties, generating very strong electric fields in strained nanostructures; as a

result, the emission is significantly red-shifted with respect to the absorption edge by the so-called confined quantum Stark effect, and the luminescence can be tuned within a wide interval from the visible range up to the near ultraviolet.

Such high-performance devices, grown using techniques recently developed, are currently fabricated and are already on the market. However, the knowledge of the structural and optical properties involved in the light emission process must be improved. So numerous experimental studies have been recently devoted to such nanostructures. Among the various techniques used for this purpose, Raman spectroscopy is known to be a powerful probe of vibrational modes (or phonons) in semiconductor materials. Measurements of phonon frequencies in nanostructures give the opportunity of determining the strain state inside their constituent layers; these results are key data, directly related to the light emission of the device. This kind of experiment is rather simple, nondestructive, and usually needs no special sample preparation. The size of the optical probe can be very small (as low as 1  $\mu\text{m}$ ). In addition, this technique is accurate and very reproducible, allowing measurements of the phonon energy within an uncertainty lower than 1  $\text{cm}^{-1}$  (about 0.1 meV).

This chapter is organized as follows: basic concepts concerning phonons in bulk nitride semiconductors and GaN-based nanostructures, as well as Raman scattering, are given in Section 1. Section 2 is devoted to the Raman studies on GaN-AlN (or GaN-GaAlN) QW structures and SLs, in non-resonant and resonant conditions. Section 3 of this chapter deals mostly with phonons in QDs stackings.

## 2. RAMAN SCATTERING IN HEXAGONAL CRYSTALS AND NANOSTRUCTURES

### 2.1. Phonons in "Bulk" GaN-Like Semiconductors

Only GaN, AlN, or AlGaIn semiconductors with wurtzite structure will be considered in the present article. Before dealing with nanostructures, we must recall briefly the vibrational properties of bulk crystals, which were recently

reviewed by Frandon et al. [1]. In fact, almost all the samples studied up until now are layers grown on a substrate and on a buffer layer, but they behave usually as “bulk” materials due to their large thickness. Hexagonal nitride crystals belong to the space group  $C_{6v}^4$ . The unit cell contains two nitrogen atoms and two Ga or Al atoms [2]. The lattice constants  $a$  and  $c$  of GaN [3] and AlN [4] are given in Table 1. In the following, the  $c$  axis of the hexagonal structure will be chosen as the  $z$  axis. Let us recall briefly how the symmetry of Raman active modes are derived in this structure. Here we are only interested in the zone center phonons, that is, characterized by a vanishing  $\mathbf{q}$  wavevector. The 12-dimensional representation of the atomic motions in the unit cell can be reduced into irreducible representations of the  $C_{6v}$  group. Besides the acoustic modes and the “silent” (inactive)  $B_1$  optic phonons, one obtains four optical modes, two nonpolar (infrared inactive), and two polar (both Raman and infrared active) phonons [5]. The nonpolar phonons exhibit the  $E_2$  symmetry, corresponding to atomic motions perpendicular to the  $z$  axis. One of them may be observed at low frequency. The other, denoted by  $E_2$  (high), shows up at a higher frequency with a high intensity in Raman spectra recorded far from resonant conditions. In addition, it cannot couple to plasmons and does not display any angular dispersion, on account of its nonpolar character. Therefore, it is frequently used as a probe of structural properties in the Raman characterization of nitride semiconductors.

Polar optic phonons are characterized by their  $A_1$  or  $E_1$  symmetries, related to atomic motions, parallel or normal to the  $z$  axis, respectively. They may be either longitudinal or transverse (LO or TO). In these ionic crystals, the long-range forces associated with the strong macroscopic electric field of longitudinal phonons are responsible for an important LO-TO splitting ( $202 \text{ cm}^{-1}$  for GaN). Moreover, due to the uniaxial properties of these crystals, the LO and one of the TO phonons are extraordinary modes, thus exhibiting an angular dispersion; their frequency varies with the angle  $\theta$  between the phonon wavevector  $\mathbf{q}$  and the  $z$  axis [6]. This variation range corresponds to the  $A_1$ - $E_1$  splitting governed by short-range interatomic forces. However, it should be noted that this variation ( $27 \text{ cm}^{-1}$  for TO phonons of GaN) is much lower than the LO-TO splitting. The symmetry of the  $\mathbf{q} = 0$  extraordinary modes depends on the value of  $\theta$ ; for a vanishing angle, the LO and TO phonons exhibit the  $A_1$  and  $E_1$  symmetry, respectively, and the reverse is found for  $\theta = 90^\circ$ . For intermediate  $\mathbf{q}$  values, the extraordinary modes called quasi-LO and TO (QLO and QTO), have a mixed symmetry. Finally, the ordinary TO phonon is nondispersive and keeps the  $E_1$  symmetry when varying the angle  $\theta$ . Table 2 gives the frequencies of the  $\mathbf{q} = 0$  phonons for relaxed “bulk” GaN and AlN [7, 8].

**Table 1.** Lattice constants  $a$  and  $c$  (nm) for wurtzite GaN and AlN.

	$a$	$c$
GaN <sup>a</sup>	0.31890	0.51864
AlN <sup>b</sup>	0.31106	0.49795

<sup>a</sup> From [3].

<sup>b</sup> From [4].

**Table 2.** Long wavelength phonon frequencies ( $\text{cm}^{-1}$ ) for wurtzite GaN and AlN.

	$E_2$ (low)	$A_1$ (TO)	$E_1$ (TO)	$E_2$ (high)	$A_1$ (LO)	$E_1$ (LO)
GaN <sup>a</sup>	144	533	561	569	735	743
AlN <sup>b</sup>	249	610	669	656	889	912

<sup>a</sup> From [7].

<sup>b</sup> From [8].

Note: The notation of phonons is that used in [5].

Note that  $\mathbf{q} \neq 0$  phonons, usually not involved in first-order Raman scattering, must be invoked in some cases, for example, when the translational symmetry is lost in the sample under study. For hexagonal GaN, the phonon dispersion  $\omega(\mathbf{q})$ , which is quite distinct from the angular dispersion previously discussed, has been calculated in the high-symmetry directions of the Brillouin zone [9, 10] and have been recently determined by X-ray inelastic scattering [11]. A scatter of results is observed, but the dispersion of published data is always found much lower for the branch starting from the  $E_2$  (high) phonon than for its LO counterpart, for example. We must keep in mind this difference when effects of phonon confinement in the nanostructures will be considered later.

For bulk-disordered AlGaN solid solutions, the evolution of phonon frequencies versus their aluminum content is characterized either by a “two-mode” or a “one-mode” behavior, depending on the symmetry of the vibrational mode. In the first case, corresponding to the  $E_2$  (high) optic phonon for example, the GaN- and AlN-like oscillators exhibit strengths of comparable orders of magnitude in most parts of the composition range. In the second case, observed for  $A_1$  (LO) and  $E_1$  (LO) phonons, the oscillator strength is strongly transferred from one to the other type of oscillators, thus allowing the observation of one mode only in the whole composition range of the alloy [12–16]. Evidence for two-mode behavior of the  $E_1$  (TO) mode has been given from infrared measurements [17]. In contrast, the case of the  $A_1$  (TO) phonon seems to be more complicated [16].

As previously mentioned, most samples are thick layers grown on a substrate (sapphire, SiC, or Si) and on a buffer layer (GaN or AlN). Due to the lattice mismatch and to the different expansion coefficients of materials constituting the nanostructure, the layers are usually submitted to a strong biaxial stress acting in the plane normal to the  $z$  axis of the hexagonal crystal. The induced strains  $\varepsilon_{zz}$  and  $\varepsilon_{xx}$ , respectively parallel and perpendicular to the  $z$  axis, modify the phonon frequencies in the layers. For the mode  $\lambda$ , the corresponding frequency shift with respect to its value in the relaxed material is given by the following linear equation

$$\delta\omega_\lambda = 2 a_\lambda \varepsilon_{xx} + b_\lambda \varepsilon_{zz} \quad (1)$$

where  $a_\lambda$  and  $b_\lambda$  are the deformation potentials of the phonon  $\lambda$ . The knowledge of these parameters is of crucial importance for evaluating the strains in the thick layers as well as in the nanostructures. For GaN, the phonon deformation potentials were measured [18–19] and calculated [20–21], but they are more controversial for AlN [22–25]. Some of the calculated and experimental values of phonon

deformation potentials are given for wurtzite GaN and AlN in Table 3.

When the material is under biaxial stress  $\sigma^B$  ( $\sigma^B > 0$  for compressive stress), one can also use the Raman stress coefficient, defined by

$$K^B = \frac{d\omega}{d\sigma^B} \quad (2)$$

If Hooke's law is obeyed,  $K^B$  can be expressed using the deformation potentials and the elastic constants only. As a rule, the observed frequency shift of phonons is positive (resp., negative) if the material is under compressive (resp., tensile) biaxial stress.

## 2.2. Phonons in GaN-Based Nanostructures

Let us consider nanostructures made of alternate layers exhibiting the wurtzite structure, grown along the  $z$  axis. Their structural and optical properties have been extensively studied during recent years. Under adequate growth conditions, the Stranski–Krastanov mechanism of strain relaxation of GaN on AlN leads to the growth of strained GaN islands on very thin (two monolayers thick) GaN wetting layers, embedded in the AlN barriers, leading to QD structures [26]. Different experimental conditions allow a two-dimensional growth, thus leading to strained QW structures or to SLs; the internal strain of the layers depends on numerous factors, including the nature of the underlying buffer layer and the thicknesses of the layers in the structure. Obviously, as a result of internal strains, the phonons from the wells and barriers will be shifted in the Raman spectra according to Eq. (1). The same equation may also be tentatively applied to QDs, assuming a nearly biaxial stress, in consideration of their pyramidal shape and their lateral size usually about 10 times larger than their height.

But new vibration modes must be considered in nanostructures. Some phonons can be confined inside one type of layer. Their properties have been extensively studied in the SLs made of III–V cubic semiconductors, such as GaAs

and AlAs [27]. Confined vibrational modes are oscillations located in one type of layer and characterized by an effective wavevector  $q_z$ . The latter is quantized, due to boundary conditions at the interfaces with the adjacent layers

$$q_z = n \cdot \frac{\pi}{d_1} \quad (3)$$

where  $n$  is an integer and  $d_1$  is the layer thickness. The frequencies of confined modes can be deduced from the LO phonon dispersion  $\omega(\mathbf{q})$  of the bulk material along the  $z$  direction; they correspond to the discrete  $q_z$  values calculated using Eq. (3). If the top of the branch of the LO branch is at the zone center  $\Gamma$ , as for the LO phonon of GaN, frequency shifts towards lower frequencies are expected and can be measured, specially for very thin (a few nanometers thick) layers. On the other hand, confinement effects should be negligible for the  $E_2$  (high) phonon, due to the weak dispersion of the corresponding branch in the Brillouin zone.

Other phonons specific to the SLs are the “folded” acoustic phonons. Indeed, if the dispersion of acoustic branches is similar in both materials, that is, when their sound velocities are not too different, acoustic waves can propagate through the whole nanostructure. Folding of the acoustic phonon branches of the constituent layers into the reduced Brillouin zone of the SL generate new vibrational modes, which are characteristic of the periodicity  $d = d_1 + d_2$  of the SL ( $d_1$  and  $d_2$  stand for the thicknesses of wells and barriers, respectively). They may show up as doublets located in the low-frequency range of the Raman spectra. The average frequencies of these doublets are given by [27]

$$\omega_n = n \cdot \frac{2\pi \cdot v}{d} \quad (4)$$

where  $n$  is an integer and  $v$  is an average sound velocity in the nanostructure calculated from the sound velocities  $v_1$

**Table 3.** Phonon deformation potentials in Wurtzite GaN and AlN.

	$a_\lambda$ (cm <sup>-1</sup> )					
	$E_2$ (low)	$A_1$ (TO)	$E_1$ (TO)	$E_2$ (high)	$A_1$ (LO)	$E_1$ (LO)
GaN, calculated <sup>a</sup>	+75	-640	-717	-742	-664	-775
GaN, measured	+115 <sup>b</sup>	-630 <sup>b</sup>	-820 <sup>b</sup>	-850 <sup>b</sup> , -818 <sup>c</sup>	-685 <sup>c</sup>	
AlN, calculated <sup>a</sup>	+149	-776	-835	-881	-739	-867
AlN, measured		-930 <sup>d</sup>	-982 <sup>d</sup>	-1092 <sup>d</sup> , -1083 <sup>c</sup>	-643 <sup>d</sup>	
	$b_\lambda$ (cm <sup>-1</sup> )					
	$E_2$ (low)	$A_1$ (TO)	$E_1$ (TO)	$E_2$ (high)	$A_1$ (LO)	$E_1$ (LO)
GaN, calculated <sup>a</sup>	4	-695	-591	-715	-881	-703
GaN, measured	-80 <sup>b</sup>	-1290 <sup>b</sup>	-680 <sup>b</sup>	-920 <sup>b</sup> , -797 <sup>c</sup>	-997 <sup>c</sup>	
AlN, calculated <sup>a</sup>	-223	-394	-744	-906	-737	-808
AlN, measured		-904 <sup>d</sup>	-901 <sup>d</sup>	-965 <sup>d</sup> , -1187 <sup>c</sup>	-1157 <sup>d</sup>	

<sup>a</sup> From [21].

<sup>b</sup> From [19].

<sup>c</sup> From [18].

<sup>d</sup> From [25].

<sup>e</sup> From [23].

and  $v_2$  in the wells and barriers of the SL according to

$$v = \frac{v_1 \cdot v_2}{(1 - \alpha)v_2 + \alpha v_1} \quad (5)$$

where  $\alpha = d_2/(d_1 + d_2)$ . The frequency difference between the components of each doublet depends on the phonon wavevector  $q_z$

$$\Delta\omega = 2 q_z \cdot v \quad (6)$$

The value of  $q_z$  is determined by the experimental geometry of Raman scattering, as it will shown in the following section.

### 2.3. Experiments

In the following, the incident (resp., scattered) light is defined by its wavevector  $\mathbf{k}_i$ , its frequency  $\omega_i$ , and its linear polarization  $\mathbf{e}_i$  (resp.,  $\mathbf{k}_s$ ,  $\omega_s$  and  $\mathbf{e}_s$ ). The experimental configuration will be indicated by the usual Porto's notation  $\mathbf{k}_i(\mathbf{e}_i \mathbf{e}_s)\mathbf{k}_s$ . For bulk crystals, conservation law between the initial and final states is obeyed both by the wavevector and the energy. In first-order Raman scattering, the wavevector  $\mathbf{q}$  and the frequency  $\omega$  of the phonon involved in the scattering process are given by

$$\mathbf{q} = \mathbf{k}_i - \mathbf{k}_s \quad (7)$$

and

$$\omega = \omega_i - \omega_s \quad (8)$$

According to Eqs. (7) and (8),  $\mathbf{q}$  is completely defined by the experimental geometry and the laser energy. In the particular case of backscattering ( $\mathbf{k}_s = -\mathbf{k}_i$ ), Eq. (7) can be written as

$$|\mathbf{q}| = 2|\mathbf{k}_i| = \frac{4\pi \cdot n}{\lambda_i} \quad (9)$$

where  $n$  is the refractive index of the material at the frequency  $\omega_i$ , and  $\lambda_i$  is the wavelength of the incident light.

Most Raman spectra of GaN-AlN or GaN-AlGaIn nanostructures reported in the literature have been recorded at room temperature. The simplest experiment is performed in a backscattering geometry along the growth axis  $z$  of the nanostructure, with polarizations of incident and scattered light either perpendicular or parallel, corresponding to the configurations  $z(xy)\underline{z}$  or  $z(xx)\underline{z}$ , respectively. In the latter case, both  $E_2$  and  $A_1$  (LO) phonons are allowed. Moreover, a micro-Raman spectrometer, using a small laser spot whose diameter is lower than  $1 \mu\text{m}$ , allows the achievement of other scattering conditions, particularly backscattering on the edge of the sample under study. In this configuration, the phonon wavevector  $\mathbf{q}$  is perpendicular to the  $z$  axis and additional phonons can be evidenced. The selection rules for all the Raman active phonons in wurtzite materials are recalled in Table 4.

The excitation of Raman scattering is usually made using the monochromatic lines of an argon or krypton laser, either in the visible or ultraviolet range (from 3.41 eV to 3.80 eV). The experimental results strongly depend on the excitation energy. If the latter corresponds to the visible range, that is,

**Table 4.** Selection rules for phonons in wurtzite crystals.

Configuration	Allowed phonons
$z(xx)\underline{z}$	$E_2, A_1$ (LO)
$z(xy)\underline{z}$	$E_2$
$x(zz)\underline{x}$	$A_1$ (TO)
$x(yy)\underline{x}$	$E_2, A_1$ (TO)
$y(zy)\underline{x}$	$E_1$ (LO)

*Note:* The notation of phonons is that used in [5].

far from any electronic resonance, the dominant electron-phonon interaction is the “deformation potential” process and the nonpolar  $E_2$  (high) optic phonon exhibits a scattering cross section much stronger than the other phonons, specially the  $A_1$  (LO) mode also allowed in the  $z(xx)\underline{z}$  configuration. Note that the Raman spectra usually contain features from the GaN QDs or QWs and from the barriers of the nanostructure, but also from the underlying thick buffer layer (usually GaN or AlN), due to the negligible optical absorption of the constituent layers in the visible range; thus an unambiguous assignment of phonons may prove difficult. However, the signature of the nanostructure itself can be obtained using a confocal set-up with a low depth of focus, as illustrated later.

On the other hand, a strong enhancement of Raman scattering by the polar LO phonon is observed under near resonant conditions, that is, if the energy of incident or/and scattered photons is close to an electronic transition energy, when the “forbidden” scattering process associated with the intraband Fröhlich electron-phonon interaction becomes dominant [28]. With the present materials, resonant conditions can be achieved in the ultraviolet range only; indeed the room temperature bandgap energy is about 3.4 eV and 6.1 eV for bulk GaN and AlN, respectively. The scattering cross section of the  $A_1$  (LO) phonon can be enhanced by several orders of magnitude [29], thus allowing the signature of very small volumes inside the sample. However, it should be noted that the penetration depth of the incident light in the sample is strongly reduced under ultraviolet excitation, due to high optical absorption. In addition, an intense photoluminescence (PL) band may show up in the spectra, making an observation of faint Raman features superimposed on the PL signal very difficult.

## 3. PHONONS IN QUANTUM WELLS AND SUPERLATTICES

### 3.1. Nonresonant Raman Scattering: Signature of Wells and Barriers in Superlattices

When Raman experiments are performed far from resonant conditions, the signal coming from the nanostructure itself is rather weak; it can be easily measured only if the sample is thick enough (about  $0.5 \mu\text{m}$ ), due to the low-scattering cross section of GaN, and specially of AlN. Actually, this kind of research study is still scarce; the main motivation is to determine the nature of the vibrational modes in the SLs and to derive the built-in strain of the constituent layers.

The first Raman study of an SL with a wurtzite structure was published by Gleize et al. [30]. This structure was made of a hundred periods of undoped GaN wells and AlN barriers, with nominal thicknesses of 6.3 nm and 5.1 nm respectively, deposited by MBE on a thick AlN buffer layer and a sapphire substrate. The layer thicknesses were large enough for neglecting the frequency shift of phonons induced by confinement, specially for the  $E_2$  mode. Micro-Raman spectra were recorded in backscattering geometry under various polarization configurations, under a 2.54 eV excitation, far from resonant conditions. Thanks to selection rules, most observed features could be unambiguously assigned to all optical phonons but the  $E_1$  (LO), either from the underlying AlN buffer layer or from each type of SLs layers. Due to internal strains, phonons from wells and barriers were found significantly shifted with respect to their frequency in relaxed materials. Using the phonon deformation potentials of GaN, a biaxial stress of 6.3 GPa and an in-plane strain  $\varepsilon_{xx} = -1.3\%$  were derived for the GaN layers of the SL from the measured shift of the  $E_2$  (high) phonon. This strain is close to the value expected for a “free-standing” state of the present nanostructure. On the other hand, the measured frequency shifts of AlN phonons, actually larger than those of GaN phonons, could not be used to determine the internal strain in the barriers of the SL, because the corresponding deformation potentials were not known at this time. Note that a feature observed at  $560\text{ cm}^{-1}$  in  $x(yy)x$  Raman spectra could not be associated to an  $A_1$  (TO) phonon from strained GaN layers, although it obeyed the regular selection rules; it was thus tentatively assigned to an interface mode. Finally, micro-Raman spectra were also recorded from place to place on a bevel made by mechanical polishing of the nanostructure; the angle between the beveled surface and the (0001) plane was about  $1^\circ$ . The strain-induced shift of the  $E_2$  (GaN) phonon was found higher in the deeper part of the SL than near the surface, giving evidence for a partial strain relaxation in the first layers of the structure.

Schubert et al. [31–32] performed other investigations combining Raman scattering and infrared ellipsometry experiments. The latter is an indirect technique for investigating the polar phonons, specially the  $E_1$  (TO) phonon when a near normal incidence is used for the measurements. A standard calculation allows the reproduction of the experimental infrared spectrum; this model needs several fitting parameters, including the TO and LO phonon frequencies of the constituent materials, together with the concentration and mobilities (parallel and perpendicular to the  $z$  axis of the SL) of free carriers. The latter data must be introduced when the sample under study is doped, intentionally or not. Indeed, the free-carrier plasmon and the LO phonon, which are both longitudinal excitations, can couple together if their energies are close to each other, thus shifting in frequency the high frequency component of the coupled mode with respect to the uncoupled phonon [33]. In [32], eight GaN-AlGaN SLs, grown by MOVPE or by MBE on thick GaN layer and on sapphire, exhibiting typical layer thicknesses of 25 nm and various aluminum contents in the barriers ( $0.08 < x < 1$ ), were compared. As expected, the strain-induced frequency shifts of the nonpolar  $E_2$  phonon for each constituent layer, derived from Raman measurements, proved that GaN (resp., AlGaN) layers were

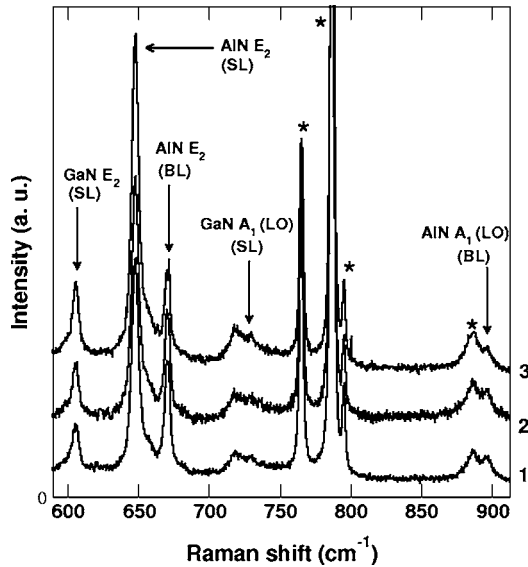
submitted to an internal compressive (resp., tensile) stress. A detailed discussion of the Raman data suggested that these SLs were in a free-standing state: both kinds of layers adopted a common in-plane lattice parameter, different from the one of the underlying thick GaN layer. The analysis of infrared ellipsometry measurements led to the determination of an electron concentration higher than  $10^{18}\text{ cm}^{-3}$  in the GaN layers of the SLs; these free carriers could originate from dislocation-activated donors or from the AlGaN layers. Moreover, the in-plane mobility introduced for fitting the infrared spectra was found higher than its out-of-plane counterpart: this result indicated a confinement of free carriers inside the wells along the  $z$  axis, the AlGaN layers of the SL acting as barriers for the free electrons as expected.

Another more recent article combining Raman and X-ray diffraction measurements [34] deals with a GaN-AlN SL grown on an AlN buffer layer and on a 6H-SiC substrate; the GaN wells were specially thin (1.5 nm) in this sample, compared to the AlN barriers (10 nm). The map of the reciprocal lattice, which was deduced from X-ray diffraction experiments, gave the average value of both lattice constants  $a$  and  $c$  of the whole SL. Figure 1 shows three micro-Raman spectra recorded in the  $z(xx)z$  configuration, when the laser spot was focused slightly higher and higher upon the surface of the sample. The variation of relative intensities of the experimental features made their assignment easy either to the SLs layers or to the underlying buffer layer, allowing the measurement of the strain-induced frequency shift of the  $E_2$  (high) phonons from the SL. Combining all these data and taking into account the measured in-plane strain of GaN layers ( $\varepsilon_{xx} = -2.35\%$ ) derived from *in-situ* RHEED experiments, both components of the biaxial strain of AlN and GaN layers could be determined. The out-of-plane strain  $\varepsilon_{zz}$  was found almost negligible for both types of layers, giving for the ratio  $\varepsilon_{zz}/\varepsilon_{xx}$  a value quite different from that predicted from the simple elastic theory ( $-2C_{13}/C_{33} = -0.51$ ). This difference is likely due to the large spontaneous and piezo-electric polarization effects which can significantly decrease this strain ratio in the hexagonal SL, as demonstrated in a calculation by Gleize et al. [35].

### 3.2. Resonant Raman Scattering: Signature of Single or Multiple QWs

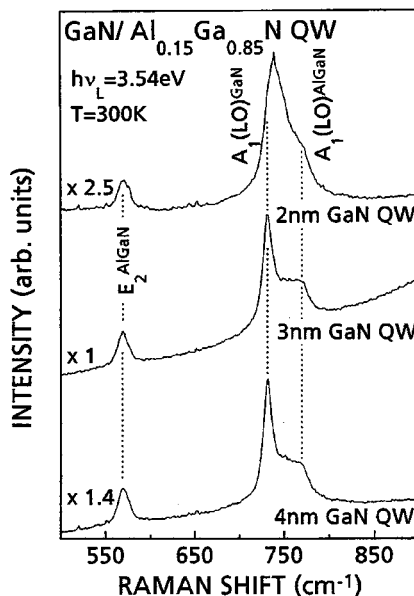
The first resonant Raman study of single GaN QWs was published by Behr et al. [36]. In these samples grown by MOCVD directly on a sapphire substrate without any buffer layer, the wells lying between thick  $\text{Ga}_{0.85}\text{Al}_{0.15}\text{N}$  layers were 2 nm, 3 nm, or 4 nm thick. As expected, only the phonons from the alloy were evidenced when the excitation was achieved in the visible range, due to the negligible volume of the QW. However, when the 3.54 eV laser line was used for the excitation, that is, for an energy close to the estimated fundamental electronic transitions in the wider QWs, the resonance conditions were nearly fulfilled and Fröhlich-induced scattering by the GaN  $A_1$  (LO) mode was favored. As can be shown in Figure 2, a Raman feature was observed at  $732\text{ cm}^{-1}$  for the structures containing the 3nm- and 4nm-wide QWs. The origin of this feature could be unambiguously assigned to the single well; its measured frequency shift was negligible, because both confinement and strain





**Figure 1.** Micro-Raman spectra recorded in backscattering along the  $z$  axis, on a GaN (1.5 nm)-AlN (10 nm) SL grown on an AlN BL and a SiC substrate. The excitation was made at 2.33 eV. Spectra 1 to 3 were obtained by focusing farther and farther away from the surface of the sample. Modes from the SL and the BL are indicated by arrows. Asterisks mark phonons from the substrate. Reprinted with permission from [34], J. Frandon et al., *Physica E* (2003). © 2003, Elsevier Science.

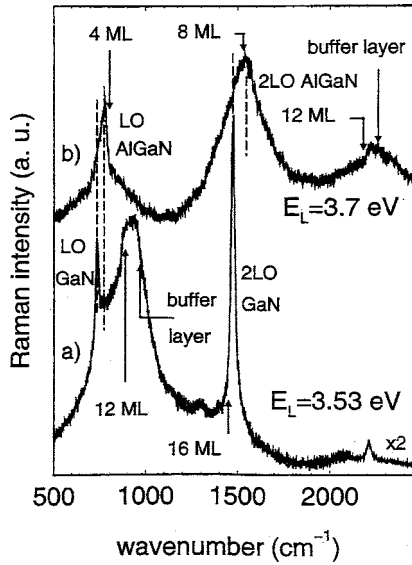
effects were probably weak in the well. In contrast, the LO feature was broadened and shifted towards higher frequencies for the 2 nm thick QW. This observation was explained by cation intermixing at the GaN-AlGaN interface, which could not be neglected in that case. Smoothing of interfaces likely due to poor growth conditions prevents the signature of confinement effects, which would induce an opposite frequency shift.



**Figure 2.** Resonant Raman spectra of GaN single QW with different widths embedded in  $\text{Al}_{0.15}\text{Ga}_{0.85}\text{N}$  barriers, recorded under the 3.54 eV excitation. Reprinted with permission from [36], D. Behr et al., *Appl. Phys. Lett.* 70, 363 (1997). © 1997, American Institute of Physics.

Further resonant scattering experiments on single or multiple GaN-AlGaN QW structures will be reported in the following. Later Ten GaN QWs of 1.5 nm width, embedded in 5 nm wide  $\text{Ga}_{0.89}\text{Al}_{0.11}\text{N}$  barriers and grown on a GaN buffer layer, have been investigated under various ultra-violet excitations [37]. In the present structure, the QWs were nearly relaxed, whereas the barriers were submitted to an internal compressive stress, due to the presence of the underlying buffer layer. As expected, first-order scattering by the  $A_1$  (LO) phonons from GaN wells, favored by the Fröhlich interaction, was found strongly enhanced by electronic resonance in the incoming channel when excitation is achieved using the 3.54 eV laser line. Indeed, the energy of the incident photon was very close to the QWs' fundamental transition, as estimated using the simple model of independent square potential wells of finite height. In these experimental conditions, the second-order scattering by the LO phonons from the thick buffer layer was dominant. Under a 3.70 eV excitation, LO phonons from GaN wells were clearly evidenced in the second-order scattering signal, due to electronic resonance in the outgoing channel; weak contributions from the barriers were also evidenced. Similar features were also observed in third-order scattering under 3.80 eV excitation.

Another study performed in resonant conditions has been devoted to a collection of four different single GaN QWs separated by 10 nm thick  $\text{Ga}_{0.83}\text{Al}_{0.17}\text{N}$  barriers and grown on a thick GaN buffer layer [38]; their thicknesses were 1 nm, 2 nm, 3 nm, and 4 nm (corresponding, respectively, to 4, 8, 12, 16 monolayers). The fundamental excitonic transitions in these wells were already determined from previous PL measurements performed at a low temperature. In this work, thick GaN and  $\text{Ga}_{0.83}\text{Al}_{0.17}\text{N}$  layers were also investigated in the same experimental conditions for comparison with the structure under study. The Raman spectra recorded at room temperature in backscattering geometry are shown in Figure 3. The PL signature of the various wells was clearly observed in the spectra, thus accurately giving the energy of the fundamental transitions in the wells at room temperature. Under excitation at 3.53 eV, first-order scattering by GaN  $A_1$  (LO) phonons confined in one of the wider QWs (3 nm) showed up in the spectra, enhanced by electronic resonance in the outgoing channel; no similar observation could be achieved on the thick GaN layer used as reference, since the excitation was too far from resonance in the bulk material. The measured frequency was close to  $734\text{ cm}^{-1}$ , corresponding to relaxed GaN, because the well involved was almost unstrained in the nanostructure. In this case, the Raman signature of the 3 nm-thick well, whose PL signal was located at 3.43 eV, close to the observed Raman feature, could be obtained. On the other hand, when the 3.70 eV excitation was used, a first-order Raman feature peaking at higher frequency ( $775\text{ cm}^{-1}$ ) and a weak contribution at lower frequency was observed. They are clearly related to phonons of the  $\text{Ga}_{0.83}\text{Al}_{0.17}\text{N}$  barriers and of the GaN wells, respectively. Scattering by vibrational modes of both layers requires an extended intermediate electronic state of the QW with a significant penetration into the barriers. This delocalization implies high-lying states whose energy is close to the bandgap of the alloy. Resonance most likely



**Figure 3.** Resonant Raman spectra of four single GaN QW in  $\text{Al}_{0.17}\text{Ga}_{0.83}\text{N}$  barriers, recorded using 3.53 eV and 3.70 eV excitations. The thicknesses of these QWs were 4, 8, 12, and 16 monolayers. Arrows mark the PL signal from the QWs. Reprinted with permission from [38], F. Demangeot, *Phys. Stat. Sol. (B)* 216, 799 (1999). © 1999, Wiley-VCH.

occurred in the incoming channel, as the incident photon energy was almost tuned on the bandgap of the alloy. Moreover, the Raman signal was found just superimposed on the PL signal from the thinner (1 nm) QW, centered at 3.60 eV; no similar Raman features could be observed with thick GaN or  $\text{Ga}_{0.83}\text{Al}_{0.17}\text{N}$  thick layers. The signal was thus likely enhanced by a double resonance effect, as the second intermediate state involved in the Raman process was a bound electronic state localized in the 1 nm-thick QW.

### 3.3. Calculations of Lattice-Dynamical Properties of Wurtzite Nanostructures

Komirenko et al. [39] first investigated the extraordinary polar phonons of wurtzite single QWs in the framework of a dielectric continuum model. The anisotropy of the materials was taken into account by introducing both components  $\varepsilon_{\perp}(\omega)$  and  $\varepsilon_z(\omega)$  of the frequency-dependant dielectric tensor of the constituent materials; the latter involve the frequencies of  $A_1$  and  $E_1$  (LO and TO) phonons, polarized along the  $z$  axis and in the  $(xOy)$  plane, respectively. The electrostatic boundary conditions on the interfaces, together with the assumption of a scalar potential vanishing far from the wells, were used. For a long wavelength phonon characterized by the in-plane  $q_{\perp}$  wavevector, the angular dispersion can be deduced from the following equation:

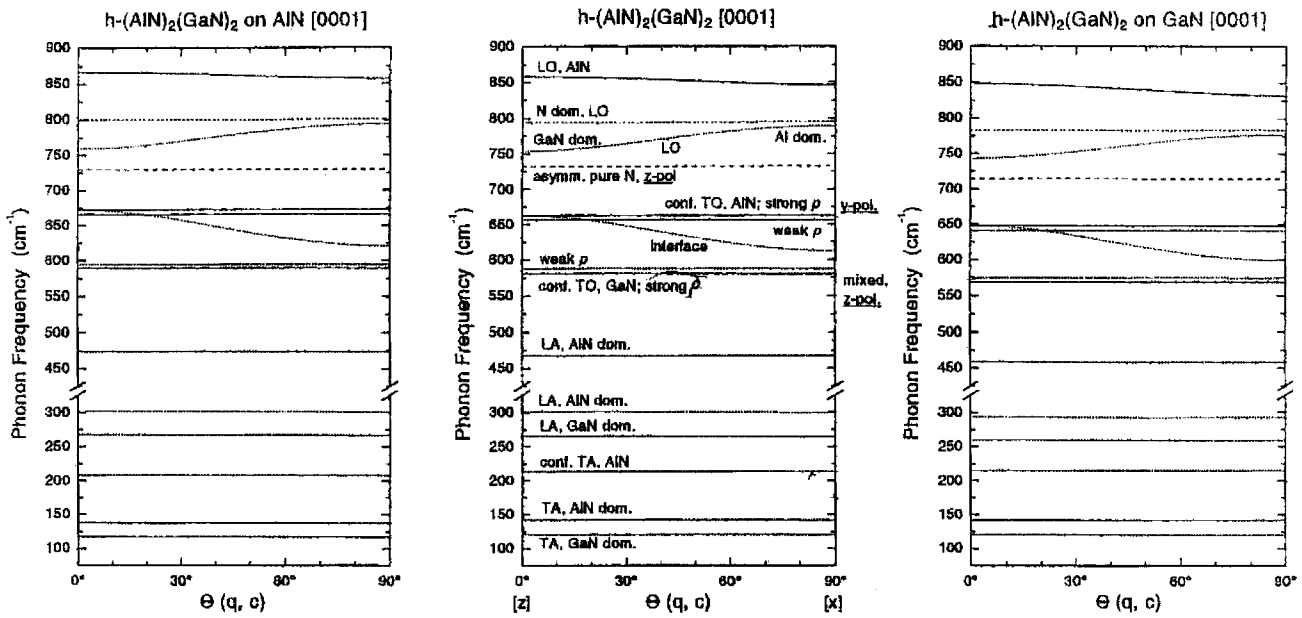
$$\varepsilon_{\perp}(\omega) \cdot q_{\perp}^2 + \varepsilon_z(\omega) \cdot q_z^2 = 0 \quad (10)$$

where  $q_z$  is the  $z$  component of an effective wavevector. Depending on the sign of the product  $\varepsilon_{\perp} \cdot \varepsilon_z$  in each medium,  $q_z$  is found either real or imaginary, leading to linear superposition of oscillating or decaying solutions, respectively. Therefore, phonons could be classified according to their localization. Confined modes are mainly located inside

the well but can penetrate significantly into the surrounding layers, interface modes decay exponentially from the interfaces in both types of layers, and propagating modes oscillate in the whole structure. Their frequency variation versus the product  $q_{\perp} \cdot d$  was given for a GaN well of width  $d$  embedded in infinite barriers made of AlN or of  $\text{Ga}_{0.85}\text{Al}_{0.15}\text{N}$ . Note that in another article, the same authors extended their study to the calculation of scattering rates by the Fröhlich electron-phonon interaction in QW structures [40].

Very few investigations of lattice dynamics in hexagonal superlattices by *ab initio* calculations have been published up until now. Wagner et al. [41] computed the structural, dielectric, and lattice-dynamical properties of short-period hexagonal GaN-AlN SLs, which were compared to their cubic counterparts. In this calculation, the widths of barriers as well as of QWs were as low as two monolayers. Both types of layers were assumed to be pseudomorphically strained on the same in-plane lattice constant; the latter could be either that of relaxed constituent materials (AlN or GaN) or an average value corresponding to an elastically relaxed SL. The goal of this work was to study the angular dispersion of phonons in the structures. The frequency  $\omega$  of the zone center phonons was calculated as a function of  $\theta$ , the tilt angle of the phonon wavevector with respect to the  $z$  axis, within the framework of the density-functional perturbation theory. Most calculated modes were assigned either to confined phonons or to interface phonons. The atoms involved in each vibration mode, together with the strength of the associated dynamical polarization, were also given. The angular dispersion of these modes is shown in Figure 4 for a GaN-AlN wurtzite SL in several strain states. Actually, only a few differences were evidenced in the angular dispersions of cubic and hexagonal SLs. In both cases, for an increasing in-plane lattice constant, all modes decrease in frequency, except the folded TA modes; the downward shift was found more pronounced for LO phonons than for the TO phonons. The only remarkable difference affects the TO modes confined in the GaN layers of the hexagonal SL, spreading in a narrower range than their counterparts in the cubic nanostructure.

However, the latter results cannot be easily checked. Indeed, experimental studies are usually performed on nanostructures with much larger periods. An alternative calculation based on the dielectric continuum model, first developed in [39] for the GaN QWs, was applied to wurtzite SLs with more realistic periods [42–44]. Within this framework, the vibrational modes were described by the dynamical polarization associated with the atomic motions in each type of layer. The Maxwell equations, the electric boundary conditions at each interface, and the Bloch's theorem, taking into account the SLs periodicity, were used together with the  $\mathbf{q} = 0$  phonon frequencies of the two types of layers in the strain state actually achieved in the SL. Note that the phonon dispersion  $\omega(\mathbf{q})$  of the bulk constituents was ignored in this model. For GaN-AlN SLs, this calculation predicted two types of polar phonons characterized by an angular dispersion  $\omega(\theta)$ . The first ones were the interface modes which have been already found for SLs of cubic structure; the corresponding amplitude of atomic motions decreases from the interface in both types of layers. Their



**Figure 4.** Angular dispersion of zone-center phonons of an ultra-thin hexagonal GaN (0.5 nm)-AlN (0.5 nm) SL calculated in different strain situations. From (l)–(r), the results are given for SLs pseudomorphic on AlN, elastically relaxed on an average in-plane lattice constant, and pseudomorphic on GaN. Reprinted with permission from [41], J. M. Wagner et al., *IPAP Conference Series* 1, 669 (2000). © 2000, Institute of Pure and Applied Physics.

dispersion is related to the anisotropy of the nanostructure. In contrast, another type of phonon, the quasi-confined modes, exhibit an angular dispersion originating from the anisotropy of the constituent materials. Indeed, the frequencies of the  $A_1$  and  $E_1$  phonons of GaN and AlN, in the TO as well in the LO range, are the limits of their spectral regions; the corresponding intervals are finite for wurtzite crystals, but vanish for isotropic materials. Quasi-confined modes correspond to oscillations in one type of SLs layers but, in contrast with confined modes in cubic SLs, the associated electric field penetrates into the adjacent layer with a decay length much larger than the lattice constant: that is why they are called “quasi-confined.” Note that modes delocalized throughout the whole nanostructure, characterized by an oscillatory behavior in both types of layers, were found only in GaN-GaAlN SLs with barriers made of Ga-rich alloys within this dielectric approach.

Very recently, Romanov et al. [45–46] calculated the polar phonons of a single GaN QD, within the framework of a macroscopic continuum dielectric model. They obtained formal analytical solutions for the surface vibrations of a GaN QD exhibiting an oblate spheroidal form, embedded in AlN. These modes are not discrete, in contrast with their counterparts in cubic GaAs-AlAs QDs, and they are found inside a continuous, allowed frequency range, due to the crystal anisotropy. In addition, two other types of phonons were found: runaway modes that freely leave the QD surface and quasi-stationary leaky modes.

The influence of strong electric fields present in GaN-AlN nanostructures has been discussed by Coffey and Bock [47]. These authors calculated the wavefunctions associated with electron and holes confined in strained GaN-AlN QWs. The influence of the electric fields (up to 1 MV/cm) induced by internal strains on these states was shown in the particular case of a 2.6 nm-thick QW: holes and electrons are

spatially separated in the QW by the confined quantum Stark effect. Strong effects on the Raman cross section by  $A_1$  (LO) phonons confined in the GaN layer were proven to proceed from the breaking of symmetry with respect to the center plane of the well. In the calculated cross section, both contributions to the electron-phonon interaction associated with deformation potentials and Fröhlich processes were taken into account. For vanishing electric fields, only confined phonons characterized by a quantum number of even parity are allowed. In contrast, it was found that confined phonons with an odd parity dominate the calculated Raman spectrum when strong fields are present in the involved layer. Therefore, it was suggested that this breakdown of parity selection rules could be used for measuring the electric field in wurtzite nanostructures. Unfortunately, the frequencies given for confined modes is questionable, considering the dispersion  $\omega(\mathbf{q})$  calculated by the authors for the LO phonon of bulk GaN, which is in agreement neither with measurements nor with calculations already published [9–11].

### 3.4. Experimental Investigations of Phonons in Nitride-Based Superlattices

As previously shown for superlattices made of cubic III–V semiconductors, the Raman signatures of disordered solid solutions and ordered nanostructures with the same mean composition are quite different, except for SLs containing ultra-thin (thinner than three monolayers) layers. Evidence for SL ordering can thus be achieved by Raman spectroscopy, which is a nondestructive technique in contrast to transmission electron microscopy (TEM) needing cross sections of the samples. However, Raman spectra of GaN-AlN SLs and AlGaIn alloys can at first sight exhibit some similarities, specially concerning the frequencies of  $E_2$  (high)

phonons, due to the “two-mode behavior” of the latter modes in the alloy (see Section 2.2). Gleize et al. [30] have observed that the ambiguity could be lifted by considering the  $A_1$  (LO) phonon which is, on the contrary, characterized in alloys by its “one-mode behavior.” Indeed, the phonon frequency expected for the  $A_1$  (LO) mode of the  $\text{Ga}_{1-x}\text{Al}_x\text{N}$  alloy with the mean Al content of the SL under study ( $x = 0.45$ ) would be  $821\text{ cm}^{-1}$  [13]. Actually, the only feature obeying the appropriate selection rules, found at a much lower frequency ( $738\text{ cm}^{-1}$ ) in Raman spectra, was assigned to  $A_1$  (LO) phonons confined in the wells, slightly shifted from the corresponding frequency in relaxed GaN by the opposite effects of confinement and strain. It should be noted that the  $A_1$  (LO) phonon confined in the barriers could not be observed, likely due to the low-scattering cross section of AlN. Finally, it was concluded that the SLs modes could be unambiguously probed by nonresonant Raman scattering.

At this point of the discussion, one can wonder if Raman experiments can determine the nature of the SL phonons, delocalized or confined in one type of layer. A simple criterion has been suggested by Davydov et al. in several articles [48–50]; if two distinct phonons of the same symmetry can be evidenced in Raman spectra from short period SLs, the corresponding modes are claimed to be confined in one type of layer. In the opposite case, the modes can be considered as delocalized. However, it should be noted that the weakness of the Raman signal coming from one type of layer can make a convenient use of this criterion difficult. The same approach has been used by Gleize et al. [30], who implicitly considered phonons confined in each type of layer, with the exception of a phonon exhibiting the  $A_1$  (TO) symmetry, assigned to an interface mode.

Chen et al. [51] claimed to obtain the first evidence for a confinement effect of the  $A_1$  (LO) phonon in GaN layers of an hexagonal superlattice. In this study, three GaN- $\text{Ga}_{0.8}\text{Al}_{0.2}\text{N}$  SLs were investigated; the thickness of the GaN layers was 1.2 nm, 2.4 nm, and 3.6 nm, respectively. The authors concentrated on the  $A_1$  (LO) mode observed in  $z(x,x)z$  micro-Raman spectra. The corresponding broad feature was slightly red shifted in frequency, compared to the relaxed material; this shift was found increasing for shrinking GaN wells. An approximate fit of the measured frequencies was obtained, using  $\omega(q_z) \approx \sin^2(q_z \cdot c/4)$  for the dispersion of the LO branch of GaN. However, it should be noted that the SLs contained only 30 periods and that the total thickness of GaN in the SL was as low as 36 nm for the thinner layers; one can thus wonder if a clear signature of the wells could be really obtained in nonresonant scattering conditions, considering the presence of an underlying thick GaN buffer layer.

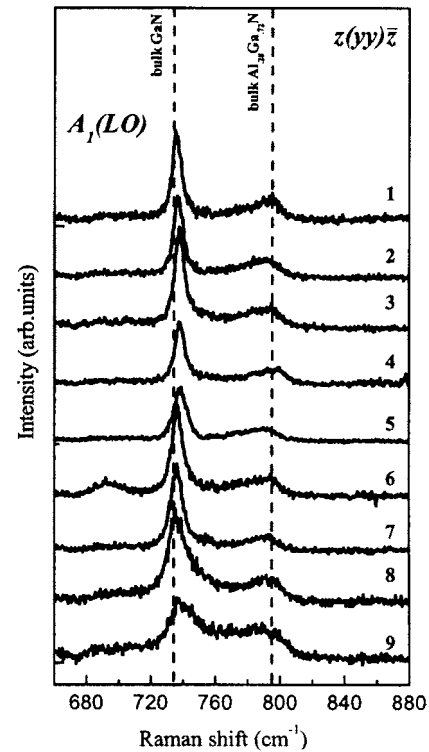
Davydov et al. [48–50] investigated by nonresonant Raman scattering a set of GaN- $\text{Ga}_{1-x}\text{Al}_x\text{N}$  superlattices, grown by MOCVD on buffer layers and sapphire substrates. The SL period was varied between 2.5 nm and 320 nm. For the sake of simplicity, the thicknesses of wells and barriers in the various nanostructures were the same in all the nanostructures investigated. The aluminum content  $x$  in the alloy of the barriers was lower than 50%. The total thickness of the SLs under study was sufficient for achieving Raman experiments in nonresonant scattering, with an excitation at 2.54 eV. In the recorded spectra,  $E_2$  (high) and  $E_1$  (TO)

phonons from GaN were observed and assigned to confined modes in the wells, whereas their counterparts could not be evidenced for the AlGaIn layers of the SL. The lack of signal from the barriers has been tentatively attributed to the low-scattering cross section by phonons of the AlGaIn alloy. On the other hand, the  $E_2$  (low) phonon confined in the barriers of the SL was also found in the low-frequency range of the spectra, together with that from GaN layers [50]. Due to its high sensitivity to the Al content (but not to the built-in strain), the  $E_2$  (low) phonon from the alloy could be used as a probe of the composition in the barriers of the SL. The same authors also gave evidence for confinement of the  $A_1$  (LO) phonon either in GaN or in GaAlN layers. In Figure 5, two modes are clearly observed in  $z(yy)z$  spectra from various SLs where the alloy content of the barriers was kept constant (28%). Note that the range of investigated periods was very wide, between 5 nm and  $3\text{ }\mu\text{m}$ .

In contrast, the behavior of  $E_1$  (LO) and  $A_1$  (TO) phonons was found quite different. Actually, each of them is always observed as a single line; its location in Raman spectra is similar to that in a  $\text{Ga}_{1-x}\text{Al}_x\text{N}$  disordered alloy, whose composition corresponds to the mean Al content in the SL

$$\langle x \rangle = x \frac{d_2}{d_1 + d_2} \quad (11)$$

where  $d_1$  and  $d_2$  are the width of wells and barriers, respectively. Accordingly, these modes are considered as delocalized in the whole structure. The frequency variations of the



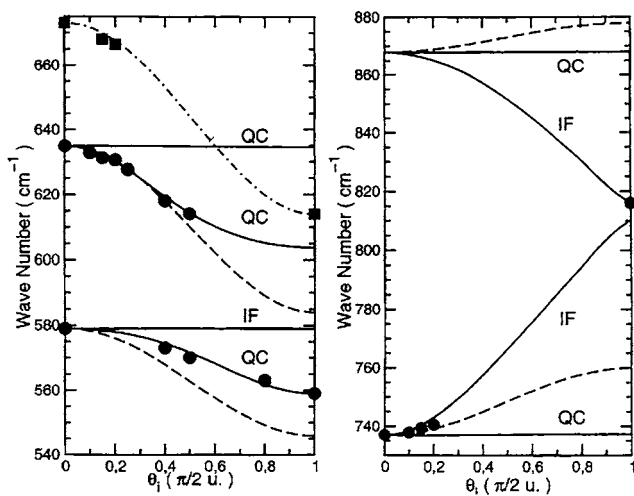
**Figure 5.** Raman spectra in the region of the  $A_1$  (LO) phonons, recorded in backscattering along the  $z$  axis, on a set of GaN- $\text{Al}_{0.28}\text{Ga}_{0.72}\text{N}$  SL with different periods: (1)  $3\text{ }\mu\text{m}$ , (2)  $640\text{ nm}$ , (3)  $320\text{ nm}$ , (4)  $160\text{ nm}$ , (5)  $80\text{ nm}$ , (6)  $40\text{ nm}$ , (7)  $20\text{ nm}$ , (8)  $10\text{ nm}$ , (9)  $5\text{ nm}$ . The thicknesses of wells and barriers in the SLs were the same (unpublished results). Reprinted with permission from V. Yu. Davydov.

$A_1$  (TO) phonons from the SLs under study and from the corresponding ternary alloy were found rather similar. The same observation was made on the  $E_1$  (LO) phonons. This kind of evolution seems to be consistent with results of a calculation performed in the framework of a dielectric continuum model, where the nanostructure was treated as an homogeneous and anisotropic crystal, characterized by an average dielectric constant  $\varepsilon_z(\omega)$ .

Another possible evidence for the nature, localized or not, of SLs phonons could be found by measuring their angular dispersion  $\omega(\theta)$  experimentally, if the latter is significantly different from that of the “bulk” material. This has been done by Gleize et al. [44] for polar phonons through an experimental study of a GaN-AlN SL, performed for checking the validity of the continuum dielectric model previously developed [42]. Micro-Raman spectra were recorded under 2.54 eV excitation, in backscattering geometry on the top surface ( $\theta = 0^\circ$ ), on the edge ( $\theta = 90^\circ$ ), and also on a bevel at  $45^\circ$  fabricated on the edge of the nanostructure by ion etching. The variation of the angle  $\theta$  around the above values was achieved by tilting the sample with respect to the incident light beam; in this experiment, the uncertainty on  $\theta$  was lower than  $5^\circ$ . The measured frequencies of various polar modes from the SL could be compared with the predicted ones. As observed in Figure 6, the agreement was found rather satisfactory, particularly for the TO modes quasi-confined in GaN and AlN layers, which could not be confused with the dispersive extraordinary TO modes from the underlying thick AlN buffer layer.

### 3.5. Folded Acoustic Phonons in Hexagonal Superlattices

The work published by Davydov et al. [49] on GaN-AlGaN superlattices has evidenced for the first time zone-center-folded acoustic phonons in hexagonal SLs, characteristic of



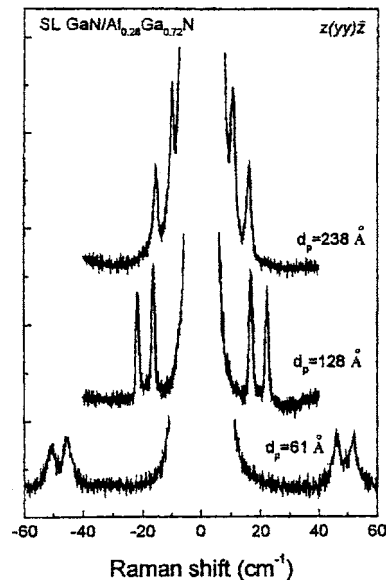
**Figure 6.** Angular dispersion of polar phonons of a GaN (5 nm)-AlN (5 nm) superlattice. Full circles and full lines correspond to the experimental values and to the calculated variation, respectively. The angular dispersion of the relaxed thick buffer layer is indicated by dashed lines. Reprinted with permission from [44], J. Gleize et al., *Phys. Stat. Sol. (A)* 195 (2003). © 2003, Wiley-VCH.

their periodicity. As shown in Figure 7, remarkable sharp Raman features were detected in the low-frequency range of the spectra recorded in the  $z(y\bar{y})\bar{z}$  scattering configuration, from a few nanostructures made of GaN and  $\text{Al}_{0.28}\text{Ga}_{0.72}\text{N}$  layers of same thicknesses, with SLs periods ranging between 6.1 nm and 23.8 nm. Actually, only the doublet expected from the first folding of acoustic branches was clearly observed in each case. As expected, the mean frequency of the doublet increases for decreasing SLs periods. The measured frequencies of both components of the doublet obeyed fairly well Eqs. (4) and (6) appearing in Section 1.2. An average sound velocity  $v = 8140$  m/s in the nanostructure was derived from these measurements. Finally, different scattering configurations were achieved for changing the  $z$  component  $q_z$  of the wavevector of the phonon involved in Raman scattering. This experiment allows the probing of the frequency dispersion of the folded acoustic modes [27]. Indeed, the authors found that the spectral spacing of both lines in the doublet was decreasing with  $q_z$ .

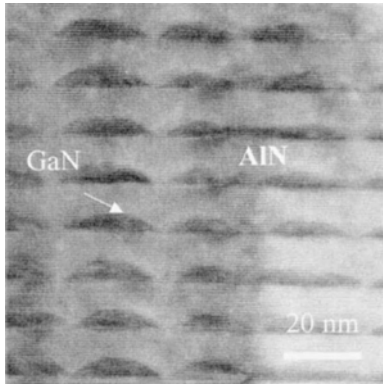
## 4. PHONONS IN QUANTUM DOTS STRUCTURES

### 4.1. Nonresonant Raman Scattering

The first Raman signature of QD structures has been published by Gleize et al. [52]. The samples were stackings of GaN-AlN QDs grown along the (0001) direction on an AlN buffer layer and a sapphire substrate. As demonstrated by TEM studies [53], GaN islands exhibited a pyramidal shape with a broad basis (about 30 nm) and a typical height of 4 nm, as shown in Figure 8. Micro-Raman spectra were recorded under 2.54 eV excitation, in a backscattering geometry along the  $z$  axis. However, the whole sample was probed



**Figure 7.** Raman spectra of GaN- $\text{Al}_{0.28}\text{Ga}_{0.72}\text{N}$  superlattices with different periods (23.8 nm, 12.8 nm, and 6.1 nm), recorded under a 2.54 eV excitation. Only the low frequency part of the spectra, exhibiting the folded acoustic phonons, is shown. Reprinted with permission from [49], *Phys. Stat. Sol. (A)*, 188, 863 (2001). © 2001, Wiley-VCH.



**Figure 8.** Cross section of a GaN-AlN QD stacking, observed by transmission electron microscopy. The typical height of GaN QDs was 4 nm. Reprinted with permission from [53], C. Adelman, *Compte-Rendus Academ. Sci. (Paris)* 1, Serie IV, 61 (2000). © 2000, Bruno Daudin.

under visible excitation and the distinction between signals originating from the stacking and the buffer layer was not straightforward. In order to overcome this difficulty, the confocal configuration was used and the laser spot was focused higher and higher above the surface, inducing a relative intensity variation of the  $E_2$  phonons from the buffer layer and from the QDs, as already illustrated for SLs. It allowed the unambiguous signature of the GaN islands. A slight (tensile) strain of the AlN spacers was deduced from the measured (negative) frequency shift of the  $E_2$  phonon. The effect of vertical correlation of QDs in these structures can be evidenced from small changes of the strain measured for the spacers.

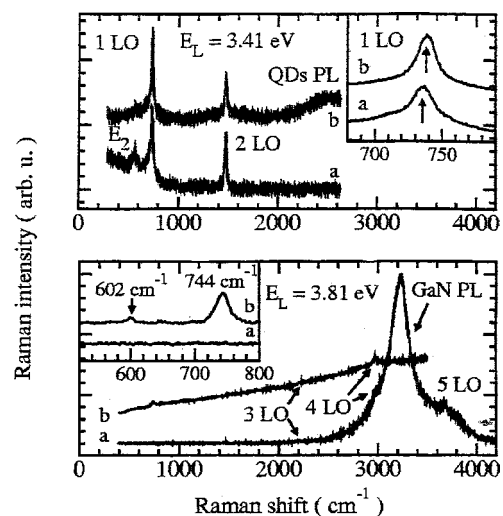
Another study has been devoted to a set of GaN-AlN QD stackings characterized by various heights and densities of dots, deposited either on sapphire or on silicon [54]. Using various backscattering geometries, most Raman-active optic phonons from the structure could be observed. Except for the  $A_1$  (LO) mode, the measured phonon frequencies were rather close to those found in the similar disordered AlGaIn alloy. The observed frequency shifts were assigned to strain effects, as in the case of SLs. An in-plane strain in GaN dots of  $-2.4\%$  or  $-2.6\%$  was estimated from the frequency shift (as high as  $+35\text{ cm}^{-1}$  or  $+38\text{ cm}^{-1}$ ) of the corresponding  $E_2$  phonon, using the corresponding deformation potentials. The QDs were found completely strained on AlN in all the structures under study, as expected. Obviously, the mean strain in the AlN spacers, tentatively derived from the experimental data, was found much lower.

## 4.2. Resonant Raman Scattering

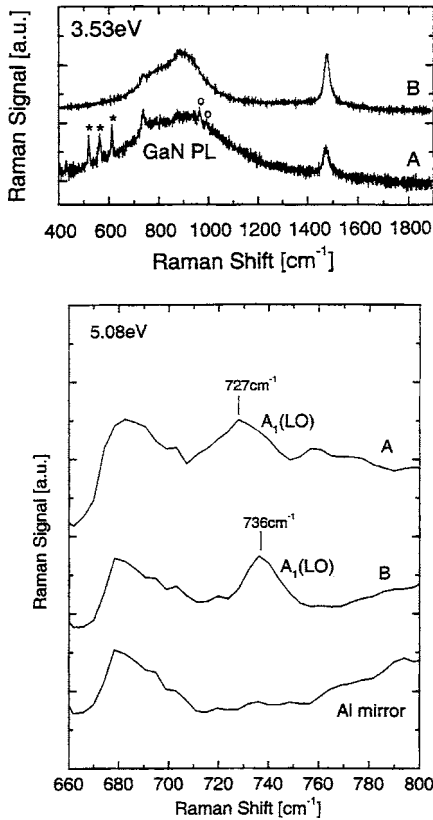
Room temperature micro-Raman experiments have been also performed on QD structures using ultraviolet laser lines, in order to enhance the scattering intensity by means of electronic resonance. In the paper by Gleize et al. [55] the sample under study was a stacking of 39 periods of GaN QDs embedded in 18 nm thick AlN spacers, grown on both GaN and AlN buffer layers and on a Si (111) substrate. A thick GaN unstrained layer was also available for comparison. Three laser lines at 3.41 eV, 3.70 eV, and 3.80 eV

were used. In fact, large internal electric fields take place in this kind of nanostructure, thus lowering the fundamental bandgap energies significantly. In the present structure, this quantum confined Stark effect was specially strong. The room temperature PL originating from GaN QDs was centered around 2.35 eV, much lower than the excitation energy, and thus did not merge the Raman signal. The more interesting result was obtained using the 3.80 eV laser line. A feature clearly showed up in the first-order scattering range at  $744\text{ cm}^{-1}$  in Raman spectra from the nanostructure, in contrast to those recorded on the GaN layer used as a reference (see Fig. 9). The observed peak, which could not originate from the underlying GaN buffer layer of the sample, was assigned to the polar  $A_1$  (LO) phonon from the QDs. A weaker Raman feature located at  $602\text{ cm}^{-1}$  was associated with the nonpolar  $E_2$  phonon from the strained dots. It should be noted that the latter mode could be observed under the 2.33 eV excitation, that is, at an energy close to the PL maximum, in contrast to the  $A_1$  (LO) phonon from QDs. These results gave evidence for a strong resonant enhancement of the scattering by polar phonons in the incoming channel at 3.80 eV, implying probably an excited state of the dots.

Another original study was carried out by Kuball et al. [56] on a single plane of self-assembled GaN QDs grown on a  $\text{Al}_{0.15}\text{Ga}_{0.85}\text{N}$  layer, using silicon as anti-surfactant. Two clearly distinct distributions of QD sizes were revealed by means of atomic force microscopy. The Raman spectra from the nanostructures are shown on the top of Figure 10. Under a 3.53 eV excitation, first-order scattering located at  $736\text{ cm}^{-1}$ , superimposed onto a broad PL band, was assigned to the  $A_1$  (LO) phonon from the “large” (about 40 nm high) dots, where confinement effects on the LO phonon frequency are almost negligible. In the same experimental conditions, a phonon was observed at the same frequency but with a lower intensity, on another sample grown in similar



**Figure 9.** Raman spectra of a thick GaN layer (a) and of a GaN-AlN quantum dot structure (b) grown on GaN and AlN buffer layers and on a Si substrate, recorded in backscattering along the  $z$  axis under 3.41 eV and 3.80 eV excitations. Reprinted with permission from [44], J. Gleize et al., *Phys. Stat. Sol. (A)*, 95 (2003). © 2003, Wiley-VCH.



**Figure 10.** Raman spectra of self-assembled GaN QDs grown on  $\text{Al}_{0.15}\text{Ga}_{0.85}\text{N}$  using Si as antisurfactant (A), and of a continuous GaN layer grown on  $\text{Al}_{0.15}\text{Ga}_{0.85}\text{N}$  (B). The spectra have been recorded at 3.53 eV (top) and at 5.08 eV (bottom). In the latter case, a reference spectrum of an Al mirror shows the system response function. Asterisks and circles mark laser plasma lines and the Raman signal from the SiC substrate, respectively. Reprinted with permission from [56], M. Kuball et al., *Appl. Phys. Lett.* 78, 987 (2001). © 2001, American Institute of Physics.

conditions but without Si, made of a continuous 0.3  $\mu\text{m}$  thick GaN layer on the alloy layer. The spectra recorded at 3.70 eV and 3.81 eV did not give any signature of the QDs. But under excitation in the far ultraviolet (5.08 eV), a significant shift (9  $\text{cm}^{-1}$ ) towards lower frequencies was observed for the  $A_1$  (LO) phonon from the GaN dots, as shown on the bottom of Figure 9. In the same experimental conditions, no frequency shift could be evidenced with the continuous GaN layer. The feature found at 727  $\text{cm}^{-1}$  was thus assigned to the  $A_1$  (LO) phonon in “small” QDs; the shift should be due to confinement effects in dots exhibiting smaller heights of about 2–3 nm. The electronic transition favoring the resonant effect under the 5.08 eV excitation was not yet identified.

### 4.3. GaN Nanowires and Pillars

Several investigations of samples containing GaN nanowires have been recently published. For example, Jun-Zhang and Lide-Zhang [57] studied by Raman spectroscopy such as nanostructures, made of nanowires embedded in the nanochannels of an anodic alumina membrane. The hexagonal structure of the nanowires was checked by X-ray

diffraction. The shift towards lower frequencies observed in the Raman spectra for the  $E_2$  (high),  $E_1$  (TO), and  $A_1$  (TO) phonons of GaN was associated with nanosize effects.

Demangeot et al. [58–59] studied structures made of nanometer-size GaN pillars designed for photonic crystals. The samples were obtained by reactive ion-etching using a mask technique on 300 nm thick GaN layers grown on a thick AlN buffer layer and on a sapphire substrate. Individual pillars of 300 nm in height, with diameters ranging between 5  $\mu\text{m}$  and 100 nm, were fabricated in this way. The samples were investigated by micro-Raman spectroscopy under a 2.54 eV excitation. No one-dimensional effects were observed as expected, considering the pillar size. Spectra recorded in the  $z(xx)\bar{z}$  configuration showed the allowed phonons from each pillar. Due to the compressive strain of the larger pillars, the  $E_2$  (high) mode was slightly shifted from the frequency of relaxed material; in contrast, strain relaxation was evidenced in smaller pillars. Moreover, the upward shift of the LO phonon in the smaller pillars could be explained by angular dispersion (see Section 2.1). Indeed, the wavevector transferred to the phonon by the incident and scattered light entering and coming out, respectively, through the facets of the pillars was tilted with respect to the  $z$  axis, leading to the observation of a shifted quasi-LO mode. The measured frequency shift was found in good agreement with the value of the facet angle (25°).

## 5. SUMMARY

Hexagonal GaN-AlN or GaN-GaN AlN QW and QD structures have been extensively studied in the last few years, on account of their important applications in opto-electronics. The lattice-dynamical properties of two-dimensional systems have been reviewed in this article. Only a few calculations of phonons in such nanostructures have been performed yet. Most articles published are actually devoted to experimental studies by Raman spectroscopy, or less often by infrared measurements. The signature of QW and QD structures has been obtained from nonpolar or polar phonons, by means of nonresonant or resonant Raman scattering, respectively. The results allowed the probing of internal strains and confinement effects in the constituent materials. Up until now, specific modes of GaN-AlN or GaN-GaN AlN SLs have been the subject of a few investigations. However, phonon confinement in layers of the structures has been evidenced for SLs in a wide range of periods. Moreover, the angular dispersion of quasi-confined and interface modes has been predicted and checked experimentally for the former. Finally, GaN pillars recently investigated by Raman spectroscopy did not exhibit lattice dynamical properties characteristic of one-dimensional systems.

## GLOSSARY

**Quantum dot (QD)** A small island made of a given semiconductor embedded in another semiconductor.

**Quantum well (QW)** A thin layer made of a given semiconductor located between two other semiconductors called barriers.

**Superlattice (SL)** A periodic array of wells and barriers.

## REFERENCES

1. J. Frandon, F. Demangeot, and M. A. Renucci, "Optoelectronic Properties of Semiconductors and Superlattices Vol. 13, III-Nitride Semiconductors Optical Properties I," pp. 333–378, (M. O. Manasreh and H. X. Jiang, Eds.). Philadelphia, Taylor & Francis, 2002.
2. R. W. G. Wyckoff, "Crystal Structures," Vol. 1, Chap. III, pp. 11–112, 2nd ed. Interscience, 1963.
3. M. Leszczynski, H. Teisseyre, T. Suski, I. Grzegory, M. Bockowski, J. Jun, S. Porowski, K. Pakula, J. M. Baranowski, C. T. Foxon, and T. S. Cheng, *Appl. Phys. Lett.* 69, 73 (1996).
4. M. Tanaka, S. Nakahata, K. Sogabe, H. Nakata, and M. Tobioka, *Japanese J. Appl. Phys. Part 2*, 36, L 1062 (1997).
5. W. Richter, *Springer Tracts in Modern Physics* 78, 121 (1976).
6. R. Loudon, *Advances in Physics*, 13, 423 (1964).
7. T. Deguchi, D. Ichiryu, K. Sekiguchi, T. Sota, R. Matsuo, T. Azuhata, M. Yamaguchi, T. Yagi, S. Chichibu, and S. Nakamura, *J. Appl. Phys.* 86, 1860 (1999).
8. J. M. Hayes, M. Kuball, Y. Shi, and J. H. Edgar, *Japanese J. Appl. Phys., Part 2*, 39, 703 (1999).
9. H. Siegle, G. Kaczmarczyk, L. Filippidis, A. P. Litvinchuk, A. Hoffmann, and C. Thomsen, *Phys. Rev. B* 55, 7000 (1997).
10. V. Yu. Davydov, Y. E. Kitaev, I. N. Goncharuk, A. N. Smirnov, J. Graul, O. Semchinova, D. Uffmann, M. B. Smirnov, A. P. Mirgorodsky, and R. A. Evarestov, *Phys. Rev. B* 58, 12899 (1998).
11. T. Ruf, J. Serrano, M. Cardona, P. Pavone, M. Pabst, M. Krisch, M. D'Astuto, T. Suski, I. Grzegory, and M. Leszczynski, *Phys. Rev. Lett.* 86, 906 (2001).
12. F. Demangeot, J. Groenen, J. Frandon, M. A. Renucci, O. Briot, S. Clur, and R. L. Aulombard, Proc. 2nd Eur. GaN Workshop *Internet J. Nitride Semicond. Res.* 2, 40 (1997).
13. F. Demangeot, J. Groenen, J. Frandon, M. A. Renucci, O. Briot, S. Clur, and R. L. Aulombard, *Appl. Phys. Lett.* 72, 2674 (1998).
14. N. Wieser, O. Ambacher, H. Angerer, R. Dimitrov, M. Stutzmann, B. Stritzker, and J. K. N. Lindler, Proc. 3rd Int. Conf. Nitride Semicond. Montpellier, France, *Phys. Stat. Sol. (B)* 216, 807 (1999).
15. A. Cros, H. Angerer, R. Handschuh, O. Ambacher, and M. Stutzmann, *Solid State Commun.* 104, 35 (1997).
16. A. A. Klochikhin, V. Yu. Davydov, I. N. Goncharuk, A. N. Smirnov, A. E. Nikolaev, M. V. Baidakova, J. Aderhold, J. Graul, J. Stemmer, and O. Semchinov, *Phys. Rev. B* 62, 2522 (2000).
17. P. Wisniewski, W. Knap, J. P. Malzac, J. Camassel, M. D. Bremser, R. F. Davis, and T. Suski, *Appl. Phys. Lett.* 73, 1760 (1998).
18. F. Demangeot, J. Frandon, M. A. Renucci, O. Briot, B. Gil, and R. L. Aulombard, *Solid State Commun.* 100, 207 (1996).
19. V. Y. Davydov, N. S. Averkiev, I. N. Goncharuk, D. K. Nelson, I. P. Nikitina, A. S. Polovnikov, A. N. Smirnov, and M. A. Jacobson, *J. Appl. Phys.* 82, 5097 (1997).
20. J. M. Wagner and F. Bechstedt, *Appl. Phys. Lett.* 77, 346 (2000).
21. J. M. Wagner and F. Bechstedt, *Phys. Rev. B* 66, 115202 (2002).
22. T. Prokofyeva, M. Seon, J. Vanbuskirk, M. Holtz, S. A. Nikishin, N. N. Faleev, H. Temkin, and S. Zollner, *Phys. Rev. B* 63, 125313 (2001).
23. A. Sarua, M. Kuball, and J. E. Nostrand, *Appl. Phys. Lett.* 81, 1426 (2002).
24. V. Darakchieva, P. P. Paskov, T. Paskova, J. Birch, S. Tungasmita, and B. Monemar, *Appl. Phys. Lett.* 80, 2302 (2002).
25. J. Gleize, M. A. Renucci, J. Frandon, E. Bellet-Amalric, and B. Daudin, *J. Appl. Phys.* 93, 2065 (2003).
26. B. Daudin, F. Widmann, G. Feuillet, Y. Samson, M. Arlery, and J. L. Rouvière, *Phys. Rev. B* 56, R 7069 (1997).
27. B. Jusserand and M. Cardona, "Light Scattering in Solids V," pp. 60–73 (M. Cardona and G. Güntherodt, Eds.). Springer-Verlag, Berlin, 1989.
28. M. Cardona, "Light Scattering in Solids II," pp. 128–135 (M. Cardona and G. Güntherodt, Eds.). Springer-Verlag, Berlin, 1982.
29. R. M. Martin and L. M. Falicov, "Light Scattering I," pp. 79–145, (M. Cardona, Ed.). Springer-Verlag, Berlin, 1983.
30. J. Gleize, F. Demangeot, J. Frandon, M. A. Renucci, F. Widmann, and B. Daudin, *Appl. Phys. Lett.* 74, 703 (1999).
31. M. Schubert, A. Kasic, J. Sik, S. Einfeldt, D. Hommel, V. Härle, J. Off, and F. Scholz, *Materials Sci. Engin. B* 82, 178 (2001).
32. M. Schubert, A. Kasic, J. Sik, S. Einfeldt, D. Hommel, V. Härle, J. Off, and F. Scholz, *Internet J. Nitride Semicond. Res.* 5, Suppl. 1 (2000).
33. G. Abstreiter, M. Cardona, and A. Pinczuk, "Light Scattering IV," pp. 18–20 (M. Cardona and G. Güntherodt, Eds.). Springer-Verlag, Berlin, 1984.
34. J. Frandon, M. A. Renucci, E. Bellet-Amalric, C. Adelman, B. Daudin, in "Proc. Int. Conf. on Superlattices, Nanostructures and Nanodevices," Toulouse, France, *Physica E* (2003), to appear.
35. J. Gleize, J. Frandon, M. A. Renucci, and F. Bechstedt, in "Proc. Mater. Res. Soc. Spring Meeting," San Francisco, CA, USA, 680 E (2001).
36. D. Behr, R. Niebuhr, J. Wagner, K. H. Bachem, and U. Kaufmann, *Appl. Phys. Lett.* 70, 363 (1997).
37. J. Gleize, F. Demangeot, J. Frandon, M. A. Renucci, M. Kuball, N. Grandjean, and J. Massies, in "Proc. Eur. Mat. Res. Soc.," Strasbourg, France, *Thin Solid Films* 364, 156 (2000).
38. F. Demangeot, J. Gleize, J. Frandon, M. A. Renucci, M. Kuball, N. Grandjean, and J. Massies, *Phys. Stat. Sol. (B)* 216, 799 (1999).
39. S. M. Komirenko, K. W. Kim, M. A. Stroschio, and M. Dutta, *Phys. Rev. B* 59, 5013 (1999).
40. S. M. Komirenko, K. W. Kim, M. A. Stroschio, and M. Dutta, *Phys. Rev. B* 61, 2034 (2000).
41. J. M. Wagner, J. Gleize, and F. Bechstedt, in "Proc. Int. Workshop on Nitride Semicond. IWN 2000," Nagoya, Japan, *IPAP Conf. Series* 1, 669 (2000).
42. J. Gleize, M. A. Renucci, J. Frandon, and F. Demangeot, *Phys. Rev. B* 60, 15985 (1999).
43. J. Gleize, J. Frandon, F. Demangeot, M. A. Renucci, M. Kuball, J. M. Hayes, F. Widmann, and B. Daudin, *Mater. Sci. and Engin. B* 82, 27 (2001).
44. J. Gleize, J. Frandon, and M. A. Renucci, in "2nd Int. Workshop Physics of Light-Matter Coupling in Nitrides," Rethimnon, Crete (2002), *Phys. Stat. Sol. (A)* 195, 605 (2003).
45. D. A. Romanov, V. V. Mitin, and M. A. Stroschio, *Phys. Rev. B* 66, 115321 (2002).
46. D. A. Romanov, V. V. Mitin, and M. A. Stroschio, *Physica B* 316–317, 359 (2002).
47. D. Coffey and N. Bock, *Phys. Rev. B* 59, 5799 (1999).
48. V. Yu. Davydov, A. A. Klochikhin, I. N. Goncharuk, A. N. Smirnov, A. S. Usikov, W. V. Lundin, E. E. Zavarin, A. V. Sakharov, M. V. Baidakova, J. Stemmer, H. Klausinger, and D. Mistele, in "Proc. Int. Workshop on Nitrides," Nagoya, Japan (2000), *IPAP Conf. Series* 1, 665 (2000).
49. V. Yu. Davydov, A. A. Klochikhin, I. E. Kozin, V. V. Emtsev, I. N. Goncharuk, A. N. Smirnov, R. N. Kyutt, M. P. Scheglov, A. V. Sakharov, W. V. Lundin, E. E. Zavarin, and A. S. Usikov, *Phys. Stat. Sol. (A)* 188, 863 (2001).
50. V. Yu. Davydov, A. N. Smirnov, I. N. Goncharuk, R. N. Kyutt, M. P. Scheglov, M. V. Baidakova, W. V. Lundin, E. E. Zavarin, M. B. Smirnov, S. V. Karpov, and H. Harima, in "Proc. Int. Workshop on Nitrides 2002," Aachen, Germany, *Phys. Stat. Sol. B* 234, 975 (2003).
51. C. H. Chen, Y. F. Chen, An Shih, S. C. Lee, and H. X. Jiang, *Appl. Phys. Lett.* 78, 3035 (2001).
52. J. Gleize, F. Demangeot, J. Frandon, M. A. Renucci, M. Kuball, F. Widmann, and B. Daudin, *Phys. Stat. Sol. B* 216, 457 (1999).
53. C. Adelman, M. Arlery, B. Daudin, G. Feuillet, G. Fishman, and Le Si Dang, *Compte-Rendus Academ. Sci. (Paris)*, 1, Serie IV, 61 (2000).



54. J. Gleize, J. Frandon, M. A. Renucci, C. Adelman, B. Daudin, G. Feuillet, B. Damilano, N. Grandjean, and J. Massies, *Appl. Phys. Lett.* 77, 2174 (2000).
55. J. Gleize, F. Demangeot, J. Frandon, M. A. Renucci, M. Kuball, B. Damilano, N. Grandjean, and J. Massies, *Appl. Phys. Lett.* 79, 686 (2001).
56. M. Kuball, J. Gleize, S. Tanaka, and Y. Aoyagi, *Appl. Phys. Lett.* 78, 987 (2001).
57. Jun-Zhang and Lide-Zhang, *J. Appl. D. Applied Phys.* 35, 1481 (2002).
58. F. Demangeot, J. Gleize, J. Frandon, M. A. Renucci, M. Kuball, D. Peyrade, L. Manin-Ferlazzo, Y. Chen, and N. Grandjean, *J. Appl. Phys.* 91, 2866 (2002).
59. F. Demangeot, J. Gleize, J. Frandon, M. A. Renucci, M. Kuball, D. Peyrade, L. Manin-Ferlazzo, Y. Chen, and N. Grandjean, *J. Appl. Phys.* 91, 6520 (2002).

# Photochemical Molecular Devices

Alberto Credi

Università degli Studi di Bologna, Bologna, Italy

## CONTENTS

1. Introduction
  2. Pseudorotaxanes, Rotaxanes, and Catenanes
  3. Artificial Photosynthetic Devices
  4. Molecular-Level Machines
  5. Molecular Devices for Information Processing
  6. Conclusion
- Glossary  
References

## 1. INTRODUCTION

In everyday life we make extensive use of *macroscopic devices*, which are assemblies of components designed to achieve a specific function. Each component of the device performs a simple *act*, while the entire device performs a more complex *function*, characteristic of the assembly. For example, the function performed by a hair dryer (production of hot wind) is the result of acts performed by a switch, a heater, and a fan, suitably connected by electric wires and assembled in an appropriate framework (Fig. 1a).

The concept of a device can be extended to the molecular level [1–4]. A *molecular-level device* can be defined as an assembly of a discrete number of molecular components (i.e., a *supramolecular* structure) designed to achieve a specific function. Each molecular component performs a single act, while the entire assembly performs a more complex function, which results from the cooperation of the various molecular components (Fig. 1b).

The extension of the concept of a device to the molecular level is of interest for the growth of nanoscience and the development of nanotechnology. Indeed, the miniaturization of components for the construction of useful

devices, which is an essential feature of modern technology, is currently pursued by the large-downward (top-down) approach [5]. This approach, however, which leads physicists and engineers to manipulate progressively smaller pieces of matter, has intrinsic limitations [6]. An alternative and promising strategy is offered by the small-upward (bottom-up) approach [7]. Chemists, by the nature of their discipline, are already at the bottom, since they are able to manipulate molecules (i.e., the smallest entities with distinct shapes and properties) and are therefore in the ideal position to develop bottom-up strategies for the construction of nanoscale devices.

### 1.1. Role of Light in Molecular-Level Devices

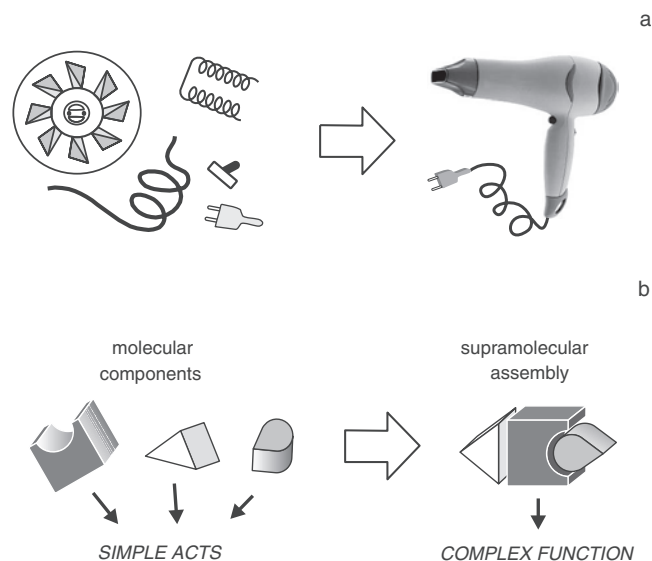
Light is made of photons, and photons are at the same time *quanta of energy* and *bits of information* [8]. This is evident in nature, where light constitutes an energy source and is consumed (converted) in massive amounts in photosynthesis, while it functions as a signal in vision-related processes, the energy used to run the operation being biologic in nature. Therefore, taking one of these two extreme views, one can think of molecular-level devices that use light as an energy supply to perform energy-expensive functions, for example, conversion into chemical energy. On the other hand, light could be used by a molecular device as an input/output signal to be processed and eventually stored and retrieved.

In general, molecular-level devices that perform light-induced functions, that is, in which photons act as an energy supply and/or input/output signals, can be termed *photochemical molecular devices* (PMDs) [2, 4, 9]. The role of light in reference to the relevant features of molecular-level devices will be discussed in more detail in the following section.

### 1.2. Characteristics of Molecular-Level Devices

Molecular-level devices operate via electronic and/or nuclear rearrangements, that is, through some kind of chemical reaction. Like their macroscopic counterpart, they are

\*This chapter first appeared in *Handbook of Photochemistry and Photobiology*, Volume 3: Supramolecular Photochemistry; Edited by H. S. Nalwa, © 2003, American Scientific Publishers.



**Figure 1.** Schematic representation of the assembly of (a) a macroscopic device and (b) a supramolecular system capable of performing as a molecular-level device.

characterized by (a) the kind of energy input supplied to make them work, (b) the way in which their operation can be monitored, (c) the possibility of repeating the operation at will (cyclic process), (d) the time scale needed to complete a cycle, and (e) the performed function.

As far as point (a) is concerned, the most obvious way to supply energy to a chemical system is through an exergonic chemical reaction. In his address to the American Physical Society, R. P. Feynman observed [10]: “An internal combustion engine of molecular size is impossible. Other chemical reactions, liberating energy when cold, can be used instead.” This is exactly what happens in our body, where the chemical energy supplied by food is used in long series of slightly exergonic reactions to power the biological machines that sustain life.

If a molecular-level device has to work by inputs of chemical energy, it will need addition of fresh reactants (“fuel”) at any step of its working cycle, with the concomitant formation of waste products [11]. Accumulation of such waste products, however, will compromise the cyclic operation of the device unless they are removed from the system, as it happens in our body as well as in macroscopic internal combustion engines. The need to remove waste products introduces noticeable limitations in the design and construction of artificial molecular-level devices based on “chemical fuel” inputs. In any case, since a molecular device has to work by repeating cycles [point (c)], a fundamental requirement is that any chemical process taking place in the system has to be reversible.

Chemical fuel, however, is not the only means by which energy can be supplied to operate molecular-level devices. As recalled in the previous section, nature shows that in green plants the energy needed to sustain the machinery of life is supplied by sunlight. Photochemical energy inputs can indeed cause the occurrence of *endergonic* chemical reactions, which can make a device work without formation of waste products. Currently there is an increasing interest in

the development of photon-powered molecular-level devices, taking advantage of the recent, outstanding progress made by supramolecular photochemistry [2, 4]. Photochemical inputs offer other advantages compared to chemical inputs. For example, they can be switched on and off easily and rapidly. It should also be noted that lasers provide the opportunity of working in very small spaces and very short time domains.

To control and monitor the device operation [point (b)], the electronic and/or nuclear rearrangements of the component parts should cause readable changes in some chemical or physical property of the system. In this regard, photochemical and electrochemical methods are very useful since both photons [2, 4] and electrons (or holes) [12, 13] can play the dual role of “writing” (i.e., causing a change in the system) and “reading” (i.e., reporting the state of the system). Luminescence spectroscopy [14], in particular, is a valuable technique since it is easily accessible and offers good sensitivity and selectivity, along with the possibility of time-resolved studies.

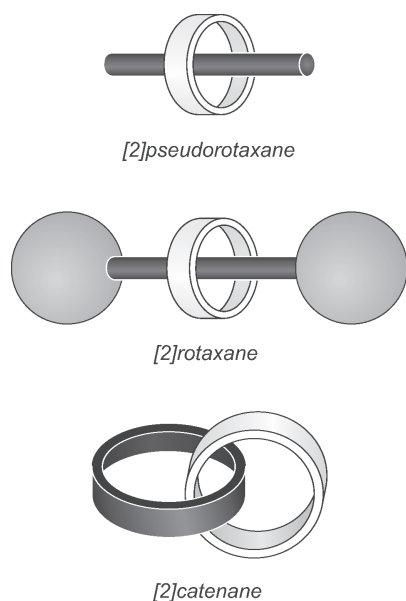
The operation time scale of molecular-level devices [point (d)] can range from less than picoseconds to seconds, depending on the type of rearrangement (electronic or nuclear) and the nature of the components involved.

Finally, as far as point (e) is concerned, the functions performed by molecular-level devices can be various and, to a large extent, still unpredictable; some specific examples will be discussed in this chapter.

In the past 10 years, a noticeable number of photochemical molecular devices based on threaded and interlocked supramolecular architectures, such as pseudorotaxanes, rotaxanes, and catenanes, have been developed. From the viewpoint of the functions performed [point (e)], PMDs of this kind can be subdivided into three categories, namely, artificial photosynthetic systems, molecular-level mechanical machines, and devices for information processing. It is worth noting that, although the energy-carrying and information-carrying aspects of light cannot be separated sharply, artificial photosynthetic devices and molecular-level mechanical machines can be regarded as “light-powered” PMDs, while the third kind of system represents “light-processing” devices. Before illustrating specific examples belonging to these categories, it is useful to recall some important features of pseudorotaxanes, rotaxanes, and catenanes.

## 2. PSEUDOROTAXANES, ROTAXANES, AND CATENANES

Research on pseudorotaxanes, rotaxanes, and catenanes has grown exponentially during the past few years [15–27]. Figure 2 shows schematically the structure of pseudorotaxanes, rotaxanes, and catenanes. The names of these compounds derive from the Latin words *rota* and *axis* for wheel and axle and *catena* for chain. In general, these species are referred to as [*n*]name, where *n* is the number of molecular components; therefore, the diagrams in Figure 2 represent [2]pseudorotaxane, [2]rotaxane, and [2]catenane.

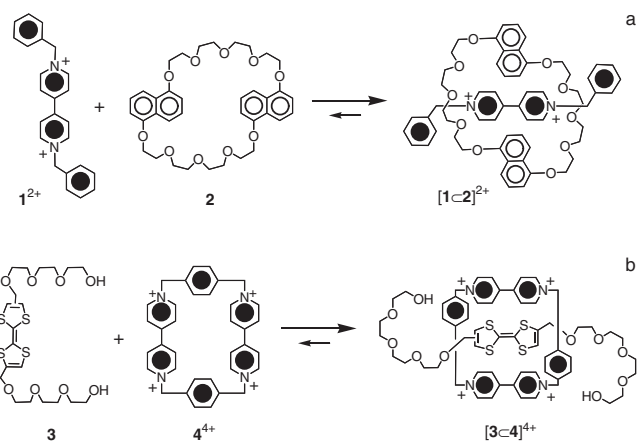


**Figure 2.** Schematic representation of a [2]pseudorotaxane, a [2]rotaxane, and a [2]catenane. The number in brackets indicates the number of molecular components.

## 2.1. Pseudorotaxanes

Pseudorotaxanes are a particularly interesting family of host-guest systems. As in the case of any host-guest complex, formation of a pseudorotaxane occurs via a molecular recognition process between two “instructed” components [1]. It is a thermodynamically controlled self-assembly process that may occur as a result of a variety of interactions deriving from the size, shape, and electronic properties of the partners. The most important types of interactions are those involving electron donor/acceptor ability, hydrogen bonding, hydrophobic/hydrophilic character,  $\pi$ - $\pi$  stacking, coulombic forces, and, on the side of the strong interaction limit, metal-ligand bonding. Usually, it is not difficult to understand which is the predominant interaction in a given system. It should be noted, however, that in some cases the strongest interaction as far as association is concerned is not that causing the most relevant changes in the properties of the system [e.g., ultraviolet-visible (UV-vis) absorption, fluorescence and NMR spectra, electrochemical behavior] on going from the separated components to the pseudorotaxane structure.

A number of pseudorotaxanes have been obtained by threading a wire-type molecule containing  $\pi$ -electron acceptor units into a macrocycle comprising  $\pi$ -electron donor units or, vice versa, a wire-type component containing electron donor units into a macrocycle that comprises electron acceptor units. Two examples are shown in Figure 3: (a) the 1,1'-dibenzyl-4,4'-bipyridinium electron acceptor dication  $1^{2+}$  threaded into the 1,5-dinaphtho-38-crown-10 (1/5DN38C10) electron donor macrocycle **2** [28] and (b) the acyclic polyether **3** containing a tetrathiafulvalene electron donor unit threaded into the electron acceptor cyclophane  $4^{4+}$  [29]. Species composed of a macrocycle covalently connected to a wirelike moiety, giving rise to self-threaded pseudorotaxane structures, are also



**Figure 3.** Two examples of self-assembling of pseudorotaxanes based on  $\pi$ -electron donor/acceptor interactions: (a) from [28] and (b) from [29].

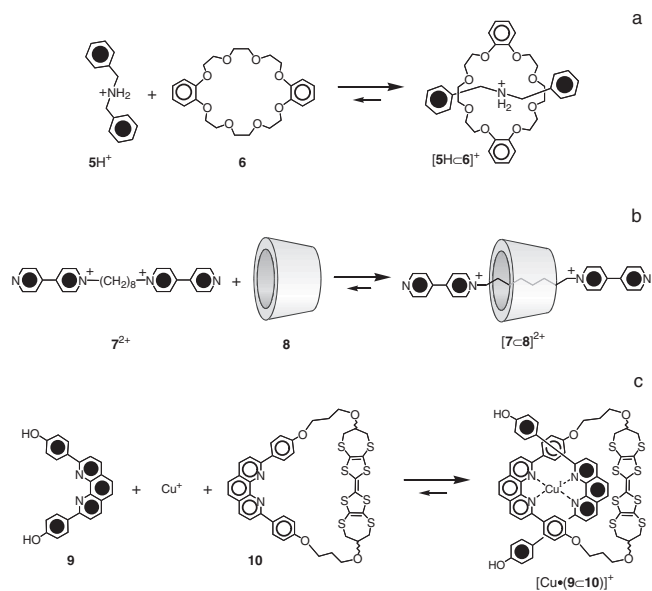
known [30]. Although in these cases a large contribution to the association driving force comes from the electron donor/acceptor interaction, other kinds of interactions, particularly hydrogen bonding, can play an important role, as clearly shown in the cases of [2]pseudorotaxanes composed of 4,4'-bipyridinium [31] or 1,2-bis(pyridinium)ethane [32] threads and crown ethers.

Several pseudorotaxanes have been obtained by threading wire-type and macrocyclic components carrying complementary hydrogen-bonding functions. Figure 4a shows, as an example, the threading of a wire-type component containing a secondary ammonium function, such as the *N,N*-dibenzylammonium ion  $5H^+$ , into a suitable crown ether like dibenzo-24-crown-8 (DB24C8), **6** (Fig. 4a) [33]. Besides hydrogen bonding, other types of interactions (e.g., ion-dipole,  $\pi$ -stacking) can contribute to stabilize the pseudorotaxane structure.

Pseudorotaxanes can also be obtained as a consequence of simple hydrophobic/hydrophilic interactions. This is the case for the since long-known species in which a wire-type component ( $7^{2+}$ ) threads the cavity of  $\alpha$ -cyclodextrin **8** (Fig. 4b) [34].

A different approach is the metal-based template method [15, 23], for example, starting from a wire (**9**) and a macrocycle (**10**), both containing a phenanthroline unit, and using  $Cu^+$  as a template (Fig. 4c) [15]. Species of this kind are essentially metal complexes and may have very large formation constants.

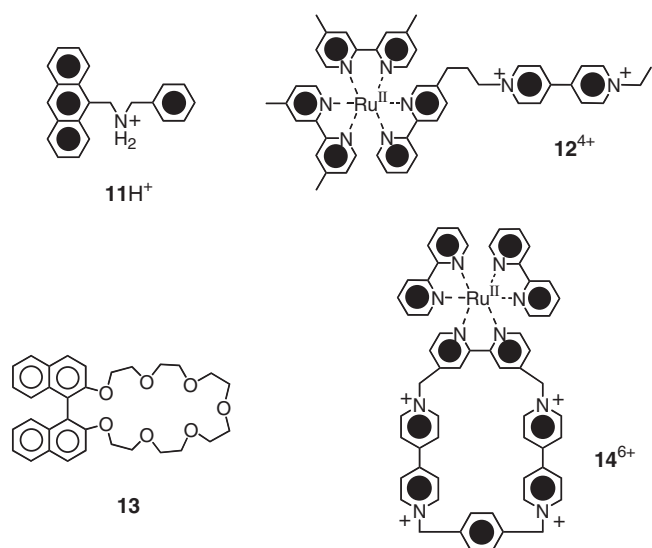
The examples reported above refer to pseudorotaxane species with a 1:1 thread/macrocycle ratio ([2]pseudorotaxanes). It is also possible to obtain species exhibiting different stoichiometric ratios, as illustrated by the fascinating [5]pseudorotaxane formed from four cyclophane  $4^{4+}$  components and a Zn(II)-phthalocyanine with appended four polyether substituents carrying  $\pi$ -electron-rich hydroquinone units [35]. Examples of pseudorotaxanes are known in which a macrocycle is threaded by two linear components [36] and a linear component threads two macrocycles [37]. Long linear arrays can be obtained by using homoditopic threads and macrocycles [38]; homogeneous or



**Figure 4.** Examples of self-assembly of pseudorotaxanes based on (a)  $[N^+ \cdots H \cdots O]$  hydrogen bonding [33], (b) hydrophobic/hydrophilic interactions [34], and (c) coordination around a metal ion [15].

heterogeneous pseudopolyrotaxanes [16] have also been prepared, as well as dendritic ones [39].

Pseudorotaxane species whose components incorporate units capable of exhibiting specific photochemical and/or redox properties are of particular interest for the purpose of constructing photochemical molecular devices. Some examples are reported in Figure 5, namely, a thread ( $11H^+$ ) with an ammonium function and a photoactive anthracene as a stopper [40];



**Figure 5.** Some pseudorotaxane components containing units capable of exhibiting specific properties. The wirelike molecule  $11H^+$ , with an ammonium center and a photoactive anthracene unit as a stopper [40]; the bipyridinium-containing wire  $12^{4+}$ , with a photo- and redox-active  $[Ru(bpy)_3]^{2+}$  moiety [41]; crown ether  $13$ , incorporating a binaphthyl unit [42]; cyclophane  $14^{6+}$ , which contains a  $[Ru(bpy)_3]^{2+}$  complex and two bipyridinium units [43].

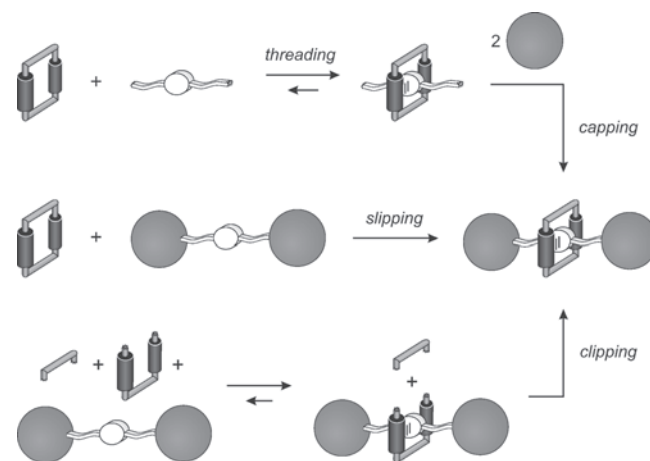
stopper [40], a bipyridinium-type wire ( $12^{4+}$ ) with a photo- and redox-active  $[Ru(bpy)_3]^{2+}$  ( $bpy = 2,2'$ -bipyridine) moiety [41], a crown ether ( $13$ ) incorporating a binaphthyl unit [42], and a cyclophane ( $14^{6+}$ ) containing a Ru complex and two bipyridinium units [43].

## 2.2. Rotaxanes and Catenanes

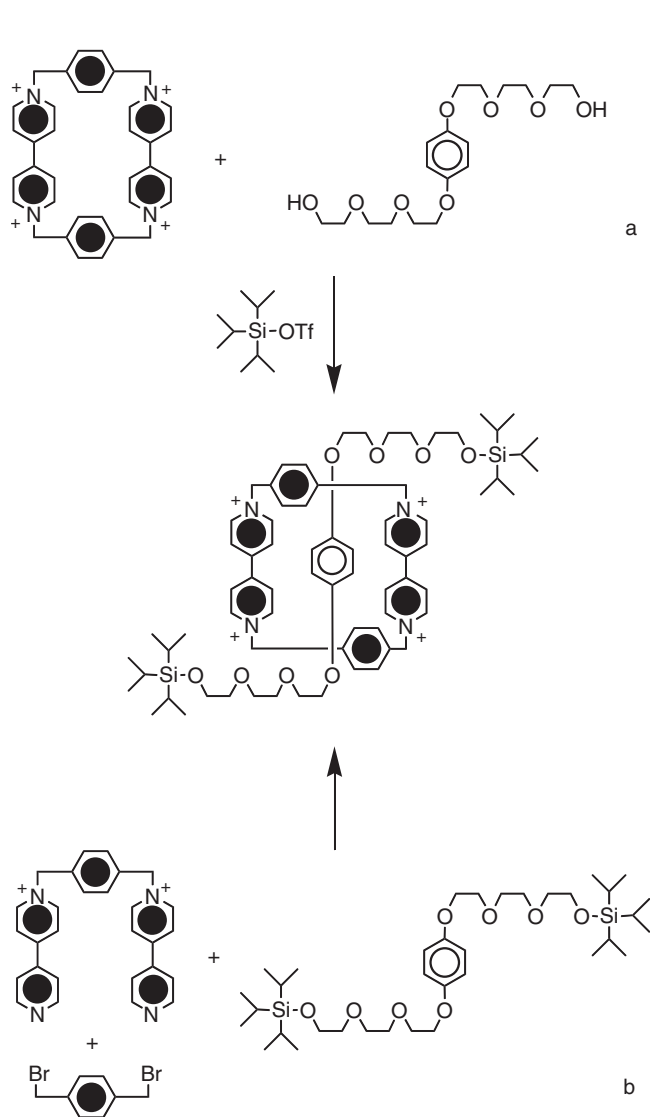
Rotaxanes and catenanes are supramolecular (multicomponent) species [1, 15] strictly related to, but also very different from, pseudorotaxanes (Fig. 2). Whereas pseudorotaxanes can undergo dissociation into their wirelike and macrocyclic components, rotaxanes and catenanes are interlocked species, whose dissociation requires breaking of a covalent bond. The general strategy to prepare rotaxanes and catenanes with high yields is based on the template effect [44], which relies on the presence of molecular recognition sites in the components to be assembled.

Figure 6 shows the routes by which components bearing suitable recognition sites lead to the formation of rotaxanes: (i) *threading* of a molecule through a preformed ring, followed by capping the end(s) of the thread; (ii) *slipping* of a preformed ring over the stoppers of a preformed dumbbell-shaped component into a thermodynamically favorable site on the rod part of the dumbbell; and (iii) *clipping* of a preformed dumbbell with a suitable U-type component that is subsequently cyclized. Figure 7 shows the synthesis of a rotaxane based on donor/acceptor interaction by the threading or the clipping approach [45]. In the first case (Fig. 7a), threading of the electron acceptor tetracationic cyclophane by a thread containing a dioxybenzene electron donor unit yields a pseudorotaxane; then, reaction of the terminal hydroxy groups of the thread with triisopropylsilyl triflate leads to the rotaxane. In the clipping approach (Fig. 7b), the rotaxane is obtained by constructing the electron acceptor cyclophane around the preformed dumbbell-shaped component.

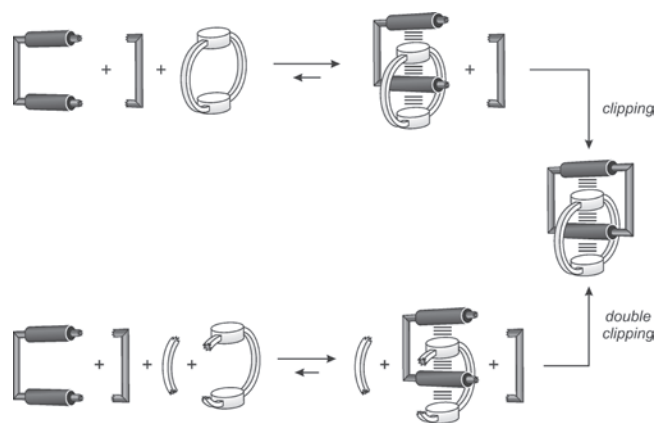
In the case of catenanes, the most rationale synthetic strategy is the clipping of a macrocycle onto a preformed one (Fig. 8). A double-clipping procedure can also be used [46]. Figure 9 shows the synthesis of a catenane templated by electron donor/acceptor interactions [45]. Reaction of a



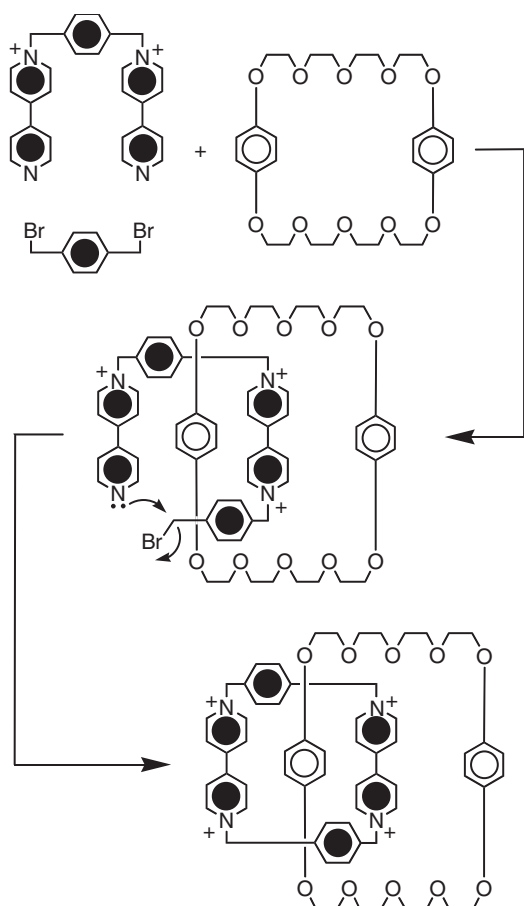
**Figure 6.** Routes for the synthesis of [2]rotaxanes.



**Figure 7.** Synthesis of a [2]rotaxane by the threading (a) and clipping (b) approaches [45].



**Figure 8.** Routes for the synthesis of [2]catenanes.



**Figure 9.** Synthesis of a [2]catenane templated by electron donor/acceptor interactions [45].

dication with a dibromide gives a tricationic intermediate, which interacts with bis-*p*-phenylene-34-crown-10 to afford a pseudorotaxane-like, or precatenane, structure. The subsequent cyclization, as a result of nucleophilic displacement of a bromide ion, gives the corresponding catenane.

In some cases, catenanes are formed from relatively small molecules by one-pot synthesis in a more or less serendipitous manner [47–49]. Figure 10 shows the one-pot synthesis of an amide-based [2]catenane from very simple compounds [48]. This synthesis is thought to involve the perpendicular preorganization of the components caused by three templating effects: (i) steric complementarity, (ii) hydrogen bonding between carbonyl oxygen atoms and amide protons, and (iii)  $\pi$ - $\pi$  interactions between the benzene rings of host and guest units. Several related amide-based rotaxanes have also been prepared [18, 21, 27].

Besides simple rotaxanes and catenanes, a great variety of more complex systems have been synthesized, including branched [*n*]rotaxanes [50], rotaxanes bearing dendritic stoppers [51], catenanes composed of three, five, and seven interlocked macrocycles [52], polyrotaxanes and polycatenanes [16–18, 24], catenanes with very special shapes [53], rotacatenanes [54], pretzelanes [55], and knots [15, 23, 27]. Some of these compounds are shown in Figure 11.

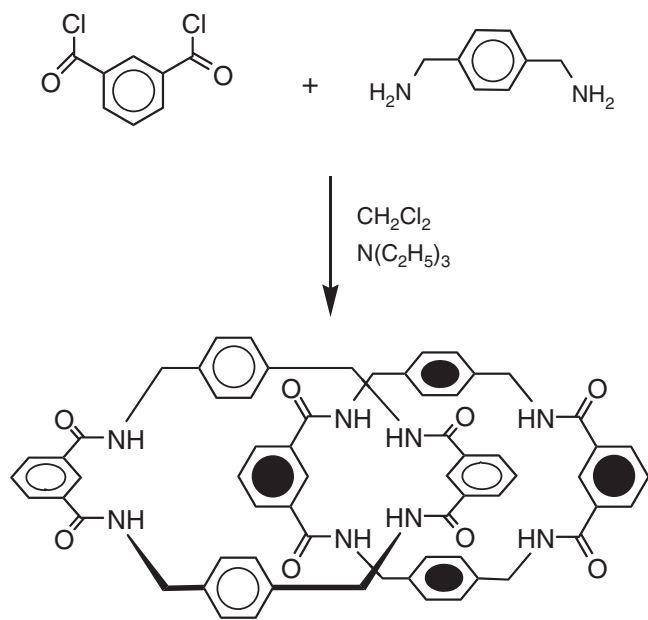


Figure 10. One-pot synthesis of an amide-based [2]catenane [48].

### 3. ARTIFICIAL PHOTOSYNTHETIC DEVICES

An intelligent approach toward the design of artificial systems for solar energy conversion (artificial photosynthetic devices) is to take the natural energy conversion sequence as a model and see whether some of the processes involved can be replaced by more convenient routes and/or the natural components can be replaced by artificial ones. In nature, a large number of light-absorbing species (pigments) deliver the excitation energy to a small number of energy-converting centers where the collected electronic energy is used to obtain charge separation [56]. This choice, made by nature, is very suitable and should therefore also be adopted in artificial systems.

Generally speaking, an artificial photosynthetic device should be made of a light-harvesting molecular array (i.e., an antenna system), a charge separation supramolecular species (a reaction center), and some kind of device capable of making use of the separated charges to produce stable, high-energy chemical species (fuels) or electricity [57–60]. Production of electricity by artificial photoelectrochromic devices has already been achieved [61], whereas photogeneration of fuels by artificial systems is a much more difficult task [62].

#### 3.1. Antenna Systems

Generally speaking, an antenna for light harvesting is an organized multicomponent system in which several chromophoric molecular species absorb the incident light and channel the excitation energy to a common acceptor component. Artificial antenna systems based on porphyrin arrays [63], multichromophoric cyclodextrins [64], polynuclear metal complexes [65, 66], dendrimers [66–68], and polymers [69, 70] have been reported. In all these systems, the chromophoric units are connected by means of covalent

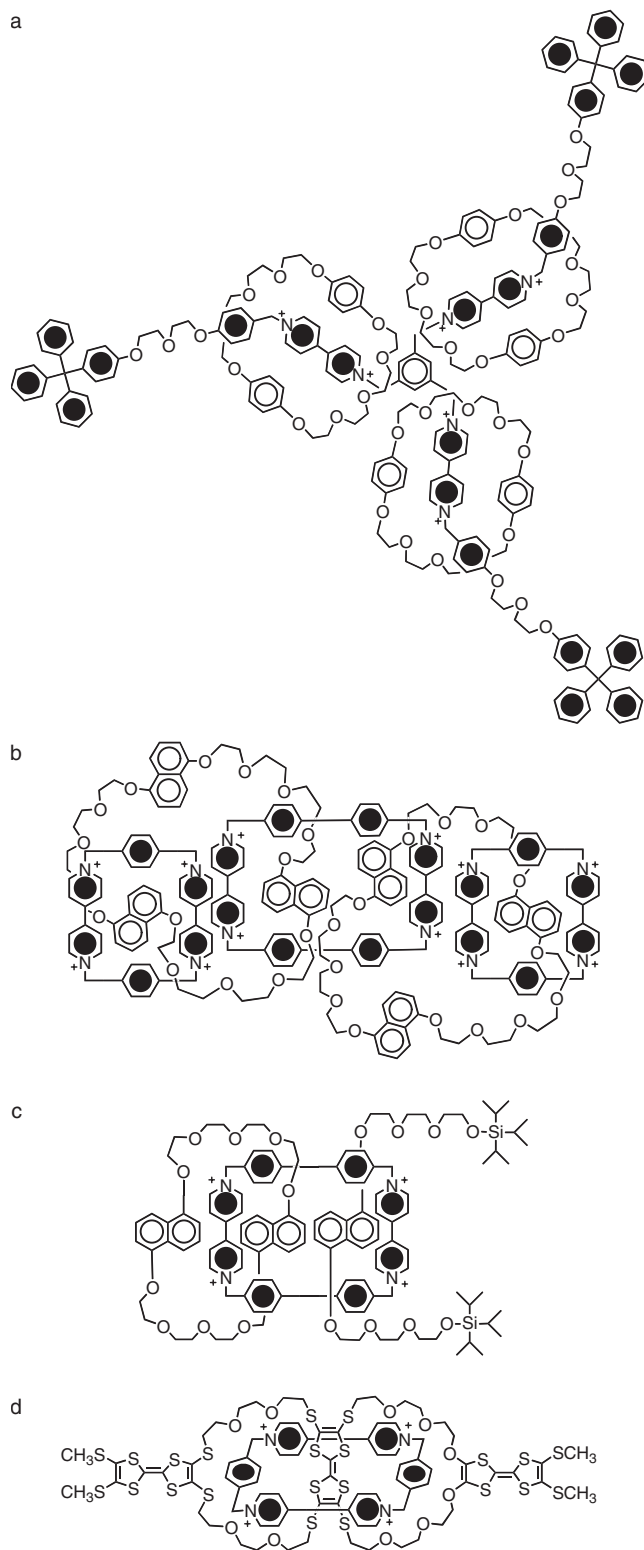


Figure 11. Examples of peculiar rotaxane and catenane structures: (a) a branched [4]rotaxane [50], (b) a [5]catenane named "olympiadane" [52], (c) a rotacatenane [54], and (d) a [2]catenane composed of three macrocyclic rings [53].

bonds, in contrast with natural photosynthetic systems where the molecular components are held together by noncovalent interactions.

Artificial antenna systems in which several chromophoric units are mechanically linked together in a polyrotaxane structure have recently been reported [71, 72]. Such species are composed of many  $\alpha$ -cyclodextrin units, each bearing one or more naphthyl chromophoric groups, threaded by a poly(ethyleneglycol) chain and stoppered by bulky groups. The polyrotaxane **15**, schematized in Figure 12 [71], contains about 15  $\alpha$ -cyclodextrins, each bearing two naphthalenesulfonate units and an axle composed of an average of 45  $[\text{OCH}_2\text{CH}_2]$  units, stoppered by two adamantane groups. When the dansyl-modified  $\beta$ -cyclodextrin **16** is added to **15** in aqueous solution at 298 K, a photoinduced energy transfer process takes place from the naphthyl chromophoric groups of **15** to the dansyl unit of **16**, which binds to the adamantane stoppers by virtue of hydrophobic interactions (Fig. 12). Such a process, evidenced by the quenching of naphthalene fluorescence and sensitization of the dansyl fluorescence, can be switched off by adding 1-adamantanol to the solution, which competes with the adamantane extremities of **15** for the cavity of **16**.

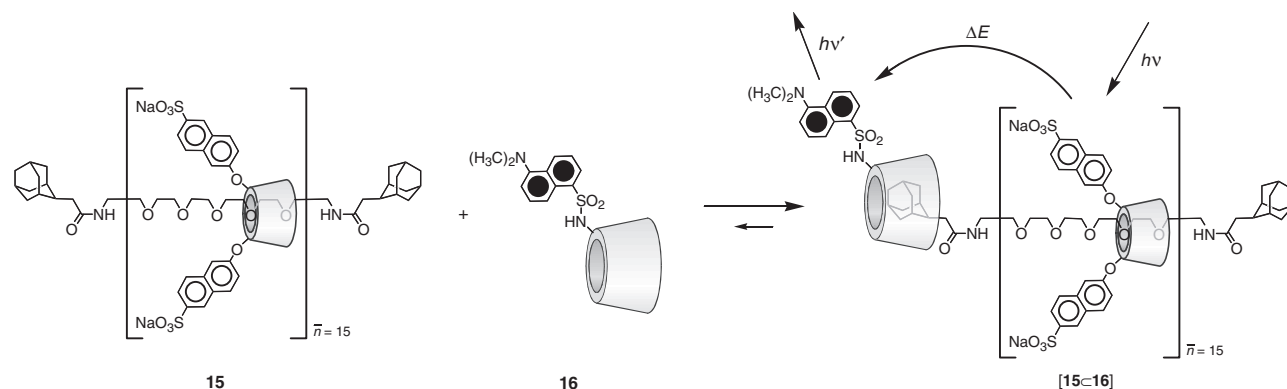
In a successive related work [72], anthracene units have been employed as stoppers for a series of polyrotaxanes; indeed, an efficient energy transfer process from the naphthalene units of the  $\alpha$ -cyclodextrin rings to the anthracene stoppers takes place within the polyrotaxanes. Fluorescence anisotropy measurements also indicate excitation energy migration between naphthalene chromophoric units. The rotaxane architecture, in conjunction with the threading procedure (Fig. 6) employed for the synthesis of this series of compounds, gives the interesting opportunity of adjusting the number of chromophores simply by changing the ratio between naphthalene-decorated and plain  $\alpha$ -cyclodextrin units during the preparation of the polyrotaxanes.

### 3.2. Charge Separation Devices

The simplest supramolecular species capable of performing a charge separation process are those containing two components (diads) [73]. A possible scheme for a diad is

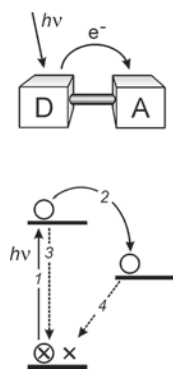
represented in Figure 13. Light excitation of the electron donor (D) (process 1) leads to an electron transfer (process 2), which produces a charge separation and is in competition with the deactivation of the excited state of D (process 3). However, the recombination of the charges in such systems (process 4) is usually very fast. To increase the lifetime of charge separation, which is of fundamental importance for utilizing the energy transiently stored in the charge separation process, more complex systems have to be considered. In particular, an additional charge stabilization step may be introduced, in which the charges are moved far apart from each other. Supramolecular species of this type are called triads [73]. Two possible schemes for charge-separating triads are shown in Figure 14. Although the scheme in Figure 14b is reminiscent of the natural photosynthetic reaction center, that of Figure 14a seems to be more popular in the field of artificial triads. In both cases, excitation of a chromophoric component (process 1) is followed by a primary photoinduced electron transfer to a primary acceptor (process 2). This is followed by a secondary thermal electron transfer (process 3) from a donor component to the oxidized chromophore (Fig. 14a) or from the primary acceptor to a secondary acceptor component (Fig. 14b). The primary process competes with excited-state deactivation (process 4), while the secondary one competes with primary charge recombination (process 5). Finally, charge recombination from remote molecular components (process 6) leads the triad back to its initial state.

Porphyrins, owing to their outstanding photophysical and redox properties [74], are extensively used for the construction of photochemical molecular devices to achieve charge separation over nanometric distance [75]. Porphyrin units have been successfully incorporated into rotaxane structures [76, 77], first playing the role of stoppers. In  $\text{CH}_3\text{CN}$  solution at room temperature, [2]rotaxane **17**<sup>2+</sup> (Fig. 15) [78, 79] undergoes a very fast (ca. 2 ps) electron transfer process from the Zn(II) to the Au(III) porphyrin upon excitation of the Zn(II) porphyrin moiety (process 1 in Fig. 15). Although direct back electron transfer from the Au(II) to the Zn(III) porphyrin indeed occurs (530 ps), the initial state is restored mainly via oxidation/reduction of the central copper unit, that is, through an electron transfer from



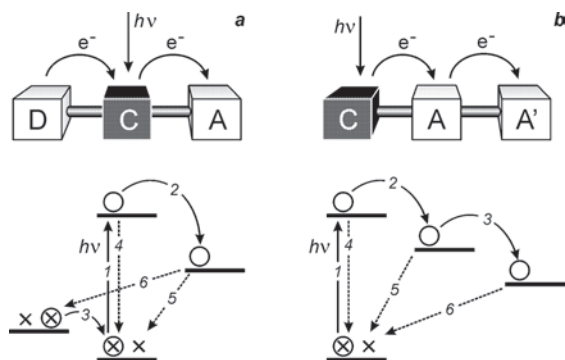
**Figure 12.** The light-harvesting polyrotaxane **15** [71] is composed of a poly(ethyleneglycol) axle encircled by an average of 15  $\alpha$ -cyclodextrin units, each bearing approximately two naphthalenesulfonate groups; therefore, **15** contains about 30 naphthyl chromophoric groups held together mechanically. In aqueous solution, the dansyl-modified  $\beta$ -cyclodextrin **16** is able to bind to the adamantane stoppers of **15**; under such conditions, a photoinduced energy transfer process from the excited naphthalenesulfonate moieties of **15** to the dansyl group of **16** is observed.



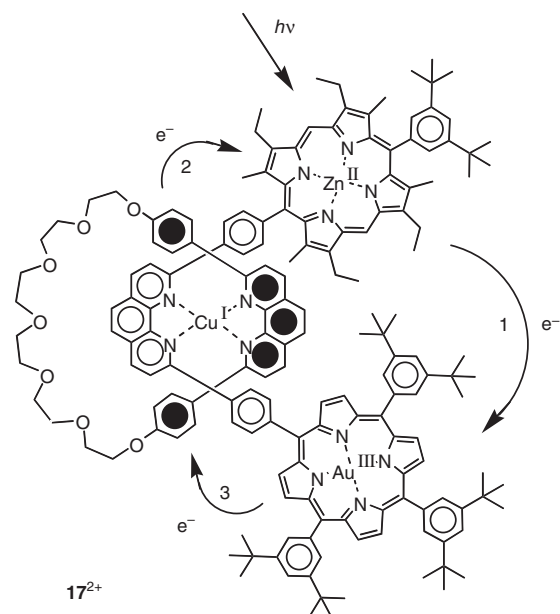


**Figure 13.** Cartoon illustration and working scheme, based on an orbital representation, of a supramolecular diad for photoinduced charge separation.

the Cu(I) unit to the oxidized Zn porphyrin (process 2; 20 ps) followed by another electron transfer from the oxidized copper site to the Au porphyrin (process 3; 2.5 ns). Interestingly, if the copper ion is removed, the so-obtained demetallated [2]rotaxane exhibits electron transfer properties similar to those of the free bis-porphyrin dumbbell components [80]. However, the very short lifetime of the primary charge-separated state and the complexity of the deactivation pattern constitute major limitations to the performance of  $17^{2+}$  as a charge separation system. Rotaxane  $18^{2+}$  (Fig. 16) [81] is composed of an axle bearing one Cu(I)-bis(phenanthroline) complex and two Zn(II) porphyrins as stoppers and a macrocyclic component that incorporates one Au(III) porphyrin. In such a compound, excitation of the Zn(II) porphyrin units ( $\text{CH}_3\text{CN}$ ; room temperature) leads to energy transfer to the central copper unit (process 1), which, in turn, transfers an electron to the Au(III) porphyrin (process 2). Since the oxidized Cu(II) moiety can be reduced by the Zn(II) porphyrin, a charge shift occurs (process 3), leading to the final charge-separated state, which lasts for 5 ns before back electron transfer from the Au(II) to the Zn(III) units (process 4) takes place [81]. Therefore, this assembly operates according to the scheme depicted in Figure 14a, except for the fact that light is absorbed by porphyrins and not by the central copper unit; however, an efficient energy transfer process takes place from the zinc porphyrin to the copper complex.

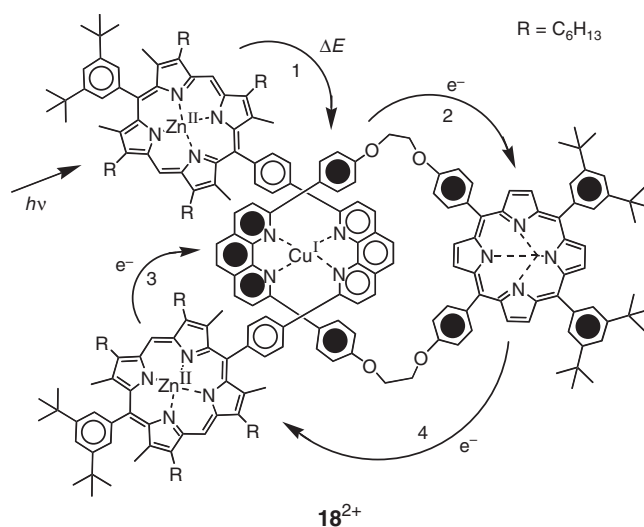


**Figure 14.** Cartoon illustrations and working schemes, based on an orbital representation, of two types of supramolecular triads for photoinduced charge separation.

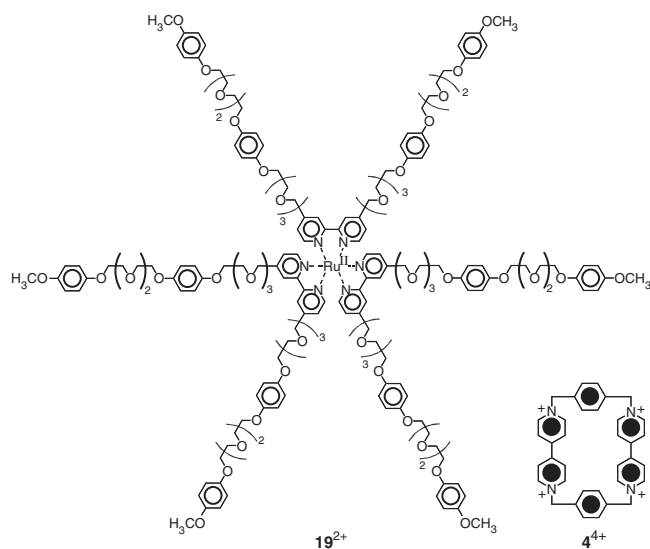


**Figure 15.** Photoinduced electron transfer processes that take place in [2]rotaxane  $17^{2+}$  [78, 79].

Among the systems proposed as models for the photosynthetic reaction center, supramolecular assemblies in which Ru(II)-polypyridine complexes and 4,4'-bipyridinium units are held together noncovalently in threaded and interlocked structures have been extensively studied [43, 82–88]. In such assemblies, connections between the molecular components rely on charge transfer interactions between the electron acceptor bipyridinium units and aromatic electron donor groups (Fig. 3). For instance, in the various pseudorotaxanes formed in acetonitrile solution at 298 K by the threading of cyclophane  $4^{4+}$  by the dioxybenzene-containing tethers of  $19^{2+}$  (Fig. 17) [84], an efficient photoinduced electron



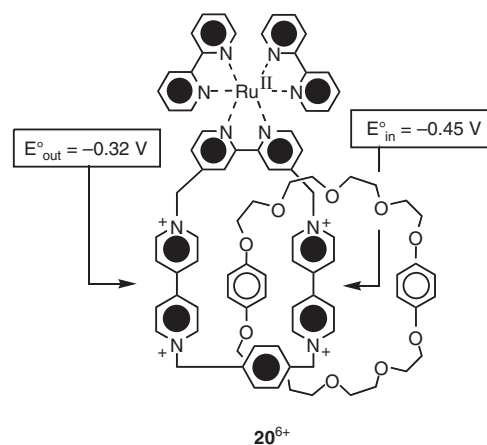
**Figure 16.** Photoinduced energy and electron transfer processes occurring in [2]rotaxane  $18^{2+}$  [81], which behaves as a triad for photoinduced charge separation according to the scheme illustrated in Figure 14a. For more details, see text.



**Figure 17.** Branched compound  $19^{2+}$  [84], which contains a  $[Ru(bpy)_3]^{2+}$  core and six pendant threadlike substituents, forms pseudorotaxanes with macrocycle  $4^{4+}$ . In such pseudorotaxane species, efficient photoinduced electron transfer takes place from the excited state of the ruthenium complex of  $19^{2+}$  to the bipyridinium units of  $4^{4+}$ .

transfer process takes place from the excited state of the  $[Ru(bpy)_3]^{2+}$  moiety of  $19^{2+}$  to a 4,4'-bipyridinium unit of  $4^{4+}$ . The back electron transfer occurs on a time scale (ca. 1  $\mu$ s) considerably longer than that found for covalently linked  $[Ru(bpy)_3]^{2+}$ /bipyridinium assemblies (nanosecond time domain), a behavior that has been attributed to increased spatial separation of the photogenerated redox pair due to repulsive electrostatic interactions between the positively charged macrocycle and Ru(II) complex [84]. It has also been found that recombination takes place within the threaded supramolecular assemblies, indicating that the pseudorotaxanes do not break apart upon light irradiation. However, in the light of the large variety of threaded species that can be formed, as well as of the relatively small stability constants of the resulting pseudorotaxanes, well-defined interlocked (catenane or rotaxane) structures might be preferred [85–88].

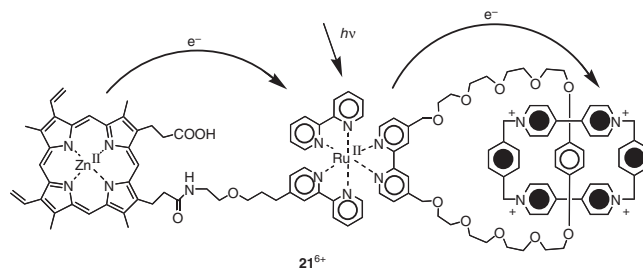
One intriguing aspect of the bacterial photosynthetic reaction center is the redox asymmetry of the cofactors; electron transfer proceeds exclusively along one branch of an almost symmetrical pair of reagents [89, 90]. The catenane structure can be exploited to reproduce such an asymmetry with artificial systems; in catenane  $20^{6+}$  (Fig. 18) [86], the two bipyridinium electron acceptors, linked to a  $[Ru(bpy)_3]^{2+}$ -type primary electron donor, possess different reduction potentials because one of them is encircled by an electron donor crown ether that both attenuates its electron acceptor affinity via charge transfer interactions and hinders access to solvent molecules. Indeed, in  $CH_3CN$  solution at 293 K, a very fast ( $k = 5.9 \times 10^{10} s^{-1}$ ) electron transfer takes place from the photoexcited  $[Ru(bpy)_3]^{2+}$  moiety to a bipyridinium unit. Although it can be anticipated with thermodynamic arguments that the redox asymmetry of the two acceptor branches in  $20^{6+}$  should result in a fivefold difference in rate constants [86], there is no means to distinguish between the two electron transfer paths by time-resolved



**Figure 18.** In [2]catenane  $20^{6+}$  [86], upon excitation of its  $[Ru(bpy)_3]^{2+}$  moiety, a very fast electron transfer process to a bipyridinium unit occurs. Owing to the catenane structure, the two bipyridinium units do not possess the same reduction potential (half-wave potential values versus SCE for the “inside” and “outside” units are indicated); such a redox asymmetry could mimic that of the cofactors in the bacterial photosynthetic reaction center.

spectroscopic techniques. In such a system, back electron transfer is also extremely rapid ( $k = 2.4 \times 10^{10} s^{-1}$ ), owing to the close proximity of the reactants, despite the fact that it should fall in the Marcus “inverted” region.

The photoinduced processes taking place in triad  $21^{6+}$  (Fig. 19), made of a Zn(II) porphyrin linked to a  $[Ru(bpy)_3]^{2+}$ -crown ether component catenated with one  $4^{4+}$  macrocycle have been studied recently ( $H_2O$ , phosphate buffer, 293 K) [88]. Upon excitation of the Zn(II) porphyrin moiety, direct electron transfer occurs from the photoexcited porphyrin to the tetracationic macrocycle. The same charge-separated state can be reached upon excitation of the Ru(II) complex followed by two electron transfer steps (Fig. 19), according to the scheme reported in Figure 14a. Two semisynthetic systems, obtained by incorporation of  $21^{6+}$  into two different proteins, namely, cytochrome  $b_{562}$  and myoglobin, were also studied [88]. Interestingly, the lifetime values for the photoinduced charge-separated state increase substantially when the heme moiety of the triad is embedded in the protein matrix: from 300 ns found for free  $21^{6+}$  to 600–900 ns of cytochrome- $b_{562}$ -( $21^{6+}$ ) and 1.1–18  $\mu$ s of myoglobin-( $21^{6+}$ ). This study not only demonstrates that protein matrix effects play a crucial role in electron transfer processes of biological importance, but also that hybrid



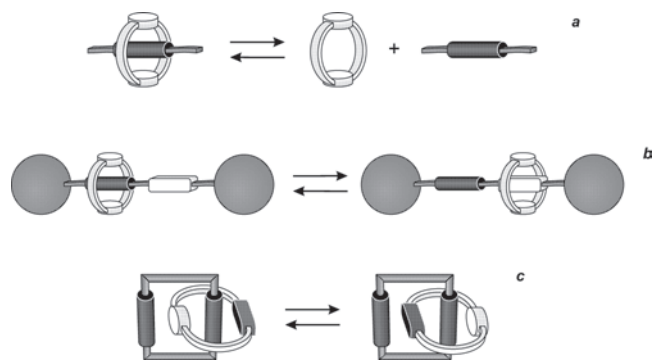
**Figure 19.** Photoinduced processes taking place in the catenane triad  $21^{6+}$  [88].

natural/artificial supramolecular assemblies are promising candidates for the realization of molecular devices to be used in artificial photosynthetic systems.

#### 4. MOLECULAR-LEVEL MACHINES

A molecular-level machine can be defined [91–93] as an assembly of a distinct number of molecular components that are designed to perform mechanical movements as a result of an appropriate external stimulation. Although there are many chemical compounds whose structure and/or shape can be modified by an external stimulus (see, e.g., photoisomerizable species), the term molecular machine is used only for systems showing large-amplitude movements of the molecular components. Chemical, photochemical, or electrochemical stimuli can be used to feed molecular-level machines [91–93]; however, for the reasons discussed in the Introduction, light is the most convenient form of energy to make molecular machines work [11]. Two kinds of light-induced processes have been used so far for this purpose: photoisomerization reactions [94] and photoinduced electron transfer processes [95]. It is very important that such molecular-level motions are accompanied by changes of some chemical or physical property of the system, resulting in a readout signal that can be used to monitor the operation of the machine. The reversibility of the movement, that is, the possibility to restore the initial situation by means of an opposite stimulus, is an essential feature of a molecular machine. Since the induced motions usually correspond to transitions between two stable structures (states), systems of this kind behave according to a binary logic and could also prove useful for information processing [3].

Threaded and interlocked compounds, owing to their peculiar structure [15–27], are attractive candidates for the construction of molecular-level machines; therefore, it is not surprising that most of the recently designed molecular-level machines are based on pseudorotaxanes, rotaxanes, and catenanes. Figure 20 shows pictorially some of the movements that can be imagined for these systems, namely, threading/dethreading of the wire and ring components of pseudorotaxanes (Fig. 20a), shuttling of the macrocyclic



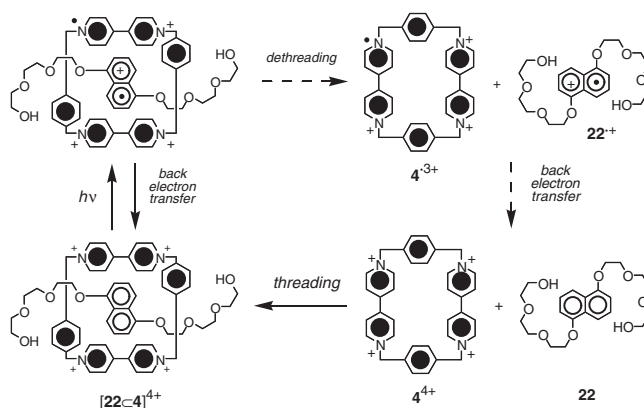
**Figure 20.** Pictorial representation of machine-like movements that can be obtained with pseudorotaxanes, rotaxanes, and catenanes: (a) dethreading/rethreading of the molecular components in a [2]pseudorotaxane, (b) shuttling of the macrocyclic component along the axle in a [2]rotaxane, and (c) ring rotation in a [2]catenane.

component along the axle in rotaxanes (Fig. 20b), and rotation of one molecular ring with respect to the other in catenanes (Fig. 20c).

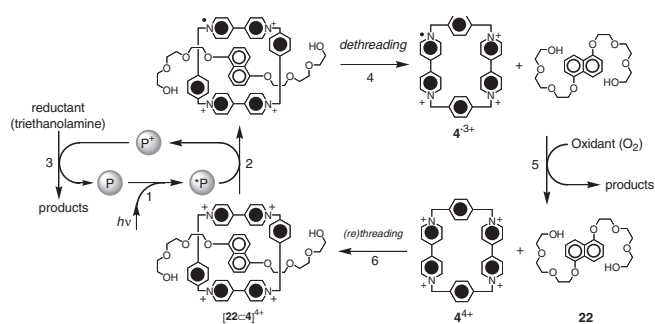
#### 4.1. Piston/Cylinder Systems

Dethreading/rethreading of the wire and ring components of a pseudorotaxane resembles the movement of a piston in a cylinder (Fig. 20a) [91]. The first attempts at designing a photochemically driven molecular machine of this type were carried out on pseudorotaxanes stabilized by electron donor/acceptor interactions (Fig. 3). In such systems, the donor/acceptor interactions introduce low-energy charge transfer (CT) excited states responsible for absorption bands in the visible region. Light excitation in these CT absorption bands leads formally to the transfer of an electron from the donor to the acceptor component, as illustrated in Figure 21 for the pseudorotaxane formed in  $\text{H}_2\text{O}$  or  $\text{CH}_3\text{CN}$  solution by the electron donor thread **22** and the electron acceptor macrocycle  $4^{4+}$ . As a consequence, particularly when this process leads to formation of charges of the same sign in the two components, one can expect destabilization of the pseudorotaxane structure followed by dethreading. In practice, however, this simple approach does not work because the back electron transfer process is much faster than the separation of the molecular components, a process that requires extended nuclear motions and solvent rearrangement. In some particular cases [96, 97], laser flash photolysis experiments have suggested that a small fraction of the irradiated pseudorotaxane may undergo dissociation.

To really achieve photoinduced dethreading, a different approach has been devised [98, 99], based on the use of an external electron transfer photosensitizer (P) and a sacrificial reductant (Red), as illustrated in Figure 22. The photosensitizer must be able to (i) absorb light efficiently and (ii) have a sufficiently long-lived and reductant excited state, so that its excitation (process 1) in the presence of the pseudorotaxane will lead (process 2) to the transfer of an electron to a bipyridinium unit of the cyclophane. The relatively fast back electron transfer from the reduced cyclophane component to the oxidized photosensitizer is prevented by the sacrificial reductant, which, if



**Figure 21.** Photochemical processes associated with [2]pseudorotaxane  $[22\text{-}c\text{-}4]^{4+}$  upon excitation in its charge transfer absorption band [98, 99]. The processes indicated by dashed arrows are unlikely to occur.

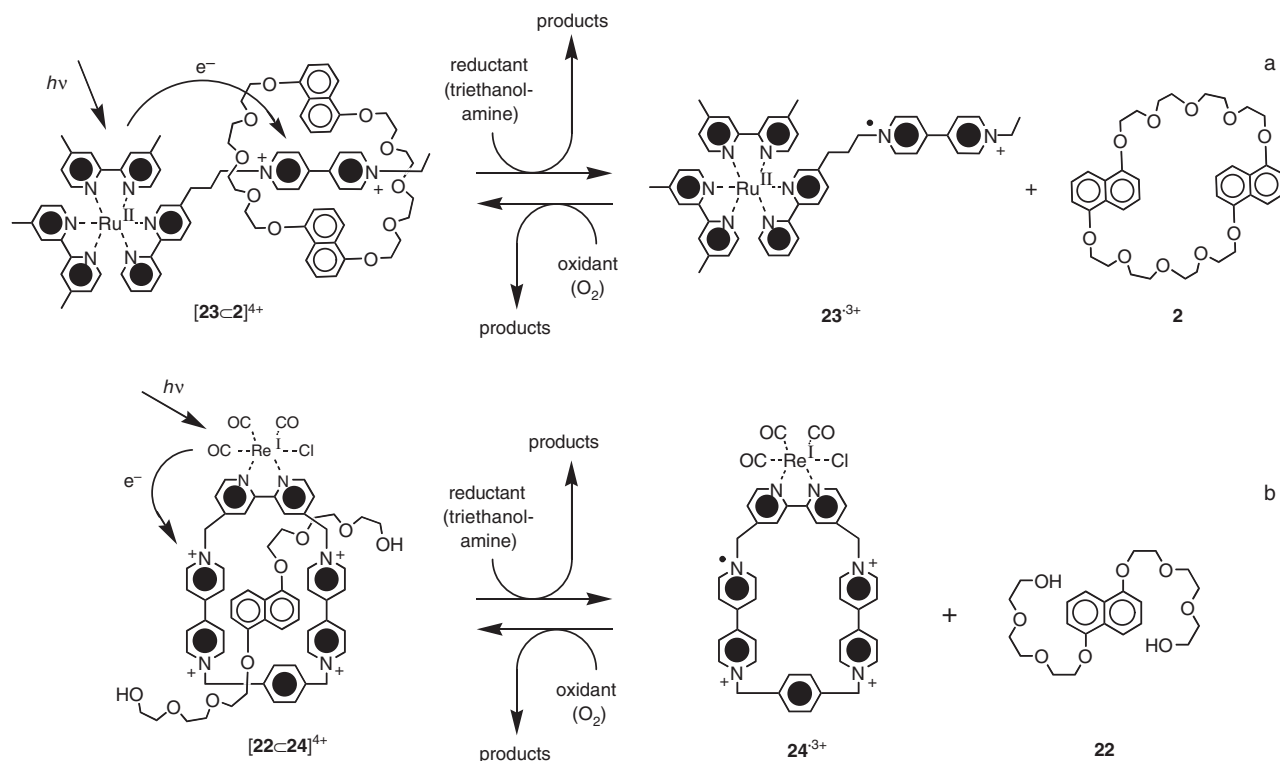


**Figure 22.** Photochemically induced dethreading of [2]pseudorotaxane  $[22\text{-}4]^{4+}$ , based on the use of an external photosensitizer (P) and a reductant scavenger. Rethreading occurs upon oxygenation of the previously deaerated solution [98, 99].

present in a sufficient amount, intercepts the oxidized photosensitizer and regenerates (process 3) its original redox state. Good candidates for the role of photosensitizer are 9-anthracenecarboxylic acid [100] and metal complexes such as  $[\text{Ru}(\text{bpy})_3]^{2+}$  [101], while efficient reductant scavengers are triethanolamine and polycarboxylate (e.g., oxalate) anions [102]. Under these conditions, the persistent reduction of a bipyridinium unit of  $4^{3+}$  is achieved and the pseudorotaxane dethreads (process 4), as evidenced by absorption spectral changes and, more important, by the increase in the intensity of the dioxynaphthalene fluorescence, which can only originate from free **22**. Oxygenation of the solution, from which  $\text{O}_2$  was initially removed, reoxidizes the macro-

cycle back to the tetracationic form (process 5), thereby promoting rethreading with **22** (process 6), as also shown by the absorption and luminescence spectra. Very recently, it has been shown that this same system can be operated in unconventional environments such as the interior pores of a sol-gel silica framework [103]. The possibility of mounting such a molecular-level machine on a solid support, by trapping the wirelike molecule onto the surface of a sol-gel film, has also been demonstrated [103].

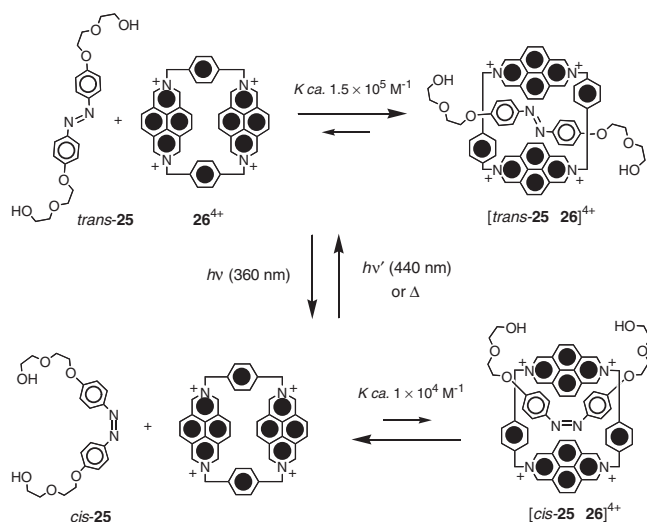
This strategy has been extended recently to second-generation pseudorotaxanes  $[23\text{-}2]^{4+}$  and  $[22\text{-}24]^{4+}$  in which the metal-complex photosensitizer (the “light-fueled” motor [104]) has been incorporated either into the thread (Fig. 23a) [41] or into the ring (Fig. 23b) [105] component. The successful operation of these pseudorotaxanes as molecular machines is the result of (i) the appropriate choice of the functional units and (ii) their covalent linking into the thread and ring components in order to achieve the correct integration of the needed functions (e.g., receptor ability, redox features, photophysical properties, etc.), the right sequence of processes, and the lack of interference between the active units. As in the case of the molecular machine shown in Figure 22, the dethreading and rethreading motions of the pseudorotaxanes represented in Figure 23 can be triggered by visible-light irradiation and oxygenation of the solution, respectively. The motions can also be easily monitored by means of UV-vis absorption and luminescence spectroscopy. The most important readout signal is the intensity of the dioxynaphthalene fluorescence associated with the free ring **2** (Fig. 23a) or free thread **22** (Fig. 23b)



**Figure 23.** Photocontrollable molecular machines based on [2]pseudorotaxanes. In these second-generation systems, the “light-fueled” motor (i.e., the photosensitizer) is part of the threadlike and of the macrocyclic components of  $[23\text{-}2]^{4+}$  and  $[22\text{-}24]^{4+}$ , respectively [41, 105]. As for the system described in Figure 22, a reductant scavenger is employed, and rethreading is performed by allowing oxygen to enter the irradiated solution.

components. It is worth noting that many [deoxygenation–irradiation (dethreading)/oxygenation (rethreading)] cycles can be performed on the same solution without any appreciable loss of signal until most of the reductant scavenger is consumed. It should also be stressed that systems that rely on this photosensitizer–scavenger strategy utilize, in addition to light energy, the irreversible decomposition of a reductant scavenger that produces “waste” species. In this regard, the search for efficient molecular machines exploiting “clean,” reversible photochemical reactions (in other words, machines that use only light as an energy supply) is of fundamental importance.

Photoisomerization reactions, particularly the well-known [94] reversible *cis/trans* photoisomerization of the azobenzene group, have long been used to exert photochemical control on chemical systems [106]. Since the early 1980s, azobenzene-containing compounds have been employed both as photocontrollable hosts [107, 108] and guests [109]. The first example of a pseudorotaxane in which dethreading/rethreading is based on such a principle and is powered exclusively by light energy, without generation of any waste products, has been reported only recently (Fig. 24) [110]. The threadlike species *trans*-**25**, which contains an electron-rich azobiphenoxy unit, and the electron acceptor macrocycle **26**<sup>4+</sup> self-assemble very efficiently in acetonitrile solution to give a pseudorotaxane, stabilized by donor/acceptor interactions. In the pseudorotaxane structure, the intense fluorescence characteristic of free **26**<sup>4+</sup> is completely quenched by the donor/acceptor interaction. Irradiation with 365 nm light of a solution containing *trans*-**25** and **26**<sup>4+</sup>, in which the majority of the species are assembled to give the pseudorotaxane, causes *trans* → *cis* photoisomerization of **25**. Since the affinity of the macrocycle for *cis*-**25** is much lower than that for *trans*-**25**, photoexcitation causes a dethreading process (Fig. 24), as indicated by a substantial increase in the fluorescence intensity of free **26**<sup>4+</sup>. On irradiation at 436 nm or by warming the solution in the dark, the *trans* isomer of **25** can be reformed and, as a result, it rethreads inside the



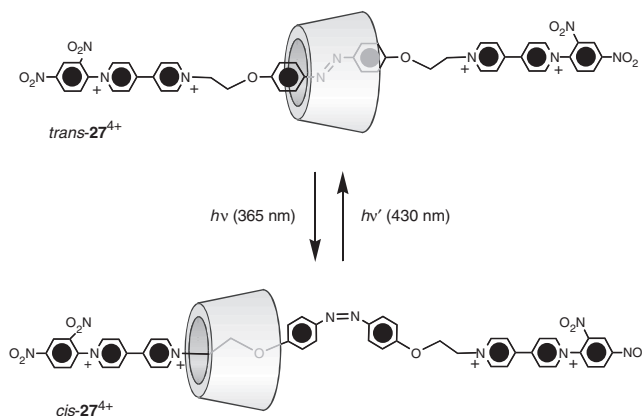
**Figure 24.** Dethreading/rethreading of [2]pseudorotaxane [**25**⊂**26**]<sup>4+</sup> as a consequence of the *cis/trans* photoisomerization of the azobenzene unit contained in the threadlike component **25** [110].

macrocycle. Owing to the full reversibility of the photoisomerization process, the light-driven dethreading/rethreading cycle can be repeated at will (Fig. 24). Another relevant feature of this system is that it exhibits profound changes of a strong fluorescence signal.

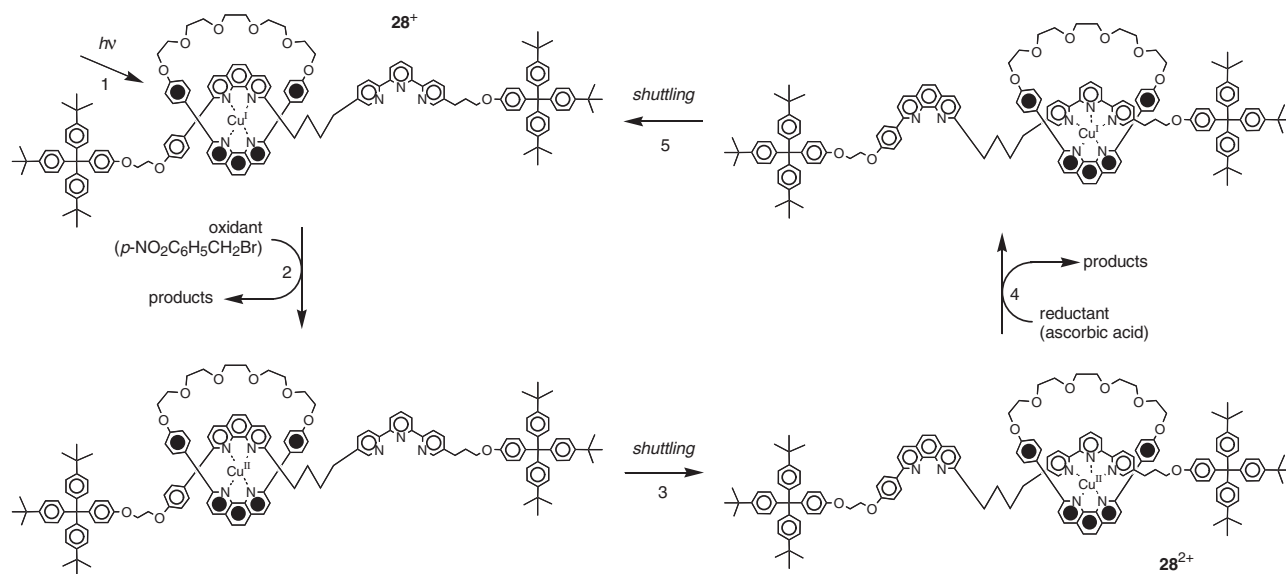
## 4.2. Molecular Shuttles

In rotaxanes containing at least two (or more) different recognition sites (“stations”) in the axle component, it is possible to switch the position of the macrocycle between the two stations by an external stimulus [91]. The [2]rotaxane *trans*-**27**<sup>4+</sup> (Fig. 25) [111] incorporates an  $\alpha$ -cyclodextrin torus and a *trans*-azobiphenoxy-containing axle. Initially, the cyclodextrin ring resides exclusively around the *trans*-azobiphenoxy recognition site. Upon irradiation at 365 nm in H<sub>2</sub>O at 278 K, the azobiphenoxy unit isomerizes [94] from *trans* to *cis*, “pushing” the  $\alpha$ -cyclodextrin component away to encircle one of the [(CH<sub>2</sub>)<sub>2</sub>O] chains. Further irradiation at 430 nm causes back isomerization of the azobiphenoxy group from the *cis* to the *trans* form, leading to the shuttling of the cyclodextrin component back to the *trans*-azobiphenoxy recognition site (Fig. 25). The photoisomerization/shuttling processes are accompanied by changes in the circular dichroism signals induced by the chiral cavity of the cyclodextrin on the azobiphenoxy  $\pi$ – $\pi^*$  transitions.

The [2]rotaxane **28**<sup>+</sup> (Fig. 26) [112] has a phenanthroline and a terpyridine unit in its axle component, and it incorporates a Cu(I) ion coordinated tetrahedrally by the phenanthroline ligand of the axle together with the phenanthroline ligand of the macrocycle. Oxidation of the tetracoordinated Cu(I) center produces a tetracoordinated Cu(II) complex; in response to the preference of Cu(II) for a pentacoordination geometry, the macrocycle shuttles away from the bidentate phenanthroline ligand of the axle and places itself on the terdentate terpyridine site. Subsequent reduction of the Cu(II) center to Cu(I) causes an opposite shuttling process, affording a return to the original structure. These movements can of course, be performed electrochemically [113], but can also be induced photochemically [114], as illustrated in Figure 26. Upon irradiation at 464 nm of an acetonitrile solution of the [2]rotaxane (process 1), the Cu(I)-based



**Figure 25.** Light-controlled reversible shuttling of the macrocyclic component of **27**<sup>4+</sup> along its axle, based on the *cis/trans* photoisomerization of the azobenzene unit [111].



**Figure 26.** Photoinduced shuttling, based on the use of an oxidant scavenger (*p*-nitrobenzylbromide), of the macrocyclic component in the copper-containing [2]rotaxane  $28^+$  [114].

chromophoric unit is excited to a metal-to-ligand charge transfer (MLCT) state. In the presence of a suitable oxidant (*p*-nitrobenzylbromide), electron transfer from the photoexcited rotaxane to the oxidant follows (process 2), which generates a tetracoordinated Cu(II) center and products deriving from reduction of *p*-nitrobenzylbromide. Such a reaction competes with the intrinsic deactivation of the MLCT excited state, which includes luminescence; therefore, emission spectroscopy is a useful tool to evaluate whether photooxidation takes place. Indeed, light excitation of the rotaxane causes spectral changes indicating the disappearance of the Cu(I) chromophore and the concomitant formation of the tetracoordinated Cu(II) center [114]; spectroscopic measurements showed that subsequent transformation of tetracoordinated Cu(II) into the more stable pentacoordinated Cu(II) species, that is, shuttling of the macrocyclic component (process 3), was slowly occurring. The cycle can be completed upon addition of an excess of ascorbic acid, which reduces the Cu(II) center back to Cu(I) (process 4), affording the shuttling of the macrocyclic ring back to its initial position (process 5). It is worth noticing that in this case the back reduction step cannot be induced by light since in Cu(II) complexes the lowest excited state decays to the ground state very rapidly and therefore cannot be involved in a bimolecular reaction with a reductant.

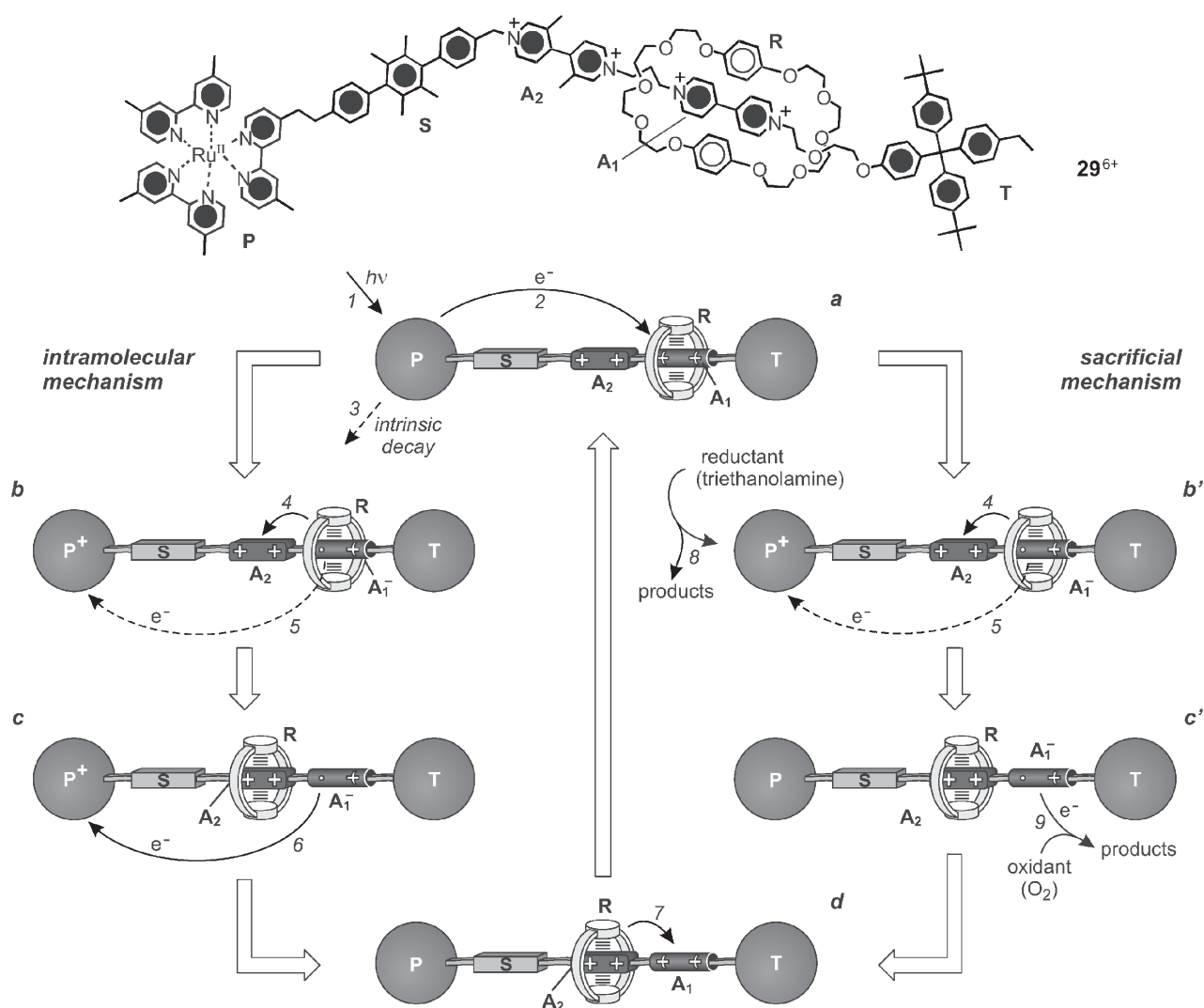
The design principles that form the basis of the light-driven molecular machines shown in Figure 23 have been employed to obtain the [2]rotaxane  $29^{6+}$  (Fig. 27) [115], specifically designed to achieve photoinduced ring shuttling. This compound is made of the electron donor macrocycle R and a dumbbell-shaped component that contains (i) [Ru(bpy)<sub>3</sub>]<sup>2+</sup> (P) as one of its stoppers, (ii) a 4,4'-bipyridinium unit (A<sub>1</sub>) and a 3,3'-dimethyl-4,4'-bipyridinium unit (A<sub>2</sub>) as electron-accepting stations, (iii) a *p*-terphenyl-type ring system as a rigid spacer (S), and (iv) a tetraaryl-methane group as the second stopper (T). The stable translational isomer of rotaxane  $29^{6+}$  is the one in which the R component encircles the A<sub>1</sub> unit, in keeping with the fact

that this station is a better electron acceptor than the other one. Two strategies have been devised in order to obtain the photoinduced abacus-like movement of the R macrocycle between the two stations A<sub>1</sub> and A<sub>2</sub>: One is based on processes involving only the rotaxane components (intramolecular mechanism), while the other one requires the use of external reactants (sacrificial mechanism).

The intramolecular mechanism, illustrated in the left part of Figure 27, is based on the following four operations [115]:

- Destabilization of the stable translational isomer.* Light excitation of the photoactive unit P (process 1) is followed by the transfer of an electron from the excited state to the A<sub>1</sub> station, which is encircled by the ring R (process 2), with the consequent “deactivation” of this station; such a photoinduced electron transfer process has to compete with the intrinsic decay of \*P (process 3).
- Ring displacement.* The ring moves from the reduced A<sub>1</sub> station to A<sub>2</sub> (process 4), a step that has to compete with the back electron transfer process from A<sub>1</sub><sup>-</sup> (still encircled by R) to the oxidized photoactive unit, P<sup>+</sup> (process 5). This is the most difficult requirement to meet in the intramolecular mechanism.
- Electronic reset.* A back electron transfer process from the “free” A<sub>1</sub><sup>-</sup> station to P<sup>+</sup> (process 6) restores the electron acceptor power to the A<sub>1</sub> station.
- Nuclear reset.* As a consequence of the electronic reset, back movement of the ring from A<sub>2</sub> to A<sub>1</sub> takes place (process 7).

The results obtained (CH<sub>3</sub>CN solution, 298 K) [115] seem to indicate that the back electron transfer (process 5) is faster than the ring displacement (process 4). It is worthwhile noticing that in a system that behaves according to the intramolecular mechanism shown in Figure 27 (left) each light input causes the occurrence of a forward and back ring movement (i.e., a full cycle) without generation of any



**Figure 27.** [2]Rotaxane  $29^{6+}$  and schematic representation of the intramolecular (left) and sacrificial (right) mechanisms for the photoinduced shuttling movement of macrocycle **R** between the two stations **A<sub>1</sub>** and **A<sub>2</sub>** located on the axle component.

waste product. In some way, it can be considered as a “four-stroke” cyclic linear motor powered by light.

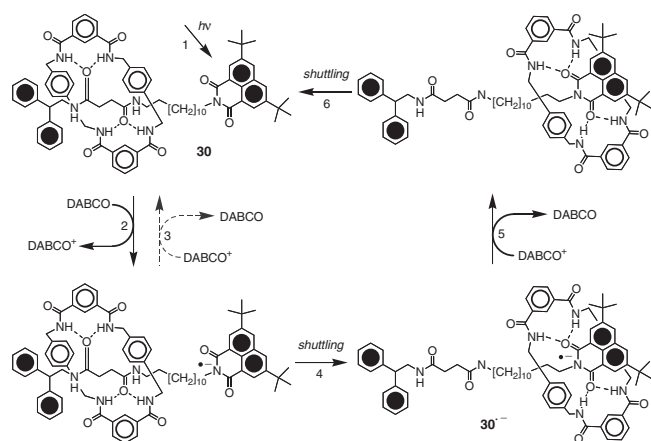
The alternative, less demanding mechanism is based on the use of external sacrificial reactants (a reductant like triethanolamine and an oxidant like dioxygen) that operate as illustrated in the right part of Figure 27:

- (a) *Destabilization of the stable translational isomer*, as in the previous mechanism.
- (b) *Ring displacement after scavenging of the oxidized photoactive unit.* Since the solution contains a suitable sacrificial reductant, a fast reaction of such species with **P<sup>+</sup>** (process 8) competes successfully with the back electron transfer reaction (process 5); therefore, the originally occupied **A<sub>1</sub>** station remains in its reduced state, **A<sub>1</sub><sup>-</sup>**, and the displacement of the ring **R** to **A<sub>2</sub>** (process 4), even if it is slow, does take place.
- (c') *Electronic reset.* After an appropriate time, restoration of the electron acceptor power of the **A<sub>1</sub>** station is obtained by oxidizing **A<sub>1</sub><sup>-</sup>** with a suitable oxidant, such as  $O_2$  (process 9).

- (d) *Nuclear reset*, as in the previous mechanism (process 7).

Such a sacrificial mechanism, although fully successful, is less appealing than the intramolecular one because it leads to the formation of waste products. However, instead of using a sacrificial reductant, that is, an electron donor molecule that undergoes a fast decomposition reaction after electron transfer has taken place, a “reversible” reductant, giving rise to a stable oxidized form, may be successfully employed, provided that the back electron transfer process can be slowed down by a wise choice of the partners.

A light-driven molecular shuttle that relies on this strategy has been reported [116]. The [2]rotaxane **30** (Fig. 28) consists of a benzylic amide macrocycle that surrounds an axle featuring two hydrogen-bonding stations, namely, a succinamide unit and a naphthalimide unit, separated by a long alkyl chain. Initially, the macrocycle resides on the succinamide station because the naphthalimide unit is a much poorer hydrogen-bonding recognition site. Light excitation at 355 nm (process 1) in acetonitrile at 298 K



**Figure 28.** Light-induced reversible shuttling of the macrocyclic component in the hydrogen-bonded [2]rotaxane **30** [117]. The operation of this system relies on the use of a reductant (DABCO). For more details, see the text.

generates the singlet excited state of the naphthalimide unit, which then undergoes high-yield intersystem crossing to the triplet excited state. Such a triplet state can be reduced in bimolecular encounters by an electron donor (1,4-diazabicyclo[2.2.2]octane; DABCO) added to the solution in a sufficiently large amount (process 2). Because the back electron transfer process (process 3) is spin forbidden and thus slow, the photogenerated ion pair can efficiently dissociate; as a matter of fact, the naphthalimide radical anion survives for hundreds of microseconds before it decays by bimolecular charge recombination with a DABCO radical cation. Since the naphthalimide anion is a much stronger hydrogen-bonding station compared to the succinamide, upon reduction of the naphthalimide unit the macrocycle is expected to shuttle from the latter to the former station (process 4); this has been demonstrated by cyclic voltammetric experiments. Laser flash photolysis studies have demonstrated that this is indeed the case; the time required for ring shuttling (ca. 1  $\mu$ s) is much shorter than the lifetime of the naphthalimide radical anion (ca. 100  $\mu$ s). After charge recombination (process 5), the macrocycle moves back to its original position (process 6). This [2]rotaxane constitutes an outstanding example of a linear molecular motor driven exclusively by light, although its operation still relies on the presence of external reactants, which, however, are not consumed. The device can be cycled at a frequency depending on the charge recombination rate of the rotaxane radical anion. It can be estimated that if the shuttle is pumped by a laser at the frequency of its “recovery stroke” (process 5), that is,  $10^4$  s $^{-1}$ , this molecular-level machine generates approximately  $10^{-15}$  W of mechanical power per molecule [116].

In a very recent work [117], the complex fluorescence behavior exhibited by a similar peptide-based [2]rotaxane bearing an anthracene unit as one of the stoppers has been interpreted in terms of a very fast (subnanosecond), short-amplitude translation of the macrocycle upon light excitation of the anthracene subunit. However, it seems that alternative explanations, such as the formation of intercomponent exciplexes [118], cannot be ruled out.

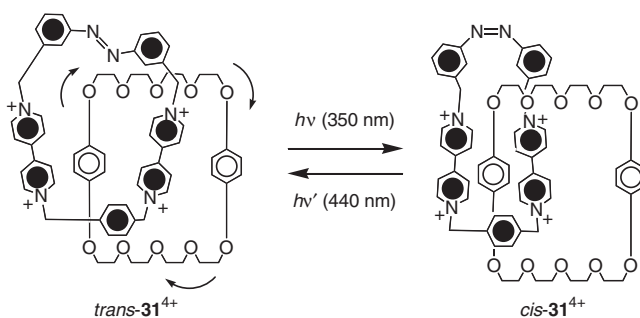
### 4.3. Ring Rotation in Catenanes

There are several examples of catenanes where ring movements can be induced by external stimulations like simple chemical reactions or homogeneous or heterogeneous electron transfer processes [91–93], but only very few cases are reported in which the stimulus employed is light. It has been shown that in azobenzene-containing [2]catenanes like **31** $^{4+}$  (Fig. 29) it is possible to control the rate of thermally activated rotation of the macrocyclic components by photoisomerization of the azobenzene moiety [119, 120]. Such systems can be viewed as molecular-level brakes operated by light.

To date, only one case has been reported in which the ring motions are induced photochemically, using the same strategy adopted to operate molecular shuttle **28** $^+$  (Fig. 26). Irradiation at 464 nm of the [2]catenane **32** $^+$  (Fig. 30) [121] in CH $_3$ CN solution at room temperature in the presence of *p*-nitrobenzylbromide causes an electron transfer process from the photoexcited [2]catenane to *p*-nitrobenzylbromide, thus generating a Cu(II) center. Owing to the preference of the Cu(II) ion for a pentacoordination geometry, the terpyridine-containing macrocycle rotates through the cavity of the other, affording a pentacoordinated Cu(II) center. Upon addition of ascorbic acid, the Cu(II) ion is reduced to Cu(I); in response to the preference of Cu(I) for tetracoordination, the terpyridine-containing macrocycle rotates again through the cavity of the other, restoring the original structure (Fig. 30).

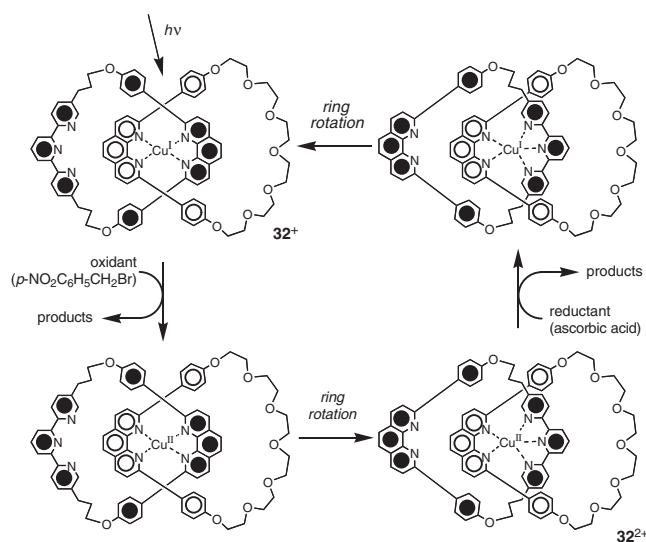
## 5. MOLECULAR DEVICES FOR INFORMATION PROCESSING

As mentioned in Section 1.1, photons represent not only quanta of energy, but also information bits, and can be used by a PMD as input/output signals, to be processed and eventually even stored and retrieved. Apart from futuristic applications related, for instance, to the construction of a chemical computer [122], the design and realization of a *molecular-level electronic set*—that is, a set of molecular-level systems capable of playing functions that mimic those performed by macroscopic components in electronic devices—is



**Figure 29.** Photocontrollable molecular-level brake. The thermally activated circumrotation of the macrocyclic polyether component of [2]catenane **31** $^{4+}$  can be modulated reversibly by *cis/trans* photoisomerization of the azobenzene unit incorporated into the tetracationic macrocycle [119, 120].





**Figure 30.** Photoinduced rotation, based on the use of an oxidant scavenger (*p*-nitrobenzyl bromide), of the terpyridine-containing macrocycle in the copper-containing [2]catenane **32<sup>+</sup>** [121]. The system is brought back to the initial structure through another ring rotation, induced chemically by reduction with ascorbic acid.

of great scientific interest because it introduces new concepts into the field of chemistry and stimulates the ingenuity of researchers engaged in the bottom-up approach to nanotechnology. In the past few years, many systems that could prove useful for information processing at the molecular level [3, 4, 6–9, 123] (e.g., wires [6, 124–127], antennas [63–70], switches [127, 128], rectifiers [129, 130], plug/socket devices [42], memories [127, 128, 131], logic gates [3, 127, 128, 132–134]) have been constructed and studied. It has already been pointed out that suitably designed pseudorotaxanes, rotaxanes, and catenanes could prove useful for information processing because they can be interconverted at will between two (or more) stable states that can be used to represent information bits on the molecular scale. In some particular cases, the relationship between the input and output signals in such molecular devices corresponds to a logic operation, opening the way to the construction of molecular-level logic gates based on pseudorotaxanes, rotaxanes, and catenanes.

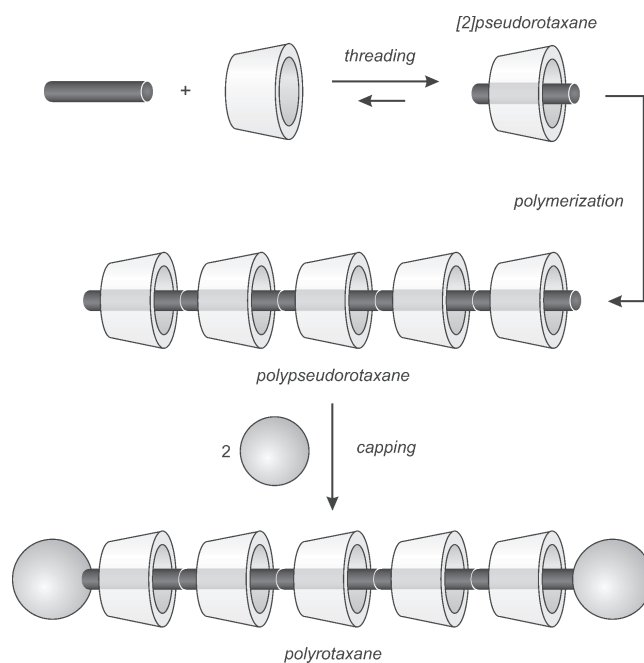
### 5.1. Molecular Wires

Very attractive candidates to play the role of wire-type compounds for the vectorial transfer of energy or electrons are linear oligo- or poly-*p*-phenylenes [135]. Such rigid rodlike conjugated molecules have been employed as spacers between chromophoric units in systems designed to achieve long-range photoinduced energy or electron transfer (photonic molecular wires) [136, 137]. It has been shown that the luminescence, stability, and processability of polymers of the poly-*p*-phenylene type can be enhanced by threading them through macrocycles to form conjugated polypseudorotaxanes and polyrotaxanes that could be viewed as “insulated molecular wires” [138, 139]. Hydrophobic binding holds the monomer inside the cavity of a macrocycle, for example, a cyclodextrin; such a [2]pseudorotaxane

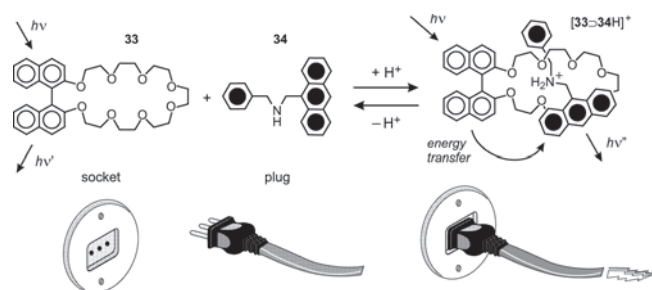
is then polymerized to form a conjugated polypseudorotaxane, which can then be stoppered at both ends to give a polyrotaxane (Fig. 31) [139]. It remains to establish, though, whether the encirclement of the molecular wire with macrocyclic rings in the polyrotaxane will result in improvement of the performance of photonic molecular wires.

### 5.2. Plug/Socket and Extension Systems

A macroscopic plug/socket system is characterized by the following features: (i) the possibility to connect/disconnect the two components in a reversible way and (ii) the occurrence of energy flow from the socket to the plug when the two components are connected. Pseudorotaxane-type supramolecular systems have been designed that may be considered as molecular-level plug/socket devices. In the system illustrated in Figure 32 [42], the plug-in function is related to the threading, driven by the formation of strong  $N^+ \cdots H \cdots O$  hydrogen bonds in dichloromethane solution [33], of ( $\pm$ )binaphthocrown ether **33** by a (9-anthracenyl)benzylammonium ion, obtained by protonation of the corresponding amine (**34**). The association process can be reversed quantitatively (plug-out) by addition of a suitable base, like tributylamine, which deprotonates the ammonium ion. In the plug-in state, which corresponds to a pseudorotaxane structure, light excitation of the binaphthyl unit of the crown causes the sensitized fluorescence of the anthracenyl unit of the thread, showing that an efficient electronic energy transfer process has occurred between the two chromophoric groups. Addition of a stoichiometric amount of base to the pseudorotaxane structure causes the revival of the binaphthyl fluorescence and the disappearance of the anthracenyl fluorescence upon excitation in the binaphthyl bands, demonstrating that plug-out has happened. The plug/socket concept at the molecular level can



**Figure 31.** Synthesis, directed by hydrophobic binding, of an “insulated molecular wire” [139].



**Figure 32.** Acid/base-controlled plug-in/plug-out of (9-anthracenyl)benzylammonium ion  $34\text{H}^+$ , obtained by protonation of the corresponding amine  $34$ , with  $(\pm)$ -binaphthocrown ether  $33$  [42]. The occurrence of photoinduced energy transfer in the plug-in state is schematized.

be extended straightforwardly to the construction of systems where (i) light excitation induces an electron flow instead of an energy flow and (ii) the plug-in/plug-out function is stereoselective (the enantiomeric recognition of chiral ammonium ions by chiral crown ethers is well known).

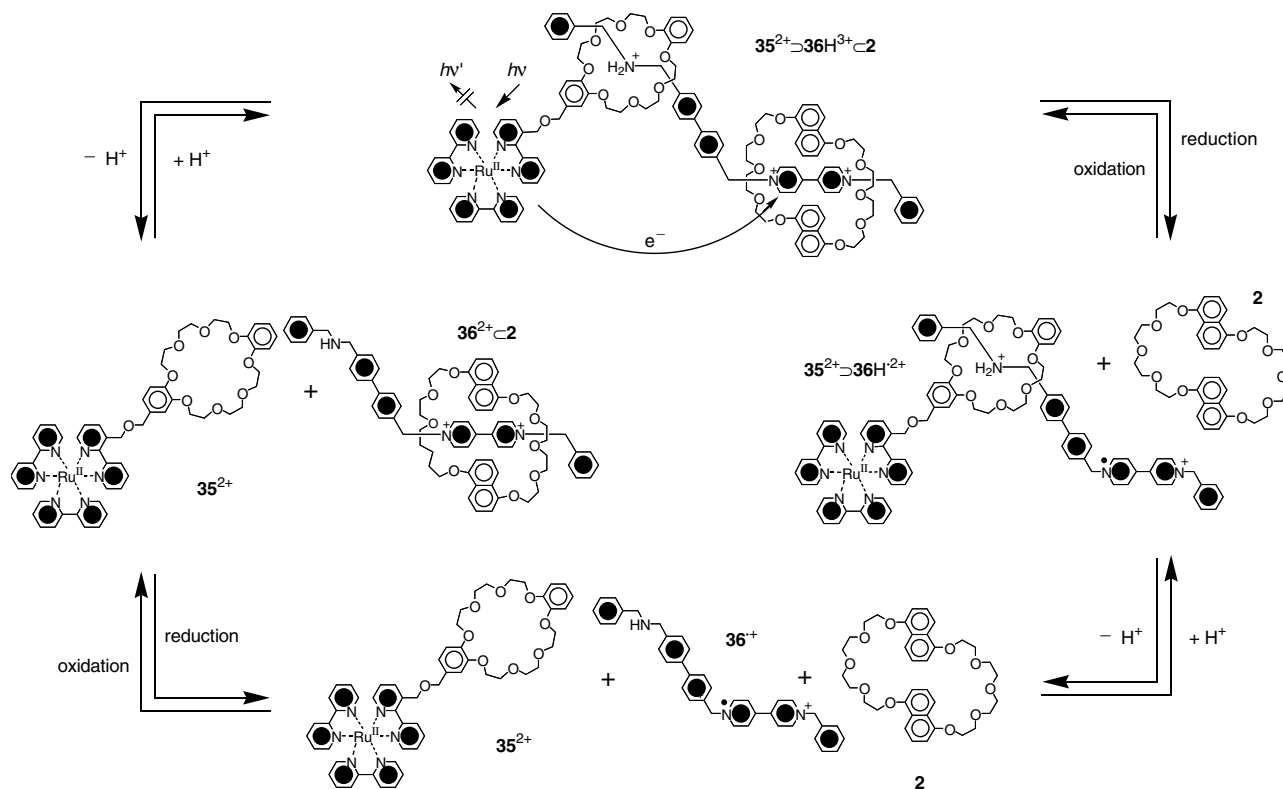
The plug/socket concept has recently been used to design and construct a self-assembling [3]pseudorotaxane that mimics at the molecular level the function played by a macroscopic extension. The system is made (Fig. 33) [140] of three components,  $35^{2+}$ ,  $36\text{H}^{3+}$ , and  $2$ . Component  $35^{2+}$  consists of two moieties—a  $[\text{Ru}(\text{bpy})_3]^{2+}$  unit, which plays the role of electron donor under light excitation, and a

DB24C8 crown ether, which plays the role of a socket. The wire-type component  $36\text{H}^{3+}$  is also made of two moieties: an ammonium unit, which, driven by hydrogen-bonding interactions, threads as a plug into the DB24C8 socket, and a bipyridinium unit, which, driven by donor/acceptor interaction, threads as a plug into the third component  $2$ , a 1/5DN38C10 crown-ether socket. In  $\text{CH}_2\text{Cl}_2/\text{CH}_3\text{CN}$  (98:2 v/v) solution, reversible connection/disconnection of the two plug/socket functions can be controlled independently by acid/base and red/ox stimulation, respectively. In the fully connected  $35^{2+} \supset 36\text{H}^{3+} \subset 2$  triad, light excitation of the  $[\text{Ru}(\text{bpy})_3]^{2+}$  unit of component  $35^{2+}$  is followed by electron transfer to the remote bipyridinium unit of component  $36\text{H}^{3+}$ , which is plugged into component  $2$ . Possible schemes to improve the system have also been discussed.

### 5.3. Logic Gates

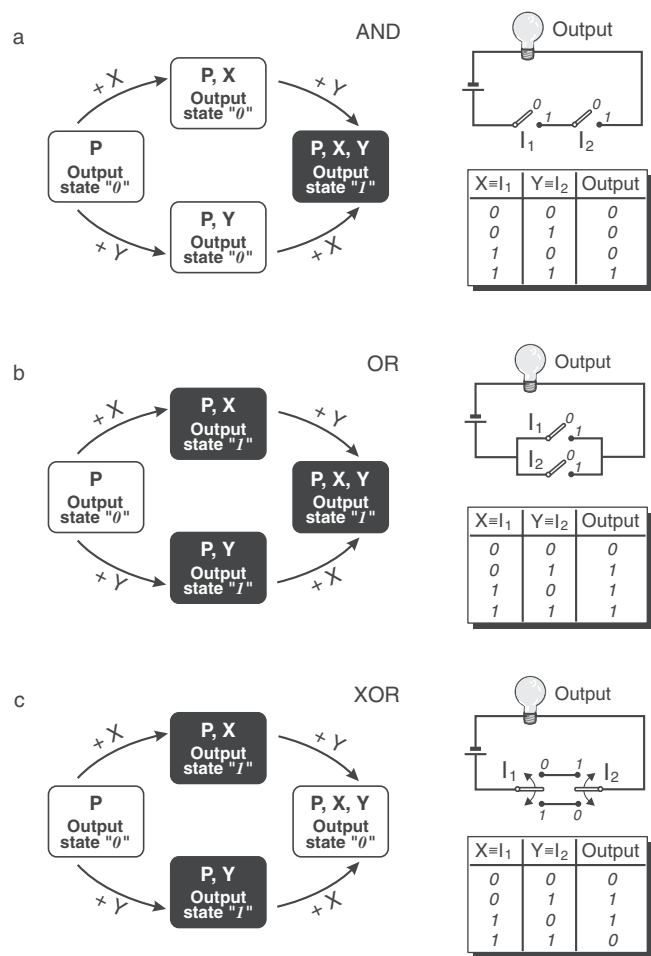
Computers are based on semiconductor logic gates that perform binary algebraic operations [141]. Logic gates are switches whose output state ( $0$  or  $1$ ) depends on the input conditions ( $0$  or  $1$ ). YES and NOT single-input gates are the simplest logic devices. A YES gate passes the input bits to the output without changes (input:  $1$ , output:  $1$ ; input:  $0$ , output:  $0$ ), while a NOT gate inverts any input data (input:  $1$ , output:  $0$ ; input:  $0$ , output:  $1$ ).

Molecular systems that can perform simple YES and NOT logic operations are very common, and luminescence



**Figure 33.** Supramolecular system that mimics the function played by a macroscopic extension [140]. The two pseudorotaxane-type connections between the three molecular components can be controlled independently by acid/base and red/ox stimulation, respectively. In the fully assembled [3]pseudorotaxane, a photoinduced electron transfer process occurs from the excited state of the  $[\text{Ru}(\text{bpy})_3]^{2+}$  moiety of  $35^{2+}$  to the bipyridinium unit of  $36\text{H}^{3+}$ , which, in turn, is plugged into crown ether  $2$ .

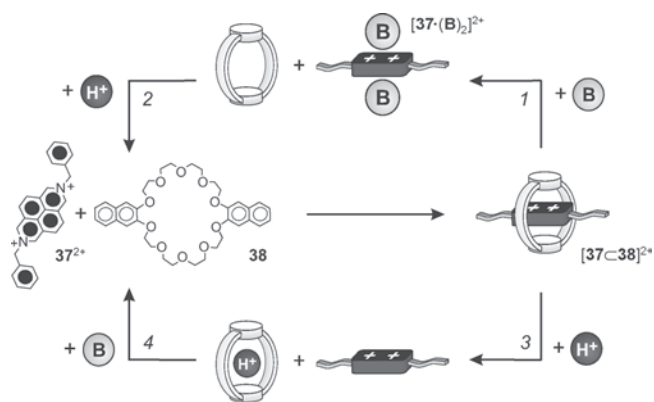
is a particularly useful signal to monitor such operations [132, 142]. To perform more complex logic operations, however, carefully designed multicomponent chemical systems are needed. Figure 34 shows schematically the changes that have to occur in a chemical system in order to perform the AND, OR, and XOR fundamental logic operations under the action of two chemical inputs (X and Y). For illustration purposes, the equivalent (from a logic viewpoint) electric circuits are also shown. The equivalent circuit of the AND gate has switches connected in series (Fig. 34a), whereas that of the OR gate has switches connected in parallel (Fig. 34b). An XOR (eXclusive OR) gate is a much more complex device, as one can understand from the fact that its equivalent circuit contains two bipolar switches (Fig. 34c). The truth table of the XOR operation is the same as that of the OR operation except that the output is 0 if both the inputs are 1. In today's processors, addition is performed with an AND gate, which gives the carry digit, and an XOR gate, which gives the sum digit. It is also important to notice that the XOR gate is actually a comparator because it can establish whether the two inputs have the same value. Interesting



**Figure 34.** Schematic representation of a chemical system (P) that performs the AND (a), OR (b), and XOR (c) logic operations under the action of two chemical inputs (X and Y). The truth tables of such operations are also shown, along with their representations based on electric circuit schemes.

examples of supramolecular systems capable of performing the AND, OR, and XOR logic operations, as well as more complex ones, and even integrating two such functions in a single supramolecular device, have been reported [132, 142–147]. In all these systems, binding of different chemical species (input) results in changes in luminescence intensity (output).

The first example of a chemical system capable of performing the XOR logic operation was based on the pseudorotaxane  $[37\subset 38]^{2+}$  illustrated in Figure 35 [148]. It results from self-assembly, in  $\text{CH}_2\text{Cl}_2/\text{CH}_3\text{CN}$  (90:10 v/v) solution, of the electron-accepting 2,7-dibenzylidiazapyrenium dication  $37^{2+}$  with the crown ether **38**, which contains two 2,3-dioxynaphthalene electron-donating units. In the pseudorotaxane structure, the electron-deficient diazapyrenium unit is sandwiched between the electron-rich 2,3-dioxynaphthalene units of **38**. Because of the electron donor/acceptor interaction, a low-energy charge transfer excited state is formed that is responsible, *inter alia*, for the disappearance of the strong fluorescence exhibited by **38** ( $\lambda_{\text{max}} = 343$  nm). Upon addition of tributylamine (**B**, Fig. 35), a 1:2 adduct,  $[37\cdot(\text{B})_2]^{2+}$ , is formed between the 2,7-dibenzylidiazapyrenium dication  $37^{2+}$  and the amine, with the consequent dethreading of **38** (process 1 in Fig. 35). This process causes large spectral changes, including the recovery of the fluorescence of free crown ether **38**. Subsequent addition of a stoichiometric amount (relative to the previously added amine) of trifluoromethanesulfonic acid unlocks  $37^{2+}$  from the  $[37\cdot(\text{B})_2]^{2+}$  adduct (process 2 in Fig. 35) and allows rethreading between dication  $37^{2+}$  and macrocycle **38** to give back the original pseudorotaxane. This process is accompanied by spectral changes opposite to those observed upon addition of amine. Processes 1 and 2 can be repeated on the same solution by repeating the addition of amine and acid; of course, the ammonium ion originated from protonation of amine **B** is also produced at the end of each cycle. As shown in Figure 35, the dethreading/rethreading cycle can also be performed by reverting the order of the two inputs. Both processes 1 and 3 cause a strong increase in emission intensity at 343 nm, which is cancelled by processes 2 and 4, respectively. Therefore, we can conclude that the chemical system described above shows the input/output



**Figure 35.** Schematic representation of the threading/dethreading pattern of [2]pseudorotaxane  $[37\subset 38]^{2+}$ , which corresponds to an XOR logic function.

relationships indicated by the truth table of the XOR logic gate (Fig. 34c): The strong fluorescent signal at 343 nm is present (output: 1) only when either amine or  $H^+$  (inputs X and Y in the truth table) are added (i.e., X: 1 and Y: 0 or vice versa); conversely, the fluorescent signal is absent (output: 0) when none or both of the inputs are present (i.e., X = Y: 0 or X = Y: 1).

## 6. CONCLUSION

The progress made in the fields of supramolecular chemistry and photochemistry, and in particular the investigations performed in the last few years on pseudorotaxanes, rotaxanes, and catenanes, has led to the design and construction of molecular-level devices capable of performing a variety of light-induced functions (photochemical molecular devices). Light stimulation is particularly convenient for operating molecular-level devices. For example, it can be switched on and off easily and rapidly and, by employing lasers, it provides the opportunity of working in small space regions and very short time domains. A further advantage offered by the use of photochemical techniques is that photons, besides supplying the energy needed to make a device work, can also be useful in reading the state of the system and thus controlling and monitoring its operation.

It should be noted, however, that the molecular-level devices described in this chapter operate in solution, that is, in an incoherent fashion. For most kinds of applications, they need to be interfaced with the macroscopic world by ordering them in some way, for example, at an interface or on a surface [103, 149], so that they can behave coherently, either in parallel or in series. Research on this topic is developing at a fast-growing rate [6, 7]. Furthermore, addressing a single molecular-scale device by instruments working at the nanometer level is no longer a dream [150, 151].

The extension of the concept of a device to the molecular level is of interest not only for the development of nanotechnology, but also for the growth of basic research. Looking at supramolecular chemistry from the viewpoint of functions with reference to devices of the macroscopic world is indeed a very interesting exercise that introduces novel concepts into chemistry as a scientific discipline.

## GLOSSARY

**Antenna for light harvesting (molecular-level)** A recognized array of molecular components (i.e., a supramolecular species) capable of absorbing light and delivering the resulting electronic energy to a predetermined component of the array; this function is often called antenna effect.

**Catenane** A supramolecular species consisting of two or more interlocked macrocyclic components.

**Charge separation** A chemical reaction, usually photoinduced, involving the transfer of an electron in a supramolecular species from a neutral component to another neutral component, leading to a species made of a positively and a negatively charged moieties.

**Logic gate (molecular-level)** A molecular or supramolecular species capable of performing a logic operation.

**Molecular device** An assembly of a discrete number of molecular components (i.e., a supramolecular species) designed to perform a specific function.

**Molecular machine** A particular type of molecular device in which the component parts display changes in their relative position as a result of some external stimulus.

**Molecular wire** A common name to indicate a long, highly conjugated molecule.

**Pseudorotaxane** An inclusion complex in which a molecular thread is encircled by a macrocyclic component; see also rotaxane.

**Rotaxane** A supramolecular species consisting of a dumbbell-shaped component and a macrocyclic component which surrounds the linear portion of the dumbbell and is trapped mechanically by bulky stoppers; when at least one of the stoppers is absent, the macrocyclic component can dethread and the supramolecular species is called pseudorotaxane.

**Supramolecular chemistry** Branch of chemistry bearing on organized entities of higher complexity that result from the association of two or more molecular components.

## ACKNOWLEDGMENTS

I am indebted to Professors Vincenzo Balzani and Margherita Venturi for their help in the preparation of the manuscript. This work was supported by the University of Bologna and the Ministero dell'Istruzione, dell'Università e della Ricerca.

## REFERENCES

1. J.-M. Lehn, "Supramolecular Chemistry." VCH, Weinheim, 1995.
2. V. Balzani and F. Scandola, "Supramolecular Photochemistry." Ellis Horwood, Chichester, 1991.
3. V. Balzani, A. Credi, and M. Venturi, in "Supramolecular Science: Where It Is and Where It Is Going" (R. Ungaro and E. Dalcanale, Eds.), p. 1. Kluwer Academic, Dordrecht, 1999.
4. V. Balzani and F. Scandola, in "Comprehensive Supramolecular Chemistry" (J. L. Atwood, J. E. D. Davies, D. D. MacNicol, and F. Vögtle, Eds.), Vol. 10, p. 687. Pergamon, Oxford, 1996.
5. G. M. Wallraff and W. D. Hinsberg, *Chem. Rev.* 99, 1801 (1999).
6. J. M. Tour, *Acc. Chem. Res.* 33, 791 (2000).
7. *Acc. Chem. Res.* 32 (1999).
8. V. Balzani, A. Credi, and F. Scandola, in "Transition Metals in Supramolecular Chemistry" (L. Fabbrizzi and A. Poggi, Eds.), p. 1. Kluwer Academic, Dordrecht, 1994.
9. V. Balzani, L. Moggi, and F. Scandola, in "Supramolecular Photochemistry" (V. Balzani, Ed.), p. 1. Reidel, Dordrecht, 1987.
10. R. P. Feynman, *Eng. Sci.* 23, 22 (1960).
11. R. Ballardini, V. Balzani, A. Credi, M. T. Gandolfi, and M. Venturi, *Acc. Chem. Res.* 34, 445 (2001).
12. P. L. Bualas, M. Gómez-Kaifer, and L. Echegoyen, *Angew. Chem., Int. Ed.* 37, 216 (1998).
13. A. E. Kaifer and M. Gómez Kaifer, "Supramolecular Electrochemistry." Wiley-VCH, Weinheim, 1999.
14. J. R. Lakowicz, "Principles of Fluorescence Spectroscopy," 2nd ed. Kluwer Academic, New York, 1999.
15. J.-C. Chambron, C. O. Dietrich-Buchecker, and J.-P. Sauvage, *Top. Curr. Chem.* 165, 131 (1993).
16. H. W. Gibson, M. C. Bheda, and P. T. Engen, *Prog. Polym. Sci.* 19, 843 (1994).

17. D. B. Amabilino and J. F. Stoddart, *Chem. Rev.* 95, 2725 (1995).
18. R. Jäger and F. Vögtle, *Angew. Chem., Int. Ed. Engl.* 36, 930 (1997).
19. S. A. Negogodiev and J. F. Stoddart, *Chem. Rev.* 98, 1959 (1998).
20. M. Fujita, *Acc. Chem. Res.* 32, 53 (1999).
21. D. A. Leigh and A. Murphy, *Chem. Ind.* 178 (1999).
22. G. A. Breault, C. A. Hunter, and P. C. Mayers, *Tetrahedron* 55, 5265 (1999).
23. J.-P. Sauvage and C. O. Dietrich-Buchecker, Eds., "Molecular Catenanes, Rotaxanes and Knots." Wiley-VCH, Weinheim, 1999.
24. F. M. Raymo and J. F. Stoddart, *Chem. Rev.* 99, 1643 (1999).
25. T. J. Hubin, A. G. Kolchinski, A. L. Vance, and D. L. Busch, *Adv. Supramol. Chem.* 5, 237 (1999).
26. T. J. Rubin and D. L. Busch, *Coord. Chem. Rev.* 200–202, 5 (2000).
27. C. Reuter, R. Schmieder, and F. Vögtle, *Pure Appl. Chem.* 72, 2233 (2000).
28. A. Credi, M. Montalti, V. Balzani, S. J. Langford, F. M. Raymo, and J. F. Stoddart, *New J. Chem.* 22, 1061 (1998).
29. M. Asakawa, P. R. Ashton, V. Balzani, A. Credi, G. Matternsteig, O. A. Matthews, M. Montalti, N. Spencer, J. F. Stoddart, and M. Venturi, *Chem.—Eur. J.* 3, 1992 (1997).
30. V. Balzani, P. Ceroni, A. Credi, M. Gómez-López, C. Hamers, J. F. Stoddart, and R. Wolf, *New J. Chem.* 25, 25 (2001) and references therein.
31. K. N. Houk, S. Menzer, S. P. Newton, F. M. Raymo, J. F. Stoddart, and D. J. Williams, *J. Am. Chem. Soc.* 121, 1479 (1999).
32. S. J. Loeb and J. A. Wisner, *Angew. Chem., Int. Ed.* 37, 2838 (1998).
33. P. R. Ashton, P. J. Campbell, E. J. T. Chrystal, P. T. Glink, S. Menzer, D. Philp, N. Spencer, J. F. Stoddart, P. A. Tasker, and D. J. Williams, *Angew. Chem., Int. Ed. Engl.* 34, 1865 (1995).
34. R. S. Wylie and D. H. Macartney, *J. Am. Chem. Soc.* 114, 3136 (1992).
35. M. Kimura, Y. Misawa, Y. Yamaguchi, K. Hanabusa, and H. Shiraï, *Chem. Commun.* 2785 (1996).
36. P. R. Ashton, R. Ballardini, V. Balzani, M. C. T. Fyfe, M. T. Gandolfi, M. V. Martínez-Díaz, M. Morosini, C. Schiavo, K. Shibata, J. F. Stoddart, A. J. P. White, and D. J. Williams, *Chem.—Eur. J.* 4, 2332 (1998).
37. P. R. Ashton, D. Philp, N. Spencer, and J. F. Stoddart, *J. Chem. Soc., Chem. Commun.* 1677 (1991).
38. N. Yamaguchi and H. W. Gibson, *Angew. Chem., Int. Ed.* 38, 143 (1998).
39. A. E. Kaifer, *Acc. Chem. Res.* 32, 62 (1999).
40. M. Montalti, R. Ballardini, L. Prodi, and V. Balzani, *Chem. Commun.* 2011 (1996).
41. P. R. Ashton, R. Ballardini, V. Balzani, E. C. Constable, A. Credi, O. Kocian, S. J. Langford, J. A. Preece, L. Prodi, E. R. Schofield, N. Spencer, J. F. Stoddart, and S. Wenger, *Chem.—Eur. J.* 4, 2411 (1998).
42. E. Ishow, A. Credi, V. Balzani, F. Spadola, and L. Mandolini, *Chem.—Eur. J.* 5, 984 (1999).
43. P. R. Ashton, V. Balzani, A. Credi, O. Kocian, D. Pasini, L. Prodi, N. Spencer, J. F. Stoddart, M. S. Tolley, M. Venturi, A. J. P. White, and D. J. Williams, *Chem.—Eur. J.* 4, 590 (1998).
44. D. H. Busch, A. L. Vance, and A. G. Kolchinski, in "Comprehensive Supramolecular Chemistry" (J. L. Atwood, J. E. D. Davies, D. D. MacNicol, and F. Vögtle, Eds.), Vol. 9, p. 1. Pergamon, Oxford, 1996.
45. P. L. Anelli, P. R. Ashton, R. Ballardini, V. Balzani, M. Delgado, M. T. Gandolfi, T. T. Goodnow, A. E. Kaifer, D. Philp, M. Pietraszkiewicz, L. Prodi, M. V. Reddington, A. M. Z. Slawin, N. Spencer, J. F. Stoddart, C. Vicent, and D. J. Williams, *J. Am. Chem. Soc.* 114, 193 (1992).
46. D. B. Amabilino, F. M. Raymo, and J. F. Stoddart, in "Comprehensive Supramolecular Chemistry" (J. L. Atwood, J. E. D. Davies, D. D. MacNicol, and F. Vögtle, Eds.), Vol. 9, p. 85. Pergamon, Oxford, 1996.
47. C. A. Hunter, *J. Am. Chem. Soc.* 114, 5003 (1992).
48. A. G. Johnston, D. A. Leigh, R. J. Pritchard, and M. D. Degan, *Angew. Chem., Int. Ed. Engl.* 34, 1209 (1995).
49. F. Vögtle, T. Dunnwald, and T. Schmidt, *Acc. Chem. Res.* 29, 451 (1996).
50. D. B. Amabilino, M. Asakawa, P. R. Ashton, R. Ballardini, V. Balzani, M. Behloradsky, A. Credi, M. Higuchi, F. M. Raymo, T. Shimizu, J. F. Stoddart, M. Venturi, and K. Yase, *New J. Chem.* 22, 959 (1998).
51. D. B. Amabilino, P. R. Ashton, V. Balzani, C. L. Brown, A. Credi, J. M. J. Fréchet, J. W. Leon, F. M. Raymo, N. Spencer, J. F. Stoddart, and M. Venturi, *J. Am. Chem. Soc.* 118, 12012 (1996).
52. D. B. Amabilino, P. R. Ashton, V. Balzani, S. E. Boyd, A. Credi, J. Y. Lee, S. Menzer, J. F. Stoddart, M. Venturi, and D. J. Williams, *J. Am. Chem. Soc.* 120, 4295 (1998).
53. Z.-T. Li, P. C. Stein, J. Becher, D. Jensen, P. Mørk, and N. Svenstrup, *Chem.—Eur. J.* 2, 624 (1996).
54. D. B. Amabilino, P. R. Ashton, J. A. Bravo, F. M. Raymo, J. F. Stoddart, A. J. P. White, and D. J. Williams, *Eur. J. Org. Chem.* 1295 (1999).
55. C. Yamamoto, Y. Okamoto, T. Schmidt, R. Jager, and F. Vögtle, *J. Am. Chem. Soc.* 119, 10547 (1997).
56. D. P. Häder and M. Tevini, "General Photobiology." Pergamon, Oxford, 1987.
57. V. Balzani, A. Credi, and M. Venturi, *Curr. Opin. Chem. Biol.* 1, 506 (1997).
58. D. Gust, T. A. Moore, and A. L. Moore, *Acc. Chem. Res.* 34, 40 (2001).
59. L. Sun, L. Hammarström, B. Åkermark, and S. Styring, *Chem. Soc. Rev.* 30, 36 (2001).
60. D. Kuciauskas, P. A. Liddell, S. Lin, T. E. Johnson, S. J. Weghorn, J. S. Lindsey, A. L. Moore, T. A. Moore, and D. Gust, *J. Am. Chem. Soc.* 121, 8604 (1999).
61. A. Hagfeldt and M. Grätzel, *Acc. Chem. Res.* 33, 269 (2000).
62. G. Steinberg-Yfrach, P. A. Liddell, S.-C. Hung, A. L. Moore, D. Gust, and T. A. Moore, *Nature* 385, 239 (1997).
63. J.-S. Hsiao, B. P. Krueger, R. W. Wagner, T. E. Johnson, J. K. Delaney, D. C. Mauzerall, G. R. Fleming, J. S. Lindsey, D. F. Bocian, and R. J. Donohoe, *J. Am. Chem. Soc.* 118, 11181 (1996) and references therein.
64. M. N. Berberan-Santos, P. Choppinet, A. Fedorov, L. Jullien, and B. Valeur, *J. Am. Chem. Soc.* 122, 11876 (2000) and references therein.
65. V. Balzani, A. Juris, M. Venturi, S. Campagna, and S. Serroni, *Chem. Rev.* 96, 759 (1996).
66. V. Balzani, P. Ceroni, A. Juris, M. Venturi, S. Campagna, F. Puntoniero, and S. Serroni, *Coord. Chem. Rev.* 219, 545 (2001).
67. A. Adronov and J. M. J. Fréchet, *Chem. Commun.* 1701 (2000).
68. M. Maus, R. De, M. Lor, T. Weil, S. Mitra, U.-M. Wiesler, A. Herrmann, J. Hofkens, T. Vosch, K. Müllen, and F. C. De Schryver, *J. Am. Chem. Soc.* 123, 7668 (2001).
69. J. E. Guillet, *Trends Polym. Sci.* 4, 41 (1996).
70. G. M. Stewart and M. A. Fox, *J. Am. Chem. Soc.* 118, 4354 (1996).
71. M. Tamura and A. Ueno, *Bull. Chem. Soc. Jpn.* 73, 147 (2000).
72. M. Tamura, D. Gao, and A. Ueno, *Chem.—Eur. J.* 7, 1390 (2001).
73. V. Balzani, Ed., "Electron Transfer in Chemistry," Vol. 3, Part II. Wiley-VCH, Weinheim, 2001.
74. K. Kalyanasundaram, "Photochemistry of Polypyridine and Porphyrin Complexes." Academic Press, London, 1992.
75. L. Flamigni, *Pure Appl. Chem.* 73, 421 (2001).
76. J.-C. Chambron, J.-P. Collin, J.-O. Dalbavie, C. O. Dietrich-Buchecker, V. Heitz, F. Odobel, N. Solladié, and J.-P. Sauvage, *Coord. Chem. Rev.* 178–180, 1299 (1998).
77. M.-J. Blanco, M. C. Jiménez, J.-C. Chambron, V. Heitz, M. Linke, and J.-P. Sauvage, *Chem. Soc. Rev.* 28, 293 (1999).

78. A. M. Brun, S. J. Atherton, A. Harriman, V. Heitz, and J.-P. Sauvage, *J. Am. Chem. Soc.* 114, 4632 (1992).
79. J.-C. Chambron, A. Harriman, V. Heitz, and J.-P. Sauvage, *J. Am. Chem. Soc.* 115, 6109 (1993).
80. J.-C. Chambron, A. Harriman, V. Heitz, and J.-P. Sauvage, *J. Am. Chem. Soc.* 115, 7419 (1993).
81. M. Linke, J.-C. Chambron, V. Heitz, J.-P. Sauvage, S. Encinas, F. Barigelletti, and L. Flamigni, *J. Am. Chem. Soc.* 122, 11824 (2000).
82. M. Seiler, H. Dürr, I. Willner, E. Joselevich, A. Doron, and J. F. Stoddart, *J. Am. Chem. Soc.* 116, 3399 (1994).
83. M. Kropf, E. Joselevich, H. Dürr, and I. Willner, *J. Am. Chem. Soc.* 118, 655 (1996).
84. E. David, R. Born, E. Kaganer, E. Joselevich, H. Dürr, and I. Willner, *J. Am. Chem. Soc.* 119, 7778 (1997).
85. Y.-Z. Hu, D. van Loyen, O. Schwarz, S. Bossmann, H. Dürr, V. Huch, and M. Veith, *J. Am. Chem. Soc.* 120, 5822 (1998).
86. A. C. Benniston, P. R. Mackie, and A. Harriman, *Angew. Chem., Int. Ed.* 37, 354 (1998).
87. Y.-Z. Hu, S. H. Bossmann, D. Van Loyen, O. Schwarz, and H. Dürr, *Chem.—Eur. J.* 5, 1267 (1999).
88. Y.-Z. Hu, H. Takashima, S. Tsukiji, S. Shinkai, T. Nagamune, S. Oishi, and I. Hamachi, *Chem.—Eur. J.* 6, 1907 (2000).
89. J. Deisenhofer and H. Michel, *Angew. Chem., Int. Ed. Engl.* 28, 829 (1989).
90. R. Huber, *Angew. Chem., Int. Ed. Engl.* 28, 848 (1989).
91. V. Balzani, A. Credi, F. M. Raymo, and J. F. Stoddart, *Angew. Chem., Int. Ed.* 39, 3348 (2000).
92. *Acc. Chem. Res.* 34 (2001).
93. *Struct. Bonding* 99 (2001).
94. H. Dürr and H. Bouas-Laurent, Eds., "Photochromism: Molecules and Systems." Elsevier, Amsterdam, 1990.
95. V. Balzani, Ed., "Electron Transfer in Chemistry." Wiley-VCH, Weinheim, 2001.
96. A. C. Benniston, A. Harriman, D. Philp, and J. F. Stoddart, *J. Am. Chem. Soc.* 115, 5298 (1993).
97. A. C. Benniston, A. Harriman, and D. S. Yufit, *Angew. Chem., Int. Ed. Engl.* 36, 2356 (1997).
98. R. Ballardini, V. Balzani, M. T. Gandolfi, L. Prodi, M. Venturi, D. Philp, H. G. Ricketts, and J. F. Stoddart, *Angew. Chem., Int. Ed. Engl.* 32, 1301 (1993).
99. P. R. Ashton, R. Ballardini, V. Balzani, S. E. Boyd, A. Credi, M. T. Gandolfi, M. Gómez-López, S. Iqbal, D. Philp, J. A. Preece, L. Prodi, H. G. Ricketts, J. F. Stoddart, M. S. Tolley, M. Venturi, A. J. P. White, and D. J. Williams, *Chem.—Eur. J.* 3, 152 (1997).
100. O. Johansen, A. W. H. Mau, and W. H. F. Sasse, *Chem. Phys. Lett.* 94, 107 (1983).
101. A. Juris, V. Balzani, F. Barigelletti, S. Campagna, P. Belser, and A. von Zelewsky, *Coord. Chem. Rev.* 84, 85 (1988).
102. E. Amouyal, *Sol. Energy Mater. Sol. Cells* 38, 249 (1995).
103. S. Chia, J. Cao, J. F. Stoddart, and J. I. Zink, *Angew. Chem., Int. Ed.* 40, 2447 (2001).
104. M. Freemantle, *Chem. Eng. News* 76, 37 (1998).
105. P. R. Ashton, V. Balzani, O. Kocian, L. Prodi, N. Spencer, and J. F. Stoddart, *J. Am. Chem. Soc.* 120, 11190 (1998).
106. S. Shinkai and O. Manabe, *Top. Curr. Chem.* 121, 76 (1984).
107. A. Ueno, H. Yoshimura, R. Saka, and T. Osa, *J. Am. Chem. Soc.* 101, 2779 (1979).
108. S. Shinkai, T. Nakaji, T. Ogawa, K. Shigematsu, and O. Manabe, *J. Am. Chem. Soc.* 103, 111 (1981).
109. A. Ueno, K. Takahashi, and T. Osa, *J. Chem. Soc., Chem. Commun.* 837 (1980).
110. V. Balzani, A. Credi, F. Marchioni, and J. F. Stoddart, *Chem. Commun.* 1861 (2001).
111. H. Murakami, A. Kawabuchi, K. Kotoo, M. Kunitake, and N. Nakashima, *J. Am. Chem. Soc.* 119, 7605 (1997).
112. P. Gaviña and J.-P. Sauvage, *Tetrahedron Lett.* 38, 3521 (1997).
113. J.-P. Collin, P. Gaviña, and J.-P. Sauvage, *New J. Chem.* 21, 525 (1999).
114. N. Armaroli, V. Balzani, J.-P. Collin, P. Gaviña, J.-P. Sauvage, and B. Ventura, *J. Am. Chem. Soc.* 121, 4397 (1999).
115. P. R. Ashton, R. Ballardini, V. Balzani, A. Credi, K. R. Dress, E. Ishow, C. J. Kleverlaan, O. Kocian, J. A. Preece, N. Spencer, J. F. Stoddart, M. Venturi, and S. Wenger, *Chem.—Eur. J.* 6, 3558 (2000).
116. A. M. Brouwer, C. Frochot, F. G. Gatti, D. A. Leigh, L. Mottier, F. Paolucci, S. Roffia, and G. W. H. Wurpel, *Science* 291, 2124 (2001).
117. G. W. H. Wurpel, A. M. Brouwer, I. H. M. van Stokkum, A. Faran, and D. A. Leigh, *J. Am. Chem. Soc.* 123, 11327 (2001).
118. M. J. MacLachlan, A. Rose, and T. M. Swager, *J. Am. Chem. Soc.* 123, 9180 (2001).
119. F. Vögtle, W. M. Müller, U. Müller, M. Bauer, and K. Rissanen, *Angew. Chem., Int. Ed. Engl.* 32, 1295 (1993).
120. M. Bauer, W. M. Müller, U. Müller, K. Rissanen, and F. Vögtle, *Liebigs Ann.* 649 (1995).
121. A. Livoreil, J.-P. Sauvage, N. Armaroli, V. Balzani, L. Flamigni, and B. Ventura, *J. Am. Chem. Soc.* 119, 12114 (1999).
122. D. Rouvray, *Chem. Br.* 34, 26 (1998).
123. J. Jortner and M. A. Ratner, Eds., "Molecular Electronics." Blackwell, Oxford, 1997.
124. A. Harriman and R. Ziessel, *Coord. Chem. Rev.* 171, 331 (1998).
125. H. L. Anderson, *Chem. Commun.* 2323 (1999).
126. F. Barigelletti and L. Flamigni, *Chem. Soc. Rev.* 29, 1 (2000).
127. M. D. Ward, *J. Chem. Educ.* 78, 1021 (2001).
128. B. L. Feringa, Ed., "Molecular Switches." Wiley-VCH, Weinheim, 2001.
129. R. M. Metzger, *Acc. Chem. Res.* 32, 950 (1999).
130. C. A. Brady and J. R. Sambles, in "Electron Transfer in Chemistry" (V. Balzani, Ed.), Vol. 5, Part I, Ch. 4. Wiley-VCH, Weinheim, 2001.
131. *Chem. Rev.* 100 (2000).
132. A. P. de Silva, D. B. Fox, T. S. Moody, and S. M. Weir, *Pure Appl. Chem.* 73, 503 (2001).
133. F. M. Raymo and S. Giordani, *J. Am. Chem. Soc.* 123, 4651 (2001).
134. F. Remacle, S. Speiser, and R. D. Levine, *J. Phys. Chem. B* 105, 5589 (2001).
135. A. J. Berresheim, M. Muller, and K. Mullen, *Chem. Rev.* 99, 1747 (1999).
136. B. Schlicke, P. Belser, L. De Cola, E. Sabbioni, and V. Balzani, *J. Am. Chem. Soc.* 121, 4207 (1999).
137. B. Schlicke, L. De Cola, P. Belser, and V. Balzani, *Coord. Chem. Rev.* 208, 267 (2000).
138. S. Anderson and H. L. Anderson, *Angew. Chem., Int. Ed. Engl.* 35, 1956 (1996).
139. P. N. Taylor, M. J. O'Connell, L. A. McNeill, M. J. Hall, R. T. Aplin, and H. L. Anderson, *Angew. Chem., Int. Ed.* 39, 3456 (2000).
140. R. Ballardini, V. Balzani, M. Clemente-León, A. Credi, M. T. Gandolfi, E. Ishow, J. Perkins, J. F. Stoddart, H.-R. Tseng, and S. Wenger, *J. Chem. Soc.*, in press.
141. C. H. Roth, Jr., "Fundamentals of Logic Design." PWS, Boston, 1995.
142. A. P. de Silva, H. Q. N. Gunaratne, T. Gunnlaugsson, A. J. M. Huxley, C. P. McCoy, J. T. Rademacher, and T. E. Rice, *Chem. Rev.* 97, 1515 (1997).
143. A. P. de Silva, H. Q. N. Gunaratne, and C. P. McCoy, *Nature* 364, 42 (1993).
144. A. P. de Silva, H. Q. N. Gunaratne, and C. P. McCoy, *J. Am. Chem. Soc.* 119, 7891 (1997).
145. H.-G. Ji, R. Dabestani, and G. M. Brown, *J. Am. Chem. Soc.* 122, 9306 (2000).

146. T. Gunnlaugsson, D. A. Mac Dónail, and D. Parker, *Chem. Commun.* 93 (2000).
147. A. P. de Silva and N. D. McClenaghan, *J. Am. Chem. Soc.* 122, 3965 (2000).
148. V. Balzani, A. Credi, S. J. Langford, and J. F. Stoddart, *J. Am. Chem. Soc.* 119, 2769 (1999).
149. C. P. Collier, G. Mattersteig, E. W. Wong, Y. Luo, K. Beverly, J. Sampaio, F. M. Raymo, J. F. Stoddart, and J. R. Heath, *Science* 289, 1172 (2000).
150. J. K. Gimzewski and C. Joachim, *Science* 283, 1683 (1999).
151. H. Shigekawa, K. Miyake, J. Sumaoka, A. Harada, and M. Komiyama, *J. Am. Chem. Soc.* 122, 5411 (2000).

# Photochemistry in Zeolite Nanocavities

Masanobu Kojima

*Shinshu University, Kami-ina, Nagano, Japan*

## CONTENTS

1. Introduction
  2. Zeolite Nanocavities as Photochemical Microreactors
  3. Influence of Brønsted and Lewis Acid Sites in Zeolite Nanocavities
  4. Characteristics of Zeolite Nanocavities Affecting Photochemical Reactions
  5. Photochemical Behavior of Alkenes in Zeolite Nanocavities
  6. Concluding Remarks
- Glossary  
References

## 1. INTRODUCTION

The spectroscopic and chemical behavior of ion radicals generated through photo-induced electron transfer reaction has attracted much attention in the last several decades. The invention of flash photolysis techniques and the improvement of laser light pulse-width made it possible for us to directly observe ion radicals with nano- and pico-second order lifetimes and to make a significant contribution to our understanding of the reaction mechanisms involved in organic photochemistry. However, now that the behavior of ion radicals has been well elucidated, the interest of researchers in photochemistry is shifting from small molecules to supramolecules.

There has been much interest in the discovery that the spectroscopic and photochemical behavior of organic small molecules included in zeolite nanocavities (zeolite supramolecules) is very different from that in solution and also that short-lived species such as ion radicals and carbocations generated spontaneously in the cavities are surprisingly stable [1–13]. These findings suggest that zeolite nanocavities have considerable potential as novel reaction vessels which can regulate the photochemical reaction of organic guest molecules. The characteristics of zeolite nanocavities affecting spectroscopic and photochemical behavior are well

understood, and as a result, it is to be expected that the cavities will be used increasingly as photoreaction vessels.

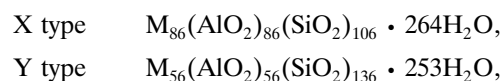
This article provides a brief summary of the spectroscopic and photochemical behavior of organic guest molecules in the cavities, mainly using aliphatic and aromatic alkenes:

1. direct (nonsensitized) photo-oxygenation by excitation of contact charge-transfer (CCT) complexes between alkenes and oxygen molecules,
2. oxygenation by singlet oxygen,
3. *cis-trans* photoisomerization,
4. photodimerization,
5. photorearrangement,
6. spectroscopy and photoreaction of short-lived species,
7. photochemical asymmetric induction.

Particular emphasis will be given to the differences between the reaction behavior in the zeolite nanocavities and that in solution. In addition, the factors influencing the excited states of guest molecules will be concisely summarized.

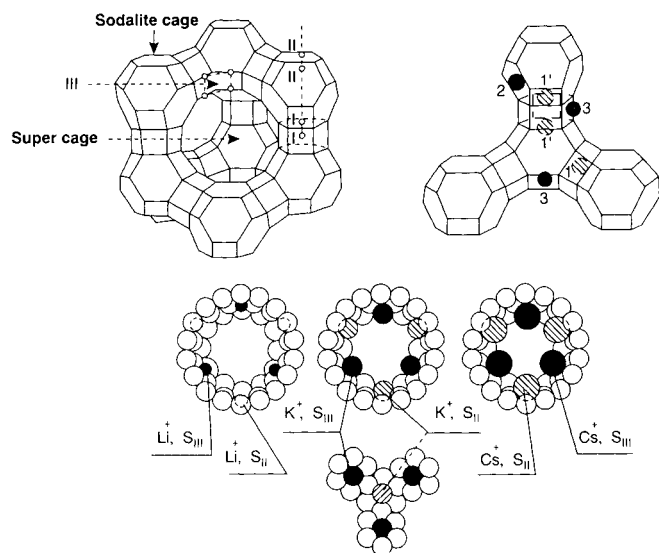
## 2. ZEOLITE NANOCAVITIES AS PHOTOCHEMICAL MICROREACTORS

Zeolites are crystalline aluminosilicates that have been widely utilized as molecular sieves and in thermal catalysis. They comprise corner-sharing  $\text{SiO}_4^{4-}$  and  $\text{AlO}_4^{5-}$  tetrahedral, and the framework contains a large number of pores, channels, and cages of various dimensions that can accommodate organic molecules of the right size. The supercage structure of X- and Y-type synthetic zeolites, and the cation location (I, II, and III) within the cages are illustrated in Figure 1 [1]. The two zeolites have the following typical unit cell compositions:



where M is a monovalent cation. These zeolites can adsorb most small organic molecules including aromatic compounds in the cavities, which have supercages (diameter, ca. 13 Å) and pore windows (ca. 7.4 Å) of sufficient size; accordingly,





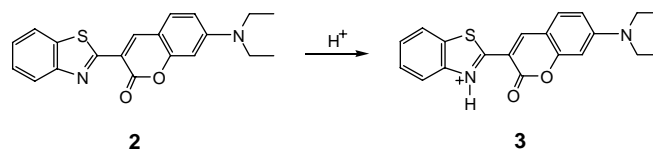
**Figure 1.** Supercage structure, cation location (I, II, III) within X and Y type zeolites. Bottom portion shows the reduction in available space (relative) within the supercage as the cation size increases. Reprinted with permission from [45], V. Ramamurthy and N. J. Turro, *J. Incl. Phenom. Mol. Recog. Chem.* 21, 239 (1995). © 1995, Kluwer Academic Publishers.

they have often been used in the photoreactions described in this article. The average number  $\langle S \rangle$  of guest molecules adsorbed in a supercage per 1 g of dry NaY zeolite can be estimated as follows [14, 15]. Because the weight of a unit cell with eight supercages is  $M_{56}(\text{AlO}_2)_{56}(\text{SiO}_2)_{136} = 12742$  g, the weight of a supercage is  $12742 \text{ g}/8 = 1593$  g. Accordingly, the number of supercages per 1 g of dry NaY is estimated to be the Avogadro number  $\times (1/1593) = \text{ca. } 3.8 \times 10^{20}$ . The supercage capacity per 1 g of dry NaY has been determined experimentally to be  $0.378 \text{ cm}^3$  [16]. When this value is divided by the volume ( $827 \text{ \AA}^3$ ) of a supercage for NaY, the number of supercages is calculated to be  $\text{ca. } 4.6 \times 10^{20}$ . This is in close agreement with the above calculated value,  $\text{ca. } 3.8 \times 10^{20}$ . Reference [1] should be referred to for other zeolites such as ZSM-5 and Mor-denite. The physical parameters of  $M^+Y$  zeolite are summarized in Table 1. As zeolites are photo-inert, the confined environment of their framework can be successfully utilized to attain remarkable selectivity in photochemical reactions [1–13].

### 3. INFLUENCE OF BRØNSTED AND LEWIS ACID SITES IN ZEOLITE NANOCAVITIES

Brønsted and Lewis acid sites in zeolite nanocavities may spontaneously generate the carbocations and ion radicals of alkenes adsorbed in the cavities [17–23]. Thus, these acid sites sometimes impede the study of the photoreaction of the guest molecules. It is very common for the acidity of Brønsted acid sites on solid surfaces to be determined by using Hammett indicators. Recently, it was found that the fluorescence and phosphorescence characteristics of organic guest molecules, such as pyrene and acetophenone, were also useful in determining the acidity in the cavities [24–27]. Kojima et al. [28] studied the influence of Brønsted and Lewis acid sites on the fluorescence lifetime of 2-quinolone (**1**) in order to estimate the acidity. The lifetimes ( $\tau$ ) of 1-Brønsted acid (1.2 ns) and 1-Lewis acid complexes (1.6 ns) have been measured in dichloromethane [29]. It was found that the acidity of the sites in zeolite nanocavities significantly affected the lifetimes of the complexes, as can be seen in Table 2. On the basis of the lifetimes, the acidity can be estimated more precisely than by using Hammett indicators. Therefore, the data provided the criteria necessary to select zeolites suitable for use in studying the photochemistry of guest molecules.

Corrent et al. [30] found that the dye coumarin 6 (**2**) was extremely sensitive to the presence of Lewis and Brønsted sites and that it could be employed to determine acidity in NaY, which was usually considered to be nonacidic, as can be seen in Figure 2 and Scheme 1. Due to the large shifts seen for the dye molecule in its neutral **2**, monocation **3**, and dication forms, both the absorption and fluorescence spectra resulted in detection of the dye species in zeolites with intermediate acidity. The ability of **2** to sense small amounts of Lewis and Brønsted sites may prove useful in studying other systems.



**Scheme 1**

**Table 1.** Dependence of physical parameters of MY zeolites on the cation.

Cation ( $M^+$ )	Ionic radius of the cation ( $\text{\AA}$ )	Electrostatic field ( $\text{V/\AA}$ ) within the case	Electrostatic potential ( $e/r$ ) of the cation	spin-orbit coupling	Vacant space within the supercage ( $\text{\AA}^3$ )	
					Y Zeolite	X Zeolite
Li	0.76	2.1	1.67		834	873
Na	1.02	1.3	1.05	27	827	852
K	1.38	1.0	0.75	87	807	800
Rb	1.52	0.8	0.67	360	796	770
Cs	1.67	0.6	0.59	840	781	732

Source: Reprinted with permission from [2], V. Ramamurthy et al., *Acc. Chem. Res.* 25, 299 (1992). © 1992, American Chemical Society.

**Table 2.** Fluorescence decay lifetimes of 2-quinolone (**1**) in solution and in zeolite.<sup>a</sup>

Condition	Lifetime ( $\tau_i$ )/ns <sup>b</sup>			Preexponential factor ( $a_i$ )			Hamett acidity <sup>c</sup>
	$\tau_1$	$\tau_2$	$\tau_3$	$a_1$	$a_2$	$a_3$	
CH <sub>2</sub> Cl <sub>2</sub> <sup>d</sup>	0.16 (0.18) <sup>g</sup>			1.0			
EtOH <sup>d</sup>	0.16	0.42		0.69	0.31		
HCl/CH <sub>2</sub> Cl <sub>2</sub> <sup>e</sup>	0.16	1.2		0.93	0.07		
BF <sub>3</sub> /CH <sub>2</sub> Cl <sub>2</sub> <sup>f</sup>	0.16	1.6 (1.6) <sup>g</sup>		0.79	0.21		
NaY	0.30	1.0		0.88	0.12		+3.3~+1.5
KL	0.33	1.1		0.94	0.06		+4.0~+3.3
HY	0.33	1.8		0.88	0.12		-3.0~-5.6
H-mordenite	0.32	2.3		0.88	0.12		-3.0~-5.6
H-ZSM-5	0.63	2.6	7.8	0.82	0.17	0.01	-5.6~-8.2

<sup>a</sup> The fluorescence decay lifetimes were determined by using a single photon counting apparatus, as reported in [149], H. Satozono, S. Suzuki, N. Tokou, H. Takehara, and Y. Uno, *J. Chem. Soc. Jpn., Chem. Indus. Chem.* 115 (1994). The decay curves were analyzed by using the equation,  $I(t) = \sum a_i \exp(-t/\tau_i)$ ; the excitation wavelengths were 320 nm for solution and 330 nm for zeolite; the emission wavelength was 373 nm.

<sup>b</sup> Measured under air.

<sup>c</sup> Determined by using Hammett indicators.

<sup>d</sup> Data for **1** =  $1.0 \times 10^{-4}$  M in the absence of HCl and BF<sub>3</sub>.

<sup>e</sup> Data for **1** =  $1.0 \times 10^{-4}$  M in the presence of 2 equiv. of HCl-OEt<sub>2</sub>.

<sup>f</sup> Data for **1** =  $1.0 \times 10^{-4}$  M in the presence of 2 equiv. of BF<sub>3</sub>-OEt<sub>2</sub>.

<sup>g</sup> Lifetime reported in [29], F. D. Lewis, G. D. Reddy, J. E. Elbert, B. E. Tillberg, J. A. Meltzer, and M. Kojima, *J. Org. Chem.* 56, 5311 (1991).

Source: Reprinted with permission from [28], M. Kojima et al., *Chem. Lett.* 675 (1999). © 1999, The Chemical Society of Japan.

## 4. CHARACTERISTICS OF ZEOLITE NANOCAVITIES AFFECTING PHOTOCHEMICAL REACTIONS

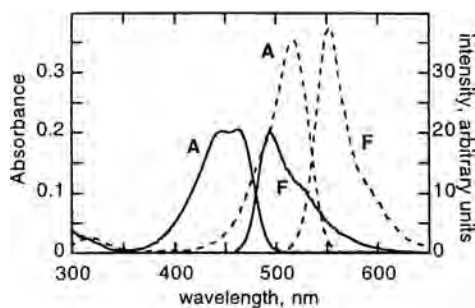
### 4.1. Adsorption Sites

The distribution of guest molecules in zeolites is more complex than in homogeneous solution. The adsorption sites for guest molecules in zeolites significantly influence the photochemical behavior of the molecules. It is thought that there are two important adsorption sites in zeolites, one of which is a pore window and the other a metal cation in the cavities. Analysis of fluorescence decay from aromatic hydrocarbons such as pyrene, naphthalene, and phenanthrene provided an insight into distribution of the sites in zeolites [14]. It was quite clear, as can be seen in Figure 3, that the distribution of lifetime measured in NaY reflected the presence of two main adsorption sites, which are heterogeneous in contrast to the homogeneous environment in solution. The width of

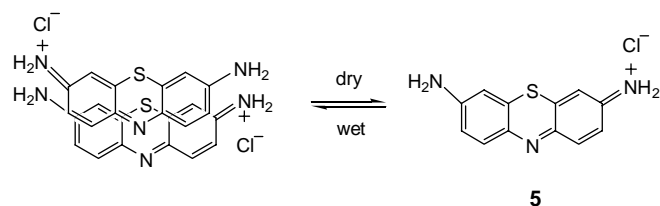
distribution of lifetime was affected by the structure of the guest molecules and co-adsorbents in NaY. The effect of the co-adsorbents was demonstrated by the results obtained in the case of pyrene with water and other solvents, as shown in Figure 4.

### 4.2. Effect of Co-Adsorbed Water

Co-adsorbed water in zeolites can impede the interaction of guest molecules with adsorption sites. For example, the formation of dimers of cationic dyes such as methylene blue (**4**) and thionin (**5**) was accelerated in NaY containing co-adsorbed water, while in dry NaY the monomers exist as a main species as shown in Figure 5 and Scheme 2 [31, 32]. The decay rate constants for fluorescence [33] and triplet excited state [16] were also greatly affected, as was the distribution of fluorescence lifetimes of aromatic hydrocarbons by co-adsorbed water as described above. Therefore, careful attention should be paid to the influence of moisture under irradiation conditions [34].



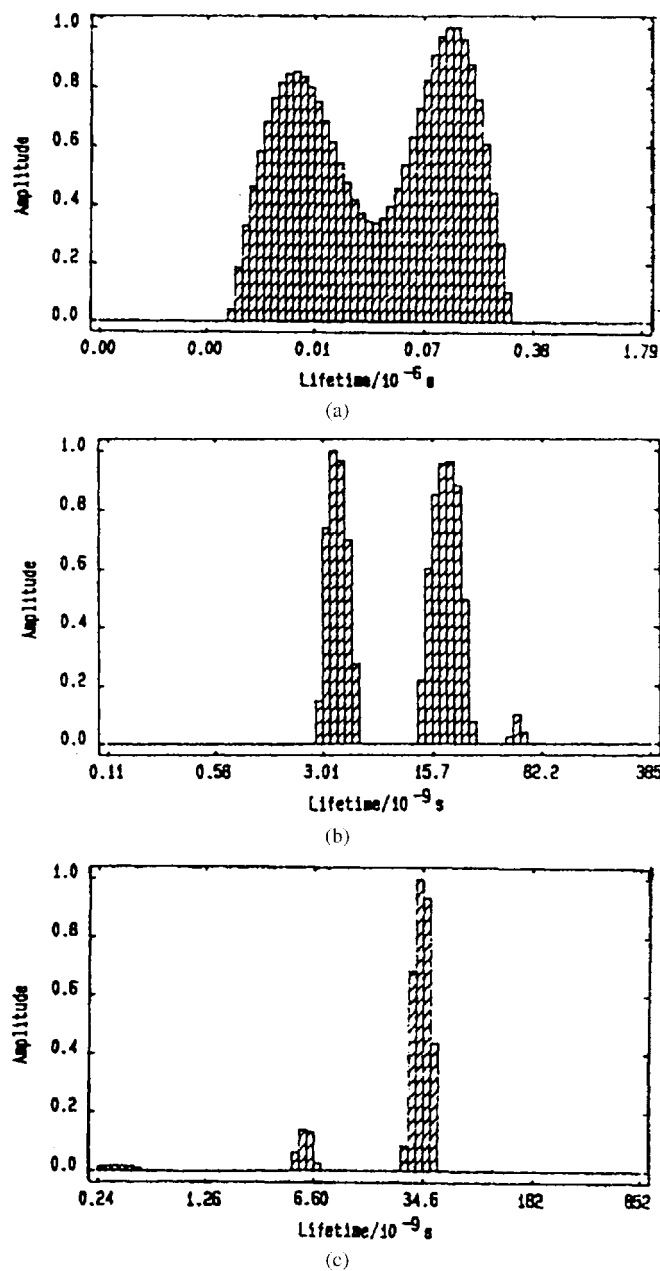
**Figure 2.** Absorption (A, left scale) and fluorescence (F, right scale) spectra of  $4 \times 10^{-6}$  M coumarin 6 in CH<sub>2</sub>Cl<sub>2</sub> for the neutral species (solid line) and for the monocation formed upon the small addition of acid (broken line). Reprinted with permission from [30], S. Corrent et al., *J. Phys. Chem. B* 102, 5852 (1998). © 1998, American Chemical Society.



Scheme 2

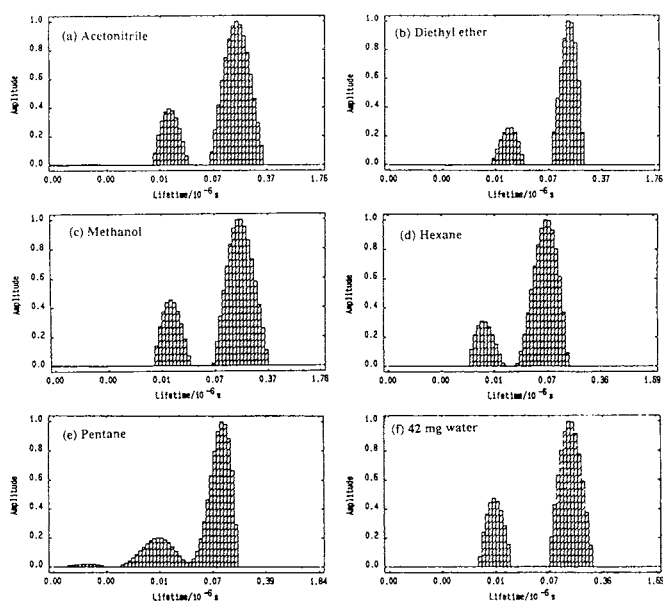
### 4.3. Acceleration of Intersystem Crossing by Metal Cations

Intersystem crossing from the excited singlet state of guest molecules to the excited triplet state is accelerated in zeolite nanocavities due to electrostatic interaction with the metal



**Figure 3.** Distribution of  $S_1$  lifetime of (a) pyrene, (b) naphthalene, and (c) phenanthrene included within "dry" NaY at room temperature. Reprinted with permission from [14], V. Ramamurthy, *Mol. Cryst. Liq. Cryst.* 240, 53 (1994). © 1994, Taylor & Francis Ltd.

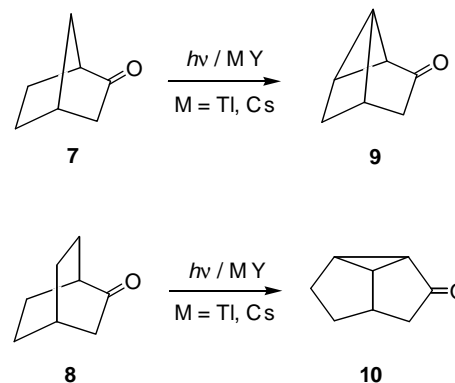
cations [35]. Measurements of the fluorescence and phosphorescence intensity of aromatic hydrocarbons like naphthalene (6) indicated that for light metal cations, such as  $\text{Li}^+$  and  $\text{Na}^+$ , the intensity was relatively unaffected by the interaction. In contrast, for heavy metal cations such as  $\text{Rb}^+$ ,  $\text{Cs}^+$ , and  $\text{Tl}^+$ , it was found that the rate of intersystem crossing increased remarkably to enhance the phosphorescence intensity, as can be seen in Figure 6. This indicates that metal cations can be used for controlling the excited state of guest molecules. On the other hand, it should be noted that the enlargement of the ion radius of a metal cation causes a decrease in the vacant space in zeolite cavities, as shown in



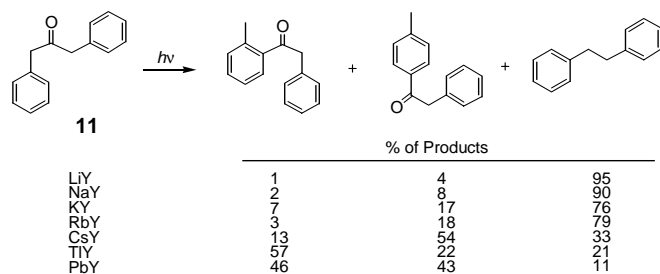
**Figure 4.** Distribution of lifetime of the excited monomer of pyrene within NaY co-included with organic solvent and water. Compare Figure 3a and note the change in distribution width. Reprinted with permission from [14], V. Ramamurthy, *Mol. Cryst. Liq. Cryst.* 240, 53 (1994). © 1994, Taylor & Francis Ltd.

Figure 1; therefore,  $\langle S \rangle$  decreases and also steric hindrance on bond formation increases. In addition, it is important to note that the strength of the electrostatic field depends on the metal cations, as shown in Table 1. These factors may affect the spectroscopic and photochemical behavior of guest molecules.

Sadeghpour et al. [36] and Pitchumani et al. [37] found that photolysis of  $\beta,\gamma$ -unsaturated ketone 7 and 8 included in MY zeolites, as shown in Scheme 3, gave the oxa-di- $\pi$ -methane products 9 and 10, which were believed to originate from the triplet state caused by heavy atom cation present in the supercage. Warriar et al. [38] observed a difference in product selectivity between dibenzyl ketones 11 and naphthyl esters in zeolites and concluded that this was due to the difference in spin of the radical pairs formed from these precursors (Scheme 4). Heavy cations present in zeolites can enhance intersystem crossing between triplet and singlet

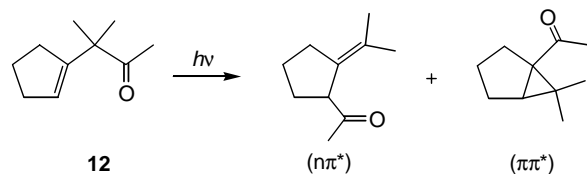


**Scheme 3**



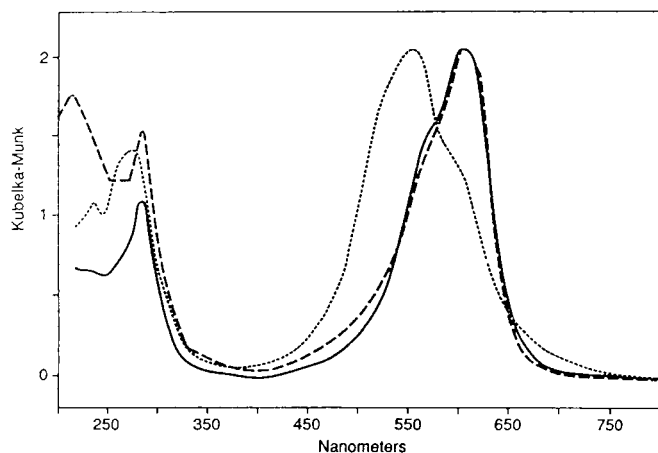
Scheme 4

geminate radical pairs. Furthermore, *ab initio* molecular orbital calculations and product analysis have shown that the nature of the lowest triplet state of enones **12** is altered by the cations present in Y zeolites (Scheme 5). Excited state energy, estimated at the CIS(D)/6-31+G\* level, indicated that the lowest triplet was  $n-\pi^*$  in character for the enones, but switched to  $\pi-\pi^*$  on coordination with alkali metal ions,

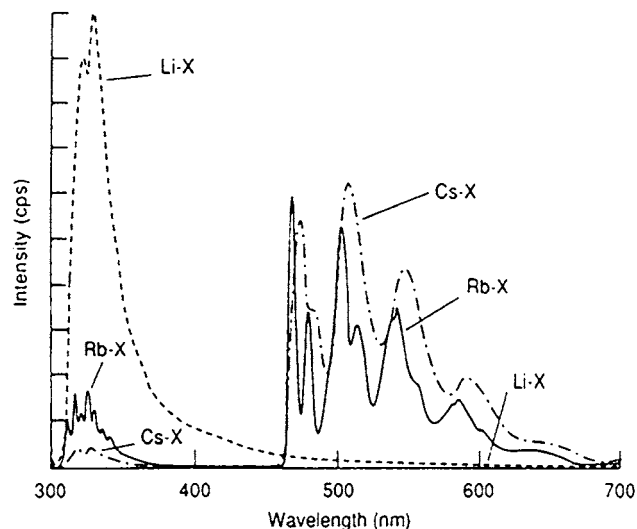


Medium	% of Products	
hexane	100%	0%
MeOH	78	22
MeCN	76	24
KX/hexane	25	75
KY/hexane	26	74

Scheme 5



**Figure 5.** Diffuse reflectance spectra of thionin include within KL and NaY. (•••) NaY, hydrated; (—) NaY, anhydrous; and (- - -) KL, hydrated or anhydrous. Reprinted with permission from [31], V. Ramamurthy et al., *J. Am. Chem. Soc.* 115, 10438 (1993). © 1993, American Chemical Society.

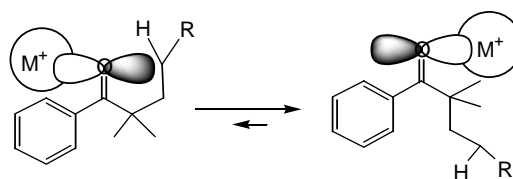


**Figure 6.** Emission spectra at 77 K of naphthalene included in LiX, RbX, and CsX (excitation  $\lambda$  285 nm). Note that the ratio of phosphorescence to fluorescence changes with the cation, but the ratio change is independent of the excitation wavelength. Reprinted with permission from [2], V. Ramamurthy et al., *Acc. Chem. Res.* 25, 299 (1992). © 1992, American Chemical Society.

such as  $\text{Li}^+$ , due to interaction with the carbonyl unit of the enones. The observed product distribution in zeolite was consistent with this theoretical prediction [39].

#### 4.4. Electrostatic Interaction of Metal Cations with Guest Molecules

Aromatic carbonyl compounds rarely undergo dark reaction due to the acid sites in zeolite cavities. Therefore, the differences between the spectroscopic and photochemical behavior in zeolite cavities and that in solution can be clearly distinguished. The data obtained from the carbonyl compounds are also useful for predicting the photochemical reaction of alkenes in zeolites. It was found for carbonyl compounds in the excited state that the selectivity of  $\alpha$ -bond fission (Norrish type-I reaction) and  $\gamma$ -hydrogen abstraction, followed by  $\beta$ -bond fission from the 1,4-biradical intermediates generated (Norrish type-II reaction), was regulated by the electrostatic interaction of the carbonyl oxygen with metal cations in the zeolite nanocavities, as illustrated in Scheme 6 [40–45]. This interaction with metal cations also influences the photochemical behavior of alkenes as described below; thus, this is one of the most important factors for regulating the photoreaction of guest molecules.



Scheme 6

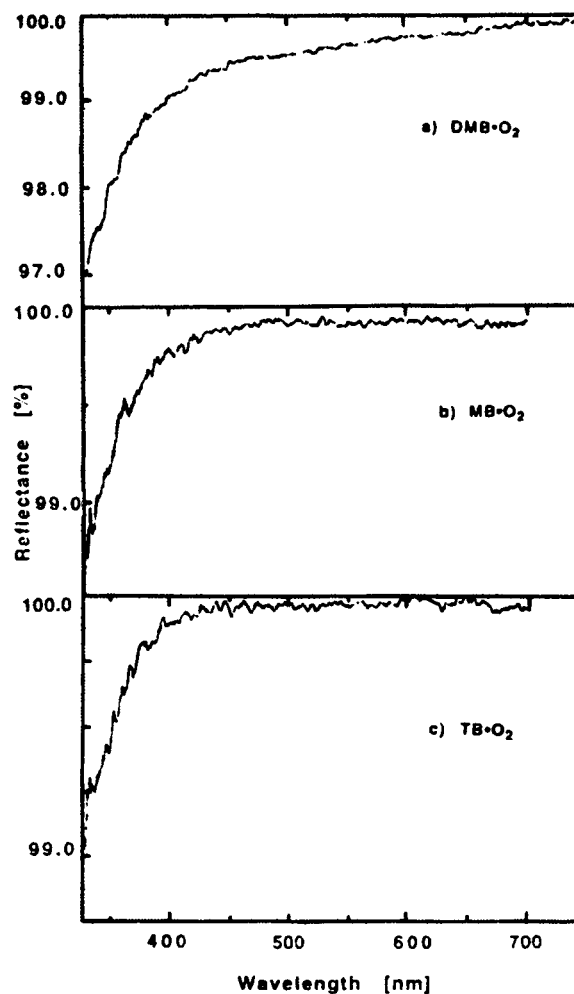
## 5. PHOTOCHEMICAL BEHAVIOR OF ALKENES IN ZEOLITE NANOCAVITIES

Although it seems likely that alkenes, which are more electron-donating compounds than ketones, are sensitive to Brønsted and Lewis acid sites in zeolite nanocavities [17–23], their photochemical behavior can be easily observed if the dark reaction is suppressed by choosing a combination of guest molecules and zeolites. For Na<sup>+</sup>- and K<sup>+</sup>-exchanged zeolites, in general, due to weak acidity in the cavities, the dark reaction of alkenes with the acid sites does not occur. However, alkenes with an electron-donating group like a methoxy group readily react with the acid sites [46–48]. Particularly, H<sup>+</sup>-exchanged zeolites often generate the carbocations and cation radicals of the alkenes.

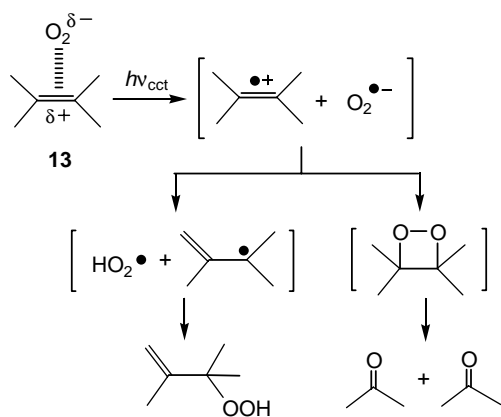
### 5.1. Direct Photo-oxygenation

In the 1950's, Evans [49] discovered the formation of CCT complexes between aromatic substrates and oxygen molecules (O<sub>2</sub>). However, the quantity of literature related to the photochemical reaction of CCT complexes is relatively small [50]. Kojima and Onodera et al. [51–56] studied the photoreaction of the CCT complexes for 4-substituted styrenes, 1-arylcyclohexenes, and 1,1-diarylethenes and found that excitation of the CCT band caused photo-induced electron transfer reaction from the alkenes to O<sub>2</sub>. For aliphatic alkenes, however, there is no report of photoreaction of the CCT complexes in solution.

Interestingly, Blatter and Sun et al. [57–68] found that hydrocarbons such as 2,3-dimethyl-2-butene (**13**), propane, cyclohexane, and toluene, formed CCT complexes with O<sub>2</sub> in zeolite NaY, the absorption band of which was observed up to the visible wavelength region, as can be seen in Figure 7. The stabilization of the CCT complexes was explained as being due to the strong electrostatic field in the zeolite nanocavities. When the CCT absorption band in the visible wavelength region was excited by using a laser light, it was suggested on the basis of infrared (IR) absorption spectra that the alkene cation radicals and superoxide anion radical (O<sub>2</sub><sup>•-</sup>) were generated through photo-induced electron transfer (Scheme 7). Myli, Xiang, Panov, and Larsen et al. [69–72] further studied the photo-oxygenation of hydrocarbons in zeolite nanocavities to find a close correlation



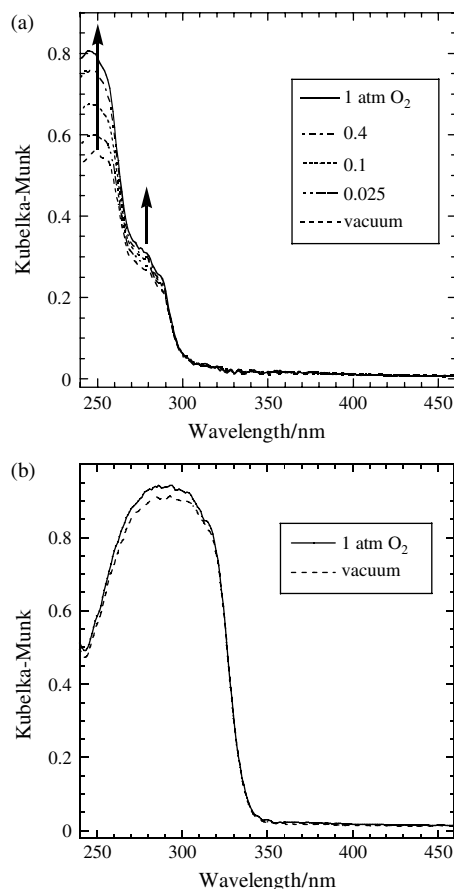
**Figure 7.** Alkene/O<sub>2</sub>/NaY diffuse reflectance spectra ratioed against alkene/N<sub>2</sub>/NaY reflectance spectra. (a) 2,3-Dimethyl-2-butene (**13**) • O<sub>2</sub>, (b) 2-methyl-2-butene • O<sub>2</sub>, and (c) *trans*-2-butene • O<sub>2</sub>. Reprinted with permission from [60], F. Blatter et al., *J. Phys. Chem.* 98, 13403 (1994). © 1994, American Chemical Society.



**Scheme 7**

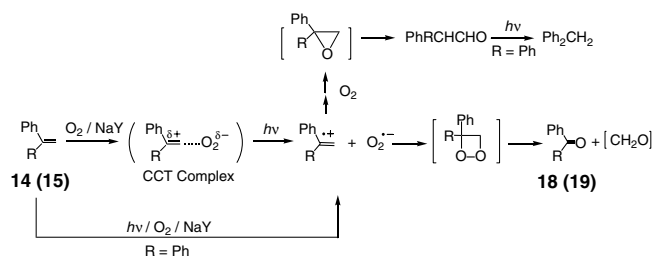
between the strength of the electrostatic field in the cavities and the distribution and yield of photo-oxygenation products.

Takeya, Kojima, and Matsubara et al. [73–76] investigated the photoreaction of CCT complexes comprising aromatic alkenes and O<sub>2</sub> formed in zeolites and compared the distribution and yield of products with those in solution. Although styrene (**14**), 1,1-diphenylethene (**15**), and *cis*- and *trans*-stilbenes (*t*-**16**), but not triphenylethene (**17**), formed their CCT complexes with O<sub>2</sub> in solutions, the CCT absorption band was observed in NaY only for **14** and **16**, as can be seen in Figure 8. Irradiation of alkenes **14–17** included in the zeolite nanocavities under O<sub>2</sub>-produced benzaldehyde (**18**) and benzophenone (**19**) as the major oxygenation products. In particular, the photo-oxygenation for **14** proceeded at the expense of the dimer formation and that for **16** and **17** competed with a photoelectrocyclic reaction, which subsequently yielded phenanthrenes (**20**) as the

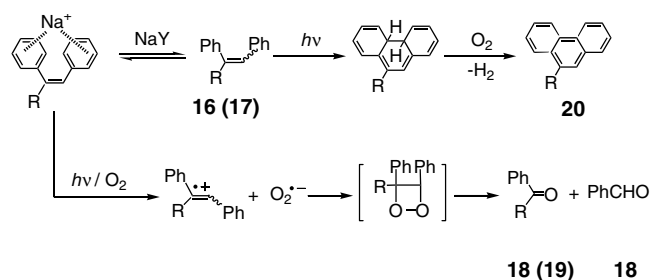


**Figure 8.** Diffuse reflectance absorption spectra for **14** (a:  $\langle S \rangle = 0.15$ ) and *t*-**16** (b:  $\langle S \rangle = 0.19$ ) in NaY observed under O<sub>2</sub> (0.025–1 atm). Reprinted with permission from [74], M. Kojima et al., *J. Chem. Soc. Perkin Trans. 2*, 1894 (2002). © 2002, The Royal Society of Chemistry.

exclusive photoproducts under O<sub>2</sub> in solution, as shown in Schemes 8 and 9, respectively. It is likely that the oxygenation products were produced through the alkene cation radicals and O<sub>2</sub><sup>-</sup> generated by excitation of the CCT complexes and/or photo-induced electron transfer from the excited alkenes to O<sub>2</sub>. Kojima et al. [74] also reported that YAG laser (266 nm) excitation of **14** included in the zeolite cavities under vacuum produced the alkene cation radical and the trapped electron, Na<sub>4</sub><sup>3+</sup>, both of which were quenched by O<sub>2</sub> (Figure 9). On the basis of semi-empirical molecular orbital calculations, it was suggested that the photo-oxygenation reaction was regulated by the electrostatic interaction between the guest molecules and alkali-metal cations in the nanocavities.

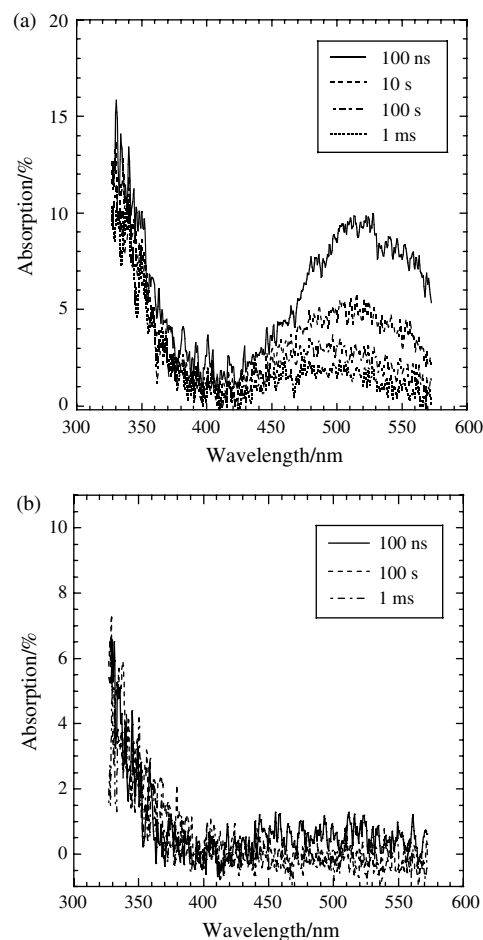


**Scheme 8**



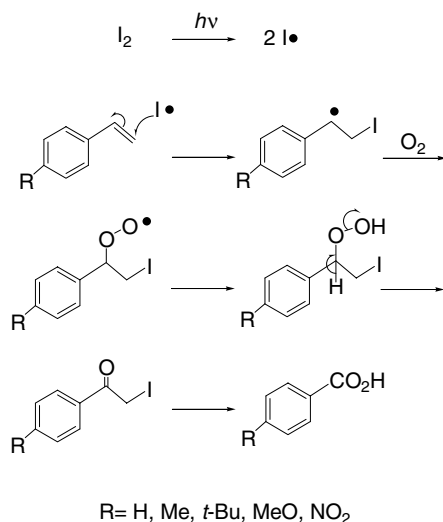
**Scheme 9**

Itoh et al. [77] found that the mesoporous silica FSM-16 is a recyclable promoter for the photo-oxidative cleavage of double bonds conjugated with an aromatic nucleus, affording the corresponding carboxylic acid in the presence of catalytic iodine in aerobic isopropyl ether. When **14** was irradiated under the same conditions, 68% benzoic acid was produced. However, **15** and **16**, which possess di-substituted double bonds, behaved differently: the former gave **19** in low yield (12%), and in the case of the latter, the starting



**Figure 9.** Transient absorption spectra observed on 266 nm laser excitation of **14** ( $\langle S \rangle = 0.46$  and  $0.61$ ) in NaY: (a) under vacuum and (b) at 0.2 atm O<sub>2</sub>. Reprinted with permission from [74], M. Kojima et al., *J. Chem. Soc. Perkin Trans. 2*, 1894 (2002). © 2002, The Royal Society of Chemistry.

material was recovered intact. Scheme 10 shows a possible path for the oxidative cleavage of double bonds with FSM-16.

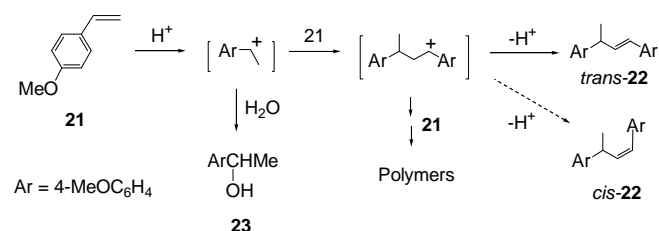


Scheme 10

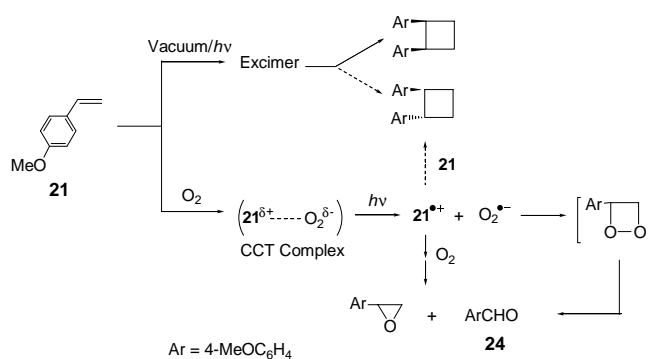
For 4-methoxystyrene (**21**), about 30% of the alkene was consumed by dark reaction with Brønsted acid sites in NaY to produce chain dimers **22** and alcohol **23** through the alkene carbocation (Scheme 11) [46–48]. The photoreaction of the **21**/NaY sample was compared to the dark reaction. As in the case of styrene (**14**) [74], the formation of dimers was a minor path in the zeolite, while the product selectivity that gave 4-methoxybenzaldehyde (**24**) increased significantly, as illustrated in Scheme 12 [75, 76]. This result was also understood in relation both to the formation of the CCT complex with O<sub>2</sub>, as can be seen in Figure 10, and to the electrostatic interaction with Na<sup>+</sup> in the nanocavities (Figure 11). Lakshminarasimhan et al. also observed the formation of CCT complex in NaY between 1,1-bis-(4-methoxyphenyl)ethene (**25**) and O<sub>2</sub> [78]. The intensity of the CCT band was much weaker than that for **21** [76]. The product distribution for **15** and **25** in NaY as hexane slurries were significantly affected by excitation wavelength and changed in comparison with that under dry conditions, reported in [74].

## 5.2. Oxygenation by Singlet Oxygen

Ramamurthy and Shailaja et al. prepared the cationic dye-exchanged zeolites X and Y using methylene blue and thionin [31, 32] and studied oxygenation of trisubstituted

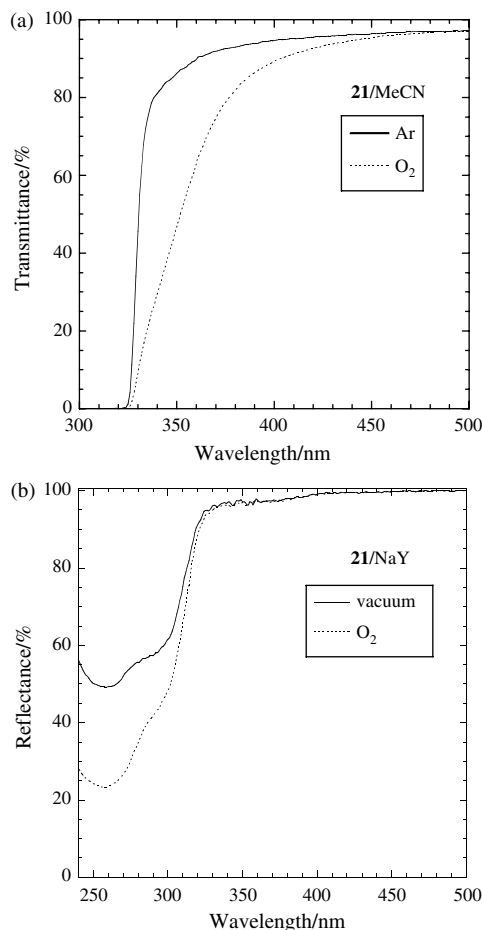


Scheme 11

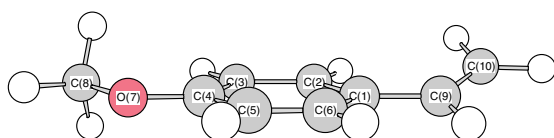


Scheme 12

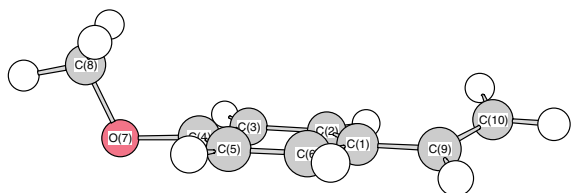
chain alkenes and 1-alkylcycloalkenes by singlet oxygen (<sup>1</sup>O<sub>2</sub>) [32, 79, 80]. It was found that the minor product in solution became the major product in the zeolites. The following two reasons were adduced to explain the high regioselectivity observed in the products: (i) because a metal cation interacted with π orbital of the carbon-carbon double (C=C) bond, <sup>1</sup>O<sub>2</sub> reacted with the alkenes from a



**Figure 10.** Absorption spectra for the CCT complexes of **21** with O<sub>2</sub>: (a) in MeCN and (b) in NaY. Reprinted with permission from [76], C. Matsubara and M. Kojima, *Res. Chem. Intermed.* 27, 975 (2001). © 2001, VSP.



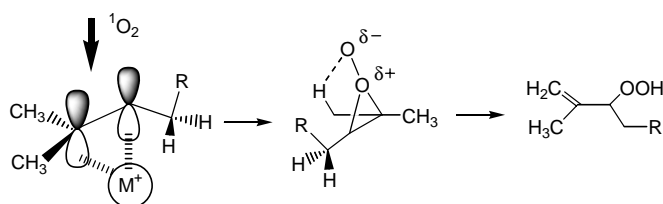
(a) **21**: C10-C9-C1-C2 = 17.6°, C8-O7-C4-C5 = 0.0°, O7-C8 = 1.423 Å, C4-O7 = 1.381 Å.



(b) **21**/Na<sup>+</sup> complex: C10-C9-C1-C2 = 21.3°, C8-O7-C4-C5 = 91.2°, O7-C8 = 1.433 Å, C4-O7 = 1.396 Å, O7, Na = 3.266 Å.

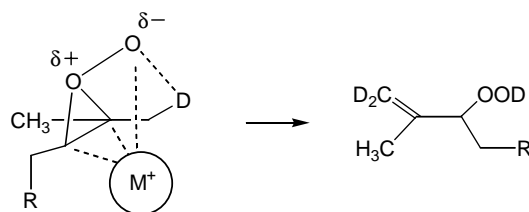
**Figure 11.** Optimum structures for **21** (a) and **21**-Na<sup>+</sup> complex (b) obtained by a semi-empirical molecular orbital calculation (AM1 method). Reprinted with permission from [76], C. Matsubara and M. Kojima, *Res. Chem. Intermed.* 27, 975 (2001). © 2001, VSP.

sterically less-hindered site, where metal cation did not exist; (ii) because the electron density on the C=C bond decreased due to interaction of the C=C bond with a metal cation, electrophilic <sup>1</sup>O<sub>2</sub> reacted selectively with a disubstituted carbon with relatively high electron density, as illustrated in Scheme 13.



**Scheme 13**

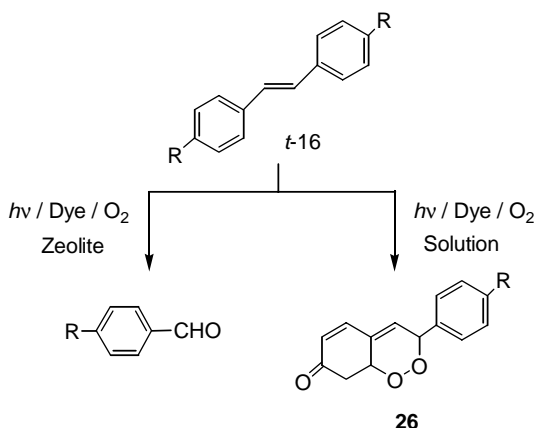
Clennan and Zhou et al. [81–84] and Stratakis and Froudakis [85] independently studied the high regioselective oxygenation by <sup>1</sup>O<sub>2</sub> in zeolites. On the basis of the correlation between distribution of products and the bulkiness of the alkyl groups on the C=C bond, they first proposed another oxygenation mechanism by <sup>1</sup>O<sub>2</sub>, whereby the high regioselectivity found in the oxygenation of trisubstituted alkenes was caused by complexation of a metal cation to the pendant oxygen in the perepoxide intermediate [81, 82, 85], as depicted in Scheme 14. However, Clennan and Sram et al. [83, 84] later revised this mechanism and explained that the novel regiochemistry of the reactions can be rationalized by invoking both cation complexation with the alkenes and electrostatic interaction between the cation and the pendant oxygen. Although further study is required in order to confirm the mechanism, the high regioselectivity in the <sup>1</sup>O<sub>2</sub>



**Scheme 14**

reaction with alkenes that occurred in the nanocavities has led to an increased interest in zeolites.

As illustrated in Scheme 15, dye-sensitized photooxygenation of stilbenes (**16**) in solution produced endoperoxide **26**, while benzaldehyde was the sole product in zeolite nanocavities [86]. The oxygenation proceeded more efficiently in Li<sup>+</sup>- and Na<sup>+</sup>-exchanged zeolites which, compared to Rb<sup>+</sup>- and Cs<sup>+</sup>-exchanged zeolites, do not have the effect of accelerating the intersystem crossing process of the guest molecules. Therefore, it is likely that this sensitized oxygenation occurred through the singlet excited state of the dyes. The oxidation in zeolites was quenched by 1,4-diazabicyclo[2.2.2]octane and N,N-dimethylaniline, but not by aliphatic alkene **13** and  $\beta$ -carotene. This supported the conclusion that the oxidizing species generated in zeolites was not <sup>1</sup>O<sub>2</sub> and that the oxygenation was initiated by photo-induced electron transfer between the dyes and the alkenes.



**Scheme 15**

### 5.3. *Cis-Trans* Photoisomerization

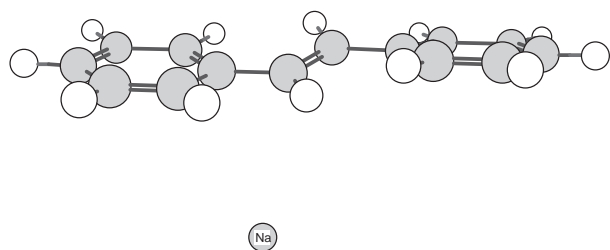
There have been many detailed studies of *cis-trans* photoisomerization in solution for C=C and nitrogen-nitrogen double (N=N) bond systems, which is one of the most important photoreactions so far discovered [87, 88]. Kuriyama et al. studied the direct (nonsensitized) photoisomerization of stilbene (**16**) adsorbed in NaY and KY zeolites [89]. Compared to the *cis-trans* isomer ratio in the photostationary state (PSS) obtained in solution using 254 nm light [(*c/t*)<sub>PSS</sub> = 76/24], the ratio of *trans* isomer in PSS in the zeolites was remarkably high [(*c/t*)<sub>PSS</sub> = 5/95].



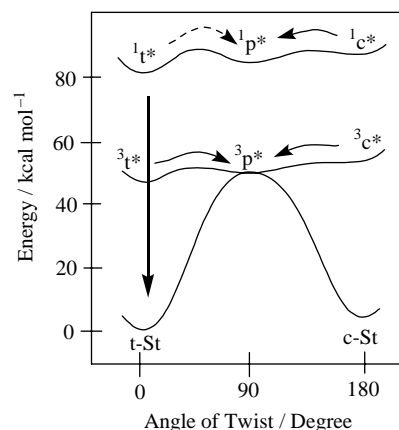
On the basis of the optimized structure of  $\text{Na}^+/t\text{-16}$  complexes calculated using semi-empirical molecular orbital calculations, it was suggested that the *trans* isomer was better stabilized than the *cis* isomer (*c*-16) due to the electrostatic interaction of  $\pi$ -electrons on the C=C bond with a metal cation, as depicted in Figure 12. Therefore, it was proposed that the interaction increased the activation energy from the excited singlet and triplet states to the ground states, as shown in Figure 13. Because of this, it was argued that deactivation from the excited states to the ground state would occur more efficiently in the zeolite cavities.

For 4-aminostilbene (**27**), on the other hand,  $(c/t)_{\text{PSS}}$  obtained in NaY using 313 nm light was in close agreement with that in solution:  $(c/t)_{\text{PSS}} = 85/15$  in solution and 75/25 in NaY [90]. The result of molecular orbital calculations suggested that the metal cation interacted electrostatically with a lone pair of the nitrogen atom, but not with the  $\pi$ -electrons on the C=C bond. Therefore, it was concluded that the activation energy from the excited state of the *trans* isomer to the twisted state was unaffected. Ramamurthy et al. [91] reported that the excited singlet state lifetime of *t*-16 adsorbed in NaY was 200 ps, which was determined by a single photon counting apparatus. Compared to the lifetime in methylcyclohexane (110 ps), the lifetime measured in NaY seemed to indicate the stabilization of the excited state of *t*-16 in the zeolite, as suggested by Kuriyama et al. [89]. However, Ellison and Thomas [92] also measured the fluorescence lifetime of *t*-16 in NaY, which was 52 ps compared to 66 ps in hexane and 32 ps in methanol. Evidently, there is a need for further study of the relation between the photoisomerization and lifetime.

Recently, Kojima et al. [93] also investigated the photoisomerization of azobenzene (**28**) adsorbed in solution. On the basis of the observation that *trans*-to-*cis* photoisomerization was very inefficient in higher concentrations and that 4-methoxyazobenzene (**29**) gave unknown products, which may be dimers in higher concentration, a novel photoisomerization mechanism through excited complexes was proposed. In zeolites  $(c/t)_{\text{PSS}}$  changed depending on the pore size as summarized in Table 3 [94]. In contrast to the photoisomerization in solution, regardless of the amount of **28** adsorbed, the *cis* isomer was produced efficiently in NaY (pore size, 7.4 Å) by irradiation using a high-pressure mercury lamp through a HOYA U-340 glass filter [ $(c/t)_{\text{PSS}} = \text{ca. } 80/20$ ]. However,  $(c/t)_{\text{PSS}}$  in Na-mordenite (7.0 × 6.5 Å) was ca. 50/50 and no photoisomerization occurred in NaZSM-5 (5.3 × 5.4 and 5.1 × 5.5 Å). On the basis of molecular orbital calculations it was suggested that the metal cation interacts



**Figure 12.** Optimum structures for *t*-16- $\text{Na}^+$  complex calculated using the AM1 method.



**Figure 13.** Potential energy surface for photoisomerization of stilbene in zeolite cage. Reprinted with permission from [89], Y. Kuriyama et al., *Chem. Lett.* 843 (1998). © 1998, The Chemical Society of Japan.

with a lone pair of one of the two nitrogen atoms, as shown in Figure 14. These results indicate that photoisomerization can be regulated by both the cavity size and the adsorption sites in guest molecules.

Hoffmann and Marlow et al. [95–97] found that *cis*-*trans* photoisomerization of **28** in molecular sieve hosts such as ALPO<sub>4</sub>-5 and ZSM-5 caused large and reversible changes in the refractive index of the composite systems. This process depended heavily on both the irradiation wavelength and the molecular sieve hosts.

Gessner et al. and Baldovi et al. achieved *cis*-to-*trans* [98] and *trans*-to-*cis* one-way photoisomerization of **16** [99], respectively, using cavity size and the shape of the zeolites. 3,4-Dimethylbenzophenone (**30**) used as a sensitizer and *c*-16 have molecular structures larger than the cavity size of silicalite S-115. Because of this, only the *trans* isomer can be adsorbed in the cavities. Thus, when an isoctane solution containing *c*-16 and **30** was irradiated with the silicalite, the *trans* isomer produced was selectively adsorbed in the nanocavities. Due to the constrained space in the cavities, the *trans*-to-*cis* photoisomerization did not occur in the cavities.

When solvent slurry containing the *trans* isomer and 4-aminoazobenzophenone adsorbed in ZSM-5 was irradiated, the *trans* isomer was sensitized by the ketone in the cavities and finally isomerized to the *cis* isomer in the solution, as illustrated in Scheme 16. The *cis* isomer was stable because the isomer did not encounter the sensitizer within the cavities due to the fact that its molecular size is larger than the cavity size. This method has considerable potential for the synthesis of *cis* isomers.

Lalitha et al. [100] described the influence of metal cations in Y zeolites in *cis*-*trans* isomerization of 4-bromophenyl styryl sulfone (**31**). The predominance of the *cis* isomer in zeolites with larger cations was attributed to the smaller cage size.

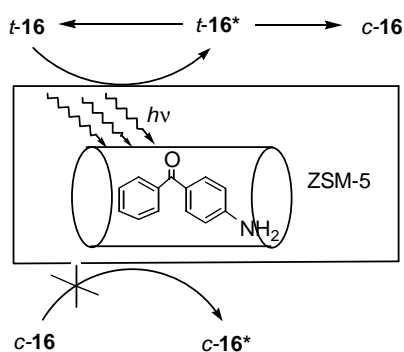
When anils (**32**) with a C=N bond was incorporated in NaY, Raman spectra analysis showed that **32** existed in the zeolite nanocavities predominantly in a zwitterionic form **33** [101] (Scheme 17). Steady state irradiation at 400 nm led to persistent changes in the diffuse reflectance UV-visible spectra with decrease of the reflectance of the band at 400 nm,

**Table 3.** *Cis/trans* isomer ratio of azobenzene (**28**) in photostationary state (PSS) in cyclohexane and NaY and Na-MOR zeolites.

Wavelength <sup>a</sup> /nm	Amount <sup>b</sup>	<i>cis/trans</i> Isomer ratio in PSS		
		C <sub>6</sub> H <sub>12</sub> <sup>d</sup>	NaY (7.4 Å) <sup>c</sup>	Na-MOR (7.0 × 6.5 Å) <sup>c</sup>
254	2 × 10 <sup>-4</sup> M	10/90		
	1 × 10 <sup>-2</sup> M	15/85		
313	2 × 10 <sup>-4</sup> M	80/20		
	1 × 10 <sup>-2</sup> M	55/45		
254	6.9 × 10 <sup>-5</sup> mol/g		20/80	
313	3.4 × 10 <sup>-5</sup> mol/g		75/25	
	6.9 × 10 <sup>-5</sup> mol/g		80/20	
	1.4 × 10 <sup>-4</sup> mol/g		80/20	
254	saturated <sup>c</sup>			20/80
313	saturated <sup>c</sup>			50/50

<sup>a</sup> Effective excitation wavelength.<sup>b</sup> Concentration of *c*- and *t*-**28** in cyclohexane and amount of *t*-**28** loaded in 1 g zeolite.<sup>c</sup> Cavities of Na-MOR were saturated by *t*-**28**.<sup>d</sup> In cyclohexane.<sup>e</sup> Pore size.Source: Reprinted with permission from [94], M. Kojima et al., *Mol. Cryst. Liq. Cryst.* 344, 179 (2000).

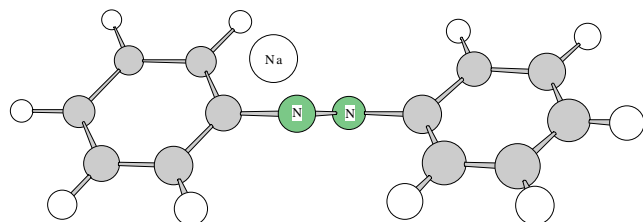
© 2000, Taylor &amp; Francis Ltd.



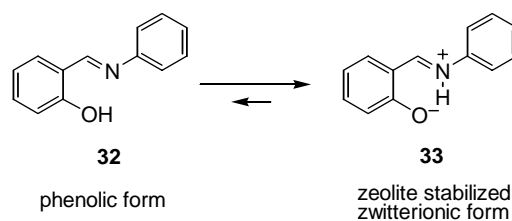
Scheme 16

as well as the appearance of a new absorption band at longer wavelengths. No photochromism was observed and this was attributed to the isomerization of the zwitterionic form to other stereoisomers, possibly by rotation about C—C or C—N bonds with partial double bond character.

Photo-induced electron transfer isomerization of *c*-**16** in Y zeolite cavities using 2,4,6-triphenylpyrylium cation (TP<sup>+</sup>), an electron accepting sensitizer, was studied by Corma et al. [102]. Isomerization of the *cis*- to *trans*-isomer occurred



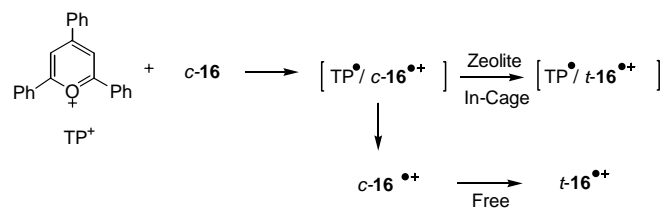
**Figure 14.** Optimized structure for *trans*-azobenzene (*t*-**28**)–Na<sup>+</sup> complex calculated using the AM1 method. Reprinted with permission from [94], M. Kojima et al., *Mol. Cryst. Liq. Cryst.* 344, 179 (2000). © 2000, Taylor & Francis Ltd.



Scheme 17

via the corresponding cation radicals. The reaction was not affected by the presence of oxygen. This contrasted with the expensive photo-oxygenation by 2,4,6-triphenylpyrylium tetrafluoroborate under homogeneous conditions. A higher contribution of the in-cage isomerization, associated with retardation of back electron transfer in the ion radical pairs, appeared to be the most noticeable characteristic of the intrazeolite process (Scheme 18). When the novel aluminosilicate MCM-41 with 20 Å monodirectional channels hexagonally arranged was used as a host, the *cis*-to-*trans* photo-induced electron transfer isomerization of **16** occurred more efficiently than in Y zeolite [103].

Lakshminarasimhan et al. [104] also studied photo-induced electron transfer isomerization of **16** with N-methylacridinium as the sensitizer and found that isomerization of *c*-**16** cation radical to *t*-**16** occurred. Their



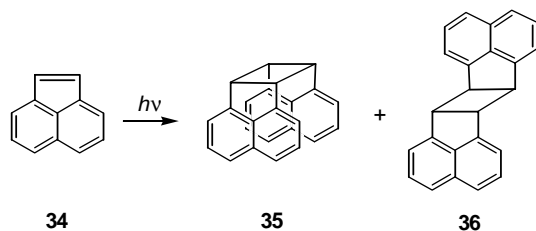
Scheme 18

proposal that a recombination of ion radicals resulted in excited triplet state **16** was based on a *cis/trans* isomer ratio in the photostationary state similar to that obtained using 2-acetonaphthone as a triplet sensitizer. Diffuse reflectance flash photolysis studies showed that independent of the isomer being sensitized only *t*-**16** cation radical is formed. However, the T-T absorption spectrum for the triplet **16**, believed to have been generated, was not observed by this time resolved spectroscopy.

#### 5.4. Photodimerization

On the basis of fluorescence spectra, it was estimated that the number of pyrene molecules per unit cell needed to form an excimer was 0.14–0.30 and 0.02–0.08 in X and Y zeolites, respectively [105, 106]. The excimer emission was observed at a value of 0.00034 in zeolite L, while only the monomer emission was seen at the same value in Mordenite [107]. It has been found that the diffusion rate of guest molecules between the cages slows considerably [108]; therefore, it seems likely that the excimer emission observed coincided with the formation of the ground state complexes. These results indicate that guest molecules do not exist homogeneously in the cavities even in the smallest quantity of adsorbed molecules.

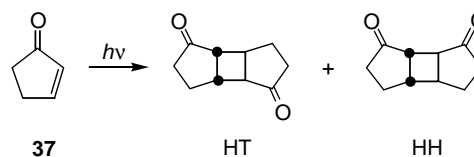
The intermolecular interaction of guest molecules is probably enhanced in zeolite nanocavities as described above. But, although numerous investigations of the photodimerization of alkenes in solution have been reported, there are few studies of this process in zeolites. Ramamurthy et al. studied [2 + 2] photodimerization of acenaphthylene (**34**) in metal-cation exchanged Y zeolites (Scheme 19) [109]. It was found that the ratio of the *cis*- (**35**) and *trans*-cyclobutane dimers (**36**) changed depending on the intersystem crossing rate enhanced by the metal cations.



Scheme 19

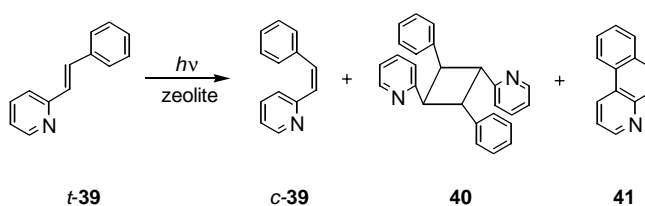
Lem et al. [110] studied regioselectivity and stereoselectivity in [2 + 2] photodimerization of cyclopentenone (**37**) and cyclohexenone (**38**) in X and Y zeolites. Both enones formed a head-to-tail [2 + 2] dimer (HT) as the major product in solution, while the major dimer produced in zeolites was a head-to-head [2 + 2] dimer (HH), as shown in Scheme 20. The ratio of HT/HH was lowest in CsX, which also had the smallest supercage volume and the weakest electrostatic interaction of the ion. However, a similar result was obtained for **37** and **38** in NaX and CsX, the relative free volumes of which were quite different. Thus, it was suggested that the complexing effect of the charge-compensating cation and the size constriction factor

in the NaY supercage probably played a role in controlling regiochemistry.



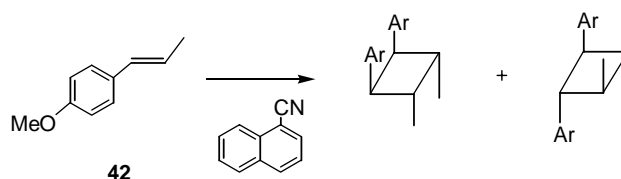
Scheme 20

Lalitha et al. [111] investigated the photodimerization of *trans*-2-styrylpyridine (*t*-**39**) in various cation-exchanged Y zeolite. At a lower loading level, *trans-cis* isomerization was the only process observed. When the loading level was increased, in addition to isomerization, significant amounts of dimerization (**40**) and cyclization products (**41**) were also observed with the product distribution, depending on the free volume available inside the cages (Scheme 21). Acidic zeolites such as HY and MgY were found to catalyze the thermal reaction of *t*-**39**.

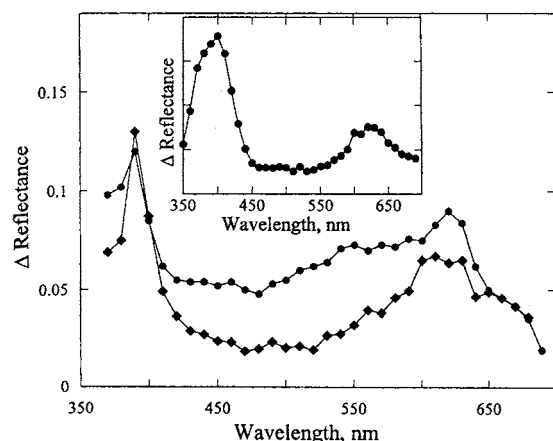


Scheme 21

Brancaleon et al. [112] studied photo-induced electron transfer reactions between excited singlet acceptors and arylalkenes included in NaX zeolites. Diffuse reflectance flash photolysis studies indicated that quenching of singlet cyanoaromatic sensitizers such as 2,3-dicyanonaphthalene and 1-cyanonaphthalene by *trans*-anethole (**42**) and **21** occurred through electron transfer and yielded relatively long-lived radical cations, which finally yielded the dimeric cyclobutane products as in solution (Scheme 22 and Figure 15). However, the dimer ratios were substantially different with the *cis*/*syn* cyclobutanes formed preferentially in the zeolite reactions, presumably as a result of the constraints imposed by the restricted space of the zeolite supercage.



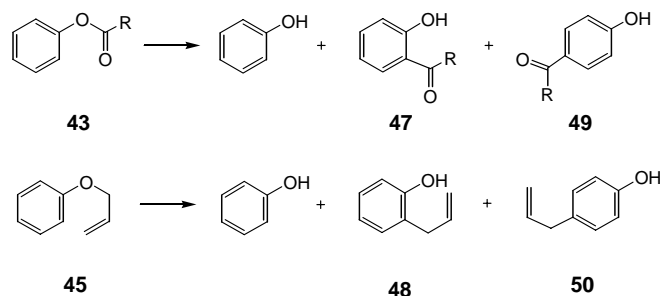
Scheme 22



**Figure 15.** Transient spectra measured after 355-nm excitation of 2,3-dicyanonaphthalene (10  $\mu\text{mol/g}$ ) plus *trans*-anethole (**42**: 52  $\mu\text{mol/g}$ ) in NaX under nitrogen ( $\bullet$ ) and oxygen ( $\blacklozenge$ ). The insert shows the spectrum obtained by direct 266-nm excitation of an oxygen-saturated sample of 10  $\mu\text{mol}$  **42** in NaX. Reprinted with permission from [112], L. Brancaloni et al., *J. Am. Chem. Soc.* 120, 4926 (1998). © 1998, American Chemical Society.

### 5.5. Photo-Fries and Photo-Claisen Rearrangements

Pitchumani and Gu et al. demonstrated by investigating photo-Fries rearrangements of phenyl acetate (**35**), phenyl benzoate (**43**) [113], and 1-naphthyl esters (**44**) [114], in addition to photo-Claisen rearrangements of allyl phenyl ether (**45**) [113] and aryl benzyl ethers (**46**) [115], that sharp selectivity consisted in a subtle matching of size and shape of reactants and/or products with the size and shape of pores, cages, and pore volumes of the intracrystalline zeolite phase. In the photorearrangements, a nearly 1 : 1 mixture of *ortho* (**47** and **48**) and *para* isomers (**49** and **50**) was normally produced in solution (Scheme 23). However, the photoreactions in zeolites were controlled selectively toward either the *ortho* or the *para* products by conducting the reactions either in faujasites X and Y or pentasils ZSM-5 and ZSM-11, respectively. For the photo-Fries reactions of phenyl acetate and phenyl benzoate in X and Y zeolites, the formation of the *ortho* isomer was highly selective (76–98%). This selectivity was not the result of shape exclusion since both the *ortho* and *para* isomers fit well within the supercage. Therefore, it was suggested that the selectivity resulted from the restrictions imposed on the mobility of the phenoxy and the acyl



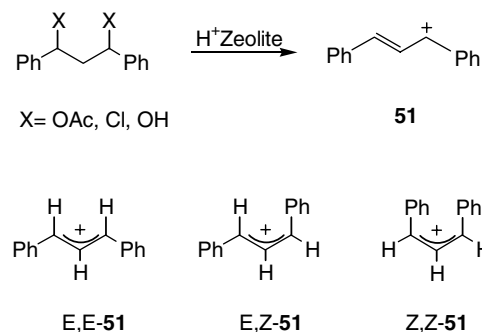
**Scheme 23**

(benzoyl) fragments by the supercage framework and also by the interaction with the cations. Vasenkov and Frei monitored a transient at 2125  $\text{cm}^{-1}$  assigned to acetyl radical generated in NaY by means of step-scan FT-infrared spectroscopy of 1-naphthyl acetate and gained a better mechanistic understanding of the photo-Fries reaction [116]. The kinetic result was interpreted in terms of a complete separation of the photogenerated pairs from the parent supercage, followed by random walks in the subspaces of the zeolite lattice imposed by the much less mobile precursor molecules. It is likely that these forced the geminate radicals to react and thereby contributed to the high selectivity of the photorearrangement.

For pentasils ZSM-5 and ZSM-11 only, the *para* isomers fit the shape and size of the zeolites. Indeed, when photolysis was conducted in water and 2,2,4-trimethylpentane, a clear preference for the *para* isomer was observed.

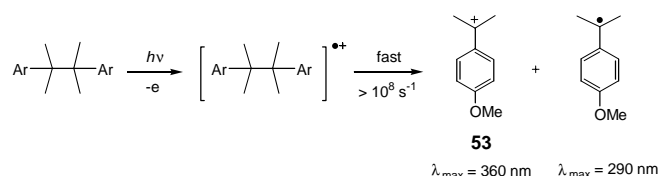
### 5.6. Spectroscopy and Photoreaction of Short-Lived Species

$\text{H}^+$ -exchanged zeolites such as HY, H-mordenite, and H-ZSM-5 have strong Brønsted acid sites. Using the strong acid sites and an electrostatic field in the zeolites, it has been possible to generate very stable carbocations in the cavities [17–23, 46–48, 117]. Garcia et al. [118] investigated the photoisomerization of 1,3-diphenylpropenylium (**51**) and 1,5-diphenylpentadienylium (**52**) ion generated within acid ZSM-5 and Mordenite zeolites as a persistent species by adsorption of  $\alpha,\omega$ -disubstituted  $\alpha,\omega$ -diphenylalkanes (Scheme 24). Irradiation of these allylic cations produced in zeolites led to *cis-trans* isomerization as the only observable process.

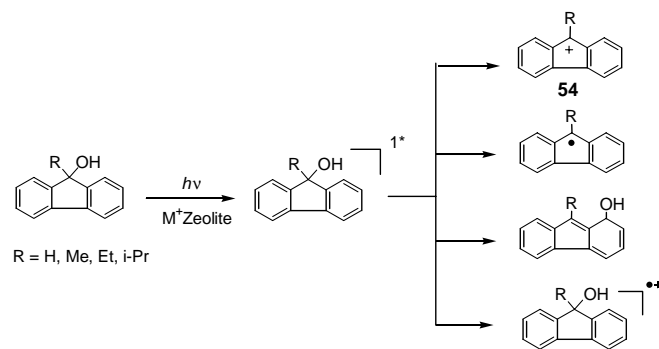


**Scheme 24**

O'Neill et al. studied the reactivity of 4-methoxycumyl cation (**53**) [119] and 9-fluorenyl cation (**54**) [120] generated in nonacidic zeolites using nanosecond laser flash photolysis (Schemes 25 and 26, respectively). In dry zeolites, the absolute reactivity of **53** was found to be heavily dependent on the nature of the alkali counterion, the Si/Al ratio, and the framework morphology, with the lifetime of the carbocation in Na $\beta$  being almost 10,000-fold longer than in CsY. The observation of the highly reactive and highly unstable **54** under these conditions afforded a remarkable example of the extraordinary ability of nonproton exchanged zeolites to provide kinetic stabilization for electrophilic guests. The



Scheme 25

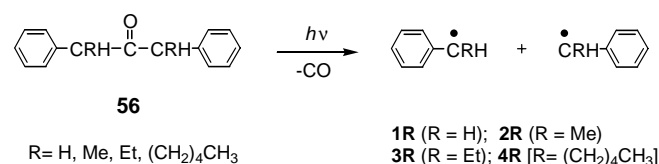


Scheme 26

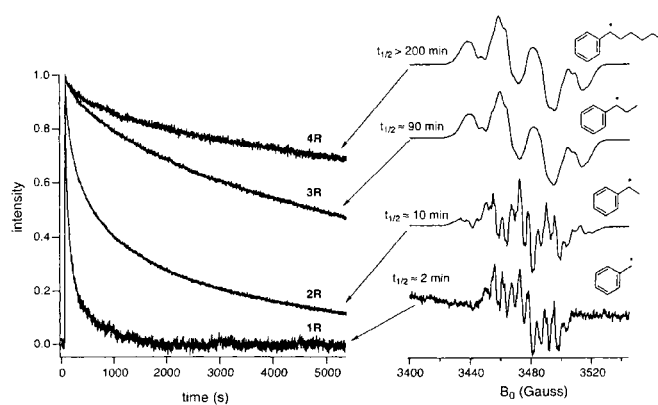
reactivity of **54** was found to be highly influenced by the nature of the alkali metal counterion, as well as by the inclusion of cosolvents within the zeolite matrix.

Turro et al. [121] investigated supramolecular effects on the dynamics of radicals generated in zeolites. Isomeric pairs of *p*, *p'*-dialkyl-substituted phenyl benzyl ketones (**55**) adsorbed on MFI zeolites (silicalite and ZSM-5) were photolyzed and investigated by electron paramagnetic resonance (EPR) spectroscopy. The photolysis produced persistent “benzoyl-type” and “benzyl-type” radicals, which depended on the length and position of the *p*-alkyl chain. The photolysis of dibenzyl ketones (**56**) adsorbed on MZSM-5 (M = Li, Na, K, Rb, Cs) zeolites also produced persistent carbon-centered radicals that were easily observed by conventional steady-state EPR spectroscopy (Scheme 27) [122, 123]. The lifetimes of the radicals increased as the group X attached to the carbon atom at the radical center increased from X = H ( $t_{1/2}$  ca. 2 min) to X = (CH<sub>2</sub>)<sub>4</sub>CH<sub>3</sub> ( $t_{1/2}$  > 200 min), as can be seen in Figure 16. In addition, it was shown that the radical lifetimes depended heavily on the size of the metal cation ( $t_{1/2}$  ca. 10 min for Li and  $t_{1/2}$  > 200 min for Cs), as can be seen in Figure 17.

Cozens et al. directly observed a single “free” benzyl radical by means of a nanosecond diffuse reflectance laser photolysis of phenylacetic acid (**57**) incorporated into cation-exchanged Y zeolites [124] (Figure 18). The spectra showed a strong absorption band centered at 315 nm and a shoulder at 305 nm that coincided with the known

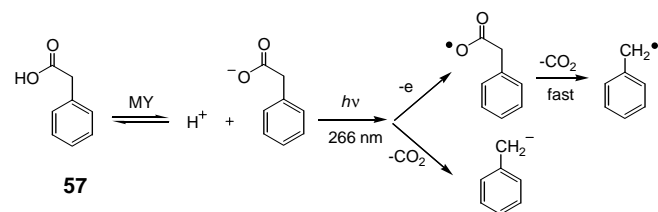


Scheme 27

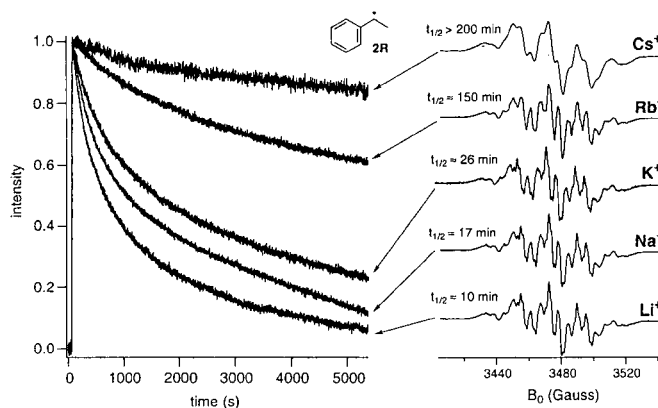


**Figure 16.** CW-EPR spectra (right) of radicals **1R–4R**@NaZSM-5 produced by photolysis of **56**@NaZSM-5 ( $\lambda_{\text{irr}} > 280 \text{ nm}$ ) and corresponding decay kinetics of the EPR signal (left) after short irradiation (10 s,  $\lambda_{\text{irr}} > 280 \text{ nm}$ ). Reprinted with permission from [123], N. J. Turro et al., *J. Org. Chem.* 67, 5779 (2002). © 2002, American Chemical Society.

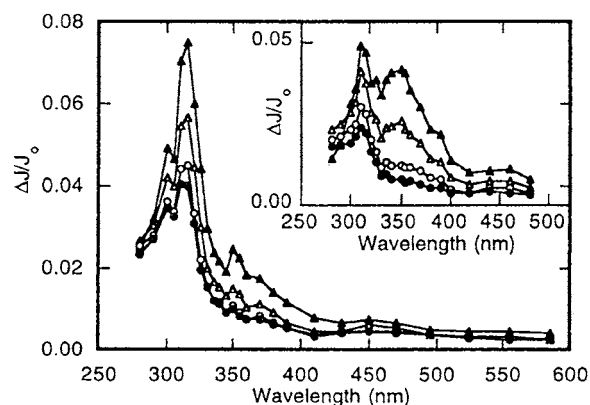
absorption spectrum for the benzyl radical in solution. The mechanism proposed for the generation of the benzyl radical is shown in Scheme 28. A second weaker absorption band at 350 nm was assigned to a benzyl anion on the basis of a quenching experiment using oxygen and product analysis. On laser photolysis of xanthene-9-carboxylate (**58**) incorporated in NaY in the absence of oxygen, prompt formation of the xanthyl radical and the xanthylum cation was observed [125]. The xanthyl radical



Scheme 28

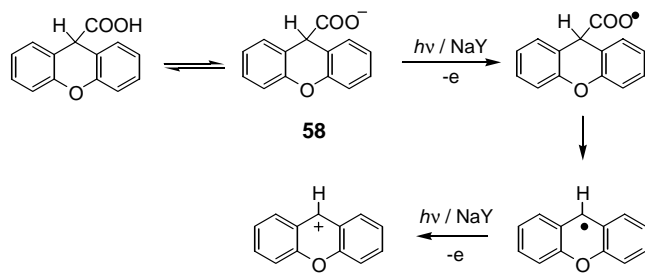


**Figure 17.** CW-EPR spectra (right) of the radical **2R** on cation-exchanged zeolites (**2R**@MZSM-5) produced by photolysis of **56**@MZSM-5 ( $\lambda_{\text{irr}} > 280 \text{ nm}$ ) and corresponding decay kinetics of the EPR signal (left) after short irradiation (10 s,  $\lambda_{\text{irr}} > 280 \text{ nm}$ ). Reprinted with permission from [123], N. J. Turro et al., *J. Org. Chem.* 67, 5779 (2002). © 2002, American Chemical Society.



**Figure 18.** Transient diffuse reflectance spectrum generated upon 266-nm laser photolysis of phenylacetic acid in evacuated ( $10^{-3}$  Torr) NaY under dry conditions. The inset shows the transient spectrum after the sample was exposed to the atmosphere for a period of 10 s and then reevacuated ( $10^{-3}$  Torr). Spectra were recorded at (▲) 0.20, (△) 0.74, (○) 1.76, and (●) 6.36  $\mu$ s after the laser pulse. Reprinted with permission from [124], F. L. Cozens et al., *J. Am. Chem. Soc.* 120, 13543 (1998). © 1998, American Chemical Society.

was formed by photoionization of **58** to the corresponding acyloxy radical, which then rapidly decarboxylates, as illustrated in Scheme 29. The xanthylium cation was produced by photoionization of the xanthy radical. In addition, in the presence of oxygen, the formation of the xanthylium cation was also heavily dependent on the zeolite counterion.



**Scheme 29**

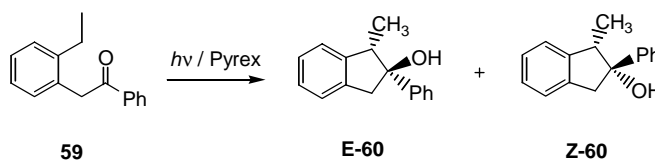
## 5.7. Photochemical Asymmetric Induction

The chiral induction of chemical reactions has been one of the main concerns of chemists for the past few decades. While great advances have been made in thermal asymmetric synthesis [126, 127], asymmetric photochemical reactions have not enjoyed the same level of success [128, 129]. However, several photochemists are exploring the possibility of employing zeolites as media for conducting chiral induction during photoreactions [130–132].

### 5.7.1. With No Chiral Inductor

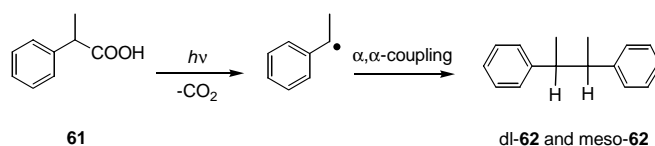
Noh et al. [133] studied the diastereoselectivity in the photocyclization of  $\alpha$ -(*o*-ethylphenyl)acetophenone (**59**) to 1-methyl-2-phenyl-2-indanol (**60**) in X and Y zeolites (Scheme 30) and made comparisons with the diastereoselectivity in isotropic solvents. The E/Z ratios in the zeolites

were much higher than in isotropic solvents. The ratios for the X zeolites were found to decrease as the cation size increased from  $\text{Li}^+$  to  $\text{Cs}^+$ , but this was not the case with the Y zeolites. The diastereoselectivity observed in the zeolites was interpreted using the conformational restriction imposed by the cavity size.



**Scheme 30**

Lalitha et al. [134] found that irradiation of 2-phenylpropionic acid (**61**) in various cation-exchanged Y zeolites led to the predominant formation of *dl*-2,3-diphenylbutane (**62**) over the *meso*-isomer, in marked contrast to photolysis in isotropic solvents (Scheme 31). This zeolite-induced diastereoselectivity was attributed to steric and electronic factors.

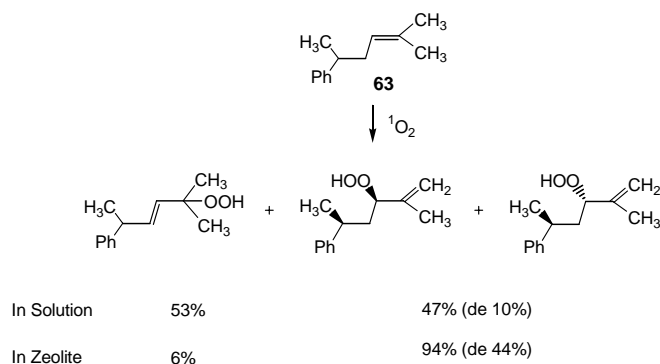


**Scheme 31**

The ene reaction of  $^1\text{O}_2$  with the chiral alkene 2-methyl-5-phenyl-2-hexene (**63**) in solution was not regioselective and exhibited very poor diastereoselectivity ( $\sim 10\%$  *de*), as shown in Scheme 32. In contrast, in thionin-supported NaY, significant enhancement of product regioselectivity (94%) and diastereoselectivity (44% *de*) was obtained [135].

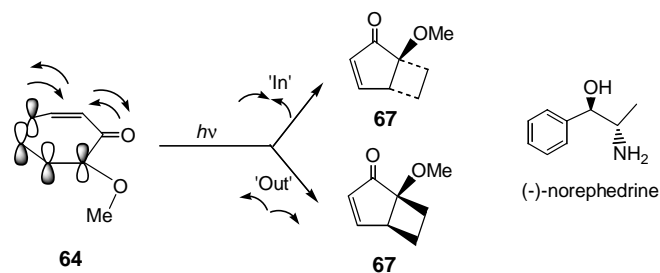
### 5.7.2. With a Chiral Inductor

Irradiation of achiral tropolone methyl ether (**64**) [130, 136], tropolone ethyl phenyl ether (**65**) [130, 137], and (*S*)-tropolone 2-methyl butyl ether (**66**) [130, 138] in solution undergoes a four  $\pi$ -electron disrotatory ring closure to yield the chiral bicycle[3.2.0] product **67**. For **64** and **65**, a racemic



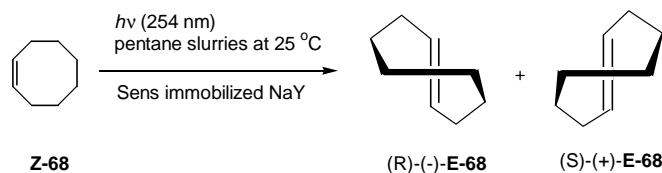
**Scheme 32**

mixture of **67** was produced as the result of an equal probability of “in” and “out” rotation, as illustrated in Scheme 33. However, irradiation of **64** with (–)-norephedrine, a chiral inductor, in NaY at –20 °C produced 50% *ee*. For **65**, it was found that the nature of the favored enantiomer was reversed between wet and dry zeolites and between NaY and NaX. The extent of *ee* depended on water content, the nature of the cation (Li<sup>+</sup>, Na<sup>+</sup>, K<sup>+</sup>, Rb<sup>+</sup>), and the number of cations (NaY versus NaX). For **66**, it was clearly shown that the cation controlled both the extent and the direction of diastereoselectivity.



Scheme 33

Wada et al. [139] reported that enantio-differentiating photoisomerization of (*Z*)-cyclooctene (**Z-68**), sensitized by (R)- or (S)-1-methylheptyl benzoate immobilized in zeolites, afforded the respective enantiomer pair, (–)- and (+)-(*E*)-isomer (**E-68**) in 5% *ee* (Scheme 34), while racemic **E-68** was obtained on photosensitization with the sensitizer pair in an isotropic solvent.

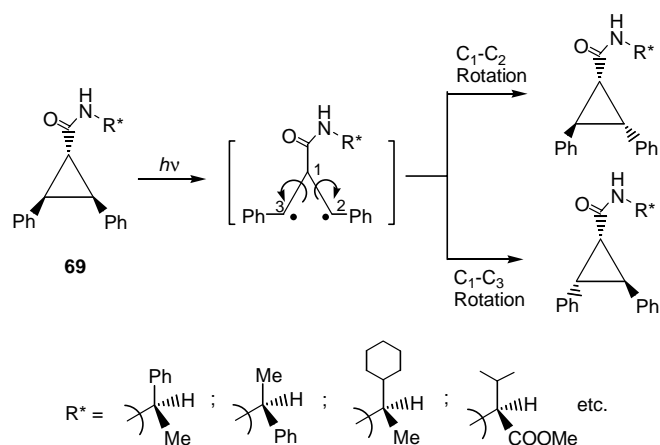


Scheme 34

### 5.7.3. With a Chiral Auxiliary

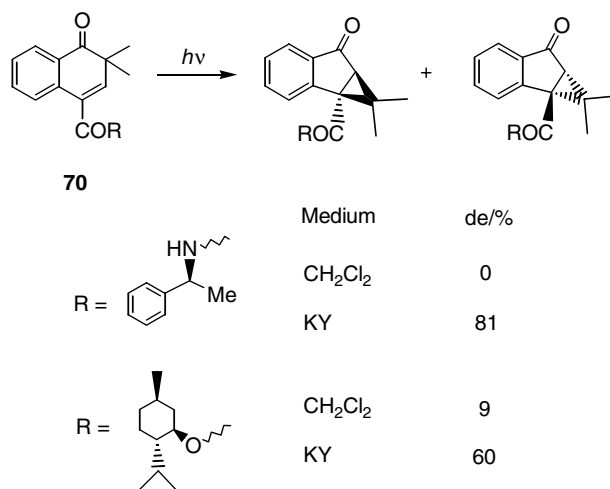
It was demonstrated by Chong and Sivaguru et al. [140, 141] that alkali metal cation-exchanged Y zeolites significantly enhanced asymmetric induction in the photoisomerization of a number of *cis*-1,2-diphenylcyclopropane derivatives (**69**) containing a chiral auxiliary (Scheme 35). The same chiral auxiliary failed to effect asymmetric induction during irradiation in solution. This fact suggested that the confined space of the zeolite was essential to force a chirally significant interaction between the auxiliary and the site of reaction on the three-membered ring. In addition, it was found that the cations present in the zeolite not only controlled the extent of diastereoselectivity but also the isomer that was being enhanced.

Jayaraman et al. further confirmed the enhancement of enatio- and diastereo-selectivities via confinement in zeolites by exploring both the photorearrangement

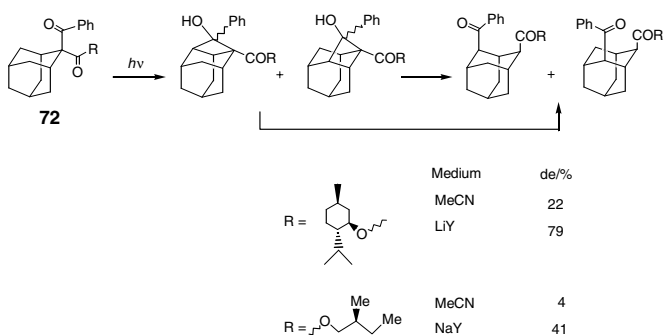


Scheme 35

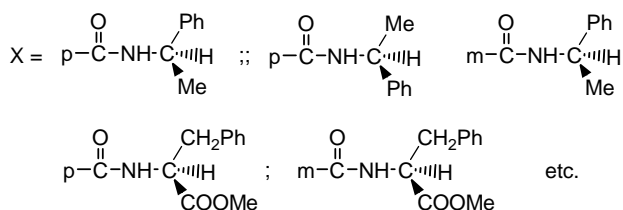
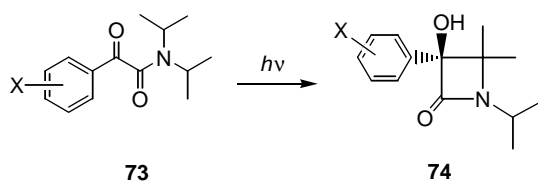
of 2,2-dimethylnaphthalenone (**70**) [142] and 2,4-cyclohexadienones (**71**) [143], and the Norrish–Yang reaction of 2-benzoyladamantane-2-carboxylic acid derivative (**72**) [142] with covalent chiral auxiliaries (Schemes 36 and 37). They also investigated the photochemical conversion of  $\alpha$ -oxoamides (**73**) into  $\beta$ -lactam derivatives (**74**) (Scheme 38) [144].



Scheme 36



Scheme 37



Scheme 38

A combination of a chiral inductor and a chiral auxiliary succeeded in boosting the photoproduct *de* for **66** [138, 145], but failed to do the same for 2β,3β-diphenylcyclopropane-1α-carboxylic acid (**75**) [146]. Although the uniqueness of zeolites as media-inducing enatio- and diastereo-selectivities has been established in the studies described above, the factors that control the high chiral induction in zeolite with respect to solution are yet to be established.

## 6. CONCLUDING REMARKS

Zeolite nanocavities continue to hold considerable attraction for photochemists because of the unique characteristics regulating the spectroscopic and photochemical behavior of included organic substrates. However, it should be noted that the acidity of Brønsted and Lewis acid sites in zeolites may change during the preparation and/or pretreatment for adsorption of organic guest molecules even if the same type of zeolite is used. This problem sometimes makes it difficult to reproduce the results obtained in another laboratory. In addition, co-adsorbents such as water and organic solvents might influence the reactivity of organic guest molecules in the ground and excited states. Therefore, experimental conditions must be carefully arranged. However, there is no doubt that zeolites have considerable potential to act as novel microreactors, which control the spectroscopic and photochemical behavior of organic guest molecules. It is also likely that the use both of transparent poly(dimethylsiloxane) or polyimide films of zeolites incorporating organic guests [147] and also zeolite-coated quartz fibers as media for photochemical and photophysical study [148] will lead to practical applications in industry and to further developments in nanotechnology.

## GLOSSARY

**Contact charge-transfer (CCT)** Electronic interaction in which the highest occupied molecular orbital of an electron donor makes contact with the lowest unoccupied molecular orbital of an electron acceptor.

**Excited singlet state** Electronically excited state in which two electrons spin in opposed directions.

**Excited triplet state** Electronically excited state in which the spin of two electrons is parallel.

**Fluorescence** The emission of light by a molecule in the excited singlet state.

**Intersystem crossing** The process of crossing from the excited singlet state to the excited triplet state.

**Laser photolysis** Photochemical reaction caused by laser light in order to measure time-resolved absorption spectra for short-lived species.

**Photophorescence** The emission of light by a molecule in the excited triplet state.

**Photostationary state (PSS)** The state of equilibrium reached photochemically in which the ratio between starting materials and products remains unchanged on further irradiation.

**Singlet oxygen** A reactive oxygen molecule in the excited singlet state.

**Zeolite supramolecule** Molecules adsorbed in zeolite cavities.

## ACKNOWLEDGMENTS

The author is grateful to Professor M. Anpo of Osaka Prefecture University for his kind encouragement in studying the photochemistry of zeolite supramolecules and also thanks Ms. M. Nakajoh and Ms. S. Nebashi for their assistance in preparing this article.

## REFERENCES

1. V. Ramamurthy, "Photochemistry in Organized and Constrained Media," VCH, New York, 1991.
2. V. Ramamurthy, D. F. Eaton, and J. V. Casper, *Acc. Chem. Res.* 25, 299 (1992).
3. V. Ramamurthy, *Chimia* 46, 359 (1992).
4. J. K. Thomas, *Chem. Rev.* 93, 301 (1993).
5. K. B. Yoon, *Chem. Rev.* 93, 321 (1993).
6. M. Anpo, "Surface Photochemistry," Wiley, Chichester, 1996, Vol. 1.
7. V. Ramamurthy, R. J. Robbins, K. J. Thomas, and P. H. Lakshminarasimhan, in "Organized Molecular Assemblies in the Solid State" (J. K. Whitesell, ed.), John Wiley & Sons, Chichester, 1999, Vol. 2, p. 63.
8. C. Tung, L. Wu, Z. Yuan, J. Guan, Y. Ying, H. Wang, and X. Xu, *Materials Science & Engineering C* 10, 75 (1999).
9. J. C. Scaiano and H. García, *Acc. Chem. Res.* 32, 783 (1999).
10. C. Tung, L. Wu, L. Zhang, H. Li, X. Yi, K. Song, M. Xu, Z. Yuan, J. Guan, H. Wang, Y. Ying, and X. Xu, *Pure Appl. Chem.* 72, 2289 (2000).
11. H. Yamashita and M. Anpo, in "Photofunctional Zeolites" (M. Anpo, ed.), Nova Science Publishers, Inc., Huntington, NY, 2000, p. 99.
12. M. Kojima, *Kokagaku* 31, 173 (2000).
13. M. Kojima, *Kagaku Kogyo* 53, 666 (2002).
14. V. Ramamurthy, *Mol. Cryst. Liq. Cryst.* 240, 53 (1994).
15. W. Zhou and E. Clennan, *J. Am. Chem. Soc.* 121, 2915 (1999).
16. S. Hashimoto, T. Miyashita, and M. Hagiri, *J. Phys. Chem. B.* 103, 9149 (1999).
17. V. Ramamurthy, J. V. Casper, and D. R. Corbin, *J. Am. Chem. Soc.* 113, 594 (1991).



18. X. Liu, K.-K. Iu, J. K. Thomas, H. He, and J. Klinowski, *J. Am. Chem. Soc.* 116, 11811 (1994).
19. J. F. Haw, J. B. Nicholas, T. Xu, L. W. Beck, and D. B. Ferguson, *Acc. Chem. Res.* 29, 259 (1996).
20. V. Ramamurthy, P. Lakshminarasimhan, C. P. Grey, and L. J. Johnston, *J. Chem. Soc. Chem. Commun.* 2411 (1998).
21. H.-M. Kao, C. P. Grey, K. Pitchumani, P. H. Lakshminarasimhan, and V. Ramamurthy, *J. Phys. Chem. A* 102, 5627 (1998).
22. P. Lakshminarasimhan, K. J. Thomas, L. Brancalone, P. D. Wood, L. J. Johnston, and V. Ramamurthy, *J. Phys. Chem. B*, 103, 9247 (1999).
23. T. Herbertz, P. S. Lakkaraju, F. Blume, M. Blume, and H. D. Roth, *Eur. J. Org. Chem.* 467 (2000).
24. W. L. Hsu and C. T. Lin, *J. Phys. Chem.* 94, 3780 (1990).
25. S. Pankasem and J. K. Thomas, *J. Phys. Chem.* 95, 7385 (1991).
26. P. Szedlaczek, S. L. Suib, M. Deeba, and G. S. Koermer, *J. Chem. Soc. Chem. Commun.* 1531 (1990).
27. X. Liu and J. K. Thomas, *Langmuir* 9, 727 (1993).
28. M. Kojima, A. Odaka, T. Nakajima, and Y. Kuriyama, *Chem. Lett.* 675 (1999).
29. F. D. Lewis, G. D. Reddy, J. E. Elbert, B. E. Tillberg, J. A. Meltzer, and M. Kojima, *J. Org. Chem.* 56, 5311 (1991).
30. S. Corrent, P. Hahn, G. Pohlars, T. J. Connolly, J. C. Scaiano, V. Fornes, and H. Garcia, *J. Phys. Chem. B* 102, 5852 (1998).
31. V. Ramamurthy, D. R. Sanderson, and D. F. Eaton, *J. Am. Chem. Soc.* 115, 10438 (1993).
32. J. Shailaja, J. Siveguru, R. J. Robbins, V. Ramamurthy, R. B. Sunoj, and J. Chandrasekhar, *Tetrahedron* 56, 6927 (2000).
33. K. Iu and J. K. Thomas, *Langmuir* 6, 471 (1990).
34. C.-H. Tung, H. Wang, and Y.-M. Ying, *J. Am. Chem. Soc.* 120, 5179 (1998).
35. V. Ramamurthy, J. V. Caspar, D. F. Eaton, E. W. Kuo, and D. R. Corbin, *J. Am. Chem. Soc.* 114, 3882 (1992).
36. R. Sadeghpour, M. Ghandi, H. M. Najafi, and F. Farzaneh, *J. Chem. Soc. Chem. Commun.* 329 (1998).
37. K. Pitchumani, M. Warriar, J. R. Scheffer, and V. Ramamurthy, *J. Chem. Soc. Chem. Commun.* 1197 (1998).
38. M. Warriar, N. J. Turro, and V. Ramamurthy, *Tetrahedron Lett.* 41, 7163 (2000).
39. S. Uppili, S. Takagi, R. B. Sunoj, P. Lakshminarasimhan, J. Chandrasekhar, and V. Ramamurthy, *Tetrahedron Lett.* 42, 2079 (2001).
40. D. R. Corbin, D. F. Eaton, and V. Ramamurthy, *J. Am. Chem. Soc.* 110, 4848 (1988).
41. V. Ramamurthy, D. R. Corbin, N. J. Turro, and Y. Sato, *Tetrahedron Lett.* 30, 5829 (1989).
42. V. Ramamurthy, D. R. Corbin, and D. F. Eaton, *J. Org. Chem.* 55, 5269 (1990).
43. V. Ramamurthy, X.-G. Lei, N. J. Turro, T. J. Lewis, and J. R. Scheffer, *Tetrahedron Lett.* 32, 7675 (1991).
44. V. Ramamurthy and D. R. Sanderson, *Tetrahedron Lett.* 33, 2757 (1992).
45. V. Ramamurthy and N. J. Turro, *J. Incl. Phenom. Mol. Recogn. Chem.* 21, 239 (1995).
46. V. J. Rao, N. Prevost, V. Ramamurthy, M. Kojima, and L. J. Johnston, *J. Chem. Soc. Chem. Commun.* 2209 (1997).
47. F. L. Cozens, R. Bogdanova, M. Régimbald, H. García, V. Martí, and J. C. Scaiano, *J. Phys. Chem. B* 101, 6921 (1997).
48. V. Fornés, H. García, V. Martí, and L. Fernández, *Tetrahedron* 54, 3827 (1998).
49. D. F. Evans, *J. Chem. Soc.* 345 (1953).
50. M. Kojima, in "Handbook of Photochemistry and Photobiology" (H. S. Nalwa, ed.). American Scientific Publishers, Stevenson Ranch, CA 2003, Vol. 2, Chap. 11, p. 501.
51. M. Kojima, H. Sakuragi, and K. Tokumaru, *Tetrahedron Lett.* 22, 2889 (1981).
52. M. Kojima, H. Sakuragi, and K. Tokumaru, *Bull. Chem. Soc. Jpn.* 62, 3863 (1989).
53. K. Onodera, G. Furusawa, M. Kojima, M. Tsuchiya, S. Aihara, R. Akaba, H. Sakuragi, and K. Tokumaru, *Tetrahedron* 41, 2215 (1985).
54. M. Kojima, H. Sakuragi, and K. Tokumaru, *Bull. Chem. Soc. Jpn.* 60, 3331 (1987).
55. M. Kojima, A. Ishida, and S. Takamuku, *Chem. Lett.* 979 (1993).
56. M. Kojima, A. Ishida, and S. Takamuku, *Bull. Chem. Soc. Jpn.* 71, 2211 (1998).
57. F. Blatter and H. Frei, *J. Am. Chem. Soc.* 115, 7501 (1993).
58. F. Blatter and H. Frei, *J. Am. Chem. Soc.* 116, 1812 (1994).
59. H. Sun, F. Blatter and H. Frei, *J. Am. Chem. Soc.* 116, 7951 (1994).
60. F. Blatter, F. Moreau, and H. Frei, *J. Phys. Chem.* 98, 13403 (1994).
61. F. Blatter, H. Sun, and H. Frei, *Catal. Lett.* 35, 1 (1995).
62. F. Blatter, H. Sun, and H. Frei, *Chem. Eur. J.* 2, 385 (1996).
63. H. Sun, F. Blatter, and H. Frei, *J. Am. Chem. Soc.* 118, 6873 (1996).
64. H. Frei, F. Blatter, and H. Sun, *Chemtech*, 26, 24 (1996).
65. H. Sun, F. Blatter, and H. Frei, *Catal. Lett.* 44, 247 (1997).
66. S. Vasenkov and H. Frei, *J. Phys. Chem. B* 101, 4539 (1997).
67. F. Blatter, H. Sun, S. Vasenkov, and H. Frei, *Catal. Today*, 41, 297 (1998).
68. S. Vasenkov and H. Frei, *Mol. Supramol. Photochem.* 5, 295 (2000).
69. K. B. Myli, S. C. Larsen, and V. H. Grassian, *Catal. Lett.* 48, 199 (1997).
70. Y. Xiang, S. C. Larsen, and V. H. Grassian, *J. Am. Chem. Soc.* 121, 5063 (1999).
71. A. G. Panov, R. G. Larsen, N. I. Totah, S. C. Larsen, and V. H. Grassian, *J. Phys. Chem. B* 104, 5706 (2000).
72. R. G. Larsen, A. C. Saladino, T. A. Hunt, J. E. Mann, M. Xu, V. H. Grassian, and S. C. Larsen, *J. Catal.* 204, 440 (2001).
73. H. Takeya, Y. Kuriyama, and M. Kojima, *Tetrahedron Lett.* 39, 5967 (1998).
74. M. Kojima, M. Nakajoh, C. Matsubara, and S. Hashimoto, *J. Chem. Soc. Perkin Trans. 2*, 1894 (2002).
75. C. Matsubara and M. Kojima, *Tetrahedron Lett.* 40, 3439 (1999).
76. C. Matsubara and M. Kojima, *Res. Chem. Intermed.* 27, 975 (2001).
77. A. Itoh, T. Kodama, Y. Masaki, and S. Inagaki, *Synlett* 522 (2002).
78. P. Lakshminarasimhan, K. J. Thomas, L. J. Johnston, and V. Ramamurthy, *Langmuir* 16, 9360 (2000).
79. X. Li and V. Ramamurthy, *J. Am. Chem. Soc.* 118, 10666 (1996).
80. R. J. Robbins and V. Ramamurthy, *J. Chem. Soc. Chem. Commun.* 1071 (1997).
81. E. L. Clennan and J. P. Sram, *Tetrahedron Lett.* 40, 5275 (1999).
82. W. Zhou and E. L. Clennan, *Org. Lett.* 2, 437 (2000).
83. E. L. Clennan and J. P. Sram, *Tetrahedron* 56, 6945 (2000).
84. E. L. Clennan, J. P. Sram, A. Pace, K. Vincer, and S. White, *J. Org. Chem.* 67, 3975 (2002).
85. M. Stratakis and G. Froudakis, *Org. Lett.* 2, 1369 (2000).
86. X. Li and V. Ramamurthy, *Tetrahedron Lett.* 37, 5235 (1996).
87. T. Arai and K. Tokumaru, *Chem. Rev.* 93, 23 (1993).
88. H. Rau, in "Photochromism: Molecules and Systems," (H. Dürr and H. Bouas-Laurent, eds.), p. 165, Elsevier, Amsterdam, 1990.
89. Y. Kuriyama, H. Takeya, S. Oishi, and M. Kojima, *Chem. Lett.* 843 (1998).
90. M. Kojima and C. Matsubara, "The Conference of Japanese Photochemical Association 2000, The Book of Abstracts," p. 35.
91. V. Ramamurthy, J. V. Casper, D. R. Corbin, D. F. Eaton and C. Dybowski, *J. Photochem. Photobiol. A: Chem.* 51, 259 (1990).
92. E. H. Ellison and J. K. Thomas, *J. Phys. Chem. B* 105, 2757 (2001).
93. M. Kojima, T. Takagi, and T. Karatsu, *Chem. Lett.* 686 (2000).
94. M. Kojima, T. Takagi, and T. Goshima, *Mol. Cryst. Liq. Cryst.* 344, 179 (2000).
95. K. Hoffmann, F. Marlow, and J. Caro, *Adv. Mater.* 9, 567 (1997).
96. F. Marlow and K. Hoffmann, *Ber. Bunsenges. Phys. Chem.* 101, 1731 (1997).

97. K. Hoffmann, U. Resch-Genger, and F. Marlow, *Microporous and Mesoporous Mater.* 41, 99 (2000).
98. F. Gessner, A. Olea, J. H. Lobough, L. J. Johnston, and J. C. Scaiano, *J. Org. Chem.* 54, 259 (1989).
99. M. V. Baldoví, A. Corma, H. García, and V. Martí, *Tetrahedron Lett.* 35, 9447 (1994).
100. A. Lalitha, K. Pitchumani, P. Kannan, and C. Srinivasan, *Tetrahedron* 54, 15667 (1998).
101. I. Casades, M. Álvaro, H. García, and M. N. Pillai, *Eur. J. Org. Chem.* 2074 (2002).
102. A. Corma, V. Fornés, H. García, M. A. Miranda, J. Primo, and M. J. Sabater, *J. Am. Chem. Soc.* 116, 2276 (1994).
103. A. Corma, V. Fornés, H. García, M. A. Miranda, and M. J. Sabater, *J. Am. Chem. Soc.* 116, 9767 (1994).
104. P. H. Lakshminarasimhan, R. B. Sunoj, S. Karthikeyan, J. Chandrasekhar, L. J. Johnston, and V. Ramamurthy, *J. Photochem. Photobiol. A: Chem.* 153, 41 (2002).
105. S. L. Suib and A. Kostapapas, *J. Am. Chem. Soc.* 106, 7705 (1984).
106. X. Liu, K.-K. Iu, and J. K. Thomas, *J. Phys. Chem.* 93, 4120 (1989).
107. X. Liu and J. K. Thomas, *Chem. Mater.* 6, 2303 (1994).
108. A. V. Barzkin and S. Hashimoto, *J. Chem. Phys.* 113, 2841 (2000).
109. V. Ramamurthy, D. R. Corbin, C. V. Kumar, and N. J. Turro, *Tetrahedron Lett.* 31, 47 (1990).
110. G. Lem, N. A. Kaprinidis, D. I. Schuster, N. D. Ghatlia, and N. J. Turro, *J. Am. Chem. Soc.* 115, 7009 (1993).
111. A. Lalitha, K. Pitchumani, and C. Srinivasan, *J. Photochem. Photobiol. A: Chem.* 134, 193 (2000).
112. L. Brancaleon, D. Brousmiche, V. J. Rao, L. J. Johnston, and V. Ramamurthy, *J. Am. Chem. Soc.* 120, 4926 (1998).
113. K. Pitchumani, M. Warriar, and V. Ramamurthy, *J. Am. Chem. Soc.* 118, 9428 (1996).
114. W. Gu, M. Warriar, V. Ramamurthy, and R. G. Weiss, *J. Am. Chem. Soc.* 121, 9467 (1999).
115. W. Gu, M. Warriar, B. Schoon, V. Ramamurthy, and R. G. Weiss, *Langmuir* 16, 6977 (2000).
116. S. Vasenkov and H. Frei, *J. Phys. Chem. A*, 104, 4327 (2000).
117. K. Pitchumani and V. Ramamurthy, *J. Chem. Soc. Chem. Commun.* 2763 (1996).
118. H. García, S. García, J. Pérez-Prieto, and J. C. Scaiano, *J. Phys. Chem.* 100, 18158 (1996).
119. M. A. O'Neill, F. L. Cozens, and N. P. Schepp, *J. Am. Chem. Soc.* 122, 6017 (2000).
120. M. A. O'Neill, F. L. Cozens, and N. P. Schepp, *Tetrahedron* 56, 6969 (2000).
121. N. J. Turro, X. Lei, S. Niu, Z. Liu, S. Jocksch, and M. F. Ottaviani, *Org. Lett.* 2, 3991 (2000).
122. N. J. Turro, X. Lei, S. Jockusch, W. Li, Z. Liu, L. Abrams, and M. F. Ottaviani, *J. Org. Chem.* 67, 2606 (2002).
123. N. J. Turro, S. Jockusch, and X. Lei, *J. Org. Chem.* 67, 5779 (2002).
124. F. L. Cozens, W. Ortiz, and N. P. Schepp, *J. Am. Chem. Soc.* 120, 13543 (1998).
125. F. L. Cozens, M. L. Cano, H. Garcia, and N. P. Schepp, *J. Am. Chem. Soc.* 120, 5667 (1998).
126. M. Avalos, R. Babiano, P. Cintas, J. L. Jimenez, and J. C. Palacios, *Chem. Rev.* 98, 2391 (1998).
127. A. Richards and R. McCague, *Chem. Ind.* 422 (1997).
128. Y. Inoue, *Chem. Rev.* 92, 741 (1992).
129. J. P. Pete, *Adv. Photochem.* 21, 135 (1996).
130. A. Joy and V. Ramamurthy, *Chem. Eur. J.* 6, 1287 (2000).
131. J. Sivaguru, J. Shailaja, S. Uppili, K. Ponchot, A. Joy, N. Arunkumar, and V. Ramamurthy, in "Organic Solid-State Reactions (F. Toda, ed.), Kluwer Academic Publishers, Dordrecht, 2002, p. 159.
132. E. Brunet, *Chirality* 14, 135 (2002).
133. T. Noh, K. Choi, H. Kwon, D. J. Chang, and B. S. Park, *Bull. Korean Chem. Soc.* 20, 539 (1999).
134. A. Lalitha, K. Pitchumani, and C. Srinivasan, *Tetrahedron* 57, 4455 (2001).
135. M. Stratakis and G. Kosmas, *Tetrahedron Lett.* 42, 6007 (2001).
136. A. Joy, A. Joy, J. R. Scheffer, D. R. Corbin, and V. Ramamurthy, *J. Chem. Soc. Chem. Commun.* 1379 (1998).
137. A. Joy, J. R. Scheffer, and V. Ramamurthy, *Org. Lett.* 2, 119 (2000).
138. A. Joy, S. Uppili, M. R. Netherton, J. R. Scheffer, and V. Ramamurthy, *J. Am. Chem. Soc.* 122, 728 (2000).
139. T. Wada, M. Shikimi, Y. Inoue, G. Lem, and N. J. Turro, *J. Chem. Soc. Chem. Commun.* 1864 (2001).
140. K. C. W. Chong, J. Sivaguru, T. Shichi, Y. Yoshimi, V. Ramamurthy, J. R. Scheffer, *J. Am. Chem. Soc.* 124, 2858 (2002).
141. J. Sivaguru, J. R. Scheffer, J. Chandrasekhar, and V. Ramamurthy, *J. Chem. Soc. Chem. Commun.* 830 (2002).
142. S. Jayaraman, S. Uppili, A. Natarajan, A. Joy, K. C. W. Chong, M. R. Netherton, A. Zenova, J. R. Scheffer, and V. Ramamurthy, *Tetrahedron Lett.* 41, 8231 (2000).
143. S. Uppili and V. Ramamurthy, *Org. Lett.* 4, 87 (2002).
144. A. Natarajan, K. Wang, V. Ramamurthy, J. R. Scheffer, and B. Patrick, *Org. Lett.* 4, 1443 (2002).
145. J. Shailaja, J. Sivaguru, S. Uppili, A. Joy, and V. Ramamurthy, *Microporous and Mesoporous Mater.* 48, 319 (2001).
146. E. Cheung, K. C. W. Chong, S. Jayaraman, V. Ramamurthy, J. R. Scheffer, and J. Trotter, *Org. Lett.* 2, 2801 (2000).
147. M. Alvaro, H. Garcia, S. Corrent, and J. C. Scaiano, *J. Phys. Chem. B* 102, 7530 (1998).
148. A. R. Pradhan, S. Uppili, J. Shailaja, J. Sivaguru, and V. Ramamurthy, *J. Chem. Soc. Chem. Commun.* 596 (2002).
149. H. Satozono, S. Suzuki, N. Tokou, H. Takehara, and Y. Uno, *J. Chem. Soc. Jpn., Chem. Indus. Chem.* 115 (1994).



# Photoconductivity of Carbon Nanotubes

Akihiko Fujiwara

*Japan Advanced Institute of Science and Technology, Tatsunokuchi, Ishikawa, Japan,  
and Japan Science and Technology Corporation, Kawaguchi, Saitama, Japan*

## CONTENTS

1. Introduction
  2. Physical Properties of Carbon Nanotubes
  3. Photoconductivity of Carbon Nanotubes
  4. Related Phenomena
  5. Summary
- Glossary  
References

## 1. INTRODUCTION

Since the discovery of carbon nanotubes (CNTs) by Iijima in 1991 [1], they have attracted great attention as potential electronic materials because of the one-dimensional tubular network structure on a nanometer scale. The variety of band structures of the CNTs, being either semiconducting or metallic, depending on the chirality and diameter of the CNT, is also a novel feature. For this reason, it is expected that CNTs become model samples for an ideal one-dimensional metal and an ideal one-dimensional semiconductor. In addition, CNTs are also expected to be one of the greatest candidates for nanotechnology materials, such as nanometer scale wirings and nanometer scale devices [2–4].

A CNT can be described as a single graphite (graphene) sheet rolled into a cylindrical shape. A concentric tubular structure can be made of two or more nanotubes with different diameters. The former and the latter are called single-wall carbon nanotubes (SWCNTs) and multiwall carbon nanotubes (MWCNTs), respectively. The thinnest CNTs are found in a most inner CNT of MWCNTs and SWCNTs grown in zeolite  $\text{AlPO}_4\text{-5}$  (AFI) single crystals; the diameter is about 0.4 nm [5, 6]. The diameter of thick CNTs is at most a few 10 nanometers. In most cases, CNTs with large diameters are MWCNTs; in the case of SWCNTs, a cross-section will not be able to maintain circular structure but it will be distorted. Moreover, in MWCNTs with large diameters, structure strongly depends on production conditions and can be not only concentric, but also the

structure in which a graphene is scrolled up—a polyhedral graphite tube with defects at the vertex and mixtures of them [7–10].

For the theoretical approach and the interpretation of experimental results, SWCNTs are suited, because interaction between layers and the effect of defects must be taken into consideration in the case of MWCNTs. Most of the experimental observation had been on MWCNTs in the beginning of research on CNTs. After the establishment of a synthesis method for high-quality SWCNTs [11–13], extensive research on SWCNTs, as well as MWCNTs, is performed. Since researches field of photoconductivity of CNTs reviewed in this article have a short history, only the research for two kinds of SWCNT samples are reported [14–19]. Photoconductivity has not been observed in MWCNT samples. Therefore, if there is no notice, there will be a discussion about the SWCNT in this article.

This chapter is organized as follows. The physical properties needed for discussion about the photoconductivity of CNTs are presented in Section 2. In Section 3, the photoconductive properties observed in two kinds of SWCNTs are shown. Here, experimental methods are also described, because introduction of this is important because it has been succeeded only with a few groups in spite of many trials. As related phenomena, two types of photo-induced current modulations are presented in Section 4. Section 5 summarizes the chapter.

## 2. PHYSICAL PROPERTIES OF CARBON NANOTUBES

A number of excellent books and review articles have summarized the physical and chemical properties of CNTs [2–4, 20, 21]. In this section, properties related to photoconductivity are briefly described.

### 2.1. Molecular Structure

A SWCNT can be made by rolling a graphene sheet into a cylindrical shape [2–4, 20–23]. Although the tubular structure with any diameter and direction can be made when

we make it from papers without a pattern on the surface, the network structure of carbon has to be taken into account for CNTs. In a graphene sheet, carbon atoms form a two-dimensional network of a six-membered ring, namely, a hexagonal (or honeycomb) lattice by connecting their three  $sp^2$  hybrid orbitals. There are two sites, A- and B-site, in the graphene: one carbon is bonded to three carbons of another site. When graphene is rolled into cylindrical shape and one carbon is put on any other carbon in the same site, a CNT can be formed in principle. Relation between these two overlapped carbon atoms on the graphene can be described by chiral vector  $C_h = na_1 + ma_2$ , where  $n, m$  are integers and  $a_1, a_2$  are the unit vectors of the graphene. The direction of the chiral vector  $C_h$  is perpendicular to the CNT axis and its length,  $L \equiv |C_h| = a(n^2 + m^2 + nm)^{1/2}$  is equal to that of circumference of the CNT, where  $a$  is the length of  $a_1$  and  $a_2$ . In actuality, because a  $sp^2$  hybrid orbital cannot be maintained for small diameters and the tubular structure is distorted for large diameters, the diameter of SWCNTs is considered to be about 0.4–2.0 nm.

## 2.2. Electronic Structure

It is intelligible when the electronic structure of a SWCNT, as well as molecular structure, is considered on the basis of a graphene sheet [20–25]. It is necessary to consider the periodic boundary conditions along the circumference of the CNT to the electronic structure of the graphene. Since the graphene sheet has a hexagonal lattice, the first Brillouin zone becomes a right hexagon. In energy-dispersion relations, the  $\pi^*$  (conduction) band and the  $\pi$  (valence) band are degenerate only at the six corners of the hexagonal first Brillouin zone,  $K$  and  $K'$  points, which the Fermi energy passes. Since the density of states at the Fermi energy is zero, the graphene is a zero-gap semiconductor. Although all the points in the first Brillouin zone are allowed for the graphene sheet, in the case of CNTs, allowed points are only on the line prolonged in the direction of the CNT axis through the  $\Gamma$  point (the center of the first Brillouin zone) and the parallel lines that separated  $2k\pi/L$  ( $k$ : integer) from this line. Therefore, when these straight lines pass through  $K$  ( $K'$ ) points, since energy dispersion will pass Fermi energy, CNTs become metallic. The distance between  $K$  ( $K'$ ) points and the allowed line through the  $\Gamma$  point is  $2\pi(2n+m)/3L$ . As a result, when  $2n+m$ , that is,  $n-m$ , is the multiple of 3, CNTs become metallic. In other cases, CNTs become semiconducting. In the energy dependence of density of states in CNTs, van Hove singularity (VHS) appears to be reflecting one-dimensional nature. Moreover, because  $\pi^*$  (conduction) and  $\pi$  (valence) bands are almost symmetrical, the density of state near the Fermi energy shows the symmetrical energy dependence in respect to the Fermi energy.

## 2.3. Optical Absorption

Theoretical prediction shows the optical transition takes place only between symmetrical bands, under the configuration that the polarization vector  $E$  is parallel to the nanotube axis by taking into account the depolarization effect [26]. Corresponding to high transition probability between the symmetric VHSs, three characteristic absorption bands in

an optical absorption spectrum are observed in the energy range from an infrared region to a visible region [13, 27]. Two absorption bands in the lower energy and one at the highest energy originate from semiconducting and metallic SWCNTs, respectively.

It is well known that the exciton binding energy becomes infinite in the limit of an ideal one-dimensional electron-hole system [28–30]. Therefore, the effect of exciton plays an important role in optical absorption for the one-dimensional system of SWCNTs. This effect is considered to mainly modify the lowest band of the optical absorption spectrum, which was predicted theoretically [31]. Experimental results of optical absorption are consistent with this prediction [13, 27].

## 2.4. Electronic Transport Properties

Although there are many findings of novel properties and functions, such as single electron transport [32, 33], spin transport [34], rectification [35, 36], switching function [37], tunable electronic structure by magnetic fields [38, 39], single molecule CNT transistors [40–42], and superconductivity [43, 44] in electron transport properties, we focus on the electron scattering—ballistic or diffusive. The ballistic conduction in CNTs even at room temperature (RT) was pointed out by observation of quantized conduction in MWCNTs at first [45]. Ballistic conduction of SWCNTs was proposed by the detailed analysis of the coulomb blockade behavior of SWCNTs which act as a quantum dot [32]. From the subsequent research for semiconducting SWCNTs, the mean-free path is estimated to be about 100 nm which is about one-tenth of the CNT length, and the result suggests diffusive conduction in semiconducting SWCNTs in spite of ballistic conduction in metallic SWCNTs [46]. This is considered to be due to the electron scattering at defects and the bending parts of CNTs.

## 3. PHOTOCONDUCTIVITY OF CARBON NANOTUBES

The research on photoconductivity for two kinds of SWCNTs has been reported. One is observed in the SWCNTs with a diameter of about 1.4 nm, being closed-packed into bundles and forming a two-dimensional triangular lattice [14–17]. Another is in the SWCNTs, with a diameter of about 0.4 nm grown in zeolite  $AlPO_4-5$  (AFI) single crystals, which are one type of the thinnest SWCNTs [18, 19]. In MWCNTs, photoconductivity has not been observed thus far.

### 3.1. Single-Wall Carbon Nanotube Bundles

Photoconductivity of CNTs has been discovered in the film sample of SWCNT bundles, and the most detailed research has been performed for this sample [14–17]. In this section, detailed experimental methods for the observation, photoconductive properties, and possible mechanisms are presented.

### 3.1.1. Experimental Technique

The samples of SWCNT bundles were synthesized by evaporation of composite rods of nickel (Ni), yttrium (Y), and graphite in helium atmosphere by arc discharge [12, 13] or ablating a graphite target containing Ni and cobalt (Co) catalysts at 1250 °C in an argon atmosphere by using a pulsed Nd:YAG laser [11]. Observations by transmission electron microscopy (TEM) revealed that soot is mainly composed of SWCNTs and also amorphous carbons and metal particles. The diameter of the SWCNTs is determined to be about  $1.4 \pm 0.2$  nm by the Raman frequency of a breathing mode and TEM observation. The typical length of SWCNT bundles estimated by scanning electron microscopy (SEM) is a few micrometers.

To prepare film samples, soot-containing SWCNTs were dispersed in methyl alcohol by an ultrasonic vibrator and suspension of SWCNTs was dropped on a glass substrate. The typical film sample size is about  $100 \mu\text{m} \times 100 \mu\text{m}$  and the thickness of the film is between 300 and 500 nm. The samples were annealed in vacuum at  $10^{-6}$  Torr and 673 K for 2 hours to remove the absorbed gases and methyl alcohol from samples. A pair of gold electrodes separated by a 10- $\mu\text{m}$  gap was evaporated in vacuum onto the surface of the film samples and connected to a DC regulated power supply (100 mV). In order to reduce the number of junctions between SWCNTs in the current pass, the narrow gap of 10  $\mu\text{m}$  was chosen because the resistance of the junctions dominates the total resistance of the sample and obscures the intrinsic transport properties of SWCNTs.

The samples were mounted in a continuous-flow cryostat and cooled by flowing the vapor of liquid He and liquid N<sub>2</sub> in the temperature range from 10 K to RT and from 100 K to RT, respectively. As a light source, an optical parametric oscillator (OPO), excited by a pulsed Nd:YAG laser, was used. The photon energy was in the range of 0.5 to 2.8 eV and the pulse duration was 5 ns. The light intensity is from a few tens nJ/pulse to 1500 nJ/pulse. The temporal profiles of the laser pulse and the photocurrent were monitored with a digitizing oscilloscope. In order to avoid spurious ringing in the fast pulse detection, we were obliged to use the input impedance of the oscilloscope (50  $\Omega$ ) as the reference resistor, despite the obvious disadvantage of lower sensitivity. The resistance of samples in the dark is ca. 100  $\Omega$  at RT and 800  $\Omega$  at around 10 K.

### 3.1.2. Observed Behaviors

The temporal evolution of photocurrent shows a Gaussian-like peak with a 5 ns width corresponding to the pulse duration of the laser. Photocurrent increases with increasing incident light intensity. When photocurrent is less than 10  $\mu\text{A}$ , the photocurrent intensity responds linearly to incident light intensity. On the other hand, it shows a saturation behavior above 10  $\mu\text{A}$ ; this saturation is often observed under intense light intensity and might be due to the lack of replenishment of carriers [47]. In photoconductivity excitation spectra estimated from the slope of the linear part in light intensity dependence of photocurrent, two clear peaks in photoconductivity excitation spectra at RT are observed around 0.7 and 1.2 eV. These energies are very close to the energy difference of first and second symmetrical pairs

of VHSs of semiconducting SWCNTs with a diameter of 1.4 nm. In addition, these spectra are very similar to the optical absorption spectra of SWCNTs prepared by the same method [13, 27].

The photoconductive response at 13.2 K is much higher than that at RT, whereas the optical absorption is hardly enhanced even at a low temperature [48]. Moreover, the enhancement strongly depends on the photon energy; the intensities of the peak in photoconductivity excitation spectra at 0.7 and 1.2 eV were enhanced by about two and one orders of magnitude, respectively. The observed photoconductive response monotonically increases with a decrease in temperature between 10 K and RT, and shows the saturation around 10 K.

### 3.1.3. Mechanism

From the correspondence between the optical absorption spectra of semiconducting carbon nanotubes and photoconductivity spectra, it is clear that the photocurrent originates from photoexcitation of electrons in semiconducting SWCNTs. Temperature dependence of photoconductivity  $\Delta\sigma(T)$  can be represented by  $\Delta\sigma(T) = \Delta n(T) \times e\mu(T) = \Delta n(T)(e^2/m^*) \{l(T)/v(T)\}$ , where  $\Delta n(T)$ ,  $e$ ,  $\mu(T)$ ,  $m^*$ ,  $l(T)$ , and  $v(T)$  are carrier numbers increased by light irradiation, carrier charge, mobility of charge carrier, effective mass of charge carrier, mean-free path, and thermal velocity [47]. Therefore, the temperature dependence of  $\Delta\sigma(T)$  should be attributed to that of  $\Delta n(T)$  and/or  $\mu(T) \propto l(T)/v(T)$ .  $T^{-3/2}$  dependence of  $\mu(T)$  is expected in conventional semiconductors with the regime of the diffusive transport due to electron-phonon interactions, because  $l(T)$  and  $v(T)$ , respectively, follow  $T^{-1}$  and  $T^{1/2}$ . On the other hand, by assuming the ballistic conduction,  $l(T)$  is expected to be limited to the nanotube length and to become independent of temperature. In this case,  $\mu(T)$  is expected to follow  $T^{-1/2}$ . Therefore,  $\Delta\sigma(T)$  is expected to follow  $T^{-3/2}$  or  $T^{-1/2}$  for the interband transition, because  $\Delta n(T)$  hardly depends on temperature. In this way, photoconductivity increases with a decrease in temperature for the interband transition, although temperature dependence of photoconductivity changes owing to the type of transport—ballistic or diffusive.

If exciton absorption is dominant in the semiconducting SWCNTs, as pointed out by the theoretical and experimental approach on optical absorption [13, 27, 31], free carriers contributing to the photoconductivity  $\Delta n(T)$  are created through thermal dissociation of excitons. In this case,  $\Delta n(T)$  will decrease with a decrease in temperature, and then,  $\Delta\sigma(T)$  will decrease, which is contrary to the experiment result. Experimental results naively support the theory that the photocarriers originate from the usual interband transition. Very recently, photoconductivity was observed in SWCNTs with the diameter of 0.4 nm [18, 19] as described in the next subsection. Since these samples have a stronger one-dimensional structure, binding energy of exciton is expected to be much larger than our samples. It is expected that the comparison of the photoconductive properties between these samples gives valuable information to solve this contradiction.

### 3.2. Single-Wall Carbon Nanotubes in Zeolite Single Crystals

Another example of observation of photoconductivity is shown in this section [18, 19]. Novel features of this type of sample are the smallest diameter and the almost perfect alignment of SWCNTs in the zeolite single crystals. For these reasons, this sample is very suitable for estimation of the effect of the one dimensionality and the optical anisotropy.

#### 3.2.1. Experimental Technique

The samples of SWCNTs in one-dimensional channels of zeolite AFI single crystals were synthesized by thermal treatment of paralyzed carbon encapsulated in the AFI crystal at 500–800 °C [6, 49]. Single-wall carbon nanotubes are grown in one-dimensional channels along the *c*-axis of AFI. Observations by TEM revealed that after dissolving the AFI framework residual materials are SWCNTs and raft-like graphite; the diameter of the SWCNTs is determined to be about  $0.42 \pm 0.2$  nm. Three possible structures,  $(n, m) = (5, 0), (3, 3), (4, 2)$ , are proposed for this type of nanotube. Typical dimensions of an AFI single crystal containing SWCNTs are 75–160  $\mu\text{m}$  in a cross-section diameter of a hexagonal face and ca. 300  $\mu\text{m}$  in length along the *c*-axis of AFI.

The gold wires of 100–150  $\mu\text{m}$  in diameter were attached to both hexagonal faces of the AFI single crystal. Bias voltage was applied between these two wires by a DC regulated power supply up to 1.5 V. Current flows along the *c*-axis of AFI, namely, the CNT axis. Linearly polarized light from a CW-Ar<sup>+</sup>-ion laser or a CW-Ti/sapphire laser pumped by an Ar<sup>+</sup>-ion laser was focused onto the central part of one surface of the AFI crystal. The direction of incident light is perpendicular to the CNT axis. The size of the illuminated spot was set about 100  $\mu\text{m}$  in diameter. The resistance of samples in the dark is around 100 M $\Omega$  at RT.

#### 3.2.2. Observed Behaviors

Conductance increases during the photo irradiation with the period of about 10 s. The response time is less than 50 ms. Photocurrent is proportional to the incident light intensity at low intensities. Although neither photon energy dependence (photoconductivity excitation spectra) nor temperature dependence have been investigated in detail, the information about optical anisotropy have been presented in this sample. By using this sample, it is confirmed that three absorption bands characteristic of CNTs are observed when a polarization vector is parallel to the *c*-axis of the AFI crystal ( $E \parallel c$ ), that is, the CNT axis, whereas optical absorption has hardly been detected for the case that the polarization vector is perpendicular to the nanotube axis ( $E \perp c$ ) [19, 50, 51], which is consistent with the theoretical prediction as described in Section 2–3 [26]. Corresponding to this, photoconductive response strongly depends on the angle between the polarization vector and the CNT axis; photocurrent for  $E \parallel c$  is about twice as large as that for  $E \perp c$ .

Intrinsic resistance of the SWCNT sample in the dark increases to more than twice the values by irradiating an intense light of about 10 mW. During the process of an increase in the resistance, the increases in photoconductive

response and in optical anisotropy are also observed. This result suggests that the intense light irradiation results not in the collapse of CNTs but in the increase in an effective semiconductor SWCNT, namely, the rearrangement of the nanotube structure within zeolite—for example, the connection of a divided semiconductor nanotubes and the structure conversion from the metallic SWCNTs to semiconducting ones.

## 4. RELATED PHENOMENA

In this section, two related phenomena, photo-induced current modulation, are presented.

### 4.1. Conductance Modulation Due to the Molecular Photodesorption

Conductance of an individual semiconducting SWCNT decreases by 10% upon ultraviolet (UV) illumination in air, NO<sub>2</sub>, and NH<sub>3</sub> atmosphere, contrary to the photoconductive response [52]. The conductance recovers after the light is turned off. This reaction occurs in reverse by repeating irradiation of light. This is caused by photodesorption of gases which acts as an electron donor or acceptor. Through photodesorption of molecules, SWCNTs becomes intrinsic semiconductors without any carrier doping and its conductance decreases. Therefore, when UV illumination is performed in a high vacuum, the conductance decreases drastically by a few orders of magnitude, and exhibit no appreciable recovery when the light was switched off.

### 4.2. Photo-Induced Tunneling Current in STM Measurements

It is expected that the local photocurrent can be measured by the scanning tunneling microscopy (STM) method [53]. A photo-induced tunneling current is observed for semiconducting and metallic SWCNTs, only when the photon energy exceeds energy difference of the first symmetrical pairs of VHS in the density of state. It is observed at both a positive and negative bias voltage of STM measurements, and increases linearly to the light intensity and is reversible. Although this behavior is preferred to observations of photoconductive response and electronic structure modulation through light irradiation in nanometer scale spatial resolution, it is necessary to clarify the extrinsic effects, such as the effect of thermal expansion of the CNT sample and the tip of STM to tunnel current, which is extremely sensitive to the distance between the sample and the tip.

## 5. SUMMARY

In this chapter, we have reviewed current states of photoconductivity of carbon nanotubes. Photoconductive properties for the bundles of SWCNTs with a diameter of 1.4 nm and the SWCNTs with a diameter of 0.4 nm in Zeolite single crystals are presented. Two types of photo-induced current modulation are also presented. The mechanism of photoconductivity is still unclear because of its short history. However, from the viewpoint both of nanoscale science and practical application for nano-scale devices, the

understanding of this phenomenon is very important. It is expected that the origin of photocarriers, the conduction characteristic of a semiconductor nanotube—ballistic or diffusive will be clarified from the detailed experiments on the temperature dependence of photoconductivity. In addition to this, the effect of the one dimensionality and the contribution of the exciton for the carrier generation will be clarified by comparing the photoconductive properties between these two types of SWCNTs with different diameters. This field is now ongoing and will develop further.

## GLOSSARY

**Carbon nanotube (CNT)** A tubular molecule made of carbon with nanometer diameter.

**Exciton** A mobile, electrically neutral, excited condition of holes and electrons in a crystal. One example is a weakly bound electron-hole pair.

**Multiwall carbon nanotube (MWCNT)** A type of carbon nanotube with the structure that a concentric tubular structure can be made of two or more nanotubes with different diameters.

**Optical parametric oscillator (OPO)** A laser-pumped crystal with nonlinear optical properties that generates coherent light whose output can be tuned continuously over wide range of wavelengths.

**Photoconductivity** An electrical conductivity increase exhibited by some nonmetallic materials, resulting from the free carriers generated when photon energy is absorbed in electronic transitions.

**Photocurrent** A current produced by photoelectric or photovoltaic effects.

**Scanning electron microscope (SEM)** A type of electron microscope that uses a beam of electrons to scan the sample surface, ejecting secondary electrons that form the picture of the sample.

**Scanning tunneling microscope (STM)** A high-resolution microscope that can detect and measure the positions and heights of individual atoms on the surface of the sample.

**Single-wall carbon nanotube (SWCNT)** A type of carbon nanotube with the structure that a single graphite (graphene) sheet rolled into a cylindrical shape.

**Transmission electronic microscope (TEM)** A type of electron microscope that uses magnetic lenses to transmit a beam of electrons through the sample; the electrons are then focused on a fluorescent screen to form an enlarged image or a diffraction image.

**van Hove singularity (VHS)** A singularity observed in energy spectrum of density of states for electrons and phonons, showing divergences of the slope.

## ACKNOWLEDGMENTS

The authors wish to thank Dr. H. Suematsu at Japan Synchrotron Radiation Research Institute and Professor K. Miyano, Professor N. Nagasawa, and Mr. N. Ogawa at the University of Tokyo for the continuous discussions and/or collaboration on this problem.

## REFERENCES

1. S. Iijima, *Nature* (London) 354, 56 (1991).
2. M. S. Dresselhaus, G. Dresselhaus, and P. Eklund, "Science of Fullerenes and Carbon Nanotubes." Academic Press, New York, 1996.
3. R. Saito, G. Dresselhaus, and M. S. Dresselhaus, "Physical Properties of Carbon Nanotubes." Imperial College Press, London, 1998.
4. P. J. F. Harris, "Carbon Nanotubes and Related Structures." Cambridge University Press, Cambridge, 1999.
5. L. C. Qin, X. Zhao, K. Hirahara, Y. Miyamoto, Y. Ando, and S. Iijima, *Nature* (London) 408, 50 (2000).
6. N. Wang, Z. K. Tang, G. D. Li, and J. S. Chen, *Nature* (London) 408, 50 (2000).
7. O. Zhou, R. M. Fleming, D. W. Murphy, C. H. Chen, R. C. Haddon, A. P. Ramirez, and S. H. Glarum, *Science* 263, 1744 (1994).
8. S. Amelinckx, D. Bernaerts, X. B. Zhang, G. Van Tendeloo, and J. Van Landuyt, *Science* 267, 1334 (1995).
9. S. Bandow, *Jpn. J. Appl. Phys.* 36, L1403 (1997).
10. Y. Maniwa, R. Fujiwara, H. Kira, H. Tou, E. Nishibori, M. Takata, M. Sakata, A. Fujiwara, X. Zhao, S. Iijima, and Y. Ando, *Phys. Rev. B* 64, 073105 (2001).
11. A. Thess, R. Lee, P. Nikolaev, H. Dai, P. Petit, J. Robert, C. Xu, Y. H. Lee, S. G. Kim, D. T. Colbert, G. Scuseria, D. Tomanek, J. E. Fischer, and R. E. Smalley, *Science* 273, 483 (1996).
12. C. C. Journet, W. K. Maser, P. Bernier, A. Loiseau, M. Lamy de la Chapelle, S. Lefrant, P. Deniard, R. Lee, and J. E. Fischer, *Nature* (London) 388, 756 (1997).
13. H. Kataura, Y. Kumazawa, Y. Maniwa, I. Umezumi, S. Suzuki, Y. Ohtsuka, and Y. Achiba, *Synth. Met.* 103, 2555 (1999).
14. A. Fujiwara, Y. Matsuoka, H. Suematsu, N. Ogawa, K. Miyano, H. Kataura, Y. Maniwa, S. Suzuki, and Y. Achiba, *AIP Conference Proceedings* 590, 189 (2001).
15. A. Fujiwara, Y. Matsuoka, H. Suematsu, N. Ogawa, K. Miyano, H. Kataura, Y. Maniwa, S. Suzuki, and Y. Achiba, *Jpn. J. Appl. Phys.* 40, L1229 (2001).
16. A. Fujiwara, Y. Matsuoka, R. Iijima, H. Suematsu, N. Ogawa, K. Miyano, H. Kataura, Y. Maniwa, S. Suzuki, and Y. Achiba, *AIP Conference Proceedings* 633, 247 (2002).
17. Y. Matsuoka, A. Fujiwara, N. Ogawa, K. Miyano, H. Kataura, Y. Maniwa, S. Suzuki, and Y. Achiba, *Sci. Technol. Adv. Mater.*, 4, 47 (2003).
18. Y. Kamada, N. Naka, N. Nagasawa, Z. M. Li, and Z. K. Tang, *Physica B* 323, 239 (2002).
19. Y. Kamada, N. Naka, S. Saito, N. Nagasawa, Z. M. Li, and Z. K. Tang, *Solid State Commun.* 123, 375 (2002).
20. M. S. Dresselhaus, G. Dresselhaus, and R. Saito, *Carbon* 33, 883 (1995).
21. M. S. Dresselhaus, R. A. Jishi, G. Dresselhaus, and R. Saito, *Mol. Mat.* 4, 27 (1994).
22. R. Saito, M. Fujita, G. Dresselhaus, and M. S. Dresselhaus, *Appl. Phys. Lett.* 60, 2204 (1992).
23. R. Saito, M. Fujita, G. Dresselhaus, and M. S. Dresselhaus, *Phys. Rev. B* 46, 1804 (1992).
24. N. Hamada, S. Sawada, and A. Oshiyama, *Phys. Rev. Lett.* 68, 1579 (1992).
25. H. Ajiki and T. Ando, *J. Phys. Soc. Jpn.* 62, 1255 (1993).
26. T. Ando and H. Ajiki, "High Magnetic Fields in Semiconductor Physics II," p. 915 (G. Landwehr and W. Ossau, Eds.). World Scientific, Singapore, 1997.
27. M. Ichida, S. Mizuno, Y. Tani, Y. Saito, and A. Nakamura, *J. Phys. Soc. Jpn.* 68, 3131 (1999).
28. R. Loudon, *Am. J. Phys.* 27, 649 (1959).
29. R. J. Elliot and R. Loudon, *J. Phys. Chem. Solids* 8, 382 (1959).
30. R. J. Elliot and R. Loudon, *J. Phys. Chem. Solids* 15, 196 (1960).
31. T. Ando, *J. Phys. Soc. Jpn.* 66, 1066 (1997).
32. S. J. Tans, M. H. Devoret, H. Dai, A. Thess, R. E. Smalley, L. J. Geerligs, and C. Dekker, *Nature* 386, 474 (1997).



33. M. Bockrath, D. H. Cobden, P. L. McEuen, N. G. Chopra, A. Zettl, A. Thess, and R. E. Smalley, *Science* 275, 1922 (1997).
34. K. Tsukagoshi, B. W. Alphenaar, and H. Ago, *Nature* 401, 572 (1999).
35. Z. Yao, H. W. Ch. Postma, L. Balents, and C. Dekker, *Nature* 402, 273 (1999).
36. R. D. Antonov and A. T. Johnson, *Phys. Rev. Lett.* 83, 3274 (1999).
37. S. J. Tans, A. R. M. Verschueren, and C. Dekker, *Nature* 393, 49 (1998).
38. A. Fujiwara, K. Tomiyama, H. Suematsu, M. Yumura, and K. Uchida, *Phys. Rev.* B60, 13492 (1999).
39. A. Fujiwara, K. Tomiyama, H. Suematsu, M. Yumura, and K. Uchida, *Physica* B298, 541 (2001).
40. H. W. Ch. Opostma, T. Teepen, Z. Yao, M. Grifoni, and C. Dekker, *Science* 293, 76 (2001).
41. V. Derycke, R. Martel, J. Appenzeller, and Ph. Avouris, *Nano Lett.* 1, 453 (2001).
42. A. Bachtold, P. Hadley, T. Nakanishi, and C. Dekker, *Science* 294, 1317 (2001).
43. M. Kociak, A. Yu. Kasumov, S. Gueron, B. Reulet, I. I. Khodos, Yu. B. Gorbatov, V. T. Volkov, L. Vaccarini, and H. Bouchiat, *Phys. Rev. Lett.* 86, 2416 (2001).
44. Z. K. Tang, L. Zhang, N. Wang, X. X. Zhang, G. H. Wen, G. D. Li, J. N. Wang, C. T. Chan, and P. Sheng, *Science* 292, 2462 (2001).
45. S. Frank, P. Poncharal, Z. L. Wang, and W. A. de Heer, *Science* 280, 1744 (1998).
46. P. L. McEuen, M. Backrath, D. H. Cobden, Y.-G. Yoon, and G. Louie, *Phys. Rev. Lett.* 83, 5098 (1999).
47. R. H. Bube, "Photoconductivity of Solids." John Wiley & Sons Inc., New York, 1960.
48. M. Ichida, S. Mizuno, Y. Saito, H. Kataura, Y. Achiba, and A. Nakamura, *Phys. Rev.* B65, 241417(R) (2002).
49. Z. K. Tang, H. D. Sun, J. Wang, J. Chen, and G. Li, *Appl. Phys. Lett.* 73, 2287 (1998).
50. Z. M. Li, Z. K. Tang, H. J. Liu, N. Wang, C. T. Chan, R. Saito, S. Okada, G. D. Li, J. S. Chen, N. Nagasawa, and S. Tsuda, *Phys. Rev. Lett.* 87, 127401 (2001).
51. N. Nagasawa, I. Kudryashov, S. Tsuda, and Z. K. Tang, *AIP Conference Proceedings* 590, 213 (2001).
52. R. J. Chen, N. R. Franklin, J. Kong, J. Cao, T. W. Tomblor, Y. Zhang, and H. Dai, *Appl. Phys. Lett.* 79, 2258 (2001).
53. S. Kazaoui, S. K. Mandal, and N. Minami, *AIP Conference Proceedings* 633, 247 (2002).

# Photodynamics of Nanoclusters

M. Belkacem, M. A. Bouchene

*Université Paul Sabatier, Toulouse, France*

P.-G. Reinhard

*Universität Erlangen, Erlangen, Germany*

E. Suraud

*Université Paul Sabatier, Toulouse, France*

## CONTENTS

1. Introduction
  2. Optical Response in Nanoclusters
  3. Nanoclusters in Intense Laser Beams
  4. Toward Quantitative Models
  5. Conclusions
- Glossary  
References

## 1. INTRODUCTION

Cluster physics is by its very nature an interdisciplinary field with connections to well established domains such as chemistry, atomic physics, molecular physics, and solid state physics [1–4]. These various branches of science have found in clusters sort of a melting pot in which several concepts and techniques have merged. For a long time, light has been preferred tool of investigation of cluster properties. Incoherent light constitutes here the simplest, natural means of approach and allows one to address the linear response domain. This is the realm of the so-called optical response, with clusters responding in the visible part of the electromagnetic spectrum, in a way similar to the response of atoms in the sky, subject to solar radiations. This linear domain provides clues on both static and dynamic properties of clusters. In particular it is an especially powerful tool of investigation of structure properties, as we shall discuss. For a few years, though, in relation to the rapid progresses in laser technology, it has also become possible to investigate truly dynamic properties of clusters subject to lasers of various intensities. Beyond the linear domain accessible to low fluence lasers one can now routinely address problems in

the truly nonlinear domain with intense laser beams. In all these situations, both in the linear and nonlinear domains, it turns out that the basic electronic response of the cluster, the aforementioned optical response, plays a key role, both in metallic systems and in nonmetals. It is thus a key issue in this field, whatever dynamical regime one wants to address. We shall thus spend some time discussing its properties in some detail, before considering more “dynamical situations.”

Large clusters at the nanometer scale contain hundreds or thousands of particles and modelling them thus constitutes a formidable task which requires simplifying assumptions. Small clusters have been attacked with a variety of detailed methods inherited mostly from chemistry and molecular physics (from the experimental as well as the theoretical points of view), and very large clusters can be studied with methods imported from solid state physics. Intermediate size clusters, typically in the nanometer range, constitute specific systems which are yet little explored in detail. They require dedicated approaches in between chemistry and bulk techniques. The building of simple and realistic models hence constitutes a key issue in the progress of the field, both to guide experiments and to understand the produced results. It is obvious that a detailed description, at the level of all electronic and ionic degrees of freedom (even when restricting the approach to the least bound electrons), is far beyond the possibilities of any practical calculation. One thus has to employ simple pictures, based on microscopic considerations, but dealing with more or less macroscopic or semi-macroscopic quantities.

Simplifications are even more crucial when one aims at describing cluster dynamics, which is a central issue for understanding photodynamics of nanoclusters. Most experiments on clusters indeed deal with light or electromagnetic

probes. The rapid development of laser technology in the last few decades has allowed the attainment of large electric fields (comparable to the ones binding clusters together) and on short time scales, typically of the order of electronic time scales [5, 6]. One is thus in a position of studying the response of clusters to short and strong electromagnetic signals which place the system far away from its ground state. In such dynamical situations, there is an urgent need for guidelines and the invention of simple tractable models is thus a key issue.

It is the aim of this chapter to discuss the response of clusters of various types to irradiations by light (in particular with various laser lights). A major goal will thus be to describe the many types of measurements performed in the various dynamical regimes attained as a function of the intensity of the excitation process. And we shall emphasize the key role played by the collective response of clusters to light, the so-called optical response. We will also discuss examples of simple models dedicated to the study of large clusters irradiated by lasers of various intensities. We shall see that “back of the envelope models,” in particular the Mie model of plasmon response, provide a key ingredient for the understanding of the coupling between light and nanoclusters. The latter model particularly allows one to understand basic physical mechanisms at work. And yet a more detailed explanation, and at least a semiquantitative approach, requires more elaborate models, which can be built in a rigorous way on the basis of well defined microscopic approaches.

The chapter is organized as follows. We first discuss the historical case of the coupling of metal clusters with light (optical response). This corresponds to a regime of small perturbation of the electron cloud. Elementary models (Mie plasmon) allow one to understand the mechanism underlying the cluster’s response, but not at a fully quantitative level. Similar plasmon behaviors are also observed in other types of clusters than in metal clusters, although with slightly different patterns, and we shall also discuss these situations. We next consider the case of more violent laser irradiations. We discuss in particular the very recent case of clusters subject to intense lasers and show that Mie plasmon again provides a key to understand the cluster behavior. However, once again details of the response go beyond simple arguments. The last part of the chapter is devoted to a discussion of how to make progress in the understanding of the cluster’s response by means of microscopic methods. We illustrate the achievements of such simplified approaches and we sketch the next steps of development to reach an even more coherent description of these various phenomena.

## 2. OPTICAL RESPONSE IN NANOCCLUSERS

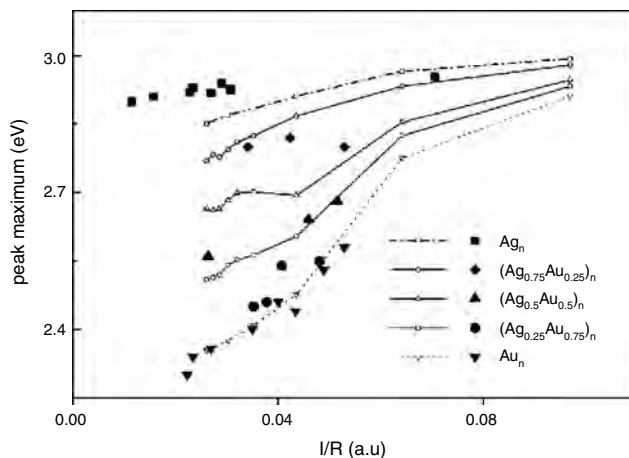
Because in metal clusters valence electrons move quasi freely, they respond particularly easily to an electromagnetic probe. This constitutes the so-called plasmon (or optical response) in metal clusters. Similar behavior can be observed in other not strictly metallic objects such as carbon systems. We shall discuss here these various aspects although

we shall particularly focus on the most important and most studied case of metals.

### 2.1. Metal Nanoclusters

#### 2.1.1. The Shining Colors of the Optical Response

Clusters have been used for practical purposes for centuries. The tailoring of fine dispersed pieces of material (clusters!) inside bulk has been turned into an art by craftworkers, from the Romans to modern artists. At least from a practical point of view, how to tune the size of dispersed particles in a glass to produce various colors has been known for a long time. The understanding of colors of such small metal particles goes back to Mie [15]. He addressed the question of the response of small particles to light, and how this response might depend on the size of the considered particle. And Mie realized immediately the potential applications of such studies for our understanding of the properties of matter. Let us briefly quote him: “Because gold atoms surely differ in their optical properties from small gold spheres [it would] probably be very interesting to study the absorption of solutions with the smallest sub-microscopical particles; thus, in a way, one could investigate by optical means how gold particles are composed of atoms” [16]. Indeed the optical response of metal clusters to light is strongly dependent on their size. This is illustrated in Figure 1 where the peak response (to light) of clusters of various sizes is plotted precisely as a function of their size. As can be clearly seen, the position of the peak response is monotonously linked to cluster’s size, which explains the reflections of various colors exhibited by glasses with metallic inclusions. In fact, what we are seeing here is just the response of a metallic sphere to an external electric field. It should thus be easy to understand the basic mechanism responsible for this effect. And we go back here to Mie’s picture. Let us briefly see how such an approach works.



**Figure 1.** Optical response of silver and gold clusters embedded in a rare gas matrix. The peak value of the response is plotted as a function of inverse cluster radius. Reprinted with permission from [14], M. Gaudry et al., *Phys. Rev. B* 64, 085407 (2001). © 2001, American Physical Society.

### 2.1.2. A Simple Model of the Optical Response in Metals

Massive metal clusters, such as the ones included in glass matrices, constitute typical examples of metallic spheres. The valence electrons form there an almost uniform electron gas not too tightly bound to the ionic background. It is thus no big surprise that a moderate external electric field as delivered by natural visible light may easily affect such clusters and possibly provide a fingerprint of some cluster properties. This is the essence of Mie theory describing the response of metallic spheres to light.

Let us consider an extremely simple model of a spherical metal cluster  $X_N$  in which the ionic background is taken as an homogeneous positively charged sphere of radius  $R$  (density  $\rho$ ). Electrons are modelled by a negatively charged sphere with the same density  $\rho$ . We thus assume that the cluster is a neutral system and that both electrons and ions occupy the same volume (which is an intuitive, although slightly excessive, approximation). In addition, we make the assumption that both electrons and ions will oscillate as rigid spheres against each other. This hypothesis may be realistic for ions. Electrons are probably not behaving that rigidly. But it fortunately turns out that the electronic response is primarily collective as long as the system is not too perturbed. Thus, the rigid sphere approximation makes sense in the regime of small excitations. If this system is put in a small uniform external electric field  $E_{\text{ext}}$  electrons will slightly separate from ions, each one going in opposite directions. Still, because ions are much heavier than electrons, they basically remain fixed and one can consider that only electrons are displaced with respect to ions. The displacement builds up a strong Coulomb field which provides a restoring force on the displaced electron cloud counterweighting the effect of the external field  $E_{\text{ext}}$ . In the limit of small values  $a$  of the electron–ion separation the net force acting on the electron cloud (along electric field  $E_{\text{ext}}$ ) becomes proportional to  $a$ ,

$$F = -N \frac{\rho e^2}{3\epsilon_0} a = NeE_{\text{ext}}$$

where  $N$  is the number of electrons. Once the external perturbation is switched off, there remains only the attracting (restoring) force between electronic and ionic clouds, proportional to the actual separation between ions and electrons. Electrons will thus undergo harmonic oscillations around ions, with a frequency

$$\omega_{\text{Mie}}^2 = \frac{\rho e^2}{3\epsilon_0 m_e} = \frac{Ne^2}{4\pi\epsilon_0 m_e R^3} \quad (1)$$

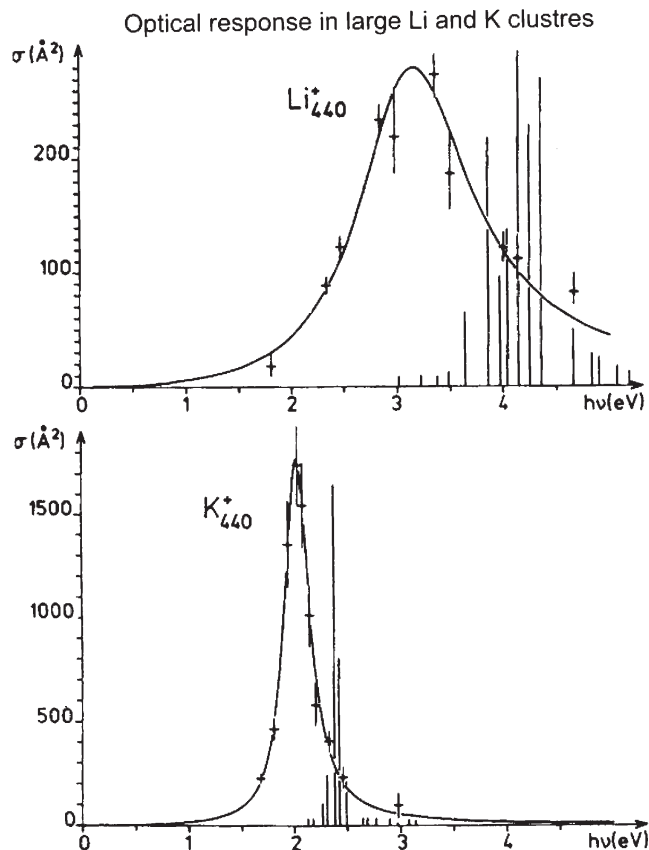
where  $m_e$  is the electron mass. This oscillation frequency  $\omega_{\text{Mie}}$  is known as the Mie frequency. When a cluster is irradiated by photons, its response will be particularly strong for light frequencies around  $\omega_{\text{Mie}}$ . In simple alkaline metals the frequency  $\omega_{\text{Mie}}$  takes values in the visible part of the electromagnetic spectrum, hence the term “optical response” to characterize this phenomenon.

The Mie model, as just outlined, does explain the gross features of the response of clusters to light, but it misses the crucial size dependence. As can be seen from Eq. (1),  $\omega_{\text{Mie}}$  only depends on the density  $\rho$  and not on the cluster

size  $N$ . The density  $\rho$  differs from one metal to the next. But metal clusters of a given material do all have the same average density. This is an effect of electron density saturation, much similar to the behavior observed for example in nuclei [17]. This saturation can be seen in terms of cluster radii  $R$  which follow a law of the form  $R \sim r_s N^{1/3}$ , where  $r_s$  is the Wigner–Seitz radius of the material. Any size dependence is obviously absent from the simple expression in Eq. (1) while experimental results do depend on cluster size. The Mie model thus provides an explanation for the basic mechanism of optical response in metal clusters but does not give access to the crucial size effects observed in this optical response. A more detailed approach is thus necessary, as we shall discuss.

### 2.1.3. Optical Response as a Function of Frequency

Our discussion has shown that the optical response of a cluster is characterized by one typical frequency for which the Mie model provides a good guess. Thus the response of the cluster will strongly depend on the color of the light used. In other words, the optical response is a resonant phenomenon. Depending on the excitation frequency, the response will be more or less strong, as in any resonant situation. This resonant behavior is illustrated in Figure 2 in the case of massive



**Figure 2.** Examples of optical response in massive Li and K clusters. Photoabsorption cross-sections are plotted as a function of photon energy. Reprinted with permission from [18], C. Bréchnac et al., *Phys. Rev. Lett.* 70, 2036 (1993). © 1993, American Physical Society.

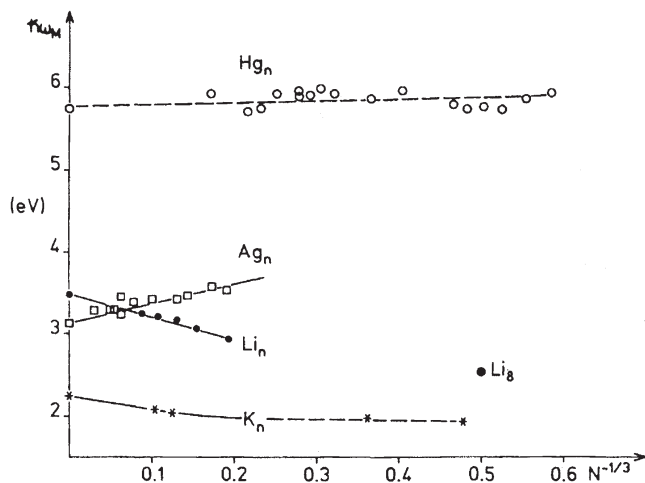
Li and K clusters. Both spectra exhibit a marked resonant behavior around a well defined peak. As a consequence one may expect a high sensitivity of the response to the excitation frequency; the stronger the response, the closer the excitation frequency to peak frequency. Practically the optical response is explored by means of a low intensity laser irradiating the metal cluster. By scanning the laser frequencies one can explore the full frequency spectrum and attain an optical response spectrum as presented in Figure 2.

### 2.1.4. Size Dependence

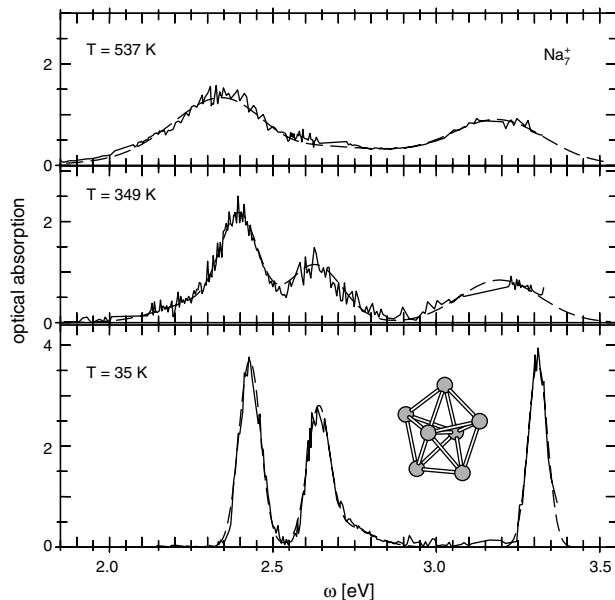
Optical spectra do depend on cluster size. The average resonance frequency follows a trend  $\omega_{\text{Mie}}(N) = \omega_{\text{Mie}}(\infty) + cN^{-1/3}$  typically down to  $N \approx 100$  and levels off for smaller clusters. The slope  $c$  is generally small with different signs depending on the material. Negative  $c$  prevail for alkalines, positive  $c$  are found for most noble metals, and Hg is an example with zero slope [20], as can be seen in Figure 3. It is due to surface effects, in fact a combination of them. In a metal cluster electrons, mostly because of their quantal nature, do occupy a volume slightly larger than ionic cores. One usually calls this effect the spill out of the electron cloud. This spill out reduces the plasmon frequency [21] and small clusters have, relatively, more surface than volume which leads to a negative slope. The spill out effect dominates for example in alkaline clusters, hence the negative slope for these materials. But in noble metals, for example, the plasmon frequency is strongly influenced by the collective dipole oscillations of the  $d$  core electrons which redshifts the resonance. This effect is inactive at the surface which means that larger surfaces yield less redshift, which favors a positive slope. The core electron effect dominates in noble metals, hence the positive slope. The two effects, core electrons and spill out, seem just to compensate for Hg.

### 2.1.5. Temperature Effects

As can be seen from Figure 4 the thermal effect plays a crucial role for the observed linewidth in optical absorption. The spectrum at low temperature shows three narrow



**Figure 3.** Mie plasmon frequencies as a function of system size for a variety of metals. Reprinted with permission from [19], C. Bréchnignac and Ph. Cahuzac, *Com. Atom. Mol. Phys.* 31, 215 (1995). © 1995, IOP Publishing.



**Figure 4.** Photoabsorption strength for  $\text{Na}_7^+$  at three different temperatures as indicated.

and well separated peaks reflecting the deformation of the considered cluster (see insert). We see here the collective splitting of the strongly oblate  $\text{Na}_7^+$  and the lower peak is furthermore Landau fragmented [26] by one close  $1ph$  state [27]. The picture changes systematically for larger temperatures. The peaks grow broader and the lower double peak merges into one. It is the temperature which causes the large width. Thermal effects at the side of the electrons cannot induce such a width because 400 K is a small energy at an electronic scale. It is the thermal ionic motion which is responsible for that line broadening. The ionic excitation energies reach down to below 100 K for  $\text{Na}_7^+$  [28]. A thermal excitation of 400 K is large on that scale. Many ionic eigenmodes are excited to rather large amplitudes. The cluster thus undergoes substantial thermal shape fluctuations. But deformation has a strong influence on the dipole spectrum; the more elongated the cluster in one direction, the lower the eigenfrequency along this direction. Thus, each member of the thermal ensemble, with its different deformation, contributes a different spectrum to the total optical response. These spectra all add up incoherently to rather broad peaks. This thermal line broadening mechanism has been discussed first in [29, 30] on the grounds of the jellium model with quadrupole shapes. The crucial impact of octupole deformations was pointed out in [31] and confirmed in the fully microscopic analysis of [32].

## 2.2. “Optical” Response in Covalent Clusters

Carbon clusters are halfway between metallic and covalent binding. The optical absorption spectra thus show pronounced resonance peaks together with a swamp of noncollective peaks. This is not so surprising. An interesting aspect of C is that its particular binding properties allow stable

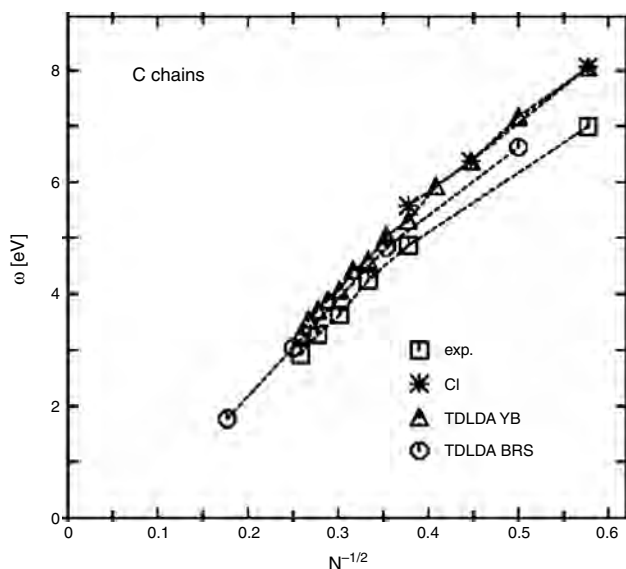
chains over a broad range of sizes. The case of C chains is thus presented in Figure 5. In a given chain the strength is distributed over a broad range of frequencies. But there sticks out a pronounced peak at low frequency. It is sort of a plasmon peak due to the metallic behavior of the  $p$  electrons which can travel freely along the whole chain, in the spirit of the Mie picture. The  $s$  electrons are more localized but take part by their large dipole polarizability (in a way similar to the  $d$  electrons in noble metals). The linear geometry of the chain altogether leads to a strong size dependence of the plasmon frequency. The picture is here that a chain of electrons is oscillating relative to the chain of ions. This produces basically a dipole field whose energy is  $\propto d^2/L$  where  $L$  is the length of the chain and  $d$  is the displacement of the cloud. The spring constant is thus  $\propto 1/L$  and so is the plasmon frequency. Figure 5 shows the trend of the low-lying dominant peak with size  $N$  of the chain. Theoretical and experimental results are in agreement and the trends line up nicely with the predicted trend  $\propto N^{-1/2}$  for the longitudinal mode.

### 3. NANOCLUSTERS IN INTENSE LASER BEAMS

#### 3.1. From Low to High Laser Intensities

##### 3.1.1. Similarity in Diversity

As we have seen, the interaction of low fluence lasers with clusters leads to different patterns from one cluster to another depending on the type of the cluster, metallic, covalent, rare gas, etc. Still, we have also seen that in many cases the electronic response exhibits a qualitatively similar, more or less collective, behavior, as exemplified by the Mie model in metal systems. With increasing laser intensity the differences between the various types of clusters tend to



**Figure 5.** Systematics of longitudinal plasmon resonance frequencies for  $N = 2-32$ . Results from various sources are compiled, experiments from [33, 34], CI calculations from [35, 36], TDLDA YB are TDLDA calculations from [37], and TDLDA BRS from [38].

be smoothed, while the Mie plasmon mechanism remains a valuable tool for understanding the qualitative behaviors of the systems. This evolution with laser intensity is not surprising. At low laser intensity the coupling to light mostly leads to electron oscillations with only occasional electron emission. In turn, for sufficiently high laser intensity the dominant primary mechanism of excitation is electron emission. But electron emission is soon slowed down by the net charge acquired by the cluster which tends to retain the electrons, otherwise ready to leave. This, at least, lasts as long as the system has not disappeared, for example by Coulomb explosion, when the net charge becomes too high. During this transient regime with quasi free electrons stripped from their parent atoms, but still bound to the cluster by its net charge, electrons more or less behave the same, whatever the type of cluster they do belong to. For example, the difference between metal and rare gas clusters (both of which under experimental investigation) thus essentially lies in the initial amount of free electrons, which turns out not to be a decisive factor for high laser intensities. In that sense, the differences between the various types of clusters tend to disappear for these large intensities. For intermediate intensities, the situation is of course a mixture, with traces of specific behaviors (to a given cluster type) and generic pattern.

##### 3.1.2. Intense Laser Domain

The investigation of the (nonlinear) dynamical properties of atomic clusters has lived up with the advent of table-top devices that produce subpicosecond laser pulses with intensities easily exceeding  $10^{17}$  W/cm<sup>2</sup> [39–45]. Due to the collective electron dynamics discussed, there may be a strong electromagnetic coupling to the Mie frequency that leads to nearly 100% absorption rates [46]. The clusters being isolated objects, no surrounding environment will absorb their excitation energy, in contrast to solids. The emission of high energy (keV) electrons [43], highly charged and very energetic ions [42] and fragments [44], as well as X-ray production [39, 47] are then the spectacular manifestations of this laser–cluster interaction.

##### 3.1.3. Basic Mechanisms at Work

Several models have been developed to explain the experimental features observed in the regime of “high” laser intensities [89–94]. All these models emphasize the major role played by the electrons inside the cluster. The basic mechanisms at work in intense laser–cluster interactions can be summarized as follows. The laser very quickly strips a sizable number of electrons from their parent atoms. These electrons form a reservoir of quasi free electrons, which can strongly couple to the laser when the electron density matches a critical value characteristic of the dipole eigenfrequency of the system (Mie resonance). The global response of the cluster is characterized by a heating of the electron cloud and electronic emission, in addition to the possibly enhanced dipole oscillations. The net charge and the high excitation energy acquired by the cluster lead to its final explosion. It should be noted that this violent scenario is, to a large extent, independent of the nature of the irradiated clusters. The general scenario we have just outlined

does not precisely specify the relative importance and the time scales of the various mechanisms at work. As a consequence, although the global scheme is generally accepted, the debate on the relative importance of the competing processes (various ionization mechanisms inside the cluster, role of the plasmon resonance, of electron temperature, of net charge, ...) remains largely open and various models are still investigated to explain experimental trends.

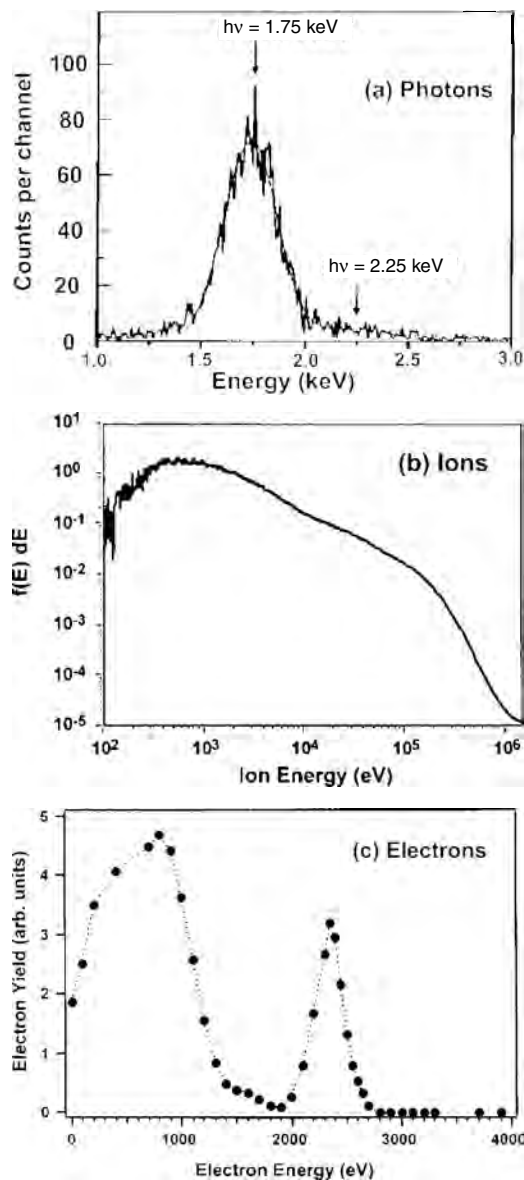
## 3.2. Rare Gas Clusters

### 3.2.1. High Energy Phenomena

Experimental studies of large rare gas clusters with high intensity lasers started in the early 1990s. Multiphoton induced X-ray emissions have been observed by McPherson et al. in Kr clusters as early as 1993 [39]. The emission of radiation in the keV energy range was clear evidence of the appearance of new phenomena specific to clusters. This was later confirmed by many other groups; see Figure 6a [47, 50]. Sustained experimental efforts were then devoted to laser-cluster interaction in the high intensity regime, mainly in the Lawrence Livermore National Laboratory, the Blackett Laboratory (Imperial College), and in the CEA-Saclay. Most of these studies dealt with rare gas clusters because of the possibility to produce such large clusters in supersonic beams. The most striking experimental results are the observation of emitted ions with charges larger than those expected for isolated atoms exposed to the same laser intensity, the appearance of extremely energetic ions, and the production of electrons with kinetic energies in the keV range. We show in Figure 6b typical results obtained for xenon clusters. Here, a cluster of 2500 xenon atoms was irradiated by a laser with a peak intensity of  $2 \times 10^{16}$  W/cm<sup>2</sup> [48]. Although most of the emitted ions have kinetic energies of a few keV, the mean kinetic energy is  $45 \pm 5$  keV. Another remarkable aspect of this energy distribution is the presence of ions with energies up to 1 MeV. Figure 6c shows the energy distribution of electrons in conditions close to the previous ones (2100 xenon clusters irradiated by a laser with  $1.5 \times 10^{16}$  W/cm<sup>2</sup> maximum intensity) [49]. Two bands appear. The first one is centered around 0.8 keV and is expected to be due to warm electrons emitted before the plasmon resonance occurs and the second one around 2.4 keV corresponds to hot electrons released by the cluster during the occurrence of plasmon resonance when important heating of electrons has been realized through collisions.

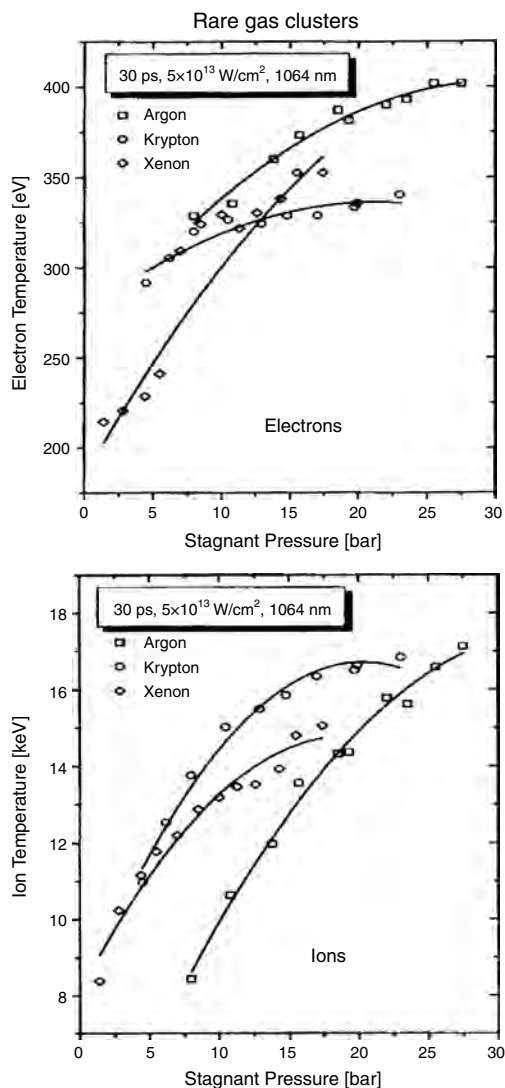
### 3.2.2. Dependence on Cluster Size and Laser Intensity

Systematic studies of the response of rare gas clusters to intense laser fields have been performed by different groups. In Figure 7, we show the results of a systematic study of average electron and ion energies as a function of the cluster-jet backing pressure, which basically fixes cluster sizes in the case of rare gas clusters irradiated by long-pulse laser fields obtained by the CEA-Saclay group [51, 52]. The results from three different clusters, argon, krypton and xenon, are shown. We note that the mean size



**Figure 6.** Experimental results obtained after irradiation of clusters by intense laser beams. (a) X-ray generation from irradiation of large krypton clusters ( $\sim 5 \times 10^5$  atoms) with 130-fs, 790-nm laser with peak intensity  $4 \times 10^{17}$  W/cm<sup>2</sup>. Reprinted with permission from [47], S. Doboş et al., *Phys. Rev. A* 56, R2526 (1997). © 1997, American Physical Society. (b) Ion energy spectrum from 2500-atom xenon clusters irradiated by a peak intensity of  $2 \times 10^{16}$  W/cm<sup>2</sup>. Reprinted with permission from [48], T. Ditmire et al., *Phys. Rev. A* 57, 369 (1998). © 1998, American Physical Society. (c) Electron energy distribution from 2100-atom xenon clusters irradiated by a laser with peak intensity  $1.5 \times 10^{16}$  W/cm<sup>2</sup>. Reprinted with permission from [49], Y. L. Shao et al., *Phys. Rev. Lett.* 77, 3343 (1996). © 1996, American Physical Society.

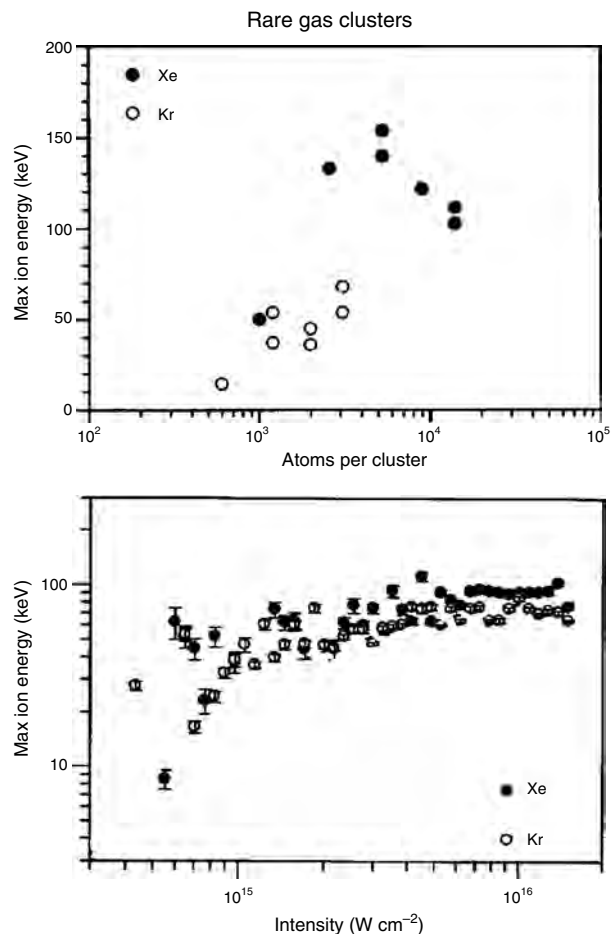
of clusters grows approximately quadratically with the stagnant pressure and goes from  $3 \times 10^4$  to  $5 \times 10^6$  atoms in the entire pressure range. It appears that the electron-to-ion energy ratio depends on the constituents of the clusters and the highest ion energies were observed for krypton clusters in combination with relatively low electron energies. The huge difference between the electron and ion energies also



**Figure 7.** Average kinetic energies of electrons (upper panel) and ions (lower panel) for various backing pressures of the cluster gas. These results were obtained by irradiating rare gas clusters with a 30-ps, 1064-nm laser pulse with peak intensity  $5 \times 10^{13} \text{ W/cm}^2$ . Reprinted with permission from [51], M. Lezius and M. Schmidt, in “Molecules and Clusters in Intense Laser Fields” (J. Posthumus, Ed.), p. 142. Cambridge Univ. Press, Cambridge, UK, 2001. © 2001, Cambridge University Press.

observed in the case of subpicosecond intense laser pulses (see Fig. 6) resists a simple interpretation but seems to lead, in this case, to the formation of a strongly heated, nonthermalized plasma.

A similar systematic investigation has been conducted by the Blackett Laboratory group at Imperial College [53–55]. Figure 8 shows the maximum ion energies obtained for krypton and xenon clusters irradiated by high-intensity laser pulses as a function of cluster size (upper panel) and as a function of laser intensity (lower panel). The maximum ion energies as a function of cluster size (upper panel) were obtained with a 170-fs laser pulse with a peak intensity of  $1.3 \times 10^{16} \text{ W cm}^{-2}$ . The maximum ion energy of Xe clusters rises from 8 keV at a cluster size of about 1000 atoms to a



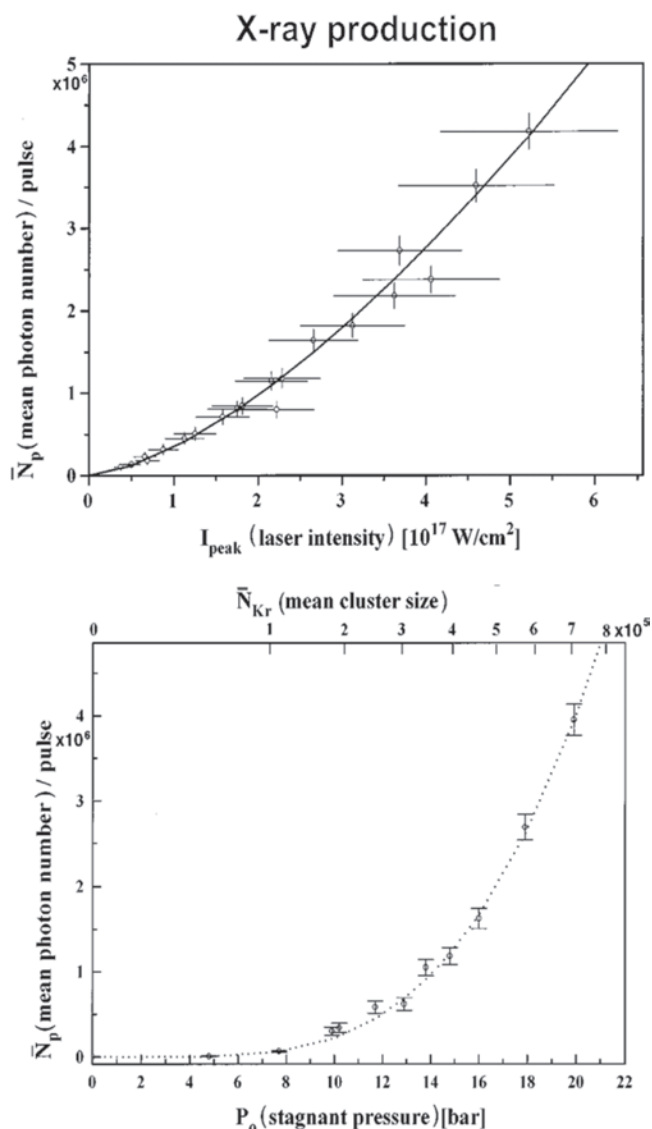
**Figure 8.** Maximum ion energies from xenon (filled circles) and krypton (open circles) clusters measured as a function of cluster size (upper panel) with a 170-fs, 780-nm laser pulse with peak intensity  $1.3 \times 10^{16} \text{ W/cm}^2$ , and as a function of laser intensity (lower panel) with a 230-fs, 780-nm laser pulse and for 5300-atom Xe and 6200-atom Kr clusters. Reprinted with permission from [53], E. Springate et al., *Phys. Rev. A* 61, 063201 (2000). © 2000, American Physical Society.

peak of 150 keV for clusters of  $\sim 5000$  atoms before falling to 100 keV as the cluster size is increased beyond 10,000 atoms. Kr clusters show a similar trend as Xe clusters, but the ion energies are lower. The experimental setup limits did not allow in this case an increase of the cluster size to the point where an optimum cluster size could be observed. The scaling of ion energies with laser intensity (lower panel) has been obtained with Xe clusters containing  $\sim 5300$  atoms (corresponding to a 43 Å radius) and Kr clusters with  $\sim 6300$  atoms (41 Å). Again, a similar behavior is observed for both rare gas species, with about 20% lower energies for Kr.

### 3.2.3. X-Ray Production

Another systematic study concerning X-ray generation has been conducted by the same CEA-Saclay group for rare gas clusters submitted to ultrashort and intense lasers [47]. Figure 9 shows the obtained mean photon number per pulse as a function of the laser intensity (upper panel) and as a





**Figure 9.** X-ray photon yield measured as a function of laser peak intensity (upper panel) for Kr clusters of estimated mean size  $7 \times 10^5$ , and as a function of backing pressure and the corresponding mean cluster size on the upper scale (lower panel) with a laser peak intensity of  $4 \times 10^{17}$  W/cm<sup>2</sup>. Reprinted with permission from [47], S. Dobosz et al., *Phys. Rev. A* 56, R2526 (1997). © 1997, American Physical Society. The solid line in the upper panel and the dashed line in the lower one represent power law fits to the experimental results (see text).

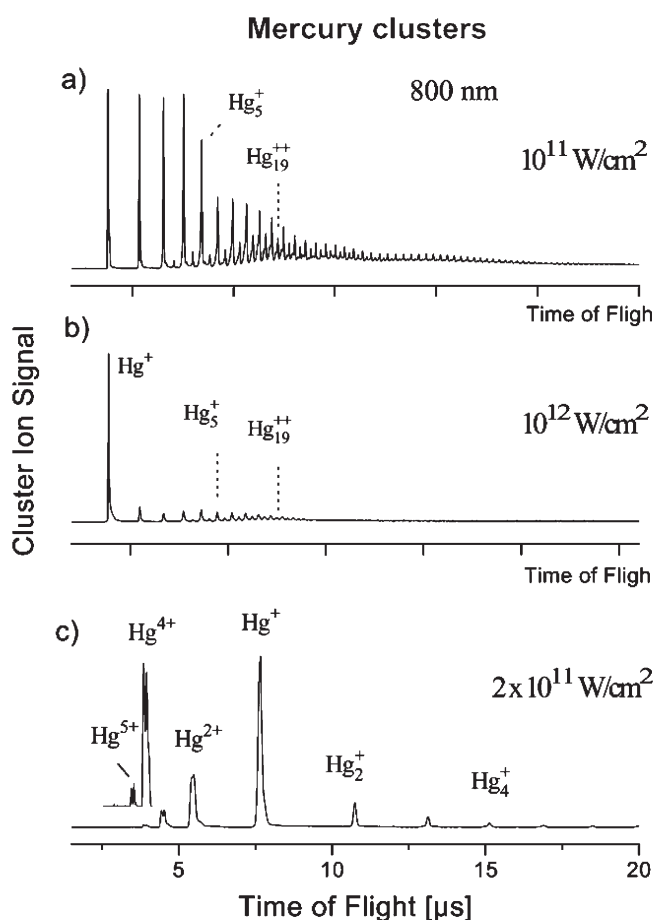
function of stagnant pressure (or cluster size, lower panel) for krypton clusters. The mean photon number as a function of laser intensity (upper panel of the figure), obtained for clusters of estimated mean size  $7 \times 10^5$  atoms corresponding to a backing pressure  $P_0 = 19.5$  bar, has been fitted by a power law  $\bar{N}_p \propto I_L^{3/2}$  (solid line). This scaling is typical for a saturated process in the focus of an intense laser field with a Gaussian intensity profile [47]. The dependence of the mean photon number on the stagnant pressure (lower panel), obtained with a laser intensity of  $4 \times 10^{17}$  W/cm<sup>2</sup>, has also been fitted with  $\bar{N}_p = (P_0 - P_c)^3$  with  $P_c \approx 3$  bar. The mean cluster size scale  $\bar{N}_{\text{Kr}}$  is also shown at the top of

the figure. Accordingly, the X-ray yield scales as  $\bar{N}_{\text{Kr}}^{3/2}$ . These results suggest that the onset of X-ray production occurs at a pressure offset of  $P_c \approx 3$  bar, corresponding to a mean cluster size  $\bar{N}_{\text{Kr}}$  close to  $10^4$  atoms. This value would then indicate the minimum cluster size for significant X-ray production in the present experimental conditions.

### 3.3. Metal Clusters

The first experiment on metal clusters in the nonperturbative regime was performed by Gerber and co-workers on mercury clusters [56, 57]. The mercury atom has a  $5d^{10} 6s^2$  closed electronic shell configuration. Diatomic and small mercury clusters are predominantly van der Waals bound systems. However, the electronic structure strongly changes with increasing cluster size and finally converges toward the bulk electronic structure where the  $6s$  and  $6p$  bands overlap, giving mercury its metallic properties.  $\text{Hg}_n$  ( $n \leq 80$ ) clusters were produced in a cold supersonic beam and were ionized by femtosecond laser pulse of 50–120 fs duration in the wavelength range from 255 to 800 nm. The originality of these experiments arises from the study of the cluster behavior in the transition region, going from the low field regime (intensity  $\sim 10^{11}$  W/cm<sup>2</sup>) to the strong field one (intensity  $\sim 10^{13}$  W/cm<sup>2</sup>). Figure 10 represents the time of flight mass spectra of the mercury clusters obtained at 800 nm. For a laser intensity of  $10^{11}$  W/cm<sup>2</sup> (Fig. 10a) a “normal” cluster size distribution is observed constituted by ionic fragments  $\text{Hg}_n^{q+}$  in the range  $q = 1, 2$ . At  $10^{12}$  W/cm<sup>2</sup> (Fig. 10b), the  $\text{Hg}^+$  signal increases while the signal of other fragments decreases. Moreover, the ratio between singly and doubly charged clusters of a given size does not change, which indicates that the small fragments come from the fragmentation of larger cluster ions. Increasing the intensity to  $2 \times 10^{12}$  W/cm<sup>2</sup> (Fig. 10c), highly charged mercury atoms (up to  $\text{Hg}^{5+}$ ) appear. Note that the direct multiphoton ionization of Hg atom requires an intensity of about one order of magnitude higher. Finally, at the highest applied intensity of  $10^{13}$  W/cm<sup>2</sup>, the signal due to molecules and clusters disappears and only atomic ions, singly and multiply charged, are observed. In this case the whole cluster breaks into pieces by Coulomb explosion. These results clearly show that the energy absorption is strongly enhanced at relatively small laser intensity and the interaction process is beyond the classical multiphoton ionization.

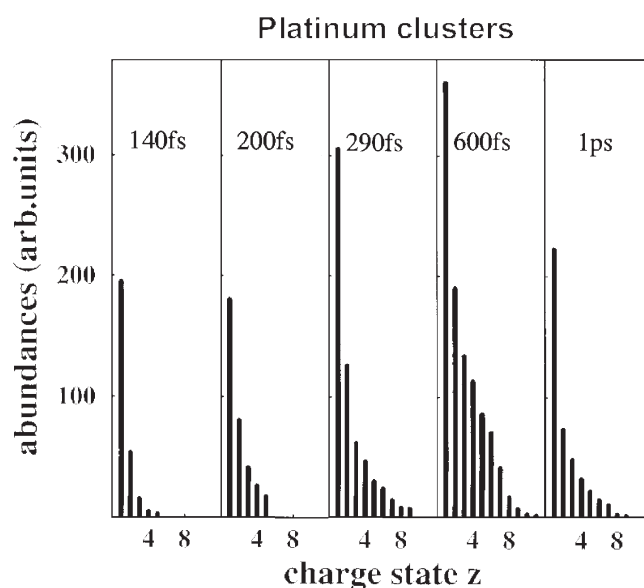
Other investigations on metal clusters have been performed with the high intensity regime. Exhaustive studies were performed at the CEA-Saclay by Lebeault et al. [58] for lead clusters exposed to an intense laser field of  $10^{15}$  W/cm<sup>2</sup> intensity, whereas platinum clusters (and lead clusters as well) excited by strong femtosecond laser pulses with intensities up to  $10^{16}$  W/cm<sup>2</sup> were studied by Meiwes-Broer and co-workers [44, 59–61]. At such high intensities, it turns out that the metallic character of the clusters does not play an important role and the results can be interpreted in terms of plasmon resonance. In the Meiwes-Broer experiments, the cluster size distribution is estimated to be below about 100 atoms. The interaction with the laser pulse makes no clusters survive the excitation. The net result is the production of highly charged ions. Ion charges as high as  $\text{Pt}^{20+}$  were observed at  $2 \times 10^{15}$  W/cm<sup>2</sup> whereas only quadruple



**Figure 10.** Time-of-flight mass spectra obtained by irradiating  $\text{Hg}_n$  clusters ( $n \leq 80$ ) with femtosecond (50–100 fs) 800-nm laser pulses with peak intensities (a)  $10^{11} \text{ W/cm}^2$ , (b)  $10^{12} \text{ W/cm}^2$ , and (c)  $2 \times 10^{12} \text{ W/cm}^2$ . Reprinted with permission from [56], B. Lang et al., *Z. Phys. D* 40, 1 (1997). © 1997, Springer-Verlag.

ionization is obtained if isolated atoms were irradiated by the same laser intensity. The production of multiply charged platinum and lead cluster ions shows a significant increase of efficiency when increasing the laser pulse length. Figure 11 shows the abundance of platinum ions as a function of the pulse width for a given pulse energy of 5 mJ. The important feature is that the optimum pulse width of 600 fs that gives the largest abundances corresponds to neither the shortest pulse width for which the highest intensity is obtained nor the longest time duration for which the interaction time is longest.

In the Saclay experiments, small size lead clusters with a few hundred of atoms are irradiated with laser pulses with duration between 60 fs and 2.5 ps and a laser intensity of about  $10^{15} \text{ W/cm}^2$ . The kinetic energies and ionic charge of fragments were studied as a function of the laser intensity and pulse duration. Highly charged  $\text{Pb}^{n+}$  ions up to  $n = 26$  have been detected with kinetic energies up to 15 keV. Moreover, the measure of the kinetic energy of ionic fragments versus the charge state exhibits a quadratic dependence for charge states lower than 10 and a linear dependence for higher charge states. These results were interpreted in the framework of the so-called nanoplasma



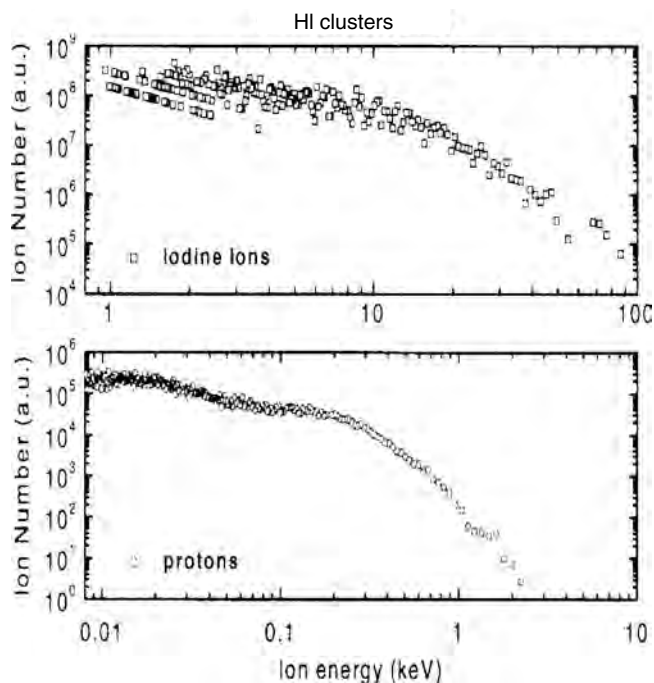
**Figure 11.** Abundances of platinum ions  $\text{Pt}^{z+}$  ( $z = 1, \dots, 11$ ) for different laser pulse widths ranging from 140 fs to 1 ps at a fixed pulse energy of 5 mJ. From left to right, the pulse intensity drops by a factor 7. Reprinted with permission from [44], L. Köller et al., *Phys. Rev. Lett.* 82, 3783 (1999). © 1999, American Physical Society.

model (see Section 4.5). One can then conclude that the fragments with charges below 10+ are driven by Coulomb forces, whereas the higher charged fragments are accelerated by hydrodynamics forces.

### 3.4. Other Materials

Experiments with molecular (or mixed species) clusters irradiated by high-intensity ultrafast laser pulses have also been conducted by several groups [63–65]. Mixed species clusters offer the advantage to allow the use of elements which may hardly bind together to form “pure” clusters. For example, the formation of large hydrogen clusters in gas jets (or its isotopes for fusion experiments; see next section) requires very high backing pressures and cryogenic cooling. Hydrogen iodide (HI) gas, investigated by Tisch et al. [63], or deuterated methane ( $\text{CD}_4$ ), investigated by Grillon et al. [65], forms large clusters very readily at low pressures even at room temperature.

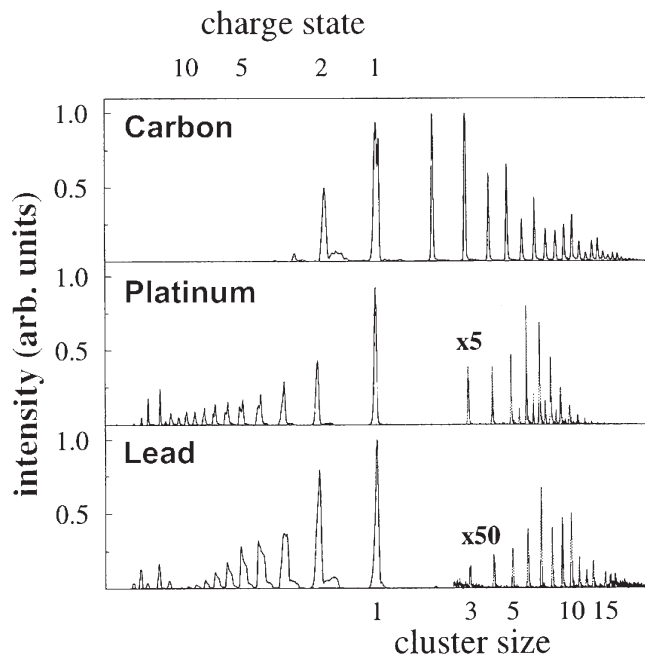
Figure 12 shows the energy spectra of iodine ions (upper panel) and protons (lower panel) obtained by irradiating HI clusters of an estimated mean size of 60,000 molecules by 260-fs, 780-nm laser pulses at a peak intensity of  $2 \times 10^{16} \text{ W cm}^{-2}$ . The maximum kinetic energy of iodine ions is  $\sim 92 \text{ keV}$ , while the mean value is about 8.6 keV. The mean and maximum kinetic energies of protons are approximately 270 eV and 2.5 keV, respectively. A monotonous increase of both iodine and proton energies was also observed with increasing the size of HI clusters [63]. The observation of energetic protons and iodine ions indicates that molecular clusters can indeed be used to produce energetic ions from a range of much broader elements than could be expected otherwise. This was also the case for the experiment by Grillon et al. [65] using deuterated methane ( $\text{CD}_4$ ) to produce energetic deuterium ions for fusion experiments.



**Figure 12.** Measured energy spectra of iodine ions (upper panel) and protons (lower panel) from explosions of 60,000-molecule HI clusters irradiated by 260-fs, 780-nm pulses at a peak intensity of  $2 \times 10^{16}$  W/cm<sup>2</sup>. Reprinted with permission from [63], J. W. G. Tisch et al., *Phys. Rev. A* 60, 3076 (1999). © 1999, American Physical Society.

Photoexcitation of other types of nanoclusters (covalent, molecular) has also been performed by several groups. Bescós et al. have studied the photoionization and photofragmentation of large neutral silicon clusters Si<sub>n</sub> with sizes up to  $n \approx 6000$  irradiated by both nanosecond pulses with intensities  $10^4$ – $10^5$  W cm<sup>-2</sup> and femtosecond pulses with intensities ranging from  $10^8$  to  $5 \times 10^{11}$  W cm<sup>-2</sup> [66]. Dobosz et al. have studied X-ray generation from carbon dioxide (CO<sub>2</sub>) clusters with sizes of 80–100 nm irradiated by a 60-fs laser pulse with peak intensity of  $10^{18}$  W cm<sup>-2</sup> [64]. Schumacher et al. have investigated the photoionization of small covalent carbon clusters submitted to strong femtosecond laser pulses with up to  $10^{16}$  W cm<sup>-2</sup> [59]. Their results are shown in Figure 13 compared to the results obtained with platinum and lead clusters submitted to the same laser pulse.

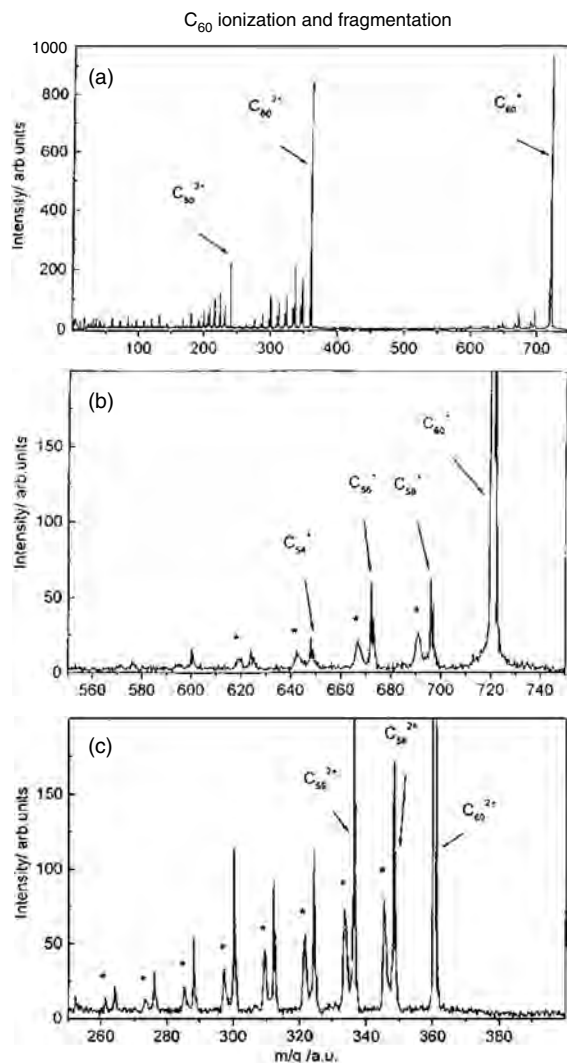
Photoionization and photofragmentation experiments of carbon fullerenes C<sub>60</sub> have also been performed using subpicosecond intense laser pulses by Campbell and co-workers [68–70]. Photoelectron as well as C<sub>60</sub><sup>n+</sup> spectra have been determined for different pulse durations and intensities. As an example, the C<sub>60</sub><sup>n+</sup> ion spectra are shown in Figure 14 for fullerenes submitted to a 35-fs, 795-nm laser pulse with a peak intensity of  $10^{14}$  W/cm<sup>2</sup>. The most striking feature of these mass spectra is the appearance of multiply charged species. Metastable fragments C<sub>60-2n</sub><sup>+</sup>, C<sub>60-2n</sub><sup>2+</sup>, and C<sub>60-2n</sub><sup>3+</sup> are also clearly observed indicating a strong coupling of electronic excitation energy to vibrational degrees of freedom leading to fragmentation.



**Figure 13.** Mass spectra of ionized carbon, platinum, and lead clusters and atomic ions after irradiation of neutral clusters by femtosecond laser pulses of  $3 \times 10^{15}$  W/cm<sup>2</sup> at 800 nm. In contrast to carbon where only a small fraction of the ion intensity originates from the higher charged ions, the metal cluster spectra show that the main intensity emerges from the abundance of atomic Pt<sup>2+</sup> and Pb<sup>2+</sup>. Reprinted with permission from [60], T. Döppner et al., *Int. J. Mass Spectr.* 192, 387 (1999). © 1999, Elsevier Science.

### 3.5. Fusion

Large opportunities are opened by the studies of laser-cluster interactions. This can be illustrated by the experimental realization of nuclear fusion in deuterium by Ditmire et al. at LLNL [67]. In this experiment one irradiates a large cluster of deuterium D<sub>2</sub> by a laser with a peak intensity of  $10^{16}$  W/cm<sup>2</sup>. The explosion of clusters results in their fragmentation into D<sup>+</sup> ions with kinetic energies of a few keV. This is sufficient to realize nuclear fusion in the collisions  $D^+ + D^+ \rightarrow He_3 + n$  that take place in the cluster beam. The detection of neutrons with 2.45 MeV kinetic energy clearly confirms the phenomenon. The experiment was later repeated by Grillon et al. using, instead of D<sub>2</sub> clusters, deuterated methane (CD<sub>4</sub>) clusters leading to much higher D<sup>+</sup> energies of the order of 45 keV compared to the 2.5 keV obtained by Ditmire et al. [65] (see Fig. 15). In this experiment, the number of neutrons generated per shot at the maximum intensity of several  $10^{17}$  W cm<sup>-2</sup> was estimated as 7000 (over the whole solid angle). The pulse width of neutrons produced by intense laser irradiation of deuterium clusters was measured by Zweiback et al. and found to be under 100 picoseconds in duration near the source [71]. Such a short time-scale neutron pulse may represent a table-top source of neutrons that enables a new class of ultrafast neutron pump-probe experiments.

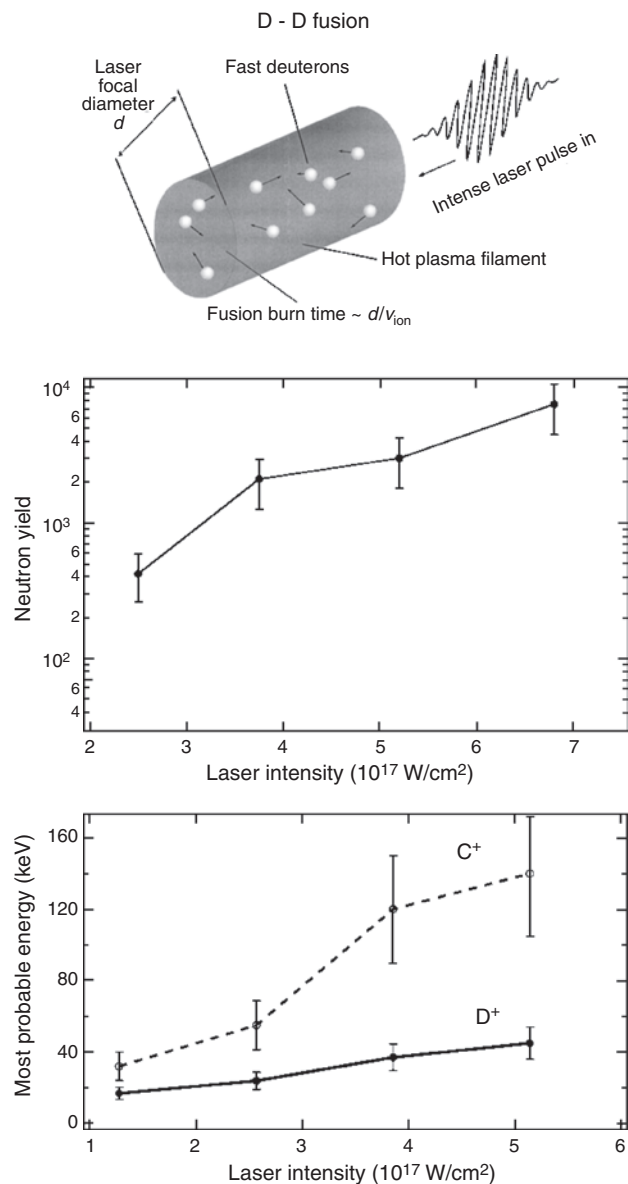


**Figure 14.** Ionization and fragmentation patterns of C<sub>60</sub> irradiated by a 35-fs, 795-nm laser pulse with a peak intensity of 10<sup>14</sup> W/cm<sup>2</sup>: (a) the whole spectrum; (b) the spectrum of singly ionized fragments; (c) the spectrum of doubly ionized fragments. Reprinted with permission from [68], M. Tchapyguine et al., *J. Chem. Phys.* 112, 2781 (2000). © 2000, American Institute of Physics.

## 4. TOWARD QUANTITATIVE MODELS

### 4.1. General Strategy

Our discussions have shown that while simple models allow one to understand basic mechanisms of interaction and qualitative behaviors of irradiated nanoclusters, they fail in providing quantitative access to experimental results. It is thus highly desirable to work out more elaborated approaches for such problems. The starting point of any quantum many body problem is, of course, the many body Schrödinger equation serving as basis for sequences of approximations. In nanometer scale systems far from equilibrium, a quantum description remains far beyond today's computers, even at an approximate level (e.g., mean field approaches). Mean field approaches, however, provide crucial guidelines for deducing simplified models [7]. It has to be remembered



**Figure 15.** Upper part: Experimental concept for an ultrafast neutron source. Reprinted with permission from [71], J. Zweiback et al., *Phys. Rev. Lett.* 85, 3640 (2000). © 2000, American Physical Society. Middle panel: Intensity dependence of the total neutron yield over the whole solid angle. Lower panel: Most probable energies of the measured distributions of C<sup>+</sup> and D<sup>+</sup>. Reprinted with permission from [65], G. Grillon et al., *Phys. Rev. Lett.* 89, 065005 (2002). © 2002, American Physical Society.

here that we want to consider situations in which electrons are deeply involved into the dynamics. Irradiating a cluster by a laser will primarily involve electrons, which will respond in various ways (collective oscillations, emission, ...) depending both on the laser characteristics and on the nature of the cluster (metallic, covalent, rare gas, ...). One thus needs to explicitly treat electronic dynamics and this eliminates the powerful approaches based on atomic molecular dynamics, which by construction cannot accommodate electronic excitations. The basic challenge is thus an efficient description of electronic dynamics. Of course, ions

will also couple to the laser field. But the ionic response takes place on a much longer time scale (typically 100–1000 fs) than the electronic one (typically 1–10 fs). A key constraint is hence to describe electronic dynamics both on the short and the long time scales and in a sufficiently simple approach to allow the study of sufficiently large systems.

Along the line of simplifying the original quantum many body problem, the step from the quantum to the semiclassical world is certainly an efficient, though reliable, step. Indeed, semiclassical methods have been developed and used in cluster physics for several years now, in particular in the case of metal clusters [8–10]. The term semiclassical deserves some explanation. By semiclassical we mean approaches in which electrons are treated as classical particles but augmented with a simplified Pauli exclusion principle (namely, a given maximal occupation in elementary phase space cells). The step from quantum to semiclassical worlds allows one to replace electronic wavefunctions by a phase space occupation function  $f(\mathbf{r}, \mathbf{p})$  representing the ensemble of all electrons together. Still, basic quantum properties such as the Pauli principle are fulfilled by  $f$ , hence the label semiclassical. A great advantage of semiclassical approaches is that they allow the treatment of large clusters [10], but with a “maximum” of microscopic inputs. Furthermore, as is well known from basic quantum mechanics, the larger the involved energies, the less necessary the quantum details. Semiclassical models thus constitute an even more justified approximation in situations far from equilibrium. Finally, it should be noted that, from the more formal side, semiclassical methods open the door to the world of kinetic theory with its well established techniques for dealing with strongly interacting particles [11]. Indeed, semiclassical approximations to quantum mean-field calculations constitute a well established starting point for going beyond a mere mean-field description by including explicit electron–electron collisions, in the spirit of kinetic theory in electronic systems. This “beyond the mean-field” path has been attacked only very recently [12, 13] but provides a useful, and sometimes indispensable, tool for investigating the dynamics of clusters in the strongly out of equilibrium domain. We shall present some of these developments at the end of this chapter. Before reaching these latest developments we shall consider even more simplified approaches and show their interest and limitations for the problems we are interested in here.

## 4.2. Quantal Framework

The simplest semiclassical approximation can be derived directly from the quantal many body problem. Even in simple small systems, solving the quantal many body problem represents a formidable task, still on the edge of modern computers. At the nanometer scale it is hardly conceivable to consider a detailed microscopic approach containing all electronic correlations. One has in any case to recur to simplified descriptions. The major difficulty lies here at the side of electrons which do behave quantally in many situations, while ions can often be treated as classical particles. A most efficient and robust, and still quantal, scheme is provided here by density functional theory [7], which

allows one to reformulate the quantum many body electronic problem in terms of an effective mean field Hamiltonian  $\hat{h}$  involving the local electronic density  $\rho_e(\mathbf{r})$  only. The many body Schrödinger equation can then be recast into a set of coupled, one-electron equations following the famous prescription of Kohn and Sham [72]. When time dependent problems are considered the former strategy can be extended and the time dependent Schrödinger equation for the many electron system replaced by a set of time dependent one-electron equations (time dependent Kohn–Sham equations). Of course a key ingredient of this approximation scheme lies in the choice of the one-electron Hamiltonian  $\hat{h}$ . We shall not discuss here the many (interesting) researches on the topic, which actually go much beyond cluster physics. Rather we shall mention the simplest approximation, the so-called LDA (local density approximation) in which  $\hat{h}$  is expressed as a function of the density  $\rho_e(\mathbf{r})$ , namely  $\hat{h} = \hat{h}(\mathbf{r}) = \hat{h}(\rho_e(\mathbf{r}))$ . This simple, although robust, approximation provides a starting point for many efficient applications, both in cluster and outside cluster physics, also in the case of time dependent problems [73].

## 4.3. Vlasov Equation

The semiclassical limit thus starts from the time dependent version of LDA, the so-called TDLDA (time dependent LDA). In terms of the one-body density operator  $\hat{\rho}$ , TDLDA takes a simple, compact form, well suited to apply semiclassical approximations [74]:

$$\dot{\hat{\rho}} = \frac{1}{i\hbar} [\hat{h}(\hat{\rho}), \hat{\rho}] \quad (2)$$

It furthermore offers a form adapted for going “beyond” the mean field in the realm of kinetic equations. The semiclassical limit of Eq. (2) is the so-called Vlasov equation, well known in plasma physics [75]. But here it emerges as a semiclassical approximation of a truly quantal equation. Following the usual recipe, it can be formally obtained from Eq. (2) by replacing the density operator  $\hat{\rho}$  by a one-body phase space distribution  $f(\mathbf{r}, \mathbf{p}, t)$  and the commutator with Poisson brackets [74]. This then leads to

$$\frac{\partial f(\mathbf{r}, \mathbf{p}, t)}{\partial t} + \{f, h\} = 0 \quad (3)$$

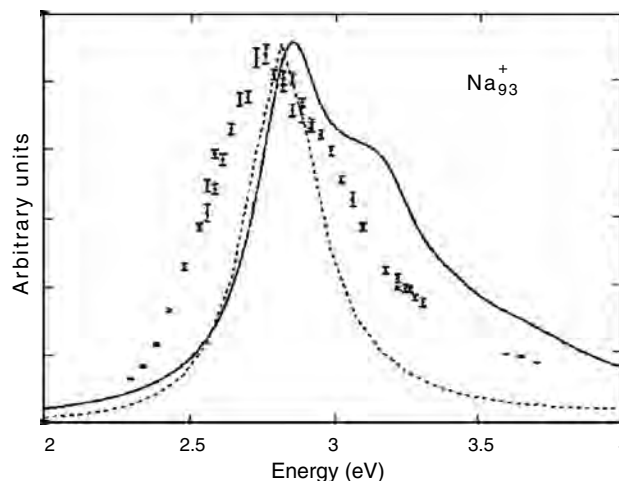
where the mean field Hamiltonian  $h$  is now classical but still a functional (or a function, in the case of LDA) of the (semiclassical) electron density  $\varrho(\mathbf{r}, t)$ . The latter is computed by integrating  $f(\mathbf{r}, \mathbf{p}, t)$  over momentum space  $\varrho(\mathbf{r}, t) = \int d^3p f(\mathbf{r}, \mathbf{p}, t)$ . It should, however, be noted that the semiclassical approximation leading from Eq. (2) to Eq. (3) has to be performed with due caution. The problem is here of a formal nature. Indeed a semiclassical approximation such as the one performed previously corresponds to the lowest order term of an expansion in terms of  $\hbar$ . And the convergence of this  $\hbar$  expansion may raise some difficulties, in particular when the mean field Hamiltonian is self-consistent, namely itself depending on the actual density  $\varrho(\mathbf{r}, t)$ . A thorough discussion of this problem can be found in [76–78] and we shall not further elaborate on it here. Another difficulty with Eq. (3) concerns the capability of

numerical simulations to preserve Fermi statistics on long times [79]. Indeed, as already mentioned, the term semiclassical precisely requires that the theory does preserve some quantal features. This holds in particular for the fermionic nature of the involved particles which is not guaranteed in a purely classical Vlasov equation. This question, however, is highly technical and we refer the reader to appropriate references on the topic [80, 81].

#### 4.4. Time-Dependent Thomas–Fermi Approximation

The Vlasov approach provides a phase-space description of electron dynamics. This allows one to treat a wide range of electronic excitations in systems of various sizes and in very different dynamical contexts. In particular it can accommodate reasonably nonlinear situations, as encountered, for example, in the interactions between clusters and intense laser beams. In particular the full phase space description provided by the phase space distribution  $f(\mathbf{r}, \mathbf{p}, t)$  allows one to treat possibly large distortions of the local Fermi sphere, a feature typical of strongly out of equilibrium dynamics. But in the case of metal clusters two effects tend to suppress these local distortions. First, the dominating presence of the Mie plasmon mode, which carries little momentum space anisotropy, tends to soften effects linked to actual distortions of the Fermi sphere. In addition, electron–electron collisions (which go beyond the actual mean field picture; see Section 4.6) act on very short time scales of order a few fs, so that they tend to remove remaining momentum sphere anisotropies very quickly. To a very good approximation, the local momentum distribution of electrons thus deviates only a little from sphericity [82]. This provides a justification for going one step further down in terms of the semiclassical approximation: integration over momentum space then leads to the so-called time dependent Thomas–Fermi (TDTF) approximation. The TDTF approach is exactly a hydrodynamical reformulation of the original problem, assuming a Thomas–Fermi kinetic energy for the electrons. It is interesting to note here that the TDTF approximation can be formally derived either from the Vlasov equation by integration over momentum space, or directly from TDLDA by a proper choice of a model wavefunction [82]. In both cases one ends up with the same set of coupled equations for the local electron density  $\rho(\mathbf{r})$  and local velocity field  $\mathbf{u}(\mathbf{r}) = \nabla\chi$  [82]. At this stage it should also be noted that TDTF represents a genuine density-functional method (see [83]), as it only involves the actual local density  $\rho(\mathbf{r})$  and its associated flow.

In cluster dynamics, the full three-dimensional (3D) electronic TDTF approximation has been explored in [82, 84]. It was shown in these publications that TDTF provides a fairly good approach to TDLDA, even for moderate excitations, as is illustrated in Figure 16. Furthermore, the simplicity of the picture allows one to treat systems of large sizes, contrarily to more detailed approaches. It is thus an ideal tool of investigation of nanocluster dynamics. It was also used in simpler versions of the theory (restricted to 1D geometry) in direct relation to irradiation by intense lasers [85–87]. Furthermore, an explicit account of the ionic background by means of pseudo-potentials allows one to accede the local



**Figure 16.** Time Dependent Thomas Fermi calculation of the optical response of a medium size metal cluster compared to experimental data. Cluster is  $\text{Na}_{93}^+$ ; experimental data have been obtained at temperature  $T = 105$  K, which explains part of the spreading of the optical peak. Reprinted with permission from [82], A. Domsps et al., *Phys. Rev. Lett.* 80, 5520 (1998). © 1998, American Physical Society.

behavior of collective currents during Mie plasmon oscillations. The TDTF picture, with its underlying hydrodynamical structure, thus provides an ideal tool of investigation of the nature (collective or not) of the optical response [84]. Coupling to ion dynamics is also possible and has already been investigated at the Born–Oppenheimer level in [88]. Extensions to nonadiabatic electron dynamics are also in reach, although they have not yet been investigated.

#### 4.5. Rate Equations and High Intensity Regime

Along the series of more and more simplified models, the next step beyond the hydrodynamical picture provided by TDTF is to consider rate equations for describing the dynamics. The relevant variables then reduce to a set of integral quantities (radius, ionization, ...), the evolution of which being followed in time. Such an oversimplified picture may, however, make sense when only gross properties of the system may be attained. This is typically the case of high intensity irradiations of clusters. At sufficiently high laser intensities, the details of the excitation mechanism tend to be washed out to the benefit of a global plasmalike behavior of the set of quasi free electrons. It is then sufficient, at least for a first step, to remain at the level of a gross description of the system, in terms of a few global variables, the primary goal being to understand the key mechanisms at work. This is the spirit of the so-called nanoplasma model developed by Ditmire et al. at Lawrence Livermore National Laboratory [95]. This model offers, at the level of global cluster characteristics, a complete scenario of the interaction process, taking into account ionization, heating, electronic emission, and cluster expansion simultaneously. In contrast to other models, it treats the polarization field radiated by the charges explicitly. In this model, the cluster is treated as a spherical plasma—a nanoplasma—where the plasmon resonance takes place. Whether the cluster can be treated as a plasma

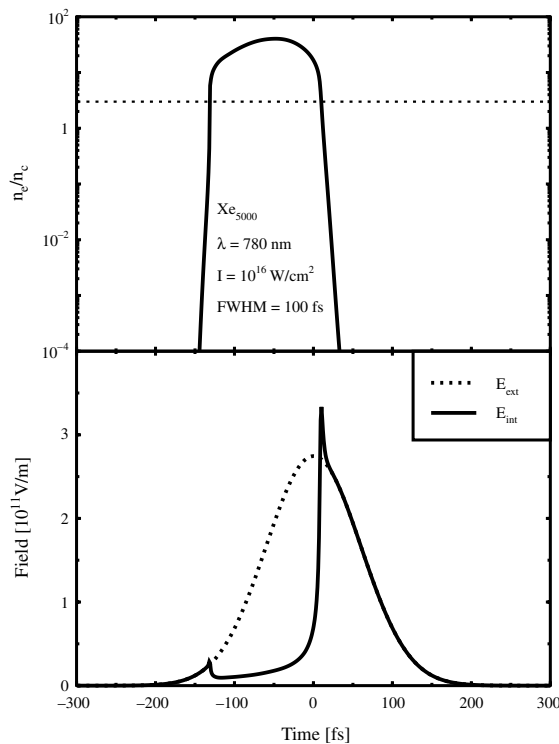
or not has given rise to a controversy, though. For example, classical dynamics simulations including the Coulomb field of the ions but neglecting the polarization field indicate that the electrons are quickly removed at the beginning of the interaction even from large clusters [96]. That makes the existence of a nanoplasma questionable. Until now there has not been any time-resolved measurement at the femtosecond scale to settle the question.

The nanoplasma model consists essentially of a few rate equations expressing the time variation of the number  $N_j$  of ions of a given charge state  $j$  due to ionization

$$\frac{dN_j}{dt} = (W_j^{\text{tun}} + W_j^{\text{coll}})N_{j-1} - (W_{j+1}^{\text{tun}} + W_{j+1}^{\text{coll}})N_j \quad (4)$$

with  $j$  running from 0 to the maximum charge state considered. Here,  $W_j^{\text{tun}}$  and  $W_j^{\text{coll}}$  represent the rate of direct optical ionization and collisional ionization of ions with charge  $j$ , respectively. These rate equations are supplemented by an additional equation expressing charge conservation inside the cluster and two other equations expressing the cluster expansion and heating. For more details, we refer the reader to the original paper [95].

As an example, the computed temporal evolution of an exploding cluster of 5000 Xe atoms irradiated by a 100-fs, 780-nm laser pulse with a peak intensity of  $10^{16}$  W/cm<sup>2</sup> is illustrated in Figure 17 [97]. Time  $t = 0$  fs is the time at which the laser reaches its maximum intensity. We have represented in the upper part of the figure the time variation



**Figure 17.** Temporal history of an exploding 5000-atom Xe cluster irradiated by a 100-fs, 780-nm laser pulse with peak intensity  $10^{16}$  W/cm<sup>2</sup>. Upper part: electron density normalized to critical density  $n_c$ ; lower part: amplitudes of internal (solid line) and external (dashed line) electric fields.

of the electron density inside the cluster normalized to the critical density  $n_c$  and in the lower part the electric field inside the cluster (solid line) together with the external one (dashed line).

At the rising edge of the pulse, quasi free electrons are produced inside the cluster from neutral atoms by tunnel ionization. The rapid increase of the number of quasi free electrons leads the system through a first modest resonance at  $t \simeq -135$  fs when the density matches three times the critical density  $n_c$ . The electric field is then shielded due to the high electron densities reached. The tunnel ionization rate falls off, but electrons are still created through thermal collisions. From times  $t \simeq -100$  fs onward, the electron temperatures are high enough for some electrons to leave the cluster leading to a fall of the density inside the cluster until time  $t \simeq 10$  fs when the second, more important resonance takes place. The inner field is then amplified to 1.5 times the external field and electronic temperature reaches 1.2 keV. The rate of electron emission increases consequently giving a highly positively charged cluster which will explode due to the huge Coulomb repulsion between ions.

Even though the model provides a good description of the gross features of the interaction of intense lasers with clusters, it fails to give a good account of all the experimental results observed, especially those far from average values. For example, the model agrees with the average ion charges observed experimentally but fails in describing the far tails of ion charge distributions which are at the origin of X-ray generation.

#### 4.6. Beyond Mean Field—The Vlasov–Uehling–Uhlenbeck Equation

As is well known, the Vlasov equation represents the basic level of the hierarchy of many body dynamical equations [98]. The TDTF approach of course does not go beyond Vlasov in that respect, as it only represents an average of the Vlasov dynamics over momentum space. Neither do, of course, rate equations, which provide an even grosser picture of the dynamics. Furthermore, as already discussed, both TDTF as well as Vlasov remain at the pure mean field level and are thus *a priori* only suited to situations where dissipative effects are not too large, actually just as the quantal cousin TDLDA. But dynamical correlations, not included in mean field, do play a key role in the dynamics of highly dissipative systems. Remembering the underlying kinetic theory picture, it is no surprise that these correlations show up at the level of two-body effects. They furthermore usually take place at a faster time scale than the mean field motion. This is the justification of treating them by instantaneous two body collisions, which formally leads to the inclusion of a Markovian collision term to complement the mean field theory. This yields the well known Vlasov–Boltzmann equation for classical systems. In the case of dense fermion systems, such as metal clusters, atomic nuclei, and liquid helium, Fermi statistics plays a central role in many situations. This then leads to the so-called Vlasov–Uehling–Uhlenbeck (VUU) scheme, as proposed in the late 1920s and early 1930s [99, 100]. This VUU scheme has furthermore been intensely studied during the last two

decades in nuclear physics [101–103]. The resulting VUU equation reads

$$\frac{\partial f}{\partial t} + \{f, h\} = I_{\text{VUU}}[f(\mathbf{r}, \mathbf{p}, t)] \quad (5)$$

with  $I_{\text{VUU}} = \int d\mathbf{p}_2 d\mathbf{p}_3 d\mathbf{p}_4 W(12, 34)(f_{12}^{\text{in}} f_{34}^{\text{out}} - f_{12}^{\text{out}} f_{34}^{\text{in}})$  where  $W(12, 34)$  is the collision rate, proportional to the elementary cross section  $d\sigma/d\omega$ , which constitutes a key ingredient of the approach. In Eq. (5), “in” and “out” label the distribution of particles entering or exiting a two body collision ( $12 \leftrightarrow 34$ ), such that  $f_{ij}^{\text{in}} = f_i f_j$ ,  $f_{kl}^{\text{out}} = (1 - f_k)(1 - f_l)$ , with the short hand notation  $f_i = f(\mathbf{r}, \mathbf{p}_i, t)$ . The weights are in a way similar to a standard Boltzmann collision term but augmented by the Pauli blocking factors in the exit channel  $f_{kl}^{\text{out}}$ . The latter terms impose that no more than one particle, or two with opposite spins, can occupy an elementary phase space cell of volume  $(2\pi\hbar)^3$ . This blocking factor plays a dramatic role for electronic systems [104], in particular at zero temperature where it fully blocks electron–electron collisions, as expected. In dynamical situations, when the system is hot or sufficiently excited, phase space opens up and two body collisions start to play a (possibly dominating) role.

It is important to note here that the VUU scheme only represents a first exploratory step in the direction of accounting for dynamical correlations. Of course one should be cautious with the possible double counting of interactions between the effective interaction in the mean field term and the collision term, an effect which has not yet been truly explored in the case of clusters. However, results obtained in related fields of physics, in which a similar question has been addressed in full detail, show that with minimal precautions one can circumvent this problem. Relying on the experience gathered in nuclear dynamics [105] and in the physics of plasmas [106], or liquid helium [107], one can assume that there is no problem as long as collisions are treated in a Markovian approximation (i.e., as instantaneous) [105]. The rule is then to use together the LDA for the mean field and a screened Coulomb cross section for the collision integral. In the case of metal clusters an explicit reevaluation of the cross section [12] actually has lead to values in agreement with the bulk values of condensed matter calculations [104]. With such an established framework, one can now envision direct applications in realistic cases [13], even with coupling to ionic molecular dynamics [108].

## 5. CONCLUSIONS

We have seen that the interaction of light with clusters may lead to various scenarios depending on the intensity of the lasers used for probing the clusters. In the optical response regime clusters are only slightly perturbed and respond in a correlatively gentle manner. Optical response nevertheless provides a bunch of interesting information on clusters, in particular because of its marked size dependence. The case of irradiations by intense lasers opens the door to a bunch of new challenging phenomena such as the production of highly energetic species (photons, electrons, ions). In this domain of physics the interaction process between the cluster and the laser is so strong that it leads to a complete destruction

of the cluster. At variance with the optical response regime it thus does not provide direct information on the clusters themselves, which constitute laboratories rather than true objects of studies. However, and this time in a similar way as in the low intensity regime, we have also seen that, again, the capability of the electron cloud to respond collectively to the external field remains a key issue. The dominant role of this plasmon is obvious for metallic systems, whatever the laser intensity. But is also indeed present in the case of rare gas clusters irradiated by sufficiently intense lasers. In this spirit irradiation of clusters by intense lasers leads us to plasma physics in the framework of the so-called nano-plasma model. The latter original model, similarly to the simple Mie model of the optical response, does provides interesting insights into the physical mechanisms at work. Both these simple models, however, only allow a qualitative description of the experiments. They miss many details, starting with the crucial finite size effects.

The step from basic simple models toward more elaborate approaches for describing these various dynamical situations is not an easy one. Indeed fully quantal calculations are much too involved to be applied to such huge systems in strongly out of equilibrium situations. One is thus bound to find appropriate approximations, keeping as much as possible of the microscopic world. Semiclassical methods offer here an appealing possibility. They have already been a little explored in the context of metal cluster dynamics, but one is still far away from having fully exploited the many opportunities they offer, in particular for large systems out of equilibrium. More developments of these methods are thus to be expected in the field of the dynamics of nanometer scale clusters irradiated by lasers of various intensities.

## GLOSSARY

**Density functional theory (DFT)** A systematic way to develop a mean-field theory with purely local potentials. It proves the existence of a local representation for the non-local exchange as well as correlation terms and it set the framework for practical approximations (see LDA).

**Landau damping or fragmentation** A mechanism, first introduced by Landau, which describes the damping of collective degrees of freedom due to their coupling to single-particle degrees of freedom.

**Local density approximation (LDA)** The most widely used realization of DFT. It uses the exchange-correlation energy of the homogeneous electron and interprets it as a function of the now local density. By density variation, one thus derives a local single-particle potential depending on the local density. The kinetic energy remains approximated (in contrast to the Time dependent Thomas-Fermi approximation) and the single-particle wavefunctions remain the relevant degrees-of-freedom.

**Mean field theory** The description of a many-particle system in terms of independent particles moving each in a common effective single-particle potential. This mean-field potential, in turn, depends on the particle density summed up from the single-particle densities. A typical example is the Hartree-Fock theory where the mean-field potential becomes non-local in the exchange term.



**Mie plasmon, Mie model** Collective description of the dominant dipole mode as small oscillations of the frozen electron cloud against the ionic background. The original formulation was done for a metal sphere using dielectric theory.

**Nanoplasma model** A phenomenological model which describes the interaction of intense laser pulses with large atomic clusters in terms of macroscopic variables. The laser field ionizes individual atoms creating a plasma of quasi-free electrons and ions of the size of the nanocluster, the nanoplasma.

**Time-dependent LDA (TDLDA)** The time-dependent generalization of the LDA employing a time-dependent variational principle instead of the stationary Ritz variational principle.

**Time dependent Thomas-Fermi approximation** An approximation to TDLDA in which one also replaces the kinetic energy by a functional of the local density, called the Thomas-Fermi kinetic energy. The system is then described purely in terms of the local one-particle density.

**Vlasov equation** The semi-classical limit of time-dependent mean-field theory. It describes the propagation of the single-particle phase-space distribution under the influence of a mean-field potential.

**Vlasov-Uehling-Uhlenbeck equation** An extension of the Vlasov equation taking into account collisions among particles (here electrons) in a Boltzmann-like collision term including Pauli exclusion principle.

## ACKNOWLEDGMENTS

We thank G. Bertsch, M. Brack, F. Calvayrac, A. Domsps, C. Guet, G. Gerber, H. Haberland, C. Kohl, S. Kümmel, K. H. Meiwes-Broer, L. Schweikardt, S. Voll, and C. Ullrich for many inspiring and motivating discussions. We also thank exchange program PROCOPE number 99074 and Institut Universitaire de France for financial support during the realization of this work.

## REFERENCES

1. Small particles and inorganic clusters, in "ISSPIC8" (H. H. Andersen, Ed.), *Z. Phys. D* 40, 1–578 (1997).
2. S. Sugano and H. Koizumi, "Microcluster Physics," Springer Series in Materials Science, Vol. 20. Springer-Verlag, Berlin, 1998.
3. T. P. Martin, "Large Clusters of Atoms and Molecules," NATO ASI Series in Applied Sciences. Plenum, New York, 1995.
4. H. Haberland, "Clusters of Atoms and Molecules 1—Theory, Experiment, and Clusters of Atoms," Springer Series in Chemical Physics, Vol. 52. Springer-Verlag, Berlin, 1994; H. Haberland, "Clusters of Atoms and Molecules 2—Solvation and Chemistry of Free Clusters, and Embedded, Supported and Compressed Clusters," Springer Series in Chemical Physics, Vol. 56. Springer-Verlag, Berlin, 1994.
5. B. Piraux, A. L'Huillier, and K. Rzazewski, "Super-intense Laser-Atom Physics," NATO ASI Series B, Vol. 316. Plenum, New York, 1993.
6. "Proceedings International Conference on Laser Physics," *Laser Phys.* 11 (2001).
7. E. K. U. Gross, J. F. Dobson, and M. Petersilka, *Top. Curr. Chem.* 181, 81 (1996).
8. M. Gross and C. Guet, *Z. Phys. D* 33, 289 (1995).
9. L. Féret, E. Suraud, F. Calvayrac, and P. G. Reinhard, *J. Phys. B* 29, 4477 (1996).
10. L. Plagne and C. Guet, *Phys. Rev. A* 59, 4461 (1999).
11. R. Balescu, "Equilibrium and Non-Equilibrium Statistical Mechanics." Wiley, New York, 1975.
12. A. Domsps, P.-G. Reinhard, and E. Suraud, *Phys. Rev. Lett.* 81, 5524 (1998).
13. A. Domsps, P.-G. Reinhard, and E. Suraud, *Ann. Phys. (NY)* 280, 211 (2000).
14. M. Gaudry, J. Lerm, E. Cottancin, M. Pellarin, J.-L. Vialle, M. Broyer, B. Prvel, M. Treilleux, and P. Mlinon, *Phys. Rev. B* 64, 085407 (2001).
15. G. Mie, *Ann. Phys. (Leipzig)* 25, 377 (1908).
16. U. Kreibig and M. Vollmer, "Optical Properties of Metal Clusters," Springer Series in Materials Science, Vol. 25. Springer-Verlag, Berlin, 1993.
17. P. Ring and P. Schuck, "The Nuclear Many-Body Problem." Springer-Verlag, Berlin, 1980.
18. C. Bréchnignac, Ph. Cahuzac, J. Leygnier, and A. Sarfati, *Phys. Rev. Lett.* 70, 2036 (1993).
19. C. Bréchnignac and Ph. Cahuzac, *Com. Atom. Mol. Phys.* 31, 215 (1995).
20. U. Kreibig and M. Vollmer, "Optical Properties of Metal Clusters," Springer Series in Materials Science, Vol. 25. Springer-Verlag, Berlin, 1993.
21. M. Brack, *Rev. Mod. Phys.* 65, 677 (1993).
22. P.-G. Reinhard, O. Genzken, and M. Brack, *Ann. Phys. (Leipzig)* 5, 1 (1996).
23. J. Babst and P.-G. Reinhard, *Z. Phys. D* 42, 209 (1997).
24. C. Yannouleas and R. Broglia, *Ann. Phys.* 217, 105 (1992).
25. C. Ellert, M. Schmidt, C. Schmitt, T. Reiners, and H. Haberland, *Phys. Rev. Lett.* 75, 1731 (1995).
26. E. M. Lifschitz and L. P. Pitaevskii, "Physical Kinetics." Pergamon Press, Oxford, 1981.
27. P.-G. Reinhard and E. Suraud, in "Metal Clusters" (W. Ekaradt, Ed.). Wiley, Chichester, UK, 1999.
28. P.-G. Reinhard and E. Suraud, *Eur. Phys. J. D* 21, 315 (2003).
29. G. F. Bertsch and D. Tomanek, *Phys. Rev. B* 40, 2749 (1989).
30. C. Yannouleas, J. M. Pacheco, and R. A. Broglia, *Phys. Rev. B* 41, 41 (1989).
31. B. Montag and P.-G. Reinhard, *Phys. Rev. B* 51, 14686 (1995).
32. M. Moseler, U. Landman, and C. Yannouleas, *Phys. Rev. Lett.* 87, 053401 (2001).
33. K. Chang and W. Graham, *J. Chem. Phys.* 77, 4300 (1982).
34. D. Forney, P. Freivogel, M. Grutter, and J. P. Maier, *J. Chem. Phys.* 104, 4954 (1996).
35. G. Pacchioni and J. Koutecky, *J. Chem. Phys.* 88, 1066 (1988).
36. M. Kolbuszewski, *J. Chem. Phys.* 102, 3679 (1995).
37. K. Yabana and G. F. Bertsch, *Z. Phys. D* 42, 219 (1997).
38. T. Berkus, P.-G. Reinhard, and E. Suraud, *Int. J. Mol. Sci.* 3, 69 (2002).
39. A. McPherson, T. S. Luk, B. D. Thompson, A. B. Borisov, O. B. Shiryaev, X. Chen, K. Boyer, and C. K. Rhodes, *Phys. Rev. Lett.* 72, 1810 (1994).
40. A. McPherson, K. Boyer, and C. K. Rhodes, *J. Phys. B* 27, L637 (1994).
41. A. McPherson, B. D. Thompson, A. B. Borisov, K. Boyer, and C. K. Rhodes, *Nature* 370, 631 (1994).
42. T. Ditmire, J. W. G. Tisch, E. Springate, M. B. Mason, N. Hay, R. A. Smith, J. Marangos, and M. H. R. Hutchinson, *Nature* 386, 54 (1997).
43. M. Lezius, S. Dobosz, D. Normand, and M. Schmidt, *Phys. Rev. Lett.* 80, 261 (1998).
44. L. Köller, M. Schumacher, J. Kohn, S. Teuber, J. Tiggesbaumker, and K. H. Meiwes-Broer, *Phys. Rev. Lett.* 82, 3783 (1999).

45. R. Schlipper, R. Kusche, B. von Issendorff, and H. Haberland, *Phys. Rev. Lett.* 80, 1194 (1998).
46. T. Ditmire, R. A. Smith, J. W. G. Tisch, and M. H. R. Hutchinson, *Phys. Rev. Lett.* 78, 3121 (1997).
47. S. Dobosz, M. Lezius, M. Schmidt, P. Meynadier, M. Perdrix, and D. Normand, *Phys. Rev. A* 56, R2526 (1997).
48. T. Ditmire, E. Springate, J. W. G. Tisch, Y. L. Shao, M. B. Mason, N. Hay, J. P. Marangos, and M. H. R. Hutchinson, *Phys. Rev. A* 57, 369 (1998).
49. Y. L. Shao, T. Ditmire, J. W. G. Tisch, E. Springate, J. P. Marangos, and M. H. R. Hutchinson, *Phys. Rev. Lett.* 77, 3343 (1996).
50. T. Ditmire, T. Donnelly, R. W. Falcone, and M. D. Penz, *Phys. Rev. Lett.* 75, 3122 (1995).
51. M. Lezius and M. Schmidt, in "Molecules and Clusters in Intense Laser Fields" (J. Posthumus, Ed.), p. 142. Cambridge Univ. Press, Cambridge, UK, 2001.
52. M. Lezius, S. Dobosz, D. Normand, and M. Schmidt, *J. Phys. B* 30, L251 (1997).
53. E. Springate, N. Hay, J. W. G. Tisch, M. B. Mason, T. Ditmire, M. H. R. Hutchinson, and J. P. Marangos, *Phys. Rev. A* 61, 063201 (2000).
54. K. J. Mendham, N. Hay, M. B. Mason, J. W. G. Tisch, and J. P. Marangos, *Phys. Rev. A* 64, 055201 (2001).
55. E. Springate, N. Hay, J. W. G. Tisch, M. B. Mason, T. Ditmire, J. P. Marangos, and M. H. R. Hutchinson, *Phys. Rev. A* 61, 044101 (2000).
56. B. Lang, A. Vierheilg, E. Wiedenmann, H. Buchenau, and G. Gerber, *Z. Phys. D* 40, 1 (1997).
57. B. Bescos, B. Lang, J. Weiner, V. Weiss, E. Wiedenmann, and G. Gerber, *Eur. Phys. J. D* 9, 399 (1999).
58. M. A. Lebeault, J. Viallon, J. Chevalyere, C. Ellert, D. Normand, M. Schmidt, O. Sublemontier, C. Guet, and B. Huber, *Eur. Phys. J. D* 20, 233 (2002).
59. M. Schumacher, S. Teuber, L. Koller, J. Kohn, J. Tiggesbaumker, and K. H. Meiwes-Broer, *Eur. Phys. J. D* 9, 411 (1999).
60. T. Döppner, S. teuber, M. Schumacher, J. Tiggesbaumkerand, and K. H. Meiwes-Broer, *Int. J. Mass Spectr.* 192, 387 (1999).
61. T. Döppner, S. teuber, M. Schumacher, J. Tiggesbaumkerand, and K. H. Meiwes-Broer, *Appl. Phys. B* 71, 357 (2000).
62. S. Teuber, T. Doppner, T. Fennel, J. Tiggesbaumker, and K.-H. Meiwes-Broer, *Eur. Phys. J. D* 16, 59 (2001).
63. J. W. G. Tisch, N. Hay, E. Springate, E. T. Gumbrell, M. H. R. Hutchinson, and J. P. Marangos, *Phys. Rev. A* 60, 3076 (1999).
64. S. Dobosz, M. Schmidt, M. Perdrix, P. Meynadier, O. Gobert, D. Normand, K. Ellert, and T. Blenski, *J. Exp. Theo. Phys.* 88, 1122 (1999).
65. G. Grillon, Ph. Balcou, J.-P. Chambaret, D. Hulin, J. Martino, S. Moustazis, L. Notebaert, M. Pittman, Th. Pussieux, A. Rousse, J.-Ph. Rousseau, S. Sebban, O. Sublemontier, and M. Schmidt, *Phys. Rev. Lett.* 89, 065005 (2002).
66. B. Bescós, R. Hoch, H.-J. Schmidtke, and G. Gerber, *Appl. Phys. B* 71, 373 (2000).
67. T. Ditmire, J. Zweiback, V. P. Yanovsky, T. E. Cowan, G. Hays, and K. B. Wharton, *Nature* 398, 489 (1999).
68. M. Tchapyguine, K. Hoffmann, O. Dühr, H. Hohmann, G. Korn, H. Rottke, M. Wittmann, I. V. Hertel, and E. E. B. Campbell, *J. Chem. Phys.* 112, 2781 (2000).
69. E. E. B. Campbell, K. Hansen, K. Hoffmann, G. Korn, M. Tchapyguine, M. Wittmann, and I. V. Hertel, *Phys. Rev. Lett.* 84, 2128 (2000).
70. E. E. B. Campbell, K. Hoffmann, H. Rottke, and I. V. Hertel, *J. Chem. Phys.* 114, 1716 (2001).
71. J. Zweiback, T. E. Cowan, R. A. Smith, J. H. Hartley, R. Howell, C. A. Steinke, G. Hays, K. B. Wharton, J. K. Crane, and T. Ditmire, *Phys. Rev. Lett.* 85, 3640 (2000).
72. W. Kohn and L. J. Sham, *Phys. Rev.* 140, 1133 (1965).
73. F. Calvayrac, P.-G. Reinhard, E. Suraud, and C. Ullrich, *Phys. Rep.* 337, 493 (2000).
74. A. Domsps, P. L'Eplattenier, P.-G. Reinhard, and E. Suraud, *Ann. Phys. (Leipzig)* 6, 455 (1997).
75. A. A. Vlasov, "Many-Particle Theory and Its Application to Plasma." Gordon & Breach, New York, 1950.
76. K. Takahashi, *Progr. Theor. Phys. Supp.* 98, 109 (1989).
77. P. L'Eplattenier, E. Suraud, and P.-G. Reinhard, *Ann. Phys. (N.Y.)* 224, 426 (1995).
78. P. L'Eplattenier, P.-G. Reinhard, and E. Suraud, *J. Phys. A* 28, 787 (1995).
79. P.-G. Reinhard and E. Suraud, *Ann. Phys. (N.Y.)* 239, 193 (1995).
80. P.-G. Reinhard and E. Suraud, *Z. Phys. A* 355, 339 (1996).
81. A. Domsps, P.-G. Reinhard, and E. Suraud, *Ann. Phys. (N.Y.)* 260, 171 (1997).
82. A. Domsps, P.-G. Reinhard, and E. Suraud, *Phys. Rev. Lett.* 80, 5520 (1998).
83. R. M. Dreizler and E. K. U. Gross, "Density Functional Theory: An Approach to the Quantum Many-Body Problem." Springer-Verlag, Berlin, 1990.
84. A. Domsps, E. Suraud, and P.-G. Reinhard, *Eur. Phys. J. D* 2, 191 (1998).
85. M. Brewczyk, K. Rzazewski, and C. W. Clark, *Phys. Rev. Lett.* 78, 191 (1997).
86. M. Brewczyk, C. W. Clark, M. Lewenstein, and K. Rzazewski, *Phys. Rev. Lett.* 80, 1857 (1998).
87. M. Brewczyk and K. Rzazewski, *Phys. Rev. A* 60, 2285 (1999).
88. P. Blaise, S. A. Blundell, and C. Guet, *Phys. Rev. B* 55, 15856 (1996).
89. K. Boyer and C. K. Rhodes, *J. Phys. B* 27, L633 (1994).
90. C. Rose-Petruck, K. J. Schafer, K. R. Wilson, and C. P. J. Barty, *Phys. Rev. A* 55, 1182 (1997).
91. K. Ishikawa and T. Blenski, *Phys. Rev. A* 62, 063204 (2000).
92. M. Rusek, H. Lagadec, and T. Blenski, *Phys. Rev. A* 63, 013203 (2001).
93. I. Last and J. Jortner, *Phys. Rev. A* 62, 013201 (2000).
94. V. P. Krainov and A. S. Roshchupkin, *J. Phys. B* 34, L297 (2001).
95. T. Ditmire, T. Donnelly, A. M. Rubenchik, R. W. Falcone, and M. D. Perry, *Phys. Rev. A* 53, 3379 (1996).
96. I. Last and J. Jortner, *J. Phys. Chem. A* 102, 9655 (1998).
97. F. Megi, M. Belkacem, M. A. Bouchene, E. Suraud, and G. Zwicknagel, *J. Phys. B* 36, 273 (2003).
98. J.-P. Hansen and I. R. MacDonald, "Theory of Simple Liquids." Academic Press, London, 1976.
99. E. A. Uehling and G. Uhlenbeck, *Phys. Rev.* 43, 552 (1933).
100. L. W. Nordheim, *Proc. Roy. Soc. London Ser. A* 119, 689 (1928).
101. G. F. Bertsch and S. Das Gupta, *Phys. Rep.* 160, 189 (1988).
102. A. Bonasera, F. Gulminelli, and J. Molitoris, *Phys. Rep.* 243, 1 (1994).
103. Y. Abe, S. Ayik, P.-G. Reinhard, and E. Suraud, *Phys. Rep.* 275, 49 (1996).
104. D. Pines and P. Nozieres, "The Theory of Quantum Liquids." Benjamin, New York, 1966.
105. K. Gütter, K. Wagner, P.-G. Reinhard, and C. Toepffer, *Ann. Phys. (N.Y.)* 225, 339 (1993).
106. S. Ichimaru et al., *Phys. Rep.* 149, 91 (1987).
107. J. W. Serene and D. Rainer, *Phys. Rep.* 101, 221 (1983).
108. E. Giglio, P.-G. Reinhard, and E. Suraud, *Ann. Phys. (Leipzig)* 11, 291 (2002).



# Photoexcitation Dynamics of Fullerenes

Mamoru Fujitsuka, Osamu Ito

Tohoku University, Sendai, Japan

## CONTENTS

1. Introduction
  2. Photoexcitation and Relaxation Processes of Fullerenes
  3. Photoinduced Reactions of Fullerenes
  4. Photoinduced Processes of Fine Particles of Fullerenes
  5. Fullerene Oligomers, Higher Fullerenes, and Metallofullerenes
  6. Charge Separation and Recombination Processes of Donor-Fullerene Linked Molecules
  7. Concluding Remarks
- Glossary  
References

## 1. INTRODUCTION

Fullerene  $C_{60}$  (Fig. 1) was found in the laser vaporization of graphite in 1985 by Kroto et al. [1]. Since the first demonstration of large scale synthesis of fullerenes in 1990 [2], quite a large number of studies on fullerenes have been carried out for clarification of their basic properties and for their applications. Up to date, in addition to  $C_{60}$ , various kinds of fullerenes such as higher fullerenes and endohedral metallofullerenes have been isolated. Furthermore, various kinds of derivatives of fullerenes have been synthesized. Thus, many kinds of compounds are included in the fullerene group. Fullerenes show interesting properties in the field of materials science: Superconductivity, photoconductivity, ferromagnetism, and nonlinear optics are examples of characteristic properties of fullerenes [3–6]. Furthermore, it should be noted that fullerenes are also attractive materials in the field of biochemistry, since the excited fullerenes are effective in cleavage of DNA in the presence of molecular oxygen and electron donors [7, 8]. Furthermore, computer simulation made clear that  $C_{60}$  would be active to HIV protease [9].

Photoexcitation dynamics of fullerenes have been also widely investigated. Nowadays, the excitation–relaxation processes of  $C_{60}$  and  $C_{70}$  have been well established [10–15]. Singlet and triplet properties have been investigated by using pico- and nanosecond laser flash photolysis techniques. One of the important photophysical properties of  $C_{60}$  and  $C_{70}$  (Fig. 1) is almost quantitative triplet generation, which results in effective photochemical bimolecular reactions [10].

From the viewpoint of photochemistry, fullerenes are good electron acceptors and many photoinduced reactions have been reported by using these fullerenes as acceptors [16–20]. The excellent acceptor ability of fullerene is a key feature of photoconductivity for fullerene-doped polymer films such as poly(*N*-vinylcarbazole) and poly(*p*-phenylene vinylene) [4, 21]. Furthermore, many derivatives of the fullerenes have been synthesized due to high reactivities of fullerenes [22]. Fullerene oligomers and polymers are interesting materials as well as pristine fullerenes [23, 24].

Utilization of fullerenes to mimic photosynthesis systems has been investigated, resulting in enhanced efficiencies of the charge separations, which relates to application of the highly efficient photovoltaic cells [25–27].

In this chapter, we review the photoexcitation dynamics of fullerenes including  $C_{60}$ ,  $C_{70}$ , higher fullerenes, endohedral metallofullerenes, and fullerene oligomers. Furthermore, photoinduced processes in the fullerene-donor linked molecules have been also reviewed, since they will serve as important molecular devices.

## 2. PHOTOEXCITATION AND RELAXATION PROCESSES OF FULLERENES

### 2.1. Excited Singlet State Properties of $C_{60}$ and $C_{70}$

$C_{60}$  and  $C_{70}$  show weak fluorescence at 700 and 660 nm (Fig. 2) [28, 29]. The quantum yield of the fluorescence of  $C_{60}$  is as low as  $3.2 \times 10^{-4}$  [30]. Small quantum yields of the fluorescence processes can be attributed to the forbidden transition due to closed shells with high symmetry ( $I_h$ -symmetry). When the symmetry of  $C_{60}$  is decreased by the introduction of a functional group, about a threefold

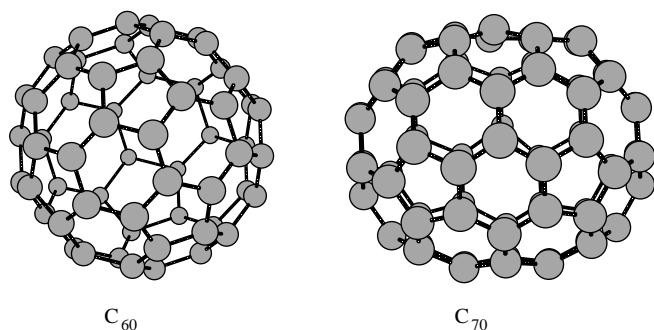


Figure 1.  $C_{60}$  and  $C_{70}$ .

increase of the fluorescence quantum yield is attained [31]. From the low symmetry,  $C_{70}$  shows a slightly larger fluorescence quantum yield ( $5.2 \times 10^{-4}$ ) than  $C_{60}$  [30]. The fluorescence lifetimes of pristine  $C_{60}$  and  $C_{70}$  are reported to be 1.2 ns and 660 ps, respectively [30].

Introduction of multiaddends to  $C_{60}$  changes fluorescence properties to a great extent. Schick et al. reported that the hexa-adduct of  $C_{60}$  ( $T_h$ -symmetry) shows a fluorescence peak at 550 nm, with high fluorescence quantum yield (0.024), which is 75 times larger than pristine  $C_{60}$  [32]. They also reported that the hexa-adduct shows apparent phosphorescence. These findings indicate that the optical devices are possible by using fullerene compounds with many addends.

By using ultrashort laser pulses, transient absorption bands due to the singlet excited states of  $C_{60}$  and  $C_{70}$  can be observed. In the case of  $C_{60}$ , the transient absorption bands due to the singlet excited state appeared around 900 nm upon ultrashort laser pulse irradiation [33]. As for the singlet excited state of  $C_{70}$ , the transient absorption spectrum shows a peak around 700 nm [34]. It has been reported that the decay rate constants of the absorption bands of the singlet excited states agreed well with the corresponding fluorescence decay rate constants. When the excitation wavelength is short enough to pump fullerenes to the higher excited states ( $S_n$ ), the lowest excited state ( $S_1$ ) should be generated after the internal conversion process (Fig. 3). In the case of  $C_{60}$ , it has been reported that the  $S_1$  state is converted with a time constant of 250 fs from the higher excited state [35]. As for  $C_{70}$ , it was confirmed that the internal conversion process proceeds within 1 ps after the excitation with the laser pulse.

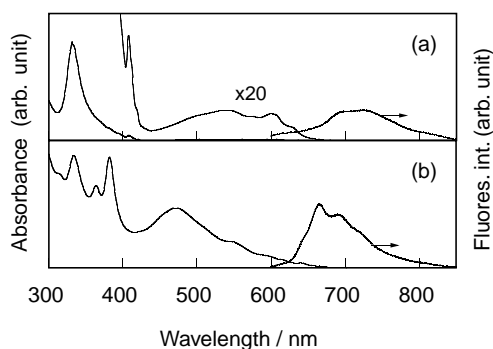


Figure 2. Absorption and fluorescence spectra of (a)  $C_{60}$  and (b)  $C_{70}$  in benzene. Reprinted with permission from [29], A. Masuhara et al., *Bull. Chem. Soc. Jpn.* 73, 2199 (2000). © 2000, Japan Chemical Society.

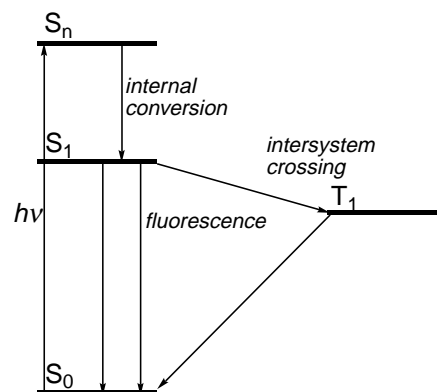


Figure 3. Schematic energy diagram of the excitation and relaxation processes of fullerenes.

## 2.2. Excited Triplet States of $C_{60}$ and $C_{70}$

Photoexcitation of  $C_{60}$  and  $C_{70}$  generates the triplet excited states almost quantitatively from the singlet excited states; that is, the quantum yields for the intersystem crossing yields ( $\Phi_{ISC}$ ) are  $>0.95$  for  $C_{60}$  and  $C_{70}$  [10, 36]. The quantitative triplet generations of the fullerenes are important in the various photochemical processes. For example, the triplet excited fullerenes are important reagents for the quantitative generation of singlet oxygen [10], which is one of the important species in the fields of photobiology.  $C_{60}$  and  $C_{70}$  in the glassy matrix of the brominated hydrocarbon at 77 K show phosphorescence at 794 and 810 nm [37], respectively, which correspond to 1.56 and 1.53 eV of the triplet energies.

Upon nanosecond laser irradiation,  $C_{60}$  shows a clear absorption band due to the triplet excited state at 750 nm (Fig. 4) [11–15], which is a good spectral probe for the photochemists who trace the photoinduced process via the triplet excited state of  $C_{60}$ , since the extinction coefficient of the transient absorption band is as large as  $16,100 \text{ M}^{-1} \text{ cm}^{-1}$  at 750 nm [15]. The decay rate of the triplet excited state of  $C_{60}$  in solution is governed by the triplet–triplet annihilation and the self-quenching processes,

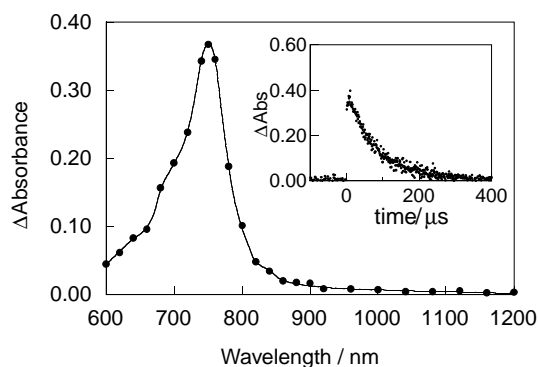
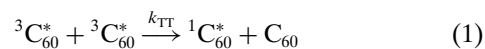


Figure 4. Transient absorption spectrum of  $C_{60}$  in toluene at 100 ns after laser light irradiation. Inset: Absorption-time profile at 750 nm.

Both processes were investigated by dependence of the decay rate of the triplet excited  $C_{60}$  on the excitation power or concentration (Fig. 5) [29, 38]. It has been reported that the bimolecular rate constants of both processes are on the order of  $10^9 \text{ M}^{-1} \text{ s}^{-1}$ , indicating that both processes are effective quenching processes of the triplet excited states. Ausman and Weisman reported that the intrinsic lifetime of the triplet excited state of  $C_{60}$  is as long as  $143 \mu\text{s}$  in toluene at room temperature [38].

In the case of  $C_{70}$ , the triplet absorption band shows peak at 980 nm, of which the extinction coefficient is  $6500 \text{ M}^{-1} \text{ cm}^{-1}$  [14]. In the case of  $C_{70}$ , the intrinsic triplet lifetime is reported by Ausman and Weisman to be as long as 11.8 ms in toluene [38].

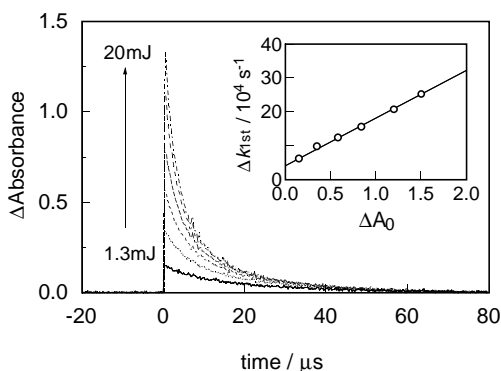
These long triplet lifetimes of  $C_{60}$  and  $C_{70}$  indicate that the wide varieties of the photoinduced reactions are expected via the triplet excited states of both fullerenes.

Triplet properties of the derivatives of  $C_{60}$  have been also reported [31]. In the case of 1,2-adducts of  $C_{60}$ , the triplet absorption band appeared around 700 nm. It has been reported that the  $\Phi_{\text{ISC}}$  values are 0.8–0.9 for these 1,2-adducts [31]. Thus, the triplet excited states of the derivatives are also good precursors for the photoinduced reactions.

### 3. PHOTOINDUCED REACTIONS OF FULLERENES

#### 3.1. Electron Acceptor Abilities of Fullerenes

The first reduction potential of  $C_{60}$  is reported to be  $-0.42 \text{ V}$  vs saturated calomel electrode (SCE) in benzonitrile [39], which is similar to the reduction potential of *p*-benzoquinone ( $-0.51 \text{ V}$  vs SCE) [40], a typical acceptor in the photosynthesis systems. The cyclic voltammogram of  $C_{60}$  shows multiple reduction waves up to sixth reduction steps [41]. From these results,  $C_{60}$  is a good electron acceptor. Its electron acceptor ability is enhanced in its excited state, since free-energy



**Figure 5.** Laser power dependence of absorption-time profiles of triplet excited  $C_{60}$  at 750 nm. Inset: Analysis of the triplet–triplet annihilation process according to the relation  $-d[\ln \Delta A_0]/dt = \Delta k_{\text{1st}} = k_{\text{1st}}^0 + (2k_{\text{2nd}}/\varepsilon_T)\Delta A_0$ , where  $\Delta A_0$ ,  $k_{\text{1st}}^0$ ,  $k_{\text{2nd}}$ , and  $\varepsilon_T$  are T-T absorbance at  $t = 0$ , an intrinsic first-order decay rate, rate constant of the T-T annihilation, and an extinction coefficient of the T-T absorption band. Reprinted with permission from [29], A. Masuhara et al., *Bull. Chem. Soc. Jpn.* 73, 2199 (2000). © 2000, Japan Chemical Society.

change for the electron transfer ( $\Delta G_{\text{et}}$ ) in the excited state [Eq. (3)] is more negative than that in the ground state [Eq. (4)] [42],

$$\Delta G_{\text{et}} (\text{excited state}) = E_{\text{ox}} - E_{\text{red}} - E_{00} - e^2/\varepsilon r \quad (3)$$

$$\Delta G_{\text{et}} (\text{ground state}) = E_{\text{ox}} - E_{\text{red}} - e^2/\varepsilon r \quad (4)$$

where  $E_{\text{ox}}$ ,  $E_{\text{red}}$ ,  $E_{00}$ , and  $e^2/\varepsilon r$  are oxidation potential of donor, reduction potential of acceptor, excitation energy, and Coulombic term, respectively. As for the oxidation, five oxidation waves were confirmed in the cyclic voltammogram, although reports on the oxidation processes of  $C_{60}$  are scarce compared to the reduction processes.

#### 3.2. Electron Transfer via the Singlet Excited States of Fullerenes

Since the decay rate constants of the singlet excited states are  $8.8 \times 10^8$  and  $1.5 \times 10^9 \text{ s}^{-1}$  for  $C_{60}$  and  $C_{70}$ , respectively, electron transfer processes via the singlet excited states become evident when a charge-transfer complex is formed in the ground state or when the concentration of the donor is as high as  $\sim 100 \text{ mM}$ .

When  $C_{60}$  or  $C_{70}$  was excited in the presence of highly concentrated amines such as dimethyl aniline and triphenyl amines,  $C_{60}$  or  $C_{70}$  showed exciplex emission. For example, the  $C_{70}$ -dimethylaniline system showed exciplex emission in the 700–800 nm region with decrease of fluorescence intensity of  $C_{70}$  in the 600–700 nm region [43]. The exciplex formation is apparent in nonpolar solvents rather than polar solvents, since the polar solvents solvate the generated radical ions as free radical ions. When the concentration of the donor is high, one-to-one charge transfer complex formation can be observed as broadening of the ground state absorption band of  $C_{60}$ . Sension et al. observed electron transfer from the singlet excited state of  $C_{60}$  within 1–2 ps by observing the absorption band around 1000 nm upon excitation of the  $C_{60}$ -dimethylaniline complex with a femtosecond laser [44]. The recombination occurs on a time scale in the range from 20 to 55 ps.

Electron transfer via the singlet excited states of the fullerenes also became evident in the solid state materials such as conjugated polymer films. Sariciftci et al. reported that the femtosecond laser irradiation on the polythiophene- $C_{60}$  composite film, in which the charge-transfer complex was formed, results in the radical ion pair formation within 1 ps [45, 46]. Thus, laser excitation on the charge transfer complex results in fast electron transfer. This kind of electron-transfer process is important in the photoconductive materials in which the substantial carriers are generated by photoirradiation. It has been reported that the photoconductivity of these composite films of fullerenes and conjugated polymer persisted about 10 ns after a short laser pulse, indicating that the charge-migration processes take place in these films.

A fast charge-separation process of the charge-transfer complex is also reported for the  $C_{60}$ -doped poly(*N*-vinylcarbazole) (PVCz) film, for which enhanced photoconductivity was also reported [4]. In the  $C_{60}$ -doped PVCz films, the electron transfer occurred immediately after the

picosecond laser pulse [47]. The decay of the initial charge-separated state with a time constant of 1.2 ns comprises three channels: the charge-recombination, the hole migration to the neighboring carbazoyl chromophores, and the formation of the local triplet excited state of  $C_{60}$  (Fig. 6).

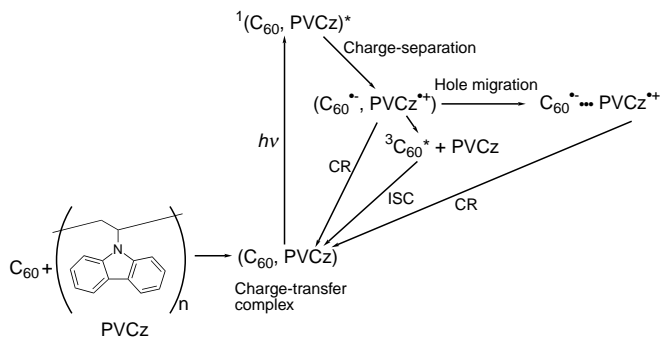
It should be noted that under low concentrations of these photoconductive polymers (<10 mM) in solution, the electron-transfer process via the triplet excited states of fullerenes or triplet excited polymers is a major process as shown below.

### 3.3. Electron Transfer via the Triplet Excited States of Fullerenes

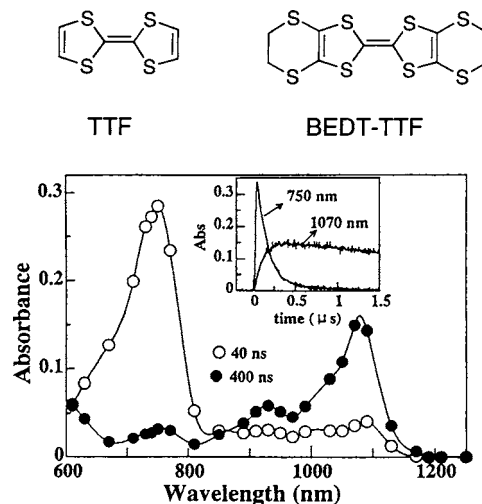
One of the important characteristics of  $C_{60}$  and  $C_{70}$  is the high quantum yield of the intersystem crossing from  $^1C_{60}^*$  ( $^1C_{70}^*$ ) to  $^3C_{60}^*$  ( $^3C_{70}^*$ ). Thus, the reaction systems including donors of lower concentrations (<10 mM) attain highly efficient electron transfer via  $^3C_{60}^*$  and  $^3C_{70}^*$ .

For observations of the electron-transfer processes via the triplet excited states of fullerenes, a nanosecond laser flash photolysis method observing transient spectra in the near-infrared (IR) region is advantageous, since the transient species of the fullerenes appeared in the near-IR regions. For example, absorption bands of the triplet excited state and radical anion of  $C_{60}$  appeared at 750 and 1080 nm, respectively. As for  $C_{70}$ , they appeared at 980 and 1360 nm, respectively. The first paper on the electron-transfer process via the triplet excited  $C_{60}$  was reported by Arbogast et al. [48]. Their studies using transient absorption spectroscopy showed the generation of the radical anion in the near-IR region. Furthermore, they showed the dependence of the rate constants for the electron-transfer processes on the free-energy changes according to the tendency described by the Rehm-Weller equation, which are calculated by the oxidation potentials of aromatic amines used as donors.

In addition to the aromatic amines, many kinds of organic compounds are known to show sufficient donor abilities. For example, tetrathiafulvalene (TTF) or bis(ethylenedithio)tetrathiafulvalene (BEDT-TTF) is a donor which shows metallic conduction when it forms a charge-transfer complex with appropriate acceptors [49].  $C_{60}$  is one of the acceptors which forms a charge-transfer complex with TTF [50]. In benzonitrile solution which contains  $C_{60}$  and TTF,

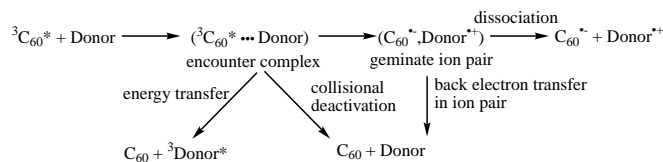


**Figure 6.** Charge-separation and charge-recombination processes of  $C_{60}$ -doped PVCz film. CR and ISC denote charge recombination and intersystem crossing, respectively.



**Figure 7.** Transient absorption spectra of  $C_{60}$  (0.1 mM) in the presence of TTF (1.0 mM) in benzonitrile. Inset: Absorption-time profiles at 750 and 1070 nm. Reprinted with permission from [51], M. M. Alam et al., *J. Photochem. Photobiol. A: Chem.* 104, 59 (1997). © 1997, Elsevier Science.

the radical ions are generated upon nanosecond laser irradiation (Fig. 7) [51]. The electron transfer was confirmed to proceed via the triplet excited state of  $C_{60}$ . The bimolecular quenching rate constant ( $k_q$ ) of the triplet excited  $C_{60}$  is  $5.0 \times 10^9 \text{ M}^{-1} \text{ s}^{-1}$ , indicating that the quenching process is a diffusion-limiting process ( $k_{\text{diff}}$  in benzonitrile is  $5.3 \times 10^9 \text{ M}^{-1} \text{ s}^{-1}$  at 298 K) because of sufficiently negative free-energy change for the electron-transfer process. On the other hand, the quantum yield for the electron transfer ( $\Phi_{\text{ET}}$ ) via the triplet excited state was evaluated to be 0.75, which was estimated as a ratio of the generated radical ions to the initial concentration of the triplet excited  $C_{60}$ ; these values can be estimated from the transient absorption spectra by using extinction coefficients of the radical ions and the triplet excited states. Since the electron-transfer rate constant ( $k_{\text{ET}}$ ) value can be estimated by using the relation  $k_{\text{ET}} = \Phi_{\text{ET}} \times k_q$ , the  $k_{\text{ET}}$  value for the  $C_{60}$  and TTF system was evaluated to be  $3.8 \times 10^9 \text{ M}^{-1} \text{ s}^{-1}$ . The  $\Phi_{\text{ET}}$  value smaller than unity indicates that other bimolecular deactivation processes of the triplet excited  $C_{60}$ , such as an energy transfer and collisional quenching, are present (Scheme 1). In the present case, the latter quenching process seems to be plausible due to the higher triplet energy of TTF compared to that of  $C_{60}$ .



**Scheme 1.** Reaction scheme for  $^3C_{60}^*$  in the presence of electron donor.

As for BEDT-TTF, the  $k_{\text{ET}}$  value was somewhat smaller than that of the  $C_{60}$ -TTF system due to the smaller free-energy change for the electron-transfer system of  $C_{60}$  and

BEDT-TTF. When the polarity of the solvent decreases, the  $\Phi_{\text{ET}}$  values decrease while the  $k_q$  values are still close to the corresponding  $k_{\text{diff}}$  values. This observation can be attributed to the difficulty of the radical ion pair dissociation in the nonpolar solvents because of poor solvation ability of the radical ion pair in these nonpolar solvents.

The electron-transfer process competitive with the energy-transfer process has been confirmed in the mixture systems of  $\text{C}_{60}$  with  $\beta$ -carotene or retinol, which is reported to be a good triplet energy acceptor [52, 53]. In nonpolar solvents, only the energy-transfer process was observed. On the other hand, the electron-transfer process also becomes evident with increasing solvent polarity. In the case of the photoinduced reaction of  $\text{C}_{60}$  with  $\beta$ -carotene in benzonitrile, the quantum yields for the electron transfer and energy transfer were estimated to be 0.84 and 0.16, respectively. As for the reaction system of  $\text{C}_{60}$  and all-*trans* retinol, the values were 0.45 and 0.55, respectively. The lower quantum yield for the electron transfer of  $\text{C}_{60}$ -retinol system can be attributed to less negative free-energy change for the electron transfer ( $-9.9$  and  $-14.1$  kcal mol $^{-1}$  for  $\text{C}_{60}$ -retinol and  $\text{C}_{60}$ -carotene systems, respectively).

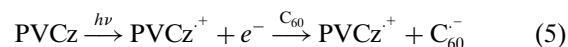
Porphyrins and phthalocyanines also act as donors for fullerenes under photoexcitation [54, 55]. It was confirmed that the electron transfer proceeded via both  $^3\text{C}_{60}^*$  and triplet excited porphyrins. Zinc-including porphyrin compounds such as tetraphenylporphyrin and octaethylporphyrin showed higher donor ability to fullerenes in comparison with copper and H incorporated porphyrins. A similar tendency was also confirmed with phthalocyanine derivatives [55].

### 3.4. Electron Transfer with Polymers

Photoconductive polymers such as PVCz and polythiophene are reported to enhance their photoconductivities upon doping of the fullerenes [4, 45]. As mentioned above, electron transfer within the charge-transfer complex in the films is responsible for the photocarrier generation upon light illumination. When the concentrations of these polymers are sufficiently lower in solution, formation of the charge-transfer complex with fullerenes in the ground state can be ignored. Under these conditions, electron-transfer processes via the triplet excited states of the fullerenes or the conjugated polymers are important.

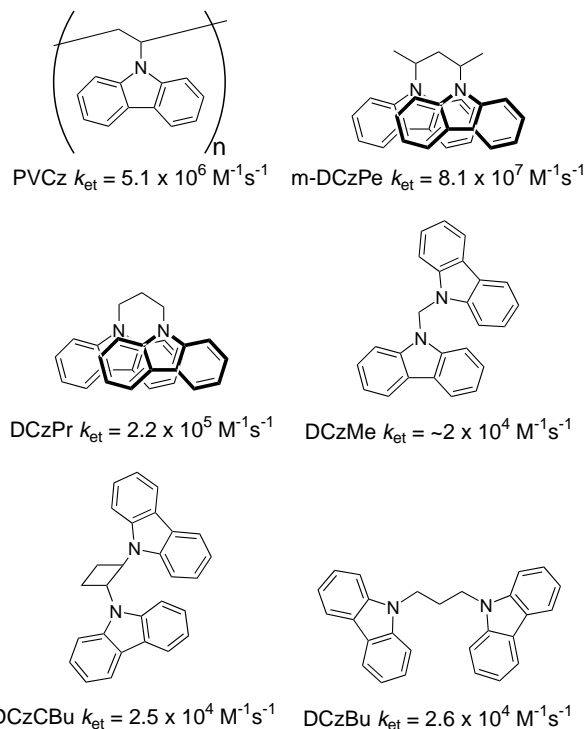
When  $\text{C}_{60}$  is photoexcited in the presence of PVCz, the electron-transfer process proceeds via two mechanisms depending on the excitation wavelength [56]. It was confirmed that electron transfer proceeds from the triplet excited state of  $\text{C}_{60}$ , when the reaction mixture is irradiated by visible light, that is, a 532-nm laser, which excites  $\text{C}_{60}$  only. The electron-transfer rate constant was estimated to be  $5.1 \times 10^6$  M $^{-1}$  s $^{-1}$ , which is ca. 1/1000 of the  $k_{\text{diff}}$  value of benzonitrile solvent. The quite slow electron-transfer rate constant can be attributed to the somewhat positive free-energy change for electron transfer. On the other hand, electron transfer proceeds more rapidly when the reaction mixture is excited with the laser pulse in the ultraviolet region, that is, a 355-nm laser, which excites both  $\text{C}_{60}$  and PVCz. The radical anion of  $\text{C}_{60}$  is generated by capturing the electron which is ejected from PVCz by excitation with

the 355-nm laser in polar benzonitrile [Eq. (5)]. This mechanism was supported by the fact that the generation rate of the  $\text{C}_{60}$  radical anion depends on the concentration of  $\text{C}_{60}$  and that PVCz radical cation is generated by the 355-nm laser irradiation even in the absence of the  $\text{C}_{60}$  in benzonitrile. The rate constant indicates that the electron-capture process by  $\text{C}_{60}$  [Eq. (5)] is the diffusion-limiting process:



The electron-transfer rate constant of the  $\text{C}_{60}$ -PVCz system is larger than the system of  $\text{C}_{60}$  and *N*-ethylcarbazole (EtCz) when  $\text{C}_{60}$  is excited by the 532-nm laser, although EtCz corresponds to the unit structure of PVCz. The larger rate constant of PVCz can be attributed to the stable radical cation of PVCz due to the stacking of the carbazole moieties in the polymer chain as observed by the charge-resonance band in the near-IR region of the transient absorption spectra. The effect of the stacking of the carbazole moieties on the electron-transfer rate constants was discussed on the basis of the data on the electron-transfer processes between  $\text{C}_{60}$  and various carbazole dimer models (Fig. 8) [57]. It has been confirmed that electron transfer proceeds effectively with the fully stacked carbazole dimers which stabilize the radical cations effectively.

In the case of the conjugated polymers such as polythiophene in polar solution, photoinduced electron transfer between fullerenes and the polymers proceeds via the triplet excited states of fullerenes or polymers rather than the charge-transfer complex. It has been well known that the oxidation potentials and triplet energies of conjugated



**Figure 8.** Carbazole dimers and the rate constants for the electron-transfer process with  $^3\text{C}_{60}^*$  in benzonitrile upon laser excitation at 532 nm.

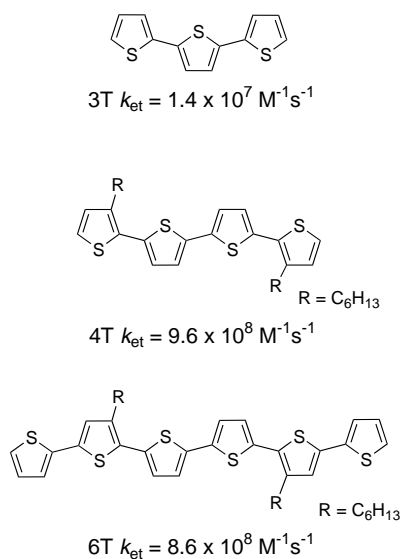
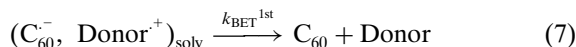
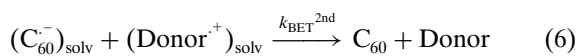


polymers depend on their conjugation length to a great extent. The studies on the electron-transfer processes with the structure-defined oligomers give important information on improvement of efficiency of the electron-transfer processes. In the electron-transfer system of fullerenes and oligothiophene, it was confirmed that the electron-transfer rate constants become large with an increase in the number of repeating units until tetramer (Fig. 9) [58]. On the other hand, a decrease in the  $k_{ET}$  values due to the smaller  $\Phi_{ET}$  values was observed for longer oligomers. This finding can be attributed to the large contribution of the energy-transfer process because of the lower triplet energies of the longer oligothiophene compared to those of fullerenes.

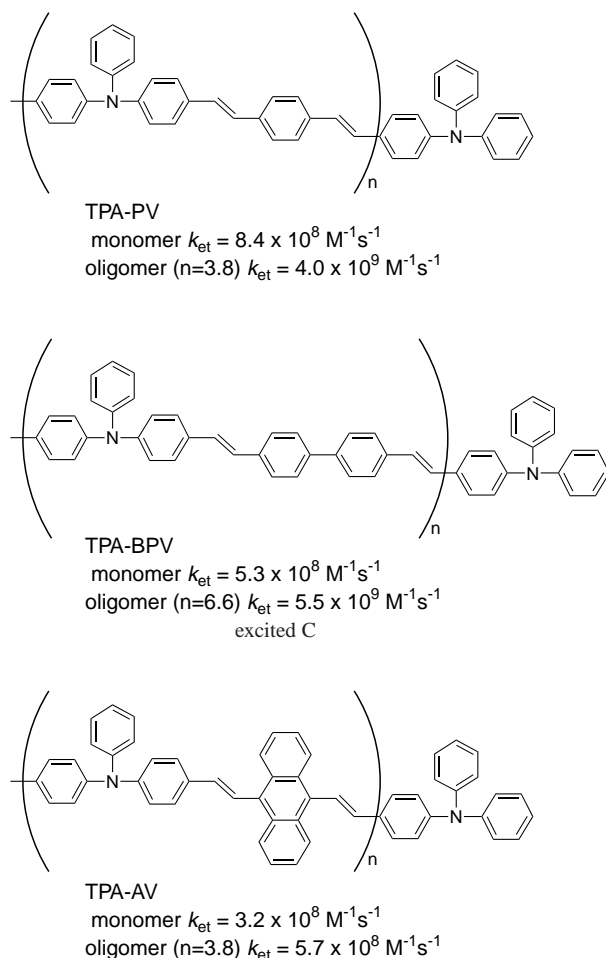
Electron-transfer processes with conjugated oligomers were also investigated in detail for the oligomers of poly(*p*-phenylenevinylene) including the triphenylamine moiety [59]. From the comparison with the monomer models of oligomers, it was revealed that the rate constants of the electron transfer with oligomers are larger due to the larger collision probability of the oligomers compared to the corresponding monomer models (Fig. 10).

### 3.5. Back Electron Transfer

When the radical cation and radical anion decay completely after laser pulse, the generated radical ion pair returns to the corresponding neutral ground state by the back electron-transfer process [60]. When the solvent is highly polar, the generated radical ions are solvated as free radical ions; thus, the back electron transfer obeys second-order kinetics [Eq. (6)]. On the other hand, in the less-polar solvents, the radical ions are present as geminate ion pairs; thus, the back electron transfer obeys first-order kinetics [Eq. (7)]:



**Figure 9.** Oligothiophenes and the rate constants for the electron-transfer process with  $C_{60}$  in benzonitrile via the triplet excited  $C_{60}$ .



**Figure 10.** Monomers and oligomers of poly(*p*-phenylenevinylene) including triphenylamine and the rate constants for the electron-transfer process with  $C_{60}$  in benzonitrile via the triplet excited  $C_{60}$ .

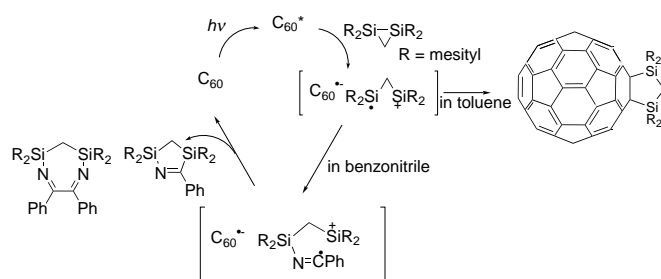
In the electron-transfer system in the solvent mixtures with moderate polarities, the back electron-transfer process by the mixed-order kinetics has been observed, suggesting selective solvation of the radical ions, because of large fullerene molecules.

### 3.6. Formation of Fullerene Adducts via Electron Transfer

Fullerenes are such active compounds that they form derivatives easily. Radical anions and cations are also intermediates for the formation reaction of the fullerene derivatives. Some examples are shown below.

Akasaka et al. reported that the photoexcited  $C_{60}$  generates [2 + 3] cycloadducts with the disilranes, such as 1,1,2,2-tetramesityl-1,2-disilirane via the electron-transfer process (Scheme 2) [61]. It is interesting to note that the adduct formation was not observed by the thermal reactions in the dark. The photoadduct formation occurs in the nonpolar toluene, suggesting that the exciplex is a plausible intermediate. When the reaction proceeds in benzonitrile, the generated radical cation of the disilirane forms 1:1 or 1:2 adducts with benzonitrile; in this case,  $C_{60}$  acts as a photocatalyst

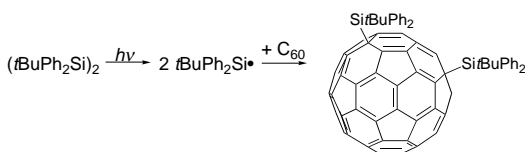
of bissilylation of benzonitrile (Scheme 2) [62]. Photocatalytic reactions of  $C_{60}$  in bissilylation were also confirmed with other carbonyl compounds used as solvents.



**Scheme 2.** Reaction scheme for  $C_{60}$  in the presence of disiliranes.

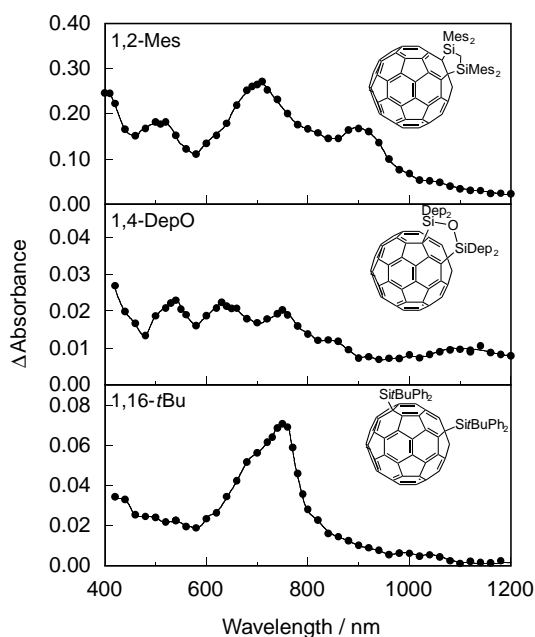
The different reactivities depending on the solvents can be attributed to the solvation of the reaction intermediate: In toluene, adduct formation is considered to proceed in the triplet exciplex; on the other hand, in benzonitrile, the solvated radical ion pair can react with solvent molecules. In the case of the reaction with the  $La@C_{82}$ , Akasaka et al. observed adduct formation in both the photo- and thermal-reaction conditions [63]. Higher reactivity of  $La@C_{82}$  can be attributed to the high electron acceptor ability of  $La@C_{82}$ . It has been reported in the electrochemical studies on metal encapsulated fullerenes that the reduction potential of  $La@C_{82}$  shifts to the anodic direction by 0.7 V in comparison with  $C_{60}$ .

With the photoirradiation on the pristine  $C_{60}$  and disilane in benzene, 1,16-addition product was obtained via the silyl radical formation (Scheme 3) [64]. These bissilylated fullerenes show lower oxidation potential due to the electron-donating nature of silicon addends. Actually, laser flash photolysis study on the photophysical properties of these bissilylated fullerenes shows a substantial change of the photoexcited state properties, such as triplet absorption and fluorescence spectra (Fig. 11) [65]. Thus, bissilylation changes properties of the fullerenes to a great extent.



**Scheme 3.** Reaction scheme for  $C_{60}$  with silyl radical.

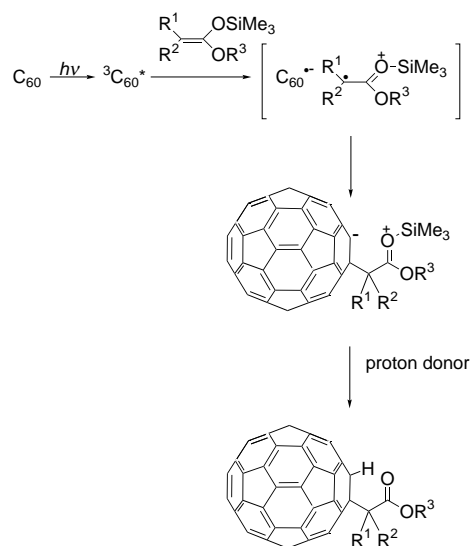
As for the C–C bond formation with fullerene, the photoinduced electron transfer with ketene silyl acetal (KSA) was reported. For example, KSA derived from ethyl acetates generated fullerene-acetates quantitatively upon photoirradiation in benzene (Scheme 4) [66]. Their reactivities to form  $C_{60}$ -adducts are studied on the basis of the oxidation potentials of the KSA, indicating adduct formation via electron transfer with triplet excited  $C_{60}$ . Furthermore, Danishefsky's diene, which is a vinyllogue of KSA, formed [4 + 2] cycloadducts of  $C_{60}$  by the Diels–Alder reaction (Scheme 5)



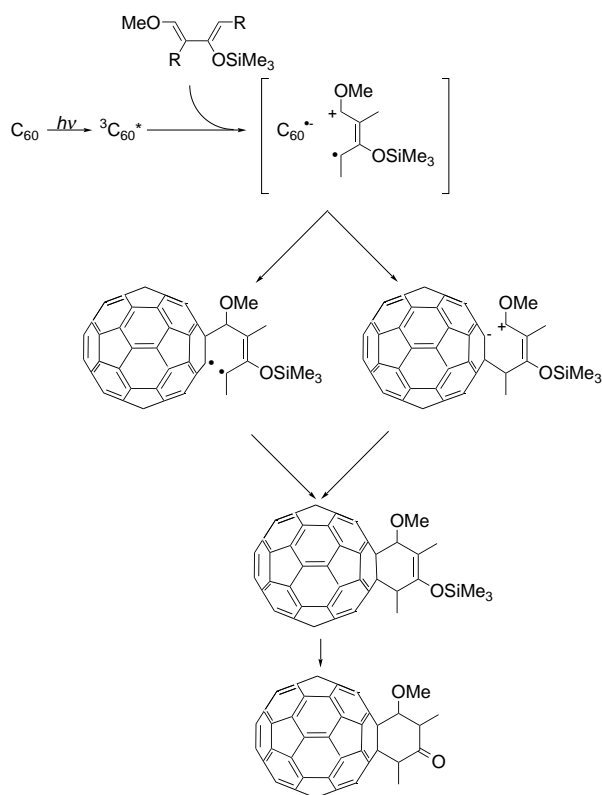
**Figure 11.** Transient absorption spectra of bissilylated  $C_{60}$  derivatives at 250 ns after the laser light irradiation. Inset: Molecular structures. Reprinted with permission from [65], M. Fujitsuka et al., *Phys. Chem. Chem. Phys.* 1, 3527 (1999). © 1999, The Royal Society of Chemistry on behalf of the PCCP Owner Societies.

[67]. In the case of this reaction, the radical anion of  $C_{60}$  was confirmed by the laser flash photolysis experiments.

Fukuzumi et al. reported that 4-*t*-butylated 1-benzyl-1,4-dihydropyridinone (BNAH) generated the anion of *t*-butylated  $C_{60}$  upon photoirradiation via the electron transfer [68]. Generated *t*-butylated  $C_{60}$  anion was quenched in the presence of acid or benzylbromide to generate 1,2-*t*-Bu $C_{60}$  or 1,4-*t*-Bu(PhCH<sub>2</sub>) $C_{60}$ , respectively. In the present

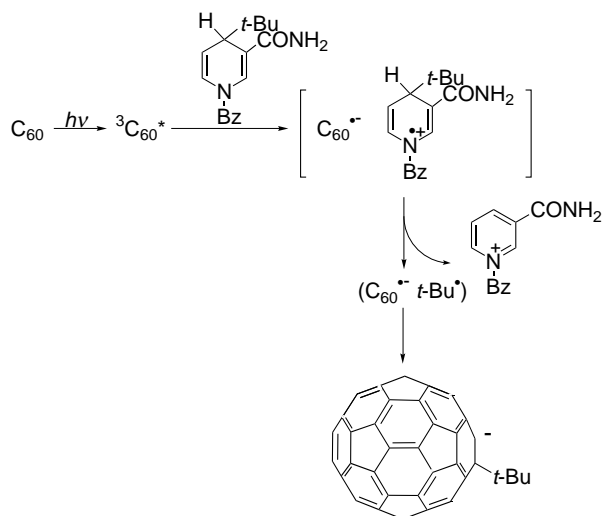


**Scheme 4.** Reaction scheme for  $C_{60}$  with ketene silyl acetals. Reprinted with permission from [66], K. Mikami et al., *J. Am. Chem. Soc.* 117, 11134 (1995). © 1995, American Chemical Society.



**Scheme 5.** Reaction scheme for  $C_{60}$  with Danishefsky's diene. Reprinted with permission from [67], K. Mikami et al., *J. Am. Chem. Soc.* 122, 2236 (2000). © 2000, American Chemical Society.

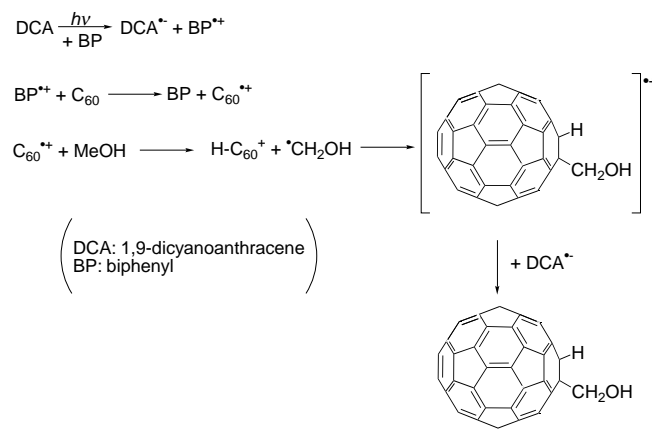
case, electron transfer via the triplet excited state of  $C_{60}$  is responsible for the adduct formation (Scheme 6). After electron transfer, the radical cation of *t*-butylated BNAH generates the *t*-Bu radical which reacts with  $C_{60}$  to generate *t*-butylated  $C_{60}$ . Using 10-methyl-9,10-dihydroacridine,



**Scheme 6.** Reaction scheme for  $C_{60}$  with 4-*t*-butylated 1-benzyl-1,4-dihydronicotinamide. Reprinted with permission from [68], S. Fukuzumi et al., *J. Am. Chem. Soc.* 120, 8060 (1998). © 1998, American Chemical Society.

generation of 1,2-dihydrofullerene was reported to be attained by a similar electron-transfer mechanism.

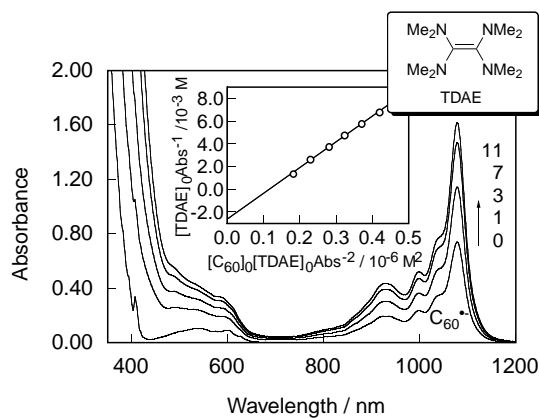
The radical cation of fullerene is also an active intermediate which generates fullerene adducts. Siedschlag et al. reported that the  $C_{60}$ -adduct generated via the radical cation of  $C_{60}$  which was formed by the cosensitizer under photoirradiation [69]. The  $C_{60}$  radical cation abstracts  $\alpha$ -proton from the alcohol to generate  $C_{60}H$  cation and alkyl radical, which forms alkylated  $C_{60}$  (Scheme 7).



**Scheme 7.** Reaction scheme for  $C_{60}$  with methanol via  $C_{60}^{\bullet+}$ .

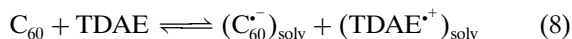
### 3.7. Electron Transfer in the Ground State

Tetrakis(dimethylamino)ethylene (TDAE) has a strong donor ability to form strong charge-transfer complexes with electron acceptors. It has been reported that charge-transfer complex salts of fullerenes with TDAE show ferromagnetism at low temperature [5]. It was revealed that  $C_{60}$  in polar solvents can be reduced in the presence of TDAE without photoirradiation (Fig. 12) [70]. From the relation between the



**Figure 12.** Steady-state absorption spectra of  $C_{60}$  and various concentrations of TDAE in deaerated *o*-dichlorobenzene at room temperature. Numbers indicate the concentration of TDAE in mM. Inset: Plot according to the relation:  $[TDAE]_0/Abs = [C_{60}]_0 [TDAE]_0/Abs^2 - 1/Ke$ . Reprinted with permission from [70], M. Fujitsuka et al., *J. Phys. Chem. B* 103, 445 (1999). © 1999, American Chemical Society.

absorption intensity of the  $C_{60}$  radical anion and the amount of TDAE, it becomes clear that  $C_{60}$  and TDAE are in equilibrium with the corresponding radical ions [Eq. (8)]. From the analysis of thermal equilibria, the equilibrium constant was estimated to be 240 for  $C_{60}$  and TDAE in benzonitrile. On the other hand, in less-polar solvents (dielectric constant  $<7$ ), the generated radical ions are solvated as radical ion pairs [Eq. (9)]:

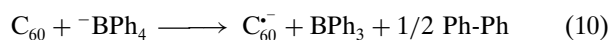


By laser irradiation on  $C_{60}$  in the solution in which  $C_{60}$  and TDAE are in equilibrium with the corresponding radical ions, other amounts of radical ions are generated photochemically, although the reaction system returns to thermal equilibrium by the back electron-transfer process. On combination of the back electron-transfer rate and the thermal equilibrium constant, the electron-transfer rate at the ground state can be estimated. For example, the rate constant of the electron-transfer process between  $C_{60}$  and TDAE in the ground state was estimated to be  $6.4 \times 10^8 \text{ M}^{-1} \text{ s}^{-1}$  in *o*-dichlorobenzene, which is about 1/3 of the rate constant between the triplet excited  $C_{60}$  and TDAE. The smaller rate constant of the electron transfer in the ground state can be attributed to the smaller free-energy change for the electron transfer in the ground state.

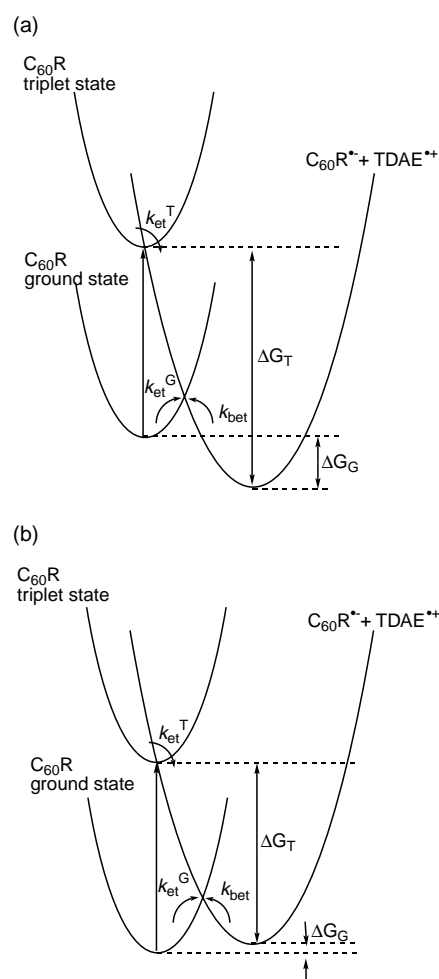
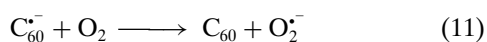
Similar electron transfer in the ground state was also confirmed with  $C_{70}$  and adducts of  $C_{60}$  [71]. In the case of the adducts of  $C_{60}$ , it was revealed that electron-transfer rate constants in the ground and the triplet states are affected by the substituents. The substituent effects of the reaction rate constants were successfully analyzed on the basis of the linear free-energy relationship. It was revealed that electron transfer in the ground state needs considerable activation energy compared to that for the electron transfer via the excited triplet state in the reaction system with TDAE (Fig. 13).

### 3.8. Electron Mediating from $C_{60}$ Radical Anion

When a donor decomposes to nonactive compounds after donating an electron to  $C_{60}$ , the radical anion of  $C_{60}$  shows a considerably long lifetime. For example, the generation rate of the superoxide anion ( $O_2^{\cdot-}$ ) via the radical anion of  $C_{60}$  can be estimated by applying this method [72]. The radical anion of  $C_{60}$  generated using tetrabutylammonium tetraphenylborate [ $^-BPh_4(^+NBu_4)$ ] as electron donor was persistent, because  $^{\cdot}BPh_4$  dissociates into less electron-accepting compounds such as  $BPh_3$  and biphenyl promptly as described by



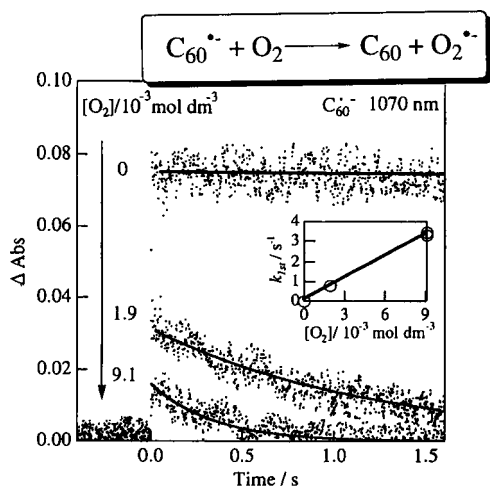
The radical anion of  $C_{60}$  also acts as an electron mediator. In the presence of molecular oxygen, the persistent radical anion of  $C_{60}$  begins to decay according to the electron-mediating process (Fig. 14)



**Figure 13.** Energy diagram of electron transfer processes of 1,2-adducts of  $C_{60}$  ( $C_{60}R$ ) and TDAE in (a) polar solvents and (b) nonpolar solvents.  $k_{et}^T$ ,  $k_{et}^G$ , and  $k_{bet}$  denote the electron transfer rate constants from the triplet excited state, and from the ground state, and back-electron-transfer rate constant, respectively.  $\Delta G_T$  and  $\Delta G_G$  indicate the free-energy changes for the electron transfer from the triplet excited state and the ground state, respectively. Reprinted with permission from [71], C. Luo et al., *Phys. Chem. Chem. Phys.* 1, 2923 (1999). © 1999, The Royal Society of Chemistry on behalf of the PCCP Owner Societies.

From the dependence of the decay rate constant of  $C_{60}^{\cdot-}$  on the concentration of  $O_2$ , the bimolecular rate constant for the generation of the superoxide anion was estimated to be  $3.7 \times 10^2 \text{ M}^{-1} \text{ s}^{-1}$  in benzonitrile. The small reaction rate constant for this electron-mediating process can be attributed to an endothermic process as estimated from the reduction potentials of  $C_{60}$  and  $O_2$  ( $-0.92$  and  $-1.2$  V vs ferrocene/ferrocenium ( $Fc/Fc^+$ ), respectively). It should be noted that the generated superoxide anion can act further as an electron mediator: In the presence of viologen dication, the superoxide anion donates an electron to generate the radical cation of viologen, although the quantum yield of the electron transfer from superoxide ion to viologen dication was somewhat small, 0.1–0.2 [73].

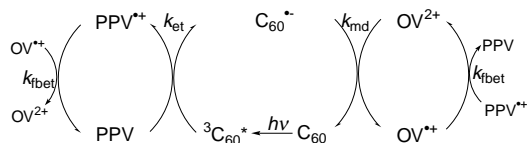
It becomes clear that triethylamine and triethanolamine also act as donors which generate the persistent radical anion of  $C_{60}$ , because the corresponding radical cations



**Figure 14.** Absorption-time profiles of  $C_{60}^-$  in the presence of the molecular oxygen. Inset: Pseudo-first-order plot. Reprinted with permission from [72], T. Konishi et al., *Chem. Lett.* 202, (2000). © 2000, The Japan Chemical Society.

easily decompose into less electron-accepting compounds, which are not identified yet. It should be noted that these donors are soluble in water. Thus, they can be employed as sacrificial donors also in aqueous systems.

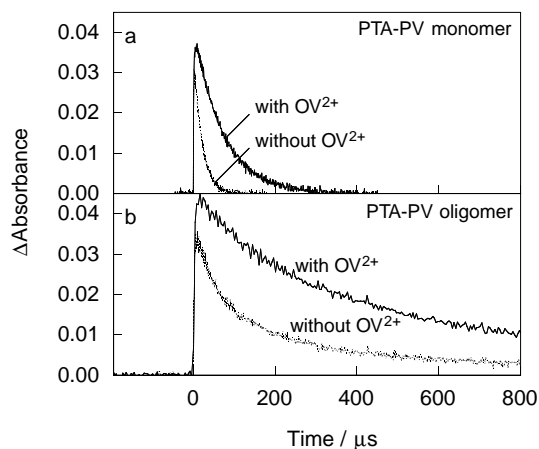
In the electron-transfer systems of the  $C_{60}$  and monomer/oligomer of poly(*p*-phenylenevinylene),  $C_{60}$  acts as a photosensitizer and electron mediator, since photoexcited  $C_{60}$  accepts an electron from the donor and mediates the electron to octylviologen dication ( $OV^{2+}$ ), another electron acceptor, efficiently [59]. In the electron-transfer system of  $C_{60}$  and monomer of TPA-PV (Fig. 10) in the presence of  $OV^{2+}$ , the generation of the radical anion of  $C_{60}$  was confirmed in the transient absorption spectra. With decrease of  $C_{60}^-$ , generation of  $OV^{\cdot+}$  was confirmed, indicating that electron transfer from  $C_{60}^-$  to  $OV^{\cdot+}$  occurs (Scheme 8). It should be noted that the radical cation of TPA-PV of the electron-mediating systems showed slow decays (Fig. 15), indicating that the back electron transfer between  $OV^{\cdot+}$  and the radical cation of the TPA-PV monomer/oligomer is retarded due to the repulsion of the positive charges of both radical cations.



**Scheme 8.** Electron-mediating system of  $C_{60}$ .

### 3.9. Water-Soluble Fullerenes

Pristine fullerenes are not soluble in water, while advantageous properties are expected in the fields of biology. Thus, much effort has been devoted to prepare water-soluble fullerenes. Sufficient solubility in water was achieved by several manners: inclusion complex formation of fullerenes with

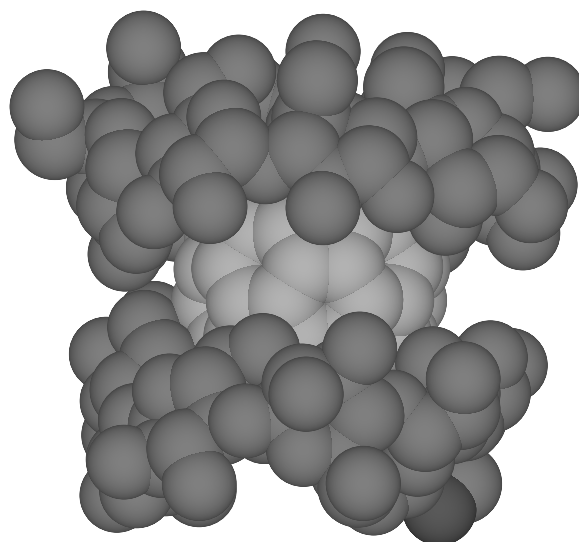


**Figure 15.** Time profiles at 1600 nm of the electron-transfer systems of (a)  $C_{60}$  and PTA-PV monomer and (b) PTA-PV oligomer in the presence and absence of  $OV^{2+}$ . Reprinted with permission from [59], H. Onodera et al., *J. Phys. Chem. A* 105, 7341 (2001). © 2001, American Chemical Society.

water-soluble compounds and introduction of water-soluble addends to fullerenes.

The water-soluble complexes with fullerenes have been achieved by using  $\gamma$ -cyclodextrin ( $\gamma$ -CD), water-soluble calixarene, miscelle, and water-soluble polymers.

Yoshida et al. reported that  $C_{60}$  forms the 1:2-complex with  $\gamma$ -CD (Fig. 16), which shows good solubility in water [74]. Andersson et al. reported that  $C_{70}$  also forms the complex with  $\gamma$ -CD [75]. Since the spectral shapes of the ground state and triplet excited state are not changed by the inclusion in  $\gamma$ -CD, the interaction between fullerenes and  $\gamma$ -CD is quite weak. It was revealed that the bimolecular excitation-relaxation and electron-transfer processes of the inclusion complex of fullerene in  $\gamma$ -CD are changed in comparison to the pristine fullerenes [29]. For example, the rate constants for the triplet-triplet annihilation processes of  $C_{60}$  and  $C_{70}$  in  $\gamma$ -CD are much smaller than



**Figure 16.**  $C_{60}$  encapsulated in  $\gamma$ -cyclodextrin.

the diffusion-limiting rate of the solvent. Furthermore, the rate constant for electron transfer of  $C_{60}$  in  $\gamma$ -CD with 1,4-diaza[2.2.2]bicyclooctane (DABCO) is 1/10–1/100 of the corresponding rate constants of the pristine fullerenes. Thus, the  $\gamma$ -CD is a retarder for the photoinduced processes of the fullerenes. Since  $\gamma$ -CD acts as retarder for the back electron-transfer process, the radical anions of fullerenes in  $\gamma$ -CD show long lifetimes compared to those of the pristine fullerenes. This aspect is favorable in the utilization of the radical anion of fullerenes as an electron mediator. Furthermore, the persistent radical anion formation was observed in the presence of triethanolamine as mentioned in Section 3.8. It was revealed that both the radical anion of  $C_{60}$  in  $\gamma$ -CD and the radical cation of methyl viologen are present at the same time as the equilibrium in water media.

Fullerenes are also known to form the inclusion complexes with calixarenes. In the case of the water-soluble inclusion complex of  $C_{60}$  and calixarene (cationic homoaxalix[3]arene), substantial interaction between fullerenes and the calixarene was observed in the ground state absorption spectrum [76]. Increase in the absorption intensity around 400–500 nm of  $C_{60}$  in calixarene can be attributed to the charge-transfer complex formation due to the  $\pi$ -electron system of calixarene. Strong interaction between the calixarene and fullerenes was also observed in the excited states. The triplet absorption peak of  $C_{60}$  in the calixarene appeared at 545 nm, which is largely blueshifted compared to that of pristine  $C_{60}$ . The triplet lifetime is as short as 50 ns. The substantial interaction between calixarene and included  $C_{60}$  was also observed in the singlet excited state as a large blueshift of the fluorescence peak.

Pristine fullerenes become soluble in water when they are incorporated in a micellar system. It was confirmed that a micellar system of poly(vinylpyrrolidone) and  $C_{60}$  showed bioactivity, such as mutagenicity, lipid peroxidation, and DNA-strand scission, upon visible-light irradiation in the presence of  $O_2$ , via generation of the active oxygen species [7].

By introduction of the hydrophilic groups such as  $COO^-$  to  $C_{60}$ , the  $C_{60}$  adducts are dissolved in water as clusters [77]. The cluster formation was excluded by using surfactants. Guldi reported that the excited singlet state properties of the clusters are not changed from the monomer state [77]. On the other hand, they showed acceleration of the decay of the triplet state of the adduct in the cluster due to triplet–triplet annihilation.

Water-soluble clusters of fullerenes were also achieved by introduction of addend with positive charge [78]. It is interesting to note that the positively charged fullerene clusters showed fast reduction of the fullerene core in a cluster due to electron-attracting force. Furthermore, it has been reported that the fullerene with cationic addend showed cleavage of double-strand DNA via generation of the active oxygen species [79].

### 3.10. Fullerodendrimers

Dendrimers have attracted wide attention because of their artificial three-dimensional nanostructures [80]. Fullerenes have been employed as a core, in branches, or as terminals of dendrimer molecules, that is, fullerodendrimers [81–87].

Introduction of dendritic branches to the fullerene core can improve solubility and processability. Furthermore, it also provides an additional functionality of the branches themselves [85].

For the fullerodendrimers, in which fullerene moieties are employed as focal points of dendrimers (Fig. 17), it has been reported that bimolecular processes of the dendrimers are varied to a great extent depending on the generation of the dendrimer moiety [86]. For example, photoinduced electron-transfer rate constants of fullerodendrimers with benzyl-ether type dendrons depend on dendrimer generation: the electron-transfer rate constants of the fourth generation were ca. 1/2–1/4 of the second generation. For the electron-transfer processes of the dendrimers, long-range electron-transfer processes were suggested from the comparison with the expectation by the semiempirical Rehm–Weller relation [42]. The findings indicate the shielding effect of the dendron groups. It should be pointed out that these shielding effects are also observed for other bimolecular processes such as triplet–triplet annihilation and energy-transfer processes and are effective for dendron groups larger than the third generation as reported for Fréchet-type dendrimers. The shielding effect of the dendrimer is important from the viewpoint of drug delivery, since it retains chemically active species for long time.

As for the monomolecular processes of the fullerene moiety of the dendrimers, such as singlet and triplet lifetimes,

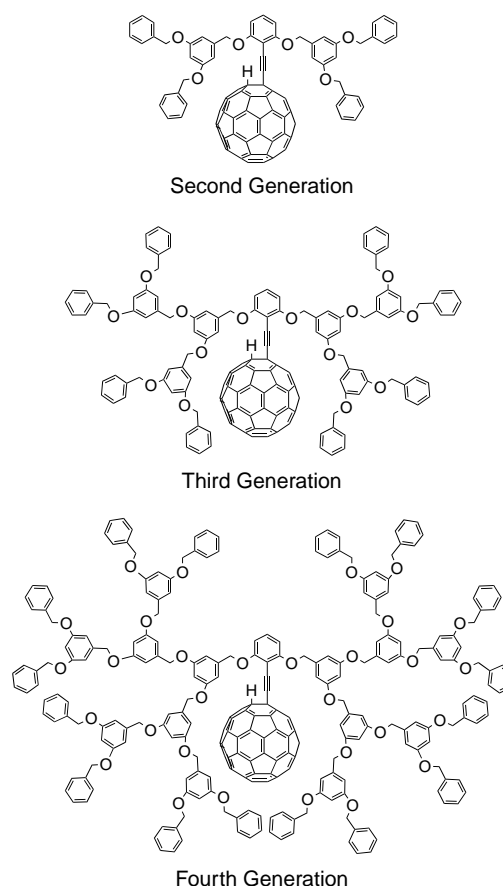


Figure 17. Molecular structures of fullerodendrimers.

substantial dependence on the dendrimer generation was not observed, indicating that the effects of the dendron groups on the excited state properties of the fullerene moiety are small [86].

Introduction of the dendrimer moiety to the fullerene is also beneficial to attain water-soluble fullerenes. Takaguchi et al. reported that fullerodendrimer bearing dendritic poly(amidoamine) substitute shows substantial solubility in water [87]. It was confirmed that the singlet oxygen was generated by the energy transfer from triplet excited fullerene moiety of the dendrimers. Furthermore, since their dendrimer generates pristine  $C_{60}$  by reversible Diels–Alder reaction, their dendrimers are interesting from the biological point of view.

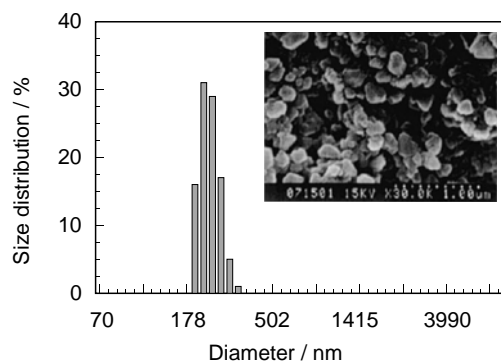
By introduction of functionality on the dendron groups, electronic interaction between the dendron groups and fullerene moiety becomes evident. Guldi et al. reported the photoinduced charge separation and energy-transfer processes in the fullerodendrimers having phenylene vinylene dendron groups [85]. The fast and highly efficiently intramolecule processes are interesting as summarized in the next section. Further interesting properties are expected for these fullerodendrimers by adding functions both to core and branch moieties.

## 4. PHOTOINDUCED PROCESSES OF FINE PARTICLES OF FULLERENES

### 4.1. Photochemistry of Fullerene Fine Particles

Fullerenes do not show sufficient solubility in the conventional organic solvents. Thus, it has been reported that fullerenes generate aggregates in poor solvents [88]. By utilizing this aspect of fullerenes, one can obtain fullerene fine particles easily.

The fine particles of the fullerenes are prepared by injection of fullerene in *o*-dichlorobenzene solution to continuously stirring ethanol [89, 90]. The fine particles of  $C_{60}$  have granular-type shape and the average diameter was estimated to be 270 nm (Fig. 18). The crystalline structure of the  $C_{60}$  fine particles was confirmed by X-ray scattering and



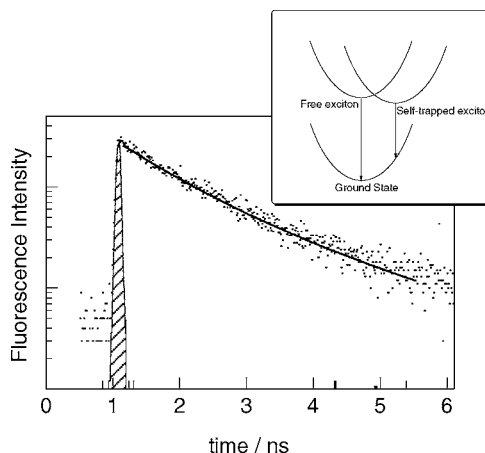
**Figure 18.** Size distribution of the fine particles of  $C_{60}$ . Inset: scanning electron microscope (SEM) picture. Reprinted with permission from [90], M. Fujitsuka et al., *J. Photochem. Photobiol. A: Chem.* 133, 45 (2000). © 2000, Elsevier Science.

transmission electron microscope (TEM) observation. In the TEM picture, it was confirmed that the crystalline structure is retained throughout the fine particle. In the case of  $C_{70}$ , the generation of the fine particles was also confirmed. The average diameter of the  $C_{70}$  fine particles is estimated to be 140 nm. It was revealed that the fine fullerene particles several tens of nanometers in diameter can be obtained by using supercritical conditions.

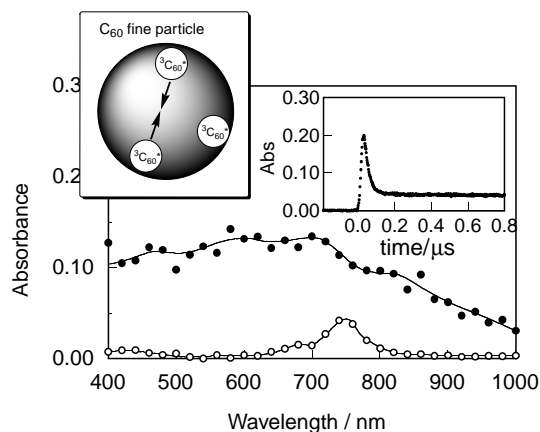
The ground state absorption spectrum of the  $C_{60}$  fine particles is quite broad compared to the isolated  $C_{60}$  in toluene. The spectral features of the  $C_{60}$  fine particles are similar to those of the  $C_{60}$  bulk crystals. These findings indicate that substantial interactions are present between the  $C_{60}$  molecules in the fine particles. It is interesting to note that the absorption peak of the  $C_{60}$  fine particles shifts to the shorter wavelength side compared to that of the  $C_{60}$  bulk crystal. The shift of the absorption peak will indicate the size effect of the fine particles as observed with the fine crystals of perylene [91].

The fine particles of  $C_{60}$  showed weak fluorescence around 700–750 nm upon excitation with a picosecond laser. The fluorescence decay profile of the  $C_{60}$  fine particles shows the two-component-decay with 0.8 and 2.1 ns of the fluorescence lifetimes (Fig. 19). The two-component-decay can be attributed to the deactivation processes of the free exciton and self-trapped exciton levels as supposed for the organic crystalline materials.

The transient absorption bands of the triplet excited state of the  $C_{60}$  fine particles can be observed by the nanosecond laser irradiation (355 nm). Immediately after the laser irradiation, the  $C_{60}$  fine particles show a quite broad absorption band around 700 nm (Fig. 20). The quite broad transient absorption band decays within 50 ns, and a sharp absorption band remains at 500 ns after the laser irradiation. From the comparison with the transient absorption spectrum of  $C_{60}$  in toluene, the sharp absorption band at 750 nm can be attributed to the localized triplet excited state of  $C_{60}$  in the fine particles. The fast-decaying component can be attributed to the triplet–triplet annihilation process in the fine particles, since the fast-decaying component can



**Figure 19.** Fluorescence decay profile of the fine particles of  $C_{60}$ . Inset: Schematic diagram of free exciton and self-trapped exciton. Reprinted with permission from [90], M. Fujitsuka et al., *J. Photochem. Photobiol. A: Chem.* 133, 45 (2000). © 2000, Elsevier Science.



**Figure 20.** Transient absorption spectra of  $C_{60}$  fine particles at 50 ns (solid circle) and 500 ns (open circle) after 355-nm laser light irradiation. Inset: absorption-time profile at 740 nm. Scheme for the T-T annihilation in the  $C_{60}$  fine particles. Reprinted with permission from [90], M. Fujitsuka et al., *J. Photochem. Photobiol. A: Chem.* 133, 45 (2000). © 2000, Elsevier Science.

be attributed to the triplet excited state from the picosecond laser flash photolysis measurements, in which generation of the broad absorption band via the intersystem crossing process was observed.

From the laser power dependence of the absorption-time profiles of the  $C_{60}$  fine particles, it was confirmed that the fast-decaying part appears when the excitation laser power becomes high; only the slow-decaying part appears with lower laser power excitation. This finding indicates that the triplet-triplet annihilation process in the fine particles becomes apparent only when the density of the triplet excited states becomes sufficiently high by the higher laser power.

On the other hand, the localized triplet excited state was not confirmed with the  $C_{70}$  fine particles. Furthermore, the fine particles of  $C_{60}$  with diameter smaller than 100 nm also did not show such localized triplet states. These findings indicate that the triplet-triplet annihilation process in the fine particles largely depends on the crystalline structure and diameter of the fine particles.

When the dispersion of the  $C_{60}$  fine particles was saturated by oxygen, the absorption band of the localized triplet excited state was quenched. The quenching of the localized triplet excited state can be attributed to the energy-transfer reaction from the triplet excited state to the oxygen generating the singlet oxygen. This finding indicates that the localized triplet excited state of the  $C_{60}$  fine particles is reactive to the substrate in the dispersion. The energy-transfer process can be observed when the dispersion solution includes  $\beta$ -carotene, a triplet energy acceptor. The energy-transfer process can be confirmed by the generation of the triplet excited state of  $\beta$ -carotene with the concomitant decay of the localized triplet excited state of the  $C_{60}$  fine particles. The bimolecular quenching rate of the energy transfer between  $\beta$ -carotene and the  $C_{60}$  fine particles was estimated to be  $1.5 \times 10^9 \text{ M}^{-1} \text{ s}^{-1}$ , indicating that the efficient energy transfer process takes place on the surface of the  $C_{60}$  fine particles.

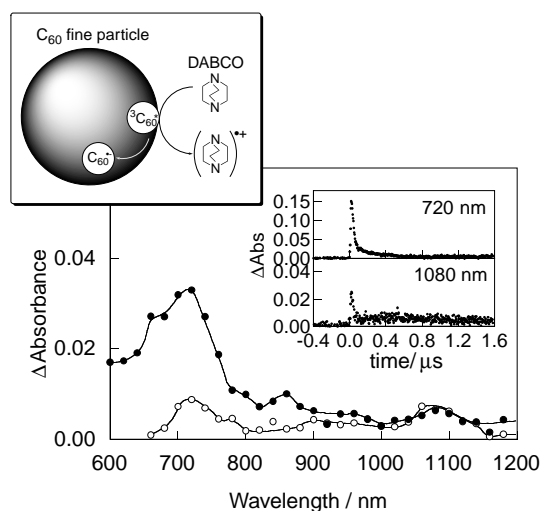
Photoinduced electron-transfer processes of the  $C_{60}$  fine particles were also confirmed in the transient absorption spectra. When the nanosecond laser light was irradiated to the solution containing the  $C_{60}$  fine particles and DABCO, an electron donor, generation of the radical anion of the  $C_{60}$  fine particles was confirmed with a decrease of the triplet excited state of  $C_{60}$  localized in the fine particles (Fig. 21). This finding indicates that the localized triplet excited state is also active to the photoinduced electron-transfer processes. The bimolecular rate constant for the present electron transfer was estimated to be  $2 \times 10^8 \text{ M}^{-1} \text{ s}^{-1}$ , which is smaller than the rate constant between  $C_{60}$  and DABCO in solution ( $4 \times 10^9 \text{ M}^{-1} \text{ s}^{-1}$ ). The smaller rate constant of the  $C_{60}$  fine particles can be attributed to the reaction process on the surface of the fine particles. The generated radical ions are finally recombined to form their neutral states. The photoinduced oxidation process of the  $C_{60}$  fine particles was also confirmed using the cosensitization reaction with the nanosecond laser flash photolysis.

These observations indicate that the localized triplet excited states of the fine particles are reactive species to the molecules in the solution both for the electron-transfer and for the energy-transfer processes, although the rate constants are somewhat smaller than those for the reaction systems, in which both donor and acceptor are isolated molecules in the solution.

## 5. FULLERENE OLIGOMERS, HIGHER FULLERENES, AND METALLOFULLERENES

### 5.1. Fullerene Dimers and Trimers

Fullerenes are also reactive to fullerene itself. Fullerene polymers have been synthesized by several methods [23, 92–94]. Investigations on properties of fullerene dimers



**Figure 21.** Transient absorption spectra of  $C_{60}$  fine particles in the presence of DABCO at 100 ns (solid circle) and 500 ns (open circle) after 355-nm laser light irradiation. Inset: absorption-time profiles. Scheme for the electron transfer process of the fine particles of  $C_{60}$ . Reprinted with permission from [90], M. Fujitsuka et al., *J. Photochem. Photobiol. A: Chem.* 133, 45 (2000). © 2000, Elsevier Science.



and trimers seem to be important to elucidate properties of one-dimensional and two-dimensional fullerene polymeric materials. From this viewpoint, several experimental and theoretical investigations have been reported on fullerene dimers and trimers. Fullerene dimer ( $C_{120}$ ) and trimer ( $C_{180}$ ) can be obtained by the high-speed vibration milling developed by Komatsu et al. (Fig. 22) [23, 95]. Ground state absorption spectra of  $C_{120}$  and  $C_{180}$  showed an absorption band around 700 nm which is characteristic of 1,2-adducts of  $C_{60}$  [96–98]. Furthermore, fluorescence spectra showed fluorescence bands similar to those of 1,2-adducts of  $C_{60}$ . Fluorescence quantum yields were in the order: 1,2-adducts of  $C_{60}$  > dimer ( $C_{120}$ ) > trimer ( $C_{180}$ ) >  $C_{60}$  polymer (Table 1). In the triplet absorption spectrum of  $C_{180}$ , substantial broadening of the transient absorption band was observed (Fig. 23). This finding indicates that the interactions between the fullerene moieties are present in the excited triplet state. It was revealed that the extinction coefficient of  ${}^3C_{180}^*$  is about 1/5 that of  $C_{60}$ . Ma et al. [96] reported that the  $C_{60}$  polymer did not show a transient absorption band upon excitation. Thus, properties of  $C_{180}$  can be regarded as intermediate between  $C_{60}$  and  $C_{60}$  polymers.

In the case of  $C_{120}O$ , spectral features of ground state absorption and fluorescence are quite similar to those of 1,2-adducts of  $C_{60}$  [99]. Thus, the interactions between the fullerene moieties are also small in the ground and excited states. As for the triplet absorption band, on the other hand, transient absorption bands appear at 630 and 480 nm, which are blueshifted compared with those of  $C_{120}$  and 1,2-adducts. Furthermore, the triplet lifetime was estimated to be 160 ns, which is quite shorter than those of  $C_{120}$  and 1,2-adducts. These findings indicate a substantial interaction between the two  $C_{60}$ -moieties. Therefore, interaction between two  $C_{60}$ -moieties depends largely on distance and orientation of two  $C_{60}$ -moieties.

When  $C_{118}N_2$ , a dimer of azafullerene  $C_{59}HN$ , is excited with the nanosecond laser, transient absorption bands appeared at 1280, 1000, 880, and 680 nm which are quite

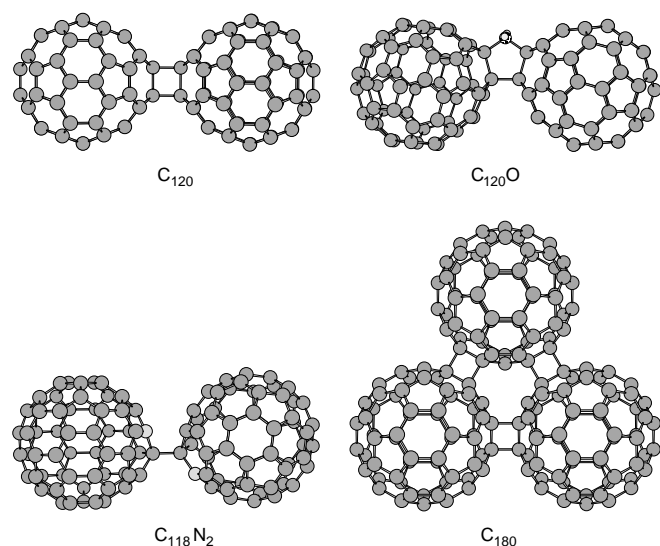
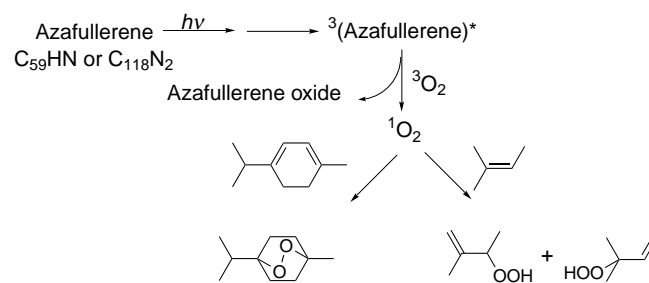


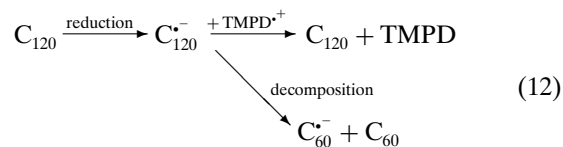
Figure 22. Molecular structures of  $C_{120}$ ,  $C_{120}O$ ,  $C_{118}N_2$ , and  $C_{180}$ .

different from azafullerene  $C_{59}HN$ :  $C_{59}HN$  shows a transient absorption peak at 750 nm along with a shoulder at 1050 nm (Fig. 24) [100]. It has been reported that the laser irradiation of  $C_{118}N_2$  generates  $C_{59}N$  radical [101]. However, it becomes clear that these absorption bands include the triplet excited state of  $C_{118}N_2$ , because these transient absorption bands are quenched in the presence of oxygen due to the triplet energy transfer generating singlet oxygen, which was observed in the near-IR emission spectra. Thus the different spectral features of the triplet excited  $C_{118}N_2$  and  $C_{59}HN$  indicate the interactions between two azafullerenyl cages. The decay lifetime of the triplet excited  $C_{118}N_2$  is 10  $\mu$ s, while that of  $C_{59}HN$  was 5  $\mu$ s. The  $\Phi_{ISC}$  values were estimated to be 0.48 for both  $C_{118}N_2$  and  $C_{59}HN$ . It has been reported that the triplet excited  $C_{118}N_2$  and  $C_{59}HN$  work as sensitizers in the oxidation reactions of olefins; 2-methyl-2-butene and  $\alpha$ -terpinene undergo ene and Diels–Alder photooxygenation reactions, respectively, to produce the corresponding peroxides in the presence of a minute amount of  $C_{118}N_2$  or  $C_{59}HN$  (Scheme 9) [102].



Scheme 9. Reaction scheme for oxidation reactions of olefins by  $C_{118}N_2$  or  $C_{59}HN$  sensitizer. Reprinted with permission from [102], N. Tagmatarchis and H. Shinohara, *Org. Lett.* 2, 3351 (2000). © 2000, American Chemical Society.

When the  $C_{120}$  is excited in the presence of *N,N,N,N*-tetramethyl-1,4-phenylenediamine (TMPD), absorption bands of the  $C_{120}$  radical anion appear with the decay of the triplet state of  $C_{120}$ , indicating the electron transfer via the triplet excited state [97]. Spectral features of the  $C_{120}$  radical anion are similar to those of the 1,2-adducts of  $C_{60}$ , indicating that interaction among fullerene cages is also negligibly small in the radical ion state. This finding indicates that a minus charge of the  $C_{120}$  radical anion is localized on one fullerene cage of the dimer molecule as in the case of the excited states. It should be noted that the radical anion of  $C_{120}$  decayed by the back electron transfer to the ground state. On the other hand, the ground state reduction of  $C_{120}$  by TDAE resulted in decomposition of the  $C_{120}$  radical anion into  $C_{60}$  and  $C_{60}$  radical anion. Thus, the decomposition of the  $C_{120}$  radical anion is a slower reaction than the back electron-transfer process between the  $C_{120}$  radical anion and the TMPD radical cation. The rate for the decomposition should be slower than the order of  $10^5$  s $^{-1}$ :



**Table 1.** Photophysical properties of  $C_{60}$ , 1,2-adduct of  $C_{60}$  ( $C_{60}R^a$ ),  $C_{120}$ ,  $C_{120}O$ , and  $C_{180}$ .

	$C_{60}$	$C_{60}R^a$	$C_{120}$	$C_{120}O$	$C_{180}$
<b>Singlet</b>					
$E_s$ (eV)	1.7	1.7~1.8	1.7	1.8	1.7
$\tau_F$ (ns)	1.2	1.2~1.3	1.6	1.7	0.9
$\Phi_F$	$3.2 \times 10^{-4}$	$(1.0\text{--}1.2) \times 10^{-3}$	$7.9 \times 10^{-4}$	$8.7 \times 10^{-4}$	$5.5 \times 10^{-4}$
<b>Triplet</b>					
$\tau_{TT}$ (nm)	750	680–700	700	680	700
$\epsilon_T$ ( $M^{-1} \text{ cm}^{-1}$ )	$1.6 \times 10^4$	$(1.4\text{--}1.6) \times 10^4$	$1.4 \times 10^4$	$7.7 \times 10^3$	$2.7 \times 10^3$
$\tau_T$ ( $\mu\text{s}$ )	55	24–29	23	0.16	24
$\Phi_{ISC}$	1.0	0.88–0.95	$0.7 \pm 0.1$	0.48	$0.74 \pm 0.1$

<sup>a</sup> $C_{60}(C_3H_6N)p-C_6H_4CHO$  [30].

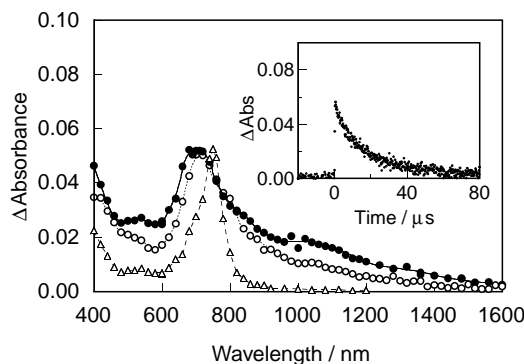
Source: Reprinted with permission from [98], M. Fujitsuka et al., *Chem. Lett.* 384 (2001); © 2001, Chemical Society of Japan and [99], M. Fujitsuka et al., *J. Phys. Chem. A* 105, 675 (2001), © 2001, American Chemical Society.

In the case of  $C_{120}O$ , electron transfer was confirmed by the appearance of a new absorption band at 1000 nm in the presence of DABCO [99]. It became clear that the generated radical ions decayed predominantly by the back electron transfer at the diffusion-limiting rate.

In Table 1, estimated properties of fullerene dimers are summarized as well as those of  $C_{60}$ , 1,2-adducts of  $C_{60}$ , and  $C_{180}$ . It becomes clear that the interaction between the fullerene moieties in the fullerene oligomers largely depends on  $C_{60}$ – $C_{60}$  distance and orientation.

## 5.2. Higher Fullerenes

Recently, photophysical and photochemical processes of  $C_{76}$ ,  $C_{78}$ ,  $C_{82}$ , and  $C_{84}$  (Fig. 25) have been investigated [103–107]. Compared with  $C_{60}$  and  $C_{70}$ , ground state absorption spectra of higher fullerenes are ranging to the near-IR region. Although absorption spectra of higher fullerenes depend on their size and symmetry, roughly saying, higher fullerenes are expected to have absorption edges at the longer wavelength side, suggesting the smaller highest occupied–lowest unoccupied molecular orbital (HOMO–LUMO) gaps. These small HOMO–LUMO gaps of the higher fullerenes also accord with the small differences between the first oxidation and reduction potentials of higher fullerenes (Table 2)

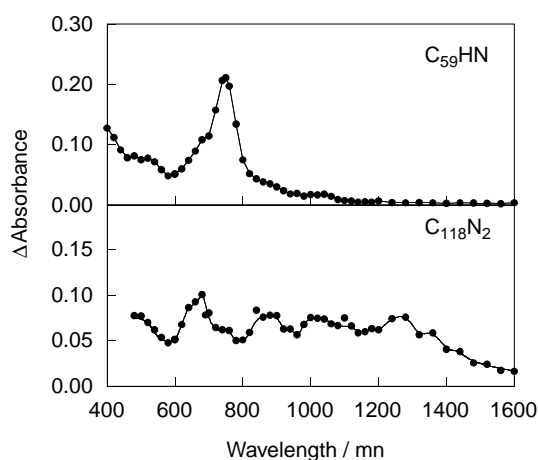


**Figure 23.** Transient absorption spectra of  $C_{60}$  (triangle),  $C_{120}$  (open circle), and  $C_{180}$  (closed circle) at 100 ns after the laser light irradiation. Inset: Absorption-time profile of  $C_{180}$  at 700 nm. Reprinted with permission from [98], M. Fujitsuka et al., *Chem. Lett.* 384 (2001). © 2001, Chemical Society of Japan.

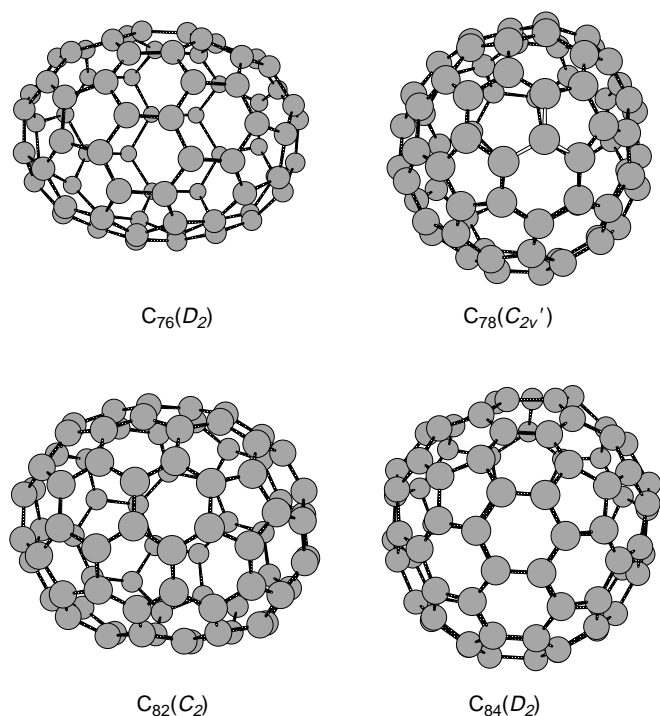
[108]. Therefore, facile oxidations of fullerenes are expected as well as easy reductions.

$C_{76}$  showed transient absorption bands at >900, 625, and 550 nm upon subpicosecond laser light irradiation at 388 nm (150 fs fwhm) as shown in Figure 26. These absorption bands decayed quickly within 100 ps, and a broad absorption band remained around 550 nm. Since the 388-nm laser light pumps  $C_{76}$  into the higher singlet excited state ( $S_n$ ), the fast-decaying component can be attributed to an internal conversion process generating the lowest singlet excited state ( $S_1$ ) from the higher singlet excited state (Fig. 3). The slow decaying component corresponds to the deactivation process of the lowest singlet excited state to the ground and the triplet excited states. The rates for the fast- and slow-decaying components correspond to 83 ps and 2.6 ns of the lifetimes of  $S_n$  and  $S_1$ , respectively. A similar two-step decay process was also observed with  $C_{78}$ .

In the triplet excited state, higher fullerenes show the absorption bands in the visible and near-IR regions (Fig. 27). It should be noted that the intensities of the transient absorption bands of higher fullerenes are quite low compared with those of  $C_{60}$  and  $C_{70}$ . These low signal intensities



**Figure 24.** Transient absorption spectra of  $C_{59}HN$  and  $C_{118}N_2$  in toluene at 100 ns after the laser light irradiation. Reprinted with permission from [100], N. Tagmatarchis et al., *J. Org. Chem.* 66, 8028 (2001). © 2001, American Chemical Society.



**Figure 25.** Molecular structures of  $C_{76}(D_2)$ ,  $C_{78}(C_{2v}')$ ,  $C_{82}(C_2)$ , and  $C_{84}(D_2)$ .

can be explained on the basis of low  $\Phi_{ISC}$  values. Quite low  $\Phi_{ISC}$  values seem to be a common feature of the higher fullerenes, in which the nonradiative deactivation process from the singlet excited states to the ground states may be an efficient pathway. The transient absorption bands of higher fullerenes are governed by the self-quenching process rather than the triplet-triplet annihilation [Eqs. (1) and (2)]. The estimated intrinsic triplet lifetimes of the higher fullerenes (Table 3) are shorter than those of  $C_{60}$  and  $C_{70}$ . Therefore, shorter triplet lifetimes seem to be a common feature of higher fullerenes.

When the higher fullerenes are treated with TDAE, the radical anions of the higher fullerenes are generated: The generation of the radical anions of higher fullerenes was confirmed by the electron paramagnetic resonance (EPR) measurements. It should be noted that the radical anion

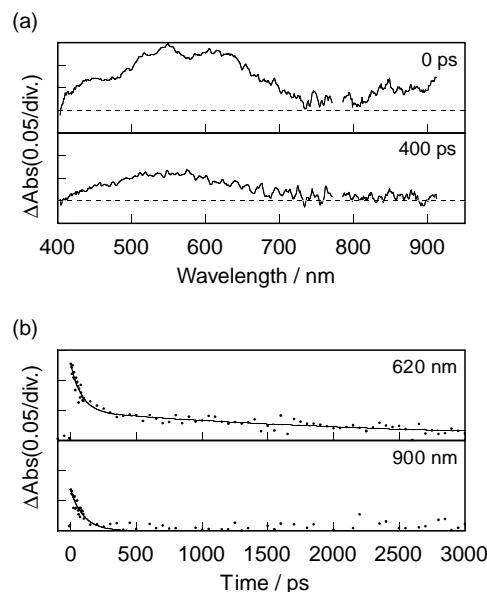
**Table 2.** Half-wave potentials and ( $E_{ox} - E_{red}$ ) for the fullerenes in 1,1,2,2-tetrachloroethane.

	$E_{1/2}$ vs $Fc/Fc^+$ in volts					$E_{ox} - E_{red}$
	+2/+1	+1/0	0/-1	-1/-2	-2/-3	
$C_{60}$	—	1.26	-1.06	—	—	2.32
$C_{70}$	1.75	1.20	-1.02	—	—	2.22
$C_{76}$	1.30	0.81	-0.83	-1.12	—	1.64
$C_{78}^a$	1.43	0.95	-0.77	-1.08	—	1.72
$C_{78}^b$	1.27	0.70	-0.77	-1.08	—	1.47
$C_{84}$	—	0.93	-0.67	-0.96	-0.96	1.60

<sup>a</sup> Major isomer.

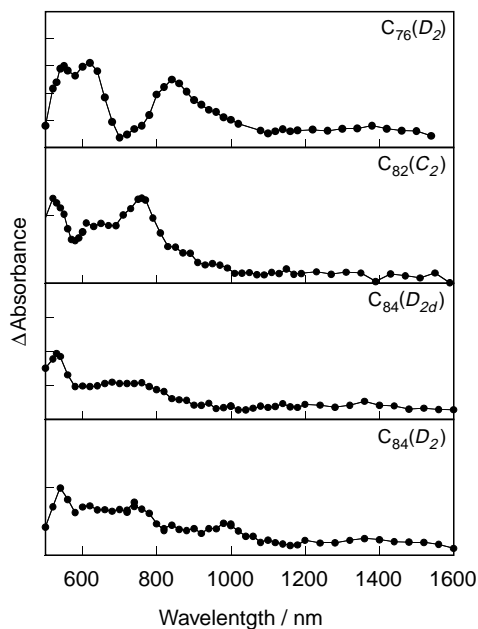
<sup>b</sup> Minor isomer.

Source: Reprinted with permission from [108], Y. Yang et al., *J. Am. Chem. Soc.* 117, 7801 (1995). © 1995, American Chemical Society.



**Figure 26.** (a) Transient absorption spectra of  $C_{76}$  in toluene upon femtosecond laser light irradiation [388 nm, full width at half maximum (FWHM) 150 fs]. (b) Absorption-time profiles.

of  $C_{82}$  is also generated by TMPD or DABCO without photoirradiation. The generation of the radical anion of  $C_{82}$  by TMPD or DABCO can be attributed to the lower reduction potential of  $C_{82}$  compared with other fullerenes such as  $C_{60}$  and  $C_{70}$ , which do not generate the radical anions in the dark.



**Figure 27.** Transient absorption spectra of higher fullerenes,  $C_{76}(D_2)$ ,  $C_{82}(C_2)$ ,  $C_{84}(D_{2d})$ , and  $C_{84}(D_2)$  in toluene at 100 ns after the laser light irradiation. Reprinted with permission from [103], M. Fujitsuka et al., *J. Phys. Chem. A* 101, 4840 (1997) and [106], *J. Phys. Chem. B* 103, 9519 (1999). © 1997, 1999, American Chemical Society.

**Table 3.** Photophysical and photochemical properties of C<sub>60</sub>, C<sub>70</sub>, C<sub>76</sub>, C<sub>78</sub>, C<sub>82</sub>, and C<sub>84</sub>.

Properties <sup>a</sup>	C <sub>60</sub>	C <sub>70</sub>	C <sub>76</sub> (D <sub>2</sub> )	C <sub>78</sub> (C <sub>2v</sub> )	C <sub>82</sub> (C <sub>2</sub> )	C <sub>84</sub> (D <sub>2d</sub> )
Singlet properties						
<i>E<sub>S</sub></i> (eV)	1.7	1.8	1.33	0.9	1.0	1.1
<i>τ<sub>S<sub>n</sub></sub></i> (ps)	0.25 <sup>c</sup>	<1	83	28		
<i>τ<sub>S1</sub></i> (ns)	1.2	0.66	2.6	1.0	1.7	
<i>Φ<sub>F</sub></i>	0.00032 <sup>d</sup>	0.00052 <sup>d</sup>	— <sup>e</sup>	— <sup>e</sup>	— <sup>e</sup>	— <sup>e</sup>
Triplet properties						
<i>E<sub>T</sub></i> (eV)	1.5	1.5	1.0–1.1	<0.9	0.9–1.0	0.9–1.0
<i>τ<sub>T</sub></i> (μs)	143 <sup>f</sup>	118,000 <sup>f</sup>	9.6	10	56	20
<i>Φ<sub>ISC</sub></i>	1.0 <sup>g</sup>	0.97 <sup>h</sup>	0.05 <sup>i</sup>	0.12 <sup>i</sup>	<0.01	<0.01
Energy transfer rates						
Oxygen <sup>b</sup>	1.6 × 10 <sup>9</sup>	9.6 × 10 <sup>8</sup>	3.5 × 10 <sup>9</sup>	n.r. <sup>j</sup>	n.r. <sup>j</sup>	1.8 × 10 <sup>9</sup>
β-carotene	2.0 × 10 <sup>9</sup>	1.2 × 10 <sup>9</sup>	2.6 × 10 <sup>9</sup>	1.9 × 10 <sup>9</sup>	1.5 × 10 <sup>9</sup>	1.6 × 10 <sup>9</sup>

<sup>a</sup> *E<sub>S</sub>*, *τ<sub>S<sub>n</sub></sub>*, *τ<sub>S1</sub>*, *Φ<sub>F</sub>*, and *E<sub>T</sub>* refer to singlet energy, lifetime of *S<sub>n</sub>*, lifetime of *S<sub>1</sub>*, fluorescence quantum yield, and triplet energy, respectively.

<sup>b</sup> In M<sup>-1</sup> s<sup>-1</sup>.

<sup>c</sup> Data from [29].

<sup>d</sup> Data from [28].

<sup>e</sup> Difficult to estimate due to weak fluorescence bands. As for relative yield, see text.

<sup>f</sup> Data from [35].

<sup>g</sup> Data from [10].

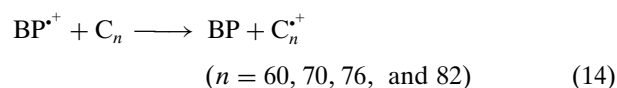
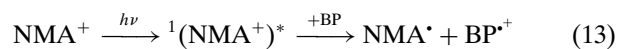
<sup>h</sup> Data from [38].

<sup>i</sup> Data from [104].

<sup>j</sup> No reaction.

The photoinduced electron-transfer processes with TMPD were also confirmed with higher fullerenes. The reaction rate constants are C<sub>60</sub> ≈ C<sub>70</sub> > C<sub>82</sub> > C<sub>76</sub> (Table 3). Based on the Rehm–Weller equation, free-energy changes for electron transfer from TMPD to the triplet excited fullerenes to TMPD are calculated to be –22, –22, –15, and –18 kcal mol<sup>-1</sup> for C<sub>60</sub>, C<sub>70</sub>, C<sub>76</sub>, and C<sub>82</sub>, respectively. Therefore, the order of reaction rate constants reflects the free-energy changes for the electron-transfer processes.

Oxidations of the higher fullerenes have been attempted by the two photoinduced processes: oxidation of excited higher fullerenes by the strong electron acceptor directly and oxidation by the sensitized reaction indirectly. For fullerenes, tetracyanoethylene (TCNE) can be utilized as an electron acceptor for direct photoinduced electron transfer. The generation of the radical cations of higher fullerenes was confirmed by their transient absorption spectra. In the case of C<sub>82</sub>, oxidation of C<sub>82</sub> in the ground state takes place with TCNE because of the lower oxidation potentials of C<sub>82</sub>. Using *N*-methylacridinium hexafluorophosphate (NMA<sup>+</sup>) and biphenyl (BP) as sensitizer and cosensitizer, respectively, the radical cations of fullerenes are generated by the following reaction schemes [109]:

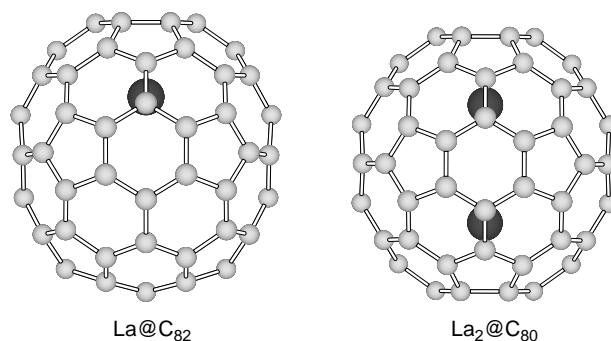


The reaction rate constants for Eq. (14) are estimated to be ~10<sup>10</sup> M<sup>-1</sup> s<sup>-1</sup> for higher fullerenes, indicating that the radical cations of higher fullerenes are formed effectively as observed with other fullerenes (C<sub>60</sub> and C<sub>70</sub>).

### 5.3. Metallofullerenes

Several kinds of endohedral metallofullerenes have been reported. Especially lanthanum-containing C<sub>82</sub>'s have been widely investigated. In the case of La@C<sub>82</sub>, it was confirmed by the EPR study that three electrons of La transfer to the C<sub>82</sub> cage, that is, La<sup>3+</sup> and C<sub>82</sub><sup>3-</sup>. Furthermore, fullerenes can also include two or three metal ions in one fullerene cage, such as La<sub>2</sub>@C<sub>80</sub>. In this section, photoexcitation and relaxation processes of La@C<sub>82</sub> and La<sub>2</sub>@C<sub>80</sub> (Fig. 28) are summarized [110].

The steady-state absorption spectra of La@C<sub>82</sub> show the absorption bands at 1412, 1002, and 636 nm, which are characteristic of the lanthanide metal-encapsulated C<sub>82</sub>-fullerenes. Since it has been reported that the change of central metal does not affect the positions of absorption maxima, the electronic transitions take place within the C<sub>82</sub><sup>3-</sup>. The absorption spectrum of La<sub>2</sub>@C<sub>80</sub> shows a broad band around 900 nm and a relatively sharp shoulder at 400–450 nm, which are characteristic bands of endohedral metallofullerenes.

**Figure 28.** Molecular structures of La@C<sub>82</sub> and La<sub>2</sub>@C<sub>80</sub>.

Immediately after the laser light irradiation, the transient absorption band appeared at 780 nm with broad bands around 1500 and 840 nm. The transient absorption band decays according to two components. The decay rate constants of the fast- and slow-decaying components were  $1.2 \times 10^7$  and  $3.4 \times 10^5$  s<sup>-1</sup>, respectively. The fast- and slow-decaying components may be due to the doublet and quartet states, respectively.

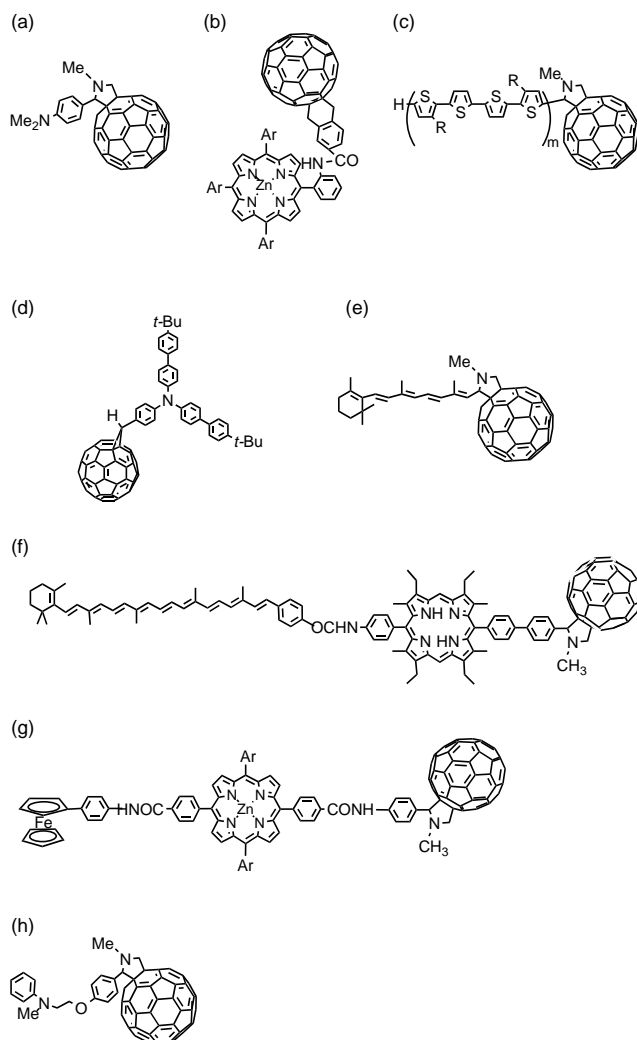
In the case of La<sub>2</sub>@C<sub>80</sub>, the decay with two steps was also observed. The fast- and slow-decaying components can be attributed to the excited singlet and triplet states, respectively. On cooling the solution as low as -30 °C, the intensity and decay rate were not increased. Thus, the movement of internal La ions does not affect the excited state properties much.

## 6. CHARGE SEPARATION AND RECOMBINATION PROCESSES OF DONOR-FULLERENE LINKED MOLECULES

### 6.1. Donor-Fullerene Dyad Molecules

Photoinduced processes of the donor-fullerene dyad molecules have been investigated widely [25–27]. In 1995, Williams et al. reported the intramolecular photoinduced charge-separation (CS) and charge-recombination (CR) processes of *N,N*-dimethylaniline-C<sub>60</sub> dyad molecules, in which the length between C<sub>60</sub> and dimethylaniline was 3 or 11  $\sigma$ -bonds (Fig. 29a) [111, 112]. They confirmed the CS process by observing a transient absorption band due to the radical cation of dimethylaniline. The CS proceeds from the singlet excited state of the C<sub>60</sub> moiety, since the fluorescence lifetime due to C<sub>60</sub> moiety becomes short. The CS rate constants were as fast as  $>1.6 \times 10^{10}$  and  $5.5 \times 10^9$  s<sup>-1</sup> for the 3- and 11-bond system, respectively, indicating that the CS process of these dyads proceeds almost quantitatively. On the other hand, the lifetime of the CS state of the 11-bond system is 0.25  $\mu$ s. Williams et al. attributed the fast CS and long lifetime of the CS state to very strong electronic coupling with the bridge by the special symmetry properties of the fullerene  $\pi$ -system.

As for the donor molecules, varieties of donors have been employed for the donor-fullerene linked molecules. Carotenoid, porphyrin, ferrocene, tetrathiafulvalene, oligothiophenes, aromatic amines, etc. have been employed for the dyad molecules [25–27, 113–124]. In these molecules, the quantum yields of the CS processes are close to unity. The lifetimes of the CS states are on the order of subnanosecond to microseconds. Imahori et al. reported that the reorganization energy of the dyad molecule including fullerene acceptor is small compared with that of reported electron acceptors such as benzoquinones due to the large  $\pi$ -electron system of fullerene. The small reorganization energy of the dyad molecules including fullerene is confirmed by analyses of the charge-transfer absorption and emission spectra of porphyrin-fullerene dyad molecules (Fig. 29b) in benzene [125]. The reorganization energy was estimated to be as small as 0.23 eV, which is comparable to the smallest values (0.22 eV) in the photosynthetic reaction

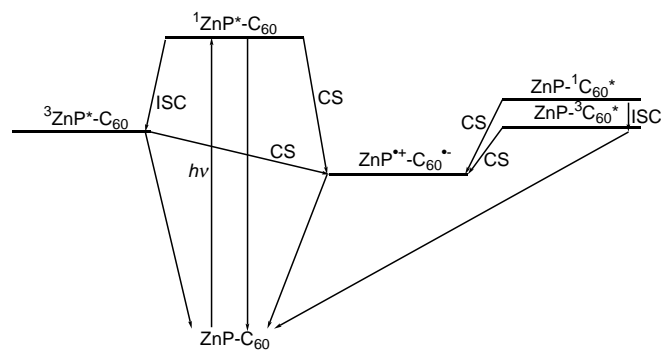


**Figure 29.** Molecular structures of dyads and triads including C<sub>60</sub>.

center. This feature seems to be one of the advantages of the fullerene-containing dyad molecules which are aiming at a long-lived CS state with high quantum yield for application to energy-storage systems or other sensitized reactions.

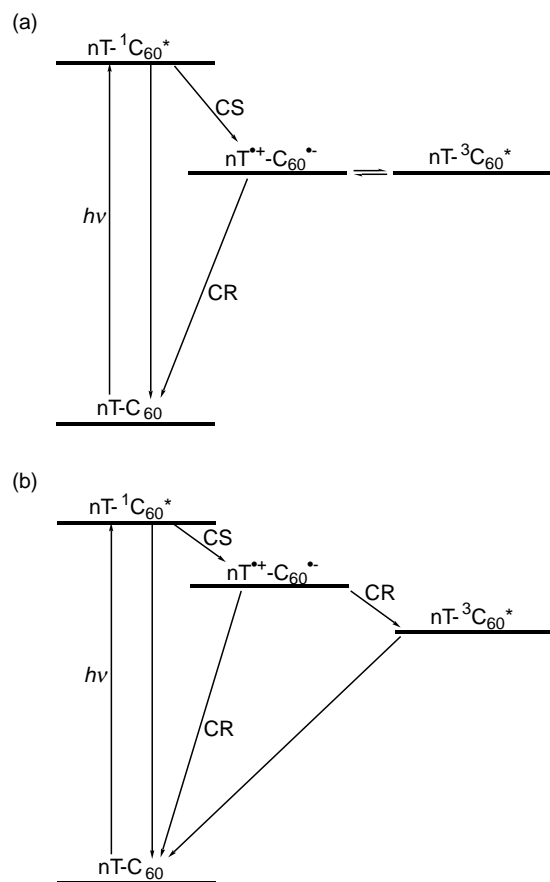
Usually, the CS process proceeds from the singlet excited state of fullerene or donor moiety. The triplet excited state of fullerene moiety is also a precursor of the long-lived CS state of the porphyrin-C<sub>60</sub> dyad [126], in which the CS rate from the triplet state was estimated to be  $5.5 \times 10^8$  s<sup>-1</sup> (Fig. 30).

In the case of the oligothiophene-fullerene dyad molecules, it has been reported that the CS state of tetrathiafulvalene-C<sub>60</sub> dyad (Fig. 29c) shows lifetimes as long as 6.3  $\mu$ s in benzonitrile due to an equilibrium between the CS state and the excited triplet state of C<sub>60</sub> (Fig. 31a) [120]. The long-lived CS states were also observed for the aromatic amine-C<sub>60</sub> and retinyl-C<sub>60</sub> dyads (Fig. 29d, e) [120–122, 124]. In the latter case the lifetime of the CS state is 20  $\mu$ s. The equilibrium between the CS state and the triplet state is supported by energetical consideration and some experimental facts, such as oxygen sensitivity and solvent polarity dependence of the CS state. The equilibrium is achieved when



**Figure 30.** Schematic energy diagram for CS processes of ZnP-C<sub>60</sub> in benzonitrile.

both states have close energy levels. When the energy level of the CS state is shifted by changing solvent polarity, the equilibrium is not obtained and the lifetime of the CS state becomes quite short, <1 ns (Fig. 31b). It should be noted that the equilibrium processes and the CR to the ground state are competitive. Thus, the long lifetime components are one part of the generated CS state. For example, in the case of octathiophene-C<sub>60</sub> dyad in benzonitrile, 85% of the CS state has lifetimes of 63 ps, while the long lifetime was 15% of the generated CS state.



**Figure 31.** Schematic energy diagrams for CS and CR processes of oligothiophene(nT)-C<sub>60</sub> in (a) polar and (b) moderately polar solvents.

## 6.2. Fullerene-Donors Triad and Tetrad Systems

The long lifetime of the CS state was also achieved by the introduction of the multistep-electron-transfer system. Liddell et al. reported that carotenoid-porphyrin-fullerene (C-H<sub>2</sub>P-C<sub>60</sub>) triad molecule (Fig. 29f) generates the final charge-separated state (C<sup>+</sup>-H<sub>2</sub>P-C<sub>60</sub><sup>-</sup>) via the C-P<sup>+</sup>-C<sub>60</sub><sup>-</sup> upon excitation of porphyrine moiety [127]. In 2-methyltetrahydrofuran, the lifetime and the quantum yield for the generation of the final CS state were 170 ns and 0.14, respectively.

The quantum yield and the lifetime become long and high in the ferrocene-zinc porphyrin-fullerene (Fc-ZnP-C<sub>60</sub>, Fig. 29g). The lifetime and the quantum yield for the generation of the CS state (Fc<sup>+</sup>-ZnP-C<sub>60</sub><sup>-</sup>) were 7.5 μs and 0.65, respectively [128].

A further long lifetime is expected for the tetramer including fullerene. The Fc-ZnP-ZnP-C<sub>60</sub> tetrad shows lifetimes as long as 19 μs in benzonitrile [129].

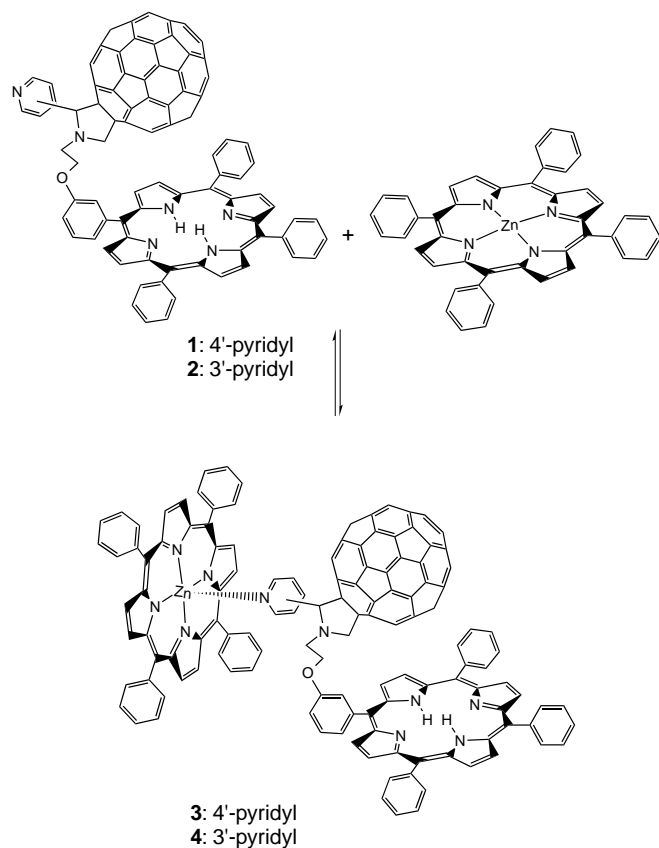
## 6.3. Supramolecular Dyad and Triad Systems

By means of metal-ligand coordinate bonds, hydrogen bonds, etc., noncovalently linked donor-acceptor molecules have been reported [130]. To date, several noncovalently linked dyads are reported for fullerene derivatives [131–135]. For example, zinc porphyrin was connected via a coordinate bond with pyridine moiety of fullerene derivatives. Intrasupramolecular charge separation processes have been confirmed by observing radical ion species in laser flash photolysis experiments. By utilization of metal coordinate bonding of zinc porphyrin, further functionalities can be donated to dyad molecules. For example, D'Souza et al. reported that supramolecular triad molecules could be obtained by forming a coordinate bond between zinc porphyrin and C<sub>60</sub>-porphyrin dyad with pyridyl group (Fig. 32) [135]. Furthermore, control of distance between the chromophores of zinc porphyrin-fullerene dyad by an axial coordination is also an interesting example of supramolecular systems [134].

Supramolecular dyad molecules are also available by utilizing host-guest chemistry. Konishi et al. reported that improvement of electron-transfer efficiencies could be attained in the electron-transfer systems composed of donors and fullerenes connected with calixarene, in which calixarene could capture the electron donor [136]. It is interesting to note that back electron transfer in these systems obeyed second order kinetics, indicating that the generated radical ions are solvated separately after electron transfer by deforming the supramolecular.

## 6.4. Light-Energy Conversion Using Donor-Fullerene Linked Molecules

The long lifetime and high quantum yield of the CS state of these donor-fullerene linked molecules seem to be efficient charge-generation species in the photoactive devices. A photoelectrochemical cell has been developed using a gold electrode which is covered by self-assembled monolayers of porphyrin-C<sub>60</sub> dyad with S-Au interaction [137].



**Figure 32.** Supramolecular triad of zinc porphyrin and fullerene-porphyrin dyad. Reprinted with permission from [135], F. D'Souza et al., *J. Phys. Chem. B* 106, 4952 (2002). © 2002, American Chemical Society.

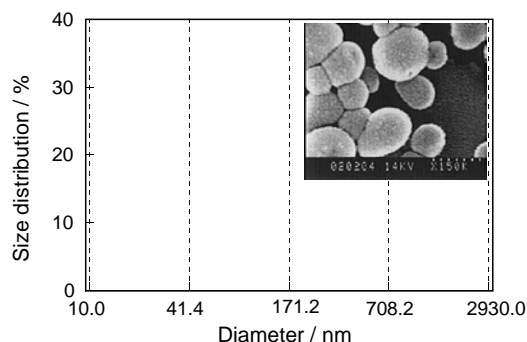
Using methylviologen as a carrier in the electrochemical cell,  $5 \text{ mW cm}^{-2}$  of photocurrent was obtained. This kind of photocurrent generation was also reported for the cell using self-assembled monolayers of oligothiophene- $\text{C}_{60}$  dyads [138].

Furthermore, the generated radical ion pair can be utilized for the electron-mediating process. For example,  $\text{C}_{60}^{\cdot-}$  moiety of  $\text{ZnP}^+-\text{C}_{60}^{\cdot-}$  dyad or  $\text{ZnP}^+-\text{H}_2\text{P}-\text{C}_{60}^{\cdot-}$  triad donates an electron to hexyl viologen to generate a radical cation. On the other hand,  $\text{ZnP}^+$  moiety of the dyad or triad oxidizes NADH analogs. Thus, both  $\text{ZnP}-\text{C}_{60}$  and  $\text{ZnP}-\text{H}_2\text{P}-\text{C}_{60}$  act as efficient photocatalysts for the uphill oxidation of NADH by hexylviologen [139].

### 6.5. Photoinduced Charge Separation and Recombination Processes of Fine Particles of Donor-Fullerene Linked Molecules

Photoinduced processes of the donor-acceptor linked molecules in condensed condition are important, since these photoactive molecules are expected to be used in a condensed form such as fine particles and assembled membranes. Thus, the investigations on the fine particles of the donor-acceptor dyad molecules give fruitful discussion on the light-energy conversion systems.

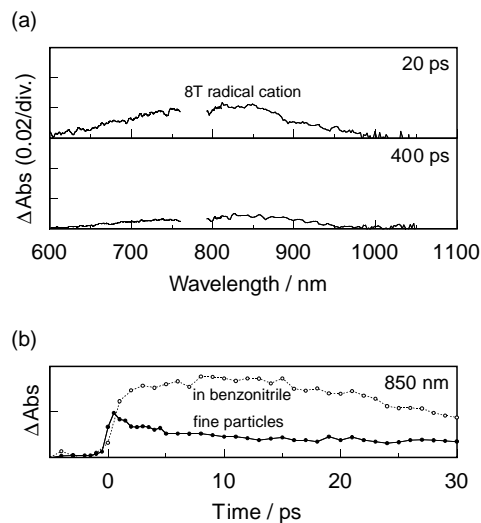
Thomas et al. reported the photoinduced CS and CR processes of aniline- $\text{C}_{60}$  dyad molecule (Fig. 29h) [140]. They



**Figure 33.** Size distribution of the fine particles of octathiophene(8T)- $\text{C}_{60}$ . Inset: SEM picture. Reprinted with permission from [141], M. Fujitsuka et al., *J. Phys. Chem. B* 105, 9930 (2001). © 2001, American Chemical Society.

found that the CS process occurs within a few nanoseconds and that CS state has a lifetime, as long as several microseconds, due to the hopping of the radical ions among the molecules in each fine particle.

In the case of fine particles of octathiophene- $\text{C}_{60}$  (8T- $\text{C}_{60}$ ) dyad (Fig. 33), the CS occurs within 1 ps upon subpicosecond laser light irradiation, indicating that the rate constant for the charge separation is quite fast ( $>1 \times 10^{12} \text{ s}^{-1}$ ), while CS in benzonitrile occurs at  $1.1 \times 10^{11} \text{ s}^{-1}$  (Fig. 34) [141]. The fast CS process can be attributed to the intermolecular charge separation within each fine particle. On the other hand, the CR process occurs by a two-step process: Fast CR within a few picoseconds can be attributed to CR between the geminate radical ion pair, while the slow CR in the nanosecond regions can be attributed to the recombination after the hopping of the radical ions. The quite fast CS and CR processes of the oligothiophene-fullerene dyads can be attributed to the molecular arrangement in the fine particles.



**Figure 34.** (a) Transient absorption spectra of fine particles of octathiophene(8T)- $\text{C}_{60}$  upon subpicosecond laser light irradiation (388 nm, FWHM 150 fs). (b) Absorption-time profiles of fine particles of 8T- $\text{C}_{60}$  (solid line) and 8T- $\text{C}_{60}$  in benzonitrile (dot line). Reprinted with permission from [141], M. Fujitsuka et al., *J. Phys. Chem. B* 105, 9930 (2001). © 2001, American Chemical Society.

In the case of oligothiophene-fullerene dyads, oligothiophene and fullerene moieties seem to be located at the closest position since both oligothiophene and fullerene moieties are hydrophobic. On the other hand, aniline-fullerene dyad is considered to form a spontaneous self-assembly in such a way that the hydrophobic fullerene moieties come together, leaving the polar aniline moiety outside, in which the distance between aniline in a dyad and C<sub>60</sub> in another dyad will be similar to that of the dyad molecule in solution. These findings indicate that the self-assembly of donor-acceptor linked molecules in the fine particles is an important factor governing the rates of the CS and CR processes.

## 7. CONCLUDING REMARKS

In the present chapter, we summarized photoexcitation dynamics of the fullerenes and related materials. In the case of the conventional fullerenes, C<sub>60</sub> and C<sub>70</sub>, their photophysical and photochemical properties were well established: A lot of photochemical reactions have been cleared and they have been employed for many applications such as photobiology and photoactive molecular devices. The fine particles of C<sub>60</sub> show interesting photophysical and photochemical properties due to the migration of the singlet and triplet excited states in each fine particle. As for the higher fullerenes and metallofullerenes, although reports on their photophysical and photochemical properties were scarce, further interesting properties are expected after accumulation of the experimental data. The dyads and triads including fullerene showed a long-lived CS state with higher quantum yield than ever reported for dyads and triads. Thus, application of the donor-acceptor linked molecules to devices such as the light-energy conversion system seems to be interesting.

## GLOSSARY

**Back electron transfer** Reverse reaction process of electron transfer. Original ground state is formed.

**Energy transfer** Process donating singlet or triplet excitation energy from an energy donor to an energy acceptor.

**Fullerenes** Molecules composed of carbon with football-like shapes. Carbon allotrope of diamond and graphite. Most famous C<sub>60</sub> was found in 1985.

**Laser flash photolysis** Spectroscopic measurement of absorption spectral change in shorter time scale upon excitation with pulsed laser. Nowadays, time resolution from femto- to millisecond region is available.

**Metallofullerenes** Fullerenes including metal ions in fullerene cage.

**Photoinduced electron transfer** Process donating an electron from an electron donor to an electron acceptor upon photoexcitation of the donor or acceptor.

## REFERENCES

- H. W. Kroto, J. R. Heath, S. C. O'Brien, R. F. Curl, and R. E. Smalley, *Nature* 318, 162 (1985).
- W. Krätschmer, L. D. Lamb, K. Fostiropoulos, and D. R. Huffman, *Nature* 347, 354 (1990).
- A. F. Hebard, M. J. Rosseinsky, R. C. Haddon, D. W. Murphy, S. H. Glarum, T. T. M. Palstra, A. P. Ramirez, and A. R. Kortan, *Nature* 350, 600 (1991).
- Y. Wang, *Nature* 356, 585 (1992).
- P. M. Allemand, K. C. Khemani, A. Koch, F. Wudl, K. Holczer, S. Konovan, G. Grüner, and J. D. Thompson, *Science* 253, 301 (1991).
- W. J. Blau, D. J. Cardin, T. J. Dennis, J. P. Hare, H. W. Kroto, R. Taylor, and D. R. M. Walton, *Phys. Rev. Lett.* 67, 1423 (1991).
- N. Miyata and Y. Yamakoshi, in "Fullerenes Vol. 5" (K. M. Kadish and R. S. Ruoff, Eds.), Vol. 97-42, p. 345. The Electrochemical Society, Pennington, NJ, 1997.
- S. Takenaka, K. Yasmashita, N. Takagi, T. Hatta, and O. Tsuge, *Chem. Lett.* 321 (1999).
- S. H. Friedman, D. L. DeCamp, R. P. Sijbesma, G. Srdanov, F. Wudl, and G. L. Keyton, *J. Am. Chem. Soc.* 115, 6506 (1993).
- J. W. Arbogast, A. P. Darmanyan, C. S. Foote, Y. Rubin, F. N. Diederich, M. M. Alvarez, S. J. Anz, and R. L. Whetten, *J. Phys. Chem.* 95, 11 (1991).
- R. J. Sension, C. M. Phillips, A. Z. Szarka, W. J. Romanow, A. R. McGhie, J. P. McCauley, A. B. Smith, and R. M. Hochstrasser, *J. Phys. Chem.* 95, 6075 (1991).
- T. W. Ebbesen, K. Tanigaki, and S. Kuroshima, *Chem. Phys. Lett.* 181, 501 (1991).
- D. K. Palit, A. V. Sapre, J. P. Mittal, and C. N. R. Rao, *Chem. Phys. Lett.* 195, 1 (1992).
- N. N. Dimitrijevic and P. V. Kamat, *J. Phys. Chem.* 96, 4811 (1992).
- L. Biczok, H. Linschitz, and R. I. Walter, *Chem. Phys. Lett.* 195, 339 (1992).
- R. J. Sension, A. Z. Szarka, G. R. Smith, and R. M. Hochstrasser, *Chem. Phys. Lett.* 185, 179 (1991).
- T. Osaki, Y. Tai, M. Yazawa, S. Tanemura, K. Inukai, K. Ishiguro, Y. Sawaki, Y. Saito, H. Shinohara, and H. Nagashima, *Chem. Lett.* 789 (1993).
- S. Nonell, J. W. Arbogast, and C. S. Foote, *J. Phys. Chem.* 96, 4169 (1992).
- H. N. Ghosh, H. Pal, A. V. Sapre, and J. P. Mittal, *J. Am. Chem. Soc.* 115, 11722 (1993).
- A. Watanabe and O. Ito, *J. Phys. Chem.* 98, 7736 (1994).
- L. Smilowitz, N. S. Sariciftci, R. Wu, C. Gettinger, A. J. Heeger, and F. Wudl, *Phys. Rev. B* 47, 13835 (1993).
- S. R. Wilson, D. I. Shuster, B. Nuber, M. S. Meier, M. Maggini, M. Prato, and R. Taylor, in "Fullerenes" (K. M. Kadish and R. S. Ruoff, Eds.), p. 91. Wiley, New York, 2000.
- G. W. Wang, K. Komatsu, Y. Murata, and M. Shiro, *Nature* 387, 583 (1997).
- A. M. Rao, P. Zhou, K. Wang, G. T. Hager, J. M. Holde, Y. Wang, W.-T. Lee, X. Bi, P. C. Eklund, D. S. Cornett, M. A. Duncan, and I. J. Amster, *Science* 259, 955 (1993).
- N. Martin, L. Sánchez, B. Illescas, and I. Pérez, *Chem. Rev.* 98, 2527 (1998).
- D. M. Guldi and P. V. Kamat, in "Fullerenes" (K. M. Kadish and R. S. Ruoff, Eds.), p. 225. Wiley, New York, 2000.
- H. Imahori and Y. Sakata, *Eur. J. Org. Chem.* 2445 (1999).
- D. Kim, M. Lee, Y. D. Suh, and S. K. Kim, *J. Am. Chem. Soc.* 114, 4429 (1992).
- A. Masuhara, M. Fujitsuka, and O. Ito, *Bull. Chem. Soc. Jpn.* 73, 2199 (2000).
- B. Ma and Y. P. Sun, *J. Chem. Soc. Perkin Trans. 2*, 2157 (1996).
- C. Luo, M. Fujitsuka, A. Watanabe, O. Ito, L. Gan, Y. Huang, and C.-H. Huang, *J. Chem. Soc. Faraday Trans. 94*, 527 (1998).
- G. Schick, M. Levitus, L. Kvetko, B. A. Johnson, I. Lamparth, R. Lunkwitz, B. Ma, S. I. Khan, M. A. Garcia-Garibay, and Y. Rubin, *J. Am. Chem. Soc.* 121, 3246 (1999).
- M. Gevaert and P. V. Kamat, *J. Phys. Chem.* 96, 9883 (1992).
- K. Tanigaki, T. W. Ebbesen, and S. Kuroshima, *Chem. Phys. Lett.* 185, 189 (1991).



35. D. McBranch, V. Klimov, L. Smilowitz, M. Grigorova, and B. R. Mattes, in "Fullerenes Vol. 3" (K. M. Kadish and R. S. Ruoff, Eds.), Vol. 96-10, p. 384. The Electrochemical Society, Pennington, NJ, 1996.
36. R. R. Hung and J. J. Grabowski, *Chem. Phys. Lett.* 192, 249 (1992).
37. R. R. Hung and J. J. Grabowski, *J. Phys. Chem.* 95, 6073 (1991).
38. K. D. Ausman and R. B. Weisman, *Res. Chem. Intermed.* 23, 4311 (1997).
39. D. Dubois, K. M. Kadish, S. Flanagan, R. E. Hauffer, L. P. F. Chibante, and L. J. Wilson, *J. Am. Chem. Soc.* 113, 4364 (1991).
40. G. J. Kavarnos and N. J. Turro, *Chem. Rev.* 86, 401 (1986).
41. Q. Xie, E. Pérez-Cordero, and L. Echegoyen, *J. Am. Chem. Soc.* 114, 3978 (1992).
42. D. Rehm and A. Weller, *Isr. J. Chem.* 8, 259 (1970).
43. Y. P. Sun, C. E. Bunker, and B. Ma, *J. Am. Chem. Soc.* 116, 9692 (1994).
44. R. S. Sension, A. Z. Szarka, G. R. Simith, and R. M. Hochstrasser, *Chem. Phys. Lett.* 185, 179 (1991).
45. N. S. Sariciftci, L. Smilowitz, A. J. Heeger, and F. Wudl, *Science* 258, 1474 (1992).
46. N. S. Sariciftci and A. J. Heeger, *Int. J. Mod. Phys. B* 8, 237 (1994).
47. A. Itaya, I. Suzuki, Y. Tsuboi, and H. Miyasaka, *J. Phys. Chem. B* 101, 5118 (1997).
48. J. W. Arbogast, C. S. Foote, and M. Kao, *J. Am. Chem. Soc.* 114, 2277 (1992).
49. H. Schwenk, S. S. P. Parkin, V. Y. Lee, and R. L. Greene, *Phys. Rev. B* 34, 3156 (1986).
50. P. Bowmer, M. Kurmoo, M. A. Green, F. P. Pratt, W. Hayes, P. Day, and K. Kikuchi, *J. Phys. Condensed Mater.* 5, 2739 (1993).
51. M. M. Alam, A. Watanabe, and O. Ito, *J. Photochem. Photobiol. A: Chem.* 104, 59 (1997).
52. Y. Sasaki, M. Fujitsuka, A. Watanabe, and O. Ito, *J. Chem. Soc. Faraday Trans.* 93, 4275 (1997).
53. Y. Sasaki, T. Konishi, M. Yamazaki, M. Fujitsuka, and O. Ito, *Phys. Chem. Chem. Phys.* 1, 4555 (1999).
54. T. Nojiri, A. Watanabe, and O. Ito, *J. Phys. Chem. A* 102, 5215 (1998).
55. T. Nojiri, M. M. Alam, H. Konami, A. Watanabe, and O. Ito, *J. Phys. Chem. A* 101, 7943 (1997).
56. M. Fujitsuka, Y. Yahata, A. Watanabe, and O. Ito, *Polymer* 41, 2807 (2000).
57. S. Komamine, M. Fujitsuka, O. Ito, and A. Itaya, *J. Photochem. Photobiol. A: Chem.* 135, 111 (2000).
58. K. Matsumoto, M. Fujitsuka, T. Sato, S. Onodera, and O. Ito, *J. Phys. Chem. B* 104, 11632 (2000).
59. H. Onodera, Y. Araki, M. Fujitsuka, S. Onodera, O. Ito, F. Bai, M. Zheng, and J.-L. Yang, *J. Phys. Chem. A* 105, 7341 (2001).
60. O. Ito, Y. Sasaki, Y. Yoshikawa, and A. Watanabe, *J. Phys. Chem.* 99, 9838 (1995).
61. T. Akasaka, W. Ando, K. Kobayashi, and S. Nagase, *J. Am. Chem. Soc.* 115, 10366 (1993).
62. T. Akasaka, Y. Maeda, T. Wakahara, M. Okamura, M. Fujitsuka, O. Ito, K. Kobayashi, S. Nagase, M. Kako, Y. Nakadaira, and E. Horn, *Org. Lett.* 1, 1509 (1999).
63. T. Akasaka, T. Kato, K. Kobayashi, S. Nagase, K. Yamamoto, H. Funasaka, and T. Takahashi, *Nature* 374, 600 (1995).
64. T. Akasaka, T. Suzuki, Y. Maeda, M. Ara, T. Wakahara, K. Kobayashi, S. Nagase, M. Kako, Y. Nakadaira, M. Fujitsuka, and O. Ito, *J. Org. Chem.* 64, 566 (1999).
65. M. Fujitsuka, O. Ito, Y. Maeda, M. Kako, T. Wakahara, and T. Akasaka, *Phys. Chem. Chem. Phys.* 1, 3527 (1999).
66. K. Mikami, S. Matsumoto, A. Ishida, S. Takamuku, T. Suenobu, and S. Fukuzumi, *J. Am. Chem. Soc.* 117, 11134 (1995).
67. K. Mikami, S. Matsumoto, Y. Okubo, M. Fujitsuka, O. Ito, T. Suenobu, and S. Fukuzumi, *J. Am. Chem. Soc.* 122, 2236 (2000).
68. S. Fukuzumi, T. Suenobu, M. Patz, T. Hirasaka, S. Itoh, M. Fujitsuka, and O. Ito, *J. Am. Chem. Soc.* 120, 8060 (1998).
69. C. Siedschlag, G. Torres-Garcia, C. Wolff, J. Mattay, M. Fujitsuka, A. Watanabe, O. Ito, L. Dunsch, F. Ziegls, and H. Luftman, in "Fullerenes Vol. 5" (K. M. Kadish and R. S. Ruoff, Eds.), Vol. 97-42, p. 296. The Electrochemical Society, Pennington, NJ, 1997.
70. M. Fujitsuka, C. Luo, and O. Ito, *J. Phys. Chem. B* 103, 445 (1999).
71. C. Luo, M. Fujitsuka, C.-H. Huang, and O. Ito, *Phys. Chem. Chem. Phys.* 1, 2923 (1999).
72. T. Konishi, M. Fujitsuka, and O. Ito, *Chem. Lett.* 202 (2000).
73. T. Konishi, M. Fujitsuka, O. Ito, Y. Toba, and Y. Usui, *Bull. Chem. Soc. Jpn.* 74, 39 (2001).
74. Z. Yoshida, H. Takekuma, S. Takekuma, and Y. Matsubara, *Angew. Chem. Int. Ed. Engl.* 33, 1597 (1994).
75. T. Andersson, M. Sundahl, G. Westman, and O. Wennerström, *Tetrahedron Lett.* 38, 7103 (1994).
76. S. D. M. Islam, M. Fujitsuka, O. Ito, A. Ikeda, T. Hatano, and S. Shinkai, *Chem. Lett.* 78 (2000).
77. D. M. Guldi, *J. Phys. Chem. A* 101, 3895 (1997).
78. D. M. Guldi, H. Hungerbühler, and K.-D. Asmus, *J. Phys. Chem. A* 101, 1783 (1997).
79. S. Takenaka, K. Yamashita, M. Takagi, T. Hatta, and O. Tsuge, *Chem. Lett.* 321 (1999).
80. S. Hecht and J. M. J. Fréchet, *Angew. Chem. Int. Ed.* 40, 74 (2001).
81. J.-F. Nierengarten, *Chem. Eur. J.* 6, 3667 (2000).
82. K. L. Wooley, C. J. Hawker, M. J. Fréchet, F. Wudl, G. Srdanov, S. Shi, C. Li, and M. Kao, *J. Am. Chem. Soc.* 114, 9836 (1993).
83. C. J. Hawker, K. L. Wooley, and M. J. Fréchet, *J. Chem. Soc., Chem. Commun.* 925, (1994).
84. E. Cloutet, Y. Gnanou, J.-L. Fillaut, and D. Astruc, *Chem. Commun.* 1565 (1996).
85. D. M. Guldi, A. Swartz, C. Luo, R. Gómez, J. L. Segura, and M. Martín, *J. Am. Chem. Soc.* 124, 10875 (2002).
86. R. Kunieda, M. Fujitsuka, O. Ito, M. Ito, Y. Murata, and K. Komatsu, *J. Phys. Chem. B* 106, 7193 (2002).
87. Y. Takaguchi, T. Tajima, K. Ohta, J. Motoyoshiya, H. Aoyama, T. Wakahara, T. Akasaka, M. Fujitsuka, and O. Ito, *Angew. Chem. Int. Ed.* 41, 827 (2002).
88. Y. P. Sun and C. E. Bunker, *Nature* 365, 398 (1993).
89. M. Fujitsuka, H. Kasai, A. Masuhara, S. Okada, H. Oikawa, H. Nakanishi, A. Watanabe, and O. Ito, *Chem. Lett.* 1211 (1997).
90. M. Fujitsuka, H. Kasai, A. Masuhara, S. Okada, H. Oikawa, H. Nakanishi, O. Ito, and K. Yase, *J. Photochem. Photobiol. A: Chem.* 133, 45 (2000).
91. K. Kasai, H. Kamatani, Y. Yoshikawa, S. Okada, H. Oikawa, A. Watanabe, O. Ito, and H. Nakanishi, *Chem. Lett.* 1181 (1997).
92. N. Takahashi, H. Dock, N. Matsuzawa, and M. Ata, *J. Appl. Phys.* 74, 5790 (1993).
93. Y. Iwasa, T. Arima, R. M. Fleming, T. Siegrist, O. Zhou, R. C. Haddon, L. J. Rothberg, K. B. Lyons, H. L. Carter Jr. A. F. Hebard, R. Tycko, G. Daggagh, J. J. Krajewski, G. A. Thomas, and T. Yagi, *Science* 264, 1570 (1994).
94. S. Pekker, A. Jánosy, L. Mihaly, O. Chauvet, M. Carrard, and L. Forró, *Science* 265, 1077 (1994).
95. K. Komatsu, K. Fujiwara, and Y. Murata, *Chem. Lett.* 1016 (2000).
96. B. Ma, J. E. Riggs, and Y.-P. Sun, *J. Phys. Chem. B* 102, 5999 (1998).
97. M. Fujitsuka, C. Luo, O. Ito, Y. Murata, and K. Komatsu, *J. Phys. Chem. A* 103, 7155 (1999).
98. M. Fujitsuka, K. Fujiwara, Y. Murata, S. Uemura, M. Kunitake, O. Ito, and K. Komatsu, *Chem. Lett.* 384 (2001).
99. M. Fujitsuka, H. Takahashi, T. Kudo, K. Tohji, A. Kasuya, and O. Ito, *J. Phys. Chem. A* 105, 675 (2001).
100. N. Tagmatarchis, H. Shinohara, M. Fujitsuka, and O. Ito, *J. Org. Chem.* 66, 8026 (2001).
101. J. C. Hummelen, B. Knight, J. Pavlovich, R. Gonzalez, and F. Wudl, *Chem. Commun.* 1554 (1996).
102. N. Tagmatarchis and H. Shinohara, *Org. Lett.* 2, 3551 (2000).

103. M. Fujitsuka, A. Watanabe, O. Ito, K. Yamamoto, and H. Funasaka, *J. Phys. Chem. A* 101, 4840 (1997).
104. D. M. Guldi, D. Liu, and P. V. Kamat, *J. Phys. Chem. A* 101, 6195 (1997).
105. M. Fujitsuka, A. Watanabe, O. Ito, K. Yamamoto, and H. Funasaka, *J. Phys. Chem. A* 101, 7960 (1997).
106. M. Fujitsuka, A. Watanabe, O. Ito, K. Yamamoto, H. Funasaka, and T. Akasaka, *J. Phys. Chem. B* 103, 9519 (1999).
107. M. Fujitsuka, O. Ito, K. Yamamoto, and T. Akasaka, *Recent Res. Devel. Phys. Chem.* 4, 135 (2000).
108. Y. Yang, F. Arias, L. Echegoyen, L. F. P. Chibante, S. Flanagan, A. Robertson, and L. J. Wilson, *J. Am. Chem. Soc.* 117, 7801 (1995).
109. S. Nonell, J. W. Arbogast, and C. S. Foote, *J. Phys. Chem.* 96, 4169 (1992).
110. M. Fujitsuka, O. Ito, K. Kobayashi, S. Nagase, K. Yamamoto, T. Kato, T. Wakahara, and T. Akasaka, *Chem. Lett.* 902 (2000).
111. R. M. Williams, J. M. Zwier, and J. W. Verhoeven, *J. Am. Chem. Soc.* 117, 4093 (1995).
112. R. M. Williams, M. Koeberg, J. M. Lawson, Y.-Z. An, Y. Rubin, M. N. Paddon-Row, and J. W. Verhoeven, *J. Org. Chem.* 61, 5055 (1996).
113. H. Imahori, S. Cardoso, D. Tatman, S. Lin, L. Noss, G. R. Seely, L. Sereno, C. Silber, T. A. Moore, A. L. Moore, and D. Gust, *Photochem. Photobiol.* 62, 1009 (1995).
114. D. Kuciauskas, S. Lin, G. R. Seely, A. L. Moore, T. A. Moore, D. Gust, T. Drovetskaya, C. A. Reed, and P. D. W. Boyd, *J. Phys. Chem.* 100, 15926 (1996).
115. H. Imahori, K. Hagiwara, M. Aoki, T. Akiyama, S. Taniguchi, T. Okada, M. Shirakawa, and Y. Sakata, *J. Am. Chem. Soc.* 118, 11771 (1996).
116. N. V. Tkachenko, L. Rantala, A. Y. Tauber, J. Helaja, P. V. Hynninen, and H. Lemmetyinen, *J. Am. Chem. Soc.* 121, 9378 (1999).
117. J. Llacay, J. Veciana, J. Vidal-Gancedo, J. L. Bourdelnde, R. González-Moreno, and C. Rovira, *J. Org. Chem.* 63, 5201 (1998).
118. N. Martin, L. Sánchez, M. A. Herranz, and D. M. Guldi, *J. Phys. Chem. A* 104, 4648 (2000).
119. T. Yamashiro, Y. Aso, T. Otsubo, H. Tang, T. Harima, and K. Yamashita, *Chem. Lett.* 443 (1999).
120. M. Fujitsuka, O. Ito, T. Yamashiro, T. Aso, and T. Otsubo, *J. Phys. Chem. A* 104, 4876 (2000).
121. M. Fujitsuka, K. Matsumoto, O. Ito, T. Yamashiro, T. Aso, and T. Otsubo, *Res. Chem. Intermed.* 27, 73 (2001).
122. S. Komamine, M. Fujitsuka, O. Ito, K. Moriwaki, T. Miyata, and T. Ohno, *J. Phys. Chem. A* 104, 11497 (2000).
123. T. Ohno, K. Moriwaka, and T. Miyata, *J. Org. Chem.* 66, 3397 (2001).
124. M. Yamazaki, Y. Araki, M. Fujitsuka, and O. Ito, *J. Phys. Chem. A* 105, 8615 (2001).
125. H. Imahori, N. V. Tkachenko, V. Vehmanen, K. Tamaki, H. Lemmetyinen, Y. Sakata, and S. Fukuzumi, *J. Phys. Chem. A* 105, 1750 (2001).
126. H. Imahori, K. Tamaki, D. M. Guldi, C. Luo, M. Fujitsuka, O. Ito, Y. Sakata, and S. Fukuzumi, *J. Am. Chem. Soc.* 123, 2607 (2001).
127. P. A. Liddell, D. Kuciauskas, J. P. Sumida, B. Nash, D. Nguyen, A. L. Moore, T. A. Moore and D. Gust, *J. Am. Chem. Soc.* 119, 1400 (1997).
128. M. Fujitsuka, O. Ito, H. Imahori, K. Yamada, H. Yamada, and Y. Sakata, *Chem. Lett.* 721 (1999).
129. H. Imahori, K. Tamaki, Y. Araki, Y. Sekiguchi, O. Ito, Y. Sakata, and S. Fukuzumi, *J. Am. Chem. Soc.* 124, 5165 (2002).
130. M. W. Ward, *Chem. Soc. Rev.* 26, 365 (1997).
131. F. D'Souza, G. R. Deviprasad, M. S. Rahman, and J.-P. Choi, *Inorg. Chem.* 38, 2155 (1999).
132. N. Armaroli, F. Diederich, L. Echegoyen, T. Habicher, L. Marconi, and J.-F. Nierengarten, *New J. Chem.* 77 (1999).
133. T. Da Ros, M. Prato, D. M. Guldi, E. Alessio, M. Ruzzi, and L. Pasimeni, *Chem. Commun.* 635 (1999).
134. F. D'Souza, G. R. Deviprasad, M. E. El-Khouly, M. Fujitaska, and O. Ito, *J. Am. Chem. Soc.* 123, 5277 (2001).
135. F. D'Souza, G. R. Deviprasad, M. E. Zandler, M. E. El-Khouly, M. Fujitaska, and O. Ito, *J. Phys. Chem. B* 106, 4952 (2002).
136. T. Konishi, A. Ikeda, T. Kishida, B. S. Rasmussen, M. Fujitsuka, and O. Ito, *J. Phys. Chem. A* 106, 10254 (2002).
137. H. Imahori, S. Ozawa, K. Ushida, M. Takahashi, T. Azuma, A. Ajavakom, T. Akiyama, M. Hasegawa, S. Taniguchi, T. Okada, and Y. Sakata, *Bull. Chem. Soc. Jpn.* 72, 485 (1999).
138. D. Hirayama, T. Yamashiro, K. Takimiya, Y. Aso, T. Otsubo, H. Norieda, H. Imahori, and Y. Sakata, *Chem. Lett.* 570 (2000).
139. S. Fukuzumi, H. Imahori, K. Okamoto, H. Yamada, M. Fujitsuka, O. Ito, and D. M. Guldi, *J. Phys. Chem. A* 106, 1903 (2002).
140. K. G. Thomas, V. Biju, D. M. Guldi, P. V. Kamat, and M. V. George, *J. Phys. Chem. B* 103, 8864 (1999).
141. M. Fujitsuka, A. Masuhara, H. Kasai, H. Oikawa, H. Nakanishi, O. Ito, T. Yamashiro, Y. Aso, and T. Otsubo, *J. Phys. Chem. B* 105, 9930 (2001).



# Photonic Crystal Lasers

John D. O'Brien, Wan Kuang, Po-Tsung Lee, Jiang Rong Cao,  
Cheolwoo Kim, Woo Jun Kim

*University of Southern California, Los Angeles, California, USA*

## CONTENTS

1. Introduction
  2. Electromagnetic Properties of Photonic Crystals
  3. Fabrication of Two-Dimensional Photonic Crystals
  4. Demonstrated Resonant Cavity Types
- Glossary  
References

## 1. INTRODUCTION

Photonic crystal lasers are lasers in which the resonant cavity is formed by a periodic dielectric constant. In this sense, they have much in common with distributed feedback lasers, which have long been an important optical source for fiber communication systems, and with vertical cavity surface emitting lasers. In this work, we take photonic crystal lasers to be lasers in which the dielectric constant is periodic in at least two dimensions. Photonic crystals came into existence as part of a program to modify spontaneous emission rates in optical microcavities by modifying the optical mode density [1]. Photonic crystals open up gaps in the optical spectrum through spatially and spectrally overlapping Bragg planes. These electromagnetic bandgaps can be, and have been, used to confine optical modes in laser cavities. These cavities can be very small. In fact, their mode volume can be made to be only a little larger than a cubic half-wavelength. In high contrast dielectric systems, only a few lattice periods may be necessary to confine an electromagnetic mode, and a lattice period has a length scale on the order of one half of the optical wavelength. More generally, photonic crystals take advantage of the nanofabrication processes which are available to pattern the dielectric function at the subwavelength scale. This patterning ability presents the possibility of designing the electromagnetic modes of photonic devices in microscopic detail. It is possible, in principle, to design laser cavities in which the optical mode's resonant frequency, spatial profile, radiation pattern, and

polarization are engineered by engineering and patterning the dielectric function at the subwavelength scale. Actually, accomplishing all of this, however, is still very challenging. In addition, because of their small volume, photonic crystal lasers can be expected to operate at very low threshold pump powers. From this aspect, they benefit both from a small cavity volume that must be inverted as well as from microcavity effects [2, 3]. This article will review the basic properties of photonic crystal lasers and the progress that has been made in their development. The first section covers the basic electromagnetic principles involved and the relevant numerical models. This will be followed by an introduction to the fabrication of semiconductor photonic crystals and a description of the progress that has been made in laser development.

## 2. ELECTROMAGNETIC PROPERTIES OF PHOTONIC CRYSTALS

In this first section, we will begin with a discussion of the electromagnetic properties of photonic crystals. This discussion is not intended to be a complete review of the electromagnetic properties of photonic crystals, but instead an overview of their properties and the relevant calculation methods that are useful in understanding their application to lasers. The discussion will proceed from calculation methods to the properties of these lattices that are of interest for semiconductor lasers.

Photonic crystals are typically modeled as a patterned dielectric structure in which the dielectric material is a source-free region in which the dielectric constant is scalar.

$$\left\{ \begin{array}{l} \nabla \times \vec{E} = -\frac{\partial \vec{B}}{\partial t} - \vec{M} \\ \nabla \times \vec{H} = \frac{\partial \vec{D}}{\partial t} + \vec{J} \\ \nabla \cdot \vec{D} = \rho \\ \nabla \cdot \vec{B} = 0 \end{array} \right.$$

This article will also take the dielectric constant to be a real number. This will later limit us to predicting, for example, the cold cavity behavior of photonic crystal resonant cavities. There have been analyses in which the nonlinear interactions have been considered [4], but in this article we focus on linear interactions. For simplicity, we also ignore any frequency dependence of the dielectric constants. Finally, we take the permeability to be unity.

$$\vec{B} = \mu_0 \vec{H}$$

Since Maxwell's equations are linear, we can expand the fields of interest into a set of time-harmonic fields

$$\begin{cases} \vec{E}(\vec{r}, t) = \vec{E}(\vec{r})e^{i\omega t} \\ \vec{H}(\vec{r}, t) = \vec{H}(\vec{r})e^{i\omega t} \end{cases}$$

The periodicity of  $\varepsilon(\vec{r})$  implies

$$\varepsilon(\vec{r} + \vec{R}) = \varepsilon(\vec{r})$$

where  $\vec{R} = m_1 a_1 + m_2 a_2 + m_3 a_3$  is a lattice vector of the direct lattice with  $\{m_i\}$  a set of arbitrary integers. The reciprocal lattice vector are given by

$$\vec{G} = l_1 \vec{b}_1 + l_2 \vec{b}_2 + l_3 \vec{b}_3$$

where

$$\vec{a}_i \cdot \vec{b}_j = 2\pi \delta_{ij}$$

and  $\{l_j\}$  are arbitrary integers and  $\delta_{ij}$  is the Kronecker delta. With these assumptions, Maxwell's equations are

$$\begin{cases} \nabla \times \vec{E}(r) = -i\omega\mu_0 \vec{H}(r) \\ \nabla \times \vec{H}(r) = i\omega\varepsilon(r) \vec{E}(r) \\ \nabla \cdot [\varepsilon(\vec{r}) \vec{E}(r)] = 0 \\ \nabla \cdot \vec{H}(r) = 0 \end{cases}$$

Finally, we can use Bloch's theorem to write the fields as Bloch waves characterized by a wave vector  $\vec{k}$  in the first Brillouin zone and a band index  $n$  as

$$\begin{cases} \vec{E}(\vec{r}) = \vec{E}_{n\vec{k}}(\vec{r}) = \vec{u}_{n\vec{k}}(\vec{r}) \exp(i\vec{k} \cdot \vec{r}) \\ \vec{H}(\vec{r}) = \vec{H}_{n\vec{k}}(\vec{r}) = \vec{v}_{n\vec{k}}(\vec{r}) \exp(i\vec{k} \cdot \vec{r}) \end{cases}$$

where  $u_{n\vec{k}}(\vec{r})$  and  $v_{n\vec{k}}(\vec{r})$  are periodic functions that satisfy

$$\begin{cases} \vec{u}_{n\vec{k}}(\vec{r} + \vec{R}) = \vec{u}_{n\vec{k}}(\vec{r}) \\ \vec{v}_{n\vec{k}}(\vec{r} + \vec{R}) = \vec{v}_{n\vec{k}}(\vec{r}) \end{cases}$$

Analytical solutions to these equations for the electromagnetic fields are not available, in general, and we are left to resort to various numerical methods to predict the electromagnetic properties of photonic crystals. Among the common numerical techniques that have been applied to these structures are the plane-wave expansion method (PWE), the finite-difference, time-domain method (FDTD), and the

finite element method (FEM). Both the plane-wave expansion and finite element methods solve the vector Helmholtz eigenvalue equation that is derived from the simplified Maxwell equations above.

$$\begin{cases} \frac{1}{\varepsilon(\vec{r})} \nabla \times [\nabla \times \vec{E}(\vec{r})] = \frac{\omega^2}{c^2} \vec{E}(\vec{r}) \\ \nabla \times \left[ \frac{1}{\varepsilon(\vec{r})} \nabla \times \vec{H}(\vec{r}) \right] = \frac{\omega^2}{c^2} \vec{H}(\vec{r}) \end{cases}$$

The finite element method has proved itself to be the fastest method in calculating photonic crystal band structure, so we will briefly describe this method. The variational procedure leads to the weak form of this equation

$$\begin{aligned} \int_{\Omega} \nabla \times \vec{W} \cdot \nabla \times \vec{E} d\Omega - k_0^2 \int_{\Omega} \varepsilon_r \vec{W} \cdot \vec{E} d\Omega \\ - \oint_{\partial\Omega} \vec{W} \cdot \nabla \times \vec{E} d\vec{S} = 0 \end{aligned}$$

where  $\vec{W}$  is the weighting function. The surface integral term vanishes on boundaries that correspond to perfect electric conductors (PEC), perfect magnetic conductors (PMC), or periodic boundaries [5]. This term will be dropped hereafter because we will apply one of those three boundary conditions. To guarantee the one-to-one mapping of the approximated nonzero eigenvalues to the physical modes, edge elements are used. Using the same basis function as those of the weighting function to approximate the vector field (Galerkin method), the electric field in any tetrahedron is expressed as

$$\vec{E} = \sum_{i=1}^6 E_i \vec{W}_i$$

Therefore, we arrive at the matrix equation

$$\int_{\Omega} \nabla \times \vec{W}_i \cdot \nabla \times \vec{W}_j d\Omega - k_0^2 \int_{\Omega} \varepsilon_r \vec{W}_i \cdot \vec{W}_j d\Omega = 0$$

which is a generalized eigenvalue equation of the form  $Ax = \lambda Bx$ . If the boundary is a PEC or a PMC, which is the case when field symmetry is used to simplify resonant cavity problems, the matrices are real and symmetric. For spatially periodic structures, the periodic boundary condition is imposed on each pair of the periodic surfaces using Bloch's theorem

$$\vec{W}_{i'} = \exp(-j\vec{\beta} \cdot \vec{\alpha}) \vec{W}_i$$

where  $i'$  is the corresponding edge number of edge  $i$  [6]. The matrix elements that correspond to the edges on the periodic surfaces are complex and this leads to a complex hermitian matrix. The matrix equation can be solved using Arpack++ (C++ interface to Arpack and direct solvers such as SuperLU and UMFPack), which is in the public domain [7].

The plane-wave expansion method solves the eigenvalue equations by Fourier expanding the electromagnetic field and the dielectric function

$$\frac{1}{\varepsilon(\vec{r})} = \sum_{\vec{G}} \kappa(\vec{G}) \exp(i\vec{G} \cdot \vec{r})$$

$$\begin{cases} \vec{E}(\vec{r}) = \sum_{\vec{G}} E_{n\vec{k}}(\vec{G}) \exp(i\vec{G} \cdot \vec{r}) \exp(i\vec{k} \cdot \vec{r}) \\ \vec{H}(\vec{r}) = \sum_{\vec{G}} \vec{H}_{n\vec{k}}(\vec{r}) \exp(i\vec{G} \cdot \vec{r}) \exp(i\vec{k} \cdot \vec{r}) \end{cases}$$

By choosing a sufficiently large number of plane waves, the eigenvalues are obtained by diagonalizing the resultant coefficient matrix which has the dimension of the number of plane waves. The plane-wave expansion method is very straightforward to utilize and thus was the first numerical method successfully applied in photonic crystal band structure calculations. However, its convergence is dependent on the number of plane waves applied, which in turn increases the computing time since the diagonalization is usually proportional to the matrix size. This is especially important in three-dimensional structures where the matrix size grows as  $N^3$ . In addition, convergence can be very slow even with a large number of plane waves, as the spatial dielectric variation is large [8, 9]. The convergence of the plane-wave expansion method can be improved by using spherical waves instead of plane waves as a basis when the photonic crystal is composed of dielectric spheres or circular cylinders [10].

The finite-difference, time-domain method, introduced by Yee in 1966 [11] is a marching-in-time procedure that simulates the continuous electromagnetic waves by volumetric sampling of the unknown fields within and surrounding the structure of interest [12]. The finite-difference, time-domain method avoids the difficulties with the linear algebra used in both the finite element method and the plane-wave expansion method which limits the size of modeling structure. It is also highly scalable because the computing time is linearly proportional to the mesh density. The finite-difference, time-domain method, however, solves the eigenvalue problem indirectly. The simulation starts from a random initial condition with a particular wavevector,  $k$ , so as not to exclude any possible modes, and propagates the fields in time. The amount of time required for this propagation depends on the precision required in the eigenmodes and eigenvalues. The eigenvalues for a given wave vector,  $k$ , are obtained by a Fourier transformation of the complex-valued field components in the time-domain recorded at various low-symmetry locations [13]. The peaks in the Fourier spectrum correspond to the eigenvalues. By applying a band-pass filter in time with its window aligned with each eigenvalues, the final steady-state eigenmode distributions are calculated by taking the time average of the time-domain solution at each mesh point.

To overcome the staircase approximation of Yee's original staggered leapfrog meshing, several alternative grids have been proposed, including hexagonal grids, tetradecahedron/dual-tetrahedron grids, and a local subcell model. Despite the significant accuracy advantage, the usage

of the alternative meshings by the finite-difference, time-domain community has been quite limited, mainly due to the additional complexity in its mesh generation and field updating.

## 2.1. Two-Dimensional Photonic Crystals

Having discussed the basic numerical modeling techniques, we will now consider the properties of these structures that are of interest for laser applications. We will begin by introducing two-dimensional photonic crystals. This will be followed by a discussion of the modes of the dielectric slab into which two-dimensional photonic crystal lattices have been patterned. Both symmetrically clad and asymmetrically clad membranes will be included in this discussion. Finally, this section will conclude with a look at resonant modes created by including defects in the lattices. Both the modes of the two-dimensional photonic crystal slab and the resonant modes introduced by defects in the lattice are of interest in photonic crystal laser design.

A two-dimensional photonic crystal is characterized by having a dielectric structure that is uniform in the  $z$  direction, while preserving a set of discrete translational symmetries in the  $x$ - $y$  plane. The electromagnetic field is characterized by an in-plane wave vector  $k_{\parallel}$  and the wave vector in the homogeneous direction  $k_z$

$$\vec{H}(\vec{r}) = e^{ik_z z} e^{i\vec{k}_{\parallel} \cdot \vec{r}_{\parallel}} u_{k_z, \vec{k}_{\parallel}}(\vec{r}_{\parallel})$$

In the case where the light is strictly propagating in the  $x$ - $y$  plane, that is,  $k_z = 0$ , solutions to Maxwell's equations can be written as solutions to two independent sets of equations. These solutions are classified conventionally as transverse electric (TE <sub>$z$</sub> ) modes and transverse magnetic (TM <sub>$z$</sub> ) modes. One field component for each of these sets,  $H_z$  for TE and  $E_z$  for TM, satisfies a scalar Helmholtz equation. The band structures for TE <sub>$z$</sub>  and TM <sub>$z$</sub>  modes can be completely different

$$\begin{cases} \frac{\partial H_z(\vec{r}_{\parallel})}{\partial y} = i\omega\varepsilon(\vec{r}_{\parallel})E_x(\vec{r}_{\parallel}) \\ \frac{\partial H_z(\vec{r}_{\parallel})}{\partial x} = -i\omega\varepsilon(\vec{r}_{\parallel})E_y(\vec{r}_{\parallel}) \\ \frac{\partial E_y(\vec{r}_{\parallel})}{\partial x} - \frac{\partial E_x(\vec{r}_{\parallel})}{\partial y} = -i\mu_0\omega H_z(\vec{r}_{\parallel}) \end{cases}$$

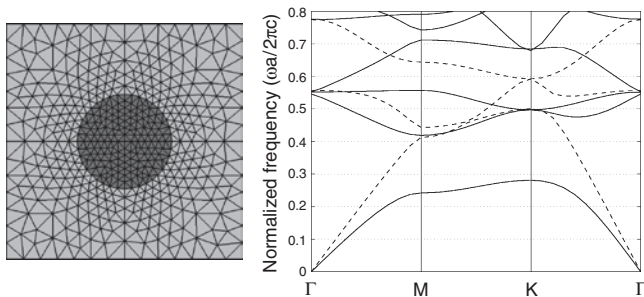
$$\begin{cases} \frac{\partial E_z(\vec{r}_{\parallel})}{\partial y} = -i\mu_0\omega H_x(\vec{r}_{\parallel}) \\ \frac{\partial E_z(\vec{r}_{\parallel})}{\partial x} = i\mu_0\omega H_y(\vec{r}_{\parallel}) \\ \frac{\partial H_y(\vec{r}_{\parallel})}{\partial x} - \frac{\partial H_x(\vec{r}_{\parallel})}{\partial y} = i\omega_0\varepsilon(\vec{r}_{\parallel})E_z(\vec{r}_{\parallel}) \end{cases}$$

Most of the investigations of photonic crystals have focused on the triangular lattice and the square lattice. However, since these structures are lithographically defined, there is in principle no need to confine the investigation to naturally occurring Bravais lattices [14]. In any case, in

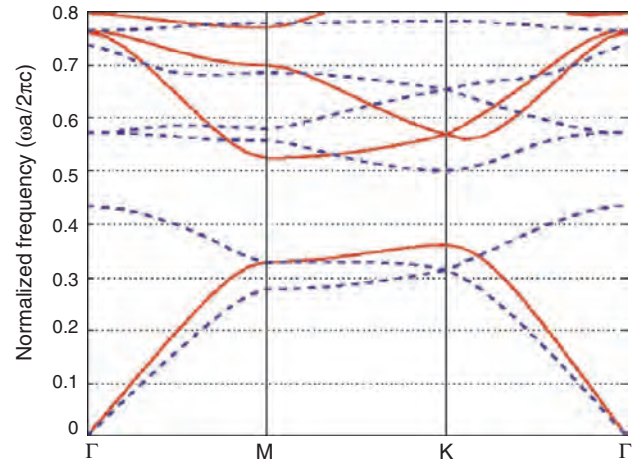
designing photonic devices formed in photonic crystals, care must be taken with choosing both the lattice and the dielectric distribution in the unit cell. A triangular lattice of air holes patterned into a high refractive index membrane creates a bandgap for both the guided TE and TM modes of the membrane for a range of hole radii. In general, a photonic lattice that consists of a connected high dielectric region is likely to exhibit a TE bandgap, while a lattice formed by disconnected high dielectric regions is more likely to exhibit a TM bandgap [15–18]. Both [18] and [19] have calculated the dispersion relations for several types of structures with a variety of lattices and unit cells.

Figure 1 shows the dispersion relation for the TE and TM modes of a two-dimensional square lattice consisting of dielectric rods. The TE dispersion relation is shown in dashed lines and the TM dispersion relation is in solid lines. Shown alongside is the conformal meshing of the unit cell that was used in this calculation. In this disconnected lattice, there is no TE bandgap, but a TM bandgap is formed. The inverse lattice consisting of low index holes in a high index matrix can be made to have both TE and TM bandgaps.

In the triangular lattice, the bandgaps for the two polarization types are formed between different bands. The first TE bandgap is formed between the first and second TE bands, while the first TM bandgap is formed between the second and third bands. Figure 2 shows the band structure for TE and TM modes of a dielectric lattice perforated by a triangular array of holes. In this figure, the dielectric constant of the background material is 13.6 and the dielectric constant of the holes is 1. The ratio of hole radius to lattice constant,  $r/a$ , is 0.47. This photonic crystal has a large TE bandgap. The frequency width of the gap is nearly 20% of the midgap frequency. The size of this gap can be changed by changing  $r/a$ . As  $r/a$  gets larger, the bottom band—called the dielectric band because at the bandedge the standing wave field is peaked in the high dielectric regions—moves up in frequency. This can be thought of as being due to the fact that this mode has a decreasing effective index as  $r/a$  increases. The second band—called the air band because the standing wave field at the bandedge is peaked in the low dielectric regions—also moves up in frequency. Since more of field of the air band is located in the low dielectric regions than the field of the dielectric band, the air band moves up in frequency with increasing  $r/a$  faster than the dielectric band and the bandgap therefore increases with increasing  $r/a$ .

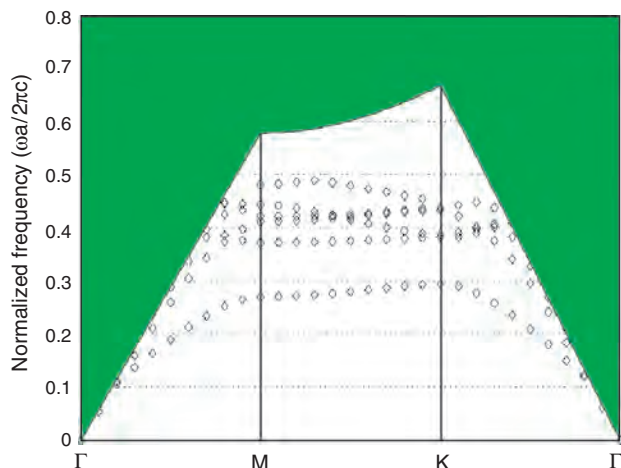


**Figure 1.** The photonic band structure of a square lattice of dielectric rods ( $n_{\text{rods}} = 12$ ) of radius of  $r/a = 0.2$  in an air background using the finite element method (left), and the conformal meshing used in the calculation (right).



**Figure 2.** The photonic band structure of a triangular lattice of air holes ( $r/a = 0.47$ ) perforating a dielectric material ( $n = 11.56$ ) using the plane-wave expansion method.

The photonic crystal structures that have been physically realized in the optical domain are not uniform in  $z$  direction, which is taken to be the epitaxial growth direction. Current etching technology often leads to lattices that are only a few microns deep. This forces the device designer to resort to membranes of photonic crystal slabs above low-index dielectric layers. The finite thickness of the photonic crystal structures complicates the electromagnetic analysis [20]. For lattices of a finite thickness, there are no longer strict TE or TM modes since the translational invariance in the  $z$  direction no longer exists. A fully three-dimensional numerical method with all six field components is required to accurately simulate a photonic crystal structure in a dielectric slab. Nevertheless, when mirror symmetry in the  $z$  direction exists, as in photonic crystals in suspended membranes, the field can be categorized as being an even or odd mode with respect to the midplane of the slab. This information can be used to help cut simulation time in half. This, of course, also requires that the layers which clad the suspended membrane be symmetric. However, in cases where the refractive index of the bottom cladding is not significantly different from air that serves as the top cladding layer at the desired working wavelength—such as sapphire and silicon dioxide at 1.55 micron—it is found that the even and odd modes describe the field reasonably accurately. To emphasize the approximation involved in the model, these modes are most often referred to in the literature as even-like or odd-like. It is worth noting that the photonic bandgap in a dielectric slab is not a three-dimensional electromagnetic bandgap [21, 22]. Since two-dimensional photonic crystals offer only lateral confinement, the lattice produces only a bandgap in the guided modes of the slab. Optical confinement depends on the index contrast in the third dimension to keep the field from radiating. The confinement of the slab is good only if the mode lies outside the light cone of the cladding. This effect is no different from what occurs in an ordinary dielectric slab waveguide [23]. In other words, a photonic bandgap exists only for those modes that are totally internally reflected at the photonic crystal membrane interfaces. Figure 3 shows the dispersion relation for a dielectric



**Figure 3.** Photonic band structure of the triangular lattice photonic crystal membrane. The light cone is mapped as a gray region.

slab in which a triangular lattice photonic crystal has been patterned. The radiation modes of the slab are shaded in the figure. The photonic crystal modes above the light line in the reduced Brillouin zone will be radiating vertically. This vertical radiation is an important element of microcavity photonic crystal laser design.

If the photonic crystal slab is placed on a low-index dielectric film instead of being symmetrically air clad, then complications are introduced into resonant cavity design. There are three major effects of breaking the symmetry about the midplane of the photonic crystal plane. These are a reduction in the effective bandgap width, an increase in the radius of the radiation cone, and the loss of a rigorous bandgap in the guided modes of the slab [24–26]. The first two of these effects are the most serious for device designers. The reduction in the bandgap occurs because the presence of a higher index substrate affects the frequency of the second band more than the lowest band. The radiation cone of the substrate is also larger than the radiation cone of the upper cladding material assuming that the substrate has a large refractive index. The third effect, the loss of the guided wave bandgap, results from the loss of strict even and odd symmetry. In a symmetrically clad membrane, the bandgap of the even guided modes and the odd guided modes are not identical. The even guided mode bandgap is usually at a lower frequency range than the bandgap for the odd guided modes. When this even and odd classification is lost, due to the asymmetric nature of the cladding, the bandgap is lost due to the spectral overlap of the dispersion relation of the modes that were formerly odd with the dispersion relation of the modes that were formerly even. The coupling between these two sets of modes is very small, however, so there is still an effective bandgap.

Most photonic devices designed to date work in the first bandgap, either in the bandgap as a result of a defect in the lattice or at one of the band edges. Band edges are useful because at the Brillouin zone boundary, the group velocity of the guided modes of the photonic crystal membrane are zero. As previously mentioned, the lower band edge mode is a standing wave with the peaks of its electric field located

in the high dielectric regions. This allows them to be used as laser modes in distributed feedback laser structures.

## 2.2. Localization of Light by Defects in the Lattice

Modes can be introduced into the electromagnetic bandgaps in photonic crystal membranes by introducing one or more defects into the lattice. The presence of defects in the lattice has the effect of pulling bandedge modes into the bandgap [27]. This phenomena is similar to formation of deep levels in an electronic bandgap of a solid due to impurities and identical to the formation of resonant modes in vertical cavity surface emitting lasers (VCSELs) by placing an active region of a precise thickness between two distributed Bragg reflectors. For example, if a high index perturbation is added to the lattice, such as by filling a hole with a high index material, then one or more modes is pulled from the upper band edge into the bandgap. This mode is sometimes referred to as a donor. Similarly, by including a low index perturbation, acceptor modes are pulled into the bandgap from the lower band edge. Thus by perturbing a single lattice site, a localized mode or group of modes is formed which have a frequency in the gap.

In analyzing these modes and designing them for laser cavities, one of the most important parameters is the  $Q$  of the resonance. The quality factor of the cavity is related to the material gain required to reach threshold through

$$\Gamma g = \frac{2\pi\bar{n}}{\lambda} \frac{1}{Q}$$

where  $\Gamma$  is the optical confinement factor and  $g$  is the threshold material gain. Three numerical methods can be used to calculate the quality factor of the cavity modes. The first method is to measure the slope of the exponential decay of the energy of a given cavity mode with time. This decay of energy from the cavity is described by  $\exp(-t/t_{ph})$ , where  $t_{ph}$  is the photon lifetime that is related to the quality factor  $Q$ , by  $Q = \omega t_{ph}$ . This method is most useful for relatively low  $Q$  modes where the slope of energy decay is visibly greater than zero.

Another method is to calculate the ratio of full width at the half magnitude of the cavity resonance in the frequency domain,  $\Delta\omega$ , to center frequency,  $\omega_0$ . However, distortion to the spectrum is often introduced because the numerical simulation terminates before the impulse response is fully evolved. This is, in effect, viewing the true time-domain response through a rectangular window, which translates mathematically into the convolution of the true spectrum with a sinc function. The convolution widens the peaks in the spectrum among other effects. Distortion can be reduced by increasing the time-response window, but at a price of longer simulation time. A better approach in addressing the problem is to apply digital signal analysis techniques to extrapolate the electromagnetic field in time-domain by 10:1 or more beyond the actual simulation window. Several methods have been proposed including Prony's method [28], generalized pencil-of-function technique [29, 30], and Padé's approximation [31]. The first two techniques extrapolate the

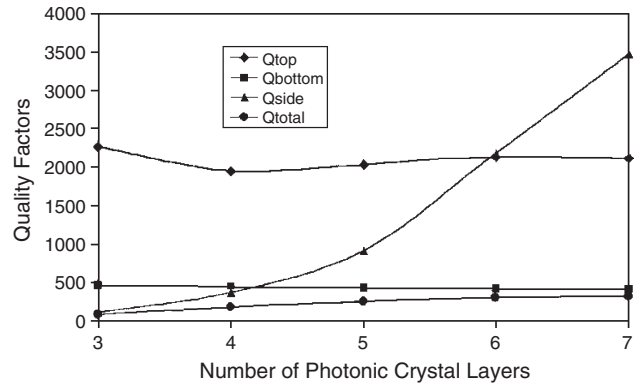


field by representing it in the time-domain as a sum of complex exponentials, while the last one uses a Padé approximation in conjunction with the fast Fourier transform. The Padé approximation technique proves itself less sensitive to the field sampling condition and thereby are more suited for general purpose extrapolation.

A third method calculates the ratio of cycle-averaged power absorbed in the boundary to the total energy in the cavity mode. This method has the advantage of being able to separate the radiation losses into different directions. For example, the effective vertical quality factor  $Q_{\perp}$  is given by the ratio of power lost to the absorber at the top and bottom  $P_{\perp}$  with respect to the total cavity energy  $U(t)$ , times the resonant frequency and effective in-plane quality factor  $Q_{\parallel}$  is similarly given by the ratio of in-plane power loss  $P_{\parallel}$  to the product of the total cavity energy and the resonant frequency. It should be noted that all of the calculations of  $Q$  in photonic crystals to date are of the cold cavity  $Q$  value. It is possible, however, to include absorption and gain in these calculations.

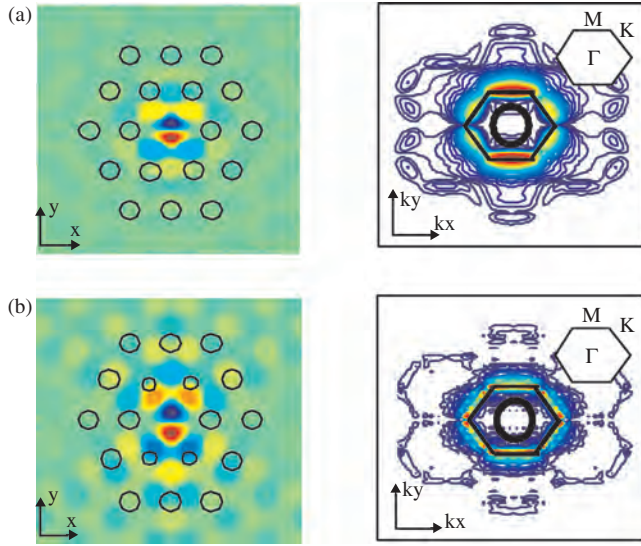
The field profile, resonant frequency, and quality factor of the modes introduced by placing defects in the lattice can be engineered. Not only can we create a defect mode with a frequency in the bandgap; we can also design a range of defect frequencies that sweep continuously across the bandgap by varying adjacent defect hole size or lattice constants [26]. Tuning the defect frequency to any value within the bandgap is one of the most important features of photonic crystal resonant cavities. One of the most common methods of creating a resonant cavity in a two-dimensional photonic crystal lattice is to fill one hole in a triangular lattice. This has the effect of introducing a doubly degenerate dipole mode into the bandgap. The resonant frequency of this mode depends on the lattice constant,  $r/a$ , and the membrane thickness in cases where the cavity is formed in an undercut membrane. The dipole mode does not have a particularly high  $Q$ . It is on the order of a few hundred. So while this mode is very easy to form, it is probably not the most interesting cavity design for laser operation. The problem with the dipole mode is that it suffers from rather large, out-of-plane radiation losses.

Understanding the role played by the in-plane and vertical radiation loss in a particular cavity is very useful in device design. The in-plane quality factor increases rapidly as the number of lattice periods increase, but for the smallest defects, the limiting factor for the cavity quality factor is usually the vertical radiation. This phenomena is illustrated in Figure 4. This figure shows the quality factors corresponding to the radiation loss in the vertical and in-plane directions as well as the total quality factor of this cavity. In this particular calculation, the cavity modeled was a single defect in a two-dimensional photonic crystal membrane. As mentioned above, the triangular lattice is often used in photonic crystal resonant cavities. This lattice has a large TE bandgap that is useful because this is the polarization that is predominantly emitted by conduction band to heavy hole radiative transitions in III-V semiconductor gain media. In addition, the larger the bandgap, the stronger the localization of the resonant fields at midgap. Because of this strong, in-plane localization, quality factors of the smallest cavities in this lattice are often dominated by out-of-plane radiation.



**Figure 4.** In-plane  $Q$ , vertical  $Q$ , and total  $Q$ . Reprinted with permission from [26], C. Kim et al., *J. Opt. Soc. Am. B* 19, 1777 (2002) © 2002, Optical Society of America.

This occurs because part of the mode overlaps the radiation cone of the slab. Since the mode is strongly localized in real space, it is spread out in wave vector space and overlaps the radiation modes of the slab. A Fourier transform of the dipole mode along with its real-space field profile is shown in Figure 5a. The figure shows the Brillouin zone boundary and the radiation cone as well. This loss can be reduced by reducing the resonant frequency of the mode. This moves the resonant mode farther away from the light cone. Equivalently, reducing the frequency of the resonant mode reduces the size of the radiation cone in  $k$ -space. This frequency reduction can be accomplished by reducing the  $r/a$  ratio of the lattice. This increases the effective index of the membrane and reduces the resonant frequencies. There is a trade-off in this, however, since reducing  $r/a$  reduces the size of the bandgap which can cause a reduction of in-plane confinement. This resonant frequency reduction can also be accomplished by increasing the thickness of the photonic crystal membrane. This also has the effect of increasing the effective index of the modes and reducing their frequencies. This strategy is effective as long as the slab does not become multimoded. Once the slab supports more than one waveguide mode, then the bandgap begins to close. This is due to the presence of the dispersion relations of the higher order slab modes. Another way in which the  $Q$  of the smallest cavities can be increased is by engineering the lattice near the missing hole. This method is the most general, but also the most open-ended. The strategy to achieve this increase in  $Q$  is most clearly illustrated by the Fourier transform of the dipole mode [32]. Again, this is shown for one of the degenerate dipole modes in the triangular lattice in Figure 5a. This figure shows that the greatest overlap of the mode with the radiation cone occurs along the  $\Gamma$ -M direction. Relaxing the in-plane confinement in this direction will allow the mode distribution in  $k$ -space to be more well localized and thereby reduce the overlap of the mode with the radiation cone. An illustration of the implementation of this design strategy is shown in Figure 5b. In this figure, the dielectric constant in the direct lattice has been modified to allow the resonant mode to expand along the  $y$  direction. This has the effect of increasing the  $Q$  by reducing the out-of-plane radiation loss. The strategy is fairly general,



**Figure 5.** The spatial profile and the Fourier transform of the dipole mode in an (a) unmodified and (b) modified, single-defect photonic crystal cavity. At right, the outer black line is the first Brillouin zone boundary and the inner black circle is the light cone in  $k$ -space.

but the particular lattice instantiation in which to achieve this increase is not unique.

Larger cavities have also been formed by removing several holes from the lattice. For these larger cavities, there are, of course, more resonant modes formed. It has not always been possible to identify the lasing modes in these larger cavities. For larger defect photonic crystal cavities, it is found that the loss of some of the defect modes is not dominated by vertical radiation loss. These modes benefit from being less tightly confined in real space and thereby spread less in reciprocal space. If the mode does not overlap the radiation cone in reciprocal space, it will not radiate out of plane. Of course, all confined modes overlap this radiation cone, but the extent of this overlap determines the out-of-plane radiation loss.

The square lattice has also been utilized in photonic crystal cavities. This lattice does not have a large TE bandgap. In fact, a complete bandgap may not even be necessary for the localization of a mode at a defect site. If the mode consists of wave vector components mainly from the region where a bandgap exists, then the mode can still be localized. In fact, quality factors from a single defect in the square lattice are thought to be higher than in a single defect in a triangular lattice [33]. This is attributed to the reduction of the in-plane confinement of the mode in the square lattice as compared to the triangular lattice. This relaxation of the in-plane confinement will then help to localize the mode in  $k$ -space, reducing the overlap of the mode with the radiation modes of the slab.

One of the more interesting features of photonic crystal lasers is that their resonant wavelength can be lithographically defined. Lithographic tuning of the wavelength can be achieved by varying the lattice constant and the hole radius. This scaling property of Maxwell's equation can be seen as follows. Assuming there is a resonant mode that satisfies the

equation,

$$\nabla \times \left( \frac{1}{\varepsilon_1(\vec{r})} \nabla \times \vec{H}_1(\vec{r}) \right) = \left( \frac{\omega_1}{c} \right)^2 \vec{H}_1(\vec{r})$$

then we can rescale the space by

$$\begin{aligned} \vec{r}' &= \alpha \cdot \vec{r} \\ \varepsilon_2(\vec{r}') &= \varepsilon_1(\alpha \vec{r}') \\ \vec{H}_2(\vec{r}') &= \vec{H}_1(\alpha \vec{r}') \end{aligned}$$

where obviously

$$\nabla' = \frac{1}{\alpha} \nabla$$

In the rescaled problem, then

$$\nabla' \times \left( \frac{1}{\varepsilon_1(\vec{r}')} \nabla' \times \vec{H}_1(\vec{r}') \right) = \left( \frac{\omega_1}{c} \right)^2 \vec{H}_1(\vec{r}')$$

Using the second and third of these equations, this last equation can be reduced to

$$\frac{1}{\alpha^2} \nabla \times \left( \frac{1}{\varepsilon_2(\vec{r})} \nabla \times \vec{H}_2(\vec{r}) \right) = \left( \frac{\omega_1}{c} \right)^2 \vec{H}_2(\vec{r})$$

then moving the denominator  $\alpha^2$  to the right side we have

$$\nabla \times \left( \frac{1}{\varepsilon_2(\vec{r})} \nabla \times \vec{H}_2(\vec{r}) \right) = \left( \frac{\omega_2}{c} \right)^2 \vec{H}_2(\vec{r})$$

where  $\omega_2 = \alpha \omega_1$  and the eigenfrequencies have been scaled.

### 3. FABRICATION OF TWO-DIMENSIONAL PHOTONIC CRYSTALS

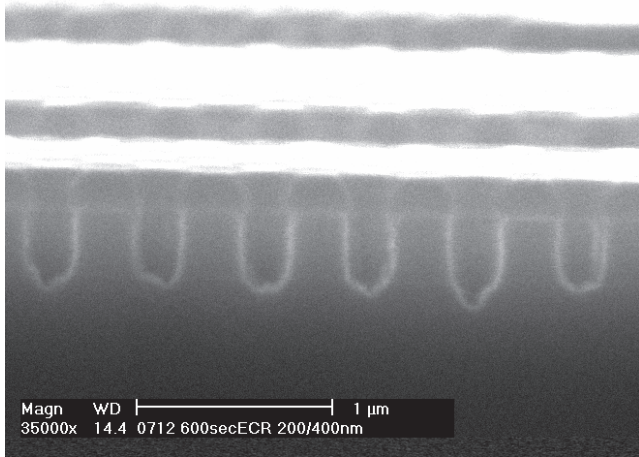
In this section, an overview of the fabrication procedures used in the formation of semiconductor photonic crystals will be presented. Most of the 2D photonic crystal lasers that have been demonstrated to date were fabricated in III–V compound semiconductors. There have been demonstrations in the AlGaAs/GaAs material system [34–36] as well as the InGaAsP/InP system [37–38]. The fabrication processes for these lasers is similar to each other even though the demonstrated lasers were designed for various types of optical modes with various physical structures. The typical semiconductor device fabrication processes include molecular beam epitaxy (MBE) or metal organic chemical vapor deposition (MOCVD) epitaxial growth of the active and waveguide materials, dielectric mask and/or metallic mask deposition for masking the pattern transfer, photolithography or electron beam lithography for defining the geometry of the laser devices, and plasma etching and/or wet chemical etching for defining the device geometry in semiconductor. Because of the similarity between the fabrication processes of all these laser devices, we are going to give the detailed description of the fabrication process of only one of the photonic crystal lasers in this article—the two-dimensional photonic crystal membrane laser in InGaAsP/InP [38]. This illustrates the basic nanofabrication process necessary to

pattern and transfer the photonic lattice into the semiconductor. The final structure consists of a 220-nm-thick, InGaAsP suspended membrane containing four quantum wells in which a triangular lattice of holes has been etched. The resonant cavity is formed in the center where there is one or more holes missing from the lattice.

To realize this structure, an epitaxial structure containing the active region, usually several quantum wells to provide TE gain, and any additional optical waveguiding layers, is deposited first. The epitaxy is capped with a thin,  $\sim 50$  nm layer that will subsequently be removed. This layer protects the active region during the etching and its removal at the end of the process guarantees a smooth top surface. The masking layers are then deposited. A silicon nitride layer that is typically on the order of 100 nm thick is deposited on top of which 100-nm of 2% polymethylmethacrylate (PMMA) is spin-coated.

The photonic lattice is defined in the PMMA by electron beam lithography. After the electron beam exposure, the PMMA is developed. At this point, the pattern is transferred through the SiN mask layer in a reactive ion etch (RIE). This nitride layer is then used to mask the pattern transfer into the semiconductor. This last pattern transfer, dry-etching step can be done using a chemically assisted, ion beam etch (CAIBE), an inductively coupled plasma etch (ICP), or an electron cyclotron resonance etch (ECR). To pattern InGaAsP/InP material, an etch recipe based on a  $\text{CH}_4/\text{H}_2/\text{Ar}$  plasma is often used, although Cl-based recipes [39–41] have also been demonstrated. For an AlGaAs/GaAs structure, a Cl-based plasma chemistry is most often used [41]. An SEM image showing the cross-sectional view of the photonic crystal lattice after a typical  $\text{CH}_4/\text{H}_2/\text{Ar}$  plasma ECR etch, is shown in Figure 6. After this step, one last plasma etch is used to remove any remaining mask materials.

At this point, the photonic lattice is transferred into the semiconductor. A wet chemical etch is used to form the suspended membrane. To remove the InP below an InGaAsP membrane, this etch is a HCl-based mixture. For example, a 4:1 HCl:H<sub>2</sub>O etch at 0 °C has been reported. This etch also removed the cap layer on the epitaxy. Care must be taken with this etch, however, because HCl is an anisotropic etch



**Figure 6.** Cross-section SEM of a triangular photonic crystal lattice in InGaAsP/InP after ECR etching.

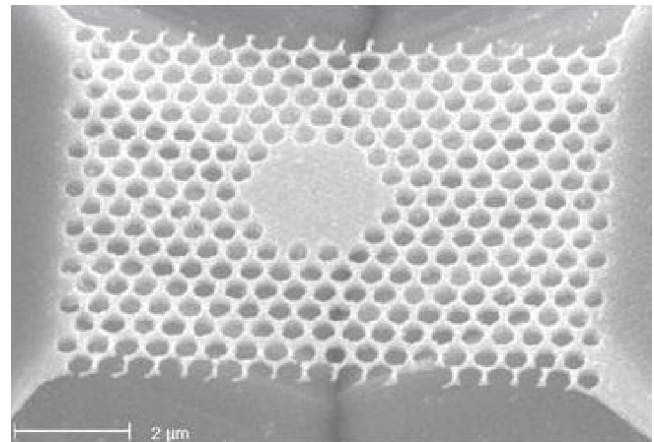
in InP [42]. The resulting membranes are suspended over a V-shaped groove that runs along the  $\langle 0, -1, -1 \rangle$  crystalline directions in the InP substrate. An electron micrograph image of a finished laser cavity is shown in Figure 7.

#### 4. DEMONSTRATED RESONANT CAVITY TYPES

A large variety of photonic crystal lasers have been demonstrated. This variety exists in both the resonant cavity design as well as in the gain material. In this section, we will review the experimental demonstrations of photonic crystal lasers. These demonstrations will be classified as lasers with photonic crystal end mirrors, lasers operating along traditional distributed feedback principles, and lasers that depend on high  $Q$  modes localized to a defect in the lattice. Most of the discussion will focus on the latter cavity type.

The simplest use of photonic crystals in laser structures is as end mirrors in a Fabry–Perot cavity. The earliest experimental demonstrations of 2D photonic crystal lasers in semiconductors were accomplished in this geometry [43]. Later, researchers conducted more detailed studies of these structures [40, 44–46] and employed an intracavity photonic crystal mirror to achieve a stable, single-mode, coupled-cavity laser. These laser structures can be straightforwardly made to be electrically pumped. The disadvantage of this geometry, however, is that the lattice must be etched deeply enough so that the lattice overlaps the entire mode profile in order to obtain the highest reflectivity [25]. There is much in common between these lasers and short-cavity, distributed Bragg reflector (DBR) lasers. Two-dimensional periodicity has the potential to offer greater mode stability, however. Quality factors in these cavities can be made very large due to a potentially long path length and therefore a potentially long photon lifetime.

Two-dimensional photonic crystal lasers have also been used in what are essentially DFB lasers as well. In these devices, the lasing occurs at the band edge of the photonic bandgap. Lasing has been observed in 2D and even in 3D periodical structures of polymers [47–49]. Many reports have observed lasing phenomenon in various types of naturally



**Figure 7.** SEM micrograph showing a tilted view of a finished, photonic crystal membrane laser cavity.

formed periodic structures in polymers. In 1998, Berggren et al. [50] and Meier et al. [51, 52] demonstrated a 2D photonic crystal DFB laser by etching a square lattice into SiO<sub>2</sub> and then spin-coating the patterns PBD doped with laser dyes.

Photonic crystal DFB lasers in semiconductor materials were demonstrated later in both triangular lattice and square lattice photonic crystals [53–56]. As reported in [53], electrically pumped DFB lasers were fabricated by directly wafer-bonding a p-InP layer containing multiple InGaAsP quantum wells, onto an n-InP substrate on which had been etched a shallow 2D photonic crystal structure. Coherent and incoherent lasing at three equivalent  $\Gamma$ -X directions was observed with different electrical pumping conditions. A more sophisticated study of mode polarization control by deforming the symmetry properties of the photonic crystal unit cell was later reported by the same group of researchers [54]. Optical pump thresholds as low as 35  $\mu$ W have been demonstrated at 80 Kelvin [55]. This demonstration utilized pulsed pumping of a 200-nm, air-clad, InGaAsP slab containing a triangular lattice photonic crystal.

Lasing in larger cavities is not strictly confined to DBR and DFB-type photonic crystal cavities. There have been other demonstrations of photonic crystal semiconductor lasers. A bent-ridge, waveguide laser cavity with two-dimensional photonic crystals as the lateral confinement has also been demonstrated [57]. The radiation loss of the waveguide bend is reduced using this method. A coupled cavity waveguide structure, formed by 40 coupled hexagonal cavities with 91 defects surrounded by two-dimensional triangular lattice photonic crystals, has also been reported [58]. Minibands inside the photonic bandgap form and single-mode lasing is observed at the first miniband edge.

The preceding photonic crystal lasers do not make use of defects in the lattice. There have been several demonstrations, however, of microcavity lasers in which the mode is formed by defects in 2D photonic crystals. These microcavities have resonant modes that exist within the electromagnetic bandgap of the photonic crystal and are localized to the immediate vicinity of a defect in the lattice. Two-dimensional photonic crystals are used to provide the in-plane localization of the mode, while the vertical confinement is provided by total internal reflection at a dielectric interface. Maximum confinement can be achieved using air as the cladding layers on both sides of a semiconductor membrane. The InP/InGaAsP material system is most often used for these demonstrations because it provides two advantages. One advantage is the relatively lower surface recombination rate, and the other is the long emission wavelength around 1.55  $\mu$ m. Surface recombination in semiconductor photonic crystals has been studied in [59]. Most of these demonstrations have been of pulsed, optically pumped lasing. Here we will first consider the smallest of these cavities, those in which the defect consists of a single missing hole in the lattice. The first two-dimensional, photonic crystal defect laser demonstration was reported by Painter et al. in June 1999 [60]. This demonstration occurred in a suspended membrane in which a triangular lattice was patterned. This device was optically pumped at 143 K. The resonant mode was formed at a single defect in the lattice. The threshold pump power and pump conditions in

this demonstration were 6.75 mW and 10 ns pulses with 250 ns period. The reported  $Q$  of this cavity was 250. This lasing mode had one of the smallest mode volumes ever reported in any laser. The cavity quality factor of this cavity was subsequently improved by a factor of approximately two or more by reducing the hole size which led to a room-temperature demonstration [61]. The highest  $Q$  mode in these single-defect, triangular lattice cavities is a doubly degenerate dipole termed the  $x$ -dipole and the  $y$ -dipole [62]. These two degenerate modes have orthogonal polarizations and have been observed experimentally. The lattice, however, can be intentionally distorted near the missing hole, thereby reducing the symmetry to break the polarization degeneracy of the dipole modes. This distortion has also been demonstrated experimentally [60, 63]. To obtain the truly single-mode operation inside the two-dimensional photonic crystal defect cavity, Park et al. proposed a new design in which a nondegenerate monopole mode is experimentally observed by reducing and pushing away the nearest six air holes from the defect cavity [64]. The measured polarization data of the monopole mode showed no preferred direction as indicated using the 3D FDTD calculation. The quality factor here was estimated to be larger than 1900. This value was obtained from the spectral linewidth at transparency. As a result of this large  $Q$  value, a low-threshold pump power of less than 0.3 mW was obtained. Various modified single-defect cavity designs have also been studied, both numerically and experimentally in [65–66].

Room-temperature, pulsed lasing action has also been realized by Ryu et al. using two-dimensional, square lattice photonic crystals [67–68]. In [67], both degenerate dipole modes and a nondegenerate quadrupole mode in the single-defect cavity are observed. The threshold pump conditions for this geometry were 0.8 mW power of optical power with a 15 ns pulse width and a 0.4% duty cycle. A FDTD calculation predicts that the quality factor of the quadrupole mode is much larger than the dipole mode and the experimental measurement yielded a quality factor of about 2000 for the quadrupole mode. Again, this measurement was obtained from the linewidth of the resonance at transparency. The nondegenerate mode has been labeled as the lowest-order whispering gallery (LWG) mode [68]. Furthermore, this mode exhibits an energy null at the center of the cavity and hence opens up a possible route of electrical pumping by putting the current contact at the cavity center. Other work towards electrically pumped photonic crystal lasers is reported by Zhou et al. [69–70]. The heterostructure in this report consisted of an undoped cavity with two compressively strained InGaAs quantum wells and a bottom DBR mirror. The photonic crystal is deeply etched through the cavity and into the bottom DBR region. Later, this group used self-organized InAs quantum dots as the active material and demonstrated photonic crystal, microcavity light-emitting diodes pumped in pulsed mode with a heat sink [71].

There has also been other recent work on incorporating quantum dot active regions into photonic crystal laser cavities. Quantum dot active regions have the potential to reduce any surface recombination loss in these cavities through the incorporation of in-plane potential wells. Two-dimensional photonic crystal defect cavities, using InAs

quantum dots as the active material, were first reported and characterized by Reese et al. [72]. Microcavities formed by removing 37 and 61 air holes out of an otherwise perfect triangular lattice photonic crystal were reported in this work. Measured photoluminescence spectra show several high  $Q$  cavity modes among the more than 100 possible resonant modes inside the cavity. Modes with quality factors higher than 1000 are obtained from the spectra. Later, photonic crystal cavities with single and seven air holes removed from the lattice with a cavity quality factor as high as 4000 were observed [3]. Yoshie et al. have published results on two-dimensional, photonic crystal, single-defect cavities using self-organized InAs quantum dots [73]. Later, this same group employed a new cavity design based on fractional edge dislocations to obtain a high-quality, single defect cavity within a two-dimensional triangular lattice photonic crystal slab [74]. Donor modes were observed and the measured quality factor as high as 2800 was achieved in a cavity using the InAs quantum dots as the emitter. Room temperature, optically pumped, InAs quantum dot photonic crystal lasers were first demonstrated using a coupled cavity design [75]. Lasing is observed for both the coupled two-defect and four-defect cavities in a square lattice photonic crystal with the threshold pump powers of 120 and 370  $\mu\text{W}$ , respectively.

Larger cavities have also been formed by removing multiple holes from the lattice. Photonic crystal defect lasers with 19 holes removed from the triangular lattice have been reported by Lee et al. [76]. An 860-nm top-emitting, vertical-cavity, surface-emitting laser (VCSEL) was used to optically pump the photonic crystal lasers. The lowest threshold pump power reported in this geometry was 0.5 mW. The corresponding threshold carrier density was estimated to be  $1.2 \times 10^{17} \text{ cm}^{-3}$  per quantum well. Approximately 2  $\mu\text{W}$  of peak output power was collected vertically and fiber coupled using this structure. This laser and the previously mentioned laser employ a photonic crystal in a suspended membrane. This has the serious disadvantage of being a very poor geometry in which to dissipate heat. To make a more thermally conductive photonic crystal defect laser structure than the suspended membrane, Hwang et al. proposed a design that involves bonding a AlAs layer to the thin slab and later oxidizing it into a low-index  $\text{AlO}_x$  layer [77]. They reported pulsed lasing action for defect cavities with 37 or more holes removed from the hexagonal lattice. Another effort of integrating the photonic crystal defect lasers with other materials was made by Monat et al. [78]. They employ the  $\text{SiO}_2$ - $\text{SiO}_2$  wafer-bonding technique to integrate the defect lasers onto a silicon wafer. The defect cavity with 61 holes removed from the hexagonal lattice was sandwiched between air and the  $\text{SiO}_2$  layer. Quality factors of the resonant modes in the cavity can be as high as 700.

Modes and their corresponding radiation patterns have also been investigated in these lasers. Shin et al. reported on investigations of the far fields and near fields of various lasing modes in photonic crystal lasers [79]. The cavities they measured are rather large with "radii" of 11, 13, 21, 29, or 31 missing holes along the  $K$  direction of the hexagonal lattice. Cavities with a "radius" of 11 lattice constants have 91 holes removed from the photonic crystal lattice. The cavity in these demonstration is, of course, hexagonal shaped and not circular. These cavities, therefore, support

dozens of resonant modes. By slightly adjusting the alignment of the optical pump beam, different lasing modes can be selectively excited. The observed lasing modes were divided into two categories: one-dimensional modes and two-dimensional modes. The one-dimensional modes were plane wave-like modes that oscillate between two parallel boundaries of the hexagonal cavity. These are TE-polarized as confirmed experimentally from the polarization-resolved emission patterns. Two-dimensional modes are observed for larger lattice constants and for cavities with at least 11 defects along the  $K$  direction. A 21-defect cavity, for example, had only one-dimensional lasing modes for lattice constants 370 nm and 400 nm. Two-dimensional lasing modes began to appear when the lattice constant was 440 nm. At the lattice constant 490 nm, only the two-dimensional mode was present. The spectrally resolved, near-field intensity distributions of the resonant modes inside the defect cavity were reported for the first time using a scanning optical microscope. The near-field images of the one-dimensional lasing modes reveal that the intensity decays within a few lattice periods into the photonic crystals. The images of the two-dimensional lasing modes indicated that intensity was mainly distributed along the cavity boundary.

All of the experimental results previously discussed were under pulsed operation at room temperature. The only continuous room temperature operation of photonic crystal defect lasers was reported by Hwang et al. [80]. This demonstration utilized the same structure as in [77], but the cavity size in this case is larger (21 defects along the  $K$  direction of the hexagonal cavity forming a cavity approximately 10  $\mu\text{m}$  in diameter). The  $\text{Al}_2\text{O}_3$  layer acts not only as the low-index cladding material but also as a thermally conductive layer to dissipate heat more efficiently.

Pulsed operation of photonic crystal lasers above room temperature has also been reported by Lee et al. [81]. The laser cavity design in this demonstration was the same as in [76]. Lasing action was observed for substrate temperatures as high as 50  $^\circ\text{C}$ . The effects of temperature on the performance of photonic crystal defect lasers were investigated in [81]. Temperature-dependent measurements of the lasing wavelength and the threshold pump power were reported. It was found that the lasing wavelength increased with substrate temperature at a rate of approximately 0.5  $\text{\AA}/\text{K}$  and the near linear red shift of the lasing wavelength was dominated by the refractive index change of the semiconductor media. The threshold input pump powers measured for substrate temperatures 20  $^\circ\text{C}$ , 35  $^\circ\text{C}$ , and 50  $^\circ\text{C}$  were 3.2 mW, 5.3 mW, and 7.4 mW, respectively.

As described earlier, one advantage of photonic crystal defect lasers is that the lasing wavelength, polarization, and emission direction of the mode can be easily engineered by lithographically changing the geometry of the devices. Using this idea, a  $10 \times 10$  multi-wavelength photonic crystal laser array of single-defect cavities was demonstrated by Painter et al. [82]. A tuning range from 1500 nm to 1625 nm with a 10-nm wavelength spacing from device to device was reported. Later Cao et al. reported a wavelength separation of approximately 4.6 nm between adjacent devices with lattice constants varying in 2 nm increments [83]. This multi-wavelength array consisted of 31 cavities. This demonstration utilized a larger cavity, 19 holes missing from the lattice.

Although multiple modes exist within such cavities, approximately 20 dB SMSR was reported in that work.

No work has been reported to date on the dynamics of these lasers. It is interesting to consider the effects of the small cavity volume that these defect photonic crystal lasers possess might have on the dynamic properties of these lasers. Experimentally, these questions will most easily be answered for lasers that can be operated CW.

Much work has been done in the last few years to make photonic crystal lasers a reality. There is a great deal of work remaining, however, if photonic crystal lasers are to become a mature, practical, photonics technology. Room temperature, CW, and electrically pumped lasing will be required. To achieve this, the investigation and minimization of absorption losses in these microcavity devices as well as innovative design strategies will be necessary. Strategies for increasing the output power from these lasers may also be required. These are daunting challenges. However, considering how far this technology has come in such a brief time, there is no reason to expect that these challenges cannot be met.

## GLOSSARY

**Compound semiconductor** Semiconductors that are composed of multiple elements.

**Finite-difference time-domain** A marching-in-time method that simulates the continuous fields by volumetric sampling of the unknown fields within and surrounding the structure of interest.

**Finite element method** An approximate method for solving partial differential equations by replacing continuous functions by piecewise approximations defined on polygons, which are referred to as elements.

**Laser** Devices that generate or amplify coherent radiation at frequencies in the infrared, visible, or ultraviolet regions of the electromagnetic spectrum.

**Microcavity** Spatial distributions of dielectric function that exhibit confinement of light.

**Photonic bandgap** A range of electromagnetic radiation frequency in which no propagation modes exist.

**Photonic crystal** Materials with a periodically varying dielectric function.

**Quantum dot** Nanoscale impurity domains in semiconductors that have quantum confinement effects on electrons in all three dimensions.

**Quantum well** Thin slab structures in semiconductors that have quantum confinement effects on electrons in the direction orthogonal to the slab.

**Resonant cavity** Microcavities that exhibit confinement on fields for certain frequencies.

## REFERENCES

1. E. Yablonovitch, *Phys. Rev. Lett.* 58, 2486 (1987).
2. J. Vuckovic, O. Painter, Y. Xu, A. Yariv, and A. Scherer, *IEEE J. Quantum Elect.* 35, 1168 (1999).
3. J.-K. Hwang, H.-Y. Ryu, and Y.-H. Lee, *Phys. Rev. B* 60, 4688 (1999).
4. See issue of *J. Opt. Soc. Am. B* 19 (2002), references contain therein.

5. C. Mias, J. P. Webb, and R. I. Ferrari, *IEE Colloquium on Semiconductor Optical Microcavity Devices and Photonic Bandgaps* 31 (Digest No. 1996/267).
6. S. P. Peet and R. L. Ferrari, in "Finite elements for Electrical Engineers" (3rd Ed.). Chap. 8. Cambridge University Press, 1996.
7. <http://www.ime.unicamp.br/%7echico/arpac+ +/>
8. H. S. Sozuer, J. W. Haus, and R. Inguva, *Phys. Rev. B* 45, 13962 (1992).
9. P. R. Villeneuve and M. Piché, *Phys. Rev. B* 46, 4969 (1992).
10. K. Ohtaka, *Phys. Rev. B* 19, 5057 (1979).
11. K. S. Yee, *IEEE Trans. Antennas Propagation* 14, 302 (1966).
12. A. Taflove and S. Hagness, in "Computational Electrodynamics—The Finite Difference Time Domain Method" (2nd Ed.). Artech House, New York, 2000.
13. D. H. Choi and W. J. R. Hofer, *IEEE Tran. Microwave Theory Tech.* 34, (1986).
14. S. David, A. Chelnokov, and J.-M. Lourtioz, *Optics Lett.* 25, 1001 (2000).
15. J. N. Winn, R. D. Meade, and J. D. Joannopoulos, *J. Mod. Optics.* 41, 257 (1994).
16. M. Pihhal and A. A. Maradudin, *Phys. Rev. B* 44, 8565 (1991).
17. P. Villeneuve and M. Piche, *Phys. Rev. B* 45, 4969 (1992).
18. J. D. Joannopoulos, R. D. Meade, and J. N. Winn, in "Photonic Crystals—Molding the Flow of Light." Princeton University Press, 1995.
19. T. Baba, *IEEE Journal of Selected Topics in Quantum Electronics* 3, 808 (1997).
20. S. G. Johnson, S. Fan, P. R. Villeneuve, and J. D. Joannopoulos, *Phys. Rev. B* 60, 5751 (1999).
21. K. M. Ho, C. T. Chan, and C. M. Soukoulis, *Phys. Rev. Lett.* 65, 3152 (1990).
22. R. D. Meade, K. D. Brommer, A. M. Rappe, and J. D. Joannopoulos, *Appl. Phys. Lett.* 61, 495 (1992).
23. D. Marcuse, in "Theory of Dielectric Optical Waveguides." Academic Press, San Diego, 1991.
24. E. Miyai and K. Sakoda, *Opt. Lett.* 26, 740 (2001).
25. B. D'Urso, O. Painter, J. O'Brien, T. Tombrello, A. Yariv, and A. Sherer, *J. Opt. Soc. Am. B* 15, 1155 (1998).
26. C. Kim, W. J. Kim, A. Stapleton, J.-R. Cao, J. D. O'Brien, and P. Daniel Dapkus, *J. Opt. Soc. Am. B* 19, 1777 (2002).
27. E. Yablonovitch, T. J. Gmitter, R. D. Meade, A. M. Rappe, K. D. Brommer, and J. D. Joannopoulos, *Phys. Rev. Lett.* 67, 3380 (1991).
28. W. L. Ko and R. Mittra, *IEEE Trans. Micro. Theory Tech.* 39, 2176 (1991).
29. Z. Bi, Y. Shen, K. Wu, and J. Litva, *IEEE Trans. Micro. Theory Tech.* 40, 869 (1992).
30. A. Monorchio and R. Mittra, *IEEE Micro. Guided Wave Lett.* 8, 93 (1998).
31. S. Dey and R. Mittra, *IEEE Micro. Guided Wave Lett.* 8, 415 (1998).
32. J. Vuckovic, M. Loncar, H. Mabuchi, and A. Sherer, *IEEE J. Quantum Electron.* 38, 850 (2002).
33. S. G. Johnson, S. Fan, A. Mekis, and J. D. Joannopoulos, *Appl. Phys. Lett.* 78, 3388 (2001).
34. K.-Y. Lim, D. J. Ripin, G. S. Petrich, L. A. Kolodziejski, E. P. Ippen, M. Mondol, H. I. Smith, P. R. Villeneuve, S. Fan, and J. D. Joannopoulos, *J. Vac. Sci. Technol. B* 17, 1171 (1999).
35. W. D. Zhou, P. Bhattacharya, J. Sabarinathan, and D. H. Zhu, *J. Vac. Sci. Technol. B* 18, 1706 (2000).
36. C. Reese, B. Gayral, B. D. Gerardot, A. Imamoğlu, P. M. Petroff, and E. Hu, *J. Vac. Sci. Technol. B* 19, 2749 (2001).
37. A. Scherer, O. Painter, B. D'Urso, R. Lee, and A. Yariv, *J. Vac. Sci. Technol. B* 16, 3906 (1997).
38. J. R. Cao, P.-T. Lee, S.-J. Choi, R. Shafiha, S.-J. Choi, J. D. O'Brien, and P. D. Dapkus, *J. Vac. Sci. Technol. B* 20, 618 (2002).

39. C. Youtsey, R. Grundbacher, R. Panepucci, I. Adesida, and C. Caneau, *J. Vac. Sci. Technol. B* 12, 3317 (1994).
40. T. D. Happ, A. Markard, M. Kamp, A. Forchel, S. Anand, J.-L. Gentner, and N. Bouadma, *J. Vac. Sci. Technol. B* 19, 2775 (2001).
41. J. Moosburger, M. Kamp, A. Forchel, R. Ferrini, D. Leuenberger, R. Houdré, S. Anand, and J. Berggren, *Nanotechnology* 13, 341 (2002).
42. L. A. Coldren, K. Furuya, and B. I. Miller, *J. Electrochem. Soc.* 31, 1918 (1983).
43. J. O'Brien, O. Painter, R. Lee, C. C. Cheng, A. Yariv, and A. Scherer, *Electron. Lett.* 32, 2243 (1996).
44. T. D. Happ, M. Kamp, F. Klopff, J. P. Reithmaier, and A. Forchel, *Semicond. Sci. Technol.* 16, 227 (2001).
45. T. D. Happ, A. Markard, M. Kamp, J. L. Gentner, and A. Forchel, *Electron. Lett.* 37, 428 (2001).
46. T. D. Happ, A. Markard, M. Kamp, A. Forchel, and S. Anand, *Appl. Phys. Lett.* 79, 4091 (2001).
47. J. Martorell and N. M. Lawandy, *Opt. Commun.* 78, 169 (1990).
48. S. Riechel, C. Kallinger, U. Lemmer, J. Feldmann, A. Gombert, V. Wittwer, and U. Scherf, *Appl. Phys. Lett.* 77, 2310 (2000).
49. M. Notomi, H. Suzuki, and T. Tamamura, *Appl. Phys. Lett.* 78, 1325 (2001).
50. M. Berggren, A. Dodabalapur, R. E. Slusher, Z. Bao, A. Timko, and O. Nalamasu, *Electron. Lett.* 34, 90 (1998).
51. M. Meier, A. Mekis, A. Dodabalapur, A. Timko, R. E. Slusher, J. D. Joannopoulos, and O. Nalamasu, *Appl. Phys. Lett.* 74, 7 (1999).
52. A. Mekis, M. Meier, A. Dodabalapur, R. E. Slusher, and J. D. Joannopoulos, *Appl. Phys. A* 69, 111 (1999).
53. M. Imada, S. Noda, A. Chutinan, T. Tokuda, M. Murata, and G. Sasaki, *Appl. Phys. Lett.* 75, 316 (1999).
54. S. Noda, M. Yokoyama, M. Imada, A. Chutinan, and M. Mochizuki, *Science* 293, 1123 (2001).
55. H. Y. Ryu, S. H. Kwon, Y. J. Lee, Y. H. Lee, and J. S. Kim, *Appl. Phys. Lett.* 80, 3476 (2002).
56. C. Monat, C. Seassal, X. Letartre, P. Regreny, P. Rojo-Remeo, P. Viktorovitch, M. Le Vassor d'Yerville, D. Cassagne, J. P. Albert, E. Jalaguier, S. Pocas, and B. Aspar, *Appl. Phys. Lett.* 81, 5102 (2002).
57. T. D. Happ, M. Kamp, F. Klopff, J. P. Reithmaier, and A. Forchel, *Electron. Lett.* 36, 324 (2000).
58. T. D. Happ, M. Kamp, A. Forchel, J.-L. Gentner, and L. Goldstein, *Appl. Phys. Lett.* 82, 4 (2003).
59. H.-Y. Ryu, J.-K. Hwang, D.-S. Song, I.-Y. Han, Y.-H. Lee, and D.-H. Jang, *Appl. Phys. Lett.* 78, 1174 (2001).
60. O. Painter, R. K. Lee, A. Scherer, A. Yariv, J. D. O'Brien, P. D. Dapkus, and I. Kim, *Science* 284, 1819 (1999).
61. J. Painter, A. Husain, A. Scherer, J. D. O'Brien, I. Kim, and P. D. Dapkus, *J. Lightwave Technol.* 17, 2082 (1999).
62. O. Painter and K. Srinivasan, *Opt. Lett.* 27, 339 (2002).
63. O. Painter, K. Srinivasan, J. D. O'Brien, A. Scherer, and P. D. Dapkus, *J. Opt. A: Pure Appl. Opt.* 3, S161 (2001).
64. H.-G. Park, J.-K. Hwang, J. Huh, H.-Y. Ryu, Y.-H. Lee, and J.-S. Kim, *Appl. Phys. Lett.* 79, 3032 (2001).
65. H.-G. Park, J.-K. Hwang, J. Huh, H.-Y. Ryu, S.-H. Kim, J.-S. Kim, and Y.-H. Lee, *IEEE J. Quantum Electron.* 38, 1353 (2002).
66. H.-Y. Ryu, H.-G. Park, and Y.-H. Lee, *IEEE J. Selected Topics in Quantum Electron.* 8, 891 (2002).
67. H. Y. Ryu, S. H. Kim, H. G. Park, Y. H. Lee, and J. S. Kim, *CLEO* 80 (2001).
68. H.-Y. Ryu, S.-H. Kim, H.-G. Park, J.-K. Hwang, Y.-H. Lee, and J.-S. Kim, *Appl. Phys. Lett.* 80, 3883 (2002).
69. W. D. Zhou, J. Sabarinathan, B. Kochman, E. Berg, O. Qasaimeh, S. Pang, and P. Bhattacharya, *Electron. Lett.* 36, 1541 (2000).
70. W. D. Zhou, J. Sabarinathan, P. Bhattacharya, B. Kochman, E. W. Berg, P.-C. Yu, and S. W. Pang, *IEEE J. Quantum Electron.* 37, 1153 (2001).
71. J. Sabarinathan, P. Bhattacharya, P.-C. Yu, S. Krishna, J. Cheng, and D. G. Steel, *Appl. Phys. Lett.* 81, 3876 (2002).
72. C. Reese, C. Becher, A. Imamoğlu, E. Hu, B. D. Gerardot, and P. M. Petroff, *Appl. Phys. Lett.* 78, 2279 (2001).
73. T. Yoshie, A. Scherer, H. Chen, D. Huffaker, and D. Deppe, *Appl. Phys. Lett.* 79, 114 (2001).
74. T. Yoshie, J. Vučković, A. Scherer, H. Chen, and D. Deppe, *Appl. Phys. Lett.* 79, 4289 (2001).
75. T. Yoshie, O. B. Shchekin, H. Chen, D. G. Deppe, and A. Scherer, *Electron. Lett.* 38, 967 (2002).
76. P.-T. Lee, J. R. Cao, S.-J. Choi, Z.-J. Wei, J. D. O'Brien, and P. D. Dapkus, *IEEE Photon. Technol. Lett.* 14, 435 (2002).
77. J.-K. Hwang, H.-Y. Ryu, D.-S. Song, I.-Y. Han, H.-W. Song, H.-K. Park, Y.-H. Lee, and D.-H. Jang, *Appl. Phys. Lett.* 76, 2982 (2000).
78. C. Monat, C. Seassal, X. Letartre, P. Viktorovitch, P. Regreny, M. Gendry, P. Rojo-Remeo, G. Hollinger, E. Jalaguier, S. Pocas, and B. Aspar, *Electron. Lett.* 37, 764 (2001).
79. D.-J. Shin, S.-H. Kim, J.-K. Hwang, H.-Y. Ryu, H.-G. Park, D.-S. Song, and Y.-H. Lee, *IEEE J. Quantum Electron.* 38, 857 (2002).
80. J. K. Hwang, H. Y. Ryu, D. S. Song, I. Y. Han, H. K. Park, D. H. Jang, and Y. H. Lee, *IEEE Photon. Technol. Lett.* 12, 1295 (2000).
81. P.-T. Lee, J. R. Cao, S.-J. Choi, J. D. O'Brien, and P. D. Dapkus, *Appl. Phys. Lett.* 81, 3311 (2002).
82. O. Painter, A. Husain, A. Scherer, P. T. Lee, I. Kim, J. D. O'Brien, and P. D. Dapkus, *IEEE Photon. Technol. Lett.* 12, 1126 (2000).
83. J. R. Cao, P.-T. Lee, S.-J. Choi, J. D. O'Brien, and P. D. Dapkus, *J. Nanosci. Nanotech.* 2, 313 (2002).

# Phthalocyanine Nanostructures

Eunyoung Kim

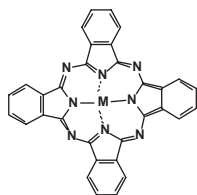
*Korea Research Institute of Chemical Technology, Yusong, Daejeon, Korea*

## CONTENTS

1. Introduction
  2. Phthalocyanine Thin Films
  3. Phthalocyanine Stacks, Molecular Arrays, and Self-Assemblies
  4. Phthalocyanine LB Films
  5. Phthalocyanine Nanocomposites and Hybrid Materials
  6. Phthalocyanine Polymers
  7. Polymeric Stacks
  8. Conclusion
- Glossary  
References

## 1. INTRODUCTION

Phthalocyanine (**1**) is a very important organic macrocycle, with many applications for its photochemical, photophysical, optical, and electrochemical properties, biological functions, and high stability [1].



**1** (M = H<sub>2</sub>, or metal oxo, metal halide, etc.)

Having mainly two characteristic absorption bands, a Soret band (300–400 nm) and a Q-band (600–800 nm), phthalocyanine (Pc) and its derivatives show characteristic color as well as photo- and electrochemical properties. They are extensively used as pigments and dyes, and they are models for biologically important species such as porphyrins, hemoglobin, and chlorophyll. They can be applied in chemical sensors, especially for the detection of NO<sub>2</sub> [2], in optoelectronic devices [3], solar cells [4], and well-behaved field

effect transistors [5], molecular metals, conducting polymers, sulfur effluent pollutant control, and in optical storage devices [1]. Their catalytic properties have been studied for some time [6], most recently for redox catalysis such as in fuel cell applications [7–9].

Recently the assemblies of phthalocyanines have attracted intense attention since the elucidation of the structure of the light-harvesting antenna LH2 in a natural purple photosynthetic bacterium [10]. Furthermore, a large number of phthalocyanine doped or bound polymers involving various metals have been prepared to enhance and tailor these properties and to facilitate the exploitation of Pcs in such applications [11]. For example phthalocyanine embedded in some organic polymers has been applied in optical recording materials, which records with the infrared (IR)-laser hole burning technique [12, 13].

An important step in the development of Pcs for these application is the precise manipulation of molecular arrangements. This precise manipulation allows directional transport of electrons, photons, and ions. In this context, a number of Pc molecules have been assembled into controlled nanoscaled structures through covalent and noncovalent bonds, by controlling the intermolecular interactions in all ranges (van der Waals, electrostatic, covalent) and molecular symmetry. For molecular self-assemblies, relatively weak and reversible noncovalent types of interactions are involved. Such interactions are electrostatic, van der Waals, hydrogen bonding, hydrophobic interaction, etc.

Covalently bonded nanoscaled Pc macromers are constructed by a polymerization method. It is a subject of great importance because it controls the aggregation of Pcs and macroscopic properties of nanoscopic molecular devices [14]. Several strategies have been explored to construct Pc polymers using different monomers and polymerization methods. The control of spatial arrangement and orientation of these planar  $\pi$ -conjugated compounds promised the creation or modification of functions and properties of molecular organizations. This chapter provides an overview on nanoscaled Pc assemblies and Pc polymers.

## 2. PHTHALOCYANINE THIN FILMS

Phthalocyanines having planar structures form thin films with a film thickness at the nanometer level. Thin films containing phthalocyanines have attracted a lot of interest



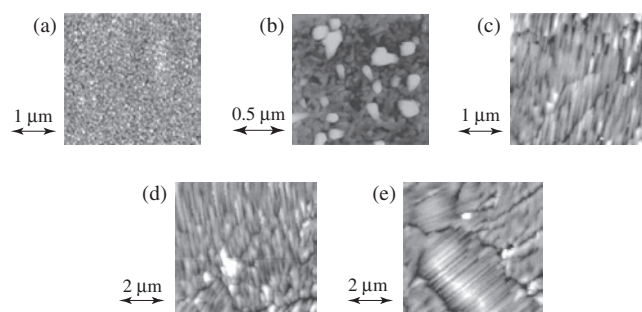
in the past decade [15–32]. Several strategies were implemented to build up phthalocyanine thin films: spin coating [33–36], casting in matrixes such as bilayer membranes or thermotropic liquid crystals [30, 37], deposition by the Langmuir–Blodgett technique [20, 23, 31, 37b–43], or self-assembly [15, 16, 18, 25–29, 44]. The latter method appears to be very attractive since it provides a stable chemical linkage between the substrate and the macrocycles. Pcs were attached to mineral substrates via electrostatic interactions [16, 25, 26, 45], sulfur-to-gold bonds [18, 27, 46], or complexation between bound ligands and metal centers [15, 28, 47].

Thin films are more generally deposited to a thin film by the vacuum deposition method [48–59]. Vacuum deposition on a highly ordered support such as MoS [60], metal [56, 59], or alkali halide surfaces (100) [61–66] tends to produce well-defined film structures. Organic molecular beam deposition (OMBE) provides various film phases of tri- and tetravalent metallophthalocyanines such as AlPcCl, InPcCl, TiOPc, and VOPc; some of these phases exhibit a highly redshifted Q-band in its electronic spectrum [67, 68]. This redshift originates from lateral stacking of the molecules in the film structure, which has been reported for cyanine aggregates [69–71] and is usually described by exciton coupling [71–73]. On the other hand, bivalent metallophthalocyanines prefer a coplanar central stacking owing to missing axial ligands and provide a blueshifted Q-band [39, 72, 74]. Nonplanar PbPc molecules were found [75] to have three adsorption phases on MoS<sub>2</sub> in ultrahigh vacuum (UHV), instead of the two phases observed for CuPc on the same surface. For CuPc, a close-packed phase with a square unit cell and a rowlike phase were observed. For PbPc, the additional adsorption phase comprised three adjacent close-packed rows separated by one or two isolated single rows. Molecularly resolved images of PbPc on MoS<sub>2</sub> show two different adsorption geometries, with the Pb atom above or below the Pc plane (the molecule is nonplanar). Different phases and structures in the Pc films depending on the metal, substituent, and the film thickness are described.

## 2.1. Metal-Free Phthalocyanine (H<sub>2</sub>Pc)

Two different polymorphic forms of free base phthalocyanine films have been grown on glass substrates by UHV organic molecular beam deposition. Postgrowth annealing of films grown at room temperature leads to transformation from the  $\alpha$  to the  $\beta_1$  phase [76]. The effects of annealing lead to a number of transition states whose morphological, structural, and spectroscopic properties can be identified using atomic force and optical interference microscopy, X-ray diffraction, and Raman and electronic absorption spectroscopy. Detailed morphological studies indicate that the transition occurs via a discrete number of nucleations and is preceded by an elongation of the  $\alpha$  crystallites. The film thickness plays a critical role and three regimes have been identified. The  $\alpha \rightarrow \beta_1$  transformation is only complete for films thicker than  $\sim 940$  Å, and thick films lead to a higher degree of orientation and larger domains.

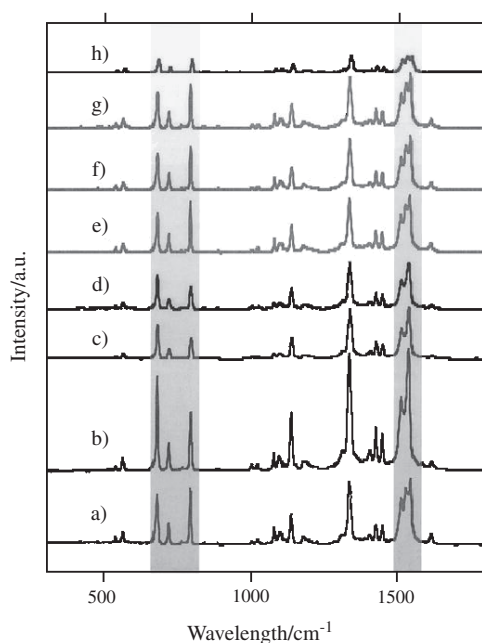
The morphology of the samples annealed for different times was assessed using atomic force microscopy (AFM) (Fig. 1). A film grown at room temperature with no annealing is shown as a reference in (a) and displays the high



**Figure 1.** AFM images of 2330 Å thick H<sub>2</sub>Pc films as a function of annealing time: (a) no anneal, (b) 1.0 h,  $\alpha$  phase, (c) 1.0 h,  $\beta_1$  phase (minor component), (d) 1.25 h and (e) 2.0 h. Reprinted with permission from [76], S. Heutz et al., *J. Phys. Chem. B* 104, 7124 (2000). © 2000, American Chemical Society.

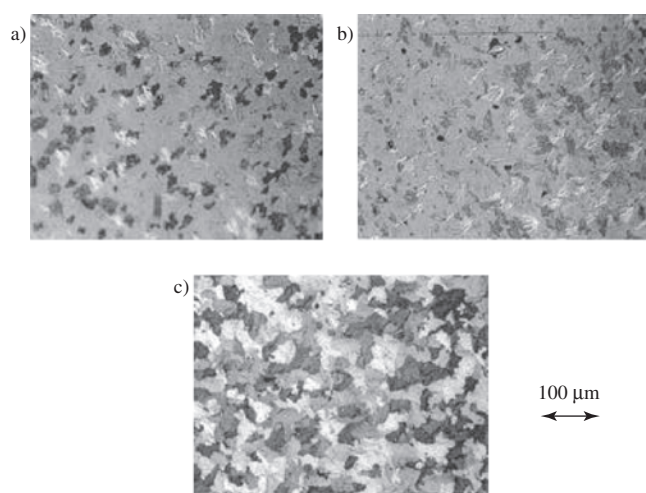
density of spherical islands that characterizes the  $\alpha$  phase [77]. The first changes become apparent after annealing for 0.75 h. The underlying surface morphology is similar to that seen for growth at room temperature, but closer inspection reveals some elongation of the spheres and the presence of several larger islands on the surface, with a typical diameter of 0.2–0.3  $\mu\text{m}$ . Elongation of the  $\alpha$  spheres becomes more pronounced after annealing for 1 h (b). This elongation prior to transformation has been reported in a previous electron microscopy study of CuPc films on muscovite [78]. Larger islands are also present on the surface, although these have not increased in size and number (number density of islands  $\cong 4 \mu\text{m}^{-2}$ ). A small proportion of the sample displays regions covered in oriented slender crystallites (c). These areas are at least 49  $\mu\text{m}^2$ , the typical area of an AFM image, and are characteristic of a pure  $\beta_1$  phase film [77]. The organized growth of the  $\beta_1$  phase therefore starts after 1 h annealing, consistent with the Raman spectra shown in Figure 2. After 1.25 h annealing the surface is completely covered with the long thin crystals of the  $\beta_1$  phase. The crystallites are parallel to each other over large areas, and a boundary between two domains of different orientations can be seen in (d). Annealing for longer times leads to no appreciable change in the surface morphology until after 2 h (e). At this point, the appearance of smooth areas between remaining islands of  $\beta_1$  crystals indicates that the  $\beta_1$  phase crystals have grown together and there only remain a few well-defined thin  $\beta_1$  crystallites, mostly arranged in columns. However, the domain boundaries are still present and there are some features reminiscent of the oriented crystallites in the smooth areas, indicating that these have been formed by the merging of the slender  $\beta_1$  crystallites.

Figure 3 shows the effect of film thickness on the larger scale morphology of the  $\beta_1$  phase. For the thinnest film for which it is possible to induce the  $\alpha \rightarrow \beta_1$  transformation, the result is isolated areas of fernlike morphology (a). There are large areas of nontransformed material between the  $\beta_1$  phase islands, and there is also space between the individual strands of the fernlike islands. When the starting film is slightly thicker, the  $\beta_1$  islands are larger, but they are still isolated from one another (b). This correlates well with the AFM results, which showed discrete domains of  $\alpha$  and  $\beta_1$  phase H<sub>2</sub>Pc. Figure 3c shows a sample that has the features



**Figure 2.** Resonance Raman spectra of 2330 Å  $H_2Pc$  films acquired with a 632.8 nm laser source. (a) and (b) are reference spectra for  $\beta_1$  and  $\alpha$  films, respectively. Different annealing times are shown: (c) 0.75 h, (d) 1.0 h,  $\alpha$  phase. (e) 1.0 h,  $\beta_1$  phase, (f) 1.25 h, (g) 1.5 h, and (h) 2.0 h. The ratio of  $\alpha$  (d) to  $\beta_1$  (e) for the film annealed for 1 h is approximately 5:2. Reprinted with permission from [76], S. Heutz et al., *J. Phys. Chem. B* 104, 7124 (2000). © 2000, American Chemical Society.

typical of all films above a critical thickness where the transformation is complete (i.e., 940 Å). The surface is covered entirely by domains of aligned  $\beta_1$  phase crystals. On close inspection this thicker film can be seen to exhibit the same fernlike fine structure as the thinner films, but there is no



**Figure 3.** Nomarski micrographs of  $H_2Pc$  films annealed for 2 h at 325 °C, for different film thicknesses: (a) 560, (b) 990, and (c) 4880 Å. The thinnest film shows nucleation of the  $\beta_1$  phase and a fernlike morphology. Increasing thickness leads to an increase in the domain size. Reprinted with permission from [76], S. Heutz et al., *J. Phys. Chem. B* 104, 7124 (2000). © 2000, American Chemical Society.

interlying space between the individual strands. It can be seen without any quantitative analysis that the size of the domains increases with film thickness for a given annealing time and temperature. This is a direct consequence of the higher degree of alignment observed of the crystallites for the thickest film.

These observations suggest three regimes of behavior for films of different thickness. The extreme case is for thin films (i.e., less than 560 Å). In this case there is not enough material to facilitate any transformation from the  $\alpha$  phase to the  $\beta_1$ . This is consistent with the suggestion that particles of the size found in these films are more stable in the  $\alpha$  phase than in  $\beta_1$ . For film thicknesses between 560 and 940 Å, only partial transformation of the film occurs, indicating that the film is thick enough to allow transformation, but there is not enough material on the surface to ensure continuity of the film during transformation. Clearly, the  $\beta_1$  phase grows at the expense of the  $\alpha$  phase directly in contact with it. The transformation occurs via discrete nucleations, since the remaining  $\alpha$  areas coexist and do not intermix with completely transformed  $\beta_1$  phase regions. It is also likely that since the transformation is very close to the sublimation point, the regions that have not been transformed are thin enough to be in the regime where the  $\alpha$  phase is more stable than the  $\beta_1$ . For film thicknesses above 940 Å, both the size of the  $\alpha$  phase crystallites and the thickness of the film (and hence its continuity) allow complete transformation of the film.

## 2.2. Copper (II) Phthalocyanine

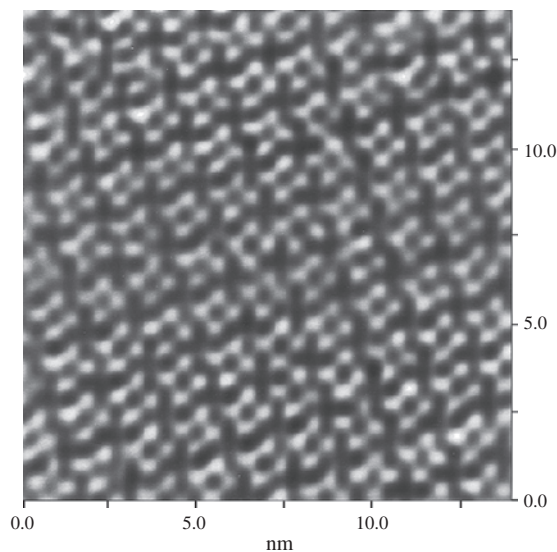
Vacume deposited thin films of metal phthalocyanines such as copper (CuPc) [52, 58, 59, 79–82], lead (PbPc) [75] cobalt (CoPc), iron (FePc), and nickel (NiPc) [83] phthalocyanines have prepared and their film structures have been examined using scanning tunneling microscopy (STM). For example, a 0.3-nm layer of copper (II) phthalocyanine could be deposited on Au (111) to form a near monolayer [56, 59]. Tanaka and co-workers [81] observed that planar CuPc molecules are bonded in a stable manner on the  $SrTiO_3$  surface in UHV, whereas CuPc can diffuse on the much less chemically active Cu (111) surface to create low-dimensional structures. Maeda et al. [58] and Kanai et al. [52] obtained similar results in UHV, showing that CuPc molecules have three adsorption configurations on the dimer row of Si (100) with the molecular plane parallel to the surface, dominated by the interaction between the aromatic rings of CuPc molecules and Si dangling bonds. Kanai et al. [52] also observed a distinctive bias-voltage dependence of the STM images of CuPc molecules on Si (111) in UHV, suggesting that there is a strong interaction between the molecule and the surface.

On the H-passivated Si (111) surface, the stacking and orientation of CuPc in UHV were found to be affected by the surface roughness [79]. On a rough surface, the CuPc molecules are stacked with the molecular columns parallel to the surface, whereas on an atomically flat surface, the CuPc molecules are stacked in columns perpendicular to the surface. Interestingly, CuPc was found [84] to induce faceting of misoriented Ag (110).

In most cases, the predominant features of the molecular image show organic material alone with an apparent hole in the center of the molecule as shown in Figure 4 for a 0.3 nm layer of CuPc on Au (111) [56].

The four-leaf pattern of the phthalocyanine ring is clearly observed, with a hole in the center of the macrocycle. The Cu atom is not participating in the tunneling process. This result was also obtained with Pt/Ir tips and a variety of bias voltages and currents. The image for H<sub>2</sub>Pc also shows an apparent hole in the center of the molecule [55]. The explanation for these “holes” was that both the occupied and unoccupied orbitals localized on Cu lay more than 1 eV from the Fermi energy, while the MPc ligand lowest unoccupied molecular orbital (LUMO) lay close to the Fermi energy [57]. As the metal in an MPc system is varied, the corresponding variation in metal *d* orbital participation near the Fermi surface should produce significant changes in the STM images. Alternatively, dramatic changes in the apparent molecular shape might also occur in systems where interactions between the metal *d* orbitals and a metallic substrate were significant. In the latter case, the metal surface density of states might “shine through,” giving enhanced height to the central metal.

Calculations [85, 86] show that the CoPc *dz<sup>2</sup>* orbital is roughly half-filled and lies very near the ligand highest occupied molecular orbital (HOMO). Calculations place the filled CuPc *dz<sup>2</sup>* orbital about 2 eV below the ligand HOMO, and there is no significant *d* orbital contribution within a band 1 eV above and 2 eV below the ligand HOMO in CuPc [85]. STM images of CoPc and CuPc on Au (111) are fully consistent both with *d* orbital contribution and with these theoretical results [87]. STM images of CoPc and CuPc show that CuPc molecules have an apparent hole in the center of the ring, while CoPc units have what appears to be a very tall atom in the center. On the basis of crude orbital

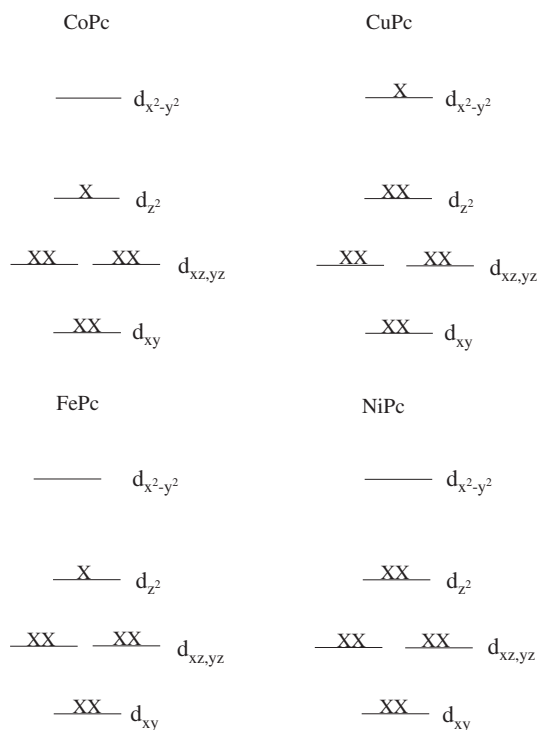


**Figure 4.** Top view STM image of a 0.3-nm layer of CuPc on Au (111) obtained with a W tip, +0.94 V sample bias, and 140 pA tunneling current. The image was Fourier filtered to reduce noise. Reprinted with permission from [56], X. Lu et al., *J. Am. Chem. Soc.* 118, 7197 (1996). © 1996, American Chemical Society.

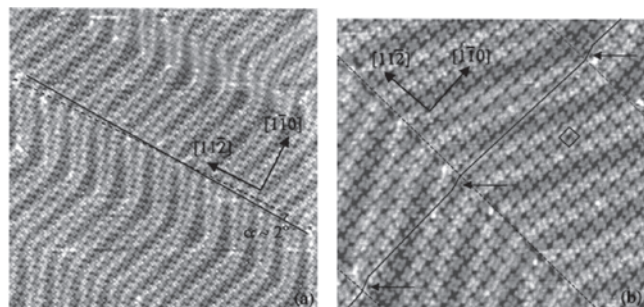
energy arguments [88] (see Fig. 5) and the expectation that tunneling from the metal substrate to the STM tip will be most enhanced when the orbitals have a spatial distribution consistent with carrying charge from below to above the molecular plane, the apparent height of Co(II) relative to the Cu(II) in MPc complexes is easily rationalized as due to the half-filled *dz<sup>2</sup>* orbital.

The influence of steps on the orientation of copper phthalocyanine monolayers on Au (111) was investigated using scanning tunneling microscopy and low-energy electron diffraction [89]. CuPc molecules adsorb with their molecular plane parallel to the surface and form a highly ordered overlayer with a square unit cell. On terraces wider than ~15 nm, the orientation of the monolayer is determined by the underlying substrate and the sides of CuPc square unit cells coincide very closely with the {112} and {110} directions of the Au (111) surface. On narrow terraces, the sides of the CuPc unit cells are aligned along the step edges. This effect is explained in terms of the maximization of coverage which favors the formation of the CuPc domains where the molecules are aligned parallel to the step edges.

Figure 6a shows an STM image of a monolayer (ML) thick CuPc film on a Au (111) surface. A monolayer is defined as the amount of deposited CuPc that entirely covers the substrate surface. As evident from this image,



**Figure 5.** Schematic orbital energy diagrams for several transition metal phthalocyanine complexes. In the case of iron (II), a single orbital configuration cannot be used to describe the ground state, and at least two configurations are required. This situation is represented diagrammatically by use of a broken × to indicate partial occupation of an orbital by an electron, while a full × represents near complete occupation by a single electron. Reprinted with permission from [56], X. Lu et al., *J. Am. Chem. Soc.* 118, 7197 (1996). © 1996, American Chemical Society.

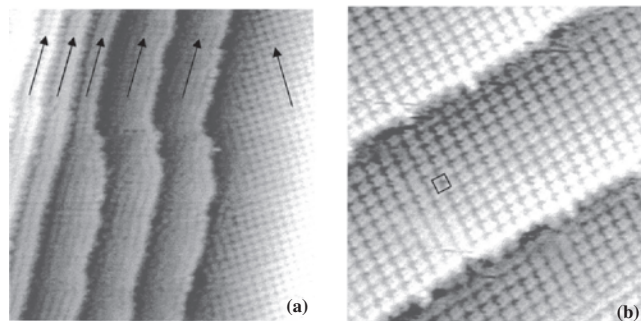


**Figure 6.** (a) STM image ( $70 \times 70 \text{ nm}^2$ , sample bias voltage  $V_s = -1.36 \text{ V}$ ,  $I = 0.14 \text{ nA}$ ) of the 1 ML CuPc film on Au(111). The dashed line marks the direction of the rows of CuPc square unit cells. The solid line follows the [112] direction of the Au(111) substrate which is defined by the line connecting the apexes of the bends of the Au(111) zigzag corrugation pattern. The CuPc molecular rows are aligned with the [112] direction within a  $\sim 2^\circ$  angle. (b) STM image ( $35 \times 35 \text{ nm}^2$ ,  $V_s = -1.50 \text{ V}$ ,  $I = 0.12 \text{ nA}$ ) of a 1 ML CuPc film. The square unit cell of the CuPc monolayer is outlined. Dashed lines follow the [112] direction of the Au(111) substrate. Arrows indicate the shifts of the CuPc molecular rows at the bends of the Au(111) zigzag corrugations. Crystalline directions of the Au(111) surface are shown on both images. Reprinted with permission from [89], I. Chizhov et al., *Langmuir* 16, 4358 (2000). © 2000, American Chemical Society.

CuPc molecules form an almost perfectly ordered layer. The molecular pattern corresponds to a square unit cell with dimensions of  $15 \text{ \AA} \times 15 \text{ \AA}$  as determined directly from the STM images (the absolute accuracy of the STM distance measurements is estimated to be  $\sim 10\%$ ). The zigzag pattern that appears in the image is due to the corrugation of the underlying reconstructed Au (111) substrate and allows for a straightforward determination of the azimuthal orientation of the molecular layer with respect to the substrate lattice directions. The sides of the CuPc unit cell are very closely oriented to the  $\{112\}$  and  $\{110\}$  crystalline directions of the Au (111) lattice. This is illustrated in Figure 6a where the solid line indicates the direction of the CuPc molecular rows and the dashed line, which connects the apexes of the bends of the Au (111) zigzag pattern, indicates the  $\{112\}$  direction of Au (111). As determined from several STM images, the angle between the CuPc rows and the  $\{112\}$  direction ranges from  $\sim 1^\circ$  to  $\sim 3^\circ$  with the average value of  $\sim 2^\circ$ .

A close-up STM image of the CuPc monolayer (Fig. 6b) shows the distinctive four-leaf shape of the CuPc molecules and their arrangement in a square unit cell (the unit cell is marked on the image). The molecular rows along the  $\{110\}$  direction undergo a lateral shift near the bend of the Au (111) zigzag corrugations, as shown by the solid lines and arrows in Figure 6b. This shift is accompanied by a change in rotational orientation of the individual CuPc molecules, as evident from Figure 6b, but without change in the unit cell dimensions.

Figure 7a covers a wide terrace on the right and narrow terraces in the center and on the left. On narrow terraces, the molecular rows are aligned parallel to the step edges and actually follow the contour of these step edges. The influence of steps on the ordering of CuPc molecules is evident also on wide terraces near the step edges, where a region of disordered CuPc molecules is seen (Fig. 7a). The width



**Figure 7.** (a) STM image ( $50 \times 50 \text{ nm}^2$ ,  $V_s = -1.70 \text{ V}$ ,  $I = 0.12 \text{ nA}$ ) of a 1 ML CuPc film in a stepped region of the Au(111) surface. Solid lines show the alignment of the CuPc molecular rows along the step edges on narrow terraces. (b) Close-up STM image ( $30 \times 30 \text{ nm}^2$ ,  $V_s = +1.32 \text{ V}$ ,  $I = 0.13 \text{ nA}$ ) of the area with two Au steps covered with 1 ML of CuPc. Reprinted with permission from [89], L. Chizhov et al., *Langmuir* 16, 4358 (2000). © 2000, American Chemical Society.

of the terraces, on which the CuPc molecules are aligned parallel to the step edges, can be as large as 15 nm.

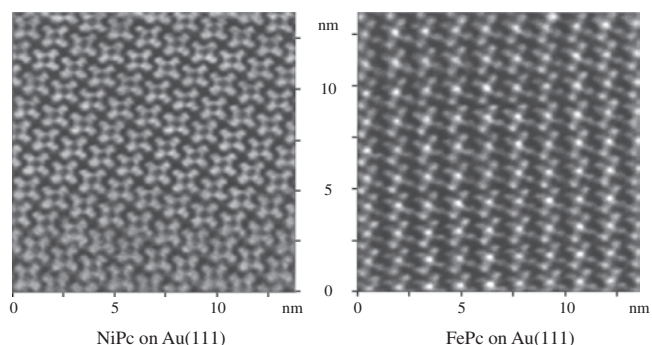
The majority of steps on Au (111) run along the  $\{110\}$  direction. Thus, the orientation of CuPc molecules on narrow terraces formed by steps running along this direction coincides with the orientation of CuPc unit cells on wider terraces, where the orientation is defined by the  $\{112\}$  and  $\{110\}$  directions of the Au (111) substrate. An STM image in Figure 7b is an example of this situation. As on wider terraces, the CuPc molecules form a square grid pattern with a square unit cell and sides parallel/perpendicular to the step edges. However, on Au (111) steps that do not run along these directions, the CuPc molecules form rows which follow the contours of the steps (see Fig. 7a).

### 2.3. NiPc and FePc

Iron(II) phthalocyanine (FePc) and nickel(II) phthalocyanine (NiPc) can be adsorbed on the Au(111) surface and provide STM images showing submolecular structure [56]. Interestingly, image contrast depended upon the identity of the central metal ion. Unlike NiPc, wherein the central metal appears as a hole in the molecular image, the iron ion in FePc is the highest point (about 0.25 nm) in the molecular image. These data are interpreted as indicating that the Fe(II)  $d^6$  system has significant  $d$  orbital character near the Fermi energy while the Ni(II)  $d^8$  system does not. This interpretation is consistent with theoretical calculations that predict a large contribution of iron  $d$  orbitals near the Fermi energy.

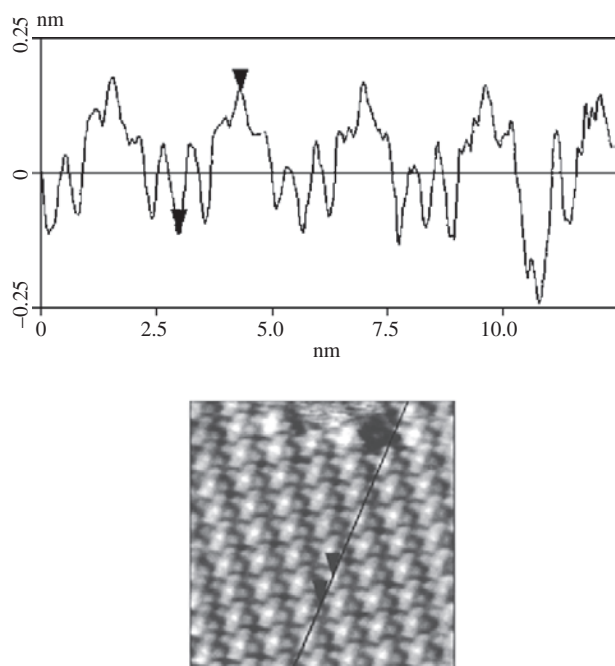
Figure 8 presents good quality images of both NiPc and FePc that had once been exposed to air. The four-leaf pattern of the phthalocyanine ring is clearly observed, as is the hole (dark area) in the center of every NiPc molecule. On the other hand, the center of every FePc has a large hill (bright spot). The FePc images were always highest in the center, while the NiPc images always appear to have holes where the Ni(II) should be.

A cross section image of a FePc sample (once exposed to air) shows the detailed variation with height observed as a function of position over the FePc as seen in Figure 9.



**Figure 8.** Top view STM images of a 0.4 nm thick layer of NiPc and of 0.3 nm of FePc on Au(111) obtained with a W tip. Both samples had MPc layers that had once been exposed to air. The gray scale extends over 0.3 nm. For NiPc the sample bias was +0.50 V and the tunneling current was 300 pA. For FePc the sample bias was +0.10 V and the tunneling current was 1.6 nA. The image was Fourier filtered to reduce noise. Reprinted with permission from [83], X. Lu and K. W. Hipps, *J. Phys. Chem. B* 101, 5391 (1997). © 1997, American Chemical Society.

The cross section was chosen to pass through the center of an FePc molecule (bottom center of image), across the benzene rings of two different arms of adjacent FePcs, and again through the center of another FePc, in a repeating pattern. In this image, the benzene rings all appear to be of roughly equal height (about 0.17 nm) and somewhat taller than the carbons of the five-member rings and the peripheral (noncoordinating) nitrogens. The  $\text{Fe}^{2+}$  ion region appears to be about 0.25 nm high, defining the total molecular height.

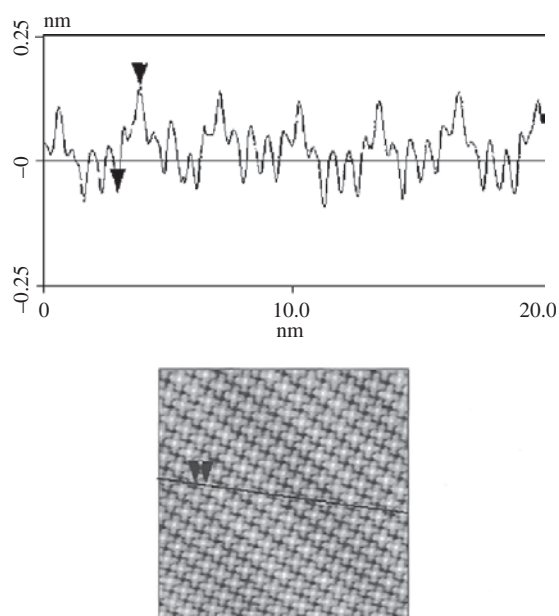


**Figure 9.** Top view and sectional STM image of a 0.3 nm thick layer of FePc adsorbed on Au (111). The FePc was once exposed to air. The image was obtained with a PtIr tip at a sample bias of +0.15 V and a fixed tunneling current of 300 pA. Reprinted with permission from [83], X. Lu and K. W. Hipps, *J. Phys. Chem. B* 101, 5391 (1997). © 1997, American Chemical Society.

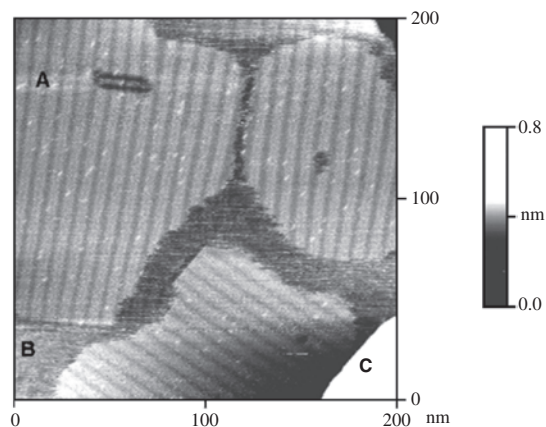
Oxygen contamination during sample transfer between UHV systems also affects the images as presented in Figure 10, wherein both a top view and sectional view are shown. While the maximum height of the FePc now appears to be about 0.20 nm, the benzene rings now appear only about 0.11 nm tall, making the relative height of the central metal even greater than in the once air exposed sample. Moreover, the relative resolution is clearly better than in Figure 9, since the drop in apparent height over the inner carbon atoms and the noncoordinating nitrogens is more clearly observed.

It is well known that both the electron density and the local density of surface states near the Fermi energy play a critical role in determining the STM image as observed for other examples [90, 91]. STM imaging of electronegative or electropositive elements, for example, can result in the observation of anomalous heights [92]. Another example is the observation of the dangling bonds on the silicon surface [93]. In the present case of Pc, the occupancy of the *d* orbitals is playing a significant role in the STM image. In these examples, Fe(II) may be acting as a conductor while Ni(II) may not be. Since the STM images reflect contours of constant current, the tip must dip toward the Au surface above the Ni(II) center and pull back from the Fe(II) in order to maintain constant current flow. There are, however, at least three separate mechanisms that could lead to the observed differences in height [83].

A different metalloporphyrin, Ni(II) octaethylporphyrin (NiOEP), was investigated by STM imaging [94]. Figure 11 is a typical constant current image of NiOEP on Au (111) observed at low resolution. In this image the individual NiOEP molecules appear as dots making up well-defined single molecule thick islands (e.g., region A). The regions



**Figure 10.** Top view and cross-sectional plot of a 0.2 nm thick FePc film on Au(111) prepared and measured in the STM UHV chamber. A PtIr tip was used at a sample bias of -0.50 V and a current of 400 pA. Reprinted with permission from [83], X. Lu and K. W. Hipps, *J. Phys. Chem. B* 101, 5391 (1997). © 1997, American Chemical Society.

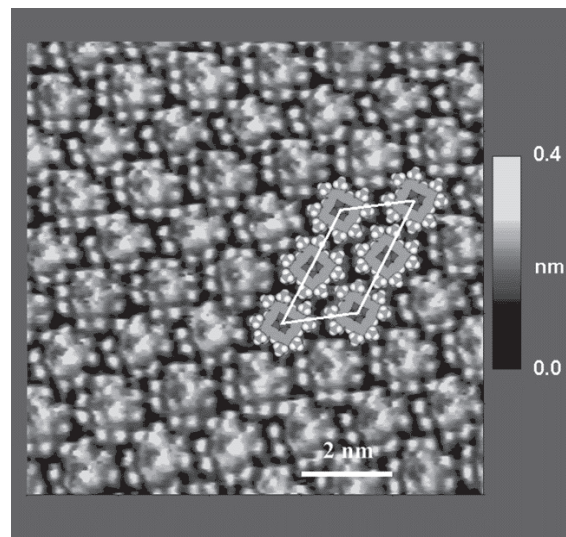


**Figure 11.** A typical constant current image of NiOEP on Au(111) observed at low resolution. The image was obtained with a W tip at a sample bias voltage of  $-1.2$  V and a set point of 300 pA. The image has been flattened. The region marked B is uncovered Au(111) and the region marked A is a single molecule thick layer of NiOEP. The area marked C is a single gold atomic step. Reprinted with permission from [94], L. Scudiero et al., *J. Phys. Chem. B* 106, 996 (2002). © 2002, American Chemical Society.

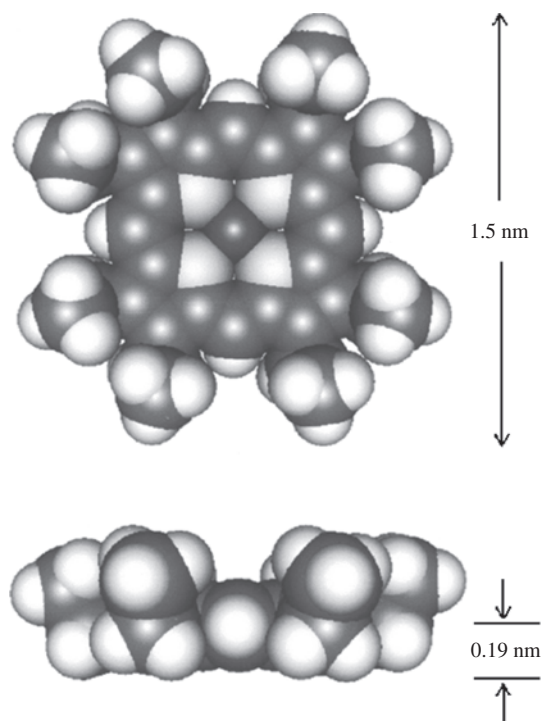
between the islands (e.g., region B) appear to be uncovered Au (111) surface and the  $I$ - $V$  curves obtained in these regions are similar to those from porphyrin-free substrates. The large height step (feature C) along the lower right side of the figure is due to a monatomic step of the Au (111) substrate. One can also observe striations running through both the NiOEP islands and portions of the uncovered surface. These are due to reconstruction of the Au (111) surface and appear as pairs of lines. The small grain gold films used in this study (about 0.3  $\mu$ m in diameter) generally have a larger reconstruction line spacing than is seen on large single-crystal Au (111) surfaces. Unlike true single-crystal gold [95], these small crystal grains show reconstruction line spacing ranging from 6.3 to about 9.0 nm.

Figure 12 is a high-resolution image of NiOEP on Au (111) that clearly shows the fourfold symmetry expected for the molecule and the somewhat dark center associated with the central Ni(II) ion. The metal ion contrast has been explained in terms of occupation of the  $d_z^2$  orbital. Also shown as an inset in Figure 12 are space filling (CPK) models of NiOEP placed to form a single primitive surface unit cell with basis vectors of length 1.65 and  $2.76 \pm 0.20$  nm. Note that there are two molecules per unit cell because of the small angular offset (ca. 15°) of alternating rows. Another interesting aspect of the NiOEP image is the prominence of the ethyl groups. While the individual hydrogens cannot be resolved, the terminal methyl groups are clearly seen with contrast similar to, but slightly greater than, the OEP ring. Moreover all the ethyl groups are turned up so that there is maximal contact between the OEP ring and the gold surface (as shown in Fig. 13).

The mechanism by which the ethyl groups attain their prominence in the STM image is of interest. The porphyrin ring shows good contrast because of both HOMO- and LUMO-mediated tunneling in the energy region close to EF (vide infra).



**Figure 12.** High-resolution constant current STM image of NiOEP at near-monolayer coverage on Au(111). The image was acquired with a W tip at  $-0.6$  V bias, with a setpoint of 0.3 nA. The image was flattened and low-pass filtered. Inset is a group of CPK models arranged as a single unit cell. Reprinted with permission from [94], L. Scudiero et al., *J. Phys. Chem. B* 106, 996 (2002). © 2002, American Chemical Society.



**Figure 13.** CPK model of a typical metal(II) OEP. The four nitrogens that bind the central metal ion are shown in light gray. The molecule is shown both in top and side view. The configuration of the ethyl groups is chosen to be consistent with the structure of NiOEP adsorbed on Au(111). Reprinted with permission from [94], L. Scudiero et al., *J. Phys. Chem. B* 106, 996 (2002). © 2002, American Chemical Society.

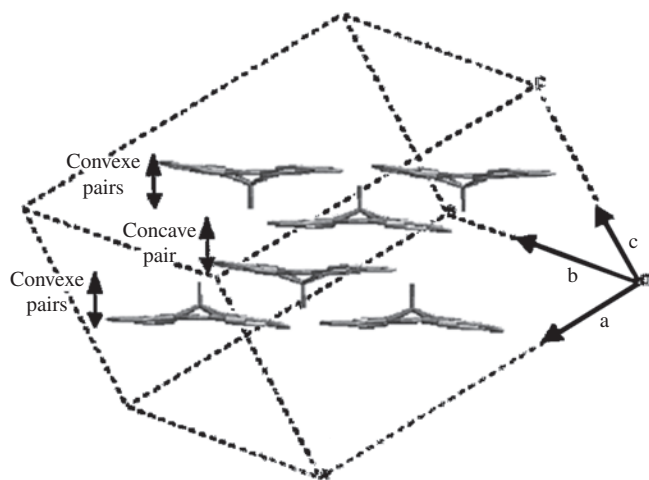
## 2.4. TiOPc

TiOPc is a nonplanar polar molecule [96] with the titanyl group located perpendicular to the macrocycle and the outer phenyl rings making an angle of  $7^\circ$  with respect to the C–N inner ring [97]. Both the nonplanarity and the dipolar character of the molecule result in a specific polymorphism that differs significantly from that of planar phthalocyanines. Crystal structures have been reported so far [1, 97, 98], a monoclinic phase I, a triclinic phase II (hereafter  $\alpha$ -TiOPc), and a triclinic phase Y (Fig. 14) [96, 98]. Moreover, in  $\alpha$ -TiOPc, the geometry of the molecule was found to be strongly distorted with respect to molecules in solution: the molecular symmetry is reduced from  $C_{4v}$  to  $C_1$ . This molecular distortion was attributed to strong  $\pi$ – $\pi$  interactions [96].

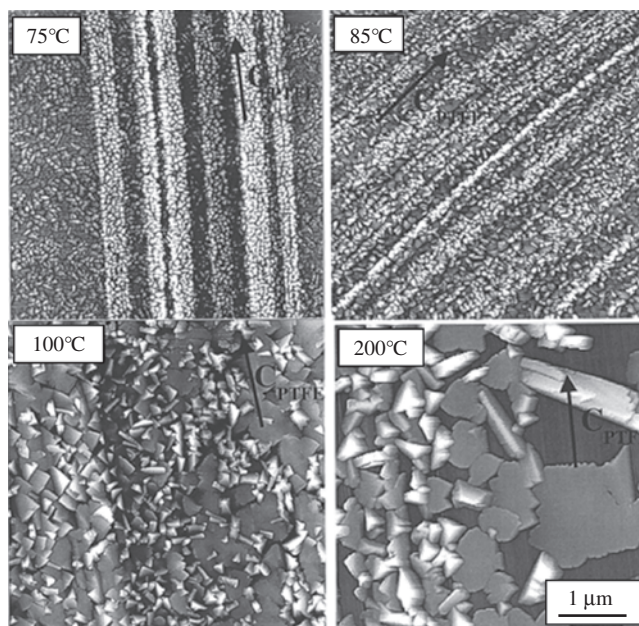
As for planar phthalocyanines, polymorphism governs the crystal packing in thin films and is found to depend strongly on the growth conditions (substrate temperature, deposition rate, and nature of the substrate) [99–102]. The optical properties (absorption, photoconductivity, and second harmonic generation) turn out to be correlated with the crystal structure of the films [100, 101, 103]. Thin films of  $\alpha$ -TiOPc (phase II) show the largest third-order nonlinear susceptibility ( $X^3 = 1.7 \times 10^{-10}$  esu) [104].

Highly oriented films of titanyl phthalocyanine (TiOPc) were obtained by high-vacuum sublimation onto an oriented poly(tetrafluoroethylene) (PTFE) substrate [99b]. In Figure 15, the evolution of the thin film morphology is depicted as probed by AFM as a function of increasing  $T_s$  in the range of 75–200 °C for films with thicknesses of 40–50 nm.

For  $T_s = 75$  °C, the films consist of a dense packing of small grains (mean radius around 35 nm) completely covering the PTFE substrate. The PTFE macrosteps are decorated by larger grains whose shape reflects that of the crystalline TiOPc phase. This observation suggests that TiOPc films grown at  $T_s < 75$  °C onto oriented PTFE consist of an amorphouslike material (hereafter  $a$ -TiOPc) with a few microcrystallites localized at the PTFE macrosteps.



**Figure 14.** Molecular model of  $\alpha$ -TiOPc (phase II) showing the concave and convex pairs. Reprinted with permission from [99b], M. Brinkmann et al., *Chem. Mater.* 14, 904 (2002). © 2002, American Chemical Society.



**Figure 15.** Evolution of the film morphology probed by AFM in TiOPc thin films of thickness in the range of 40–50 nm grown onto an oriented PTFE substrate. Films were obtained at different substrate temperatures in the range of 75–200 °C at a constant deposition rate of 0.8–1.0 nm/min. Reprinted with permission from [99b], M. Brinkmann et al., *Chem. Mater.* 14, 904 (2002). © 2002, American Chemical Society.

The grain size distribution is rather broad and suggests that coarsening has already occurred during growth.

For  $T_s = 85$  °C (Fig. 15), two type of grains are observed: (i) small spherically shaped aggregates of radius  $< 40$  nm and (ii) larger crystalline domains of size 50–150 nm with a wedgelike shape. The majority of the crystalline domains are not preferentially oriented on the PTFE. Similar to the observations for  $T_s = 75$  °C, the larger crystalline domains are located along the PTFE macrosteps. A closer examination of the film morphology reveals that the larger crystalline domains do not have flat surfaces but are composed of smaller aggregates that have coalesced. The preferential location of the larger crystalline domains along PTFE terraces suggests that nucleation of  $a$ -TiOPc is heterogeneous.

The morphology is found to change drastically around  $T_s = 100$  °C. The films show a continuous (coverage close to 100%) and polycrystalline texture consisting of large trapezoidal crystallites. The ratio of the film thickness to the in-plane size of the microcrystallites lies in the range of 0.1–0.3. This indicates that the platelet-shaped microcrystallites lie flat on the PTFE substrate. Well-oriented pyramid-like microcrystallites protrude on the surface of the uniform textured film. These crystallites likely correspond to secondary nuclei grown in a homoepitaxial manner on the underlying TiOPc film. The absence of depletion zones around existing crystallites in conjunction with the continuous film texture suggests again that growth is not driven by Ostwald ripening.

Increasing  $T_s$  to 200 °C results in a loss of uniformity in the surface coverage, which decreases to approximately 60–75%. The grains show a variety of shapes and orientations. Amid a majority of flat-lying crystallites, a few

crystallites are in an edge-on orientation and are seen by transmission electron microscopy (TEM) as darker needle-shaped crystals. The latter observation is indicative of a progressive loss of preferential orientation with increasing  $T_s$ , in agreement with the appearance of additional diffraction spots in the electron diffraction (ED) pattern. At  $T_s = 100\text{ }^\circ\text{C}$ , an original growth mechanism was observed whereby *a*-TiOPc microcrystallites were formed by the static coalescence and reorganization of small amorphous aggregates in close contact. Nucleation of *a*-TiOPc is initiated at the PTFE macrosteps from which oriented crystallization propagates, leading to uniform *a*-TiOPc films with a twinned texture and a dense (0 1 0) contact plane. The molecules are in an edge-on orientation, with their molecular plane oriented parallel to the PTFE chains. At the mesoscale, the nucleation of crystalline *a*-TiOPc involves the alignment and oriented coalescence of amorphous prenucleation aggregates along the PTFE macrosteps (i.e., a graphoepitaxial process). At the molecular scale, it is proposed that the TiOPc orientation and the preferential nucleation of the *a* polymorph are enforced by the topography and structure of the PTFE macrosteps in conjunction with the requirement for a minimal nucleation free energy. The optical absorption of the films in the near infrared is found to be strongly correlated with the structural and morphological modifications in the films. The oriented character of the *a*-TiOPc films results in a strong polarization of the 850-nm band perpendicular to the PTFE chain axis direction.

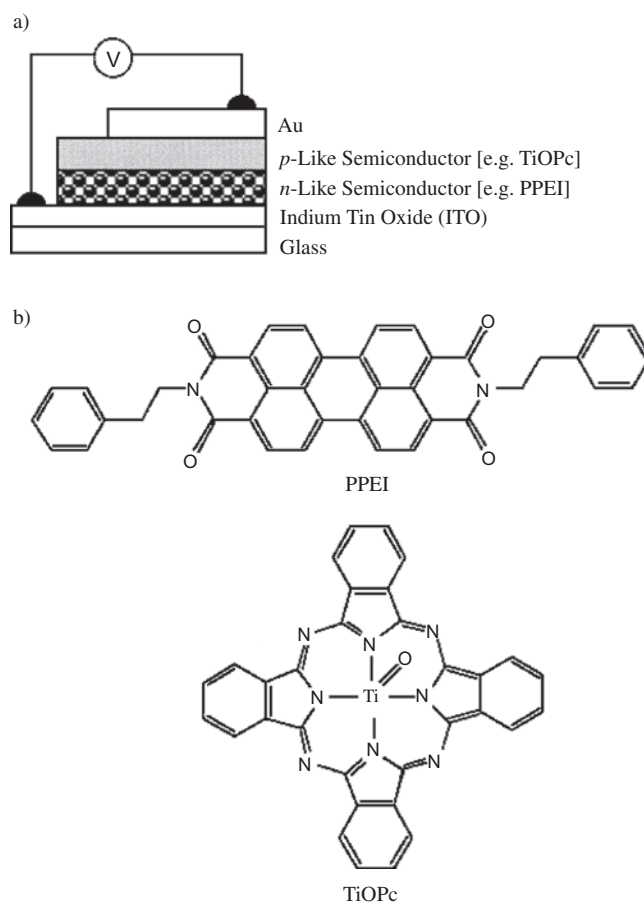
A perylene phenethylimide/titanyl phthalocyanine bilayer (PPEI/TiOPc) is a typical example of an *n*-like/*p*-like molecular semiconductor heterojunction as depicted in Figure 16 [105]. The complex morphologies of the PPEI, TiOPc, and PPEI/TiOPc thin films, at various stages of solvent-vapor annealing, have been directly and spatially resolved by a variety of fluorescence and transmission near-field scanning optical microscopy experiments.

The topographical image of a 10-nm TiOPc film that was annealed for 24 h is shown in Figure 17a. The image shows that the initially amorphous film has restructured to a highly porous film of nanocrystallites ranging in height from the level of the substrate (0 nm) to over 100 nm. The flat profile of the fiber probe is responsible for making the TiOPc crystals appear bigger in the film plane due to a so-called tip artifact. These images reveal sharp pointed TiOPc nanocrystals that are not fully resolved even with sharp AFM tips. The typical in-plane cross-sections of these TiOPc nanocrystals range from <10 to 30 nm. The heights of the crystals, in contrast, are not distorted by the shear-force images and range up to 100 nm.

## 2.5. Fluorophthalocyanines

Alkali halide surfaces (100) have proven to be useful substrates for studies of organic pigment thin films [61–66]. In particular thin films of fluorinated Pcs have been prepared on an alkali halide surfaces.

Thin films of hexadecafluorophthalocyaninatozinc ( $F_{16}\text{PcZn}$ ) are prepared on amorphous  $\text{SiO}_2$  (quartz glass) and on well-ordered NaCl, KCl, and KBr (100) surfaces and are studied by optical absorption and atomic force microscopy [106]. Figure 18 shows the results of a 0.7-nm thin film of

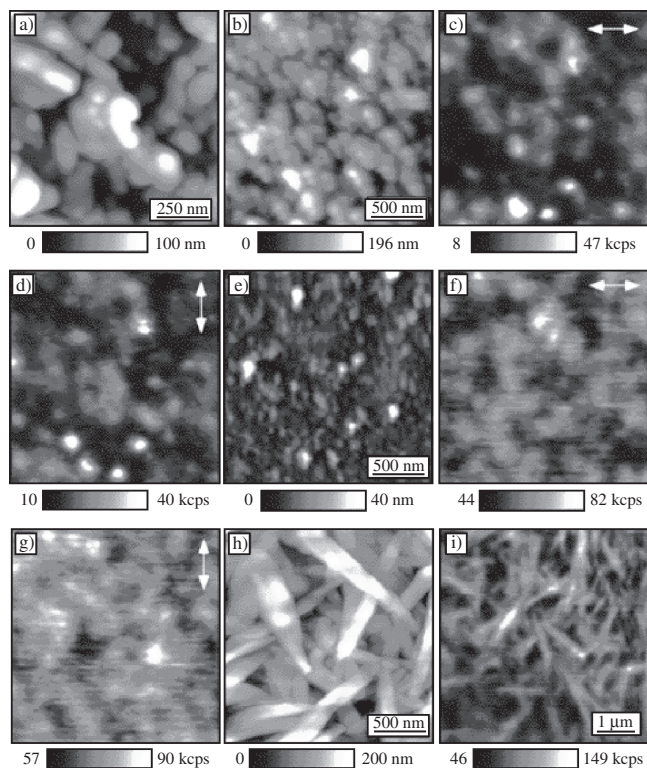


**Figure 16.** (a) Schematic drawing of a typical geometry for a molecular semiconductor based heterojunction photovoltaic device. (b) Chemical structures of perylene phenethylimide (PPEI) and titanyl phthalocyanine (TiOPc). Reprinted with permission from [105], M. Adams et al., *J. Am. Chem. Soc.* 119, 10608 (1997). © 1997, American Chemical Society.

$F_{16}\text{PcZn}$  on NaCl (100) with the {010} and {001} azimuth directions of the substrate indicated in the figure and two height profiles of single scans. Two different classes of  $F_{16}\text{PcZn}$  particles are observed. A rather high concentration of small but high (3 nm) particles is seen in areas of high densities of NaCl steps, especially found in the directions {010} and {001}. Such behavior was also observed earlier under comparable conditions for the growth of tetrapyrrodotetraazaporphyrins (TPyTAP) on alkali halide surfaces [65]. Also found, however, are rather extended flat areas (up to about 200 nm in length or width) with a uniform thickness of about 1.2 nm.

In Figure 19 two films (0.7 and 18 nm average thickness) of  $F_{16}\text{PcZn}$  on KBr are compared. For the thin film, rather small particles, again growing at step edges of the substrate, are observed to be of approximately spherical geometry. Some larger ensembles of particles are detected with an orientation of  $27^\circ$  relative to the KBr {010}. The thicker film mainly consists of well-defined particles of triangular shape with edges about 100–300 nm long, rather flat when compared to the spherical particles of the thinner film. One angle within the triangles almost always equals  $90^\circ$ ; the two others often are found between  $45^\circ$  and  $50^\circ$ . The triangular



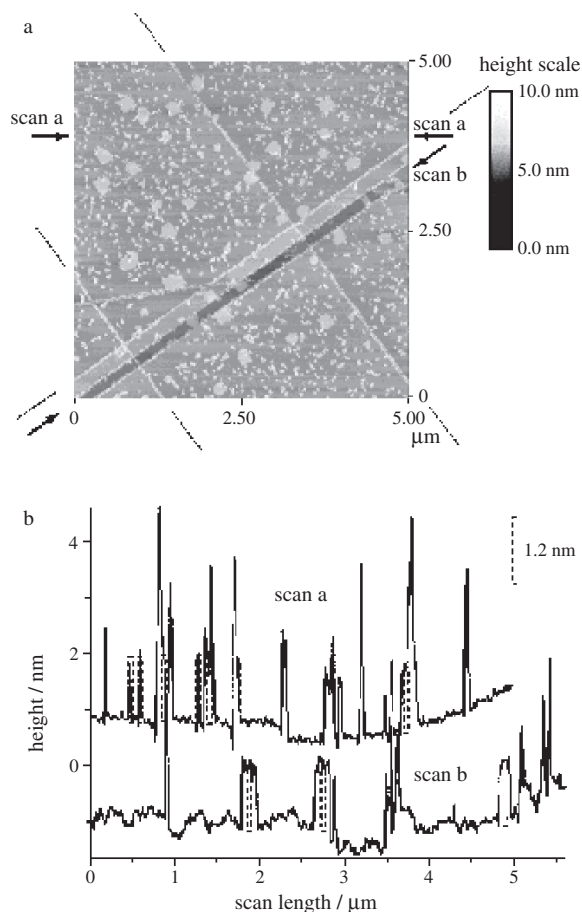


**Figure 17.** (a) Topographic image of a 10 nm TiOPc thin film which was vapor-annealed in  $\text{CH}_2\text{Cl}_2$  for 24 h. Topographic (b) and corresponding polarized fluorescence [(c) and (d)] images of a bilayer assembly PPEI/TiOPc, where a film of PPEI has been vacuum-deposited onto an annealed TiOPc surface [as in (a)] and subsequently vapor-annealed for only 30 min. Topographic (e) and corresponding polarized fluorescence [(f) and (g)] images of PPEI on glass which has been vapor-annealed for 30 min. (h) Topographic image of 300 nm thick film of PPEI on glass which has been vapor-annealed for 48 h. (i) Fluorescence image of an annealed 300 nm PPEI film similar to that shown in image (h). Reprinted with permission from [105], M. Adams et al., *J. Am. Chem. Soc.* 119, 10608 (1997). © 1997, American Chemical Society.

objects as a whole have a preferential orientation of 15–25° of one of their edges relative to KBr {010}, with angles around 18° and 22° most frequently found.

Atomic force microscopy performed on the films grown on the alkali halide surfaces allows further conclusions to be drawn. On NaCl large plateaus of about 1.2-nm height are seen (Fig. 18) aside from a high number of smaller grains of rather unspecific orientation relative to the substrate. The height of 1.2 nm would be explained by arrays of molecules stacked vertical to the surface with two of the benzene moieties in contact with the surface when the size of a  $\text{F}_{16}\text{PcZn}$  molecule is calculated from the distance of 1.32–1.46 nm as detected earlier in crystal lattices [62, 107].

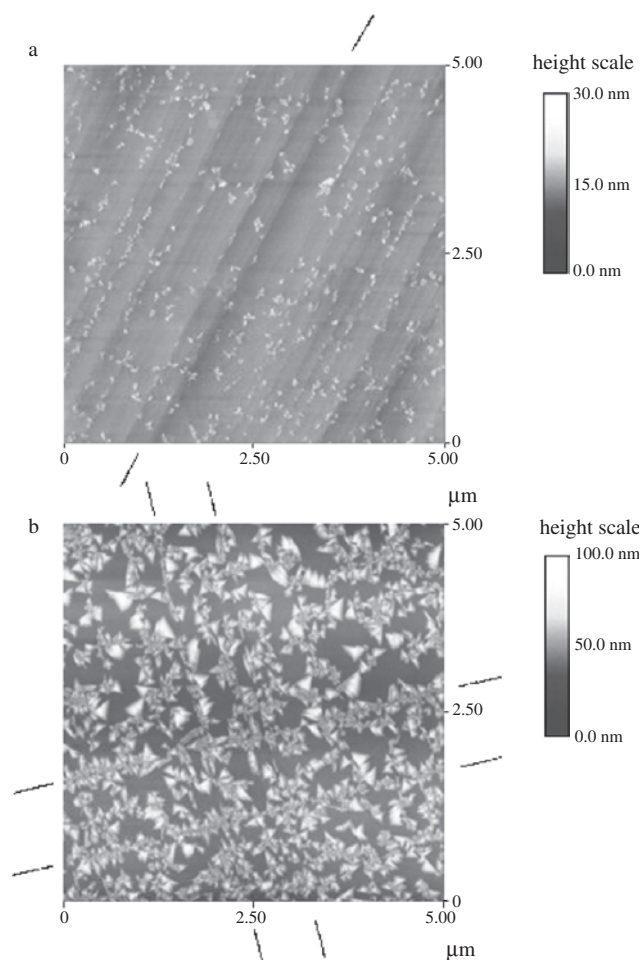
On KBr, a crystallization of  $\text{F}_{16}\text{PcZn}$  along step edges of the substrate is seen (Fig. 19a) as also observed for the growth of TPyTAP on alkali halides [65]. In thicker films, however, well-shaped domains are formed (Fig. 19b) which show a preferential orientation relative to the substrate lattice. To discuss the characteristic angles of 90° and 45–50° within the  $\text{F}_{16}\text{PcZn}$  crystals as well as the preferential alignment of crystal edges along 18° and 22° relative to the {010} of the KBr substrate, calculations were made by considering



**Figure 18.** (a) Height image of 0.7-nm  $\text{F}_{16}\text{PcZn}$  on NaCl as obtained by AFM in tapping mode with the substrate [010] and [001] azimuth directions indicated as straight lines and (b) single height scans as marked by the arrows. Reprinted with permission from [106], D. Schlettwein et al., *Chem. Mater.* 12, 989 (2000). © 2000, American Chemical Society.

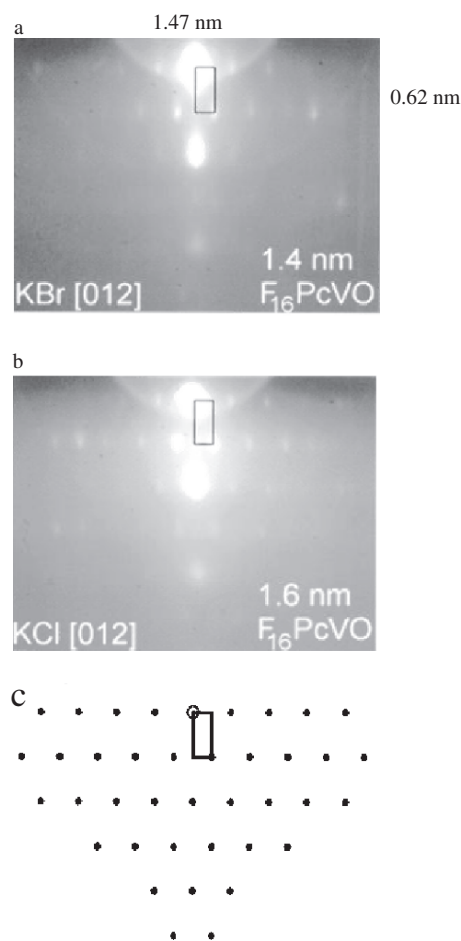
the relative alignment of crystal lattices. In the range of lattice constants (1.32–1.46 nm) as reported for  $\text{F}_{16}\text{PcZn}$ , two commensurate square lattices were found relative to the KBr surface mesh, namely  $2\sqrt{2} \times 2\sqrt{2}$ ,  $R = 45^\circ$  (A) and  $\sqrt{10} \times \sqrt{10}$ ,  $R = 18.4^\circ$  (B). Both square lattices would explain the angle of 90° often observed within the crystals as arising from the {100} and {010} axes of the  $\text{F}_{16}\text{PcZn}$  lattice. Angles around 45° would then correspond to the angle between {100} and {110} of the  $\text{F}_{16}\text{PcZn}$  lattice. Two  $\text{F}_{16}\text{PcZn}$  molecules would be spaced at 1.32 nm in A and at 1.47 nm in B. A distance of 1.32 nm in A is not consistent with the splitting as observed in the ultraviolet-visible (UV-vis) absorption spectra. A lattice constant that small was only detected for films having a considerably larger splitting of the band, redshifting it to 820 nm, a significantly longer wavelength than measured in the present experiments. Further, a preferred orientation of  $\text{F}_{16}\text{PcZn}$  [100] at 26.6° relative to KBr [010] in B is more compatible with the angles of the  $\text{F}_{16}\text{PcZn}$  crystals relative to the substrate as detected in the AFM images.

Thin films of hexadecafluorophthalocyaninatooxovanadium ( $\text{F}_{16}\text{PcVO}$ ) were vapor-deposited under OMBE conditions on the (100) surfaces of NaCl, KCl, and KBr and on



**Figure 19.** AFM height image of (a) 0.7-nm and (b) 18-nm (b)  $F_{16}PcZn$  on KBr with the substrate [010] and [001] as straight lines. Reprinted with permission from [106], D. Schlettwein et al., *Chem. Mater.* 12, 989 (2000). © 2000, American Chemical Society.

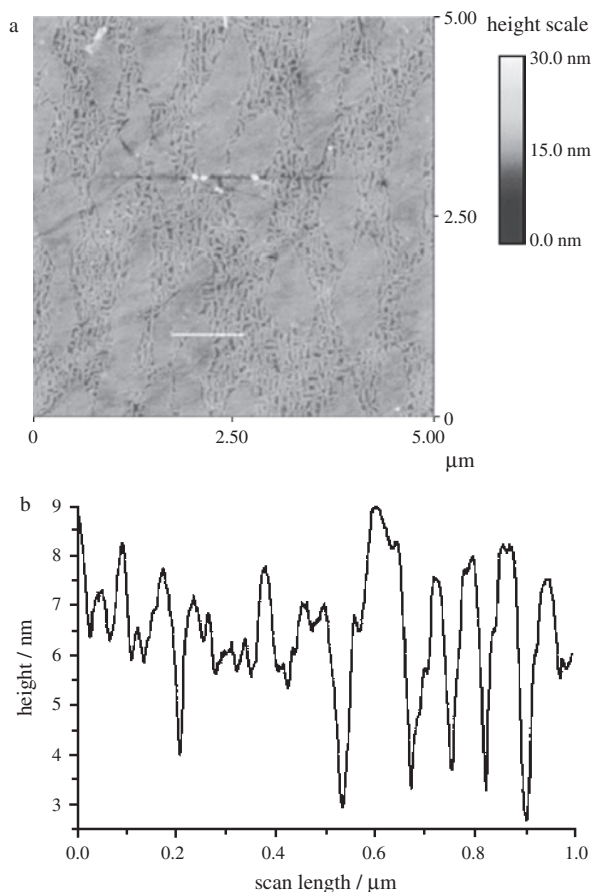
quartz glass and were analyzed by AFM and reflection high energy electron diffraction (RHEED) [108]. Beginning at submonolayer coverages and extending to a film thickness of several tens of nanometers the film structure is determined *in-situ* by RHEED. Figure 20 shows the results obtained at 1.4 and 1.6 nm  $F_{16}PcVO$  in the {012} azimuth directions of KBr and KCl. Highly ordered growth of crystalline domains of  $F_{16}PcVO$  with dimensions in the micrometer range leading to films of quite uniform thickness is observed. On KBr a commensurate  $\sqrt{10} \times \sqrt{10}$ ,  $R = 18.4^\circ$  square lattice is seen in RHEED of the first monolayers with the molecules parallel to the substrate surface which is also preserved at higher film thickness. On KCl a surface lattice of the same size is formed which is, however, understood as a result of point-on-line coincidence. Diffraction of transmitted electrons yields a constant three-dimensional crystal structure of the films on KBr and KCl with a tetragonal unit cell of  $a = b = 1.47$  nm and  $c = 0.62$  nm. On NaCl with its smaller lattice constant no ordered relative orientation is possible and hence an increased part of the film appears amorphous. On quartz glass, on the other hand, ordered films are formed with the molecular planes predominantly oriented cofacially parallel to each other and vertical to the surface.



**Figure 20.** RHEED in the [012] azimuth orientation of (a) 1.4 nm  $F_{16}PcVO$  on KBr, (b) 1.6 nm  $F_{16}PcVO$  on KCl, and (c) the pattern of expected spots considering the appropriate extinction rules of diffraction. Reprinted with permission from [108], D. Schlettwein et al., *Langmuir* 16, 2872 (2000). © 2000, American Chemical Society.

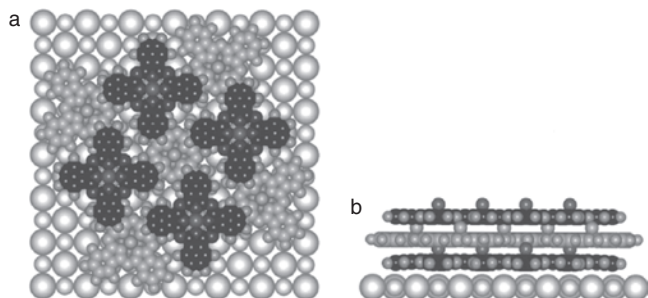
In Figure 21a an AFM image as obtained at a 24 nm film of  $F_{16}PcVO$  on quartz glass is shown with a typical cross section in Figure 21b. The film consists of two different kinds of domains, rather small walls and larger plateaus. The walls of 50–100 nm diameter are found to reach about 5–10 nm height above a rather flat level and are oriented at angles close to  $90^\circ$  relative to each other which is quite remarkable in view of the amorphous substrate that the film was grown on. Even the plateaus show orientation parallel to each other with some preferred angles (about  $40^\circ$  and  $50^\circ$ ) at, however, less pronounced edges when compared to the films on KBr or KCl. The detailed positions of the molecules are proposed as the structure depicted in Figure 22, as concluded from RHEED and UV-vis analysis.

Metallophthalocyanines have been demonstrated to possess remarkable semiconducting properties [109, 110]. However, the transistor properties of metallophthalocyanines have received less attention presumably because of their low reported mobilities (ca.  $10^{-4}$   $\text{cm}^2/\text{V}^{-1}$  s), for example, in the case of nickel phthalocyanine (Ni-Pc) [111–113]. It is known that in order for a material to transport electrons (*n*-channel), it needs to have an accessible LUMO



**Figure 21.** Plateaus and walls of  $F_{16}PcVO$  as detected by AFM at a 24 nm film grown on (a) quartz glass and (b) a height profile at the location indicated by the white line in plot (a). Reprinted with permission from [108], D. Schlettwein et al., *Langmuir* 16, 2872 (2000). © 2000, American Chemical Society.

level for electron injection and sufficient  $\pi$ -overlaps to achieve reasonable charge carrier mobilities [114]. Therefore, molecules with strong electron-withdrawing groups and extended  $\pi$ -systems are good candidates for  $n$ -channel semiconductors.

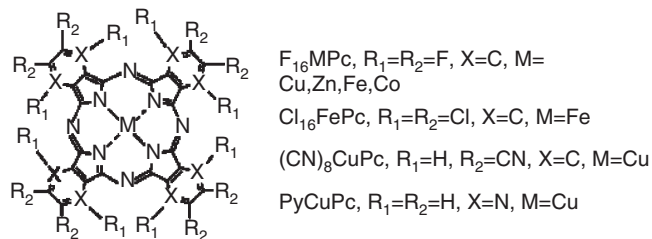


**Figure 22.** Structure of an array of four molecules in the (dark) uneven numbered monolayers and five molecules of the even (gray) numbered monolayers. The molecules are optimized in position ( $mm^+$ ) within the lattice as obtained by RHEED on KBr and KCl. A “top” view vertical to the substrate surface is shown in plot (a) and a view parallel to the surface in (b). Reprinted with permission from [108], D. Schlettwein et al., *Langmuir* 16, 2872 (2000). © 2000, American Chemical Society.

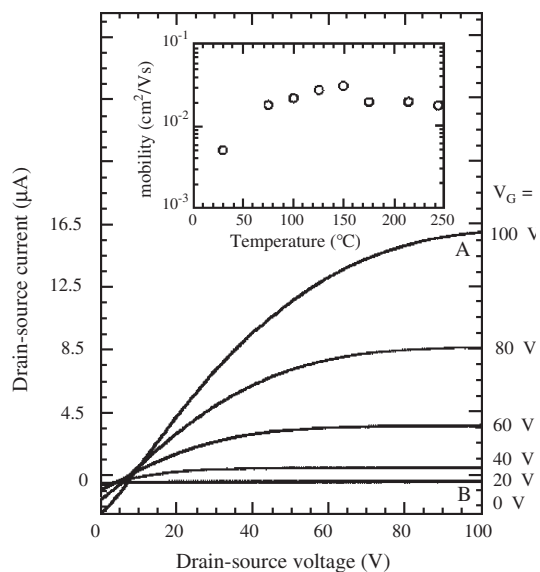
Copper octafluorophthalocyanine ( $F_8CuPc$ ) has been found to form a rectifying junction with  $p$ -type unsubstituted MPcs [115, 116]. Among the metallophthalocyanines with strong electron-withdrawing groups, hexadecahalogenated metallophthalocyanines (Fig. 23) were found to function as air-stable  $n$ -channel semiconductors with a maximum electron field-effect mobility of  $0.03 \text{ cm}^2 \text{ V}^{-1} \text{ s}^{-1}$  (Fig. 24) [117]. The same field-effect mobilities as in vacuum ( $10^{-3}$  Torr) can be obtained when measured in air.

Electron-withdrawing groups are known to lower the HOMO and LUMO energy levels of molecules. The LUMO level of  $F_{16}MPC$  has previously been shown to be ca. 1.6 eV lower than its unsubstituted counterpart by ultraviolet photoelectron spectroscopy (UPS) measurement and UV-vis data and this makes it less susceptible to oxidation. In addition, since all the  $F_{16}MPC$ s adopt the edge-on conformations in their thin films the fluorine atoms are in contact with air and could help to block moisture from penetrating through the films.

X-ray diffraction measurements (Fig. 25) indicate that the as-deposited thin films of  $F_{16}CuPc$  on  $Si/SiO_2$  are highly ordered with a sharp diffraction peak at  $2\theta$  of ca.  $6.02^\circ$  corresponding to an interplane distance of  $14.6 \text{ \AA}$ , which is similar to the reflection from the (200) lattice planes of  $\alpha$ -form  $CuPc$ , but in an expanded unit cell as is expected from the larger van der Waals radius of F over H [109]. The major peak visible under electron diffraction (Fig. 25, inset) is around  $3\text{--}4 \text{ \AA}$ , which corresponds to the  $\pi$ -stacking distance of the phthalocyanine rings. Therefore, the  $F_{16}CuPc$  molecules are standing and essentially perpendicular to the  $SiO_2$  surface; this renders the  $\pi$ -overlap direction of  $F_{16}CuPc$  the same as the current flow direction, which provides an efficient path for charge transport. The mechanisms for charge transport in these metallophthalocyanines and other polycrystalline organic semiconductors are believed to undergo a hopping mechanism at room temperature. Therefore, the morphology of films can greatly affect charge carrier mobilities due to the grain boundary effect [109]. It is found that the samples deposited at  $T_d$  above  $75^\circ \text{C}$  are nodular with a mean diameter of about 50 nm. In contrast to  $CuPc$ , the nodules do not change to large, separated crystals around  $150^\circ \text{C}$  but remain in good contact, becoming only more elongated. Thus, the good mobilities at high  $T_d$  may be the result of the very smooth, flat films, with close contact of the elongated nodules. These materials should be of great interest as all-organic complementary circuits and ring oscillators,  $n$ -channel semiconductors in photovoltaic



**Figure 23.** Electron transport. Reprinted with permission from [117], Z. Bao et al., *J. Am. Chem. Soc.* 120, 207 (1998). © 1998, American Chemical Society.



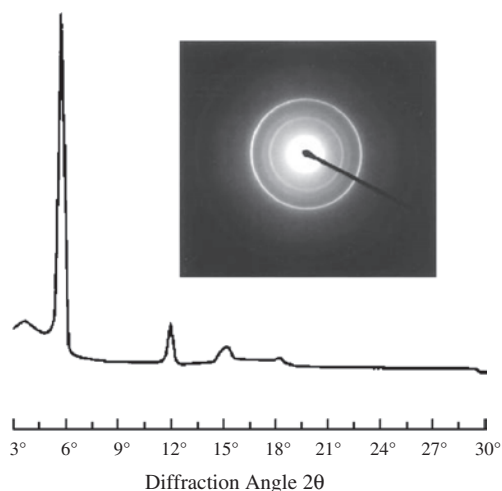
**Figure 24.** Drain-source current-voltage characteristics at different gate voltages of an *n*-channel transistor fabricated from  $F_{16}CuPc$ . Reprinted with permission from [117], Z. Bao et al., *J. Am. Chem. Soc.* 120, 207 (1998). © 1998, American Chemical Society.

devices, and electron-transporting materials in light-emitting diode applications.

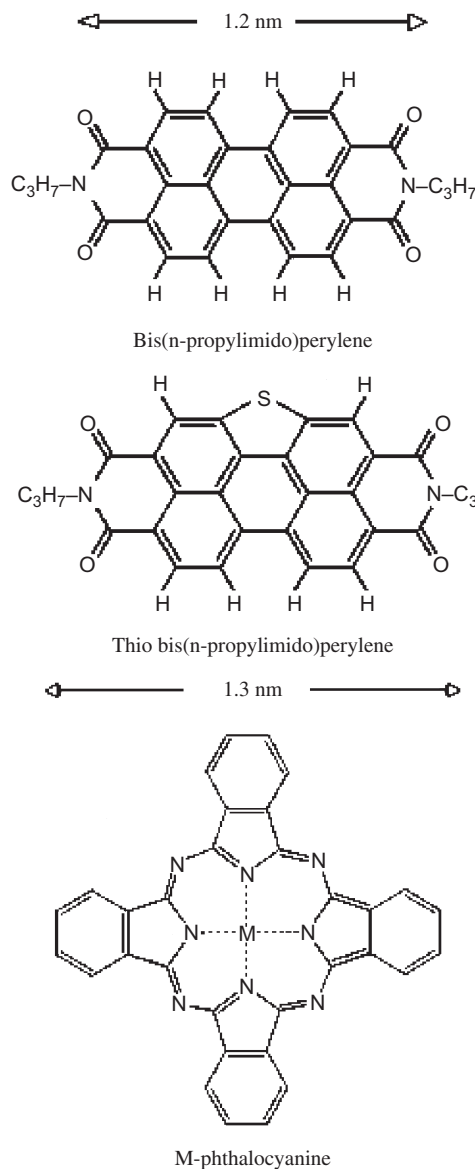
## 2.6. Phthalocyanine Mixed Thin Solid Films

Thin solid mixed films of phthalocyanine (chloroindium, chlorogallium, copper, cobalt, zinc, and metal-free phthalocyanine), bis(*n*-propylimido)perylene, and thio-bis(*n*-propylimido)perylene derivatives (Fig. 26) were fabricated by vacuum co-evaporation onto glass and silver island films [118].

The resonant Raman scattering (RRS) and surface-enhanced resonance Raman scattering (SERRS) spectra of the mixed film bis-perylene tetracarboxylic derivatives (PTCD)/ $ClInPc$  obtained with the 514.5 nm laser line and



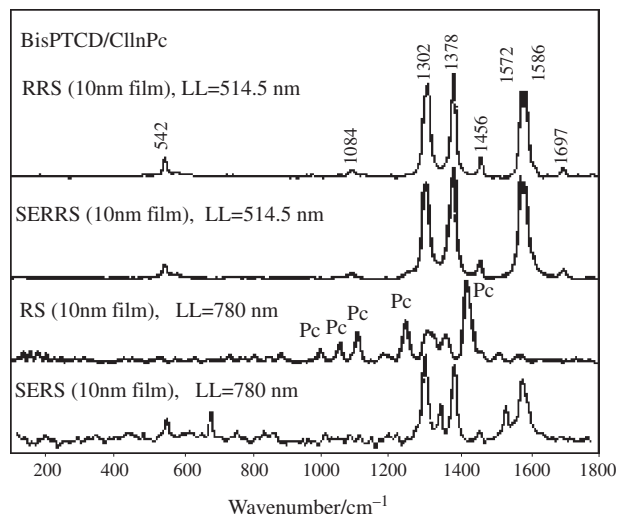
**Figure 25.** X-ray and electron (inset) diffractograms of  $F_{16}CuPc$  deposited on  $SiO_2$ . Reprinted with permission from [117], Z. Bao et al., *J. Am. Chem. Soc.* 120, 207 (1998). © 1998, American Chemical Society.



**Figure 26.** Molecular structure of  $MPc$  and  $PTCD$  molecules. Reprinted with permission from [118], A. P. Kam et al., *Chem. Mater.* 13, 4463 (2001). © 2001, American Chemical Society.

the baseline corrected spectra are presented in Figure 27. The fundamental mode observed at  $542\text{ cm}^{-1}$  is due to the perylene ring deformation. The C-H bend is observed at  $1084\text{ cm}^{-1}$ , while perylene ring stretches appear at  $1291(\text{sh.})$ ,  $1302$ ,  $1378$ , and  $1456\text{ cm}^{-1}$ . The ring C=C stretches are observed at  $1572$  and  $1586\text{ cm}^{-1}$ , and the symmetric C=O stretch is at  $1697\text{ cm}^{-1}$ . The SERRS spectrum obtained for this mixed film is clearly the enhanced version of the RRS spectrum and occurs when the  $PTCD$  moiety is physisorbed onto the silver island substrate. Physical adsorption means that there is no strong interaction (bonding) of the organic with the metal surface.

The Raman scattering (RS) of the mixed film of bis- $PTCD/ClInPc$  taken with the 780 nm laser line is presented in Figure 27. It becomes apparent on comparing the Raman spectra of this mixed film that the spectrum at 780 nm (RS)



**Figure 27.** RRS, SERRS, RS, and SERS spectra of mixed thin solid films of bisPTCD/ClInPc molecules. Reprinted with permission from [118], A. P. Kam et al., *Chem. Mater.* 13, 4463 (2001). © 2001, American Chemical Society.

contains characteristic bands of both ClInPc and bis-PTCD. In the RS spectrum, the most intense characteristic vibration observed at  $1453\text{ cm}^{-1}$  belongs to the ClInPc moiety. The surface-enhanced Raman scattering (SERS) spectrum of the mixed film, obtained with the 780 nm line, also shown in Figure 27, consists of a combination of ClInPc and perylene chromophore vibrations. However, the intensity of the bis-PTCD SERS is again higher than that of the Pc molecule. Therefore, characteristic vibrations of the perylene moiety are used to discuss the SERS (780 nm) spectrum in an attempt to extract the effect of intermolecular interactions from the mixed film spectra. The predominant perylene bands in the SERS (780 nm) spectrum are observed at  $1689$ ,  $1594$ ,  $1577$ ,  $1439$ ,  $1379$ ,  $1295$ , and  $531\text{ cm}^{-1}$ . Taking the  $531\text{ cm}^{-1}$  band as a reference, a comparison of the SERS (780 nm) to the RS spectra of bis-PTCD/ClInPc mixed films indicates an increase in the relative intensities of four in-plane ring-stretching vibrations, in particular in that of the  $1577\text{ cm}^{-1}$  vibration. Furthermore, in the SERS (780 nm) spectrum, the full width at half-maximum (FWHM) remained constant for all vibrational bands with the exception of  $1379$  and  $1439\text{ cm}^{-1}$ . In the RS spectrum, the bandwidth doubles for the  $1379$  and  $1439\text{ cm}^{-1}$  bands. This indicates the presence of doublets, not resolved in the spectrum due to band overlap. When the vibrational band at  $542\text{ cm}^{-1}$  is used to normalize the spectra obtained with the 514.5 nm laser line, the relative intensities of the C–H bend and C=C stretching vibrational bands, at  $1084$  and  $1586\text{ cm}^{-1}$ , respectively, decreased in the SERRS spectrum with respect to the RRS spectrum. A comparative analysis of the FWHM bandwidths shows that the bandwidth of the  $1295\text{ cm}^{-1}$  vibrational band in the SERS (780 nm) spectra is double relative to that in the RRS spectrum.

A similar approach in analysis was utilized for the other thio-PTCD/MpC mixed films that were studied. The most noteworthy system is that of the thio-PTCD/CoPc mixed films, in which there are relative intensity deviations when comparisons are made between the RRS and the SERRS

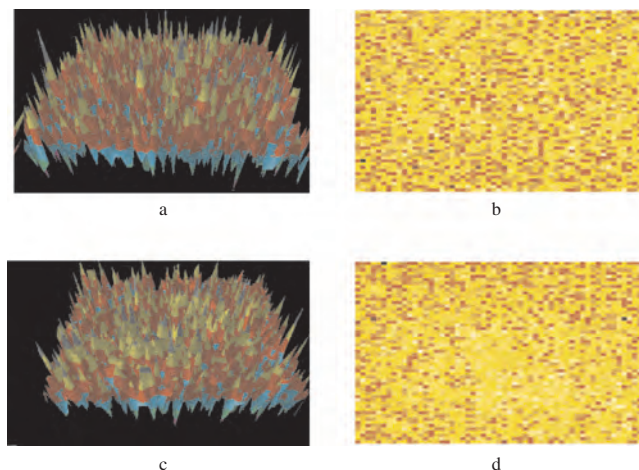
spectra and the RS and the RRS spectra of this mixture. Surprisingly, a comparison of the RS to RRS spectra of thio-PTCD/CoPc mixed films reveals no change in FWHM bandwidths.

The extent of the spectral changes on the perylene moiety upon mixing with phthalocyanine was deduced by comparing relative intensities and FWHM bandwidths for Raman spectra of neat films of bis-PTCD and thio-PTCD. Such analysis reveals similar deviations (for RS, SERS, RRS, and SERRS) in both relative intensities and bandwidths that are observed for the characteristic vibrational bands of the perylene chromophore in the neat films. Therefore, the perylene moiety in mixed films appears to retain the same molecular organization as in the neat film. This provides conclusive evidence for a lack of molecular mixing between phthalocyanine and perylene in these co-evaporated mixed films.

Global images of the SERRS signal from mixed films of bis-PTCD and various phthalocyanine derivatives as well as thio-PTCD/Pc on silver island films were obtained using the 633 nm laser line. The global images from the mixed film samples were captured using the filtered Raman scattered light of the fundamental vibrational wavenumber at  $1300\text{ cm}^{-1}$  for bis-PTCD, at  $1380\text{ cm}^{-1}$  for thio-PTCD perylene, and at  $680\text{ cm}^{-1}$  for phthalocyanine.

Representative images were selected (Fig. 28a and c) to illustrate the three-dimensional distribution of the bis-PTCD SERRS signal from the mixed film on silver islands. The bis-PTCD/ClInPc film presents a homogeneous distribution of aggregates of bis-PTCD (and ClInPc) in the film as shown in the three-dimensional image (Fig. 28a), where the bright coloration corresponds to the higher relative intensity of the SERRS signal from the bis-PTCD center at  $1300\text{ cm}^{-1}$ . The aggregation or phase separation with a homogeneous distribution of aggregates is also seen in the three-dimensional images taken from films of thio-PTCD/ClInPc (Fig. 28c). Similar results were obtained for all the other PTCD/Pc mixed films that were fabricated.

The point-to-point maps confirm the results from wide field images showing that the structure of the mixed thin



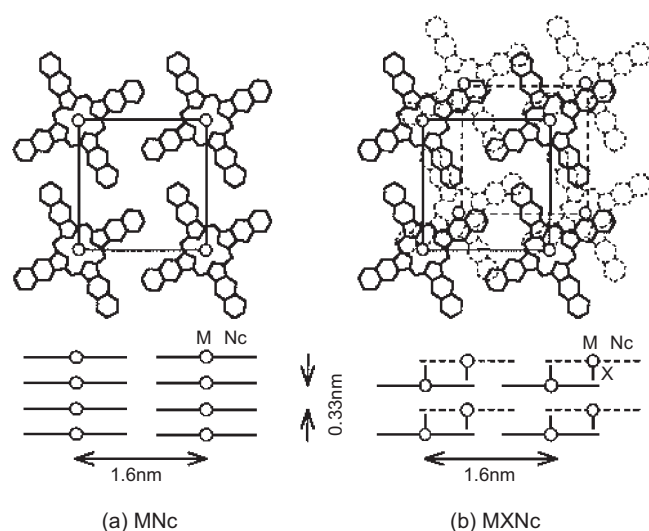
**Figure 28.** Global field images [(a) and (c)] and point-to-point bit map images [(b) and (d)] of mixed films of bisPTCD/ClInPc and thioPTCD/ClInPc, respectively, molecules. Reprinted with permission from [118], A. P. Kam et al., *Chem. Mater.* 13, 4463 (2001). © 2001, American Chemical Society.

films is a distribution of aggregates from both materials. Thus global images provide a powerful analytical technique to determine the degree of mixing or phase separation within micrometer spatial resolution.

## 2.7. Naphthalocyanine Thin Films

The naphthalocyanine (Nc) ligand can also coordinate various metals, as Pc does, in the central position, which are classified by the valency of the central metal. In the epitaxial films deposited on the alkali halide surface, two types of molecular stacking have been found depending upon the central coordination structure, as schematically shown in Figure 29 [119]. Metal-free Nc ( $H_2Nc$ ) and divalent metal Ncs like ZnNc take on the face-to-face, eclipsed stacking in which the planar molecules are packed in a tetragonal unit cell and piled up cofacially along the molecular column holding the molecular planes parallel to the substrate surface (Fig. 29a). On the other hand, trivalent and tetravalent metal Ncs (MXNcs) like chloroaluminum Nc (AlClNc), fluorogallium Nc (GaFNc), and vanadyl Nc (VONc) crystallize in the slipped stacking (Fig. 29b). This different stacking structure is caused by the axial ligand (X) with halogen or oxygen atoms protruding out of the Nc molecular plane. The interplanar distance between the stacked MXNc molecules,  $\sim 0.33$  nm, determined from their X-ray diffraction pattern [119c] suggested that the axial ligands alternated up and down to form a dimeric structure as shown in Figure 29b, since the M–X bond would occupy a longer spacing if the MXNc molecules were piled up in the eclipsed stacking as in the case of divalent MNcs. The two types of molecular stacking in the MNc and MXNc films have also been proven from their high-resolution electron microscopy and electron diffraction [118].

These different stacking modes in the organic thin films relate to their superior photoelectric characteristics [120]. Furthermore, the crystal growth and molecular orientation

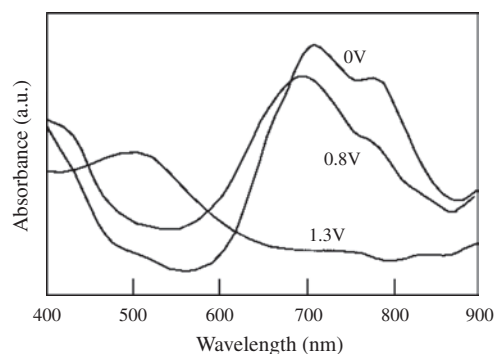


**Figure 29.** Molecular stacking in the epitaxially oriented films of (a) MNc and (b) MXNc. Reprinted with permission from [122], T. Kouzeki et al., *J. Phys. Chem.* 100, 20097 (1996). © 1996, American Chemical Society.

in the epitaxial organic films have a significant influence on their optical, electrochemical, and photovoltaic properties [121].

Orientation-controlled naphthalocyanine thin films showed electrochromism [122]. The amorphous ZnNc film deposited on an indium tin oxide (ITO) coated glass electrode exhibited an irreversible electrochromic oxidation in 0.1 M KCl. This reaction gave rise to swelling of the film surface due to expansion of grains caused by incorporation of charge-compensating anions between the aggregated molecules. Epitaxially oriented films were prepared by deposition onto the (001) cleavage surface of NaCl and then transferred onto the ITO electrode. The epitaxial ZnNc film, in which the planar molecules are piled up in columns taking on the face-to-face, eclipsed stacking, exhibited both electrochromic reduction and oxidation. This electrochromic activity was attributed to a reversible incorporation of counterions through hollow channels between the molecular columns, which was accompanied by rearrangement in the molecular stacking. By contrast, no electrochromic reaction occurred for the epitaxial VONc film, where the alternately slipped dimeric structure did not facilitate a penetration of counterions into the stacked molecules.

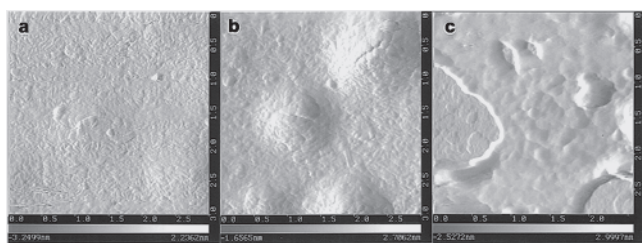
Figure 30 shows *in-situ* visible spectral change during the oxidation process for the amorphous ZnNc film electrode. The original green film (at 0 V in Fig. 30) shows absorption peaks at 710 and 780 nm which are assigned to the  $\pi$ – $\pi^*$  transition of the conjugating Nc macrocycle [123]. This spectral shape resembles the Q-band absorption of the  $\alpha$ -form of vapor-deposited MPc films [124]. It suggests that the original ZnNc film is in a state where some neighboring molecules aggregate with an  $\alpha$ -polymorphic interaction similar to that of MPc films. In the irreversible oxidation process, these Q-band absorption peaks start to decrease at potentials above 0.8 V vs Ag/AgCl. Upon further oxidation up to 1.0–1.3 V vs Ag/AgCl, the Q-band disappears while an absorption band goes up at around 500 nm. This absorption spectrum no longer changed even if a reverse negative potential was applied to the film. The amorphous VONc film exhibited an electrochromic behavior similar to that for the amorphous ZnNc film. These electrochromic changes of the amorphous film imply an irreversible incorporation of counterions from electrolyte solution.



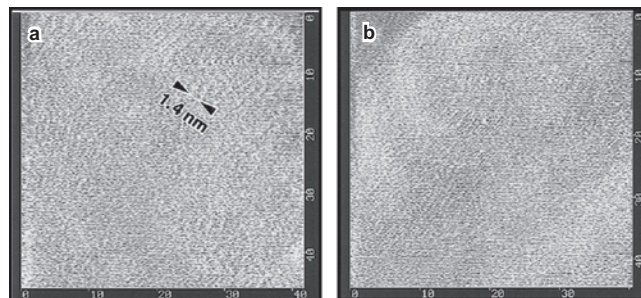
**Figure 30.** UV-vis absorption spectra of amorphous ZnNc film upon the oxidation process in 0.1 M KCl. Reprinted with permission from [122], T. Kouzeki et al., *J. Phys. Chem.* 100, 20097 (1996). © 1996, American Chemical Society.

Figure 31 shows AFM images taken for the ZnNc amorphous film deposited on ITO at a substrate temperature of 25 °C. The AFM image taken before applying bias potentials (Fig. 31a) indicates that the amorphous ZnNc film consists of grains with size less than 100 nm, and the surface morphology is considerably smooth with a maximum roughness of about 5 nm. This surface morphology was not changed in the negative potentials at which the cyclic voltammogram indicated no reduction peak. On the other hand, an application of positive potentials gave rise to a significant change in the film structure. Figure 31b shows an AFM image taken at 1.0 V vs Pt at which the film is totally oxidized. On the surface, swelling bumps and cracks appeared, which seems to suggest that the film is upheaved. Upon oxidation the films accumulate charges, and counteranions, Cl<sup>-</sup> in this case, penetrate into the film. This incorporation of charge-compensating Cl<sup>-</sup> ions gives rise to an expansion of grains as previously pointed out [125, 126], which is considered to result in swelling the film surface. When a further anodic bias was applied up to 1.2 V vs Pt, the film was seriously damaged and peeled off the ITO substrate as seen in the *in-situ* electrochemical processes (EC)-AFM image in Figure 31c.

Using a polycrystalline ZnNc film deposited on ITO at substrate temperature of 250 °C, a microscopic change in the film structure upon electrochromic oxidation was observed at high resolution by EC-AFM. The polycrystalline film was composed of larger grains of submicrometer size. The ED pattern taken from this original film indicated the Debye-Scherrer rings corresponding to the spacings of 0.33 and 1.4 nm. It suggests that the crystalline grains consist of the molecular columns lying on the substrate with an intercolumnar distance of 1.4 nm; therefore, most of the planar ZnNc molecules are standing normal to the substrate surface. This columnar structure of the original, polycrystalline ZnNc film can be observed in the EC-AFM image before applying bias potentials as is shown in Figure 32a. The stripe images with a distance of 1.4 nm agree with the columnar structure confirmed by the ambient AFM and transmission electron microscopic techniques. The polycrystalline ZnNc film exhibited a reversible electrochromic activity similar to that of the epitaxially oriented film mentioned in the previous section. When the film was biased at reduction potentials up to -1.0 V vs Pt in the EC-AFM, the columnar image was still observed similar to that at 0 bias potential as shown in Figure 32b. On the other hand,



**Figure 31.** EC-AFM images (scales in  $\mu\text{m}$ ) of amorphous ZnNc film electrode at (a) 0 bias potential, (b) 1.0 V, and (c) 1.2 V vs Pt in an electrolyte solution of 0.1 M KCl. Reprinted with permission from [122], T. Kouzeki et al., *J. Phys. Chem.* 100, 20097 (1996). © 1996, American Chemical Society.



**Figure 32.** EC-AFM images (scales in nm) of polycrystalline ZnNc film electrode at (a) 0 bias potential and (b) -1.0 V vs Pt in an electrolyte solution of 0.1 M KCl, showing the molecular columns with a spacing of 1.4 nm. Reprinted with permission from [122], T. Kouzeki et al., *J. Phys. Chem.* 100, 20097 (1996). © 1996, American Chemical Society.

when a positive potential was applied to oxidize the film, the columnar structure was no longer observed.

### 3. PHTHALOCYANINE STACKS, MOLECULAR ARRAYS, AND SELF-ASSEMBLIES

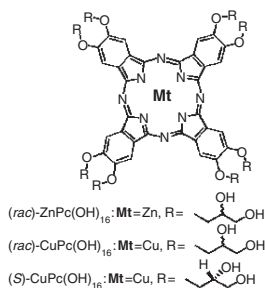
#### 3.1. Phthalocyanine Stacks, Pc Nanorod, and Nanoscaled Fibrous Assemblies

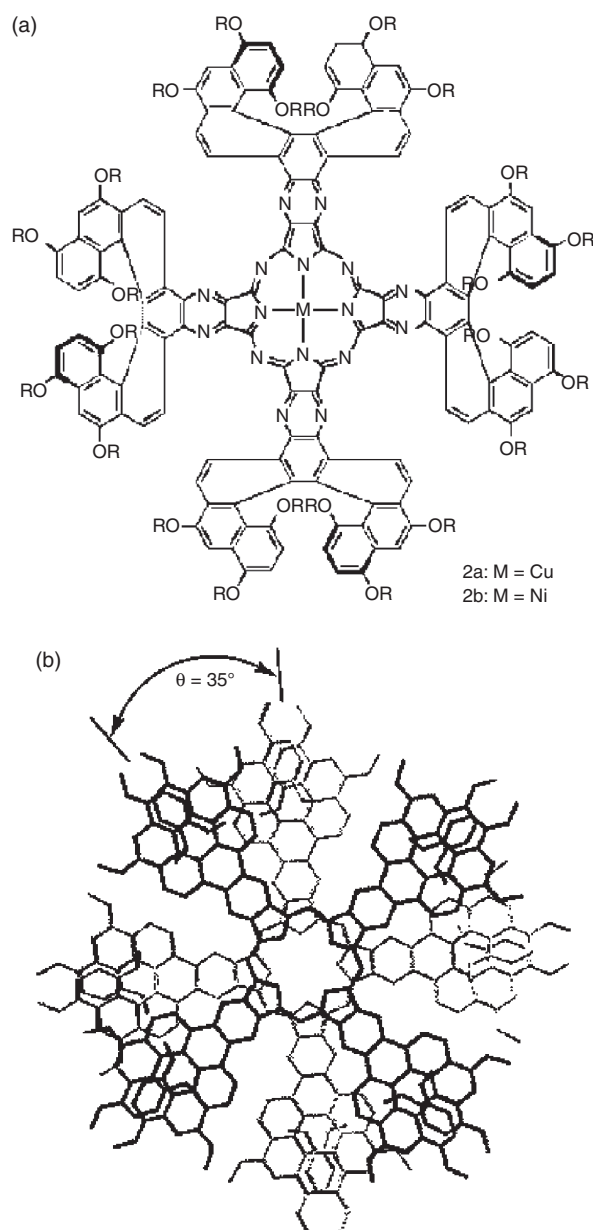
Disc-shaped rigid Pcs and MPcs can easily stack through strong  $\pi$ - $\pi$  interaction and form one-dimensional rodlike assemblies with interesting electronic and optic properties [127-130]. Cofacially stacked Pc aggregates are present even in dilute solution for some examples [130].

Pc-based superstructures were constructed by  $\pi$ - $\pi$  interaction of Pc molecules in which the cores of copper and nickel octaazaphthalocyanines are fused to four nonracemic [7] helicenes according to Figure 33 [127].

A calculation by molecular mechanics shows that the energy is minimized when the Pc molecules stack in a chiral superstructure with a core-to-core distance of ca. 3.4 Å as shown in Figure 33b. Atomic force microscopic images shown in Figure 34 are in accord with the calculated structure (Figure 33b) if on the surface of mica the stacks are isolated and perpendicular to the surface. In Langmuir films, however, the molecules stack in the opposite way, with the stacking axis parallel to the water.

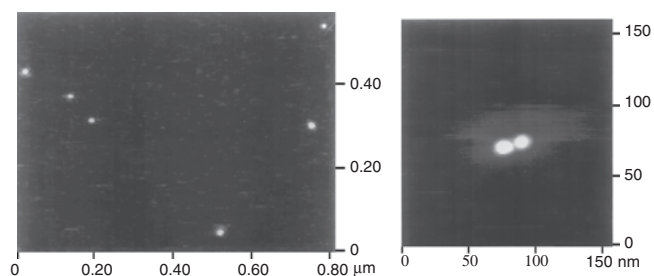
A family of copper and zinc phthalocyanine-based amphiphilic (3) possessing racemic and optically active diol units, (*rac*)-ZnPc(OH)<sub>16</sub>, (*rac*)-CuPc(OH)<sub>16</sub>, and (*S*)-CuPc(OH)<sub>16</sub>, show self-assembling properties in aqueous solution [128].





**Figure 33.** Chemical structure (a) and calculated stacked structure (b) of Pc molecules in which the cores of copper and nickel octaaza-phthalocyanines are fused to four nonracemic [7] helicenes. The lowest energy conformation of two phthalocyanine ligands of structure 2, as calculated with the MacroModel program and MM3 force field. The darker phthalocyanine is on top. Redrawn with permission from [127], J. M. Fox et al., *J. Am. Chem. Soc.* 121, 3453 (1999). © 1999, American Chemical Society.

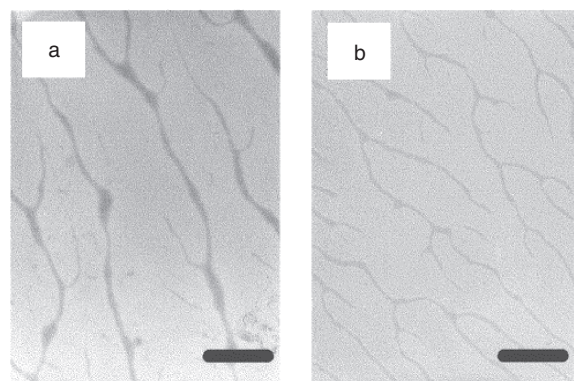
The copper complexes produced nanosized fibrous assemblies from aqueous solutions through two noncovalent bondings:  $\pi$ - $\pi$  interaction among phthalocyanine rings and hydrogen bonds among diol units, as shown in Figure 35. The formation of fibrous assemblies strongly depends on the central metal of the phthalocyanine complex. The optically active (*S*)-CuPc(OH)<sub>16</sub> is stacked and arranged in a left-handed helix. The chirality of diol units in (*S*)-CuPc(OH)<sub>16</sub> also affects the intercolumnar lattice of phthalocyanine stacks.



**Figure 34.** (a) Atomic force microscopic height image of six stacks of phthalocyanines **2b** on mica. As the coordinate out of the plane of the page increases to its maximum, 3 nm, the shade becomes lighter. (b) Atomic force microscopic height image of two stacks of phthalocyanines **2a**. As the coordinate out of the plane of the page increases to its maximum, 7 nm, the shade becomes lighter. Reprinted with permission from [127], J. M. Fox et al., *J. Am. Chem. Soc.* 121, 3453 (1999). © 1999, American Chemical Society.

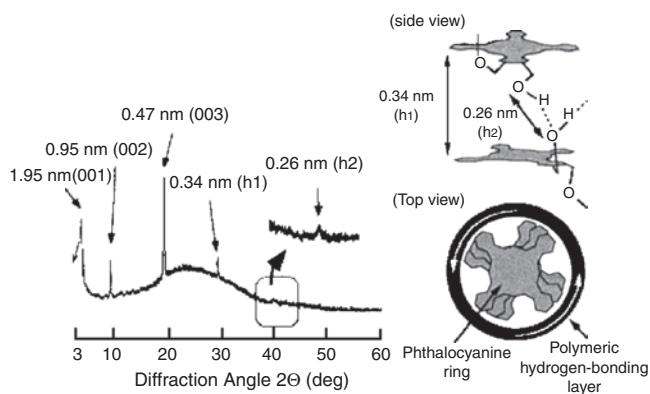
The X-ray diffraction pattern of (*S*)-CuPc(OH)<sub>16</sub> film is remarkably different from that of the racemic mixture, possibly due to the reflections from a discotic lamellar structure [131]. The chirality of amphiphilic copper phthalocyanine affected the lattice of the assembly of phthalocyanine stacks and stabilization of micellar fibers: (i) the chiral amphiphilic phthalocyanine can form a helical arrangement in the phthalocyanine stack, and (ii) the intercolumnar lattice of the phthalocyanine stacks transferred from the hexagonal lattice to the lamellar structure introducing chiral side chains as substituent groups. As a result of the intercolumnar hydrogen bonding, the phthalocyanine stacks assemble to form the hexagonal lattice. On the other hand, the chirality of the diol unit controls the direction of hydrogen bonding among hydroxyl groups. The regularity of the hydrogen-bonding direction results in the helical arrangement of the phthalocyanine rings. The X-ray reflection peak at 0.26 nm for (*S*)-CuPc(OH)<sub>16</sub> in Figure 36 corresponds to the regular packing of the diol units.

The polymeric hydrogen bonding between diol units may be formed within the phthalocyanine stack, contributing to the formation of the helical arrangement. The helical arrangement will induce the distance separating



**Figure 35.** Transmission electron micrographs of fibrous assemblies made of (a) (*rac*)-CuPc(OH)<sub>16</sub> and (b) (*S*)-CuPc(OH)<sub>16</sub> (bar = 400 nm). Reprinted with permission from [128], M. Kimura et al., *Langmuir* 16, 2078 (2000). © 2000, American Chemical Society.

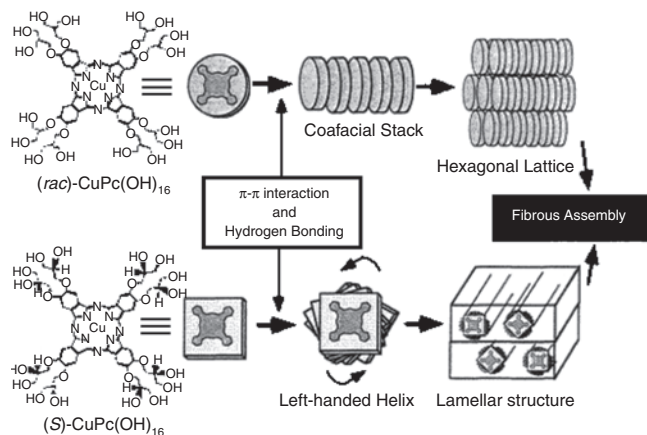




**Figure 36.** Diffraction pattern of X-ray reflected from a glass surface coated with  $(S)$ -CuPc(OH)<sub>16</sub> and assigned Miller indices ( $hkl$ ).  $h_1$  = stacking distance between phthalocyanine rings.  $h_2$  = distance between the peripheral side chains. Reprinted with permission from [128], M. Kimura et al., *Langmuir* 16, 2078 (2000). © 2000, American Chemical Society.

of phthalocyanine stacks and alter the intercolumnar structure. Engelkamp et al. reported the helical arrangement of optically active phthalocyanines and proposed three types of helical structures [132]. The X-ray reflection of the stacking distance was only observed at 0.34 nm, and the CD spectra of  $(S)$ -CuPc(OH)<sub>16</sub> implied that the dipoles of the phthalocyanine rings were arranged in the form of a left-handed helix. Pathways for the formation of fibrous assemblies are speculated in Figure 37.

Similarly, crown ether-substituted Pcs were used to create nanoscaled fibrous assemblies possessing an electron conduction wire and ion transport channels [133]. Furthermore, side-chain-modified Pcs [(2,3,9,10,16,17,23,24-octakis((2-benzyloxy)ethoxy)phthalocyaninato)copper, CuPcOC<sub>2</sub>OBz] form long rodlike stacks on substrates [134]. CuPcOC<sub>2</sub>OBz exhibits cofacial stacking in its aggregates, with a ring spacing of ca. 3.36 Å, as determined by wide-angle X-ray diffraction measurements [129]. These molecules showed cofacially stacked Pc aggregates even in dilute solution, as evidenced by broadened and blueshifted visible solution spectra [130]. Visible absorption spectra, consistent with



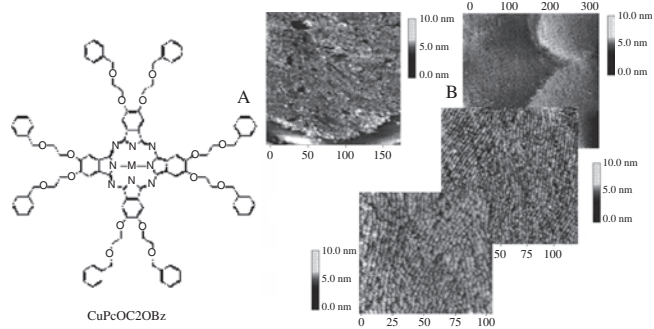
**Figure 37.** Speculated pathways for the formation of fibrous assemblies. Reprinted with permission from [128], M. Kimura et al., *Langmuir* 16, 2078 (2000). © 2000, American Chemical Society.

monomeric CuPcOC<sub>2</sub>OBz, are observed in CHCl<sub>3</sub> for solutions below ca. 10<sup>-6</sup> M, while more concentrated solutions (10<sup>-4</sup> M) show a high degree of aggregation. H<sub>2</sub>PcOC<sub>2</sub>OBz exhibits similar behavior. Figure 38 shows STM images of CuPcOC<sub>2</sub>OBz.

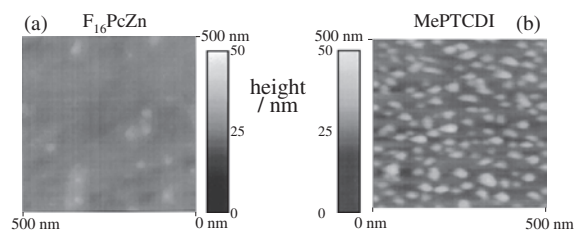
In films of metallophthalocyanine stacks, the Pc rings are spaced by van der Waals distances and exciton coupling of neutral–electronic transitions between neighboring macrocycles becomes very efficient. The characterization of the dynamics of the exciton motion together with the related exciton–exciton annihilation at high excitation densities has been an area of active theoretical and experimental research [135–139]. For large exciton densities, nonexponential bimolecular exciton–exciton annihilation has been observed by femtosecond spectroscopy studies in H<sub>2</sub>Pc thin films [136], FALPc thin films [137], VOPc films [138], and Langmuir–Blodgett films of SiPc polymers [139]. The analyses of these data are based on the assumption of unidimensional exciton transport, a condition not well fulfilled in films because of the interactions between the Pc stacks. In addition, local heating of thin films may affect the exciton dynamics. These factors impede considerably the elucidation of exciton transport dynamics in metallophthalocyanine films. On the other hand, linear polymers of (phthalocyaninato)siloxane in solution strictly limit the exciton transport to one dimension and heating effects can be avoided in flowing solutions.

Chemical modification of the core of phthalocyanines provides a high versatility in molecule structure and hence intermolecular interactions. The film structure as well as electrical and optical characteristics can be adjusted in a rather wide range. Perfluorinated phthalocyanines (F<sub>16</sub>Pc) is an example showing such influence on the position of molecular energy levels as well as solid-state structure. A cofacial parallel orientation of molecules and layered growth, for example, could be obtained for F<sub>16</sub>Pc in thin films on SiO<sub>2</sub> [107, 140–142]. Figures 39 and 40 show the morphology and the space-filling model of F<sub>16</sub>PcZn, respectively.

Structural variations in F<sub>16</sub>Pc thin films can be expected to lead to significant changes in electrical properties as observed for films of unsubstituted phthalocyanines in a series of time-of-flight measurements. The result revealed



**Figure 38.** Structure and STM images of CuPcOC<sub>2</sub>OBz monolayer (A) and bilayer (B) films on Au(111)/mica substrates. The vertical axes in these images were parallel to the compression barrier direction. The horizontal axes indicate distance in nanometers. Redrawn with permission from [134], P. Smolenyak et al., *J. Am. Chem. Soc.* 121, 8628 (1999). © 1999, American Chemical Society.

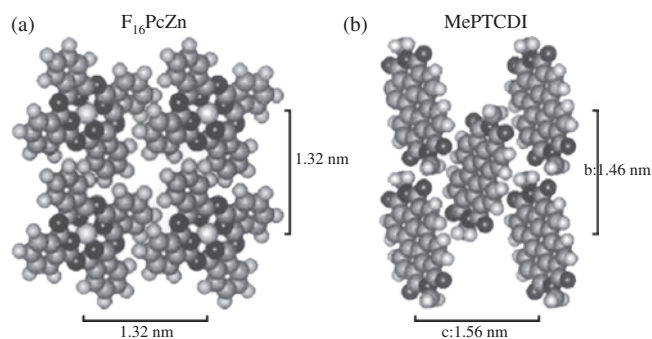


**Figure 39.** Morphology of 0.7 nm thin films [(a)  $F_{16}PcZn$ ; (b) MePTCDI] deposited on quartz glass at 300 K as obtained from tapping mode AFM with a Si tip. Reprinted with permission from [107], D. Schlettwein et al., *J. Phys. Chem. B* 103, 3078 (1999). © 1999, American Chemical Society.

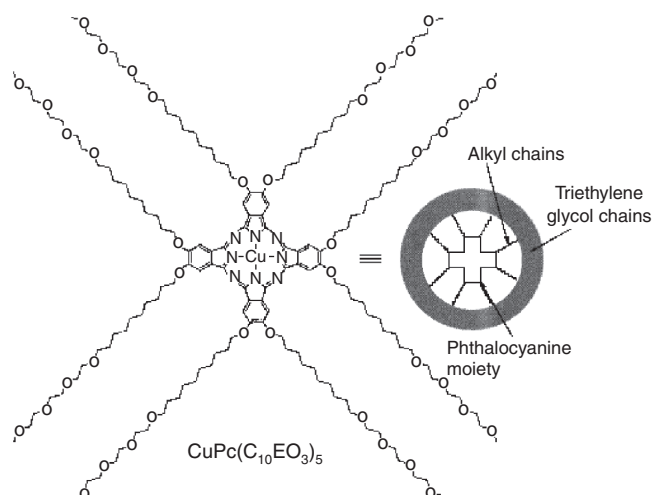
changes in defect and excess electron mobilities dependent on temperature-induced structural reorganization in the films detected by changes in optical absorption spectra [142–145]. The high electronegativity of the F atoms leads to a stabilization of the frontier orbitals as seen by shifts in the redox potentials in solution and in thin films [146] and by UPS [147, 148]. This ease of reduction leads to *n*-type doping of films during film preparation by physical vapor deposition even under UHV conditions [149, 150]. The decrease in conductivity following exposure to air is explained by compensation of this *n*-doping by oxygen [142, 149–151] while the mobility of charge carriers was found to be constant during this change [141].

Single-crystalline substrates offer a regular structure that was found to influence the growth of molecular materials considerably [152]. Commensurate or coincident lattices of crystalline molecular thin films can be formed and were found in many examples of Pc and related materials [153]. Alkali halide surfaces are most suitable to provide a well-ordered optically transparent substrate. Epitaxial relationships could be established in the past for Pc and related molecules. Especially the optical absorption properties are changed considerably by the intermolecular orientation and hence chromophore coupling [60, 65, 154, 155].

Amphiphilic disklike molecule  $CuPc(C_{10}EO_3)_8$  compounds contain a central phthalocyanine core, eight decoxy spacers, and eight peripheral triethylene glycol chains (Fig. 41) [156]. These compounds contain a central Pc core, eight decoxy spacers, and eight peripheral eight triethylene



**Figure 40.** Space-filling model of  $F_{16}PcZn$  as concluded from XRD and UV-vis analysis and of MePTCDI as reported in the Cambridge Structural Database. Reprinted with permission from [107], D. Schlettwein et al., *J. Phys. Chem. B* 103, 3078 (1999). © 1999, American Chemical Society.

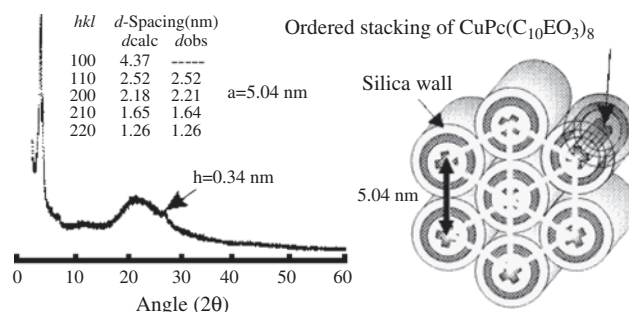


**Figure 41.** Reprinted with permission from [156], M. Kimura et al., *J. Am. Chem. Soc.* 123, 2438 (2001). © 2001, American Chemical Society.

glyco chains. The nonionic surfactants and block polymers containing oligo- and poly(ethylene glycol) headgroups have been widely used as templates for the preparation of mesoporous silica [157]. The introduction of triethylene glycol chains into the disklike molecules can induce the assembly of inorganic sources. The synthesized phthalocyanine derivatives exhibited excellent solubility in polar and non-polar solvents except for hydrocarbons. Figure 42 shows the UV-vis spectra of  $CuPc(C_{10}EO_3)_8$  in  $CH_2Cl_2$  and a mixture of  $CH_2Cl_2$  and ethanol. The UV-vis spectrum in  $CH_2Cl_2$  had a strong sharp peak at 677 nm, typical of nonaggregated phthalocyanine [158]. When ethanol was admixed, the Q-band was broadened, and the maximum was blueshifted. These spectral changes can be ascribed to the formation of phthalocyanine stacks having a cofacial arrangement. By increasing polarity of the solvent, the hydrophobic phthalocyanine cores come closer and form a cofacial one-dimensional stack in polar solvents.

### 3.2. Phthalocyanine Molecular Arrays

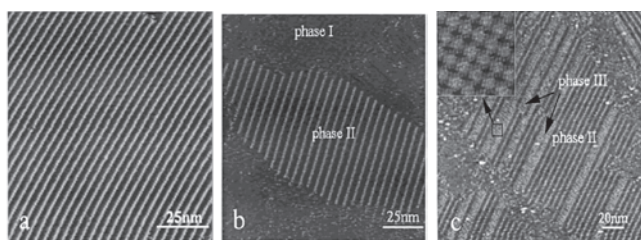
Single molecular arrays of Pc have been obtained with templates of two-dimensional (2D) alkane lamella of nanometer scale using  $C_{18}X$  ( $X = Cl, Br, I, CN$ ) and  $C_{18}SH$ . When Pc



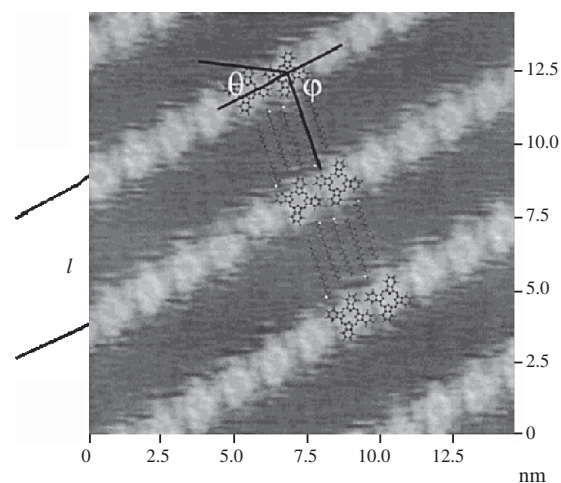
**Figure 42.** Powder XRD patterns of the organic-inorganic composite containing  $CuPc(C_{10}EO_3)_8$  and silica and assigned Miller indices (*hkl*). Reprinted with permission from [156], M. Kimura et al., *J. Am. Chem. Soc.* 123, 2438 (2001). © 2001, American Chemical Society.

and alkane derivatives ( $C_{18}SH$  and  $C_{18}X$ ,  $X = Cl, Br, I, CN$ ) were coadsorbed from solution onto HOPG (highly oriented pyrolytic graphite), a new phase of homogeneous molecular assembly of Pc with  $C_{18}SH$  and  $C_{18}X$  was found in addition to the typical segregated domains [159, 160]. By adjusting the molar ratio of Pc to alkane derivatives to about 1:3, homogeneous intercalation of Pc in the length scale of sub-micrometers can become the main form of Pc on a graphite surface. Figure 43a shows a homogeneous molecular assembly of Pc with  $C_{18}SH$ . In the image, the bright lines correspond to Pc molecular lines. The line width is about 1.5 nm, consistent with the side width of the Pc molecule. The dark bands in the image correspond to  $C_{18}SH$  lamellae and the 2.5 nm width of them is in accordance with the molecular length of  $C_{18}SH$ . On the surface the molecular lines can extend to several hundred nanometers. On the large-scale image, the domain boundary can be detected. The angle between the orientations of these domains is measured to be nearly  $60^\circ$  or  $120^\circ$ , indicating that the orientation of the domain is determined by the registry of alkane chains of thiols to the substrate. By altering the molar ratio of Pc to  $C_{18}SH$ , multirow bands of Pc (phase III) or single molecular line of Pc (phase II) surrounded by  $C_{18}SH$  lamellae (phase I) can be obtained corresponding to concentrations of Pc above or below the optimal ratio, respectively (Fig. 43b and c). High-resolution images obtained on the multirow band regions of Pc are consistent with the adsorption structure of Pc reported on HOPG [51]. Pcs joggle together in the molecular array as in the 2D domain. Though the uniform assembly structures can become dominant by adjusting the molar ratio of Pc to alkane derivatives to nearly 1:3, one can still observe structures as shown in Figure 43b and c, in some area of the surface. This is attributed to the fluctuation of the molar ratio of Pc to alkane derivatives during the volatilization of the solvent, and this is considered to be an indication that the deposition from solution is a dynamic equilibrium process, where kinetic factors are attributed to the nonuniform regions.

The homogeneous assembly of Pc with  $C_{18}SH$  is stable enough to endure repeated scanning and high-resolution images could be obtained on this assembly as shown in Figure 44. The Pc molecule in the line can be observed to



**Figure 43.** (a) A large-scale image of the uniform assembly of Pc with  $C_{18}SH$  when the molar ratio has been adapted to 1:3 (667 mV, 1.019 nA). (b) Coexistence of phase I (domain of pure thiol) and phase II (uniform assembly) when the molar ratio was below 1:3 ( $-431$  mV, 677 pA). (c) Coexistence of phase II and phase III (pure Pc domain) when the molar ratio was above 1:3 (715 mV, 1.136 nA), (inserted) high-resolution image obtained on the Pc domain. Redrawn with permission from [159], S. B. Lei et al., *J. Phys. Chem. B* 105, 12272 (2001). © 2001, American Chemical Society.



**Figure 44.** High-resolution image of the uniform assembly of Pc with  $C_{18}SH$  (560 mV, 1.019 nA). The imaging condition was optimized for the observation of Pc. Parameters defining this assembly were defined on this image. Reprinted with permission from [159], S. B. Lei et al., *J. Phys. Chem. B* 105, 12272 (2001). © 2001, American Chemical Society.

tilt for  $32 \pm 4^\circ$  from the lamellae direction and the  $C_{18}SH$  molecules adsorb on the surface with its carbon chain parallel to the surface and nearly perpendicular to the Pc lines  $75 \pm 6^\circ$ . The repeating period ( $l$ ) is measured to be  $4.0 \pm 0.2$  nm, in accordance with the length of one  $C_{18}SH$  molecule plus the width of one Pc molecule. It can also be counted that on each side of one Pc molecule there exist three  $C_{18}SH$  molecules (Fig. 44), so the Pc vs  $C_{18}SH$  ratio can be measured to be 1:3 from the STM image in the intercalated structure.

According to these STM results, the groove between  $C_{18}X$  lamellae appears to be a favorable site for Pc molecules to stay. On the basis of the observations, it was suggested that when  $C_{18}X$  is excessive, the co-adsorption of Pcs with  $C_{18}X$  results in uniform assembly of  $C_{18}X$  and Pc molecules that are surrounded by lamellae formed by  $C_{18}X$ . As the stoichiometry of Pc increases, Pc molecule arrays extend in the boundary of  $C_{18}X$  lamellae and the size of uniform assemblies also increases until Pc is excessive. At this time, Pc molecules crystallize along the Pc arrays of the uniform assembly and multirow Pc bands formed. This provides a qualitative illustration of the assembly process and rigorous elucidation of this process needs quantitative simulations.

Many of phthalocyanine 3D and 2D nanostructures are connected by hydrogen bonding [161]. The hydrogen bonds have the advantage of selectivity and directionality, which are important in building biological nanostructures. Although phthalocyanine nanostructures have been constructed using other interactions, such as van der Waals and hydrophobic interaction, they received little attention due to lack of directional selectivity [162, 163].

### 3.3. Phthalocyanine Self-Assemblies

Thin films of phthalocyanines [47, 164–168] and porphyrins [15, 168–171] obtained by the self-assembly method rely on the covalent anchoring of the macrocycles on various

substrates by a predetermined number of sites. It is thus possible to reach a high degree of control on the organization of the molecules within the film, allowing complex molecular architectures to be built [15, 47, 168, 172]. Such structures could find interesting applications for energy transfer devices [173, 174] or two-dimensional conjugated polymers.

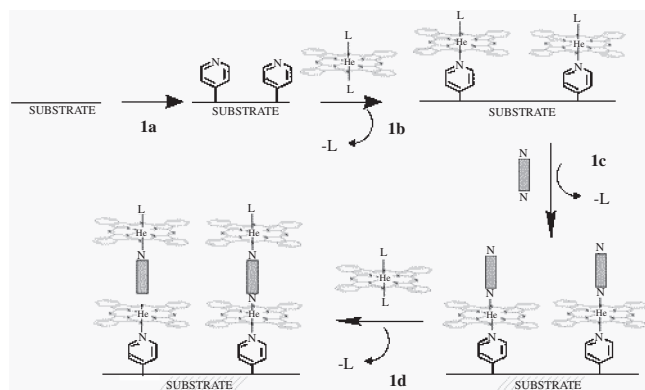
For example ruthenium phthalocyanine (RuPc) monolayers were obtained by self-assembly on pyridino-functionalized metal oxide substrates, by coordination between the ruthenium ions and the pyridino groups [175]. Figure 45 shows formation of RuPc multilayers.

Figure 46 shows an AFM image of a  $[\text{SiO}_2/\text{Py}/\text{RuPc}]$  sample. The film appears homogeneous and regular even on a large scale, with an experimental roughness of 0.5 nm (as for the pristine  $[\text{SiO}_2/\text{Py}]$  sample) consistent with the absence of stacked or aggregated macrocycles. This observation indicates that unspecifically adsorbed materials are actually removed by washing. The observed thickness (AFM contact mode) is 1.8 nm, consistent with the expected one for a  $\text{SiO}_2/\text{Py}/\text{RuPc}$  layer.

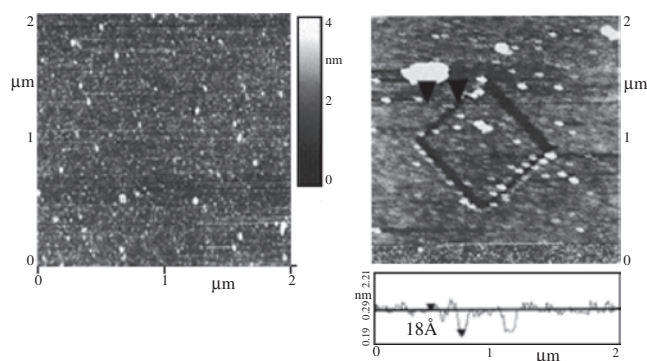
The recently developed technique of layer-by-layer (LBL) assembly of oppositely charged materials has been used to fabricate multilayers on various substrates. LBL assembly has been applied in the construction of materials with well-controlled, nanometer-scale architecture [45, 176]. The key to the construction of multilayers is the interface between adjacent layers, and hence, interface properties are crucial to the self-assembled systems [177] and their physical properties.

Using a layer-by-layer self-assembly technique, multilayers of nickel phthalocyanine tetrasulfonate (NiPc) and poly(diallyldimethylammonium chloride) (PDDA) onto transparent substrates were prepared [45, 178]. In an aqueous solution, PDDA forms a uniform, nanometer-thick thin film on a silica substrate, because PDDA is attracted to the negatively charged substrate surface [179].

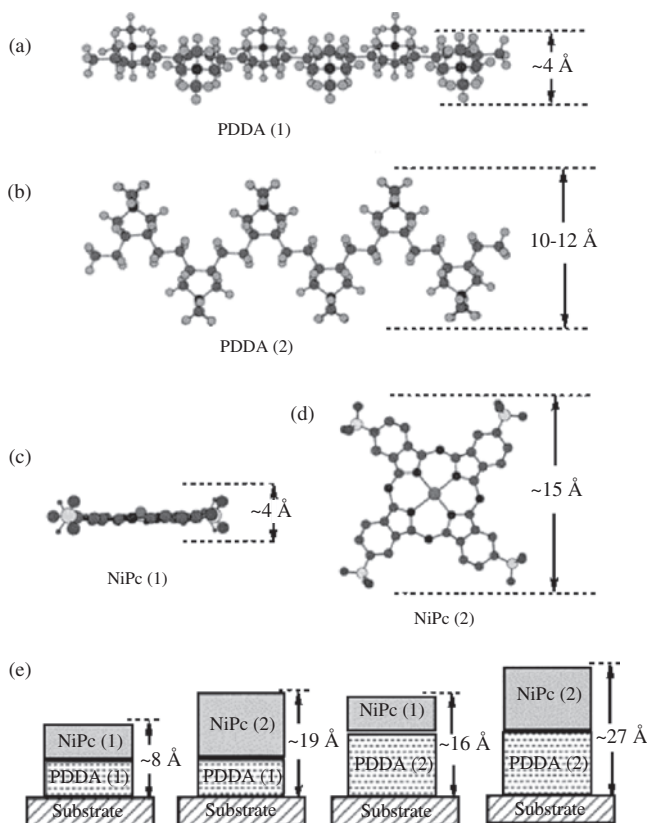
A negatively charged NiPc macrocycle binds to the dispersed positively charged polymeric PDDA monolayer. Multilayer thin films can be obtained by alternately dipping the sample in solutions of PDDA and NiPc. The idealized structure of NiPc and PDDA layers is shown in Figure 47. The



**Figure 45.** Scheme of the formation of ruthenium phthalocyanine multilayers by sequential ligand exchange reactions. L stands for benzonitrile and the bidentate ligands (pyrazine or bipyridine are represented by  $\blacksquare$ ). Reprinted with permission from [175], V. Huc et al., *Langmuir* 17, 1928 (2001). © 2001, American Chemical Society.



**Figure 46.** AFM study of a  $[\text{SiO}_2/\text{Py}/\text{RuPc}]$  sample. The left image shows that no significant difference can be observed on the topography of the surface upon grafting of the phthalocyanine; the experimental roughness remains around 0.5 nm, as for the pristine  $[\text{SiO}_2/\text{Py}]$  surface. The right image allows a measurement of the thickness of the film, which was found to be 1.8 nm (see the line cut below the image). The poor quality of the right image comes from the pollution of the tip resulting from scratching the film to draw the square feature. Reprinted with permission from [175], V. Huc et al., *Langmuir* 17, 1928 (2001). © 2001, American Chemical Society.



**Figure 47.** The idealized linear structure of PDDA lying flat or PDDA(1) gives a thickness of  $\sim 4$  Å (a). The idealized linear structure of PDDA standing up or PDDA(2) yields a higher thickness value of  $\sim 10$ – $12$  Å (b). The structure of NiPc lying flat or NiPc(1) gives a thickness of  $\sim 4$  Å (c). The structure of NiPc standing on edge or NiPc(2) yields a higher thickness value of  $\sim 15$  Å (d). Four idealized layer-pair combinations between PDDA and NiPc yield  $\sim 8$ , 16, 19, and 27 Å thickness values, respectively (e). Reprinted with permission from [45], D. Q. Li et al., *J. Am. Chem. Soc.* 120, 8797 (1998). © 1998, American Chemical Society.

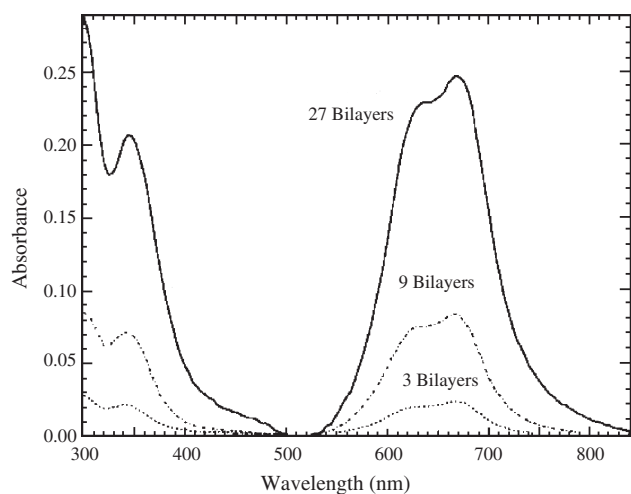
growth of multilayer films was monitored by measuring the absorption of 630 and 665 nm light (Fig. 48) [45].

Surface topography and amplitude images of 3-, 9-, and 27-layer-pair films are shown in Figure 49. As the film thicknesses increase from 3 layer-pairs to 9 and 27 layer-pairs, root mean square (rms) roughnesses also increase from 5.3 to 6.9 and 14.7 Å.

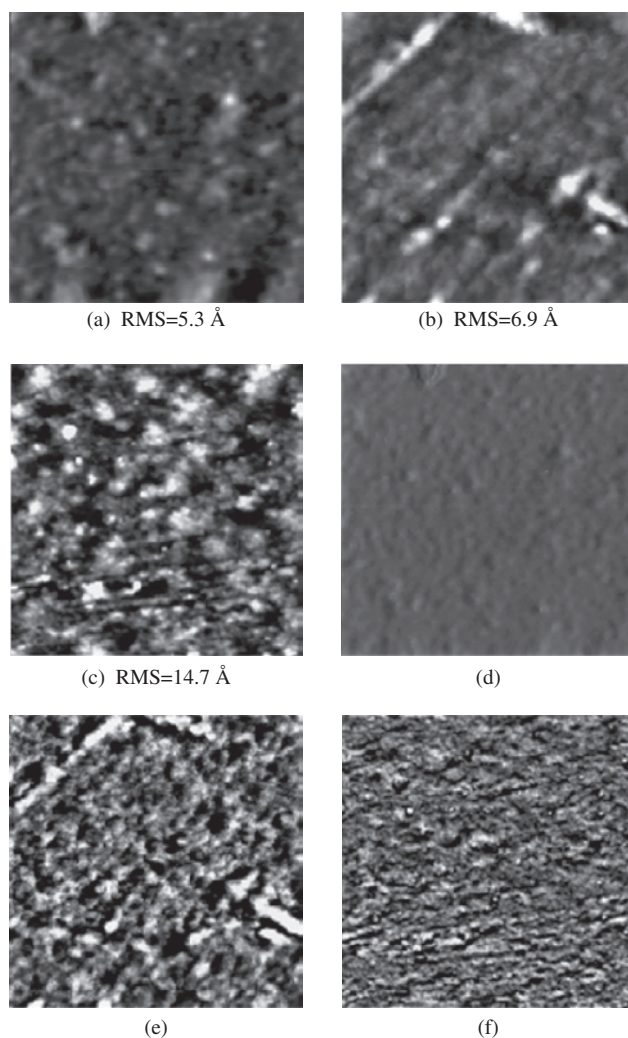
Similarly Li et al. deposited multilayers of nickel phthalocyanine tetrasulfonate and PDDA onto indium tin oxide (ITO) and ITO/TiO<sub>2</sub> substrates, respectively [178]. To probe charge-transfer properties of these self-assembled multilayers on conductive and semiconductive surfaces, Kelvin probe and surface photovoltage measurements have been carried out. The formation of both ionic multilayers and covalent multilayers was well characterized [45, 179, 180].

An *en face* self-assembly of monomeric PcCoDS monolayers on dioctadecylammonium bromide (DODAB) was reported [181]. The water-soluble anionic dye, cobalt phthalocyanine disulfonate (PcCoDS), was used to prepare  $\pi$ -electron terminated model monolayers with a high surface free energy. The water-soluble PcCoDS self-assembles into a  $\pi$ -electron rich overlayer. In water, the large hydrophilic central atom, cobalt, and two polar charged anionic peripheral substituents in PcCoDS (Fig. 50b, d) reduce the tendency to adsorb edge-on or to form large aggregates [182, 183]. UV-vis spectroscopy measurements of phthalocyanine self-association established that PcCoDS adsorbs onto DODAB Langmuir–Blodgett (LB) films predominantly in the monomeric form [183–186].

The adhesion between the dye monolayers was nearly two orders of magnitude greater than that between pure DODAB films. Adhesive contact altered the optical absorption spectrum, as observed upon the cofacial dimerization of phthalocyanine dyes. The adhesion also increased in proportion to the dye coverage. The dye-dependent increase in the range of the van der Waals force between the membranes is



**Figure 48.** Optical absorption of 3 layer-pairs of PDDA-NiPc (dashed), 9 layer-pairs of PDDA-NiPc (dash-dot), and 27 layer-pairs of PDDA-NiPc (solid). The  $\alpha$  and  $\beta$  absorptions at 630 and 665 nm are due to the  $\pi$ -\* electronic transitions in NiPc molecules. Reprinted with permission from [45], D. Q. Li et al., *J. Am. Chem. Soc.* 120, 8797 (1998). © 1998, American Chemical Society.

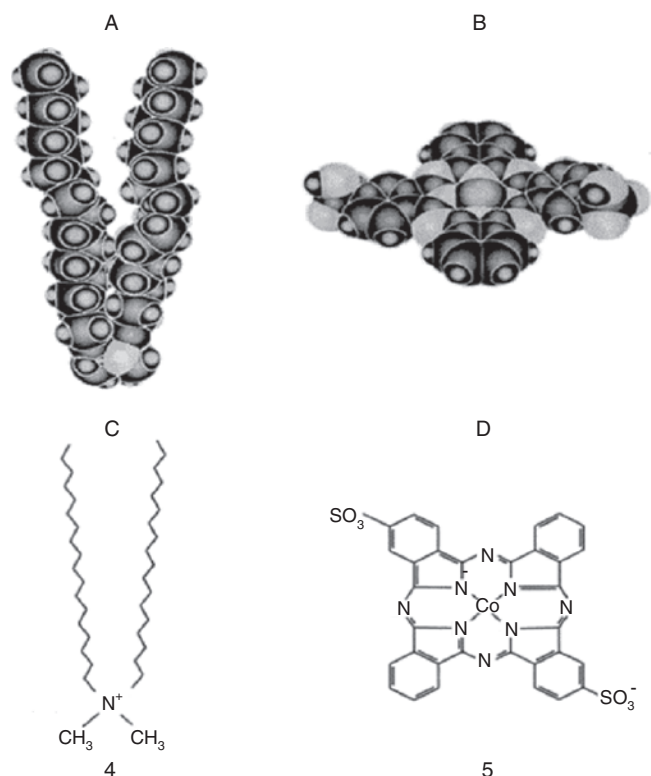


**Figure 49.** AFM images ( $1 \mu\text{m} \times 1 \mu\text{m}$ ) of the surfaces of 3-, 9-, and 27-layer-pair films. Images (a)–(c) are topographs of the surface structure for 3, 9, and 27 layer-pairs; images (d)–(f) are simultaneously taken amplitude images of the same films, respectively. The latter images are pseudoderivatives of the structural data, used to emphasize fine structural information. Reprinted with permission from [45], D. Q. Li et al., *J. Am. Chem. Soc.* 120, 8797 (1998). © 1998, American Chemical Society.

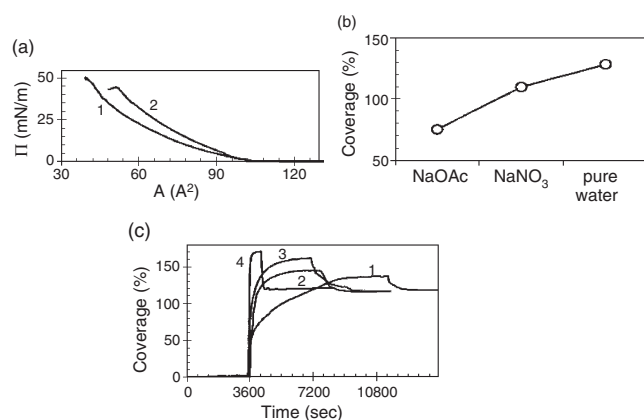
predicted by Lifschitz theory for the multilayer system. Flocculation measurements were then used to confirm that the measured intermembrane forces alter vesicle aggregation in aqueous solutions.

Changes in the surface pressure versus area isotherms of DODAB monolayers on water, after the addition of PcCoDS to the subphase, indicated that PcCoDS binds to DODAB monolayers (Fig. 51a). The DODAB on a pure water subphase exhibited a stable isotherm (Figure 51a, curve 1) as was evident from the absence of changes in the surface pressure at constant film area. After the addition of 0.05 mM PcCoDS to the subphase, the isotherm was measured every 10 min, without exceeding the collapse pressure. The monolayer expanded noticeably 20 min after the dye addition.

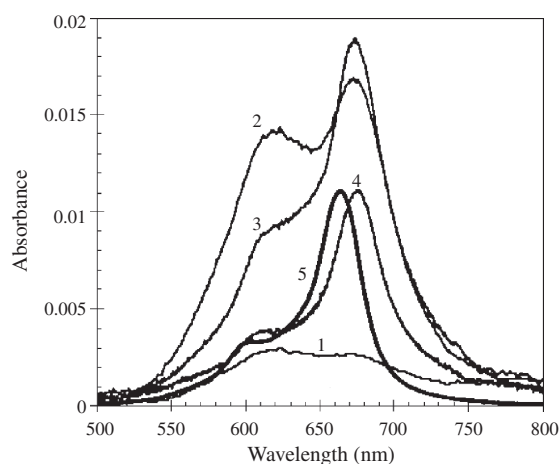
The samples exhibited two peaks at 615 and 670 nm characteristic for the Q-band in phthalocyanines (Fig. 52)



**Figure 50.** Chemical structures (C, D) and molecular models (A, B) of the water-soluble anionic phthalocyanine derivative, PcCoDS, and cationic surfactant, DODAB. Reprinted with permission from [181], N. Lavrik and D. Leckband, *Langmuir* 16, 1842 (2000). © 2000, American Chemical Society.



**Figure 51.** Adsorption of PcCoDS on DODAB monolayers. (a) shows the changes in the surface pressure–area isotherm of a DODAB monolayer in the presence of PcCoDS counterions in the subphase. (b) shows the % coverage of PcCoDS on DODAB monolayers in 1 mM NaNO<sub>3</sub>, 1 mM NaOAc, and pure water, as determined by SPR. (c) shows the kinetics of PcCoDS binding onto DODAB, as monitored by SPR. PcCoDS adsorption was carried out from 0.05 mM solutions containing the following concentrations of NaNO<sub>3</sub>: (1) 0 mM, (2) 0.1 mM; (3) 10 mM; (4) 100 mM. DODAB. Reprinted with permission from [181], N. Lavrik and D. Leckband, *Langmuir* 16, 1842 (2000). © 2000, American Chemical Society.



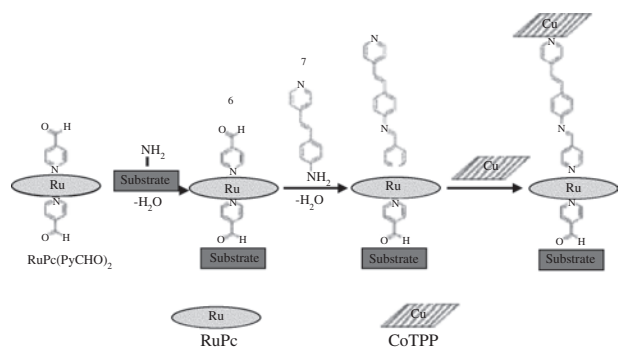
**Figure 52.** Comparison of the electronic absorption spectra of PcCoDS adsorbed on different substrates. The adsorbed samples correspond to the following preparation procedures. Curve 1: ionisorption onto pre-adsorbed poly-L-lysine on glass; curve 2: ionisorption onto protonated aminosilanzed glass; curve 3: physisorption onto hydrophobized glass; curve 4: ionisorption onto DODAB monolayers on glass. Curve 5 shows the scaled spectrum of a 0.05 mM aqueous solution of PcCoDS. DODAB. Reprinted with permission from [181], N. Lavrik and D. Leckband, *Langmuir* 16, 1842 (2000). © 2000, American Chemical Society.

[183–188], which showed different features depending on the preparation procedures.

Strong interactions between plate-shaped, aromatic phthalocyanine macrocycles promote their association into cofacially stacked structures [183–188]. As a result, phthalocyanine species typically self-assemble on surfaces with the macrocycles nearly perpendicular to the substrate plane [182, 189] and thus present their edges to the medium.

The spectral features within the Q-band measured with the different phthalocyanine assemblies reflected differences both in the organization within the films and in the forces between the macrocycles and the substrates. On positively charged, hydrophilic poly-L-lysine, the dye exhibits a low apparent coverage and/or a macrocycle orientation perpendicular to the substrate. The film also contained a high fraction of aggregated PcCoDS. Similar Q-band properties were observed for substituted PcCu sulfonate assembled electrostatically on poly-L-lysine [184]. The dye self-association was also very pronounced on protonated, aminosilane layers. However, the greater dye coverage suggests that both electrostatics and the substrate hydrophobicity are important for binding and orienting the macrocycles. The high dimer fractions in PcCoDS layers on both poly-L-lysine and aminosilane modified surfaces is attributed to the molecular disorder and microroughness of the substrates [190]. The roughness of the glass substrates might also contribute to the aggregation.

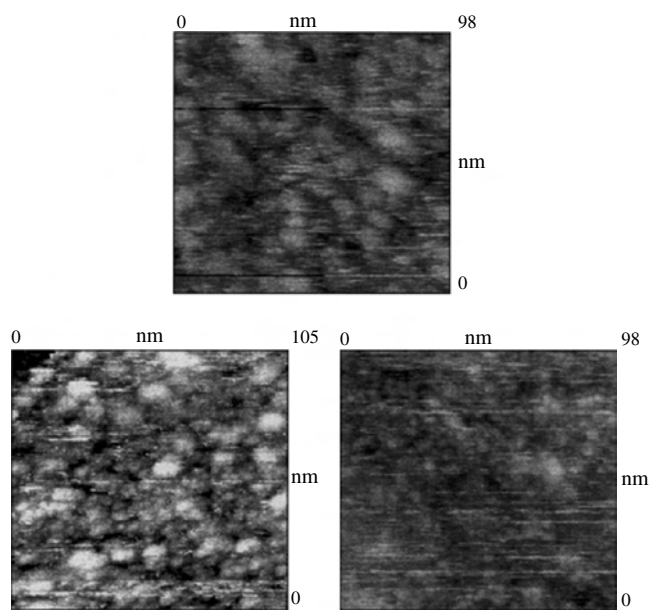
Pc thin films prepared by chemical linkage between the substrate and the macrocycles show that ligand exchange occurs upon the binding of the Pc ring to the surface in several examples [15, 47, 185–191]. Exceptional stability was observed in ruthenium phthalocyanines axially complexed by pyridine ligands, the preparation of which is shown in Figure 53.



**Figure 53.** Scheme of the strategy developed for grafting metallic macrocycles on glass or gold substrates using apical ligands as linkers. Reprinted with permission from [168], V. Huc et al., *Langmuir* 16, 1770 (2000). © 2000, American Chemical Society.

Figure 54 exhibits STM images recorded at ambient temperature on the  $[\text{SC}_6\text{H}_4\text{NH}_2\text{-RuPc}]$  bilayer. The images taken after the grafting of RuPc complexes clearly evidence small grains (ca. 2 nm in diameter) of ca. round shape superimposed on the larger pattern exhibited by the STM image of the same sample before the grafting. Those small objects can be assumed to be the Pc rings, locally ordered by groups of 6–7 molecules.

Thin films of silicon phthalocyanine dichloride ( $\text{SiPcCl}_2$ ) could be deposited from solution on to the H-passivated Si(111) surface [192]. In a high coverage film, clusters of about  $5.5 \text{ nm} \times 4.5 \text{ nm}$  in size are observed. These clusters are believed to partially stack on each other, suggesting a tilted growth mechanism of the layers on the surface. In a low coverage film, well-ordered monolayers are found, with a close structural similarity to the bulk crystal structure

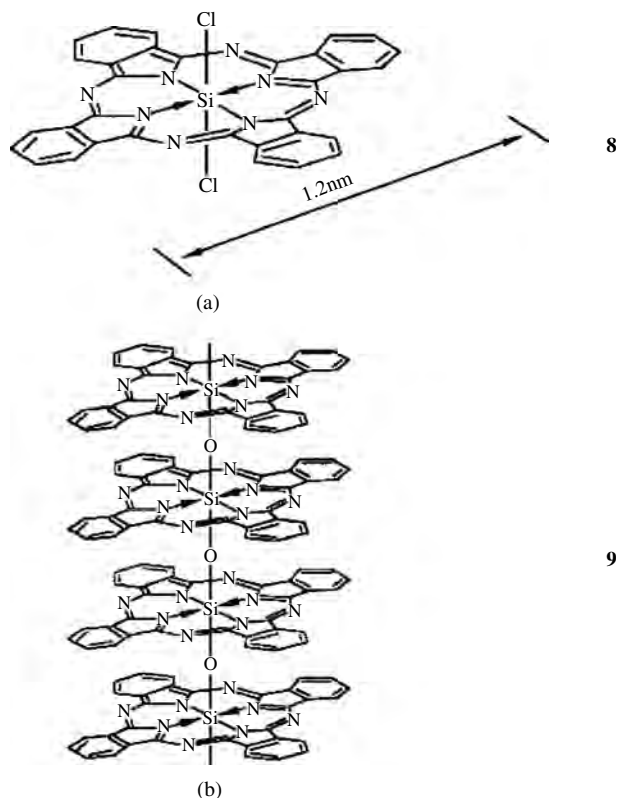


**Figure 54.** STM images recorded at ambient temperature on a  $[\text{SC}_6\text{H}_4\text{NH}_2]$  SAM (top) and a  $\text{SC}_6\text{H}_4\text{NH}_2\text{-RuPc}$  bilayer (bottom) on flat gold. Full  $z$  scale is 10.2 nm (top), 10.6 nm (bottom left), and 15.8 nm (bottom right). Reprinted with permission from [168], V. Huc et al., *Langmuir* 16, 1770 (2000). © 2000, American Chemical Society.

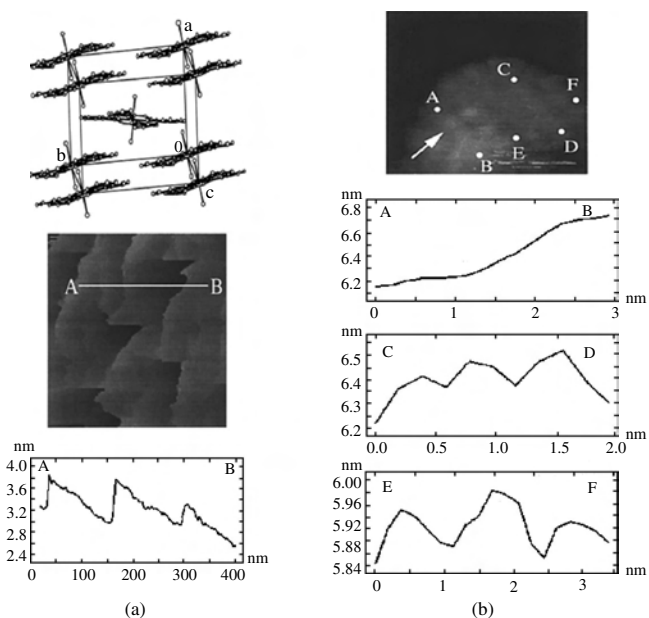
of  $\text{SiPcCl}_2$ . The bulk crystal structure of  $\text{SiPcCl}_2$  (Fig. 55) was determined directly from powder X-ray diffraction data using the Monte Carlo method. The results of STM manipulation and the observation of well-ordered  $\text{SiPcCl}_2$  layers on the Si(111) surface indicate a weaker interaction between the  $\text{SiPcCl}_2$  molecules and the substrate than between the  $\text{SiPcCl}_2$  molecules (Fig. 56a).

The scanning tunneling spectroscopy (STS)  $I$ - $V$  curve was analyzed to investigate the nature of the  $\text{SiPcCl}_2$  films on the surface. The  $I$ - $V$  curve measured in the ordered area in Figure 56b shows marked rectifying behavior. This behavior was duplicated at all points tested over both the monolayer and multilayer films; no local states were observed at different positions on the films. Such rectifying behavior has been observed by Pomerantz et al. [80] and Ottaviano et al. [193] in STS studies of CuPc on graphite and NiPc on Si(111), respectively. This behavior is to be expected for a film that acts as an organic  $p$ -type semiconductor (due to oxygen doping) on a  $p$ -doped semiconductor surface. Thus rectifying behavior could be attributed to the H-passivated silicon surface.

Application of two-dimensional PC monolayer assemblies for light harvesting is discussed in [21]. The air/water interface structure was characterized with X-ray specular reflectivity and on solid substrates by optical absorption spectroscopy.



**Figure 55.** (a) Molecular structure of silicon phthalocyanine dichloride ( $\text{SiPcCl}_2$ ). The lateral dimension in the plane of the phthalocyanine molecule is about 1.2 nm. (b) The  $(\text{SiPcO})_n$  chain after polymerization of  $\text{SiPc(OH)}_2$ . Reprinted with permission from [192], P. Miao et al., *J. Phys. Chem. B* 104, 1285 (2000). © 2000, American Chemical Society.



**Figure 56.** (a) STM image (500 nm  $\times$  500 nm) of the H-passivated Si(111) surface before the deposition of SiPcCl<sub>2</sub>. Tunneling conditions:  $V = +1.680$  V,  $I = 0.35$  nA, constant current mode. A sequence of zigzag steps is clearly resolved, with an average terrace width of about 150 nm. On the wide terraces, the corrugation is measured to be about 0.3 nm, which indicates a very flat surface. (b) 5 nm  $\times$  5 nm STM image of a separated cluster island of SiPcCl<sub>2</sub> molecules on the H-passivated Si(111) surface. Tunneling conditions:  $V = +1.680$  V,  $I = 0.35$  nA, constant current mode. Well-ordered layers are visible in the image. Corresponding surface profiles show that the thickness of one monolayer is about 0.6 nm (along AB). Reprinted with permission from [192], P. Miao et al., *J. Phys. Chem. B* 104, 1285 (2000). © 2000, American Chemical Society.

### 3.4. Discotic Mesophase Phthalocyanines

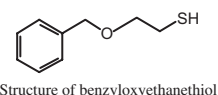
Rodlike self-assembling organic materials have attracted significant attention due to their unique electro- and photoactive properties. These properties have been shown to be dependent on both the long-range order and molecular orientation within thin films of these materials, as evaluated in field-effect transistors [118, 194], photovoltaics [195], and polarized emission light-emitting diodes [196].

Discotic mesophase phthalocyanines, such as CuPcO-C<sub>2</sub>OBz in Figure 38, self-assembled in parallel columnar structures [134, 197]. Discotic mesophase materials in general are attractive for these technologies if the coherence length achievable in rodlike aggregates of these materials exceeds the expected separation distance between source/drain (OFET) or anode/cathode (PV) contacts. (Generally a minimum coherence length of 100 nm is required.) Under these conditions, charge mobilities along the rod axis greater than 0.01 cm<sup>2</sup> V<sup>-1</sup> s<sup>-1</sup> are expected [198].

It was reported that thin films of CuPcOC<sub>2</sub>OBz contain the Pc oriented nearly “edge-on” to the substrate plane, with coherence lengths in individual rods averaging ca. 40 nm. A key feature of these molecules which leads to the stiff nature and coherence of each bilayer film is the benzyl termination in the eight side chains, which appears to reinforce the interactions between adjacent Pc rings and

between adjacent Pc columns [134, 197]. No other Pc material capable of forming a discotic mesophase, held in place by noncovalent interactions, has to date demonstrated such long-range order and thin film coherence. The structural perfection in the individual Pc columns rivals that seen in the rodlike polymers of silicon phthalocyanines developed by Wegner and co-workers [199].

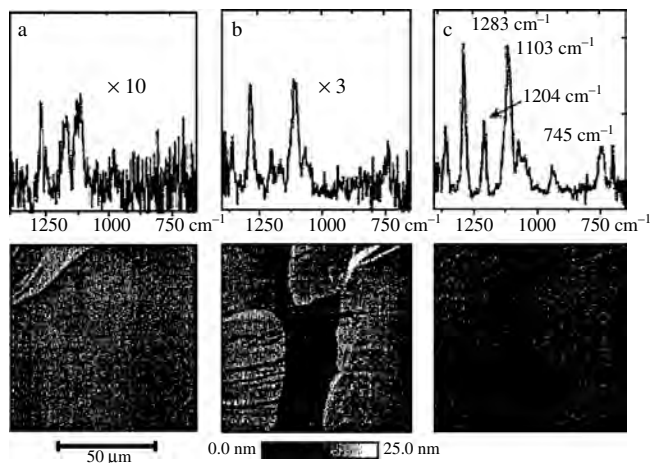
Phenyl–phenyl interactions between a surface modifier and the Pc assembly played a critical role in the efficient transfer of coherent thin films of these Pc assemblies to metal, silicon/silicon oxide, and transparent conducting oxide substrates [134]. Molecular assemblies with phenyl termination are believed to interact through both cofacial and edge-to-face arrangement of the aromatic groups [200], which can strongly affect the type and coherence of the resultant molecular aggregate structures [201]. Modification of gold surfaces with a new phenyl-terminated thiol (2), which mimics the side chain composition of these Pcs, leads to a greater efficiency in transfer of CuPcOC<sub>2</sub>OBz to a gold surface, vs the efficiency of transfer seen for a CH<sub>3</sub>-terminated alkanethiol self-assembled monolayer [197]. Such phenyl surface modifications also influence the orientation of individual Pcs as determined by reflection–absorption IR spectroscopy (RAIRS). Analogous modification of the oxide surfaces of silicon wafers, with a mixture of 1,1,1,3,3,3-hexamethyldisilazane (HMDS) and 1,3-diphenyl-1,1,3,3-tetramethyldisilazane (DPTMDS), shows a higher degree of transfer vs the unmodified surfaces. The presence of phenyl groups in the surface modifier leads not only to higher efficiency in transfer but also to more ordered/optically anisotropic thin films.



Representative RAIRS spectra are shown in Figure 57 and show the greatest contrast observed between film transfers over three experimental trials. The small IR signal in Figure 57a and the corresponding AFM image are evidence that only small portions of a bilayer of CuPcOC<sub>2</sub>OBz are transferred effectively to this type of surface. The remaining material is left on the LB trough or picked up as highly folded and defective film segments. Figure 57a shows a corner section of the Pc bilayer film whose dimensions were less than 250  $\mu$ m  $\times$  250  $\mu$ m and a larger bare Au region features typical of transfer to an unmodified Au surface. Film segments, transferred to the unmodified Au surface, may interact through nonspecific interactions with carbonaceous contamination.

Figure 57b reflects the improved transfer of a single bilayer of CuPcOC<sub>2</sub>OBz due to nonspecific hydrophobic interactions with the methyl-terminated octanethiol, although a continuous film is still not achieved, as seen in the corresponding AFM image. Bilayer islands are seen across the surface, with average dimensions of 500  $\mu$ m  $\times$  500  $\mu$ m. Comparable results are obtained using octadecanethiol; therefore, chain length in the self-assembled monolayer (SAM) cannot by itself be a contributing factor in determining Pc transfer efficiency to a methyl-terminated Au surface.





**Figure 57.** RAIRS spectra of a single bilayer film of CuPcOC<sub>2</sub>CBz onto (a) a clean Au slide, (b) a Au slide modified with octanethiol, and (c) a Au slide modified with benzyloxyethanethiol. The Pc-O-C (1204, and 1283 cm<sup>-1</sup>) and out-of-plane bending transitions (Pc-H = 745 cm<sup>-1</sup>) have been marked. Corresponding AFM images, shown in the lower half of the figure, are considered representative for transfer to each type of surface and were obtained by tapping mode AFM in an aqueous solution. The majority of the surface shown with (a) is bare Au, with only a small amount of CuPcOC<sub>2</sub>CBz (upper left-hand corner) present on the surface in this region. Larger, islandlike deposits of CuPcOC<sub>2</sub>CBz in (b) are typical for Au substrates that have been hydrophobized and had rms roughness values of ca. 3 nm, while the coherent, conformal deposits in (c) are typical for those obtained on hydrophobized Au surfaces with the addition of phenyl moieties and had rms roughness values of ca. 2 nm. Reprinted with permission from [197], R. A. P. Zangmeister et al., *Langmuir* 17, 7071 (2001). © 2001, American Chemical Society.

Figure 57c shows the marked improvement in a single bilayer transfer of CuPcOC<sub>2</sub>OBz to the Au surface modified with benzyloxyethanethiol. The transfer efficiency on Au surfaces modified with benzyloxyethanethiol is consistently a factor of ca. 10 vs the bare gold surface and a factor of ca. 3 vs the gold surfaces modified with CH<sub>3</sub>-terminated SAMs. These estimates are made from AFM imaging and the maximum IR absorbance for each film at 1283 cm<sup>-1</sup>. The corresponding AFM image to Figure 57c shows a complete bilayer transfer of CuPcOC<sub>2</sub>OBz over a 100 μm × 100 μm area. Images of continuous film features are acquired from scans taken at random over the entire sample, within the physical limits of the imaging scan head (ca. 1 mm<sup>2</sup>). The entire area of the transferred Pc film is ca. 1 cm<sup>2</sup>. The scan image shown in Figure 57c also reveals small “ridges” in the bilayer film. This image was specifically chosen to show the maximal corrugation observed in the Pc film. The ridges run from the lower left to the upper right sides of the image, and the average step height of these ridges was 7 ± 2 nm, or approximately 2–3 Pc column diameters [134].

#### 4. PHTHALOCYANINE LB FILMS

The Langmuir–Blodgett technique, which often utilizes derivatized Pcs for solubility, produces controllable morphologies on large areas. Properties of LB films consisting of Pcs are significantly influenced by the orientation

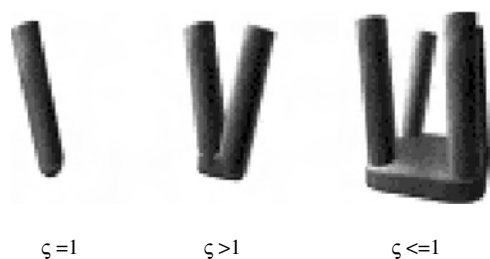
and aggregation of Pcs [202, 203]. Thus many spectroscopic measurements have been carried out in order to elucidate molecular ordering of Pcs in thin films [204–215]. Various studies indicate that substituents in Pcs play an important role in determining the orientation of Pcs. Pcs form aggregated columns and exhibit an edge-on conformation with respect to substrates in monolayers, except for the case where an amphiphilic porphyrazine was used, as observed by Palacin et al. [32]. It was also reported that the introduction of tetracarboxyl residues in Pc rings results in high in-plane anisotropy [23, 216–219].

Selectively oriented multilayers of precisely controlled thickness can be reproducibly prepared by customizing the hydrophobic and hydrophilic regions of the molecule by derivatization of the phthalocyanine rings. Although the electronic and optical properties of many of these films have been studied extensively, the nature of the interaction of Pc films with the substrate, water, or layer interfaces is less well understood. Because underivatized phthalocyanines or those with added nonpolar groups tend to form irregular or poorly transferred films, an amphiphilic transfer promoter such as octadecanol is typically added to facilitate reproducible film transfer and to stabilize and homogenize films deposited by the Langmuir–Blodgett technique.

LB films have been obtained from both substituted and unsubstituted phthalocyanines [220], though a comprehensive understanding of their organization at the air–water interface has yet to be developed for deriving a packing arrangement–property relationship in the ultrathin LB films [221]. Monomolecular films of substituted amphiphilic phthalocyanines can readily be obtained using the method of Langmuir–Blodgett [24, 39, 74, 220, 222].

A survey of the literature on phthalocyanine monolayers at the air–water interface shows considerable dispersion in the results for similar phthalocyanines and in some cases even for the same phthalocyanine [223–230]. Experimental conditions such as subphase temperature, spreading solvent, and even the type of measuring system can cause major changes in the monolayer characteristics of these “nonclassical” monolayer materials.

The major characteristic of Langmuir and LB films (i.e., the out-of-plane orientation of the molecules) is a direct consequence of the amphiphilic character of the molecules and the organizing role of the air–water interface [231]. The key parameter is the ratio  $\zeta$  between the projection on the water surface of the volume filled by the aliphatic chain(s) vs the area filled at the air–water interface by the polar head(s) (Fig. 58).  $\zeta$  is strongly related to the *critical packing parameter* introduced by Ninham for short-chain surfactant molecules that self-organize in water either as micelles, lamellar structures, vesicles, or reverse micelles [232, 233]. Phthalocyanine derivatives, however, do not generally fit with those geometrical rules, and their orientation at the air–water interface is totally monitored by the location and nature of the substituents grafted on the periphery of the macrocycle. Unsubstituted Pcs are very likely to form aggregates at the air–water interface, because no attractive interaction with the water subphase is possible for those purely aromatic molecules. Similar disordered LB films were obtained with soluble Pcs, bearing bulky alkyl or aryl substituents because the Langmuir monolayers built from



**Figure 58.** Schematic definition of the ratio  $\zeta$ . Three typical cases are given: a single-chain compound such as a fatty acid ( $\zeta = 1$ ), a double-chain compound with a small polar head ( $\zeta > 1$ ), and the four-chain phthalocyanine ( $\zeta < 1$ ). Reprinted with permission from [268], S. Palacin, *Adv. Colloid Interface Sci.* 87, 165 (2000). © 2000, Elsevier Science.

those nonamphiphilic molecules are actually multilayers [234–242]. It is commonly assumed that those molecules are not really suitable for LB film formation since they show little evidence of conventional hydrophilic/hydrophobic character in their chemical constitution [243]. Highly ordered LB films containing Pcs described in the literature are all based on truly amphiphilic Pc derivatives (i.e., phthalocyanines bearing both polar groups and aliphatic chains).

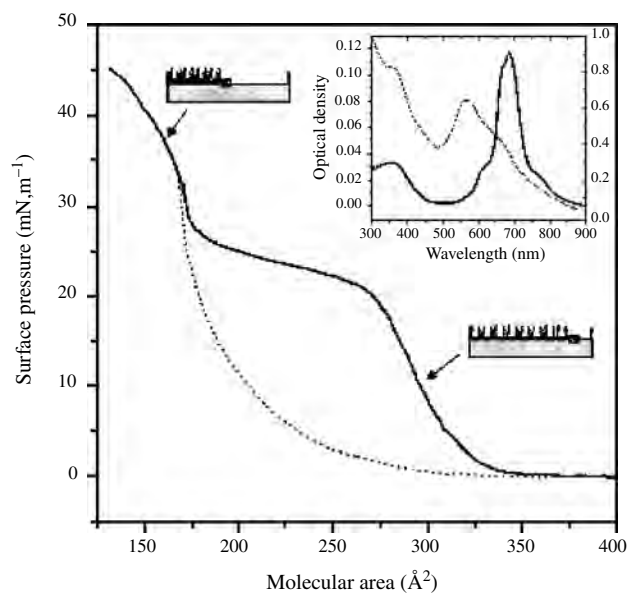
Two extreme orientations of Pc derivatives in Langmuir monolayers and LB films can be discussed: in the first one, the Pc rings lie parallel to the water surface (or the substrate in the resulting LB films); in the second one, the Pc rings exhibit an edge-on orientation. The latter geometry favors face-to-face interactions between neighboring Pc rings and is particularly useful in conductometric applications. The former geometry cannot be obtained without the LB technique and was used to form a true two-dimensional polymer exhibiting outstanding mechanical properties [244].

Another unique characteristic of the LB technique is the ability to induce in-plane anisotropy in the lamellar structure. As rationalized by Minari et al. [245] and Schwiegk et al. [246], the in-plane anisotropy observed in some LB films arises from the flow effect during the transfer of the floating monolayer onto solid substrates. Rigid rod polymers [247, 248] and linear aggregates of discotic mesogens [249–252] are the two major families of molecules that exhibit in-plane anisotropy in LB films. In both cases, the molecular or supramolecular objects to be dynamically aligned during the transfer exhibit an anisotropic shape at the air–water interface [253, 254].

#### 4.1. Pc Rings with a Tetrapyrroline Bearing Four Octadecyl Chains (Flat-Lying Pc Rings)

The Pc ring is rigid, conjugated, and hydrophobic. It is prone to aggregation in face-to-face dimers, at least when the central metallic ion does not bear any bulky axial ligand. Thus, anchoring the Pc ring parallel to the water surface requires strong polar substituents, either in the center or on the periphery of the macrocycle. However, phthalocyanines bearing strong polar groups on their periphery were much more studied and many Langmuir and Langmuir–Blodgett films were built [32, 255–268].

Pc rings with a tetrapyrroline porphyrane bearing four octadecyl chains on its periphery ( $MS_{18}$ , with M the metallic ion located in the center of the macrocycle) is the first example of a Langmuir monolayer based on flat lying [260]. As shown by the surface–pressure isotherms (Fig. 59) and by various orientational studies performed by electron spin resonance (ESR), linear dichroism, and X-ray diffraction on the LB films built up from that monolayer, the porphyrane rings lie almost parallel to the water surface but as dimers. Figure 59 shows that the formation of the face-to-face dimers is irreversible, since the decompression isotherm does not match the first compression isotherm [268]. UV-visible spectra recorded on LB films formed before and after the plateau of the first compression isotherm confirm that  $MS_{18}$  is in a monomeric state at low pressure and dimerizes at high surface pressure (Fig. 59, inset). The dimerization brings the  $\zeta$  ratio closer to 1, since the dimer bears eight octadecyl chains for a dimeric polar head filling  $310 \text{ \AA}^2$  at the air–water interface and allows the monolayer to be transferred correctly onto solid substrates. Orientational studies performed on the resulting LB films indicate that the macrocycles are slightly tilted with respect to the substrate. Similar results were also observed with tetrapyrroline porphyrins that share many geometrical characteristics with the described porphyranes [269]. Thus, taking into account that the geometry of the porphyrane rings is fixed by the



**Figure 59.** Surface pressure vs molecular area isotherms recorded with  $CuS_{18}$  at room temperature on a KBr 0.05 M water solution. Solid line: first compression, 30 min after spreading. Dotted line: decompression isotherm. Schematic views of the monomeric and dimeric monolayers are given. Inset: UV-visible absorption curves observed on LB films deposited from the  $CuS_{18}$  monolayer on a KBr 0.05 M water solution. Solid line: 16 LB layers deposited at  $10 \text{ mN m}^{-1}$  (left vertical axis). Dotted line: 110 LB layers deposited from the same monolayer at  $30 \text{ mN m}^{-1}$  (right vertical axis). The solid line spectrum is characteristic of the monomeric state of  $CuS_{18}$ . The dotted line spectrum is characteristic of a dimer of  $CuS_{18}$  molecules. Reprinted with permission from [268], S. Palacin, *Adv. Colloid Interface Sci.* 87, 165 (2000). © 2000, Elsevier Science.

anchoring of the four pyridinium groups to the water surface, the molecules are forced to dimerize for the monolayer to reach a reasonable compactness.

#### 4.2. Pc Ring with Esters, Amides, and Ethers (Tilted with Respect to the Water Surface)

Contrary to the pyridinium groups involved in the previous examples, weak polar groups grafted on the periphery of the Pc ring such as esters [41, 256], amides [255, 262], or ethers [130, 236, 240, 257, 270, 271] are not polar enough to anchor the macrocycle parallel to the water surface. The macrocycles are thus tilted with respect to the water surface and able to self-organize in columnar assemblies. The actual orientation of such molecules at the air–water interface generally depends on their association numbers (i.e., the average number of molecules involved in the self-assembled stacks. When the association number is small (typically less than 10), the monolayer is quite disordered. Indeed, a competition occurs between the self-association in columnar assemblies and the affinity of the polar groups for the water surface. The tilt angles are thus small (30–60°; with respect to the plane of the interface) and the monolayer exhibits a polycrystalline behavior, since the self-assembled columns are not long enough to be in-plane oriented. When the association number is high (typically higher than 100), the Pc rings form well-defined columnar assemblies at the air–water interface, which can be in-plane oriented by the transfer process.

The LB films of tetraamido metallophthalocyanines, bearing four tertiary amide groups on their periphery, exhibited in-plane dichroism when the metallic ion was either Cu or Ni and the multilayers deposited at high surface pressure [263]. On the contrary, no in-plane dichroism was observed with Co and Zn. In the former case, the tilt angle was high (i.e., the macrocycles were almost perpendicular to the plane of the substrate). In the latter case, the tilt angle was low.

These results indicate that if designing a phthalocyanine ring able to lie parallel to the water surface at the air–water interface only requires enough strong polar groups located on the periphery of the aromatic cores, designing flat-lying phthalocyanines able to form stable monolayers and well-organized LB films requires one also to take into account the  $\zeta$  factor of the monolayer (i.e., the actual role played within the monolayer by each component of the molecule).

#### 4.3. Edge-on Pcs in Langmuir and LB Films

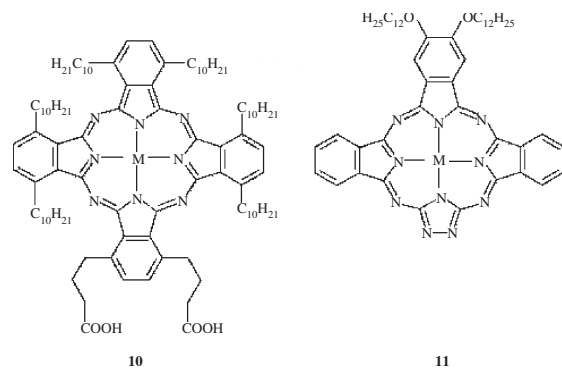
The orientation obtained from Pc molecules bearing weak polar groups is very difficult to predict, since it results from the competition between the affinity of the polar substituents for the water surface and the aggregation ability of the Pc derivatives. Three different strategies were designed to get edge-on Pc rings in LB films: (i) using unsymmetrically substituted phthalocyanines, which bear strong polar groups only on one part of its core; (ii) preparing LB films from polymeric phthalocyanines such as phthalocyaninatosiloxanes; or (iii) relying on mesogenic phthalocyanines, able to form stable columnar assemblies at the air–water interface.

Cook's team developed both synthetic pathways leading to unsymmetrically substituted phthalocyanines and characterization of the resulting LB films [24, 259, 272].

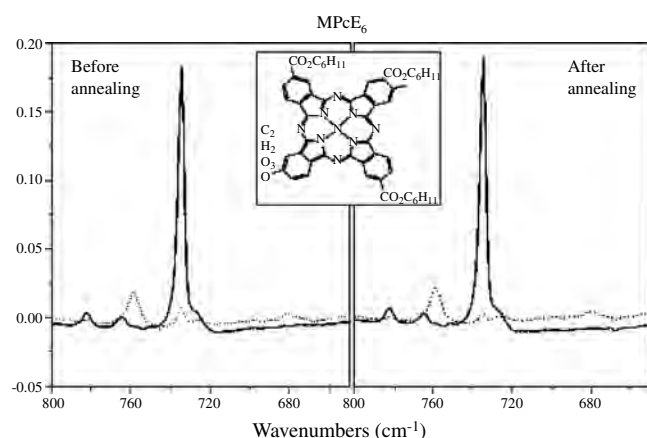
The Pcs are unsymmetrically substituted, generally bearing only one or two substituent groups that contain a terminal hydrophilic moiety, grafted on the same benzenoid ring of the phthalocyanine and alkyl or alkoxy chains on the three other benzenoid rings (Fig. 60a). The area per molecule lies in the range 80–120 Å<sup>2</sup>, depending on the number and the length of the chains, which is consistent with the molecules standing more or less perpendicular to the water subphase. X-ray diffraction, UV-visible, and infrared absorption measurements performed on the LB multilayers indicate that, in the case of Pc rings bearing alkyl chains on three of their four benzenoid rings, highly ordered multilayers are formed: the Pc rings are perpendicular to the plane of the substrate and tilted from the axis of the dipping direction with an average angle of 25°. On the contrary, LB films based on Pc rings bearing alkoxy chains are almost disordered. These results show that properly designed phthalocyanines can form well-ordered mono- and multilayers exhibiting edge-on macrocycles.

A similar design strategy was followed recently in the triazolephthalocyanine family, where one of the four benzene ring is replaced by a triazole (Fig. 60b) [273]. As in the previous example, columnar assemblies are expected to form spontaneously at the air–water interface and to be aligned during the transfer process, but this self-organization requires nickel(II) ions in the subphase.

Well-ordered Langmuir and Langmuir–Blodgett films with high order parameters were observed from mesomorphic Pc bearing four hexyl chains grafted to the benzenoid rings through ester functions (MPcE<sub>6</sub>, inset in Fig. 61). As shown by Albouy [274], the MPcE<sub>6</sub> molecule forms columns in the bulk solid state, with a basic repeat distance of 3.365 Å. The packing of the columns in a two-dimensional square lattice exhibits a regular distance of 20.8 Å, and a typical domain dimension along the axes perpendicular to the columns is 290 Å. In the columns, there is no tilt of one molecule with respect to its neighbors, which means each



**Figure 60.** Examples of phthalocyanine derivatives specifically designed for an edge-on orientation in Langmuir and LB films. (a) Unsymmetrically substituted phthalocyanine designed and synthesized by Cook et al. [272g]. (b) Triazolephthalocyanines designed and synthesized by Torres et al. [273]. Reprinted with permission from [268], S. Palacin, *Adv. Colloid Interface Sci.* 87, 165 (2000). © 2000, Elsevier Science.

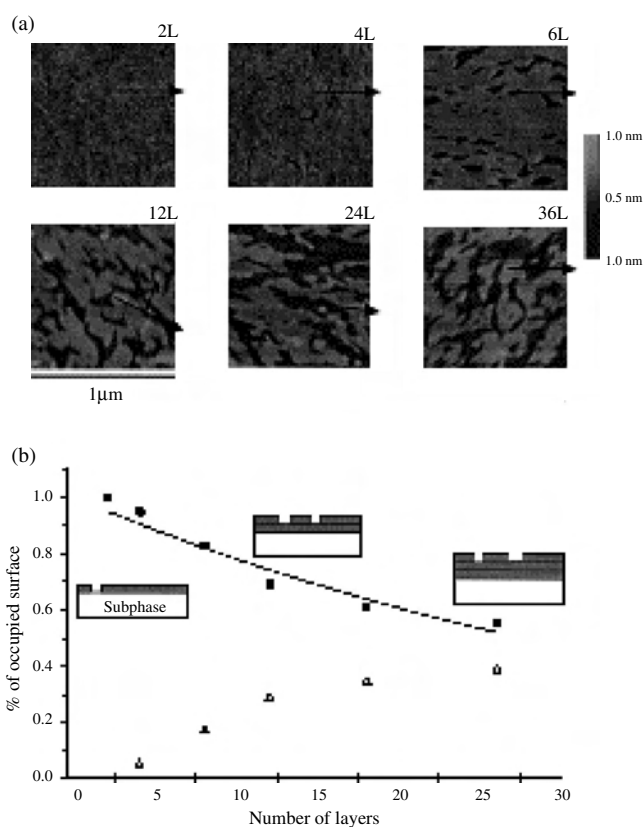


**Figure 61.** Infrared linear dichroism spectra recorded before and after annealing on LB films built from NiPcE<sub>6</sub>. The electric field of the incident infrared light is either parallel (dotted lines) or perpendicular (solid lines) to the axis of the transfer. The inset gives the structure of the MPcE<sub>6</sub> molecule. Reprinted with permission from [274], P. A. Albouy, *J. Phys. Chem.* 98, 8543 (1994). © 1994, American Chemical Society.

column keeps a fourfold symmetry. In the crystal cell, the benzenoid rings are pointing to the diagonal of the square cell.

A columnar structure, similar to the bulk state one, is found within LB films and the columns are aligned with the dipping direction. This latter result was confirmed by Bourgoïn et al. [275], using infrared linear dichroism. The experimental order parameter is 0.94, which indicates that the average angle between the columns and the axis of transfer is less than 10°. Interestingly, the LB multilayers keep their lamellar structure and their in-plane anisotropy upon severe annealing. When the LB multilayers are heated at 200 °C for 2 h under nitrogen, the in-plane anisotropy is actually improved and the order parameter even reaches unity, as evidenced by infrared linear dichroism on the band at 740 cm<sup>-1</sup> polarized within the plane of the Pc ring (Fig. 61).

Another peculiar behavior of these LB films is revealed by AFM [275]. In the tapping mode, the morphology of the outer surface of the lamellar assembly can be investigated. Figure 62a gives the topographic images recorded for several thicknesses of NiPcE<sub>6</sub> LB films. The darker areas are one monolayer deeper than the brighter ones. It is clear from the images that the area occupied by defects (the darker regions) increases regularly with the number of deposited layers. These defects arise from a solid state reorganization that occurs during and after the transfer of the monolayers onto the substrate. As the transfer ratio is actually slightly lower than 1, each freshly deposited layer exhibits monolayer-thick defects. However, the topographic images in Figure 62 indicate that the defects in the underlayers are filled by the upper ones. Thus all the defects “add” in the topmost layer. According to this simple model, the *n*th layer should fill  $\alpha^n$  of the total area of the sample, with  $\alpha$  the transfer ratio. Figure 62b shows that the model is in correct agreement with the results, assuming  $\alpha = 0.975$ . This result implies that PcE<sub>6</sub> molecules are able to slide easily from one column to a neighboring one.



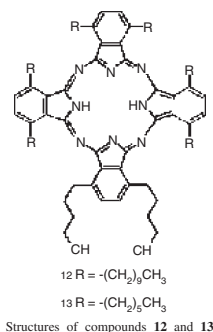
**Figure 62.** (a) Topographic images (1  $\mu\text{m} \times 1 \mu\text{m}$ ) recorded on 2-, 4-, 8-, 12-, 18-, and 26-layer samples of NiPcE<sub>6</sub> LB multilayers. The vertical scale is common to all the images. The black arrow is the direction of the transfer. (b) Percentage of the surface occupied by the topmost *n*th layer (solid squares) and the (*n*-1)th layer (open triangles). The solid curve gives the theoretical percentage  $\alpha^n$  derived from the model detailed in the text. Inset: Schematics of the summation of the defects in the topmost layer. Reprinted with permission from [275], J. P. Bourgoïn et al., *Langmuir* 12, 6473 (1996). © 1996, American Chemical Society.

It is noteworthy that the LB films based on PcE<sub>6</sub> molecules, that were built up by the Langmuir–Blodgett technique via a Y-type deposition, do not exhibit the classical Y-type structure, with a bilayer periodicity. The actual periodicity is one monolayer and these films behave as lamellar liquid crystals, owing to the mesomorphic properties of the molecule in the bulk. The upstroke and downstroke depositions occur only on hydrophobic substrates, which is clearly evidenced by selective deposition on patterned substrates [276]. It is even possible to peel off the multilayers one monolayer after the other using the AFM tip as a plow [277]. This example is thus at the limit between LB films and bulk materials, since the molecular packing is exactly the same in both cases. It should, however, be remembered that the in-plane orientation arises from the LB transfer, without any rubbing of the substrate before the deposition, and that the in-plane orientation is stable upon severe annealing. The LB technique appears to be a good alternative to sample preparation for in-plane alignment of liquid crystals.

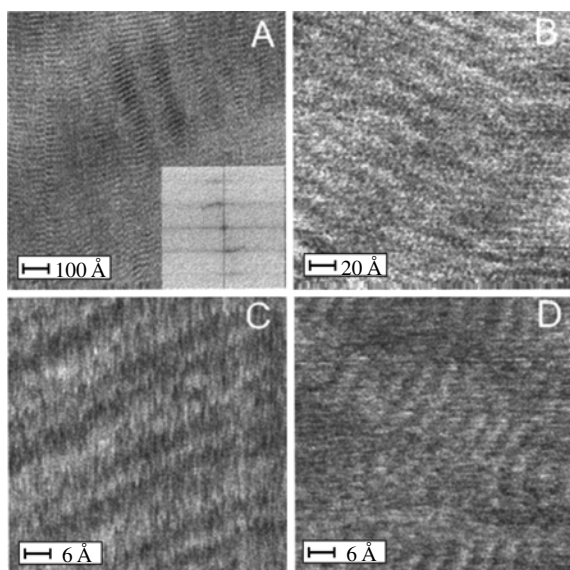
#### 4.4. Octasubstituted Amphiphilic Phthalocyanines

Unsubstituted and lightly substituted phthalocyanine molecules show a strong propensity to form columnar structures in which the planar aromatic nucleus of one molecule is either fully cofacial or partially offset from the nucleus of its neighbor [278].

Y-type Langmuir–Blodgett films of the octasubstituted amphiphilic phthalocyanines **12** and **13** deposited onto hydrophobic glass show a columnar arrangement of the molecules in the surface layer [279].



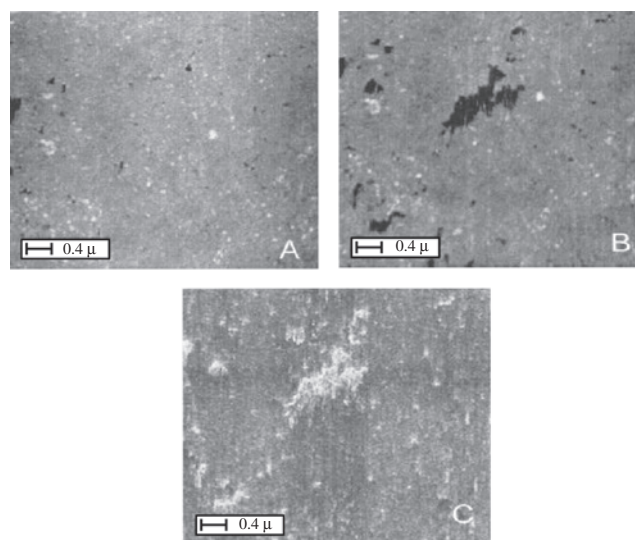
This columnar arrangement is observed on the surface of films with one, two, and three Y-type bilayers. Figure 63A



**Figure 63.** Higher magnification friction images of the surface of a two-bilayer film. The scanning direction was along the  $y$  axis in parts A and C and along the  $X$  axis in parts B and D. Panel A shows a  $1000 \text{ \AA} \times 1000 \text{ \AA}$  area with domains of different columnar orientations. The insert is the 2D Fourier transform showing spots that correspond to the different domains with an intercolumnar distance of  $21 \pm 2 \text{ \AA}$ . The horizontal and vertical lines through the center and the spots are noise due to the raster scanning and the finite image size. (B) Smaller area where the columnar packing and individual molecules within the columns can be observed. (C) Small area scanned with the tip at more than  $60^\circ$  with respect to the columnar axis (see text for explanation). (D) A zone in (B). Reprinted with permission from [279], M. Velez et al., *Langmuir* 14, 4221 (1998). © 1998, American Chemical Society.

depicts an area where columns with different orientations come together. The inset is the Fourier transform of the image showing spots that correspond to the spacing and orientation of the different columnar domains. The intercolumnar distance is measured in Fourier space and corresponds to  $21 \pm 2 \text{ \AA}$  ( $n = 60$  images). When the surface of these columns is scanned in the direction of their longitudinal axis, the friction images show the edges of individual molecules (Fig. 63B, D). The distance between the molecules averaged  $5.0 \pm 0.6 \text{ \AA}$  from 118 individual measurements done on nine different images. In these higher resolution images, if the scanning direction of the tip is more perpendicular to the columnar axis, a thinner column between the  $21 \text{ \AA}$  spaced columns appears (Fig. 63C), but there is no evidence of the individual molecules within the columns. After repeated scanning in this tip–column orientation, the distances between the columns and their integrity are perturbed.

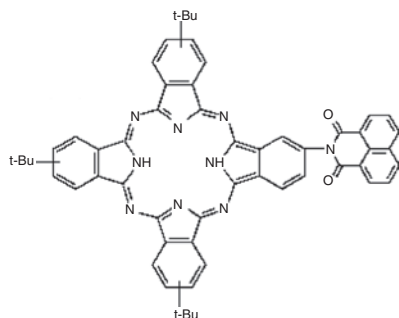
The Y-type deposition of the molecules onto a hydrophobic surface implies that the first molecular monolayer deposited has the hydrophobic tails, the R groups, in contact with the surface with the hydroxyl headgroups exposed for H-bonding with the hydroxy headgroups of the second monolayer. The bilayer so formed then has a hydrophobic surface of R groups exposed at the commencement of the second dip. It was observed during the AFM experiments on films of **12** that the technique was able to distinguish between the hydrophobic surface of a bilayer and the surface remaining once parts of the outer monolayer were removed by the tip, exposing the hydroxy headgroups of the monolayer below [280]. Thus the friction images (Fig. 64C) indicate that the most external surface of the bi- or multilayers interacts less with the tip (more hydrophobic behavior) than the surface exposed after removing the outermost monolayer.



**Figure 64.** (A) AFM topographical image of a  $4.8 \mu\text{m} \times 4.8 \mu\text{m}$  area of a two-bilayer film before and after (B) its central part has been scanned (total height range is 10 nm). (C) Friction image of the same area shown in (B). Lighter regions represent areas that have a stronger interaction with the scanning tip. Reprinted with permission from [279], M. Velez et al., *Langmuir* 14, 4221 (1998). © 1998, American Chemical Society.

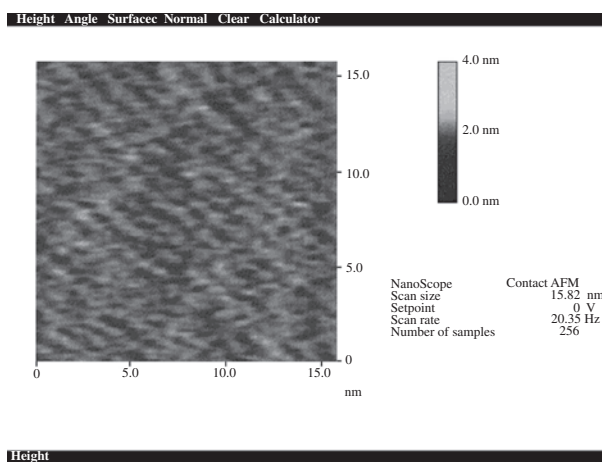
#### 4.5. Metal-Free Asymmetrically Substituted Phthalocyanine

Langmuir–Blodgett films of a metal-free asymmetrically substituted phthalocyanine, 1,8-naphthalimide-tri-*tert*-butylphthalocyanine (NaBuPc), showed that the asymmetrically substituted Pc not only possesses good solubility in common organic solvents but also possesses an ideal LB film forming ability [281].

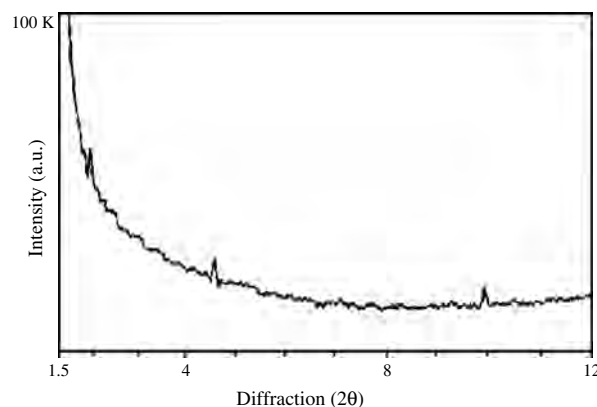


The atomic force microscopy topography of a NaBuPc LB monolayer on a muscovite substrate is shown in Figure 65. The molecular structure of individual molecules was observed for this LB film, which indicates a smooth and steady film can be obtained through the LB technique. From this picture the diameter of NaBuPc molecules was measured to be about 0.84 nm. If we further assume that the molecules of NaBuPc are cubic in structure, the area per molecule should be about  $70 \text{ \AA}^2$ . This is completely in accordance with the result estimated from the surface pressure–area isotherm of NaBuPc, indicating that a highly oriented LB film was obtained on this substrate.

Figure 66 depicts a small-angle X-ray diffraction (SAXRD) pattern of a 28-layer Y-type LB film of NaBuPc on glass. The SAXRD pattern shows several reflections at  $2\theta = 2.14, 4.54, \text{ and } 9.98$  corresponding to (001), (002),



**Figure 65.** AFM image of the NaBuPc LB film, scan size:  $16 \times 16 \text{ nm}^2$ , AFM: contact mode, set point: 0 V, scan rate: 20.35 Hz. Reprinted with permission from [281], Y. Q. Liu et al., *J. Phys. Chem. B* 104, 11859 (2000). © 2000, American Chemical Society.



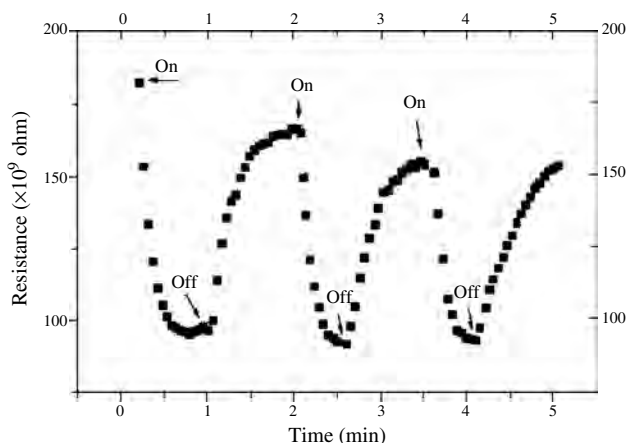
**Figure 66.** Small-angle X-ray diffraction pattern of a 28-layer LB film of NaBuPc on glass. Reprinted with permission from [281], Y. Q. Liu et al., *J. Phys. Chem. B* 104, 11859 (2000). © 2000, American Chemical Society.

and (005) Bragg diffraction, respectively, demonstrating a well-defined layered structure of the LB film. From the diffraction pattern, the bilayer  $d$  spacing of the LB film is calculated to be about  $40 \text{ \AA}$ ; thus, the thickness of a single-layer film is  $20 \text{ \AA}$ . As mentioned the NaBuPc molecules are densely stacked in a face-to-face orientation and edge-on to the water surface with a tilt angle of about  $72^\circ$  using a naphthalimide group as the hydrophilic moiety. The longer diagonal distance across the NaBuPc molecule is approximately  $21.1 \text{ \AA}$ . Therefore, the thickness of the NaBuPc monolayer on the water surface should be about  $20 \text{ \AA}$ . The thickness values obtained both from surface pressure–area isotherms and from SAXRD agree well. The SAXRD result, on one hand, provides additional evidence for the configuration of NaBuPc molecules at the air–water interface. On the other hand, it indicates that the orientation of the phthalocyanine molecules was maintained during the LB transfer process.

For second-harmonic generation (SHG) nonlinear optical (NLO) materials, there are three requirements: (1) a highly polarizable electron conjugation system; (2) an electron-donating substituent and an electron-withdrawing substituent on the aromatic ring or other conjugated system; (3) a noncentrosymmetric structure. Phthalocyanine is an 18-electron conjugated molecule, and the other two requirements can be realized by chemical modification of phthalocyanine molecules and by the LB technique with X- or Z-type deposition models.

The LB films of NaBuPc exhibited SHG activity. The SH intensity of NaBuPc relative to a Y-cut quartz wedge is about 1.76 and the second-order susceptibility and the molecular hyperpolarizability values of a three-layer LB film are  $8.32 \times 10^{-9}$  and  $5.97 \times 10^{-30}$  esu, respectively.

At room temperature, the response and recovery curves of the gas sensor of a five-layer LB film of NaBuPc in 10 ppm  $\text{NO}_2/\text{N}_2$  atmosphere are shown in Figure 67. When  $\text{NO}_2$  was introduced into the test cell, the resistance of the sensor decreased. The equilibrium was reached in less than 1 min, demonstrating relatively large adsorption and desorption velocities for  $\text{NO}_2$  molecules on NaBuPc films. This is probably due to the fact that the LB sensor films are ultrathin.



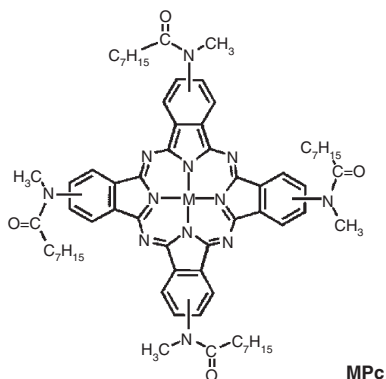
**Figure 67.** Influences of  $\text{NO}_2$  on the resistance of the  $\text{NO}_2$  gas sensor consisting of a five-layer LB film of NaBuPc in 10 ppm  $\text{NO}_2/\text{N}_2$  at room temperature. Reprinted with permission from [281], Y. Q. Liu et al., *J. Phys. Chem. B* 104, 11859 (2000). © 2000, American Chemical Society.

They can be rapidly saturated by the gas molecules, reaching a maximum response value.

Different metals, substituents, transfer promoters, or solvents have been shown to produce different orientations of the plane of the phthalocyanine relative to the surface. For example, Fryer et al. [282] assert that copper tertbutyl substituted phthalocyanines [ $\text{CuPcBu}_4$ ] lie with the plane of the molecule inclined but close to normal to the surface, which is consistent with previous work done by Lloyd et al. [283]. However, the lead analog lies parallel to the surface [240]. Without an amphiphilic promoter, islands of crystals within a disordered structure are observed for both metal chelated  $\text{PcBu}_4$ 's.

#### 4.6. Metallophthalocyanines Bearing Amide Side Chains

Metallophthalocyanines in Figure 68 (MPcs) [M being one of the following metal ions: Co(II), Ni(II), Cu(II), or Zn(II)], bearing amide side chains and being highly soluble

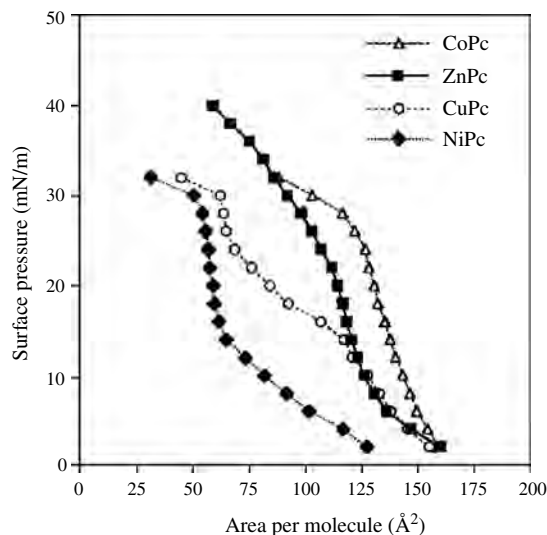


**Figure 68.** Tetraamidometallophthalocyanines MPc. M(II) = Co(II), Cu(II), Ni(II), or Zn(II). Reprinted with permission from [284], S. Fouriaux et al., *J. Phys. Chem.* 100, 16984 (1996). © 1996, American Chemical Society.

in organic solvents, have been synthesized by starting from the corresponding phthalonitrile. All four compounds can form Langmuir and Langmuir–Blodgett films, but interestingly, their behavior as monolayers was shown to be very much dependent on the central metal ion [284]. The study of  $\Pi$ - $A$  isotherms, low-angle X-ray diffraction patterns, and IR dichroism showed that cobalt and zinc phthalocyanines are coordinated with water molecules and therefore orient with an angle of around  $60^\circ$  normal to the air–water interface or to the substrate. On the other hand, nickel phthalocyanine is not coordinated with water; it forms columns that orient in the transfer direction during the deposition process. The copper phthalocyanine is an intermediate case. For low surface pressures, it behaves like Co and Zn compounds; the square planar copper (II) is certainly liganded with water molecules. At higher surface pressures, the water molecules are ejected and the macrocycles can orient more vertically (angle of around  $30^\circ$  between macrocycle and normal to the air–water interface) and form oriented columnar structures when deposited onto substrates.

The  $\Pi$ - $A$  isotherms at  $21^\circ\text{C}$  are shown in Figure 69. For a given temperature, ZnPc, NiPc, and CuPc present very nicely reproducible curves whereas that of CoPc shows a rather large instability.

The curves corresponding to CoPc and ZnPc are very similar: a not very clear solid phase followed by a slow collapse at around  $26\text{ mN/m}$ . The area per molecule in the middle of the solid phase ( $18\text{ mN/m}$ ) is respectively of  $140$  and  $120\text{ \AA}^2$ . Theoretical molecular dimensions derived from molecular models (Chem 3D molecular modeling calculation program) give section values of  $40\text{ \AA}^2$  if macrocycles are oriented vertically and of  $170\text{ \AA}^2$  if they are flat at the air–water interface. The molecular sections observed in the solid phase suggest that CoPc and ZnPc belong to the second type. Metallomacrocycle/water interactions are dominant over  $\Pi$  interactions.



**Figure 69.** Surface pressure/molecular area isotherm ( $21^\circ\text{C}$ ) of the MPcs. The measurements were performed in equilibrium conditions by steps of  $2\text{ mN/m}$ . Reprinted with permission from [284], S. Fouriaux et al., *J. Phys. Chem.* 100, 16984 (1996). © 1996, American Chemical Society.

For NiPc, there is a slow increase corresponding to the liquid phase until rather high surface pressures (14 mN/m). For higher pressures, there is an almost vertical part in the curve corresponding to the solid phase of a rather rigid monolayer for a molecular area of around  $60 \text{ \AA}^2$ . A clear collapse is observed at 30 mN/m.

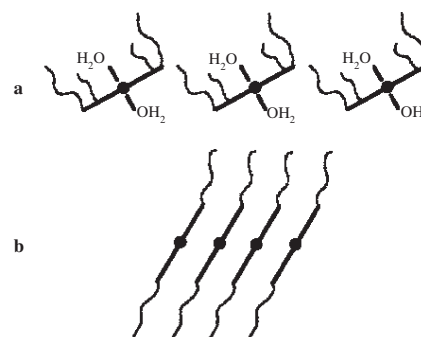
The behavior of the CuPc monolayer seems to be intermediate between that of ZnPc and that of NiPc. For low pressures, the CuPc  $\Pi$ - $A$  isotherm can be superimposed on that of ZnPc; however, at 16 mN/m, after a very short solid phase, a first collapse is observed followed by a clear second solid phase between 25 and 30 mN/m. At these surface pressures, the area per molecule is similar to that observed in the case of the nickel compound.

It is noticeable that, for low surface pressures, the  $\Pi$ - $A$  curves of CuPc and NiPc were found to be very much dependent on the subphase temperature. Interestingly, the arrangement of the macrocycles at the air-water interface appeared to be very much dependent on the nature of the central metal.

For the nickel compound, the macrocycles start also to interact when they are still almost in a horizontal position; however, the area per molecule ( $60 \text{ \AA}^2$ ) that is obtained in the solid phase corresponds to macrocycles almost vertically oriented at the air-water interface. In this case,  $\pi$ - $\pi$  interactions between macrocycles should be more important than in the previous case.

For low surface pressures, the  $\Pi$ - $A$  curve of the copper phthalocyanine is similar to that of ZnPc, suggesting that the macrocycles are oriented almost flat at the interface; however, for surface pressures around 16 mN/m, the layer becomes unstable. This first collapse leads to a new solid phase whose area per molecule is very similar to the one observed in the case of NiPc. This can be easily interpreted as a reorientation of the macrocycles. However, for similar compounds [213], the presence of several solid phases in the  $\Pi$ - $A$  curve has been interpreted as multilayer formation. This explanation would fit very well to our case since the area per molecule shifts from  $130 \text{ \AA}^2$  in the first solid phase to about one-half its value in the second solid phase.

This strong metal dependence of molecular organization at the air-water interface and after deposition onto solid substrates can be interpreted from the coordination number of these central metal ions. Indeed, as Co(II) and Zn(II) are penta- or hexacoordinate ions, it can be expected that CoPc and ZnPc, in contact with water molecules, will be strongly coordinated by one or two apical  $\text{OH}_2$  which prevent  $\pi$ - $\pi$  interactions between macrocycles and favor their rather horizontal organization in the monolayers (see Fig. 70a). The presence of water in the films of CoPc and ZnPc analyzed by IR spectroscopy confirms this hypothesis. The absence of clear diffraction peaks by low-angle X-ray reflection spectroscopy can then be understood, since uncharged macrocycles are very poor LB film candidates if they cannot aggregate via  $\pi$ - $\pi$  interactions. In the other hand, Ni(II) is a tetracoordinate ion fully satisfied with a phthalocyanine ligand.  $\pi$ - $\pi$  interactions are then possible and NiPc forms very good quality LB films with 100% transfer ratio and clear interlayer spacing corresponding to macrocycles standing almost vertical on the substrate (see Fig. 70b). Finally, Cu(II) is square planar, which is a deformed octahedral



**Figure 70.** Interaction of MPC with water. Reprinted with permission from [284], S. Fouriaux et al., *J. Phys. Chem.* 100, 16984 (1996). © 1996, American Chemical Society.

structure. At low surface pressures, CuPc is certainly coordinated by one or two apical  $\text{OH}_2$ ; the absence of clear X-ray diffraction bands confirms this. However, contrary to the case of CoPc and ZnPc, the  $\text{OH}_2$  ligands are ejected from the monolayer during the first collapse at 16 mN/m. Consequently, for higher surface pressure, the macrocycles can fully afford  $\pi$  interactions and reorient in a more vertical position.

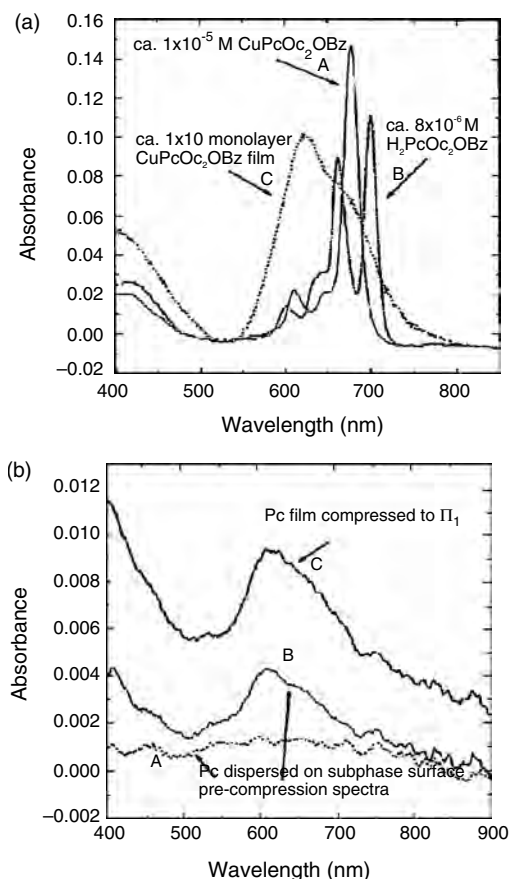
#### 4.7. $\text{CuPcOC}_2\text{OBz}$ and $\text{H}_2\text{PcOC}_2\text{OBz}$

(2,3,9,10,16,17,23,24-Octakis((2-benzyloxy)ethoxy)phthalocyaninato)copper and its dihydrogen analog form highly ordered Langmuir-Blodgett thin films, where the phthalocyanine rings orient with the plane of the ring nearly perpendicular to the compression direction on the LB trough [271]. The resultant thin films show remarkable mechanical stability on the trough, and atomic force microscopy studies show that the transferred thin films, in their fully compressed states, consist of stable bilayers of the Pc. X-ray diffraction studies indicate partial overlap of the benzyl-terminated side chains in adjacent Pc columns.

Solutions of  $\text{CuPcOC}_2\text{OBz}$  produced well-defined Langmuir surface pressure-area isotherms with two distinct phase transitions [130]. These films, once compressed, show a remarkable degree of mechanical stability, which affects their transfer to various substrates and which ultimately exerts some control over their spectroscopic and electrochemical properties. Langmuir films transferred to optically transparent ITO electrodes, at pressures corresponding to both of the observed phase transitions, show a high degree of reversibility for the oxidation processes of these Pc thin films, in perchlorate supporting electrolytes. Studies suggest the oxidation of both aggregated and monomerlike Pcs occurs within the thin films. There is evidence that the onset of oxidation of the Pc aggregates results in film phase transformations, which yields less aggregated or even monomeric Pcs, which are oxidized at correspondingly higher potentials.

Spectroscopic characterization of  $\text{CuPcOC}_2\text{OBz}$  and  $\text{H}_2\text{PcOC}_2\text{OBz}$  indicates that these Pcs do not behave as typical LB amphiphiles. Solution and thin film spectra, shown in Figure 71a, illustrate the spectroscopic properties of monomeric and aggregated forms. Monomeric  $\text{CuPcOC}_2\text{OBz}$  in dilute solution has a narrow absorbance band with a maximum at 677 nm, while  $\text{H}_2\text{PcOC}_2\text{OBz}$





**Figure 71.** (a) Solution and thin film spectra: solid line (A), CuPcOC<sub>2</sub>OBz ca.  $1 \times 10^{-5}$  M in CHCl<sub>3</sub>; dot-dash line (B), H<sub>2</sub>PcOC<sub>2</sub>OBz ca.  $8 \times 10^{-6}$  M in CHCl<sub>3</sub>; dotted line (C), CuPcOC<sub>2</sub>OBz ca.  $10^{-6}$  M in CHCl<sub>3</sub>; dashed line, CuPcOC<sub>2</sub>OBz ca.  $10^{10}$  monolayers on ITO. (b) Time/pressure dependent CuPcOC<sub>2</sub>OBz on trough spectra: dotted line (A), dispersed Pc precompression (ca. 15 min after Pc introduction to trough); solid line (B), dispersed Pc precompression "Pc island" (ca. 18 min); dot-dash line (C), partial compression ca. 10 mN/m. Reprinted with permission from [271], P. E. Smolenyak et al., *Langmuir* 13, 6568 (1997). © 1997, American Chemical Society.

exhibits the expected splitting of the monomer peak with absorbance maxima at 662 and 700 nm. The strongly blueshifted Q-band spectrum seen for concentrated solutions and thin films of these materials, with an absorbance maximum at ca. 625 nm, arises from cofacial aggregation of the Pcs, as predicted by the molecular exciton model for dyes in close proximity [60, 154, 155, 285]. On-trough spectroscopic characterization of these Pc films at submonolayer coverage indicates that the aggregation behavior of these molecules, seen in concentrated solutions, is sustained for noncompressed Langmuir films after initial spreading on the LB trough.

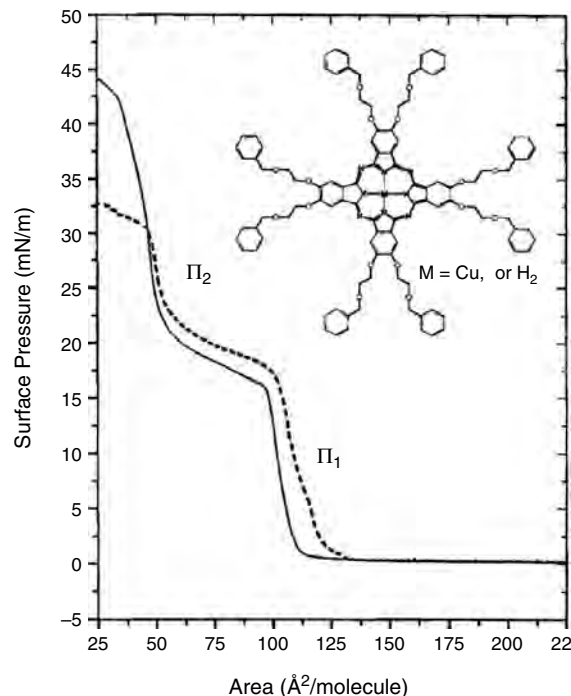
Figure 71b shows on-trough Q-band spectra, collected prior to and after film compression. The intensity and absorbance maxima of the spectra vary with time. Spectra recorded at random time intervals, after solvent evaporation, show either a presence or absence of Pc. The absence of absorbing species occurs because the Pc is not homogeneously distributed on the subphase surface. When absorbing species are present aggregated Pcs are indicated.

Islandlike regions of aggregated Pc are thought to be diffusing on the subphase surface and occasionally drifting into the light path of the spectrometer. On-trough spectra found for the compressed CuPcOC<sub>2</sub>OBz and H<sub>2</sub>PcOC<sub>2</sub>OBz films are comparable to those found for Langmuir–Blodgett and cast films of these materials.

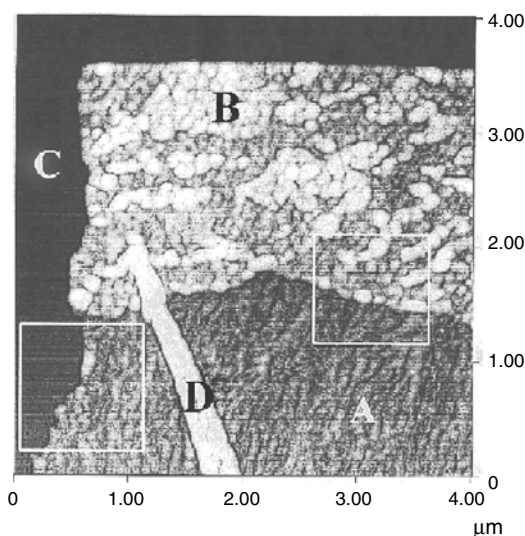
CuPcOC<sub>2</sub>OBz and H<sub>2</sub>PcOC<sub>2</sub>OBz on water form Langmuir films exhibiting two distinct phase transitions (Fig. 72). An area of ca.  $120 \text{ \AA}^2/\text{molecule}$  at the first phase transition (1) suggests the Pc molecules are cofacially stacked into columnar aggregates, on edge, with Pc rings oriented at a small angle to the normal of the subphase surface. The second phase transition (2), at ca.  $60 \text{ \AA}^2/\text{molecule}$ , is smaller than the area required for a single Pc in a closest packed monolayer of these materials. The observed molecular area at this transition suggests the formation of a Pc bilayer of ordered columns, on the subphase surface.

Fully compressed films of CuPcOC<sub>2</sub>OBz and H<sub>2</sub>PcOC<sub>2</sub>OBz are quite rigid and affect the response of the Wilhelmy balance. Reproducibility of pressure–area isotherms on LB troughs of different geometry is dependent on the position, and motion, of the compression barriers and the placement of the Wilhelmy balance.

The AFM image shown in Figure 73 reveals a region of film, labeled B, that has folded back onto itself along the patterned edge. The corrugated texture seen in region A is typical of images in continuous bilayer film regions. Roughness analysis averaged over a  $1 \mu\text{m}^2$  area in this region gave



**Figure 72.** Room temperature pressure–area isotherms (ca. 23 °C): solid line, CuPcOC<sub>2</sub>OBz; dashed line, H<sub>2</sub>PcOC<sub>2</sub>OBz. 1 = two-dimensional liquid–solid condensed phase transition; 2 = monolayer–bilayer phase transition. Inset shows the structure of the octakis(benzyloxyethoxy)-substituted Pcs. Reprinted with permission from [271], P. E. Smolenyak et al., *Langmuir* 13, 6568 (1997). © 1997, American Chemical Society.



**Figure 73.** Tapping mode AFM image of a patterned bilayer film edge and edge defects on an HOPG substrate. Region A corresponds to a single bilayer. Region B shows the bilayer folded back onto itself. Region C is the uncoated HOPG substrate. Feature D appears to be a “buckled” region in the continuous bilayer. Bilayer film thickness calculated from the height data of the boxed areas was ca. 70 Å. Reprinted with permission from [271], P. E. Smolenyak et al., *Langmuir* 13, 6568 (1997). © 1997, American Chemical Society.

a mean of 13.0 Å. Values of 10.0–13.0 Å were typical for film regions away from defect sites. The feature labeled D in Figure 73 appears to correspond to a “buckled” region in the continuous bilayer. These features are commonly encountered and are thought to be precursors of fibers that form upon collapse of the on-trough film bilayer [129]. A film thickness of ca. 76 Å relative to the graphite surface, labeled C, was determined for the pattern edge shown in the lower left boxed region of the image. The upper right boxed region shows the contact between regions A and B, where a step edge of ca. 80 Å was determined. Step heights of 55–75 Å relative to the graphite surface were typical for the edge sites of these patterned films. X-ray scattering measurements of collapsed LB films of this material indicate an intercolumnar distance of 28 Å. Small-angle X-ray data for multilayer horizontally CuPcOC<sub>2</sub>OBz films transferred to Si(100) indicate a monolayer repeat distance of 24 Å. Using this value, a thickness of ca. 50–60 Å is expected for a closest packed single bilayer film in intimate contact with the graphite surface.

The extraordinary stability of these compressed films is thought to be due to the terminal benzyl functionality on the peripheral substituents of the CuPcOC<sub>2</sub>OBz and H<sub>2</sub>PcOC<sub>2</sub>OBz molecules. Interaction of the Pc macrocycle electrons is the principal director of order in these systems, while the benzyl functionality introduces an additional opportunity for interaction not previously observed in peripherally substituted Pc systems. Cofacial columnar aggregation of the macrocycles in liquid crystalline Pcs is well known, but only few materials are sufficiently stable to allow for mechanical on-trough patterning [286–288]. The terminal benzyl functionality could contribute to the

extraordinary stability in the *x, y* plane of these thin films, through intra- and intercolumnar arene–arene interaction.

The degree of order and stiffness in these thin films, as aligned on the LB trough, and as transferred by the horizontal dipping method, leads to a strongly dichroic material, one that sustains its mechanical properties even as a single bilayer thin film. X-ray scattering analysis of LB films of this material suggests that the Pc rings are packed closer together than would be expected without interdigitation of the side chains, by ca. 4 Å. A column-to-column distance of ca. 24 Å is consistent with the partial overlap of the terminal benzene rings.

#### 4.8. Application of Pc LB Films

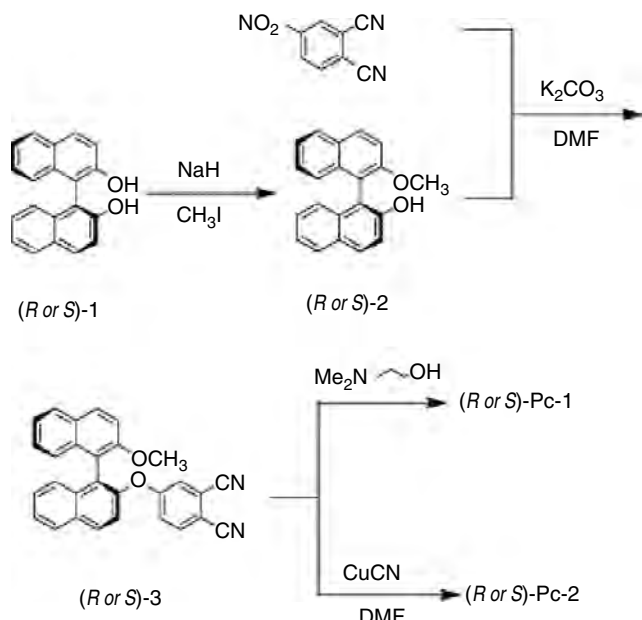
Three substituted phthalocyanines, two asymmetrical and one symmetrical, named amino-tri-*tert*-butyl-phthalocyanines (AmBuPc), 1,8-naphthalimide-tri-*tert*-butyl-phthalocyanine (NaBuPc), and tetra-*iso*-propoxy-phthalocyaninato copper(II) (*i*-Pro-CuPc), were used as semiconductor layers in OFETs based on their LB films [289]. These substituted Pcs possess good solubility in common organic solvents. From the long-wavelength absorption edge of their UV-vis absorption spectra and their electrochemical data, the highest occupied molecular orbital and the lowest unoccupied molecular orbital were determined and the energy band diagram of their OFETs was deduced. The narrower energy gaps of them indicated stronger electron donor–acceptor ability than other symmetrical Pcs because of the substituents at the peripheral ring. The results of their OFETs demonstrated that the LB films of these substituted Pcs can be used as semiconducting layers of OFETs functioning as *p*-channel accumulation devices. From the electrical characteristics of their OFETs, the channel carrier mobilities of AmBuPc, NaBuPc, and *i*-Pro-CuPc were calculated to be about  $2.84 \times 10^{-5}$ ,  $4.42 \times 10^{-4}$ , and  $3.25 \times 10^{-4}$  cm<sup>2</sup> V<sup>-1</sup> s<sup>-1</sup>, respectively.

Optical SHG from films of phthalocyanine derivative deposited on metal (aluminum) and glass substrate has been investigated [290]. In spite of the existence of the inversion center, for both Al and glass substrates, the bulk characteristic of the SHG was confirmed by the thickness dependence of the SH intensity. Drastic enhancement of the signal intensity for Pc/Al sample was also observed.

The optically active phthalocyanines substituted with chiral 2'-methoxy-1,1'-binaphthoxyl were synthesized according to Figure 74 [291].

The metal-free and metal phthalocyanines modified with optically active binaphthyl can form stable monolayers at the air–water interface. In these layers, the phthalocyanines planes are stacked in an edge-on arrangement.

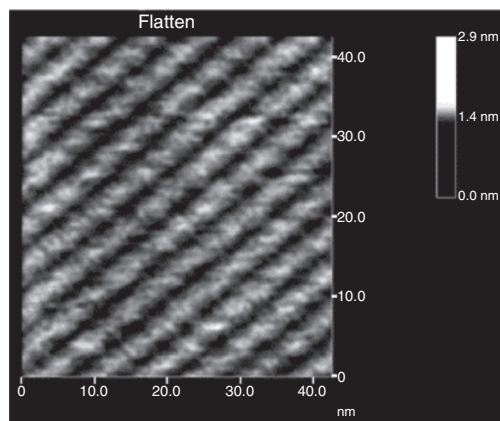
Figure 75 shows an AFM image of the nine-layer LB film of (*R*)-Pc-2 after vertical transfer to a mica substrate at 20 mN m<sup>-1</sup>. This higher resolution image provides evidence for the long-range highly ordered striped arrangement of the molecules of (*R*)-Pc-2 in the surface layer. The AFM image depicts that most of molecules are stacked in an edge-on arrangement, which is consistent with the result that the Q-band is broad and blueshifted to 640 nm for (*R*)-Pc-2 in the UV-vis spectra. In addition, the striations



**Figure 74.** The synthesis of the optically active (R or S)-Pc. Reprinted with permission from [291], H. Liu et al., *Synthetic Metals* 131, 135 (2002). © 2002, Elsevier Science.

in the AFM image show a strong tendency to form helical strips as a result of the substitution groups of chiral 2'-methoxy-1, 1'-binaphthoxyl of neighboring molecules partially offset from each other. On the other hand, Figure 75 also provides an image of individual molecules which are parallel to the surface with a diameter of  $2.52 \pm 0.2$  nm, which is in agreement with the calculation by molecular modeling.

Pcs are electron donating molecules and they undergo charge transfer interactions with electron acceptor gases (such as NO<sub>2</sub>). This produces partially charged species which must interact with their surroundings in order to become stable. A possible model which describes the mechanisms of gas sensing suggest that uniform films are preferable in gas sensing. To date, the most extensively studied Pcs with respect



**Figure 75.** AFM images of a nine-layer LB film of (R)-Pc-2. Reprinted with permission from [291], H. Liu et al., *Synthetic Metals* 131, 135 (2002). © 2002, Elsevier Science.

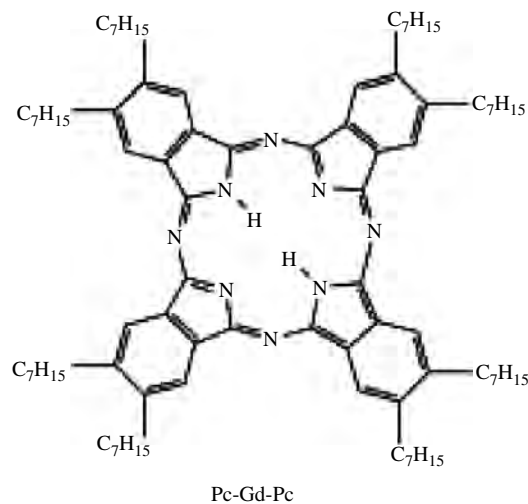
to gas sensing applications are CuPcs and PbPcs although other metals including Ni and Zn have also been studied [292]. A range of deposition techniques, such as evaporation, laser vacuum sublimation, and the LB technique, have also been reported in the literature using these compounds.

Conductometric gas sensing with devices fabricated by ultrafast LB deposition using a gadolinium bis-phthalocyanine [Gd(Pc)<sub>2</sub>] are shown in Figure 76 [292a].

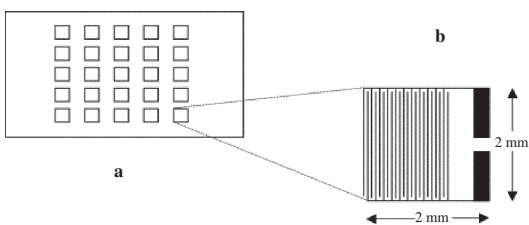
The devices fabricated for these experiments consisted of a Gd(Pc)<sub>2</sub> LB film on gold interdigitated electrodes. The interdigitated electrodes consisted of 25 pairs of  $2 \times 2$  mm<sup>2</sup> gold (on chrome) electrodes mounted on glass (Fig. 77). The fingers on each device were 10 μm in diameter and separated by 25 μm gaps.

Figure 78 shows the surface topography of the film on two different scan sizes ( $100 \times 100$  μm and  $5 \times 5$  μm). In particular, Figure 78a reports an image of the morphology of the LB layers deposited onto interdigitated electrodes. Figure 78b and c reports the morphology of the sample on the gold finger and between the finger respectively. The film surface appears quite rough with a rms roughness value of  $(21 \pm 2.5)$  nm. Large grains with a diameter ranging between 0.5 and 1.0 μm and height 10–100 nm have been revealed on different regions of the surface. Although Figure 78 shows surface roughness and nonuniformity in the nanoscale, in the macroscale a layer by layer repeatability becomes evident. The change in optical absorbance of the sample as a function of the number of excursions of the dipping arm [i.e., layers of Gd(Pc)<sub>2</sub>] was increased. Figure 79 shows the magnitude of the response to NO<sub>2</sub> at concentrations ranging from 0.25 to 1.0 ppm. Both the speed and the magnitude of the response are shown to be concentration dependent. From the initial value of  $\sim 0.14$  μA, the current rises sharply upon exposure to NO<sub>2</sub> and then stabilizes as the device approaches equilibrium. Surface adsorption is responsible for the initial fast response and diffusion effects for the slower process.

The feasibility of using thin films, either LB or evaporated films of lanthanide bisphthalocyanines for the detection of



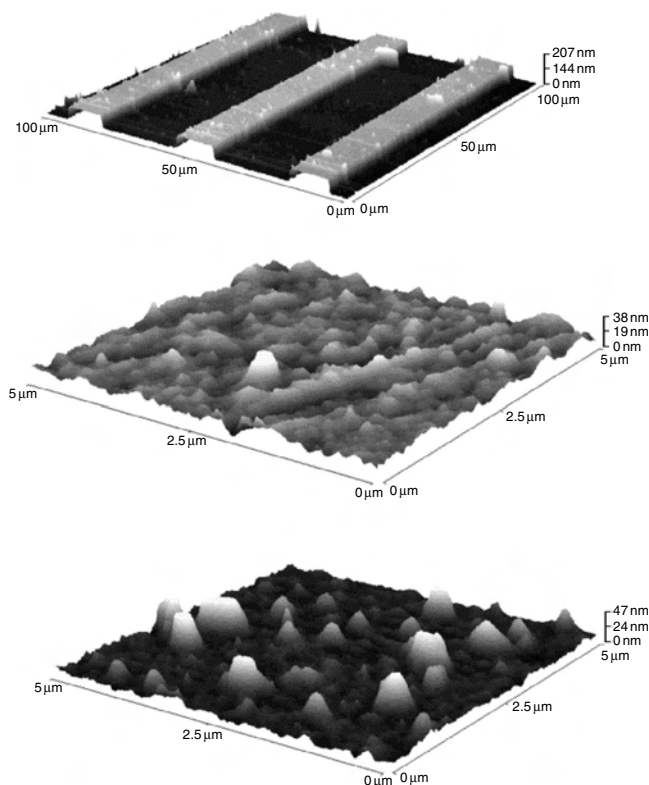
**Figure 76.** Chemical structure of Gd(Pc)<sub>2</sub>. Reprinted with permission from [292a], C. M. Dooling et al., *Colloids Surfaces A* 198, 791 (2002). © 2002, Elsevier Science.



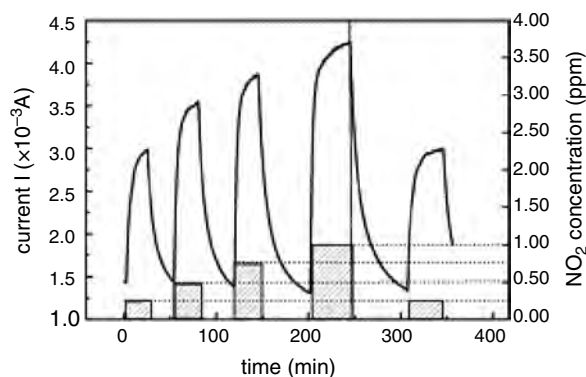
**Figure 77.** (a) A  $5 \times 5$  array of gold on chrome interdigitated electrodes. (b) Close up view of single pair of electrodes. Reprinted with permission from [292a], C. M. Dooling et al., *Colloids Surfaces A* 198, 791 (2002). © 2002, Elsevier Science.

volatile organic compounds (VOCs) such as alcohols, aldehydes, esters, and acids, has been demonstrated [293].

Several examples in the literature demonstrate the success of using arrays of sensors formed by metal oxide semiconductors or conducting polymers coupled with pattern recognition techniques for the detection of food and beverage odors [294]. Sensor arrays formed by conducting polymers able to discriminate among olive oils with well-defined organoleptic characteristics have been described [295]. Similarly a sensor array based on Langmuir–Blodgett bisphthalocyanines films including unsubstituted bisphthalocyanines with different central metal atom ( $\text{PrPc}_2$  and  $\text{LuPc}_2$ ) and an octatertbutyl substituted bisphthalocyanine



**Figure 78.** Atomic force microscope image of 20 layer  $\text{Gd}(\text{Pc})_2$  LB film: (a)  $100 \times 100 \mu\text{m}$  resolution, (b)  $5 \times 5 \mu\text{m}$  resolution on gold finger, (c)  $5 \times 5 \mu\text{m}$  resolution between the fingers. Reprinted with permission from [292a], C. M. Dooling et al., *Colloids Surfaces A* 198, 791 (2002). © 2002, Elsevier Science.

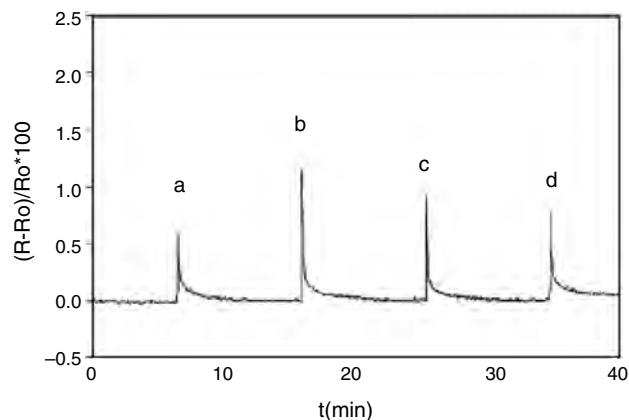


**Figure 79.** Current versus time of 20 layer  $\text{Gd}(\text{Pc})_2$  LB film for exposure and recovery cycles at varied gas concentrations. Reprinted with permission from [292a], C. M. Dooling et al., *Colloids Surfaces A* 198, 791 (2002). © 2002, Elsevier Science.

( $\text{PrPc}'_2$ ) has been designed aiming to discriminate among diverse virgin olive oils [296].

Langmuir–Blodgett films of  $\text{LuPc}_2$ ,  $\text{PrPc}_2$ , and  $\text{PrPc}'_2$  have been deposited onto glass substrates covered with ITO microelectrodes. The high conductivity of the  $\text{LnPc}_2$  allows one to obtain films with measurable resistances even if only 5 monolayers are deposited onto electrodes with a spacing of  $75 \mu\text{m}$ . The resistance increases during the first days after the preparation, due to drying processes, and after 10–15 days, a plateau is reached and the sensors are stable [293].

The response of  $\text{LnPc}_2$ -based sensors toward the headspace of olive oil samples is illustrated in Figure 80 for  $\text{LuPc}_2$ . The exposure of the LB films to the olive oil aroma causes a fast increase of the resistivity of the films [expressed as the fractional change of resistance  $(\Delta R/R) \times 100$ ]. The change is reversible and the baseline is reached after a few seconds. As observed in the figure, the sensors show a degree of selectivity toward the different classes of olive oils. The intensity of the response produced by the lampante olive oil



**Figure 80.** Typical response of a  $\text{LuPc}_2$  LB film expressed as the fractional change in resistance  $(\Delta R/R) \times 100$  toward: (a) refined olive oil, (b) lampante olive oil, (c) extra virgin olive oil, and (d) ordinary olive oil. Reprinted with permission from [296], N. Gutierrez et al., *Sens. Actuators B* 77, 437 (2001). © 2001, Elsevier Science.

was higher than that observed for the ordinary, the extra virgin, and the refined olive oils.

Sensors generated from different bisphthalocyanines show different sensitivities toward the headspace of the olive oil. Besides the differences in the intensity of the responses, the unsubstituted bisphthalocyanines PrPc<sub>2</sub> and LuPc<sub>2</sub> showed a similar pattern of responses and follow the previously described trend, lampante > extravirgin > ordinary > refined. In contrast, the sensors based on the tertbutyl substituted PrPc<sub>2</sub> show a different pattern of response. In this case, the change in conductivity provoked by the headspace of the ordinary olive oil is bigger than the variation produced by the extra virgin olive oil. This behavior can be related to the electron donor character of the tertbutyl groups, which can affect the redox process between the volatile components and the sensitive material. The difference can also be related to the different structure of the monolayer due to the presence of the tertbutyl groups that can affect the mobility of the charge carriers.

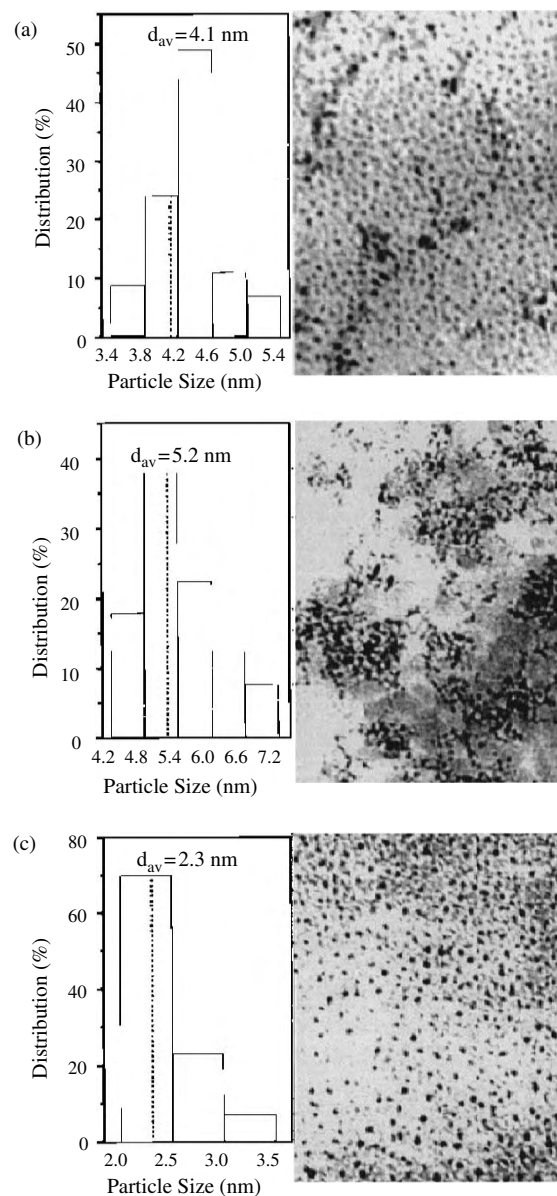
## 5. PHTHALOCYANINE NANOCOMPOSITES AND HYBRID MATERIALS

Complex films composed of nanoscopic particles of Pcs with nanostructured materials have been successfully prepared by coating the mixture of nanostructured materials with Pcs on glass substrates [297–301].

A “ship-in-a-bottle” synthesis where encapsulation of copper phthalocyanines into mesoporous channels of silicate MCM-41 was achieved by chemical vapor deposition (CVD) using 1,2-dicyanobenzene (DCNB) [297]. Silanol protons of MCM-41 were ion-exchanged with copper ions before CVD, and when the initial amount of DCNB was much larger than that of copper ions, CuPc molecules in the channels were found to form a cofacial structure that was confirmed by diffuse reflectance spectra.

Complex films composed of nanoscopic particles of phthalocyanine and titanium dioxide have been prepared by coating the mixed colloids of titanium dioxide and phthalocyanine on glass substrates [298]. Nanoscopic colloids of TiO<sub>2</sub> were prepared by hydrolyzing titanium isopropoxide [299]. Nanoscopic phthalocyanine colloids were synthesized by adding a solution of Pc (H<sub>2</sub>Pc or VOPc) dissolved in concentrated H<sub>2</sub>SO<sub>4</sub> to the aqueous solution of a surfactant [C<sub>16</sub>H<sub>33</sub>N(CH<sub>3</sub>)<sub>3</sub>Br] to give a transparent blue colloidal solution. The obtained colloidal solution was then washed to neutral pH with water by using an ultrafilter. A colloidal mixture of titanium dioxide/phthalocyanine solution was prepared by mixing the TiO<sub>2</sub> colloid with the H<sub>2</sub>Pc colloid.

The mixed colloidal solution was transparent indicating that the dispersion of nanoparticles is in nanoscale. The colloidal mixture could be coated on a glass by the spin coating technique and the resultant film was dried to give transparent titanium dioxide/phthalocyanine complex films. Figure 81 shows the TEM photographs and particle size distributions of the TiO<sub>2</sub>, H<sub>2</sub>Pc, and VOPc colloids. The particle sizes of TiO<sub>2</sub> (3.4–5.4 nm;  $d_{av} = 4.1$  nm) are a little larger than those of VOPc (2.0–3.5 nm;  $d_{av} = 2.3$  nm) and similar to those of H<sub>2</sub>Pc (4.2–7.2 nm;  $d_{av} = 5.1$  nm). The

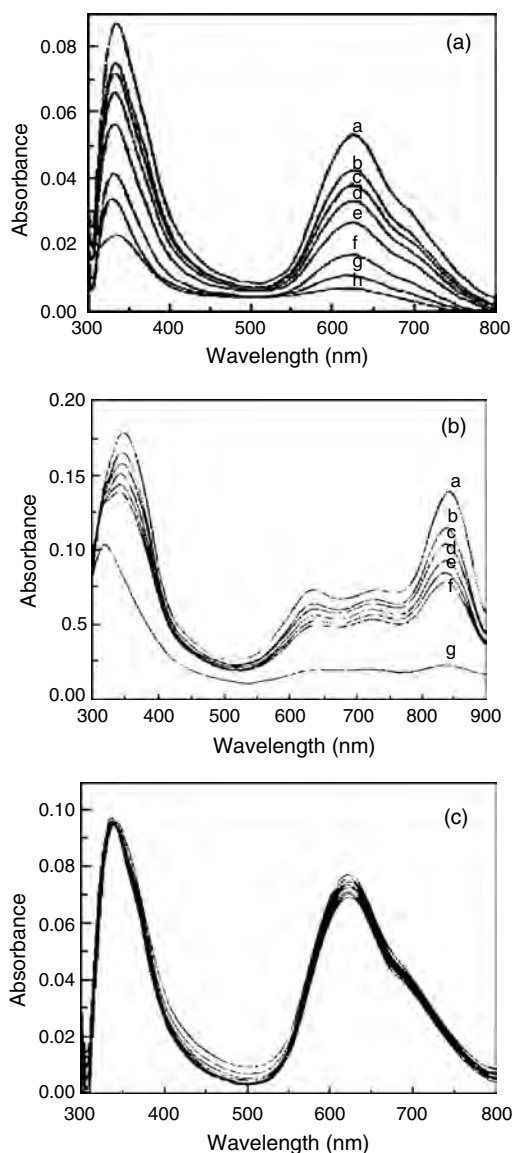


**Figure 81.** TEM micrographs of colloids: (a) TiO<sub>2</sub>, (b) H<sub>2</sub>Pc, (c) VOPc. Reprinted with permission from [298], W. Liu et al., *Langmuir* 15, 2130 (1999). © 1999, American Chemical Society.

particles in the TiO<sub>2</sub> colloid and the VOPc colloid are well separated from each other without heavy aggregation. The first particles of H<sub>2</sub>Pc can be clearly observed although there are some aggregates that may be formed during the desiccation process of TEM samples. This suggests that the dispersability of the H<sub>2</sub>Pc particles is poorer than that of metal phthalocyanine (such as VOPc) particles.

The obtained transparent blue complex films are bleached when illuminated with UV light due to the UV-light-induced catalysis of the titanium dioxide particles for the oxidizing decomposition of phthalocyanine. These nanoscopic materials are important for UV-light-induced decoloration of a new kind of UV-light recording material that is a complex film composed of nanoscopic particles of titanium dioxide and phthalocyanine.

Figure 82a–c shows the UV-vis spectra of the VOPc/TiO<sub>2</sub>, H<sub>2</sub>Pc/TiO<sub>2</sub>, and H<sub>2</sub>Pc/PVA complex films, respectively, which are illuminated and measured under the same conditions. The complex films of VOPc/TiO<sub>2</sub> and H<sub>2</sub>Pc/TiO<sub>2</sub> are obviously bleached after being illuminated by the UV light; however, the spectra of the H<sub>2</sub>Pc/PVA film did not change significantly. This clearly shows the light-induced catalytic activity of the TiO<sub>2</sub> particles in the complex films. Further evidence for the light-induced catalytic decomposition process is that the complex film decolorized very slowly when covered by a piece of quartz glass having a coating film of TiO<sub>2</sub> on it, while the complex film covered by quartz glass



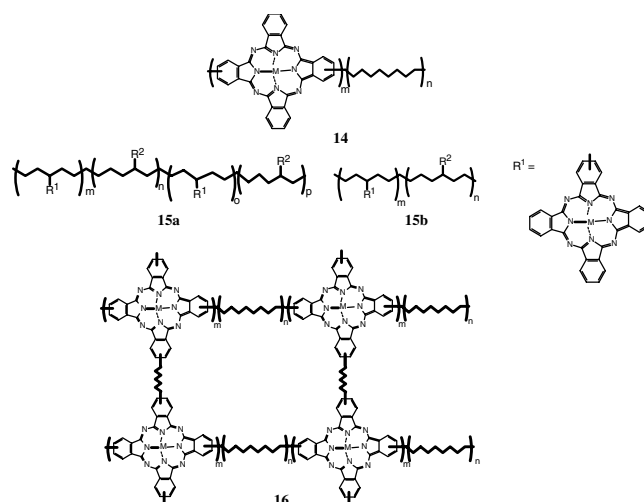
**Figure 82.** UV-vis spectra of TiO<sub>2</sub>/phthalocyanine complex films. (a) TiO<sub>2</sub>/H<sub>2</sub>Pc: a, before illumination; b–e, each after additional 10 min of illumination; f–h, each after additional 20 min of illumination. (b) TiO<sub>2</sub>/VOPc: a, before illumination; b–f, each after additional 10 min of illumination; g, after additional 120 min of illumination. (c) PVA/H<sub>2</sub>Pc, measured under the same conditions of (a) VOPc. Reprinted with permission from [298], W. Liu et al., *Langmuir* 15, 2130 (1999). © 1999, American Chemical Society.

itself decolorized just as the quartz glass did not exist. These results prove that the light in the UV region (about 280 nm) absorbed by TiO<sub>2</sub> leads to the light-induced decoloration of the film.

Since the dispersion is in nanoscale, the titanium dioxide/phthalocyanine film has high transparency, which is requisite for optical device application. Similarly, a phthalocyanine-sensitized nanostructure was reported [300]. In this example, phthalocyanine substituted with ester groups was anchored onto nanostructured TiO<sub>2</sub> films. Thus TiO<sub>2</sub> film is pre-treated with (CH<sub>3</sub>)<sub>3</sub>COLi to change the surface hydroxyl groups (-OH) into oxygen anions (-O<sup>-</sup>), to allow the surface to be more reactive toward the ester functionalities of the dye. The dye can then be anchored onto the semiconductor surface through the produced carboxylate group(s). The amount of anchored dye on the semiconductor shows a dependence on both the time of base treatment and the time of dye treatment. Electrodes treated with the free base phthalocyanine and zinc Pc were characterized by absorption spectroscopy, photocurrent action spectroscopy, and photocurrent–photovoltage measurements. The homogeneous blue–green color and the absorption bands in the far-red region are indicative of an attachment of the dye on TiO<sub>2</sub> film. A monochromatic incident photo-to-current conversion efficiency of 4.3% was achieved at 690 nm for a cell where the base-treated electrode was treated with ZnPcBu.

## 6. PHTHALOCYANINE POLYMERS

Covalently bound phthalocyanine nanostructures are constructed by polymerization. The type of Pc polymers are (1) linear polymer (**14–15**) including block or random copolymer and comblike side chain, (2) ladder (network) type (**16**), and (3) cofacial one-dimensional type (**17**) (Figs. 83 and 84). As described in the previous section, many examples of ordered stacks, produced through only noncovalent bonds, are known. These stack structures have low kinetic stability. Therefore, the covalent linkage of side chains needs to be enhanced to increase the stability of ordered stacks. Only a few examples of such polymeric Pc materials are known to date [302, 303].



**Figure 83.** Linear and network type of polymeric phthalocyanines.

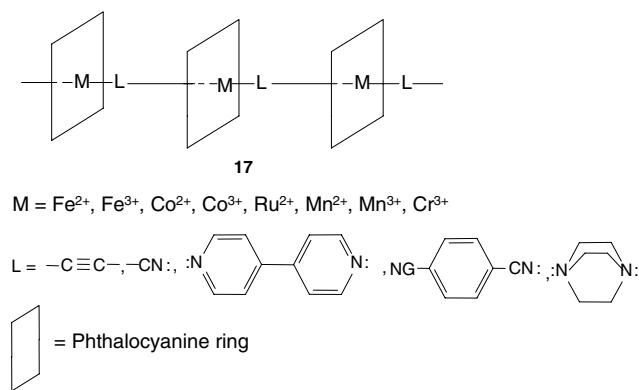


Figure 84. Cofacial 1-D type of polymeric phthalocyanines.

### 6.1. Synthesis of Soluble Phthalocyanine Polymers

Network type phthalocyanine polymers are synthesized from tetramerization of dianhydride and urea as has been well documented [1, 11, 304]. These polymers are usually insoluble and thus structures of them are not well characterized. In order to increase solubility a solubilizing group was introduced into the network polymer as a spacer, or a linear type of phthalocyanine polymers has been synthesized by using a mixture of dianhydride (for the construction of Pc ring) and monoanhydride (for linearity).

Soluble phthalocyanine polymers were prepared from tetramerization of hexafluoroisopropylidene-benzenetetracarboxylic acid dianhydride and urea in the presence of Ti(OBu)<sub>4</sub> and (NH<sub>4</sub>)<sub>2</sub>MoO<sub>4</sub> [305]. Modification of end groups and bridging groups between the phthalocyanine rings of the polymer has allowed development of soluble phthalocyanine polymers. A general scheme for the synthesis of poly(titanyloxo-phthalocyanines), PTiOPc, is summarized in Figure 85. The resultant polymer was deep blue-green in color with a metallic glint and soluble in DMF. It was noteworthy that PTiOPc with carboxylic acid end groups (**19**) showed higher solubility in DMF than the imide type. Polymers with imide end groups (**18**) were stable up to ~350 °C

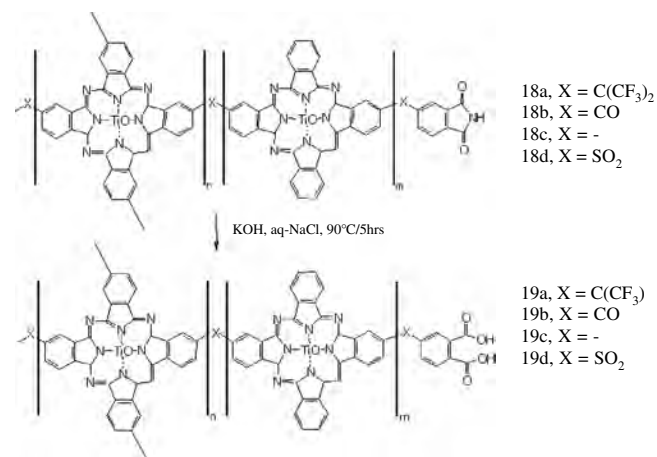


Figure 85. General scheme for the synthesis of poly(titanyloxo-phthalocyanines). Reprinted with permission from [305c], D. S. Han et al., *Synthetic Metals* 101, 62 (1999). © 1999, Elsevier Science.

and temperatures for 10% weight loss ( $T_{10}$ ) were 386, 454, 386, and 458 °C for **18a**, **18b**, **18c**, and **18d**, respectively.

Figure 86 shows UV-vis spectra of poly(titanyloxo-phthalocyanines) in DMF solution ( $\sim 1.0 \times 10^{-6}$  M). In dilute chloroform solution, poly(titanyloxo-phthalocyanines) are present mainly as monomers, characterized by the sharp absorption bands in the Soret (350–400 nm) and in the Q-band region (around 680 nm) [306, 307]. For the sample with carbonyl bridged (**18b**), the Q-band is broadening and the maximum shifts slightly to around 670 nm, which is ascribed to the Q-band(s) of the polymer aggregates [304]. The intensity of the Q-band(s) of the polymer was significantly reduced when the bridging group was sulfone (**18d**), possibly due to the insolubility of the polymer **18d** in DMF. However, the absorbance of the sulfone-bridged polymer was much increased after end group modification to carboxylic acid (**19d**) as shown in Figure 86b.

It was noteworthy that PTiOPc with carboxylic acid end groups showed higher solubility in DMF than the imide type.

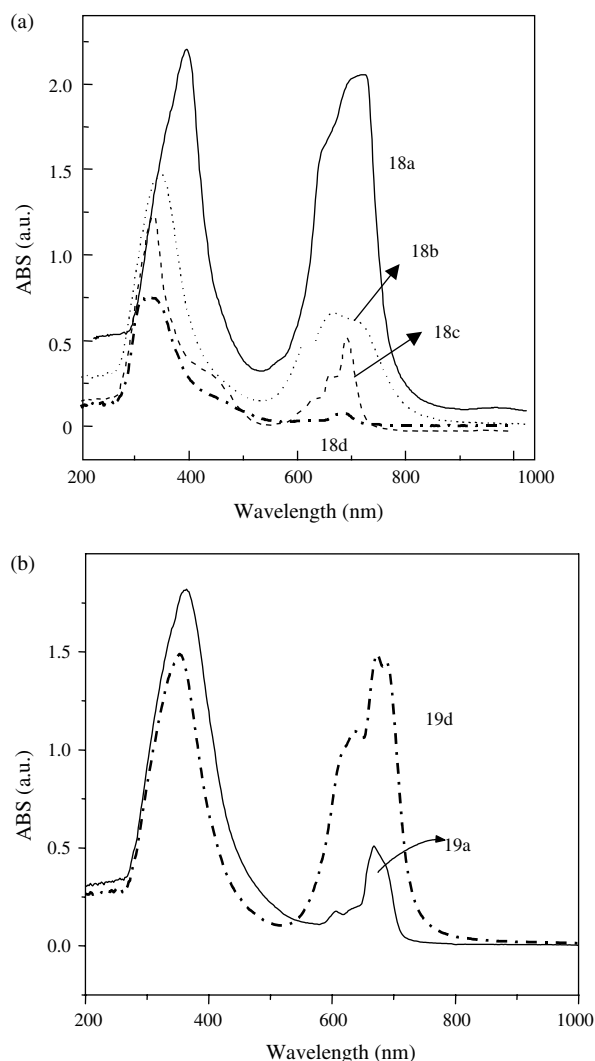


Figure 86. UV-vis spectra of poly(titanyloxo-phthalocyanines) in DMF solution. (a) Imide end group. (b) Carboxylic acid end group. Reprinted with permission from [305c], D. S. Han et al., *Synthetic Metals* 101, 62 (1999). © 1999, Elsevier Science.

The surface of the film prepared by the spin coating method showed a homogeneous surface with an average pore size of less than 0.2  $\mu\text{m}$ .

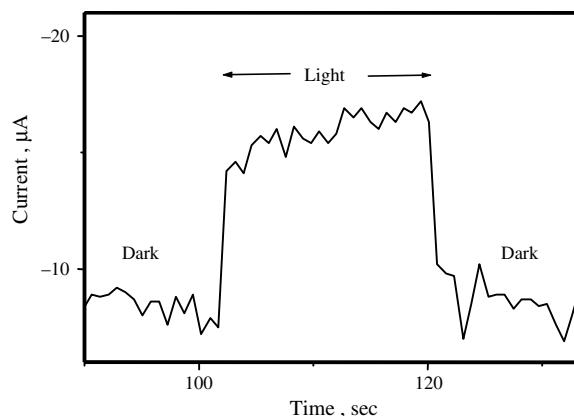
The soluble phthalocyanine polymers could be processed to a thin film without binder by the spin coating method. The resultant film was transparent, indicating that the aggregation of Pc polymer is much reduced and the dispersion of Pc is in nanoscale.

Irradiation of the films of poly(titanyl-oxo-phthalocyanines) under the potential of 0.6 V (vs Ag/Ag/Cl) resulted in photocurrent generation. Figure 87 shows photoamperometric measurement of an ITO glass coated with **18b** prepared by the solution coating method.

As potential was stepped from  $-0.2$  to 0.6 V, current pulse was decayed under dark. Photocurrent was generated when the electrode was irradiated and the anodic current was decayed in the dark. The photocurrent generation was repetitive by a light and dark switching under a potential of 0.6 V. Such current generation can be ascribed to a redox process of hydroquinone and quinone [304], which can quench the photogenerated hole carrier from PTiOPc film. Relative efficiency ( $\eta_{\text{rel}}$ ) was defined as the ratio of photocurrent of the polymer film ( $i_p$ ) and that of TiOPc ( $i_r$ ):  $\eta_{\text{rel}} = i_p/i_r$ , and  $i_T$  were determined as  $i_p$  (or  $i_T$ ) =  $i/(Al)$ , where  $I$ ,  $A$ , and  $l$  are observed photocurrent, area, and thickness of the film (cm), respectively. Thus  $\eta_{\text{rel}}$  reflects relative charge carrier generation efficiency of PTiOPc. The current intensity was linearly dependent on the film thickness up to 1.5  $\mu\text{m}$ .

Table 1 summarizes the photocurrent generation for different poly(titanyl-oxo-phthalocyanines). Films of PTiOPc showed higher photoconductivity than that of the monomeric  $\alpha$ -type titanium oxophthalocyanine ( $\alpha$ -TiOPc) dispersed in polyvinyl butyral (PVB).

Photocurrent could be affected by the charge generation efficiency of the phthalocyanine chromophores in the polymers and by the charge mobility between the polymer chains. Particularly important are the structure and arrangement of the polymer in film. In the film of **18b**, smaller bridging of C=O induces ordering of polymer chains, resulting in high photocurrent generation. On the other hand, large hexafluoroisopropylidene groups in **18a** favor amorphous irregular structures, resulting in low photocurrent for **18a**. Indeed



**Figure 87.** Photocurrent of an ITO glass coated with **20b** (film thickness of 0.54  $\mu\text{m}$ ). Reprinted with permission from [305c], D. S. Han et al., *Synthetic Metals* 101, 62 (1999). © 1999, Elsevier Science.

**Table 1.** Photocurrent generation of the films of PTiOPc.

Polymer	Thickness ( $\mu\text{m}$ )	$i_{\text{hv}}$ ( $\mu\text{A}/\text{cm}^2$ )	$\eta_{\text{rel}}$
TiOPc	1.05	2.67	1
<b>18a</b>	0.23	1.07	1.8
<b>18b</b>	0.54	10.27	7.5
<b>18c</b>	0.51	2.00	1.5
<b>18d</b>	0.64	5.33	3.3
<b>19a</b>	1.29	2.07	0.6
<b>19b</b>	0.47	4.67	3.9
<b>19c</b>	0.54	2.00	1.5
<b>19d</b>	0.58	2.67	1.8

Note: Film prepared by a milling method using a mixture of  $\alpha$ -TiOPc (40 wt%) and PVB (60 wt%).

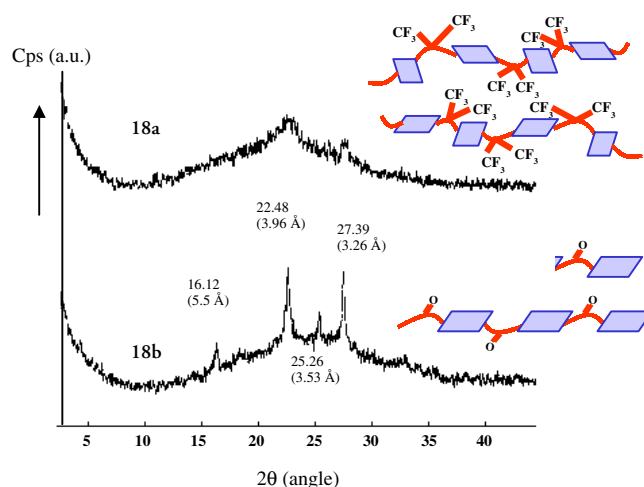
Source: Reprinted with permission from [305c], D. S. Han et al., *Synthetic Metals* 117, 203 (2001). © 2001, Elsevier Science.

XRD of the polymer films indicated higher ordering in **18b** than in **18a** as shown in Figure 88.

## 6.2. Polymeric Pc Nanocomposite

Although the previous soluble phthalocyanine polymers could be used in the preparation of photoconductive film with high optical clarity, the hardness of the film (pencil strength  $<B$ ) and adhesion property on a surface has limited extensive application of PTiOPc, particularly in a process requiring multilayer film preparation. To improve such mechanical properties of PTiOPc phthalocyanine polymer hybrid silica nanocomposite was investigated using a sol-gel process [308].

The fundamental requirement for the sol-gel method is that phthalocyanine molecules must have nanosized particles or dissolve into the solution for the sol-gel process. Otherwise, the film would show bulk phase separation between the macrocycles and the host, impeding effective transfer of photocarrier. To improve photocurrent generation efficiency plus solubility, the end group of the polymer **19** was modified to an alkyl or a polyethylene glycol unit.



**Figure 88.** XRD of PTiOPc film. Reprinted with permission from [305c], D. S. Han et al., *Synthetic Metals* 101, 62 (1999). © 1999, Elsevier Science.

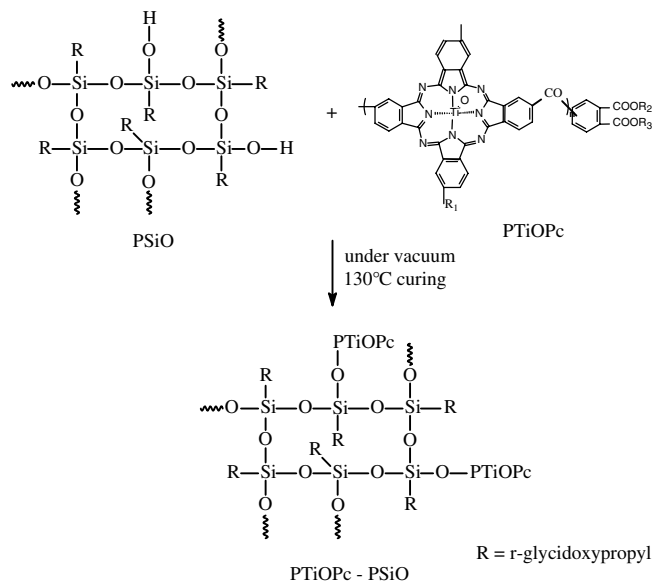


The solution for the silica hybrid film consisted of soluble PTiOPc and a sol solution prepared from the hydrolysis of *r*-glycidoxypropyl-trimethoxysilane and methyl trimethoxysilane. A general scheme for the synthesis of phthalocyanine polymers and silica hybrid film is summarized in Figure 89. Phthalocyanine polymers modified with alkyl group showed higher solubility in organic solvent than the unsubstituted PTiOPc, to allow a sol-gel process. Thin films prepared by using a mixture of phthalocyanine polymer in silica solution showed homogeneous surface morphology. Surface roughness of PTiOPc-silica hybrid film was estimated as lower than 10 nm by an  $\alpha$ -step and scanning electron microscopy (SEM).

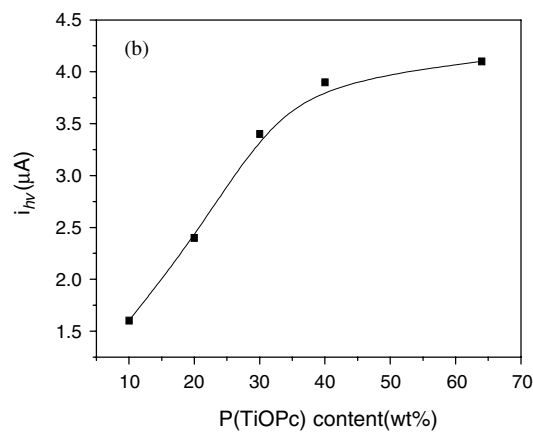
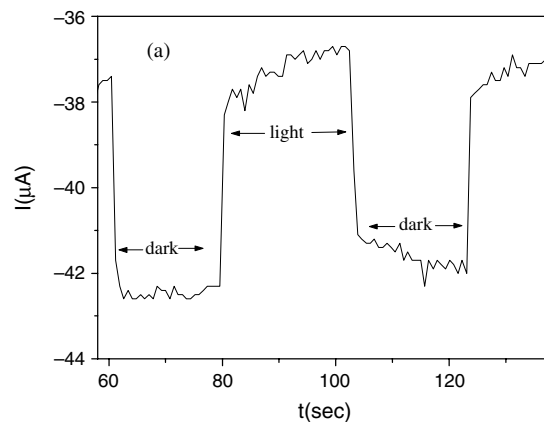
Interestingly, PTiOPc-silica nanocomposite film showed high pencil hardness of 3-H when coated on a glass substrate. Furthermore the film was adherent on a substrate to allow a multilayer coating process. Absorption spectra of the PTiOPc-silica hybrid films were characterized by the appearance of a Q-band at  $\sim 690$  nm similar to that of PTiOPc films. Irradiation of the Q-bands of PTiOPc-PSiO film under the potential of 0.6 V (vs Ag/AgCl) resulted in photocurrent generation. Figure 90a shows chrono-amperometric measurement of an ITO glass coated with PTiOPc-PSiO film.

As potential was stepped from  $-0.2$  to  $0.6$  V, current pulse was decayed under dark. Photocurrent was generated when the electrode was irradiated. The current generation was repetitive by a light/dark switching under the bias potential of  $0.6$  V. Such current generation can be rationalized by a redox process of hydroquinone/quinone [304], which can quench the photogenerated hole carrier from PTiOPc-PSiO film.

As shown in Figure 90b, the photocurrent generation was dependent on the content of PTiOPc up to 40 wt%. Such a photocurrent generation was related to the absorbance of



**Figure 89.** Preparation of phthalocyanine polymers and silica hybrid film  $R_2$  or  $R_3$  = octyl or PEG ( $M_w = 350$ ). Reprinted with permission from [308a], D. S. Han et al., *Synthetic Metals* 117, 203 (2001). © 2001, American Chemical Society.



**Figure 90.** (a) Photocurrent of an ITO glass coated with PTiOPc-silica hybrid. (b) Plot of the photocurrent vs content of PTiOPc (wt%). Reprinted with permission from [308a], D. S. Han et al., *Synthetic Metals* 117, 203 (2001). © 2001, American Chemical Society.

the film, indicating that the photocurrent generation originates from the carrier generation by photoexcited phthalocyanine units. Above 40 wt%, however, the dependence of photocurrent on the content became less important, possibly due to a saturation effect. Interestingly, the photocurrent generation from PTiOPc-silica hybrid was larger than the film of TiOPc doped PVB matrix as compared in Table 2. However, the photocurrent was not much affected by the end groups or substituent on the phthalocyanine ring. This result implies that the octyl or PEGM units do not alter the macroscopic structure for photocarrier generation. The quenching of the carrier by hydroquinone is very fast in a liquid electrolyte system, in which the charge transport is usually diffusion controlled.

Photocurrent generation of phthalocyanine polymer-silica hybrid films in double layered solid cells was determined from an all-solid-type photoconductor, assembled using benzidine, oxadiazole, or butadiene derivatives as CTM. The structure of the solid cell is shown in Figure 91. Irradiation of the solid type cell resulted in photocurrent generation higher than  $10$  nA/cm<sup>2</sup> when potential was stepped from 7 to 10 V. Figure 92 shows chrono-amperometric measurement of a cell structured as PTiOPc-CR ( $R_2, R_3$  = octyl)/PSiO/BT.

Interestingly the current generation from the solid cell was much affected by the CTM as summarized in Table 3.

**Table 2.** Photocurrent of PTiOPc-PSiO hybrid films.

NO	R <sub>1</sub>	R <sub>2</sub> , R <sub>3</sub>	Thickness (μm)	i <sub>hv</sub> (μA/cm <sup>2</sup> )	η <sub>rel</sub>
1	TiOPc <sup>a</sup>		1.1	2.6	1
2	octyl	H	1.2	4.3	1.6
3	octyl	octyl	1.0	4.1	1.5
4	PEGM	H	1.2	4.4	1.7
5	PEGM	PEGM	1.2	4.3	1.6

<sup>a</sup> Monomeric dispersed in PVB (60 wt%).

Note: Film prepared by using a mixture of PTiOPc (40 wt%) in silica matrix (area 1.5 cm<sup>2</sup>).

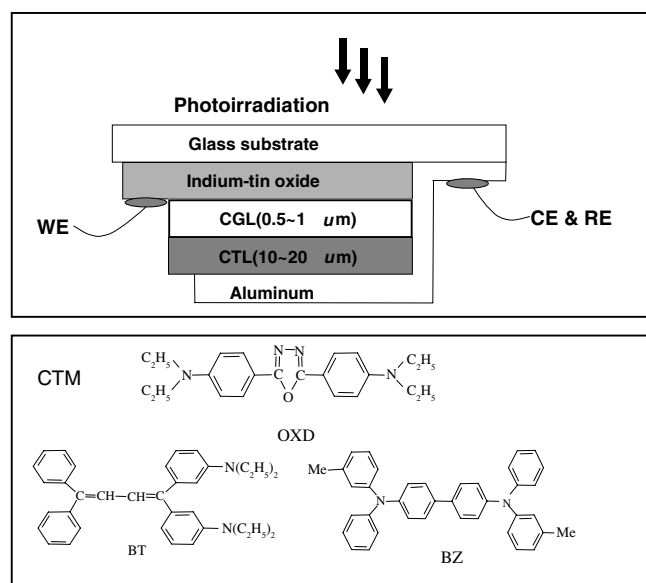
Source: Reprinted with permission from [308a], D. S. Han et al., *Synthetic Metals* 117, 203 (2001). © 2001, Elsevier Science.

Furthermore, the current generation from the solid cell prepared from PEGMe end groups (PTiOPc-CR; R<sub>2</sub>, R<sub>3</sub> = PEGMe) was larger than that from octyl end groups (PTiOPc-CR; R<sub>2</sub>, R<sub>3</sub> = octyl). Such an end group effect on the photocurrent may be attributed to the effective carrier transport by the ethylene oxy group in solid media, since ethylene oxy group could host a hole carrier by an electron donating oxygen center. If so, the hole carrier generated from the PTiOPc unit could be transported through the ethylene oxy group to CTM. Addition to this plasticizing effect by the PEGMe group may have an effect on the photocurrent generation.

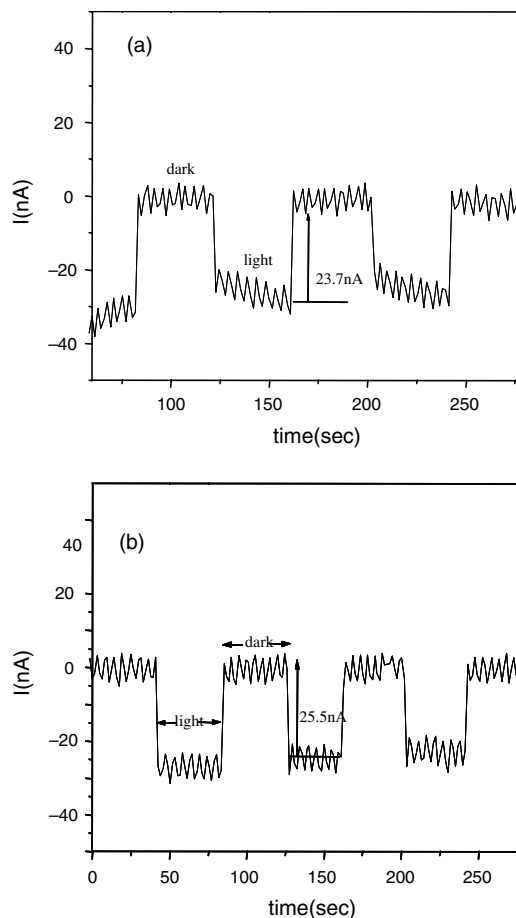
Those two effects are important in a solid medium, in which carrier generation is subjective to the polymer segmental motion and free volume around the carrier.

### 6.3. Phthalocyanine Centered Polymers

One-dimensional polymers of octasubstituted phthalocyanines were synthesized from the tetramerization of a dinitrile phthalocyanine precursor, 4-(2,3,4,5,6-pentaphenylbenzene)phthalonitrile [309], to give β-tetrakis (2,3,4,5,6-pentaphenylbenzene) phthalocyanine (Fig. 93) [309].



**Figure 91.** Structure of a solid photocell (CGM:PTiOPc-CR, CTM:BT, OXD, and BZ).



**Figure 92.** Photocurrent generation from a solid cell prepared from PTiOPc-CR (R<sub>2</sub>, R<sub>3</sub> = PEGMe) in contact to CTL containing (a) BZ and (b) BT.

The polyphenylated Pcs and MPcs exhibit different physical properties, but all maintain similar electronic properties. All the materials synthesized are soluble in common organic solvents such as aromatic and chlorinated hydrocarbons, ethers, and hydrocarbons such as hexane and cyclohexane. The high solubility is outstanding for Pcs and MPcs. The unsubstituted polyphenylated Pc **20a** is crystalline, but Pcs **20b** and **20e** are more amorphous and form films readily from solution.

The ground-state electronic absorption spectra of **20b** and **20d**, in toluene, are shown in Figure 94. The metal-free derivative **20b** shows a split Q-band with λ<sub>max</sub> at 712 nm. This absorption is redshifted ~40 nm compared to unsubstituted Pc. Alkoxy substitution of the pentaphenylbenzene substituent has no additional effect on the λ<sub>max</sub> of the Q-band absorption. As expected, the positions of the Q-band and B-band are influenced by the presence of a metal. The lead derivative **20d** has the farthest redshifted Q-band, placed at 724 nm.

Third-order NLO value (X<sup>(3)</sup>) of Pc **20a** was determined as X<sup>(3)</sup> = 0.52 × 10<sup>-10</sup> esu and ⟨γ⟩ = 6.12 × 10<sup>-32</sup> esu (measured at 1064 nm), which is among the highest X<sup>(3)</sup> values reported for tetrasubstituted Pcs. The X<sup>(3)</sup> is comparable to naphthalocyanines [310]. Such an enhancement in the X<sup>(3)</sup> value is believed to originate from the polyaromatic

**Table 3.** Photocurrent of PTiOPc-CR in solid photocells.

PTiOPc-CR	CTM	$i_{hv}$ (nA/cm <sup>2</sup> )
R <sub>2</sub> ,R <sub>3</sub> = octyl	OXD	9.8
	BZ	10.9
	BT	17.8
R <sub>2</sub> ,R <sub>3</sub> = PEGMe	OXD	12.8
	BZ	23.7
	BT	25.5

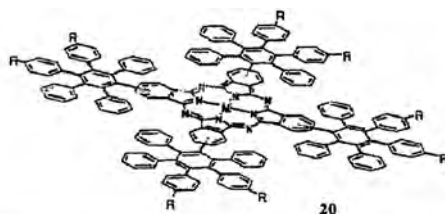
Note: Film prepared by using a mixture of PTiOPc-CR (40 wt%) and PSiO (film area 1.5 cm<sup>2</sup>).

Source: Reprinted with permission from [308a], D. S. Han et al., *Synthetic Metals* 117, 203 (2001). © 2001, Elsevier Science.

substituents on the phthalocyanine core, as evidenced by the redshifted Q-band in the electronic absorption spectrum.

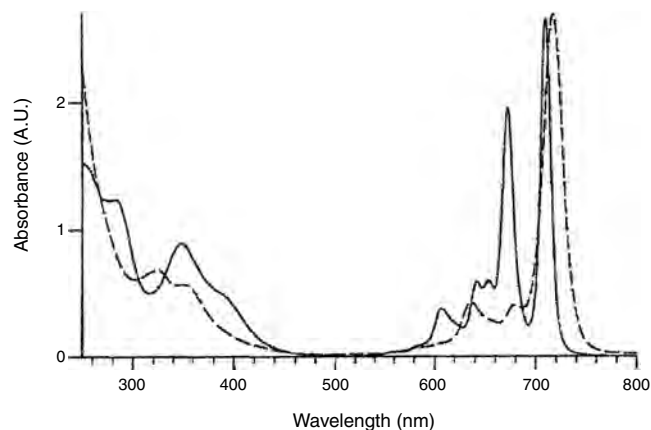
The Pc-centered poly(oxyethylenes) with four to eight side chains were prepared by the synthetic route shown in Figure 95 [311]. Pc-centered poly(oxyethylenes) containing four or eight side chains, with average lengths of 8, 12, and 16 oxyethylene subunits, were prepared from poly(oxyethylene) monomethyl ethers of average molecular masses 350, 550, and 750 Da, respectively.

The Pc-centered poly(oxyethylenes) have interesting properties due to the strong tendency of the Pc cores to self-associate. In particular, the macromolecules containing four polymer side chains **21–23** display columnar lyotropic behavior despite the absence of a stable thermotropic mesophase. Figure 96 shows a photomicrograph ( $\times 100$ , crossed polarizers) of the lyotropic mesophases formed from an aqueous solution of **21** at 50 °C. A concentration gradient was established by evaporation of water from the edge of the slide (left). The columnar nematic mesophase ( $N_c$ ), forming as droplets, lies at the boundary of the isotropic solution (right) and the  $C_H$  mesophase. A dark band of isotropic, dry



compound	R	M	Yield(%)
<b>20a</b>	H	2H	10
<b>20b</b>	-OC <sub>4</sub> H <sub>9</sub>	2H	21
<b>20c</b>	-OC <sub>4</sub> H <sub>9</sub>	Ni	25
<b>20d</b>	-OC <sub>4</sub> H <sub>9</sub>	Pb	27
<b>20e</b>	-OC <sub>12</sub> H <sub>25</sub>	2H	20

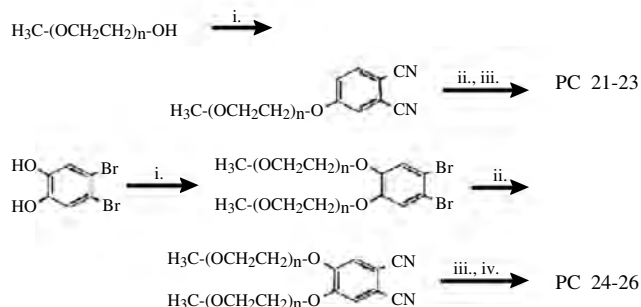
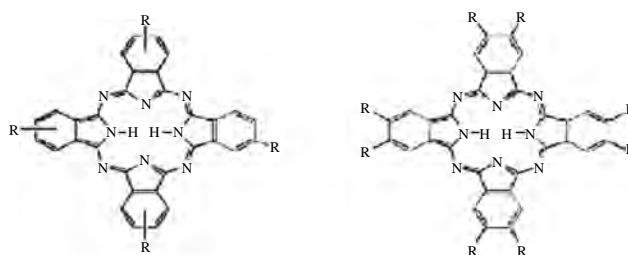
**Figure 93.** Structures of  $\beta$ -tetrakis(2,3,4,5,6-pentaarylbenzene)phthalocyanines, **20a–e**. Redrawn with permission from [309], C. J. Walsh and B. K. Mandal, *Chem. Mater.* 12, 287 (2000). © 2000, American Chemical Society.



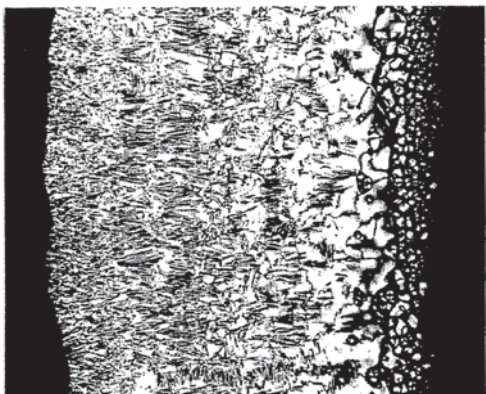
**Figure 94.** The ground-state electronic absorption spectra of **20b** (solid line) and **20d** (dashed line), in toluene. Redrawn with permission from [309], C. J. Walsh and B. K. Mandal, *Chem. Mater.* 12, 287 (2000). © 2000, American Chemical Society.

material has formed between the edge of the slide and the  $C_H$  mesophase.

Only Pc **24** exhibits a pure (i.e., nonbiphasic) thermotropic mesophase and shows a columnar structure with two-dimensional hexagonal ordering of the Pc stacks (as indicated by two small-angle diffraction rings with  $d$ -spacings in the ratio  $1:\sqrt{3}$ ) by X-ray diffraction study. The intercolumnar distance was calculated to be 38.8 Å. A sharp diffraction ring corresponding to a  $d$ -spacing of 3.4 Å is consistent with the strong intracolumnar periodicity associated with the  $D_{ho}$  mesophase commonly encountered in alkoxy-substituted Pcs [312]. In addition, the mixture of homeotropic regions and fanlike optical texture exhibited by the mesophase **24**, observed by polarizing



**Figure 95.** Structure and synthesis of Pc-centered poly(oxyethylenes) with four to eight side chains. Redrawn with permission from [311], G. J. Clarkson et al., *Macromolecules* 29, 1854 (1996). © 1996, American Chemical Society.



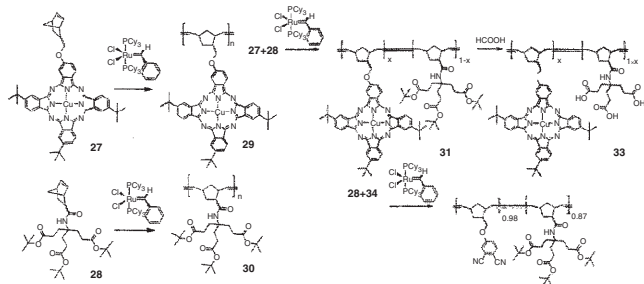
**Figure 96.** Photomicrograph ( $\times 100$ , crossed polarizers) of the lyotropic mesophases formed from an aqueous solution of **21** at  $50^\circ\text{C}$ . A concentration gradient was established by evaporation of water from the edge of the slide (left). The columnar nematic mesophase ( $N_C$ ), forming as droplets, lies at the boundary of the isotropic solution (right) and the  $C_H$  mesophase. A dark band of isotropic, dry material has formed between the edge of the slide and the  $C_H$  mesophase. Redrawn with permission from [311], G. J. Clarkson et al., *Macromolecules* 29, 1854 (1996). © 1996, American Chemical Society.

optical microscopy, is characteristic of a  $D_{ho}$  structure [313]. Pc material containing four uniform side chains has a well-defined thermotropic mesophase stable up to  $170^\circ\text{C}$ , suggesting that the thermotropic columnar mesophase is severely destabilized by the presence of side chains of nonuniform length.

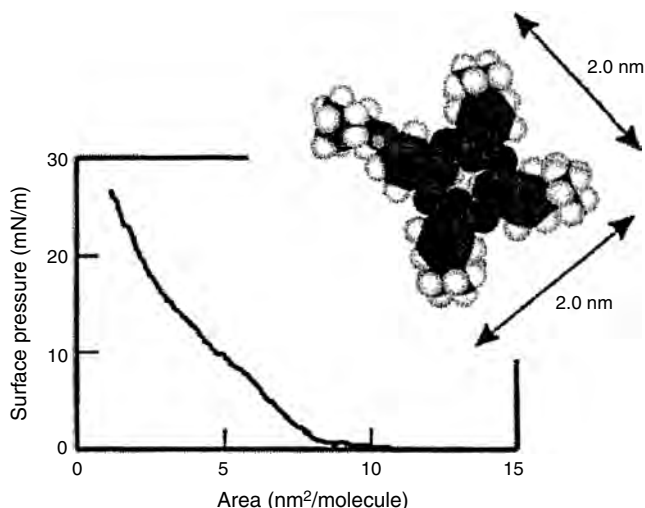
#### 6.4. Poly(norbornenes) Containing Copper Phthalocyanines

Kimura et al., synthesized poly(norbornenes) containing copper phthalocyanines (polymer **29–32**) as a pendant group through a ring-opening metathesis reaction [314]. Figure 97 shows the synthetic scheme of the polymers with the initiator  $(\text{PCy}_3)_2\text{Cl}_2\text{Ru}(=\text{CHC}_6\text{H}_5)$  [315].

The amphiphilic block copolymer **33** was synthesized by the treatment of **31** with formic acid [316]. The amphiphilic character of **33** favors the alignment of the phthalocyanine planes parallel to the water surface, as indicated in Figure 98 which shows the  $\pi$ - $A$  isotherm of **33** on pure water as the subphase. Surface pressure begins to rise at a molecular area of ca.  $10\text{ nm}^2$ , and the pressure is slowly increased up to



**Figure 97.** Synthetic scheme of poly(norbornenes) containing copper phthalocyanines. Redrawn with permission from [314], M. Kimura et al., *Langmuir* 18, 7683 (2002). © 2002, American Chemical Society.



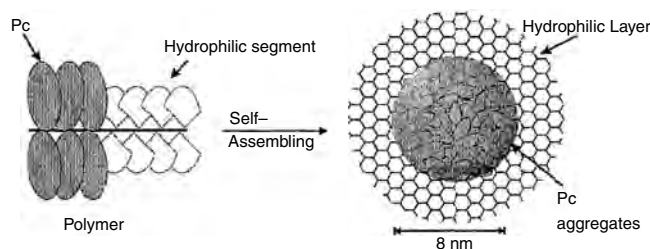
**Figure 98.** Surface pressure vs area per molecule isotherms for **33** on triply distilled water at  $25^\circ\text{C}$ . Redrawn with permission from [314], M. Kimura et al., *Langmuir* 18, 7683 (2002). © 2002, American Chemical Society.

$25\text{ mN/m}$  on further compression. The limiting molecular area per molecule of **33** is estimated as ca.  $8\text{ nm}^2$  which is nearly twice the molecular dimension of the phthalocyanine plane ( $3.9\text{ nm}^2$ ) estimated by the Corey–Pauling–Koltun molecular model (Fig. 99).

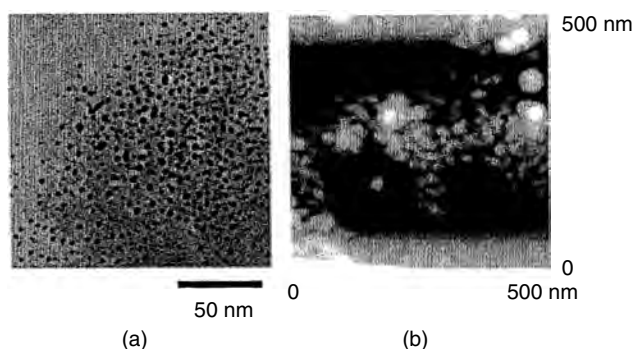
The amphiphilic diblock copolymer **33** showed spherical objects with a diameter of approximately  $8\text{ nm}$  in a TEM image (Fig. 100a), in which the dark image is ascribed to highly concentrated phthalocyanine moieties. Similarly AFM images also show many particles with an average size of  $14.0\text{ nm}$  (Fig. 100b). These results support that the amphiphilic diblock copolymer **33** self-organized in aqueous media to produce micellar aggregates by segregation between a hydrophobic polymeric phthalocyanine segment and a hydrophilic ionized segment, as shown in Figure 99.

#### 6.5. Poly(phthalocyanine-co-sebacic anhydride)

Phthalocyanine-containing biodegradable copolymers, poly(phthalocyanine-co-sebacic anhydride) (Pc-SA), have been synthesized [317]. The synthetic scheme is summarized in Figure 101.



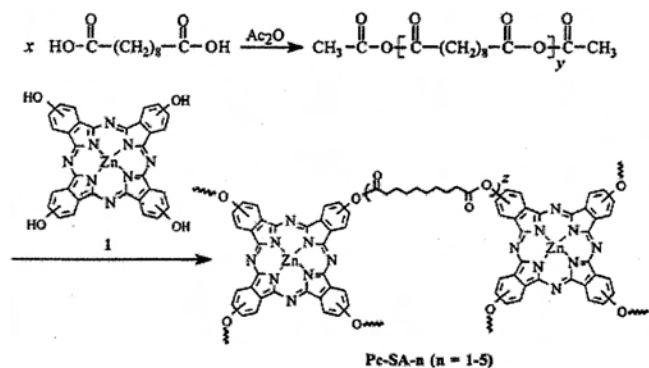
**Figure 99.** Schematic illustration of the spherical organization of **33** in an alkaline aqueous solution. Redrawn with permission from [314], M. Kimura et al., *Langmuir* 18, 7683 (2002). © 2002, American Chemical Society.



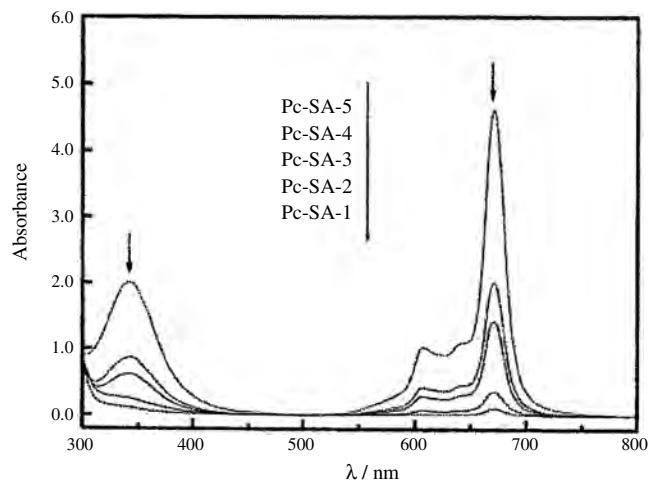
**Figure 100.** (a) Transmission electron micrograph of spherical organizations made of **33**. (b) Atomic force microscopic image of an assembly of **33** on mica. As the coordinate out of the plane of the page increases to its maximum, 7.8 nm, the shade becomes lighter. Reprinted with permission from [314], M. Kimura et al., *Langmuir* 18, 7683 (2002). © 2002, American Chemical Society.

Nanoparticles with an average hydrodynamic radius of 166 nm have been prepared from the copolymer Pc-SA-5, which has a Pc to sebacic acid molar ratio of 0.01, via a microphase inversion method. The collapse of polymer chains in the formation of Pc-SA-5 nanoparticles leads to aggregation of the Pc rings inside. The aggregation tendency decreases upon degradation of the nanoparticles in alkaline media, giving ultimately monomeric species. The degradation kinetics of Pc-SA-5 nanoparticles have been investigated by a combination of static and dynamic laser light scattering. It has been found that the rate of degradation increases with the pH and temperature. By using absorption and fluorescence spectroscopies, the release of Pc can be monitored, which occurs almost simultaneously with the degradation. The results suggest that this novel polymer-based colloidal system is potentially useful for the delivery and release of photosensitizers in photodynamic therapy.

The absorption spectra of the copolymers Pc-SA- $n$  ( $n = 1-5$ ) in chloroform given in Figure 102 are typical for monomeric phthalocyanines [318, 319]. The spectra show the B-band at 343 nm, the Q-band at 673 nm, and the two vibronic bands at 607 and 640 nm. As expected, the intensities of these bands are higher for copolymers with a higher Pc content. Upon excitation at 610 nm, all these copolymers



**Figure 101.** Synthesis of poly(phthalocyanine-co-sebacic anhydride), Pc-SA-5. Reprinted with permission from [317], J. Fu et al., *Langmuir* 18, 3843 (2002). © 2002, American Chemical Society.



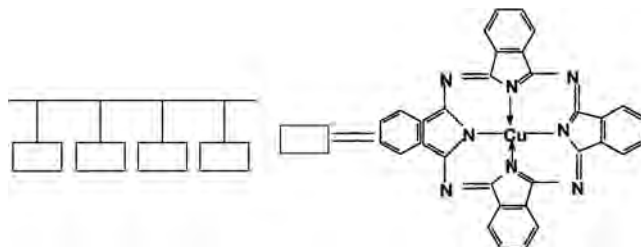
**Figure 102.** UV-vis spectra of Pc-SA- $n$  ( $n = 1-5$ ) in chloroform with a concentration of  $3.30 \times 10^{-4} \text{ g cm}^{-3}$ . Reprinted with permission from [317], J. Fu et al., *Langmuir* 18, 3843 (2002). © 2002, American Chemical Society.

fluoresce at ca. 680 nm. The fluorescence quantum yield decreases initially with increasing Pc content, attaining a saturated value of ca. 0.22. This observation suggests that as the Pc content increases, the macrocycles in the polymer matrix exhibit a higher aggregation tendency.

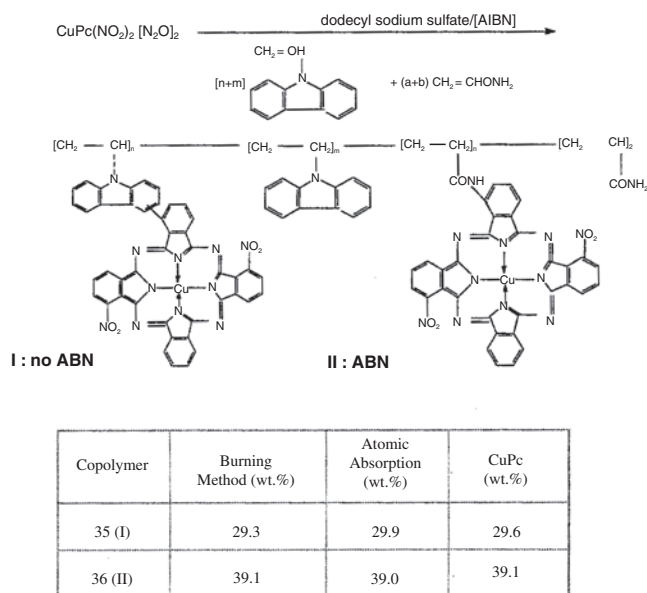
A Zimm plot for the sodium dodecyl sulfate (SDS)-stabilized Pc-SA-5 nanoparticles in water showed that the nanoparticles are composed of loosely aggregated polymer chains with a large number of water molecules entrapped inside. The average hydrodynamic radius of the Pc-SA-5 nanoparticles in water was determined to be 166 nm by dynamic laser light scattering. The results show that this biocompatible polymer-based colloidal system is potentially useful for the delivery and release of photosensitizers in photodynamic therapy (PDT).

## 6.6. Poly(vinylcarbazole) Bonded Pc

Wang et al. have reported a linear type copolymer containing CuPc, the structure of which is shown in Figure 103 [320]. The copolymer consisting of poly(vinylcarbazole-co-acrylamide)-bonded CuPc(NO<sub>2</sub>)<sub>2</sub> was synthesized by the reaction of the diazonium salt of dinitro-diamino copper phthalocyanine with vinylcarbazole and acrylamide as described in Figure 104. The polymer (VK-AA) showed



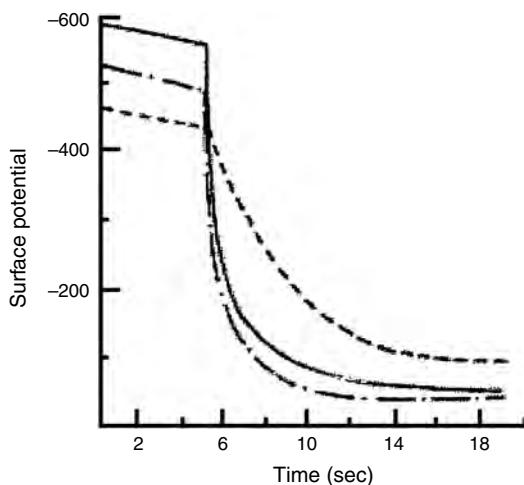
**Figure 103.** Structure of the polymer-bonded phthalocyanines. Reprinted with permission from [320], M. Wang et al., *J. Photochem. Photobiol. A* 88, 183 (1995). © 1995, Elsevier Science.



**Figure 104.** Synthesis of VK-AA copolymer containing CuPc. Reprinted with permission from [320], M. Wang et al., *J. Photochem. Photobiol. A* 88, 183 (1995). © 1995, Elsevier Science.

good photoconductivity, much better than that of the corresponding phthalocyanine monomer  $\text{CuPc}(\text{NO}_2)_4$ .

Figure 105 shows the photoinduced discharge curve of the polymer films prepared from **35** and **36** in contact with a charge transport layer. Polymers **35** and **36** have good charge acceptance ( $V_0$ ) of 588 and 523 V respectively and low residual potential ( $V_r$ ) of 76 and 62 V respectively. The surface potentials decrease suddenly at the beginning of exposure. The rates of dark discharge ( $R_d$ ) are 19 and 25  $\text{V s}^{-1}$ , the rates of photodischarge ( $R_p$ ) are 250 and 312  $\text{V s}^{-1}$ , the half-discharge times ( $t_{1/2}$ ) are 0.438 and 0.975 s, and the percentages of potential discharge after 1 s of exposure ( $\Delta V_1$ ) are 71.4% and 79.2% for **35** and **36** respectively. These values indicate that both polymers **35** and **36** have good charge



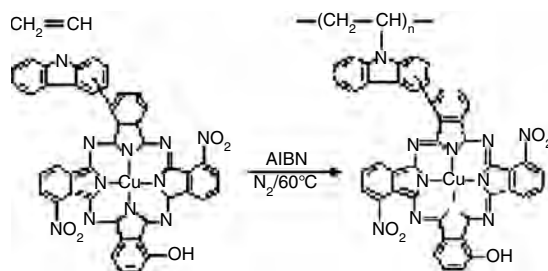
**Figure 105.** PIDC of P/R from polymers **35** (—) and **36** (---) and  $\text{CuPc}(\text{NO}_2)_4$  (-.-). CTM is TPD:PVK:PMMA = 5:2.5:1 (by weight). Reprinted with permission from [320], M. Wang et al., *J. Photochem. Photobiol. A* 88, 183 (1995). © 1995, Elsevier Science.

acceptance, small  $R_d$ , and large  $R_p$ , showing good photoconductivity. Compared with the  $\text{CuPc}(\text{NO}_2)_4$  monomer, polymers **35** and **36** have bigger values of  $R_p$ , smaller  $R_d$ , and shorter  $t_{1/2}$ , indicating that polymers **35** and **36** have much better photoconductivity than the  $\text{CuPc}(\text{NO}_2)_4$  monomer.

It was suggested that bigger conjugated systems are formed between  $\text{CuPc}(\text{NO}_2)_2$  and the P(VK-co-AA) main chain, which could enhance the activity of electrons so that they could be excited more easily [321]. Furthermore, there are strong electron acceptor groups ( $-\text{NO}_2$ ) on the phthalocyanine rings and also electron donor groups ( $\equiv\text{N}:$ ) on the same polymer chain P(VK-co-AA). The interaction of the electron acceptor and electron donor groups may help the charge carriers move, hence increasing the photoconductivity [321, 322].

Similarly a linear type of Pc polymer was synthesized starting from the monomer of vinylcarbazole bonded to copper phthalocyanine (VKCuPc), which was synthesized by diazo-reaction of vinylcarbazole (VK) and the diazonium salt of dinitro-diamine copper phthalocyanine [ $\text{CuPc}(\text{NO}_2)_2(\text{NH}_2)_2$ ] [323].

VKCuPc monomer is stable at room temperature owing to the steric effect caused by the huge phthalocyanine ring. It can be initiated by azoisobutyronitrile (AIBN) to homopolymerize without air at 80 °C in the following way:



However, the polymerization degree is low because of the sterically hindered phthalocyanine ring. The average  $n$  value is only about 3 measured by vapor pressure osmometry. The content of Cu determined from the atomic absorption analysis is 6.12 wt%, slightly smaller than the theoretical value (7.33 wt%), which may explain the low polymerization degree. PVKCuPc is soluble in DMF and THF.

Table 4 shows the photoconductivity of the P/Rs from PVKCuPc, VKCuPc monomer, and CuPc. PVKCuPc has good charge acceptance ( $V_0 = 589$  V), a small rate of dark discharge ( $R_d = 26$   $\text{V s}^{-1}$ ), and a fast rate of photodischarge ( $R_p = 187$   $\text{V s}^{-1}$ ). The percentage of potential discharge

**Table 4.** Photoconductivity of PVKCuPc, VKCuPc monomer, and CuPc.

CGM	$V_0$ (V)	$R_d$ ( $\text{V s}^{-1}$ )	$R_p$ ( $\text{V s}^{-1}$ )	$\Delta V_1$ (%)	$t_{1/2}$ (s)	$t_{1/2}^{-1}$ ( $\text{s}^{-1}$ )
PVKCuPc	589	26	187	59.8	0.625	1.600
VKCuPc	375	15	156	50.5	0.938	1.066
CuPc	598	35	147	36.4	4.840	0.210

Note: CTM is TPD:PVK:PC = 5:5:1 (by weight). The thicknesses of the interface layer (IFL), charge generation layer (CGL), and charge transport layer (CTL) are about 1.5, 1.5, and 10  $\mu\text{m}$  respectively.

Source: Reprinted with permission from [323], M. Wang et al., *J. Photochem. Photobiol. A* 94, 249 (1996). © 1996, Elsevier Science.

after 1 s of exposure is  $\Delta V_1 = 59.8\%$ , and the time of half-discharge is  $t_{1/2} = 0.625$  s.

The differences of the photoconductivity of PVKCuPc, VKCuPc monomer, and CuPc may result from their different structures as described for polymers **35** and **36** [320]; that is, in the case of VKCuPc monomer, a bigger pi-conjugated system is formed between the phthalocyanine ring and VK, which could enhance the cativity of electrons so that they could be more easily excited [322]. Hence the photoconductivity increases greatly compared with that of CuPc. When VKCuPc monomers are homopolymerized, the photoconductivity of PVKCuPc increases further, compared which that of VKCuPc monomer.

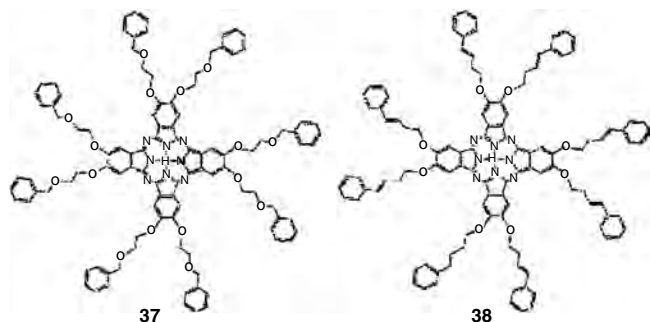
## 7. POLYMERIC STACKS

One-dimensional polymeric stacks were prepared using reactive octasubstituted phthalocyanines [324, 325]. The key to this strategy is the placement of the reactive site(s) along the side chains of the disklike monomer, rather than at the periphery, because the later approach can result in cross-linking of the discotic columns [302b].

The stacking of phthalocyanines can be controlled by putting certain metals in the middle [197], as shown in Figure 84 (compound **17**). The bridging ligands can be organic ligands with unsaturated or heteroatom containing aromatic molecules for high charge transport. A better conductor has been made by substituting biphenyl to separate the porphyrin rings. The spacing of this material will also control the nature of the conductivity. These materials can also be doped to make them semiconductors.

### 7.1. Polymeric Pc Stacks by Olefin Metathesis

Among the synthetic targets selected prepare polymeric Pc stacks by cross-linking of the discotic columns is Pc **38** in Figure 106, which preserves the freedom to utilize a variety of transition metals, M, at the Pc core. Pc **38** contains eight  $\beta$ -alkyl styryl groups that can react via photostimulated [2+2] cycloaddition. The precedence for this strategy comes from the observations of Zhao and co-workers, who demonstrated that photolysis of LB multilayers of fatty acids and lipids derived from  $\beta$ -substituted styrenes produced dimers via cyclobutane formation [326]. The thin film behavior of



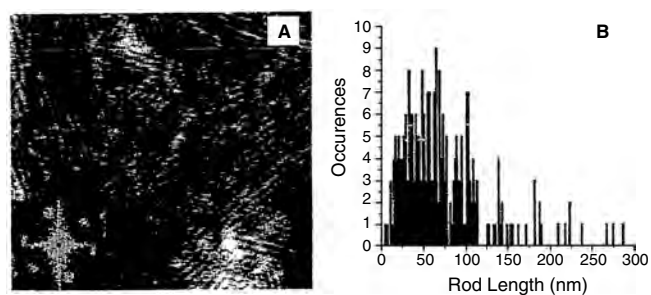
**Figure 106.** Disklike monomers for 1D polymers. Redrawn with permission from [324], A. S. Drager et al., *J. Am. Chem. Soc.* 123, 3595 (2001). © 2001, Elsevier Science.

**38** at the air–water interface was similar to that reported for **37** [134].

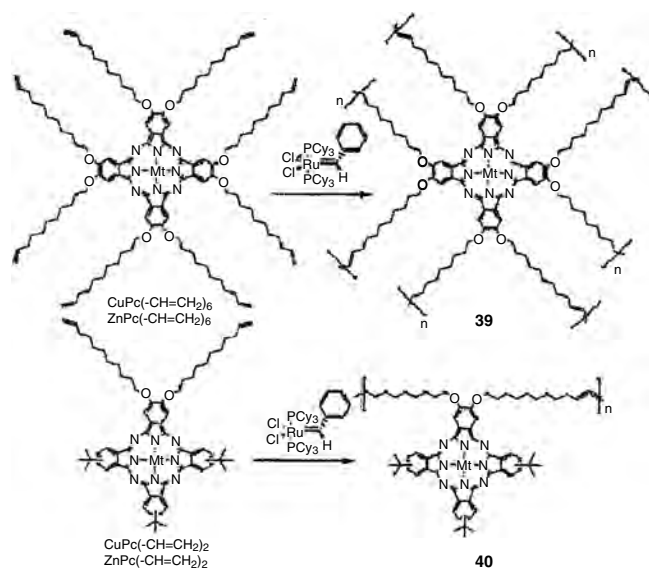
Figure 107A shows a typical image of rodlike structures found in the cast film. Rod lengths were measured within a  $500 \text{ nm} \times 500 \text{ nm}$  area that includes the image area of Figure 107A. Only rods with distinct end points were measured and are included in a histogram (Figure 107B) that shows the large variation of rod lengths, with a mean rod length of 72 nm. Both the matrix-assisted laser desorption ionization (MALDI) and AFM data indicate the presence of macromolecules consistent with Pc rod lengths of 10–40 nm. In addition the AFM data clearly suggest that considerably larger Pc rods are formed during irradiation, with lengths up to 290 nm. The observed column-to-column distance between adjacent Pc rods was  $6.4 \pm 0.2$  nm, which is approximately twice the expected column diameter for **37** [134]. The Pc polymer rods are arranged in domains of 8–10 rods each, aligned along the three principal crystallographic axes of HOPG, suggesting that these rods adopt epitaxial relationships with the HOPG substrate.

Phthalocyanine polymers **39** and **40** (Fig. 108) were prepared from two phthalocyanine monomers CuPc(-CH=CH<sub>2</sub>)<sub>8</sub> and CuPc(-CH=CH<sub>2</sub>)<sub>2</sub> bearing eight and two terminate olefin groups, respectively, through olefin metathesis reaction using a ruthenium initiator (PCy<sub>3</sub>)<sub>2</sub>Cl<sub>2</sub>Ru(=CHC<sub>6</sub>H<sub>5</sub>) developed by Grubbs et al. [325]. The polymers resulting from two Pc monomers **39** and **40** bear the Pc rings in the polymeric network and the main polymer chain, respectively, by the intermolecular formation of carbon–carbon double bonds. A linear polymer **40** prepared from CuPc(-CH=CH<sub>2</sub>)<sub>2</sub> produced a rodlike nanostructure in which the copper phthalocyanine moieties were stacked with the regular stacking distance.

Matrix-assisted laser desorption ionization-time of flight-mass (MALDI-TOF-Ms) spectroscopy for polymerized samples indicated that all of the olefin groups were intramolecularly linked through the olefin metathesis reaction at a high-diluted condition (Fig. 109). The GPC analysis of **40** revealed a high molecular weight  $M_n = 55,000$  with a wide polydispersity PDI = 3.0 (relative to monodispersed

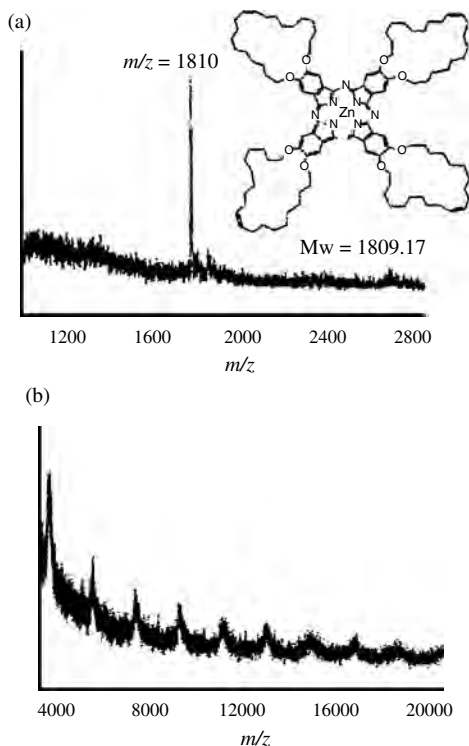


**Figure 107.** (A) Tapping mode AFM image (sample in water) of cast photolyzed material on HOPG. The image is  $250 \text{ nm} \times 250 \text{ nm}$ , with a height scale of 2.0 nm. A Fourier domain transformation (inset) of the AFM image indicates the three-fold symmetry packing of the rodlike structures. (B) A histogram of molecular object length measured within a  $500 \text{ nm} \times 500 \text{ nm}$  scan area. Only complete molecular objects with defined end points were measured with lengths ranging from 5 to 290 nm, with a mean length of 72 nm. Redrawn with permission from [324], A. S. Drager et al., *J. Am. Chem. Soc.* 123, 3595 (2001). © 2001, Elsevier Science.

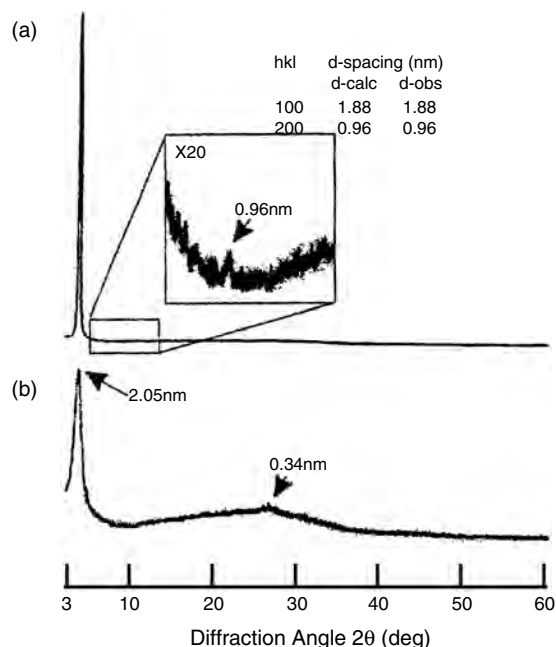


**Figure 108.** Polymerization process of phthalocyanine monomers through olefin metathesis process. Reprinted with permission from [303], M. Kimura et al., *Macromolecules* 34, 4706 (2001). © 2001, American Chemical Society.

polystyrene standards). The intermolecular formation of carbon–carbon double bonds through the olefin metathesis reaction gave a high molecular weight polymer material containing a Pc moiety.



**Figure 109.** MALDI-TOF-MS spectra of polymerized samples from  $\text{ZnPc}(-\text{CH}=\text{CH}_2)_8$  at the two initial concentrations:  $[\text{ZnPc}(-\text{CH}=\text{CH}_2)_8] = 60.0 \text{ mM}$  (a) and  $[\text{ZnPc}(-\text{CH}=\text{CH}_2)_8] = 7.5 \text{ mM}$  (b). Reprinted with permission from [303], M. Kimura et al., *Macromolecules* 34, 4706 (2001). © 2001, American Chemical Society.



**Figure 110.** Diffraction patterns of X-ray reflected from a glass surface coated with  $\text{CuPc}(-\text{CH}=\text{CH}_2)_2$  (a) and **40** (b). Reprinted with permission from [303], M. Kimura et al., *Macromolecules* 34, 4706 (2001). © 2001, American Chemical Society.

The X-ray diffraction pattern of linear polymer **40** is shown in Figure 110. The regular spacing of 0.34 nm among Pc moieties within the columns can be derived from the oriented reflection in the wide-angle region. This value of 0.34 nm is a common stacking distance in planar aromatic compounds [132b, 327]. The 0.34 nm spacing value indicates the formation of highly ordered stacks among Pc moieties within **40**. The diffuse halo at around 0.43 nm is characteristic for liquidlike order of the alkyl chains. The small-angle reflection at 2.05 nm is related to ordering of the columns [328]. The covalent linkage of side chains in  $\text{CuPc}(-\text{CH}=\text{CH}_2)_2$  results in the formation of a columnar structure consisting of one-dimensional ordered stacks of numerous Pc moieties.

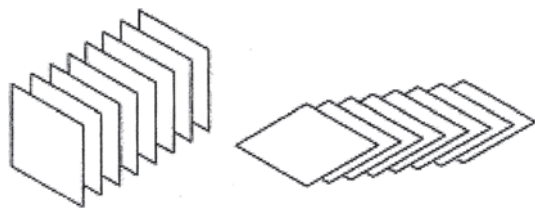
The morphologies of the aggregates examined by TEM showed irregular nanostructures for polymer **39** (Fig. 111a) and rodlike structures for linear polymer **40** with a width of ca. 2.0 nm (Fig. 111b). The rods in each domain were almost orientated along a regular direction. Therefore, the covalent linkage of side chains in the unsymmetrical Pc monomer allows the direct observation of columnar densely packed Pc stacks bearing 300–500 nm lengths. These long ordered Pc stacks might open new possibilities toward the construction of molecular wires.

## 7.2. Cofacial Arrangement of Phthalocyanine Rings in Phthalocyaninato–Polysiloxanes

There has been much research on LB films of Pcs and their applications in electronic devices following the first report by Baker et al. [234]. Among the many types of Pcs,

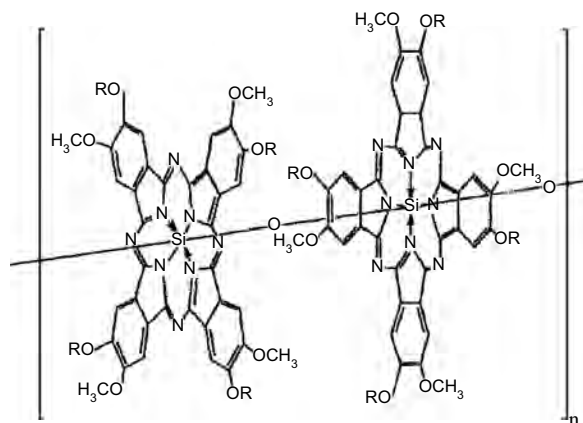






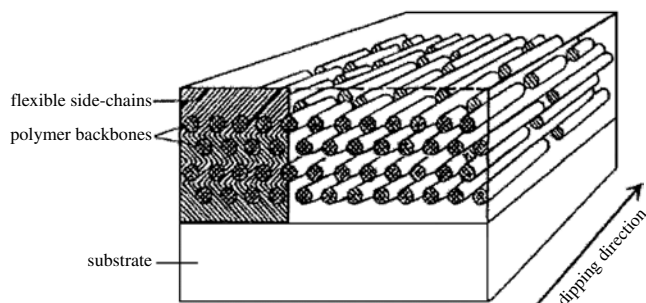
**Figure 113.** Schematic representation of the proposed face-to-face (left) and J-like (right) arrangements of the monomer both at the air-water interface and in the LB films. Each square represents a macrocycle ring of the monomer. Reprinted with permission from [231], P. L. Chen et al., *Colloids Surfaces A* 175, 171 (2000). © 2000, Elsevier Science.

Cofacial arrangement properties of phthalocyaninato-polysiloxanes have been analyzed by electrical dark conductivity experiments and by pulse-radiolysis time-resolved microwave conductivity (PR-TRMC) measurements [341, 342]. PcPS (**41**) consists of phthalocyanine rings which are covalently connected in a cofacial geometry. The strong steric interaction between the disk-shaped repeat units forces the polysiloxane backbone to become rigid, resulting in a repeat distance of 0.33 nm [341]. This close cofacial arrangement also induces an electromagnetic coupling of the chromophore units. In the polymer the Q-band is considerably broadened and blueshifted to 540–560 nm while the monomer exhibits the Q-band at 680 nm. These spectral changes can be explained by the theory of molecular excitons as given by Kasha et al. [285].



**41** (PcPS, with R=C<sub>8</sub>H<sub>17</sub> and R=C<sub>18</sub>H<sub>37</sub>)

On peripheral alkoxy chain substitution, the polymers are soluble and can be processed by the Langmuir–Blodgett technique into thin films [334a, 342a, 343]. The backbone of the hairy rod molecules is oriented parallel to the substrate surface. Consecutive transfer of monolayers leads to PcPS LB films with a layered structure and a monolayer thickness of approximately 2.2 nm. Upon annealing the structure of PcPS films changed to a highly oriented hexagonal packing of the cylinders of cofacially stacked conjugated macrocycles in a disordered matrix of aliphatic side chains as shown in Figure 114 [344, 345]. TEM measurements have shown that PcPS LB films consist of microdomains with dimensions of several tens of nanometers and a strictly parallel alignment of the molecules. The flow conditions on the



**Figure 114.** The structure of PcPS Langmuir–Blodgett films with hexagonal packing of the PcPS rods. Reprinted with permission from [341], P. Gattinger et al., *J. Phys. Chem. B* 103, 3179 (1999). © 1999, American Chemical Society.

Langmuir trough generate a preferential alignment of the long axis of the PcPS molecules along the dipping direction [346]. This structural order is responsible for the pronounced anisotropy of various properties of these films [43, 246, 286b, 347].

Due to its excellent thermal and particularly good electrochemical stability [348] PcPS has been examined with respect to electrical and photoelectrical properties [246, 286b, 347, 349]. In contrast to films of monomeric Pc, where different polymorphic structures can be present depending on the method of preparation, the covalent link in PcPS forces the macrocycles into a strict cofacial stacking. Even though there is no orbital overlap between the Pc macrocycles it is expected that electron motion within the core of the stack will be rapid compared to the motion perpendicular to the polymer backbone which would involve tunneling through the aliphatic side chains. This makes PcPS a model system for the study of charge transport in materials with an intrinsically one-dimensional conductivity. The layer-wise deposition of the PcPS molecules enables the control of the molecular orientation within the films.

Depending on the voltage, either an Ohmic or space-charge-limited current (SCLC) should be observed [347a]. At low fields the current density  $j$  is described by Ohm's law

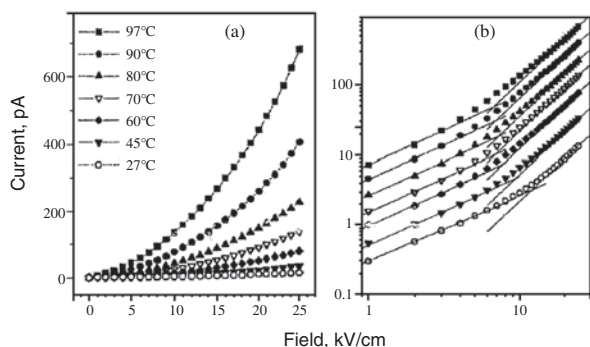
$$j_{\Omega} = ne\mu \frac{U}{d} \quad (1)$$

whereas at higher fields Child's law for SCLC applies:

$$j_{\text{SCLC}} = \frac{9}{8} e_0 e_{\mu} \frac{U^2}{d^3} \quad (2)$$

Here,  $\mu$ ,  $d$ , and  $e$  denote the mobility, the electrode separation, and the dielectric constant.  $n$  is the charge carrier density initially present in the material at low voltages, which is introduced by doping, impurities, or by thermal activation. In the well-annealed samples the Ohmic conductivity is low and a SCLC regime could be clearly resolved, as shown in Figure 115.

The double-logarithmic plot of Figure 115b reveals the transition from ohmic to space-charge-limited behavior. The straight lines represent the ohmic and space-charge-limited regime according to Eqs. (1) and (2), respectively. The onset of the transition from the Ohmic to the SCLC region shifts only slightly to lower fields with increasing temperature.



**Figure 115.**  $I/U$  characteristics of a film of 11 LB layers of  $C_1C_8$  on interdigitated electrodes recorded at different temperatures. The electrode distance is  $10\ \mu\text{m}$ . Reprinted with permission from [341], P. Gättinger et al., *J. Phys. Chem. B* 103, 3179 (1999). © 1999, American Chemical Society.

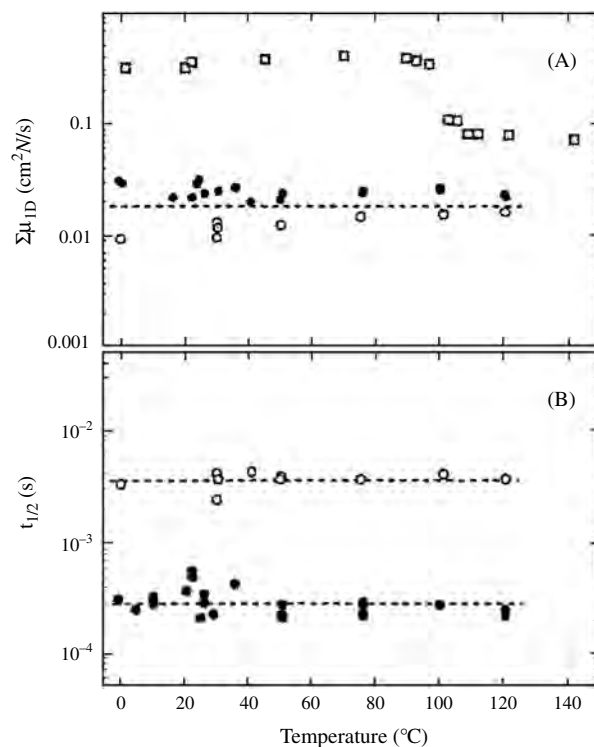
According to Eq. (2) the charge carrier mobility  $\mu$  can be deduced from the current density in the SCLC regime. The data of Figure 115 yield a temperature dependence of the mobility with values ranging between  $3.6 \times 10^{-7}$  at  $27^\circ\text{C}$  and  $2.1 \times 10^{-5}\ \text{cm}^2/\text{Vs}$  at  $97^\circ\text{C}$ . Knowing  $\mu$ , the initial density of charge carriers  $n$  can be calculated from the Ohmic part of the curve according to Eq. (1). For the set of data shown in Figure 115 values for  $n$  are approximately  $1 \times 10^{13}\ \text{cm}^{-3}$  ( $1.9 \times 10^{13}\ \text{cm}^{-3}$  at  $27^\circ\text{C}$ ,  $8.9 \times 10^{12}\ \text{cm}^{-3}$  at  $97^\circ\text{C}$ ). In contrast to the increase in mobility by two orders of magnitude upon raising the temperature, the carrier density  $n$  in the Ohmic region remains almost constant.

From the PR-TRMC transients for the  $C_1C_{18}$  derivative, the end-of-pulse conductivity per unit dose ( $D\ \text{J/m}^3$ ) and  $\Delta\sigma_{\text{eop}}/D$  were determined and used to determine the one-dimensional, intracolumnar mobility  $\sum\mu_{1D}$  that can be derived using the following relationship:

$$\sum\mu_{1D} = 3E_p(\Delta\sigma_{\text{eop}}/D)/F_{\text{eop}} \quad (3)$$

The values of the pair formation energy  $E_p = 25\ \text{eV}$  and the end-of-pulse pair survival probability  $F_{\text{eop}} = 0.35$  ( $C_1C_8$ ) and  $0.46$  ( $C_1C_{18}$ ) were estimated [351] and used to calculate the values of  $\sum\mu_{1D}$  given in Figure 116. As can be seen,  $\sum\mu_{1D}$  ( $\approx 2 \times 10^{-2}\ \text{cm}^2/\text{Vs}$ ) is almost independent of temperature from  $0$  to  $120^\circ\text{C}$ . In addition, similar values are found for both the  $C_1C_8$  and  $C_1C_{18}$  compounds. This supports the assumption that the mobility does indeed refer to intracolumnar charge transport (i.e., it is independent of the average distance between the columns  $L$  which varies from  $22$  to  $37\ \text{\AA}$ ). The average value of  $\sum\mu_{1D}$ , given by the horizontal straight line in Figure 116A, is  $0.018\ \text{cm}^2/\text{Vs}$ .

Similarly, in a  $C_9C_9$  polysiloxane derivative the mobility was also found to display only a small temperature dependence [352]. The independence of  $\mu_{1D}$  on the side chain length indicates that only transport parallel to the chain axis is involved. The absolute value of  $\mu_{1D}$  for the  $C_9C_9$  polysiloxane derivative, however, was a factor of 3 larger than the average value for the  $C_1C_8$  compounds, possibly due to an additional degree of disorder in the  $C_1C_8$  and  $C_1C_{18}$  compounds resulting from the random nature of substitution of the two different alkoxy side chains.

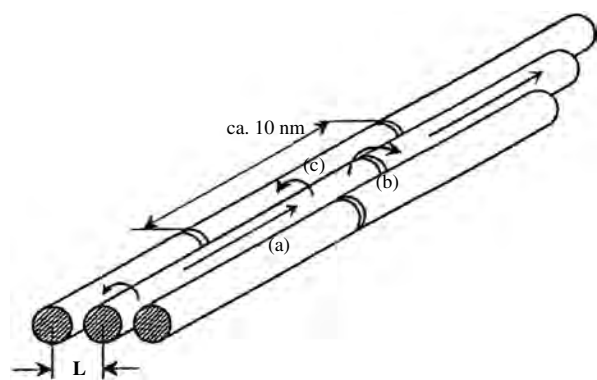


**Figure 116.** (A) The temperature dependence of the one-dimensional, intracolumnar mobility calculated from  $e_{\text{eop}}/D$  for  $C_1C_8$  (filled circles) and  $C_1C_{18}$  (open circles). Data for the monomeric  $C_9C_9$  compound (open squares) are included for comparison. (B) The temperature dependence of the first half-life of the conductivity transients for  $C_1C_8$  and  $C_1C_{18}$  using the same symbols as in (A). Reprinted with permission from [341], P. Gättinger et al., *J. Phys. Chem. B* 103, 3179 (1999). © 1999, American Chemical Society.

For comparison, mobility data for the monomeric, uniformly substituted  $C_9C_9$  compound [351] are displayed in Figure 116A. These are significantly larger than for the polymeric compounds over the entire temperature range and clearly display the sharp decrease at the crystalline solid to liquid crystal transition which has been found to be characteristic of the  $n$ -alkyl, substituted monomeric compounds.

TEM measurements on monomolecular layers of the  $C_1C_{18}$  compounds have shown the existence of microdomains of several tens of nanometers in length and width with strictly parallel alignment of the molecules [350, 353]. The independence of  $\mu_{1D}$  on the side chain length indicates that only transport parallel to the chain axis is involved (Fig. 117). Mobilities over macroscopic distances of PcPS LB films parallel to the preferential chain orientation are approximately  $10^{-7}$ – $10^{-6}\ \text{cm}^2/\text{Vs}$  at room temperature.

Charge carrier transport perpendicular to the polymer chains involves tunneling through the aliphatic side chain regions. From PR-TRMC relaxation times a temperature-independent value of  $\mu_{2D} = 10^{-5}\ \text{cm}^2/\text{Vs}$  is derived. This is three orders of magnitude smaller than the intracolumnar mobility  $\mu_{1D}$  and proves that charge transport on a microscopic scale, for example, within a domain of highly oriented PcPS chains must be highly anisotropic. In agreement with this, the dark conductivity “strictly” perpendicular to the polymer backbones is smaller by approximately three orders



**Figure 117.** Schematic representation of charge transport within a domain of parallel oriented PcPS molecules. Redrawn with permission from [341], P. Gatteringer et al., *J. Phys. Chem. B* 103, 3179 (1999). © 1999, American Chemical Society.

of magnitude than the corresponding in-plane conductivity and it follows an Arrhenius-type temperature dependence with  $E_a \sim 0.36$  eV. This value is similar to that of the temperature dependent in-plane conductivity.

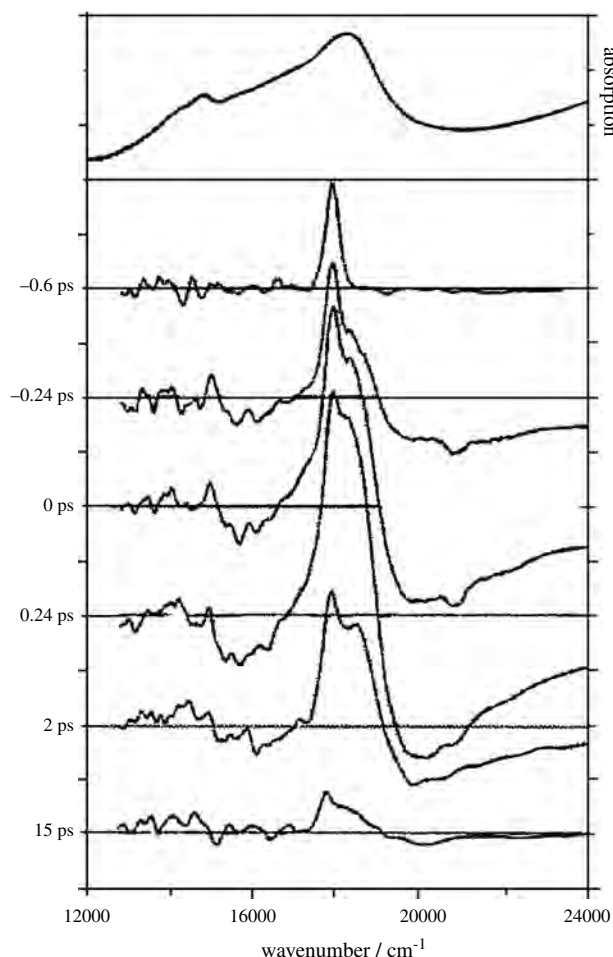
Langmuir–Blodgett multilayer structures of PcPS exhibit high photoconductivity and strong light absorption in the visible, properties that are the basis for the successful development of photoactive devices such as photodiodes and sensors. The photogeneration of charges in PcPS films has been the subject of intense research for many years [220a, 349a, 354]. There are several issues of central importance in studying the photogeneration of charge carriers as well as the transport dynamics of excited states and charge carriers. The proper characterization of the relaxation dynamics of the initially excited electronic states and, in particular, of the exciton transport dynamics is of great interest in this regard.

(Phthalocyaninato)polysiloxane composed of siloxane-polymerized, cofacially stacked phthalocyanines, staggered at an angle of  $36^\circ$ , is a one-dimensional molecular conductor [354]. The linear stacking and the rather small ring–ring interplanar spacing of about 0.33 nm [43, 135, 354] favor efficient intermacrocycle interactions, so that optical excitation is expected to lead to extensive excitonic coupling between the extended-conjugated electron systems of the phthalocyanine cycles [43, 348, 349b].

[Tetramethoxytetrakis(octylxy)phthalocyaninato]polysiloxane is a linear polymer consisting of an average of  $32^\circ$  cofacially stacked oxo-bridged silicon phthalocyanine rings with stacking distances of  $d_{\text{Si-O-Si}} = 0.33$  nm and constitutes fairly rigid rods of ca. 11 nm length [43, 135]. The temporal evolution of the singlet exciton states created at different excitation energy densities between ca. 0.5 and 2.5 mJ/cm<sup>2</sup> was studied by femtosecond transient absorption spectroscopy [355]. Both photoinduced bleaching and transient absorption were observed, and decay dynamics, which strongly depend on the excitation energy density, are nonexponential. At higher excitation densities, the observed relaxation dynamics in PcPS are dominated by exciton–exciton annihilation. The excited state lifetime of singly excited chains is ca. 4.5 ps, drops to about 0.5 ps for doubly excited chains, and becomes less than the instrumental

resolution of 150 fs at higher excitation densities. An analysis of the decay dynamics was made in terms of a model, which has been successfully utilized to rationalize the exciton transport dynamics in VOPc films and PbPc films, and in which the exciton–exciton annihilation rate is time dependent ( $t^{-1/2}$ ) [354, 356]. For low excitation densities the decay behavior can be well reproduced, while at higher densities the recovery of the ground state is faster than predicted. This fast recovery is supposed to originate from the creation of charge-separated states, which efficiently quench all excited states of a polymer chain.

Figure 118 displays the time evolution of the transient spectra of PcPS in tetrahydrofuran solution recorded between  $-0.6$  and  $+15$  ps. The wavelength of the pump laser is 555 nm ( $18,020$  cm<sup>-1</sup>) and the excitation density is ca. 0.5 mJ/cm<sup>2</sup>. Analogous transient absorption measurements on solutions of PcPS indeed demonstrated that the spectra were independent of the polarization conditions.



**Figure 118.** Time evolution of transient spectra of PcPSi in tetrahydrofuran excited with a 120 fs pump pulse at 555 nm ( $18,020$  cm<sup>-1</sup>) with an excitation density of ca. 0.5 mJ/cm<sup>2</sup>. The spectrum at  $D = -0.6$  ps constitutes the baseline with T1 except for the range of the scattering light of the pump pulse between 18,020 and 17,700 cm<sup>-1</sup> where  $T > 1$ . Bleaching and absorption bands are recognized as increases and decreases with respect to the baseline, respectively. Reprinted with permission from [355], J. Ern et al., *J. Phys. Chem. A* 103, 2446 (1999). © 1999, American Chemical Society.

## 8. CONCLUSION

The nanostructure of phthalocyanines and their polymers has been controlled through covalent and noncovalent bonds, by controlling the intermolecular interactions in all ranges. Thus phthalocyanine thin films, nanorods and stacks, molecular arrays of Pc with templates, self-assembly, layer-by-layer assembly of oppositely charged materials, Langmuir–Blodgett films, and other methods have been developed for construction of nanostructured phthalocyanines, as a noncovalent method. Complex film composed of nanoscopic particles of Pcs with nanostructured materials is also an example of a noncovalent method of nanostructured Pcs. Since the dispersion is in nanoscale, the titanium dioxide/phthalocyanine film has high transparency, which is requisite for optical device application.

Having planar structures in the central ring, phthalocyanines easily form thin films with a film thickness on the nanometer level, by deposition methods. STM images of the thin films were highly dependent on the electron density and the local density of surface states near the Fermi energy.

Disk-shaped rigid phthalocyanines and metallophthalocyanines can easily stack through strong  $\pi$ – $\pi$  interaction and form one-dimensional rodlike assemblies with interesting electronic and optic properties. Such cofacially stacked Pc aggregates are present even in dilute solution for some examples. In the Langmuir and Langmuir–Blodgett films containing phthalocyanine derivatives, it is shown that the molecular parameters of the amphiphilic Pc derivative (i.e., the nature, the number, and the location of the polar substituents, the number and the location of the aliphatic chains) strongly affect the orientation of the molecules at the air–water interface and in the LB multilayers. Two extreme examples are given: LB films containing Pc molecules lying parallel to the substrate and LB films containing Pc molecules standing edge-on. In both cases, good-quality and well-ordered LB films are only obtained when the packing parameter  $s$  is sufficiently close to unity. It is shown that “sacrificial” single-chain amphiphilic molecules, mixed with the Pc derivatives, can significantly improve the quality of the mono- and multilayers and in some cases modify the inner structure of the film. Methods for the identification of the nanostructures are developed using various techniques such as STM, AFM, surface-enhanced Raman scattering spectrum, and UV-vis spectral methods. Such methods enable the precise manipulation of molecular arrangements and photoelectronic properties of Pcs in nanoscale.

In films of metallophthalocyanine stacks, the Pc rings are spaced by van der Waals distances and exciton coupling of neutral–electronic transitions between neighboring macrocycles becomes very efficient. On the other hand, linear polymers of (phthalocyaninato)siloxane in solution strictly limit the exciton transport to one dimension and heating effects can be avoided in flowing solutions.

Chemical modification of the core of phthalocyanines by electron withdrawing groups such as fluorine provides a high versatility in molecule structure and hence intermolecular interactions. The film structure as well as electrical and optical characteristics can be adjusted in a rather wide range.

Several polymeric nanostructures are achieved by cofacial arrangement of Pc stacks by bridging with an organic

spacer, linear, or network type by, for example, using olefin metathesis and condensation polymerization methods. The stacking of phthalocyanines can be controlled by putting certain metals in the middle. The bridging ligands can be organic ligands with unsaturated or heteroatoms containing aromatic molecules for high charge transport. A better conductor has been made by substituting biphenyl to separate the porphyrin rings. Among those, phthalocyanine-polysiloxanes are one example showing edge-on phthalocyanine structures, which are linked through a siloxane chain by their centers, thus forming a rigid rod nanostructures. These are promising for designing molecular devices because of their one-dimensionality and high stability.

Although polymeric Pc nanostructures are rare, compared to the monomeric stacks, the polymer stacks ensure increased stack stability, processibility, and wider applications. The control of spatial arrangement and orientation of these nanostructured Pc materials allowed directional transport of electrons, photons, and ions, to improve photoelectronic properties of phthalocyanines.

Judging from the unique properties of Pc and availability of nanoscaled manipulations, there will be increasing applications of nanoconstruction based on Pc in the future.

## GLOSSARY

**Fermi energy ( $E_F$ )** When a number of electrons are put into an energy level, electrons will occupy higher energy levels when the lower ones are filled up.  $E_F$  is the energy level of the highest occupied state at zero temperature.

**Langmuir–Blodgett film** A set of monolayers, or layers of organic material one molecule thick, deposited on a solid substrate. An LB film can consist of a single layer or many, up to a depth of several visible-light wavelengths.

**Layer-by-layer (LBL) assembly** Assembly of oppositely charged materials.

**Molecular self-assemblies** Spontaneous formation of molecules into covalently bonded, well-defined, stable structures via electrostatic, van der Waals, hydrogen bonding, hydrophobic interaction, etc.

**Molecular wire** A common name to indicate a long, highly conjugated molecule.

**Monolayer** A one-molecule thick insoluble layer of an organic material spread onto an aqueous subphase.

## REFERENCES

1. K. Y. Law, *Chem. Rev.* 93, 449 (1993); M. J. Stillman and T. Nyokong, “Phthalocyanines, Properties and Applications” (C. C. Leznoff and A. B. P. Lever, Eds.), Ch. 3. VCH, New York, 1989.
2. R. A. Collins and K. A. Mohammed, *J. Phys. D* 21, 14 (1988); C. Hamann, M. Hietschold, A. Mrwa, M. Mueller, M. Starke, and R. Kilper, *Top. Mol. Organ. Eng.* 7, 129 (1991).
3. B. W. Flynn, A. E. Owen, and J. Mayor, *J. Phys. C* 10, 405 (1977).
4. A. H. Ghosh, D. L. Morel, T. Feng, R. F. Shaw, and C. A. Rowe, *J. Appl. Phys.* 1, 20 (1974).
5. R. Madru, G. Guillaud, M. Sadoun, M. Maitrot, J. J. Andre, J. Simon, and R. Even, *Chem. Phys. Lett.* 145, 343 (1988); M. Maitrot, G. Guillaud, B. Boudjema, J. J. Andre, H. Strzelecka, J. Simon, and R. Even, *Chem. Phys. Lett.* 133, 59 (1987).

6. H. Kropf and F. Steinbach, "Katalyse an Phthalocyaninen." Georg Theme Verlag, Stuttgart, 1973.
7. S. Mho, B. Ortiz, S. M. Park, D. Ingersoll, and N. Doddapaneni, *J. Electrochem. Soc.* 142, 1436 (1995).
8. J. H. Zagal, *Coord. Chem. Rev.* 119, 89 (1992).
9. A. L. Thomas, "Phthalocyanine Research and Applications." CRC Press, Boca Raton, FL, 1990.
10. G. McDermott, S. M. Prince, A. A. Freer, A. M. Hawthornthwaite-Lawless, M. Z. Papiz, R. J. Cogdel, and N. W. Isaacs, *Nature* 374, 517 (1995).
11. "Phthalocyanines, Properties and Applications" (C. C. Leznoff and A. B. Lever, Eds.). VCH, New York, 1993.
12. J. Seto, S. Tamura, N. Asai, N. Kishii, Y. Kijima, and N. Matsuzawa, *Pure Appl. Chem.* 68, 1429 (1996).
13. J. Fabian, H. Nakazumi, and M. Matsuoka, *Chem. Rev.* 92, 1197 (1992); Y. Tooru, *JP* 09 58, 129 [97, 58, 129] (1997); N. Yoshuki, N. Hideki, and K. Hisamitsu, *JP* 08, 287, 514 [96, 287, 514] (1996); K. Shuichi, K. Tetsuya, M. Shinichiro, and S. Mare, *JP* 09, 202, 047 [97, 202, 047] (1997); S. Noboru, T. Tatsuya, U. Yasunobu, and S. Tsutomu, *JP* 09, 226, 249 [97, 226, 249] (1997).
14. "Supramolecular Materials and Technologies" (D. N. Reinhoudt, Ed.), Perspectives in Supramolecular Chemistry, Vol. 4. Wiley, New York, 1999.
15. D. A. Offord, S. B. Sachs, M. S. Ennis, T. A. Eberspacher, J. H. Griffin, C. E. D. Chidsey, and J. P. Collman, *J. Am. Chem. Soc.* 120, 4478 (1998).
16. M. Lutt, M. R. Fitzsimmons, and D. Q. Li, *J. Phys. Chem. B* 102, 400 (1998).
17. M. A. Diaz-Garcia, G. Rojo, and F. Agullo-Lopez, *Proc. SPIE* 3473, 91 (1998).
18. D. L. Pilloud, C. C. Moser, K. S. Reddy, and P. L. Dutton, *Langmuir* 14, 4809 (1998).
19. B. Bottger, U. Schindewolf, D. Mobius, J. L. Avila, M. T. Martin, and R. Rodriguez-Amaro, *Langmuir* 14, 5188 (1998).
20. F. Armand, B. Cabezon, M. V. Martinez-Diaz, A. Ruau-del-Teixier, and Torres, *J. Mater. Chem.* 7, 1741 (1997).
21. B. W. Gregory, D. Vaknin, J. D. Gray, B. M. Ocko, P. Stroeve, T. M. Cotton, and W. S. Struve, *J. Phys. Chem. B* 101, 2006 (1997).
22. C. F. Van Nostrum, *Mol. Cryst. Liq. Cryst. A* 302, 1291 (1997).
23. J. P. Bourgoin, F. Doublet, S. Palacin, and M. Vandevyver, *Langmuir* 12, 6473 (1996).
24. M. J. Cook, *J. Mater. Chem.* 6, 677 (1996).
25. K. Araki, M. J. Wagner, and M. S. Wrighton, *Langmuir* 12, 5293 (1996).
26. Y. Sun, X. Zhang, C. Sun, Z. Wang, J. Shen, D. Wang, and T. Li, *Chem. Commun.* 2379 (1996).
27. W. Han, S. Li, S. M. Lindsay, D. Gust, T. A. Moore, and A. L. Moore, *Langmuir* 12, 5742 (1996).
28. D. Li, L. W. Moore, and B. I. Swanson, *Langmuir* 10, 1177 (1994).
29. M. Pomerantz, A. Aviram, R. A. Mccorkle, L. Li, and A. G. Schrott, *Science* 255, 1115 (1992).
30. Y. Ishikawa and T. Kunitake, *J. Am. Chem. Soc.* 113, 621 (1991).
31. C. Bubeck, D. Neher, A. Kaltbeitzel, G. Duda, T. Arndt, T. Sauer, and G. Wegner, *NATO ASI Ser. E* 162, 185 (1989).
32. S. Palacin, P. Lesieur, I. Stefanelli, and A. Barraud, *Thin Solid Films* 159, 83 (1988).
33. G. C. Bryant, M. J. Cook, T. J. Ryan, and A. J. Thorne, *J. Chem. Soc. Chem. Commun.* 467 (1995).
34. M. J. Cook, D. A. Mayes, and H. Poynter, *J. Mater. Chem.* 5, 2233 (1995).
35. S. M. Critchley, D. C. Davies, K. J. Markland, and M. R. Willis, *Synth. Met.* 1447, 41 (1991).
36. M. Fujiki, H. Tabei, and T. Kurihara, *Langmuir* 4, 1123 (1988).
37. (a) S. Michaeli, M. Hugerat, H. Levanon, M. Bernitz, A. Natt, and R. Neumann, *J. Am. Chem. Soc.* 114, 3612 (1992). (b) P. A. Albouy, *J. Phys. Chem.* 98, 8543 (1994).
38. M. J. Cook, M. F. Daniel, K. J. Harrison, N. B. Mckeown, and A. Thomson, *J. Chem. Commun.* 1148 (1987).
39. G. Granito, L. M. Goldenberg, M. R. Bryce, A. P. Monkman, L. Troisi, L. Pasimeni, and M. C. Petty, *Langmuir* 12, 472 (1996).
40. A. A. Kalachev, T. Sauer, V. Vogel, N. A. Plate, and G. Wegner, *Thin Solid Films* 188, 341 (1990).
41. K. Ogawa, S. Kinoshita, H. Yonehara, H. Nakahara, and K. Fukuda, *J. Chem. Soc. Chem. Commun.* 477 (1989).
42. J. Ouyang and A. B. P. Lever, *J. Phys. Chem.* 95, 5272 (1991).
43. Th. Sauer, Th. Arndt, D. N. Batchelder, A. A. Kalachev, and G. Wegner, *Thin Solid Films* 187, 357 (1990).
44. K. Uosaki, T. Kondo, Z. Q. Zhang, and M. Yanagida, *J. Am. Chem. Soc.* 119, 8367 (1997).
45. D. Q. Li, M. Lutt, M. R. Fitzsimmons, R. Synowicki, M. E. Hawley, and G. W. Brown, *J. Am. Chem. Soc.* 120, 8797 (1998).
46. T. R. E. Simpson, D. J. Revell, M. J. Cook, and D. A. Russell, *Langmuir* 13, 460 (1997).
47. V. Huc, J. P. Bourgoin, C. Bureau, F. Valin, G. Zalczer, and S. Palacin, *J. Phys. Chem. B* 103, 10489 (1999).
48. J. K. Gimzewski, E. Stoll, and R. R. Schlittler, *Surf. Sci.* 181, 267 (1987).
49. R. Moeller, R. Coenen, A. Esrlinger, and B. Kaslouski, *J. Vac. Sci. Technol. A* 8, 659 (1990).
50. P. H. Lippel, R. J. Wilson, M. D. Miller, C. Woell, and S. Chiang, *Phys. Rev. Lett.* 62, 171 (1989).
51. C. Ludwig, R. Strohmaier, J. Petersen, B. Gompf, and W. Eisenmenger, *J. Vac. Sci. Technol. B* 12, 1963 (1994).
52. M. Kanai, T. Kawai, K. Motai, X. D. Wang, T. Hashizume, and T. Sakura, *Surf. Sci.* 329, L619 (1995).
53. T. Fritz, M. Hara, W. Knoll, and H. Sasabe, *Mol. Cryst. Liq. Cryst. A* 252, 561 (1994).
54. V. Petracek, *Int. J. Electron.* 78, 267 (1995).
55. J. Freund, O. Probst, S. Grafstroem, S. Dey, J. Kowalski, R. Neumann, M. Woertge, and G. zu Putlitz, *J. Vac. Sci. Technol. B* 12, 1914 (1994).
56. X. Lu, K. W. Hipps, X. D. Wang, and U. Mazur, *J. Am. Chem. Soc.* 118, 7197 (1996).
57. U. Mazur and K. W. Hipps, *J. Phys. Chem.* 99, 6684 (1995); U. Mazur and K. W. Hipps, *J. Phys. Chem.* 98, 8169 (1994).
58. Y. Maeda, T. Matsumoto, M. Kasaya, and T. Kawai, *Jpn. J. Appl. Phys.* 2 35, L405 (1996).
59. T. Fritz, M. Hara, W. Knoll, and H. Sasabe, in "Atomic Force Microscopy/Scanning Tunneling Microscopy" (S. H. Cohen and M. L. Lightbody, Eds.), Vol. 2, p. 99. Plenum, New York, 1997.
60. L. K. Chau, C. D. England, S. Chen, and N. R. Armstrong, *J. Phys. Chem.* 97, 2699 (1993).
61. A. Schmidt, L. K. Chau, A. Back, and N. R. Armstrong, in "Phthalocyanines: Properties and Applications" (C. C. Leznoff and A. B. P. Lever, Eds.). VCH, New York, 1996.
62. Z. Bao, A. J. Lovinger, and J. Brown, *J. Am. Chem. Soc.* 120, 207 (1998).
63. T. Morioka, H. Tada, and A. Koma, *J. Appl. Phys.* 73, 2207 (1993).
64. H. Tada and S. Mashiko, *Jpn. J. Appl. Phys.* 34, 3889 (1995).
65. D. Schlettwein, H. Tada, and S. Mashiko, *Thin Solid Films* 331, 117 (1998).
66. D. Schlettwein, A. Back, T. Fritz, B. Schilling, and N. R. Armstrong, *Chem. Mater.* 10, 601 (1998).
67. A. Schmidt, R. Schlaf, D. Louder, L. Chau, S. Chen, T. Fritz, M. F. Lawrence, B. A. Parkinson, and N. R. Armstrong, *Chem. Mater.* 7, 2127 (1995).
68. A. Yamashita, T. Maruno, and T. Hayashi, *J. Phys. Chem.* 98, 12695 (1994).
69. A. Yamashita, T. Maruno, and T. Hayashi, *J. Phys. Chem.* 97, 4567 (1993).
70. L. Dähne, *J. Am. Chem. Soc.* 117, 12855 (1975).
71. F. Nüesch, J. E. Moser, V. Shklover, and M. Grätzel, *J. Am. Chem. Soc.* 118, 5420 (1996).

72. V. Czikkely, H. D. Försterling, and H. Kuhn, *Chem. Phys. Lett.* 6, 207 (1970).
73. V. Czikkely, G. Dreizler, H. D. Försterling, H. Kuhn, J. Sondermann, P. Tillmann, and J. Z. Wiegand, *Naturforsch.* 24a, 1821 (1969).
74. M. Rikukawa and M. F. Rubner, *Langmuir* 10, 519 (1994).
75. R. Strohmaier, C. Ludwig, J. Petersen, B. Gompf, and W. J. Eisenmenger, *J. Vac. Sci. Technol. B* 14, 1079 (1996).
76. S. Heutz, S. M. Bayliss, R. L. Middleton, G. Rumbles, and T. S. Jones, *J. Phys. Chem. B* 104, 7124 (2000).
77. S. M. Bayliss, S. Heutz, G. Rumbles, and T. S. Jones, *Phys. Chem. Chem. Phys.* 1, 3673 (1999).
78. R. O. Loutfy, *Can. J. Chem.* 59, 549 (1981).
79. M. Nakamura, Y. Morita, Y. Mori, A. Ishitani, and H. Tokumoto, *J. Vac. Sci. Technol. B* 14, 1109 (1996).
80. M. Pomerantz, A. Aviram, R. A. McCorkle, L. Li, and A. G. Schrott, *Science* 255, 1115 (1992).
81. H. Tanaka and T. Kawai, *Jpn. J. Appl. Phys.* 35, 3759 (1996).
82. F. Rochet, G. Dufour, H. Roulet, N. Motta, A. Sgarlata, M. Piancastelli, and M. D. Crescenzi, *Surf. Sci.* 319, 10 (1994).
83. X. Lu and K. W. Hipps, *J. Phys. Chem. B* 101, 5391 (1997).
84. B. Mathias, R. Berndt, and W. D. Schneider, *Phys. Rev. B* 55, 1384 (1996).
85. A. Rosa and E. J. Baerends, *Inorg. Chem.* 33, 584 (1994).
86. P. A. Reynolds and B. N. Figgis, *Inorg. Chem.* 30, 2294 (1991).
87. K. W. Hipps, X. Lu, D. Wang, and U. Mazur, *J. Phys. Chem.* 100, 11207 (1996).
88. M. Scrocco, C. Ercolani, and A. M. Paoletti, *J. Electron Spectrosc. Relat. Phenom.* 63, 155 (1993); H. J. Joswig, H. H. Schmidt, F. Steinbach, and R. Stritzel, in "Proc. Int. Congr. Catal.," 6th ed. (G. C. Bond, P. B. Wells, and F. C. Tompkins, Eds.), Vol. 1, pp. 583–592. Chemical Society, Letchworth, UK, 1997.
89. I. Chizhov, G. Scoles, and A. Kahn, *Langmuir* 16, 4358 (2000).
90. J. A. Stroscio and W. J. Kaiser, "Scanning Tunneling Microscopy." Academic Press, New York, 1993.
91. R. Wiesendanger and H. J. Guntherodt, "Scanning Tunneling Microscopy II." Springer-Verlag, New York, 1992.
92. R. M. Tromp, E. J. Van Loenen, J. E. Demuth, and N. D. Lang, *Phys. Rev. B* 37, 9042 (1988).
93. R. J. Hamers, *Annu. Rev. Phys. Chem.* 40, 531 (1989).
94. L. Scudiero, D. E. Barlow, and K. W. Hipps, *J. Phys. Chem. B* 106, 996 (2002).
95. J. V. Barth, H. Brune, G. Ertl, and R. Behm, *J. Phys. Rev. B* 42, 9307 (1990).
96. Z. Mizugushi, G. Rihs, and H. R. Karfunkel, *J. Phys. Chem.* 99, 16217 (1995).
97. W. Hiller, J. Strahle, W. Kobel, and M. Z. Hanack, *Kristallogr.* 159, 173 (1982).
98. K. Oda, O. Okada, and K. Nukada, *Jpn. J. Appl. Phys.* 31, 2181 (1992).
99. (a) H. Yonehara, H. Etori, M. K. Engel, M. Tsushima, N. Ikeda, and T. Ohno, *Chem. Mater.* 13, 1015 (2001). (b) M. Brinkmann, J. C. Wittmann, M. Barthel, M. Hanack, and C. Chaumont, *Chem. Mater.* 14, 904 (2002).
100. A. Yamashita, T. Maruno, and T. Hayashi, *J. Phys. Chem.* 97, L4567 (1993).
101. A. Yamashita, T. Maruno, and T. Hayashi, *J. Phys. Chem.* 98, 12695 (1994).
102. H. Yanagi, T. Mikami, H. Tada, T. Terui, and S. Mashiko, *J. Appl. Phys.* 81, 7306 (1997).
103. A. Yamashita, S. Matsumoto, S. Sakata, T. Hayashi, and H. Kanbara, *J. Phys. Chem. B* 102, 5165 (1998).
104. H. S. Nalwa, T. Saito, A. Kakuta, and T. Iwayanagi, *J. Phys. Chem.* 97, 10515 (1993).
105. M. Adams, Kerimo, J. C. Olson, Zaban, A. Gregg, and F. Barbara, *J. Am. Chem. Soc.* 119, 10608 (1997).
106. D. Schlettwein, K. Hesse, H. Tada, S. Mashiko, U. Storm, and J. Binder, *Chem. Mater.* 12, 989 (2000).
107. D. Schlettwein, H. Graaf, J. P. Meyer, T. Oekermann, and N. I. Jaeger, *J. Phys. Chem. B* 103, 3078 (1999).
108. D. Schlettwein, H. Tada, and S. Mashiko, *Langmuir* 16, 2872 (2000).
109. Z. Bao, A. J. Lovinger, and A. Dobabalapur, *Appl. Phys. Lett.* 69, 3066 (1996).
110. Z. Bao, A. J. Lovinger, and A. Dobabalapur, *Adv. Mater.* 9, 42 (1997).
111. G. Guillaud and J. Simon, *Chem. Phys. Lett.* 219, 123 (1994).
112. G. Guillaud, R. Ben Chaabane, C. Jouve, and M. Gamoudi, *Thin Solid Films* 258, 279 (1995).
113. A field-effect mobility of 0.015 cm<sup>2</sup>/V s was reported by Guillaud et al. for lutetium bisphthalocyanine after annealing in air at 150 °C for 2 days. G. Guillaud, M. A. Sadoun, and M. Maitrot, *Chem. Phys. Lett.* 167, 503 (1990).
114. D. M. De Leeuw, M. M. J. Simenon, A. R. Brown, and R. E. F. Einerhand, *Synth. Met.* 87, 53 (1997).
115. T. L. Anderson, G. C. Komplin, and W. J. Pietro, *J. Phys. Chem.* 97, 6577 (1993).
116. W. Pietro, *J. Adv. Mater.* 6, 239 (1994).
117. Z. Bao, A. J. Lovinger, and J. Brown, *J. Am. Chem. Soc.* 120, 207 (1998).
118. A. P. Kam, R. Aroca, and J. Duff, *Chem. Mater.* 13, 4463 (2001).
119. (a) H. Yanagi, M. Ashida, J. Elbe, and D. Wöhrle, *J. Phys. Chem.* 94, 7056 (1990). (b) H. Yanagi, T. Kouzeki, M. Ashida, T. Noguchi, A. Manivannan, K. Hashimoto, and A. Fujishima, *J. Appl. Phys.* 71, 5146 (1992). (c) H. Yanagi, T. Kouzeki, and M. Ashida, *J. Appl. Phys.* 73, 3812 (1993).
120. C. H. Griffiths, M. S. Walker, and P. Goldstein, *Mol. Cryst. Liq. Cryst.* 33, 149 (1976).
121. T. J. Klofta, P. C. Rieke, C. L. Linkous, W. J. Buttner, A. Nanthakumar, T. D. Mewborn, and N. R. Armstrong, *J. Electrochem. Soc.* 132, 2134 (1985); T. J. Klofta, J. Danziger, P. Lee, J. Pankow, K. W. Nebesney, and N. R. Armstrong, *J. Phys. Chem.* 91, 5646 (1987); H. Yanagi, M. Ashida, Y. Harima, and K. Yamashita, *Chem. Lett.* 385 (1990); H. Yanagi, S. Douko, Y. Ueda, M. Ashida, and D. Wöhrle, *J. Phys. Chem.* 96, 1366 (1992); L. K. Chau, C. Arbour, G. E. Collins, K. W. Nebesney, P. A. Lee, C. D. England, N. R. Armstrong, and B. A. Parkinson, *J. Phys. Chem.* 97, 2690 (1993); M. Era, T. Tsutsui, and S. Saito, *Appl. Phys. Lett.* 67, 2436 (1995).
122. T. Kouzeki, S. Tatezono, and H. Yanagi, *J. Phys. Chem.* 100, 20097 (1996).
123. S. A. Mikhaleenko and E. A. Luk'yanets, *Zh. Obshch. Khim.* 39, 2554 (1969); B. L. Wheeler, G. Nagasubramanian, A. J. Bard, L. A. Schechtman, D. R. Dininny, and M. E. Kenny, *J. Am. Chem. Soc.* 106, 7404 (1984); D. Wöhrle, J. Gitzel, G. Krawczyk, E. Tsuchida, H. Ohno, I. Okura, and T. Nishisaka, *J. Macromol. Sci. Chem. A* 25, 1227 (1988); M. L. Kaplan, A. J. Lovinger, Jr., W. D. Reents, and P. H. Schmidt, *Mol. Cryst. Liq. Cryst.* 112, 345 (1984).
124. E. A. Lucia and F. D. Verderame, *J. Phys. Chem.* 48, 2674 (1968).
125. V. I. Gavrilov, N. V. Butasova, E. A. Luk'yanets, and I. V. Shelpein, *Electrokhimiya* 16, 1611 (1980); J. M. Green and L. R. Faulkner, *J. Am. Chem. Soc.* 105, 2950 (1983).
126. (a) M. Shimura, K. Satoh, T. Idenuma, and Y. Shimura, *Hyomen Gijutsu* 41, 938 (1990). (b) H. Yanagi and M. Toriida, *J. Electrochem. Soc.* 141, 64 (1984).
127. J. M. Fox, T. J. Katz, S. V. Elshocht, T. Verfirst, M. Kauranen, A. Persoon, T. Thongpanchang, T. Krauss, and L. Brus, *J. Am. Chem. Soc.* 121, 3453 (1999).
128. M. Kimura, T. Muto, H. Takimoto, K. Wada, K. Ohta, K. Hanabusa, H. Shirai, and N. Kobayashi, *Langmuir* 16, 2078 (2000).
129. E. J. Osburn, A. Schmidt, L. K. Chau, S. Chen, P. Smolenyak, N. R. Armstrong, and D. F. O'Brien, *Adv. Mater.* 8, 926 (1996).

130. E. J. Osburn, L. K. Chau, S. Y. Chen, N. Collins, D. F. O'Brien, and N. R. Armstrong, *Langmuir* 12, 4784 (1996).
131. K. Ohta, R. Higashi, M. Ikejima, I. Yamamoto, and N. Kobayashi, *J. Mater. Chem.* 8, 1979 (1998).
132. (a) H. Engelkamp, C. F. Van Nostrum, S. J. Picken, and R. Nolte, *Chem. Commun.* 979 (1998). (b) C. F. Van Nostrum, A. W. Bosman, G. H. Gelinck, P. G. Schouten, J. M. Warman, A. P. M. Kentgens, M. A. C. Devillers, A. Meijerink, S. J. Picken, U. Sohling, A. J. Schouten, and R. Nolte, *Chem. Eur. J.* 1, 171 (1995).
133. C. F. Van Nostrum, S. J. Picken, A. J. Schouten, and R. Nolte, *J. Am. Chem. Soc.* 117, 9957 (1995); H. Engelkamp, S. Middelbeek, and R. Nolte, *Science* 284, 765 (1999).
134. P. Smolenyak, R. Peterson, K. Nebesny, M. Törker, D. F. O'Brien, and N. R. Armstrong, *J. Am. Chem. Soc.* 121, 8628 (1999).
135. T. Inabe, J. G. Gaudiello, M. K. Mofuel, J. W. Lyding, R. L. Burton, W. J. McCarthy, C. R. Kannewurf, and T. J. Marks, *J. Am. Chem. Soc.* 108, 7595 (1986).
136. B. I. Greene and R. R. Millard, *Phys. Rev. Lett.* 55, 1331 (1985).
137. Z. Z. Ho and N. Peyghambarian, *Chem. Phys. Lett.* 148, 107 (1988).
138. A. Teresaki, M. Hosoda, T. Wada, H. Tada, A. Koma, A. Yamada, H. Sasabe, A. F. Garito, and T. Kobayashi, *J. Phys. Chem.* 96, 10534 (1992).
139. M. K. Casstevens, M. Samoc, J. Pflieger, and P. N. Prasad, *J. Chem. Phys.* 92, 2019 (1990).
140. S. Isoda, S. Hashimoto, T. Ogawa, H. Kurata, S. Moriguchi, and T. Kobayashi, *Mol. Cryst. Liq. Cryst.* 247, 191 (1994).
141. Z. Bao, A. J. Lovinger, and J. Brown, *J. Am. Chem. Soc.* 120, 207 (1998).
142. J. P. Meyer, Dissertation, Universität Bremen, Bremen, 1997.
143. A. Ioannidis and J. P. Dodelet, *J. Phys. Chem. B* 101, 891 (1997).
144. A. Ioannidis and J. P. Dodelet, *J. Phys. Chem. B* 101, 901 (1997).
145. A. Ioannidis and J. P. Dodelet, *J. Phys. Chem. B* 101, 5100 (1997).
146. K. Hesse and D. Schlettwein, *J. Electroanal. Chem.* 476, 148 (1999).
147. S. Hiller, D. Schlettwein, N. R. Armstrong, and D. Wöhrle, *J. Mater. Chem.* 8, 945 (1998).
148. E. Karmann, J. P. Meyer, D. Schlettwein, N. I. Jaeger, M. Anderson, A. Schmidt, and N. R. Armstrong, *Mol. Cryst. Liq. Cryst.* 283, 283 (1996).
149. D. Schlettwein, D. Wöhrle, E. Karmann, and U. Melville, *Chem. Mater.* 6, 3 (1994).
150. D. Schlettwein, N. R. Armstrong, P. A. Lee, and K. W. Nebesny, *Mol. Cryst. Liq. Cryst.* 253, 161 (1994).
151. J.-P. Meyer, D. Schlettwein, D. Wöhrle, and N. I. Jaeger, *Thin Solid Films* 258, 317 (1995).
152. S. R. Forrest, *Chem. Rev.* 57, 11793 (1997).
153. A. Schmidt, L. K. Chau, A. Back, and N. R. Armstrong, in "Phthalocyanines: Properties and Applications" (C. C. Leznoff and A. B. P. Lever, Eds.), VCH, New York, 1996.
154. R. Hochstrasser and M. Kasha, *Photochem. Photobiol.* 3, 317 (1964).
155. M. Kasha, in "Spectroscopy of the Excited State" (B. Di Bartolo, Ed.), Plenum, New York, 1976.
156. M. Kimura, K. Wada, K. Ohta, K. Hanabusa, H. Shirai, and N. Kobayashi, *J. Am. Chem. Soc.* 123, 2438 (2001).
157. S. A. Bagshaw, W. Prouzet, and T. J. Pinnavaia, *Science* 269, 1242 (1995); D. Zhao, J. Feng, Q. Huo, N. Melosh, G. H. Fredrickson, B. F. Chmelka, and G. D. Stucky, *Science* 279, 548 (1998); P. Yang, D. Zhao, D. I. Margolese, B. F. Chmelka, and G. D. Stucky, *Nature* 396, 152 (1998); P. Feng, X. Bu, G. D. Stucky, and D. J. Pine, *J. Am. Chem. Soc.* 122, 994 (2000).
158. M. J. Stillman and T. Nyokong, in "Phthalocyanines Properties and Applications" (C. C. Leznoff and A. P. Lever, Eds.), Vol 1, p. 135. VCH, New York, 1989.
159. S. B. Lei, C. Wang, S. X. Yin, and C. L. Bai, *J. Phys. Chem. B* 105, 12272 (2001).
160. B. Xu, S. Yin, C. Wang, X. Qui, Q. Zeng, and C. Bai, *J. Phys. Chem. B* 104, 10502 (2000).
161. J. P. Rabe and S. Buchhiz, *Science* 253, 424 (1991); S. D. Feyter, P. C. M. Grim, M. Rucker, P. Vanoppen, C. Meiners, M. Sieffert, S. Valiyaveetil, K. Mullen, and F. C. D. Schryver, *Angew. Chem. Int. Ed. Commun.* 37, 1223 (1998); P. Bhyrappa, S. R. Wilson, and K. S. Suslick, *Supramol. Chem.* 9, 169 (1998); R. K. Kumar, S. Balasubramanian, and I. Goldberg, *Inorg. Chem.* 37, 541 (1998); Y. Diskin-Posner and I. Goldberg, *Chem. Commun.* 1961 (1996); Y. Diskin-Posner, R. K. Kumar, and I. Goldberg, *New J. Chem.* 23, 885 (1999).
162. D. M. Cyr, B. Venbataraman, G. W. Flynn, A. Black, and G. W. Whitesides, *J. Phys. Chem.* 100, 13747 (1996); L. Giancarlo, D. Cyr, K. Muyskens, and G. W. Flynn, *Langmuir* 14, 1465 (1998).
163. M. Hibino, A. Sumi, and I. Hatta, *J. Appl. Phys.* 34, 3354 (1995); C. L. Claypool, F. Faglioni, W. A. Goddard, and N. S. Lewis, *J. Phys. Chem. B* 103, 7077 (1999); C. L. Claypool, F. Faglioni, W. A. Goddard, H. B. Gray, N. S. Lewis III, and R. A. Marcus, *J. Phys. Chem. B* 101, 5978 (1997).
164. T. R. E. Simpson, D. A. Russell, I. Chambrier, M. J. Cook, A. B. Horn, and S. C. Thorpe, *Sens. Actuators B* 29, 353 (1995).
165. I. Chambrier, M. J. Cook, and D. A. Russell, *Synthesis* 1283 (1995).
166. T. R. E. Simpson, D. J. Revell, M. J. Cook, and D. A. Russell, *Langmuir* 13, 460 (1997).
167. M. J. Cook, R. Hersans, J. McMurdo, and D. A. Russell, *J. Mater. Chem.* 6, 149 (1996).
168. V. Huc, M. Saveyroux, J. P. Bourgoin, F. Valin, G. Zalczer, P. A. Albouy, and S. Palacin, *Langmuir* 16, 1770 (2000).
169. D. Li, L. W. Moore, and B. I. Swanson, *Langmuir* 10, 1177 (1994).
170. F. DaCruz, K. Driaf, C. Berthier, J. M. Lameille, and F. Armand, *Thin Solid Films* 349, 155 (1999).
171. F. Armand, P. A. Albouy, F. Da Cruz, M. Normand, V. Huc, and E. Goron, *Langmuir*, in press.
172. A. Ulman, "An Introduction to Ultrathin Organic Films: From Langmuir-Blodgett to Self-Assembly." Academic Press, San Diego, CA, 1991.
173. T. H. Tran-Thi, S. Palacin, and B. Clergeot, *Chem. Phys. Lett.* 157, 92 (1989).
174. T. H. Tran-Thi, J. F. Lipskier, D. Houde, C. Pepin, R. Langlois, and S. Palacin, *J. Chem. Soc.* 88, 2529 (1992).
175. V. Huc, F. Armand, J. P. Bourgoin, and S. Palacin, *Langmuir* 17, 1928 (2001).
176. G. Decher, *Science* 277, 1232 (1997); D. M. Kaschak, J. T. Lean, C. C. Waraksa, B. S. Geoffrey, H. Usami, and T. E. Mallouk, *J. Am. Chem. Soc.* 121, 3435 (1999); J. W. Ostrander, A. A. Mamedov, and N. A. Kotov, *J. Am. Chem. Soc.* 123, 1101 (2001); Y. J. Liu, A. Wang, and R. O. Claus, *J. Phys. Chem. B* 101, 1385 (1997); Y. J. Liu and R. O. Claus, *J. Appl. Phys.* 85, 419 (1999).
177. D. Q. Li, A. Bishop, Y. Gim, X. B. Shi, M. R. Fitzsimmons, and Q. X. Jia, *Appl. Phys. Lett.* 73, 2645 (1998); J. B. Schlenoff, D. Laurent, and H. Ly, *J. Adv. Mater.* 10, 347 (1998).
178. Q. X. Jia, L. S. Li, and D. Q. Li, *Chem. Mater.* 14, 1159 (2002).
179. L. S. Li, R. Wang, M. Fitzsimmons, and D. Q. Li, *J. Phys. Chem. B* 104, 11195 (2000).
180. D. Q. Li, M. A. Ratner, T. J. Marks, C. H. Zhang, J. Yang, and G. K. Wong, *J. Am. Chem. Soc.* 112, 7389 (1990).
181. N. Lavrik and D. Leckband, *Langmuir* 16, 1842 (2000).
182. S. Fouriaux, F. Armand, O. Araspin, A. Ruoudelteixier, E. M. Maya, P. Vazquez, and T. Torres, *J. Phys. Chem.* 100, 16984 (1996).
183. V. I. Vlaskin, O. P. Dimitriev, Z. I. Kazantseva, and A. V. Nabok, *Thin Solid Films* 286, 40 (1996).
184. T. M. Cooper, A. L. Campbell, and R. L. Crane, *Langmuir* 11, 2713 (1995).
185. A. Ferencz, D. Neher, M. Schulze, G. Wegner, L. Viaene, and F. C. Deschryver, *Chem. Phys. Lett.* 245, 23 (1995).
186. M. Abkowitz and A. R. Monahan, *J. Chem. Phys.* 58, 2281 (1972); Y. Sakakibara, K. Saito, and T. Tani, *Jpn. J. App. Phys. I* 37, 695 (1998).



187. J. P. A. Heuts, E. Schipper, P. Piet, and A. L. German, *Theochem. J. Mol. Struct.* 333, 39 (1995).
188. J. Souto, Y. Gorbunova, M. L. Rodriguezmendez, S. Kudrevich, J. E. Vanlier, and J. A. Desaja, *J. Raman Spectrosc.* 27, 649 (1996).
189. M. Burghard, M. Schmelzer, S. Roth, P. Haisch, and M. Hanack, *Langmuir* 10, 426 (1994).
190. E. T. Vandernberg, L. Bertilsson, B. Liedberg, K. Uvdal, R. Erlandsson, H. Elwing, and I. Lundstrom, *J. Colloid Interface Sci.* 174, 103 (1991).
191. D. L. Pilloud, C. C. Moser, K. S. Reddy, and P. L. Dutton, *Langmuir* 14, 4809 (1998).
192. P. Miao, A. W. Robinson, R. E. Palmer, B. M. Kariuki, and K. D. M. Harris, *J. Phys. Chem. B* 104, 1285 (2000).
193. L. Ottaviano, S. Santucci, S. Di Nardo, L. Lozzi, M. Passacantando, and P. Picozzi, *J. Vac. Sci. Technol.* 15, 1014 (1997).
194. P. Dyreklev and G. Gustafsson, *O. Inganas. Synth. Met.* 55, 4093 (1993); Y. Y. Lin, D. J. Gundlach, S. F. Nelson, and T. N. Jackson, *IEEE Electron Device Lett.* 18, 606 (1997); D. J. Gundlach, T. N. Jackson, D. G. Schlom, and S. F. Nelson, *Appl. Phys. Lett.* 74, 3302 (1999); Z. Bao, A. J. Lovinger, and A. Dodabalapur, *Adv. Mater.* 9, 42 (1997); G. Xu, Z. Bao, and J. T. Groves, *Langmuir* 16, 1834 (2000); H. Sirringhaus, R. J. Wilson, R. H. Friend, M. Inbasekaran, W. Wu, E. P. Woo, M. Grell, and D. D. C. Bradley, *Appl. Phys. Lett.* 77, 406 (2000).
195. R. N. Marks, R. Zamboni, and C. Taliani, *Mater. Res. Soc. Symp. Proc.* 413, 425 (1996); C. Videlot and D. Fichou, *Synth. Met.* 102, 885 (1999).
196. M. Era, T. Tsutsui, and S. Shogo, *Appl. Phys. Lett.* 67, 2436 (1995); P. Dyreklev, M. Berggren, O. Inganas, M. R. Andersson, Wennerstrom, and T. Hjertberg, *Adv. Mater.* 7, 43 (1995); G. Wegner, D. Neher, M. Remmers, V. Cimrova, and M. Schulze, *Mater. Res. Soc. Symp. Proc.* 413, 23 (1996); M. Grell, W. Knoll, D. Lupo, A. Meisel, T. Miteva, D. Neher, H. G. Nothofer, U. Scherf, and A. Yasuda, *Adv. Mater.* 11, 671 (1999); X. L. Chen, Z. Bao, B. J. Sapjeta, A. J. Lovinger, and B. Crone, *Adv. Mater.* 12, 344 (2000).
197. R. A. P. Zangmeister, P. E. Smolenyak, A. S. Drager, D. F. O'Brien, and N. R. Armstrong, *Langmuir* 17, 7071 (2001).
198. A. M. van de Craats and J. Warma, *Adv. Mater.* 13, 130 (2001).
199. S. J. Tans, L. J. Geerligs, C. Dekker, J. Wu, and G. Wegner, *J. Vac. Sci. Technol. B* 15, 586 (1997); J. Wu, G. Lieser, and G. Wegner, *Adv. Mater.* 8, 151 (1996).
200. K. C. Janda, J. C. Hemminger, J. S. Winn, and S. E. Novick, *J. Chem. Phys.* 63, 1419 (1975); J. M. Steed, T. A. Dixon, and W. Klemperer, *J. Chem. Phys.* 70, 4940 (1979); G. Karlstrom, P. Linse, A. Wallqvist, and B. Jonsson, *J. Am. Chem. Soc.* 105, 3777 (1983); S. K. Burley and G. A. Petsko, *Science* 229, 23 (1985); M. C. Grosel, A. K. Cheetham, D. A. O. Hope, and S. C. Weston, *J. Org. Chem.* 58, 6654 (1993); S. Paliwal, S. Geib, and C. S. Wilcox, *J. Am. Chem. Soc.* 116, 4497 (1994).
201. D. G. Whitten, L. Chen, H. C. Geiger, J. Perlstein, and X. Song, *J. Phys. Chem. B* 102, 10098 (1998).
202. C. C. Leznoff and A. B. P. Lever, "Phthalocyanines: Properties and Applications," Vols. 1–4, VCH, New York, 1989, 1993, 1996.
203. A. Ulman, "An Introduction to Ultrathin Organic Films." Academic Press, San Diego, CA, 1991; M. C. Petty, "Langmuir–Blodgett Films, An Introduction." Cambridge Univ. Press, Cambridge, UK, 1996.
204. R. Aroca, C. Jennings, G. J. Kovacs, O. Loutfy, and P. S. Vincett, *J. Phys. Chem.* 89, 4051 (1985).
205. D. P. Dilella, W. R. Barger, A. W. Snow, and R. R. Smardzewski, *Thin Solid Films* 133, 207 (1985).
206. D. W. Kalina and S. W. Crane, *Thin Solid Films* 134, 109 (1985).
207. G. J. Kovacs, R. O. Loutfy, P. S. Vincett, C. Jennings, and R. Aroca, *Langmuir* 2, 689 (1986).
208. G. J. Kovacs, C. A. Jennings, R. O. Loutfy, and P. S. Vincett, *Langmuir* 4, 518 (1988).
209. H. Oyanagi, M. Yoneyama, K. Ikegami, M. Sugi, S. Kuroda, T. Ishiguro, and T. Matsushita, *Thin Solid Films* 159, 435 (1988).
210. W. Barger, J. Dote, M. Klusty, R. Mowery, R. Price, and A. Snow, *Thin Solid Films* 159, 369 (1988).
211. E. Byrnda, I. Koropeckey, L. Kalvoda, and S. Nespurek, *Thin Solid Films* 199, 375 (1991).
212. M. Burgard, M. Schmelzer, S. Roth, P. Haisch, and M. Hanack, *Langmuir* 10, 4265 (1994).
213. P. A. Albouy, *J. Phys. Chem.* 98, 8543 (1994).
214. M. J. Cook, M. F. Daniel, A. J. Dunn, A. A. Gold, and A. J. Thomson, *J. Chem. Soc. Chem. Commun.* 863 (1986).
215. M. J. Cook, A. J. Dunn, A. A. Gold, and A. J. Thomson, *J. Chem. Soc. Dalton Trans.* 1583 (1988).
216. K. Ogawa, S. Kinoshita, H. Yonehara, H. Nakahara, and K. Fukuda, *J. Chem. Soc. Chem. Commun.* 4779 (1989).
217. K. Ogawa, H. Yonehara, T. Shoji, S. Kinoshita, E. Maekawa, H. Nakahara, and K. Fukuda, *Thin Solid Films* 178, 439 (1989).
218. L. Pasimeni, M. Meneghetti, R. Rella, L. Valli, C. Granito, and L. Troisi, *Thin Solid Films* 265, 58 (1995).
219. L. Pasimeni, U. Segre, A. Toffoletti, L. Valli, and A. Marigo, *Thin Solid Films* 284/285, 656 (1996).
220. (a) T. Saue, W. Caseri, G. Wegner, A. Vogel, and B. Hoffmann, *J. Phys. D* 23, 79 (1990). (b) H. Wang and J. B. Land, *Langmuir* 10, 790 (1994). (c) D. G. Zhu and M. C. Petty, *Sens. Actuators B* 2, 265 (1990). (d) T. Kume, S. Hayashi, H. Ohkuma, and K. Yamamoto, *Jpn. J. Appl. Phys.* 1 34, 6448 (1995). (e) G. Mchale, M. I. Newton, P. D. Hooper, and M. R. Willis, *Opt. Mater.* 6, 89 (1996).
221. S. G. Liu, Y. Q. Liu, Y. Xu, D. B. Zhu, A. C. Yu, and X. S. Zhao, *Langmuir* 14, 690 (1998).
222. X. D. Chai, K. Tian, H. J. Chen, X. Y. Tang, T. J. Li, Z. Q. Zhu, and D. Mobius, *Thin Solid Films* 178, 221 (1989).
223. M. Rikukawa and M. F. Rubner, *Thin Solid Films* 210/211, 274 (1992).
224. R. Rella, A. Serra, P. Siciliano, A. Tepore, L. Valli, and A. Zocco, *Thin Solid Films* 286, 256 (1996).
225. W. C. Moreira and R. Aroca, *Spectrochim. Acta A* 51, 2325 (1995).
226. R. Aroca, H. Bolourchi, D. Battisti, and K. Najafi, *Langmuir* 9, 3138 (1993).
227. K. R. Rickwood, D. R. Lovett, B. Lukas, and J. Silver, *J. Mater. Chem.* 5, 725 (1995).
228. J. Souto, M. L. Rodríguez-Méndez, J. de Saja-González, and J. de Saja, *Thin Solid Films* 284, 888 (1996).
229. R. E. Clavijo, D. Battisti, R. Aroca, G. J. Kovacs, and C. A. Jennings, *Langmuir* 8, 113 (1992).
230. M. Petty, D. R. Lovett, J. M. O'connor, and J. Silver, *Thin Solid Films* 179, 387 (1989); "Langmuir–Blodgett Films" (G. Roberts, Ed.). Plenum Press, New York, 1990; A. Ulman, "An Introduction to Ultrathin Organic Films—From Langmuir–Blodgett to Self-Assembly." Academic Press, New York, 1991; M. I. Governado-Mitre, R. Aroca, and J. A. DeSaja, *Langmuir* 11, 547 (1995).
231. P. Chen, D.-h Tang, X. Wang, H. Chen, M. Liu, J. Li, and X. Liu, *Colloids Surfaces A* 175, 171 (2000).
232. J. N. Israelachvili, D. J. Mitchell, and B. W. Ninham, *J. Chem. Soc. Faraday Trans. I* 72, 1525 (1976).
233. J. N. Israelachvili, "Intermolecular and Surface Forces." Academic Press, San Diego, 1992.
234. S. Baker, M. C. Petty, G. G. Roberts, and M. V. Twigg, *Thin Solid Films* 99, 53 (1983).
235. R. Aroca and D. Battisti, *Langmuir* 6, 250 (1990).
236. W. R. Barger, A. W. Snow, H. Wohltjen, and N. L. Jarvis, *Thin Solid Films* 133, 197 (1985).
237. R. A. Hann, S. K. Gupta, J. R. Fryer, and B. L. Eyres, *Thin Solid Films* 134, 35 (1985).
238. J. H. Kim, T. M. Cotton, R. A. Uphaus, and C. C. Leznoff, *Thin Solid Films* 159, 141 (1988).
239. K. Miyano, *Langmuir* 6, 1254 (1990).

240. K. Nichogi, K. Waragai, A. Taomoto, Y. Saito, and S. Asakawa, *Thin Solid Films* 179, 297 (1989).
241. G. G. Roberts, M. C. Petty, S. Baker, M. T. Fowler, and N. J. Thomas, *Thin Solid Films* 132, 113 (1985).
242. A. W. Snow and N. L. Jarvis, *J. Am. Chem. Soc.* 106, 4706 (1984).
243. G. Roberts, "Langmuir-Blodgett Films." Plenum Press, New York/London, 1990.
244. D. Lefevre, F. Porteu, P. Balog, M. Roullay, G. Zalcer, and S. Palacin, *Langmuir* 9, 150 (1993).
245. N. Minari, K. Ikegami, S. Kuroda, K. Saito, M. Saito, and M. Sugi, *J. Phys. Soc. Jpn.* 58, 222 (1989).
246. S. Schwiegk, T. Vahlenkamp, Y. Xu, and G. Wegner, *Macromol.* 25, 2513 (1992).
247. G. Wegner, *Thin Solid Films* 216, 105 (1992).
248. M. Seufert, C. Fakirov, and G. Wegner, *Adv. Mater.* 7, 52 (1995).
249. M. Matsumoto, T. Sekiguchi, H. Tanaka et al., *Chem. Lett.* 1085 (1988).
250. P. A. Albouy, M. Vandevyver, J. Perez, C. Ecoffet, D. Markovitsi, M. Veber, C. Jallabert, and H. Strzelecka, *Langmuir* 8, 2262 (1992).
251. M. Vandevyver, P. A. Albouy, C. Mingotaud, J. Perez, and A. Barraud, *Mol. Cryst. Liq. Cryst. A* 235, 51 (1993).
252. M. Vandevyver, P.-A. Albouy, C. Mingotaud, J. Perez, and A. Barraud, *Langmuir* 9, 1561 (1993).
253. C. Jegou, B. Agricole, M.-H. Li, E. Dupart, H. T. Nguyen, and C. Mingotaud, *Langmuir* 14, 1516 (1998).
254. C. Jegou, E. Dupart, P.-A. Albouy, and C. Mingotaud, *Thin Solid Films* 327/329, 1 (1998).
255. M. Fujiki, H. Tabei, and T. Kurihara, *Langmuir* 4, 1123 (1988).
256. H. Itoh, T. Koyama, K. Hanabusa, E. Masuda, H. Shirai, and T. Hayakawa, *J. Chem. Soc. Dalton Trans.* 1543 (1989).
257. D. W. Kalina and S. W. Crane, *Thin Solid Films* 134, 109 (1985).
258. Y. M. Lvov, O. B. Gurskaja, T. S. Berzina, and V. I. Troitsky, *Thin Solid Films* 182, 283 (1989).
259. N. B. McKeown, M. J. Cook, A. J. Thomson, K. J. Harrison, M. F. Daniel, R. M. Richardson, and S. J. Roser, *Thin Solid Films* 159, 469 (1988).
260. S. Palacin, A. Ruau-del-Teixier, and A. Barraud, *J. Phys. Chem.* 90, 6237 (1986).
261. S. Palacin, A. Ruau-del-Teixier, and A. Barraud, *Mol. Cryst. Liq. Cryst.* 156, 331 (1988).
262. S. Palacin, A. Ruau-del-Teixier, and A. Barraud, *J. Phys. Chem.* 93, 7195 (1989).
263. S. Fouriaux, F. Armand, O. Araspin, A. Ruau-del-Teixier, E. Maya, P. Vazquez, and T. Torres, *J. Phys. Chem.* 42, 16984 (1996).
264. M. Fukui, N. Katayama, Y. Ozaki, T. Araki, and K. Iriyama, *Chem. Phys. Lett.* 177, 247 (1991).
265. J. Liu, L. Xu, S. Shen, Q. Zhou, T. Li, and H. Xu, *J. Photochem. Photobiol. A* 71, 275 (1993).
266. M. A. Mohammed, P. Ottenbreit, W. Prass, G. Schnurpfeil, and D. Woehrl, *Thin Solid Films* 213, 285 (1992).
267. H. Nakahara, K. Z. Sun, K. Fukuda, N. Azuma, H. Nishi, H. Uchida, and T. Katsube, *J. Mater. Chem.* 5, 395 (1995).
268. S. Palacin, *Adv. Colloid Interface Sci.* 87, 165 (2000).
269. F. Porteu, S. Palacin, A. Ruau-del-Teixier, and A. Barraud, *J. Phys. Chem.* 95, 7438 (1991).
270. M. J. Cook, A. J. Dunn, M. F. Daniel, R. C. O. Hart, R. M. Richardson, and S. J. Roser, *Thin Solid Films* 159, 395 (1988).
271. P. E. Smolenyak, E. J. Osburn, S. Y. Chen, L.-K. Chau, D. F. O'Brien, and N. R. Armstrong, *Langmuir* 13, 6568 (1997).
272. (a) G. C. Bryant, M. J. Cook, C. Ruggiero, T. G. Ryan, A. J. Thorne, S. D. Haslam, and R. M. Richardson, *Thin Solid Films* 243, 316 (1994); (b) A. Cole, R. J. McLlroy, S. C. Thorpe, M. J. Cook, J. McMurdo, and A. K. Ray, *Sens. Actuators B* 13, 416 (1993); (c) M. J. Cook, M. F. Daniel, K. J. Harrison, N. B. McKeown, and A. J. Thomson, *J. Chem. Soc. Chem. Commun.* 1148 (1987); (d) M. J. Cook, N. B. McKeown, A. J. Thompson, and K. J. Harrison, in "Anal. Appl. Spectrosc. [Proc. Int. Conf.]" (C. Creaser, Ed.), R394, 1988; (e) M. J. Cook, N. B. McKeown, J. M. Simmons, A. J. Thomson, M. F. Daniel, K. J. Harrison, R. M. Richardson, and S. J. Roser, *J. Mater. Chem.* 1, 121 (1991); (f) M. J. Cook, *J. Mater. Sci. Mater. Electron.* 5, 117 (1994); (g) O. Omar, A. K. Ray, A. K. Hassan, Z. Ghassemlooy, and M. J. Cook, *Proc. SPIE* 2852, 81 (1996).
273. F. Armand, M. V. Martinez-Diaz, B. Cabezón, P. A. Albouy, A. Ruau-del-Teixier, and T. Torres, *J. Chem. Soc. Chem. Commun.* 1673 (1995); F. Armand, B. Cabezón, M. V. Martinez-Diaz, A. Ruau-del-Teixier, and T. Torres, *J. Mater. Chem.* 7, 1741 (1997).
274. P. A. Albouy, *J. Phys. Chem.* 98, 8543 (1994).
275. J. P. Bourgoïn, F. Doublet, S. Palacin, and M. Vandevyver, *Langmuir* 12, 6473 (1996).
276. J. P. Bourgoïn and S. Palacin, *Langmuir* 14, 3967 (1998).
277. J. P. Bourgoïn, R. V. Sudiwala, and S. Palacin, *J. Vacuum Sci. Technol. B* 14, 3381 (1996).
278. A. W. Snow and W. R. Barger, in "Phthalocyanines: Properties and Applications" (C. C. Leznoff and A. B. P. Lever, Eds.), p. 345. VCH, New York, 1989.
279. M. Velez, S. Vieira, I. Chambrier, and M. J. Cook, *Langmuir* 14, 4221 (1998).
280. J. E. Frommer, *Angew. Chem. Int. Ed. Engl.* 31, 1298 (1992).
281. Y. Q. Liu, W. P. Hu, Y. Xu, S. G. Liu, and D. B. Zhu, *J. Phys. Chem. B* 104, 11859 (2000).
282. J. R. Fryer, C. M. McConnell, R. A. Hann, B. L. Eyres, and S. K. Gupta, *Philos. Mag. B* 61, 843 (1990).
283. J. P. Lloyd, C. Pearson, and M. C. Petty, *Thin Solid Films* 160, 431 (1988).
284. S. Fouriaux, F. Armand, O. Araspin, A. Ruau-del-Teixier, E. M. Maya, P. Vazquez, and T. Torres, *J. Phys. Chem.* 100, 16984 (1996).
285. M. Kasha, H. R. Rawls, and M. A. El-Bayoumi, *Pure Appl. Chem.* 11, 371 (1965).
286. (a) J. Simon and P. Bassoul, in "Phthalocyanines: Properties and Applications" (A. B. P. Leznoff, Ed.), Vol. 2, p. 223. VCH, New York, 1993. (b) G. Wegner, *Mol. Cryst. Liq. Cryst.* 235, 1 (1993). (c) M. K. Engel, P. Bassoul, L. Bosio, H. Lehmann, M. Hanack, and J. Simon, *Liquid Cryst.* 15, 709 (1993). (d) C. F. van Nostrum, A. W. Bosman, G. H. Gelinck, P. G. Schouten, J. M. Warman, P. M. Kentgens, M. A. C. Devillers, A. Meijerink, S. J. Picken, U. Sohling, A. J. Shouten, and R. J. M. Nolte, *J. Chem. Eur.* 1, 171 (1995). (e) M. Hanack, A. Beck, and H. Lehmann, *Synthesis* 703 (1987). (f) G. Pawlowski and M. Hanack, *Synthesis* 287 (1980). (g) M. J. Cook, *J. Mater. Sci. Mater. Electron.* 5, 117 (1994).
287. T. Toupance, V. Ahsen, and J. Simon, *J. Am. Chem. Soc.* 116, 5352 (1994); J. Vacus and J. Simon, *Adv. Mater.* 7, 797 (1995); T. Toupance, M. Bassoul, L. Mineau, and J. Simon, *J. Phys. Chem.* 100, 11704 (1996); G. J. Clarkson, N. B. McKeown, and K. E. Treacher, *J. Chem. Soc. Perkin Trans.* 1, 1817 (1995); C. Piechocki and J. Simon, *Nuovo. Chim.* 9, 159 (1985).
288. C. F. van Nostrum, S. J. Picken, R. J. Nolte, and M. Angew. Chem. Int. Ed. Engl. 33, 2173 (1994); C. F. van Nostrum, S. J. Picken, A. J. Schouten, and R. J. M. Nolte, *J. Am. Chem. Soc.* 117, 9957 (1995).
289. Y. Liu, W. Hu, W. Qiu, Y. Xu, S. Zhou, and D. Zhu, *Sensors Actuators B* 80, 20 (2001).
290. T. Manaka and M. Iwamoto, *Thin Solid Films* 393, 119 (2001).
291. H. Liu, Y. Liu, C. Zhu, M. Liu, C. Wang, C. Chen, and F. Xi, *Synthetic Metals* 131, 135 (2002).
292. (a) C. M. Dooling, T. H. Richardson, L. Valli, R. Rella, and J. Jiang, *Colloids Surfaces A* 198, 791 (2002). (b) R. Rella, A. Serra, P. Siciliano, A. Tepore, L. Troisi, and L. Valli, *Thin Solid Films* 870, 284 (1996). (c) Y. H. Ju, C. Hsieh, and C. J. Liu, *Thin Solid Films* 342, 238 (1999). (d) P. D. Hooper, M. I. Newton, G. McHale, and M. R. Willis, *Semicond. Sci. Technol.* 12, 455 (1997). (e) J. P.

- Germain, A. Pauly, C. Maleysson, J. P. Blanc, and B. Schöllhorn, *Thin Solid Films* 333, 253 (1998).
293. M. L. Rodríguez-Méndez, J. Souto, R. de Saja, J. Martínez, and J. A. de Saja, *Sens. Actuators B* 58, 544 (1999).
  294. K. Persaud and G. H. Dodd, *Nature* 299, 352 (1982); P. N. Bartlett, N. Blair, and J. W. Gardner, in "ASIC 15 Colloque Montpellier," p. 478, 1993; P. N. Bartlett, J. M. Elliot, and J. W. Gardner, *Food Technol.* 51, 44 (1997); E. Schaller, J. O. Bosser, and F. Escher, *Chimia* 53, 98 (1999); H. Ulmer, J. Mitrovics, G. Noetzel, U. Weimar, and W. Göpel, *Sens. Actuators B* 43, 24 (1997).
  295. A. Guadarrama, M. L. Rodríguez Méndez, J. A. de Saja, J. J. Ríos, and J. M. Olías, *Sens. Actuators B* 69, 276 (2000); R. Stella, J. N. Barisci, G. Serra, G. G. Wallace, and D. De-Rossi, *Sens. Actuators B* 63, 1 (2000).
  296. N. Gutierrez, M. L. Rodríguez-Méndez, and J. A. de Saja, *Sens. Actuators B* 77, 437 (2001).
  297. Y. Tanamura, T. Uchida, N. Teramae, M. Kikuchi, K. Kusaba, and Y. Onodera, *Nano Lett.* 1, 387 (2001).
  298. W. Liu, Y. Wang, L. Gui, and Y. Tang, *Langmuir* 15, 2130 (1999).
  299. V. Shklover, M. K. Nazeeruddin, S. M. Zakeeruddin, C. Barbè, A. Kay, T. Haibach, W. Steurer, R. Hermann, H. U. Nissen, and M. Grätzel, *Chem. Mater.* 9, 430 (1997).
  300. He, Hagfeldt and Lindquist, *Langmuir* 17, 2743 (2001).
  301. J. Texter and M. Leleental, *Langmuir* 15, 654 (1999).
  302. (a) N. B. McKeown, *J. Mater. Chem.* 10, 1979 (2000). (b) J. F. Van der Pol, E. Neelman, J. C. Van Mitenburg, J. W. Zwikker, R. J. M. Nolte, and W. Drenth, *Macromolecules* 23, 155 (1990).
  303. M. Kimura, K. Wada, K. Ohta, K. Hanabusa, H. Shirai, and N. Kobayashi, *Macromolecules* 34, 4706 (2001).
  304. W. J. Buttner, P. C. Reike, and N. R. Armstrong, *J. Phys. Chem.* 89, 1116 (1985).
  305. (a) J. Lim and E. Kim, *J. Korean Soc. Imaging Sci.* 3, 24 (1997). (b) J. Lim and E. Kim, *J. Korean Soc. Imaging Sci.* 4, 13 (1998). (c) D. S. Han, Y. J. Li, and E. Kim, *Synthetic Metals* 117, 203 (2001).
  306. "Phthalocyanine Materials" (N. B. McKeown, Ed.). Cambridge Univ. Press, New York, 1998.
  307. D. Schlettwein, T. Oekermann, T. Yoshida, M. Tochimoto, and H. Minoura, *J. Electroanal. Chem.* 481, 42 (2000).
  308. (a) D. S. Han, Y. J. Lee, J. S. Kim, and E. Kim, *Synthetic Metals* 117, 203 (2001). (b) E. Kim, Y. J. Li, D. S. Han, S. N. Lee, and M. J. Moon, *J. Korean Soc Imaging Sci.* 6, 21 (2000).
  309. C. J. Walsh and B. K. Mandal, *Chem. Mater.* 12, 287 (2000).
  310. H. S. Nalwa, in "Non-Linear Optics of Organic Molecules and Polymers" (H. S. Nalwa and S. Miyata, Eds.), pp. 611–797. CRC, Boca Raton, 1997.
  311. G. J. Clarkson, B. M. Hassan, D. R. Maloney, and N. B. McKeown, *Macromolecules* 29, 1854 (1996).
  312. J. F. Van der Pol, E. Neeleman, J. W. Zwikker, R. J. M. Nolte, W. Drenth, J. Aerts, R. Visser, and S. J. Picken, *Liq. Cryst.* 6, 577 (1989).
  313. C. Destrade, P. Foucher, H. Gasparoux, N. H. Tinh, A. M. Levelut, and J. Malthete, *Mol. Cryst. Liq. Cryst.* 106, 121 (1984).
  314. M. Kimura, H. Ueki, K. Ohta, K. Hanabusa, H. Shirai, and N. Kobayashi, *Langmuir* 18, 7683 (2002).
  315. B. R. Maughon, M. Weck, B. Mohr, and R. H. Grubbs, *Macromolecules* 30, 257 (1997); H. D. Maynard, S. Y. Okada, and R. H. Grubbs, *Macromolecules* 33, 6239 (2000).
  316. G. R. Newkome, R. K. Behara, C. N. Moorefield, and G. R. Baker, *J. Org. Chem.* 26, 7126 (1991).
  317. J. Fu, X. Li, D. K. P. Ng, and C. Wu, *Langmuir* 18, 3843 (2002).
  318. M. T. M. Choi, P. P. S. Li, and D. K. P. Ng, *Tetrahedron* 56, 3881 (2000).
  319. A. C. H. Ng, X. Y. Li, and D. K. P. Ng, *Macromolecules* 32, 5292 (1999); X. Y. Li, X. He, A. C. H. Ng, C. Wu, and D. K. P. Ng, *Macromolecules* 33, 2119 (2000); T. Ngai, G. Z. Zhang, X. Y. Li, D. K. P. Ng, and C. Wu, *Langmuir* 17, 1381 (2001); Z. Chen, X. Y. Li, T. Ngai, C. Wu, and D. K. P. Ng, *Langmuir* 17, 7957 (2001).
  320. M. Wang, H. Z. Chen, and S. L. Yang, *J. Photochem. Photobiol. A* 88, 183 (1995).
  321. H. Z. Chen, M. Wang, L. X. Feng, and S. L. Yang, *J. Appl. Polym. Sci.* 46, 1033 (1992).
  322. H. Z. Chen, M. Wang, L. X. Feng, and S. L. Yang, *J. Polym. Sci. A* 31, 1165 (1993); H. Z. Chen, M. Wang, L. X. Feng, and S. L. Yang, *J. Appl. Polym. Sci.* 49, 679 (1993); H. Z. Chen, M. Wang, L. X. Feng, and S. L. Yang, *J. Photochem. Photobiol. A* 70, 179 (1993).
  323. M. Wang, H. Z. Chen, J. L. Shen, and S. L. Yang, *J. Photochem. Photobiol. A* 94, 249 (1996).
  324. A. S. Drager, R. A. P. Zangmeister, N. R. Armstrong, and D. F. O'Brien, *J. Am. Chem. Soc.* 123, 3595 (2001).
  325. S. T. Nguyen, L. K. Johnson, R. H. Grubbs, and J. W. Ziller, *J. Am. Chem. Soc.* 114, 3974 (1992); E. L. Dias, S. T. Nguyen, and R. H. Grubbs, *J. Am. Chem. Soc.* 119, 3887 (1997).
  326. X. M. Zhao, J. Perlstein, and D. G. Whitten, *J. Am. Chem. Soc.* 116, 10463 (1994).
  327. C. Piechochi, J. Simon, A. Skoulios, D. Guillon, and P. Weber, *J. Am. Chem. Soc.* 104, 5245 (1982).
  328. M. Weck, B. Mohr, B. R. Maughon, and R. H. Grubbs, *Macromolecules* 30, 6430 (1997); D. Janietz, *J. Mater. Chem.* 8, 265 (1998); H. Ringsdorf, R. Wüstefeld, E. Zerta, M. Ebert, and J. H. Wendorff, *Angew. Chem. Int. Ed. Engl.* 28, 914 (1989); T. Wang, D. Yan, E. Zhou, O. Karthaus, and H. Ringsdorf, *Polymer* 39, 4509 (1998); P. H. J. Kouwer, W. F. Jager, W. J. Mijs, and S. J. Picken, *Macromolecules* 33, 4336 (2000).
  329. O. E. Sielcken, L. A. Van de Kuil, W. Drenth, J. Schoonman, and R. J. M. Nolte, *J. Am. Chem. Soc.* 112, 3086 (1990).
  330. G. Wegner, *Ber. Bunsenges. Phys. Chem.* 95, 11, 1326 (1991).
  331. M. Hanack and M. Lang, *Adv. Mater.* 6, 11, 819 (1996).
  332. D. Neher, *Adv. Mater.* 7, 8, 691 (1995).
  333. E. Orthmann and G. Wegner, *Angew. Chem. Int. Engl.* 25, 12, 1105 (1986).
  334. (a) A. Kalachev, T. Sauer, V. Vogel, N. A. Plate, and G. Wegner, *Thin Solid Films* 188, 341 (1990). (b) R. G. M. Crockett, A. J. Campbell, and F. R. Ahmed, *Polymer* 31, 602 (1990).
  335. M. Suzuki, A. Ferencz, S. Iida, V. Enkelmann, and G. Wegner, *Adv. Mater.* 5, 359 (1993).
  336. S. Iida, M. Schaub, M. Schulze, and G. Wegner, *Adv. Mater.* 5, 564 (1993).
  337. M. Schulze, *Trends Polym. Sci.* 2, 120 (1994).
  338. M. Büchel, Z. Sekkat, S. Paul, B. Weichart, H. Menzel, and W. Knoll, *Langmuir* 11, 4460 (1995).
  339. C. D. Henry, H. Tebbe, G. Wegner, F. Armand, and A. Ruau-del-Teixier, *Adv. Mater.* 9, 805 (1997); C. Henry, F. Armand, O. Araspin, J. P. Bourgoin, and G. Wegner, *Chem. Mater.* 11, 1024 (1999).
  340. M. Nicolau, C. Henry, M. V. Martínez-Díaz, T. Torres, F. Armand, S. Palacin, A. Ruau-del-Teixier, and G. Wegner, *Synthetic Metals* 102, 1521 (1999).
  341. P. Gattinger, H. Rengel, D. Neher, M. Gurka, M. Buck, A. M. van de Craats, and J. M. Warman, *J. Phys. Chem. B* 103, 3179 (1999).
  342. (a) Th. Sauer and G. Wegner, *Mol. Cryst. Liq. Cryst.* 162, 97 (1998). (b) W. Casei, T. Sauer, and G. Wegner, *Makromol. Chem. Rapid Commun.* 9, 651 (1988). (c) T. Sauer, W. Caseri, and G. Wegner, *Mol. Cryst. Liq. Cryst.* 183, 387 (1990).
  343. E. Orthmann and G. Wegner, *Angew. Chem.* 98, 1114 (1986).
  344. P. A. Albouy, M. Schaub, and G. Wegner, *Acta Polymer* 45, 210 (1994).
  345. S. Mittler-Neher, D. Neher, G. I. Stegeman, F. W. Embs, and G. Wegner, *Chem. Phys.* 161, 289 (1992); M. Cha, D. Neher,

- F. W. Embs, S. Mittler-Neher, and G. Stegeman, *Chem. Phys. Lett.* 202, 44 (1993).
346. G. Wegner and K. Mathauer, *Mater. Res. Soc. Symp. Proc.* 274, 767 (1992).
347. (a) P. Gattinger, H. Rengel, and D. J. Neher, *Appl. Phys.* 84, 3731 (1998). (b) C. Bubeck, D. Neher, A. Kaltbeitzel, G. Duda, T. Arndt, T. Sauer, and G. Wegner, in "Nonlinear Optics in Polymers" (J. Messier, F. Kajzar, P. Prasad, and P. Ulrich, Eds.), NATO ASI Ser. E, Vol. 162, p. 185. Kluwer Academic, Dordrecht, 1989. (c) S. Schwiegk, H. Fischer, Y. Xu, F. Kremer, and G. Wegner, *Makromol. Chem. Makromol. Symp.* 46, 211 (1991). (d) R. Back, L. Kalvoda, D. Neher, A. Ferencz, J. Wu, and G. Wegner, *Chem. Mater.* 10, 2284 (1998).
348. Ferencz, N. R. Armstrong, and G. Wegner, *Macromolecules* 27, 1517 (1994).
349. (a) L. Kalvoda, R. Back, A. Ferencz, D. Neher, and G. Wegner, *Mol. Cryst. Liq. Cryst.* 252, 223 (1994). (b) P. Gattinger, H. Rengel, and D. Neher, *Synth. Met.* 83, 245 (1996).
350. A. M. Van de Craats, J. M. Warman, M. P. de Haas, D. Adam, J. Simmerer, D. Haarer, and P. Schuhmacher, *Adv. Mater.* 8, 823 (1996).
351. P. G. Schouten, J. M. Warman, M. P. de Haas, C. F. van Nostrum, G. H. Gelinck, R. J. M. Nolte, M. J. Copyn, J. W. Zwikker, M. K. Engel, M. Hanack, Y. Chang, and W. T. Ford, *J. Am. Chem. Soc.* 116, 6880 (1994).
352. P. G. Schouten, J. M. Warman, and M. P. de Haas, *J. Phys. Chem.* 97, 9863 (1995); J. M. Warman and P. G. Schouten, *Appl. Organomet. Chem.* 10, 637 (1996).
353. K. Yase, S. Schwiegk, G. Lieser, and G. Wegner, *Thin Solid Films* 210/211, 22 (1992).
354. C. W. Dirk, T. Inabe, K. F. Schoch, and T. J. Marks, *J. Am. Chem. Soc.* 105, 1539 (1983).
355. J. Ern, A. Bock, L. Oddos-Marcel, H. Rengel, H. P. Trommsdorff, G. Wegner, and C. Kryschi, *J. Phys. Chem. A* 103, 2446 (1999).
356. V. Gulbinas, M. Chachisvilis, L. Valkunas, and V. Sundstrom, *J. Phys. Chem.* 100, 2213 (1996).



# Plasma Chemical Vapor Deposition of Nanocrystalline Diamond

Katsuyuki Okada

National Institute for Materials Science, Tsukuba, Ibaraki, Japan

## CONTENTS

1. Introduction
  2. Growth of Nanocrystalline Diamond
  3. Spectroscopic Characterization
  4. Plasma Diagnostics
- Glossary  
References

## 1. INTRODUCTION

Covalently bonded disordered thin-film materials have been of considerable interest from fundamental and applied perspectives in the last twenty years, since the chemical vapor deposition (CVD) of diamond was developed, followed by fullerenes and carbon nanotubes [1, 2]. Amorphous and nanostructured carbon films are being extensively studied for electron emitters, cold-cathode sources, hard low-friction coatings, etc. From fundamental perspectives, on the other hand, the structure of these materials contains both three-fold coordinated ( $sp^2$ -bonded) and four-fold coordinated ( $sp^3$ -bonded) carbon atoms. Nanocrystalline diamond films have also drawn remarkable attention [3] because they have a low coefficient of friction and low electron emission threshold voltage. The small grain size (approximately 5–100 nm) gives films valuable tribology and field-emission properties, compared with those of conventional polycrystalline diamond films. Furthermore, it has been proposed that applications for microelectromechanical systems (MEMS) devices, metal-semiconductor field effect transistors MESFETs, electrochemical electrodes, and biochemical devices can be created by taking advantage of these excellent properties [4–6].

Recent plasma dry processes (e.g., deposition, coating, etching) require a wide area and high density plasma at low pressures (<1 Torr) [7]. An electron cyclotron resonance (ECR) plasma was first developed to meet these conditions. Subsequently, a helicon-wave excited plasma was employed.

It was found [8] that the density of an inductively coupled plasma (ICP) becomes high at low pressures. Amorim et al. [9] reported that the plasma density of ICP after the transition from a low-density E-discharge to a high-density H-discharge reaches  $10^{12} \text{ cm}^{-3}$ . It is necessary in plasma-enhanced chemical vapor deposition (PE-CVD) to get a sufficient radical flux for deposition. Thus the ICP is thought to be a promising method for PE-CVD at low pressures.

In this review article, the synthesis of nanocrystalline diamond by low-pressure ICP-CVD and its spectroscopic characterizations are mainly described. Plasma diagnostics with a Langmuir probe are also reviewed.

## 2. GROWTH OF NANOCRYSTALLINE DIAMOND

### 2.1. Conventional Microwave Plasma CVD

A microwave plasma is most commonly used for the PE-CVD of diamond films [10], in which the conventional pressure of deposition is on the order of a few 10 Torr. A  $\text{CH}_4/\text{H}_2$  mixture, in which the  $\text{CH}_4$  content ( $[\text{CH}_4]$ ) is usually less than 5%, leads to micrometer-size polycrystalline diamond films. One methodology for synthesizing nanocrystalline diamond films is to increase the  $[\text{CH}_4]$  to 10% while the substrate temperature is kept constant [11–13]. The resultant morphology changes from faceted microcrystals to ball-shaped nanocrystals.

Another methodology is to substitute a noble gas for hydrogen while the  $[\text{CH}_4]$  is kept constant. Gruen et al. [14, 15] demonstrated the synthesis of nanocrystalline diamond films in a  $\text{CH}_4/\text{Ar}$  or  $\text{C}_{60}/\text{Ar}$  microwave discharge, without the addition of hydrogen. Extensive characterizations with X-ray diffraction (XRD), transmission electron microscopy (TEM), and electron energy loss spectroscopy (EELS) showed [16] that the films consist of a pure crystalline diamond phase with a grain size ranging from 3 to 20 nm. They also proposed from the plasma diagnostics [17] and the theoretical calculations [18] that the  $\text{C}_2$  dimer could

be responsible for the growth of the very fine-grained diamond films, whereas the  $\text{CH}_3$  radical is generally believed to be a precursor for the diamond growth.

Recently Butler et al. [4] reported the deposition of nanocrystalline diamond films with the conventional deposition conditions for micrometer-size polycrystalline diamond films. The substrate pretreatment by the deposition of a thin H-terminated a-C film, followed by the seeding of nanodiamond powder, increased the nucleation densities to more than  $10^{12}/\text{cm}^2$  on a Si substrate. The resultant films were grown to thicknesses ranging from 100 nm to 5  $\mu\text{m}$ , and the thermal conductivity ranged from 2.5 to 12 W/cm K.

In addition to microwave plasma, direct current (dc) plasma [19], hot-filament [20], magnetron sputtering [21], and radiofrequency (rf) [22–24] plasmas were utilized for nanocrystalline diamond deposition. Amaratunga et al. [23, 24], using  $\text{CH}_4/\text{Ar}$  rf plasma, reported that single-crystal diffraction patterns obtained from nanocrystalline diamond grains all show {111} twinning.

From a theoretical point of view, the stability of nanocrystalline diamond was discussed by several authors. Badziag et al. [25] pointed out that, according to semi-empirical quantum chemistry calculations, sufficiently small nanocrystalline diamond (3–5 nm in diameter) may be more stable than graphite by forming C-H bonds at the growing surface. Barnard et al. [26] performed the *ab initio* calculations on nanocrystalline diamond up to approximately 1 nm in diameter. The results revealed that the surfaces of cubic crystals exhibit reconstruction and relaxations comparable to those of bulk diamond, and the surfaces of the octahedral and cubooctahedral crystals show the transition from  $\text{sp}^3$  to  $\text{sp}^2$  bonding.

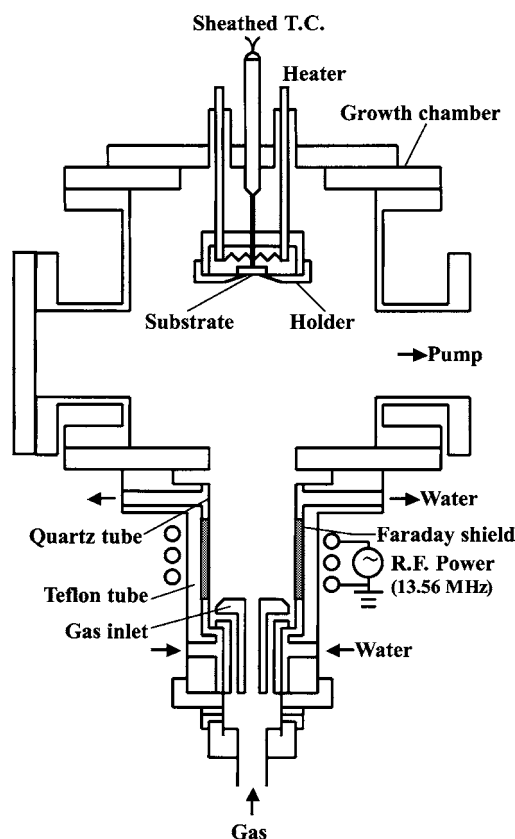
## 2.2. Low-Pressure Plasma CVD

Whereas a microwave plasma is most commonly used for the PE-CVD of diamond films, an ECR is the only plasma that is used for diamond deposition below 1 Torr [27–29]. Although Bozeman et al. [30] reported diamond deposition at 4 Torr with the use of a planar ICP, there have been a few reports that describe the synthesis of diamond by low-pressure ICP. Okada et al. [31–33] first reported the synthesis of nanocrystalline diamond particles in a low-pressure  $\text{CH}_4/\text{CO}/\text{H}_2$  ICP, followed by Teii and Yoshida [34], with the same gas-phase chemistry.

In the PE-CVD of diamond films, the addition of oxygen to a  $\text{CH}_4/\text{H}_2$  system was intended to get a high growth rate and/or an improvement of the quality of resultant films [35–38]. Several authors proposed the role of oxygen in the diamond growth. Mucha et al. [37] pointed out that oxygen additions to a  $\text{CH}_4/\text{H}_2$  system increase the concentration of atomic hydrogen; correspondingly, amorphous and graphitic carbon, which would otherwise inhibit diamond growth, is better suppressed. From a detailed chemical kinetics model that describes both gas-phase and surface processes occurring in diamond CVD, Frenklach and Wang [38] postulated that OH radicals and atomic oxygen are considered to gasify  $\text{sp}^2$  carbon and to suppress the formation of aromatic species in the gas phase. Teii et al. [39] pointed out that the OH radicals resulting predominantly from loss reactions of the

by-product O atoms with  $\text{H}_2$  and  $\text{CH}_4$  are highly responsible for the enhanced diamond growth.

A 13.56-MHz low-pressure ICP system [31–33] has been utilized as a radical source for PE-CVD and applied to the preparation of diamond films from a  $\text{CH}_4/\text{H}_2$  plasma. CO has been added to a  $\text{CH}_4/\text{H}_2$  plasma to clarify the effect of oxygen-containing radicals on the diamond growth. A schematic view of the apparatus is given in Figure 1. It consisted of a water-cooled quartz tube surrounded by a Teflon tube and a stainless-steel growth chamber. An inductively coupled plasma was generated by applying 13.56-MHz rf powers of 1 kW to a three-turn helical coil wound around the Teflon tube. The chamber was pre-evacuated to  $5 \times 10^{-5}$  Torr by a turbo molecular pump (200 liters/s). A Faraday shield was inserted between the rf coil and the quartz tube to rule out electrostatic coupling from the rf coil to the plasma. The quartz tube was wrapped with a grounded copper plate slitted at regular intervals along the azimuthal direction. A substrate holder was manipulated from the top of the chamber. Molybdenum plates and silicon (100) wafers ( $\phi$  10 mm) were used as a substrate. The substrate was heated by a tungsten filament. The substrate temperature ( $T_s$ ) was monitored with a sheathed thermocouple and kept at a prescribed temperature within  $\pm 1$  °C by a proportional integral derivative (PID) controller. The deposition conditions were as follows. The flow rates of  $\text{CH}_4$  and  $\text{H}_2$  were kept at 4.5 and 75 sccm, respectively, whereas



**Figure 1.** Schematic description of the low-pressure inductively coupled rf plasma CVD system. Adapted with permission from [33], K. Okada et al., *J. Mater. Res.* 14, 578 (1999). © 1999, Materials Research Society.

the flow rate of CO ( $[CO]$ ) was varied between 0, 1.0, 5.0, and 10 sccm, respectively. The total gas pressure ( $P_r$ ) was varied from 45 to 50 mTorr. The  $T_s$  was kept at 900 °C. The deposition duration was 2 h.

### 3. SPECTROSCOPIC CHARACTERIZATION

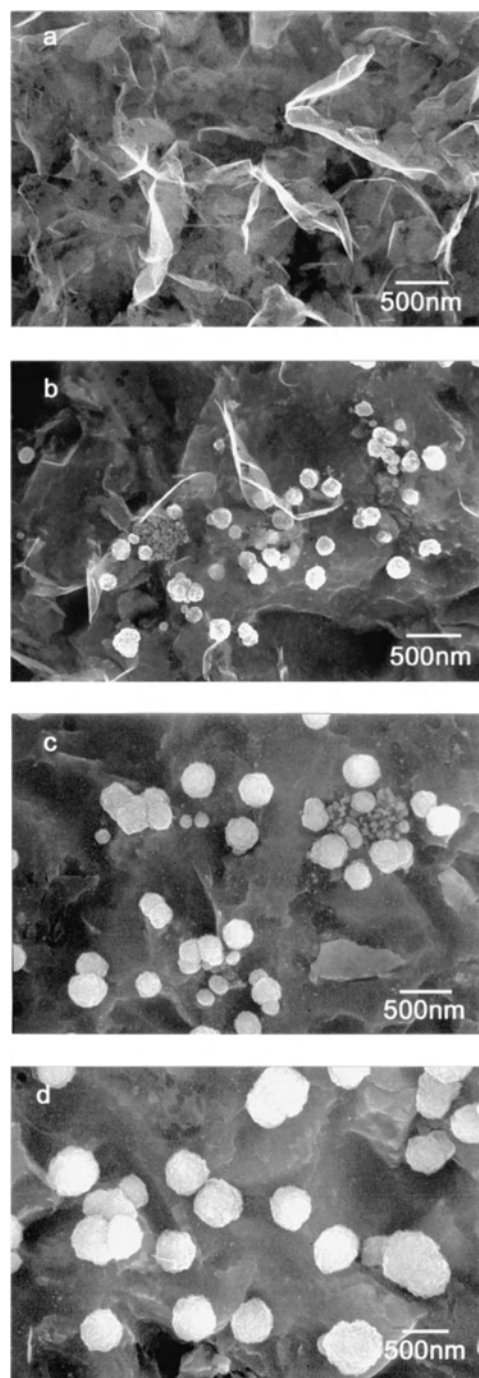
#### 3.1. SEM and TEM

Figure 2 presents the SEM photographs of the resultant deposits on a Si(100) substrate. Figure 2a, b, c, and d correspond to  $[CO] = 0, 1.0, 5.0,$  and 10 sccm, which are labeled as samples A, B, C, and D, respectively. The morphology of sample A was scale-like as shown in Figure 2a, and crystal facets were not clearly seen. When CO was added to a  $CH_4/H_2$  plasma, particles 200–300 nm in diameter with scale-like deposits appeared as shown in Figure 2b. With the increase in  $[CO]$ , only particles were deposited as shown in Figure 2c and d. The background of the particles was the substrate. The diameter of the particles was 200–700 nm. The detailed observation reveals that the particles consist of small particles about several tens of nanometers in diameter, and that the sizes are almost the same regardless of increasing  $[CO]$ . It is therefore speculated that increasing  $[CO]$  makes the supersaturation degree of carbon large, and then the number of encountered particles is increased.

The TEM image of sample B is shown in Figure 3a. Figure 3b shows the transmission electron diffraction (TED) pattern corresponding to Figure 3a. In the TEM image, a scale-like deposit was mainly observed. The ring pattern in the TED indicates that the deposit is composed of a large number of microcrystallites. Figure 4a presents the TEM image of sample C. The corresponding TED pattern is presented in Figure 4b. Only particles 200–500 nm in diameter were observed in the TEM image. The TED pattern was spotty compared with that of Figure 3b. The TEM images clearly show that each particle is composed of small particles about several tens of nanometers in diameter. The interplanar spacings ( $d$  values) obtained from the TED patterns are summarized in Table 1, where they are compared with the experimental values reported for diamond. The agreement between the values obtained and those for diamond is within the experimental error. No reflections due to nondiamond planes were observed in the patterns of sample C, whereas the reflections of nondiamond planes were observed in the pattern of sample B. Although these reflections are not always assigned to graphite, it is speculated that they are attributed to disordered microcrystalline graphite. From the TEM image of sample B, the size of the disordered microcrystalline graphite was estimated to be about several hundred nanometers. It is therefore concluded that scale-like deposits consist of disordered microcrystalline graphite, whereas particles are composed of only diamond microcrystallites.

#### 3.2. XRD

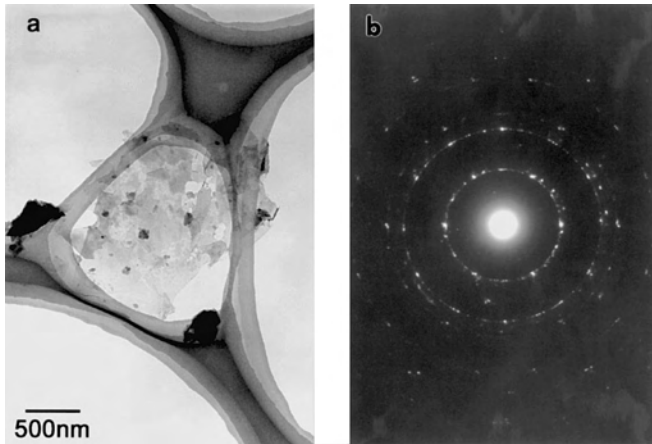
The X-ray diffraction (XRD) pattern for sample D is shown in Figure 5. D(111) and D(220) denote the diffraction peaks of the diamond plane. The diffraction peaks of the silicon



**Figure 2.** SEM micrographs of the obtained deposits. (a)  $[CH_4]/[CO] = 4.5/0$  sccm. (b)  $[CH_4]/[CO] = 4.5/1.0$  sccm. (c)  $[CH_4]/[CO] = 4.5/5.0$  sccm. (d)  $[CH_4]/[CO] = 4.5/10$  sccm. Reprinted with permission from [33], K. Okada et al., *J. Mater. Res.* 14, 578 (1999). © 1999, Materials Research Society.

substrate also appeared. Although the incident X-ray angle was quite shallow, it reached the substrate because of the imperfect coverage of the deposit as shown in Figure 2d. The peaks corresponding to graphite were not observed. Although no clear crystal facets can be seen in the SEM observations, the diffraction pattern clearly reveals that the deposit is neither amorphous carbon nor graphite, but diamond. The crystallite size was estimated to be approximately

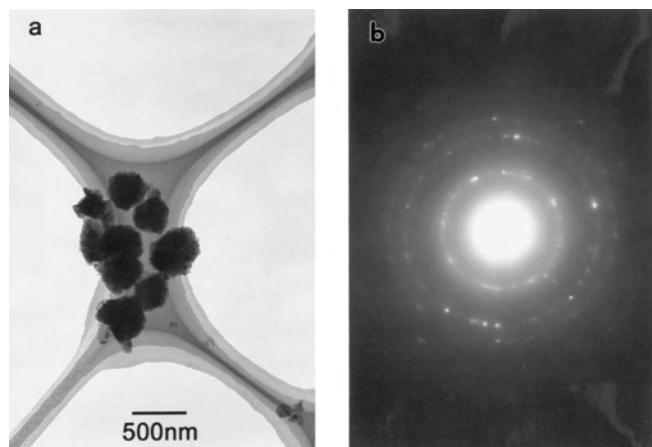




**Figure 3.** (a) TEM micrograph of sample B ( $[\text{CH}_4]/[\text{CO}] = 4.5/1.0$  sccm). (b) TED pattern corresponding to (a). Reprinted with permission from [33], K. Okada et al., *J. Mater. Res.* 14, 578 (1999). © 1999, Materials Research Society.

20 nm from the full width at half-maximum (FWHM) of the diamond peaks with the use of Scherrer's equation [40]. It accordingly implies that the particles that are several hundred nanometers in diameter consist of smaller particles several tens of nanometers in diameter. This is consistent with the TEM observation.

The addition of CO to  $\text{CH}_4/\text{H}_2$  plasmas is considered to produce oxygen-containing radicals, such as atomic oxygen, the OH radical, and the CO radical itself, in plasmas. As mentioned previously, the morphological change from a scale-like deposit to a particle took place with the CO additive. Furthermore, the number of particles encountered increased with an increase in [CO]. According to the TED and XRD patterns, nondiamond carbon was effectively removed with an increase in [CO]. We therefore presume that oxygen-containing radicals produced by the addition of CO play an effective role in the removal of nondiamond carbon in the diamond growth conditions and that the CO



**Figure 4.** (a) TEM micrograph of sample C ( $[\text{CH}_4]/[\text{CO}] = 4.5/5.0$  sccm). (b) TED pattern corresponding to (a). Reprinted with permission from [33], K. Okada et al., *J. Mater. Res.* 14, 578 (1999). © 1999, Materials Research Society.

**Table 1.** Interplanar spacings from the TED patterns and the reported values.

Sample B	Sample C	Diamond <sup>a</sup>	(hkl)
0.207	0.207	0.206	(111)
0.124	0.124	0.126	(220)
0.114			
0.106	0.106	0.10754	(311)
0.090		0.08916	(400)
0.081		0.08182	(331)
0.072		0.07280 <sup>b</sup>	(422)
0.061		0.06864 <sup>b</sup>	(511), (333)

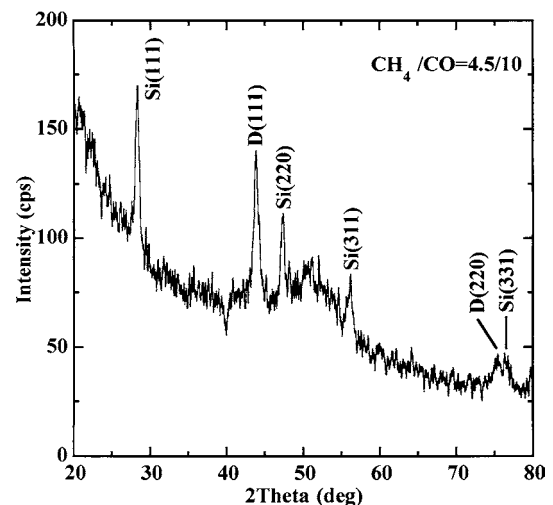
<sup>a</sup> Joint Committee on Powder Diffraction Standards (JCPDS) Powder Diffraction File, 6-675.

<sup>b</sup> Values are calculated from  $a = 0.3567$  nm.

additive makes the supersaturation degree of carbon large. This is consistent with the previously reported hypotheses [37, 38] that OH radicals and atomic oxygen gasify  $\text{sp}^2$  carbon and that they suppress the formation of amorphous carbon and graphitic carbon.

### 3.3. Raman Spectroscopy

Raman spectroscopy is a nondestructive method for the study of the vibrational band structure of materials. It has been extensively used for the characterization of diamond [41–44], graphite [45], and diamond-like carbon (DLC) [42, 43, 46–49]. So far Raman scattering is the most popular technique for identifying  $\text{sp}^3$  bonding in diamond and  $\text{sp}^2$  bonding in graphite and DLC. Although Raman scattering should represent the phonon density of state (PDOS), weighted by a coupling parameter, Raman spectroscopy of  $\text{sp}^2$ -bonded carbon with excitation wavelength in the visible range (514, 488 nm, etc.) does not provide a good representation of the PDOS [50]. Since the local  $\text{sp}^2$ -bonded carbon energy gap of  $\sim 2$  eV is comparable to the energy of visible Raman excitation, the  $\text{sp}^2$ -bonded carbon network exhibits the electronic  $\pi$ - $\pi^*$  transition resonance enhancement in the Raman cross section [43, 48–50]. On the other

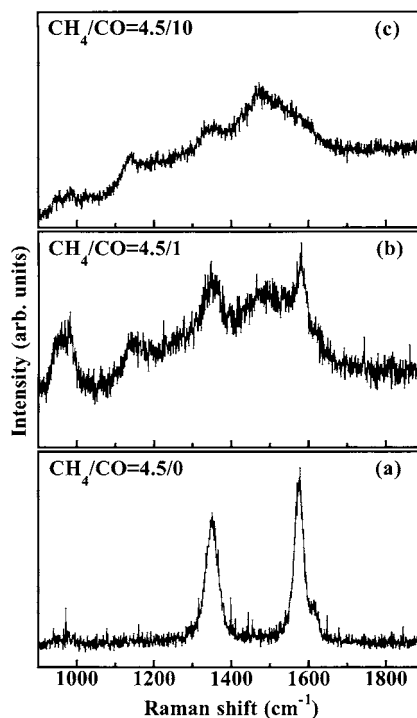


**Figure 5.** XRD pattern of sample D ( $[\text{CH}_4]/[\text{CO}] = 4.5/10$  sccm). Reprinted with permission from [57], K. Okada et al., *J. Appl. Phys.* 88, 1674 (2000). © 2000, American Institute of Physics.

hand, the  $sp^3$ -bonded carbon does not exhibit such a resonance effect because of the higher local gap of  $\sim 5.5$  eV. As a result, the Raman spectra obtained with visible excitation are completely dominated by the  $sp^2$ -bonded carbon. However, Raman spectroscopy with ultraviolet (UV) excitation has recently been used to characterize DLC [50–53]. The advantage of UV Raman spectroscopy is to eliminate the resonance effect of  $sp^2$ -bonded carbon. Excitation of 244 nm (5.1 eV) is far from the energy of previously mentioned  $sp^2$ -bonded carbon resonance. It is accordingly expected that the resonance Raman scattering from  $sp^2$ -bonded carbon is suppressed and that the signal from  $sp^3$ -bonded carbon is possibly increased. UV Raman spectra of tetrahedral amorphous carbon (t-aC) films containing  $sp^3$  bonding dominantly exhibit a peak at  $\sim 1150$   $cm^{-1}$  attributed to an  $sp^3$ -bonded carbon network [50–52]. Okada et al. [54] first applied UV Raman spectroscopy to the characterization of bonding structures of nanocrystalline diamond. Sun et al. [55] reported UV Raman characteristics of nanocrystalline diamond films with different grain sizes from 120 to 28 nm. They pointed out that the downshift and broadening of the diamond peak with decreasing grain size are consistent with the phonon confinement model. On the other hand, Praver et al. [56] reported the visible Raman spectra of nanocrystalline diamond powder with a size of  $\sim 5$  nm. The peaks at 500, 1140, 1132, and 1630  $cm^{-1}$  are compared with the calculated VDOS of diamond, and the origin of features in the vibrational spectrum from nanocrystalline diamond is suggested.

In Raman measurements [57], the 514-nm line of an  $Ar^+$  laser, the 325-nm line of a He-Cd laser, and the 244-nm line of an intracavity frequency-doubled  $Ar^+$  laser were employed. The incident laser beam was directed onto the sample surface under the back-scattering geometry, and the samples were kept at room temperature. In the 514-nm excitation, the scattered light was collected and dispersed in a SPEX 1403 double monochromator and detected with a photomultiplier. The laser output power was 300 mW. In the 325- and 244-nm excitations, the scattered light was collected with fused silica optics and was analyzed with a UV-enhanced CCD camera, using a Renishaw micro-Raman system 1000 spectrometer modified for use at 325 and 244 nm, respectively. A laser output of 10 mW was used, which resulted in an incident power at the sample of approximately 1.5 mW. The spectral resolution was approximately 2  $cm^{-1}$ . That no photoalteration of the samples occurred during the UV laser irradiation was ensured by confirming that the visible Raman spectra were unaltered after the UV Raman measurements.

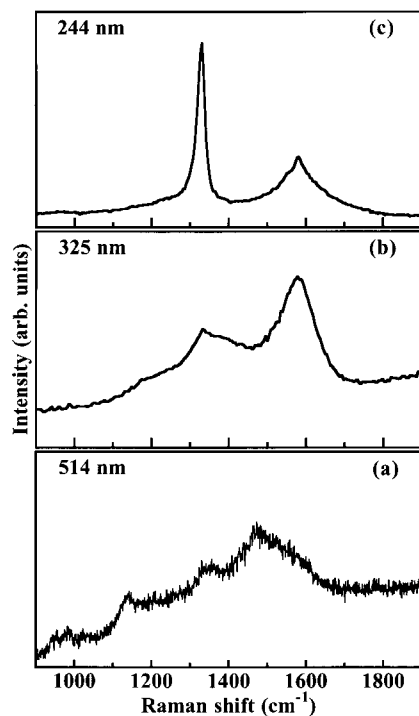
Figure 6 shows the 514-nm excited Raman spectra. Figure 6a, b, and c corresponds to sample A, sample B, and sample D, respectively. The Raman spectrum of sample A exhibits two peaks at  $\sim 1355$   $cm^{-1}$  ( $D$  peak) and  $\sim 1580$   $cm^{-1}$  ( $G$  peak) assigned to  $sp^2$  bonding [45]. New peaks appear at  $\sim 1150$   $cm^{-1}$  and  $\sim 1480$   $cm^{-1}$  in sample B. The former peak is due to  $sp^3$  bonding. Nemanich et al. [42, 44] assigned the peak at  $\sim 1150$   $cm^{-1}$  to microcrystalline or amorphous diamond. Praver and Nugent [58] attributed the peak at 1100–1150  $cm^{-1}$  to the surface phonon mode of diamond from the EELS studies of the nanophase diamond powder. On the



**Figure 6.** 514-nm excited Raman spectra of the deposits obtained with different gas mixtures. (a)  $[CH_4]/[CO] = 4.5/0$  sccm. (b)  $[CH_4]/[CO] = 4.5/1.0$  sccm. (c)  $[CH_4]/[CO] = 4.5/10$  sccm. Reprinted with permission from [57], K. Okada et al., *J. Appl. Phys.* 88, 1674 (2000). © 2000, American Institute of Physics.

other hand, Ferrari and Robertson [59] have recently proposed another interpretation, that the peak at  $\sim 1150$   $cm^{-1}$  is not attributable to nanocrystalline diamond but to  $sp^2$  bondings of a trans-polyacetylene oligomer of a given conjugation length. The peak at  $\sim 1480$   $cm^{-1}$  is probably related to amorphous  $sp^2$  structures [44], though it is downshifted from the  $G$  peak. Both the  $D$  and  $G$  peaks become relatively small compared with those of sample A. A peak at  $\sim 950$   $cm^{-1}$  is derived from scattering by two transverse-optical (TO) phonons of silicon substrate [43]. The incident laser beam reached the substrate because the substrate was not fully covered with the deposit as shown in Figure 2b. In the Raman spectrum of sample D, the  $G$  peak turns into a shoulder and the  $D$  peak becomes faint, whereas the peak at  $\sim 1480$   $cm^{-1}$  has a maximum intensity and the peak at  $\sim 1150$   $cm^{-1}$  still remains. However, the three spectra in Figure 6 do not clearly exhibit the 1332  $cm^{-1}$  diamond peak. These features of Raman spectra imply that the deposit from  $CH_4/H_2$  predominantly contains  $sp^2$  bonding; the addition of CO to  $CH_4/H_2$  produces a mixture of  $sp^2$  and  $sp^3$  bondings; the increase in  $[CO]$  brings about the increase in  $sp^3$  bonding. These tendencies are consistent with the TEM and XRD observations, which reveal that the increase in  $[CO]$  improves the crystallinity of the deposit.

Figure 7 shows a sequence of Raman spectra from sample D with different excitation wavelengths. Figure 7a, b, and c corresponds to 514 nm, 325 nm, and 244 nm, respectively. Compared with the spectrum of 514-nm excitation, the 325-nm excited Raman spectrum exhibits a clear peak at 1332  $cm^{-1}$  and the remarkable enhancement of the



**Figure 7.** Raman spectra of sample D ( $[\text{CH}_4]/[\text{CO}] = 4.5/10$  sccm) with different excitation wavelengths. (a) 514 nm. (b) 325 nm. (c) 244 nm. Reprinted with permission from [57], K. Okada et al., *J. Appl. Phys.* 88, 1674 (2000). © 2000, American Institute of Physics.

peak at  $\sim 1580 \text{ cm}^{-1}$ , while the peak at  $\sim 1150 \text{ cm}^{-1}$  turns into a shoulder. In a 244-nm excited Raman spectrum, the peak at  $1332 \text{ cm}^{-1}$  is only enhanced, whereas the peak at  $\sim 1580 \text{ cm}^{-1}$  is weakened. Neither a peak nor a shoulder can be recognized at  $\sim 1150 \text{ cm}^{-1}$ . The Raman spectra in Figure 7a are superimposed on a broad photoluminescence background. The luminescence background diminishes with increasing excitation photon energy as shown in Figure 7b and c.

The TED and XRD patterns revealed that the deposit is not amorphous carbon but nanocrystalline diamond. Nonetheless, the 514-nm excited Raman spectra do not exhibit a clear diamond peak at  $1332 \text{ cm}^{-1}$ , though the peak due to the  $\text{sp}^3$ -bonded carbon network appears at  $\sim 1150 \text{ cm}^{-1}$ . The Raman cross section of the  $\text{sp}^2$ -bonded carbon network with visible excitation is resonantly enhanced [43, 48–50]. It consequently makes the  $1332 \text{ cm}^{-1}$  diamond peak overlap with the peaks due to  $\text{sp}^2$ -bonded carbon.

The suppression of the dominance of the resonance Raman effect in the 514-nm excitation and the possible increase in the signal from  $\text{sp}^3$ -bonded carbon are expected to occur in higher photon energies. Wagner et al. [43] mentioned that a resonance enhancement of scattering by  $\text{sp}^3$ -bonded carbon is expected at an incident photon energy of 4.8 eV, which is close to the onset of the  $\sigma$ - $\sigma^*$  transition in both  $\text{sp}^2$ - and  $\text{sp}^3$ -bonded carbon. Gilkes et al. [51] stated that the 244-nm photon energy is sufficient to excite the  $\sigma$ - $\sigma^*$  transition of both  $\text{sp}^2$  and  $\text{sp}^3$  sites. The enhancement of the peaks at both  $1332 \text{ cm}^{-1}$  and  $\sim 1580 \text{ cm}^{-1}$  in the 325-nm excitation suggests that the resonance

enhancement of the Raman cross section due to  $\text{sp}^2$ -bonded carbon still remains and that the  $\sigma$ - $\sigma^*$  transition in both  $\text{sp}^2$ - and  $\text{sp}^3$ -bonded carbon is possibly induced. The remarkable enhancement of the peak at  $1332 \text{ cm}^{-1}$  and the diminution of the peak at  $\sim 1580 \text{ cm}^{-1}$  in the 244-nm excitation reveals that the resonance Raman effect due to  $\text{sp}^2$ -bonded carbon is suppressed, whereas the resonant enhancement due to the  $\sigma$ - $\sigma^*$  transition of  $\text{sp}^3$ -bonded carbon is predominantly attained.

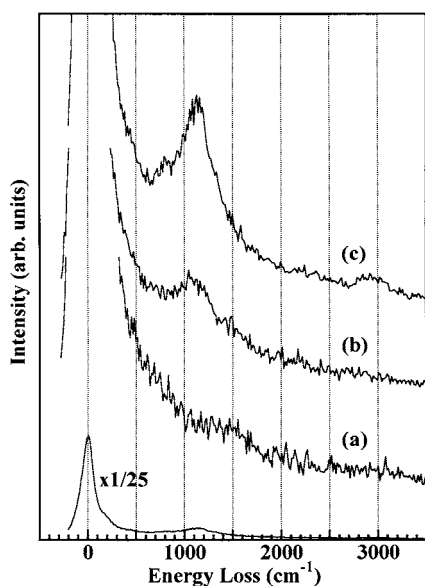
The 244-nm excited Raman spectra of t-aC films exhibit the appearance of the peak at  $\sim 1150 \text{ cm}^{-1}$  and the increase in the intensity proportional to the amount of  $\text{sp}^3$  bonding in the films [50, 51]. However, the diamond peak at  $1332 \text{ cm}^{-1}$  is not enhanced in this study because the deposit obtained is not amorphous carbon but nanocrystalline diamond. The peak at  $\sim 1150 \text{ cm}^{-1}$  is probably disappearing because of the striking enhancement of the diamond peak at  $1332 \text{ cm}^{-1}$ .

### 3.4. HREELS

High-resolution electron energy loss spectroscopy (HREELS) is a method for the study of the vibrational motion of atoms and molecules on and near the surface by the analysis of the energy spectrum of low-energy electrons back-scattered from it [60]. With developments in modern ultra-high-vacuum (UHV) technology and increasing interest in the physical properties of clean and adsorbate-covered surfaces and of the chemical phenomena occurring on these surfaces, scientific interest in HREELS has increased dramatically, and the method has been widely used in recent years [60–65].

HREELS experiments [66] were performed in a UHV chamber. The chamber was pre-evacuated by polyphenylether-oil diffusion pump; the base pressure reached  $\sim 2 \times 10^{-8}$  Torr. The HREELS spectrometer consisted of a double-pass electrostatic cylindrical-deflector-type monochromator and the same type of analyzer. The energy resolution of the spectrometer is 4–6 meV ( $32\text{--}48 \text{ cm}^{-1}$ ). A sample was transferred from the ICP growth chamber to the HREELS chamber in the atmosphere. It was clipped by a small tantalum plate, which was suspended by tantalum wires. The sample was radiatively heated in vacuum by a tungsten filament placed at the rear. The sample temperature was measured by an infrared ( $\lambda = 2.0 \mu\text{m}$ ) optical pyrometer. All HREELS measurements were taken at room temperature. The electron incident and detection angles were each  $72^\circ$  to the surface normal. The primary electron energy was 15 eV.

Figure 8 presents the HREELS spectra of heated films. Figure 8a, b, and c corresponds to sample A, sample B, and sample D, respectively. In Figure 8a without CO additive, the spectrum has a faint peak at  $\sim 1500 \text{ cm}^{-1}$  derived from the C=C stretching mode of threefold bonded carbon atoms [60]. The whole spectrum is similar to that of a single crystal graphite (0001) surface [63]. With CO additive as shown in Figure 8b, one can see a peak at  $\sim 1100 \text{ cm}^{-1}$ , which is assignable to the C-C stretching mode of fourfold bonded carbon atoms [42, 60]. The peak at  $\sim 1500 \text{ cm}^{-1}$  disappeared. With increasing [CO] as shown in Figure 8c, the intensity of the peak at  $\sim 1100 \text{ cm}^{-1}$  became strong. In addition, a shoulder centered at  $\sim 700 \text{ cm}^{-1}$  appeared. These features of the VDOS are consistent with the theoretical results



**Figure 8.** HREELS spectra of the nanocrystalline diamond and diamond-like carbon films with various  $[\text{CH}_4]/[\text{CO}]$ . (a)  $[\text{CH}_4]/[\text{CO}] = 4.5/0.0$ . (b)  $[\text{CH}_4]/[\text{CO}] = 4.5/1.0$ . (c)  $[\text{CH}_4]/[\text{CO}] = 4.5/10$  sccm. The elastic peak for (c), reduced by a factor of 25, is shown for comparison. Reprinted with permission from [66], K. Okada et al., *Diamond Relat. Mater.* 10, 1991 (2001). © 2001, Elsevier Science.

for random network models of t-aC. Tight binding molecular dynamics (TBMD) simulations for a sample with 75% fourfold atoms predict two major broad peaks at  $\sim 700 \text{ cm}^{-1}$  and  $\sim 1100 \text{ cm}^{-1}$ , respectively, corresponding to the bending and stretching vibrations in the network [67]. A rather similar form of the PDOS is obtained in *ab initio* calculations with a 90%  $\text{sp}^3$  fraction [68].

According to the characterizations by TEM and XRD, the sample prepared from a  $\text{CH}_4/\text{H}_2$  plasma was composed of nanocrystalline diamond and disordered microcrystalline graphite. Then nondiamond carbon was effectively removed with an increase in  $[\text{CO}]$ . It is therefore concluded that the VDOS of the nanocrystalline diamond and DLC films extracted from the HREELS data is in qualitative agreement with the characterizations of TEM and XRD. Although the HREELS probes only the region near the surface, the agreement suggests that the surface dynamics do not differ dramatically from those of the bulk.

### 3.5. EELS Mapping

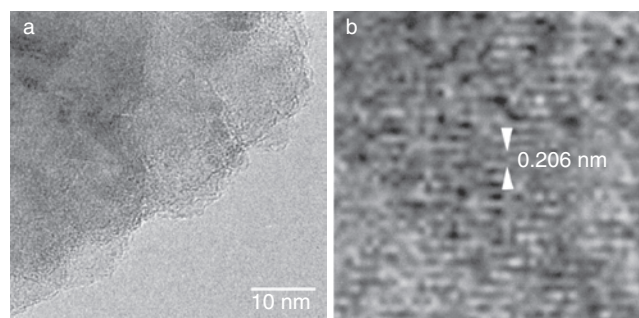
EELS in TEM has been demonstrated to be a powerful technique for performing microanalysis and studying the electronic structure of materials [69]. The energy loss near edge structures (ELNES) is sensitive to the crystal structure. The C-K edge of diamond and that of graphite are typical examples. For trigonal  $\text{sp}^2$ -bonded carbon, the spectrum within the first 30 eV of the edge can be separated into two broad features, corresponding to the  $\pi^*$  states between 282 and 288 eV and the  $\sigma^*$  states between 290 and 320 eV, whereas for tetrahedral  $\text{sp}^3$ -bonded carbon only the  $\sigma^*$  peak is observed between 289 and 320 eV [70]. Therefore, one can easily distinguish between diamond and diamond-like carbon with the help of ELNES. Muller et al.

[71] acquired the mapping of  $\text{sp}^2$  and  $\text{sp}^3$  states across the silicon-diamond interface by scanning transmission electron microscopy (STEM) and parallel acquisition electron energy loss spectroscopy (PEELS). Bruley's two-window technique [72], by integrating intensities of the  $\pi^*$  and  $\sigma^*$  peaks, has demonstrated the quantitative analysis of the  $\text{sp}^2$  content in the samples. Bursill et al. [73–75] carefully performed the structural analysis on nanocrystalline diamond powder and studied the surface and bulk plasmon response derived from the low-loss spectra by using high-resolution TEM (HR-TEM)/PEELS and STEM/PEELS. Praver et al. [56, 76] also reported the EEL spectra of nanocrystalline diamond synthesized by detonation and ion implantation.

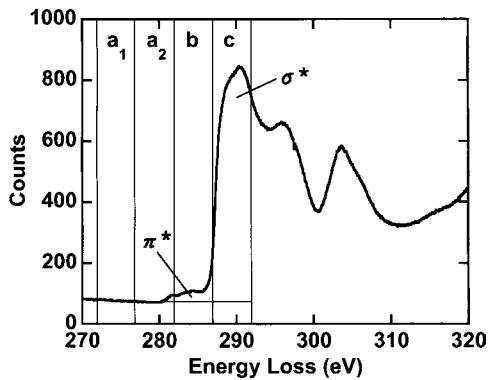
The HR-TEM observations [77] were performed on a Hitachi HF-3000 at 297 keV, and the EELS measurements [77] were made with a post-column energy filter (GATAN, GIF2002). The vacuum of the microscope was less than  $1.2 \times 10^{-6} \text{ Pa}$ , in which the samples were not contaminated with carbon during TEM observations. Two-dimensional arrays of charge-coupled devices (CCDs) were used for the digital recording of TEM images, EEL spectra, and chemical maps. The typical CCD readout times were 5 s for the acquisition of EEL spectra and 50 s for chemical mappings, respectively. The energy resolution of the instrument was approximately 0.5 eV measured as the zero-loss FWHM.

Figure 9a shows a HR-TEM image of an outer part of a nanocrystalline diamond particle. Lattice fringes clearly appeared in the enlargement of the left-hand side of the sample as shown in Figure 9b. The  $d$  values were 0.206 nm, corresponding to (111) spacings of diamond. The diffractogram derived from the Fourier transformation of the HR-TEM image exhibited a ring pattern, which means the observed sample is polycrystalline. Furthermore, careful observation reveals that the particle consists of smaller subgrains approximately 20–50 nm in diameter. Thus the boundaries are not surface steps of a single crystal. The size of subgrains is comparable to the grain sizes of nanocrystalline diamond films previously reported by several authors [15, 23, 29, 78], in which the grain sizes were found to be in the range of 3–50 nm.

The EEL spectrum corresponding to Figure 9a is shown in Figure 10. It exhibits a peak at 290 eV due to  $\sigma^*$  states, and a slight peak appears at  $\sim 285 \text{ eV}$ , corresponding to  $\pi^*$  states. The ELNES above 290 eV is similar to that of diamond [70] and is obviously different from that of graphite or  $\text{sp}^3$ -rich



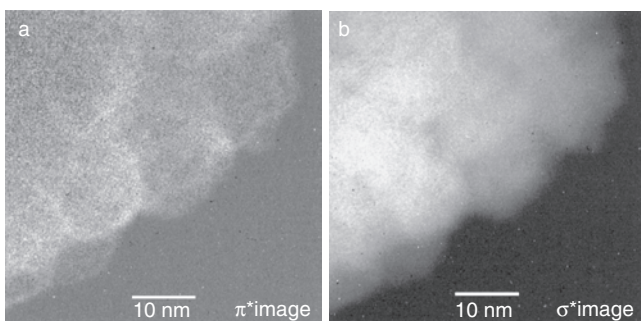
**Figure 9.** (a) High-resolution transmission electron microscope image of an outer part of a nanocrystalline diamond particle and (b) enlargement of the left-hand side of (a).



**Figure 10.** Electron energy loss spectrum corresponding to Figure 9a.  $a_1$ ,  $a_2$ , b, and c indicate the four energy windows: 272–277 eV, 277–282 eV, 282–287 eV, and 287–292 eV, respectively.

tetrahedral amorphous carbon [72]. The intensity of the  $\pi^*$  peak is much lower than that of the  $\sigma^*$  peak. Although the  $\sigma^*$  peak in general includes contributions from both  $sp^2$  and  $sp^3$  bondings, the  $\sigma^*$  peak of the EEL spectrum in Figure 10 is considered to be mainly due to  $sp^3$  bondings. The use of a narrow energy window positioned on the ELNES signal allows the mapping of the variation in intensity as a function of position within the microstructure. The conventional so-called *three-window method* [69] was employed to remove the background contribution. The two pre-edge images (272–277 eV and 277–282 eV) (indicated by  $a_1$  and  $a_2$  in Fig. 10) were used to obtain an extrapolated background image. The subtraction of the extrapolated background image from the post-edge images (282–287 eV and 287–292 eV) (indicated by b and c) produces the  $\pi^*$  image and the  $\sigma^*$  image, respectively, with removal of the background contribution.

The  $\pi^*$  image and the  $\sigma^*$  image corresponding to the TEM image of Figure 9a are shown in Figure 11a and b, respectively. Since the intensity of the  $\pi^*$  image was weak compared with that of the  $\sigma^*$  image, the former was multiplied by 5. The  $\pi^*$  image reveals that the intensity is strong around the subgrains, whereas the  $\sigma^*$  image shows that the intensity is strong within the subgrains. Although  $sp^2$ -bonded graphitic layers do not appear clearly with the limitation of resolution of the HR-TEM image, these energy-filtered  $\pi^*$  and  $\sigma^*$  images imply that  $sp^2$  bondings are localized around 20–50-nm subgrains. The  $sp^2$  bondings around the subgrains are considered to contribute the slight peak at  $\sim 285$  eV in



**Figure 11.** (a)  $\pi^*$  image corresponding to Figure 9a. (b)  $\sigma^*$  image corresponds to Figure 9a.

the ELNES. The width of the  $sp^2$  bondings is estimated to be approximately 1 nm from the  $\pi^*$  image in Figure 11a. Fallon and Brown reported [79] the presence of amorphous carbon at the grain boundaries of CVD diamond films by TEM observation and EELS analysis. The amorphous carbon is shown to contain almost complete  $sp^2$  bonding and to be nonhydrogenated. It was also demonstrated from a theoretical point of view [80] that  $sp^2$  bondings are energetically stable in grain boundaries of nanocrystalline diamond. It is consequently considered that the  $sp^2$  bondings are possibly localized in the grain boundaries of 20–50-nm subgrains.

#### 4. PLASMA DIAGNOSTICS

A Langmuir probe has been utilized to measure plasma parameters (plasma potential ( $V_p$ ), electron temperature ( $T_e$ ), electron density ( $N_e$ ), and electron energy distribution function (EEDF)) [81–84]. Although there has been much controversy about the interpretation of Langmuir probe characteristics of rf plasmas, the recent development of a sophisticated Langmuir probe system [85] enables one to obtain reproducible plasma parameters precisely. However, only a few works have been carried out on actual process plasmas used for etching or deposition, because it is difficult to maintain the initial condition of probe tips and/or chamber walls for the measurement reproducibility. Cali et al. [86] reported the Langmuir probe characterization of a low-pressure capacitively coupled  $CH_4/H_2$  rf plasma. The structure of an EEDF can help one to understand the electron distribution and the heating mechanism in a rf plasma. The EEDF of a low-pressure rf plasma generally consists of two Maxwellian distributions, fast and slow electrons [87]. This feature is due to the stochastic electron heating on the oscillating plasma-sheath boundary.

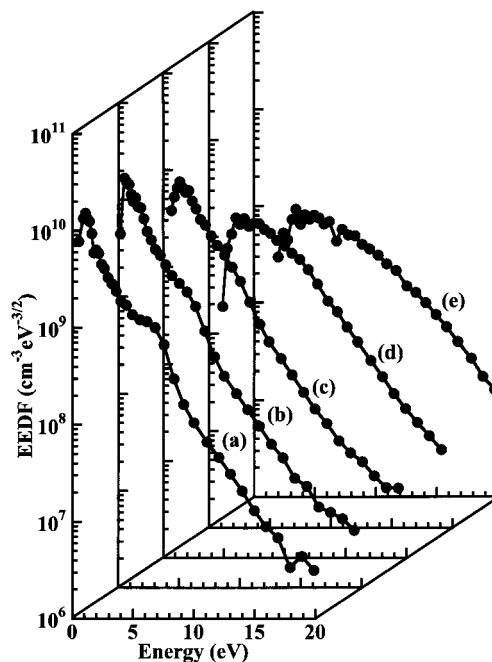
A Langmuir probe was inserted [88] through one of the side flanges of the chamber as shown in Figure 1. The probe was a cylindrical tungsten wire, which was 0.19 mm in radius and 10 mm in length. The probe tip was supported by a ceramic tube, which was 2.5 mm in diameter and was enclosed by a stainless-steel casing capacitively coupled to the probe tip. Since the mean free path of an electron is large compared with the diameter of the ceramic tube for all investigated pressures, the collisionless sheath approximation can be applied [89]. When the plasma was in the high-density regime ( $10^{11}$  to  $10^{12}$   $cm^{-3}$ ), the tip length was shortened to 4 mm to prevent the probe tip from glowing red. The rf fluctuations of the plasma potential were compensated for by self-resonant inductors [85]. The reference probe, which was a stainless-steel casing mounted on the probe shaft, automatically compensated for the plasma-ground sheath impedance, plasma potential shifts, and low-frequency noise [85]. The plasma-ground sheath impedance can be significant when nonconducting layers (e.g., carbon layers in this study) coat the chamber wall. A single  $I$ - $V$  characteristic curve was taken, averaging 120 samples per data point. Between scans the probe tip was cleaned by electron bombardment by pulse biasing it to +150 V. Before every probe measurement, the chamber was cleaned with an  $O_2$  plasma, which removed contamination of thin carbon layers on the chamber wall. This probe and chamber cleaning made the

obtained  $I-V$  characteristics reproducible, without the need for time-dependent hysteresis.

Figure 12a-c shows the variation in the  $V_p$ , the  $T_e$ , and the  $N_e$  of a  $CH_4/H_2$  plasma with pressure. The  $V_p$  and  $N_e$  decrease with increasing pressure up to 40 mTorr and inversely increase at 50 mTorr. The  $N_e$  increases with increasing pressure up to 40 mTorr and inversely decreases at 50 mTorr. The pressure dependence of the  $V_p$ , the  $T_e$ , and the  $N_e$  of a  $CH_4/H_2$  plasma is the same as that of an Ar plasma up to 40 mTorr. Therefore, these features in a  $CH_4/H_2$  plasma up to 40 mTorr can be explained by the same hypotheses of Ar plasma [83, 84], whereas the opposite feature at 50 mTorr should let us assume different phenomena in a  $CH_4/H_2$  plasma.

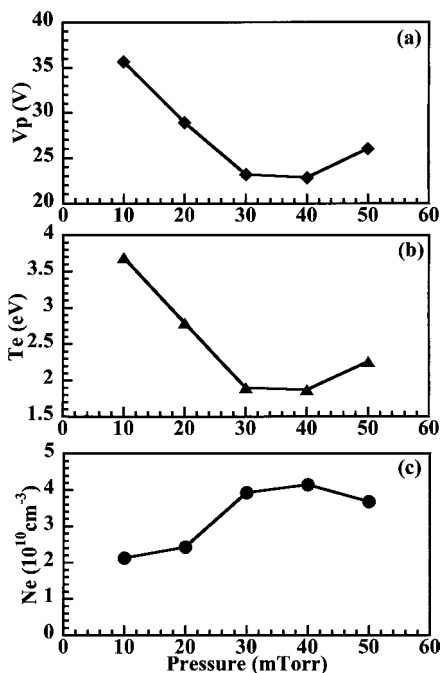
Figure 13a-e shows the EEDFs of a  $CH_4/H_2$  plasma as a function of pressure. The shape of the EEDF at 50 mTorr corresponding to Figure 13a is different from that of an Ar plasma at the same pressure. There is a hump at  $\sim 6$  eV. The hump gradually disappears with decreasing pressure. The shape of the EEDF at 30 mTorr in Figure 13c is almost a straight line, which means a Maxwellian distribution. The shape of the EEDF at 20 mTorr in Figure 13d deviates from a straight line and comes close to a Druyvesteyn distribution. It still keeps a Druyvesteyn distribution at 10 mTorr in Figure 13e. Accordingly, the transition from a Maxwellian distribution to a Druyvesteyn distribution occurs at 20 mTorr in a  $CH_4/H_2$  plasma.

Turner and Hopkins [90] previously reported an unusual structure of the EEDF. They found a dip at  $\sim 4$  eV in the EEDF of a  $N_2$  plasma. They interpreted the dip as the electric absorption of a  $N_2$  molecule corresponding to the resonant peak of the vibrational excitation cross section.

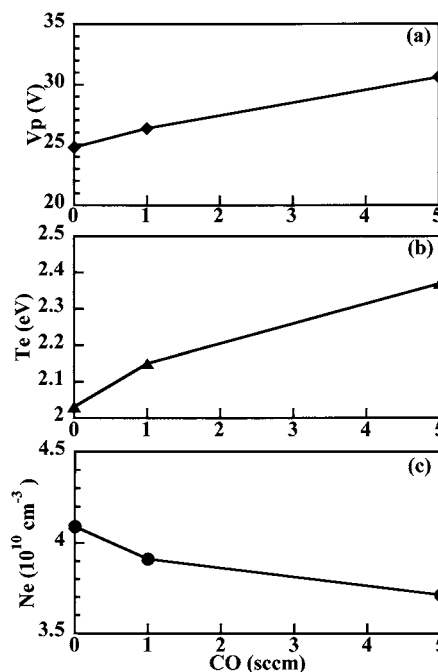


**Figure 13.** Electron energy distribution functions of a  $CH_4/H_2$  plasma as a function of pressure. (a) 50 mTorr. (b) 40 mTorr. (c) 30 mTorr. (d) 20 mTorr. (e) 10 mTorr. Reprinted with permission from [88], K. Okada et al., *J. Vac. Sci. Technol., A* 17, 721 (1999). © 1999, American Institute of Physics.

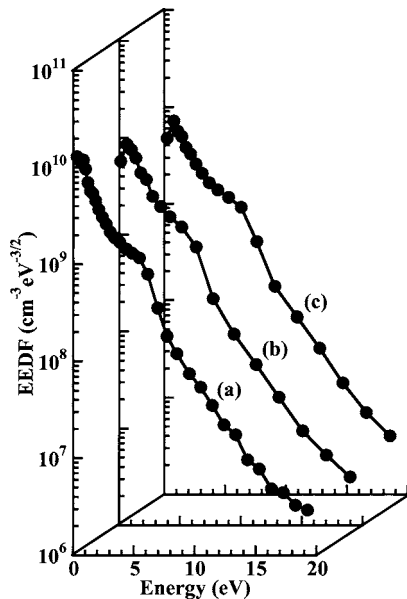
Cali et al. [86] reported a similar dip at  $\sim 6$  eV in the EEDF of a  $CH_4/H_2$  plasma. In the  $CH_4$  vibrational excitation cross sections,  $\sigma_v(1, 3)$  and  $\sigma_v(2, 4)$  have a peak at  $\sim 6$  eV [91]. The dip can be attributed to the electric absorption of a  $CH_4$



**Figure 12.** Variation of the plasma parameters of a  $CH_4/H_2$  plasma with pressure. (a) Plasma potential. (b) Electron temperature. (c) Electron density. Reprinted with permission from [88], K. Okada et al., *J. Vac. Sci. Technol., A* 17, 721 (1999). © 1999, American Institute of Physics.



**Figure 14.** Variation of the plasma parameters of a  $CH_4/CO/H_2$  plasma with [CO] content. (a) Plasma potential. (b) Electron temperature. (c) Electron density.



**Figure 15.** Electron energy distribution functions of a  $\text{CH}_4/\text{CO}/\text{H}_2$  plasma as a function of  $[\text{CO}]$  content. (a)  $[\text{CO}] = 0$  sccm. (b)  $[\text{CO}] = 1.0$  sccm. (c)  $[\text{CO}] = 5.0$  sccm.

molecule analogous to the vibrational absorption of  $\sim 4$  eV electrons of a  $\text{N}_2$  molecule. Although the unusual structure in the EEDF of a  $\text{CH}_4/\text{H}_2$  plasma at 50 mTorr is not a clear dip but a hump, it is presumably equivalent to the energy corresponding to the resonant peak of the vibrational excitation cross section of a  $\text{CH}_4$  molecule. Since the electron mean free path becomes longer with decreasing pressure and the EEDF is expected to be relatively insensitive to the electron impact cross sections [90], the hump gradually disappears with decreasing pressure. Thus the hump is considered to bring about the opposite feature of the  $V_p$ , the  $T_e$ , and the  $N_e$  of a  $\text{CH}_4/\text{H}_2$  plasma at 50 mTorr.

Figure 14a–c shows the variation in the  $V_p$ , the  $T_e$ , and the  $N_e$  of a  $\text{CH}_4/\text{CO}/\text{H}_2$  plasma with  $[\text{CO}]$ . While the  $V_p$  and  $T_e$  increase with increasing  $[\text{CO}]$ , the  $N_e$  decreases with increasing  $[\text{CO}]$ . Figure 15a–c shows the EEDFs of a  $\text{CH}_4/\text{CO}/\text{H}_2$  plasma as a function of  $[\text{CO}]$ . The hump at  $\sim 6$  eV still appears with the addition of CO, and the spectrum shape retains almost the same feature. The inclinations below 6 eV become slow with increasing  $[\text{CO}]$ , which means that the  $T_e$  increases with increasing  $[\text{CO}]$ . It is consistent with the result of Figure 14b. The electron impact dissociation of CO produces  $\text{O}^-$  ( $\text{CO} + e \rightarrow \text{C} + \text{O}^-$ ) in a  $\text{CH}_4/\text{CO}/\text{H}_2$  plasma. It is therefore assumed that the increase in negative ions reduces the  $N_e$  relatively to satisfy the charge balance in a plasma, and that the decrease in  $N_e$  leads to the increase in  $V_p$  and  $T_e$ .

## GLOSSARY

**Electron energy distribution function** The distribution function of electrons in a plasma. That of a low-pressure radiofrequency plasma generally consists of two Maxwellian distributions, that is, fast and slow electrons.

**Electron energy loss spectroscopy** An analytical technique used to characterize the chemistry, bonding, and electronic structure of thin samples of materials. It is normally performed in a transmission electron microscope. The inelastically scattered electron beams are spectroscopically analyzed to give the energy spectrum of electrons after the interaction.

**Inductively coupled plasma** Plasmas generated by application of radiofrequency power to a nonresonant inductive coil and maintained by an inductive electromagnetic field. Low-pressure ICP is a high-density plasma source.

**Langmuir probe** One of the most useful tools for diagnosing a plasma, in which a metal probe is inserted in a discharge and is biased positively or negatively to draw electron or ion current. The plasma potential, electron temperature, electron density, and electron energy distribution function are obtained from the current-voltage characteristics.

**Nanocrystalline diamond** Diamond crystallites or films in which the crystal grains range between several nm and several hundred nanometers in diameter.

**Plasma CVD** Plasma chemical vapor deposition. Technique for synthesizing materials in which chemical components in vapor phase excited by plasma react to form a solid film at some surface.

**Raman spectroscopy** A nondestructive method for the study of the vibrational band structure of materials, which has been extensively used for the characterization of diamond, graphite, and diamond-like carbon. Raman spectroscopy is so far the most popular technique for identifying  $\text{sp}^3$  bonding in diamond and  $\text{sp}^2$  bonding in graphite and diamond-like carbon.

## ACKNOWLEDGMENTS

The author thanks Drs. S. Komatsu, H. Kanda, K. Kimoto, T. Aizawa, R. Souda, and S. Matsumoto of Advanced Materials Laboratory/National Institute for Materials Science (AML/NIMS) for their cooperation in experiments and the fruitful discussion of the results.

## REFERENCES

1. J. Robertson, *Prog. Solid State Chem.* 21, 199 (1991).
2. M. P. Siegal, W. I. Milne, and J. E. Jaskie, Eds., *Mater. Res. Soc. Symp. Proc.* 498 (1998).
3. D. M. Gruen, *Annu. Rev. Mater. Sci.* 29, 211 (1999).
4. J. E. Butler, D. S. Y. Hsu, B. H. Houston, X. Lui, J. Vignola, T. Feygelson, J. Wang, and C. T.-C. Nyguen, "8th International Conference on New Diamond Science and Technology," Melbourne, 2002, p. 116.
5. J. A. Carlisle, J. Birrell, J. E. Gerbi, O. Auciello, J. M. Gibson, and D. M. Gruen, "8th International Conference on New Diamond Science and Technology," Melbourne, 2002, p. 129.
6. G. M. Swain, A. B. Anderson, and J. C. Angus, *MRS Bull.* 56 (1998).
7. M. A. Lieberman and A. J. Lichtenberg, "Principles of Plasma Discharges and Materials Processing." Wiley, New York, 1994.
8. J. Hopwood, *Plasma Sources Sci. Technol.* 1, 109 (1992).
9. J. Amorim, H. S. Maciel, and J. P. Sudano, *J. Vac. Sci. Technol.* B9, 362 (1991).
10. M. Kamo, Y. Sato, S. Matsumoto, and N. Setaka, *J. Cryst. Growth* 62, 642 (1983).

11. R. Erz, W. Dotter, D. Jung, and H. Ehrhardt, *Diamond Relat. Mater.* 2, 449 (1993).
12. J. Lee, B. Hong, R. Messier, and R. W. Collins, *Appl. Phys. Lett.* 69, 1716 (1996).
13. T. Sharda, M. M. Rahaman, Y. Nukaya, T. Soga, T. Jimbo, and M. Umeno, *Diamond Relat. Mater.* 10, 561 (2001).
14. D. M. Gruen, S. Lui, A. R. Krauss, J. Luo, and X. Pan, *Appl. Phys. Lett.* 64, 1502 (1994).
15. D. Zhou, T. G. McCauley, L. C. Qin, A. R. Krauss, and D. M. Gruen, *J. Appl. Phys.* 83, 540 (1998).
16. D. Zhou, D. M. Gruen, L. C. Qin, T. G. McCauley, and A. R. Krauss, *J. Appl. Phys.* 84, 1981 (1998).
17. A. N. Goyette, J. E. Lawler, L. W. Anderson, D. M. Gruen, T. G. McCauley, D. Zhou, and A. R. Krauss, *J. Phys. D: Appl. Phys.* 31, 1975 (1998).
18. P. C. Redfern, D. A. Horner, L. A. Curtiss, and D. M. Gruen, *J. Phys. Chem.* 100, 11654 (1996).
19. V. I. Konov, A. A. Smolin, V. G. Ralchenko, S. M. Pimenov, and E. D. Obratsova, *Diamond Relat. Mater.* 4, 1073 (1995).
20. A. V. Khomich, V. I. Polyakov, P. I. Perov, V. P. Varnin, and I. G. Terenetskaya, *Mater. Res. Soc. Symp. Proc.* 423, 723 (1996).
21. S. N. Kundu, M. Basu, A. B. Maity, S. Chaudhuri, and A. K. Pal, *Mater. Lett.* 31, 303 (1997).
22. D. V. Fedoseev, V. L. Bukhovets, I. G. Varshavskaya, and Y. N. Tolmachev, *Russ. J. Phys. Chem.* 70, 1594 (1996).
23. G. Amaratunga, A. Putnis, K. Clay, and W. Milne, *Appl. Phys. Lett.* 55, 634 (1989).
24. G. A. J. Amaratunga, S. R. P. Silva, and D. A. McKenzie, *J. Appl. Phys.* 70, 5374 (1991).
25. P. Badziag, W. S. Verwoerd, W. P. Ellis, and N. R. Greiner, *Nature* 343, 244 (1990).
26. A. S. Barnard, S. P. Russo, and I. K. Snook, *Diamond Relat. Mater.*, in press.
27. J. Wei, H. Kawarada, J. Suzuki, and A. Hiraki, *J. Cryst. Growth* 99, 1201 (1990).
28. C. R. Eddy, D. L. Youchison, B. D. Sartwell, and K. S. Grabowski, *J. Mater. Res.* 7, 3255 (1992).
29. M. Zarrabian, N. Fourches-Coulon, G. Turban, C. Marhic, and M. Lancin, *Appl. Phys. Lett.* 70, 2535 (1997).
30. S. P. Bozeman, D. A. Tucker, B. R. Stoner, J. T. Glass, and W. M. Hooke, *Appl. Phys. Lett.* 66, 3579 (1995).
31. K. Okada, S. Komatsu, T. Ishigaki, and S. Matsumoto, *Mater. Res. Soc. Symp. Proc.* 363, 157 (1995).
32. K. Okada, S. Komatsu, T. Ishigaki, and S. Matsumoto, "Proceedings of the 12th International Symposium on Plasma Chemistry," Minnesota, 1995, p. 2261.
33. K. Okada, S. Komatsu, and S. Matsumoto, *J. Mater. Res.* 14, 578 (1999).
34. K. Teii and T. Yoshida, *J. Appl. Phys.* 85, 1864 (1999).
35. Y. Hirose and Y. Terasawa, *Jpn. J. Appl. Phys.* 25, L519 (1986).
36. T. Kawato and K. Kondo, *Jpn. J. Appl. Phys.* 26, 1429 (1987).
37. J. A. Mucha, D. L. Flamm, and D. E. Ibbotson, *J. Appl. Phys.* 65, 3448 (1989).
38. M. Frenklach and H. Wang, *Phys. Rev. B* 43, 1520 (1991).
39. K. Teii, H. Ito, M. Hori, T. Takeo, and T. Goto, *J. Appl. Phys.* 87, 4572 (2000).
40. M. von Laue, *Z. Kristallogr.* 64, 115 (1926).
41. S. A. Solin and A. K. Ramdas, *Phys. Rev. B* 1, 1687 (1970).
42. R. J. Nemanich, J. T. Glass, G. Lucovsky, and R. E. Shroder, *J. Vac. Sci. Technol., A* 6, 1783 (1988).
43. J. Wagner, M. Ramsteiner, Ch. Wild, and P. Koidl, *Phys. Rev. B* 40, 1817 (1989).
44. R. E. Shroder and R. J. Nemanich, *Phys. Rev. B* 41, 3738 (1990).
45. F. Tuinstra and J. L. Koenig, *J. Chem. Phys.* 53, 1126 (1970).
46. A. C. Ferrari and J. Robertson, *Phys. Rev. B* 61, 14095 (2000).
47. M. Nakamizo, R. Kammereck, and P. L. Walker, Jr., *Carbon* 12, 259 (1974).
48. M. Yoshikawa, G. Katagiri, H. Ishida, A. Ishitani, and T. Akamatsu, *Appl. Phys. Lett.* 52, 1639 (1988); *J. Appl. Phys.* 64, 6464 (1988).
49. M. Yoshikawa, N. Nagai, M. Matsuki, H. Fukuda, G. Katagiri, H. Ishida, and A. Ishitani, *Phys. Rev. B* 46, 7169 (1992).
50. V. I. Merkulov, J. S. Lannin, C. H. Munro, S. A. Asher, V. S. Veerasamy, and W. I. Milne, *Phys. Rev. Lett.* 78, 4869 (1997).
51. K. W. R. Gilkes, H. S. Sands, D. N. Batchelder, J. Robertson, and W. I. Milne, *Appl. Phys. Lett.* 70, 1980 (1997).
52. K. W. R. Gilkes, S. Praver, J. Robertson, and H. S. Sands, *Mater. Res. Soc. Symp. Proc.* 498, 49 (1998).
53. D. R. Tallant, T. A. Friedmann, N. A. Missert, M. P. Siegal, and J. P. Sullivan, *Mater. Res. Soc. Symp. Proc.* 498, 37 (1998).
54. K. Okada, H. Kanda, S. Komatsu, and S. Matsumoto, *Mater. Res. Soc. Symp. Proc.* 593, 459 (2000).
55. Z. Sun, J. R. Shi, B. K. Tay, and S. P. Lau, *Diamond Relat. Mater.* 9, 1979 (2000).
56. S. Praver, K. W. Nugent, D. N. Jamieson, J. O. Orwa, L. A. Bursill, and J. L. Peng, *Chem. Phys. Lett.* 332, 93 (2000).
57. K. Okada, H. Kanda, S. Komatsu, and S. Matsumoto, *J. Appl. Phys.* 88, 1674 (2000).
58. S. Praver and K. W. Nugent, in "Amorphous Carbon: State of the Art" (S. R. P. Silva, J. Robertson, and G. A. Amaratunga, Eds.), p. 199. World Scientific, Singapore, 1998.
59. A. C. Ferrari and J. Robertson, *Phys. Rev. B* 63, 121405 (2001).
60. H. Ibach and D. L. Mills, "Electron Energy Loss Spectroscopy and Surface Vibrations." Academic Press, London, 1982.
61. B. J. Waclawski, D. T. Pierce, N. Swanson, and R. J. Celotta, *J. Vac. Sci. Technol.* 21, 368 (1982).
62. C. Oshima, R. Souda, M. Aono, and Y. Ishizawa, *Rev. Sci. Instrum.* 56, 227 (1985).
63. C. Oshima, T. Aizawa, R. Souda, and Y. Ishizawa, *Solid State Commun.* 65, 1601 (1988).
64. T. Aizawa, R. Souda, S. Otani, Y. Ishizawa, and C. Oshima, *Phys. Rev. Lett.* 64, 768 (1989).
65. T. Aizawa, T. Ando, K. Yamamoto, M. Kamo, and Y. Sato, *Diamond Relat. Mater.* 4, 600 (1995).
66. K. Okada, T. Aizawa, R. Souda, S. Komatsu, and S. Matsumoto, *Diamond Relat. Mater.* 10, 1991 (2001).
67. C. Z. Wang and K. M. Ho, *Phys. Rev. Lett.* 71, 1184 (1993).
68. D. A. Drabold, P. A. Fedders, and P. Stumm, *Phys. Rev. B* 49, 16415 (1994).
69. R. Brydson, "Electron Energy Loss Spectroscopy." Springer-Verlag, New York, 2001.
70. R. F. Egerton and M. J. Whelan, *J. Electron Spectrosc. Relat. Phenom.* 3, 232 (1974).
71. D. A. Muller, Y. Tzou, R. Raj, and J. Silcox, *Nature* 366, 725 (1993).
72. J. Bruley, D. B. Williams, J. J. Cuomo, and D. P. Pappas, *J. Microsc.* 180, 22 (1995).
73. L. A. Bursill, J. L. Peng, and S. Praver, *Philos. Mag. A* 76, 769 (1997).
74. R. P. Fehlhaber and L. A. Bursill, *Philos. Mag. B* 79, 477 (1999); *Phys. Rev. B* 60, 14147 (1999); *Phys. Rev. B* 62, 17094 (2000).
75. J. L. Peng, R. P. Fehlhaber, L. A. Bursill, and D. G. McCulloch, *J. Appl. Phys.* 89, 6204 (2001).
76. S. Praver, J. L. Peng, J. O. Orwa, J. C. McCallum, D. N. Jamieson, and L. A. Bursill, *Phys. Rev. B* 62, 16360 (2000).
77. K. Okada, K. Kimoto, S. Komatsu, and S. Matsumoto, "8th International Conference on New Diamond Science and Technology," Melbourne, 2002, p. 187.
78. R. Erz, W. Dotter, D. Jung, and H. Ehrhardt, *Diamond Relat. Mater.* 2, 449 (1993).
79. P. J. Fallon and L. M. Brown, *Diamond Relat. Mater.* 2, 1004 (1993).
80. P. Keblinski, D. Wolf, S. R. Phillpot, and H. Gleiter, *J. Mater. Res.* 13, 2077 (1998).
81. J. Hopwood, C. R. Guarnieri, S. J. Whitehair, and J. J. Cuomo, *J. Vac. Sci. Technol., A* 11, 152 (1993).
82. L. J. Mahoney, A. E. Wendt, E. Barrios, C. J. Richards, and J. L. Shohet, *J. Appl. Phys.* 76, 2041 (1994).



83. P. A. Miller, G. A. Hebner, K. E. Greenberg, P. D. Pochan, and B. P. Aragon, *J. Res. Natl. Inst. Stand. Technol.* 100, 427 (1995).
84. A. Schwabedissen, E. C. Benck, and J. R. Roberts, *Phys. Rev. E* 55, 3450 (1997).
85. M. B. Hopkins, *J. Res. Natl. Inst. Stand. Technol.* 100, 415 (1995).
86. F. A. Cali, P. A. F. Herbert, and W. M. Kelly, *J. Vac. Sci. Technol., A* 13, 2920 (1995).
87. V. A. Godyak and R. B. Piejak, *Phys. Rev. Lett.* 65, 996 (1990).
88. K. Okada, S. Komatsu, and S. Matsumoto, *J. Vac. Sci. Technol., A* 17, 721 (1999).
89. L. Schott, in "Plasma Diagnostics" (W. Lochte-Holtgreven, Ed.), North-Holland, Amsterdam, 1968.
90. M. M. Turner and M. B. Hopkins, *Phys. Rev. Lett.* 69, 3511 (1992).
91. W. L. Morgan, *Plasma Chem. Plasma Process.* 12, 477 (1992).

# Polyacetylene Nanostructures

Kevin K. L. Cheuk, Bing Shi Li, Ben Zhong Tang

*Hong Kong University of Science and Technology,  
Clear Water Bay, Kowloon, Hong Kong, China*

## CONTENTS

1. Introduction
  2. Unsubstituted Polyacetylene
  3. Polyacetylenes with Amino Acid Ester Pendants
  4. Polyacetylenes with Amino Acid Pendants
  5. Polyacetylenes with Ethylene Oxide Pendants
  6. Conclusions
- Glossary  
References

## 1. INTRODUCTION

Many complicated biological tasks, such as transforming chemicals in localized areas, transporting materials between cells or organs, and defending against foreign enemies, are handled by functionalized biopolymers. As can be seen from enzymes, hemoglobin, liposomes, etc. [1, 2], nature has tailored each of the biomacromolecules with a suitable structure and arranged or assembled the structural components in an organized way. To achieve an organizational structural hierarchy, the living world relies on a noncovalent architecture. Self-assembly is the organizational motif that is ubiquitously utilized by biological systems and underlies the formation of a wide variety of complex biological structures. The process obviously affords high flexibility, high efficiency, etc., but, importantly, still allows precise control over the formation of structural morphologies [3, 4].

Many of the concepts of biological self-assembly are derived from studies of tobacco mosaic virus, which is a helical assembly composed of 2130 identical protein units [5]. Though forming this complex protein requires a delicate management among the molecular interactions (van der Waals, electrostatic, hydrophobic, and steric interactions, hydrogen and coordination bonds, etc.), the assembly mechanism has exemplified that the association process is entropically driven [5, 6] and the final bioassembly

occupies the state of a thermodynamic minimum. In general, the success of organizing structures by self-assembly depends on how successfully these interactions can be utilized to bind molecules together. Supramolecular chemistry is inspired by the study of the basic features of these secondary interactions, which contributes to our understanding not only of living systems, but also nonliving systems. Based on these interactions, supramolecular chemistry has assembled a number of well-defined, regular nonbiological architectures [7–16], which are expected to generate new properties and to create new materials [17–19].

Making precise nano- and mesoscopic structures is still one of the greatest challenges now facing scientists and technologists. Molecular self-assembly is one of the feasible ways of approaching this goal. Although self-assembly originated from the study of small molecules, it should also be a strategy that is applicable to big molecules. Through cooperative self-assembly processes, macromolecular chains may also be hierarchically organized into large and complex but precise and ordered structures. Nature has presented wonderful examples in this regard: the  $\alpha$ -helix and  $\beta$ -sheet of proteins assemble into defined tertiary and quaternary structures. The natural process is truly amazing, and judiciously designed nonnatural systems should be able to mimic the bioprocesses to self-assemble into biomimetic structures. There are many successful reports addressing this idea. In this article, we will review the biomimetic hierarchical structures generated by unsubstituted and substituted polyacetylenes.

## 2. UNSUBSTITUTED POLYACETYLENE

Polyacetylene is the simplest linear conjugated macromolecule and is one of the best-known organic conductors [20–24]. The discovery of the metallic conductivity of doped polyacetylene has opened up a fascinating field of research, conductive macromolecules, which have brought us to a plastic-electronics revolution, with many exciting implications in high technologies, as evidenced by the award of the Nobel Prize in chemistry in 2000. High-molecular-weight

polyacetylene can be synthesized from the acetylene polymerization initiated by the Ziegler–Natta catalyst (Chart 1) [25, 26], but under “normal” conditions, only a featureless morphology can be produced [27–29]. The fundamental norm lasted until Akagi, Shirakawa, and co-workers investigated the asymmetric polymerization of acetylene [30]. Through mixing of a chiral nematic mesogen (*R*)- or (*S*)-**2** (Chart 2) with an organometallic catalyst, multistranded helical polyacetylene fibers, a few hundred nanometers in diameter, were successfully prepared. It was observed that the polymerization conducted in the presence of the (*R*)-form nematic liquid crystals led to the formation of left-handed helical fibrillar morphologies (Fig. 1), whereas that in the presence of the (*S*)-form gave polymer fibrils twisting in the opposite direction. With control over optical purity or the type of chiral dopant, it was possible to generate helical morphologies with different helical pitches.



Chart 1

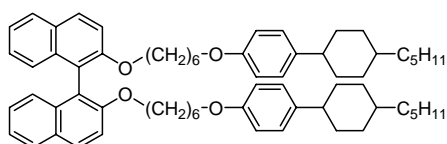
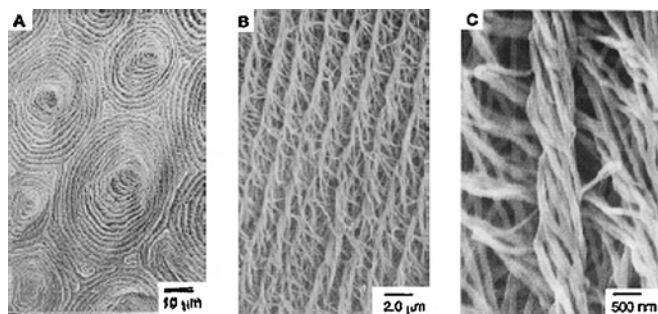
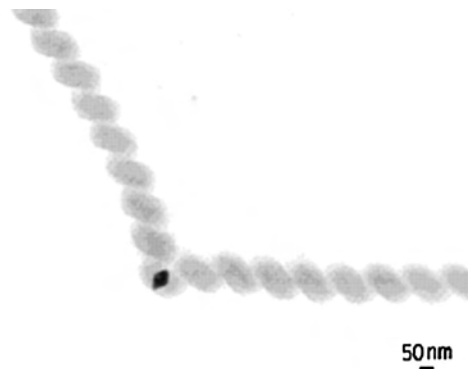
*(R)*-(+)- or (*S*)-(-)-**2**

Chart 2

Another helical structure of polyacetylene was prepared at high temperatures (~250 °C) [31]. Similar to the Akagi and Shirakawa reaction, Qin et al. also used an asymmetric condition to build the helical polymers (Fig. 2). However, the catalyst system used by Qin is different from that used by Akagi and Shirakawa: the former used a native asymmetric catalyst, copper tartrate, and the latter used an achiral catalyst blended with a chiral dopant. The fibers obtained were obviously different; the former afforded single-stranded and more regular helical structures. Interestingly, the fibers were formed in such a way that two helical strands simultaneously grew on a single copper nanocrystal. The two strands were opposites in an absolute helical sense but identical in cycle



**Figure 1.** SEM micrographs of left-handed helical polyacetylene fibers prepared in a chiral nematic reaction field. Reprinted with permission from [30], K. Akagi et al., *Science* 282, 1683 (1998). © 1998, American Association for the Advancement of Science.



**Figure 2.** TEM image of two regular coiled fibers, symmetrically grown on a single copper crystal and prepared by polymerization of acetylene at ~250 °C. Reprinted in part with permission from [31], Y. Qin et al., *Org. Lett.* 4, 18 (2002). © 2002, American Chemical Society.

number, node diameter, node length, helix pitch, and fiber diameter. A small amount of the acetylene monomer may have initially bound to the chiral catalyst in an asymmetrical way, and the chiral chains propagated with other monomer molecules also inserted in an asymmetrical fashion.

### 3. POLYACETYLENES WITH AMINO ACID ESTER PENDANTS

The two examples discussed above clearly demonstrate that the formation of regular helical structures closely relates to the asymmetrical force field. Chirality is a structural feature of many natural constituent components (amino acids, saccharides, etc.), and biological systems exhibit helicity at all organizational levels (e.g.,  $\alpha$ -helix of proteins, double helix of DNA, triple helix of collagen, and spiral bacterium of *Spirillum*). Obviously, rather than using an external stimulus, nature has put an asymmetrical field in internal building units, permitting better control over the final assembly structures. Many scientists have taken this approach and used asymmetrical building blocks to construct chiral polymers [32–64].

The (unsubstituted) polyacetylene chain is symmetrical and achiral. However, when pendant groups are introduced, the chain symmetry is broken. Theoretical computation suggests that the chain segments of a substituted polyacetylene bearing bulky appendages can take on helical conformations [65]; a majority of the chain segments with long persistence lengths will rotate in one preferred screw sense when the appendages are chiral species. In addition to fusing the chiral species into the polymer structure at the molecular level by covalent bonds, the polyacetylene chains could also spirally rotate in asymmetrical force fields when the  $\pi$  electrons of the conjugated backbone and/or the functional groups of the achiral substituents experience molecular interactions with external chiral species [66]. With the aim of preparing asymmetrical polyacetylenes for the study of hierarchiral structures, Shinohara, Shigeka, and co-workers synthesized an optically active polyphenylacetylene bearing menthoxy-carbonylamino groups (Chart 3), which possessed a high molecular mass ( $1 \times 10^6$  Da) and a high stereoregularity (*Z* content ~90 mol%) [67]. Under the influence of the

chiral pendants, the achiral main chain of **3** became CD active and absorbed strongly in the long-wavelength region ( $\sim 400$  nm). A possible reason for this is the formation of a secondary structure with an excess of one-handed helical structure. Further investigation of its higher-order structure by scanning probe microscopy revealed that the polymer afforded a helical quaternary structure. From Figure 3a, it can be seen that the two polymer strands are intertwined to form a right-handed double-helical structure. Each strand is also helically rotating and has a width of 9 Å, which matches the width of the polyphenylacetylene backbone with a *Z* configuration, as suggested by the molecular mechanics calculation.

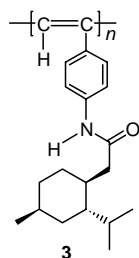
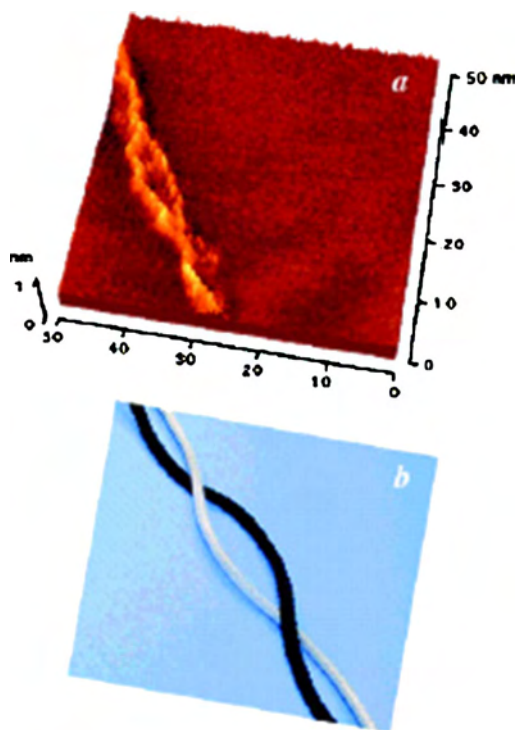


Chart 3

The  $\alpha$ -helix of the polypeptide chain exemplifies nature's ability to construct complex chiral structures by making use of hydrogen bonding provided by each amino acid residue. Inspired by this phenomenon, in 1997, our group embarked on a research program on the development of



**Figure 3.** (a) Low-current STM height image of interwound polymer chains of **3** on highly oriented pyrolytic graphite at room temperature. (b) String model of the interwinding polymer chains. Reprinted with permission from [67], K. Shinohara et al., *J. Am. Chem. Soc.* 123, 3619 (2001). © 2001, American Chemical Society.

new biomimetic polymers, using amino acids as chiral ingredients. Through the incorporation of the naturally occurring building blocks into the conjugated polymer structure, we synthesized a variety of new amphiphilic polyacetylenes [66], examples of which are given in Charts 4 and 5. The amino acid substituents not only conferred helical conformations on the polyacetylene chains but also endowed them with hydrogen bonding capacity, which is an important secondary force for self-assembly. The polymers were therefore able to self-fold into higher-order structures. An example of the organizational morphologies is shown in Figure 4. By a simple process of solvent evaporation, polymer **4**, which bears isoleucine appendages, organized into helical cables with left-handed twists. The atomic force microscope (AFM) image revealed that the helical fibrils were, on average,  $>500$  nm in length and  $\sim 20.5$  nm in width. These sizes are much bigger than the dimensions of a single chain, indicating that nanofibrils are assemblies of multiple strands of polymer chains. Similar to the fibrous proteins of  $\alpha$ -keratin [68], the helical chains of **4** may have been plaited together via a folding process aided by noncovalent interactions such as interstrand hydrogen bonding [69]. The involvement of noncovalent forces in the assembly process was clearly confirmed by the partially unraveled helices generated by the repeated horizontal scans of the AFM tip on the surface of mica in the direction perpendicular to the long axes of the nanofibers. The unraveled morphology was obviously due to the breakage of the physical bonds that had glued the chain segments together.

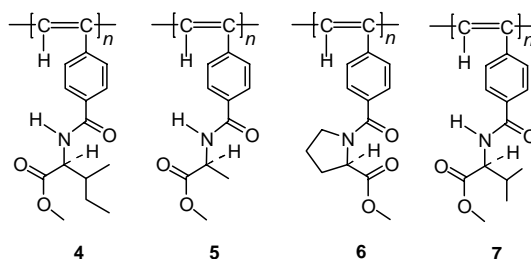


Chart 4

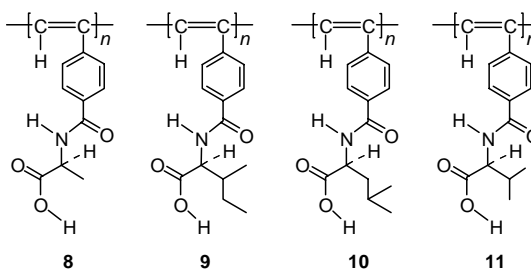
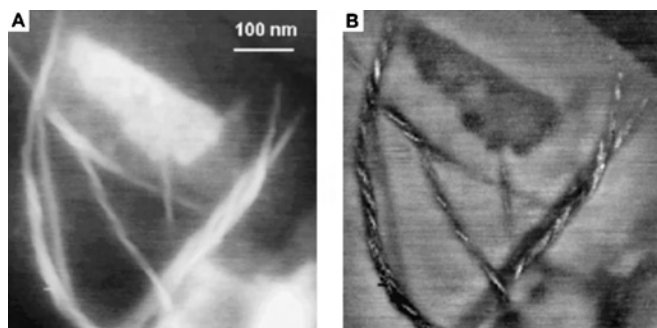


Chart 5

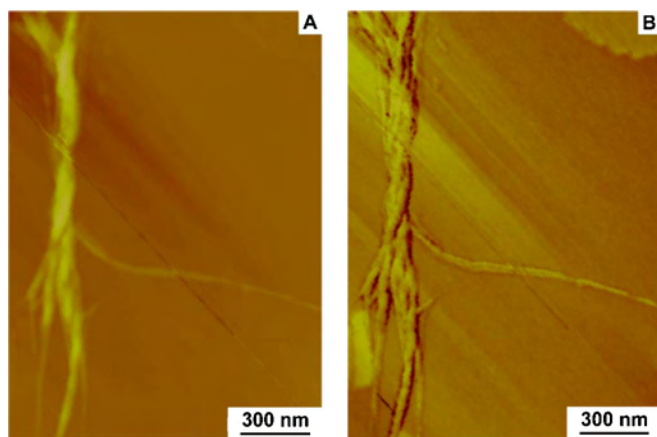
Similarly, polymer **5**, which bears smaller pendants of alanine groups, also formed helical fibrils. The structural details are different, however; the helical cables of **5** are right-handedly winding, which is different from the left-handed twisting observed in **4**, and the cables of **5** ( $\sim 100$  nm in diameter) are on average thicker than those of **4**. Why the assembly behavior of **5** is different from that of **4** is unclear, but it may be related to the packing process benefiting from



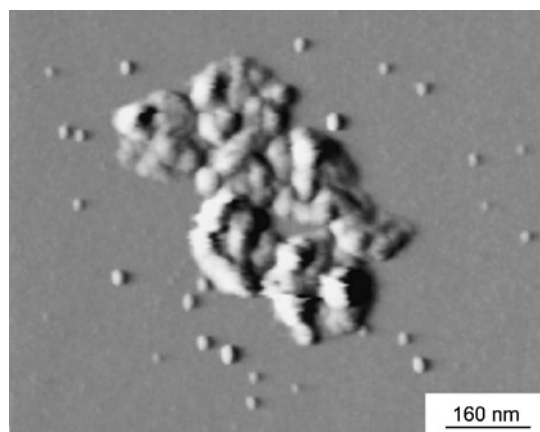
**Figure 4.** AFM (A) height and (B) phase images of left-handed helices formed upon natural evaporation of a methanol solution of **4** ( $36.6 \mu\text{M}$ ) on newly cleaved mica. Reprinted with permission from [62], B. S. Li et al., *Polym. Prepr.* 42, 248 (2001). © 2001, American Chemical Society.

the molecular structure of **5**. The smaller pendants in **5** may facilitate close packing and interchain hydrogen bonding between the polymer chains due to a less pronounced steric effect arising from the side groups. Thus, more polymer chains can associate together to form single strands, as verified by the thicker strands, which eventually fold up to form the multistranded cables.

With the proline appendages, **6** is incapable of forming hydrogen bonds. It is thus of interest to know whether the macromolecular chains can associate into defined structures without the involvement of this noncovalent interaction. Although **6** in methanol displayed only weak CD activity [70], when its dilute solution ( $38.9 \mu\text{M}$ ) was dropped onto freshly cleaved mica, tortuously twisted cables of double-stranded helical fibrils were formed, an example of which is shown in Figure 6. The morphology is composed of two helical strands ( $\sim 150 \text{ nm}$  in width), which braid together to form the final supercoils. Each of the strands seems to be the result of winding of many single-stranded fibers, and the whole structure bears a good likeness to the superhelical structure formed by the menthol-containing polymer (**3**) already discussed (cf. Fig. 3). The similarity suggests that the



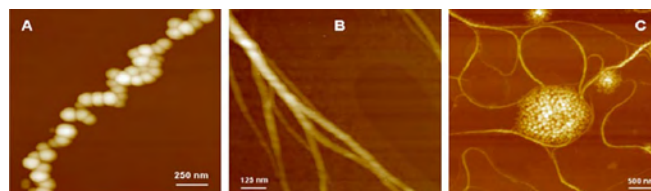
**Figure 5.** AFM (A) height and (B) phase images of self-assembly morphologies of multistranded right-handed helices formed upon natural evaporation of a dilute methanol solution of **5** ( $43.2 \mu\text{M}$ ) on newly cleaved mica. Reprinted with permission from [62], B. S. Li et al., *Polym. Prepr.* 42, 248 (2001). © 2001, American Chemical Society.



**Figure 6.** AFM deflection images of tortuously twisted nanofibers formed upon natural evaporation of a methanol solution of **6** ( $38.9 \mu\text{M}$ ) on freshly cleaved mica. Reprinted with permission from [42], K. K. L. Cheuk, Ph.D. Dissertation, Hong Kong University of Science & Technology, 2002.

cyclic molecular structures in the polymers favor the formation of the loose double-helical quaternary structure.

Molecular information, such as amino-acid sequence and chain chirality and amphiphilicity, encoded in the primary structures of biomacromolecules plays a primary role in determining their native folding structures; for example, L-glutamic acid segments in proteins often give  $\alpha$ -helix structure, whereas L-isoleucine segments most frequently induce  $\beta$ -sheet formation [1, 2, 71]. The folding structures can, however, be varied or denatured by the changes in the environmental surroundings of the biopolymers, because of the noncovalent nature of the supramolecular assembly. Loss of body fluid, for example, can transmute organizational structures of proteins by dehydration or deprivation. Similar phenomena have also been observed in the self-assembly processes of the amino acid-containing polyacetylenes. For example, whereas a methanol solution of **7** gave pearl-shaped structures upon natural evaporation, its tetrahydrofuran (THF) solution gave helical cables with a clear left-handed twist under similar assembly conditions (Fig. 7). The polymer chains of **7** may take an extended conformation in THF because THF is a good solvent of both the backbone and the pendants of the polymer. During the aggregation process accompanying solvent evaporation, the extended helical chains may twine around each other via interchain



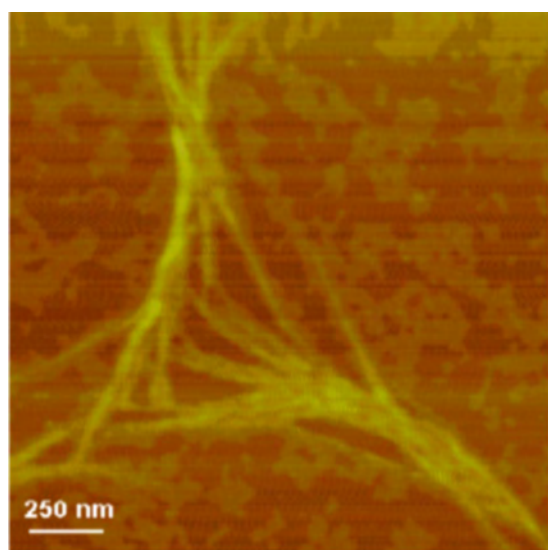
**Figure 7.** AFM images of (A) clustered pearls, (B) helical cables, and (C) clustered pearls plus helical cables formed upon natural evaporation of (A) methanol, (B) THF, and (C) methanol/THF (1:7 by volume) solutions of **7** on the surfaces of newly cleaved mica. Scale bars (nm): (A) 250, (B) 125, (C) 500. Concentration of polymer solutions:  $\sim 1\text{--}5 \text{ mM}$ . Reprinted with permission from [72], Li et al., *Macromolecules* 36, 77 (2003). © 2003, American Chemical Society.

hydrogen bonding to give twisted strands, further association of which in different multiplicities (doublet, triplet, etc.) will give thicker fibrils of different diameters—this assembly mechanism is clearly suggested by the image shown in Figure 7B. It is envisioned that evaporation of a methanol/THF solution of **7** may generate transition morphologies containing both micellar and fibrillar structures. This was indeed the case; as shown in Figure 7C, the organizational morphologies obtained from the mixture solvent system showed combined features of the assembly structures obtained from the individual solvent systems.

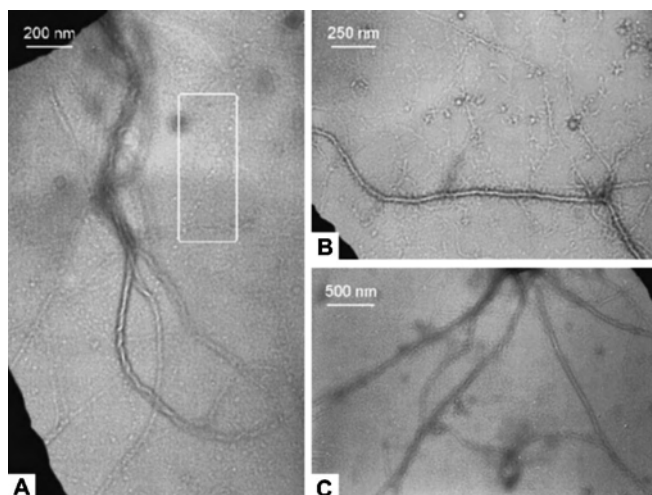
#### 4. POLYACETYLENES WITH AMINO ACID PENDANTS

Whereas the amino acid pendants of polymers **4–7** are esterified, polymers **8–11** carry “free” amino acid pendants. The change in the molecular structure is expected to affect the assembly structures of the polymers. Different from its “polyester” counterpart **5** (cf. Fig. 5), “polyacid” **8** formed pigtail-like nanofibers upon the natural evaporation of its methanol solution under ambient conditions (Fig. 8). A number of fibrils were bundled together to form plaits with loose tails. Each fibril comprised many polymer chains that were stuck together through interchain hydrogen bonds.

“Polyacid” **9** also formed helical fibrils. Close examination by transmission electron microscopy (TEM), however, revealed that the fibrils possessed a hollow structure (Fig. 9); that is, the fibrils were actually nanotubes. The tubes wound around each other to give twisted hollow structures. As marked by the rectangle in Figure 9A, there are many hollow rings or spherical vesicles in addition to the twisting tubes. These structures are remarkable, because nanotubes and vesicles have seldom been formed by homopolymers,



**Figure 8.** AFM height image of pigtail-like nanofibers formed upon natural evaporation of a methanol solution of **8** ( $46.0 \mu\text{M}$ ) on newly cleaved mica. Reprinted with permission from [62], B. S. Li et al., *Polym. Prepr.* 42, 248 (2001). © 2001, American Chemical Society.

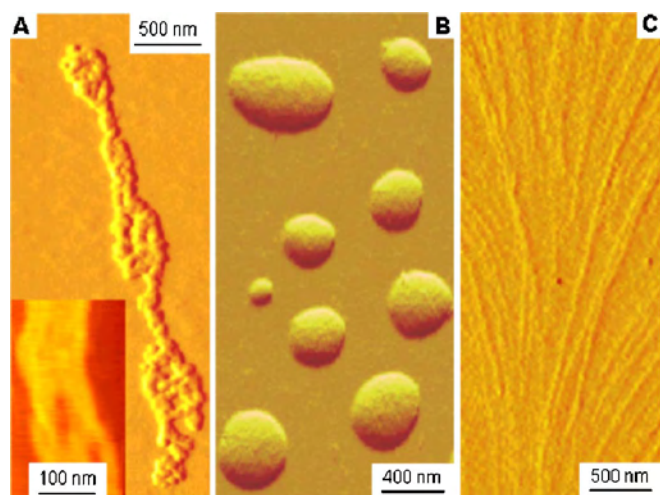


**Figure 9.** TEM images of vesicles and nanotubes formed upon natural evaporation of a methanol solution of **9** ( $19.3 \mu\text{M}$ ) on a carbon-coated grid under ambient conditions. Reprinted with permission from [42], K. K. L. Cheuk, Ph.D. Dissertation, Hong Kong University of Science & Technology, 2002.

although they have been observed in a few copolymer systems [13, 73–79]. The coexistence of the vesicular and tubular structures suggests that the vesicles are the building units of the nanotubes; stringing the former together leads to the formation of the latter.

In the polar solvent of methanol, the polyacetylene main chains of **9** may associate together with their pendants facing outward, in an effort to minimize the exposure of their hydrophobic backbones to the polar environment [80]. Curling of the bi- or multilayer sheets would result in the formation of a closed vesicular structure. Following the mechanism of coalescence [81], the vesicles may fuse together to form the tubular structure, the shells of which are covered by the isoleucine pendants. During the thickening of the solution accompanying the solvent evaporation, the tubes may grow in length by the linear fusion of more vesicles, and the lengthened nanotubes may twine round each other via hydrogen bonding of the pendants on the outer shells to give the helical cables of nanotubes.

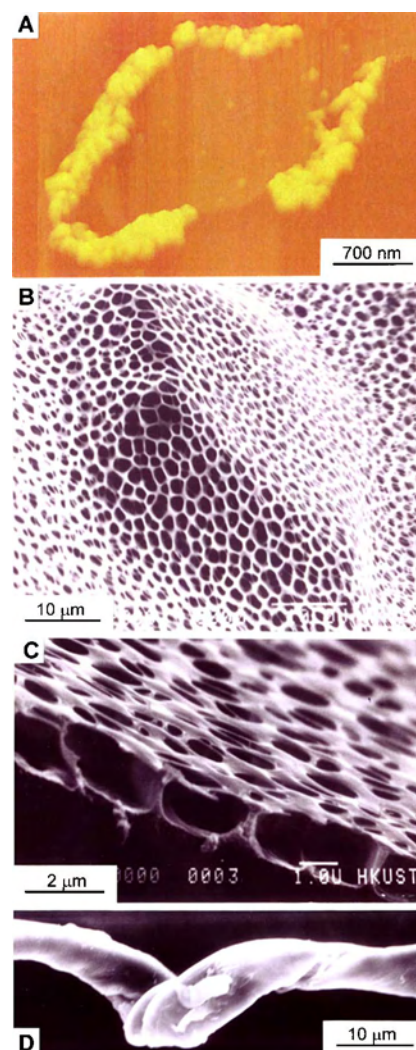
The previous mechanism should be solvent dependent; changing the solvent or environment would affect the assembly process because of the perturbation of the interactions between the polymer chains. A more comprehensive study was conducted on the self-assembly processes of **10**, which carries leucine pendants [66]. When methanol was used, twisted cables of helical fibrils were formed, an example of which is shown in Figure 10A. Close inspection of the cable structure reveals that the fibrils fold back to form knobs or  $\beta$  bends at two ends of the cable. When a dilute solution was used, the aggregation of the macromolecules was further suppressed and the resultant morphology looked like long threads or helical chains, each pair of which twist over and under each other to form a double helix (inset of Fig. 10A). When the solvent was changed to chloroform, the morphology obtained from the solution of similar concentration ( $9.6 \mu\text{M}$ ) became distinctly different. Instead of forming helical cables, the chloroform solution gave oval eggs or



**Figure 10.** AFM images of self-assembly morphologies formed upon natural evaporation of dilute solutions of **10** on newly cleaved mica. (A) A multistranded cable from a  $12.8 \mu\text{M}$  methanol solution (inset: duplex braids from a  $2.6 \mu\text{M}$  solution). (B) Spherical vesicles from a  $9.6 \mu\text{M}$  chloroform solution with 0.5% methanol. (C) Extended filaments from  $12.8 \mu\text{M}$  methanol containing  $25.5 \mu\text{M}$  KOH. Reprinted with permission from [66], B. Z. Tang, *Polym. News* 26, 262 (2001).

spherical vesicles (Fig. 10B). This difference is, however, not totally unexpected. Unlike methanol, chloroform is a poor solvent of amino acids, and the polymer chains would self-fold to minimize their exposure to the solvent. When the solvent evaporates, the elementary “foldamers” may cluster together to form compactly packed larger spheres in an effort to minimize their surface area in contact with the air. The morphology changed not only with solvent but also with pH. The addition of KOH to the methanol solution disassembled the helical cables and gave extended filaments (Fig. 10C). The complexation of the  $\text{K}^+$  ions with the polymer chains partially dissociates the amino acid groups, thus hindering the hydrogen bond formation. The electrostatic repulsion of the closely located charged chains cannot easily bend but takes an extended conformation.

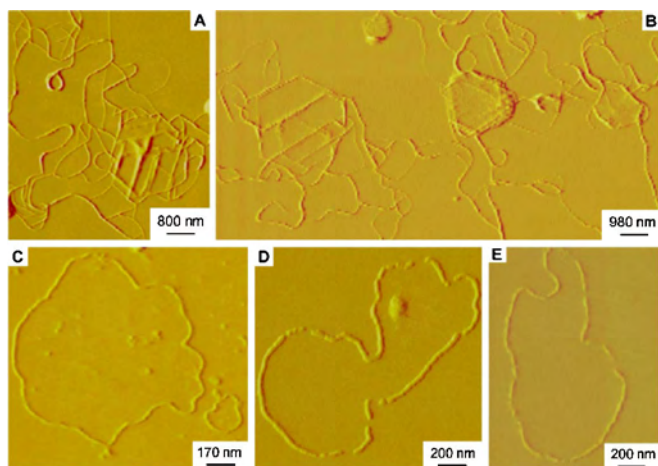
Concentration is also a critical parameter in determining the final morphological structure; overcrowding may cause post-fusion of the polymer aggregates, leading to the formation of even higher-order structures. For example, evaporation of a dilute solution of **10** gave crescent helical fibers (Fig. 11A). The closely located helical cables may be interconnected by interstrand hydrogen bonds of the amino acid groups, but the solvent molecules, on the other hand, try to push the polymer chains apart; the balance of the two antagonistic forces results in the formation of a fence-like structure. If the concentration of the polymer solution is increased, more polymer chains will stick together to construct more closed fences or cages, and the neighboring cages may merge to form a continuous structure. Indeed, when a THF solution of **10** with a relatively high concentration ( $28.9 \mu\text{M}$ ) was used, a mesoporous, honeycomb-like, thin solid film comprising interconnected cages was formed (Fig. 11B). The interconnection of the cages was three-dimensional in nature, as clearly revealed by a scanning electron microscope image of the tilted sample (Fig. 11C). Figure 11D shows a partial view of a long fiber of **10**



**Figure 11.** (A) AFM image of crescent helices formed by a diluted solution of **10** ( $12.8 \mu\text{M}$ ). (B) Scanning electron microscope (SEM) image of a honeycomb pattern generated from a concentrated THF solution of **10** ( $28.9 \mu\text{M}$ ), whose 3D nature is clearly revealed by the enlarged side view (C) with the sample tilted  $60^\circ$  from the electron beam axis. (D) SEM micrograph of a twisted fiber formed upon diffusion of ether into a methanol solution of **10** ( $3.9 \mu\text{M}$ ). A and D are reprinted with permission from [85], F. Salhi et al., *J. Nanosci. Nanotechnol.* 1, 137 (2001). © 2001, American Scientific Publishers. B and C are reprinted with permission from [66], B. Z. Tang, *Polym. News* 26, 262 (2001).

obtained from a diffusion process. When ether was diffused into a methanol solution of **10**, left-handed helical ribbons were formed. The image proves that the polymer is capable of building a large helical structure, even in the micrometer domain.

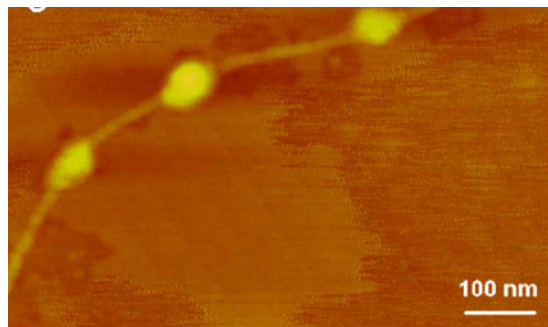
The folding structures of biopolymers are affected by external perturbations in addition to internal factors. The supercoiling of DNA is affected, for example, by small changes in the local ionic strength, which can cause the reversal of the helical twist in the DNA coils [82]. Similar phenomena have been observed in our nonnatural polymer system. The pH effect on the assembly behaviors of polymer **11** is shown in Figure 12. Changing the medium pH from “neutral” to “basic” changed the organizational



**Figure 12.** AFM deflection images of (A and B) helical nanofibers formed by **11** upon natural evaporation of its methanol solution ( $7 \mu\text{g/ml}$ ) on freshly cleaved mica under ambient conditions. The nanofibers can be unraveled by adding a 1 M equivalent of KOH (i.e.,  $\text{KOH}/\mathbf{11} = 1:1$ ) to the methanol solution of the polymer ( $4 \mu\text{g/ml}$ ), as shown in C–E. Reprinted with permission from [83], Li et al., *Nano-Letters* 1, 323 (2001). © 2001, American Chemical Society.

morphology of the polymer from continuous helical cables to discrete random threads [83]. The random threads showed almost no macroscopic screw sense. This example illustrates how ionization of the carboxyl groups by the potassium ions breaks the hydrogen bonds, which are believed to maintain the long, thick helical structure of the polymer chains.

By partially hydrolyzing “polyester” **7**, we succeeded in generating a valine-containing polymer consisting of both ester and acid repeat units, poly[(4-ethynylbenzoyl-L-valine methyl ester)-*co*-(4-ethynylbenzoyl-L-valine)]. This hybrid polymer afforded self-assembly structures with organizational features of both the “polyester” and the “polyacid.” While “polyester” **7** assembled into pearl-shaped morphological structures upon natural evaporation of its dilute methanol solution (cf. Fig. 7), under similar conditions



**Figure 13.** AFM images of string beads formed upon natural evaporation of methanol solutions of a partially hydrolyzed **7**, poly[(4-ethynylbenzoyl-L-valine methyl ester)-*co*-(4-ethynylbenzoyl-L-valine)], on the surfaces of newly cleaved mica. Scale bars (nm): 100; concentration:  $\sim 2 \mu\text{g/ml}$ ; temperature:  $\sim 23^\circ\text{C}$ . Reprinted with permission from [72], Li et al., *Macromolecules* 36, 77 (2003). © 2003, American Chemical Society.

“polyacid” **11** associated into helical ropes (cf. Fig. 12). The hybrid polymer gave an intermediate structure with spherical beads strung together on a filamentary string (Fig. 13). In methanol, the coiled chains of **7** may pack together to minimize the exposure of its hydrophobic backbones to the polar solvent, forming micelle-like structures with their outer shells decorated by the hydrophilic amide and ester functional groups. On the other hand, the strong solvation power of the methanol solvent toward **11** may force the helical chains to take on an extended conformation. During the solvent evaporation, the micelles may grow in size and stick together to give the clustered pearls, whereas the individual helical chains may aggregate in a side-by-side fashion to form spirally twisting fibrils. This aggregation is reminiscent of protein folding. Particular types of amino acids tend to form a relatively small number of local structural motifs [84], whereas aggregate in the proteins in such a way that the hydrophobic and hydrophilic regions are respectively out of, and in, contact with water.

## 5. POLYACETYLENES WITH ETHYLENE OXIDE PENDANTS

The previous results clearly show that not only molecular asymmetry but also chain amphiphilicity plays important roles in the self-assembly processes of chiral acetylene polymers. In this section we focus our discussion on the self-organization of polymers solely with the latter property (amphiphilic achiral species). A few examples of such amphiphilic polyacetylenes are given in Chart 6, in which polar hydrophilic substituents are appended to nonpolar polyacetylene backbones.

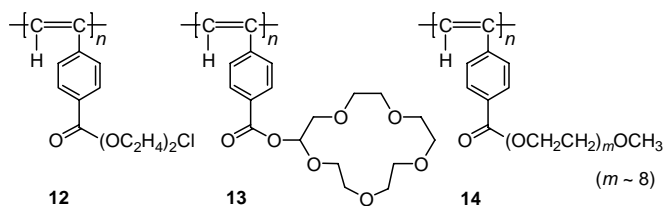
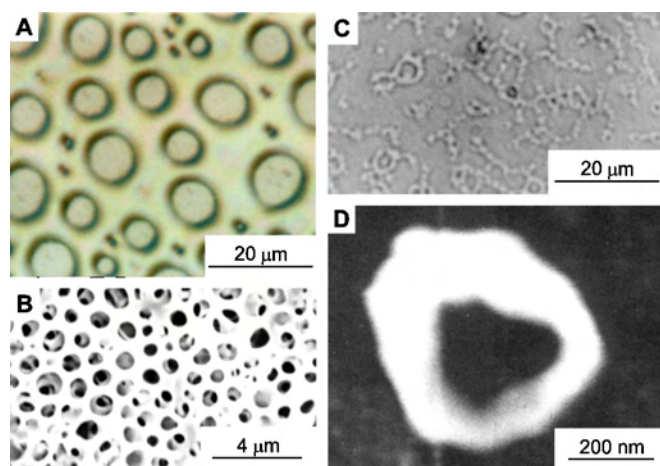


Chart 6

When a tiny drop of a THF/hexane solution of **12**, which bears short ethylene oxide pendants, was deposited on a glass slide, a microporous thin film ( $\sim 2\text{--}10 \mu\text{m}$  in pore diameter) was instantly formed upon solvent evaporation (Fig. 14A). When the solvent was changed to a mixture of dichloromethane (DCM) and hexane and when the solution concentration was increased, a three-dimensional porous thin solid film with a smaller pore size ( $\sim 1 \mu\text{m}$  in diameter) was formed (Fig. 14B). When a dilute solution was used, the evaporation process afforded the elementary building blocks for a three-dimensional higher-order structure: bagel-like vesicles [86, 87], whose sizes varied from several hundred nanometers to a few micrometers (Fig. 14C and D). This primary structure may help us understand the assembly mechanism: when deposited on a glass substrate in the three-dimensional space, the horizontally oriented vesicles may merge into porous layers that are parallel to the substrate accompanying the solvent evaporation, whereas

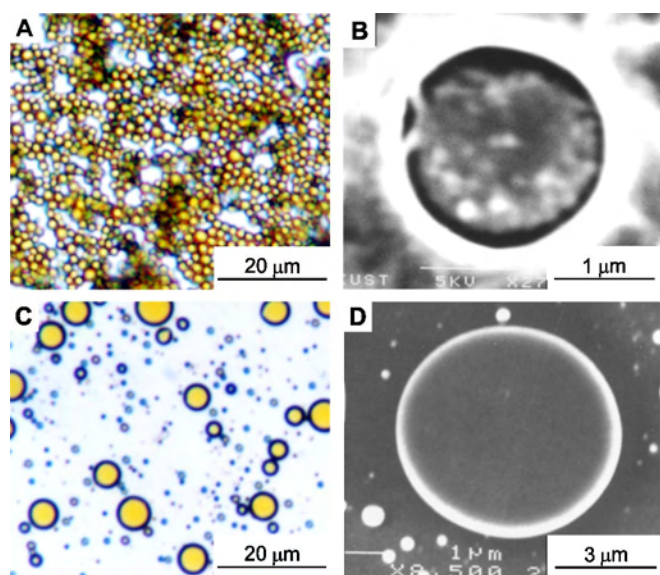




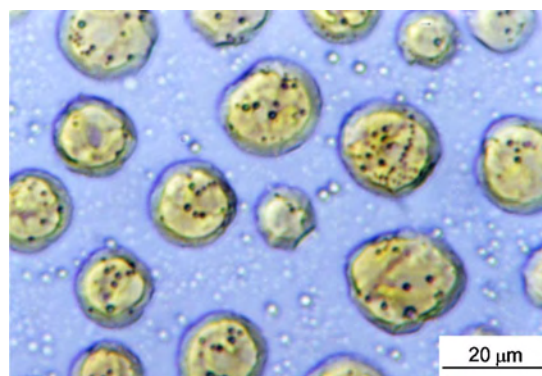
**Figure 14.** Microporous films formed by natural evaporation of (A) THF/hexane ( $\sim 1:1$  by volume) and (B) DCM/hexane ( $\sim 1:1$  by volume) solutions of **12** on glass slides. Concentrations of **12**: (A)  $\sim 1$ , (B)  $\sim 2$  mg/ml. (C, D) Vesicular structures formed by the evaporation of a dilute solution of **12** ( $\sim 0.3$  mg/ml) in the DCM/hexane mixture. The morphologies shown in (A, C) and (B, D) are POM and SEM images, respectively. Reprinted with permission from [85], F. Salhi et al., *J. Nanosci. Nanotechnol.* 1, 137 (2001). © 2001, American Scientific Publishers.

convergence of the vesicles with other orientations would produce the interlayer pores, leading to the formation of the multilayer porous structure.

The self-association of **12** is also solvent-sensitive: when relatively polar solvents were used, discrete microspheres, rather than regular pores, were formed. Upon solvent evaporation, a THF solution of **12** afforded spheres with an



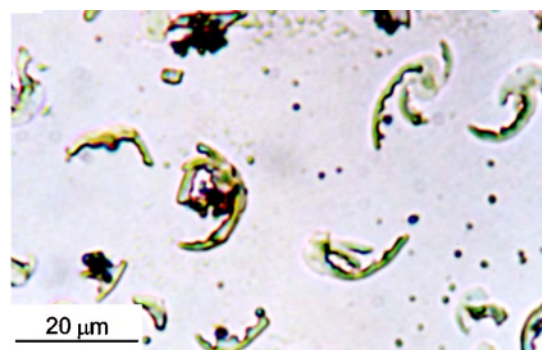
**Figure 15.** Microspheres formed by natural evaporation of (A, B) THF and (C, D) DCM/acetone ( $\sim 1:1$  by volume) solutions of **12** on glass slides. Concentration of **12**:  $\sim 1$  mg/ml. The morphologies shown in (A, C) and (B, D) are POM and SEM images, respectively. Reprinted with permission from [85], F. Salhi et al., *J. Nanosci. Nanotechnol.* 1, 137 (2001). © 2001, American Scientific Publishers.



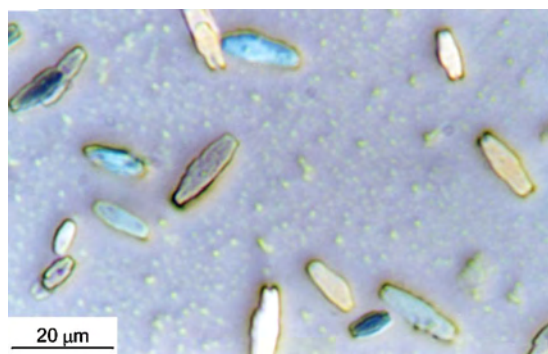
**Figure 16.** POM image of the microcrystals of carbazole formed inside microspheres of **12** by natural evaporation of a DCM/acetone solution of **12**/carbazole on a glass slide. Concentration of **12**/carbazole:  $\sim 6$  mg/ml; weight ratio of **12**/carbazole: 2:1; volume ratio of DCM/acetone:  $\sim 1:1$ . Reprinted with permission from [46], K. K. L. Cheuk et al., *Polym. Mater. Sci. Eng.* 82, 54 (2000).

average diameter of  $\sim 1.5$   $\mu\text{m}$  (Fig. 15A and B) [85]. Similarly, a DCM/acetone mixture of **12** also gave microspheres (Fig. 15C and D). The hydrophobic polyacetylene main chains of **12** may have aggregated together to form the core of the spheres that are surrounded by its hydrophilic ethylene oxide side chains under polar conditions, whereas the amphiphilic polymer may have formed bi-, tri-, or multilayers and/or even vesicular structures [76, 87] to reduce the surface area in the nonpolar environments.

Biomimetalization has attracted much interest in recent years [88–95]. Molding of inorganic crystals into appropriate shapes and sizes has created a variety of different material properties. The amphiphilic polyacetylenes were found to regulate the growth of organic crystals. For example, evaporation of a DCM/acetone mixture of **12** and carbazole gave regular spherical microcrystals of carbazole  $\sim 20$   $\mu\text{m}$  in diameter (Fig. 16). Under similar conditions, when a drop of a DCM/ethanol solution of carbazole/**13**, which contains crown ether appendages, was deposited on a glass slide, isolated sickle-like crystals,  $\sim 20$   $\mu\text{m}$  in length, were formed (Fig. 17). Replacing **13** with **14**, which bears long oligo(ethylene oxide) appendages, led to the generation of



**Figure 17.** POM images of the microcrystals of carbazole formed inside microreservoirs of **13** by natural evaporation of DCM/ethanol ( $\sim 1:1$  by volume) solutions of **13**/carbazole on a glass slide. Concentrations of **13**/carbazole:  $\sim (0.25$  mg/0.5 mg)/ml. Reprinted with permission from [46], K. K. L. Cheuk et al., *Polym. Mater. Sci. Eng.* 82, 54 (2000).



**Figure 18.** POM images of microcrystals of carbazole in a polymer matrix of **14** formed by natural evaporation of DCM/ethanol solutions of carbazole/**5** on a glass slide. Volume ratio of DCM/ethanol: ~1:1; concentration of **14**: ~1 mg/ml; weight of carbazole added to 1 ml of the polymer solution: 2 mg. Reprinted with permission from [46], K. K. L. Cheuk et al., *Polym. Mater. Sci. Eng.* 82, 54 (2000).

crystal bars, ~8 to 20  $\mu\text{m}$  in length (Fig. 18). The formation of these defined crystal structures is probably achieved by a micelle-like self-assembly process. When solvent evaporates, carbazole molecules pack together to form a crystal. However, in the presence of amphiphilic polymers, the packing process may be slowed down because the carbazole molecules may be wrapped in the amphiphilic chains. The polymer backbones may solvate the carbazole molecules in the inner core, with the polar ethylene oxide groups exposed to the solvent environment. The separate micelle-like complexes may thus in turn give the microcrystals that are covered by, or sheathed in, the amphiphilic polymer chains. Different pendants bring about different degrees of repulsion or steric effects. The different properties of the micelle-like aggregates may have eventually guided the carbazole molecules to grow in different patterns.

## 6. CONCLUSIONS

It is generally agreed that it is difficult to form supra-molecular assemblies of defined architecture from synthetic homopolymers [96]. In this review, we have proved, however, that homopolyacetylenes can self-organize into macromolecular architectures with well-defined three-dimensional structures. Both the unsubstituted and substituted polyacetylenes spontaneously assembled into various mechanically robust organizational morphologies reminiscent of natural hierarchical structures: helices, vesicles, fibrils, etc. This clearly demonstrates that synthetic homopolymers with rationally designed molecular structures can be used to fabricate biomimetic morphologies, whose size, shape, and pattern can be readily tuned by simple morphosynthetic processes. The organizational morphologies changed with the variations in the pendant hydrophilicity, solvent polarity, and pH value, suggesting a proteomimetic adoptability [97] and demonstrating the tunability of the hierarchical structures by internal perturbations and external stimuli.

Unlike “conventional” vinyl polymers, the acetylene polymers consist of alternating double bonds, whose structural cousins are highly photoconductive [98–100]. Cytotoxicity assays have revealed that the amphiphilic polyacetylenes

are biocompatible, and some of them can even stimulate the growth of living cells [101–103]. Their photoelectronic and biological properties make the polyacetylenes promising candidates for biomaterials; they may be found to be useful in potential applications in such biotechnological systems as artificial nervous networks, photosynthesis devices, and phototherapy processes.

## GLOSSARY

**Achiral** An object that is superposable on its mirror image.

**Amphiphilic** A molecule with a hydrophilic end that dissolves in polar solvents and another, hydrophobic end that dissolves in nonpolar solvents.

**Chiral** An object that is nonsuperimposable to its mirror image.

**Circular dichroism (CD)** A change from planar to elliptic polarization when an initially plane-polarized light wave traverses an optically active medium.

**Helicity** The sense of twist of a helix, propeller, or screw.

**Micelle** An aggregate formed by amphiphilic molecules in, e.g., water such that their polar ends are in contact with water and their nonpolar portions are on the interior.

**Vesicle** A small, thin-walled bladderlike cavity.

**Z (zusammen)** One of the stereochemical descriptors for alkenes or for other double-bond systems with at least two nongeminal substituents (other than H) at the two ends of the double bonds. If the pertinent substituents are on the same side, the descriptor is *Z*. *E* (*entgegen*) denotes that the substituents of highest Cahn-Ingold-Prelog (CIP) priority at each end of the double bond are on opposite sides. In the polyacetylene system, there exist four theoretically possible stereostructures for the repeat units, that is, *E-s-E*, *E-s-Z*, *Z-s-Z*, and *Z-s-E* isomeric structures.

**Z content** The content (%) of the stereoisomers with a *Z* configuration.

## ACKNOWLEDGMENTS

We thank the financial support from the Hong Kong Research Grants Council (projects HKUST 6187/99P, 6121/01P, and 6085/02P), the University Grants Committee of Hong Kong (project AoE/P-10/01-1-A), and Esquel Enterprises Ltd., Hong Kong (project EGC 001.02/03). We are indebted to Prof. Xudong Xiao of the Department of Physics of our university and Prof. Chunli Bai of the Chinese Academy of Sciences, Beijing, for their helpful discussions. We are grateful to Mr. Jacky W. Y. Lam and Drs. Fouad Salhi, Qunhui Sun, Gao Li, Junwu Chen, Jingdong Luo, and John A. K. Cha of our research group for their technical assistance.

## REFERENCES

1. G. B. Johnson, “The Living World,” 2nd ed. McGraw-Hill, Boston, 2000.
2. M. K. Campell, “Biochemistry,” 2nd ed. Saunders College Publishing, New York, 1995.
3. D. Philip and J. F. Stoddart, *Angew. Chem. Int. Ed.* 35, 1155 (1996).

4. P. Ball, "The Self-Made Tapestry: Pattern Formation in Nature." Oxford University Press, Oxford, 1999.
5. A. Klug, *Angew. Chem. Int. Ed. Engl.* 22, 565 (1983).
6. M. A. Lauffer, "Entropy-Driven Processes." Springer-Verlag, New York, 1975.
7. G. M. Whitesides and B. Grzybowski, *Science* 295, 2418 (2002).
8. T. Ishi-I, M. Crego-Calama, P. Timmerman, D. N. Reinhoudt, and S. Shinkai, *Angew. Chem. Int. Ed.* 41, 1924 (2002).
9. G. M. Whitesides and M. Boncheva, *Proc. Natl. Acad. Sci. U.S.A.* 99, 4769 (2002).
10. J. Stahl, J. C. Bohling, E. B. Bauer, T. B. Peters, W. Mohr, J. M. Martín-Alvarez, F. Hampel, and J. A. Gladysz, *Angew. Chem. Int. Ed.* 41, 1872 (2002).
11. E. D. Sone, E. R. Zubarev, and S. I. Stupp, *Angew. Chem. Int. Ed.* 41, 1706 (2002).
12. L. Brunsveld, B. J. B. Folmer, E. W. Meijer, and R. P. Sijbesma, *Chem. Rev.* 101, 4071 (2001).
13. D. T. Bong, T. D. Clark, J. R. Granja, and M. R. Ghadiri, *Angew. Chem. Int. Ed.* 40, 988 (2001).
14. T. Kawasaki, M. Tokuhira, N. Kimizuka, and T. Kunitake, *J. Am. Chem. Soc.* 123, 6792 (2001).
15. F. M. Raymo, M. D. Bartberger, and J. F. Stoddart, *J. Am. Chem. Soc.* 123, 9264 (2001).
16. A. E. Rowan and R. J. M. Nolte, *Angew. Chem. Int. Ed.* 37, 63 (1998).
17. O. Ikkala and G. T. Brinke, *Science* 295, 2407 (2002).
18. G. A. Ozin, *Chem. Commun.* 419 (2000).
19. J. M. Lehn, *Science* 260, 1762 (1993).
20. M. Aldissi, Ed., "Intrinsically Conducting Polymers: An Emerging Technology." Kluwer, Dordrecht, the Netherlands, 1993.
21. H. G. Kiess, Ed., "Conjugated Conducting Polymers." Springer-Verlag, Berlin, 1992.
22. I. V. Krivoshei and V. M. Skorogotov, "Polyacetylene and Polyarylenes: Synthesis and Conducting Properties." Gordon and Breach Science, New York, 1991.
23. T. A. Skotheim, Ed., "Handbook of Conducting Polymers." Dekker, New York, 1986.
24. J. C. W. Chien, "Polyacetylene." Academic Press, New York, 1984.
25. G. Natta, G. Mazzanti, G. Pregaglia, and M. Peraldo, *Gazz. Chim. Ital.* 89, 465 (1959).
26. G. Natta, G. Mazzanti, and P. Pino, *Angew. Chem.* 69, 685 (1957).
27. S. Shibahara, M. Yamane, K. Ishikawa, and H. Takezoe, *Macromolecules* 31, 3756 (1998).
28. J. W. Hall and G. A. Arbuckle, *Macromolecules* 29, 546 (1996).
29. H. Shirakawa, Y.-X. Zhang, T. Okuda, K. Sakamaki, and K. Akagi, *Synth. Met.* 65, 93 (1994).
30. K. Akagi, G. Piao, S. Kaneko, K. Sakamaki, H. Shirakawa, and M. Kyotani, *Science* 282, 1683 (1998).
31. Y. Qin, H. Li, Z. Zhang, and Z. Cui, *Org. Lett.* 4, 18 (2002).
32. H. Goto, Y. Okamoto, and E. Yashima, *Macromolecules* 35, 4590 (2002).
33. B. Erdogan, J. N. Wilson, and U. H. F. Bunz, *Macromolecules* 35, 7863 (2002).
34. K. Morino, K. Maeda, Y. Okamoto, E. Yashima, and T. Sato, *Chem. Eur. J.* 8, 5112 (2002).
35. T. Sato, K. Terao, A. Teramoto, and M. Fujiki, *Macromolecules* 35, 2141 (2002).
36. R. Nomura, J. Tabei, and T. Masuda, *J. Am. Chem. Soc.* 123, 8430 (2001).
37. E. Yashima, K. Maeda, and O. Sato, *J. Am. Chem. Soc.* 123, 8159 (2001).
38. C.-Y. Huang, J. W. Klemke, Z. Getahun, W. F. DeGrado, and F. Gai, *J. Am. Chem. Soc.* 123, 9235 (2001).
39. R. B. Prince, J. S. Moore, L. Brunsveld, and E. W. Meijer, *Chem. Eur. J.* 7, 4150 (2001).
40. J. M. Hannink, J. J. L. M. Cornelissen, J. A. Farrera, P. Foubert, F. C. De Schryver, N. A. J. M. Sommerdijk, and R. J. M. Nolte, *Angew. Chem. Int. Ed.* 40, 4732 (2001).
41. I. M. Khan, Ed., "Synthetic Macromolecules with Higher Structural Order," ACS Symposium Series, Vol. 812, American Chemical Society, Washington, DC, 2001.
42. K. K. L. Cheuk, Ph.D. Dissertation, Hong Kong University of Science & Technology, 2002.
43. K. K. L. Cheuk, J. W. Y. Lam, Q. Sun, J. A. K. Cha, and B. Z. Tang, *Polym. Prepr.* 40, 653 (1999).
44. B. S. Li, K. K. L. Cheuk, D. Yang, J. W. Y. Lam, L. Wan, C. Bai, and B. Z. Tang, *Macromolecules* 36, 5447 (2003).
45. K. K. L. Cheuk, J. W. Y. Lam, Q. Sun, J. A. K. Cha, and B. Z. Tang, *Polym. Prepr.* 40, 655 (1999).
46. K. K. L. Cheuk, J. W. Y. Lam, J. A. K. Cha, and B. Z. Tang, *Polym. Mater. Sci. Eng.* 82, 54 (2000).
47. K. K. L. Cheuk, J. W. Y. Lam, and B. Z. Tang, *Polym. Mater. Sci. Eng.* 82, 56 (2000).
48. K. K. L. Cheuk, J. W. Y. Lam, J. A. K. Cha, and B. Z. Tang, *Polym. Prepr.* 41, 131 (2000).
49. J. W. Y. Lam, K. K. L. Cheuk, and B. Z. Tang, *Polym. Prepr.* 41, 912 (2000).
50. J. W. Y. Lam, K. K. L. Cheuk, and B. Z. Tang, *Polym. Prepr.* 41, 969 (2000).
51. K. K. L. Cheuk, J. W. Y. Lam, Q. Sun, J. A. K. Cha, and B. Z. Tang, *Polym. Prepr.* 41, 981 (2000).
52. K. K. L. Cheuk, F. Salhi, J. W. Y. Lam, and B. Z. Tang, *Polym. Prepr.* 41, 1567 (2000).
53. F. Salhi, K. K. L. Cheuk, J. W. Y. Lam, and B. Z. Tang, *Polym. Prepr.* 41, 1590 (2000).
54. F. Salhi, J. W. Y. Lam, K. K. L. Cheuk, J. A. K. Cha, and B. Z. Tang, *Polym. Prepr.* 41, 1185 (2000).
55. B. S. Li, K. K. L. Cheuk, J. Zhou, Y. Xie, J. A. K. Cha, X. Xiao, and B. Z. Tang, *Polym. Prepr.* 42, 543 (2001).
56. K. K. L. Cheuk, J. Luo, J. W. Y. Lam, and B. Z. Tang, *Polym. Prepr.* 42, 545 (2001).
57. B. S. Li, K. K. L. Cheuk, J. A. K. Cha, X. D. Xiao, and B. Z. Tang, *Polym. Mater. Sci. Eng.* 84, 396 (2001).
58. K. K. L. Cheuk, B. S. Li, F. Salhi, J. W. Y. Lam, J. A. K. Cha, and B. Z. Tang, *Polym. Mater. Sci. Eng.* 84, 516 (2001).
59. K. K. L. Cheuk, B. S. Li, F. Salhi, J. W. Y. Lam, J. A. K. Cha, and B. Z. Tang, *Polym. Mater. Sci. Eng.* 84, 536 (2001).
60. B. S. Li, K. K. L. Cheuk, X. Xiao, C. Bai, and B. Z. Tang, *Polym. Mater. Sci. Eng.* 85, 39 (2001).
61. K. K. L. Cheuk, B. S. Li, J. Chen, and B. Z. Tang, *Polym. Prepr.* 42, 234 (2001).
62. B. S. Li, K. K. L. Cheuk, X. Xiao, C. Bai, and B. Z. Tang, *Polym. Prepr.* 42, 248 (2001).
63. J. W. Chen, J. W. Y. Lam, K. K. L. Cheuk, Z. L. Xie, H. Peng, L. M. Lai, and B. Z. Tang, *Polym. Mater. Sci. Eng.* 86, 179 (2002).
64. J. W. Chen, K. K. L. Cheuk, Z. L. Xie, J. W. Y. Lam, and B. Z. Tang, *Polym. Prepr.* 43, 690 (2002).
65. J. W. Y. Lam, L. Y. Ngai, T. W. H. Poon, Z. Y. Lin, and B. Z. Tang, *Polym. Prepr.* 41, 289 (2000).
66. B. Z. Tang, *Polym. News* 26, 262 (2001).
67. K. Shinohara, S. Yasuda, G. Kato, M. Fujita, and H. Shigeoka, *J. Am. Chem. Soc.* 123, 3619 (2001).
68. G. L. Zubay, "Biochemistry," 4th ed. Wm. C. Brown Publishers, Boston, 1998.
69. B. Brutschy and P. Hobza, *Chem. Rev.* 100, 3861 (2000).
70. J. Luo, K. K. L. Cheuk, J. W. Y. Lam, and B. Z. Tang, *Polym. Prepr.* 42, 541 (2001).
71. R. H. Pain, Ed., "Mechanisms of Protein Folding," 2nd ed. Oxford University Press, New York, 2000.

72. B. S. Li, K. K. L. Cheuk, L. Ling, J. Chen, X. Xiao, C. Bai, and B. Z. Tang, *Macromolecules*, 36, 77 (2003).
73. M. S. Spector, R. R. Price, and J. M. Schnur, *Adv. Mater.* 11, 337 (1999).
74. L. Zhang and A. Eisenberg, *J. Am. Chem. Soc.* 118, 3168 (1996).
75. Y.-Z. Liang, Z.-C. Li, and F.-M. Li, *New J. Chem.* 24, 323 (2000).
76. W. Meier, *Chem. Soc. Rev.* 29, 295 (2000).
77. S. Stewart and G. Liu, *Angew. Chem. Int. Ed.* 39, 340 (2000).
78. S. Vauthey, S. Santoso, H. Gong, N. Watson, and S. Zhang, *Proc. Natl. Acad. Sci. USA* 99, 5355 (2002).
79. X. H. Yan, G. J. Liu, F. T. Liu, B. Z. Tang, H. Peng, A. B. Pakhomov, and C. Y. Wong, *Angew. Chem. Int. Ed.* 40, 3593 (2001).
80. Y. Moroi, "Micelles: Theoretical and Applied Aspects." Plenum, New York, 1992.
81. K. Yu and A. Eisenberg, *Macromolecules* 31, 3509 (1998).
82. Z. Reich, L. Zaidmann, S. B. Gutman, T. Arad, and A. Minski, *Biochemistry* 33, 14177 (1994).
83. B. S. Li, K. K. L. Cheuk, F. Salhi, J. W. Y. Lam, J. A. K. Cha, X. Xiao, C. Bai, and B. Z. Tang, *NanoLetters* 1, 323 (2001).
84. J. M. Thornton and S. P. Gardner, *Trends Biol. Sci.* 14, 300 (1989).
85. F. Salhi, K. K. L. Cheuk, Q. Sun, J. W. Y. Lam, J. A. K. Cha, G. Li, B. Li, J. Chen, and B. Z. Tang, *J. Nanosci. Nanotechnol.* 1, 137 (2001).
86. C. J. Brinker, Y. Lu, A. Sellinger, and H. Fan, *Adv. Mater.* 11, 579 (1999).
87. H. Ringsdorf, B. Schlarb, and J. Venzmer, *Angew. Chem. Int. Ed. Engl.* 27, 113 (1988).
88. G. J. de A. A. Soler-Illia, C. Sanchez, B. Lebeau, and J. Patarin, *Chem. Rev.* 102, 4093 (2002).
89. S. Mann, "Biom mineralization: Principles and Concepts in Bioinorganic Materials Chemistry." Oxford University Press, New York, 2002.
90. J. Aizenberg, G. Lambert, S. Weiner, and L. Addadi, *J. Am. Chem. Soc.* 124, 32 (2002).
91. K. Naka and Y. Chujo, *Chem. Mater.* 13, 3245 (2001).
92. L. A. Estroff and A. D. Hamilton, *Chem. Mater.* 13, 3227 (2001).
93. S. Mann, *Angew. Chem. Int. Ed.* 39, 3392 (2000).
94. D. B. DeOliveira and R. A. Laursen, *J. Am. Chem. Soc.* 119, 10627 (1997).
95. S. Mann, Ed., "Biomimetic Materials." VCH, New York, 1996.
96. S. M. Yu, C. M. Soto, and D. A. Tirrell, *J. Am. Chem. Soc.* 122, 6552 (2000).
97. K. B. Storey and J. M. Storey, Eds., "Protein Adaptations and Signal Transduction." Elsevier, Amsterdam, 2001.
98. B. Z. Tang, J. W. Y. Lam, X. Kong, P. P. S. Lee, X. Wan, H. S. Kwok, Y. M. Huang, W. Ge, H. Chen, R. Xu, and M. Wang, "Liquid Crystals III" (I. Khoo, Ed.), p. 62. SPIE, Bellingham, WA, 1999.
99. B. Z. Tang, H. Chen, R. Xu, J. W. Y. Lam, K. K. L. Cheuk, H. N. C. Wong, and M. Wang, *Chem. Mater.* 12, 213 (2000).
100. J. Sun, H. Chen, R. Xu, M. Wang, J. W. Y. Lam, and B. Z. Tang, *Chem. Commun.* 1222 (2002).
101. B. Z. Tang, *Polym. Prepr.* 43, 48 (2002).
102. K. K. L. Cheuk, B. S. Li, J. W. Chen, Y. Xie, and B. Z. Tang, "Proceedings of the 5th Asian Symposium on Biomedical Materials," 2001, p. 514.
103. B. S. Li, K. K. L. Cheuk, J. Zhou, Y. Xie, and B. Z. Tang, *Polym. Mater. Sci. Eng.* 85, 401 (2001).



# Polyaniline Fractal Nanocomposites

Reghu Menon, A. K. Mukherjee

*Indian Institute of Science, Bangalore, India*

## CONTENTS

1. Introduction
  2. Preparation of Conducting Polymers and Composites
  3. Conducting Polymer Nanocomposites
  4. Conducting Polyaniline Fractal Nanocomposites
  5. Applications
  6. Conclusions
- Glossary  
References

## 1. INTRODUCTION

Typical composites consist of two components, in which the host material determines mechanical and processing properties of the system and the guest material imparts special physical and chemical properties to the intricately mixed host-guest blend. The host material is supposed to have a wide range of facile processing options so that the guest material can be easily incorporated into the host system to obtain the desired properties. Toward this end, polymers are considered to be excellent host systems, because a wide range of physical and chemical properties can be observed in polymers; moreover, they can be easily processed and blended with a variety of materials. Hence, several polymer composites have been extensively studied for the past few decades for use in various applications [1]. Some of the well-known composites are glass, carbon, or metal fiber reinforced polymers [2] and elastomers reinforced with various types of particles like carbon [3].

In previous generation polymer composites, the size of the guest material was usually on the order of microns. In such composites, it was difficult to optimize the physical properties, because intimate and homogenous mixing of guest-host materials is hard to achieve; moreover, the processibility is not versatile enough for subtle applications. Hence it is highly desirable to have nanoscopic and even molecular level mixing of guest-host materials, so that it is easier to fine-tune the physical and chemical properties, and this could pave the way for several innovative applications.

In recent years, the advent of well-defined nanoparticles of metallic, magnetic, semiconducting, and insulating materials has facilitated the preparation of a wide range of well-tailored nanocomposites with specific properties [4–6]. Moreover, it is possible to attain much lower values for the percolation threshold (according to classical percolation theory, the volume fraction of spherical particles required to make quasi-contact with each other in a composite is nearly 16%, which is considered to be the threshold for percolative processes among particles) in composites containing nanoscopic materials rather than mesoscopic ones [7]. This is mainly due to the self-organizational properties of nanoparticles, as shown by Michels et al. for carbon nanoparticle composites [8]. Furthermore, it is possible to obtain an aspect ratio (ratio of the length to the diameter of the particle, which is 1 for a spherical particle) above 1 for nanoparticles. It is well known that by increasing the aspect ratio of particles it is possible to bring down the value of the percolation threshold ( $f_c$ ), which means that the quasi-contact between particles can be attained at a much lower volume fraction of filling than the conventional 16% for spherical particles [9–11]. The advantage of attaining a lower volume fraction of filling and percolation threshold is that the pristine mechanical and processing properties of host matrix can be retained in the blend, and the design of composites becomes easier with lower cost.

Although conventional polymer composites are highly tractable with excellent mechanical properties, host polymer matrices such as polyethylene have rather poor electrical and thermal properties. In typical composites, the host matrix plays the role of inert support for the active guest material, which effectively determines the electrical and optical properties of composites. Moreover, in previous generation composites, inorganic or ceramic guest materials were not that compatible with the organic polymer host matrix, and this usually led to the formation of inhomogeneous composites with poor mechanical and physical properties. In recent years several organic/polymeric materials (for example, conducting polymers, ferroelectric polymers, photoconductive polymers, light-harvesting polymers, photorefractive polymers, and nonlinear optical materials) have shown interesting electrical and optical properties (analogous to those in inorganic materials) [12–14], and these materials are much

more compatible with the polymer matrix. Hence a new opportunity has come for making nanoscopic and molecular level polymer composites that show a wide range of solid-state physical properties.

The conducting polymer consists of polyconjugated chains  $[(\text{—C}=\text{C—C}=\text{C—C}=\text{C—})_n]$  with alternating single ( $\sigma$ -bonds) and double bonds ( $\pi$ -bonds). The  $\pi$ -electrons are highly delocalized and easily polarizable, and these features play important roles in the electrical and optical properties of polyconjugated systems. Moreover, the intrinsic quasi-one-dimensional nature and the extent of both intra- and interchain delocalization of  $\pi$ -electrons play significant roles in the structural, electrical, and optical properties of polyconjugated systems. The chemical structure of some of the well-known conducting polymers including polyacetylene (PA), polyaniline (PANI), polypyrrole (PPy), polythiophenes (PTs), poly(*p*-phenylene vinylene), poly(*p*-phenylene) (PPP), polythienylene vinylene (PTV), and others, are shown in Figure 1 [13].

Polyconjugated chains are stiff and less tractable, unlike conventional polymers, which are highly processible. Usually polyconjugated systems are made processible by substituting solublizable side groups to the main chain or with the help of modified counterions in dopant species. For example, in the case of polythiophenes, the alkyl group substitution makes them soluble, and in the case of polyaniline, the surfactant counterion in protonic acids makes it soluble in several organic solvents [15]. Hence by co-dissolving conjugated and host polymers in a suitable solvent, it is possible to make conducting polymer nanocomposites in an insulating polymer matrix. Also, chemical modification of guest materials such as inorganic semiconductor nanoparticles (e.g., cadmium, selenide, and titanium dioxide) [16], fullerene ( $\text{C}_{60}$ )

[17], or carbon nanotubes [18, 19], can disperse well in conjugated polymer solutions, so that nanocomposites of these materials in conjugated polymer matrices can be prepared. These types of composites have interesting optical properties and application in optoelectronic devices.

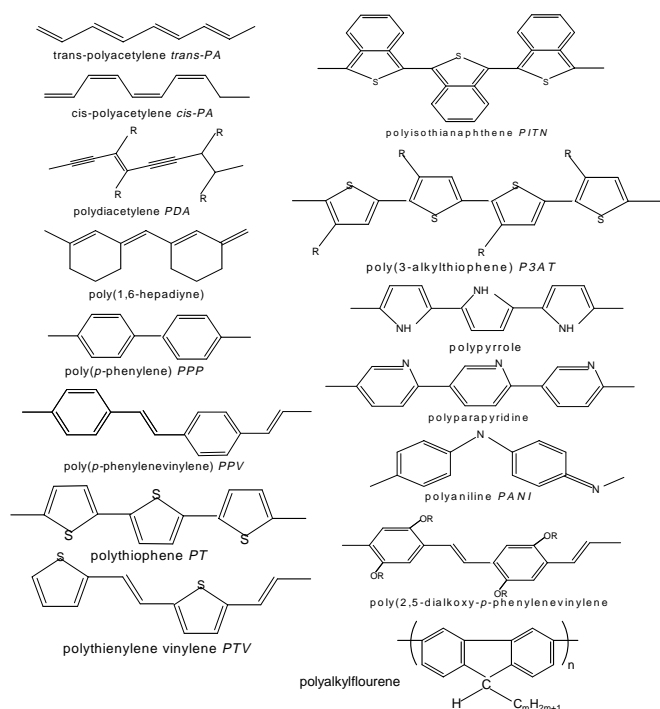
In this chapter, a general introduction to conducting polymer nanocomposites is given, with some detailed descriptions for several of them. From the fundamental science point of view, the main objective of this chapter is to tie up the concepts of nanocomposites, conducting polymers, morphology, fractal structures, percolation process, and charge transport in novel nanosystems. In conducting polymer nanocomposites many of the above-mentioned ideas come together in a very interesting manner unlike in nanoparticle systems. In one of the most exciting types of conducting polymer nanocomposites the chains self-assemble to form an interpenetrating fibrillar fractal network, which is rather unique in nanosystems. In such a nanoscale fibrillar fractal network, the electrical charge transport properties have several interesting features. However, the optical and magnetic properties are not that different from those observed in bulk systems, because it is well known that in conducting polymers the optical and magnetic properties are mainly governed by molecular level features that are nearly identical in both macro- and nanosystems.

Among, the various conducting polymers, only for surfactant counterion processed polyaniline is this nanoscale fibrillar fractal network formed well in a controllable fashion and also being investigated systematically. In this unique nanoscale fibrillar fractal network the conducting polyaniline chains are self-assembled by subtle interactions of the polymer chain, surfactant counterion, and solvent. Although a wide range of nanostructures, from a fibrillar fractal network to phase-segregated aggregates, can be obtained by changing the host polymer matrix and processing parameters, among them the most interesting morphological and electrical properties are observed only with the nanoscale fibrillar fractal network. Hence this chapter is largely devoted to the structural and electrical charge transport properties of this special type of polyaniline fractal nanocomposites. Moreover, they have several interesting electrical and optical applications, as mentioned later in the chapter.

## 2. PREPARATION OF CONDUCTING POLYMERS AND COMPOSITES

Usually the synthesis of conjugated polymers is carried out by one of two procedures: chemical synthesis or electropolymerization. The chemical route is further subdivided into catalytic polymerization, noncatalytic polymerization, precursor methods, and organometallic coupling. Various synthetic routes for the preparation of some of the well-known conjugated polymers are given below [20].

PA can be synthesized by the following routes: catalytic polymerization, noncatalytic polymerization, catalytic polymerization of monomers other than acetylene, and precursor methods. For the catalytic polymerization routes, five types of catalysts can be used to yield PA in the form of a uniform film. These are Zeiglar–Natta catalyst  $[\text{Ti}(o\text{-}n\text{-C}_4\text{H}_9)_4$  and  $(\text{C}_2\text{H}_5)_3\text{Al}]$ , Luttinger catalyst  $(\text{NaBH}$



**Figure 1.** Structures of various conjugated polymers.

and nickel chloride) [21], metathesis catalyst  $[\text{WCl}_6$  and  $(\text{C}_6\text{H}_5)_4\text{Sn}$  in toluene] [22], single component catalyst  $[\text{Cp}_2\text{Ti}(\text{PMe}_3)_2]$  [23], Rh and Re catalysts [e.g.,  $\text{Rh}(\text{COD})\text{Cl}$  and  $\text{Rh}(\text{NBD})\text{Cl}$ , where COD is cycloocta-1,5-diene and NBD is bicyclo[2.2.1]hepta-2,5-diene] [24]. For the non-catalytic route, irradiation of acetylene gas with ultraviolet or ionization radiation has shown to produce PA [25]. Monomers such as 1,3,5,7-cyclooctatetraene with a metathesis catalyst  $\text{W}[\text{OCH}(\text{CH}_2\text{Cl})_2]_n\text{Cl}_{6-n}-(\text{C}_2\text{H}_5)_2\text{AlCl}$  ( $n = 2$  or 3) also yield PA [26] through the ring open polymerization reaction. The precursor route makes use of a prepolymer that can be thermally converted to PA [27]. The process basically consists of three steps. The first step is the synthesis of the monomer 7,8-bis(trifluoromethyl)tricyclo[4.2.2.0<sup>2,5</sup>]deca-3,7,9-triene by the thermal reaction between hexafluorobut-2-yne and cyclooctatetraene. The second step is the polymerization reaction carried out in presence of ring open metathesis polymerization initiators to form a high molecular weight precursor polymer. The third step is the thermal conversion of the precursor polymer to PA.

PPP can be synthesized by the following routes: direct oxidation of benzene, direct synthesis, organometallic coupling, precursor methods, and electropolymerization. The procedure of direct oxidation of benzene consists of dehydro coupling of benzene nuclei by catalyst-oxidant systems, leading to the formation of C—C bonds. The reagent for the polymerization is either a binary system of a Lewis acid such as  $\text{AlCl}_3$  and an oxidant such as  $\text{CuCl}_2$  [28],  $\text{CuCl}$  [29],  $\text{MnO}_2$ ,  $\text{PbO}_2$ , and  $\text{NO}_2$  [30] or a simple reagent with both Lewis acid and oxidizing properties such as  $\text{FeCl}_3$ ,  $\text{MoCl}_5$ ,  $\text{AsF}_5$ , and  $\text{SbF}_5$  [31–36]. The direct synthesis route makes use of Bergman cyclization of enediyne followed by thermal treatment of an enediyne yielding a PPP derivative with a molecular weight of 1500–2000 [37]. The organometallic synthesis is basically classified into two categories: the Yamamoto-Colon route or Suzuki coupling. The first method makes use of Ni(II) complexes such as  $\text{NiCl}_2(\text{bpy})$ , where bpy is 2,2'-bipyridine, and  $\text{NiBr}_2(\text{PPh}_3)_2$  [38–43] whereas the second method involves coupling of Pd catalysts with various bromobenzene derivatives with benzene boronic acid [44, 45]. Precursor-based synthesis of PPP has also been carried out. Some of the precursors are Marvel's precursor [46, 47], ICI precursor [48], and Grubb's precursor [49, 50]. PPP has also been synthesized through anodic electrochemical oxidation. The electropolymerization has been carried out in various media and electrolytes. For example, Rubinstein [51, 52] used a strongly acidic medium—an  $\text{HF}/\text{H}_2\text{SO}_4$  two-phase system. Organic aprotic media such as dichloromethane, nitrobenzene, nitromethane, phenylacetonitrile, acetonitrile, and propylene carbonate, along with various simple and complex electrolytes such as  $\text{P}_2\text{O}_5$ ,  $\text{CuCl}_2$ ,  $\text{LiBF}_4 + \text{CuCl}_2$ , and  $\text{LiAsF}_6 + \text{CuCl}_2$  [53–61], have also been used for the electrosynthesis of PPP.

The basic synthesis procedures for PT can be considered in parallel with those for PPP. PT and poly-(3-alkylthiophene) (P3AT) can be prepared through direct oxidative coupling with various oxidizing agents such as  $\text{Fe}(\text{III})$ ,  $\text{Mo}(\text{V})$ , and  $\text{Ru}(\text{III})$  [62–66]. Polyalkoxythiophenes were prepared by  $\text{Cu}(\text{ClO}_4)_2$  oxidation of bithiophenes [67]. The organometallic coupling reactions can be basically classified into two categories: Ni-catalyzed coupling and

Pd-catalyzed coupling. The former can be subdivided into four methods, viz., the Yamamoto method [68], the Colon method [69], the McCulloch method [70], and the Rieke method [71]. The latter can be further subdivided into two routes: the Curtis method [72] and the Stille method [73]. The most conductive PTs have been prepared electrochemically in rigorously anhydrous aprotic solvents of high dielectric constant and low nucleophilicity such as acetonitrile [74], benzonitrile [75], nitrobenzene [76], and propylene carbonate [77] in the presence of small anions derived from strong acids such as  $\text{ClO}_4^-$ ,  $\text{PF}_6^-$ ,  $\text{BF}_4^-$ , and  $\text{AsF}_6^-$  associated with lithium and tetraalkylammonium cations [77–80]. Partial crystallinity has been observed in poly-3-methylthiophene grown in acetonitrile with  $\text{CF}_3\text{SO}_3^-$  [81, 82].

For the synthesis of PPy, two routes have been used: chemical synthesis and electropolymerization. Because pyrrole is one of the most easily oxidized monomers, a variety of oxidizing agents are available for the preparation of pyrrole such as  $\text{FeCl}_3$ ,  $\text{Fe}(\text{NO}_3)_3$ ,  $\text{Fe}(\text{ClO}_4)_3$ ,  $\text{Fe}_2(\text{SO}_4)_3$ ,  $\text{K}_3\text{Fe}(\text{CN})_6$ ,  $\text{FeBr}_3$ ,  $\text{CuCl}_2$ , and  $\text{CuBr}_2$  [83–90]. Effective catalytic processes have also been favored for mass production at low cost and extensive post-treatment steps.  $\text{CuCl}/\text{AlCl}_3/\text{O}_2$  is a typical system [91] applied to synthesize PPy chemically. The electrochemical synthesis method has also been adopted for the preparation of PPy, and it is basically an oxidative process. Therefore, it is of fundamental importance that the electrode does not oxidize to compete with pyrrole. Most PPy has been prepared with inert electrodes, such as platinum [92], gold [93], and glassy carbon [94]. Among the organic solvents, acetonitrile and propylene carbonate have been most extensively used for their poor nucleophilic characters, along with electrolytes such as tetraethylammonium tetrafluoroborate and tetrabutylammonium hexafluorophosphate [95, 96]. High-quality films have been obtained even with nucleophilic aprotic solvents such as dimethylsulfoxide, dimethylformamide, and hexamethylphosphoramide [97–99].

Because this chapter is mainly concerned with PANI and its composites, a detailed description of the synthesis of PANI is given here. The anhydrous salt of LiCl was dissolved while 125 ml of 1.0 M HCl was stirred in to prepare a 2.0 M salt solution. Dissolution of the salt is exothermic. Aniline ( $\text{C}_6\text{H}_5\text{NH}_2$ , 5.0 ml, 0.0548 mol) added to 75 ml of the 2.0 M salt/HCl solution which was then cooled while being stirred at 0 °C in an ice bath to obtain a homogeneous solution. Ammonium peroxydisulfate  $[(\text{NH}_4)_2\text{S}_2\text{O}_8]$ , 2.75 g, 0.0126 mol] dissolved in the remaining 50 ml of the 2 M HCl solution and cooled to 0 °C, and then added to the aniline/salt/HCl solution with constant stirring for 1 min. A homogeneous solution was obtained. The temperature remained between 0 and 3 °C throughout the entire polymerization reaction. By using the potential profiling technique [100, 101], which involves placement of a platinum electrode and a saturated calomel reference electrode in the reaction vessel to measure the potential changes during the reaction, the open circuit potential ( $V_{\text{oc}}$ ) was continuously monitored. The synthesis was discontinued when  $V_{\text{oc}}$  reached a value of 0.43 V. The approximate time taken to reach 0.43 V was 3 h. An intense blue-green precipitate with a coppery glint was formed in each case. This precipitate was collected on a Buchner funnel with water (9 cm



diameter, Whatman no. 4 filter paper) using an aspirator. It was washed approximately 10 times with 1.0 M HCl (80 ml portions) until the filtrate became colorless. Care was taken to ensure that the precipitate cake was always covered by a thin layer of the washing solution and that it was never allowed to develop cracks during this washing process, which would impair the washing efficiency. This as-synthesized emeraldine hydrochloride was partially dried for 15 min by sucking air through the filter cake in the Buchner funnel, then transferred to a Petri dish, and dried for 24 h in a desiccator under dynamic vacuum.

Similar to the preparation of conducting polymers, the preparation for composites is also divided into two categories: electrochemical route and chemical route. For small-scale preparation, the electrochemical route is used whereas the chemical route allows large-scale synthesis of composites. The electrochemical route encompasses two methods: electrode coating or codeposition. The former method uses three electrodes (reference, working, and counter) in a one-compartment cell containing the electrolyte and the monomer solution. To obtain blends, the working electrode is coated with a film of insulating polymer, before the anodic deposition of conducting film. The codeposition method is similar to the electrode coating method, but the insulating polymer host is dissolved in the electrolyte solution, which also contains the monomer of the conductive polymer. As the conductive polymer film is anodically deposited on the surface of the electrode, it becomes soaked with the insulating polymer solution. Blends of poly(vinyl chloride) (PVC) with pyrrole [102], thiophene [103], and 3-methylthiophene [104] can be prepared by the electrochemical method. There are two methods for the chemical synthesis of conductive polymer blends: mechanical mixing of the blend components (PANI-PVC blend [105]) and polymerization of the conductive polymer in the insulating polymer matrix. An oxidizing agent is used to polymerize the heterocyclic monomer that is either embedded in the insulating polymer matrix or mixed with it in a common solvent. Various PPy blends with latex [106], poly(2-vinyl pyridine) [107], and others are prepared by this method.

This chapter also focuses on blends of PANI; thus, the procedures for preparation of various PANI blends is given in detail. Conductive blends of PANI with low-density polyethylene (PE), high-density PE, polystyrene, and polypropylene [108] can be prepared by melt processing of PANI doped with dodecylbenzenesulfonic acid (DBSA) in a miniature counter-rotating double-screw extruder; this thermoplastic blend, with conductivity values of  $\sim 0.1$  S/cm, is commercially known as Neste complex. A PANI-PVC blend is also prepared by the above-mentioned procedure and is commercially known as Versicon [109]. Blends of PANI with cellulose acetate can be prepared by two methods. In one of the methods, a fine powder of chemically prepared PANI is suspended in an acid solution of insulating polymer, and the films obtained by casting this solution are brittle in nature. The electrode coating method was also used and it improved the adhesion of PANI to an optically transparent electrode, facilitating spectroelectrochemical measurements [110]. Fibrils of PANI were prepared by the polymerization of aniline in a gel

of poly(acrylic acid) using  $\text{FeCl}_3$  as oxidant [111]. Scanning electron micrography revealed a diameter of 50 nm for the fibrils having a length of 1–5  $\mu\text{m}$ . Monofilaments of conductive fibers from a blend of PANI and poly(*p*-phenylene-terephthalamide) were obtained at different concentrations of PANI through the process of wet-spinning from a solution of the component polymers in sulfuric acid into a 1 N sulfuric acid solution [112]. Electroactive polymer blends of PANI and polystyrene or poly(methylmethacrylate-*co*-butadiene-*co*-styrene) (MBS) are prepared via various techniques [113]. The methods used were *in-situ* oxidative polymerization in aqueous dispersion of the insulating host, coagulation of latex of the thermoplastic in an acidic dispersion of PANI, or dry blending (casing from a solution containing both components). A blend of polyaniline and nitrilic rubber has been prepared by coating a platinum working electrode with a thin film of nitrilic rubber (29% acrylonitrile) and polymerizing aniline by the potentiodynamic method. Because aniline polymerization must be performed at low pH, nitrilic rubber was chosen for its resistance to acid attack [114]. The melt mixing procedure was used to disperse PANI doped with DBSA in poly(styrene-*co*-butadiene-*co*-styrene) (SBS rubber) [115] and thermoelastic polymer poly(styrene-ethylene/butylene-styrene) [108]. Conductivity values of 2 and 0.1 S/cm at volume fractions of PANI of 50 and 2%, respectively, can be obtained [108, 115]. PANI doped with poly(*p*-styrene sulfonic acid) can also be viewed as a polymer blend and can be electrochemically deposited onto a working electrode surface using an aqueous solution containing *p*-styrene sulfonic acid as an electrolyte [116].

### 3. CONDUCTING POLYMER NANOCOMPOSITES

Conducting polymer nanocomposites can be prepared in several ways. Either conjugated polymers can be dispersed in a host matrix such as conventional polymers, inorganic glassy materials, porous materials, on layered structures, or molecular/nanoparticle guest materials such as  $\text{C}_{60}$ , carbon nanotubes, titanium dioxide, cadmium selenide, or biological materials, can be dispersed in a conjugated polymer matrix. Moreover, the morphology of the composite can be easily altered by varying the self-organization/self-assembly features of the guest–host matrix, and this also significantly affects its physical properties. Typically, undoped conjugated polymers are semiconductors with bandgaps varying from 1 to 4 eV. The conductivity can be varied by 10 orders of magnitude, from insulator to metal, by doping, as shown in Table 1 [27, 75, 117–154]. The electrical and optical properties can be fine-tuned by varying the  $\pi$ -electron delocalization, interchain interactions, or disorder. Hence it is possible to obtain a wide range of interesting electrical and optical properties in conducting polymer nanocomposites.

Of the various types of conducting polymer nanocomposites, the doped conjugated polymers in the insulating polymer matrix have been the most extensively studied. In these composites, either the dispersion of insoluble conducting polymer particles or the formation of a tenuous interpenetrating network of soluble conducting polymers in an insulating polymer matrix can be achieved. In the latter,

**Table 1.** Room temperature conductivity of various doped conducting polymers [117–154].

Polymer	Dopant	Conductivity (S/cm)	
Polyacetylene (Naarmann route)	I <sub>2</sub>	10 <sup>5</sup>	
Polyacetylene (liquid crystal)	I <sub>2</sub>	1.2 × 10 <sup>4</sup>	
Polyacetylene (Shirakawa)	I <sub>2</sub>	10 <sup>3</sup>	
Polyacetylene (Durham)	I <sub>2</sub>	10–10 <sup>2</sup>	
Polypyrrole	[Ti(Obu) <sub>4</sub> –AlEt <sub>3</sub> ]	1–100	
	I <sub>2</sub>	1–100	
	FeCl <sub>3</sub>	1–100	
	AsF <sub>5</sub>	1–100	
	Rb	1–100	
	PF <sub>6</sub>	200–1500	
	HClO <sub>4</sub>	4 × 10 <sup>2</sup>	
	<i>p</i> -Toluenesulfonic acid	200–230	
	HClSO <sub>3</sub>	2 × 10 <sup>2</sup>	
	ClO <sub>4</sub> <sup>-</sup> , BF <sub>6</sub> <sup>-</sup> , TsO <sup>-</sup> , and HSO <sub>4</sub>	50–200	
	Poly(3-methylthiophene)	PF <sub>6</sub>	1975
		ClO <sub>4</sub>	750
Poly(3-methylthiophene)	SO <sub>3</sub> CF <sub>3</sub>	30–100	
Polythiophene	PF <sub>6</sub>	370	
	BF <sub>4</sub>	270	
	ClO <sub>4</sub>	10–100	
	AsF <sub>6</sub>	97	
Poly(3-octylthiophene)	FeCl <sub>3</sub>	1–180	
Poly(thienylthiophene)	I <sub>2</sub>	315	
Poly( <i>p</i> -phenylene)	AsF <sub>5</sub>	500	
	Naphthyl K <sup>+e</sup>	50	
Poly(2-butoxy-5-methoxy-4-phenylene vinylene)	FeCl <sub>3</sub>	5.7 × 10 <sup>2</sup>	
Poly(2,5-diheptyl-1,4-phenylene vinylene)	SbF <sub>5</sub>	2.8 × 10 <sup>4</sup>	
Poly(phenylene vinylene)	FeCl <sub>3</sub>	35	
Polyaniline	HCl/CSA/DBSA/MSA	10 <sup>1</sup> –220	
	H <sub>3</sub> PO <sub>4</sub>	58	
	Diphenyl phosphate	65	
	Phosphoric acid	40	

the aspect ratio of the conducting polymer network can be controlled by varying the processing conditions, because the nanoscopic level self-assembly of the conducting polymer chains depends on molecular scale interactions. In this way, it is possible to attain very low percolation thresholds and also to observe a novel charge transport mechanism in these nanoscopic networks of conducting polymer chains. Moreover, these conducting networks have interesting applications, as discussed in Section 4. Hence this chapter is largely focused on the morphology and charge transport properties of conducting polymer networks in an insulating polymer matrix, although a brief overview of several other types of conjugated polymer nanocomposites is given.

Over the past 10 years, several types of conducting polymer nanocomposites with interesting electrical properties have been prepared, for example, poly(3-octylthiophene)/polyethylene (P3OT–PE), polyacetylene/polyvinyl butyral (PA–PVB), poly(3,4-ethylenedioxythiophene)/polystyrene sulfonate (PEDOT–PSS) or polyvinyl pyrrolidone (PEDOT–

PVP), and polyaniline–camphor sulfonic acid/polymethyl methacrylate [PANI–CSA/PMMA] [155–158]. Several of these composites show a finite conductivity at volume fractions of conducting polymers as low as 1%, which is much below the classical percolation threshold of 16% conducting material in the matrix. To a large extent, the distribution of conducting networks in the insulating matrix depends on the interaction between conducting and insulating polymers, which in turn is quite sensitive to the processing parameters. For example, in solution and gel processing routes the conducting polymer can get adsorbed to the connected gel network, and this leads to the formation of a two-dimensional network of conducting pathways in the insulating matrix [159]. Similarly, the chemical functionality of the guest–host matrix can influence the morphology from fractal networks to phase-segregated granular type formations. The structure of the conducting polymer chain plays a significant role in composite formation. The connectivity and conductivity of network are influenced by the flexibility

and mobility of the conducting polymer chains in the matrix. Either via the molecular level interaction of functional groups in guest–host polymer chains or via cross-linking of the guest and host polymers through covalent bonds, it is possible to control the extent of interpenetration in the network. In this way, the domain size, the nature of the interfacial region, and morphology can be controlled. Some typical examples are given in the following paragraphs.

PA is the simplest of all of the conducting polymers because of its chemical structure, and doped films of PA have shown conductivity on the order of  $10^5$  S/cm, typical to that observed in conventional metals. However, PA is intractable and unstable at ambient atmosphere. Recently, fairly stable blends of PA were synthesized by blending it with PVB as the host insulating polymer matrix, with conductivity values of  $\sim 1$  S/cm [156].

PEDOT is another well-known conducting polymer because of its stability, semitransparent conducting properties, wide range of bandgap tuning (1.4–2.5 eV), and processibility. PEDOT when doped with poly(styrene sulfonic acid) (PSS) yields a soluble polyelectrolyte complex with positively charged PEDOT chains and negatively charged PSS ions, and it forms a fine dispersion in several solvents including water. The conductivity of PEDOT–PSS composites can be enhanced by several orders of magnitude (from  $10^{-4}$  to  $10^2$  S/cm) under special processing conditions as mentioned in the literature [160]. In recent years, PEDOT composites have received a lot of attention because of their special electrical and optical properties [148].

Conducting polymer blends of PPy can be prepared by several different techniques. For example, PPy–Nafion and PPy–PMMA are made by interfacial polymerization [161, 162], PPy–nylon and PPy–cellulose [163, 164] are made by vapor-phase polymerization of pyrrole in the insulating polymer matrix containing the required oxidant, PPy–PVC and PPy–poly(vinyl alcohol) can be prepared by solution-phase polymerization of monomer, host polymer, and oxidant in a common solvent [165, 166], and PPy–PVC and PPy–Aramid can be prepared by electropolymerization of the monomer adsorbed into the host matrix [167]. All of these techniques usually yield PPy composites at  $\sim 1$  S/cm.

Nanocomposites of poly(2-methoxy, 5-(2'-ethyl-hexoxy)-*p*-phenylene vinylene) (MEH–PPV) in PE can be prepared by the solution or gel processing route [168]. Both MEH–PPV and PE are dissolved in xylene at elevated temperatures and form a gel upon cooling down to room temperatures. Free-standing films of MEH–PPV–PE, containing a volume fraction of MEH–PPV as low as 0.1%, can be prepared by stretch orienting the gel. These films show a high degree of anisotropy in polarized absorption and photoluminescence along the direction of tensile drawing with ratios in excess of 150:1 and 60:1, respectively. The MEH–PPV chains are highly oriented in the PE matrix and the delocalized  $\pi$ -electronic states are over 100 Å, which corresponds to several tens of monomer units [168, 169].

During the last decade, much work has been carried out in the field of conjugated polymer composite-based photosensors and photovoltaic devices [170]. For example, blends

of conjugated polymers as the electron donor with  $C_{60}$  as the acceptor have shown very interesting photoinduced charge transfer processes [171–174]. A nanocomposite of a conducting polymer and  $C_{60}$  has a high interfacial area for efficient charge separation through the control of morphology of phase separation in the interpenetrating network of donor and acceptor. Polyblends of PPV and  $C_{60}$  have shown a conversion efficiency of 2.9% [175]. Also, interpenetrating networks of two conjugated polymers, for example, MEH–PPV as a donor and a cyano group-substituted PPV as an acceptor have a quantum efficiency of 15% [175]. Furthermore, quite efficient large area photodiodes have been fabricated from these molecular-scale composites. Also, poly(3-octylthiophene) and fullerene composites have shown interesting photophysical properties [176]. Recently, composites of PPV derivatives and carbon nanotubes have improved the performance of devices, because the presence of nanotubes can enhance the mobility of carriers [19].

Conducting polymer nanocomposites with inorganic nanoparticles have been prepared and have several interesting physical properties. For example, PPy– $ZrO_5$ , PPy– $Fe_2O_3$ , and PANI– $TiO_2$ , the dielectric properties can vary significantly [5].

Nanocomposites of PANI or PPy with  $Fe_2O_3$  have shown interesting magnetic properties [5]. For example, laser action has been reported in films of MEH–PPV– $TiO_2$  in polystyrene [177]. It has been observed that the presence of  $TiO_2$  nanocrystals significantly narrows the emission spectrum of MEH–PPV. For MEH–PPV/CdS the presence of CdS has improved the quantum yield for charge separation [178]. CdSe dispersed in MEH–PPV has enhanced the photoluminescence characteristics of the latter owing to efficient charge transfer [179]. It has been observed that the incorporation of semiconductive inorganic nanocrystals such as CdS or CdSe in MEH–PPV-based devices has improved the device performance.

Conducting polymers such as PPy or PANI, can be incorporated into the porous structure of zeolite systems. Composites of PPy with zeolites such as faujasite and mordenite [180, 181] have conductivity on the order of  $10^{-4}$  S/cm. PANI has been incorporated in layered zeolites such as  $V_2O_5 \cdot nH_2O$  [182] (known as oxide bronze) to form a layered conducting polymer–zeolite nanocomposite system, in which the conductivity is nearly 4 orders of magnitude larger with respect to the pristine oxide, with a room temperature conductivity as high as 0.1 S/cm. Conducting polymer composites have been prepared with various types of elastomers too. For example, blends of poly(3-methyl thiophene)/nitrile rubber has been prepared by the electrode coating method, with a conductivity of  $\sim 0.1$  S/cm [183]. Composites of poly(3,4-dialkylpyrrole) or poly(3-alkylthiophene) with natural or nitrile rubber have conductivity as high as 1 S/cm [183].

Among the various conducting polymer nanocomposites, only for surfactant counterion-processed PANI systems has a systematic and rigorous investigation been carried out. In particular, for the PANI–CSA/PMMA fractal nanocomposite, a detailed study on the morphology and charge transport has been done, as described in Section 4.

#### 4. CONDUCTING POLYANILINE FRACTAL NANOCOMPOSITES

PANI is ideal for making conducting polymer nanocomposites owing to its ease of processing and inexpensive method of synthesis with high yield, good stability, and wide variation of conductivity. The conductivity of PANI can be varied by 10 orders of magnitude by altering the protonation level, with a high value of conductivity of  $\sim 500$  S/cm by doping with camphor sulfonic acid (CSA). The chemical structures of protonated PANI (emeraldine salt) and CSA are shown in Figure 2. Emeraldine base is a semirigid polymer that is sparingly soluble in a few solvents such as *N*-methylpyrrolidone and concentrated sulfuric acid. However, by doping emeraldine base with functionalized protonic acids (e.g., CSA or DBSA) the conducting form of PANI can be made soluble in several solvents such as *meta*-cresol or xylene. Functionalized protonic acids have a chemical structure consisting of  $H^+(M-R)^-$  where the counterion consists of an ionic group such as  $SO_3^-$  and a functional group such as dodecylbenzyl or camphor [15]. The role of the counterion  $(M-R)^-$  is to act as a surfactant in which  $M^-$  attaches ionically to the positively charged polymer and the R group imparts solubility in solvents and also makes it processible. This counterion-induced processibility of PANI in various organic solvents has opened up the possibility of codissolving it with a host polymer matrix in a suitable solvent, and this yields a nanoscopic/molecular level control on the morphology of the composite. This has significantly improved the electrical and optical properties of PANI blends. Moreover, the conducting PANI blends can be easily cast from solution to obtain free-standing films and fibers.

Conducting PANI nanocomposites have been prepared with some well-known polymers such as polymethylmethacrylate, nylon, polycarbonate, polystyrene, polysulfone, polyvinyl acetate, polypropylene, polyvinyl chloride, and acrylonitrile-butadiene-styrene copolymer [15]. In each of these polyblends the morphology of the PANI network is slightly different, because the molecular level interactions come into play and this determines the nanoscale structures. In some of the polyblends guest-host chains are highly interpenetrating; whereas in others a phase-segregated structure can be observed. For example, polyblends with ultra-high molecular weight polyethylene, polyvinyl alcohol, or polyacetonitrile (PAN) are optically clear and transparent for low volume fractions of PANI, because the typical width of PANI interconnects in the network are less than  $200 \text{ \AA}$ ; as a result the scattering losses are less [184]. Moreover, these polyblends can be stretched to high draw ratios, and this makes the PANI chains well aligned within the matrix. This has been verified by X-ray diffraction and polarized absorption spectra studies [15]. These types of polyblends can be used in flexible infrared (IR) polarizers. PANI chains form well-ordered conducting lines in a PAN matrix because the chains can be easily aligned by tensile drawing, and the scattering losses are less in the IR range [184]. The phase-segregated morphology in the PANI-PAN blend is being facilitated by the polar CN groups in the host polymer, which is a classic example to show how the molecular level interactions can alter the morphology and physical properties of these systems. Whereas, in the less polar PMMA host matrix, the

interpenetrated nanostructure can be controlled by varying the processing parameters such as the surfactant counterions, molecular weight of PMMA, and solvents, and this helps to investigate the interesting correlation between morphology and physical properties. This correlation is rigorously studied for PANI-PMMA composites, as discussed in Section 4.1.

#### 4.1. Morphology of PANI-PMMA Fractal Nanocomposites

Cao and co-workers [185–188] were the first to perform a detailed systematic study of the nature and properties of surfactant counterion-processed PANI composites. Although composites with several host polymer matrices have been prepared, those with PMMA are the best in terms of very fine controls on composition, morphology, and physical properties. For example, by varying the molecular weight of PMMA, the diffusion of PANI-CSA in PMMA (hereafter PANI-PMMA) can be controlled, and this affects the formation of nano- or microstructures during the slow liquid-liquid phase separation process at temperatures around  $50^\circ\text{C}$ . Hence, the dynamics of the diffusion of PANI-CSA in PMMA plays a significant role in the formation of the self-assembled interpenetrating fibrillar network that determines its physical properties. For example, in optimally processed composites with nanoscopic level intricate connectivity, it is possible to obtain conductivity values of  $\sim 1$  S/cm for a 1% volume fraction of PANI-CSA in PMMA, which is one of the amazing properties of these systems. The best results are obtained by using modest molecular weight PMMA with

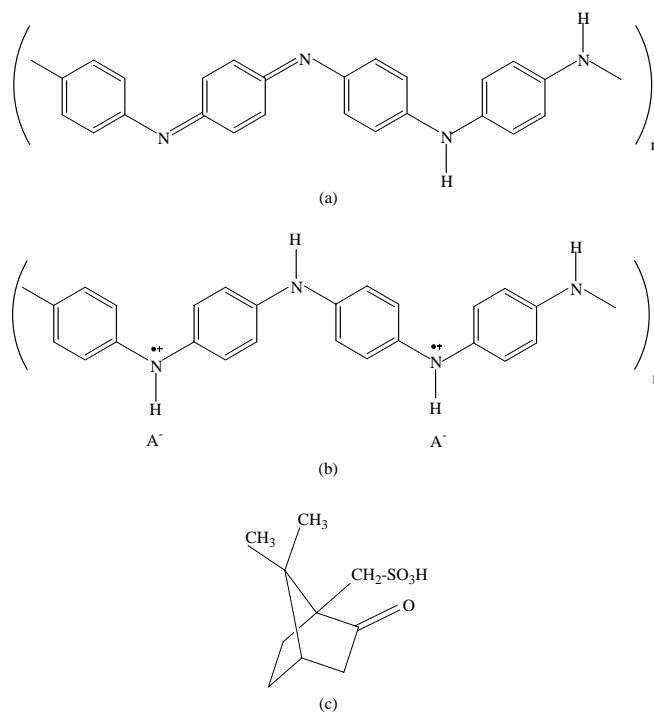
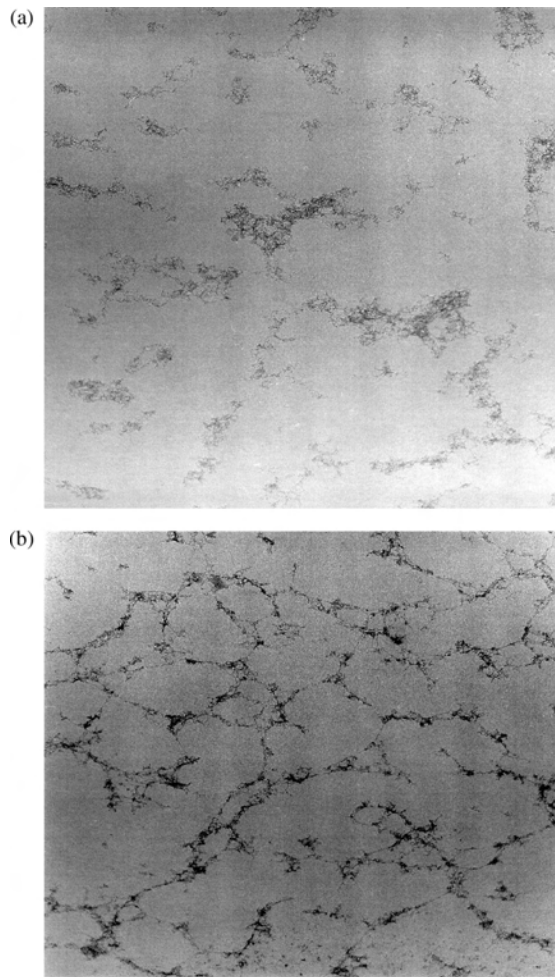


Figure 2. Chemical structures of (a) emeraldine base, (b) emeraldine salt, and (c) 10-camphor sulfonic acid.

*meta*-cresol as the solvent. The extent of polarity of the surfactant counterion, host polymer, and solvent and processing conditions such as temperature and solution viscosity play significant roles in nanoscopic level morphology and the associated physical properties.

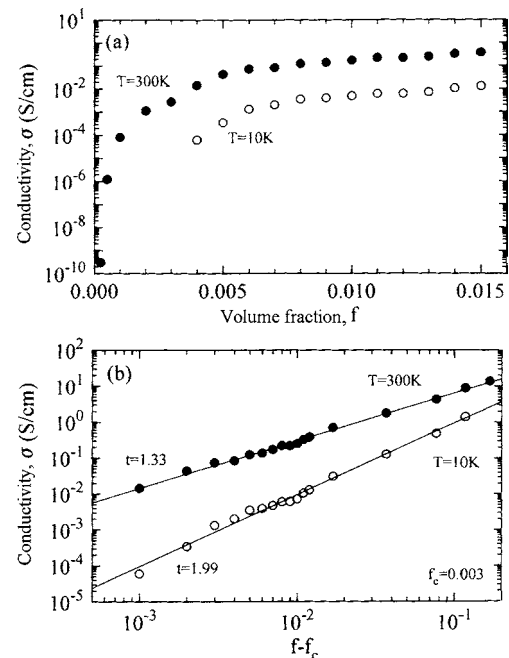
Transmission electron micrographs of PANI-PMMA nanocomposites containing volume fractions ( $f$ ) of 0.25 and 0.5% of PANI-CSA are shown in Figure 3. These micrographs clearly show the distribution pattern of PANI, as expected for a percolating medium, with the formation of "links" (PANI-CSA fibrils), "nodes" (intersection point of two fibrils), and "blobs" (bundled-up dense regions), especially for 0.5% PANI-CSA. The links have diameters of  $\sim 100$ – $500$  Å. However, as  $f$  is lowered to 0.25%, the number of links connecting the blobs rapidly decreases, as shown in Figure 3b. This suggests that as the links thin down, by lowering the volume fraction of PANI-CSA, the network falls apart to disconnected blobs. What exactly triggers this instability and makes the network unsustainable is not yet clearly understood. It seems that there is some critical diameter



**Figure 3.** Transmission electron micrographs of PANI-CSA/PMMA blends for volume fractions, (a)  $f = 0.005$  and (b)  $f = 0.0025$  of PANI-CSA. Scale: 1 cm = 50 nm. Reprinted with permission from [186], R. Menon et al., *Phys. Rev. B* 50, 13931 (1994). © 1994, American Physical Society.

around  $100$  Å for the links to hold the network together; and below this number the links become fragile and a significant volume fraction of PANI-CSA tends to stay within the blobs. Hence, in this processing route, with several optimized parameters such as the molecular weight of PMMA, the percolation threshold volume fraction ( $f_c$ ) is between 0.5 and 0.25% of PANI-CSA and the conductivity near the percolation threshold is  $\sim 10^{-3}$  S/cm, as shown in Figure 4 [186]. These values are quite remarkable with respect to the composites consisting of intractable PANI particles dispersed in PMMA, in which the conductivity at  $f_c \sim 8\%$  is  $\sim 10^{-8}$  S/cm [186]. Moreover, it seems that the processing parameters can be optimized further, and this could yield PANI nanocomposites with  $f_c \sim 0.1\%$ , and conductivity at  $f_c$  of  $\sim 1$  S/cm.

Detailed investigations of transmission electron micrographs of PANI-PMMA composites have been carried out for a wide range of compositions of PANI-CSA [186]. When these micrographs are examined at different magnifications, the structure of the interconnected fibrillar network appears to be self-similar at all length scales, and this is especially so near the percolation threshold. This finding is consistent with the view that all systems exhibit self-similarity near the percolation threshold due to its fractal structure, which has been verified by numerical analysis of transmission electron micrographs. The numerical analysis is performed by mapping the mass distribution as a function of distance in the micrographs [186]. Usually in a homogeneous medium, the mass  $M(r)$  increases as a function of distance ( $r$ ) from a chosen origin; for example, in two dimensions,  $M(r) \propto r^2$ . Similarly, for a fractal structure the mass distribution is given by  $M(r) \propto r^D$ , where  $D$  is the fractal dimension. Typically,  $M(r)$  is estimated by scanning and digitizing



**Figure 4.** (a) Conductivity versus volume fraction of PANI-CSA in PMMA. (b) Conductivity as a function of difference from critical volume fraction. Reprinted with permission from [186], R. Menon et al., *Phys. Rev. B* 50, 13931 (1994). © 1994, American Physical Society.

the surface area of the network as a function of successively larger scanned areas, from any arbitrary starting point in the micrograph, which are then sampled and averaged out, as given in [185]. The log-log plots of surface area versus distance yield straight lines, and the slope of these lines depends on the volume fraction of PANI-CSA in the composite. For example, the typical values obtained from the above analysis for  $D$  with  $f = 3.7, 1.96,$  and  $0.96\%$  are 1.99, 1.75, and 1.53, respectively [186]. Hence, by decreasing  $f$  of PANI-CSA toward the percolation threshold, the value of  $D$  also decreases, and this suggests the presence of a self-similar structure with holes on every length scale. The estimate of  $D$  for the two-dimensional scanned slice of the three-dimensional object is  $\sim 1.5$ . The fractal dimension of the three-dimensional network at the percolation threshold (i.e.,  $f_c \sim 0.5\%$ ) can be estimated by adding 1 to the value of  $D$  obtained from the above analysis for the two-dimensional slice; that is,  $1 + 1.5 = 2.5$ . This number suggests that the network is open, porous, and self-similar on every length scale. Hence, this yields a large surface area for a fractal network, which is quite useful for several applications, as described in Section 5.

### 4.2. Electrical Properties of PANI-PMMA Fractal Nanocomposites

The typical values of room temperature conductivity and resistivity ratios  $\rho_r [\rho_r = \rho(4.2 \text{ K})/\rho(300 \text{ K})]$  for PANI-PMMA composites at various  $f$  values of PANI-CSA are presented in Table 2. The conductivity versus  $f$  plot is shown in Figure 4. The smooth and continuous increase in conductivity as a function of  $f$  is rather special to these systems. This suggests that as the connectivity of conducting channels gets denser, the movement of charge carriers becomes easier. When one compares this with classical percolating systems, in which the conductivity increases abruptly at the percolation threshold and then quickly saturates at higher values of  $f$ , it is possible to get very fine control of the value of conductivity as a function of  $f$  in PANI-PMMA nanocomposites. Hence the conductivity can be easily varied by nearly 10 orders of magnitude as a function of  $f$ . The precise determination of a percolation threshold can be obtained by fitting the data to the well-known “scaling

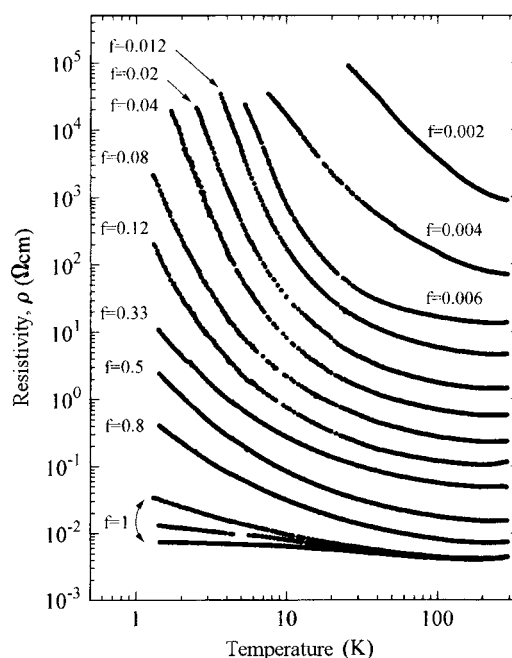
law” of percolation theory [i.e.,  $\sigma(f) \approx \sigma_T |f - f_c|^t$ , where  $\sigma_T$  is a conductivity constant and  $t$  is the critical exponent (usually  $t \approx 1$  and 2 for two- and three-dimensional systems, respectively)] [189]. The fit is shown in Figure 4b. At 10 K,  $t = 1.99 \pm 0.04$  ( $f_c = 0.3 \pm 0.05\%$ ), which is close to  $t = 2$  for three-dimensional systems, although the room temperature data give  $t = 1.33 \pm 0.02$  ( $f_c = 0.3\%$ ), which can be attributed to thermally assisted hopping transport of charge carriers among the weakly connected parts of network. The temperature dependence of  $t$  is an interesting feature of PANI-PMMA nanocomposites, which is not usually observed in classical percolating systems.

The temperature dependence of conductivity of PANI-PMMA composites for a wide range of  $f$  values ( $0.002 \leq f \leq 1$ ) is shown in Figure 5 [186]. The temperature coefficient of resistivity (TCR) for 100% PANI-CSA is quite weak with the typical metallic positive TCR above 150 K, and the resistivity minima vary according to the extent of disorder present in the system [190]. Upon increasing the dilution of PANI-CSA with PMMA, although the negative TCR became stronger at low temperatures, the intrinsic metallic positive TCR of PANI-CSA at temperatures above 200 K was observed even in samples containing volume fractions of PANI-CSA as low as  $f \sim 0.3\%$ , which is remarkable. For  $f > 0.006$ , the temperature dependence of conductivity was weak for  $T > 50$  K, as shown in Figure 5. The temperature dependence of conductivity is characterized by the resistivity ratios ( $\rho_r$ ) at various volume fractions as shown in Table 1. For  $f > 0.006$ , the network is well connected and the barrier due to disorder is rather weak at  $T > 50$  K. However, at very low temperatures, the charge carriers have to hop across the random disorder potential barriers, and the exponential temperature dependence of conductivity is indicative

**Table 2.** Room temperature conductivity [ $\sigma(300 \text{ K})$ ] and resistivity ratio [ $\rho(4.2 \text{ K})/\rho(300 \text{ K})$ ] of PANI-CSA/PMMA blends at various volume fractions ( $f$ ) of PANI-CSA.

$f$	$\sigma(300 \text{ K})(\text{S/cm})$	$\rho(4.2 \text{ K})/\rho(300 \text{ K})$
1	200–400	1.3–10
0.67	110	13
0.33	21	19
0.12	9	30
0.04	1.8	210
0.012	0.22	2200
0.008	0.12	
0.003	0.003	
0.001	$10^{-4}$	

Source: Reprinted with permission from [186], R. Menon et al., *Phys. Rev. B* 50, 13931 (1994). © 1994, American Physical Society.



**Figure 5.** Resistivity versus temperature at various volume fractions. Reprinted with permission from [186], R. Menon et al., *Phys. Rev. B* 50, 13931 (1994). © 1994, American Physical Society.

of thermally activated hopping transport among localized states at various energy levels.

Usually in disordered systems, the low temperature dependence of resistivity due to hopping transport is exponential in behavior {i.e.,  $\rho(T) = \rho_0 \exp[(T_0/T)^\gamma]$ , where  $\gamma = 1/(d + 1)$  and  $d$  is the dimensionality of the system, and  $T_0 = q/[k_B N(E_F)L_c^3]$ , where  $q$  is a numerical coefficient,  $N(E_F)$  is the density of states at the Fermi level,  $L_c$  is the localization radius of states (rate of fall-off of the envelope of the wavefunction of localized states) near the Fermi level}. As temperature decreases, the average hopping length [ $r \sim L_c(T_0/T)^\gamma$ ] increases as  $T^{-1/4}$ ; hence, this type of transport is usually referred as variable range hopping (VRH). In VRH, a carrier just below the Fermi level jumps to a state just above it, and the farther it jumps the greater is the choice of states available, and usually it jumps to a state for which the energy  $\{E \sim [4.2r^3 N(E_F)]\}$  required is as small as possible. Whereas in nearest-neighbor hopping [ $\rho = \rho_0 \exp(A/k_B T)$ ] with a constant activation energy ( $A$ ), the average hopping length is on the order of the mean separation between localized states, and it does not vary with temperature. The value of  $T_0$  in VRH gives an estimate of how far the system has moved to the insulating side. Moreover, the localization length can be determined from  $T_0$ , which gives some idea about the length scale of the localized wavefunctions and the extent of disorder present in the system [13].

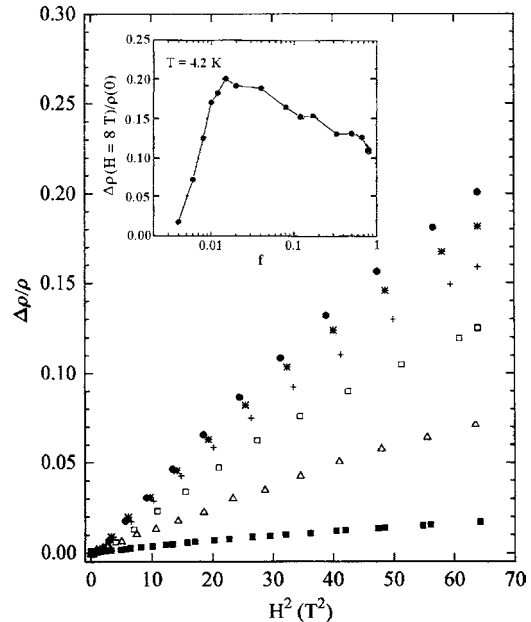
The values of  $\gamma$  and  $T_0$  give some idea about the hopping transport mechanism in disordered systems. However, for the convoluted and multiply connected PANI-CSA network, the complex fractal morphology plays a significant role in the hopping mechanism. For example, in these systems the value of  $\gamma$  systematically increases from 0.25 to 1 upon varying  $f$  from 0.012 to 1, which is not expected in the conventional VRH model. Nevertheless, this behavior is expected in systems in which the fractal structure modifies the wavefunctions of the localized states, and accordingly  $\gamma$  varies as the fractal dimensionality of the system changes. Details about the charge transport mechanism in fractal structures, as in PANI-PMMA, are described in [186]. Hence, conducting polymer nanocomposites offer the possibility of investigating novel charge transport mechanisms in fractal network structures.

Among various charge transport properties, magnetoresistance (MR), the change of resistance as a function of magnetic field, which especially occurs at low temperatures, is well known for providing additional information on the nanoscopic scale charge transport mechanism. In particular, this gives insight into the underlying relationship between nanostructure and scattering and relaxation mechanisms of charge carrier dynamics. The classical transverse MR is mainly due to the bending of the charge carrier trajectory by a Lorentz force, and it is proportional to the square of the field, with the proportionality constant expressed as a function of charge transport scattering time [185]. In typical metals the dominant contribution to the weak positive MR (usually less than a 5% increase in resistance at 4.2 K) is due to the classical orbital motion of charge carriers. Moreover, the MR gives information about the second derivative of the density of states at the Fermi level. Because MR probes the local charge carrier dynamics in conducting systems, the MR

data can be used to determine the nanoscopic transport property parameters, for example, the elastic and inelastic scattering length and scattering time. Furthermore, the MR results are supplementary to conductivity data; hence it is essential to check the internal consistency of the models used to understand the charge transport properties.

The MR data at 4.2 K for PANI-PMMA nanocomposites are shown in Figure 6 [187]. The normalized variation in MR is plotted as a function of  $H^2$  for PANI-PMMA samples with  $0.015 < f < 0.004$  that are just above the percolation threshold, and in these the fractal structure is observed to be prominent. The  $H^2$  dependence of the positive MR at low fields is due to the shrinkage in the overlap of wavefunctions of localized states in the presence of a magnetic field, which is usually observed in VRH transport. The positive MR decreases considerably by lowering  $f$  from 0.015 to 0.004, as shown in Figure 6. The MR shows a maximum at  $f \sim 0.015$  at 4.2 K. As the system approaches the percolation threshold, the connectivity of the network decreases; as a result the carriers find it increasingly difficult to hop from site to site in the presence of the magnetic field, and the value of MR decreases considerably for  $f < 0.015$ . Whereas for  $f > 0.015$  the connectivity increases at higher volume fractions, and the effect of field on hopping transport gradually decreases; hence the value of MR is less. This shows that MR is an ideal probe to investigate the role of nanoscopic level morphology in the charge transport properties in conducting polymer nanocomposites. The detailed analysis of MR results is described in [186].

Thermoelectric power [or thermopower ( $S$ )] is another phenomena to explore the charge transport mechanism in metallic and semiconducting systems. In the thermoelectric effect or Seebeck effect, a temperature gradient at the



**Figure 6.** Magnetoresistivity versus square of magnetic field for  $f = 0.015$  ( $\bullet$ ),  $0.012$  ( $*$ ),  $0.01$  ( $+$ ),  $0.008$  ( $\square$ ), and  $0.006$  ( $\triangle$ ). The inset shows magnetoresistivity versus volume fraction at 4.2 K. Reprinted with permission from [186], R. Menon et al., *Phys. Rev. B* 50, 13931 (1994). © 1994, American Physical Society.

ends of a sample gives rise to an electric field opposite to the direction of the temperature gradient [192]. Usually the sign of thermopower is consistent with a positive or negative charge of the carrier. The diffusion thermopower ( $S_d$ ) in metallic systems is a function of the first derivative of density of states at Fermi level. Although the temperature dependence of thermopower [ $S(T)$ ] is supposed to be linear in metals, it is usually complicated by scattering processes. However, in high quality metallic conducting polymers a quasilinear temperature dependence of thermopower has been observed down to 8 K, which is quite remarkable when the extent of disorder present in these systems is considered. In several conducting polymer composites a linear temperature dependence of thermopower has been observed, but only down to 100 K [13].

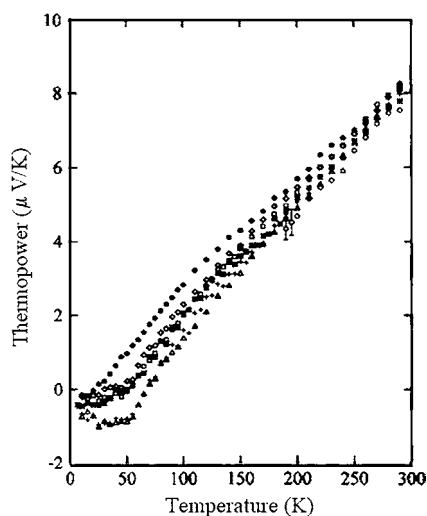
The  $S(T)$  of PANI-PMMA nanocomposites is shown in Figure 7 [193]. The thermopower at room temperature is nearly  $8 \mu\text{V/K}$  for all volume fractions, and it is positive for  $T > 80 \text{ K}$ . The data show the typical metallic linear temperature dependence over a wide range of volume fractions of PANI-CSA in PMMA; however, there is a clear deviation from linearity below 100 K, and this deviation increases as  $f$  is lowered. The characteristic U-shaped dependence of  $S(T)$  below 100 K indicates the onset of the breakup of the conducting network into disconnected regions, and the thermally activated hopping transport [ $S_{\text{hop}}(T) \propto T^{1/2}$  for VRH] across these regions dominates over the metallic diffusion thermopower [ $S_d(T) \propto T$ ]. Because thermopower is a zero current transport coefficient, it is relatively less sensitive to the electrical conduction paths between the disconnected regions, and this is mainly due to the fact that nanoscopic level thermoelectric voltages sum up together as long as the thermal gradients take place across the conducting paths. Hence investigating the low temperature U-shape in thermopower can give some insight into how well the conducting network is connected at the nanoscopic level. Thus  $S(T)$  is another useful probe to investigate the correlation between

morphology and charge transport mechanism in conducting polymer nanocomposites.

## 5. APPLICATIONS

Conducting polymer nanocomposites are used for a wide range of applications as indicated in the following [194]:

1. PANI nanocomposites have a wide range of applications for antistatic coating, electromagnetic interference shielding, and anticorrosive coatings. In particular, the fibrillar fractal network of PANI nanocomposite has high conductivity at low volume fractions of PANI and hence is ideal for these types of electrical applications.
2. PEDOT-PSS is most widely used by photographic film and electronics packaging industries. An antistatic coating of PEDOT-PSS on films (photographic/electronics packaging) having a surface resistance less than  $10^9 \Omega/\text{m}^2$ , eliminates the risk of static charge buildup, which may damage the films. Interestingly, more than 100 million square meters of photographic films are coated by PEDOT-PSS every year. Also, PEDOT-PSS is widely used for transparent conducting electrodes [157].
3. Conducting polymer-coated fibers such as polyester or nylon have applications in electromagnetically camouflaged nets in stealth devices [183].
4. Conducting polymer composites with various nanocrystals have had interesting applications in light-emitting diodes, solar cells, lasing medium, and electrochromic devices. For example, MEH-PPV/perylene bis(phenthylimide)-based photovoltaic cells show an open circuit voltage of 0.58 V and their performance is better than that of MEH-PPV/CN-PPV-based photovoltaic devices [195]; PPV/carbon nanotube-based photovoltaic devices show a quantum efficiency of 1.8%, which is twice that of standard ITO-based devices, with an open circuit voltage of 0.9 V [19]. Nanocomposites based on MEH-PPV and  $\text{TiO}_2$  nanocrystals show higher quantum efficiency of 12% [16].  $\text{TiO}_2$  dispersed in an MEH-PPV/polystyrene blend acts as a lasing medium that shows excited emission at wavelengths of 532 and 435 nm [177]. Blends of PPy and epichlorohydrin and ethylene oxide (Hydrin C) show excellent electrochromicity and are used in electrochromic devices [183].
5. Networks of PANI blends filled with semiconducting polymers can be used as grid electrodes in a polymer grid triode [196]. The open structures of fibrillar fractal networks of PANI nanocomposite have large active surface area for devices.
6. Conducting polymer nanocomposites have shown potential for use in molecular sensors, biosensors, and molecular electronics applications [197, 198].



**Figure 7.** Thermopower versus temperature for various concentrations ( $y$ ) of PANI-CSA in PMMA:  $y = 100\%$  ( $\bullet$ ),  $66.6\%$  ( $\diamond$ ),  $33.3\%$  ( $\square$ ),  $9.09\%$  ( $*$ ),  $4.76\%$  ( $+$ ),  $2.43\%$  ( $\Delta$ ), and  $1.24\%$  ( $\circ$ ). Reprinted with permission from [193], C. O. Yoon et al., *Phys. Rev. B* 48, 14080 (1993). © 1993, American Physical Society.

## 6. CONCLUSIONS

In conclusion, conducting polymer nanocomposites have broadened the horizon of conventional polymer composites. In usual polymer composites the physical and chemical properties of the composite are limited, and the volume fraction of guest material is above the percolation threshold



(16% volume fraction), which restricts the processibility and mechanical properties of the composite. Moreover, it is hard to attain uniform distribution of nano or meso particles in composites due to various problems with compatibility, and this usually leads to inhomogeneity in the physical properties. It is possible to overcome several of these shortcomings with the breakthrough in the self-assembled fibrillar fractal network of guest polymer chains in the host matrix. This is very well illustrated for the conducting PANI-CSA fibrillar fractal network in a PMMA matrix in which the nanoscale morphology and the associated physical properties can be controlled rather well. The connected network forms at a volume fraction of PANI-CSA as low as 0.3%, with conductivity values of  $\sim 10^{-3}$  S/cm. The network is quite robust in that it remains well connected even after the removal of the host polymer. This large open area conducting fractal network is quite useful as an electrode in various applications, for example, in polymer grid triodes. It is possible to obtain excellent control of the electrical and optical properties of this network by subtle variations in the composition of the nanocomposite as demonstrated by the temperature dependence of conductivity, magnetoresistance, thermoelectric power, and optical transmission features. Further molecular scale engineering and functionalization of conjugated polymer chains, and fabrication of this type of self-assembled fractal networks can widen the scope of this category of nanostructured systems, which are rather unique compared with other types of nanosystems.

## GLOSSARY

**Conducting polymer** A long chain carbon polymer consisting of alternating single and double bonds, in which delocalized  $\pi$ -electrons determine the physical and chemical properties.

**Fractal** A system that looks self-similar at all length scales, in which the dimensionality has noninteger values [integer value means 1, 2 and 3 dimensions for Euclidean geometry].

**Localization** A phenomenon in which the wavefunctions associated with the electronic states get localized, to a few interatomic distances, by the random disorder potential fluctuations so that there is hardly any overlap with nearest-neighbor wavefunctions.

**Lorentz force** The force (**F**) experienced by a charge carrier  $q$  in electric (**E**) and magnetic field intensity (**B**), and it is given by the following relation:  $\mathbf{F} = q(\mathbf{E} + \mathbf{v} \times \mathbf{B})$  where  $\mathbf{v}$  is the velocity of charge.

**Magnetoresistance** The variation of resistance as a function of magnetic field. It is mainly due to the bending of charge carrier trajectory by Lorentz force, which is usually proportional to the square of the field, with the proportionality constant expressed as a function of scattering time.

**Nanocomposite** A nearly homogenous mixture of two or more components, in which the physical size of components is typically below 100 nm, and this imparts special size-dependent properties.

**Percolation threshold** The minimum volume fraction of guest component in a composite, at which the physical properties increase by several orders of magnitude due to the connectivity of guest material. For example, for conducting

spherical particles, at around 16% volume fraction, the electrical conductivity increases by several orders of magnitude.

**Resistivity** A basic property of a material that signifies the measure of resistance offered by it to the flow of charge carriers. Resistivity ( $\rho$ ) is defined as  $\rho = R(A/l)$ , where  $R$  is the resistance,  $l$  is the length of the sample, and  $A$  is the cross-sectional area. The SI unit is  $\Omega \cdot \text{m}$ .

**Thermopower** In the Seebeck effect, a temperature gradient at the ends of a sample gives rise to an electric field in the opposite direction as the temperature gradient. It is a measure of the rate of change of potential difference across a material as a function of unit change in temperature gradient.

## REFERENCES

1. F. Carmona, *Physica A* 157, 461 (1989).
2. R. M. Norman, "Conductive Rubbers and Plastics." Elsevier, New York, 1970.
3. E. Sichel, "Carbon-Black Polymer Composites." Dekker, New York, 1982.
4. D. Godovsky, V. Sukhorev, A. Volkov, and M. A. Moskvina, *J. Phys. Chem. Solids* 54, 1613 (1993).
5. B. Z. Tang, Y. Geng, J. M. Y. Lam, B. Li, X. Jing, X. Wang, F. Wang, A. B. Pakhomov, and X. X. Zhang, *Chem. Mater.* 11, 1518 (1999).
6. C. B. Murray, D. J. Norris, and M. G. Bawendi, *J. Am. Chem. Soc.* 115, 8708 (1993).
7. R. Zallen, "Physics of Amorphous Solids." Wiley, London, 1998.
8. M. A. J. Michels, J. C. M. Brokken-Zijp, W. M. Groenewoud, and A. Knoester, *Physica A* 157, 529 (1989).
9. I. Balberg and S. Bozowski, *Solid State Commun.* 44, 551 (1984).
10. D. M. Bigg, *Polym. Eng. Sci.* 19, 1188 (1978).
11. F. Carmona and A. E. Amarti, *Phys. Rev. B* 47, 3284 (1987).
12. H. S. Nalwa, in "Handbook of Organic Conductive Molecules and Polymers" (H. S. Nalwa, Ed.), Vol. 2, p. 261. Wiley, New York, 1997.
13. R. Menon, C. O. Yoon, D. Moses, and A. J. Heeger, in "Handbook of Conducting Polymers," 2nd ed. (T. A. Skotheim, R. Elsenbaumer, and J. R. Reynolds, Eds.), p. 27. Dekker, New York, 1998.
14. B. O. Regan and M. Gratzel, *Nature (London)* 353, 737 (1991).
15. Y. Cao, P. Smith, and A. J. Heeger, *Synth. Met.* 48, 91 (1992).
16. S. S. Salafsky, W. H. Lubberhuizen, and R. E. I. Schropp, *Chem. Phys. Lett.* 290, 297 (1991).
17. G. Yu, K. Pakbaz, and A. J. Heeger, *Appl. Phys. Lett.* 64, 3422 (1994).
18. M. Hughes, M. S. P. Shaffer, A. C. Renouf, C. Singh, G. Z. Chen, D. J. Frey, and A. J. Windle, *Adv. Mater.* 14, 382 (2002).
19. H. Ago, K. Petritsch, M. S. P. Shaffer, A. H. Windle, and R. H. Friend, *Adv. Mater.* 11, 1281 (1999).
20. R. Kiebooms, R. Menon, and K. H. Lee, in "Handbook of Advanced Materials for Electronics and Photonics," Vols. 1–10, (H. S. Nalwa, Ed.), Vol. 8, p. 1. Academic Press, San Diego, 2001.
21. T. Ito, H. Shirakawa, and S. Ikeda, *J. Polym. Sci., Chem. Ed.* 12, 11 (1974).
22. M. Aldissi, C. Linaya, J. Sledz, F. Shue, L. Giral, J. M. Fabre, and R. M. Rolland, *Polymer* 23, 243 (1982).
23. H. G. Alt, A. J. Signorelli, G. P. Pez, and R. H. Baughman, *J. Chem. Phys.* 69, 106 (1978).
24. F. Cataldo, *Polym. Commun.* 33, 3073 (1992).
25. Y. Tabata, B. Saito, H. Shiboni, H. Sobue, and K. Oshima, *Makromol. Chem.* 76, 89 (1964).
26. Y. V. Karshak, V. v. Karshak, G. Kanischka, and H. Hocker, *Makromol. Chem., Rapid Commun.* 6, 685 (1985).
27. J. H. Edwards, W. J. Feast, and D. C. Bott, *Polymer* 25, 395 (1984).

28. P. Kovacic and A. Kyriakis, *J. Am. Chem. Soc.* 85, 454 (1963).
29. N. Tushima, K. Kanaka, A. Koshirai, and H. Hirai, *Bull. Chem. Soc. Jpn.* 61, 2551 (1988).
30. P. Kovacic and R. J. Hopper, *J. Polym. Sci., Part A: Polym. Chem.* 4, 1445 (1966).
31. P. Kovacic and F. Koch, *J. Org. Chem.* 28, 1836 (1963).
32. P. Kovacic and R. M. Lange, *J. Org. Chem.* 28, 968 (1963).
33. P. Kovacic, F. Koch, and C. E. Stephan, *J. Polym. Sci., Polym. Chem. Ed.* 2, 1196 (1964).
34. G. A. Olah, P. Schilling, and I. M. Gross, *J. Am. Chem. Soc.* 96, 876 (1974).
35. J. Simitzis and C. Dimopolou, *Makromol. Chem.* 185, 2553 (1984).
36. F. Teraoka and T. Takahashi, *J. Macromol. Sci. Phys. B* 18, 73 (1980).
37. J. A. John and J. M. Tour, *J. Am. Chem. Soc.* 116, 5011 (1992).
38. T. Yamamoto, *Prog. Polym. Sci.* 17, 1153 (1992).
39. T. Yamamoto, in "Organic Conductive Molecules and Polymers" (H. S. Nalwa, Ed.), Vol. 2, p. 171. Wiley, New York, 1997.
40. M. Kumada, *Pure Appl. Chem.* 52, 669 (1980).
41. E. Negishi, *Pure Appl. Chem.* 53, 2333 (1981).
42. J. K. Still, *Angew. Chem., Int. Ed. Engl.* 25, 508 (1986).
43. K. Tamao, K. Sumitani, and K. Kumada, *J. Am. Chem. Soc.* 94, 4374 (1972).
44. N. Miyaoura, T. Yanagi, and A. Suzuki, *Synth. Commun.* 11, 513 (1981).
45. R. B. Miller and S. Dugar, *Organometallics* 3, 1261 (1984).
46. P. E. Cassidy, C. S. Marvel, and S. Ray, *J. Polym. Sci., Part A: Polym. Chem.* 3, 1553 (1965).
47. C. S. Marvel and G. E. Hartzell, *J. Am. Chem. Soc.* 81, 448 (1959).
48. D. G. H. Ballard, A. Courtis, I. M. Shirley, and S. C. Taylor, *Macromolecules* 21, 294 (1988).
49. D. L. Gin, V. P. Conticello, and R. H. Graubs, *J. Am. Chem. Soc.* 116, 10507 (1994).
50. D. L. Gin, V. P. Conticello, and R. H. Graubs, *J. Am. Chem. Soc.* 116, 10934 (1994).
51. I. Rubenstein, *J. Polym. Sci., Polym. Chem. Ed.* 21, 3035 (1985).
52. I. Rubenstein, *J. Electrochem. Soc.* 130, 1506 (1983).
53. S. Aeiyaich and P. C. Lacaze, *J. Chem. Phys.* 86, 143 (1989).
54. S. Aeiyaich and P. C. Lacaze, *J. Polym. Sci., Chem. Ed.* 27, 515 (1989).
55. V. Gutmann and R. Schmied, *Coord. Chem. Rev.* 12, 263 (1974).
56. K. Imanishi, M. Satoh, Y. Yasuda, R. Tsushima, and S. Aoki, *J. Electroanal. Chem.* 242, 203 (1988).
57. K. Kobayashi, T. X. Yang, K. Muraiyama, M. Shimomura, and S. Miyauchi, *Synth. Met.* 69, 475 (1995).
58. G. Froyer, F. Maurice, P. Bernier, and P. McAndrew, *Polymer* 23, 1103 (1982).
59. M. A. Sato, K. Klaeriyama, and K. Someno, *Makromol. Chem.* 184, 2248 (1983).
60. M. Satoh, M. Tabata, K. Kaneto, and K. Yoshino, *J. Electroanal. Chem.* 195, 203 (1985).
61. M. Satoh, M. Tabata, F. Vesugi, K. Kaneto, and K. Yoshino, *Synth. Met.* 17, 595 (1987).
62. H. B. Gu, S. Nakajima, R. Sugimoto, and K. Yoshino, *Jpn. J. Appl. Phys.* 27, 311 (1988).
63. R. Sugimoto, S. Takeda, H. B. Gu, and K. Yoshino, *Chem. Express* 1, 635 (1986).
64. K. Yoshino, S. Nakajima, and R. Sugimoto, *Jpn. J. Appl. Phys.* 26, L1038 (1986).
65. K. Yoshino, S. Nakajima, M. Fujii, and R. Sugimoto, *Polym. Commun.* 28, 309 (1987).
66. K. Yoshino, D. H. Park, B. K. Park, M. Onada, and R. Sugimoto, *Solid State Commun.* 67, 1119 (1988).
67. M. C. Gallazi, L. Castellani, R. A. Marin, and G. Zerbi, *J. Polym. Sci., Polym. Chem. Ed.* 31, 3339 (1993).
68. T. Yamamoto, K. Senechika, and A. Yamamoto, *J. Polym. Sci., Polym. Lett. Ed.* 18, 9 (1980).
69. I. Colon and G. T. Kwiatkowski, *J. Polym. Sci., Polym. Chem. Ed.* 28, 367 (1990).
70. R. D. McCullough and R. D. Lowe, *J. Chem. Soc. Chem. Commun.* 70 (1992).
71. X. Wu, T. A. Chen, and R. D. Rieke, *Macromolecules* 28, 2101 (1995).
72. M. D. McClain, D. A. Whittington, D. J. Mitchel, and M. D. Curtis, *J. Am. Chem. Soc.* 117, 3887 (1995).
73. M. J. Marsella and T. M. Swager, *J. Am. Chem. Soc.* 115, 12214 (1993).
74. G. Tourillon and F. Garnier, *J. Electroanal. Chem.* 135, 173 (1982).
75. K. Kaneto, Y. Kohno, K. Yoshino, and Y. Inuishi, *J. Chem. Soc., Chem. Commun.* 382 (1983).
76. S. Hotta, T. Hosaka, and W. Shimotsuma, *Synth. Met.* 6, 317 (1983).
77. M. Sato, S. Tanaka, and K. Kaeriyama, *Synth. Met.* 14, 279 (1986).
78. M. Sato, S. Tanaka, and K. Kaeriyama, *J. Chem. Soc., Chem. Commun.* 713 (1985).
79. J. Roncali, F. Garnier, M. Lemaire, and R. Carreau, *Synth. Met.* 15, 323 (1986).
80. A. Yassar, J. Roncali, and F. Garnier, *Macromolecules* 22, 804 (1989).
81. F. Garnier, G. Tourillon, J. Y. Barraud, and H. Dexpert, *J. Mater. Sci.* 161, 51 (1984).
82. L. F. Warren, J. A. Walker, D. P. Anderson, and C. G. Rhodes, *J. Electrochem. Soc.* 136, 2286 (1989).
83. M. G. Kanatzidis, L. M. Tonge, T. K. Marks, H. O. Marcy, and C. R. Kannewurf, *J. Am. Chem. Soc.* 109, 3797 (1987).
84. M. Zagorska and A. Pron, *Synth. Met.* 18, 43 (1987).
85. S. Rapi, V. Bocchi, and G. P. Gardini, *Synth. Met.* 24, 217 (1988).
86. S. Machida, S. Miyata, and A. Techagumpuch, *Synth. Met.* 31, 311 (1989).
87. Y. A. Bubitsky, B. A. Zhubanov, and G. G. Maresch, *Synth. Met.* 41-43, 375 (1991).
88. S. P. Armes, *Synth. Met.* 20, 365 (1987).
89. T. H. Chao and J. March, *J. Polym. Sci., Polym. Chem.* 26, 743 (1988).
90. E. T. Kang, K. G. Neoh, Y. K. Ong, K. L. Tan, and B. T. G. Tan, *Macromolecules* 24, 2822 (1991).
91. N. Tushima and J. Tayanagi, *Chem. Lett.* 1369 (1990).
92. R. A. Bull, F. R. F. Fan, and A. J. Bard, *J. Electrochem. Soc.* 129, 1009 (1982).
93. M. L. Daroux, E. B. Yeager, M. Kalaji, N. H. Cuong, and A. Bewick, *Makromol. Chem., Macromol. Symp.* 8, 127 (1987).
94. B. R. Scharifker, E. Garcia-Pastoriza, and W. Marino, *J. Electroanal. Chem.* 300, 85 (1991).
95. A. F. Diaz, K. K. Kanazawa, and G. P. Gardini, *J. Chem. Soc., Chem. Commun.* 635 (1979).
96. K. K. Kanazawa, A. F. Diaz, W. D. Gill, P. M. Grant, G. B. Street, G. P. Gardini, and J. F. Kwak, *Synth. Met.* 1, 329 (1980).
97. A. F. Diaz and J. Bargon, in "Handbook of Conducting Polymers" (T. A. Skotheim, Ed.), Vol. 1, p. 81. Dekker, New York, 1986.
98. T. F. Otero and A. H. Arevalo, *Synth. Met.* 66, 25 (1994).
99. T. F. Otero, C. Santamaria, and B. K. Bunting, *J. Electroanal. Chem.* 380, 291 (1995).
100. S. K. Manohar, A. G. MacDiarmid, and A. J. Epstein, *Synth. Met.* 41-43, 711 (1991).
101. A. G. MacDiarmid, S. K. Manohar, J. G. Masters, Y. Sun, H. Weiss, and A. J. Epstein, *Synth. Met.* 41-43, 621 (1991).
102. K. Uosaki, K. Okazaki, and H. Kita, *J. Polym. Sci.: Part A: Polym. Chem.* 28, 399 (1990).
103. O. Niwa and T. Tamamura, *Synth. Met.* 20, 235 (1987).
104. J. Roncali and F. Garnier, *J. Phys. Chem.* 92, 833 (1988).
105. C. K. Subramaniam, A. B. Kaiser, P. W. Gilberd, and B. Wessling, *J. Polym. Sci.: Polym. Phys. Ed.* 31, 1425 (1993).
106. A. Yassar, J. Roncali, and F. Garnier, *Polym. Commun.* 28, 103 (1987).
107. S. P. Armes and M. Aldissi, *Polymer* 31, 569 (1990).

108. O. T. Ikkala, J. Laakso, K. Vakiiparta, E. Viranen, H. Rouhonen, H. Jarvinen, T. Taka, P. I. Passiniemi, and J.-E. Osterholm, *Synth. Met.* 69, 97 (1995).
109. S. Roth and W. Graupner, *Synth. Met.* 55–57, 3623 (1993).
110. M. A. De Paoli, E. A. R. Duek, and M. A. Rodrigues, *Synth. Met.* 41–43, 973 (1991).
111. J.-M. Liu and S. C. Yan, *J. Chem. Soc., Chem. Commun.* 1529 (1991).
112. A. Andreatta, A. J. Heeger, and P. Smith, *Polym. Commun.* 31, 275 (1990).
113. L. Terlemezyan, M. M. Hailkov, and B. Ivanova, *Polym. Bull.* 29, 283 (1992).
114. E. L. Tassi and M.-A. De Paoli, *J. Chem. Soc., Chem. Commun.* 155 (1990).
115. S. J. Davies, T. G. Ryan, C. J. Wilde, and G. Beyer, *Synth. Met.* 69, 209 (1995).
116. H. Tsumani, S. Fukuzawa, M. Ishikawa, M. Morita, and Y. Matsuda, *Synth. Met.* 72, 231 (1995).
117. H. Naarman and H. Theophilou, *Synth. Met.* 22, 1 (1987).
118. K. Akagi, S. Katayama, H. Shirakawa, K. Araya, A. Mukoh, and T. Narahara, *Synth. Met.* 17, 241 (1987).
119. H. Shirakawa and S. Ikeda, *J. Polym. Sci., Polym. Chem. Ed.* 12, 929 (1974).
120. D. Bott, C. Brown, C. Chai, N. Walker, W. Feast, P. Foot, P. Calvert, N. Billingham, and R. Friend, *Synth. Met.* 14, 245 (1986).
121. J. Tsukamoto and A. Takahashi, *Synth. Met.* 41–43, 7 (1991).
122. N. Foxonet, J. L. Ribet, N. Coustel, and M. Galtier, *Synth. Met.* 41–43, 85, (1991).
123. D. Wang, S. Hasegawa, M. Shmizu, and J. Tanaka, *Synth. Met.* 46, 85 (1992).
124. H. Shirakawa, Y.-K. Zhang, T. Okuda, K. Sakamaki, and K. Akagi, *Synth. Met.* 65, 93 (1991).
125. H. Kaneko, Y. Nogami, T. Isohiguro, H. Nishiyama, H. Ishimoto, A. Takahashi, and J. Tsukamoto, *Synth. Met.* 57, 4888 (1993).
126. C. O. Yoon, R. Menon, A. J. Heeger, E. B. Park, W. W. Park, K. Akagi, and H. Shirakawa, *Synth. Met.* 69, 79 (1995).
127. Y. Cao, P. Smith, and A. J. Heeger, *Synth. Met.* 41–43, 181 (1991).
128. R. Zozuk, S. Roth, and F. Kremeer, *Synth. Met.* 41–43, 193 (1991).
129. H. Kaneko and T. Ishiguro, *Synth. Met.* 65, 141 (1994).
130. W. Tütthart and G. Leising, *Synth. Met.* 57, 4878 (1993).
131. E. B. Park, J. S. Yoo, J. Y. Park, Y. W. Park, K. Akagi, and H. Shirakawa, *Synth. Met.* 69, 61 (1995).
132. M. Yamamura, K. Sato, and T. Hagiwara, *Synth. Met.* 41–43, 439 (1991).
133. R. Menon, C. O. Yoon, D. Moses, and A. J. Heeger, *Synth. Met.* 64, 53 (1994).
134. S. Masubuchi, S. Kazama, K. Mizoguchi, F. Shimizu, K. Kume, R. Matsushita, and T. Matsuyama, *Synth. Met.* 69, 71 (1995).
135. J. H. Lee and I. J. Chung, *Synth. Met.* 53, 245 (1993).
136. S. Masubuchi, S. Kazama, R. Matsushita, and R. Matsuyama, *Synth. Met.* 69, 345 (1995).
137. J. Roncali, A. Yassar, and F. Garnier, *J. Chem. Soc., Chem. Commun.* 581 (1988).
138. S. Hotta, *Synth. Met.* 22, 103 (1988).
139. G. Tourillon and F. Garnier, *J. Phys. Chem.* 87, 2289 (1983).
140. J. Roncali, A. Yassar, and F. Garnier, *J. Chem. Phys.* 86, 85 (1989).
141. M. Sato, S. Tanaka, and K. Kaeriyama, *J. Chem. Soc., Chem. Commun.* 185 (1984).
142. G. Tourillon and F. Garnier, *J. Electroanal. Chem.* 135, 173 (1995).
143. G. W. Heffer and D. S. Pearson, *Synth. Met.* 44, 341 (1991).
144. H. Ishikawa, K. Amame, A. Kobayashi, M. Satoh, and E. Hasegawa, *Synth. Met.* 64, 49 (1994).
145. H. Jarvinen, L. Lahtinen, I. Nasman, O. Hormi, and A. L. Tammi, *Synth. Met.* 69, 299 (1995).
146. J. Moulton and P. Smith, *Synth. Met.* 40, 13 (1991).
147. K. Y. Jen, C. C. Han, and R. L. Elsenbaumer, *Mol. Cryst. Liq. Cryst.* 189, 169 (1990).
148. D. M. Ivory, G. G. Miller, J. M. Sowa, L. W. Schacklette, R. R. Chance, and R. H. Baughman, *J. Chem. Phys.* 1506 (1979).
149. L. Athouel, Y. Pelous, G. Froyer, G. Louarn, and S. Lefrant, *J. Chem. Phys.* 89, 1285 (1992).
150. Y. W. Park, E. B. Park, K. H. Kim, C. K. Park, and J. I. Jin, *Synth. Met.* 41–43, 315 (1991).
151. R. Mertens, P. Nagels, R. Callaerts, M. V. Roy, J. Briers, and H. J. Geise, *Synth. Met.* 51, 55 (1992).
152. S. K. Jeong, J. S. Suh, E. J. Oh, W. W. Park, C. Y. Kim, and A. G. MacDiarmid, *Synth. Met.* 69, 171 (1995).
153. G. Baora and M. Spargaglione, *Synth. Met.* 72, 135 (1995).
154. C. O. Yoon, J. H. Kim, H. K. Sung, K. Lee, and H. Lee, *Synth. Met.* 81, 75 (1996).
155. A. Fizazi, J. Moulton, K. Pakbaz, S. D. D. V. Rughooputh, P. Smith, and A. J. Heeger, *Phys. Rev. Lett.* 64, 2180 (1990).
156. N. S. Sariciftci, V. M. Kobrayanskii, R. Menon, L. Smilowitz, C. Halvorson, T. W. Hagler, D. Mihailovic, and A. J. Heeger, *Synth. Met.* 53, 161 (1993).
157. L. B. Groenendaal, F. Jonas, D. Feitag, H. Pielartzik, and J. R. Reynolds, *Adv. Mater.* 12, 481 (2000).
158. S. Ghosh, J. Rasnmussan, and O. Ingnas, *Adv. Mater.* 10, 1097 (1998).
159. L. H. Sperling, "Interpenetrating Polymer Networks and Related Materials." Plenum, New York, 1981.
160. P.-H. Aubert, L. Groenendaal, F. Louwet, L. Lutsen, D. Vanderzande, and G. Zotti, *Synth. Met.* 126, 193 (2002).
161. T. Iyoda, A. Ohtani, K. Honda, and T. Shimudzu, *Macromolecules* 23, 1971 (1990).
162. M. Morita, I. Hashida, and M. Nishimura, *J. Appl. Polym. Sci.* 36, 1639 (1988).
163. Y. Chen, R. Qian, G. Li, and Y. Li, *Polym. Commun.* 32, 189 (1991).
164. V. Bocchi, G. P. Gardini, and S. Rapi, *J. Mater. Sci. Lett.* 6, 1283 (1987).
165. T. Ueno, H. D. Arntz, S. Flesh, and L. Bargon, *J. Makromol. Sci. Chem. A* 25, 1557 (1988).
166. F. Jouseem and L. Olmedo, *Synth. Met.* 41–43, 385 (1981).
167. M. A. de Paoli, R. J. Waltman, A. F. Diaz, and J. Bargon, *J. Chem. Soc., Chem. Commun.* 1015 (1984).
168. T. W. Hagler, K. Pakbaz, K. F. Voss, and A. J. Heeger, *Phys. Rev. B* 44, 8652 (1991).
169. T. W. Hagler, K. Pakbaz, and A. J. Heeger, *Phys. Rev. B* 49, 10968 (1994).
170. R. H. Friend and N. C. Greenham, in "Handbook of Conducting Polymers" (T. A. Skotheim, R. Elsenbaumer, and J. R. Reynolds, Eds.), p. 823. Dekker, New York, 1998.
171. S. Morita, A. A. Zakhidov, and K. Yoshino, *Jpn. J. Appl. Phys.* 32, L873 (1993).
172. N. S. Sariciftci, D. Braun, C. Zhang, V. I. Srdanov, A. J. Heeger, G. Stucky, and F. Wudl, *Appl. Phys. Lett.* 62, 585 (1993).
173. J. J. M. Halls, K. Pickler, R. H. Friend, S. C. Moratti, and A. B. Holmes, *Appl. Phys. Lett.* 68, 3120 (1996).
174. G. Yu, J. Gao, J. C. Hummelen, F. Wudl, and A. J. Heeger, *Science (Washington, DC)* 270, 1789 (1995).
175. J. J. M. Halls, C. A. Walsh, N. C. Greenham, E. M. Morsegella, R. H. Friend, S. C. Moratti, and A. B. Holmes, *Nature (London)* 376, 498 (1995).
176. G. Yu, Y. Cao, J. Wang, J. McElvain, and A. J. Heeger, *Synth. Met.* 102, 904 (1999).
177. F. Hide, B. J. Schwartz, M. A. Diaz-Garcia, and A. J. Heeger, *Chem. Phys. Lett.* 256, 424 (1996).
178. V. I. Colvin, M. C. Schlamp, and A. P. Alivisatos, *Nature (London)* 370, 354 (1994).

179. N. C. Greenham, X. Peng, and A. P. Alivisatos, *Phys. Rev. B* 54, 24 (1996).
180. P. Enzel and T. Bein, *J. Phys. Chem.* 93, 6270 (1989).
181. T. Bein and P. Enzel, *Angew. Chem. Int. Ed. Engl.* 28, 1692 (1989).
182. M. G. Kanatzidis, C.-G. Wu, H. O. Marcy, and C. R. Kannewurf, *J. Am. Chem. Soc.* 111, 4139 (1989).
183. M. A. de Paoli, in "Handbook of Organic Conductive Molecules and Polymers" (H. S. Nalwa, Ed.), Vol. 2, p. 773. Wiley, New York, 1997.
184. Y. Cao, N. Colaneri, A. J. Heeger, and P. Smith, *Appl. Phys. Lett.* 65, 2001 (1994).
185. R. Menon, C. O. Yoon, C. Y. Yang, D. Moses, A. J. Heeger, and Y. Cao, *Macromolecules* 26, 7245 (1996).
186. R. Menon, C. O. Yoon, C. Y. Yang, D. Moses, P. Smith, A. J. Heeger, and Y. Cao, *Phys. Rev. B* 50, 13931 (1994).
187. C. O. Yoon, R. Menon, A. J. Heeger, and Y. Cao, *Synth. Met.* 63, 47 (1996).
188. C. Y. Yang, R. Menon, A. J. Heeger, and Y. Cao, *Synth. Met.* 79, 27 (1996).
189. A. Aharony and D. Stauffer, "Introduction to Percolation Theory," 2nd ed. Taylor and Francis, London, 1993.
190. R. Menon, in "Handbook of Organic Conductive Molecules and Polymers," Vols. 1-4 (H. S. Nalwa, Ed.), Vols. 4, p. 47. Wiley, New York, 1997.
191. N. F. Mott and E. A. Davis, "Transport in Non-Crystalline Solids." Oxford University Press, Oxford, 1979.
192. C. Kittel, "Introduction to Solid State Physics." Wiley, New York, 1996.
193. C. O. Yoon, R. Menon, D. Moses, A. J. Heeger, and Y. Cao, *Phys. Rev. B* 48, 14080 (1993).
194. Y. Yang and A. J. Heeger, *Nature (London)* 372, 244 (1994).
195. J. J. Dittmer, K. Petritsch, E. A. Marseglia, R. H. Friend, H. Host, and A. B. Holmes, *Synth. Met.* 102, 879 (1999).
196. A. J. Heeger, *TRIP* 3, 39 (1995).
197. R. G. Freeman, K. C. Grabar, K. J. Allison, R. M. Bright, J. A. Davis, M. A. Jackson, P. C. Smith, D. G. Walter, and M. J. Natan, *Science (Washington, DC)* 267, 1629 (1995).
198. G. Schmid, *Chem. Rev.* 2, 1709 (1992).



# Polymer Electrolyte Nanocomposites

Mikrajuddin Abdullah<sup>1</sup>, Wuled Lenggoro, Kikuo Okuyama

*Hiroshima University, Hiroshima, Japan*

## CONTENTS

1. Introduction
  2. Conductivity Enhancement in Polymer Electrolytes
  3. Development of Polymer Electrolyte Nanocomposites
  4. Preparation Methods
  5. Important Parameters
  6. Charge Transport Characterizations
  7. Spectroscopic Characterizations
  8. Microscopic Analysis
  9. Thermal Characterizations
  10. Density Method
  11. Electrical Properties
  12. Mechanical Properties
  13. Thermal Properties
  14. Luminescent Composites
  15. Conclusion
- Glossary  
References

## 1. INTRODUCTION

Rechargeable cells are key components in mobile technologies, such as portable consumer electronics and electric vehicles [1]. A search for batteries that provide high energy density and multiple rechargeability has been a subject of considerable attentions. Even though battery technology developed one hundred years ago, progress and improvements in technology have been slow, particularly when compared to the growth of computer technology [2].

A Li-based battery provides a high density and flexibility of design. Today's lithium battery has a high specific energy ( $>130 \text{ W h kg}^{-1}$ ), a high energy density ( $>300 \text{ W h L}^{-1}$ ),

<sup>1</sup> Permanent address: Department of Physics, Bandung Institute of Technology, Jalan Ganeca 10 Bandung 40132, Indonesia.

high cell voltage (3.5 V), as well as a long cycle life (500–1000) charge/discharge. Worldwide production of such devices exceeded 200 million in 1997 and it will be approximately three times that number during 2001 [1]. Since lithium produces an explosion reaction with water-based electrolytes, a search for nonaqueous electrolytes is critically important to the production of the next-generation lithium battery, using electrolytes in a solid phase in an effort to develop more environmentally friendly materials. Polymer electrolytes are potential candidates for replacing the conventional aqueous electrolytes in lithium batteries. Polymers containing esters, ethers, or mixtures thereof which have the ability to dissolve salts are the base materials for polymer electrolytes. Polymer electrolytes are generally prepared by mixing high molecular weight polymers (HMWPs) with a salt solution. The polymer serves as solid solvent, thus permitting the salt to dissociate into anions and cations. Since the mass of a cation is much smaller than that of an anion, the electrical conductivity is dominated by cation transfer. Lithium salts are usually used for this purpose since they are the most electropositive of materials ( $-3.04 \text{ V}$  relative to the standard hydrogen electrodes) as well as the lightest metal (atomic mass 6.94 g/mol, and density  $0.53 \text{ g/cm}^3$ ) and thus facilitate the design of storage systems with high energy density (Watt hour/kg) [1]. Table 1 shows a comparison of the electrochemical properties of several metals.

Until presently, however, no polymer electrolyte-based lithium batteries are commercially available in the market. Therefore, worldwide research is being focused on the development of high power and high energy density polymer electrolytes with a major attention to safety, performance, and reliability. A battery contains two electrodes: positive and negative (both sources of chemical reactions), separated by an electrolyte that contains dissociated salts through which ion carriers flow. Once these electrodes are connected to external circuits, chemical reaction appears at both electrodes to result in a deliverance of electrons to the external circuits. The properties of a battery thus strongly depend on the electrolyte, anode, and cathode. With the use of polymer electrolytes in lithium batteries, high specific energy and specific power, safe operation, flexibility in packaging, and low cost in fabrication as well as low internal voltage drop at relatively large current withdraw is expected [3].

**Table 1.** Electrochemical properties of several metals that have potential applications for use in batteries.

Metal	Atomic weight [g/mol]	Valence charge	Specific charge [A h kg <sup>-1</sup> ]	Electrode potential [V]
Li	6.94	1	3862	3.05
Na	22.99	1	1166	2.71
Mg	24.31	2	2205	2.38
Zn	65.38	2	820	0.76
Cd	112.41	2	477	0.40
Pd	207.20	2	250	0.13

Realization of commercial polymer electrolyte batteries is actively investigated in many companies worldwide. A major effort to develop advanced polymer batteries for electric vehicles began in the early 1990s by 3M and Hydro-Quebec [4]. The battery contains a lithium metal anode, a polyethylene oxide (PEO)-based polymer electrolyte, and a vanadium oxide (VO<sub>x</sub>) cathode. The reversibility of lithium intercalation and deintercalation in the VO<sub>x</sub> is quite good but the average discharge of the cell is low. PolyPlus Battery company in the United States is developing polymer electrolyte-based lithium battery which would operate at room temperature with specific energy as high as 500 W h kg<sup>-1</sup> [3]. In a prototype cell, using cathode made of lithium intercalated disulfide polymer, a specific energy as high as 100 W h kg<sup>-1</sup> and charge and discharge cycles almost reproducible for over 350 cycles were observed at 90 °C [5]. Moltec company reported a specific density of 180 W h kg<sup>-1</sup> for an AA-sized battery based on organosulfur cathode [6]. Ultrafine Battery company reported a room-temperature solid polymer battery based on intercalation type electrode with a specific energy 125 W h kg<sup>-1</sup> and charge/discharge cycling time of 500 [3]. This performance is still below the consumer expectation threshold. In 1995, Turrentine and Kurani in the United States did a survey on demand for alternative fuel cell for vehicles and found that consumers agreed to buy electric vehicles which would run for at least 200 km per battery [7].

## 2. CONDUCTIVITY ENHANCEMENT IN POLYMER ELECTROLYTES

It is believed that in the polymer electrolytes, the cations are coiled by polymer segment leaving the anions to occupy separate positions [8]. Battery performance is limited by the speed of cation diffusion. The transport of cations takes place if there is a relaxation of the polymer segments so that cations are released from a segment and then occupy another segment. Segmental relaxation requires the presence of free volume in the polymer matrix, a condition that can be attained if the polymer is in an amorphous state. Unfortunately, most HMWPs crystallize at ambient temperatures. Ions are transported with difficulty in a crystalline matrix since no chain relaxation occurs and, as a result, the conductivity of polymer electrolytes in this phase (at ambient temperature) is depressed. The transport of ions in this state is dominated by the jumping of cations to the nearest location, which depends on the blocking potential (activation energy). This is similar to the jump of charge carriers in

crystalline solids. The characteristic time for jumping is proportional to the exponential of the blocking potential. This results in a conductivity of the order of 10<sup>-8</sup> S/cm, a value that is far below the desired value of about 10<sup>-4</sup> S/cm [9]. When it enters the amorphous state, that is, at temperatures above the melting point, a high conductivity appears. For a commonly used polymer, that is, polyethylene oxide, the melting temperature is 65 °C. This is, of course, impractical since the operating temperature for most electronic devices is room temperature. In addition, at temperatures above the melting point, the polymer becomes soft, causing the solid-state properties to degrade. Initiated by the work of Wright and Armand [10–12], several kinds of polymer electrolytes have been intensively investigated around the world. Table 2 displays examples of polymer electrolytes and their measured conductivities at 20 °C [13].

Improvements in the electrical conductivity of polymer electrolytes at ambient temperature is therefore of critical importance for technological applications. Several approaches have been explored to realize this aim. Some frequently used methods will be explained briefly here.

### 2.1. Preparing Low Degree of Crystallinity Polymers

By considering that the presence of amorphous state is strictly important for improving the conductivity, the main strategy is to enhance the amorphous state at low temperatures. The first approach is to prepare low degree of crystallinity polymer from initial. It includes cross-linking of two polymers [13, 14], synthesis of new polymer, cross-linking high molecular weight polymer through  $\gamma$ -irradiation [15, 16], addition of plasticizers in polymer electrolytes, addition of fillers, and bending of two polymers [17, 18]. Another strategy is to prepare an amorphous polymer so as to obtain a polymer that is composed of four to five monomeric units. For this system, the chains must be sufficiently long to effectively complex cations but too short to crystallize at low temperatures. Thus the matrix would still be in the amorphous state even at low temperatures. The polymer host serves as a solvent and does not include any organic liquids.

### 2.2. Addition of Side Chains

An alternative way to decrease the crystallinity of polymer matrix is to introduce side chain to the polymer main chain. Theoretically, chain ends and branch can be thought of as impurities, which depress the melting point of the polymer. Simple mathematical formulation can be used to explain the melting point lowering by the presence of chain ends and branch. If  $X_i$  is the mole fraction of impurities (chain ends, side chains, and branch), then the melting point of polymer,  $T_m$ , decreases according to [19]

$$\frac{1}{T_m} - \frac{1}{T_m^o} = \frac{R}{\Delta H_u} \ln(1 - X_i) \quad (1)$$

where  $T_m^o$  = melting point of polymer containing only polymer chain with infinite chain length,  $R$  = gas constant, and  $\Delta H_u$  = enthalpy of fusion per mole of repeat unit. Chung and Sohn showed that the XRD intensity of polymer

**Table 2.** Examples of polymer electrolytes with their corresponding electrical conductivities at 20 °C.

Polymer host	Repeat unit	Example polymer electrolyte	Conductivity (S/cm) at 20 °C
Poly(ethylene oxide), PEO	$\text{-(CH}_2\text{CH}_2\text{O)}_n\text{-}$	$(\text{PEO})_8\text{:LiClO}_4$	$10^{-8}$
Poly(oxymethylene), POM	$\text{-(CH}_2\text{O)}_n\text{-}$	$\text{POM:LiClO}_4$	$10^{-8}$
Poly(propylene oxide), PPO	$\text{-(CH}_2\text{CH}_2\text{CH}_2\text{O)}_n\text{-}$	$(\text{PPO})_8\text{LiClO}_4$	$10^{-8}$
Poly(oxymethylene-oligo-ethylene), POO	$\text{-(CH}_2\text{O)(CH}_2\text{CH}_2\text{O)}_n\text{-}$	$(\text{POO})_{25}\text{:LiCF}_3\text{SO}_3$	$3 \times 10^{-5}$
Poly(dimethyl siloxane), DMS	$\text{-(CH}_3\text{)}_2\text{SiO)}_n\text{-}$	$\text{DMS:LiClO}_4$	$10^{-4}$
Unsaturated ethylene Oxide segmented, UP	$\text{-(HC=CH(CH}_2\text{)}_4\text{O(CH}_2\text{CH}_2\text{O)}_n\text{(CH}_2\text{)}_4\text{)}_x\text{-}$	$\text{UP:LiClO}_4$ (EO:Li <sup>+</sup> = 32 : 1)	$10^{-5}$
Poly[(2-methoxy)ethyl glycidyl ether], PMEGE	$\text{-(CH}_2\text{CHO)}_n\text{-}$   $\text{CH}_2\text{(OCH}_2\text{CH}_2\text{)}_2\text{OCH}_3$	$(\text{PMEGE})_8\text{:LiClO}_4$	$10^{-5}$
Poly[(methoxy) poly(ethylene glycol)] methacrylate, PMG <sub>n</sub> (EO:Li <sup>+</sup> = 18:1)	$\text{-(CH}_2\text{C(CH}_3\text{)}_2\text{)}_n\text{-}$   $\text{C=O}$   $\text{O-(CH}_2\text{CH}_2\text{O)}_x\text{CH}_3$	$\text{PMG}_{22}\text{:LiCF}_3\text{SO}_3$	$3 \times 10^{-5}$
(PEO-PPO-PEO)-SC SC = siloxane crosslinked	$\text{PEO-(CH}_2\text{)}_3\text{-Si(CH}_3\text{)}_2\text{-O-Si(CH}_3\text{)}_2\text{-(CH}_2\text{)}_3\text{-PEO}$     $\text{O O}$     $\text{PEO-(CH}_2\text{)}_3\text{-Si(CH}_3\text{)}_2\text{-O-Si(CH}_3\text{)}_2\text{-(CH}_2\text{)}_3\text{-PEO}$     $\text{CH}_3 \text{ CH}_3$	$(\text{PEO-PPO-PEO})\text{-SC:LiClO}_4$ (4:1 molar)	$1\text{-}3 \times 10^{-5}$
PEO grafted polysiloxane, PGPS	$\text{-(SiO)}_n\text{-}$   $\text{CH}_2\text{CH}_2\text{PEO}$	$\text{PGPS:LiClO}_4$	$10^{-4}$
Poly[bis-2-(2-methoxyethoxy) ethoxy]phosphazene, MEEP	$\text{-(P=N)}_n\text{-}$     $\text{OCH}_2\text{CH}_2\text{OCH}_2\text{CH}_2\text{OCH}_3$     $\text{OCH}_2\text{CH}_2\text{OCH}_2\text{CH}_2\text{OCH}_3$	$(\text{MEEP})_4\text{:LiBF}_4$ $(\text{MEEP})_4\text{:LiN(CF}_3\text{SO}_2)_4$ $(\text{MEEP})_4\text{:LiC(CF}_3\text{SO}_2)_4$	$2 \times 10^{-5}$ $5 \times 10^{-5}$ $10^{-4}$

decreases with the increase in the length of chain of comb-shaped polymer [20].

Despite depressing the melting point of polymer, the presence of side chain also promotes the solvating of a salt as reported by Ikeda and co-workers [21, 22]. The side chain has shorter relaxation time compared to the main chain. The coupling of the side chain with the ion carrier, therefore, results in an increase in the conductivity. Watanabe et al. designed comb-shaped polyether host with short polyether side chain [23]. However, the mechanical properties decreased even as the conductivity increased. High conductivity with good mechanical properties was obtained by designing a polymer of high molecular weight with trioxyethylene side chain as reported also by Ikeda et al. [24]. With 18 mol.% of side chain, the conductivity was measured to be  $1.5 \times 10^{-4}$  S/cm at 40 °C and raised to  $1.4 \times 10^{-3}$  S/cm at 80 °C.

Composite of polymer with room-temperature molten salt is also an interesting approach to improve the conductivity of polymer electrolytes. Watanabe et al. reported the composite

consisting of chloroaluminate molten salt that possesses a conductivity of  $2 \times 10^{-3}$  S/cm at 303 K [25, 26]. However, the disadvantage of chloroaluminate is its hygroscopic properties such that it is impractical in application. The use of non-chloroaluminate molten salt, therefore, is required to avoid the hygroscopic problem. Tsuda et al. reported a conductivity of  $2.3 \times 10^{-2}$  S/cm in composite of polymer and room-temperature molten fluorohydrogenates [27].

### 2.3. Addition of Plasticizers

Another approach to improve the conductivity is by addition of additional material into the host polymer. This approach appears to be the simplest since a pre-produced polymer can be used to make the polymer electrolytes. Previously, low molecular weight polymers were usually used to reduce the operation temperature of polymer electrolytes. The low molecular weight polymers which were added to the matrix of HMWP to reduce the crystallinity at low temperatures are frequently known as liquid plasticizers.



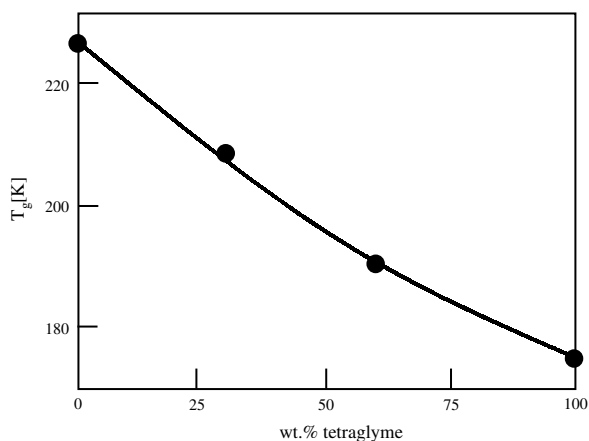
Feullade and Perche demonstrated the idea of plasticizing the polymer with an aprotic solution containing alkali metal salt in which the organic solution of the alkali metal salt remained trapped within the matrix of solid polymer matrix [28]. Such mixing results in formation of gels with ionic conductivity close to the liquid electrolytes. Less evaporating solvents such as ethylene carbonate (EC), propylene carbonate (PC), dimethyl formamide (DMF), diethyl phthalate (DEP), diethyl carbonate (DEC), methyl ethyl carbonate (MEC), dimethyl carbonate (DMC),  $\gamma$ -butyrolactone (BL), glycol sulfide (GS), and alkyl phthalates have been commonly investigated as plasticizers for the gel electrolytes.

Figure 1 shows the effect of plasticizer content tetraglyme (tetraethylene glycol dimethyl ether) on the glass temperature of a system of PEO-co-PPO (3:1):LiClO<sub>4</sub> [29]. The decrease in the glass temperature can be simply explained using a Fox equation:

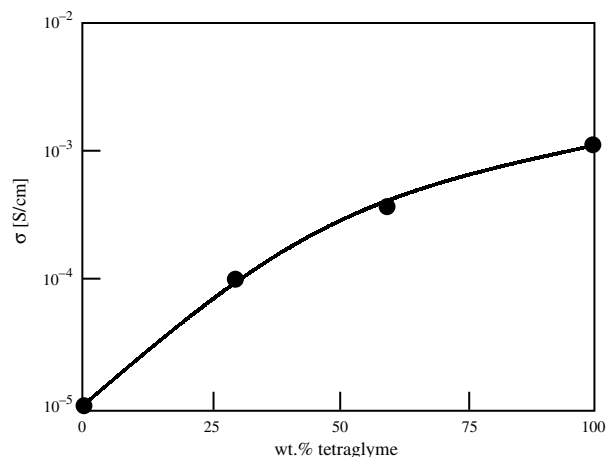
$$\frac{1}{T_g} = \frac{W_1}{T_{g1}} + \frac{W_2}{T_{g2}} \quad (2)$$

where  $W_1$  and  $W_2$  denote the weight fractions of component 1 and component 2, respectively, and  $T_{g1}$  and  $T_{g2}$  are their corresponding glass transitions. This equation tells that the glass temperature of the composite locates between the glass temperature of the components. This relation is also applicable for copolymer where  $T_{g1}$  and  $T_{g2}$  denote the glass temperature of polymers forming the copolymer. Reduction in the glass temperature means the enhancement in the amorphous state at low temperature, and therefore improves the conductivity at low temperatures. Figure 2 shows the enhancement of conductivity by the addition of plasticizer tetraglyme on the system of PEO-co-PPO (3:1):LiClO<sub>4</sub>, measured at 25 °C [29]. The decrease in the glass transition results in the improvement in the fraction of amorphous state at room temperature, therefore improving the conductivity.

However, an improvement in conductivity is adversely accompanied by a degradation in solid-state configuration and a loss of compatibility with the lithium electrode [9],

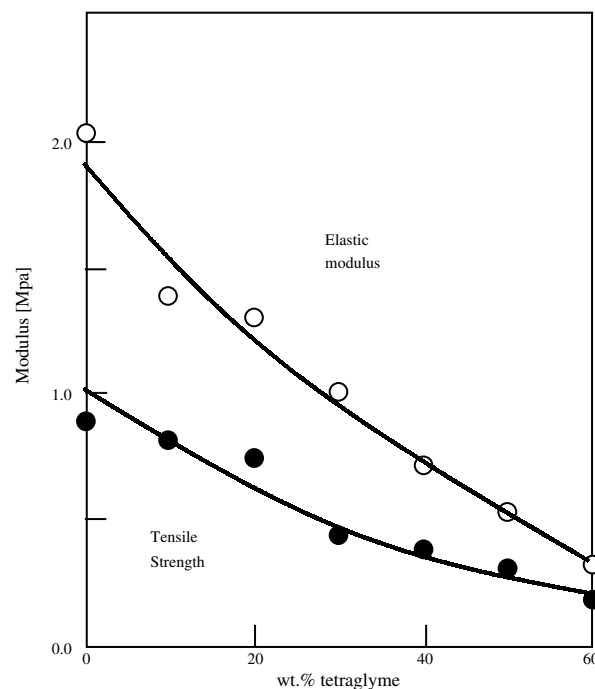


**Figure 1.** Effect of plasticizer weight fraction on the glass temperature of a PEO-co-PPO (3:1):LiClO<sub>4</sub> using plasticizer tetraglyme (tetraethylene glycol dimethyl ether). Data points were derived from [29], D. R. MacFarlane et al., *Electrochim. Acta* 40, 2131 (1995).



**Figure 2.** Effect of plasticizer weight fraction on the conductivity at 25 °C of a PEO-co-PPO (3:1):LiClO<sub>4</sub> using plasticizer tetraglyme (tetraethylene glycol dimethyl ether). Data points were extracted from [29], D. R. MacFarlane et al., *Electrochim. Acta* 40, 2131 (1995).

particularly when the fraction of plasticizers is too high. For example, the modulus of elasticity and elastic strength significantly decreases by addition of plasticizers. This is because the plasticizers are usually low molecular weight polymer having low mechanical strength. Therefore, addition of plasticizers decreases the mechanical strength of the host polymer. Figure 3 shows the effect of plasticizer tetraglyme content on the elastic modulus and tensile strength of PEO-co-PPO (3:1):LiClO<sub>4</sub> [29]. The use of moderate or large quantities of plasticizer results in the production of



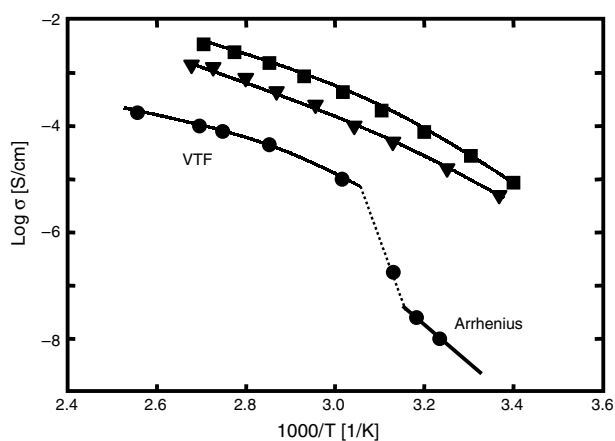
**Figure 3.** Effect of plasticizer weight fraction on the modulus of a PEO-co-PPO (3:1):LiClO<sub>4</sub> using plasticizer tetraglyme (tetraethylene glycol dimethyl ether). Data points were extracted from [29], D. R. MacFarlane et al., *Electrochim. Acta* 40, 2131 (1995).

gel electrolyte. The presence of some plasticizer may also give rise to problems caused by its reaction with the lithium anode. The poor mechanical stability was accounted to be mainly due to the solubility of the polymer matrix in the plasticizer [30]. Cross-linking of the polymer with ultraviolet radiation [31], thermally [32], by photopolymerization [33], or electron beam radiation polymerization [34] was found to reduce the solubility of polymer in the solvent and also helped to trap liquid electrolytes within the polymer matrix.

### 3. DEVELOPMENT OF POLYMER ELECTROLYTE NANOCOMPOSITES

Currently, one popular approach to improve the conductivity involves dispersing ceramic fillers (solid plasticizers) in the polymer matrix, producing what is currently known as composite polymer electrolytes. This approach was first introduced by Weston and Steele [35]. Ceramic filler was used to reduce the glass transition temperature and crystallinity of the polymer and thus allow the amorphous polymer to maintain the liquid-like characteristic at the microscopic level. Ceramic fillers that are frequently used have particle sizes in the range of about several ten nanometers up to several micrometers. Fortunately, such filler materials are commercially available in various sizes at low prices. Figure 4 shows the effect of filler content on the conductivity of polymer electrolytes PEO:LiClO<sub>4</sub> [9]. Table 3 displays examples of polymer electrolyte nanocomposites and their conductivities at around room temperature.

The inorganic filler also acts as a support matrix for the polymer, so that even at high temperature, the composite remains solid. However, at the microscopic level, it maintains a liquid-like structure, which is important for sufficient conductivity. The filler particles, due to high surface area, prevent the recrystallization of polymer when annealed above the melting point. The acid-base interaction between the filler surface group and the oxygen of the PEO leads to a Lewis acid characteristic of the inorganic filler and favors



**Figure 4.** Arrhenius plot of electrical conductivities of: (solid) ceramic-free PEO:LiClO<sub>4</sub>, (triangle) PEO:LiClO<sub>4</sub> containing 10 wt.% Al<sub>2</sub>O<sub>3</sub> (5.8 nm), and (square) PEO:LiClO<sub>4</sub> containing 10 wt.% TiO<sub>2</sub> (13 nm). Data points were extracted from [9], F. Croce et al., *Nature* 394, 456 (1998).

**Table 3.** Examples of polymer electrolyte nanocomposites with their corresponding electrical conductivities at around room temperature.

Polymer electrolytes	Fillers	Conductivity at around rt (S/cm)	Ref.
PEO:LiBF <sub>4</sub>	nano-sized-Al <sub>2</sub> O <sub>3</sub>	~10 <sup>-4</sup>	[36]
	micro-sized-Al <sub>2</sub> O <sub>3</sub>	~10 <sup>-5</sup>	
PEO:LiClO <sub>4</sub>	SiC	~10 <sup>-7</sup>	[37]
EO-co-PO:LiCF <sub>3</sub> SO <sub>3</sub>	Li <sub>1.3</sub> Al <sub>0.3</sub> Ti <sub>1.7</sub> (PO <sub>4</sub> ) <sub>3</sub>	~2 × 10 <sup>-4</sup> (40 °C)	[38]
Brached-poly(ethylene imine):H <sub>3</sub> PO <sub>4</sub>	silica (12 nm size)	~10 <sup>-7</sup>	[39]
PEO:LiClO <sub>4</sub>	α-Al <sub>2</sub> O <sub>3</sub>	~10 <sup>-5</sup>	[40]
PEO:LiClO <sub>4</sub>	AlCl <sub>3</sub>	~10 <sup>-5</sup>	[40]
PEO:LiClO <sub>4</sub>	NNPAAM	>~10 <sup>-5</sup>	[40]
PEO-PEG:LiI	Al <sub>2</sub> O <sub>3</sub>	~10 <sup>-6</sup>	[41]
PEO-PMMA:EC:LiI	Al <sub>2</sub> O <sub>3</sub>	~10 <sup>-8</sup>	[41]
PEG:LiCF <sub>3</sub> O <sub>4</sub>	SiO <sub>2</sub>	~10 <sup>-5</sup>	[42]
PEG:LiCF <sub>3</sub> O <sub>4</sub>	C <sub>12</sub> H <sub>25</sub> OSO <sub>3</sub> Li coated-SiO <sub>2</sub>	~5 × 10 <sup>-5</sup>	[43]
EC:PC:PAN:LiAsF <sub>6</sub>	porous zeolite	~10 <sup>-3</sup>	[44]
PEO:LiClO <sub>4</sub>	AlN, BaTiO <sub>3</sub> , Bi <sub>2</sub> O <sub>3</sub>	~10 <sup>-7</sup> -10 <sup>-6</sup>	[46]
	B <sub>4</sub> C, BN, CaSiO <sub>3</sub>		
	CeO <sub>2</sub> , Fe <sub>2</sub> O <sub>3</sub> , MoS <sub>2</sub> ,		
	PbTiO <sub>3</sub> , Si <sub>3</sub> N <sub>4</sub> ,		
	carbon black		
PEO:Li[(SO <sub>2</sub> CF <sub>3</sub> ) <sub>2</sub> N]	γ-LiAlO <sub>2</sub>	~4 × 10 <sup>-6</sup>	[47]
PEO:PMMA:EC:LiI	MgO	~10 <sup>-7</sup>	[48]
PEO:AgSCN	Al <sub>2</sub> O <sub>3</sub>	~8.8 × 10 <sup>-4</sup>	[49]
PEO:AgSCN	Fe <sub>2</sub> O <sub>3</sub>	~1.1 × 10 <sup>-5</sup>	[50]
PEO:AgSCN	SO <sub>2</sub>	~3 × 10 <sup>-6</sup>	[51]
PEO:NaClO <sub>4</sub>	Na <sub>2</sub> SiO <sub>3</sub>	~2 × 10 <sup>-6</sup>	[52]
PEO:LiCF <sub>3</sub> SO <sub>3</sub>	mineral clay	~10 <sup>-3</sup>	[53]
PEO:NH <sub>4</sub> I	PbS	~0.99 × 10 <sup>-6</sup>	[54]
PEO:NH <sub>4</sub> I	CdS	~0.96 × 10 <sup>-6</sup>	[54]
PEO:NH <sub>4</sub> I	Pb <sub>x</sub> Cd <sub>1-x</sub> S	~0.63-0.84 × 10 <sup>-6</sup>	[54]

the formation of complexes with PEO. The filler then acts as cross-linking center for the PEO, reducing the tension of the polymer for self-organization and promoting stiffness. On the other hand, the acid-base interaction between the polar surface group of the filler and electrolyte ions probably favors the dissolution of the salt.

Another potential application of polymer electrolyte nanocomposites is for making solar cells [55]. Dye-sensitized solar cells have attracted great scientific and technological interest as potential alternatives to classical photovoltaic devices. The cell operation mechanism involves absorption of visible light by the chemisorbed dye, followed by the electron injection from the excited synthesizer into the semiconductor conduction band. The selection of liquid electrolytes, usually containing organic solvent such as acetonitrile and propylene carbonate, assures the perfect regeneration of the dye by direct interaction of the dye oxidized state and I<sup>-</sup>/I<sub>3</sub><sup>-</sup> redox couple and leads to impressively high solar-to-electrical conversion efficiencies (7–11%) [56, 57]. However, the stability and long-term operation of the cell are affected by solvent evaporation or leakage. Thus commercial exploitation of these devices needs the replacement of the liquid electrolyte by a solid charge transport medium, which not only offers hermetic sealing and stabilization but also reduces design restriction and endows the cell

with shape choices and flexibility. Katsaros et al. investigated solid-state dye-sensitized solar cells using composite polymer electrolytes using PEO and  $\text{TiO}_2$  in the presence of  $\text{I}^-/\text{I}_3^-$  redox couple [55]. Initially, dye:Ru(dcbpy) $_2$ (NCS) $_2$  (dcbpy is 4,4'-dicarboxylic acid-2-2'-bipyridine) was attached on the surface of  $\text{TiO}_2$  nanoparticles by immersion of the  $\text{TiO}_2$  thin-film electrode overnight in ethanolic solution of the complex, followed by drying. The functionalized  $\text{TiO}_2$  nanoparticles,  $\text{I}^-/\text{I}_3^-$ , and PEO were put in acetonitrile, followed by heating and drying to evaporate the solvent. Maximum incident photon to current efficiencies as high as 40% were obtained at 520 nm, only two times lower than that obtained using liquid electrolytes [58]. The overall conversion efficiency was 0.96%. For all-solid-state devices, such efficiency can be considered to be sufficiently high [59].

## 4. PREPARATION METHODS

Now we will briefly explain several methods of preparation of polymer electrolyte nanocomposites that are commonly used. Which method should be used, of course, depends on the materials and the form of sample to be formed. One method can only produce sample in the form of thick film, and another one can produce a sample in the form of film of submicrometer thickness.

### 4.1. Casting Method

This method is frequently used due to its simplicity. It can produce polymer film from several micrometers up to several millimeters thickness. Generally, this method includes the following steps:

- dispersion of ceramic fillers in a salt solution,
- addition of a specified amount of polymer to the mixture,
- mixing by means of stirrer or ultrasonic equipment to disperse the particles homogeneously in the polymer matrix,
- casting the mixture on a substrate,
- finally drying in vacuum or in an atmosphere of argon.

All these steps are usually performed in a glove box filled with argon gas and excluding oxygen and water to levels below 20 parts per million (ppm), to avoid the possible occurrence of a "dangerous reaction" between water and lithium. The solvent must be water-free and should be common solvent for both the salt and the polymer. Since the melting point of several polymers is as high as 65 °C, the solvent must also easily evaporate so that drying can be performed at temperatures of around 65 °C. Organic solvents such as acetonitrile, cyclopentanone, and propylene carbonate, plus inorganic solvents such as thionyl chloride ( $\text{SOCl}_2$ ), are typically used.

Sometimes, the insertion of salt is performed after casting the film. For example, Ardel et al. prepared PVDF 2801 (Kynar)-based polymer electrolyte composites according to the following steps [60]. First, Kynar was dissolved into cyclopentanone. Nanoparticles of silica were added and the mixture was mixed for 24 h at room temperature to get homogeneous slurry. After complete dissolution, the slurry was cast on the Teflon support and spread with the use of

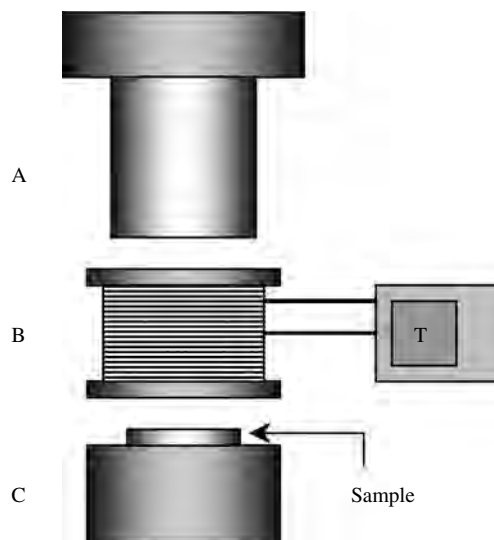
doctor blade technique. To prevent surface irregularities, the film was then covered with a box pierced with holes that allowed a slow evaporation of the cyclopentanone. After complete evaporation of the cyclopentanone, the polymer membrane was soaked in a lithium ion solution for 48 h. Several fresh lithium solutions for each soaking can be used to ensure a complete impregnation of lithium ion into the membrane.

### 4.2. Spin Coating

The spin-coating method is very similar to the casting method. Instead of casting the film on a substrate, in this method, the mixture is dropped on a substrate and placed in a spin coater that can be rotated at adjustable rotation speed. The film thickness can be controlled easily by adjusting the viscosity (concentration) of the mixture and the speed of rotation. However, this method is only available if the viscosity of the mixture is not too high. For a gel mixture, the spin coater rotation is not enough to spread the mixture droplet to form thin film.

### 4.3. Hot Press

Hot press technique equipment is illustrated in Figure 5. The equipment consists of: (A) weighing cylinder, (B) heating chamber, (C) base, and (T) temperature controller. Proper amounts of polymer, salt, and filler are mixed in a mortar for about several minutes. The powder mixture is then sandwiched between two sheets of Mylar or other materials, and positioned inside the heating chamber that is controlled at temperatures lightly above the melting point of the polymer. If PEO is used as polymer matrix, temperature of 80 °C is suitable [61]. The sample is then pressed overnight with a pressure that can be controlled by weighing cylinder. After heating and pressing, the sample is then slowly cooled to room temperature. The sample is then separated from the Mylar sheet and placed in a glove box.

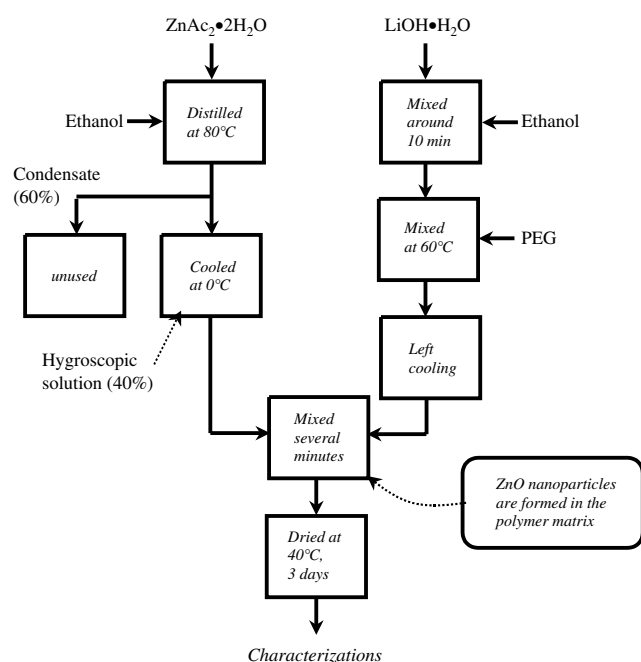


**Figure 5.** Illustration of hot press equipment: (A) weighing cylinder, (B) heater, (C) base, and (T) temperature controller.

#### 4.4. In-situ Preparation

*In-situ* preparation explained here is the preparation of nanoparticles in the polymer matrix. Mikrajuddin et al. produced polymer electrolytes of polyethylene glycol with lithium ion by *in-situ* production of ZnO nanoparticles in the polymer matrix [62, 63]. The preparation methods will be briefly described as follows. Zinc acetate dihydrate,  $(\text{CH}_3\text{COO})_2\text{Zn} \cdot 2\text{H}_2\text{O}$  0.1 M in 100 mL ethanol 99.5, was heated with stirring in distillation equipment at temperature of 80 °C to produce about 60 mL condensate and 40 mL of hygroscopic solution. Lithium hydroxide monohydrate,  $\text{LiOH} \cdot \text{H}_2\text{O}$ , of various concentrations was suspended in 40 mL ethanol and stirred until all the granular material dissolved. Polyethylene glycol (PEG) ( $M_n = 2,000,000$ ) was suspended into each LiOH solution and then stirred with heating at around 60 °C until homogeneous gel-type mixtures were obtained. The mixture temperatures were then left to go down several minutes, after which 10 mL of hygroscopic  $\text{CH}_3\text{COO}_2\text{Zn} \cdot 2\text{H}_2\text{O}$  solution was added into each mixture. The new mixtures were then homogeneously mixed and then dried in an oven that was kept at temperature of 40 °C during three days. The schematic of sample preparations is displayed in Figure 6.

There are many differences between the present method and the commonly used ones. In the present approach: (a) Nanoparticles are grown *in-situ* in polymer matrix. (b) The size of dispersed particles is controllable. (c) Ion carriers are inserted *in-situ* in the polymer matrix during the growing process. (d) Finally, since the grown nanoparticles are luminescent, we obtain a new class of polymer electrolytes, namely luminescent polymer electrolytes with nanoparticles as luminescence centers. Based on the TEM picture, we found that the size of ZnO nanoparticles was 5 nm.



**Figure 6.** Diagram of *in-situ* preparation of PEG:Li containing nanoparticles of ZnO. Adapted with permission from [62], Mikrajuddin et al., *J. Electrochem. Soc.* 149, H107 (2002). © 2002, Elsevier.

Chandra et al. produced polymer electrolytes PEO:NH<sub>4</sub>I containing nanometer-sized semiconductor particles PbS, CdS, Pb<sub>x</sub>Cd<sub>1-x</sub>S [54]. Methanolic solution of PEO and NH<sub>4</sub>I was first stirred roughly at 40 °C for 8–10 h, which resulted in viscous solution of the ion conducting complexes of PEO/NH<sub>4</sub>I. To this solution, a solution Pb(CH<sub>3</sub>COO)<sub>2</sub>, Cd(CH<sub>3</sub>COO)<sub>2</sub>, or Pd(CH<sub>3</sub>COO)<sub>2</sub> + Cd(CH<sub>3</sub>COO)<sub>2</sub> in a desired fraction was added. The stirring was continued until the viscosity was back to the value it was before adding the acetate compounds. Subsequently, H<sub>2</sub>S was bubbled through it giving PbS, CdS, or Pb<sub>x</sub>Cd<sub>1-x</sub>S. The final viscous solution was poured in a petri dish for obtaining solution-cast film. Then the film was dried in vacuum.

## 5. IMPORTANT PARAMETERS

To bring polymer electrolytes as well as polymer electrolyte composites, these materials should provide enough values of several properties as follows.

### 5.1. Electrical Conductivity

Conductivity defines the density of current that can be transported in the material by applying a certain electric field. If electric field  $E$  is applied in the material, the current density will be proportional to the applied electric field, where the proportional constant is the conductivity, or,

$$J = \sigma E \quad (3)$$

with  $J$  the current density ( $\text{A/m}^2$ ) and  $\sigma$  ( $\text{S/m}$  or  $\text{S/cm}$ ) the electrical conductivity. It is clear that high conductivity material will produce high current density upon applying a certain electric field. The value of conductivity is determined by the density of mobile ions (ion carriers) in the material ( $n$ ), the scattering time of the ion ( $\tau$ ), the ion charge ( $q$ ), as well as the mass of ion carrier ( $m$ ), according to a relation

$$\sigma = \frac{nq^2\tau}{m} \quad (4)$$

This equation gives the reason why most polymer electrolytes use lithium ions as ion carriers. The mass of lithium is the smallest among all metals, so it produces the highest conductivity.

For industrial application, the conductivity of polymer electrolytes must be as high as  $10^{-2}$  S/cm. However, until presently, this conductivity can only be achieved at high temperatures in which the polymer is present in the soft phase, or even liquid phase. The conductivity at room temperature of most reported polymers is still below  $10^{-4}$  S/cm.

### 5.2. Transference Number

Since the electrochemical process in lithium batteries involves the intercalation and de-intercalation of lithium cations throughout host compound lattice, solid polymer electrolytes with cation transference number ( $t^+$ ) approaching unity are desirable for avoiding a concentration gradient during repeated charge-discharge cycles. The reported  $t^+$  value for dried polymer electrolytes range from 0.06 to 0.2 [64]. For a gel polymer system,  $t^+$  value of 0.4–0.5 has

been found for poly(bis-methoxy ethoxy)phosphazene [65], and 0.56 in a system of UV-cured gel polymer electrolytes based on polyethylene glycol diacrylate/polyvinylidene fluoride [66].

Transference number of a particle is defined as the ratio of the conductivity due to it and the total conductivity. Assume the total conductivity  $\sigma$  is due to ionic,  $\sigma_{\text{ion}}$ , and to electronic,  $\sigma_e$ , then

$$\sigma = \sigma_{\text{ion}} + \sigma_e \quad (5)$$

The ionic and electronic transference numbers are then

$$t_i = \frac{\sigma_{\text{ion}}}{\sigma} \quad (6)$$

and

$$t_e = \frac{\sigma_e}{\sigma} \quad (7)$$

For pure ionic,  $t_i = 1$ , and for pure electronic,  $t_e = 1$ . For polymer electrolyte composites, a general condition satisfied is  $0 < t_i, t_e < 1$ .

### 5.3. Crystallinity

Crystallinity plays an important role in determining the conductivity of polymer electrolytes. At crystalline phase, the transport of ion carriers is very difficult so that the conductivity is very low. At amorphous phase, there is a segmental motion of polymer chain that also assists the displacement of ions. As a result, the transport of ions is relatively easy. Thus, high conductivity will result. One major route to improve the conductivity of polymer electrolytes is by increasing the fraction of amorphous states. Addition of ceramic fillers, addition of plasticizer, and production of branch polymer are efforts to improve the amorphous state in the polymer.

### 5.4. Mechanical Strength

One objective of the use of polymer electrolyte is to make a battery or fuel cell with a strength comparable to that of liquid electrolytes. Therefore, it is expected that the improvement of conductivity is not accompanied by a decrease in the mechanical strength. It is why the addition of ceramic filler has received more attention, since the conductivity and the mechanical strength can be improved simultaneously. In contrast, the use of liquid plasticizer, although it can enhance the conductivity much higher than the addition of ceramic filler, involves such a degradation in the mechanical strength as to make this approach less interesting.

### 5.5. Storage Time

Battery or fuel cell made from polymer electrolytes should have to operate several weeks or several months. Thus, the properties of polymer electrolytes should not change too much during this time. For example, the conductivity should not depend so much on the storage time. Ideally, the properties should be time independent. However, in reality, the properties tend to degrade with storage time.

## 6. CHARGE TRANSPORT CHARACTERIZATIONS

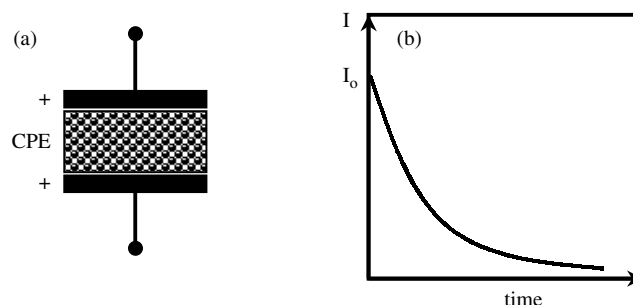
Electrical conductivity is the critical parameter for polymer electrolyte composites. One target of the present research in this field is to produce polymer electrolyte nanocomposites that exhibit a high electrical conductivity, especially at room temperature. Conductivity at around  $10^{-2}$ – $10^{-3}$  S/cm is required to bring this material into industry. The electrical conductivity relates to the value of current that can be produced by the battery. The potential produced by the battery depends on the reaction of the battery with the electrode. Even though the electrode reaction can produce high electrical potential, the use of low conductive electrolytes can produce only small amount of electric current. And since the power can be calculated simply by the relation  $Power = Voltage \times Current$ , the use of low conductive materials will produce a low specific energy battery.

### 6.1. d.c. Conductivity

Ideally, the d.c. conductivity should be measured in order to be sure that the values pertain to long-range ion movement instead of dielectric losses such as would be associated with limited or localized rattling of ions within cages. However, the difficulty in making a d.c. measurement is in finding an electrode material that is compatible with the electrolyte composites. For example, if stainless steel electrodes are attached to an electrolyte composite, as displayed in Figure 7a, and small voltage is applied across the electrodes,  $\text{Li}^+$  ions migrate preferentially toward the cathode, but pile up without being discharged at the stainless/electrolyte interface. A  $\text{Li}^+$  ion deficient layer forms at the electrolyte/stainless steel interface.

The cell therefore behaves like a capacitor. There is an accumulation of ions at interface region of electrode and composite. A large instantaneous current  $I_0$  presents when the cell is switched on, whose magnitude is related to the applied voltage and the resistance of the electrolytes but then falls exponentially with time, as illustrated in Figure 7b. The characteristic time of current decreasing is relatively fast so that it is difficult to make an accurate measurement.

Therefore, the a.c. method is commonly used in the present to make measurement over a wide range of frequencies. The d.c. value can be extracted from the a.c. data. Many a.c. measurements are performed with blocking



**Figure 7.** (a) Polymer electrolyte composites sandwiched between two blocking electrodes. (b) The decay of current when a constant d.c. voltage is applied between two electrodes.

electrode such that no discharge or reaction occurs at the electrode/electrolyte interface. Because the current will flow back and forth, no ions pile up on electrode surface, especially when using a high a.c. frequency. This is why the a.c. resistance (impedance) tends to decrease with increase in the frequency. The electrodes that are commonly used are platinum, stainless steel, gold, and indium tin oxide (ITO) glass. The complex impedance method is widely used to determine the resistance of the sample. The principle of the method is based on measurements of cell impedance, which are taken over a wide range of frequency and then analyzed in the complex impedance plane which is useful for determining the appropriate equivalent circuits for a system and for estimating the values of the circuit parameters.

Impedance is nothing but the a.c. resistance of the cell. The value in general contains the real and the imaginary part. An electrochemical cell, in general, exhibits resistive, capacitive, as well as inductive properties. The resistive property contributes to the real part of the impedance, while the capacitive and the inductive properties contribute to the imaginary part of the impedance. Therefore, an electrochemical cell can be considered as a network of resistor, capacitor, as well as conductor. Which arrangement for which cell is usually determined after performing a measurement, by analyzing the form of impedance curve. A capacitor that presents as an open circuit in a d.c. network and an inductor that appears as a straight conductor wire in a d.c. circuit, both appear as imaginary resistors in the a.c. circuit. Until presently, the inductive properties of the electrochemical cell are ignored so that the polymer electrolyte composite is considered only as a network of resistor and capacitor.

The complex impedance can be written in a general form as

$$Z(\omega) = Z'(\omega) - iZ''(\omega) \tag{8}$$

where  $\omega$  is the frequency,  $Z'(\omega)$  is the real part of impedance, contributed by resistive part,  $Z''(\omega)$  is the imaginary part of impedance, contributed by capacitive part, and  $i = \sqrt{-1}$ , the imaginary number.

As an illustration, Figure 8 shows examples of simple RC circuits and the corresponding plot of impedance (Nyquist plot). For a serial arrangement of a resistor and a capacitor, as displayed in Figure 8b left, the impedance can be written as

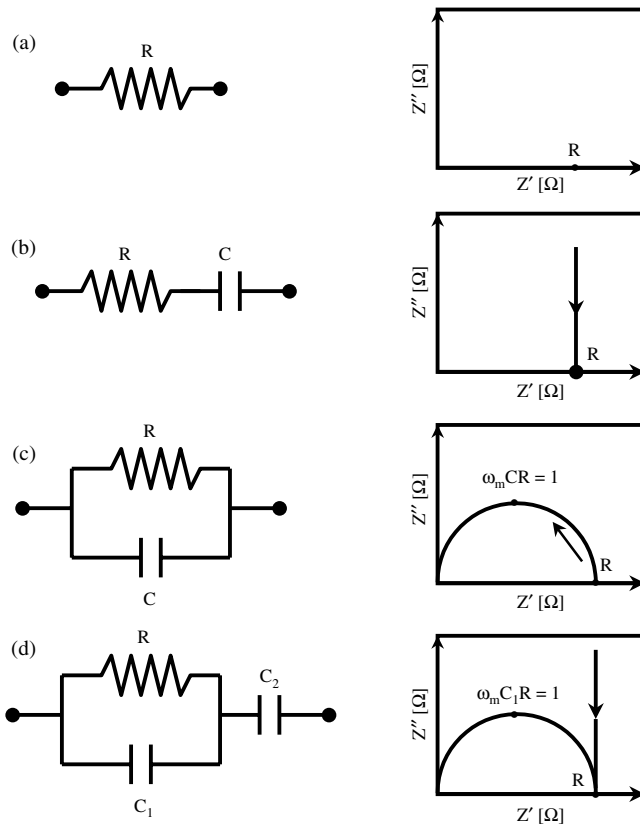
$$Z = R - \frac{i}{\omega C} \tag{9}$$

or

$$Z' = R \tag{10a}$$

$$Z'' = \frac{1}{\omega C} \tag{10b}$$

It is clear that the real part of impedance is constant, independent of the frequency, while the imaginary part depends on the frequency. For very small frequency, the imaginary part is very large and this value decreases inversely with frequency. For frequency approaches to infinity, the imaginary part of impedance closes to zero and the impedance



**Figure 8.** Examples of simple RC circuits and the corresponding impedance (Nyquist) plots.

value at this very high frequency equals to resistance. Thus the Nyquist plot for this arrangement appears as a vertical straight line, starting from a lower frequency value at the upper part downwards when the frequency increases, as shown in Figure 8b right. The intersection of this line with horizontal axis (the real value of impedance) corresponds to the resistance.

For a parallel arrangement of resistor  $R$  and capacitance  $C$ , as appears in Figure 8c left, the real and imaginary parts of the impedance are given by

$$Z' = \frac{R}{1 + (\omega RC)^2} \tag{11a}$$

and

$$Z'' = R \frac{\omega RC}{1 + (\omega RC)^2} \tag{11b}$$

and the corresponding Nyquist plot appears in Figure 8c right. The Nyquist plot appears as an arc. The intersection of this arc with the vertical axis at a low frequency (right arc) corresponds to the resistance. The frequency at the peak of the arc,  $\omega_m$ , satisfies the relation

$$\omega_m RC = 1 \tag{12}$$

From the intersection point at the low frequency region and the position of the arc peak, the resistance and the capacitance of the system can be determined.

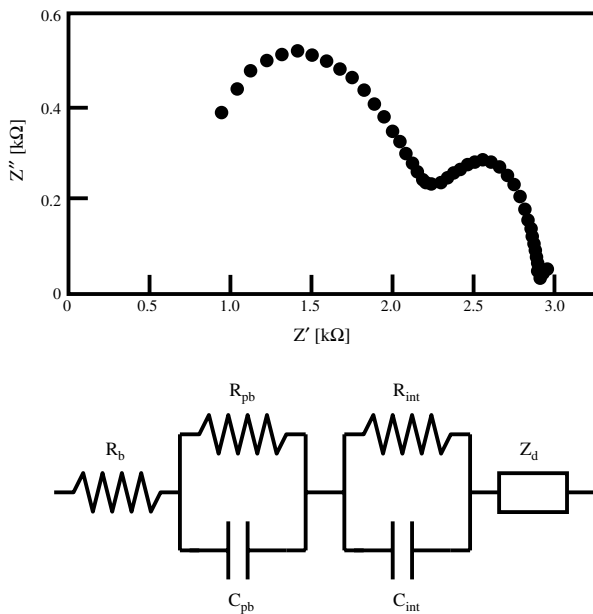
More complex arrangements, have a more complex expression for the impedance. For example, a combination of serial and parallel circuit as appears in Figure 8d left has the impedance as

$$Z = \left( \frac{1}{R} + i\omega C_1 \right)^{-1} + \frac{1}{i\omega C_2} \quad (13)$$

with the corresponding Nyquist plot appearing in Figure 8d right. It contains a vertical line that intersects the horizontal axis at  $Z' = R$ , and an arc with the peak satisfies  $\omega_m RC_1 = 1$ . Again, from these two values, one can determine  $R$  and  $C_1$ . The value of  $C_2$  is determined by measuring the vertical component of impedance at a certain frequency, say  $\omega^*$ . If the vertical component of impedance at this point is  $Z''^*$ , the value of  $C_2$  satisfies

$$Z''^* = \frac{1}{\omega^* C_2} \quad (14)$$

Sometimes, the form of curve is not as simple as that described here. However, in principle, we can find some circuit arrangement such that the theoretical Nyquist plot is in agreement with the measured data. Some computer software is commercially available for extracting the equivalent circuit for measured data. As an example, the impedance measurement of a system of PEO:LiCF<sub>3</sub>SO<sub>3</sub> containing Li<sub>1.4</sub>Al<sub>0.4</sub>Ge<sub>1.6</sub>(PO<sub>4</sub>)<sub>3</sub> fillers is displayed in Figure 9a [67]. The corresponding a.c. circuit that can produce this impedance data appears in Figure 9b, with  $R_b$  = bulk resistance,  $R_{pb}$  = phase boundary resistance,  $R_{int}$  = interfacial resistance,  $C_{pb}$  = phase boundary capacity,  $C_{int}$  = interfacial capacity,  $Z_d$  = diffusive impedance. The corresponding parameter values that can properly fit the measured data are



**Figure 9.** (Top) Impedance plot PEO:LiCF<sub>3</sub>SO<sub>3</sub> containing Li<sub>1.4</sub>Al<sub>0.4</sub>Ge<sub>1.6</sub>(PO<sub>4</sub>)<sub>3</sub> obtained from experiment. Data points were extracted from [67], C. J. Leo et al., *Solid State Ionics* 148, 159 (2002). (Bottom) The suggested RC circuit for data in (a). See text for the explanation of symbols.

$R_b = 593 \Omega$ ,  $R_{pb} = 1637 \Omega$ ,  $C_{pb} = 31 \text{ nF}$ , and  $C_{int} = 1.9 \mu\text{F}$  [67].

From the measured resistance of polymer electrolytes, the electrical conductivity can be calculated using a simple equation

$$\sigma = \frac{1}{R_e} \frac{\ell}{A} \quad (15)$$

where  $R_e$  = resistance of polymer electrolyte,  $\ell$  = material thickness (electrode spacing), and  $A$  = material cross section.

The common procedure for measuring the temperature dependence of conductivity is as follows.

- Heat the sample at a required temperature. Sometimes, it needs a half hour or more to equilibrate the sample temperature.
- Measure the impedance at all range of frequency. Sometimes, it can take from tens of mHz up to several MHz. The computerized measurement is usually performed since a great number of data should be collected for each setting temperature.
- Change the setting temperature, and again collect the impedance data in all frequency regions.
- Analyze the collected data and find the equivalent circuit.
- Determine the resistance of the electrolytes based on the impedance plot and the equivalent circuit at each setting temperature.
- Calculate the conductivity at each setting temperature.

## 6.2. a.c. Conductivity

Despite the d.c. conductivity, the a.c. conductivity sometimes gives important information such as the dielectric properties of the composites. The frequency dependence of a.c. conductivity in polymer electrolytes can be written as [38]

$$\sigma_{ac}(\omega) = \sigma_{dc} + A\omega^n \quad (16)$$

where  $\sigma_{dc}$  = d.c. conductivity,  $A$  and  $n$  are the material parameters,  $0 < n < 1$ , and  $\omega$  is an angular frequency.

The curve might consist of three regions, a spike at low frequency, followed by a plateau at medium frequency, and another spike at high frequency. The high frequency part corresponds to bulk relaxation phenomena, while the plateau region is connected to d.c. part of conductivity. The lower spike is connected to electrode/electrolyte phenomena. Fitting the curve with Eq. (16), one can determine the parameters  $A$  and  $n$ , and from those parameters, the hopping frequency [68],

$$\omega_p = \left( \frac{\sigma_{dc}}{A} \right)^{1/n} \quad (17)$$

By fitting the experimental data of  $\sigma_{ac} - \omega$ , one can determine the  $\sigma_{dc}$  and  $\omega_p$  at each temperature. Using this approach, Siekierski et al. [69] found in a system of

PEO<sub>3</sub>:LiClO<sub>4</sub> + α-Al<sub>2</sub>O<sub>3</sub>, that both  $\sigma_{dc}$  and  $\omega_p$  satisfy the Arrhenius expression

$$C = C_o \exp\left[-\frac{E}{kT}\right] \quad (18)$$

where  $C$  is either  $\sigma_{dc}$  or  $\omega_p$ , and  $C_o$  is the corresponding prefactor.

Furthermore, the temperature-dependent dielectric constant can also be obtained from the  $\sigma_{ac}$  data. The real part of the dielectric constant,  $\epsilon'$ , can be expressed as

$$\epsilon' = \frac{\sigma''_{ac}}{\omega\epsilon_o} \quad (19)$$

where  $\sigma''_{ac}$  is the imaginary part of the a.c. conductivity, and  $\epsilon_o$  is the permittivity of vacuum. The complex dielectric constant can be written as  $\epsilon(\omega) = \epsilon'(\omega) + i\epsilon''(\omega)$ , and the imaginary part can be obtained from the real part using a Kramer–Kronig relation

$$\epsilon''(\omega) = -\frac{2\omega}{\pi} P \int_0^\infty \frac{\epsilon'(s)}{s^2 - \omega^2} ds \quad (20)$$

where  $P$  denotes the principal part of the integral [70]. On the other hand, if the imaginary part has been known, the real part can be determined using a relation

$$\epsilon'(\omega) = \frac{2}{\pi} P \int_0^\infty \frac{s\epsilon''(s)}{s^2 - \omega^2} ds \quad (21)$$

### 6.3. Diffusion Coefficient

Electrical conductivity can also be determined by measuring the diffusion coefficient. From the temperature-dependent diffusion coefficient, the temperature dependence of electrical conductivity can be determined using Nerst–Einstein equation

$$\sigma = \frac{ne^2D}{kT} \quad (22)$$

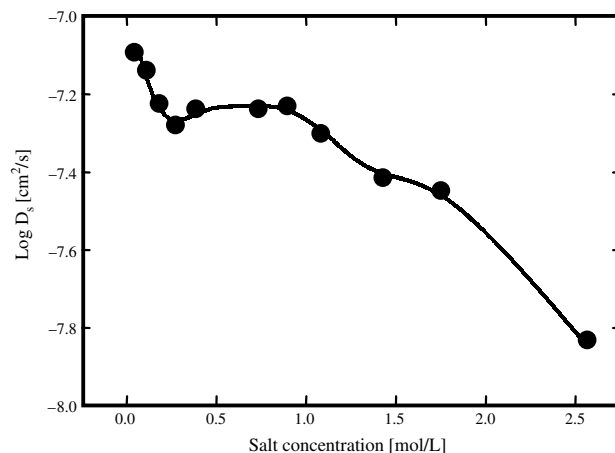
where  $n$  = charge carrier concentration  $e$  = electron charge, and  $D$  = diffusion coefficient.

Salt diffusion coefficient can be obtained by galvanostatically polarizing a symmetric cell containing no-blocking electrode for a short period of time. For example, assume a cell containing Li-based polymer electrolytes and lithium electrodes at both sides. When the current is turned off, the induced concentration profile is allowed to relax. At long time after the current interrupt, the following equation is applicable [71]:

$$\ln \Delta\Phi = \frac{\pi^2 D_s}{L^2} t + A_1 \quad (23)$$

where  $\Delta\Phi$  = measured cell potential,  $D_s$  = salt diffusion coefficient,  $L$  = electrolyte thickness,  $t$  = time, and  $A_1$  = a constant.

It appears that  $D_s$  is proportional to the slope of curve  $\ln \Delta\Phi$  with respect to  $t$ . The dependence of salt diffusion constant on the salt concentration is displayed in Figure 10 [71] for system of PEO:NaCF<sub>3</sub>SO<sub>3</sub> at 83 °C. The  $D_s$  decreases



**Figure 10.** Effect of salt concentration on the diffusion coefficient for PEO:NaCF<sub>3</sub>SO<sub>3</sub> system at 83 °C. Data points were extracted from [71], Y. Ma et al., *J. Electrochem. Soc.* 142, 1859 (1995).

as the salt concentration increases from about  $8 \times 10^{-8}$  cm s for dilute solution.

Diffusion coefficient can also be determined from the Nyquist plot as discussed by Strauss et al. [72]. The medium frequency arc is attributed to the solid/electrolyte interface. At lower frequencies, the impedance is affected by concentration gradient (diffusion) and ionic aggregates. The diffusion impedance of symmetric electrolyte with no-blocking electrode, such as Li/CPE/Li, can be written as

$$D = \frac{RTL}{n^2 F^2 C_b Z_{DC}} \quad (24)$$

where  $R$  = the gas constant,  $n$  = ratio of EO/cations,  $F$  = Faraday number,  $C_b$  = bulk concentration of cation,  $T$  = temperature, and  $L$  = electrolyte thickness.

Lorimer also introduced another formula for calculating the diffusion constant, that is [73],

$$D = \frac{\omega_m L^2}{2.54} \quad (25)$$

where  $\omega_m$  = the frequency at the maxima of low frequency arc, and  $L$  = electrolyte thickness. The values predicted by Eq. (25), however, are around 6–10 times as large as that predicted by Eq. (14). The error can be contributed by the shift of  $\omega_m$  due to the formation of ion pairs [72].

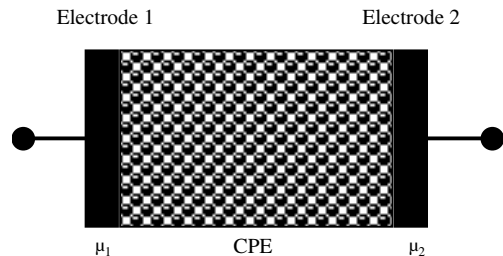
### 6.4. Transference Number

Transference number can be calculated by analyzing the arc impedance spectrum of symmetrical cell with no blocking electrode. The transference number can be calculated by comparing the width of the skew low frequency semicircle,  $Z_d$ , with the value of the bulk resistance, that is [74],

$$t_+ = \frac{1}{1 + Z_d/R_b} \quad (26)$$

Transference number can also be determined by measurement of the electrochemical potential of the cell as illustrated in Figure 11 [75]. Suppose the polymer composite is





**Figure 11.** A simple experiment for determining the transference number to electrodes with differential chemical potentials.

sandwiched between two electrodes with different chemical potential  $\mu_1$  and  $\mu_2$ . The electrochemical potential across this cell is given by

$$E = \frac{1}{|z|F} \int_{\mu_1}^{\mu_2} t_i d\mu = \frac{1}{|z|F} t_i (\mu_2 - \mu_1) \quad (27)$$

where  $|z|$  = absolute value of the valence of the mobile ion in the electrolyte; and  $F$  = Faraday number.

For pure ionic composite,  $t_i = 1$  so that

$$E_{\text{pure}} = (\mu_2 - \mu_1) |z|^{-1} F^{-1} \quad (28)$$

Thus

$$E = t_i E_{\text{pure}} \quad (29)$$

By measuring  $E$  and calculating  $E_{\text{pure}}$ , we can obtain  $t_i$ .

Another method based on a combination of d.c. polarization and a.c. impedance has been introduced by Evans et al. This method involves measuring the resistance and current across a symmetrical Li/electrolyte/Li cell polarized by a d.c. voltage [76]. The  $t^+$  is given by

$$t^+ = \frac{I_S(V - I_o R_o)}{I_o(V - I_S R_S)} \quad (30)$$

where  $V$  = d.c. voltage applied to the cell,  $R_o$  = initial resistance of the passivating layer,  $R_S$  = steady-state resistance of the passivating layer,  $I_o$  = initial current, and  $I_S$  = steady-state current.

The d.c. polarization potential usually used is several tens of millivolts. This equation is applicable for ideal, dilute solutions. However, Doyle and Newman state that although this equation is not strictly applicable in concentrated electrolytes, the ratio of steady-state to initial current provides useful information on the contribution by organic additives to the ionic conductivity of polymer electrolytes [77]. The simplification of Eq. (30) was also used, that is,  $t^+ = I_{SS}/I_o$ . However, significant errors resulted from neglect of kinetic resistances at the electrode/electrolyte interface [78]. Transference numbers of some composites appear in Table 4.

## 7. SPECTROSCOPIC CHARACTERIZATIONS

### 7.1. NMR Spectroscopy

A moving ion would substantially modify the interaction of electromagnetic waves with matter. Investigating this interaction gives a better understanding of ion dynamics on

**Table 4.** Transference number of several composites.

Composites	Transference number	Temperature	Ref.
PEO:LiCF <sub>3</sub> SO <sub>3</sub> + $\gamma$ -LiAlO <sub>2</sub> (4 $\mu$ m)	0.29	90 °C	[79]
PEO:LiBF <sub>4</sub> + $\gamma$ -LiAlO <sub>2</sub> (4 $\mu$ m)	0.26	90 °C	[79]
PEO:LiClO <sub>4</sub> + TiO <sub>2</sub> (13 nm)	0.5–0.6	90 °C	[79]
PEO:LiClO <sub>4</sub> + Al <sub>2</sub> O <sub>3</sub> (6 nm)	0.31–0.33	90 °C	[80]
(PEO) <sub>30</sub> LiClO <sub>4</sub>	0.18–0.19	100 °C	[80]
(PEO) <sub>8</sub> LiClO <sub>4</sub>	0.19–0.20	90 °C	[80]
(PEO) <sub>8</sub> LiClO <sub>4</sub> + SiO <sub>2</sub>	0.22–0.23	100 °C	[80]

a microscopic scale. An example of method for studying the ion dynamics is nuclear magnetic resonance (NMR) spectroscopy. This method probes the spin of ion using an electromagnetic wave in radio frequency. In amorphous single-phase polymer electrolytes, there is usually found a straight relationship between polymer segmental motion and ionic mobility by observing a strong correlation between the onset of NMR line-narrowing and the glass transition [81]. NMR has contributed significantly to the understanding of the physical properties of the composite polymer electrolytes mainly because it offers the possibility to selectively study the ionic and polymer chain dynamics. For example, measurement of the temperature dependence of <sup>7</sup>Li lineshapes and spin-lattice relaxation allows the determination of the activation energy and the correlation time of the cation motion. Gang et al. described the <sup>7</sup>Li line-narrowing in the composite of PEO:LiBF<sub>4</sub> +  $\gamma$ -LiAlO<sub>2</sub> (10–30 wt%) in the temperature range of 270–270 K [82]. Dai et al. reported wide line and high resolution solid-state <sup>7</sup>Li NMR [83].

In material, each spin interacts with other spins, giving rise to spin-spin interaction or relaxation time  $T_2$ . Furthermore, a new thermal equilibrium distribution of the spin, which has to be mediated through lattice, is forced by the magnetic field. The characterization time required for the excess energy to be given to the lattice or for attainment of new thermal equilibrium is expressed in terms of spin-lattice or thermal relaxation time  $T_1$ . Under simultaneous application of static and radio frequency magnetic field in perpendicular direction,

$$H_z = H_o \quad (31a)$$

$$H_x = 2H_1 \cos \omega t \quad (31b)$$

The interaction of this magnetic field with the nuclear spin results in the Bloch susceptibility [84]

$$\chi' = \frac{1}{2} \chi_o \omega_o T_2 \frac{T_2(\omega_o - \omega)}{1 + T_2^3(\omega_o - \omega)^2 + \gamma^2 H_1^2 T_1 T_2} \quad (32a)$$

$$\chi'' = \frac{1}{2} \chi_o \omega_o T_2 \frac{1}{1 + T_2^2(\omega_o - \omega)^2 + \gamma^2 H_1^2 T_1 T_2} \quad (32b)$$

where  $\omega_o = \gamma H_o$ , and  $\gamma$  is the gyromagnetic ratio of the spin. For low RF field  $H_1$ ,  $\gamma^2 H_1^2 T_1 T_2 \ll 1$ , then Eqs. (32a) and (32b) give the familiar absorption curve with half-width

$$\Delta\omega = \omega_o - \omega \cong 1/T_2 \quad (33)$$

However, the exact lineshape and linewidth can be determined using Van Vleck method of moment. This method

allows the connection of the absorption line with the motional behavior of the nuclei. The second moment,  $M_2$  is given by

$$M_2 = \int_{-\infty}^{\infty} (\omega - \omega_o)^2 f(\omega) d\omega$$

$$= \frac{3}{4} \gamma^4 \hbar^2 I(I+1) \sum \frac{(1 - 3 \cos \theta_{ij})^2}{r_{ij}^6} \quad (34)$$

where  $I$  is the nuclear spin [85].

Nuclear spin and NMR frequencies of some nuclei at  $H_o = 10,000$  Gauss are given in Table 5 [86]. Based on this data, we can select the magnetic field  $H_o$  at around 10,000 Gauss (1 Tesla) and frequency  $\omega_o$  of around 16.574 MHz, so that the absorption of the target spin can be observed. For example, in order to detect the absorption of lithium ion in the lithium-based polymer electrolyte, the magnetic field  $H_o$  can be set at around 16,574 Gauss.

If the spins are in motion, such as in fluid or intramolecular motion of liquid-like lattice, the value of  $M_2$  is small because of the small time-average local field component (the average of  $\cos^2 \theta_{ij} = 1/3$ ). The linewidth decreases as

$$(\omega - \omega_o) \propto M_2^{1/2} \quad (35)$$

If  $\tau_c$  is the fluctuation time,  $M_2^{1/2} \tau_c \ll 1$  corresponds to rigid lattice and motional narrowing corresponds to  $M_2^{1/2} \tau_c \gg 1$ . The region with  $1/\tau_c$  approximate to  $M_2^{1/2}$  represents, the region of the onset of motional narrowing. Motional narrowing is used to study the ionic motion. Considerable line-narrowing takes place above a certain temperature, indicating diffusional motion.

A rough estimation of the activation energy for motion can be obtained by using a modified Bloembergen, Purcell, and Pound expression [87]:

$$\nu_c = \frac{1}{\tau_c} = \frac{\alpha \gamma \Delta \omega}{\tan \left[ \frac{\pi}{2} \left( \frac{\Delta \omega^2 - B^2}{A^2 - B^2} \right) \right]} \quad (36)$$

where  $\nu_c$  = jump frequency,  $\Delta \omega$  = measured linewidth at temperature  $T$ ,  $A$  = unnarrowed linewidth of the rigid lattice,  $B$  = fully narrowed linewidth, and  $\alpha$  is a constant.

**Table 5.** Nuclear spin and resonance frequency at 10,000 Gauss of several nuclei.

Nuclei	Nuclear spin	Magnetic resonance frequency (MHz) at 10,000 Gauss
<sup>1</sup> H	1/2	42,577
<sup>6</sup> Li	1	6,265
<sup>7</sup> Li	3/2	16,574
<sup>17</sup> O	5/2	5,72
<sup>19</sup> F	1/2	40,055
<sup>23</sup> Na	3/2	11,262
<sup>39</sup> K	3/2	1,987
<sup>41</sup> K	3/2	1,092
<sup>63</sup> Cu	3/2	11,285
<sup>65</sup> Cu	3/2	12,090
<sup>107</sup> Ag	1/2	1,220
<sup>109</sup> Ag	1/2	1,981

Fitting  $\nu_c/\alpha$  with Arrhenius expression,

$$\frac{\nu_c}{\alpha} = \frac{\nu_o}{\alpha} \exp \left[ -\frac{\Delta E}{kT} \right] \quad (37)$$

one obtains the value of  $\Delta E$  based on the Arrhenius plot of  $\nu_c/\alpha$ .

Another expression for determining the activation energy is given by Hendrickson and Bray [88]:

$$\ln \left( \frac{1}{\Delta \omega - D} - \frac{1}{A} \right) = -\frac{\Delta E}{kT} + \ln \left( \frac{1}{B} - \frac{1}{A} \right) \quad (38)$$

where  $D$  is a temperature-independent constant of a line-broadening term.

The relation between spin-lattice relaxation time  $T_1$  and the fluctuation time  $\tau_c$  can be written as [89]

$$\frac{1}{T_1} = S \left( \frac{\tau_c}{1 + \omega_o^2 \tau_c^2} + \frac{4\tau_c}{1 + 4\omega_o^2 \tau_c^2} \right) \quad (39)$$

where  $S$  is a constant. For an approximate case, in which relaxation from a pair of nuclei of fixed internuclear spacing  $r$  only is considered, one obtains [90]

$$S = \left( \frac{2}{5r^6} \right) \gamma^4 \hbar^2 I(I+1) \quad (40)$$

The spin-spin relaxation time  $T_2$  is given by [87]

$$\frac{1}{T_2} = S \left( \frac{5}{2} \frac{\tau_c}{1 + \omega_o^2 \tau_c^2} + \frac{\tau_c}{1 + 4\omega_o^2 \tau_c^2} + \frac{3}{2} \tau_c \right) \quad (41)$$

To study dynamics, the relaxation time is measured as a function of temperature so that  $\tau_c$  can be calculated. Using an Arrhenius relation

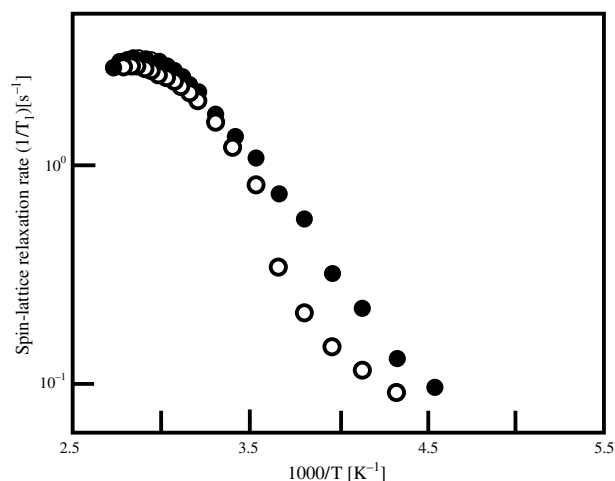
$$\tau_c = \tau_o \exp(\Delta E/kT) \quad (42)$$

the activation energy can be calculated.

Many NMR experiments have been performed on polymer electrolyte nanocomposites [91–95]. Figure 12 shows the Arrhenius plot of spin-lattice relaxation time for PEO<sub>8</sub>:LiClO<sub>4</sub> polymer electrolytes and the composite prepared with 5.3 wt.%  $\gamma$ -Al<sub>2</sub>O<sub>3</sub> detected at a Larmor frequency of  $\omega_o = 155.4$  MHz [96]. The attempt frequency  $1/\tau_o$  can be interpreted as a vibrational frequency, of order of optical phonon frequency ( $10^{12}$ – $10^{13}$  Hz). It can be calculated (e.g., using Mathematica software) that the function  $1/T_1$  finds a maximum value at  $\omega_o \tau_c = 0.613$ . The maximum value of  $1/T_1$  appears at temperature of  $T \cong 330$  K for both samples. Using a Larmor frequency of  $\omega_o = 155.4$  MHz, one obtains  $\tau_c = 0.613/(1.554 \times 10^8) = 3.94 \times 10^{-9}$  s. For composite of PEO:LiClO<sub>4</sub> + carbon black, Franco et al. estimated the relation time of about  $4.4 \times 10^{-9}$  s based on the <sup>1</sup>H resonance measurement [97]. Using Eq. (42) and assuming  $1/\tau_o \cong 10^{12}$ , we have  $\Delta E \cong 0.24$  eV for both samples.

The electrical conductivity can be determined from Eq. (42) and different form of Nernst–Einstein equation, that is,

$$\sigma = \frac{Nd^2 q^2}{6\tau_c kT} \quad (43)$$



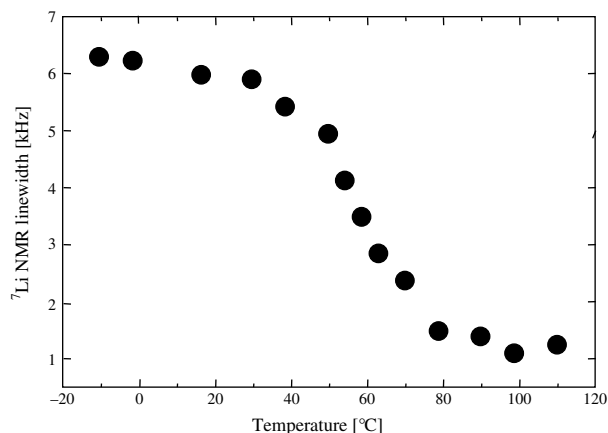
**Figure 12.** Arrhenius plot of spin-lattice relaxation time ( $1/T_1$ ) of  $^7\text{Li}$  NMR spectra for (open circle) PEO: $\text{LiClO}_4$  and (solid circle) PEO: $\text{LiClO}_4$  containing carbon black. Data points were extracted from [96], A. C. Bloise et al., *Electrochim. Acta* 46, 1571 (2001).

where  $N$  = lithium concentration per unit volume,  $d$  = average ionic jump distance, and  $q$  = ionic charge.

For example, the value of  $N$  in  $\text{PEO}_8:\text{LiClO}_4$  was determined from the molecular weights of PEO and  $\text{LiClO}_4$  and the density of the electrolytes ( $\rho \approx 1.3 \text{ g/cm}^3$ ) [96], to result in  $N \approx 1.7 \times 10^{21} \text{ cm}^{-3}$ . Considering the average Li-Li distance of  $\sim 4 \text{ \AA}$  [96], the conductivity at 300 K is about  $7.1 \times 10^{-4} \text{ S/cm}$ .

Temperature-dependent linewidth of composite of  $\text{PO}_{1.5}\text{LiI} + 6 \text{ v\% Al}_2\text{O}_3$  is displayed in Figure 13 [83]. It can be seen that there is a drastic change in the line-width when temperature is changed from 30 °C to 50 °C. It is assumed that the onset of the motional narrowing is at temperature of 40 °C. At  $-20$  °C the sample exhibits a rigid limit lineshape with baseline due to a distribution of  $^7\text{Li}$  nuclear quadrupole satellite transition [98]. As the temperature is raised, partial line-narrowing results.

Forsyth et al. reported the effect of filler content on the  $^7\text{Li}$  linewidth for a composite of copolymer trihydroxypoly(ethylene oxide-co-propylene oxide) with an EO/PO



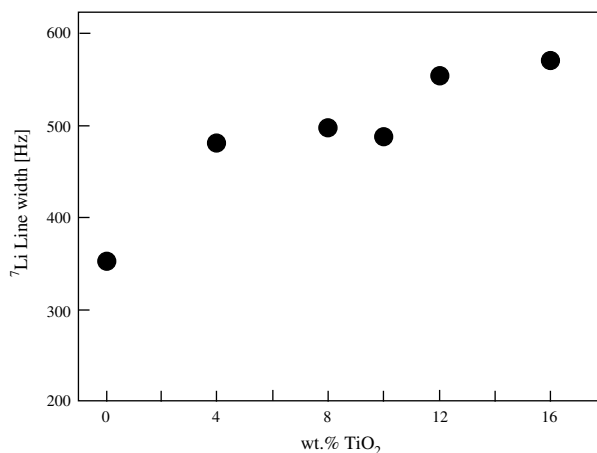
**Figure 13.** Temperature dependence of  $^7\text{Li}$  NMR linewidth of  $\text{PEO}_{1.5}\text{LiI}$  containing 6 vol.%  $\text{Al}_2\text{O}_3$ . Data points were extracted from [83], Y. Dai et al., *Electrochim. Acta* 43, 1557 (1998).

ratio of 3:1 containing  $\text{LiClO}_4$  and  $\text{TiO}_2$  nanoparticles [99]. The linewidth increases with increase in the filler content and reaches a plateau after about 10 wt.%, as observed in Figure 14. Although the linewidth relates to the mobility of lithium ion, in which the line-narrowing represents mobile ion, an interpretation that the increase of linewidth relates to decrease in the mobility of lithium ions will be contradictory with the reported result. The reported result confirmed that addition of filler at lower content increases the lithium ion mobility and therefore increases the conductivity. A possible interpretation is the lithium ion environment changes with the addition of filler and the linewidth changes are more likely to reflect the changing environment rather than the changing mobility. A possible interpretation is chemical shift dispersion, that is, lithium ion occupying many different state environments (but magnetically degenerate) such that a distribution of chemical shift is obtained.

The broad signal of resonance is attributed to crystalline state, while the narrow component is attributed to amorphous phase. This difference contribution can be used to predict the crystallinity of polymer in composite. For example, Singh et al. observed the  $^1\text{H}$  resonance of a system of  $\text{PEG}_{46}:\text{LiClO}_4 +$  nanoparticles of  $\text{Mn}_{0.03}\text{Zn}_{0.97}\text{Al}_2\text{O}_4$  [95]. They fitted the broad part of the signal with a Gaussian function and the narrow component with the Lorentzian function. The crystallinity of the polymer equals to the fraction of the area of narrow and broad components of the signal. For pure PEG they found a crystalline of about 83% using this method.

## 7.2. Raman Scattering

Raman spectroscopy is important to probe molecules with anisotropic polarizability. The vibrating atoms are not able to follow the incident radiation frequency if it is much higher than the phonon frequency. However, the electron cloud of the vibrating atom can interact with the frequency of the incident radiation. These oscillating dipoles can absorb energy from the radiation field and re-emit radiation of the same frequency. This radiation is detected as scattered light



**Figure 14.** Effect of filler weight fraction on the  $^7\text{Li}$  NMR linewidth of copolymer of trihydroxypoly(EO-co-PO) with (EO/PO = 3/1) containing  $\text{LiClO}_4$  and  $\text{TiO}_2$  nanoparticles. Data points were extracted from [99], M. Forsyth et al., *Solid State Ionics* 147, 203 (2002).

and is known as Rayleigh scattering. Moreover, the oscillating dipoles see the force field of the vibrating atomic nuclei also as the nuclei oscillate around the equilibrium position; the deformability of the electron cloud varies with the oscillation frequency of the nuclei.

The Raman scattering is described in a simple term here. If a time-dependent electric field,  $E(t)$ , is applied to a molecule, it produces an induced dipole moment,  $\mu(t)$ ,

$$\mu(t) = \alpha(t)E(t) \quad (44)$$

where  $\alpha(t)$  is the polarizability of molecule. If the incident frequency and the polarizability of the molecule change between  $\alpha_{\min}$  and  $\alpha_{\max}$  of frequency  $\omega_{\text{int}}$  as a result of its rotation and vibration, we can write [100]

$$\mu(t) = \left( \alpha + \frac{1}{2} \Delta\alpha \cos \omega_{\text{int}} t \right) E_o \cos \omega t \quad (45)$$

with

$$\Delta\alpha = \alpha_{\max} - \alpha_{\min} \quad (46)$$

Therefore, we obtain,

$$\begin{aligned} \mu(t) = & \alpha E_o \cos \omega t + \frac{1}{2} \Delta\alpha E_o \\ & \times [\cos(\omega + \omega_{\text{int}})t + \cos(\omega - \omega_{\text{int}})t] \end{aligned} \quad (47)$$

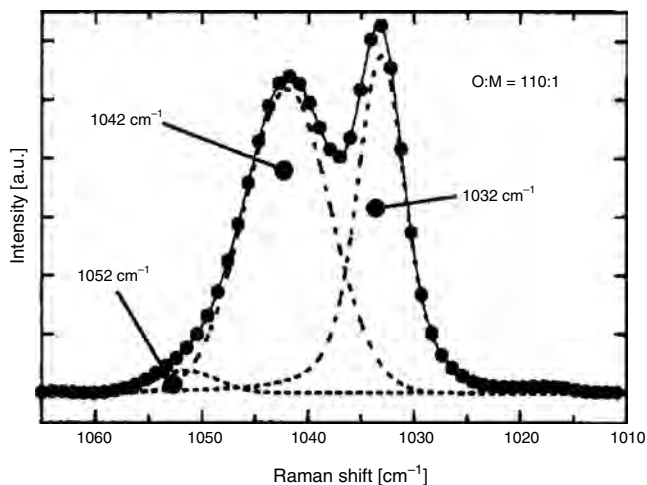
The induced dipole moment has then components as follows: unshifted frequency,  $\omega$ , known as Rayleigh line; lower frequency,  $\omega - \omega_{\text{int}}$ , known as Stokes line; and higher frequency,  $\omega + \omega_{\text{int}}$ , known as anti-Stokes line.

Raman spectra can be used to determine the concentration of free ions in the electrolytes. For example, the Raman spectra of  $\text{LiCF}_3\text{SO}_3$  have been tabulated as appear in Table 6 [101]. A composite containing  $\text{SO}_3$ , the Raman spectrum of the  $\nu_s(\text{SO}_3)$  spectral region of the triflate anion of poly(ethylene oxide) dimethyl ether (400) complexed with  $\text{LiCF}_3\text{SO}_3$ , along with the three-component curves fit are shown in Figure 15. It was explained that the component observed at  $1032 \text{ cm}^{-1}$  corresponds to free anions not interacting directly with lithium cations. The component of  $1042 \text{ cm}^{-1}$  has been attributed to contact pair and the component of  $1052 \text{ cm}^{-1}$  has been attributed to  $\text{Li}_2\text{CF}_3\text{SO}_3$  triple ions [102].

Because of the multicomponent nature of the spectrum, it can be concluded that the ion-ion interaction is present in

**Table 6.**  $\text{LiCF}_3\text{SO}_3$  vibrational assignments.

Band	Wavenumber ( $\text{cm}^{-1}$ )	Assignment
$\nu_s(\text{SO}_3)$	1033	free ion
	1043	monodenate ion pairs, $\text{LiX}$ , also $\text{LiX}_2^-$ and $\text{LiX}_3^{2-}$
	1053	$\text{Li}_2\text{X}^+$ aggregate
	1062	$\text{LiX}_3^{2-}$
$\nu_{\text{as}}(\text{SO}_3)$	1272	free ion
	1257, 1302	monodenate ion pairs, $\text{LiX}$ , also $\text{LiX}_2^-$ , $\text{LiX}_3^{2-}$
	1270, 1308	$\text{Li}_2\text{X}^+$ aggregate
	1288	$\text{Li}_3\text{X}^{2+}$ aggregate



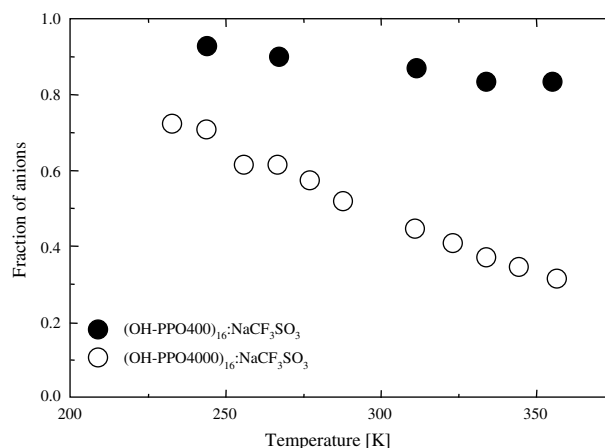
**Figure 15.** Raman spectra of  $\text{LiCF}_3\text{SO}_3$ . Reprinted with permission from [102], A. Ferry et al., *Electrochim. Acta.* 43, 1471 (1998). © 1998, Elsevier Science.

the system even down to the concentration of O:M = 563:1. The relative amount of anions not interacting directly with lithium ions, that is, spectroscopically free, increases with increasing concentration from approximately 22% at O:M 563:1 to 40% at O:M = 110 and then falls off slightly at higher concentration. The  $1042 \text{ cm}^{-1}$  band initially decreases in relative intensity with increasing concentration and then levels off at 54% in the upper concentration range.

The fraction of free ion obtained from Raman spectra in a system of PPO: $\text{NaCF}_3\text{SO}_3$  is displayed in Figure 16 [103], for a system of hydroxyl end capped PPO with  $\text{NaCF}_3\text{SO}_3$ .

### 7.3. FTIR Spectroscopy

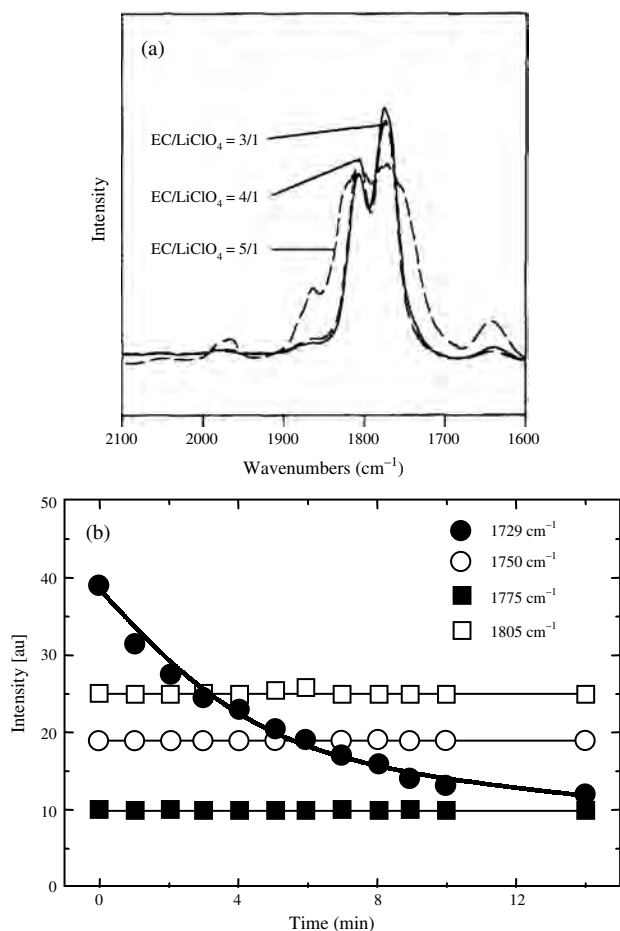
Atoms in solid vibrate at frequency approximately  $10^{12}$ – $10^{13}$  Hz. Vibration mode involving pairs of groups of bonded atoms can be excited to higher energy by absorption of radiation at appropriate frequency. In the infrared (IR) technology, the frequency at the incident radiation is varied and the



**Figure 16.** Effect of temperature on the fraction of anions obtained from the Raman spectrometry. Data points were extracted from [103], H. Ericson et al., *Electrochim. Acta* 43, 1401 (1998).

quantity of radiation absorption or transmission by sample is observed. In the Raman technique, on the other hand, the sample is illuminated with monochromatic light, usually generated by a laser. In order for a particular mode to be IR active, the associated dipole moment must vary during the vibrational cycle. Therefore, centrosymmetric vibrational modes are IR inactive. The principal selection rule for a vibrational mode to be Raman active is that the nuclear motions involved must produce a change in polarizability.

*In-situ* FTIR spectroscopy can also be used to determine the conductivity of ion in composites. For example, a system of poly(methyl methacrylate-co-alkali metal methacrylate)-ethylene carbonate:LiClO<sub>4</sub> is displayed in Figure 17a. A typical spectrum of carbonyl stretches region to appear in four peaks at 1730 cm<sup>-1</sup>, 1751 cm<sup>-1</sup>, 1775 cm<sup>-1</sup>, and 1806 cm<sup>-1</sup> [104]. The evolution of carbonyl peak was observed with time under the application of d.c. field such that the ion transport in the composite is shown in Figure 17b [104]. The change in the intensity of carbonyl group in the ethylene carbonate represents the different chemical environments within the composites. The intensities of the peak at 1730 cm<sup>-1</sup>, 1775 cm<sup>-1</sup>, and 1806 cm<sup>-1</sup> were found to be fairly



**Figure 17.** (a) IR spectra of poly(methyl methacrylate-co-alkali metal methacrylate)-ethylene carbonate:LiClO<sub>4</sub> and (b) the decay of the observed peaks when the applied d.c. potential was switched off. Data points we extracted from [104], C. H. Kim et al., *Electrochim. Acta* 43, 1421 (1998).

constant with time under the electric field. It indicated that these three peaks might not be correlated with movement of charge carriers. However, the intensity of the 1750 cm<sup>-1</sup> peak decreased with the time, eventually reaching a limit value. The decrease in the intensity of the 1750 cm<sup>-1</sup> peak related to the change in the concentration of the plasticizer solvating the salt. The change in the peak intensity corresponding to various chemical environments is due to the migration of the charge carrier. The concentration of the plasticizer to solvate the salt was found to decrease, which implies that the movement of cations in the electrolytes is strongly correlated with the motion of the plasticizers.

The change in the peak intensity of the plasticizer solvating salt can be analyzed solving the following transport equation [104]:

$$\frac{\partial C}{\partial t} = D \frac{\partial^2 C}{\partial x^2} - \mu E \frac{\partial C}{\partial x} \quad (48)$$

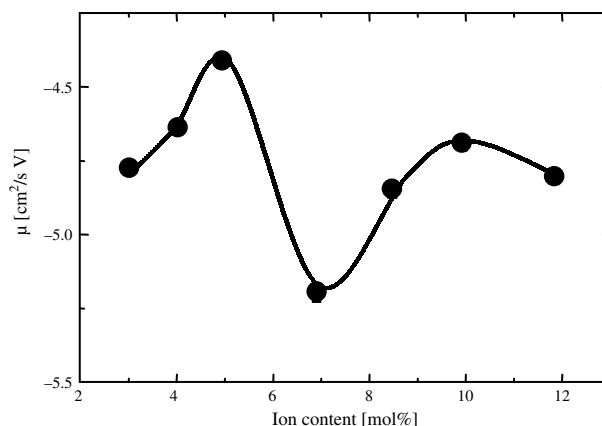
where  $C$  = concentration of charge carriers, represented by the intensity of the 1750 cm<sup>-1</sup> peak,  $D$  = diffusion coefficient,  $\mu$  = mobility of the charge carriers, and  $E$  = electric field.

The solution of Eq. (48) at a fixed position,  $x = 0$ , can be expressed as

$$C(x = 0, t) = A + B \exp\left[-\frac{(\mu E)^2}{4D} t\right] \quad (49)$$

where  $A$  and  $B$  are constants. From the slope of curve intensity of 1750 cm<sup>-1</sup> peak, one can determine the mobility of the ion carriers. Measuring the mobility at various ion concentrations, we can determine the mobility at various ion concentrations as appears in Figure 18 [104].

The ion movement can also be analyzed based on the change in the intensity of 624 cm<sup>-1</sup>, arising from ClO<sub>4</sub><sup>-</sup> stretching band [105]. Kim et al. showed the dependence of 624 cm<sup>-1</sup> intensity on time at 25 °C and found that the mobility calculated from that data is similar to that obtained from the 1750 cm<sup>-1</sup> absorption of ethylene carbonate [104]. The change of anionic mobility with the ion content of ionomers was found to be nearly the same as that of cation mobility.



**Figure 18.** The effect of ion content on the mobility of poly(methyl methacrylate-co-alkali metal methacrylate)-ethylene carbonate:LiClO<sub>4</sub> determined from the decay curve of 1729 cm<sup>-1</sup> peak. Data points we extracted from [104], C. H. Kim et al., *Electrochim. Acta* 43, 1421 (1998).

For the infrared spectra of PEG:LiClO<sub>4</sub>:AlBr<sub>3</sub> 1 mass%, the  $\nu_4(\text{ClO}_4^-)$  spectra can be separated into two contributions with maxima at 623 and 633 cm<sup>-1</sup> [106]. The 623 cm<sup>-1</sup> band is attributed to free anions and the 633 cm<sup>-1</sup> peak is related to bound or contact (ClO<sub>4</sub><sup>-</sup>) [107]. The fraction of free anions can be calculated as the fraction of area under 623 cm<sup>-1</sup> mode to the total area of  $\nu_4(\text{ClO}_4^-)$  envelope. Compared to composite in the absence of AlBr<sub>3</sub>, there is a dramatic increase in the fraction of free anions when AlBr<sub>3</sub> is dispersed in the electrolytes.

#### 7.4. X-ray Photoelectron Spectroscopy

X-ray photoelectron spectroscopy (XPS) is a powerful technique for studying the surface of solids. The data obtained using this technique are mainly used to extract the information regarding the bonding energies of various core-level electrons from different elements of solid materials. These values are then interpreted as the bonding between the element under consideration with their neighbor. Information about the local structure and interaction of an element with its neighbor can be extracted from the XPS data [108]. In the development of battery, the interaction between the electrolyte and the electrode determines the performance of the battery. Understanding this interaction is important to optimize the preparation parameters for realizing high-performance batteries. Therefore, surface studies, for example using XPS, may be of great significance to understand the interaction of polymer electrolytes with electrode.

In principle, this technique measures the kinetic energy of electrons that are emitted from matter as a consequence of bombardment with ionizing radiation or high-energy particles. If the process results in an ionization of electrons from the bombarded material, the kinetic energy of the electron will satisfy

$$E_k = h\nu - E_b \quad (50)$$

where  $h\nu$  = energy of incident radiation, and  $E_b$  = binding energy of electron.

For a given atom, a range of  $E_b$  values is possible corresponding to ionization of electrons from different inner and outer valence shells. Measurement of the value of  $E_k$ , and therefore  $E_b$ , provides a means of identification of atoms. In the XPS method, the ionizing radiation is usually MgK $\alpha$  (1254 eV) or AlK $\alpha$  (1487 eV) monochromatic radiation.

Using XPS method, Vosshage and Chowdary investigated the interaction of salt with the polymer chain in the systems of PEO<sub>*n*</sub>LiCF<sub>3</sub>SO<sub>3</sub> and PEO<sub>*n*</sub>Cu(CF<sub>3</sub>SO<sub>3</sub>)<sub>2</sub> [108]. There is evidence of the interaction of the carbon from -CH<sub>2</sub>-CH<sub>2</sub>-O- polymer chains with the cation of the salt through the ether oxygen of PEO and anion of the salt. A complex between the action of the salt and the oxygen of the PEO is identified using this method. It is also observed that for the PEO<sub>*n*</sub>Cu(CF<sub>3</sub>SO<sub>3</sub>)<sub>2</sub> system, the change in the nature of the complex occurs at low salt concentrations. However, for PEO<sub>*n*</sub>LiCF<sub>3</sub>SO<sub>3</sub> system, such a change is identified at higher salt concentration.

Liu et al. prepared polymer electrolyte nanocomposites using SiO<sub>2</sub> filler and 2-[methoxy(polyethylenoxy)-propyl] trimethoxy silane coated SiO<sub>2</sub> [109]. The XPS method has

been utilized to confirm the success of coating. During treatment with 2-[methoxy(polyethylenoxy)-propyl] trimethoxy silane, the OH- groups of the surface of the SiO<sub>2</sub> react with partially hydrolyzed silane. For the untreated SiO<sub>2</sub>, the XPS data can be fitted by band centering at 284.6 eV, which is often characteristic of adventitious CH<sub>2</sub> species in the measurement chamber. On the other hand, the coated SiO<sub>2</sub> can be fitted with two bands, centered at 284.6 eV and 286.2 eV. The former corresponds to the adventitious CH<sub>2</sub> species while the latter corresponds to C-O-C group that appears as a result of the functionalization reaction.

#### 7.5. X-ray Diffraction

X-rays are electromagnetic radiation with a wavelength around 1 Å (10<sup>-10</sup> m). The X-rays which are used in almost all diffraction experiments are produced by accelerating an electron beam through 30000 V and permitting it to strike a metal target, such as copper. The incident electron has sufficient energy to ionize some of the copper 1s (K shell) electrons. An electron in an outer orbital (2*p* or 3*p*) immediately drops down to occupy the vacant 1s level and the energy released in the transition appears as X-radiation. The transition energies have fixed values and so create the spectra of characteristic X-radiation. For copper, the 2*p* → 1s transition, called K $\alpha$ , has a wavelength of 1.5418 Å and the 3*p* → 1s transition, K $\beta$ , has a wavelength of 1.3922 Å.

If the average crystalline size is below a critical limit (~200 nm diameter), a broadening of diffraction X-ray beam occurs [110]. The commonly accepted formula for particle size broadening is the Scheerer formula

$$d = \frac{0.9\lambda}{B \cos \theta_B} \quad (51)$$

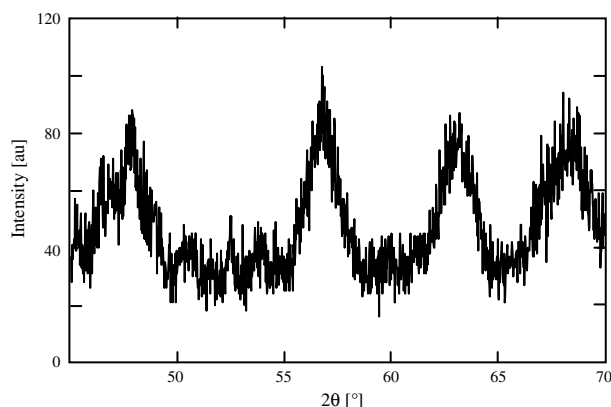
where  $d$  = crystalline radius,  $\lambda$  = X-ray wavelength,  $\theta_B$  = Bragg angle,  $B$  = the line-broadening, given by Warren formula

$$B^2 = B_M^2 - B_S^2 \quad (52)$$

where  $B_M$  = measured peak width in radiation at half peak height,  $B_S$  = width of a peak of a standard material mixed with the sample, whose particle size is considerably greater than 200 nm and which has a diffraction peak near the relevant peak of the sample. For relatively large particle, the width of peak (unbroadened peak) is very small, so that  $B_M \gg B_S$ . Therefore, it is often possible to approximate  $B$  with  $B_M$ .

Figure 19 shows the XRD spectra of polyethylene glycol-based polymer electrolyte nanocomposites containing ZnO nanoparticles [62]. Using  $\langle 110 \rangle$  with a position at around  $2\theta_B \cong 56.7^\circ$ , and the width of the peak of around  $\Delta(2\theta_B) \cong 1.25^\circ$ , we obtain  $\theta_B \cong 0.5$  rad and  $\Delta\theta_B \cong 0.022$  rad. Thus the predicted nanoparticle size is around  $d \cong 7.2$  nm.

The degree of crystallinity of polymer can be determined also by wide-angle X-ray scattering (WAXS). Figure 20 illustrates the XRD spectra of polymer, where the relatively sharp peaks are due to scattering from the crystalline regions and the broad underlying hump is due to scattering from noncrystalline region. The degree of crystallinity can be predicted based on the measurement of the area under the sharp peak ( $A_c$ ) and the broad hump ( $A_a$ ) and using a



**Figure 19.** XRD pattern of PEG containing Li ions and ZnO nanoparticles. Data were extracted from [62], Mikrajuddin et al., *J. Electrochem. Soc.* 149, H107 (2002).

simple equation

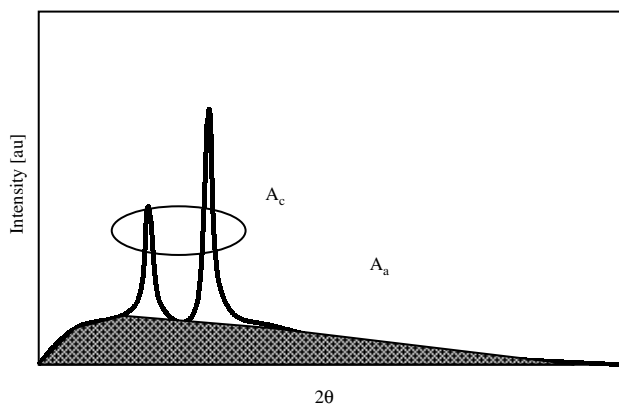
$$x_c = \frac{A_c}{A_c + A_a} \quad (53)$$

Shin et al. observed the effect of filler content on the XRD pattern on PEO in a system of  $\text{PEO}_{10}\text{LiCF}_3\text{SO}_3$  containing  $\text{Ti}_n\text{O}_{2n-1}$ . As observed in Figure 21, the PEO peak intensities decrease by the increase in the volume fraction of filler content [111]. It indicates that the crystallinity of the sample decreases by increasing the volume fraction of filler content. Similar results have also been reported by Leo et al. in a system of  $\text{PEO}:\text{LiCF}_3\text{SO}_3$  containing filler of  $\text{Li}_{1.4}(\text{Al}_{0.4}\text{Ge}_{1.6})(\text{PO}_4)_3$  [112]. With addition of filler, the intensity of the crystalline peaks has decreased and a noticeable broadening of the area under the peak was observed. It is a clear indication of the reduction of the crystallinity of the polymer.

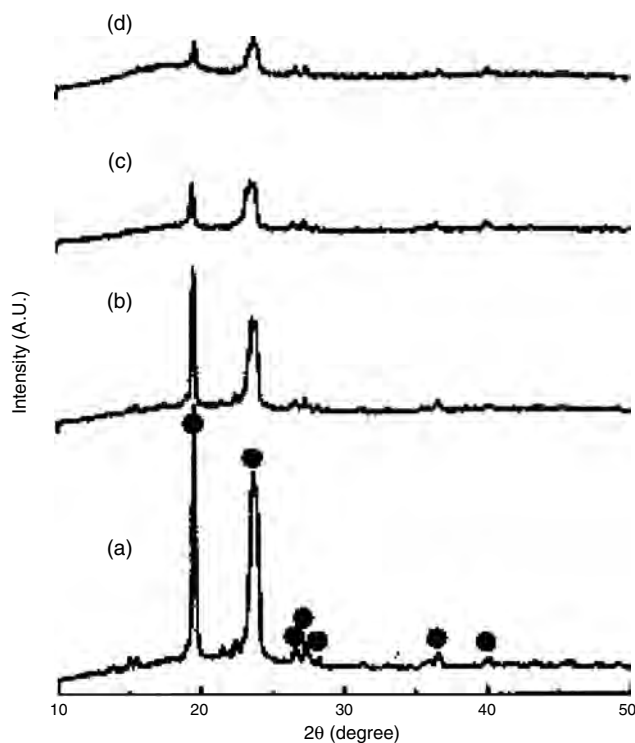
## 8. MICROSCOPIC ANALYSIS

### 8.1. Scanning Electron Microscopy

The morphology of the sample surface can be observed using scanning electron microscopy (SEM). The surface smoothness and the presence of holes in the scale down to

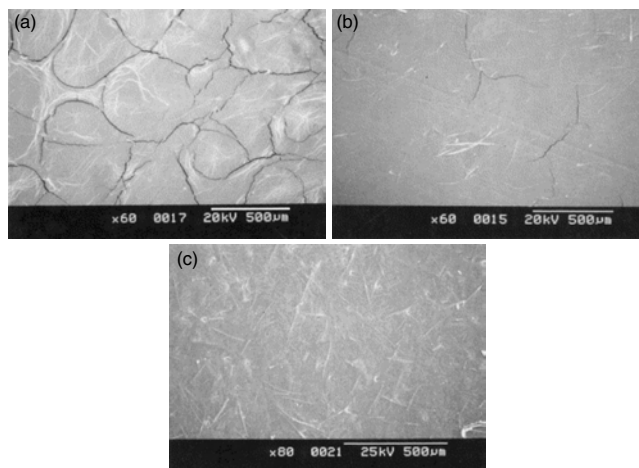


**Figure 20.** Typical form of XRD pattern of high molecular weight polymer.



**Figure 21.** XRD patterns of  $\text{PEO}_{10}\text{LiCF}_3\text{SO}_3$  polymer electrolytes with (a) 0, (b) 5, (c) 10, and (d) 15 wt.%  $\text{Ti}_n\text{O}_{2n-1}$ . (●, crystalline of PEO). Reprinted with permission from [111], J. H. Shin et al., *Mater. Sci. Eng. B* 95, 148 (2002). © 2002, Elsevier Ltd.

several tens of nanometers can be viewed using the advanced field emission SEM. Wen et al. compared the SEM picture of  $\text{PEO}:\text{LiClO}_4$  and  $\text{PEO}:\text{LiClO}_4$  containing alumina whisker. For  $\text{PEO}:\text{LiClO}_4$ , great amounts of microcracks were observed on the surface, as observed in Figure 22a [113]. The size of islands are several micrometers, compared to the PEO spherulite [114]. Addition of 10 wt.%



**Figure 22.** SEM photograph of (a)  $\text{PEO}:\text{LiClO}_4$ , (b)  $\text{PEO}:\text{LiClO}_4$  containing 10 wt.% whisker, and (c)  $\text{PEO}:\text{LiClO}_4$  containing 20 wt.% whisker. Reprinted with permission from [113], Z. Wen et al., *Solid State Ionics* 148, 185 (2002). © 2002, Elsevier Ltd.

whisker in the polymer electrolytes inhibited the formation of microcracks inside the composite polymer electrolytes (Fig. 22b). Further addition of the amount of the whisker, for example 20 wt.%, is more effective in avoiding the formation of microcracks (Fig. 22c).

Golodnitsky et al. observed the SEM picture of filler-free PEO<sub>n</sub>:LiI and PEO<sub>n</sub>:LiI containing alumina [115]. PEO<sub>n</sub>:LiI containing high concentration salt is made up of units whose area is hundreds of square microns. Addition of alumina causes a minor reduction in the grain size. In a PVdF gel polymer electrolyte containing CuO filler, Wang and Gu found that the surface presented a multitude of PVdF grains and pores of average size of about 2–4 μm in diameter [116]. They assumed the CuO nanoparticles distributed uniformly in the polymer matrix.

### 8.2. Transmission Electron Microscopy

In the case of polymer electrolyte nanocomposites, transmission electron microscopy (TEM) is usually used for determining the dispersion of nanoparticles in the polymer matrix and the size of nanoparticles. Capiglia et al. showed that larger filler (submicron size) is quite well dispersed in the polymer matrix while the smaller filler (tens of nanometers size) is not well distributed in the polymer matrix [61]. Instead, the small filler is condensed in large blocks of size up to 1 μm. Based on the TEM photograph, Mikrajuddin et al. showed that PEG based polymer electrolyte nanocomposites made by *in-situ* growth of ZnO nanoparticles in the polymer matrix and *in-situ* insertion of lithium ion during nanoparticles growth have particle size of about 6 nm [63]. This result is consistent with the calculation of the particle size using size-dependent bandgap equation [117–119]. Chandra et al. also observed the size of nanoparticles synthesized *in-situ* in polymer electrolyte nanocomposites using TEM and found that small content nanoparticles (about 1 wt.%) have smaller size [54].

### 8.3. Atomic Force Microscopy

There are not many reports on the atomic force microscopy (AFM) investigation of polymer electrolytes. Instead of investigating the polymer electrolytes themselves, Granvalet-Manchini et al. investigated the change in the surface of lithium electrode when making contact with polymer electrolytes [120]. After about three days' contact with polymer electrolytes, self-assembled polymer layer is developed on the surface of lithium electrode.

### 8.4. Optical Microscopy

Optical microscopy characterization of polymer electrolyte nanocomposites was not reported too much. To date, Kim et al. reported the optical micrograph of a system of PEO<sub>16</sub>:LiClO<sub>4</sub> containing various filler content, taken under crossed polarizers [121]. They observed well-defined spherulitic morphologies. The spherulites were observed in thin films deposited on the glass substrate whose typical thickness was about 20 μm. They proposed that the size and the morphology of the spherulites can be related to the melting point or glass temperature of the composites. This was based on the

fact that the spherulites have a lamellar structure for almost all polymers and the increase in the lamella thickness results in the increase in the melting temperature [122].

## 9. THERMAL CHARACTERIZATIONS

### 9.1. Thermogravimetry

Thermogravimetry (TG) is a technique for measuring the change in the weight of a substance as a function of temperature or time. The result usually appears as a continuous chart record, as displayed in Figure 23. The sample, usually a few milligrams in weight, is heated at a constant rate, typically 1–20 °C/min. It has constant weight until it begins to decompose at temperature  $T_i$ . Decomposition usually takes place over a range of temperature  $T_i$  to  $T_f$  and second constant plateau is then observed above  $T_f$ , which corresponds to the weight of residue.

A TGA curve of composite made by PEO:LiBF<sub>4</sub> containing 2-[methoxy(polyethylenoxy)-propyl]trimethoxy silane-coated SiO<sub>2</sub> nanoparticles is displayed in Figure 24 [109]. At temperatures below 180–200 °C, the sample experiences only a small weight loss due to removal of residual water on the surface of SiO<sub>2</sub>. At increasing temperatures, the OH groups on the SiO<sub>2</sub> surfaces begin to decompose to give rise to slight increase in the weight loss. In addition to the decomposition of the OH groups, another weight loss take place at about 350 °C that can be attributed to the decomposition of silane molecules that are bonded on the surface of SiO<sub>2</sub>. Liu et al. suggested that the adsorption of containing 2-[methoxy(polyethylenoxy)-propyl]trimethoxy silane on the surface of SiO<sub>2</sub> is likely to give a sub-monolayer coverage [109].

### 9.2. Differential Thermal Analysis

Differential thermal analysis (DTA) is a technique in which the temperature of a sample is compared with that of inert reference material during a programmed change of temperature. The temperature of sample and reference should be the same until some thermal event such as melting, decomposition, or change in crystal structure occurs in the sample.

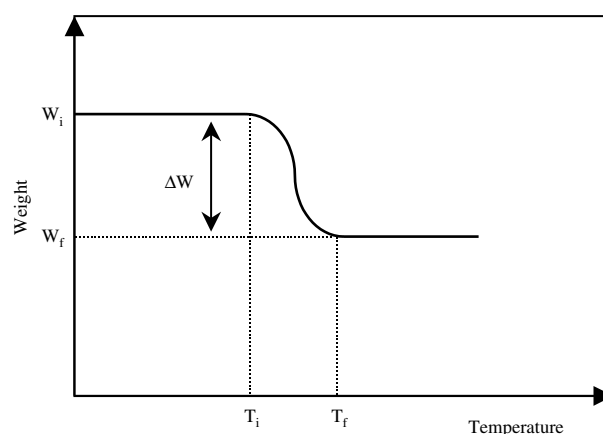
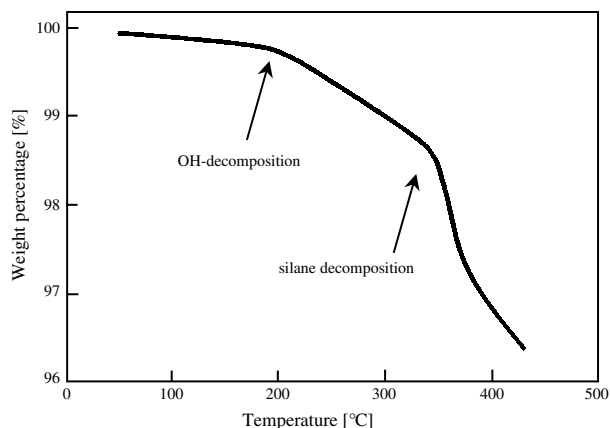


Figure 23. Typical form of TGA curve.



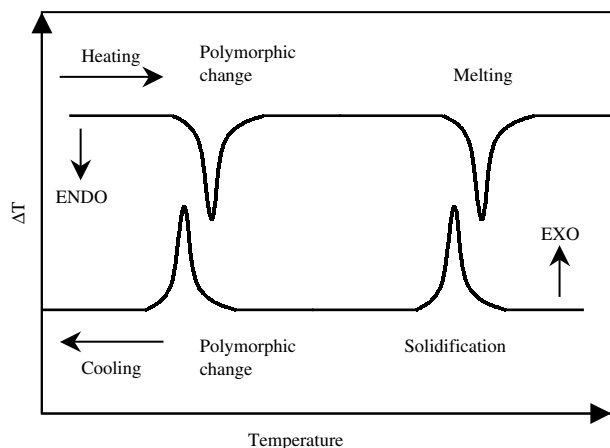


**Figure 24.** TGA curve of PEO:LiBF<sub>4</sub> containing 2-[methoxy (polyethyl-enoxy)-propyl]trimethoxy silane coated SiO<sub>2</sub> nanoparticles. The curve was replotted from [109], Y. Liu et al., *J. Power Sources* 109, 507 (2002).

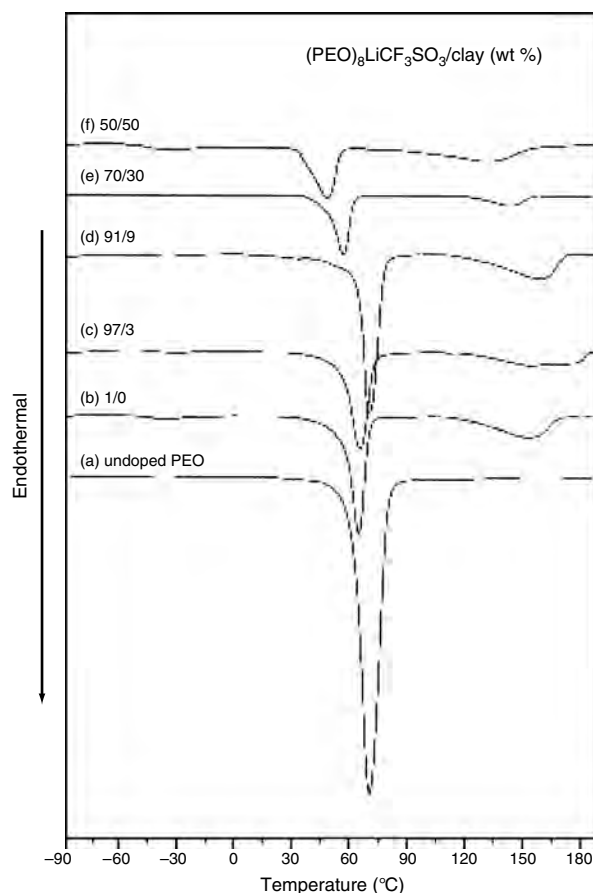
If the sample temperature lags behind the reference temperature, the process is called endothermic. On the contrary, if the sample temperature leads the reference temperature, the process is known as exothermic. The sample size is usually a few milligrams and heating and cooling rate is usually 1–50 °C/min. The difference in the sample and reference temperature will appear as Figure 25.

If calorimetric data is required, it is better to use differential scanning calorimetry (DSC). DSC is very similar to DTA. A sample and an inert reference are also used in DSC system but the cell is designed differently. The sample and the reference are maintained at the same temperature during the heating program and extra heat input to the sample (or to the reference if sample undergoes an exothermic change) is required to maintain this balance. Enthalpy changes are therefore measured directly.

Examples of DSC curves for various PEO:LiCF<sub>3</sub>SO<sub>3</sub> + clay composites are displayed in Figure 26 [123]. From this figure, we can extract several parameters like the glass temperature, the melting point, and enthalpy. These values were found to depend on the filler content, as summarized in Table 7. A pure PEO has one first-order endothermic transition at around 70 °C, corresponding to the melting of the



**Figure 25.** Typical form of DTA curve.



**Figure 26.** DSC curve of PEO:LiCF<sub>3</sub>SO<sub>3</sub> containing clay. Reprinted with permission from [123], H.-W. Chen and F.-C. Chang, *Polymer* 42, 9763 (2001). © 2001, Elsevier Ltd.

PEO crystalline phase. When salt is added, a second minor endothermic transition was observed at around 140–150 °C, due to the melting of crystalline complex phase formed by PEO and LiCF<sub>3</sub>SO<sub>3</sub> [124–126]. The melting temperature of the crystalline PEO phase depends on the filler content. The  $T_m$  initially shifted to higher temperature when the filler content increased, and reached the highest value at 9 wt.% clay, and then decreased with further increase in the clay content.

**Table 7.** The parameters of polymer electrolyte nanocomposites extracted from the DSC curve.

Samples	$T_g$ (K)	$T_m$ (K)	$\Delta H$ (J/g)	$X_c$	$T_{mc}$ (K)
PEO		70.50	165.5		
PEO:LiCF <sub>3</sub> SO <sub>3</sub>	–46	69.84	59.9	36.2	152.0
PEO:LiCF <sub>3</sub> SO <sub>3</sub> + clay 3 wt%	–50	71.58	68.9	41.6	149.7
PEO:LiCF <sub>3</sub> SO <sub>3</sub> + clay 9 wt%	–43	77.4	77.8	47.0	156.9
PEO:LiCF <sub>3</sub> SO <sub>3</sub> + clay 30 wt%	–46	54.93	40.1	24.2	142.6
PEO:LiCF <sub>3</sub> SO <sub>3</sub> + clay 50 wt%	–48	45.99	29.1	17.6	132.4

Adapted with permission from [123], H.-W. Chen and F.-C. Chang, *Polymer* 42, 9763 (2001). © 2001, Elsevier.

The PEO crystallinity (expressed by the area covered by transition curve) is also dependent on the clay content. The PEO crystallinity initially increases with increasing clay content up to 9 wt.% and then decreases with further increase in the clay content.

Melt-crystallized polymers are never completely crystallized. This is because there are an enormous number of chain entanglements in the melt and it is impossible for the organization to form 100% crystalline polymer during crystallization. The degree of crystallinity is therefore of great technological importance. The degree of crystallinity can be deduced from the DTA data, in which the melting enthalpy can be obtained. The crystallinity can be calculated using a simple equation [127]:

$$X_c = \frac{\Delta H_m}{\Delta H_{m,c}} \times f_{\text{PEO}} \quad (54)$$

where  $\Delta H_m$  = melting enthalpy measured,  $\Delta H_{m,c}$  = melting enthalpy of 100% crystalline (for PEO,  $\Delta H_{m,c} = 196.4$  J/g), and  $f_{\text{PEO}}$  = weight fraction of PEO in polymer electrolytes.

## 10. DENSITY METHOD

Another method for determining the crystallinity is based on the knowledge of density of crystalline and amorphous phases as well as the density of the polymer specimen. The crystallization of polymer from melt is accompanied by the reduction in the volume due to an increase in density. The crystals have a higher density than the molten or non-crystalline polymer since the last two contain also free volume. Based on this difference, the density method can be utilized to determine the degree of crystallinity.

If  $V$  is volume of polymer specimen, and  $V_a$  and  $V_c$  are volumes of amorphous and crystalline regions, respectively, we have  $V = V_a + V_c$ . The relation of polymer specimen mass and the amorphous and the crystalline region masses is given by

$$\rho V = \rho_a V_a + \rho_c V_c \quad (55)$$

where  $\rho$  = density of polymer specimen,  $\rho_a$  = density of amorphous region, and  $\rho_c$  = density of crystalline region.

By defining the crystallinity as  $x_c = \rho_c V_c / \rho V$ , we obtain

$$x_c = \frac{\rho_c}{\rho} \left( \frac{\rho - \rho_a}{\rho_c - \rho_a} \right) \quad (56)$$

The density of polymer specimen can be determined by simply measuring the volume and weighing the mass. The density of crystalline region can be calculated from the knowledge of the crystal structure. The density of amorphous phase can be determined by measuring the density of almost completely amorphous polymer, such as polymer obtained by rapid cooling from polymer melt.

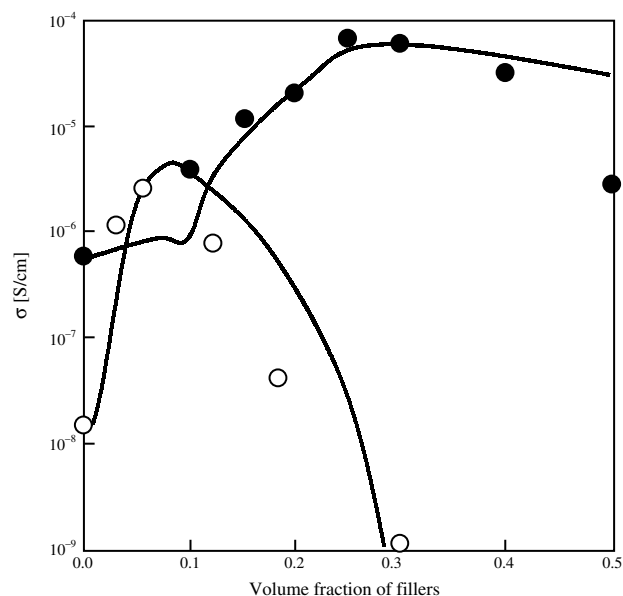
Equation (56), however, is valid if polymer specimen contains no holes which are often present in molded samples. In addition, since packing of the molecules in amorphous region is random, it is likely that the density of amorphous phase depends on the thermal treatment of the specimen.

## 11. ELECTRICAL PROPERTIES

### 11.1. Effect of Filler Content on Conductivity

The role of the ceramic filler is to influence the recrystallization kinetics of the polymer matrix chains, thereby ultimately promoting localized amorphous regions and thus enhancing the transport of cations [9]. To produce a high fraction of amorphous state in the composite, the as-prepared composite is first heated above the melting point so that all parts of the polymer are converted to the amorphous state. During the cooling process, the matrix part around particles remains in the amorphous state, even when the temperature drops below the melting point. Therefore, a high electrical conductivity would be expected to appear at ambient temperatures. Indeed, enhancement in conductivity of up to about three orders of magnitude at low temperatures and about one order of magnitude at high temperatures has been reported for the system of poly(ethylene oxide)-LiClO<sub>4</sub> containing ceramic fillers [9]. In addition, composites containing ceramic fillers in the nanoscale particle size exhibit both excellent mechanical stability (promoted by the network of the fillers into the polymer bulk) and high ionic conductivity (promoted by the high surface area of the dispersed filler).

The volume fraction of filler particles affects the conductivity of a composite. The symbols in Figure 27 display the effect of filler loading on the electrical conductivity of a poly(ethylene oxide)/NaI containing filler of  $\Theta$ -Al<sub>2</sub>O<sub>3</sub> [128]. The conductivity increases with an increase in the volume fraction of fillers, reaches a maximum at a certain value of filler particles, and then decreases toward zero for further increases in the volume fraction of fillers. This observation



**Figure 27.** Effect of filler volume fraction on the electrical conductivity at 25 °C for composites of (open circle) PEO:LiClO<sub>4</sub>+PAAM and (solid circle) PEO:NaI+ $\Theta$ -Al<sub>2</sub>O<sub>3</sub>. Date points were extracted from Y. Liu et al., *J. Power Sources* 109, 507 (2002). Curves were obtained from theoretical calculation to fit the data using ( $t/R = 0.6$ ) for fitting the open circle data and ( $t/R = 1.16$ ) for fitting the solid circle data. Curves were replotted from [128], J. Przulski et al., *Electrochim. Acta* 40, 2102 (1995).

can be explained as follows. By increasing the fraction of fillers, the total amount of amorphous state around the fillers increases since the surface area increases, thus increasing the conductivity. If the filler content is so high, some of the filler agglomerates (making contact) so that the surface area is reduced, thus reducing the fraction of amorphous state around the filler, thereby reducing the conductivity. At a specified amount of filler fraction, the continuous network of amorphous state disappears so that the transport of cations is blocked. The conductivity of composites can be approximated with the conductivity of filler particles.

The effective medium approximation was used to explain the conductivity enhancement in polymer electrolyte composites [128]. Dispersed ceramics create an amorphous layer around the particles, which have a high conductivity. The composite is considered to be a two-phase system: particles and amorphous layer as one phase and the rest of the polymer as the other phase. The conductivity of the second phase (polymer matrix) is equal to the conductivity of the polymer electrolytes free of dispersed particles. The conductivity of the particle–amorphous layer can be calculated using Maxwell–Garnett equation [129],

$$\sigma_c = \sigma_1 \frac{2\sigma_1 + 2Y(\sigma_2 - \sigma_1)}{2\sigma_1 + \sigma_2 - Y(\sigma_2 - \sigma_1)} \quad (57)$$

where  $\sigma_1$  = conductivity of the interface layer,  $\sigma_2$  = conductivity of dispersed grain, and  $Y$  = volume fraction of filler in the composite, according to equation [128]

$$Y = \frac{1}{(1 + t/R)^3} \quad (58)$$

where  $t$  = thickness of the conducting layer, and  $R$  = radius of filler.

The system is analogous to a system containing conducting particles dispersed in a polymer matrix in which the conducting particles correspond to the particle–amorphous layer. The improved conductivity of grain and polymer medium is calculated by the Nakamura [130] or Nan and Smith [131, 132] equation,

$$\sigma_c^a = 2\sigma_c \frac{V_c}{3 - V_c} \quad (59a)$$

$$\sigma_a^e = 2\sigma_e \frac{1 - V_c}{2 + V_c} \quad (59b)$$

where  $V_c = V_2/Y$ , and  $V_2$  = volume fraction of filler in a bulk electrolyte.

The dependence of composite conductivity on the load fraction of dispersed particles and particle size can be calculated using the effective medium theory [133]:

$$\left(\frac{V_2}{Y}\right) \frac{\sigma_c^a - \sigma_m}{\sigma_m + p_c(\sigma_c^a - \sigma_m)} + \left(1 - \frac{V_2}{Y}\right) \frac{\sigma_e^a - \sigma_m}{\sigma_m + p_c(\sigma_e^a - \sigma_m)} = 0 \quad (60)$$

where  $\sigma_m$  is the conductivity of the composite and  $p_c$  is the continuous percolation threshold for the composite grain.  $P_c$  can be taken to be 0.28 on the basis of general percolation theory [131, 132]. Lines in Figure 27 are the theoretical prediction for a system of PEO:LiClO<sub>4</sub>+PAAM and

PEO:NaI +  $\Theta$ -Al<sub>2</sub>O<sub>3</sub> [128]. The data were collected at 25 °C. The theoretical curves were calculated using  $t/R = 0.6$  for solid line and  $t/R = 1.16$  for dashed line.

However, this theory cannot explain the enhancement of conductivity at high temperatures compared to polymer electrolytes which are free of filler as shown in Figure 4. An alternative approach has been used to explain conductivity enhancement due to filler dispersion [134]. The presence of a filler induces the formation of an amorphous layer around the filler particles as well as the presence of an ionic layer around the particles. Typically, an amorphous layer around the filler particles is effectively created if the polymer containing a filler is heated above the melting point and then cooled down. The presence of a ceramic filler inhibits the recrystallization of a polymer layer around the particles so that layer remains in the amorphous state after the polymer reaches room temperature. That means that, without heating above the melting point, the conductivity of polymer electrolytes containing a filler is close to that of filler-free polymer electrolytes. However, by assuming the presence of an ionic layer around the filler which has a conductivity higher than that when the ionic layer is absent, the conductivity is then enhanced even though all parts of the polymer are in the crystalline phase or in the amorphous phase. This assumption explains the enhancement in conductivity at high temperatures even when all parts of the polymer are in the amorphous state.

This approach is similar to the observation of conductivity enhancement in solid-state ionic composites, into which ceramic fillers are dispersed [135]. The ionic transport in solid-state ionics is very similar to polymer electrolytes. Polymer electrolytes in the crystalline phase can be thought of as analogous to solid-state ionics having a low conductivity, and polymer electrolytes in the amorphous phase can be analogous to solid-state ionics having a high conductivity. Therefore, since the ionic layer is assumed to be present in solid-state ionic materials when the fillers are dispersed, a similar layer would be expected to appear in polymer electrolytes containing a ceramic filler. The conductivity of the ionic layer can be roughly approximated with  $\sigma_l = \sigma_\infty + \Delta\sigma$ , in which  $\sigma_\infty$  is the conductivity of the medium around the particles in the absence of an ionic layer, and  $\Delta\sigma$  is the excess conductivity due to the presence of a charged layer. Thus, if the polymer around the filler is in the crystalline state, the conductivity of the layer around the particles would be higher than the conductivity of this crystalline state. If the polymer medium around the particles is in the amorphous state, the conductivity of the ionic layer would be higher than the conductivity of the amorphous polymer. Mikrajuddin et al. calculated the loading effect on the electrical conductivity of composites by assuming a simple cubic packing of filler particles and obtained a bell-shaped conductivity variation [134], similar to that obtained experimentally.

Most of fillers used for making polymer electrolyte composites are restricted to nonconductive materials. Recent reports of the addition of small amount of conducting materials such as carbon (1.5 wt.%) with surface area of 60 m<sup>2</sup>/g showed an enhancement of conductivity and interfacial stability compared to carbon-free composites [136].

## 11.2. Effect of Salt Concentration on Conductivity

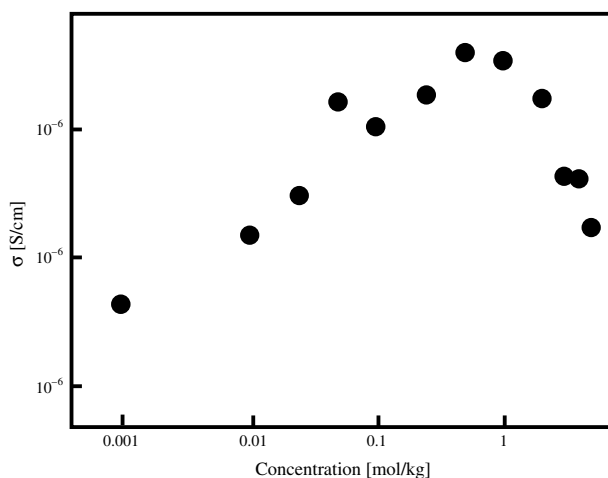
Another potential approach is to increase the concentration of salt ions in the matrix. However, this approach is unpredictable. Figure 28 shows the effect of ion content on the electrical conductivity of a system of PEG:LiClO<sub>4</sub> + α-Al<sub>2</sub>O<sub>3</sub> at 25 °C [137]. By increasing the concentration of salt ions, the electrical conductivity initially increases, followed by a decrease after passing a specified salt concentration. Explanations have been proposed to explain this observation. Doeff et al. explained this behavior in terms of a trade-off between an increasing number of charge carriers and ion aggregation and increased viscosity due to ionic cross-linking, which lowers the conductivity as the salt concentration passes a critical value [138]. Dupon et al. explained this dependence as being due to strong ion pairing, which effectively traps the mobile cations, and therefore significantly reduces the ionic conductivity relative to non-ion-paired complexes on a similar structure [139].

Marcinek [137] found that up to LiClO<sub>4</sub> concentration equal to 0.25 mol/kg, the conductivity of both systems PEG:LiClO<sub>4</sub> and PEG:LiClO<sub>4</sub> + α-Al<sub>2</sub>O<sub>3</sub> system of PEG:LiClO<sub>4</sub> + α-Al<sub>2</sub>O<sub>3</sub> do not differ from each other by more than 30–40%. However, for high salt concentrations, the conductivity of electrolytes containing α-Al<sub>2</sub>O<sub>3</sub> are much higher. The difference rises up to 30–40 times for a system with the highest salt concentration.

## 11.3. Effect of Temperature on Conductivity

Since the transport of ions in the amorphous state is assisted by chain segment relaxation, the temperature dependence for ion transport in this state follows the temperature dependence of chain relaxation. A Vogell–Tamman–Fulcher (VTF) dependence of electrical conductivity then results, that is,

$$\sigma(T) = \frac{A}{\sqrt{T}} \exp\left[-\frac{B}{T - T_o}\right] \quad (61)$$



**Figure 28.** Effect of salt concentration on the conductivity at 25 °C of PEG:LiClO<sub>4</sub> + α-Al<sub>2</sub>O<sub>3</sub>. Data points were extracted from [137], M. Marcinek et al., *Solid State Ionics* 136–137, 1175 (2000).

in which  $A$ ,  $B$ , and  $T_o$  are constants and  $T$  is the temperature. The value of the constant parameter depends on the type of composites as well as the conditions used in preparing the polymer. The value of  $T_o$  depends on the glass transition of the polymer. A generally accepted relation is  $T_o = T_g + 50$ , in which  $T_g$  denotes the glass transition of the polymer [140]. The glass transition of most polymers is related to the melting point that satisfies  $T_g/T_m = 0.5–0.8$  [19]. Parameter  $B$  can be expressed as a linear function of  $T_o$  [134].

The value of VTF parameters was found to depend on the concentration of salt. For example, in a system of PPG4000:AgCF<sub>3</sub>SO<sub>3</sub>, the value of VTF parameters at various salt concentrations was reported by Eliasson et al. [141]. The VTF parameters also depend on the salt type, as reported by Florzanczyk et al. [142].

On the other hand, since the transport of ions in the crystalline state is dominated by ion carriers jumping to the nearby locations, the temperature dependence of conductivity then follows the Arrhenius law,

$$\sigma(T) = A \exp\left[-\frac{E_a}{kT}\right] \quad (62)$$

in which  $E_a$  is the activation energy. The value of  $E_a/q$ , in which  $q$  is the charge of the ion carrier, represents the blocking potential that must be overcome for an ion carrier to jump to the nearest locations. For polymer electrolytes only (free of ceramic fillers), a VTF behavior of conductivity is observed at temperatures above the melting point; Arrhenius behavior prevails at low temperatures. A drastic depression of electrical conductivity occurs at temperatures where the VTF behavior changes to Arrhenius behavior [9]. Since the dispersion of filler particles will generate amorphous states even at low temperatures, VTF behavior is observed even at low temperatures for conductivity, as can also be seen in Figure 2. Continuing the VTF behavior up to ambient temperature overcomes a drastic depression of conductivity so that high conductivity prevails at low temperatures.

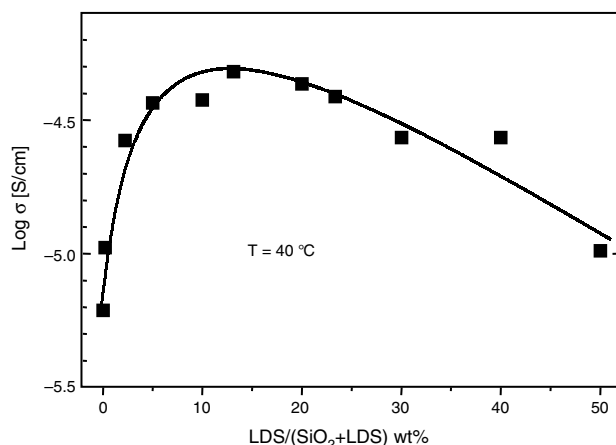
## 11.4. Effect of Particle Surface on Conductivity

As observed in Figure 4, at high temperatures where all parts of the polymer are in an amorphous state, the conductivity of a composite is higher than that of polymer electrolytes which are free of fillers. This indicates that the amorphous layer around filler particles should not be the only contributor to conductivity enhancement. It has been proposed that the surface properties of the dispersed filler also play a significant role in the electrical conductivity of polymer electrolyte nanocomposites. Prior to use, the fillers are usually cleaned by drying at certain temperatures in vacuum or washing with a solution followed by drying in vacuum to remove contaminants on the surface. Matsuo and Kuwano observed an enhancement in conductivity by a factor of five to ten when a lithium dodecylsulfate surfactant was added to the surface of an SiO<sub>2</sub> in a system of PEG-LiCF<sub>3</sub>SO<sub>3</sub>-SiO<sub>2</sub> [43]. Prior to the synthesis of composites, the silica nanoparticles were dispersed in a

solution of the surfactant to produce a self-assembly of surfactant molecules on the particle surface. Figure 29 shows the effect of surfactant content (lithium dodecylsulfate, LDS ( $C_{12}H_{25}OSO_3Li$ )) on the electrical conductivity of a system of poly(ethylene oxide)- $LiCF_3SO_3$ - $SiO_2$ . The ionic conductivity rapidly increases with increasing LDS content and then decreases after reaching a critical value at a certain weight fraction of LDS. The weight fraction of LDS to produce the conductivity peaks is the amount necessary for producing a monolayer on the surface of  $SiO_2$ . Further increases in LDS content led to a reduction in conductivity.

Functionalization of  $SiO_2$  in a poly(ethylene glycol)-based polymer electrolyte using 2-[methoxy(polyethylenoxy)propyl] trimethoxy silane was reported to enhance electrical conductivity as well as the tensile strength of composites (the tensile strength was increased by about 1 Mpa compared to that using pristine  $SiO_2$ ) [109]. A small improvement in conductivity compared to pristine  $SiO_2$  was observed for small loading levels of surfactant. It was assumed that silane moieties attached on the  $SiO_2$  surface effectively prevent coagulation of the  $SiO_2$  particles during blending because of steric repulsive forces. It then increases the dispersibility of  $SiO_2$  powder in the PEO matrix [109]. The relaxation of chain segments is also improved by adding treated  $SiO_2$ . In poly(ethylene oxide)-based electrolytes,  $Li^+$  ions are coordinated to oxygen atoms in the polymer chains. Movement of the dissociated  $Li^+$  ions can be constrained by multiple oxygen atoms coordinated to the same  $Li^+$  central ion. Upon the addition of functionalized  $SiO_2$ , the oxygen atoms from the short polyether units on the surface of  $SiO_2$  compete with the oxygen atoms from the polymer chains for complexation with  $Li^+$ . The result is a more relaxed coordination between oxygen atoms and  $Li^+$  ions, which in turn, facilitates the transport of  $Li^+$  ions through the polymer.

Croce et al. observed a difference in conductivity when acidic, neutral, and basic  $Al_2O_3$  were used as fillers [143]. A specific interaction between the surface group of ceramic particles and both the PEO segment and lithium salt ions



**Figure 29.** Effect of surfactant weight fraction on the electrical conductivity of PEG: $LiCF_3SO_3$  containing LDS coated  $SiO_2$  nanoparticles. Data points were extracted from [43], Y. Matsuo and J. Kuwano, *Solid State Ionics* 79, 295 (1995).

was assumed to exist, which can be attributed to Lewis acid-base interactions. This interaction may act as cross-linking centers for the PEO segments and for the  $X^-$  anions to lower the PEO reorganization tendency and thus promoting the structure modification of the polymer chains. The effect promotes  $Li^+$  conducting pathways at the ceramic surface. Second, Lewis acid-base interactions between the electrolyte ionic species lower ionic coupling. The expected result is the promotion of salt dissociation via a type of “ion-ceramic complex” formation. The surface of the filler also affects the transference number of ion in the composites. Table 8 shows the effect of acid-base properties of the filler on the transference number in a system of  $P(EO)_{20}LiCF_3SO_3$  containing  $Al_2O_3$  [143].

Capiglia et al. investigated the properties of composite electrolytes consisting of  $SiO_2$  powder with different surface features in PEO: $LiClO_4$  system. They removed the hydroxyl groups on  $SiO_2$  by calcinations at 900 °C in order to reduce the hygroscopic properties of the particles. The reduction of hydroxyl group on the particle surface was found to increase the ionic conductivity [144]. Walls et al. prepared series of  $SiO_2$  material with hydrophilic and hydrophobic surface groups and used them as filler in PEGDM system. They showed clearly a cause and effect relationship between the observed properties and the surface chemistry [145]. Fan et al. attached different surface group to the silica and used the functionalized particles in PEGDM-based composite electrolyte. They found that the silica surface chemistry affected mostly the rheological properties, but not the ionic conductivity [146].

## 11.5. Effect of Particle Size on Conductivity

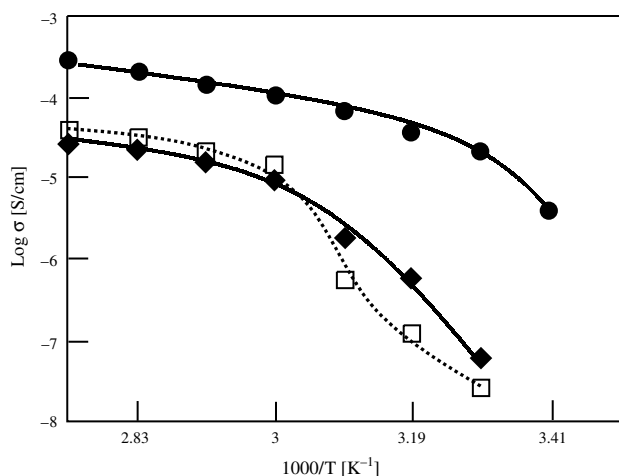
The use of nanometer- and micrometer-sized  $Al_2O_3$  in a system of PEO: $LiBF_4$  improved the electrolyte mechanical and electrochemical performance with decreasing size of ceramic filler. Nanometer-sized particles provide an order increase in conductivity compared to micrometer-sized filler [36]. Chandra et al. observed a decrease in the conductivity at 333 K of two orders of magnitude when particle size was increased from 10 to 100  $\mu m$ . However, only a small decrease was observed at 373 K when the particle size was increased in the same range [147]. Wiczorek et al. reported a decrease in conductivity when the particle size is increased from 2 to 7  $\mu m$  [148]. Figure 30 shows the Arrhenius plot of electrical conductivity of a system of PEO-based polymer electrolyte nanocomposites at different filler sizes [148].

The dependence of conductivity on the filler size can be described qualitatively using a space-charge layer concept

**Table 8.** Lithium transference number at 95 °C.

Samples	$t^+$
$P(EO)_{20}LiCF_3SO_3$	0.46
$P(EO)_{20}LiCF_3SO_3 + 10\%Al_2O_3$ (basic)	0.48
$P(EO)_{20}LiCF_3SO_3 + 10\%Al_2O_3$ (neutral)	0.54
$P(EO)_{20}LiCF_3SO_3 + 10\%Al_2O_3$ (acidic)	0.63

Adapted with permission from [143], F. Croce et al., *Electrochim. Acta* 46, 2457 (2001). © 2001, Elsevier.



**Figure 30.** Arrhenius plot of (square) PEO:LiBF<sub>4</sub>, (diamond) PEO:LiBF<sub>4</sub> containing 10 wt.% Al<sub>2</sub>O<sub>3</sub> (micrometer size), and (circle) PEO:LiBF<sub>4</sub> containing 10 wt.% Al<sub>2</sub>O<sub>3</sub> (nanometer size). Data points were extracted from [148], W. Wiczeorek et al., *Electrochim. Acta* 40, 2251 (1995).

that is commonly used to explain similar effect in a composite of solid-state ionics. The origin of space-charge layer is ascribed to the difference in the free energy formation of the individual vacancies in case of Schottky disorder and of the vacancies and the interstices in the case of Frenkel disorder. The space-charge layer for a two-phase composite of solid-state ionics has been introduced by Maier, who found the enhanced conductivity of the composite material as [149]

$$\sigma = (1 - \phi)\sigma_o + (3\sqrt{2})\beta_L \left(\frac{\phi}{r}\right) \sqrt{\frac{\varepsilon\varepsilon_o RT}{V_m}} \mu_v \sqrt{N_{vo}} \quad (63)$$

where  $\sigma_o$  = conductivity of filler-free polymer electrolytes,  $\phi$  = volume fraction of filler,  $\beta_L$  = a constant to account for the topology of filler,  $r$  = filler particle radius,  $\varepsilon$  = dielectric constant,  $\varepsilon_o$  = permittivity of vacuum,  $V_m$  = bulk molar volume of the matrix phase,  $\mu_v$  = the mobility of dominant defect, and  $N_{vo}$  = the mole fraction of dominant defect at the interface. This equation can fit the data of conductivity of NaCl containing various sizes of Al<sub>2</sub>O<sub>3</sub> [150].

### 11.6. Effect of Plasticizers on Conductivity

The plasticizers have a great influence on the electrical, chemical, and electrochemical properties of the polymer electrolyte composites. The addition of ethylene carbonate results in a more homogeneous and transparent film. Golodnitsky et al. observed a conductivity enhancement by a factor of two in system of Li:PEO<sub>9</sub>PMMA<sub>0.5</sub> + 6 vol.% Al<sub>2</sub>O<sub>3</sub> when ECl is added [151]. Enhancement about seven times was observed in a system of Li:PEO<sub>6</sub>PMMA<sub>0.5</sub> + 6 vol.% Al<sub>2</sub>O<sub>3</sub> if PEG<sub>0.5</sub> is added as appears in Table 9 [151].

Leo et al. [152] observed the different temperature dependence of conductivity when plasticizer is added into the polymer composites. Different weight percent of plasticizer alters the shape of log  $\sigma$  against  $1/T$ . The temperature dependence of conductivity below 50 °C shows an Arrhenius

**Table 9.** Effect of EC and PEG plasticizers on the electrical conductivity at 120 °C.

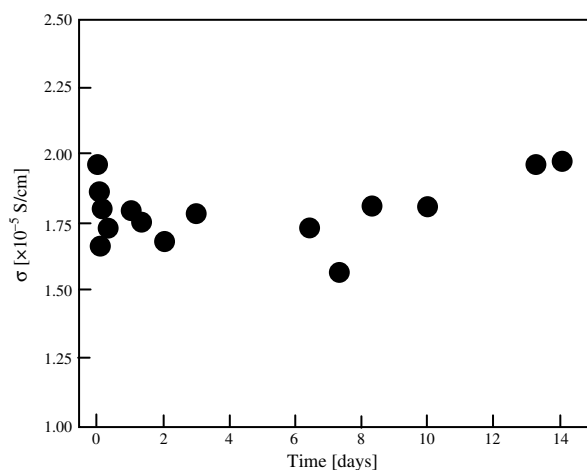
Electrolytes	Plasticizer	Filler	Conductivity (S/cm)
PEO <sub>9</sub> PMMA <sub>0.5</sub> :LiI		Al <sub>2</sub> O <sub>3</sub> 6 wt.%	0.6×10 <sup>-3</sup>
PEO <sub>9</sub> PMMA <sub>0.5</sub> :LiI	ECl	Al <sub>2</sub> O <sub>3</sub> 6 wt.%	1.2×10 <sup>-3</sup>
PEO <sub>6</sub> PMMA <sub>0.6</sub> :LiI		Al <sub>2</sub> O <sub>3</sub> 6 wt.%	0.4×10 <sup>-3</sup>
PEO <sub>6</sub> PMMA <sub>0.6</sub> :LiI	PEG <sub>0.5</sub>	Al <sub>2</sub> O <sub>3</sub> 6 wt.%	1.0×10 <sup>-3</sup>

Adapted with permission from [151], D. Golodnitsky et al., *Solid State Ionics* 85, 231 (1996). © 1996, Elsevier.

type for all plasticizer content. However, above 50 °C, the temperature dependence of conductivity seems to change with the change in the content of plasticizer. For 5 wt.% plasticizer (ethylene carbonate), there is a temperature  $T_m$  above which the Arrhenius plot of conductivity was observed and below which a qualitative change in the curve was observed. The discontinuity in the slope of the curve of the unplasticized composite disappears. At higher plasticizer content, a distinct change in the temperature-dependent conductivity was observed.

### 11.7. Effect of Storage Time on Conductivity

Shin et al. measured the effect of storage time on the electrical conductivity of polymer electrolyte composites of PEO<sub>10</sub>:LiCF<sub>3</sub>SO<sub>3</sub> containing 5–15 wt.% of Ti<sub>n</sub>O<sub>2n-1</sub> stored at 90 °C. The conductivity increased with increase in the storage time until approximately 5 h, when the conductivity reached a steady-state value. The conductivity of polymer electrolytes containing ceramics reaches the steady-state value faster than ceramic-free polymer electrolytes [153]. The conductivity of PEO<sub>8</sub>:LiClO<sub>4</sub> containing 10 wt.% SiO<sub>2</sub> is relatively stable up to two weeks storage as displayed in Figure 31 [154]. Croce et al. suggested that the recrystallization may occur with kinetics which appear to be critically dependent on the annealing condition [9].



**Figure 31.** Effect of storage time on the conductivity of PEO<sub>8</sub>:LiClO<sub>4</sub> containing 10 wt.% SiO<sub>2</sub>. Data points were extracted from [154], G. Appetecchi et al., *Electrochim. Acta* 45, 1481 (2000).

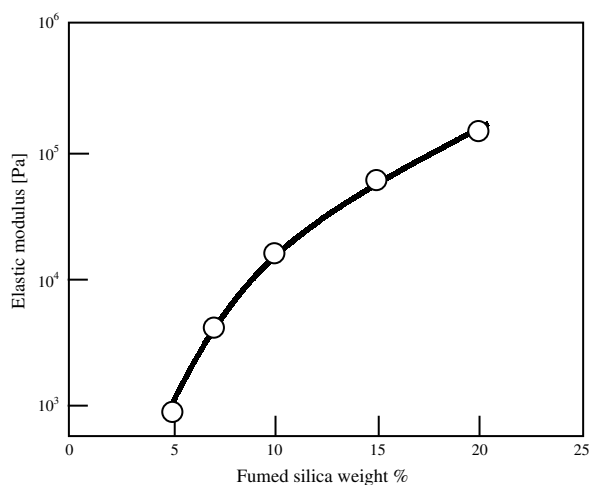
Appetecchi et al. compared the conductivity of EC-DMC-PAN:LiPF<sub>6</sub> containing 6 wt.% Al<sub>2</sub>O<sub>3</sub> and EC-DMC-PAN:LiPF<sub>6</sub> free of Al<sub>2</sub>O<sub>3</sub>. They found that, after 30 days aging at 75 °C, there was no significant change in the conductivity of ceramics containing polymer electrolytes, while the ceramic-free polymer suffered a depression in conductivity to become about 10% of the initial value [155].

## 12. MECHANICAL PROPERTIES

### 12.1. Effect of Filler Content

Weston and Steele used ceramic filler to improve the mechanical properties of PEO films [156]. Addition of ceramic filler to improve the mechanical properties of polymer is not new. The addition of carbon black filler can extend the lifetime of tires from 5,000 miles if no carbon black is used to a potential 80,000 miles in some current tires. Figure 32 shows the effect of filler content on the elastic modulus of a system of poly(ethylene glycol) dimethyl ether:LiN(CF<sub>3</sub>SO<sub>2</sub>)<sub>2</sub> containing fumed silica with a surface group modified to become Si-C<sub>8</sub>H<sub>17</sub> instead of Si-OH. Increasing the concentration of the filler generates a stronger network structure with the modulus increasing by two orders of magnitude [157].

Although addition of filler is effective in hardening the polymer electrolytes at lower temperature, the effectiveness becomes lower at temperatures higher than the melting point of the matrix. Wen et al. used a whisker to improve the mechanical strength of polymer electrolyte composites. The work is based on the morphology of whisker which has a special shape similar to rigid network formed inside the polymer electrolytes. The mechanical strength of the polymers was evaluated with their thermal creep behavior, indicated by the relative resistance change of the polymer electrolyte films after being kept for some time under a certain pressure [113]. Addition of ceramic filler in a composite of PEO<sub>8</sub>:LiClO<sub>4</sub> remarkably affected their



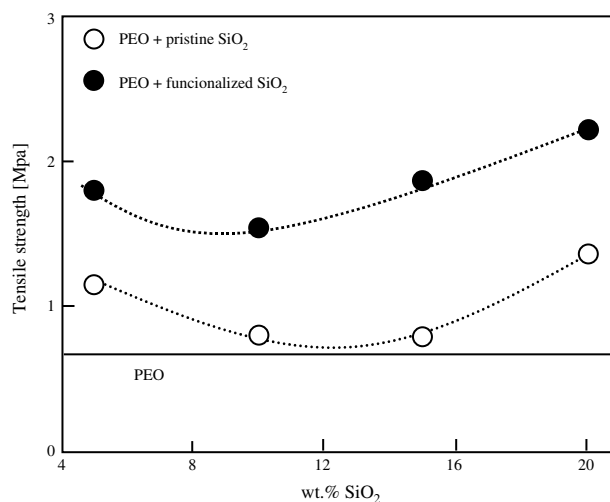
**Figure 32.** Effect of weight fraction of filler on the elastic modulus of PEG dimethyl ether:LiN(CF<sub>3</sub>SO<sub>2</sub>)<sub>2</sub> containing C<sub>8</sub>H<sub>17</sub> coated fumed silica. Data points were extracted from [152], C. J. Leo et al., *Solid State Ionics* 148, 159 (2002).

thermal creep properties, in particular at high temperatures. The electrolytes containing whisker filler are much more mechanically stable than those containing nanosized  $\gamma$ -Al<sub>2</sub>O<sub>3</sub>. However, at low temperatures (below the melting point), the thermal creep properties of both composites are similar.

Leo et al. observed improvement of mechanical strength of PEO-based polymer electrolytes by a factor of three when 7.5 wt.% Nasicon glass-ceramic fillers is added [152]. This filler content also increased the glass temperature of about 14 °C. It is suggested that the addition of filler increases the stiffness of polymer segment, thereby suppressing the polymer chain motion [158].

### 12.2. Effect of Particle Surface

Inorganic fillers are actually bonded to the molecular chain and thereby immobilize the polymer chain. The degree of adhesion between the polymer matrix and the fillers, the surface area of the filler, and the packing characteristic of the filler are important factors that determine the mechanical characteristics of the composites [159]. Liu et al. compared the effect of tensile strength of composites of PEO:LiBF<sub>4</sub>+SiO<sub>2</sub> containing pristine SiO<sub>2</sub> and organic coated SiO<sub>2</sub> [109]. The SiO<sub>2</sub> was coated using 2-[methoxy(polyethylenoxy)-propyl] trimethoxy silane. Figure 33 shows the effect of filler loading on the tensile strength. It can be seen that the trend in the tensile strength variation is similar for both composites. However, the tensile strength of composite made using coated SiO<sub>2</sub> filler is always larger than that of material made by pristine SiO<sub>2</sub>. A double enhancement was observed in all filler loading region. Functionalized SiO<sub>2</sub> might be considered as a filler which carries a pendant coupling agent. The coupling agent has two types of functional groups, one capable of forming chemical bond with the surface of the filler and the other capable of entangling with PEO chains [160].



**Figure 33.** Effect of filler content on the tensile strength of PEO:LiBF<sub>4</sub> containing pristine SiO<sub>2</sub> (open circle) and functionalized SiO<sub>2</sub> (solid circle). Data points were extracted from [109], Y. Liu et al., *J. Power Sources* 109, 507 (2002), and lines are for eye guide.

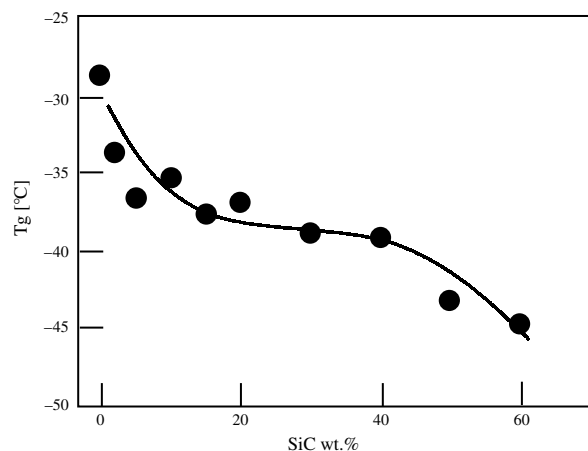
## 13. THERMAL PROPERTIES

### 13.1. Effect of Filler Content on the Glass Temperature

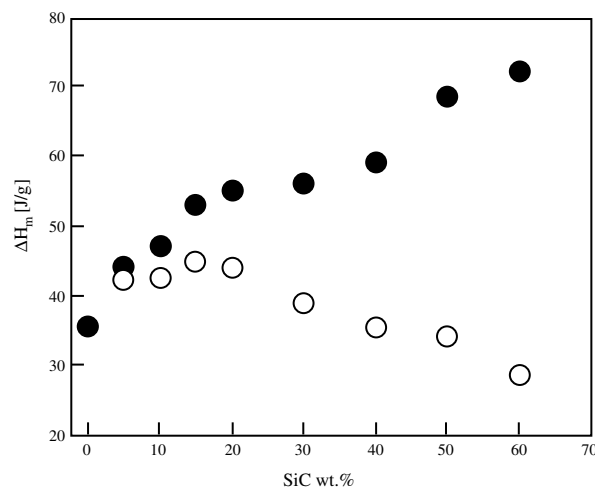
Franco et al. observed the reduction in the glass transition temperature in composite of PEO:LiClO<sub>4</sub> containing carbon black (conducting filler) [97].  $T_g = 220$  K was observed for composite containing 10 wt.% carbon black, 210 K for that containing 20 wt.% carbon black, and 202 K for that containing 30 wt.% carbon black. Choi and Shin measured the effect of the filler loading on the glass temperature of a system of PEO<sub>16</sub>:LiClO<sub>4</sub>+SiC.  $T_g$  first decreases rapidly with the increase in the filler content and then reaches a plateau beyond which it further drops as can be seen in Figure 34 [161].

On the contrary, Chung and Sohn observed also an enhancement of glass temperature as the concentration of salt increases in a system of polymer comb-shaped polymer matrix by attaching triethoxyethylene side chain on the main chain of polyethylene oxide [162]. Wiczorek et al. observed that the SiO<sub>2</sub> filler which enhanced the conductivity raised the  $T_g$  [163], while the  $\alpha$ -Al<sub>2</sub>O<sub>3</sub> filler which reduced the conductivity above room temperature lowered the  $T_g$  [164]. The data indicated that the variation of  $T_g$  neither exhibits systematic results nor meets the expected variation of conductivity.

Filler content also affects the melting enthalpy of composites. Figure 35 shows the effect of filler loading on the melting enthalpy extracted from DCS curve for system of PEO<sub>16</sub>:LiClO<sub>4</sub>+SiC, and the normalization relative to the mass fraction of pure (PEO)<sub>16</sub>:LiClO<sub>4</sub> [161]. Using Eq. (54) and remembering  $\Delta H_{m,c}$  is proportional to mass fraction of pure (PEO)<sub>16</sub>:LiClO<sub>4</sub>, curve (b) reflects the crystallinity of the composite. It is clear that the crystallinity increases with the loading of the filler at low loading and then decreases with further increase in the filler content. Choi and Shin proposed the enhancement of crystallinity with the loading content of filler is due to the role of the filler which may act as nucleation centers of crystalline polymer phase. The



**Figure 34.** Effect of filler content on the glass temperature of PEO<sub>16</sub>:LiClO<sub>4</sub> containing SiC. Data points were extracted from [161], B. Choi and K. Shin, *Solid State Ionics* 86–88, 303 (1996), and line is for eye guide.

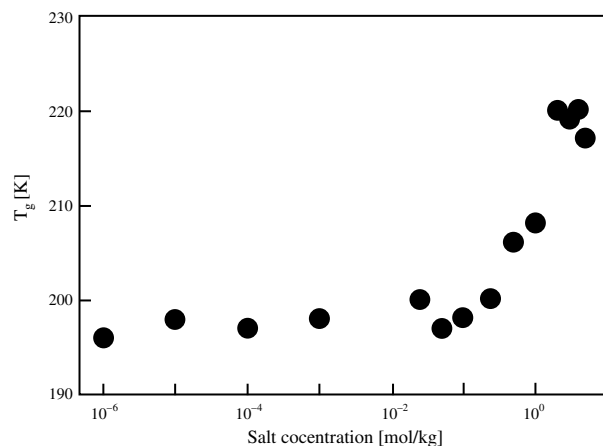


**Figure 35.** Effect of filler content on the melting enthalpy (solid circle) and crystallinity (open circle) of PEO<sub>16</sub>:LiClO<sub>4</sub> containing SiC. Data points were extracted from [161], B. Choi and K. Shin, *Solid State Ionics* 86–88, 303 (1996).

nucleation effect was considered to be sufficient to overcome the hindrance of crystallization due to the enhancement of the segmental motion of the PEO [161].

### 13.2. Effect of Salt Concentration on the Glass Temperature

Marcinek et al. observed the effect of salt concentration of the system of PEG:LiClO<sub>4</sub> +  $\alpha$ -Al<sub>2</sub>O<sub>3</sub> and found that the glass temperature also increases with the salt concentration as appears in Figure 36 [137]. For concentrations up to 0.25 mol/kg salt concentration, the  $T_g$  is almost constant. At higher salt concentrations, the plot of  $T_g$  with respect to the logarithm of salt concentration likely increases with an exponential trend. They also compared the variation of glass temperature of system free of filler and found that at up to 0.26 mol/kg salt concentration, the  $T_g$  of both samples is almost similar.



**Figure 36.** Effect of salt concentration on the glass temperature of PEG:LiClO<sub>4</sub> containing  $\alpha$ -Al<sub>2</sub>O<sub>3</sub>. Data points were extracted from [137], M. Marcinek et al., *Solid State Ionics* 136–137, 1175 (2000).



At higher salt concentration, the  $T_g$  of filler-free samples is higher than that of sample containing filler. Sun et al. found that the glass temperature of a system of poly(*N,N*-dimethylaminoethyl methacrylate)-tetraglyme:LiClO<sub>4</sub> polymer electrolytes increases strongly with the increasing salt concentration over the first 0.5 mol/kg addition of LiClO<sub>4</sub>. Further addition of salt results in only a minor increase in the glass temperature [165].

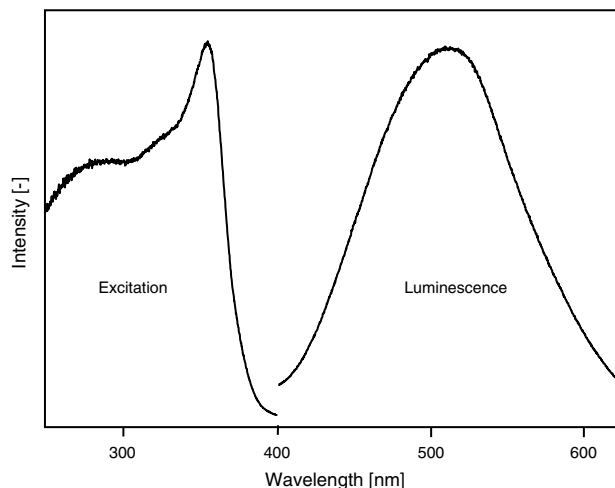
## 14. LUMINESCENT COMPOSITES

Most fillers used in polymer electrolyte nanocomposites are “optically inactive,” that is, they do not have any luminescence properties. It would be interesting to investigate the properties of composite if the fillers loaded in polymer emit luminescence. This approach would have interesting applications such as the possibility of obtaining information regarding the degradation of battery or fuel cells using such composites, for example based on the luminescence intensity emitted by the filler. Changes in properties of the polymer when the battery or fuel cell degrades from the initial performance would be expected. This indicates that the properties of the medium around the filler would change when the battery or fuel cell degrades. It would affect the detected luminescence intensity emitted by the filler change. Based on this detected luminescence, the current performance of the battery or fuel cell could be determined.

Zinc oxide (ZnO) is one of the promising materials for preparing composite polymer electrolytes that are luminescent. ZnO nanoparticles play a role as an agent for reducing the tendency of the polymer matrix to crystallize and simultaneously as luminescence centers. Since the luminescence spectra of ZnO are dependent on crystalline size (quantum size effect), the emitted wavelength can be controlled by adjusting the size of the ZnO nanocrystallites. ZnO particles of different sizes can be produced easily using, for example, a colloidal process, so that the “color” of the composite can be easily tuned. A “blue composite” can be prepared using smaller ZnO nanoparticles, while a “yellow composite” can be produced using large ZnO particle size. This composite has also considerable potential for fabricating devices that simultaneously produce both electrical current and light, such as luminescent electrochemical cells, self-powered displays, etc.

Figure 37 (right) shows an example of a photoluminescence (PL) spectrum of composite polymer electrolytes containing ZnO nanoparticles [62]. The sample produced a highly intense green luminescence. The color of those samples can clearly be observed by the naked eye even using a hand-held UV lamp as background illumination in the laboratory. The PL peaks can be shifted to lower or higher wavelengths by altering the concentration of the precursors. The luminescence spectrum was produced by an electron transition from the bottom of conduction band to a state located near the center of the band.

The corresponding excitation spectra of the samples are shown in Figure 37 (left). A peak is related to the band-edge transition. The wavelength peak is smaller than that observed for bulk ZnO, which shows a peak at 365 nm (energy about 3.4 eV). The shift of the band-edge peak to lower wavelengths indicates the presence of a quantum size



**Figure 37.** Left: Excitation spectra of PEG:Li containing ZnO nanoparticles. Right: The corresponding luminescence spectra. Data were extracted from [62], Mikrajuddin et al., *J. Electrochem. Soc.* 149, H107 (2002).

effect of the optical bandgap. Using the size-dependent optical bandgap equation, the size of ZnO nanoparticles in the matrix is estimated to be around 6 nm.

The *in-situ* growth of nanoparticles in the polymer matrix ensures the dispersion of nanoparticles in polymer bulk easily without the need for an intensive mixing process. The selection of a precursor containing lithium ions permits the insertion of cations during the growth process. This approach has been used to produce composite polymer electrolytes containing ZnO nanoparticles using lithium hydroxide as one precursor and a hygroscopic solution of zinc acetate as another precursor. A high molecular weight polyethylene glycol was first mixed with a solution of lithium hydroxide and then further mixed with a hygroscopic solution of zinc acetate. Since lithium did not participate in the formation of zinc oxide, lithium ions were left in the polymer matrix and were then able to take part as ion carriers.

## 15. CONCLUSION

Stable and high electrical conductivity polymer electrolytes are required for fabricating flexible and environmentally friendly fuel cells and batteries. Some important parameters critical to polymer electrolytes in order to bring this material into industries have been discussed in this review. Although high electrical conductivity of polymer electrolytes usually appears at high temperatures, many efforts to improve the electrical conductivity at room temperature have been introduced by researchers all around the world. They include the synthesis of amorphous polymer matrix, addition of second phase in the host polymer matrix (plasticizers) like low molecular weight polymers, and addition of size chains. The most popular approach now is the addition of ceramic filler in nanometer scale. This approach becomes interesting since the addition of nanometer-sized ceramic filler improves not only the electrical conductivity of polymer electrolytes but also the mechanical properties. This material, usually named

as polymer electrolyte nanocomposite, attracts a lot of attention because of the simplicity in the processing. Various kinds of polymer in a lot of molecular weights as well as various kinds of ceramic filler in a lot of sizes are available in the market. The process of production of composites is relatively simple, that is, by just mixing the polymer, salt, and filler in a common solution, ended with drying. Methods of preparation of polymer electrolyte nanocomposites were briefly discussed in this review.

Characterizations of the prepared films are important to understand the properties as well as to find the optimum preparation conditions. Various methods of characterization, including electrical, spectroscopic, microscopic, and thermal characterizations, were discussed briefly. Detailed explanations of the methods might be found in some analytical chemistry books.

In the final part, we discussed some parameters which affect the properties of polymer electrolyte composites. It was found that the properties of the composites are sensitive to the preparation condition as well as material used for making the composites. For example, the electrical conductivity is greatly dependent on the volume fraction of fillers, surface property, filler size, type of salt, side chain, etc. Also the mechanical properties are affected by filler content, surface property, and salt concentration.

## GLOSSARY

**Anion** An ionic species having a negative charge.

**Battery** A device that stores energy and makes it available in an electrical form.

**Blending** Physically mixing several types of materials so thoroughly that they appear to be indistinguishable from each other in the product.

**Casting method** A method of forming sheets of composite materials by pouring fluid materials onto a flat surface.

**Cation** An ionic species having a positive charge.

**Charging** Supply electric current to a battery.

**Copolymerization** Polymerization with two or more different monomers.

**Cycle life** The number of charge/discharge cycles that are possible before failure occurs.

**Differential scanning calorimetry** A materials characterization laboratory technique by which the temperature of a sample of the substance in question is raised in increments while a reference is heated in the same rate. The amount of heat that is required to heat the sample and the reference to each temperature is recorded and can be plotted. From these plots, melting points, phase change temperatures, chemical reaction temperatures, and glass transition temperature of polymers can be determined.

**Discharging** Withdrawing charge from a battery.

**Doctor blade technique** A technique using a flat bar used for regulating the amount of liquid material on the rollers of a coating machine, or to control the thickness of a coating after it has been applied to a substrate.

**Electrical conductivity** A measure of how well a material accommodates the transport of electric charge.

**Energy density** The energy obtainable per unit volume.

**Energy efficiency** (energy released on discharge)/(energy required for charge).

**Filler** Inorganic particles added to polymer matrix.

**Fourier transform spectroscopy** 1A measurement technique whereby spectra are collected based on the response from a pulse of electromagnetic radiation. Fourier transform spectroscopy is more sensitive and has a much shorter sampling time than conventional spectroscopic techniques.

**Free volume** The extrapolated differences in volume between a glass and the extrapolation of the melt curve is called the free volume. The free volume is associated with the space between molecules in a sample.

**Glass transition temperature ( $T_g$ )** The temperature below which molecules have very little mobility. On a larger scale, polymers are rigid and brittle below their glass transition temperature and elastic above it.  $T_g$  is usually applicable to amorphous phases and is commonly applicable to glasses and plastics.

**Hot press** The forming of a compact material at temperatures sufficiently high to cause concurrent sintering.

**Melting point** The temperature at which it changes state from solid to liquid. When considered as the temperature of the reverse change, the temperature is referred to as the freezing point.

**Nuclear magnetic resonance (NMR)** A physical phenomenon described independently by Felix Bloch and Edward Mills Purcell in 1946. It involves the interaction of atomic nuclei placed in an external magnetic field with an applied electromagnetic field oscillating at a particular frequency. Magnetic conditions within the material are measured by monitoring the radiation absorbed and emitted by the atomic nuclei. NMR is used as a spectroscopy technique to obtain physical, chemical, and electronic properties of molecules. It is also the underlying principle of Magnetic Resonance Imaging. NMR is one of the techniques used to build quantum computers.

**Number average molecular weight** A way of determining the molecular weight of a polymer. Polymer molecules, even ones of the same type, come in different sizes (chain lengths, for linear polymers), so we have to take an average of some kind. The number average molecular weight is the common average of the molecular weights of the individual polymers. It is determined by measuring the molecular weight of  $n$  polymer molecules, summing the weights, and dividing by  $n$ . The number average molecular weight of a polymer can be determined by osmometry, end-group titration, and colligative properties.

**Plasticizers** Materials added to polymer matrix to improve the fraction of amorphous state.

**Polymer electrolytes** Electrolytes which using polymer as a media to dissociate ions.

**Rechargeable batteries** Batteries that can be restored to full charge by the application of electricity. They come in many different designs using different chemistry.

**Small angle x-ray scattering** A laboratory technique in which photons are elastically scattered from a sample. The sample can not be too thick. Liquids can be examined. Features on the nanometer length scale can be examined.

**Specific energy** The energy obtainable per unit weight.

**Weight average molecular weight** A way of determining the molecular weight of a polymer. Polymer molecules, even if of the same type, come in different sizes (chain lengths, for linear polymers), so we have to take an average of some kind. For the weight average molecular weight, this is done as follows: weigh a number of polymer molecules, add the squares of these weights, and then divide by the total weight of the molecules. Intuitively, if the weight average molecular weight is  $w$ , and you pick a random monomer, then the polymer it belongs to will have a weight of  $w$  on average. The weight average molecular weight can be determined by light scattering, small angle neutron scattering (SANS), and by sedimentation velocity.

**Wide angle x-ray scattering** An X-ray diffraction technique that is often used to determine the crystalline structure of polymers.

## ACKNOWLEDGMENT

Japan Society for the Promotion of Science (JSPS) Postdoctoral Fellowship for Mikrajuddin Abdullah is gratefully acknowledged.

## REFERENCES

- J. O. Besenhard and M. Winter, *ChemPhysChem* 3, 155 (2002).
- J.-M. Tarascon and M. Armand, *Nature* 414, 359 (2001).
- F. B. Dias, L. Plomp, and J. B. J. Veldhuis, *J. Power Sources* 88, 169 (2000).
- M. Gauthier, M. Armand, and L. Krause, "Proceedings of the 7th International Meeting on Lithium Batteries," 1994, abstract p. 177.
- M. Liu, S. J. Visco, and L. C. De Jonghe, *J. Electrochem. Soc.* 138, 1891 (1991).
- H. Oman, "Proceedings of the 12th Annual Battery Conference on Applications and Advances," 1997, p. 31.
- T. Turrentine and K. Kurani, Report UCD-ITS-RR-95-5, Institute of Transportation Studies, 1995.
- P. Lightfoot, M. A. Metha, and P. G. Bruce, *Science* 262, 883 (1993).
- F. Croce, G. B. Appetecchi, L. Persi, and B. Scrosati, *Nature* 394, 456 (1998).
- D. E. Fenton, J. E. Parker, and P. V. Wright, *Polymer* 14, 589 (1973).
- P. V. Wright, *Br. Polym. J.* 7, 319 (1975).
- M. B. Armand, J. M. Chabagno, and M. J. Duclot, in "Fast Ion Transport in Solids" (M. J. Duclot, P. Vashishta, J. M. Mundy, and G. K. Shenoi, Eds.), Elsevier, North Holland, Amsterdam, 1979.
- F. B. Dias, L. Plomp, and J. B. J. Feldhuis, *J. Power Sources* 88, 169 (2000).
- J. R. MacCallum, M. J. Smith, and C. A. Vincent, *Solid State Ionics* 11, 307 (1981).
- M. Watanabe, S. Nagano, K. Sanui, and N. Ogata, *J. Power Sources* 35, 327 (1987).
- Y. Song, X. Peng, Y. Lin, B. Wang, and D. Chen, *Solid State Ionics* 76, 35 (1995).
- O. Inganas, *Br. Polym. J.* 20, 233 (1988).
- D. W. Kim, J. K. Park, and H. W. Rhee, *Solid State Ionics* 83, 49 (1996).
- R. J. Young and P. A. Lovell, "Introduction to Polymers," 2nd ed., p. 297. Chapman & Hall, London, 1991.
- J.-S. Chung and H.-J. Sohn, *J. Power Sources* 112, 671 (2002).
- A. Nishimoto, M. Watanabe, Y. Ikeda, and S. Kohjiya, *Electrochim. Acta* 43, 1177 (1998).
- Y. Ikeda, Y. Wada, Y. Mataba, S. Murakami, and S. Kohjiya, *Electrochim. Acta* 45, 1167 (2000).
- K. Motogami, M. Kono, S. Mori, M. Watanabe, and N. Ogata, *Electrochim. Acta* 37, 1725 (1992).
- Y. Ikeda, H. Masuo, S. Syoji, T. Sakashita, Y. Matoba, and S. Kohjiya, *Polym. Int.* 43, 269 (1997).
- M. Watanabe, S. Yamada, K. Sanui, and N. Ogata, *J. Chem. Soc. Chem. Commun.* 929 (1993).
- M. Watanabe, S. Yamada, and N. Ogata, *Electrochim. Acta* 40, 2285 (1995).
- Y. Tsuda, T. Nohira, Y. Nakamori, K. Matsumoto, R. Hagiwara, and Y. Ito, *Solid State Ionics* 149, 295 (2002).
- G. Feullade and P. Perche, *J. Appl. Electrochem.* 5, 63 (1975).
- D. R. MacFarlane, J. Sun, P. Meakin, P. Fasoulopoulos, J. Hey, and M. Forsyth, *Electrochim. Acta* 40, 2131 (1995).
- S. Chintapalli and R. French, *Solid State Ionics* 86-88, 341 (1996).
- H. W. Rhee, W. I. Jung, M. K. Song, S. Y. Oh, and J. W. Choi, *Mol. Cryst. Liq. Cryst. Sci. Technol. A* 294, 225 (1997).
- M. Morita et al., *J. Electrochem. Soc.* 137, 3401 (1990).
- D. W. Xia, D. Soltz, and J. Smidt, *Solid State Ionics* 14, 221 (1984).
- M. S. Michael, M. M. E. Jacob, S. R. S. Prabaharan, and S. Radhakrishna, *Solid State Ionics* 98, 167 (1997).
- J. E. Weston and B. C. H. Steele, *Solid State Ionics* 7, 75 (1982).
- W. Krawiec, L. G. Scanlon, Jr., J. P. Fellner, R. A. Vaia, S. Vasudevan, and E. P. Gianellis, *J. Power Sources* 54, 310 (1995).
- B. K. Choi and K. H. Shin, *Solid State Ionics* 86-88, 303 (1996).
- K. Nairn, M. Forsyth, H. Every, M. Greville, and D. R. MacFarlane, *Solid State Ionics* 86-88, 589 (1996).
- G. K. R. Sanadeera, M. A. Careem, S. Skaarup, and K. West, *Solid State Ionics* 85, 37 (1996).
- W. Wieczorek, J. R. Stevens, and Z. Florzanczyk, *Solid State Ionics* 85, 67 (1996).
- D. Golodnisky, G. Ardel, and E. Peled, *Solid State Ionics* 85, 231 (1996).
- E. Peled, D. Golodnisky, G. Ardel, and V. Eshkenazy, *Electrochim. Acta* 40, 2197 (1995).
- Y. Matsuo and J. Kuwano, *Solid State Ionics* 79, 295 (1995).
- M. Slane and M. Solomon, *J. Power Sources* 55, 7 (1995).
- Y. W. Kim, W. Lee, and B. K. Choi, *Electrochim. Acta* 45, 1473 (2000).
- J. M. Pernaut and A. L. deOliveira, *Synth. Met.* 84, 443 (1997).
- M. C. Borghini, M. Mastragostino, and A. Zanelli, *J. Power Sources* 68, 52 (1997).
- G. Ardel, G. Golodnitsky, E. Stauss, and E. Peled, *J. Power Sources*, in press.
- S. S. Sekhon, G. S. Sandhar, S. A. Agnihotri, and S. Chandra, *Bull. Electrochem.* 12, 415 (1996).
- S. S. Sekhon and A. Singh, *Bull. Electrochem.* 12, 671 (1996).
- S. S. Sekhon and G. S. Sandhar, *Eur. Polym. J.* 34, 435 (1998).
- S. A. Hashmi, A. K. Thakur, and H. M. Upadhyaya, *Eur. Polym. J.* 34, 1277 (1998).
- H. W. Chen and F. C. Chang, *Polymer* 42, 9763 (2001).
- A. Chandra, P. K. Singh, and S. Chandra, *Solid State Ionics*, 154-155, 15 (2002).
- G. Katsaros, T. Stergiopolous, I. M. Arabatzis, K. G. Papagodokostaki, and P. Falaras, *J. Photochem. Photobiol. A* 149, 191 (2002).
- B. O'Regan and M. Gratzel, *Nature* 353, 737 (1991).
- M. K. Nazeeruddin, A. Kay, I. Rodicio, R. Humphry-Baker, E. Muller, P. Liska, N. Vlachopoulos, and M. Gratzel, *J. Am. Chem. Soc.* 115, 6382 (1993).
- M. K. Nazeeruddin, A. Kay, I. Rodicio, R. Humphry-Baker, E. Muller, P. Liska, N. Vlachopoulos, and M. Gratzel, *J. Am. Chem. Soc.* 115, 6382 (1993).
- A. F. Nogueira, J. R. Durrant, and M.-A. De Paoli, *Adv. Mater.* 11, 826 (2001).

60. G. Ardel, D. Golodnitsky, K. Freedman, E. Peled, G. B. Appetecchi, P. Romagnoli, and B. Scrosati, *J. Power Sources* 110, 152 (2002).
61. C. Capiglia, J. Yang, N. Imanishi, A. Hirano, Y. Takeda, and O. Yamamoto, *J. Power Sources* (in press).
62. Mikrajuddin, I. W. Lenggoro, F. G. Shi, and K. Okuyama, *J. Electrochem. Soc.* 149, H107 (2002).
63. Mikrajuddin, I. W. Lenggoro, F. G. Shi, and K. Okuyama, *J. Phys. Chem. B*, 107, 1957 (2003).
64. J. B. Goodenough, *Solid State Ionics* 69, 184 (1994).
65. K. M. Abraham and M. Alamgir, *Chem. Mater.* 3, 339 (1991).
66. M. K. Song, J. Y. Cho, B. W. Cho, and H. W. Rhee, *J. Power Sources* 110, 209 (2002).
67. C. J. Leo, G. V. S. Rao, and B. V. R. Chowdary, *Solid State Ionics* 148, 159 (2002).
68. D. P. Almond and A. R. West, *Solid State Ionics* 23, 27 (1987).
69. M. Siekierski, W. Wiczorek, and J. Przulski, *Electrochim. Acta* 43, 1339 (1998).
70. C. Kittel, "Introduction to Solid State Physics," 7th ed., p. 310. John Wiley, New York, 1996.
71. Y. Ma, M. Doyle, T. Fuller, M. M. Doeff, L. C. DeJonghe, and J. Newman, *J. Electrochem. Soc.* 142, 1859 (1995).
72. S. Strauss, D. Golodnitsky, G. Ardel, and E. Peled, *Electrochim. Acta* 43, 1315 (1998).
73. J. W. Lorimer, *J. Power Sources* 26, 491 (1989).
74. P. R. Sorensen and T. Jacobson, *Electrochim. Acta* 27, 1671 (1982).
75. K. Kiukkola and C. Wagner, *J. Electrochem. Soc.* 104, 308 (1957); 104, 379 (1957).
76. J. Evans, C. A. Vincent, and P. G. Bruce, *Polymer* 28, 2324 (1987).
77. M. Doyle and J. Newman, *J. Electrochem. Soc.* 142, 3465 (1995).
78. P. G. Bruce, M. T. Hardgrave, and C. A. Vincent, *Electrochim. Acta* 37, 1517 (1992).
79. F. Croce, L. Persi, F. Ronci, and B. Scrosati, *Solid State Ionics* 135, 47 (2000).
80. S. Chung, Y. Wang, L. Persi, F. Croce, S. G. Greenbaum, B. Scrosati, and E. Plichta, *J. Power Sources* 97–98, 644 (2001).
81. S. D. Brown, S. G. Greenbaum, M. G. McLin, M. C. Wintersgill, and J. J. Fontanella, *Solid State Ionics* 67, 257 (1994).
82. W. Gang, J. Roos, D. Brinkmann, F. Capuano, F. Croce, and B. Scrosati, *Solid State Ionics* 53–56, 1102 (1992).
83. Y. Dai, Y. Wang, S. G. Greenbaum, S. A. Bajue, D. Golodnitsky, G. Ardel, E. Strauss, and E. Peled, *Electrochim. Acta* 43, 1557 (1998).
84. S. Chandra, "Superionic Solids." North-Holland, Amsterdam, 1981.
85. P. A. Allen, in "International Review of Science—Physical Chemistry" (C. A. McDowell, Ed.), Ser. 1, Vol. 4. Butterworths, London and Boston, 1972.
86. G. E. Pake, in "Advances in Solid State Physics" (F. Seitz and D. Turnbull, Eds.), Vol. 2, Academic Press, New York, 1956.
87. A. Abragam, "The Principles of Nuclear Magnetic Resonance." Oxford Univ. Press, London, 1961.
88. J. R. Hendrickson and P. J. Bray, *J. Magn. Reson.* 9, 341 (1973).
89. N. Bloembergen, E. M. Purcell, and R. V. Pound, *Phys. Rev.* 73, 679 (1948).
90. P. Mansfield, "Progress in NMR Spectroscopy," Vol. 8. Pergamon, Oxford, 1971.
91. S. Wong, R. A. Vaia, E. P. Giannelis, and D. B. Zax, *Solid State Ionics* 86–88, 547 (1996).
92. S. Wong and D. B. Zax, *Electrochim. Acta* 42, 3513 (1997).
93. F. Croce, G. B. Appetecchi, S. Slane, M. Salomon, M. Tavares, S. Arumugam, Y. Wang, and S. G. Greenbaum, *Solid State Ionics* 86–88, 307 (1996).
94. C. G. Joo, L. M. Bronstein, R. L. Karlinsey, and J. W. Zwanziger, *Solid State Nucl. Magn. Res.* 22, 235 (2002).
95. T. J. Singh, T. Mimani, K. C. Patil, and S. V. Bhat, *Solid State Ionics*, 154–155, 21 (2002).
96. A. C. Bloise, C. C. Tambelli, R. W. A. Franco, J. P. Donoso, C. J. Magon, M. F. Souza, A. V. Rosario, and E. C. Pereira, *Electrochim. Acta* 46, 1571 (2001).
97. R. W. A. Franco et al., *Solid State Ionics* 136–137, 1181 (2000).
98. S. D. Brown, S. G. Greenbaum, M. G. McLin, M. C. Wintersgill, and J. J. Fontanella, *Solid State Ionics* 67, 257 (1994).
99. M. Forsyth, D. R. MacFarlane, A. Best, J. Adebahr, P. Jacobson, and A. J. Hill, *Solid State Ionics* 147, 203 (2002).
100. P. W. Atkins and R. S. Friedman, "Molecular Quantum Mechanics." Oxford Univ. Press, London, 1997.
101. W. Huang, R. French, and R. A. Wheeler, *J. Phys. Chem.* 98, 100 (1994).
102. A. Ferry, G. Oradd, and P. Jacobsson, *Electrochim. Acta.* 43, 1471 (1998).
103. H. Ericson, B. Mattsson, L. M. Torell, H. Rinne, and F. Sundholm, *Electrochim. Acta* 43, 1401 (1998).
104. C. H. Kim, J. K. Park, S. I. Moon, and M. S. Yoon, *Electrochim. Acta* 43, 1421 (1998).
105. A. Beronson and J. Lindgre, *Solid State Ionics* 60, 37 (1993).
106. A. Borkowska, A. Reda, A. Zalewska, and W. Wiczorek, *Electrochim. Acta* 46, 1731 (2001).
107. M. Solomon, M. Xu, E. M. Eyring, and S. Petrucci, *J. Phys. Chem.* 98, 8234 (1994).
108. D. M. Vossage and B. V. R. Chowdary, *Electrochim. Acta* 40, 2109 (1995).
109. Y. Liu, J. Y. Lee, and L. Hong, *J. Power Sources* 109, 507 (2002).
110. A. R. West, "Basic Solid State Chemistry." Wiley, Chichester, 1988.
111. J. H. Shin, K. W. Kim, H. J. Ahn, and J. H. Ahn, *Mater. Sci. Eng. B* 95, 148 (2002).
112. C. G. Leo, G. V. S. Rao, and B. V. R. Chowdary, *Solid State Ionics* 148, 159 (2002).
113. Z. Wen, M. Wu, T. Itoh, M. Kubo, Z. Lin, and O. Yamamoto, *Solid State Ionics* 148, 185 (2002).
114. Z. Y. Wen, T. Itoh, N. Hirata, M. Ikeda, M. Kubo, and O. Yamamoto, *J. Power Sources* 90, 20 (2000).
115. D. Golodnitsky, G. Ardel, and E. Peled, *Solid State Ionics* 47, 141 (2002).
116. B. Wang and L. Gu, *Mater. Lett.* 57, 361 (2002).
117. L. E. Brus, *J. Phys. Chem.* 90, 2555 (1986).
118. L. E. Brus, *J. Chem. Phys.* 79, 5566 (1983).
119. L. E. Brus, *J. Chem. Phys.* 80, 4403 (1984).
120. M. L. Granvalet-Manchini, T. Hanrath, and D. Teeters, *Solid State Ionics* 135, 283 (2000).
121. Y. W. Kim, W. Lee, and B. K. Choi, *Electrochim. Acta* 45, 1473 (2000).
122. J. H. Magill, in "Treatise on Materials Science and Technology" (J. M. Schultz, Ed.), Vol. 10A. Academic Press, New York, 1977.
123. H.-W. Chen and F.-C. Chang, *Polymer* 42, 9763 (2001).
124. W. Wiczorek, D. Raducha, A. Zalewska, and J. R. Stevens, *J. Phys. Chem. B* 102, 8725 (1998).
125. W. Wiczorek, A. Zalewska, D. Raducha, Z. Florzanczyk, and J. R. Stevens, *Macromolecules* 29, 143 (1996).
126. W. Wiczorek, A. Zalewska, D. Raducha, Z. Florzanczyk, and J. R. Stevens, *J. Phys. Chem. B* 102, 352 (1998).
127. G. Drezzen, D. A. Ivanov, B. Nysten, and G. Groeninckx, *Polymer* 41, 1395 (2000).
128. J. Przulski, M. Siekierski, and W. Wiczorek, *Electrochim. Acta* 40, 2102 (1995).
129. J. C. Maxwell, "A Treatise in Electricity and Magnetism," Vol. 1, Chapter XI. Clarendon, London, 1892.
130. M. Nakamura, *Phys. Rev. B* 29, 3691 (1984).
131. C. W. Nan, *Prog. Mater. Sci.* 37, 1 (1993).
132. C. W. Nan and D. M. Smith, *Mater. Sci. Eng. B* 10, 99 (1991).
133. S. Kirkpatrick, *Rev. Mod. Phys.* 45, 574 (1973).
134. Mikrajuddin, F. G. Shi, and K. Okuyama, *J. Electrochem. Soc.* 147, 3157 (2000).

135. C. C. Liang, *J. Electrochem. Soc.* 120, 1289 (1973).
136. G. B. Appetecchi and S. Passerini, *Electrochim Acta* 45, 2139 (2000).
137. M. Marcinek, A. Zalewska, G. Zukowska, and W. Wieczorek, *Solid State Ionics* 136–137, 1175 (2000).
138. M. M. Doeff, P. Georen, J. Qiao, J. Kerr, and L. C. De Jonghe, *J. Electrochem. Soc.* 146, 2024 (1999).
139. R. Dupon, B. L. Papke, M. A. Ratner, D. H. Whitmore, and D. F. Shriver, *J. Am. Chem. Soc.* 104, 6247 (1982).
140. P. Jeevanandam and S. Vasudevan, *J. Phys. Chem. B* 102, 4753 (1998).
141. H. Eliasson, I. Albinsson, and B. E. Mellander, *Electrochim. Acta* 43, 1459 (1998).
142. Z. Florzanczyk, E. Zygado-Monikowska, E. Rogalska-Joska, F. Krok, J. R. Dygao, and B. Misztal-Faraj, *Solid State Ionics*, 152–153, 227 (2002).
143. F. Croce, L. Persi, B. Scrosati, F. Serraino-Fiory, E. Plichta, and M. A. Hendrickson, *Electrochim. Acta* 46, 2457 (2001).
144. C. Capiglia, P. Mustarelli, E. Quartarome, C. Tomasi, and A. Magistris, *Solid State Ionics* 118, 73 (1999).
145. H. J. Walls, J. Zhou, J. A. Yerian, P. S. Fedkiw, S. A. Khan, M. K. Stowe, and G. L. Baker, *J. Power Sources* 89, 156 (2000).
146. J. Fan, S. R. Rafhavan, X. Y. Yu, X. A. Khan, P. S. Fedkiw, J. Hou, and G. L. Baker, *Solid State Ionics* 111, 117 (1998).
147. A. Chandra, P. C. Srivastava, and S. Chandra, *J. Mater. Sci.* 30, 3633 (1995).
148. W. Wieczorek, Z. Florzanczyk, and J. R. Stevens, *Electrochim. Acta* 40, 2251 (1995).
149. J. Maier, *J. Phys. Chem. Solids* 46, 309 (1985).
150. A. Kumar and K. Shahi, *Solid State Commun.* 94, 813 (1995).
151. D. Golodnitsky, G. Ardel, and E. Peled, *Solid State Ionics* 85, 231 (1996).
152. C. J. Leo, G. V. S. Rao, and B. V. R. Chowdari, *Solid State Ionics* 148, 159 (2002).
153. J. H. Shin, K. W. Kim, H. J. Ahn, and A. H. Ahn, *Mater. Sci. Eng. B* 95, 148 (2002).
154. G. Appetecchi, F. Croce, L. Persi, F. Ronci, and B. Scrosati, *Electrochim. Acta* 45, 1481 (2000).
155. G. B. Appetecchi, P. Romagnoli, and B. Scrosati, *Electrochem. Commun.* 3, 251 (2001).
156. J. W. Weston and B. C. H. Steele, *Solid State Ionics* 7, 75 (1982).
157. H. J. Wals, J. Zhou, J. A. Yerian, P. S. Fedkiw, S. A. Khan, M. K. Stowe, and G. L. Baker, *J. Power Sources* 89, 156 (2000).
158. B. Kumar and L. G. Scanlon, *J. Electroceram.* 5, 127 (2000).
159. R. B. Seymour, "Reinforced Plastics: Properties and Applications," p. 52. American Society of Metals, Int., Metals Park, OH, 1991.
160. F. M. Gray, "Solid Polymer Electrolytes." VCH, Weinheim, 1991.
161. B. Choi and K. Shin, *Solid State Ionics* 86–88, 303 (1996).
162. J.-S. Chung and H.-J. Sohn, *J. Power Sources* 112, 671 (2002).
163. W. Wieczorek, K. Such, S. H. Chung, and J. R. Stevens, *J. Phys. Chem.* 98, 9047 (1994).
164. J. Przyluski, K. Such, H. Wycislik, W. Wieczorek, and Z. Florzanczyk, *Synth. Metals* 35, 241 (1990).
165. J. Sun, D. R. MacFarlane, and M. Forsyth, *Electrochim. Acta* 40, 2301 (1995).

# Polymer Nanostructures

Liming Dai

The University of Akron, Akron, Ohio, USA

## CONTENTS

1. Introduction
  2. Polymer Nanoparticles
  3. Polymer Nanowires, Nanotubes,  
and Nanofibers
  4. Polymer Nanofilms
  5. Nanostructured Polymers with Special  
Architectures
  6. Concluding Remarks
- Glossary  
References

## 1. INTRODUCTION

As the term implies, polymer (or macromolecule) refers to a molecule of extraordinarily large size (typically >1000 in molecular weight). Although polymer molecules are large, they are made up of individual, repeating units termed monomers. The overall properties of a given polymeric material depend on: (i) the constituent monomer units and the way they are arranged in the macromolecule and (ii) the spatial arrangement of the constituent macromolecular chains and the nature of the intermolecular interactions that hold them together [1]. These interesting structure–property relationships provide a broad basis to allow the development of various polymeric materials (e.g., polymer fibers, films, powders) with different properties from the same macromolecules.

Polymers have been widely used in all aspects of our daily life. After all, our clothes are made from synthetic fibers, car tires from rubbers, and computer chips from plastics. It is now difficult to imagine what our life would be like if there were no polymers. With the recent significant advances in nanoscience and nanotechnology, various nanostructured polymers have been devised for a wide range of advanced applications. Examples include the use of polymer nanoparticles as drug delivery devices, polymer nanofibers as conducting wires, and polymer thin films and periodically structured polymeric structures for optoelectronic devices.

Like most other nanomaterials [2, 3], nanostructured polymers could also possess interesting mechanical, electronic, optical, and even magnetic properties that are different from those of the bulk materials, depending on their size, shape, and composition.

The development of nanostructured polymers has opened up novel fundamental and applied frontiers, which has attracted tremendous interest in recent years. This chapter provides an overview on the rapidly developing field of polymer nanostructures. We will first discuss the preparation of polymer nanoparticles, with an emphasis on their potential applications for controlled drug delivery. We will then describe the preparation of fiberlike polymers (i.e., nanowires, nanotubes, and nanofibers) of potential applications in electronic devices. Finally, we will examine the use of polymer thin films (nanofilms or nanosheets) in organic optoelectronic devices, along with the periodically structured polymers as photonic crystals.

## 2. POLYMER NANOPARTICLES

Polymer nanoparticles are of special interest in medical applications. In particular, the recent development of polymer nanoparticles as effective drug delivery devices is revolutionizing the way in which medical treatments are performed. Encapsulating or incorporating drugs in polymer nanoparticles allows effective delivery of the drug molecules to the target site and their controlled release, leading to an increase in the therapeutic benefit and reduction of the side effects [4]. Significant advances in polymer science and biomedical engineering have facilitated the development of new synthetic approaches to polymer nanoparticles.

Depending on the method of preparation, polymer nanospheres or nanocapsules can be obtained. These polymer nanoparticles, usually having a diameter ranging from 10 to 300 nm, can be prepared by various techniques, including *in-situ* polymerization, dispersion of preformed polymers, and self-assembling. The *in vitro* and *in vivo* performances of various polymer nanoparticles as drug delivery devices have recently been discussed in several excellent review articles [5, 6]. In what follows, we provide a status summary of the preparation of polymer nanoparticles.

## 2.1. Polymer Nanospheres by Polymerization

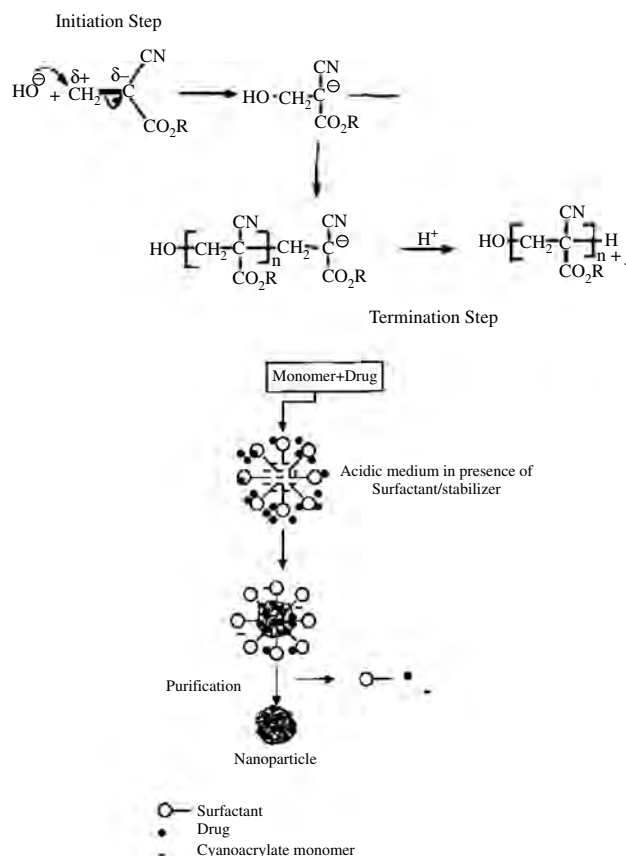
While conventional emulsion polymerization has been widely used to produce polymer particles with the size range of 0.1–1  $\mu\text{m}$ , miniemulsion and microemulsion polymerization methods have recently been developed for the preparation of polymer nanoparticles in the ranges of 50–200 and 15–50 nm, respectively [7, 8]. Using polymerizable amphiphilic PEO macromonomers [i.e.,  $\text{CH}_3\text{O}-(\text{CH}_2\text{CH}_2\text{O})_n-(\text{CH}_2)_{11}-\text{OOC}(\text{CH}_3)=\text{CH}_2$ ,  $n = 10, 15$ , or 40; designated as C1-PEO-C11-MA- $n$ ] as stabilizers in dispersion/emulsion polymerizations, for example, Gan and co-workers have successfully prepared polymer [e.g., polystyrene (PS), poly(methyl methacrylate) (PMMA)] microlatexes with particle sizes ranging from 15 to 200 nm [9–11]. A large amount of surfactants, however, is normally required for these emulsion polymerization, though high solid-contents up to 40 wt% have been reported [12, 13]. The relatively high content of surfactant in the dispersions often limits their biomedical applications [14–16].

Recently, considerable efforts have been devoted to investigating ways to minimize the amount of surfactant used and to maximize the solid content. In this context, both solution and interfacial polymerization methods have been used to encapsulate drug molecules in polymer nanoparticles. For example, Couvreur and co-workers [16], synthesized poly(alkylcyanoacrylate) nanoparticles by polymerizing methyl or ethyl cyanoacrylate in aqueous acidic medium in the presence of polysorbate-20 as a surfactant. The polymerization follows an anionic mechanism and the schematic representation of the procedure used for the production of poly(alkylcyanoacrylate) nanoparticles is given in Figure 1.

For controlled release purposes, drug molecules can be dissolved in the polymerization medium either before or after the polymerization reaction. The resulting suspension of polymer nanoparticles is then purified by ultracentrifugation or by resuspending the nanoparticles in an isotonic surfactant-free medium.

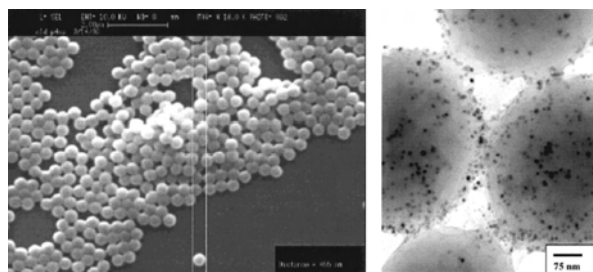
More recently, Lowe and Temple [17] have used the interfacial polymerization technique originally proposed by Al-Khoury Fallouh, et al. [18] to prepare poly(isobutyl cyanoacrylate) nanoparticles for encapsulating calcitonin. In this case, isobutyl cyanoacrylate monomers and calcitonin were dissolved in an ethanol solution containing Myglol® 812 oil. The oil solution was then added dropwise into an aqueous solution of poloxamer 188 under stirring for the interfacial polymerization to take place at the surface of the Myglol® droplets. The resulting poly(isobutyl cyanoacrylate) nanoparticles were separated from other preparation additives by diafiltration [19]. Calcitonin was found to be incorporated into the poly(isobutyl cyanoacrylate) nanoparticles with an efficiency of 90%.

Along with these efforts in preparing polymer nanoparticles via polymerization, nanoparticles with tailor-made surface properties (e.g., chemical, electrical, mechanical) by surface engineering have been reported [20]. For instance, Dokoutchaev and co-workers [21] have developed several methods to deposit metal colloids (e.g., Pt, Pd, Ru, Ag, Au) onto the surface of polymer micro- and nanoparticles.



**Figure 1.** Schematic representation of poly(alkylcyanoacrylate) nanoparticle production by anionic polymerization of alkylcyanoacrylate. Reprinted with permission from [16], P. Couvreur et al., *J. Pharm. Pharmacol.* 31, 331 (1979). © 1979, Kluwer/Academic Plenum.

Examples include the controlled hydrolysis of surface acetoxy groups to generate hydroxyl functionalities for specific adsorption silver and ruthenium nanoparticles [22], electrostatic deposition of Au colloids on positively charged polymer micro/nanoparticles [21, 23], and simple adsorption of Pd nanoparticles on poly(vinylpyridine) nanospheres [24]. As shown in Figure 2, these polymer micronanospheres (0.2–3  $\mu\text{m}$  in diameter) functionalized with metal nanoparticles



**Figure 2.** (a) Scanning electron microscopy (SEM) image of poly(4-vinylpyridine) microspheres and (b) transmission electron microscopy (TEM) micrographs showing the surface coverage of poly(4-vinylpyridine) microspheres with colloidal palladium nanoparticles. Reprinted with permission from [24], S. Pathak et al., *Chem Mater.* 12, 1985 (2000). © 2000, American Chemical Society.

(1–10 nm in diameter) possess a high ratio of surface area to volume and are promising for various potential applications, especially as efficient catalysts, chemical/electronic/optical sensors, active substrates for surface enhanced Raman scattering, and photocatalysts for solar energy conversion.

## 2.2. Dispersion of Preformed Polymers

Several other related methods involving the dispersion of preformed polymers, such as those based on the use of emulsifying agents [25–28] and supercritical fluids [29–33], have also been used to prepare polymer nanoparticles.

### 2.2.1. Polymer Nanosphere by Emulsifying Dispersion

In this case, a preformed polymer is dissolved in an organic solvent, which is then emulsified into an aqueous solution, with or without the presence of drug molecules, to make an oil (O) in water (W) emulsion (O/W emulsion) by using a surfactant/emulsifying agent [25, 26]. Upon the formation of a stable emulsion, the organic solvent is evaporated at room temperature by continuous stirring or by heating to produce the polymer nanoparticles.

In order to control the size of the resultant nanoparticles, a modified version of the W/O method has been developed that uses both water-insoluble organic solvent and water-soluble solvent (e.g., acetone, methanol). In this case, the spontaneous diffusion of water-soluble solvent could cause an interfacial turbulence between the two phases to create smaller particles. Therefore, the increase in the concentration of water-soluble co-solvent was shown to cause a considerable decrease in the nanoparticle size [27].

### 2.2.2. Polymer Nanospheres by Supercritical Fluid Method

These methods inevitably involve the use of organic solvents that are hazardous to the environment and physiological systems [28]. The need for environmentally safer encapsulation has been a driving force for the development of new methods for the preparation of polymer nanoparticles with desired physicochemical properties. In this regard, the supercritical fluid technique has been an attractive alternative for generating polymer nanoparticles of high purity without any trace amount of the organic solvent [29]. As detailed discussions on supercritical fluid technology are beyond the scope of this chapter, interested readers are referred to specialized reviews and monographs [31–33]. Briefly, in a typical supercritical fluid method the solute of interest is solubilized in a supercritical fluid. The solution is then expanded through a nozzle to reduce the solvent power of the supercritical fluid, resulting in the precipitation of the solute. Although the supercritical fluid method has advantages due to its solvent-free nature, further research breakthroughs are required before any commercial applications will be realized as most polymers exhibit little or no solubility in supercritical fluids.

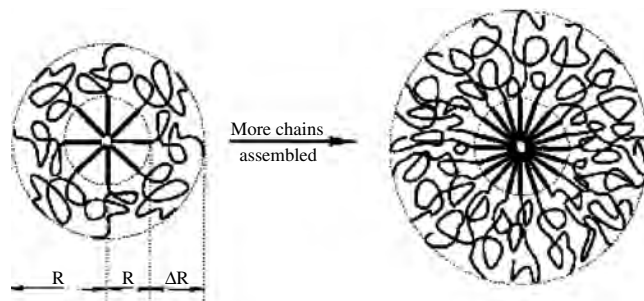
## 2.3. Self-Assembling of Preformed Polymers

Self-assembly involves the aggregation of molecules or macromolecules to thermodynamically stable structures that are held together by weak noncovalent interactions. These weak noncovalent interactions include hydrogen bonding,  $\pi$ - $\pi$  stacking, electrostatic forces, van der Waals forces, and hydrophobic and hydrophilic interactions. Because of the fast dynamic and very specific noncovalent interactions involved, self-assembling processes are usually very fast. The resulting supramolecules could undergo spontaneous and continuous de-assembly and re-assembly processes under certain conditions due to the noncovalent nature. Supramolecular materials can, therefore, select their constituents in response to external stimuli or environmental factors and behave as adaptive materials. Although self-assembling (or complexation) of small molecules has for decades been an active research area, self-assembling of polymeric chains is a recent development. Various supramolecular aggregates with unusual structures [34–38], including shell-core and shell-hollow core, have been successfully prepared which are difficult to form by conventional chemical reactions.

### 2.3.1. Shell-Core Polymer Nanoparticles

Self-assembling of diblock copolymers in a selective solvent, in which only one block is soluble, can form shell-core nanoparticles (Fig. 3).

To demonstrate this concept, several groups have carried out detailed studies on various amphiphilic copolymers, including poly(ethylene oxide)-*block*-poly(propylene oxide), PEO-PPO, and poly(*N*-isopropylacrylamide)-*block*-poly(ethylene oxide), PNIPAM-*b*-PEO [39–44]. It was demonstrated that the formation of shell-core architectures in the copolymer systems can be induced by changes in temperature, solvent composition, ionic strength, and/or pH. For example, self-assembled shell-core polymer nanoparticles consisting of PNIPAM core and PEO shell have been prepared in water above  $\sim 32$  °C. While both PNIPAM and PEO blocks dissolve in water at room temperature, PNIPAM becomes hydrophobic and undergoes an “coil-to-globule” transition at temperatures higher than  $\sim 32$  °C [45, 46]. By



**Figure 3.** Schematic representation of a core-shell nanostructure formed by a self-assembly of coil-rod diblock copolymer chains in a selective solvent. Reprinted with permission from [39], G. Zhang et al., *Acc. Chem. Res.* 34, 249 (2001). © 2001, American Chemical Society.



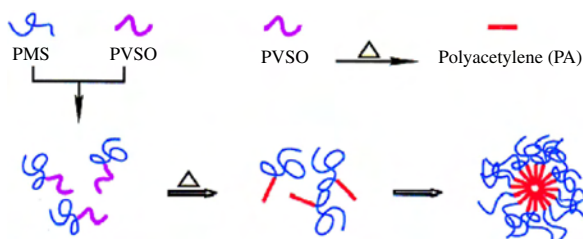
controlling the heating rate, Zhu and Napper [45] have prepared core-shell nanoparticles of a narrow size distribution from PNIPAM-*b*-PEO block copolymers.

The core-shell formation from appropriate diblock copolymers has also been induced by certain chemical reactions. Of particular interest, Wu et al. [47] have used the soluble poly(4-methylstyrene-*block*-phenylvinylsulfoxide), PMS-*b*-PVSO, as the starting material in THF. Thermal elimination of phenylsulfenic acid converted the soluble and flexible PVSO block into an insoluble rodlike polyacetylene (PA) block [48, 49], leading to the formation of core-shell nanoparticles with the conducting PA core surrounded by the THF soluble PMS shell (Fig. 4). Nanoparticles with conducting polymers either as the core or shell have also been prepared by colloidal chemistry [50].

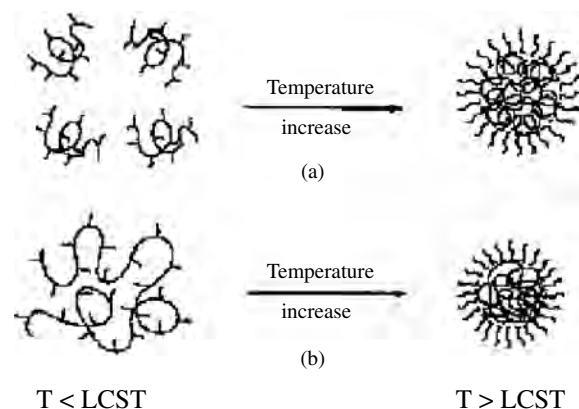
Although the block copolymer approach to the core-shell nanoparticles is an effective method and has recently been extended to include the use of triblock copolymers to form polymer nanoparticles with a multilayered shell structure [50], the general application of this method is largely limited by the rather delicate synthesis of diblock copolymers with well-defined chemical and physical structures.

To eliminate the use of block copolymers, Qiu and Wu [51] investigated the temperature-induced self-assembly of PNIPAM and PEO *graft* copolymers. They have demonstrated that the size of nanoparticles formed by the PNIPAM chains grafted with short PEO chains is inversely proportional to the number of the PEO short chains on individual PNIPAM polymer backbones (Fig. 5a) [51]. By suppressing the interchain association, these authors have even prepared single-chain core-shell nanoparticles, as schematically shown in Figure 5b [52].

Apart from the formation of core-shell nanoparticles from pure grafted polymers, the self-assembly in mixture systems of a homopolymer and a graft copolymer has also been effectively exploited as an alternative “block-copolymer-free” approach to polymer core-shell nanoparticles. Based on the homopolymer and graft polymer approach, Liu and co-workers [53] have recently reported an interesting approach to hollow nanospheres (i.e., shell-hollow core nanoparticles). These authors first prepared core-shell nanoparticles by self-assembling a polymer pair of poly( $\epsilon$ -caprolactone) (PCL) and a graft copolymer of methylacrylic acid and methyl methacrylate (MAF) in water. The resulting nanoparticles have a PCL core stabilized by the MAF shell with its short PCL branches anchored onto the core (Fig. 6a).



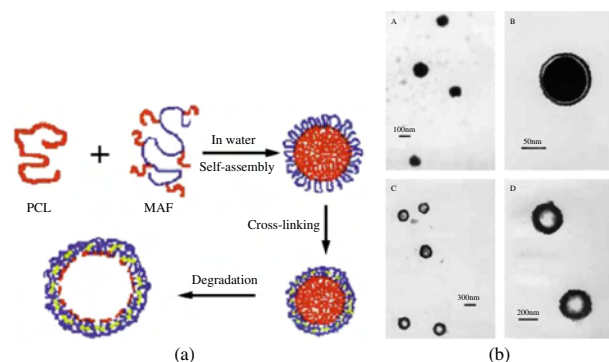
**Figure 4.** Schematic representation of chemical reaction-induced self-assembly of PMS-*b*-PVSO diblock copolymer chains in solution upon heating. Reprinted with permission from [47], C. Wu et al., *J. Am. Chem. Soc.* 121, 1954 (1999). © 1999, American Chemical Society.



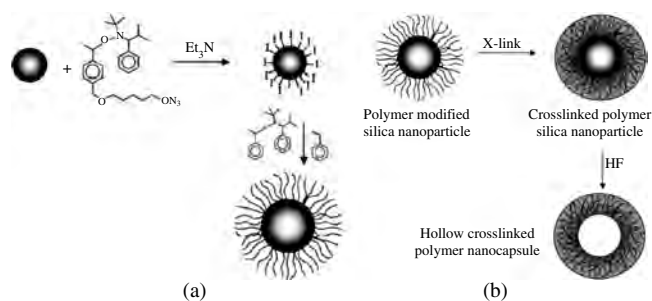
**Figure 5.** Schematic representation of the formation of (a) core-shell polymer nanoparticles from PNIPAM-*g*-PEO graft copolymers and (b) a single chain core-shell nanostructure through the coil-to-globule transition of the chain backbone of PNIPAM-*g*-PEO. Reprinted with permission from [52], X. Qiu and C. Wu, *Phys. Rev. Lett.* 80, 620 (1998). © 1998, American Chemical Society.

These authors then chemically cross-linked the micellar shell to form the so-called “shell-cross-linked knedel-like nanoparticles” [54], while they biodegraded the core with an enzyme to produce the hollow core (Fig. 6a). The morphologies of the nanoparticles before (A&B) and after (C&D) core degradation are shown by the TEM micrographs in Figure 6b. Careful examination of the nanoparticles shown in Figure 6b indicates that the particles have expanded significantly to from ca. 100 to 300 nm in diameter and a shell thickness from ca. 10 to 100 nm, suggesting a swelling effect associated with the core removing process.

Closely related to this study, Blomberg and co-workers [55] have successfully prepared hollow polymeric nanocapsules through surface-initiated living free-radical polymerization. In particular, these authors first attached trichlorosilyl-substituted alkoxyamine initiating groups onto the surface silanol groups of silica nanoparticles. They then carried out living free-radical polymerization from the surface initiating groups, resulting in the formation of core-shell morphology (Fig. 7a).



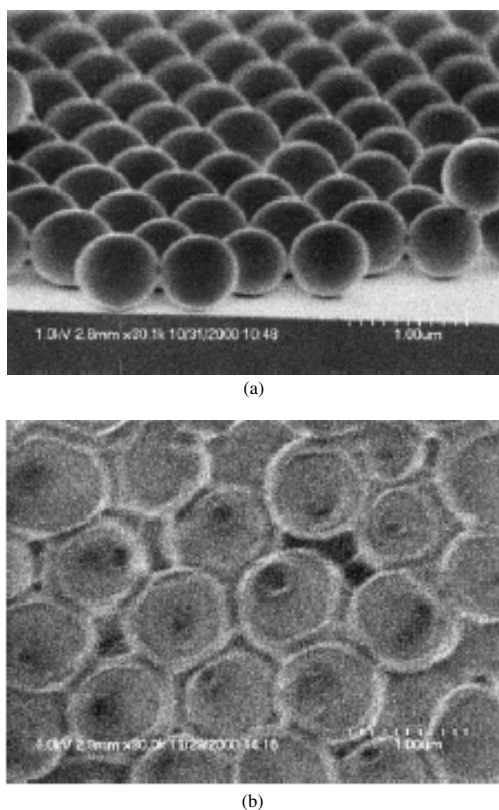
**Figure 6.** (a) A schematic illustration of the processes of self-assembly, cross-linking, and degradation. (b) TEM images of MAF-2/PCL (1:1, w/w) nanoparticles before (A and B) and after (C and D) biodegradation of the PCL core. Reprinted with permission from [53], X. Liu et al., *Angew. Chem. Int. Ed.* 41, 2950 (2002). © 2002, Wiley-VCH.



**Figure 7.** Schematic representation of (a) the polymer-modified silica nanoparticles and (b) the formation of hollow, cross-linked polymer nanocapsules from the polymer-modified silica nanoparticles. Reprinted with permission from [55], S. Blomberg et al., *J. Polym. Sci. A 40*, 1309 (2002). © 2002, Wiley-VCH.

Thermal or chemical cross-linking of the polymeric shell, followed by removal of the silica core with HF led to stable hollow polymeric nanocapsule (Fig. 7b). Figure 8a and b shows field-emission scanning electron microscopic (FESEM) images for cross-linked poly(styrene-*co*-vinylbenzocyclobutene)-modified nanoparticles before and after removal of the silica core, respectively.

Similar hollow nanospheres have been previously prepared through self-assembling *block* copolymers in selective solvents followed by cross-linking of the micellar shell and



**Figure 8.** FESEM images for cross-linked poly(styrene-*co*-vinylbenzocyclobutene)-modified nanoparticles before (a) and after (b) removal of the silica core. Reprinted with permission from [55], S. Blomberg et al., *J. Polym. Sci. A 40*, 1309 (2002). © 2002, Wiley-VCH.

removing the core via chemical degradation [56–59], though the “block-copolymer-free” approaches discussed may be regarded as a simpler and more economic approach. Given that the hollow polymer nanospheres can be used to encapsulate a large variety of guest molecules, including many catalysts and drugs, there has been increasing interest in the research and development of polymer hollow nanoparticles. Clearly, a promising potential for future research and application exists in this area.

### 3. POLYMER NANOWIRES, NANOTUBES, AND NANOFIBERS

Just as polymer nanoparticles have broadened the potential applications of polymer materials, polymer wires, tubes, and fibers of diameters down to a nanometer scale have also been studied for a large variety of potential applications. Polymer nanowires, nanotubes, and nanofibers are useful as both “building blocks” for nanodevices and “connecting components” between the nanoscale entities and the macroscale world. In this regard, conducting polymer nanowires, nanotubes, and nanofibers are of particular interest as they have been shown to possess the processing advantages of plastics and the optoelectronic properties of inorganic semiconductors or metals. We provide an overview on the syntheses, properties, and potential applications of polymer nanowires, nanotubes, and nanofibers, with an emphasis on those based on conducting polymers.

#### 3.1. Tip-Assisted Syntheses of Polymer Nanowires

The use of a scanning tunneling microscope (STM) and scanning electrochemical microscope (SECM) for generation and manipulation of polymer structures as small as a few nanometers has been well documented [49, 60]. The polymerization of pyrrole onto specific regions of graphite substrates at a submicrometer resolution was achieved by using the STM tip as an electrode. Polypyrrole strips with a linewidth of 50  $\mu\text{m}$  and length of 1 mm were produced by a SECM [61], as were micrometer-sized polypyrrole towers [62]. By spin-coating a solution of Nafion and anilinium sulfate onto a Pt electrode in a SECM unit, Wu et al. [63] polymerized aniline into a micrometer scale structure. Borgwarth et al. [64] successfully prepared a 20  $\mu\text{m}$  wide polythiophene line by using the tip of a SECM as an electrode for region-specific oxidation of bromide into bromine, followed by the diffusion of the bromine into a conductive substrate covered with a thiophene derivative, to produce localized oxidative polymerization of thiophene monomers.

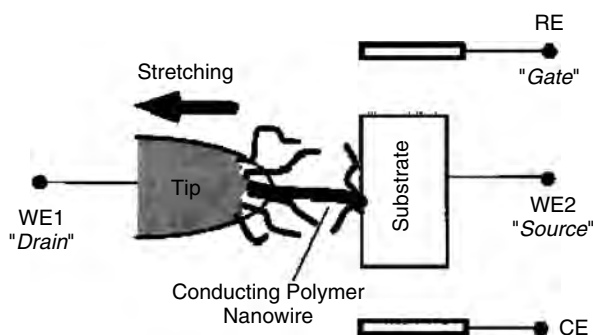
Aiming for polymer structures at the nanometer scale, Nyffenegger and Penner [65] produced electrochemically active polyaniline particles with a size ranging from 10 to 60 nm in diameter and 1 to 20 nm in height by using the Pt tip of a scanning tunneling microscope as an electrode for the electropolymerization of aniline. Maynor and co-workers [66] used an electrochemical reaction at an atomic force microscope tip for region-specific deposition of conducting polymer *nanowires* with diameters in the range from 50 to 500 nm on semiconducting and insulating substrates.

Bumm et al. [67] demonstrated the use of a STM tip to probe electrical properties of individual conjugated conducting molecules ("molecular wires") dispersed into a self-assembled monolayer film of nonconducting alkanethiolate molecules. In a closely related but separate study, He and co-workers [68] have electrochemically deposited a conducting polyaniline nanowire bridge between a STM tip and a gold electrode by region-selectively coating the STM tip with an insulation layer so that only a few nm<sup>2</sup> at the tip end was exposed for localized growth of the polyaniline bridge (Fig. 9) [68].

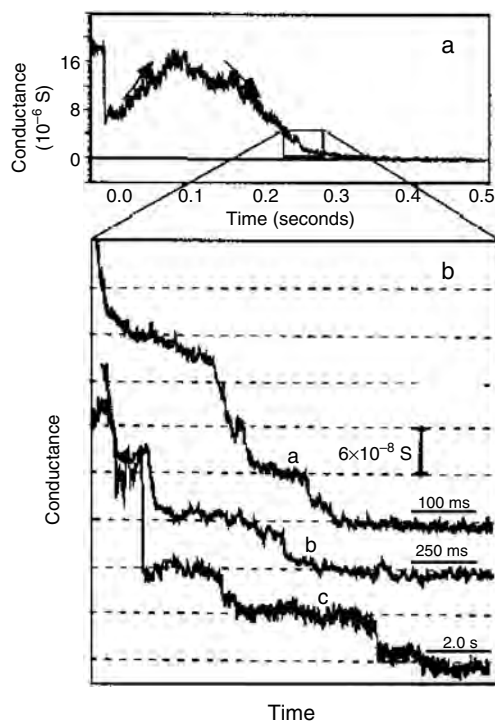
Upon stretching the polymer nanowire by moving the STM tip away from the Au electrode, these authors observed a stepwise decrease in the conductance (Fig. 10), resembling that reported for metallic nanowires [69, 70].

The initial increase in the conductance seen in Figure 10a is attributed to the stretching-induced alignment of the polymer chains in the nanowire, since aligned conducting polymers have been demonstrated to show higher conductivities. The observed smaller conductance step height ( $<2e^2/h$ ) and wider plateaus than those of metal nanowires may indicate the occurrence of polymer chains sliding in the polyaniline nanowires during stretching. The conductance of the polyaniline nanowires with various diameters was measured as a function of the electrochemical potential by stopping the stretching at different conductance steps.

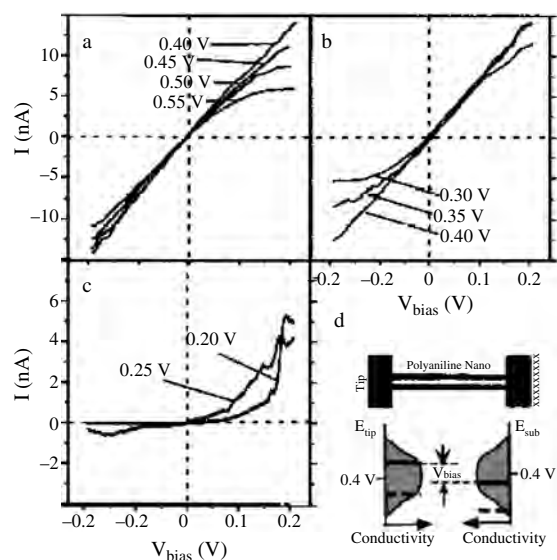
In analogy to the control of the gate voltage in semiconductor devices [70], He et al. [68] measured the current-voltage curves by sweeping the tip-substrate bias voltage ( $V_{\text{bias}}$ ) while maintaining the electrochemical potential of the substrate electrode (or the tip electrode) at different values. The resulting  $I-V_{\text{bias}}$  curves show a nearly linear relationship when the substrate potential is kept between 0.30 and 0.55 V (Fig. 11a and b). As seen in Figure 11c, however, the polyaniline nanowire exhibits rectifying characteristics at 0.25 V; the current is small at negative bias whereas it increases when the bias is positive. The observed rectifying characteristics become more pronounced when the potential is reduced to 0.2 V. The observed transition from ohmic to rectifying characteristics can be understood by considering



**Figure 9.** Schematic drawing of the experimental setup. The electrochemical potential of the nanowire was controlled with respect to a reference electrode (RE) in the electrolyte. A counter-electrode was used as in a standard electrochemical setup. In comparison to a field effect transistor, the RE, WE1, and WE2 electrodes are analogous to the gate, source, and drain electrodes. Reprinted with permission from [68], H. X. He et al., *Appl. Phys. Lett.* 78, 811 (2001). © 2001, American Institute of Physics.



**Figure 10.** (a) Conductance of a polyaniline nanowire during an entire stretching process. The arrows point to the initial increase and followed by a stepwise decrease in the conductance. (b) A zoom in of the stepwise decrease. For clarity, curves (a) and (b) are shifted upward by 2 and 3 divisions, respectively. The substrate and tip potentials were held at 0.45 and 0.5 V, respectively. Reprinted with permission from [68], H. X. He et al., *Appl. Phys. Lett.* 78, 811 (2001). © 2001, American Institute of Physics.



**Figure 11.** (a-c) Current ( $I$ ) through a polyaniline nanowire as a function of the tip-substrate bias voltage ( $V_{\text{bias}}$ , drain-source voltage). (d) A model that explains the observed  $I-V_{\text{bias}}$  characteristics. The shaded bell curves represent conductivity of the nanowire at points near the tip and the substrate electrodes, respectively. Reprinted with permission from [68], H. X. He et al., *Appl. Phys. Lett.* 78, 811 (2001). © 2001, American Institute of Physics.

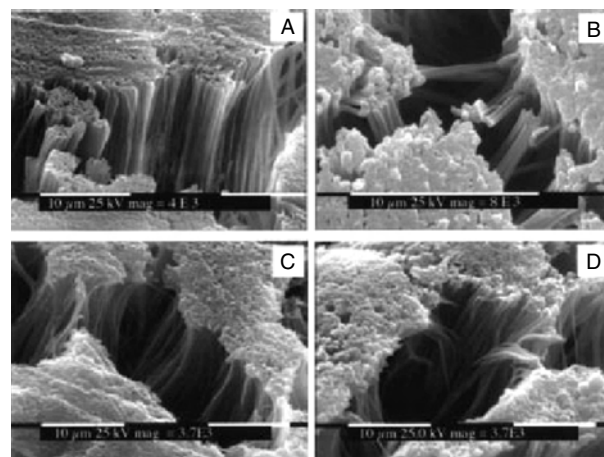
the situation described in Figure 11d, which shows that the polyaniline nanowire has one end attached to the tip and the other connected to the substrate. Therefore, the electrochemical potentials of the two ends are fixed at  $E_{\text{sub}}$  and  $E_{\text{tip}}$ . As polyaniline is in the oxidized conducting form at the electrochemical potentials close to or slightly higher than 0.3 V [71], both portions of the polyaniline nanowire near the substrate and tip are conducting at  $E_{\text{sub}} = 0.40$  V with a small  $V_{\text{bias}}$  ( $E_{\text{tip}} = E_{\text{sub}} + V_{\text{bias}}$ ) so that the  $I$ - $V$  curve is ohmic. At 0.25 V, however, a negative sweep moves the  $E_{\text{tip}}$  to potentials lower than the redox potential of polyaniline (ca. 0.3 V) so that the polymer is in the nonconducting reduced form while a positive sweep of bias moves  $E_{\text{tip}}$  to the highly conductive region, leading to the rectifying behavior. The controllable conductance of the conducting polymer nanowires, together with their mechanical flexibility and rectifying characteristics, should have important implications for the use of polymer nanowires in various micro/nanoelectronic devices and many other applications.

### 3.2. Template Syntheses of Polymer Nanowires, Nanotubes, and Nanofibers

Polymer nanowires with interesting nanometer-scale architectures have also been fabricated using porous membranes or supramolecular nanostructures as templates. For instance, Smith et al. [72] have recently developed a process for producing nanocomposites with well-defined poly(*p*-phenylene vinylene) (PPV) nanowires within self-organizing liquid-crystal matrixes. This process involves self-assembling of a polymerizable liquid-crystal monomer (e.g., acrylate) into an ordered hexagonal array of hydrophilic channels (ca. 4 nm in diameter) filled with a precursor polymer of PPV, followed by photopolymerization to lock in the matrix architecture and thermal conversion to form PPV nanofibers in the channels. As a result, significant fluorescence enhancement was observed, most probably due to the much reduced interchain-exciton quenching achieved by separating the PPV molecules from the polymer matrix.

More generally, polymer nanowires and nanotubes with improved order and fewer structural defects can be synthesized within a template formed by the pores of a nanoporous membrane [73] or the nanochannels of a mesoporous zeolite [74]. Template synthesis often allows the production of polymeric wires or tubules with controllable diameters and lengths (Fig. 12) [75]. Template synthesis of conjugated polymers, including polyacetylene, polypyrrole, polythiophene, polyaniline, and PPV, may be achieved by electrochemical or chemical oxidative polymerization of the corresponding monomers. While the electrochemical template synthesis can be carried out within the pores of a membrane that is precoated with metal on one side as an anode [73], the chemical template synthesis is normally performed by immersing the membrane into a solution containing the desired monomer and oxidizing agent, with each of the pores acting as a tiny reaction vessel.

It is noted with interest that if the pores of polycarbonate membranes are used as the template, highly ordered polymeric tubules are produced by preferential polymerization along the pore walls [76] due to the specific solvophobic



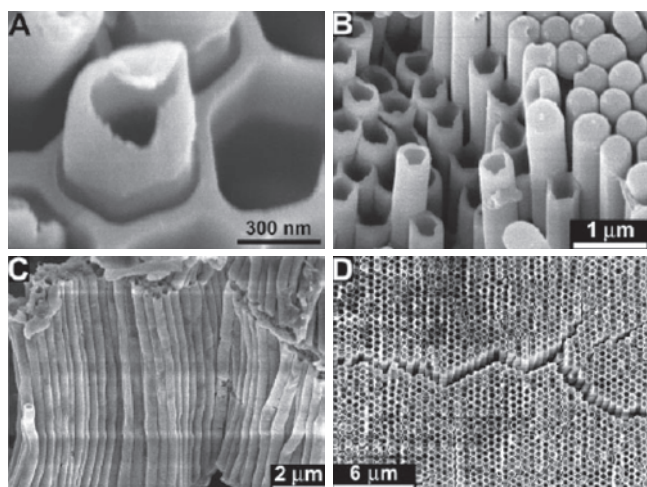
**Figure 12.** Scanning electron micrographs of microfibrils prepared in the alumina template membrane: (A) PS, (B) poly(vinylidene fluoride) (PVDF), (C) poly(phenylene oxide), and (D) PMMA. Reprinted with permission from [75], V. M. Cepak and C. R. Martin, *Chem. Mater.* 11, 1363 (1999). © 1999, American Chemical Society.

and/or electrostatic interactions between the polymer and the pore wall [73]. These conducting polymer tubules show a wide range of electrical conductivities, increasing with decreasing pore diameter [77, 78]. This is because the alignment of the polymer chains on the pore wall can enhance conductivity, and the smaller tubules contain proportionately more of the ordered material.

By wetting ordered porous templates with polymer solution or melts, Steinhart et al. [79] have developed another simple technique for the fabrication of polymer nanotubes with a monodisperse size distribution and uniform orientation.

Figure 13 shows polymer nanotubes formed by melt-wetting of ordered porous alumina and oxidized macroporous silicon templates with narrow pore size distribution. The method can be used to produce polymer nanotubes of narrow size distribution from almost all melt-processible polymers, their blends, or multicomponent solutions. More recently, conjugated conducting polymer nanotubes were synthesized using “template-free” polymerization that involves a self-assembled supramolecular template [80, 81]. These studies are of particular interest because high-temperature graphitization of the polymer nanotubes could transform them into carbon nanotubes of superior electronic and mechanical properties [82], as demonstrated by polyacrylonitrile nanotubules synthesized in the pores of an alumina membrane or in zeolite nanochannels [83, 84].

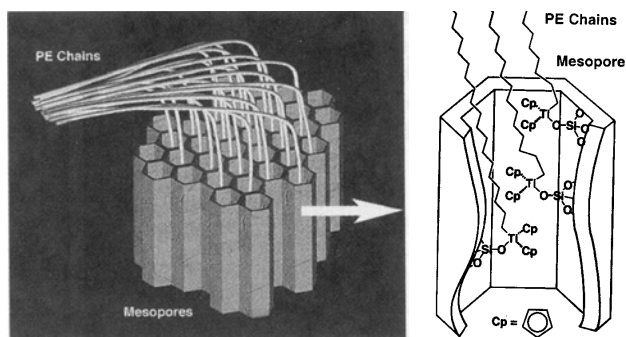
On the other hand, Kageyama and co-workers [85] prepared crystalline nanofibers of ultrahigh molecular weight polyethylene by extruding the polymer through porous nanoscale reactors as it was synthesized. In particular, these authors coated the hexagonal pores (27 Å) of mesoporous silica fiber reactors with the classic polymerization catalyst titanocene. After activating the catalyst, they then pressurize the vessel containing the reactors with ethylene gas. Being confined within the narrow pores, the resulting polymer chains were forced to grow out of the framework, much like spaghetti extruding from a pasta maker [86] (Fig. 14).



**Figure 13.** Scanning electron micrographs of nanotubes obtained by melt-wetting. (A) Damaged tip of a PS nanotube. (B) Ordered array of tubes from the same PS sample after complete removal of the template. (C) Array of aligned polytetrafluoroethylene (PTFE) tubes. (D) PMMA tubes with long-range hexagonal order obtained by wetting of a macroporous silicon pore array after complete removal of the template. Reprinted with permission from [79], M. Steinhart et al., *Science* 296, 1997 (2002). © 2002, American Association for the Advancement of Science.

### 3.3. Electrospinning of Polymer Nanofibers

While the potential applications of polymer nanowires and nanotubes have yet to be fully exploited, polymer nanofibers have been demonstrated to be attractive for a large variety of potential applications, including as high performance filters, scaffolds in tissue engineering, wound dressings, sensors, and drug delivery systems [87–90]. However, the large-scale fabrication of polymer nanowires/nanofibers at a reasonably low cost has been a big challenge toward the realization of commercial applications of polymer nanofibers. Electrospinning, a technique which was first patented in 1934 [91], has recently been reexamined, notably by Reneker and co-workers [87–90], as an effective method for large scale fabrication of ultrafine polymer fibers.

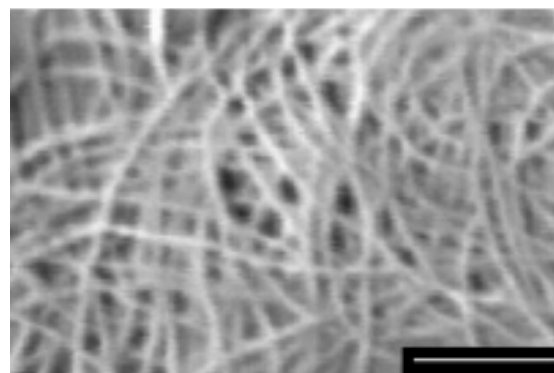


**Figure 14.** Conceptual scheme for the growth of crystalline fibers of polyethylene by mesoporous silica-assisted extrusion polymerization. Reprinted with permission from [85], K. Kageyama et al., *Science* 285, 2113 (1999). © 1999, American Association for the Advancement of Science.

The electrospinning process involves the application of a high electric field between a droplet of polymer fluid and a metallic collection screen at a distance of 5–50 cm from the polymer droplet. An electrically charged jet flows from the polymer droplet toward the collection screen when the voltage reaches a critical value (typically, ca. 5–20 kV) at which the electrical forces overcome the surface tension of the polymer droplet. The electrical forces from the charge carried by the jet further cause a series of electrically driven bending instabilities to occur as the fluid jet moves toward the collection screen. The repulsion of charge on adjacent segments of the fluid jet causes the jet to elongate continuously to form ultrafine polymer fibers. The solvent evaporates and the stretched polymer fiber that remains is then collected on screen as a nonwoven sheet composed of one fiber many kilometers in length. The electrospun polymer fibers thus produced have diameters ranging from several micrometers down to 50 nm or less. This range of diameters overlaps conventional synthetic textiles and extends through diameters two or three orders of magnitude smaller.

Reneker and co-workers have made significant advances on both theoretical and experimental fronts. They have carried out detailed theoretical studies on the formation of electrically charged polymer jet and its bending instability [92–94] and have also prepared a large number of novel polymer fibers with diameters from few nanometers to micrometers by electrospinning various synthetic and natural polymers from either solution or melts. Various polymers ranging from conventional synthetic polymers, through conducting and liquid crystalline polymers, to biopolymers have been electrospun into polymer nano/microfibers [89, 95]. A typical microscopic image of the resulting polymer nanofibers is shown in Figure 15 [96].

The electrospun fiber mats possess a high surface area per unit mass, low bulk density, and high mechanical flexibility. These features make the electrospun fibers very attractive for a wide range of potential applications. Among them, the use of electrospun polymer fibers for electronic applications is of particular interest. The high surface to volume ratio associated with electrospun *conducting polymer* fibers makes them excellent candidates for electrode materials since the rate of electrochemical reaction is proportional

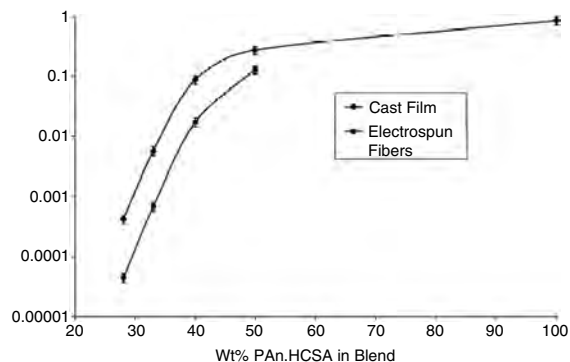


**Figure 15.** Typical SEM image of electrospun polystyrene fibers with an average diameter of 43 nm. Scale bar: 1000 nm. Reprinted with permission from [96], A. G. MacDiarmid et al., *Synth. Met.* 119, 27 (2001). © 2001, Elsevier Science.

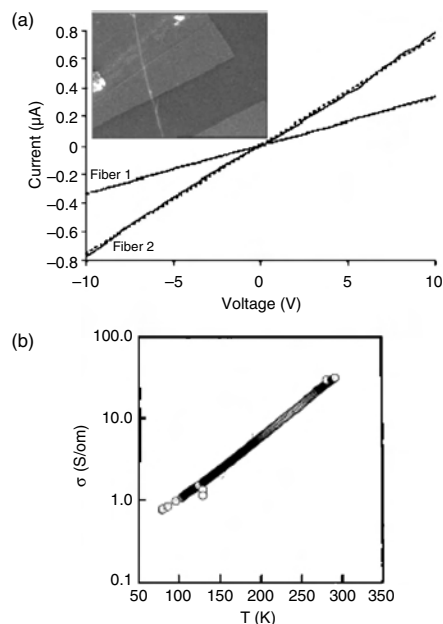
to the surface area of an electrode and diffusion rate of the electrolyte. Reneker and co-workers [97] have reported the pyrolysis of electrospun polyacrylonitrile nanofibers into conducting carbon nanofibers. They have also prepared conducting polymer nanofibers by electrospinning polyaniline from sulfuric acid into a coagulation bath and characterized them by scanning tunneling microscopy, electron microscopy, and electron diffraction.

Norris et al. [98] prepared camphorsulfonic acid doped polyaniline (HCSA-PANI) and polyethylene oxide composite thin fibers (ca.  $0.95\text{--}2\ \mu\text{m}$  in diameter) by the electrospinning technique from a mixed solution. The four-point probe method [99] was used to measure the conductivity of the nonwoven fiber *mat* and was cross-checked with measurements of the conductivity of cast films produced from the same solution. Figure 16 shows the effect of the weight percentage content of HCSA-PANI on the room temperature conductivity obtained from the HCSA-PANI/PEO electrospun fibers and film [98]. As can be seen in Figure 16, the conductivity of the electrospun fiber mat was lower than that for a cast film, though they have very similar ultraviolet-visible (UV-vis) absorption characteristics. The lower conductivity values for the electrospun fibers than those of cast films can be attributed to the porous nature of the nonwoven electrospun fiber mat as the four-probe method measures the volume resistivity rather than the conductivity of an individual fiber. Although the measured conductivity for the electrospun mat of conducting nanofibers is relatively low, their porous structure, together with the high surface-to-volume ratio, enables faster de-doping and re-doping in both liquids and vapors.

In order to measure the conductivity of an individual nanofiber, MacDiarmid and co-workers [96] have also collected a *single* electrospun HCSA-PANI/PEO nanofiber on a silicon wafer coated with a thin layer of  $\text{SiO}_2$  and deposited two separated gold electrodes  $60.3\ \mu\text{m}$  apart on the nanofiber (two-probe method). The current–voltage ( $I$ – $V$ ) curves thus measured for single 50 wt% HCSA-PANI/PEO fibers with diameters of 600 and 419 nm are shown in Figure 17a (i.e., Fiber 1 and Fiber 2, respectively), which give a more or less straight line with a conductivity



**Figure 16.** The effect of the weight percentage content of HCSA-PANI on the room temperature conductivity obtained from the HCSA-PANI/PEO electrospun fibers and cast films. Reprinted with permission from [98], I. D. Norris et al., *Synth. Met.* 114, 109 (2000). © 2000, Elsevier Science.



**Figure 17.** (a) Current–voltage curve for a single 50 wt% HCSA-PANI/PEO nanofiber. (b) Temperature dependence of the conductivity for a single 72 wt% HCSA-PANI/PEO nanofiber. Reprinted with permission from [96], A. G. MacDiarmid et al., *Synth. Met.* 119, 27 (2001). © 2001, Elsevier Science.

of ca. 0.1 S/cm. The temperature dependence of the conductivity for a single 72 wt% HCSA-PANI/PEO electrospun fiber with a diameter of  $1.32\ \mu\text{m}$  given in Figure 17b also shows a linear plot with a room-temperature conductivity of 33 S/cm (295 K). This value of conductivity is much higher than the corresponding value of about 0.1 S/cm for a cast film (Fig. 16), suggesting a highly aligned nature of the PANI chains in the electrospun fiber.

## 4. POLYMER NANOFILMS

Polymer thin films with their thickness at the nanometer scale (i.e., polymer nanofilms or nanosheets) are an important class of materials from the point views of both scientific fundamental and practical applications. For instance, the immobilization of a thin layer of biomacromolecules onto the surfaces of polymeric biomaterials could produce bioactivities [100], while conjugated polymer thin films play vital roles in organic optoelectronic devices, including polymer thin film transistors [101–103], photoconductors [104], photovoltaic cells [105], and light-emitting diodes (LEDs) [106, 107]. In this section, we choose polymer thin films formed by solution casting, plasma deposition, Langmuir–Blodgett deposition, and physical adsorption as a few examples to illustrate their importance to various practical applications with a focus on polymer LEDs.

### 4.1. Polymer Nanofilms by Solution Casting

The syntheses of soluble conjugated polymers offer excellent possibilities for advanced device fabrications using various solution-processing methods (e.g., spin-coating) [49]. The

simplest single layer LED devices consist of a thin solution-cast layer of electroluminescent conjugated polymer (e.g., poly[2-methoxy-5-(2'-ethyl-hexyloxy)-*p*-phenylene vinylene]) sandwiched between two electrodes (an anode and a cathode). Among the two electrodes, at least one should be transparent or semitransparent. In practice, a transparent indium-tin-oxide (ITO) coated glass is often used as the anode and a layer of low work-function metal (e.g., aluminum, calcium) acts as the cathode.

Upon application of an electrical voltage onto the electroluminescence (EL) polymer layer in a LED device, electrons from the low work-function cathode (e.g., Al) and holes from the high work-function anode (e.g., ITO) are injected respectively into the lowest unoccupied molecular orbital and the highest occupied molecular orbital of the polymer, resulting in the formation of a singlet exciton that produces luminescence at a longer wavelength (the Stokes shift) through radiative decay. To maintain a low operation voltage, a very thin polymer layer (ca. 100 nm) is usually used. The wavelength (and hence the color) of the photons thus produced depends on the energy gap of the organic light-emitting material, coupled with a Stokes shift. Since conjugated polymers can have  $\pi$ - $\pi^*$  energy gaps over the range between 1 and 4 eV (1240–310 nm), polymer-based LEDs should, in principle, emit light across the whole spectrum from ultraviolet to near infrared with a good color tunability by controlling the energy gap through molecular engineering [106, 107]. Indeed, polymer LEDs with a wide range of emission colors and with reasonably high quantum efficiencies (a few percentage) are now reported. For detailed discussion on the current state of the art in the development of polymeric LEDs, interested readers are referred to specialized reviews and conference monographs [108–111].

Although the solution-processing technique provides a simple and attractive approach for polymer thin film formation, it may cause a number of problems related to the quality of polymer films thus formed. These include difficulty in choosing suitable solvent(s) for preparing pinhole-free single layer or multilayer polymer thin films, in controlling the film thickness and polymer chain conformation. Consequently, various other methods, including plasma polymerization, the Langmuir–Blodgett technique, and layer-by-layer adsorption, for the formation of polymer nanofilms have been developed.

## 4.2. Polymer Nanofilms by Plasma Polymerization

To circumvent those problems intrinsically associated with the solution-processing technique, plasma polymerization has been used as an alternative thin-film-formation method. Radio-frequency glow-discharge is formed when gaseous monomers are exposed to a radio-frequency electric field at low pressure (<10 Torr) [112, 113]. During the glow-discharge process, energy is transferred from the electric field to free electrons, which inelastically collide with molecules leading to generation of more electrons, ions, and free radicals in the excited state. These plasma species are very reactive toward surfaces, causing surface modification in the case of plasma treatment and polymer deposition in

the case of plasma polymerization. Although the electrons activated for generating charged particles may have a very high electron temperature (e.g., 2 eV = 23,200 K), they are not at thermodynamic equilibrium with gas molecules in the so-called “cold” plasma process [112]. Therefore, plasma treatment and plasma polymerization can be carried out with the gas molecules being at ambient temperature, and thus without thermal degradation of the sample surface and/or the plasma-polymerized layer. Plasma polymerization has been widely demonstrated to generate thin, cohesive, adhering, pinhole-free polymer thin films, which are often used as protective coatings or adhesion promoting layers and have potential applications in optical wave guides, sensor technology, and electronic/photonics devices [113]. Although plasma polymerization, in most cases, produces an electrically insulating organic film, a few approaches to semiconducting plasma polymer films have been reported. Along with others [114, 115], we have plasma-polymerized polyaniline thin films (ca. 350 nm) [116]. The plasma polyaniline films thus prepared are smooth and free of oxidant and solvents, having improved physicochemical characteristics compared with polyaniline films formed by electrochemical polymerization or chemical synthesis followed by spin-coating, solvent casting, or melt extrusion. The presence of conjugated sequences in the plasma-polyaniline films was confirmed by UV-vis, Fourier transform infrared and electron spin resonance measurements, which allow the conductivity of the plasma-polyaniline films to be enhanced by 3 orders of magnitude through HCl treatment. It was further demonstrated that the atomic ratios of C/N both higher and lower than that of aniline (C/N = 6) can be obtained by choosing appropriate discharge conditions, indicating the possibility of tailoring the structure and properties of the plasma-polyaniline films by optimizing the discharge conditions.

Although the advantages of the plasma-generated semiconducting polymer thin films for electronic applications remain to be demonstrated, an oxygen or nitrogen plasma treatment of a PPV layer at the PPV/Al interface in a LED device with the Cr/PPV/Al structure has been demonstrated to cause the disappearance of the rectifying behavior and an increase in the current by many orders of magnitude [117]. Similarly, the efficiency, brightness, and lifetime of LEDs were shown to be significantly improved by an air or argon plasma treatment on the ITO surface, presumably due to the removal of contaminants coupled with an increase in the work function of ITO [118, 119]. A hydrogen plasma, on the other hand, was found to increase the turn-on voltage and reduce the efficiency largely due to a decrease in the work function of ITO [118–121]. Thus, the plasma technique shows much promise for interfacial engineering in LEDs [120, 121]. Furthermore, a few studies have reported the use of plasma polymers as emitting layers in LED devices [122]. There is no doubt that the plasma polymerization of semiconducting organic films and plasma surface modification demonstrated previously will have potential implications for making novel electronic and photonic devices. The ease with which multilayered polymer nanofilms and microsized patterns of organic materials can be made by the plasma technique could add additional benefits to this approach [123].

### 4.3. Polymer Nanofilms by Langmuir–Blodgett Deposition

Although the solution-processing and plasma polymerization techniques discussed provide simplified approaches for polymer nanofilm formation, they provide no means of controlling the orientation of polymer chains in the resulting films. The Langmuir–Blodgett (LB) method involves the formation of a Langmuir film at the gas/liquid interface, followed by a dipping process to transfer the polymer thin film onto a solid substrate [124]. In addition to the ease with which the number of molecular layers (and hence the thickness of films) can be controlled at the molecular level, the LB technique has another major advantage for controlling the film structure in three dimensions [125] as the orientation of polymer chains in each of the layers can be independently controlled by anisotropic compression of the corresponding Langmuir film during the dipping process [126]. The oriented and/or patterned LB films [127] can be further used as substrates, for example, for controlling liquid crystal alignment [127]. As a consequence, the LB technique has been widely used for making manometer-thick multilayer films with well defined structures and ordered molecular organizations from amphiphilic conjugated polymers, nonconjugated precursor polymers, and even certain non-surface-active conjugated polymers.

LB films of highly anisotropic conducting polymers can be prepared through: (a) the manipulation of amphiphilic macromolecules comprising an alkyl chain as the hydrophobic group and with a conjugated polymer being attached to its hydrophilic end [128], (b) the manipulation of mixed monolayers consisting of a surface-active agent (e.g., dopant) and non-surface-active conjugated polymer [129], or (c) the direct synthesis of conducting polymers at the air–water interface or within a preformed multilayer film. To mention but a few examples, Shimidzu et al. [130–133] have prepared conducting LB films containing polypyrrole [130], polyaniline [131], or poly(3-alkylthiophene) [132]. Among them, multilayer LB films (200 layers) of a substituted polypyrrole showed an anisotropic conductivity as high as  $10^{10}$  (i.e.,  $\sigma_{\parallel} = 10^{-1}$  S/cm and  $\sigma_{\perp} = 10^{-11}$  S/cm) [131]. Well characterized LB films of various conjugated polymers including poly(3-alkylthiophene) have also been reported by Chung et al. [129] for which the readers are referred to the excellent review by Rubner and Skotheim [134].

More recently, PPV-type LB films have also recently been prepared from the sulphonium precursor of PPV [135, 136] and some of its soluble derivatives [137–139]. Also, LEDs with polarized EL emissions have been fabricated using certain LB films as the EL material [140, 141]. On this basis, Grüner et al. [142] have precisely determined the location of the exciton recombination zone [143] in LEDs by making multilayer LB films of soluble PPP derivatives with two regions of perpendicular macroscopic orientation, followed by quantifying the emission profile through the analysis of the EL anisotropy.

### 4.4. Polymer Brushes by End Adsorption

End-adsorbed polymer brushes consist of another major class of oriented polymer thin films, in which the constituent polymer chains aligned *perpendicularly* on the substrate sur-

face [144–147]. Just as the in-plan orientation of polymer chains in the LB films has brought new properties and hence broadened the scope for using polymer thin films in optoelectronic devices, the surface-bound polymer brushes have facilitated polymer thin films for many technological applications [144–150], such as in controlling the stability of colloidal dispersions, regulating the permeability of a cell membrane, metabolism, the transmission of information, the biocompatibility of biomaterials, and molecular separation by liquid chromatography. For instance, capsule membranes with end-grafted temperature/pH-responsive polymer chains [e.g., poly(*N*-isopropylacrylamide) or poly(glutamic acid)] may be used as thermoselective drug release devices and/or pH-sensitive gates via a conformational change of the end-grafted polymer brushes [151, 152]. Furthermore, end-adsorbed polymer chains have also been shown to be useful for regulating the frictional forces between solid surfaces, the spreading properties of liquids, and the stability of thin films on solid surfaces [153, 154]. Knowledge of macromolecular conformations and conformational transitions of surface-bound polymer chains is essential for a detailed understanding of their performance at the molecular level. Recent developments, on both experimental and theoretical fronts [144–147, 155–158] in the investigation of adsorbed polymer brought the goal of structural testing against theories within reach.

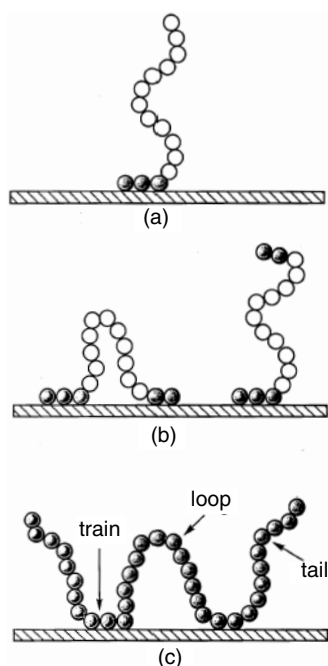
Generally speaking, the conformation of polymer chains adsorbed at the liquid/solid interface differs from that in a bulk solution [144–147]. This is particularly true for end-adsorbed polymer chains in a good solvent, where random coils of the macromolecules in solution may become highly stretched polymer “brushes” at the liquid/solid interface.

While end-adsorbed homopolymers and diblock copolymers form polymer brushes in which the chains can only exist in a “tail” conformation (Fig. 18a), end-adsorbed triblock copolymers, ABA (the A blocks represent short “sticking” segments, whereas the B block does not adsorb), can form either a “loop” or a “tail” depending on the sticking energy of the A block and the surface coverage at the liquid/solid interface [159] (Fig. 18b). Adsorbed homopolymer, on the other hand, forms a more complicated conformational structure (Fig. 18c) due to the random adsorption of its constituent monomers onto the surface.

Along with others, we have carried out the structural investigation of adsorbed polymers at the liquid/solid interface using surface force apparatus [159–161] (SFA) and neutron reflectometry [162–164]. The surface force apparatus contains two molecularly smooth mica sheets, mounted in a crossed cylinder configuration, being used as substrates for polymer adsorption [160]. The surface separation,  $D$ , can be varied by mechanical or piezoelectric transducers and is measured with the aid of interferometry to an accuracy of ca. 3 Å. The corresponding force,  $F(D)$ , between the mica substrates is measured directly by observing the deflection of a leaf spring of known spring constant bearing one of the mica sheets. The results are presented in the form  $F(D)/R$  vs  $D$ , where  $R$  is the geometric mean radius of curvature of the two mica surfaces, and the value of  $F(D)/R$  gives the interaction energy per unit area of surface,  $E(D)$  [159–161].

The use of SFA for measuring the interactions between adsorbed homopolymer surfaces at a high surface coverage

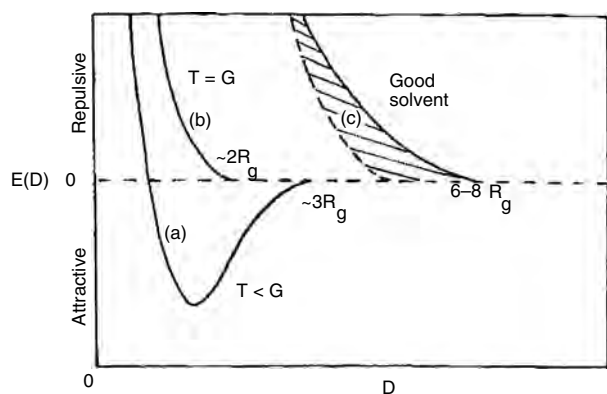




**Figure 18.** Conformations of adsorbed polymer chains. (a) “Tail-like” conformation of end-adsorbed homopolymer or diblock copolymer. (b) “Loop-like” or “tail-like” conformation of end-adsorbed triblock copolymer. (c) “Tail-loop-train” conformation of adsorbed homopolymer.

in a wide variety of solvency conditions has been reviewed elsewhere [165, 166]. Without repetition of the numerical discussions, the main results from the SFA studies are summarized in Fig. 19, which shows only schematic smooth curves instead of the actual  $F(D)$  data for reasons of clarity.

As can be seen from curve (a) of Figure 19, the interaction between surfaces bearing adsorbed polymer chains in a poor solvent (e.g., polystyrene in cyclohexane at  $T = 24\text{ }^\circ\text{C}$ ,  $T_\theta = 35\text{ }^\circ\text{C}$ ) is characterized by a deep, long-ranged (ca.  $3R_g$ ,  $R_g$  is the radius of gyration of a polymer coil) [167–169] attractive force, well-originating from the monomeric attraction in the poor solvent, followed by a repulsion at



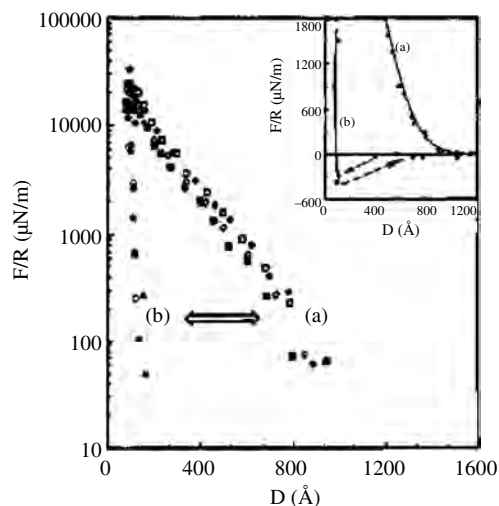
**Figure 19.** Summary of interaction profiles between surfaces with adsorbed homopolymers in various solvency conditions at high surface coverage. Reprinted with permission from [165], J. Klein, in “Molecular Conformation and Dynamics in Condensed Systems” (M. Nagasawa, Ed.). Elsevier Science, Amsterdam, 1988. © 1988, Elsevier Science.

lower  $D$  values due to reduced available configurations for the adsorbed polymer chains in the gap because of excluded volume effects. At the theta temperature,  $T_\theta$ , the attractive forces disappear [curve (b) of Fig. 19], reflecting the absence of the segment–segment interactions at the theta point. The onset distance for interactions reduces from  $3R_g$  for the poor solvent case to around  $2R_g$ . In a good solvent, the interaction becomes monotonically repulsive with a longer ranged onset distance of  $6\text{--}8R_g$  [region (c) of Fig. 19], attributable to the repulsive monomer–monomer interactions (i.e., the osmotic repulsion) associated with the positive second virial coefficient in the good solvent.

Using a symmetric polystyrene–polyvinylpyridine (PS–PVP) diblock copolymer, Hadziioannou and co-workers [170] demonstrated that the nonadsorbing PS chains can be held onto the mica surface by the covalently linked adsorbing PVP blocks, with the PS chains being stretched out to form a polymer brush at the mica/toluene interface. To mimic a layer of end-grafted polymer chains more closely, Taunton et al. [155] used end-functionalized PS–X homopolymers and highly asymmetric  $\text{PS}_m\text{--PEO}_n$  diblock copolymers for the surface force measurements, where PS–X denotes linear polystyrene chains with one end terminated by the zwitterionic group  $[-(\text{CH}_2)_3\text{N}^+(\text{CH}_2)_2-(\text{CH}_2)_3\text{SO}_3^-]$  and  $\text{PS}_m\text{--PEO}_n$  denotes polystyrene–poly(ethylene oxide) diblock copolymers [ $m$  and  $n$  are weight-averaged degrees of polymerization for polystyrene and poly(ethylene oxide) blocks, respectively, and  $n$  is small]. These authors demonstrated that the strong interaction between the zwitterionic or ethylene oxide groups and the mica surface can also terminally anchor the nonadsorbing PS block, as a dangling chain, at the mica/solvent (e.g., toluene) interface. At a higher surface coverage the PS chains are shown to be strongly stretched, to give a monotonic repulsive interaction between two such polymer “brushes,” consistent with theoretical predictions [155, 171, 172].

We have explored the conformational transitions of the end-adsorbed PS–PEO diblock copolymer chains by directly measuring the interactions of a *single* layer of the end-adsorbed PS–PEO diblock copolymer chains against a *bare* mica surface in pure toluene (good solvent) and pure cyclohexane (poor solvent,  $T_\theta = 34\text{ }^\circ\text{C}$ ) [159]. The results are given in Figure 20 on a log-linear scale, in which no attraction is observed and strong repulsive forces are seen.

The effective layer thickness of ca.  $1000\text{ \AA}$  deduced from Figure 20a indicates that the  $\text{PS}_{1420}\text{--PEO}_{51}$  chains are terminally attached to the mica surface via the short PEO segments with the PS chains extending into the solution to form a polymer brush. Figure 20b gives the force–distance curve that was measured on the same end-adsorbed PS layer after the toluene was thoroughly replaced by pure cyclohexane. In comparison with Figure 20a, Figure 20b shows a steeper repulsive wall commencing at a much shorter separation distance, which demonstrates unambiguously that the end-adsorbed PS brush has collapsed in the poor solvent to form a more compact polymer layer at the cyclohexane/mica interface. Furthermore, the transitions between Figure 20a and Figure 20b with changing solvent quality are characterized by fast dynamics, suggesting potential applications, for example in polymeric valves, sensors, and liquid chromatography [173, 174].



**Figure 20.** Force–distance profiles on a log–linear scale for an end-adsorbed PS<sub>1420</sub>–PEO<sub>51</sub> diblock copolymer single layer against a bare mica surface during the first few compression–decompression cycles: (a) in toluene before and after having been immersed in cyclohexane; (b) in cyclohexane. The open double-arrow indicates that the transition between (a) and (b) is practically reversible. The inset shows the corresponding force profiles as (a) and (b), respectively, on a linear–linear scale. Reprinted with permission from [159], L. Dai et al., *Macromolecules* 28, 5512 (1995). © 1995, American Chemical Society.

Although the surface force apparatus serves as a good experimental technique for probing conformations and conformational transitions of macromolecular chains within the adsorbed polymer thin film at the liquid/solid interface [159, 175], the force measurements cannot determine the distribution of segment density normal to the surface. Neutron reflection experiments provide information on the density profile normal to the interface [164, 176]. In this regard, we investigated the segment density profiles of the surface-bound polymers normal to the interface by reflectometry, choosing neutrons as the radiation because of important contrast effects which can operate at the molecular level [164]. For terminally anchored polymer chains in a good solvent, two regimes are anticipated. If the grafting density is low, the tethered chains do not interact with each other and exist as separate “mushrooms.” If the grafting density is high, with a distance between anchor points less than the Flory radius of the chains (i.e.,  $s < R_F$ ), the polymers take up a more extended configuration to form a semidilute “brush” [162, 163].

In the mushroom regime, each chain may be thought of as occupying roughly a hemisphere, with a radius comparable to the Flory radius for a polymer coil in a good solvent [162, 163, 177]. In the brush regime, however, the reflectivity profile of an end-adsorbed PS<sub>1700</sub>–PEO<sub>167</sub> from toluene onto quartz can be fitted by a parabolic function, consistent with the theoretical prediction for semidilute polymer brushes [178–180]. Our recent neutron reflectivity measurements on telechelic *triblock* copolymer chains [181] have demonstrated, to a very good approximation, that ABA-type end-tethered chains behave in a manner equivalent to their AB-type counterparts of half their molecular weight and they adsorb predominantly in a loop conformation for

copolymers with sufficiently strong sticking A blocks, consistent with the SFA measurements [159, 175].

## 5. NANOSTRUCTURED POLYMERS WITH SPECIAL ARCHITECTURES

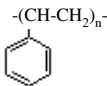
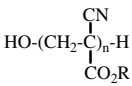
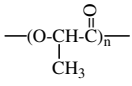
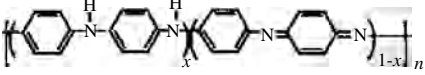
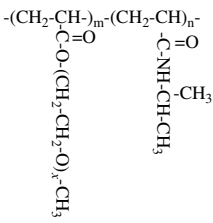
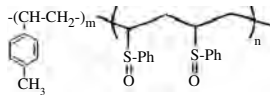

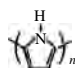

Just as microchips have revolutionized computers and electronics, nanotechnology has the potential to revolutionize many industrial sectors. As discussed, various polymer nanostructures (e.g., polymer nanoparticles, nanofibers, nanofilms; see Table 1) have been prepared to possess useful physicochemical properties for device applications. However, considerable efforts are required to design, construct, and operate new devices at the nanometer scale, as the technology for making proper connections from nanoscale entities to the macroscale world still remains a big challenge. In particular, electrically conducting nanofibers with diameters at the nanometer scale and lengths in kilometers are both useful “building blocks” for nanodevice construction and ideal connections between the nanoscale entities and the macroscale world. Effective fabrication of *ordered* nanostructured polymers is a pre-requisite for the intergration of nanostructured materials into useful “building blocks” and various functional units/nanodevices of practical significance. As we shall see later, techniques, including colloidal self-assembling, phase separation, and nanopatterning, have been devised to construct polymer materials and functional systems of multidimensional *ordered* nanostructures.

### 5.1. Self-Assembly of Ordered Nanoporous Polymers

Polymers with periodically modulated mechanical, optical, electronic, or magnetic properties have potential applications in many areas, including sensors, displays, microelectronics, data storage devices, and nonlinear optics [182, 183]. For instance, polymers with periodic dielectric media, like photonic crystals, could be used to manipulate and control light [184, 185]. Therefore, the fabrication of thin films with three-dimensional (3D) periodic arrays by incorporation of large quantities of monodisperse domains in an organized fashion within appropriate matrices or using self-organization (i.e., self-assembling) of colloid nanoparticles has rapidly become the forefront of development in materials science. Consequently, many novel nanostructured polymers of multidimensional periodic structures have been reported. To mention but a few examples, Kumacheva and co-workers [186] have used the self-assembling approach to producing nanostructured polymers with a 3D periodic structure (Fig. 21).

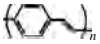
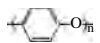
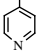
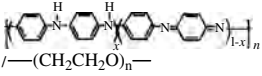
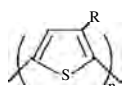
As can be seen in Figure 21a, Kumacheva et al. [186] first synthesized a core–shell latex consisting of a hard core-forming polymer and a soft shell-forming polymer. They then packed these core–shell latex particles into thin layers of 3D structures by, for example, precipitation, centrifugation, or electrodeposition followed by latex drying. The resulting materials were finally annealed at high temperature to melt the soft shells, leading to the formation of nanostructured polymer thin films consisting of 3D nanoparticle assemblies. The laser confocal fluorescent microscopy

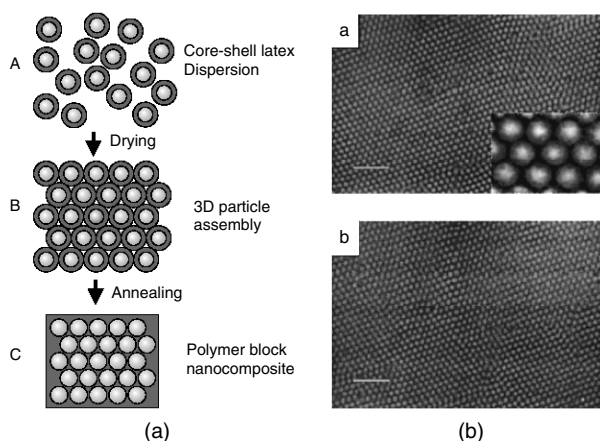
**Table 1.** Examples of polymer nanostructures.

Polymer (name and structure)	Nanostructure	Size (nm)	Ref.
Polystyrene 	nanospheres nanowires nanotubes nanofibers polymer brushes	15–200 ~300 ~40	[9–11] [75] [79] [96] [155–159]
Poly(alkylcyanoacrylate) 	nanospheres	~200	[16]
Poly(lactide) 	nanospheres	200–250	[25–27]
Polyaniline 	nanoparticles nanowires nanotubes nanofilms LB films	10–60 100–200 ~350	[51] [68] [80, 81] [116] [131]
PNIPAM- <i>g</i> -PEO 	core-shell nanospheres	15–250	[40–45, 51, 52]
PMS- <i>b</i> -PVSO 	core-shell nanospheres	30–60	[58, 49]
PCL/MAF mixtures 	core-shell nanospheres	100–300	[53]
Polypyrrole 	nanowires LB films	50 μm	[61] [130]
Polythiophene 	nanowires	20 μm	[64]

continued

Table 1. Continued.

Polymer (name and structure)	Nanostructure	Size (nm)	Ref.
PPV 	nanowires nanofilms LB films	4 ~100	[72] [106–111] [135, 136]
PVDF $-(CF_2CH_2)_n-$	nanowires	>30	[75]
Poly(phenylene oxide) 	nanowires	>30	[75]
PMMA $-(CH_2-\overset{\text{CH}_3}{\underset{\text{COOCH}_3}{\text{C}}})_n-$	nanowires nanotubes	~300	[75] [79]
PTFE $-(CF_2CF_2)_n-$	nanotubes	~300	[79]
Polyethylene $-(CH_2CH_2)_n-$	nanofibers	~3	[83]
Poly(4-vinylpyridine) $-(CH_2-\overset{\text{CH}}{\underset{\text{N}}{\text{C}}})_n-$ 	micro/nanospheres	0.2–3 μm	[24]
Polyacrylonitrile $-(CH_2-\overset{\text{H}}{\underset{\text{CN}}{\text{C}}})_n-$	nanotubes nanofibers	>30	[83, 84] [97]
Polyaniline/PEO mixtures 	nanofibers	1–2 μm	[98]
Poly(3-alkythiophene) 	LB films	1–5	[132]
Poly(meta-phenylene isophthalamide)/aluminum $-(\text{HN}-\text{C}_6\text{H}_3-\text{NHOC}-\text{C}_6\text{H}_3-\text{CO})_n-$ / Al	coaxial nanowires	100–200	197



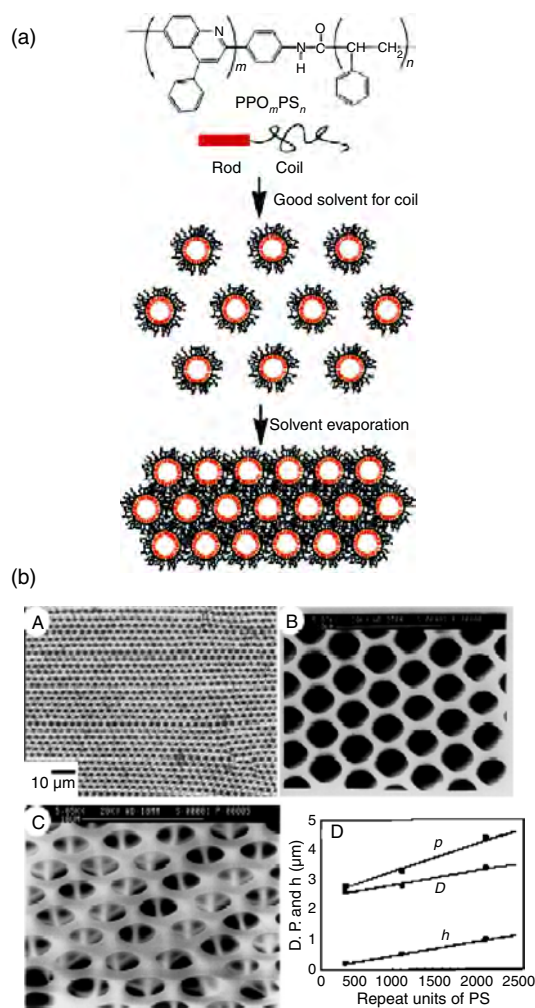
**Figure 21.** (a) Schematic representation of the approach for producing nanostructured polymers with 3D ordered structure. (A) Synthesis of the core-shell polymer nanoparticles with hard functional cores and soft inert shells; (B) self-assembling of the polymer nanoparticles into a 3D compact; and (C) heat treatment of the compact to induce melting of the soft shells to form polymer nanocomposite with nanostructured spheres. (b) Laser confocal fluorescent microscopy images of the surface and the bulk morphology of the 3D nanostructured polymer films. *Top:* Composite morphology at the surface of the sample; inset shows the same structure with the width of the area being  $3.3 \mu\text{m}$ . *Bottom:* Polymer structure in the layer located 30 mm below the surface. Scale bar is  $10 \mu\text{m}$ . Reprinted with permission from [186], E. Kumacheva, et al., *Adv. Mater.* 11, 231 (1999). © 1999, Wiley-VCH.

images of the surface and the bulk morphology of the 3D nanostructured polymer films thus prepared are given in Figure 21b, which shows a highly ordered structure in the  $z$ -direction as well as in the lateral domains. These highly ordered nanostructured polymers with 3D periodic structures have been demonstrated to be promising media for data storage.

On the other hand, Jenekhe and Chen [187] have prepared multidimensional ordered mesoporous polymer materials by self-assembling hollow spherical micelles made by self-organized rod-coil diblock copolymers in a selective solvent. Figure 22a schematically shows the approach used with the morphology of the resulting materials given in Figure 22b. Although micropores were observed in this particular case (Figure 22b), the diameter, periodicity, and wall thickness of the ordered arrays of spherical holes were demonstrated to depend on the copolymer molecular weight and composition, indicating the possibilities of forming porous polymer films with nanostructured holes for a variety of applications ranging from size/shape-selective separation to photonic modulation.

## 5.2. Coaxial Polymer Nanowires and Nanofibers

5.2 The formation of ordered structures from metal nanowires and carbon nanotubes has been an active research area for some years. Various nano- and microfabrication techniques have been developed. Examples include the use of electric and magnetic fields for aligning suspended metallic nanowires [188–190], the combination of fluidic alignment with patterned surface structures (e.g., microchannels)

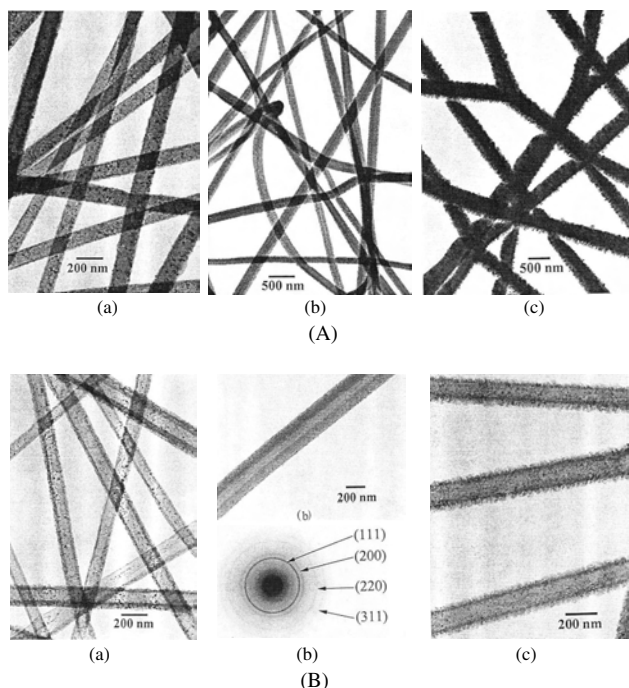


**Figure 22.** (a) Schematic illustration of its hierarchical self-assembly into ordered microporous materials. (b) Polarized optical and (B and C) scanning electron micrographs of microporous micellar films obtained from a diblock solution by solution casting on a glass slide (A) and an aluminum substrate (B and C). (D) The molecular weight dependence of geometric parameters of the pores: the diameter,  $D$ ; minimum wall thickness,  $h$ ; center-to-center hole periodicity,  $p$  ( $h = p - D$ ). Reprinted with permission from [187], S. A. Jenekhe and X. L. Chen, *Science* 283, 372 (1999). © 1999, American Association for the Advancement of Science.

for nanowire patterning, [191, 192] and the lithographic patterning of aligned carbon nanotubes [193]. The effective fabrication of ordered polymer nanowires or nanofibers is a more recent development. While a few aligned polymer nanowires prepared by synthesizing them at a scanning microscope tip or by using a template were described (Section 3), the possibility of forming aligned *electrospun* nanofibers by using a rotating cathode collector has recently been reported [194, 195]. Nonconducting electrospun polymer fibers have also been used as “templates” for coating with appropriate conducting polymers and for deposition of a metal layer from solution or vapor [196]. MacDiarmid and co-workers [96] reported the uniform coating of an electrospun polyacrylonitrile nanofiber with a layer of conducting polypyrrole (20 to 25 nm thick) by immersing the

electrospun fibers in an aqueous solution of polymerizing polypyrrole. These authors also prepared gold coated polyacrylonitrile nanofibers through treatment of the electrospun fibers with a solution of  $\text{AuS}_2\text{O}_3$  and ascorbic acid.

Reneker and co-workers [197] coated electrospun poly(*meta*-phenylene isophthalamide) nanofibers with subnanometer thick coatings of various other materials (e.g., carbon, Cu, and Al) by chemical and physical vapor deposition. They also prepared nanotubes consisting of pure aluminum or mixtures of aluminum and aluminum oxide by coating the electrospun poly(*meta*-phenylene isophthalamide) nanofiber with an aluminum layer, followed by selectively removing the polymer nanofiber core via solvent dissolution or thermal degradation [197]. During thermal degradation of the poly(*meta*-phenylene isophthalamide) nanofiber cores, the aluminum coated layer was subjected to a limited degree of oxidation, which produced nanotubes of mixed aluminum and aluminum oxide. The aluminum coated layers did not oxidize when the template fiber core was removed by dissolution. Figure 23A(a–c) shows TEM images of aluminum-coated poly(*meta*-phenylene isophthalamide) fibers with the coating thickness increasing from ca. 10 to 100 nm. As seen in Figure 23B(a–c), aluminum nanotubes remained after dissolution of the fiber cores of poly(*meta*-phenylene isophthalamide) with *N,N*-dimethylacetamide solvent. The electron diffraction pattern associated with the aluminum nanotubes shown

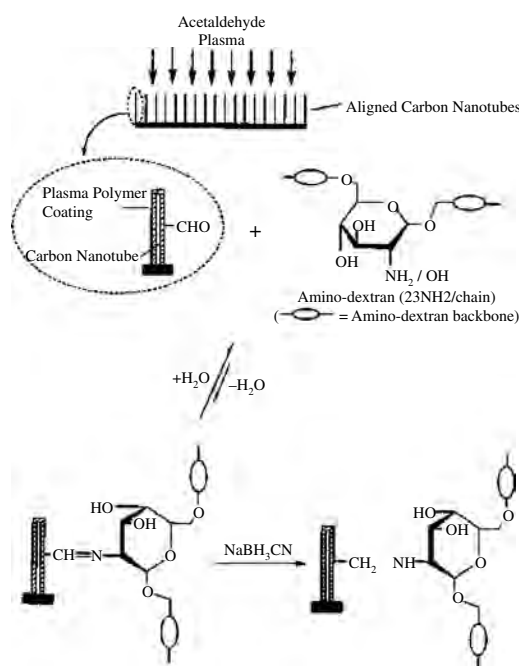


**Figure 23.** (A) (a–c) TEM images of aluminum-coated poly(*meta*-phenylene isophthalamide) electrospun nanofibers with the coating thickness increasing from about 10 nm in (a) to nearly 100 nm in (c). (B) (a–c) TEM images of Al nanotubes prepared by solvent dissolution of the poly(*meta*-phenylene isophthalamide) core. (d) Electron diffraction pattern of nanotubes associated with the aluminum nanotubes shown in Figure 24B(a). Reprinted with permission from [197], W. Liu et al., *J. Mater. Res.* 17, 3206 (2002). © 2002, Materials Research Society.

in Figure 23B(a) is given in Figure 23B(d), in which all the *d*-spacings are characteristic of the aluminum crystal unit cell.

Another interesting area closely related to the fabrication of polymer nanowires and nanofibers is the synthesis of coaxial nanowires of polymers and carbon nanotubes. We have recently prepared large-scale aligned carbon nanotubes perpendicular to the substrate surface by pyrolysis of iron (II) phthalocyanine ( $\text{FeC}_{32}\text{N}_8\text{H}_{16}$ , designated as FePc) under  $\text{Ar}/\text{H}_2$  at 800–1100 °C and developed a novel approach for chemical modification of aligned carbon nanotubes [198]. Radio-frequency glow-discharge plasma treatment activated the surface of the nanotubes for subsequent reactions characteristic of the plasma-induced surface groups. We then successfully grafted polysaccharide chains onto the plasma-activated aligned carbon nanotubes through Schiff-base formation, followed by reductive stabilization of the Schiff-base linkage with sodium cyanoborohydride (Fig. 24).

The resulting amino-dextran grafted nanotube film showed zero air/water contact angles. The (acetaldehyde) plasma treated carbon nanotube film gave relatively low advancing ( $90^\circ$ ), sessile ( $78^\circ$ ), and receding ( $45^\circ$ ) air/water contact angles compared to the advancing ( $155^\circ$ ), sessile ( $146^\circ$ ), and receding ( $122^\circ$ ) angles for an untreated sheet of aligned carbon nanotubes. The glucose units within the surface-grafted amino-dextran chains (Fig. 24) can be further converted into dialdehyde moieties by periodate oxidation [199], thereby providing a method for creating multilayer coaxial structures.



**Figure 24.** Scheme showing the grafted polysaccharide chains onto plasma activated aligned carbon nanotubes through Schiff-base formation, followed by reductive stabilization of the Schiff-base linkage with sodium cyanoborohydride. Reprinted with permission from [198], Q. Chen et al., *J. Phys. Chem. B* 105, 618 (2001). © 2001, American Physical Society.

In addition to the chemical grafting of polymer chains onto the carbon nanotube surface, we recently used the aligned carbon nanotubes as nanoelectrodes for making novel conducting coaxial nanowires by electrochemically depositing a concentric layer of an appropriate conducting polymer uniformly onto each of the aligned nanotubes to form the aligned conducting polymer coated carbon nanotube coaxial nanowires (CP-CNT) [200]. The SEM image for these CP-CNT coaxial nanowires given in Figure 25b shows the same features as the aligned nanotube array of Figure 25a, but the tubes had a larger diameter due to the presence of the newly electropolymerized polypyrrole coating. The presence of the conducting polymer layer was also clearly evident in TEM images [200] (Fig. 25c). The aligned CP-CNT coaxial nanowires were demonstrated to show much stronger redox responses than the conventional conducting polymer electrode [200]. The coaxial structure allows the nanotube framework to provide mechanical stability [201, 202] and efficient thermal and electrical contact with the conducting polymer layer [203, 204]. The large interfacial surface area per unit mass obtained for the nanotube-supported conducting polymer layer is potentially useful in many optoelectronic applications, for example in sensors, organic light-emitting diodes, and photovoltaic cells where the charge injection and separation are strongly limited by the interfacial area available in more conventional devices [49].

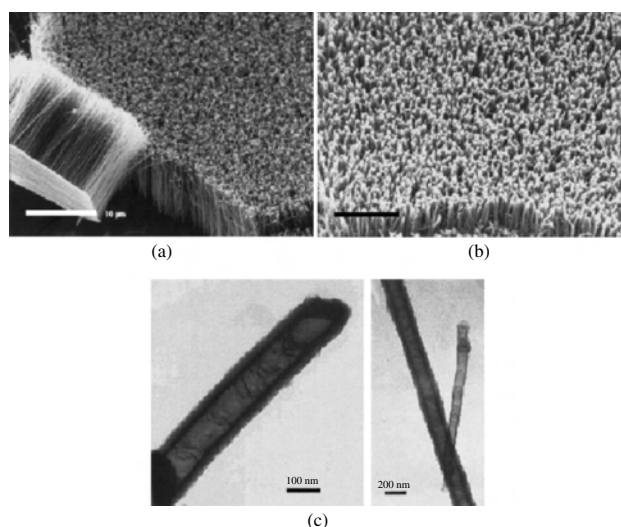
To demonstrate the potential sensing applications for the CP-CNT coaxial nanowires, we have also immobilized glucose oxidase ( $\text{GO}_x$ ) onto the aligned carbon nanotube substrate by electropolymerization of pyrrole in the presence of glucose oxidase [205]. The glucose oxidase-containing polypyrrole-carbon nanotube coaxial nanowires were used to monitor the concentration change of hydrogen peroxide ( $\text{H}_2\text{O}_2$ ) generated from the glucose oxidation reaction by measuring the increase in the electro-oxidation current at the oxidative potential of  $\text{H}_2\text{O}_2$  (i.e., the amperometric

method) [205]. The amperometric response was found to be much higher than that of more conventional flat electrodes coated with glucose oxidase-containing polypyrrole films under the same conditions. The CP-CNT nanowire sensors were also demonstrated to be highly selective for glucose with their amperometric responses being almost unchanged even in the presence of some interference species including ascorbic acid, urea, and D-fructose. Therefore, the CP-CNT nanowires could be used for making new glucose sensors with a high sensitivity, selectivity, and reliability, which is clearly an area in which future work would be of value.

### 5.3. Multilayered Polymer Nanofilms

Polymer-based multilayer thin films have recently received significant attention due to their potential use as photonic crystals for manipulation and control of light. Indeed, certain multilayer polymer nanostructures with the phase-separated lamellar domains of different refractive indices have been used as 1D optical reflectors for reflecting a band of frequencies for both TE and TM polarized light regardless of angle of incidence [206, 207]. Apart from the multilayer film formation by polymer phase separation to be discussed, the construction of multilayer polymer nanofilms has also been achieved by the LB technique (Section 4.3) and a layer-by-layer self-assembly process developed by Ferreira and Rubner [208]. The principle of the layer-by-layer process lies in the alternate spontaneous adsorption of oppositely charged polymers from dilute solutions. This technique has been successfully used to generate multilayer thin films comprised of sequentially adsorbed layers of partially doped polyaniline and a polyanion (e.g., sulphonated polystyrene), leading to conductivities comparable to those obtained with spin-cast films (0.5–1.0 S/cm) after having been doped with strong acids such as HCl and methanesulfonic acid [209]. Based on the layer-by-layer adsorption process, Rubner et al. [210–212] have also constructed multilayer LEDs from PPV and poly(styrene sulfonic acid), (SPS), or poly(methacrylic acid) (PMA) and found that the type of polyanion used has a significant effect on the performance of the LED devices fabricated with Al and ITO as electrodes. In particular, LEDs fabricated from PMA/PPV multilayers were found to exhibit luminance levels in the range of 20–60  $\text{cd/m}^2$  with a thickness dependent turn-on voltage and rectification ratios greater than  $10^5$ , whereas the SPS/PPV counterparts showed nearly symmetric  $I$ – $V$  curves with a thickness independent turn-on voltage and much lower luminance levels. The observed difference in the device performance can be attributed to a doping effect associated with the sulfonic acid groups in SPS. Furthermore, these authors have recently extended the layer-by-layer adsorption process to include the hydrogen-bonding interactions between the polyaniline and poly(vinylpyrrolidone), poly(vinyl alcohol), poly(acrylamide), or poly(ethylene oxide) [213]. By using preordered/prepatterned substrates, the layer-by-layer absorption process should, in principle, lead to the construction of oriented/patterned conjugated polymers.

Another interesting area closely related to the polymer-polymer multilayer structure is the intercalation of polymer chains into the layered structures of clay nanoparticles,

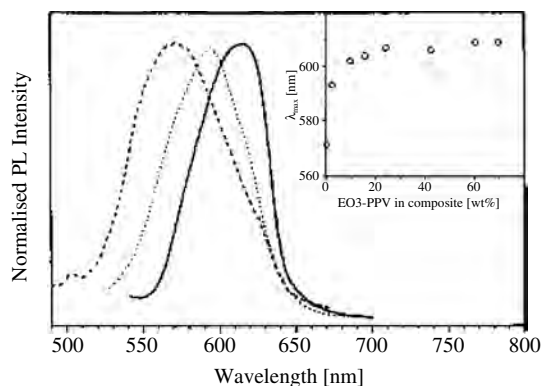


**Figure 25.** (a) Aligned nanotubes, (b) CP-CNT coaxial nanowires, and (c) TEM images of the CP-CNT coaxial nanowires. Reprinted with permission from [200], M. Gao et al., *Angew. Chem. Int. Ed.* 39, 3664 (2000). © 2000, Wiley-VCH.

leading to the formation of organic–inorganic hybrid multilayer films [214]. Organic–inorganic hybrid composites constitute a new class of materials, possessing properties characteristic of both constituent components with potential synergistic effects [215–217]. Owing to their unusual properties, organic–inorganic hybrid nanocomposites have attracted increased attention in recent years. Consequently, various polymers including poly(ethylene oxides) [218, 219], poly(olefins) [220], polyimide [221], polypyrrole [222], and polyaniline [223, 224] have been incorporated into clay nanoparticles through either a solution or a melt intercalation process [225, 226]. The most widely used clay is montmorillonite, which consists of an alumina octahedral and two silica tetrahedral sheets stacking into the layered structure with a gallery gap of ca. 1 nm between the layers. The galleries are normally occupied by cations (e.g.,  $Na^+$ ,  $Ca^{2+}$ ,  $Mg^{2+}$ ), which can be easily replaced through alkylammonium ion exchange reaction to form the so-called organoclay. The alkylammonium ions in the organoclay layered structure facilitate the intercalation of polymer chains. At high intercalation levels, the clay may exfoliate into their nanoscale building blocks to disperse uniformly in the polymer matrices, forming exfoliated polymer–clay nanocomposites. The organic–inorganic hybrid nanocomposites thus prepared have been demonstrated to show improved environmental stability, mechanical strength, and lower permeability for gases with respect to corresponding pure polymers [227–229].

On the other hand, certain electroluminescent organic–inorganic hybrid materials have also been prepared by sol–gel chemistry [230]. In this context, we have recently intercalated conjugated conducting and light-emitting polymers into clay nanoparticles at an intercalation level below the critical value required for the clay exfoliation to explore the conformational effects on their optoelectronic properties. As is well known, the band gap energies of conjugated polymers, and hence the related optoelectronic properties, depend strongly on their chain conformations [71]. Therefore, the conformational changes of light-emitting polymer backbones could be exploited as an alternative approach to color tuning, in addition to chemical modification of the polymer structure, in polymer light-emitting diodes. On this basis, we intercalated light-emitting poly[1,4-(2,5-bis(1,4,7,10-tetraoxaundecyl)phenylenevinylene)] ( $EO_3$ -PPV), into clay nanoparticles for light-emitting measurements [231].

The intercalation process is experimentally revealed by a steady increase in the height of the clay galleries as determined by X-ray diffraction [231]. The photoluminescent (PL) spectra of the composites at several different intercalation levels are given in Figure 26. As can be seen, the PL emission shows a redshift with increasing intercalation level. Included in the inset of Figure 26 is the dependence of the PL peak position ( $\lambda_{max}$ ) on the polymer content, which shows that the  $\lambda_{max}$  continuously increases with increasing polymer content to a limiting value of ca. 610 nm, characteristic of  $EO_3$ -PPV, at ca. 20% (w/w), then remains unchanged despite further intercalation. These features could be attributed to an intercalation-induced conformational transition from a “compact coil” to “expanded coil,” which should lead to an increase in the effective con-



**Figure 26.** PL emissions from the  $EO_3$ -PPV intercalated clay nanoparticles at different intercalation levels. Reprinted with permission from [231], B. Winkler et al., *J. Mater. Lett.* 18, 1539 (1999), © 1999, Plenum.

jugation length, and hence a concomitant decrease in the bandgap energy.

Our results from a single layer LED device based on the  $EO_3$ -PPV intercalated nanoparticles showed an EL spectrum similar to the PL emission. As expected, the similarity between the EL and PL emissions suggested that the same singlet excitons were generated upon both the PL and EL excitation.

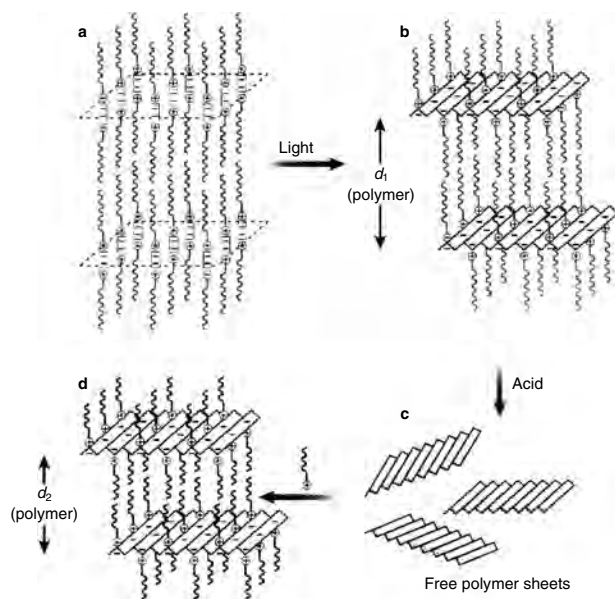
Closely related to the preparation of layered nanocomposites consisting of polymer thin films interspersed with clay sheets, Matsumoto and co-workers [232] have moved a step further forward by showing novel polymer sandwiches with different fillings. In so doing, these authors first created layered structures consisting of layers of muconate anions (i.e., reactive dienes with carboxylate group at either end) sandwiched between layers of alkylammonium cations (Fig. 27). They then polymerized the layered muconate anions into molecule-thick polymer sheets by exposure to ultraviolet light. Upon exposure of the “synthetic clay” to acid, the alkylammonium cations were removed to free the uncharged polymer sheets. The released polymer sheets can be “glued” together again by one of the many alkylammonium ions for a large variety of potential applications, ranging from molecular recognition to chemical purification.

#### 5.4. Nanostructured Polymers by Phase Separation and Nanopatterning

Apart from the discussed *isolated* polymer nanostructures (e.g., nanoparticles, nanofibers, and nanofilms) and their assemblies, nanostructured polymer domains consisting of an intrinsic part of the polymer morphology (hence cannot be separated from other features of the polymer material) have also been prepared through, for example, polymer phase separation and nanopatterning.

Like the self-assembling technique discussed, polymer phase separation plays an important role in fabrication of nanostructured polymers, as it provides the opportunity for nanoscale structuring that otherwise is difficult by lithographic techniques [233, 234]. The conditions necessary for microphase separation in immiscible polymer mixtures depend on their molecular architectures, nature of

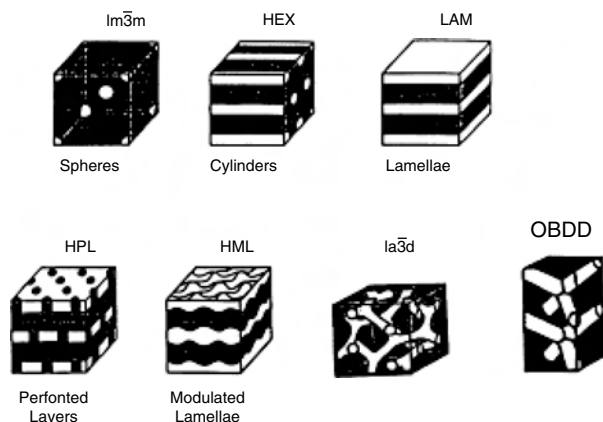




**Figure 27.** Schematic representation showing how to build molecular sandwiches with different fillings. Reprinted with permission from [232], A. Matsumoto et al., *Nature* 405, 328 (2000). © 2000, Macmillan Magazines Ltd.

monomers, compositions, and molecular weights [235, 236]. By varying polymer structures and phase separation conditions, at least seven well-defined microdomain structures with sizes typically in the range of a few tens of nanometers have been observed in polymer materials (Fig. 28).

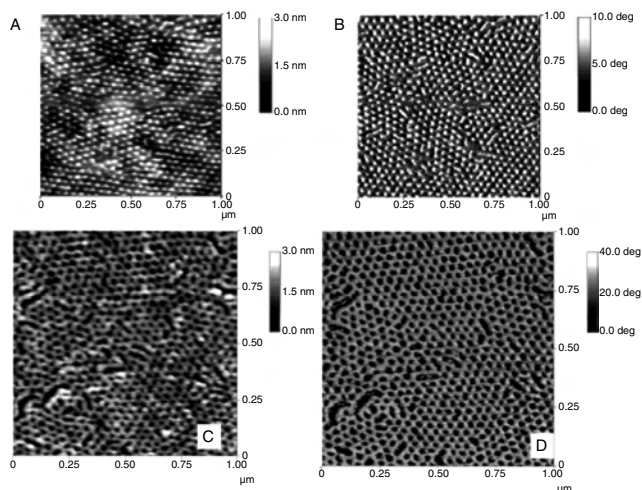
Among these well-defined microdomain structures observed in phase separated polymer systems, cylindrical microdomains formed by block copolymers are of particular interest as the selective removal of either the minor or major component can transform thin polymer films into an array of nanopores or nanoscopic posts. The resultant polymer nanostructures could be used as membranes for molecular separation and/or as templates for preparing electronic and magnetic nanostructured materials.



**Figure 28.** Experimentally observed nanostructure form by phase separation of diblock copolymers. Reprinted with permission from [236], T. P. Lodge and M. Muthukumar, *J. Phys. Chem.* 100, 13275 (1996). © 1996, American Chemical Society.

The phase separation of block copolymers has been the subject of intensive study over the past several decades [233–236]. It has recently been demonstrated that cylindrical microdomains in certain phase-separated block copolymer thin films can be oriented normal to the substrate surface by either controlling interfacial interactions between the copolymer and substrate with anchored random copolymers [237, 238] or by applying an external electric field normal to the surface [239–241]. Figure 29A and B shows atomic force microscope (AFM) images for a phase-separated asymmetric polystyrene and poly(methyl methacrylate) (PS-*b*-PMMA, ca. 30% volume fraction of PMMA) block copolymer thin film (40 nm thick) spin-cast onto Si substrates precoated with a random copolymer of PS and PMMA having a PS fraction of 0.60 [242]. Cylindrical microdomains oriented in the direction perpendicular to the substrate are clearly evident, especially in the phase image of Figure 29B. The corresponding AFM height and phase images for the same PS-*b*-PMMA film after selectively removing the PMMA component by deep UV radiation and dissolution in a selective solvent (i.e., acetic acid for PMMA) are given in Figure 29C and D, respectively. Both show an ordered array of circular nanopores perpendicularly oriented in the polymer film.

By adding PMMA homopolymers with appropriate molecular weights into the PS-*b*-PMMA matrices, Jeong et al. [243] were able to tune the size of the cylindrical microdomains (and hence the circular holes) formed in the block copolymer films without perturbing their spatial order and orientation. They found that pore diameters either larger or smaller than those achievable with the pure copolymer could be obtained by selective removal of the homopolymer and corresponding block of the copolymer or the homopolymer only. By so doing, both 6 and 22 nm diameter pores have been prepared from the same block copolymer film.



**Figure 29.** AFM image for a PS-*b*-PMMA block copolymer thin film on a neutral substrate after annealing at 170 °C in tapping mode before [(A) shows the height image and (B) the phase image] and after [(C) shows the height image and (D) the phase image] removal of the PMMA cylinders. Holes at the original locations of the cylinders are clearly seen. Reprinted with permission from [242], T. Thurn-Albrecht et al., *Adv. Mater.* 12, 787 (2000). © 2000, Wiley-VCH.

More interestingly, these authors have recently used the phase-separated PS-*b*-PMMA nanoporous films and nanoscopic posts as templates for producing metal nanodots and nanoporous metal films, respectively, by evaporation metal (e.g., Cr, Au) thin films on these polymer nanostructures, followed by selective removal of the polymer templates [244].

Based on polymer phase separation, Berggren et al. [245] have also demonstrated the formation of submicrometer-sized domains having a range of compositions and emission characteristics by self-organization (i.e., phase separation) in polymer blends consisting substituted polythiophenes with different bandgaps. As a result, a voltage-controlled multiple-color emission was achieved, suggesting an attractive way for making future polymeric electroluminescent color screens.

Like the soluble substituted polythiophenes, polyacetylene can be solubilized by making copolymers with polyisoprene, polystyrene, or polybutadiene via the so-called anionic to Ziegler-Natta route [49]. The polyisoprene-polyacetylene (PI-PA) diblock copolymers thus prepared present an unusual situation where the high flexibility and solubility associated with polyisoprene chains and the stiffness and conductivity characteristic of insoluble conjugated polyacetylene chains are combined into one macromolecule. Due to the large difference in physical properties between these two blocks, the copolymers of PI-PA are expected to show phase separation in solution and domain structure in the solid state [246, 247]. Indeed, we have recently found that I<sub>2</sub> doping of the PI-PA copolymer films leads to the formation of a pseudo interpenetrating polymer network (PIPn) [247]. The aggregated structures (especially the PIPn network) play an important role in regulating the electrical properties of the PI-PA copolymers [247], and the doping-induced phase separation process may have potential implications for making various multiphase conducting polymers with different ordered structures ranging from the nanometer to micrometer scale.

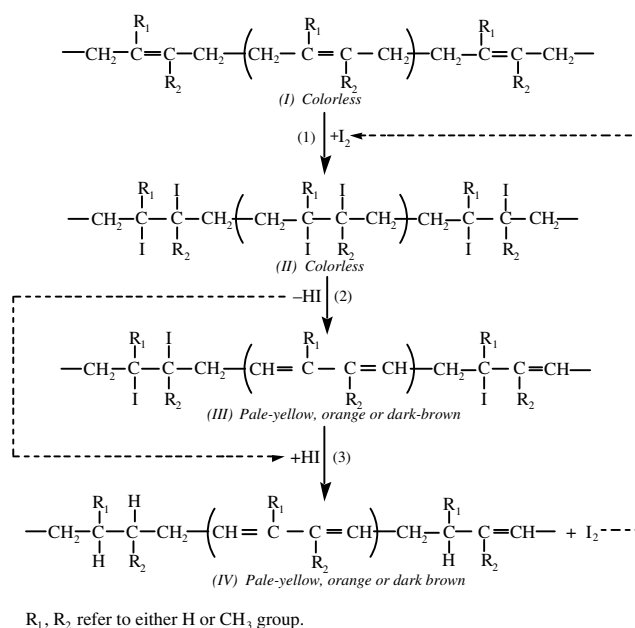
Furthermore, the chain segregation has also been either experimentally observed or theoretically predicted for block copolymers confined between two constituent homopolymer layers [248], two foreign walls [249–252], or end attached at the liquid/solid interface [253, 254], suggesting a considerable scope for patterning of polymer chains through polymer phase separation. To mention but a few examples, Zhao and co-workers [255] have experimentally demonstrated nanopattern formation by tethered PS-*b*-PMMA brushes upon treatment with selective solvents, while a number of other groups have reported the patterning of polymer brushes by various lithographic techniques [256].

As is well known, photolithographic processing has been widely used for the pattern formation in semiconducting industries (e.g., for delineating the circuit elements in today's large-scale integrated devices) for many years with an ultimate resolution at the submicrometer scale. Recent work on photolithographic patterning of conducting polymers and carbon nanotubes [100, 257] has demonstrated that photolithographic techniques, coupled with appropriate chemical reactions, could provide effective means for the micro/nanopattern formation of various organic electronic materials [100, 257, 258]. For instance, in 1988, Thakur

reported that the conductivity of nonconjugated *cis*-1,4-polyisoprene (i.e., natural rubber) could be increased by about 10 orders of magnitude upon "doping" with iodine [259]. In view of the ease with which conducting rubber can be made and the potential challenge of Thakur's claim to modern theory of conducting polymers, Thakur's work received complimentary comments from several scientific journals [260–262]. Meanwhile, various other polymers with isolated (nonconjugated) double bonds, such as *trans*-1,4-polyisoprene, 1,4-poly-(2,3-dimethylbutadiene), and *trans*-1,4-polybutadiene, have also been found to become dark in color and conductive when "doped" with iodine in the solid state. Surprisingly, however, *cis*-1,4-polybutadiene does not change color or become conductive upon "I<sub>2</sub> doping" under the same conditions [260–262]. We were the first to demonstrate that "I<sub>2</sub> doping" of 1,4-polyisoprene produces conjugated sequences of unsaturated double bonds in the polyisoprene backbone through polar addition of I<sub>2</sub> into the isolated double bonds in the polymer chain, followed by HI elimination [263].

The reaction mechanism for the I<sub>2</sub>-induced conjugation is shown in Figure 30, and the conjugated sequences thus produced have been shown to be responsible for the high conductivity of the "I<sub>2</sub>-doped" polyisoprene. The reactions shown in Figure 30 have been confirmed by optical and other spectroscopic measurements reported by several groups, including ours [263–267].

In our further investigation of conducting polydienes [264], we have found that *cis*- and *trans*-1,4-polybutadiene exhibit different behavior toward the reactions of Figure 30. For *cis*-1,4-polybutadiene the reaction sequence given in Fig. 30 terminated, at room temperature, at product (II), whereas for the *trans*-isomer the reaction sequence proceeded toward product (III) and/or (IV) thus leading to the



**Figure 30.** Reactions of polydiene with iodine, leading to the formation of conjugated sequences. Reprinted with permission from [263], L. Dai and J. W. White, *Polymer* 32, 2120 (1991). © 1991, Elsevier Science.

formation of conjugated sequences which confer electrical conductivity. Spectroscopic measurements and molecular orbital calculations demonstrated that it was an unfavorable combination of electronic and steric interactions within the iodinated *cis*-1,4-polybutadiene backbone (product II) that inhibited the elimination of hydrogen iodide through the E-2 elimination mechanism [reaction (2) of Fig. 30] at room temperature and hence halted the formation of conjugated sequences in the case of *cis*-1,4-polybutadiene [264]. However, *cis*-1,4-polybutadiene can be photoisomerized into the *trans*-isomer [268], and the isomerized material is then amenable to “I<sub>2</sub> doping.” This discovery provides means for photolithographic generation of conducting patterns from *cis*-1,4-polybutadiene films through region-specific photoisomerization of the *cis*-isomer into its *trans*-counterpart and subsequent I<sub>2</sub>-induced conjugation of the photoisomerized *trans*-1,4-polybutadiene chains [269]. The conducting patterns thus formed are colored and show strong fluorescence emission, which enables visualization of the conducting polymer regions.

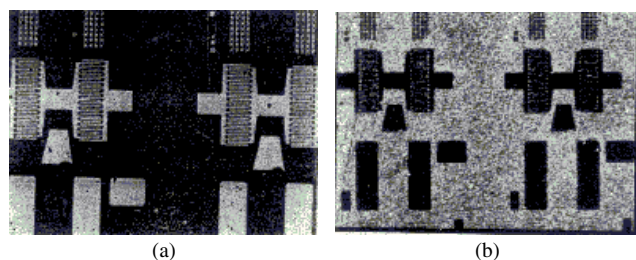
An example of the conducting patterns thus generated is shown in Figure 31a. It is a close replication of the photomask structure, and conducting wires on a micrometer scale are clearly evident. A corresponding fluorescence microscopic image of the conducting pattern is given in Figure 31b. It shows the same features as the optical micrograph (Fig. 31a), but with inverse intensities in the image. The dark regions characteristic of the “I<sub>2</sub>-doped” *trans*-1,4-polybutadiene in Figure 31a gave rise to bright fluorescence emission in Figure 31b, consistent with the fluorescence emission originating from the conjugated structures [270, 271]. The dark regions in Figure 31b represent nonfluorescent components associated with the *cis*-isomer. The resolution obtained in this study is limited by the light wavelength and photomask structure, which can, in principle, be improved for generation of polymer patterns with a submicron resolution.

More recently, we have also demonstrated that lithographic techniques could be applied to the pattern formation of carbon nanotubes. Although carbon nanotubes synthesized by most of the common techniques often exist in a randomly entangled state, [272, 273] aligned carbon nanotubes have been prepared either by postsynthesis

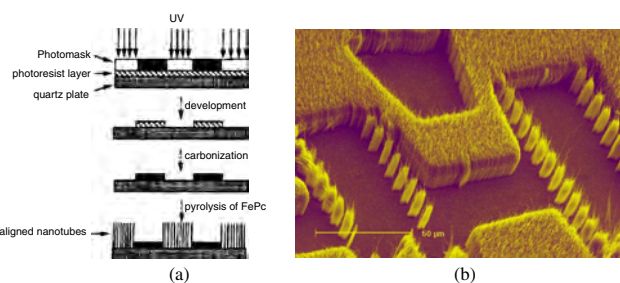
fabrication or by synthesis-induced alignment [100]. As briefly mentioned in Section 5.2, we, among others [274–278], have prepared large-scale aligned carbon nanotube arrays *perpendicular* to the substrate surface by pyrolysis of iron(II) phthalocyanine onto the pristine quartz glass plates [279]. Subsequently, we have also developed microfabrication methods for patterning the aligned carbon nanotubes with a submicrometer resolution [280]. Our method allows not only the preparation of micropatterns and substrate-free films of the perpendicularly aligned nanotubes but also their transfer onto various substrates, including those which would otherwise not be suitable for nanotube growth at high temperatures (e.g., polymer films) [279]. In one study, we have developed a novel method for photolithographic generation of the perpendicularly aligned carbon nanotube arrays with resolutions down to a micrometer scale [281].

Figure 32a shows the steps of the photolithographic process. In practice, we first photolithographically patterned a positive photoresist film of diazonaphthoquinone (DNQ)-modified cresol novolak onto a quartz substrate. Upon UV irradiation through a photomask, the DNQ-novolak photoresist film in the exposed regions was rendered soluble in an aqueous solution of sodium hydroxide due to photogeneration of the hydrophilic indenecarboxylic acid groups from the hydrophobic DNQ via a photochemical Wolff rearrangement [282]. We then carried out the pyrolysis of FePc, leading to region-specific growth of the aligned carbon nanotubes in the UV exposed regions (Fig. 32b). In this case, the photolithographically patterned photoresist film, after an appropriate carbonization process, acts as a shadow mask for the patterned growth of the aligned nanotubes. This method is fully compatible with existing photolithographic processes [283].

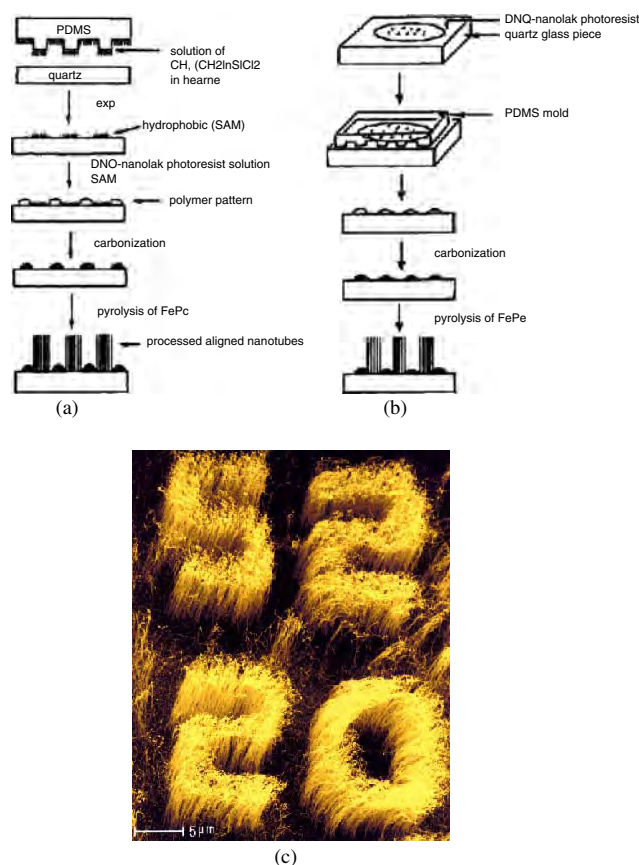
Furthermore, we have also used the micro-contact printing ( $\mu$ CP) and micromolding techniques [284] to prepare micropatterns of carbon nanotubes aligned in a direction normal to the substrate surface [285]. While the  $\mu$ CP process involves the region-specific transfer of self-assembling monolayers (SAMs) of alkylsiloxane onto a quartz substrate and subsequent adsorption of polymer chains in the SAM-free regions (Fig. 33a), the micromolding method allows the formation of polymer patterns through solvent evaporation from a precoated thin layer of polymer solution confined between a quartz plate and a polydimethylsiloxane (PDMS)



**Figure 31.** (a) Optical microscopy image of a pattern obtained by “I<sub>2</sub> doping” of the photoisomerized *trans*-1,4-polybutadiene regions in the iodinated *cis*-1,4-polybutadiene matrix. The dark areas are regions of “I<sub>2</sub>-doped” polybutadiene, and the width of the white rectangles at the bottom part of the picture is 18  $\mu$ m. (b) Fluorescence micrograph of the conducting pattern. Reprinted with permission from [269], L. Dai et al., *Macromolecules* 29, 282 (1996). © 1996, American Chemical Society.



**Figure 32.** (a) Schematic representation of the micropattern formation of aligned carbon nanotubes by photolithographic process. (b) Typical SEM micrographs of patterned films of aligned nanotubes prepared by the pyrolysis of FePc onto a photolithographically prepatterned quartz substrate. Reprinted with permission from [281], Y. Yang et al., *J. Am. Chem. Soc.* 121, 10832 (1999). © 1999, American Chemical Society.



**Figure 33.** Schematic illustration of the procedure for fabricating patterns of aligned carbon nanotubes by (a) microcontact printing and (b) solvent assisted micromolding. (c) A typical SEM image of aligned nanotube pattern prepared by the pyrolysis of FePc onto the photoresist prepatterned quartz via micromolding technique. Reprinted with permission from [285], S. Huang et al., *J. Phys. Chem. B* 104, 2193 (2000). © 2000, American Chemical Society.

elastomer mold (Fig. 33b). The DNO-novolak photoresist patterns formed in both cases were then carbonized into carbon black for region-specific growth of the aligned nanotubes in the polymer-free regions by pyrolysis of iron(II) phthalocyanine under Ar/H<sub>2</sub> atmosphere at 800–1100 °C (Fig. 33c), as is the case for the aforementioned photolithographic patterning. The spatial resolution is limited by the resolution of the mask used and submicrometer features were obtained.

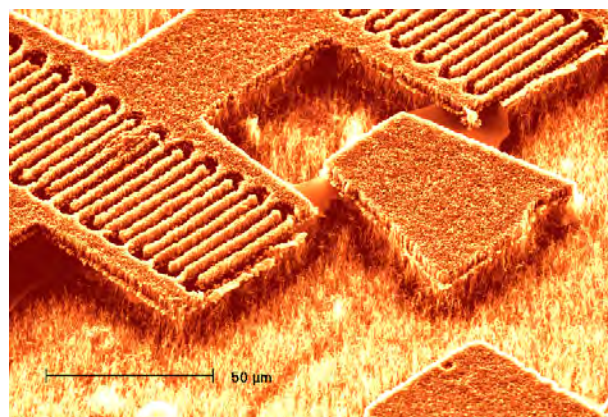
Subsequently, we found that 3D micropatterns of well-aligned carbon nanotubes can also be prepared by pyrolysis of FePc onto appropriate photopatterned substrates [286]. In this particular case, the photopatterning was achieved by photolithographic cross-linking of a chemically amplified photoresist layer spin-cast on a quartz plate or a Si wafer, coupled with a solution development to generate a negative photoresist pattern. Owing to an appropriate surface characteristic, the patterned photoresist layer was found in this case to support the aligned carbon nanotube growth by pyrolysis of FePc, as were the photoresist-free substrate surfaces. The difference in chemical nature between the surface areas covered and uncovered by the photoresist film, how-

ever, caused a region-specific growth of the nanotubes with different tubular lengths and packing densities (Fig. 34).

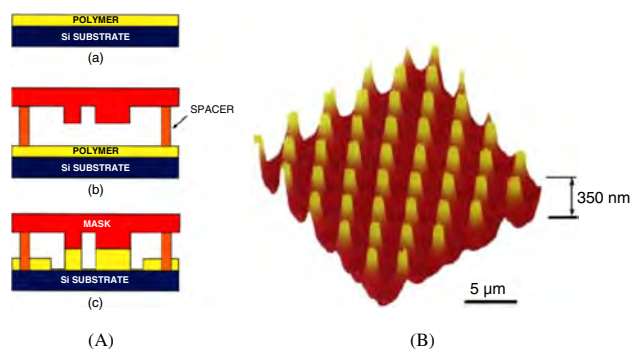
As can be seen from this discussion, micropatterns of aligned nanotubes with resolutions down to a submicrometer scale, suitable for fabrication of various electronic and photonic devices, have been prepared by lithographic techniques. These lithographic patterning methods, coupled with the ease with which polymer chains can be chemically and/or electrochemically attached onto the carbon nanotube wall (Section 5.2), should allow the formation of the nanostructured polymer-nanotube coaxial nanowires in a patterned fashion, attractive for constructing various on-tube optoelectronic devices and sensor arrays.

On the other hand, three-dimensional polymer nanopatterns have also been prepared by some nonconventional lithographic techniques. Notably, a mask-induced self-assembling (MISA) process has been applied to the nanopattern formation in polymer films [287–290]. In this process, a mask with protruded patterns is placed at a certain distance above the top surface of a polymer melt (e.g., PMMA, PS), in the presence or absence of an external field (e.g., thermal or electrical field), allowing attraction of an excess amount of polymer chains to the area below the mask protrusions. Subsequent solidification of the polymer melt thus leads to the formation of polymer patterns with a lateral dimension identical to that of the mask protrusions. Using the MISA patterning technique, 3D polymer patterns with feature size down to nanometer scales can be prepared [288]. Figure 35A shows schematically a typical procedure for the MISA patterning. An AFM image of polymer nanopatterns produced by the MISA technique is given in Figure 35B, which shows well-defined 3D nanopatterned structures.

As can be seen, the MISA method is a straightforward and feasible technique for fabricating polymer patterns with submicrometer/nanometer features. Continued research efforts in this embryonic field could give birth to a flourishing area of nanopatterning technologies.



**Figure 34.** Typical SEM micrographs of the 3D aligned carbon nanotube micropattern. Reprinted with permission from [286], Q. Chen and L. Dai, *J. Nanosci. Nanotechnol.* 1, 43 (2001). © 2001, American Scientific Publishers.



**Figure 35.** (A) Schematic of MISA: (a) a thin polymer film cast on a flat silicon substrate, (b) a mask with protruding patterns placed a distance above the polymer film, and (c) the polymer film self-constructs into a mesa under a mask protrusion. The mesa has a lateral dimension identical to that of the mask protrusion, a height equal to the distance between the mask and the substrate. (B) AFM image of the PMMA pillars formed by MISA. Each PMMA pillar is formed under each dot protrusion on the mask. Reprinted with permission from [288], S. Y. Chou et al., *Appl. Phys. Lett.* 75, 1004 (1999). © 1999, American Institute of Physics.

## 6. CONCLUDING REMARKS

An overview of the recent progress in research and development of nanostructured polymers was presented. As can be seen, nanostructured polymers, including nanoparticles, nanowires, nanotubes, nanofibers, nanofilms, and their derivatives, possess interesting biomedical, electronic, optical, and mechanical properties for use in many potential applications. In order to realize their commercial applications, nanopatterning of polymer materials and self-assembling of nanostructured polymers have also been developed for effective incorporation of polymer nanostructures into nanodevices, and proper connections of the nanoscale structures and devices to the macroscale world. With the promising approaches already reviewed in this chapter, and more to be developed, practical applications of nanostructured polymers are imminent.

## ABBREVIATIONS

**AFM** Atomic force microscopy.  
**CP-CNT** Conducting polymer-carbon nanotube.  
**DNQ** Diazonaphthoquinone.  
**EL** Electroluminescence.  
**EO<sub>3</sub>-PPV** Poly[1,4-(2,5-bis(1,4,7,10-tetraoxaundecyl)phenylenevinylene)].  
**ESR** Electron spin resonance.  
**FePc** Iron(II) phthalocyanine.  
**FTIR** Fourier transform infrared.  
**GO<sub>x</sub>** Glucose oxidase.  
**HCSA** Camphorsulfonic acid.  
**ITO** Indium tin oxide.  
**LB** Langmuir-Blodgett.  
**LED** Light-emitting diode.  
**MAF** Graft copolymer of methylacrylic acid and methyl methacrylate.

**MISA** Mask-induced self-assembling.  
**NR** Neutron reflectivity.  
**PAN** Polyacrylonitrile.  
**PANI** Polyaniline.  
**PCL** Poly( $\epsilon$ -caprolactone).  
**PEO** Poly(ethylene oxide).  
**PI-PA** Polyisoprene-polyacetylene diblock copolymer.  
**PIPn** Pseudo interpenetrating polymer network.  
**PL** Photoluminescence.  
**PMA** Poly(methylacrylic acid).  
**PMMA** Poly(methyl methacrylate).  
**PMS** Poly(4-methylstyrene).  
**PNIPAM** Poly(*N*-isopropylacrylamide).  
**PPV** Poly(*p*-phenylene vinylene).  
**PS** Polystyrene.  
**PTFE** Polytetrafluoroethylene.  
**PVDF** Poly(vinylidene fluoride).  
**PVP** Polyvinylpyridine.  
**PVSO** Poly(phenylvinylsulfoxide).  
**SECM** Scanning electrochemical microscope.  
**SEM** Scanning electron microscope.  
**SFA** Surface force apparatus.  
**SPS** Poly(styrene sulfonic acid).  
**STM** Scanning tunneling microscope.  
**TEM** Transmission electron microscope.  
 **$\mu$ CP** Microcontact printing.  
**UV-vis** Ultraviolet-visible.

## GLOSSARY

**Carbon nanotube** An elongated tubular structure consisting of carbon hexagons arranged in a concentric manner with a diameter at the nanometer scale.  
**Electroluminescence** The emission of light by a substance upon the excitation by an applied voltage.  
**Fluorescence** The emission of light by a substance immediately after the absorption of energy from light of usually shorter wavelength.  
**Nanostructure** Structural entities with at least one dimension down to a nanometer scale.  
**Polymer** A chain-like molecule of large size in which the atoms are held together by covalent bonds.  
**Polymer brush** An assembly of end-anchored polymer chains at the liquid-solid interface in which each of the constituent polymer chains adopts an extended linear chain conformation.  
**Self-assembling** The spontaneous generation of well-defined supramolecular architectures through non-covalent aggregation of macromolecular or low molecular weight compounds.  
**Template synthesis** The production of materials with controllable structures by synthesizing them within the pores of a template membrane.

## ACKNOWLEDGMENT

I thank my colleagues and many others who made contributions to the work that is reviewed in this chapter.

## REFERENCES

1. P. J. Flourey, "Principle of Polymer Chemistry." Cornell Univ. Press, New York, 1953.
2. S. N. Hanna, in "Handbook of Nanophases Materials" (A. N. Goldstein, Ed.). Dekker, New York, 1997.
3. T. Liu, J. Tang, H. Q. Zhao, Y. P. Deng, and L. Jiang, *Langmuir* 18, 5624 (2002).
4. "Colloidal Drug Delivery Systems" (J. Krueger, Ed.). Decker, New York, 1994.
5. See, for example: K. S. Soppimath, T. M. Aminabhavi, A. R. Kulkarni, and W. E. Rudzinski, *J. Controlled Release* 70, 1 (2001), and references cited therein.
6. E. Allemann, J.-C. Leroux, and R. Gurny, *Adv. Drug Delivery Rev.* 34, 171 (1998).
7. G. Teng and M. D. Soucek, *Polymer* 42, 2849 (2001), and references cited therein.
8. C. M. Miller and M. S. El-Aasser, *NATO ASI Ser. E* 335 (1997).
9. X. J. Xu, K. S. Siow, M. K. Wong, and L. M. Gan, *Colloid Polym. Sci.* 279, 879 (2001).
10. X. J. Xu, K. S. Siow, M. K. Wong, and L. M. Gan, *Langmuir* 17, 4519 (2001).
11. J. Liu, L. M. Gan, C. H. Chew, W. K. Teo, and L. H. Gan, *Langmuir* 13, 6421 (1997).
12. X. J. Xu, C. H. Chew, K. S. Siow, M. K. Wong, and L. M. Gan, *Langmuir* 15, 8067 (1999).
13. M. Rabelero, M. Zacarias, E. Mendizábal, J. E. Puig, J. M. Dominguez, and I. Katime, *Polym. Bull.* 38, 695 (1997).
14. G. Birrenbach and P. P. Speise, *J. Pharm. Sci.* 65, 1763 (1976).
15. J. Hearn, M. C. Wilkinson, and A. R. Goodall, *Adv. Colloid. Inter. Sci.* 14, 173 (1981).
16. P. Couvreur, B. Kante, M. Roland, P. Goit, P. Bauduin, and P. Speiser, *J. Pharm. Pharmacol.* 31, 331 (1979).
17. P. J. Lowe and C. S. Temple, *J. Pharm. Pharmacol.* 46, 547 (1994).
18. N. Al-Khoury Fallouh, L. Roblot-Treupel, H. Fessi, J. P. Devissaguet, and F. Puisieux, *Int. J. Pharm.* 28, 125 (1986).
19. G. Tishchenko, K. Luetzow, J. Schauer, W. Albrecht, and M. Bleha, *Separation Purification Technol.* 22, 403 (2001).
20. See, for example: F. Caruso, *Adv. Mater.* 13, 11 (2001), and references cited therein.
21. A. Dokoutchaev, J. T. James, S. C. Koene, S. Pathak, G. K. S. Prakash, and M. E. Thompson, *Chem. Mater.* 11, 2389 (1999).
22. M. T. Greci, S. Pathak, K. Mercado, G. K. S. Prakash, M. E. Thopson, and G. A. Olah, *J. Nanosci. Nanotechnol.* 1, 3 (2001).
23. A. Dokoutchaev, V. V. Krishnan, M. E. Thompson, and M. Balasubramanian, *J. Mol. Struct.* 470, 191 (1998).
24. S. Pathak, M. T. Greci, R. C. Kwong, K. Mercado, G. K. S. Prakash, G. A. Olah, and M. E. Thompson, *Chem. Mater.* 12, 1985 (2000).
25. M. F. Zambaux, F. Bonneaux, R. R. Gref, P. Maincent, E. Dellacherie, M. J. Alonso, P. Labrude, and C. Vigneron, *J. Control. Rel.* 50, 31 (1998).
26. T. Niwa, H. Takeuchi, T. Hino, N. Kunou, and Y. Kawashima, *J. Control. Rel.* 25, 89 (1993).
27. P. Wehrle, B. Magenheimer, and S. Benita, *J. Pharm. Biopharm.* 41, 19 (1995).
28. D. T. Birnbaum, J. D. Kosmala, D. B. Henthorn, and L. B. Peppas, *J. Control. Rel.* 65, 375 (2000).
29. J. W. Tom and P. G. Debenedetti, *J. Aerosol Sci.* 22, 555 (1991).
30. T. W. Randolph, A. D. Randolph, M. Mebes, and S. Yeung, *Biotechnol. Progr.* 9, 429 (1993).
31. C. Kropf, H. Dolhaine, T. Forster, K. Schaber, M. Turk, S. Cihlar, and P. Christophliemk, *PCT Int. Appl.* (2000).
32. J. W. Tester, R. L. Danheiser and R. D. Weinstein, in "Green Chemical Syntheses and Processes" (P. T. Anastas, L. G. Heine, and T. C. Williamson, Eds.). ACS, Washington, DC, 2000.
33. R. Noyori and T. Ikariya, in "Stimulating Concepts in Chemistry" (F. Vgötle, J. F. Stoddart, and M. Shibasaki, Eds.). Wiley-VCH, Weinheim, 2000.
34. S. I. Stupp, V. LeBonheur, K. Walker, L. S. Li, K. E. Huggins, M. Keser, and A. Amstutz, *Science* 276, 384 (1997).
35. M. Moffitt, K. Khougaz, and A. Eisenberg, *Acc. Chem. Res.* 29, 95 (1996).
36. S. E. Webber, *J. Phys. Chem. B* 102, 2618 (1998).
37. J. T. Chen, E. L. Thomas, C. K. Ober, and G. P. Mao, *Science* 273, 343 (1996).
38. G. J. Liu, *Curr. Opin. Colloid. Inter.* 3, 200 (1998).
39. G. Zhang, A. Niu, S. Peng, M. Jiang, Y. Tu, M. Li, and C. Wu, *Acc. Chem. Res.* 34, 249 (2001).
40. K. B. Thurmond, T. Koalewski, and K. L. Wooley, *J. Am. Chem. Soc.* 118, 7239 (1996).
41. A. Harada and K. Kataoka, *Science* 283, 65 (1999).
42. S. A. Jenekhe and S. A. Chen, *Science* 279, 1903 (1998).
43. P. W. Zhu and D. H. Napper, *Macromol. Chem. Phys.* 200, 1950 (1999).
44. H. A. Klok and S. Lecommandoux, *Adv. Mater.* 13, 1217 (2001) and references cited therein.
45. P. Zhu and D. H. Napper, *Langmuir* 16, 8543 (2000).
46. H. G. Schild, *Progr. Polym. Sci.* 17, 163 (1992).
47. C. Wu, A. Niu, and L. M. Leung, *J. Am. Chem. Soc.* 121, 1954 (1999).
48. R. S. Kanga, T. E. Hogen-Esch, E. Randrianalimanana, A. Soum, and M. Fontanille, *Macromolecules* 23, 4235 (1990).
49. L. Dai, *J. Macromol. Sci., Rev. Macromol. Chem. Phys.* 39, 273 (1999).
50. S. Liu and S. P. Armes, *J. Am. Chem. Soc.* 123, 9910 (2001).
51. X. Qiu and C. Wu, *Macromolecules* 30, 7921 (1997).
52. X. Qiu and C. Wu, *Phys. Rev. Lett.* 80, 620 (1998).
53. X. Liu, M. Jiang, S. Yang, M. Chen, D. Chen, C. Yang, and K. Wu, *Angew. Chem. Int. Ed.* 41, 2950 (2002).
54. K. B. Thurmond, T. Kowalewski, and K. L. Wooley, *J. Am. Chem. Soc.* 119, 6656 (1997).
55. S. Blomberg, S. Ostberg, E. Harth, A. W. Bosman, B. V. Horn, and C. J. Hawker, *J. Polym. Sci. A* 40, 1309 (2002).
56. S. Stewart and G. J. Liu, *Chem. Mater.* 11, 1048 (1999).
57. Q. Zhang, E. E. Remsen, and K. L. Wooley, *J. Am. Chem. Soc.* 122, 3642 (2000).
58. S. A. Jenekhe and X. L. Chen, *Science* 283, 372 (1999).
59. J. Zhou, Z. Li and G. Liu, *Macromolecules* 35, 3690 (2002).
60. R. Yang, D. F. Evans, and W. A. Hendrickson, *Langmuir* 11, 211 (1995).
61. C. Kranz, H. E. Gaub, and W. Schuhmann, *Adv. Mater.* 8, 634 (1996).
62. C. Kranz, M. Ludwig, H. E. Gaub, and W. Schuhmann, *Adv. Mater.* 7, 568 (1995).
63. Y.-M. Wu, F. R. F. Fan, and A. J. Bard, *J. Electrochem. Soc.* 136, 885, (1989).
64. K. Borgwarth, C. Ricken, D. G. Ebling, and J. Heinze, *Ber. Bunsen. Ges. Phys. Chem.* 99, 1421, (1995).
65. R. M. Nyffenegger and R. M. Penner, *J. Phys. Chem.* 100, 17041, (1996).
66. B. W. Maynor, S. F. Filocamo, M. W. Grinstaff, and J. Liu, *J. Am. Chem. Soc.* 124, 522 (2002).
67. L. A. Bumm, J. J. Arnold, M. T. Cygan, T. D. Dunbar, T. P. Burgin, L. Jones II, D. L. Allara, J. M. Tour, and P. S. Weiss, *Science* 271, 1705 (1996).
68. H. X. He, C. Z. Li, and N. J. Tao, *Appl. Phys. Lett.* 78, 811 (2001).

69. J. I. Pascual, J. Mendez, J. Gomez-Herrero, A. M. Baro, N. Garcia, and V. T. Binh, *Phys. Rev. Lett.* 71, 1852 (1993).
70. U. Landman, W. D. Luedtke, N. A. Burman, and R. J. Colton, *Science* 248, 454 (1990).
71. "Handbook of Conducting Polymers" (T. A. Skotheim, J. Reynolds, and R. Elsenbaumer, Eds.), 2nd ed., Dekker, New York, 1998.
72. R. C. Smith, W. M. Fischer, and D. L. Gin, *J. Am. Chem. Soc.* 119, 4092 (1997).
73. See, for example: C. R. Martin, *Acc. Chem. Res.* 28, 61 (1995), and references cited therein.
74. C. G. Wu and T. Bein, *Science* 266, 1013 (1994).
75. V. M. Cepak and C. R. Martin, *Chem. Mater.* 11, 1363 (1999).
76. C. R. Martin, *Adv. Mater.* 3, 457 (1991).
77. Z. Cai, J. Lei, W. Liang, V. Menon, and C. R. Martin, *Chem. Mater.* 3, 960, (1991).
78. R. V. Parthasarathy and C. R. Martin, *Chem. Mater.* 6, 1627, (1994).
79. M. Steinhart, J. H. Wendorff, A. Greiner, R. B. Wehrspohn, K. Nielsch, J. Schilling, J. Choi, and U. Gösele, *Science* 296, 1997 (2002).
80. M. X. Wan and J. C. Li, *J. Polym. Sci. A* 37, 4605 (1999).
81. H. Qiu, M. Wan, B. Matthews, and L. Dai, *Macromolecules* 34, 675 (2001).
82. R. Saito, G. Dresselhaus, and M. S. Dresselhaus, "Physical Properties of Carbon Nanotubes." Imperial College Press, London, 1998.
83. R. V. Parthasarathy, K. L. N. Phani, and C. R. Martin, *Adv. Mater.* 7, 896 (1995).
84. T. Kyotani, T. Nagai, S. Inoue, and A. Tomita, *Chem. Mater.* 9, 609 (1997).
85. K. Kageyama, J.-I. Tamazawa, and T. Aida, *Science* 285, 2113 (1999).
86. M. Rouhi, *C&E News*, Sept. 27, 10 (1999).
87. J. Doshi, G. Srinivasan, and D. H. Reneker, *Polym. News* 20, 206 (1995).
88. J. Doshi and D. H. Reneker, *J. Electrostat.* 35, 151 (1995).
89. D. H. Reneker and I. Chun, *Nanotechnology* 7, 216 (1996).
90. D. H. Reneker, A. L. Yarin, H. Fong, and S. Koombhongse, *J. Appl. Phys.* 87, 4531 (2000).
91. A. Formhals, U.S. Patent 1, 975, 504, 1934.
92. A. F. Spivak, Y. A. Dzenis, and D. H. Reneker, *Mech. Res. Commun.* 27, 37 (2000).
93. A. L. Yarin, S. Koombhongse, and D. H. Reneker, *J. Appl. Phys.* 89, 3018 (2001).
94. A. L. Yarin, S. Koombhongse, and D. H. Reneker, *J. Appl. Phys.* 90 4836 (2001).
95. H. Fong, I. Chun, and D. H. Reneker, *Polymer* 40, 4585 (1999).
96. A. G. MacDiarmid, W. E. Jones, Jr., I. D. Norris, J. Gao, A. T. Johnson, Jr., N. J. Pinto, J. Hone, B. Han, F. K. Ko, H. Okuzaki, and M. Llaguno, *Synth. Met.* 119, 27 (2001).
97. I. Chun, D. H. Reneker, H. Fong, X. Fang, J. Deitzel, N. B. Tan, and K. Kearns, *J. Adv. Mater.* 31, 36 (1996).
98. I. D. Norris, M. M. Shaker, F. K. Ko, and A. G. MacDiarmid, *Synth. Met.* 114, 109 (2000).
99. L. J. van der Pauw, *Philips Res. Rep.* 13, 1 (1958).
100. L. Dai and A. W. H. Mau, *J. Phys. Chem. B* 104, 1891 (2000).
101. A. J. Lovinger and L. J. Rothberg, *J. Mater. Res.* 11, 1581 (1996).
102. H. E. Katz, *J. Mater. Chem.* 7, 369 (1997).
103. G. Horowitz, *Adv. Mater.* 10, 365 (1998).
104. V. S. Mylnikov, *Adv. Polym. Sci.* 115 (1994).
105. S. Sariciftci and A. J. Heeger, *Int. J. Mod. Phys. B* 8, 237 (1994).
106. A. Kraft, A. C. Grimsdale, and A. B. Holmes, *Angew. Chem. Int. Ed.* 37, 402 (1998).
107. L. Dai, B. Winkler, L. Dong, L. Tong, and A. W. H. Mau, *Adv. Mater.* 13, 915 (2001).
108. N. C. Greenham and R. H. Friend, *Solid State Phys.* 49, 1 (1995).
109. Q. Pei, Y. Yang, G. Yu, Y. Cao, and A. J. Heeger, *Synth. Met.* 85, 1229 (1997).
110. Z. Yang and F. Karasz, *Macromol. Symp.* 83, 83 (1997).
111. R. H. Friend, R. W. Gymer, A. B. Holmes, J. H. Burroughes, R. N. Marks, C. Taliani, D. D. C Bradley, D. A. Dos Santos, J. L. Brédas, M. Lögdlund, and W. R. Salaneck, *Nature* 397, 121, (1999).
112. H. Yasuda, "Plasma Polymerization." Academic Press, New York, 1985.
113. "Plasma Deposition, Treatment, and Etching of Polymers" (R. d'Agostino, Ed.). Academic Press, New York, 1990.
114. K. Tanaka, Y. Matsuura, S. Nishio, and T. Yamabe, *Synth. Met.* 63, 221 (1994).
115. E. T. Kang, K. Kato, Y. Uyama, and Y. Ikada, *J. Mater. Res.* 11, 1570 (1996).
116. X. Gong, L. Dai, A. W. H. Mau, and H. J. Griesser, *J. Polym. Sci. A* 36, 633 (1998).
117. T. P. Nguyen, P. Le Rendu, K. Amgaard, M. Cailler, and V. H. Tran, *Synth. Met.* 72, 35 (1995).
118. K. Furukawa, Y. Terasaka, H. Ueda, and M. Matsumura, *Synth. Met.* 91, 99 (1997).
119. C. C. Wu, J. C. Sturm, and A. Kahn, *Appl. Phys. Lett.* 70, 1348 (1997).
120. B. Hu and F. E. Karasz, *Chem. Phys.* 227, 263 (1998).
121. W. R. Salaneck, S. Stafström, and J. L. Brédas, "Conjugated Polymer Surfaces and Interfaces." Cambridge Univ. Press, Cambridge, UK, 1996.
122. "Proc. Int. Workshop Electroluminescence (EL'94)" (X. Xu, X. Luo, Y. Xie, and H. Zhou, Eds.). Science Press, Beijing, 1995.
123. L. Dai, *Rad. Phys. Chem.* 62, 55 (2001).
124. "Langmuir-Blodgett Films" (G. G. Roberts, Ed.). Plenum Press, New York, 1990.
125. S. Schwiegk, T. Vahlenkamp, Y. Xu, and G. Wegner, *Macromolecules* 25, 513 (1992).
126. A. Aoki and T. Miyashita, *Adv. Mater.* 9, 361 (1997).
127. M. Suzuki, A. Ferencz, S. Iida, V. Enkelmann, and G. Wegner, *Adv. Mater.* 5, 359 (1993).
128. J. Paloheimo, P. Kuivalainen, H. Stubb, E. Vuorimaa, and P. Ylilähti, *Appl. Phys. Lett.* 56, 1157 (1990), and references cited therein.
129. J. H. Cheung, E. Punkka, M. Rikukawa, R. B. Rosner, A. T. Royappa, and M. F. Rubner, *Thin Solid Films* 211, 246 (1992).
130. T. Shimidzu, T. Iyoda, M. Ando, A. Ohtani, T. Kaneko, and K. Honda, *Thin Solid Films* 160, 67 (1988).
131. T. Iyoda, M. Ando, T. Kaneko, A. Ohtani, T. Shimidzu, and K. Honda, *Langmuir* 3, 1169 (1987).
132. M. Ando, Y. Watanabe, T. Iyoda, K. Honda, and T. Shimidzu, *Thin Solid Films* 179, 225 (1989).
133. S. Sagisaka, M. Ando, T. Iyoda, and T. Shimidzu, *Thin Solid Films* 230, 65 (1993).
134. M. F. Rubner and T. A. Skotheim, in "Conjugated Polymers" (J. L. Brédas and R. Silbey, Eds.). Kluwer Academic, Dordrecht, 1991.
135. M. Era, H. Shinozaki, S. Tokito, T. Tsutsui, and S. Saito, *Chem. Lett.* 1097 (1988).
136. Y. Nishikata, M.-A. Kakimoto, and Y. Imai, *Thin Solid Films* 179, 191 (1989).
137. K. Kamiyama, M. Era, T. Tsutsui, and S. Saito, *Jpn. J. Appl. Phys.* 29, L840 (1990).
138. T. Vahlenkamp and G. Wegner, *Macromol. Chem. Phys.* 195, 1933 (1994).
139. M. Remmers, M. Schulze, and G. Wegner, *Macromol. Rapid Commun.* 17, 239 (1996).
140. V. Cimrová, M. Remmers, D. Neher, and G. Wegner, *Adv. Mater.* 8, 146 (1996).
141. A. Bolognesi, G. Bajo, J. Paloheimo, T. Östergard, and H. Stubb, *Adv. Mater.* 9, 121 (1997).
142. J. Grüner, M. Remmers, and D. Neher, *Adv. Mater.* 9, 964 (1997).

143. "Solid State Luminescence: Theory, Materials, and Devices" (A. H. Kitai, Ed.). Chapman & Hall, New York, 1993.
144. S. Patel and M. Tirrell, *Annu. Rev. Phys. Chem.* 40, (1989).
145. A. Halperin, M. Tirrell, and T. P. Lodge, *Adv. Polym. Sci.* 100, 31 (1992).
146. S. T. Milner, *Science* 251, 905 (1991).
147. P. F. Luckham and B. A. Costello, *Adv. Colloid. Interface Sci.* 44, 183 (1993).
148. D. H. Napper, "Polymeric Stabilization of Colloidal Dispersions." Academic Press, London, 1983.
149. C. R. Cantor and P. R. Schimmel, "Biophysical Chemistry." Freeman New York, 1980.
150. "Surface Modification of Polymeric Biomaterials" (B. D. Ratner and D. G. Castner, Eds.). Plenum Press, New York, 1996.
151. Y. Okahata, H. Noguchi, and T. Seki, *Macromolecules* 19, 494 (1986).
152. Y. Ito, Y. Ochiai, Y. S. Park, and Y. Imanishi, *J. Am. Chem. Soc.* 119, 1619 (1997).
153. J. Klein, E. Kumacheva, D. Mahalu, D. Perahia, and L. J. Fetters, *Nature* 370, 634 (1994).
154. J. I. Martin, Z.-G. Wang, and M. Schick, *Langmuir* 12, 4950 (1996).
155. H. J. Taunton, C. Toprakcioglu, L. J. Fetters, and J. Klein, *Macromolecules* 23, 571 (1990).
156. H. J. Taunton, C. Toprakcioglu, L. J. Fetters, and J. Klein, *Nature* 332, 712 (1988).
157. L. Dai and C. Toprakcioglu, *Europhys. Lett.* 16, 331 (1991).
158. C. Toprakcioglu, L. Dai, M. A. Ansarifar, M. Stamm, and H. Motschmann, *Progr. Colloid Polym. Sci.* 91, 83 (1993).
159. L. Dai, C. Toprakcioglu, and G. Hadziioannou, *Macromolecules* 28, 5512 (1995).
160. J. Israelachvili, "Intermolecular and Surface Forces." Academic Press, London, 1992.
161. D. Sarid, "Scanning Force Microscopy: with Applications to Electric, Magnetic and Atomic Forces." Oxford Univ. Press, New York, 1991.
162. J. B. Field, C. Toprakcioglu, L. Dai, G. Hadziioannou, G. Smith, and W. J. Hamilton, *J. Phys. II (France)* 2, 2221 (1992).
163. J. B. Field, C. Toprakcioglu, R. C. Ball, H. B. Stanley, L. Dai, W. Barford, J. Penfold, G. Smith, and W. Hamilton, *Macromolecules* 25, 434 (1992).
164. J. S. Higgins and H. C. Benoît, "Polymers and Neutron Scattering." Clarendon Press, Oxford, 1994.
165. J. Klein, in "Molecular Conformation and Dynamics of Macromolecules in Condensed Systems" (M. Nagasawa, Ed.). Elsevier Science, Amsterdam, 1988.
166. B. Bhushan, J. N. Israelachvili, and U. Landman, *Nature* 374, 607 (1995).
167. H. Yamakawa, "Modern Theory of Polymer Solutions." Harper & Row, New York, 1971.
168. H. Mattoussi and F. E. Karasz, *J. Chem. Phys.* 99, 9188 (1993).
169. L. Dai, *Eur. Polym. J.* 29, 645 (1993), and references cited therein.
170. G. Hadziioannou, S. Patel, S. Granick, and M. Tirrell, *J. Am. Chem. Soc.* 108, 2869 (1986).
171. S. Alexander, *J. Phys. (Paris)* 38, 983 (1977).
172. S. Milner, T. Witten, and M. Cates, *Macromolecules* 21, 2610 (1988).
173. P. Auroy and L. Auvray, *Macromolecules* 25, 4134 (1992).
174. P.-Y. Lai and A. Halperin, *Macromolecules* 25, 6693 (1992).
175. L. Dai and C. Toprakcioglu, *Macromolecules* 25, 6000 (1992).
176. J. Penfold, R. M. Richardson, A. Zarbakhsh, J. R. P. Webster, D. G. Bucknall, A. R. Rennie, R. A. L. Jones, T. Cosgrove, R. K. Thomas, J. S. Higgins, P. D. I. Fletcher, E. Dickinson, S. J. Roser, I. A. McLure, A. R. Hillman, R. W. Richards, E. J. Staples, A. N. Burgess, E. A. Simister, and J. W. White, *J. Chem. Soc., Faraday Trans.* 93, 3899 (1997).
177. P. G. de Gennes, *Macromolecules* 13, 1069 (1980).
178. S. T. Milner and T. A. Witten, *Macromolecules* 25, 5495 (1992).
179. W. H. Tang and T. A. Witten, *Macromolecules* 29, 4412 (1996).
180. T. Haliloglu and W. L. Mattice, *Macromol. Theory Simul.* 6, 667 (1997).
181. D. L. Anastassopoulos, A. A. Vradis, C. Toprakcioglu, G. S. Smith, and L. Dai, *Macromolecules* 31, 9369 (1998).
182. V. V. Tsukruk, *Progr. Polym. Sci.* 22, 247 (1997).
183. G. A. C. B. Murray, C. R. Kagan, and M. G. Bawendi, *Science* 270, 1335 (1995).
184. A. A. Zakhidov, R. H. Baughman, Z. Iqbal, C. Cui, I. Khayrullin, S. O. Dantas, J. Marti, and V. G. Ralchenko, *Science* 282, 897 (1998).
185. "Optics of Nanostructured Materials" (V. Markel and T. George, Eds.) Wiley, New York, 2001.
186. E. Kumacheva, O. Kalinina, and L. Lilge, *Adv. Mater.* 11, 231 (1999).
187. S. A. Jenekhe and X. L. Chen, *Science* 283, 372 (1999).
188. P. A. Smith, D. N. Christopher, N. J. Thomas, T. S. Mayer, B. R. Martin, J. Mbindyo, and T. E. Mallouk, *Appl. Phys. Lett.* 77, 1399 (2000).
189. X. Duan, Y. Huang, J. Wang, and C. M. Lieber, *Nature* 409, 66 (2001).
190. M. Tanase, L. A. Bauer, A. Hultgren, D. M. Silevitch, L. Sun, D. H. Reich, P. C. Searson, and G. J. Meyer, *Nano Lett.* 1, 155 (2001).
191. Y. Huang, X. Duan, Q. Wei, and C. M. Lieber, *Science* 291, 630 (2001).
192. B. Messer, J. H. Song, and P. Yang, *J. Am. Chem. Soc.* 122, 10232 (2000).
193. S. Huang and L. Dai, *J. Nanoparticle Res.* 4, 145 (2002).
194. A. Theron, E. Zussman, and A. L. Yarin, *Nanotechnology* 12, 384 (2001).
195. J. A. Matthews, G. E. Wnek, D. G. Simpson, and G. L. Bowlin, *Biomacromolecules* 3, 232 (2002).
196. M. Bognitzki, W. Czado, T. Frese, A. Schaper, M. Hellwig, M. Steinhart, A. Greiner, and J. H. Wendorff, *Adv. Mater.* 13, 70 (2001).
197. W. Liu, M. Graham, B. V. Satola, E. A. Evans, and D. H. Reneker, *J. Mater. Res.* 17, 3206 (2002).
198. Q. Chen, L. Dai, M. Gao, S. Huang, and A. W. H. Mau, *J. Phys. Chem. B* 105, 618 (2001).
199. L. Dai, H. A. W. StJohn, J. Bi, P. Zientek, R. C. Chatelier, and H. J. Griesser, *Surf. Interf. Anal.* 29, 46 (2000).
200. M. Gao, S. Huang, L. Dai, G. Wallace, R. Gao, and Z. Wang, *Angew. Chem. Int. Ed.* 39, 3664 (2000).
201. P. Poncharal, Z. L. Wang, D. Ugarte, and W. A. de Heer, *Science* 283, 1513 (1999).
202. R. Gao, Z. L. Wang, Z. Bai, W. A. de Heer, L. Dai, and M. Gao, *Phys. Rev. Lett.* 85, 622 (2000).
203. Frank, P. Poncharal, Z. L. Wang, and W. A. de Heer, *Science* 280, 1744 (1998).
204. T. W. Odom, J.-L. Huang, P. Kim, and C. M. Lieber, *J. Phys. Chem. B* 104, 2794 (2000), and references cited therein.
205. M. Gao, L. Dai, and G. G. Wallace, *Electroanalysis* 15, 1089 (2003).
206. Y. Lansac, M. A. Glaser, N. A. Clark, and O. D. Lavrentovich, *Nature* 398, 54, (1999).
207. B. H. Cumpston, S. P. Ananthavel, S. Barlow, D. L. Dyer, J. E. Ehrlich, L. L. Erskine, A. A. Heikal, S. M. Kuebler, I.-Y. S. Lee, M.-M. Sandy, Dianne, J. Qin, H. Rockel, M. Rumi, X.-L. Wu, S. R. Marder, and J. W. Perry, *Nature* 398, 51 (1999).
208. M. Ferreira and M. F. Rubner, *Macromolecules* 28, 7107 (1995).
209. J. H. Cheung, W. B. Stockton, and M. F. Rubner, *Macromolecules* 30, 2712 (1997).
210. A. C. Fou, O. Onitsuka, M. Ferreira, M. F. Rubner, and B. R. Hsieh, *J. Appl. Phys.* 79, 7501 (1995).
211. O. Onitsuka, A. C. Fou, M. Ferreira, B. R. Hsieh, and M. F. Rubner, *J. Appl. Phys.* 80, 4067 (1996).
212. M. Ferreira, O. Onitsuka, A. F. Fou, B. R. Hsieh, and M. F. Rubner, *Mater. Res. Soc. Symp. Proc.* 413, 49 (1996).
213. W. B. Stockton and M. F. Rubner, *Macromolecules* 30, 2717 (1997).



214. E. P. Giannelis, *Adv. Mater.* 8, 29 (1996).
215. G. A. Ozin, *Adv. Mater.* 4, 612 (1992).
216. J. H. Fendler and F. C. Meldrum, *Adv. Mater.* 7, 607 (1995).
217. "Hybrid Organic-Inorganic Composites" (J. E. Mark, C. Y.-C. Lee, and P. A. Bianconi, Eds.), ACS Symp. Ser. 585. ACS, Washington, DC, 1995.
218. P. Aranda and E. Ruiz-Hitzky, *Chem. Mater.* 4, 1395 (1992).
219. E. Ruiz-Hitzky and P. Arando, *Adv. Mater.* 2, 545 (1990).
220. S. A. Johnson, E. S. Brigham, P. J. Ollivier, and T. E. Mallouk, *Chem. Mater.* 9, 2448 (1997).
221. K. Yano, A. Usuki, and A. Okada, *J. Polym. Sci. A: Polym. Chem.* 35, 2289 (1997).
222. K. Ramachandran and M. M. Lerner, *J. Electrochem. Soc.* 144, 3739 (1997).
223. K. A. Carrado and L. Xu, *Chem. Mater.* 10, 1440 (1998).
224. L. Dai, Q. Wang, and M. X. Wan, *J. Mater. Sci. Lett.* 19, 1645 (2000).
225. P. Aranda and E. Ruiz-Hitzky, *Chem. Mater.* 4, 1395 (1992).
226. E. Ruiz-Hitzky, *Adv. Mater.* 5, 334 (1993).
227. W. P. Chang and W.-T. Whang, *Polymer* 37, 4229 (1996).
228. T. D. De Morais, F. Chaput, K. Lahlil, and J.-P. Boilot, *Adv. Mater.* 11, 107 (1999).
229. L. D. Carlos, V. De Zea Bermudez, R. A. Sa Ferreira, L. Marques, and M. Assunçao, *Chem. Mater.* 11, 581 (1999).
230. "sol-gel Science: Physics and Chemistry of sol-gel Processing" (C. J. Brinker and G. Scherrer, Eds.). Academic Press, San Diego, 1989.
231. B. Winkler, L. Dai, and A. W. H. Mau, *J. Mater. Lett.* 18, 1539 (1999).
232. A. Matsumoto, T. Odani, K. Sada, M. Miyata, and K. Tashiro, *Nature* 405, 328 (2000).
233. G. H. Fredrickson and F. S. Bates, *Annu. Rev. Mater. Sci.* 26, 503 (1996).
234. M. Park, C. Harrison, P. M. Chaikin, R. A. Register, and D. H. Adamson, *Science* 276, 1401 (1997).
235. P. G. de Gennes, "Scaling Concepts in Polymer Physics." Cornell Univ. Press, Ithaca, NY, 1979.
236. T. P. Lodge and M. Muthukumar, *J. Phys. Chem.* 100, 13275 (1996).
237. P. Mansky, Y. Liu, E. Huang, T. P. Russell, and C. J. Hawker, *Science* 275, 1458 (1997).
238. E. Huang, L. Rockford, T. P. Russell, C. J. Hawker, and J. Mays, *Nature* 395, 757 (1998).
239. T. L. Morkved, M. Lu, A. M. Urbas, E. E. Ehrichs, H. M. Jaeger, P. Mansky, and T. P. Russell, *Science* 273, 932 (1996).
240. T. Thurn-Albrecht, J. Schotter, A. Kästle, N. Emley, T. Shibauchi, L. Krusin-Elbaum, K. Guarini, C. T. Black, M. T. Tuomine, and T. P. Russell, *Science* 290, 2126 (2000).
241. T. Thurn-Albrecht, J. Derouchey, T. P. Russell, and H. M. Jaeger, *Macromolecules* 33, 3250 (2000).
242. T. Thurn-Albrecht, R. Steiner, J. DeRouchey, C. M. Stafford, E. Huang, M. Bal, M. Tuominen, C. J. Hawker, and T. P. Russell, *Adv. Mater.* 12, 787 (2000).
243. U. Jeong, H.-C. Kim, R. L. Rodriguez, I. Y. Tsai, C. M. Christopher, M. Stafford, J. K. Kim, C. J. Hawker, and T. P. Russell, *Adv. Mater.* 14, 274 (2000).
244. K. Shin, K. A. Leach, J. T. Goldbach, D. H. Kim, J. Y. Jho, M. Tuominen, C. J. Hawker, and T. P. Russell, *Nano Lett.* 2, 934 (2002).
245. M. Berggren, O. Inganäs, G. Gustafsson, J. Rasmusson, M. R. Andersson, T. Hjertberg, and O. Wennerström, *Nature* 372, 444 (1994).
246. L. Dai and J. W. White, *J. Polym. Sci., Part B, Polym. Phys.* 31, 3 (1993).
247. L. Dai and J. W. White, *Polymer* 38, 775 (1997).
248. K. D. Jandt, C.-A. Dai, and E. J. Kramer, *Adv. Mater.* 8, 660 (1996), and references cited therein.
249. E. B. Zhulina, C. Singh, and A. C. Balazs, *Macromolecules* 29, 6338 (1996).
250. N. Koneripalli, R. Levicky, and F. S. Bates, *Langmuir* 12, 6681 (1996).
251. W. H. Jo, H. K. Nam, and J. C. Cho, *J. Polym. Sci., Part B: Polym. Phys.* 34, 2169 (1996).
252. P. Mansky, T. P. Russell, C. J. Hawker, M. Pitsikalis, and J. Mays, *Macromolecules* 30, 6810 (1997).
253. E. Zhulina and A. C. Balazs, *Macromolecules* 29, 2667 (1996).
254. J. P. Spatz, M. Möller, M. Noeske, R. J. Behm, and M. Pietralla, *Macromolecules* 30, 3874 (1997).
255. B. Zhao, W. J. Brittain, W. Zhou, and S. Z. D. Cheng, *Macromolecules* 122, 2407, (2000).
256. M. husemann, M. Morrison, D. Benoit, J. Frommer, C. M. Mate, W. D. Hinsberg, J. L. Hedrick, and C. J. Hawker, *J. Am. Chem. Soc.* 122, 1844 (2000), and references cited therein.
257. L. Dai, B. Winkler, L. Dong, L. Tong, and A. W. H. Mau, *Adv. Mater.* 13, 915 (2001).
258. S. Holdcroft, *Adv. Mater.* 13, 1753 (2001).
259. M. Thakur, *Macromolecules* 21, 661 (1988).
260. P. Calvert, *Nature* 333, 296 (1988).
261. S. Borman, *C&E News*, May 7, 53 (1990).
262. T. Rothman, *Sci. Am.*, August, 12 (1988).
263. L. Dai and J. W. White, *Polymer* 32, 2120 (1991).
264. L. Dai, A. W. H. Mau, H. J. Griesser, and D. A. Winkle, *Macromolecules* 27, 6728 (1994).
265. L. Dai, *J. Phys. Chem.* 96, 6469 (1992).
266. E. D. Owen and H. S. M. Al-Mohd, *Polymer* 38, 3533 (1997).
267. I. Schopov and V. Sinigersky, *Macromol. Symp.* 121, 35 (1997), and references cited therein.
268. M. A. Golub and D. B. Parkinson, *Macromol. Synth.* 3, 32 (1968).
269. L. Dai, H. J. Griesser, X. Hong, A. W. H. Mau, T. H. Spurling, Y. Yang, and J. W. White, *Macromolecules* 29, 282 (1996).
270. N. F. Colaneri, D. Bradely, R. H. Friend, P. L. Burn, A. B. Holmes, and C. W. Spangler, *Phys. Rev. B* 42, 11670 (1990).
271. B. Xu and S. Holdcroft, *Macromolecule* 26, 4457 (1993).
272. T. Ebbesen, "Carbon Nanotubes." CRC Press, Boca Raton, 1997.
273. R. Saito, G. Dresselhaus, and M. S. Dresselhaus, "Physical Properties of Carbon Nanotubes." Imperial College Press, London, 1998.
274. S. Fan, M. G. Chapline, N. R. Franklin, T. W. Tomber, A. M. Cassell, and H. Dai, *Science* 283, 512 (1999).
275. W. Z. Li, S. S. Xie, L. X. Qian, B. H. Chang, B. S. Zou, W. Y. Zhou, R. A. Zhao, and G. Wang, *Science* 274, 1701 (1996).
276. C. N. R. Rao, R. Sen, B. C. Satishkumar, and A. Govindaraj, *J. Chem. Soc., Chem. Commun.* 1525 (1998).
277. Z. F. Ren, Z. P. Huang, J. H. Xu, P. B. Wang, M. P. Siegal, and P. N. Proencio, *Science* 282, 1105 (1998).
278. B. Q. Wei, R. Vajtai, Y. Jung, J. Ward, R. Zhang, G. Ramanath, and P. M. Ajayan, *Nature* 416, 495 (2002).
279. S. Huang, L. Dai, and A. W. H. Mau, *J. Phys. Chem. B* 103, 4223 (1999).
280. L. Dai, A. Patil, X. Gong, Z. X. Guo, L. Liu, Y. Liu, and D. B. Zhu, *Chem. Phys. Chem.* 4, 1150 (2003).
281. Y. Yang, S. Huang, H. He, A. W. H. Mau, and L. Dai, *J. Am. Chem. Soc.* 121, 10832 (1999).
282. J. March, "Advanced Organic Chemistry," 4th ed. Wiley, New York, 1992.
283. G. M. Wallraff and W. D. Hinsberg, *Chem. Rev.* 99, 1801 (1999).
284. R. J. Jackman and G. M. Whitesides, *CHEMTECH* 18 (May 1999).
285. S. Huang, A. W. H. Mau, T. W. Turney, P. A. White, and L. Dai, *J. Phys. Chem. B* 104, 2193 (2000).
286. Q. Chen and L. Dai, *J. Nanosci. Nanotechnol.* 1, 43 (2001).
287. E. Schäffer, T. Thurn-Albrecht, T. P. Russell, and U. Steiner, *Nature* 403, 874 (2000).
288. S. Y. Chou, L. Zhuang, and L. Guo, *Appl. Phys. Lett.* 75, 1004 (1999).
289. S. Y. Chou and L. Zhuang, *J. Vac. Sci. Technol. B* 17, 3197 (1999).
290. P. Deshpande, X. Sun, and S. Y. Chou, *Appl. Phys. Lett.* 79, 1688 (2001).

# Polymer/Clay Nanocomposites

Masami Okamoto

*Toyota Technological Institute, Tempaku, Nagoya, Japan*

## CONTENTS

1. Introduction
  2. Structure of Clay and Its Modification with Surfactants
  3. Preparative Methods and Structure of Polymer/Clay Nanocomposites
  4. Characterization of Polymer/Clay Nanocomposites
  5. Types of Polymers Used for Polymer/Clay Nanocomposite Preparation
  6. Materials Properties of Polymer/Clay Nanocomposites
  7. Crystallization of Polymer/Clay Nanocomposites
  8. Melt Rheology of Polymer/Clay Nanocomposites
  9. Processing Operations of Polymer/Clay Nanocomposites
  10. Conclusions
- Glossary  
References

## 1. INTRODUCTION

Polymer/clay *nanocomposites* (PCNs) are a new class of materials which have attracted much attention from both scientists and engineers in recent years due to their excellent properties such as high dimensional stability, heat deflection temperature, gas barrier performance, reduced gas permeability, optical clarity, flame retardancy, and enhanced mechanical properties when compared with the pure polymer or conventional composites (micro- and macrocomposites) [1–15]. The first successful PCN appeared about 10 years ago through the pioneering efforts of a research team from Toyota Central Research & Development Co. Inc. (TCRD) in the form of a Nylon 6/clay hybrid [1, 2].

Earlier attempts to prepare polymer/clay composites are found in almost half-a-century old patent literatures [16, 17]. In such cases, incorporation of 40 to 50 wt% clay mineral (bentonite, hectorite, etc.) into a polymer was attempted but ended with unsatisfactory results: The maximal modulus enhancement was only around 200%, although the clay loading was as much as 50 wt%. The failure was obvious because they failed to achieve good dispersion of clay particles in the matrix, in which clay minerals existed as agglomerated tactoids. Such a poor dispersion of the clay particles could improve the material rigidity but certainly sacrifice the strength, the elongation at break, and the toughness of the material [16, 17].

A prime reason for this impossibility of improving the tactoid dispersion into well-dispersed exfoliated monolayers of the clay is obviously due to the intrinsic incompatibility of hydrophilic layered silicates with hydrophobic engineering plastics. One attempt at circumventing this difficulty was made by Unitika Ltd. [18] about 30 years ago in preparing Nylon 6/clay composites (not nanocomposites) via *in-situ* polymerization of  $\epsilon$ -caprolactam with montmorillonite, but the results were not very good.

The first major breakthrough of the problem was brought about in 1987, when Fukushima and Inagaki of TCRD, via their detailed study of polymer/layered silicate composites, persuasively demonstrated that *lipophilization*, by replacing inorganic cations in galleries of the native clay with alkylammonium surfactant, successfully made them compatible with hydrophobic polymer matrices [19]. The modified clay was thus called *lipophilized* clay, *organo-phillic* clay, or simply *organo-clay* (organoclay). Furthermore, they found that the lipophilization enabled one to expand clay galleries and exfoliate the silicate layers into single layers of a nanometer thickness.

Six years later, in 1993, Usuki, Fukushima, and their colleagues at TCRD successfully prepared, for the first time, *exfoliated* Nylon 6/clay hybrid (NCH) via *in-situ* polymerization of  $\epsilon$ -caprolactam, in which alkylammonium-modified organoclay was thoroughly dispersed in advance [1, 2]. The resulting composite of the loading of only 4.2 wt% clay possessed a doubled modulus, a 50% enhanced strength, and an increase in heat distortion by 80 °C compared to the neat Nylon 6, as shown in Table 1. This invention opened up a

**Table 1.** Mechanical and thermal properties of Nylon 6/clay hybrid.

Properties	Nylon 6 nanocomposite	Neat Nylon 6
Clay content (wt%)	4.2	0
Specific gravity	1.15	1.14
Tensile strength (MPa)	107	69
Tensile modulus (GPa)	2.1	1.1
Impact (kJ/m <sup>2</sup> )	2.8	2.3
HDT (°C at 1.8 MPa)	147	65

new era of engineering materials, which we may call “polymer/clay nanocomposites.”

Thus, along the stream of development in PCN technologies, many studies have been devoted to PCNs since their intrinsically excellent properties of polymer should have attractive potential for continuous expansion of application versatility.

Apart from this, rheological behavior, especially elongational and shear flow behavior in the molten state and crystallization behavior under supercooled state of PCNs, has not well been reported yet, although such knowledge should be indispensable in relation with their performance in processing operations. One objective of this chapter is to focus on a profound understanding of PCNs for their innovations in practical material production. For this purpose, it is indispensable to illuminate the nanostructure as well as rheological properties of PCNs to assess appropriate processing conditions for designing and controlling their hierarchical nanostructure, which must be closely related to their material performance.

## 2. STRUCTURE OF CLAY AND ITS MODIFICATION WITH SURFACTANTS

The commonly used clays for the preparation of PCNs belong to the same general family of 2:1 layered or phyllosilicates. (see Table 2.) Their crystal structure consists of layers made up of two silica tetrahedral fused to an edge-shared octahedral sheet of either aluminum or magnesium hydroxide. The layer thickness is around 1 nm and the lateral dimensions of these layers may vary from 30 nm to several micrometers and even larger depending on the particular layered silicate. Stacking of the layers leads to a regular van der Waals gap between the layers called the *interlayer* or

**Table 2.** Chemical formula and characteristic parameter of commonly used 2:1 phyllosilicates.

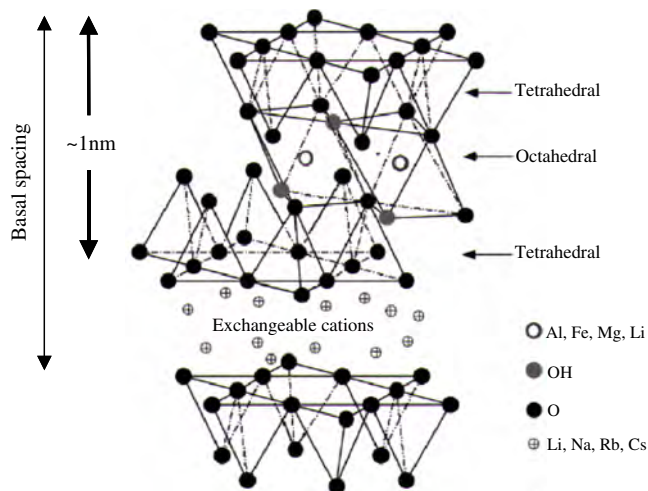
2:1 Phyllosilicates	Chemical formula <sup>a</sup>	CEC (mequiv /100 gm)	Particle length (nm)
Montmorillonite	$M_x(Al_{4-x}Mg_x)Si_8O_{20}(OH)_4$	110	100–150
Hectorite	$M_x(Mg_{6-x}Li_x)Si_8O_{20}(OH)_4$	120	200–300
Saponite	$M_xMg_6(Si_{8-x}Al_x)Si_8O_{20}(OH)_4$	86.6	50–60

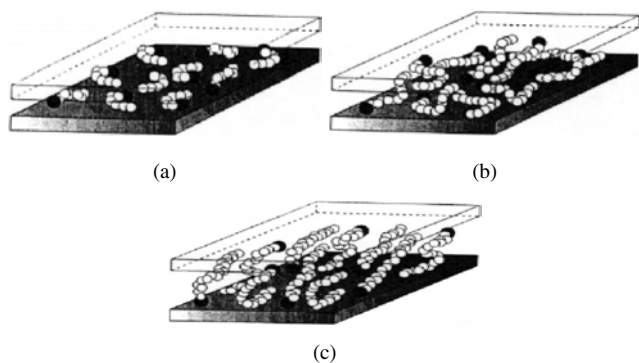
<sup>a</sup> M = monovalent cation; x = degree of isomorphous substitution (between 0.3 and 1.3).

*gallery*. Isomorphous substitution within the layers (for example, Al<sup>3+</sup> replaced by Mg<sup>2+</sup> or by Fe<sup>2+</sup>, or Mg<sup>2+</sup> replaced by Li<sup>+</sup>) generates negative charges that are counterbalanced by alkali and alkaline earth cations situated inside the galleries, as shown in Figure 1.

The most commonly used layered silicates are montmorillonite (MMT) hectorite and saponite having different chemical formulas, respectively,  $M_x(Al_{4-x}Mg_x)Si_8O_{20}(OH)_4$ ,  $M_x(Mg_{6-x}Li_x)Si_8O_{20}(OH)_4$ , and  $M_x(Si_{8-x}Al_x)Si_8O_{20}(OH)_4$  ( $x = 0.3–1.3$ ). The type of clay is characterized by a moderate surface charge (cation exchange capacity) (CEC of 80–120 mequiv/100 gm) and layer morphology. These clays are only miscible with hydrophilic polymers, such as poly(ethylene oxide) (PEO) [20] and poly(vinyl alcohol) (PVA) [21]. To improve miscibility with other polymer matrices, one must convert the normally hydrophilic silicate surface to organophilic, which makes possible intercalation of many engineering polymers. Generally, this can be done by ion-exchange reactions with cationic surfactants including primary, secondary, tertiary, and quaternary alkyl ammonium or alkylphosphonium cations. The role of alkylammonium or alkylphosphonium cations in the organosilicates is to lower the surface energy of the inorganic host and improve the wetting characteristics with the polymer matrix and results in a larger interlayer spacing. One can evaluate that about 100 alkylammonium salt molecules are localized near the individual silicate layers ( $\sim 8 \times 10^{-15} \text{ m}^2$ ) and active surface area ( $\sim 800 \text{ m}^2/\text{g}$ ). Additionally, the alkylammonium or alkylphosphonium cations could provide functional groups that can react with the polymer matrix or in some cases initiate the polymerization of monomers to improve the strength of the interface between the inorganic and the polymer matrix [22, 23].

Vaia et al. [24] have shown that alkyl chains can vary from liquidlike to solidlike, with the liquidlike structure dominating as the interlayer density or chain length decreases (see Fig. 2), or as the temperature increases by using Fourier transform infrared spectroscopy (FTIR). This is due to the relatively small energy differences between the *trans* and

**Figure 1.** Structure of 2:1 phyllosilicates. Adapted with permission from [32], E. P. Giannelis et al., *Adv. Polym. Sci.* 138, 107 (1999). © 1999, Springer-Verlag.



**Figure 2.** Alkyl chain aggregation models. (a) Short chain lengths: the molecules are effectively isolated from each other. (b) Medium lengths: quasi-discrete layers form with various degrees of in-plane disorder and interdigitation between the layers. (c) Long lengths: interlayer order increases leading to a liquid-crystalline polymer environment. Open circles represent the CH<sub>2</sub> segments while cationic head groups are represented by filled circles. Reprinted with permission from [24], R. A. Vaia et al., *Chem Mater.* 6, 1017 (1994). © 1994, American Chemical Society.

gauche conformers; the idealized models described earlier assume all *trans* conformations. In addition, for the longer chain length surfactants, the surfactants in the layered silicate can show thermal transition akin to melting or liquid-crystalline to liquidlike transitions upon heating.

### 3. PREPARATIVE METHODS AND STRUCTURE OF POLYMER/CLAY NANOCOMPOSITES

So far there have been much literature available devoted to developing PCNs with different combinations of organoclays and matrix polymers such as epoxy polymer resin [5], polyurethanes (PU) [6], PEI [7], polybenzoxazine [8], polypropylene (PP) [9, 14, 15, 25], polystyrene (PS) [10, 11], poly(methyl methacrylate) (PMMA) [11, 12], and poly( $\epsilon$ -caprolactone) (PCL) [13] liquid crystalline polymers (LCP) [26] by employing somewhat different technologies appropriate to each. The technologies are broadly classified into three main categories.

#### 3.1. Intercalation of Polymer or Prepolymer from Solution

This is based on a solvent system in which polymer or prepolymer is soluble and the silicate layers are swellable. The layered silicate is first swollen in a solvent, such as water, chloroform, toluene, etc. When the polymer and layered silicate solutions are mixed, the polymer chains intercalate and displace the solvent within the interlayer of the silicate. Upon solvent removal, the intercalated structure remains, resulting in PCNs.

#### 3.2. *In-situ* Intercalative Polymerization Method

In this method, the organoclay is swollen within the liquid monomer or a monomer solution so that the polymer formation can occur in between the intercalated sheets.

Polymerization can be initiated either by heat or radiation, by the diffusion of a suitable initiator, or by an organic initiator or catalyst fixed through cation exchange inside the interlayer before the swelling step by the monomer.

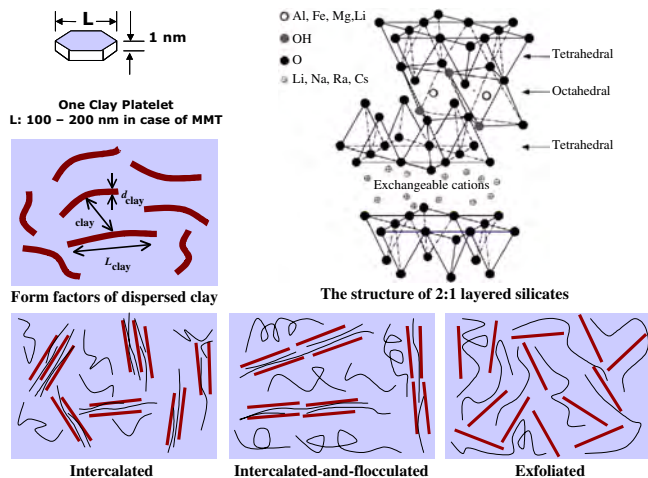
#### 3.3. Melt Intercalation Method

This method involves annealing, statically or under shear, a mixture of the polymer and organoclay above the softening point of the polymer. This method has great advantages over either *in-situ* intercalative polymerization or polymer solution intercalation. First, this method is environmentally benign due to the absence of organic solvents. Second, it is compatible with current industrial process, such as extrusion and injection molding. The melt intercalation method allows the use of polymers which were previously not suitable for *in-situ* polymerization or the solution intercalation method.

Other possibilities are exfoliation-adsorption [21, 27] and template synthesis [28, 29]. Nowadays this solvent-free method is much preferred for practical industrial material production for its high efficiency and possibility of avoiding environmental hazards.

#### 3.4. Structure of PCNs

The *in-situ* polymerization is employed for the first time in NCH production [1, 2], and the melt intercalation is the direct blending of organoclay into modified polymer matrix such as used in PP/clay nanocomposite [9, 14, 15, 25, 30]. Since Vaia et al. [31] found that the melt compounding of polymers with clay is possible without using organic solvent, nanocomposite preparations via this method have been widely used in practice, especially for polyolefin-based nanocomposites. This process involves annealing, statically or under shear, a mixture of the polymer and organoclay above the softening point of the polymer. During the anneal, the polymer chains diffuse from the bulk polymer melt into the galleries between the silicate layers. Depending on the degree of penetration of the matrix into the organically modified layered silicate galleries, nanocomposites are obtained with structures ranging from *intercalated* to *exfoliated*. Polymer penetration resulting in finite expansion of the silicate layers produces intercalated nanocomposites consisting of well-ordered multilayers with alternating polymer/silicate layers and a repeat distance of few nanometers (intercalated; see Fig. 3) [30]. On the other hand, extensive polymer penetration resulting in disordered and eventual delamination of the silicate layers produces *near to* exfoliated nanocomposites consisting of individual silicate layers dispersed in polymer matrix (exfoliated) [32]. Under some conditions, the intercalated nanocomposites exhibit flocculation because of the hydroxylated edge-edge interaction of silicate layers (intercalated and flocculated). The length of the oriented collections in the range of 300–800 nm is far larger than original clay (mean diameter  $\cong$  150 nm) [33, 34]. Such flocculation presumably is governed by an interfacial energy between polymer matrix and organoclays and is controlled by ammonium cation-matrix polymer interaction. The polarity of the matrix polymer is of fundamental importance in controlling the nanoscale structure.



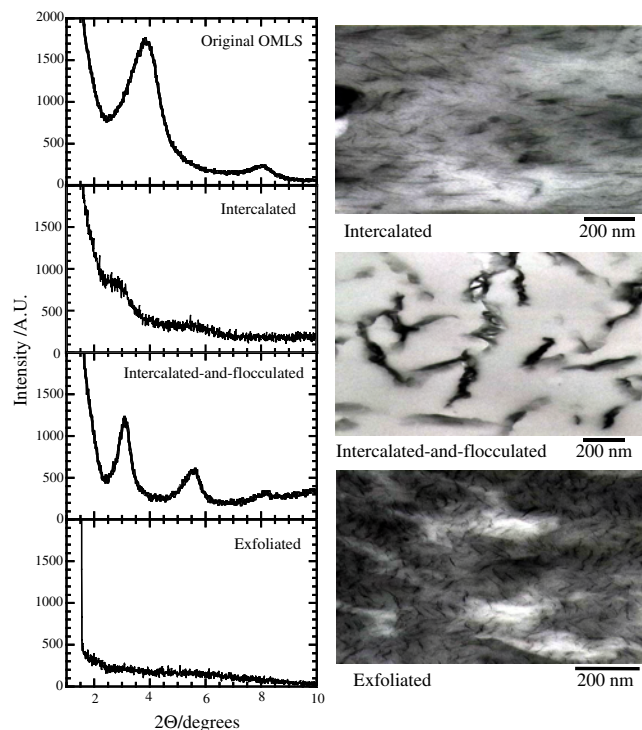
**Figure 3.** Schematic illustration of three different types of thermodynamically achievable polymer/clay nanocomposites. Reprinted with permission from [327], S. Sinha Ray et al., *Macromolecules* 36, 2355 (2003). © 2003, American Chemical Society.

#### 4. CHARACTERIZATION OF POLYMER/CLAY NANOCOMPOSITES

Generally the structure of the PCNs has typically been established using a wide-angle X-ray diffraction (WAXD) analysis and transmission electron microscope (TEM) observation. Due to its easiness and availability WAXD is most commonly used to probe the PCN structure and sometimes to study the kinetics of the polymer melt intercalation. By monitoring the position, shape, and intensity of the basal reflections from the distributed silicate layers, the PCN structure, either *intercalated* or *exfoliated*, may be identified. For example, in case of *exfoliated* nanocomposites, the extensive layer separation associated with the delamination of the original silicate layers in the polymer matrix results in the eventual disappearance of any coherent X-ray diffraction from the distributed silicate layers. On the other hand, for *intercalated* nanocomposites, the finite layer expansion associated with the polymer intercalation results in the appearance of a new basal reflection corresponding to the larger gallery height.

Although WAXD offers a convenient method to determine the interlayer spacing of the silicate layers in the original layered silicates and in the intercalated nanocomposites (within 1–4 nm), little can be said about the spatial distribution of the silicate layers or any structural inhomogeneities in the PCNs. Additionally, some layered silicates initially do not exhibit well-defined basal reflection. Thus, peak broadening and intensity decreases are very difficult to study systematically. Therefore, conclusions concerning the mechanism of nanocomposite formation and their structure based solely on WAXD patterns are only tentative.

On the other hand, TEM allows a qualitative understanding of the internal structure, spatial distribution of the various phases, and defect structure through direct visualization. However, special care must be exercised to guarantee a representative cross section of the sample. The WAXD patterns and corresponding TEM images of three different types of nanocomposites are presented in Figure 4.



**Figure 4.** (Left) WAXD patterns and (Right) TEM images of three different types of nanocomposites.

#### 5. TYPES OF POLYMERS USED FOR POLYMER/CLAY NANOCOMPOSITE PREPARATION

##### 5.1. Vinyl Polymers

These include the vinyl addition polymers derived from common monomers like methyl methacrylate (MMA) [11, 33, 35–44], methyl methacrylate copolymers [12, 33, 45, 46], other acrylates [47–49], acrylic acid [50, 51], acrylonitrile [52–55], styrene (S) [10, 11, 31, 56–80], 4-vinylpyridine [81], acrylamide [82, 83], and tetrafluoro ethylene [84]. In addition, selective polymers like PVA [21, 85–87], poly(*N*-vinyl pyrrolidone) [88, 89], poly(vinyl pyrrolidinone) [90–93], poly(vinyl pyridine) [94], poly(ethylene glycol) (PEG) [95], poly(ethylene vinyl alcohol) [96], poly(vinylidene fluoride) [97], poly(*p*-phenylenevinylene) [98], polybutadiene [99], poly(styrene-*co*-acrylonitrile) (SAN) [100], ethyl vinyl alcohol copolymer [101], polystyrene–polyisoprene diblock copolymer [102, 103], and others [104] have also been used.

##### 5.1.1. PMMA/Clay Nanocomposites

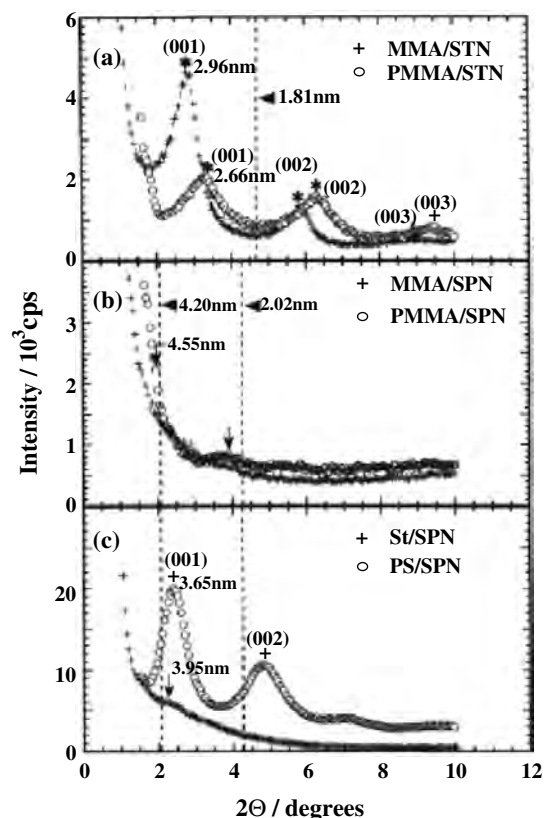
Okamoto et al. [11, 33] used organically modified smectite clays for the preparation of PMMA and PS nanocomposites. Organically modified smectite clays (SPN and STN) were prepared by replacing  $\text{Na}^+$ -smectite with QA (quaternary), oligo (oxypropylene) diethylmethylammonium cation (SPN) or methyltriocylammonium cation (STN) by exchange reaction. In a typical synthesis, both lipophilized smectite clays were (SPN and STN) dispersed in MMA and S via ultrasonication at 25 °C for 7 h to obtain suspensions. After that *t*-butyl peroxy-2-ethylhexanate and/or 1,1-bis(*t*-butyl peroxy)

cyclohexane as an initiator was added to the suspensions and then free-radical polymerization was carried out in the dark at 80 °C for 5 h (for MMA) and at 100 °C for 16 h (for S) in a silicon oil bath. For comparison authors also prepared PMMA and/or PS including QA as the reference under the same conditions and procedure. WAXD analyses were performed directly from the suspensions of MMA/SPN, MMA/STN, and S/SPN, and corresponding nanocomposites.

From WAXD patterns of MMA/STN suspension (see Fig. 5a), the higher order peaks of interlayer spacing corresponding to  $d_{(002)}$  and  $d_{(003)}$  are clearly observed along with basal spacing  $d_{(001)}$  peak, suggesting MMA intercalated into the STN gallery without the loss of layer structure, while the corresponding nanocomposite, PMMA/STN, exhibits rather broad Bragg peaks, indicating the formation of disordered intercalated structure.

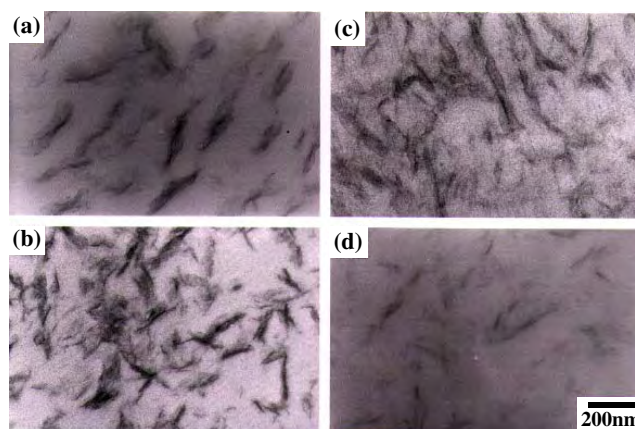
In contrast, for MMA/SPN suspension (see Fig. 5b), the absence of any Bragg diffraction peaks indicates that the clay has been completely exfoliated or delaminated in the suspension. A similar pattern was observed in case of corresponding PMMA/SPN nanocomposite but with a small remnant shoulder as shown in Figure 5b.

Further studies by the same group [33] have demonstrated the effect of the nature of co-monomers on the structure

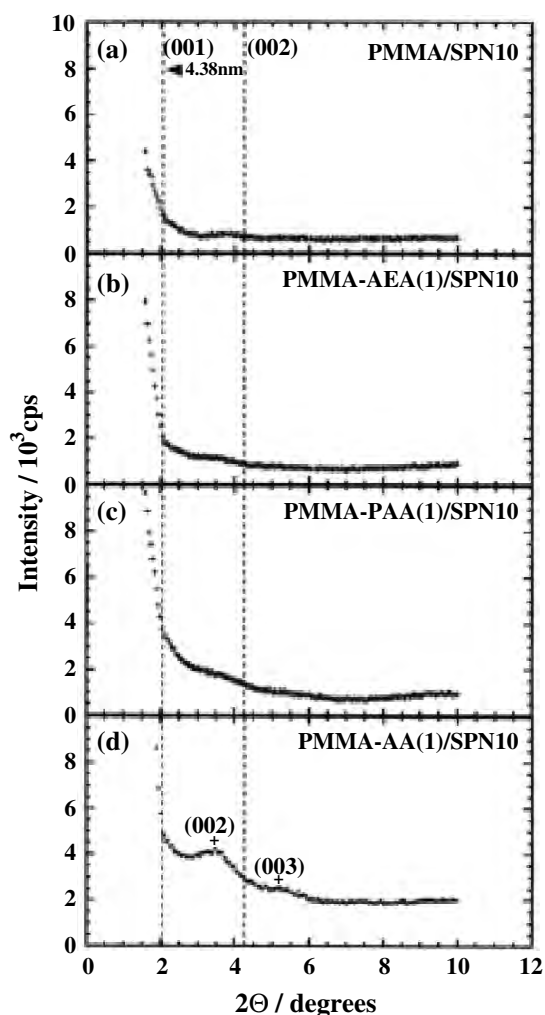


**Figure 5.** WAXD patterns of various monomer/organoclay suspensions and corresponding polymer/clay nanocomposites. The dashed lines indicate the location of the silicate (00 $l$ ) reflection of organoclay from suspensions and nanocomposites. The asterisk indicates the position of (00 $l$ ) reflections from suspensions and nanocomposites. The arrows indicate a small shoulder or a weak peak. Reprinted with permission from [11], M. Okamoto et al., *Polymer* 41, 3887 (2000). © 2000, Elsevier Science.

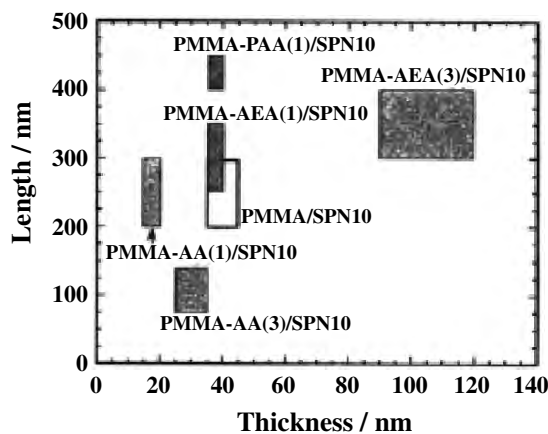
of PMMA nanocomposites prepared via *in-situ* free-radical co-polymerization of MMA in presence of lyophilized smectite clays (each containing 10 wt%). They used three different types of co-monomers (each 1 mol%) such as *N,N*-dimethylaminopropyl acrylamide (PAA), *N,N*-dimethylaminoethyl acrylate (AEA), and acrylamide (AA) for the free-radical polymerization of MMA. Figure 6 represents the results of WAXD patterns of various nanocomposites (each containing 10 wt% of SPN clay). The same behavior of the stacked is observed but the thickness of the aggregation slightly decreased compared to that of PMMA/SPN10. In case of PMMA-PAA(1)/SPN10 (see Fig. 7c), individual silicate layers connected through the edge are clearly observed in the PMMA-PAA(1) matrix and large anisotropy of the dispersed clay is observed. In contrast, the PMMA-AA(1)/SPN10 nanocomposite (see Fig. 7d) exhibited less stacking of 4–5 silicate layers with a distance of about 5 nm as a fine dispersion in the PMMA-AA(1) matrix. The coherent orders of the silicate layers in this system are higher than that in other systems and are consistent with the WAXD patterns (see Fig. 6). They also prepared PMMA/SPN10 nanocomposite with a high content (3 mol%) of AA and AEA co-monomers and then tried to find out the effect of nanocomposite morphology on co-monomer amount. The length versus thickness schemes of randomly dispersed silicate layers in the nanocomposites nicely demonstrate the characteristic effects of the polar group in each co-monomer on the morphology (see Fig. 8). Incorporation of 1 mol% of AEA co-monomer possessing a dimethyl amine group appears to lead to a slight edge-edge interaction. On the other hand, the introduction of the AA co-monomer having an amide group appears to play an important role in delaminating the silicate layers. However, incorporation of 3 mol% of AEA and AA lead to the stacking of the layers compared to the corresponding 1 mol% copolymer matrix systems. We believe this behavior may be due to the formation of strong hydrogen bonding between the polar groups. For the PAA co-monomer having both polar groups, a much stronger flocculation takes place.



**Figure 6.** Bright Field TEM images of: (a) PMMA/SPN, (b) PMMA-AEA (1 mol%)/SPN, (c) PMMA-PAA (1 mol%)/SPN, and (d) PMMA-AA (1 mol%)/SPN. Each contains 10 wt% SPN. Reprinted with permission from [33], M. Okamoto et al., *Polymer* 42, 1201 (2001). © 2001, Elsevier Science.



**Figure 7.** WAXD patterns of various nanocomposites. Reprinted with permission from [33], M. Okamoto et al., *Polymer* 42, 1201 (2001). © 2001, Elsevier Science.



**Figure 8.** Plots of length vs thickness of the dispersed clay particles in various copolymer matrices estimated from TEM images. The estimated values are located within the shaded area. Reprinted with permission from [33], M. Okamoto et al., *Polymer* 42, 1201 (2001). © 2001, Elsevier Science.

### 5.1.2. PS/Clay Nanocomposites

The same method recently was used by Zeng et al. [77] for the preparation of PS-based nanocomposites. S-monomer was first intercalated into the interlayer space of organoclay. Upon the intercalation, the complex was subsequently polymerized in the confinement environment of the interlayer space with a free-radical initiator, 2,2-azobisobutyronitrile. Akelah and Moet [57, 60] have used this *in-situ* intercalative polymerization technique for the preparation of PS-based nanocomposites. They modified  $\text{Na}^+$ -MMT and  $\text{Ca}^{+2}$ -MMT with vinylbenzyltrimethyl ammonium cation by the ion exchange reaction and these modified MMTs were used for the preparation of nanocomposites. They first disperse and swell modified clays in various solvent and co-solvent mixtures such as acetonitrile, acetonitrile/toluene, and acetonitrile/THF by stirring for 1 h under  $\text{N}_2$  atmosphere. To the stirred solution S and *N-N'*-azobis (isobutyronitrile) (AIBN) were added, and polymerization of S was carried at 80 °C for 5 h. The resulting composites were isolated by precipitation of the colloidal suspension in methanol, filtered off, and dried. In this way, intercalated PS/MMT nanocomposites were produced and the extent of intercalation completely depends on the nature of solvent used. Although the PS is well intercalated, a drawback of this procedure remains that the macromolecule produced is not a pure PS but rather a copolymer between S and vinylbenzyltrimethylammonium cations. For the preparation of PS based nanocomposites, Doh and Cho [63] have more commonly used MMT. They compared the ability of several tetra-alkylammonium cations incorporated in  $\text{Na}^+$ -MMT through the exchange reaction to promote the intercalation of PS through the free-radical polymerization of S initiated by AIBN at 50 °C. They found that the structural affinity between S monomer and the surfactant of modified MMT plays an important role in the final structure and the properties of nanocomposites. This concept has, however, been nicely achieved by Weimer et al. [67] for the preparation of PS/MMT nanocomposites. They modified  $\text{Na}^+$ -MMT by anchoring an ammonium cation bearing a nitroxide moiety known for its ability to mediate the controlled/"living" free-radical polymerization of S in bulk. The absence of WAXD peaks in the low angle area together with the TEM observations of silicate layers randomly dispersed within the PS matrix attest to the complete exfoliation of the layered silicate.

PS was also the first polymer used for the preparation of nanocomposite using the melt intercalation technique with alkylammonium cation modified MMT [31]. In a typical preparative method, PS first was mixed with host organoclay powder, the mixture was pressed into a pellet, and then the pellet was heated in a vacuum at 165 °C. This temperature is well above the bulk glass transition temperature of PS ensuring the presence of a polymer melt. The WAXD patterns of the hybrid before heating show peaks characteristic of the pure organoclay and during heating the organoclay peaks were progressively reduced while a set of new peaks corresponding to the PS/clay appeared. After 25 h, the hybrid shows the WAXD patterns corresponding predominantly to that of intercalated structure. The same authors also carried out the same experiment under the same experimental conditions using  $\text{Na}^+$ -MMT, but WAXD patterns did

not show any intercalation of PS into the silicate galleries emphasizing the importance of polymer/clay interactions. They also attempt to intercalate PS in the toluene with the same organoclay as used for melt intercalation resulting in intercalation of the solvent instead of PS. Therefore, direct melt intercalation enhances the specificity for the polymer by eliminating the competing host-solvent and polymer-solvent interaction. The schematic illustration of polymer chains intercalated in organoclay is presented in Figure 9.

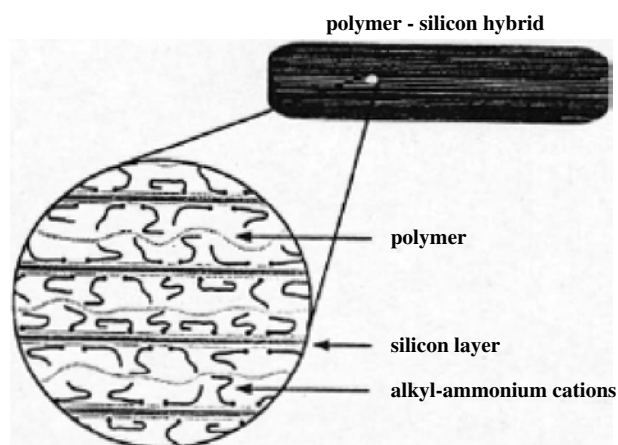
Syndiotactic polystyrene (s-PS)/organoclay nanocomposites have also been prepared by the solution intercalation technique by mixing pure s-PS and organoclay with adsorbed cetyl pyridium chloride [75]. The WAXD analyses and TEM observations clearly established the near exfoliate structure of the prepared nanocomposites.

### 5.1.3. SAN/Clay Nanocomposites

Kim et al. [100] used this method for the preparation of SAN/clay nanocomposites using PCL as a compatibilizer. They used a two-step mixing sequence for the preparation of SAN nanocomposites. PCL/clay master batches with different degrees of intercalation were first prepared and then were melt-mixed with SAN, where PCL is miscible with SAN. The intercalation behavior of PCL in the master batches was investigated in terms of the type of organoclay and mixing conditions. Longer mixing time and lower mixing temperature were required for the preparation of PCL master batches with exfoliated structure. As the degree of exfoliation of organoclay becomes better, the stiffness reinforcement effect of the organoclay increases in both PCL/clay master batches and their blends with SAN.

### 5.1.4. PVA/Clay Nanocomposites

More recently, Strawhecker and Manias [87] have used this method in attempts to produce PVA/MMT nanocomposite films. PVA/MMT nanocomposite films were cast from MMT/water suspension where PVA was dissolved. Room temperature distilled water was used to form a suspension of Na<sup>+</sup>-MMT. The suspension was first stirred for 1 h and then sonicated for 30 min. Low viscosity, fully



**Figure 9.** Schematic illustration of polymer chains intercalated in organoclay. Reprinted with permission from [31], R. A. Vaia et al., *Chem. Mater.* 5, 1694 (1993). © 1993, American Chemical Society.

hydrolyzed atactic PVA was then added to the stirring suspensions such that the total solid (silicate plus polymer) was  $\leq 5$  wt%. The mixtures were then heated to 90 °C to dissolve the PVA and again sonicated for 30 min, and finally films were cast in a closed oven at 40 °C for 2 days. The recovered cast films were then characterized by both WAXD and TEM. Both the *d*-spacing and their distribution decrease systematically with increasing MMT wt% in the nanocomposites. The TEM photograph of 20 wt% clay containing nanocomposite reveals the coexistence of silicate layers in the intercalated and the exfoliated states.

### 5.1.5. Block Copolymer/Clay Nanocomposites

Krishnamoorti et al. [102, 103] prepared the block copolymer-based layered silicate nanocomposites. Disordered polystyrene-polyisoprene block copolymer/layered silicate nanocomposites were prepared by solution mixing of appropriate quantities of finely ground dimethyldioctadecylammonium cation modified MMT (2C18-MMT) and an anionically synthesized monodisperse polystyrene-1,4-polyisoprene (7 mol% 3,4 and 93 mol% 1,4) diblock copolymer (PSPI18) in toluene at room temperature. The homogeneous solution was dried extensively at room temperature and subsequently annealed at 100 °C in a vacuum oven for  $\sim 12$  h to remove any remaining solvent and to facilitate complete polymer intercalation between the silicate layers. The WAXD patterns of PSPI18/2C18-MMT or PS/2C18-MMT clearly indicate the formation of intercalated structure, whereas composite prepared with 1,4-polyisoprene showed no change in gallery height. The intercalation of PS into the silicate layers may be due to the slight Lewis base character imparted by the phenyl ring in PS, leading to the favorable interactions with the 2C18-MMT layers. Further, the interlayer gallery spacing for the PSPI18/2C18-MMT composites is independent of the silicate loading. All the hybrids exhibit clear regular layered structure, demonstrated by the presence of the  $d_{001}$  and higher order diffraction peaks. This independence in gallery height on the silicate loading is consistent with the results obtained by Vaia and co-workers on model PS-based nanocomposite systems.

## 5.2. Condensation Polymers and Rubbers

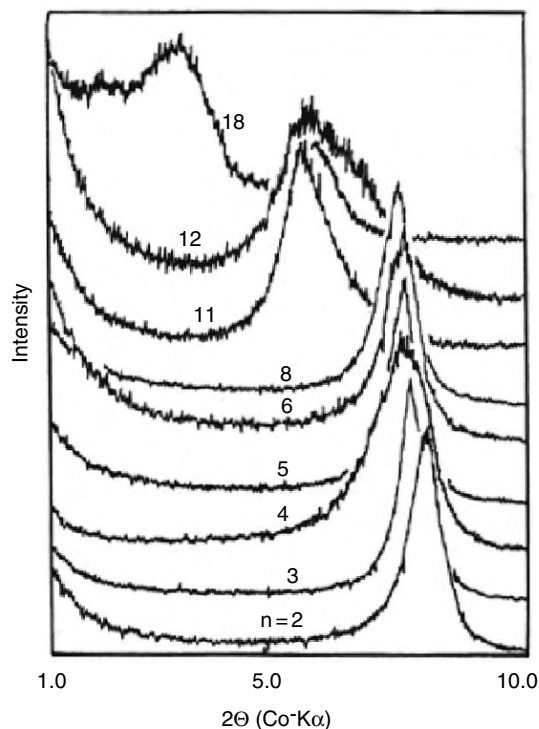
Several technologically important polycondensates have also been used in the nanocomposite preparation with layered silicate. These include Nylon 6 [1, 2, 105–125], several others polyamides [126–132], PCL [13, 133–140], poly(ethylene terephthalate) (PET) [141–147], poly(butylene terephthalate) (PBT) [148], polycarbonate (PC) [149, 150], PEO [20, 151–168], ethylene oxide copolymers [169], poly(ethylene imine) [170], poly(dimethyl siloxane) (PDMS) [171–176], LCP [26, 177] polybenzoxazole (PBO) [178], butadiene copolymers [179–181], epoxidized natural rubber [182, 183], epoxy polymer resins (EPR) [184–204], phenolic resins [205], PU [206–209], polyurethane urea (PUU) [210], polyimides [211–226], poly(amic acid) [227–229], polysulphone [230], and polyetherimide [231, 232].



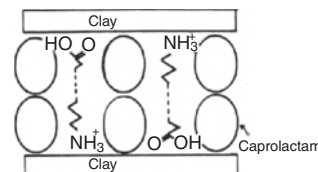
### 5.2.1. Nylon/Clay Nanocomposites

TCRD first reported [1] the ability of  $\alpha, \omega$ -amino acid  $[\text{COOH}-(\text{CH}_2)_{n-1}-\text{NH}_2^+]$ , with  $n = 2, 3, 4, 5, 6, 8, 11, 12, 18$  modified  $\text{Na}^+$ -MMT to be swollen by the  $\epsilon$ -caprolactam monomer at  $100^\circ\text{C}$  and subsequently to initiate its ring-opening polymerization to obtain Nylon 6/MMT nanocomposites. For the intercalation of  $\epsilon$ -caprolactam, they chose the ammonium cation of  $\omega$ -amino acids because these acids catalyze ring-opening polymerization of  $\epsilon$ -caprolactam. The number of carbon atoms in  $\alpha, \omega$ -amino acids has a strong effect on swelling behavior as reported in Figure 10, indicating the extent of intercalation of  $\epsilon$ -caprolactam monomer is high when the number of carbon atoms in  $\omega$ -amino acid is high. Figure 11 represents the conceptual view of swelling behavior of  $\alpha, \omega$ -amino acid modified  $\text{Na}^+$ -MMT by  $\epsilon$ -caprolactam.

In a typical synthesis, 12-aminolauric acid modified MMT (12-MMT) and  $\epsilon$ -caprolactam were mixed in a motor. The content of 12-MMT ranged from 2 to 70 wt%. These were then heated at  $250\text{--}270^\circ\text{C}$  for 48 h to polymerize  $\epsilon$ -caprolactam, using 12-MMT as catalyst. A small amount of 6-aminocaproic acid was added to the mixture to confirm the ring-opening polymerization of  $\epsilon$ -caprolactam, and 12-MMT content in the mixture become less than 8 wt%. A typical procedure used was as follows: A 3 L three-necked separable flask, coupled with a mechanical stirrer, was used as the reaction vessel. In the vessel, 509 g of  $\epsilon$ -caprolactam, 29.7 g of 12-MMT, and 66 g of 6-aminocaproic acids were placed under nitrogen. The mixture was heated at  $100^\circ\text{C}$  in an oil bath while being stirred for 30 min, followed by heating at  $250^\circ\text{C}$  for 6 h. The products were mechanically



**Figure 10.** XRD patterns of  $\omega$ -amino acid  $[\text{NH}_2(\text{CH}_2)_{n-1}\text{COOH}]$  modified  $\text{Na}^+$ -MMT. Reprinted with permission from [1], A. Usuki et al., *J. Mater. Res.* 8, 1174 (1993). © 1993, Materials Research Society.

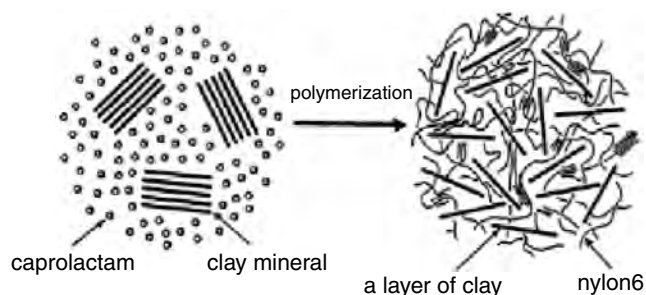


**Figure 11.** Swelling behavior of  $\omega$ -amino acid modified MMT by  $\epsilon$ -caprolactam. Reprinted with permission from [1], A. Usuki et al., *J. Mater. Res.* 8, 1174 (1993). © 1993, Materials Research Society.

crushed, washed with 2 L of water at  $80^\circ\text{C}$  for 1 h, and dried at  $80^\circ\text{C}$  overnight. A conceptual scheme for the synthetic method is presented in Figure 12 [105]. Further works have demonstrated that intercalative polymerization of  $\epsilon$ -caprolactam could be realized without the necessity to render the MMT surface organophilic. In attempts to carry out the whole synthesis in one pot [107], the system has proved to be sensitive to the nature of the acid used to promote the intercalation of  $\epsilon$ -caprolactam. Reichert et al. have also used same method for the preparation of Nylon 12/MMT nanocomposites [127].

For the preparation of Nylon 6/clay nanocomposites people generally used an *in-situ* intercalative polymerization technique. Liu et al. [114] first used this technique for the preparation of commercially available Nylon 6 with  $\text{C}_{18}$ -MMT nanocomposites by using a twin-screw extruder. They prepared nanocomposites with MMT content from 1 to 18 wt%. WAXD patterns and TEM observations respectively indicated that nanocomposites prepared with MMT less than 10 wt% lead to the exfoliated structure but more than 10 wt% MMT leads to the formation of intercalated structure. WAXD and differential scanning calorimetry (DSC) analyses also showed that exfoliated structures strongly influenced the nature of the Nylon 6 crystallization, favoring the formation of  $\gamma$ -crystals in addition to the crystals of the  $\alpha$ -form observed in the native Nylon 6 matrix, and they also have a strong heterophase nucleation effect. After that VanderHart et al. [121] prepared Nylon 6/clay nanocomposites using the melt intercalation method.

Recently, Fornes et al. [119] have reported the preparation of Nylon 6/clay nanocomposites using a twin-screw extruder under molten state. They used three different molecular grades of Nylon 6 for the preparation of nanocomposites with bis(hydroxyethyl)(methyl)-rapeseed quaternary ammonium  $[(\text{HE})_2\text{M}_1\text{R}_1]$  modified MMT and tried to



**Figure 12.** Schematic illustration for synthesis of Nylon 6/clay nanocomposite. Reprinted with permission from [1], A. Usuki et al., *J. Mater. Res.* 8, 1179 (1993). © 1993, Materials Research Society.

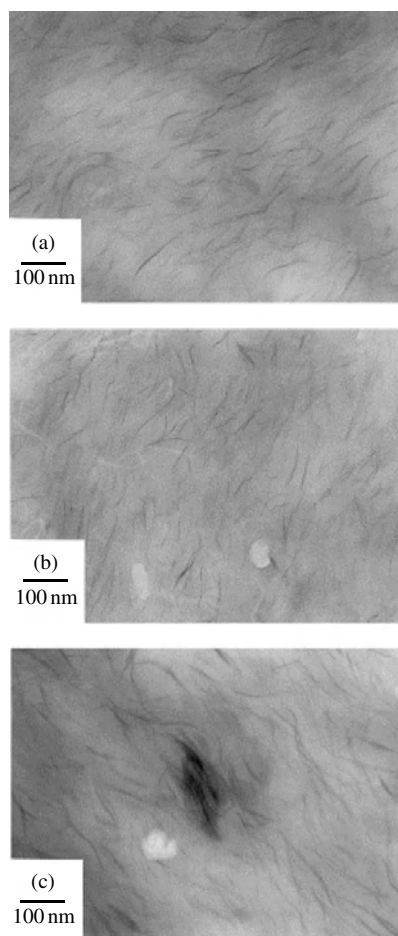
find effects of matrix molecular weights on structure, properties, rheology, etc. Nanocomposites were prepared using a Haake, co-rotating, intermeshing twin-screw extruder, which was operated at 240 °C with a screw speed of 280 rpm and a feed rate of 980 g/h.

They reported the WAXD patterns of  $(HE)_2M_1R_1$  based MMT and the nanocomposites based on the three Nylon 6 matrixes of low molecular weight (LMW), medium molecular weight (MMW), and high molecular weight (HMW), having an approximate MMT concentration of 1.5 wt%. TEM images of various nanocomposites corresponding to the WAXD patterns are presented in Figure 13. WAXD patterns and TEM observations collectively revealed a mixed structure for the LMW based nanocomposites, while the MMW and HMW based nanocomposites revealed well-exfoliated structures. The average number of platelets per stack is shown to decrease with increasing matrix molecular weight. The mechanical properties of the nanocomposites were consistent with the morphological structure found via WAXD and TEM analyses.

In further study [123], they examined the effect of organoclay structure on Nylon 6 nanocomposite morphology and properties. In order to understand this, a series of organic

amine salts were ion exchanged with  $Na^+$ -MMT to form organoclays varying in amine structure or exchange level relative to the MMT. Each organoclay was melt-mixed with a HMW Nylon 6 using a twin-screw extruder operated under the same conditions as described previously; some organoclays were also mixed with LMW Nylon 6. The structure and corresponding nomenclature of various amine compounds that were used for the modification of  $Na^+$ -MMT using an ion exchanged method are presented in Figure 14. They conclude that three distinct surfactant effects were identified that lead to greater extents of exfoliation, higher stiffness, and increased yield strengths for nanocomposites based on the HMW Nylon 6: (a) one long alkyl tail on the ammonium ion rather than two, (b) methyl groups on the amine rather than 2-hydroxy-ethyl groups, and (c) an equivalent amount of amine surfactant on the clay opposed to an excess amount.

Very recently, Gilman et al. [79] reported the preparation of Nylon 6- and PS-based nanocomposites of MMT modified with trialkylimidazolium cation in order to expect high stability of OMLS at high processing temperature. Figure 15 represents various kinds of imidazolium salts used for the modification of MMT. For the preparation of nanocomposites they used a miniextruder, which was operated at 10 °C above the melting point of the polymer with a residence time of 3–5 min and screw speed of 200–300 rpm. WAXD analyses and TEM observations respectively established the formation of exfoliated structure in case of Nylon 6-based nanocomposite whereas there was intercalated structure with the PS/MMT system.

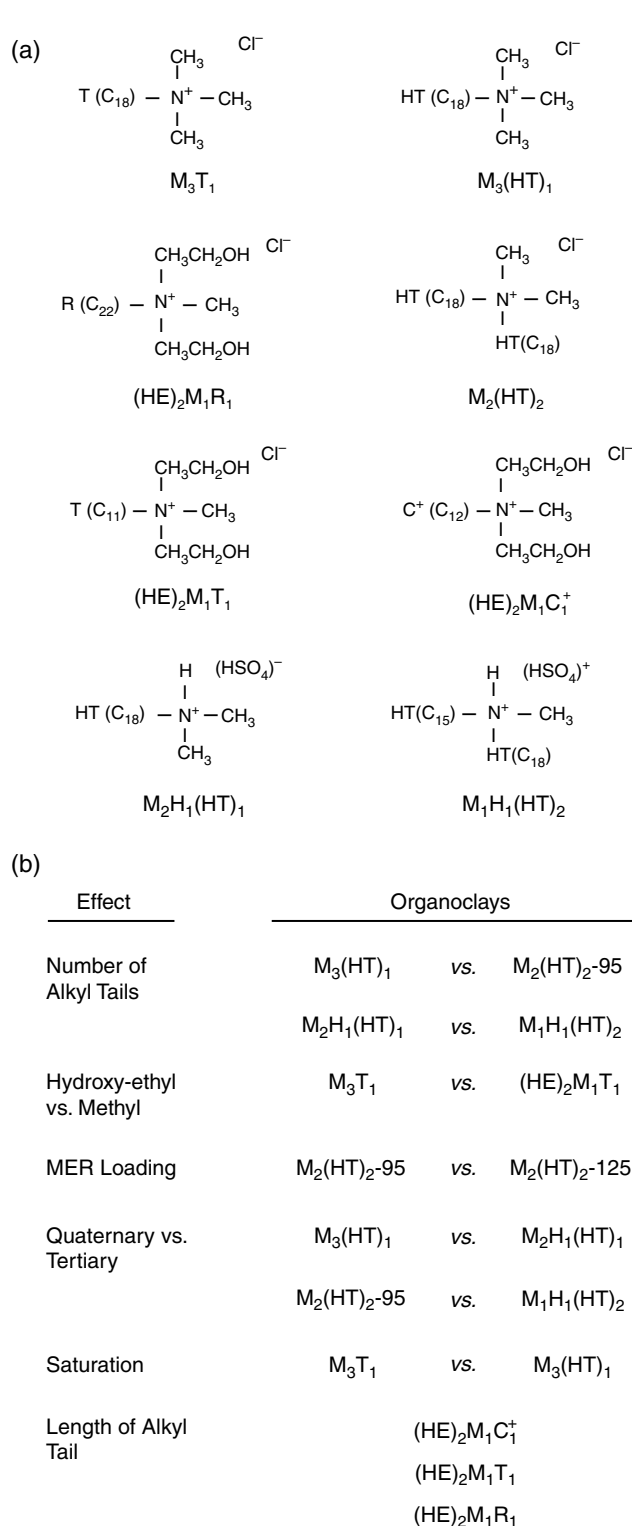


**Figure 13.** Bright field TEM images of melt compounded nanocomposites containing ~3 wt% MMT based on (a) HMW, (b) MMW, and (c) LMW Nylon 6. Reprinted with permission from [119], T. D. Fornes et al., *Polymer* 42, 9929 (2001). © 2001, Elsevier Science.

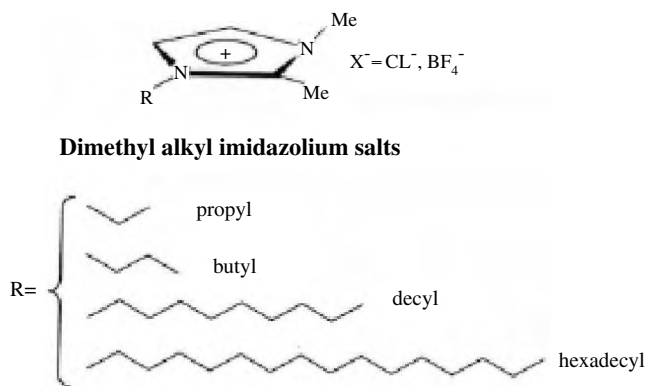
### 5.2.2. PCL/Clay Nanocomposites

For the preparation of PCL-based nanocomposites, Messersmith and Giannelis [133] modified MMT with protonated aminolauric acid and dispersed the modified MMT in liquid  $\epsilon$ -caprolactone before polymerizing at high temperature. The nanocomposites were prepared by mixing up to 30 wt% of the modified MMT with dried and freshly distilled  $\epsilon$ -caprolactone for a couple of hours followed by ring-opening polymerization under stirring at 170 °C for 48 h. The same authors [13] have also reported on the  $\epsilon$ -caprolactone polymerization inside a  $Cr^{+3}$ -exchanged fluorohectorite at 100 °C for 48 h.

Pantoustier et al. [137, 138] used this *in-situ* intercalative polymerization method. They used both pristine MMT and  $\omega$ -amino dodecanoic acid modified MMT for the comparison of prepared nanocomposite properties. For nanocomposite synthesis, in a polymerization tube, the desired amount of pristine MMT was first dried under vacuum at 70 °C for 3 h. A given amount of  $\epsilon$ -caprolactone was then added under nitrogen and the reaction medium was stirred at room temperature for 1 h. A solution of initiator  $[Sn(Oct)_2$  or  $Bu_2Sn(Ome)_2$ ] in dry toluene was added to the mixture in order to reach a  $[monomer]/[Sn]$  molar ratio equal to 300. The polymerization was then allowed to proceed for 24 h at room temperature. After polymerization, a reverse ion-exchange reaction was used to isolate the PCL chains from the inorganic fraction of the nanocomposite. A colloidal suspension was obtained by stirring 2 g of the nanocomposite in 30 mL of THF for 2 h at room



**Figure 14.** (a) Molecular structure and nomenclature of amine salts used to organically modify  $\text{Na}^+$ -MMT by ion exchange. The symbols M (methyl), T (tallow), HT (hydrogenated tallow), HE:2 (hydroxy-ethyl), R (rapeseed), C (coco), and H (hydrogen) designate the substituents on the nitrogen. (b) Organoclay used to evaluate the effect of structural variations of the amine cations on nanocomposite morphology and properties. Reprinted with permission from [123], T. D. Fornes et al., *Polymer* 43, 5915 (2002). © 2002, Elsevier Science.



**Figure 15.** Structures of various imidazolium salts used to treat  $\text{Na}^+$ -MMT. Reprinted with permission from [79], J. W. Gilman et al., *Chem. Mater.* 14, 3776 (2002). © 2002, American Chemical Society.

temperature. Separately, a solution of 1 wt% of LiCl in THF was prepared. The nanocomposite suspension was added to 50 mL of the LiCl solution and left to stir at room temperature for 48 h. The resulting solution was centrifuged at 3000 rpm for 30 min. The supernatant was then decanted and the remaining solid washed by dispersing in 30 mL of THF followed by centrifugation. The combined supernatant was concentrated and precipitated from petroleum ether.

The polymerization of CL with pristine MMT gives PCL with a molar mass of 4800 g/mol and a narrow distribution. For comparison, authors also conducted the same experiment without MMT, but there is no polymerization of CL. These results demonstrate the ability of MMT to catalyze and to control CL polymerization at least in terms of molecular weight distribution which remains remarkably narrow. For the mechanism of polymerization, authors assume that the CL is activated through the interaction with acidic site on the clay surface and the polymerization is likely to proceed via the activated monomer mechanism by the cooperative function of Lewis acidic aluminum and Bronsted acidic silanol functionalities on the initiator walls. On the other hand, in the polymerization of CL with the protonated  $\omega$ -amino dodecanoic acid modified MMT, the molar mass is 7800 g/mol with a monomer conversion of 92% and again a narrow molecular weight distribution. The WAXD patterns of both nanocomposites indicate the formation of intercalated structure. In another recent publication [139, 140], the same group prepared PCL/MMT nanocomposites by using *in-situ* ring-opening polymerization of CL using dibutyl tin dimethoxide as an initiator/catalyst.

### 5.2.3. PET/Clay Nanocomposites

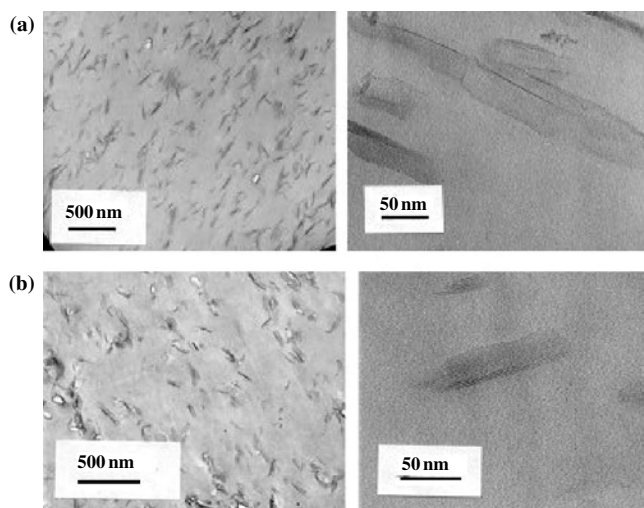
There are many reports on the preparation and characterization of PET/clay nanocomposites [141–147] using this method. Unfortunately no reports give a detailed description of the preparative method. There is one report concerning the preparation of a PET nanocomposite by *in-situ* polymerization of a dispersion of organoclay in water; however, characterization of the resulting composite was not reported [141]. This report claims that water serves as a dispersing aid for the intercalation of monomers into the galleries of the organoclay and discloses that a wide variety of small molecules can serve as dispersing aids in place

of, or in combination with, water. There is another route developed by Nanacor, Inc. [167] that was based on novel exfoliation of clays into ethylene glycol, one of the basic monomers for PET. The key to this approach includes finding a suitable surfactant that gives exfoliation of clay into ethylene glycol and also finding polymerization conditions that permit polymerization while retaining the exfoliation of the clay. Recently Imai et al. [147] reported the preparation of higher modulus PET/expandable fluorine mica nanocomposites with a novel reactive compatibilizer. Details regarding synthetic route are presented in [147].

Davis et al. [146] first reported the preparation of PET-based nanocomposites using the melt intercalation method. They used 1,2-dimethyl-3-*N*-alkyl imidazolium salt modified MMT (hexadecyl-MMT) for nanocomposite preparation with PET. PET/MMT nanocomposites were compounded via melt blending in a corotating mini twin-screw extruder operated at 285 °C. WAXD analyses and TEM (see Fig. 16) observations respectively established that the formation of mixed delaminated/intercalated structure is achieved in the nanocomposites.

#### 5.2.4. PBT/Clay Nanocomposites

Like PET nanocomposites, this method was successfully applied by Chisholm et al. [148] for the preparation PBT/clay nanocomposites. They used sulfonated PBT for the preparation of nanocomposites. Because of the ionic nature of the  $-\text{SO}_3\text{Na}$  groups and the expected insolubility of the  $-\text{SO}_3\text{Na}$  groups in the polyester matrix, it was thought that the presence of the  $-\text{SO}_3\text{Na}$  groups may provide a thermodynamic driving force for the production of nanocomposites derived from MMT. But after preparation and characterizations of nanocomposites it was found that degree of intercalation was not strongly dependent on the amount of  $-\text{SO}_3\text{Na}$  groups; however, the mechanical properties increased significantly with increasing  $-\text{SO}_3\text{Na}$  content.



**Figure 16.** TEM images of: (a) CD12 showing high levels of dispersion and exfoliation, average tactoids of four sheets per stack and (b) CD13 showing similar levels of dispersion and delamination as compared to CD12. Reprinted with permission from [146], C. H. Davis et al., *J. Polym. Sci. B* 40, 2661 (2002). © 2002, Wiley-VCH.

This behavior indicates that with high  $-\text{SO}_3\text{Na}$  content the number of interactions increases between the clay particles and the matrix via strong specific interactions involving the  $-\text{SO}_3\text{Na}$  groups.

#### 5.2.5. PC/Clay Nanocomposites

Recently, Huang et al. [149] reported the synthesis of a partially exfoliated bisphenol A PC nanocomposite using carbonate cyclic oligomers and ditallowdimethyl-exchanged MMT. WAXD patterns indicate that exfoliation of this organoclay occurs after mixing with the cyclic oligomers in a brabender mixer for 1 h at 180 °C. Subsequent ring-opening polymerization of the cyclic oligomers converts the matrix into the linear polymer without the disruption of the nanocomposite structure. The TEM image revealed that a little exfoliation is obtained, although no indication of layer correlation is observed in WAXD.

Mitsunaga et al. [150] also reported intercalated PC/clay nanocomposites prepared through the melt intercalation method in the presence of compatibilizer. The morphology of these nanocomposites and degradation of the PC matrix after nanocomposites preparation could be controlled by varying surfactants used for the modification of clay and compatibilizers. The intercalated PC/clay nanocomposites exhibited remarkable improvements of mechanical properties when compared with PC without clay.

#### 5.2.6. PEO/Clay Nanocomposites

In 1992, Aranda and Ruiz-Hitzky [20] first reported the preparation of PEO/MMT nanocomposites by using this method. They have carried out a series of experiments to intercalate PEO ( $M_w = 10^5$  g/mol) into  $\text{Na}^+$ -MMT using different polar solvents [e.g., water, methanol, acetonitrile, mixtures (1:1) of water/methanol and methanol/acetonitrile]. In this method the nature of solvents is very crucial to facilitate the insertion of polymers between the silicate layers, polarity of the medium being a determining factor for intercalations. The high polarity of water causes swelling of  $\text{Na}^+$ -MMT provoking the cracking of the films. Methanol is not suitable as a solvent for high molecular weight PEO, whereas water/methanol mixtures appear to be useful for intercalations, although cracking of the resulting materials is frequently observed. PEO intercalated compounds derived from the homoionic  $\text{M}^{+n}$ -MMT and  $\text{M}^{+n}$ -hectorite can satisfactorily be obtained using anhydrous acetonitrile or methanol/acetonitrile mixture as solvents.

The resulting PEO/clay nanocomposites show good stability toward treatment with different solvents (e.g., acetonitrile, methanol, ethanol, water, etc.) in experiments carried out at room temperature for long time periods (>24 h). In addition, the lack of PEO replacement by organic compounds having high affinity toward the parent silicate, such as dimethyl sulfoxide and crown ethers, indicates again the high stability of PEO-intercalated nanocomposites. On the other hand, treatment with salt solutions provokes the replacement of the interlayer cations without disruption of PEO. For example,  $\text{Na}^+$  ions in PEO/ $\text{Na}^+$ -MMT are easily replaced by  $\text{NH}_4^+$  or  $\text{CH}_3(\text{CH}_2)_2\text{NH}_3^+$  ions, after treatment (2 h) at room temperature with aqueous solution of their

chloride, perchlorate, and thiocyanate salts (1 N solutions), in a reversible process.

After that, Wu and Lerner [151] reported the intercalation of PEO in Na<sup>+</sup>-MMT and Na<sup>+</sup>-hectorite by using this method in acetonitrile, allowing stoichiometric incorporation of one or two polymer chains in between the silicate layers and increasing the intersheet spacing from 0.98 to 1.36 and 1.71 nm respectively. Study of the chain conformation using two-dimensional double-quantum nuclear magnetic resonance on <sup>13</sup>C enriched PEO intercalated in Na<sup>+</sup>-hectorite reveals that the conformation of the “-OC-CO-” bonds of PEO is 90 ± 5% *gauche*, inducing constraints on the chain conformation in the interlayer [157].

Recently, Choi et al. [162] prepared PEO/MMT nanocomposites by a solvent casting method using chloroform as a co-solvent. WAXD analyses and TEM observations respectively established the intercalated structure of these nanocomposites. Various other authors [163, 168] have also used same method and solvent for the preparation PEO/clay nanocomposites.

Vaia et al. [152] also applied the same method to intercalate PEO in Na<sup>+</sup>-MMT layers. Intercalation of PEO in layered silicate was accomplished by heating the PEO with the Na<sup>+</sup>-MMT at 80 °C. The WAXD patterns before any heating contain peaks characteristic of both Na<sup>+</sup>-MMT and crystalline PEO. After heating to 80 °C, the intensity of the peaks corresponding to the unintercalated silicate and crystalline PEO is progressively reduced while a set of new peaks corresponding to the PEO-intercalated MMT are observed signifying the completion of intercalation. Very recently Shen et al. [167] reported the preparation of PEO/OMLS nanocomposites using melt intercalation technique.

In order to discover the effect of thermal treatment on the amount of PEO and PE-PEG diblock copolymer intercalated into the layers of Na<sup>+</sup>-MMT and on ionic conductivity of PEO/Na<sup>+</sup>-MMT, Liao et al. [164] prepared PEO/Na<sup>+</sup>-MMT and PE-PEG diblock copolymer/Na<sup>+</sup>-MMT nanocomposites using a melt intercalation technique. It was found that PEO can be intercalated into the layers of Na<sup>+</sup>-MMT by simple mechanical blending and part of PE in PE-PEG diblock copolymers was also intercalated into the layers of Na<sup>+</sup>-MMT. The intercalated amount increases with thermal treatment time, which ultimately improves the ionic conductivity of the PEO/Na<sup>+</sup>-MMT nanocomposites. Recently, this method was successfully applied by Artzi et al. [101] for the preparation of ethylene-vinyl alcohol copolymer/clay nanocomposites.

### 5.2.7. PDMS/Clay Nanocomposites

PDMS/clay nanocomposites were synthesized by sonicating a mixture of silanol-terminated PDMS and a commercial organoclay at room temperature for 2 min [171]. Delamination of the silicate particles in the PDMS matrix was accomplished by suspending the organosilicate in PDMS at room temperature and sonicating. WAXD analyses of various nanocomposites revealed no distinct features in the low 2θ ranges indicating the formation of exfoliated nanocomposites.

### 5.2.8. LCP/Clay Nanocomposites

Vaia and Giannelis [26] reported the reversible intercalation between organoclay and LCP in the nematic state. Melt intercalation of a model main chain liquid crystalline co-polymer based on 4,4'-dihydroxy-*a*-methylstilbene and a 50:50 mole ratio mixture of heptyl/nonyl alkyl dibromide was accomplished by annealing a powder mixture of the polymer and organoclay within the nematic region of the polymer.

In another report, Chang et al. [177] have prepared nanocomposites of thermotropic liquid crystalline polyester (TLCP) and Cloisite 25A using a melt intercalation method above the melt transition temperature of the TLCP. Liquid crystallinity of the nanocomposites was observed when organoclay content was up to 6 wt%.

### 5.2.9. PBO/Clay Nanocomposites

Zhu et al. [76] used phosphonium salt for the first time for the modification of clay and then tried to find the differences between organo ammonium and phosphonium salt treatments of clay fillers in nanocomposites toward thermal stability.

This technique was successfully applied by Hsu and Chang [178] in order to prepare PBO/clay nanocomposite from a PBO precursor, polyhydroxyamide (PHA), and an organoclay. The PBO precursor was made by the low temperature polycondensation reaction between isophthaloyl chloride and 2,2-bis(3-amino-4-hydroxyphenyl) hexafluoropropane with an inherent viscosity of 0.5 dl/g. For the preparation of PBO/clay nanocomposite, the organoclay was first dispersed in dimethylacetamide in which PHA was dissolved. The PHA/clay film was obtained from solution casting and dried at 80 °C under vacuum. Finally PBO/clay nanocomposite was obtained by curing the film at 350 °C to form a benzoxazole ring. The WAXD pattern and TEM observation respectively established that silicate layers were delaminated in PBO/clay nanocomposite film.

### 5.2.10. Thermoset Epoxy/Clay Nanocomposites

The studies of thermoset epoxy (EPR) systems were concerned with the ring-opening polymerization of epoxides to form polyether nanocomposites. This chemistry was followed by studies of both rubbery and glassy thermoset EPR/clay nanocomposites using different types of amine curing agents. The mechanisms leading to the monolayer exfoliation of clay layers in thermoset epoxy systems have been greatly elucidated. In addition, the polymer/clay interfacial properties have been shown to play a dominant role in determining the performance benefits derived from nanolayer exfoliation.

Messersmith and Giannelis [184] first reported the preparation of epoxy resin based nanocomposites of organoclay. They have analyzed the effect of different curing agents and curing conditions in the formation of nanocomposites based on the diglycidyl ether of bisphenol A (DGEBA) and a MMT modified by bis(2-hydroxyethyl) methyl hydrogenated to allow alkylammonium cation. They found that this modified clay dispersed readily in DGEBA when sonicated for a short time period as determined by the increase in viscosity at relatively low shear rates and the transition of the

suspension from opaque to semitransparent. The increase in viscosity was attributed to the formation of a so-called "house-of-cards" structure in which edge-to-edge and edge-to-face interactions between dispersed layers form a percolation structure. WAXD patterns of uncured clay DGEBA also indicate that intercalation occurred during and that this intercalation improves going from room temperature to 90 °C.

After that Wang and Pinnavaia [186] reported the preparation of PCNs of epoxy resin in the DGEBA, and the concomitant delamination of acidic forms of MMT at elevated temperature using the self-polymerization technique. They used a series of acidic cation such as  $H^+$ ,  $NH_4^+$ , and acidic onium ions of the type  $[H_3N(CH_2)_{n-1}COOH]^+$ ,  $[H_3N(CH_2)_nNH_2]^+$ ,  $[H_3N(CH_2)_nNH_3]^{+2}$  ( $n = 6$  and  $12$ ) for the modification of MMT, carried out the polymerization-delamination process over the temperature range of 198–287 °C, and found that the EPR-clay delamination temperature (PDT) was dependent on the heating rate and nature of the cation used for the modification of clay. In general, the PDT increased with decreasing cation acidity and basal spacing of the clay.

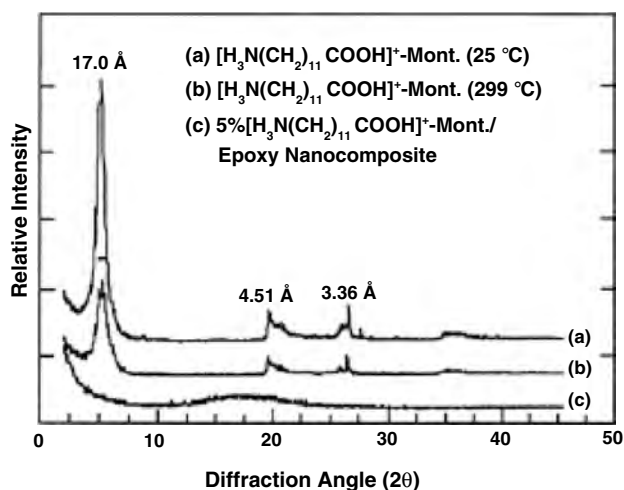
The delamination of MMT in the polymerized epoxy resin was confirmed by X-ray powder diffraction (XRD) as shown by the powder patterns in Figure 17a and b where  $[H_3N(CH_2)_{11}COOH]^+$ -MMT remains crystalline over the temperature range 25–229 °C. However, no diffraction peaks were observed for a 5:95 (w/w) clay/polyether nanocomposite formed from  $[H_3N(CH_2)_{11}COOH]^+$ -MMT at 229 °C (see Fig. 17c). Only a very diffuse scattering characteristic of the amorphous polyether appears in the XRD pattern of the composite. The absence of a 17-Å peak for  $[H_3N(CH_2)_{11}COOH]^+$ -MMT suggests that the clay particles have been exfoliated and the 9.6-Å-thick clay layers dispersed at the molecular level. TEM provides unambiguous evidence for the delamination of the MMT in the polyether

matrix. PDT values and thermodynamic data for MMT-polyether nanocomposites formed from bifunctional onium ion MMT, onium ion  $NH_4^+$ , and  $H^+$  MMT are respectively presented in Tables 3 and 4.

In another study, Lan and Pinnavaia [185] have reported the preparation of PCNs with a rubber-epoxy matrix obtained from DGEBA derivatives cured with a diamine so as to reach subambient glass transition temperatures. It has been shown that depending on the alkyl chain length of modified MMT, an intercalated and partially exfoliated or a totally exfoliated nanocomposite can be obtained. Lan et al. [187] have also studied other parameters such as the nature of alkyl ammonium cations present in the gallery and the effect of the cation exchange capacity of the MMT when DGEBA was cured with *m*-phenylene diamine. The same kind of study was also conducted by Zilg et al. [194] who cured DGEBA with hexahydrophthalic acid anhydride in the presence of different types of clays and also modified them with a wide variety of surfactants.

Recently, Kornmann et al. [201] reported the synthesis of epoxy-based nanocomposites using two different types of MMT clays with different CECs in order to investigate the influence of the CEC of the MMT clay on the synthesis and structure of nanocomposites. The CEC of any clay is a very important factor during nanocomposite synthesis because it determines the amount of surfactants which can be intercalated between the silicate layers. In this context, the swelling behavior is of critical importance to the final nanocomposite structure. For the preparation of nanocomposites both MMT clays were modified with octadecylammonium cation, and a nanocomposite synthesis procedure was the same as that used by previous authors. From WAXD patterns, it has been found that an MMT with a low CEC is exfoliated already during swelling in the epoxy resin prior to curing. A possible mechanism explaining this phenomenon is homopolymerization of the EPR during the swelling phase, causing diffusion of new epoxy molecules into the clay galleries. The large amount of space available between the layers favors the diffusion. The swelling duration of the clay with high CEC is shown to be critical for the synthesis of an exfoliated nanocomposite. Regarding the structure, TEM observations reveal interlamellar spacing of 90 Å (low CEC) and 110 Å (high CEC). However, multiplatelets of nonexfoliated layers were also observed. In summary, these nanocomposites contain clay/polymer composite particles consisting of inhomogeneously distributed silicate layer aggregates with polymer between these layers.

A group of researchers [203] from Australia has recently reported the morphology, thermal relaxation, and mechanical properties of PCNs of high-functionality epoxy resins. Three different types of resins used were bifunctional DGEBA, trifunctional triglycidyl *p*-amino phenol (TGAP), and tetrafunctional tetraglycidyl diamino diphenylmethane (TGDDM) and all were cured with diethyltoluene diamine (DETDA). The structures of all resins and curing agents are presented in Table 5. MMT modified with octadecylammonium cation was used for the preparation of nanocomposites. The PCNs were prepared using the previously reported method. In a typical synthesis, organoclay was first dispersed in the resin at 80 °C using a stirrer at 500 rpm.



**Figure 17.** XRD powder patterns for a freeze-dried  $[H_3N(CH_2)_{11}COOH]^+$ -MMT, (b)  $[H_3N(CH_2)_{11}COOH]^+$ -MMT freeze-dried and then heated at 229 °C, and (c) clay-polyether nanocomposite containing 5 wt%  $[H_3N(CH_2)_{11}COOH]^+$ -MMT. Reprinted with permission from [186], M. S. Wang and T. J. Pinnavaia, *Chem. Mater.* 7, 468 (1995). © 1995, American Chemical Society.

**Table 3.** PDT values and thermodynamic data for polyether/clay nanocomposites formed from bifunctional onium ion-MMT.

Interlayer cation	Initial basal spacing (Å)	PDT <sup>a</sup> (°C)	Heat of reaction (J/g)	Heat of polym <sup>b</sup> (kJ/mol)
[H <sub>3</sub> N(CH <sub>2</sub> ) <sub>11</sub> COOH] <sup>+</sup>	17.0 ± 0.1	229 ± 1	572 ± 16	228 ± 6
[H <sub>3</sub> N(CH <sub>2</sub> ) <sub>5</sub> COOH] <sup>+</sup>	13.3 ± 0.0	248 ± 1	565 ± 06	225 ± 2
[H <sub>3</sub> N(CH <sub>2</sub> ) <sub>12</sub> NH <sub>3</sub> ] <sup>2+</sup>	13.4 ± 0.1	271 ± 1	566 ± 08	225 ± 3
[H <sub>3</sub> N(CH <sub>2</sub> ) <sub>6</sub> NH <sub>3</sub> ] <sup>2+</sup>	13.1 ± 0.1	273 ± 2	568 ± 07	226 ± 3
[H <sub>3</sub> N(CH <sub>2</sub> ) <sub>12</sub> NH <sub>2</sub> ] <sup>+</sup>	13.5 ± 0.0	281 ± 2	563 ± 07	224 ± 3
[H <sub>3</sub> N(CH <sub>2</sub> ) <sub>6</sub> NH <sub>2</sub> ] <sup>+</sup>	13.2 ± 0.1	287 ± 2	557 ± 03	222 ± 2

Note: The clay:polymer composition was 5:95 (w/w).

<sup>a</sup> PDT is the onset temperature for epoxide polymerization–clay delamination at a heating of 20 °C/min.

<sup>b</sup> Heat of reaction for two epoxide equivalents.

Source: Reprinted with permission from [186], M. S. Wang and T. J. Pinnavaia, *Chem. Mater.* 7, 468 (1995). © 1995, American Chemical Society.

After mixing the resin–organoclay blend for 30 min the curing agent was added and the system kept under vacuum for another 60–90 min at around 70 °C. The blends were then cured for 2 h at 100 °C, 1 h at 130 °C, 12 h at 160 °C followed by a postcure for 2 h at 200 °C.

The morphology of the cured samples was investigated using WAXD and different microscopy techniques. Figure 18a represents the WAXD patterns of the MMT concentration series showing that the organoclay with an initial *d*-spacing of 2.3 nm is mainly exfoliated in the DGEBA-based system. On the other hand, high content (10 wt%) organoclay shows intercalated structure, while for DGEBA-based systems, resins of higher functionality show distinctive peaks even at low organoclay loading, indicating that these nanocomposites have a lower degree of exfoliated structure. WAXD patterns are shown in Figure 18b for TGAP and Figure 18c for TGADDM based nanocomposites of MMT. In case of any nanocomposite system, the peak observed around 2.5 nm correlates to the (002) plane and therefore represents only half the distance of the *d*-spacing.

Figure 19a and b represents atomic force microscopy (AFM) phase contrast images of the DGEBA nanocomposite containing 5 wt% layered silicate. Individual layers cannot be seen by AFM as they usually are by the TEM. A striated structure, however, can be seen with increasing phase intervals at the top of the picture. So from the AFM images it is established that silicate layers are not homogeneously distributed in the matrix, and some stacked layers are present.

Very recently, Chen et al. [204] synthesized epoxy-MMT nanocomposite using a surface initiated method in order to understand the interlayer expansion mechanism and

thermal–mechanical properties of these nanocomposites. MMT modified with bis-2-hydroxyethyl methyl tallow ammonium cation (C30B) was used as OMLS for nanocomposite synthesis. 3,4-Epoxycyclohexylmethyl-3,4-epoxycyclohexane carboxylate was used as epoxy monomer, and hexahydro-4-methylphthalic anhydride (HHMPA), ethylene glycol (EG), and benzyldimethylamine (BDMA) were respectively used as curing agent, initiator, and catalyst during synthesis. In a typical preparative method, the epoxy monomer HHMPA was mixed in a molar ratio of epoxide groups to HHMPA of 1:0.87. The resulting mixture was denoted as the *resin* by the authors. To the resin was added a specific weight percent of the resin weight either as EG, BDMA, or C30B. All materials were then blended using an orbital mixture, until the blend become bubble free and homogeneously mixed. The blended samples were then immediately cured first isothermally for up to 8 h at temperatures ranging from 70 to 140 °C, followed by 8 h at 180 °C, and finally 12 h at 220 °C under vacuum.

The curing mechanism for an epoxy-anhydride system with an alcohol initiator is shown in Figure 20. Amine catalysts like BDMA were added to the mixture to accelerate the reaction by facilitating the ring opening of epoxy groups. Several published papers indicate that intragallery onium ions can catalyze the epoxy curing reaction and thus lead to favorable conditions for obtaining exfoliated PCNs. To understand fully in case of this system, Chen et al. [204] verify that the cross-linking reactions in the presence of C30B were due to hydroxy initiation and not due to catalytic reactions. For this reason, the extent of reaction of a resin containing C30B was compared to the extent of reaction for a neat resin and resins containing either EG

**Table 4.** PDT values and thermodynamic data for polyether/clay nanocomposites formed from onium ion, NH<sub>4</sub><sup>+</sup>, and H<sup>+</sup> MMT.

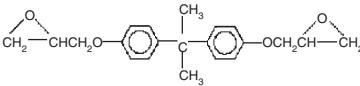
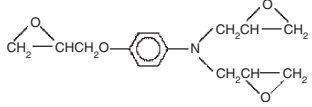
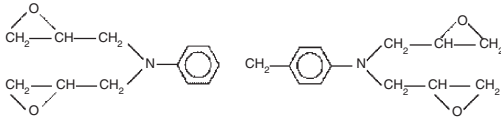
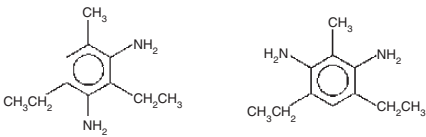
Interlayer cation	Initial basal spacing (Å)	PDT <sup>a</sup> (°C)	Heat of reaction (J/g)	Heat of polym <sup>b</sup> (kJ/mol)
[H <sub>3</sub> N(CH <sub>2</sub> ) <sub>11</sub> CH <sub>3</sub> ] <sup>+</sup>	15.9 ± 0.2	198 ± 1	550 ± 3	219 ± 2
[H <sub>3</sub> N(CH <sub>2</sub> ) <sub>5</sub> CH <sub>3</sub> ] <sup>+</sup>	14.9 ± 0.1	287 ± 1	554 ± 6	220 ± 3
NH <sub>4</sub> <sup>+</sup>	12.5 ± 0.1	247 ± 1	554 ± 5	220 ± 2
H <sup>+</sup>	13.9 ± 0.1	231 ± 1	555 ± 12	221 ± 5

<sup>a</sup> The PDT is the onset temperature for epoxide polymerization–clay delamination at a heating rate of 20 °C/min and a composite a clay:polymer composition of 5:95 (w/w).

<sup>b</sup> Heat of polymerization for two epoxide equivalents.

Source: Reprinted with permission from [186], M. S. Wang and T. J. Pinnavaia, *Chem. Mater.* 7, 468 (1995). © 1995, American Chemical Society.

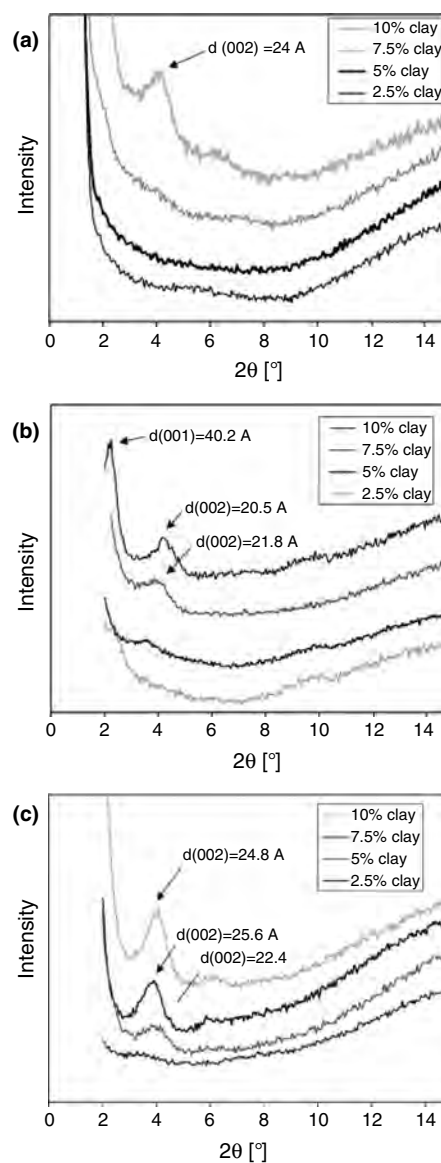
**Table 5.** Epoxy resins and hardener as used for nanocomposite synthesis.

Substance	Formula
DGEBA	
TGAP	
TGDDM	
DETDA	

Source: Reprinted with permission from [203], O. Becker et al., *Polymer* 43, 4365 (2002). © 2002, Elsevier Science.

or BDMA. As seen in Figure 21, the curing kinetics of the resin-C30B system more closely resembles the curing kinetics of the resin-EG system than the resin-BDMA system. This is a direct indication that the nanocomposites predominantly cured via initiation by the surfactant hydroxy groups and not by catalytic means. Figure 21 also shows that the curing rate of the pristine resin is significantly lower than the other mixtures. This highlights an important prerequisite for interlayer expansion, which is that extragallery polymerization rates should be slower than intragallery polymerization rates.

Time-resolved high-temperature XRD was used to probe the expansion behavior of the silicate layers during curing of the PCNs, and Figure 22 represents a plot of the results of a PCN containing 15 wt% C30B held isothermally at 70 °C. In Figure 23, the changes in *d*-spacing are plotted against the isothermal cure time for various clay loadings and cure temperature. On the basis of various characterization methods, the authors proposed an exfoliation mechanism of surface-initiated epoxy nanocomposites consisting of three stages. In the first stage, the interlayer expansion induced by intragallery polymerization must overcome any polymer chains that bridge the silicate layers. The interlayer expansion cannot proceed beyond the first stage if the number of bridging units becomes too great. The second stage was characterized by a steady and linear increase in interlayer spacing and accounts for the majority of the total expansion realized. During this stage, the silicate layers could be monitored via isothermal DSC experiments. Also, for samples that exhibited a large increase in interlayer expansion, it was found that the activation energy associated with the interlayer expansion was less than the activation energy associated with the curing. The reverse was true for samples that showed no increase in interlayer spacing. In the



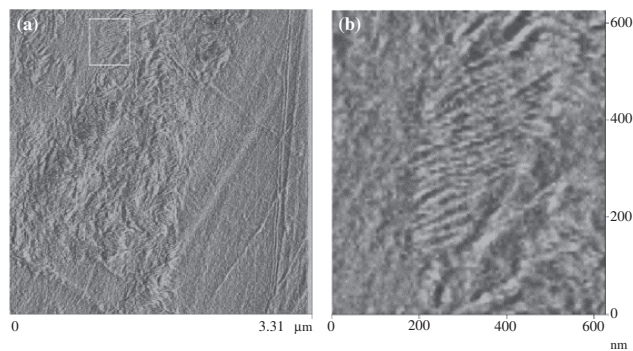
**Figure 18.** WAXD patterns of (a) DETDA cured DGEBA nanocomposites, (b) DETDA cured TGAP nanocomposites, and (c) DETADA cured TGDDM nanocomposites containing 0–10 wt% organoclay. Reprinted with permission from [203], O. Becker et al., *Polymer* 43, 4365 (2002). © 2002, Elsevier Science.

third stage, the interlayer expansion slowed then stopped, and in some cases decreased slightly. This was ascribed to the evolving modulus of the extragallery polymer such that the interlayer expansion stopped when the modulus of the extragallery polymer became equal to or exceeded the modulus of the intragallery polymer.

### 5.2.11. PU/Clay Nanocomposites

Chen et al. [207] have used a PCL-based nanocomposite synthesis technique for the preparation of novel segmented PU/clay nanocomposites articulated on diphenylmethane diisocyanate, butanediol, and preformed polycaprolactone diol. Even if the mechanism proposed for the chemical link

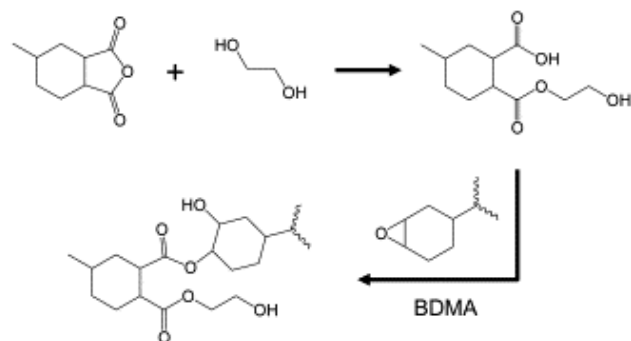




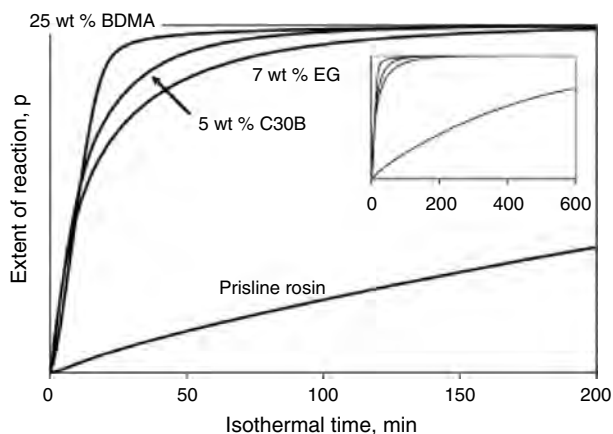
**Figure 19.** Phase contrast AFM images of DETDA cured DGEBA containing 5 wt% organoclay. Reprinted with permission from [203], O. Becker et al., *Polymer* 43, 4365 (2002). © 2002, Elsevier Science.

between the nanofiller surface and the polymer does not appear appropriate, they succeeded in producing a material where the nanofiller acts as a multifunctional chain extender inducing the formation of star-shaped segmented polyurethane. Recently, Wang and Pinnavaia [206] reported the preparation of polyurethane-MMT nanocomposites using a direct *in-situ* intercalative polymerization technique. More recently, Yao et al. [209] reported the preparation of a novel kind of PU/MMT nanocomposite using a mixture of modified 4, 4'-di-phenylmethylete diisocyanate (M-MDI), modified polyether polyol (MPP), and Na<sup>+</sup>-MMT. In a typical synthetic route a known amount of Na<sup>+</sup>-MMT was first mixed with 100 mL of MPP and then stirred at 50 °C for 72 h. Then the mixture of MPP and Na<sup>+</sup>-MMT was blended with a known amount of M-MDI and stirred for 30 s at 20 °C, and finally curing was conducted at 78 °C for 168 h.

Biomedical PUU/MMT (modified with dimethyl ditalow ammonium cation) nanocomposites were prepared by adding organoclay suspension in toluene dropwise to the solution of PUU in *N, N*-dimethylacetamide (DMAC) [210]. The mixture was then stirred overnight at room temperature. The solution was degassed, and then films were cast on to round glass Petri dishes. The films were air-dried for 24 h and subsequently dried under vacuum at 50 °C for 24 h. WAXD analyses indicated the formation



**Figure 20.** Schematic illustration of generalized curing reaction involving the epoxy monomer, HHMPA, EG, and BDMA. Reprinted with permission from [204], J. S. Chen et al., *Polymer* 43, 4895 (2002). © 2002, Elsevier Science.



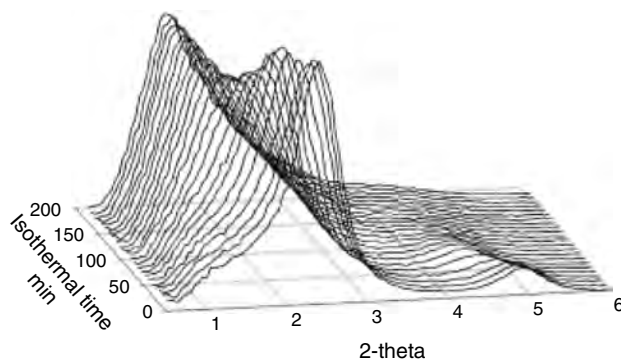
**Figure 21.** Extent of reaction of a neat resin and resins containing either C30B, EG, or BDMA. The inset shows the same data but for longer reaction. Reprinted with permission from [204], J. S. Chen et al., *Polymer* 43, 4895 (2002). © 2002, Elsevier Science.

of intercalated nanocomposites but they did not report any TEM photographs.

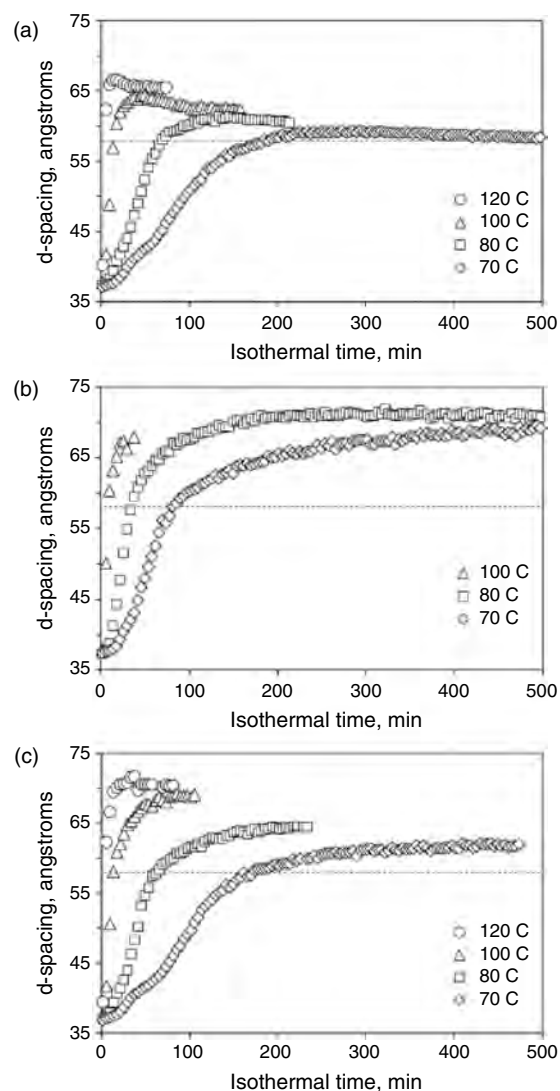
### 5.2.12. Polyimide/Clay Nanocomposites

Yano et al. [209] have conducted the preparation of polyimide/MMT nanocomposites from a DMAC solution of poly(amic acid) and a DMAC dispersion of MMT modified with dodecylammonium cation. Table 6 shows the dispersibility of various kinds organically modified MMTs in DMAC and the average diameter of organophilic MMTs obtained from the dynamic light scattering experiment. In case of 12CH<sub>3</sub>-MMT, MMT appeared to disperse in DMAC homogeneously and the average diameter of the dispersed MMT particles was the smallest of all. Another interesting aspect is that as the carbon number of the surfactant increases, the hydrophilicity of the organophilic MMT decreases. Table 6 also indicates that 10–12 carbon atoms are appropriate for organophilic MMT to be dispersed in DMAC.

In another report [226] polyimide/MMT nanocomposites were prepared using a solvent cast method from solution of poly(amic acid) precursors and the dodecyl-MMT using



**Figure 22.** TT-XRD of a resin containing 15 wt% C30B held isothermally at 70 °C. Reprinted with permission from [204], J. S. Chen et al., *Polymer* 43, 4895 (2002). © 2002, Elsevier Science.



**Figure 23.** Changes in  $d_{001}$  as a function of the curing time and temperature: (a) 5, (b) 10, and (c) 15 wt% silicate loading. The dashed lines denote the quantitative detection limit of the TT-XRD setup. Reprinted with permission from [204], J. S. Chen et al., *Polymer* 43, 4895 (2002). © 2002, Elsevier Science.

*N*-methyl-2-pyrrolidone as a solvent. The cured films of the rigid-rod polyimide/MMT nanocomposites as characterized by FTIR, TEM, and WAXD were exfoliated nanocomposites at low MMT content and partially exfoliated structure at high MMT content.

### 5.2.13. Polyetherimide/Clay Nanocomposites

PEI/MMT nanocomposites were prepared by melt blending of hexadecylamine modified MMT and PEI at 350 °C [231, 232]. WAXD patterns of various nanocomposites show no peaks but TEM observations show relatively stacked silicate layers not homogeneously dispersed in the polymer matrix. According to the authors, due to the strong interaction between PEI and organoclay, the nanocomposites exhibited a substantial increase at glass transition tem-

**Table 6.** Dispersibility and average diameter of organically modified MMT in DMAC.

Intercalated salts	Dispersibility of organophilic MMT in DMAC	Average diameter <sup>a</sup> ( $\mu\text{m}$ )
<i>n</i> -Octyltrimethylammonium chloride	not dispersible	—
Ammonium salt of dodecylamine (12CH <sub>3</sub> -MMT)	dispersible	0.44
Ammonium salt of 12-aminododecanoic acid (12COOH-MMT)	partly dispersible	3.75
<i>n</i> -Decyltrimethylammonium chloride (C10A-MMT)	„	0.61
<i>n</i> -Dodecyltrimethylammonium chloride	not dispersible	—
<i>n</i> -Hexadecyltrimethylammonium chloride	„	—
<i>n</i> -Dioctadecyldimethylammonium chloride	„	—
<i>n</i> -Triocetyltrimethylammonium chloride	„	—
<i>n</i> -Benzyltrimethylammonium chloride	„	—

<sup>a</sup> Values of average diameter are much bigger than 200 nm, because an average diameter from light scattering measurement includes solvent around a substance.

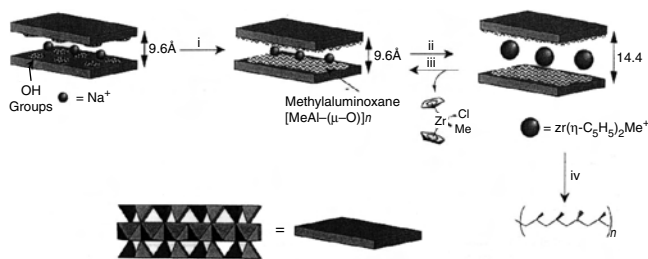
perature  $T_g$ , thermal decomposition temperature, a drastic decrease in solvent uptake, etc., compared to the virgin PEI but they did not check the stability of intercalated salt in organoclay at this high temperature of mixing.

### 5.3. Polyolefins

PP [9, 14, 15, 25, 30, 233–266], PE [267–273], polyethylene oligomers [274], copolymers like poly(ethylene-co-vinyl acetate) (EVA) [275], and ethylene propylene diene methylene linkage rubber (EPDM) [276, 277] have also been used.

#### 5.3.1. PP/Clay Nanocomposites

Tudor et al. [235] first used this *in-situ* intercalative polymerization method for the preparation of PP/clay nanocomposites. They have demonstrated the ability of soluble metallocene catalyst to intercalate inside silicate layers and to promote the coordination polymerization of propylene. Accordingly, a synthetic hectorite (Laponite RD) was first treated with methylaluminoxane (MAO) in order to remove all the acidic protons and to prepare the inter-layer spacing to receive the transition metal catalyst. It has to be noted that MAO is commonly used in association with metallocenes to produce coordination catalysts active in olefin polymerizations. During this first treatment step, WAXD analysis showed no noticeable increase of the layer spacing, although the diffraction peak broadened slightly, but the increase in Al content and complete disappearance of Si–OH signals from infrared spectra agree with the MAO reaction/adsorption inside the layered silicate galleries. Upon the addition of the metallocene catalyst ( $[\text{Zr}(\eta\text{-C}_3\text{H}_5)_2\text{Me}(\text{THF})]^+$ ), a cation exchange reaction occurs between Na<sup>+</sup> in MAO treated hectorite and the metallocene catalyst as demonstrated by an increase in the inter-layer spacing of 0.47 nm, consistent with the size of the species. Details can be seen in Figure 24. Using a synthetic fluorinated mica-type layered silicate that is deprived from any protons in the galleries, the catalyst was even



**Figure 24.** Schematic illustration of the modification and ion exchange of Laponite with  $[\text{Zr}(\eta\text{-C}_3\text{H}_5)_2\text{Me}(\text{thf})]\text{BPh}_4$  and propene polymerization. Details regarding the reagent and conditions are shown in relevant reference. Reprinted with permission from [235], J. Tudor et al., *Chem. Commun.* 2031 (1996). © 1996, Royal Chemical Society.

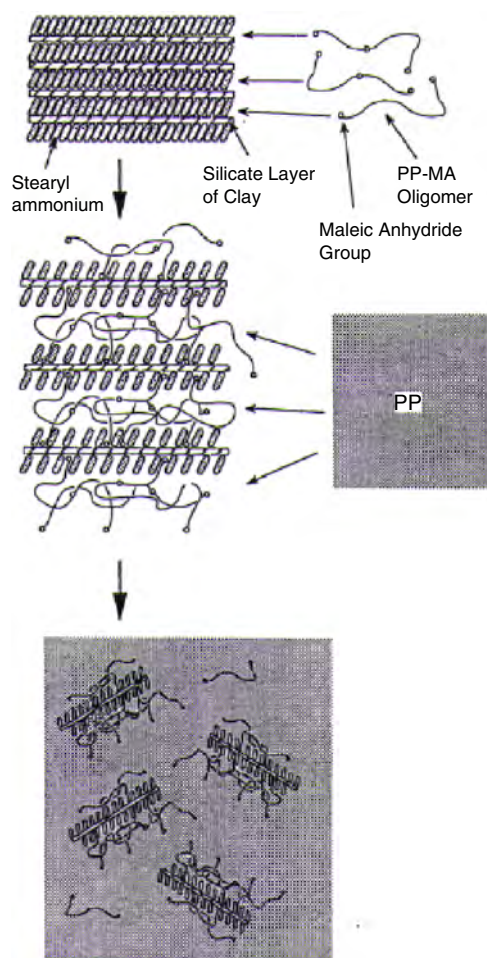
intercalated directly within the silicate layers without the need for MAO treatment. These two modified layered silicates catalyzed with reasonably high activity with the polymerization of propylene when contacted with an excess of MAO, producing PP oligomers. Unfortunately, the authors did not report any characterization of these composites, so one cannot make claims about the morphology. In another recent publication, Sun and Garces [259] have reported the preparation of PP/clay nanocomposites by *in-situ* intercalative polymerization with metallocene/clay catalysts.

Usuki et al. [239] first reported a novel approach to prepare PP/clay nanocomposites using functional oligomer with polar telechelic OH groups (PP-OH) as compatibilizer.

In this approach, first PP-OH intercalates between the layers of  $2\text{C}_{18}$ -MMT, the second step was the melt mixing of PP-OH/ $2\text{C}_{18}$ -MMT with PP, and the nanocomposite with intercalated structure was obtained. Further study by the same group [14] reported the preparation of PP/MMT nanocomposites by melt blending of PP, maleic anhydride grafted PP oligomer (PP-MA), and clays modified with stearyl ammonium using a twin-screw extruder. In their study, they used two different types of maleic anhydride modified PP oligomer with different amounts of maleic anhydride groups and two types of organically modified clays to understand the miscibility effect of the oligomers on the dispersibility of the organoclay in PP matrix, and to study the effect of hybridization on their mechanical properties when compared with neat PP and PP/clay nanocomposites without oligomers.

WAXD analyses and TEM observations respectively established the intercalated structure for all nanocomposites. On the basis of WAXD patterns and TEM images, they proposed a possible mechanism for dispersion of intercalated clay layers in the PP matrix. Figure 25 shows a schematic presentation of the mixing process of the three components (i.e., PP, PP-MA, and OMLS) into the nanocomposites. Authors believe that the driving force of the intercalation originates from the maleic anhydride group and the oxygen groups of the silicate through hydrogen bond.

In a recent report, Hasegawa et al. [240] found that PP-MA was able to intercalate into the intergalleries of OMLS, as like the functional oligomer, and they described a facile approach for the preparation of PP/clay nanocomposite using a PP-MA and organically modified clay by a melt intercalation technique. In a typical preparative

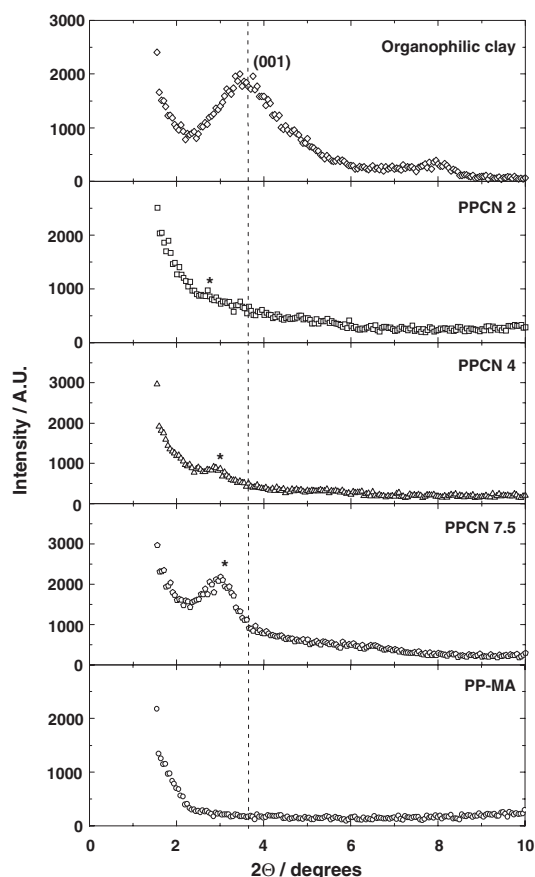


**Figure 25.** Schematic representation of the dispersion process of the organoclay in the PP matrix with the aid of PP-Mas. Reprinted with permission from [239], A. Usuki et al., *J. Appl. Polym. Sci.* 63, 137 (1997). © 1997, Wiley-VCH.

method, PP/clay nanocomposite pellets were prepared by a melt blending of pellets of PP-MA and the powder of  $\text{C}_{18}$ -MMT at  $200\text{ }^\circ\text{C}$  using a twin-screw extruder.

The same authors [245] also prepared polyethylene-propylene rubber (EPR)/ $\text{C}_{18}$ -MMT nanocomposites by melt blending of EPR-g-MA and  $\text{C}_{18}$ -MMT powder using a twin-screw extruder, and then tried to compare the morphology of EPR based nanocomposites with PP/clay nanocomposites.

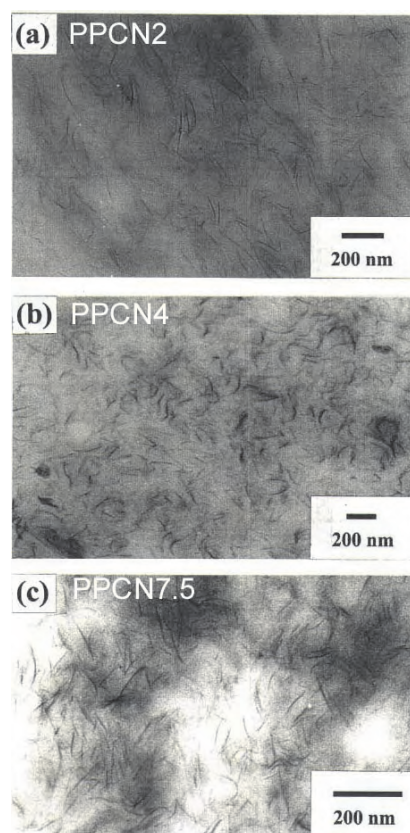
Recently, Nam et al. [30] prepared PP/MMT nanocomposites using the same method as used by previous authors. For example a mixture of PP-MA (0.2 wt% MA) and  $\text{C}_{18}$ -MMT was melt extruded at  $200\text{ }^\circ\text{C}$  in a twin-screw extruder. They prepared PCNs with three different amounts of clay content (inorganic part) of 2, 4, and 7.5 wt%, which were correspondingly abbreviated as PPCN2, PPCN4, and PPCN7.5 respectively. The WAXD patterns of  $\text{C}_{18}$ -MMT, PP-MA, and various PPCNs are presented in Figure 26. WAXD patterns clearly established near to exfoliate structure is formed with PPCN2, disordered intercalated nanocomposite is formed in case of PPCN4, while PPCN7.5 represents an ordered intercalated structure. These features are clearly observed with bright field



**Figure 26.** WAXD patterns for organoclay, PP-MA, and various PPCNs. The dashed lines indicate the location of the silicate (001) reflection of organoclay. The asterisks indicate a remanent shoulder for PPCN2 or a small peak for PPCN4. Reprinted with permission from [30], P. H. Nam et al., *Polymer* 42, 9633 (2001). © 2001, Elsevier Science.

TEM images of various PPCNs as shown in Figure 27. In order to understand the hierarchical structure of PPCNs they also used polarizing optical microscopy, light scattering, and small angle X-ray diffraction for the characterization of PPCNs along with WAXD and TEM. On the basis of these analyses they demonstrated the dispersed clay and interfibril structure of PPCNs. The schematic illustration of this structure is presented in Figure 28.

In another publication [253], Liu and Wu have reported the preparation of PPCN via grafting-melt compounding using a new type of co-intercalated organophilic clay which has a larger interlayer spacing than the ordinarily organophilic clay that is only modified with alkyl ammonium cation. One of the co-intercalation monomers is unsaturated so it could tether on the PP backbone by virtue of grafting reaction. The co-intercalated organophilic clay (EM-MMT) was prepared as follows: 130 g hexadecylammonium modified MMT ( $C_{16}$ -MMT) and 20 g epoxypropyl methacrylate were mixed in a Hake Reocorder 40 mixer for 1 h. Before mixing with clay, the initiator of grafting reaction, dibenzoyl peroxide, and donor agent were dissolved in epoxypropyl methacrylate. The nanocomposites were prepared using a twin-screw extruder with a screw speed of 180 rpm and operated at temperature around 200 °C. WAXD patterns

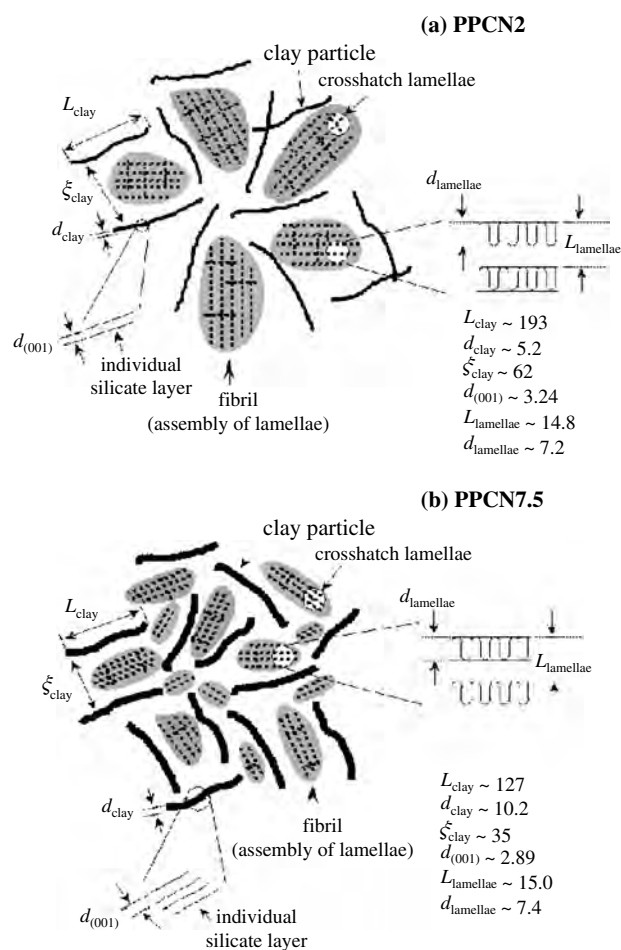


**Figure 27.** Bright field TEM images of PPCNs: (a) 2, (b) 4, and (c) 7.5 wt% MMT. The dark lines are the cross sections of silicate layers and the bright areas are the PP-MA matrix. Reprinted with permission from [30], P. H. Nam et al., *Polymer* 42, 9633 (2001). © 2001, Elsevier Science.

and TEM observations established that the larger interlayer spacing and strong interaction caused by grafting can improve the dispersion effect of silicate layers in the PP matrix.

Recently, Manias et al. [254] reported the preparation of PP/organically modified MMT, having a coexisting intercalated and exfoliated structure by the melt intercalation technique. They prepared nanocomposites two different ways: (a) by introducing functional groups in PP and using common alkylammonium MMT and (b) by using neat/unmodified PP and a semifluorinated surfactant modification for the MMT.

Kaempfer et al. [264] reported the preparation of new PCNs via melt compounding of syndiotactic polypropylene (sPP) containing organoclay and *in-situ* formed core/shell nanoparticles. Melt compounding of sPP with organohectorite, obtained via cation exchange of fluohectorite with octadecylammonium cation, in a co-rotating twin-screw extruder represents an attractive new route to reinforced sPP with considerably higher stiffness. The matrix reinforcement is achieved by *in-situ* formation of silicate nanoparticles via exfoliation combined with simultaneous *in-situ* encapsulation of the resulting nanosilicates in a thin shell of iPP-graft-MA. The resulting anisotropic core/shell type nanoparticles, containing stacks of organohectorite layer as



**Figure 28.** The schematic illustration for dispersed clay structure and the interfibrillar structure for PPCNs with: (a) 2 and (b) 7.5 wt% MMT. Reprinted with permission from [30], P. H. Nam et al., *Polymer* 42, 9633 (2001). © 2001, Elsevier Science.

core and iPP-graft-MA as shell, represent a very effective new class of nucleating agents for sPP crystallization.

### 5.3.2. PE/Clay Nanocomposites

PE/clay nanocomposites have also been prepared by the *in-situ* intercalative polymerization of ethylene using so-called polymerization filling technique [272]. Pristine MMT and hectorite were first treated with trimethyl-aluminum-depleted methylaluminumoxane before being contacted by a Ti-based constrained geometry catalyst. The nanocomposite was formed by addition and polymerization of ethylene. In the absence of a chain transfer agent, ultrahigh molecular weight polyethylene was produced. The tensile properties of these nanocomposites were poor and essentially independent of the nature and content of the silicate. Upon hydrogen addition, the molecular weight of the polyethylene was decreased with parallel improvement of mechanical properties. The formation of exfoliated PCNs was established using WAXD and TEM analyses. In another report, Heinemann et al. [268] prepared (co)polyolefin/clay nanocomposites using this method.

MA grafted polyethylene (PE-MA)/clay nanocomposites were also prepared by a melt intercalation technique [271].

The extent of exfoliation and intercalation completely depends on the hydrophilicity of polyethylene grafted with MA and the chain length of the organic modifier in the clay. When the number of methylene groups in alkylamine (organic modifier) was larger than 16, the exfoliated nanocomposite was obtained, and the maleic anhydride grafting level was higher than about 0.1 wt% for the exfoliated nanocomposite with the clay modified with dimethyl dehydrogenated tallow ammonium cation or octadecylammonium cation.

Very recently, EPDM/clay nanocomposites have been prepared by mixing EPDM with OMLS via a vulcanization process [276]. They used thiuram and dithiocarbamate for the vulcanization accelerator.

## 5.4. Specialty Polymers

In addition to the aforementioned conventional polymers, several interesting developments have also taken place in the preparation of nanocomposites of layered silicates with some specialty polymers including the *N*-heterocyclic polymers like polypyrrole (PPY) [278–283], poly(*N*-vinylcarbazole) (PNVC) [284, 285], and polyaromatics such as polyaniline (PANI) [286–300], poly(*p*-phenylene vinylene) [301], and related polymers [302]. PPY and PANI are known to display electric conductivity [303], and PNVC is well known for its high thermal stability and characteristic optoelectronic properties [304–307]. Some research has also been initiated with liquid crystalline polymer based nanocomposites [308–312] and hyperbranch polymers (HBP) [313].

### 5.4.1. PNVC/Clay Nanocomposites

Biswas and Sinha Ray [284] first reported the preparation of PNVC/MMT nanocomposites by direct polymerization of *N*-vinylcarbazole (NVC) (solid or in solution) in the presence of MMT without the use of any free-radical initiator. Melt polymerization of NVC in MMT (at 70 °C) as well as solution (in benzene) polymerization of NVC in the presence of MMT at 50 °C resulted in the formation of PNVC/MMT nanocomposite with intercalated structure. After repeated benzene extraction of prepared nanocomposites, intercalated PNVC could not be removed, while all the surface-adsorbed PNVC was extracted with benzene. WAXD analyses confirmed intercalation of PNVC in MMT interlayer galleries.

According to the authors, the initiation in the NVC/MMT system was suggested to be cationic involving Brønsted acid sites in MMT arising from the dissociation of interlayer water molecules coordinated to the exchangeable cations [284]. Yet another possibility, especially with NVC, was that the transition metal oxides ( $\text{Fe}_2\text{O}_3/\text{TiO}_2$ ) present in MMT could also lead to cationic initiation of NVC. The same authors subsequently reported that direct interaction of MMT with pyrrole led only to ca. 5% yield of PPY in 3 h while ANI could not be polymerized by MMT [281]. According to them, such a trend is possibly not surprising since NVC is relatively more susceptible to cationic polymerization compared to the latter monomers.

Further work by Sinha Ray and Biswas, in the study of a NVC/MMT polymerization/nanocomposite formation

system, the addition of  $\text{FeCl}_3$  was considered to be interesting. Results of a recent study [285] indicated that in a NVC-MMT polymerization/nanocomposite formation system addition of  $\text{FeCl}_3$  increased the percentage loading of PNVC in the composite.

#### 5.4.2. PANI/Clay and PPY/Clay Nanocomposites

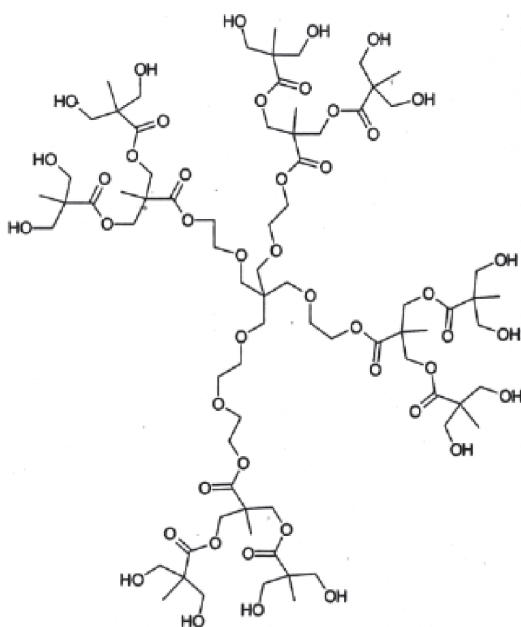
Polymerization vis-a-vis nanocomposite formation in PY/MMT-water and ANI/MMT-water systems was possible after using  $\text{FeCl}_3$  and  $(\text{NH}_4)_2\text{S}_2\text{O}_8$  [281, 287] as oxidant respectively in the two systems.

Kim et al. [286] first used this method for the preparation of PANI/MMT nanocomposite using dodecylbenzenesulfonic acid (DBSA) and camphorsulphonic acid (CSA) as dopant. In a typical synthetic method,  $\text{Na}^+$ -MMT was first dispersed in an aqueous medium and then sonicated by using an ultrasonic generator. The DBSA or CSA dopants were dissolved in distilled water and mixed with ANI monomer solution at a 1:1 molar ratio; then the emulsion solutions were mixed in a four-neck reactor by stirring while the temperature was kept at 25 °C. The oxidant initiator,  $(\text{NH}_4)_2\text{S}_2\text{O}_8$  solution, was dropped into the reactor. The WAXD analysis clearly indicates the formation of intercalated nanocomposites.

In another recent publication, Kim et al. [283] reported the preparation of intercalated PPY/ $\text{Na}^+$ -MMT nanocomposite via an inverted emulsion pathway method.

#### 5.4.3. HBP/Clay Nanocomposites

Very recently, Plummer et al. [313] have used this method for the preparation of HBP/MMT nanocomposites. The chemical structure of the HBP is presented in Figure 29. The



**Figure 29.** Chemical structure of the dendrimer analog of the second pseudo-generation HBP. Reprinted with permission from [313], C. J. G. Plummer et al., *Chem. Mater.* 14, 486 (2002). © 2002, American Chemical Society.

PCNs were prepared by introducing the required amount of  $\text{Na}^+$ -MMT to 10 g of HBP dispersed in 75 mL of boiling deionized water. The mixture was stirred in air at 50 °C with a magnetic stir bar. After evaporation of half the water, the resulting gel was transferred to an open silicone rubber mold and dried in air for 2 days at 50 °C. The remaining solid was then dried for another 2 days at 120 °C under vacuum, ground, and pressed into 25-mm diameter, 1-mm thick disks at 60 °C for WAXD analyses. At high  $\text{Na}^+$ -MMT contents, WAXD analyses indicated 2.5–2.8, 2.8–3, and 3.6–3.9 nm silicate layer basal spacing for the second, third, and fourth pseudo-generation HBPs, respectively, as opposed to 1.06 nm for the as-received  $\text{Na}^+$ -MMT. The corresponding WAXD peaks disappeared as the clay content was reduced to below 20 wt% for all the HBPs, consistent with the previous study by Strawhecker and Manias [87]. TEM images of nanocomposite containing 20 wt%  $\text{Na}^+$ -MMT revealed stacks of 5–10 silicate layers with a relatively well-defined spacing, interspersed with exfoliated silicate layers. At 10 wt% MMT, however, exfoliation was confirmed to dominate.

### 5.5. Biodegradable Polymers

Recently, some groups have started the preparation, characterization, and materials properties of various kinds of biodegradable polymers/nanocomposites having properties suitable for a widerange of applications. So far reported biodegradable polymers for the preparation of nanocomposites are polylactide (PLA) [34, 314–324], poly(butylene succinate) (PBS) [325–328], PCL [13, 133–140], unsaturated polyester [329], polyhydroxy butyrate [330], and aliphatic polyester [331–334].

#### 5.5.1. PLA/Clay Nanocomposites

Sinha Ray et al. [34, 315] first reported the preparation of intercalated PLA/layered silicate nanocomposites. For nanocomposite (PLACNs) preparation  $\text{C}_{18}$ -MMT and PLA were first dry mixed by shaking them in a bag. The mixture was then melt-extruded by using a twin-screw extruder operated at 190 °C to yield very light gray color strands of PLACNs. Nanocomposites loaded with a very small amount of oligo-PCL as a compatibilizer were also prepared in order to understand the effect of oligo-PCL on the morphology and properties of PLACNs [34]. The compositions of various nanocomposites of PLA with  $\text{C}_{18}$ -MMT are summarized in Table 7. WAXD patterns of a series of nanocomposites are shown in Figure 30. Figure 31 represents the TEM photographs of nanocomposites corresponding to the WAXD patterns. On the basis of WAXD analyses and TEM observation, they calculated form factors (see Table 8), that is, average length ( $L_{\text{clay}}$ ), thickness ( $d_{\text{clay}}$ ) of the stacked intercalated silicate layers, and the correlation length ( $\xi_{\text{clay}}$ ) between them (see Fig. 3). These data clearly established that silicate layers of the clay were intercalated and randomly distributed in PLA matrix. Incorporation of very small amount of oligo-PCL as a compatibilizer in the nanocomposites lead to a better parallel stacking of the silicate layers and also much stronger flocculation due to the hydroxylated edge–edge interaction of the silicate layers. Owing to the interaction between clay platelets and

**Table 7.** Composition and characteristic parameters of various PLACNs based on PLA, oligo-PCL, and C<sub>18</sub>-MMT.

Sample	Composition (wt%)			$M_w \times 10^{-3}$ (g/mol)	$M_w/M_n$	$T_g$ (°C)	$T_m$ (°C)	$\chi_c$ (%)
	PLA	Oligo-PCL	C <sub>18</sub> -MMT <sup>b</sup>					
PLACN1	97		3 [2.0]	178	1.81	60.0	169	50.65
PLACN2	95		5 [3.0]	185	1.86	60.0	170	39.01
PLACN3	93		7 [4.8]	177	1.69	59.8	170	43.66
PLACN4	94.8	0.2	5 [3.3]	181	1.76	58.6	170	41.47
PLACN5	94.5	0.5	5 [3.3]	181	1.76	57.6	169	32.91
PLACN6	93	2.0	5 [2.8]	180	1.76	54.0	168	—
PLACN7	92	3.0	5 [2.4]	181	1.77	51.0	168	—
PLA <sup>a</sup>	100			187	1.76	60.0	168	36.24
PLA1	99.8	0.2		180	1.76	58.0	168.5	46.21
PLA2	99.5	0.5		180	1.76	57.0	168.8	52.51
PLA3	98	2.0		180	1.76	54.7	169	—

<sup>a</sup>  $M_w$  and PDI of extruded PLA (at 190 °C) are  $180 \times 10^3$  (g/mol) and 1.6 respectively.

<sup>b</sup> Values in brackets indicate the amount of clay (inorganic part) content after burning.

<sup>c</sup> The degree of crystallinity.

the PLA matrix in the presence of a very small amount of oligo-PCL, the disk–disk interaction plays an important role in determining the stability of the clay particles and hence the enhancement of mechanical properties of such nanocomposites.

In their further research [316–318, 324], they prepared a series of PLACNs with various types of organoclay in order to investigate the effect of organoclay on the morphology, properties, and biodegradability of PLACNs. Four different types of pristine layered silicates were used and each of them was modified with a different type of surfactant. Detailed specifications of various types of organoclay was used by them are presented in Table 9. On the basis of WAXD analyses and TEM observations, the authors concluded the formation of four different types of PLACNs. Ordered intercalated-and-flocculated nanocomposites were obtained when ODA was used as organoclay, disordered intercalated structure was found in case of PLA/SBE4 nanocomposite, PLA/SAP4 nanocomposite shows near to exfoliate nanocomposite, while the coexistence of stacked intercalated and exfoliated nanocomposite structure is found with PLA/MEE4 nanocomposite. So the nature of OMLS has a strong effect on the final morphology of PLA-based nanocomposites.

In a very recent work, Maiti et al. [319] have prepared a series of PLACNs with three different types of pristine layered silicate such as saponite, MMT, and mica, and each of them was modified with alkylphosphonium salts having various chain lengths. In their work they first try to find the effect of alkylphosphonium modifier of different chain lengths on the properties of organoclay and how the different clays behave differently having same organic modifier. Second, they study the effects of dispersion, intercalation, and aspect ratio of clay on materials properties. From the WAXD patterns it is clearly observed that the  $d$ -spacing (001) increases with increasing modifier chain length and for a fixed modifier it increases with increasing lateral dimension of the clay particle. We believe there are two reasons to observe this type of behavior: one is the CEC value and the other is the lateral size of various pristine layered silicates, and in both cases layered silicates follow the order

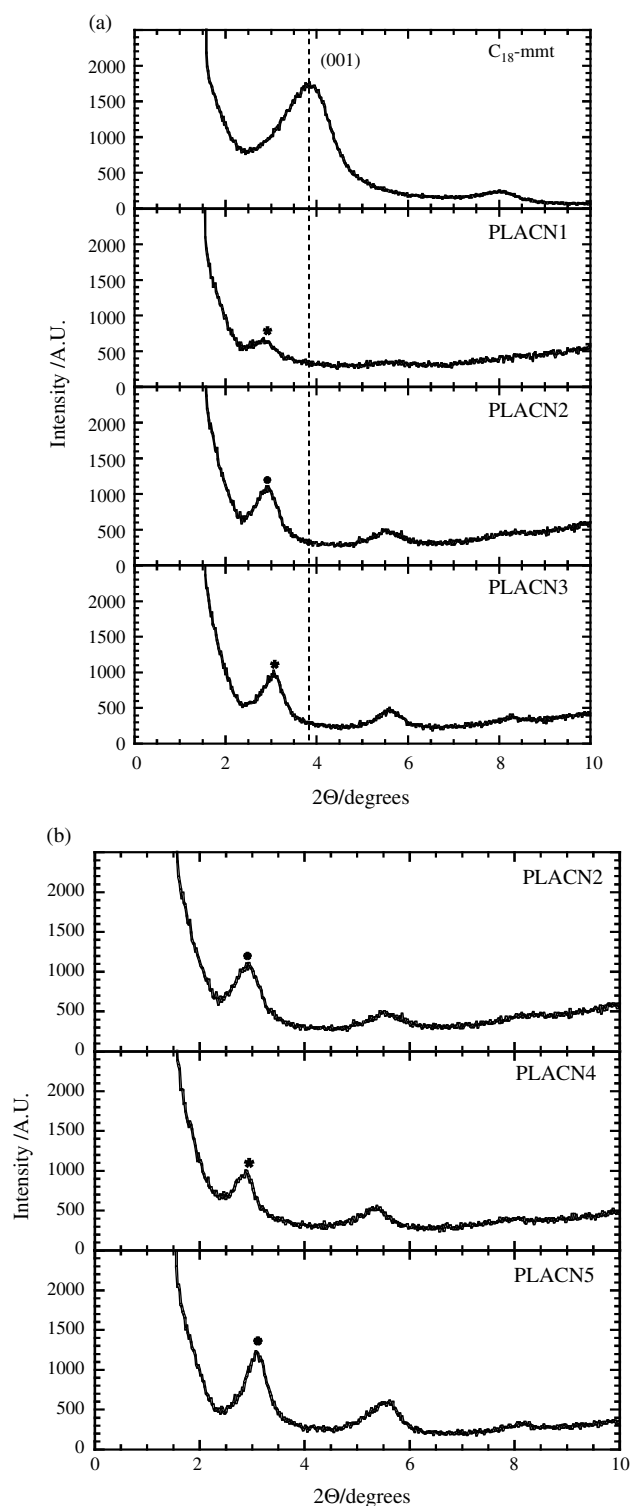
mica > MMT > saponite. According to the authors, out of two factors, the former factor is more important in controlling the  $d$ -spacing/stacking of silicate layers than that of the latter. Since mica has a high lateral size and also a high amount of surfactant molecules due to its high CEC value, surfactant chains inside the intergallery have restricted conformation due to physical jamming. According to them this physical jamming is smaller in case of saponite due to its lower CEC and smaller in lateral size. Therefore, the situation for OMLS, based on TEM and WAXD analyses, is schematically illustrated in Figure 32.

Figure 33 compares the WAXD patterns of nanocomposites with different clay dimensions having the same clay [ $n$ -hexadecyl tri- $n$ -butyl phosphonium bromide (C<sub>16</sub>)-modified] content (3 wt%). For MMT-based nanocomposite, the peaks are sharp and crystallite sizes are slightly less than those of the corresponding organoclay, indicating an almost ordered structure of MMT in nanocomposite. The peaks of the nanocomposites prepared with mica clay are very sharp, similar to those of corresponding organoclay, and slightly larger crystallite sizes indicate that the number of stacked silicate layers is the same to that of original organoclay but some amount of PLA is intercalated between the galleries, giving rise to a larger crystallite size. On the basis of WAXD patterns and crystallite size, stacking of silicate layers in the organoclays and in various nanocomposites prepared with three different organoclays is presented schematically in Figure 34.

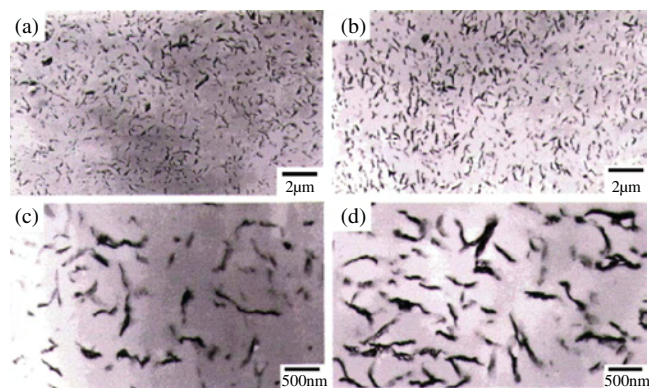
More recently Dubois et al. [320, 322] reported the preparation of plasticized PLA/MMT nanocomposites. The OMLS used was MMT modified with bis-(2-hydroxyethyl)methyl (hydrogenated tallowalkyl) ammonium cations. WAXD analyses have confirmed the formation of intercalated nanocomposites.

### 5.5.2. PBS/Clay Nanocomposites

Like PLA, PBS is also an aliphatic thermoplastic polyester with many interesting properties, including biodegradability, melt processability, and thermal and chemical resistance. Although these properties show the potential applications of PBS, some of the other properties such as softness, gas



**Figure 30.** WAXD patterns for  $C_{18}$ -MMT and various PLACNs: (a) without oligo-PCL and (b) with oligo-PCL. The dashed line in each figure indicates the location of the silicate (001) reflection of  $C_{18}$ -MMT. The asterisks indicate the (001) peak for  $C_{18}$ -MMT dispersed in PLA matrices. Reprinted with permission from [34], S. Sinha Ray et al., *Macromolecules* 35, 3104 (2002). © 2002, American Chemical Society.



**Figure 31.** TEM bright field images: (a) PLACN2 ( $\times 10000$ ), (b) PLACN4 ( $\times 10000$ ), (c) PLACN2 ( $\times 400000$ ), and (d) PLACN4 ( $\times 40000$ ). The dark entities are the cross section of intercalated organoclay, and the bright areas are the matrices. Reprinted with permission from [34], S. Sinha Ray et al., *Macromolecules* 35, 3104 (2002). © 2002, American Chemical Society.

barrier properties, flexural properties, etc. are frequently not enough for a wide range of applications. Sinha Ray et al. [325, 326] first reported the preparation of PBS/MMT nanocomposites (PBSCNs) by simple melt extrusion of PBS and OMLS, having properties suitable for a wide range of applications. MMT modified with octadecylammonium chloride was used as organoclay for nanocomposite preparation. In recent publications [327, 328], the same authors also reported the details of structure–property relationships in case of PBSCNs.

Recently, Lee et al. [332] have reported the preparation of biodegradable aliphatic polyester (APES)/organoclay nanocomposites using a melt intercalation method. Two kinds of organoclays, Cloisite 30B and Cloisite 10A with different ammonium cations located in the silicate galleries, were chosen for the nanocomposites preparation. The WAXD analyses and TEM observations respectively showed a higher degree of intercalation in case of APES/Cloisite 30B nanocomposites as compared to that of APES/Cloisite 10A nanocomposites. According to the authors, this behavior may be due the hydrogen-bonded interaction between APES and hydroxyl group in the galleries of Cloisite 30B nanocomposites than for the APES/Cloisite nanocomposites.

**Table 8.** Comparison of form factors between PLACN2 and PLACN4 obtained from WAXD patterns and TEM observations.

Form factors	PLACN2	PLACN4
<b>WAXD</b>		
$d_{001}$ (nm)	3.03	2.98
$d_{\text{clay}}$ (nm)	13	10
<b>TEM</b>		
$d_{\text{clay}}$ (nm)	$38 \pm 17.25$	$30 \pm 12.5$
$L_{\text{clay}}$ (nm)	$448 \pm 200$	$659 \pm 145$
$L_{\text{clay}}/d_{\text{clay}}$	12	22
$\xi_{\text{clay}}$ (nm)	$255 \pm 137$	$206 \pm 92$



**Table 9.** Specifications and designation of organoclay used for the preparation of PLACNs.

Clay codes	Pristine clay	Particle length (nm)	CEC (mequiv/100 gm)	Organic salt used for the modification of clay	Suppliers
ODA	MMT	150–200	110	octadecylammonium cation	Nanocor Inc., USA
SBE	MMT	100–130	90	trimethyloctadecylammonium cation	Hojun Yoko Co., Japan
MEE	synthetic F-mica	200–300	120	dipolyoxyethylene alkyl(coco) methylammonium cation	CO-OP Chemicals, Japan
SAP	Saponite	50–60	86.6	tributylhexadecylphosphonium cation	CO-OP Chemicals, Japan

## 6. MATERIALS PROPERTIES OF POLYMER/CLAY NANOCOMPOSITES

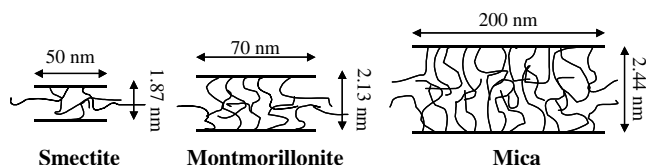
PCNs consisting of a polymer and clay (modified or not) frequently exhibit remarkably improved mechanical and materials properties as compared to those of pristine polymers containing a small amount of ( $\leq 5$  wt%) layered silicate. Improvements can include high moduli, increased strength and heat resistance, decreased gas permeability and flammability, and increased biodegradability of biodegradable polymers. The main reason for these improved properties in PCNs is interfacial interaction between matrix and layered silicate as opposed to conventional filler reinforced systems.

### 6.1. Mechanical Properties

#### 6.1.1. Dynamic Mechanical Analysis

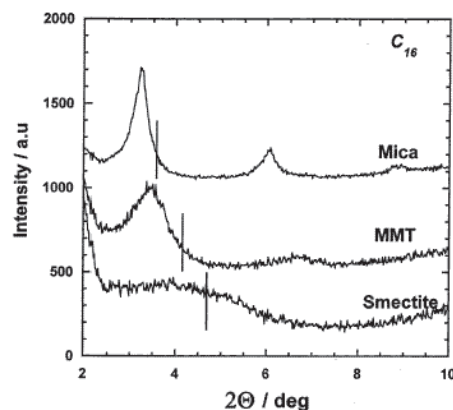
Dynamic mechanical analysis (DMA) measures the response of a given material to a cyclic deformation (here in tension–torsion mode) as a function of temperature. DMA results are expressed by three main parameters: (a) the storage modulus ( $G'$ ) corresponding to the elastic response to the deformation; (b) the loss modulus ( $G''$ ) corresponding to the plastic response to the deformation, and (c)  $\tan \delta$ , that is, the ( $G''/G'$ ) ratio, useful for determining the occurrence of molecular mobility transitions such as the glass transition temperature ( $T_g$ ).

In the temperature dependence of storage modulus  $G'$  and loss factor  $\tan \delta$  of the relevant PCNs, below the glass transition region, both samples exhibit high  $G'$  and restriction of a substantial drop in  $G'$  with increasing temperature.  $G'$  in the glassy region below  $T_g$  is approximately 50–100% higher in the nanocomposite compared with the blend systems without clays. The shift of  $\tan \delta$  reaches to higher temperatures and a decrease of the value indicates an increase in nanocomposite  $T_g$ . In some cases, the magnitude of the shift estimated by  $\tan \delta$  is about 10 °C or more [12]. These indicate that the interaction between polymer and silicate layers at the interface of layers and polymer

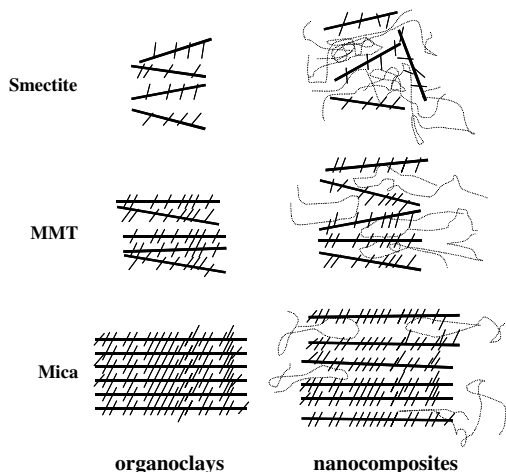


**Figure 32.** Schematic representation of organoclays with  $C_{16}$  ion. Reprinted with permission from [319], P. Maiti et al., *Chem. Mater.* 14, 4654 (2002). © 2002, American Chemical Society.

matrix could suppress the mobility in the polymer segments near the interface. That is, in both systems the intercalated nanocomposites are formed. The large aspect ratio of the structural hierarchy in the nanoscale level might lead to such a large enhancement in  $G'$  throughout the glassy and rubbery region. The temperature dependence of  $G'$  of the PPCNs is reported (Fig. 35) [30]. For all PPCNs, there is a strong enhancement of moduli in the investigated temperature range, which indicates that the plastic and as well as elastic response of PP toward deformation is strongly influenced in the presence of organoclay. Below,  $T_g$ , the enhancement of  $G'$  is clear in the intercalated PPCNs. The clay content dependence of  $G'$  is also reported (Fig. 36) [30].  $G'_{PPCN}$  and  $G'_{PP-MA}$  are the moduli of the intercalated PPCNs and the PP-MA, respectively. The large reinforcement in  $G'$  is observed in the figure. The essential factor governing the enhancement of mechanical properties is the aspect ratio of the dispersed clay particles. According to the Halpin–Tai theoretical expression on the enhancement of  $G'$  [335], the Einstein coefficient  $k_E$  was estimated by selecting an appropriate value for the best fit to the experimentally obtained  $G'_{PPCN}/G'_{PP-MA}$  versus volume fraction of the clay plots. The estimated values of  $k_E$  are about 60 for PPCN4 and about 31 for PPCN2 and PPCN7.5. In the intercalated PPCNs, the explanation for the enhancement of  $G'$  by only the  $k_E$  factor as discussed in the previous case of PMMA/clay nanocomposites [33] is hampered because each PPCN exhibits a different value of  $k_E$ , despite the different clay contents. In the case of intercalated PPCNs, the enhancement of  $G'$  is



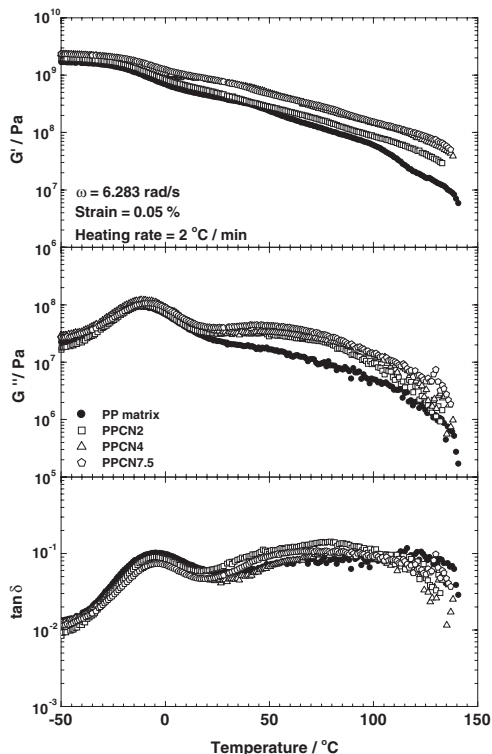
**Figure 33.** WAXD patterns of smectite, MMT, and mica nanocomposites with  $C_{16}$  organoclay and same clay content (3 wt%). Reprinted with permission from [319], P. Maiti et al., *Chem. Mater.* 14, 4654 (2002). © 2002, American Chemical Society.



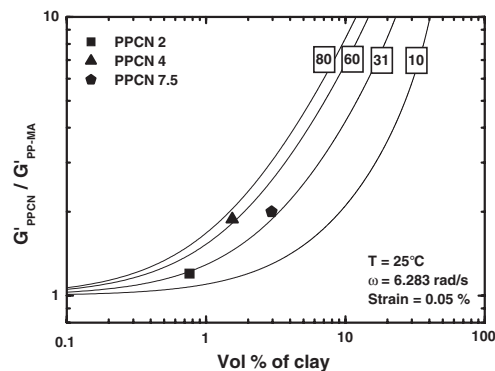
**Figure 34.** Schematic presentation of silicate layers in organoclay and in various nanocomposites. Reprinted with permission from [319], P. Maiti et al., *Chem. Mater.* 14, 4654 (2002). © 2002, American Chemical Society.

due to both the degree of the intercalation and the aspect ratio of the dispersed clay particles.

The two-dimensional aspect ratios of the dispersed clay particles  $L_{\text{clay}}/d_{\text{clay}}$  estimated from TEM observation are reported to be 37 for PPCN2, 20 for PPCN4, and 12 for PPCN7.5, respectively. In the PPCN4, despite the lower value of  $L_{\text{clay}}/d_{\text{clay}}$  compared to PPCN2 and low addition of the clay compared to PPCN7.5, this nanocomposite shows the highest value of  $k_E$ , suggesting that much higher



**Figure 35.** Temperature dependence of  $G'$ ,  $G''$ , and  $\tan \delta$  for PP-MA matrix and various PPCNs. Reprinted with permission from [30], P. H. Nam et al., *Polymer* 42, 9633 (2001). © 2001, Elsevier Science.



**Figure 36.** Plots of  $G'_{\text{PPCN}}/G'_{\text{PP-MA}}$  vs vol% of clay for PPCNs. The value of Einstein coefficient  $k_E$  was shown in the box. The theoretical lines show the results calculated by the Halpin–Tai expression with various  $k_E$ . Reprinted with permission from [30], P. H. Nam et al., *Polymer* 42, 9633 (2001). © 2001, Elsevier Science.

efficiency of the intercalation for the reinforcement is attained. The details were also reported in PBS/clay nanocomposites [325].

The remarkable improvement in  $G'$  related to the strong interaction between matrix and organoclay is clearly observed in case of Nylon 6/clay nanocomposites [336]. Table 10 represents the temperature dependence of  $G'$  and the thermal expansion coefficient ( $\alpha$ ) of the Nylon 6 matrix and various nanocomposites (N6CNs). They summarized the details in a dynamic temperature RAM test for neat Nylon 6 and various N6CNs. All N6CNs show a very high increment of moduli at all temperature ranges.

Increased  $G'$  related to the dimension of the dispersed clay particles is further demonstrated in case of PLACNs [34]. In order to understand the effect of compatibilizer on morphology and mechanical properties, the authors also prepared PLACNs with a very small amount of oligo-PCL. The details of composition and designation of various types of nanocomposites are presented in Table 7. The enhancement in  $G'$  clearly appears in different magnitudes at investigated temperature ranges for all PLACNs. This behavior indicates that the elastic properties of PLA are significantly affected in the presence of  $C_{18}$ -MMT. Below  $T_g$ , the enhancement of  $G'$  is also clear in case of various intercalated PLACNs. On the other hand, all PLACNs show much higher increments of  $G'$  at high temperature ranges compared to that of PLA matrices. This is due to both mechanical reinforcement by the clay particles and extended intercalation at high temperature [260]. Above  $T_g$ , when materials become soft, the reinforcement effect of the clay particles becomes prominent, due to restricted movement of the polymer chains, and hence strong enhancement of  $G'$ .

At the other extreme, PLACN4 and PLACN5 exhibit strong enhancement of  $G'$  as compared to that of the PLACN2 with comparable clay loading and PLA/o-PCL matrices containing 0.2 and 0.5 wt% oligo-PCL (see Table 8 and Fig. 31b). The presence of small amounts of oligo-PCL does not lead to a big shift and broadening of the  $\tan \delta$  curves. However, a large increment in  $G'$  above  $T_g$  became clear, indicating that the large anisotropy of the dispersed particles due to the flocculation enhanced the loss component.

**Table 10.** Summary of DMA test for Nylon 6 and various N6CNs under different temperature ranges.

Sample	Term	0 °C	25 °C	50 °C	100 °C	150 °C	200 °C
Nylon 6	$\alpha \times 10^5$ /cm/cm. °C	9.5	12	14	22	31	48
	$G'$ (GPa)	1.04	0.94	0.52	0.16	0.11	0.065
N6CN1.6	$\alpha \times 10^5$ /cm/cm. °C	8.9	9.7	11	16	22	60
	$G'$ (GPa)	1.2	1.1	0.8	0.41	0.27	0.01
N6CN3.7	$\alpha \times 10^5$ /cm/cm. °C	6.4	6.6	8.7	8.5	14	67
	$G'$ (GPa)	1.9	1.8	1.2	0.74	0.52	0.18
N6CN4.4	$\alpha \times 10^5$ /cm/cm. °C	7.1	7.7	9.8	11	15	42
	$G'$ (GPa)	1.4	1.3	0.95	0.56	0.38	0.14

The  $G'$  values of various PLACNs and corresponding matrices without clay at different temperature ranges are summarized in Table 11. PLACNs with a very small amount of oligo-PCL (PLACN4 and PLACN5) exhibit very high enhancement of mechanical properties as compared to that of PLACNs with comparable clay loading (PLACN2). The essential factor governing the enhancement of mechanical properties of the nanocomposites is the aspect ratio of the dispersed clay particles [335]. From the TEM figures (see Fig. 31) it is clearly indicated that, in the presence of a very small amount of oligo-PCL, flocculation of the dispersed clay particles took place again due to the edge-edge interaction of the clay particles. The two-dimensional aspect ratios of the dispersed clay particles  $L_{\text{clay}}/d_{\text{clay}}$  estimated from TEM observation are 22 for PLACN4 and 12 for PLACN2 (see Table 8) and there is hence strong enhancement of mechanical properties.

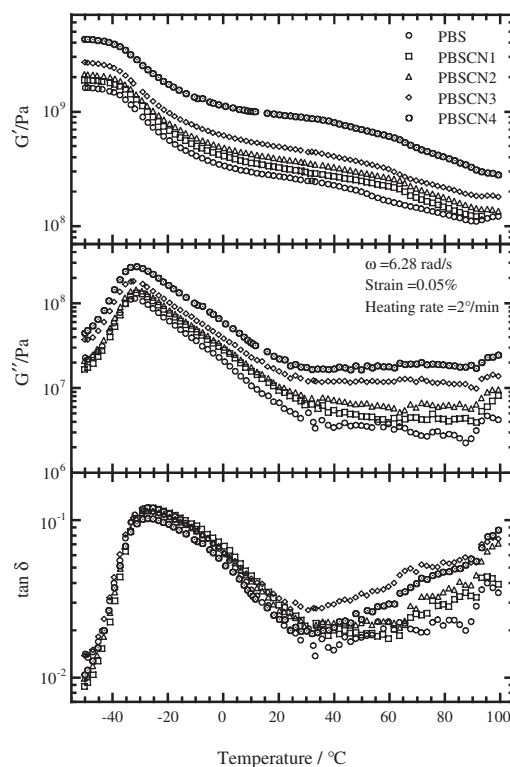
The increment in  $G'$  directly depends upon the aspect ratio of dispersed clay particles and is also clearly observed in case of PBSCNs. The temperature dependence of  $G'$  of PBS and various PBSCNs are reported (Fig. 37). The nature of enhancement of  $G'$  in PBSCNs with temperature is somewhat different from well-established intercalated PPCNs [30] and well-known exfoliated N6CN systems [105]. In the latter system, there is a maximum of 40–50% increment of  $G'$  compared to that of matrix at well below  $T_g$ , and above  $T_g$  there is a strong enhancement ( $>200\%$ ) in  $G'$ . This behavior is common for so far reported nanocomposites and the reason is the strong reinforcement effect of the clay

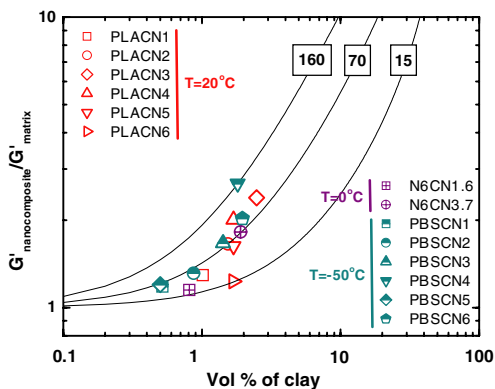
particles above  $T_g$  when materials become soft. But in case of PBSCNs, the order of enhancement of  $G'$  is almost same below and above  $T_g$ , and this behavior may be due to the extremely low  $T_g$  ( $-29$  °C) of PBS matrix. At the temperature range of  $-50$  to  $-10$  °C, the increments in  $G'$  are 18% for PBSCN1, 31% for PBSCN2, 67% for PBSCN3, and 167% for PBSCN4 compared to that of neat PBS. Furthermore at room temperature, PBSCN3 and PBSCN4 respectively show higher increments in  $G'$  of 82% and 248% than that of neat PBS, while those of PBSCN1 and PBSCN2 are 18.5% and 44% higher. At 90 °C, only PBSCN4 exhibits very strong enhancement of  $G'$  compared to that of the other three PBSCNs.

In Figure 38, Okamoto summarized the clay content dependence of  $G'$  of various types of nanocomposites obtained well below  $T_g$ . The Einstein coefficient  $k_E$  derived

**Table 11.**  $G'$  value of various PLACNs and corresponding matrices without clay at different temperature ranges.

Samples	Storage modulus $G'$ (GPa)			
	$-20$ °C	$40$ °C	$100$ °C	$145$ °C
PLACN1	2.32	2.07	0.16	0.09
PLACN2	2.90	2.65	0.25	0.10
PLACN3	4.14	3.82	0.27	0.19
PLACN4	3.71	3.21	0.43	0.16
PLACN5	3.04	2.60	0.32	0.16
PLACN6	2.08	1.97	0.23	0.08
PLACN7	1.86	1.76	0.16	0.07
PLA	1.74	1.60	0.13	0.06
PLA1	1.73	1.60	0.13	0.06
PLA2	1.68	1.55	0.12	0.06
PLA3	1.67	1.62	0.12	0.06

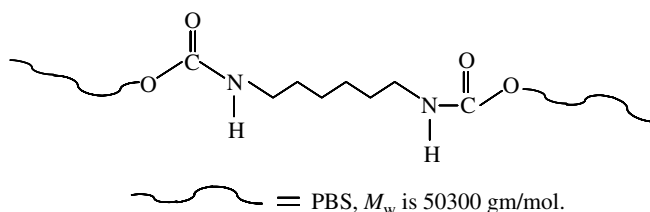
**Figure 37.** Temperature dependence of  $G'$ ,  $G''$ , and their ratio  $\tan \delta$  for PBSCNs (prepared with  $C_{18}$ -MMT) and neat PBS. Reprinted with permission from [328], K. Okamoto et al., *J. Polym. Sci. B*, in press.



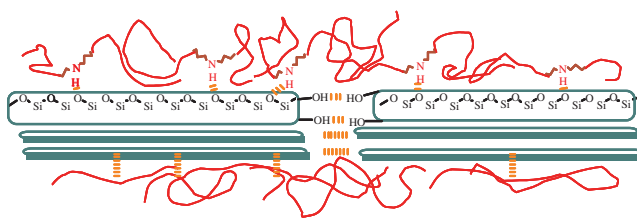
**Figure 38.** Plots of  $G'_{\text{nanocomposite}}/G'_{\text{matrix}}$  vs vol% of clay for various nanocomposites. The Einstein coefficient  $k_E$  is shown with the number in the box. The lines show the calculated results from the Halpin–Tai theory with various  $k_E$ .

using Halpin and Tai’s theoretical expression modified by Nielsen is shown in the figure and represents the aspect ratio ( $L_{\text{clay}}/d_{\text{clay}}$ ) of dispersed clay particles without intercalation.

From this figure, it is clearly observed that PBSCNs show very high increment in  $G'$  compared to other nanocomposites having the same content of clay in the matrix. PPCNs are well known for intercalated systems, N6CNs are well-established exfoliated nanocomposites, PLACNs are going to establish intercalated-and-flocculated nanocomposites, while PBSCNs are intercalated-and-extended flocculated nanocomposites systems [327, 328]. Due to the strong interaction between hydroxylated edge-edge groups, the clay particles are sometimes flocculated in the polymer matrix. As a result of this flocculation the length of the clay particles increases enormously and hence the overall aspect ratio. For the preparation of high molecular weight PBS, di-isocyanate end groups are generally used as a chain extender [336]. These isocyanate end group chain extenders make urethane bonds with hydroxy terminated low molecular weight PBS, and each high molecular weight PBS chain contains two such kinds of bonds (see schematic illustration in Fig. 39). These urethane type bonds lead to strong interaction with the silicate surface by forming hydrogen bonds and hence strong flocculation (see Fig. 40). For this reason, the aspect ratio of dispersed clay particles is much higher in case of PBSCNs compared to all nanocomposites, and hence there is a high enhancement of modulus.



**Figure 39.** Formation of urethane bondings in high molecular weight PBS.



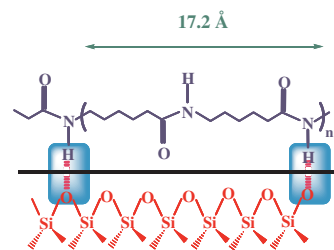
**Figure 40.** Formation of hydrogen bonds between PBS and clay, which leads to the flocculation of the dispersed silicate layers.

### 6.1.2. Tensile Properties

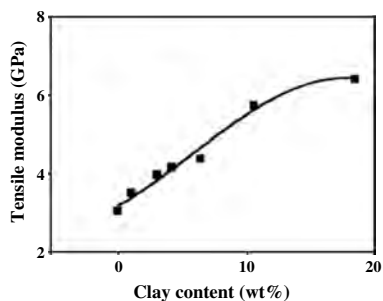
The tensile modulus of a polymeric material expressing the stiffness has shown to be remarkably improved when nanocomposites are formed with layered silicates. N6CNs prepared through the intercalative ring opening polymerization of  $\epsilon$ -caprolactam, leading to the formation of exfoliated nanocomposites, exhibit a drastic increase in the tensile properties at rather low filler content. The main reason for the drastic improvement of modulus in case of N6CNs is to the strong interaction between matrix and silicate layers via formation of hydrogen bonds as shown in Figure 41.

In case of nanocomposites, the extent of improvement of modulus directly depends upon the average length of the dispersed clay particles, hence the aspect ratio. Figure 42 represents the dependence of tensile modulus ( $E$ ) measured at 120 °C for exfoliated N6CNs with various clay contents obtained by *in-situ* intercalative polymerization of  $\epsilon$ -caprolactam in the presence of protonated aminododecanoic acid-modified MMT and saponite [2, 114]. Moreover, the difference in the extent of exfoliation, as observed for Nylon 6-based nanocomposite synthesized by *in-situ* intercalative polymerization of  $\epsilon$ -caprolactam using  $\text{Na}^+$ -MMT and various acids, strongly influenced the final modulus of nanocomposites.

In Table 12 we summarized the tensile modulus of 1pot-NCH together with neat Nylon 6 and N6CN (=NCH) [107]. The excellent modulus in case of 1pot-NCH can be considered to have its origin in the uniformly dispersed silicate layers. Furthermore, 1pot-NCH has much improved mechanical properties compared with NCH. The polymer matrix in nanocomposites prepared by 1pot synthesis is only the homopolymer of Nylon 6, whereas NCH prepared via intercalative ring-opening polymerization is a copolymer of Nylon 6 and a small amount of Nylon 12. The presence of Nylon 12 may give the low modulus. Various kinds of acids have been used to catalyze the polymerization. One



**Figure 41.** Schematic illustration of formation of hydrogen bonds in Nylon 6/MMT nanocomposite.

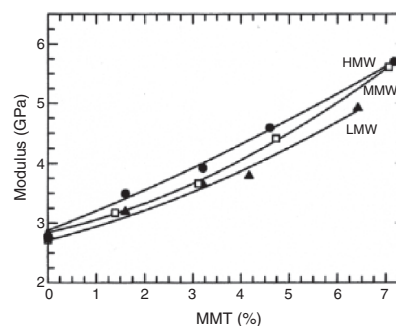


**Figure 42.** Dependence of tensile modulus ( $E$ ) on clay content measured at 120 °C. Reprinted with permission from [114], L. M. Liu et al., *J. Appl. Polym. Sci.* 71, 1133 (1999). © 1999, Wiley.

can observe variation of the modulus of the nanocomposites [107]. On the other hand, the WAXD peak intensity ( $I_m$ ) that is inversely related to the exfoliation of clay particles also depends on the nature of the acid used to catalyze the polymerization process. For an increase in the  $I_m$  values, a parallel decrease in the modulus is observed, indicating that exfoliated layers are the main factor responsible for the stiffness improvement, while intercalated particles, having a less important aspect ratio, rather play a minor role.

The effect of MMT content and N6 molecular weight on the tensile modulus of nanocomposites prepared using MMT modified with  $(HE)_2M_1R_1$  is shown in Figure 43 [119, 123]. The addition of organoclay leads to substantial improvement in stiffness for the composites based on each three Nylon 6 (e.g., LMW, MMW, and HMW). Interestingly, the stiffness increases with increasing matrix molecular weight at any given concentration even though the moduli of the neat Nylon 6 are all quite similar. In Table 13 we summarized the moduli and other mechanical properties of the virgin materials and selected  $(HE)_2M_1R_1$  Nylon 6/clay nanocomposites. The slightly larger modulus of 2.82 GPa for LMW may be the result of a higher degree of crystallinity resulting in faster crystallization kinetics during the cooling of the specimen during injection molding.

Similar trends with respect to the level of organoclay content and molecular weight are evident in the yield strength result. The dependence of yield strength on MMT content and molecular weight is shown in Figure 44. Yield strength increases with the content of MMT. However, the levels of strength improvement for the pure Nylon 6 are nearly



**Figure 43.** Effect of MMT content on tensile modulus for LMW-, MMW-, and HMW-based nanocomposites. Reprinted with permission from [119], T. D. Fornes et al., *Polymer* 42, 9929 (2001). © 2001, Elsevier Science.

identical. The HMW- and MMW-based nanocomposites show a steady increase in strength with content of clay, while the LMW-based nanocomposites show a less pronounced effect. The differences in strength improvement with respect to molecular weight are very prominent at the highest clay content. The increase in strength relative to the virgin matrix for the HMW composite is nearly double that of the LMW composite.

The relationship between MMT content and elongation at break for the different matrices is shown in Figure 45 for two different rates of extension. Figure 45a shows that the virgin polyamides are very ductile at a test rate of 0.51 cm/min. With increasing clay content the ductility gradually decreases; however, the HMW and MMW based composites show reasonable levels of ductility at MMT concentration as high as 3.5 wt%. Elongation at breaks for the LMW based nanocomposites decreases rapidly at low MMT content at around 1 wt%. The larger reduction in the LMW-based systems may be due to the presence of stacked silicate layers. On the other hand, at the higher testing rate of 5.1 cm/min, shown in Figure 45b, similar trends are observed, but the absolute levels of elongation at break values are significantly lower. Interestingly, the strain at break for LMW composites is relatively independent of rate of extension, similar to what has been observed in case of glass fiber reinforced composites. Even at the highest clay content, the HMW composite exhibits ductile fracture, whereas the LMW- and MMW-based nanocomposites fracture in a brittle manner at the highest clay content.

**Table 12.** Mechanical properties of 1pot-NCH synthesized in presence of phosphoric acid.

Mechanical properties	Method used	Nylon 6	NCH <sup>a</sup> (MMT = 4.7 wt%)	1pot-NCH (MMT = 4.1 wt%)
Tensile modulus (GPa)				
23 °C	ASTM-D 638M	1.11	1.87	2.25
120 °C	JIS-K 7113	0.19	0.61	0.67
Tensile strength (MPa)				
23 °C	ASTM-D 638M	68.6	97.2	102
120 °C	JIS-K 7113	26.6	32.3	34.7
HDT (°C at 1.82 MPa)	ASTM-D 648	65	152	160

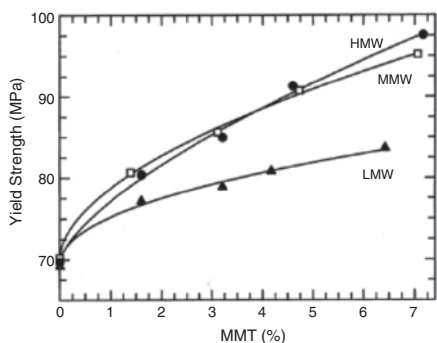
<sup>a</sup> Prepared by *in-situ* intercalative method.

**Table 13.** Mechanical properties of some Nylon 6/(HE)<sub>2</sub>M<sub>1</sub>R<sub>1</sub> nanocomposites.

N6/(HE) <sub>2</sub> M <sub>1</sub> R <sub>1</sub> Nanocomposites	Modulus (GPa)	Yield strength (MPa)	Strain <sup>a</sup> (%)	Elongation at break (%)		Izod impact strength (J/m)
				Crosshead speed		
				0.51 cm/min	5.1 cm/min	
<b>LMW</b>						
0.0 wt% MMT	2.82	69.2	4.0	232	28	36.0
3.2 wt% MMT	3.65	78.9	3.5	12	11	32.3
6.4 wt% MMT	4.92	83.6	2.2	2.4	4.8	32.0
<b>MMW</b>						
0.0 wt% MMT	2.71	70.2	4.0	269	101	39.3
3.1 wt% MMT	3.66	86.6	3.5	81	18	38.3
7.1 wt% MMT	5.61	95.2	2.4	2.5	5	39.3
<b>HMW</b>						
0.0 wt% MMT	2.75	69.7	4.0	3.4	129	43.9
3.2 wt% MMT	3.92	84.9	3.3	119	27	44.7
7.2 wt% MMT	5.70	97.6	2.6	4.1	6.1	46.2

<sup>a</sup> Strain at yield point measured during modulus and yield strength testing using a crosshead speed of 0.51 cm/min.  
 Source: Reprinted with permission from [119], T. D. Fornes et al., *Polymer* 42, 9929 (2001). © 2001, Elsevier Science.

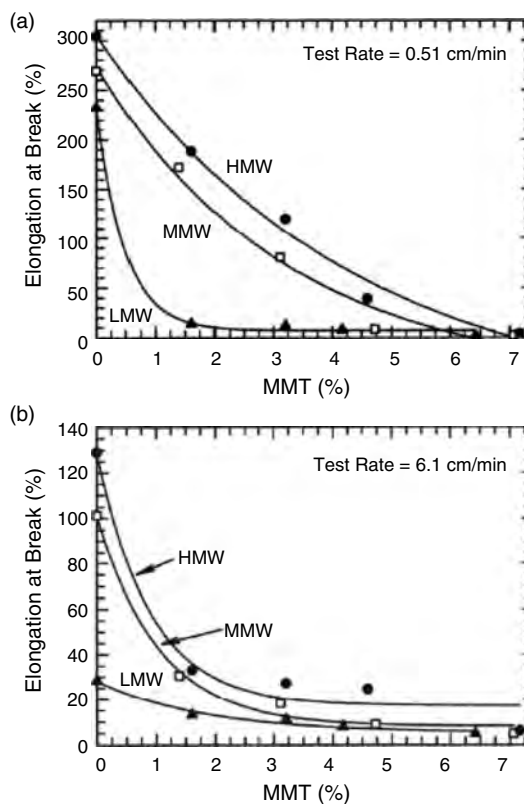
In case of PPCNs, most of the studies report tensile properties as a function of clay content [254]. Figure 46 shows an Instron study of a neat-PP/f-MMT (modified by alkyltrichlorosilane) composite compared to a PP/2C<sub>18</sub>-MMT “conventional” composite. In case of PPVNs, there is a sharp increase of tensile modulus for very small clay loading (≤3 wt%) followed by a much slower increase beyond clay loading of 4 wt%, and this is the characteristic behavior of PCNs. With increase clay content, the strength does not change markedly compared to the neat-PP value and there is only a small decrease in the maximum strain at break. PP systems—conventionally filled, with no nanometer-level dispersion by similar fillers—do not exhibit as strong improvement in their tensile modulus. On the other hand, as the PP/layered silicate interaction is improved, for example when MA functional groups are incorporated in the polymer, the stresses are much more effectively transferred from the polymer matrix to the inorganic filler, and thus a higher increase in tensile properties is expected. Figure 47a and b respectively represents MMT content dependence of tensile modulus and strength of various PPCNs prepared by melt extrusion of PP-MA and C<sub>18</sub>-MMT. The modulus of PPCNs systematically increases with



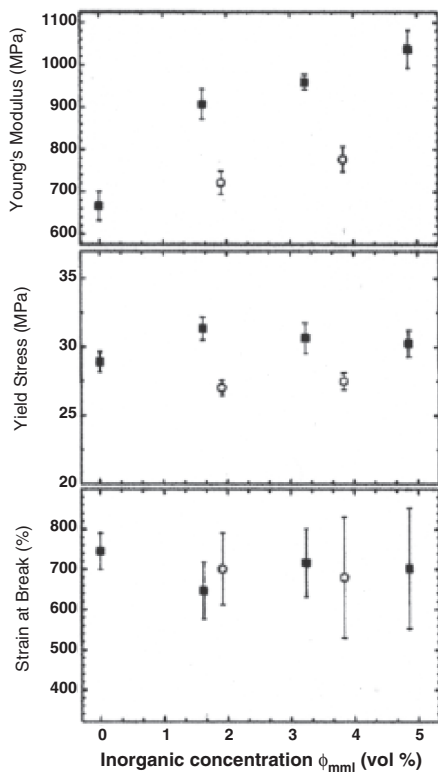
**Figure 44.** Effect of MMT content on yield strength for LMW-, MMW-, and HMW-Nylon 6 based nanocomposites. Reprinted with permission from [119], T. D. Fornes et al., *Polymer* 42, 9929 (2001). © 2001, Elsevier Science.

increasing clay content. The tensile strength also increases with increasing clay content up to 4 wt% and then levels off.

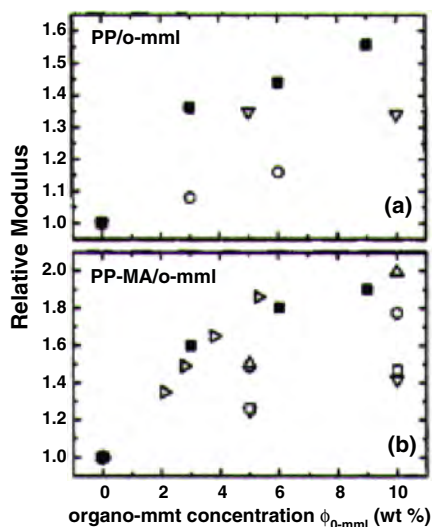
In case of nanocomposites if the systems are not thermodynamically favorable, these properties will be changed during processing because the nanocomposite structure will be changed during processing. A recent work by Reichert et al. [337] showing a systematic study of the dependencies



**Figure 45.** Effect of MMT content on elongation at break for LMW-, MMW-, and HMW-Nylon 6 based nanocomposites at a crosshead speed of (a) 0.51 and (b) 5.1 cm/min. Reprinted with permission from [119], T. D. Fornes et al., *Polymer* 42, 9929 (2001). © 2001, Elsevier Science.



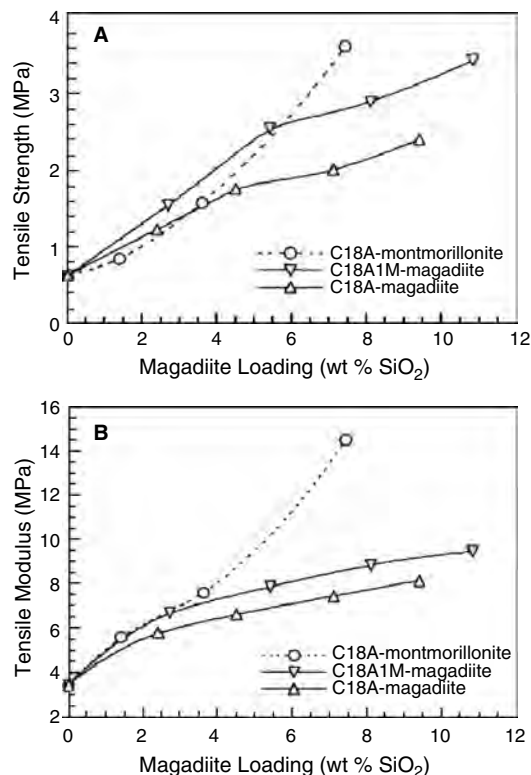
**Figure 46.** Tensile characterization of the PP/f-MMT nanocomposites (■) by Instron. For comparison, conventionally filled PP/2C<sub>18</sub>-MMT “macro” composites are also shown (○). Reprinted with permission from [254], E. Manias et al., *Chem. Mater.* 13, 3516 (2001). © 2001, American Chemical Society.



**Figure 47.** Relative moduli of various PP-based nanocomposites, each normalized by modulus of the respective neat PP. (a) PP-based nanocomposites with: f-MMT (■), C<sub>18</sub>-MMT (▽), and 2C<sub>18</sub>-MMT (○). (b) PP-MA/2C<sub>18</sub>-MMT nanocomposite (■) and PP hybrids with various PP-g-MA pretreated organically modified MMT: C<sub>18</sub>-MMT (right triangle open), C<sub>18</sub>-MMT (○, △), and C<sub>8</sub>-MMT (▽, □). Reprinted with permission from [254], E. Manias et al., *Chem. Mater.* 13, 3516 (2001). © 2001, American Chemical Society.

on compatibilizer functionality and organic modification revealed that considerable enhancement of tensile properties could be achieved only when appropriate PP-MA compatibilizers are used to pretreat the OMLS in conjunction with specific organic modification of the MMT. Similar materials under different processing conditions showed much smaller improvements in the practical materials properties [337].

The evolution of the tensile modulus for the epoxy matrix with three different types of layered silicates loading is presented in Figure 48 [191]. A C<sub>18</sub>-MMT, a C<sub>18</sub>A-magadiite, and magadiite modified with methyl-octadecylammonium cation (C<sub>18</sub>A1M-magadiite) were used for nanocomposite preparation. This figure shows much significant increase of the modulus for the MMT-based nanocomposites with the filler content of 4 wt%. According to the present authors, this behavior is due the difference in layer charge in magadiite and MMT. Organomagadiites have a higher layer charge density and subsequently higher alkylammonium content than organo-MMT. As the alkylammonium ions interact with the epoxy resin while polymerizing, dangling chains are formed, and more of this chain is thus formed in the presence of organomagadiites. These dangling chains are known to weaken the polymer matrix by reducing the degree of network cross-linking, then compromising the reinforcement effect of the silicate layer exfoliation.



**Figure 48.** A comparison of (A) the tensile strengths and (B) tensile moduli for epoxy nanocomposites prepared from C<sub>18</sub>A-MMT, C<sub>18</sub>A-magadiite, and C<sub>18</sub>A1M-magadiite. The silicate loading was determined by calcining the composites in air at 650 °C for 4 h at a heating rate of 2 °C/min. Reprinted with permission from [191], Z. Wang and T. J. Pinnavaia, *Chem. Mater.* 10, 1820 (1998). © 1998, American Chemical Society.

For thermoset matrices, a significant enhancement in the tensile modulus is observed for an exfoliated structure when alkylammonium cations with different chain length modified MMTs were used for nanocomposites preparations, with the exception that MMT modified with butylammonium only gives an intercalated structure with a low tensile modulus.

Zilg et al. [194] have reported the correlations between polymer morphology, silicate structures, stiffness, and toughness of thermoset nanocomposites as a function of layered silicate type and content. According to them, the main factor for the matrix stiffness improvement resides in the formation of supramolecular assemblies obtained by the presence of dispersed anisotropic laminated nanoparticles. They also described a stiffening effect when the MMT is modified by a functionalized organic cation (carboxylic acid or hydroxyl groups) that can strongly interact with the matrix during curing.

The tensile properties of APES/Cloisite 30B and APES/Cloisite 10A nanocomposites at various clay contents are presented in Table 14 [338]. In comparison to the APES, the tensile strength and modulus have been improved with little decrease of elongation at break. APES/Cloisite 30B nanocomposites exhibit much higher tensile strength and modulus compared to the APES/Cloisite 10A nanocomposites. This is also attributed to the strong interaction between APES matrix and Cloisite 30B. These results further confirm the importance of strong interaction between matrix and clay, which ultimately leads to the better overall dispersion as already observed by TEM observations.

### 6.1.3. Flexural Properties

Nanocomposite researchers are generally interested on tensile properties of final materials and there are very few reports concerning the flexural properties of neat polymer and its nanocomposite with OMLS. Very recently, Sinha Ray et al. [324] reported detailed measurements of flexural properties of neat PLA and various PLACNs. They conducted flexural properties measurements with injection-molded samples and according to the ASTM D-790 method. Table 15 shows the flexural modulus, flexural strength, and distortion at break of neat PLA and various PLACNs measured at 25 °C. There is a significant increase in flexural modulus for PLACN4 compared to that of neat PLA followed by a much slower increase with increasing OMLS content, and a maximum of 21% in case of PLACN7. On the other hand, flexural strength and distortion at break remarkably increase with PLACN4 then gradually decrease with organoclay loading. According to the authors this behavior

**Table 14.** Tensile properties of APES/Cloisite 30B nanocomposites.

Cloisite 30B content (wt%)	Modulus (kgf/cm <sup>2</sup> )	Strength (kgf/cm <sup>2</sup> )	Elongation at break (%)
0	106.7	131.7	12.45
1	112.3	139.0	12.25
3	114.4	144.1	11.95
5	118.2	149.8	11.40
10	129.5	157.7	10.90
20	144.4	190.8	11.30
30	173.8	213.5	12.25

**Table 15.** Comparison of materials properties between neat PLA and various PLACNs prepared with trimethyl octadecylammonium modified MMT.

Materials properties	PLA	PLACN4	PLACN5	PLACN7
Bending modulus (GPa)	4.8	5.5	5.6	5.8
Bending strength (MPa)	86	134	122	105
Distortion at break (%)	1.9	3.1	2.6	2

may be due to high organoclay content leading to a brittleness of materials.

### 6.1.4. Heat Distortion Temperature

Heat distortion temperature (HDT) of a polymeric material is an index of heat resistance toward applied load. Most of the PCNs studies report HDT as a function of clay content, characterized by ASTM D-648. Kojima et al. [2] first show that HDT of pure N6 increases up to 80 °C after PCN preparation with MMT. In their further work [106] they report clay content dependence of HDT of NCH. In case of NCH there is a marked increase in HDT, from 65 °C for the neat N6 to 150 °C for 4.7 wt% nanocomposite; beyond that wt% of MMT, the HDT of nanocomposite levels off. They also conducted HDT tests of various NCHs prepared with clays having different lengths and found that HDT also depends upon the aspect ratio of dispersed clay particles [2]. Like all other mechanical properties, 1potNCH also shows higher HDT than that of NCH prepared by *in-situ* intercalative polymerization.

Since the degree of crystallinity of Nylon 6/clay nanocomposite is independent of the amount and nature of clay, the HDT of Nylon 6/clay nanocomposite is due to the presence of a strong interaction between matrix and silicate surface by forming hydrogen bonds (see Fig. 41). Although Nylon 6 in nanocomposite stabilizes in a different crystal phase ( $\gamma$ -phase) than that found in pure Nylon 6, this different crystal phase is not responsible for higher mechanical properties of Nylon 6/clay nanocomposites because  $\gamma$ -phase is a very soft crystal phase. On the other hand, increased mechanical properties of NCH with increasing clay content is due to the mechanical reinforcement effect.

The nanodispersion of MMT in the PP matrix also promotes a higher HDT [254]. In Table 16 we summarized the HDT of PP and its PCNs based on f-MMT and alkylammonium modified MMT. Like previous systems, there is a significant increase in HDT, from 109 °C for the neat PP to 152 °C for a 6 wt% of clay; after that the HDT of nanocomposite levels off. This improvement in HDT of neat PP after nanocomposite preparation originates from the better mechanical stability of the nanocomposite compared to the neat PP since there is no increment of melting point of neat PP after PCN preparation.

Sinha Ray et al. examined the HDT of neat PLA and various PLACNs with different load conditions. As seen in Figure 49a [324], in case of PLACN7 (inorganic clay content = 5 wt%), there is marked increase of HDT with intermediate load of 0.98 MPa, from 76 °C for the neat PLA to 98 °C for PLACN4 (inorganic clay content = 3 wt%). The value of HDT gradually increases with increasing organoclay



**Table 16.** HDT of PP/clay nanocomposites and the respective unfilled PP.

Organically modified MMT (wt%)	HDT (°C)	
	PP/f-MMT	PP/alkyl-MMT
0	109 ± 3	109 ± 3
3	144 ± 5	130 ± 7 <sup>a</sup>
6	152 ± 5	141 ± 7 <sup>b</sup>
9	153 ± 5	

<sup>a</sup> C<sub>18</sub>-MMT filler, extruder processed.

<sup>b</sup> 2C<sub>18</sub>-MMT filler, twin-head mixer.

Source: Reprinted with permission from [254], E. Manias et al., *Chem. Mater.* 13, 3516 (2001). © 2001, American Chemical Society.

content, and in case of PLACN7, the value increases up to 111 °C.

On the other hand, imposed load dependence on HDT is clearly observed in case of PLACNs. Figure 49b shows the typical load dependence in case of PLACN7. The increase of HDT of neat PLA due to nanocomposite preparation is a very important property improvement, not only from the industrial point of view but also molecular control on the silicate layers, that is, crystallization through interaction between PLA molecules and SiO<sub>4</sub> tetrahedral layers in the MMT. In case of high load (1.81 MPa), it is very difficult to achieve high HDT enhancement without strong interaction between polymer matrix and organo-MMT [2]. In case of all PLACNs studied here, the values of the melting temperature  $T_m$  do not change significantly as compared to that of neat PLA. So the improvement of HDT with intermediate load (0.98 MPa) originates from the better

mechanical stability of the PLACNs due to mechanical reinforcement by the dispersed clay particles, higher value of the degree of crystallinity  $\chi_c$ , and intercalation. This is qualitatively different from the behavior of the NCH system, where the MMT layers stabilize in a different crystalline phase ( $\gamma$ -phase) [106] than that found in the neat Nylon 6, with the strong hydrogen bondings between the silicate layers and Nylon 6 as a result of the discrete lamellar structure on both sides of the clay (see Fig. 41).

## 6.2. Thermal Stability

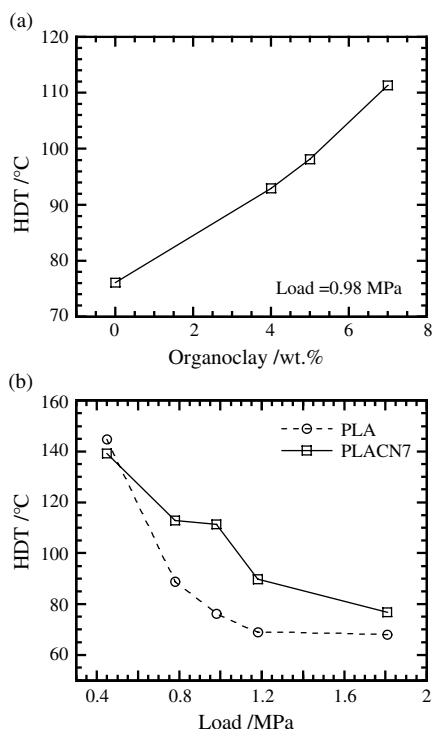
The thermal stability of polymeric materials is usually studied by thermogravimetric analysis (TGA). The weight loss due to the formation of volatile degradation products is monitored as a function of temperature ramp. When the heating is operated under an inert gas flow, a nonoxidative degradation occurs while the use of air or oxygen is allowed following the oxidative degradation of the samples. Generally the incorporation of clay in the polymer matrix enhanced the thermal stability by acting as a superior insulator and mass transport barrier to the volatile products generated during decomposition.

Blumstein [35] first reported the improved thermal stability of a PCN that combined PMMA and MMT. PMMA intercalated ( $d$ -spacing increase of 0.76 nm) between the galleries of MMT clay resisted the thermal degradation under conditions that would otherwise completely degrade pure PMMA. These PMMA nanocomposites were prepared by free-radical polymerization of MMA intercalated in the clay. TGA data reveal that both linear PMMA and cross-linked PMMA intercalated into MMT layers have a 40–50 °C higher decomposition temperature. Blumstein argues that the stability of the PMMA nanocomposite is due not only to its different structure but also restricted thermal motion of the PMMA in the gallery.

Recently, there have been lots of reports concerned with the improved thermal stability of nanocomposites prepared with various types of organoclay and polymer matrices [339–341]. Recently Zanetti et al. [275] published the details TG analyses of nanocomposites based on EVA. The inorganic phase was flohectorite or MMT, both exchanged with octadecylammonium cation. According to them the deacylation of EVA in nanocomposites is accelerated and may occur at temperatures lower than those for the pure polymer or corresponding microcomposite due to catalysis by the strongly acid sites created by thermal decomposition of the silicate modifier. These sites are active when there is an intimate contact between the polymer and the silicate. Slowing down of the volatilization of the deacylated polymer in nitrogen may be due to the labyrinth effect of the silicate layers in the polymer matrix [342].

In air, the nanocomposite presents a significant delay of weight loss that may derive from the barrier effect due to diffusion of both the volatile thermo-oxidation products to the gas and oxygen from the gas phase to the polymer. According to Gilman et al. this barrier effect increases during volatilization owing to ablative reassembly of the reticular of the silicate on the surface [343].

The thermal stability of the PCL-based nanocomposites has also been studied by TGA. Generally, the degradation

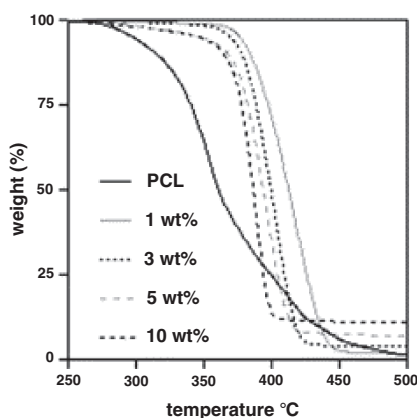


**Figure 49.** (a) Organoclay (wt%) dependence of HDT of neat PLA and various PLACNs. (b) Load dependence of HDT of neat PLA and PLACN7. Reprinted with permission from [324], S. Sinha Ray et al., *Polymer* 44, 857 (2003). © 2003, Elsevier Science.

of PCL fits a two-step mechanism [140]: first there is a statistical rupture of the polyester chains by pyrolysis of ester groups with the release of  $\text{CO}_2$ ,  $\text{H}_2\text{O}$ , and hexanoic acid and in the second step,  $\epsilon$ -caprolactone (cyclic monomer) is formed as a result of an unzipping depolymerization process. The thermograms of nanocomposites prepared with organoclay and pure PCL recovered after clay extraction are presented Figure 50. Both intercalated and exfoliated nanocomposites show higher thermal stability when compared to the pure PCL or the corresponding microcomposites. The nanocomposites exhibit a 25 °C rise in decomposition temperature at 50% weight loss. The shift of the degradation temperature may be ascribed to a decrease in oxygen and volatile degradation product permeability/diffusivity due to the homogeneous incorporation of clay sheets, to a barrier of these high aspect ratio fillers, and to char formation. The thermal stability of the nanocomposites systematically increases with increasing clay; however, above a loading of 5 wt%, the thermal stability is not improved anymore.

But completely different behavior is observed in case of synthetic biodegradable aliphatic polyester (BAP)/clay nanocomposite systems, in which the thermal degradation temperature and thermal degradation rate are systematically increased with an increasing amount of organoclay up to 15 wt% [344]. Like PS-based nanocomposites, a small amount of clay also increased the residual weight of BAP/OMMT because of the restricted thermal motion of the polymer in the silicate layers. The residual weight of various materials at 450 °C increased in the order BAP < BAP03 < BAP06 < BAP09 < BAP15 (here number indicates wt% of clay). This kind of improved thermal property is also observed in other systems like SAN [345], the intercalated nanocomposites prepared by emulsion polymerization.

Many researchers believe the role of clay in the nanocomposite structure might be the main reason for the difference in TGA results of these systems compared to the systems reported thus far. The clay acts as a heat barrier, which could enhance the overall thermal stability of the system, as well as assisting in the formation of char after thermal decomposition. Thereby, in the beginning stage of



**Figure 50.** Temperature dependence of the weight loss under an air flow for neat PCL and PCL nanocomposites containing 1, 3, 5, and 10 wt% (relative to inorganics) of MMT-Alk (heating rate: 20 K/min). Reprinted with permission from [140], B. Lepoittevin et al., *Polymer* 43, 1111 (2002). © 2002, Elsevier Science.

thermal decomposition, the clay could shift the decomposition temperature higher. However, after that, this heat barrier effect would result in a reverse thermal stability. In other words, the stacked silicate layers could hold accumulated heat that could be used as a heat source to accelerate the decomposition process, in conjunction with the heat flow supplied by the outside heat source.

### 6.3. Fire Retardant Properties

The cone calorimeter is the most effective bench-scale method for studying the fire retardant properties of polymeric materials. Fire-relevant properties, measured by the cone calorimeter, such as heat release rate (HRR), peak HRR, and smoke and CO yield, are vital to the evaluation of the fire safety of materials.

Gilman et al. reviewed the flame retardant properties of nanocomposites in detail [346, 347].

Table 17 represents the cone calorimeter data of three different kinds of polymers and their nanocomposites with MMT. From Table 17 we can see that all MMT-based nanocomposites reported here show reduced flammability. Peak HRR is reduced by 50–75% for Nylon 6, PS, and PP-MA nanocomposites [347]. According to the authors the MMT must be nanodispersed for it to affect the flammability of the nanocomposites. However, the clay need not be completely delaminated for it to affect the flammability of the nanocomposite. In general, the nanocomposite flame retardant mechanism is that a high-performance carbonaceous-silicate char builds up on the surface during burning; this insulates the underlying material and slows the mass loss rate of decomposition products.

For a PPCN with 4 wt% organoclay [347], there is a 75% reduction in flammability compared to the neat matrix (see Fig. 51).

### 6.4. Gas Barrier Properties

Nanoclays are believed to increase the barrier properties by creating a maze or “tortuous path” (see Fig. 52) that retards the progress of the gas molecules through the matrix resin. The direct benefit of the formation of this type of path is clearly observed in polyimide/clay nanocomposite by showing dramatically improved barrier properties with simultaneous decrease in thermal expansion coefficient [211, 213]. The polyimide/layered silicate nanocomposites revealed a several-fold reduction in the permeability of small gases (e.g.  $\text{O}_2$ ,  $\text{H}_2\text{O}$ , He,  $\text{CO}_2$ , and the organic vapor ethylacetate) with the presence of a small fraction of organoclay. For example, at 2 wt% clay loading, the permeability coefficient of water vapor was decreased tenfold for the synthetic mica relative to pristine polyimide. By comparing nanocomposites made with layered silicates of various aspect ratios the permeability was noted to decrease with increasing aspect ratio.

The  $\text{O}_2$  gas permeability was measured for the exfoliated PLA/synthetic mica nanocomposites prepared by Sinha Ray et al. [348]. The relative permeability coefficient value (i.e.,  $P_{\text{PLACN}}/P_{\text{PLA}}$  where  $P_{\text{PLACN}}$  and  $P_{\text{PLA}}$  stand for the nanocomposite and pure PLA permeability coefficient, respectively) has been plotted as a function of the wt% of clay. The curve fitting has been achieved by using Nielsen theoretical

**Table 17.** Cone calorimeter data of various polymers and their nanocomposites with organoclay.

Sample (structure)	% Residue yield ( $\pm 0.5$ )	Peak HRR (kW/m <sup>2</sup> ) ( $\Delta\%$ )	Mean HRR (kW/m <sup>2</sup> ) ( $\Delta\%$ )	Mean $H_c$ (MJ/kg)	Mean SEA (m <sup>2</sup> /kg)	Mean CO yield (kg/kg)
Nylon 6	1	1010	603	27	197	0.01
N6 nanocomposite 2% (delaminated)	3	686 (32)	390 (35)	27	271	0.01
N6 nanocomposite 5% (delaminated)	6	378 (63)	304 (50)	27	296	0.02
PS	0	1120	703	29	1460	0.09
PS-silicate mix 3% (immiscible)	3	1080	715	29	1840	0.09
PS-nanocomposite 3% (intercalated/delaminated)	4	567 (48)	444 (38)	27	1730	0.08
PSw/DBDPO/Sb <sub>2</sub> O <sub>3</sub> 30%	3	491 (56)	318 (54)	11	2580	0.14
PP-MA	5	1525	536	39	704	0.02
PP-MA nanocomposite 2% (intercalated/delaminated)	6	450 (70)	322 (40)	44	1028	0.02
PP-MA nanocomposite 4% (intercalated/delaminated)	12	381 (75)	275 (49)	44	968	0.02

<sup>a</sup> Heat flux, 35 kW/m<sup>2</sup>.  $H_c$ , specific heat of combustion; SEA, specific extinction area. Peak heat release rate, mass loss rate, and SEA data, measured at 35 kW/m<sup>2</sup>, are reproducible to within  $\pm 10.5$ . The carbon monoxide and heat of combustion data are reproducible to within  $\pm 15\%$ .

Source: Reprinted with permission from [347], J. W. Gilman et al., *Chem. Mater.* 12, 1866 (2000). © 2000, American Chemical Society.

expression [349] allowing the prediction of gas permeability in function of the length and width of the filler particles as well as their volume fraction within the PLA matrix (see Fig. 53).

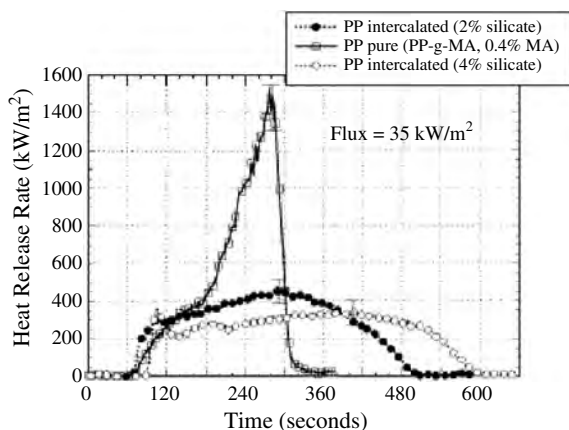
In the Nielsen model [349], platelets of length ( $\cong L_{\text{clay}}$ ) and width ( $\cong D_{\text{clay}}$ ) of the clay are dispersed parallel in polymer matrix; then the tortuosity factor ( $\tau$ ) can be expressed as

$$\tau = 1 + (L_{\text{clay}}/2D_{\text{clay}})\phi_{\text{clay}} \quad (1)$$

where  $\phi_{\text{clay}}$  is the volume fraction of dispersed clay particles. Therefore, the relative permeability coefficient ( $P_{\text{PCN}}/P_{\text{Neat}}$ ) is given by

$$P_{\text{PCN}}/P_{\text{Neat}} = \tau^{-1} = 1/[1 + (L_{\text{clay}}/2D_{\text{clay}})\phi_{\text{clay}}] \quad (2)$$

where  $P_{\text{PCN}}$  and  $P_{\text{Neat}}$  are the permeability coefficient of PCN and neat polymer, respectively.

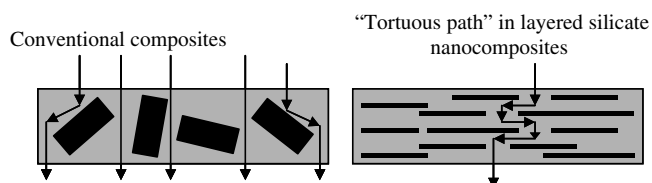


**Figure 51.** Heat release rate during cone-calorimetry combustion of heat PP-MA and PPCNs. Reprinted with permission from [347], J. W. Gilman et al., *Chem. Mater.* 12, 1866 (2000). © 2000, American Chemical Society.

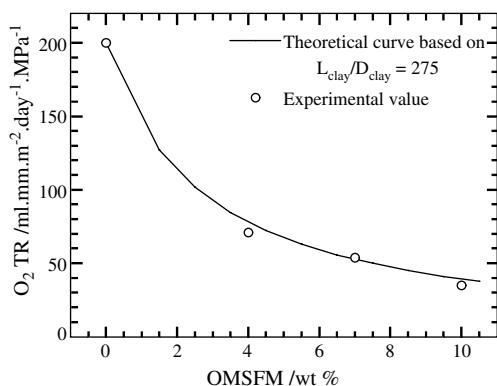
The H<sub>2</sub>O-vapor permeability for the PUU/clay nanocomposites is presented by Xu et al. in terms of  $P_c/P_o$ , that is, the permeability coefficient of the nanocomposite ( $P_c$ ) relative to that of the neat PUU ( $P_o$ ) [350]. The nanocomposite formation results in a dramatic decrease in H<sub>2</sub>O-vapor transmission through the PUU sheet. The solid lines are based on the argument of the tortuosity model for the aspect ratio of 300 and 1000. A comparison between the experimental values and the theoretical model prediction suggests a gradual change in the effective aspect ratio of the filler ( $L_{\text{clay}}/D_{\text{clay}}$ ).

## 6.5. Ionic Conductivity

Solvent-free electrolytes are of much interest because of their charge-transport mechanism and their possible applications in electrochemical devices. With this background, Vaia et al. [152] have considered the preparation of PEO/clay nanocomposites to fine tune ionic conductivity of PEO. An intercalated nanocomposite prepared by melt intercalation of PEO (40 wt%) into Li<sup>+</sup>-MMT (60 wt%) has shown to enhance the stability of the ionic conductivity at lower temperature when compared to a more conventional PEO/LiBF<sub>4</sub> mixture. This improvement in conductivity is explained by the fact that PEO is not able to crystallize when intercalated, hence eliminating the presence of crystallites, nonconductive in nature. The higher conductivity at room temperature compared to conventional



**Figure 52.** Formation of tortuous path in polymer/clay nanocomposites.



**Figure 53.** Oxygen gas permeability of neat PLA and various PLACNs as a function of organoclay content measured at 20 °C and 90% relative humidity. The filled circles represent the experimental data. Theoretical fits based on Nielsen tortuosity model.

PEO/LiBF<sub>4</sub> electrolytes with a single ionic conductor character makes those nanocomposites new promising electrolyte materials. The same type of behavior in ionic conductivity is also observed in case of poly[bis(methoxy-ethoxy) ethoxy phosphazene]/Na<sup>+</sup>-MMT nanocomposite as prepared by Hutchison et al. [351].

In a recent report, Okamoto et al. [12] have reported the correlation between internal structure and ionic conductivity behavior of PMMA/clay and PS/clay nanocomposites having various dispersed morphologies of the clay layers by using an impedance analyzer in the temperature range of 90–150 °C. The nanocomposites having finer dispersion of the clay layers exhibit higher ionic conductivity rather than the other systems such as PMMA/clay nanocomposite with stacking layer structure. The activation energy of the conductivity in finer dispersed morphology systems becomes larger than the other systems and the corresponding organoclay solids.

## 6.6. Optical Transparency

Although layered silicates are micrometer in lateral size, they are just 1 nm thick. Thus, when single layers are dispersed in a polymer matrix, the resulting nanocomposite is optically clear in the visible region. Strawhecker and Manias have reported the ultraviolet (UV)/visible transmission spectra of pure PVA and PVA/Na<sup>+</sup>-MMT nanocomposites with 4 and 10 wt% MMT [87]. The spectra show that the visible region is not affected at all by the presence of the silicate layers and retains the high transparency of the PVA. For the UV wavelengths, there is strong scattering and/or absorption, resulting in very low transmission of the UV light. This behavior is not surprising as the typical MMT lateral sizes are 50–1000 nm.

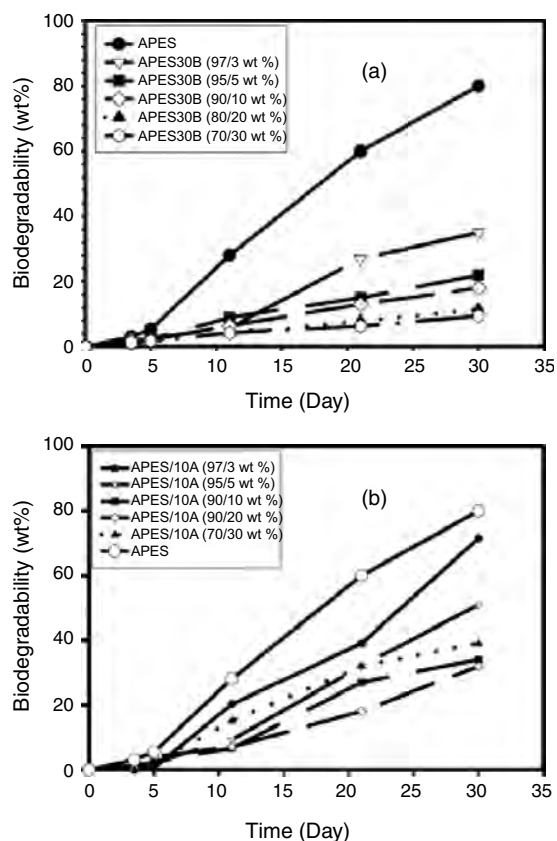
Like PVA, various other polymers also show optical transparency after nanocomposite preparation with organoclay [254].

## 6.7. Biodegradability of Green Polymeric Nanocomposites

Another most interesting and exciting aspect of nanocomposite technology is the significant improvement of biodegradability of biodegradable polymers after nanocomposite preparation with organoclay. There is a need for

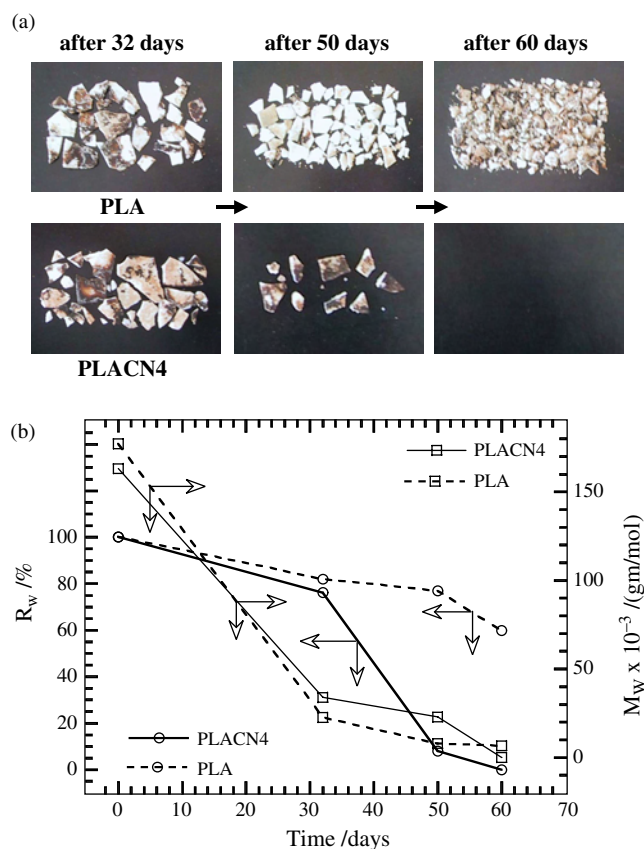
the development of *green polymeric materials* that would not involve the use of toxic or noxious components in their manufacture and could be degraded in the natural environment or easily recycled. Aliphatic polyesters are among the most promising materials for the production of environmentally friendly biodegradable plastics. Biodegradation of aliphatic polyester is well known, in that some bacteria degrade them by producing enzymes, which attack the polymer. Tetto et al. [352] first reported some results about the biodegradability of nanocomposites based on PCL, where the authors found that the PCL/clay nanocomposites showed improved biodegradability compared to pure PCL. According to them, the improved biodegradability of PCL after nanocomposite formation may be due to the catalytic role of the organoclay in the biodegradation mechanism. But still it is unclear how the clay increases the biodegradation rate of PCL.

Recently, Lee et al. [332] reported the biodegradation of aliphatic polyester based nanocomposites under compost. Figure 54a and b respectively represents the clay content dependence of biodegradation of APES based nanocomposites prepared with two different types of clays. They assumed that the retardation of biodegradation is due to the improvement of the barrier properties of the aliphatic APES after nanocomposites preparation with clay. However, there are no data about permeability.



**Figure 54.** Biodegradability of APES nanocomposites with: (a) Closite 30B and (b) Closite 10A. Reprinted with permission from [332], S. R. Lee et al., *Polymer* 43, 2495 (2002). © 2002, Elsevier Science.

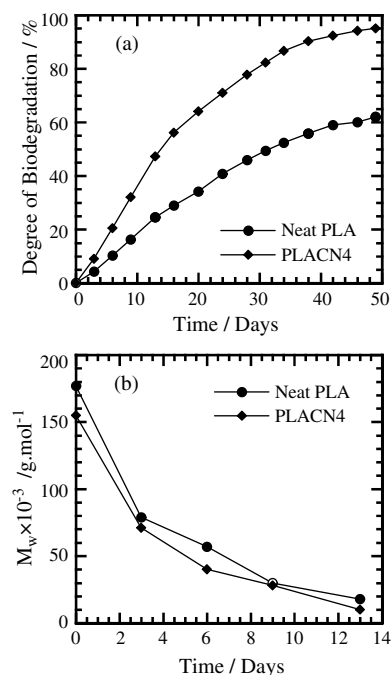
Very recently, Sinha Ray et al. [318, 324] first reported the biodegradability of neat PLA and corresponding nanocomposites prepared with trimethyl octadecylammonium modified MMT ( $C^3C_{18}$ -MMT) with detailed mechanisms. The compost used was prepared from food waste and tests were carried out at temperature of  $58 \pm 2$  °C. Figure 55a shows the real picture of the recovered samples of neat PLA and PLACN4 ( $C^3C_{18}$ -MMT = 4 wt%) from compost with time. The decreased  $M_w$  and residual weight percentage  $R_w$  of the initial test samples with time are also reported in Figure 55b. The biodegradability of neat PLA is significantly enhanced after PCN preparation. Within one month, both extent of  $M_w$  and extent of weight loss are at almost the same level for both PLA and PLACN4. However, after one month, a sharp change occurs in weight loss of PLACN4, and within two months, it is completely degraded in compost. The degradation of PLA in compost is a complex process involving four main phenomena, namely: water absorption, ester cleavage and formation of oligomer fragments, solubilization of oligomer fragments, and finally diffusion of soluble oligomers by bacteria [353]. Therefore, the factor that increases the hydrolysis tendency of PLA ultimately controls the degradation of PLA. They expect the presence of terminal hydroxylated edge groups of the silicate layers may be one of the factors responsible for



**Figure 55.** (a) Real picture of biodegradability of neat PLA and PLACN4 recovered from compost with time. Initial shape of the crystallized samples was  $3 \times 10 \times 0.1$  cm<sup>3</sup>. (b) Time dependence of residual weight  $R_w$  and of matrix  $M_w$  of PLA and PLACN4 under compost at  $58 \pm 2$  °C. Reprinted with permission from [324], S. Sinha Ray et al., *Polymer* 44, 857 (2003). © 2003, Elsevier Science.

this behavior. In case of PLACN4, the stacked ( $\sim 4$  layers) and intercalated silicate layers are homogeneously dispersed in the PLA matrix (from TEM image) and these hydroxy groups start heterogeneous hydrolysis of the PLA matrix after absorbing water from compost. This process takes some time to start. For this reason, the weight loss and degree of hydrolysis of PLA and PLACN4 are almost same up to one month (see Fig. 55b). However, after one month there is a sharp weight loss in case of PLACN4 compared to that of PLA. That means one month is a critical value to start heterogeneous hydrolysis, and due to this type of hydrolysis the matrix becomes very small fragments and disappears with the compost. This assumption was confirmed by conducting the same type of experiment with PLACN prepared by using dimethyl dioctadecyl ammonium salt modified synthetic mica which has no terminal hydroxylated edge group, and the degradation tendency was almost the same with neat PLA [354].

They also conducted respirometric testing to study degradation of the PLA matrix in compost environment at  $58 \pm 2$  °C. For this test the compost used was made from bean-curd refuse, food waste, and cattle feces. Unlike weight loss, which reflects the structural changes in the test sample, CO<sub>2</sub> evolution provides an indicator of the ultimate biodegradability of PLA in PLACN4 (prepared with *N*(cocoalkyl)*N*, *N*-[bis(2-hydroxyethyl)]-*N*-methylammonium modified synthetic mica), that is, mineralization, of the samples. Figure 56 shows the time dependence of the degree of biodegradation of neat PLA and PLACN4, indicating that the biodegradability of PLA in PLACN4 is enhanced significantly. The presence of organoclay may thus cause a different mode of attack on the PLA



**Figure 56.** Degree of biodegradation (i.e., CO<sub>2</sub> evolution), and (b) time-dependent change of matrix  $M_w$  of neat PLA and PLACN4 (MEE clay = 4 wt%) under compost at  $58 \pm 2$  °C. Reprinted with permission from [317], S. Sinha Ray et al., *Macromol. Rapid Commun.* 23, 943 (2002). © 2002, Wiley-VCH.

component, which might be due to the presence of hydroxy groups. Details regarding the mechanism of biodegradability are presented in relevant literature [317, 354].

## 6.8. Other Properties

Another property of polymer that is strongly affected by the incorporation of layered silicates is a sharp increase of the scratch resistance [254], dimensional stability [355], and solvent resistance [355] via nanocomposite technology.

## 7. CRYSTALLIZATION OF POLYMER/CLAY NANOCOMPOSITES

### 7.1. Spherulitic Texture and Growth

Crystallization of PCNs might be a good tool for controlling the structure of PCNs and thereby the various properties. Maiti et al. [260] have reported an example of the time variation of the diameter of the spherulite  $D$  for PP-MA and PP/clay nanocomposites at 135 °C (see Fig. 57). A linear growth of  $D$  is seen in a range of  $t$  scale for PP-MA, PPCN2, and PPCN7.5. The linear growth rate  $G$  [ $=1/2(dD/dt)$ ], defined as the initial slope of the plots, slightly increases with increasing clay content. From the extrapolation of  $D$  vs  $t$  plots, we estimated the onset time  $t_0$ , which corresponds to the induction time of the crystallization. The  $t_0$  of both PPCNs decreases with clay content compared to the PP-MA matrix without clay. The reduction of  $t_0$  in the PPCNs is attributed to the nature of the clay as the nucleating agent. For PPCNs,  $G$  shows almost the same value compared to PP-MA without clay. In spite of the increase in clay content, the dispersed clay particles have not much effect on the crystallization and no big acceleration of  $G$  in the crystallization of the PPCNs is seen. In the changes in  $t_0$  with crystallization temperature  $T_c$ , the PPCNs show remarkably short time especially at high  $T_c$ , suggesting that the dispersed clay particles have some contribution to enhance the nucleation as mentioned. The primary nucleation density of the

spherulites (i.e., the number of heterogeneous nuclei  $N$ ) was given by

$$N = (3/4\pi)(D_m/2)^{-3} \quad (3)$$

where  $D_m$  is the maximum diameter of the spherulite (i.e., the attainable diameter before impingement). The calculated values of  $N$  at 130 °C were  $4 \times 10^{-8}$  for PP-MA,  $50 \times 10^{-8}$  for PPCN2, and  $200 \times 10^{-8} \mu\text{m}^{-3}$  for PPCN7.5, respectively. The time variation of the volume fraction of the spherulites increases in proportion to  $NG^3$  ( $\cong$  overall crystallization rate). This fact suggests that the overall crystallization rate of the PPCNs is about one or two orders of magnitude higher than that of matrix PP-MA without clay.

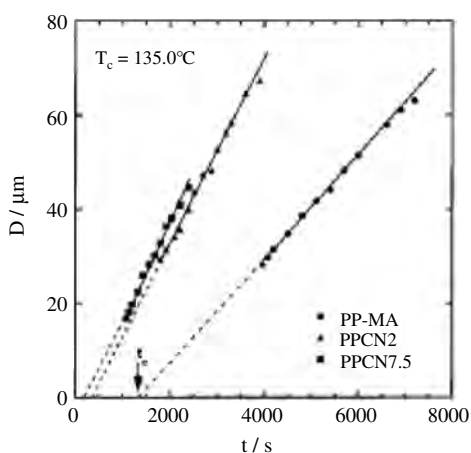
### 7.2. Formation of $\gamma$ -Form in PPCNs

Maiti et al. [261] have reported the temperature dependence of the fraction of  $\gamma$ -form  $f_\gamma$ . The value of  $f_\gamma$  was calculated from the area of the specific peak, compared to the total area of  $\alpha$  and  $\gamma$ -forms. At low  $T_c$  ( $<100$  °C) PP-MA does not exhibit  $\gamma$ -crystals, but their content increases with increasing  $T_c$ . The fraction of  $\gamma$ -form consistently increases with clay content in PPCNs, compared to PP-MA, at every  $T_c$ . Lotz et al. [356] reported that  $\gamma$  crystals are nucleated on the lateral (010) faces of  $\alpha$  crystal and appear to be favored by, or linked to, the absence of chain folding. The mobility of the PP-MA matrix is significantly reduced in the presence of maleic anhydride grafting in the main chain, which causes lowering of chain folding especially at high  $T_c$ . In the presence of clay particles in PPCNs, the movements of polymer chains inside the clay particles are restricted. The correlation length of the clay particles is roughly the same as that of radius of gyration of the matrix [30]. Thus, the formation of  $\gamma$ -phase is enhanced in the presence of clay particles.

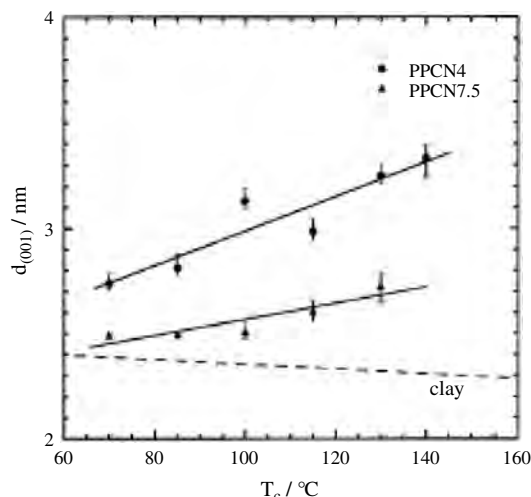
### 7.3. Intercalation during Crystallization

In the PPCNs, at high  $T_c$  ( $\geq 110$  °C), where the crystallization rate is low enough to solidify the system, the intercalation should be anticipated in the melt state during crystallization [31]. The driving force of the intercalation originates from strong hydrophilic interaction between the MA group and the polar clay surfaces [30, 245]. With increasing  $T_c$ , the small peak and shoulder shift toward the smaller angle region in the PPCNs, suggesting that the extent of intercalation takes place with crystallization [260].

Figure 58 shows  $d_{(001)}$  of the clay gallery quantitatively, as a function of  $T_c$ , obtained from their respective Bragg reflections. Here, in case of PPCN2, the peak is not prominent. The dotted line shows the effect of annealing on the  $d_{(001)}$  value of organoclay. The  $d_{(001)}$  increases with  $T_c$  for both PPCN4 and PPCN7.5 systems and PPCN4 always exhibits a significantly higher value than that of PPCN7.5. These imply that intercalation proceeds at  $T_c$  and increases with decreasing clay content. Further decrease of clay content from 4 to 2 wt% in PPCN2 leads to a partially exfoliated system as discussed in Section 3.1. That is, the PPCN with low clay content crystallized at high  $T_c$  ( $\geq 110.0$  °C) exhibits a higher amount of intercalation than that with high clay content crystallized at any  $T_c$ .



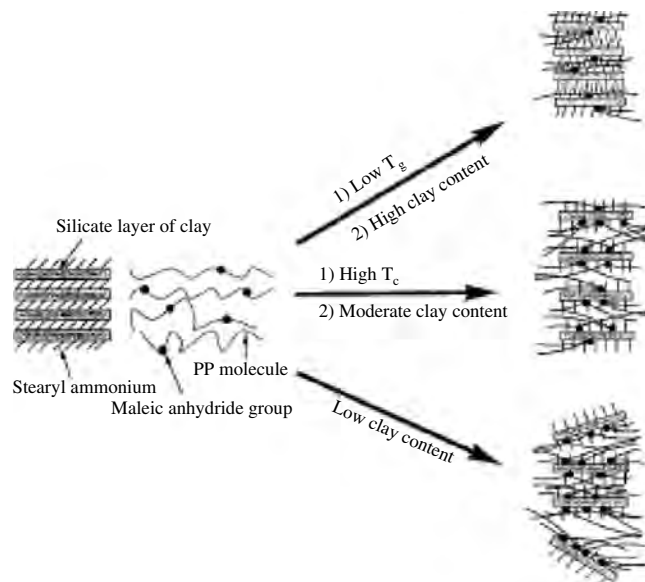
**Figure 57.** Spherulitic diameter as a function of crystallization time at  $T_c = 130.0$  °C. The arrow indicates the induction time of crystallization for PP-MA. Reprinted with permission from [260], P. Maiti et al., *Macromolecules* 35, 2042 (2002). © 2002, American Chemical Society.



**Figure 58.**  $T_c$  dependence of the interlayer spacing of PPCN4 and PPCN7.5. The broken line shows the annealing effect on organoclay. Reprinted with permission from [260], P. Maiti et al., *Macromolecules* 35, 2042 (2002). © 2002, American Chemical Society.

At high  $T_c$  ( $\geq 110$  °C) (low crystallization rate), the melt state exists for quite a long time and PP-MA chains have enough time to intercalate before crystallization can occur in the bulk. Then the enhanced intercalation is produced. The extent of intercalation is strongly dependent on the time of the molten state. In other words, the intercalated PPCNs are not equilibrated. By decreasing the clay content in the nanocomposites, the virtual gallery space in the silicate layers decreases and consequently, the PP-MA molecules would try to accommodate, through interaction, in the minimum space causing higher intercalated species. For sufficiently low clay content, a system like PPCN2, having less gallery space, is partially exfoliated due to the high number density of the tethering junction.

There are two possible ways to order polymer chains inside the silicate gallery. Either (1) polymer molecules escape from gallery and crystallize outside (*diffuse out*) or (2) molecules may penetrate into the silicate gallery when they are in the molten state (*diffuse in*). When PPCN4 is directly crystallized from the melt at 70.0 °C for two different times of 30 min and 17 h, the interlayer spacing is the same (2.75 nm). If PPCN4 melt is annealed at 150.0 °C, just above  $T_m$  ( $=145.0$  °C) for sufficiently long time and then subsequently crystallized at 70.0 °C for 30 min, the interlayer spacing increases to 2.96 nm. Furthermore, when PPCN4 is crystallized from the melt at 30 °C, where the crystallization rate is slow enough, the interlayer spacing becomes 3.08 nm. All these experiments indicate that the extent of intercalation is strongly dependent on the time of the molten state, and ordering of polymer chains occurs through a *diffuse-in* mechanism. In other words, a slower crystallization rate makes a more intercalated species as molten polymer molecules have sufficient time to diffuse into the silicate gallery. Based on the WAXD and TEM micrographs, the nature of intercalation has been represented by Maiti et al. [260, 261] in Figure 59. Thus, by suitably crystallizing the PPCNs we can control the fine structure (*confined orientation*) of the PCNs.



**Figure 59.** The illustration for a diffuse-in mechanism by suitable crystallization. Reprinted with permission from [260], P. Maiti et al., *Macromolecules* 35, 2042 (2002). © 2002, American Chemical Society.

#### 7.4. Effect of Intercalation on Enhancement of Dynamic Modulus

According to the prediction of Khare et al. [357], the confinement of polymer chains increases the viscosity and mechanical properties of the system significantly. One can expect some difference in mechanical properties with the change of the degree of intercalation in the PPCNs vis-à-vis the clay content and  $T_c$  (see Table 18). It is clear from the table that for a particular  $T_c$ ,  $G'$  increases with increasing clay content. The PP-MA crystallized at 130 °C exhibits a 9.9% increase in  $G'$  compared to the sample crystallized at 70.0 °C. PPCN7.5 and PPCN4 show 13.3 and 30.6% increases, respectively, in the same condition. The effect of  $T_c$  on  $G'$  is in the order of PP-MA < PPCN7.5 < PPCN4. It may be recalled that the  $T_c$  dependence of  $d_{(001)}$  showed the order of intercalation PPCN7.5 < PPCN4 in Figure 58. This implies that much higher efficiency of the intercalation for the reinforcement is attained in the PPCN4. For PPCN2, owing to the partial exfoliation, the degree of intercalation decreases and hence the modulus decreases compared to the low  $T_c$  condition ( $=70$  °C). Here, it should be mentioned that the crystallinity increases a little bit with increasing  $T_c$  for both PP-MA and PPCNs and the extent is almost same for all the systems. So it is believed that not the crystallinity but the degree of intercalation does affect the storage modulus.

#### 7.5. Crystallization Controlled by Silicate Surfaces

The formation of  $\gamma$ -form in the presence of clay in the NCH system is well known [117]. The essential difference between the  $\gamma$ -form and the  $\alpha$ -form is the molecular packing; in the  $\alpha$ -form hydrogen bondings are formed between antiparallel chains while the molecular chains have to twist away

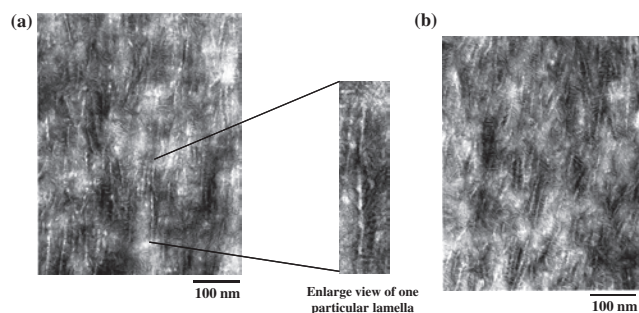
**Table 18.** Dynamic storage modulus of PP-MA and PPCNs at  $T = 50$  °C crystallized at different temperatures.

System	$T_c$ °C	$G' \times 10^{-8}$ (Pa)	% Increase
PP-MA	70	2.92	9.9
	130	3.21	
PPCN2	70	4.79	30.6
	130	4.50	
PPCN4	70	5.16	13.3
	130	6.74	
PPCN7.5	70	7.49	8.49
	130	8.49	

Source: Reprinted with permission from [260], P. Maiti et al., *Macromolecules* 35, 2042 (2002). © 2002, American Chemical Society.

from the zigzag planes to form the hydrogen bonds among the parallel chains in  $\gamma$ -form giving rise to lesser interchain interaction as compared to the  $\alpha$ -form.

The lamellar morphology and distribution of clay particles in NCH (N6CN3.7) (MMT = 3.7 wt%), crystallized at 170 and 210.0 °C have been reported by Maiti et al. [358] in Figure 60. The white strips (Fig. 60a) represent the discrete lamellar pattern, and after a close look, a black clay particle inside the lamella is clearly observed. In other words, lamellar growth occurs on both sides of the clay particles (i.e., the clay particle is sandwiched by the formed lamella). This is a unique observation of lamellar orientation on the clay layers. In the semicrystalline polymer generally stacked lamellar orientation takes place. The lamellar pattern at high  $T_c$  (Fig. 60b) is somehow similar but along with the sandwiched structure, branched lamellae are formed which are originated from the parent sandwiched lamella. There are no clay particles found inside the branch lamella and the  $\gamma$ -phase having irregular chain packing with distortion ( $\gamma^*$ -phase) is formed as revealed by WAXD which one can observe only in case of high  $T_c$  crystallized nanocomposites. This epitaxial growth ( $\gamma^*$ -phase) on the parent lamella forms the shish-kebab-type of structure, which virtually enhances the mechanical properties of the nanocomposites. From this sandwiched structure the accurate determination of long spacing and lamellar thickness of N6CN3.7 from small angle X-ray scattering is questionable [116]! It has to be remembered that Nylon 6 has the highest capability of forming hydrogen bonding to form a hydrogen-bonded sheet. The pseudo-hexagonal packing is favored with the hydrogen



**Figure 60.** TEM micrographs of N6C3.7 crystallized at (a) 170 and (b) 210 °C. The black strip inside the white part is clay. (b) The typical shish-kebab type of structure.

bonding between the silicate layers and Nylon 6. As a result the induction time of N6CN3.7 becomes very short, as compared to neat Nylon 6. Once one molecular layer is nucleated on the clay surface, other molecules may form the hydrogen bonding on the already formed hydrogen-bonded molecule to the silicate surface giving rise to the discrete lamellar structure on both side of the clay. This unique mechanism can well explain the higher crystallization rate of PCNs along with morphology and developed internal structure. This sandwiched structure (each silicate layer is strongly covered by polymer crystals) makes the system very rigid. As a result the HDT increases up to 80 °C but the surrounding excess amorphous part (lower crystallinity of N6CN3.7 as compared to neat Nylon 6) can easily retain the polymeric properties like impact strength and ultimately makes a improved/perfect system in PCNs.

## 8. MELT RHEOLOGY OF POLYMER/CLAY NANOCOMPOSITES

### 8.1. Linear Viscoelastic Properties

The measurement of rheological properties of the PCNs under molten state is crucial to gain a fundamental understanding of the nature of the processability and the structure–property relationship for these materials. Dynamic oscillatory shear measurements of polymeric materials are generally performed by applying a time dependent strain of  $\gamma(t) = \gamma_o \sin(\omega t)$  and the resultant shear stress is  $\sigma(t) = \gamma_o [G' \sin(\omega t) + G'' \cos(\omega t)]$ , with  $G'$  and  $G''$  being the storage and loss modulus, respectively.

Generally, the rheology of polymer melts strongly depends on the temperature at which the measurement is carried out. It is well known that for the thermorheological simplicity, isotherms of storage modulus ( $G'(\omega)$ ), loss modulus ( $G''(\omega)$ ), and complex viscosity ( $|\eta^*(\omega)|$ ) can be superimposed by horizontal shifts along the frequency axis:

$$b_T G'(a_T \omega, T_{\text{ref}}) = b_T G'(\omega, T)$$

$$b_T G''(a_T \omega, T_{\text{ref}}) = b_T G''(\omega, T)$$

$$|\eta^*(a_T \omega, T_{\text{ref}})| = |\eta^*(\omega, T)|$$

where  $a_T$  and  $b_T$  are the frequency and vertical shift factors, and  $T_{\text{ref}}$  is the reference temperature. All isotherms measured for pure polymer and for various PCNs can be superimposed along the frequency axis.

In case of polymer samples, it is expected, at the temperatures and frequencies at which the rheological measurements were carried out, that the polymer chains should be fully relaxed and exhibit characteristic homo-polymer-like terminal flow behavior (i.e., curves can be expressed by a power law of  $G' \propto \omega^2$  and  $G'' \propto \omega$ ).

The rheological properties of *in-situ* polymerized nanocomposites with end-tethered polymer chains were first described by Krisnamoorti and Giannelis [135]. The flow behavior of PCL- and Nylon 6-based nanocomposites differed extremely from that of the corresponding neat matrices, whereas the thermorheological properties of the nanocomposites were entirely determined by that behavior of matrices [135]. The slope of  $G'(\omega)$  and  $G''(\omega)$  versus  $a_T \omega$



is much smaller than 2 and 1, respectively. Values of 2 and 1 are expected for linear homodispersed polymer melts, and large deviations especially in the presence of a very small amount of layered silicate loading may be due to the formation of network structure in the molten state. However, such nanocomposites based on the *in-situ* polymerization technique exhibit fairly broad molar mass distribution of the polymer matrix, which hides the structure relevant information and impedes the interpretations of the results.

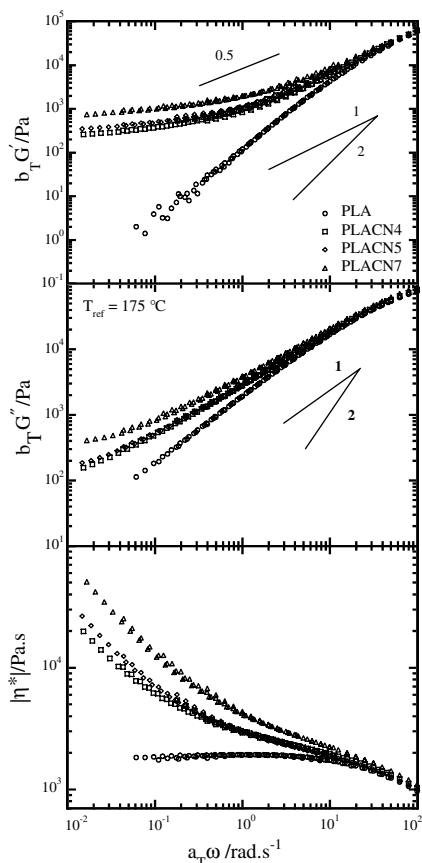
To date, the melt state linear dynamic oscillatory shear properties of various kinds of nanocomposites have been examined for a wide range of polymer matrices including Nylon 6 with various matrix molecular weights [119], PS [71], PS-PI block copolymers [102, 103], PCL [140], PP [25, 248, 265], PLA [34, 324], PBS [326–329], and so on [359–361].

The linear dynamic viscoelastic master curves for the neat PLA and various PLACNs are shown in Figure 61 [324]. The linear dynamic viscoelastic master curves were generated by applying a time–temperature superposition principle and shifted to a common temperature  $T_{\text{ref}}$  using both frequency shift factor  $a_T$  and modulus shift factor  $b_T$ . The moduli of the PCNs increase with increasing clay loading at all frequencies  $\omega$ . At high  $\omega$ 's, the qualitative behavior of  $G'(\omega)$  and  $G''(\omega)$  is essentially the same and unaffected by frequencies. However, at low frequencies  $G'(\omega)$  and  $G''(\omega)$

increase monotonically with increasing clay content. In the low frequency region, the curves can be expressed by power law of  $G'(\omega) \propto \omega^2$  and  $G''(\omega) \propto \omega$  for neat PLA, suggesting that this is similar to those of the narrow  $M_w$  distribution homopolymer melts. On the other hand, for  $a_T < 5 \text{ rad s}^{-1}$ , the viscoelastic response [particularly  $G'(\omega)$ ] for all the nanocomposites displays significantly diminished frequency dependence as compared to the matrices. In fact, for all PLACNs,  $G'(\omega)$  becomes nearly independent at the low  $a_T\omega$  and exceeds  $G''(\omega)$ , characteristic of materials exhibiting a pseudo-solid-like behavior [135]. The terminal zone slopes values of both neat PLA and PLACNs are estimated at the lower  $a_T\omega$  region ( $< 10 \text{ rad s}^{-1}$ ) and are presented in Table 19. The lower slope values and the higher absolute values of the dynamic moduli indicate the formation of “spatially linked” structures in the PLACNs under the molten state [362]. Because of this structure or highly geometric constraints, the individual stacked silicate layers are incapable of freely rotating and hence by imposing small  $a_T\omega$ , the relaxations of the structure are prevented almost completely. This type of prevented relaxation due to the highly geometric constraints of the stacked and intercalated silicate layers leads to the presence of the pseudo-solid-like behavior as observed in PLACNs. This behavior probably corresponds to the shear-thinning tendency, which strongly appears in the viscosity curves ( $a_T\omega < 5 \text{ rad s}^{-1}$ ) ( $|\eta^*|$  vs  $a_T\omega$ ) [57]. Such a feature strongly depends on the shear rate in the dynamic measurement because of the formation of the shear-induced alignment of the dispersed clay particles [363].

The temperature dependence frequency shift factors ( $a_T$ , Williams–Landel–Ferry type [364]) used to generate master curves shown in Figure 61 are shown in Figure 62. The dependence of the frequency shift factors on the silicate loading suggests that the temperature-dependent relaxation process observed in the viscoelastic measurements is somehow affected by the presence of the silicate layers [135]. In case of N6CN3.7, where the hydrogen bonding occurs on the already formed hydrogen-bonded molecule to the silicate surface, the system exhibits large value of flow activation energy (estimated from the slope in Fig. 62a) near one order higher in magnitude compared with that of neat Nylon 6 [365].

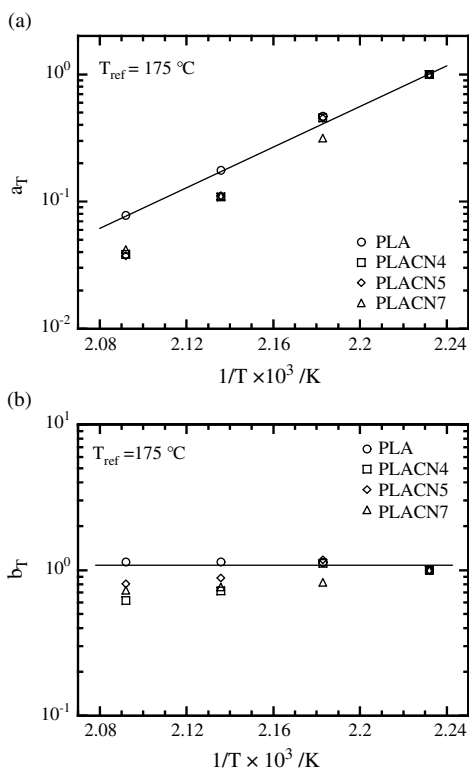
The shift factor  $b_T$  shows a large deviation from a simple density effect; it would be expected that the values would not vary far from unity [364]. One possible explanation is an internal structure development occurring in PLACNs during measurement (shear process). The alignment of the silicate layers probably supports PCN melts to withstand the shear force, thus leading to the increase in the absolute values of  $G'(\omega)$  and  $G''(\omega)$ .



**Figure 61.** Reduced frequency dependence of storage modulus, loss modulus, and complex viscosity of neat PLA and various PLACNs. Reprinted with permission from [324], S. Sinha Ray et al., *Polymer* 44, 857 (2003). © 2003, Elsevier Science.

**Table 19.** Terminal slopes of  $G'$  and  $G''$  vs  $a_T\omega$  for PLA and various PLACNs.

System	$G'$	$G''$
PLA	1.3	0.9
PLACN4	0.2	0.5
PLACN5	0.18	0.4
PLACN7	0.17	0.32



**Figure 62.** (a) Frequency shift factors  $a_T$  and (b) modulus shift factor  $b_T$  as a function of temperature.

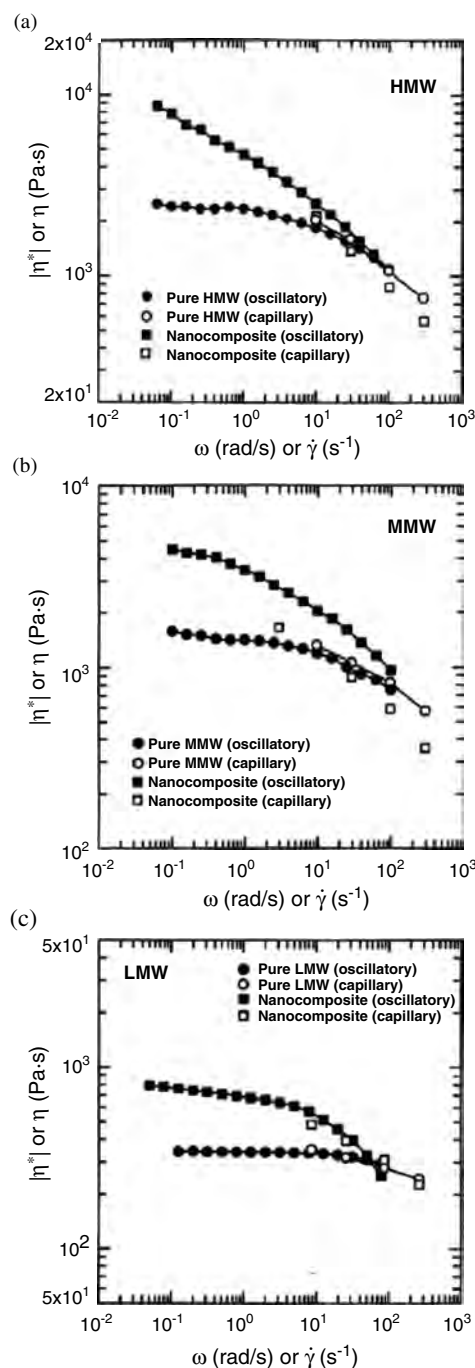
Galgali et al. [248] have also shown that the typical rheological response in nanocomposites arises from frictional interactions between the silicate layers and not due to the immobilization of confined polymer chains between the silicate layers. They have also shown a dramatic decrease in the creep compliance for the PPCH6 prepared with PP-MA and 6 wt% MMT. On the other hand, for PPCH9 prepared with PP-MA and 9 wt% of MMT, Galgali et al. [248] showed a dramatic three order of magnitude drop in the zero shear viscosity beyond the apparent yield stress, suggesting that the solidlike behavior in the quiescent state is a result of the percolated structure of the layered silicate.

Ren et al. [102] measured the viscoelastic behavior of a series of nanocomposites of disordered PS-PI block copolymer and MMT. Dynamic moduli and stress relaxation measurements indicate solidlike behavior for nanocomposites with more than 6.7 wt% MMT, at least on a time scale in the order of 100 s. According to them, this solidlike behavior is due to the physical jamming or percolation of the randomly distributed silicate layers at a surprisingly low volume fraction due to their anisotropic nature. The fact that alignment of the silicate layers by large shear stresses results in a more liquidlike relaxation behavior supports the percolation agreement.

A solidlike rheological response is also observed for PCL-based nanocomposites with organoclay content of 3 wt% or more [140].  $G'(\omega)$  and  $G''(\omega)$  in the terminal region are substantially increased for all the studied nanocomposites compared with neat PCL and or PCL-based microcomposites.

Recently, Fornes et al. [119] have conducted dynamic and steady shear capillary experiments of pure Nylon 6

with different molecular weights and their nanocomposites with organoclay over a large range of frequencies and shear rates. Figure 63 shows logarithmic plots of complex viscosity,  $|\eta^*|$  vs  $\omega$  at  $240^\circ C$  for pure Nylon 6 and



**Figure 63.** Complex viscosity vs frequency from a dynamic parallel plate rheometer (solid points) and steady shear viscosity vs shear rate from a capillary rheometer (open points) at  $240^\circ C$  for (a) pure HMW-Nylon 6 and its nanocomposite with (HE)<sub>2</sub>M<sub>1</sub>R<sub>1</sub> organoclay, (b) pure MMW-Nylon 6 and its nanocomposite with (HE)<sub>2</sub>M<sub>1</sub>R<sub>1</sub> organoclay, and (c) pure LMW-Nylon 6 and its nanocomposite with (HE)<sub>2</sub>M<sub>1</sub>R<sub>1</sub> organoclay. The content of MMT in each nanocomposite = 3 wt%. Reprinted with permission from [119], T. D. Fornes et al., *Polymer* 42, 9929 (2001). © 2001, Elsevier Science.

(HE)<sub>2</sub>M<sub>1</sub>R<sub>1</sub> nanocomposites based on (a) HMW, (b) MMW, and (c) LMW obtained using the parallel plate oscillating rheometer. Figure 63 also shows a plot of steady-state shear viscosity  $\eta$  versus shear rate  $\dot{\gamma}$  obtained using a capillary rheometer. From the figure we can see a significant difference between the nanocomposites particularly at low frequencies. The HMW-based nanocomposites show very strong non-Newtonian behavior and this is more pronounced at the low frequency region. On the other hand, this non-Newtonian behavior gradually decreases with decreasing molecular weight of the matrix, and with LMW it behaves like pure polymer. This particular trend is more clearly observed in plot of  $G'$  vs  $\omega$  due to the extreme sensitivity of  $G'$  toward dispersed morphology under the molten state [119]. The difference in terminal zone slopes may be due to the different extent of exfoliation of the clay particles in three types of matrices.

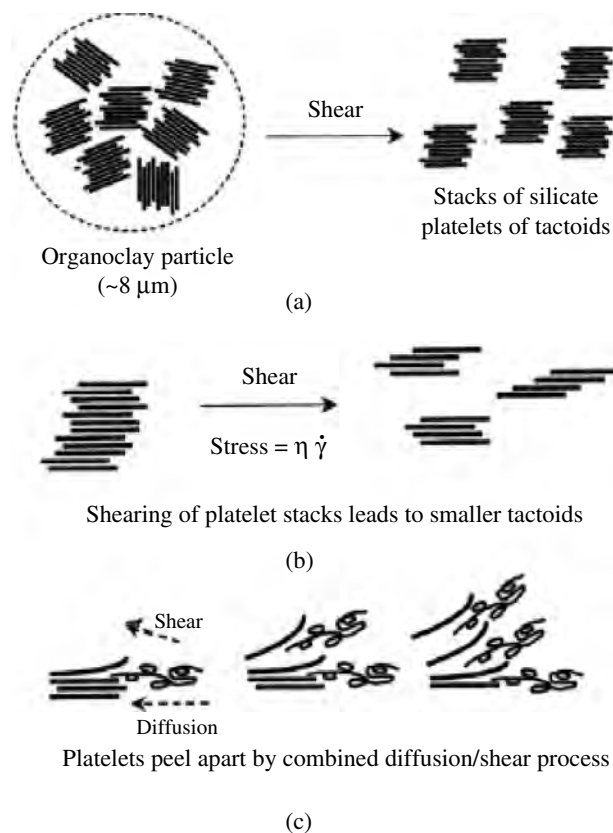
At the other extreme, the steady shear capillary shows a trend with respect to the matrix molecular weight. The HMW- and MMW-based nanocomposites show lower viscosities compared to that of their corresponding matrices, whereas viscosities of LMW-based nanocomposites are lower than pure matrix. According to them, this behavior also due the higher degree of exfoliation in case of HMW- and MMW-based nanocomposites compared to the LMW-based nanocomposite.

Finally they considered the differences in the melt viscosity among the three systems. Over the range of frequencies and shear rates tested, the melt viscosity of the three systems follow the order HMW > MMW > LMW, and hence the resulting shear stresses exerted by the pure polymers also follows same order. Therefore, during melt mixing, the level of stress exerted on the organoclay by the LMW polyamide is significantly lower than those developed in presence of HMW or MMW polyamides. As a result the breakup of clay particles is much easier in case of HMW polyamide and ultimately improved the clay particle dispersion.

Figure 64 shows schematic suggestions of various roles that shear stress may play during the melt compounding of nanocomposites. Therefore, the role of polymer molecular weight is believed to stem from the fact that a melt viscosity exerts the taller stacks into shorter ones. The final step in exfoliation involves peeling the platelets of the stacks one by one, and this takes time and requires a strong matrix–organoclay interaction to cause spontaneous wetting.

## 8.2. Steady Shear Flow

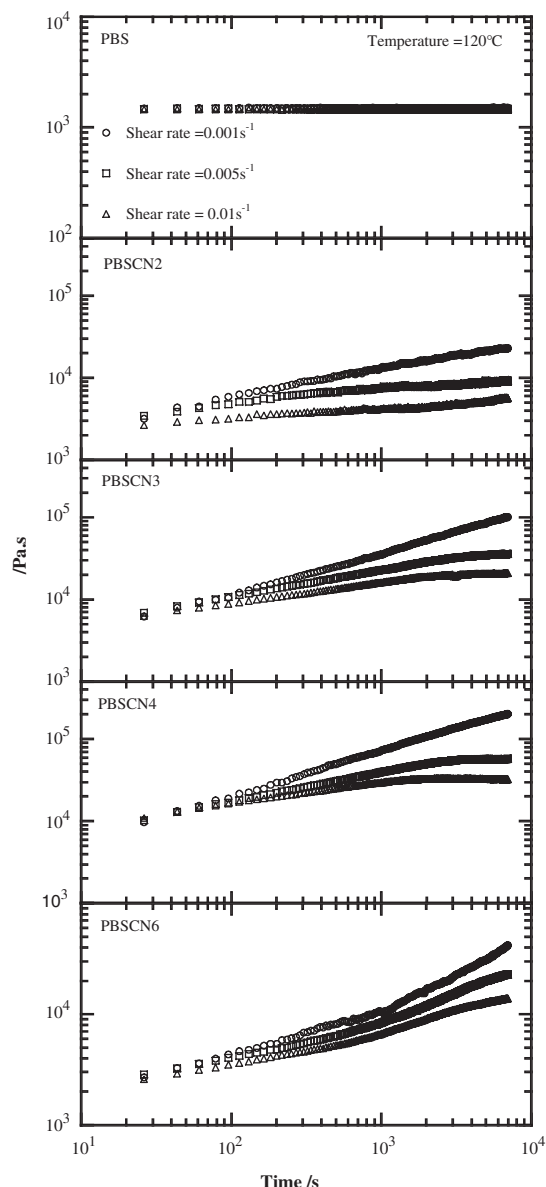
The steady shear rheological behaviors of neat PBS and various PBSCNs are shown in Figure 65. The steady viscosity of PBSCNs is enhanced considerably at all shear rates with time and at a fixed shear rate increases monotonically with increasing silicate loading [327]. On the other hand, all intercalated PBSCNs exhibit strong rheopexy behavior, and this becomes prominent at low shear rates, while neat PBS exhibits a time independent viscosity at all shear rates. With increasing shear rates, the shear viscosity attains a plateau after a certain time, and the time required to attain this plateau decreases with increasing shear rates. The possible



**Figure 64.** Stemwise mechanism of clay platelets exfoliation during melt compounding: (a) organoclay breakup, (b) intercalated organoclay tactoid breakup, and (c) platelet exfoliation. Reprinted with permission from [119], T. D. Fornes et al., *Polymer* 42, 9929 (2001). © 2001, Elsevier Science.

reasons for this type of behavior may be the planer alignment of the clay particles toward the flow direction under shear. When the shear rate is very slow ( $0.001 \text{ s}^{-1}$ ), clay particles take longer to attain complete planer alignment along the flow direction, and this measurement time (1000 s) is too short to attain such alignment and hence shows strong rheopexy behavior. On the other hand, under high shear rates ( $0.005$  or  $0.01 \text{ s}^{-1}$ ) this measurement time is considerable enough to attain such alignment, and hence nanocomposites show time independent shear viscosity after a certain time.

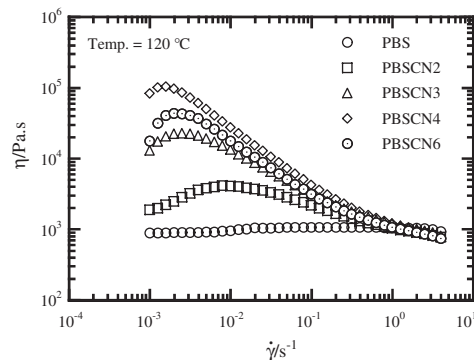
Figure 66 shows shear rate dependence of viscosity for neat PBS and corresponding nanocomposites measured at  $120^\circ\text{C}$ . The neat PBS exhibits almost Newtonian behavior at all shear rates, whereas nanocomposites exhibited non-Newtonian behavior. At very low shear rates, shear viscosity of nanocomposites initially exhibits some shear-tickening behavior and this corresponds to the rheopexy behavior as we observed at very low shear rates (see Fig. 65). After that all nanocomposites show very strong shear thinning behavior at all shear rates and this behavior is analogous to the results obtained in case of dynamic oscillatory shear measurements [324]. Additionally, at very high shear rates, the viscosities of nanocomposites are comparable to that of neat PBS. These observations suggest that the silicate layers are strongly oriented toward the flow direction at high shear rates, and



**Figure 65.** Time variation of shear viscosity for PBSCN. Reprinted with permission from [327], S. Sinha Ray et al., *Macromolecules* 36, 2355 (2003). © 2003, American Chemical Society.

shear thinning behavior at high shear rates is dominated by that of neat polymer.

The PCNs always exhibit significant deviation from Cox–Merz relation [366], while all neat polymers nicely obey the empirical Cox–Merz relation, which requires that for  $\dot{\gamma} = \omega$ , the viscoelastic data should obey the relationship  $\eta(\dot{\gamma}) = |\eta^*(\omega)|$ . We believe there are two possible reasons for the deviation from the Cox–Merz relation in case of nanocomposites: first of all this rule is only applicable for homogenous systems like homopolymer melts but nanocomposites are heterogeneous systems. For this reason this relation is nicely obeyed in case of neat polymer [327]. Second, the structure formation is different when nanocomposites are subjected to dynamic oscillatory shear and steady shear measurements.

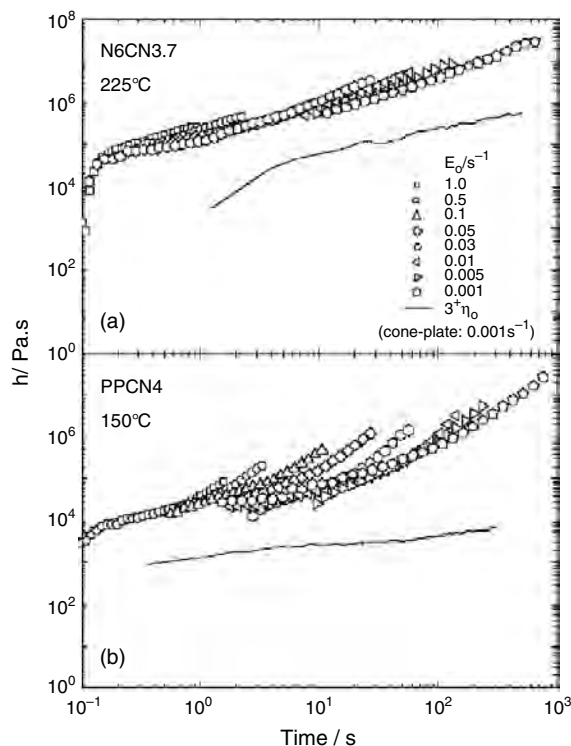


**Figure 66.** Shear viscosity as a function of shear rates for the shear rate sweep test. Reprinted with permission from [327], S. Sinha Ray et al., *Macromolecules* 36, 2355 (2003). © 2003, American Chemical Society.

### 8.3. Elongational Flow and Strain-Induced Hardening

Okamoto et al. [256] first conducted elongation tests of PP/clay nanocomposites (PPCN4) under molten state at constant Hencky strain rate  $\dot{\epsilon}_0$  using an elongation flow optorheometry [367], and also they attempted to control the alignment of the dispersed silicate layers with nanometer dimensions of an intercalated PPCNs under uniaxial elongational flow.

Figure 67 shows double logarithmic plots of transient elongational viscosity  $\eta_E(\dot{\epsilon}_0; t)$  against time  $t$  observed for



**Figure 67.** Time variation of elongational viscosity  $\eta_E(\dot{\epsilon}_0; t)$  for (a) N6CN3.7 melt at 225 °C and for (b) PPCN4 at 150 °C. The solid line shows three times the shear viscosity,  $3\eta_E(\dot{\gamma}; t)$ , taken at a low shear rate  $\dot{\gamma} = 0.001 \text{ s}^{-1}$  on a cone-plate rheometer.

a Nylon 6/clay system (N6CN3.7) and PPCN4 (MMT = 4 wt%) with different Hencky strain rates  $\dot{\epsilon}_0$  ranging from 0.001 to 1.0  $\text{s}^{-1}$ . The solid curve represents time development of threefold shear viscosity,  $3\eta_0(\dot{\gamma}; t)$ , at 225 °C with a constant shear rate  $\dot{\gamma} = 0.001 \text{ s}^{-1}$ . In  $\eta_E(\dot{\epsilon}_0; t)$  at any  $\dot{\epsilon}_0$ , N6CN3.7 melt shows a weak tendency of *strain-induced hardening* as compared to that of PPCN4 melt. A strong behavior of strain-induced hardening for the PPCN4 melt originated from the perpendicular alignment of the silicate layers to the stretching direction as reported by Okamoto et al. [256].

From TEM observations (see Fig. 60), the N6CN3.7 forms a fine dispersion of the silicate layers of about 100 nm in  $L_{\text{clay}}$ , 3 nm thickness in  $d_{\text{clay}}$ , and  $\xi_{\text{clay}}$  of about 20–30 nm between them. The  $\xi_{\text{clay}}$  value is one order of magnitude lower than the value of  $L_{\text{clay}}$ , suggesting the formation of spatially linked like structures of the dispersed clay particles in Nylon 6 matrix. For N6CN3.7 melt, the silicate layers are densely dispersed into the matrix and hence difficult to align under elongational flow. Under flow fields, the silicate layers might translationally move, but not rotationally in such a way that the loss energy becomes minimum. This tendency was also observed in PPCN7.5 melt having a higher content of MMT (=7.5 wt%) [365].

On the other hand, one can observe two features for the shear viscosity curve. First, the extended Trouton rule,  $3\eta_0(\dot{\gamma}; t) \cong \eta_E(\dot{\epsilon}_0; t)$ , does not hold for both N6CN3.7 and PPCN4 melts, as opposed to the melt of ordinary homopolymers. The latter,  $\eta_E(\dot{\epsilon}_0; t)$ , is more than 10 times larger than the former,  $3\eta_0(\dot{\gamma}; t)$ . Second, again unlike ordinary polymer melts,  $3\eta_0(\dot{\gamma}; t)$  of N6CN3.7 melt increases continuously with  $t$ , never showing a tendency of reaching a steady state within the time span (600 s or longer) examined here. This *time-dependent thickening* behavior may be called *anti-thixotropy* or *rheopexy*. Via slow shear flow ( $\dot{\gamma} = 0.001 \text{ s}^{-1}$ ),  $3\eta_0(\dot{\gamma}; t)$  of N6CN3.7 exhibits a much stronger rheopexy behavior almost two orders of magnitude higher than that of PPCN4. This reflects a fact that the shear-induced structural change involved a process with an extremely long relaxation time as well as for other PCNs having rheopexy behavior [325, 327], especially under weak shear field.

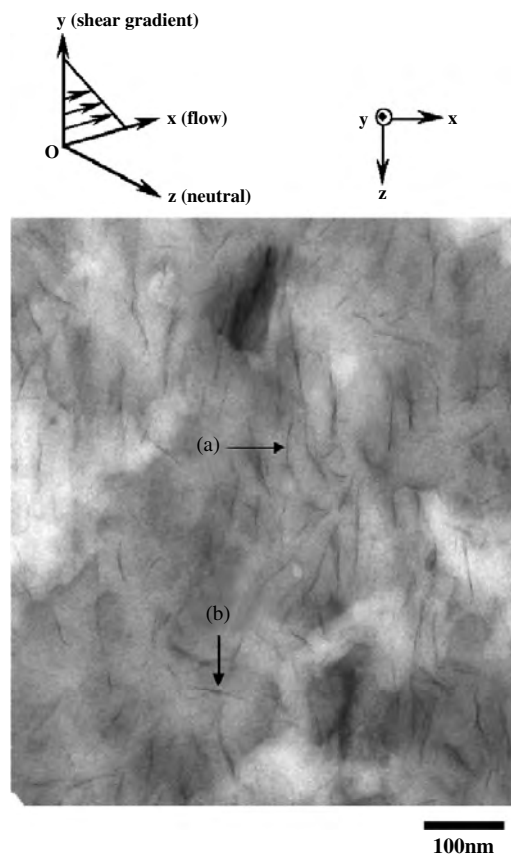
#### 8.4. Alignment of Silicate Layers

The orientation of silicate layers and Nylon 6 crystallites in injection molded N6CN3.7 using WAXD and TEM is examined [111]. Kojima et al. have found three regions of different orientations in the sample as a function of depth. Near the middle of the sample, where the shear forces are minimal, the silicate layers are oriented randomly and the Nylon 6 crystallites are perpendicular to the silicate layers. In the surface region, shear stresses are very high, so both the clay layers and the Nylon 6 crystallites are parallel to the surface. In the intermediate region, the clay layers, presumably due to their higher aspect ratio, still orient parallel to the surface and the Nylon 6 crystallites assume an orientation perpendicular to the silicate. Very recently, Medellin-Rodriguez et al. [117] reported that the molten N6CN samples showed planar orientation of silicate layers along the flow direction, which is strongly dependent

on shear time as well as clay loading, reaching a maximally orienting level after being sheared for 15 min with  $\dot{\gamma} = 60 \text{ s}^{-1}$ .

Okamoto et al. conducted TEM observations for the sheared N6CN3.7 with  $\dot{\gamma} = 0.0006 \text{ s}^{-1}$  for 1000 s [368]. The edges of the silicate layers laying along the  $z$ -axis [marked with the arrows (a)] or parallel alignment of the silicate edges to the shear direction ( $x$ -axis) [marked with the arrows (b)] rather than assuming random orientation in the Nylon 6 matrix is observed, but in fact, one cannot see these faces in this plane (Fig. 68). Here, it should be emphasized that the planar orientation of the silicate faces along the  $x$ - $z$  plane does not take place prominently. For the case of rapid shear flow, the commonly applicable conjecture of the planar orientation of the silicate faces along the shear direction was first demonstrated to be true by Kojima et al. [111].

In uniaxial elongational flow (converging flow) for a PPCN4, the formation of a *house-of-cards* structure is found by TEM analysis [256]. The perpendicular (but *not* parallel) alignment of disklike clay particles with large anisotropy toward the flow direction might sound unlikely but this could be the case especially under an elongational flow field, in which the extensional flow rate is the square of the converging flow rate along the thickness direction, if the assumption of *affine* deformation without volume change is valid. Obviously under such conditions, the energy dissipation rate due



**Figure 68.** TEM micrograph in the  $x$ - $z$  plane showing N6CN3.7 sheared at 225 °C with  $\dot{\gamma} = 0.0006 \text{ s}^{-1}$  for 1000 s. The  $x$ -,  $y$ -, and  $z$ -axes correspond respectively to flow, shear gradient, and neutral direction.

to viscous resistance between the disk surface and the matrix polymer is minimal, when the disks are aligned perpendicular to the flow direction.

Moreover, Lele et al. [265] recently reported the *in-situ* rheo-X-ray investigation of flow-induced orientation in syndiotactic PP/layered silicate nanocomposite melt.

Some 20 years ago van Olphen [369] pointed out that the electrostatic attraction between the layers of natural clay in aqueous suspension arises from higher polar force in the medium. The intriguing features such as yield stress thixotropy and/or rheopexy exhibited in aqueous suspensions of natural clay minerals may be taken as a reference to the present PCNs.

### 8.5. Electrorheology

Electrorheological fluids (ERFs), sometimes referred to as “smart fluids,” are suspensions consisting of polarizable particles dispersed in insulating media [370]. A mismatch in conductivity or dielectric constant between the dispersed particle and the continuous medium phase induces polarization upon application of an electric field. The induced particle dipoles under the action of an electric field tend to attract neighboring particles and cause the particles to form fibril-like structures, which are aligned to the electric field direction [371].

Among various materials [372–374], semiconducting polymer is one of the novel intrinsic ER systems since it has the advantage of a wide range of working temperature, reduced abrasion of device, low cost, and relatively low current density. As a result, development of a high-performance ER fluid followed by conducting polymer optimization and tuning has been the subject of considerable interest for practical applications as a new electromechanic interface. Nevertheless, the yield stress and modulus of ER fluids are lower than those of magnetorheological fluids. Thus the performance of conducting polymer-based ER fluids is still insufficient for the successful development of specific application devices.

On this basis of this information, Kim et al. [286] first introduced nanocomposite as ERFs using PANI/clay nanocomposites with intercalated structure. Though PANI/clay intercalated nanocomposites are a new material for application of ER materials, yield stresses of the system showed less than 100 Pa at 1.2 kV/mm (20 wt% suspensions). This value is a little lower than the yield stress of a pure PANI particle system [374]. In other words, no synergistic effect of clay on yield stress was shown.

Recently, Park et al. [375] observed remarkable enhancement of yield stress for electrorheological fluids in PANI-based nanocomposites of clay. In further study [376], they fabricated three kinds of ERFs containing different contents of PANI/clay nanocomposite and pure PANI particles in order to investigate the effect of nanocomposite particles on the enhancement of yield stress more systematically. They observed that there is an optimum content ratio between nanocomposite and pure PANI particles to produce minimum yield stress. Details regarding data collection and explanations are presented in [376].

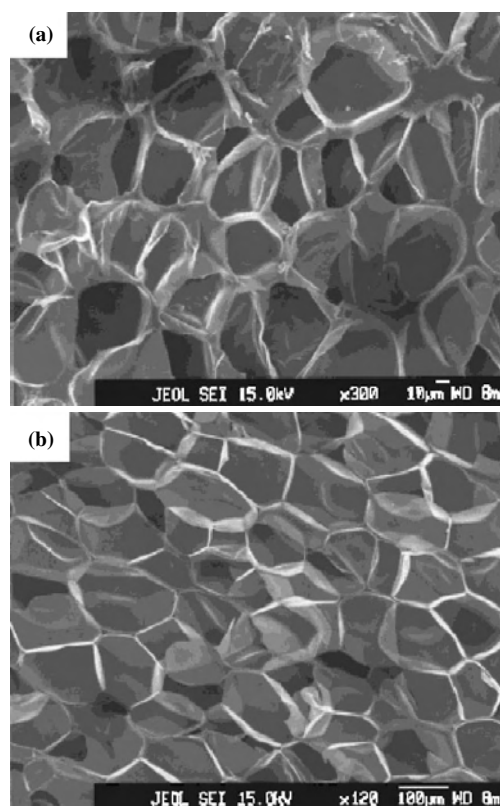
## 9. PROCESSING OPERATIONS OF POLYMER/CLAY NANOCOMPOSITES

The flow-induced internal structural change occurs in both shear and elongational flow, but they almost differ from each other, as judged from the previous results on  $\eta_E(\dot{\epsilon}_0; t)$  and  $3\eta_0(\dot{\gamma}; t)$  (see Fig. 67). Thus, with these rheological features of the PCNs and the characteristics of each processing operation, which process type should be selected for a particular nanocomposite for the enhancement of its mechanical properties?

For example, the strong strain-induced hardening in  $\eta_E(\dot{\epsilon}_0; t)$  is requisite for withstanding the stretching force during the processing, while the rheopexy in  $3\eta_0(\dot{\gamma}; t)$  suggests that for such PCN a promising technology is processing in confined space such injection molding where shear force is crucial.

### 9.1. Foam Processing Using Supercritical CO<sub>2</sub>

Via batch processing in an autoclave, the foam processing on PPCNs having different contents of clay by using supercritical CO<sub>2</sub> as foaming agent under 10 MPa at various temperatures is reported [257]. Figure 69 shows the typical results of scanning electron microscope (SEM) images of the fracture surfaces of the PPCN4 and PP-MA without clay. Both foams exhibit the polygon closed-cell structures having pentagonal



**Figure 69.** SEM micrographs for (a) PPCN4 and (b) PP-MA foamed at 134.7 °C. Reprinted with permission from [257], M. Okamoto et al., *Nano Lett.* 1, 503 (2001). © 2001, American Chemical Society.

and hexagonal faces, which express the most energetically stable state of polygon cells. The morphological parameters of the cells are listed in Table 20. The function for determining cell density  $N_c$  is defined as [377]

$$N_c \cong \frac{1 - \frac{\rho_f}{\rho_p}}{10^{-4}d^3} \quad (4)$$

The mean wall thickness  $\delta$  is given by

$$\delta = d \left( \frac{1}{\sqrt{1 - \frac{\rho_f}{\rho_p}}} - 1 \right) \quad (5)$$

where  $\rho_p$ ,  $\rho_f$ , and  $d$  are the density of the polymer (prefoamed materials), the density of the foam (post-foamed samples) in  $\text{g/cm}^3$ , and the mean cell size in mm, respectively. The PPCN4 foam shows smaller  $d$  and larger  $N_c$  compared to PP-MA foam, suggesting that the dispersed clay particles act as nucleating sites for cell formation and lowering of  $d$  with increasing clay content [262]. The final  $\rho_f$  is controlled by the competitive process in the cell nucleation, its growth, and coalescence. Cell nucleation, in a heterogeneous nucleation system such as PPCN4 (MMT = 4 wt%) foam, took place in the boundary between the matrix PP-MA and the dispersed clay particles. The cell growth and coalescence are strongly affected by the modulus and the loss modulus ( $\cong$ viscosity component) of the materials during processing. As mention in Section 8.3, the strain-induced hardening behavior is probably strong enough to increase the extensional viscosity under biaxial flow and to protect the cell from its breakage at high temperature. Therefore, the strain-induced hardening leads to the high cell wall thickness in the PPCN4 foam.

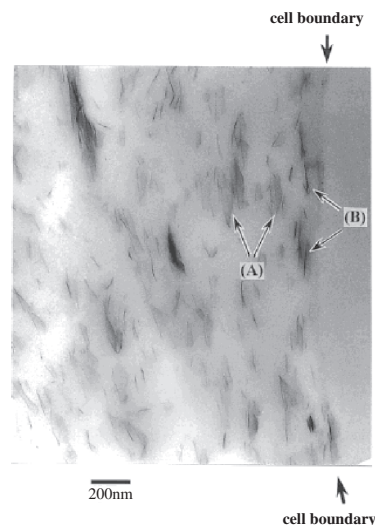
The alignment of the dispersed clay particles under biaxial flow in the foam processing is also observed (Fig. 70). Due to the biaxial flow of material during the foam process, the clay particles either turned their face [marked with the arrows (A) in Fig. 70] or had fixed face orientation [marked with the arrows (B) in Fig. 70] and aligned along the flow direction of materials (i.e., along the cell boundary). The interesting point here is that such aligning behavior of the clay particles may help cells to withstand the stretching force from breaking the thin cell wall, in other words, to improve the strength of foam in mechanical properties. The clay particles seem to act as a secondary cloth layer to protect the cells from being destroyed by external forces. The compression modulus  $K'$  of the PPCN foams appears higher than

**Table 20.** Morphological parameters and compression modulus of PP-MA and PPCN foams.

Foam samples	$\rho_f$ ( $\text{g/cm}^3$ )	$d$ ( $\mu\text{m}$ )	$N_c \times 10^{-6}$ ( $\text{cell/cm}^3$ )	$\delta$ ( $\mu\text{m}$ )	$K'^a$ (MPa)
PP-MA	0.06	155.3	2.49	5.6	0.44
PPCN2	0.06	133.0	3.94	4.6	1.72
PPCN4	0.12	93.4	9.64	11.9	1.95
PPCN7.5	0.13	33.9	220	2.7	2.80

<sup>a</sup> At 25 °C.

Source: Reprinted with permission from [257], M. Okamoto et al., *Nano Lett.* 1, 503 (2001). © 2001, American Chemical Society.



**Figure 70.** TEM micrographs for PPCN4 foamed at 134.7 °C (monocell wall). Reprinted with permission from [257], M. Okamoto et al., *Nano Lett.* 1, 503 (2001). © 2001, American Chemical Society.

that of PP-MA foam even though its at same  $\rho_f$  level (see Table 20). This may create the improvement of mechanical properties for polymeric foams through PCNs.

Recently, some literature has become available [378] related to the reactive extrusion foaming of various nanocomposites.

## 9.2. Slow Shear Flow Processing

Very slow shear processing for the Nylon 6/clay system (N6CN3.7) (MMT = 3.7 wt%) is examined with the expectation that it would result in an excellent material having enhanced mechanical properties of the PCN [368]. As anticipated, N6CN3.7 subjected to shear processing shows strong enhancement in relative modulus as compared to the corresponding Nylon 6 matrix (Table 21). For example, after having been sheared with  $\dot{\gamma} = 0.0006 \text{ s}^{-1}$  for 1000 s, the modulus of N6CN3.7 at 30 °C was 2.6 times higher, while for the presheared N6CN3.7 the modulus was only 1.8 times higher than that of neat Nylon 6. To improve the modulus, the silicate layers seem to act as an internal bone layer to protect the materials from being bent by external forces.

## 9.3. Electrospinning Processing

Fibers and nanofibers of N6CN (diameter of 100–500 nm) were electrospun from HFIP solution and collected as nonwoven fabrics or as aligned yarns [379]. The

**Table 21.** Bending modulus for N6CN3.7 and neat Nylon 6.

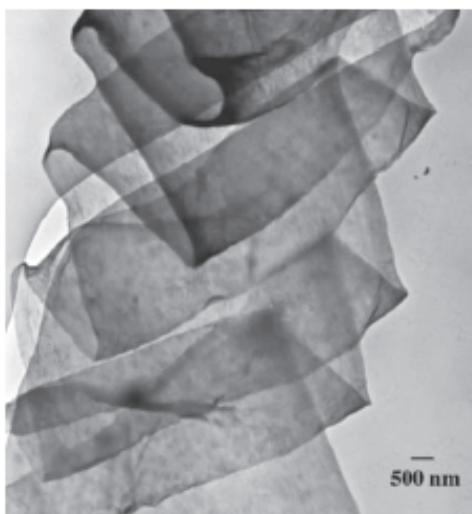
Sample $T^a$ °C	Modulus of N6CN3.7 (GPa)		Modulus of Nylon 6 (GPa)	
	Preshear	Postshear	Preshear	Postshear
30	2.69	4.00	1.51	1.54
150	1.76	2.22	0.46	0.52

<sup>a</sup> Measuring temperature.

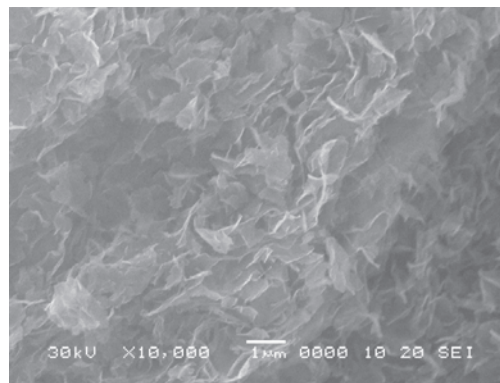
electrospinning process resulted in highly aligned MMT particles and Nylon 6 crystallites. The cylindrical shaped fibers, nanofibers, and ribbon shaped fibers were also found in the products (Fig. 71). The electrospinning can be expected to align other nanofillers such as carbon nanotubes.

#### 9.4. Porous Ceramic Materials via PCNs

Very recently, a new route for the preparation of porous ceramic material from thermosetting epoxy/clay nanocomposite was first demonstrated by Brown et al. [380]. This route offers an attractive potential for diversification and application of the PCNs. Sinha Ray and co-workers have reported the results on the novel porous ceramic material via burning of the PLA/clay system (PLACN) [315]. The SEM image of the fractured surface of porous ceramic material prepared from simple burning of the PLACN in a furnace up to 950 °C is shown in Figure 72. After complete burning, as seen in the figure, the PLACN becomes a white mass with a porous structure. The bright lines in the SEM image correspond to the edge of the stacked silicate layers. In the porous ceramic material, the silicate layers form a house-of-cards structure, which consists of large plates having lengths of ~1000 nm and thicknesses of ~30–60 nm. This implies that the further stacked platelet structure is formed during burning. The material exhibits the open-cell-type structure having 100–1000 nm diameter voids, BET surface area of 31 m<sup>2</sup> g<sup>-1</sup>, and low density of porous material of 0.187 g ml<sup>-1</sup> estimated by the buoyancy method. The BET surface area value of MMT is 780 m<sup>2</sup>/g and that of the porous ceramic material is 31 m<sup>2</sup>/g, suggesting about 25 MMT plates stacked together. When MMT is heated above 700 °C (but below 960 °C) first all OH groups are eliminated from the structure and thus MMT is decomposed into that of a nonhydrated aluminosilicate. This transformation radically disturbs the crystalline network of the MMT, and the resulting diffraction pattern is indeed often typical of an amorphous (or noncrystalline) phase.



**Figure 71.** TEM micrograph of a ribbon shaped nanofiber. Reprinted with permission from [379], P. H. Fong et al., *Polymer* 43, 775 (2002). © 2002, Elsevier Science.



**Figure 72.** SEM image of porous ceramic material after coated with platinum layer (~10 nm thickness). Reprinted with permission from [315], S. Sinha Ray et al., *Nano Lett.* 2, 423 (2002). © 2002, American Chemical Society.

The estimated rough value of compression modulus  $K$  is in the order of ~1.2 MPa, which is five orders of magnitude lower than the bulk modulus of MMT (~10<sup>2</sup> GPa) [33]. In the stress–strain curve, the linear deformation behavior is nicely described in the early stage of the deformation (i.e., the deformation of the material closely resembles that of ordinary polymeric foams) [381]. This open-cell-type porous ceramic material consisting of the house-of-cards structure is expected to provide strain recovery and excellent energy dissipation mechanism after unloading in the elastic region up to 8% strain; probably each plate bends like a leaf spring. This porous ceramic material is an elastic and very lightweight new material. This new route for the preparation of porous ceramic material via burning of nanocomposites can be expected to pave the way for a much broader range of applications of the PCNs.

## 10. CONCLUSIONS

Development of the PCNs is one of the latest evolutionary steps of polymer technology. PCNs offer attractive potential for diversification and application of conventional polymeric materials. Since the possibility of direct melt intercalation first demonstrated by Vaia et al. [31], the melt intercalation method has become the mainstream preparation for intercalated polymer nanocomposites without *in-situ* intercalative polymerization. It is a quite effective technology for the case of the PCN industry. Some of PCNs are already commercially available and applied in industrial products. Biodegradable polymer based PCNs seem to have a very bright future for a wide range of applications such as high performance biodegradable materials. Undoubtedly, the unique properties originating from the controlled nanostructure pave the way for a much broader range of applications.

Although a significant amount of work has already been done on various aspects of PCNs, a lot of research still remains to be carried out in order to understand the structure–property relationship in various PCNs. On the other hand, we have to conduct rheological measurements of various PCNs under molten states in detail, in order to



discover the processing conditions of these materials, and this is the final goal of any polymeric material.

Finally, PCNs show concurrent improvement in various materials properties at very low clay content together with the ease of preparation through simple processes such as melt intercalation, directly by melt extrusion, or injection molding, opening a new dimension for plastics and composites.

## GLOSSARY

**Clay** General family of 2:1 layered- or phyllosilicates. Their crystal structure consists of layers made up of two silica tetrahedral fused to an edge-shared octahedral sheet of either aluminium or magnesium hydroxide. The layer thickness is around 1 nm and the lateral dimensions of these layers may vary from 30 nm to several microns and even larger depending on the particular layered silicate.

**Exfoliation** Extensive polymer penetration resulting in disordered and eventual delamination of the silicate layers produces *near* to exfoliated nanocomposites consisting of individual silicate layers dispersed in polymer matrix.

**Flocculation** Conceptually this is same with intercalated nanocomposites, however, silicate layers are sometimes flocculated due to hydroxylated edge-edge interaction of the silicate layers (intercalated and flocculated).

**Green polymeric materials** These would not involve the use of toxic or noxious components in their manufacture, and could be degraded in natural environment or easily recycled. Aliphatic polyesters are among the most promising materials for the production of environmentally friendly biodegradable plastics.

**Intercalation** Polymer penetration resulting in finite expansion of the silicate layers produces intercalated nanocomposites consisting of well-ordered multilayers with alternating polymer/silicate layers and a repeat distance of few nanometers.

**Montmorillonite** One of the most commonly used layered silicates ( $M_{1/3}(Al_{5/3}Mg_{1/3})Si_4O_{10}(OH)_2$ ). This clay is only miscible with hydrophilic polymers, such as poly (ethylene oxide) and poly (vinyl alcohol).

**Nanocomposite** Phase mixing of at least two dissimilar materials (e.g., polymer and inorganic filler) occurs on a nanometer scale. The nanocomposite exhibits remarkable improvement of materials properties.

**Organo-clay** To improve miscibility with other polymer matrices, one must convert the normally hydrophilic silicate surface to organophilic, which makes possible intercalation of many engineering polymers. Generally, this can be done by ion-exchange reactions with cationic surfactants including primary, secondary, tertiary, and quaternary alkyl ammonium or alkylphosphonium cations.

## REFERENCES

1. A. Usuki, Y. Kojima, A. Okada, Y. Fukushima, T. Kurauchi, and O. Kamigaito, *J. Mater. Res.* 8, 1174 (1993).
2. Y. Kojima, A. Usuki, M. Kawasumi, A. Okada, Y. Fukushima, T. Kurauchi, and O. Kamigaito, *J. Mater. Res.* 8, 1185 (1993).

3. P. C. LeBaron, Z. Wang, and T. Pinnavaia, *J. Appl. Clay Sci.* 15, 11 (1999).
4. E. Manias, A. Touny, L. Wu, K. Strawhecker, B. Lu, and T. C. Chung, *Chem. Mater.* 13, 3561 (2001).
5. T. Lan, D. K. Padmananda, and T. J. Pinnavaia, *Chem. Mater.* 7, 2144 (1995).
6. Y. I. Tien and K. H. Wei, *Polymer* 42, 3213 (2001).
7. J. C. Huang, Z. Zhu, J. Yin, X. Qian, and Y. Sun, *Polymer* 42, 873 (2001).
8. T. Agag and T. Takeichi, *Polymer* 41, 7083 (2000).
9. G. Galgali, C. Ramesh, and A. Lele, *Macromolecules* 34, 852 (2001).
10. X. Fu and S. Qutubuddin *Polymer* 42, 807 (2001).
11. M. Okamoto, S. Morita, H. Taguchi, Y. H. Kim, T. Kotaka, and H. Tateyama, *Polymer* 41, 3887 (2000).
12. M. Okamoto, S. Morita, and T. Kotaka, *Polymer* 42, 2685 (2001).
13. P. Messersmith and E. Giannelis, *J. Polym. Sci., Polym. Chem.* 33, 1047 (1995).
14. M. Kawasumi, N. Hasegawa, M. Kato, A. Usuki, and A. Okada, *Macromolecules* 30, 6333 (1997).
15. N. Hasegawa, M. Kawasumi, M. Kato, A. Usuki, and A. Okada, *J. Appl. Polym. Sci.* 67, 87 (1998).
16. National Lead Co., U.S. Patent 2, 531, 396, 1950.
17. Union Oil Co., U.S. Patent 3, 084, 117, 1963.
18. Unitika Ltd., Japanese Kokai Patent Application 109998, 1976.
19. Y. Fukushima and S. Inagaki, *J. Incl. Phen.* 5, 473 (1987).
20. P. Aranda and E. Ruiz-Hitzky, *Chem. Mater.* 4, 1395 (1992).
21. D. J. Greenland, *J. Colloid Sci.* 18, 647 (1963).
22. A. Blumstein, *J. Polym. Sci. A* 3, 2653 (1965).
23. Krishnamoorti, R. A. Vaia, and E. P. Giannelis, *Chem. Mater.* 8, 1728 (1996).
24. R. A. Vaia, R. K. Teukolsky, and E. P. Giannelis, *Chem. Mater.* 6, 1017 (1994).
25. M. J. Solomon, A. S. Almusallam, K. F. Seefeld, S. Somwangthanoj, and P. Varadan, *Macromolecules* 34, 1864 (2001).
26. R. A. Vaia and E. P. Giannelis, *Polymer* 42, 1281 (2001).
27. J. Billingham, C. Breen, and Yarwood, *J. Vibr. Spectrosc.* 14, 19 (1997).
28. C. O. Oriakhi, I. V. Farr, and M. M. Lerner, *Clay Clay Minerals* 45, 194 (1997).
29. M. Alexandre and P. Dubois, *Mater. Sci. Eng. R* 28, 1 (2000).
30. P. H. Nam, P. Maiti, M. Okamoto, T. Kotaka, N. Hasegawa, and A. Usuki, *Polymer* 42, 9633 (2001).
31. R. A. Vaia, H. Ishii, and E. P. Giannelis, *Chem. Mater.* 5, 1694 (1993).
32. E. P. Giannelis, R. Krishnamoorti, and E. Manias, *Adv. Polym. Sci.* 138, 107 (1999).
33. M. Okamoto, S. Morita, Y. H. Kim, T. Kotaka, and H. Tateyama, *Polymer* 42, 1201 (2001).
34. S. Sinha Ray, P. Maiti, M. Okamoto, K. Yamada, and K. Ueda, *Macromolecules* 35, 3104 (2002).
35. A. Blumstein, S. L. Malhotra, and A. C. Watterson, *J. Polym. Sci. A* 8, 1599 (1970).
36. D. C. Lee and L. W. Jang, *J. Appl. Polym. Sci.* 61, 1117 (1996).
37. G. Chen, X. Chen, Z. Lin, W. Ye, and K. Yao, *J. Mater. Sci. Lett.* 18, 1761 (1999).
38. G. Chen, K. Yao, and J. Zhao, *J. Appl. Polym. Sci.* 73, 425 (1999).
39. A. Tabtiang, S. Lumlong, and R. A. Venables, *Eur. Polym. J.* 36, 2559 (2000).
40. A. Tabtiang, S. Lumlong, and R. A. Venables, *Polym. Plast. Technol. Eng.* 39, 293 (2000).
41. S. Bandyopadhyay and E. P. Giannelis, *Polym. Mater. Sci. Eng.* 82, 208 (2000).
42. X. Huang and W. J. Brittain, *Macromolecules* 34, 3255 (2001).
43. C. Zeng and L. J. Lee, *Macromolecules* 34, 4098 (2001).
44. N. Salahuddin and M. Shehata, *Polymer* 42, 8379 (2001).

45. C. Forte, M. Geppi, S. Giamberini, G. Ruggeri, C. A. Veracini, and B. Mendez, *Polymer* 39, 2651 (1998).
46. F. Dietsche, Y. Thomann, R. Thomann, and R. Mulhaupt, *J. Appl. Polym. Sci.* 75, 369 (2000).
47. T. Seckin, Y. Onal, I. Aksoy, and M. E. Yakinci, *J. Mater. Sci.* 31, 3123 (1996).
48. F. Dietsche and R. Mulhaupt, *Polym. Bull.* 43, 395 (1999).
49. Z. Chen, C. Huang, S. Liu, Y. Zhang, and K. Gong, *J. Appl. Polym. Sci.* 75, 796 (2000).
50. J. Billingham, C. Breen, and Yarwood, *J. Vib. Spectrosc.* 14, 19 (1997).
51. J. Lin, J. Wu, Z. Yang, and M. Pu, *Macromol. Rapid Commun.* 22, 422 (2001).
52. R. Blumstein, A. Blumstein, and K. K. Parikh, *Appl. Polym. Symp.* 25, 81 (1994).
53. Y. Sugahara, S. Satakawa, K. Kuroda, and C. Kato, *Clays Clays Miner.* 36, 343 (1988).
54. F. Bergaya and F. Kooli, *Clay Miner.* 26, 33 (1991).
55. Y. S. Choi, K. H. Wang, M. Xu, and I. J. Chung, *Chem. Mater.* 14, 2936 (2002).
56. C. Kato, K. Kuroda, and H. Takahara, *Clays Clay Miner.* 29, 294 (1981).
57. A. Akelah, in "Polymers and Other Advanced Materials: Emerging Technologies and Business Opportunities" (P. N. Prasad, J. E. Mark, and F. J. Ting, Eds.), p. 625. Plenum, New York, 1995.
58. R. A. Vaia, K. D. Jant, E. J. Kramer, and E. P. Giannelis, *Chem. Mater.* 8, 2628 (1996).
59. R. Krishnamoorti, R. A. Vaia, and E. P. Giannelis, *Chem. Mater.* 8, 1728 (1996).
60. A. Akelah and M. Moet, *J. Mater. Sci.* 31, 3589 (1996).
61. M. Sikka, L. N. Cerini, S. S. Ghosh, and K. I. Winey, *J. Polym. Sci. B* 34, 1443 (1996).
62. M. Laus, M. Camerani, M. Lelli, K. Sparnacci, F. Sandrolini, and O. F. Francescangeli, *J. Mater. Sci.* 33, 2883 (1998).
63. J. G. Doh and I. Cho, *Polym. Bull.* 41, 511 (1998).
64. T. L. Porter, M. E. Hagerman, B. P. Reynolds, and M. E. Eastman, *J. Polym. Sci. B* 36, 673 (1998).
65. N. Hasegawa, H. Okamoto, M. Kawasumi, and A. Usuki, *J. Appl. Polym. Sci.* 74, 3359 (1999).
66. M. W. Noh and D. C. Lee, *Polym. Bull.* 42, 619 (1999).
67. M. W. Weimer, H. Chen, E. P. Giannelis, and D. Y. Sogah, *J. Am. Chem. Soc.* 121, 1615 (1999).
68. X. Fu and S. Qutubuddin, *Polymer* 42, 807 (2000).
69. G. Chen, S. Liu, S. Zhang, and Z. Qi, *Macromol. Rapid Commun.* 21, 746 (2000).
70. Y. T. Lim and O. O. Park, *Macromol. Rapid Commun.* 21, 231 (2000).
71. B. Hoffman, C. Dietrich, R. Thomann, C. Friedrich, and R. Mulhaupt, *Macromol. Rapid Commun.* 21, 57 (2000).
72. C. Zilg, R. Thomann, M. Baumert, J. Finter, and R. Mulhaupt, *Macromol. Rapid Commun.* 21, 1214 (2000).
73. H. D. Wu, C. R. Tseng, and F. C. Chang, *Macromolecules* 34, 2992 (2001).
74. P. Xiao, M. Xiao, and K. Gong, *Polymer* 42, 4813 (2001).
75. C.-R. Tseng, J.-Y. Wu, H.-Y. Lee, and F.-C. Chang, *Polymer* 42, 10063 (2001).
76. J. Zhu, A. B. Morgan, F. J. Lamelas, and C. A. Wilkie, *Chem. Mater.* 13, 3774 (2001).
77. Q. H. Zeng, D. Z. Wang, A. B. Yu, and G. Q. Lu, *Nanotechnology* 13, 549 (2002).
78. F. L. Beyer, N. C. B. Tan, A. Dasgupta, and M. E. Galvin, *Chem. Mater.* 14, 2983 (2002).
79. J. W. Gilman, W. H. Awad, R. D. Davis, J. Shields, R. H. Harris, Jr., C. Davis, A. B. Morgan, T. E. Sutto, J. Callahan, P. C. Trulove, and H. C. DeLong, *Chem. Mater.* 14, 3776 (2002).
80. M. Y. Gelfer, H. S. Hyun, L. Liu, B. S. Haiao, B. Chu, M. Rafailovich, M. Si, and V. Zaitsev, *J. Polym. Sci. B* 41, 44 (2003).
81. H. Z. Friedlander and C. R. Frink, *J. Polym. Sci. B* 2, 457 (1964).
82. N. A. Churochkina, S. G. Starodoubtsev, and A. R. Khokhlov, *Polym. Gels Networks* 6, 205 (1998).
83. D. Gao, R. B. Heimann, M. C. Williams, L. T. Wardhaugh, and M. Muhammad, *J. Mater. Sci.* 34, 1543 (1999).
84. A. Wheeler, U.S. Patent 2, 847, 391, 1958.
85. N. Ogata, S. Kawakage, and T. Ogihara, *J. Appl. Polym. Sci.* 66, 573 (1997).
86. H. Matsuyama and J. F. Young, *Chem. Mater.* 11, 16 (1999).
87. K. E. Strawhecker and E. Manias, *Chem. Mater.* 12, 2943 (2000).
88. C. W. Francis, *Soil Sci.* 115, 40 (1973).
89. K. A. Carrado and L. Xu, *Chem. Mater.* 10, 1440 (1998).
90. Y. Komori, Y. Sugahara, and K. Kuroda, *Chem. Mater.* 11, 3 (1999).
91. R. Levy and C. W. Francis, *J. Colloid Interface Sci.* 50, 442 (1975).
92. A. Nisha, M. K. Rajeswari, and R. Dhamodharan, *J. Appl. Polym. Sci.* 76, 1825 (2000).
93. C. M. Koo, H. T. Ham, M. H. Choi, S. O. Kim, and I. J. Chung, *Polymer* 44, 681 (2003).
94. K. G. Fournaris, M. A. Karakassides, and D. Petridis, *Chem. Mater.* 11, 2372 (1999).
95. R. L. Parfitt and D. J. Greenland, *Clay Miner.* 8, 305 (1970).
96. X. Zhao, K. Urano, and S. Ogasawara, *Colloid Polym. Sci.* 267, 899 (1989).
97. L. Priya and J. P. Jog, *J. Polym. Sci. B* 41, 31 (2003).
98. C. O. Oriakhi, X. Zhang, and M. M. Lerner, *Appl. Clay Sci.* 15, 109 (1999).
99. N. Nugay, Kusefoglus, and B. Erman, *J. Appl. Polym. Sci.* 66, 1943 (1997).
100. S. W. Kim, W. H. Jo, M. S. Lee, M. B. Ko, and J. Y. Jho, *Polymer* 42, 9837 (2001).
101. N. Artzi, Y. Nir, M. Nakris, and A. Seigmann, *J. Polym. Sci. B* 40, 1741 (2002).
102. J. Ren, A. S. Silva, and R. Krishnamoorti, *Macromolecules* 33, 3739 (2000).
103. C. A. Mitchell and R. Krishnamoorti, *J. Polym. Sci. B* 40, 1434 (2002).
104. N. Schamp and Huylebroeck, *J. Polym. Sci. Polym. Symp.* 42, 553 (1973).
105. A. Usuki, Y. Kojima, M. Kawasumi, A. Okada, Y. Fukushima, T. Kurauchi, and O. Kamigaito, *J. Mater. Res.* 8, 1179 (1993).
106. Y. Kojima, A. Usuki, M. Kawasumi, A. Okada, T. Kurauchi, and O. Kamigaito, *J. Polym. Sci. A* 31, 983 (1993).
107. Y. Kojima, A. Usuki, M. Kawasumi, A. Okada, T. Kurauchi, and O. Kamigaito, *J. Polym. Sci. A* 31, 1755 (1993).
108. Y. Kojima, A. Usuki, M. Kawasumi, A. Okada, T. Kurauchi, and O. Kamigaito, *J. Appl. Polym. Sci.* 49, 1259 (1993).
109. A. Okada and A. Usuki, *Mater. Sci. Eng. C* 3, 109 (1995).
110. Y. Kojima, A. Usuki, M. Kawasumi, A. Okada, T. Kurauchi, O. Kamigaito, and K. Kaji, *J. Polym. Sci. B* 32, 625 (1994).
111. Y. Kojima, A. Usuki, M. Kawasumi, A. Okada, T. Kurauchi, O. Kamigaito, and K. Kaji, *J. Polym. Sci. B* 33, 1039 (1995).
112. A. Usuki, A. Koiwai, Y. Kojima, M. Kawasumi, A. Okada, T. Kurauchi, and O. Kamigaito, *J. Appl. Polym. Sci.* 55, 119 (1995).
113. "Polymer-Clay Nanocomposites" (T. J. Pinnavaia and G. W. Beall, Eds.). Wiley, New York, 2000.
114. L. M. Liu, Z. N. Qi, and X. G. Zhu, *J. Appl. Polym. Sci.* 71, 1133 (1999).
115. S. H. Wu, F. Y. Wang, C.-C. M. Ma, W. C. Chang, C. T. Kuo, H. C. Kuan, and W. J. Chen, *Mater. Lett.* 49, 327 (2001).
116. D. M. Lincoln, R. A. Vaia, Z. G. Wang, and B. S. Hsiao, *Polymer* 42, 1621 (2001).
117. F. J. Medellin-Rodriguez, C. Burger, B. S. Hsiao, B. Chu, R. A. Vaia, and S. Phillips, *Polymer* 42, 9015 (2001).
118. H. R. Dennis, D. L. Hunter, D. Chang, S. Kim, J. L. White, J. W. Cho, and D. R. Paul, *Polymer* 42, 9513 (2001).

119. T. D. Fornes, P. J. Yoon, H. Keskkula, and D. R. Paul, *Polymer* 42, 9929 (2001).
120. J. S. Shelley, P. T. Mather, and DeVries, *Polymer* 42, 5849 (2001).
121. D. L. VanderHart, A. Asano, and J. W. Gilman, *Chem. Mater.* 13, 3781 (2001).
122. Q. Wu and X. Liu, *Polymer* 43, 1933 (2002).
123. T. D. Fornes, P. J. Yoon, D. L. Hunter, H. Keskkula, and D. R. Paul, *Polymer* 43, 5915 (2002).
124. M. R. Kamal, N. K. Borse, and A. Garcia-Rejon, *Polym. Eng. Sci.* 42, 1883 (2002).
125. M. N. Bureau, J. Denault, K. C. Cole, and G. D. Enright, *Polym. Eng. Sci.* 42, 1897 (2002).
126. Y. Ding, D. J. Jones, P. Maireles-Torres, and J. Roziere, *Chem. Mater.* 7, 562 (1995).
127. P. Reichert, J. Kressler, R. Thomann, R. Mulhaupt, and G. Stoppelmann, *Acta Polym.* 49, 116 (1998).
128. B. Hoffman, J. Kressler, G. Stoppelmann, C. Friedrich, and G. M. Kim, *Colloid Polym. Sci.* 278, 629 (2000).
129. E. Giza, H. Ito, T. Kikutani, and N. Okui, *J. Polym. Eng.* 20, 403 (2000).
130. G. M. Kim, D. H. Lee, B. Hoffmann, J. Kresler, and G. Stoppelmann, *Polymer* 42, 1095 (2001).
131. S. V. Nair, L. A. Goettler, and B. A. Lysek, *Polym. Eng. Sci.* 42, 1872 (2002).
132. X. Liu, Q. Wu, Q. Zhang, and Z. Mo, *J. Polym. Sci. B* 44, 63 (2003).
133. P. B. Messersmith and E. P. Giannelis, *Chem. Mater.* 5, 1064 (1993).
134. G. Jimenez, N. Ogata, H. Kawai, and T. Ogihara, *J. Appl. Polym. Sci.* 64, 2211 (1997).
135. R. Krishnamoorti and E. P. Giannelis, *Macromolecules* 30, 4097 (1997).
136. G. Jimenez, N. Ogata, H. Kawai, and T. Ogihara, *J. Appl. Polym. Sci.* 64, 2211 (1997).
137. N. Pantoustier, M. Alexandre, P. Degee, C. Calberg, R. Jerome, C. Henrist, R. Cloots, A. Rulmont, and P. Dubois, *Polymer* 9, 1 (2001).
138. N. Pantoustier, B. Lepoittevin, M. Alexandre, D. Kubies, C. Calberg, R. Jerome, and P. Dubois, *Polym. Eng. Sci.* 42, 1928 (2002).
139. B. Lepoittevin, N. Pantoustier, M. Devalckenaere, M. Alexandre, D. Kubies, C. Calberg, R. Jerome, and P. Dubois, *Macromolecules* 35, 8385 (2002).
140. B. Lepoittevin, M. Devalckenaere, N. Pantoustier, M. Alexandre, D. Kubies, C. Calberg, R. Jerome, and P. Dubois, *Polymer* 43, 1111 (2002).
141. Y. Ke, C. Long, and Z. Qi, *J. Appl. Polym. Sci.* 71, 1139 (1999).
142. D. J. Sekelik, S. Stepanov Enazarenko, D. Schiraldi, A. Hiltner, and E. Baer, *J. Polym. Sci. B* 37, 847 (1999).
143. J. C. Matayabas, Jr., S. R. Turner, B. J. Sublett, G. W. Connell, and R. B. Barbee, (Eastman Chemical Co.), PCT Int. Appl. Wo 98/29499, 1998.
144. T. Takekoshi, F. F. Khouri, J. R. Campbell, T. C. Jordan, and K. H. Dai, (General Electric Co.), U.S. Patent 5, 530, 052, 1996.
145. M. Okamoto, Y. Shinoda, T. Okuyama, A. Yamaguchi, and T. Sekura, *J. Mater. Sci. Lett.* 15, 1178 (1996).
146. C. H. Davis, L. J. Mathias, J. W. Gilman, D. A. Schiraldi, J. R. Shields, P. Trulove, T. E. Sutto, and H. C. Delong, *J. Polym. Sci. B* 40, 2661 (2002).
147. Y. Imai, S. Nishimura, E. Abe, H. Tateyama, A. Abiko, A. Yamaguchi, T. Aoyama, and H. Taguchi, *Chem. Mater.* 14, 477 (2002).
148. B. J. Chisholm, R. B. Moore, G. Barber, F. Khouri, A. Hempstead, M. Larsen, E. Olson, J. Kelley, G. Balch, and J. Caraher, *Macromolecules* 35, 5508 (2002).
149. X. Huang, S. Lewis, W. J. Brittain, and R. A. Vaia, *Macromolecules* 33, 2000 (2000).
150. M. Mitsunaga, K. Hironaka, and M. Okamoto, *Polym. Preprints Japan* 51, 2645 (2002); *Macromol. Mater. Eng.* 288, 543 (2003).
151. J. Wu and M. M. Lerner, *Chem. Mater.* 5, 835 (1993).
152. R. A. Vaia, S. Vasudevan, W. Krawiec, L. G. Scanlon, and E. P. Giannelis, *Adv. Mater.* 7, 154 (1995).
153. S. Wong, S. Vasudevan, R. A. Vaia, E. P. Giannelis, and D. Zax, *J. Am. Chem. Soc.* 117, 7568 (1995).
154. R. A. Vaia, B. B. Sauer, O. K. Tse, and E. P. Giannelis, *J. Polym. Sci. B* 35, 59 (1997).
155. H. L. M. Hatharasinghe, M. V. Smalley, J. Swenson, C. D. Willians, R. K. Heenan, and S. M. King, *J. Phys. Chem. B* 102, 6804 (1998).
156. L. Hernan, J. Morales, and J. Santos, *J. Solid State Chem.* 141, 327 (1998).
157. D. J. Harris, T. J. Bonagamba, and K. Schmidt-Rhor, *Macromolecules* 32, 6718 (1999).
158. W. Chen, Q. Xu, and R. Z. Yuan, *J. Mater. Sci. Lett.* 18, 711 (1999).
159. J. Bujdak, E. Hackett, and E. P. Giannelis, *Chem. Mater.* 12, 2168 (2000).
160. G. Schmidt, A. I. Nakatani, P. D. Butler, A. Karim, and C. C. Han, *Macromolecules* 33, 7219 (2000).
161. Y. Xiao, K. A. Hu, Q. C. Yu, and R. J. Wu, *J. Appl. Polym. Sci.* 80, 2162 (2001).
162. H. Y. Choi, S. G. Kim, Y. H. Hyun, and M. S. Jhon, *Macromol. Rapid Commun.* 22, 320 (2001).
163. Y. H. Hyun, S. T. Lim, H. Y. Choi, and M. S. Jhon, *Macromolecules* 34, 8084 (2001).
164. B. Liao, M. Song, H. Liang, and Y. Pang, *Polymer* 42, 10007 (2001).
165. H. W. Chen and F. C. Chang, *Polymer* 42, 9763 (2001).
166. H. W. Chen, C. Y. Chiu, H. D. Wu, I. W. Shen, and F. C. Chang, *Polymer* 43, 5011 (2002).
167. Z. Shen, G. P. Simon, and Y. B. Cheng, *Polymer* 43, 4251 (2002).
168. S. K. Lim, J. W. Kim, I. Chin, Y. K. Kwon, and H. J. Choi, *Chem. Mater.* 14, 1989 (2002).
169. H. R. Fischer, L. H. Gielgens, and T. P. M. Koster, *Acta Polym.* 50, 122 (1999).
170. L. Wei, M. Rocci-Lane, P. Brazis, C. R. Kannevorf, Y. I. Kim, W. Lee, J. H. Choy, and M. G. Kanatzidis, *J. Am. Chem. Soc.* 122, 6629 (2000).
171. S. D. Burnside and E. P. Giannelis, *Chem. Mater.* 7, 1597 (1995).
172. S. Wang, C. Long, X. Wang, Q. Li, and Z. Qi, *J. Appl. Polym. Sci.* 69, 1557 (1998).
173. H. Takeuchi and C. Cohen, *Macromolecules* 32, 6792 (1999).
174. S. D. Burbside and E. P. Giannelis, *J. Polym. Sci. B* 38, 1595 (2000).
175. L. Bokobza and N. Nugay, *J. Appl. Polym. Sci.* 81, 215 (2001).
176. M. A. Osman, A. Atallah, M. Muller, and U. W. Suter, *Polymer* 42, 6545 (2001).
177. J. H. Chang, B. S. Seo, and D. H. Hwang, *Polymer* 43, 2969 (2002).
178. S. L. C. Hsu and K. C. Chang, *Polymer* 43, 4097 (2002).
179. A. Akelah, M. A. El-Borai, M. F. A. El-Aal, A. Rehab, and M. S. Abou-Zeid, *Macromol. Chem. Phys.* 200, 955 (1999).
180. L. Zhang, Y. Wang, Y. Wang, Y. Sui, and D. Yu, *J. Appl. Polym. Sci.* 78, 1873 (2000).
181. Y. Wang, L. Zhang, C. Tang, and D. Yu, *J. Appl. Polym. Sci.* 78, 1879 (2000).
182. A. K. Manna, D. K. Tripathy, P. P. De, S. K. De, M. K. Chatterjee, and D. G. Pfeiffer, *J. Appl. Polym. Sci.* 72, 1895 (1999).
183. Y. T. Vu, J. E. Mark, L. H. Pham, and M. Engelhardt, *J. Appl. Polym. Sci.* 82, 1391 (2001).
184. P. B. Messersmith and E. P. Giannelis, *Chem. Mater.* 6, 1719 (1994).
185. T. Lan and T. J. Pinnavaia, *Chem. Mater.* 6, 2216 (1994).
186. M. S. Wang and T. J. Pinnavaia, *Chem. Mater.* 7, 468 (1995).
187. T. Lan, P. D. Kaviratna, and T. J. Pinnavaia, *Chem. Mater.* 7, 2144 (1995).
188. Z. Wang, T. Lan, and T. J. Pinnavaia, *Chem. Mater.* 8, 2000 (1996).
189. H. Shi, T. Lan, and T. J. Pinnavaia, *Chem. Mater.* 8, 1584 (1996).
190. T. J. Pinnavaia, T. Lan, Z. Wang, H. Shi, and P. D. Kaviratna, in "Nanotechnology: Molecularly Designated Materials" (G.-M. Chow and K. E. Gonsalves, Eds.), Vol. 622, p. 250. American Chemical Society, Washington, DC, 1996.
191. Z. Wang and T. J. Pinnavaia, *Chem. Mater.* 10, 1820 (1998).

192. J. Massam and T. J. Pinnavaia, in "Chemical and Pyrolytic Routes to Nanostructured Powders and Their Industrial Application" (G. Beaucage, G. Burns, D.-W. Hua, and J. E. Mark, Eds.), Vol. 520, p. 223. Materials Research Society, Warrendale, PA, 1998.
193. D. C. Lee and J. W. Jang, *J. Appl. Polym. Sci.* 68, 1997 (1998).
194. C. Zilg, R. Mulhaupt, and J. Finter, *Macromol. Chem. Phys.* 12, 8000 (2000).
195. X. Kornmann, H. Lindberg, and L. A. Berglund, *Polymer* 42, 1303 (2001).
196. L. Jiankun, K. Yucai, Q. Zongneng, and Y. Xiao-Su, *J. Polym. Sci. B* 39, 115 (2001).
197. I. J. Chin, T. T. Albrecht, H. C. Kim, and J. Wang, *Polymer* 42, 5947 (2001).
198. X. Kornmann, H. Lindberg, and L. A. Berglund, *Polymer* 42, 4493 (2001).
199. A. S. Zerda and A. J. Lesser, *J. Polym. Sci. B* 39, 1137 (2001).
200. I. J. Chin, T. T. Albrecht, H. C. Kim, T. P. Russell, and J. Wang, *Polymer* 42, 5947 (2001).
201. X. Kornmann, R. Thomann, R. Mulhaupt, J. Finter, and Berglund, *Polym. Eng. Sci.* 42, 1815 (2002).
202. W. Feng, A. Ait-Kadi, and B. Riedl, *Polym. Eng. Sci.* 42, 1827 (2002).
203. O. Becker, R. Varley, and G. Simon, *Polymer* 43, 4365 (2002).
204. J. S. Chen, M. D. Poliks, C. K. Ober, Y. Zhang, U. Wiesner, and E. P. Giannelis, *Polymer* 43, 4895 (2002).
205. M. H. Choi, I. J. Chung, and J. D. Lee, *Chem. Mater.* 12, 2977 (2000).
206. Z. Wang and T. J. Pinnavaia, *Chem. Mater.* 10, 3769 (1998).
207. T. K. Chen, Y. I. Tien, and K. H. Wei, *J. Polym. Sci. A* 37, 2225 (2000).
208. Y. I. Tien and K. H. Wei, *Polymer* 42, 3213 (2001).
209. K. J. Yao, M. Song, D. J. Hourston, and D. Z. Luo, *Polymer* 43, 1017 (2002).
210. R. Xu, E. Manias, A. J. Snyder, and J. Runt, *Macromolecules* 34, 337 (2001).
211. K. Yano, A. Usuki, A. Okada, T. Kurauchi, and O. Kamigaito, *J. Polym. Sci. A* 31, 2493 (1993).
212. T. Lan, P. D. Kaviratna, and T. J. Pinnavaia, *Chem. Mater.* 6, 573 (1994).
213. K. Yano, A. Usuki, and A. Okada, *J. Polym. Sci. A* 35, 2289 (1997).
214. Z.-K. Zhu, Y. Yang, J. Yin, X. Y. Wang, Y. C. Ke, and Z. N. Qi, *J. Appl. Polym. Sci.* 73, 2063 (1999).
215. Y. Yang, Z. K. Zhu, J. Yin, X. Y. Wang, and Z. E. Qi, *Polymer* 40, 4407 (1999).
216. H. L. Tyan, K. H. Wei, and T. E. Hsieh, *J. Polym. Sci. B* 38, 2873 (2000).
217. J. C. Huang, Z. K. Zhu, J. Yin, X. F. Qian, and Y. Y. Sun, *Polymer* 42, 873 (2001).
218. A. Gu and F. C. Chang, *J. Appl. Polym. Sci.* 79, 289 (2001).
219. A. Gu, S. W. Kuo, and F. C. Chang, *J. Appl. Polym. Sci.* 79, 1902 (2001).
220. S. H. Hsiao, G. S. Liou, and L. M. Chang, *J. Appl. Polym. Sci.* 80, 2067 (2001).
221. H. L. Tyan, C. M. Leu, and K. H. Wei, *Chem. Mater.* 13, 222 (2001).
222. J. C. Huang, Z. K. Zhu, X. D. Ma, X. F. Qian, and J. Yin, *J. Mater. Sci.* 36, 871 (2001).
223. T. Agag, T. Koga, and T. Takeichi, *Polymer* 42, 3399 (2001).
224. A. B. Morgan, J. W. Gilman, and C. L. Jackson, *Macromolecules* 34, 2735 (2001).
225. C. M. Leu, Z. W. Wu, and K. H. Wei, *Chem. Mater.* 14, 3016 (2002).
226. R. Magaraphan, W. Lilayuthalart, Sirivat, and J. W. Schwank, *Compos. Sci. Technol.* 61, 1253 (2001).
227. H. L. Tyan, Y. C. Liu, and K. H. Wei, *Polymer* 40, 4877 (1994).
228. J. Kim, R. Ahmed, and S. J. Lee, *J. Appl. Polym. Sci.* 80, 592 (2001).
229. J. H. Chang, D. K. Park, and K. J. Ihn, *J. Polym. Sci. B* 39, 471 (2001).
230. G. S. Sur, H. L. Sun, S. G. Lyu, and J. E. Mark, *Polymer* 42, 9783 (2001).
231. J. Lee, T. Takekoshi, and E. P. Giannelis, *Mater. Res. Soc. Symp. Proc.* 457, 513 (1997).
232. J. C. Huang, Z. K. Zhu, X. F. Q, and Y. Y. Sun, *Polymer* 42, 873 (2001).
233. Y. Kurokawa, H. Yasuda, and A. Oya, *J. Mater. Sci. Lett.* 15, 1481 (1996).
234. N. Furuichi, Y. Kurokawa, K. Fujita, A. Oya, H. Yasuda, and M. Kiso, *J. Mater. Sci.* 31, 4307 (1996).
235. J. Tudor, L. Willington, D. O'Hare, and B. Royan, *Chem. Commun.* 2031 (1996).
236. Y. Kurokawa, H. Yasuda, M. Kashiwagi, and A. Oya, *J. Mater. Sci. Lett.* 16, 1670 (1997).
237. M. R. Nyden and J. W. Gilman, *Com. Theor. Polym. Sci.* 7, 191 (1997).
238. M. Kato, A. Usuki, and A. Okada, *J. Appl. Polym. Sci.* 66, 1781 (1997).
239. A. Usuki, M. Kato, A. Okada, and T. Kurauchi, *J. Appl. Polym. Sci.* 63, 137 (1997).
240. N. Hasegawa, H. Okamoto, M. Kato, and A. Usuki, *J. Appl. Polym. Sci.* 78, 1918 (2000).
241. A. Oya, Y. Kurokawa, and H. Yasuda, *J. Mater. Sci.* 35, 1045 (2000).
242. J. W. Lee, Y. T. Lim, and O. O. Park, *Polym. Bull.* 45, 191 (2000).
243. Q. Zhang, Q. Fu, L. Jiang, and Y. Lei, *Polym. Int.* 49, 1561 (2000).
244. J. M. Garces, D. J. Moll, J. Bicerano, R. Fibiger, and D. G. McLeod, *Adv. Mater.* 12, 1835 (2000).
245. N. Hasegawa, H. Okamoto, M. Kawasumi, M. Kato, A. Tsukigase, and A. Usuki, *Macromol. Mater. Eng.* 280/281, 76 (2000).
246. S. Hambir, N. Bulakh, P. Kodgire, R. Kalgaonkar, and J. P. Jog, *J. Polym. Sci. B* 39, 446 (2001).
247. M. Zanetti, G. Camino, P. Reichert, and R. Mulhaupt, *Macromol. Rapid Commun.* 22, 176 (2001).
248. G. Galgali, C. Ramesh, and A. Lele, *Macromolecules* 34, 852 (2001).
249. J. M. Gloaguen and J. M. Lefebvre, *Polymer* 42, 5841 (2001).
250. J. M. Garcia-Martinez, O. Laguna, S. Areso, and E. P. Collar, *J. Appl. Polym. Sci.* 81, 625 (2001).
251. C. I. Park, O. O. Park, J. G. Lim, and H. J. Kim, *Polymer* 42, 7465 (2001).
252. P. Reichert, B. Hoffman, T. Bock, R. Thomann, R. Mulhaupt, and C. Friedrich, *Macromol. Rapid Commun.* 22, 519 (2001).
253. X. Liu and Q. Wu, *Polymer* 42, 10013 (2001).
254. E. Manias, A. Touny, K. E. Strawhecker, B. Lu, and T. C. Chung, *Chem. Mater.* 13, 3516 (2001).
255. E. Manias, *Mater. Res. Soc. Bull.* 26, 862 (2001).
256. M. Okamoto, P. H. Nam, P. Maiti, T. Kotaka, N. Hasegawa, and A. Usuki, *Nano Lett.* 1, 295 (2001).
257. M. Okamoto, P. H. Nam, M. Maiti, T. Kotaka, T. Nakayama, M. Takada, M. Ohshima, A. Usuki, N. Hasegawa, and H. Okamoto, *Nano Lett.* 1, 503 (2001).
258. S. Hambir, N. Bulakh, P. Kodgire, R. Kalgaonkar, and J. P. Jog, *J. Polym. Sci. B* 39, 446 (2001).
259. T. Sun and J. M. Garces, *Adv. Mater.* 14, 128 (2002).
260. P. Maiti, P. H. Nam, M. Okamoto, T. Kotaka, N. Hasegawa, and A. Usuki, *Macromolecules* 35, 2042 (2002).
261. P. Maiti, P. H. Nam, M. Okamoto, T. Kotaka, N. Hasegawa, and A. Usuki, *Polym. Eng. Sci.* 42, 1864 (2002).
262. P. H. Nam, P. Maiti, M. Okamoto, T. Kotaka, T. Nakayama, M. Takada, M. Ohshima, A. Usuki, N. Hasegawa, and H. Okamoto, *Polym. Eng. Sci.* 42, 1907 (2002).
263. S. Hambir, N. Bulakh, and J. P. Jog, *Polym. Eng. Sci.* 42, 1800 (2002).

264. D. Kaempfer, R. Thomann, and R. Mulhaupt, *Polymer* 43, 2909 (2002).
265. A. Lele, M. Mackley, G. Galgali, and C. Ramesh, *J. Rheol.* 46, 1091 (2002).
266. Q. Zhang, Y. Wang, and Q. Fu, *J. Polym. Sci. B* 41, 1 (2003).
267. H. G. Jeon, H. T. Jung, S. W. Lee, and S. D. Hudson, *Polym. Bull.* 41, 107 (1998).
268. J. Heinemann, P. Reichert, R. Thomsaa, and R. Mulhaupt, *Macromol. Rapid Commun.* 20, 423 (1999).
269. V. P. Privalko, F. J. B. Calleja, D. I. Sukhorukov, E. G. Privalko, R. Walter, and K. Friedrich, *J. Mater. Sci.* 34, 497 (1999).
270. J. Rong, J. Jing, H. Li, and M. Sheng, *Macromol. Rapid Commun.* 22, 329 (2001).
271. K. H. Wang, M. H. Choi, C. M. Koo, Y. S. Choi, and I. J. Chung, *Polymer* 42, 9819 (2001).
272. M. Alexandre, P. Dubois, T. Sun, J. M. Graces, and R. Jerome, *Polymer* 43, 2123 (2002).
273. T. G. Gopakumar, J. A. Lee, M. Kontopoulou, and J. S. Parent, *Polymer* 43, 5483 (2002).
274. M. A. Osman, G. Seyfang, and U. W. Suter, *J. Phys. Chem.* 104, 4433 (2000).
275. M. Zanetti, G. Camino, R. Thomann, and R. Mulhaupt, *Polymer* 42, 4501 (2001).
276. A. Usuki, A. Tukigase, and M. Kato, *Polymer* 43, 2185 (2002).
277. S. D. Wangle and J. P. Jog, *J. Polym. Sci. B* 41, 1014 (2003).
278. A. I. Nazzal and G. B. Street, *J. Chem. Soc. Chem. Commun.* 375 (1985).
279. Y. Sun and E. Ruckenstein, *Synth. Met.* 72, 261 (1995).
280. L. Wang, P. Brazis, M. Rocci, C. R. Kanneurf, and M. G. Kanatzidis, in "Organic/Inorganic Hybrid Materials" (R. M. Laine, C. Sanchez, J. F. Brinker, and E. Giannelis, Eds.), Vol. 519, p. 257. Materials Research Society, Warrendale, PA, 1998.
281. S. Sinha Ray and M. Biswas, *Mater. Res. Bull.* 35, 1187 (1999).
282. B.-H. Kim, J.-H. Jung, J. Joo, J.-W. Kim, and H.-J. Choi, in "Nanocomposites 2001" Proceedings.
283. J. W. Kim, F. Liu, H. J. Choi, S. H. Hong, and J. Joo, *Polymer* 44, 289 (2003).
284. M. Biswas and S. Sinha Ray, *Polymer* 39, 6423 (1998).
285. S. Sinha Ray and M. Biswas, *J. Appl. Polym. Sci.* 73, 2971 (1999).
286. J. M. Kim, S. G. Kim, H. J. Choi, and M. S. Jhon, *Macromol. Rapid Commun.* 20, 450 (1999).
287. M. Biswas and S. Sinha Ray, *J. Appl. Polym. Sci.* 77, 2948 (2000).
288. L. Dai, Q. Wang, and M. Wan, *J. Mater. Sci. Lett.* 19, 1645 (2000).
289. D. Lee, S. H. Lee, K. Char, and J. Kim, *Macromol. Rapid Commun.* 21, 1136 (2000).
290. Q. Wu, Z. Xue, Z. Qi, and F. Wang, *Polymer* 41, 2029 (2000).
291. S. Uemura, M. Yoshie, N. Kobayashi, and T. Nakahira, *Polym. J.* 32, 987 (2000).
292. B. H. Kim, J. H. Jung, J. Joo, J. W. Kim, and H. J. Choi, *J. Korean Phys. Soc.* 36, 366 (2000).
293. J. M. Yeh, S. J. Liou, C. Y. Lai, P. C. Wu, and T. Y. Tsai, *Chem. Mater.* 13, 1131 (2001).
294. B. Feng, Y. Su, J. Song, and K. Kong, *J. Mater. Sci. Lett.* 20, 293 (2001).
295. J. W. Kim, S. G. Kim, H. J. Choi, M. S. Suh, M. J. Shin, and M. S. Jhon, *Int. J. Mod. Phys.* 15, 657 (2001).
296. B. H. Kim, J. H. Jung, J. W. Kim, H. J. Choi, and J. Joo, *Synth. Met.* 17, 115 (2001).
297. H. J. Choi, J. W. Kim, J. Joo, and B. H. Kim, *Synth. Met.* 21, 1325 (2001).
298. M. S. Cho, H. J. Choi, K. Y. Kim, and W. S. Ahn, *Macromol. Rapid Commun.* 23, 713 (2002).
299. B. H. Kim, J. H. Jung, S. H. Hong, J. Joo, A. J. Epstein, K. Mizoguchi, J. W. Kim, and H. J. Choi, *Macromolecules* 35, 1419 (2002).
300. G. Nascimento, V. R. L. Constantino, and M. L. A. Temperini, *Macromolecules* 35, 7535 (2002).
301. B. Winkler, L. Dai, and A. W.-H. Mau, *J. Mater. Sci. Lett.* 18, 1539 (1999).
302. S. Ke, M. Ying, C. Ya-An, C. Zhao-Hui, J. Xue-hai, and Y. Jian-niah, *Chem. Mater.* 13, 250 (2000).
303. "Handbook of Conducting Polymers," 2nd ed. (T. A. Skotheim, R. L. Elsenbaumer, and J. R. Reynolds, Eds.), Ch. 25. Dekker, New York.
304. R. C. Pennwell, B. N. Ganguly, and T. W. Smith, *J. Polym. Sci. Macromol. Rev.* 13, 63 (1973).
305. M. Biswas and S. K. Das, *Polymer* 23, 1706 (1982).
306. M. Biswas and A. Majumder, *J. Appl. Polym. Sci.* 41, 1489 (1991).
307. M. Biswas and P. Mitra, *J. Appl. Polym. Sci.* 41, 1989 (1991).
308. G. Lagaly, *Clay Miner.* 16, 1 (1981).
309. M. Kawasumi, N. Hasegawa, A. Usuki, and A. Okada, *Mater. Sci. Eng. C* 6, 135 (1998).
310. R. A. Vaia and E. P. Giannelis, *Polymer* 42, 1281 (2001).
311. W. Zhou, J. E. Mark, M. R. Unroe, and F. E. Arnold, *J. Macromol. Sci. Pure Appl. Chem. A* 38, 1 (2001).
312. J. H. Chang, B. S. Seo, and D. H. Hwang, *Polymer* 43, 2969 (2002).
313. C. J. G. Plummer, L. Garamszegi, Y. Leterrier, M. Rodlert, and J.-A. E. Manson, *Chem. Mater.* 14, 486 (2002).
314. N. Ogata, G. Jimenez, H. Kawai, and T. Ogihara, *J. Polym. Sci. B* 35, 389 (1997).
315. S. Sinha Ray, K. Okamoto, K. Yamada, and M. Okamoto, *Nano Lett.* 2, 423 (2002).
316. S. Sinha Ray, M. Okamoto, K. Yamada, and K. Ueda, *Polym. Preprints Japan* 155 (2002).
317. S. Sinha Ray, K. Yamada, A. Ogami, M. Okamoto, and K. Ueda, *Macromol. Rapid Commun.* 23, 493 (2002).
318. S. Sinha Ray, M. Okamoto, K. Yamada, and K. Ueda, *Nano Lett.* 2, 1093 (2002).
319. P. Maiti, K. Yamada, M. Okamoto, K. Ueda, and K. Okamoto, *Chem. Mater.* 14, 4654 (2002).
320. M. Pluta, A. Caleski, M. Alexandre, M.-A. Paul, and P. Dubois, *J. Appl. Polym. Sci.* 52, 1497 (2002).
321. S. Sinha Ray, K. Yamada, M. Okamoto, A. Ogami, and K. Ueda, *Chem. Mater.* 15, 1456 (2003).
322. M.-A. Paul, M. Alexandre, P. Degee, C. Henrist, A. Rulmont, and P. Dubois, *Polymer* 44, 443 (2003).
323. J.-H. Chang, Y. Uk-An, and G. S. Sur, *J. Polym. Sci. B* 41, 94 (2003).
324. S. Sinha Ray, K. Yamada, M. Okamoto, and K. Ueda, *Polymer* 44, 857 (2003).
325. S. Sinha Ray, K. Okamoto, and M. Okamoto, *J. Nanosci. Nanotech.* 2, 171 (2002).
326. S. Sinha Ray, K. Okamoto, and M. Okamoto, in "Nanocomposites 2002" Proceedings, ECM.
327. S. Sinha Ray, K. Okamoto, and M. Okamoto, *Macromolecules* 36, 2355 (2003).
328. K. Okamoto, S. Sinha Ray, and M. Okamoto, *J. Polym. Sci. B* 41, 3160 (2003).
329. X. Kornmann, L. A. Berglund, J. Sterete, and E. P. Giannelis, *Polym. Eng. Sci.* 38, 1351 (1998).
330. H. J. Choi, J. H. Kim, and J. Kim, *Macromol. Symp.* 119, 149 (1997).
331. S. H. Park, H. J. Choi, S. T. Lim, T. K. Shin, and M. S. Jhon, *Polymer* 42, 5737 (2001).
332. S. R. Lee, H. M. Park, H. L. Lim, T. Kang, X. Li, W. J. Cho, and C. S. Ha, *Polymer* 43, 2495 (2002).
333. R. K. Bharadwaj, A. R. Mehrabi, C. Hamilton, C. Trujillo, M. Fan Murga, A. Chavira, and A. K. Thompson, *Polymer* 43, 3699 (2002).
334. S. T. Lim, Y. H. Hyun, and H. J. Choi, *Chem. Mater.* 14, 1839 (2002).
335. L. E. Nielsen, "Mechanical Properties of Polymers and Composites." Dekker, New York, 1975.
336. T. Yasuda and E. Takiyama, U.S. Patent 5,391,644, 1995.

337. P. Reichert, H. Nitz, S. Klinke, R. Brandsch, R. Thomann, and R. Mulhaupt, *Macromol. Mater. Eng.* 275, 8 (2000).
338. T. Mitsunaga, K. Okada, and Y. Nagase, in "PPS 2002 Proceedings," Taipei, p. 139.
339. M. Biswas and S. Sinha Ray, *Adv. Polym. Sci.* 155, 167 (2001).
340. E. P. Giannelis, *Appl. Organomet. Chem.* 12, 675 (1998).
341. J. M. Gilman, *Appl. Clay Sci.* 15, 31 (1999).
342. G. Camino, R. Sgobbi, S. Colombier, and C. Scelza, *Fire Mater.* 24, 85 (2000).
343. J. W. Gilman, T. Ksahiwagi, E. P. Giannelis, E. Manias, S. Lomakin, J. D. Lichtenhan, and P. Jones, in "Chemistry and Technology of Polymer Additives" (S. Al-Malaika, A. Golovoy, and C. A. Wilkie, Eds.), Ch. 14. Blackwell Science, Oxford, 1999.
344. S. T. Lim, Y. H. Hyun, and H. J. Choi, *Chem. Mater.* 14, 1839 (2002).
345. J. T. Yoon, W. H. Jo, M. S. Lee, and M. B. Ko, *Polymer* 42, 329 (2001).
346. J. W. Gilman, *Appl. Clay Sci.* 15, 31 (1999).
347. J. W. Gilman, C. L. Jackson, A. B. Morgan, R. Harris, Jr., E. Manias, E. P. Giannelis, M. Wuthenow, D. Hilton, and S. H. Phillips, *Chem. Mater.* 12, 1866 (2000).
348. S. Sinha Ray, K. Yamada, M. Okamoto, A. Ogami, and K. Ueda, *Polymer* 44, 6631 (2003).
349. L. Nielsen, *J. Macromol. Sci. Chem. A* 1, 929 (1967).
350. R. Xu, E. Manias, A. J. Snyder, and J. Runt, *Macromolecules* 34, 337 (2001).
351. J. C. Hutchison, R. Bissessur, and D. F. Shiver, *Chem. Mater.* 8, 1597 (1996).
352. J. A. Tetto, D. M. Steeves, E. A. Welsh, and B. E. Powell, in "ANTEC'99," p. 1628.
353. J. W. Liu, Q. Zhao, and C. X. Wan, *Space Med. Med. Eng.* 14, 308 (2001).
354. S. Sinha Ray, K. Yamada, M. Okamoto, and K. Ueda, *Macromol. Mater. Eng.* 288, 936 (2003).
355. J. Massam, Z. Wang, T. J. Pinnavaia, T. Lan, and G. Beall, *Polym. Mater. Sci. Eng.* 78, 274 (1998).
356. B. B. Lotz, S. Graff, and J. C. Wittmann, *J. Polym. Sci. B* 24, 2017 (1986).
357. R. Khare, J. J. de Pablo, and A. Yethiraj, *Macromolecules* 29, 7910 (1996).
358. P. Maiti and M. Okamoto, *Macromol. Mater. Eng.* 288, 440 (2003).
359. R. Krishnamoorti and E. P. Giannelis, *Langmuir* 17, 1448 (2001).
360. R. Krishnamoorti, J. Ren, and A. S. Silva, *J. Chem. Phys.* 15, 4968 (2001).
361. R. Krishnamoorti and K. Yurekli, *Current Opinion Colloid Interface Sci.* 6, 464 (2001).
362. J. Ren, A. S. Silva, and R. Krishnamoorti, *Macromolecules* 33, 3739 (2000).
363. M. Okamoto, H. Taguchi, H. Sato, T. Kotaka, and H. Tatayama, *Langmuir* 16, 4055 (2000).
364. M. L. Williams, R. F. Landel, and J. D. Ferry, *J. Amer. Chem. Soc.* 77, 3701 (1955).
365. P. H. Nam, Master Thesis, Toyota Technological Institute, 2001.
366. W. P. Cox and E. H. Merz, *J. Polym. Sci.* 28, 619 (1958).
367. T. Kotaka, A. Kojima, and M. Okamoto, *Rheol. Acta* 36, 646 (1997).
368. M. Okamoto, P. H. Nam, and P. Maiti, unpublished results, 2003.
369. H. van Olphen, "An Introduction to Clay Colloid Chemistry." Wiley, New York, 1977.
370. H. Block and J. P. Kelly, *J. Phys. D* 21, 1661 (1998).
371. W. M. Winslow, *J. Appl. Phys.* 20, 1137 (1992).
372. T. C. Halsey, *Science* 258, 761 (1992).
373. M. Trau, S. Sankaran, D. A. Saville, and I. A. Aksay, *Nature* 374, 437 (1995).
374. J. W. Kim, M. H. Noh, H. J. Choi, D. C. Lee, and M. S. Jhon, *Polymer* 41, 1229 (2000).
375. J. H. Park, Y. T. Lim, and O. O. Park, *Macromol. Rapid Commun.* 22, 616 (2001).
376. Y. T. Lim, J. H. Park, and O. O. Park, *J. Colloid Interface Sci.* 245, 198 (2002).
377. D. Klempner and K. C. Frisch, "Handbook of Polymeric Foams and Foam Technology." Hanser, Munich/Vienna, 1991.
378. T. Abiko, H. Kawato, T. Kanai, T. Oda, and H. Saito, in "Nanocomposites 2002 Proceedings,"
379. H. Fong, W. Liu, C. S. Wang, and R. A. Vaia, *Polymer* 43, 775 (2002).
380. J. M. Brown, D. B. Curliss, and R. A. Vaia, in "Proceedings of the PMSE Spring Meeting," San Francisco, 2000, p 278.
381. "Cellular Solids" (L. J. Gibson and M. F. Ashby, Eds.), p. 8. Pergamon, New York, 1988.



# Polymeric Nano/Microgels

Piotr Ulanski, Janusz M. Rosiak

*Technical University of Lodz, Poland*

## CONTENTS

1. Introduction
  2. Synthesis
  3. Methods Used  
for Studying Microgels
  4. Applications
- Glossary  
References

## 1. INTRODUCTION

Soft nanomaterials—polymeric nanogels and microgels—have had a fast and brilliant career from an unwanted by-product of polymerization processes to an important and fashionable topic of interdisciplinary research in the fields of polymer chemistry and physics, materials science, pharmacy, and medicine. Together with their larger analogs—macroscopic gels, most known in the form of water-swelling hydrogels—they have a broad field of actual and potential applications ranging from filler materials in coating industry to modern biomaterials.

There are at least two ways of defining polymeric *nanogels* and *microgels*. One of them originates from the definition of polymer gels. A *polymer gel* is a two-component system consisting of a permanent three-dimensional network of linked polymer chains, and molecules of a solvent filling the pores of this network. *Nanogels* and *microgels* are particles of polymer gels having the dimensions in the order of nano- and micrometers, respectively. The other definition says that a *nanogel* or a *microgel* is an internally cross-linked macromolecule. This approach is based on the fact that, in principle, all the chain segments of a nanogel or microgel are linked together, thus being a part of one macromolecule. It also reflects the fact that such entities can be synthesized either by intramolecular cross-linking of single linear macromolecules or in a single polymerization event (e.g., initiated by one radical) that in the absence of cross-linking would lead to the formation of a single linear polymer chain.

The latter definition allows us to consider nano- and microgels as a specific form of macromolecules, along with linear, branched, comblike, circular, star-shaped, dendrimer,

and other forms (Fig. 1). Since usually the shape of a nano- or microgel resembles a linear macromolecule in a coiled conformation, these structures are often seen as permanently “frozen” polymer coils.

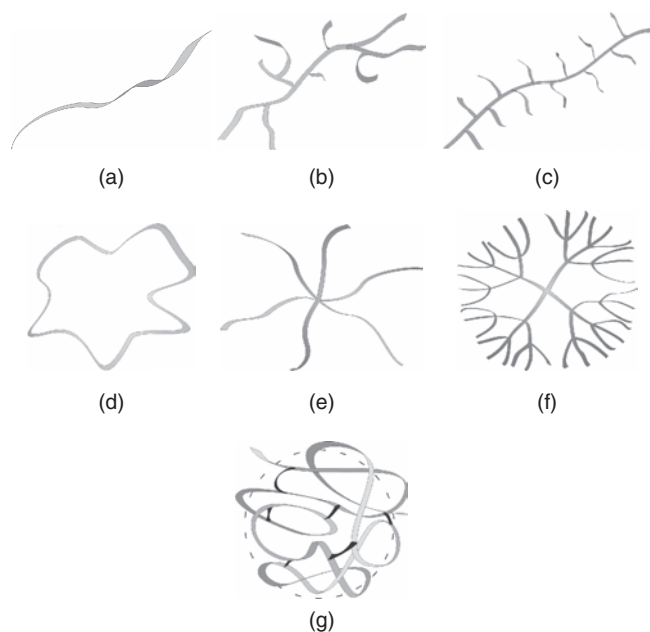
In fact, molecular weights and dimensions of swollen nanogels are often similar to these of typical single macromolecules in solution, but the presence of internal bonds results in different physicochemical properties, including fixed shape, different rheological behavior, higher resistance to degradation, and the ability to trap other molecules within their structure.

It seems logical to use the term *nanogel* to describe gel particles of submicrometer size and to limit the use of *microgel* to particles over micrometer size. This rule has, however, not established itself in the literature. More often than not, the more popular term *microgels* is used to describe all small gel structures, including those having the dimensions of several tens or hundreds of nm. Anyway, a strict differentiation between these two groups is not always unambiguous (shall we measure the particles in their dry or swollen forms?), reasonable, and useful, since many properties, synthetic methods, etc. are common. Therefore, in the following we will use the word *microgel* as a general term denoting all over-micrometer and submicrometer gel particles, limiting the use of the term *nanogel* to a subclass of small microgels formed by internal cross-linking of single macromolecules (see Section 2.2).

Microgels belong to the large family of cross-linked polymeric *microparticles*. Their distinct property is the ability to swell in a suitable solvent. Certainly, the choice of such a solvent is a function of the chemical structure of the polymer network. Therefore a cross-linked microparticle that remains impermeable and does not swell in contact with a group of solvents may become a microgel in another group of solvents.

Very important and perhaps most studied so far are microgels composed of hydrophilic polymers, thus capable of swelling in water. Such gels, irrespective of their dimensions, form a large group of compounds named *hydrogels*. Typical hydrogel-forming polymers are those containing hydrophilic groups as —OH, —COOH, —NH<sub>2</sub>, —CONH<sub>2</sub>, —CONH—, —SO<sub>3</sub>H, or ether linkages. In principle, nearly all water-soluble polymers, including those of natural origin,





**Figure 1.** Macromolecules of various architectures: (a) linear, (b) branched, (c) comblike, (d) circular, (e) star-shaped, (f) dendrimer, (g) microgel.

can be transformed into hydrogels. Macroscopic hydrogels have been extensively studied since the 1960s [1], and to date a number of large-scale applications emerged from this field (contact lenses, drug-delivery systems, wound dressings, etc.) [2–5]. Hydrogels, due their good biocompatibility and ability to mimic the properties of some tissues like cartilage and muscles, are especially suitable for use as biomaterials (see Section 4.1).

All polymer gels, macro- and microscopic, can be divided in two classes with respect to the character of the bonds linking the chains. In a *physical gel* or *pseudogel*, the links may be relatively weak van der Waals forces, hydrophobic or electrostatic interactions, or hydrogen bonds. Such gels are usually weak and can be destroyed (reversibly or not) by, for example, increasing the temperature or changing the solvent. Gelatin-based gels may serve as an example of such structures. It should be noted that many polymers in specific solution conditions tend to aggregate or self-assemble, thus forming physical microgels [6–13]. These phenomena will not be discussed here. *Chemical gels* or *permanent gels* are polymer networks where the links between the chains are covalent bonds. Therefore, such gels cannot be easily destroyed or dissolved, since their destruction would require the covalent bonds to be broken. The scope of this chapter is limited to the permanent gels only.

A further differentiation comes from the fact that, besides homogeneous microgels composed either of a single polymer or a copolymer, there is a growing interest in non-homogeneous, complex structures. These are either single microgel particles of a special architecture (e.g., core and shell of different composition and properties), or materials where microgels serve as building blocks for larger organized structures.

A distinct class of microgels is stimuli-sensitive (“smart,” “intelligent”) structures. They are able to react, usually by a pronounced change in dimensions and swelling ability, to external stimuli such as temperature, pH, ionic strength, concentration of a given substance, electric field, light, etc. Such structures may find applications in controlled or self-regulating drug delivery, signal transmission, or micromachinery (see Sections 4.1 and 4.3).

First reports regarding microgels date from 1930s, when Staudinger described the formation of a styrene-divinylbenzene microgel [14, 15]. Since then, hundreds of reports have been published on this topic. For a full insight, the reader is directed to the excellent review papers by Funke et al. [16] and Saunders and Vincent [17], covering most of the relevant aspects, as well as to a number of reviews dedicated to more specific issues [18–20].

In this chapter we will first discuss the methods used to synthesize microgels, then list the techniques used in studying their properties, and finally briefly review their actual and potential applications.

## 2. SYNTHESIS

A multitude of techniques have been described for the synthesis of polymeric microgels. Most of them can be classified in two groups. The first one are techniques based on concomitant polymerization and cross-linking (where the substrates are monomers or their mixtures), called by some authors “cross-linking polymerization.” The second group is methods based on intramolecular cross-linking of macromolecules (where the starting material is not a monomer, but a polymer).

### 2.1. Formation of Microgels by Cross-Linking Polymerization

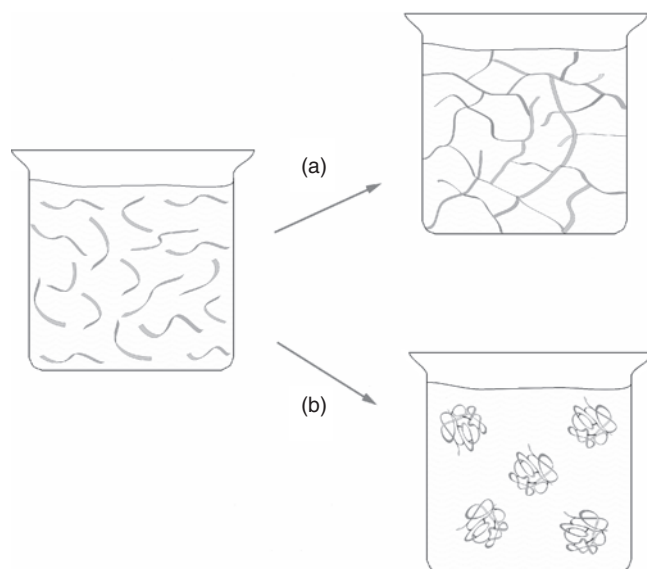
Cross-linking polymerization is the most common process used to synthesize polymeric networks. The substrate is usually a mixture of monomers, where at least one of the components contains two or more polymerizable functions. For example, in the case of free-radical cross-linking polymerization of vinyl compounds this would require that at least one of the monomers contains two or more vinyl groups. When radicals are generated in such a system, in the process of propagation monomer molecules add one after another to the free radical at the end of the growing chain. Since some monomer molecules bear two or more active groups, upon incorporation in the (initially) linear chain, some of their functionalities are not yet used and form pendant active groups along the macromolecule. Therefore, the propagating chain may react not only with monomer molecules but also with these pendant groups. If the pendant group belongs to another chain, the two chains become linked together (intermolecular cross-linking). If the propagating radical reacts with a pendant group localized on its own chain, a closed loop is formed (intramolecular cross-linking). Intermolecular cross-linking leads to the formation of branched structures and finally to macroscopic gel filling the whole volume of the reaction vessel (“wall-to-wall” gel). In an ideal case,

after all the functionalities reacted, the final product would be a single molecule occupying the whole reaction vessel, with all chain segments linked together (Fig. 2a). On the other hand, pure intramolecular cross-linking leads to separate, highly internally cross-linked single macromolecules, that is, nanometer-size microgels (Fig. 2b). In practice we can speak about prevailing inter- or intramolecular cross-linking. Most microgels synthesized by cross-linking polymerization are formed by combination of these two processes.

### 2.1.1. Cross-Linking Polymerization in Solution

Most of the work on the microgel synthesis by cross-linking polymerization in solution has been done on the systems reacting according to the free-radical mechanism. An alternative is the synthesis by anionic cross-linking polymerization in solution (Section 2.1.1).

**Free-Radical Polymerization** Free-radical cross-linking polymerization in solution, although less commonly used than emulsion-based techniques, is a subject of considerable interest, in the areas of both gelation theories and experimental studies. This seems to result from the fact that it is probably the simplest available method for the preparation of microgels, has a broad range of applications, is highly versatile, and does not require the use of surfactants. The latter, employed in most versions of emulsion polymerization techniques (see Section 2.1.2), may be present in the final product and may need to be removed in a separate purification step, thus making the synthetic procedure more complex. On the other hand, microgel formation by cross-linking polymerization in solution requires a very careful choice of reaction parameters. In general, it provides less precise control of the size of the products and yields microgels of broader size distribution than emulsion polymerization.



**Figure 2.** Two modes of polymer cross-linking: (a) intermolecular, leading to the formation of macroscopic gel in the whole reaction volume (“wall-to-wall” gel), (b) intramolecular, leading to the formation of microgels.

In order to obtain microgels by cross-linking copolymerization in solution, it is necessary to control the competition between propagation of linear chains, intermolecular cross-linking, and intramolecular cross-linking in such a way that microgels of desired average molecular weight and/or dimensions are formed, but no macrogelation occurs. One of the decisive factors is the concentration of the monomer mixture. In a dilute solution where the growing chains are separated, the local concentration of the pendant reactive groups within the macromolecule is much higher than their average concentration in the whole reaction volume. Therefore, reaction of the growing chain end with a pendant group belonging to its own chain is much more probable than a reaction with a pendant group of another chain. Thus, intramolecular cross-linking is promoted and, at a certain stage, the system contains mainly microgels. On the contrary, in a concentrated solution where the coils of both growing and dead chains overlap, the probability of the chain end reacting with a “foreign” pendant group may be higher than with its own one. This promotes intermolecular cross-linking and, in consequence, macrogelation, often not being preceded by a distinct microgelation stage. For a detailed description of the phenomena related to microgel formation in free-radical cross-linking polymerization, consult the review paper by Funke et al. [16] and a recent theoretical study by Okay [21].

In the course of a cross-linking polymerization reaction proceeding through a microgelation stage, two factors tend to shift the competition between intra- and intermolecular cross-linking toward the latter process. The first factor is that the number (and concentration) of microgels increases, making the interparticle contact and reaction more probable. The second is that within a microgel particle the number of pendant groups available for further intramolecular cross-linking events decreases (probably not only due to their actual decay in the cross-linking reaction, but also due to the increasing sterical constraints within the internally cross-linked structure). Therefore, even in the relatively dilute systems where intramolecular cross-linking initially prevails, one can finally expect macrogel formation.

A practical message from this reasoning is that in order to avoid macrogelation and obtain microgels one has to work in a dilute solution (typically below 5%) and stop the synthesis before the formed gel microparticles start to react with each other. The latter means that usually one has to terminate the process well before all of the monomer functionalities have reacted.

The works of Graham and co-workers [22–27] indicates that the previously described general picture is not always fully applicable and that some of the formulated precautions may be too conservative. They postulate that for every system where a carefully selected solvent is used with respect to the solubility of the polymer being formed, a “critical gelation concentration” (CGC) can be found, below which no macrogelation takes place, even at a complete monomer conversion. What is surprising is that this CGC may be in some cases as high as 90% (w/w), although values in the order of 20% seem to be more typical. It has been also shown that by varying the concentration at which microgels are prepared, their molecular weight may be controlled. A reason that is evoked for the existence

of CGCs and for their relatively high values is that in a good solvent (or solvent combination) the dead chains, polymerizing chains, and polymer loops extending out of the microgel particle being formed act as very effective steric stabilizers that prevent contact between the microgel particles. As a result of that, particle–particle interactions and interparticle cross-linking are hampered, thus preventing macrogelation and shifting the competition to the side of intramolecular cross-linking. The previously described hypothesis has been tested for many polymerizing systems [e.g., for radical polymerization of 2-hydroxyethyl methacrylate with diethyleneglycol methacrylate and for step-growth polymerization of poly(ethylene glycol), 1,2,6-hexanetriol, and biscyclohexylmethane-4,4'-diisocyanate] in various solvent compositions.

These observations emphasize the importance of solvent selection in the formation of microgels by this technique. In a recent work, the question of solvent composition and its influence on the microgel formation has been addressed by Frank et al. [28]. They have shown that in the cross-linking copolymerization of divinylbenzene and maleic anhydride at low monomer concentration in methyl ethyl ketone/heptane mixtures, products of three distinct morphologies are formed, depending primarily upon solvent composition. With increasing MEK contents the properties of the obtained cross-linked structures change from microspheres and microgels to macroscopic networks.

Basic, extensive research on the mechanism of cross-linking polymerization in solution has been done by Funke and co-workers [16, 29, 30] and other groups [21, 31–35], mostly on 1,4-divinylbenzene and its copolymers.

Recent studies on the applications of this method to synthesize microgels include copolymerization of various divinyl compounds with derivatives of maleic and fumaric acids [36], synthesis of functionalized microgels based on sulfoethylmethacrylate, able to bind metal ions (the bound ions can be subsequently reduced to form stabilized metal colloids) [37], and synthesis of reactive microgels as a semiproduct in the formation of oxazaborolidine-based dispersed catalysts for enantioselective reduction reactions [38]. Microgelation of the acrylamide/*N,N'*-methylene bis(acrylamide) system has been extensively investigated by Kara and Pekcan, using special techniques enabling real-time observation of the reaction progress [39–41] and precise monitoring of the accompanying thermal effects [42].

An interesting example illustrating how versatile this method may be is the first report on the synthesis of fullerene-containing microgel structures [43]. Fullerenes, acting as multifunctional monomers, were co-polymerized, in a free-radical process in *o*-dichlorobenzene solutions, with 4-vinylbenzoic acid, as well as with 2- and 4-vinylpyridine to form submicrometer and micrometer size microgels of interesting rheological and electroactive properties.

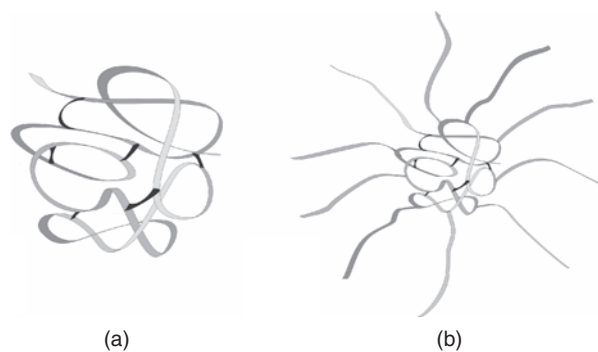
A promising modification of cross-linking polymerization in solution may be the use of chain transfer agents [32, 33, 44, 45]. The aim of this approach is to limit macrogelation processes and in this way to allow the synthesis of highly branched chains and possibly also microgels to be carried out to high degrees of monomer conversion and/or at relatively high monomer concentrations. Catalytic chain transfer agents such as cobalt porphyrin have been shown to perform

much better in preventing macrogelation than conventional chain transfer agents exemplified by mercaptans [44, 45].

Another new and elegant way to control the kinetics and yields of free-radical cross-linking polymerization reactions is the idea of radical living polymerization [46–52]. In this technique, a spin-trapping agent (iniferter) is present in the polymerizing system that can reversibly combine with the propagating radical at the end of a growing polymer chain. The free chains, spin trap, and their product—blocked, inactive (“dormant”) radical—are in equilibrium. As a result, at given polymerization conditions the momentary concentration of active propagating (or cross-linking) radicals can be kept at a much lower level than in the absence of the iniferter. This concentration may be controlled by varying the concentration of the spin trap. The use of living polymerization is rapidly expanding in polymer synthesis due to its many advantages (e.g., precisely controlled average molecular weight and molecular weight distribution) and has also found its way to the field of synthesis of microgels. Abrol and co-workers have demonstrated the application of nitroxides as trapping agents in the free-radical formation of *t*-butylstyrene-*co*-1,4-divinylbenzene microgels [53, 54]. It has been found that living free-radical polymerization helps one to avoid the macrogelation problem and provides much better control over the formation of microgels compared to classical free-radical polymerization. Both random (homogeneous) and core-shell type microgels (Fig. 3) can be formed using the living polymerization approach. Ward et al. described the use of this method for cross-linking polymerization of multifunctional glycol methacrylates, with *p*-xylene bis(*N,N'*-diethyldithiocarbamate) as the iniferter [55], while Baek et al. carried out detailed studies on the application of metal-ion-mediated living radical polymerization to obtain star polymers with microgel cores [56–60].

A specific case of cross-linking polymerization in solution is precipitation polymerization, when the microgels being formed in solution have a tendency toward deswelling and precipitation. Since the further growth and cyclization reactions are limited mostly to the surface and the inner sphere of such a phase-separated particle (that can be considered a deswollen, collapsed microgel), the resulting products are often nearly monodisperse.

It should be noted that use of the term precipitation polymerization is not limited to solution polymerization. There are also special cases of emulsion polymerization



**Figure 3.** Microgels of various architectures: (a) random (homogeneous), (b) core-shell.

(especially the surfactant-free emulsion polymerization; see Section 2.1.2) which are frequently classified as precipitation polymerization [18].

It seems that precipitation polymerization is especially suitable for preparing thermosensitive microgels, since one can control the precipitation/deswelling tendency by changing temperature. For example, for a polymer that undergoes a phase transition leading to precipitation above a given temperature (lower critical solution temperature, LCST), it is possible to carry out precipitation polymerization above LCST and subsequently resolubilize the product by lowering the temperature.

In a broad study on stimuli-sensitive microgels, a range of microgels composed of *N*-vinyl caprolactam and its copolymers with sodium acrylate has been synthesized in aqueous solution using this method [61–66]. Precipitation polymerization carried out at temperatures above the LCST is also frequently used to obtain thermoresponsive microgels of poly(*N*-isopropylacrylamide) and poly(*N*-isopropylmethacrylamide) [18, 67–70]. Other examples of utilization for this technique include the synthesis of ionic microgels based on methacrylic and acrylic acids [71–75].

Fukutomi et al. employed a modification of this technique to obtain microgels of poly(vinyl alcohol) [76]. In this case one cannot start from the (nonexistent) monomer. Instead, vinyl acetate was co-polymerized in solution with *N,N'*-dimethyl-*N,N'*-divinyl-sebacoyldiamide to yield a precipitate of cross-linked poly(vinyl acetate) microparticles. Upon alkaline hydrolysis of this material, poly(vinyl alcohol) microgels were formed.

Recent studies indicate that precipitation polymerization can be also used to fabricate a sort of imprinted microgel structure [77], per analogy to the molecularly imprinted nonswellable microspheres of broad biomedical use, synthesized by a similar technique [78].

**Anionic Polymerization** In ionic polymerization (cf. [79–82]), the active centers participating in chain growth are not radicals, but ions. In principle, three groups of monomers can be used: hydrocarbon (including vinyl), polar (acrylates, methacrylates), and cyclic (oxiranes, lactones, etc.).

Although the ring-opening polymerization of the latter group of compounds is a promising technique used to obtain microspheres [83], so far only the first two groups have gained some attention in the field of microgel synthesis. The carbanions being the active centers in anionic polymerization usually do not undergo any spontaneous deactivation; thus such a process may be considered as a living polymerization. However, since carbanions react rapidly with any substances bearing reactive H atoms (water, carboxylic acids, alcohols), a prerequisite of performing a living polymerization is high purity of the reactant mixture. Since even traces of water from air can prevent the polymerization and in general the concentration of impurities should be kept at a submicromolar level, this requirement is one of the main difficulties encountered when using this technique. In the case of polar monomers, polymerization is often carried out at a low temperature (e.g., below  $-75\text{ }^{\circ}\text{C}$ ) in order to eliminate side reactions. One of the main advantages of anionic polymerization is the possibility to obtain precisely defined

products of narrow molecular weight distribution. Moreover, block copolymers or other structures of special architecture can be synthesized in this way.

In order to obtain a microgel by anionic polymerization, one has to use a bifunctional monomer compatible with this technique. Up to now, most studies in this area concentrated on ethylene glycol dimethacrylate and divinylbenzenes.

Studies on the anionic polymerization of ethylene glycol dimethacrylate (EGDMA) revealed interesting features indicating two distinct phases of the process (cf. [16] and references cited therein). In the first phase, just after the formation of growing chains, no strong increase in molecular weight is observed, while the number of pendant unsaturated groups decreases. In this stage, intramolecular reactions (cyclization) dominate, with only minor participation of intermolecular cross-linking. It has been estimated that ca. 50% of the structural units participate in cyclization. The products are “living” microgels that possess the active centers and reactive vinyl groups. At a later stage, as the free volume decreases, these entities come into contact and undergo intermolecular cross-linking, evidenced by a steep increase in average molecular weight. Other works on this topic have indicated a strong influence of the solvent-initiator system on the reaction kinetics as well as on the general possibility of directing the reaction into the formation of microgels rather than insoluble macroscopic networks and avoiding excessive side reactions [84]. A toluene/*n*-BuLi system works apparently better than most of the other tested combinations.

In contrast to the EGDMA system, in the polymerization of 1,4-divinylbenzene in THF cyclization reactions are not very effective, at least at low concentrations of an initiator (*n*-BuLi, lithium diisopropylamide) [16, 85]. Instead, in the first stage mostly linear polymer is formed, with the pendant vinyl groups left largely unreacted. However, upon an increase in *n*-BuLi concentration over 2%, a gradual increase in cyclization yield is observed resulting in the formation of microgels. At initiator concentration higher than 15%, insoluble macrogels are formed. The tendency to form microgels is a function of both initiator and monomer concentration. The shapes of these complex dependencies (cf. also [86–88]), and the locations of “microgel formation regions” can be satisfactorily predicted based on kinetic considerations [89]. The resulting microgels are in the size range of 3–30 nm.

In comparison with 1,4-divinylbenzene, anionic polymerization of 1,3-divinylbenzene is much faster. Due to the much higher reactivity of pendant vinyl groups in the latter isomer, a strong tendency for cyclization is observed; thus the formation of microgels is favored over reactions leading to the linear chains and macroscopic gels [16].

Another polymer that has been used to obtain microgels by anionic polymerization is 1,4-diisopropenylbenzene [85, 90].

The technique of anionic polymerization, due to the formation of (theoretically) infinitely long-lasting active centers, is particularly useful in the synthesis of structured microgels, mostly based on block copolymers. A typical approach is a two-step procedure. In the first step, only one monomer (A) is polymerized until the monomer is used up but the active centers at the chain ends are still present.

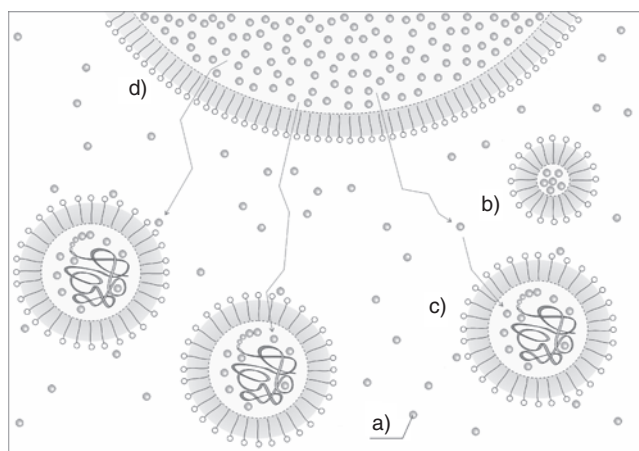
Upon addition of a second monomer (B), the polymerization continues. In a simplest case, a block copolymer of the structure  $(A)_n-(B)_m$  is formed. If A is a bifunctional monomer and B is a monofunctional one, this approach leads to the formation of core-shell star-shaped structures, with a microgel as a core and linear chains bound as branches. This technique (called by some authors “core-first”) has been applied to the systems where the microgel core is built of 1,4-divinylbenzene [91–95]. A reverse technique (“arm-first”), where the bifunctional monomer is added to the living linear chains, was used, for example, to synthesize products having EGDMA microgel core and poly(*t*-butyl acrylate) arms [96]. Much work has been done on the microgel formation in another block copolymer system, *t*-butylstyrene-divinylbenzene (TBS-DVB) [97–101]. Various versions of the synthetic procedure have been tested. In one of them the reaction was performed in *n*-heptane, which is a good solvent for polyTBS but not for polystyrene or the resulting copolymer. The reaction was started by the formation of reactive polyTBS chains. Upon addition of DVB the block copolymers formed precipitated from the solution and further reaction proceeded in this separated phase. This method yields star-shaped microgels with polyTBS arms having gel nuclei molar fractions up to 35%. One could regulate the properties of these entities by changing the length of the living polyTBS chains used in the synthesis. The choice of solvent is an important factor in these syntheses. By selecting THF as a solvent where no precipitation occurs, the molecular weight distribution can be better controlled.

It may be expected that in the future anionic polymerization will be one of the methods used to construct even more complex microgels of well-defined architecture. For example, in a recent work a complex triblock poly(2-hydroxyethylmethacrylate-*b*-styrene-*b*-2-hydroxyethylmethacrylate) was synthesized forming a “flower-type” microgel (cf. [102–106]) with closed-loop arms fixed to a polystyrene shell and an additional function enabling precise ultraviolet (UV)-induced cutting of these loops into two equal linear arms [107].

### 2.1.2. Emulsion Polymerization

**Macroemulsion** In the synthesis of microgels by polymerization in solution, the most important difficulty is how to avoid macrogelation (i.e., how to confine the cross-linking reactions into small, separated spaces). This problem can be overcome by using emulsion polymerization, where each micelle may serve as a separate microreactor, protected from the contact with other micelles by the stabilizing action of a surfactant. Thus, in such a confined space the polymerization and cross-linking reactions can be carried out to a high degree of monomer conversion, resulting in a single microgel particle, with no or very limited macrogel formation. Because of this advantage, emulsion polymerization is a very popular method of microgel fabrication.

In a classical free-radical emulsion polymerization [108, 109]. (Fig. 4), the system initially consists of monomer molecules that are dispersed in the liquid phase (usually water) in the form of micelles (of a size in the order of a few nm) and monomer droplets, typically of the size



**Figure 4.** Classical emulsion polymerization, at moderate surfactant concentration: (a) monomer molecules in solution, (b) inactive monomer micelles, (c) active monomer micelles with growing polymer chain(s), (d) monomer droplet. Arrows denote the monomer transport toward the active micelles.

of 0.1–1 mm. Such a microheterogeneous system is stabilized by the presence of surfactants. The radicals are generated in the liquid phase. In some systems, initiation and first propagation steps also take place in the solution. As the growing chain has the tendency to become phase-separated, surfactant-protected polymer–monomer particles are being formed, where the further polymerization and cross-linking steps take place. In other systems (especially when monomers are poorly soluble in water), initiation may occur within a monomer-filled micelle by an initiator radical that diffuses into the micelle from solution. During the chain growth, monomer molecules diffuse from the droplets and any inactive micelles to the active particles containing growing chain(s). After these outer monomer sources are used up and only the rest of the monomers inside the active particles react, these particles do not grow any longer (or may even contract due to internal cross-linking when multifunctional monomers are present) and, upon nearly complete consumption of the monomer, the process is finally terminated.

Emulsion polymerization of monofunctional monomers leads to the formation of coagulated polymer particles (latexes), while in the presence of multifunctional monomers internally cross-linked particles—microgels—are formed, having the ability to swell in a good solvent.

Extensive comparative studies on both processes, mostly employing styrene and divinylbenzene, revealed marked differences in the kinetics, mechanism, and product properties [16, 110–114]. Cross-linking polymerization leads to the formation of smaller particles, due to intraparticle cross-linking and to the hampered diffusion of monomer molecules into the structure. The number of polymer particles is higher than in the polymerization of monofunctional monomers, due to the fact that the particle growth rate decreases upon cross-linking, the monomer consumption from the inactive micelles is slower, and their lifetime is longer. Thus, in consequence, their chance of capturing a radical and being transformed into a new polymer particle is higher. A stronger tendency to form interparticle aggregates has

been observed, which is attributed to the possibility of the reaction of pendant groups with the propagating radical of the neighboring particle. Moreover, a tendency of polymer formation in the monomer droplets is evidenced, in contrast to the emulsion polymerization of corresponding monofunctional monomers. It has been suggested that this is due to the fact that if some radicals enter a monofunctional monomer droplet, polymerization is rapidly terminated, but in the case of multifunctional monomer, the onset of gelation slows down termination processes, thus favoring further propagation and cross-linking events. Apart from these effects, size distribution of microgels is narrower than for non-cross-linked particles formed of chemically similar monomers.

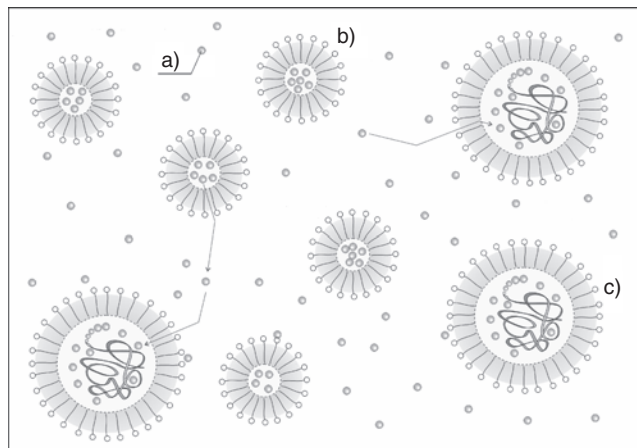
Recent research on emulsion polymerization in microgel synthesis includes broad studies by Matsumoto and co-workers on allyl methacrylate (an interesting monomer bearing two different vinyl groups), polymerized alone and in the presence of various comonomers (diallyl terephthalate, allyl benzoate, methyl methacrylate) and comparative studies on vinyl methacrylate [115–120]. The same group also investigated microgel formation by emulsion polymerization of lauryl methacrylate/trimethylolpropane trimethacrylate [121]. Ishii synthesized new emulsifiers which, when applied for emulsion co-polymerization of mono- and bifunctional monomers, yielded microgel emulsions of better shelf stability than in the case of a conventional emulsifier, sodium dodecylbenzene sulfonate [122]. Other examples are the synthesis of microgels based on methyl methacrylate/butanediol dimethacrylate [123], *N*-ethylacrylamide/*N,N'*-methylenebisacrylamide [124], *N*-vinylcaprolactam [125, 126], as well as ionic microgels made of methyl methacrylate, 2-ethoxyethyl methacrylate, ethylene glycol methacrylate, and 2-(tetradecyldimethylammonio)ethyl methacrylate bromide [127].

The emulsion polymerization technique is also employed as one of the synthetic steps in preparation of complex microgel-based particles of core-shell morphology [128], and in fabrication of reactive microgels having film-forming abilities than can be applied in coating technology [129]. Last but not least, it is applied for the formation of polyorganosiloxane microgels by polycondensation of trimethoxymethylsilane in aqueous emulsions [130–132].

An insight into the kinetics, mechanism, molecular weight distributions, etc. in emulsion polymerization of multifunctional monomers may be gained by performing simulations based on the Monte Carlo method, as demonstrated by Tobita et al. [133, 134] and Jabbari [135]. It is expected that an approach based on a combination of theoretical considerations, simulations, and experimental data (cf. [134]) will lead to a more detailed understanding of this complex process.

**Microemulsion** Some of the disadvantages of the classical emulsion polymerization can be avoided by using miniemulsion of microemulsion polymerization (cf. [16, 20, 136, 137], Fig. 5).

In a monomer-containing emulsion, with increasing surfactant concentration the amount of monomer stored in the droplets decreases while more monomer molecules form micelles. When a critical value of emulsifier concentration is reached, no monomer droplets are left, with all the



**Figure 5.** Polymerization in microemulsion, at high surfactant concentration: (a) monomer molecules in solution, (b) inactive monomer micelles, (c) active monomer micelles with growing polymer chain(s). No monomer droplets present (compare Fig. 4). Arrows denote the monomer transport toward the active micelles.

monomer being present in micelles (and to some extent in the solution). Such a transparent micellar solution is a starting point for the polymerization in microemulsion. In such a system the polymerization in monomer droplets is avoided. In the absence of this side effect known from the macroemulsion technique, nearly monodisperse microgels can be easily synthesized.

Microemulsion polymerization has been used to prepare styrene/1,4-divinylbenzene and styrene/1,3-diisopropenylbenzene microgels of different sizes and swelling abilities [16, 138, 139]. The styrene-based structures formed by this method may be subsequently chemically modified to yield polyelectrolyte microgels of various, defined sizes [140, 141].

**Inverse Emulsion** Most of the emulsion polymerization syntheses are performed in systems where the continuous liquid phase is water or aqueous solution, and the monomers and polymers are of relatively hydrophobic character. Certainly, it is possible to reverse this situation and polymerize hydrophilic monomers in organic, hydrophobic liquid phase.

The mechanism and kinetics of microgel formation in inverse emulsion polymerization have been extensively studied in the case of acrylamide [142]. The influences of the kind of solvent, kind and concentration of emulsifier, monomer content, agitation speed, etc. on the rate of process and product properties were described.

Besides synthesizing neutral hydrophilic microgels (cf. [142, 143]), this technique is especially well suited for producing polyelectrolyte microgels of uniform size. For example, spherical gel microparticles of acrylic acid copolymerized with diethylene glycol diacrylate have been fabricated by inverse miniemulsion polymerization [20]. The products had various diameters, depending on the surfactant concentration, and a polydispersity lower than 10%.

Neyret and Vincent co-polymerized in inverse microemulsion *N,N'*-methylenebisacrylamide with equimolar or nonequimolar amounts of cationic [2-(methacryloyloxy)ethyl]trimethylammonium chloride (MADQUAT) and anionic sodium 2-acrylamido-2-methylpropanesulfonate

and obtained polyampholyte microgels of very interesting swelling and flocculation properties [144].

**Surfactant-Free Emulsion Polymerization** Emulsion polymerization, besides its numerous advantages, has also some shortcomings, the most important being the presence of surfactants that usually have to be removed from the products in a separate step after the synthesis. A complete removal of a surfactant is not always possible, since its molecules may be in some cases incorporated (bound or trapped) into the products. This problem is especially pronounced in the case of microemulsion polymerization, where relatively large quantities of emulsifiers must be used in order to force all monomer to be present in micelles.

A way out of this problem, although limited to some particular systems, is the use of a technique called by some authors “surfactant-free emulsion polymerization,” where the stabilization of emulsions is provided by the monomer and/or polymer itself. This can be realized in at least two ways: either the initiator of free-radical polymerization is an ion that, when incorporated into a growing oligomeric chain, causes this molecule to be surface active, or the substrates for polymerization are unsaturated (i.e., polymerizable) oligomers bearing ionized groups at one or two ends.

The application of the former technique in microgel synthesis evolved from a method used for preparation of nonswellable polystyrene latex particles [145, 146]. It has been first used by Pelton and Chibante to synthesize temperature-sensitive poly(*N*-isopropylacrylamide) microgels [147], and since then it has become the method of choice in the fabrication of these materials [148–152]. Other examples of microgels that can be obtained in this way are systems based on poly(methyl methacrylate) and polystyrene, alone or as a copolymer with methacrylic acid [153–155].

The synthesis is usually carried out with a persulfate salt as the initiator that decomposes into  $\text{SO}_4^{\cdot -}$  radicals capable of adding to monomer molecules and initiating chain growth [17]. The growing oligomer radicals bear the anionic sulfate group at the dead end and behave like a surfactant. The presence of surface-active compounds combined with the tendency of polymer chains to undergo a phase separation (cross-linking polymerization of *N*-isopropylacrylamide—NIPAM—is carried out above the LCST) results in formation of stabilized particles containing the growing and cross-linking chains. Internally cross-linked particles obtained in this way form swollen microgels when transferred into a good solvent. In the case of poly(NIPAM), the switching from a poor to a good solvent is accomplished simply by lowering the temperature below the LCST. It is possible to synthesize NIPAM-based copolymer microgels by incorporating water-soluble vinyl monomers like acrylamide [147], acrylic acid [152, 156], *N*-acryloylglycine [157], or 2-aminoethylmethacrylate hydrochloride [158].

The version of surfactant-free emulsion polymerization where self-emulsifying reactive oligomers are used has been extensively studied by Funke and co-workers on unsaturated polyesters [16, 159–161]. In this approach, unsaturated polyester molecules having carboxylic groups at both chain ends were used. For effective self-emulsification, as well as for emulsification of their mixture with comonomers,

the average molecular weight of these compounds must lie within a certain range. Molecules of too low molecular weight do not provide the desired solubilization efficiency, while for too long chains their own solubility is insufficient. For example, in one of the systems studied where the polyesters were made of maleic anhydride and 1,6-hexanediol, the optimum molecular weight of these oligomers for solubilization of styrene as a hydrophobic comonomer was in the range 1.7–2.2 kDa [162].

Also the way the initial emulsion is prepared and the relation between the comonomer ratios and overall monomer concentration must be carefully chosen to avoid formation of insoluble fraction (macro gels or agglomerates) [163].

A common property of the products synthesized by surfactant-free emulsion polymerization is the presence of ionic groups at the microgel surface which may be used for further modification, binding various compounds, or interparticle cross-linking.

### 2.1.3. Cross-Linking Polymerization in the Bulk

Bulk polymerization is a possible but, in general, not particularly suitable way of synthesizing microgels, primarily since the polymerizing and cross-linking system tends to form a macroscopic “wall-to-wall” gel in the whole reaction volume. According to classical gelation theory [164] involving homogeneous growth of linear chain and their subsequent linking together, formation of distinct microgels as intermediate stages should not take place. However, in reality most polymerizing and cross-linking systems are not strictly homogeneous (see a brief general discussion in [16] and references cited therein). If, before macrogelation is reached, the polymerization and cross-linking processes proceed through stages characterized by inhomogeneous density of cross-links [i.e., when microgels are formed that are not (yet) linked together], there is some chance that they could be potentially separated.

A recent example showing that this may in fact be possible is a study on free-radical bulk polymerization of tetraethoxylated bisphenol A dimethacrylate with styrene or divinylbenzene, where various populations of microgels at different stages of cross-linking (single microgels in the range of 10–40 nm and large microgel clusters) have been observed by atomic force microscopy and by dynamic light scattering upon dissolution of the samples [165, 166]. Also recent works on simulation of polymerization in systems containing multifunctional monomers clearly indicate the onset of structural heterogeneity and the formation of microgels ([167], cf. also [168, 169]).

### 2.1.4. Polymerization with Nonclassical Initiation

Most of the work on the synthesis of microgels by combined polymerization and cross-linking has been done using classical initiation methods, that is, with chemical initiators, which, when activated (mostly thermally decomposed) give rise to reactive intermediates capable of initiating the chain reactions of polymerization and cross-linking. This

approach, although most commonly used, has some disadvantages. First of all, the initiator or its fragments usually remain in the products, either chemically bound or entrapped within the polymer structure. This may pose serious problems in these applications where purity of the material is of high importance (biomaterials, optics, electronics). Second, in some cases the heating of the reaction mixture in order to activate the initiator may be undesirable. Therefore there is a need for alternative techniques where initiation is provided by other means. One may envisage that the techniques already used in polymerization processes, like photopolymerization, radiation polymerization, initiation by the action of ultrasound, or microwaves, will find an application in the microgel synthesis as well.

Photopolymerization and photocuring are very intensely studied synthetic techniques, widely used in industry (cf. reviews [170, 171]). Photoinduced polymerization combined with cross-linking can be used to produce macroscopic polymer gels based, for example, on 2-hydroxyethyl methacrylate [172], *N*-isopropylacrylamide [173], acrylic acid, and *N*-vinylpyrrolidone [174]. Microgels of poly(ethylene glycol) (PEG) were synthesized by photopolymerization, using a method where a mixture of poly(ethylene glycol) dimethacrylates and a photoinitiator was sprayed over a double-layer liquid bath [175]. The droplets formed in the upper layer were subsequently UV-illuminated in the lower layer to form internally cross-linked PEG spheres, able to swell in water. Kazakov et al. proposed an interesting procedure where monomers (acrylamide, *N*-isopropylacrylamide, vinylimidazole) were encapsulated into liposomes and subsequently polymerized and cross-linked with UV light, resulting in microgels of 30–300 nm size [176].

Radiation-induced polymerization is a well-established, versatile synthetic technique used in polymer science and, to a limited extent, also in technology (for reviews see [177–184]). Polymerization initiated by ionizing radiation (typically gamma rays from isotope sources or fast electrons generated by accelerators) is quite similar to the classical one and can be performed in the bulk, in solution, in emulsion, etc., the main difference being only the initiation step. Ionizing radiation can interact with monomers and polymers by direct or indirect effects. In the former, the energy is absorbed by a monomer molecule, which may result in a radical formation, in the latter the energy is absorbed by the solvent, and reactive products (mostly radicals) resulting from this event may in turn attack monomer to initiate polymerization. In the case of aqueous systems, the species initiating the polymerization is most often the hydroxyl radical.

Ionizing radiation can be used in the synthesis of polymer gels (both macro- and microscopic) in two general ways: either by inducing cross-linking polymerization of monomers or by inducing cross-linking of polymer chains in the absence of monomers. The latter technique has some important advantages and will be discussed separately in Section 2.2.2. It is important to know that at late stages of radiation-induced polymerization, when only low quantities of free monomer molecules are left in the system and the radicals are still generated randomly along the chains, intermolecular recombination (cross-linking) reactions may occur with a

considerable yield even in the total absence of any bifunctional monomer. Therefore, by using ionizing radiation it is possible to obtain a polymer gel starting from monofunctional monomers. More often than not, multifunctional monomers are used anyway, usually in order to increase the yield of cross-linking and thus reduce the radiation dose necessary to produce a gel of a given cross-link density. Applications of this technique range from the formation of gels based on relatively simple compounds (e.g., acrylamide [185] or *N*-vinylpyrrolidone [4]) to complex stimuli-sensitive “smart” gels targeted for advanced biomedical purposes (cf. [186–190]).

Examples of radiation-induced polymerization employed to synthesize internally cross-linked polymer microparticles are the works of Yoshida et al. [191–195] and Naka et al. [196–198]. Various monomer mixtures, mainly containing diethylene glycol dimethacrylate, were irradiated without any auxiliary substances in organic solution to yield products that were suitable for derivatization or immobilization of biomolecules and intended for biomedical applications. Microgels can be also synthesized by radiation-induced cross-linking polymerization in emulsion, as shown on the example of styrene-based gels co-polymerized with cationic polymerizable surfactants [199].

Ultrasound is often used in microgel or microparticle synthesis, albeit not for initiating chemical reactions, but rather as a tool for solubilization, agitation, homogenization, formation of miniemulsions, etc. It seems that the well-known fact that the same ultrasound can induce polymerization (for reviews see [200–202]) has so far largely escaped the attention of researchers working on microgel synthesis.

Ultrasound waves propagating in a liquid may cause the formation of free radicals. This effect is due to the phenomenon of cavitation (i.e., the formation of small gas bubbles). Their collapse and their compression phase of oscillations in the ultrasonic wave are adiabatic processes leading to local, transient increase in temperature inside the bubble, lasting for fractions of microseconds. Since these temperatures may reach over 3000 K, [203, 204] a fraction of solvent molecules (or other molecules) present in the gas phase is decomposed into free radicals. These can diffuse to the liquid phase and initiate chemical reactions, including polymerization. In the case of aqueous systems, hydroxyl radicals are generated [205–212] that are very efficient initiators of polymerization. The efficiency of cavitation and of radical formation in particular depends on frequency and intensity of ultrasound, as well as on temperature, external pressure, presence of gases in the liquid, etc. [200, 212].

Ultrasound-induced polymerization in solution has been mostly performed on vinyl polymers, namely styrene [213–221], methyl methacrylate [213, 215–219, 222, 223], *n*-butyl methacrylate [221], vinyl acetate [213], vinyl chloride [224], acrylamide [222, 223], *N*-vinylcarbazole [225], and *N*-vinylpyrrolidone [200]. Moreover, the suitability of this technique for synthesis of some special polymers has been demonstrated (e.g., polysilylenes [226] and phthalocyanine polymers [227]).

Although no extensive studies on the possibility of microgel synthesis by ultrasound have been made so far, there are first reports on the possibility of ultrasound-induced



polymerization of bifunctional monomers [228] and fabrication of microspheres [229].

It has been shown that concomitant action of ionizing radiation and ultrasound may lead to interesting results in the synthesis of internally cross-linked microspheres (that would become microgels in a suitable solvent). In a radiation-induced cross-linking polymerization of diethyleneglycol dimethacrylate in ethyl acetate, the action of ultrasound affects the size and shape of formed particles, probably by promoting interparticle interactions [230].

## 2.2. Intramolecular Cross-Linking of Polymer Chains: Monomer-Free Techniques

In most research work and applications, microgels are synthesized using procedures based on polymerization processes starting from monomers as the basic substrates. This is, however, not the only possible way. An alternative approach to the synthesis of microgels, in particular the *nanogels* of small size (typically  $<0.1 \mu\text{m}$ ), is intramolecular cross-linking of individual macromolecules. An obvious and important advantage of this method is the absence of monomer. This is of great value when the product is intended for biomedical use, where even small quantities of residual monomer may be potentially harmful and thus unacceptable. Furthermore, intramolecular cross-linking may provide means to obtain cross-linked structures of various molecular weight and size, including very small structures, depending on the molecular weight of the parent polymer. Such nanogels obtained from single macromolecules are interesting physical forms of polymers as they are a sort of “frozen” polymer coil of limited segmental mobility. One can also expect that a combination of intra- and intermolecular cross-linking (cf. [231–233]) will provide a tool for synthesizing nanogels and microgels of independently chosen molecular weight and dimensions (various internal densities). Last but not least, intramolecular cross-linking of individual macromolecules is an interesting reaction. A number of questions regarding this process, particularly its kinetics, have not been answered yet (cf. [234–236]).

Given the commercial availability of a multitude of polymers, including food- and medical-grade products, starting from a polymer rather than from a monomer can be a reasonable synthetic option. Moreover, in some cases, where monomers do not exist [like poly(vinyl alcohol)] or polymerization is either impossible or very difficult (carbohydrates), intramolecular cross-linking of polymers may be the best way to produce microgels.

### 2.2.1. Chemical Intramolecular Cross-Linking

Intramolecular cross-linking, similar to polymerization, can be performed either as a thermally initiated chemical reaction or as a photo- or radiation-induced process. Chemical intramolecular cross-linking of individual polymer chains can be achieved in at least two ways. One is to prepare linear or branched polymer with pendant reactive (e.g., vinyl) groups and initialize the cross-linking by a suitable initiator. Batzilla and Funke synthesized linear poly(4-vinyl styrene) and subsequently carried out a cross-linking of this polymer

in dilute solution using 2,2'-azobis(isobutyronitrile) (AIBN) as an initiator [237]. Reaction conditions and time could be chosen where intramolecular cross-linking prevailed. In a similar way, microgels can be made of preformed polymers by photo-cross-linking [238].

Another way does not require any special substrate preparation (no polymerizable pendant groups needed). It has been shown that intramolecular cross-linking of single chains of water-soluble polymers can be carried out by reacting them with a suitable cross-linking agent in dilute solutions. The cross-linker must be capable of reacting with the functional groups ( $-\text{OH}$ ,  $-\text{COOH}$ , etc.) of the polymer and should be at least bifunctional. Synthesis is carried out in solution. Polymer concentration must be chosen sufficiently low to avoid intermolecular cross-linking (i.e., it must be significantly lower than the coil overlap concentration). By varying the concentration of the cross-linker one can influence the internal cross-link density. Burchard et al. used this approach to synthesize internally cross-linked single macromolecules (nanogels) of poly(vinyl alcohol) with glutaraldehyde as the crosslinker [239] and of poly(allylamine) cross-linked with 1,4-dimethoxybutane-1,4-diimine dihydrochloride [240] (cf. also [241, 242]). A similar approach is used to obtain microgels of polysaccharides. For example, hydroxypropylcellulose microgels can be produced by (presumably mostly intramolecular) cross-linking of linear chains with divinylsulfone [243]. Analogous processes are utilized for the synthesis of commercially produced preparations of internally cross-linked hyaluronic acid [244–247].

### 2.2.2. Radiation-Induced Cross-Linking

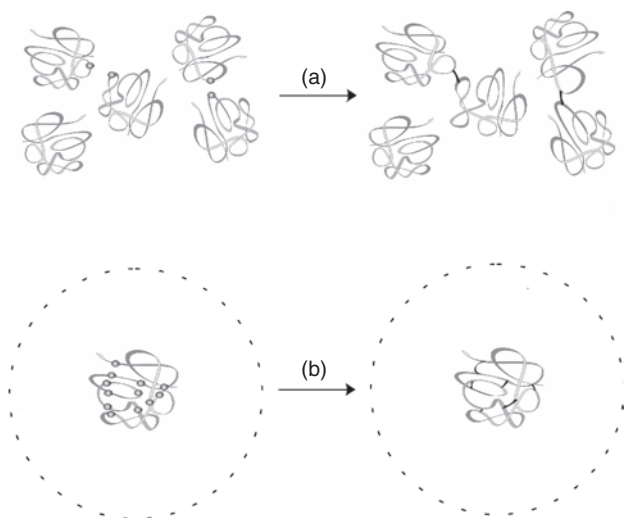
Synthesis of nano/microgels by intramolecular cross-linking of individual polymer chains can be also initiated by ionizing radiation. The main advantage of this method is that it can be carried out in a pure polymer/solvent system, free of any monomers, initiators, cross-linkers, or any other additives. Therefore it seems to be especially well suited for the synthesis of high-purity products for biomedical use. In this approach, to be discussed in more detail, pure aqueous solution of a polymer is subjected to a short (a few microseconds), intense pulse of ionizing radiation. In this way, many radicals are generated simultaneously along each polymer chain, and their intramolecular recombination leads to the formation of nanogels. This approach has been first tested on neutral water-soluble polymers—poly(vinyl alcohol) [235], polyvinylpyrrolidone [248], and poly(vinyl methyl ether) [249, 250]—and later expanded to poly(acrylic acid) as an exemplary polyelectrolyte [236, 251].

The main parameter influencing the competition between inter- and intramolecular recombination of polymer radicals in dilute solutions is the average number of radicals present at each macromolecule at the same time [234]. If this number, under the given synthesis conditions, is much lower than 1, there is only a meager chance that a radical will find a reaction partner within the same chain. In such cases, recombination is only possible between radicals localized on two separate macromolecules. On the other hand, when there are tens of radicals present along each chain, the probability of intramolecular encounters and reactions

is higher than that of intermolecular ones. The latter processes are relatively slow, since they require that two large entities—polymer coils—diffuse toward each other.

In the case of the radiation-induced radical formation, these two opposite conditions (i.e., a very low or very high number of radicals per chain) can be fulfilled by means of a proper choice of irradiation conditions. Continuous irradiation at a relatively low dose rate, such as typical irradiation with gamma rays from isotope sources, leads to a steady-state concentration of polymer radicals in the order of  $10^{-7}$  M. When the concentration of polymer coils is significantly higher than this value (this condition is usually easily fulfilled), the average number of radicals per chain is much lower than unity and intermolecular cross-linking is observed (Fig. 6a). In order to promote intramolecular cross-linking, short, intense pulses of radiation can be employed, such as pulses of fast electrons from an accelerator, generating radical concentrations in the order of  $10^{-4}$ – $10^{-3}$  M. If the concentration of polymer coils is low (that is to say,  $10^{-6}$ – $10^{-4}$  M), many radicals are generated on each macromolecule (typically many tens or even over a hundred), and the conditions for intramolecular recombination are fulfilled (Fig. 6b). Certainly, this does not mean that intermolecular reactions are totally eliminated in such a case. Some coils may come into contact before all the radicals decay, and if there is an uneven number of radicals on a chain, at least one of them must finally find a reaction partner at a neighboring macromolecule.

The data on changes in molecular weight, viscosity, and radius of gyration following the pulse irradiation of dilute polymer solutions clearly indicate that strongly internally cross-linked nanogels are formed which, in comparison with the starting macromolecules, have somewhat higher molecular weight but at the same time significantly lower



**Figure 6.** Gel formation by recombination of polymer-derived radicals under two different experimental conditions: (a) *intermolecular* cross-linking leading to macrogelation (high polymer concentration, low steady-state concentration of radicals  $\Rightarrow$  momentary average number of radicals per chain is lower than one), (b) *intramolecular* cross-linking leading to microgelation (low polymer concentration, pulse-generated high concentration of radicals  $\Rightarrow$  momentary average number of radicals per chain is much higher than one).

dimensions [235, 236, 248, 251]. While the main reason for the increase in molecular weight is the intermolecular cross-linking occurring in the system with very low yields in parallel to intramolecular recombination, the latter process is the dominant reason for the reduction in coil dimensions.

A balance between inter- and intramolecular recombination of polymer radicals may be also maintained when continuous irradiation is used. Therefore it is possible to synthesize microgels by cross-linking in a solution using isotope sources, as has been experimentally demonstrated and supported by simulations for poly(vinyl alcohol) by Wang et al. [231–233, 252].

### 2.3. Disruption of Macroscopic Networks

The idea of obtaining microscopic gel particles by disrupting continuous “wall-to-wall” gels seems to be conceptually the simplest of all synthetic approaches, since the procedures used to obtain macroscopic networks are usually simple, with less parameters to be controlled than in the previously described typical microgel synthesis methods—there is no need to control the micelle size or to observe the precautions necessary to avoid macrogelation. A disadvantage of this “nonelegant” method is that the size distribution is very broad (however, for microgels in the scale of many micrometers it can be reduced, e.g., by using mechanical sieves); one cannot usually expect to produce extremely small gel particles in this way nor obtain products of a regular, spherical shape. On the other hand, the disruption method may be of some advantage for synthesizing microgel fractions of various diameters but precisely the same crosslink density (since they are derived from one specimen of a macroscopic gel) [253]. In the authors’ laboratory this method is used routinely to fabricate large amounts of coarse polyvinylpyrrolidone microgel of dimensions below  $50 \mu\text{m}$ , following radiation-induced synthesis of macroscopic gel in the bulk [254]. A gel disruption process has been reported to yield cross-linked polysaccharide microgels (of dimensions in the 100 nm range), as one of the steps to construct polysaccharide/phospholipide biovectors for drug delivery [255].

It should be noted that important final steps of almost all synthetic procedures used to obtain microgels are purification and drying. It has been clearly demonstrated that drying methods and conditions may have significant influence on the final structure and properties of microgels [143, 256].

## 3. METHODS USED FOR STUDYING MICROGELS

Since most microgels of micrometer and submicrometer size are soluble in a suitable solvent, their properties can be conveniently studied by the methods developed for macromolecules in solution. These include various versions of viscometry, static and dynamic light scattering, gel permeation chromatography (GPC), and, to a lesser extent, ultracentrifugation and osmometry.

Relative changes in hydrodynamic dimensions of microgels, related to their average molecular weight, structure, and size, can be followed by *viscosity measurements* in dilute

solutions, using simple equipment such as an Ubbelohde viscometer.

Determination of an intrinsic viscosity of a polymer solution  $[\eta]$  is one of the simplest and most common ways to determine average molecular weight of a polymer (precisely the viscosity-average molecular weight,  $M_v$ ). Correlation between these values is known as the Mark–Houwink equation,  $[\eta] = KM^\alpha$ , where  $K$  and  $\alpha$  are parameters which are constant for a given linear polymer/solvent pair at a defined temperature and can be found in handbooks (e.g., [257]). Since a microgel particle is more compact than a coil of the same linear polymer, viscosity of microgel solution is lower than that of linear macromolecules of equal concentration. As a result of that, viscosity measurements do not yield proper values of molecular weight for microgels, at least when  $K$  and  $\alpha$  values for linear chains are used.

Although the Mark–Houwink parameters for some microgels have been determined, their practical use is very limited, since the real dependence of viscosity on molecular weight is influenced by cross-link density, way of synthesis etc., and therefore it may vary from one to another preparation. Anyway, it is worth noting that the values of the exponent  $\alpha$  for microgels are low (e.g., 0.16 for microgels of poly(vinyl alcohol) [241], 0.25 for microgels based on polystyrene copolymers [258], 0.09 to 0.24 for divinylbenzene-based gels [16, 29]) when compared with values typical for random coils of flexible macromolecules in good solvents (0.5–0.8), indicating only a weak dependence of viscosity on molecular weight.

Despite the previously described disadvantage, viscosity is a very convenient tool to measure volume changes in gel structures of constant average molecular weight. Examples of such experiments are synthesis of microgels from linear chains by intramolecular cross-linking [231, 232, 235] or changes in volume of stimuli-sensitive microgels [251]. Senff and Richtering provided large data collections and detailed discussions on the temperature influence on viscosity and rheology of thermosensitive poly(*N*-isopropylacrylamide) microgels [259, 260]. An extensive study of viscosity-related phenomena in polyelectrolyte microgels has been presented by Antonietti et al. [140, 141, 261].

Viscosity measurements are also frequently used to follow the changes in size of microgels during the synthesis based on polymerization and cross-linking, often in parallel with other methods, indicating the changes in molecular weight. Such studies have been done, for example, on polyacrylamide [142], poly(allyl methacrylate) [115–118], poly(*t*-butyl acrylate) [96], polyurethanes [22], and poly(vinyl methacrylate) [117].

Relatively low viscosity of microgel solutions is one of the factors that makes them suitable for high-solid-content organic coatings (see Section 4.2), since to maintain the desired viscosity level of a solution or dispersion, higher concentration of microgels than linear chains can be used.

Another viscosity-related field of studies is *rheology* of microgel solutions or dispersions. The information gained is related to the compactness and stiffness of gel particles and their susceptibility to flow-induced deformation, solvent permeability, as well as the interactions between the particles. For some compact microgels (e.g., based on polyester copolymers), almost Newtonian flow has been observed

even at concentrations of 40 wt% indicating low interparticle interaction and low deformation [16]. Solutions of other microgel structures show pronounced deviations from the Newtonian behavior, mostly behaving as pseudoplastic, shear-thinning fluids. Discussions on structure–rheology relationships of microgel solutions can be found in [19, 259, 260]. Rheological tests provide valuable information on the behavior of the outer layer of complex microgels—for example, in a core–hair structure one can follow the tendency of the hairs to become extended in a given solvent [262]. Data on the solutions of thermoresponsive microgels of poly(*N*-isopropylacrylamide) show pronounced temperature dependence of rheological properties, reflecting the change in volume fraction occupied by gel microparticles [18, 263]. Changes in rheological properties of the reaction mixture can yield important information on the mechanism and kinetics of cross-linking polymerization [264]. Precise knowledge on how the composition and synthetic procedures influence the rheological properties of final products is essential for fabrication of microgels used in coating technology [265–268].

*Static light scattering*, based on the laws discovered and methods developed by Rayleigh, Debye, and Zimm, is an absolute method of determination of weight-average molecular weight of any dissolved macromolecular structure [269–271]. In this method, a laser light beam is passed through a solution of macromolecules or microgels, and the (time-averaged) intensity of scattered light is measured, in relation to the intensity of the incident beam, at various angles, for a few different concentrations of the polymer in the sample. Double extrapolation of these data to zero angle and zero concentration yields the weight-average molecular weight. One has to stress that this method is of particular value for studying microgels, since many other methods (viscometry, simple gel permeation chromatography without light-scattering detection) that require calibration can yield incorrect molecular weights of microgels when calibrated on linear polymer samples. Certainly, static light scattering also has some limitations. The most important in the present context is the upper limit of molecular weight that can be determined. Molecules or gel particles of  $M_w$  higher than a few million Da cannot be usually analyzed by this method. Another limitation is uncertainty whether one of the calculation parameters, the refractive index increment ( $dn/dc$ ), undergoes significant changes when linear chains of a given polymer are transformed into microgels. This problem, often neglected, still requires detailed studies. Examples of static light-scattering measurements on microgels are listed, arranged according to the main chemical component of the microgel: hyaluronic acid [247], organosilicon compounds [131], poly(acrylic acid) [236, 251], poly(allyl aniline) [240], poly(allyl methacrylate) [115–118, 120, 272], polyethylene [273], poly(lauryl methacrylate) [121], poly(methacrylic acid) [274], poly(methyl methacrylate) [275], poly(*N*-isopropylacrylamide) [151, 259, 260, 274], poly(*N*-vinylcaprolactam) [61, 63, 64, 66, 125], poly(vinyl alcohol) [231, 235, 239], poly(vinyl methacrylate) [117], and polyvinylpyrrolidone [248].

Static light scattering is not only a tool for determining the weight-average molecular weight, but it yields as well

the radius of gyration (a very important parameter in analysis of microgels) and a second virial coefficient, which is useful for investigating polymer-solvent vs. polymer-polymer interactions. For example, a negative value of this parameter indicates a tendency of polymer chains or microgels to undergo reversible aggregation in a given solvent.

Static light-scattering techniques can be also used for real-time study of the kinetics of microgel formation. This can be done by coupling a pulse-radiolysis setup with a laser light scattering photometer [276–279]. Cross-linking and/or polymerization reactions are initiated by short (a few microseconds) pulse of ionizing radiation in the form of fast electrons generated by an electron accelerator, and subsequent changes in the intensity of scattered light caused by changes in molecular weight and/or radius of gyration can be recorded, analyzed, and, when possible, recalculated into rate constants of participating reactions.

It is worth mentioning that *in-situ*, real-time monitoring of microgel formation is possible not only by following the increase in the intensity of scattered light but also by measuring the decrease in intensity of transmitted light. A description of the latter technique and its applications can be found in the works of Kara and Pekcan [39–41].

*Dynamic light scattering*, based on temporal correlations of the intensity of light scattered by the solution of macromolecular structures, does not yield (at least directly) molecular weights, but average values and distributions of diffusion coefficients [271, 280–282]. These data can be recalculated into average values and distributions of hydrodynamic diameters—again very important characteristics of a microgel sample. The range of sizes that can be measured is more shifted toward large structures when compared with static light scattering (up to a few micrometer). It should be stressed that the average radius of gyration determined by static light scattering and the average hydrodynamic radius calculated from dynamic light scattering are different physical parameters. The relation between these two values is a valuable indicator of microgel structure [239, 240]. Examples of application of dynamic light scattering for analyzing microgels can be found in the following papers, arranged according to the main component of the studied material: dextran [283], hydroxypropyl cellulose [243], organosilicon gels [132, 284], polyacrylamide and its derivatives [71, 285], poly(acrylic acid) [285, 286], poly(allyl aniline) [240], poly(*n*-butyl acrylate) [129], polyesters [287], poly(ethylene oxide) [8], poly(2-hydroxyethyl methacrylate-*b*-styrene-*b*-2-hydroxyethyl methacrylate) [107], poly(methacrylic acid) [274], MADQUAT [144], poly(methyl methacrylate) [123], poly(methyl vinyl ether) [250], poly(*N*-isopropylacrylamide) [70, 148–150, 152, 259, 260, 274, 288–295], poly(*N*-vinylcaprolactam) [126], poly(sodium 2-acrylamido-2-methylpropanesulfonate) [144], polystyrene [129, 139, 296], poly-(tetramethoxylated bisphenol A dimethacrylate) [165], poly(vinyl alcohol [231, 232, 239]), poly(2-vinylpyridine) [297, 298], and poly(2-vinyl pyridine-*b*-styrene-*b*-2-vinyl pyridine) [299].

Surface charge effects like electrophoretic mobility can be investigated by measuring the *zeta potential* or by *phase analysis light scattering* [67, 144, 300].

A method that in some aspects resembles light scattering is the *small angle neutron scattering* technique (SANS).

Neutrons of suitable energy range are scattered by atomic nuclei of a polymeric sample and give rise to scattering patterns similar to those obtained by light scattering. An advantage of neutron scattering is that it can be used not only in solutions but also in gels and even in the condensed phase, when appropriate samples are used (e.g., containing a small fraction of deuterated macromolecules). This method allowed detection of structural differences in gels of the same chemical composition but synthesized by different methods (chemical and  $\gamma$ -ray initiation) [301]. Temperature-dependent SANS measurements were applied to follow the structural changes in thermoresponsive microgels of poly(*N*-isopropylacrylamide) [17, 148, 294, 302].

Microgels can be also studied by GPC (size exclusion chromatography; for general reviews see [303, 304]). This method is routinely used in research and industry to determine molecular weight distribution and number-, weight-, and *z*-average molecular weights of polymers. In its basic form, GPC is not an absolute method and requires calibration on monodisperse polymer standards of precisely known molecular weight. Since macromolecules or microgels are segregated on GPC columns according to their size (hydrodynamic volume) and not molecular weight, the same precautions as mentioned previously for viscometry must be applied if the method is to be used for determination of molecular weight distribution of microgels, since linear polymer standards and microgels of the same molecular weight may have very different dimensions and retention volumes. This problem can be partially overcome in modern GPC setups equipped with a light-scattering detector that in principle allows for absolute determination of molecular weight of each polymer or microgel fraction. Still, the use of right-angle laser light scattering detectors with microgel samples may lead to some systematic errors, since the algorithms for recalculation of the data to zero angle are based on the theory of polymer coils, not microgels. On the other hand, detection at a low angle (multiangle or low-angle detectors) usually gives noisy signals, especially in aqueous solutions. Nevertheless, the method is fast, efficient and for sure a valuable tool in microgel analysis. Exemplary applications described in the literature refer to microgels based on poly(allyl methacrylate) [272], poly(divinylbenzene) [305], poly(methyl methacrylate) [23], polystyrene and poly(*t*-butyl styrene) [101, 306], polystyrene and poly(butyl acrylate) copolymers [307], poly(*t*-butyl styrene-*co*-divinylbenzene) [100], and poly(vinyl alcohol) [232]. Gel permeation chromatography may be also applied for preparative purposes. Microgels based on polyethyleneimine and poly(ethylene glycol) have been successfully fractionated by this technique [308].

Chemical composition of microgels can be determined by any regular analytical technique used for polymers. UV-visible or infrared (IR) spectroscopy is often used to control the conversion of monomers during the microgel synthesis. The use of IR spectroscopy may be facilitated by the fact that many microgels form films that may be analyzed directly. Concentration and structures of polymer-derived free radicals during polymerization or cross-linking can be followed, in some cases, by electron paramagnetic resonance [165, 309–312]. Classical methods of instrumental analysis

as conductometric and potentiometric titration may be very useful for analyzing ion-bearing microgels [155, 297].

*Nuclear magnetic resonance (NMR) spectroscopy* can be used for determination of the chemical structure of microgels [68, 120, 125, 313–316]. Another application of a related technique in the field of polymer systems is the pulsed-NMR measurements of *spin-spin nuclear magnetic relaxation* times. They yield valuable data regarding polymer structure, crosslink, and/or entanglement density in solid polymers [317–319], polymer melts [320], and gels [321–323].

*Visualization* of microgels can be realized by various microscopic techniques. While the use of optical microscopy is limited to the relatively large structures, most studies are based on transmission electron microscopy (TEM, selected reviews: [324, 325]), scanning electron microscopy (SEM, [325, 326]) and atomic force microscopy (AFM, [327–330]).

Transmission electron microscopy is widely used to study microgels. Usually it does not require any complicated sample preparation. In a typical procedure, a drop of dilute microgel dispersion or solution is cast on a suitable support (often a carbon-film-coated copper mesh) and dried at room temperature (RT). This method is well suited for observation of single gel particles or their monolayers. Exemplary applications of TEM in studying microgels are visualization of simple gel particles based on polyacrylamide [142], poly(2-acrylamido-2-methylpropanesulfonate-*co*-(2-(methacryloyloxy)ethyl)trimethylammonium chloride) [144], poly(divinylbenzene-*co*-maleic anhydride) [28], poly(*N*-ethylacrylamide) [124], poly(*N*-isopropylacrylamide) [149, 150, 156], polyurethanes [22], as well as more complex structures and effects, like core-shell microgels [69, 128, 262, 293], loading of nanogels with drugs [308], binding metal or metal oxide particles [37, 331, 332], and template influence on the synthesis of polysilane microgels [333].

More complex microgel structures, multilayers, foils, and surface features of microgel-based materials can be visualized by scanning electron microscopy. SEM enables the analysis of thick, nontransparent (in the sense of TEM) samples and due to its large focus depth gives sharp pictures of structurally complex materials. Sample preparation is not as simple as in TEM, since here coating the sample with a thin layer of a conducting material is necessary. Examples of applications of SEM in the field of microgels include a study on the influence of monomer ratio on the properties of poly(*N*-isopropylacrylamide-*co*-acrylic acid) gel particles [152], thermally induced structural changes in poly(*N*-isopropylacrylamide) microgels [294], various morphologies of poly(divinylbenzene-*co*-maleic anhydride) [28] and poly(divinylbenzene-*co*-4-methylstyrene) gels [305], binding microgels onto TiO<sub>2</sub> pigments [122] and aluminum surfaces [332], structures of microgel-based ion-exchange resins [334], structure of polypyrrole particles obtained by template polymerization in the presence of poly(vinyl methyl ether) microgels [335], and structural effects accompanying inverse emulsion cross-linking polymerization of acrylamide [142].

AFM is a development of scanning tunneling microscopy. These techniques differ from electron microscopy both in operating principles and in many aspects of their application. Sample preparation is simple, no metal sputtering or vacuum environment, etc. is needed and the native

sample structure in its natural environment (e.g., air, liquid) can be visualized. AFM has been successfully used for imaging of polymer systems, from surfaces through colloidal particles and dendrimeric structures down to single macromolecules (extensive review: [336]) In the field of microgels, the AFM technique has been used for example, for studying surface topology of vinyl/dimethacrylate networks [165, 166], poly(acrylic acid) films based on linear chains and on nanogels (see Fig. 9 in Section 4.3) [251], films based on polystyrene and poly(*n*-butyl acrylate-*co*-acetoacetoxy ethyl methacrylate) gel particles [129], cluster formation in organosilicon micronetworks [284], structures of polystyrene graft microparticles [337], and the fibrous nature of polysaccharide gels [338]. An interesting modification of the AFM technique allowing for measurement of interparticle forces (that might be possibly used in future for measuring the forces between microgel particles) has been described by Sigmund et al. [339]. Another application of AFM that may be of interest in the present context is the determination of elastic properties of microparticles [340].

## 4. APPLICATIONS

### 4.1. Biomaterials

The possibilities of employing macroscopic polymer gels as biomaterials, mostly in the form of hydrogels based on synthetic polymers, have been explored since 1960s, when these materials were first synthesized [1]. Since then, a number of products reached the stage of commercial application, soft contact lenses, drug delivery systems, and wound dressings being the most widely known examples. Given the number of research groups involved and progress being made in this field, one may anticipate that in the future the number of hydrogel-based biomedical products on the market will be constantly increasing.

Broad although not very recent publications on the medical use of hydrogels are the collective works edited by Peppas [2] and DeRossi et al. [341]. Park et al. reviewed the narrower field of biodegradable hydrogels [342]. Out of more recent books and book chapters on this subject [343] provides a more general outlook, while the scope of [344] is limited to silicone-based hydrogels. For exemplary review papers on the medical applications of hydrogels, see [3, 345–352].

Although certainly the characteristics of hydrogels differ from one to another formulation, a few common properties can be listed that make these materials suitable for biomedical applications. In their high water content and hydrophilicity hydrogels are similar to tissues. They also mimic some properties of soft tissues as reversible swelling and elasticity. Due to their network structure they may be loaded with a drug which can be subsequently released at a controlled rate. This rate can be adjusted, one of the main factors being the mesh size. The latter parameter allows also construction of semipermeable membranes or containers, for example an outer shell of a hybrid artificial organ (an implant containing living cells) allowing the transport of water, oxygen, nutrients, and enzymes, but being impermeable to larger entities such as immunoglobulins and other components of the

immune system (cf. [353–355]). Due to their fair to excellent biocompatibility, hydrogels are usually well tolerated as implants.

An example of a mature biomaterial technology based on classical, homogeneous hydrogels is the large-scale production of wound dressings, by a technique combining radiation-induced cross-linking of polyvinylpyrrolidone and concomitant sterilization of the final product [4, 356]. A number of other products based on similar technology (e.g., systems for local delivery of anticancer drugs and for induction of childbirth) have successfully passed clinical tests [347, 355, 357, 358].

While “regular” hydrogels are already common components of biomaterials, current efforts of the researchers are now concentrated on the stimuli-sensitive (“intelligent,” “smart”) gels (reviews: [5, 18, 341, 359–363]). These materials are able to respond to external stimuli, such as temperature, pH, ionic strength, light, electric field, or even (selective) changes in the concentration of a given chemical species. The latter property can be used, for example, in glucose-responsive insulin-releasing devices [314] or antigen-responsive systems [364]. The response to the stimulus, being induced by conformational changes of the polymer chain segments, usually manifests itself as a pronounced change in the gel volume (strong contraction or expansion) and in the amount of bound liquid (decrease or increase in the degree of swelling). Due to these properties, stimuli-sensitive gels are tested for applications such as sensors, actuators, chemical valves, controllable or self-regulating drug-delivery systems, or even artificial muscles. Certainly, there is still some gap between the artificial hydrogel fish that moves by swinging its tail in a laboratory bath [365] or electrically driven gel finger working in the air [366] and a future implementation of a hydrogel-based muscle, but fast developments in the field of stimuli-sensitive hydrogels allow one to expect that biomaterials based on these materials will be implemented very soon.

Microgels are also intensely studied with respect to their biomedical applications (reviews: [16, 18, 361, 362, 367–370], exemplary patents: [371–375]). Of course, the product range is different than that of macroscopic gels, although there is a significant overlap in the field of controlled drug delivery. The most important microgel applications in the biomedical field are carriers for enzymes, antibodies, etc. used in diagnostics (e.g., immunoassays), drug carriers for therapeutic purposes (local, controlled drug delivery), and, potentially, microdevices (see Section 4.3), artificial biological fluids, and synthetic vectors for drug delivery.

Coupling microgels with selective biochemicals leads to materials applicable in biological testing [16, 18, 376]. This technique has been used for some time with solid nanospheres [368, 376, 377]. In some cases, in comparative tests microgels performed better than polystyrene-based microsphere supports, providing testing material of higher sensitivity [378]. A typical action of the microgel-based immunoassay is based on an aggregation of antibody-bearing microgels with the specific antigens. The large particles formed in this way can be detected by microscopic techniques. In a modified immunoassay, magnetic microgels can be applied, containing an encapsulated polymer core with adsorbed magnetic nanoparticles [371, 379]. Magnetically

labeled cells can be separated from a cell mixture by applying magnetic field, for example in a section of tubing in which the cell mixture is flowing.

Although there is a broad field of potential biomedical applications of conventional microgels, a strong tendency is observed to focus the research on complex microgels and on stimuli-sensitive systems. The preference for using stimuli-sensitive gels is even more pronounced for microgels than for the “wall-to-wall” gels. One of the important reasons is much shorter response time. While the reaction of macroscopic responsive gels to a stimulus is sometimes unacceptably slow (for example, when the molecules of a chemical stimulus have to diffuse into the whole volume of a gel slab), microgels, due to their small dimensions and high surface-to-volume ratio, respond much faster.

Temperature-sensitive microgels are tested for controlled binding of biomolecules. It has been shown that poly(*N*-isopropylacrylamide)—pNIPAM—microgels can bind various proteins by physical sorption above the phase transition temperature (i.e., at ca. 40 °C) and release them upon lowering the temperature to 25 °C [380, 381]. Proteins can be also covalently bound to such gels, and their activity can be controlled by temperature changes [382]. In complex systems such as described by Yasui et al. [383], one can achieve high enzyme activity within a defined, relatively narrow (a few degrees) temperature range. Pichot and co-workers demonstrated the possibility of using thermo- and pH-responsive microgels for binding nucleic acids [362, 384]. It has been shown that the interaction of temperature-sensitive microgels with elements of the immune system like granulocytes (foreign-body attacking cells) can be moderated by changes in temperature [385]. It is worth noting that the interaction of pNIPAM gel particles was much weaker than that of polystyrene microspheres, which may indicate that, in the context of attack by immune system cells, these microgels have higher biocompatibility than solid microspheres.

Thermosensitive microgels have been also tested as drug carriers. The structure and hydrophilic/hydrophobic properties of the drug have been identified as important factors influencing the phase transitions and uptake/release characteristics of poly(*N*-vinyl caprolactam) gel particles [126]. In order to achieve the desired release profile, composite microgels may be used, for example combined nonporous silica/pNIPAM gels [386]. The rate of the thermally triggered drug release may then be controlled by changing the composition of this hybrid product. Another interesting example of a composite structure based on drug-loaded thermosensitive microgels is a wound dressing, where drug-bearing pNIPAM gel particles are incorporated into a self-adhesive film [387]. The product combines adhesive and temperature-controlled absorptive functions and is easy to peel off after use.

Compositions containing poly(*N*-vinylcaprolactam-co-sodium acrylate) microgels and gelatin undergo a reversible macrogelation upon temperature increase above ca. 32 °C [65]. Such materials, liquid (injectable) at RT but forming a gel at the temperature of the human body, are considered for applications in surgery and drug delivery.

Another group of responsive materials tested for use as biomaterials are pH-sensitive and/or ionic-strength-sensitive microgels. For these products, there are at least two mechanisms allowing for controlled drug delivery. One can load

the gel particles with a drug at a pH where the particles are fully swollen (expanded), trap it inside by a pH change leading to the collapse of the microgel, and subsequently allow the drug to diffuse out at a pH-controlled rate. A similar mechanism applies as well to the systems where ionic strength is the stimulus for expansion and collapse, or where both pH and ionic strength effects are operating. Another mechanism is pH-dependent reversible ionic binding of drugs. Drug and protein binding and release from anionic microgels have been studied, for example, by Eichenbaum et al. [73, 74] and Soppimath et al. [388], while Vinogradov et al. [308, 375, 389] described the synthesis and properties of some cationic systems.

A sophisticated drug-delivery system, mimicking the action of secretory granules, has been constructed by Kiser et al. [390–392]. The core is an anionic microgel particle based on methacrylic acid, loaded with a drug. Subsequently, by lowering pH, a collapse of the microgel is induced. In this form, the particle is coated with a lipid bilayer, to simulate the natural secretory granule and to protect the particle from premature swelling. Poration of the lipid bilayer (e.g., by applying electric field) causes the gel to swell, allowing release of the drug. A different synthetic procedure leading to similar systems is based on encapsulation of hydrogel-forming components into liposomes and subsequent polymerization [176]. A further example of this kind is a group of products intended for drug delivery of vaccine formulations, consisting of cross-linked polysaccharide microgel core surrounded by a lipid bilayer [255].

A pH-sensitive microgel preparation based on poly(methacrylic acid-*co*-ethyl acrylate) has been devised for oral delivery of a novel drug being a HIV-1 protease inhibitor [393]. It has been demonstrated that the absorption of this poorly water soluble drug from the tested system was much better than from the suspension of a free drug.

Solid sustained release devices for oral delivery of drugs can be obtained by compressing microgels. Such a system based on polyurethane microgels has been shown to retain its integral structure but become microporous on swelling with water [374].

Microgels can be functionalized not only by coupling them with biomolecules, but also by molecular imprinting. This process leads to microgels bearing structural binding sites specific to target molecules. A general procedure of molecular imprinting of a polymer is as follows. Monomers being in contact with a template molecule are polymerized and cross-linked, the template is removed, and the polymer network contains a complementary binding site able to rebind the same template or analogous molecules. Ye et al. and Biffis et al. demonstrated the applicability of this procedure for synthesizing molecularly imprinted microgels and proved their binding performance [77, 78, 394].

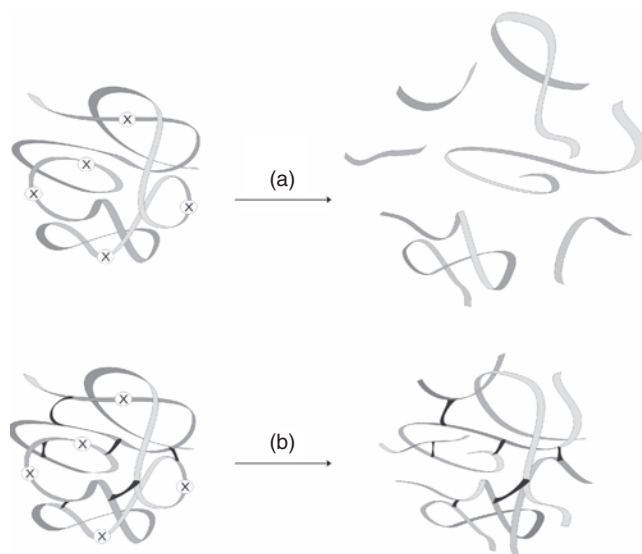
Stability of shape and dimensions of microgels when compared with linear polymer chains may be helpful in their potential use for blocking dental microchannels in cases when there is a need to use a synthetic substitute for the natural gel-like substance performing this function [395].

An interesting and potentially valuable property of microgels is their enhanced resistance against degradation when compared to linear macromolecules [251, 396]. This effect

is illustrated in Figure 7. As a result of any intense or long-lasting stimulus inducing chain breakage (a mechanochemical action, ultrasound, the formation of peroxy radicals along the chain, etc.), a linear macromolecule is easily degraded to short fragments. The same number of chain breaks formed in a microgel may cause no or very little fragmentation, since the chain segments are linked together in many points and will not fall apart as a result of a single chain break.

This effect has been demonstrated on microgels of poly(acrylic acid) (PAA) [251, 397]. Aqueous solutions of linear chains and microgels of PAA were subjected to the action of ionizing radiation in the presence of oxygen. Under such conditions, no cross-linking takes place in the system. Initially formed carbon-centered radicals are rapidly converted into the corresponding peroxy radicals, which in turn initiate processes leading to chain scission. As the concentrations of linear and cross-linked chains of similar average molecular weight were identical, the yield of scission events should be equal for both samples. However, the changes in molecular weight and in the radius of gyration in the case of linear and microgel PAA revealed striking differences. While linear PAA is easily degraded even at relatively low doses, which is evidenced by parallel decrease in weight-average molecular weight and radius of gyration, microgels, within the same dose range, seem to remain intact, their molecular weight and radius of gyration being constant.

This degradation resistance combined with suitable rheological properties may be used in fabricating materials for medical applications. A commercialized example of such a product is a polymer drug based on microgels of a natural polysaccharide used to enhance the viscoelastic performance of synovial fluid [246]. These macromolecules are subjected to mechanochemical stress and to the attack of reactive oxygen species, mainly free radicals. It has been shown that under such conditions internally cross-linked



**Figure 7.** Enhanced degradation resistance of microgels (b) when compared to linear macromolecules (a). Upon several chain scission events at locations marked with  $\otimes$  a linear chain is cut into pieces, while the segments of a microgel do not fall apart.

macromolecules perform better than the corresponding linear ones [247]. Preliminary tests on a substitute synovial fluid containing microgels made of a synthetic polymer proved the high degradation resistance and proper viscoelastic properties of this product [398].

First tests have been performed on the application of microgels as synthetic, nonvirial vectors in gene delivery. The latter is regarded as a powerful tool for curing some hereditary diseases and treating genetically based disorders. Certainly, the issue is a very complex one, since such vectors must be capable of performing many processes such as binding DNA fragments, attachment to cells, internalization, and intracellular plasmid release. First attempts using microgel-like structures for gene delivery were based mainly on chitosan, but synthetic structures based on 2-(dimethylamino)ethyl methacrylate, *N*-vinylpyrrolidone, and *N*-isopropylacrylamide have been tested as well, with promising results [369].

There are also projects to design microgel-based intravenous drug carriers that could remain in blood for a suitable period of time, facilitate the cellular uptake, and possibly also selectively deliver the drug to a target site. Animal tests have shown that by varying properties of such structures (chemical composition, hydrophilicity) one can change the biodistribution patterns of the microgels and that drug-loaded microgels were more efficient than equivalent concentrations of free drug in curing melanoma in mice [369].

Some further perspectives in the application of nano- and microsized particles and devices in drug delivery are discussed in [370].

## 4.2. Coatings

Where actual, large-scale applications of microgels are concerned, the surface coatings industry seems to be the most prominent field. The hundreds of research papers published and patents issued (for a few representative examples see [399–415]) dealing with microgel-containing coatings emphasize the significance of this application. The interest in the use of microgels as components of coatings originated mainly from environment protection needs and regulations. In order to reduce the amount of volatile organic compounds in the coating formulations, the manufacturers tend to increase the total solid content. This is, however, problematic if polymer components of a given molecular weight range are used in binders, since the viscosity of formulations becomes too high. When microgels are used, viscosity can be maintained at a desired level. Another approach besides the high-solid products is to use water-borne coating systems. Microgels can be used both in solvent-borne and water-borne coating products. Besides their advantageous rheological properties, they often exert a reinforcing effect on the cured coating. The use of microgels in coating technologies has been the subject of concise but informative reviews [16, 267] (cf. also book chapters in [416, 417]).

Microgel-containing solutions and dispersions are usually characterized by pseudoplastic, strongly non-Newtonian rheological properties. They are highly viscous at low shear rate (they do not flow at a zero shear rate), but their viscosity decreases remarkably with increasing shear rate. This is in a

perfect accordance with the needs for a typical paint application process. In the storage tank (no or low shear rate) the viscosity should be high to prevent pigment settling, during the gun-spraying (high shear rate) low viscosity is desired, and at the object surface (no or low shear rate again) viscosity should increase rapidly so that no sagging effect occurs, even for films of high thickness. Another useful property of microgels is their positive influence on the orientation of flake pigments in metal effect coatings.

Microgels also have a positive influence on the mechanical properties of cured paint films such as stone chip resistance, impact flexibility, and elasticity. This is attributed to the cross-linked polymer structure, the high molecular weight of gel particles, and the microheterogeneous structure of the microgel-containing polymer film that probably allow the impact energy to be more efficiently dissipated [267].

In the automotive industry, the primer coating layer is often applied by electrodeposition. It has been shown that compositions containing amine-based cationic microgels, mostly in the form of aqueous dispersions, can be used for electrocoating [418, 419].

Problems that have been recently investigated with respect to the use of microgels in coatings include deeper understanding of the relationship between microgel structure and rheological properties (and ways to adjust the latter) [265], the influence of substrate composition and synthetic procedures on the shelf stability of the product and affinity between microgels and pigments [122], influence of microgels on the drying time [142], and ability to form films suitable for drying at ambient temperatures [129].

Microgels can be used not only as constituents of regular coatings but also as self-adsorbing and self-organizing film-forming layers for protecting metal surfaces against corrosion. It has been shown that core-shell microgels based on styrene, butyl acrylate, and phosphate-substituted acrylates form a layer of a structured molecular order on a surface of technical aluminum and provide efficient protection against corrosion in standard tests [332, 420].

Although the use of synthetic microgels in coatings started in the late 1960s [421] or, depending on what we consider a true microgel, perhaps rather in the 1970s [422, 423], one should mention that physical and chemical studies on a highly durable ancient oriental lacquer used in Asia for millennia revealed a structure containing self-formed, natural core-shell-like microgel particles [424].

## 4.3. Miscellaneous

Besides their applications in coatings (biggest market) and in biomaterials (perhaps the most promising direction for the future), microgels are used or tested for use in a number of other fields.

Besides large-scale use of microgels in the coating industry, similar properties make them interesting for the manufacturers of *cosmetics*, namely nail varnishes [425, 426]. In varnishes based on organic solvents, organophilic clays are used to prevent pigment sedimentation. These compounds, however, exert some unwanted side effects and usually require toluene as a component of the formulation. The presence of microgels allows reduction or elimination of the



use of clays while maintaining the proper rheological properties of the varnish and preventing the precipitation of the pigments.

Historically one of the first applications of microgels was in *papermaking* [427–429]. In manufacturing quality products starch and other polysaccharides used as paper and paper-board sizes may be replaced with poly(vinyl alcohol) (PVAL) for better performance. It has been demonstrated that microgels of PVAL show clear advantages over the same polymer in a linear form (e.g., they have lower tendency to penetrate into paper, which is an undesirable effect). Several microgel-containing preparations were used, based either on pure PVAL gels or gel components combining PVAL and polysaccharides. Anionic polysilicate microgels in combination with organic polymers are used to flocculate pulp and filler fines in the water-removal step of the papermaking process [430].

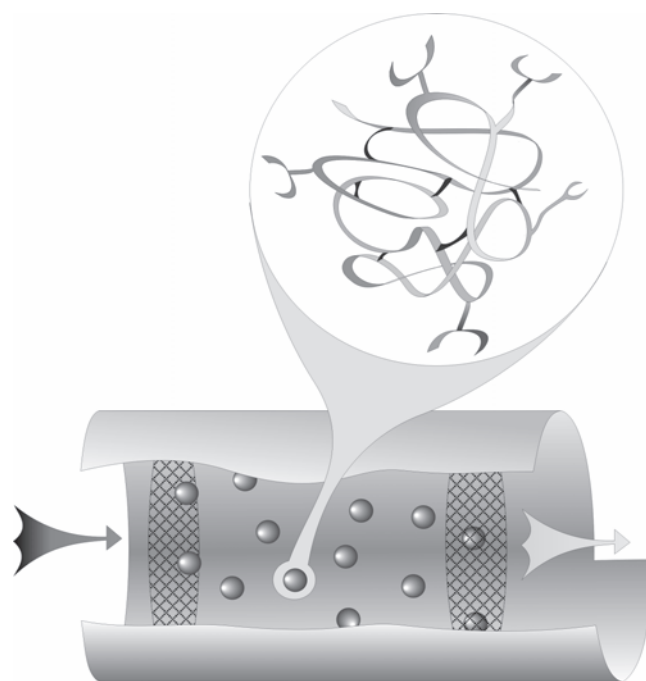
Microgels can be a valuable component of *fibers*. An exemplary application is the admixture of vinylidene chloride gels to an acrylic fiber, significantly improving the flame retardancy [431]. Similar gels have been shown to improve load-bearing properties and flame retardancy of polyurethane *foams* [432].

Microgels can be also applied as supports in *catalysis*. Organo-aluminum compounds coupled to organopolysiloxane microgel particles serve as co-catalysts in the polymerization of olefins [433, 434]. Enantioselective reduction of prochiral ketones can be catalyzed by microgel-bound oxazaborolidines [38]. Good solubility and, at the same time, low viscosity of the solution are the important advantages of microgel-supported catalyst, while the catalytic action and selectivity are comparable to those of low-molecular-weight analogs. Microgels bearing trialkylammonio groups have been demonstrated to catalyze alkaline hydrolysis of aryl laurate esters [127].

By using microgel-supported catalyst, a homogeneous catalysis in a flow reactor may be carried out (Fig. 8). If the inlet and outlet of the reactor are equipped with membranes that the gel particles cannot pass, the reactants are in a constant flow but the catalyst remains in the reactor, despite it being present in a nearly molecular dispersion.

Particular rheological properties as well as higher mechanochemical resistance of microgel solutions when compared to the solutions of linear chains are the basis of their applications in the fields of liquid thickening, *oil recovery*, and *hydraulics*. Solutions of relatively inexpensive polyacrylamide-based microgels are used as thickening agents and agents for restricting the flow of liquids through subterranean formations [435]. Microgel solutions can be applied as a non-Newtonian, shear-resistant, nonleaking hydraulic fluid for hydraulic energy transmission systems and devices absorbing mechanical energy (liquid springs, shock absorbers) [436].

Due to their swelling and water-retaining properties, hydrophilic microgels have been postulated and tested, with good results, for use as *soil conditioners* [437–439]. In the case of preparations consisting only of homogeneous microgels, one may encounter a problem of poor mixing with soil and spontaneous separation (gel particles come up to the surface of soil), due to differences in specific gravity of soil components and gels. This can be avoided if structured



**Figure 8.** A schematic illustration of a homogeneous catalysis in a flow reactor, based on catalyst coupled to microgel particles, trapped between two membranes.

microgels are used, consisting of solid filler grains of high specific gravity embedded in gel particles [439]. While gel-based soil conditioners are well suited for use in flower pots or on the lawn of a golf course, their price does not allow them to be used in large-scale projects like desert reclamation in countries with very limited financial resources, even if economical synthesis routes are taken into consideration (e.g., radiation-cross-linking of acrylamide in bulk followed by mechanical grinding).

An extensively tested and potentially broad field of microgel application is in *printing* and *photographic technology*. Since the rheological properties of microgel can be tailored to meet specific needs (a sophisticated method of viscosity adjustment may be varying the hair length of core-hair type microgels), they may be useful in liquid photopolymer formulations used to cover the screen in the screen printing technique [262]. Incorporation of microgels in the photosensitive layer of a kind of modern lithographic plate leads to a product that can be developed directly on a printing press, without a postexposure wet development step [440]. This technology allows one to save time and labor as well as reduce the use of volatile organic compounds. Another technology has been elaborated to obtain printing plates for flexographic printing [441, 442]. Microgel-based photosensitive resin allows the plates to be water-developable, thus eliminating the use of harmful halogen-containing solvents used to develop the plates in a conventional technique. A variety of photosensitive compositions for use in printing and manufacture of printed circuit boards employ microgels to enhance physical properties, eliminate cold flow, improve storage stability, enhance photospeed, and render these materials suitable for water processing [443–446]. A further interesting example is the use of reactive microgels

that constitute a chemically active compound of a hardenable resin composition [447, 448].

Some inks and electrographic liquid developers contain finely dispersed microparticles of magnetic substances. Several problems have to be overcome in producing these "magnetic fluids," one the most important being the poor dispersion stability. This can be significantly improved when incorporating these solid microparticles, during synthesis, into polymeric microgels [449].

Macroscopic polymer gels can be made photosensitive, not only by introducing chromophores that undergo permanent changes (e.g., cross-linking) upon irradiation, but also by incorporating structures that enable reversible photochemical switching of properties (reversible cross-linking) [450]. This indicates that also microgels themselves can be turned into photosensitive materials, either by using suitable monomers or by postsynthesis modification. In fact, coumarin-containing organosilicon microgels have been demonstrated to undergo photoinduced cluster formation [284]. So far, most often microgels are used in photography and imaging as auxiliary substances, either as binding agents improving the physical properties of the film layers or as additives that help to incorporate the photographically active or other (e.g., antistatic) substances into the photographic layers [451, 452].

Debord et al. have demonstrated that relatively simple microgels made of poly(*N*-isopropylacrylamide) can be manipulated to form colloidal crystals of specific colors depending on the fabrication parameters [70]. In another approach, polymeric nanospheres are incorporated into a stimuli-sensitive hydrogel [453]. Under the action of a chemical stimulus, the distances between the nanospheres can be varied, thus causing shifts of the wavelength of the Bragg peak of the diffracted light. This leads to the changes in color of the specimen. It is expected that such colloidal crystals can find a wide range of applications in *photonics* and *chemical sensing*.

One may expect that in the near future interesting applications will be found for the recently described *electrically conducting microgels* based on pyrrole and aniline polymers bound to a gel core [454]. The products have promising properties in the aspects of electrical conduction, electromagnetic frequency interference shielding, and electrostatic prevention.

*Sorption* and *binding* of a variety of compounds is an intensely studied application field of polymer gels. Most research in this area concerns the use of hydrogels. Exemplary applications of macroscopic hydrogels being investigated, besides the drug-delivery systems described in Section 4.1, include, for example, binding of metal ions [455], selective removal of pollutants (arsenate and selenite [456], textile dyes [457], organic substances [458]), or collection of uranyl ions from seawater [459]. Reversible sorption of water by hydrogels is tested for an application in sludge dewatering [460].

A number of studies revealed the potential application of microgels in *metal ion binding* and *ion exchange*. An advantage of using micro- instead of macrogels is primarily the binding kinetics—in microgels the binding groups are easily accessible, in contrast to most macroscopic gel

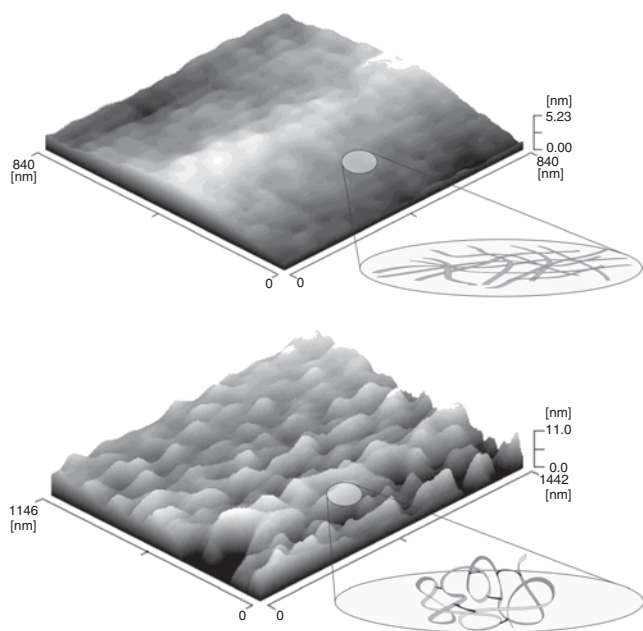
structures, where considerable time is needed for the substrates to diffuse into the gel volume. Gel particles bearing carboxylate groups bind divalent alkali earth cations ( $\text{Mg}^{2+}$ ,  $\text{Ca}^{2+}$ ,  $\text{Sr}^{2+}$ ,  $\text{Ba}^{2+}$ ) more effectively than monovalent cations (as  $\text{Na}^+$ ) [75]. Binding of calcium ions has been studied in more detail [63, 65]. Other studies have shown that there may be a pronounced selectivity in binding divalent metal ions. For example, binding of  $\text{Hg}^{2+}$  cations by poly(*N*-vinylcaprolactam-*co*-sodium acrylate) microgels is much stronger than binding of  $\text{Cu}^{2+}$  and divalent alkali metal ions [64]. Strong, albeit reversible, binding of  $\text{Pb}^{2+}$  by microgels of poly(*N*-isopropylacrylamide-*co*-sodium acrylate) has been reported as well [149, 288]. These observations indicate that microgel-based systems may be used for selective ion binding. Various microgel-containing selective ion-exchange materials have been fabricated. Examples are commercially available macroporous polymeric anion and cation exchangers where every exchanger particle (having the diameter of a fraction of mm) consists of a large number of submicrometer size microgels (cf. [461–463]). Such systems may be applied for example for eliminating trace concentrations of organic compounds that exist in water in an ionic form.

It is postulated that thermosensitive microgels may serve as valuable binding/separation agents, due to the ability of these materials to absorb various chemical species below the conformational transition temperature and to release them at elevated temperatures due to the contraction of microgels. The compounds being reversibly absorbed include metal ions [288, 464], polymers [465], and surfactants [18, 150, 302, 466–468]. Most studies in this area have been done on poly(*N*-isopropylacrylamide)-based gels. Besides, the interactions between surfactants and poly(*N*-vinylcaprolactam) microgels have been investigated [61].

One of the most fascinating prospective uses of stimuli microgels is in *microdevices* and *micromachinery*. Due to their fast response time, they may be used, for example, as self-regulated, pH- or temperature-controlled microvalves. Contrary to conventional microactuators (electromagnetic, electrostatic, thermopneumatic, etc.), microgel-based valves are simple and do not require external power for operation. Fully operational exemplary devices of this kind, having short response times, have been recently presented by Beebe et al. [469].

Microgels can be used as building bricks for constructing complex polymer structures and materials. A simple example may be fabrication of a polymer material (foil, coating, etc.) of a well-developed, rough (in the microscale) surface. This may be carried out just by casting a foil from a microgel solution. Such a surface, even after drying and collapse of microgels due to a loss of solvent, remains structured when compared to analogous sample obtained from solution of linear chains of the same polymer (Fig. 9) [251].

Chen et al. have demonstrated that styrene-based microgels bearing carboxyl group could be easily self-organized into ordered multilayered films or latex crystals [155]. Calcium ions may be used to form large structures of spherical poly(*N*-vinylcaprolactam-*co*-sodium acrylate) microgels [63]. Poly(vinyl methyl ether) (PVME) microgels can be used as specific nanoporous templates in the polymerization of pyrrole [335]. The resulting products were large,



**Figure 9.** Surfaces of films obtained by casting and drying solutions of poly(acrylic acid): (a) film of linear PAA, (b) film of PAA microgels, as observed by atomic force microscopy.

needle-like particles, in contrast to small spherical particles obtained with linear PVME. Microgel-like, internally cross-linked rubber particles have a high reinforcing effect when incorporated into regular rubber materials [470, 471]. Materials constructed of microgels that are embedded in continuous polymer matrix are considered for use as membranes, filters, and absorbents [472].

## GLOSSARY

**Chemical gel (permanent gel)** A gel where the polymer network is composed of polymer chains connected by permanent, covalent bonds.

**Critical gelation concentration (CGC)** 1. The highest monomer concentration at which no macroscopic gel is formed even at a complete monomer conversion (in the crosslinking processes starting from polymers). 2. The highest polymer concentration at which no macroscopic gel can be obtained (in the crosslinking processes starting from polymers).

**Cross-linking** A process of formation of permanent links (covalent bonds) between two separate macromolecules or between two segments of same macromolecule.

**Cross-linking polymerization** A process where polymerization and cross-linking take place side-by-side; a typical phenomenon for polymerization of systems containing multifunctional monomers.

**Gel** A two-component material consisting of a (permanent or labile) network of linked polymer chains and a solvent filling the pores of this network. In this chapter this term is used to denote only the chemical (permanent) gels.

**Hydrogel** A two-component material consisting of a (permanent or labile) network of linked hydrophilic polymer

chains and water (or aqueous solution) filling the pores of this network. In this chapter this term is used to denote only the chemical (permanent) hydrogels.

**Intermolecular cross-linking** A process of formation of permanent links (covalent bonds) between two separate macromolecules.

**Intramolecular cross-linking** A process of formation of permanent links (covalent bonds) between two segments of same macromolecule.

**Ionizing radiation** Any form of radiation (electromagnetic radiation or fast particles) having sufficiently high energy to cause ionization of matter. Gamma rays from isotope sources and beams of accelerated electrons are commonly used in radiation-based polymer technology.

**Lower critical solution temperature (LCST)** Lowest temperature at which the polymer-solvent system becomes phase-separated (for polymer-solvent systems that become immiscible upon temperature increase).

**Macroscopic gel** A continuous gel phase of macroscopic dimensions. It can be easily seen with a naked eye. Macroscopic gel can be filling the whole volume of the sample or the reaction vessel (a “wall-to-wall” gel).

**Microgel** A gel particle of microscopic dimensions (or in other words, an internally cross-linked polymer microparticle), able to swell, without disintegration, in a suitable solvent. In this chapter this term is used to denote only the chemical (permanent) gel particles. For a more detailed discussion of the microgel definition—see Introduction.

**Microparticle (polymeric)** Any polymer particle of microscopic dimensions, regardless of the presence or absence of any links and the nature of the forces acting between the individual polymer chains.

**Nanogel** 1. A gel particle of submicrometer size. 2. A subclass of small microgels formed by intramolecular cross-linking of single macromolecules. In this chapter this term is used to denote only the chemical (permanent) gel particles. For a more detailed discussion of the nanogel definition—see Introduction.

**Physical gel (pseudogel)** A gel where the polymer network is composed of polymer chains connected by weak, usually reversible, binding phenomena (ionic bonds, hydrogen bonds, van der Waals forces, entanglements).

**Surfactant-free emulsion polymerization** A particular kind of emulsion polymerization where the emulsifying action is provided not by an added surfactant but by the monomer and/or polymer itself.

## ACKNOWLEDGMENTS

This work has been supported in part by the State Committee for Scientific Research (Poland), grants 3 T09B 053 19, 3 T09A 128 22, and PBZ-KBN-004/CD/T11/2000, as well as by the International Atomic Energy Agency, research project 302-F2-POL-11513 (F2.20.34). The valuable assistance of Renata Czechowska-Biskup, Katarzyna Filipczak, Artur Henke, Jadwiga Ignaczak, Dr. Ireneusz Janik, Sławomir Kadlubowski, Marek Kozicki, Dr. Piotr Kujawa, and Dr. Przemysław Stasica in collecting literature,

managing the reference database, and preparing the drawings is gratefully acknowledged.

## REFERENCES

- O. Wichterle and D. Lim, *Nature* 185, 117 (1960).
- N. A. Peppas, "Hydrogels in Medicine and Pharmacy." CRC Press, Boca Raton, 1986.
- N. A. Peppas and J. J. Sahlin, *Biomaterials* 17, 1553 (1996).
- J. M. Rosiak, in "Radiation Effects on Polymers" (R. C. Clough and S. W. Shalaby, Eds.), ACS Book Series Vol. 475, p. 271. Am. Chem. Soc., Washington, DC, 1991.
- O. Hirasa, *J. Intelligent Mater. Syst. Struct.* 4, 538 (1993).
- P. Molyneux, "Water-Soluble Synthetic Polymers. Properties and Applications." CRC Press, Boca Raton, 1987.
- G. N. Kormanovskaya, I. N. Vlodec, and P. A. Rebinder, *Dokl. Akad. Nauk SSSR* 183, 348 (1968).
- S. Rangelov and W. Brown, *Polymer* 41, 4825 (2000).
- P.-D. Hong, C.-M. Chou, and J.-C. Chen, *Polymer* 41, 5847 (2000).
- X. Zheng, Z. Tong, X. Xie, and F. Zeng, *Polym. J.* 30, 284 (1998).
- C. Esquenet and E. Buhler, *Macromolecules* 35, 3708 (2002).
- S. Jiang, K.-Q. Xia, and G. Xu, *Macromolecules* 34, 7783 (2001).
- T. Aubry, F. Bossard, and M. Moan, *Polymer* 43, 3375 (2002).
- H. Staudinger and W. Heuer, *Chem. Ber.* 67, 1164 (1934).
- H. Staudinger and E. Husemann, *Chem. Ber.* 68, 1618 (1935).
- W. Funke, O. Okay, and B. Joos-Müller, *Adv. Polym. Sci.* 136, 139 (1998).
- B. R. Saunders and B. Vincent, *Adv. Colloid Polym. Sci.* 80, 1 (1999).
- R. Pelton, *Adv. Colloid Interface Sci.* 85, 1 (2000).
- M. Antonietti, *Angew. Chem.* 100, 1813 (1988).
- M. Antonietti and K. Landfester, *Prog. Polym. Sci.* 27, 689 (2002).
- O. Okay, *Polymer* 40, 4117 (1999).
- N. B. Graham and J. Mao, *Colloid Surface A* 118, 211 (1996).
- N. B. Graham and A. Cameron, *Pure Appl. Chem.* 70, 1271 (1998).
- N. B. Graham, U.K. Patent 290264B, 1984.
- N. B. Graham and C. M. G. Hayes, *Macromol. Symp.* 93, 293 (1995).
- N. B. Graham, *Colloid Surface A* 118, 211 (1996).
- N. B. Graham, J. Mao, and A. Urquhart, *Angew. Makromol. Chem.* 240, 113 (1996).
- R. S. Frank, J. S. Downey, K. Yu, and H. D. H. Stoever, *Macromolecules* 35, 2728 (2002).
- O. Okay, M. Kurz, K. Lutz, and W. Funke, *Macromolecules* 28, 2728 (1995).
- Y. Huang, U. Seitz, and W. Funke, *Makromol. Chem.* 186, 273 (1985).
- M. Antonietti and C. Rosenauer, *Macromolecules* 24, 3434 (1991).
- H. Chen, K. Ishizu, T. Fukutomi, and T. Kakurai, *J. Polym. Sci. Chem.* 22, 2123 (1984).
- K. Ishizu, S. Kuwabara, H. Chen, H. Mizuno, and T. Fukutomi, *J. Polym. Sci., Polym. Chem. Ed.* 24, 1735 (1986).
- K. Ishizu, M. Nunomura, and T. Fukutomi, *J. Polym. Sci., Polym. Lett. Ed.* 24, 607 (1986).
- K. Ishizu, M. Nunomura, and T. Fukutomi, *J. Polym. Sci., Polym. Chem. Ed.* 25, 1163 (1987).
- L. Y. Tsarik, O. N. Novikov, and V. V. Magdinets, *J. Polym. Sci. A* 36, 371 (1998).
- A. Biffis, *J. Mol. Catal. A* 165, 303 (2001).
- C. Schunicht, A. Biffis, and G. Wulff, *Tetrahedron* 56, 1693 (2000).
- S. Kara and O. Pekcan, *Polymer* 41, 6335 (2000).
- S. Kara, O. Okay, and O. Pekcan, *Polym. Bull.* 45, 281 (2000).
- S. Kara and O. Pekcan, *Polymer* 41, 3093 (2000).
- O. Pekcan and S. Kara, *Polymer* 42, 7411 (2001).
- P. L. Nayak, S. Alva, K. Yang, K. Dhal Pradeep, J. Kumar, and S. K. Tripathy, *Macromolecules* 30, 7351 (1997).
- P. A. Costello, I. K. Martin, A. T. Slark, D. C. Sherrington, and A. Titterton, *Polymer* 43, 245 (2002).
- N. O'Brien, A. McKee, D. C. Sherrington, A. T. Slark, and A. Titterton, *Polymer* 41, 6027 (2000).
- D. Greszta, D. Mardare, and K. Matyjaszewski, *Macromolecules* 27, 638 (1994).
- D. Mardare and K. Matyjaszewski, in "Polymeric Materials Encyclopedia" (J. C. Salomone, Ed.), Vol. 5, p. 3840. CRC Press, Boca Raton, 1996.
- T. E. Patten, J. Xia, T. Abernathy, and K. Matyjaszewski, *Science* 272, 866 (1996).
- K. Matyjaszewski, *ACS Symp. Ser.* 85, 2 (1998).
- S. G. Gaynor, K. Beers, S. Coca, A. Muhlenbach, J. Qiu, J. Xia, X. Zhang, and K. Matyjaszewski, *ACS Symp. Ser.* 765, 52 (2000).
- "Controlled/Living Radical Polymerization" (K. Matyjaszewski, Ed.), ACS Symp. Ser. Vol. 768. Am. Chem. Soc., Washington, DC, 2000.
- K. Matyjaszewski, J. Qiu, D. Shipp, and S. G. Gaynor, *Macromol. Symp.* 155, 15 (2000).
- S. Abrol, P. A. Kambouris, M. G. Looney, and D. H. Solomon, *Macromol. Rapid Commun.* 18, 755 (1997).
- S. Abrol, M. J. Caulfield, G. G. Qiao, and D. H. Solomon, *Polymer* 42, 5987 (2001).
- J. H. Ward, A. Shahar, and N. A. Peppas, *Polymer* 43, 1745 (2002).
- K.-Y. Baek, M. Kamigaito, and M. Sawamoto, *Macromolecules* 34, 7629 (2001).
- K.-Y. Baek, M. Kamigaito, and M. Sawamoto, *Macromolecules* 34, 215 (2001).
- K.-Y. Baek, M. Kamigaito, and M. Sawamoto, *J. Polym. Sci. A* 40, 2245 (2002).
- K.-Y. Baek, M. Kamigaito, and M. Sawamoto, *J. Polym. Sci. A* 40, 633 (2002).
- K.-Y. Baek, M. Kamigaito, and M. Sawamoto, *Macromolecules* 35, 1493 (2002).
- Y. Gao, S. C. F. Au-Yeung, and C. Wu, *Macromolecules* 32, 3674 (1999).
- S. Peng and C. Wu, *Macromol. Symp.* 159, 179 (2000).
- S. Peng and C. Wu, *Macromolecules* 34, 6795 (2001).
- S. Peng and C. Wu, *Polymer* 42, 6871 (2001).
- S. Peng and Ch. Wu, *J. Phys. Chem. B* 105, 2331 (2001).
- S. Peng and C. Wu, *Macromolecules* 34, 568 (2001).
- D. Duracher, A. Elaissari, and C. Pichot, *Macromol. Symp.* 150, 305 (2000).
- A. Guillerme, J. P. Cohen Addad, J. P. Bazile, D. Duracher, A. Elaissari, and C. Pichot, *J. Polym. Sci. B* 38, 889 (2000).
- C. D. Jones and L. A. Lyon, *Macromolecules* 33, 8301 (2000).
- J. D. Debord, S. Eustis, S. B. Debord, M. T. Lofye, and L. A. Lyon, *Adv. Mater.* 14, 658 (2002).
- H. Kawaguchi, M. Kawahara, N. Yaguchi, F. Hoshino, and Y. Ohtsuka, *Polym. J.* 20, 903 (1988).
- M. Kashiwabara, K. Fujimoto, and H. Kawaguchi, *Colloid Polym. Sci.* 273, 339 (1995).
- G. M. Eichenbaum, P. F. Kiser, D. Shah, S. A. Simon, and D. Needham, *Macromolecules* 32, 8996 (1999).
- G. M. Eichenbaum, P. F. Kiser, A. V. Dobrynin, S. A. Simon, and D. Needham, *Macromolecules* 32, 4867 (1999).
- G. M. Eichenbaum, P. F. Kiser, D. Shah, W. P. Meuer, D. Needham, and S. A. Simon, *Macromolecules* 33, 4087 (2000).
- T. Fukutomi, K. Asakawa, and N. Kihara, *Chem. Lett.* 1997, 783 (1997).
- L. Ye, P. A. G. Cormack, and K. Mosbach, *Anal. Chim. Acta* 435, 187 (2001).
- L. Ye and K. Mosbach, *React. Funct. Polym.* 48, 149 (2001).
- M. Szwarc, "Carboanions, Living Polymers and Electron Transfer Processes." Interscience, New York, 1968.
- M. Szwarc, "Ions and Ions Pairs in Organic Reactions." Wiley Interscience, New York, 1974.

81. M. Szwarc and M. Van Beylen, "Ionic Polymerization and Living Polymers." Kluwer Academic, Dordrecht, 1993.
82. H. L. Hsieh and R. P. Quirk, "Anionic Polymerization: Principles and Practical Applications." Dekker, New York, 1996.
83. S. Slomkowski, S. Sosnowski, and M. Gadzinowski, *Macromol. Symp.* 123, 45 (1997).
84. W. Straehle and W. Funke, *Makromol. Chem.* 179, 2145 (1978).
85. J. C. Hiller and W. Funke, *Angew. Makromol. Chem.* 76/77, 161 (1979).
86. H. Eschwey, M. L. Hallensleben, and W. Burchard, *Makromol. Chem.* 73, 235 (1973).
87. H. Eschwey and W. Burchard, *J. Polym. Sci., Polym. Symp.* 53, 1 (1975).
88. P. Lutz and P. Rempp, *Makromol. Chem.* 191, 1051 (1988).
89. O. Okay and W. Funke, *Makromol. Chem.* 191, 1565 (1990).
90. A. Okamoto and I. Mita, *J. Polym. Sci., Polym. Chem. Ed.* 16, 1187 (1978).
91. D. J. Worsfold, J. G. Zilliox, and P. Rempp, *Can. J. Chem.* 42, 3379 (1969).
92. A. Kohler, J. G. Zilliox, P. Rempp, J. Pollacek, and I. Koessler, *Eur. Polym. J.* 8, 627 (1972).
93. L. K. Bi and L. J. Fetters, *Macromolecules* 9, 732 (1976).
94. R. N. Young and L. J. Fetters, *Macromolecules* 11, 899 (1978).
95. F. A. Taromi and P. Rempp, *Makromol. Chem.* 190, 1791 (1989).
96. D. Held and A. H. E. Muller, *Macromol. Symp.* 157, 225 (2000).
97. O. Okay and W. Funke, *Makromol. Chem. Rapid Commun.* 11, 583 (1990).
98. O. Okay and W. Funke, *Macromolecules* 23, 2623 (1990).
99. L. Pille and D. H. Solomon, *Macromol. Chem. Phys.* 195, 2477 (1994).
100. S. Abrol and D. H. Solomon, *Polymer* 40, 6583 (1999).
101. M. Nguyen, R. Beckett, L. Pille, and D. H. Solomon, *Macromolecules* 31, 7003 (1998).
102. S. Krause, *J. Phys. Chem.* 68, 1948 (1964).
103. W. T. Tang, G. Hadziioannou, P. M. Cotts, B. A. Smith, and C. W. Frank, *Polym. Prepr.* 27, 107 (1986).
104. N. P. Balsara, M. Tirell, and T. P. Lodge, *Macromolecules* 24, 1975 (1991).
105. R. Saito, S. Yoshida, and K. Ishizu, *J. Appl. Polym. Sci.* 63, 849 (1997).
106. R. Saito and K. Ishizu, *Polymer* 38, 225 (1997).
107. R. Saito, Y. Akiyama, and K. Ishizu, *Polymer* 40, 655 (1999).
108. I. Piirma, "Emulsion Polymerization." Academic Press, New York, 1982.
109. "Emulsion Polymerisation and Emulsion Polymers" (P. A. Lovell and M. S. El Aasser, Eds.), Wiley, Chichester, UK, 1997.
110. W. Obrecht, U. Seitz, and W. Funke, *Makromol. Chem.* 175, 3587 (1974).
111. W. Obrecht, U. Seitz, and W. Funke, *Makromol. Chem.* 176, 2771 (1975).
112. W. Obrecht, U. Seitz, and W. Funke, *Makromol. Chem.* 177, 1877 (1976).
113. W. Obrecht, U. Seitz, and W. Funke, *Makromol. Chem.* 177, 2235 (1976).
114. H. Kast and W. Funke, *Makromol. Chem.* 182, 1567 (1981).
115. A. Matsumoto, K. Kodama, Y. Mori, and H. Aota, *J. Macromol. Sci., Pure Appl. Chem. A* 35, 1459 (1998).
116. A. Matsumoto, K. Kodama, H. Aota, and I. Capek, *Eur. Polym. J.* 35, 1509 (1999).
117. A. Matsumoto, T. Shimatani, and H. Aota, *Polym. J.* 32, 871 (2000).
118. A. Matsumoto, M. Fujihashi, and H. Aota, *Polym. J.* 33, 636 (2001).
119. A. Matsumoto, *Prog. Polym. Sci.* 26, 189 (2001).
120. A. Matsumoto, *Macromol. Symp.* 179, 141 (2002).
121. A. Matsumoto, N. Murakami, H. Aota, J. Ikeda, and I. Capek, *Polymer* 40, 5687 (1999).
122. K. Ishii, *Colloid Surface A* 153, 591 (1999).
123. A. Mura-Kuentz and G. Riess, *Macromol. Symp.* 150, 229 (2000).
124. J. S. Lowe, B. Z. Chowdhry, J. R. Parsonage, and M. J. Snowden, *Polymer* 39, 1207 (1998).
125. A. Laukkanen, S. Hietala, S. L. Maunu, and H. Tenhu, *Macromolecules* 33, 8703 (2000).
126. H. Vihola, A. Laukkanen, J. Hirvonen, and H. Tenhu, *Eur. J. Pharm. Sci.* 16, 69 (2002).
127. D. J. Evans, A. Williams, and R. J. Pryce, *J. Molec. Catal. A* 99, 41 (1995).
128. S. Kirsch, A. Doerk, E. Bartsch, H. Sillescu, K. Landfester, H. W. Spiess, and W. Maechtle, *Macromolecules* 32, 4508 (1999).
129. Y.-J. Park, M. J. Monteiro, S. van Es, and A. L. German, *Eur. Polym. J.* 37, 965 (2001).
130. F. Baumann, M. Schmidt, B. Deubzer, M. Geck, and J. Dauth, *Macromolecules* 27, 6102 (1994).
131. F. Baumann, B. Deubzer, M. Geck, J. Dauth, and M. Schmidt, *Macromolecules* 30, 7568 (1997).
132. G. Lindenblatt, W. Schaertl, T. Pakula, and M. Schmidt, *Macromolecules* 33, 9340 (2000).
133. H. Tobita and K. Yamamoto, *Macromolecules* 27, 3389 (1994).
134. H. Tobita, M. Kumagai, and N. Aoyagi, *Polymer* 41, 481 (2000).
135. E. Jabbari, *Polymer* 42, 4873 (2001).
136. M. Antonietti, R. Basten, and S. Lohmann, *Macromol. Chem. Phys.* 196, 441 (1995).
137. F. Candau, in "Polymerization in Organic Media" (E. C. Paleos, Ed.), p. 215. Gordon & Breach, Philadelphia, 1992.
138. M. Antonietti, W. Bremser, and M. Schmidt, *Macromolecules* 23, 3796 (1990).
139. E. Bartsch, M. Antonietti, W. Schupp, and H. Sillescu, *J. Chem. Phys.* 97, 3950 (1992).
140. F. Groehn and M. Antonietti, *Macromolecules* 33, 5938 (2000).
141. M. Antonietti, A. Briel, and F. Groehn, *Macromolecules* 33, 5950 (2000).
142. L.-W. Chen, B.-Z. Yang, and M.-L. Wu, *Prog. Org. Coatings* 31, 393 (1997).
143. S.-Y. Lin, K.-S. Chen, and L. Run-Chu, *Polymer* 40, 6307 (1999).
144. S. Neyret and B. Vincent, *Polymer* 38, 6129 (1997).
145. J. W. Goodwin, R. H. Ottewill, R. Pelton, and G. Vianello, *Br. Polym. J.* 10, 173 (1978).
146. J. W. Goodwin, R. H. Ottewill, and R. Pelton, *Colloid Polym. Sci.* 257, 61 (1979).
147. R. H. Pelton and P. Chibante, *Colloids Surf.* 20, 247 (1986).
148. H. M. Crowther, B. R. Saunders, J. S. Mears, T. Cosgrove, B. Vincent, S. M. King, and G.-E. Yu, *Colloid Surface A* 152, 327 (1999).
149. B. R. Saunders, H. M. Crowther, G. E. Morris, S. J. Mears, T. Cosgrove, and B. Vincent, *Colloid Surface A* 149, 57 (1999).
150. N. C. Woodward, B. Z. Chowdhry, S. A. Leharne, and M. J. Snowden, *Eur. Polym. J.* 36, 1355 (2000).
151. Y. Zhao, G. Zhang, and C. Wu, *Macromolecules* 34, 7804 (2001).
152. K. Kratz, Th. Hellweg, and W. Eimer, *Colloid Surface A* 170, 137 (2000).
153. B. R. Saunders, H. M. Crowther, and B. Vincent, *Macromolecules* 30, 482 (1997).
154. B. R. Saunders and B. Vincent, *Colloid Polym. Sci.* 275, 9 (1997).
155. X. Chen, Z. Cui, Z. Chen, K. Zhang, G. Lu, G. Zhang, and B. Yang, *Polymer* 43, 4147 (2002).
156. M. J. Snowden, B. Z. Chowdhry, B. Vincent, and G. E. Morris, *J. Chem. Soc. Faraday Trans.* 92, 5013 (1996).
157. H. S. Choi, J. M. Kim, K. Lee, and Y. C. Bae, *J. Appl. Polym. Sci.* 69, 5013 (1998).
158. F. Meunier, A. Elaissari, and C. Pichot, *Polym. Adv. Technol.* 6, 489 (1994).
159. W. Funke, R. Koltz, and W. Straehle, *Makromol. Chem.* 180, 2797 (1979).
160. Y. Ch. Yu and W. Funke, *Makromol. Chem.* 103, 187 (1982).
161. Y. Ch. Yu and W. Funke, *Makromol. Chem.* 103, 203 (1982).
162. W. Funke and K. Walther, *Polymer J.* 17, 179 (1985).
163. M. Miyata and W. Funke, *Makromol. Chem.* 184, 755 (1983).

164. P. J. Flory, *J. Am. Chem. Soc.* 63, 3083 (1941).
165. L. Rey, J. Galy, and H. Sautereau, *Macromolecules* 33, 6780 (2000).
166. L. Rey, J. Duchet, J. Galy, H. Sautereau, D. Vouagner, and L. Carrión, *Polymer* 43, 4375 (2002).
167. J. B. Hutchison and K. S. Anseth, *Macromol. Theory Simul.* 10, 600 (2001).
168. M. Ghiass, A. D. Rey, and B. Dabir, *Macromol. Theory Simul.* 10, 657 (2001).
169. M. Ghiass, A. D. Rey, and B. Dabir, *Polymer* 43, 989 (2002).
170. J.-P. Fouassier, "Photoinitiation, Photopolymerization, and Photocuring: Fundamentals and Applications." Hanser Gardner, Munich, 1995.
171. "Photopolymerization: Fundamentals and Applications" (A. B. Scranton, C. Bowman, and R. W. Peiffer, Eds.), ACS Symposium Ser. Vol. 673. Am. Chem. Soc., Washington, DC, 1997.
172. S. Lu and K. S. Anseth, *J. Controlled Release* 57, 291 (1999).
173. H. Kubota and A. Fukuda, *J. Appl. Polym. Sci.* 65, 1313 (1997).
174. J. Jakubiak, J. Nie, L. A. Linden, and J. F. Rabek, *J. Polym. Sci. A* 38, 876 (2000).
175. R. J. Russell, A. C. Axel, K. L. Shields, and M. V. Pishko, *Polymer* 42, 4893 (2001).
176. S. Kazakov, M. Kaholek, I. Teraoka, and K. Levon, *Macromolecules* 35, 1911 (2002).
177. A. Charlesby, "Atomic Radiation and Polymers." Pergamon Press, Oxford, 1960.
178. M. Dole, "The Radiation Chemistry of Macromolecules." Academic Press, New York, 1972.
179. J. E. Wilson, "Radiation Chemistry of Monomers, Polymers and Plastics." Dekker, New York, 1974.
180. "CRC Handbook of Radiation Chemistry" (Y. Tabata, Y. Ito, and S. Tagawa, Eds.). CRC Press, Boca Raton, 1991.
181. "Radiation Processing of Polymers" (A. Singh and J. Silverman, Eds.). Carl Hanser, Munich, 1992.
182. V. S. Ivanov, "Radiation Chemistry of Polymers." VSP, Utrecht, The Netherlands, 1992.
183. R. J. Woods and A. K. Pikaev, "Applied Radiation Chemistry: Radiation Processing." Wiley Interscience, New York, 1993.
184. "Recent Trends in Radiation Polymer Chemistry" (S. Okamura, Ed.), Advances in Polymer Science, Vol. 105, Springer, Berlin, 1993.
185. J. Rosiak, K. Burczak, W. Pekala, N. Pislewski, S. Idziak, and A. Charlesby, *Radiat. Phys. Chem.* 32, 793 (1988).
186. I. Kaetsu, K. Uchida, Y. Morita, and M. Okubo, *Radiat. Phys. Chem.* 40, 157 (1992).
187. N. Nagaoka, A. Safranji, M. Yoshida, H. Omichi, H. Kubota, and R. Katakai, *Macromolecules* 26, 7386 (1993).
188. Z.-L. Ding, M. Yoshida, M. Asano, Z.-T. Ma, H. Omichi, and R. Katakai, *Radiat. Phys. Chem.* 44, 263 (1994).
189. M. Carenza and F. M. Veronese, *J. Controlled Release* 29, 187 (1994).
190. G. A. Mun, Z. S. Nurkeeva, V. V. Khutorianskiy, A. D. Sergaziyev, and J. M. Rosiak, *Radiat. Phys. Chem.* 65, 67 (2002).
191. Y. Morita, M. Yoshida, M. Asano, and I. Kaetsu, *Colloid Polym. Sci.* 265, 916 (1987).
192. M. Yoshida, T. Yokota, M. Asano, and M. Kumakura, *Colloid Polym. Sci.* 267, 986 (1989).
193. M. Yoshida, T. Yokota, M. Asano, and M. Kumakura, *Eur. Polym. J.* 26, 121 (1990).
194. A. Safranji, S. Kano, M. Yoshida, H. Omichi, R. Katakai, and M. Suzuki, *Radiat. Phys. Chem.* 46, 203 (1995).
195. M. Yoshida, M. Asano, I. Kaetsu, and Y. Morita, *Yakuzaigaku* 42, 137 (1982).
196. Y. Naka, Y. Yamamoto, and K. Hayashi, *Radiat. Phys. Chem.* 40, 83 (1992).
197. Y. Naka and Y. Yamamoto, *J. Polym. Sci. A* 30, 1287 (1992).
198. Y. Naka and Y. Yamamoto, *J. Polym. Sci. A* 30, 2149 (1992).
199. M. Dreja, W. Pyckhout-Hintzen, and B. Tieke, *Macromolecules* 31, 272 (1998).
200. G. J. Price, in "Chemistry under Extreme or Non-classical Conditions" (R. van Eldik and C. D. Hubbard, Eds.), p. 381. Wiley/Spektrum Akademischer Verlag, New York/Heidelberg, 1997.
201. T. J. Mason and J. P. Lorimer, "Sonochemistry: Theory and Uses of Ultrasound in Chemistry." Ellis Horwood, Chichester, UK, 1988.
202. "Current Trends in Sonochemistry" (G. J. Price, Ed.). Royal Society of Chemistry, Cambridge, UK, 1992.
203. K. S. Suslick, D. A. Hammerton, and R. E. J. Cline, *J. Am. Chem. Soc.* 108, 5641 (1986).
204. E. B. Flint and K. S. Suslick, *Science* 253, 1397 (1991).
205. K. Makino, M. M. Mossoba, and P. Riesz, *J. Phys. Chem.* 87, 1369 (1983).
206. K. Makino, M. M. Mossoba, and P. Riesz, *J. Am. Chem. Soc.* 104, 3537 (1982).
207. A. Henglein and C. Kormann, *Int. J. Radiat. Biol.* 48, 251 (1985).
208. X. Fang, G. Mark, and C. von Sonntag, *Ultrasonics Sonochem.* 3, 57 (1996).
209. G. Mark, A. Tauber, R. Laupert, H.-P. Schuchmann, D. Schulz, A. Mues, and C. von Sonntag, *Ultrasonics Sonochem.* 5, 41 (1998).
210. A. Tauber, G. Mark, H.-P. Schuchmann, and C. von Sonntag, *J. Chem. Soc. Perkin Trans.* 2 1129 (1999).
211. C. von Sonntag, G. Mark, H.-P. Schuchmann, J. von Sonntag, and A. Tauber, in "Chemical Processes under Extreme or Non-Classic Conditions" (J.-L. Luche, C. Balny, S. Bénéfice, J. M. Denis, and C. Pétrier, Eds.), p. 11. E.U. Directorate General, Science, Research and Development, Luxembourg, 1998.
212. C. von Sonntag, G. Mark, A. Tauber, and H.-P. Schuchmann, *Adv. Sonochem.* 5, 109 (1999).
213. H. W. Melville and A. Murray, *Trans. Faraday Soc.* 46, 996 (1950).
214. T. Miyata and F. Nakashio, *J. Chem. Eng. Japan* 8, 463 (1975).
215. P. Kruus, *Ultrasonics* 21, 193 (1983).
216. P. Kruus and T. J. Patraboy, *J. Phys. Chem.* 89, 3379 (1985).
217. P. Kruus, J. Lawrie, and M. L. O'Neill, *Ultrasonics* 26, 352 (1988).
218. P. Kruus, M. L. O'Neill, and D. Robertson, *Ultrasonics* 28, 304 (1990).
219. P. Kruus, *Adv. Sonochem.* 2, 1 (1991).
220. G. J. Price, P. F. Smith, and P. J. West, *Ultrasonics* 29, 166 (1991).
221. G. J. Price, D. J. Norris, and P. J. West, *Macromolecules* 25, 6447 (1992).
222. J. O. Stoffer, O. C. Sitton, and H. L. Kao, *Polym. Mater. Sci. Eng. Prepr.* 65, 42 (1991).
223. J. O. Stoffer, O. C. Sitton, and Y. H. Kim, *Polym. Mater. Sci. Eng. Prepr.* 67, 242 (1992).
224. H. Fujiwara, T. Kikyū, H. Nanbu, and T. Honda, *Polymer Bull.* 33, 317 (1994).
225. J. P. Lorimer, T. J. Mason, and D. Kershaw, *J. Chem. Soc., Chem. Commun.* 1217 (1991).
226. K. Matyjaszewski, D. Greszta, J. S. Hrkach, and H. K. Kim, *Macromolecules* 28, 59 (1995).
227. M. D. Hohol and M. W. Urban, *Polymer* 34, 1995 (1993).
228. H. Fujiwara and K. Goto, *Polymer Bull.* 25, 571 (1991).
229. K. S. Suslick, M. W. Grinstaff, K. J. Kolbeck, and M. Wong, *Ultrasonics Sonochem.* 1, 65 (1994).
230. Y. Naka and Y. Yamamoto, *Kobunshi Ronbunshu.* 50, 287 (1993).
231. B. Wang, S. Mukataka, M. Kodama, and E. Kokufuta, *Langmuir* 13, 6108 (1997).
232. B. Wang, S. Mukataka, E. Kokufuta, M. Ogiso, and M. Kodama, *J. Polym. Sci. B* 38, 214 (2000).
233. B. Wang, S. Mukataka, E. Kokufuta, and M. Kodama, *Radiat. Phys. Chem.* 59, 91 (2000).
234. P. Ulanski, Zainuddin, and J. M. Rosiak, *Radiat. Phys. Chem.* 46, 917 (1995).
235. P. Ulanski, I. Janik, and J. M. Rosiak, *Radiat. Phys. Chem.* 52, 289 (1998).

236. P. Ulanski, S. Kadlubowski, and J. M. Rosiak, *Radiat. Phys. Chem.* 63, 533 (2002).
237. T. Batzilla and W. Funke, *Makromol. Chem. Rapid Commun.* 8, 261 (1987).
238. Y. Shindo, T. Sugimura, K. Horie, and I. Mita, *J. Photopolym. Sci. Technol.* 1, 155 (1988).
239. U. Brasch and W. Burchard, *Macromol. Chem. Phys.* 197, 223 (1996).
240. M. Frank and W. Burchard, *Makromol. Chem., Rapid Commun.* 12, 645 (1991).
241. W. Arbogast, A. Horvath, and B. Vollmert, *Makromol. Chem.* 181, 1513 (1980).
242. B. Gebben, H. W. A. van der Berg, D. Bargeman, and C. A. Smolders, *Polymer* 26, 1737 (1985).
243. X. Lu, Z. Hu, and J. Gao, *Macromolecules* 33, 8698 (2000).
244. E. A. Balazs and A. Leschiner, U.S. Patent 4, 582, 865, 1986.
245. E. A. Balazs, A. Leschiner, and E. A. Leschiner, U.S. Patent 4, 713, 448, 1987.
246. E. A. L. Balazs, in "Cellulosics Utilisation" (H. P. Inagaki, Ed.), p. 233. Elsevier Applied Science, London, 1989.
247. S. Al-Assaf, G. O. Phillips, D. J. Deeble, B. Parsons, H. Starnes, and C. von Sonntag, *Radiat. Phys. Chem.* 46, 207 (1995).
248. P. Ulanski and J. M. Rosiak, *Nucl. Instrum. Methods B* 151, 356 (1999).
249. S. Sabharwal, H. Mohan, Y. K. Bhardwaj, and A. B. Majali, *Radiat. Phys. Chem.* 54, 643 (1999).
250. K.-F. Arndt, T. Schmidt, and R. Reichelt, *Polymer* 42, 6785 (2001).
251. S. Kadlubowski, J. Grobelny, W. Olejniczak, M. Cichomski, and P. Ulanski, *Macromolecules*, 36, 2484 (2003).
252. K. S. Schmitz, B. Wang, and E. Kokufuta, *Macromolecules* 34, 8370 (2001).
253. R. Czechowska-Biskup, M.Sc. Thesis, Technical University of Lodz, Poland, 2002.
254. R. Czechowska-Biskup, A. Henke, I. Ignaczak, J. M. Rosiak, and P. Ulanski, unpublished data.
255. N. C. Santos, A. M. A. Sousa, D. Betbeder, M. Prieto, and M. A. R. B. Castanho, *Carbohydr. Res.* 300, 31 (1997).
256. C. B. Agbugba, B. A. Hendriksen, B. Z. Chowdhry, and M. J. Snowden, *Colloid Surface A* 137, 155 (1998).
257. "Polymer Handbook" (J. Brandrup and E. H. Immergut, Eds.), 3 ed. Wiley, New York, 1989.
258. B. H. Zimm, F. P. Price, and J. P. Bianchi, *J. Phys. Chem.* 62, 979 (1958).
259. H. Senff and W. Richtering, *J. Chem. Phys.* 111, 1705 (1999).
260. H. Senff and W. Richtering, *Colloid Polym. Sci.* 278, 830 (2000).
261. M. Antonietti, A. Briel, and S. Foerster, *Chem. Phys.* 105, 7795 (1996).
262. T. Takahashi, H. Watanabe, N. Miyagawa, S. Takahara, and T. Yamaoka, *Polym. Adv. Technol.* 13, 33 (2002).
263. D. M. Kiminta, P. F. Luckham, and S. Lenon, *Polymer* 36, 4827 (1995).
264. G. Van Assche, E. Verdonck, and B. Van Mele, *Polymer* 42, 2959 (2001).
265. C. Raquois, J. F. Tassin, S. Rezaiguia, and A. V. Gindre, *Progr. Org. Coatings* 26, 239 (1995).
266. S. Fridrikh, C. Raquois, J. F. Tassin, and S. Rezaiguia, *J. Chim. Phys. Phys. Chim. Biol.* 93, 941 (1996).
267. D. Saatweber and B. Vogt-Birnbrich, *Progr. Org. Coatings* 28, 33 (1996).
268. M. Osterhold, *Progr. Org. Coatings* 40, 131 (2000).
269. P. Kratochvil, "Classical Light Scattering from Polymer Solutions." Elsevier, Amsterdam, 1987.
270. "Light Scattering from Polymer Solutions" (M. B. Hughlin, Ed.). Academic Press, New York, 1972.
271. K. S. Schmitz, "Dynamic Light Scattering by Macromolecules." Academic Press, New York, 1990.
272. A. Matsumoto, N. Kawasaki, and T. Shimatani, *Macromolecules* 33, 1646 (2000).
273. M. Helmstedt, J. Stejskal, and W. Burchard, *Macromol. Symp.* 162, 63 (2000).
274. S. Zhou and B. Chu, *J. Phys. Chem. B* 102, 1364 (1998).
275. B. Hirzinger, M. Helmstedt, and J. Stejskal, *Polymer* 41, 2883 (2000).
276. R. Lubis, J. Olejniczak, J. Rosiak, and J. Kroh, *Radiat. Phys. Chem.* 36, 249 (1990).
277. K. Burczak, R. Lubis, J. Rosiak, and J. Kroh, in "Proceedings of the 7th Tihany Symposium on Radiation Chemistry" (J. Dobo, L. Nyikos, and R. Schiller, Eds.), p. 355. Akademiai Kiado, Budapest, 1991.
278. P. Ulanski, E. Bothe, J. M. Rosiak, and C. von Sonntag, *Macromol. Chem. Phys.* 195, 1443 (1994).
279. P. Kujawa, P. Ulanski, and J. M. Rosiak, *Radiat. Phys. Chem.* 52, 389 (1998).
280. C. S. Johnson and D. A. Gabriel, "Laser Light Scattering." Dover, New York, 1994.
281. P. Stepanek, in "Dynamic Light Scattering: The Method and Some Applications" (W. Brown, Ed.), p. 177. Oxford Science Publications/Clarendon Press, Oxford, UK, 1993.
282. B. Chu, "Laser Light Scattering: Basic Principles and Practice." Academic Press, New York, 1991.
283. I.-S. Kim, Y.-I. Jeong, and S.-H. Kim, *Int. J. Pharm.* 205, 109 (2000).
284. C. Graf, W. Schaertl, and N. Hugenberg, *Adv. Mater.* 12, 1353 (2000).
285. P. Bouillot and B. Vincent, *Colloid Polym. Sci.* 278, 74 (2000).
286. M. Dauben, K. Platkowski, and K.-H. Reichert, *Angew. Makromol. Chem.* 250, 67 (1997).
287. J. S. Chen and T. L. Yu, *J. Appl. Polym. Sci.* 69, 871 (1998).
288. G. E. Morris, B. Vincent, and M. J. Snowden, *Progr. Colloid Polym. Sci.* 105, 16 (1997).
289. H. M. Crowther and B. Vincent, *Colloid Polym. Sci.* 276, 46 (1998).
290. E. Abuin, A. Leon, E. Lissi, and J. M. Varas, *Colloid Surface A* 147, 55 (1999).
291. E. Daly and B. R. Saunders, *Langmuir* 5546 (2000).
292. E. Daly and B. R. Saunders, *Phys. Chem. Chem. Phys.* 2, 3187 (2000).
293. N. Hatto, T. Cosgrove, and M. J. Snowden, *Polymer* 41, 7133 (2000).
294. K. Kratz, T. Hellweg, and W. Eimer, *Polymer* 42, 6631 (2001).
295. K. Kratz, A. Lapp, W. Eimer, and T. Hellweg, *Colloid Surface A* 197, 55 (2002).
296. A. Stipp, C. Sinn, T. Palberg, I. Weber, and E. Bartsch, *Progr. Colloid Polym. Sci.* 115, 59 (2000).
297. A. Fernandez-Nieves, A. Fernandez-Barbero, B. Vincent, and F. J. de las Nieves, *Macromolecules* 33, 2114 (2000).
298. A. Fernandez-Nieves, A. Fernandez-Barbero, B. Vincent, and F. J. de las Nieves, *Progr. Colloid Polym. Sci.* 115, 134 (2000).
299. R. Saito and K. Ishizu, *Polymer* 38, 225 (1997).
300. J. F. Miller, K. Schaetzel, and B. Vincent, *J. Colloid Int. Sci.* 143, 532 (1991).
301. T. Norisuye, N. Masui, Y. Kida, D. Ikuta, E. Kokufuta, S. Ito, S. Panyukov, and M. Shibayama, *Polymer* 43, 5289 (2002).
302. S. J. Mears, Y. Deng, T. Cosgrove, and R. Pelton, *Langmuir* 13, 1901 (1997).
303. W. W. Yau, J. J. Kirkland, and D. D. Bly, "Modern Size-Exclusion Liquid Chromatography: Practice of Gel Permeation and Gel Filtration Chromatography." Wiley, New York, 1979.
304. S. Mori and H. G. Barth, "Size Exclusion Chromatography." Springer-Verlag, Weinheim, 1999.
305. J. S. Downey, G. McIsaac, R. S. Frank, and H. D. H. Stoeber, *Macromolecules* 34, 4534 (2001).
306. L. Pille, A. G. Jhingran, E. P. Capareda, and D. H. Solomon, *Polymer* 37, 2459 (1996).

307. S. Podzimek, M. Kaska, and J. Sruparek, *Macromol. Symp.* 151, 543 (2000).
308. S. Vinogradov, E. Batrakova, and A. Kabanov, *Colloid Surface B* 16, 291 (1999).
309. B. C. Gilbert, J. R. L. Smith, C. E. Milne, A. C. Whitwood, and P. Taylor, *J. Chem. Soc. Perkin Trans. 2* 1759 (1994).
310. I. Janik, P. Ulanski, K. Hildenbrand, J. M. Rosiak, and C. von Sonntag, *J. Chem. Soc. Perkin Trans. 2* 2041 (2000).
311. P. Ulanski, E. Bothe, K. Hildenbrand, J. M. Rosiak, and C. von Sonntag, *J. Chem. Soc. Perkin Trans. 2* 13 (1996).
312. P. Ulanski, E. Bothe, K. Hildenbrand, and C. von Sonntag, *Chem. Eur. J.* 6, 3922 (2000).
313. M. Akashi, S. Saihata, E. Yashima, S. Sugita, and K. Marumo, *J. Polym. Sci. A* 31, 1153 (1993).
314. D. Shiino, Y. Murata, K. Kataoka, Y. Koyama, M. Yokoyama, T. Okano, and Y. Sakurai, *Biomaterials* 15, 121 (1994).
315. K. R. Morgan, C. J. Roberts, S. J. B. Tendler, M. C. Davies, and Ph. M. Williams, *Carbohydr. Res.* 315, 169 (1999).
316. K. J. McGrath, C. M. Roland, and M. Antonietti, *Macromolecules* 33, 8354 (2000).
317. A. Charlesby and J. Steven, *Int. J. Radiat. Phys. Chem.* 8, 719 (1976).
318. A. Charlesby, P. Kafer, and R. Folland, *Radiat. Phys. Chem.* 11, 83 (1978).
319. A. Charlesby and B. J. Bridges, *Radiat. Phys. Chem.* 19, 155 (1982).
320. R. Folland and A. Charlesby, *J. Polym. Sci.* 16, 339 (1978).
321. A. Charlesby and R. Folland, *Radiat. Phys. Chem.* 15, 393 (1980).
322. B. Nystroem, M. E. Moseley, W. Brown, and J. Roots, *J. Appl. Polym. Sci.* 26, 3385 (1981).
323. J. Rosiak, K. Burczak, W. Pekala, N. Pislewski, and S. Idziak, *Radiat. Phys. Chem.* 32, 793 (1988).
324. C. B. Carter and D. B. Williams, "Transmission Electron Microscopy: A Textbook for Material Science." Plenum, New York, 1996.
325. S. L. Flegler, J. W. Heckman, and K. L. Klomparens, "Scanning and Transmission Electron Microscopy: An Introduction." Oxford Univ. Press, London, 1997.
326. L. Reimer, T. Tamir, and A. L. Schawlow, "Scanning Electron Microscopy: Physics of Image Formation and Microanalysis." Springer-Verlag, Weinheim, 1998.
327. "Atomic Force Microscopy/Scanning Tunneling Microscopy" (S. H. Cohen and M. L. Lightbody, Eds.). Plenum, New York, 1999.
328. E. Meyer, "Atomic Force Microscopy: Fundamentals to Most Advanced Applications." Springer-Verlag, Weinheim, 2002.
329. "Atomic Force Microscopy in Cell Biology" (B. P. Jena and J. K. H. Horber, Eds.), *Methods in Cell Biology*, Vol. 68. Academic Press, San Diego, 2002.
330. K. S. Birdi, "Scanning Tunneling Microscopy and Atomic Force Microscopy: Applications in Surface and Colloid Chemistry." CRC Press, Boca Raton, 2003.
331. T. M. Chou, P. Prayoonthong, A. Aitouchen, and M. Libera, *Polymer* 43, 2085 (2002).
332. A. Henke, E. Jaehne, and H.-J. P. Adler, *Macromol. Symp.* 164, 1 (2001).
333. I. M. Papisov, K. I. Bolyachevskaya, A. A. Litmanovich, V. N. Matveenko, and I. L. Volchkova, *Eur. Polym. J.* 35, 2087 (1999).
334. F. M. B. Coutinho, D. L. Carvalho, M. L. La Torre Aponte, and C. C. R. Barbosa, *Polymer* 42, 43 (2001).
335. A. Pich, Y. Lu, H.-J. P. Adler, T. Schmidt, and K.-F. Arndt, *Polymer* 43, 5723 (2002).
336. S. S. Sheiko, *Adv. Polym. Sci.* 151, 61 (2000).
337. M. A. Hempenius, W. F. Zoetelief, M. Gauthier, and M. Moller, *Macromolecules* 31, 2299 (1998).
338. V. J. Morris, A. R. Kirby, and A. P. Gunning, *Progr. Colloid Polym. Sci.* 114, 102 (1999).
339. W. M. Sigmund, J. Sindel, and F. Aldinger, *Progr. Colloid Polym. Sci.* 105, 23 (1997).
340. R. W. Stark, T. Drobek, M. Weth, J. Fricke, and W. M. Heckl, *Ultramicroscopy* 75, 161 (1998).
341. "Polymer Gels: Fundamentals and Biomedical Applications" (D. DeRossi, K. Kajiwara, Y. Osada, and A. Yamauchi, Eds.). Plenum Press, New York, 1991.
342. K. Park, W. S. W. Shalaby, and H. Park, "Biodegradable Hydrogels for Drug Delivery." Technomic, Lancaster, 1993.
343. "Hydrogels and Biodegradable Polymers for Bioapplications" (R. M. Ottenbrite, S. J. Huang, and K. Park, Eds.), ACS Symposium Series 627. American Chemical Society, Washington, DC, 1996.
344. "Silicone Hydrogels: The Rebirth of Continuous Wear Contact Lenses" (D. Sweeney, Ed.). Butterworth-Heinemann Medical, Oxford, 2000.
345. A. S. Hoffman, in "Macromolecules" (H. Benoit and P. Rempp, Eds.), p. 321, 1982.
346. K. R. Kamath and K. Park, *Adv. Drug Delivery Rev.* 11, 59 (1993).
347. J. M. Rosiak, *J. Controlled Release* 31, 9 (1994).
348. J. M. Rosiak, P. Ulanski, L. A. Pajewski, F. Yoshii, and K. Makuuchi, *Radiat. Phys. Chem.* 46, 161 (1995).
349. N. A. Peppas, P. Bures, W. Leobandung, and H. Ichikawa, *Eur. J. Pharm. Biopharm.* 50, 27 (2000).
350. M. E. Byrne, K. Park, and N. A. Peppas, *Adv. Drug Delivery Rev.* 54, 149 (2002).
351. A. S. Hoffman, *Adv. Drug Delivery Rev.* 54, 3 (2002).
352. N. B. Graham, *Chem. Ind.* 15, 482 (1990).
353. K. Burczak, T. Fujisato, M. Hatada, and Y. Ikada, *Proc. Japan Acad. Ser. B* 67, 83 (1991).
354. M. Kozicki, P. Kujawa, L. A. Pajewski, M. Kolodziejczyk, J. Narebski, and J. M. Rosiak, *Eng. Biomater.* 2, 11 (1999).
355. P. Ulanski, I. Janik, S. Kadlubowski, M. Kozicki, P. Kujawa, M. Pietrzak, P. Stasica, and J. M. Rosiak, *Polym. Adv. Technol.* 13, 951 (2002).
356. J. M. Rosiak, A. Rucinska-Rybus, and W. Pekala, U.S. Patent 4, 871, 490, 1989.
357. J. M. Rosiak, W. Dec, and A. J. Kowalski, *Med. Sci. Monit.* 2, 78 (1996).
358. J. M. Rosiak, A. J. Kowalski, and W. Dec, *Radiat. Phys. Chem.* 52, 307 (1998).
359. A. S. Hoffman, *Mater. Res. Soc. Bull.* 42 (1991).
360. J. Ed. Dusek, "Responsive Gels: Volume Transitions," *Adv. Polym. Sci.* Vol. 109. Springer, Berlin, 1993.
361. R. Langer, *Nature* 392, 5 (1998).
362. C. Pichot, A. Elaissari, D. Duracher, F. Meunier, and F. Sauzedde, *Macromol. Symp.* 175, 285 (2001).
363. R. Yoshida, K. Sakai, T. Okano, and Y. Sakurai, *Adv. Drug Delivery Rev.* 11, 85 (1993).
364. T. Miyata, N. Asami, and T. Urugami, *Nature* 399, 766 (1999).
365. T. Shiga, Y. Hirose, A. Okada, T. Kurauchi, and O. Kamigaito, in "Proc. 1st Japan International SAMPE Symposium," p. 659, 1989.
366. T. Shiga, Y. Hirose, A. Okada, and T. Kurauchi, *J. Intelligent Mater. Syst. Struct.* 4, 553 (1993).
367. A. Rembaum, S. P. S. Yen, and W. Volksen, *Chemtech* 182 (1978).
368. A. Rembaum and Z. A. Tokes, "Microspheres: Medical and Biological Applications." CRC Press, Boca Raton, 1988.
369. S. Mitra, T. K. De, and A. Maitra, in "Encyclopedia of Surface and Colloid Science" (P. Somasundaran, Ed.), p. 2397. Dekker, New York, 2002.
370. D. Lavan, D. Lynn, and R. Langer, *Nature Drug Discovery* 1, 77 (2002).
371. S. P. S. Yen, A. Rembaum, and R. S. Molday, U.S. Patent 4, 157, 323, 1979.
372. A. Rembaum, S. P. S. Yen, and W. J. Dreyer, U.S. Patent 4, 138, 383, 1979.
373. M. Nair and J. S. Tan, U.S. Patent 5, 078, 994, 1992.



374. N. B. Graham and J. Mao, U.S. Patent 5, 994, 492, 1999.
375. A. V. Kabanov and S. V. Vinogradov, U.S. Patent 6, 333, 051, 2001.
376. A. Rembaum, S. P. S. Yen, E. Cheong, S. Wallace, R. S. Molday, I. L. Gordon, and W. J. Dreyer, *Macromolecules* 9, 328 (1976).
377. P. Guiot and P. Couvreur, "Polymeric Nanoparticles and Microspheres." CRC Press, Boca Raton, 1986.
378. T. Delair, F. Meunier, A. Elaissari, M. H. Charles, and C. Pichot, *Colloid Surface A* 153, 341 (1999).
379. F. Saucedo, A. Elaissari, and C. Pichot, *Colloid Polym. Sci.* 277, 1041 (1999).
380. H. Kawaguchi, K. Fujimoto, and Y. Mizuhara, *Colloid Polym. Sci.* 270, 53 (1992).
381. K. Fujimoto, Y. Mizuhara, N. Tamura, and H. Kawaguchi, *J. Intelligent Mater. Syst. Struct.* 4, 184 (1993).
382. T. Shiroya, N. Tamura, M. Yasui, K. Fujimoto, and H. Kawaguchi, *Colloid Surface B* 4, 267 (1995).
383. M. Yasui, T. Shiroya, K. Fujimoto, and H. Kawaguchi, *Colloid Surface B* 8, 311 (1997).
384. A. Elaissari, L. Holt, C. Voisset, C. Pichot, B. Mandrand, and C. Mabilat, *J. Biomater. Sci., Polym. Ed.* 10, 403 (1999).
385. K. Achiha, R. Ojima, Y. Kasuya, K. Fujimoto, and H. Kawaguchi, *Polym. Adv. Technol.* 6, 534 (1995).
386. Y. Shin, J. H. Chang, J. Liu, R. Williford, Y.-K. Shin, and G. J. Exarhos, *J. Controlled Release* 73, 1 (2001).
387. S.-Y. Lin, K.-S. Chen, and L. Run-Chu, *Biomaterials* 22, 2999 (2001).
388. K. S. Soppimath, A. R. Kulkarni, and T. M. Aminabhavi, *J. Controlled Release* 75, 331 (2001).
389. S. V. Vinogradov, T. K. Bronich, and A. V. Kabanov, *Adv. Drug Delivery Rev.* 54, 135 (2002).
390. P. F. Kiser, G. Wilson, and D. Needham, *Nature* 394, 459 (1998).
391. P. F. Kiser, G. Wilson, and D. Needham, *J. Controlled Release* 68, 9 (2000).
392. R. A. Siegel, *Nature* 394, 427 (1998).
393. F. De Jaeghere, E. Allemann, F. Kubel, C. Galli, R. Cozens, E. Doelker, and R. Gurny, *J. Controlled Release* 68, 291 (2000).
394. A. Biffis, N. B. Graham, G. Siedlaczek, S. Stalberg, and G. Wulff, *Macromol. Chem. Phys.* 202, 163 (2001).
395. L.-A. Linden, in "Proc. 5th Int.Symp. Chemistry Forum'99" (M. Jarosz, Ed.), p. 65. Warsaw University of Technology, Warsaw, 1999.
396. S. Kadlubowski, A. Henke, and P. Ulanski, unpublished data.
397. S. Kadlubowski and P. Ulanski, unpublished data.
398. A. Henke, M.Sc. Thesis, Technical University of Lodz, Poland, 2002.
399. D. S. Gibbs, J. F. Sinicola, and D. E. Ranck, U.S. Patent 4, 324, 714, 1982.
400. H. J. Wright, D. P. Leonard, and R. A. Ezzell, U.S. Patent 4, 377, 661, 1983.
401. H. J. Wright, D. P. Leonard, and R. A. Ezzell, U.S. Patent 4, 414, 357, 1983.
402. W. T. Short, R. A. Ottaviani, and D. J. Hart, U.S. Patent 4, 570, 734, 1985.
403. K. G. Olson, S. K. Das, and R. Dowbenko, U.S. Patent 4, 540, 740, 1985.
404. T. Kurauchi, K. Ishii, A. Yamada, and J. Nozue, U.S. Patent 4, 563, 372, 1986.
405. C. Gajria and Y. Ozari, U.S. Patent 4, 567, 246, 1986.
406. K. G. Olson, S. K. Das, and R. Dowbenko, U.S. Patent 4, 611, 026, 1986.
407. Y. Tsuchiya and K. Tobinaga, U.S. Patent 5, 200, 461, 1993.
408. G. P. Craun, D. J. Telford, and H. J. DeGraaf, U.S. Patent 5, 508, 325, 1996.
409. G. P. Craun and V. V. Kaminski, U.S. Patent 5, 554, 671, 1996.
410. W. Dannhorn, L. Hoppe, E. Luhmann, and H.-J. Juhl, U.S. Patent 5, 565, 504, 1996.
411. G. P. Craun, U.S. Patent 5, 576, 361, 1996.
412. G. P. Craun, U.S. Patent 5, 733, 970, 1998.
413. G. P. Craun, B. A. Smith, and N. S. Williams, U.S. Patent 5, 877, 239, 1999.
414. H.-D. Hille, S. Neis, and H. Muller, U.S. Patent 5, 977, 258, 1999.
415. M. Roth, Q. Tang, and S. H. Eldin, U.S. Patent 5, 994, 475, 1999.
416. "Automotive Paints and Coatings" (G. Fettes, Ed.). VCH Verlagsgesellschaft, Weinheim, 1995.
417. "Polymer Dispersions and Their Industrial Applications" (D. Urban and K. Takamura, Eds.). Wiley-VCH, Weinheim, 2002.
418. V. G. Corrigan and S. R. Zawacky, U.S. Patent 5, 096, 556, 1992.
419. P. W. Uhlianuk, U.S. Patent 5, 407, 976, 1995.
420. A. Henke, *Farbe und Lack* 106 (2000).
421. N. D. P. Smith, U.K. Patent 1, 242, 054, 1967.
422. W. Funke, *J. Oil Col. Chem. Assoc.* 60, 438 (1977).
423. S. Porter, Jr. and B. N. McBane, U.S. Patent 4, 075, 141, 1978.
424. J. Kumanotani, *Progr. Org. Coatings* 34, 135 (1998).
425. J.-F. Tranchant, H.-G. Riess, and A. Meybeck, U.S. Patent 6, 280, 713, 2001.
426. A. Kuentz, H.-G. Riess, A. Meybeck, and J.-F. Tranchant, U.S. Patent 5, 711, 940, 1998.
427. J. C. Solenberger, U.S. Patent 3, 941, 728, 1976.
428. J. C. Solenberger, U.S. Patent 3, 941, 730, 1976.
429. A. J. Deyrup, U.S. Patent 4, 012, 352, 1977.
430. J. D. Rushmere, U.S. Patent 5, 185, 206, 1993.
431. D. S. Gibbs, U.S. Patent 4, 164, 522, 1979.
432. D. S. Gibbs, J. H. Benson, and R. T. Fernandez, U.S. Patent 4, 232, 129, 1980.
433. H. Alt, F. Baumann, J. Weis, and A. Koppl, U.S. Patent 6, 358, 876, 2002.
434. A. Köppl, H. G. Alt, and R. Schmidt, *J. Organometal. Chem.* 577, 351 (1999).
435. M. L. Zweigle and J. C. Lamphere, U.S. Patent 4, 172, 066, 1979.
436. B.-L. Lee and L. C. Hrusch, U.S. Patent 6, 237, 333, 2001.
437. R. A. Herrett and P. A. King, U.S. Patent 3, 336, 129, 1967.
438. S. N. Yen and F. D. Osterholtz, U.S. Patent 3, 900, 378, 1975.
439. K. Tanaka, U.S. Patent 5, 013, 349, 1991.
440. S.-M. Cheng, R.-C. Liang, and Y.-H. Tsao, U.S. Patent 5, 811, 220, 1998.
441. S. Satake, Y. Yatsuyanagi, M. Fuji, and I. Imagawa, U.S. Patent 5, 545, 694, 1996.
442. S. Satake, Y. Yatsuyanagi, M. Fuji, and I. Imagawa, U.S. Patent 5, 547, 999, 1996.
443. M. Fryd and T. R. Suess, U.S. Patent 4, 726, 877, 1988.
444. M. Fryd and T. R. Suess, U.S. Patent 4, 753, 865, 1988.
445. M. Fryd, E. Leberzammer, and S. A. R. Sebastian, U.S. Patent 5, 075, 192, 1991.
446. K. Kanda, Y. Ichinose, S. Arimatsu, K. Konishi, and T. Hase, U.S. Patent 5, 393, 637, 1995.
447. Y. Fukuchi, U.S. Patent 5, 120, 796, 1992.
448. Y. Fukuchi, U.S. Patent 5, 229, 434, 1993.
449. A. Kitahara and K. Konno, U.S. Patent 4, 749, 506, 1988.
450. D. Kuckling, I. G. Ivanova, H.-J. P. Adler, and T. Wolff, *Polymer* 43, 1813 (2002).
451. G. Helling, U.S. Patent 4, 513, 080, 1985.
452. M. Nair, L. A. Lobo, and T. K. Osburn, U.S. Patent 6, 001, 549, 1999.
453. J. H. Holtz and S. A. Asher, *Nature* 389, 829 (1997).
454. Y.-B. Kim, C.-H. Park, and J.-W. Hong, U.S. Patent 6, 399, 675, 2002.
455. G. C. Rex and S. Schlick, *J. Phys. Chem.* 89, 3598 (1985).
456. J. H. Min and J. G. Hering, U.S. Patent 6, 203, 709, 2001.
457. S. Duran, D. Solpan, and O. Guven, *Nucl. Instrum. Methods B* 151, 196 (1999).
458. H. Ichijo, R. Kishi, O. Hirasa, and Y. Takiguchi, *Polym. Gels Networks* 2, 315 (1994).
459. T. Caykara, R. Inam, and C. Ozyurek, *J. Polym. Sci. A* 39, 277 (2001).

460. H. Unno, X. Huang, T. Akehata, and O. Hirasa, in "Polymer Gels. Fundamentals and Biomedical Applications" (D. DeRossi, Ed.), p. 183. Plenum Press, New York, 1991.
461. P. Li and A. K. Sengupta, *React. Funct. Polym.* 44, 273 (2000).
462. E. F. Meitzner and J. A. Oline, U.S. Patent 4, 501, 826, 1985.
463. E. F. Meitzner and J. A. Oline, U.S. Patent 4, 256, 840, 1981.
464. M. J. Snowden, D. Thomas, and B. Vincent, *Analyst* 118, 1367 (1993).
465. M. J. Snowden, *J. Chem. Soc., Chem. Commun.* 803 (1992).
466. G. Wang, R. Pelton, and J. Zhang, *Colloid Surface A* 153, 335 (1999).
467. K. C. Tam, S. Ragaram, and R. H. Pelton, *Langmuir* 10, 418 (1994).
468. C. Wu, S. Zhou, S. C. F. Au-Yeung, and S. Jiang, *Angew. Makromol. Chem.* 240, 123 (1996).
469. D. J. Beebe, J. S. Moore, J. M. Bauer, Q. Yu, R.-H. Liu, C. Devadoss, and B.-H. Jo, *Nature* 404, 588 (2000).
470. W. Obrecht and W. Jeske, U.S. Patent 6, 399, 706, 2002.
471. W. Obrecht and W. Jeske, U.S. Patent 6, 372, 857, 2002.
472. T. Fukutomi, Y. Sugito, M. Takizawa, S. Mizoguchi, M. Nakamura, H. Takeuchi, N. Oguma, M. Maruyama, and S. Horiguchi, U.S. Patent 5, 770, 631, 1998.



# Polymeric Nanoparticles

Bobby G. Sumpter, Donald W. Noid, Michael D. Barnes

*Oak Ridge National Laboratory, Oak Ridge, Tennessee, USA*

Joshua U. Otaigbe

*University of Southern Mississippi, Hattiesburg, Mississippi, USA*

## CONTENTS

1. Introduction
  2. Synthetic Routes for Polymeric Nanoparticles
  3. Supercritical Fluid-Based Particle Production
  4. Droplet and Aerosol Techniques
  5. Gas Atomization Approaches
  6. Dendrimers, Hyperbranched Polymers, or Star Polymers
  7. Molecular Imprint Polymers
  8. Simulation and Modeling of Polymer Particles
  9. Applications of Polymer Particles
  10. Polymer Particle Patent Review
  11. Conclusions
- Glossary  
References

## 1. INTRODUCTION

Science and technology continue to witness enormous attention focused on the production of new materials on the micrometer and nanometer scale that have tunable material, electrical, and optical properties. Polymer particles, polymer particle alloys, or polymeric composites provide one viable avenue for the production of these highly desired systems. Currently, polymer particles can be produced in a variety of ways, some of which allow easily controllable particle size and composition as well as a number of crucial physical properties [1–12]. In addition, recent results have shown that polymeric particles in the micro- to submicrometer range can be formed such that dynamical confinement effects result in interesting nanostructures and properties that cannot be produced using conventional methods [2].

Polymer particle wires and arrays, “supramolecular particle structures,” have also been produced which offer another set of exciting possibilities [4]. These combined capabilities open the door to a variety of novel uses, such as electro-optic and luminescent devices, magnetic coatings, thermoplastics and conducting materials, hybrid inorganic–organic polymer alloys, polymer-supported heterogeneous catalysis, high-energy-density materials, information materials, and a whole host of applications in the biomedical field [6–16]. In this chapter we review some of the recent progress in the production and characterization of polymer particles and provide examples of a number of relevant applications. Our intent is to provide a general overview of the various areas and methods relevant to polymeric particles. Since there is a very large literature base for each of the topics discussed in the following sections, we have tried to provide some general references where more extensive literature citations can be found.

## 2. SYNTHETIC ROUTES FOR POLYMERIC NANOPARTICLES

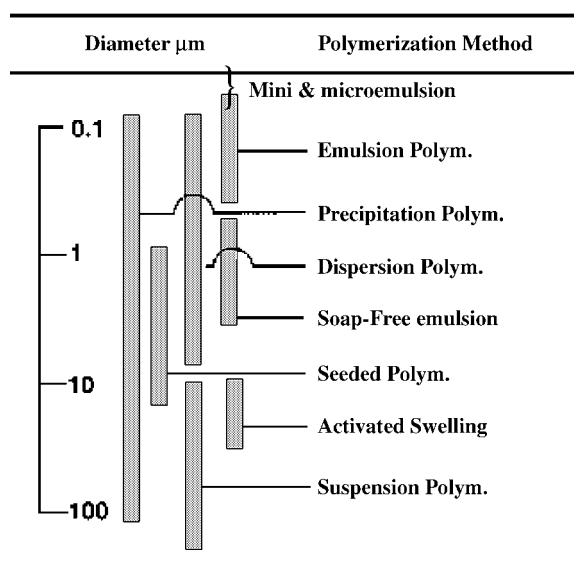
The synthesis of polymeric nanoparticles in large and homogeneous quantities has received considerable attention in polymer and materials science [17–73]. Much of the motivation has been derived from the incredibly broad and often unique applications of polymeric particles (see later sections for details). To date most of the synthetic production of polymer particles generally falls within two primary approaches. The first approach is based on the emulsification of the water-immiscible organic solution of the polymer by an aqueous phase containing a surfactant, followed by evaporation of the solvent. The second approach is based on the precipitation of a polymer after addition of a nonsolvent of the polymer. On the other hand, nanoparticles formed of natural macromolecules are generally obtained by thermal denaturing proteins (such as albumin) or by a gelification process, as in the case of alginates.

In the past, polymer latexes (suspensions or dispersions of polymer particles) were largely made by conventional emulsion polymerization but this method is mostly suitable for only radical homopolymerization of a narrow set of barely water-soluble monomers. To broaden the range of possible polymeric systems a number of new techniques for generating micro- and miniemulsions, phase inversions, secondary dispersions, and suspension polymerizations have been developed and successfully implemented. Figure 1 illustrates some of the types of polymerization methods available for producing polymer particles and the corresponding particle size range. We discuss a number of these techniques and their applicability to the production of polymeric nanoparticles. Our discussion is only meant to give a flavor of the various polymerization routes for producing polymer particles. There are a number of reviews and books dedicated to these methods and more complete details are better obtained from those references and references cited therein [17–26].

## 2.1. Emulsion Polymerization

Emulsion polymerization as a conventional preparation method can make polymeric particles in the size range of 100–1000 nm, a range that has been gradually broadened [17, 18, 27–39]. For example, the seeded emulsion polymerization technique was developed to make latexes larger than 1000 nm, while the miniemulsion and microemulsion polymerizations were designed to prepare particles in the ranges 50–200 and 20–50 nm, respectively (see Fig. 1).

Emulsion polymerization is a widely used industrial process for making coatings, paints, adhesives, and resins. Monomers used in emulsion polymerization are typically only sparingly soluble in water although a few percent of water-soluble co-monomers are often added to enhance stability. Both ionic, such as sodium dodecyl sulfate or sodium dodecyl benzene sulfonate, and nonionic surfactants are used to produce the emulsions. A typical polymer emulsion



**Figure 1.** Particle size range achieved for different synthetic polymerization techniques.

formulation contains a water-soluble initiator such as potassium persulfate, an organic phase consisting of monomers dispersed in 1–20 micrometer droplets, and a surfactant that is above its critical micelle concentration. The surfactant causes a high concentration of monomer-swollen micelles to form in the aqueous phase. As the system is heated, the initiator decomposes to give aqueous phase radicals that propagate with small amounts of monomer dissolved in the aqueous phase. The newly forming radicals become hydrophobic very quickly and enter the micelles where they initiate polymerization of particles. Particle nucleation continues until all of the micelles either have been nucleated to form polymer particles or have been dispersed. As long as there are monomer droplets in the system, homogeneous nucleation can continue to take place. Once the micelles have been depleted, the polymer particles continue to grow by using monomer diffusing through the aqueous phase. Particle growth is continued until all of the monomers in the aqueous phase have been depleted.

One of the critical elements of emulsion polymerization is the formation of micelles which act as compartmentalized reaction chambers. This is how emulsion polymerization can produce reasonably small particles. Polymerization conducted in dispersed aqueous systems, such as suspension polymerization, produces relatively large polymer particles (20–1000 µm).

### 2.1.1. Soap-Free Emulsion Polymerization

In emulsion polymerization, surfactants play important roles such as maintaining the polymer particle stability, controlling the particle size, distribution, latex surface tension, and latex rheological properties. Clearly the choice and amount of surfactants significantly affect the polymer latex performance. For example, improper surfactant choice may lead to foaming, which in turn causes surface defects and decreased water resistance. Also the amount of the surfactants is the key factor to control new particle generation in the case of seeded polymerization. Unfortunately, surfactant molecules used in emulsion polymerization do not always stay tightly on the surface of particles but repetitively undergo desorption and absorption. These molecules are not easily removed from the final latex product and can often interfere with applications to systems that are not compatible with this type of latex contaminant. To overcome this type of problem, two techniques were developed, soap-free emulsion polymerization or the use of polymerizable surfactants [30, 31]. Soap-free emulsion polymerization can produce functional polymer particles in the submicrometer size range. Water is usually used as the continuous phase in soap-free polymerization. The polymer particles formed during soap-free emulsion polymerization retain their stability by electrorepulsive forces between ionic fragments on the particle surfaces or sequences.

### 2.1.2. Miniemulsion Polymerization

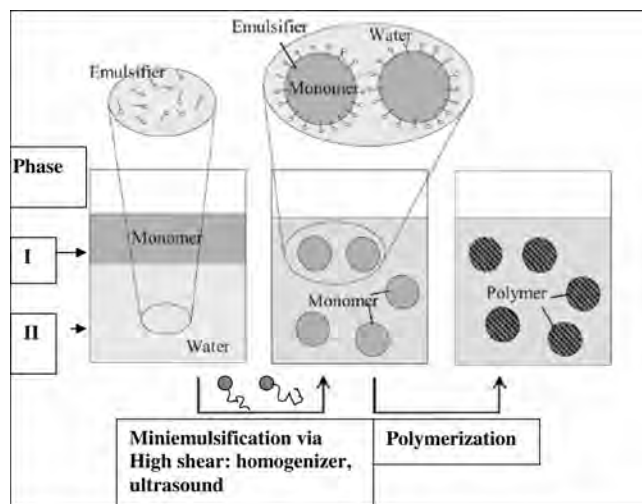
Miniemulsion polymerization shares many of the fundamental principles with emulsion polymerization, most importantly compartmentalization [19, 32, 33]. Miniemulsions are specially formulated heterophase systems where stable nanodroplets of one phase are dispersed in a second

continuous phase (see Fig. 2). This system is created by using an appropriate combination of high shear treatment, surfactants, and the presence of an osmotic pressure agent that is insoluble in the continuous phase. Nanodroplet stability is obtained by adding an agent that dissolves in the dispersed phase but that is not soluble in the continuous phase. A simple example is a typical oil–water miniemulsion, where oil, a hydrophobic agent, an emulsifier, and water are homogenized by high shear to obtain homogenous and monodisperse droplets in the size range of 30 to 500 nm.

The generality and potential of the miniemulsion method lay in the fact that since each of the droplets is basically an individual batch reactor, a whole variety of polymerization reactions can be performed, thus significantly extending the profile of classical emulsion polymerization. Radical homopolymerization, copolymerization, catalytic chain transfer, controlled free radical polymerization, polyaddition reactions, metal catalyzed reaction, among others have all been utilized to produce polymer particles using the miniemulsion technique. Due to this large range of possible polymerization reactions and the nearly unlimited number of possible monomers that can be used for the formation of particles, a wide variety of polymeric particles have been produced using miniemulsion technology. Examples include numerous homopolymers, in particular polystyrene, poly(methyl methacrylate), poly(vinyl chloride), poly(acrylic acid), poly(*n*-methylol acrylamide), polyacrylonitrile, etc., polymer–polymer hybrids, encapsulated pigments, carbon black, and liquid, silica, and composite particles.

A useful list of characteristics for determining if a system represents a miniemulsion has been compiled by Antonietti and Landfester [19]. They discuss seven items that should be present.

- (1) Dispersed miniemulsions in a steady state are stable against diffusional degradation but critically stabilized with respect to colloidal stability.
- (2) The interfacial energy between the oil and water phase is significantly greater than zero and the surface coverage of the droplets by surfactant molecules is incomplete.



**Figure 2.** Fundamental principles involved in miniemulsion polymerizations.

- (3) The formation of a miniemulsion requires high mechanical agitation to reach a steady state.
- (4) The stability of droplets against diffusional degradation originates from an osmotic pressure within the droplets that controls the solvent or monomer evaporation.
- (5) Polymerization occurs by droplet nucleation only.
- (6) The growth of droplets during polymerization can be suppressed.
- (7) The amount of surfactant or inherent surface stabilizing groups required to form a polymerizable miniemulsion is small compared to other polymerizations.

### 2.1.3. Microemulsion Polymerization

Miniemulsions are defined by the mode of operation instead of a size range and are fairly easy to distinguish among most other heterophase polymerization methods. However, it can be confusing to find in the literature another method called microemulsion polymerization. Microemulsions are formed by mixing water, a hydrophobic compound, and suitable emulsifiers [20, 34, 35]. The medium is a multicomponent liquid that exhibits long-term stability, has low viscosity, and is optically transparent and isotropic. In microemulsions, the polymerization starts from a thermodynamically stable state that is spontaneously formed. This is generally achieved by using large amounts of specialized surfactants or mixtures that have an interfacial tension at the oil–water interface that is near zero. The microdroplets formed consist of a spherical organic core surrounded by a monomolecular shell of emulsifier molecules whose polar groups are in contact with the continuous aqueous phase. Initiation of polymerization is not simultaneously obtained in all of the microdroplets and therefore only some of the droplets contain the first polymer chains formed. These chains influence the stability of the microemulsion and can lead to an increase in the particle size and secondary nucleation. Latexes formed via microemulsions typically consist of relatively small polymer particles in the range of 5–50 nm but the particles are often mixed among numerous empty micelles. However, a variety of elaborate surfactants (mixtures of cationic and anionic salts) have been utilized to significantly alter the final polymer particle size, surfactant content, and distribution. The essential features of microemulsion polymerization are: (1) polymerization proceeds under nonstationary state conditions; (2) size and particle concentration increase throughout polymerization; (3) chain transfer to monomer/exit of transferred monomeric radical–radical reentry events are operative; and (4) molecular weight is independent of conversion and distribution of the resulting polymer broad. Microemulsion and inverse microemulsion polymerization have been used to produce a variety of polyacrylate latex particles, water-soluble nanoparticles, and conductive polymeric particles.

### 2.1.4. Inverse Emulsions

The advantage gained by emulsion stabilization is not restricted to only direct micro- and miniemulsions but can easily be extended to inverse emulsions [21, 36, 37]. Polymer

spheres in the nanometer range, below 200 nm in diameter, can be produced through this standard technique that involves the use of an inverse emulsion—a clear mixture of water in oil also containing a surfactant. The water-in-oil inverse emulsion contains pools of water surrounded by oil molecules. These water droplets can be used as miniature nanoreactors to produce nanoparticles by adding the right amount of monomer into the solution. The chemical thermodynamics governing the emulsion drives the monomer molecules added into the solution directly into the water droplets. The polymerization reaction occurs inside the water droplets, triggered by the addition of an appropriate initiator substance into the system. The microscopic polymerization process inside the tiny water droplet is similar to macroscopic polymerization. One advantage at this stage of particle formation is that drug molecules can be taken up and effectively encapsulated. The nanoparticles formed assume the spherical shape of the water droplet with the size of the resulting nanoparticle being restricted by the diameter of the water droplet.

Applications of the inverse emulsion polymerization to micro- and miniemulsions are the most common. For miniemulsions, osmotic pressure is built up by an insoluble agent such as an ionic compound, in the continuous phase. The droplet size finds an equilibrium state which is characterized by a dynamic equilibrium rate between fusion and fission of the droplets and the droplet size seems to be only dependent on the quantity of the osmotic agent. There appears to be a zero effective droplet pressure that results from a balance between the osmotic pressure and the Laplace pressure. As such, inverse miniemulsions do not appear to be as critically stabilized as that for direct miniemulsions but instead are stable systems. Nevertheless, surfactants can be used in a relatively efficient manner for inverse miniemulsion polymerization, especially when compared to inverse microemulsion and inverse suspension polymerizations.

## 2.2. Suspension Polymerization

Another polymerization method that has many similarities to the emulsion methods is suspension polymerization [22, 38]. In this synthetic method a water-insoluble monomer is dispersed in the continuous phase as liquid droplets via vigorous stirring. An oil-soluble initiator is used to begin polymerization inside the monomer droplets. Droplets are kept from adhesion and coalescence by the presence of a small amount of stabilizer. Nearly all of the nucleation occurs in the droplets which act as isolated batch polymerization reactors. The larger droplet size causes the droplet pressures to be much smaller which leads to Ostwald ripening at a considerably slower rate than in miniemulsions. The final polymer particle size has been found to depend on the stirring speed, volume ratio of the monomer to water, concentration of the stabilizer, the viscosity of both phases, and the design of the reaction vessel. When a properly designed reactor and well-stabilized suspension is used, monodisperse polymer particles can be produced. The final product is generally limited to polymeric particles in the size range of 20–2000  $\mu\text{m}$ . The main difference between

miniemulsion and suspension polymerization is that suspension polymerization utilizes much larger monomer droplets dispersed in the continuous phase.

## 2.3. Precipitation and Dispersion Polymerization

Dispersion polymerization can be considered an intermediate technique between homogenous and heterogenous polymerizations [24, 39–43]. All reagents are initially soluble in the medium and produce an insoluble polymer which precipitates out as the polymerization proceeds. By using soluble polymer stabilizers, polymer particles can be produced. The particle stability is primarily controlled by steric effects. A good example of successful dispersion polymerization is the preparation of polyphenol particles. In this work, peroxidase-catalyzed dispersion polymerization was performed by using a water-soluble polymer stabilizer in aqueous 1,4-dioxane and poly(vinyl methyl ether) in a 40% phosphate buffer solution as a steric stabilizer. This work produced relatively monodisperse particles in the submicrometer range. Similar particles of *m*- and *p*-cresols and *p*-phenylphenol have also been produced using the same type of synthetic procedure.

In precipitation polymerization, a polymer is generally precipitated out of solution by adding a nonsolvent of the polymer [25]. The primary polymer particles do not form into colloids but remain in a loose slurrylike form. This occurs since no stabilizer or block copolymer is added to the medium and therefore no steric barrier for particle stability is formed. Polymerization can occur in both the continuous and dispersed phase. Careful control of the kinetics can give polymer materials with a wide range of particle sizes (see Fig. 1). For example polymeric spherical particles with an average size of 160 nm have been prepared by precipitation of the particles which was facilitated by the increasing molecular weight of the polymer or from increased cross-linking.

## 2.4. Seeded Polymerization

Polymerization based on using a previously formed polymer particle or one that is created during the process but altered by swelling followed by chemical reactions is usually referred to as seeded polymerization. Seeded polymerization can be accomplished using many of the previously discussed synthesis techniques, in particular emulsion and dispersion polymerization [23, 34–42]. Synthesis based on seeded polymerization can be used to produce porous polymer particles as well as composite, core-shell, and hollow structures. The porosity of the particles produced by a seeded polymerization technique has been found to be dependent on the molecular weight of the seed polymer. As the molecular weight of the seed increases, the porous particles produced can become macroporous.

One drawback of seeded polymerization is that the final particle diameter is limited by the size of the initial polymer particle seed. Monodisperse submicrometer polymer particles are not easily obtained using seeded polymerization but particles from 1 to several hundreds of micrometers appear to be readily producible. For example, extremely uniform

polymeric particles have been successfully produced using the seeded polymerization techniques. In a rather elaborate study, a repeated seeded emulsion polymerization in a non-gravitational field was used to generate uniform polymeric microspheres up to 100  $\mu\text{m}$  in size. Ugelstad et al. performed a two-step swelling technique and achieved similar results [42, 43]. This method is characterized by the use of an oligomer of extremely low solubility in water as an effective swelling agent. In order to produce larger particles, from 0.5 to 100  $\mu\text{m}$ , which have applications in areas such as polymer coating emulsions that are resistant to shear thinning, Ito et al. used a seeded emulsion polymerization procedure [47]. Controlled coagulation induced by the formation of secondary polymers with opposite charge to the surface of the seed particles was achieved. They studied and characterized the effects of agitation rate, size of the polymer seed particles, and the pH or the reaction mixture.

A variety of seeded polymerization methods have been used to produce monodisperse micrometer-sized polymeric particles. Many of these studies were based on using a swelling stage during the overall process. For example, a dynamic swelling method makes the seed polymer absorb a large amount of swelling monomers by treating the monomer soluble in the medium with slow, continuous, dropwise addition of water. Many of the conventional emulsion and dispersion seeded polymerization techniques use seed particles consisting of linear polymers for the initial swelling stage. This is due to difficulty associated with preparing micrometer-sized seed particles with a cross-linked network structure. Some success has been reported in using a two-stage swelling process of cross-linked seed particles. The effect of seed cross-linking on monomer swelling and final particle morphology reveals a strong dependence.

Core-shell composite polymer particles can also be efficiently produced using seeded polymerization. A seeded dispersion polymerization method was reported to yield micrometer-sized monodisperse polymethyl methacrylate (PMMA)/polystyrene (PS) composite particles consisting of a PMMA core and a PS shell. This study suggested that seeded dispersion polymerization, in which almost all monomers and initiators exist in the medium with seed particles having higher glass transition temperature than polymerization temperature, has an advantage for producing core-shell polymer particles. In particular, polymer layers tend to accumulate in their order of formation, even if the morphology is unstable thermodynamically.

## 2.5. Self-Assembly of Block and Ionic Polymers

Surfactant-free polymeric nanoparticles, something that is extremely difficult to achieve via most synthetic routes, can be produced by taking advantage of the self-assembly of block copolymers and ionomers in a selective solvent [26, 53–73]. Self-assembly of block copolymers can be successfully induced by a variety of methods including chemical reaction, polymer-polymer complexation, microphase inversion, temperature control, and a microwave method. Most of these techniques produce core-shell nanoparticles

but have the advantage that nanoparticles are surfactant-free. In addition, core-shell structures are often desirable for many uses in biomedicine (see later sections).

Poly(styrene-block-(2, bis-[4-methoxyphenyl]oxycarbonyl)styrene) nanoparticles have been prepared via self-assembly by using temperature control. The particles are formed with a core-shell structure by using temperature and *p*-xylene as a solvent. The temperature-induced self-organization is achieved due to the solubility of the rod-shaped poly([4-methoxyphenyl]oxycarbonyl)styrene block in *p*-xylene (soluble above 100 °C). Temperature controlled self-organization was also used to produce nanoparticles of poly(*N*-isopropylacrylamide) (PNIPAM) grafted with short poly(ethylene oxide) chains. Both of these polymers are soluble in water at room temperature, but at higher than 32 °C, PNIPAM becomes hydrophobic and undergoes an intrachain coil-to-globule transition and an interchain aggregation to form nanoparticles. By controlling the formation conditions, interchain association can be completely suppressed and a single-chain core-shell nanoparticles are formed.

Core-shell poly(ethylene oxide-block- $\epsilon$ -caprolactone) (PEO-b-PCL) diblock copolymer nanoparticles that are stable in water have also been produced using a microphase inversion technique. In this work, tetrahydrofuran was used as the primary solvent which was suddenly replaced by a nonsolvent, water. This leads to the aggregation of the water insoluble polymeric block, PCL, and to the formation of a core, while the soluble block, PEO, formed a protective corona. Since these core-shell nanoparticles have been shown to be biodegradable in the presence of Lipase PS, they have important applicability to drug delivery.

Complexation between multiple polymer blocks has been used to generate stable core-shell nanoparticles. Polyacrylate and PMMA can be complexed with hydroxyl-containing polystyrene [PS-(OH)] in toluene to form insoluble particles. Successful implementation of this concept was achieved by using poly(styrene-block-methyl methacrylate) diblock copolymer complexed with hydroxyl containing polystyrene. Complexation of the PMMA block and the PS-(OH) led to an insoluble core, while the soluble PS blocks prevent macroscopic precipitation. The final product was stable nanoparticles whose particle size could be regulated by the initial concentrations of the two components and by the mixing order.

Microwave irradiation can also be used to facilitate the formation of polymeric nanoparticles. Stable polystyrene nanoparticles were formed by using microwave radiation in the presence of potassium persulfate in water. This method substantially reduces the reaction time (factor of 20) and produces narrowly distributed nanoparticles. Particle size can be controlled by varying the monomer-to-initiator weight ratio.

## 2.6. Polyanionic Solution-Based

Both continuous and batch processes have been developed which use a polyanionic solution that is atomized into a swirling polycationic solution to form polymeric nanoparticles [74–81]. This method of production is often referred to as titration since a sequential addition of one polymer into another is performed. By varying the ratios of



polyanion to polycation, a variety of nanoparticle compositions can be produced. One advantage of this method is that all solutions are made using water as a solvent which eliminates the possibility of having trace amounts of organic solvents of surfactants within the nanoparticles (a serious problem for medical applications).

The polyanionic method is intimately effective for generating core-shell nanoparticles. In a typical process, the anionic solution (droplet-forming) forms the core and the cationic solution (receiving solution) forms the corona or shell. This is the most common setup and is often referred to as the standardized system; however, there are examples of the reverse where a droplet-forming cationic solution is mixed with an anionic receiving solution.

A typical batch system is composed of a needle connected to a syringe that is inserted into an ultrasonic hollow titanium probe with a conical tip. The probe is connected to a transducer and power generator which is used for nebulizing the solution. An anionic polymer solution is introduced into the syringe and slowly extruded through the needle and the probe tip where it is atomized by the transducer. The atomized anionic mist is released into air above a container of the cationic solution which is vigorously swirled during the reaction (1–2 min). As mentioned previously the anionic solution is generally used as the droplet-forming internal phase mixture (core polymer) and the cationic solution is used as the receiving batch mixture (corona or shell polymer). A reverse system simply uses the same setup but introduces a cationic mixture into the syringe to form the mist that is received by an anionic solution.

The batch system described can be modified into a continuous system by using two inflow lines, one for the anionic solution and one for the cationic solution, and one overflow line to keep the receiving bath volume constant. This mode of operation produces nanoparticles of similar quality to the batch system.

## 2.7. Polyelectrolyte Complexes

Polymeric nanoparticles formed from macroscopic homogeneous colloidal systems can be prepared by aggregates of a high molar mass polyion species of weak charge density (called the host) with a much shorter lower mass macromolecular counterion (called guest) [82, 83]. Through continuous addition of the guest reactant, polymer nanoparticles form as colloidal particles that aggregated and precipitate. By altering the ratio of the host to guest, a variety of compositions can be produced. This technique is similar to the polyanionic solution based methods described previously and share similar advantages. In particular, multipolymeric water-soluble mixtures of two interacting pairs enable a template assembly of the nanoparticles. There is no use of organic solvents or surfactants and the process offers a high flexibility in choosing reacting pairs.

## 3. SUPERCRITICAL FLUID-BASED PARTICLE PRODUCTION

Supercritical fluids (SCFs) are substances that are above their critical temperature and critical pressure [84]. These substances often have densities and solvating capabilities

similar to those of a typical liquid but have diffusivity and viscosity comparable to that of gases, making them ideal solvents. These unique properties provide great promise as a versatile, environmentally acceptable replacement for conventional solvents. Indeed SCFs have been used fairly extensively for extractions, in particular for coffee and tea decaffeination, natural product extraction, and chromatography. More recent applications of SCF technology have been in the area of processing such as mixing, impregnation, encapsulation, reaction, crystal growth, etc. [85–97]. The most used SCF has been carbon dioxide (CO<sub>2</sub>). This is primarily because supercritical carbon dioxide (scCO<sub>2</sub>) has an easily achievable critical point of 31.1 °C and 73.8 bars and is nontoxic, cheap, nonflammable, and environmentally acceptable and may be recycled.

The use of SCFs in polymer science has begun to witness an increase in popularity and a number of successful production techniques for polymeric particles have been reported [75–87]. Recently polymer-based nanoparticles have been produced by these alternative methods using supercritical fluid technology. Particles that have been produced using SCF technology tend to have characteristics that are strongly influenced by the properties of the solute, the type of SCF used, and the processing parameters (such as flow rate of solute and solvent phase, temperature and pressure of the SCF, pre-expansion temperature, nozzle geometry, and the use of coaxial nozzles). For example, polymer properties such as polymer concentration, crystallinity, glass transition temperature, and polymer composition are important factors that determine the final morphology of the particles. An increase in the polymer concentration can lead to the formation of less spherical and fiberlike particles. In an antisolvent process, the rate of diffusion of antisolvent gas is higher in a crystalline polymer compared to an amorphous polymer leading to high mass transfer rates in crystalline polymers that produces high supersaturation ratios and small particles with a narrow size distribution. Since SCFs act as plasticizers for polymers by lowering their glass transition temperatures (*T<sub>g</sub>*), polymers with a low *T<sub>g</sub>* tend to form particles that become sticky and aggregate together. A change in polymer chain length, chain number, chain composition, and branching ratio can alter polymer crystallinity and thus the particle morphology.

Core-shell particle structures can be produced by using an intimate mixture under pressure of the polymer material with a core material either before or after SCF solvation of the polymer, followed by an abrupt release of pressure which leads to solidification of the polymeric material around the core material. This technique has been successfully used to microencapsulate infectious Bursal Disease virus vaccine in a polycaprolactone or a poly(lactic-co-glycolic acid) matrix.

There have been a reasonable number of drug and polymeric microparticles prepared using SCFs as both solvents and antisolvents. Particles from 5 to 100 μm were the first to be produced using an array of solutes including lovastatin, polyhydroxy acids, and mevinolin. Further work in the past decade has led to the simultaneous co-precipitation of two solutes, a drug, an excipient, and poly(lactic acid) (PLA) particles of lovastatin and naproxen. In these studies, supercritical CO<sub>2</sub> was passed through an extraction vessel containing a mixture of drug and polymer, and the CO<sub>2</sub>

containing the drug and the polymer was then expanded through a capillary tube. In another process, PLA and clonidine were dissolved in methylene chloride, and the mixture was expanded by supercritical carbon dioxide to precipitate polymeric drug particles.

Similar to polymeric particles produced using SCF technology, the properties of the drugs such as solubility and partitioning of the drug into SCF determine the properties of the particles formed. For example, if the drug is soluble in a SCF under the operating conditions, it will then be extracted into the SCF and will not precipitate out. It has been observed that steroids with  $\log P$  (the log of the partition coefficient) values between 1.6 to 3.9 formed spherical nonporous particles, whereas steroids with  $\log P$  of 4.2 or 4.3 were extracted out into the SCF. The properties of the drugs also play an important role during encapsulation of a drug in a polymer matrix. There are strong influences of the properties of the drug on the drug loading. PLA-microparticle formation using an antisolvent process with supercritical  $\text{CO}_2$  indicated that an increase in  $\log P$  decreases the loading efficiency as well as release rate, possibly because lipophilic drugs can be entrained by supercritical  $\text{CO}_2$  during SCF precipitation. Nucleation and growth rate influence the effective encapsulation and morphology of the particles. If the initial nucleation and growth rate of the drug is rapid and the polymer precipitation rate is relatively slow, then the drugs can form needles encapsulated in polymeric coat.

SCF technology is currently claimed to be useful in producing particles in the 5 to 2000 nm range. U.S. Patent 6, 177, 103 describes a process that rapidly expands a solution of the compound and phospholipid surface modifiers in a liquefied gas into an aqueous medium, which may contain the phospholipid. By expanding into an aqueous medium, particle agglomeration and growth are prevented, thereby producing particles of a narrow size distribution. An additional step may be required to remove the aqueous phase if the final product is a dry powder.

To achieve commercial success, the methods or techniques developed need to be scaled up to produce batch quantities for conducting further research or for marketing the product. The advances in the understanding of the mechanism of supercritical particle formation and SCF mass transfer are forming the basis for efficient scale-up of the laboratory-scale processes. While many laboratory investigators were only able to produce milligrams of the product, a scaled process that was capable of producing 200 g of biodegradable PLA particles in the size range of 6 to 50  $\mu\text{m}$  has been developed. Cost of manufacturing at the pilot scale with SCF technology has been claimed to be comparable to several conventional techniques, such as single-stage spray drying, micronization, crystallization, and milling batch operations. Thus from the perspective of scale-up, SCF technology appears to offer some advantages. The processing equipment can be a single stage, totally enclosed process that is free of moving parts and constructed from high-grade stainless steel, allowing easy maintenance. It offers reduced solvent requirements and particle formation occurs in a light-, oxygen-, and possibly moisture-free atmosphere, minimizing these often confounding factors.

## 4. DROPLET AND AEROSOL TECHNIQUES

Many nonsynthetic methods for producing polymeric particles are based on nebulization or piezoelectric droplet generation of very dilute polymer solutions [98–111]. Over the last several years, advances in microdroplet production technology for work in single-molecule detection and spectroscopy in droplet streams has resulted in generation of droplets as small as 2–3  $\mu\text{m}$  with a size dispersity of better than 1%. In the context of polymer particle generation, droplet techniques are attractive since particles of essentially arbitrary size (down to the single polymer molecule limit) can be produced by adjusting the size of the droplet of polymer solution, or the weight fraction of the polymer in solution. While droplet production in the size range of 20–30  $\mu\text{m}$  (diameter) is more or less routine (several different on-demand droplet generators are now available commercially), generation of droplets smaller than 10  $\mu\text{m}$  remains nontrivial especially under the added constraint of high monodispersity. Small droplets (<10  $\mu\text{m}$ ) are especially attractive as a means for producing multicomponent polymer-blend and polymer-composite particles from solution since solvent evaporation can be made to occur on a millisecond time scale, thus inhibiting phase separation in these systems. The primary condition for suppression of phase separation in these systems is that solvent evaporation must occur on a time scale that is faster than the self-organization times of the polymers. This implies time scales for particle drying on the order of a few milliseconds implying droplet sizes <10  $\mu\text{m}$  (depending on solvent, droplet environment, etc.). It was shown recently that a microdroplet approach can be used to form homogeneous composites of co-dissolved bulk immiscible polymers using instrumentation developed in our laboratory for probing single fluorescent molecules in droplet streams. In addition to a new route to forming nanoscale polymer composites, a microparticle format offers a new tool for studying multicomponent polymer blend systems confined to femtoliter and attoliter volumes, where high surface area-to-volume ratios play a significant role in phase separation dynamics.

Several different choices exist for producing micrometer and submicrometer droplets of solution—each with certain trade-offs in terms of volume throughput, nominal size, and size dispersity. There are additional trade-offs associated with sampling and interrogation facility that should be considered as well. Two familiar methods of droplet production include electrospray generation and aerosol generation using a vibrating orifice coupled to a high-pressure liquid stream. In electrospray generation, a liquid stream is forced through a needle biased at approximately 1 kV (nom.). Charge carriers induced on the surface of the liquid stream eventually come close enough during solvent evaporation for Coulomb repulsion to occur (the Taylor cone), resulting in fragmentation, or explosion, of the liquid stream. This results in a cloud of charged liquid droplets whose size can be made quite small (<1  $\mu\text{m}$ ). The obvious drawback is that it is difficult to isolate individual particles for study, and size dispersity tends to be highly sensitive to experimental parameters. Another common method of

producing liquid droplets is the technique of vibrating orifice aerosol generation (VOAG). Invented by Berglund and Liu back in the 1970s, the VOAG is unmatched in terms of volume throughput ( $>100$  nanoliters per second) and size dispersity ( $<0.1\%$  depending on experimental conditions). This technique works by introducing a high-frequency (10 to 100 kHz) instability in a high-pressure liquid stream applied by a piezoelectric transducer (PZT). The resulting fragmentation of the stream produces highly monodisperse droplets that are ultimately limited by the purity of the radio frequency (rf) signal applied to the PZT. Some disadvantages of this mode of production are that the droplets travel at high speeds (several meters/second) and are quite close together (typically no more than 3 droplet diameters apart). This makes isolation and spectroscopic interrogation of individual droplets difficult. A more serious problem is in the significant particle size limitations associated with this technique. A VOAG works best at a size range of 30–50  $\mu\text{m}$  but can function down to about 12–15  $\mu\text{m}$ . Because of the way droplets are produced, however, there is a concomitant increase in the rf frequency that can be problematic.

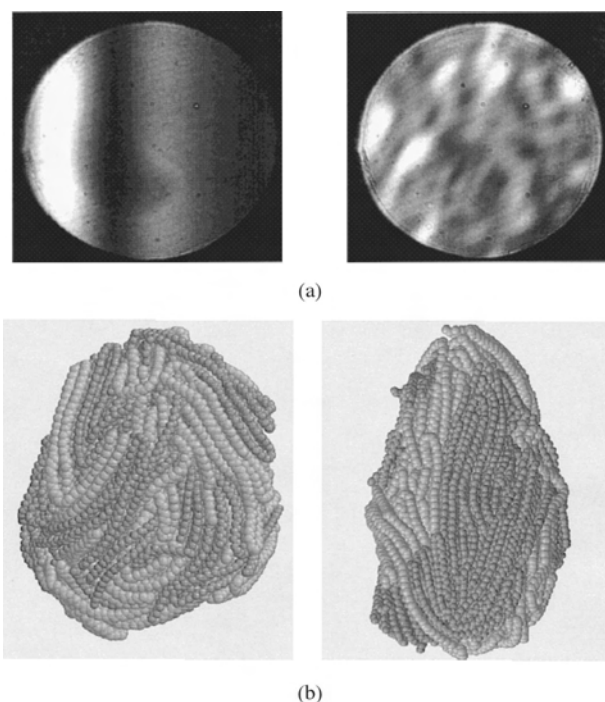
The method we have chosen in our experiments is an “on-demand” or droplet ejection device. Like a VOAG, it also uses piezoelectric transduction but at much lower frequencies. The physics of droplet production is completely different for the two methods: The VOAG operates by generating a high (and fixed) frequency instability in a liquid stream; the on-demand droplet generator functions by the application of an acoustic wave to a static solution, which forces (ejects) a droplet out of a micrometer sized orifice. We use Pyrex or quartz tubing that is heated, drawn, cut, and polished to produce a tapered orifice that can range in size from 1 to 50  $\mu\text{m}$ . The droplet sizes are comparable (usually slightly larger) to the orifice diameter and, depending on the quality of the orifice, size dispersity less than 1% can be achieved. Droplet production rates tend to be significantly lower than the aforementioned techniques. Ultimately, droplet rates are limited by piezoelectric relaxation times (10 kHz); practically, however, under conditions of high monodispersity, droplet rates are typically much lower (20–100 Hz). The advantages of this technique are small size and on-demand production that makes single droplet/particle manipulation and interrogation straightforward.

#### 4.1. Tailoring the Properties of Polymer Particles

Composite polymer particles, or polymer alloys, with specifically tailored properties could find many novel uses in a number of fields. However, the problem of phase separation from bulk-immiscible components in solution often poses a significant barrier to producing many commercially and scientifically relevant homogeneous polymer blends [112–114]. The typical route taken in trying to form homogeneous blends of immiscible polymers is to use compatibilizers to reduce interfacial tension. A number of different groups have examined phase separation in copolymer systems to fabricate fascinating and intricate meso- and microphase separated structures with a rich variety of morphologies [115, 116].

Recently some interest has focused on trying to suppress phase separation in mixed polymer systems by very rapid solvent evaporation from small ( $\leq 10 \mu\text{m}$  diameter) droplets of dilute polymer solution. Using instrumentation developed for probing single fluorescent molecules in 1–10  $\mu\text{m}$  diameter droplet streams [117], detailed exploration of microdroplets to form homogeneous polymer composites without compatibilizers as a possible route to new materials with tunable properties has been accomplished [118]. From these studies it has been shown the primary condition for suppression of phase separation in such systems is that solvent evaporation must occur on a time scale that is fast compared to self-organization times of the polymers. This implies time scales for particle drying on the order of a few milliseconds which would require droplet sizes  $\leq 10 \mu\text{m}$  (depending on solvent, droplet environment, etc.). In addition to this new route to forming nanoscale polymer particle composites, a microparticle format offers a new tool for studying multicomponent polymer blend systems confined to femtoliter and attoliter volumes where high surface area-to-volume ratios play a significant role in phase separation dynamics.

Figure 3a illustrates qualitatively the effect of phase separation on optical diffraction fringe contrast and definition for two polymer-blend particles prepared from different sized droplets of co-dissolved polymers (polyvinyl chloride and polystyrene) in tetrahydrofuran. The particle on the left is homogeneous as evidenced by uniform fringe intensity, and high-fringe contrast and definition. Moreover, the scattering data can be matched quantitatively to Mie theory calculations that assume a homogeneous and spherical particle. The particle on the right has no discernible fringe structure but does display interesting periodic “island” structure implying some order and uniformity of phase-separated domains.



**Figure 3.** (a) See [118, 119]. (b) See [119].

Figure 3b shows molecular dynamics simulations of a stable polymer-blend particle (10 nm diameter) composed of immiscible components. The leftmost particle remains homogeneous throughout a broad temperature range. For phase separation to occur (right), an enormous amount of thermal energy must be supplied in order to overcome the surface energy barrier. This result agrees qualitatively with the observation that homogeneous blends of bulk-immiscible polymers can be formed in spherical microparticles. The composite particle was calculated to have a *single* melting temperature of 190 K and glass transition temperature of 90 K which is different than either of the polymer components ( $T_m$  218 K,  $T_g$  111 K for light and  $T_m$  162 K,  $T_g$  81 K for dark). The segregated particle has two melting points and glass transition temperatures that correspond to within 10 K of the individual components. Formation of homogeneous polymer-blend composites from bulk-immiscible co-dissolved components using droplet techniques has two requirements. First, solvent evaporation must occur on a relatively short time scale compared to polymer translational diffusion. Second, the polymer mobility must be low enough so that, once the solvent has evaporated, the polymers cannot overcome the surface energy barrier and phase-separate. It was previously shown definitively the effects of droplet size and solvent evaporation, and the second requirement is almost always satisfied even for modest molecular weight polymers.

To explore effects of polymer mobility in detail, composite particles of poly(ethylene glycol) (PEG) oligomers (MW 200, 400, 1000, and 3400) with medium molecular weight (14 K) atactic poly(vinyl alcohol) (PVA) were produced [120]. This type of system allowed systematic examination of the phase separation behavior where one component (PEG) had substantially different viscosities (specified as 4.3, 7.3, and 90 cSt at room temperature, respectively).

Higher molecular weight PEG polymer-blend particles were shown to be homogeneous by utilizing bright-field microscopy, optical diffraction, and fluorescence imaging. Blend particles prepared with the 200 molecular weight PEG were observed to form sphere-within-a-sphere particles with a PVA central core. Figure 4 shows diffraction data acquired from particles at successive 10 min intervals from a 10  $\mu\text{m}$  diameter PEG[200]/PVA[14 K] (80:20 w/w) particle. As shown in the first frame, the particle is initially homogeneous. The second and third frames indicate that the composite particle undergoes phase separation into an inhomogeneous particle as evidenced by the fringe distortion. Interestingly, the structure in the two-dimensional (2D) diffraction data for this system is much different than those observed for large phase-separated

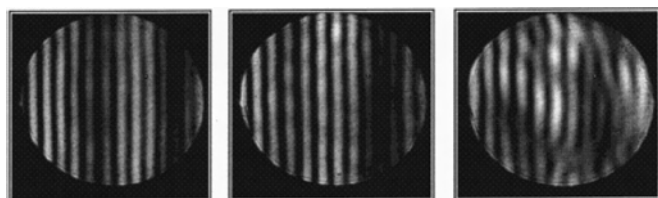


Figure 4. See [119].

PVC/PS particles that presumably coalesce into submicrometer spheroidal domains. On the basis of fluorescence and phase-contrast imaging data, PEG[200]/PVA[14 K] particles form spherically symmetric (sphere-within-a-sphere) heterogeneous structures, which should also produce well-defined diffraction fringes. The interpretation of these data was that diffusional motion of the PVA core in the PEG host particle, combined with rotational diffusion of the particle, breaks the spherical symmetry and thereby introduces distortion in the diffraction pattern. This observation is entirely consistent with our model of polymer-composite formation where heterogeneous particles may be formed provided that the mobility of one of the polymers is low enough to overcome the surface energy barrier. From the 20 min time scale for phase separation in the low molecular weight PEG system, we estimate a diffusion coefficient of  $10^{-10}$   $\text{cm}^2/\text{s}$ , which is consistent with recent molecular modeling results. For a diffusion coefficient,  $D$ , of  $10^{-10}$   $\text{cm}^2/\text{s}$  and 1200 s time scale, the average diffusion distance  $r = (6Dt)^{1/2} = 8.5$   $\mu\text{m}$ , which is comparable to the particle diameter. Composite particles formed from the higher molecular weight PEG (>1000) form homogeneous composite particles with PVA.

Another interesting aspect of this work comes from Mie analysis of the scattering data for homogeneous composite particles. Observations for several different polymer blend systems reveal that the material dielectric constant (manifested in both the real and imaginary parts of the refractive index) can be tuned by adjusting the relative weight fractions of the polymers in the mixture. Both  $\text{Re}(n)$  and  $\text{Im}(n)$  for the polymer-blend microparticles are intermediate between the values determined for pure single-component particles and can be controlled by adjusting the weight fractions of polymers. For both miscible and (bulk) immiscible polymers that have been combined in homogeneous microparticles, the measured refractive index was observed to be very close to estimates obtained from a simple mass-weighted average of the two species.

Although the microdroplet technique is well suited for producing nearly arbitrarily small particles (down to a single molecule limit), optical diffraction is obviously not suitable for probing particles smaller than a few hundred nanometers. To complement experimental effort on polymeric particles, investigation of various dynamical and steady-state properties of smaller polymer and polymer blend nanoparticles (1–10 nm diameter) has been examined using molecular dynamics tools. These traditionally reliable and accurate simulations allow development of considerable insight into the structure, and properties of polymer-blend particles, as well as aiding in interpretation of experimental results and guiding future experiments. Results have been reported from classical molecular dynamics techniques; polymer nanoparticles of varying size (up to 300,000 atoms), chain lengths (between 1 and 200 monomers), and intermolecular interaction energy have been examined which allows the systematic study of size-dependent physical properties and time dependence of segregation/equilibration of these particles [119]. Some of these studies are discussed in more detail in later sections of this chapter.

## 5. GAS ATOMIZATION APPROACHES

The production of micro- and nanometer-sized polymer powders from molten polymers is an attractive, facile, low energy, and economic process. Polymer powders with tailored characteristics such as particle shape, size distribution, and purity can be directly prepared from the molten state of polymers such as polyethylene-based waxes that cannot be ground using conventional methods [121–126]. The gas atomization process (GAP) for mass-producing high quality spherical polymer powders involves using high pressure (approximately 7.6 MPa maximum) nitrogen gas and a specifically designed nozzle to atomize a molten stream of polymer into fine droplets that cool to form spherical powders. Powders with properties tailored to varying applications can be efficiently produced in short cycles by changing a few process control variables in a contamination-free environment, making the GAP a useful alternative to conventional grinding processes. These benefits of the process together with its flexibility, high throughput, and facile nature should make it highly attractive to industrial processes that must be capable of mass production and safe, environmentally benign operation.

The targeted applications of the powders include uses as powder spray coatings [1], formulating ingredients for functional coatings, and as raw materials for solid-state compacting of polymer alloys and composites [1, 127]. For these applications, the required properties of the powders include purity, uniform micrometer-sized particles with uniform size distribution, and spherical shape. These properties are essential for free-flowing powders with optimal surface area, leading to products with improved handling and performance capabilities.

Commercial organic polymer powders are produced by conventionally grinding extruded polymer pellets, often under cryogenic temperature conditions. Grinding is undesirable because it is expensive, highly energy-intensive, and susceptible to contamination from the grinding equipment and environmental pollution. Because of the erratic nature of the grinding process, it is almost impossible to control the quality and distribution of the powders and the size and shape of the particles.

The GAP method is an alternative route to mass producing polymer powders that eliminates most of the problems of conventional grinding operations. In addition, the simplicity and versatility of the GAP means that the equipment can be constructed from readily available construction materials such as steel (used in the crucible) and impact-resistant crystal-clear polycarbonate (used in the atomization chamber). The optical clarity of the latter allows direct real time visualization of the atomization of the molten polymer as it exits the crucible. This process involves heating the material in a crucible until the desired atomization temperature is reached. Once the material reaches this temperature, it is forced out of the crucible through a circular channel (the pour tube) into the atomization nozzle, where it is atomized into fine particles by the high pressure nitrogen gas. The particles cool as they fall through the atomization chamber, forming micrometer-sized powders that collect in a vented chamber. Additional details of the GAP process has been reported [121–126].

GAP feasibility studies and process development efforts focused on using commercial polyethylenes (e.g., Hoechst Celanese's PE130 and PE520) [128] as the model material because they are presently the largest volume commodity plastics used in the United States (over  $9 \times 10^9$  kg are produced annually). The high consumption, low toxicity, low molecular weights (2000 to 10,000 g/mol), and low melting temperatures (approximately 200 °C) of the PE130 and PE520 make them ideal materials for atomization. Thus far, only the low molecular weight polyethylenes have been atomized into fine powders with changeable particle shapes and size distributions (0–250  $\mu\text{m}$ ). The studies conducted to date show that the quality and properties of the product powders depend on three key processing variables: (1) polymer melt temperature, (2) gas atomization pressure, and (3) melt stream size or pour tube diameter. Unlike particles produced by conventional grinding, the particles in gas-atomized powders are spherical with smooth surfaces and near uniform sizes. Other particle shapes—such as whiskers and elongated spheres—can be produced under specific processing conditions such as using low atomization pressures (approximately 2 MPa). Typically, the whiskers have diameters of about 100 nm and lengths of a few millimeters.

To expand the GAP method to produce powders from other polymers with tailored powdered characteristics for wide applications, computer simulations of the process are needed. As mentioned, potential applications of the product powders include use as formulation ingredients for functional coatings tailored to specific biochemical engineering application areas, such as personal hygiene and beauty care products, packaging, and other disposable and/or recyclable plastic products. Other applications include polymer dispersions or emulsions in environmentally friendly solvents, feedstock for solid-state compacting of polymer alloys, and powder spray coatings. As an example, the PE520 is designed for use in paints to increase matting effects and to mar resistance of the painted surface. Other advantages of using polymer powder additives in paints are improved sanding ability smoothness, and rheological properties; prevention of pigment settling and metal marking; and water repellence. Because of the flexibility, versatility, and economy offered by GAP, it should be attractive to polymer manufacturers, processors, and end-users.

Because the polymers (PE130 and PE520) can be atomized in a relatively narrow temperature range (190–220 °C), temperature control in GAP must be precise to avoid potential thermal degradation of the molten polymer prior to atomization. This can be achieved by heating the polymer in the crucible under a blanket of nitrogen gas using precisely controlled band heaters with thermocouples strategically placed in the melt. Obviously, polymers that show different rheological properties under conditions that they are likely to encounter during atomization can be expected to atomize differently. At low pressures (approximately 2 MPa), for example, the shear induced by the gas jets on the molten polymer at the instant of melt disintegration is not enough to completely overcome the internal elastic stresses present in the molten polymer. This leads to the formation of whiskers and elongated spheres rather than absolute spheres. For the polyethylenes studied thus far, it has been found that the formation of whiskers and elongated spheres can be

avoided by using high gas atomization pressures (approximately 7.6 MPa). It appears that a mixture of whiskers and spheres would be ideal for making self-reinforced polymer powders that can be used for applications requiring improved mechanical properties. Investigations on expanding the use of GAP to other polymers with vastly different thermal and rheological properties are needed.

More recently, 50/50 blends of PE130 and ultralow melting phosphate glass composition have been successfully atomized under conditions that were used to atomize the pure PE130 polymer. This result confirms the expectation of the broad application of GAP to many fields, such as producing polymer alloys, glass-polymer alloys, *in-situ* composites, and related products with tailored properties. These products could be used in many areas, such as for decorative or protective coatings, for polymer-supported heterogeneous catalysts, and in producing lightweight structural composites. The structural composites can be easily fabricated by applying established solid-state powder compaction methods to the gas-atomized composite powders to form compacts with varying shapes and sizes.

The research conducted thus far has provided valuable insight into GAP diagnostic control systems, dynamics, and mechanisms of powder formation. This knowledge can be used to expand the method to include the production of other kinds of materials with desirable properties for beneficial uses. The desirable properties of the powders include the following: purity, particle shape, particle size, and size distribution. The many initial problems of GAP when applied to polymers and composites are now understood and can be controlled and managed in order to produce powders with tailored characteristics. The technology of GAP has now advanced to a stage of finding more applications in the areas of polymer engineering and composite engineering and of scaling up to mass production of the fine polymer powders.

## 6. DENDRIMERS, HYPERBRANCHED POLYMERS, OR STAR POLYMERS

Dendrimers, hyperbranched polymers, or star polymers offer capabilities similar to polymeric nanoparticles since they generally form relatively small spherical materials, often with core-shell structures (generally a hollow core) [129–173]. As such it is important to recognize this new class of macromolecular materials in a chapter on polymeric nanoparticles. The interest in dendrimers and hyperbranched polymers has substantially increased since the pioneering work of Vogtel, Tomalia, and Newkome [132–136]. A broad range of dendrimers and hyperbranched polymers are now available and there has been enormous interest in their uses and applications. Many of these applications, such as the development of self-assemblies, electroactive and electroluminescent devices, sensors, molecular devices, catalysts, pharmaceuticals and biochemicals, analytical chemical applications, nanoscale building blocks, micelle mimics, and performance materials are synergistic with those of polymeric particles. This is due to the similarities in fundamental size and shape as well as compositions.

Dendrimers and hyperbranched polymers represent a novel class of structurally controlled macromolecules derived from a branch-upon-branch structural motif. Dendrimers are well defined, highly branched macromolecules that radiate from a central core and are synthesized through a stepwise, repetitive reaction sequence that guarantees complete shells for each generation, leading to polymers that are highly monodisperse. The synthetic procedures developed for dendrimer preparation permit nearly complete control over the critical molecular design parameters, such as size, shape, surface/interior chemistry, flexibility, and topology. These synthetic methods are more closely related to organic chemistry than to traditional polymer synthesis. There are basically two different synthetic strategies for the synthesis of dendrimers: a divergent and a convergent approach to construct dendritic frameworks. Both methods use step-by-step synthesis (activation or protection of monomers, condensation reactions, purification) and require quantitative coupling reactions to construct high generation dendrimers. More recently, a number of methods have been developed that reduce the number of synthetic steps for producing dendrimers in high yields: a double-stage convergent growth approach; a hypercore monomer approach; double-exponential dendrimer growth; orthogonal coupling strategies.

Hyperbranched polymers offer an advantage over dendrimers in their ease of synthesis. On the other hand the degree of branching and the structure is less controllable than for dendrimers. The simplest branched material is a star polymer in which several linear polymer chains are attached to only one branching point. These polymers can contain chemically the same or different arms linked to a core. Star-block copolymers have also been made in which the arms consist of block or triblock copolymers. Various types of hyperbranched polymers, with multiple branching points, have been synthesized, including polyesters, poly(ether ketones), polyuretanes, polyamides, polycarbosilanes, etc.

Many properties of dendrimers have been found to differ from their linear polymer analogs. In general, dendrimers are more soluble in common solvents and less viscous compared to analogous linear polymers. The solubility depends predominantly on the properties of their surface groups which can to a large degree be controlled. Dendrimers with hydrophobic interiors such as polyethers and polycarbosilanes can be made water soluble by introducing hydrophilic groups into their surface groups. The opposite can also be achieved, that is, changing a water soluble dendrimer into an insoluble material by converting the hydrophilic surface groups into hydrophobic surface groups.

Another interesting and useful feature of dendrimers is the intrinsic viscosity in solution, and melt is lower than linear analogs. The main reason for this difference appears to be due to the lack of chain entanglements. Results have shown that intrinsic viscosity of a dendrimer does not obey the well known Mark-Houwink-Sakurada behavior. This has been associated to a transition from an extended structure for lower generation dendrimers to a globular shape at higher generations. Similar trends are also found for hyperbranched polymers, where the viscosity depends on the degree of branching: polymers having high branching

display behavior similar to dendrimers while those with low branching can have chain entanglements and behave more like linear polymers.

Other properties that differ are hydrodynamic volume which is larger for dendrimers, the degree of crystallinity (dendrimers are amorphous), and the glass transition temperature. The glass transition temperature has been found to be a function of the backbone depending on the structure, the number of end-groups, and the number of cross-links or branching points. The glass transition temperature decreases with an increase in the number of end-groups but it increases with increasing number of branch points and the polarity of the end-groups. For hyperbranched polymers, the glass transition temperature appears to depend more on the chain length between the branching points. This means that systems with short chain lengths will have low glass transition temperatures even though the total molecular weight may be quite large.

The rich source of possible surface functionality for dendrimers makes them very attractive for nanometer building blocks and carrier molecules. They are also important in technologies such as coatings and inks where their unusual viscosity characteristics play an important role. Xerox has a number of patents which use dendrimers in ink and toner applications. Dendrimers have also found an increasing role as additives to commodity plastics where they improve the drying of plastic fibers.

## 7. MOLECULAR IMPRINT POLYMERS

With the increased interest in chemical and biosensors within the field of modern analytical chemistry as well as medical and environmental science, methods for generating materials suitable for these applications based on biomimics have been introduced. Systems with large surface areas populated by large numbers of reactive or binding sites are optimal. Polymeric particles offer such possibilities due to their inherent large surface area and the possibility of functionalization. Dendrimers, hyperbranched polymers, or star polymers also provide numerous advantages for this area of interest. Another possibility has come from using synthetic polymers as templates for imprinting an image of a molecule, a technique known as molecular imprinting (an antibody mimic) [174–191]. The final product generally consists of a bulk polymer which is then processed into a fine powder, the smaller the particles comprising the powder the better.

There are basically two distinct approaches to molecular imprinting. A prepolymerization complex between imprint molecule and functional monomers can be formed via noncovalent interactions or they can be covalently coupled. The covalent imprint method offers more homogeneous population of binding sites and a higher yield of binding sites relative to the amount of imprint molecule utilized. Noncovalent imprinting is somewhat more flexible when it comes to selecting the functional monomers, possible target molecules, and the use of the imprinted materials. Hybrid methods have also been suggested which attempt to combine the advantages of covalent and noncovalent molecular imprinting methods.

A common method for preparing molecular imprint polymers is by using solution polymerization followed by mechanical grinding of the polymeric solid to give small particles with diameters generally in the micrometer range. Particles can also be prepared directly in the form of spherical beads by using, for example, a two-phase system using perfluorocarbons instead of water as the continuous phase. Polymeric particles synthesized in this way can also be made magnetic by inclusion of iron oxide particles. Another method for synthesizing molecular imprint polymer particles without requiring mechanical grinding is based on using dispersion polymerization. This method can generate aggregates of spherical particles and if the system is sufficiently dilute one can get reasonably controllable and uniform sized particles. Other methods have been reported where the polymeric particles that are imprinted are formed *in-situ*, inside a chromatography column or in a capillary.

## 8. SIMULATION AND MODELING OF POLYMER PARTICLES

Molecular modeling provides a way of visualizing processes at a submacromolecular level that also connects theory and experiment. Particularly attractive from a computational point of view is that many polymer particles are very close to the size scale where a complete atomistic model can be studied without using artificial constraints such as periodic boundary conditions. Yet these particles are often too small for traditional experimental structure/property determination. Polymeric particles in the micro- and nanometer size range show many new and interesting properties due to size reduction to the point where critical length scales of physical phenomena become comparable to or larger than the size of the structure itself. This size-scale mediation of the properties (mechanical, physical, electrical, etc.) opens a facile avenue for the production of materials with predesigned properties.

The primary computational tool used to date for the study of polymeric nanoparticles, in particular, their atomistic-based structure and dynamics, has been molecular-dynamics-based algorithms for generating and modeling polymer nanoparticles [192–208]. Some efforts using Monte Carlo techniques have also been pursued [209]. Structural and dynamical details of polymer processes at the atomic or molecular level have been studied and linked to experimentally accessible macroscopic properties of materials. A number of these studies will be discussed.

Since the smaller sized particles have more surface atoms than the larger ones (larger surface area to volume ratio), a decrease of the diameter increases the ratio. The large ratio of surface atoms to the total number of atoms leads to a reduction of the nonbonded interactions between the polymer chains on the surface layer; hence the cohesive energy is dramatically dependent on the size. In addition, the ratio of surface chain ends to total number of chain ends for the particles is much larger than that of the bulk system, leading to enrichment of chain ends at surface. This observation is consistent with analysis of thin films. With regard to an effect of the side chain atoms, the increase in these atoms corresponds to a decrease in the ratio of surface atoms and therefore represents an increase of cohesive energy of the system.

The increase in cohesive energy is due to the increase in the number of atoms that are inside the spherical particle versus on the surface. This phenomenon is a result of the finite sized spherical confinement of the particle and is different than what is observed in the corresponding bulk systems (side chains tend to lower the cohesive energy).

The large proportional surface area leads to large surface free energy, which is described by per unit of surface area ( $\text{J}/\text{nm}^2$ ). The surface is irregular and has many cavities that may introduce unique (catalytic or interpenetrating) properties of polymer fine particles. The free volume (cavities) and molecular packing can be important in a diffusion rate of a small molecule trapped in the particles. It also suggests that nanoscale polymer particles are loosely packed and can show dynamical flexibility (e.g., compressive modulus of the particles is much smaller than that of the bulk system).

Simulations have also been performed on models for bulk polyethylene (PE). The radial distribution function for the simulated bulk PE, which provides information on the intra- and intermolecular structure, was in very good agreement with experimental data. Comparing a bulk system with the nanoscale spherical particles reveals the effects of conformational changes of the particles due to the size reduction and the shape. The most notable difference was in the amount of gauche conformations as signified by the magnitude of a peak at 3.2 Å. For the smaller particles this peak was almost entirely missing. The larger particles tended to have a somewhat higher concentration of gauche conformations but were still significantly less than the bulk. This reduction in the conformational disorder as the diameter of the particle decreases is a surface induced phenomenon. As the particle diameter decreases the surface area to volume ratio increases and the polymer chains are forced to lie mostly on the surface of the spherical particle. The surface tends to cause the polymer chains to form a pseudocrystalline layer; that is, the polymers fold in a nearly all-*trans* configuration.

Several simulations have been applied to study the morphology of single or multiple chains with different chain lengths and compositions. The surface chains of the polymer nanoparticles tend to straighten and align at temperatures below the melting point; the preferential morphology for the small polymer particle with a long chain length is a rodlike shape. This stretching of the chains leads to a reduction of the cohesive energy and an increase in volume. Studies on the effects of chain length show that the particles with the shortest chain length (see Fig. 5) have the most spherical shape.

For a transition from the amorphous (solid) to the melt phase (liquid) and a glass–rubber transition, the volume increases owing to conformational disorder of the polymer particles. Energy, temperature, and volume are calculated while annealing the system gradually by scaling the momenta with a constant scaling factor. Thermal analysis has provided a great deal of practical and important information about the molecular and material world relating to equations of state, critical points, and other thermodynamics quantities. Figure 6a shows the dependence of the melting point and glass transition temperature on the diameter of the particle. The dramatic reduction of the melting point for the polymer particles is an important example of surface effects and

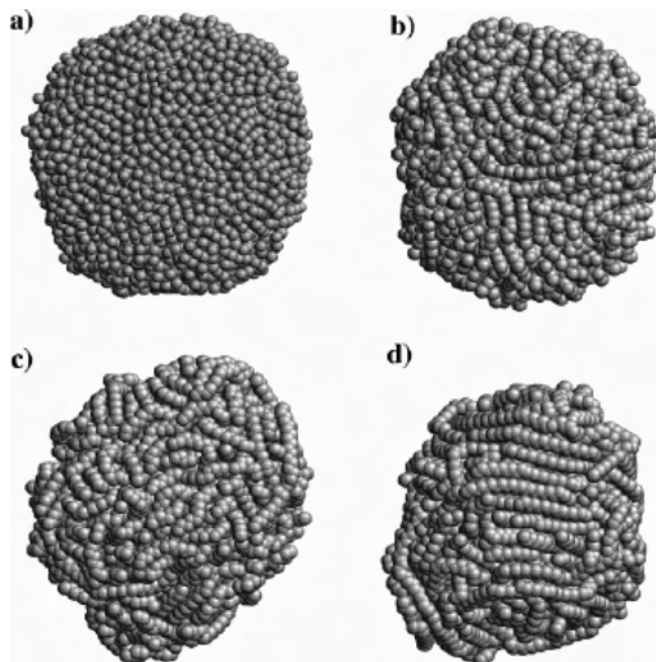


Figure 5. See [206].

shows the importance of size. Since the large ratio of surface atoms to the total number leads to a significant reduction of the nonbonded interactions (lower cohesive energy), the melting point decreases with decreasing size. Figure 6b

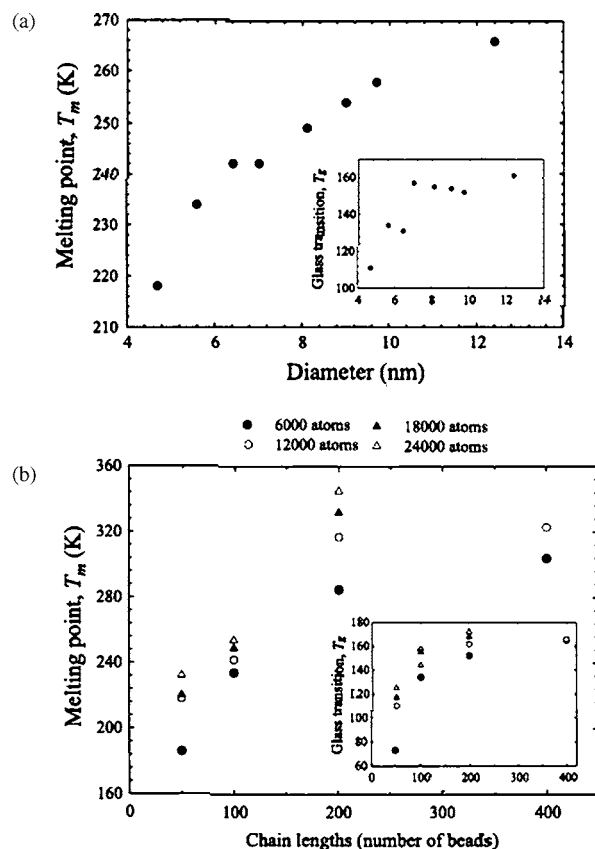


Figure 6. See [194].



shows the effect of chain length on these transition temperatures. A strong dependence of the melting point and the glass transition temperature on chain length is attributed to molecular weight and nonbonded energy of each chain.

From an atomistic thermodynamic analysis, the melting point of a polymer particle (6000 atoms) with chain lengths of 50 and 100 beads was found to be 186 and 232 K, respectively. The melting point was higher than the temperature at which the surface chains experienced a significant change in mobility. There appear to be two steps in the melting transition. The first step (mechanical melting) is at a temperature of 200 K and the second (thermodynamic melting) is 230 K. The first step is an early melting stage at which all chains in the particle start moving. The second step is the fusion stage of a solid. There is a plateau region between the first and second stages. The mobility of the chains in the outer layers increases rapidly after this region. In contrast, the chains in the core layer do not have the second step and increase linearly.

In the past, numerous calculations have been performed for the mechanical property of bulklike crystalline PE polymer using force field semiempirical, *ab initio* calculation, and *ab initio* molecular dynamics (MD) methods. The compressive (bulk) modulus for the amorphous polymer particles was calculated in order to get an idea of their stiffness and strength. The compressive modulus and yield point for the PE particles were investigated by applying an external force in MD simulations. It is known that values of the tensile modulus of bulk polyethylene are between 210 and 340 GPa and the compressive modulus is generally higher than the tensile modulus. In addition, the bulk and tensile strength or yield point are always much smaller than the modulus for a thermoplastic such as polyethylene. In a MD study of polymer nanoparticles, a compressive modulus was found to be several magnitudes of order smaller than the bulk values, and a yield point that was much larger than the modulus. The stress-strain curve actually looked more like a curve for an elastomer. However, the initial deformation caused by the compression (that which gives the modulus) is not reversible. What occurs during this phase is the deformation of a spherical particle to an oblate top. This structure is stable but it lies at a slightly higher energy than that for a spherical particle. Thus, the modulus for compression in this region is actually more a measure of the force required to deform the spherical polymer particle into an oblate top (pancakelike structure). Further deformation tends to be reversible up to the point of rupture. This deformation is actually more closely related to the bulk modulus since the stress is due to the cohesive energy and not a microstructure. This leads to a yield point that is significantly larger than the modulus.

## 9. APPLICATIONS OF POLYMER PARTICLES

Polymeric particles offer a number of unique properties that make their range of possible applications quite broad: small size and volume; large and specific surface area; high

diffusibility and mobility; stable dispersions; uniform size, shape, morphology, surface chemistry; and the fact that they can be produced in various sizes, shapes, and compositions. To date many of the applications include examples from the biomedical, optical and optoelectrical, chemical, and rheological fluid fields. We briefly discuss some of these applications and provide extensive references for anyone interested in further details.

### 9.1. Biomedical Applications

Dramatic progress in biomedical engineering has recently led to the development of new macromolecular drugs which hold great promise for successful therapeutics. Medicinal uses of polymeric materials have been fairly broad and continue to grow. For example, biodegradable polymers have been used for sutures, artificial skin, and materials for covering wounds. Other medical and biochemical applications have included the use of polymer particles in absorbents, latex diagnostics, affinity bioseparators, and drug and enzyme carriers. In particular, the use of nanoparticles as drug delivery vehicles has enjoyed significant activity and research. Drugs or other biologically active molecules have been dissolved, entrapped, encapsulated, adsorbed onto surfaces, and chemically attached to polymeric particles as a means for delivery [14–16, 210–239]. Controlled drug release formulations have been tried in various forms depending on the specific end use. Controlled drug release offers many advantages over other types of delivery including the ability to supply more constant drug levels, to enable more efficient utilization of the drug, and to locally deliver the agent to a confined area. In addition, decreased costs and frequency of administration add to the attractive features of these types of drug delivery systems. To date, polymer micro- and nanoparticles have been the most extensively utilized system for these purposes. When suitably encapsulated, a pharmaceutical can be delivered to the appropriate site, its concentration can be maintained at proper levels for long periods of time, and it can be prevented from undergoing premature degradation. Nanoparticles offer the advantage that they provide a better penetration into the body and are small enough that they can be injected into the circulatory system or delivered via the respiratory system or through traditional oral intake.

#### 9.1.1. Drug Delivery

Modern pharmaceutical development makes extensive use of high-throughput screening, genomics, combinatorial chemistry, and other techniques. This has led to the synthesis of new chemical compounds that are bringing new challenges and opportunities to pharmaceutical development. One of the largest new set of drugs being developed is proteins and peptides, macromolecules which are often poorly permeable, poorly soluble, and unstable in physiological fluids and have unfavorable pharmacokinetics. These drugs generally need special care and require specific delivery systems. One of the most common degradation pathways is physical damage to proteins in the form of aggregation or precipitation. Unfortunately protein aggregates can form during the formulation process, long-term storage, or shipping and delivery. This can have dramatic impact on the final efficacy of the drug.

Currently some of the largest challenges, are in improving solubility, enhancing the chemical/enzymatic stability, reducing adsorption to containers, minimizing aggregation, assisting with refolding of proteins, and improving absorption. Presently, there are at least 75 protein or peptide-based products approved for marketing in the United States alone that can be used in the treatment of cancer, diabetes, multiple sclerosis, and growth deficiencies. With more than 100 other such drugs in human clinical trials, the market for protein-based drugs will continue to grow clearly defining the importance of designing appropriate drug delivery vehicles.

Polymeric nanoparticles offer promising technologies that overcome many of the problems presented for protein/peptide delivery and stability [14–16, 210–239]. Compared to other colloidal carriers, polymeric particles have a higher stability when in contact with biological fluids, and their polymeric nature (system of very large molecules) allows for the desired controlled and sustained drug release. Polymeric particles also represent drug delivery systems suitable for most of the administration routes (inhalation, oral, circulatory system), even if a rapid recognition by the immune system may limit their use as injectable carriers. Indeed there has already been some success in using polymeric-based particles for peptide drug delivery. The first microparticle extended-release formulation of a peptide to be approved by the U.S. Food and Drug Administration consists of poly(lactic-co-glycolic) acid microparticles that encapsulate the leuteinizing-hormone-releasing hormone agonist, leuporelin acetate. This particular formulation is used for diseases such as endometriosis and prostate cancer. Another approved formulation used the same microparticle to encapsulate recombinant human growth hormone for the treatment of growth hormone disorders.

A substantial amount of research has focused on using polymeric nanoparticles, in particular PEG derivatives, for drug delivery. PEG is a simple, water-soluble, nontoxic polymer that is nonimmunogenic (the immune system does not recognize it and it is not metabolized) and has been approved in a number of products for human administration by mouth, injection, and topical application. PEG-based systems have been shown to entrap up to 45% by weight of a drug within the nanoparticle and to have extended circulation times due to decreased uptake by the mononuclear phagocyte system. A controlled release system that uses an injectable polymer vehicle has been employed by a number of researchers and has also been commercialized by Schering-Plough and Roche. The polymer protects the protein from rapid hydrolysis or degradation within the body thereby prolonging its action. Pioneering research on systems where PEG polymer chains were chemically attached to drug substances showed that by increasing their size there was an associated improvement in their delivery. When PEG is attached to a drug it can often extend the length of action in the body from minutes to hours or days depending on the molecular weight of the PEG molecules.

Further advances using PEG in conjunction with other polymers are already in development to improve injectable polymer systems. In one technique, a low-molecular-weight biodegradable polymer that is a viscous liquid at room temperature is prepared. This is then mixed with the therapeutic protein and injected. PLA-PEG and poly(orthoester) have

been used in this system. Low-molecular-weight PLA-PEG has delivered bone morphogenetic protein (a bone growth factor used in the regeneration of bone tissue) into rats, with the polymer being degraded within three weeks and replaced by bone. Simply varying the viscosity of the polymer by changing either polymer concentration or polymer molecular weight may control the release of protein from this system. These polymers break down by hydrolysis, and further studies need to be undertaken to assess protein stability in this system and possible inflammatory responses in target tissues. In a second technique, a biodegradable polymer is dissolved in a physiologically acceptable solvent, suspending the protein particles, and this suspension is then injected into the tissue or patient. On entering the tissue, the solvent diffuses in the aqueous environment while the polymer precipitates out and entraps the protein particles. This injectable polymer depot has been explored using poly(lactic co-glycolic acid) with *N*-methyl pyrrolidone or glycofurol as the solvent. The rate of release may be adjusted by such parameters as the weight percentage of polymer in solution, the ratio of polylactide to polyglycolide, molecular weight, and protein loading. The release kinetics from this system was found to be favorable and there has been no reported loss in activity of human soluble tumor factor receptor.

Some other applications in the research sector of the drug delivery arena have included: the use of chitosan particles as a cancer chemotherapeutic carrier for adriamycin; chitosan particles used for oral sustained delivery of nifedipin, ampicillin, and various steroids; ocular drug delivery via a suspension composed of hydrogels and particles which enhances the bioavailability of ocular drugs; a particle gel for extending precorneal residence time of ocular drugs; treatment of infiltrating brain tumors such as oligodendrogliomas by using IdUrd loaded poly(D,L-lactide-co-glycolide) particles and intracranial implantation via stereotactic injection; use of alginate-poly-L-lysine particles for possible treatments of insulin-dependent diabetes mellitus; polyalkylcyanoacrylate nanocapsules for the delivery of insulin and indomethacin; biodegradable particles for drug delivery based on 1,5-dioxepan-2-one and D,L-diactide; glutamate and the tripeptide TRH-impregnated polyanhydride-based particles for stimulation of trigeminal motoneurons; a simple, cost effective, and scalable method that is based on albumin microparticles (biodegradable, nontoxic, and nonimmunogenic) for drug release (such as chlorothiazide); microcapsules of polyelectrolyte complexes for PH controlled release; chitosan/gelatin network polymer particles for controlled release of cimetidine; block copolymers of biodegradable poly(L-lactic acid) and poly(DL-lactide-co-glycolide) with poly(ethylene glycol) for controlled drug delivery and targeting; polymer-based gene delivery systems; drug delivery platforms based on synthetic polypeptides; aliphatic polyanhydrides for drug carriers; biodegradable gelatin particles for treatment of kidney disease.

Clearly there has been intensive research into the use of polymer-based systems for controlled drug delivery and release [14–16, 210–239]. While there are currently only a

few clinically approved polymeric systems, the use of polymeric systems for oral extended release has a relatively large research base. Nano- and microparticle systems have been the most extensively used/studied formulations for controlled drug release and the field is primed for technology development for moving these bench studies into the clinical arena. Nanoparticle delivery systems have been demonstrated to provide a better penetration of the particles inside the body. Owing to their size, delivery via intravenous injection is possible and therefore they can be used for intramuscular or subcutaneous applications. In addition, the nanoscale of these systems also can minimize irritant reactions at the injection site. Nanoparticle systems also exhibit greater stability, in both longer shelf storage lives and uptake times. These synthetic systems are extremely versatile and can be designed to elicit the desired kinetics, uptake, and response from the body. Nanoparticulate drug delivery systems have even been recommended for the broad application of vaccination. Currently, immunization often requires multiple injections (MMR, hepatitis, tetanus, etc.) and there may be a high preponderance of people to put off or to miss these boosters, leading to limitations in the efficacy of the immunization. A more efficacious vaccine that would only require a single dosage or an oral controlled release system is highly desired and some success has been reported by using nanoparticulate drug delivery systems [16, 232].

In summary, extensive research has shown that polymeric particles offer enormous advantages to drug delivery systems due to: (1) there is the possibility to functionalize the particle; (2) the large size of the polymer molecule(s) making up the particle make it possible for them to remain at delivery site for longer time (protection against premature metabolism and reduced immunogenicity); (3) drugs can be released slowly and/or in a controlled manner by (a) diffusion of a carrier polymer, (b) deposition of the carrier itself, (c) osmotic force, (d) swelling of the carrier/delivery system, and (e) chemical reaction; (4) multiple administration routes, such as inhalation, injection, or oral, are feasible.

### 9.1.2. Immunoassays

Since the first demonstration in 1979 that proteins could be transferred to microporous nitrocellulose membranes and detected using antibodies, development of rapid immunoassays using these high-surface-area materials has proliferated [16, 240–265]. Initially much investigation centered on understanding the interactions between proteins and polymers and the requirements for blocking nonspecific interactions on the membrane and on developing a series of detection methodologies and strategies. This work has led to a variety of immunoassay delivery systems for detecting a large menu of analytes.

The determination of antigens in biofluids is generally accomplished through heterogeneous immunoassays. The most common methods require the separation of the antigen–antibody complexes from the medium, followed by measurement of the quantity of antigen. One technique, called the sandwich method, uses an immobilized antibody and a labeled antibody. The carriers of the antibodies require large surface areas in order to allow the formation of the desired antigen–antibody complex. Polymer particles have been found to be very applicable in this regard

and plates with immobilized polyacrolein particles have been developed and used to covalently bind antibodies. In addition, polymer particle dispersions offer similar capabilities. Latex agglutination tests are the quickest, easiest methods among immunoassays. They can be sensitive, depending on the method of determination, and are comparable to other methods. Some of the first latex particles to be used were based on poly(styrene) derivatives. The ability of polystyrene to bind protein molecules without significantly changing the biochemical activities is the basis for most polymer particle immunoassays. Polystyrene can be used as the backbone of these particles and is crucial for the easy assimilation of these particles into most binding protocols. Other studies have used poly(hydroxyethyl methacrylate) and poly(glycidyl methacrylate) particles. Results have shown that in addition to the biospecific attractive force between the antigen and antibody, the electrostatic interactions between antibody–polymer particle and antigen–polymer particle have strong influence on agglutination rate. New latex designs consist of particles having a heterogeneous surface in a microdomain structure.

By doping magnetic materials, such as iron oxides, into polymer particles, the resulting particles retain some magnetic properties and can be used as solid supports for immunoassays in single use or automated assays. Automated assays using magnetic particles can quickly wash or separate the reaction components to reduce assay time or increase performance. Sorting of cells or cellular isolation has also been accomplished using these types of magnetic particles. Immunoglobulins targeting the desired material can be attached to the surface of the particles for directed isolation. A suspension of magnetic particles is mixed with a preparation of the target molecule or cell. Once the target has bound to the affinity group, a magnet is used to separate the target-bound particles from the solution. The unbound material can then be washed away from the particles. Depending on the application, the target molecules or cells can then, if needed, be detached from the magnetic particles. Some of the biomedical applications of these types of magnetic particles are: cell separation, mRNA separation, protein purification, immunoassays, affinity purification, ion exchange, PCR clean-up, solid-phase cDNA library construction, isolation of single or double stranded DNA, solid-phase DNA sequencing, hybridization procedures, charcoal trapping, sequence-specific magnetic particle probes, plasmid purification, and genomic DNA separation.

Biochemicals such as DNA, hormones, proteins, and ligands are also immobilized for diagnostics. DNA diagnosis uses DNA-carrying particles, composed of single stranded DNA, which subsequently binds to its complementary DNA or RNA. Research has shown some enhanced capabilities for 20-mer DNA on latex particles. These systems were capable of binding to complementary DNA faster than free DNA, presumably due to the restriction of dynamic motion of the chains (DNA attached to a particle is difficult to hybridize). The interactions between proteins, DNA, enzymes, antibodies, and substrates such as polymer particles have been an active area of research, driven by the desire for rapid and accurate diagnostics and for the development of ultrasensitive biosensors.

### 9.1.3. Polymeric Particles for In Vivo and In Vitro Analysis

Labeled polymer particles have been used to determine cardiac output and regional blood flow [266–284]. This has been achieved in mice by radioactively labeling the polymer particles and detecting the amount deposited by the blood into body tissues. Alternatives to this procedure that offer better safety included using polystyrene impregnated with dyes which could be measured with spectrometry, fluorescence labeling of the particles, and using air filled albumin particles that can be determined by ultrasound contrast. Some interesting trends on the effects of particle size on tissue distribution have been observed. Particles larger than 10  $\mu\text{m}$  can be targeted to lung tissues and those smaller than a micrometer are typically engulfed by Kupffer cells in the liver.

A fascinating application of polymeric particles is their use in preoperative embolization. Such procedures can facilitate surgical removal of tumors by reducing their volume and vascularity as well as decreasing blood loss during surgery. Biodegradable particles composed of starch and poly(D,L) lactide have shown some success in emboluses. Other candidates come from thermosensitive polymers such as poly(*N*-isopropylacrylamide) which precipitates out at certain temperatures and occludes capillary vessels.

Polymeric particles have also been utilized for the analysis of activity of phagocytes such as macrophages and leukocytes. These assessments were performed by using latex particles as inert invaders which the phagocytes would ultimately engulf. The latex particles were fluorescently labeled and were easily detectable inside of the phagocytes. The susceptibility of polymeric particles to phagocytosis is a crucial aspect to understand since drug delivery via these particles must reach its intended site. Research has mapped out a number of the influences of polymer particle size, composition, morphology, and surface chemistry.

## 9.2. Optical and Optoelectronic Applications

For many years, researchers in materials and photonics have been interested in the design and fabrication of structures that confine and manipulate electromagnetic fields on length scales comparable to optical wavelengths. The ultimate goal is an all-optical information processing and computation platform using photons in ways analogous to electrons in silicon devices on similar length scales. Specific focus areas such as wafer-scale integration, parallel processing, and frequency management (e.g., add-drop filters) on micro- or submicrometer length scales are active areas of photonics research. While a great deal of progress has been made in the burgeoning field of *microphotonics*, we are still a long way off from realizing important goals such as the optical transistor and all-optical integrated circuits [285].

One of the critical issues faced by researchers trying to engineer high-density photonic device and optical computing/information processing structures is the problem of “turning” the path of the photon. Waveguide structures work well as long as the path is straight; however, including turns with bend radii comparable to propagation wavelength is seriously problematic since the losses tend to be unacceptably high. Typically, minimum bend radii in such structures

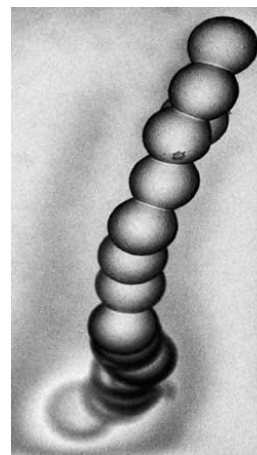
are on the order of several tens of micrometers (at least) to avoid scattering and retroreflection losses at the turn.

### 9.2.1. Photonic Molecules

A new strategy has recently emerged for confining and manipulating electromagnetic fields with precise frequency and spatial control. Based on coupled optical microcavities, these new photonic structures have been called photonic molecules (PMs) by virtue of the similarity between the field eigenmodes and electronic structure in real molecules [286]. In contrast with waveguides in photonic bandgap (PBG) crystals (fabricated by introducing line defects) where a broad range of frequencies are allowed to propagate within the band gap, PM structures permit transmission only at cavity resonance frequencies. Furthermore because the resonance  $Q$ 's (energy storage factors) can be made quite high ( $>10^4$ ), it is conceivable that these kinds of structures can function as amplifiers, switches, and add-drop filters.

A recent discovery that lends fascinating and interesting materials properties describes the use of a simple water-soluble polymer blend to generate a new kind of polymer microsphere-based structure which was called a photonic polymer [287]. In the course of screening different water-soluble polymer blends for high-density ordered microsphere array applications [288], it was discovered that particles made from polyethylene glycol ( $\approx 10$  k MW) and polyvinyl alcohol (14 k MW) in a 4:1 mass ratio had a tendency to stick together in clumps of two, three, or multiple particles. Under higher magnification, we observed that the “sticking” was in fact a partial merging of the particle surfaces shown in Figure 7. The particle binding was so robust that under high-precision particle focusing conditions, we were able to “stack” particles in nearly perfect columnar structures up to  $\approx 20$  particles high. Other types of two- and three-dimensional architectures were explored using an electric quadrupole and computer-controlled 2D translation stage for particle positioning.

One of the most surprising aspects of this work was the observation of sharp resonance features (distinct from “monomer” resonances) in fluorescence from dye doped



**Figure 7.** Electron micrograph of a photonic polymer structure made from merged polymer-blend microspheres [287]. There are about 30 individual spheres in the vertical chain that has folded near the top.

into the particles. Interestingly, the optical properties of merged-sphere systems were considered theoretically several years earlier by Videen and co-workers [289]. Resonance features in emission were also observed in transient merging-droplet experiments by Moon et al. [290]. What is surprising about the observation of shared optical resonances from merged spheres (especially with the large solid angle of intersection) is that a large segment of the dielectric boundary which confines the electromagnetic wave has been removed. Geometric optics calculations of long-lived trajectories in merged spheres show clearly that high- $Q$  resonances are *not* supported for (plane) angles of intersection exceeding more than a few degrees. Calculations on bispheres of differing sizes have shown an interesting antinodal structure that includes an interaction between states with significantly different angular momenta, but with very low  $Q$ . Only in the special case where the contact angle is very small—similar to the physisorbed sphere case—are high- $Q$  coupled resonances in the equatorial plane supported.

In the experimental case, typical plane angles of intersection can be more than 50 degrees; yet the structures clearly support high- $Q$  resonances. Using a combination of three-dimensional ray optics and surface-of-section techniques [291], robust periodic trajectories that make a quasi-helical path around the particle chain axis have been demonstrated. These coupled resonances were highly robust with respect to overlap angle, deviations from collinearity, and size along the axis of the polymer structure.

### 9.2.2. Light Scattering Devices and Lenses

Light scattering by polymeric particles dispersed in different polymeric matrices can be used for the fabrication of a high efficiency back-light for liquid crystalline displays. Multimode scattering depends on the correlation length of the heterogeneous domains. The brightness of the back-light has been increased by a factor of 1.5 over conventional designs by using particles in a polymer film. Light diffusers, blinds, and shades can be developed if the polymer particles have a refractive index differing from the polymer matrix [292–294].

Lens effects have also been observed from polymer particles [292–294]. Amorphous polymer particles are generally transparent and the spherical texture can give a lens effect at the microscopic level. Polymer particles having a radial graded refractive index can be prepared by a dynamic seeded polymerization technique. These particles have a composition gradient decreasing toward the center of the particle which causes an increasing refractive index. Excellent light focusing properties have been observed. Other reports on lens effects of polymer particles have focused on using a close-packed structure of polystyrene microparticles on a glass slide. With this arrangement, standard optical microscopy was used to clearly view the insides of the particles.

### 9.2.3. Electroluminescent Devices

Organic electroluminescent devices based on polymer layers have attracted much attention because of low operating voltages, the ability to tune the color of the emitting light, and

ease of fabrication. The phenomenon known as electroluminescence (EL) is caused by the emission of light generated from the recombination of electrons and holes electrically injected into a semiconductor. Traditionally most conventional and marketable electroluminescent devices have been inorganic semiconductors but developments dating back to the late 1990s have opened the door to a broad range of organic materials [295–306].

One of the most exciting developments in the field of conducting polymers occurred in the early 1990s with the discovery that conducting polymers such as poly(phenylene vinylene) (PPV) could be used as the emissive layer in light emitting diodes (LEDs). High-efficiency surface emission across the whole visible spectral range could be obtained relatively easily and researchers were able to achieve the emission of many different colors of light using these devices. The first polymer LEDs used PPV as the emitting layer [306]. Many different polymers have now been shown to emit light under the application of an electric field (EL). PPV and its derivatives are still the most commonly used materials, but *polythiophenes*, *polypyridines*, and *polyphenylenes* are now being tested for higher efficiency, longer lifetime, and lower power requirements.

Despite the extensive studies in this field, the quantum efficiency and brightness of polymeric LEDs still remain modest. In addition, one of the problems associated with such devices is that the lifetime of the cell is too short to use for many practical purposes, due to degradation of the cell caused by the gradual crystallization. Polymeric nanoparticles and nanoparticle composites may provide new possibilities for optimizing quantum efficiency and brightness as well as the LED lifetime [302]. Enhancement of current densities, radiances, and power efficiencies in polymer light emitting devices have been observed from using polymers mixed with oxide nanoparticles.

The semiconducting polymer PPV has attracted the most attention as an electroactive material. In general compounds with shorter conjugation lengths have a higher photoluminescence quantum yield. Precise control of the conjugated chain lengths could lead to very useful organic structures. Recently, research into semiconducting polymeric nanoparticles, in this case (poly[2-methoxy-5-(2'-ethyl-hexyloxy)-1,4-phenylene vinylene]) (MEH-PPV), has demonstrated the capability of possible control of the chain length and therefore the fluorescence emission spectra. This research is beginning to shed some light on the structural characteristics and luminescence properties which point toward many promising possibilities. An organic analog of inorganic quantum rods has been produced using droplet techniques and results indicate linearly polarized fluorescence with a narrow Gaussian-like emission spectra having a discrete distribution of center frequencies. The luminescence dynamics of these particles were found to be qualitatively similar to those of thin films but had a significantly higher photostability.

The luminescence properties of these newly discovered organic quantum rods might have important applications to biomedical imaging. For *in vitro* studies, a fluorescent microscope could be used to follow the time dependent activities of proteins, enzymes, or cells that have been tagged with organic quantum rods of different lengths. Rods that have different lengths are composed of polymer molecules that

differ in the number of monomeric repeat units which cause them to have different fluorescent emission. Currently visualization of proteins and cells is achieved by labeling them with organic fluorescent dyes, or fluorophores, such as the popular green fluorescent protein (GFP). But this approach has some rather significant limitations. To make GFP produce green light, a laser of a shorter wavelength, such as blue light, must be used. But if another dye that fluoresces in the blue wavelength were being used at the same time, then its signal would be lost in the blue light needed to trigger the first dye. This type of spectral overlap limits the use of fluorophores to two, or perhaps three, for any given experiment. Another major limitation of fluorophores is that their emission does not last long enough.

The unique physical properties of organic quantum rods should be able to overcome these obstacles. Simply by altering their size, they can be engineered to produce light at many different wavelengths. Spectral overlap is not such an issue because the rods can have very similar light absorption/excitation profiles and there should not be a limit to the number of quantum rods one could use in an experiment. In addition, quantum rods should not stop fluorescence even after being visualized for very long periods of time. While traditional inorganic quantum dots or rods also exhibit these properties and provide similar capabilities, they have serious limitations concerning their hydrophobic nature. For inorganic quantum dots to mix with the aqueous contents of a cell, they have to possess a hydrophilic coat. Organic quantum rods are made of semiconducting polymers that can have numerous side groups (ethers, methoxyls, hydroxyls, etc.) which can be hydrophilic and therefore may not suffer this problem to the extent of the inorganic quantum dots. The side groups also provide chemical sites for attaching protein specific antibodies or aptamers which can be used as targeting molecules for specific delivery. In addition it is relatively easy to produce composites or blends of the semiconducting polymers without loss of the fluorescence properties.

### 9.3. Chemical Applications

Ion exchange resins, polymer supported transition metal catalysts, and phase transfer catalysts are the most common chemical use of polymeric particles [307–316]. Increasing applications can be found in enzyme immobilization where polymer particles can be used to absorb, entrap, or chemically bind enzymes [307, 308]. This procedure appears to improve the durability of some enzymes. Other applications are related to batchwise separation and some column chromatography (particles > 3 $\mu$ m). In addition, polymeric particles have also found some applications in xerographic toners and as expandable beads for commodity materials. Polymeric particles are also one of the main constituents of polymer colloids, a class of polymers manufactured in the form of fine dispersions of polymer particles in aqueous or nonaqueous media. This class of polymers has found wide commercial applications in synthetic rubber (for tires, running shoes, and so on; Teflon, neoprene for fan belts and wet suits), surface coatings, paints, adhesives, impact modifiers, soil conditioners, toners for image development,

and the biomedical and biotechnical fields. Polymer colloids is one of the largest areas of polymer research and includes emulsion polymerization of acrylic monomers to form latex paints, suspension polymerization of divinylbenzene and comonomers to form ion-exchange and other porous resins, and micro- and miniemulsion polymerization to form submicrometer spheres for biodiagnostic uses. We have not included a specific section on polymeric or functional polymer colloids but have discussed many of the applications and synthetic production methods relevant to this field. A good source to get a more complete view on functional polymer colloids is provided in [309].

#### 9.3.1. Supported Catalysts

Supported homogeneous and heterogeneous catalysts are used extensively in industrial manufacturing of fine chemicals such as drugs, perfumes, pesticides, food additives, petrochemicals, etc. [309–312]. The use of inorganic catalyst supports such as activated carbon, silica, silica gel, alumina, etc. unfortunately provide little flexibility for tailoring which often leads to catalysts that do not have satisfactory selectivity. Organic polymer supports, on the other hand, provide a much larger degree of flexibility for tailoring. Cross-linked polymers with specific properties are widely used as catalyst supports since they are inert, non-toxic, nonvolatile, and often recyclable. Specific control over catalytic and complexing ability of ligands can be induced and the amount of metal present on the surface of such catalysts is very small, which is of economic significance in the case of expensive catalytic metals such as Ru and Pd. For these reasons, polymer supported catalysts have generated a considerable amount of interest in research. Examples can be found in selective hydrogenation of polyunsaturated cycloolefines and unsaturated carbonyl compounds where a functional polystyrene-supported metal (Ru, Rh, Pd) catalyst was successfully produced. In addition a number of applications have used commercially available resins as supports and ligands to produce effective polymer-supported catalysts. Again, the advantage of using polymer supports is the possibility to influence product selectivity by support and ligand composition. This applies to both homogeneous and heterogeneous catalyst systems.

Clearly, polymeric particles offer notable advantages for catalyst supports due to their high surface area to volume ratio, a crucial element for efficient catalysis. In addition, the intimate control of particle size and composition provides flexible parameters for tailoring the selectivity of the supported catalyst.

#### 9.3.2. Ion Exchange Resins

Ion exchange is a process whereby anions or cations from solution replace anions or cations held on a solid sorbent [313]. The exchange process is reversible in that the exchanged ions can be released by treating the sorbent with a suitable stripping reagent. Natural soils contain solids with charged sites that exchange ions, and certain minerals called zeolites are quite good exchangers. Ion exchange also takes place in living materials because cell walls, cell membranes, and other structures have charges. Ion exchange materials

include silicates, phosphates, flourides, humus, wool, proteins, cellulose, alumina, glass, and many others. The first industrial ion exchangers were inorganic aluminum silicates, used for softening water and treating sugar solutions. Later it was discovered that sulfonated coal was a relatively effective ion exchange material, but these types of materials are fragile and useful only under restricted operating conditions. Now nearly all ion exchange applications use synthetic polymer resins.

Ion exchange resins are polymers with electrically charged sites where ions may replace others [313]. These synthetic ion exchange resins are usually cast as porous beads with considerable external and pore surface where ions can attach. Absorption plays an important role whenever there is a large surface area and if a substance is adsorbed to an ion exchange resin, no ion is liberated.

Polystyrene-based ion exchange resins are the most common. These are generally insoluble spherical or irregular porous particles grafted with negatively (sulfonic or carboxylic) or positively (quarternary, tertiary, secondary, or primary amino) charged groups and the particles generally have excellent chemical, mechanical, and in most cases thermal stability. Typical applications of polymer particle-based ion exchange resins have included: water treatment, sugar refinement, preparation and purification of pharmaceuticals, catalysts, etc.

### 9.3.3. Calibration Standards and Chromatography

Polymer particles, in particular, polystyrene particles, which can be produced with quality size standards are often used for calibration of flow cytometers, particle and hematology analyzers, confocal laser scanning microscopes, and zeta-potential measuring instruments. In addition, monodisperse polymer particles provide advantages for support materials in high performance liquid chromatography [314–317]. By using precise sized polymer particles, uniform packing of the chromatographic columns can be achieved and allows operation under lower pressures with an associated high efficiency of separation capacity.

Another example of the advantage of using monodisperse polymer particles is in size exclusion chromatography. Size exclusion chromatography (SEC), is commonly used to obtain molecular weight distributions of polymers. Many biopolymers, including a large number of polysaccharides, have very large hydrodynamic sizes that may prevent an efficient use of SEC. By using macroporous, highly monodisperse polymer particles the range of molecular sizes accessible for aqueous SEC has been extended toward larger values.

## 9.4. Rheological Fluids

Viscosity control can be achieved by using particles whose volume changes with environmental conditions [318–333]. For example, the volume of carboxylated latex particles increases with increasing pH so that the viscosity of the dispersion increases [318]. Ethyl acrylate-methacrylic acid copolymer latex is one of the most popular thickeners. Other variables used to influence viscosity have been temperature, poly(*N*-isopropylacrylamide) particles, and electric fields [318, 319].

### 9.4.1. Electrorheological Fluids

The use of electric fields to control viscosity of polymer particle-based fluids is known as electrorheological fluids [318]. These fluids are composed of particles from 1 to 100  $\mu\text{m}$  in diameter that are suspended in a nonconducting liquid. The particles align themselves into structures along the direction of an applied electric field which dramatically changes its rheological properties. This is similar to a sol–gel transition but one that is controlled with an electric field. The extent of the alignment of polymeric particles has been found to depend mainly on the difference in dielectric constants of the liquid medium and the particle. Poly(methacrylic acid) particles in various media, paraffin oil, poly(dimethyl siloxane), chlorinated paraffin, and transformer oil, were also found to give increasing yield stress as a function of increasing particle diameter up to 900 nm. Applications of these fluids are expected to be mainly in the area of mechanical devices such as novel switches, actuators, clutches, etc.

### 9.4.2. Magnetorheological Fluids

Magnetorheological (MR) fluids are considerably less well known than electrorheological (ER) fluids. Both fluids are noncolloidal suspensions of polarizable particles having a size on the order of a few micrometers that respond to external MR or ER fields with a change in rheological behavior [318–333]. Typically, this change is manifested by the development of a yield stress that monotonically increases with applied field. Interest in magnetorheological fluids originates from their ability to provide simple, quiet, rapid-response interfaces between electronic controls and mechanical systems [318–333]. Many researchers believe magnetorheological fluids have the potential to radically change the way electromechanical devices are designed and operated.

The magnetorheological response of MR fluids results from the polarization induced in the suspended particles by application of an external field. The interaction between the resulting induced dipoles causes the particles to form columnar structures, parallel to the applied field. These chainlike structures restrict the motion of the fluid, thereby increasing the viscous characteristics of the suspension. The mechanical energy needed to yield these chainlike structures increases as the applied field increases resulting in a field dependent yield stress. In the absence of an applied field, MR fluids exhibit Newtonian-like behavior.

While the commercial success of ER fluids has remained relatively elusive, MR fluids have seen an increasing commercial success. A number of MR fluids and various MR fluid-based systems have been commercialized including an MR fluid brake for use in the exercise industry (stationary bikes), a controllable MR fluid damper for use in truck seat suspensions, and an MR fluid shock absorber for oval track automobile racing.

## 10. POLYMER PARTICLE PATENT REVIEW

There has been a relatively large number of patents on production methods and applications of polymer micro- and nanoparticles (on the order of 400 from 1996 to 2002).

A similar trend has been witnessed in the dendrimer and hyperbranched polymer area: approx. 433 patents issued during 1996–2000 on uses and production of dendrimers with an incredible growth rate giving a projection of well over 1000 patents before 2005. Such vibrant activity is clear evidence of the importance and applicability these materials to a broad range of fields. We provide a brief overview of some relevant patents in the area of polymer particles. The purpose is to give a brief overview of the various types of patent disclosures issued, not to discuss all of the various patents. Intricate details of the patents we discuss can best be obtained from the actual patent disclosures and supporting literature contained therein.

A continuous process for the preparation of inorganic and organic bead polymers using a static micromixer was disclosed by Eisenbeiss et al. [334]. According to this invention the bead polymers obtainable by the process have a very uniform particle size distribution, which can be set in a range of between 0.1 and 300  $\mu\text{m}$ . The process is based on the mixing of liquid streams of suitable, usually immiscible component solutions in a micromixer, giving spherical particles in a continuous procedure with extremely improved volume yield, large particle yield with particle size range which can be set to a specific value, simplified temperature program, and reduced consumption of chemicals.

A composite paramagnetic particle and method for production was recently disclosed [335]. In one aspect of the invention, a particle comprised of a multitude of submicrometer polymer bead aggregates covalently cross-linked to each other to form larger diameter particles is presented. Distributed throughout the composite paramagnetic particle are vacuous cavities. Each submicrometer polymer bead has distributed throughout its interior and surface submicrometer magnetite crystals. In another aspect of the invention, composite particles are produced by using high energy ultrasound during polymerization of one or more vinyl monomers. In one embodiment, high energy ultrasound is used during an emulsification step and during the early stages of the polymerization process to produce micrometer sized composite paramagnetic particles. The particles according to the invention exhibit a high percent magnetite incorporation and water and organic solvent stability.

A method reported for the preparation of polymer particles includes: (a) forming an organic phase by dissolving a polymer material in a solvent; (b) dispersing the organic phase in an aqueous phase comprising a particulate stabilizer and homogenizing the resultant dispersion, thereby forming spherical particles having a selected particle and uniform particle size distribution; (c) following the homogenizing, adding a particle shape-modifying surface active material to the spherical particles; and (d) removing the solvent, thereby producing irregularly shaped polymer particles having mainly the same selected particle size and distribution as the spherical particles [336].

A process has been reported for the preparation of polyvinylarene polymer particles by suspension polymerization, where (a) vinylarene monomers are suspended in an aqueous medium to yield a suspension; (b) the temperature of the suspension is adjusted to a temperature above 50 °C, at which temperature an initiator is added; (c) subsequently, the reaction temperature is increased by 5 to 30 °C

per hour until a temperature of at least 120 °C is reached; and (d) the temperature is retained at least 120 °C until the polymerization is complete [337].

Wu describes polymer particles made from copolymers of multifunctional (meth)acrylate monomer and multifunctional aromatics [338]. He also described methods of improving the compression characteristics of (meth)acrylate polymer particles by copolymerizing with a multifunctional (meth)acrylate monomer a multifunctional aromatic monomer. The particles are of a size, are of a uniformity, and contain physical characteristics that make them ideally suitable for use as spacers in liquid crystal display devices.

Particles of a copolymer of a vinyl arene and a copolymerizable compound containing a polar moiety and a vinyl moiety containing water may be prepared by forming a mixture of monomers and small amounts of water and polymerizing under agitation to 20 to 70% conversion and then suspending the mass in water and finishing the polymerization. The resulting polymer beads contain finely dispersed water which is useful as an environmentally acceptable blowing agent [339].

An aqueous microemulsion polymerization procedure is described in which very small colloidal polymer particles are produced from tetrafluoroethylene monomer. The polymerization procedure involves adding a free radical initiator to a mixture of a microemulsion of at least one liquid saturated organic compound, and tetrafluoroalkyl ethylene [340].

A composition that includes a plurality of microcapsules each with one to five particles in a liquid droplet, and a complex coacervation induced shell encapsulating the liquid droplet and the one to five particles, has been reported [341]. There is also a composition comprised of a plurality of microcapsules each including a single particle in a liquid droplet, and a complex coacervation induced shell encapsulating the liquid droplet and the single particle. The authors also describe an encapsulation process [342] that includes (a) forming an emulsion composed of a continuous phase comprising a liquid, a cationic material, and an anionic material, and a disperse phase composed of a plurality of droplets of a second liquid, wherein a number of the droplets includes therein one to five particles; and (b) inducing complex coacervation of the cationic material and the anionic material.

A polymer packing material suitable for liquid chromatography and a method for producing it was described by Kimura et al. [343]. The polymer packing material was based on polymer particles with a styrene skeleton and had a monodispersed particle distribution that could be obtained by hydrophilic treatment of an inner surface of a micropore existing in a fine pore of the polymer packing material, or subsequent introduction of a hydrophobic group into the inner hydrophilic surface by chemical modification. A method for producing the polymer packing material suitable for liquid chromatography includes the step of polymerizing glycerol dimethacrylate as a cross-linking agent and 2-ethylhexyl methacrylate as a monomer according to a two-step swelling polymerization process. Alternatively, the producing method includes the step of cross-linking and polymerizing only glycerol dimethacrylate to form a polymer and introducing the hydrophobic group into the polymer by



chemical modification to form a shell around each of the droplets [343].

An inorganic dispersant having a high specific surface area and a high surface activity which comprises a calcium phosphate type compound having a specific particle composition, particle shape, particle size and dispersibility, and specific surface area was recently disclosed. When used as a suspension polymerization stabilizer, it provides polymer particles having a uniform and sharp particle size distribution, and when the polymer particles are contained in an unsaturated polyester resin composition and a toner composition, the obtained compositions have excellent quality [344].

A seeded microemulsion polymerization procedure in which colloidal polymer particles are produced from tetrafluoroethylene or tetrafluoroethylene/comonomer or other polymerizable monomers was described by Wu. The particles have an average diameter between 1 to 100 nm. A microemulsion is formed of a liquid monomer in water and a gaseous monomer is added either before or after polymerization is initiated [345].

An efficient method was disclosed for obtaining polymer particles by evaporating an organic solvent while maintaining a solution of a polymer in the organic solvent in contact with polymer particles, using a simple apparatus and a simple procedure. The polymer particles (powder) produced by the method have a small particle diameter, a high bulk density, and a small amount of residual solvent. The method includes introducing the organic solvent solution of the polymer into a particle producing zone which does not substantially contain steam, wherein an atmosphere is maintained in which the organic solvent is vaporizable and the particles are stirred. The organic solvent is evaporated, while maintaining the solution in contact with the polymer particles [346].

A phase inversion process for preparing nanoparticles and microparticles has been reported. The process involves forming a mixture of a polymer and a solvent, wherein the solvent is present in a continuous phase, and introducing the mixture into an effective amount of a nonsolvent to cause the spontaneous formation of microparticles [347].

Microspheres have been prepared by providing a solution of the polymer and of the active principal in a water-immiscible solvent which is more volatile than water and mixing with an aqueous solution of the surface-active agent, followed by evaporation of the solvent [348]. Biocompatible microspheres containing one or more active principals, a biodegradable and biocompatible polymer and a surface-active agent which is also biodegradable and biocompatible, contain less than 10 ppm of heavy metals.

A method of making polymeric particles having a predetermined and controlled size and size distribution is described by M. Nair, Z. R. Pierce, and C. Sreekumar (U.S. Patent 4, 833, 060, 1989). This disclosure describes a process which comprises dissolving a polymer in a solvent immiscible in water to form a solution, forming a suspension of small droplets of said solution in water containing a promoter which is water soluble and silica particles having an average particle size of from 0.001 to 1  $\mu\text{m}$  by high shear agitation. The promoter affects the hydrophilic/hydrophobic balance of the silica particles in the water suspension, removing the

solvent from the droplets and separating the solidified polymer particles from the water.

Otaigbe et al. [349] described a method for making polymer microparticles, such as spherical powder and whiskers (a whisker is defined here as a polymer microfiber of <100  $\mu\text{m}$  in length and with a diameter of <10  $\mu\text{m}$ ). The method involves melting a polymer under conditions that avoid thermal degradation of the polymer, atomizing the melt in a special gas atomization nozzle assembly in a manner to form atomized droplets, and cooling the droplets to form polymer microparticles. The gas atomization parameters can be controlled to produce polymer microparticles with desired particle shape, size, and distribution.

Handyside and Morgan [350] used rotary, two-fluid, or ultrasonic wave melt atomization processes to prepare thermosetting polymer powder compositions suitable for powder coating processes. The thermosetting resin may consist of polyester or epoxy polymer containing a curing agent and one or more coloring agents. The melt-atomized powder is characterized by improved particle size distribution and by a generally rounded particle shape.

Noid et al. [351] used a new device called a microdroplets-on-demand generator (MODG) to produce polymer micro- and nanoparticles from solution. The proof of concept was demonstrated using poly(ethylene glycol) microparticles generated with the MODG and captured in a microparticle levitation device. The potential application of the MODG in materials science and technology was eluded to in the previous sections. There are several key advantages to this method for polymeric particle production: (1) It is relatively simple to produce particles of nearly any size and composition, including composites and novel blends. Many of these compositions are not obtainable by more conventional methods. (2) The technique lends itself to clean and efficient operation. There are no synthetic procedures requiring specialized knowledge or experience and there are generally no chemical by-products. (3) The technique is very controllable and arrays of particles or even intricate nanostructures can be quickly produced on any surface. (4) Encapsulation of chemicals, drugs, or other particles into a polymer particle is also relatively straightforward.

Aoki et al. [352] developed a method for making aqueous dispersions of ultrafine cross-linked diallyl phthalate polymer particles with average diameter 10–300 nm by polymerizing aqueous solutions containing up to 15% diallyl phthalates in the presence of 7–30% (on diallyl phthalate) water-soluble polymerization initiators without the presence of surfactants. The dispersions are useful as modifiers for rubbers and plastics. Organic monomers such as MMA or oligomers, optionally containing polymerization initiators, can be sublimed into reactors *in vacuo* in inert atmospheres and irradiated with ultraviolet (UV) light to give ultrafine PMMA particles (3000 to 5000 Å particle sizes) with good purity [353].

A method for manufacturing spherical and uniform-size polyolefin ultrafine particles is reported by Yamazaki and Takebe [354]. In this method, the ultrafine particles (approximately 1.5  $\mu\text{m}$  particle size), useful for supports of absorbents, antiblocking agents, etc., are prepared by blending polyolefins in liquid organic compounds, melting the

blends, cooling to form spherical polyolefin particles, and removing the organic compounds by extraction.

In another method [355], electrically conductive polymer ultrafine particles (0.5 to 10  $\mu\text{m}$  particle size) are prepared by mixing an organic solvent solution of a metal salt with another organic solvent solution of a thermoplastic polymer, cooling or pouring this mixed solution into water or a poor solvent of the thermoplastic polymer to separate the metal salt-containing thermoplastic polymer particles, and conducting the precipitation of metal from the metal salt by the difference of ionization or by the addition of a reducing agent. Powdered poly(tetrafluoroethylene) (PTFE) with a specific surface area of 2 to 4  $\text{m}^2/\text{g}$  and a low pressure molding coefficient of 20–150 is ultrasonically ground to give powdered PTFE that has a specific surface area of 4 to 9  $\text{m}^2/\text{g}$  and a low pressure molding coefficient of <20 [356]. The PTFE powders are useful for moldings having high density (e.g., 2.1872) and good surface smoothness.

Polymeric ultrafine particle-adsorbed structures with anti-static, low-friction, and abrasion-resistant properties were prepared by Akaishi et al. [357]. The structures are comprised of various substrates laminated with charged polymeric thin films on which charged polymer ultrafine particles, prepared by a macromonomer method, are adsorbed. The structures are manufactured by immersing charged polymeric thin-film-laminated substrates into a solution containing dispersed charged polymeric ultrafine particles prepared by the macromonomer method to adsorb the particles on the thin films. As an example of this invention by Akaishi et al. [357], a quartz oscillator microbalance as a substrate was alternately immersed 10 times into solutions of polyallylamine hydrochloride and Na styrenesulfonate homopolymer to form multilayer films having the homopolymer layer as the outermost layer. This was immersed in a solution containing dispersed *N*-vinylacetamide-grafted styrene polymer ultrafine particles in the presence of NaCl to give a polymeric particle-adsorbed structure in which the adsorption of particles depended on the concentration of NaCl. For a review of the macromonomer method for preparing polymer particles, the reader is referred to the classic, elegant review by Ito and Seigou [358, 359]. Printing inks and products made from them employ polymer and inorganic ultrafine particles. In one method, Yamada [360] mixed UV-curable resins with ultrafine Fe-based strong magnetic powders to give ink that could be printed on flexible films, fabrics, or paper to form electromagnetic shields. Polyester acrylate, epoxy acrylate, or urethane acrylate resins were used as the UV-curable binder and the ultrafine magnetic powder was mixed at 80–100 vol% (based on the binder resins) [360]. In a second method, Suwabe et al. [361] prepared aqueous inkjet inks, with good anticlogging ability and smudge prevention, by mixing aqueous dispersion of non-film-forming ultrafine inorganic or synthetic polymer particles (e.g., PMMA particles) with pigments and film-forming resin fine particles. In a third method, Uraki et al. [362, 363] prepared inkjet aqueous dispersion inks containing dispersed colored resin particles with an average diameter of 50–300 nm that were prepared by kneading organic pigments with water-soluble inorganic salts and water-soluble solvents in water and mixing with aqueous dispersions containing fine resin particles. The inks were easily

filtered through a 0.45- $\mu\text{m}$  membrane to form ink showing good discharge ability and transparency.

Composite structures consisting of metallic nanoparticles coated with organic polymers or organic polymer blend nanoparticles have been reported [364–369]. Funaki et al. [364] prepared a metal-organic polymer composite (especially porous) structure composed of a microphase-separated structure from a block copolymer in which a metalphilic polymer chain and a metalphobic polymer chain are bonded together at each end, and ultrafine metal particles (<10 nm) were contained in the metalphilic polymer phase of the microphase-separated structure. Preferred polymers are a poly(2-vinylpyridine) and 2-vinylpyridineisoprene block copolymer. The composite structures just mentioned are useful as functional material (e.g., catalyst) in heterogeneous catalysis. Ehrat and Watriner [365] prepared thermoplastic polyolefin or olefin copolymer powders with average particle size of 80 to 120  $\mu\text{m}$  by grinding in an impact mill together with fillers, such as Al, Mg, and/or Ca hydroxides, carbonates, or oxides. The composite mixtures are useful as highly filled molding compositions for battery electrodes or as powder coatings. Tamura [366] developed anisotropic magnetic-permeable composites. The composite contains ultrafine particles of ferromagnetic Fe oxide that are smaller than single domain sizes dispersed in a solid organic polymer as oriented in the domain direction of the particles and substantially separated from each other. The composites are prepared by dispersing the particles in a monomer and polymerizing the monomer in a magnetic field. Far-infrared (IR) radiation-emitting bodies from polymer microparticles and inorganic compounds have been reported [367]. The bodies are prepared from polymer particles with ultrafine inorganic particles (e.g.,  $\text{Al}_2\text{O}_3$  or  $\text{SiO}_2$ ) bonded to their surfaces. The bodies are useful for accelerating fermentation, preserving fresh food, and promoting plant growth. A typical method for producing the radiation-emitting bodies involves mixing an aqueous dispersion of PVC particles (2  $\mu\text{m}$ ) with  $\text{AlCl}_3$  and  $\text{NH}_4\text{OH}$  to give polyvinylchloride (PVC) particles with adhering alumina hydrate particles (0.01  $\mu\text{m}$ ). The product can be extruded to give a film that is capable of far-IR radiation emission. The preparation of composite ultrafine organic polymer mixture particles has been reported by Kagawa [368]. The composite particles were prepared by dissolving two different organic polymers in a solvent with a boiling point higher than the melting point of the polymers and collision crushing with pressure to give particles with diameter <0.05  $\mu\text{m}$ . The composite particles have good film-forming property (e.g., formed 5–10  $\mu\text{m}$  film on Al foil that can be readily peeled off from the foil). Ultrafine polystyrene particles and their composites with other materials can be prepared by adding dropwise polystyrene (weight-average molecular weight 3,840,000) solution (approximately 0.0002% in  $\text{C}_6\text{H}_6$ ) to the surface of  $\text{H}_2\text{O}$  and the solvent evaporated to give a thin layer of ultrafine particles which could be collected by moving barriers. The particles are cumulated on a chrome plate at a surface pressure of 1 to 50  $\text{dyne}/\text{cm}^2$  to give composite materials having area occupied with the particles ranging from 11 to 90%.

Hayashi et al. [370] and Suda et al. [371] developed low-temperature, glass coloring agents containing ultrafine

noble metal particle—polymer composite and ultrafine colored polymer particles, respectively. The former coloring agents contain a composite of ultrafine Au, Pt, Pd, Rh, or Ag particles dispersed in a polymer without coagulation, an organometallic compound for fixing the ultrafine particles in glass, a printing binder, glass powder, and an organic solvent [370]. The low-coloring temperature decreases strain in the colored glass and improves its cutting property. The ultrafine colored polymer particles developed by Suda et al. [371] are useful for electrostatic photographic image developing agents or cosmetics. The particles are prepared by mixing the pigments with COOH (or ester)-containing polyolefins and nonaqueous solvents and precipitating. Stirring the pigment-coated carbon black, Zn naphthenate, and saponified EVA polymer in organic solvents, evaporating, and precipitating resulted in particles with a median diameter of 1.564  $\mu\text{m}$ .

Superparamagnetic composites have been developed by Tamura [372]. The superparamagnetic composite material consists of ultrafine particles of ferromagnetic Fe oxide smaller than sizes of single domain structures dispersed as substantially separated in an organic polymer and prepared by dispersing the particles in a monomer and polymerizing the monomer. An aqueous dispersion of the ultrafine particles is prepared by a chemical reaction, hydrophobic coating of the particles by adding a surfactant to the dispersion, separating the particles, and adding the mixture to the monomer. The resulting composite has an extremely low residual magnetization and coercive force [372].

Ultrafine polymer particles can be prepared from vinyl polymers [373, 374], polyisocyanates and acrylates [375], polystyrene [376], and polyacrylates [377–379] by graft copolymerization [373], spreading and curing [375], dispersion polymerization [376], and emulsion polymerization [374–379]. The resulting particles are useful for water-resistant coatings and films [373, 375, 377], adhesives [376, 378, 379], and freeze–thaw cycle resistant films [374]. Ultrafine particle polymer latex is obtained by emulsion polymerization using a redox-type polymerization initiator in the presence of a compound serving as polymerization inhibitor solution in the monomer [380]. Coagulation of rubber-modified polymer latexes has been reported by Kitayama et al. [381]. In [381], a 30% acrylonitrile-butadiene-Me methacrylate-styrene graft copolymer (melting temperature 90 °C) latex was coagulated with an aqueous solution of  $\text{CaCl}_2$  (11 mmol/L) at a concentration of 12 mmol/L and 95 °C, separated, water washed, dewatered, and dried to form a powdered polymer without any particles. Ultrafine, particulate polymer latex based on unsaturated monomers with an average size <100 nm, a cross-linked structure, and glass transition temperature lower than that calculated by weight fraction method can be used to give a film excellent transparency, smoothness, tack, water resistance, and mechanical strength [382]. The polymer particle properties are dependent on the surfactant used. The latex is useful as a component in paints, adhesives, binder, additive for hydraulic inorganic material, fiber processing, reinforcement for optical glass fiber, electroconductive film, paper making, and photosensitive compositions [382]. Stable, aqueous colorants, useful in cosmetics, writing inks, and textiles, are prepared by encapsulating ultrafine, primary particles with

polymers which are not substantially altered in the process [383].

Artificial stone compositions for high-gloss products resistant to chemicals, water, and weathering can be prepared by mixing: (1) hydraulic inorganic material, (2)  $\text{SiO}_2$ -based by ash with an average particle size 1–20  $\mu\text{m}$ , (3) water-dispersible ultrafine granular acrylic polymer with an average particle size 50–2000 nm, and (4) pigment [384]. The ultrafine granular acrylic polymer was prepared by emulsion polymerization.

Ultrafine particles can be dispersed in organic polymers to form composites that exhibit good transparency and stability, making the composites useful for selective wavelength-shielding optical filters and nonlinear optical materials [385, 386]. Yao and Hayashi [385] prepared ultrafine particle-dispersing polymer compositions from the reaction (which forms ultrafine particles) of metal compounds and chalcogenation agents in an organic solution of polymer bearing pyrrolidone groups and stabilizer, followed by removal of the solvent. A typical preparation of the ultrafine particle-dispersing polymer compositions consists of injecting 0.5 ml  $\text{H}_2\text{S}$  (g) into a tube containing 3.08 mg  $\text{Cd}(\text{NO}_3)_2 \cdot 2.4\text{H}_2\text{O}$  and 0.01 g polyvinylpyrrolidone in 5 ml MeOH. Displacing the  $\text{H}_2\text{S}$  with nitrogen gave a product containing dispersed CdS with size 60 Å, which showed absorbency at 510 nm. In another patent, Yao and Hayashi [386] reported cuprous halide-dispersed polymer compositions and manufacture of polymer compositions dispersed with ultrafine cuprous halide powders to give a transparent film containing ultrafine CuBr particles with average diameter of 8.5 nm.

Giannelis et al. [387] have published a comprehensive review covering recent references on polymer–silicate nanocomposites. Recently, considerable attention has been paid to this type of nanocomposite to afford model systems to study confined polymers or polymer brushes and because of various applications in technical and biomedical fields.

## 11. CONCLUSIONS

In this chapter, we have reviewed recent progress and discussed new insights into generating, characterizing, and modeling polymer micro- and nanoparticles. A wide range of electronic, optical, physical, chemical, and mechanical properties of single and multicomponent polymer particles have been used to fulfill needs for a broad spectrum of applications. Even with the large amount of work done in the past and currently occurring, there still remains tremendous potential in the future development of multicomponent polymer particles with tailored properties and particles for controlled release and delivery of pharmaceuticals.

One exciting area is in the observation that polymer particle structures suggest the capability of manipulation of optical waves in a wide variety of 2D and 3D photonic wire structures that can be tailored to a particular application. We anticipate a number of interesting applications of these type of structures including 3D conductive vertical wires/supports and sensor technologies. By tuning the particle intersection (via adjustment of polymer blend composition), one can turn on (or off) coupling between orthogonal particle chain segments where the bend radius is close to the particle radius

(e.g., 1 to 4  $\mu\text{m}$ ). Losses should be comparable to single (linear) chain coupling which has already been shown to be low. From a purely scientific point of view, photonic molecules represent a new field of study that incorporates a variety of disciplines including materials science, optics, and electronic structure. A number of challenges remain, however. Most polymeric materials are strongly absorbing at near infrared (i.e., telecommunications) frequencies so it remains a nontrivial task to find polymer-blend systems that are transmissive in this important frequency range but also retain the material properties similar to the PEG:PVA blend used in the studies summarized here. Further challenges include engineering an optical (or electronic) interface to the photonic molecule or polymer structure with specific frequency input-output requirements. This new class of structures may ultimately complement photonic bandgap crystal technology and add a new component to the toolbox for microphotonics.

Another developing and extremely important area that can benefit enormously from polymeric particle technology is that of drug delivery. More than 80% of all drugs are currently delivered in a powder format. Although tablets and capsules clearly play key roles in drug delivery, they can often be quite unsuitable for effective processing and delivery of macromolecules, especially proteins, peptides, monoclonal antibodies, antisense drugs, interleukins, cytokines, enzymes, and gene medicines. Preparation of fine powders of these types of macromolecules presents a significant problem to drug manufacturers since formation directly by precipitation from solution can cause numerous difficulties in filtering and drying the minute particles. Currently processors harvest larger particles from crystallizers and then dry and mill them to the desired size. This frequently damages the structure and surface of the drug and can also generate highly charged particles that stick to each other, making further processing very difficult. These types of difficulties in using conventional manufacturing processes to prepare fine particles with specific, preferred characteristics could also significantly constrain the design of new, promising drug delivery systems. Use of polymeric particles and the associated production technology can offer solutions to many of these current difficulties. In addition, the unique capabilities of nanoparticle delivery systems to protect drugs from degradation, prolong their residence time, withstand heat sterilization, have better storage life, remain stable in harsh conditions, and provide controlled release make this technology very attractive. It is clear that micro- and nanoparticulate systems have the potential to have a revolutionary impact on drug delivery and several other areas in the biomedical field. Already proof-of-concept studies have yielded some very encouraging results but further improvements are needed in order to employ a larger range of the available therapeutic macromolecules (gene therapy agents and sensitive proteins).

Other biomedical applications that may depend/benefit on new advances in polymer particle technology are medical imaging, bioassays, and biosensors. The incorporation of functional nanoparticles can be highly advantageous for the performance of numerous bioassays. The tremendous increase in surface area offers the ultimate ability for binding to target molecules such as proteins and enzymes. These

same particles offer complementary advantages for the production of highly sensitive biosensors. In addition, polymer particles can be produced out of conjugated molecules that fluoresce. With future advances in the functionalization of these so-called organic quantum rods, noninvasive biomedical imaging could be substantially improved.

Finally, in the ultimate search for new and improved materials, polymeric particles offer the unique possibility of producing new alloys of polymers that do not typically mix. This capability opens the door to a nearly unlimited number of polymer blend and composite molecular systems of which the properties and dynamic behavior remain to be explored.

## GLOSSARY

**Biomedical engineering** An integration of physical, chemical, mathematical, and computational sciences and engineering principles to study biology, medicine, behavior and health.

**Catalysis** A substance that increases the rate of a chemical reaction without being consumed.

**Colloidal dispersion** A system in which particles (solid, liquid, or gas) of colloidal size are dispersed in a *continuous phase* of a different composition or state.

**Drug delivery** The method and route used for administration of medicinal therapeutics.

**Electroluminescence** The nonthermal conversion of electrical energy into light in a liquid or solid substance.

**Emulsion** A system in which liquid droplets and/or liquid crystals are dispersed in a liquid.

**Fluorescence** The emission of light or other electromagnetic radiation of longer wavelengths by a substance as a result of the absorption of some other radiation of shorter wavelength. Fluorescent emission continues only as long as the stimulus producing it is maintained.

**Immunoassay** A process that measures and identifies a specific biological substance such as an antigen.

**Latex** An emulsion or sol in which each colloidal particle contains a number of macromolecules.

**Molecular modeling** Computational methods used to simulate and model simple and complex systems.

**Nanoparticle** A particle that has size dimensions on the nanometer scale.

**Optoelectronic** Any device that functions as an electrical-to-optical or optical-to-electrical transducer.

**Photonics** The technology of generating and harnessing light and other forms of radiant energy whose quantum unit is the photon.

**Polyelectrolytes** A polymeric substance which, on dissolving in an ionizing solvent, dissociates to give *polyions* together with an equivalent amount of ions of small charge and opposite sign.

**Polymer** Long-chain molecules of high molecular weight consisting of many repeating monomer units.

**Polymerization** A synthetic technique for producing polymers.

**Semiconducting polymers** Polymers that are semiconductors (typically having conductivities in the range of  $10^{-7}$  to  $10^{-3}$  S/cm).

**Suspension** A system in which solid particles are dispersed in a liquid.

**Supercritical fluid** Substances that are above their critical temperature and pressure.

## ACKNOWLEDGMENTS

This work was sponsored by the Division of Materials Science, Office of Basic Energy Sciences, U.S. Department of Energy, under contract DE-AC05-00OR22725 with Oak Ridge National Laboratory, managed and operated by UT-Battelle, LLC. Financial support of J.U.O.'s research from the U.S. National Science Foundation (through grants 992088 and 0242754) and Huntsman Chemical Corporation and the research of work of his former students are gratefully acknowledged.

## REFERENCES

- J. Otaigbe, M. D. Barnes, K. Fukui, B. G. Sumpter, and D. W. Noid, *Adv. Polym. Sci.* 154, 1 (2000).
- M. D. Barnes, K. C. Ng, K. Fukui, B. G. Sumpter, and D. W. Noid, *Mater. Today* 2, 25 (1999).
- B. G. Sumpter, K. Fukui, M. D. Barnes, and D. W. Noid, *Mater. Today* 2, 3 (1999).
- M. D. Barnes, K. Runge, B. Hathorn, S. Mahurin, B. G. Sumpter, and D. W. Noid, *Mater. Today* 5, 20 (2002).
- "Polymer Powder Technology" (M. Narkis and N. Rosenzweig, Eds.). Wiley, New York, 1999.
- T. A. Misev, "Powder Coatings Chemistry and Technology." Wiley, New York, 1991.
- "Polymeric Reagents and Catalysts" (W. T. Ford, Ed.). Am. Chem. Soc., Washington, DC, 1986.
- W. T. Ford et al., *Pure Appl. Chem.* 60, 395 (1988).
- J. M. J. Frechet et al., *Pure Appl. Chem.* 60, 353 (1998).
- "Preparative Chemistry Using Supported Reagents" (P. Laszlo, Ed.). Academic Press, New York, 1987, and pertinent references contained therein.
- C. Adachi, S. Hibino, T. Koyama, and Y. Taniguchi, *J. Appl. Phys.* 2, L827 (1997).
- M. Granstrom and O. Inganas, *Appl. Phys. Lett.* 68, 147 (1996).
- J. Hanes, J. L. Cleland, and R. Langer, *Adv. Drug Delivery Rev.* 28, 97 (1997).
- H. Kawaguchi, *Progr. Polym. Sci.* 25, 1171 (2000).
- M. N. V. Ravi Kumar, N. Kumar, A. J. Domb, and M. Arora, *Adv. Polym. Sci.* 160, 45 (2002).
- A. Prokop, E. Kozlov, G. Carlesso, and J. M. Davidson, *Adv. Polym. Sci.* 160, 119 (2002).
- D. C. Blackley, "Polymer Lattices," 2nd ed. Chapman & Hall, London, 1997.
- "Emulsion Polymerization and Emulsion Polymers" (P. A. Lovell and M. S. El-Aasser, Eds.), Wiley, New York, 1997.
- M. Antonietti and K. Landfester, *Progr. Polym. Sci.* 27, 689 (2002).
- I. Capek, *Adv. Col. Int. Sci.* 92, 195 (2001).
- D. J. Hunkeler and J. Hernandez-Barajas, "Inverse-Emulsion/Suspension Polymerization in Organized Media." Gordon & Breach, Philadelphia, 1992.
- J. V. Dawkins, *Comprehensive Polym. Sci.* 4, 231 (1989).
- I. Fuminori, M. Guanghai, N. Masatoshi, and O. Shinzo, *Col. Sur.* 201, 131 (2002).
- "Dispersion Polymerization in Organic Media" (K. E. J. Barrett, Ed.), Wiley, 1974.
- C. Bunyakan and D. Hunkeler, *Polymer* 40, 6213 (1999).
- G. Zhang, A. Niu, S. Peng, M. Jiang, Y. Tu, M. Li, and C. Wu, *Acc. Chem. Res.* 34, 249 (2001).
- R. Arshady, *Polym. Engn. Sci.* 33, 865 (1993).
- R. G. Gilbert, "Emulsion Polymerization: A Mechanistic Approach." Academic Press, New York, 1995.
- G. Odian, "Principles of Polymerization," 3rd ed. Wiley, New York, 1991.
- M. B. Urquiola, E. D. Sudol, V. L. Dimonie, and M. S. El-Aasser, *J. Polym. Chem.* 31, 1403 (1993).
- D. Cochin and F. Candau, *Macromolecules* 26, 5755 (1993).
- K. Landfester, *Adv. Mater.* 13, 765 (2001).
- F. J. Schork, G. W. Poehlein, S. Wang, J. Reimers, J. Rodrigues, and C. Samer, *Colloid Surf. A* 153, 39 (1999).
- M. Antonietti, R. Basten, and S. Lohmann, *Macromol. Chem. Phys.* 195, 441 (1995).
- F. Candau, M. Pabon, and J.-Y. Anquetil, *Colloid Surf. A* 153, 47 (1999).
- K. Landfester, M. Willert, and M. Antonietti, *Macromolecules* 33, 2370 (2000).
- F. Candau, *Macromol. Symp.* 92, 169 (1995).
- H. G. Yuan, G. Kalfas, and W. H. Ray, *J. Macromol. Sci. Rev. Macromol. Chem. Phys. C* 31, 215 (1991).
- M. Okubo and J. Izumi, *Col. Sur.* 153, 297 (1999).
- K. Jin-Woong and S. Kyung-Do, *Polymer* 41, 6181 (2000).
- J. W. Vanderhoff, M. S. El-Aasser, F. J. Micale, E. D. Sudol, C. M. Tseng, H. R. Scheu, and D. M. Cornfeld, *ACS Polym. Preprint* 28, 455 (1986).
- J. Ugelstad, F. K. Kaggerud, F. K. Hansen, and A. Berge, *Macromol. Chem.* 180, 737 (1979).
- J. Ugelstad, *Makromol. Chem.* 179, 815 (1978).
- M. Okubo, M. Shiozaki, M. Tsujihiro, and Y. Tsukuda, *Col. Polym. Sci.* 269, 222 (1991).
- M. Okubo and T. Nakagawa, *Col. Polym. Sci.* 270, 853 (1992).
- M. Okubo and M. Shiozaki, *Polym. Int.* 30, 469 (1993).
- F. Ito, M. Guanghai, N. Masatoshi, and O. Shinzo, *Col. Sur. A* 201, 131 (2002).
- Y. Almong, S. Reich, and M. Levy, *Br. Polym. J.* 14, 131 (1982).
- C. K. Ober, K. P. Lok, and M. L. Hair, *J. Polym. Sci. Lett. Ed.* 23, 103 (1985).
- C. M. Tseng, Y. Y. Lu, M. S. El-Aasser, and J. W. Vanderhoff, *J. Polym. Sci. Polym. Chem. Ed.* 24, 2995 (1986).
- M. Okubo, K. Ikegami, and Y. Yamamoto, *Col. Polym. Sci.* 267, 193 (1989).
- H. Uyama, H. Kurioka, and Kobayashi, *Col. Sur. A* 153, 189 (1999).
- A. Harada and K. Kataoka, *Science* 283, 65 (1999).
- S. A. Jenekhe and X. L. Chen, *Science* 283, 372 (1999).
- M. Svensson, P. Alexandridis, and P. Linse, *Macromolecules* 32, 637 (1999).
- J. Kritz, J. Plestil, Z. Tuzar, H. Pospisil, J. Brus, J. Jakes, B. Masar, P. Jicek, and D. Doskocilova, *Macromolecules* 32, 397 (1999).
- K. Matsumoto, M. Kubota, H. Matsuoka, and H. Uamaoka, *Macromolecules* 32, 7122 (1999).
- Z. Zhou, B. Chu, and D. G. Peiffer, *Macromolecules* 26, 1876 (1993).
- K. Mortensen and W. Brown, *Macromolecules* 26, 4128 (1993).
- R. Nagarajan and K. Ganesh, *Macromolecules* 22, 4312 (1989).
- Q. F. Zhou, X. Zhu, and Z. Wen, *Macromolecules* 22, 491 (1989).
- Y. X. Liu, D. Zhang, X. H. Wan, and Q. F. Zhou, *Chin. J. Polym. Sci.* 16, 283 (1998).
- X. Wan, Y. Tu, D. Zhang, and Q. F. Zhou, *Chin. J. Polym. Sci.* 16, 377 (1998).
- R. L. Jones and R. J. Spontak, *J. Chem. Phys.* 103, 5137 (1995).
- X. Qui and C. Wu, *Macromolecules* 30, 7921 (1997).
- X. Qui and C. Wu, *Phys. Rev. Lett.* 80, 620 (1998).

67. C. Wu, A. Niu, and L. M. Leung, *J. Am. Chem. Soc.* 121, 1954 (1999).
68. L. M. Leung and K. H. Tan, *Polym. Commun.* 35, 1556 (1994).
69. M. Jiang, X. Qui, W. Qin, and L. Fei, *Macromolecules* 28, 730 (1995).
70. Y. Zhang, M. Xiang, M. Jiang, and C. Wu, *Macromolecules* 30, 2035 (1997).
71. M. Xiang, M. Jiang, Y. Zhang, and C. Wu, *Macromolecules* 16, 3712 (2000).
72. Z. Gan, T. F. Jim, M. Li, Y. Zhao, S. Wang, and C. Wu, *Macromolecules* 32, 590 (1999).
73. W. Zhang, J. Gao, and C. Wu, *Macromolecules* 30, 6388 (1997).
74. R. M. Fitch, "Polymer Colloids: A Comprehensive Introduction." Academic Press, San Diego, 1997.
75. P. Calvo, C. Remunan-Lopez, J. L. Vila-Jato, and M. J. Alonso, *Pharmaceut. Res.* 14, 1431 (1997).
76. P. Calvo, C. Remunan-Lopez, J. L. Vila-Jato, and M. J. Alonso, *J. Appl. Polym. Sci.* 63, 125 (1997).
77. S. Deacon, *J. Clin. Pathol.* 29, 749 (1976).
78. A. Prokop, C. A. Holland, E. Kozlov, B. Moore, and R. D. Tanner, *Biotechnol. Bioeng.* 15, 228 (2001).
79. P. K. Smith, R. I. Krohn, G. T. Hermanson, A. K. Mallia, F. H. Gartner, M. D. Provenzano, E. K. Fujimoto, N. M. Goeke, B. J. Olson, and D. C. Klenk, *Anal. Biochem.* 150, 76 (1985).
80. R. Fagnani, M. S. Hagan, and R. Bartholomew, *Cancer Res.* 50, 3638 (1990).
81. A. Prokop, U.S. Patent 6, 482, 439, 2002.
82. A. V. Kabanov and V. A. Kabonov, *Bioconj. Chem.* 6, 7 (1995).
83. G. F. Pierce, J. E. Tarpley, D. Janagihar, T. A. Mustoe, G. M. Fox, and A. Thomason, *Amer. J. Pathol.* 140, 1375 (1992).
84. A. A. Clifford, "Fundamentals of Supercritical Fluids." Oxford Univ. Press, London, 1998.
85. P. G. Jessop and W. Leitner, "Chemical Synthesis Using Supercritical Fluids." Wiley-VCH, Weinheim, 1999.
86. S. G. Kazarian, *Polym. Sci. Ser. C* 42, 78 (2000).
87. A. I. Cooper and J. M. DeSimone, *Curr. Opin. Solid State Mater. Sci.* 1, 761 (1996).
88. A. I. Cooper, J. D. Londono, G. Wignall, J. B. McClain, E. T. Samulski, J. S. Lin, and A. Dobrynin, *Nature* 389, 368 (1997).
89. M. Rubinstein, A. L. C. Burke, J. M. J. Frichet, and J. M. DeSimone, *Nature* 389, 368 (1997).
90. S. M. Frederick and J. D. Wang, *Inorg. Chim. Acta* 294, 214 (1999).
91. S.-D. Yeo, G.-B. Lim, P. G. Debenedetti, and H. Bernstein, *Biotech. Bioeng.* 41, 341 (1993).
92. B. Subramaniam, R. A. Rajewski, and K. Snavely, *J. Pharm. Sci.* 86, 885 (1997).
93. J. W. Tom and P. G. Debenedetti, *J. Aerosol Sci.* 22, 555 (1991).
94. B. L. Knutson, P. G. Debenedetti, and J. W. Tom, "Preparation of Microparticulates Using Supercritical Fluids" (S. Cohen, and H. Bernstein, Eds.) Dekker, New York, 1996.
95. L. Benedetti, A. Bertucco, and P. Pallado, *Biotech Bioeng.* 53, 232 (1997).
96. L. Frederiksen, K. Anton, P. van Hoogevest, H. R. Keller, and H. Leuenberger, *J. Pharm. Sci.* 86, 921 (1997).
97. R. Chang and E. J. Davis, *J. Coll. Inter. Sci.* 54, 352 (1976).
98. E. J. Davis and A. K. Ray, *J. Coll. Inter. Sci.* 75, 566 (1980).
99. A. K. Ray, A. Souyri, E. J. Davis, and T. M. Allen, *Appl. Opt.* 30, 3974 (1991).
100. J. F. Widmann, C. L. Aardahl, and E. J. Davis, *Am. Lab.* 28, 35 (1996).
101. See also the review by E. J. Davis, *Aer. Sci. Tech.* 26, 212 (1997).
102. P. Chylek, V. Ramaswamy, A. Ashkin, and J. M. Dziedzic, *Appl. Opt.* 22, 2302 (1983).
103. H. C. Van de Hulst and R. T. Wang, *Appl. Opt.* 30, 4755 (1991).
104. G. Konig, K. Anders, and A. Frohn, *J. Aerosol Sci.* 17, 157 (1986).
105. A. R. Glover, S. M. Skippon, and R. D. Boyle, *Appl. Opt.* 34, 8409 (1995).
106. J. F. Widmann and E. J. Davis, *Colloid Polym. Sci.* 274, 525 (1996).
107. T. Kaiser, S. Lange, and G. Schweiger, *Appl. Opt.* 33, 7789 (1994).
108. S. Holler, Y. Pan, R. K. Chang, J. R. Bottinger, S. C. Hill, and D. B. Hillis, *Opt. Lett.* 23, 1489 (1998).
109. J. F. Widmann, C. L. Aardahl, T. J. Johnson, and E. J. Davis, *J. Coll. Int. Sci.* 199, 197 (1998).
110. M. D. Barnes, N. Lermer, W. B. Whitten, and J. M. Ramsey, *Rev. Sci. Instrum.* 68, 2287 (1997).
111. N. Lermer, M. D. Barnes, C.-Y. Kung, W. B. Whitten, and J. M. Ramsey, *Anal. Chem.* 69, 2115 (1997).
112. C. Koning, M. van Duin, C. Pagnouille, and R. Jerome, *Progr. Polym. Sci.* 23, 707 (1998).
113. J. W. Yu, J. F. Douglas, E. K. Hobbie, S. Kim, and C. C. Han, *Phys. Rev. Lett.* 78, 2664 (1997).
114. A. H. Marcus, D. M. Hussey, N. A. Diachun, and M. D. Fayer, *J. Chem. Phys.* 103, 8189 (1996).
115. S. A. Jenekhe and X. L. Chen, *Science* 279, 1903 (1998); 283, 372 (1999).
116. F. S. Bates and G. H. Fredrickson, *Phys. Today* 52, 32 (1999), and references cited therein.
117. C.-Y. Kung, M. D. Barnes, N. Lermer, W. B. Whitten, and J. M. Ramsey, *Appl. Opt.* 38, 1481 (1999).
118. M. D. Barnes, C.-Y. Kung, K. Fukui, B. G. Sumpter, D. W. Noid, and J. U. Otaigbe, *Opt. Lett.* 24, 121 (1999).
119. M. D. Barnes, K. C. Ng, K. Fukui, B. G. Sumpter, and D. Noid, *Macromolecules* 32, 7183 (1999).
120. K. Fukui, B. G. Sumpter, M. D. Barnes, D. W. Noid, and J. U. Otaigbe, *Macromol. Theory Sim.* 8, 38 (1999).
121. J. U. Otaigbe, D. W. Noid, and B. G. Sumpter, *Adv. Polym. Technol.* 17, 161 (1998).
122. J. U. Otaigbe and J. McAvoy, *Adv. Polym. Technol.* 17, 145 (1998).
123. J. U. Otaigbe and J. McAvoy, *Mater. World* 5, 383 (1997).
124. J. U. Otaigbe, J. M. McAvoy, A. I. Enderson, J. Ting, J. Mi, and R. Terpstra, U.S. Patent 6, 171, 433, 1997.
125. J. M. McAvoy and J. U. Otaigbe, Gas atomization of polymers, in "SPE 55th ANTEC Papers," 1997.
126. J. M. McAvoy, M. S. Thesis, Iowa State University, 1997.
127. J. P. Jog, *Adv. Polym. Tech.* 12, 281 (1993).
128. Hoechst waxes for technical applications technical brochure, Hoechst Celanese Corporation, Summit, NJ, pp. 1-33, 1993.
129. K. Inoue, *Progr. Polym. Sci.* 25, 453 (2000).
130. O. A. Matthews, A. N. Shipway, and J. F. Stoddart, *Progr. Polym. Sci.* 23, 1 (1998).
131. J. Roovers and B. Comanita, *Adv. Polym. Sci.* 142, 180 (1999).
132. D. A. Tomalia and H. D. Durst, *Top. Curr. Chem.* 165, 193 (1993).
133. E. Buhleier, W. Wehner, and F. Vogtle, *Synthesis* 155 (1978).
134. D. A. Tomalia, H. Barker, J. R. Dewald, M. Hall, G. Kallos, S. Martin, J. Roeck, J. Ryder, and P. Smith, *Polym. J.* 17, 117 (1985).
135. D. A. Tomalia, H. Barker, J. R. Dewald, M. Hall, G. Kallos, S. Martin, J. Roeck, J. Ryder, and P. Smith, *Macromolecules* 19, 2466 (1986).
136. G. R. Newkome, Z.-Q. Yao, G. R. Baker, and V. K. Gupta, *J. Org. Chem.* 50, 2003 (1985).
137. F. Zeng and S. C. Zimmerman, *Chem. Rev.* 97, 1681 (1997).
138. C. J. Hawker and J. M. J. Fréchet, *J. Am. Chem. Soc.* 112, 7638 (1990).
139. Y. H. Kim, *Polym. Chem. Ed.* 36, 1685 (1998).
140. E. Malmstrom and A. Hult, *JMS Rev. Macromol. Chem. Phys. C* 37, 555 (1997).
141. H. Ihre, M. Johansson, E. Malmstrom, and A. Hult, in "Advances in Dendritic Macromolecules" (G. R. Newkome, Ed.), Vol. 3, p 1. JAI Press, Greenwich, CT, 1996.
142. H. Ihre, A. Hult, and E. Soderlind, *J. Am. Chem. Soc.* 118, 6388 (1996).
143. M. Trollsas, J. Hedrick, D. Mecerreyes, R. Jerome, and P. Dubois, *J. Polym. Sci. Polym. Chem. Ed.* 36, 3187 (1998).

144. C. J. Hawker and F. Chu, *Macromolecules* 29, 4370 (1996).
145. A. Morikawa, *Macromolecules* 31, 5999 (1996).
146. A. Kumar and S. J. Ramakrishnan, *J. Polym. Sci. Polym. Chem. Ed.* 34, 839 (1996); R. Spindler and J. M. J. Frechet, *Macromolecules* 26, 4809 (1993).
147. H. R. Kricheldorf, O. Bolender, and T. Stukenbrock, *Macromol. Chem. Phys.* 198, 2651 (1997).
148. M. Ohta and J. M. J. Frechet, *J. Mater. Sci. A* 34, 2025 (1997).
149. G. Yang, M. Jikei, and M. Kakimoto, *Macromolecules* 31, 5964 (1998).
150. A. M. Muzafarou, M. Golly, and M. Moller, *Macromolecules* 28, 8444 (1995).
151. R. A. Gossage, E. M. Martinez, and G. van Koten, *Tetrahedron Lett.* 39, 2397 (1998).
152. I. L. Rushkin, Q. Shen, S. E. Lehman, and L. V. Interrante, *Macromolecules* 30, 3141 (1997).
153. C. Lach, P. Muller, H. Frey, and R. Mulhaupt, *Macromol. Rapid Commun.* 18, 253 (1997).
154. F. Morgenroth and K. Mullen, *Tetrahedron* 53, 15349 (1997).
155. C. A. Martinez and A. S. Hay, *J. Mater. Sci. A* 35, 57 (1998).
156. M. Pitsikalis, S. Pispas, J. W. Mays, and N. Hadjichristidis, *Adv. Polym. Sci.* 135, 1 (1998).
157. C. J. Hawker, R. Lee, and J. M. J. Frechet, *J. Am. Chem. Soc.* 113, 4583 (1991).
158. P. J. Flory, *J. Am. Chem. Soc.* 74, 2718 (1952).
159. C. N. Moorefield and G. R. Newkome, in "Advances in Dendritic Macromolecules" (G. R. Newkome, Ed.), Vol. 1, p. 1. JAI Press, Greenwich, CT, 1994.
160. T. H. Mourey, S. R. Turner, M. Rubinstein, J. M. J. Frechet, C. J. Hawker, and K. L. Wooley, *Macromolecules* 25, 2401 (1992).
161. C. J. Hawker, P. J. Farrington, M. E. Mackay, K. L. Wooley, and J. M. J. Frechet, *J. Am. Chem. Soc.* 117, 4409 (1995).
162. P. J. Farrington, C. J. Hawker, J. M. J. Frechet, and M. E. Mackay, *Macromolecules* 31, 5043 (1998).
163. C. J. Hawker, K. L. Wooley, and J. M. J. Frechet, *J. Am. Chem. Soc.* 115, 4375 (1996).
164. J. K. Young, G. R. Baker, G. R. Newkome, K. F. Morris, and C. S. Johnson, Jr., *Macromolecules* 27, 3464 (1994).
165. G. R. Newkome, J. K. Young, G. R. Baker, R. L. Potter, L. Audoly, D. Cooper, C. D. Weis, K. Morris, and C. S. Johnson, Jr., *Macromolecules* 26, 2394 (1993).
166. M. Murat and G. S. Grest, *Macromolecules* 29, 1278 (1996).
167. S. Stechemesser and W. Eimer, *Macromolecules* 30, 2204 (1997).
168. V. A. Kabonov, A. B. Zezin, V. B. Rogacheva, Zh G. Gulyaeva, M. F. Zansochova, J. G. H. Joosten, and J. Brackman, *Macromolecules* 31, 5142 (1998).
169. K. L. Wooley, C. J. Hawker, J. M. Pochan, and J. M. J. Frechet, *Macromolecules* 26, 1514 (1993).
170. H. Stutz, *J. Polym. Sci., Polym. Phys. Ed.* 28, 1483 (1990).
171. C. J. Hawker and F. Chu, *Macromolecules* 29, 4370 (1996).
172. Y. H. Kim and O. W. Webster, *Macromolecules* 25, 5561 (1992).
173. C. J. Hawker, E. E. Malmstrom, C. W. Frank, and K. P. Kampf, *J. Am. Chem. Soc.* 119, 9903 (1997).
174. K. Haupt and K. Mosbach, *Chem. Rev.* 100, 2495 (2000).
175. G. Wulff, *Chemtech*, November issue, p. 19 (1998).
176. P. A. G. Cormack and K. Mosbach, *Reac. Func. Polym.* 41, 115 (1999).
177. N. Masque, R. M. Marce, and Borrul, *Trends Anal. Chem.* 20, 477 (2001).
178. B. Sellergren, *Angew. Whcme. Int. Ed. Engl.* 39, 1031 (2000).
179. G. Wulf, *Angew. Chem. Int. Ed. Engl.* 34, 1812 (1995).
180. K. Mosbach and O. Ramstrom, *Bio Tech.* 14, 163 (1996).
181. M. J. Whitcombe, M. E. Rodriguez, P. Villar, and E. N. Vulfson, *J. Am. Chem. Soc.* 117, 7105 (1995).
182. J. U. Klein, M. J. Whicombe, F. Mulholland, and E. N. Vulfson, *Angew. Chem. Int. Ed. Engl.* 38, 2057 (1999).
183. E. Yilmaz, K. Haupt, and K. Mosbach, *Angew. Chem. Int. Ed. Engl.* 39, 2115 (2000).
184. K. Hosoya, K. Yoshihako, Y. Shirasu, K. Kimata, T. Araki, N. Tanaka, and J. Haginaka, *J. Chromatogr.* 728, 139 (1996).
185. M. A. Vorderbruggen, K. Wu, and C. M. Breneman, *Chem. Mater.* 8, 1106 (1996).
186. A. G. Mayes and K. Mosbach, *Anal. Chem.* 68, 3769 (1996).
187. R. J. Ansell and K. Mosbach, *Analyst* 123, 1611 (1998).
188. B. Sellegren, *J. Chromatogr. A* 673, 133 (1994).
189. L. Ye, P. A. G. Cormack, and K. Mosbach, *Anal. Commun.* 36, 35 (1999).
190. J. Matsui, T. Kato, T. Takeuchi, M. Suzuki, K. Yokoyama, E. Tamiya, and I. Karube, *Anal. Chem.* 65, 2223 (1993).
191. L. Schweitz, L. I. Anderson, and S. Nilsson, *Anal. Chem.* 69, 1179 (1997).
192. K. Fukui, B. G. Sumpter, M. D. Barnes, D. W. Noid, and J. U. Otaigbe, *Macromol. Theory Simul.* 8, 38 (1999).
193. K. Fukui, B. G. Sumpter, K. Runge, C. Y. Kung, M. D. Barnes, and D. W. Noid, *Chem. Phys.* 244, 339 (1999).
194. K. Fukui, B. G. Sumpter, M. D. Barnes, and D. W. Noid, *Comput. Theor. Polym. Sci.* 9, 245 (1999).
195. S. K. Gray, D. W. Noid, and B. G. Sumpter, *J. Chem. Phys.* 101, 4062 (1994).
196. M. L. Connolly, *J. Am. Chem. Soc.* 107, 1118 (1985).
197. S. N. Kreitmeier, G. L. Liang, D. W. Noid, and B. G. Sumpter, *J. Therm. Anal.* 46, 853 (1996).
198. K. Runge, B. G. Sumpter, D. W. Noid, and M. D. Barnes, *J. Chem. Phys.* 110, 594 (1999).
199. K. Runge, B. G. Sumpter, D. W. Noid, and M. D. Barnes, *Chem. Phys. Lett.* 299, 352 (1999).
200. B. C. Hathorn, B. G. Sumpter, D. W. Noid, R. E. Tuzun, and C. Yang, *J. Phys. Chem. A* 106, 9174 (2002).
201. B. C. Hathorn, B. G. Sumpter, M. D. Barnes, and D. W. Noid, *Polymer* 43, 3115 (2002).
202. B. C. Hathorn, B. G. Sumpter, D. W. Noid, and M. D. Barnes, *Macromolecules* 35, 1102 (2001).
203. B. C. Hathorn, B. G. Sumpter, M. D. Barnes, and D. W. Noid, *J. Phys. Chem. B* 105, 11468 (2001).
204. S. K. Gray, B. G. Sumpter, D. W. Noid, and M. D. Barnes, *Chem. Phys. Lett.* 333, 308 (2001).
205. K. Fukui, B. G. Sumpter, M. D. Barnes, and D. W. Noid, *Macromolecules* 33, 5982 (2000).
206. K. Fukui, B. G. Sumpter, D. W. Noid, C. Yang, and R. E. Tuzun, *J. Polym. Sci. B* 38, 1812 (2000).
207. K. Fukui, B. G. Sumpter, D. W. Noid, C. Yang, and R. E. Tuzun, *J. Phys. Chem. B* 104, 526 (2000).
208. K. Fukui, B. G. Sumpter, M. D. Barnes, and D. W. Noid, *Polym. J.* 31, 664 (1999).
209. V. Vao-soongnern, R. Ozisik, and W. L. Mattice, *Macromol. Theory Simul.* 10, 553 (2001).
210. H. Okada, *Adv. Drug Deliv. Rev.* 28, 43 (1997).
211. D. Luo and W. M. Saltzman, *Nature Biotechnol.* 18, 33 (2000).
212. N. S. Yang and W. H. Sun, *Nature Med.* 2, 481 (1995).
213. N. S. Yang, J. Burkholder, B. Roberts, B. Martinell, and D. McCabe, *Proc. Nat. Acad. Sci. USA* 87, 9568 (1990).
214. J. L. Cleland, O. L. Johnson, S. Putney, and A. J. S. Jones, *Adv. Drug Deliv. Rev.* 28, 71 (1997).
215. R. A. Jain, R. Hontz, and J. R. Swanson, *Proc. Int. Symp. Control. Release Bioact. Mater.* 26, 883 (1999).
216. R. Gref, Y. Minamitake, M. T. Peracchia, V. Trubetskoy, V. Torchilin, and R. Langer, *Science* 263, 1600 (1994).
217. H. Cohen, R. J. Levy, J. Gao, I. Fishbein, V. Kousaev, S. Sosnowski, S. Slomkowski, and G. Golomb, *Gene Ther.* 7, 1896 (2000).
218. W. F. Anderson, *Nature* 392, S25 (1996).
219. K. L. Wooley, *J. Polym. Sci. A* 38, 1397 (2000).

220. G. B. Sukhorukov, E. Donath, S. Moya, A. S. Sussha, A. Voigt, J. Hartmann, and H. Mohwald, *J. Microencapsulation* 17, 177 (2000).
221. S. M. Marinakos, *J. Am. Chem. Soc.* 121, 8518 (1999).
222. E. Merisko-Liversidge, P. Sarpotdar, J. Bruno, S. Hajj, L. Wei, N. Peltier, J. Rake, J. M. Shaw, S. Pugh, L. Polin, J. Jones, T. Corbett, E. Cooper, and G. G. Liversidge, *Pharm. Res.* 13, 272 (1996).
223. K. B. Thurmond, E. E. Remsen, T. Kowalewski, and K. L. Wooley, *Nucleic Acids Res.* 27, 2966 (1999).
224. G. G. Liversidge and K. C. Cundy, *Int. J. Pharm.* 125, 91 (1995).
225. M. Tobio, R. Gref, A. Sanchez, R. Langer, and M. J. Alonso, *Pharm. Res.* 15, 270 (1998).
226. L. Dahne, S. Leporatti, E. Donath, and H. Mohwald, *J. Am. Chem. Soc.* 123, 5431 (2001).
227. C. Allen, D. Maysinger, and A. Eisenberg, *Colloid Surf. B* 16, 3 (1999).
228. H. Takeuchi, H. Yamamoto, and Y. Kawashima, *Adv. Drug Deliv. Rev.* 47, 39 (2001).
229. X. Qiu, S. Leporatti, E. Donath, and H. Mohwald, *Langmuir* 17, 5375 (2001).
230. J. S. Patton, P. Trinchero, and R. M. Platz, *J. Control. Release* 28, 79 (1994).
231. D. Lemoine and V. Preat, *J. Con. Rel.* 54, 15 (1998).
232. D. A. Edwards, J. Hanes, G. Caponetti, J. Hrkach, A. Ben-Jebria, M. L. Eskew, J. Mintzes, D. Deaver, N. Lotan, and R. Langer, *Science* 276, 1868 (1997).
233. S. Dumitriu and M. Dumitriu, "Polymeric Biomaterials." Dekker, New York, 1994.
234. B. D. Ratner, "Biomaterials Science: An Introduction to Materials in Medicine." Academic Press, San Diego, 1997.
235. P. Guiot and P. Couvreur, "Polymeric Nanoparticles and Microspheres." CRC Press, Boca Raton, FL, 1986.
236. J. L. Cleland, A. Daugherty, and R. Mrsny, *Curr. Opinion Biotechnol.* 12, 212 (2001).
237. D. D. Breimer, *Adv. Drug Del. Rev.* 33, 265 (1998).
238. P. R. Lockman, R. J. Mumper, M. A. Kahn, and D. D. Allen, *Drug Dev. Ind. Pharm.* 28, 1 (2002).
239. K. E. Byrd, A. J. Domb, A. J. Sokoloff, and E. L. Hamilton-Byrd, *Polym. Adv. Tech.* 3, 337 (1992).
240. Y. Dolizky, S. Sturchak, B. Nizan, B. A. Sela, and S. Margel, *Anal. Biochem.* 220, 257 (1994).
241. D. L. Marshall and G. K. Bush, *Am. Biotech. Lab.* 5, 48 (1987).
242. J. M. Singer, in "Future Directions in Polymer Colloids" (M. S. El-Aasser, Ed.), p. 315. Nijhoff, Dordrecht, 1987.
243. J. M. Singer and C. M. Plotz, *Am. J. Med.* 21, 888 (1956).
244. A. Rembaum, S. P. S. Yen, and W. Volksen, *Chemtech.* March, 182 (1978).
245. S. Hosaka, Y. Murao, S. Masuko, and K. Miura, *Immunol. Commun.* 12, 509 (1983).
246. A. A. Harchali, P. Montagne, J. Ruf, M. L. Cuilliere, M. C. Bene, G. Faure, and J. Duheile, *Clin. Chem.* 40, 442 (1994).
247. A. Kondo, S. Uchimura, and K. Higashitani, *J. Ferment. Bioeng.* 78, 164 (1994).
248. J. Ugelstad, R. Schmid, A. Berge, O. Aune, J. Bjørgum, L. Kilaas, P. Stenstad, A. Skjeltorp, T. Lindmo, and L. Korsnes, in "The Polymer Materials Encyclopedia 6" (J. C. Salamone, Ed.), pp. 4501-4519. CRC Press Inc., Boca Raton, FL, 1996.
249. J. Ugelstad, A. Berge, T. Ellingsen, J. Bjørgum, R. Schmid, P. Stenstad, O. Aune, T. N. Nilsen, S. Funderud, and K. Nustad, *NATO ASI Ser. E* 138, 355 (1987).
250. M. Uhlem, E. Hornes, and O. Olsvik, "Advances in Biomagnetic Separation." Biotechnology Press, 1994.
251. M. Okubo and H. Hattori, *Colloid Polym. Sci.* 271, 1157 (1993).
252. T. Maehara, Y. Eda, K. Mitani, and S. Matsuzawa, *Biomaterials* 11, 122 (1990).
253. M. Hatakeyama, S. Iwato, K. Fujimoto, H. Handa, and H. Kawaguchi, *Colloids Surf. B* 10, 171 (1998).
254. M. Hatakeyama, S. Iwato, H. Hanashita, K. Nakamura, K. Fujimoto, and H. Kawaguchi, *Colloids Surf. A* 153, 445 (1999).
255. H. Hakala, E. Maki, and H. Lonnberg, *Bioconj. Chem.* 9, 316 (1998).
256. A. M. Rudolph and M. A. Heymann, *Circ. Res.* 21, 163 (1997).
257. U. B. Bruckner and K. Messmer, *Biorheology* 27, 903 (1990).
258. R. W. Barbee, B. D. Perry, R. N. Re, and J. P. Murgu, *Am. J. Physiol.* 263, R728 (1992).
259. V. E. Hjortdal, E. S. Hansen, T. B. Henriksen, D. Kjolseth, K. Soballe, and J. C. Djurhuus, *Plast. Reconstr. Surg.* 89, 116 (1992).
260. M. J. Lyon and H. H. Wanamaker, *Hearing Res.* 67, 157 (1993).
261. D. P. Arnstein, G. S. Berke, T. K. Trapp, T. Bell, and M. Natividad, *Otolaryngol. Head Neck Surg.* 103, 371 (1990).
262. P. Kowallik, R. Schulz, B. D. Guth, A. Schade, W. Paffhausen, R. Gross, and G. Heusch, *Circulation* 83, 974 (1991).
263. N. Kobayashi, K. Kobayashi, K. Kondo, S. Horinaka, and S. Yagi, *Am. J. Physiol.* 266, H1910 (1994).
264. Y. Morita, B. D. Payne, G. S. Aldea, C. McWatters, W. Nusseini, H. Mori, J. I. Hoffman, and L. Kaufman, *Am. J. Physiol.* 258, H1573 (1990).
265. F. W. Prinzen and R. W. Glenny, *Cardiovasc. Res.* 28, 1467 (1994).
266. H. Mori, S. Haruyama, Y. Shinozaki, H. Okino, A. Iida, R. Takanashi, I. Sakuma, W. K. Hussein, B. D. Payne, and J. I. Hoffman, *Am. J. Physiol.* 263, H1946 (1992).
267. C. Christiansen, H. Kryvi, P. C. Sontum, and T. Skotland, *Biotech. Appl. Biochem.* 19, 307 (1994).
268. P. Walday, H. Tolleshaug, Y. Gjoen, G. M. Kindberg, T. Berg, and T. Skotland, *Biochem. J.* 299, 437 (1994).
269. A. Bol, J. A. Melin, J. L. Vanoverschelde, T. Baudhuin, D. Vogelaers, M. DePauw, C. Michel, A. Luxen, D. Laber, and M. Cogneau, *Circulation* 87, 512 (1993).
270. K. Riggi, M. B. Wood, and D. M. Ilstrup, *J. Orthop. Res.* 8, 909 (1990).
271. P. Naredi, J. Mattsson, and L. Hafstrom, *Int. J. Microcirc. Exp.* 10, 169 (1991).
272. R. Sandin, U. Feuk, and J. Modig, *Acta Anaesthesiol. Scand.* 34, 457 (1990).
273. S. Sanchez, J. C. Bandi, and R. Mastai, *Proc. Soc. Exp. Biol. Med.* 200, 375 (1992).
274. T. Uchida, T. Takano, and S. Hosaka, *J. Immunol. Methods* 77, 55 (1985).
275. F. L. Jordan, H. J. Wynder, and W. E. Tomas, *J. Neurosci. Res.* 26, 74 (1990).
276. H. Kawaguchi, N. Koiwai, Y. Ohtsuka, M. Miyamoto, and S. Sasakawa, *Biomaterials* 8, 113 (1986).
277. L. Illum, L. O. Jacobsen, R. H. Muller, E. Mak, and S. S. Davis, *Biomaterials* 8, 113 (1987).
278. S. Yasukawa, H. Oshima, N. Matsumura, and T. Kondo, *J. Microencapsul* 7, 179 (1990).
279. Y. Tabata and Y. Ikada, *Adv. Polym. Sci.* 94, 107 (1990).
280. Y. Ishikawa, N. Muramatsu, H. Oshima, and T. Kondo, *J. Biomater. Sci. Polym. Ed.* 2, 53 (1991).
281. A. G. A. Coombes, P. D. Scoles, M. C. Davies, L. Illum, and S. S. Davis, *Biomaterials* 15, 673 (1994).
282. Y. Urakami, Y. Kasuya, K. Fujimoto, M. Miyamoto, and H. Kawaguchi, *Colloids Surf. B* 3, 183 (1994).
283. T. Kasuya, K. Fujimoto, M. Miyamoto, and H. Kawaguchi, *Biomaterials* 15, 673 (1994).
284. R. S. Hasan, H. M. Dockrell, S. Jamil, T. J. Chiang, and R. Hussain, *Infect. Immunol.* 61, 3724 (1993).
285. See for example, L. Marshall and G. Kra, The processing power of light, *Opt. Photon. News*, March 2002.
286. M. Bayer, T. Gutbrod, J. P. Reithmayer, A. Forchel, T. L. Reinecke, P. A. Knipp, A. A. Dremin, and V. D. Kulakovskii, *Phys. Rev. Lett.* 81, 2582 (1998).
287. M. D. Barnes, S. Mahurin, A. Mehta, B. G. Sumpter, and D. W. Noid, *Phys. Rev. Lett.* 88, 015508 (2002).



288. K. C. Ng, J. V. Ford, S. C. Jacobson, J. M. Ramsey, and M. D. Barnes, *Rev. Sci. Instrum.* 71, 2497 (2000).
289. G. Videen, D. Ngo, and M. B. Hart, *Opt. Comm.* 125, 275 (1996).
290. H.-J. Moon, G.-H. Kim, Y.-S. Lim, C.-S. Go, J.-H. Lee, and J.-S. Chang, *Opt. Lett.* 21, 913 (1996).
291. S. Mahurin, A. Mehta, B. G. Sumpter, D. W. Noid, K. Runge, and M. D. Barnes, *Opt. Lett.* 27, 610 (2002).
292. Y. Koike and E. Nihei, in "Proc. 3rd IUMRS Int. Conf. Adv. Mat.," 1993.
293. S. Hayashi, Y. Kumamoto, T. Suzuki, and T. Hirai, *J. Colloid Int. Sci.* 144, 538 (1991).
294. Y. Koike, Y. Sumi, and Y. Ohtsuka, *Appl. Opt.* 25, 19 (1986).
295. J. H. Burroughes, D. D. C. Bradley, A. R. Brown, R. N. Marks, K. Mackay, R. H. N. Friend, P. L. Burn, and A. B. Homes, *Nature* 347, 539 (1990).
296. P. Chandrasekhar, "Conducting Polymers." Kluwer Academic, Boston, 1999.
297. R. H. Friend, J. H. Burroughes, and T. Shimoda, *Phys. World* June 1998, p. 35.
298. K. Ziemelis, *Nature* 399, 408 (1999).
299. A. Kraft, A. C. Grimsdale, and A. B. Holmes, *Angew. Chem. Int. Ed.* 37, 402 (1998).
300. R. H. Friend, R. W. Gymer, A. B. Holmes, J. H. Burroughes, R. N. Marks, C. Taliani, D. D. C. Bradley, D. A. D. Santos, J. L. Bredas, M. Logdlund, and W. R. Salaneck, *Nature* 397, 121 (1999).
301. Y. Yang, *Mater. Res. Soc. Bull.* 22, 31 (1997).
302. S. A. Carter, J. C. Scott, and P. J. Brock, *Appl. Phys. Lett.* 71, 1145 (1997).
303. G. Yu, J. Gao, J. C. Hummelen, F. Wudl, and A. J. Heeger, *Science* 270, 1789 (1995).
304. N. C. Greenham, P. Xiaogan, and A. P. Alivisatos, *Phys. Rev. B* 54, 17628 (1996).
305. J. J. M. Halls, C. A. Walsh, N. C. Greenham, and E. A. Marseglia, *Nature* 376, 498 (1995).
306. D. Y. Kim, H. N. Cho HN, and C. Y. Kim, *Progr. Polym. Sci.* 25, 1089 (2000).
307. K. G. I. Nilsson, *J. Immunol. Methods* 122, 273 (1989).
308. M. Yasui, T. Shiroya, J. Fujimoto, and H. Kawaguchi, *Colloids Surf. B* 8, 311 (1997).
309. "Functional Polymer Colloid Polymers and Microparticles" (R. Arshady, Ed.), Vol. 4. 1999.
310. H. Li and B. He, *Reactive Funct. Polym.* 26, 61 (1995).
311. F. Ciardelli, C. Carlini, P. Pertici, and G. Valentini, *J. Macromol. Sci. Chem. A* 26, 237 (1989).
312. R. Mani, V. Mahadevan, and M. Srinivasan, *J. Macromol. Sci. Pure Appl. Chem. A* 30, 251 (1993).
313. S. D. Alexandratos, in "Ion Exchange and Solvent Extraction" (A. SenGupta, Ed.), Vol. 14. Dekker, New York, 2000; S. D. Alexandratos and S. Natesan, *European Polym. J.* 35, 431 (1999); see also Ion exchange, in "Ullmann's Encyclopedia of Industrial Chemistry," 6th ed., Wiley-VCH Electronic Release, 2001.
314. E. Meehan, in "Column Handbook for Size Exclusion Chromatography" (C.-S. Wu, Ed.). Academic Press, New York, 1999.
315. "Chromatography of Polymers: Characterization by SEC and FFF" (T. Provder, Ed.). Am. Chem. Soc., Washington, DC, 1993.
316. "Strategies in Size Exclusion Chromatography" (M. Potschka and P. L. Dublin, Eds.). Am. Chem. Soc., Washington, DC, 1996.
317. J. Ugelstad, L. Söderberg, A. Berge, and J. Bergström, *Nature* 303, 95 (1983).
318. P. Brrradna, P. Stern, O. Quadrat, and J. Snuparek, *Colloid Polym. Sci.* 273, 324 (1995).
319. M. J. Garcia-Salinas and F. J. de las Nieves, *Progr. Colloid Polym. Sci.* 110, 134 (1998).
320. R. Pool, *Science* 35/36, 327 (1990).
321. T. G. Duclos, *Mech. Design* 21, 42 (1988).
322. W. M. Winslow, *J. Appl. Phys.* 1137 (1949).
323. *Design News*, Dec. 4 (1995).
324. J. D. Carlson et al., U.S. Patent 5, 277, 282; U.S. Patent 5, 284, 330, 1994.
325. J. D. Carlson and K. D. Weiss, *Machine Design* Aug. 1994, p. 61.
326. V. D. Chase, *Appliance Manuf.* May 1996, p. 6.
327. M. R. Jolly, J. D. Carlson, and B. C. Muñoz, *Smart Mater. Struct.* 5, 607 (1996).
328. W. Kordonsky, *J. Magn. Mater.* 122, 395 (1993).
329. Lord Corporation, Rheonetic Linear Damper—RD-1001/RD-1004 Product Information Sheet, Lord Corp. Pub. No. PS RD-1001/4, 1997.
330. J. Rabinow, *AIEE Trans.* 67, 1308 (1948).
331. J. Rabinow, *Nat. Bureau Standards Tech. News Bull.* 32, 54 (1948).
332. E. M. Shtarkman, U.S. Patent 4, 992, 360, 1991, and U.S. Patent 5, 167, 850, 1992.
333. K. D. Weiss, J. D. Carlson, and D. A. Nixon, *J. Intell. Mater. Syst. Struct.* 5, 72 (1994).
334. F. Eisenbeiss, J. Kinkel, and H.-D.-J. Muller, U.S. Patent 6, 492, 471, 2002.
335. I. Sucholeiki, N.-H. Sung, and J. Y. Lee, U.S. Patent 6, 423, 410, 2002.
336. T. C. Zion, D. E. Smith, H. Yoon, and M. C. Ezenyilimba, U.S. Patent 6, 380, 297, 2002.
337. A. C. Poppelaars and J. M. Zijderfeld, U.S. Patent 6, 262, 193, 2001.
338. J.-C. Wu, U.S. Patent 6, 187, 440, 2001.
339. J. J. Crevecoeur, E. W. J. Neijman, L. N. Nelissen, and J. M. Zijderfeld, U.S. Patent 6, 242, 540, 2001.
340. H. S. Wu, J. Hegenbarth, X. K. Chen, and J. G. Chen, U.S. Patent 5, 895, 799, 1999.
341. N. Chopra, P. M. Kazmaier, and F. E. Torres, U.S. Patent 6, 492, 025, 2002.
342. N. Chopra, P. M. Kazmaier, and P. J. Gerroir, U.S. Patent 6, 488, 870, 2002.
343. T. Kimura, M. Teramachi, K. Hosoya, and Y. Ohtsu, U.S. Patent 6, 482, 867, 2002.
344. H. Shibata, Y. Takahashi, H. Kasahara, M. Aoyama, and S. Takiyama, U.S. Patent 6, 482, 881, 2002.
345. H. S. Wu, U.S. Patent 5, 523, 346, 1999.
346. M. Okamoto, N. Kunishi, and Y. Koyama, U.S. Patent 5, 583, 166, 1999.
347. E. Mathiowitz, D. Chickering III, Y. S. Jong, and J. S. Jacob, U.S. Patent 6, 235, 224, 2001.
348. G. Spenlehauer, M. Veillard, and T. Verrechia, U.S. Patent 6, 120, 805, 2001.
349. J. U. Otaigbe et al., U.S. Patent 6, 171, 433, 2001.
350. T. M. Handyside and A. R. Morgan, GB Patent 2, 246, 571, 1992.
351. D. W. Noid, J. U. Otaigbe, M. D. Barnes, B. G. Sumpter, and C. Y. Kung, U.S. Patent 6, 461, 546, 1998.
352. K. Aoki, K. Koide, and A. Matsumoto, Jpn Patent 08, 157, 532, 1996.
353. M. Oda and K. Setoguchi, Jpn Patent 02, 097, 501, 1990.
354. M. Yamazaki and K. Takebe, Jpn Patent 01, 198, 634, 1989.
355. M. Shigemitsu, Jpn Patent 01, 006, 035, 1989.
356. Y. Kometani, S. Fumoto, and S. Tanigawa, Ger Patent 2, 063, 635, 1972.
357. M. Akaiishi, T. Serizawa, and K. Taniguchi, Jpn Patent 10, 337, 794, 1998.
358. K. Ito, *Progr. Polym. Sci.* 23, 581 (1998).
359. K. Ito and K. Seigou, *Adv. Polym. Sci.* 142, 129 (1999).
360. H. Yamada, Jpn Patent 10, 330, 670, 1998.
361. Y. Suwabe, T. Mikami, and M. Fukuda, Jpn Patent 10, 140, 057, 1996.
362. H. Uraki, S. Sawada, Y. Iida, T. Fujigamori, and S. Hazama, Jpn Patent 09, 053, 035, 1997.
363. H. Uraki, J. Satake, Y. Iida, T. Fujigamori, and S. Hazama, Jpn Patent 09, 053, 036, 1997.

364. Y. Funaki, K. Tsutsumi, T. Hashimoto, and M. Harada, Euro Patent 864, 362, 1998.
365. R. Ehrat and H. Watrinet, Euro Patent 761, 743, 1997.
366. H. Tamura, Jpn Patent 04, 025, 102.
367. H. Nakai and S. Edakawa, Jpn Patent 02, 202, 922, 1990.
368. A. Kagawa, Jpn Patent 63, 120, 740, 1988.
369. J. Kumaki, Euro Patent 197, 461, 1986.
370. S. Hayashi, S. Murakami, K. Goto, T. Noguchi, and Y. Yamaguchi, Jpn Patent 07, 025, 642, 1995.
371. Y. Suda, M. Murakami, and K. Makino, Jpn Patent 06, 287, 313, 1994.
372. H. Tamura, Jpn Patent 03, 163, 805, 1991.
373. K. Kawazu, K. Seike, T. Kawamura, H. Kiyata, and H. Onoyama, Jpn Patent 09, 286, 948, 1997.
374. A. Katsushima, Jpn Patent 06, 073, 334, 1994.
375. T. Fujiwa and S. Urabe, Jpn Patent 09, 255, 914, 1997.
376. T. Yoshihara, Jpn Patent 09, 110, 909, 1997.
377. Z. Kishimoto, Jpn Patent 02, 212, 562, 1990.
378. H. Morita, Y. Ishizaki, and J. Azuma, Jpn Patent 01, 170, 677, 1989.
379. S. Myanaga, Y. Doi, and J. Tsunoda, Jpn Patent 08, 259, 846, 1996.
380. A. Shichizawa and Ii-H. Aachi, Jpn Patent 07, 138, 304, 1995.
381. T. Kitayama, N. Takami, K. Urabe, and T. Fukuda, Jpn Patent 06, 256, 405, 1994.
382. H. Morita, E. Hirota, and Y. Ishizaki, Euro Patent 273, 605, 1988.
383. F. J. Micale, U.S. Patent 4, 665, 107, 1987.
384. S. Yamaguchi, T. Takabe, T. Ito, N. Kobayashi, and H. Morita, Jpn Patent 05, 254, 906 1993.
385. H. Yao and T. Hayashi, Jpn Patent 04, 300, 946, 1992.
386. H. Yao and T. Hayashi, Jpn Patent 05, 287, 116, 1993.
387. E. P. Giannelis, R. Krishnamoorti, and E. Manias, *Adv. Polym. Sci.* 138, 107, 1999, and references therein.

